SECOND EDITION

Handbook of Laser Technology and Applications

VOLUME II

Lasers Design and Laser Systems

edited by
Chunlei Guo • Subhash Chandra Singh

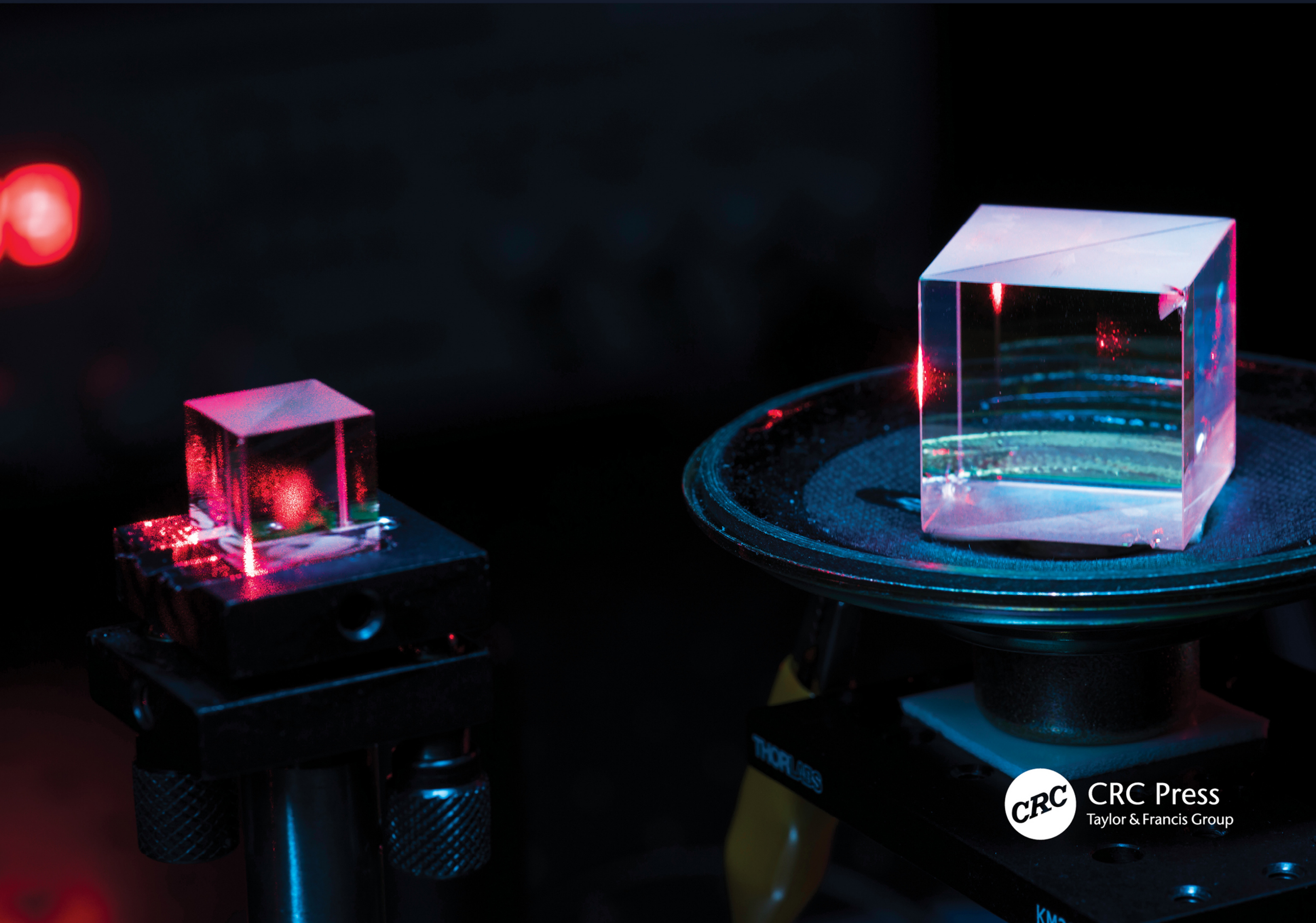

CRC Press
Taylor & Francis Group

Handbook of Laser Technology and Applications

Handbook of Laser Technology and Applications

Lasers: Principles and Operations (Volume One)
Second Edition

Lasers Design and Laser Systems (Volume Two)
Second Edition

Lasers Application: Material Processing and Spectroscopy (Volume Three)
Second Edition

Laser Applications: Medical, Metrology and Communication (Volume Four)
Second Edition

Handbook of Laser Technology and Applications

Lasers Design and Laser Systems (Volume Two)

Second Edition

Edited by

Chunlei Guo

Subhash Chandra Singh

CRC Press
Taylor & Francis Group
Boca Raton London New York

CRC Press is an imprint of the
Taylor & Francis Group, an **informa** business

Second edition published 2021
by CRC Press
6000 Broken Sound Parkway NW, Suite 300, Boca Raton, FL 33487-2742

and by CRC Press
2 Park Square, Milton Park, Abingdon, Oxon, OX14 4RN

© 2021 Taylor & Francis Group, LLC

First edition published by IOP Publishing 2004

CRC Press is an imprint of Taylor & Francis Group, LLC

Reasonable efforts have been made to publish reliable data and information, but the author and publisher cannot assume responsibility for the validity of all materials or the consequences of their use. The authors and publishers have attempted to trace the copyright holders of all material reproduced in this publication and apologize to copyright holders if permission to publish in this form has not been obtained. If any copyright material has not been acknowledged please write and let us know so we may rectify in any future reprint.

Except as permitted under U.S. Copyright Law, no part of this book may be reprinted, reproduced, transmitted, or utilized in any form by any electronic, mechanical, or other means, now known or hereafter invented, including photocopying, microfilming, and recording, or in any information storage or retrieval system, without written permission from the publishers.

For permission to photocopy or use material electronically from this work, access www.copyright.com or contact the Copyright Clearance Center, Inc. (CCC), 222 Rosewood Drive, Danvers, MA 01923, 978-750-8400. For works that are not available on CCC please contact mpkbookspermissions@tandf.co.uk.

Trademark notice: Product or corporate names may be trademarks or registered trademarks and are used only for identification and explanation without intent to infringe.

Library of Congress Cataloging-in-Publication Data
Names: Guo, Chunlei, editor. | Singh, Subhash Chandra, editor.
Title: Handbook of laser technology and applications : four volume set /
[edited by] Chunlei Guo and Subhash Chandra Singh.
Description: 2nd edition. | Boca Raton : CRC Press, 2021- |
Series: Handbook of laser technology and applications | Includes bibliographical
references and index. | Contents: v. 1. Lasers: principles and operations —
v. 2. Laser design and laser systems — v. 3. Lasers applications: materials processing —
v. 4. Laser applications: medical, metrology a [?].
Identifiers: LCCN 2020037189 (print) | LCCN 2020037190 (ebook) |
ISBN 9781138032613 (v. 1 ; hardback) | ISBN 9781138032620 (v. 2 ; hardback) |
ISBN 9781138033320 (v. 3 ; hardback) | ISBN 9780367649173 (v. 4 ; hardback) |
ISBN 9781138196575 (hardback) | ISBN 9781315389561 (v. 1 ; ebook) |
ISBN 9781003127130 (v. 2 ; ebook) | ISBN 9781315310855 (v. 3 ; ebook) |
ISBN 9781003130123 (v. 4 ; ebook)
Subjects: LCSH: Lasers.
Classification: LCC TK7871.3 .H25 2021 (print) | LCC TK7871.3 (ebook) |
DDC 621.36/6—dc23
LC record available at https://lccn.loc.gov/2020037189
LC ebook record available at https://lccn.loc.gov/2020037190

ISBN: 978-1-138-03262-0 (hbk)
ISBN: 978-0-367-64979-1 (pbk)
ISBN: 978-1-003-12713-0 (ebk)

Typeset in Times
by codeMantra

Contents

Preface ix

Editors xi

Contributors xiii

1. **Solid-State Lasers: Section Introduction** 1
   R. C. Powell

2. **Transition Metal Ion Lasers—Cr^{3+}** 3
   Georges Boulon

3. **Transition Metal Ion Lasers Other Than Cr^{3+}** 25
   Stephen A. Payne

4. **Rare-Earth Ion Lasers—Nd^{3+}** 35
   A. I. Zagumennyi, V. A. Mikhailov, and I. A. Shcherbakov

5. **Rare-Earth Ions—Miscellaneous: Ce^{3+}, U^{3+}, Divalent, etc.** 55
   Gregory J. Quarles

6. **Ti:sapphire: Material, Lasers and Amplifiers** 69
   Peter F. Moulton, Alan R. Fry, and Peter Fendel

7. **Lanthanide Series Lasers—Near-Infrared** 83
   Norman P. Barnes

8. **Lasers Based on Non-Linear Effects** 101
   Fabienne Pellé

9. **Solid-State Raman Lasers** 127
   T. T. Basiev and R. C. Powell

10. **Colour Centre Lasers** 151
    T. T. Basiev, P. G. Zverev, and S. B. Mirov

11. **Laser Diodes: Section Introduction** 167
    Ian White

12. **Basic Principles of Laser Diodes** 169
    Niloy K. Dutta

13. **Spectral Control in Laser Diodes** 195
    Markus-Christian Amann

14. **High-Speed Laser Diodes** 211
    Peter P. Vasil'ev

15. **High-Power Laser Diodes and Laser Diode Arrays** 225
    Peter Unger

16. **Visible Laser Diodes: Properties of III–V Red-Emitting Laser Diodes** 235
    Peter Blood

17. Visible Laser Diodes: Properties of Blue Laser Diodes 251
Robert Martin

18. Long-Wavelength Laser Diodes 263
S. Anders, G. Strasser, and E. Gornik

19. Semiconductor Lasers and Optical Amplifiers for Switching and Signal Processing 273
Hitoshi Kawaguchi

20. Silicon-Based Lasers 287
Qiang Li, Bei Shi, and Yu Han

21. Gas/Vapour Lasers: Section Introduction 299
Julian Jones

22. Atomic Gas Lasers: Helium–Neon Lasers 301
Alan D. White and Lisa Tsufura

23. Metal vapor Lasers: Helium–Cadmium Laser 309
William T. Silfvast

24. Copper and Gold Vapour Lasers 315
Colin Webb

25. Ion Lasers: Argon and Krypton Ion Lasers 325
Malcolm H. Dunn and Tony Gutierrez

26. Carbon Dioxide Lasers 337
Denis R. Hall

27. Excimer Lasers: F_2, N_2 and H_2 Lasers 365
W. J. Witteman

28. High-Brightness Excimer Lasers and Extreme Conditions They Produce 403
Sándor Szatmári

29. Optically Pumped Mid-IR Lasers: NH_3, C_2H_2 419
Mary S. Tobin

30. Far-IR Lasers: HCN, H_2O 433
Wilhelm Prettl

31. Diode-Pumped Alkali Lasers (DPALs) 441
Boris Zhdanov and Randall Knize

32. Chemical Lasers:Section Introduction 449
Julian Jones

33. Chemical Lasers: COIL 451
B. D. Barmashenko and S. Rosenwaks

34. Chemical Lasers: HF/DF 467
Lee H. Sentman

35. Fiber and Waveguide Lasers: Section Introduction 475
R. C. Powell

36. Fibre Lasers 477
Wei Shi, Shijie Fu, and Qiang Fang

37. High-Power Fibre Lasers 489
Christophe A. Codemard and M. N. Zervas

38. Raman Fibre Lasers 501
Igor Bufetov and Sergey Babin

39. Solitons and Dissipative Solitons for Ultrafast Lasers 521
Ph Grelu

40. Bismuth-Doped Fibre Lasers and Optical Amplifiers 535
Evgeny Dianov, Mikhail Melkumov, and Sergei Firstov

41. Erbium and Other Doped Fibre Amplifiers 557
Kevin Cordina

42. High-Power Planar Waveguide Lasers 571
J. I. Mackenzie and D. P. Shepherd

43. MEMS-Based Swept Laser Source 585
John O. Gerguis, Yasser M. Sabry, Haitham Omran, and Diaa Khalil

44. Dye Lasers: Section Introduction 599
Colin Webb

45. Liquid Lasers 601
David H. Titterton

46. Solid-State Dye Lasers 623
David H. Titterton

47. Other Lasers: Section Introduction 637
Colin Webb, Subhash Chandra Singh, and Chunlei Guo

48. Free-Electron Lasers and Synchrotron Light Sources 639
P. G. O'Shea and J. B. Murphy

49. X-Ray Lasers 653
Jorge J. Rocca

50. Terahertz Lasers 671
Taiichi Otsuji

Index 685

Taylor & Francis
Taylor & Francis Group
http://taylorandfrancis.com

Preface

This updated Handbook comes at the time when the world just celebrated the 60th anniversary of the laser. Compared to most fields in science and technology, the laser is still a relatively young one, but its developments have been astonishing. Today, hardly any area of modern life is left untouched by lasers, so it is almost impossible to provide a complete account of this subject.

As challenging as it is, this updated Handbook attempts to provide a comprehensive coverage on modern laser technology and applications, including recent advancements and state-of-the-art research and developments. The main goal of developing this Handbook is to provide both an overview and details of ever-expanding technologies and applications in lasers.

We want this Handbook to be useful for both newcomers and experts in lasers. To meet these goals, the chapters in this Handbook are typically developed in a style that does not require advanced mathematical tools. On the other hand, they are written by the experts in each area so that the most important concepts and developments are covered.

The first edition of the Handbook was released in 2003. It has been hugely popular and ranked as one of the top ten most referenced materials by the publisher. Eighteen years later, although a relatively short period for many more established scientific fields, the Handbook has become outdated, and an update is overdue. The rapid changes in lasers are certainly reinforced by my own experience of teaching and researching the subject in the Institute of Optics at University of Rochester. Flipping through my old lecture notes on lasers, I am often amazed at how much progress we have witnessed in this field over the years.

I am indebted to the editors of the first edition, Colin Webb and Julian Jones, who brought this original Handbook into existence. When I was asked to take over this second edition, it laid before me a daunting task of how to rejuvenate the Handbook while keeping its original flavour. Since many of the fundamental principles of the laser are well established, we tried to honour the original authors by keeping the chapters on fundamental concepts where possible. If a revision is needed, we usually started by asking the original authors for the revision but if impossible, we brought in new authors to revise these chapters.

As the laser shines in modern applications, we added a large number of new chapters reflecting the most recent advancements in laser technologies. Throughout the Handbook, entirely new sections were added, including sections on materials processing, laser spectroscopy and lasers in imaging and communications. Nearly all chapters in these sections are either entirely new or substantially revised. On the other hand, some of the topics previously included have seen dwindling relevance today. We had to make the hard decision to let go of some of these outdated chapters from the first edition. Despite these deletions, this new Handbook still grows significantly from the original three volumes to the current four volumes.

Bringing this large project to its conclusion is the collective efforts of many individuals. It began with the encouragement and guidance of Lu Han, the then managing editor of this Handbook. I know how much Lu cared about this project. I still remember an initial phone call with Lu, we finished it at a late afternoon past 5 pm. Over the phone, I was told that I would receive the first edition of this Handbook. To my surprise, I had the handbooks in my hand the next morning. At CRC press, this project was later passed onto Carolina Antunes and finally to Lara Spieker, who has been essential in bringing this project to its conclusion.

Many people have provided me with indispensable help. My co-editor, Subhash Chandra Singh, at the University of Rochester, helped chart the layout of this new edition and worked along with me throughout this project. Ying Zhang, who was a senior editor at Changchun Institute of Optics, Fine Mechanics, and Physics (CIOMP) in China, spent a half year with us in Rochester, where his years of professional editorial experience helped move this project forward significantly. Lastly, my thanks go to Pavel Redkin of CIOMP, who made significant contributions in communicating with the chapter authors and guiding them throughout the project. Additionally, my appreciation goes to Kai Davies, Sandeep K. Maurya, Xin Wei, and Wenting Sun for their help in this Handbook project.

Chunlei Guo
Editor-in-Chief
University of Rochester

Taylor & Francis
Taylor & Francis Group
http://taylorandfrancis.com

Editors

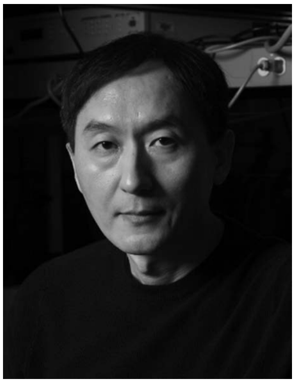

Chunlei Guo is a Professor in The Institute of Optics and Physics at the University of Rochester. Before joining the Rochester faculty in 2001, he earned a PhD in Physics from the University of Connecticut and did his postdoctoral training at Los Alamos National Laboratory. His research is in studying femtosecond laser interactions with matter, spanning from atoms and molecules to solid materials.

His research at University of Rochester has led to the discoveries of a range of highly functionalized materials through femtosecond laser processing, including the so-called black and colored metals and superhydrophillic and superhydrophobic surfaces. These innovations may find a broad range of applications, and have also been extensively featured by the media, including multiple New York Times articles. Lately, he devoted a significant amount of efforts to developing technologies for global sanitation by working with the Bill & Melinda Gates Foundation. Through this mission, he visited Africa multiple times to understand humanitarian issues. To further expand global collaboration under the Gates project, he helped establish an international laboratory at Changchun Institute of Optics, Fine Mechanics, and Physics in China. He is a Fellow of the American Physical Society, Optical Society of America, and International Academy of Photonics & Laser Engineering. He has authored about 300 referred journal articles.

Subhash Chandra Singh is a scientist at the Institute of Optics, University of Rochester and an Associate Professor at Changchun Institute of Optics, Fine Mechanics, and Physics. Dr. Singh earned a Ph.D. in Physics from University of Allahabad, India in 2009. Prior to working with the Guo Lab, he was IRCSET-EMPOWER Postdoctoral Research Fellow at Dublin City University, Ireland for 2 years and a DST-SERB Young Scientist at University of Allahabad for 3 years. He has more than 10 years of research experience in the fields of laser-matter interaction, plasma, nanomaterial processing, spectroscopy, energy applications, plasmonics, and photonics. He has published more than 100 research articles in reputable refereed journals and conference proceedings. His past editor experience includes serving as the main editor for Wiley-VCH book *Nanomaterials; Processing and Characterization with Lasers* and guest editor for special issues of a number of journals.

Taylor & Francis
Taylor & Francis Group
http://taylorandfrancis.com

Contributors

Markus-Christian Amann
S. Anders
Sergey Babin
B. D. Barmashenko
Norman P. Barnes
T. T. Basiev
Peter Blood
Georges Boulon
Igor Bufetov
Christophe Codemard
Kevin Cordina
Evgeny Dianov
Malcolm H. Dunn
Niloy K. Dutta
Qiang Fang
Peter Fendel
Sergei Firstov
Alan Fry
Shijie Fu
John O. Gerguis
E. Gornik
Ph Grelu
Chunlei Guo
Tony Gutierrez
Denis R. Hall
Yu Han
Julian Jones
Hitoshi Kawaguchi
Diaa Khalil
Randall Knize
Qiang Li
J. I. Mackenzie
Robert Martin
Mikhail Melkumov
V. A. Mikhailov
S. B. Mirov
Peter Moulton
J. B. Murphy
P. G. O'Shea
Haitham Omran
Taiichi Otsuji
Stephen A. Payne
Fabienne Pellé
R. C. Powell
Wilhelm Prettl
Gregory J. Quarles
Jorge J. Rocca
S. Rosenwaks
Yasser M. Sabry
Lee H. Sentman
I. A. Shcherbakov
D. P. Shepherd
Bei Shi
Wei Shi
William T. Silfvast
Subhash Chandra Singh
G. Strasser
Sándor Szatmári
Szeged, Hungary
David H. Titterton
Mary S. Tobin
Lisa Tsufura
Peter Unger
Peter P. Vasil'ev
Colin Webb
Ian White
Alan D. White
W. J. Witteman
A. I. Zagumennyi
Michalis N. Zervas
Boris Zhdanov
P. G. Zverev

Taylor & Francis
Taylor & Francis Group
http://taylorandfrancis.com

1

Solid-State Lasers: Section Introduction

R. C. Powell

Lasers can be categorized by whether their active medium is a solid, liquid, or gas. Solid-state lasers were the first type of lasers to be invented (ruby lasers). They have the advantage of being rugged, compact systems that make them useful in non-laboratory environments. Technically, both dielectric host materials with dopants or point defects and semiconductors are solid-state lasers; however, the common terminology is to use the name 'solid state lasers' for the former and 'semiconductor lasers' for the latter. This chapter deals with solid-state lasers while semiconductor lasers are discussed in Chapter 11.

There are a wide variety of laser host materials, including oxide and fluoride crystals and glasses. Similarly, there are many types of dopants including transition metal ions, rare-earth ions, and colour centres. It is the combination of specific dopants or point defects with specific host materials that determines the fundamental properties of the laser. These combinations can operate as three-level, four-level, and vibronic lasers spanning the near-ultraviolet, visible, and near-infrared spectral regions. They can be pulsed or continuous wave, discrete line or tunable, and mode-locked or operating in Q-switched modes. The ruggedness and versatility of solid-state lasers have led to their use in many practical applications.

This section describes the fundamental science and technology of the most common solid-state lasers and provides information on their systems design and laser operating parameters. One way to extend the spectral range of solid-state lasers is through non-linear optical effects. This section describes the use of several types of non-linear optical effects in solid-state lasers. The laser material for the systems described in this section is in the form of a rod or slab. Other configurations of solid-state lasers such as fibres and waveguides are discussed in Chapter 35.

Taylor & Francis
Taylor & Francis Group
http://taylorandfrancis.com

2

Transition Metal Ion Lasers—Cr^{3+}

Georges Boulon

CONTENTS

2.1 Introduction 3
2.2 Free-Ion Energy Levels 4
2.3 Crystal-Field Splitting: Ligand-Field Action 6
  2.3.1 Crystal-Field Expression in the Octahedral Symmetry Site 6
  2.3.2 Calculations of the Cr^{3+} Energy Levels 7
2.4 The Dynamic Effect of the Ligand: Electron–Phonon Interaction 10
  2.4.1 Configuration-Coordinate Diagram 10
  2.4.2 Optical Band Shapes 11
  2.4.3 Radiative and Non-Radiative Transitions. Energy Transfer Processes 11
    2.4.3.1 Radiative and Non-Radiative Transitions 11
    2.4.3.2 Role of Radiative and Non-Radiative Energy Transfers in the Concentration-Quenching Processes 12
2.5 Emission Sharp Line of the Cr^{3+} Ion in the Ruby Laser: A Strong Crystal-Field Model and a Three-Level Scheme 13
2.6 Emission Broadband Cr^{3+} Laser Crystals: A Weak Crystal-Field Model and a Four-Level Scheme 16
  2.6.1 Spectroscopic Approach 16
  2.6.2 Alexandrite Laser Crystal 17
  2.6.3 Colquiriite Solid-State Laser 18
2.7 Conclusion 23
References 23

2.1 Introduction

The most popular centres in inorganic solids are probably Cr^{3+} optical ones. As with many transition metal ions, Cr^{3+} is used as a colouring agent in the glass industry and in jewellery where beautiful mineral stones, such as ruby (Al_2O_3 sapphire), alexandrite ($BeAl_2O_4$ chrysoberyl), emerald ($Be_3Al_2(SiO_3)_6$), as well as several garnets containing aluminium or gallium, are used. Colour characteristics can easily be connected to our light environment, with visible and strong broadband absorption. In solid-state laser sources, Cr^{3+} ions, which are dispersed in a host crystal as an impurity in the place of aluminium octahedral symmetry sites, can be pumped inside the usual absorption bands with an appropriate xenon flashlamp or with argon and krypton laser energy sources. The optical excitation energy is absorbed by raising electrons of 3d^3 Cr^{3+} configuration from the ground level to one of the pump absorption bands. It is then transformed by fast radiationless transitions into the lowest excited level. During this process, the energy lost by the electron of the excited Cr^{3+} ion is carried into the lattice by phonons. In the last step of the process, the electrons return to the ground state through spontaneous emission or fluorescence if the pump intensity is below the laser threshold. Laser emission, that is to say, stimulated radiation that produces the expected output beam, only occurs when the pump intensity is above the laser threshold, and then the necessary inversion of the population begins to be reached between the ground level and the involved excited level. One of the advantages of Cr^{3+}-doped crystals is to show visible emission in the deep red spectral range where eyes are still sensitive. It is truly fascinating to detect the passage between spontaneous emission in all space and the directional stimulated emission in ruby at 694.3 nm (0.6943 µm). Theodore H. Maiman [1] saw it for the first time in 1960 at the Hughes Research Laboratories in Malibu, California, by using a rod of synthetic ruby coated on the two opposite sides and pumped by a pulsed helical xenon flashlamp. Maiman's demonstration of the ruby laser, before the gas laser and the dye laser, opened the laser era.

The understanding of Cr^{3+}-doped crystals is thus connected with the physical properties of Cr^{3+} activator ions, the host materials and relevant physical processes including:

i. static electron–lattice interactions, to ascertain how the electronic energy levels of the free ions are perturbed by the electrostatic crystal field of the nearest-neighbour host ions;
ii. electron–photon interactions, to determine absorption and emission of light radiation between energy levels, which can be classified as so-called allowed or forbidden transitions;

iii. electron–phonon interactions, due to the thermal vibrations of the host ions, which modulate the local crystal field at the Cr^{3+} site and then are strongly dependent on the temperature seen in shifts and broadening of spectral lines; and

iv. ion–ion interactions, strongly dependent on the activator concentration leading to either non-radiative energy transfer accompanied by concentration quenching, which is very well known in luminescent materials, or radiative energy transfer, so-called radiative trapping. An example of radiative trapping can be found in Cr^{3+} centres of ruby due to the presence of the resonant absorption–emission lines.

All these static and dynamic processes strongly affect the spectroscopic properties of Cr^{3+} ions due to the nature of the optically active electrons belonging to the $3d^3$ outer configuration. As a result, the absorption and emission spectra are characterized by the usual broadbands and sharp lines, which are useful for laser operations, as we shall demonstrate.

This chapter is divided into five parts. The first three summarize the general concepts of determining the energy levels for the $3d^3$ Cr^{3+} ion, first as a free ion and then as an impurity ion in the usual octahedral crystal field in which the stabilization energy is maximum. The last two explain the main physical properties, first of ruby as an example of a strong field Cr^{3+} laser crystal emitting $^2E \rightarrow {}^4A_2$ sharp line in the three-level scheme of Cr^{3+} laser crystals, second of alexandrite as an example of an intermediate field Cr^{3+} laser crystal emitting both $^2E \rightarrow {}^4A_2$ sharp line and $^4T_2 \rightarrow {}^4A_2$ broadband and finally of garnets and fluorides as examples of a weak crystal-field Cr^{3+} laser crystal model emitting a $^4T_2 \rightarrow {}^4A_2$ broadband useful for tunable solid-state lasers in the four-level scheme.

2.2 Free-Ion Energy Levels

A detailed development of the theoretical description of electronic energy levels of atoms and ions can be found in several books [2–7]. The energy E and eigenfunction ψ of transition metal-free ions can be obtained by solving Schrödinger's equation:

$$H_{\text{fi}}\psi = E\psi \tag{2.1}$$

$$H_{\text{fi}} = H_1 + H_{\text{e}} + H_{\text{s-o}}. \tag{2.2}$$

H_1 is the kinetic and potential energy of the optical active i electron in the spherically symmetric ion nucleus:

$$H_1 = \sum_i \frac{\hat{p}_i^2}{2m} - \frac{Ze^2}{4\pi\varepsilon_0 r_i} \tag{2.3}$$

H_{e} is the electrostatic Coulomb interaction between the electrons, which configures the electrons into L and S terms:

$$H_{\text{e}} = \sum_{i\rangle j} \frac{e^2}{4\pi\varepsilon_0 r_{ij}}. \tag{2.4}$$

$H_{\text{s-o}}$ is the spin–orbit interaction which is the relativistic effect that couples the magnetic moment of the spinning electrons and the magnetic field caused by the orbital motion of the electrons which forms J terms:

$$H_{\text{s-o}} = \sum_i \xi(r_i)\hat{\boldsymbol{l}}_i \cdot \hat{\boldsymbol{s}}_i \tag{2.5}$$

The interelectron Coulomb interaction is simplified to a spherically averaged potential term, by the central field approximation

$$H_{\text{e}} = \left\langle \sum_{j\neq i} \frac{e^2}{4\pi\varepsilon_0 r_{ij}} \right\rangle = U_i(r_i). \tag{2.6}$$

If the spin–orbit interaction is neglected and the central field approximation is used, then the free ion Hamiltonian becomes

$$H_{\text{fi}} = H_{\text{o}} \sum_i \frac{\hat{p}_i^2}{2m} - \frac{Z_e^2}{4\pi\varepsilon_0 r_i} + U_i(r_i) = V_i(r_i) \tag{2.7}$$

which is referred to as the central field Hamiltonian, where $V_i(r_i)$ is the combined nuclear and interelectron potential energy term. The solutions to Schrödinger's equation are separable for each of the electrons, and the wavefunction, in polar coordinate form, can be written as:

$$u_i = R_{ni,li}(r_i) \cdot Y_{ii}^{m_{zi}}(\theta_i, \Phi_i) \cdot S(s_{zi}) \tag{2.8}$$

$$= |n\ell m_z\rangle_i |s_z\rangle_i = | n\ell m_z s_z\rangle_i \tag{2.9}$$

where $R_{ni,li}(r_i)$ is the solution to the radial equation of the central field potential, $V_{(ri)}$ for the ith electron. $Y_{li}^{m_{zi}}(\theta_i, \Phi_i)$ are the spherical harmonics of the ith electron and $S_{(szi)}$ is the spin state of the ith electron. The solutions are parametrized by the four quantum numbers n, l, m_z and s_z as can be seen in Table 2.1.

The Pauli exclusion principle states that no two electrons in an ion can occupy the same quantum state characterized by the four quantum numbers.

Since the electron is a spin ½ particle, such as a fermion, the N electron wavefunction built from single-particle states $u_1(1) \ldots u_n(N)$ must be antisymmetric and is given by the Slater determinant as linear combinations of products of the single-electron wavefunction. This wavefunction is antisymmetric because an interchange of the spatial and spin coordinates of two particles (say u_1 and u_2) is equivalent to interchanging two rows, so that the sign of the determinant changes. The energy of the state $\sum E_{n,e}$ depends on the set of n_i, ℓ_i values. This set, $n_i\ell_i$, is called the electron configuration. In each $n\ell$ orbital, there is a maximum of $2(2\ell + 1)$ electrons.

The electron configuration of a Cr atom with 24 electrons is $1s^22s^22p^63s^23p^63d^54s$. Thus, the Cr^{3+} ion has given up three electrons from the outer shells leaving three unshielded electrons in the 3d orbitals. These are the electrons that play the dominant role in determining the optical properties of the ion, with each electron having quantum numbers $n = 3$ and $\ell = 2$.

Finally, it can be observed that the energy of the states does not depend on the m_z and s_z values, and, as for the

TABLE 2.1

Quantum Numbers Associated with Solutions to Schrödinger's for Atoms and Ions

Quantum Number	Allowed Values	Purpose
Principal, n	1,2,3 . . .	Indicates the energy and size of the orbital.
Orbital, l	$(n-1), (n-2), \ldots, 0$	Indicates the shape of the orbital and the electronic angular momentum.
Magnetic, l_z	$\pm l, \pm(l-1), \ldots 0$	Indicates the direction of an orbital and the electron's behaviour in a magnetic field.
Spin state, S_z	$\pm 1/2$	Indicates the axial angular momentum of the electron.

single electron functions, these eigenstates have a large energy degeneracy. Since H_0 commutes with ℓ_i the orbital angular momenta vectors, it will also commute with the total orbital angular momentum $L = \sum_i \ell_i$ and M_z. Likewise, H_0 commutes with s_i and hence the total spin angular momentum $S = \sum_i s_i$ and S_z, so that the eigenstates of H_0 can be classified by the set of quantum numbers $(n_i\ell_i)$ L S M_z S_z with corresponding ketl$(n_i\ell_i)$ $LSM_zS_z\rangle$.

These L and S angular momenta vectors can then be coupled to give the total angular momentum for the ion, $J = L + S$. A second alternative to add up the angular momenta is to first sum up the individual orbital and spin angular momenta for each electron to form the total $j_i = \ell_i + s_i$ and then sum up j_i over all electrons to give $J = \sum j_i$. Note that the size of the spin–orbit interaction determines which coupling scheme gives a better zero-order approximation to the actual spectrum. The first approach is more appropriate for transition metal ions such as Cr^{3+}. A diagram of the energy splittings due to the electronic and spin–orbit interactions is given in Figure 2.1.

The final degeneracy due to the $2J + 1$ different possible spatial orientations for the angular momentum can be partially or totally lifted only by an external perturbation such as an applied electric field (the Stark effect as in the octahedral symmetry crystallographic site of the hosts, as we shall see later) or magnetic field (the Zeeman effect). In the usual spectroscopic term designated by ^{2S+1}L, the superscript is called the multiplicity of the term. The spectroscopic notation S, P, D, F, . . . is used for $L = 0, 1, 2, 3, \ldots$, respectively. When the spin–orbit interaction is taken into account, each term is split into states having specific values of J designated by $^{25+l}L_J$, called multiplets. In the Russell–Saunders approximation, or L–S coupling, L and S are still treated as good quantum numbers.

The energy value of the energy levels for each spectral term can theoretically be obtained by calculating the interaction of multielectrons. Slater, Condon and Shortley used three parameters, F_0, F_2 and F_4, as radical integrators of static interaction, to denote the level position of the 3d^n electron configuration. These are known as the Slater parameters. Based on group theory, Racah used A, B and C to denote the parameters. These are known as the Racah parameters. The relationship between these two sets of parameters are $A = F_0 - 49\ F_4$, $B = F_2 - 5\ F_4$ and $C = 35\ F_4$. A is the same for all the energy levels and only contributes as a shift. Table 2.2 gives level energies of 3d^3 (Cr^{3+}) spectral terms.

The eight terms have to be ordered with respect to their energies. Hund's rules require that the ground-state term has the greatest multiplicity possible and the greatest orbital angular

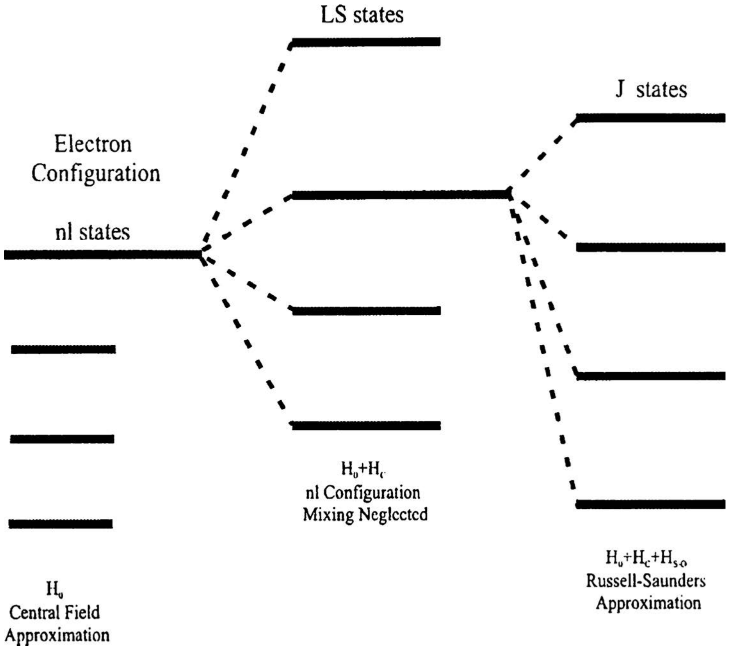

FIGURE 2.1 Splitting of free-ion states by *LS* coupling and spin–orbit coupling.

TABLE 2.2

Level Energies of $3d^3$ (Cr^{3+}) Spectral Terms

Spectral Terms	Level Energies
^2H	$3A - 6B + 3C$
^2G	$3A - 11B + 3C$
^4F	$3A - 15B$
^2F	$3A + 9B + 3C$
2D	$3A + 5B + 5C \pm (193B^2 + 8BC + 4C^2)^{1/2}$
4P	$3A$

momentum value consistent with that multiplicity. Therefore the ground state is the ^4F term. Finally, all energies measured relative to the ground state yield:

$$\frac{E(^4F)}{C} = -15\frac{B}{C} \tag{2.10}$$

$$\frac{E(^4P)}{C} = 0 \tag{2.11}$$

$$\frac{E(^2H)}{C} = -6\frac{B}{C} + 3 \tag{2.12}$$

$$\frac{E(^2P)}{C} = -6\frac{B}{C} + 3 \tag{2.13}$$

$$\frac{E(^2G)}{C} = -11\frac{B}{C} + 3 \tag{2.14}$$

$$\frac{E(^2F)}{C} = 9\frac{B}{C} + 3 \tag{2.15}$$

$$\frac{E(^2D)}{C} = 5\frac{B}{C} + 5 - \sqrt{193\left(\frac{B}{C}\right)^2 + 8\frac{B}{C} + 4} \tag{2.16}$$

$$\frac{E(^2D')}{C} = 5\frac{B}{C} + 5 + \sqrt{193\left(\frac{B}{C}\right)^2 + 8\frac{B}{C} + 4} \tag{2.17}$$

These expressions are plotted in units of E/C and B/C as shown in Figure 2.2 [3]. By measuring the optical absorption and emission spectra of a specific type of $3d^3$ ion such as Cr^{3+}, the energy-level splittings shown on the right-hand side of the figure have been found and identified with the designated terms. This fixes the value of B/C for Cr^{3+} at 0.222 as shown in the broken vertical line. Racah parameters for $3d^3$ Cr^{3+} ion are $B = 918\,\text{cm}^{-1}$, $C = 4133\,\text{cm}^{-1}$ and $C/B = 4.50$.

The free-ion terms are further split by spin–orbit interaction. However, for $3d^3$ ions in general and Cr^{3+} in particular, this is a smaller effect than the crystal-field splitting.

2.3 Crystal-Field Splitting: Ligand-Field Action

2.3.1 Crystal-Field Expression in the Octahedral Symmetry Site

When a free ion is put into a crystal host as an impurity, it is no longer in an environment of complete spherical symmetry. Instead, it is surrounded by a set of nearest-neighbour ions, or ligands, in a geometric configuration. With the Cr^{3+} ion, the stabilization energy is maximum in the specific type of octahedral symmetry environment, which can be described as a regular octahedron possessing a centre of inversion as shown in Figure 2.3 and denoted by group theory as the O_h point group symmetry.

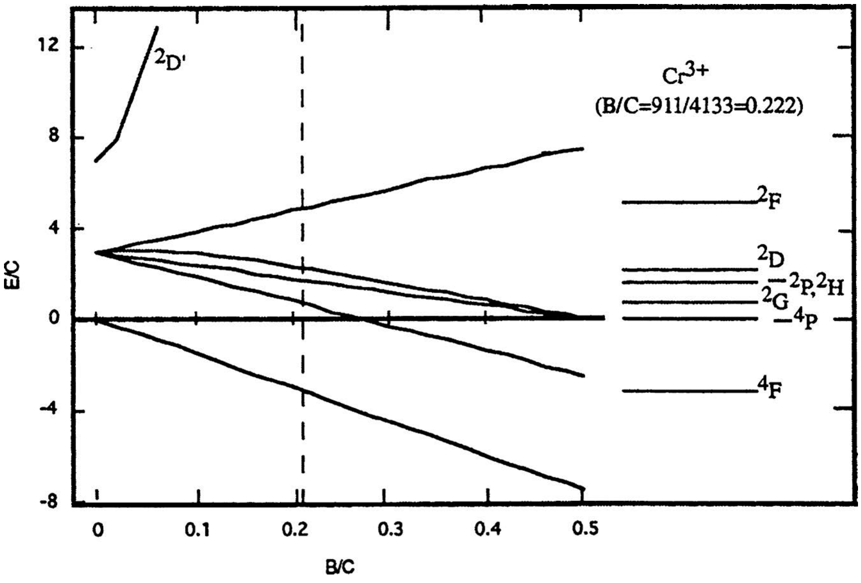

FIGURE 2.2 Free-ion terms of a d^3 ion and energy levels for Cr^{3+} [3].

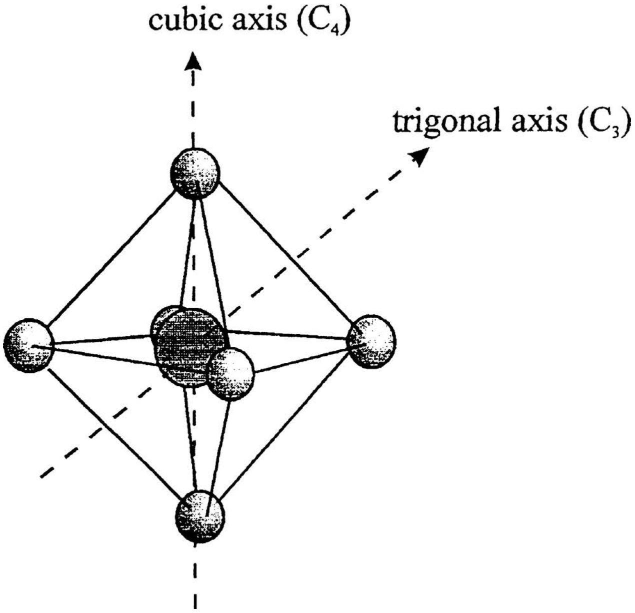

FIGURE 2.3 The Cr^{3+} ion in an octahedral ligand field. The cubic axis (C_4) and trigonal axis (C_3) are shown.

All point groups are characterized by character tables giving the irreducible representations. The Mulliken notation is the one most commonly used: *A* and *B* denote one-dimensional representations, *E* denotes two-dimensional representations and *T* denotes three-dimensional representations. For groups with a centre of inversion, subscripts g and u are used to indicate representations that are symmetric (g for gerade) or antisymmetric (u for ungerade) with respect to the inversion operation respectively. For the O_h point group, the eight main representations are A_{1g}, A_{2g}, E_g, T_{1g}, T_{2g}, $E_{1/2g}$, $E_{3/2g}$ and G_g. In Bethe's notation, the first five representations are symbolized by Γ_1, Γ_2, Γ_3, Γ_4 and Γ_5.

The Hamiltonian of the Cr^{3+} ion in an octahedral symmetry crystal field is given by the same expression [8] as well as the V_c crystal-field energy term, assuming that all six neighbouring ions (oxygen or fluorine) can be approximated by point charges, each with the amount $-Z_pe$, fixed at their average positions $R_p(0) = (a_p, \theta_p, \Phi_p)$:

$$H = H_1 + H_e + H_{s-o} + V_c \tag{2.18}$$

$$V_c = \sum_i^6 \sum_{p=1}^6 \frac{1}{4\ \pi\varepsilon_0} \frac{Ze}{\left|R_p(0) - r_i\right|}. \tag{2.19}$$

The *i*th electron is at $\boldsymbol{r}_i = (r_i, \theta_i, \Phi_i)$. If we assume that $a_i < a_k$, we can expand V_c in terms of spherical harmonics according to the standard multipole expansion:

$$\frac{1}{r_{ij}} = \sum_k \sum_{p=1}^{+k} \frac{4\pi}{2k+1} \frac{r^k}{a^{k+1}} Y_k^m\left(\theta_2, \varphi_2\right). \tag{2.20}$$

The potential function at the central ion due to the six ligands located at distance '*a*' is then yielded by:

$$V_c = \sum_i \sum_{p=1}^{6} \sum_{\ell=0}^{\infty} \sum_{m=-\ell}^{\ell} \frac{4\pi Ze}{2\ell+1} \cdot \frac{r_i^{\ell}}{a_p^{\ell+1}} \cdot Y_\ell^{m*}(\theta_i, \varphi_i) \cdot Y_\ell^m(\theta_j, \varphi_j). \tag{2.21}$$

One obtains:

$$\begin{aligned} V_c &= \frac{Ze}{4\pi\varepsilon_0}\left[\frac{6}{a_p} + \frac{7r_i^4}{2a_p^5}\right. \\ &\left.= \left\{C_0^{(4)}(\theta_i\varphi_i) + \sqrt{\frac{5}{14}}\left(C_4^{(4)}(\theta_i, \varphi_i) + C_{-4}^{(4)}(\theta_i, \varphi_i)\right)\right\}\right] \\ &= r_i^6 \text{terms} + \cdots \end{aligned} \tag{2.22}$$

where

$$C_t^{(k)}(\theta, \varphi) = \left(\frac{4\pi}{2k+1}\right)^{1/2} Y_k^t(\theta, \varphi). \tag{2.23}$$

This expression is of even parity as expected with the inversion symmetry of the local arrangement.

2.3.2 Calculations of the Cr^{3+} Energy Levels

In the expression of the Hamiltonian *H*, the best way to calculate the energy level positions is to estimate the relative values of each term by applying the perturbation procedure. The perturbations are then treated from the highest to the lowest magnitude.

Usually, there are three types of treatment.

1. *Weak crystal field* ($V_c < H_{s-o} < H_e$): the correct quantum numbers *J* and M_J are taken from the free ion, and the crystal field acts as a perturbation that causes Stark splitting of the free-ion multiplets. This is the case for the 4f configuration of optically active rare earths shielded by the 5s^{2}5p^6 outer-shell electrons.
2. *Intermediate crystal field* ($H_{s-o} < V_c < H_e$): this is the case of outer 3d electrons of optically active transition metal ions such as Cr^{3+}. Calculations of the energy levels can be made by neglecting both the crystal-field Hamiltonian, V_c, and the spin–orbit Hamiltonian, H_{s-o}, and by considering only the *LS* terms of the Coulomb Hamiltonian, $H_1 + H_e$, representing the interaction between the electrons. The correct quantum numbers are *L*, *S*, M_L and M_S. The crystal field is a perturbation that splits the free-ion terms, and the H_{s-o} interaction is an additional perturbation that determines further splitting of the energy levels.
3. *Strong crystal field* (H_{s-o}, $H_e < V_c$): this is the case with 4d or 5d optically active electrons. The intermediate crystal-field procedure involved with Cr^{3+} ion is much more complicated than the other two. However, an illustrated model of d orbitals is very useful to interpret the spectroscopic data. As can be seen in Figure 2.4, the angular forms of the five-fold degenerate d orbitals ($\ell = 2$ and $2\ell + 1 = 5$) of even parity in an octahedral crystal field can be divided into two

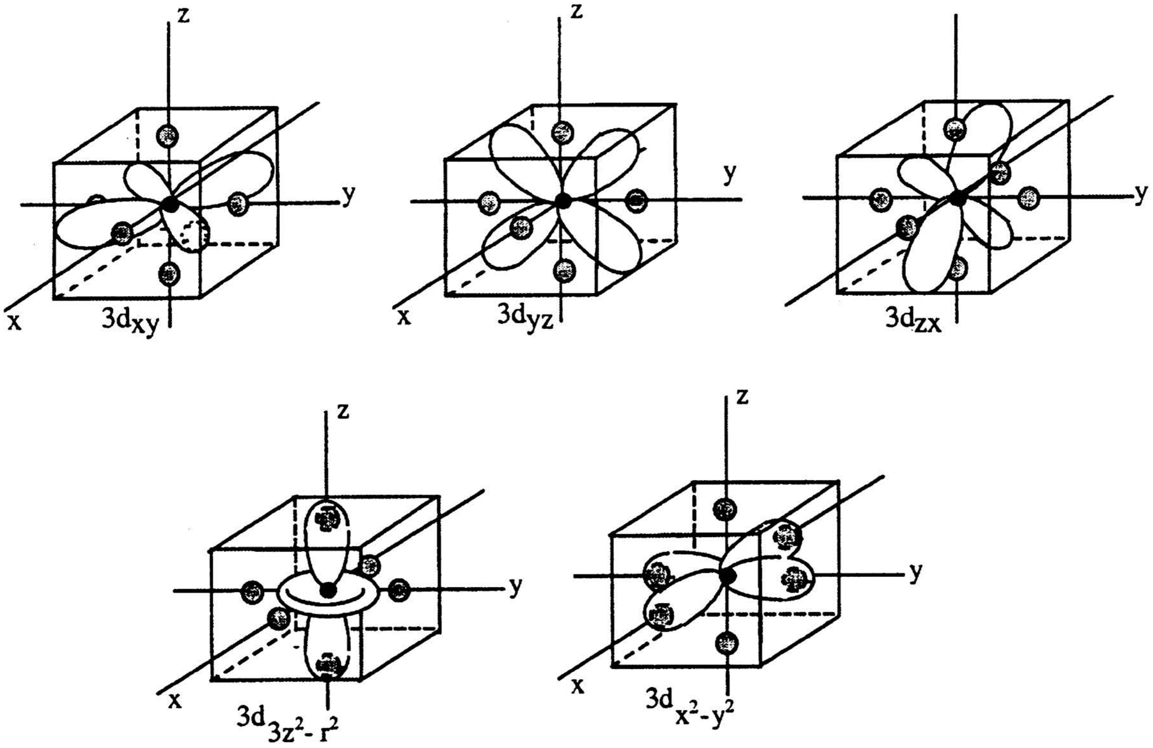

FIGURE 2.4 3d orbital angular forms of even parity in an octahedral crystal field.

types of levels labelled t_{2g} functions for the three-fold degenerate t_2 level (d_{xy}, d_{yz}, d_{zx}) and e_g functions for the two-fold degenerate e level $\left(d_x^2 -_y^2, d_z^2\right)$. It is easy to understand that the t_{2g} orbitals, which are directed between the ligands, are less strongly coupled to the lattice and have lower energy than the e_g orbitals, which are directed towards the ligands. The usual representation of t_{2g} and e_g is shown in Figure 2.5, where the energy difference is designated by $10D_q$, D_q being the parameter characterizing the strength of the crystal field.

$\Delta = 10D_q$ has been estimated by using the static electric theory

$$\Delta = \frac{5eqr^{-4}}{3R^5} \tag{2.24}$$

$$e/r$$

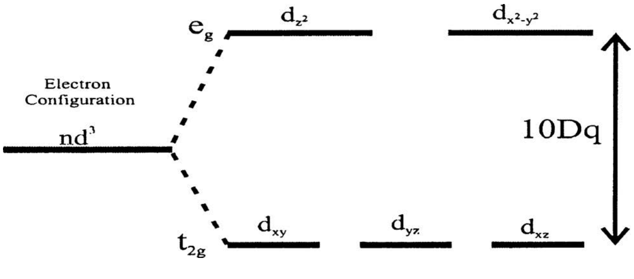

FIGURE 2.5 The two sets of d orbitals e_g (two-fold degenerate e level) and t_{2g} (three-fold degenerate t_2 level). The energy difference between the two sets is $10D_q$.

where e is the electric charge and r is the average distance from the metal ion nucleus to the electron in its d orbital. q is the ligand charge and R is the distance of the metal ion to the centre of the ligand.

The Cr^{3+} ground state is t_{2g} with the maximum number of electrons (three for $3d^3$) and, according to Hund's rule, the maximum number of parallel spins (↑↑↑). We can get two kinds of transitions: intraconfigurational transition inside the t_{2g} configuration with a change of only one spin direction and interconfigurational transitions between t_{2g} and e_g with the same alignment of the three spin directions (Figure 2.6).

This is a very important aspect of Cr^{3+} spectroscopy because it is needed to interpret absorption and emission spectra composed of broadbands and sharp lines as we shall see when we consider the coupling between the electrons of the Cr^{3+} ion and the lattice vibrations. In addition to these general considerations, we use the notation of the eight irreducible representations of the O_h octahedral symmetry group to label the eigenstates. The irreducible representations of the free-ion terms are reduced in terms of the irreducible representations of the O_h group as given in Table 2.3.

The last step is to find the quantitative values of each term. Tanabe and Sugano [9,10] calculated the energy states by considering the effect of the crystal-field Hamiltonian V_c, before the Coulomb interaction between the outer electrons, H_e, that is to say in the strong field. This approach yields results similar to those of the intermediate field approach because the effects of the interaction terms of the Hamiltonian, V_c and $H_1 + H_e$, are comparable.

The energies of the crystal-field multiplets can be expressed in terms of the Racah parameters B and C and the crystal-field

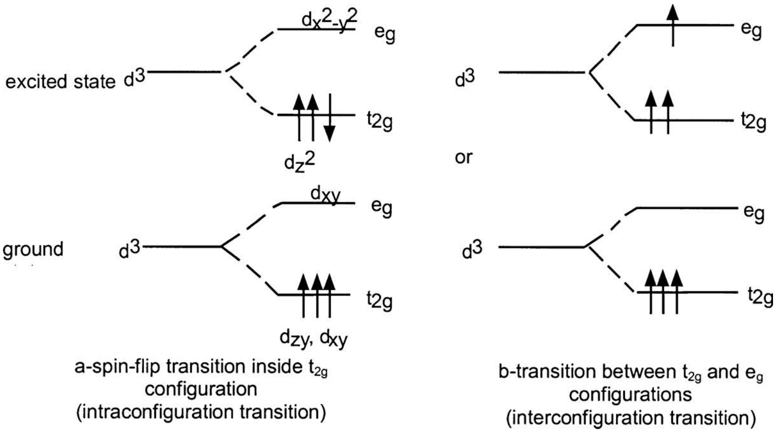
excited state
d3
dx2-y2
eg
t2g
dz2
ground
d3
dxy
eg
t2g
dzy, dxy
a-spin-flip transition inside t2g configuration (intraconfiguration transition)
d3
eg
t2g
or
d3
eg
t2g
b-transition between t2g and eg configurations (interconfiguration transition)

FIGURE 2.6 The two types of transitions of d^3 electrons in an octahedral crystal field.

TABLE 2.3

Irreducible Representations of the O_h Group

Spectral Terms (*LS* Coupling)	Irreducible Representations
^{2}H	$^2E + 2^2T_1 + ^2T_2$
^{2}G	$^2A_{ig} + ^2E_g + T_{1g} + T_{2g}$
^{4}F	$^4A_{2g} + ^4T_{1g} + ^4T_{2g}$
^{2}F	$^4A_{2g} + ^4T_{1g} + ^4T_{2g}$
^{2}D	$^2E_g + ^2T_{2g}$
^{2}D′	$^2E_g + ^2T_{2g}$
^{4}P	$^4T_{1g}$
^{2}P	$^4T_{1g}$

TABLE 2.4

Energies of the Crystal-Field Multiplets Expressed in Terms of the Racah Parameters *B* and *C* and the Crystal-Field Splitting $10D_q$

t_2^3 Configuration	t_2^2e Configuration
$E(^4A_2) = 3A - 15B - 12D_q$	$E(^2A_1) = 3A - 11B + 3C - 2D_q$
$E(^2E) = 3A - 6B + 3C - 12D_q$	$E(^4T_1) = 3A - 3B - 2D_q$
$E(^2T_1) = 3A - 6B + 3C - 12D_q$	$E(^4T_2) = 3A - 15B - 2D_q$
$E(^2T_2) = 3A + 5C - 12D_q$	

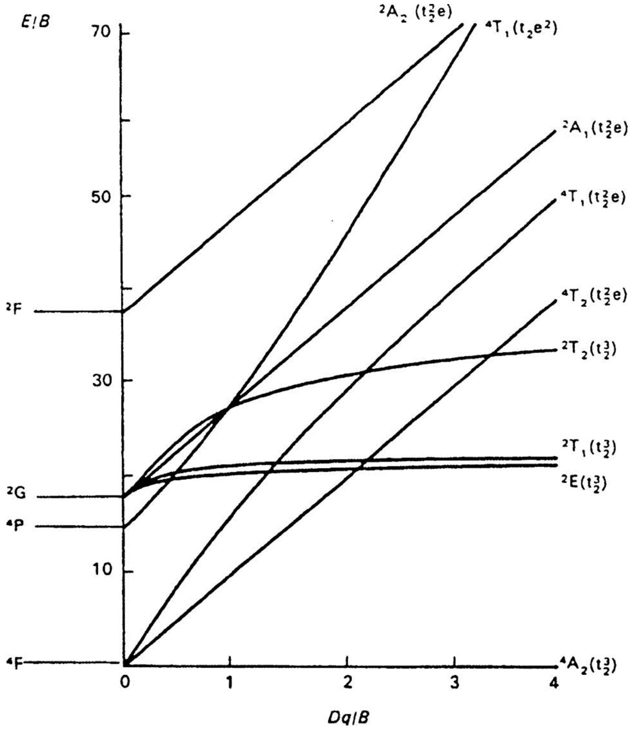

FIGURE 2.7 The Tanabe–Sugano diagram showing energy levels *E*/*B* of the Cr^{3+} ion in an octahedral crystal field as a function of the crystal-field strength D_q/B. The theoretical free-ion levels are shown on the left by taking $D_q = 0$ [9,10].

splitting $10D_q$ previously introduced with e_g and t_{2g} orbitals. The results are shown in Table 2.4 for the main *LS* term involved in the optical transitions.

The strength of the crystal field, $10D_q$, is characterized by the energy difference between the $^4A_2$ and $^4T_2$ states. Figure 2.7 shows the Tanabe–Sugano diagram for Cr^{3+}, which is very well known by spectroscopists. It can be seen that levels, which are derived from the same electronic configuration t_{2g}^3, as the ground state $^4A_2$, ^2E, $^2T_1$ and $^2T_2$ are almost independent of D_q for strong crystal fields and appear as horizontal lines. Figure 2.7 also shows that the lowest excited state is dependent on the strength of the crystal field: for strong field hosts, it is the ^2E state giving $^4A_2 \Leftrightarrow {}^2E$ transition, which is observed as a narrow spin-forbidden line ($\Delta S \neq 0$). For weak field hosts, the $^4T_2$ is the lowest giving the $^4A_2 \Leftrightarrow {}^4T_2$ transition, which is observed as spin-allowed broadband ($\Delta S = 0$). The separation in energy between the lowest vibrational levels of $^4T_2$ and ^2E determines the nature of the Cr^{3+} ion emission. $D_q/B = 2.3$ is the point that separates weak and strong crystal fields.

In this theoretical part, we have assumed a perfect octahedral symmetry labelled as the O_h point group. However, the oxygen octahedron is slightly disturbed along the three-fold axis, which is the *c* axis of the crystal (see Figure 2.3), so that the site symmetry is lowered to C_{3v}. A more correct analysis of Cr^{3+}-ion spectroscopy should be done with the C_{3v} character table and direct-product representations as well as with C_{3v} selection rules for forced electric dipole transitions. From these tables, the distinction between the two kinds of

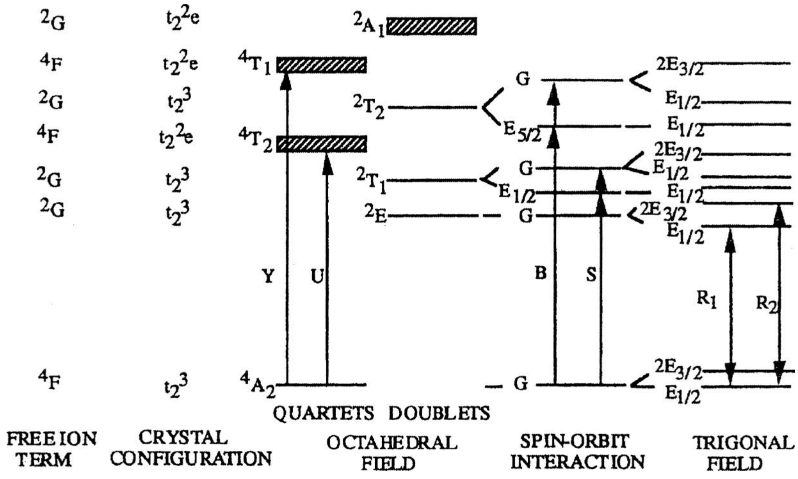

FIGURE 2.8 Cr^{3+} energy levels in the C_{3i} octahedral symmetry, spin–orbit interaction and trigonal field action are shown [7].

polarization, light polarized parallel and perpendicular to the *c* axis, can be made for each transition. Figure 2.8 summarizes all energy levels occurring within the C_{3v} symmetry site of Cr^{3+} ion in ruby. In addition to the octahedral Stark field within the two t_{2g} and e_g configurations, we have also mentioned the spin–orbit interaction and the trigonal field distortion which was described just above. The separation between the two sublevels is 0.38 cm^{-1} for the $^4A_2$ ground state and 29 cm^{-1} for the ^2E excited state in ruby. At room temperature, only ^2E splitting can be seen in the absorption spectrum with the use of a well-resolved spectrophotometer.

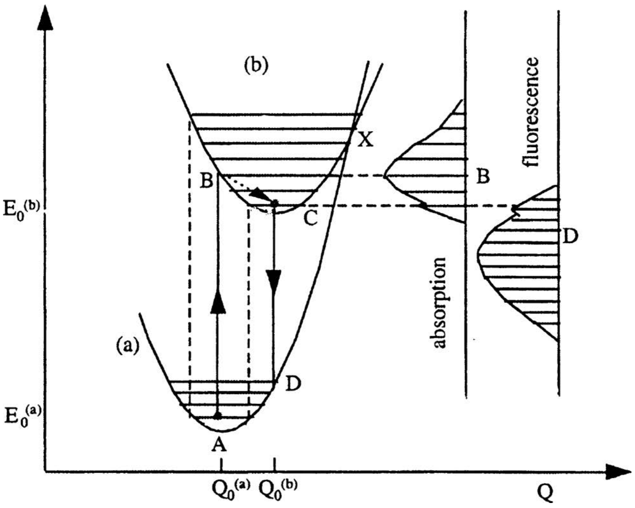

FIGURE 2.9 The usual single configuration coordinate diagram interprets absorption and luminescence properties of activator centres in solids. The zero-phonon line can be seen between $E_0^{(a)}$ and $E_0^{(b)}$ in both absorption and emission spectra.

2.4 The Dynamic Effect of the Ligand: Electron–Phonon Interaction

2.4.1 Configuration-Coordinate Diagram

The interaction of the optically active electrons of impurity ions with the lattice vibrations is most easily described using the single configuration coordinate diagram shown in Figure 2.9 in which the configurational coordinate *Q* represents the collective position of the lattice relative to the optical ion. Although this is a great oversimplification of the true situation, it is still quite useful in explaining some aspects of the optical spectra of ions in solids. It is assumed that the lattice vibrates about the active ion in a totally symmetric 'breathing mode' such that the electronic states have additional energy due to the vibrations, which are represented by a harmonic oscillator potential. In the configurational coordinate model, the harmonic oscillator energies are quantized so that:

$$E_{\text{vibr.}} = (n + 1/2)\hbar\omega \tag{2.25}$$

where $\hbar\omega$ is the phonon energy and *n* is the phonon order.

The potential curves are described by parabolas in the harmonic approximation assuming the same frequency ω for the phonon energy of both ground state E_g and excited state E_e.

$$E_g = \frac{1}{2}k\left(Q - Q_o^g\right)^2 \tag{2.26}$$

and

$$E_e = \frac{1}{2}k\left(Q - Q_o^g\right)^2 + E_o \tag{2.27}$$

$$\omega = \left(\frac{k}{M}\right)^{1/2} \tag{2.28}$$

where *M* is the mass of atoms involved in the vibration. The difference of configurational coordinates $Q_o^e - Q_o^g$ means the sensitivity difference of the two electronic levels to the host environment. This is expressed by the Huang–Rhys dimensionless parameter *S*:

$$\frac{1}{2}M\omega^2\left(Q_o^e - Q_o^g\right)^2 = S\hbar\omega \tag{2.29}$$

The Huang–Rhys parameter can also be used to characterize the difference in the strength of vibronic coupling between the two states in terms of the Stokes shift between absorption and emission lines:

$$\text{Stokes shift} = 2S\hbar\omega \tag{2.30}$$

2.4.2 Optical Band Shapes

We find then that absorption and emission line shapes both become broadband by taking into account the vibrational state interaction. The quantum mechanical approach shows that the band shape is Pekarian evaluated as proportional to:

$$\frac{\exp(-S)S^m}{m!}$$

which is plotted in Figure 2.10 for various values of S. As S increases, the band shape becomes more Gaussian.

The previous parts of this chapter have shown that electronic transitions of Cr^{3+} ions involve two types of orbitals e_g and t_{2g} in an octahedral crystal field. The transitions between the same type of orbital (t_{2g}), which correspond to the spin-flip case, are not strongly coupled to vibrations, so that S is small. The optical spectra are dominated by transitions that are purely electronic in nature, not involving phonons. This is the case for the so-called R_1 and R_2 lines associated with $^4A_2 \Leftrightarrow {}^2E$ transitions in absorption and emission occurring at the same wavelength (694.3 and 692.9nm, respectively in ruby).

The transitions between the two types of orbitals e_g and t_{2g}, which involve a change in the spatial orbital, have strong electron–phonon coupling and hence, large values of S. The absorption and emission spectra are composed of a zero-phonon line at the same energy in each and a vibronic broadband, which is Stokes-shifted in the emission spectrum. An example of this is the $^4A_2 \Leftrightarrow {}^4T_2$ transition of the Cr^{3+} ion.

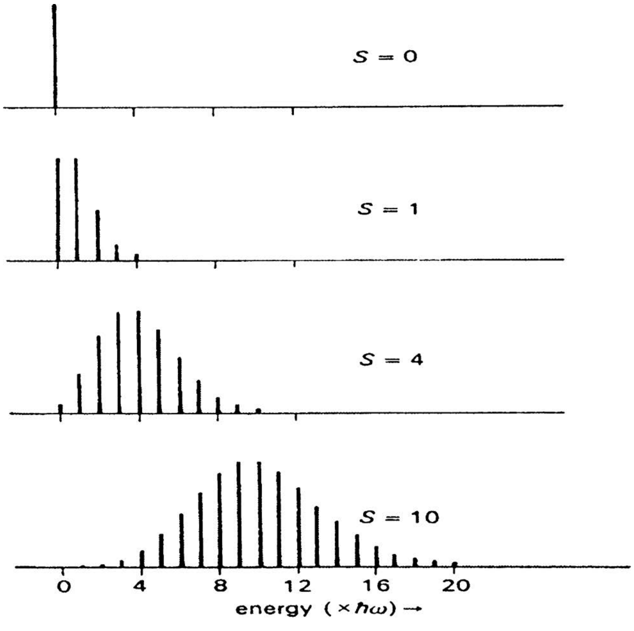

FIGURE 2.10 The relative intensities of the different electronic vibrational lines change with the strength of the coupling. S is the Huang–Rhys parameter.

Finally, from this description, only three levels are needed to interpret the absorption and emission spectra of the Cr^{3+} ion. Besides the $^4A_2$ ground state, the $\bar{E}$ component of ^2E and the $^4T_{2g}$ level, which are the two lowest excited states, are systematically used to explain laser operations. Figure 2.11 shows a schematic representation of the three types of crystal-field models usually met in Cr^{3+}-doped crystals. In ruby, which is a strong crystal-field model shown in Figure 2.9a, $\bar{E}$ is the lowest excited state and the laser transition is interpreted as $\bar{E} \rightarrow {}^4A_2$ at 693.3nm, whereas in almost all other Cr^{3+}-doped crystals, $^4T_2$ is the lowest excited state giving rise to $^4T_2 \rightarrow {}^4A_2$ transition of a tunable solid-state laser between 700 and 1250nm depending on the nature of the host. The parameter playing the main role is the distance R between the Cr^{3+} ion and the ligand occurring in the $10D_q$ formula as a result of the static electric theory, so that R increases progressively from a to b and c in Figure 2.11. The crystal-field dependence can be measured by the gap between $^4T_2$ and ^2E levels from either intensity or lifetime thermal dependence. For example, characteristics in Cr^{3+}-doped garnets are given in Table 2.5, confirming the relationship between ε and the cell parameter a_o of the cubic structure in garnets.

2.4.3 Radiative and Non-Radiative Transitions. Energy Transfer Processes

2.4.3.1 Radiative and Non-Radiative Transitions

As the Cr^{3+} transition metal ion of $3d^3$ configuration is characterized by strong absorption associated with the $^4A_2 \rightarrow {}^4T_2$ and $^4A_2 \rightarrow {}^4T_1$ spin-allowed transitions of vibronic nature, there can be efficient pumping, thanks to broad xenon flashlamp or laser visible sources. In the examples shown in Figure 2.11, under $^4T_2$ pumping, populating the excited state of the laser transition requires efficient radiationless relaxation down to the lowest state in each case. The dynamics of the non-radiative decays between $^4T_1$, $^4T_2$ and ^2E excited states have been analysed by applying the four-wave mixing technique in several hosts [13,14,18]. The time scale between vibrational levels is very fast, within tens of picoseconds. Therefore, radiative transition provides spontaneous emission and stimulated emission in lasers. The quantum efficiency η of the emitting level $\left(\eta = \frac{\tau \exp}{\tau \mathrm{rad}}\right)$ is an important parameter in the search for efficient radiative emission. η depends on both the experimental fluorescence (τ exp) lifetime and the radiative lifetime (τ rad) which is very often difficult to measure. Calculations of oscillator strength (f), absorption cross section (σ abs) and stimulated emission cross sections (σ) of the transition are detailed in many references [6,7,15]. However, such a description considers isolated ions in the host material, but experience reveals a strong concentration dependence of the optical properties due to ion–ion interaction, which is a function of the distance of two neighbour ions. The main consequence is the energy transfer process, which takes place when distances are less than ~2nm. The interactions known are dipole–dipole, dipole–quadrupole and quadrupole–quadrupole. Two types of energy transfers have been observed: resonant and non-resonant or phonon-assisted energy transfers. The energy transfers may lead to energy diffusion through resonant-radiative processes and to

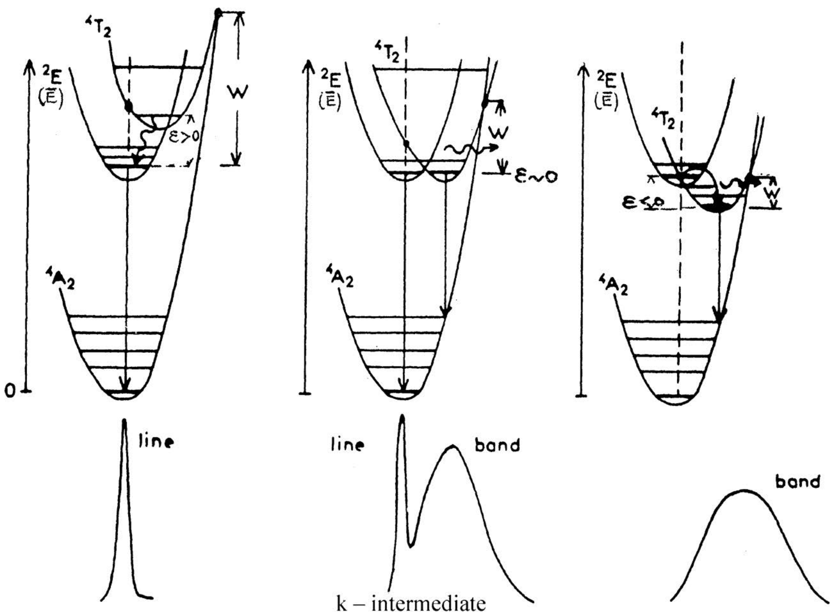

a – high crystal field
ε > 0

k – intermediate
crystal field
ε ~ 0

c – low crystal field
ε < 0

FIGURE 2.11 The three main types of crystal-field strength ion. Cr^{3+}-doped crystals can be measured by the energy gap ε between the lowest vibrational levels of ${}^2E$ and ${}^4T_2$ electronic levels.

TABLE 2.5

Spectroscopic Parameters and Cell Parameters in Garnets

Garnet Host	ε (cm^{-1})	a_o (Å)	R-line ${}^2E \rightarrow {}^4A_2$ (nm)	Wavelength of the Maximum of ${}^4T_2 \rightarrow {}^4A_2$ (nm)	τ (μs)
$Y_3Al_5O_{12}$ [11,12]	1000	12.005	680	720	9000
$Y_3Ga_5O_{12}$ [7]	600		693	720	240
$Gd_3Ga_5O_{12}$ [13,14]	380	12.376		769	160
$Y_3(Sc,Ga)_2Ga_3O_{12}$ [15]	250		696.3–694.9	740	145
$(Gd,Ca)_3(Ga,Mg,Zr)_2$ Ga_3O_{12} [16]	100	12.50		760	106
$Gd_3(Sc,Ga)_2Ga_3O_{12}$ [15]	50		690	760	120
$Gd_3Sc_2Ga_3O_{12}$ [17]	50	12.567	696.4–695.0 694.2–693.2 (4K)	785	245–340 530–330 (4K)
$La_3Lu_2Ga_3O_{12}$ [13,14]	−1000			830	68

concentration quenching when a sensitizer ion transfers the excitation to an unexpected and unexcited activator ion. These processes have to be understood in doped crystals. Especially in the high crystal-field schema of Cr^{3+} ion in which ${}^2E \leftrightarrow {}^4A_2$ resonant transition occurs, lifetime measurements provide useful information.

2.4.3.2 Role of Radiative and Non-Radiative Energy Transfers in the Concentration-Quenching Processes

Resonant-radiative energy transfer is well known for acting as a radiation trap. Resonant transitions permit a long-range energy diffusion between identical ions by successive re-absorption/re-emission processes. This serial mechanism affects the experimental excited state decay because it leads to a lengthening of the fluorescence lifetime measured over the volume of the sample relative to the lifetime of a single isolated ion. The strong spectral overlap between the fluorescence and absorption spectra enhances fluorescence re-absorption. Examples of resonant laser transitions in this class are ${}^2E \leftrightarrow {}^4A_2$ of Cr^{3+} in crystals and glasses like in ruby at 694.3 nm, more generally any resonant zero-phonon lines of transition metal ions and rare-earth ions such as ${}^5I_7 \leftrightarrow {}^5I_8$ in Ho^{3+} at 2.1 μm, ${}^3F_4 \leftrightarrow {}^3H_6$ in Tm^{3+} at 2.0 μm, ${}^4I_{13/2} \leftrightarrow {}^4I_{15/2}$ in Er^{3+} at 1.5 μm and ${}^2F_{5/2} \leftrightarrow {}^2F_{7/2}$ in Yb^{3+} at 980 nm. The size and the concentration of the sample are critical factors since the probability of a re-absorption/re-emission event depends on the distance that the emitted light has to travel in the sample. Depending on the nature of the sample, micro-crystal or bulky single crystal, large variations in lifetimes can be found [19,20].

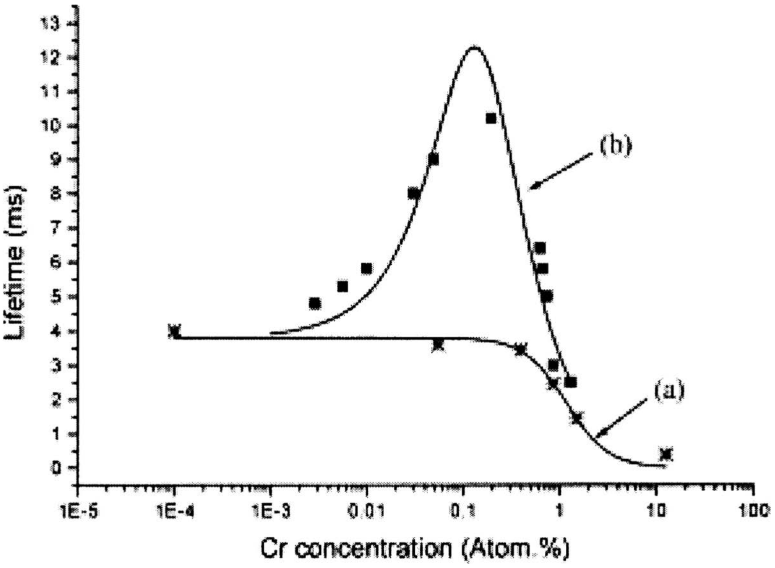

FIGURE 2.12 Self-quenching of ruby at 77 K. (*a*) Comparison of experimental points for powder from Ref. [19] with theory as given from Ref. [21] with $\tau_w = 3.8$ ms and $N_0 = 1.4\%$. (*b*) Comparison of experimental points for a bulk crystal from Ref. [20] with theory as given from Ref. [21] with $\tau_w = 3.8$ ms and $N_0 = 0.2\%$.

Figure 2.12 shows the observed experimental results lifetime *versus* the dopant concentration for the ruby. Identifying the origin of the observed lifetime variations allows the understanding of the excited state dynamics. The fluorescence lifetime increases from 4.2 ms at 10^{-3} weight% Cr_2O_3 up to 10.5 ms at 0.2 weight% Cr_2O_3 and decreases to 2 ms at 1 weight% Cr_2O_3 [19]. The curve can be divided into two regimes: in the lowest concentration range the experimental lifetime increases as the dopant concentration increases, whereas for the higher concentration range, measured lifetime decreases when the doping rate increases.

Consequently, the two behaviours seen from curve (b) in Figure 2.12 are, respectively:

- fluorescence re-absorption; the so-called self-trapping process between resonant transitions, which results from radiative energy transfer in the case of $^2E \rightarrow {}^4A_2$ and $^4A_2 \rightarrow {}^2E$ transitions. Experimentalists have to be careful to record purely radiative lifetime due to the strong influence of the concentration as observed in Figure 2.12, since a wrong estimation of the lifetime can be the source of some error for the application to laser cavities;
- the usual quenching process as it can frequently be seen in luminescent materials; in a general way, fluorescence extinction is mainly due to energy migration through the excited level of the emitting ion either to the same neighbour ions (forming pairs and clusters) or to impurities such as transition metal ions for which oscillator strengths of the optical transition (3d configuration) are much higher than those of rare-earth ions (4f configuration) and even to unknown intrinsic defects.

We can say that the same behaviour is observed with a rare-earth ion (Ho^{3+}, Tm^{3+}, Er^{3+} and Yb^{3+}) presenting resonant transitions between the first excited level and the fundamental state, by using concentration-gradient fibres [22]. The originality of concentration-gradient samples is that one fibre contains a collection of single crystals of different concentration spread along its axis. Such single-crystalline fibres present a dopant concentration varying continuously between two chosen compositions. Gradient concentration fibres are synthesized by the laser-heated pedestal growth (LHPG) technique from a special ceramic feeding rod and the concentration distribution is analysed by EDX microprobe at regular intervals along the axis of the fibre. These procedures could be applied to Cr^{3+}-doped crystals to evaluate the concentration-quenching processes and the measurement of the intrinsic radiative lifetime.

It is worthwhile reminding readers that the linewidth of the transition at very low temperature should simply reflect the radiative lifetime of the state as is required by the uncertainty principle. Fluorescence line narrowing (FLN), optical hole burning and optical coherent transients have all been employed in the study of this problem in dilute systems such as ruby [23]. The high-resolution laser spectroscopy technique has determined a width of ~100 MHz, which is therefore likely to contain residual inhomogeneous components.

2.5 Emission Sharp Line of the Cr^{3+} Ion in the Ruby Laser: A Strong Crystal-Field Model and a Three-Level Scheme

The ruby laser occupies a special place in laser science: a rod of synthetic ruby produced the first laser emission demonstrated by Maiman in 1960 [1] in the deep red at 694.3 nm and, even nowadays, it is one of the rare solid-state laser media emitting in the visible range. The ruby story will stay with us as one of the best examples of scientists being obstinate in their approach because, before 1960, it was claimed that the ruby laser would not work. Sixty years later, however, such laser sources are still useful for certain applications such as pulsed holography, interferometry, non-destruction tests and plasma measurements. Ruby consists of a sapphire Al_2O_3 single crystal with a corundum structure in which approximately 0.05 weight% of Al^{3+} cations have been replaced by Cr^{3+} active ions, i.e. 1.58×10^{19} ions cm^{-3}. This substitution is possible because of the same 3+ valence and an ionic radius (62 pm) similar to that of aluminium (53 pm). Depending on the initial concentration of Cr^{3+}, pink or red rods are available from 3 to 25 mm in diameter and up to 20 cm long. They can be grown either by the Verneuil method, used since the beginning of the century, or by the more recent Czochralski method, which gives better optical quality samples. The ruby's success is associated with its excellent mechanical, chemical and thermal properties and, obviously, to the possibility of getting inversion of the population between the $^4A_2$ ground state and the ^2E excited state of Cr^{3+} ions. Sapphire is, in fact, a hard, refractory, unalterable material. The optical transparency between UV fundamental absorption and usual infrared absorption of the sapphire host is large. The fundamental absorption occurs near 165 nm, i.e. at a band gap of 6.2 eV so that excited-state absorption of the laser emission from the Cr^{3+} emitting levels to the conduction band is inefficient. The thermal conductivity is the largest of the laser crystals, 42 W m^{-1} K^{-1} at room temperature, much higher than YAG (11 W m^{-1} K^{-1}), which is considered as the reference. The main drawback of the ruby laser is the operation as a three-level scheme, the ground state also playing the role of the terminal level of the laser transition considerably limiting the laser output energy. Therefore, such a laser is characterized by a high threshold. Finally, only three levels are important for the usual interpretation of Cr^{3+} absorption and emission spectra. Besides the $^4A_2$ ground state, the $\bar{E}$ component of the ^2E and $^4T_{2g}$ levels, which are the two lowest excited states, will be used to understand laser operations. In ruby, $\bar{E}$ is the lowest excited state, and therefore, the laser transition is interpreted as $^2E \rightarrow {}^4A_2$ at 694.3 nm. In almost all other Cr^{3+}-doped crystals, $^4T_2$ is the lowest excited state, giving rise to a $^4T_2 \rightarrow {}^4A_2$ tunable solid-state laser between 700 and 1200 nm depending on the nature of the host.

The spectroscopic properties of ruby can be interpreted in Figure 2.13 within Tanabe and Sugano's strong crystal-field model, which has been explained in the first part of this article. $^4T_2$ and $^4T_1$ visible broad absorption bands are pumped from the $^4A_2$ ground state with xenon flashlamps. The non-radiative processes between $^4T_2$, $^4T_1$ and ^2E are much higher in probability than the direct transition to the ground state. The transition $^2E \rightarrow {}^4A_2$, which appears as two sharp emission lines at 694.3 and 692.9 nm, belongs to the same t_{2g} configuration and represents a forbidden electronic dipole transition and even spin-forbidden transition. The ^2E excited state is then a metastable level with a lifetime of 3 ms.

Figures 2.14 and 2.15 show the absorption spectra of $^4A_2 \rightarrow {}^4T_1$, $^4A_2 \rightarrow {}^4T_2$ and $^4A_2 \rightarrow {}^2E$ transitions analysed as a function of the polarized pump beam, parallel or perpendicular to the optic axis *c* of the uniaxial sapphire crystal. $^4A_2 \rightarrow {}^4T_1$ and $^4A_2 \rightarrow {}^4T_2$ absorption broadbands, which match nicely a large part of the visible spectral range except in the red, are at the origin of the very well-known colour of the ruby crystal.

Such a long lifetime allows high-energy storage, much higher than with Nd^{3+}-YAG in which the $^4F_{3/2}$ excited state lifetime is only 0.25 ms. This is the main advantage of the ruby laser, producing high-energy Q-switched pulses.

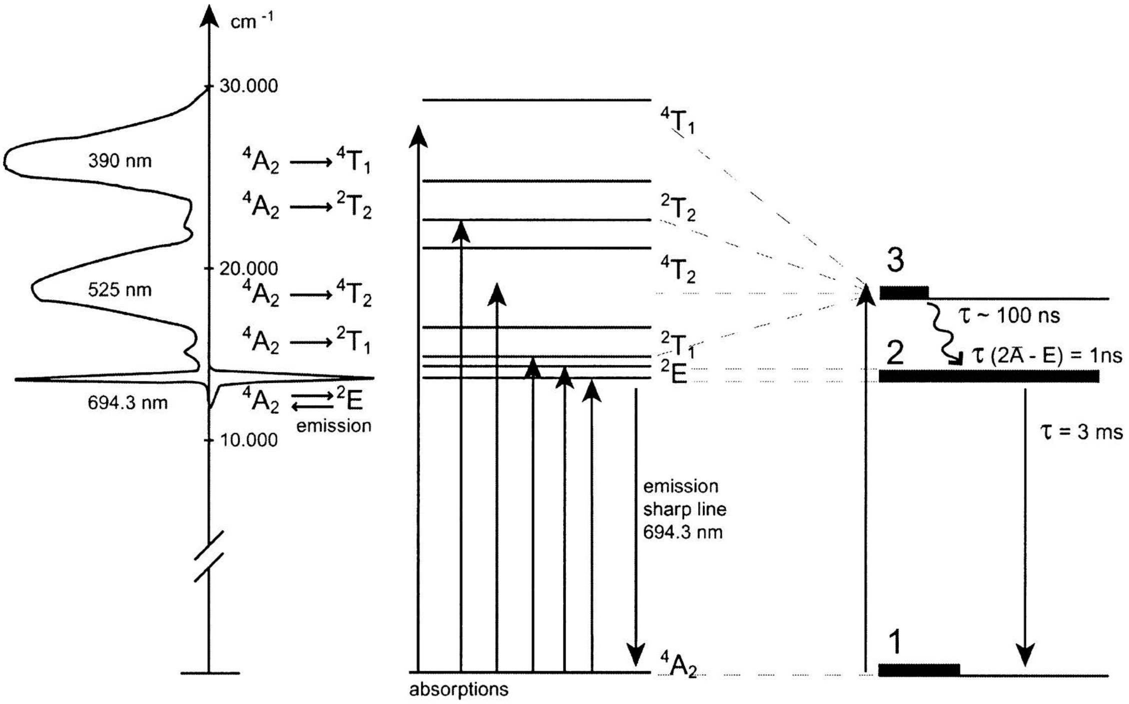

FIGURE 2.13 The absorption coefficient and absorption cross section of ruby for the incident beam polarized parallel and orthogonal to the *c* axis (Cr^{3+} concentration is 1.88×10^{19} at cm^{-3}) [24].

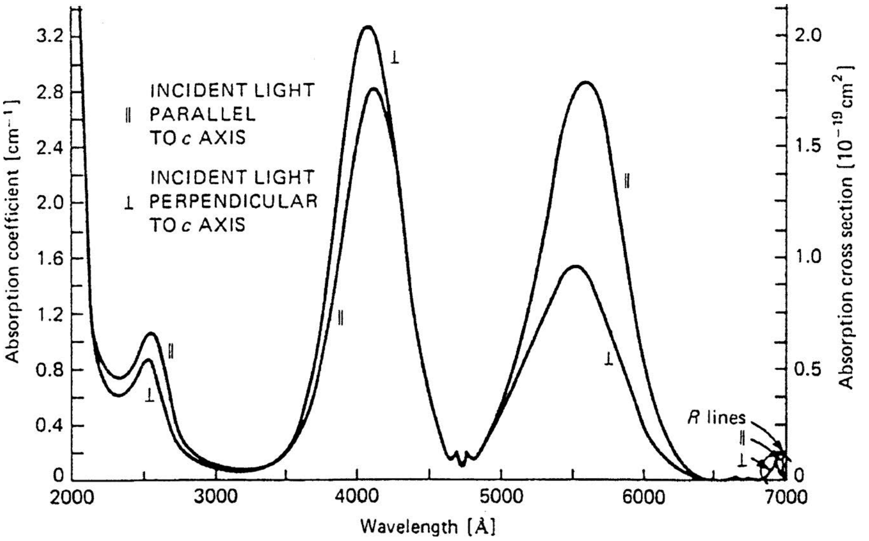

FIGURE 2.14 The absorption coefficient and absorption cross section of the R_1 and R_2 lines in ruby for an incident beam polarized parallel and orthogonal to the c axis (Cr^{3+} concentration is 1.58×10^{19} at cm^{-3}) [25].

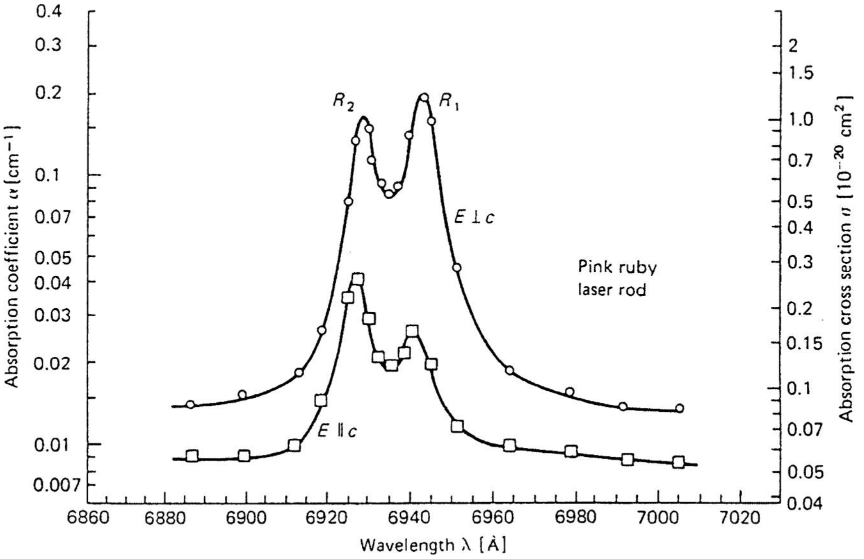

FIGURE 2.15 An interpretation of the absorption and emission spectra of ruby by the schematic three-level system.

The ruby laser can operate in either an oscillator (Figure 2.16) or oscillator–amplifier configuration in one of the three-pulse modes [26,27]:

i. the long-pulse mode called normal or conventional mode, ranging from 0.3 to a few milliseconds long depending on the length of the light pulse from the pump lamp. The generation of spikes during the pulse is known as a peculiar feature of the ruby laser since the first observation of stimulated emission in this system. One application of instantaneous pulses is in drilling holes in ruby samples, applied in watches for instance;
ii. the Q-switched mode with a usual Pockels cell or even a passive saturable dye. Pulse durations of 10 to 35 ns can be obtained with peak power in the 100 MW range or 1 GW in the oscillator–amplifier system and
iii. mode-locked, ruby lasers can produce a train of 20–30 pulses each as short as 3–4 ps. Each pulse has energy around 1 mJ, so peak power can reach hundreds of megawatts but are highly unstable.

Finally, we can say that, even within the most difficult three-level scheme operation, the ruby laser's initial success at room temperature was the result of favourable conjunctions. These are the two broad and intense absorption bands in the visible spectrum ($^4A_2 \rightarrow {}^4T_1$ at ~400 nm and $^4A_2 \rightarrow {}^4T_2$ at ~550 nm) and a unique emission line in the red ($^2E \rightarrow {}^4A_2$ at 694.3 nm) with a relatively narrow linewidth (330 GHz = 0.53 nm), a very

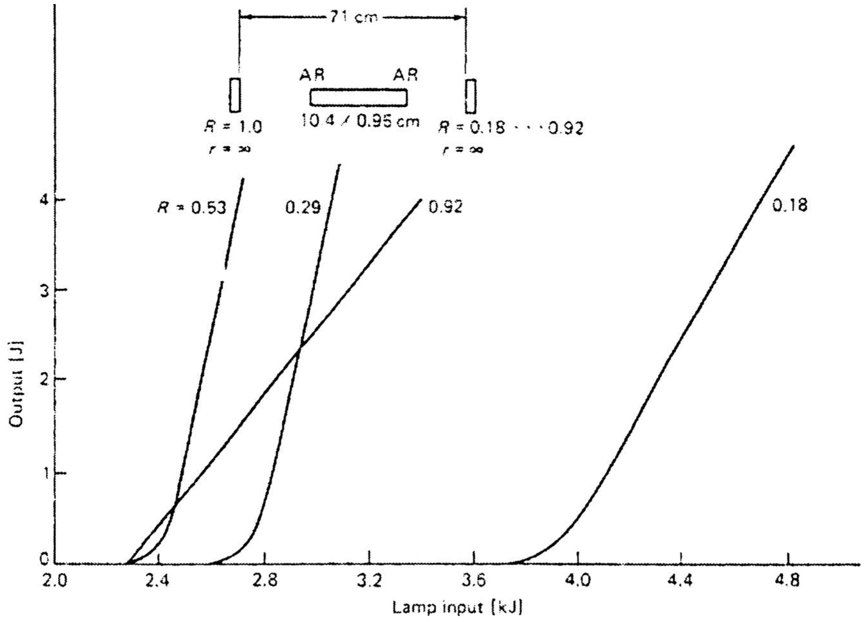

FIGURE 2.16 Oscillator output *versus* lamp input with output coupling as parameters [20,21].

long excited-state lifetime (3 ms) and a high radiative quantum efficiency of 0.7. Within the visible part of the spectrum, characterizations were easier than in UV or IR with the use of sensitive photomultipliers. In addition, we recall that ruby is the simplest host for Cr^{3+} doping due to its natural substitution of Al^{3+} by Cr^{3+} in the desirable octahedral position. The growth of ruby by the pioneering experiments of Verneuil, who developed the so-called flame fusion technique one century ago, gave at one's early disposal, good optical quality samples and more recently, even better samples by using the Czochralski method. All of these features strongly contributed to the outcome of the first laser operation in 1960 by Maiman, which was followed by the impressive development of solid-state laser engineering and the discovery of new laser media.

2.6 Emission Broadband Cr^{3+} Laser Crystals: A Weak Crystal-Field Model and a Four-Level Scheme

2.6.1 Spectroscopic Approach

We have seen that the ruby laser emits only a sharp line associated with $^2E \rightarrow {}^4A_2$ emission, which is resonant with the $^4A_2 \rightarrow {}^2E$ absorption line. ^2E and $^4A_2$ belong to orbitals within the t_{2g} configuration corresponding to lobes between ligand directions, as a spin-flip transition. As a result, configuration-coordinate diagrams use parabolas centred on the same vertical energy axis, without any Stokes shift, and with a Huang–Rhys parameter $S \sim 0$ (Figure 2.10). At room temperature, no trace of the $^4T_2 \rightarrow {}^4A_2$ emission broadband can be detected owing to the large gap of 2300 cm^{-1} between the ^2E level and the $^4T_2$ upper level. Such a broadband is only seen at higher temperatures when ^2E high-vibrational levels occupy the same energy as those of the $^4T_2$ level. The only way to observe $^4T_2 \rightarrow {}^4A_2$ broadband variation is to control it with the crystal-field strength between Cr^{3+} and neighbour ligands in different hosts, i.e. to adjust the distance R between Cr^{3+} and the centre of the ligand and therefore the parameter $\Delta = \dfrac{5eq\bar{r}^4}{3R^5}$ given previously. If R increases, Δ decreases and, therefore, for some Cr^{3+}-doped crystals, the $^4T_2$ parabola can be drawn at the same energy level as the ^2E level and even below the ^2E level. In this case, after relaxational processes between both the ^2E and $^4T_2$ levels, the observed emissions are associated with both the $^2E \rightarrow {}^4A_2$ sharp line as well as the transitions between the $^4T_2$ lowest vibrational levels and the $^4A_2$ vibrational levels. In addition, a Stokes shift is associated with the electron–phonon coupling in the $^4T_2$ level which is stronger than in ^2E, because $^4T_2$ belongs to orbitals transformed as e_g, corresponding to lobes along the ligand directions.

Besides ruby, other Cr^{3+}-doped crystals can show R laser lines in the strong crystal-field model at room temperature, such as spinel $MgAl_2O_4$ (14 660 cm^{-1}), $Y_3Al_5O_{12}$ (YAG) (14 530 cm^{-1}) and alexandrite $BeAl_2O_4$ (14 706 cm^{-1}), compared to 14 400 cm^{-1} in ruby. However, as we have just demonstrated, broadband fluorescence occurs from the $^4T_2$ level in some hosts where the crystal field is weaker. This can be used for vibronic tunable lasers. It has the advantage of a four-level scheme built up with vibrational levels of both $^4A_2$ and $^4T_2$ electronic states (Figure 2.17), thanks to optical pumping within intense and broadbands in the visible range. Solid-state vibronic lasers, which work similarly to dye lasers, were considered to be much more simple, compact and robust. The development of this media is strongly dependent on the success of the single laser crystal growth techniques from melts, with severe requirements such as high optical quality of the crystal, homogeneous distribution of Cr^{3+} active ions, large sizes for rods and slabs, as well as low loss at laser wavelengths in the red and near-infrared and absence of laser-induced damage.

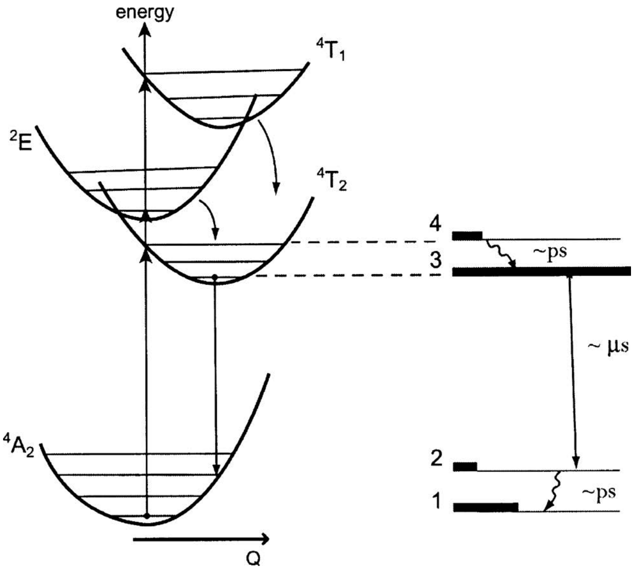

FIGURE 2.17 An interpretation of Cr^{3+} centres in the weak crystal-field model by the schematic four-level system. Relaxation times have been shown.

Thus, since the 1970s, researchers have been very keen to discover new Cr^{3+}-doped crystals characterized by a weak crystal-field model. Table 2.6 gives the main crystals grown and shows slope efficiency measurements of the $^4T_2 \rightarrow {}^4A_2$ peak lasing wavelength under the laser-pumped configuration [28]. It can be seen that emerald, LiCAF and LiSAF fluorides and alexandrite are at the top of the evaluation. Unfortunately, emerald is too difficult to grow for industrial development. We shall only illustrate this part with the two main crystal families under consideration today, alexandrite and LiCAF or LiSAF fluorides.

2.6.2 Alexandrite Laser Crystal

The first vibronic lasers were reported in 1963 by Bell Labs researchers [29,30] using the transition-metal ions Ni^{2+}, Co^{2+} and V^{2+} in MgF_2, MgO, ZnF_2 or $KMgF_3$ hosts, which only work when cooled to cryogenic temperatures. This is why the first vibronic laser to reach the market, in 1979, working at room temperature, was the alexandrite crystal or Cr^{3+}-doped $BeAl_2O_4$ [31]. $BeAl_2O_4$ (also named chrysoberyl) has a hexagonal close-packed structure isomorphous with olivine in the orthorhombic space group D_{2h}^{16}. The Al^{3+} ions are octahedral, coordinated by the oxygen ions, and occupy two inequivalent crystallographic sites, one with mirror symmetry (C_s point group) occupied by 78% of Cr^{3+} ions and one with inversion symmetry (C_i point group) occupied by 22% of Cr^{3+} ions. The concentration of Cr^{3+} dopant is usually between 0.05 and 0.3 at% (0.1 at% represents 3.51×10^{19} ions cm^{-3}). Alexandrite is optically and mechanically similar to ruby. High thermal conductivity (23 W m^{-1} K^{-1}, two-thirds that of ruby and twice that of YAG) enables alexandrite rods to be pumped at high average powers without thermal fracture.

Absorption and emission spectra are shown in Figure 2.18 for the three types of polarizations $E \parallel a$, $E \parallel b$ and $E \parallel c$ since alexandrite is biaxial (*a*, *b* and *c* are the usual crystallographic axes). Laser radiation is emitted from $E \parallel b$ as can be seen in Figure 2.18. Both $^2E \rightarrow {}^4A_2$ sharp lines of the two crystallographic sites and $^4T_2 \rightarrow {}^4A_2$ broadbands are observed. By analogy with ruby, alexandrite can operate at room temperature as a three-level scheme with mirror symmetry Cr^{3+} ions: Rm lines at 680.4 nm with a lifetime of 1.54 ms. The other crystallographic site, which is occupied by 22% of Cr^{3+} ions, is characterized by inversion symmetry and then optical transitions are strongly forbidden. As a result, the lifetime is 63 ms below 130 K, one of the longest known lifetimes. The stimulated emission cross section σ_{RM} of the Cr^{3+} ions in used

TABLE 2.6

The Measured Efficiencies of Cr^{3+} Vibronic Lasers Utilizing the Laser-Pumped Laser Configuration

Host material	Name	Peak Lasing Wavelength (nm)	Slope Efficiency (%)
$Be_3Al_2(SiO_3)_6$	Emerald	768	64
$LiCaAlF_6$	LiCAF	780	54
$BeAl_2O_4$	Alexandrite	752	51
$LiSrAlF_6$	LiSAF	825	36
$ScBeAlO_4$	Scalexandrite	792	30
$ScBO_3$	Borate	843	29
$Gd_3Sc_2Ga_3O_{12}$	GSGG	785	28
$Na_3Ga_2Li_3F_{12}$	GFG	791	23
$Y_3Sc_2Al_3O_{12}$	YSAG	767	22
$Gd_3Sc_2Al_3O_{12}$	GSAG	784	19
$SrAlF_5$	Pentafluoride	932	15
$KZnF_3$	Perovskite	820	14
$ZnWO_4$	Tungstate	1035	13
$La_3Ga_5SiO_{14}$	LGS	968	10
$Gd_3Ga_5O_{12}$	GGG	769	10
$Ca_3Ga_{5.5}Nb_{0.5}O_{14}$	Niobate	1040	5
$Y_3Ga_5O_{12}$	YGG	(740)	5
$Y_3Sc_2Ga_3O_{12}$	YSGG	(750)	5
$La_3Lu_2Ga_3O_{12}$	LLGG	830	3

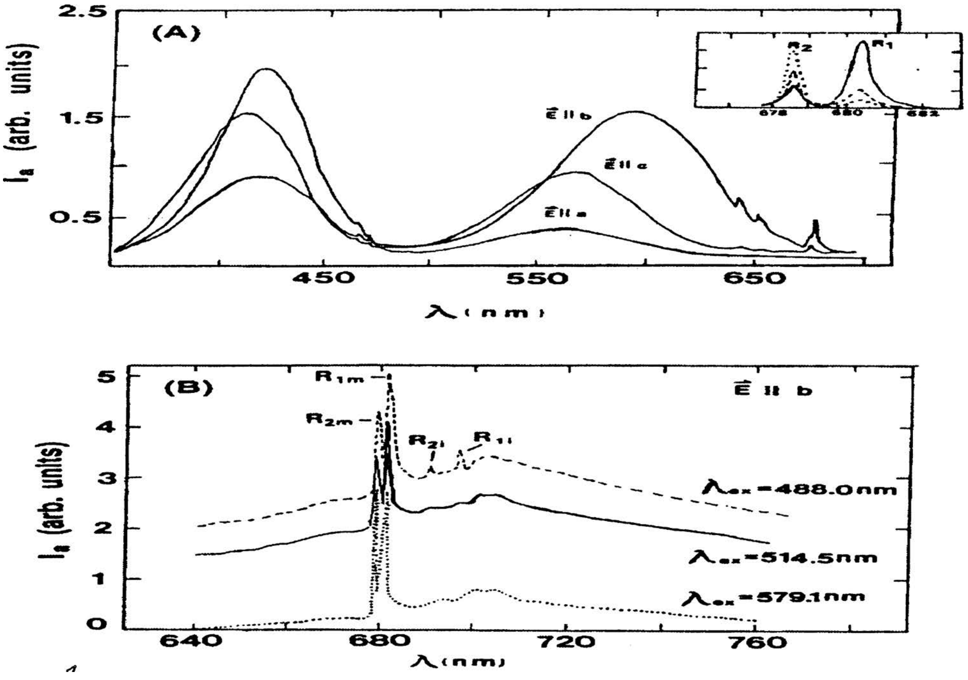

FIGURE 2.18 The absorption and emission spectra of alexandrite at room temperature for incident beam polarized parallel to the *a*, *b*, *c* axes, respectively [30].

mirror symmetry sites is ten times larger ($3 \times 10^{-19} cm^2$) than in ruby. However, the main interest of alexandrite is associated with the $^4T_2 \rightarrow {}^4A_2$ broadband, which allows laser tunability between 700 and 826 nm. The $^4T_2$ lifetime is 260 s and the stimulated emission cross section σ_m (band) is $1.0 \times 10^{-20} cm^2$. Alexandrite is pumped by either xenon flashlamp or mercury arc sources into the $^4T_1$ and $^4T_2$ absorption broadbands between 380 and 630 nm. The tunable output can reach 100 W average under pulsed pumping and 50 W under CW pumping [32].

An interesting spectroscopic feature has to be mentioned regarding the broadband emission of alexandrite crystal. Laser photons in the cavity can be absorbed by excited-state absorption of the ^2E long-lived metastable state [33]. Obviously excited-state absorption adds a supplementary loss to the photopopulation rates and additional heating of the crystal. However, in this compound the excited-state absorption spectrum exhibits a broad minimum area that exactly matches the $^4T_2 \rightarrow {}^4A_2$ broadband tunable laser emission. This effect represents 10% at the peak maximum and the only detected limitation is observed for the long-wavelength laser range.

Temperature dependences of the output laser energy in Figures 2.19 and 2.20 show strong effects. As the temperature increases and the gain of alexandrite increases, the laser wavelength shifts to longer wavelength and the fluorescence lifetime decreases. This is connected with the Boltzmann distribution of the $^4A_2$, ^2E and $^4A_2$ states which produces an inversion population between the $^4T_2$ and $^4A_2$ states. The stimulated cross section increases since, in addition to the usual pumping *via* $^4T_1$ and $^4T_2$ vibrational levels, $^4T_2$ is also populated *via* the ^2E vibrational levels only separated by 800 cm^{-1}, thereby increasing the population of the initial laser level. However, raising the temperature also populates the $^4A_2$ vibrational levels, and so conflicting effects occur. The result is that performance is only positively affected by temperature increases for wavelengths above 730 nm [26].

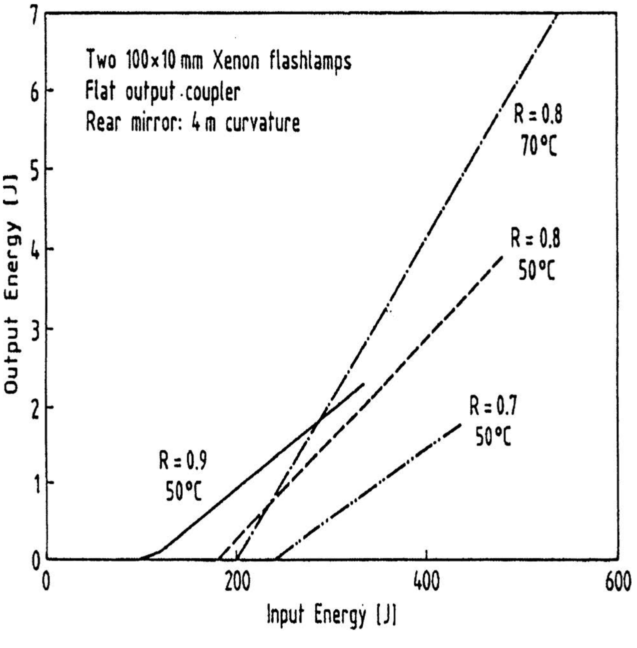

FIGURE 2.19 Output energy *versus* input energy for the alexandrite laser at 50°C and 70°C, respectively [26].

2.6.3 Colquiriite Solid-State Laser

Cr^{3+}-doped fluoride crystals also show a vibronic emission, which is used for tunable solid-state lasers. The optical transparency of fluorides is higher than that of oxides,

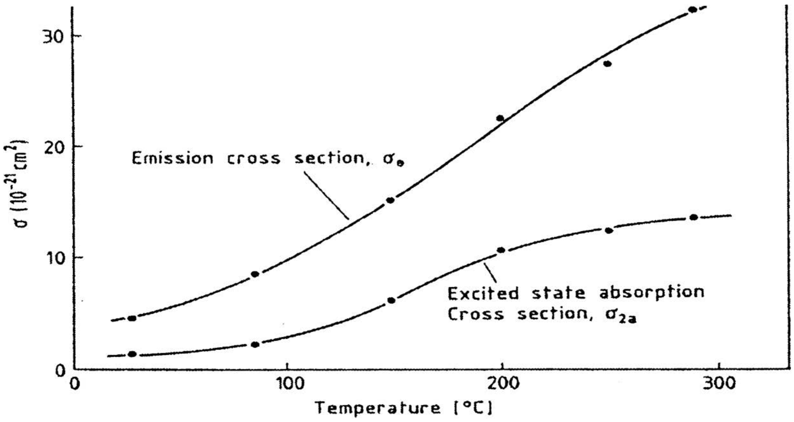

FIGURE 2.20 The temperature dependence of emission and excited-state absorption cross section at 790 nm [26].

which is important to reduce any excited-state absorption of the laser emission from the Cr^{3+} emission level. Thus, nonradiative transitions *via* the conduction band can be neglected. An important advance has been made with the discovery of LiCaA1F$_6$ (LiCAF) and LiSrA1F$_6$ (LiSAF) of the colquiriite family by the Lawrence Livermore group [34,35]. In particular, the Cr^{3+}-doped LiCAF laser appears to be as efficient as alexandrite when pumped by other lasers [36] (seen in Tables 2.6 and 2.7), or by flashlamps [37]. The second of the colquiriite-structure crystals to be lased was Cr^{3+}-doped LiSAF [35]. Here, Sr^{2+} is used to replace the Ca^{2+} ion of the LiCAF host crystal. Absorption and emission cross sections are shown in Figure 2.21 under polarized optical pumping.

Although the efficiency of Cr^{3+}-LiSAF was found to be slightly less than that of Cr^{3+}-LiCAF (see Tables 2.6 and 2.7), it has, nevertheless, drawn more attention due to its higher emission cross section, broader tuning range and, in addition, the option of being doped to high Cr^{3+} concentrations giving the first Cr^{3+} stoichiometric laser crystal [38]. The tuning range of this laser crystal has been demonstrated to be from 780 to 1010 nm. The high emission cross section of 4.8×10^{-20} cm^2 and the emission lifetime of 67 s have resulted in successful Q-switching [39]. The absorption bands have also permitted laser action by pumping with visible A1GaInP diodes at 670 nm [40]; laser output performances are given in Table 2.8, Cr^{3+}-Nd^{3+}:GSGG garnet has been listed for comparison with the neodymium solid-state laser.

Colquiriite crystals can be an attractive alternative to Ti^{3+}:Al$_2$O$_3$ sapphire since they can be pumped with a diode and exhibit greater energy storage and lower laser threshold. Obviously, diode laser pumping on the low-energy side of the $^4T_2$ broadband minimizes the so-called quantum defect between photon energies of excitation and emission transitions, which is an important limitation of the efficiency. Since 1995, it is possible to find on the market CW diode-pumped, single frequency (resolution limited linewidth < 20 MHz), Cr^{3+}-doped LiSAF micro-lasers and diode-pumped sub-100 femtoseconds (fs) passive mode-locked lasers. Due to the broadband absorption, which overlaps with the emission bands of xenon flashlamps, and longer luminescence lifetime in comparison with Ti^{3+}:Al$_2$O$_3$, Cr^{3+}:LiSAF and Cr^{3+}:LiCAF are suitable amplifier media for flashlamp pumping. A terawatt class system with a Cr^{3+}:LiSAF regenerative amplifier to produce 150 fs pulses with outputs of 15 mJ was designed as shown in the schematic diagram of Figure 2.22 [41].

Also a self-starting, self-mode-locked, femtosecond, diode-pumped Cr^{3+}:LiSAF laser has been demonstrated [42] with a Kerr-lens, mode-locked, diode-pumped crystal that starts with a simple mirror and produces 70 fs pulses at 850 nm with an average power of 50 mW, as shown in Figure 2.23. The same

TABLE 2.7

Laser Efficiency Optical and Thermal Properties of Cr^{3+}-Doped Colquiriite Structure Crystals

Host	**LiCaAlF$_6$**	**LiSrGaF$_6$**	**LiSrAlF$_6$**
Name	**LiCAF**	**LiSGAF**	**LiSAF**
Intrinsic efficiency η_0 (%)	67	52	53
Quantum intrinsic efficiency η_{0q} (%)	82	66	67
π emission cross section, σ_{em} (10^{-20}cm^{-2})	1.3	3.3	4.8
Emission peak (nm)	763	835	846
Emission lifetime τ (μs)	170	88	67
Zero-phonon line (nm)	678	699	699
Expansion α_c coefficient	3.6	0	−10
(10^{-6}/°C) α_a	22	12	25
Melting point (°C)	810	716	766

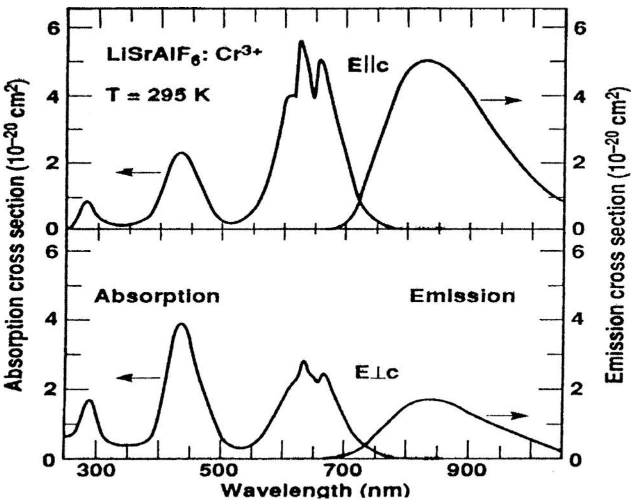

FIGURE 2.21 Absorption and emission spectra at room temperature of Cr^{3+}:LiSAF for two incident beam polarized parallel and orthogonal to the *c* axis [35].

group has developed a Cr^{3+}:$LiSrGaF_6$ laser that produces, in Q-switched operation, four times as much energy (12 μJ at 10 kHz) as a Cr^{3+}:LiSAF laser under the same pumping conditions (four red diodes emitting 400 mW) [43].

We would like to mention that the development of the colquiriite family of laser crystals is the result of a proper scientific approach. Laser performances of Cr^{3+}-doped crystals tend to be best when Cr^{3+} ions are substituted for small cations such as Al^{3+} at octahedral sites and when the host is composed of small and more highly charged cations constituting a stiff lattice. The comparison between $LiSrGaF_6$, $LiSrAlF_6$, $LiCaAlF_6$ and $LiCaGaF_6$ compounds shows that the nearest-neighbour (nn) cations (Sr^{2+} or Ca^{2+}) impact on the Cr^{3+} properties more significantly than the identity of the substitutional site (Al^{3+} or Ga^{3+}). Two qualitative explanations for this observation have been given: (i) lattice relaxation at the Cr^{3+} ion compensates for the change in the size of the substitutional site and (ii) the nn cation serves to displace the six fluorines surrounding Cr^{3+}. This latter change is not compensated for by lattice relaxation. The nn cations impose a t_{2u}-type distortion on the fluorines at the Cr^{3+} site. The t_{2u} twist angles θ_{tw} have been measured and may be related to the observed Cr^{3+} emission lifetime τ_{em} (Figure 2.24).

The comparison with $Na_3Ga_2Li_3F_{12}$ (GFG) garnet is interesting because the Cr^{3+} ion substitutes for the Ga^{3+} ion, which is in a site of almost regular octahedral symmetry C_{3i}, with inversion-site symmetry. Consequently, the fluorescence lifetime is longer (310 μs) than in Cr^{3+}:LiSAF (67 μs) and the emission cross section is much lower ($0.6 \times 10^{-20} cm^2$).

TABLE 2.8

Laser Output Performances of Diode Laser-Pumped Cr^{3+}:LiSAF and Cr^{3+}:LiCAF [15]

Laser	Output Power (mW)	1 W Diode-Pumped Slope Efficiency (%)	Maximum Slope Efficiency (%)	Optical Conversion Efficiency (%)	Overall Electrical Efficiency (%)
Cr:LiCAF	158	28	50	19	1.7
Cr:LiSAF	176	25	45	21	1.9
Cr,Nd:GSGG	173	23	42	21	1.9

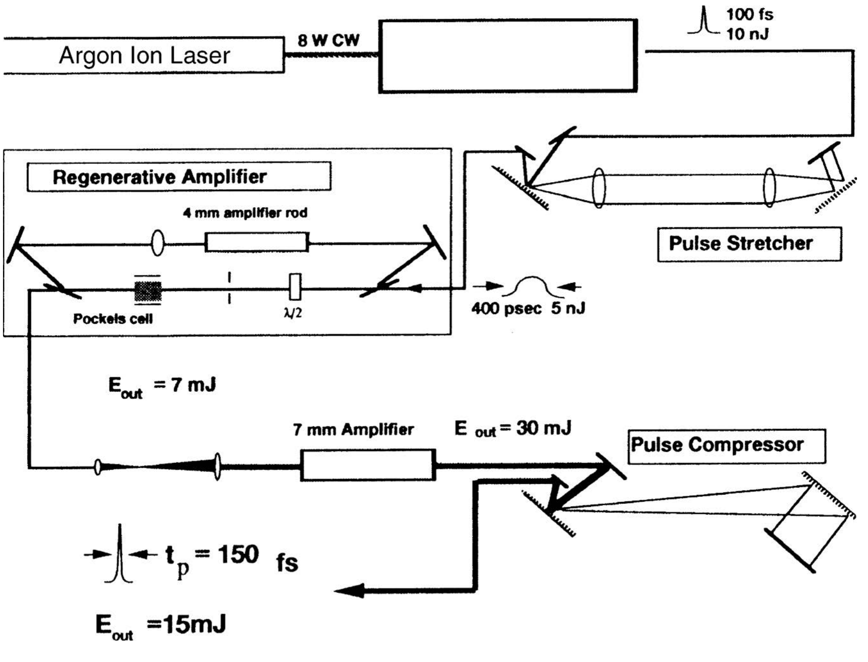

FIGURE 2.22 An example of the Cr^{3+}:LiSAF laser optical layout [41].

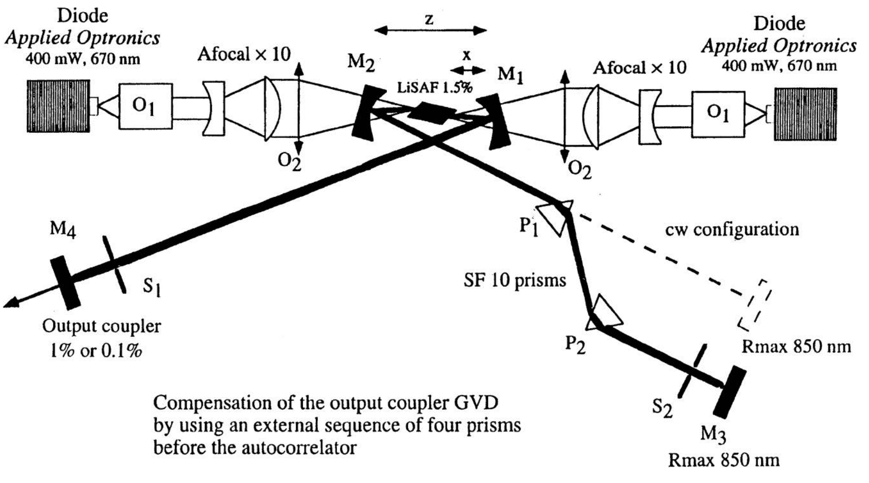
Diode
Applied Optronics
400 mW, 670 nm
Afocal × 10
O1
O2
M2
z
x
LiSAF 1.5%
M1
Afocal × 10
Diode
Applied Optronics
400 mW, 670 nm
O1
O2
M4
S1
Output coupler
1% or 0.1%
P1
cw configuration
SF 10 prisms
P2
Rmax 850 nm
S2
M3
Rmax 850 nm
Compensation of the output coupler GVD
by using an external sequence of four prisms
before the autocorrelator

FIGURE 2.23 The x-fold cavity configuration used in a compact diode-pumped Kerr-lens, mode-locked Cr^{3+}:LiSAF laser [42]. M, mirrors; O, objectives; P, prisms; S, slits.

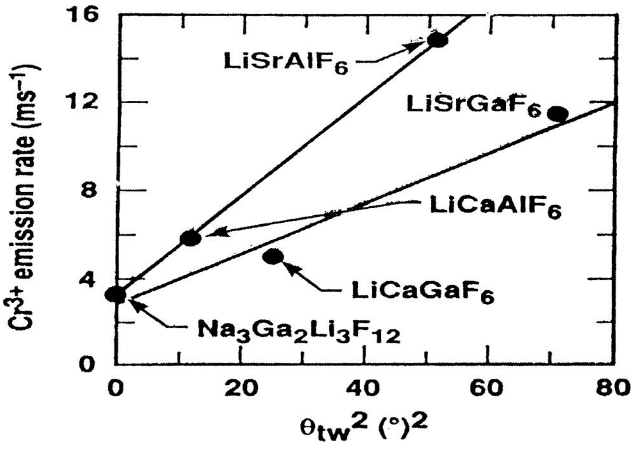

FIGURE 2.24 Cr^{3+} emission rate in m s^{-1} as a function of θ_{tw}^2 in (°)^2 for fluoride garnet and colquiriite crystals.

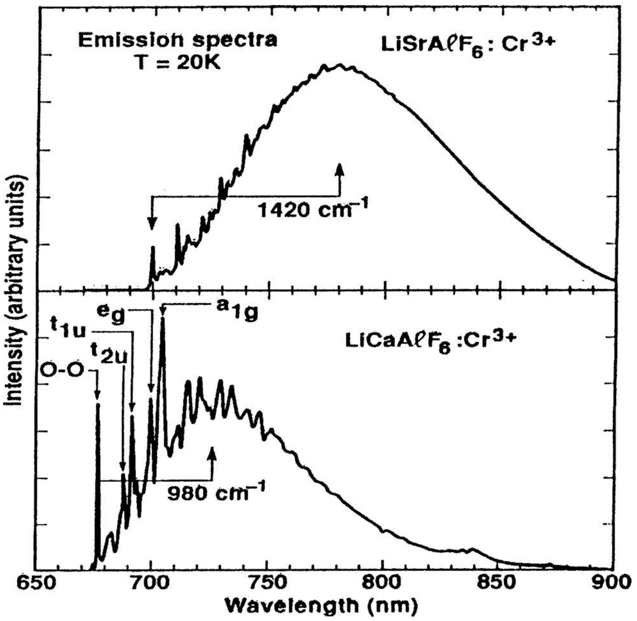

FIGURE 2.25 Emission spectra at 20 K of Cr^{3+}:LiSAF and Cr^{3+}:LiCAF. Zero-phonon lines of the $^4T_2 \rightarrow {}^4A_2$ broadband are denoted by 0–0 (699 nm in LiSAF and 678 nm in LiCAF). The difference between zero-phonon lines and the emission peak is also noted (1420 cm^{-1} in LiSAF and 980 cm^{-1} in LiCAF) as an indication of the Stokes shift. The vibronic structure can be interpreted in the lower Stokes shift crystal by t_{2u}, t_{1u}, e_g and a_{1g}.

In Figure 2.24, two straight lines are observed for each family in accordance with θ_{tw}^2 so that the transition rate increases from 3.23 to 14.93 ms^{-1} in the series GFG, LiCAF, LiSAF. Moreover, the temperature independence of the decay rate (14.93 ms^{-1} from τ = 67 μs) of the $^4T_2$ state in Cr^{3+}:LiSAF implies that the transition probability is dominated by the static contribution of the trigonal distortion. Referring to the configurational coordinate diagrams in Figure 2.11, the temperature dependence of the $^4T_2$ state is dependent on an 'activation energy' *W*, which is determined by the crystal-field strength. In this case, *W* is unusually high, with quenching occurring only at higher than room temperatures; thus, non-radiative decay processes are not efficient in the fluorescence quenching. Another feature of Cr^{3+}:colquiriite crystals is the larger Stokes shift of the Cr^{3+}:LiSAF emission compared to Cr^{3+}:LiCAF (Figure 2.25), probably indicating that the Jahn–Teller effect is larger for LiCAF with, in addition, opposite shifts of the $^4T_2$ and $^4T_1$ excited states (the Jahn–Teller effect can be seen in crystals where strong electron–phonon coupling lifts electronic state degeneracy through a splitting of the vibronic energy levels). The result of such opposite distortion in $^4T_2$ and $^4T_1$ is that excited state absorption between $^4T_2$ and $^4T_1$ is unusually broadband but, fortunately, characterized by a low cross section. A theoretical model proves that up-conversion and thermal quenching of fluorescence strongly limit small-signal gain in a CW pumped Cr^{3+}:LiSAF laser [44]. The pumping configuration of a 3% doped Cr^{3+}:LiSAF pumped by two red laser diodes emitting 400 mW has been optimized. In Q-switched operation, this laser produces tunable nanosecond pulses with an energy up to 6.5 μJ. Finally, the emission broadband at 20 K in Cr^{3+}:LiCAF shows vibronic structure in Figure 2.24 analysed in terms of the splitting of the $^4T_2$ level with t_{2u}, t_{1u}, t_{1u},

e_g and a_{1g} representations in the O_h point group. Recently, the shortest pulse ever produced of 15 fs from an all solid-state mode-locked Cr^{3+}:LiSAF laser has been demonstrated [45].

To summarize, Cr^{3+}:LiCAF and Cr^{3+}:LiSAF laser crystals can be efficiently pumped by flashlamps, diodes or lasers. Cr^{3+} has a unity distribution coefficient and crystal growth conditions are relatively easy at around 800°C. The tunability is relatively large (~200 nm for Cr^{3+}:LiSAF) and the emission cross section is high ($3.2 \times 10^{-20} cm^2$ for Cr^{3+}:LiSAF). Long energy storage lifetimes allow Q-switching and amplifier configurations.

After the discovery of the first solid-state laser sources (Ruby, 1960; Nd^{3+}-doped YAG ($Y_3Al_5O_{12}$), 1964) researchers have tried to point out solar-pumped Nd^{3+}-doped YAG crystal, the most common solid-state laser material emitting in the near-IR at 1064 nm. Possible solar laser applications are space-to-earth power transmission, free-space laser communications [46] or solar-pumped laser-induced magnesium production from magnesium oxide [47]. The excitation efficiency is low due to the weak overlap of the narrow 4f Nd^{3+} absorption lines and the broad emission spectrum of the sunlight so that the natural idea was to improve the matching of these spectra by co-doping with Cr^{3+} ions as sensitizer ions showing large ${}^4A_2 \rightarrow {}^4T_1$ and ${}^4A_2 \rightarrow {}^4T_2$ absorption bands in the visible spectral range. The overlap between the Cr^{3+} and Nd^{3+} ions co-doped YAG absorption spectra and the solar emission spectrum can reach about 40% and the energy transfer between Cr^{3+} and Nd^{3+} ions occurs by both radiative (resonance between 4f Nd^{3+} sharp absorption lines and the broad ${}^4T_2 \rightarrow {}^4A_2$ emission band) and non-radiative (shortening of the Cr^{3+} decays) processes [48]. The overlapping of the ${}^2E \rightarrow {}^4A_2$ sharp emission line of the strong crystal field in Cr^{3+}-doped YAG is too narrow and the intensity of the ${}^4T_2 \rightarrow {}^4A_2$ emission band is too weak to be efficient. The best theoretical solution should be found with a weaker crystal field giving rise to an intense broad ${}^4T_2 \rightarrow {}^4A_2$ emission band by changing the composition of the garnet as already mentioned in this Handbook [49] with $Gd_3Sc_2Ga_3O_{12}$ (GSGG) and $Y_3Sc_2Ga_3O_{12}$ (YSGG). However, these crystals are much more expensive to develop with the use of Sc^{3+} ion and difficult to grow due to the use of volatile Ga^{3+} ion, compared to YAG.

The first success of 1 W output was reported by Young in 1966 [50]. Then, a collection efficiency of 6.7 W m^{-2} was achieved by pumping an Nd^{3+}-doped YAG rod through a heliostat-parabolic mirror system in 2003 [51].

Cr^{3+}-Nd^3-co-doped YAG ceramic/crystal materials have attracted more attention in recent years. For single-shot laser operation with a 0.1 at% Cr^{3+} and 1.0 at% Nd^{3+}-co-doped YAG ceramic rod, the laser efficiency was found to be more than twice that of a 1.0 at% Nd^{3+}-doped YAG ceramic rod. At low repetition rates, the average output power of a Cr^{3+}-Nd^{3+}-co-doped YAG rod was higher than that of Nd^{3+}-doped YAG. However, this ratio gradually decreased with increasing repetition rates. The thermal effect of the Cr^{3+}-Nd^{3+}-co-doped YAG rod was also higher than that of Nd^{3+}-doped YAG in high-repetition operation. Although the Cr^{3+}-Nd^{3+}-co-doped YAG rod was more efficient for low-repetition rate application, it might not be much more efficient than the Nd^{3+}-co-doped YAG medium for high repetition rate and CW laser operations. As a result of the effectiveness of Nd^{3+}-doped YAG single-crystal rods for solar laser operation, there still exist some concerns about the advantages of Cr^{3+} and Nd^{3+} co-doped YAG in solar-pumped lasers [46,52]. Only a moderate, but not significant, advantage of Cr^{3+} and Nd^{3+} co-doped YAG ceramic over Nd^{3+}-doped YAG single-crystal medium has been experimentally observed in both solar laser conversion and slope efficiency.

Another way has been investigated to increase the laser efficiency of Nd^{3+}-doped YAG by adding both Ce^{3+} and Cr^{3+} effective sensitizers to Nd^{3+} ions [48,53,54]. Two intense excitation bands of Ce^{3+} ions are involved in UV at 340 nm and blue at 450 nm with the allowed electronic transitions from the 4f (${}^2F_{5/2}$) ground state to the different crystal-field splitting bands of excited 5d state (Figure 2.26). Ce^{3+} ions bring indeed an additional absorption to sunlight, which is converted into two broad yellow 5d $\rightarrow$ ${}^2F_{7/2}$, ${}^2F_{5/2}$ bands around 525 nm transmitted to 4f sharp absorption lines of Nd^{3+} ions and also to Cr^{3+} ${}^4T_1 \rightarrow {}^4A_2$ broad absorption bands. Finally, the main ${}^4F_{3/2} \rightarrow {}^4F_{11/2}$ Nd^{3+} laser line at 1064 nm can be increased. The optimum concentration set of Ce^{3+} (0.9 mol%)/Cr^{3+} (8.0 mol%)/Nd^{3+} (1.0 mol%)-doped YAG increases four times as large as the Cr^{3+}-Nd^3-co-doped YAG one. The effective fluorescence lifetime of Nd^{3+} at 1064 nm in the optimum concentration is 200 µs, which enables the laser action. These results show that a small amount of Ce^{3+} can effectively improve the sunlight absorption by at least two 5d broadbands at around 350 and 450 nm, and, as a result, an Nd^{3+}-doped YAG laser is expected to be remarkably improved. In addition, Ce^{3+} ions have the ability to prevent colour centre generation by UV irradiation [55].

At last, some hope is made with new transparent ceramics able to contain higher concentrations of dopants in garnets. A future power plant in space might take benefit of these advanced materials.

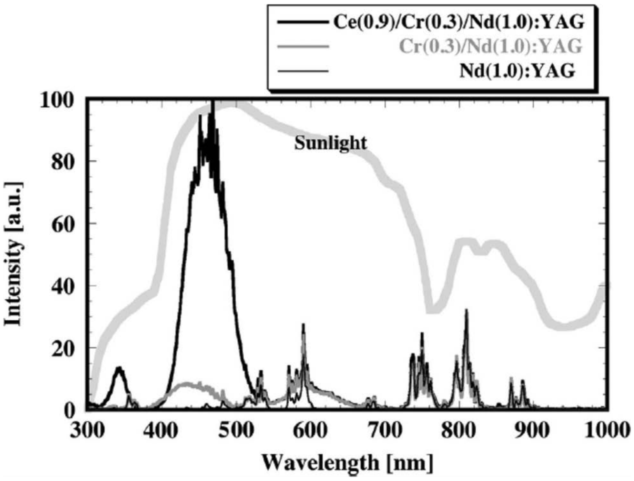

FIGURE 2.26 Excitation spectra of Ce^{3+}(0.9)/Cr^{3+}(0.3)/Nd^{3+}(1.0)-doped YAG (bold black lines), Cr^{3+}(0.3)/Nd^{3+}(1.0)-doped YAG (grey) and Nd^{3+}(1.0)-doped YAG (black) by monitoring Nd^{3+} emission line at 1064 nm used for laser. We clearly see absorption of Ce^{3+} 5d broadbands in UV and blue, Cr^{3+} ${}^4T_1$ and ${}^4T_2$ broadbands in visible and Nd^{3+} 4f sharp lines, respectively [53].

TABLE 2.9

Typical Operating Characteristics of the Main Cr^{3+}-Doped Laser Crystals

Crystals	**Ruby Al_2O_3**	**Alexandrite $BeAl_2O_4$**	**Garnet $Gd_3Sc_2Al_3O_{12}$**	**Emerald $Be_3Al_2(SiO_3)_6$**	**Colquiriite LiCAF $LiCaAlF_6$**	**Colquiriite LiSAF $LiSrAlF_6$**
Crystal field	Strong	Intermediate	Intermediate	Intermediate	Weak	Weak
ε ($^4T_2$-^2E) (cm^{-1})	2300	800	-	400	<0	<0
R emission line	694.3	680	-	-	-	-
$^2E \rightarrow {}^4A_2$ (nm)		696				
Emission broadband	-	752	785	768	780	825
$^4T_2 \rightarrow {}^4A_2$ (nm)						
Laser tunability (nm)	-	700–826	750–840	750–760	720–840	760–920
Slope efficiency (%)		71	28	64	36	54
Quantum efficiency	0.70	0.76	0.28	0.86	0.82	0.67
Lifetime of the excited level at RT	3 ms	240 μs and 63 ms	150 μs	65 μs	170 μs	67 μs
Emission cross	2.5×10^{-19}	1.1×10^{-20}	0.70×10^{-20}	1.9×10^{-20}	1.3×10^{-20}	4.8×10^{-20}
section (cm^2)	19					
Pump	Flashlamp	Flashlamp	Flashlamp	Flashlamp or Kr laser	Laser diode or Kr laser	Laser diode
Examples of performances	ms-fixed Q pulses of 100 J	CW50 W	CW250 mW	CW320 mW	(see Table 2.8)	15 fs pulses (see Table 2.8)
Main drawback	Three-level scheme	Difficulties in growing the crystals	Sc high cost	Difficulties in growing the crystals	-	-

2.7 Conclusion

In this chapter, our main objective was to describe the concepts that allow us to understand the optical properties of the Cr^{3+} metal transition ion in inorganic oxide and fluoride crystals applied to laser sources. Typical operating characteristics of the main Cr^{3+} laser crystals are summarized in Table 2.9. Laser science history retains the Cr^{3+} ion not only as the first demonstration of laser radiation in the famous experiment on the ruby, Cr^{3+}:Al_2O_3 laser crystal, by Maiman in June 1960 and then on alexandrite, Cr^{3+}:$BeAl_2O_4$ the first tunable vibronic solid-state laser, but also as the activator ion which triggered scientific discussions on the truest physical models which have to be adopted in laser source research. An important advantage of the Cr^3+ ion is connected with the two sets of orbitals, e_g and t_{2g} belonging to the $3d^3$ configuration which offer the three types of crystal-field strengths in the octahedral symmetry site of oxide and fluoride host crystals: strong crystal fields giving rise to the red sharp line $^2E \rightarrow {}^4A_2$; intermediate crystal fields for which the $^2E \rightarrow {}^4A_2$ and the $^4T_2 \rightarrow {}^4A_2$ broadband appear and weak crystal fields in crystals in which only the $^4T_2 \rightarrow {}^4A_2$ broadband is observed and which has allowed tunable solid-state lasers to be developed. By playing with the crystal-field strength, all possibilities are met with the Cr^{3+} ion under flashlamp, laser or diode pumping sources: CW or pulsed operations in the millisecond to femtosecond range.

Another important interest of research on the Cr^{3+} ion in host crystals has been to stimulate basic knowledge in spectroscopy on other chromium oxidation states and other metal transition ions to provide a new laser radiation. Among them, we can mention the following:

- The Cr^{4+} ($3d^2$)-doped forsterite (Mg_2SiO_4), which was discovered while looking for a Cr^{3+} dopant and is now commercialized as a tunable solid-state laser emitting between 1167 and 1345 nm, and also Cr^{4+}-doped YAG as a tunable solid-state laser and a mainly saturable absorber crystal;
- Cr^{2+} ($3d^4$)-doped ZnSe, which works between 2000 and 2800 nm;
- Cr^{5+} ($3d^1$) now known for its infrared fluorescence broadband around 1400 nm in the tetrahedral symmetry site of silicates and phosphates and
- Ti^{3+} ($3d^1$)-doped sapphire (Al_2O_3) now the most developed tunable solid-state laser emitting between 660 and 1060 nm.

These laser ions will be presented in the next chapters.

REFERENCES

1. Maiman H 1960 *Nature* **187** 493.
2. Condon E U and Shortley G H 1935 *The Theory of Atomic Spectra* (London: Cambridge University Press).
3. Griffith J S 1961 *The Theory of Transition Metal Ions* (London: Cambridge University Press).
4. Prather J L 1961 *Atomic Energy Levels in Crystals* (Washington, DC: Department of Commerce).
5. Cotton F A 1963 *Chemical Applications of Group Theory* (New York: Wiley).
6. Di Bartolo B 1968 *Optical Interactions in Solids* (New York: Wiley).
7. Powell R 1998 *Physics of Solid-State Laser Materials* (New York: Springer).

8. Imbush F 1987 *Spectroscopy of Solid-State Laser-Type Materials (Ettore Majorana International Science Series Physical Sciences 30)* ed B Di Bartolo (New York: Plenum) p 141.
9. Tanabe Y and Sugano S 1954 *J. Phys. Soc. Japan* **9** 753.
10. Sugano S, Tanabe Y and Kamimura H 1970 *Multiplets of Transition Metal Ions in Crystals* (New York: Academic).
11. Nie W, Monteil A and Boulon G 1990 *Opt. Quantum Electron.* **22** S227–45.
12. Monteil A, Nie W, Madej C and Boulon G 1990 *Opt. Quantum Electron.* **22** S247–57.
13. Monteil A, Garapon C and Boulon G 1988 *J. Luminesc.* **39** 167.
14. Boulon G, Garapon C and Monteil A 1987 *Optical Science and Engineering—Series 8—Advances in Laser Science—Conference Proceedings* vol 160 (Seattle, WA: American Institute of Physics) p 87.
15. Gan F 1995 *Laser Mater.* (Singapore: World Scientific).
16. Hasmi F, Ver Steeg K, Durville F, Powell R C and Boulon G 1990 *Phys. Rev. B* **42** 3818.
17. Hasmi F, Powell R C and Boulon G 1992 *Opt. Mater.* **1** 281.
18. Boulon G 2001 Advances in energy transfer processes *Book of the International School of Atomic and Molecular Spectroscopy (Erice, June 1999)* ed B Di Bartolo and X Chen (Singapore: World Scientific).
19. Imbusch G F 1967 *Phys. Rev.* **153** 326.
20. Tolstoi N A and Shun'-Fu L 1962 *Opt. Spectrosc. (URSS)* **13** 224.
21. Auzel F, Bonfigli F, Gagliari S and Baldacchini G 2001 *J. Luminesc.* **94–95** 293–7.
22. Laversenne L, Goutaudier C, Guyot Y, Cohen-Adad M T and Boulon G 2002 *J. Alloys Compounds* **341** 214–9.
23. Yen W M and Selzer P M (ed) 1981 *Laser Spectroscopy of Solids (Topics in Applied Physics 49)* (Berlin: Springer-Verlag) pp 141–88.
24. Maiman T H, Hoskins R H, D'Haenens I T, Asawa C K and Eotuhov V 1961 *Phys. Rev.* **123** 1151.
25. Cronemeyer O C 1964 *J. Opt. Soc. Am.* **56** 1703.
26. Koechner W 1992 *Solid-State Laser Engineering* 3rd edn. (New York: Springer).
27. Hecht J 1986 *The Laser Guidebook* (New York: McGraw-Hill).
28. Payne S A and Chase L L 1989 *J. Appl. Phys.* **66** 1051.
29. Johnson L F, Dietz R E and Guggenheim H J 1963 *Phys. Rev. Lett.* **11** 318–20.
30. Johnson L F, Dietz R E and Guggenheim H J 1966 *Phys. Rev. Lett.* **17** 13–15.
31. Boulon G 1989 *Disordered Solids—Structures and Processes (Ettore Majorana International Science Series 46)* ed B DiBartolo (New York: Plenum) pp 317–41.
32. Walling J C, Jenssen H P, Morris R C, O'Dell E W and Peterson O G 1979 *Opt. Lett.* **4** 182.
33. Powell R C, Xi L, Gang X, Quarles G J and Walling J C 1985 *Phys. Rev. B* **32** 2788.
34. Payne S A, Chase L L, Neivkirk H W, Smith L K and Krupke W F 1988 *IEEE J. Quantum Electron.* **QE-24** 2243–52.
35. Payne S A, Chase L L, Smith L K, Kway W L and Neivkirk H N 1989 *J. Appl. Phys.* **66** 1051–6.
36. Payne S A, Chase L L, Atherton L J, Caird J A, Kway W L, Shinn M D, Hughes R S and Smith L K 1990 *SPIE* **1223** 84–93.
37. Payne S A, Chase L L, Smith L K and Chai B H T 1990 *Opt. Quantum Electron.* **22** S259–68.
38. Stalder M, Chai BHT and Bass M 1991 *Appl. Phys. Lett.* **58** 216–8.
39. Scheps R, Myers J F and Payne S A 1990 *IEEE Photon. Technol.* **2** 626–8.
40. Scheps R 1992 *Opt. Mater.* **1** 1.
41. Beaud P, Richardson M, Miesak E J and Chai B H T 1993 *Opt. Lett.* **18** 1550.
42. Falcoz F, Balembois F, Georges P and Brun A 1995 *Opt. Lett.* **20** 1874.
43. Falcoz F, Balembois F, Georges P and Brun A 1997 *Opt. Lett.* **22** 387.
44. Falcoz F, Balembois F, Kerboull F, Druon F, Georges P and Brun A 1997 *IEEE J. Quantum Electron.* **QE-33** 269.
45. Vemura S and Torizuka K 1999 *Advanced Solid-State Lasers (OSA TOPS 26)* (Washington, DC: OSA) pp 410–4.
46. Liang D, Almeida J and Garcia D 2013 *Proceedings Volume 8785, 8th Iberoamerican Optics Meeting and 11th Latin American Meeting on Optics, Lasers, and Applications* 87859Y doi:10.1117/12.2027673.
47. Takashi Y, Tomomasa O, Thanh Hung D, Hiroki K, Junichi N and Kauta O 2012 *Proceedings of a Symposium on "Magnesium Technology 2012," TMS 2012 Annual Meeting & Exhibition*, Orlando, FL, pp. 55–58.
48. Mares J A, Jacquier B, Pedrini C and Boulon G 1988 *Czech. J. Phys. B* **38** 802.
49. Zagumennyi A I, Mikhailov V A and Scherbakov I A 2003 *The Handbook of Laser Technology and Applications* 1st edn. chapter B1.3 (London: CRC Press) p 353.
50. Young C G 1966 *Appl. Opt.* **5** (6) 993.
51. Lando M, Kagan J, Linyekin B and Dobrusin V 2003 *Opt. Commun.* **222** 371–81.
52. Almeida J, Liang D and Guillot E 2012 *Opt Laser Technol.* **44** 2115–9.
53. Fujioka K, Saiki T, Motokoshi S, Fujimoto Y, Fujita H and Nakatsuka M 2013 *J. Luminesc.* **143** 10–13.
54. Quarles G J *This Handbook* chapter B1.5, p 411.
55. Laroche M, Girard S, Moncorge R, Bettinelli M, Abdulsabirov R and Semashko V 2003 *Opt. Mater.* **22** 147.

3

Transition Metal Ion Lasers Other Than Cr^{3+}

Stephen A. Payne

CONTENTS

3.1 Introduction 25
3.2 Survey of Transition Metal Lasers 25
  3.2.1 Ti^{3+} Lasers 25
  3.2.2 Transition Metal Lasers: V^{2+}, Co^{2+} and Ni^{2+} Ions in Octahedral Sites 26
  3.2.3 Transition Metal Lasers: Cr^{4+}, Cr^{2+}, Fe^{2+} and Mn^{5+} Ions in Tetrahedral Sites 26
  3.2.4 Tabulation of Transition Metal Lasers 26
3.3 Physics and Engineering Issues 26
  3.3.1 Electronic Structure 26
  3.3.2 Absorption and Emission 27
  3.3.3 Excited-State Absorption 29
  3.3.4 Radiative Rates and Non-Radiative Losses 30
  3.3.5 Optical Loss 30
  3.3.6 Laser Gain and Oscillation 31
  3.3.7 Host Properties 31
3.4 Summary 32
References 32

3.1 Introduction

In this chapter, the background and status of transition-metal-based solid-state lasers are discussed [1,2]. The transition metal ions that have been demonstrated to lase include Ti^{3+}, V^{2+}, Cr^{2+}, Cr^{3+}, Cr^{4+}, Mn^{5+}, Fe^{2+}, Co^{2+} and Ni^{2+}. All of these ions will be discussed in this chapter with the exception of Cr^{3+}. These transition metal ions have been demonstrated to laser oscillate in a cavity, by serving as the activators in various host media including oxide, fluoride, sulphide and selenide crystals. Laser oscillation has never been reported for any transition-metal-doped glass: all known laser systems are based on crystalline host media. They are incorporated onto sites of either fourfold or sixfold coordination, referred to as tetrahedral and octahedral sites, respectively. In terms of their practical use, Ti^{3+} in sapphire ($Ti:Al_2O_3$) is, by a wide margin, the most common transition metal laser. The next most common transition metal lasers include the Cr^{3+} lasers, alexandrite and Cr:LiSAF, forsterite (Cr^{4+} in Mg_2SiO_4) and $Co:MgF_2$. Several other materials are still being explored. Lasers based on V^{2+} and Ni^{2+} do not seem to have taken hold significantly, in spite of the many years that have elapsed since the initial demonstration of their lasing capability. Some ions have been reported to exhibit gain but an ability to oscillate has not yet been demonstrated, for example Rh^{2+} [3] and Cu^{+} [4], as discussed later.

3.2 Survey of Transition Metal Lasers

3.2.1 Ti^{3+} Lasers

The Ti:sapphire laser is, undoubtedly, the most ubiquitous solid-state laser based on a transition metal ion dopant [5]. In a way, its emergence may be construed as the confluence of two essential discoveries: that of vibronic (broadband emitter) lasers and the ruby laser. By replacing the chromium ion in ruby with titanium (i.e. changing $Cr^{3+}:Al_2O_3$ to $Ti^{3+}:Al_2O_3$), broadband laser operation becomes possible while the favourable thermo-mechanical properties of the sapphire host can simultaneously be exploited. Ti:sapphire can be a continuous wave (cw) pumped by powerful Ar ion lasers with 488 and 514 nm output lines, as well as with doubled Nd:YAG lasers. In fact, with the commercialization of high-power diode-pumped Nd:YAG and $Nd:YVO_4$ lasers, all-solid-state versions of these laser systems are now available. Ti^{3+} has also been shown to lase in chrysoberyl, or $BeAl_2O_4$, although inadequate information is available to assess the true potential of this material [6,7].

Another critical discovery ensued, which was the discovery that Kerr lens mode-locking provided a simple, robust means of generating femtosecond pulses with Ti:sapphire [8–10]. The Kerr lens mode-locked oscillator inspired a fresh realization that transition-metal-doped solid-state lasers could be unique as well as practical. Since then, Ti:sapphire has served as the workhorse of short-pulse lasers, often arranged with several stages of amplification to operate at average powers of more than 10 W [11].

The tuning range was found to be extraordinary, reaching beyond 0.66–1.18 µm, encompassing the 1.05 µm wavelength typical of Nd:glass lasers and permitting their use in hybrid systems (Ti:sapphire master oscillator with Nd:glass power amplifiers). The material properties of sapphire are outstanding, in light of its high thermal conductivity and high fracture toughness. Ti:sapphire lasers are most commonly pumped by argon ion and doubled Nd:YAG lasers, although other approaches such as flashlamps have been explored with some success. It is conceivable that Ti:sapphire may one day be pumped by nitride-based semiconductor lasers, if their brightness can be increased considerably beyond their current value.

3.2.2 Transition Metal Lasers: V^{2+}, Co^{2+} and Ni^{2+} Ions in Octahedral Sites

The V^{2+} ion [12,13] has only been lased in fluoride hosts, including V:MgF_2, $KMgF_3$ and$CsCaF_3$, primarily because of the difficulty in stabilizing the divalent oxidation state of vanadium in oxide media. The efficiencies have generally been found to be quite low, however, because of the presence of excited-state absorption (ESA) losses. Vanadium lasers operate in the range of 1.1–1.3 µm.

Ni:MgF_2 has been demonstrated to lase [14–16] in several hosts including $KMgF_3$, MgF_2 and $CaY_2Mg_2Ge_3O_{12}$, although the sub-ambient temperatures together with the low efficiencies (due to low luminescent efficiencies and ESA losses) have limited their practical utility. Nickel lasers operate in the range of 1.4–1.8 µm.

The most common Co^{2+} laser [17–19] is, undoubtedly, Co:MgF_2, which has been effectively pumped by a 1.31 µm Nd:YAG laser on a time scale shorter than the room temperature storage time of the medium (~37 µs). The tuning range for Co:MgF_2 is impressive, being 1.5–2.5 µm. The broad tuning range has enabled Nd:YAG-pumped Co:MgF_2 lasers to service a niche scientific market. Low-temperature operation of Co:$KZnF_3$ has also been reported [20,21].

3.2.3 Transition Metal Lasers: Cr^{4+}, Cr^{2+}, Fe^{2+} and Mn^{5+} Ions in Tetrahedral Sites

It is interesting that, following much activity leading to the identification of over a dozen Cr^{3+} lasers, further exploratory work found that both Cr^{2+} and Cr^{4+} ions were also interesting and practical lasers. While Cr^{3+} is exclusively found in six-fold coordinated sites, the new divalent and tetravalent species appear only in fourfold sites. Cr^{2+} has been found to lase in the 2.1–2.9 µm range in ZnS, ZnSe, CdSe and $Cd_{0.85}Mn_{0.15}Se_2$ hosts [22–28]. Cr^{2+} lasers are actively being explored and developed and these have been pumped by Tm lasers, Co:MgF_2 and by 1.7 µm laser diodes. Fe^{2+} has been discovered to lase in ZnSe in the 4.0–4.5 µm region below about 200 K [29], although the first report of laser action dates back to 1983 [30], for Fe in the semiconductor InP and for 2 K (pumping above the bandgap).

Cr^{4+} lasers operate in the near-infrared at 1.2–1.6 µm and have been reported in such hosts as Mg_2SiO_4, Ca_2GeO_4, Y_2SiO_5 and $Y_3Al_5O_{12}$ [31–39]. These lasers can be conveniently pumped with a 1.06 µm Nd:YAG laser. The original material representing this new class of gain media is known as forsterite (Cr:Mg_2SiO_4). Several watts of power are presently available from this class of materials and both Cr:YAG and forsterite have been mode-locked [40–43].

Mn^{5+} lasers operate as the so-called three-level lasers, similar to the original ruby laser, where the laser transition at 1.18 µm terminates near the ground state of the ion. Mn^{5+} has been studied in the $Ba_3(VO_4)_3$ host crystal thus far, where a scientific observation of laser action has been reported [44].

3.2.4 Tabulation of Transition Metal Lasers

A summary of the known laser materials based on transition metals other than Cr^{3+} appears in Table 3.1. It should be noted that there is a diversity of host materials and ions and that there are certainly many more media yet to be discovered.

3.3 Physics and Engineering Issues

3.3.1 Electronic Structure

Transition metals occupy three rows of the periodic table of the elements. Thus far, only the ‘first-row’ elements have demonstrated the ability to lase as an oscillator, although gain has been reported for Rh^{2+} [3] (second-row ion). The treatment of the electronic structure begins with the atomic species, which is described as $3d^n$ for the first row. Because the atomic interactions are the strongest, including the nuclear, repulsive and exchange interactions, the atomic states are the starting point of consideration [45].

For a $3d^1$ ion such as Ti^{3+}, the *only* electronic state that arises from this configuration is the ^2D state. The upper left superscript is the multiplicity (or degeneracy) of the spin, given as $2S+1$, while the ‘D’ stands for the $L = 2$ orbital angular momentum. Since there is only a single electron (with spin 1/2), $2S+1=2$, which is known as a *doublet*. If we now consider the Cu^{2+} ion, which has a $3d^9$ configuration, we may regard this as being one electron short of the $3d^{10}$ fully symmetric closed shell. Therefore, the $3d^9$ structure is characterized as having one *hole* and also yields the ^2D atomic state. For more complicated transition metal ions, for example, those with the $3d^2$ configuration, numerous states result including the ^1S, ^3P and ^1D states, where certain singlet and triplet states are excluded by the requirement of antisymmetrization for the overall electronic wavefunction. Again, d^8 ions give rise to these same states as a consequence of the electron–hole symmetry noted earlier.

Once the atomic state is specified, the crystal field in which the ion is situated must be accounted for. The crystalline environment of transition metal ions is simplified however, since they occur mainly in fourfold or sixfold coordinated sites, referred to as tetrahedral or octahedral sites, respectively, see Figure 3.1. Furthermore, it is often the case that the sites do not deviate far from perfect sites (metal ion at the centre of the

TABLE 3.1

Laser Properties of Transitional Metal Lasers Other Than Cr^{3+}

Laser ion	Laser Crystal	Electronic Transition	Wavelength, μm (temp., if <R_T)	References
Ti^{3+}	Al_2O_3	^2E–$^2T_2$	0.66–1.18	[5]
	$BeAl_2O_4$		0.80	[6,7]
V^{2+}	$CsCaF_3$	$^4T_2$–$^4T_2$	1.24–1.33 (80 K)	[12]
	MgF_2		1.07–1.16 (80 K)	[13]
Cr^{4+}	Mg_2SiO_4	$^3T_2$–$^3T_2$	1.17–1.35	[31–33]
	Ca_2GeO_4		1.35–1.48	[34]
	$Y_3Al_5O_{12}$		1.33–1.57	[35,36]
	$Y_3Sc_xAl_{5-x}O_{12}$		1.39–1.63	[37]
	Y_2SiO_5		1.25–1.35 (77–300 K)	[38,39]
Cr^{2+}	ZnS	^5E–$^5T_2$	2.35	[23]
	ZnSe		2.1–2.8	[22,23,26] [28]
	$Cd_{0.85}Mn_{0.15}Se_2$		2.3–2.66	[24,25]
	CdSe		2.3–2.9	[27]
Mn^{5+}	$Ba_3(VO_4)_3$	^1E–$^3A_2$	1.181	[44]
Fe^{2+}	n-InP	$^5T_2$–^5E	3.53 (2 K)	[30]
	ZnSe		3.98–4.54 (20–170 K)	[29]
Co^{2+}	MgF_2	$^3T_2$–$^3A_2$	1.5–2.5 (80–300 K)	[17–19]
	$KZnF_3$		1.63–2.08 (25–150 K)	[20,21]
Ni^{2+}	$KMgF_3$	$^3T_2$–$^3A_2$	1.59 (80 K)	[15]
	MgF_2		1.63, 1.73–1.75 (20–200 K)	[14]
	$CaY_2Mg_2Ge_3O_{12}$		1.46 (80 K)	[16]

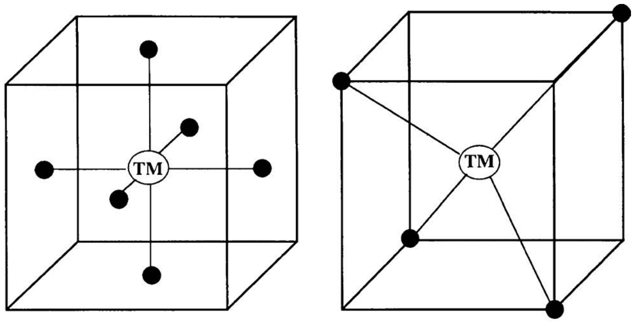

Octahedral Coordination   Tetrahedral Coordination

FIGURE 3.1 Depiction of a transitional metal ion in octahedral and tetrahedral sites in a crystalline lattice.

cube, with the anions at the centre of the six faces for an octahedron or at four of the corners of the cube for a tetrahedron).

The octahedral or tetrahedral sites further split the orbital component of the atomic state into *crystal field* states. For example, a D state is split into E and T_2 states, although the S and P states are not split further but become identified as A_1 and T_1 states, respectively. The rules governing crystal field splitting are encompassed within the discipline of group theory and the magnitude of the effect is encompassed in the well-known Tanabe–Sugano diagrams [45]. As an example of the result of this procedure, the d^8 configuration of Ni^{2+} in an octahedral coordination appears in Figure 3.2. The abscissa of the Tanabe–Sugano diagram represents the magnitude of the crystal field, so at the furthest left-hand position, the energy levels are simply the atomic states. As a final note, it should be mentioned that a sign reversal in crystal field splitting occurs in two situations: incorporating the ion into a tetrahedral as opposed to an octahedral site and considering electrons instead of holes. In other words, the diagram in Figure 3.2 also represents a d^2 ion in a tetrahedral environment.

3.3.2 Absorption and Emission

As an example of the type of absorption and emission spectra exhibited by all of the ions of interest in this chapter, the data for Cr^{2+}:ZnSe are plotted in Figure 3.3. One of the features of the spectra is the approximate 'mirror image' quality of the absorption and emission spectra, where they appear to be roughly symmetrically disposed about a line of reflection. In principle, the material can be pumped anywhere within the wavelength range of the absorption band and the material may then be expected to emit photons according to the emission spectrum. Nearly all of the transition metal lasers operate in the vibronic mode by emitting vibrations during the emission process, with the exceptions of Mn^{5+} and high-field Cr^{3+}

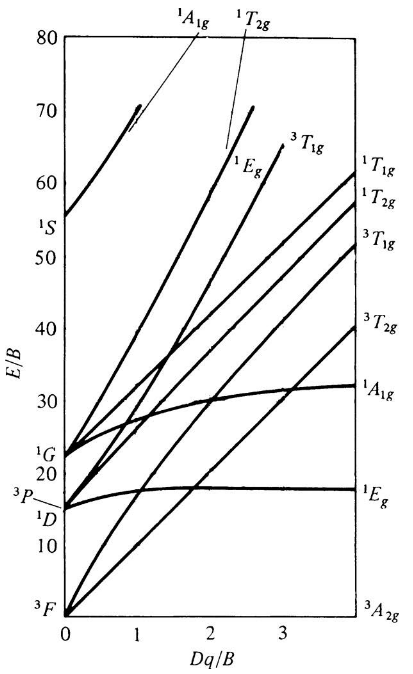

FIGURE 3.2 Tanabe–Sugano diagram for a d8 ion (such as Ni^2) in an octahedral coordination.

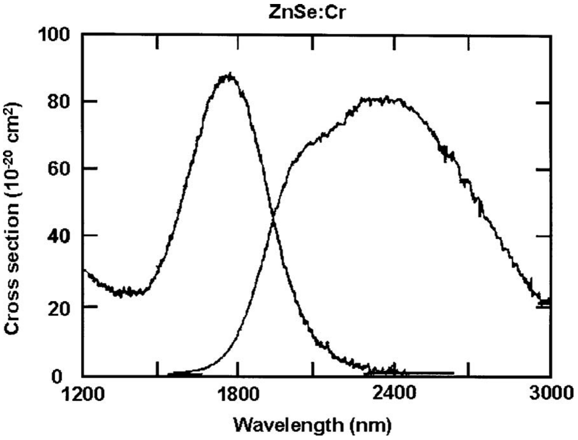

FIGURE 3.3 Absorption and emission spectra of Cr^{2+}:ZnSe, serving as an illustration of the vibronic nature of the emission band and revealing the appearance of a mirror image of the absorption and emission features.

(as in for the ruby laser). As a consequence, we will focus on broad-band vibronic emitters in this section.

A 'configuration coordinate' diagram description of absorption and emission is sketched in Figure 3.4.

The essence of this conceptual diagram is that the Gaussian distribution of interatomic distances in the initial state is unchanged in the course of the electronic transition to the other state, so the distribution is mapped via the vertical intersection with the other curve (up for absorption, down for emission) and then to the energy axis. The shape of the potential energy surfaces is regarded as approximately harmonic in nature, given as [46]

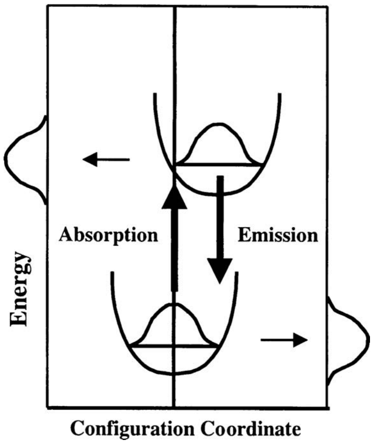

FIGURE 3.4 Idealized configuration coordinate diagram describing the absorption and emission processes for an ion embedded in a host medium.

$$V = \frac{1}{2} k_{\text{gnd}} Q^2 \tag{3.1}$$

for the ground state and as

$$V = \frac{1}{2} k_{\text{ex}} (Q - \Delta Q)^2 \tag{3.2}$$

for the displaced excited state. Q is regarded as the embodiment of the generalized configuration coordinate representing the internuclear separation between the transition metal and the host anion and ΔQ is the displacement between the two electronic states. If, for simplicity, we assume that the ground and excited states have the same shape (i.e. $k_{\text{gnd}} = k_{\text{ex}}$), then the 'Stokes shift' between the absorption and emission peaks is given as $2\text{Sh}\nu_{\text{ph}}$, where S is known as the Huang–Rhys factor and $\text{h}\nu_{\text{ph}}$ is the characteristic phonon energy of the host material. At low temperature, the spectral width of the absorption or emission feature is given as $\Delta = S^{1/2}\text{h}\nu_{\text{ph}}$, so a greater ΔQ shift between the ground and excited potential energy surfaces leads to broader spectral features. To a higher degree of specificity, the lineshape can be described by a Pekarian function:

$$L_{\text{ph}}(p) = S^p exp(-S)/p! \tag{3.3}$$

where p is the number of phonons, which are converted to photon energy via the relationship $E = p\ \text{h}\nu_{\text{ph}} + E_{\text{ZPL}}$ by including the energy of the zero-phonon line (ZPL).

The emission bandshape is a critical aspect of the laser properties of the system since it determines the possible tuning range and has a major consequence on the magnitude of the emission cross section, which is given by [5]

$$\sigma_{\text{em}} = \lambda^2 / \left(8\pi n^2 \tau_{\text{rad}} \Delta\nu_{\text{em}}\right) \tag{3.4}$$

where λ is the wavelength, n is the refractive index, τ_{rad} is the radiative lifetime and $\Delta\nu_{\text{em}}$ is the spectral width of the transition in s^{-1}. It is, therefore, easy to see that, with other factors held constant, the emission cross section must necessarily be reduced to capture the advantage of greater tuning range for the laser. In addition, the potential to generate short pulses also requires the availability of bandwidth, in that the shortest achievable pulsewidth is limited by the uncertainty principle

$$\tau_{\text{lase}} > 0.3/\Delta\nu_{\text{lase}} \tag{3.5}$$

and the laser pulsewidth must naturally be less than that of the emission band ($\Delta\nu_{\text{lase}} \ll \Delta\nu_{\text{em}}$). For the case of an amplifier having gain G, the bandwidth is given by

$$\Delta\nu_{\text{lase}} = \Delta\nu_{\text{em}} / \left(\ln G\right)^{1/2} \tag{3.6}$$

For example, if a multi-pass regenerative amplifier is operating with G = 10^6, then the gain-narrowing factor is 3.7, indicating an attainable pulsewidth of 12 fs. Work with Ti:sapphire oscillators has yielded a pulsewidth of ~5 fs [10] (close to the limit imposed by the emission bandwidth of $\Delta\nu_{\text{em}}$ ~ 3 fs).

3.3.3 Excited-State Absorption

ESA is one of the more subtle aspects of laser materials that needs to be understood to determine whether it can offer net gain at the laser wavelength. The ESA cross section is directly subtracted from the emission cross section of Equation (2.4) to yield the net gain cross section:

$$\sigma_{\text{gain}} = \sigma_{\text{em}} - \sigma_{\text{ESA}} \tag{3.7}$$

In other words, the light passing through the gain medium can either experience stimulated emission, pump-induced loss or both, depending on whether the ion undergoes a transition from the excited state to a lower-lying level or to a higher level, respectively. For some ions such as Ti^{3+}, there is no ESA, simply because there are no accessible excited states above the metastable pumped energy level of the ion. Other ways to avoid the negative impact of ESA for ions include situations where the ESA is either wavelength-shifted from the emission band such that it does not significantly overlap it or for cases where it possesses a significantly weaker cross section. We can consider several examples to compare these cases:

- no relevant higher-lying excited states—Ti:sapphire (octahedral site);
- weak ESA that is spin-forbidden—Cr^{2+} in ZnSe (tetrahedral site) and
- strong ESA which reduces the laser efficiency—Ni^{2+} and V^{2+} ions (octahedral site) and Cr^{4+} (tetrahedral site) in certain crystals.

The energy levels for each of these cases are shown in Figure 2.5. Ti^{3+} is the simplest case because the valence electronic configuration consists only of a single 3d electron. Then, we can imagine that the octahedral crystal field surrounding the ion splits the orbitals into two types: t_{2g} and e_g (t_{2g} orbitals 'point' between the oxygens, while the e_g orbitals point at them and, therefore, have higher energy). So, since there is a single electron, the states become the $^2T_{2g}$ ground state and the ^2E_g excited state, and the laser transition is the transition between them as pictured in Figure 3.5.

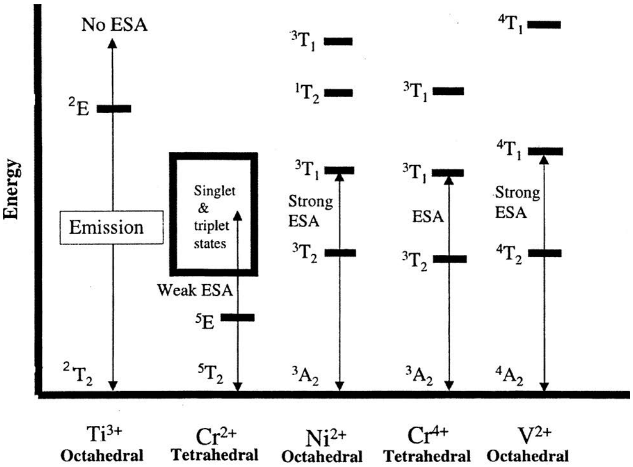

FIGURE 3.5 Energy levels of Ti^{3+} (octahedral); Cr^{2+} (tetrahedral); Ni^{2+} (octahedral); Cr^{4+} (tetrahedral) and V^{2+} (octahedral). The laser and ESA transitions are noted.

Cr^{2+} also does not suffer from extensive ESA losses [23], even though there are a great many excited states above the pumped metastable level. Cr^{2+} has four 3d electrons, so we can imagine that it is one 3d electron short of a half-filled shell—describable as a 3d hole. So with a 3d hole, the two lowest electronic states again become the T_{2g} and E_g states with a spin multiplicity of $2S+1 = 5$. The laser transition occurs between the $^5T_{2g}$ and ^5E_g states. It is coincidentally the same orbital transition as for Ti^{3+} due to two inversions of its nature: because it is a hole rather than an electron and because it is a tetrahedral rather than an octahedral arrangement of host anions. The important point relevant to ESA is that all of the other excited states (of which there are many) must necessarily be either spin triplets or singlets and are, therefore, spin-forbidden from the excited state. For this reason, Cr^{2+} ions in a tetrahedral coordination experience little ESA loss. In contrast, Mn^{2+} and Fe^{3+} (d^5) in octahedral sites do not lase because the ESA transitions are spin-allowed while the emission is forbidden—the opposite of the favourable condition that exists for Cr^{2+} in tetrahedral sites.

For the $3d^8$ Ni^{2+} laser ion situated in an octahedral environment [47,48] or the $3d^2$ Cr^{4+} ion in a tetrahedral site, the emission transition ($^3T_2$–$^3A_2$) may be expected to have roughly the same transition strength as the ESA transition ($^3T_2$–$^3T_1$). Similar considerations apply to V^{2+} although the electronic states are spin quartets rather than triplets [49,50]. In both cases, because the transitions are spin-allowed they derive their transition strength from vibrational interactions with odd-parity phonons that break the symmetry. (While there is sometimes a magnetic dipole contribution to the strength of d–d transitions, the vibrational component normally dominates.) It turns out that the σ_{em} and σ_{ESA} values are approximately comparable for these three systems, although, by serendipity, the emission cross section can sometimes be somewhat larger leading to efficient laser performance. For example, for forsterite (Cr^{4+}:Mg_2SiO_4), the emission cross section turns out to be significantly larger than that of the ESA for one of three polarizations. In contrast, Cr^{4+}:$LiAlO_2$ [51] does not exhibit any net gain since the crystal is isotropic and it appears that $\sigma_{ESA} > \sigma_{em}$. Another way in which the emission 'beats' the ESA is by reducing the temperature below ambient. This effect is apparent for Ni^{2+}:MgO where the emission features sharpen up and thereby rise above the ESA. The efficiency of V^{2+} lasers is also negatively impacted by ESA.

3.3.4 Radiative Rates and Non-Radiative Losses

The emission rate experienced by a metal ion doped into a host medium is the sum of the radiative and non-radiative rates. The basic equation governing the radiative rate is known as Fermi's Golden Rule [2]:

$$W_{\text{rad}} = \left(8\pi^3/h^2\right)\left|\langle I|H_{\text{ph}}|F\rangle\right|^2 g(v) \qquad (3.8)$$

where the initial and final states, *I* and *F*, are linked via the photon field, H_{ph}, and *g*(*v*) is the lineshape function in units of s. For transition metal ions, the relevant electronic states are all derived from the $3d^n$ electronic shell, so the transitions are nominally symmetry-forbidden on the atomic basis. That is to say that the electronic states are both of even parity and, together in consideration of the odd parity of the photon operator, the overall integral is identically zero. However, for the case where the crystalline field is tetrahedral, the inversion symmetry of the ion is destroyed and the 3d–3d transition becomes allowed. This is the nature of the radiative transitions for Cr^{4+}, Cr^{2+}, Fe^{2+} and Mn^{5+} ions, all of which lase when they occupy the tetrahedral sites of certain host media. For Cr^{4+}, Cr^{2+} and Fe^{2+}, the radiative lifetimes are of the order of 1–100 μs for their spin-allowed laser transitions, while it is longer (about 1 ms) for Mn^{5+} because the laser transition is also spin-forbidden. In referring back to Equation (2.8), we see that the radiative rate can be seen as arising from the admixture of opposite parity states into the initial and final states, as a consequence of the crystal field.

For transition metals doped into an octahedral crystal field, the radiative rate can arise from the small residual acentric component of the crystal field and the dynamically induced transition strength resulting from the vibrations that destroy the centre of inversion. Magnetically induced dipole strength can also play a role as in the $^4T_2$–$^4A_2$ emission transition of V^{2+}. Ti:sapphire is an example of the first case, since the sixfold coordinated site of Al_2O_3 has a significant asymmetric component. The dynamic component of the radiative rate is more important for materials where the transition metal site is most purely octahedral such as for $KMgF_3$.

Non-radiative decay is generally described as a thermally activated process for transition metal ions, where the excited state is thermally promoted to a very high vibrational level of the lower ground state and then subsequently decays to the ground state. At this point, the excitation energy is deactivated into vibrational energy and then heat. The competition between radiative and non-radiative decay can be described by

$$k_{\text{em}} = k_{\text{rad}} + k_{\text{nr}} \qquad (3.9)$$

where the non-radiative component is usually given by $k_{nr} = A_{nr} \exp(-E_{nr}/kT)$. The main issue is the magnitude of the 'quenching temperature', T_q, where the radiative and non-radiative rates become comparable. As an example of this type of data, the emission lifetimes of Cr^{2+}:ZnSe and Fe^{2+}:ZnSe are plotted in Figure 3.6. T_q is about 170 and 380 K for these two materials [23]. For comparison, it is 500 [52], 300 [12] and 370 K [53] for Ni^{2+}:MgO, V^{2+}:$CsCaF_3$ and Ti^{3+}:Al_2O_3, respectively.

The Cr^{4+} ion offers some insight into how it can sometimes be difficult to have both favourable emission efficiency and low ESA in a single material. The ion–host combination, Cr^{4+}:$LiAlO_2$, proved to be >30% radiative at room temperature [51] (while the standard forsterite laser material Cr^{4+}:Mg_2SiO_4 is only about 13% efficient) [31–33]. As a result, there was initially much excitement based on the hope that a more efficient Cr^{4+} laser was about to emerge. In spite of the enhanced emission, researchers were unable to lase Cr^{4+}:$LiAlO_2$. It was eventually recognized that ESA was more prominent in $LiAlO_2$ because it did not have the advantage of a strong polarization dependence which can favour low ESA in a particular polarization.

3.3.5 Optical Loss

Optical loss in laser crystals can be due to crystal imperfections and the presence of impurities that absorb at the laser wavelength. In addition, absorption can arise from the differing oxidation states of the doped laser ion. Finally, poor optical quality of the gain element can, in effect, lead to diffraction of the light out of cavity mode so that it is registered as a loss (or a reduction in the beam quality of the oscillator or amplifier). Reducing the optical loss to ~ 0.1% cm^{-1} often requires several years of crystal growth development and, therefore, must be warranted on the basis of the anticipated properties of the laser material. Such was the case, for example, for Ti:sapphire, where eventually Ti^{4+} was eliminated using carefully controlled growth conditions, which reduced the losses to a favourable level. Some host materials such as $Y_3Al_5O_{12}$, MgF_2 and ZnSe had been developed partly for other reasons and are available as high-quality optical materials.

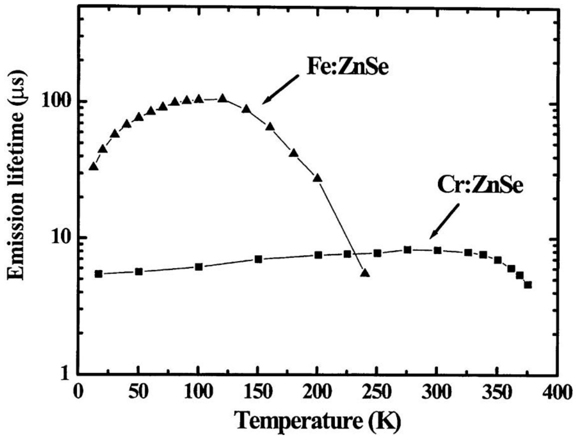

FIGURE 3.6 Emission lifetimes of Cr^{2+} and Fe^{2+} in ZnSe. The precipitous drop in the lifetime is due to the onset of non-radiative decay.

3.3.6 Laser Gain and Oscillation

Laser materials can naturally be arranged to operate in a wide variety of configurations, although we will consider the simple case of a cw longitudinally pumped material. The gain afforded by a laser material can be written as

$$G = T_{\text{surf}} \exp\left[\left(\sigma_{\text{gain}} N_{\text{ex}} - \alpha_{\text{loss}}\right) d\right] \tag{3.10}$$

where N_{ex} is the excited-state population, α_{loss} is the distributed loss in the material, d is the pathlength of the light in the material and T_{surf} is the surface transmission factor. The excited-state population is given as

$$N_{\text{ex}} = \alpha_{\text{abs}} I_{\text{pump}} \tau_{\text{em}} / h\nu_{\text{pump}} \tag{3.11}$$

where α_{abs} is the pump absorption coefficient, I_{pump} is the pump intensity, $h\nu_{\text{pump}}$ is the energy of the pump photon and τ_{em} is the emission lifetime of the excited state. By employing equations (2.10) and (2.11) and allowing for the gain to just equal the loss in an oscillator, the threshold condition can be derived:

$$P_{\text{th}} = \pi\omega^2 h\nu_{\text{pump}} \left(T_{\text{OC}} + T_{\text{loss}}\right) / 4\sigma_{\text{gain}} \tau_{\text{em}} \tag{3.12}$$

where P_{th} is the minimum threshold pump power for the oscillator, ω is the pump laser radius, T_{OC} is the output coupling, T_{loss} is the total double-pass transmission of the gain medium, which accounts for the passive losses, and the emission lifetime accounts for the negative impact of non-radiative decay since $\tau_{\text{em}}^{-1} = k_{\text{rad}} + k_{\text{nr}}$. Thus, Equation (2.9) reveals that losses, ESA (recall $\sigma_{\text{gain}} = \sigma_{\text{em}} - \sigma_{\text{ESA}}$) and non-radiative decay all lead to an increase in the laser threshold of the oscillator, by attenuating the light intensity, reducing the gain and reducing the inversion density, respectively.

3.3.7 Host Properties

Solid-state lasers operating in an 'average power' mode must appropriately manage the repercussions of the thermal gradients existing in the medium, which lead to thermal aberrations (sometimes mainly a spherical lens) and the potential to fracture the gain element. Assuming that the thermal gradients are fully developed in time (i.e. in equilibrium), then the allowed thermal flux that can safely be removed from the surface of a symmetrical thin slab without fracture is [54]

$$Q_{\text{th}} = 6bR_{\text{T}}/d \tag{3.13}$$

where d is the thickness of the slab and b is the safety factor (usually taken as 20%). An overall measure of a material's ability to resist fracture is quantified with the parameter:

$$R'_{\text{T}} = \kappa(1-\nu)K_{1\text{c}}/\alpha E \tag{3.14}$$

where κ is the thermal conductivity, ν is Poisson's ratio (0.2–0.3 for most materials), K_{1c} is related to the material's propensity to resist crack propagation, α is the expansion coefficient and E is Young's modulus. Finally, R_T, the fracture toughness, is given by

$$R_{\text{T}} = R'_{\text{T}} / a^{1/2} \tag{3.15}$$

where a is the radius of the surface flaws, which is usually taken to be a = 25 μm. Some typical values of R'_{T} and κ are listed in Table 3.2 [54,55].

Another important impact of the thermal gradients within the optical material is the introduction of a thermal lens. This effect arises from the stresses, strains and temperature rise within the material. For simplicity, we can consider the case of an unstressed optical element, where the pathlength due to temperature variation of ΔT is given by

$$\Delta p = \left[\alpha(n-1)\mathrm{d}n/\mathrm{d}T\right] L\Delta T. \tag{3.16}$$

The magnitude of the change in refractive index with temperature dn/dT is an important parameter in determining the amount of thermal lensing exhibited by the material. From the data in Table 3.2, it should be noted that MgF_2, for example, has a much lower dn/dT than ZnSe. The thermal gradient that occurs in the material generally gives rise to a large spherical wavefront distortion, which can be partially mitigated with additional optics.

Lastly, the magnitudes of several non-linear refractive indices are listed in Table 3.2 [56]. The n_2 becomes important for pulsewidths of the order of nanoseconds or less, since it leads to an intensity-dependent refractive index and lensing effect. The non-linear index, n_2, is defined by

$$n = n_0 + n_2 \left\langle E^2 \right\rangle \tag{3.17}$$

where E is the electric field of the laser beam. The non-linear indices generally follow the rule of fluorides < oxides < selenides.

TABLE 3.2

Thermal, Mechanical and Optical Properties of Host Media

	Thermo-mechanical		Optical	
Crystal	**Thermal Conductivity, κ (W m K^{-1})**	**Fracture Toughness, R_T (W m$^{-1/2}$)**	**Index Change dn/dT (10^{-6} K^{-1})**	**Non-linear Index n_2 (10^{-13} esu)**
Al_2O_3	28	22	12	1.2
$Y_3Al_5O_{12}$	10	4.6	9	2.7
Y_2SiO_5	4.5	1.9	6, 7, 9 (anisotropic)	3.7
Mg_2SiO_4	8	-	-	-
MgF_2	21	7.6	0.3, 0.9	0.3
ZnSe	18	5.3	70	170

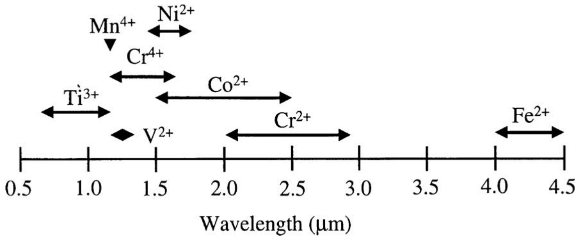

FIGURE 3.7 Summary of tuning ranges offered by known laser ions.

The non-linear index is also responsible for Kerr lens mode-locking by virtue of the slight difference in the oscillator stability that arises from the intensity-dependent focusing power, causing the mode-locked state to be preferred over cw output.

3.4 Summary

In this chapter, the nature and scope of transition metal ion lasers (excluding Cr^{3+}) have been summarized, as they are embodied in today's solid-state laser systems. Ti:sapphire is by far the most common transition-metal-based solid-state laser, and it has led to many new opportunities for short-pulse lasers. Co^{2+}:MgF_2 lasers are commercially available and Cr^{4+} and Cr^{2+} lasers are growing in importance. Research in transition metal lasers is continuing, as the vibronic laser Fe^{2+}:ZnSe was first reported to lase in 1999 and many of the second- and third-row ions are yet to be explored in depth. The electronic structure, absorption and emission spectra, ESA, radiative properties, optical gain/loss and host properties have been described. The tuning ranges encompassed by the known transition metal ions are pictured in Figure 3.7.

Work is done under the auspices of the US Department of Energy by the University of California Lawrence Livermore National Laboratory under Contract W-7405-ENG-48.

REFERENCES

1. Caird J A and Payne S A 1991 *Handbook of Laser Science and Technology. Supplement 1: Lasers* ed M J Weber (Boca Raton, FL: Chemical Rubber Company) p 1.
2. Powell R C 1998 *Physics of Solid-State Laser Materials* (New York: Springer).
3. Powell R C, Quarles G J, Martin J J, Hunt C A and Sibley W A 1985 Opt. Lett. **10** 212–4.
4. Barrie J D, Stafsudd O M and Nelson P 1987 J. Luminesc. **37** 303.
5. Moulton P F 1986 J. Opt. Soc. Am. B **3** 125–33.
6. Pestryakov E V, Trunov V I and Alimpiev A I 1987 Sov. J. Quantum Electron. **17** 585–6.
7. Segawa Y, Sugimoto A, Kim P H, Namba S, Yamagishi K, Anzai Y and Yamaguchi Y 1987 Japan. J. Appl. Phys. **36** L291–2.
8. Keller U 1994 Appl. Phys. B **58** 347–63.
9. French P M W 1996 Contemp. Phys. **37** 283–301.
10. Morgner U, Kaertner F X, Cho S H, Chen Y, Haus H A, Fujimoto J G, Ippen E P, Scheuer V, Angelow G and Tschudi T 1999 Opt. Lett. **24** 411–3.
11. Wang H, Backus S, Chang Z, Wagner R, Kim K, Wang X, Umstadter D, Lei T, Murnane M and Kapteyn H 1999 J. Opt. Soc. Am. **16** 1790–4.
12. Brauch U and Durr U 1985 Opt. Commun. **55** 35–40.
13. Moulton P F 1982 Appl. Phys. **28** 233.
14. Moulton P F, Mooradian A and Reed T B 1978 Opt. Lett. **3** 164–6.
15. Johnson L F, Guggenheim H J and Bahnck D 1983 Opt. Lett. **8** 371–3.
16 Moulton P F 1982 IEEE J. Quantum Electron. **18** 1185–8.
17. Moulton P F 1985 IEEE J. Quantum Electron. **21** 1582–95.
18. Fox A M, Maciel A C and Ryan J F 1986 Opt. Commun. **59** 142–4.
19. Wedford D and Moulton P F 1988 Opt. Lett. **13** 975–7.
20. Kunzel W, Knierim W and Durr U 1981 Opt. Commun. **36** 383–6.
21. German K R, Durr U and Kunzel W 1986 Opt. Lett. **11** 12–4.
22. Page R H, Schaffers K I, DeLoach L D, Wilke G D, Patel F D, Tassano J B, Payne S A, Krupke W F, Chen K-T and Burger A 1997 IEEE J. Quantum Electron. 33 609–19.
23. DeLoach L D, Page R H, Wilke G D, Payne S A and Krupke W F 1996 IEEE J. Quantum Electron. **32** 1–11.
24. Hoemmerich U, Wu X, Davis V R, Trivedi S B, Grasza K, Chen R J and Kutcher S 1997 Opt. Lett. **22** 1180–2.
25. Seo J T, Hoemmerich U, Trivedi S B, Chen R J and Kutcher S 1998 Opt. Commun. **153** 267–70.
26. Podlipensky A V, Shcherbitsky V G, Kuleshov N V, Mikhailov V P, Levchenko V I, Yakimovich V N, Postnova L I and Konstantinov V I 1999 Opt. Commun. **167** 129–32.
27. McKay J, Schepler K L and Catella G C 1999 Opt. Lett. **24** 1575–7.
28. Wagner G J, Carrig T J, Page R H, Schaffers K I, Ndap J-O, Ma X and Burger A 1999 Opt. Lett. **24** 19–21.
29. Adams J J, Bibeau C, Page R H, Krol D M, Furu L H and Payne S A 1999 Opt. Lett. **24** 1720–2.
30. Klein P B, Furneaux J E and Henry R L 1983 Appl. Phys. Lett. **42** 638–40.
31. Petricevic V, Gayen S K, Alfano R R, Yamagishi K, Anzai H and Yamaguchi Y 1988 Appl. Phys. Lett. **52** 1040–2.
32. Petricevic V, Gayen S K and Alfano R R 1989 Opt. Lett. **14** 612–4.
33. Carrig T J and Pollock C R 1991 Opt. Lett. **21** 1662–4.
34. Petricevic V, Bykov A B, Evans J M and Alfano R R 1996 Opt. Lett. **21** 1750–2.
35. Eilers H, Dennis W M, Yen M, Kueck S, Petermann K, Huber G and Jia W 1993 IEEE J. Quantum Electron. **29** 258–12.
36. Sennaroglu A, Pollack C R and Nathel H 1995 J. Opt. Soc. Am. B **12** 930–7.
37. Kueck S, Petermann K, Pohlmann U, Schoenhoff U and Huber G 1994 Appl. Phys. B **58** 153–6.
38. Deka C, Chai B H T, Shimony Y, Zhang X X, Munin E and Bass M 1992 Appl. Phys. Lett. **61** 2141–3.
39. Koetke J, Kueck S, Petermann K, Huber G, Cerullo G, Danailov M, Magni V, Qian L F and Svelto O 1993 Opt. Commun. **101** 195–8.

40. Seas A, Petricevic V and Alfano R R, 1992 Opt. Lett. **17** 937–9.
41. Robertson A, Fuchs H, Ernst U, Wallenstein R, Scheuer V and Tschudi T 2000 J Opt. Soc. Am. B **17** 668–71.
42. French P M W, Rizvi N H, Taylor J R and Shestakov A V 1993 Opt. Lett. **18** 39–41.
43. Sennaroglu A, Pollack C R and Nathel H 1994 Opt. Lett. **19** 390–2.
44. Merkle L, Pinto A, Verdun H R and McIntosh B 1992 Appl. Phys. Lett. **61** 2386–8.
45. Sugano S, Tanabe Y and Kamimura H 1970 *Multiplets of Transition Metal Ions in Crystals* (New York: Academic).
46. DiBartolo B 1975 *Optical Properties of Ions in Solids* (New York: Plenum).
47. Koetke J, Petermann K and Huber G 1993 J. Luminesc. **60–61** 197–200.
48. Payne S A 1990 Phys. Rev. B **41** 6109–16.
49. Payne S A and Chase L L 1987 J. Luminesc. **38** 187–9.
50. Moncorgé R and Benyattou T 1988 Phys. Rev. B **37** 9177–85.
51. Kuck S, Hartung S, Petermann K and Huber G 1995 Appl. Phys. B **61** 33–6.
52. Iverson M V, Windscheif J C and Sibley W A 1980 Appl. Phys. Lett. **36** 183–4.
53. Albers P, Stark E and Huber G J. Opt. Soc. Am. B 3 134–9.
54. Albrecht G F and Payne S A 1994 *Electro-Optics Handbook* ed R Waynant and M Ediger (New York: McGraw-Hill).
55. Krupke W F, Shinn M D, Marion J E, Caird J A and Stokowski S E 1986 J. Opt. Soc. Am. B **3** 102–14.
56. Adair R, Chase L L and Payne S A 1989 Phys. Rev. **39** 3337–50.

Taylor & Francis
Taylor & Francis Group
http://taylorandfrancis.com

4

Rare-Earth Ion Lasers—Nd^{3+}

A. I. Zagumennyi, V. A. Mikhailov, and I. A. Shcherbakov

CONTENTS

4.1 Spectroscopic and Laser Properties of Nd^{3+} Ions 35
4.2 Nd:YAG Laser Crystal 35
  4.2.1 Energy Levels of Nd^{3+} Ions in a YAG Crystal 37
  4.2.2 The Lifetime of Nd^{3+} Ions in YAG 38
  4.2.3 Effective Emission Cross Sections of Laser Transitions 39
  4.2.4 Absorption Spectra and Pump Levels of Nd:YAG Crystals 39
  4.2.5 Properties of the Basic $^4F_{3/2} \rightarrow {}^4I_{11/2}$ Transition at 1064 nm 40
  4.2.6 Concentration Quenching of Emission for High Neodymium Doping Levels 40
4.3 Polycrystalline Nd:YAG Ceramic Laser 43
4.4 Nd:YLF Laser Crystal 45
4.5 Nd:Vanadate Laser Crystals 45
  4.5.1 Preparation of the Nd:YVO$_4$ and Nd:GdVO$_4$ Crystals 46
  4.5.2 Absorption and Emission of Nd:GdVO$_4$ 47
  4.5.3 Nd:YVO$_4$ and Nd:GdVO$_4$ Lasers 48
4.6 Nd:Cr:GSGG and Nd:Cr:YSGG Crystals 50
4.7 Nd:LSB Crystal 51
4.8 Nd^{3+}-Doped Glass 51
References 52

4.1 Spectroscopic and Laser Properties of Nd^{3+} Ions

In this chapter the basic physical, spectroscopic and laser properties of Nd:$Y_3Al_5O_{12}$, Nd:ceramics, Nd:$YLiF_4$, Nd:YVO_4, Nd:$GdVO_4$, Nd:$YAlO_3$, Nd:Cr:GSGG, Nd:Cr:YSGG, Nd:LSB crystals and Nd:glass will be discussed.

4.2 Nd:YAG Laser Crystal

The Nd:YAG laser is by far the most commonly used type of commercial solid-state laser. Neodymium-doped yttrium aluminium garnet $Y_{3-x}Nd_xAl_5O_{12}$ (Nd:YAG) possesses a combination of properties uniquely favourable for laser operation. Undoped pure $Y_3Al_5O_{12}$ is a colourless, optically isotropic crystal which possesses a cubic structure characteristic of garnets. Its optical properties are isotropic: the refractive index does not depend on the direction of the light nor its polarization. The cubic structure of YAG favours a narrow fluorescence linewidth, which results in a high gain and a low threshold for laser operation. The YAG host is hard, is of good optical quality and has a high thermal conductivity. The basic physical and chemical properties of YAG crystals are summarized in Table 4.1.

The major laser activator ion for YAG is Nd^{3+}, which replaces isomorphic Y^{3+} ions. As the Nd^{3+} ion radius (0.98 Å) exceeds that of the Y^{3+} ion (0.90 Å), the entry of neodymium ions into the YAG lattice is limited, up to a concentration of a few per cent. In Nd:YAG, trivalent neodymium substitutes for trivalent yttrium, so charge compensation is not necessary.

It is possible to grow a transparent Nd^{3+}:YAG crystal with an atomic concentration of Nd^{3+} of up to 1.5% with the substitution of Y^{3+} ions. The Nd doping level in YAG is sometimes expressed in different concentration units: a concentration of 1.0% Nd atoms in the lattice is equivalent to 0.727% Nd or 0.848 wt% Nd_2O_3, respectively. The concentration of Nd^{3+} sites in these cases is 1.386×10^{20} cm^{-3}. The growth is carried out by the Czochralski (CZ) method (pulling from a melt) using iridium crucibles. The high-quality crystal must be grown with a very slow growth rate (0.5 mm h^{-1}).

The difference in the ion radii of Nd^{3+} and Y^{3+} determines the distribution coefficient of neodymium ions in the melt–crystal system. The concentration of Nd ions in the growing crystal is much less than the concentration in the melt, because

TABLE 4.1

Comparison of Nd:YAG, Nd:YLF and Nd:$YAlO_3$

Crystal	YAG	$YAlO_3$	YLF
Crystal class	Cubic	Orthorhombic	Tetragonal
Space group	I_{a3d}	P_{bnm}	$I4_{1/a}$
Doping limit (at %)	0.3–1.6	1–3	1–2
Lattice parameters (Å)	12.01	$a = 5.176$	$a = 5.26$
		$b = 5.307$	$c = 10.94$
		$c = 7.355$	
Melting point (°C)	1970	1870	825
Density (undoped) (g cm^{-3})	4.56	5.35	3.99
Hardness (Mohs)	8.5	8.0	4–5
Thermal conductivity with 1 at% Nd (W m^{-1} K^{-1})	11.1	9.1	6.0
Thermal conductivity of undoped crystal at 300 K (W m^{-1} K^{-1})	13.0	11.0	6.3
Refractive index at laser wavelength	1.818	$n_\alpha = 1.929$	1.470(e)
		$n_\beta = 1.943$	1.448(o)
		$n_\gamma = 1.952$	
Lasing wavelength (nm)	1064.2	1079.6 (*b*-axis)	1047.0 (π)
		1064 (*c*-axis)	1053.0 (σ)
Linewidth (nm)	0.6	1.1	1.2
Radiative lifetime (μs)	255	190 (0.1 at%)	520
Lifetime for 1 at% Nd ions (μs)	220	170	460
Effective laser cross section (10^{-19} cm^2)	2.8	3.1 ‖ *a*-axis	1.87 (π)
		3.9 ‖ *b*-axis	1.25 (σ)
		2.3 ‖ *c*-axis	
Diode pump peak wavelength (nm)	807.5	803 E ‖ *c*-axis	792
		807 E ‖ *a*-axis	
Peak absorption coefficient with 1 at% Nd (cm^{-1})	8.0	14	32.1 (π)
			8.6 (σ)
FM75%—absorption bandwidth at 1 at% Nd (nm)	2.5	2.8 ‖ *a*-axis	6 (π)
Thermal change of indices at 1064 nm (10^{-6} K^{-1})	9.0	9.7(α)	−4.3 (e)
		14.5 (γ)	−2.0 (o)
Linear expansion coefficient (10^{-6} K^{-1})	7.3	9.5 ‖ *a*-axis	8.3 ‖ *c*-axis
		4.3 ‖ *b*-axis	13.3 ‖ *a*-axis
		10.8 ‖ *c*-axis	

π, E ‖ *c*-axis.
σ, $E \perp$ *c*-axis.
e, extraordinary polarization; o, ordinary polarization.

the distribution coefficient is only ~0.18. Because the Nd distribution coefficient is low, not all Nd:YAG crystal boules are uniformly doped. This problem arises as a result of the crystal-growth mechanism. In substituting the larger Nd^{3+} for a Y^{3+} in $Y_3Al_5O_{12}$, the Nd^{3+} is preferentially retained in the melt. The increase in the concentration of Nd from the seed to the terminus of a 20-cm long boule is about 20%–25%. For a laser rod 3–8 cm long, this end-to-end variation may be 0.05–0.10 wt% of Nd_2O_3.

In addition to CZ growth from iridium crucibles, crystals can also be grown by zone melting in molybdenum containers. However, the highest quality crystals are produced by CZ growth. In this method, the melt is induction heated via the iridium crucible, which contains the starting materials. The growth process originates on the seed rod. Since the temperature of the seed crystal is lower than the temperature of the melt, the melt gradually crystallizes on the seed crystal during the slow lift and rotation rates (10–20 rev min^{-1}). The crystal orientation of the growing boule reproduces that of the seed crystal. For the crystal growth process, the melt temperature must be maintained above the melt temperature of YAG (1970°C) with a very high degree of accuracy. At such high melt temperatures, one difficulty is the crucible material. For Nd:YAG, the best material is iridium, although its high cost and rarity pose serious problems in the manufacture of Nd:YAG crystals. The CZ growth of Nd:YAG is a capital-intensive process. A single iridium crucible for growing large-sized crystals costs almost US $100,000. Even worse, a significant portion of the crucible is unrecoverable, as it is ‘burned-up’ during use, limiting its lifetime. The capital investment is increased by the additional need for protection systems to ensure a continuous supply of electrical power, cooling water and other utilities essential for maintaining a reasonable productivity level. Therefore, the Nd:YAG rod, particularly a slab-shaped crystal, is often one of the most expensive components in the laser system.

YAG crystals grow in an inert atmosphere of nitrogen or argon. At the optimum growth rate of 0.5 mm h^{-1}, the manufacture of the average size Nd:YAG crystal boules (a length of about 150 mm with a diameter of about 100 mm) takes about 300 h, i.e. about 2 weeks. The CZ growth enables production of large Nd:YAG crystals. The biggest Nd:YAG crystal grown to date is 100 mm in diameter and 300 mm long.

During growth, defects form in the central part of the crystal, giving rise to mechanical and optical distortions. Electron microprobe studies have revealed that, in the core region, the Nd concentration can be as much as twice as high as in the surrounding areas. The core originates from the presence of facets on the growth interface, which have a different Nd^{3+} distribution coefficient from the surrounding growth surface. These compositional differences cause corresponding differences in the thermal expansion coefficients, which, in turn, give rise to the stress patterns observed as the crystals cool down from the growth temperature. Annealing does not seem to eliminate the core and, thus far, no way has been found to prevent the formation of facets on the growth interface. Therefore, active elements are cut out from the peripheral parts of Nd:YAG crystals. As a rule, the active elements are made in the form of long thin cylinders with their axis directed along the growth of the crystal boule. By changing the orientation of the seed rod, it is possible to change the orientation of the crystallographic axes in an active element. Cylindrical elements produced from Nd:YAG have, as a rule, diameters of 3, 4, 5, 6.3, 8 or 10 mm and lengths of 32, 40, 50, 65, 80, 100, 125, 150 or 200 mm.

In specifying Nd:YAG rods, the emphasis is on size, dimensional tolerance, doping level and passive optical tests of rod quality. Cylindrical rods with flat ends are typically finished to the following specifications: ends flat to $\lambda/10$, ends parallel to ±4 arcsec, perpendicularity to rod axis to ±5 min and rod axis parallel to within ±5° to the [111] direction. Dimensional tolerances typically are ±0.5 mm in length and ±0.025 mm in diameter. Most suppliers furnish laser crystals with a photograph showing the fringe pattern of the crystal as examined by a Twyman–Green interferometer. A double-pass Twyman–Green interferometer quickly reveals any strained areas, small defects or processing errors. The optical quality of such rods is normally quite good and comparable to the best quality of optical glass. For example, 6 mm by 100 mm rods cut from the outer sections of 20 mm by 150 mm boules typically may show only one to two fringes in a Twyman–Green interferometer.

Usually, lamp-pumped Nd:YAG lasers with an average output power of up to 500 W use a single rod up to 10 mm in diameter and 150 mm long. Higher-power systems with outputs of 2–3 kW can have up to four or, less-commonly, six pump heads with a laser rod up to 200 mm long. Later rectangular slab configuration crystals with up to 10 mm by 25 mm cross-sectional dimensions and lengths in excess of 200 mm have entered the market (Figure 4.1).

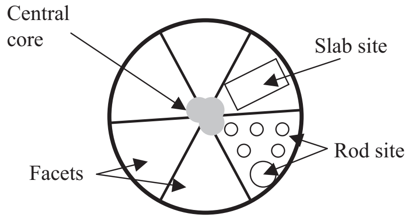

FIGURE 4.1 Nd:YAG boule cross section showing the facet regions and location of slab and rod sites.

The spectroscopic properties of Nd:YAG are determined by the basic properties of an Nd^{3+} ion, as slightly modified by the YAG crystalline matrix. Neodymium is a rare-earth metal. The optical and laser properties of trivalent neodymium, as well as other rare-earth ions, are determined by the transitions inside the 4f-electronic shell (Figure 4.2). Under the action of the electrostatic crystal field of the lattice, the energy levels split into Stark levels, which vary from crystal to crystal, and while the lines broaden as a result of interactions with the phonons of the crystal lattice. At room temperature, the main 1.06 μm line in Nd:YAG is homogeneously broadened by thermally activated lattice vibrations.

The structure of the energy-level-free Nd^{3+} ion is determined by the electrons' Coulomb interactions with the nucleus and with each other, and also with the spin and orbital moments of the electrons. The lowest Nd^{3+} ion energy level belongs to a ${}^4I_J$ atomic state. This means that three electrons of the Nd^{3+} ion, being on the 4f shell, have a total spin moment S of 3/2 and an orbital moment L of 6. As a result of the spin–orbital interaction, the 4f multiplet is split into four Stark levels with total moment J from $L - S = 6 - 3/2 = 9/2$ up to $L + S = 6 + 3/2 = 15/2$.

In Figure 4.2, the splitting of the lowest ${}^4I$ levels of Nd^{3+} with various spin–orbits and Stark splits by the crystal field in a YAG crystal is shown. The energy levels of a free Nd^{3+} ion are also shown.

4.2.1 Energy Levels of Nd^{3+} Ions in a YAG Crystal

A detailed diagram of the Nd^{3+} energy levels in YAG is given in Ref. [1]. All levels of the free ion in crystals split as a consequence of the Stark effect arising from the crystal field. Each term is split into $(2J + 1)/2$ components, in particular: ${}^4I_{9/2}$ into 5, ${}^4I_{11/2}$ into 6, ${}^4I_{13/2}$ into 7 and ${}^4I_{15/2}$ into 8. Energy splitting between components lies in the ranges of about 10–100 cm^{-1}. In Figure 4.2, the energy-level diagram for the Nd^{3+} ion in a YAG crystal is shown at a temperature T of 300 K; however, the Stark splitting is only shown for levels that directly participate in laser generation. The number of levels from the Stark splitting is large, compared to those for the free ion. However, the weak splitting of the levels is grouped around the free ion energy. As a result of the low symmetry of the local crystal field of the Nd^{3+} ion in YAG, the degeneracy of levels in YAG is removed completely, except for Kramer's degeneracy of the J_z projection, which can be removed only by using an external magnetic field.

According to parity selection rules, optical transitions are forbidden between the energy levels in one electronic shell. In our case, this means that either the probability of all optical transitions between levels is small or the time for spontaneous optical transitions between levels is large (in comparison with the time constant of permitted optical transitions, being of the

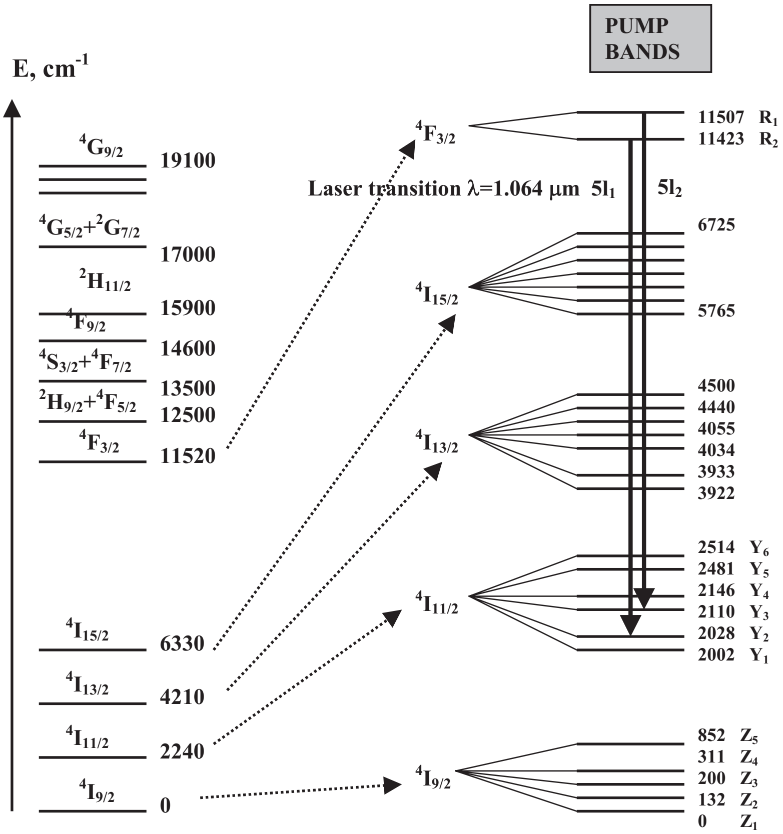

FIGURE 4.2 Energy-level diagram of the free ion and the splitting of the Nd^{3+} ion inside the crystal field of YAG.

order of 10^{-8}–10^{-9} s). For Nd^{3+} ions, all transitions between levels of the 4f shell are weak. Their intensity differs from zero as a consequence of mixing the 4f shell with a shell with opposite parity (for example, the 5d shell) under the action of odd harmonics arising from the crystal field. The intensity of transitions strongly varies from crystal to crystal and is defined by the specific properties of the matrix.

4.2.2 The Lifetime of Nd^{3+} Ions in YAG

In the general case, the lifetime of the energy levels is determined, as noted earlier, by radiative and non-radiative relaxation between levels, which has been investigated by many research groups. We shall consider them more in detail.

According to the energy levels of Nd^{3+} ions in garnet crystals, optical transitions can occur from the metastable levels, including the $^4F_{3/2}$ level, downwards, to the $^4I_{9/2}$–$^4I_{15/2}$ multiplets. All these transitions are forbidden and their characteristic lifetimes are about 10^{-3}–10^{-4} s. The energy distances between the pump levels above the $^4F_{3/2}$ level are rather small in comparison with the YAG phonon energy. Therefore, the probabilities for non-radiative transitions between them are great and the lifetimes are accordingly small ($\ll 10^{-6}$ s). Thus, the Nd^{3+} ions, upon being excited to pump levels, relax to the $^4F_{3/2}$ level quickly, in practice completely non-radiatively.

The $^4F_{3/2}$ level is metastable because the next lower level is separated from it by 4698 cm^{-1}. Therefore, non-radiative transitions downwards from the $^4F_{3/2}$ level have a small probability. They can be made only through multi-phonon relaxation requiring close to six phonons; the probability of such transitions is small and the lifetime is great, about 1–3×10^{-2} s. As the radiative time for the $^4F_{3/2}$ level transition is also great (about 2.5×10^{-4} s), this level is, therefore, metastable—a long-lived level which is convenient for use as the upper level in a four-level scheme for lasers.

It is worthwhile noting that the ratio $\eta = (\tau_{em})^{-1}/[(\tau_{em})^{-1} + (\tau_\sigma)^{-1}]$ determining the quantum yield of emission from the upper laser $^4F_{3/2}$ level in YAG is greater than 99.5% with a fluorescence lifetime of 230 μs.

For the lower $^4I_{9/2}$–$^4I_{15/2}$ multiplets, the energy distances within and between them are less or comparable to the maximum phonon energy (850 cm^{-1}). The transitions within and between these multiplets experience non-radiative relaxations with a short time constant of about 10^{-8} s.

Thus, in view of the energy distances and lifetimes for Nd^{3+} ions in YAG, the laser scheme (see Figure 4.2) will be close to the ideal four-level system. The pump level ‘4’ includes all levels lying above the $^4F_{3/2}$ level. The metastable transition level ‘3’ is served by the $^4F_{3/2}$ state, split into two Stark levels: R_1 at 11 423 cm^{-1} and R_2 at 11 507 cm^{-1}. The ‘2’ transitions can be served by any levels of the $^4I_{11/2}$–$^4I_{15/2}$ multiplets. Moreover, at last, the lowest level is comprised from a set of Stark levels from the $^4I_{9/2}$ multiplet. Hence, laser generation on the four-level scheme can occur over the whole range of channels formed by the different Stark levels in the multiplets.

4.2.3 Effective Emission Cross Sections of Laser Transitions

The emission cross sections of the basic laser transitions of Nd:YAG are well investigated and are described in Ref. [1]. In Table 4.2 the basic lines for Nd:YAG laser generation, the emission cross sections of transitions σ and factors of branching emission β are given. The ratio β shows the relative intensity of the emission for transitions between levels *i* and *j*. The sum β_{ij} of all transitions between the $^4F_{3/2}$ multiplet and all multiplets is equal to one. Stronger transitions give a larger β_{ij} coefficient. As it can be seen from Table 4.2, even among the strongest transitions there can be large distinctions in the emission cross sections observed, which are reflected in light amplification of the active laser rod and in the thresholds for laser generation. The branching ratio of emission from $^4F_{3/2}$ is as follows: $^4F_{3/2} \to {}^4I_{9/2} = 0.25$, $^4F_{3/2} \to {}^4I_{11/2} = 0.60$, $^4F_{3/2} \to {}^4I_{13/2} = 0.14$ and $^4F_{3/2} \to {}^4I_{15/2} < 0.01$. This means that almost all the ions transferred from the ground level to the pump bands end up at the upper laser level and 60% of the ions at the upper laser level cause fluorescence output to the $^4I_{11/2}$ manifold. Therefore, in commercial lasers in basic use, only the strongest transitions with wavelengths of 1064.15, 1318.4 and 1338.1 nm are used.

4.2.4 Absorption Spectra and Pump Levels of Nd:YAG Crystals

As previously noted and shown in Figure 4.2, $^4F_{3/2}$ and higher levels are used to pump Nd:YAG crystals. These levels consist of Stark levels that are broadened by the influence of lattice fluctuations on the neodymium ions. It is obvious that the wider transitions absorb the pump light more strongly and, as a result, are more effective for laser operation. The absorption coefficient of the pumping light is determined by the effective cross section of the transitions.

As an overwhelming number of the neodymium ions are located in the $^4I_{9/2}$ level (more precisely, the Z_1–Z_4 sublevels), light absorption practically only occurs from this level. The intensity of the absorption lines is dictated by the cross section of the transitions. In addition to the neodymium ions, the pumping light can be absorbed into the matrix of the YAG crystal. The YAG matrix is transparent in the range of 240–5500 nm. Therefore, in the range of visible and near-infrared radiation, where the strongest absorption lines are located, the absorption by the matrix is not relevant. The matrix absorption spectrum may be caused by impurities or defects. In the light of these remarks, we shall consider the absorption spectrum of Nd:YAG crystals, shown in Figure 4.3. As can be seen from the spectrum, the basic absorption is given by five main peaks, arising from transitions to the following pump levels:

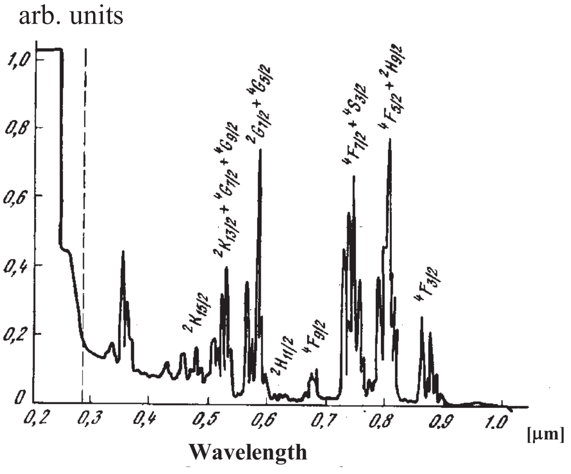

FIGURE 4.3 Absorption spectra of an Nd:YAG crystal.

1. $^4F_{3/2}$: $\lambda \simeq 880$ nm;
2. $^4F_{3/2} + {}^2H_{9/2}$: $\lambda \simeq 810$ nm;
3. $^4F_{7/2} + {}^4S_{3/2}$: $\lambda \simeq 750$ nm;
4. $^2G_{7/2} + {}^4G_{5/2}$: $\lambda \simeq 580$ nm;
5. $^2K_{13/2} + {}^2G_{7/2} + {}^4G_{9/2}$: $\lambda \simeq 520$ nm.

The other absorption peaks have a small effect on the laser pumping process because of their small cross sections. The two most intense peaks are located in the spectral range of the basic pump source. The ultraviolet area is characterized by absorption peaks 360 and 260 nm while the wing of the matrix absorption begins at 400 nm and rises strongly to 240 nm (i.e. the absorption edge of the transparent crystal/matrix). As the pump light absorbed by the matrix does not contribute to useful laser radiation and only results in heating, the ultraviolet pumping radiation in real lasers is absorbed by a special light filter, to prevent it from impinging upon the Nd:YAG laser rod. The UV filter is necessary to avoid the generation of colour centres from residual impurities and defects and, in particular, from iron ions. Such colour centres absorb pump and laser radiation and sharply reduce the efficiency of the laser.

TABLE 4.2

Wavelength, branching emission, β_{ij} and cross sections, σ, for the strongest Nd^{3+} ion transitions in YAG at T = 300 K

Transition	Bottom Level (cm^{-1})	Wavelength (nm)	β_{ij}	σ, 10^{-20} cm^2
^{4}F3/2 → $^4I_{13/2}$	3922	1318.4 (R_2)	0.021	1.5
	3933	1335.1 (R_1)	0.015	0.92
	4034	1338.1 (R_2)	0.023	1.5
	2028	1052.1 (R_2)	0.041	2.7
	2002	1051.5 (R_1)	0.091	4.7
$^4F_{3/2} \to {}^4I_{11/2}$	2110	1064.15 (R_2)	0.125	7.1
	2028	1064.4 (R_1)	0.041	1.9
	2146	1068.2 (R_2)	0.040	1.8
	2110	1073.7 (R_2)	0.062	2.6
	2146	1078.0 (R_1)	0.043	1.2
$^4F_{3/2} \to {}^4I_{9/2}$	852	938.5 (R_2)	0.041	0.81
	852	946.4 (R_1)	0.049	1.34

The R_1 and R_2 transitions arise according to 11 507 and 11 423 cm^{-1} Stark levels of the $^4F_{3/2}$ multiplet.

4.2.5 Properties of the Basic $^4F_{3/2} \rightarrow {}^4I_{11/2}$ Transition at 1064 nm

The Nd:YAG emission line at 1064.15 nm offers the maximum emission cross section and efficiency. It is possible, however, to obtain oscillation at other wavelengths by inserting etalons or dispersive prisms in the resonator, by utilizing a specially designed resonant reflector as an output mirror or by employing highly selective dielectrically coated mirrors. These elements suppress laser oscillation at the undesirable wavelength and provide optimum conditions at the desired wavelength. With this technique, over 20 transitions have been made to lase in Nd:YAG (Table 4.2).

The 1.064 and 1.061 μm lines of the $^4F_{3/2} \rightarrow {}^4I_{11/2}$ provide the lowest threshold in Nd:YAG. At room temperature, the 1.064 μm line $R_2 \rightarrow Y_3$ is dominant, while at low temperatures, the 1.061 μm line $R_1 \rightarrow Y_1$ has the lower threshold. If the flashlamp-pumped laser crystal is cooled, additional laser transitions are obtained, most notably the 0.946 μm line. Diode-pumped Nd:YAG lasing is very effective at the 0.946 μm line for a temperature of 300 K (Table 4.8).

The 1.064 and 1.061 μm lines are caused by two transitions close in frequency: $5l_2$ between levels 11 507 cm^{-1} ($^4F_{3/2}$) and 2110 cm^{-1} ($^4I_{11/2}$) and $4l_1$ between levels 11 423 cm^{-1} ($^4F_{3/2}$) and 2028 cm^{-1} ($^4I_{11/2}$) (Figure 4.2 and Table 4.2). The energy and wavelengths of these transitions are (i) $5l_2$: 9397 cm^{-1} (1064.17 nm) and (ii) $4l_1$: 9395 cm^{-1} (1064.4 nm). The linewidth for room temperatures is equal to 6.5 cm^{-1}, which appreciably exceeds the distance between them (2 cm^{-1}). Therefore, the line contours are strongly blocked by each other, hence forming a total contour, which is only slightly distinguishable from a Lorentzian function. The intensity of the $4l_1$ line is weaker than the $5l_2$ line $(\sigma_{4l_1} \simeq 1.9\times10^{-19}\,\text{cm}^2, \sigma_{4l_2} = 7.1\times10^{-19}\,\text{cm}^2)$ and, consequently, the centre of the total line is closer to the centre of the stronger line corresponding to a wavelength of 1064.15 nm. The effective cross section slightly exceeds the cross section of the stronger line at 8.8×10^{-19} cm^2. At room temperature (300 K), the Maxwell–Boltzmann fraction in the upper Stark sublevel is 0.427 for Nd:YAG. The effective stimulated emission cross section is the spectroscopic cross section multiplied by the occupation of the upper laser level relative to the entire $^4F_{3/2}$ manifold population.

Heating the crystal displaces the line to a longer wavelength. For temperature intervals of ±60°C, which are of interest for practical applications, this displacement can be well described by a linear function with a slope of $d\lambda/dT = 5 \times 10^{-3}$ nm K^{-1} and the line centre is located at 1064.15 nm at room temperature (300 K).

4.2.6 Concentration Quenching of Emission for High Neodymium Doping Levels

For Nd lasers to function effectively, the activator ions should absorb the maximum amount of pump radiation. As the absorption lines of rare-earth ions in crystals are weak, increasing the activator concentration is of interest. However, at an increased activator concentration, we encounter the phenomenon of concentration quenching of the emission, which appears as a short non-exponential fluorescence decay and a fall in the quantum efficiency. In Figure 4.4a the dependence of the $^4F_{3/2}$ level lifetime on the Nd^{3+} concentration in the YAG crystal is shown. Up to 1 at%, the lifetime does not depend on concentration and is about 250 μs; at $C_{\text{Nd}} > 1$ at%, there is a sharp reduction in lifetime. Similarly at $C_{\text{Nd}} = 1$ at%, the maximum emission intensity is observed (Figure 4.4b). This drop at very low concentrations is connected with a reduction in absorbed pump light and at large concentrations with the fall in the quantum efficiency due to non-radiative relaxation. The concentration of neodymium (by at%) in YAG has been limited to 1.0%–1.5%. Higher doping levels tend to shorten the fluorescence lifetime, broaden the linewidth and cause strain in the crystal, resulting in poor optical quality. There is an optimum concentration $C_{\text{Nd}} = 1$ at% corresponding to the minimum threshold for laser generation.

The nature of the concentration quenching of the emission, as previously specified, is connected to the interaction of Nd^{3+} ions with each other. Two closely located Nd^{3+} ions are coupled with each other by a dipole–dipole interaction, which strongly depends on distance ($W \simeq 1/R^{-6}$). A pair of Nd^{3+} ions is capable of creating an additional channel for non-radiative relaxation of Nd^{3+} ions from the $^4F_{3/2}$ level. The performance of an Nd:YAG laser can be somewhat improved by choosing the optimum Nd concentration. As a general guideline, it can be stated that a

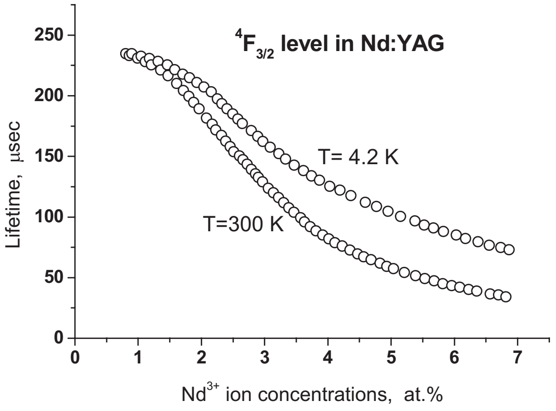

(a)

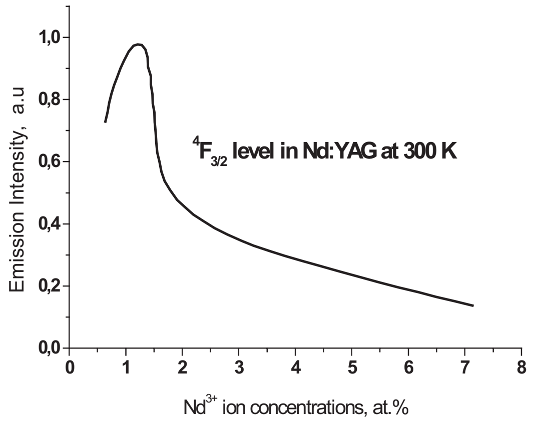

(b)

FIGURE 4.4 (a) Lifetime dependence of $^4F_{3/2}$ level on Nd^{3+} ions concentration in YAG crystals. (b) The concentration quenching of the $^4F_{3/2}$ level emission.

high doping concentration (approximately 1.2 at%) is desirable for Q-switched operation because this will lead to high energy storage. For continuous-wave (cw) operation, a lower doping concentration (0.6–0.8 at%) is usually chosen to obtain good beam quality and the minimum lasing threshold.

The design, fabrication and properties of many lasers based on different Nd^{3+}-doped crystals are described in the papers presented at Advanced Solid State Lasers conferences [2–11]. The performance of a laser-diode-pumped solid-state laser is superior to that of a flashlamp-pumped solid-state laser including such characteristics as high efficiency, high beam quality and high output power stability. It is more difficult to develop a high-power laser with high output parameters. Diode-pumped solid-state lasers operating at high cw power levels are attractive light sources for various applications ranging from material processing to sophisticated fundamental physics experiments.

A design for a diode-pumped cw Nd:YAG laser [12] with an output power of up to 750 W is shown in Figure 4.5. The output power of the laser at 1.06 μm is plotted in Figure 4.6. The design features and performance are summarized in Table 4.3.

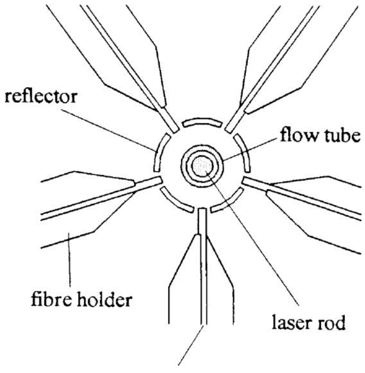

FIGURE 4.5 A diode-pumped Nd:YAG laser.

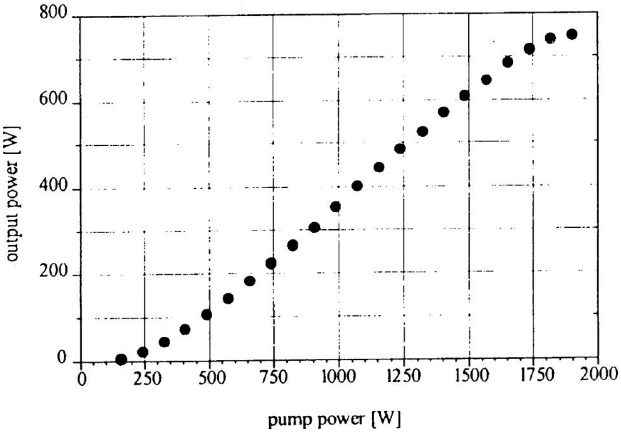

FIGURE 4.6 Output power at 1.06 μm.

TABLE 4.3

Parameters of a Side-Pumped Nd:YAG Laser

Design Feature	Performance Summary
Side pumped 0.5% Nd:YAG rod	Optical-to-optical efficiency = 40% for P_{out} = 750 W
6 mm diameter rod	Efficiency with respect to electrical input = 10%
CW-fibre coupled diode	Output power = 750 W in multi-mode
Power = 10 W, core diameter = 800 μm	Output power = 80 W in TEM$_{00}$ mode
Numerical aperture = 0.20	
Maximum pump power = 2 kW	

A multi-kilowatt, high brightness, diode-pumped laser for precision laser machining [13] is presented schematically in Figure 4.7 and Table 4.4. The laser gain uses a 0.5 × 3.6 × 17 cm Nd:YAG slab. Figure 4.8 shows the output–input energy of a high-power module containing the zigzag Nd:YAG slab pumped by a stacked quasi-cw diode array. The zigzag geometry is already well known to minimize thermal lensing. The Brewster-cut slab allows nearly fulfilled minimizing regions of unextracted gain due to the slab geometry, which means that no coating is required on the crystal end faces. The input faces of the slab are anti-reflection coated and cooled directly with water. An unstable resonator using a hyper-Gaussian variable reflectance mirror enables the laser to run in a single transverse mode with the beam quality limited by a single pass of the gain modules. The resonator magnification was 1.5 and the cavity length was approximately 1 m. Figure 4.9 summarizes the beam quality of the laser as a function of output power.

A high brightness mode-locked Nd:YAG end-pumped zigzag slab laser has been developed with a mode-locked master oscillator and high-power amplifier using a novel architecture [14]. The laser emitted 150 W of linearly polarized power with an average M^2 beam quality of 1.25. A schematic layout of the laser system is shown in Figure 4.10. The gain module uses a 5.6 × 1.7 × 67 mm (height × thickness × length) composite zigzag slab. The central 49 nm length of the slab is 0.2% doped Nd:YAG with 9 mm long, diffusion-bonded, undoped YAG end caps on each side to reduce end effects by confining

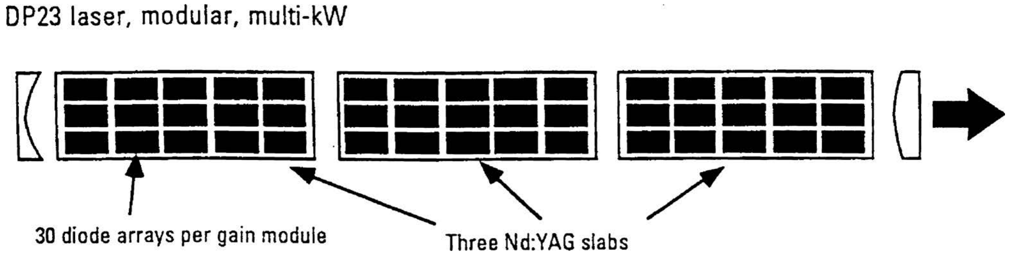
DP23 laser, modular, multi-kW
30 diode arrays per gain module
Three Nd:YAG slabs

FIGURE 4.7 Laser diode pumping and resonator configuration of an Nd:YAG laser.

TABLE 4.4

Multi-kilowatt, High Brightness, Diode-Pumped Nd:YAG Laser

Design Feature	Performance Summary
Pump source = 30 diode laser arrays	Beam quality = 2–4 times diffraction limited
Each array = 1 cm × 2 cm package	Output = 1100 W with beam 2.4 × DL
Package = 16 of 1 cm quasi-cw bar	Output power = 3600 W with beam 3.5 × DL
Peak power per bar = 50 W and duty cycles = 20%	Optical efficiency = 25% for P_{out} = 3600 W Output power = 5000 W in multi-mode operation
Diode pulse duration from 100 μs to 1 ms	Optical efficiency = 35% in multi-mode operation
Average power per array = 4800 W	
Laser gain module = zigzag Nd:YAG slab	
Size = 0.5 × 3.6 × 17 cm	
Active gain volume = 3 × 0.5 × 11 cm	

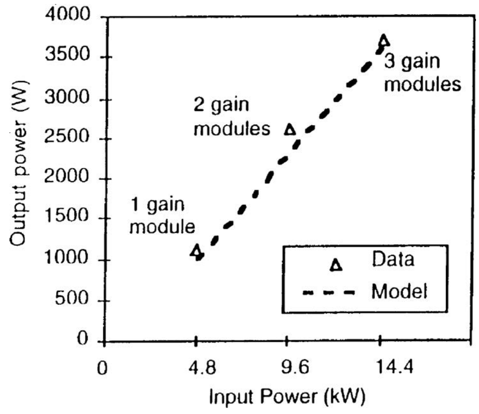

FIGURE 4.8 Laser output as a function of diode power.

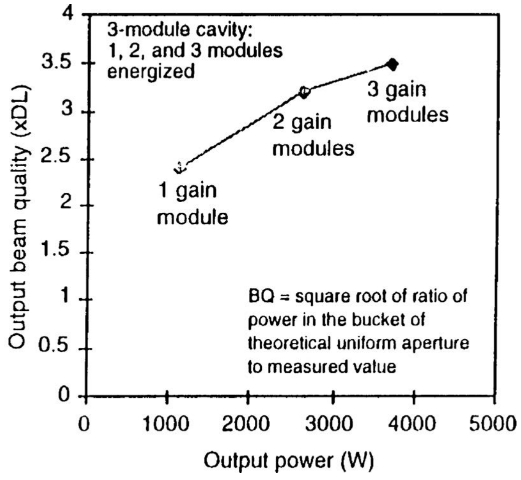

FIGURE 4.9 Laser beam quality as a function of output power.

heat generation to the centre section. The slab ends are cut at 45° and anti-reflection coated for 1064 nm. The total internal reflection (TIR) faces have 3 μm thick, SiO_2 evanescent wave coatings, which allow the faces to be contacted and conduction cooled. Water-cooled copper microchannel coolers are thermally contacted to the slab's TIR faces using a low thermal resistance interface. The slab is pumped from both ends by 805 nm cw diode arrays. Microlenses collimate the fast axis of each diode bar and a lens duct with a 93% throughput concentrates the pump light to a 1.5 × 5 mm area. The diode light is injected through the first TIR footprint, where the evanescent wave coating also acts as an anti-reflection coating at 805 nm. The pump light undergoes a TIR reflection from the 45° input face of the slab and is guided down the length of the slab by the TIR for efficient and uniform end pumping. Approximately 85% of the total pump light is absorbed in the slab. The total diode pump power is 1200 W and the Nd:YAG laser operated with an optical efficiency of 12.5%.

Efficient, cw-pumped TEM_{00} mode infrared beam sources are of interest in both industrial and scientific applications, e.g. optical communications, material processing, gravitational wave detection and so on. Furthermore, cw-pumped TEM_{00} mode of 1064 nm beam sources is in high demand in the information technology field, where frequency-converted ultraviolet or visible high-repetition-rate Q-switched laser beams are used for drilling or trimming the printed circuit boards mounted in mobile phones and computers. Various attractive schemes for TEM_{00} mode cw diode-pumped Nd:YAG lasers have been proposed [15–18]: their highest single-transverse-mode power was less than 100 W with an electrical efficiency of less than 10%.

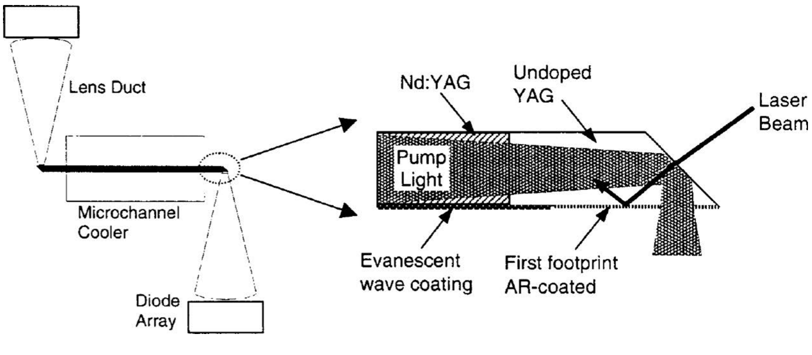

FIGURE 4.10 Schematic diagram of a condition-cooled, end-pumped zigzag slab architecture.

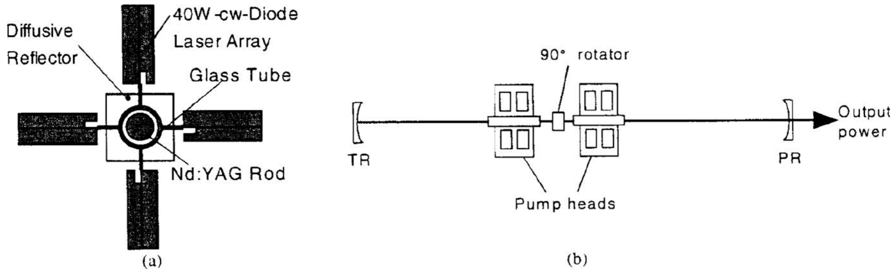

FIGURE 4.11 Schematic diagram of (a) the pump module and (b) the resonator configuration.

CW 153 W output power in the TEM$_{00}$ mode at 1064 nm generated by a laser-diode-pumped Nd:YAG rod laser with an electrical efficiency of 10.9% and beam quality $M^2 = 1.18$ is described in Ref. [19]. Figure 4.11 shows the laser design. A quartz 90° polarization rotator was placed between two uniformly pumped Nd:YAG rods for polarization-dependent bifocusing compensation [20]. The pump heat consisted of two modules. Each module contained four 1 cm long linear cw diode arrays (808 nm wavelength and 40 W average output power). One module was rotated 22.5° from the other around the optical axis to produce a uniform pump-light distribution within the rod cross section. Each Nd:YAG rod (4 mm in diameter and 70 mm in length, with 0.6% Nd doping) was surrounded by a flow tube and a diffusive reflector. In Figure 4.12, a high-order ($M^2 = 40$) laser performance in two mode-multi-transverse and TEM$_{00}$ at 1064 nm operation are compared. In both cases, the transmittance of the output coupler was 20%–25%.

Based on the calculation reported in Ref. [18], the 950-mm long concave–concave resonator was designed to provide stable operation near the highest diode pump power of 700 W. A maximum TEM$_{00}$ output power of 153 W was generated with 682 W total diode pump power and 1409 W electrical input power into the laser diodes, corresponding to an electrical efficiency of 10.9% and an optical-to-optical conversion efficiency of 22.4%.

The use of diode-laser bars as efficient high-power pump sources for end-pumped Nd:YAG solid-state lasers is now well established [21–24]. Slope efficiencies reaching 50%–60% at 1064 nm have been reported for end-pumped Nd:YAG lasers by fibre-coupled diodes or a beam-shaped diode bar, the maximum attainable power was limited by the rod diameter and space for the diode. The side pumping has been favourable for scaling to a high output power, for it is convenient to use a large number of diode arrays and reduce the thermal loading problems, but the slope efficiency is reduced to 25%–40%; the lower slope efficiency is usually caused by imperfect matching between the laser mode volume and the diode pumping volume.

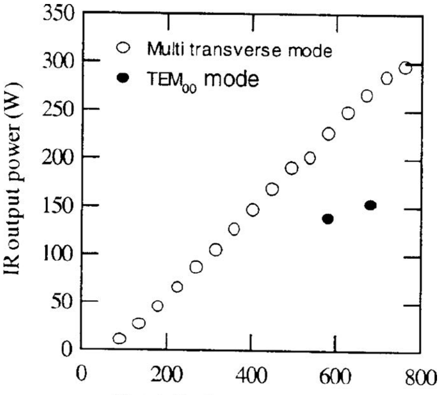

FIGURE 4.12 Multi-transverse and TEM$_{00}$ mode laser performances.

4.3 Polycrystalline Nd:YAG Ceramic Laser

Highly transparent nanocrystalline Nd:$Y_3Al_5O_{12}$ (Nd:YAG) is a new type of inorganic laser media for a new generation of solid-state lasers. A polycrystalline ceramic laser material is an aggregate of crystalline grains, each randomly oriented with respect to neighbouring grains. Polycrystalline Nd:YAG has received much attention since the quality of ceramics Nd:YAG has been improved greatly and highly efficient laser oscillation can be obtained [25–32]. Compared to single-crystal Nd:YAG, the ceramic Nd:YAG laser material has several advantages:

1. its ease of fabrication;
2. it is less expensive;
3. large sizes and high neodymium concentrations can be fabricated;
4. it has a multi-layer and multi-functional ceramic structure and
5. it can be mass produced.

The first solid-state laser based on a ceramic polycrystalline fluoride material (Dy:CaF) was reported in the middle of the 1960s. But only in the last decade have ceramic Nd:YAG laser materials received much attention, after highly transparent nanocrystalline $Y_3Al_5O_{12}$ (YAG) doped with Ln activators, in particular Nd ions, were developed (see, for example, Refs. [25–27]). The first Nd:$Y_3Al_5O_{12}$ (Nd:YAG) ceramic laser was reported in 1995 [28]. High-power and highly efficient lasers with laser-diode pumping were constructed [29–33] from ceramics of Nd:YAG.

The room-temperature absorption spectra of ceramics and single-crystal Nd:YAG are shown in Figure 4.13. For both single-crystal and ceramic Nd:YAG, the absorption peaks are centred at 808.6 nm.

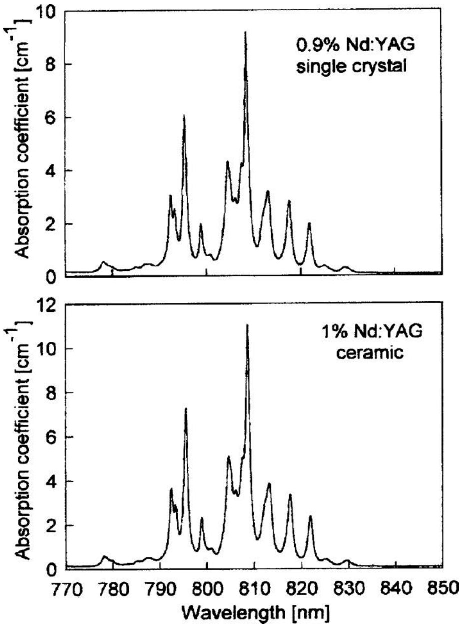

FIGURE 4.13 Absorption spectrum: single crystal 0.9% Nd:YAG and ceramic 1% Nd:YAG.

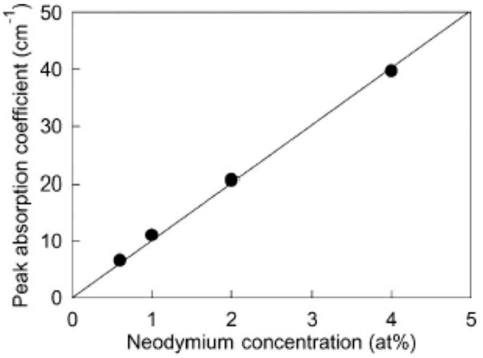

FIGURE 4.14 Peak absorption coefficient of ceramics Nd:YAG around 808 nm *versus* neodymium concentration.

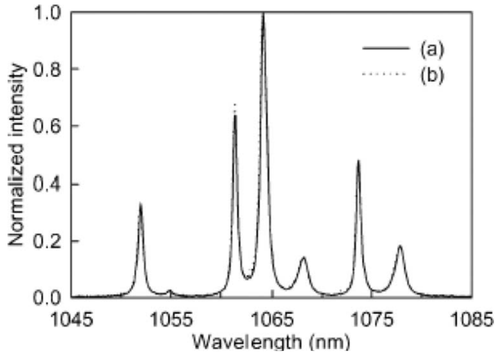

FIGURE 4.15 Fluorescence spectrum: (a) ceramic 1% Nd:YAG and (b) single crystal 0.9% Nd:YAG.

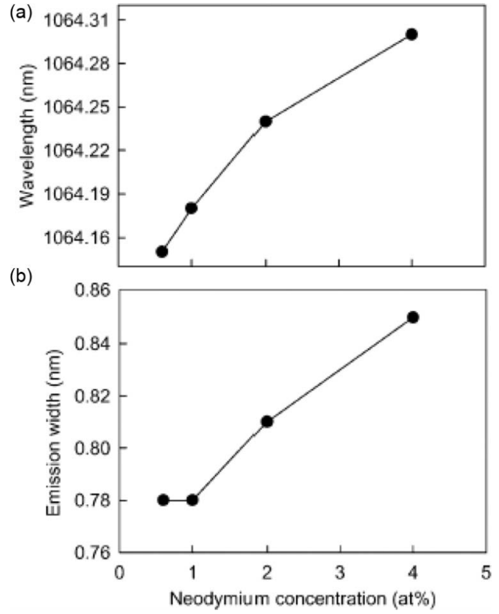

FIGURE 4.16 (a) Fluorescence redshift and (b) FWHM at 1064 nm *versus* neodymium concentration.

The FWHMs (full widths at half maximum) of the absorption coefficients are both 1.04 nm. Room-temperature absorption spectra for 0.6%, 2% and 4% ceramics Nd:YAG have also been measured. Not much difference has been observed except that the absorption coefficient increases with an increase in Nd^{3+} concentration. Figure 4.14 shows the peak absorption coefficient of ceramic Nd:YAG around 808.6 nm *versus* neodymium concentration. From this figure, one can see that the relationship between the peak absorption coefficient and neodymium concentration is linear.

Figure 4.15 shows the room-temperature fluorescence spectrum for the $^4F_{3/2} \rightarrow {}^4I_{11/2}$ transition of a 1% Nd:YAG single crystal and ceramic, respectively. To have a clear comparison, the fluorescence spectra for the single crystal and ceramic were normalized and put together. From this figure, these two spectra are almost identical. The main emission peak is at 1064.18 nm. The FWHM is 0.78 nm.

Emission spectra for 0.6%, 2% and 4% Nd:YAG ceramics have also been measured [29]. A small wavelength redshift has been observed with increasing concentration because of a slight change in the crystal field. Figure 4.16a shows the main fluorescence peak spectra at 1064 nm for 0.6%, 1%, 2% and 4% Nd:YAG ceramics, respectively.

The four emission peaks are centred at 1064.15, 1064.18, 1064.24 and 1064.30 nm for 0.6%, 1%, 2% and 4% Nd:YAG ceramics, respectively. The redshift from 0.6% to 4% Nd:YAG ceramics is 0.12 nm. Because of the fluorescence quenching effect, the fluorescence emission linewidth at 1064 nm is also slightly broadened with concentration increases greater than 1%. Figure 4.16b shows the FWHM of the 1064 nm fluorescence peak. The FWHMs are 0.78, 0.78, 0.81 and 0.85 nm for 0.6%, 1%, 2% and 4% Nd:YAG ceramics, respectively. The linewidths for 0.6% and 1% Nd:YAG ceramics are identical. This means that the fluorescence quenching effect is very weak for neodymium concentrations less than 1%, which is similar to that of a single crystal.

Figure 4.17 shows the fluorescence lifetime of single crystal and Nd:YAG ceramics *versus* neodymium concentration.

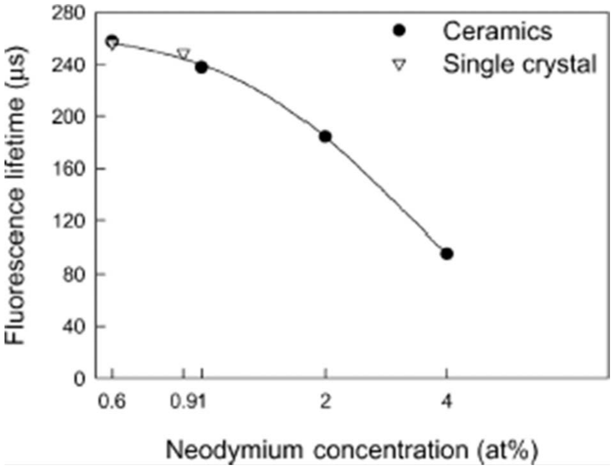

FIGURE 4.17 Fluorescence lifetime of ceramic and single-crystal Nd:YAG *versus* neodymium concentration. The full curve is the *fitted curve* for the ceramic fluorescence lifetime.

The fluorescence lifetime for a single-crystal 0.6% Nd:YAG (procured from Litton-Airtron Inc.) and that for a single-crystal 0.9% Nd:YAG are 256.3 and 248.6 µs, respectively.

Fluorescence lifetimes of 257.6, 237.6, 184.2 and 95.6 µs have been measured, respectively, for 0.6%, 1%, 2% and 4% ceramics Nd:YAG. These data agree well with the results in Ref. [1]. The fluorescence lifetime decreases dramatically when the neodymium concentration exceeds 1%. The fluorescence lifetimes for the 0.6% doped single crystal and the ceramics are almost identical (only 1.3 µs difference). The fluorescence lifetime difference between 0.9% Nd:YAG single crystal and 1% Nd:YAG ceramic is 11 µs. We could predict that for the same concentration for single-crystal and ceramic Nd:YAG, for example, a concentration of 0.9%, the lifetime difference should be less than 11 µs. From the fitted curve for the ceramic fluorescence lifetimes, the lifetime for the 0.9% Nd:YAG ceramic is 244.2 µs, which is only 4.4 µs different from that of the single-crystal 0.9% Nd:YAG [29].

A 1.46 kW Nd:YAG ceramic laser was demonstrated by the Toshiba Corporation, Japan [34]. The optical-to-optical conversion efficiency is 42%. The dependence of output power on pump power is shown in Figure 4.18. The data on the single-crystal Nd:YAG laser are also shown on the same graph to allow a comparison. An output power of 1.72 kW was obtained for the single-crystal laser, with an optical-to-optical conversion efficiency of 49%. Although the laser efficiency of the ceramic Nd:YAG laser is still less than that of the single-crystal Nd:YAG laser, it shows that it could possibly be used in industry in the near future.

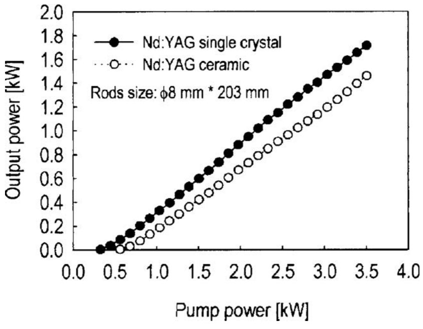

FIGURE 4.18 Laser outputs of ceramic and single-crystal Nd:YAG lasers as a function of pump power.

Nanocrystalline Nd:YAG ceramics, as the new generation of laser materials, will before long become a very good alternative to the widely used Nd:YAG single crystals for different types of solid-state lasers, including multi-kW industrial lasers.

4.4 Nd:YLF Laser Crystal

Nd:YLF is a good candidate for certain specialized applications because the output is polarized and the crystal exhibits a lower thermal birefringence [35,36]. Nd:YLF has a higher energy storage capability (due to its lower gain coefficient) compared to Nd:YAG and its output wavelength matches that of phosphate Nd:glass; therefore mode-locked and Q-switched Nd:YLF lasers [37] have become the standard oscillators for the large glass lasers employed in fusion research.

Some of the important physical properties of Nd:YLF are listed in Table 4.1, together with its optical and laser parameters.

Nd:YLF is grown utilizing a modified CZ technique. The as-grown crystals are then processed into laser rods or slabs.

The favourable features of Nd:YLF are:

- a large product of the stimulated emission cross section and lifetime for a low cw threshold,
- high-power, low-beam-divergence, efficient single-mode operation,
- high average power Q-switched operation at a moderate repetition rate,
- linearly polarized resonators for Q-switching and frequency doubling,
- potential uniform mode for large diameter rods or slabs and
- the 1053 nm output matches the gain curves of Nd:glass and performs well as an oscillator and pre-amplifier for this type of laser.

4.5 Nd:Vanadate Laser Crystals

For small and efficient diode-laser-pumped solid-state laser systems, it is desirable to decrease the requirement for temperature control of the diode-laser pump and to increase the tolerance in the wavelength selection. Therefore, it is necessary that the laser material features a high absorption coefficient and a large absorption linewidth. Disordered crystals, for instance, offer broad absorption lines but have the disadvantage of low cross sections due to the inhomogeneous broadening of the transitions. Therefore, the advantage of low-temperature sensitivity of the pumping process and the corresponding increased tolerance in pump-wavelength selection is correlated in such crystals with decreased inhomogeneous emission cross sections.

In vanadate crystals like Nd:YVO$_4$ [38–41] and Nd:GdVO$_4$ [42], both broad homogeneous absorption lines and homogeneous emission lines feature high peak cross sections (Table 4.5). As we know, the accidental degeneracy of the $^4F_{3/2}$ level in GdVO$_4$ enhances the emission cross sections because the spectra condense into fewer emission lines [43].

4.5.1 Preparation of the Nd:YVO$_4$ and Nd:GdVO$_4$ Crystals

Laser quality crystals of vanadate doped with neodymium can be grown by the CZ technique. Yttrium vanadate and gadolinium vanadate belong to the group of oxide compounds crystallizing in a ZrSiO$_4$ structure with the tetragonal

TABLE 4.5

Comparison of Nd: YVO$_4$ and Nd: GdVO$_4$ [44–46]

General Information		
Composition of 1 at% Nd-doped crystal	$Y_{0.99}Nd_{0.01}VO_4$	$Gd_{0.99}Nd_{0.01}VO_4$
Concentration (for 1 at% Nd) (×10^{20} Nd atom cm^{-3})	1.252	1.25
Nd doping limit (%)	3	3
Nd segregation coefficient	0.35	0.9
Crystal structure	Tetragonal	Tetragonal
Lattice parameters (Å)	$a = 7.12$	$c = 7.21$
	$a = 6.29$	$c = 6.35$
Space group	I4$_1$/*amd*	I4$_1$/*amd*
Crystal type	Positive uniaxial	Positive uniaxial
Structure type	Zircon	Zircon
Optical Properties		
Indices of refraction (n_e, n_o):	$n_e = 2.168$ at 1064 nm	$n_e = 2.192$ at 1063 nm
	$n_o = 1.958$ at 1064 nm	$n_o = 1.972$ at 1063 nm
Birefringence ($n_e - n_o$):	+0.21	+0.24
Transparency range (μm)	0.4–5.0 μm	0.4–5.0 μm
Optical activity:	None	None
Absorption coefficient (cm^{-1})		74 ($E \parallel c$-axis,
(*a*-cut at 808 nm)	20 (0.7 at%)	1.3 at% Nd)
	31 (1.1 wt%)	10 cm^{-1} ($E \perp c$-axis,
	54 (1.78 wt%)	1.3 at% Nd)
	72 (2.02 wt%)	
	110 (3.0 at%)	
Thermal Properties		
Melting point (°C)	1810	1800
Thermal conductivity (W m^{-1}K^{-1})	5.2 (∥ to *c*-axis) [47]	12.3 (∥ to *c*-axis)
Undoped crystal at 300 K	5.1 (⊥ to *c*-axis) [47]	9.9 (∥ to *a*-axis)
	9.6 (∥ to *a*-axis)	
Thermal conductivity		11.7 (along ⟨011⟩
Nd-doped crystal at 300 K	-	1.3 at% Nd)
		9.63 (∥ to *a*-axis, 1.3 at% Nd)
Thermal expansion coefficient (×10^{-6} K^{-1})	4.43(*a*-axis)	1 (*a*-axis)
	11.37 (*c*-axis)	6.3 (*c*-axis)
Refractive index change (×10^{-6} K^{-1})		
(dn_o/dT)	(8.5 ± 0.9)	4.7±
(dn_e/dT)	2.9	
Laser Properties		
Emission cross sections	15.6 at 1064 nm	7.6 at 1064 nm
π-polarization (×10^{-19} cm^2)	7.61 at 1342 nm	1.8 at 1342 nm
Lasing wavelength (nm)	1064.3	1062.9
Optical-to-optical efficiency (%)	>60	65
Polarized laser emission	Yes ($E \parallel c$), π-polarization	Yes ($E \parallel c$), π-polarization
Intrinsic loss at laser wavelength (cm^{-1})	0.04	0.01
Laser linewidth (nm)	1.3 (at 1.06 μm)	1.25 (at 1.06 μm)

(*Continued*)

TABLE 4.5 (*Continued*)

Comparison of Nd: YVO_4 and Nd: $GdVO_4$ [44–46]

		2.15 (at 1.34 µm)
Excited-state absorption	None	None
Spectroscopic Data		
Absorption bandwidth (FWHM) (nm)	748–760 803–813 877–881	748–760 803–813 877–881
FW75% (wavelength range where at least 75% of diode light is absorbed) (nm)	15.7 (1.1 at% Nd)	13.5 (1.0 at% Nd)
Branching ratios (experimental)	$\beta = 0.422$ at 0.9 µm $\beta = 0.464$ at 1.06 µm $\beta = 0.112$ at 1.34 µm	-
Metastable splitting at 300 K (cm^{-1})	14	~0
Fluorescence linewidth (cm^{-1})	7	6
Radiative lifetime (µs)	115	110
Fluorescence lifetime (µs)	100 (0.87 wt% Nd) 90 (1.1 wt% Nd) 50 (1.8 wt%Nd) 47 (2.2 wt%Nd)	90 (1.2 at% Nd) 40 (4 at% Nd) 20 (6.9 at% Nd)
Mechanical Properties		
Hardness (Mohs)	5.5 ± 0.5	5
Knoop hardness (kg mm^{-2})	480	470
Density (g cm^{-3})	4.22	5.47

space group $I4_1/amd$. The fourfold symmetry axis is the crystallographic *c*-axis. Perpendicular to this axis are the two undistinguishable *a*- and *b*-axes. The rare-earth ion, which is surrounded by eight oxygen atoms, has site symmetry 42m.

In comparison with YVO_4, the replacement of Y^{3+} ions by the larger Gd^{3+} ions increases the distances between the dodecahedral lattice sites. This decreases the ion–ion interactions between neighbouring ions and also makes the segregation coefficient of Nd^{3+} ions closer to unity.

The YVO_4 and Nd:$GdVO_4$ crystals are grown by the CZ method along the *c*-axis or *a*-axis. As growth parameters it used a pulling rate of 1–2 mm h^{-1}, a rotation rate of 10–30 rev min^{-1} and an atmosphere of nitrogen containing 2% oxygen by volume. The crystals were then annealed at 1200°C for 10 h in air. The melting point of Nd:$GdVO_4$ was measured with an optical pyrometer to be 1800°C ± 20°C.

4.5.2 Absorption and Emission of Nd:$GdVO_4$

The uniaxial crystal Nd:$GdVO_4$ shows strong polarization-dependent absorption transitions due to the anisotropic crystal field. At 808.4 nm, the peak absorption coefficient in π-polarization is 78 cm^{-1} for a 1.2% neodymium doping level, resulting in an effective absorption cross section of 5.2×10^{-19} cm^2 [42,43]. For σ-polarization, the absorption coefficient is only 17 cm^{-1}. The absorption spectra as a function of wavelength for both polarizations are shown in Figure 4.19.

The half-width of the absorption at 808.4 nm is 1.6 nm. At the same neodymium concentration, the absorption coefficient of Nd:$GdVO_4$ is seven times higher and the transition line is 80% broader in comparison with Nd:YAG.

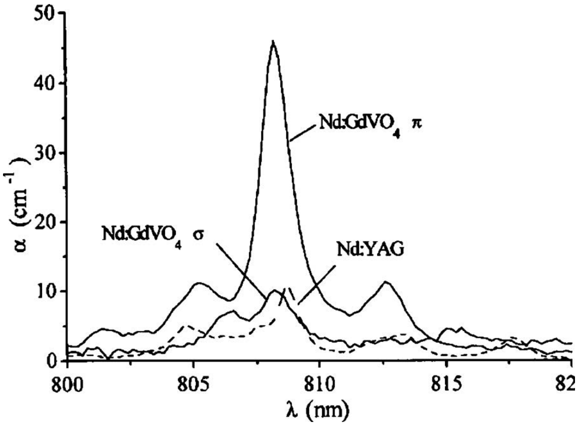

FIGURE 4.19 Absorption spectra for Nd:$GdVO_4$ in π- and σ-polarization. The absorption spectrum of Nd:YAG is shown for comparison.

Figure 4.20 shows an enlarged plot of the $^4F_{3/2} \rightarrow {}^4I_{11/2}$ in π-polarization in comparison with a corresponding spectrum of Nd:YAG. The total Stark splitting of the $^4F_{3/2}$ multiplet is about one-third of that in Nd:YAG. In addition, the number of transition lines is reduced in Nd:$GdVO_4$. Transition pairs, resulting from the $^4F_{3/2}$ splitting (indicated by arrows in the Nd:YAG spectrum), are not assignable in the spectrum of Nd:$GdVO_4$. This leads to the assumption that the upper laser level $^4F_{3/2}$ is completely degenerate, resulting in a reduction of transition lines by a factor of two, which could be verified by the measurements at 12 K. For completeness the detected energy levels derived from corresponding 77 K spectra of Nd:$GdVO_4$ are listed in Table 4.6.

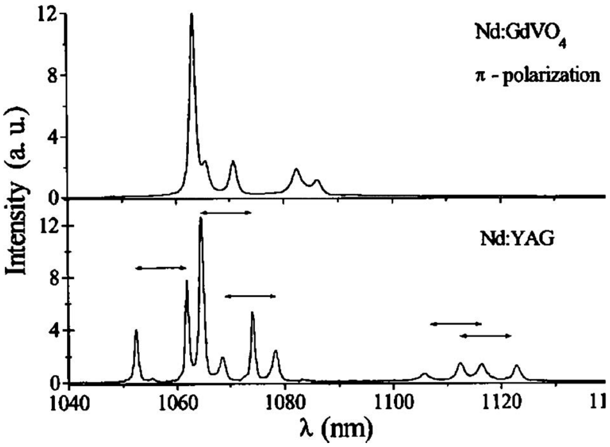

FIGURE 4.20 Fluorescence spectra of the $^4F_{3/2} \rightarrow {}^4I_{11/2}$ in π-polarization in comparison with Nd:YAG at 300 K.

TABLE 4.6

Splitting of the ^4I and ^4F Terms of Nd^{3+} in $GdVO_4$ at 77 K

Multiplets	Energy (cm^{-1})
$^4I_{9/2}$	0, 107, 173, 267, 409
$^4I_{11/2}$	1967, 1987, 2035, 2137, 2165
$^4I_{13/2}$	3915, 3932, 3970, 4022, 4075, 4146
$^4I_{15/2}$	5839, 5900, 5914, 5933, 6055, 6235, 6294
$^4I_{3/2}$	11 375 (degenerate)
$^4F_{5/2}$	12 372, 12 403, 12 413

We do not know other laser crystals with $^4F_{3/2}$ degeneracy. Nd:YVO$_4$, which is a similar compound, has a $^4F_{3/2}$ splitting of 18 cm^{-1}. Therefore, the effective emission cross section, in the case of Nd:GdVO$_4$, is identical to the atomic emission cross section. This is illustrated in Figure 4.21, which shows the splitting of the materials Nd:YAG, Nd:YVO$_4$ and Nd:GdVO$_4$, by the transition lines of the $^4F_{3/2}$ level, into a single level of the $^4F_{3/2}$ multiplet.

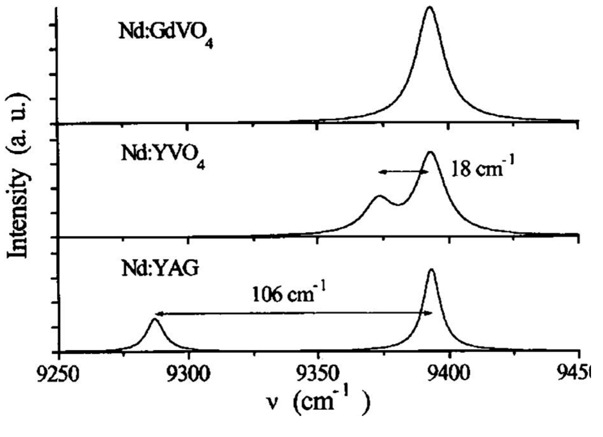

FIGURE 4.21 Merging of transition lines for the three crystals—Nd:YAG, Nd:YVO$_4$ and Nd:GdVO$_4$ at 300 K. A splitting of the $^4I_{3/2}$ level in Nd:GdVO$_4$ could not be detected.

4.5.3 Nd:YVO$_4$ and Nd:GdVO$_4$ Lasers

Neodymium-doped gadolinium vanadate (Nd:GdVO$_4$) is an attractive and very efficient laser material for diode pumping and has been receiving considerable attention [42–46]. Compared with Nd:YAG crystal, Nd:GdVO$_4$ has a sevenfold larger absorption cross section (5.2×10^{-19}cm^2, $E \parallel c$) and a threefold larger emission cross section at 1.06 μm (7.6×10^{-19}cm^2, $E \parallel c$). More importantly, the Nd:GdVO$_4$ thermal conductivity (12.3 W m^{-1} K^{-1}, direction ‖ to the c-axis) is very good and comparable to that of YAG. Such unique spectroscopic and thermal properties make the Nd:GdVO$_4$ crystal a promising substitute for Nd:YAG diode-pumped compact solid-state lasers [48–50].

The laser output power [48] of an Nd:GdVO$_4$ at 1.06 mm was 14.3 W at the highest pump power of 26 W, the light–light conversion efficiency was 54.8%, the pumping threshold was 0.32 W and the slope efficiency was 62%. Figure 4.22 gives a schematic diagram of the laser and Figure 4.23 shows its input–output power.

Passively Q-switched laser output of an Nd:GdVO$_4$ crystal at 1.06 μm has been demonstrated [49].

An actively acousto-optical Q-switched diode-pumping Nd:GdVO$_4$ laser (Figure 4.24) is described in Ref. [48]. The average Q-switched (60 kHz) laser output power at 1.06 μm was 7.3 W at a pump power of 19 W, the pumping threshold was 1.3 W, the optical–optical conversion efficiency was 38.1% and the average slope efficiency was 42.9%.

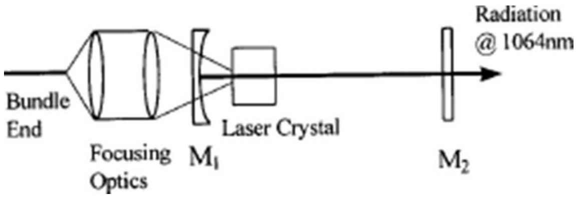

FIGURE 4.22 Schematic diagram of a diode-pumped Nd:GdVO$_4$ crystal lasing at 1063 nm. M$_1$, M$_2$, mirrors.

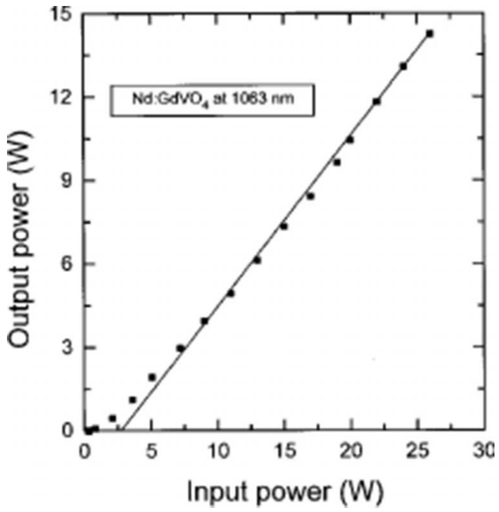

FIGURE 4.23 Output power of an Nd:GdVO$_4$ crystal at 1063 nm.

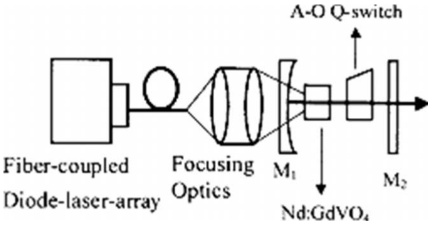

FIGURE 4.24 Schematic diagram of an end-pumped Q-switched 1.06 μm Nd:GdVO$_4$ laser. A–O, acousto-optical; M$_1$, M$_2$, mirrors.

TABLE 4.7

TEM$_{00}$ Laser Properties of Q-switched Operation [50]

		Pulse length (ns)		Efficiency (%)	
Crystal	**Output Power (W)**	**10 kHz**	**20 kHz**	**Real**	**Optical**
Nd:YVO$_4$	9	5	8	36	53
Nd:YAG	8.5	8	12	32	50
Nd:YLF	8	11	16	34	47

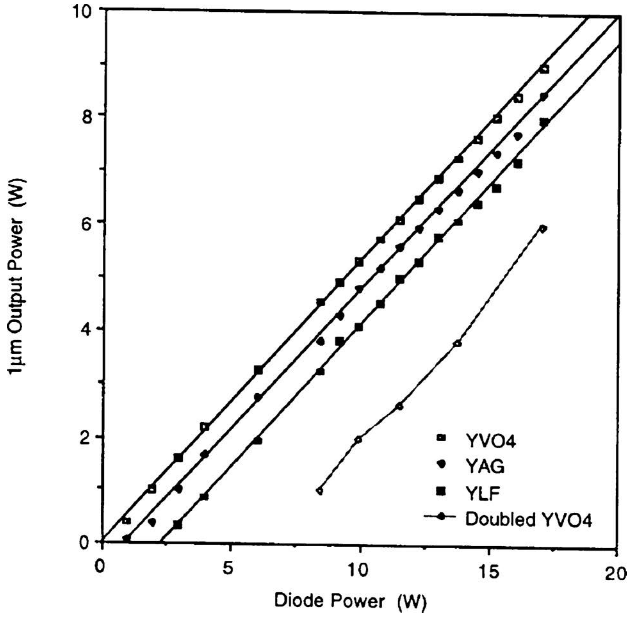

FIGURE 4.26 Performance characteristics of an actively Q-switched end-pumped laser for a short cavity design.

Some important parameters of an Nd:GdVO$_4$ crystal have been calculated or estimated [48]: dn/dT = 4.7×10^{-6} K^{-1}, material constant = 3.5×10^{-6}m^{2}s^{-1}, FOM of the thermal stress resistance > 5.73 W cm^{-1} and power per unit length at the stress limit = 51.6 W cm^{-1}.

New-generation diode pump sources allow end-pumped cw lasers to achieve gain levels previously reached only in quasi-cw diode-pumped systems. A very effective cw pumping oscillator layout is shown in Figure 4.25 [50]. The short cavity lengths and high pump intensity ensured very short pulse Q-switched operation (Table 4.7). The end-pumped Nd:YVO$_4$ (or Nd:YAG or Nd:YLF) lasers with single-pass small-signal gain G = 10 produce Q-switched output at the 16 W level in 6 ns pulses at 20Hz (Table 4.7).

One of the major advantages of Nd:YVO$_4$ (Nd:GdVO$_4$) is its ability to retain short pulse output even at a very high peak rate frequency (prf). The Nd:YVO$_4$ demonstrated sub-20 ns pulses at 100kHz prf. However, the usual laser scheme based on Nd:YVO$_4$ and Nd:GdVO$_4$ performs poorly at lower prf; while Nd:YAG and Nd:YLF perform well at 10kHz, the Nd:YVO$_4$ drops in output power by 50% compared to operation at 100kHz. The use of short-cavity laser design on Figure 4.26 allows highly efficient Q-switched operation with a very low threshold at low and high prf to be obtained.

Now many companies in the world produce commercial low and middle-power lasers based on vanadate crystals. A≈diode-pumped laser with two Nd:YVO$_4$ rods and four diode bars produces an output power of about 35 W at 1064nm, 20 W at 532nm and 8 W at 355 nm—all with a beam quality $M^2 < 1.3$ (Spectra-Physics, Tucson, AZ, USA).

Diode-pumped Nd:GdVO$_4$ lasers at 1.06 μm have demonstrated an output power of ~25 W with a slope efficiency of 60% with beam quality $M^2 = 1.55$. In such lasers, vanadate crystals about 3 × 3 × 4mm in size and cut with the *a*-axis parallel to the optical axis of the laser system are used.

A diode-pumped quasi-three-level Nd^{3+} laser operating on $^4F_{3/2} \rightarrow {}^4I_{9/2}$ has been realized for Nd:YAG, Nd:YAlO$_3$, Nd:YVO$_4$ and Nd:GdVO$_4$ crystals (Table 4.8). The three-level scheme for Nd^{3+} lasing in a GdVO$_4$ host is shown in Figure 4.27.

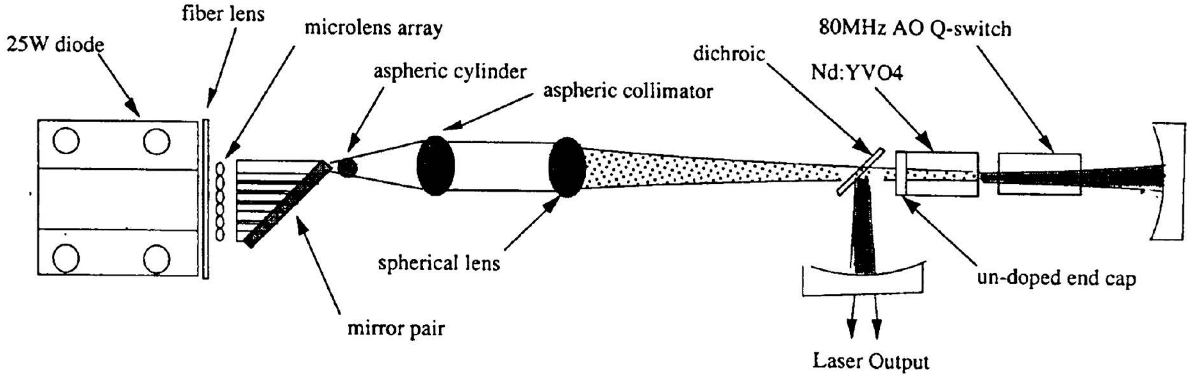

FIGURE 4.25 A high-gain end-pumped Nd:YVO$_4$ laser.

TABLE 4.8

Performance of cw Diode-Pumped Quasi-Three-Level Lasers

Crystal	Lasing Wavelength (nm)	Output Power (mW)	Slope Efficiency (%)	Reference
Nd:GdVO$_4$	912	2900	48	[46]
Nd:YVO$_4$	915	98	9	[46]
Ng:YAG	946	7400	32	[51]
Nd:YAlO$_3$	930	800	40	[52]

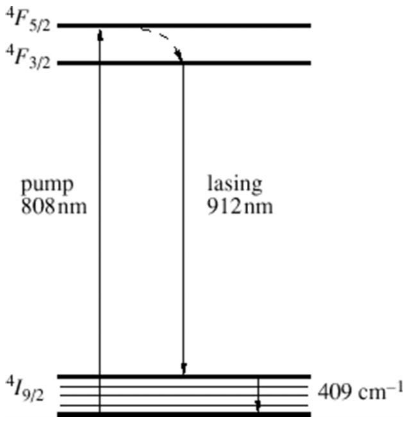

FIGURE 4.27 Diagram of the levels and energy transformation in Nd:GdVO$_4$ crystals during lasing at 912nm upon the $^4F_{3/2} \rightarrow {}^4I_{9/2}$ transition.

4.6 Nd:Cr:GSGG and Nd:Cr:YSGG Crystals

Soon after the invention of the Nd:YAG laser, attempts were made to increase the efficiency in transferring radiation from the pump source to the laser crystal by utilizing a second dopant called a 'sensitizer'. A particularly attractive sensitizer is Cr^{3+} [53,54] because the broad absorption bands of chromium can efficiently absorb light throughout the whole visible region of the spectrum (Figure 4.28). The concept of improving efficiency by co-doping an Nd:laser crystal with Cr^{3+} ions is based on transferring excitation [55,56], absorbed by the broad Cr^{3+} absorption bands, over to the Nd^{3+} ions. No improvement was achieved with the host crystal YAG because all the Cr^{3+} excitation was deposited in the ^{2}E level and the spin-forbidden nature of the $^2E \rightarrow {}^4A_2$ transition resulted in an inefficient transfer process.

However, measurements at the author's laboratory have shown that nearly 100% transfer efficiency could be achieved in the co-doped garnet crystal $Gd_3Sc_2Ga_3O_{12}$ (GSGG) and $Y_3Sc_2Ga_3O_{12}$ (YSGG). Unlike YAG, a large percentage of the Cr^{3+} excitation in GSGG and YSGG appears in the $^4T_2$ state and non-radiative transfer to Nd^{3+} ions can occur via the $^4T_2 \rightarrow {}^4A_2$ transition, which is spin-allowed and has a good spectral overlap with the Nd^{3+} levels (Figure 4.29).

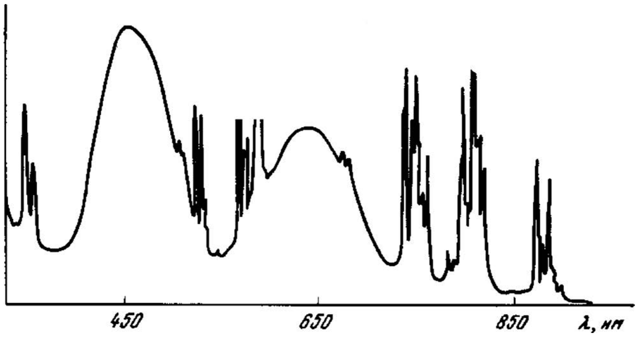

FIGURE 4.28 Absorption spectra of an Nd:Cr:GSGG crystal.

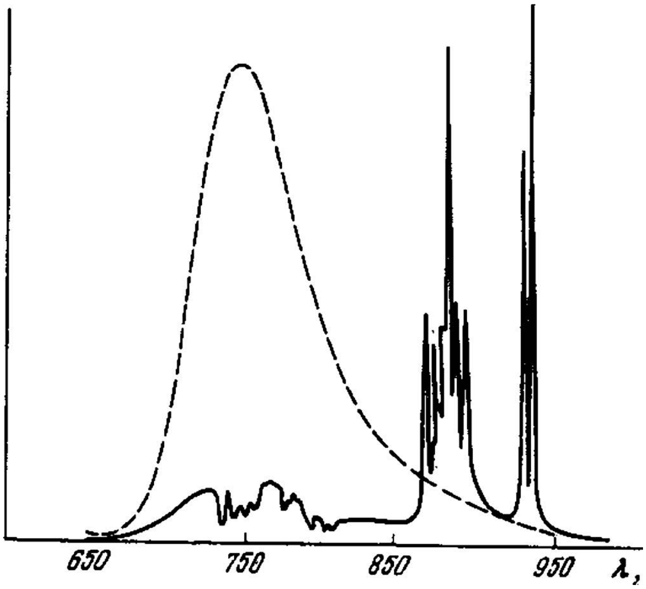

FIGURE 4.29 Emission spectra of Cr:GSGG crystals (dotted line) and emission spectra of Nd:Cr:GSGG crystal (full) at temperature 300 K.

Experiments performed in some studies [53–56] showed, with the flashlamp-pumped operation, nearly a factor-of-three improvement in slope efficiency for the doubly doped garnet compared to an Nd:YAG crystal. For an Nd:Cr:YSGG laser rod 6.3mm in diameter and 100mm in length, we have achieved an output energy of 2J, electrical efficiency of 7.7% and a slope efficiency of 8.8%, which is the highest slope efficiency yet reported for flashlamp-pumped solid-state lasers. It was found that the pumping efficiency improvement is not a strong function of the Cr concentration for the range 1–2 × 10^{20}cm^{-3}. The higher pump efficiency of Nd:Cr:GSGG and Nd:Cr:YSGG does not automatically translate into better system performance because Nd:Cr:GSGG does exhibit much stronger thermal focusing and stress birefringence, compared to Nd:YAG (see Tables 4.1 and 4.9). The absorption efficiency and heat deposition rate for the Cr:Nd:GSGG rod are almost three times those of Nd:YAG, a consequence of the broad red and blue absorption bands of the Cr^{3+} sensitizer. As a consequence, the thermal focusing power as a function of lamp input power has been reported to be several times larger in Cr:Nd:GSGG or Cr:Nd:YSGG than in Nd:YAG. Therefore, if beam brightness is the criterion, rather than output energy, some of the advantages of Cr:Nd:GSGG and Cr:Nd:YSGG are offset, particularly at medium average powers. Now Nd:Cr:GSGG and Nd:Cr:YSGG laser rods are widely used in compact military range-finders. Measurements have shown that under single-shot and low-repetition-rate operation, a factor of two higher beam brightness is achieved in a GSGG or YSGG system compared to a YAG system.

Active elements manufactured from Nd:Cr:GSGG and Nd:Cr:YSGG crystals are optimum materials for low- and medium-power flashlamp-pumped lasers with low repetition rates of up to several cycles per second. The advantages of YSGG and GSGG crystals compared with YAG crystals are lost when large-size elements are used because of the worse thermal characteristics of Nd:Cr:GSGG and Nd:Cr:YSGG crystals [57,58].

High-optical-quality Nd:Cr:GSGG and Nd:Cr:YSGG crystals up to 13 cm in diameter and 23 cm long are grown commercially in Russia and the USA by the CZ technique [57].

4.7 Nd:LSB Crystal

Neodymium-doped lanthanum scandium borate (Nd:LaSc$_3$(BO$_3$)$_4$ or Nd:LSB) is one of the most efficient laser crystals for diode pumping as well as for flashlamp pumping [58,59]. It is a new laser crystal with improved spectral properties stipulated by the possibility of the introduction of high Nd^{3+} concentrations (up to 50 at%) into the crystalline host.

These properties make the Nd:LSB crystal indispensable in the design of low-power (up to 150 mW at 531 nm), highly efficient compact diode-pumped solid-state laser systems because they allow the effect of temperature drift of the wavelength of the pumping laser diode to be reduced and the stability of the radiated laser frequency to be increased because of the wide absorption line of Nd ions at the 808 nm wavelength. The maximum absorption and radiation cross section are similar to those of Nd:YAG but the bands are five times wider. The absorption coefficient of 10 at% Nd^{3+}:LSB crystals is three times higher than that in Nd:YAG crystals. This allows Nd:LSB active elements to be used in end-pumped microchip configurations just about 1 mm long. The optical slope efficiency of the Nd:LSB laser at 1062 nm is about ~67%.

Investigation of Nd:LSB crystals shows a high efficiency for the use of these crystals for intracavity frequency doubling with potassium titanyl phosphate crystals. The corresponding optical efficiency is greater than 25%, and the efficiency of conversion of the basic frequency into the second harmonic is 55% [60–62]. The comparative spectroscopic data of Nd:LSB (at room temperature) are given in Table 4.9.

4.8 Nd^{3+}-Doped Glass

There are several characteristics that distinguish Nd:glass from Nd-doped crystals [63–65]. A wide variety of Nd-doped laser glasses depending on the composition of the glass is known. Many compositions of oxide, fluoride and sulphide glasses have been developed. The commercial Nd:glasses are the oxide glasses, silicate and phosphate glasses (i.e. SiO$_2$ and P$_2$O$_5$-based glasses). Table 4.10 lists some important spectroscopic, optical and thermal properties of typical silicate and phosphate glasses.

TABLE 4.9

Comparison of Nd:Cr:GSSG, Nd:Cr:YSSG and Nd:LSB Crystals

Crystal	**Cr:Nd:GSSG**	**Cr:Nd:YSGG**	**Nd:LSB**
Crystal class	Cubic	Cubic	Monoclinic
Space group	I_{a3d}	I_{a3d}	C2/*c*
Doping limit (at% or atom cm^{-3})	Cr: (1–2)10^{20}	Cr: (1–2)10^{20}	5–50 at%
	Nd: (1–3)10^{20}	Nd: (1–3)10^{20}	
Lattice parameters (Å)	12.57	12.42	$a = 9.778$
			$c = 7.929$
Melting point (°C)	1825	1850	1600
Density (undoped) (g cm^{-3})	6.50	5.2	3.8
Hardness (Mohs)	~7	>7	7
Thermal conductivity at 300 K (W m^{-1} K^{-1})	6.0	7.9	2.8
Thermal conductivity of undoped crystal at 300 K (W m^{-1} K^{-1})	6.4	8.3	3.2
Refractive index at laser wavelength	1.943 (1060 nm)	1.926 (1060 nm)	$n_x = 1.828$
	1.955 (750 nm)		$n_y = 1.827$
			$n_z = 1.828$
Lasing wavelength (nm)	1061.2	1058.5	1800
			1348
			1062
			905
Linewidth (nm)	1.8	1.6	4
Radiative lifetime (μs)	280	270	118 (10 at% Nd)
Effective laser cross section (10^{-19} cm^2)	1.5	1.5	1.3
Diode pump peak wavelength (nm)	808	808	808
Thermal change of indices at 1064 nm (10^{-16} K^{-1})	10.9	12.3	-
Linear expansion coefficient (10^{-6} K^{-1})	7.4	8.3	-

TABLE 4.10

Optical, Physical and Spectroscopic Properties of Nd-Doped Glasses

	Glass Type					
Properties	**Silicate NS-0835 (Illinos)**	**Silicate Q-246 (Kiger)**	**Silicate LSG-91H (Hoya)**	**Phosphate LHG-5 (Hoya)**	**Phosphate LHG-6 (Hoya)**	**Silicate LG-630 (Schott)**
Nd^{3+} concentration (10^{20} cm^{-3})	4.6	4.5	3.04	3.174	3.397	2.8
Peak wavelength (nm)	1060	1062	1062	1054	1054	1061
Cross section ($\times 10^{20}$)	2.8	2.9	2.7	4.1	4.2	2.7
Fluorescent lifetime (µs)	330	340	310	290	315	350
Linewidth FWHM (nm)	26	27.7	25.2	18.6	20.1	27.8
Thermal conductivity (W m K^{-1})	0.91	1.3	1.2	1.19	0.98	1.35
Density (g cm^{-3})	2.63	2.55	2.81	2.68	2.83	2.54
Index of refraction	1.5196	1.568	1.5498	1.539	1.528	1.561
Non-linear index n_2 [10^{-13}]	1.5	1.4	1.59	1.28	1.13	1.41
dn/dt (10^{-6} °C^{-1})	−2.2	2.9	1.8	8.6	−5.3	2.9
Optical thermal coefficient (10^{-6} °C^{-1})	8.5	8.0	7.9	4.6	0.6	8.0
Thermal expansion coefficient (20°C–40°C) (10^{-6} °C^{-1})	10.3	9.0	10.5	8.6	12.7	9.3
Softening point (°C)	661	518	505	455	485	468
Specific heat (J g^{-1} K^{-1})	0.9	0.93	0.91	0.71	0.75	0.92
Knoop hardness	490	600	590	497	321	490
Young's modulus (kg mm^{-2})	9910	8570	8890	6910	5109	6249

The physical, spectroscopic and laser properties of Nd:glass are isotropic. There are two important differences between Nd glasses and Nd crystals. First, the thermal conductivity of the glass is much lower than that of most crystal hosts. (The high thermal conductivity is a more important parameter for the Nd:YAG crystal: it is the reason this laser crystal has taken up to 70% of the laser market.) Second, the emission lines of Nd^{3+} in glasses are considerably broader than in crystals. A wider line increases the threshold for laser lasing and the amplification value. In contrast, this broadening has an advantage because the broader laser lines are used to obtain and amplify very short light pulses. In addition, a broader line permits larger amounts of energy to be stored in the amplifying Nd:glass medium for the same linear amplification coefficient.

An Nd:crystal host is a better material for cw or very high-repetition-rate operation, because the commercial crystals provide higher gain and greater thermal conductivity. Nd:glasses with their low thermal conductivity are more suitable for high-energy pulse operation because of their large size and broadened fluorescence line. Nd^{3+}-doped glasses have been made in a variety of shapes and sizes, from a fibre a few micrometres in diameter, to rods 2 m long and 7.5 cm in diameter and discs up to 1 m in diameter and 10 cm thickness.

The Lawrence Livermore National Laboratory (USA) has developed the world's largest Nd:glass laser system, which comprises 192 beam lines that will deliver 1.8 MJ, 500 TW to the fusion target where internal fusion ignition and burn was demonstrated [65]. In the present design, the short pulse amplifiers comprise bundles of 4 cm thick Nd:glass slabs positioned at the Brewster angle, arranged in columns four slabs high, two columns wide and eleven deep in the 'regenerative' four-pass section and five deep in the single-pass 'booster' section. Each beam line has an aperture of 40 × 40 cm.

REFERENCES

1. Kaminskii A A 1990 *Laser Crystal (Springer Series in Optical Science 14)* 2nd edn (Berlin: Springer).
2. Optical Society of America 1993 *OSA Proceedings of Topical Meeting (New Orleans)* vol 15 (Washington, DC: Optical Society of America).
3. Optical Society of America 1994 *OSA Proceeding on Advanced Solid State Lasers (ASSL'94)* vol 20 (Washington, DC: Optical Society of America).
4. Optical Society of America 1995 *OSA Proceedings on Advanced Solid State Lasers (ASSL'95)* vol 24 (Washington, DC: Optical Society of America).
5. Optical Society of America 1996 *OSA Trends in Optics and Photonics, Advanced Solid State Lasers (ASSL'96)* vol 1 (Washington, DC: Optical Society of America).
6. Optical Society of America 1997 *OSA Trends in Optics and Photonics, Advanced Solid State Lasers (ASSL'97)* (Washington, DC: Optical Society of America).
7. Optical Society of America 1998 *OSA Trends in Optics and Photonics, Advanced Solid State Lasers (ASSL'98)* vol 19 (Washington, DC: Optical Society of America).
8. Optical Society of America 1999 *OSA Trends in Optics and Photonics, Advanced Solid State Lasers (ASSL'99)* vol 26 (Washington, DC: Optical Society of America).
9. Optical Society of America 2000 *OSA Trends in Optics and Photonics, Advanced Solid State Lasers (ASSL)* vol 34 (Washington, DC: Optical Society of America).
10. Optical Society of America 2001 *OSA Trends in Optics and Photonics, Advanced Solid State Lasers (ASSL)* (Washington, DC: Optical Society of America).
11. Optical Society of America 2002 *OSA Trends in Optics and Photonics, Advanced Solid State Lasers (ASSL)* (Washington, DC: Optical Society of America).

12. Schone W et al 1997 *Advanced Solid State Lasers (ASSL'97)* p 292.
13. Machan J, Moyer R, Hoffmaster D, Zamel J, Burchman D, Tinti R, Holleman G, Marabella L and Injeyan H 1988 *Advanced Solid State Lasers (ASSL'98)* pp 263–5.
14. Pealese S, Harkenrider J, Long W, Chui F, Hoffmaster D, Burt W and Injean H 2001 *Advanced Solid State Lasers (ASSL)* pp 300–22.
15. Tidwell S C, Seamans J F and Bowers M S 1993 *Opt. Lett.* **18** 116–18.
16. Golla D, Bode M, Knoke S, Schone S and Tunnerman A 1996 *Opt. Lett.* **21** 53–55.
17. Shine R J, Alfrey A J and Byer R L 1995 *Opt. Lett.* **20** 459–61.
18. Konno S, Fujikawa S and Yasui K 1997 *Appl. Phys. Lett.* **70** 2650–951.
19. Konno S, Fujikawa S and Yasui K 2001 *Advanced Solid State Lasers (ASSL)* pp 9–11.
20. Yasui K 1996 *Appl. Opt.* **35** 2566–96.
21. Shannon D and Wallace R 1991 *Opt. Lett.* **16** 318–20.
22. Clarkson W A and Hanna D C 1996 *Opt. Lett.* **21** 869–71.
23. Kopf D, Keller U, Emanuel M A, Beach R J and Skidmore J A 1997 *Opt. Lett.* **22** 99–101.
24. Du. K, Liano Y and Loosen P 1997 *Opt. Commun.* **140** 53–6.
25. Sekita M, Haneda H, Yanagitani T and Shiransaki S 1990 *J. Appl. Phys.* **67** 453.
26. Sekita M, Haneda H, Shiransaki S and Yanagitani T 1991 *J. Appl. Phys.* **69** 3709.
27. Ikesue A, Kamata K and Yoshida K 1995 *J. Am. Ceram. Soc.* **78** 3545.
28. Ikesue A, Kinoshita T, Kamata K and Yoshida K 1995 *J. Am. Ceram. Soc.* **78** 1033.
29. Lu J, Prabhu M, Song J, Li C, Xu J, Ueda K, Kaminskii A A, Yagi H and Yanagitani T 2000 *Appl. Phys. B* **71** 469–73.
30. Lu J, Song J, Prabhu M, Xu J, Ueda K, Yagi H, Yanagitani T and Kudryashov A 2000 *Japan. J. Appl. Phys.* **39** L1048.
31. Lu J, Prabhu M, Xu J, Ueda K, Yagi H, Yanagitani T and Kaminskii A A 2000 *Appl. Phys. Lett.* **77** 3707.
32. Lu J, Prabhu M, Song J, Li C, Xu J, Ueda K, Yagi H, Yanagitani T and Kaminskii A A 2001 *Japan. J. Appl. Phys.* **40** L552.
33. Lu J, Murai T, Takaichi K, Uematsu T, Misiwa K, Prabhu M, Xu J, Ueda K, Yagi H, Yanagitani T, Kaminskii A A and Kudryashov A 2001 *Appl. Phys. Lett.* **78** 3586.
34. Lu J, Ueda K, Yagi H, Yanagitani T, Akiyama Y and Kaminskii A A 2002 *J. Alloys Compounds* **341** 220–5.
35. Harmer A L, Linz A and Gabbe D 1969 *J. Phys. Chem. Solids* **30** 1483–91.
36. Heinz P, Seilmeir A and Piskarskas A 1997 *Opt. Commun.* **136** 433.
37. Fluck R, Zhang G, Keller U, Weingarten K and Moser M 1996 *Advanced Solid State Lasers (ASSL'96)* vol 1 (Washington, DC: Optical Society of America) pp 274–6.
38. O'Conner P R 1966 *Appl. Phys. Lett.* **9** 407–9.
39. Bagdasarov H S, Bogomolova G A and Popov A A 1968 *Dokl. Acad. Nauk. (DAN) SSSR* **180** 1347–50.
40. Fields R A, Birnbaum M, Fincher CL 1987 *Appl. Phys. Lett.* **51** 1885.
41. Chai B H, Loutts G, Lefaucheur J, Zhang X X, Hong P, Bass M, Shcherbakov I A and Zagumennyi A I 1994 *OSA Proc. Adv. Solid-State Lasers* **20** 41.
42. Zagumennyi A I, Ostroumov V G, Shcherbakov I A, Jensen T, Meyn J P and Huber G 1992 *Quantum Electron.* **22** 1071–2.
43. Jensen T, Meyn J P, Huber G, Ostroumov V G, Zagumennyi A I and Shcherbakov I A 1993 *OSA Proceedings of Topical Meeting (New Orleans)* vol 15 (Washington, DC: Optical Society of America) p 64.
44. Zagumennyi A I, Zavartsev Yu.D, Studenikin P A, Shcherbakov I A, Umyskov A F and Popov P A 1996 *SPIE* **2698** 182–92.
45. Zagumennyi A I, Mikhailov V A and Shcherbakov I A 1996 *Laser Phys.* **6** 582–8.
46. Zagumennyi A I, Mikhailov V A, Vlasov V I, Sirotkin A A, Podreshetnikov V I, Kalachev Yu L, Zavartsev Yu D, Kutovoi S A and Shcherbakov I A 2003 *Laser Phys.* **13** 1–8.
47. Klei P H and Croft W J 1967 *J. Appl. Phys.* **38** 1603.
48. Zhang H, Liu J, Wang J, Wang C, Zhu L, Shao Z, Meng X, Hu X and Jiang M 2002 *J. Opt. Soc. Am. B* **19** 18.
49. Song C, Shen D, Kim N and Ueda J 2000 *Appl. Phys. B* **70** 471–4.
50. Fuller M, Matthews D and Marshal L R 1998 *Advanced Solid State Lasers, Technical Digest* (Washington, DC: Optical Society of America) p 252.
51. Abraham M, Bar-Lev A, Epshtein H, Goldring A, Zimmerman Y, Lebiush E and Lavi R 2001 *Advanced Solid State Lasers, Technical Digest* (Washington, DC: Optical Society of America) p 357.
52. Kellner T, Heine F, Struve B, Ostroumov V, Peterman K and Huber G 1996 *OSA Topics Advanced Solid-State Lasers* (Washington, DC: Optical Society of America)p 356.
53. Zharikov E V, Zhitnyk V A, Zverev G V, Kalitin S R, Kuratev I I, Laptev V V, Osiko V V, Pashkov V A, Prokhorov A M, Shestakov A V and Shcherbakov I A 1982 *Sov. J. Quantum Electron.* **12** 1652–3.
54. Zharikov E V, Osiko V V, Prokhorov A M and Shcherbakov I A 1984 *Izv. Akad. Nauk SSSR Ser. Fiz.* **48** 1330.
55. Caird J A, Shinn M D, Kirchoff T A, Smith L K and Wilder R E 1986 *Appl. Opt.* **25** 4294–304.
56. Ostroumov V G, Privis Yu S, Smirnov V A and Shcherbakov I A 1988 *J. Opt. Soc. Am.* **3** 81.
57. Stokowski S E, Randles M H and Morris R C 1988 *IEEE J. Quantum Electron.* **24** 934–48.
58. Jackel S, Moshe I and Lallouuz P 1997 *Opt. Eng.* **36** 2031.
59. Kutovoi S A, Laptev V V and Matsnev S Yu 1991 *Quantum Electron.* **18** 149–50.
60. Meyn J P, Jensen T and Huber G 1994 *IEEE J. Quantum Electron.* **30** 913–7.
61. Laser Focus World June 1997 p 70.
62. Ostroumov V G, Heine F and Kuck S et al 1997 *Appl. Phys. B* **64** 301–5.
63. Aus de Au J, Kopf D and Keller U 1997 *Opt. Lett.* **22** 307.
64. Stuart B C, Perry M D and Wharton K 1997 *Opt. Lett.* **22** 242.
65. Zapata L, Rotter M, Marshall C and Erlandson A 1998 *Tops Advanced Solid-State Lasers* p 206.

Taylor & Francis
Taylor & Francis Group
http://taylorandfrancis.com

5

Rare-Earth Ions—Miscellaneous: Ce^{3+}, U^{3+}, Divalent, etc.

Gregory J. Quarles

CONTENTS

5.1 Introduction 55
5.2 Trivalent Cerium Lasers 55
5.3 Trivalent Uranium Lasers 60
5.4 Divalent Rare-Earth Ion Lasers 64
5.5 Summary 65
References 65
Further Reading 68

5.1 Introduction

Major advances have been made during the last two decades in the development of rare-earth-activated solid-state laser systems. Much of this effort has focused upon improving the efficiencies of near-infrared lasers utilizing trivalent neodymium or several of the other ions, which directly exhibit laser action in the near-infrared. However, since the beginning of studies in the late 1950s of rare-earth-activated solid-state materials for laser systems, ions other than just neodymium have played a key role in the evolution of this field. Much of the initial research and spectroscopy of lanthanide and actinide ions in solids were focused on investigations of hosts and activators for the phosphor industry. These investigations evolved to looking at ions other than those that emitted in the visible region and expanded into the ultraviolet (UV) and infrared regions of the electromagnetic spectrum.

This chapter will initially review the cerium ion, which exhibits the only directly pumpable, tunable, UV 5d–4f stimulated emission in the rare-earth ion series. The trivalent uranium ion, which has brought about such historical trends as the second ion ever lased, the only actinide ion ever to exhibit stimulated emission and the first recorded diode-pumped solid-state laser, will also be covered. Both of these ions have seen a revitalization in their interest to the solid-state laser community in the 1990s, after virtually no research in the 1980s. New and efficient solid-state lasers have been demonstrated for both cerium (in the 290 nm region of the spectrum) and uranium (at approximately 2.8 μm). The final section in this chapter will overview the history of the search for other rare-earth lasers utilizing divalent, rather than trivalent activator ions, including divalent dysprosium, europium, samarium and thulium.

The chapter is divided into three primary sections, with each section providing a historical overview of the spectroscopy, historical investigations, development and demonstrations of the stimulated emission for each of the ions in a variety of hosts. There has been an attempt in each section to provide an overview of the significance of the research, the applications of the laser in the industrial and scientific fields and the future directions for research with each ion. A beginning review will be presented of the energy levels, the absorption and emission spectra, the pertinent upper state lifetimes and the spectroscopic assets and deficiencies for each ion. Finally, a review of the laser performance demonstrated for each ion in the continuous wave (cw) and pulsed regimes will be summarized in each section.

There have been many excellent papers and texts written reviewing rare-earth-activated solid-state laser research over the past years. I have also referenced several books, manuscripts and chapters that are considered noteworthy with summaries covering the topics to be reviewed in this chapter in the Further Reading section. For any reader interested in a more in-depth review of these divalent and trivalent lanthanide and actinide ions, it is strongly suggested that these seminal and historical reviews be read. These reviews provide a comprehensive summary and bring together all aspects from basic materials science and crystallography to stimulated emission spectroscopy and solid-state laser design and engineering.

5.2 Trivalent Cerium Lasers

Investigations involving the cerium ion have had several cyclical periods of intense interest during the past years. The primary driver for this interest is the fact that the cerium ion exhibits direct UV absorption and emission and can provide tunable stimulated emission in the proper choice of host crystal. The interest in these UV sources has spanned several applications, including photolithography, medical, detection of biological and chemical agents and lidar. If the laser were to emit in the UV and demonstrate tunability, then the applications become even more vast. Many groups have attempted for decades to develop a superior UV laser source but material limitations consistently seem to provide obstacles. These limitations can be as simple as the band edge of the host being too close to upper laser levels and limiting the UV transmission to UV-induced colour centres and UV-activated defects that diminish or impede the stimulated emission.

Most of the previously studied tunable solid-state lasers have included transition metal ions such as trivalent titanium (Ti^{3+}) and chromium (Cr^{3+}) in a variety of oxide and fluoride hosts [1–3]. These transition metal ions typically exhibit broadband emission in the visible to near-infrared regions of the spectrum due to vibronic transitions within the 3d shell. Most trivalent lanthanide rare-earth ions exhibit very sharp absorption and emission bands throughout the spectrum based upon 4f–4f transitions [4,5]. However, with cerium in a trivalent state (Ce^{3+}), the excited state is a 5d level and the emission from this state can be broad and efficient. This is due to the electronic configuration of the trivalent cerium ion and the separation between the 5d and 4f energy levels [2–5]. The Ce^{3+} ion has been activated into a number of different fluoride and oxide hosts and the laser efficiencies are varied. The proximity of the band edge in some hosts has impacted the performance, as well as the fact that the allowed 5d → 4f transitions are very fast, typically with lifetimes of the order of nanoseconds. This severely limits the possibility of coupling flashlamp technologies as an excitation source. Research into hosts that have crystal fields that give rise to cerium absorptions, which match well with commercially available gas and solid-state laser sources, has caused a tremendous increase in the past decade of cerium-activated solid-state lasers.

The electronic configuration of Ce^{3+} consists of a palladium core with 46 electrons and with a $4f^15s^25p^65d^16s^2$ outer electron configuration. The inner 4f shell is unfilled, with a single electron, and the filled 5s and 5p outer shells shield this 4f shell. For the typical trivalent rare-earth ion, the Coulomb interactions and spin–orbit coupling are both larger than the magnitude of the crystal field, because of this shielding of the optically active 4f electrons [4,6–8]. In a self-consistent field approximation, it is assumed that the electrons move in a centrally symmetric field, brought about by the other electrons and the nucleus. In this approximation, the spin–orbit coupling adheres to the rule of $L + S \geq J \geq |L - S|$. If $L \geq S$, then J can have the values of $2S + 1$, whereas for $L < S$, J equals $2L + 1$. The designation for the energy levels is then derived from the form $^{2S+1}L_J$ [2].

Additional imposed criteria include that if the principal quantum number, n, is related to the orbital angular momentum quantum number, l, by $n = 2l + 1$, then there is no multiplet splitting of the energy levels. However, if $n > 2l + 1$ or $n < 2l + 1$, the multiplet splittings are inverted or normal, respectively. The standard selection rules state that electric dipole transitions are allowed within these rare-earth ions if the following angular momenta relations hold: $\Delta J = 0$ and $J + J' \geq 1$. For the Ce^{3+} ion, utilizing the Russell-Saunders coupling approximations [2], for the 4f shell, we obtain $n = 4$, $l = 3$, $s = \pm 1/2$, $m = 0, \pm 1, \pm 2, \pm 3$ and $j = l + s$, which yields $j = 7/2$ and $5/2$. Utilizing these quantum numbers, it is possible to formulate the splitting of the 4f shell into its two components, the $^2F_{7/2}$ excited state and the $^2F_{5/2}$ ground state, as illustrated in Figure 5.1.

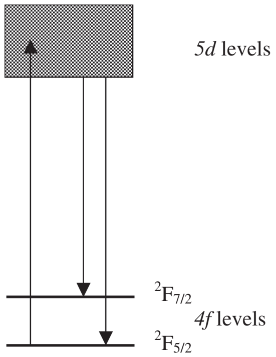

FIGURE 5.1 Partial Ce^{3+} energy level diagram (after Castillo [9]).

The splitting of the $^2F_{7/2}$ and $^2F_{5/2}$ energy levels is influenced by the ligand field in which the ion resides. This changes from host to host and the splitting of these levels can be between 1500 and 3000 cm^{-1} for trivalent cerium [8]. The single electron for the trivalent cerium is located in the 5d shell and gives rise to the 5d level situated (Figure 5.1) approximately 50 000 cm^{-1} above the ground state in fluoride hosts and it can be as low as 35 000 cm^{-1} in oxide hosts. The UV emission associated with the cerium ion originates from the 5d upper manifold and has electric-dipole-allowed 5d–4f transitions to the split ground-state energy levels. Fluorescence for nearly all cerium ions is composed of two peaks in the UV, with each of the peaks corresponding to a 5d → $^2F_{7/2}$ emission and a 5d → $^2F_{5/2}$ emission. Because of the nature of the 5d wavefunction, the resulting emission is generally a vibrationally broadened spectrum, as compared to those normally observed with the narrow emission of the electric-dipole-forbidden 4f–4f transitions in other rare-earth ions.

Over the past four decades, there have been numerous investigations of the spectroscopic and stimulated emission properties of the trivalent cerium ion in a variety of hosts. The trend that has been observed is that the fluorescence is generally very intense but the stimulated emission faces many potential loss mechanisms, including solarization, colour centre and defect formation and excited-state absorption (ESA) processes. All of these can limit or even totally prevent the laser process. The oxide hosts have shown the greatest tendencies towards having multiple detrimental mechanisms inherent in their nature, although similar mechanisms have also been observed in the fluorides.

The oxide host with the largest degree of characterization is most likely Ce^{3+}-activated $Y_3Al_5O_{12}$ (YAG) [7,10–17]. Cerium doped in the YAG matrix was investigated heavily in the late 1960s for use as phosphors in cathode-ray tubes for the colour television market. In the YAG host, the trivalent cerium ion enters a distorted cubic site with a D_2 symmetry, causing the 5d levels to be very low lying, and it also provides a large crystal field to dramatically split the $^2F_{7/2}$ and $^2F_{5/2}$ energy levels. This low-lying 5d level causes the energy gap to be decreased between the upper and lower levels and shifts the emission into the visible (yellow) region of the spectrum in YAG. Table 5.1 lists the various crystal properties for Ce in YAG, as well as in other hosts. The absorption, emission and energy level schemes for Ce:YAG are illustrated in Figure 5.2.

TABLE 5.1

Crystal Properties of Selected Cerium-Doped Hosts, after Castillo [9]

Crystal	Space Group	Local Site Symmetry	Optical Absorption (nm)	Refractive Index	Reference
$Y_3Al_5O_{12}$	O_h^{10}	D_2	210–500	1.83	[11,15]
LaF_3	D_{3d}^4	C_2	160–260	1.64	[19]
$LiYF_4$	C_{4h}^6	S_4	190–300	1.47	[20]
Rb_2NaYF_6	O_h^5	O_h	150–320	-	[21]
CaF_2	O_h^5	C_{4v}, O_h	180–320	1.47	[22]
BaY_2F_8	C_{2h}^3	C_{2h}	205–315	1.50	[23]
$LiCaAlF_6$		D_3	250–280	1.39	[24,25]
$LiSrAlF_6$	D_{3d}^2	D_3	250–280	1.41	[24,25]

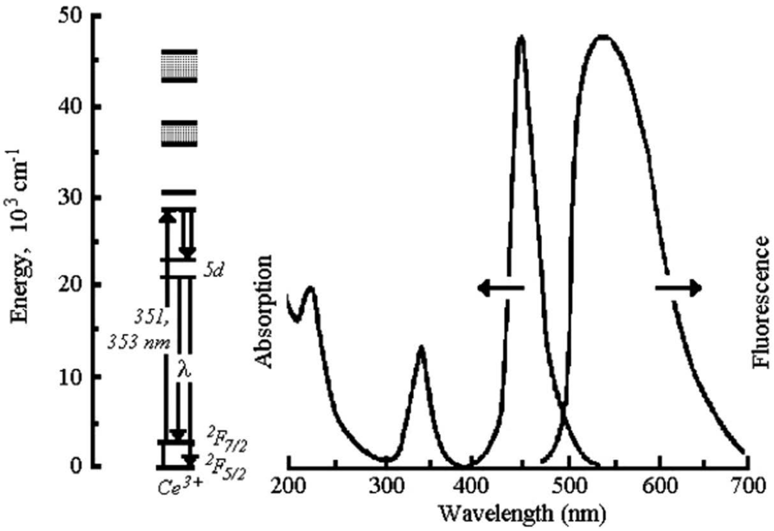

FIGURE 5.2 Ce:YAG absorption and emission spectra (after Jacobs et al. [11]).

The onset of the bandgap in YAG is visible with the tail of absorption beginning at 275 nm [17,18], while the absorption peaks at nominally 350 and 450 nm correspond to the absorption between the ground state and the upper 5d manifolds. The band at 220 nm has been identified by Wong et al. [14] as intrinsic lattice defects, as the same peaks can be observed in some undoped samples of YAG [16]. The broad emission spanning from approximately 500 to 700 nm arises from the direct transitions from the 5d upper-level manifolds to the split $^2F_7/_2$ and $^2F_5/_2$ ground-state energy levels. The wavelengths for the absorption peaks, emission peaks and the fluorescent lifetimes for trivalent cerium in a variety of hosts are brought together for the reader in Table 5.2.

The Ce ion in YAG has never been shown to exhibit stimulated emission, even with the significant quantity of research conducted in this field. The primary issue preventing the operation of Ce:YAG as a solid-state laser is the ESA, which is observed through the overlap of the absorption and emission bands as shown in Figure 5.2. The ESA can be reduced through cooling the crystal but lasing is still not achieved [11–13,15]. The radiation from the pump source, even at low temperature, excited the electrons into the phonon-coupled states and into the conduction band and served as a primary loss mechanism for excitation energy [13,15].

Several other oxide hosts have been activated with the cerium ion for investigation of the potential for stimulated emission. Studies showed that if the charge, ionic radius and the ionization potential of the activator ion (Ce^{3+}) and the host cation were similar, the chances for ESA would be minimized [13]. New oxide hosts studied included Ce^{3+}:$YAlO_3$ (YALO) [27], Ce^{3+}:Y_2O_3 [28] and Ce^{3+}:$LaPO_4$ [29]. The crystal field of the YALO shifted the upper-state manifolds to higher energy and gave broad emission from 325 to 400 nm but stabilization of the cerium ions was problematic. No laser action was ever observed in Ce:YALO. The cerium ion in Y_2O_3 and $LaPO_4$ proved to exhibit strong emission and tremendous phosphor potential; however, none of these oxide hosts could sustain stimulated emission either.

The failure of any of these oxide hosts to lase led researchers to concentrate most of their studies on the fluoride hosts. As compared to the oxides, the fluorides are more strongly insulating and characteristically have larger energy gaps between the various levels. They also tend to exhibit higher-energy conduction bands, resulting in better UV transmission. Optically, the fluoride host matrix is greatly influenced by the weak metal-to-fluorine bonds, the high electronegativity and small polarizability of the fluorine. These effects combine to give rise to typically lower refractive indices than the oxides,

TABLE 5.2

Trivalent Cerium Crystal Absorption, Emission and Fluorescence Lifetime Properties in Selected Hosts after Hammons et al. [26]

Host Material	Peak Absorption Wavelength (nm)	Peak Emission Wavelength (nm)	Lifetime (ns)
Lu_2SiO_5	357	395	40
Y_2SiO_5	356	388	37
Gd_2SiO_5	340	402	60
$Y_3Al_5O_{12}$	457	527	65
$Lu_3Al_5O_{12}$	447	517	85
$LiSrAlF_6$	266	290	28
$SrAlF_5$	248	285	43
$LiYF_4$	287	310	40
$LiGdF_4$	289	310	41
KYF_4	287	218	38

weaker crystal fields, wider transmission bands, lower melting temperatures and a general shift of the 4f levels to shorter wavelengths [9]. The earliest research with a fluoride host involved the LaF_3 fluoride matrix [19,30,31]. Researchers reported broadband fluorescence from 270 to 450 nm. The C_2 site symmetry causes the 5d state to split into five levels and exhibit a broad emission with two peaks corresponding to the splitting of the ground state. The upper-state lifetime for this electric-dipole-allowed d–f transition was a rapid 20 ns. The first demonstration of laser performance was published by Ehrlich et al. [19], in which they used a 40-mJ KrF excimer pump source at 249 nm to pump the Ce absorption bands at room temperature. Stimulated emission was measured at a peak wavelength of 285.5 nm, with a laser oscillation threshold of 3 mJ. Ehrlich et al. also demonstrated tunability of the laser from 275 to 315 nm but the manuscript stated that the performance was inferior due to poor crystal quality. Minimal follow-up research has taken place with a LaF_3 host doped with trivalent cerium.

Another fluoride host investigated thoroughly was the $LiYF_4$ host (YLF). The initial report of laser operation in Ce:YLF was also reported at room temperature by Ehrlich and colleagues [20] using an identical pumping scheme with the KrF laser. The Ce:YLF laser operated at 325.5 nm and produced an estimated tuning range of 305–335 nm. In the YLF host, the S_4 site symmetry splits the 5d state into four levels, all of which can be seen in the UV absorption spectrum (as shown in Figure 5.3).

The broken curve is the fluorescence spectrum, with two peaks indicating the transitions from the 5d manifold to the split $^2F_{7/2}$ and $^2F_{5/2}$ ground-state energy levels. This radiative lifetime is again very rapid, measured as 40 ns in the YLF host, and listed in Table 5.2. It is interesting to note that, because of the allowed transitions, the stimulated emission cross-sections for trivalent cerium actually rival those found in dye lasers, of the order of $7–9 \times 10^{-18}\,cm^{-2}$. Subsequent studies of the Ce:YLF laser material determined that the gain and pump rate were influenced by ESA of the pump light, which led to the formation of transient and stable colour centres [32]. The rate at which the defects and transients evolved impacted the gain saturation, slope efficiency and laser threshold. It is interesting to note that the ESA influenced the Ce:YAG system so strongly that there was no stimulated emission possible, whereas in the Ce:YLF system, tunable laser action was still feasible. Aside from this initial research with Ce:YLF, there has been very little investigation on the material later.

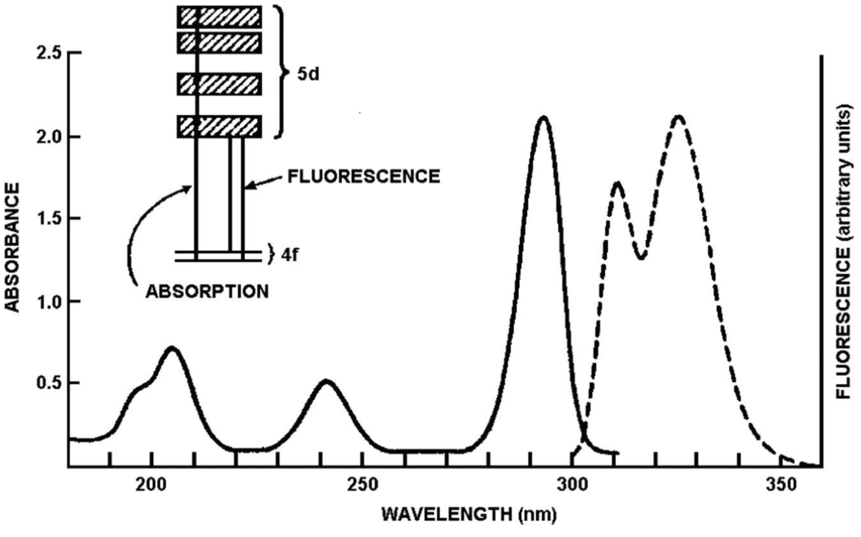

FIGURE 5.3 Absorption (full curve) and fluorescence (broken curve) spectra of Ce^{3+}:$LiYF_4$ (after Ehrlich et al. [20]).

Spectroscopic and laser research was conducted during the same time period with Ce^{3+}:CaF_2 but similar ESA issues plague this host [22]. The fluorescence lifetime for this crystal is also around 40 ns. It was observed that the Ce^{3+}:CaF_2 crystal would actually turn from a clear water white to a reddish-brown colour during UV excitation, signifying the formation of the colour centres. This colouration could be reversed with heating of the crystal or by photo-bleaching at a wavelength absorbed by the colour centres [22]. Tables 5.1 and 5.2 list other fluoride and oxide hosts not discussed in detail here due to either a lack of stimulated emission or repeated incidences of ESA being problematic in the laser operation.

Two final hosts of note will be reviewed in the remainder of the section. One is an isomorph of YLF, namely $LiLuF_4$. This host doped with the cerium ion produces fluorescence peaks at 308 and 327 nm and also exhibits a radiative lifetime of roughly 40 ns [33–41]. Compared to Ce^{3+}:$LiYF_4$, the Ce^{3+}:$LiLuF_4$ compound is more photochemically stable and has better optomechanical properties. This Ce^{3+}:$LiLuF_4$ gain material has been shown to be efficient as a 308 nm emitting solid-state laser pumped by either a Ce:$LiSrAlF_6$ (LiSAF) pump source at 290 nm, a second-harmonic from a copper-vapour laser 289 nm or as an amplifier for a KrF laser at 248 nm. The efficiencies for the LiSAF-pumped device exceed 55% [37], while output powers of greater than 1.25 W have been demonstrated by McGonigle et al. [38–41]. Prism tuning of this source was demonstrated from 305.5 to 316 nm and a second band was tuned from 323 to 331 nm [39]. The only two noted drawbacks are that the cost of the LuF_3 for the growth of this material is generally very expensive and some colour centre formation, albeit slight, has been observed. More future research with Ce^{3+}:$LiLuF_4$ should be forthcoming, as this is a relatively new host and dopant combination.

The final Ce-activated hosts presented in this section are a series of isomorphs, based upon the colquiriite family of materials, including $LiSrAlF_6$ (LiSAF), $LiCaAlF_6$ (LiCAF), $LiSrGaF_6$ (LiSGaF) and the other isomorphs. LiCAF was first investigated and characterized at Lawrence Livermore National Laboratory in 1988 and was activated with trivalent chromium [42]. Although the colquiriite hosts have proven to be intriguing new laser materials when activated with chromium, success when doping with other transition metal ions or rare-earth ions has been limited, prior to the investigations with trivalent cerium. In a colquiriite host, the cerium takes on a charge of 3+ and carries an ionic radius of roughly 1.15 Å. The trivalent aluminium ion in this type of structure has a much smaller ionic radius, approaching 0.67 Å; thus, it is assumed that the Ce^{3+} might prefer to reside on the Sr^{2+} or Ca^{2+} sites, since their radii are more nearly equivalent at 1.27 and 1.14 Å, respectively [24,43–46].

The initial investigations of UV laser properties of the Ce-doped LiSAF and LiCAF hosts were conducted by Dubinskii et al. [47–50] in 1993, followed up shortly thereafter by parallel research at the Naval Research Laboratory (NRL) [51,52] and Lawrence Livermore National Laboratory (LLNL) [25,43,53,54]. Utilizing well-oriented slabs of LiSAF and LiCAF, both the NRL and LLNL groups were able to demonstrate high efficiencies and broad tunability using two different resonator configurations. Efficiencies for Ce:LiSAF in a gain-switched, side-pumped configuration were approximately 17% when pumped at NRL with a fourth-harmonic Nd:YAG laser at 266 nm [51,52]. In an end-pumped, nearly confocal resonator configuration investigated at LLNL, efficiencies as high as 29% and 21% were measured with Ce:LiSAF and Ce:LiCAF, respectively [25,53].

The research by Marshall et al. [43] was one of the initial works describing the energy levels and interactions within the Ce-colquiriites. The ground state in the colquiriites may be split into three nearly doubly degenerate levels by the crystal field of the host. The crystal field also splits the 5d orbital into its two components, the t_{2g} and the e_g levels. Because of the sixfold coordinate octahedral field present at the Ca and Sr sites (potential sites for the Ce ion), the t_{2g} is assumed to be the lower of the split levels of the excited state. Figure 5.4 shows the absorption and emission cross-section spectra as a function of wavelength and polarization for these uniaxial materials. The Ce^{3+} absorption has a weak polarization dependence for both hosts. These peaks are also slightly shifted with each polarization, occurring at 266 nm for $\pi(E \parallel c)$ and at 272 nm for $\sigma(E \perp c)$ polarizations in LiSAF, and at 267 and 271 nm in LiCAF. These spectra are for 1 mol% CeF_3 and exhibit extremely high absorption and emission cross sections. The measured fluorescence lifetime of the 5d–4f transition in LiSAF is nominally 28 ns at 290 nm [25,52–54]. Just as with many of the other Ce-activated solids, colour centres exist in this family of hosts, more strongly in LiSAF than in LiCAF [43,54]. Co-doping and charge compensation have shown signs of minimizing these effects in the colquiriite isomorphs [9,43,45,46,54].

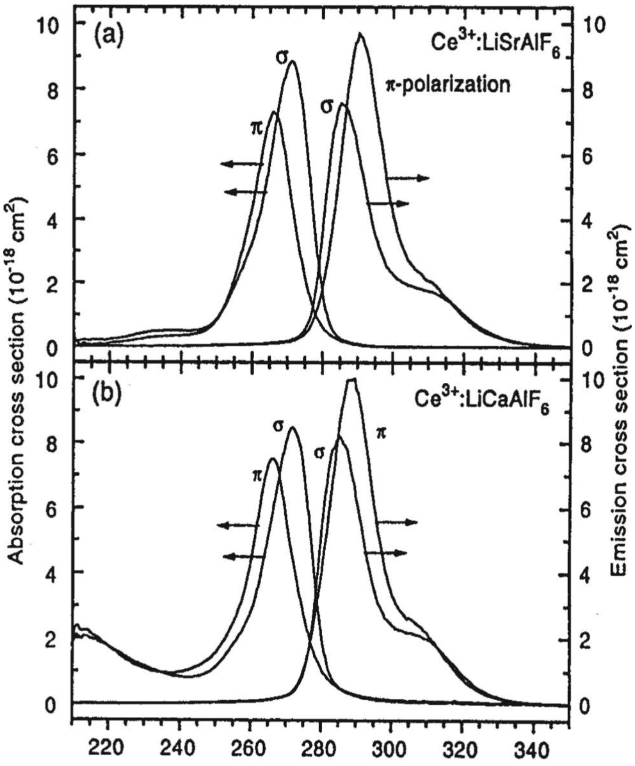

FIGURE 5.4 Ce-doped (a) LiSAF and (b) LiCAF absorption and emission cross-section spectra, as a function of polarization (after Marshall et al. [43]).

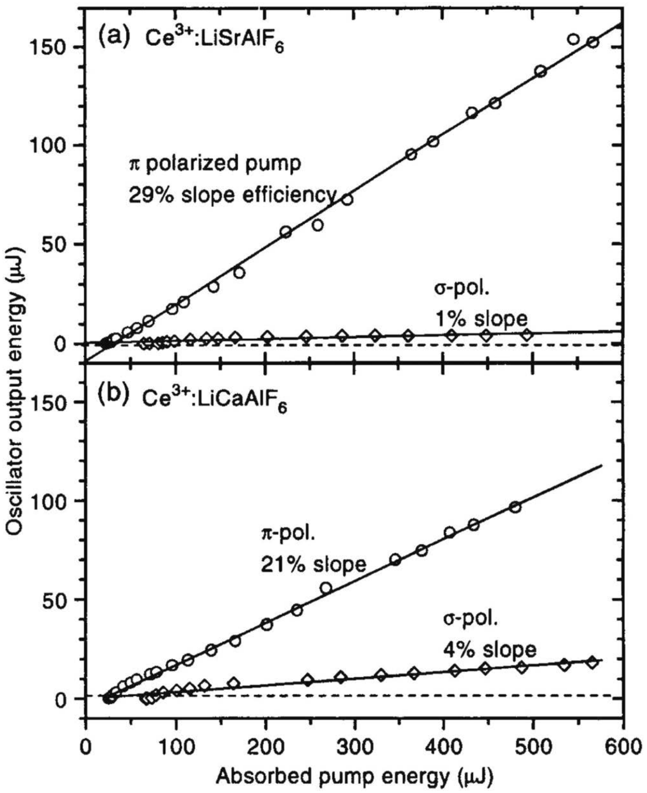

FIGURE 5.5 Laser output energies at ~292 nm as a function of absorbed 266 nm pump energy in Ce-doped (a) LiSAF and (b) LiCAF (after Marshall et al. [43]).

Figure 5.5 shows the strong polarization dependence observed in the output of both LiCAF and LiSAF, with the σ-polarization showing strongly decreased laser output [43]. Figure 5.6 shows the broad tunability of the LiSAF and LiCAF lasers from NRL data utilizing a prism in the cavity. Tunability has been investigated by several groups [43,55–57] and the output follows the profile of the stimulated emissions cross sections plotted previously in Figure 5.4. Finally, besides use as an oscillator material, Ce-doped LiCAF and LiSAF have been used by several groups as a high-peak-power amplifier for femtosecond pulses [58–62], which may open up a variety of UV-based applications, including high-field physics and materials processing.

Spectroscopic and laser investigations of the trivalent cerium ion have led to efficient pulsed lasers operating in the 280–330 nm region of the UV. To date, there have been no oxide-based hosts that have supported stimulated emission but all Ce-doped lasers have originated in the fluoride hosts. Lasers using these fluoride crystals are just starting to emerge from the laboratory and are being utilized in hardened systems for field experiments. These newly investigated hosts and dopants show promise for consideration for future commercial tunable solid-state UV systems.

5.3 Trivalent Uranium Lasers

Trivalent uranium (U^{3+}) activated into various laser hosts has played an interesting and important role in the history and evolution of solid-state lasers. The spectroscopy of the uranium ion doped into CaF_2 was first investigated in the late 1950s by Galkin and Feofilov [63,64] and simultaneously by Conway [65]. The intense early interest was due to the vast number of visible and near-infrared absorption bands and the strong fluorescence bands between 2.0 and 2.8 μm. Most of these early studies focused on the spectroscopy of CaF_2 [63–79], LiF^- [80], SrF_2 [63,64,67,77], BaF_2 [63,64,77] and $LaCl_3$ [81,82], while later spectroscopy has dealt with trivalent uranium in $LiYF_4$ [83–86]. These studies of uranium in $LiYF_4$ involved researchers investigating materials and their spectroscopic properties to find crystals that would allow efficient diode- or laser-pumping of transitions in the near-infrared, with a focus on lasing these transitions in the 2–3 μm wavelength region [83–87], competing with the Er^{3+} ion. Much of the focus on U^{3+}-activated hosts evolves from the search for materials for radar and medical applications operating in the infrared, with broad outputs which may give rise to tunability. It is interesting to note that after the

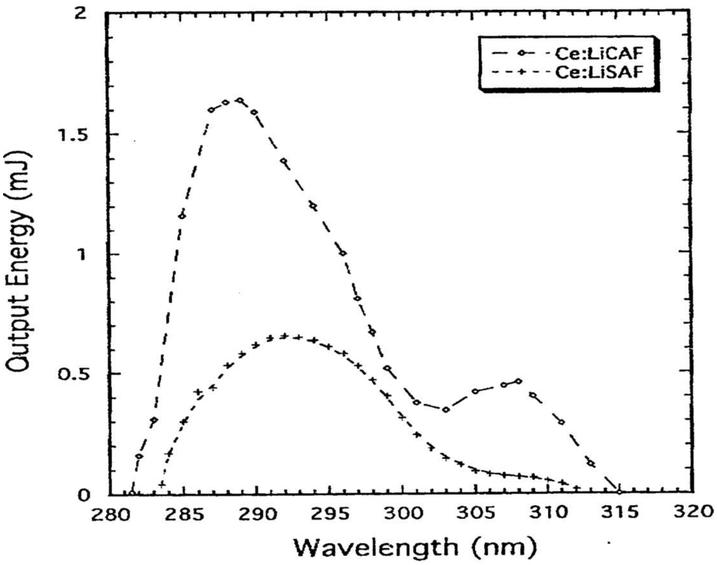

FIGURE 5.6 Laser tuning spectra and output energy of Ce-doped LiCAF and LiSAF, pumped at 266 nm at room temperature (after Pinto et al. [55]).

advent of the ruby laser in 1960, a laser based upon U^{3+}:CaF_2 was the second laser ever demonstrated (also in 1960) [66]. One of the major notable differences was that ruby is a three-level laser, whereas the actinide-based U^{3+} ion behaves as a four-level laser. It is also interesting to note that the uranium ion is the only actinide ion ever to have stimulated emission reported, during these past years of intense solid-state laser research.

One issue that has always been of concern with spectroscopists and crystal growth scientists relative to the uranium ion is that of charge compensation. Since the desired valence state for the uranium ion for these infrared laser transitions is the trivalent state, and in CaF_2, SrF_2 and BaF_2 hosts the uranium ion resides on a divalent site, there is naturally a charge mismatch. This has often given rise to multiple valence states of uranium residing in the host lattice to provide a charge-neutral lattice. Uranium has been spectroscopically identified in the various hosts in the U^{2+}, U^{3+}, U^{4+} and U^{6+} valence states [67,73,74,77–84].

The U^{3+} ion is a member of the actinide series of elements, having a partially filled 5f shell, making its $5f^3$ configuration of energy levels nearly analogous and actually iso-electronic to those found in its $4f^3$ counterpart trivalent neodymium (Nd^{3+}). Since there are three electrons in the unfilled 5f shell, by Hund's rules, the lowest term of an f^3 configuration is a ^4I_J term, with the $J = 9/2$ state being the lowest-lying state. The shielding of the 5f levels from the crystalline field is much weaker than that of the 4f shell but it has a greater spin–orbit interaction, which gives rise to larger splittings between the ^4I_J levels than those found with Nd^{3+}. It has been determined quantitatively that the actinide ions exhibit crystal field strengths nearly twice as strong as those for the lanthanides and that the cross sections for the absorptions of the 5f–5f transitions are sometimes two orders of magnitude larger than those of their lanthanide 4f–4f counterparts [87].

As with their lanthanide counterparts in the rare-earth series, the absorption and emission lines are sharp and well defined. These sharp lines can be attributed to the transitions occurring between configurations of an unfilled inner f-electron shell that, as alluded to previously, is partially shielded. Transitions between these well-split ^4I_J levels involve a violation of the Laporte rule of $\Delta l = \pm 1$ for electric dipole transitions. This larger spacing between the ^4I_J levels also allows for a reduction in the non-radiative decay between the adjacent ^4I_J levels, which results in the potential for laser transitions in the 2.5–2.9 μm range between the $^4I_{11/2}$ and the $^4I_{9/2}$ levels of U^{3+}. Figure 5.7 illustrates this energy level scheme and the wide splittings of the ^4I_J levels for the U^{3+} ion in CaF_2.

This diagram highlights the ^4I multiplets of the trivalent uranium ion in a typical fluoride host crystal field, identifying three of the major ^4I_J energy manifolds located throughout the visible and near-infrared portions of the spectrum. The upward arrows illustrate potential excitation paths in the 500 nm region (20 000 cm^{-1}) and in the 850–950 nm region (into the $^4I_{15/2}$ manifold at approximately 11 000 cm^{-1}). Representative absorption coefficient spectra as a function of wavelength for these manifolds in U^{3+}:$LiYF_4$ (YLF) are illustrated in Figures 5.8 and 5.9. Because of the uniaxial nature of YLF, there are two distinct polarization-dependent spectra in each wavelength region, one corresponding to $E \perp c$ and the other for $E \parallel$ to the c-axis. These two figures, shown at room temperature, illustrate the breadth of the absorption spectrum, which is due to the multiple transitions between the individual Stark levels.

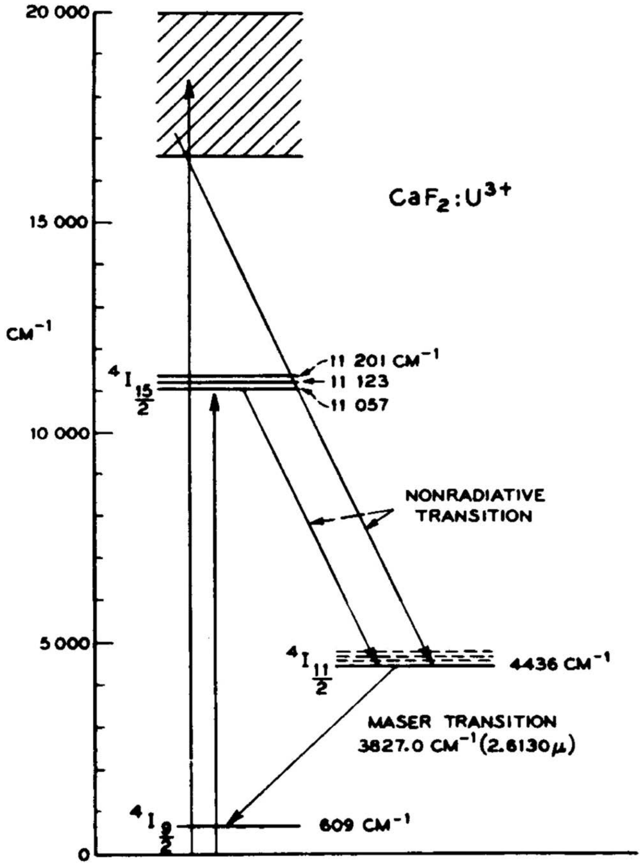

FIGURE 5.7 The absorption, fluorescence and laser transitions of the 2.613 μm transition in CaF_2:U^{3+} (after Boyd et al. [88]).

As exhibited in Figure 5.7, there is a broadband of energy levels in YLF corresponding to the $^4I_{11/2}$ manifold located at approximately 5000 cm^{-1}. The crystal-field splitting of this ground-state manifold is particularly large compared to that of the U^{3+} ion in CaF_2, measured as 1113 versus 602 cm^{-1}, respectively. The optical absorption between the $^4I_{9/2}$ and the $^4I_{11/2}$ energy levels can give rise to absorptive losses on the high-energy side of the emission spectra, which define the region of the laser transition from the $^4I_{11/2}$ upper laser level to the $^4I_{9/2}$ ground state. These absorption transitions between the $^4I_{9/2}$ and the $^4I_{11/2}$ levels are illustrated in Figure 5.10 and are typical for trivalent uranium in a fluoride-based host. At room temperature, these absorption losses diminish past 2.6 μm, thus allowing any laser transitions at greater than 2.6 μm to be very efficient with minimal intrinsic or ground-state absorptive losses. Figure 5.10 illustrates these absorption transitions between the ground state and first excited state, while Figure 5.11 is representative of the broad fluorescence spectrum originating from the $^4I_{11/2}$ to $^4I_{9/2}$ transitions occurring at room temperature in U^{3+}:YLF.

As with any transition when trying to determine the probability for stimulated emission, the lifetime of the metastable upper laser level plays a key role. If pumping with a pulsed source, optimization is most efficient with an excitation source

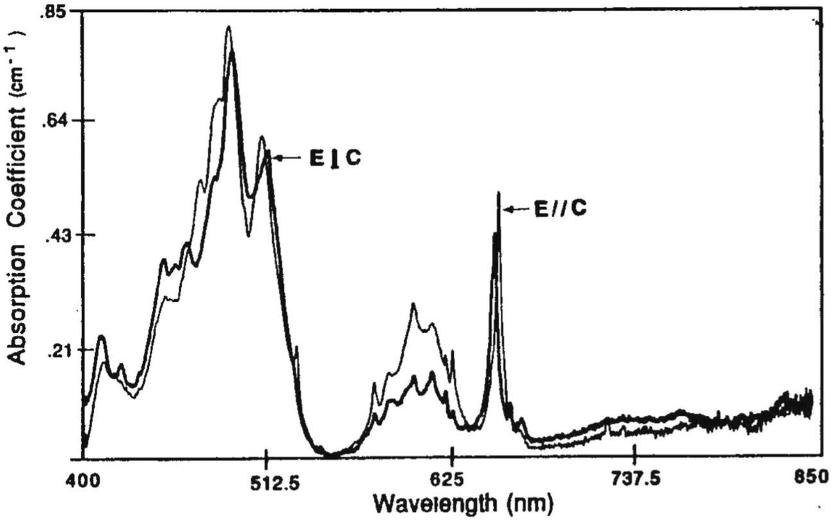

FIGURE 5.8 The polarized absorption spectra of U^{3+}:YLF in the visible region at 300 K (after Quarles et al. [83]).

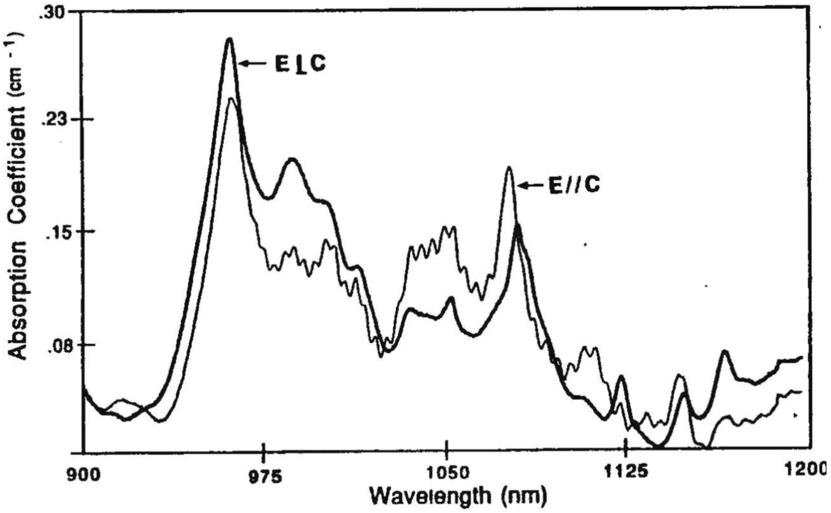

FIGURE 5.9 The polarized absorption spectra of U^{3+}:YLF in the near-infrared region at 300 K (after Quarles et al. [83]).

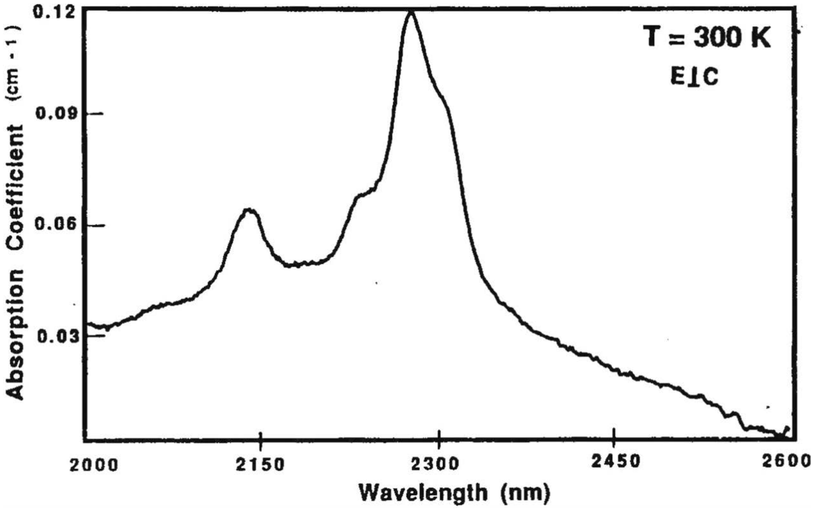

FIGURE 5.10 The $E \perp c$ polarized ${}^4I_{9/2}$–${}^4I_{11/2}$ absorption spectra of U^{3+}:YLF at 300 K (after Quarles et al. [83]).

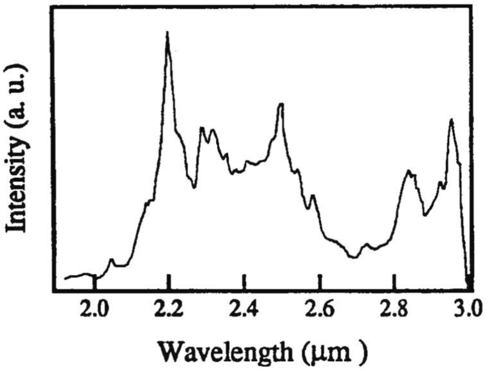

FIGURE 5.11 The $^4I_{11/2}$–$^4I_{9/2}$ fluorescence spectra of U^{3+}:YLF at 300 K (after Louis et al. [87]).

that is nearly matched to this lifetime. Since the $^4I_{11/2}$–$^4I_{9/2}$ emission arises as a Laporte forbidden transition, the lifetimes are reasonable and typically single exponential. For the CaF_2 family of hosts, the lifetimes measured at room temperature are of the order of 15 μs [88], whereas for the YLF host, these same transitions exhibit lifetimes an order of magnitude longer at 175–192 μs [83,87]. The difference between these two reported $^4I_{11/2}$ lifetime values could be attributed to concentration effects. Compared to the lanthanides, the actinides (such as trivalent uranium) can exhibit concentration quenching of the upper-state lifetimes at much lower concentrations. This, as referenced earlier in this section, can be due to the fact that the oscillator strengths for the actinide ions are one to two orders of magnitude larger than those for the lanthanides and, thus, the probability for energy transfer from ion to ion can occur at a much lower concentration [21]. If there is ion-to-ion energy transfer, this could be exhibited by a measurable decrease in the upper-state lifetime and occur in concentrations as low as 0.1% in an actinide-activated material.

Laser action in the trivalent uranium ion was first observed by Sorokin and Stevenson in 1960 [66] in the CaF_2 host. A review of the literature shows that there were many simultaneous studies and various reports of different lasing conditions and different wavelengths. Several groups measured room temperature, pulse-pumped lasing in CaF_2 at 2.61 μm [66,73,89–91], at 2.57 μm [73] and 2.51 μm [73,89,90]. Others have measured the pulse-pumped lasing at reduced temperatures (77 K) at wavelengths of 2.24 μm in CaF_2 [67–69], 2.41 μm in SrF_2 [71] and 2.56 μm in BaF_2 [70,92]. In most of these cases, xenon pumping was utilized to provide a strong overlap between the xenon output and the high-quantum-efficiency infrared absorption bands. The various wavelengths of laser operation recorded can most likely be attributed to transitions oscillating on various components between the Stark-split manifolds. Likewise, since the crystals can be stressed during both growth and the pumping process, this may cause perturbations, which may make some of the transitions less forbidden and, thus, give rise to different research groups measuring slightly different laser oscillation wavelengths. Finally, as exhibited in Figures 5.10 and 5.11, any changes in the ground-state absorptive losses in the laser host crystal can impact the intracavity laser losses and, thus, the threshold operating conditions for the various transitions.

The cw excitation also leads to lasing of the trivalent uranium ion in tests in the early 1960s. The first cw lasing was accomplished by Boyd et al. [88] using a cw mercury lamp to excite the uranium ions at approximately 900 nm. The laser output was also measured at 2.61 μm for CaF_2 in a cw operating condition. One of the most significant breakthroughs recorded in solid-state laser history also occurred with cw excitation of the uranium ion. In 1963, Keyes and Quist became the first scientists to successfully excite a solid-state laser with GaAs diodes [93]. An artist's rendition of this first diode-pumped solid-state laser is illustrated in Figure 5.12. They utilized cw diodes operating at 840 nm and demonstrated that the $^4I_{9/2}$–$^4I_{15/2}$ transition in U^{3+}:CaF_2 could efficiently be excited to lase at 2.631 μm. Even though this lasing took place at 4.2 K, this was the first demonstration of the efficient use of semiconductor laser diodes as an excitation source for solid-state lasers. Later research has led to the demonstration of titanium:sapphire-pumped cw lasers based upon U^{3+}:YLF as the host material [87,94]. These studies have shown that lasing could be achieved at 2.827 μm when pumped at room temperature between 810 and 890 nm. The efficiency of this cw

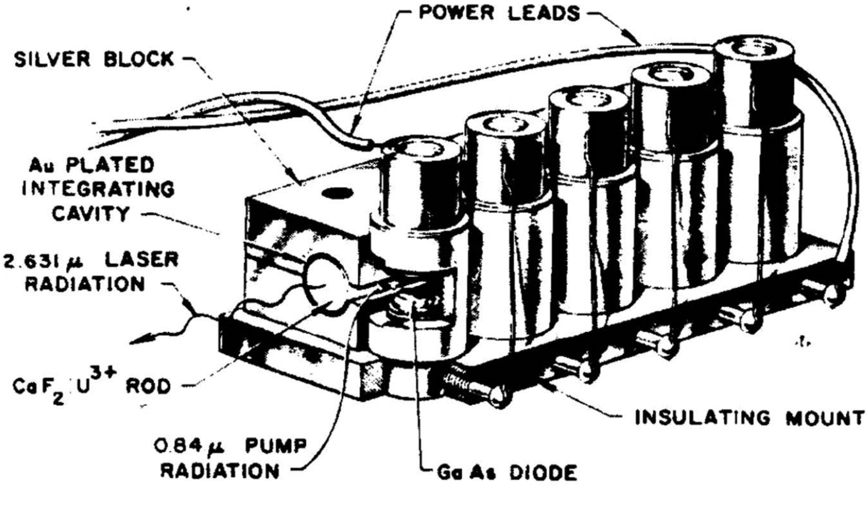

FIGURE 5.12 An artist's rendition of the first diode-pumped solid-state laser—GaAs-pumped U:CaF_2 (after Keyes et al. [93]).

pumping approaches 0.3%. As can be seen in a comparison of Figures 5.10 and 5.11, this lasing represents a four-level laser scheme when operating at the longer wavelengths of the $^4I_{11/2}$–$^4I_{9/2}$ transition.

Spectroscopic and laser investigations of the trivalent uranium ion have led to efficient pulsed and cw lasers operating in the 2.5–2.9 μm wavelength region. Significant historical and scientific studies have documented the stimulated emission of the U^{3+}-based 5f–5f transitions in various fluoride hosts. Of historical note is that U^{3+} in CaF_2 was the second solid-state laser ever reported (the same year as the ruby laser); it is the first and only actinide ever reported to exhibit stimulated emission and it has set historical precedence in the now-booming field of diode-pumped solid-state lasers as the first solid ever lased using diode pumping. Even though there is not a proliferation of these lasers in the commercial marketplace, their place in the historical context of solid-state lasers is noteworthy.

5.4 Divalent Rare-Earth Ion Lasers

In the previous sections, it has been shown how trivalent lanthanide rare-earth ions can exhibit stimulated emission on both the f-to-f transitions and the d-to-f transitions. There exists another group of rare-earth ions that carry a divalent charge, which have also shown laser action in previous studies. Amongst these divalent ions are samarium (Sm^{2+}), dysprosium (Dy^{2+}) and thulium (Tm^{2+}). As with the trivalent ions, the electronic configuration consists of a palladium core with 46 electrons and with a $4f^n5s^25p^65d^16s^2$ outer electron configuration, where for $4f^n$, $n = 6$ for Sm^{2+}, $n = 10$ for Dy^{2+} and $n = 13$ for Tm^{2+}. This filling sequence for the $4f^n$ shell makes Sm^{2+} isoelectronic to Eu^{3+}, Dy^{2+} isoelectronic to Ho^{3+} and Tm^{2+} isoelectronic to Yb^{3+}. Just as with the trivalent ions, this inner 4f shell is partially filled, and the 5s and 5p outer shells are completely filled, shielding the 4f shell. One important difference of the divalent lanthanide ions, compared with those of the trivalent lanthanides, is that the energy levels of the $4f^{n-1}5d$ configurations will typically occur at lower energies. Examples of the placement of these energy levels are shown in Figure 5.13 for the divalent Sm (in two different hosts), Dy and Tm ions.

In some of the host materials investigated by various groups, the 4f–5d transitions occur in the visible region of the spectrum (such as in the Sm and Tm examples illustrated in Figure 5.13) and can support visible to near-infrared stimulated emission. For ions such as divalent Sm, the 5d–4f laser transitions are spectrally broadened by the interaction of the 5d electron level and the crystalline host. These 5d–4f laser transitions are also electric-dipole-allowed transitions, similar to those described in the earlier section with the trivalent cerium ion and, thus, have much stronger oscillator strengths. As is clearly seen in Figure 5.13, many divalent rare-earth ions, when activated in fluoride-based hosts, have 4f energy levels high enough in energy that radiationless decay processes can occur efficiently from the 5d to the 4f levels. The one exception to this case involves the Sm^{2+} ion, and the choice of host. The specific crystal host and, thus, the crystal field strength determine whether the upper laser level belongs to the $^5D_0$ f-orbital (as shown in Figure 5.13 for Sm^{2+} in SrF_2) or to the 5d level (as with CaF_2 in Figure 5.13).

One divalent ion, which has been studied extensively but has never exhibited stimulated emission, is the divalent europium ion (Eu^{2+}), which is a close analogue of Sm^{2+}. Many researchers have anticipated being able to make Eu^{2+} lase, especially

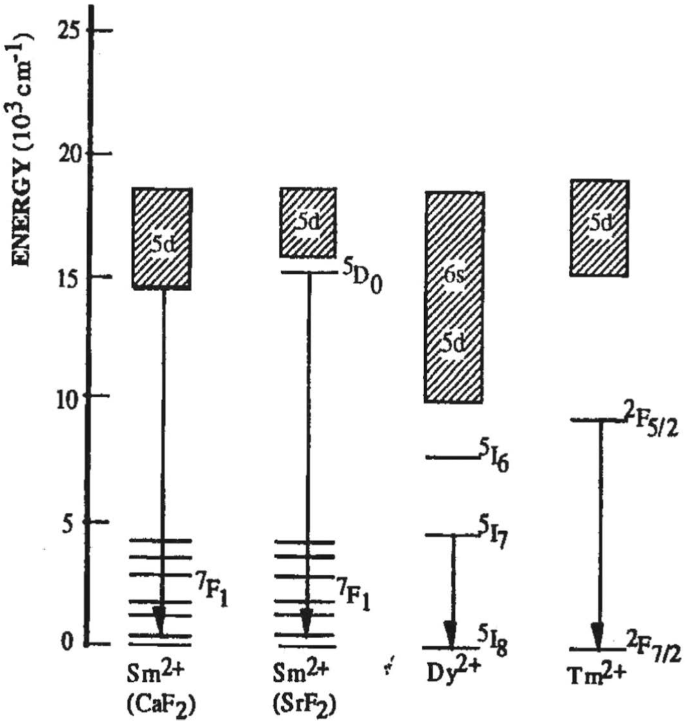

FIGURE 5.13 Partial energy level diagrams for the divalent rare earths: Sm^{2+}, Dy^{2+} and Tm^{3+} (after Powell [2]).

because of its very strong fluorescence, but all efforts have been hampered by extremely strong ESA [95,96]. Even though in most hosts the Eu^{2+} ion emits from an allowed-electric-dipole 5d–4f transition, the ESA has completely overwhelmed the possibility of reaching population inversion.

The first divalent rare-earth ion studied in great detail was the Sm^{2+} ion in CaF_2. The early pioneers of the trivalent uranium studies were also the pioneers of the divalent samarium ion, namely Feofilov [97,98] and, separately, Sorokin and Stevenson [99]. Sorokin and Stevenson went on to be the first researchers to demonstrate stimulated emission with the Sm^{2+} ion in CaF_2, exciting with a pulsed Xe lamp and the crystal at 20 K [97–101]. The output wavelength was 708.5 nm, on the allowed 5d–4f transition. The measured upper-state lifetime for this transition was a very short 1.4 μs. Subsequent studies have shown that the Sm ion in CaF_2 can be lased on various lines between 708.3 and 745 nm when excited with a pulsed ruby laser excitation source, at temperatures ranging from 65 to 210 K [102]. Studies were also conducted on the SrF_2 host activated with divalent Sm. In 1962, Sorokin et al. [103] followed up their Sm:CaF_2 laser studies of 1961, with evidence of stimulated emission of Sm in SrF_2. The divalent Sm ion in SrF_2 lased on the $^5D_0$–$^7F_1$ transition at 696.9 nm, at a temperature of 4.2 K. The upper state lifetime for this d–d transition was much longer than the transition in CaF_2, measured to be 10 ms. Following these initial publications, Sm:SrF_2, was also lased using a pulsed ruby excitation source [104,105]. Subsequent research over the next three decades has determined that significant ESA, defect-induced losses and non-radiative decay processes severely limit the utility of the divalent Sm ion at other than cryogenic temperatures [106–110].

Another ion that was studied heavily during the 1960s was the divalent dysprosium ion [111–113]. Just as with its Sm^{2+} counterpart, the Dy^{2+} ion was initially excited with a Xe lamp in an attempt to induce stimulated emission. As is seen in Figure 5.13, the Dy^{2+} ion lases on an f–f transition between the $^5I_7$ and $^5I_8$ manifolds, at nominally 2.358 μm. The Dy^{2+} ion was first lased in the CaF_2 host in 1962 under both cw [114,115] and pulsed [116] conditions. The pulsed laser demonstration occurred with a Hg lamp as the excitation source and the crystal was held at 77 K [116], while for the cw experiments [114,115], a Xe lamp was used and the crystal temperature was lower at 4 K. Other pumping sources included a tungsten (W) lamp (cw, between 4 and 77 K) [117,118] and a Xe lamp at 20–77 K [119,120]. One of the Xe lamp excited systems was with an SrF_2 host [120], which exhibited a slightly longer wavelength of 2.3659 μm. There were other pumping configurations, including a pulsed system [121], a cw system with giant pulses [122] and a giant pulsed system with a very high repetition rate [123]. Finally, there were several unique and intriguing pumping schemes explored with the divalent Dy ion in CaF_2 and SrF_2 hosts, including ones utilizing sunlight focused in a cw scheme to achieve laser oscillation with the crystal temperature held at 77 K [124–126] and a scheme whereby the laser was excited in a quasi-cw manner using a pyrotechnic detonation [127]. All of these studies led to unique laser systems, but none of them exhibited stability or room temperature operation.

One final divalent rare-earth ion that has been moderately investigated is the thulium ion (Tm^{2+}). As mentioned previously, the Tm^{2+} ion is isoelectronic to the Yb^{3+} ion and operates as a laser between the $^2F_{5/2}$ and $^2F_{7/2}$ transitions at 1.116 μm. There has been no reported laser research involving the divalent thulium ion since 1980. The reports by Kiss and Duncan [117,128,129] were for pulsed pumping with a Xe lamp at 4.2 K and for cw operation, pumped with a Hg lamp at crystal temperatures between 2.7 and 4.2 K. Neither of these operating schemes showed any promise for commercialization because of the low temperatures required to stabilize the ion in the fluoride host.

All of the divalent rare-earth ions investigated and reported in this section have exhibited deficiencies when considered for solid-state lasers. Even though stimulated emission was possible with each ion in a variety of fluoride hosts, none of the combinations can overcome the limitations of ESA, optical instability and defect-induced losses. It can be stated that the Tm^{2+}, Dy^{2+} and Sm^{2+} ions all indeed exhibit laser operation but none is efficient or robust enough to warrant significant research or development over the past two decades.

5.5 Summary

The purpose of this chapter is to highlight the research involving several lesser-known, yet historically significant, trivalent and divalent rare-earth-activated solid-state lasers. Laser action in the UV region of the spectrum has been observed in fluorides doped with the trivalent cerium ion. These lasers are tunable and highly efficient, with some of the highest stimulated emission cross sections for any rare-earth-doped solids. The trivalent uranium ion holds several historically significant records in the evolution of solid-state crystalline lasers. Trivalent uranium is the first and only actinide ion to exhibit stimulated emission, it is also the first ion ever to be lased by direct diode excitation and, finally, it is the second ion ever lased, immediately following the discovery of the ruby laser. This trivalent ion, like its cerium counterpart, is broadly tunable, except that it demonstrates stimulated emission in the 2.0–2.8 μm region of the infrared. Finally, a tremendous amount of research has gone into attempting to understand divalent rare-earth ions such as Tm, Dy and Sm. Each has exhibited stimulated emission and in some unusual configurations, such as solar-pumped or pyrotechnic pulsed, because of instabilities, ESA and defects, none of the divalent systems has shown promise as a robust system for commercial applications.

REFERENCES

1. Koechner W 1988 *Solid-State Laser Engineering* (Berlin: Springer).
2. Powell R C 1998 *Physics of Solid-State Laser Materials* (New York: Springer).
3. Weber MJ (ed) 1982 *CRC Handbook of Laser Science and Technology, Volume 1: Lasers and Masers* (Boca Raton, FL: Chemical Rubber Company).
4. Deike G H 1968 *Spectra and Energy Levels of Rare-Earth Ions in Crystals* (New York: Wiley-Interscience).

5. Wyborne B G 1965 *Spectroscopic Properties of Rare Earths* (New York: Wiley–Interscience).
6. Hamilton D S 1985 *Tunable Solid State Lasers* ed P Hammerling, A B Budgor and A Pinto (New York: Springer) pp 80–90.
7. Weber M J 1973 *Solid State Commun.* **12** 741–4.
8. Dorenbos P 2000 *J. Lumin.* **91** 155–76.
9. Castillo V K 2002 PhD Thesis University of South Florida
10. Blasse G and Bril A 1967 *J. Chem. Phys.* **47** 5139–46.
11. Jacobs R R, Krupke W F and Weber M J 1978 *Appl. Phys. Lett.* **33** 410–12.
12. Miniscalco W J, Pellegrino J M and Yen W M 1978 *J. Appl. Phys.* **49** 6109–11.
13. Owen J F, Dorain P B and Kobayasi T 1981 *J. Appl. Phys.* **52** 1216–23.
14. Wong S M, Rotman S R and Warde C 1984 *Appl. Phys. Lett.* **44** 1038–40.
15. Hamilton D S, Gayen S K, Pogatshnik G J, Ghen R D and Miniscalco W J 1989 *Phys. Rev. B* **39** 8807–15.
16. Rotman S R, Tuller H L and Warde C 1992 *J. Appl. Phys.* **71** 1209–14.
17. Doroshenko M E, Ivanov M A, Sigachev V B and Timoshechkin M I 1992 *Sov. J. Quantum Electron.* **22** 588–90.
18. Tomiki T, Akamine H, Gushiken M, Kinjoh Y, Miyazato M, Togokawa N, Hiraoka M, Hirata N, Ganaha Y and Futemma T 1991 *J. Phys. Soc. Japan* **60** 2437–45.
19. Ehrlich D J, Moulton P F and Osgood R M Jr 1980 *Opt. Lett.* **5** 339–41.
20. Ehrlich D J, Moulton P F and Osgood R M Jr 1979 *Opt. Lett.* **4** 184–6.
21. Aull B F and Jenssen H P 1986 *Phys. Rev. B* **34** 6647–55
22. Pogatshnik G J and Hamilton D S 1987 *Phys. Rev. B* **36** 8251–7.
23. Kaminskii A A, Kochubei S A, Naumochkin K N, Pestryakov E V, Trunov V I and Uvarova T V 1989 *Sov. J. Quantum Electron.* **19** 340–3.
24. Wannemacher R and Meltzer R S 1989 *J. Lumin.* **43** 251–60.
25. Marshall C D, Payne S A, Speth J A, Krupke W F, Quarles G J and Castillo V 1994 *OSA Proc. Advanced Solid-State Lasers (TOPS 20)* (Washington, DC: Optical Society of America) pp 389–94.
26. Hammons D A, Richardson M C, Chai B H T, Bass M, Quarles G J and Castillo V 1995 *OSA Annual Meeting Proc.* (Washington, DC: Optical Society of America) p 158.
27. Li G, Wu J, Chen Y, Chen J, Shi Z and Xiao C 1993 *Chinese J. Lasers B* **2** 91–6.
28. Nolas G S, Tsoukala V G, Gayen S K and Slack G A 1994 *Opt. Lett.* **19** 1574–6.
29. Benderskaya L P, Voloshinovskii A S, Novikova T P, Pidzyrailo N S and Pashchuk I P 1991 *Opt. Spectrosc. (USSR)* **70** 198–200.
30. Elias L R, Heaps W S and Yen W M 1973 *Phys. Rev. B* **8** 4989–95.
31. Yang K H and DeLuca J A 1977 *Appl. Phys. Lett.* **31** 594–6
32. Lim K-S and Hamilton D S 1989 *J. Opt. Soc. Am. B* **6** 1401–6.
33. Dubinskii M A, Abdulsabirov R Yu, Korableva S L, Naumov A K and Semashko V V 1992 *18th Int. Quantum Electron. Conf., OSA Technical Digest* (Washington, DC: Optical Society of America) pp 548–50.
34. Sarukura N, Liu Z, Segawa Y, Edamatsu K, Suzuki Y, Itoh T, Semashko V V, Naumov A K, Korableva S L, Abdulsabirov R Y and Dubinskii M A 1994 *OSA Proc. Advanced Solid-State Lasers (TOPS 20)* (Washington, DC: Optical Society of America) pp 395–9.
35. Sarakura N, Liu Z, Segawa Y, Semashko V V, Naumov A K, Korableva S L, Abdulsabirov R Yu and Dubinskii M A 1995 *Opt. Lett.* **20** 599–601.
36. Sarakura N, Liu Z, Segawa Y, Edamatsu K, Suzuki Y, Itoh T, Semashko V V, Naumov A K, Korableva S L, Abdulsabirov R Yu and Dubinskii M A 1995 *Opt. Lett.* **20** 294–6.
37. Rambaldi P, Moncorgé R, Wolf J P, Pedrini C and Gesland J Y 1998 *Opt. Commun.* **146** 163–6.
38. McGonigle A J S, Coutts D W and Webb C E 1999 *Opt. Lett.* **24** 232–4.
39. McGonigle A J S, Coutts D W and Webb C E 1999 *OSA Proc. Advanced Solid-State Lasers (TOPS 26)* (Washington, DC: Optical Society of America) pp 123–9.
40. McGonigle A J S, Coutts D W and Webb C E 1999 *IEEE J. Selected Topics Quantum Electron.* **5** 1526–31.
41. McGonigle A J S, Coutts D W, Webb C E, Girard S and Moncorgé R 1999 *Electron. Lett.* **35** 1640–1.
42 Payne S A, Chase L L, Newkirk H W, Smith L K and Krupke W F 1988 *IEEE J. Quantum Electron.* **24** 2243–53.
43. Marshall C D, Speth J A, Payne S A, Krupke W F, Quarles G J, Castillo V and Chai B H T 1994 *J. Opt. Soc. Am. B* **11** 2054–65.
44. Castillo V K and Quarles G J 1995 *UV and Visible Lasers and Laser Crystal Growth, San Jose (Proc. SPIE 2380)* (Bellingham, WA: SPIE) pp 43–50.
45. Castillo V K, Quarles G J and Chang R S F 2001 *J. Cryst. Growth* **225** 445–8.
46. Castillo V K and Quarles G J 1997 *J. Cryst. Growth* **174** 337–41.
47. Dubinskii M A, Semashko V V, Naumov A K, Abdulsabirov R Yu and Korableva S L 1993 *Laser Phys.* **3** 216–17.
48. Dubinskii M A, Semashko V V, Naumov A K, Abdulsabirov R Yu and Korableva S L 1993 *J. Mod. Opt.* **40** 1–5.
49. Dubinskii M A, Semashko V V, Naumov A K, Abdulsabirov R Yu and Korableva S L 1994 *Laser Phys.* **4** 480–4.
50. Dubinskii M A, Abdulsabirov R Y, Korableva S L, Naumov A K and Semashko V V 1993 *OSA Proc. Advanced Solid-State Lasers (TOPS 15)* (Washington, DC: Optical Society of America) pp 195–8.
51. Pinto J F, Esterowitz L, Rosenblatt G H and Quarles G J 1993 *LEOS '93 Conf. Technical Proceedings* Post-deadline paper PD1.4, pp 7–8.
52. Pinto J F, Rosenblatt G H, Esterowitz L, Castillo V and Quarles G J 1994 *Electron. Lett.* **30** 240–1.
53. Marshall C D, Payne S A, Speth J A, Tassano J B, Quarles G J and Castillo V 1994 Presented at *OE/LASE'94 Conf., Los Angeles* Session 2115, Paper 2115–02.
54. Bayramian A J, Marshall C D, Wu J H, Speth J A, Payne S A, Quarles G J and Castillo V K 1996 *J. Lumin.* **69** 85–94.
55. Pinto J F, Esterowitz L and Quarles G J 1995 *Electron. Lett.* **31** 2009–11.
56. Rambaldi P, Douard M and Wolf J P 1995 *Appl. Phys. B* **61** 117–20.
57. Pinto J F, Esterowitz L and Carrig T J 1998 *Appl. Opt.* **37** 1060–1.

58. Sarakura N, Liu Z, Ohtake H, Segawa Y, Dubinskii M A, Abdulsabirov R Yu, Korableva S L, Naumov A K and Semashko V V 1997 *Opt. Lett.* **22** 994–6.
59. Sarakura N, Dubinskii M A, Zhenlin L, Semashko V V, Naumov A K, Korableva S L, Abdulsabirov R Yu, Edamatsu K, Suzuki Y, Itoh T and Segawa Y 1995 *IEEE J. Selected Topics Quantum Electron.* **1** 792–804.
60. Sarakura N, Liu Z, Segawa Y, Semashko V V, Naumov A K, Korableva S L, Abdulsabirov R Yu and Dubinskii M A 1995 *Appl. Phys. Lett.* **67** 602–4.
61. Shimamura K, Baldochi S L, Mujilatu N, Nakano K, Liu Z, Sarukura N and Fukuda T 2000 *J. Cryst. Growth* **211** 302–7.
62. Liu Z, Kozeki T, Suzuki Y, Sarukura N, Shimamura K, Fukuda T, Hirano M and Hosono H 2001 *IEEE J. Selected Topics Quantum Electron.* **7** 542–50.
63. Galkin L N and Feofilov P P 1957 *Sov. Phys. Dokl.* **2** 255–7.
64. Galkin L N and Feofilov P P 1959 *Opt. Spectrosc. (USSR)* **1** 492–3.
65. Conway J G 1959 *J. Chem Phys.* **31** 1002–4.
66. Sorokin P P and Stevenson M J 1960 *Phys. Rev. Lett.* **5** 557–9.
67. Title R S, Sorokin P P, Stevenson M J, Pettit G D, Scardefield J E and Lankard J R 1962 *Phys. Rev.* **128** 62–6.
68. Yariv A 1962 *Phys. Rev.* **128** 1588–92.
69. Johnson L F, Boyd G and Nassau K 1962 *Proc. IRE* **50** 86.
70. Porto S P S and Yariv A 1962 *Proc. IRE* **50** 1542–3.
71. Porto S P S and Yariv A 1962 *Proc. IRE* **50** 1543–4.
72. Porto S P S and Yariv A 1962 *J. Appl. Phys.* **33** 1620–1.
73. Wittke J P, Kiss Z J, Duncan R C Jr and McCormick J J 1963 *Proc. IEEE* **51** 56–62.
74. Meredith R E and Jenney J A 1963 *J. Chem Phys.* **39** 3127–30.
75. Bazhulin P A, Malyshev V I, Markin A S, Rakov A V and Bagdasarov Kh S 1964 *Opt. Spectrosc. (USSR)* **16** 291–2
76. Porto S P S and Yariv A 1964 *Quant. Elect. III, Paris* vol 1 (New York: Columbia University Press) pp 717–23.
77. Hargreaves W A 1967 *Phys. Rev.* **156** 331–42.
78. Hargreaves W A 1970 *Phys. Rev. B* **2** 2273–84.
79. Hargreaves W A 1991 *Phys. Rev. B* **44** 5293–95.
80. Feofilov P P 1959 *Opt. Spectrosc. (USSR)* **1** 493–4.
81. Gruber J H, Morrey J R and Carter D G 1979 *J. Chem. Phys.* **71** 3982–7.
82. Crosswhite H M, Crosswhite H, Carnall W T and Paszek A P 1980 *J. Chem. Phys.* **72** 5103–17
83. Quarles G J, Esterowitz L, Rosenblatt G H, Uhrin R and Belt R F 1992 *OSA Proc. Advanced Solid-State Lasers (TOPS 13)* (Washington, DC: Optical Society of America) pp 306–9.
84. Jenssen H P, Noginov M A and Cassanho A 1993 *OSA Proc. Advanced Solid-State Lasers (TOPS 15)* (Washington, DC: Optical Society of America) pp 463–7.
85. Simoni E, Louis M, Gesland J Y and Hubert S 1996 *J. Lumin.* **65** 153–61.
86. Hubert S, Simoni E, Louis M, Zhang W P and Gesland J Y 1994 *J. Lumin.* **65** 245–9.
87. Louis M, Simoni E, Hubert S, Auzel F, Meichenin D and Gesland J Y 1995 *OSA Proc. Advanced Solid-State Lasers (TOPS 24)* (Washington, DC: Optical Society of America) pp 141–5.
88. Boyd G D, Collins R J, Porto S P S, Yariv A and Hargreaves W A 1962 *Phys. Rev. Lett.* **8** 269–72.
89. Sorokin P P and Stevenson M J 1961 *Advances in Quantum Electronics* ed J Singer (New York: Columbia University Press) pp 65–76.
90. Duncan R C, Jr, Kiss Z J and Wittke J P 1962 *J. Appl. Phys.* **33** 2568–9.
91. Miles P A 1961 *Advances in Quantum Electronics* ed J Singer (New York: Columbia University Press) p 76.
92. Bostick H A and O'Connor J R 1962 *Proc. IRE* **50** 219–20.
93. Keyes R J and Quist T M 1964 *Appl. Phys. Lett.* **4** 50–2.
94. Meichenin D, Auzel F, Hubert S, Simoni E, Louis M and Gesland J Y 1994 *Electron. Lett.* **30** 1257.
95. Owen J F, Dorain P B and Kobaysi T 1981 *J. Appl. Phys.* **52** 1216–23.
96. Lawson J K and Payne S A 1992 *OSA Proc. Advanced Solid-State Lasers (TOPS 13)* (Washington, DC: Optical Society of America) pp 330–2.
97. Feofilov P P 1956 *Opt. Spektrosk.* **1** 992–9.
98. Feofilov P P and Kaplyanskii A A 1962 *Opt. Spektrosk.* **12** 493–500
99. Sorokin P P and Stevenson M J 1961 *IBM J. Res. Dev.* **5** 56–8.
100. Kaiser W, Garrett C G B and Wood D L 1961 *Phys. Rev.* **123** 766–76.
101. Anan'yev Yu A, Grezin A K, Mak A A, Sedov B M and Yudina Ye N 1968 *Sov. J. Opt. Technol.* **35** 313–16.
102. Vagin Y U S, Marchenko V M and Prokhorov A M 1969 *Sov. Phys. JETP* **28** 904–9.
103. Sorokon P P, Stevenson M J, Lankard J R and Pettit G D 1962 *Phys. Rev.* **127** 503–8.
104. Konyukhov V K, Marchenko V M and Prokhorov A M 1966 *Opt. Spectrosc. (USSR)* **20** 299–300.
105. Konyukhov V K, Marchenko V M and Prokhorov A M 1966 *IEEE J. Quantum Electron.* **2** 541–2.
106. Forrester P A, Green G M and Sampson D F 1965 *Br. J. Appl. Phys.* **16** 1209–10.
107. Malkin B Z, Ivanenko Z I and Aizenberg I B 1970 *Sov. Phys. Solid State* **12** 1491–6.
108. Payne S A, Chase L L, Krupke W F and Boatner L A 1988 *J. Chem. Phys.* **88** 6751–6.
109. Chase L L, Payne S A and Wilke G D 1987 *J. Phys. C: Solid State Phys.* **20** 953–65.
110. Lawson J K, Lee H W H, Payne S A and Boatner L A 1991 *OSA Proc. Advanced Solid-State Lasers (TOPS 10)* (Washington, DC: Optical Society of America) pp 386–9.
111. Galaktionova N M, Egorova V F, Zubkova V S, Mak A A and Prilezhaev D S 1967 *Opt. Spektrosk.* **23** 949–53.
112. Voronko Yu K, Osiko V V, Prokhorov A M and Shcherbakov I A 1974 *Proc. P.N. Lebedev Phys. Inst.* vol 60, ed D V Skobeltsin (New York: Consultants Bureau) pp 1–30.
113. Zolotov E M 1974 *Proc. P.N. Lebedev Phys. Inst.* vol 60, ed D V Skobeltsin (New York: Consultants Bureau) pp 87–132.
114. Johnson L F 1962 *Proc. IRE* **50** 1691–2.
115. Yariv A 1962 *Proc. IRE* **50** 1699–1700
116. Kiss Z J and Duncan R C 1962 *Proc. IRE* **50** 1531–2.
117. Kiss Z J 1964 *Quant. Elect. III, Paris* vol 1 (New York: Columbia University Press) pp 805–15.
118. Pressley R J and Wittke J P 1967 *IEEE J. Quantum Electron.* **QE-3** 116–29.
119. Hatch S E, Parson W E and Weagle R J 1964 *Appl. Phys. Lett.* **5** 153–4.

120. Zolotov E M, Osiko V V, Prokhorov A M and Shipulo G P J 1972 *Appl. Spectrosc. (USSR)* **8** 627–8.
121. Isaev S K, Kornienko L S, Lariontsev E G and Khritankov M S 1973 *Sov. J. Quantum Electron.* **2** 335–8.
122. Konyukhov V K, Kostin B B, Kulevskii L A, Murina T M and Prokhorov A M 1965 *Dokl. Akad. Nauk. SSSR* **165** 1056–8.
123. Kostin V V, Kulevsky L A, Murina T M, Prokhorov A M and Tikhonov A A 1966 *IEEE J. Quantum Electron.* **2** 611–12.
124. Kiss Z J, Lewis H R and Duncan R C 1963 *Appl. Phys. Lett.* **2** 93–6.
125. Kaminskii A A, Kornienko L S and Prokhorov A M 1965 *Dokl. Akad. Nauk. SSSR* **161** 1063–4.
126. Kozlov N A, Mak A A and Sedov B M 1966 *Opt. Mekh. Prom.* **N11** 25–9.
127. Bodretsova A I, Kaminskii A A, Levikov S I and Osiko V V 1967 *Sov. Phys. Dokl.* **12** 507–8.
128. Duncan R C and Kiss Z J 1963 *Appl. Phys. Lett.* **3** 23–4.
129. Kiss Z J and Duncan R C 1962 *Proc. IRE* **50** 1532–3.

FURTHER READING

Caird J A and Payne S A 1990 Crystalline paramagnetic ion lasers *CRC Handbook of Laser Science and Technology* ed M J Weber (Boca Raton, FL: Chemical Rubber Company).

Deike G H 1968 *Spectra and Energy Levels of Rare-Earth Ions in Crystals* (New York: Wiley–Interscience).

DiBartolo B 1968 *Optical Interactions in Solids* (New York: Wiley).

Kaminskii A A 1984 *Izves. Akad. Nauk. SSSR, Neorgan. Mat.* **6** 901–24.

Kaminskii A A 1981 *Laser Crystals, Their Physics and Properties* (Berlin: Springer).

Kaminskii A A and Osiko V V 1970 *Izv. Akad. Nauk. SSSR, Neorgan. Mat.* **6** 629–96

Koechner W 1988 *Solid-State Laser Engineering* (Berlin: Springer).

Mak A A, Anan’ev A and Ermakov B A 1968 *Sov. Phys.–Usp.* **92** 419–52.

Moulton P F 1982 Paramagnetic ion lasers *CRC Handbook of Laser Science and Technology, Volume 1: Lasers and Masers* ed M J Weber (Boca Raton, FL: Chemical Rubber Company).

Penzkofer A 1988 *Prog. Quantum Electron.* **12** 291–427

Powell R C 1998 *Physics of Solid-State Laser Materials* (New York: Springer).

Reisfeld R and Jørgensen C K 1977 *Lasers and Excited States of Rare Earths* (Berlin: Springer).

Uitert L G 1966 *Luminesence of Inorganic Solids* (New York: Academic) pp 465–539.

Walling J C 1987 Tunable paramagnetic-ion solid state lasers *Tunable Lasers* ed L F Mollenauer and J C White (Berlin: Springer).

Weber M J 2001 *CRC Handbook of Lasers* (Boca Raton, FL: Chemical Rubber Company).

Weber M J (ed) 1982 *CRC Handbook of Laser Science and Technology Volume 1: Lasers and Masers* (Boca Raton, FL: Chemical Rubber Company).

Wyborne B G 1965 *Spectroscopic Properties of Rare Earths* (New York: Wiley–Interscience).

Yariv A 1985 *Optical Electronics* (New York: CBS College Publishing).

6

Ti:sapphire: Material, Lasers and Amplifiers

Peter F. Moulton, Alan R. Fry, and Peter Fendel

CONTENTS

6.1 Introduction 69
6.2 Laser Material Properties 69
    6.2.1 Material Physics, Properties and Growth 71
6.3 Laser Systems 71
    6.3.1 Oscillators 71
        6.3.1.1 Tunable cw Lasers 71
        6.3.1.2 Short-Pulse Laser 73
        6.3.1.3 Dispersion Management 74
        6.3.1.4 Frequency Combs and Carrier Envelope Phase 74
    6.3.2 Amplifiers 75
        6.3.2.1 Amplifier Design 75
        6.3.2.2 Regenerative Amplifiers 76
        6.3.2.3 Multipass and Multi-stage Amplifiers 77
6.4 Exotica 77
    6.4.1 Petawatt Systems 77
    6.4.2 Cryogenically Cooled Systems 77
References 78

6.1 Introduction

The Ti:Al_2O_3 (Ti:sapphire) laser has several ancestors, including the first laser [1], based on the crystal ruby, formally Cr^{3+} ions doped into sapphire (Al_2O_3). Ti:sapphire employs the same robust host crystal as in ruby, which is crucial for the ruby laser to operate under the intense optical pumping from flashlamps, required by the three-level nature of the ruby laser transition. Another class of ancestors were the first broadly tunable solid-state lasers, based on divalent transition-metal ions, such as Ni^{2+} and Co^{2+}, doped into mainly fluoride host crystals, such as MgF_2 [2–5]. While these types of lasers could be tuned over an impressive range of wavelengths (1600–2500 nm in the case of Co:MgF_2 [6]), the low gain and the general need to operate under cryogenic cooling were drawbacks that limited their utility. Finally, another Cr^{3+}-doped crystal, alexandrite ($BeAl_2O_4$), developed in the late 1970s [7,8] showed that tunable solid-state lasers could be made with robust host crystals and operate at room temperature. Later variations of the alexandrite laser, providing broader tuning ranges, included Cr^{3+}-doped fluoride materials [9,10], such as $LiCaAlF_6$ (LiCAF) and $LiSrAIF_6$ (LiSAF).

Presently, the Ti:sapphire laser has become the most widely employed tunable and ultrafast-pulse solid-state laser, and in the following brief review of solid-state laser fundamentals, we explain how its unique set of properties have enabled its widespread use.

6.2 Laser Material Properties

The unique combination of good spectroscopic and material properties is the major reason that Ti:sapphire became and still remains a widely used crystal for tunable laser systems.

Table 6.1 lists the room-temperature (unless noted) spectroscopic properties of several common solid-state laser materials. Ti:sapphire emerges as having similar cross sections and saturation fluences to Nd:YAG ($Y_3Al_5O_{12}$), one of the most widely used conventional (i.e. non tunable) solid-state materials. It also has the largest gain linewidth of all the materials shown,

TABLE 6.1

Spectroscopic Properties of Selected Solid-State Laser Materials at 300 K, Unless Indicated

Material	Peak Wavelength (nm)	Storage Time (ms)	Cross Section at Peak (cm^2)	Gain Linewidth (nm)	Saturation fluence (J cm^{-2})
Nd:YAG	1064	0.24	2.8×10^{-19}	0.6	0.66
Yb:CaF$_2$	1030	2.4	3.0×10^{-21}	50	64
Co:MgF$_2$ (77 K)	1900	1.4	1.5×10^{-21}	600 (50 THz)	68
Cr:BeAl$_2$O$_4$	755	0.26	7×10^{-21}	55 (29 THz)	37
Cr:LiSAF	850	0.067	5.0×10^{-21}	190 (85 THz)	4.7
Ti:Al$_2$O$_3$	800	0.0032	2.5×10^{-19}	225 (100 THz)	1.0

supporting generation and amplification of pulses as short as 5 and 20 fs, respectively. A few the materials also have large linewidths but, in addition, high saturation fluences, limiting their use in pulse amplifiers.

Table 6.2 is another comparison table showing important thermo-optical and thermo-mechanical properties of some of the solid-state laser materials listed in Table 6.1. For non-isotropic materials, the values given represent those for the most favorable orientation and polarization.

A comparison of sapphire with the other materials points out the advantage of the crystal in high-power operation, as it has the highest thermal conductivity (with some variations in published data, as shown) and the highest thermal shock parameter. All of the properties in Table 6.2 for sapphire vary favorably at lower temperatures, as we discuss in more detail later in this chapter. The LiSAF material, which otherwise has excellent spectroscopic parameters, has limits to high-power operation, primarily from a low thermal conductivity.

Figure 6.1 shows the Ti:sapphire absorption (gray) and emission (black) cross sections as a function of wavelength. The solid lines are older line shape data [17] corrected for an

TABLE 6.2

Physical Properties of Selected Solid-State Laser Materials

Material	κ (W m^{-1}°C^{-1}) 300 K	κ (W/m^{-1}°C^{-1}) 100 K	α (10^{-6}°C^{-1})	dn/dt (10^{-6}°C^{-1})	E (GPa)	RT (W/m)	Refs.
YAG	10	58	6.7	8.9	282	1100	[11–13]
MgF$_2$	21	100	15	2.0	138	1300	[11,12]
BeAl$_2$O$_4$	23		4.4 (a) 6.8 (b) 6.9 (c)	9.4 (a) 8.3 (b)	446	2350	[12,13]
LiSAF	3.1		−8.1 (c) 26 (a)	−4.5 (n_o) −9.1 (n_e)	109	84 (a) 160 (c)	[14,15]
Al$_2$O$_3$	28–42	380	6.7 (‖ to c)	12.8 (‖ to c)	405	3400	[11,12,16]

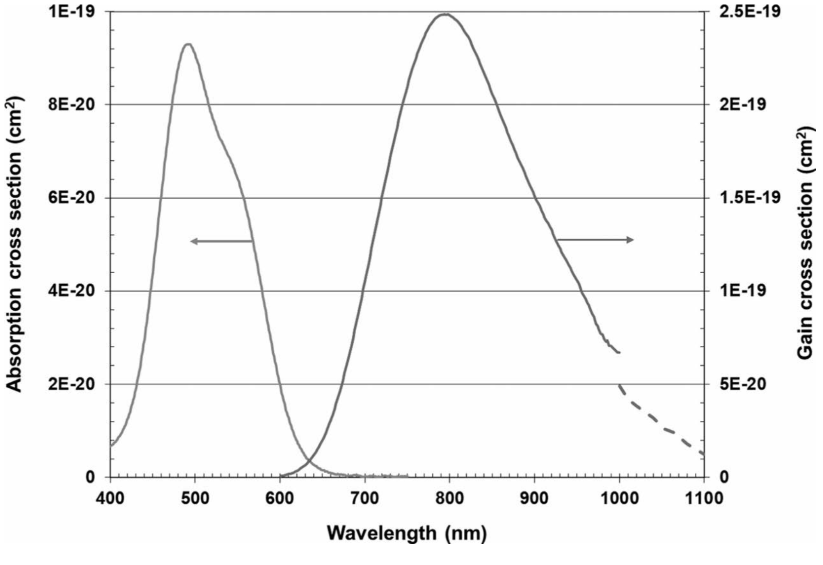

FIGURE 6.1 Data on Ti:sapphire absorption and gain cross sections as a function of wavelength, for π-polarized light.

absorption cross-section scale (left axis) derived by a newer, more accurate analysis [18], while the gain cross-section scale (right axis) reflects the consensus of several measurements [19–21]. Gain data at wavelengths longer than 1000 nm from [17] have been omitted due to the increasing level of noise from the detector used in the original measurements. However, included in the plot (dashed lines) are long-wavelength gain cross-section data derived from direct gain measurements [20].

The absorption band in Figure 6.1 shows that optical pumping of Ti:sapphire can be accomplished through the use of a variety of different lasers. Early cw operation with pumping by argon-ion gas lasers (488–515 nm) has been superseded by use of frequency doubled, Nd-doped and Yb-doped solid-state lasers, or by optically pumped semiconductor lasers (OPSL). Pulsed pumps include the same solid-state lasers operating in the nanosecond-pulse regime, and, for very high-energy systems, doubled Nd:glass lasers. Recently, GaN-based diode lasers have become available with sufficient power and brightness to pump Ti:sapphire lasers, and future diode developments may provide a path to more efficient, compact and inexpensive systems.

6.2.1 Material Physics, Properties and Growth

The Ti:sapphire laser transition occurs between energy levels associated with the single 3d-electron in the outer shell of the Ti^{3+} ion. The normally five-fold degenerate, free-space 3d-electronic state is split when the ion sits in the sapphire crystal at a site normally occupied by an Al^{3+} ion. That field at the site is nearly cubic in symmetry, with a strong trigonal component. The lowest-energy state ($^2T_2$) is a three-fold nearly degenerate level and splits slightly into two main levels by the trigonal field, with the lower level splitting further by a spin-orbit interaction [22–24]. The two-fold-degenerate upper laser level (^2E) interacts with the host crystal through the Jahn-Teller interaction to split into two spatially disjoint, but equal-energy states.

We have listed some of the properties of the host crystal, sapphire, in Table 6.2, and there is ample literature on other properties, as the material finds widespread use, ranging from substrates for semiconductor devices, protective covers on cellphone cameras to windows on military equipment such as tanks. It is produced in yearly quantities of several hundred tons. In terms of hardness, sapphire is below only diamond and silicon carbide. The crystal structure is of the trigonal space group $R\underline{3}c$, and is uniaxial, with a slight birefringence of about 0.008, and an index of about 1.76–1.77 [25]. Optical properties are given with respect to polarization either parallel to the crystal c-axis (pi-polarized) or perpendicular (sigma-polarized). In Ti:sapphire, the absorption and emission properties are strongly polarized in favor of pi-polarized light for both absorption and emission [15].

From the standpoint of laser design, one important practical material property is the absorption coefficient (typically in cm^{-1}) of the pump-band light. This is proportional to the Ti^{3+} concentration in the crystal. Unfortunately, there are several different ways to specify this, including the actual ion density (ions/cm^3), Ti^{3+} doping in molecular % or weight %, Ti_2O_3 doping in molecular % or weight %, and sometimes just a % doping, with no indication of what the % signifies. As an example of one relationship, if α_{490} is the absorption at 490 nm for π-polarized light, then

$$\text{Weight\% } Ti_2O_3 = (0.032 \pm 0.003)\alpha_{490}, \tag{6.1}$$

where the presumption is that all of the Ti ions are in the 3+ state [18].

In specifying material, the safest approach is to specify the desired pi-polarized absorption coefficient. In some cases, vendors may quote absorption at 514 nm (α_{514}), a convention from the period when argon-ion lasers were widely used as pump sources, and the absorption there is about 0.875 of the value at 490 nm.

In terms of material growth, commercial materials have been prepared using variations in the Czochralski crystal-pulling-from-the-melt technique, with the use of post-growth annealing to improve the FOM [26]. Another widely utilized approach is the Heat-Exchanger Method (HEM) [27], which has been used to grow very large-size materials needed for high-energy laser systems.

6.3 Laser Systems

After reviewing some basic material properties of Ti:sapphire in the previous section, the rest of this chapter will focus on the use of Ti:sapphire as a gain material in laser oscillators and amplifiers. Because of its favorable thermal and spectroscopic properties, Ti:sapphire has been used in countless different laser and amplifier configurations. Only the most common are described below, and references are given for those who want to get a more comprehensive overview.

6.3.1 Oscillators

6.3.1.1 Tunable cw Lasers

Under cw pumping conditions, and with no loss due to excited-state absorption of the pump or other complications, the cw gain per unit length, g_0, of a laser material with uniform pumping can be expressed as follows:

$$g_0 \propto \alpha \; W_p \lambda_p^4 / n^4 \Delta\lambda, \tag{6.2}$$

where W_p is the pump rate in excitations/($cm^3 s^{-1}$), λ_p is the peak gain wavelength, and $\Delta\lambda$ is the gain linewidth of the transition, given in units of wavelength. For a broad-linewidth material such as Ti:sapphire, achieving sufficient gain for laser action requires relatively high optical pumping rates. This leads to the use of cw lasers as pump sources, focused to high intensities in the Ti:sapphire laser medium.

For laser-pumped materials pumped along the direction of the laser beam (longitudinal pumping), the pump power (P_{th}) required to reach the threshold of laser action can be approximated by the following equation [28]:

$$P_{th} = \eta_c \frac{\pi h \nu_p}{4\sigma_p \tau} \left(T + L_{cav} + L_{XTL}\right)\left(w_0^2 + w_p^2\right)\left[1 - \exp(-\alpha l)\right]^{-1}, \tag{6.3}$$

where η_c is the coupling efficiency of the pump beam into the laser crystal, which accounts for losses in the optical elements between the pump laser and the inside of the laser material; h is Planck's constant; ν_p is the frequency of the pump laser; σ_p and τ are the peak gain cross section and upper-state lifetimes discussed above, respectively; T is the transmission of the (assumed single) output-coupling (OC) mirror; L_{cav} is the total loss in the optical cavity from other than the output coupler and laser crystal; L_{XTL} is the loss in the crystal; w_0 and w_p are the mode radii of the laser and pump beams in the crystal, respectively; α is the absorption coefficient in the crystal for pump light; and l is the length of the crystal. The equation assumes the use of a standing-wave resonator, where the losses are calculated per round-trip (i.e. two-pass) in the cavity and crystal. For a ring-cavity system, the factor 4 in the equation must be changed to 2, since the laser beam is only amplified in one pass through the crystal, but this is mitigated by the reduced losses due to single passes in the cavity and crystal.

The assumption in Equation (6.3) is that the pump and laser beams are Gaussian in cross section and the mode sizes are uniform inside the crystal, i.e. the confocal lengths of the pump and laser beams are longer than the crystal, or the inverse of α, when the latter is large compared to the crystal length. Good design practice is to limit the length of the crystal such that αl is in the range of 2–3, as longer crystals provide marginally lower thresholds and can increase the threshold due to crystal loss. When the assumption of uniform pump and laser beam sizes in the crystal is not appropriate, the threshold increases and calculations become more complex [29]. The use of a single-mode pump laser leads to the lowest thresholds, since it allows smaller radii pump beams that still maintain a uniform beam size in the crystal.

For cw Ti:sapphire lasers, typical pump-beam mode radii are in the 25–50 μm region, to obtain thresholds on the order of a Watt with output couplers in the 2%–10% transmission range. This requires optical resonators designed to match the laser cavity mode size to this relatively small beam. The design is complicated by the desire to operate the gain medium at Brewster's angle to the resonator axis, minimize reflection losses over a wide wavelength range and eliminate the need for anti-reflection coatings that can suffer optical damage. The presence of a Brewster's angle element adds astigmatism (different optical paths for beam transverse axes in the Brewster plane of incidence and perpendicular to it) that can produce an elliptical cross section, rather than round output beam for resonators with a small mode size.

With the use of a Brewster's angle crystal, Equation (6.3) must be multiplied by n, the Ti:sapphire index of refraction (about 1.76), since the pump and laser beams inside the crystal are elongated in one dimension by this factor, thus reducing the pump intensity and gain by the same amount.

Figure 6.2 shows the typical cavity designs used for cw-pumped Ti:sapphire lasers. Both standing-wave and ring-cavity designs are illustrated. The standing-wave design is the so-called "W" configuration, with an alternative, the "Z" arrangement, achieved by rotating one of curved mirrors about the axis established by the beam in the crystal. The designs provide tight focusing for the cavity mode in the laser crystal and also, through the use of off-axis mirrors, correction for the astigmatism created by Brewster's angle laser crystal in between the two focusing mirrors. This approach was first developed for cw lasers based in liquid dyes [30] with a three-mirror design, subsequently improved to a four-mirror design that provided a single focal spot in the laser medium [31]. The four-mirror design has been readily adapted for cw Ti:sapphire lasers. Cavity designers often employ the ABCD matrix approach [32] to work out the correct choice of mirror curvatures and spacings, with the addition of the ABCD matrix for off-axis curved mirrors [33]. The technique becomes increasingly necessary for even more complex designs than in Figure 6.2, involving other curved mirrors to produce added intracavity small spot sizes for use with nonlinear crystals or high-speed acousto-optic modulators. The designs also provide cavity beams between the focusing mirrors and HR or OC mirrors that have relatively large, nearly uniform mode sizes. The cavity parameters are relatively insensitive to the exact optical path for the beams, allowing insertion of Brewster's angle optics with minimal addition of astigmatism to the cavity mode. The ring-cavity design facilitates single-frequency operation through elimination of spectral hole-burning (for more details, see Refs. [34–38]).

With the desire to use a low-transmission output coupler to keep the threshold low, it becomes important that other optics in the cavity also have low losses. One key intracavity optic for Ti:sapphire lasers is the tuning element. While Brewster's angle prisms are one option, birefringent filters (BRFs), another technology with origins from cw dye lasers [39], are more common. The filters are based on uniaxial birefringent crystals placed at Brewster's angle to the resonator beam (Figure 6.2) to provide a low-loss tuning element. BRFs can be viewed as a variation of the etalon concept. When ab interference between the transmitted and reflected beams creates a wavelength-varying transmission in an etalon, a BRF operates on the interference between the two linearly and orthogonally polarized beams that represent the general state of polarization

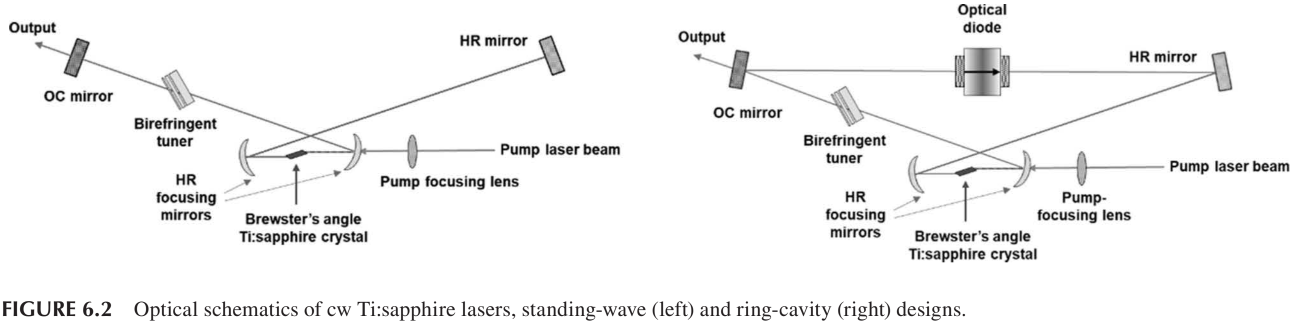

FIGURE 6.2 Optical schematics of cw Ti:sapphire lasers, standing-wave (left) and ring-cavity (right) designs.

inside a birefringent crystal. With a given thickness, orientation and birefringence for single BRF crystal, a cavity optical beam with incoming linear polarization will generally exit the BRF with elliptical polarization, due to the optical phase difference between the two orthogonally polarized beams. Only when the wavelength of the beam produces a phase difference that is an integer multiple of π (a resonance for the BRF), the beam polarization state will remain linear and not suffer loss at the exiting Brewster surface. Modern designs [40] use off-axis plates to enable broad tuning ranges. Details of BRF designs can be found in Refs. [41–46].

Figure 6.3 shows the tuning curve for a commercial cw Ti:sapphire laser, showing coverage from 670 to 1100 nm, possible through the use of three different sets of cavity mirrors. The challenge is clear to designing a BRF that covers this range and provides enough spectral rejection to permit operation at either extreme of the gain region.

The earliest cw Ti:sapphire lasers employed argon-ion lasers as pumps, but they have been replaced by cw, frequency-doubled solid-state lasers, typically based on diode-pumped, Nd:YVO$_4$ lasers and doubled Yb:fiber lasers, and frequency-doubled, OPSLs. Recently, InGaN-based semiconductor lasers have become available with sufficient brightness for pumping cw lasers [48–52] and at present are capable of producing Ti:sapphire powers around 0.5 W. Published work indicates that use of 450 nm-region diodes can induce extra loss in the Ti:sapphire crystal [48] and yields lower efficiency than expected [52]. Thus, diodes at longer wavelengths are more desirable. The reason for this effect has been recently identified, and optimal diode wavelengths for pumping are at 490 nm and longer [53,54].

6.3.1.2 Short-Pulse Laser

The relation between pulse duration $\Delta\tau$ and the bandwidth $\Delta\omega$ required to support such pulse is described through the time-bandwidth product: $\Delta\omega \times \Delta\tau = \text{const}$ [55]. One of the key properties of Ti:sapphire is its broad gain spectrum, which covers several hundred nanometers, thus supporting extremely short, on the order of 5 fs, laser pulses.

In general, a laser cavity only supports a discrete spectrum. Each longitudinal cavity mode needs to satisfy the geometrical condition $n\lambda/2 = L$ (n being an integer and L the optical path length). The mode spacing is given by the inverse of the cavity round-trip time and lies typically based on geometric considerations in between 10 MHz and 1 GHz, which corresponds to a cavity length of approximately 15 m and 15 cm, respectively, for a linear cavity.

Combining this with the requirements imposed by the time-bandwidth product a short-pulse laser cavity needs to lase on a large number (>10^4) of modes to cover the required bandwidth for an fs pulse. Lasing on many modes, however, is necessary but not sufficient to generate short pulses from a laser cavity.

It is well known that light with different frequencies propagates with different phase velocities through space except when in vacuum, a phenomenon called dispersion. As a consequence, unless dispersion is managed properly (see below), no short-pulse formation in a laser cavity is possible as different parts of the spectrum (different modes) would have slightly different round-trip times leading to the pulse spreading out in time. But even if the dispersion is managed properly in a laser cavity, it is not guaranteed for the laser to produce short pulses. In order to do that, all longitudinal modes in the cavity need to be forced into "lock-step" with each other so that they add up coherently and produce a single short pulse.

Various methods are used in scientific and commercial lasers to lock the cavity modes together. Most techniques rely on a cavity design which favors high peak power operation over steady-state cw operation by either increasing the gain or reducing the interactivity losses when the laser produces ultrashort pulses. For Ti:sapphire lasers, the most common mode-locking mechanism is the Kerr Lens mode locking [56,57], though other techniques like using a saturable absorber [58] also exist. A comprehensive discussion of mode locking can be found in Refs. [59–63].

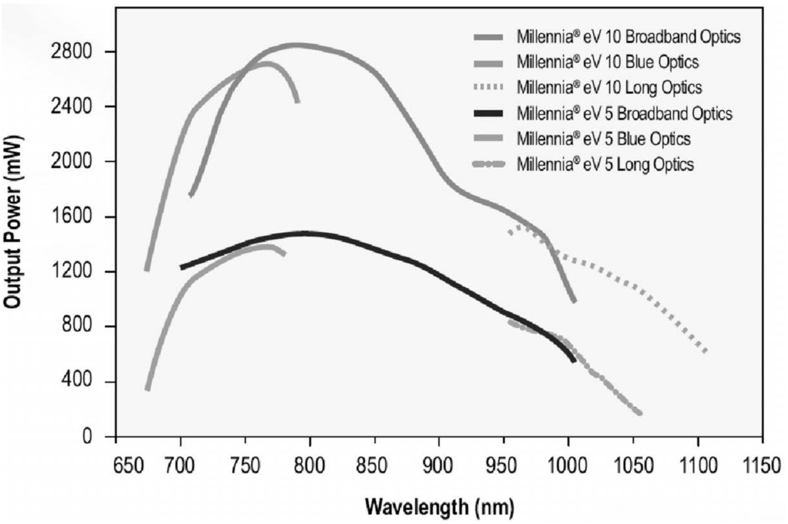

FIGURE 6.3 Tuning curve for commercial Ti:sapphire laser (Spectra-Physics 3900S) with three different optics sets (Broadband, Blue and Long) and with 5 W, and 10 W, 532 nm pump powers (Millenia eV 5 and 10) [47].

6.3.1.3 Dispersion Management

Many techniques for managing the dispersion in Ti:sapphire laser resonators have been developed over the past two decades. Unfortunately in the operating wavelength region of a Ti:sapphire laser, no negative dispersion materials, i.e. materials in which blue light travels faster than red light, are readily available. The three most common ways to introduce negative dispersion in the near IR are the Gires–Tournois interferometers [64], a combination of 2 or 4 prisms [65,66] and chirped mirrors [67].

Prisms are an easy and versatile way to control dispersion in a laser cavity. Two basic geometries employing either 2 or 4 prisms are possible, and both have been used in commercial laser systems. A typical 2-prism cavity is shown in Figure 6.4. The idea behind any dispersion management tool is to introduce a wavelength-dependent optical path length or phase difference. In case of prisms, each wavelength travels on a different trajectory through the prism assembly accumulating slightly different phase along the way. The prism material, degree of prism insertion and the distance between the two prisms determine the amount of dispersion the assembly introduces.

A detailed derivation of the dispersion of such prism assemblies introduce can be found [65]. The GDD is approximated by

$$\mathrm{GDD}(\lambda) \approx -4\ d\ \frac{\lambda_0^3}{2\pi c^2}\left(\frac{dn}{d\lambda}\Big|_{\lambda_0}\right)^2 + D\frac{\lambda_0^3}{2\pi c^2}\frac{d^2n}{d\lambda^2}\Big|_{\lambda_0}$$

with d being the separation between the two prisms and D being the insertion. In order to avoid the Fresnel reflection losses, the prism should be used under Brewster's angle [68]. The apex angle α itself should follow this equation to minimize losses also on the second prism surface:

$$\alpha = 180° - 2\theta_B$$

θ_B being the Brewster angle for the material the prism is made from.

Prisms work well for lasers with pulse durations above 12 fs. However, the dispersion manipulation prisms can provide is insufficient once the simultaneous lasing bandwidth approaches 100 nm. In this case, not only second and third orders but higher orders of dispersion terms also need to be managed [69,70]. A state-of-the-art solution is a chirped mirror [67]. A chirped mirror is a dielectric mirror which in addition to being a high reflector also alters the spectral phase of the reflected light in a controlled manner. The phase response or dispersion of a chirped mirror is given by the interference inside of the layer stack and not – to first order – by the material of the layer stack itself. This allows laser designers a lot of freedom in shaping the dispersion of the laser cavity and to carefully control higher-order dispersion terms which is essential for sub 10 fs laser operation.

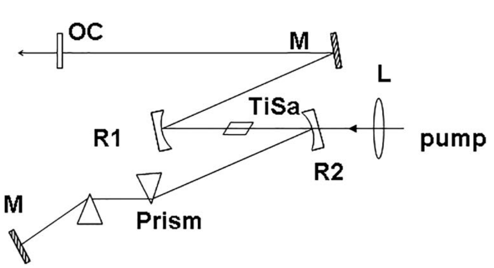

FIGURE 6.4 Typical cavity layout for a Ti:sapphire laser using prisms for dispersion compensation.

The basic and greatly simplified operating principle of a chirped mirror relies on the principle that different colors experience different penetration depths into the thin film layer stack (see Figure 6.5). For negatively chirped mirrors, short-wavelength light is reflected on top of the mirror, while the long part of the spectrum penetrates deep into the layer stack accumulating a phase delay compared to the blue part of the spectrum. The dispersion of such a mirror is opposite to material dispersion in the near IR and can hence be used for dispersion management.

6.3.1.4 Frequency Combs and Carrier Envelope Phase

The concept of frequency combs or carrier envelope phase is not limited to Ti:sapphire lasers but applies to all mode locked lasers. Ti:sapphire lasers, however, were the first lasers in which a fully stabilized, self-referenced comb was demonstrated [71,72].

A detailed description about frequency combs can be found in Refs. [73–75]. The seminal work on this topic by Hall and Hänsch in the late 1990s is of long reaching significance for the ultrafast as well as the frequency metrology community enabling, e.g., optical clocks [76] or the generation of attosecond pulses [77].

The most difficult part in realizing a frequency comb was to measure and control the phase and the phase slip between the carrier wave and the envelope function, the so-called carrier envelope phase (CEP) or the carrier envelope offset frequency f_{ceo} [78,79] (see Figure 6.6). The shift in CEP from pulse to pulse originates from the fact that the carrier propagates with its phase velocity, i.e., speed of light, while the amplitude function propagates only with the group velocity.

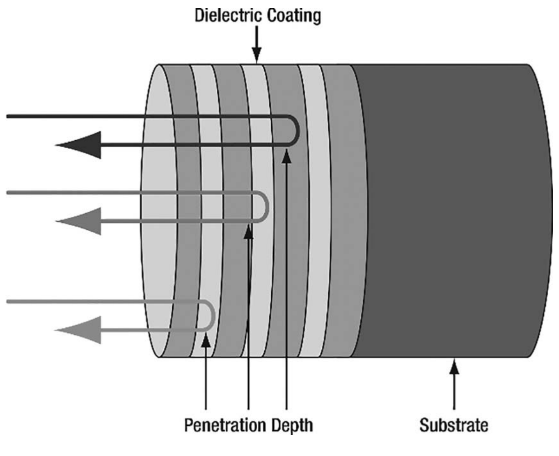

FIGURE 6.5 In a chirped mirror, different wavelength experience diffrenet penetration depths into the dielectric coating and hence chirped mirrors introduce dispersion.

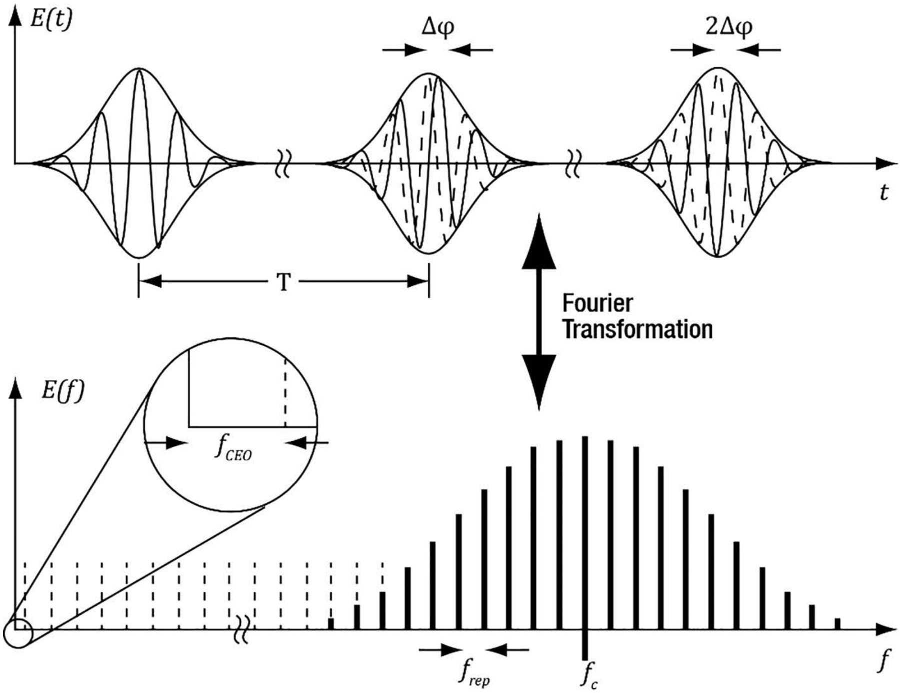

FIGURE 6.6 An fs pulse train and a frequency comb are linked through Fourier transformation. The mode spacing is given by the repetition rate [74].

For particular applications like high harmonic or attosecond pulse generation, it is vital that one generate femtosecond pulses with a specific and constant carrier envelope offset phase [77].

6.3.2 Amplifiers

Femtosecond pulse oscillators typically operate with pulse energies in the range of a few nJ up to hundreds of nJ in gain-switched Ti:sapphire oscillators. A number of schemes have been developed to increase the energy of Ti:sapphire systems, spanning several orders of magnitude in repetition rate and pulse energy, ranging from hundreds of kHz at μJ energy to tens of J in single-shot configurations. The most common commercial Ti:sapphire systems are configured in a well-established and widely adopted middle range of a few to tens of mJ operating at a few kHz repetition rate, e.g. 1 kHz, 5 mJ, 5 W average power. The pulse duration of a Ti:sapphire amplifier can also span several orders of magnitude from <10 fs to >1 ps, with the most common commercial systems operating in the range of 30–50 fs FWHM.

In most applications of amplified ultrafast laser pulses, the key parameter is the pulse intensity rather than the pulse energy or average power. This requires that amplified beams have a “clean” spatial profile that can be focused to the desired spot size to achieve the necessary intensity. In some cases, particularly in very high-intensity applications, it is also necessary to have a “clean” temporal profile, free of pre- and post-pulses.

Nearly every Ti:sapphire amplifier utilizes the technique of chirped pulse amplification (CPA), in which the seed laser pulse from a Ti:sapphire oscillator is temporally stretched by several orders of magnitude in a dispersive optical system, amplified and then recompressed in another dispersive optical system. The chirped-pulse amplification technique [80] was developed to reduce the peak power in high-energy Nd:glass amplifiers [81] and was quickly adapted to Ti:sapphire systems [82].

6.3.2.1 Amplifier Design

The laser designer will optimize the energy of a Ti:sapphire laser amplifier by achieving the highest possible gain for a given pump energy without introducing temporal or spatial distortions to the amplified pulse. The amplified pulse should reach the saturation fluence for the highest efficiency and the highest shot-to-shot energy stability, as well as to ensure that the dispersion associated with the amplification is linear across the temporally chirped pulse to achieve consistent recompression. Over-saturation of the pulse can result in changes in the pulse intensity profile, specifically higher amplification of the temporally leading edge of the pulse, and in a CPA configuration, this effect will also result in a spectral reshaping of the amplified pulse due to the longer wavelengths temporally preceding the shorter wavelengths.

Ti:sapphire amplifier designs must also optimize the overall dispersion of the CPA system including the total group velocity dispersion (GVD) of the optical elements in the amplifier. High GVD due to a large number of optical elements is significantly more challenging for very short (<30 fs) laser pulses with correspondingly large (>30 nm) bandwidths, and many amplifier designs are fine-tuned in terms of the selection of the type and thickness of materials used in the amplifier stages.

Gain narrowing is an important consideration in amplifier design, but it is not commonly a significant problem for Ti:sapphire due to its extremely broad gain bandwidth. Again it is only in applications that require extremely broad bandwidths (e.g. >100 nm for a <10 fs pulse), or in cases where it is desirable to shift the center wavelength of the output of the Ti:sapphire amplifier by many tens of nm away from the peak of the gain near 800 nm. It is more often the case that the bandwidth of the Ti:sapphire amplifier is limited by the spectral bandwidth of other elements of the Ti:sapphire amplifier, such as the reflectivity of the dielectric coatings of the mirrors.

A more detailed descriptions about the general architecture of CPA systems, e.g. strechter and compressor designs, can be found in Ref. [83].

6.3.2.2 Regenerative Amplifiers

The regenerative amplifier [84] (commonly abbreviated "regen") is the first most commonly used amplification stage in commercial Ti:sapphire systems. A typical Ti:sapphire regenerative amplifier configuration is shown in Figure 6.7. In this figure, the pump beam is shown in green, and the seed and amplified Ti:sapphire beams are shown in red. Two Pockels cells are used as electro-optical switches, and two polarizers are used: one to inject the seed beam and the other to eject the amplified beam after the last round-trip, both arranged for transmission in P-polarization. When the regen cavity is inactive, seed laser pulses are continuously injected into the regen cavity, reflecting in S-polarization off the input polarizer (P1) into the cavity. These pulses double-pass through the input Pockels cell (PC1) and quarter waveplate (QWP) for a net rotation of half-wave to P-polarization. The pulses then make a complete round-trip through the regen cavity, through the Ti:sapphire crystal, the output polarizer (P2), the output Pockels cell (PC2), and then back through the entire cavity. Upon making a second round-trip through the QWP, the pulse is again S-polarized and is rejected from the cavity from the input polarizer (P1). During amplification, the typical sequence of events follows: first, the Ti:sapphire crystal is pumped by a pulsed or CW pump source. When the Ti:sapphire is sufficiently pumped to achieve the necessary gain, the input Pockels cell (PC1) is activated to produce a quarter-wave rotation, so that in combination with the QWP, there is net-zero round-trip change in the polarization state of a P-polarized seed pulse making its return trip through the cavity (similarly, any subsequent seed pulses entering the cavity stay in their S-polarization state and are rejected from the input polarizer after a single half-round-trip). The selected, P-polarized seed pulse then makes multiple round-trips through the cavity, continuing to extract the stored energy in the Ti:sapphire crystal. When the maximum gain and saturation of the amplifier are achieved, the output Pockels cell (PC2) is activated a quarter-wave rotation so that when the amplified pulse makes a round-trip through this Pockels cell, the net half-wave rotation switches the pulse to S-polarization, and it is rejected from the cavity through the output Pockels cell (P2).

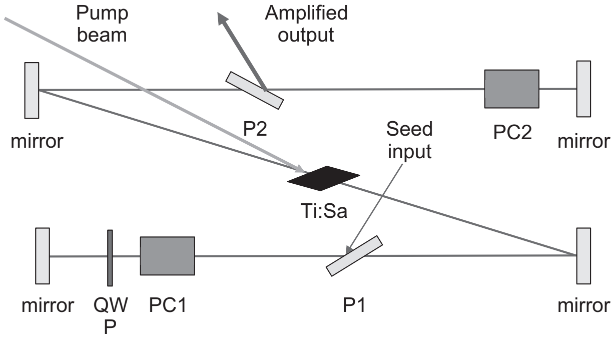

FIGURE 6.7 Schematic layout of a regenerative amplifier cavity.

To maximize efficiency in any regenerative amplifiers, it is necessary to use optical elements that have low losses for the amplified beam, e.g. high-reflectivity cavity mirrors, high-transmission Pockels cells, waveplate, and Ti:sapphire crystal. Polarizers must have high transmission in P-polarization and simultaneously high reflectivity in S-polarization. The coatings for the optics in Ti:sapphire regen amplifiers can be especially challenging due to the broad-bandwidth Ti:sapphire; these coatings must have correspondingly broad-bandwidth as well as relatively flat spectral phase characteristics. An additional requirement for these coatings is moderate to high damage threshold as the peak fluence and peak intensity the amplified pulses in the cavity can become quite high. In general, optical coatings with the broadest bandwidth and flattest spectral phase have lower damage threshold than coatings with narrower bandwidth, and it can be necessary to trade-off between these features and to consider cavity designs that increase the amplified spot size on critical optics.

Another practical consideration for the selection of components in Ti:sapphire regenerative amplifiers is the total chromatic dispersion and accumulated higher-order spectral phase from transmission through the intracavity components. Normally, the stretcher/compressor system is designed to accommodate this dispersion over some range of round-trips, and changes in the dispersion of a different number of round-trips can be compensated with a small adjustments, e.g. to the compressor grating separation and/or grating angle.

In a typical, commercial, 1 kHz Ti:sapphire regenerative amplifier pumped with 20 mJ of 527 nm light from a Q-switched, frequency-doubled Nd:YLF laser, a seed pulse of a few nanojoules energy is amplified to >5 mJ in ~15 round-trips, corresponding to a total net gain of ~10^6 and a net round-trip gain of ~3. For a seed pulse with a bandwidth of >50 nm, FWHM (Gaussian) gain narrowing from amplification and the transmission and reflection bandwidth of intracavity optics will typically reduce the spectral bandwidth to around 30 nm FWHM (Gaussian), corresponding to a transform-limited pulse duration of ~30 fs FWHM.

A broader spectrum and narrower pulse duration can be achieved by means of intra-cavity elements with specifically tailored spectral response to increase losses near the peak of the Ti:sapphire gain to effectively "flatten" the spectral reshaping from the gain narrowing; such systems can achieve ~20 fs, with singular demonstrations as low as 12 fs [85–87].

Similarly, Ti:sapphire regen amplifiers can be configured to operate with amplified pulses having a peak at nearly any wavelength within the broad gain bandwidth, albeit with narrower spectral bandwidth. Cavity optics coated to have high loss at the peak of the gain of Ti:sapphire (~800 nm) and high reflectivity at another wavelength range can produce, for example, pulses centered at 760 nm [88] for the LCLS photoinjector, or at 1053 nm [20] for seeding a high-energy Nd:glass amplifier system.

6.3.2.3 Multipass and Multi-stage Amplifiers

In a multipass amplifier [89,90], a set of mirrors are arranged to provide multiple, slightly offset beam paths through the pumped region of the Ti:sapphire crystal in a fixed number of passes. This is a conceptually simple configuration with the advantage of having a smaller GVD compared to a regenerative amplifier, but can become difficult to align and optimize is the number of passes through the Ti:sapphire is high. Consequently, multipass amplifiers are better suited to systems requiring very high pulse energy in which the input pulse energy is already high relative to the saturation fluence of the amplifier, and saturation can be reached within 2–10 passes.

The most common commercial, few mJ Ti:sapphire laser systems are comprised of a single stage of amplification, either a regenerative amplifier or a multipass amplifier. Nearly, all higher-energy systems delivering 10 mJ or more are comprised of multiple stages of amplification, often with each stage having its own pump source, and operating at its own maximum rep-rate. A typical commercial configuration for a system generating pulses of 100 mJ energy would have an oscillator seeding a 1 kHz regenerative (or multipass) amplifier pumped by a q-switched, diode-pumped, frequency-doubled Nd:YLF laser to produce 5 mJ which would be picked down to a 10 Hz pulse train to seed a multipass amplifier pumped by a 10Hz q-switched, flashlamp-pumped, frequency-doubled Nd:YAG laser to produce 130 mJ before compression.

6.4 Exotica

6.4.1 Petawatt Systems

Scaling of CPA Ti:sapphire systems to very high peak powers, 1 PW (10^{15} W), and higher, has been accomplished, typically with compressed pulse energies of >30 J, and pulse widths on the order of 20–30 fs. The approach involves a series of amplifier stages, each pumped by higher-energy pumps. As the stages scale up in energy, they use larger-aperture beams and crystals to avoid optical damage to the laser medium and associated optics.

Early PW-class systems started with a Ti:sapphire femtosecond oscillator, typically followed by a Ti:sapphire-based regenerative amplifier, and then by staged amplifiers, with multipassing used to assure efficient extraction of pulse energy. For most scientific applications, it is very important to obtain a very high contrast (>10^{10}) between the main output pulse and any other pulse energy on either temporal side of that pulse. PW-class systems include a variety of techniques to improve pulse contrast. Some recent designs have employed optical parametric chirped pulse amplifiers (OPCPAs), which, under the right operating conditions [91], provide a unique combination of very high gain, broad gain bandwidth, and relatively low background pulse energy. Other techniques to improve pulse contrast include the addition of a cross-polarized wave (XPW) nonlinear element at some point in the amplifier chain [92]. The device operation is based on the use of third-order nonlinearity in a crystal, and hence is effective at suppressing low-energy content in the amplified pulse.

High-energy operation of Ti:sapphire brings challenges from the large-aperture crystals needed to avoid optical damage. They can lose energy stored from the pump laser through amplified spontaneous emission (ASE) along the transverse dimension of the laser crystal. Standard ASE-mitigation techniques include the use of absorbing media placed at the outer edge of the laser crystal. Another technique is to stagger the pump pulses in time to avoid too high a stored energy, and extract energy during the pumping process, a technique referred to as extraction during pumping (EDP) [93,94].

At the time of this writing, the field of PW-class Ti:sapphire lasers is dynamic, with new systems being developed and installed worldwide. One former (2017) peak-power record (5.4 PW) for any laser was set by a Ti:sapphire system [94], and in 2019, one of the 10-PW systems under construction [95–97] reached operational status at ELI-NP to set a new record.

A report from the U.S. National Academies of Sciences provides a more detailed technical discussion of PW-class Ti:sapphire lasers, with information on the status as of 2017 [98].

6.4.2 Cryogenically Cooled Systems

Ti:sapphire has unusually favorable properties regarding thermal effects, having a high thermal conductivity, which leads to lower thermal gradient in the crystal for a given level of power dissipation, and also a high stress-fracture limit. At high-enough powers, the material does exhibit optical distortion, mostly from the refractive index change. (Sapphire is naturally birefringent, and stress-induced birefringence in the material is small compared to the inherent birefringence, so losses in polarized resonators are not an issue. This is in comparison to isotropic materials such as YAG or glasses.) At sufficiently high powers, the refractive index distortion in Ti:sapphire can be enough to create unwanted changes in the cavity mode properties, in the case of oscillators, or the output-beam properties, in the case of amplifiers.

Cooling the Ti:sapphire crystal to cryogenic temperatures results in a dramatic change in the thermal, optical and mechanical properties that all relate to refractive-index distortion created by laser operation.

Table 6.3 compares important properties of sapphire at 300 and 100 K. Besides the dramatic increase in thermal conductivity, the change of refractive index with temperature undergoes a significant reduction, so that thermal gradients that do exist have a reduced effect on the refractive index. In addition, the major reduction in thermal expansion greatly reduces stresses in the material. This reduction also minimizes changes in the shape of the material surface, which can also modify its optical properties.

The major disadvantage with cooling is the reduced heat capacity. For a pulsed pump source, such as the ns-duration Q-switched laser pumps used for high-energy lasers, the initial temperature rise is much faster than the time it takes for heat to flow out of the pumped region and is thus mainly determined

TABLE 6.3

Sapphire Properties at 300 and 100 K [99]

Property	300 K	100 K
Thermal conductivity, κ (W cm^{-1} K^{-1})	0.33	10
Index change with temperature, dn/dT (K^{-1})	12.8×10^{-6}	1.9×10^{-6}
Thermal expansion coefficient, α (K^{-1})	5.0×10^{-6}	0.34×10^{-6}
Volumetric heat capacity (J K^{-1}cm^{-3})	3.1	0.25
Thermal diffusivity (cm^{2}s^{-1})	0.1	40

by the heat capacity of the material. At 100 K, the initial heat rise would be about ten times higher than at 300 K. This is mitigated by the reduction in index change this rise will create, as well as the reduced thermal expansion and hence stress. In addition, the very large increase in thermal diffusivity at 100 K means that the heat flows very quickly away from the pumped volume, so, except at very high pulse rates, or for large pump volumes, the material settles back to the overall heat rise set by the average heat dissipation. In one case, calculations showed that steady state would be reached in 30 μs at 100 K, but this number is highly dependent on the dimensions of pump and laser beams in the crystal [99].

Another important consideration for Ti:sapphire lasers is the rapid reduction in upper-state lifetime above 300 K. This results in additional heating in the material under pumping conditions, as the reduction is associated with non-radiative transitions from the upper to lower laser levels. This can lead to a "thermal runaway" as higher temperatures lead to higher non-radiative losses and hence even more heating. The use of cryogenic cooling assures that except for the most extreme conditions, thermal runaway will not be present in the laser system.

Cryogenic cooling has enabled power scaling of Ti:sapphire regenerative amplifiers used in moderate-energy ultrafast laser systems. Before compression, a 10 kHz-rate amplifier produced 40 W of average power with a 180 W-average-power pump laser, leading to 26 W average-power compressed pulses with 58 fs pulse width [100]. A cryo-cooled, higher rate (100 kHz) system has produced up to 4.8 W of power before compression through use of a 37 W-average-power pump, with 3 W of compressed power with 22 fs pulses [101]. Commercial products based on an ultrafast oscillator and a single, cryogenically cooled regenerative amplifier provide average powers in the 10–12 W range, for pulse rates from 1 to 300 kHz, and pulse widths ≤40 fs [102].

At present, commercial, cryogenically cooled, single multipass amplifier systems produce as much as 5 mJ of compressed energy at 1 kHz and 1 mJ at 10 kHz, for 10 W of average power, with ≤25 fs pulses. Systems with two to three multipass stages generate as much as 20 mJ of energy at 1 kHz and 5 mJ at 10 kHz (50 W of average power), also with ≤25 fs pulses [103]. Similar performance is available from commercial systems combining regenerative and multipass amplifiers, but the pulse widths are specified as ≤40 fs [104].

In lower-pulse-rate, higher-energy systems, a four-pass amplifier, with 200 mJ of input, generated 3.5 J of energy with 9.8 J of 532 nm pump energy, leading to a compressed output of 2.5 J in 25 fs pulses, at a 10 Hz rate [105]. Another system with a 40 mm-diameter crystal and 6.5 J of 532 nm pump energy produced 3.2 J of output energy with a 260 mJ input, also at a 10 Hz rate [106].

REFERENCES

1. T. H. Maiman, "Stimulated optical radiation in ruby," *Nature*, vol. 187, p. 493, 1960.
2. L. F. Johnson, R. E. Dietz, and H. J. Guggenheim, "Optical maser oscillation from N^{2+} in MgF_2, involving simultaneous emission of phonons," *Phys. Rev. Lett.*, vol. 11, no. 7, pp. 318–320, Oct. 1963, doi: 10.1103/PhysRevLett.11.318.
3. L. F. Johnson, R. E. Dietz, and H. J. Guggenheim, "Spontaneous and stimulated emission from Co^{2+} ions in MgF_2 and ZnF_2," *Appl. Phys. Lett.*, vol. 5, no. 2, pp. 21–22, Jul. 1964, doi: 10.1063/1.1754029.
4. L. F. Johnson, H. J. Guggenheim, and R. A. Thomas, "Phonon-terminated optical masers," *Phys. Rev.*, vol. 149, p. 179, 1966.
5. L. F. Johnson and H. J. Guggenheim, "Phonon terminated coherent emission from V^{2+} ions in MgF_2," *J. App. Phys.*, vol. 38, p. 4837, 1967.
6. P. F. Moulton, "Tunable solid state lasers," *Proc. IEEE*, vol. 80, p. 348, 1992.
7. J. C. Walling, H. P. Jenssen, R. C. Morris, E. W. O'Dell, and O. G. Peterson, "Tunable-laser performance in $BeAl_2O_4:Cr^{3+}$," *Opt. Lett.*, vol. 4, no. 6, pp. 182–183, Jun. 1979, doi: 10.1364/OL.4.000182.
8. J. C. Walling, O. G. Petersen, H. P. Jenssen, R. C. Morris, and E. W. O'Dell, "Tunable alexandrite lasers," *IEEE J. Quantum Electron.*, vol. 16, p. 1302, 1980.
9. S. A. Payne, L. L. Chase, H. W. Newkirk, L. K. Smith, and W. F. Krupke, "$LiCaAlF_6:Cr^{3+}$: a promising new solid-state laser material," *IEEE J. Quantum Electron.*, vol. 24, no. 11, pp. 2243–2252, Nov. 1988, doi: 10.1109/3.8567.
10. S. A. Payne, L. L. Chase, L. K. Smith, W. L. Kway, and H. W. Newkirk, "Laser performance of $LiSrAlF_6:Cr^{3+}$," *J. Appl. Phys.*, vol. 66, p. 1051, 1989.
11. W. F. Krupke, "Insulator materials in high power lasers for inertial fusion: present and future," in *MRS Proceedings*, vol. 24, p. 401, Jan. 1983, doi: 10.1557/PROC-24-401.
12. W. F. Krupke, M. D. Shinn, J. E. Marion, J. A. Caird, and S. E. Stokowski, "Spectroscopic, optical, and thermomechanical properties of neodymium- and chromium-doped gadolinium scandium gallium garnet," *J. Opt. Soc. Am.*, vol. B3, p. 102, 1986.
13. B. W. Woods, S. A. Payne, J. E. Marion, R. S. Hughes, and L. E. Davis, "Thermomechanical and thermo-optical properties of the $LiCaAlF_6:Cr^{3+}$ laser material," *J. Opt. Soc. Am.*, vol. B8, p. 970, 1991.
14. S. A. Payne et al., "Properties of $Cr:LiSrAlF_6$ crystals for laser operation," *Appl. Opt.*, vol. 33, p. 5526, 1994.
15. R. D. Peterson, A. T. Pham, H. P. Jenssen, A. Cassanho, and V. Castillo, "Thermo-optical comparison of LiSAF, LiCAF, and LiSGaF," in *OSA Trends in Optics and Photonics Vol. 26, Advanced Solid State Lasers*, M. M. Fejer, H. Injeyan, and U. Keller, Eds. Washington, DC: Optical Society of America, 1999, vol. 26, pp. 647–651.
16. M. G. Holland, "Thermal conductivity of several optical laser materials," *J. Appl. Phys.*, vol. 33, p. 2910, 1962.

17. P. F. Moulton, "Spectroscopic and laser characteristics of Ti:Al_2O_3," *J. Opt. Soc. Am. B*, vol. 3, p. 125, 1985.
18. R. L. Aggarwal, A. Sanchez, R. E. Fahey, and A. J. Strauss, "Magnetic and optical measurements on Ti:Al_2O_3 crystals for laser applications: concentration and absorption cross section of Ti^{3+} ions," *Appl. Phys. Lett.*, vol. 48, p. 1345, 1986.
19. N. P. Barnes and D. K. Remelius, "Amplifier and line-narrowed oscillator performance of Ti:Al_2O_3," in *Tunable Solid-State Lasers II*, A. B. Budgor, Ed. Berlin Heidelberg: Springer-Verlag, 1986, p. 318.
20. B. C. Stuart, S. Herman, and M. D. Perry, "Chirped-pulse amplification in Ti:sapphire beyond 1 μm," *IEEE J. Quantum Electron.*, vol. 31, p. 528, 1995.
21. K. Ertel, C. Hooker, S. J. Hawkes, B. T. Parry, and J. L. Collier, "ASE suppression in a high energy Titanium sapphire amplifier," *Opt. Exp.*, vol. 16, p. 8039, 2008.
22. E. D. Nelson, J. Y. Wong, and A. L. Schawlow, "Far infrared spectra of Al_2O_3:Cr^3+ and Al_2O_3:Ti^{3+}," *Phys. Rev.*, vol. 156, pp. 298–308, 1967.
23. R. R. Joyce and P. L. Richards, "Far infrared spectra of Al_2O_3 doped with Ti, V and Cr," *Phys. Rev.*, vol. 179, pp. 375–380, 1969.
24. R. M. MacFarlane, J. Y. Wong, and M. D. Sturge, "Dynamic Jahn-Teller effect in octahedrally coordinated d^1 impurity systems," *Phys. Rev.*, vol. 166, pp. 250–258, 1968.
25. I. H. Malitson and M. J. Dodge, "Refractive index and birefringence of synthetic sapphire," *Latter Appears Handb. Opt. Mater.*, vol. 62, p. 1405, 1972.
26. J. F. Pinto, L. Esterowitz, G. H. Rosenblatt, M. Kokta, and D. Peressini, "Improved Ti:sapphire laser performance with new high figure of merit crystals," *IEEE J. Quantum Electron.*, vol. 30, p. 2612, 1994.
27. F. Schmid and C. P. Khattak, "Growth of Co:MgF_2, and Ti:Al_2O_3 crystals for solid state laser applications," in *Tunable Solid State Lasers*, P. Hammerling, A. B. Budgor, and A. Pinto, Eds. New York: Springer, 1985, pp. 122–128.
28. J. Harrison, A. Finch, D. M. Rines, G. A. Rines, and P. F. Moulton, "Low-threshold, cw, all-solid-state Ti:Al_2O_3 laser," *Opt. Lett.*, vol. 16, p. 581, 1999.
29. A. J. Alfrey, "Modeling of longitudinally pumped cw Ti:sapphire laser oscillators," *IEEE J. Quantum Electron.*, vol. 25, p. 760, 1989.
30. H. Kogelnik, P. I. E, A. Dienes, and C. V. Shank, "Astigmatically compensated cavities for cw dye lasers," *IEEE J. Quantum Electron.*, vol. 8, p. 373, 1972.
31. W. D. Johnston and P. K. Runge, "An improved astigmatically compensated resonator for CW dye lasers," *IEEE J. Quantum Electron.*, vol. 8, p. 724, 1972.
32. H. Kogelnik, T. Li, A. Massey, and A. E. Siegman, "Laser beams and resonators," *Appl. Opt.*, vol. 5, p. 1550, 1966.
33. J. Harrison, A. Finch, D. M. Rines, G. A. Rines, and P. F. Moulton, "Low-threshold, cw, all-solid-state Ti:Al_2O_3 laser," *Opt. Lett.*, vol. 16, p. 581, 1991.
34. C. L. Tang, H. Statz, and G. deMars, "Spectral output and spiking behavior of solid-state lasers," *J. Appl. Phys.*, vol. 34, p. 2289, 1963.
35. A. R. Clobes and M. J. Brienza, "Single-frequency traveling-wave Nd:YAG laser," *Appl. Phys. Lett.*, vol. 21, p. 265, 1972.
36. P. A. Schulz, "Single-frequency Ti:Al_2O_3 ring laser," *IEEE J. Quantum Electron.*, vol. 24, p. 1039, 1988.
37. T. F. Johnston, Jr. and W. Proffitt, "Design and performance of a broad-band optical diode to enforce one-direction traveling-wave operation of a ring laser," *IEEE J. Quantum Electron.*, vol. 16, p. 483, 1980.
38. W. Vassen, C. Zimmermann, R. Kallenbach, and T. W. Hansch, "A frequency-stabilized titanium sapphire laser for high-resolution spectroscopy," *Opt. Commun.*, vol. 75, p. 435, 1990.
39. J. M. Yarborough and J. L. Hobart, "Tuning apparatus for an optical oscillator," US Patent 3,934,210. Note that Fig. 4 incorrectly indicates Brewster's angle.
40. U. Demirbas, "Off-surface optic axis birefringent filters for smooth tuning of broadband lasers," *Appl. Opt.*, vol. 56, p. 7815, 2017.
41. D. Bruneau, H. Cazeneuve, C. Loth, and J. Pelon, "Double-pulse dual-wavelength alexandrite laser for atmospheric water vapor measurement," *Appl. Opt.*, vol. 30, p. 3932, 1991.
42. G. Holtom and O. Teschke, "Design of a birefringent filter for high-power dye-lasers," *IEEE J. Quantum Electron.*, vol. 10, p. 577, 1974.
43. I. J. Hodgkinson and J. I. Vukusic, "Birefringent filters for tuning flashlamp-pumped dye lasers: simplified theory and design," *Appl. Opt.*, vol. 17, no. 12, pp. 1944–1948, Jun. 1978, doi: 10.1364/AO.17.001944.
44. S. Lovold, P. F. Moulton, D. K. Killinger, and N. Menyuk, "Frequency tuning characteristics of a Q-switched Co:MgF_2 laser," *IEEE J. Quantum Electron.*, vol. 21, p. 202, 1985.
45. K. Naganuma, G. Lenz, and E. P. Ippen, "Variable bandwidth birefringent filter for tunable femtosecond lasers," *IEEE J. Quantum Electron.*, vol. 28, p. 2142, 1992.
46. S. M. Kobtsev and N. A. Sventsitskay, "Application of birefringent filters in continuous-wave tunable lasers: a review," *Opt. Spectrosc.*, vol. 73, p. 114, 1992.
47. Spectra-Physics Model 3900S Data Sheet SP-DS-20150918. Permission to use granted by MKS/Spectra-Physics. All rights reserved, 2015.
48. P. W. Roth, A. J. Maclean, D. Burns, and A. J. Kemp, "Directly diode-laser-pumped Ti:sapphire laser," *Opt. Lett.*, vol. 34, p. 3334, 2009.
49. P. W. Roth, A. J. Maclean, D. Burns, and A. J. Kemp, "Direct diode-laser pumping of a mode-locked Ti:sapphire laser," *Opt. Lett.*, vol. 36, p. 304, 2011.
50. C. G. Durfee et al., "Direct diode-pumped Kerr-lens mode-locked Ti:sapphire laser," *Opt. Express*, vol. 20, p. 13677, 2012.
51. K. Gürel et al., "Green-diode-pumped femtosecond Ti:sapphire laser with up to 450 mW average power," *Opt. Express*, vol. 23, 30043, 2015.
52. R. Sawada, H. Tanaka, N. Sugiyama, and F. Kannari, "Wavelength-multiplexed pumping with 478- and 520-nm indium gallium nitride laser diodes for Ti:sapphire laser," *Appl. Opt.*, vol. 56, p. 1654, 2017.
53. P. F. Moulton, J. G. Cederberg, K. T. Stevens, G. Foundos, M. Koselja, and J. Preclikova, "Optimized InGaN-diode pumping of Ti:sapphire crystals," *Opt Mater. Express*, vol. 9, pp. 2131–2146, 2019.
54. P. F. Moulton, J. G. Cederberg, K. T. Stevens, G. Foundos, M. Koselja, and J. Preclikova, "Characterization of absorption bands in Ti:sapphire crystals," *Opt. Mater. Express*, vol. 9, pp. 2216–2251, 2019.

55. J.-C. Diels and W. Rudolph, *Ultrashort Laser Pulse Phenomena: Fundamentals, Techniques, and Applications on a Femtosecond Time Scale*. Amsterdam: Elsevier, 2006.
56. L. Dahlström, "Passive mode-locking and Q-switching of high power lasers by means of the optical Kerr effect," *Opt. Commun.*, vol. 5, pp. 157–162, 1972.
57. E. G. Lariontsev and V. N. Serkin, "Possibility of using self-focusing for increasing contrast and narrowing of ultrashort light pulses," *Sov. J. Quantum Electron.*, vol. 5, p. 796, 1975.
58. L. R. Brovelli, "Self-starting soliton modelocked Ti-sapphire laser using a thin semiconductor saturable absorber," *Electron. Lett.*, vol. 31, pp. 287–289, 1995.
59. H. A. Haus, "Mode-locking of lasers," *IEEE J. Sel. Top. Quantum Electron.*, vol. 6, pp. 1173–1185, 2000.
60. P. G. Drazin and R. S. Johnson, *Solitons: An Introduction*. Cambridge: Cambridge University Press, 1989.
61. G. L. Lamb, *Elements of Soliton Theory*. New York: Wiley, 1980.
62. J. Herrmann, "Theory of Kerr-lens mode locking: role of self-focusing and radially varying gain," *JOSA B*, vol. 11, pp. 498–512, 1994.
63. U. Keller, "Semiconductor saturable absorber mirrors (SESAM's) for femtosecond to nanosecond pulse generation in solid-state lasers," *IEEE J. Sel. Top. Quantum Electron.*, vol. 2, pp. 435–453, 1996.
64. F. Gires and P. Tournois, "An interferometer useful for pulse compression of a frequency modulated light pulse," *CR Acad. Sci.*, vol. 258, pp. 6112–6115, 1964.
65. R. L. Fork, O. E. Martinez, and J. P. Gordon, "Negative dispersion using pairs of prisms," *Opt. Lett.*, vol. 9, pp. 150–152, 1984.
66. M. Ramaswamy-Paye and J. G. Fujimoto, "Compact dispersion-compensating geometry for Kerr-lens mode-locked femtosecond lasers," *Opt. Lett.*, vol. 19, pp. 1756–1758, 1994.
67. R. Szipöcs, C. Spielmann, F. Krausz, and K. Ferencz, "Chirped multilayer coatings for broadband dispersion control in femtosecond lasers," *Opt. Lett.*, vol. 19, pp. 201–203, 1994.
68. M. Cervantes, "Brewster angle prisms: a review," *Opt. Laser Technol.*, vol. 20, pp. 297–300, 1988.
69. B. E. Lemoff and C. P. J. Barty, "Cubic-phase-free dispersion compensation in solid-state ultrashort-pulse lasers," *Opt. Lett.*, vol. 18, pp. 57–59, 1993.
70. R. Ell, "Generation of 5-fs pulses and octave-spanning spectra directly from a Ti:sapphire laser," *Opt. Lett.*, vol. 26, pp. 373–375, 2001.
71. R. Holzwarth, "Optical frequency synthesizer for precision spectroscopy," *Phys. Rev. Lett.*, vol. 85, pp. 2264–2267, 2000.
72. D. J. Jones, "Carrier-envelope phase control of femtosecond mode-locked lasers and direct optical frequency synthesis," *Science*, vol. 288, pp. 635–639, 2000.
73. J. L. Hall, "Nobel lecture: defining and measuring optical frequencies," *Rev. Mod. Phys.*, vol. 78, pp. 1279–1295, 2006.
74. T. W. Hänsch, "Nobel lecture: passion for precision," *Rev. Mod. Phys.*, vol. 78, pp. 1297–1309, 2006.
75. J. Ye and S. T. Cundiff, *Femtosecond Optical Frequency Comb: Principle, Operation and Applications*. Boston, MA: Springer Science & Business Media, 2005.
76. R. Holzwarth, M. Zimmermann, T. Udem, and T. W. Hansch, "Optical clockworks and the measurement of laser frequencies with a mode-locked frequency comb," *IEEE J. Quantum Electron.*, vol. 37, pp. 1493–1501, 2001.
77. P. B. Corkum and F. Krausz, "Attosecond science," *Nat. Phys.*, vol. 3, p. 381, 2007.
78. J. Reichert, R. Holzwarth, Th. Udem, and T. W. Hänsch, "Measuring the frequency of light with mode-locked lasers," *Opt. Commun.*, vol. 172, no. 1, pp. 59–68, Dec. 1999, doi: 10.1016/S0030-4018(99)00491-5.
79. F. Lücking, A. Assion, A. Apolonski, F. Krausz, and G. Steinmeyer, "Long-term carrier-envelope-phase-stable few-cycle pulses by use of the feed-forward method," *Opt. Lett.*, vol. 37, pp. 2076–2078, 2012.
80. D. Strickland and G. Mourou, "Compression of amplified chirped optical pulses," *Opt. Commun.*, vol. 56, no. 3, pp. 219–221, Dec. 1985, doi: 10.1016/0030-4018(85)90120-8.
81. P. Maine, D. Strickland, P. Bado, M. Pessot, and G. Mourou, "Generation of ultrahigh peak power pulses by chirped pulse amplification," *IEEE J. Quantum Electron.*, vol. 24, no. 2, pp. 398–403, Feb. 1988, doi: 10.1109/3.137.
82. M. Pessot, J. Squier, G. Mourou, and D. J. Harter, "Chirped-pulse amplification of 100-fs pulses," *Opt. Lett.*, vol. 14, no. 15, pp. 797–799, Aug. 1989, doi: 10.1364/OL.14.000797.
83. S. Backus, C. Durfee, and M. Murnane, "High power ultrafast lasers," *Rev. Sci. Instrum.*, vol. 69, p. 1207, Jun. 1998, doi: 10.1063/1.1148795.
84. J. E. Murray and W. H. Lowdermilk, "Nd:YAG regenerative amplifier," *J. Appl. Phys.*, vol. 51, no. 7, pp. 3548–3556, 1980, doi: 10.1063/1.328194.
85. C. P. J. Barty et al., "Regenerative pulse shaping and amplification of ultrabroadband optical pulses," *Opt. Lett.*, vol. 21, no. 3, pp. 219–221, Feb. 1996, doi: 10.1364/OL.21.000219.
86. C. P. J. Barty et al., "Generation of 18-fs, multiterawatt pulses by regenerative pulse shaping and chirped-pulse amplification," *Opt. Lett.*, vol. 21, no. 9, pp. 668–670, May 1996, doi: 10.1364/OL.21.000668.
87. H. Takada, M. Kakehata, and K. Torizuka, "High-repetition-rate 12fs pulse amplification by a Ti:sapphire regenerative amplifier system," *Opt. Lett.*, vol. 31, no. 8, pp. 1145–1147, Apr. 2006, doi: 10.1364/OL.31.001145.
88. M. P. Minitti et al., "Optical laser systems at the Linac coherent light source," *J. Synchrotron. Radiat.*, vol. 22, no. 3, Art. no. 3, May 2015, doi: 10.1107/S1600577515006244.
89. W. H. Lowdermilk and J. E. Murray, "The multipass amplifier: theory and numerical analysis," *J. Appl. Phys.*, vol. 51, no. 5, pp. 2436–2444, May 1980, doi: 10.1063/1.328014.
90. C. L. Blanc, G. Grillon, J. P. Chambaret, A. Migus, and A. Antonetti, "Compact and efficient multipass Ti:sapphire system for femtosecond chirped-pulse amplification at the terawatt level," *Opt. Lett.*, vol. 18, no. 2, pp. 140–142, Jan. 1993, doi: 10.1364/OL.18.000140.
91. F. Tavella, A. Marcinkevičius, and F. Krausz, "Investigation of the superfluorescence and signal amplification in an ultrabroadband multiterawatt optical parametric chirped pulse amplifier system," *New J. Phys.*, vol. 8, p. 219, 2006.

92. A. Jullien et al., “10^{-10} temporal contrast for femtosecond ultraintense lasers by cross-polarized wave generation,” *Opt. Lett.*, vol. 30, p. 920, 2005.
93. V. Chvykov, J. Nees, and K. Krushelnick, “Transverse amplified spontaneous emission: the limiting factor for output energy of ultra-high power lasers,” *Opt. Commun.*, vol. 312, p. 216, 2014.
94. Z. Gan et al., “200 J high efficiency Ti:sapphire chirped pulse amplifier pumped by temporal dual-pulse,” *Opt. Express*, vol. 25, p. 5169, 2017.
95. D. N. Papadopoulos et al., “The Apollon 10 PW laser: experimental and theoretical investigation of the temporal characteristics,” *High Power Laser Sci. Eng.*, vol. 4, p. 34, 2016.
96. R. Dabu, “High power femtosecond lasers at ELI-NP,” in *AIP Conference Proceedings* vol. 1645, p. 219., 2015, doi: 10.1063/1.4909578.
97. F. Lureau et al., “Latest results of 10 petawatt laser beamline for ELi nuclear physics infrastructure,” *Proc. SPIE*, vol. 9726, p. 972613, 2016.
98. National Academies of Sciences, Engineering, and Medicine. *Opportunities in Intense Ultrafast Lasers: Reaching for the Brightest Light*. Washington, DC: The National Academies Press, 2017.
99. P. A. Schulz and S. R. Henion, “Liquid-nitrogen-cooled Ti:Al_2O_3 laser,” *IEEE J. Quantum Electron.*, vol. 27, p. 1139, 1991.
100. I. Matsushima, H. Yashiro, and T. Tomie, “10 kHz 40W Ti:sapphire regenerative ring amplifier,” *Opt. Lett.*, vol. 31, p. 2066, 2006.
101. J. H. Sung, H. W. Lee, C. H. Nam, and S. K. Lee, “100-kHz 22-fs Ti:sapphire regenerative amplification laser with programmable spectral control,” *Appl. Phys. B*, vol. 122, p. 125, 2016.
102. KMLabs, *Wyvern Product Line*. Boulder, CO: KMLabs.
103. KMLabs, *Dragon and Red-Dragon Product Lines*. Boulder, CO: KMLabs.
104. KMLabs, *Red-Wyvern Product Lines*. Boulder, CO: KMLabs.
105. M. Pittman, S. Ferré, J. P. Rousseau, L. Notebaert, J. P. Chambaret, and G. Chériaux, “Design and characterization of a near-diffraction-limited femtosecond 100-TW 10-Hz high-intensity laser system,” *Appl. Phys. B*, vol. 74, no. 6, pp. 529–535, Apr. 2002, doi: 10.1007/s003400200838.
106. H. Kiriyama et al., “High temporal and spatial quality petawatt-class Ti:sapphire chirped-pulse amplification laser system,” *Opt. Lett.*, vol. 35, p. 1497, 2010.

Taylor & Francis
Taylor & Francis Group
http://taylorandfrancis.com

7

Lanthanide Series Lasers—Near-Infrared

Norman P. Barnes

CONTENTS

7.1 Introduction 83
7.2 Quantum Mechanics and Spectroscopy 84
7.3 Energy Transfer and Diffusion 85
7.4 Properties of Laser Materials 87
7.5 Pump and Population Inversion 89
7.6 Basic Laser Equations 92
7.7 Tuning 95
7.8 Laser Performance 96
7.9 Summary 98
References 98

7.1 Introduction

Lanthanide series solid-state lasers that operate in the near- to mid-infrared region of the spectrum are explored in this chapter. Lanthanide series lasers that produce wavelengths longer than ~1.4 µm are analysed here, in particular, lasers having lanthanide series atoms of Dy, Ho, Er and Tm. Lasers producing wavelengths longer than 1.4 µm enjoy an advantage with regard to eye safety because these wavelengths are absorbed volumetrically in the vitreous humour of the eye. Therefore, the laser radiation is not focused onto the retina of the eye, which greatly increases the radiation level required for eye damage. These active atoms also often have other common properties including a dependence on energy transfer processes. Specifically the population of various manifolds or groups of closely spaced energy levels are populated through the transfer of quanta of energy from other manifolds. Energy transfer processes will also be covered in this chapter. Topics not covered here include lanthanide series lasers in glasses or fibre lasers, including lasers utilized for communication purposes.

Lanthanide series solid-state lasers have several advantages over most other types of lasers, advantages which are associated with their spectroscopic properties. A primary advantage of these lasers is their ability to store energy over relatively long time intervals. Virtually all solid-state lasers are optically pumped, either with a lamp or laser diodes. With the capability to store energy, solid-state lasers can behave like an optical integrator, storing the optical energy in the active atoms. Having stored the pump energy for time intervals up to many milliseconds, most of it can be released in a single pulse with characteristics tailored to the specific application. This optical integration ability is virtually unique with solid-state lasers.

Solid-state lasers also have the ability to concentrate the pump radiation into a nearly diffraction-limited beam, a narrow spectral bandwidth or both. While laser diode arrays are more efficient than solid-state lasers, the ability of solid-state lasers to produce high power or energy in a very narrow spectral bandwidth or diffraction-limited beam is often a reason to select them. Also, solid-state lasers have the ability to generate a wide range of pulse lengths and pulse repetition frequencies, ranging from a continuous beam to a pulse repetition frequency up to ~1.0 GHz while pulse lengths can be as short as tens of femtoseconds.

Although Nd:YAG is useful for many applications, particular wavelengths generated by other lanthanide series lasers may be sought because they interact with matter differently. A different interaction may be important, for example yielding increased eye safety. Some wavelengths are strongly absorbed by water, such as the 2.9 µm Er:YAG laser, and thus useful for medical applications. In contrast, lasers in the blue-green region of the spectrum may be sought because they are transmitted by water. Other laser materials and active atoms are selected for particular properties including the ability to store energy, produce a polarized output or generate a minimum amount of heat internal to the laser.

In the following sections of this chapter, the physics and spectroscopy of lanthanide series solid-state lasers are reviewed along with energy transfer processes and diffusion. Laser performance, in either continuous or pulsed modes, can usually be characterized by a threshold and slope efficiency. Possible laser transitions are presented next, along with a method for determining which particular transition will oscillate. Examples of Er, Tm, Ho and Dy lasers are presented in Section 7.7 with thresholds and slope efficiencies reported in the literature. Finally, Section 7.8 will summarize the results.

7.2 Quantum Mechanics and Spectroscopy

Lanthanide series lasers are characterized by the particular lanthanide series atom employed and, to a lesser degree, on the particular laser material in which the atom resides. Electron shells in the lanthanide series atoms are filled between 1s and 4d. Laser transitions for these elements occur between various energy levels of the 4f electrons. In addition, lanthanide series atoms have completely filled 5s and 5p shells. Usually electrons in the 6s shell as well as one electron from the 4f shell form the bonding electrons. Because the 5s and 5p shells are completely filled, they shield the 4f electrons from the electric field produced by the laser material. Thus, the electric field of the laser material exerts only a relatively weak effect on the 4f electrons. This insensitivity of the 4f energy levels on the particular laser material allows lanthanide series atoms to be arranged in an energy level chart for facile reference [1], often referred to as a Dieke chart. An abridged Dieke chart for the atoms of interest is shown in Figure 7.1.

Energy levels of lanthanide series lasers are determined primarily by the quantum mechanics of the individual lanthanide series atom. A spherically symmetric central attractive force is provided by the nucleus and the core electrons, that is the 1s–4d electrons. This attractive force is the dominant mechanism in lanthanide series atoms. Next, in order of importance, is the mutual repulsion of the 4f electrons. Because of the mutual repulsion of the electrons, they couple to make the total angular momentum, *L*, and total spin, *S*, approximately good quantum numbers. Next, in order of importance, is the spin–orbit coupling. Spin–orbit coupling makes the total angular momentum, *J*, an approximately good quantum number. In many cases, the spin–orbit effect is nearly equal to the mutual repulsion term. Taken together, these interactions are not sufficient to remove all of the energy level degeneracy. Finally, the electric field of the laser material, or crystal field, splits the various free atom energy levels slightly, removing most of the remaining degeneracy. A set of energy levels associated with a particular *L*, *S* and *J* are referred to as a manifold. Manifold splittings are sufficiently small that they appear in a Dieke diagram only as a broadening of the line that represents the manifold. A figure showing the relative magnitude of the various interactions is given in Figure 7.2.

Manifolds are designated in terms of the Russell–Saunders notation. Typically, the manifold has the notation $^{2S+1}L_J$, where *S* is the total spin quantum number, *J* is the total angular momentum quantum number while *L* designates the total angular momentum quantum number. With Russell–Saunders notation, the letters S, P, D, F, G, H, I, . . . represent the total angular momentum 0, 1, 2, 3, 4, 5, 6 . . . If the total spin quantum number is an integer, the maximum for the total number of levels in a manifold is $(2J+1)$. If the total spin quantum

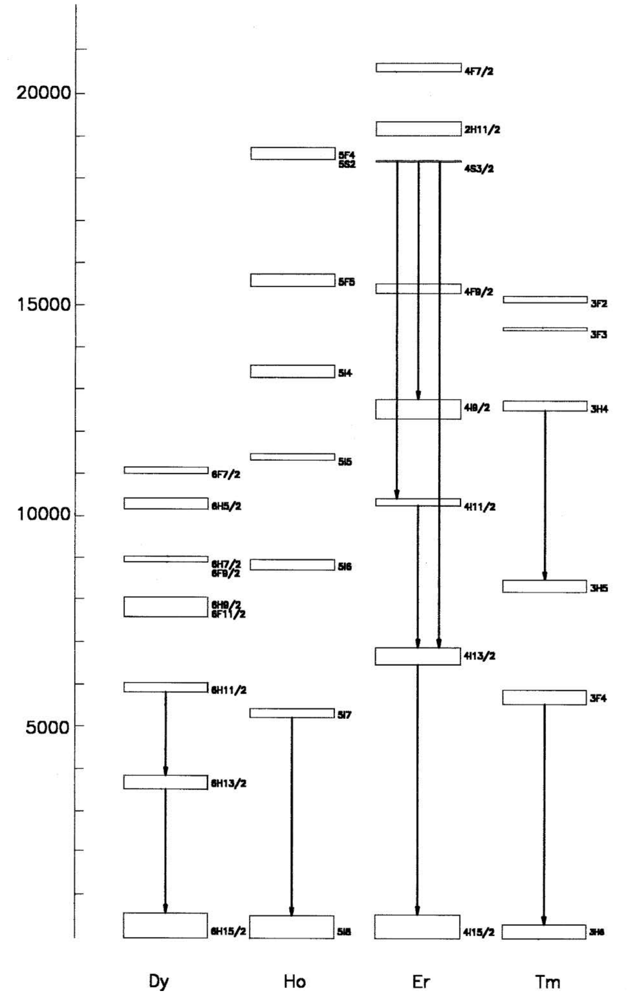

FIGURE 7.1 Abridged Dieke diagram for Dy, Ho, Er and Tm. Common laser transitions are indicated.

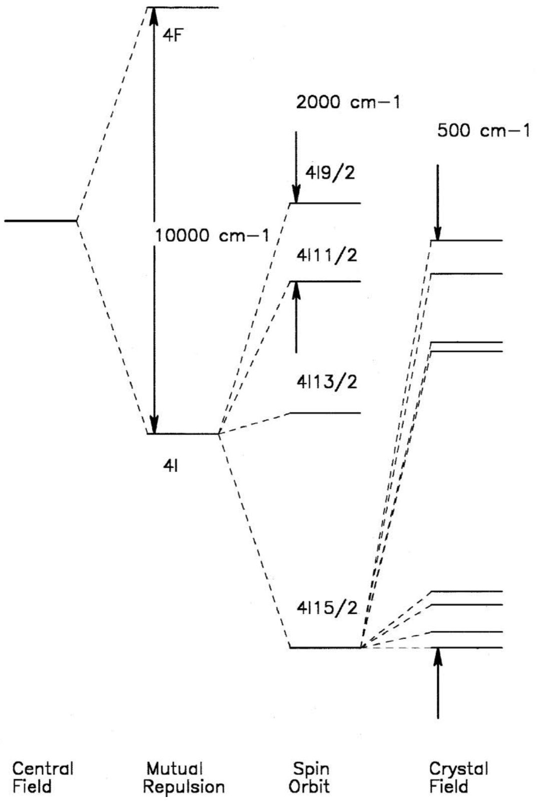

FIGURE 7.2 Magnitude of the various quantum mechanical interactions.

number is a half-integer, in the crystalline field, all of the levels are doubly degenerate, reducing the maximum number of levels to $(2J+1)/2$. Often this condition is referred to as Kramers' degeneracy.

Crystal-field effects can be characterized by a set of crystal-field parameters, B_{nm}. Crystal-field parameters result from the electric field effects which neighbouring atoms have on the active atom. In crystalline laser materials, the crystal-field parameters depend on the symmetry imposed by the neighbouring atoms. Crystals have an ionic character so that an ionic charge is associated with each neighbouring atom. Crystal-field parameters can, in principle, be calculated given the position and charge of neighbouring atoms. Usually, however, the energy levels of a lanthanide series atom in a laser material are measured spectroscopically and the crystal-field parameters are adjusted to reflect the experimental data.

Laser transitions are primarily electric dipole transitions. Transition probabilities between a set of levels can be forbidden and occur only because the specific levels are not pure levels but have some other levels included in the wavefunctions. While the contribution of other levels which are included can be relatively small, it is sufficient to allow the transition to occur. As a result of this mixing of levels, selection rules are rarely strictly observed. In general, however, the rule that the total spin of the level does not change during the transition does have some validity. Although magnetic dipole transitions are much weaker than electric dipole transitions under normal circumstances, in the case of lanthanide series atoms, magnetic dipole contributions to a transition can be noticeable.

Laser transitions in lanthanide series atoms are usually from a single level within a manifold to another single level in another manifold. For closely spaced energy levels, more than one pair of levels may contribute to a particular transition. An individual transition can be approximated by a Lorentzian lineshape, that is

$$g(\nu)=\left(\Delta\nu/2\pi\right)\left[\left(\nu-\nu_0\right)^2+\left(\Delta\nu/2\right)^2\right]^{-1}$$

where $\Delta\nu$ is the linewidth and ν_0 is the centre frequency. However, many lines have some variation in the centre wavelength. Thus, a Voigt profile is often a better approximation. The linewidth of the Lorentzian lineshape function is dependent on the temperature and is of the order of 10 cm^{-1} at room temperature. Linewidths become narrower as the temperature is reduced.

If the crystal does not have sufficient symmetry, the laser transitions are polarized. For example, in uniaxial crystals the laser transition is usually different if the electric field of the emitted radiation is polarized perpendicular to or parallel to the optical axis of the crystal. If a polarized laser is desired, the polarization dependence of the transition can be used to advantage.

7.3 Energy Transfer and Diffusion

Lanthanide series lasers are often made efficient by energy transfer processes. If the energy difference between a pair of manifolds in one atom is nearly equal to the energy difference between a pair of manifolds of a neighbouring atom, the atom in the excited manifold can transition to a lower energy manifold while simultaneously raising the neighbouring atom from a low-energy manifold to a higher energy manifold. A classic case of an energy transfer process involves the exchange between the first excited manifolds of Ho and Tm. A Tm atom, which initially resides in the first excited manifold, $^3F_4$, transitions to the ground manifold, $^3H_6$, while a neighbouring Ho atom transitions from the ground manifold, $^5I_8$, to the first excited manifold, $^5I_7$, shown as process H in Figure 7.3. No photons are emitted and reabsorbed, rather there is an energy exchange between two atoms. For historical reasons, atoms donating the excitation are denoted as sensitizers while atoms receiving the excitation are denoted as active atoms.

Energy transfer usually occurs between neighbouring atoms by a dipole–dipole interaction. Dipole fields decrease as the inverse cube of the distance separating the dipoles. Consequently, the dipole–dipole interaction depends on the inverse sixth power of the distance. Dipole–quadrupole and quadrupole–quadrupole interactions are possible but they decrease as the inverse eighth and inverse tenth power of the

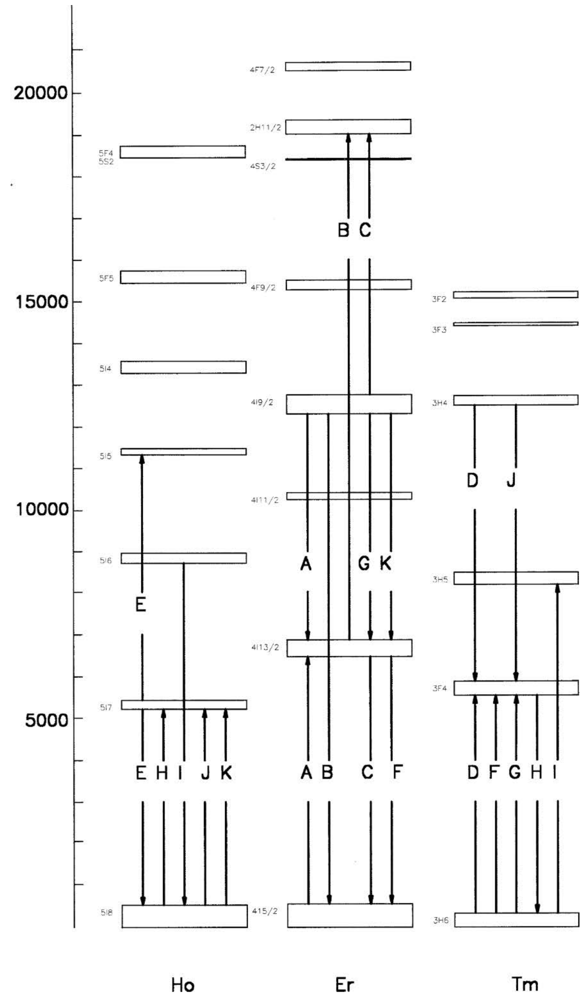

FIGURE 7.3 Abridged Dieke diagram for Ho, Er and Tm. Forward energy transfer interactions are indicated by a pair of lettered arrows. Reverse energy transfer interactions are represented by reversed arrows.

distance. Because of the distance dependence and strength of the interactions, the dipole–dipole mechanism is usually responsible for energy transfer.

Historically, energy transfer was analysed by Forster [2] and Dexter [3]. Energy transfer parameters were simply calculated by integrating over the product of the sensitizer emission spectra and the active atom absorption spectra. The strength of this interaction depends on the orientation of the atoms with respect to each other and the orientation of both dipoles with a vector connecting the atoms. In the classical approach, all possible orientations were averaged. In addition, all possible distances separating the interacting atoms were also averaged. Because of the inverse sixth power dependence of the interaction on the distance, the selection of the nearest possible distance for the dipoles becomes very critical. These approximations are valid for fluids, to which these models were initially applied. However, they are not strictly applicable to crystals where the distances and orientations are fixed by the crystal lattice. An energy transfer model has been developed which takes into account the restrictions set by the crystal lattice [4].

Energy transfer parameters have been modelled for crystalline laser materials by starting with a knowledge of the energy levels of the particular laser material. Utilizing a quantum mechanical model, level-to-level transition probabilities or lifetimes can be calculated. It is necessary to know the level-to-level lifetimes, rather than the manifold-to-manifold lifetimes, because energy transfer is greatly enhanced by a resonance between the interacting levels. Thus, pairs of energy levels that are in resonance or near resonance can contribute heavily when they have adequate transition probabilities. To calculate the energy transfer parameters, all possible transitions between all of the upper manifold and lower manifold levels must be known for both the sensitizer and active atom. Rather than integrating over the emission and absorption spectra, a summation over all possible pairs of transitions can be performed. In addition, a summation over all possible sites for the sensitizer and active atom can be performed. Possible sites and the allowed orientation of the dipole are both determined by the crystal lattice. When performing the summation over the sites, it was observed that for common laser materials, YAG and YLF, the nearest similar neighbours contributed about three-quarters of the total sum.

Active atoms or sensitizers which have a next nearest similar neighbour that is also an active atom or sensitizer usually have a substantially different lifetime from atoms, which do not enjoy this condition. Because of the shielding of the 4f electrons from the crystal field and because the next similar neighbours are usually not very close, the occupancy of these sites has little effect on the energy levels and transition probabilities. However, the existence of a close cooperative neighbour can have a significant effect on the energy transfer process. An energy transfer process can shorten the fluorescent lifetime of neighbouring similar atoms. To describe the dynamics of the active atoms or sensitizers, the atoms can be divided into two or more groups depending on the distance to a cooperative atom.

Atoms can be divided into distinctive groups. An atom may have no nearest similar site occupied by a cooperative atom, called a singlet, or may have a single nearest similar site occupied by a cooperative atom, called a doublet. Or, the concentration of cooperative atoms may not be constant, as they prefer to form clusters. In fact, experimental data indicate that this occurs in some solid-state lasers. In either case, the decay could be described with similar mathematics. In these cases, the decay of the manifolds may be described by a sum of exponentials, an exponential term for atoms having cooperative atoms close and another for atoms having cooperative atoms further away.

Many energy transfer processes are possible, as displayed in Figure 7.3. Energy transfer from Tm to Ho, described earlier, is an example. In addition, Ho in the $^5I_7$ manifold can also transition to the $^5I_8$ manifold while it raises a neighbouring Tm atom from the $^3H_6$ to the $^3F_4$ manifold. Obviously, this is simply the reverse of the first process and is sometimes referred to as back transfer. In self-quenching, the sensitizer and the active atom are the same types of atom. As an example, a Tm atom in the $^3H_4$ manifold can transition to the $^3F_4$ manifold while raising a neighbouring Tm atom from the $^3H_6$ manifold to the $^3F_4$ manifold, process D. Finally, the opposite processes can occur, that is two Tm atoms both initially in the $^3F_4$ manifold can interact promoting one of the Tm atoms to the $^3H_4$ manifold while the other Tm atom transitions to the $^3H_6$ manifold. Because the final state of one of the initial Tm atoms is an energy manifold higher than the original excited manifold, this process is referred to as up-conversion.

Energy transfer can be described using a set of differential equations. For example, the differential equations for Tm and Ho forward and back energy transfer are given. Denoting the Tm $^3H_6$, Tm $^3F_4$, Ho $^5I_7$ and Ho $^5I_8$ manifolds as 1, 2, 7 and 8, respectively, the differential equations describing the population densities of the various manifolds, N_i, are:

$$\frac{dN_7}{dt} = -\frac{N_7}{\tau_7} - P_{71}N_7N_1 + P_{28}N_2N_8$$

$$\frac{dN_2}{dt} = -\frac{N_2}{\tau_2} + P_{71}N_7N_1 - P_{28}N_2N_8.$$

In this approximation, the energy transfer rate is proportional to the product of the number density of atoms in the manifold which donates the excitation and the number density of atoms in the manifold which receives the excitation. P_{ij} is referred to as the energy transfer parameter. The subscripts i and j refer to the initial manifolds of the atom acting as the sensitizer and the atom acting as the active atom. If more than a single site for the cooperative atoms exists, similar differential equations can be written for each. A fraction of the population inversion can be associated with each site. The total manifold population is then described by the sum of the solutions.

Energy transfer and back energy transfer are related and their ratio is a function of temperature. In general, for every energy transfer process there is a reverse energy transfer process. Often the excited manifold of one atom has a higher average energy than the excited manifold of the other atom. Given these differences in energy, the interacting levels have a different thermal occupation or Boltzmann factors. As a consequence, the difference in the thermal occupation factors favours the forward energy transfer over the back energy transfer. Again, the classical case is the energy transfer processes between the Tm $^3F_4$ and the Ho $^5I_7$ manifolds. If the partition function of a manifold is defined as

$$Z_i = \sum_j \exp\left(-E_{ij}/kT\right)$$

where the summation is over all energy levels in the manifold, k is Boltzmann's constant and T is the temperature. Using this, the ratio of the forward-to-backward energy transfer rates can be shown to be [5]

$$P_{71}/P_{28} = \left(Z_2 Z_8/Z_1 Z_7\right)\exp\left(-\left(E_{ZL2} - E_{ZL7}\right)/kT\right)$$

where the subscripts 1, 2, 7 and 8 again refer to the Tm $^3H_6$, Tm $^3F_4$, Ho $^5I_7$ and Ho $^5I_8$ manifolds, respectively, and E_{zl2} and E_{ZL7} are the energies of the lowest or zero level of manifolds 2 and 7, respectively.

Diffusion can affect the energy transfer of the various atoms by permitting the excitation to migrate among the same types of atoms. Diffusion is a special case of energy transfer where the sensitizer and active atom are the same types and the interacting manifolds are the same. As an example of diffusion, a Tm atom in the $^3H_4$ manifold can interact with a neighbouring Tm atom in the $^3H_6$ manifold. The first atom transitions to the $^3H_6$ manifold while promoting the second atom to the $^3H_4$ manifold. On average, no energy is lost in this process and the same number of Tm atoms remains in the $^3H_4$ manifold. Diffusion tends to be orders of magnitude faster compared with the more general energy transfer because all pairs of energy levels have at least one resonance. Diffusion can assist other transfer processes by allowing transfer to a pair of atoms where energy transfer can occur faster.

Several authors have proposed various models to describe the effects of diffusion on the decay of atoms affected by energy transfer processes. A static transfer model describes the decay of an initially excited manifold described by $\exp[-t/\tau - k_S(C_{DA}t)^{1/2}]$, where k_S is a constant and C_{DA} is the sensitizer to active atom transfer constant. However, this model neglects diffusion and back energy transfer. A diffusion-limited model describes decay by $\exp[-t/\tau - k_D(C_{DA}t)^{1/2} f(x)]$, where k_D is a constant and $f(x)$ is a ratio of polynomials in x while x is $Dt^{2/3}/C_{DA}^{1/3}$. This model assumes that diffusion is much slower than energy transfer, a condition usually contrary to the previous analysis, and neglects back energy transfer. A migration-assisted model describes decay by $\exp[-t/\tau - k_M(C_{DA}t)^{1/2} - Wt]$, where k_M and W are constants. This model assumes that migration is essentially a random walk fast enough to maintain the same relative distribution but neglects back energy transfer.

Experimental decay curves can often be fitted almost equally well with several of these models. The sum of exponentials approach has the attraction of using simple rate equations to describe the processes and has proven to work rather well for practical laser applications [6].

7.4 Properties of Laser Materials

Although the choice of the laser material makes only a small change in the position of the energy levels, it can make a large difference in other properties, such as cross sections and thermal properties. Properties of interest can be grouped into optical, mechanical and thermal properties. Each is discussed here along with some germane effects. A table of laser material properties is given in Table 7.1 for an oxide, $Y_3Al_5O_{12}$ or YAG, and a fluoride, $YLiF_4$ or YLF.

Optical properties include a range of transparency, refractive index and variation in the refractive index with temperature. For efficient operation, the laser material must be transparent at both the pump and laser wavelengths. In most cases, pump wavelengths are shorter than laser wavelengths. The ultraviolet absorption features of laser materials do not have a sharp cut-off wavelength; thus, some laser material absorption may extend into the pump region. Because absorption by the laser material does not contribute to the laser process but does add to the heat deposited in the laser material, some short wavelengths may be filtered out, especially for flashlamp-pumped systems.

Refractive indices are usually best described by a Sellmeier equation. Specifically, the refractive index, n, is related to the wavelength, λ, by

$$n^2 = A + B\lambda^2/\left(\lambda^2 - C\right) + D\lambda^2/\left(\lambda^2 - E\right)$$

where A, B, C, D and E are constants and λ is almost always in µm. Some materials are birefringent; that is the index of refraction is dependent on the polarization. In this case, a set of Sellmeier coefficients is associated with each different polarization. In addition, the variation of the refractive index with temperature is important because of thermal focusing effects which are discussed later. When a linearly polarized output is desired, a birefringent material is often selected. Birefringent

TABLE 7.1

Laser Material Properties

Parameter	YAG	YLF(a)	YLF(c)	Units
Transparency	0.24–5.5	0.12–7.3		µm
Refractive index	1.819	1.450	1.471	
Sellmeier				
A	2.08745	1.38757	1.31021	
B	1.20810	0.70757	0.84903	
C	0.02119	0.00931	0.00876	
D	17.2049	0.01885	0.53607	
E	1404.45	50.997	134.957	
dn/dT	10.4	–0.7	–2.3	10^{-6} K^{-1}
Lattice constant	1201	516.8	10.736	pm
Density	4560	3980		kg m^{-3}
Lanthanide sites	1.38	1.39		10^{28} m^{-3}
Phonon maximum	860	560		cm^{-1}
Young's modulus	3.6	0.075		TPa^{-1}
Poisson's ratio	0.25	≈0.33		
Strength	0.20	0.033		GPa
Melting point	1940	819		°C
Specific heat	590	791		J/kg
Conductivity	13	5.8	7.2	W mK^{-1}
Thermal expansion	7.8	8.3	13.3	10^{-6} mK^{-1}
Thermal shock	790	180		W m^{-1}

materials usually produce a polarized laser output because the transition probability and, thus, the gain are dependent on the polarization. Also, the natural birefringence, usually being much larger than the thermally induced birefringence, swamps any thermal variations that tend to scramble the polarization.

Lattice parameters set the size of the cell that forms the basic building block of the laser material lattice. In general, there are more atoms in a unit cell than can be found in one chemical formula. The number density of potential active atom sites can be determined using the lattice parameters. If there are n chemical formulae of atoms in the unit cell and the chemical formula has x atoms for which the active atom could be substituted, the number density of potential sites, N_S, can be expressed as

$$N_S = nx/abc$$

where a, b and c are the lattice parameters along the axes of a rectangular lattice. For example, YAG has eight chemical formulae contained in a unit cell and there are three Y atoms in the chemical formula. Because YAG is a cubic lattice, a, b and c are equal and the number density of potential sites is $24/a^3$. The density is the mass per unit volume of the laser material and is also obviously dependent upon the lattice parameters.

The response of the laser material to an applied stress can be described by the mechanical parameters: Young's modulus and Poisson's ratio. Young's modulus, E, is the ratio of applied tensile stress, or force per unit area, to strain, or change in length per unit length. While the laser material elongates in response to the applied tensile stress, it simultaneously shrinks along the lateral dimensions. Poisson's ratio, v, is the ratio describing the decrease in the lateral dimensions to the increase in the length. The strength of the laser material is the maximum stress that can be applied without inducing permanent changes. Crystalline laser materials usually fail in tension with the appearance of a crack originating on the surface. The strength of the laser material depends heavily on the surface finish, smoother surfaces producing a higher strength.

The lifetime of a laser manifold depends strongly on the maximum phonon energy. The lifetime of a manifold depends on the radiative decay and non-radiative quenching. In non-radiative quenching, an atom drops from a high manifold to the manifold directly below it with the emission of one or more phonons. If two laser manifolds are separated by an energy about five times the maximum phonon energy, non-radiative quenching of the upper lifetime is usually small. Manifolds that are not non-radiatively quenched often possess long lifetimes and are referred to as metastable manifolds. Fluoride laser materials tend to have lower maximum phonon energies than oxide laser materials.

Thermal parameters, including the coefficient of thermal expansion and thermal conductivity, may depend on the orientation with respect to the crystal axes. Because resonant frequencies depend on the optical length of the resonator, a change in the temperature can cause a change in the exact laser wavelength. The optical length of a laser material changes according to

$$\frac{\Delta(n\ell)}{n\ell} = \left[\frac{1}{n}\frac{\mathrm{d}n}{\mathrm{d}T} + \alpha\right]\Delta T$$

where n and α are the appropriate refractive index and coefficient of thermal expansion and ℓ is the length. In an open resonator, an expansion of the laser material implies a decrease in the air pathlength, which must be included in the resonator length calculations. Because laser materials are pumped volumetrically and cooled on the lateral surfaces, pumping causes thermal gradients. With circular symmetry, uniform pumping causes parabolic temperature profiles. When the laser material has different thermal conductivities in different lateral directions, even uniform pumping produces complex thermal profiles.

A temperature gradient, from the centre to the surface of the laser material, causes thermal lensing because of the variation in the refractive index with temperature and stress. (A temperature gradient causes a gradient in the index of refraction and thus in the optical pathlength, that is a lensing effect.) For isotropic laser rods, the thermally induced focal length, f, is approximated by [7,8]

$$\frac{1}{f} = \frac{P_H}{2\pi a^2 k_c}\left[\frac{\mathrm{d}n}{\mathrm{d}T} + 2n^3\alpha C\right]$$

where P_H is the heat generation rate in the laser rod, k_c is the thermal conductivity, a is the radius of the laser rod, α is the coefficient of thermal expansion and C is a constant depending on the polarization and the photoelastic constants. In oxide laser materials such as YAG, both the first and second terms in the square brackets are positive. In this case, thermal lensing can be large and positive. In fluoride laser materials such as YLF, the first term is negative and the second term is positive. In the latter case, the terms tend to cancel and the thermal lensing can be small and possibly negative. Because of the decreased thermal lensing, fluoride laser materials may be selected for applications where thermal focusing is a concern. For diode-pumped lasers, the heat-generation rate is roughly linearly proportional to the pump power. However, for flashlamp-pumped lasers, the heat-generation rate may increase faster than the pump power.

Thermal gradients can cause depolarization in isotropic laser materials. In isotropic laser rods, depolarization is associated with the photoelastic term, the C term mentioned earlier. Linearly polarized radiation incident on a thermally stressed laser rod can be resolved into radial and tangential components on the laser rod ends. Because of small differences in the radial and tangential refractive indices, an initially linearly polarized beam becomes elliptical upon exiting the laser rod. Generally, a portion of the elliptically polarized beam will be rejected by a linear polarizer in the laser resonator, causing a loss. This depolarization loss has to be averaged over the laser beam cross section because the radial and tangential directions as well as the phase difference, $\Delta\phi$, vary over the cross section. For a material like YAG, the maximum phase difference is

$$\Delta\phi_0 = \left(2n_0^3\alpha P_H/k_c\lambda\right)\left[\left(p_{11} - p_{12} + 4p_{44}\right)\left(v+1\right)/48\left(1-v\right)\right]$$

and the phase difference varies with the radial position as $\Delta\phi_0(\rho/a_r)^2$. Losses have been calculated for both Gaussian and uniform beams [9] and are plotted in Figure 7.4. Losses for a

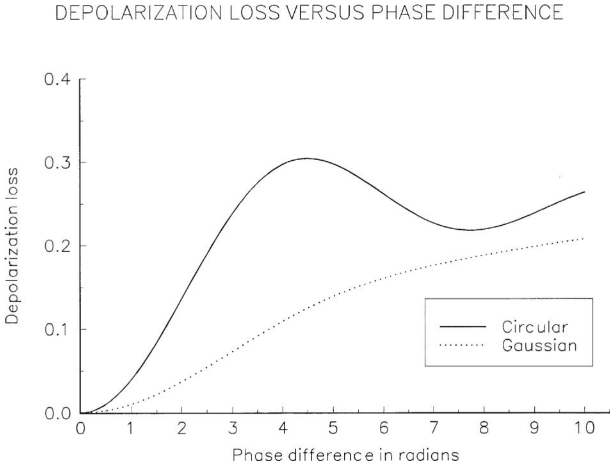

FIGURE 7.4 Depolarization loss versus phase difference.

Gaussian beam are smaller because the beam is concentrated in the centre of the laser rod where the phase difference is small. Conversely, losses for a uniform beam can be as high as 0.33.

7.5 Pump and Population Inversion

Population inversions in solid-state lasers are created almost exclusively using optical pumping. Optical pumping can be achieved by various methods including noble gas discharges, laser diodes and sometimes another laser. Optical pump radiation is absorbed by the laser material, which uses the absorbed energy to promote active atoms to the upper laser level. Establishing a higher population density in the upper laser level rather than in the lower laser level, that is a population inversion, may require several processes. When more active atoms reside in the upper laser level than in the lower laser level, laser action is possible. Solving the laser pumping problem is the first step in determining the laser output.

The laser process can be either continuous or pulsed. If it is pulsed, lasing can occur during the pumping process, referred to as normal mode, or lasing can occur in a single short pulse near the end of the pump pulse, referred to as Q-switched mode. In the latter case, a fast optical shutter, that is a Q-switch, is needed to prevent lasing before the pumping is completed. Although the pumping and energy conversion processes are the same in all cases, different approaches are taken to calculate the laser output.

Noble gas discharges, similar to the flashlamps associated with photography, were the first optical pumps. In fact, they are still extensively used today with little modification from early configurations. While Kr and Ar flashlamps have been used, Xe is the most commonly used gas. Lamps are usually fabricated in a thin cylinder and laser rods are often configured in a similar manner to facilitate optical coupling between the lamp and laser rod. In a continuous discharge mode, the optical spectrum of Xe has a low-level blackbody spectrum with superimposed emission lines of Xe. In a pulsed discharge, the blackbody component becomes dominant but broad Xe emission features can still be recognized. Xe emission lines are grouped in the near-infrared. Conversion of electrical energy to optical energy can be relatively efficient, approximately 0.3–0.5, depending on the lamp and the discharge parameters. But because the emission spectrum of the lamp and the absorption spectrum of the laser material usually do not match well, lamp pumping has a limited efficiency. Arc-lamp lifetimes are usually in the hundreds of hours and flashlamp lifetimes are in the range of 10^7–10^8 shots, depending on the discharge and the lamp design.

Laser diodes and laser diode arrays can improve both the efficiency and reliability of lasers and are becoming increasingly common. Laser diodes can efficiently convert electrical energy into optical radiation, roughly 0.3–0.5. However, the spectral emission can be rather narrow, of the order of a few nm. By matching the laser diode emission spectrum with an absorption feature of the laser material, pump radiation can be efficiently absorbed. Initially, most laser diodes used GaAlAs technology and were confined to the 0.78–0.88 μm region. Presently, driven by communications applications, laser diodes can cover the spectral region between ~0.6 and 2.1 μm. Laser diode wavelengths and technologies are listed in Table 7.2. High average power laser diodes and laser diode arrays are available primarily around 0.80, 0.98 and 0.67 μm. Laser diode lifetimes are often in the range of 10 000 h or more and pulsed diodes last for 10^8–10^9 shots, depending on the current pulses.

Laser diode arrays for laser pumping applications are often fabricated from edge-emitting bars with multiple emitting stripes. Bars are usually 10 mm in length and can be stacked to form arrays. Because the emitting stripes of edge-emitting laser diodes are only a few micrometres by tens of micrometres, the radiation pattern is not symmetric. The mode pattern perpendicular to the junction is often single mode but highly divergent, ~35°, because of the small size of the emitting stripe in this plane. The transverse mode pattern in the perpendicular plane is highly multi-mode but not as divergent, ~10°. For pumping applications, glass fibre lenses are often mounted in front of each bar to collimate the highly divergent component of the beam effectively.

Laser pumping is often employed for lasers with short upper laser level lifetimes or if laser diodes with the proper wavelength are not available. Pumping a laser with another laser has other advantages associated with the relatively good beam quality of the pump laser. It is often possible to match the pumped volume with the TEM_{00} laser mode volume, thereby

TABLE 7.2

Wavelengths of Commercial Laser Diodes

Material System			
Active Region	**Substrate**	**Minimum**	**Maximum**
InGaAlP	GaAs	0.61	0.69
GaAlAs	GaAs	0.78	0.88
InGaAs	GaAs	0.88	1.10
InGaAsP	GaAs	0.69	0.88
InGaAsP	InP	1.10	1.60
InGaAs	InP	1.60	2.10

enhancing good beam quality. If the laser transition possesses a short upper laser lifetime, a pump laser can deliver the pump energy in a short Q-switched pulse. Because Q-switched pulses are typically shorter than most upper laser manifold lifetimes, energy storage losses can be obviated and a Q-switched-like pulse produced. This is referred to as gain switching.

Given a pump source, the optical pump radiation is used to create a population inversion. Pump radiation is coupled to the laser material, absorbed, transferred to the upper laser manifold and stored until the laser pulse evolves. Each process is assigned an efficiency and these efficiencies are often nearly independent of the pumping level. The efficiency of the laser system is roughly proportional to the product of these various efficiencies.

Lamps are coupled to the laser material utilizing specular or diffuse cavities. Specular cavities are usually in the form of a conic section, such as an elliptical cylinder. Lamps are usually near one focus of the ellipse and the laser rod is near the other focus. Radiation from the lamp is focused onto the laser material in this arrangement. The coupling efficiency, η_C, of specular cavities, can be high, many above 0.9 [10,11]. Conversely, diffuse cavities are constructed from extremely high reflecting materials such as $BaSO_4$. Pump radiation essentially fills the cavity and reflects until either it is absorbed by the laser rod and reabsorbed by the lamp or it finds another way to escape, such as propagating into a hole in the cavity wall. Diffuse cavities are often thought to produce a more nearly uniform absorbed pump distribution.

Laser diodes are coupled to the laser material in several ways including merely being in close proximity to the laser material. For laser materials with reasonable absorption, the efficiency of this method is difficult to surpass. For laser materials with low absorption, the high brightness of laser diodes can be used to good advantage. Pump radiation is admitted into a highly reflecting cavity through a small slit. On average, it makes many passes through the laser material before it can escape.

After being coupled to a laser material, the pump radiation must be absorbed to be useful. The absorption efficiency relates energy stored in the upper laser manifold to incident pump energy. To calculate the absorption efficiency, the absorption coefficients must be known as a function of the pump wavelength. The absorption efficiency, η_A, can be approximated as [12]

$$\begin{aligned}\eta_A = &\int_0^\infty \int_0^\pi \int_0^{2\pi} P(\lambda_P)(1-\exp(-\beta_{1A}Cl))\eta_Q \\ &\times (\lambda_P/\lambda_L)F(\theta,\phi)\sin(\theta)\mathrm{d}\phi\,\mathrm{d}\theta\,\mathrm{d}\lambda \\ &\times \left(\int_0^\infty \int_0^\pi \int_0^{2\pi} P(\lambda_P)F(\theta,\phi)\sin(\theta)\mathrm{d}\phi\,\mathrm{d}\theta\,\mathrm{d}\lambda\right)^{-1}\end{aligned}$$

under the assumption of limited depletion of the ground manifold. $P(\lambda_P)$ is the pump power as a function of wavelength, β_{1A} is the absorption coefficient normalized to unity concentration, C is the concentration of absorbing atoms, η_Q is the quantum efficiency, l is the absorption length and $F(\theta, \phi)$ is the distribution of incident angles for the pump photons. A factor of (λ_P/λ_L) is needed because every absorbed photon creates one atom in the pump manifold. Obviously, longer pump wavelengths can be more efficient. This assumes that the ground manifold is not significantly depleted. If depletion occurs, the absorption coefficient will decrease as will the absorption efficiency.

The absorption coefficients β_{1A} for the lanthanide series atoms of interest appear in Figures 7.5–7.7. Although absorption spectra were taken for lightly doped materials, the

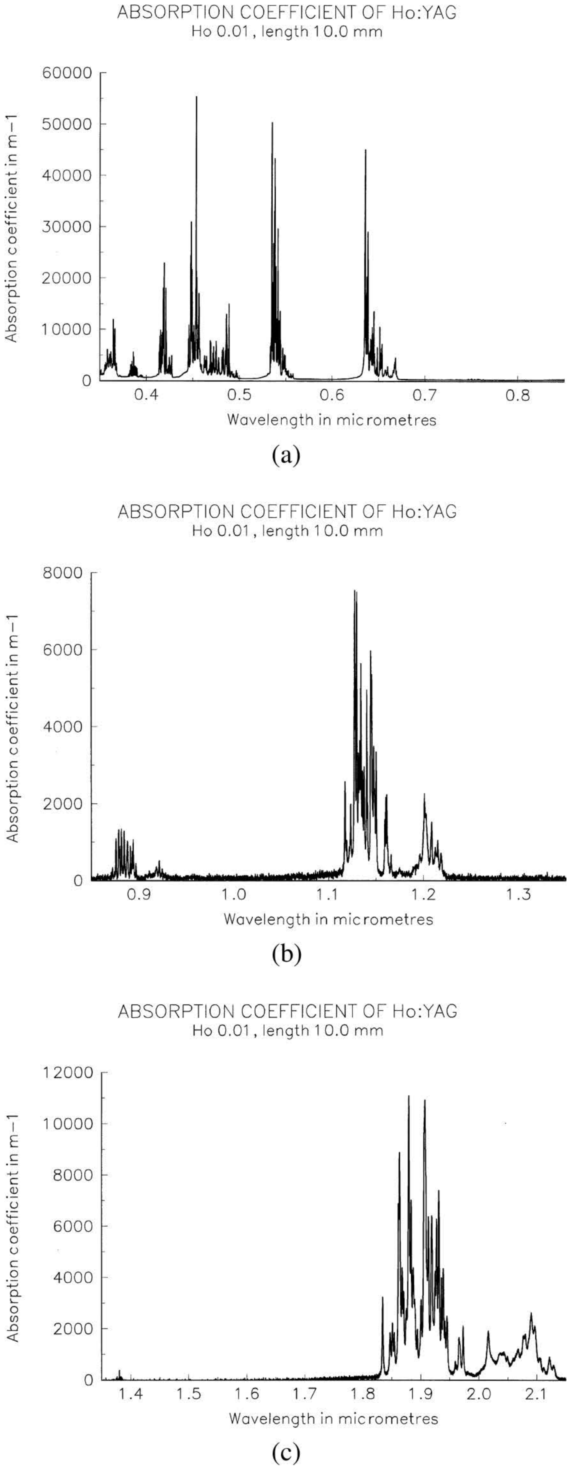

FIGURE 7.5 Normalized absorption coefficient for Ho:YAG.

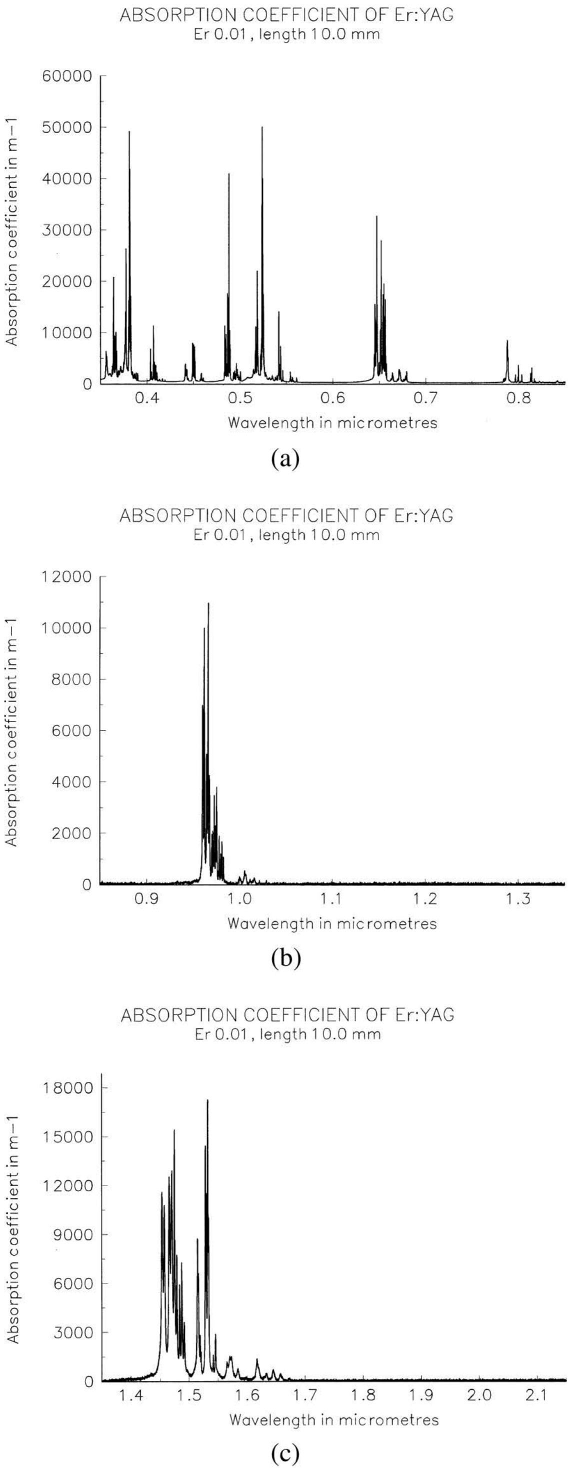

(a)

(b)

(c)

FIGURE 7.6 Normalized absorption coefficient for Er:YAG.

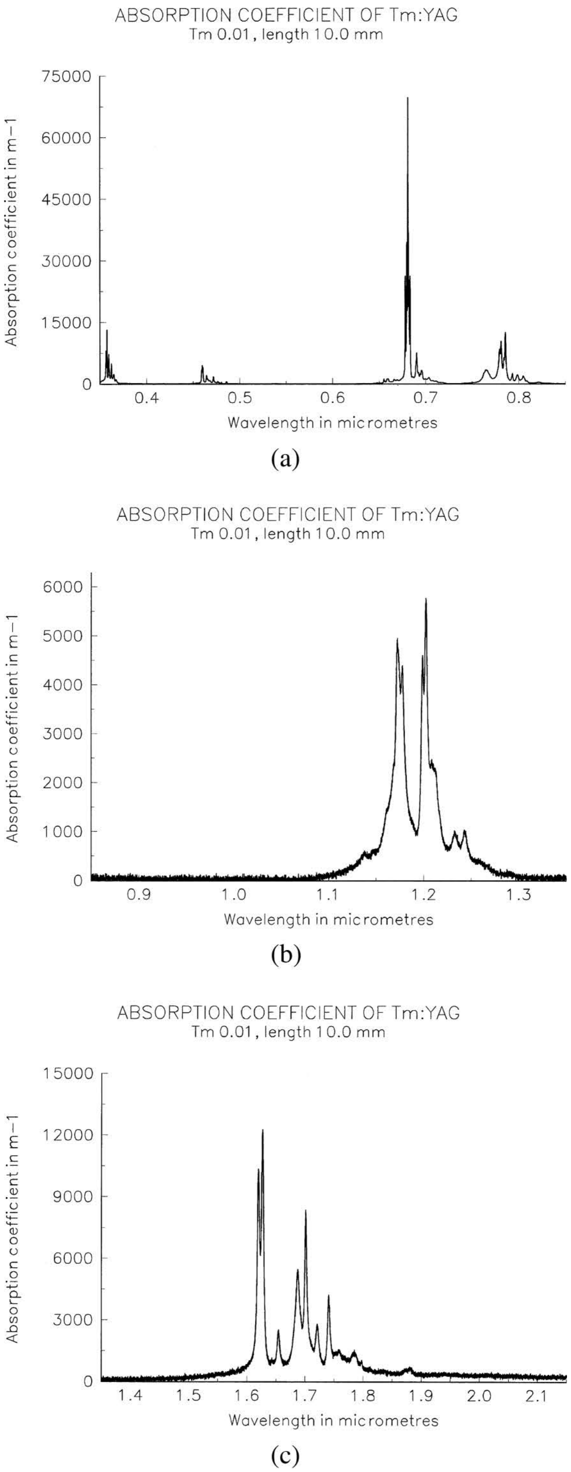

(a)

(b)

(c)

FIGURE 7.7 Normalized absorption coefficient for Tm:YAG.

calculated absorption coefficient was divided by the concentration of active atoms to yield the normalized results, which are shown in the figures.

Sensitizers are sometimes used to increase the absorption efficiency of weakly absorbing active atoms. To be effective, the sensitizer must absorb the pump radiation and transfer the absorbed energy to the active atom with high efficiency. For example, Tm absorbs pump radiation in the $^3H_4$ manifold from GaAlAs laser diodes and subsequently pumps the Ho $^5I_7$ manifold. As another example, Cr absorbs flashlamp radiation and subsequently pumps the Tm $^3F_4$ manifold. Because Cr is a transition metal atom, rather than a lanthanide series atom, the absorption features are broad, as shown in Figure 7.8. By covering much of the visible region, Cr is a very good absorber of flashlamp radiation.

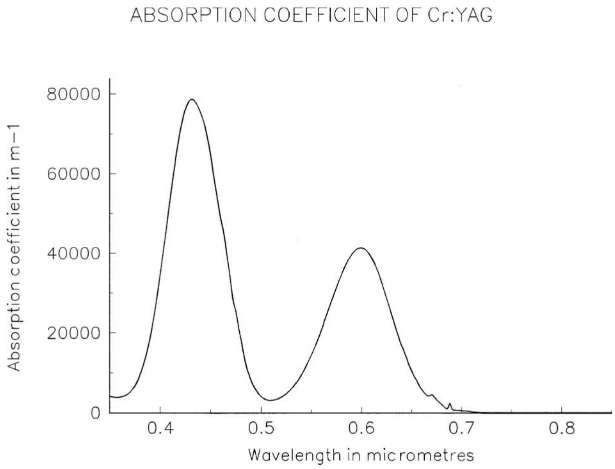

FIGURE 7.8 Normalized absorption coefficient for Cr:YAG.

For complex systems, absorption transfer efficiency can be roughly approximated by assigning a quantum efficiency, which may be greater than unity, to each manifold [13]. In this approximation, the absorption efficiency integration over pump wavelengths is split into a sum of integrals, one over each pump manifold. Each pump manifold is assigned a quantum efficiency, η_Q. Because of the nature of the lanthanide series spectra, absorption features may be sufficiently separated making identification of the absorbing manifold straightforward. Manifolds which have beneficial energy transfer effects may have a quantum efficiency greater than unity.

In the Q-switched case, the atoms in the upper laser manifold must be stored until the laser operation commences. A storage efficiency, η_S, for a square pump pulse

$$\eta_S = (\tau_2/\tau_1)\,\left(1 - \exp(-\tau_1/\tau_2)\right)$$

where τ_1 is the length of the pump pulse and τ_2 is the upper laser manifold lifetime. In essence, some active atoms excited to the upper laser manifold may decay away before the Q-switch opens. For a half-sinusoid pump pulse, the storage efficiency is quite similar.

To approximate the energy transfer effects better, the pumping of every manifold and all subsequent energy transfer processes are described with a set of laser pumping equations. Pumping rates are calculated for every manifold by determining the pump power at the appropriate wavelengths and calculating the manifold absorption efficiency. Pumping rates for each manifold, R_i, are proportional to n_{Ai} P_i, where P_i is the pump power at the appropriate wavelengths. Lifetimes, τ_i, and energy transfer parameters, P_{ij}, must be known for each manifold.

To illustrate these processes, consider a Tm laser and, for the nonce, neglect the $^3H_5$ manifold, as shown in Figure 7.9. If the $^3H_4$ manifold is pumped, the laser pumping equations describing the evolution of the relevant manifolds are:

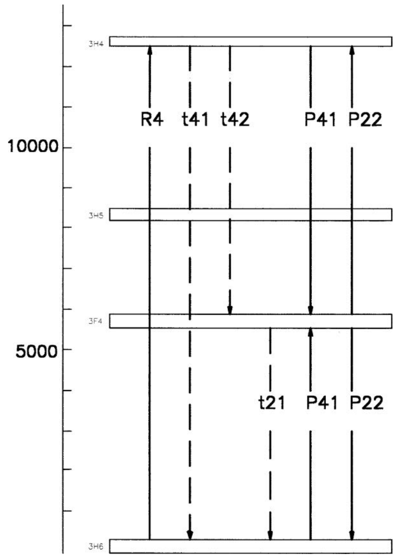

FIGURE 7.9 Simplified Dieke diagram for Tm showing pumping and dynamics.

$$\frac{dN_4}{dt} = -\frac{N_4}{\tau_4} - P_{41}N_4N_1 + P_{22}N_2^2 + R_4$$

$$\frac{dN_2}{dt} = -\frac{N_2}{\tau_2} + \frac{\beta_{42}N_4}{\tau_4} + 2P_{41}N_4N_1 - 2P_{22}N_2^2$$

$$N_1 + N_2 + N_4 = C_T N_S$$

$$1/\tau_4 = 1/\tau_{41} + 1/\tau_{42} = \beta_{41}/\tau_4 + \beta_{42}/\tau_4\,.$$

β_{ij} is the branching ratio, that is the fraction of the decaying population density of manifold N_i, which ends up increasing the population density of manifold N_j. Energy transfer out of manifold 4, $^3H_4$, by self-quenching process P_{41}, depends on the number density in manifold 4, the manifold which donates the energy and the number density in manifold 1, $^3H_6$, the manifold which receives the energy. Conversely, the up-conversion, process P_{22}, depends on the number density in manifold 2 squared because atoms in this manifold both donate and accept the energy. A factor of 2 appears with the energy transfer processes in the second equation because 2 Tm atoms in the $^3F_4$ manifold are created at a time. Energy transfer processes P_{41} and P_{22} are inverse processes. Every energy transfer process has an inverse process although one of the energy transfer parameters, P_{ij}, may be significantly larger than its corresponding inverse energy transfer parameter. The third equation replaces the differential equation for the ground manifold by noting that the number of Tm atoms must remain constant, equal to $C_T N_S$, where C_T is the concentration of Tm atoms. Note that the storage efficiency is automatically included in the solution of the laser pumping equations.

7.6 Basic Laser Equations

To calculate the laser output, the differential equations describing the laser pumping and the laser dynamics are solved.

Differential equations describe the manifold population densities rather than the level population densities. This approximation is usually valid because the levels within a manifold equilibrate in very short time intervals, on the order of a ps. Thus, even though energy is taken from only one level, the entire manifold contributes to the output. For different temporal operating modes, methods of solution will differ.

Strictly speaking, solutions for the different operating modes may not produce a linear relationship between the laser output power or energy and the electrical power or energy. Nevertheless, a linear relationship is a rather good approximation. Therefore, laser performance can be approximated using a threshold power, P_{ETH}, or energy, E_{ETH}, and a slope efficiency, σ_{S}. The threshold power or energy is the electrical power or energy required for the laser to begin lasing. The slope efficiency is the rate at which the laser output power or energy increases as electrical power or energy increases above the threshold. A plot of typical normal mode laser output energy versus electrical energy for a TEM_{00} Ho:Tm:Cr:YAG laser is shown in Figure 7.10. A curve fit, also shown, yields the threshold and slope efficiency for various output mirror reflectivities.

Ho, Er and Tm can operate on transitions, which have a small but non-negligible thermal population in the lower laser level and are referred to as quasi-four-level lasers. In three-level lasers, extraction of a photon decreases the population inversion by two, a decrease of one from the upper laser level and an increase of one into the lower laser level. In contrast, in four-level lasers, extraction of a photon decreases the population by one, a decrease of one from the upper laser level. The lower laser level has no thermal population and it relaxes quickly. Thus, there is virtually zero population in the lower laser level. For intermediate cases, the extraction of a photon decreases the population by a factor of γ. If γ is closer to one than two, the laser is termed a quasi-four-level laser, which is the case for the lasers considered here.

When laser pumping can be approximated by a pair of pumping rates, the differential equations governing the laser dynamics can be approximated as

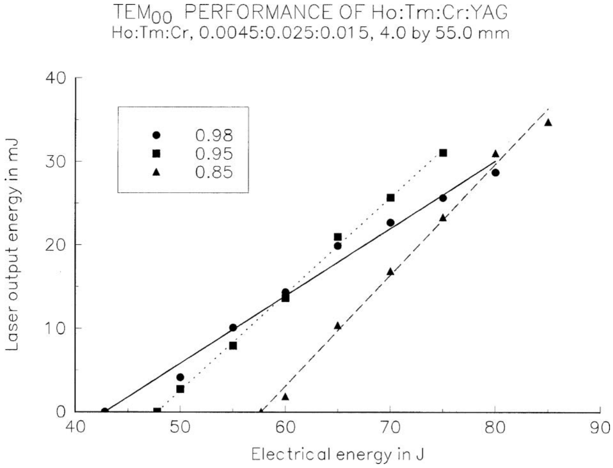

FIGURE 7.10 Typical laser output energy versus pump energy.

$$\frac{\partial N_2}{\partial t} = -\frac{N_2}{\tau_2} - \frac{\sigma c}{n}\left(Z_2 N_2 - Z_1 N_1\right) N_{\text{P}} + R_2$$

$$\frac{\partial N_1}{\partial t} = -\frac{N_1}{\tau_1} + \frac{\beta_{21} N_2}{\tau_2} + \frac{\sigma c}{n}\left(Z_2 N_2 - Z_1 N_1\right) N_{\text{P}} + R_1$$

$$\frac{\partial N_{\text{P}}}{\partial t} + \frac{c}{n}\frac{\partial N_{\text{P}}}{\partial z} = \frac{\sigma c}{n}\left(Z_2 N_2 - Z_1 N_1\right) N_{\text{P}}$$

Here, N_2 and N_1 are the upper and lower laser manifold population densities, τ_2 and τ_1 are the lifetimes and R_2 and R_1 are the pump rates of the upper and lower laser manifolds. Further, Z_2 and Z_1 are the thermal occupation or Boltzmann factors for the upper and lower laser levels, σ is the emission cross section, c is the speed of light, n is the index of refraction and N_{P} is the photon density. The γ factor is

$$\gamma = 1 + Z_1 / Z_2 .$$

For quasi-four-level lasers, the lower laser level is in the ground manifold and the term $(-N_1/\tau_1)$ disappears. To a good approximation in many cases, the active atoms reside either in the upper or lower laser manifolds, that is

$$N_1 + N_2 \approx C N_{\text{S}}$$

where C is the concentration of the active atoms while N_{S} is the number density of potential active atom sites. Thus, CN_{s} is the number density of active atoms. Optical transparency is defined by the population density in the upper laser manifold necessary to overcome the thermal population density in the lower laser level. Without optical pumping, the laser material displays a loss, caused by the population density in the lower laser level. With optical pumping, the population density in the upper laser level increases, offsetting the loss. At optical transparency, the gain which results from the population density in the upper laser level Z_2N_2 balances the loss caused by the population density in the lower laser level Z_1N_1, so there is no net gain or loss. Using this relation, optical transparency occurs when the upper laser level population density, $N_{2\text{T}}$, is

$$N_{2\text{T}} = C N_{\text{S}} (\gamma - 1) / \gamma .$$

With quasi-four-level lasers, the differential equation for the population density of the lower laser level can be eliminated permitting closed-form approximations for the laser performance. When the active atoms are primarily in the upper or lower laser manifolds, the derivative of one quantity is simply the negative of the other. Integrating the laser dynamics equations along the length of the resonator and accounting for the photon losses,

$$\frac{\partial N_2}{\partial t} = -\frac{N_2}{\tau_2} - \frac{2\sigma_{\text{e}}\ell_{\text{c}}}{n}\frac{c}{2\ell_{\text{c}}}\left[\gamma N_2 - (\gamma - 1) C N_{\text{S}}\right] N_{\text{P}} + R_2$$

$$\frac{\partial N_{\text{P}}}{\partial t} = 2\sigma_e \ell \frac{c}{2\ell_{\text{c}}}\left(\gamma N_2 - (\gamma - 1) C N_{\text{S}}\right) N_{\text{P}} + \frac{c}{2\ell_{\text{c}}} N_{\text{P}} \ln(R_{\text{M}} R_{\text{L}})$$

where σ_e is the effective emission cross section, that is $Z_2\sigma$, ℓ and ℓ_c are the lengths of the laser rod and the laser resonator, R_M is the reflectivity of the output mirror and R_L represents the losses. Integration along the length of the resonator is straightforward when the output mirror reflectivity is reasonably high, usually a good approximation for the lasers considered here.

Different methods are used to calculate the laser performance in different operating modes. For continuous operation, a steady-state laser output is of interest. Thus, the temporal derivatives of the laser pumping and laser dynamics equations are set equal to zero and the resulting algebraic equations solved for the photon population density. For the other extreme, for Q-switching, the laser pumping equations are solved with no laser photons present. Population densities of the upper and lower laser manifolds at the instant of Q-switching serve as initial conditions in the solution of the laser dynamics equations for the photon population density. For normal mode operation, the laser pumping equations for all germane manifolds and the laser dynamics equations are solved simultaneously to obtain the laser output [4]. Normal-mode lasing occurs somewhat after the pump pulse commences. Initial temporal behaviour often appears as a series of damped short pulses while the laser output relaxes to quasi-continuous operation. These initial pulses are referred to as relaxation oscillations. When the laser operates in a single transverse mode, both the frequency and the exponential damping constant of the relaxation oscillations can be predicted [13,14].

Solving the laser dynamics equations for the continuous case [13], the laser output power, P_{LO}, is related to the pump rate by

$$P_{LO} = \pi w^2 \ell \frac{hc}{\lambda_L} \frac{\ln(R_M)}{\ln(R_M R_L)} (R_2 - R_{2TH})$$

$$R_{2TH}\tau_2 = \left[(\gamma - 1)CN_S/\gamma - \ln(R_M R_L)/2\sigma_e \ell \gamma\right]$$

while the pump rate many times above the threshold is approximated as

$$R_2 = \eta_E \eta_C \eta_A \left(P_E \lambda_L / hc\pi a_r^2 \ell\right)$$

where η_E is the efficiency with which electrical power is converted to optical pump power and λ_L is the laser wavelength. For operation close to the threshold, the pump rate is approximated as being linearly related to the electrical power. To obtain some closed-form solutions, it is assumed that the laser material is a right circular cylinder with radius a_r and the laser output has a circular beam profile, that is a constant intensity to a radius of w. Gaussian beam profiles can also be handled but space does not allow its presentation. Using these equations, the threshold and slope efficiency are

$$P_{ETH} = \pi a_r^2 \ell \left(hc/\lambda_L \tau_2\right) \times \left[(\gamma - 1)CN_S/\gamma - \ln(R_M R_L)/2\sigma_e \ell \gamma\right] / \eta_E \eta_C \eta_A$$

$$\sigma_S = \left(\pi w^2 / \pi a_r^2\right)\left[\ln(R_M)/\ln(R_M R_L)\right]\eta_E \eta_C \eta_A.$$

The threshold is a combination of overcoming the population in the lower laser level and the optical losses in the resonator. The slope efficiency is a product of the overlap factor, that is the ratio of the cross-sectional area of the mode to the cross-sectional area of the laser rod, multiplied by the ratio of the output to the total loss.

The threshold of quasi-four-level lasers is quite sensitive to the temperature, primarily through the factor $(\gamma - 1)$. Noting that this factor is Z_1/Z_2 and the nearly exponential nature of Z_1, the critical temperature dependence becomes apparent. Most initial experiments with quasi-four-level lasers were performed at reduced temperatures, down to cryogenic temperatures. But, with aggressive pumping, it was found that quasi-four-level lasers performed well at room temperatures even though some cooling still improves the performance.

One general closed-form solution for normal-mode operation is not practical because of the variety of particular systems under analysis. Typically lasing commences somewhat after the pump pulse begins. Initial lasing undergoes relaxation oscillations, characterized by a series of regularly spaced temporal pulses with exponentially decreasing amplitude. If the laser is confined to a single transverse mode, relaxation oscillations are often observed. If the laser is not confined to a single transverse mode, several sets of relaxation oscillations complicate the temporal picture. As the oscillations damp out, laser output may relax to a quasi-continuous power output. Both the period between and damping constants of the relaxation oscillations are calculated for quasi-four-level lasers [13].

For Q-switched operation, the laser pumping equations are solved with no energy extraction by laser photons. Solutions for population densities of the upper and lower laser manifolds at the instant the Q-switch opens are then used as the initial conditions for the laser dynamics equations. Because the Q-switched pulse evolution time interval and pulse length are short compared with energy transfer time intervals, energy transfer occurring during these time intervals can be ignored in most cases. Solving the laser dynamics equations for the population density of the upper laser manifold by eliminating the photon density [13],

$$\frac{N_{20} - N_{2F}}{N_{20} - N_{2T}} = \frac{\ln(R_M R_L)}{2\sigma_e \ell \gamma (N_{20} - N_{2T})} \ln\left(1 - \frac{N_{20} - N_{2F}}{N_{20} - N_{2T}}\right)$$

where N_{20} and N_{2F} are the initial and final population densities of the upper laser manifold. Under the approximation that the upper laser manifold population density is directly proportional to the electrical pump energy and uniformly distributed

$$N_{20} = \left(\eta_E \eta_C \eta_A E_E\right)\left(\lambda_L/hc\right)/\pi a_r^2 \ell.$$

Given the ratio of gain coefficient and length product to losses $2\sigma_e\ell\gamma(N_{20}-N_{2T})/\ln(R_M R_L)$, the normalized ratio of the difference between the initial and final population densities of the upper laser manifold, $(N_{20}-N_{2F})/(N_{20}-N_{2T})$, can be calculated using the previous transcendental equation above. The results of the solution are given in Figure 7.11.

With the solution of the transcendental equation, the laser output energy, E_{LO}, and the pulse length, τ_P, can be determined

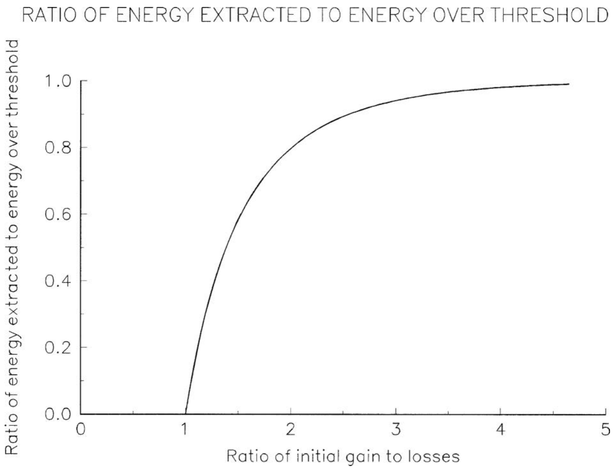

FIGURE 7.11 Differential population inversion versus ratio of loss to gain.

using closed-form approximations. Laser output energy can be expressed as

$$E_{\mathrm{LO}} = \frac{w^2}{a_{\mathrm{r}}^2} \frac{\ln(R_{\mathrm{M}})}{\ln(R_{\mathrm{M}} R_{\mathrm{L}})} (E_{\mathrm{SO}} - E_{\mathrm{ST}}) \frac{N_{20} - N_{2\mathrm{F}}}{N_{20} - N_{2\mathrm{T}}}$$

where

$$E_{\mathrm{S0}} = \pi a_{\mathrm{r}}^2 \ell h c N_{20} / \lambda_{\mathrm{L}}$$

$$E_{\mathrm{ST}} = \pi a_{\mathrm{r}}^2 \ell h c N_{2\mathrm{T}} / \lambda_{\mathrm{L}}$$

are the initial stored energy and the stored energy required to reach optical transparency.

The pulse length can be approximated as $E_{\mathrm{LO}}/P_{\mathrm{LOmax}}$, where P_{LOmax} is the peak power in the laser pulse. The latter quantity is available through the examination of the laser dynamics equations [13,52]. With this,

$$\tau_{\mathrm{P}} = -\frac{2\ell_{\mathrm{c}}}{c \ln(R_{\mathrm{M}} R_{\mathrm{L}})} \frac{N_{20} - N_{2\mathrm{F}}}{N_{20} - N_{2\mathrm{T}}} \times \left[1 + \frac{\ln(R_{\mathrm{M}} R_{\mathrm{L}})}{2\sigma_{\mathrm{e}} \ell \gamma (N_2 - N_{2\mathrm{T}})} \left(1 + \ln\left(\frac{-\ln(R_{\mathrm{M}} R_{\mathrm{L}})}{2\sigma_{\mathrm{e}} \ell \gamma N_2 - N_{2\mathrm{T}}}\right)\right)\right]^{-1}.$$

Thus, with a knowledge of some basic laser material parameters and the initial population density in the upper laser manifold, both the laser output energy and the pulse length can be calculated under the assumption of a uniform excitation density.

Quasi-four-level lasers can be effective laser amplifiers for Q-switched lasers. The laser pumping equations are solved as a function of time with no laser photons present. Upper and lower laser manifold population densities at the time of Q-switching are used as the initial conditions for the amplifier. The Frantz–Nodvik equations, modified for quasi-four-level lasers, are then solved for the gain and energy extraction of the amplifier [14]. A diode-pumped Ho:Tm:YLF laser demonstrated a large signal gain greater than 12 following this procedure. In another case, the small signal gain of Ho:Tm lasers was measured versus pump energy and compared with the gain versus pump energy predicted by simultaneously solving the energy transfer equations for the four lowest Ho and four lowest Tm manifolds [6]. Good agreement was found for a variety of Ho and Tm concentrations and for both polarizations of this birefringent laser material.

7.7 Tuning

While individual transitions of lanthanide series lasers are relatively narrow, the multiplicity of individual levels promotes virtually continuous tuning. For example, the upper laser manifold of Ho:YAG, the $^5I_7$ manifold, has 15 individual levels while the lower laser manifold of Ho:YAG, the $^5I_8$ manifold, has 17 individual levels. Of the 255 possible transitions, some may be forbidden or relatively weak, depending on the laser material. Nevertheless, transitions essentially cover the spectral range between 1.85 and 2.12 μm almost continuously, except for two relatively small gaps near 2.0 μm. However, because of the thermal populations, only the longer wavelengths will operate.

The laser wavelength depends on the strength of allowed laser transitions, the temperature and, for some modes, the level of pumping. For a lanthanide laser material like Nd:YAG operating on the $^4F_{3/2}$–$^4I_{11/2}$ transition, there is essentially no population density in the lower laser level. Consequently, the wavelength of the laser tends to be independent of pumping. However, for quasi-four-level lasers, the transition with the highest gain depends on the strength of the transition and the population density of both the upper and lower laser levels. For resonator configurations with a high output mirror reflectivity, overcoming the thermal population in the lower laser level is often the largest threshold factor. In this case, typically the transition with the longest wavelength reaches the threshold first. The longest wavelength usually indicates that the lower laser level is the highest in the ground manifold and, therefore, has the lowest thermal population. However, for resonator configurations with a lower output mirror reflectivity, overcoming the optical losses becomes the largest threshold factor. In this case, the transition with a larger emission cross section may be favoured.

Which transition dominates depends on the level of pumping in the Q-switched mode while, in the normal mode, whichever transition reaches the threshold first will dominate. In normal mode, at some instant during the pump pulse, one of the transitions will reach the threshold. At this point, the population inversion will be limited to the threshold value of the operating transition. By limiting the population inversion, competing transitions will not achieve threshold. In the Q-switched mode, the Q-switch will prevent all transitions from reaching the threshold during the pump pulse. When the Q-switch finally opens, pulses for all transitions will begin to evolve. The transition with the highest net gain will achieve a high power level first, extract much of the population inversion and limit the gain of competing transitions. Thus, the population inversion will be depleted before the other transitions can extract a significant amount of energy. A high net gain is a combination of a large emission cross section and population inversion and low losses. Because the population inversion is a function of both the wavelength and the level of pumping, the dominant wavelength may change with a change in the level of pumping.

Which transition will dominate in normal-mode operation also depends on the design of the laser resonator. The threshold occurs when the round trip gain is unity, that is

$$R_{\mathrm{M}}R_{\mathrm{L}}\exp\left[2\sigma_{\mathrm{e}}\left(\gamma N_2-(\gamma-1)CN_{\mathrm{S}}\right)\ell\right]=1.$$

However, both σ_{e} and γ are dependent on the particular transition. Thresholds are competitive where [15]

$$\left[(\gamma_{\lambda1}-1)/\gamma_{\lambda1}-(\gamma_{\lambda2}-1)/\gamma_{\lambda2}\right]2CN_S\ell$$
$$=\left[1/(\sigma_{\mathrm{e}\lambda1}\gamma_{\lambda1})-1/(\sigma_{\mathrm{e}\lambda2}\gamma_{\lambda2})\right]\ln(R_{\mathrm{M}}R_{\mathrm{L}})$$

In a plot of the concentration and length product, $CN_{\mathrm{S}}\ell$, versus the losses, $\ln(R_{\mathrm{M}}R_{\mathrm{L}})$, lines defined by this equation separate the regions where the particular transitions would operate. For example, Ho has transitions at 2.122, 2.097 and 2.091 µm. The effective emission cross section is the smallest for the longest wavelength transition and increases upon going towards the shorter wavelengths. For low loss cases, overcoming the thermal population density in the lower laser level is the dominant effect. Thus, in this case, the 2.122 µm transition is the strongest because it has the lowest population in the lower laser level. Conversely, for high loss cases, overcoming the losses is the dominant effect. In this case, the 2.091 µm transition is the strongest because it has the largest effective emission cross section. For intermediate losses, the 2.097 µm transition operates. In fact, measurements of the operating wavelengths for various Ho concentrations and output mirror reflectivities support this analysis [15].

Atmospheric conditions also affect the laser wavelength. In this region of the spectrum, many atmospheric absorption features exist. H_2O and CO_2 are the primary contributors to the atmospheric absorption in the near and mid-infrared region of the spectrum. If strong atmospheric absorption features exist in the vicinity of the laser wavelength, continuous tuning of the laser may be hampered by the existence of these absorption features. When tuning is tried, the laser is apt to skip over the wavelengths, where the absorption features are strong. This has been observed for Ho lasers [16].

7.8 Laser Performance

Laser operation utilizing several lanthanide series atoms was demonstrated soon after the discovery of the laser itself. A partial list of laser performance parameters appears in Table 7.3. By cooling to liquid nitrogen temperatures, laser operation was demonstrated in Ho:YAG on the ${}^5I_7$–${}^5I_8$ transition, in Er:YAG on the ${}^4I_{13/2}$–${}^4I_{15/2}$ transition and in Tm:YAG on the ${}^3F_4$–${}^3H_6$ transition using flashlamp pumping [17]. The importance of energy transfer processes and the possibility of using up-conversion to produce visible photons from infrared pump photons were identified [18].

Efficient operation on the Ho ${}^5I_7$–${}^5I_8$ transition in multiply doped laser materials was demonstrated at cryogenic temperatures by several groups. With a Ho:Tm:Er:YAG laser rod with a low Ho concentration, a continuous laser demonstrated a threshold of ~200 W and a slope efficiency of 0.065 using an incandescent W–I lamp [19]. Both normal-mode and Q-switched operations were demonstrated in Ho:Tm:Er:YLF [20] and Ho:Tm:Er:YAG [21]. Normal-mode thresholds were 14 and 30 J while slope efficiencies were 0.029 and 0.012, respectively, in a good quality beam, often TEM_{00}. Because of Ho:Tm sharing, slope efficiencies for Q-switched operation were somewhat lower.

Although Ho:YLF has a higher thermal population than Ho:YAG, better performance was achieved at room temperature with the former. Ho:Tm:Er:YLF and Ho:Tm:Er:YAG laser rods, with similar concentrations and dimensions, were evaluated in a flashlamp-pumped system. Normal-mode thresholds were 100 and 155 J while slope efficiencies were 0.0013 and 0.0004, respectively [22]. Substantially higher normal-mode efficiency was demonstrated by using Cr for a sensitizer in a Ho:Tm:Cr:YAG laser. Thresholds were reduced to ~45 J and slope efficiency was increased to 0.051 [23]. Because Cr substitutes for Al in YAG, Cr has not been tried in YLF.

Continuous laser operation near room temperature was obtained using laser diode pumping. With a laser diode at 0.785 µm to pump the Tm in an end-pumped configuration, a Ho:Tm:YAG laser had an optical threshold of ~52 mW and a slope efficiency of ~0.06 at −10°C [24]. With a similar configuration, single wavelength operation was achieved [25]. Single wavelength operation is important for seeding purposes and heterodyne detection. By using laser diodes operating at 1.9 µm and end pumping, a Ho:YAG laser had a threshold of ~0.55 W and a slope efficiency of 0.35, optical to optical [26]. In this case, the laser was cooled to −53°C and the optical power was the pump power incident on the laser material.

Normal-mode and Q-switched operation of diode-pumped Ho:Tm:YAG were demonstrated in a side-pumped arrangement at room temperature. The optical-to-optical threshold was ~2.4 J while the slope efficiency was ~0.026 and ~0.0023 for normal-mode and Q-switched operation, respectively. A Q-switched slope efficiency substantially closer to normal mode was obtained by permitting multiple Q-switched pulses [27]. Normal-mode and Q-switched operation of diode-pumped Ho:Tm:YLF in a side-pumped arrangement at 16°C were achieved. Here, the optical-to-optical thresholds were 1.5 and 2.5 J while the slope efficiency was 0.124 and 0.060 for the normal-mode and Q-switched operations [28]. Using similar hardware, a Ho:Tm:YLF diode-pumped amplifier demonstrated 0.6 J/pulse [29].

Because up-conversion between Tm and Ho was recognized to be deleterious, a Tm:YAG laser pumping a Ho:YAG laser was tried. By placing both laser materials in the same resonator, a continuous threshold of 0.19 W and a slope efficiency of 0.42 were achieved where the input power is the absorbed optical power [30]. In a similar vein, a pulsed Ho:LuAG laser pumped by a $\mathrm{Co{:}MgF_2}$ laser demonstrated a 4.3 mJ threshold and a slope efficiency of 0.82, absorbed optical to optical [31].

Although Er:YAG operated on the ${}^4I_{13/2}$–${}^4I_{15/2}$ transition at liquid nitrogen temperatures, limited work has been performed

TABLE 7.3

Near to Mid-Infrared Laser Performance

Laser	Pump	Mode	Temperature	Threshold	Slope
$^5I_7$–$^5I_8$					
Ho:Tm:Er:YAG	Lamp	Continuous	≈77 K	≈200 W	0.065
Ho:Tm:Er:YAG	Lamp	NM, QS	≈77 K	30 J	0.012
Ho:Tm:Er:YLF	Lamp	NM, QS	≈77 K	14 J	0.029
Ho:Tm:Er:YAG	Lamp	NM	Room temperature	155 J	0.0004
Ho:Tm:Er:YLF	Lamp	NM	Room temperature	100 J	0.0013
Ho:Tm:Cr:YAG	Lamp	NM	Room temperature	≈45 J	0.051
Ho:Tm:YAG	Diode	Continuous	−10°C	52 mW	≈0.06
Ho:Tm:YAG	Diode	NM	Room temperature		0.026
Ho:Tm:YAG	Diode	QS	Room temperature		0.0023
Ho:Tm:YLF	Diode	NM	16°C	1.5 J	0.124
Ho:Tm:YLF	Diode	QS	16°C	2.5 J	0.060
$^4I_{13/2}$–$^4I_{15/2}$					
Er:YAG	Lamp	NM	≈77 K		
Er:Yb:YAG	Lamp	NM	Room temperature	75 J	
$^4I_{11/2}$–$^4I_{13/2}$					
Er:YAG	Lamp	NM	Room temperature	17.4 J	
Er:YAlO$_3$	Lamp	NM	Room temperature	8.9 J	
Er:YSGG	Lamp	NM	Room temperature	30 J	0.012
Er:YSGG	Lamp	NM	Room temperature	≈10 J	≈0.01
$^4S_{3/2}$–$^4I_{9/2}$					
Er:YAlO$_3$	Lamp	NM	Room temperature	55 J	0.00015
Er:YLF	Lamp	NM	Room temperature	14 J	0.006
Er:YLF	Lamp	NM	Room temperature	16 J	0.004
$^4S_{3/2}$–$^4I_{13/2}$					
Er:YLF	Lamp	NM	Room temperature	≈100 J	≈0.012
$^3F_4$–$^3H_6$					
Tm:Cr:YAG	Lamp	NM	Room temperature	73 J	0.045
Tm:YAG	Diode	Continuous	−15°C	17 W	0.33
Tm:YAG	Diode	Continuous	Room temperature	50 W	0.40
Tm:YAG	T_i:Al$_2$O$_3$	Continuous	Room temperature	0.23 W	0.59
Tm:YAlO$_3$	T_i:Al$_2$O$_3$	Continuous	Room temperature	0.1 W	0.44
Tm:Sc$_2$O$_3$	Diode	Continuous	Room temperature	0.30 W	0.18
Tm:Y$_2$O$_3$	Diode	Continuous	Room temperature	0.48 W	0.08
Tm:LuAG	Diode	NM	Room temperature	0.78 J	0.144
Tm:LuAG	Diode	QS	Room temperature	0.78 J	0.050
$^3H_{13/2}$–$^3H_{15/2}$					
Dy:BaY$_2$F$_8$	Lamp	NM	≈77 K	510 J	
$^3H_{11/2}$–$^3H_{13/2}$					
Dy:YLF	Er:YLF	NM	Room temperature	0.015 J	0.07

on this transition. Operation on this transition at higher temperatures is somewhat difficult, partially because of excited-state absorption between the $^4I_{13/2}$ and $^4I_{9/2}$ manifolds. Using a low Er concentration and a Yb sensitizer, flashlamp-pumped, room temperature operation was achieved with a threshold of ~75 J. Lasing which originates on the $^4I_{11/2}$ and $^4S_{3/2}$ manifolds was also reported.

Efficient operation on the $^4I_{11/2}$–$^4I_{13/2}$ transition in Er:YAG and Er:YSGG has been demonstrated. Although the lower laser level is not thermally populated, the lower laser manifold has a lifetime much longer than the upper laser manifold. Because the lower laser manifold does not decay quickly, lasing can be terminated as this manifold populates. Nevertheless, with similar Er:YAG and Er:YAlO$_3$ laser rods, normal-mode thresholds of 17.4 and 8.9 J were possible in a resonator having very low output coupling [32]. Utilizing Er:YSGG, a 30 J threshold and a 0.012 slope efficiency in a flashlamp-pumped system have been demonstrated [33]. Subsequently, work was done on optimizing the pump pulse length and a threshold of ~10 J and a slope efficiency of ~0.01 were achieved [34]. Diode pumping of this transition has been achieved using a two-dimensional laser diode array at 0.973 μm. With 4.0 ms quasi-continuous pump pulses, an ~20 W threshold and 0.029 incident optical-to-optical efficiency were obtained [35].

Seeking room temperature operation on the $^4I_{13/2}$–$^4I_{15/2}$ transition, an Er:YAlO$_3$ laser with a very low Er concentration was aggressively pumped. Rather than observing this, the $^4S_{3/2}$–$^4I_{9/2}$ transition was observed at 1.663 μm instead. A 53 J threshold was obtained in a resonator with two highly reflecting mirrors [36]. On the same transition in Er:YAlO$_3$ but at 1.677 μm, a threshold of ~55 J and a slope efficiency of ~0.00015 were observed. In an Er:YLF laser, the $^4S_{3/2}$–$^4I_{9/2}$ transition at 1.73 μm achieved both normal-mode and Q-switched outputs. Thresholds of 14 and 16 J and slope efficiencies of 0.006 and 0.004, respectively, were achieved [37]. Also in an Er:YLF laser, the $^4S_{3/2}$–$^4I_{13/2}$ transition at ~0.85 μm was observed with a threshold of ~100 J and a slope efficiency of ~0.012 [38]. Operation of the $^4S_{3/2}$–$^4I_{11/2}$ transition at 1.23 μm was also observed in Er:YLF.

Er:YLF is suitable for up-conversion lasers as well. Using a pulsed 1.53 μm Er:glass laser as a pump, a three-step up-conversion process created a population inversion in the $^4S_{3/2}$ manifold. A three-step process excites the $^2H_{11/2}$ manifold, which subsequently decays quickly to the $^4S_{3/2}$ manifold, which serves as a metastable level. The most efficient operation was achieved at 1.73 μm, where the total efficiency was 0.11, optical to optical, at 110 K [39]. Conversely, a 0.797 μm laser diode generated a population inversion on the $^4S_{3/2}$–$^4I_{15/2}$ transition at 48 K. At this temperature, a continuous 0.55 μm laser resulted in a threshold of ~0.4 W and a slope efficiency of 0.08 [40].

Efficient, flashlamp-pumped, normal-mode operation using Cr as a sensitizer has been demonstrated in Tm:Cr:YAG. Operating on the $^3F_4$–$^3H_6$ transition at 2.016 μm, a room temperature Tm:Cr:YAG laser achieved a threshold of 73 J and a slope efficiency of 0.045 [41]. Operation on the $^3H_4$–$^3H_5$ transition at 2.274 μm was demonstrated in Tm:Cr:YAlO$_3$ using flashlamp pumping. The threshold was ~70 J but the highly reflecting resonator provided little output to determine a slope efficiency [42].

Continuous operation of a diode-pumped Tm:YAG laser provided a high power output at 2.013 μm. Utilizing laser diodes in an end-pumped configuration, continuous operation had a threshold of 1.7 W and a slope efficiency of 0.33 at –15°C [43]. Utilizing a high power laser diode array and a lens duct to concentrate the pump radiation into an internally reflecting laser rod, a threshold of ~50 W and a slope efficiency of 0.40 was achieved, where the pump power is considered to be the power delivered to the laser rod [44]. The power produced by this arrangement in a highly multi-mode beam was 115 W.

Using a Ti:Al$_2$O$_3$ laser in an end-pumped configuration, high slope efficiencies were achieved. Operating on the $^3F_4$–$^3H_6$ transition, thresholds of ~0.23 and ~0.1 W and slope efficiencies of 0.59 and 0.44 were achieved in Tm:YAG [45] and Tm:YAlO$_3$ [46], absorbed and incident optical to optical, respectively. The laser wavelengths were 2.105 and 1.94 μm for the two laser materials. High slope efficiencies verified that the quantum efficiency was greater than unity when pumping the $^3H_4$ manifold.

Continuous operation was also achieved in Tm:Y$_2$O$_3$ and Tm:Sc$_2$O$_3$ using laser diode pumping in an end-pumped scheme. Both lasers operated on the $^3F_4$–$^3H_6$ transition but the wavelengths were ~2.05 and ~2.15 μm in the two laser materials. Thresholds were 0.30 and 0.48 W and slope efficiencies 0.18 and 0.08, absorbed optical to optical, respectively. It was suggested that better quality laser material would benefit the operation [47].

Both normal-mode and Q-switched operation were demonstrated in Tm:LuAG using laser diode pumping. In a side-pumped configuration, the $^3F_4$–$^3H_6$ transition at 2.023 μm produced a threshold of 0.78 J and slope efficiencies of 0.144 and 0.050, optical to optical, for normal mode and Q-switched operation [48].

A Dy:BaY$_2$F$_8$ laser operating on the $^6H_{13/2}$–$^6H_{15/2}$ transition was achieved by cooling the laser rod to liquid nitrogen temperatures. The threshold for this device was 510 J and the wavelength was 3.022 μm [49]. By using an Er:YLF laser as a pump, a Dy:YLF laser operated at 4.340 μm on the $^6H_{11/2}$–$^6H_{13/2}$ transition [50]. The threshold was less than 0.015 J while the slope efficiency was greater than 0.07, optical to optical at room temperature.

7.9 Summary

Solid-state lasers can generate a variety of wavelengths in the near to mid-infrared region of the spectrum with respectable efficiencies. Although some of these lasers are quasi-four-level lasers, room temperature operation is practical. But to achieve room temperature operation, aggressive pump techniques are required.

These lasers are more complicated than their Nd counterparts primarily because of the importance of the energy transfer processes, which include energy transfer to different atoms and back transfer, self-quenching, upconversion and diffusion. For some lasers, the energy transfer processes are vital to the operation and, in other cases, they are detrimental. Energy transfer processes are well described with a rate equation approach, similar to the laser dynamics rate equations. Solutions depend on the mode of operation: continuous, normal mode or Q-switched mode. Usually laser dynamics equations must include any non-negligible population density in the lower laser level.

A number of examples of laser performance for Dy, Ho, Er and Tm have been presented. Performance is characterized here by the threshold and slope efficiency. While lamp pumping has been used to achieve the requisite high levels of pumping, laser diode pumping is becoming more common.

For further information on the physics of solid-state lasers, the reader is encouraged to refer [1]. For further information on the engineering of solid-state lasers, Ref. [51] may be referred.

REFERENCES

1. Powell R C 1998 *Physics Of Solid State Laser Materials* (New York: Springer).
2. Forster T 1947 Experimentalle Und Theoretische Untersuchung Des Zwischenmolerkularen Ubergangs Von Elektronenregungsenergie *Naturfurshung* **4A** 321–7.
3. Dexter D L 1953 A theory of sensitizer luminescence in solids *J. Chem. Phys.* **21** 836–50.
4. Barnes N P, Filer E D, Morrison C A and Lee C J 1996 Ho:Tm lasers I: theoretical *IEEE J. Quantum Electron.* **QE-32** 92–103.

5. Walsh B M, Barnes N P and DiBartolo B 1997 On the distribution of energy between the Tm $^3F_4$ And Ho$^5I_7$ manifolds in Tm sensitized Ho luminescence *J. Luminescence* **75** 89–98.
6. Barnes N P, Rodriguez W J and Walsh B M 1996 Ho:Tm:YLF laser amplifiers performance *J. Opt. Soc. Am.* ***B*** **13** 2872–82.
7. Foster J D and Osterink L M 1970 Thermal effects in a Nd:YAG laser *J. Appl Phys.* **41** 3656–63
8. Koechner W 1970 Thermal lensing in a Nd:YAG laser rod *Appl. Opt.* **9** 2548–53.
9. Williams-Byrd J A and Barnes N P 1990 Laser performance, thermal focusing and depolarization effects in Nd:Cr:GSGG and Nd:YAG *Proc. Solid State Lasers* **1223** 237–46.
10. Bowness C 1965 On the efficiency of single and multiple elliptical laser cavities *Appl. Opt.* **4** 103–7
11. Schuldt S B and Aagard R L 1963 An analysis of radiation transfer by means of elliptical cylinder reflectors *Appl. Opt.* **2** 509–13.
12. Barnes N P, Storm M E, Cross P and Skolaut M W Jr 1990 Efficiency of Nd laser materials with laser diode pumping *IEEE J. Quantum Electron.* **QE-26** 558–69.
13. Barnes N P, Murray K E and Jani M G 1997 Flash lamp pumped Ho:Tm:Cr:YAG and Ho:Tm:Er:YLF lasers: modeling of a single, long pulse length comparison *Appl. Opt.* **36** 3363–74.
14. Singh U N, Yu J, Petros M, Barnes N P, Williams-Byrd J A, Lockard G E and Modlin E A 1998 Injection seeded, room temperature, diode pumped Ho:Tm:YLF laser with output energy of 600 mJ at 10 Hz *Proc. Advanced Solid State Laser Conference* (Washington, DC: Optical Society of America) pp 194–6.
15. Lee C J, Han G and Barnes N P 1996 Ho:Tm Lasers II: experiments *IEEE J. Quantum Electron.* **QE-32** 104–11
16. Barnes N P, Jani M G, Murray K E and Harrel S R 1994 Diode pumped Ho:Tm:YLF laser pumping an AgGaSe$_2$ parametric oscillator *J. Opt. Soc. Am. B* **11** 2422–6
17. Johnson L F, Geusic J E and van Uitert L G 1965 Coherent oscillation from Tm^{3+}, Ho^{3+}, Yb^{3+} and Er^{3+} in yttrium aluminum garnet *Appl. Phys. Lett.* **7** 127–9.
18. Johnson L F, Guggenheim H J, Rich T C and Ostermayer F W 1972 Infrared to visible conversion by rare earths in crystals *J. Appl. Phys.* **43** 1125–37.
19. Beck R and Gurs K 1975 Ho laser with 50 W output and 6.5% slope efficiency *J. Appl. Phys.* **46** 5224–5.
20. Barnes N P 1979 TEM mode Ho:YLF laser *Proc. SPIE* **190** 297–304
21. Barnes N P 1981 Pulsed Ho:YAG oscillator and amplifier *IEEE J. Quantum Electron.* **QE-17** 1303–8.
22. Chicklis E P, Naiman C S, Folweiler R C and Doherty J C 1972 Stimulated emission in multiply doped Ho^{3+}:YLF and YAG–A comparison *IEEE J. Quantum Electron.* **QE–8** 225–30.
23. Quarles G J, Rosenbaum A, Marquardt C L and Esterowitz L 1989 High efficiency 2.09 μm flashlamp pumped laser *Appl. Phys. Lett.* **55** 1062–5.
24. Kintz G J, Esterowitz L and Allen R 1987 CW Diode-pumped Tm^{3+}:Ho^{3+}:YAG 2.1 μm room-temperature laser *Electron. Lett.* **22** 616.
25. Storm M E and Rohrbach W W 1989 Single longitudinal mode lasing of Ho:Tm:YAG at 2.09 μm *Appl. Opt.* **28** 4965–7.
26. Nabors C D, Ochoa J, Fan T Y et al 1995 Ho:YAG laser pumped by 1.9 μm diode laser *IEEE J. Quantum Electron.* **QE-31** 1063–5.
27. Bowman S R, Lynn J G, Searles S K et al 1993 High average power operation of a Q-switched diode pumped holmium laser *Opt. Lett.* **18** 1724–6.
28. Jani M G, Naranjo F L, Barnes N P et al 1995 Diode pumped, long pulse length Ho:Tm:YLF laser at 10 Hz *Opt. Lett.* **20** 872–4.
29. Singh U N, Williams-Byrd J A, Barnes N P et al 1997 Diode pumped 2.0 μm solid state lidar transmitter for wind measurements *Proc. SPIE* **3104** 173–8
30. Stoneman R C and Esterowitz L 1992 Intracavity pumped 2.09 μm Ho:YAG laser *Opt. Lett.* **17** 736–8
31. Hart D W, Jani M and Barnes N P 1996 Room temperature lasing of end pumped Ho:Tm:Lu$_3$ Al$_5$O$_{12}$ *Opt. Lett.* **21** 728–30.
32. Breguet J, Umyskov A F, Semenkov S G et al 1992 Comparison of threshold energy of selectively excited YAlO$_3$:Er and YAG:Er lasers *IEEE J. Quantum Electron.* **QE-28** 2563–6.
33. Zharikov E V, Il'ichev N N, Kalitan S P et al 1986 Spectral, luminescence, and lasing properties of yttrium scandium gallium garnet activated with chromium and erbium *Sov. J. Quantum Electron.* **16** 635–9.
34. Moulton P F, Manni J G and Rines G A 1988 Spectroscopic and laser characteristics of Er,Cr:YSGG *IEEE J. Quantum Electron.* **QE-24** 960–73.
35. Waarts R, Nam N and Sanders S 1994 Two dimensional Er:YSGG microlaser array pumped with a monolithic two dimensional laser diode array *Opt. Lett.* **19** 1738–40.
36. Weber M J, Bass M and DeMars G A 1971 Laser action and spectroscopic properties of Er in YAlO$_3$*J. Appl. Phys.* **42** 301–5.
37. Barnes N P and Allen R A 1986 Operation of an Er:YLF laser at 1.73 μm *IEEE J. Quantum Electron.* **QE-22** 337–43
38. Chicklis E P, Naiman C S and Linz A 1972 Stimulated emission at 0.85 μm in Er:YLF, *Dig. Tech. Papers VII International Quantum Electronics Conference* (Montreal, Canada: OSA Publishing).
39. Pollack S A, Chang D B and Birnbaum M 1989 Threefold upconversion laser at 0.85, 1.23 and 1.73 μm in Er:YLF pumped with a 1.53 μm Er:glass laser *Appl. Phys. Lett.* **54** 869–71.
40. Stephens R R and McFarlane R A 1993 Diode pumped upconversion laser with 100 mW output power *Opt. Lett.* **18** 54–7.
41. Quarles G J, Rosenbaum A, Marquardt C L and Esterowitz L 1990 Efficient room temperature operation of a flashlamp pumped Cr:Tm:YAG laser at 2.01 μm *Opt. Lett.* **15** 42–4.
42. Caird J A, DeShazer L G and Nella J 1975 Characteristics of room temperature 2.3 μm laser emission from Tm in YAG and YAlO$_3$ *IEEEJ. Quantum Electron.* **QE-11** 874–80.
43. Kmetec J D, Kubo T S and Kane T J 1994 Laser performance of diode pumped thulium doped Y$_3$Al$_5$O$_{12}$, (Y,Lu)$_3$Al$_5$O$_{12}$, and Lu$_3$Al$_5$O$_{12}$ crystals *Opt. Lett.* **19** 186–8.

44. Honea E C, Beach R J, Sutton S B et al 1997 115 W Tm:YAG CW diode pumped solid state laser *Advanced Solid State Laser Conference (Orlando, FL)* (Washington, DC: Optical Society of America).
45. Stoneman R C and Esterowitz L 1990 Efficient, broadly tunable, laser pumped Tm:YAG and Tm:YSAG CW lasers *Opt. Lett.* **15** 486–8.
46. Stoneman R C and Esterowitz L 1989 Efficient 1.94 μm Tm:$YAlO_3$ laser *IEEE J. Selected Topics* **1** 78–81.
47. Fornasiero L, Berner N, Dicks B M et al 1999 Broadly tunable laser emission from Tm:Y_2O_3 and Tm:Sc_2O_3 *Advanced Solid State Laser Conference (Boston, MA)* (Washington, DC: Optical Society of America).
48. Barnes N P, Jani M G and Hutcheson R L 1995 Diode pumped, room temperature Tm:LuAG laser *Appl Opt.* **34** 4290–4.
49. Johnson L F and Guggenheim H J 1973 Laser emission at 3 µm from Dy^{3+} in BaY_2F_8 *Appl. Phys. Lett.* **23** 96–8.
50. Barnes N P and Allen R E 1991 Room temperature Dy:YLF laser operation at 4.34 μm *IEEE J. Quantum Electron.* **QE-27** 277–82.
51. Koechner W 1976 *Solid State Laser Engineering* (New York: Springer).
52. Jani M G, Barnes N P and Murray K E 1997 Flash lamp pumped Ho:Tm:Cr:YAG and Ho:Tm:Er:YLF lasers: experimental *Appl. Opt.* **36** 3357–62.
53. Datwyler M, Luthy W and Weber H P 1987 New wavelength of the $YAlO_3$:Er laser *IEEE J. Quantum Electron.* **QE-23** 158–9.

8

Lasers Based on Non-Linear Effects

Fabienne Pellé

CONTENTS

8.1 Introduction 102
8.2 Physical Background 102
  8.2.1 Non-linear Polarization 102
  8.2.2 Second-Harmonic Generation 102
  8.2.3 Phase Matching 103
    8.2.3.1 Phase Matching in Uniaxial Crystals 104
    8.2.3.2 Phase Matching in Biaxial Crystals 104
    8.2.3.3 Limiting Parameters of the Doubling Efficiency 105
8.3 Self-Frequency Doubled Lasers *versus* Intracavity Frequency Doublers 106
  8.3.1 Intracavity Frequency Doubling 107
    8.3.1.1 Nd^{3+}-Crystals as the Gain Medium 107
    8.3.1.2 Type of Non-linear Crystals 107
    8.3.1.3 Output Power of the Second Harmonic 107
    8.3.1.4 Modelling the Behaviour of a Solid-State Laser with Reabsorption as an Additional Loss: Example of Nd^{3+} 946 nm Laser Emission 108
  8.3.2 Designs 109
    8.3.2.1 Optimization of the Diode End-Pumped Lasers 109
    8.3.2.2 Optimization of Second-Harmonic Generation: Conditions to Achieve an Efficient Laser Source 109
  8.3.3 Self-Frequency Doubled Lasers 110
  8.3.4 Nature of Crystals 110
    8.3.4.1 Requirements in Finding Crystals 110
  8.3.5 Nd^{3+} and Yb^{3+} Uses 111
    8.3.5.1 Nd^{3+} Ion Spectroscopy 111
    8.3.5.2 Evaluation of Yb^{3+} Ion Emission Parameters 112
    8.3.5.3 Refractive Indices Measurements 113
  8.3.6 Comparison between Both Systems 113
  8.3.7 Periodically Poled Structures 115
8.4 Ion–Host Combination, Non-linear Coefficients 115
  8.4.1 Ion–Host Combination: How to Choose the Best Host with Nd^{3+} or Yb^{3+} Dopants 115
  8.4.2 Non-linear Coefficients 116
    8.4.2.1 Case of KTP: Analysis of the Electronic Hyperpolarizability Tensor 116
    8.4.2.2 Modelling Chemical Substitutions 117
    8.4.2.3 Case of Borates: Calculation of Microscopic Hyperpolarizability 117
8.5 System Configurations: Resonator Designs and Pumping 118
  8.5.1 Modelling Intracavity Frequency-Doubled Lasers 118
    8.5.1.1 Diode End-Pumped Lasers 118
    8.5.1.2 Fibre-Coupled Laser-Diode End-Pumped Lasers: Coupling and Resonator 119
  8.5.2 Resonator Designs: Examples of Intracavity-Frequency-Doubled Lasers 120
    8.5.2.1 Ring Cavity 121
    8.5.2.2 Three-Mirror Folded Cavity 121
    8.5.2.3 Hemispherical Cavity 122
    8.5.2.4 Microchip 122
  8.5.3 Resonator Designs: Self-Doubling Lasers 122
8.6 Typical Operating Characteristics 124
References 125

8.1 Introduction

Advances in semiconductor laser diodes have given a new impulse in the research for visible solid-state laser sources with the opportunity to realize compact devices. There is an important potential interest for compact visible sources emitting in the blue, green or red in many applications. Low-power compact continuous-wave (cw) visible lasers are the key components in the development of undersea optical communications, high brightness displays, high-speed printers, high-density data storage, for medical applications and the environment (control of pollution), while high-power (cw or pulsed visible) devices are required for spectroscopy, materials treatment or surgery. Semiconductor laser diodes emitting in the near-infrared operating stably at room temperature require simple electric power supplies providing ideal excitation sources for miniaturized devices. Several optical processes such as parametric oscillation, stimulated Raman scattering or frequency mixing, or frequency conversion in a non-linear crystal, allow laser emission in the infrared range to be converted into visible laser radiation. Frequency conversion or, more precisely, second-harmonic generation (SHG) in a non-linear crystal will be the subject of this chapter. An infrared cw laser emission can be converted into a visible laser light either by intracavity frequency doubling (ICFD) or by self-doubling. These new approaches are promising in work to achieve compact all-solid-state lasers emitting in the blue-green spectral range. The basic principles of SHG will be given in the first part. Then ICFD will be compared to self-doubling in their principles and performances. For a deeper understanding, the reader can refer to several reference textbooks on non-linear optics [1–5], laser materials [6] and engineering [7,8].

8.2 Physical Background

8.2.1 Non-linear Polarization

As an introduction, we will consider the propagation of electromagnetic radiation in a medium with non-linear dielectric properties. In such a medium, when subjected to an electric field $\boldsymbol{E}$, the induced polarization $\boldsymbol{P}$ is not proportional to the applied field but should be expressed as an expansion in powers of the applied field $\boldsymbol{E}$:

$$\boldsymbol{P} = \varepsilon_0\left(\chi^{(1)}\boldsymbol{E} + \chi^{(2)}\boldsymbol{E}^2 + \chi^{(3)}\boldsymbol{E}^3 + \ldots\right) \tag{8.1}$$

with ε_0 the dielectric constant of the medium and $\chi^{(k)}$ the kth susceptibility tensor of rank (k). In the following, we will restrict the non-linearity to the second order since we are concerned only with the SHG. Consider two electromagnetic waves incident on the non-linear medium. They are taken as plane waves propagating along the z-direction with wavevector $\boldsymbol{k}_l$, amplitude $\boldsymbol{E}_l$ and frequency ω_l (l = 1, 2).

$$\boldsymbol{E}_l^{w_l} = \frac{1}{2}\mathrm{Re}\left(\boldsymbol{E}_l \exp\left[i\left(\omega_l t - \boldsymbol{k}_l \cdot \boldsymbol{r}\right)\right]\right) \tag{8.2}$$

The contribution of the quadratic term of Equation (8.1) is then given by:

$$\boldsymbol{P}^{(2)} = \varepsilon_0\chi^{(2)}\left[\frac{1}{2}\left(\boldsymbol{E}_1^2 + \boldsymbol{E}_2^2\right) + \frac{1}{2}\boldsymbol{E}_1^2\cos\left(2\omega_1 t\right) + \frac{1}{2}\boldsymbol{E}_2^2\cos\left(2\omega_2 t\right) + \boldsymbol{E}_1\boldsymbol{E}_2\left[\cos\left(\omega_1+\omega_2\right)t + \cos\left(\omega_1-\omega_2\right)t\right]\right]. \tag{8.3}$$

The non-linear response of the medium results in an exchange of energy between electromagnetic fields of different frequency. Then, the second-order susceptibility gives rise, in addition to a constant polarization, to oscillating components at the second harmonics, $2\omega_1$, $2\omega_2$ and components at the sum or difference frequencies ($\omega_1 \pm \omega_2$). The last components have important applications, i.e. parametric oscillation $\omega_3 = \omega_1 + \omega_2$ and the generation of tunable coherent sources $\omega_3 = \omega_1 - \omega_2$.

8.2.2 Second-Harmonic Generation

In this section, we will focus our interest on SHG. The non-linear polarization is usually written more compactly: the ith component of the induced polarization is determined by the tensor component $\chi_{ijk}^{(2)}$ with the components of the incident field following:

$$P_i^{\omega_3} = \varepsilon_0 \sum_{j,k=1}^{3} \chi_{i,j,k}^{(2)} E_j^{\omega_1} E_k^{\omega_2} \tag{8.4}$$

where i, j and k run from 1 to 3 and stand for x, y and z, respectively, and $\omega_3 = \omega_1 + \omega_2$.

SHG is the limiting case of a three-wave interaction, where the two fundamental harmonics have the same frequency ($\omega_1 = \omega_2$). An alternative notation $d_{ijk}^{(2)}$ for the non-linear tensor is often used; $d_{ijk}^{(2)}$ is related to $\chi_{ijk}^{(2)}$ as follows:

$$d_{ijk}^{(2)} = \frac{1}{2}\chi_{ijk}^{(2)}. \tag{8.5}$$

In the interaction process between the two fields, no physical significance can be attached to the exchange of E_j and E_k. Therefore, it is possible to replace the product of subscripts k and j by a single symbol, to reduce the number of subscripts in the formula. The Voigt notation is commonly adopted. In this convention, the first indices, x, y and z, are replaced by 1, 2 and 3 respectively, while the second and third indices are replaced by one index taking the following values:

$$xx = 1 \quad yy = 2 \quad zz = 3 \quad yz = zy = 4$$
$$zx = xz = 5 \quad xy = yx = 6. \tag{8.6}$$

The contracted $d_{ijk}^{(2)}$ tensor has 3×6 components instead of 27 for the $d_{ijk}^{(2)}$. The non-vanishing components of the induced polarization are determined by the form of the tensor and the components of the incident fields. The first condition for a crystal to exhibit a quadratic non-linear susceptibility (i.e. a non-vanishing $d^{(2)}$) is the lack of an inversion centre in its structure. The form of this tensor (i.e. the non-vanishing components) is linked to the point group symmetry of the crystal. In addition to these symmetry-imposed restrictions on the number of non-vanishing d_{ij} elements, other restrictions arise, since the d_{ij} elements should be invariant under each symmetry operation. This introduces relationships between the components and further reduces the number of independent coefficients. As an example, dihydrogen phosphate KH_2PO_4 (KDP), one of the most popular non-linear crystals, belongs to the $\bar{4}2m$ point group symmetry; then its non-linear susceptibility is reduced to

$$d_{ij}=\begin{vmatrix} 0 & 0 & 0 & d_{14} & 0 & 0 \\ 0 & 0 & 0 & 0 & d_{25} & 0 \\ 0 & 0 & 0 & 0 & 0 & d_{36} \end{vmatrix} \qquad (8.7)$$

In this case, only a few components of the tensor are non-vanishing and further symmetry consideration simply that $d_{14} = d_{25}$.

From this example and Equation (8.4), it is easy to deduce that the direction of the induced non-linear polarization may be different from those of the applied electromagnetic field. Consider an incident wave propagating in a direction perpendicular to the optic axis $\boldsymbol{E}(E_x, E_y, 0)$. The induced non-linear polarization will be $\boldsymbol{P}^{(2\omega)}(0, 0, P_z)$ with $P_z^{2\omega} = 2\varepsilon_0 d_{36} E_x^{(\omega)} E_y^{(\omega)}$ (see Figure 8.1).

8.2.3 Phase Matching

The macroscopic SH wave will result from the summation of individual contributions generated by atoms at different positions (x, y, z) on the path of the fundamental beam in the non-linear medium. Then, the SH wave will have an appreciable intensity if the vectors of the phase velocities of the fundamental wave and the polarization wave are properly matched, i.e. $\upsilon_{\text{ph}}^{(\omega)} = \upsilon_{\text{ph}}^{(2\omega)}$ with $\upsilon_{\text{ph}} = \omega_i / k^{(\omega_i)} = c / n^{(\omega_i)}$. This phase-matching condition can be written as

$$\Delta \boldsymbol{k} = \boldsymbol{k}(\omega_1 + \omega_2) - \boldsymbol{k}(\omega_1) - \boldsymbol{k}(\omega_2) = 0 \qquad (8.8)$$

which may be interpreted as momentum conservation for the three photons participating in the mixing process (Figure 8.2). In the limiting case of SHG, the phase-matching condition reduces to $\boldsymbol{k}(2\omega) = 2\boldsymbol{k}(\omega)$. The maximum exchange of energy between the fundamental and the second harmonic will be obtained for a collinear propagation of the waves, which implies that their phase velocity must be equal.

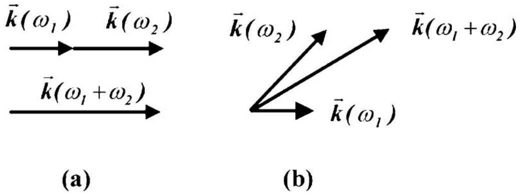

(a) **(b)**

FIGURE 8.2 Phase-matching condition as momentum conservation for (a) collinear propagation and (b) non-collinear propagation of waves.

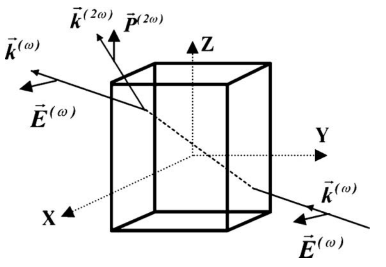

FIGURE 8.1 The effect of non-linear susceptibility in a uniaxial crystal: an incident wave, propagating in a plane perpendicular to the optic axis, with electric field $\boldsymbol{E}^{(\omega)}(E_x, E_y, 0)$ induces a polarization, at frequency $2\omega, \boldsymbol{P}^{2(\omega)}\left(0,0,P_z^{(2\omega)}\right)$ (i.e. parallel to the optic axis).

The phase-matching condition is not easily fulfilled in crystals because of phase velocity dispersion. Let us consider the general case $\Delta(\boldsymbol{k}) \neq 0$, which means $\upsilon_{\text{ph}}(\omega) \neq \upsilon_{\text{ph}}(2\omega)$. If the incident wave propagates in the z-direction in a non-linear medium, a phase difference between the fundamental wave and the wave generated at 2ω will increase and, after travelling a path l, it will be $\Delta k = |k(2\omega) - k(\omega)| l$. To simplify the analysis, we consider the general case of a low conversion efficiency (undepleted regime). In this case, the amplitude of the incident wave remains constant along the pathlength through the non-linear crystal. The total amplitude of the SH wave for a crystal length L results from the summation of the microscopic contribution $\mathrm{d}E(2\omega, z)$ from $z = 0$ to $z = L$. The intensity of the SH wave at the output of the crystal is then

$$I(2\omega,L) = I(\omega)^2 \frac{2\omega^2 \left|d_{\text{eff}}^2\right| L^2}{n^3 c^3 \varepsilon} \sin c^2\left(\Delta k L/2\right) \ \text{with} \sin c(x) = \sin(x)/x. \qquad (8.9)$$

A maximum in the intensity of the second harmonic is obtained for $\Delta k l/2 = \pi$. Half of the distance between two adjacent peaks of this interference pattern (also called Maker fringes) corresponds to the so-called *coherence length* l_c. Using $k^{\omega} = \omega n^{\omega}/c$, l_c is given by

$$l_c = \frac{2\pi}{\Delta k} = \frac{\lambda}{4\left[n^{(2\omega)} - n^{(\omega)}\right]} \qquad (8.10)$$

where λ is the free-space wavelength of the fundamental wave.

The coherence length represents the maximum distance over which the fundamental and the SH waves are in phase and interfere constructively (i.e. the distance along which the second amplitude increases). For $l > l_c$, destructive interference occurs which reduces the SH amplitude. From a practical point of view, the difference $n(2\omega) - n(\omega)$ should be as small as possible to provide a large coherence length compared to the crystal length. This can be achieved by taking advantage of the wave propagation in birefringent crystals and satisfying the condition in Equation (8.8).

Let $\boldsymbol{E}$ be the electric field incident on an anisotropic medium—from Equation (8.4) the induced polarization $\boldsymbol{P}$ is not necessarily parallel to $\boldsymbol{E}$. The electric displacement vector $\boldsymbol{D}$ is related to $\boldsymbol{E}$ through the dielectric tensor ε_{kl} as follows:

$$D_k = \varepsilon_{kl} E_l \qquad (8.11)$$

where k and l refer to the Cartesian coordinates (x, y, z) fixed with respect to the crystal axes. An axis transformation is used to diagonalize the tensor ε_{kl}. In the new system, $D_i = \varepsilon_i \boldsymbol{E}_i$ with $i = x, y, z$, the principal dielectric axes. Defining the principal refractive indices n_i such as $n_i^2 = \varepsilon_i$, the equation of a general ellipsoid is then obtained:

$$\frac{x^2}{n_x^2} + \frac{y^2}{n_y^2} + \frac{z^2}{n_z^2} = 1. \tag{8.12}$$

According to Equation (8.12), it is possible to determine the refractive index associated with a plane wave propagating along an arbitrary direction in a crystal.

8.2.3.1 Phase Matching in Uniaxial Crystals

In *uniaxial* crystals, z is taken along the symmetry axis (also referred to as the optic axis). The principal plane is defined by the z-axis and the wavevector $\boldsymbol{k}$ of the propagating wave. The *ordinary beam* 'o' propagates with a polarization perpendicular to the optic axis and the *extraordinary beam* 'e' is polarized in the principal plane. Thus, Equation (8.12) is simplified since $n_x = n_y = n_\mathrm{o}$ and $n_z = n_\mathrm{e}$:n_o, n_o is the ordinary index of refraction and n_e the extraordinary one. By definition, the optic axis is the direction in which the o- and e-rays propagate with the same velocity. For a *positive* uniaxial crystal $n_\mathrm{o} < n_\mathrm{e}$, while $n_\mathrm{o} > n_\mathrm{e}$ for the *negative* uniaxial crystal (Figure 8.3). Consider a wave propagating along an arbitrary direction, n_o remains constant whatever the beam polarization and its propagation direction, whereas n_e will depend on θ, the angle between the optic axis and the direction of propagation, following

$$\frac{1}{n_\mathrm{e}(\theta)^2} = \frac{\cos^2(\theta)}{n_\mathrm{o}^2} + \frac{\sin^2(\theta)}{n_\mathrm{e}^2}. \tag{8.13}$$

Both n_o and n_e are functions of the frequency. There exists an angle which satisfies the phase-matching condition $\left(n_\mathrm{e}^{2\omega} = n_\mathrm{o}^{\omega}\right)$. This *phase-matching angle* θ_m is determined by the intersection of the sphere corresponding to the index surface of the ordinary beam at ω with the index ellipsoid associated to the extraordinary beam at 2ω (see, for example, the case of the negative uniaxial crystal in Figure 8.3). θ_m is then obtained by solving

$$\frac{1}{\left(n_\mathrm{o}^{\omega}\right)^2} = \frac{\cos^2\theta_\mathrm{m}}{\left(n_\mathrm{o}^{2\omega}\right)^2} + \frac{\sin^2\theta_\mathrm{m}}{\left(n_\mathrm{e}^{\omega}\right)^2}. \tag{8.14}$$

Different types of interaction processes in the harmonic generation can be encountered depending on the two possible orientations for the linear polarization of the fundamental beam. These are summarized in Table 8.1. A complete calculation of the phase-matching angles in uniaxial crystals is developed in Ref. [5].

8.2.3.2 Phase Matching in Biaxial Crystals

The propagation of light waves in *biaxial* crystals is much more complex. A complete description can be found in Ref. [5]. The dependence of the refractive indices on the light

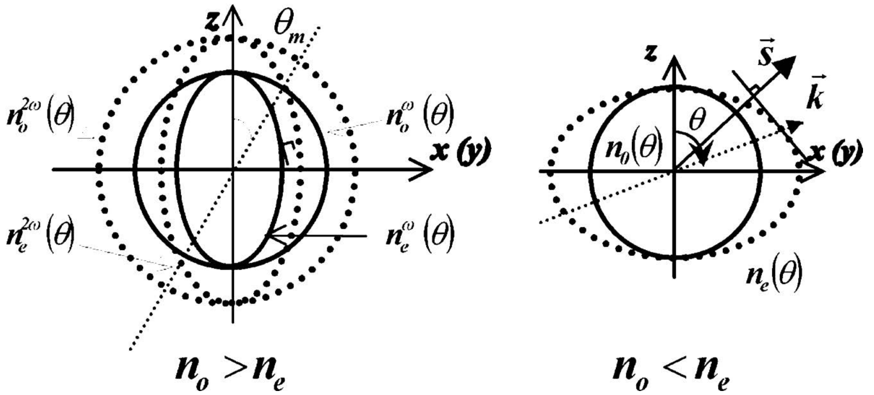

FIGURE 8.3 Uniaxial crystals: the dependence of the ordinary (n_o) and extraordinary (n_e) indices on the angle θ between the wavevector k and the optic axis. Phase matching is for SHG in a negative birefringent crystal (n_o < n$_\mathrm{e}$). The illustrated energy and wave propagations are for a positive birefringent crystal (n_o < n$_\mathrm{e}$).

TABLE 8.1

Types of Phase Matching in Uniaxial Crystals

ω_1	ω_2	SH (ω_3)	Crystal	SH Type
o	O	e	Negative	I
e	E	o	Positive	I
o	E	e	Negative	II
e	O	e	Negative	II
e	E	o	Positive	II
e	O	o	Positive	II

propagation direction is described by surfaces in a coordinate system (X, Y, Z) defined as *crystallophysical*, which differs from the crystallographic one (a, b, c). In the (X, Y, Z) system, (XY), (XZ) and (YZ) are defined as principal planes. The crystallophysical axes are obtained in such a way that the considered optic axis always belongs to the XZ principal plane. The optic axis direction is given by the intersection of the ellipse and circle in XZ (Figure 8.4). The angle V_Z between one of the optic axes and the Z-axis is given by

$$\sin V_Z = \frac{n_Z}{n_Y}\left(\frac{n_Y^2 - n_X^2}{n_Z^2 - n_X^2}\right)^{(1/2)} \text{for } n_X < n_Y < n_Z \qquad (8.15)$$

$$\cos V_Z = \frac{n_X}{n_Y}\left(\frac{n_Y^2 - n_Z^2}{n_X^2 - n_Z^2}\right)^{(1/2)} \text{for } n_X > n_Y > n_Z \qquad (8.16)$$

Different phase-matching types are possible depending on the direction of the light propagation in the principal planes (Table 8.2). The corresponding equations for calculating phase-matching angles are detailed in Ref. [5]. A systematic review of phase matching in uniaxial and biaxial crystals is developed in Ref. [9].

The efficiency of SH conversion is not independent of the azimuthal angle ϕ measured between the x-axis and the projection in the xy-plane of the phase-matching direction. Thus, the effective non-linear coefficient d_{eff} will be generally expressed as a combination of several d_{ij} components of the non-linear tensor, θ_{m} and ϕ. As an example, in the case of BBO (a negative uniaxial crystal), phase matching is achieved for a type I interaction (see Table 8.1) and d_{eff} is given by $d_{\text{ooe}} = d_{31} \sin\theta - d_{22}\cos\theta\sin 3\phi$.

8.2.3.3 Limiting Parameters of the Doubling Efficiency

For an extraordinary wave propagating in an anisotropic crystal, the directions of wave propagation (***k***) and energy propagation (***s***) are generally different. The energy propagation direction is defined by the normal to the tangent at the intersection of (***k***) and the $n_{\text{o}}(\theta)$ curve (Figure 8.3). Therefore, the angle ρ between ***k*** and ***s*** (called the *birefringence angle* or, more usually, the *walk-off angle*) is given by

$$\rho(\theta) = \pm\arctan\left[\left(n_{\text{o}}/n_{\text{e}}\right)^2 \tan\theta\right] \mp \theta \qquad (8.17)$$

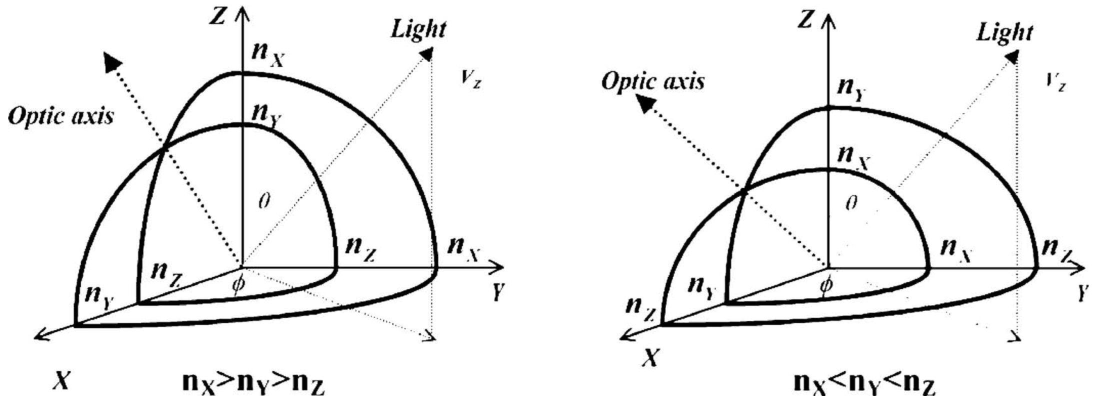

FIGURE 8.4 Indicatrices of refractive indices in biaxial crystals.

TABLE 8.2

Types of Phase Matching in Biaxial Crystals

	$n_X < n_Y < n_Z$		$n_X > n_Y > n_Z$	
Principal Plane	**Interaction**	**Phase Matching**	**Interaction**	**Phase Matching**
XY	Ooe	I	eeo	I
	Eoe	II	oeo	II
	Oee	II	eoo	II
YZ	Eeo	I	ooe	I
	Oeo	II	eoe	II
	Eoo	II	oee	II
$ZX(\theta < V_Z)$	Ooe	I	eeo	I
	Eoe	II	oeo	II
	Oee	II	eoo	II
$ZX(\theta > V_Z)$	eeo	I	ooe	I
	oeo	II	eoe	II
	eoo	II	oee	II

(the upper and lower signs refer to negative and positive crystals, respectively).

A laser beam with an arbitrary linear polarization entering a crystal will be split into two beams, which propagate with orthogonal polarizations, i.e. an *ordinary* beam and an *extraordinary* beam. If L is the crystal length, at the output face of the crystal, the two beams will be separated by δ given by

$$\delta = L \tan \rho \tag{8.18}$$

with ρ (the *walk-off angle*) the angle between the two beams (Figure 8.5).

The walk-off effect effectively decreases the interaction length and can, of course, be minimized if the beams are propagating in a direction along which $\boldsymbol{k}$ is parallel to $\boldsymbol{s}$.

However, if the phase matching is achieved for an angle θ_m other than 90° with respect to the optic axis of a uniaxial crystal, there will be double refraction: the incident beam will split into two beams with orthogonal polarizations. The beams will be completely separated after a distance $l_{d_\mathrm{f}} = d_{f\rho^{-1}}$, with d_f the diameter of the fundamental beam. l_{d_f} is called the *aperture length*. This case corresponds to *critical phase matching*. Otherwise, the case $\theta_\mathrm{m} = 90°$ corresponds to *non-critical phase matching* because the effect of limiting factors to the conversion efficiency is much smaller than in the previous case. Provided $n_\mathrm{o}^{\omega} \sim n_\mathrm{e}^{2\omega}$ and $\mathrm{d}\left(n_\mathrm{o}^{\omega} - n_\mathrm{e}^{2\omega}\right)/\mathrm{d}T \neq 0$, non-critical phase matching can be achieved by tuning the temperature of the crystal (this is the case of $\mathrm{LiNbO_3}$).

In real situations, other factors can affect perfect phase matching such as the divergence and spectral width of the fundamental beam or temperature variations in the non-linear crystal. These factors are of fundamental importance for the applications in which we are interested in this chapter. Following the analysis of Dmitriev et al. [5], the dependence of Δk on these different effects can be expressed in the linear approximation as

$$\Delta k \simeq \Delta k(0) + \frac{\partial(\Delta k)}{\partial T}\Delta T + \frac{\partial(\Delta k)}{\partial\partial(\delta\theta)}\Delta\theta + \frac{\partial(\Delta k)}{\partial \nu}\Delta\nu \tag{8.19}$$

where $\Delta k(0)$ is the mismatch to exact phase matching: the partial derivatives with respect to one argument are taken with the assumption that the other two are constant and $\Delta k(0) = 0$. From Equation (8.9), the conversion efficiency ($I_{2\omega}/I_\omega$) is reduced to half its value for sin c^2 ($\Delta kL/2$) = 0.5 or $\Delta k = 0.886\pi\, L^{-1}$. Then, the angular ($\Delta\theta$), thermal ($\Delta T$) and spectral ($\Delta\nu$) bandwidths can be written as

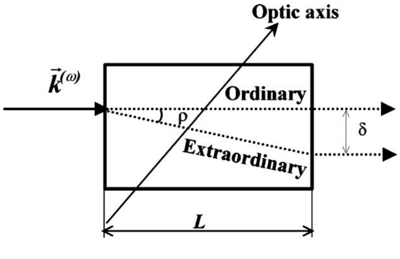

FIGURE 8.5 Walk-off effect in a uniaxial crystal.

$$\Delta\theta = 1.772\pi L^{-1}\left[\frac{\partial(\Delta k)}{\partial(\delta\theta)}\right]^{-1}_{\theta=\theta_\mathrm{pm}} \tag{8.20}$$

$$\Delta T = 1.772\pi L^{-1}\left[\frac{\partial(\Delta k)}{\partial T}\right]^{-1}_{T=T_\mathrm{pm}} \tag{8.21}$$

$$\Delta\nu = 1.772\pi L^{-1}\left[\frac{\partial(\Delta k)}{\partial \nu}\right]^{-1}_{\nu=\nu_\mathrm{pm}} \tag{8.22}$$

In Equation (8.20), $[\partial(\Delta k)/\partial(\delta\theta)]_{\theta=\theta\mathrm{pm}}$ defines the angular sensitivity (β_θ). Since $\Delta k = (4\pi/\lambda)(n^{2\omega} - n^{\omega})$, the different derivatives in Equations (8.20)–(8.22) will depend on the dispersion of the refractive indices and on the type of phase matching. If in the case of non-critical phase matching, the first derivative with respect to θ equals 0, then the second one becomes important; in this case, $\Delta\theta \propto (\partial^2(\Delta k)/\partial(\delta\theta)^2)^{-1}]^{1/2}$. The equations for calculating $\Delta\theta$, ΔT and $\Delta\nu$ are given in Ref. [5] for all types of phase matching and interactions. The relevant parameters for non-linear crystals of interest in this chapter are summarized in Table 8.3. Furthermore, frequency doubling with focused Gaussian beams is discussed in Refs. [10,11]. This is the case for ICFD and the principal results are given in Section 8.3.1.

8.3 Self-Frequency Doubled Lasers *versus* Intracavity Frequency Doublers

Optical harmonic generation has been widely developed to extend the spectrum of laser sources. In particular, in the field of solid-state lasers, considerable efforts have been devoted to the harmonic generation of $\mathrm{Nd^{3+}}$ lasers for visible and UV laser radiations. Large conversion efficiency requires high power densities not available with cw sources. For this reason, Q-switched or mode-locked lasers delivering high peak powers were used as fundamental radiation, the harmonic generator being external to the cavity. In this way, visible and UV sources were available in the nanosecond and picosecond regimes. In 1968, the possibility of using the high intracavity power for efficient frequency conversion and a continuous 532 nm laser source (350 mW) was demonstrated with a non-linear crystal ($\mathrm{Ba_2NaNb_5O_{15}}$, also called ‘Banana’) inside the cavity of an Nd:YAG laser delivering 1 W at 1.064 μm [14]. Furthermore, with the appearance of semiconductor laser diodes (LD), LD-pumped cw lasers with intracavity SHG is a promising approach for the development of compact visible laser sources. Later, another promising approach for compact all-solid-state lasers in the blue–green wavelength range was developed with the use of a gain medium which simultaneously acts as a harmonic generator (self-frequency doubling (SFD)). In a first step, we will focus our interest on ICFD, then on SFD. Finally, we will compare the advantages and drawbacks of both systems.

TABLE 8.3

Frequency Doublers: Physical Properties and Tolerance Parameters: Angular Δθ (mrad cm−1), Thermal ΔT (° cm−1) and Spectral Δλ (nm cm−1)

							Tolerance Factors				
		$\lambda_{fund.}$ (µm)	θ_{PM} (°)	d_{eff} (pm V^{-1})	n^{ω}	Transparency (µm)	$\rho^{(\omega)}$	$\Delta\theta$	ΔT	$\Delta\lambda$	
Banana	ooe	1.06	74	13.2[a]		0.37–5	-	2.4	0.8	0.3	[5]
(*mm*2)[c]				14.6[b]							
KTP	eoe	1.06	24.3	3.18	1.74	0.35–4.5	0.26	25	25	0.56	[8]
(*mm*2)[d]											
BBO	ooe	1.06	22.8	1.94	1.65	0.198–2.6	3.19	0.5	55	0.66	[8]
(3m)[e]		0.946		2.08	1.658		3.5	0.42	23	0.43	[12]
$LiNbO_3$[f]	ooe	1.06	90	4.7	2.23	0.33–5.5	0	2.3	0.6	0.23	[8]
(3m)[e]								3.1	1.1	0.3	[5]
$LiIO_3$	ooe	1.06	30.2	4.1	1.85	0.3–6	4.26	0.7	-	-	[8]
(6)[e]		0.946	34.3	4.01	1.861		4.6	0.28	20	0.16	[12]
LBO	ooe	0.946	19.5	0.92	1.6077	0.16–2.6	0.7	2.29	8	0.63	[12]
(*mm*2)[e]											
$KNbO_3$	eeo	0.946	30	16.4		0.4–4.5	-	-	-	-	[13]
(*mm*2)[c]											

[a] Along *Y*.
[b] Along *X*.
[c] Negative biaxial.
[d] Positive biaxial.
[e] Negative uniaxial.
[f] Temperature tuning at 107°C.

8.3.1 Intracavity Frequency Doubling

8.3.1.1 Nd^{3+}-Crystals as the Gain Medium

Up to now, ICFD has been developed with Nd^{3+}-doped crystals as the gain medium, most of them being LD pumped (see Section 8.5). In addition to the well-known 1.064 µm laser emission due to the $^4F_{3/2} \rightarrow {}^4I_{11/2}$ transition, the Nd^{3+} ion exhibits other laser transitions at 1.32 µm ($^4F_{3/2} \rightarrow {}^4I_{13/2}$) and 946 nm ($^4F_{3/2} \rightarrow {}^4I_{9/2}$), which can be used to achieve SHG for red and blue radiations, respectively. The fundamental wavelength is provided by Nd^{3+} emission in crystals commonly used for infrared laser sources: $Y_3Al_5O_{12}$ (YAG), YVO_4, $YAlO_3$ (YAP) and $LiYF_4$ (YLF). ICFD has also been achieved in $Sr_5(PO_4)_3F$ (S-FAP) and $LaSc_3(BO_3)_4$ (see Tables 8.4 and 8.8).

8.3.1.2 Type of Non-linear Crystals

The most important criterion for selecting the non-linear crystal is the dependence of the effective non-linear coefficient on the fundamental wavelength. As an example, KTP, widely used as a frequency-doubling crystal for the 1.064 µm laser transition, cannot be used for frequency doubling the 946 nm radiation since it exhibits a high non-linearity at 1.064 µm but a low d_{eff} coefficient at 946 nm. In this case, $KNbO_3$, $LiIO_3$ or β-BaB_2O_4 (BBO) or LiB_3O_5 (LBO) are used as non-linear crystals for harmonic generation in the blue [12,15]. Other factors for the selection of a particular crystal have also to be considered such as spectral, temperature and angular acceptance bandwidths and walk-off angle (Table 8.3). For example, $KNbO_3$ exhibits a high non-linearity and a possibility of non-critical phase matching but severe drawbacks limit its use: very small temperature and spectral acceptance bandwidths, photorefractivity leading to optical damage. Furthermore, the possibility of domain reversal has been reported particularly for non-critical phase matching, where the crystal has to be heated up to 180°C [12]. BBO and $LiIO_3$ exhibit a large temperature bandwidth; then temperature control is not necessary. $LiIO_3$ has the highest non-linear coefficient; however, it has also the smallest spectral acceptance bandwidth. The small angular acceptance bandwidth and the large walk-off angle of these crystals limit their use. LBO is a promising candidate with respect to walk-off angle and spectral and angular acceptance bandwidths even if its non-linear coefficient is less than that of BBO and $LiIO_3$.

8.3.1.3 Output Power of the Second Harmonic

For ICFD, the non-linear crystal is placed inside the cavity. To optimize the output power of the second harmonic, the output mirror of the cavity should reflect 100% of the fundamental radiation and be totally transparent at the SH wavelength. Therefore, in addition to the linear loss of the cavity due to absorption scattering, imperfect mirror coatings and so on, one must consider the non-linear loss due to the SHG, since in this case, a non-negligible fraction of the power at ω is converted. The detailed theory of internal optical SHG is described at length in Ref. [16]. We will only briefly give the most important results. The pump and the laser beams are assumed to have a Gaussian profile and be collinear in the crystal. If the laser crystal length L is much shorter than the distance in which the beam section area doubles relative to its value at the waist, the waist radius of the pump beam is taken to be approximately constant within the crystal. The effect of the non-linear crystal in the cavity is taken into account by introducing a power-dependent loss. Then, under steady-state conditions and for small-signal gain G_0, the round-trip saturated gain of the laser equals the loss of the cavity:

$$\frac{2G_0 l}{1+2SI} = \beta_L + KI \tag{8.23}$$

where the term on the right-hand side corresponds to the gain in the cavity, the term on the left to the losses (β_L being associated to the total round-trip linear loss due to the different components of the cavity and KI the round-trip non-linear loss due to frequency conversion by the non-linear crystal in the cavity). The factor 2 takes account of the saturation in the forward and backward directions in the gain medium of length l, and S is the saturation term given by

$$S = \frac{1}{I_\mathrm{sat}} = \frac{\sigma_\mathrm{em}\tau}{\hbar\omega} \tag{8.24}$$

where σ_em is the emission cross section, τ the emission lifetime and $\hbar\omega$ the laser frequency. The round-trip non-linear loss of the cavity, which is the sum of the SHG power in the forward and backward directions, is given by [16]

$$P^{(2\omega)} = KP_\mathrm{c}^{(\omega)} \frac{P_\mathrm{c}^{(\omega)}}{\pi\omega_\mathrm{c}^2} \tag{8.25}$$

with K defined as the non-linear coupling term. For simplicity, the direction of propagation is assumed to be along the principal axis, and the effects of double refraction are then neglected. With this hypothesis, K is expressed as (MKS units):

$$K = k \sin c^2\left(\frac{\Delta k L_\mathrm{n}}{2}\right) \text{with}\, k = 4\frac{\omega_\mathrm{c}^2}{\omega_\mathrm{n}^2}\left(\frac{\mu_0}{\varepsilon_0}\right)^{1/2} \frac{\omega_1^2 d_\mathrm{eff}^2 L_\mathrm{n}^2}{n_1^2 n_2 c^2} \tag{8.26}$$

where ω_c and ω_n are the beam waist in the cavity and non-linear crystal respectively, ω_1 is the radian frequency of the fundamental, $n_1 = n^\omega$ and $n_2 = n^{2\omega}$, d_eff is the relevant non-linear coefficient and L_n is the length of the non-linear crystal.

From Equation (8.25), the conversion efficiency ($P^{(2\omega)}/P_\mathrm{c}^{(\omega)}$) depends on the non-linear coupling term and the fundamental power density in the non-linear crystal. The non-linear coupling term includes the length of the non-linear crystal and the phase mismatch. To optimize the cavity, the thermal lens effect, which appears at high power density, should be taken into account especially with YAG and YVO_4 crystals.

When the conversion efficiency exceeds 20%, the depletion of the fundamental power should be taken into account. In the case of depleted input, Equation (8.25) should be replaced by [1]

$$\frac{P^{(2\omega)}}{P_\mathrm{c}^{(\omega)}} = \tan h^2\left[k^{1/2}\left(\frac{P_\mathrm{c}^{(\omega)}}{\pi\omega_\mathrm{c}^2}\right)^{1/2} \sin c\left(\Delta kl/2\right)\right]. \tag{8.27}$$

8.3.1.4 Modelling the Behaviour of a Solid-State Laser with Reabsorption as an Additional Loss: Example of Nd^{3+} 946 nm Laser Emission

In practice, the output harmonic power can be lower than the expected value. This is explained by other processes such as reabsorption, which introduce additional losses. Reabsorption is especially important for low gain lasers of interest for ICFD. This is the case for the 946 nm laser transition in which the effective emission cross section is lower by about one order of magnitude than that of 1.06 μm and corresponds to a quasi-four-level system. The lower laser level is the upper crystal field component of the $^4I_{9/2}$ ground-state multiplet. Then, due to the small energy gap (for example, 857 cm^{-1} in YAG), there is a significant reabsorption loss owing to the population of this state at room temperature [17].

A room-temperature cw operation in a short gain medium with a low threshold can be achieved by using end pumping, which allows a high inversion efficiency in a small volume that helps to overcome the reabsorption loss. The detailed modelling of the behaviour of a solid-state laser with reabsorption loss is reported in Ref. [18] providing a comprehensive understanding of mode-overlap effects in longitudinally pumped lasers. In particular, the effects of reabsorption loss on the threshold and on the slope are analysed in detail. The threshold as expressed in terms of incident pump power is given by [17,18]

$$P_\mathrm{th,inc} = \frac{\pi h\nu_\mathrm{p}\left(\omega_\mathrm{c}^2 = \omega_\mathrm{p}^2\right)}{4\sigma f\tau\left(1-\exp\left(-\alpha_\mathrm{p} l\right)\right)}\left(L_\mathrm{c} + T + 2N_1^0\sigma l\right) \tag{8.28}$$

where σ is the gain cross section, N_1^0 the equilibrium population density of the lower laser level, ω_c the laser beam waist in the cavity, ω_p the pump beam radius, ν_p the pump frequency, τ the upper-state lifetime, α_p the absorption coefficient at the pump wavelength, l the laser crystal length, L_c the fixed cavity loss, T the output coupling and f the fraction of the total $^4F_{3/2}$ population that stays in the lower crystal-field component of the $^4F_{3/2}$ multiplet.

From Equation (8.28), reabsorption is just like an additional loss leading to an increase in the threshold. It can also be deduced from Equation (8.28) that making the pump-beam waist ω_p and laserbeam waist ω_c as small as possible will reduce the threshold. Furthermore, it follows from Equation (8.28) that the optimum crystal length l_0 results from a compromise between large absorption of the pump and minimum reabsorption of the laser emission. The length of the laser crystal that minimizes the threshold can be calculated by differentiating Equation (8.28), provided that the other factors are known:

$$\alpha_\mathrm{P} \exp\left(-\alpha_\mathrm{p} l_\mathrm{o}\right)\left(\frac{2\sigma N_1^0}{\alpha_\mathrm{p}} + L + T - 2\sigma N_1^0 l_0\right) - 2\sigma N_1^0 = 0. \tag{8.29}$$

As an example, an optimum length l_0 equal to 1.2 mm is obtained for a 1.1% doped Nd:YAG ($N_1^0 = 1.1 \times 10^{18}$ ions cm^{-3}) and pumping by a dye laser ($\alpha_{\mathrm{p}=} 0.95$ cm^{-1}), $\sigma = 4 \times 10^{-20}$ cm^2, assuming $L = 0.001$ and $T = 0.0085$ [17].

The key parameter for the internal slope efficiency (s_{int}) is $r_{\text{waist}} = \omega_p/\omega_c$ for a laser with reabsorption loss. There is an optimum value r^0_{waist} that maximizes the slope efficiency. r^0_{waist} depends on both the internal laser power and the reabsorption loss, i.e. it will increase as the reabsorption loss or the internal power increases. Anyway, for an appropriate value of r_{waist} and large internal laser powers, the reabsorption loss is saturated and the slope efficiency is comparable with that of a laser without reabsorption loss. Another parameter for the choice of the output coupler of the cavity is the external slope efficiency defined as [18]

$$\frac{dP_{\text{out}}}{dP_p} = \frac{T}{T+L}\frac{\nu_c}{\nu_p}\eta_a s_{\text{int}} \tag{8.30}$$

where η_a is the efficiency with which incident pump photons are absorbed (corresponding to $[1-\exp(-\alpha_p l)]$ in Equation (8.28)), s_{int} is the efficiency with which absorbed pump photons are converted to laser photons, ν_c/ν_p is the quantum defect associated to this conversion, T is the output coupler transmittance and L is the total optical round-trip loss of the cavity. Then, $T/(T+L)$ represents the fraction of laser photons that are emitted through the output coupler.

8.3.2 Designs

8.3.2.1 *Optimization of the Diode End-Pumped Lasers*

Several models have been proposed to optimize the design of diode end-pumped lasers. Simple design criteria were given for longitudinally pumped lasers operating in TEM_{00}, using a circular or elliptical Gaussian beam to simulate the laser diode beam distribution [19]. An analytical model has been developed for fibre-coupled laser-diode end-pumped lasers, by including the effect of pump-beam quality into the mode overlap integrals [20,21]. From this model, a simple procedure to optimize the design of the laser resonator and the optical coupling system has been derived. In another approach [22], the pump beam coming from the optical fibre is considered as Gaussian and its propagation is described by its M^2 factor [23]. This model allows a straightforward procedure to design the optimum laser resonator and the coupling optics. These models are briefly presented in Section 8.5.

8.3.2.2 *Optimization of Second-Harmonic Generation: Conditions to Achieve an Efficient Laser Source*

Another problem to be solved for intracavity doubling is the optimization of SHG. As we have previously noted, the walk-off effect reduces the efficiency of the frequency conversion. Taking this effect into account [11] and assuming a focused Gaussian beam, the non-linear coupling term K is then given by

$$K = \frac{2\omega^2 d_{\text{eff}}^2 L_n h k_\omega}{\epsilon_0\, c^3 \pi_\omega^3} \tag{8.31}$$

where h is a non-linear function depending on the walk-off angle ρ, the length of the non-linear crystal (L_n), the fundamental laser beam waist (ω_c) and the fundamental wavevector k_ω inside this crystal. In the case of non-critical phase matching, $h = 1$. For non-critical phase matching, if the fundamental beam waist is such as $\lambda/\rho\pi n_\omega < \omega_c < \rho L_n/(24)^{1/2}$, then h is expressed as

$$h = \frac{\sqrt{\pi}}{2B\sqrt{\xi}}\arctan(\xi) \tag{8.32}$$

with B the walk-off parameter and ξ the focusing parameter given by:

$$B = \rho/2\frac{\sqrt{\pi n L_n}}{2\lambda} \text{ and } \xi = \frac{L_n \lambda}{2\pi\omega_0^2 n_\omega}. \tag{8.33}$$

An example of the analytical solution of h for BBO and $LiIO_3$ crystals [12] is given in Figure 8.6.

In conclusion, to achieve an efficient visible laser source by ICFD, the laser crystal should have a large emission cross section, a long emission lifetime, a low passive loss, an effective absorption bandwidth (important in the case of diode pumping) and an optimized length to reduce the reabsorption loss, if any. The non-linear crystal should obviously have a large non-linear coefficient but a small walk-off angle. Visible laser sources with ICFD have been realized by optimizing all the parameters important to achieve a large SH output power. Some examples are given in Tables 8.4 and 8.8 (in Section 8.6). As shown in Table 8.8, the best optical conversion efficiency is obtained for the YAG-Banana system due to the large non-linear coefficient of this frequency doubling crystal compared to the others (Table 8.3). However, Banana has a poor optical quality and a low damage threshold which prevents its commercial use. The absorption cross section of the Nd^{3+} $^4I_{15/2} \rightarrow {}^4F_{3/2}$ transition is lower in YAG than in YVO_4. In addition, the absorption bandwidth is larger in YVO_4, thus this material is more appropriate to realize miniaturized devices such as diode-pumped microchips. Different designs and pumping devices are detailed in Section 8.5.

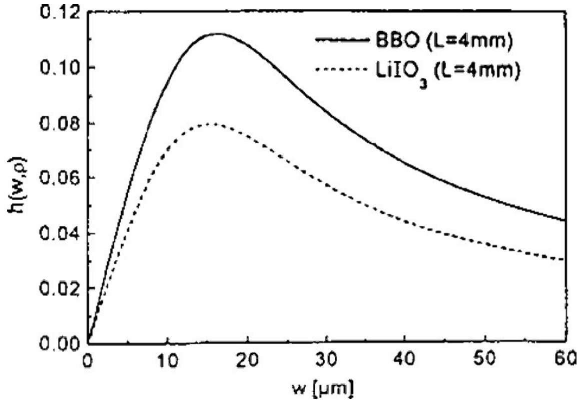

FIGURE 8.6 Dependence of the non-linear coupling function h on the fundamental beam waist for $LiIO_3$ and BBO (length of both crystals L = 4 mm) (after Ref. [12]).

TABLE 8.4

Lasers with Intracavity-Doubling Frequency

Laser Crystal	Length (mm)	Frequency Doubler	Length (mm)	Cavity	λ_{SH} (nm)	Other Data	Ref.
YAG		Banana T=83°C	2.8	~H (L = 450 mm)	532		[14]
YAG	1	$LiIO_3$		H	473	$\omega_l = 40$ μm	[17]
YAG[a]	3	$LiIO_3$	4	A (L < 70 mm)	473	$P_{th}^{(SH)} = 10\,mW$	[12]
YAG[a]	3	BBO	4	A	473		[12]
YAG[a]	3	LBO	4	A	473		[12]
YAG (1.1 at%)	10	KTP	15	C	532	$\omega_p = 290$ μm $\omega_l = 90$ μm	[24]
YAG (0.6 at%)	115	KTP	5	A (L = 560 mm)[b] EO Q-switch (F = 20 kHz, τ = 500 ns)	532	Beam quality (Fund.) Function of P_{pump} $0.92 < \frac{M_x^2}{M_y^2} < 1.06$	[25]
YAG	8	KTP	5	A(L = 330 mm)	532		[26]
YAG	1	$KNbO_3$	3.7	H[c]	473	$\omega_l = 40$ μm	[13]
YAG (1.1 at%)	1	$KNbO_3$	1.5		473	$\omega_0 = 45$ μm	[27]
YAG	3	$KNbO_3$	6.5	B	473	$\frac{\omega_p}{\omega_l} = 0.5$	[28]
YVO_4 (1 at%)	0.5	LBO	2	M	671		[29]
YVO_4 (1.1 at%)	1	KTP	5	D (L = 21 mm)	532	$M_x^2 = 1.2$ $M_y^2 = 1.3$	[30]
YVO_4 (1.1 at%)	1	KTP	5	H (L=21 mm)[c] AO Q-switch (F = 100 Hz)	532	$P_{th}^{(SH)} = 100\ mW$	[31]
YVO_4 (3 at%)	0.5	KTP	2	P			[32]
YVO_4 (1 at%)	6	KTP	5	C (L = 330 mm)	532		[26]
YVO_4 (1 at%)	1	KTP	5	H(L = 100 mm)[c]	532	Beam quality (?) $M^2\left(\parallel_{\mathbf{cYV0_4}}\right) = 1.1$ $M^2\left(\perp_{\mathbf{cYV0_4}}\right) = 1.2$	[33]
YVO_4 (1 at%)	1	KTP	10	P (L = 7 mm) Q-switch[d]	532		[34]
S-FAP	3	KTP	3	H[c] (L = 45 mm)	529.5		[35]
LSB	1.2	KTP	1	P (L = 3 mm)	531		[36]
YLF (0.5 at%)	15	LBO T=162.6º C		C	526.5	$TEM_{00}M^2 < 1.2$ $\omega_c = 60$ μm	[37]
YAP	77	KTP	10	C (L = 140 cm)	540	$\frac{\omega_0^{inKTP}}{\omega_l^{inYAP}} = 0.061$	[38]

A, three-mirror folded; B, standing-wave; C, ring; D, concentric; H, hemispherical (plane-concave); M, microchip; P, plane parallel.

[a] Composite laser rod: 3 mm long Nd:YAG with two diffusion-bonded 3-mm long undoped cap ends.

[b] Side-pumped.

[c] Front mirror = coated face of the crystal.

[d] Passive Q-switch with Cr^{4+}:YAG (L = 1.5 mm).

8.3.3 Self-Frequency Doubled Lasers

There is another approach to realizing blue–green or red, compact, solid-state laser sources. It is possible to combine the laser properties and the quadratic non-linear characteristics into a single element. SFD is an attractive alternative to intracavity doubling. Though the first self-frequency-doubled laser was demonstrated in Tm^{3+}:$LiNbO_3$ [39], most of the systems have been developed with Nd^{3+}- or Yb^{3+}-doped crystals. Except for the evident interest of Nd^{3+} ions, the development of strained InGaAs diode lasers emitting around 980 nm has given renewed interest to Yb^{3+}-doped materials for compact solid-state laser devices.

8.3.4 Nature of Crystals

8.3.4.1 Requirements in Finding Crystals

If self-doubling appears more simple than intracavity doubling, the problem lies in finding a crystal satisfying several requirements. These crystals should have a large non-linearity, a broad transparency range and a high optical damage threshold. Large crystals of good optical and mechanical quality are required. The structure should offer suitable sites for rare-earth ions (RE) and accept high RE concentrations. Furthermore, the doped laser crystal should exhibit good laser performance in the phase-matching orientation. As for intracavity doubling, other parameters such as walk-off, spectral, thermal and angular acceptances are of fundamental importance.

Up to now, only a few crystals have simultaneously exhibited good laser properties and quadratic non-linear susceptibility. SFD has been demonstrated in MgO:LiNbO$_3$ [40–44] periodically poled (PP) [45], LiTaO$_3$ (PP) [46], BaCaBO$_3$F [47], YAl(BO$_3$)$_4$ (YAB) [44,48–55], YCa$_4$O(BO$_3$)$_3$ (YCOB) [56–58], GdCa$_4$O(BO$_3$)$_3$ (GdCOB) [59–62], Gd$_2$(MoO$_4$)$_3$ [63], LaBGeO$_5$ [44,64] and Ce$_{1-x}$Gd$_x$Sc$_3$(BO$_3$)$_4$ (CSB) [65].

8.3.5 Nd^{3+} and Yb^{3+} Uses

A visible laser radiation is obtained by self-doubling the infrared laser emission provided by Nd^{3+} or Yb^{3+}. If, in both cases, the laser emission occurs in a quite similar spectral range, the optical properties of Nd^{3+} and Yb^{3+} are quite different. The energy levels of the 4f^3 configuration of Nd^{3+} ions extend from 0 to, at least, 40 000 cm^{-1} while the level scheme of the 4f^{13} configuration of Yb^{3+} ions is very simple: only one excited state (^{2}F$_{5/2}$) $\simeq$ 10 000 cm^{-1} above the ground-state multiplet (^{2}F$_{7/2}$). So, the well-known Nd^{3+} 1.06 μm laser emission is obtained in a four-level system while for Yb^{3+}, the infrared laser emission is obtained in a three- or quasi-four-level scheme depending on the splitting of the ground-state multiplet. This provides advantages and drawbacks, which we will discuss in the following sections.

8.3.5.1 Nd^{3+} Ion Spectroscopy

First of all, in both cases, the three parameters (absorption and stimulated emission cross sections, σ_{abs} and σ_{em}, and the emission lifetime, τ) related to the potential performance of the laser material are evaluated as usual. Moreover, the laser properties of the crystal should be investigated in the appropriate direction corresponding to the phase-matching conditions. σ_{abs} and σ_{em} are evaluated from polarized absorption and emission spectra and application of the Judd–Ofelt (JO) theory (in the case of Nd^{3+} ions) or using the Füchtbauer–Ladenburg (FL) equation or the method of reciprocity (for Yb^{3+}). So, absorption and emission spectra are recorded in $\sigma(E \perp c, H \parallel c)$ and $\pi(E \parallel c)$ polarizations for uniaxial crystals, ***c*** being the optic axis. For biaxial crystals, the spectra are recorded with absorption or emission light polarized along each of the three principal axes of the optical indicatrix, i.e. *X*, *Y* and *Z*.

Besides the assessment of laser performance, the study of the absorption spectra is an important step to determine the best pumping spectral range to reduce the energy difference between the pump and stimulated emission photons (i.e. a small quantum defect). A small quantum defect allows low thermal loading of the crystal to be achieved. Typically, the relevant absorption extends from 700 to 800 nm for the (^{4}I$_{9/2}$ → ^{4}F$_{3/2}$) Nd^{3+} transition and from 900 to 1100 nm for the (^{2}F$_{7/2}$ → ^{2}F$_{5/2}$) Yb^{3+} absorption. In both cases, pumping can be achieved using infrared laser diodes. However, due to additional 4f energy levels, Nd^{3+} ions suffer several drawbacks compared to Yb^{3+}. The pumping efficiency can be reduced by excited-state absorption (ESA) of the pump from the ^{4}F$_{3/2}$ manifold to upper levels. However, it is noteworthy that resonant absorption of the SH can occur from the ground state to upper levels, thus lowering the self-doubling efficiency. Furthermore, the broadening of the spectral features due to the interaction between the 4f electrons and the vibrations of the host is more pronounced for Yb^{3+} due to a larger electron–phonon coupling than for other rare earths. Then, Yb^{3+} exhibits a large absorption bandwidth (for example, FWHM= 19 nm in BaCaBO$_3$F [47]) compared to Nd^{3+} (FWHM = 5.5 nm in CSB [65]). Yb^{3+}-doped crystals appear to be more suitable for diode pumping in contrast to their Nd^{3+} counterparts; due to their wide absorption bandwidth they offer less sensitivity to the laser diode output wavelength affected by temperature changes. Yb^{3+} also exhibits a large emission bandwidth, which opens the possibility of tunability and generation of ultra-short pulses.

The absolute radiative properties of Nd^{3+}-doped materials can be computed from simple and accurate absorbance measurements. The line strength $S_{\text{q}}^{\text{meas}}$ $(J \to J')$ of an electric-dipole transition is related to its optical density through the following relation:

$$S_{\text{q}}^{\text{meas}}(J \to J') = \frac{3ch}{8\pi^3 e^2}\frac{(2J+1)}{N}\frac{9n}{(n^2+2)^2}\frac{1}{\bar{\lambda}}\int_{J\to J'} k_q(\lambda)\,\mathrm{d}\lambda \tag{8.34}$$

where *e* is the electron charge, *c* the light velocity, *N* the Nd^{3+} concentration, $\bar{\lambda}$ the mean absorption wavelength of the transition, *n* the refractive index of the crystal at $\bar{\lambda}$, *J* (*J*′) the total momentum quantum number of the initial (final) multiplet and $k_q(\lambda)$ the absorption coefficient at λ; *q* stands for the electric field polarization with respect to the optic axis or of the optical indicatrix *X*, *Y* or *Z*. According to the JO theory [66,67], the line strength of an electric dipole transition between the initial manifold, $|(S, L)J\rangle$, and the final $|(S', L')J'\rangle$ state can be written in the form

$$S_{\text{q}}^{\text{meas}}\left(\left|(S,L)J\right\rangle \to \left|(S',L')J'\right\rangle\right) = \sum_{t=2,4,6} \Omega_t \left|\left\langle (S,L)J \parallel U^{(t)} \parallel (S',L')J' \right\rangle\right|^2 \tag{8.35}$$

where $\left\langle \parallel U^{(t)} \parallel \right\rangle$ are the doubly reduced unit tensor operators calculated in the intermediate coupling approximation. The numerical values of the unit tensor operators have been calculated by Carnall et al. [68]. The intensity parameters Ω_t (with $t = 2$, 4 and 6) include the odd-symmetry crystal-field terms, radial integrals and perturbation denominators. These phenomenological parameters, determined by least-square fitting between experimental and calculated line strengths, allow the different characteristics required to assess the potential laser performance of the doped crystal to be calculated.

- The probability for a transition from initial *J*′ manifold to $\bar{J}$ final manifold is given by

$$A\left[(S',L')J';(\bar{S},\bar{L})\bar{J}\right] = \frac{64\pi^4 e^2}{3h(2J'+1)\bar{\lambda}^3}\frac{n\left(n^2+2\right)^2}{9} \sum_{t=2,4,6} \Omega_t \left|\left\langle (S',L')J' \parallel U^{(t)} \parallel \left(\bar{S}',\bar{L}'\right)\bar{J}' \right\rangle\right|^2 . \tag{8.36}$$

- The fluorescence branching ratios for transitions originating from an initial $|(S', L')J'\rangle$ manifold are:

$$\beta\left[(S',L')J';(\bar{S},\bar{L})\bar{J}\right]=\frac{A\left[(S',L')J';(\bar{S},\bar{L})\bar{J}\right]}{\sum_{(\bar{S},\bar{L})\bar{J}}A\left[(S',L')J';(\bar{S},\bar{L})\bar{J}\right]} \quad (8.37)$$

  where the summation is over all the possible terminal states.
- The spontaneous radiative lifetime

$$\tau_{\text{rad}}=\left(\sum_{\bar{S},\bar{L},\bar{J}}A\left[(S',L')J';(\bar{S},\bar{L})\bar{J}\right]^{-1}\right). \quad (8.38)$$

- The radiative quantum efficiency of the $|(S', L')J'\rangle$ manifold is

$$\eta=\frac{\tau_{\text{f}}}{\tau_{\text{rad}}} \quad (8.39)$$

  where τ_{f} is the measured fluorescence lifetime. η is usually less than 1 since τ_{f} is reduced by multi-phonon and ion–ion relaxation processes. Due to the small energy gap ($\Delta\epsilon \sim 4800\,\text{cm}^{-1}$) between the $^4F_{3/2}$ emitting level and the next lower $^4I_{15/2}$ multiplet, several phonons $p = \Delta\epsilon/\hbar\omega$ ($\hbar\omega$ being the effective phonon frequency) are required to bridge the gap; then the non-radiative de-excitation by multi-phonon relaxation has a high probability. Thus, the lifetime is reduced, which obviously decreases the quantum efficiency. As examples, $\eta = 0.26$ for Nd:YAB as a result of a high multi-phonon relaxation probability involving three effective phonons of $1346\,\text{cm}^{-1}$ [69], $\eta = 0.15$ in GdCOB ($\hbar\omega = 1472\,\text{cm}^{-1}$). These are rather low compared to that in YAG (0.88–1) or in YAP (0.88) ($\hbar\omega_{\text{YAG}} = 857\,\text{cm}^{-1}$, $\hbar\omega_{\text{YAP}} = 750\,\text{cm}^{-1}$). At high concentration, Nd–Nd interaction leads to concentration quenching through cross-relaxation, further reducing τ_{f}.
- Finally, the stimulated emission cross section can be calculated from the radiative rate and the lineshape of the fluorescence using the FL relation:

$$\sigma_q^{(J\to J')}(\nu)=\frac{\lambda^2 g_q(\nu)}{8\pi n^2\tau_{\text{rad}}} \quad (8.40)$$

  where $g_q(\nu)$ is the normalized lineshape function obtained in polarization q. For anisotropic crystals, $g_q(\nu)$ is thus given by

$$g_q(\nu)=\frac{I_q(\nu)}{\frac{1}{3}\sum_q I_q} \quad (8.41)$$

  where I_q is the integrated fluorescence intensity recorded with electric polarization along the optical indicatrix X, Y or Z.

However, it should be noted that the JO theory assumes that all the Stark levels of the initial manifold are equally populated. This assumption is usually not valid for temperatures near 300 K except in the case of low crystal-field splitting [70]. In Equation (8.40), in addition to this approximation, it is assumed that all the transitions have the same strength regardless of the Stark components involved. However, the values determined this way are roughly not so far from the real ones.

8.3.5.2 Evaluation of Yb^{3+} Ion Emission Parameters

The emission cross section of Yb^{3+} ions can be determined using either the method of reciprocity or the FL relation [71]. The reciprocity method is used if absolute polarized absorption cross sections, the energy and the degeneracy of the Stark components in the ground and excited manifolds are known; otherwise, the FL relation (Equation (8.40)) is employed. Since only one absorption transition is available within the 4f^{13} configuration, the radiative probability cannot be deduced from absorption and the JO theory. However, owing to the simple energy level scheme, the shortening of the lifetime is less probable in the case of Yb^{3+} ions, since up-conversion by energy transfer or a cross-relaxation process is unlikely to occur. Furthermore, due to the large energy gap between the excited manifold and the ground state ($\sim 10\,000\,\text{cm}^{-1}$), a great number of phonons is required to bridge the gap even for materials that have a large phonon cut-off frequency; the multi-phonon process has then a low probability. Thus, in most materials, it is assumed that $\tau_{\text{rad}} = \tau_{\text{f}}$. Unlike Nd^{3+}, Yb^{3+} ions do not suffer from concentration quenching and the multi-phonon relaxation process that adds to the thermal loading of the crystal. In addition, the small energy difference between the pump and the emitted photons results in negligible heat generation, about four times less than that of Nd^{3+} for unit pump power. However, lifetime measurement requires some precautions due to the radiative trapping effect occurring in thick samples or highly concentrated ones due to a significant reabsorption of the emission. The trapping effect produces an apparent lengthening of the lifetime and then leads to an underestimation of the emission cross section. Lifetime measurements done on very thin samples or lightly doped crystals are more representative of the intrinsic lifetime.

Yb^{3+}-based lasers are expected to be quasi-four-level systems. Then, the major problem is a non-negligible ground-state absorption at the laser wavelength, as for the 946 nm Nd^{3+} laser transition we have previously discussed. One important parameter for a quasi-four-level system is β_{min}, the minimum fraction of ions that must be excited to balance exactly the gain with the ground-state absorption at λ_{ext} (the extraction wavelength of the laser) and the Yb-doped crystal becomes transparent at λ_{ext}. β_{min} is related to the absorption and the emission cross sections at λ_{ext} following:

$$\beta_{\text{min}}=\frac{\sigma_{\text{abs}}(\lambda_{\text{ext}})}{\sigma_{\text{abs}}(\lambda_{\text{ext}})+\sigma_{\text{em}}(\lambda_{\text{ext}})}. \quad (8.42)$$

It is then possible to evaluate the minimum absorbed pump intensity I_{min} required to get a lossless material and to reach the threshold. I_{min} is related to β_{min} and the pump saturation intensity I_{sat} as given by Equation (8.24) in which σ_{em} is replaced by σ_{abs} (λ_{ext}):

$$I_{\text{min}}=\beta_{\text{min}}I_{\text{sat}} \quad (8.43)$$

Low thresholds will be obtained for small $\beta_{\min}$ values corresponding to minimal resonant losses at λ_{ext}. Such a condition is achieved for large splitting of the $^2F_{7/2}$ ground state, otherwise cooling is necessary to reduce the ground-state absorption at λ_{ext}, improving the laser performance. The splitting is linked to the Yb^{3+} site symmetry and the nature of the ligands, as we will see in Section 8.4. The relevant spectroscopic parameters of Nd^{3+} and Yb^{3+} in the different self-doubler crystals are summarized in Tables 8.5 and 8.6.

8.3.5.3 Refractive Indices Measurements

Measurements of the refractive indices ($n_{o,\,e}$ for uniaxial and $n_{X,\,Y,\,Z}$ for biaxial crystals) and determination of the dispersion curves in the entire transparency range, especially in the range of the laser emission wavelengths selected for frequency doubling, are needed for further estimation of the phase-matching directions. The wavelength dependence of the refractive index is given by the Sellmeier equation:

$$n(\lambda^2) = A + \frac{B}{\lambda^2 - C} - D\lambda^2 \tag{8.44}$$

where A, B, C and D are obtained by least-square fit to experimental data. Using equations given by Dmitriev et al. [5] for calculating the phase-matching angles for the group symmetry of the crystal and the Sellmeier fit of the refractive indices, one can find all the phase-matching configurations for SHG of fundamental radiation in the near- or mid-infrared range. As an example, from phase-matching curves calculated for GdCOB, a biaxial crystal, represented in Figure 8.7, we can deduce that type I and II phase-matching are possible in all the principal planes for fundamental wavelengths ranging from 830 nm to 2.7 μm, but frequency doubling at 1.064 µm is allowed only for type I in the XY (with $\theta_{PM} = 90°$ and $\phi_{PM} = 45.99°$) and the ZX (with $\theta_{PM} = 19.68°$ and $\phi_{PM} = 0°$) planes [59].

According to the linear and non-linear properties of the SFD crystal, a suitable orientation to get a good compromise between high cross sections and large non-linear optic (NLO) coefficients is determined and the cavity design improved. Formulas (8.28) and (8.30) used to calculate the threshold and output power (given in Section 8.3.1 and derived from [18]) also apply for self-frequency-doubled laser cavity. Furthermore, in this case also, if the SH is generated by a focused Gaussian fundamental input beam, then $P^{2\omega}$ is expressed by Equation (8.31). Theoretical models of a self-doubling laser have been developed taking into account end pumping, radially varying laser gain, beam-waist data, walk-off effect and the reabsorption of the second harmonic waves by Nd^{3+} ions [72]. Technical details on cavity configuration are developed in Section 8.5. In Table 8.7, the characteristics of the more popular systems are summarized.

8.3.6 Comparison between Both Systems

From Tables 8.8 and 8.9, it appears that ICFD allows us to achieve a more powerful visible laser source than self-doubling. However, an SFD laser provides a more compact system with reduced losses due to reflection and scattering. Both suffer from the same drawback due to many oscillating longitudinal modes and large amplitude fluctuations, which strongly modulate the SH output power. The instability of intracavity frequency-doubled lasers arises from the coupling of longitudinal modes. In multi-longitudinal-mode lasers, the doubling process can occur either by direct doubling of individual longitudinal modes or by frequency mixing of two different modes. Then the coupling between modes can lead to chaotic intensity fluctuations which are often called the ‘green problem’.

TABLE 8.5

Nd3+-Doped Self-Doubling Crystals: Spectroscopic Parameters (Peak Absorption Cross Section, Emission Cross Section, Fluorescence Lifetime and Quantum Efficiency)

	$LiNbO_3$:MgO [44]	**YAB [44]**	**$LaBGeO_5$ [44]**	**GdCOB [60]**	**YAB [50][a]**
Concentration	0.2 at.%	5.6 at.%	1.4 at.%	7 at.%	5.6 at.%
λ_{abs} (nm)	807.5 $^{(\sigma)}$	807.3 $^{(\sigma)}$	798.4 $^{(\sigma)}$	811	
	812.19 $^{(\pi)}$	807.4 $^{(\pi)}$	798.4 $^{(\pi)}$		
σ_{abs} (× 10^{20} $\text{cm}^{2)}$	2.3 $^{(\sigma)}$	2.58 $^{(\sigma)}$	2.36 $^{(\sigma)}$	2.23 $^{(Z)}$	
	2.7 $^{(\pi)}$	0.94 $^{(\pi)}$	2.2 $^{(\pi)}$	1.57 $^{(Y)}$	
				1.86 $^{(X)}$	
	0.08 (σ_{SH})	0.31 (σ_{SH})	0.438 (σ_{SH})	0.23 (σ_{SH})	
	0.058 (σ_{ESA})	0.018 (σ_{ESA})	0.003 (σ_{ESA})	0.008 (σ_{ESA})	
λ_{em} (nm)	1094 $^{(\sigma)}$	1062 $^{(\sigma)}$	1049 $^{(\sigma)}$	1060	1338.4 $^{(\sigma)}$
	1085 $^{(\pi)}$	1060 $^{(\pi)}$	1049 $^{(\pi)}$		1337.8$^{(\pi)}$
σ_{em} (×10^{20} cm^2)	7.8 $^{(\sigma)}$	9.7 $^{(\sigma)}$	7.6 $^{(\sigma)}$	4.2 $^{(Z)}$	2.46 $^{(\sigma)}$
	27 $^{(\pi)}$	13.7 $^{(\pi)}$	11.3 $^{(\pi)}$	2.1 $^{(Y)}$	2.56 $^{(\pi)}$
				1.9 $^{(X)}$	
Fluorescence lifetime (µs)	95	53	280	98	
Quantum efficiency (η)	0.94	0.18	0.89	0.15	

[a] $\lambda_{\text{em}} = 1338$ nm.

TABLE 8.6

Yb3+-Doped Self-Doubling Crystals: Spectroscopic Parameters (Peak Absorption Cross Sections, Emission Cross Section and Fluorescence Lifetime) and Laser Parameters Defined in Section 8.3.1 (Isat, βmin and Imin)

	$LiNbO_3$:MgO [43][a]	GdCOB [62]	BCBF [47]
Concentration	1 at.%	7 at.%	2–3 at.%
λ_{abs} (nm)	980	902	912
$\Delta\lambda_{abs}$ (nm)	5	15	19
σ_{abs} ($\times 10^{20}$ cm^2)	1.13 $^{(\sigma)}$ 0.87 $^{(\pi)}$	0.41	1.1
λ_{em} (nm)	1063.9	1032 1052[b] 1082[c]	1034
σ_{em} ($\times 10^{20}$ cm^2)	0.55$^{(\sigma)}$ 0.24$^{(\pi)}$	0.55	1.53
Fluorescence lifetime (ms)	0.540	2.6	1.17
I_{sat} (KW cm^{-2})	33.2	25.5	17
β_{min}	0.106	0.06 0.03[b] 0.007[c]	0.097
I_{min} (KW cm^{-2})	3.51	1.54 0.67[b] 0.19[c]	1.064

[a] Since self-frequency doubling can only be achieved for the fundamental ordinary beam (i.e. σ polarization), only the laser parameters of interest in our purpose are given in this table.

[b] Refers to 1052 emission line.

[c] Refers to 1082 emission line.

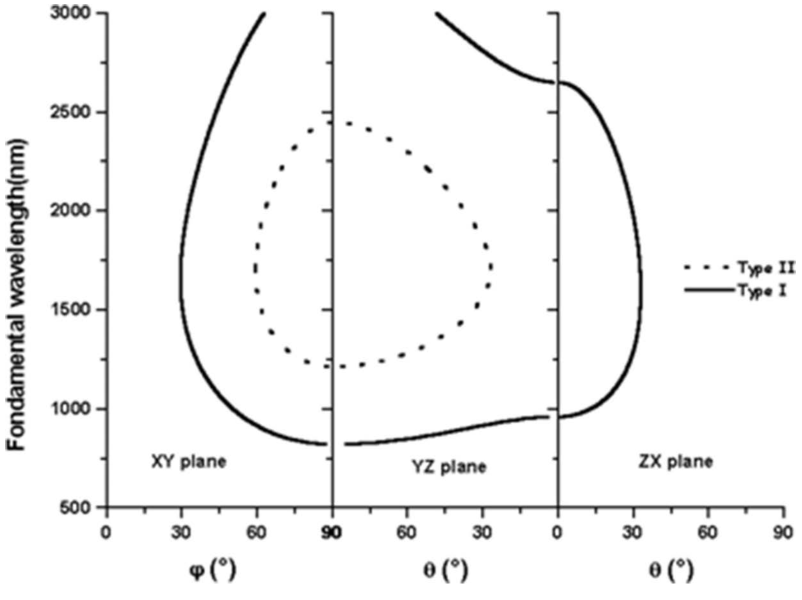

FIGURE 8.7 Phase-matching curves for propagation of the fundamental wavelength on the GdCOB *XY*, *YZ* and X principal planes: broken curve, type I phase matching; full curve, type II phase matching (after Ref. [59]).

In addition to the restrictions due to transparency in the UV or poor acceptance angles, frequency-doubling crystals used for ICFD suffer from other limitations such as their maximum available size and hygroscopy. SFD crystals have better chemical stability and can be grown as large crystals since most of them are obtained with congruent fusion (except YAB and CSB). Their limitations come from the stability of the structure with regard to the introduction of a high RE concentration. As an example, when the Yb^{3+} concentration exceeds 50% in YCOB, large crystals cannot be obtained due to incongruent melting.

TABLE 8.7

Self-Doubling Crystals: Point Group Symmetry (S), Phase Matching (PM), Effective Non-linear Coefficient d_{eff}, Phase-Matching Angle θ_{PM}, Walk-Off Angle (ρ) and Tolerance Parameters: Angular Sensitivity β_θ, Angular Bandwidth $\Delta\theta$ and Temperature Sensitivity ΔT. (All Data Are Given for a Fundamental Wave at 1.064 µm, Data Concerning Single-Domain $LiNbO_3$ Are Reported in Table 8.3.)

	S	PM	d_{eff}	θ_{PM}	*P* (°)	β_θ (cm^{-1} mrad)	Δθ (mrad cm)	Δ*T* (°C cm)	
YAB	R_{32}	Type I	1.27	$\theta = 33°, \phi = 0°$		8.69	8.7		[49,73]
		Type II	0.73	$\theta = 46°, \phi = 90°$					
YAB[a]		Type I						50	[50]
GdCOB	C_m	Type I							
		ZX plane	1	$\theta = 19.7°, \phi = 0°$	0.87		2.6	> 50	[74]
		XY plane	0.5	$\theta = 90°, \phi = 46°$	0.87		1.7		
YCOB	C_m	Type I							
		ZX plane	1.1	$\theta = 33.95°, \phi = 0°$	0.61		1.3	65	[75]
		XY plane	0.5	$\theta = 90°, \phi = 35.3°$	0.86		1.3	65	[75]
$LaBGeO_5$	P_{321}	Type I	0.296^b	$\theta = 54°$	1.15		1.47	10.08	[76]
CSB	R_{32}	Type I	2–3d(KDP)	$\theta = 33°$					[65]
		Type II	2–3d(KDP)	$\theta = 48°$					
$Gd2(MoO_4)_3$	P_{ba2}	Type I	1.9	$\theta = 60°, \phi = 45°$					[77]
BCBF	P_{62m}	Type I	0.26	$\theta = 37°$		5.75			[47]
$LiNbO_3$:MgO		QPM	21.6						[45]

[a] At 1.048 µm.

8.3.7 Periodically Poled Structures

Progress was reported with periodically poled (PP) structures with ferroelectric oxides such as $LaTiO_3$ [46] and $LiNbO_3$ [45], where ferroelectric domains alternate. As an example, the use of quasi-phase matching (QPM) in PP structures offers the possibility of using π-polarized fundamental laser oscillation for SH generation. This represents two advantages compared to a single-domain Yb:$LiNbO_3$:MgO system, where the fundamental beam should have a σ-polarization to achieve SH generation in type I phase matching. First, the π-polarized beam cross section is much higher than the σ-polarized one. In addition, QPM with $\boldsymbol{E} \parallel \boldsymbol{c}$ allows us to access the d_{33} component of the non-linear tensor, increasing the effective non-linear coefficient from 5.6 (type I) to 21.6 pm V^{-1}, and avoid the walk-off effect. Under non-optimal conditions, a conversion of 18% of infrared to visible output power was obtained, which is higher than in NYAB (14%) [51] or in Nd:YCOB (15%) [58]. If the problem linked to the accurate control of the domain period length remains to be solved, this should allow the SFD performances of lasers based on $LiNbO_3$:RE^{3+} to be enhanced.

In comparison with Nd^{3+}, Yb^{3+} has a simple energy level diagram, which avoids detrimental complications such as ESA, up-conversion, concentration quenching effect and ground-state resonant absorption of the SH (especially important in the case of NYAB). The long fluorescence lifetime of the $^2F_{5/2}$ emitting level and the low quantum defect offer long energy storage and a weak thermal loading of the system. Pumping with high-power laser diode can result in local heating of the crystal. This local heating can induce a thermal lens effect but also a phase mismatching between the fundamental and SH beams which reduces the SH output power and affects the beam pattern [78]. Yb^{3+}-doped materials should be more suitable for high-power laser applications than Nd^{3+}-doped one. Moreover, the drawback of Yb^{3+} compared to Nd^{3+} is a significant ground-state absorption of the laser emission, which can be avoided either by cooling or by choosing the host providing a large splitting of the ground state as we will discuss in the next section.

8.4 Ion–Host Combination, Non-linear Coefficients

8.4.1 Ion–Host Combination: How to Choose the Best Host with Nd^{3+} or Yb^{3+} Dopants

For SFD, the choice of the ion–host combination is a fundamental factor to achieve simultaneously good laser and NLO properties. The chemical problem of the substitution of Nd^{3+} or Yb^{3+} into a non-linear crystal has to be taken into consideration. First of all, the structure of the host should allow RE ion doping at a high concentration without disorder of the substitution and distortion of the site. This is especially important for Nd^{3+}-doped materials, where increasing the RE concentration results in the formation of clusters, which favour energy transfer between RE ions leading to a lower quantum efficiency. The best condition to avoid the concentration quenching effect is to consider a crystal where Nd^{3+} or Yb^{3+} replaces another rare earth (La^{3+}, Y^{3+}, Sc^{3+} or Gd^{3+}) of similar ionic radius and chemical properties. This explains why the oxyborates have shown significant results compared to $LiNbO_3$ for which, in addition to photorefractive damage,

RE^{3+} substitutes Li^+ resulting in multiple site symmetries for RE^{3+} due to charge compensation and RE^{3+} can only be introduced with a rather low concentration. Furthermore, $LiNbO_3$ suffers from optical damage due to the photorefractive effect. Doping $LiNbO_3$ with MgO (5%) allows this drawback to be overcome, reducing the photorefractive effect [79], but prevents the introduction of a high Re^{3+} concentration [44].

Other important factors to take into account when choosing a host material are its symmetry and the crystal-field strength, which greatly influence the polarized spectroscopic features and the Stark splitting of the excited and ground-state multiplets. The crystal field is a key parameter, especially for Yb^{3+} ions, to achieve a quasi-four-level system. The case of $Yb:BaCaBO_3F$ is a beautiful example to illustrate the role of charge compensation at the Yb^{3+} site [47]. In this case, Yb^{3+} occupies sevenfold-coordinated Ca^{2+} sites. The coordination polyhedron consists of five O^{2-} from the coplanar borate groups and two F^- located on the ***c***-axis above and below this plane. The O^{2-} replacing one of the F^- ions gives rise to a large crystal-field splitting and a strong polarization dependence for the spectra, which are both favourable for laser performance. A figure-of-merit has been developed, which can be useful in predicting the laser performance of the crystal.

Finally, the electron–phonon coupling has also to be considered since it prevails over the thermal shift and the broadening of the spectral lines, which is favourable for diode pumping, but also favours multi-phonon relaxation, which competes with the radiative channel. The last effect would be detrimental to the emission efficiency especially in the case of Nd^{3+} due to the rather small energy gap between the emitting level and the next lower multiplet (~4800 cm^{-1}). The order of the multi-phonon process is mainly determined by the highest-energy vibrational mode; hence, crystals with a high phonon cut-off frequency should be avoided. As an example, in the YAB structure, Nd^{3+} ions are shielded by the B–O–Al triangular prism and separated from each other. In this case, the Nd–Nd interaction is expected to be weak. However, the quantum efficiency is low resulting from the high non-radiative probability due to the high phonon cut-off frequency of borate compounds mediating the multi-phonon process.

8.4.2 Non-linear Coefficients

Several approaches have been developed to understand the structure–property relationships in non-linear materials. In oxides such as KTP, the optical non-linearity is linked to O–Ti–O bonds running along extended chains, while in borate systems, the origin of the non-linear properties is ascribed to boron–oxygen oxoanions which can be treated as molecular crystals. In the following sections, we will summarize these different approaches and illustrate them with two examples.

8.4.2.1 Case of KTP: Analysis of the Electronic Hyperpolarizability Tensor

A systematic analysis of the electronic hyperpolarizability of KTP has been performed since its non-linear properties are well characterized and its structure is well suited for theoretical study using the techniques of quantum chemistry. The structure of KTP consists of distorted TiO_6 octahedra and PO_4 tetrahedra, which are linked in a three-dimensional framework through shared corners. The orthorhombic structure that results contains chains of –Ti–O–Ti–O– atoms running parallel to the crystallographic ***a***-axis, one oxygen being shared between every two adjacent TiO_6 octahedra. Along these chains derived from distorted TiO_6 octahedron, long (~2.10 Å), intermediate (~1.96 Å) and short (~1.74 Å) Ti–O distances alternate. Early studies using bond-parameter models for the KTP non-linear properties identified the distorted TiO_6 octahedron as a key contributor to the microscopic hyperpolarizability. The theoretical calculations of the hyperpolarizability tensor of KTP, developed in Refs. [80–82], were undertaken essentially to identify basic patterns in the non-linear response and to estimate the influence of the Ti–O bond length, in a first step, of the Ti–O–Ti angle, and in a second step, of the magnitude and the direction of the changes in the non-linear microscopic susceptibility when replacing K or Ti by other cations. The authors were more interested in drawing the main tendency following these parameter variations rather than calculating the exact value of the non-linear coefficient.

At the microscopic scale, the components of the dipole moment, induced in a molecule by electric fields, are related to the microscopic polarizability tensors through a relation similar to Equation (8.1), where the macroscopic $\chi^{(n)}$ susceptibilities are replaced by microscopic parameters (keeping the usual summation convention for repeated indices):

$$p_i = \alpha_{ij} E_j(\omega) + \beta_{ijk} E_j(\omega_1) E_k(\omega_2) \ldots \qquad (8.45)$$

Second-order non-linear effects are governed by the hyperpolarizability tensor. The standard perturbative expression of the individual components β_{ijk} of the hyperpolarizability tensor involves excited states, energies and dipole transition moments. Evaluation of β_{ijk} under the sum-over-state approach thus implies computing the matrix elements and supplying the energies of the molecular orbitals. Details of the sum-over-states formalism, including a description of its implementation using LCAO-MO can be found in Ref. [81].

First of all, to understand the origins and the structural dependence of the electronic hyperpolarizability tensor, the theoretical calculations of electronic hyperpolarizability β were performed using a perturbative sum-over-states formalism together with extended Hückel wavefunctions for TiO_2 and $(TiO_6)^{8-}$ entities. Indeed, these asymmetric species can be considered as the smallest sub-units of the crystal that are expected to be responsible for the non-linear properties [81]. TiO_2 has a linear structure with long and short Ti–O distances along the z-axis; Δ, the asymmetry parameter, is defined as their difference. In TiO_6, the remaining four oxygens and the titanium belong to the xy-plane. In this frame, many of the orbitals identified in TiO_2 are found in $(TiO_6)^{8-}$ as well, appropriately modified to reflect the participation of the equatorial oxygen atoms in the xy-plane. To study the origin of the electronic hyperpolarizability, evaluation of β was done by considering separately the contribution from excitations in π and σ bonding and non-bonding orbital systems. State-by-state analysis reveals that NLO effects arise almost entirely from excitations within the π system. From all β_{ijk}, the β_{zzz} component has the largest magnitude in both TiO_2 and TiO_6, as an obvious consequence of an asymmetric O–Ti–O axis (β_{zzz} corresponds to both incident and second harmonic radiations polarized along the asymmetric O–Ti–O axis). To investigate the influence of bond lengths, extended Hückel/sum-over-states calculations of electronic hyperpolarizability were made as a function of Δ. In TiO_6, only the Ti–O axial distances are varying while equatorial ones are left constant. In both TiO_2 and $(TiO_6)^{8-}$, β_{zzz} is remarkably sensitive to bond length. The net hyperpolarizability results from the near cancellation of large contributions with opposite signs. Specific contributions to the hyperpolarizability classified into three major π families and three major σ families typically pass through minima and maxima as Δ is increased. As we have already mentioned, the σ contribution to β is almost equal to zero. From the behaviour of individual π terms with Δ, one can understand that the SHG intensities observed for the KTP isomorphs vary over wide ranges, while the TiO_6 octahedra in the crystal structures appear to exhibit almost insignificant variations with composition. As examples, the substitution of arsenic for phosphorus ($KTiOAsO_4$) seems to enhance SHG by up to approximately 15%, although replacing Ti by Sn leads to significant degradation of the performance. No net tendency is observed replacing K by other cations (Na, Rb, Cs, Tl, Ag or NH_4). Therefore, the last step of these theoretical investigations concerns the influence of the original electronic distribution on the hyperpolarizability as a result of the possible chemical substitutions [82]. A systematic assessment of the effect of changing the Ti–O–Ti angle and oxygen electronegativity on the electronic hyperpolarizability has been performed. So, a larger system made of three adjacent TiO_6 octahedra was considered. This system is the minimum necessary to explore the effect of the Ti–O–Ti angle. The analysis is focused on the local non-linear response of the central TiO_6unit placed in the context of an extended chain. This condition implies the determination of the molecular orbitals of the complete system. The microscopic hyperpolarizability was computed only for the central unit using the molecular orbitals truncated to include those atomic orbitals within the considered octahedron. Furthermore, the atoms within the central unit are not allowed to move, so any variation of the local β results from a purely electronic effect and cannot be due to geometrical effects. To compare this with experiments, isotropic averages of the squared hyperpolarizability tensor, $\langle\beta^2\rangle$, are calculated since they should be proportional to powder SHG intensity. An increase of 25% is obtained as the Ti–O–Ti angle in the chain goes from 125° to 145°. Most of the increase is taken by the β_{zzz} component. This non-linear response enhancement follows from the perturbed local electronic structure at the different angles, as reflected by changes in the electronic third moment. This result is consistent with the correlation between SHG efficiency and Ti–O–Ti angle that has been observed experimentally for the KTP isomorphs. In $KTiOP_{(1-x)}As_xO4$, the SHG powder signal increased by 17% for $_x$ going from 0 to 1, while the Ti–O–Ti angle increases by 5.5%. In the $K_{(1-x)}NaxTiOPO4$ system, the SHG signal is almost unchanged as $_x$ varies from 0 up to 0.5, but falls by an order of magnitude as $_x$ approaches 1. The Ti–O–Ti angle remains almost constant for $0 < x < 0.5$ and decreases for $x > 0.5$. All these results exhibit the same trends as predicted by theoretical calculations.

8.4.2.2 Modelling Chemical Substitutions

Modelling chemical substitutions can be achieved by changing the oxygen electronegativity. For the original system (i.e. KTP), contributions to the sum over states are distributed over the entire range of occupied orbitals. Increasing the electronegativity of the oxygen relative to the titanium, however, results in the formation of localized oxygen orbitals at lower energies. Most of the terms in the sum then originate from these perturbed levels and SHG in the model system is reduced as a result. When, by contrast, the oxygen electronegativity is decreased, the energies of the uppermost oxygen orbitals are raised leading to a significant near-resonant enhancement of the non-linear response. However, it should be mentioned that, in real systems, there is a correlation between the Ti–O–Ti angle and the electronegativity of the substituent cations, although changes in the angle may have different origins depending on whether the site substitution is within the framework (phosphorus atom) or is outside the framework (potassium atom). This consideration means that the two effects—namely the variation of $\langle\beta^2\rangle$ with both the angle and the ionization potential of the chain oxygens—act cooperatively and, hence, cannot be examined separately in real systems. The changes observed in $\langle\beta^2\rangle$ should be larger than those predicted from either of the calculations taken in isolation. If the macroscopic coefficient cannot be derived from these calculations, it is possible to derive general trends that can help synthesize new inorganic frequency-doubling crystals.

8.4.2.3 Case of Borates: Calculation of Microscopic Hyperpolarizability

In the case of borate systems, the optical non-linear property arises from conjugate bonds within BO groups and the macroscopic χ^2 susceptibility can be calculated from the microscopic hyperpolarizability of the group and application of anion group theory [83]. SHG coefficients calculated, in this way, are in good agreement with experimental data. So, structural criteria were proposed to select, from the borate family, crystals with NLO properties. According to anionic group theory, the NLO susceptibility in a crystal results from the interaction between incident photons and electrons of anionic groups (for inorganic crystals) or molecules (for organics). The overall SHG coefficient is assumed to be the geometric superposition of all individual coefficients of the relevant groups, following

$$\chi_{i,j,k}(2\omega) = N\sum_{p=1}^{n}\sum_{i',j',k'}\alpha_{ii'}\alpha_{jj'}\beta^{(p)}_{i',j',k'}(2\omega) \tag{8.46}$$

where N is the number of cells per unit volume, n is the number of groups in the unit cell, $\alpha_{ii'}$, $\alpha_{jj'}$ and $\alpha_{kk'}$ are the direction cosines of the Cartesian system axes of the group with the crystallographic axes and $\beta^{(p)}_{i',j',k'}(2\omega)$ is the microscopic hyperpolarizability of the pth group in the unit cell.

As previously mentioned, the microscopic hyperpolarizability is calculated using the standard perturbative theory but, here, the wavefunctions are the localized wavefunctions of the group.

Owing to the multiple discrete and condensed oxoanions, borate compounds can be synthesized with very different structures. Keszler et al. [84] have proposed an overview of the structural chemistry of non-centrosymmetric borates selected for their NLO properties. This analysis of the structure–NLO properties relationship is based on anion group theory and provides important guidelines for the synthesis of new solid-state inorganic crystals of interest in NLO applications. The widely used BBO and LBO have no derivative chemistry; hence, it is impossible to slightly alter their physical properties. However, new structural types that could be chemically derived would allow subtle control over both non-linear and linear properties (i.e. susceptibility coefficients and the magnitude of birefringence) through atomic substitutions within a given structural type.

For example, YAB, BBO and LBO belong to the orthoborate type but their structure differs by the arrangement of the orthoborate anion: independent BO_3 groups in YAB, isolated B_3O_6 rings in BBO and condensed B_3O_7 rings in LBO. However, each of these anion groups belongs to the D_{3h} symmetry. In Ref. [84], the orientational dependencies of the group hyperpolarizability coefficients are derived. In BBO, B_3O_6 planar rings are tilted from the local z-axis. Then, from the structural data and anion group theory, the NLO coefficient (d_{22} = 2.3 pm V^{-1}) is only 67% of the optimal value expected for planar groups parallel to the z-axis. Following the same analysis, from the BO_3 group alignment with respect to the z-axis in YAB, the NLO coefficient observed (d_{11} = 1.5 pm V^{-1}) represents 49% of the optimal value. The maximum non-linearity of an orthoborate crystal is expected to be approximately 3 pm V^{-1}. Since the microscopic hyperpolarizability β_{zzz} is invariant to rotation about the B–O bond along the z-axis, a variety of orthoborate structural arrangements are expected to produce an optimal non-linearity. In particular, it should be possible to synthesize an orthoborate with a non-linearity that is comparable to that of BBO while maintaining a smaller birefringence, providing a smaller sensitivity to phase matching and an enhanced conversion efficiency for the production of UV light. In this goal, $BaCaBO_3F$ (BCBF) has been synthesized [84]. When doped with Yb^{3+} ions, this crystal behaves as self-doubler [47] as we mentioned in Section 8.3.3. From the relative orientation of the BO_3 groups in the BCBF hexagonal structure, the number density of BO_3 groups and the hyperpolarizability β_{zzz} of that group derived from YAB, a non-linear coefficient d_{11} equal to 0.4 pm V^{-1} is predicted. Furthermore, because of the coplanar arrangement of the BO_3 groups in that structure, a birefringence similar to that of BBO is expected. For type I phase matching, θ_m is expected between 20° and 30°, which would produce d_{eff} = 0.35 pm V^{-1}. It is remarkable to note the good agreement between this predicted value and the experimental one (0.26 pm V^{-1}) measured on Yb:BCBF [47]. To improve the linear property, the lack of coplanarity of the BO_3 groups would allow the birefringence to be reduced. A smaller birefringence can be achieved if the coplanarity of the BO_3 groups is disrupted while maintaining a small tilted angle between each of the BO_3 group and the c-axis.

Other structures, such as pyroborates of the type $AMOB_2O_5$ ($A \equiv$ K, Rb and Cs, $M \equiv$ Nb and Ta), were demonstrated to be a unique means for examining the structural interrelationship of linear and NLO properties [84]. As the size of the alkali metal decreases, the B_2O_5 groups adopt non-linear geometries by twisting about the central B–O bond and the coplanarity of the group, observed in the Cs–Nb derivative, is severely disturbed. From consideration of the alignment of the B_2O_5 groups, the highest non-linearity and birefringence are expected with the Cs derivative. Another interesting feature of these structures is the presence of chains of alternating short–long M–O interactions that extend approximately orthogonal to the B_2O_5 planes. These chains, of course, are reminiscent of the Ti–O distances in KTP that contribute, as we have already discussed, to its high non-linearity. In the borates, however, the chains are not expected to contribute significantly to the non-linearity as pairs of chains are related by an approximate centre of symmetry, i.e. the sequence long–short–long M–O distances in one chain alternates with a short–long–short one in a neighbouring chain. This analysis demonstrates the feasibility for controlling the linear and NLO properties and synthesizing new non-centrosymmetric borates for NLO applications.

8.5 System Configurations: Resonator Designs and Pumping

8.5.1 Modelling Intracavity Frequency-Doubled Lasers

As we have already mentioned in Section 8.3.1, a key parameter for efficient intracavity doubling is the beam waist in the non-linear crystal, especially for critical phase matching (see Equations (8.32) and (8.33)). The actual trend is to develop compact laser sources and then the pumping is achieved using laser diodes. Several models [19–22,31,85] were proposed, which allow simple criteria to optimize coupling optics and the resonator geometry to be derived. These analyses demonstrate that the most important parameter, for laser efficiency and output power, is the spatial overlap between the pump beam and the laser mode in the active medium.

8.5.1.1 Diode End-Pumped Lasers

The first model [19], based on a space-dependent rate equation analysis for a four-level system, was investigated to study the influence of the optimum ratio between mode and pump spot size on input power. In this analysis, Gaussian and elliptic beam profiles of the pump are considered. This treatment is particularly well adapted for diode laser end pumping because asymmetric pump distribution is taken into account. This model provides a convenient way to calculate the optimum spot size for the available input pump power and pumping configuration for a plano-concave resonator. Integrating Equation (8.30) gives

$$P_{out} = \frac{T}{2\gamma}\frac{J_1^2}{J_2}\eta_p\left[P_{in} - P_{th}\right] \tag{8.47}$$

with γ the total logarithmic loss per pass, J_1^2/J_2 a geometrical factor accounting for the overlapping efficiency, η_p the pumping efficiency and P_{in} and P_{th} the incident and threshold power, respectively.

The geometrical factor is expressed from overlap integrals between the normalized mode distribution $s_1(x, y, z)$ and the normalized pump distribution in the active medium $r_{\mathrm{p}}(x, y, z)$:

$$\frac{J_1^2}{J_2}=\frac{\left(\iiint s_1(x,y,z)\,r_{\mathrm{p}}(x,y,z)\,\mathrm{d}v\right)^2}{\iiint s_1^2(x,y,z)\,r_{\mathrm{p}}(x,y,z)\,\mathrm{d}v}. \tag{8.48}$$

The pumping efficiency η_{p} corresponds to the ratio between the power incident on the active medium and the power emitted by the source. It is related to the transfer efficiency η_{t}, η_{a} as defined in Equation (8.30) and the quantum defect by the following relation:

$$\eta_{\mathrm{p}}=\eta_{\mathrm{t}}\eta_{\mathrm{a}}\frac{\nu_{\mathrm{c}}}{\nu_{\mathrm{p}}}. \tag{8.49}$$

In Ref. [19], two parameters, ζ and δ, are introduced to obtain an explicit expression for the output power depending on the ellipticity of the pump beam:

- $\zeta=\left(\omega/\bar{\omega}_{\mathrm{p}}\right)^2$ (ω is the mode spot size and ω_{p} the minimum spot size allowed by the given configuration) and
- δ, the ratio between the minor and the major spot size ($0 \le \delta \le 1$), accounts for the ellipticity of the beam ($\delta = 1$ for a circular Gaussian beam).

Calculation of both J_1 and J_2 in a closed form allows P_{out} to be expressed as

$$P_{\mathrm{out}}=\frac{T}{2\gamma}\eta_{\mathrm{p}}P_{\mathrm{tho}}f_1(\zeta,\delta)\left[\xi-f_0(\zeta,\delta)\right] \tag{8.50}$$

where $P_{\mathrm{tho}}=\pi\gamma I_{\mathrm{sat}}\omega_{\mathrm{p}}^{-2}/2\eta_{\mathrm{p}}$ is the threshold limit obtained in the ideal case of vanishing mode area, its value is determined by the spectroscopic parameters of the crystal: $\xi = P_{\mathrm{in}}/P_{\mathrm{tho}}$ corresponds to the amount by which the threshold limit is exceeded. f_0 is the normalized threshold given by

$$f_0=\frac{1}{\delta}\left[\left(\zeta\delta^2+1\right)\left(\zeta+1\right)\right]^{\frac{1}{2}}; \tag{8.51}$$

f_1 is the overlapping efficiency, expressed as

$$f_1=\frac{\zeta\delta\left[\left(\zeta\delta^2+2\right)\left(\zeta+2\right)\right]^{\frac{1}{2}}}{\left[\left(\zeta\delta^2+1\right)\left(\zeta+1\right)\right]}. \tag{8.52}$$

From the plot of the normalized output power $P_{\mathrm{out}}/[(\mathrm{T}/2\gamma)\eta_{\mathrm{p}}P_{\mathrm{tho}}]$ as a function of ξ for different values of ellipticity δ, the optimum mode size can be easily calculated, for the available input pump power and pumping configuration, which determines $\bar{\omega}_{\mathrm{p}}$. The corresponding threshold power $P_{\mathrm{th}}^{\mathrm{opt}}=P_{\mathrm{th}}(1+\zeta)$ and slope efficiency are also readily obtained. For a beam coming from the fibre with a circular Gaussian profile, Equation (8.47) becomes

$$P_{\mathrm{out}}\left(P_{\mathrm{in}},\zeta,\bar{\omega}_{\mathrm{p}}\right)=\frac{T\eta_{\mathrm{p}}}{2\gamma}\frac{\zeta(\zeta+2)}{(\zeta+1)^2}\left[P_{\mathrm{in}}-\frac{\pi\gamma I_{\mathrm{sat}}\omega_{\mathrm{p}}^{-2}}{2\eta_{\mathrm{p}}}(\zeta+1)\right]. \tag{8.53}$$

Experimental results for an Nd:YAG laser pumped by a 500-mW diode array have shown a fairly good agreement with the predictions of this model. This analysis gives a straightforward procedure for designing the resonator but the effect of some parameters, such as the divergence and the focus position of the pumping light, are not considered. These parameters are important for fibre-coupled laser-diode end-pumped lasers. Therefore, an analytical model was proposed to design the laser resonator and to optimize the optical coupling system by taking into account the beam quality.

8.5.1.2 Fibre-Coupled Laser-Diode End-Pumped Lasers: Coupling and Resonator

In this analysis [20,21], the minimum value of $\bar{\omega}_{\mathrm{p}}$ is limited, as previously mentioned, by the properties of the gain medium but also by the pump-beam quality and the focus position in the active medium, whereas in the Laporta and Brussard treatment [19], the minimum spot size $\bar{\omega}_{\mathrm{p}}$ was assumed to be constant and depended only on the resonator configuration. In the frame of this second analysis, $\bar{\omega}_{\mathrm{p}}$ depends on the z-coordinate due to the divergence of the beam coming out from the fibre, then it is expressed, based on the paraxial approximation, as:

$$\omega_{\mathrm{p}}(z)=\omega_{\mathrm{p0}}+\theta_{\mathrm{p}}\left|z-z_0\right| \tag{8.54}$$

where ω_{p0} is the radius at the waist, θ_{p} the far-field angle and z_0 the focal plane in the active medium. The beam waist for a given beam is related to its associate far-field angle by the brightness theorem, therefore $\theta_{\mathrm{p}} = C/n\omega_{\mathrm{p0}}$ (C is a constant characterizing the beam quality). For a given value ω_{p0} of the pump beam waist in an active medium of length L and an absorption coefficient α at λ_{p}, the average spot size is simply expressed as:

$$\bar{\omega}_{\mathrm{p}}\left(\beta,\omega_{\mathrm{p0},}\xi_0\right)=\omega_{\mathrm{p0}}+\frac{\beta}{\omega_{\mathrm{p0}}}\left(\xi_0-1+2\exp(\xi_0)\right)$$
$$\text{with } \xi_0=\alpha z_0 \text{ and } \beta=C/n\alpha. \tag{8.55}$$

The parameter β accounts for the pump-beam quality and spectroscopic properties of the active medium. With β and ω_{p0} fixed, the optimum focal position, which minimizes $\bar{\omega}_{\mathrm{p}}$ is simply derived by setting the first derivative of $\bar{\omega}_{\mathrm{p}}$ with respect to ξ_0 equal to 0, then $z_{0,\mathrm{opt}} = \ln(2)/\alpha$. This allows the minimum spot size $\omega_{\mathrm{p0,opt}}$ to be determined using Equation (8.55) with $\xi_{0,\mathrm{opt}}$ and the condition $\partial\bar{\omega}_{\mathrm{p}}/\partial\omega_{\mathrm{p0}}=0$,

$$\omega_{\mathrm{p0,opt}}=\sqrt{\frac{C\ln(2)}{n\alpha}} \quad \text{then } \theta_{\mathrm{p,opt}}=\sqrt{\frac{C\alpha}{n\ln(2)}}. \tag{8.56}$$

Then, the minimized average spot size is simply derived: $\bar{\omega}_{\mathrm{p,min}}=2\sqrt{\beta\ln(2)}$. The output power in the condition of minimum average pump size is obtained by substituting $\zeta=\left(\omega_{\mathrm{p0}}/\bar{\omega}_{\mathrm{p,min}}\right)^2$ (at fixed β) in Equation (8.47). These simple expressions are useful guidelines for designing the coupling system.

To design the resonator, all the optimized parameters are replaced in Equation (8.47) and the optimum mode size for a given β and input power P_{in} is obtained for $\partial P_{\text{out}}(P_{\text{in}}, \beta, \omega_{\text{p0}})/\partial\omega_{\text{p,0}})/\partial\omega_{\text{p,0}} = 0$:

$$\omega_{\text{p,opt}} = \sqrt{4\beta\ln(2)\left[g_{+}(\chi,\beta) - g_{-}(\chi,\beta) - 1\right]} \quad (8.57)$$

where

$$g\pm(\chi,\beta) = \left[\frac{\sqrt{3}\sqrt{27\left(\chi/4\beta\ln(2)\right)^2 + 1}}{9} \pm \frac{\chi}{4\beta\ln(2)}\right]^{1/3} \quad \text{with}$$

$$\chi = \frac{P_{\text{in}}}{\left(\pi\gamma I_{\text{sat}}/2\eta_{\text{p}}\right)}. \quad (8.58)$$

The value of χ is determined from the spectroscopic properties of the gain medium, the total resonator losses and the pumping efficiency. This analytical model provides a simple way to design the coupling optics and the resonator of fibre-coupled laser-diode end-pumped lasers.

These previous models considered the transversal pump beam's distribution as a Gaussian one with the longitudinal propagation described by its divergence. Another treatment has been proposed, which makes use of the M^2 formalism to describe the longitudinally pump-beam propagation in the active medium [22,85].

The output-to-input characteristics and mode-matching efficiency are defined by the overlap between the spatial distribution of the pump energy and the spatial distribution of the laser photons in the active medium as previously noted. Using the M^2-factor, the propagation of pump-beam spot size $\omega_{\text{p}}(z)$ is expressed as [23]:

$$\omega_{\text{p}}(z) = \omega_{\text{p0}}\left[1 + \frac{M^2\lambda_{\text{p}l}}{n\pi\omega_{\text{p}^0}^2}\left(\frac{z}{l} - b\right)^2\right]^{1/2} \quad (8.59)$$

where λ_{p} and ω_{p0} are the wavelength and beam waist of the pump respectively, the non-dimensional parameter $b = z/l$ is introduced to describe the focusing position in the active medium. From the mode-overlap integrals, the optimum focusing conditions that ensure a minimum threshold pump power and a maximum overlap efficiency, at a defined laser beam spot size, were determined by numerical simulations for different values of M^2, b and r^{waist} (the pump-beam waist ratio as defined in Section 8.3.1). Analytical expressions could be derived for an optimum beam waist ratio, focusing positions and maximum overlap efficiency.

- *Optimum beam waist ratio*

$$r_{\text{waist}}^{\text{opt}} = (A_1 - A_2\alpha_{\text{a}}l)\left(M^2 - 1\right)^{(A_1 - A_4\alpha_{\text{a}}l)}. \quad (8.60)$$

- *Optimum focusing position*

$$b_{\text{opt}} = (B_1 - B_2\alpha_{\text{a}}l)(B_3 - B_4\alpha_{\text{a}}l)\log\left(M^2 - 1\right). \quad (8.61)$$

- *Optimum overlap efficiency*

$$\eta_{\text{m}}^{\text{opt}} = (\eta_1 + \eta_2\alpha_{\text{a}}l)(\eta_3 + \eta_4\alpha_{\text{a}}l)M^2 \quad (8.62)$$

where the different parameters A_i, B_i and η_i are functions of the laser beam volume $V_l = \pi\omega_{\text{c}}^2 l$. In the same way, an expression for the optimum threshold can be obtained $F_{\text{th}}^{\text{opt}} = P_1 + P_2\left(r_{\text{waist}}^{\text{opt}}\right)^2$, where $P_i = f(V_l)$. Good agreements were obtained between predicted values and experimental measurements [22,85]. This method provides a very simple procedure (schematized in Figure 8.8) for the design of the coupling optics and the resonator.

8.5.2 Resonator Designs: Examples of Intracavity-Frequency-Doubled Lasers

Intracavity doubling is achieved by introducing a non-linear crystal into the laser resonator. Almost all ICFD crystals are longitudinally pumped. The input mirror has, as usual, a high transmission at the pump wavelength and high reflectance at the fundamental but also at the SH wavelength. Since high

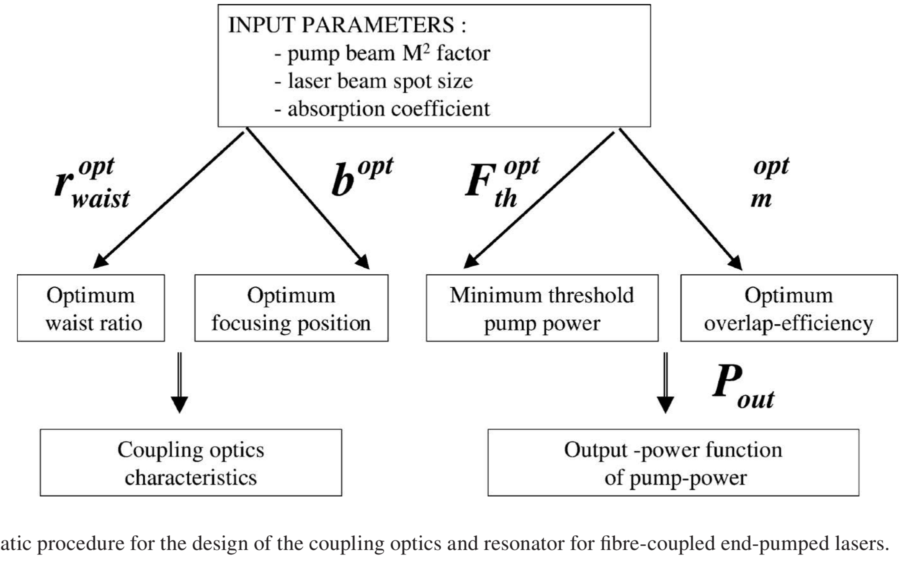
INPUT PARAMETERS :
- pump beam M² factor
- laser beam spot size
- absorption coefficient
r opt waist
b opt
F opt th
opt m
Optimum waist ratio
Optimum focusing position
Minimum threshold pump power
Optimum overlap-efficiency
P out
Coupling optics characteristics
Output -power function of pump-power

FIGURE 8.8 Schematic procedure for the design of the coupling optics and resonator for fibre-coupled end-pumped lasers.

conversion efficiency requires a high power density, the output mirror should be 100% reflective at the pump and fundamental laser wavelengths and totally transmitting at the SH wavelength.

For a laser oscillation at 946 nm, the output mirror has a sufficient transmission at 1.06 μm to suppress the $^4F_{3/2} \rightarrow {}^4I_{11/2}$ laser transition. The pump side of the crystal is anti-reflection coated at the pump wavelength and high reflection coated at both the fundamental and the SH wavelengths to act as an input mirror of the cavity. The opposite side is anti-reflection coated at the fundamental wavelength. The non-linear crystal is anti-reflection coated at the fundamental to reduce the passive loss of the cavity. As we have already seen, from Equation (8.25) in Section 8.3.1, the SH power is proportional to the fundamental power density and the fundamental power. Then, the beam waist inside the non-linear crystal should be as small as possible to increase the fundamental power density. Concurrently, the intracavity beam must be large enough inside the laser rod to utilize the maximum volume that can contribute to the laser oscillation. This generally requires that the beam cross-sectional area be at least one order of magnitude larger inside the laser rod than inside the non-linear crystal.

Four major types of resonators are used to develop ICFD lasers. Ring and three-mirror folded cavities are more appropriate to generate high SH powers. Hemispherical cavity and microchip delivers lower SH power and is used to realize miniaturized visible laser sources. In the following, we will give the basic configuration of each of them. They operate in cw mode, a pulsed regime can be achieved by either using the non-linear crystal, which simultaneously acts as frequency doubler and electro-optic (EO) Q-switch (this is possible with KTP [31]), or adding an acousto-optic (AO) Q-switch or a saturable absorber (Cr^{4+}:YAG [34], for example).

8.5.2.1 Ring Cavity

High-power visible sources were demonstrated in ICFD ring lasers (Tables 8.4 and 8.8). A 'bowtie' ring resonator provides a tight focus at the location of the frequency-doubler crystal and a good mode matching with the pump in the rod. With this configuration, the pump spot size in the rod can be adjusted to optimize the fundamental power while avoiding thermal effects (thermal lensing). Furthermore, the travelling-wave resonator eliminates the spatial hole burning due to the standing-wave distribution of the intensity in conventional oscillators. Compact pumping sources such as high-power, beam-shaped diode bars [24,37] can be used to give a well-confined pump spot, collimated over the length of the laser rod. A Faraday rotator is placed inside the cavity to enforce unidirectional single-frequency laser operation, thus suppressing the chaotic fluctuation behaviour known as the 'green problem'. Half-wave plates are added on each side of the frequency-doubler crystal to align the polarization in the proper direction for SHG before entering the crystal and one at the output face to rotate the laser polarization back to its initial orientation. A schematic diagram of an Nd:YLF ring laser resonator pumped from opposite ends by two beam-shaped diode bars is represented in Figure 8.9.

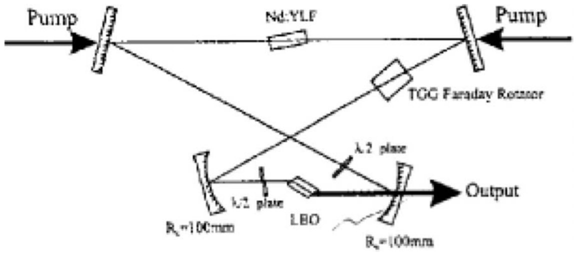

FIGURE 8.9 Schematic diagram of an Nd:YLF ring resonator, with a TGG Faraday rotator and a LBO frequency-doubling crystal (after Ref. [37]).

A standing-wave laser cavity has been used instead of a ring cavity to simplify longitudinal pumping. A frequency-stabilized laser emission was obtained at 946 nm with harmonics at 473 nm and 237 nm [28].

8.5.2.2 Three-Mirror Folded Cavity

A schematic diagram of a three-mirror folded cavity is represented in Figure 8.10. The cavity is folded by a harmonic separator with a high reflectance and a high transmittance at the fundamental and SH wavelengths, respectively. The laser rod is in the first arm of the cavity, close to the front mirror and the non-linear crystal in the second arm between the folded and the rear mirror. This configuration also allows the beam radius in the laser rod and in the non-linear crystal to be adjusted independently. High SH powers are obtained by combining the forward and reverse SH beams into one single output beam.

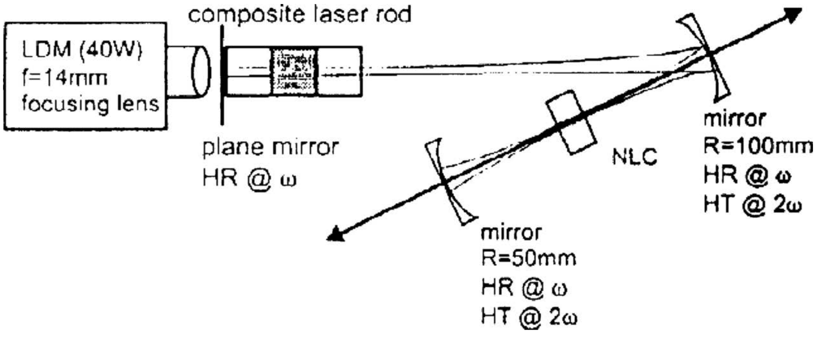

FIGURE 8.10 Schematic diagram of a three-mirror folded cavity (after Ref. [12]).

8.5.2.3 Hemispherical Cavity

A hemispherical cavity is appropriate to realize compact laser-diode-pumped visible sources. The input coupler can be a coated mirror or the coated front face of the laser crystal, the output coupler being a curved mirror with a high transmission at the SH wavelength. In this case, the beam radii cannot be adjusted separately, the laser crystal is placed near the front mirror and the non-linear crystal is placed close to the gain medium near the cavity waist. To achieve an efficient conversion, the pump beam is tightly focused (~40–60 μm). Due to the moderate pumping power, the thermal lens effect is not so critical as in previous designs [13,31,35]. In Figure 8.11, a compact EO Q-switch ICFD laser is schematized.

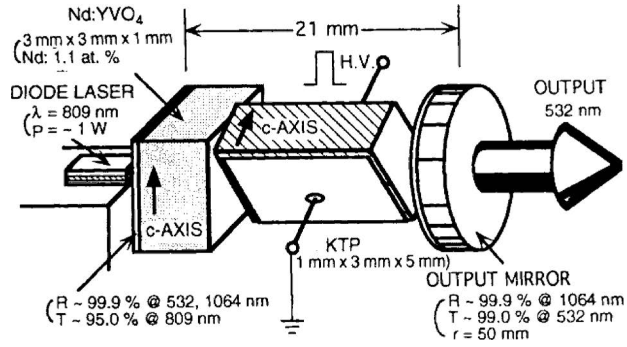
Nd:YVO$_4$
3 mm x 3 mm x 1 mm
Nd: 1.1 at. %
21 mm
H.V.
DIODE LASER
λ = 809 nm
P = ~ 1 W
c-AXIS
c-AXIS
OUTPUT
532 nm
KTP
1 mm x 3 mm x 5 mm)
OUTPUT MIRROR
R ~ 99.9 % @ 532, 1064 nm
T ~ 95.0 % @ 809 nm
R ~ 99.9 % @ 1064 nm
T ~ 99.0 % @ 532 nm
r = 50 mm

FIGURE 8.11 Schematic diagram of a diode-laser-pumped ND:YVO$_4$ laser. A single KTP crystal functioned as the intrafrequency doubler and the EO Q-switcher (HV high voltage) (after Ref. [31]).

8.5.2.4 Microchip

A composite-material microchip is the most compact device. The laser crystal is cut in a plane-parallel chip in close contact with the plane-parallel non-linear crystal. The surfaces of the composite material are coated to have a high reflectance at λ_{fund} and a high transmittance at the SH wavelength for the output face. An example of a microchip laser is represented in Figure 8.12.

8.5.3 Resonator Designs: Self-Doubling Lasers

In this case, the laser crystal is both the laser active medium and the non-linear medium for frequency doubling; the waist size of the cavity mode as well as the focusing of the pump radiation into the crystal being the most critical parameters. Pump focusing and the configuration of the laser cavity have, thus, to be compromised between the focusing required for optimum laser performance and the waist size of the TEM$_{00}$, which provides optimum frequency doubling. The threshold and visible output power are given by Equations (8.28) and (8.25), respectively, or Equations (8.25) using (8.32) and (8.33) for a focused Gaussian fundamental beam (see Section 8.3.1). According to Equation (8.28), the minimization of P_{th} requires minimized radii for the pump (ω_{p}) and laser mode (ω_{c}). The pump mode radius is minimized by an appropriate choice of the focusing system, while the radius of the laser modes can be minimized by increasing the cavity length inside the stability region of the optical resonator. The hemispherical cavity is one of the designs that minimize ω_{c}. The minimum threshold can be further decreased by the use of a concentric cavity to reduce the ω_{c} *and also anti-reflection coatings on the elements*. Modelling self-doubled lasers is simpler than for ICFD lasers and predictions of their performance can be achieved by numerical analysis based on the conventional rate equations

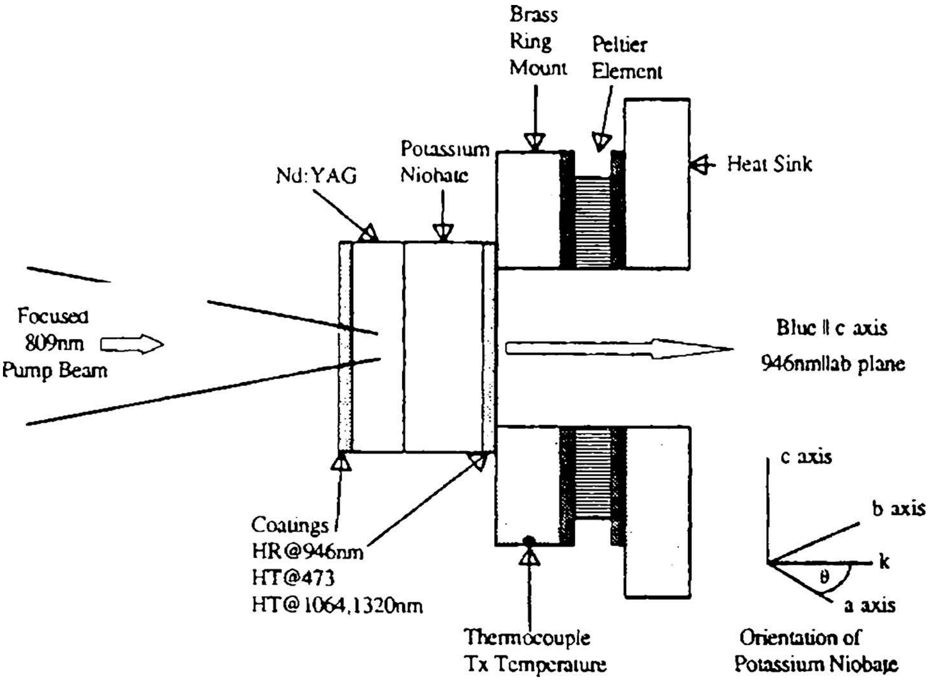
Brass Ring Mount
Peltier Element
Heat Sink
Potassium Niobate
Nd:YAG
Focused 809nm Pump Beam
Blue ∥ c axis
946nm∥ab plane
c axis
b axis
k
θ
a axis
Coatings
HR@946nm
HT@473
HT@1064,1320nm
Thermocouple Tx Temperature
Orientation of Potassium Niobate

FIGURE 8.12 Composite-cavity microchip scheme (after Ref. [27]).

with additional terms to account for the conversion of the fundamental beam (see [41,51,72,86,87,90–95], for example).

The first model was developed by Dmitriev et al. [86,87]. In this model, the spatial dependence of the pumping rate is not taken into account. Therefore, it is more appropriate for flash-lamp side pumping. Later, Brenier [72] has modified this theoretical investigation to describe cw laser-diode end-pumped Nd^{3+} SFD lasers. Then, a forward and backward fundamental wave and a second harmonic wave are considered to propagate in the crystal and the non-linear equations are solved numerically giving their spatial dependence. The laser operation is described by rate equations for a four-level system with additional terms to take counter-propagating fundamental and SH waves into account, together with the reabsorption of the SH wave by the laser emitting ions. This model was applied to NYAB and $LiMgO_3$:MgO:Nd^{3+} using the optical and spectroscopic data published in the literature. The influence of the cavity parameters (ω_p, ω_1 and ω_2) and the length of the crystal on the green output power was investigated.

The model previously presented for fibre-coupled, laser-diode, end-pumped lasers [20,21] also applies to determine the optimum pumping condition for SFD lasers taking into account the pump-beam quality. This analysis was performed for NYAB using spectroscopic data (τ, σ_p, α_p) and round-trip cavity losses [53]. The threshold was calculated as a function of the pump-beam waists for different fibre-coupled laser diodes. The coupling optics are chosen to match this optimum pumping condition. The experimental set-up is schematized in Figure 8.13. The theoretical predictions are in excellent agreement with the experimental data as shown in Figure 8.14.

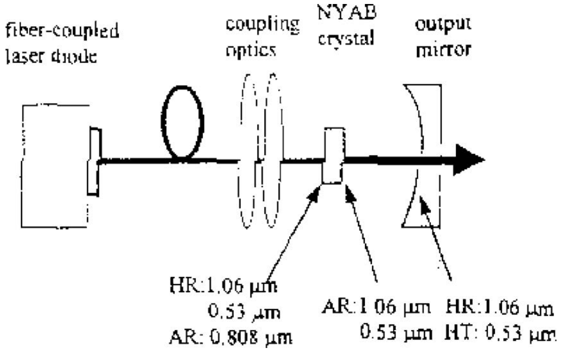

FIGURE 8.13 Fibre-coupled diode pumping experimental set-up (after Ref. [53]).

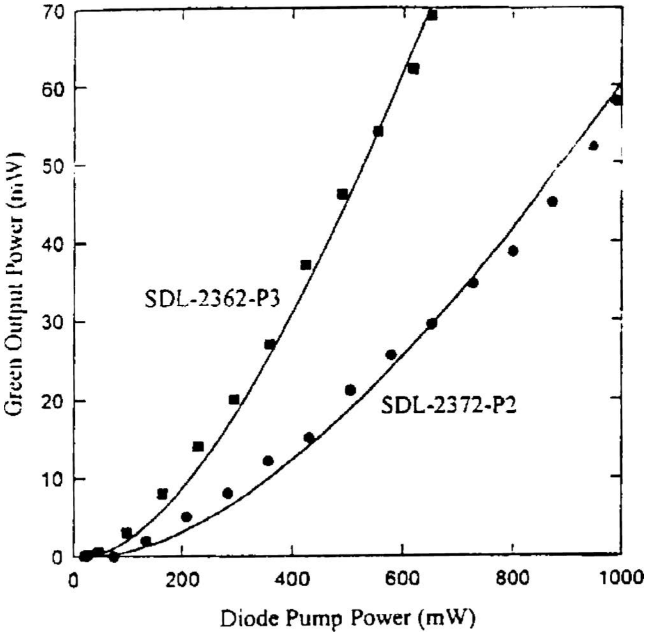

FIGURE 8.14 SH output power *versus* optical pump power of an NYAB laser: experimental (symbols) and theoretical results (full curves) (after Ref. [53]).

8.6 Typical Operating Characteristics

TABLE 8.8

Lasers with Intracavity Doubling Frequency

	Pump	λ_{pump} (nm)	$T_{\mathrm{out}\,(\%)}$	λ_{fund} (nm)	$P_{\mathrm{SH}}/P_{\mathrm{pump}}$	ζ (%)	Ref.
YAG:Banana				1064	0.350 W/1 W	35	[14]
YAG:LiO$_3$	2×SDL-2420	808	50	946	50 μW		[17]
YAG[a]:LiIO$_3$	LDA (2 × 20 W)	804		946	0.520 W/2.4 W	21.7	[12]
YAG[a]:BBO	LDA (2 × 20 W)	804		946	0.550 W/2.580 W	21.3	[12]
YAG[a]:LBO	LDA (2 × 20 W)	804		946	0.372 W/2.4 W	15.5	[12]
YAG:KTP				1064	3 W/14 W	21.4	[24]
YAG:KTP	LDA (2 × 20 W)	808		1064	20 W[b]/0.141 W	14.2	[25]
YAG:KTP	LDA (2 × 20 W)	808		1064	2 W/11.2 W	17.8	[26]
					4 W/27 W (unstable)		
YAG:KNbO$_3$	SDL-303V	809	85	946	3.1 mW/420 mW	0.74	[13]
YAG:KNbO$_3$	Ti-Sa(cw)	808.5		946	3.6 mW/870 mW	0.41	[27]
YAG:KNbO$_3$	SDL-2473 (2 W)		HT	946	100 mW/250 mW$^{\mathrm{IR}}$		[28]
YVO$_4$:LBO	SDL-2362 (1.2 W)		60	1342	10 mW/750 mW$^{\mathrm{abs}}$		[29]
YVO$_4$:KTP	810-CT100(1 W)	809	99	1064	230 mW/780 mW	29.5	[30]
YVO$_4$:KTP	ML 812-4D(1 W)	809	99	1064	105 mW/900 mW	11.5	[31]
YVO$_4$:KTP	SDL2432(0.5 W)	809		1064	50 mW/380 mW	13	[32]
YVO$_4$:KTP	LDA (2 × 20 W)	808		1064	1 W/10 W	10	[26]
YVO$_4$:KTP	MDL-100(1 W)	808	>95	1064	286.5 mW/881.4 mW	32.5	[33]
YVO$_4$:KTP	SDL-2372-P3	808	HT	1064	0.350 W/1.2 W	29.2	[34]
Passive Q-switch		808			240 W[b]/1.5 W		
S-FAPF-KTP	QW1000	805	HT	1059	40 mW/400 mW	10	[35]
LSB-KTP	SDL-2482(2 W)	808	M	1062.5	0.522 W/2.05 W	25	[36]
YLF LBO	LDA (2 × 20 W)	792	91	1053	6.2 W/28 W	22	[37]
YAP-KTP	High-pressure Kr lamp			1080	1 W$^{\mathrm{(SH)}}$		[38]

T_{out}, output coupler transmission at λ_{SH}; ζ, linear optical–optical conversion efficiency.

[a] Composite laser rod: 3-mm long Nd:YAG with two diffusion-bonded 3-mm long undoped cap ends.

[b] Peak power.

TABLE 8.9

Self-Frequency Doubled Lasers: Performance

Nd-Doped	Pump	λ_p (nm)	$T_{\mathrm{out}}^{\mathrm{SH}}$(%)	Cavity	λ_{fund} (nm)	η (%)	P_{th} (mW)	$P_{\mathrm{SH}}/P_{\mathrm{abs}}$ (mW/mW)	ζ (%)	
YAB	Ti-Sa	807 (o)	60	H	1338	16	98	0.6/750	0.1	[50]
YAB	SDL-2430-H1	800	>85	H[c]	1060		40	6/420	1.4	[88]
									20W[d]	
YAB	SDL-2362-P2	808	>HT	H	1063		40	67/650$^{\mathrm{pump}}$		[89]
									20 W[d]	
YAB[a]	SDL-2362-P2	808	>90	H	1063		~11	67/650	10.3	[53]
YAB[a]	2×(SFH-487401)	807	88	H	1062			225/1610	14	[51]
	Ti-Sa							450/2200	20.5	
YAB[a]	2×(SDL-2462-P1)	808	86	CC	1063			51/1380	3.7	[49]
Gd$_2$(MoO$_4$)$_3$[a]	SDL-2460	807	85	SC	1060.6			0.48/420$^{\mathrm{pump}}$		[77]
YCOB[a]	POL-5100BW	812	>96	H	1060	51		62/900	7	[58]
LiNbO$_3$:MgO[a]	SDL-2482-P1	809	>98	H	1093		220	8/870	1	[42]
LiNbO$_3$:MgO[a]	SDL-5412-H1	813	>90	H	1093		5.2	0.2/33	0.8	[41]

(*Continued*)

TABLE 8.9 (*Continued*)

Self-Frequency Doubled Lasers: Performance

Nd-Doped	Pump	λ_p (nm)	T_{out}^{SH}(%)	Cavity	λ_{fund} (nm)	η (%)	P_{th} (mW)	P_{SH}/P_{abs} (mW/mW)	ζ (%)	
	Ti-Sa	809		M[b]		2.4	7.7	0.2/100	0.2	
Yb-doped										
YCOB 20 at.%	Ti-Sa	900	>96	H	1090	35.8	370	1/900		[57]
$LiNbO_3$:MgO 1 at.%(4 mm)	Ti-Sa	980	80	CC	1060	47	101	30/560		[43]
$LiNbO_3$:MgO^{PP} 1 at.%	Ti-Sa	980	50	H	1060	7.5		10.5/1400		[45]

CC, concentric resonator; *H*, hemispherical cavity (plane-concave); η, slope efficiency for the infrared; P_{th}, threshold power; T_{out}^{SH}, output coupler transmission at λ_{SH}; ζ, linear optical–optical conversion efficiency.

[a] Face coated.

[b] Monolithic laser: the flat and spherical faces of the crystal are coated with dielectric mirrors.

[c] Acousto-optic Q-switch (repetition rate 16 kHz).

[d] Peak power (τ_{pulse} = 25 ns).

REFERENCES

1. Blombergen N 1965 *Nonlinear Optics* (New York: Benjamin).
2. Yariv A 1975 *Quantum Electronics* 2nd edn (New York: Wiley).
3. Shen Y R 1984 *The Principles of Nonlinear Optics* (New York: Wiley).
4. Levenson M D and Kano S S 1988 *Introduction to Nonlinear Laser Spectroscopy (Quantum Electronics—Principles and Applications)* revised edn, ed P F Lia and P Kelley (New York: Academic).
5. Dmitriev V G, Gurzadyan G G and Nikogosyan D N 1991 *Handbook of Nonlinear Optical Crystals (Springer Series in Optical Sciences)* ed A E Siegman (Berlin: Springer).
6. Kaminskii A A 1990 *Laser Crystals: Their Physics and Properties (Springer Series in Optical Sciences)* 2nd edn, ed D L MacAdam (Berlin: Springer).
7. Demtröder W 1996 *Laser Spectroscopy: Basic Concepts and Instrumentation* 2nd enlarged edn (New York: Springer).
8. Koechner W 1996 *Solid State Engineering* 4th edn (New York: Springer).
9. Hobden M V 1967 *J. Appl. Phys.* **38** 4365–72.
10. Kleinman D A, Ashkin A and Boyd G D 1966 *Phys. Rev.* **145** 338–79.
11. Boyd G D and Kleinman D A 1968 *J. Appl. Phys.* **39** 3597–639.
12. Kellner T, Heine F and Huber G 1997 *Appl. Phys. B* **65** 789–92.
13. Risk W P, Pon R and Lenth W 1989 *Appl. Phys. Lett.* **54** 1625–7.
14. Geusic J E, Levinstein H J, Singh S, Smith R G and van Uitert L G 1968 *IEEE J. Quantum Electron.* **QE-4** 352–3.
15. Fan T Y and Byer R L 1987 *Opt. Lett.* **12** 809–11.
16. Smith R G 1970 *IEEE J. Quantum. Electron.* **QE-6** 215–23.
17. Risk W P and Lenth W 1987 *Opt. Lett.* **12** 993–5.
18. Risk W P 1988 *J. Opt. Soc. Am. B* **5** 1412–23.
19. Laporta P and Brussard M *IEEE J. Quantum Electron.* **QE-27** 2319–26.
20. Chen Y F, Lio S T, Kao C F, Huang T M, Lin K H and Wang S C 1996 *IEEE J. Quantum Electron.* **QE-32** 2010–16.
21. Chen Y F, Kao C F and Wang S C 1997 *Opt. Commun.* **133** 517–24.
22. Pavel N, Kurimura S and Taira T 1999 *Advanced Solid State Lasers* vol 26, ed M M Fejer, H Injeyan and U Keller (Washington, DC: OSA Publishing) pp 253–9.
23. Sasnett M W 1992 Propagation in multimode laser beams—the M2 factor *The Physics and Technology of Laser Resonator* ed D R Hall and P E Jackson (Bristol: IOP) pp 132–42.
24. Martin K I, Clarkson W A and Hanna D C 1996 *Opt. Lett.* **21** 875–7.
25. Konno S and Yasui K 1998 *Appl. Opt.* **37** 551–4.
26. Yelland C and Sibbett W 1996 *J. Mod. Opt.* **43** 893–901.
27. Matthews D G, Conroy R S, Sinclair B D and MacKinnon N 1996 *Opt. Lett.* **21** 198–200.
28. Hollemann G, Peik E and Walther H 1994 *Opt. Lett.* **19** 192–4.
29. Conroy R S, Kemp A J, Friel G J and Sinclair B D 1997 *Opt. Lett.* **22** 1781–3.
30. Pavel N, Taira T and Furuhata M 1998 *Opt. Laser Technol.* **30** 275–80.
31. Taira T and Kobayashi T 1995 *Appl. Opt.* **34** 4298–301.
32. MacKinnon N and Sinclair B D 1994 *Opt. Commun.* **105** 183–7.
33. Shen D, Liu A, Song J and Ueda K 1998 *Appl. Opt.* **37** 7785–8.
34. Chen Y F 1998 *IEEE Photon. Technol. Lett.* **10** 669–71.
35. Zhao S, Wang Q, Zhang X, Wang S, Zhao L, Sun L and Zhang S 1997 *Opt. Eng.* **36** 3107–10.
36. Meyn J P and Huber G 1994 *Opt. Lett.* **19** 1436–8.
37. Hardman P J, Clarkson W A and Hanna D C 1998 *Opt. Commun.* **156** 49–52.
38. Pan Q, Zhang T, Zhang Y, Li R, Peng K, Yu Z and Lu Q 1998 *Appl. Opt.* **37** 2394–6.
39. Johnson L F and Ballman A A 1969 *J. Appl. Phys.* **40** 297–302.
40. Fan T Y, Cordova-Plaza A, Digonnet M J F, Byer R L and Shaw H J 1986 *J. Opt. Soc. Am. B* **3** 140–7.

41. Ishibashi S, Itoh H, Kaino T, Yokohama I and Kubodera K 1996 *Opt. Commun.* **125** 177–85.
42. Zhang K, Xie C, Guo R, Wang J and Pen K 1996 *Appl. Opt.* **35** 3200–2.
43. Montoya E, Capmany J, Bausá L E, Kellner T, Diening A and Huber G 1999 *App. Phys. Lett.* **74** 3113–15.
44. Jaque D, Capmany J, Sanz García J A, Brenier A, Boulon G and García Solé J 1999 *Opt. Mater.* **13** 147–57.
45. Capmany J, Montoya E, Bermúdez V, Callejo D, Diéguez E and Bausá L 2000 *Appl. Phys. Lett.* **76** 1374–6.
46. Abedin K S, Tsuritani T, Sato M and Hiromasa I 1996 *Appl. Phys. Lett.* **70** 10–12.
47. Schaffers K I, DeLoach L D and Payne S A 1996 *IEEE J. Quantum. Electron.* **QE-32** 741–8.
48. Lu B S, Wang J, Pan H F, Jiang M H, Liu E Q and Hou X Y 1989 *J. Appl. Phys.* **66** 6052–4.
49. Hemmati H 1992 *IEEE J. Quantum Electron.* **QE-28** 1169–71.
50. Jaque D, Capmany J and García Solé J 1999 *Appl. Phys. Lett.* **74** 1788–90.
51. Bartschke J, Knappe R, Boller K J and Wallenstein R 1997 *IEEE J. Quantum. Electron.* **QE-33** 2295–300.
52. Bartschke J, Boller K J, Wallenstein R, Klimov I V, Tsvetkov V B and Shcherbakov I A 1997 *J. Opt. Soc. Am. B* **14** 3452–6.
53. Chen Y F, Wang S C, Kao C F and Huang T M 1996 *Appl. Opt.* **37** 514–17.
54. Wang C L, Lin K H, Hwang T M, Chen Y F, Wang S C and Pan C L 1998 *Appl. Opt.* **37** 3282–5.
55. Jaque D, Capmany J, García Solé J, Luo Z D and Jiang A D 1998 *J. Opt. Soc. Am. B* **15** 1656–62.
56. Jang W K, Ye Q, Eichenholz J M, Richardson M C and Chai B H T 1998 *Opt. Commun.* **155** 332–4.
57. Hammons D A, Eichenholz J M, Ye Q, Chai B H T, Shah L, Peale R E, Richardson M and Qiu H 1998 *Opt. Commun.* **156** 327–30.
58. Eichenholz J M, Hammons D A, Shah L, Ye Q, Peale R E and Richardson M 1999 *Appl. Phys. Lett.* **74** 1954–6.
59. Aka G, Kahn-Harari A, Mougel F, Vivien D, Salin F, Coquelin P, Colin P, Pelenc D and Damelet J P 1997 *J. Opt. Soc. Am. B* **14** 2238–47.
60. Mougel F, Aka G, Kahn-Harari A, Hubert H, Benitez J M and Vivien D 1997 *Opt. Mater.* **8** 161–73.
61. Mougel F, Augé F, Aka G, Kahn-Harari A, Vivien D, Balembois F, Georges P and Brun A 1998 *Appl. Phys. B* **67** 533–5.
62. Mougel F, Dardenne K, Aka G, Kahn-Harari A and Vivien D 1999 *J. Opt. Soc. Am. B* **16** 164–72.
63. Kaminskii A A, Ueda K, Bagaev S N, Pavlyuk A A, Song J, Nishioka H, Uehara N and Musha M 1996 *Quantum Electron.* **26** 379–80.
64. Capmany J, Jaque D, García Solé J and Kaminskii A A 1998 *Appl. Phys. Lett.* **72** 531–3.
65. Ostroumov V, Petermann K, Huber G, Ageev A A, Kutovoj S, Kuzmin O, Panyutin V, Pfeifer E and Hinz A 1997 *J. Luminesc.* **72/74** 826–8.
66. Judd B R 1962 *Phys. Rev.* **127** 750–61.
67. Ofelt G S 1962 *J. Chem. Phys.* **37** 511–20.
68. Carnall WT, Crosswhite H and Crosswhite H M 1977 *Energy level structure and transition probabilities of the rare earth lanthanides in LaF_3: Internal Report* (John Hopkins University, Baltimore, MD).
69. Jaque D, Munõz J A, Cussó F and García Solé J 1998 *J. Phys.: Condens. Matter* **10** 7901–5.
70. Krupke W F 1974 *IEEE J. Quantum Electron.* **QE-10** 450–7.
71. DeLoach L D, Payne S A, Chase L L, Smith L K, Kway W L and Krupke W F 1993 *IEEE J. Quantum Electron.* **QE 29** 1179–91.
72. Brenier A 1997 *Opt. Commun.* **141** 221–8.
73. Fan Y X, Schlecht R, Qiu M W, Luo D, Jiang A D and Huang Y C 1992 *Proc. Adv. Solid State Lasers* **13** 371–5.
74. Aka G, Kahn-Harari A, Vivien D, Benitez J M, Salin F and Godart J 1996 *Eur. J. Solid State Inorg. Chem.* **33** 727–36.
75. Iwai M, Kobayashi T, Furuya H, Mori Y and Sasaki T 1997 *Japan J. Appl. Phys.* **36** 276–9.
76. Capmany J and García Solé J 1997 *Appl. Phys. Lett.* **70** 2517–19.
77. Kaminskii A A, Bagaev S N, Ueda K, Pavlyuk A A and Musha M 1997 *Quantum Electron.* **27** 657–8.
78. Omatsu T, Kato Y, Shimosegawa M, Hasegawa A and Ogura I 1995 *Opt. Commun.* **118** 302–8.
79. Bryan D A, Gerson R and Tomaschke H E 1984 *Appl. Phys. Lett.* **44** 847–9.
80. Jarman R H, Munowitz M and Harrison J F 1991 *J. Crystal Growth* **109** 353–60.
81. Munowitz M, Jarman R H and Harrison J F 1992 *Chem. Mater.* **4** 1296–304.
82. Munowitz M, Jarman R H and Harrison J F 1993 *Chem. Mater.* **5** 1257–67.
83. Chen C, Wu Y C, Li R K 1985 *Chim. Phys. Lett.* **2** 389–92.
84. Keszler D A, Akella A, Schaffers K I and Alekel T 1994 *New Materials for Advanced Solid State Lasers Symposium* ed B H T Chai, S A Payne, T Y Fan, A Cassanho and T H Allik (Pittsburgh, PA: Materials Research Society) pp 85–94.
85. Pavel N and Taira T 1999 *Opt. Eng.* **38** 1806–13.
86. Dmitriev V G and Zenkin V A 1976 *Sov. J. Quantum Electron.* **6** 984–6.
87. Dmitriev V G, Zenkin V A, Kornienko N E, Ryzhkov A I and Strizhevskii 1978 *Sov. J. Quantum Electron.* **8** 1356–61.
88. Li Z, Fan Q, Hou F, Ma J and Xue Q 1994 *Opt. Eng.* **33** 1138–41.
89. Chen Y F, Wang S C, Kao C F and Huang T M 1996 *IEEE Photon. Techol. Lett.* **8** 1313–15.
90. Belabaev K G, Kaminskii A A and Sarkisov S E 1975 *Phys. Stat. Sol. a* **28** K17–20.
91. Risk W P, Baumert J C, Bjorklund G C, Schellenberg F M and Lenth W 1988 *Appl. Phys. Lett.* **52** 85–7.
92. Risk W P and Lenth W 1989 *Appl. Phys. Lett.* **54** 789–91.
93. Kretschmann H M, Huber G, Batchko R G, Meyn J P, Fejer M M and Byer R L 1999 *Laser Phys.* **9** 293–8.
94. Ye Q, Shah L, Eichenholz J M, Hammons D A, Richardson M, Chin A and Chai B H T 1999 *Advanced Solid State Lasers* vol 26 ed M Fejer, H Injeyan and U Keller (Boston, MA: OSA Publishing) pp 100–3.
95. Kaminskii A A, García-Solé J, Bagaev S N, Jaque D and Capmany J 1998 *Quantum Electron.* **28** 1031–3

9

Solid-State Raman Lasers

T. T. Basiev and R. C. Powell

CONTENTS

9.1 Introduction 127
9.2 Theoretical Background 128
9.3 Visible Nanosecond SRS Based on $Ba(NO_3)_2$ Crystals 131
9.4 Infrared SRS Shifters and Raman Lasers Based on $Ba(NO_3)_2$ 132
9.5 IR-Pumped $LiIO_3$ Raman Laser 134
9.6 Picosecond Raman Frequency Shifters Based on KGW ($KGd(WO_4)_2$) Crystals 135
9.7 Nanosecond Raman Lasers Based on KGW Crystals 136
9.8 New $BaWO_4$ SRS Crystals 137
9.9 IR $BaWO_4$ and $SrWO_4$ Nanosecond Raman Lasers 138
9.10 $BaWO_4$ Yellow Raman Shifters and Lasers 138
9.11 $BaWO_4$ Picosecond Raman Frequency Shifters 139
9.12 $PbWO_4$ SRS Shifters and Raman Lasers 140
9.13 Raman Laser Applications 140
9.14 Conclusions 146
Acknowledgements 146
References 146
Further Reading 149

9.1 Introduction

In 1928, two research groups in Russia and India simultaneously (with a difference of a week) and independently observed an important non-linear optical process—Raman scattering. Since then the field of non-linear optics has increased in importance and provided us with a significant amount of information about fundamental light–matter interactions and enabled the development of sophisticated new types of optical devices including optical parametric amplifiers and Raman lasers.

Raman scattering is a process involving the inelastic scattering of light by a material occurring simultaneously with the absorption or emission of thermal energy (phonons). Conservation of energy requires that the energy of the scattered photon differs from that of the incident photon by an amount equal to the energy of the phonon that is absorbed or emitted. The two Indian scientists who first observed Raman scattering, C. V. Raman and K. S. Krishnan, were performing light-scattering experiments on molecular liquids [1]. The two Russian scientists who simultaneously observed the same effect, G. S. Landsberg and L. I. Mandelshtam, were investigating light scattering in crystals [2]. Since then Raman light scattering has also been observed in many types of gases.

Initially the investigations of Raman scattering centred on trying to understand the fundamental physics associated with the process. This included the mechanism by which the incident light beam interacts with the atoms of the material and the electron–phonon interaction causing some of the light energy to be converted to thermal energy. The details of these interactions differ depending on the type of material being used as the Raman medium. Once the physics of the process was understood, Raman scattering became useful as a spectroscopic tool to study the vibrational, structural and chemical properties of molecules and solids. The Raman spectrum of different molecules is so distinct that Raman spectroscopy has become a common method used for chemical analysis. In 1962 Woodbury and Ng [3] reported frequency shifting of a ruby laser beam through Raman scattering. In this case, the intensity of the incident light beam was great enough to result in stimulated Raman scattering (SRS). Raman wavelength shifters made from gas cells with long path lengths have become a normal accessory for lasers. Since stimulated scattering is a process similar to stimulated emission, it was a logical step to place a Raman gas cell in an optical resonator to obtain a Raman laser. Solid-state Raman lasers are of greatest interest because of the ability to build them in a compact, rugged, low-maintenance format. Some of the properties of crystals used for Raman lasers and amplifiers are discussed here and then some potential Raman laser applications are described. Raman scattering is a third-order non-linear optical process in a medium. It does not require phase matching. The resonance characteristics of the process allow it to be useful for investigating the microscopic physics of the atoms, ions or molecules of the medium and for the generation of new frequencies of light. Efficient Raman scattering requires high-power laser sources and materials that have very specific properties. Molecular gases such as H_2 are useful as Raman media because they have high-frequency vibrational modes and narrow spectral linewidths. These properties lead to large Raman frequency shifts and large Raman scattering cross sections as discussed later. However, gas media have a low particle concentration, $N \approx 10^{20}\,\mathrm{cm}^{-3}$ even for high pressures, and low thermal conductivity. This requires optical interaction lengths of up to a few metres to achieve a significant Raman signal or SRS gain and achieving a pump intensity that exceeds the SRS threshold (>1.0 GW cm^{-2}) along the entire length of a gas cell is difficult. The use of constant gas flow cells to overcome thermal problems is also cumbersome.

Liquid media have a higher density of active particles than gases but the broadening of the vibrational transitions due to fluctuations in bond lengths, bond angles and coupling constants as well as particle rotations and collisions is much larger. In general, the increased density outweighs the increased linewidth, resulting in higher Raman gain coefficients for liquid media compared to gas media. Low thermal conductivity is a major drawback of a liquid Raman medium since flowing cell techniques have problems associated with obtaining the homogeneous laminar flows that are required for laser transmission. In addition, thermal lensing and self-focusing of the pump laser beam can be a major problem in liquid Raman cells.

Many of the problems associated with gas and liquid media are avoided by using crystalline solids as the Raman medium. The high density of solids ($N \approx 10^{22}\,\mathrm{cm}^{-3}$) along with narrower spectral linewidths results in high Raman gains and this allows for a more precise resonance enhancement effect. A great variety of crystals have been investigated for Raman scattering and these provide Raman frequency shifts from 10 to 3000 cm^{-1} in the spectral range from the ultraviolet to the infrared.

Raman scattering in solids occurs because the light wave travelling through the medium is frequency modulated by optical phonons or molecular vibrations. This creates sidebands on the light wave shifted by an amount equal to the vibrational frequency at higher (anti-Stokes) and lower (Stokes) frequencies. The spectral width of the Raman sidebands depends on the lifetime of the vibrational excitation and their intensity depends on the effective scattering cross section describing the light–matter interaction. Conservation of the wavevector determines the direction of the Raman scattered beam of light. Monodirectional gain in a collinear pumping scheme results in SRS in the near forward or backward directions compared to the incident light beam.

9.2 Theoretical Background

The theory of SRS follows the usual treatment of third-order non-linear optical processes [4] with the non-linear polarization, in this case given by

$$P^{\mathrm{NL}} = N\left(\partial\alpha/\partial q\right) q_{\mathrm{av}} E \tag{9.1}$$

where N is the density of scattering centres, q_{av} is the average value for the displacement operator of the normal vibrational mode, E is the electric field of the optical beam and α is the polarizability.

In the steady-state regime, when the pump duration t_{p} is much longer than the Raman mode dephasing time $T_{\mathrm{R}}\left(t_{\mathrm{p}} \gg T_{\mathrm{R}}\right)$, solving the coupled differential equations for q_{av} and the electric fields of the light beams propagating through the media leads to an expression for the gain coefficient g that causes the build-up of the Stokes beam I_{S}, due to SRS. After travelling a length L in the Raman medium, the Stokes beam intensity is given by

$$I_{\mathrm{S}}(L) = I_{\mathrm{S}}(0)\,\exp\left[g I_{\mathrm{p}} L\right] \tag{9.2}$$

in the non-pump-depletion region, where I_{p} is the intensity of the incident laser pump beam and the gain coefficient is

$$g = \frac{\lambda_{\mathrm{p}}\lambda_{\mathrm{S}}^2 N}{\pi c \hbar n_{\mathrm{S}}^2 \Delta\nu_{\mathrm{R}}}\left(\frac{\mathrm{d}\sigma}{\mathrm{d}\Omega}\right). \tag{9.3}$$

Here, λ_{p} and λ_{S} are the wavelengths of the laser pump beam and the Stokes Raman beam, respectively, and $\Delta\nu_{\mathrm{R}}$ is the full-width at half maximum of the Raman spectral line in units of s^{-1}. The gain coefficient is the most important parameter for solid-state laser applications and its magnitude is usually given in units of cm GW^{-1}. These expressions show that the intensity of the Raman beam increases with the intensity of the pump laser and the interaction length and is greater for higher scattering cross sections. In addition, the gain is greatest for materials with a high density and a small Raman linewidth [5]. In the transient case, when the pump pulse duration is smaller than the dephasing time and the pump spectral width is broader than that of the Raman line ($t_{\mathrm{p}} < 10T_{\mathrm{R}}$; $\Delta\nu_{\mathrm{p}} \gg \Delta\nu_{\mathrm{R}}$), the analytical expression for the Stokes intensity for large amplification gain, in the non-pump-depletion region, can be written as [6]

$$I_{\mathrm{S}}(L) = I_{\mathrm{S}}(0)\exp\left(-\frac{t_{\mathrm{p}}}{T_{\mathrm{R}}}\right)\exp 2\left[I_{\mathrm{p}} t_{\mathrm{p}} L \frac{\lambda_{\mathrm{p}}\lambda_{\mathrm{S}}^2 N}{\hbar n_{\mathrm{S}}^2}\left(\frac{\mathrm{d}\sigma}{\mathrm{d}\Omega}\right)\right]^{1/2}. \tag{9.4}$$

Comparing expression (9.4) with (9.1) and (9.2), one can see that the Raman gain has a slower (square root) dependence on the crystal length L and the total integral Raman scattering cross section, $\mathrm{d}\sigma/\mathrm{d}\Omega$, and does not depend on the Raman linewidth, $\Delta\nu_{\mathrm{R}}$, at all. The linear pump intensity dependence for steady-state regimes changes to the pump pulse energy ($W = I_{\mathrm{p}}t_{\mathrm{p}}$) square root dependence for the transient regime described by Equation (9.4). The transient regime is very important when one tries to realize short-pulse picosecond and femtosecond Raman shifting and lasing.

The width of a Stokes Raman line is determined by the lifetime of the vibrational mode produced in the Raman interaction $\Delta\nu_{\mathrm{R}} = (\pi C T_{\mathrm{R}})^{-1}$ and is strongly temperature dependent. This decay or dephasing of a phonon mode is generally associated with phonon–phonon interactions in which the initial phonon decays into two other phonon modes with conservation of energy and wavevector. This takes place through anharmonic coupling of the vibrational modes represented by the interaction Hamiltonian H_A. The expression for the width of a Stokes Raman line is [7]

$$\Delta\tilde{v}_R \sim \int \mathrm{d}\kappa \sum_{s,s'} \left| \langle n_{s\kappa_1}+1,\ n_{s'\kappa_2}+1,\ n_0=0 \middle| H_\mathrm{A} \middle| n_{s\kappa_1},\ n_{s'\kappa_2},\ n_0=1 \rangle \right|^2$$

$$\times \delta\left(\omega_0-\omega_{s\kappa_1}-\omega_{s'\kappa k_2}\right)\delta\left(\kappa-\kappa_1-\kappa_2\right) \qquad (9.5)$$

where the phonon wavevectors and frequencies are given by κ and ω, respectively. The rate at which a phonon decay process occurs, thus, depends on the strength of the anharmonic coupling in the lattice and the phonon density of states. Thus, materials that have a small anharmonicity parameter will have a small Raman linewidth and, therefore, a high gain coefficient [5].

The second material parameter affecting the Raman gain is the scattering cross section, which depends on the strength of the photon–phonon coupling. This can be expressed in terms of the laser-induced modulation of the local polarizability through the relationship

$$\left(\frac{\mathrm{d}\sigma}{\mathrm{d}\Omega}\right) = \frac{\hbar\omega_\mathrm{S}^4}{2m\omega_\mathrm{R}c^4}\left(\frac{\partial\alpha}{\partial q}\right)^2. \qquad (9.6)$$

Here ω_R is the frequency of the vibrational mode. Thus, materials that have a high value of polarizability and vibrational modes that induce a large modulation of this polarizability will have a large Raman scattering cross section and, thus, a high Raman gain. Because of the resonant denominator appearing in the quantum mechanical expression for the dipole moment in the polarizability, materials with low-energy electronic transitions (such as molecular crystals with charge transfer bands) will have a high polarizability. In addition, the rate of the Raman scattering processes involves the matrix element of polarizability between initial and final states and this leads to symmetry selection rules with directional properties for each vibrational mode [7]. Totally symmetric 'breathing modes' of vibration produce the greatest degree of modulation of the polarizability. In addition, lattice structures such as diamond, zinc-blende and wurtzite are favourable for covalent bonding and allow for a greater vibrational modulation of the polarizability than ionic binding.

The two-photon nature of Raman transitions results in a very small scattering cross section for the process. To attain high efficiency for the stimulated Raman conversion starting from spontaneous noise of very low intensity, we must provide a very high increment $I_\mathrm{p}gL \simeq 30$ in Equation (9.2). For a typical crystal length of about 3 cm, this leads to a very high gain value $I_\mathrm{p}g \simeq 10\,\mathrm{cm}^{-1}$. This estimate means that, even for high gain materials with $g \simeq 10\,\mathrm{cm\ GW}^{-1}$, we must use a very high pump density at the level of 1 GW cm^{-2} without laser damage to the Raman crystal. For low gain materials, the pump density must be even higher. One of the best examples of a new synthetic solid-state Raman material is $\mathrm{Ba(NO_3)_2}$ operating on the A_{1g} nitrate molecular ion breathing mode [8–14]. This provides a frequency shift of 1046 cm^{-1} with an extraordinarily small linewidth at room temperature of 0.4 cm^{-1}, leading to a Raman gain of as high as 47 cm GW^{-1} for green (0.532 μm) and 11 cm GW^{-1} for infrared (1.064 μm) pumping. $\mathrm{Ba(NO_3)_2}$ crystals are now available in large sizes with high optical quality and a laser damage threshold higher than 1 GW cm^{-2}.

Measuring and analysis of the temperature dependencies of the spectral line broadening and dephasing time for the A_{1g} Raman active vibrational mode provide a better understanding of the unique narrow linewidth feature of $\mathrm{Ba(NO_3)_2}$ crystals [13,15,16]. The forbiddance of fast three-phonon splitting processes in dephasing and line broadening (which is the main process for most other materials) together with very small inhomogeneous linewidth results in the extraordinarily small Raman linewidth, Δv_R, and strong temperature dependence of the linewidth. The latter is well explained by a four-phonon relaxation and dephasing process with a much smaller relaxation rate [13,15,16].

Another good synthetic crystal with practically the same Raman frequency shift ($v_\mathrm{R} = 1069\,\mathrm{cm}^{-1}$) is $\mathrm{NaNO_3}$. The broader linewidth of $\mathrm{NaNO_3}$ ($\Delta v_\mathrm{R} = 1.0\,\mathrm{cm}^{-1}$) results in a lower gain coefficient in the steady-state regime compared to $\mathrm{Ba(NO_3)_2}$.

For natural crystals, the best Raman properties are exhibited by diamond and calcite ($\mathrm{CaCO_3}$) crystals providing high-frequency shifts of 1333 and 1086 cm^{-1}, respectively. Unfortunately, size, optical quality and the price of natural crystals limit their applications. The quality of natural crystals causes the inhomogeneous widths of their Raman lines to vary greatly from 1.5 to 2.7 cm^{-1} for diamond and from 1.2 to 1.6 cm^{-1} for calcite [17]. This leads to significant variations in gain.

$\mathrm{KGd(WO_4)_2}$ synthetic crystals have a smaller Raman frequency shift and much broader Raman lines, 5–8 cm^{-1}. These have been useful for picosecond pulse applications.

Lithium iodate ($\mathrm{LiIO_3}$) and niobate ($\mathrm{LiNbO_3}$) synthetic crystals were among the most popular Raman materials at the beginning of the Raman laser era. However, due to the large linewidth, 5–20 cm^{-1}, and moderate laser damage threshold, 0.1–0.5 GW cm^{-2}, they did not find wide practical applications.

To estimate the potential of a specific crystal as a Raman laser material, it is important to compare the frequency and spectral width of the Raman line, as well as the peak and integrated cross sections for the two-photon Raman transition. For a great number of prospective Raman materials, a comparative study was undertaken [17–20] and some of the results are presented in Table 9.1. The materials that were analysed included carbonate, nitrate, phosphate, tungstate, niobate, iodate, bromide, borate and silicate crystals. The frequencies and linewidths of the most intense and narrow quasi-molecular Raman vibrations of $[\mathrm{CO_3}]$, $[\mathrm{NO_3}]$, $[\mathrm{WO_4}]$, $[\mathrm{MoO_4}]$, $[\mathrm{NbO_6}]$, $[\mathrm{NbO_4}]$, $[\mathrm{IO_3}]$, $[\mathrm{PO_4}]$, $[\mathrm{C1O_3}]$, $[\mathrm{B_3O_6}]$, $[\mathrm{BrO_3}]$, $[\mathrm{SiO_2}]$, $[\mathrm{SO_4}]$ anion and $[\mathrm{NH_4}]$ cation groups were compared. The relative intensities (integral and peak) of SRS lines were measured for more than 30 synthetic crystals in comparison with a reference diamond crystal (100%). The RS line intensities were studied for various orientations of the crystals with respect to the exciting and scattered beams (see Table 9.1). As can be seen from the table, the highest gain for the steady-state regime (peak intensity) compared to diamond (100%) is found in $\mathrm{Ba(NO_3)_2}$ (63%), $\mathrm{BaMoO_4}$ (64%) and $\mathrm{BaWO_4}$ (63%). For $\mathrm{SrMoO_4}$ and

TABLE 9.1

Parameters of Spontaneous Raman Scattering in Crystals[a] [17]

Material	Lattice Space Group	Molecular Group	Raman Frequency ν_R (cm^{-1})	Raman Linewidth $\Delta\nu_R$ (cm^{-1})	Integral Cross Section (au)	Peak Intensity (au)	Geometry of Excitation Scattering	
							K	*E*
Diamond	O_h^7	-	1332.9	2.7	100	100	$\parallel C_3$	$\perp C_3$
Nitrates and Calcites								
$Ba(NO_3)_2$	Th^6	$[NO_3]$	1048.6	0.4	21	63	$\parallel C_4$	$\perp C_4$
$NaNO_3$	D_{3d}^6	$[NO_3]$	1069.2	1.0	23	44	$\parallel C_3$	$\perp C_3$
$CaCO_3$	D_{3d}^6	$[CO_3]$	1086.4	1.2	6.0	10.6	$\parallel C_3$	$\perp C_3$
Tungstates								
$CaWO_4$	C_{4h}^6	$[WO_4]$	910.7	6.95	52	18.6	$\perp C_4$	$\parallel C_4$
$SrWO_4$	C_{4h}^6	$[WO_4]$	921.5	2.74	50	41	$\perp C_4$	$\parallel C_4$
$BaWO_4$	C_{4h}^6	$[WO_4]$	926.5	1.63	47	64	$\perp C_4$	$\parallel C_4$
$KGd(WO_4)2$	C_{2h}^6	$[WO_6]$	901	5.4	50	35	$\perp C_2$	$\perp C_2$
$KGd(WO_4)2$	C_{4h}^6	$[WO_6]$	768	6.4	59	37	$\perp C_2$	$\parallel C_2$
Molybdates								
$CaMoO_4$	C_{4h}^6	$[MoO_4]$	879.3	5.0	64	34	$\perp C_4$	$\parallel C_4$
$SrMoO_4$	C_{4h}^6	$[MoO_4]$	887.7	2.8	55	51	$\perp C_4$	$\parallel C_4$
$BaMoO_4$	C_{4h}^6	$[MoO_4]$	892.4	2.1	52	64	$\perp C_4$	$\parallel C_4$
Iodate and Niobates								
$LiIO_3$	C_6^6	$[IO_3]$	821.6	5.0	54	25	$\parallel C_2$	$\perp C_2$
$LiNbO_3$	C_{3v}^6	$[NbO_6]$	872	21.4	44	5	$\parallel C_3$	$\perp C_3$
$LiNbO_3$	C_{3v}^6	$[NbO_6]$	632	27	166	18	$\perp C_3$	$\parallel C_3$
$LiNbO_3$	C_{3v}^6	$[NbO_6]$	250	28	-	22	$\perp C_3$	$\parallel C_3$
$LaNbO_4$	C_{2h}^3	$[NbO_4]$	805	9	22	7.1	$\perp C_2$	$\parallel C_2$
Phosphates								
$Ca_5(PO_4)_3F$	C_{6h}^2	$[PO_4]$	964.7	2.8	3.4	3.8	$\perp C_6$	$\parallel C_6$
$Sr_5(PO_4)_3F$	C_{6h}^2	$[PO_4]$	950.3	2.8	3.4	3.8	$\perp C_6$	$\parallel C_6$
$Li_3PO_4^a$	-	$[PO_4]$	951	7.7	-	-	-	-
Other								
$Ba_3(B_3O_6)_2$	C_{3v}^6	$[B_3O_6]$	636	4.5	1	0.6	$\parallel C_3$	$\perp C_3$
TiO_2	D_{4h}^{14}		612	48	159	9.8	$\perp C$	$\parallel C$
ZnO	C_{6v}^4		438	6.0	7.14	2.7	$\parallel C$	$\perp C$
Y_2O_3			379	4.0	3.3	2.16		
SiO_2	D_3^6	$[SiO_4]$	464	7	2.2	1.2	$\perp C_3$	$\parallel C_3$
$Y_3Al_5O_{12}$			783	8	3	1.0		
Al_2O_3			419	2	0.05	0.07		
CdF_2			318	21	0.16	0.2		
CaF_2			323	8.4	0.07	0.21		

[a] Line with inhomogeneous splitting.

other tungstates, iodates and niobates, the gain is between 50% and 20% and for calcite it is only about 10%. In the transient regime or for femto- and picosecond operation, where the integrated scattering cross section is the most important parameter, the record holder is expected to be $LiNbO_3$ (166%) and rutile TiO_2 (159%); the next is diamond (100%), and then the molybdates, tungstates and iodates (70%–54%). Nitrates $Ba(NO_3)_2$ and $NaNO_3$ show only 21%–23%, and calcite $CaCO_3$ is even smaller at 6%.

An analysis of the data given in Table 9.1 shows that the best crystals for low-threshold SRS frequency converters should have both a large integral RS cross section and a small RS transition broadening. Two promising classes for this purpose are tungstates and molybdates, which possess large integral

RS cross sections (40%–60%) and a great variety of line broadenings (1.6–15 cm^{-1}).

Since the line broadening (both due to the up-conversion and decay dephasing) of high-frequency SRS-active vibrational modes relates to their interaction with lattice phonons, the authors of Refs. [21–24] selected the crystals with the heaviest cations to reduce the frequencies of phonon modes. In Refs. [21–24], simple tungstates of alkaline-earth metals (Ca, Sr and Ba) with a scheelite structure were synthesized and investigated. As is evident from Table 9.1, the $CaWO_4$ crystal frequently encountered in the scientific literature has a modest peak scattering cross section, equal to 18%, which is three times smaller than in the $Ba(NO_3)_2$ crystal and almost two times smaller than in $KGd(WO_4)_2$. This results from the significant broadening of its RS line, $\Delta\nu_R = 6.95\,cm^{-1}$, at room temperature. Replacement of the small-size and low-mass calcium ions for larger, heavier strontium and barium ions resulted in a much lower relaxation rate and the several times narrower spectral line (2.74 and 1.63 cm^{-1}) of $[WO_4]^{2-}$ Raman vibrations at room temperature.

As the cation mass increases in the sequence Ca, Sr and Ba, the maximum frequency ω_{lat} of lattice phonons decreases from 274 to 194 cm^{-1}. In addition, the increase in the cation radius and lattice constant results in the higher frequency of the totally symmetric A_{1g} mode of the $[WO_4]^{2-}$ complex (see Table 9.1). These two factors weaken the vibron–lattice interactions and considerably narrow the spectrum of Raman vibration, which should manifest itself in a growth of the peak scattering cross section and the steady-state SRS gain.

A detailed study of the RS fine structure of the A_{1g} mode in scheelites [23] shows that due to the largest lattice constants and the W–W distances for the $BaWO_4$ crystal (as well as for $Ba(NO_3)_2$), the Davydov splitting (DS) for these crystals is very small, $\Delta E_{DS} \approx 0.5\text{–}1\,cm^{-1}$ [23]. A very low acoustic phonon density at this frequency, $h\omega_{ph} = \Delta E_{DS} = 0.5\text{–}1\,cm^{-1}$, cannot provide fast dephasing and strong broadening of these DS components by means of direct single-phonon bridge processes. Conversely, in $CaWO_4$ and partly in $SrWO_4$ crystals with smaller lattice constants, the DS was found to be much higher—50 and 28 cm^{-1}, respectively. This can explain the much faster dephasing and stronger broadening (6.9 and 2.74 cm^{-1}) in these crystals due to direct single-phonon bridge processes from one DS component to another with absorption or emission of acoustic phonons with 30–50 cm^{-1} frequencies, whose density (ρ) can be rather high $\left(\rho \approx \omega_{ph}^2\right)$.

Similar regularities were observed in the series of alkaline-earth molybdates with a scheelite structure, $CaMoO_4$, $SrMoO_4$ and $BaMoO_4$. Table 9.1 demonstrates the relative values of integral and peak scattering coefficients. As is seen, even with the broader RS lines, the new crystals $BaWO_4$ and $BaMoO_4$ surpass the unique $Ba(NO_3)_2$ crystal in the peak cross section, while the $SrWO_4$ and $SrMoO_4$ crystals are only slightly below.

The data on the peak cross sections of spontaneous RS found by the comparative study were subsequently confirmed by direct measurements of SRS gain and thresholds [17,21,22,24]. This proved the high potential of the newly developed crystals for applications in SRS amplifiers and lasers, which will be discussed later.

9.3 Visible Nanosecond SRS Based on $Ba(NO_3)_2$ Crystals

One of the first studies of visible SRS in synthetic nitrate crystals $Ba(NO_3)_2$, $Pb(NO_3)_2$ and $NaNO_3$ in comparison with natural $CaCO_3$ crystals was reported in Ref. [8]. SRS crystals 15 mm long were studied in a single-pass scheme under 530 nm excitation. The pump laser, consisting of an Nd-glass master oscillator with passive Q-switching, a double-stage amplifier and a second-harmonic generator, produced pulses of green radiation with an energy of 0.8 J and a duration of 15 ns. The pump energy density was increased from 1 J cm^{-2} to the point of laser damage of the SRS crystal, which is 6–15 J cm^{-2}. For the $Ba(NO_3)_2$ crystal, the minimum SRS threshold energies were about 1 J cm^{-2} for the first Stokes and 3 J cm^{-2} for the second Stokes, and the highest total conversion efficiency was equal to 26%. The first Stokes maximum output energy was as high as 0.15 J at the pump energy density of about 8 J cm^{-2}, which was close to the surface damage threshold. For the $Pb(NO_3)_2$ crystal, the SRS thresholds were approximately double, while the maximum conversion efficiency was lower by about 20%, and the first Stokes output of about 70 mJ was reached at the pump density of 6–7 J cm^{-2}, starting the bulk damage of the sample. The $NaNO_3$ and $CaCO_3$ crystals showed even higher SRS thresholds of about 4–5 J cm^{-2} and also had a higher laser damage threshold of 14 J cm^{-2}. The output energies were measured to be 0.15 J with a conversion efficiency of 17% for $NaNO_3$ and 0.12 J with 14% efficiency for $CaCO_3$. Thus, by the first and second Stokes frequency shifts of 1045–1085 cm^{-1}, all these crystals can provide highly efficient yellow (560 nm) and orange (598 nm) visible radiation, but the best performance was shown by the $Ba(NO_3)_2$ crystal.

Raman lasers based on the $Ba(NO_3)_2$, $NaNO_3$ and $CaCO_3$ crystals under external pumping by nanosecond (t_p = 10 ns) 532 nm radiation were studied in Ref. [10]. In a 26-cm long flat resonator with the reflection coefficients of mirrors R1 ≈ 100% and R2 = 8%, the threshold pump densities were equal to 5–7 MW cm^{-2} for nitrate crystals and 20 MW cm^{-2} for calcites (the crystals were 5–8 cm long). These data correlate well with the directly measured SRS gain coefficients: $g_{Ba(NO_3)_2} = 47 \pm 5$ cm GW^{-1}, $g_{CaCO_3} = 13 \pm 3$ cm GW^{-1} and $g_{NaNO_3} = 47 \pm 5$ cm GW^{-1}.

At a pump density exceeding the threshold by fivefold, the efficiency of the pump conversion to all the Stokes components reached a maximum of 50%–65%. Since the variations in R2 from 4% to 20% did not change the conversion efficiency, the exit face of the Raman crystal can be used instead of the output mirror. The maximum conversion efficiency in the $Ba(NO_3)_2$ crystal was 40% for the first Stokes component and 25% for the second Stokes component at single-pass pumping. It was shown that an increase in the number of pump beam passes in the cavity resulted in a better selection and an increase in the conversion efficiency (up to 50% for the first Stokes component at two-pass pumping). The second Stokes component in a flat and unstable resonator can be efficiently suppressed by the on-coming pumping.

Visible SRS lasers with a much higher repetition rate were studied in Ref. [25]. The authors for the first time obtained

SRS conversion under copper vapour laser pumping with a repetition rate of 16 kHz and a mean power of 1.9 W at a wavelength of 510.6 nm and 1.8 W at 578.2 nm. The beam divergence of the copper vapour laser was rather low, 2×10^{-4} rad, and the pulse duration was short, 14 ns. In a $Ba(NO_3)_2$ crystal 5 cm long, the SRS radiation at $\lambda_{Stokes} = 539.4$ nm had a power of 600 mW and a conversion efficiency of 38%, and the radiation at $\lambda_{Stokes} = 615.4$ nm was obtained with a power of 300 mW and a conversion efficiency of 18%. Using monochromatic pumping, the yellow band had a higher SRS threshold than the green band, which correlates with the spectral dependence of the gain coefficient. Using biharmonic pumping, the yellow band SRS threshold was reduced to that of the green band. The summed efficiency of the high order (second and third) Stokes components did not exceed 2%–3%. The power of the backward SRS radiation was fourfold weaker than the power of the direct SRS. The authors observed thermally induced birefringence and offered methods to eliminate it. It was supposed that additional Stokes losses appear due to non-linear absorption. The life of the SRS crystals before laser damage was found to depend on the quality and purity of the chemical reagents used for the synthesis of $Ba(NO_3)_2$ crystals. By summing the pump and SRS frequencies in the KDP and DKDP crystals, ten lines of UV radiation were obtained in the region 203–308 nm with a mean power of 1–80 mW.

Airborne or space-based LIDAR transmitters with two UV on-line and off-line outputs for ozone measurements can be developed on the basis of a $Ba(NO_3)_2$ Raman laser emitting the first (563 nm) and second (599 nm) Stokes frequencies under 532 nm pumping, with the following frequency doubling to 281 and 299 nm. This approach was proposed in Ref. [26]. The authors used a compact frequency-doubled Q-switched Nd:YAG laser with a pulse duration of 8 ns and a repetition rate of up to 30 Hz. The $Ba(NO_3)_2$ crystal 5 cm long was placed in a separate 15 cm Raman cavity, consisting of a flat high-reflecting end mirror and a 10 m radius concave output coupler. With a small pump beam spot diameter (1 mm), a pump energy of 10–30 mJ and a pump flux of 1–4 J cm^{-2}, the output energy for the first and second Stokes frequencies was up to 6–8 mJ with a conversion efficiency of 20%–30%. There was only a small difference in the characteristics for the 1 and 10 Hz repetition rates. For a higher pump energy (20–70 mJ) and larger pump spot diameter (2.5 mm), at half the flux and with an optimized output coupler, first and second Stokes radiation with a power, respectively, of 25 and 32 mJ was obtained with a high conversion efficiency of 40%–48%. The total conversion efficiency into the two Stokes frequencies was more than 65% at the repetition rate of 30 Hz.

Amplification of 563 nm laser radiation using a barium nitrate Raman oscillator/amplifier was measured in Ref. [27]. As the pump source, the authors used the second harmonic ($\lambda = 532$ nm) of an Nd:YAG laser with a pulse duration of 5–7 ns and a beam diameter of 1.8 mm. The dependence of the amplified first Stokes energy on the pump energy (5–25 µJ) was measured for the two seed energies (2 and 35 µJ) of the first Stokes beam. In both cases, the output energy was virtually the same and reached 3.5 mJ. Hence, the experiments demonstrated a high, from 100 to 1600, Raman gain of the single-pass $Ba(NO_3)_2$ Raman amplifier.

The experiments described here demonstrate the excellent performance of $Ba(NO_3)_2$ crystals as SRS materials for visible-frequency Raman shifting at nanosecond pumping of high peak power (the steady-state regime of SRS).

Transient SRS in $Ba(NO_3)_2$ crystals was first studied in Ref. [28] under pumping by 532 nm second-harmonic radiation of an Nd:YAG laser. The pump pulse duration was about 22±2 ps, which is less than the dephasing (transverse) relaxation time T_2 (= 28 ps) of internal symmetrical vibrations of quasi-molecular $(NO_3)^-$ complexes of $Ba(NO_3)_2$ crystals. In the single-pass scheme, SRS threshold intensities of $Ba(NO_3)_2$ crystals 50 and 40 mm long were estimated to be 1.1 and 1.45 GW cm^{-2}, respectively, which are much higher than for the steady-state nanosecond oscillation regime. This corresponds to an approximately tenfold decrease in the picosecond Raman gain in comparison with steady nanosecond pumping. It should be noted that the overall conversion efficiency of a $Ba(NO_3)_2$ crystal at a pump density of 2 GW cm^{-2} was 25% for the first Stokes Raman shifting ($\lambda_{IST} = 563$ nm) and 5% for the second Stokes ($\lambda_{IIST} = 599$ nm).

These data, restrict the application of $Ba(NO_3)_2$ crystals for picosecond SRS, especially in the infrared spectral region.

9.4 Infrared SRS Shifters and Raman Lasers Based on $Ba(NO_3)_2$

Solid-state Raman lasers, discretely or continuously tunable, are of special importance for the IR spectral region, where no dye lasers with high quantum yield and good photo and thermal stability exist and only a few IR bands are covered by available tunable solid-state lasers based on impurity-doped and radiatively coloured crystals.

At the same time, SRS becomes a much more complicated problem when moving to the IR spectral region, because the SRS gain cross section decreases with an increase in the pump wavelength. For example, the $Ba(NO_3)_2$ crystal has $g = 47$ cm GW^{-1} for $\lambda = 532$ nm and $g = 11$ cm GW^{-1} for $\lambda = 1064$ nm [12,13].

By the early 1980s, unique tunable lasers for the near-IR range were developed by employing LiF crystals with F_2^- and F_2^+ colour centres [29–31]. These lasers were tunable in the 0.82–1.28 µm IR region. To extend the tuning range further into the IR region, new SRS-active crystals, $Ba(NO_3)_2$ and $KGd(WO_4)_2$, were offered [32]. The investigations described in Refs. [32–34] have shown that $Ba(NO_3)_2$ crystals operate advantageously in the near-IR range up to 1.7 µm with efficiencies as high as 60% under nanosecond pumping, with power densities well below the laser damage threshold. Further extension into the IR is restricted by $Ba(NO_3)_2$ fundamental absorption beginning at approximately 1.8 µm. The $KGd(WO_4)_2$ crystals have a much wider transparency region, up to 5 µm, and also can convert the IR radiation to the Stokes region, but the four times smaller steady-state gain coefficient and low laser radiation resistance restrain their application in nanosecond lasers.

The development of SRS shifters based on $Ba(NO_3)_2$ crystals enabled the spectral range of tunable solid-state lasers to be extended to the 1.3–1.7 μm IR region and, as a result, to develop a solid-state laser spectrometer for a very wide near-IR region (from 0.82 to 1.7 μm). This spectrometer also covered the visible (0.42–0.82 μm) and UV (0.25–0.45 μm) regions by using the second and higher harmonics of tunable IR radiation [31–34]. It was the first all-solid-state laser spectrometer operating in all the three spectral regions—UV, visible and IR.

Interest in SRS lasers was rekindled in the early 1990s, when solid-state lasers based on impurity-doped crystals found so many applications that there was a need to prevent the human eye from being hurt by a laser beam. The laser wavelength determined to be safe for the human eye was standardized to be $\lambda = 1.54$ μm and the radiation of the majority of lasers was found to be in the prohibited wavelength area with $\lambda < 1.5$ μm (as an example, Nd:YAG laser crystals operate at 0.53, 1.06 and 1.32 μm, ruby at 0.69 μm, alexandrite at around 0.78 μm and Ti:sapphire at 0.7–1.1 μm). In this respect, the development of SRS frequency shifters for laser radiation available at the eye-safe wavelength of 1.54 μm is of great importance.

The small atmospheric absorption and the high transmittance of fibres at this wavelength also allow wide applications in such devices as LIDARs, free-space communication and fibre links.

One of the simplest and most effective ways to obtain 1.54 μm radiation was proposed in 1993–1994 in Refs. [35–42], where a $Ba(NO_3)_2$ Raman laser was pumped by the 1.064 and 1.320 μm radiation of a Q-switched neodymium laser. Under 1064 nm nanosecond pumping, a $Ba(NO_3)_2$ crystal 30–50 mm long in a compact cavity with dichroic mirrors, specifically designed for optimum lasing of the first, second and third Stokes waves, produced a single-mode radiation at new, including eye-safe, wavelengths (1.2–1.4 μm and 1.5–1.6 μm), with a light-to-light conversion efficiency of 20%–50% [35–38].

Application of a single-pass $Ba(NO_3)_2$ SRS converter in combination with an amplifier on an LiF crystal with F_2^- colour centres is described in Ref. [43]. In this work, a SRS converter produced a weak (with an efficiency of 1%) nanosecond signal of the first Stokes component at 1197 nm, which was then amplified in an LiF: F_2^-crystal 12 cm long. The same Nd:YAG laser with an energy of 60 mJ and a pulse duration of 12 ns at 1064 nm, used as the pump source for the converter and amplifier, and a good spectral overlap of the generation and amplification regions provided a high total efficiency for the system, of up to 35% from the pump energy. No beam focusing to the SRS crystal was used and the second Stokes component was completely absent. In the intracavity pumping scheme, when both the SRS and LiF: F_2^- crystals were placed inside the Nd:YAG cavity, the conversion efficiency was improved by up to 50% [44]. When the Nd:YAG crystal was replaced with Nd:YAP, a conversion efficiency of 50% was recorded for frequency shifting in both the pump (1078 nm) and first Stokes (1216 nm) radiation. Using a KGW:Nd crystal in the same cavity, operating both as the active laser and SRS element, the authors [43] had the first Stokes radiation at 1180 nm with an efficiency of 50%. The oscillation train contained 1–15 pulses with an energy of 45–10 mJ, each depending on the initial transmittance of the LiF: F_2^- crystal, which worked as the passive Q-switch, converter to the first Stokes radiation and amplifier.

The 1.320-μm nanosecond intracavity pumping of a $Ba(NO_3)_2$ crystal, when the pump and Raman laser had one common cavity or two optically coupled cavities, enabled the conversion efficiency to the first Stokes frequency at 1.5 μm to be increased up to 90% [39–42]. In this case, the effect of non-linear cavity dumping makes it possible to shorten the pump pulse a few times and to increase the peak power. An important additional advantage of SRS lasers is that their output beam can have a much better spatial quality and smaller beam divergence (‘beam clean-up’) and, hence, higher brightness than the pump beam [36–38,45].

A diffraction-limited high-energy (0.25 J) eye-safe Raman laser with wavelengths of 1535 and 1560 nm was developed in 1995 [46,47] when an intracavity $Ba(NO_3)_2$ crystal was pumped by a high-power nanosecond Nd:YAG laser operating at 1.318–1.338 μm. The two standing-wave resonators, a pump cavity 69 cm long and a Raman cavity 20 cm long were coupled by a dichroic beamsplitter. Using a 50-mm uncoated $Ba(NO_3)_2$ crystal, the authors [46,47] had 12 mJ of Raman laser output with 48% conversion efficiency at a pump power of 25 mJ. The SRS pulse was about half that of the 10 ns pump pulse. Non-linear Raman beam clean-up was observed in the near and far fields of the 1.5 μm beam profile. The second Stokes radiation at 1.820–1.860 μm was generated through a cascaded SRS process. In an enhanced (more powerful) system with an Nd:YAG rod Ø7 × 110 mm and two flashlamp pump cavities, the output diffraction-limited eye-safe radiation had a power of 0.25 J at a repetition rate of 1 Hz. The repetition rate was limited by the thermal effects due to the low thermal conductivity of $Ba(NO_3)_2$ crystals.

The optical scheme and characteristics of a typical eye-safe Raman laser with increased pulse repetition rate are shown in Figure 9.1.

An attempt to develop 20 Hz eye-safe cascaded Raman lasers on $Ba(NO_3)_2$ crystals with 140 mJ, 1064 nm Nd:YAG laser pumping was done in Ref. [48]. The authors used an external pumping scheme with a 50-mm long $Ba(NO_3)_2$ crystal placed in a 20-cm, flat-mirror Raman laser cavity. In the double-pass pumping scheme with an output coupling of $T = 82\%$, they obtained a threshold energy of 50 mJ (1.3 J cm^{-2}) and an SRS output energy of 28 mJ for the first Stokes radiation at $\lambda = 1197$ nm. For the second Stokes 1369 nm laser cavity with an output coupler transmission of $T = 62\%$, the output energy was 27 mJ. Using highly reflecting mirrors for the first and second Stokes wavelengths and the output coupler for the third Stokes with $T = 71\%$, the authors had 8.5 mJ of the third Stokes radiation at the eye-safe wavelength of 1.598 μm. The pulsewidth decreased from 30 ns of the pump pulse to 11 ns for the first and to 9.5 ns for the third Stokes. Substantial energy drops of 7%, 46% and 76% for the first, second and third Stokes, respectively, were observed due to the thermal load increasing in the $Ba(NO_3)_2$ crystal at a repetition rate of 20 Hz and a pump energy of 140 mJ.

To develop a marine-based LIDAR laser transmitter, operating around 580 nm, for the very turbid water of a surf zone, the authors of Ref. [49] have studied and optimized a $Ba(NO_3)_2$ SRS laser with intracavity pumping by an Nd:YLF laser and

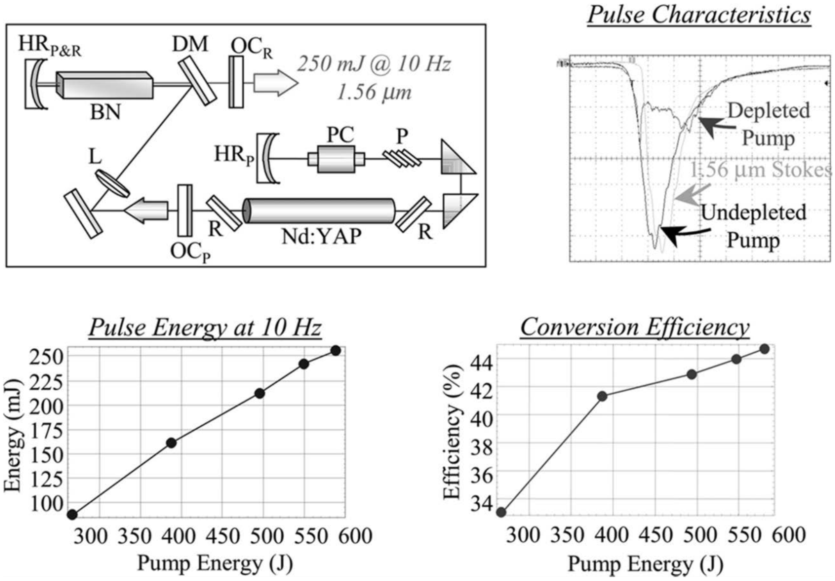

FIGURE 9.1 Optical scheme and typical characteristics of an eye-safe solid-state Raman laser. (Data provided by J M Murray and W Austin, Lite Cycles, Inc.)

with second-harmonic generation by an LBO crystal. With an Nd:YAG rod ø7× 76 mm and a T-shaped high-Q pump laser cavity coupled with a low-Q Raman cavity (400 and 85 mm in length, respectively), the authors of Ref. [49] realized non-linear cavity-damping regimes. They used a 20-mm long MgF_2 AR-coated $Ba(NO_3)_2$ SRS crystal and a Raman cavity output coupler with $R = 25\%$. With 50 J of flashlamp pump energy and 10 Hz, the maximum output for a Raman wavelength of 1176 nm was 150 mJ, which was transferred into 90 mJ of yellow (588 nm) radiation by the LBO (type I) crystal 12 mm long. To stop pulse modulation and frequency cascading, the authors included a prism in the Raman cavity. In this case, they had 1.5-ns pulsed radiation at 588 nm wavelength, which is well suited for coastal water LIDAR applications.

Application of a single-mode, single-frequency Nd:YAG laser with very high spectral and spatial brightness as a pump source allowed an average output power of 4.7 W to be reached by a $Ba(NO_3)_2$ Raman laser under 33 W pump power, which corresponds to a slope efficiency of about 19% (see Figure 9.2) [33]. Simultaneously, the second Stokes radiation was observed with a power of 0.4 W at a slope efficiency of 2.1%. The pump laser beam produced five-pulse trains with a repetition rate of 30 Hz. The train energy was 1.1 J at a pulse energy of 0.22 J and a peak power of 4.4 MW. The laser beam in the $Ba(NO_3)_2$ crystal was 2 mm in diameter. The Raman laser cavity 6.5 cm long was formed by flat mirrors: the first mirror had a high transmission for the pump wavelength and high reflection for the first Stokes radiation, while the output coupler had a reflectivity of 77% for 1.064 nm and 35% for the first Stokes radiation.

At the lower repetition rate of 10 Hz and a single-pulse train, the maximum conversion efficiency to the first Stokes radiation was 35% and the maximum output energy reached was 30 mJ. At the same time, the second Stokes energy was as high as 16 mJ with an efficiency of about 10%.

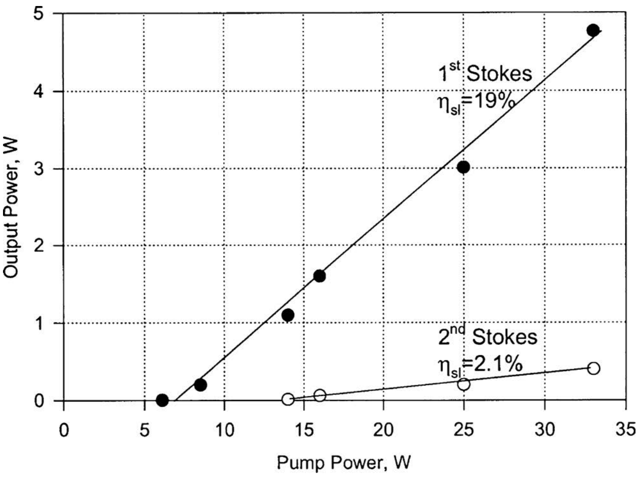

FIGURE 9.2 Pump-to-output average power dependences for the first and second Stokes radiation of $Ba(NO_3)_2$ Raman lasers under 1064 nm high-power Nd:YAG pumping.

9.5 IR-Pumped $LiIO_3$ Raman Laser

The $LiIO_3$ crystalline Raman laser operating in the IR region at a high repetition rate was first described in Refs. [50,51]. The pumping Nd:YAG laser operated in a quasi-continuous-wave (cw) mode at 1080 nm with a repetition rate of 1–10 kHz and a pulse duration of 100 ns. In a shared two-mirror cavity with a $LiIO_3$ SRS crystal 25 mm long, cut at $\theta \approx 20.5°$, the first Stokes radiation (the Raman shift $\nu_R = 818\,\text{cm}^{-1}$) had an average output power of 1.26 W and a pulse duration of 50 ns. In a separate experiment, a second Stokes radiation of 1310 nm was obtained with a power of 0.55 W and a pulse duration of 15 ns [50].

Using a three-mirror coupled cavity, the author of Ref. [51] had a strong pulse shortening, $t_{p(1St)}$ = 4–8 ns with an average output power of 0.9 W, a peak power of 7 kW and a conversion efficiency of 77%. After optimization, the second Stokes pulse duration was even shorter, $t_{p(2St)}$ = 2 ns with an average power of 0.2 W and a peak power of 100 kW.

A picosecond Raman laser on a $LiIO_3$ SRS crystal was studied in Ref. [52]. The authors used a Y-cut lithium iodate crystal 10 mm long and, as the source of synchronous pumping, a self-mode-locked neodymium phosphate glass laser operating at $\lambda = 1054$ nm. The pump pulses had a duration of 6–10 ps at an axial interval of 6.7 ns and the duration of the train envelope was about 200 ns.

A Raman laser cavity 1 m long was formed by an entrance edge mirror with $R_{1.05\mu} = 25\%$ and $R_{1.14c} = 98\%$, an output mirror with $R_{(1.05\mu,1.14\mu)} = 50\%$ and a two-lens intracavity telescope with a $LiIO_3$ crystal in between. The first Stokes component was observed at 1.143 μm with a frequency shift of 760 cm^{-1}. In the vicinity of the SRS threshold (1 mJ), the output train consisted of 25 pulses and had a total duration of 170 ns. Varying the Raman cavity length, the authors found that the maximum shortening (by a factor of 7–8) of the SRS pulses in comparison with the pump pulses occurs when the Raman cavity length is equal to the length of the pump cavity. The minimum SRS pulse duration was 1 ps at an energy conversion efficiency of 30%. The maximum conversion efficiency reached 40%.

A series of studies [53–58] have been devoted to the practical development of Raman lasers based on the $LiIO_3$ crystal, operating in the yellow spectral region at a wavelength of around 580 nm, which is efficiently absorbed by haemoglobin and only slightly absorbed by the melanin of human skin.

With flashlamp quasi-cw (3 kHz) Nd:YAG intracavity pumping, the authors of Ref. [53] obtained a 770-cm^{-1} Raman frequency shift and a first Stokes radiation at the wavelength of 1179 nm with an average power of 1.8 W, a pulse duration of 40 ns and a conversion efficiency of 50%. After frequency doubling in an LBO crystal, the radiation had a wavelength of 580 nm and an average power of 550 mW. By using a transversely diode-pumped Nd:YAG laser, the authors [54–56] reached a power of 2.7 W for the first Stokes output radiation at 1155 nm with an electrical-to-optical efficiency of 10%. The second-harmonic output power at 577 nm was 0.96–1.2 W at a repetition rate of 7–10 kHz, a pulse duration of 8 ns and an overall electrical-to-optical efficiency of 13%. The thermal lensing in the intracavity-pumped $LiIO_3$ Raman laser was measured in Ref. [55] under excitation by a cw lamp-pumped, acousto-optically Q-switched Nd:YAG laser operated at 1064 nm by 200 ns pulses with a typical power of 2.7 kW and a repetition rate of 3 kHz. The intracavity-pumped $LiIO_3$ crystal oscillated in the same cavity with an average power of 1 W at 1157 nm. The power of the negative thermal lens in the $LiIO_3$ crystal was observed to be linearly dependent on the first Stokes average power with a slope of $-4.2\, m^{-1}\, W^{-1}$ and almost independent of the output coupler reflectivity R = 25%–50%. Longitudinal diode pumping of the Nd:YAG-$LiIO_3$ Raman laser and optimization of the thermal lensing resulted in an increase in the output average power of yellow radiation to 1.42 W at 20 ns pulse duration and an 8 kHz repetition rate with an electrical-to-optical efficiency of 7.5% [57].

Among the limitations and shortcomings of the $LiIO_3$ SRS crystal, we should mention its low thermal conductivity, moisture resistance and laser damage threshold.

9.6 Picosecond Raman Frequency Shifters Based on KGW ($KGd(WO_4)_2$) Crystals

A specific feature of picosecond Raman converters is that they cannot successfully work in a compact cavity a few cm long, which is the order of a Raman crystal length. In addition, SRS has a non-stationary character when the pump pulse duration is less than or equal to the time of phase relaxation of the Raman oscillation ($t_p \leq 10T_R$). At the same time, the laser damage threshold of non-linear crystals is much higher when the crystal is irradiated by picosecond laser pulses than by nanosecond ones, i.e. the picosecond operation mode allows pumping with a higher power density without crystal damage. As was shown earlier, with non-stationary pumping, the Raman gain coefficient sharply decreases in comparison with the steady-state regime, loses its dependence on the scattering peak cross section and pump power and keeps only the slow square root dependence on the integral Raman scattering cross section and picosecond pump pulse energy density.

The first results on SRS in Nd:$KY(WO_4)_2$ (Nd:KYW) and Nd:$KGd(WO_4)_2$ (Nd:KGW) crystals were obtained during 1984–85 [58] under picosecond pumping. At the same time, it was also the first study where the Raman material worked simultaneously both as an active and non-linear material.

At about 20 J flashlamp pump energy, active elements 5 mm in diameter and 50 mm long oscillated at the fundamental Nd^{3+} wavelength of 1067 nm in a single-mode regime, producing a train of about 10 ultrashort pulses, each having a duration of 11–12 ps, at a spectral width of 1.8 cm^{-1} and an energy of 0.5 mJ. The efficiency of stimulated Raman self-conversion to the first Stokes component (λ = 1182.7 nm) for a single picosecond pulse from the beginning of the train was 6.14% of the total energy and reached 35% in the middle of the train. In the case when two Nd:KYW crystals were used (one as the lasing and self-converting Raman master oscillator and the second as the synchronously laser-pumped Raman amplifier (without flashlamp pumping)), the authors had a maximum conversion efficiency $\eta_{1St} = 37\%$ to the first Stokes, $\eta_{2St} = 16\%$ to the second Stokes (λ_{2St} = 1323.7 nm) and $\eta_{aS} < 5\%$ to the anti-Stokes (λ_{aS} = 947.9 nm). When the Nd:KYW amplifier was additionally pumped by 30 J of flashlamp radiation, the total output energy increased to 11 mJ. For the two Nd:KGW crystals 50 mm long used in one laser cavity, the conversion efficiency of the whole train to the Raman scattering radiation was not so high, $\eta_{1St} = 3.84\%$ (λ_{1St} = 1180.5 nm), probably due to the quality of the crystals, and was improved with an SRS amplifier to $\eta_{1St} = 16.58\%$, $\eta_{2St} = 0.96\%$ and $\eta_{aS} = 0.03\%$.

The authors also briefly mentioned an oscillation observed in Nd:$K(MoO_4)_2$ and Nd:$NaLa(MoO_4)_2$ crystals. The pulse duration at the fundamental wavelength was 5–6 ps and, at the first Stokes component, 1.5–2.5 ps, with a conversion efficiency of $\eta_{1St} = 40\%$.

Almost simultaneously with [58], intracavity SRS generation from Nd:KGd(WO$_4$)$_2$ crystals was reported in Ref. [59]. The authors studied the frequency doubling of the picosecond radiation of an Nd:KGW laser with passive mode-locking. New radiation wavelengths of 1180 and 1320 nm were found, corresponding, respectively, to the first and second Stokes components of the SRS conversion of the Nd^{3+} fundamental wavelength (1067 nm) in an Nd:KGW crystal with a frequency shift of $900 \pm 10\,\text{cm}^{-1}$. This was verified by the SRS radiation from an Nd:KGW crystal that was placed in the picosecond Nd:YAG laser cavity and was not flashlamp pumped. Estimates of the SRS conversion efficiency showed that only 10% of the total energy belonged to the 1180 nm radiation and the other 90% falls to the 1067 nm radiation. The SRS pulse duration was 3.8 ± 0.4 ps, which was considerably shorter, by a factor of 2.5, than the pump pulse.

The SRS of undoped KGW crystals with different orientations in an external pumping scheme under 30 ps Nd:YAG laser pumping was studied later in Ref. [60]. In the 1.06–1.32 μm spectral region, the SRS radiation from 12 new spectral lines with different combinations of Stokes shifts of 84, 767 and 901.5 cm^{-1} was recorded. The normalized thresholds and gain coefficients for different polarization orientations were measured. The maximum gain coefficients were measured to be 6.4 cm GW^{-1} for the 901.5 cm^{-1} Stokes frequency shift and 4.3 cm GW^{-1} for 767 cm^{-1}. With increasing pump density, the SRS radiation of the higher Stokes components, up to the fourth component with a wavelength $\lambda_{4\text{St}} = 1730\,\text{nm}$, was recorded.

The SRS pulse compression in Nd:KGW and Nd:KYW picosecond lasers was especially investigated in Ref. [61,62]. In a cavity 1.3 m long formed by the back dichroic mirror with $R_{1064\,\text{nm}} = 99.94\%$ and $R_{1180\,\text{nm}} = 72.6\%$ and by a glass plate as the output coupler, the first Stokes radiation comprised 22%–40% of the pump pulse energy at the middle of the pulse train, the first Stokes pulse duration was as short as $t_{1\text{St}} = 1.3$ ps, and the pump pulse duration was also shortened to 3.9 ps. Application of the SRS amplifier on an Nd:KGW crystal with a synchronous laser pumping in a passive regime (without flashlamp pumping of the Nd^{3+} ions) allowed the authors to shorten the Stokes pulse to a minimum value of 0.9 ps and increase the conversion efficiency to above 40%. With active amplifying, the Stokes pulse duration grew continuously from 1.1 to 6 ps as the energy of the Nd:KGW amplifier pumping E_p increased from 25 to 80 J. The duration of the Nd laser fundamental radiation pulse decreased from 10 to 4.4 ps.

A detailed review of the KGW crystal structure, lattice cell parameters, atomic positions and coordinates and interatomic distances can be found in Refs. [63,64]. A spectroscopic study of spontaneous and SRS in KGW crystals with different orientations of the pump beam direction and polarization with respect to the crystallographic axes was also presented. The Stokes components of the SRS, from the first (1162.2 nm) to the fourth (1734.8 nm) ones, were observed under pumping by 1064 nm radiation from an Nd:YAG laser with a pulse duration of 30 ps. The threshold power was 4.8–24.3 GW cm^{-2}. The threshold pump density for the KGW first Stokes with shifts of 767 and 901.5 cm^{-1} was measured for different orientations and compared with those measured for CaWO$_4$ and Ba(NO$_3$)$_2$ crystals. The normalized SRS threshold for KGW was measured to be from 3.9 to 14.8 GW cm^{-2} depending on the crystal orientation, which was much less than 23–25 GW cm^{-2} for CaWO$_4$ crystals. The SRS threshold pump density measured for Ba(NO$_3$)$_2$ crystals of 6.2 GW cm^{-2} is much less than that for CaWO$_4$ but higher than the minimum value for KGW at the optimum orientation.

The non-stationary gain coefficient calculated from the measured thresholds turned out to be minimal for the CaWO$_4$ crystals (g = 1–1.1 cm GW^{-1}), four times higher than for the Ba(NO$_3$)$_2$ crystals (g = 4 cm GW^{-1}) and the highest for KGW crystals for the optimal orientation *p[mm]p* (g = 6.4 cm GW^{-1} for the 901.5 cm^{-1} Stokes shift). For the KGW Stokes shift of 767 cm^{-1} and the orientation *q[pp]q*, this value was g = 5.2 cm^{-1}. These data on KGW and KYW Raman lasing properties demonstrate the very efficient operation of these crystals in the pico- and sub-picosecond regimes of oscillation, where high-density pumping (1–10 GW cm^{-2}) can be used without radiation damage to the crystal. These crystals demonstrate multi-wavelength frequency shifts of coherent radiation to the hard-to-reach IR region from 1 to 1.7 μm with a high conversion efficiency (about 40%) and a very effective radiation pulse shortening (more than ten times) to femtosecond durations.

The compression of pump laser pulses by backward SRS in KGW crystals has been studied in Ref. [65]. The KGW crystals were pumped by 19 ps pulses of 532 nm radiation. At the optimized focusing conditions (a focusing angle of 75 mrad) and pumping exceeding the SRS threshold by two to three times, the authors obtained the 555 nm radiation of the first Stokes component with a total conversion efficiency of about 30% with an output pulse duration of 1.6–1.7 ps, which corresponds to the high, by a factor of 11–12, compression of 3–5 μJ pump pulses to 1 μJ output pulses.

9.7 Nanosecond Raman Lasers Based on KGW Crystals

The main problem associated with the use of KGW crystals as Raman shifters for nanosecond IR laser radiation is a rather high SRS threshold (due to the low Raman gain) in combination with a low laser damage threshold for nanosecond pumping. The narrow gap between the SRS and laser damage thresholds essentially restricts the SRS conversion efficiency and imposes strong requirements upon the pump radiation profile and the optical quality of the crystal and all the elements of the Raman cavity.

The first paper in which the authors succeeded in realizing nanosecond intracavity SRS generation with an Nd:KGW crystal was [66]. The pulse duration of the fundamental radiation was t_p = 7.5 ns and the duration of the first Stokes pulse at 1180 nm was measured to be threefold shorter, t_SRS = 2.5 ns. The intracavity SRS threshold was estimated to be 150–300 MW cm^{-2}. However, no data on the conversion efficiency and output energy were reported.

Nanosecond SRS in KGW crystal in a single-pass scheme with external pumping was also studied in Refs. [67,68]. The SRS gain coefficients for both Stokes shifts of 901.5 and

767.3 cm^{-1} were found to be 6 cm GW^{-1} when pumped by an Nd:YAG laser with a radiation wavelength of 1064 nm. For nanosecond (t_p = 10 ns) pumping by an Nd:KGW laser in a single-pass scheme, the total efficiency of SRS conversion to both (first and second) Stokes was 70% with an output energy of 10 mJ. These results did not depend on whether the Stokes shift frequency was 767.3 or 901.5 cm^{-1}.

Application of KGW crystals for SRS frequency shifting of nanosecond radiation with longer wavelengths, 1.1–1.4 μm, where the gain coefficient is much weaker, was first demonstrated in Ref. [32]. A KGW crystal 40 mm long was used for tunable nanosecond SRS frequency conversion of a solid-state colour-centre laser MALSAN-201. Using the single-pass Raman shifting scheme with a pump pulse duration of 8 ns, an energy of about 20 mJ and a spectral width of 0.1 cm^{-1}, the authors observed the tunable radiation in new spectral regions, 1.23–1.37 μm (first Stokes) and 1.43–1.6 μm (second Stokes). The LiF : F_2^- colour-centre laser radiation was tunable from 1.1 to 1.23 μm with a pump density of about 1 GW cm^{-2}. The maximum conversion efficiency reached 30% for the first Stokes radiation and 20% for the second. These results were among the first experiments on solid-state Raman lasers operated in the eye-safe spectral region (1.54 μm). It should be noted that the laser damage threshold was only two to three times higher than the SRS threshold, which strongly limited the reported operation.

Ten years later, a compact flashlamp-pumped solid-state laser for a range finder operating in the eye-safe spectral region at 1538 nm was developed in Refs. [68,69] with the application of SRS in an Nd:KGW active crystal self-pumped by 1350-nm (the fundamental wavelength) Nd^{3+} laser radiation. The authors used the Nd:KGW active non-linear elements with dimensions of Ø3 × 50 mm and Ø4 × 65 mm. The cavity mirrors had the reflectivity $R1 = R2 = 99.99\%$ at the fundamental wavelength of 1351 nm and the exit mirror has a 35%–40% reflectivity at the first Stokes wavelength of 1538 nm. Passive polymer and electro-optical LiNbO$_3$ Q-switches were used.

In the case of an Nd:KGW crystal with small dimensions, Ø3 × 50 mm, the threshold pump energy of the single-pulse mode changed from 2.5 to 5.5 J and the energy of the 40 ns SRS pulse increased from 1 to 6 mJ, as the passive Q-switch transmission changed from 45% to 33%. The KGW crystal with dimensions of Ø4 × 65 mm allowed an increase in the output energy to 9 mJ at the pump energy of 7.5 J. With electro-optical Q-switching by a Brewster-cut LiNbO$_3$ crystal, the output energy of the 12 ns pulses reached 13.5–15 mJ at a pump energy of 10 J. The overall efficiency was quite high—0.15%.

Using diode laser pumping of Nd-doped laser crystals, one can build compact and efficient solid-state lasers for IR and green spectral regions. A transversely diode-pumped Nd:KGd(WO$_4$)$_2$ Raman laser with self-frequency conversion is described in Ref. [70]. An AlGaAs/GaAs quasi-cw diode laser operating at 808 nm with a power of 300 W and a pulse duration of 300 μs was used for side pumping an Nd:KGd(WO$_4$)$_2$ crystal rod 4 mm in diameter and 22 mm in length. The plano-concave Raman laser cavity with an acousto-optical Q-switch inside had a high reflectivity for the fundamental wavelength (1067 nm) and an output coupler transmission of 5% for the first Stokes wavelength (1162 nm). As a result, the first Stokes pulsed radiation had an energy of 0.1 mJ for a pulse duration of 50 ns, while the pump pulse duration was 140 ns with a repetition rate of 47 Hz. The second-harmonic radiation (581 nm) was generated with a 30% efficiency by a LiB$_3$O$_5$ crystal with non-critical phase matching at a temperature of 54°C. The second-harmonic pulses were threefold shortened to 16 ns.

Intracavity self-frequency conversion in a microchip composed from Yb:KGW and Yb:KYW crystals was reported by two groups of authors [71,72]. They used 1.7 and 1.1-mm thick plates of Yb-doped laser crystals, pumped by a 980 nm laser diode and a Cr^{4+}:YAG plate as the saturable absorber. With an output coupler reflectivity of 7% and 5%, the authors obtained nanosecond pulses of the first Stokes radiation at a wavelength of 1139 nm with an average power of 7 and 2 mW and a repetition rate of 17 and 49 kHz, respectively.

This historical review of the best SRS materials for nano- and picosecond Raman lasers shows that, up until the mid-1990s, there was no clear understanding as to why one SRS material is better for nanosecond operation and another operates better in the picosecond regime. There was no complete comparative analysis of the major fundamental properties of SRS materials, which would allow one to select the most suitable materials among the known synthetic crystals or to develop SRS materials with the required properties.

9.8 New BaWO$_4$ SRS Crystals

The newly developed BaWO$_4$ crystals for SRS exhibit many advantages in comparison with the two previously discussed best synthetic crystals, Ba(NO$_3$)$_2$ and KGd(WO$_4$)$_2$ (the characteristics of these crystals are compared in Table 9.1). As one can see, the BaWO$_4$ crystal has a much higher hardness, thermal conductivity and moisture resistance than Ba(NO$_3$)$_2$. The transparency range in the IR is also much wider for BaWO$_4$ than for Ba(NO$_3$)$_2$ crystals. The Raman scattering integral cross section of BaWO$_4$ is at least double, which is important for picosecond application, where BaWO$_4$ can provide a much higher gain than Ba(NO$_3$)$_2$. The extremely small Raman line broadening (0.4 cm^{-1}) in Ba(NO$_3$)$_2$ results in the record high gain in the nanosecond (steady-state) regime of SRS but at the same time restricts the steady-state regime to the picosecond time scale. As the result, the Raman gain of Ba(NO$_3$)$_2$ falls steeply down on shortening the picosecond pulse duration due to the transient character of SRS ($t_p < 10T_R$).

For nanosecond pulses, the BaWO$_4$ crystal exhibits only slightly smaller SRS peak cross sections and gain coefficients than those of Ba(NO$_3$)$_2$ crystals, but, due to the four times larger linewidth (1.6 cm^{-1}) and correspondingly four times shorter dephasing time T_r, its steady-state regime can be extended to the four times shorter laser pulses on the picosecond time scale.

Comparing the BaWO$_4$ crystal with KGd(WO$_4$)$_2$, one can see almost equally high hardness, thermal conductivity, moisture resistance and wide transparency range. The integral cross sections of these two crystals are also quite similar and high. A difference can be found only in the line broadening and the dephasing time. Due to the three times broader Raman line, the KGd(WO$_4$)$_2$ crystals have a much lower nanosecond (steady-state) SRS cross section and gain coefficient than $Ba(NO_3)_2$ and $BaWO_4$ crystals. Even for the picosecond region 10^{-11}–10^{-9} s, the new $BaWO_4$ crystal can show much better SRS operation than $KGd(WO_4)_2$. Only with few-picosecond or sub-picosecond pumping can KGW crystals overcome the $BaWO_4$ crystal in gain and efficiency, due to the deeper transient behaviour and faster gain decrease in $BaWO_4$ in comparison with KGW.

Similar properties are demonstrated by the $SrWO_4$ crystal, whose line broadening and dephasing time lie between those of $BaWO_4$ and KGW crystals and define the intermediate values of $SrWO_4$ SRS cross section and Raman gain, which are better than those for KGW and poorer than for $BaWO_4$ in the nano and picosecond steady-state regime.

9.9 IR $BaWO_4$ and $SrWO_4$ Nanosecond Raman Lasers

IR SRS laser oscillation in the newly developed $BaWO_4$ crystal and two well-known non-linear crystals were comparatively studied in Ref. [24], using a 9-cm long Fabry–Pérot cavity formed by two plane dielectric mirrors, an input mirror with $R_{1.064} < 5\%$ and $R_{1.1-1.25} > 98\%$ and an output mirror with $R_{1.0-1.2} \approx 55\%$.

A pulsed single-mode Nd:YAG laser passively Q-switched by an $LiF:F_2^-$ crystal was used as the pump source. The pump laser operated by 12 ns pulses with a repetition rate of 10 Hz. The pump beam was focused on the centre of an SRS crystal by a lens with a focal length of 50 cm. The beam's focal diameter was measured by a CCD camera to be 90 μm at half maximum. The beam shape was close to Gaussian.

The real Raman laser efficiency reaches 26% for $Ba(NO_3)_2$ and 20.5% for $BaWO_4$. In both cases, the slope efficiency exceeds 75% and the laser thresholds are very close. At the same time, no efficiency saturation is observed for $BaWO_4$ with increasing pump power; hence, one can expect further improvement of the laser characteristics. The best results are obtained at the $BaWO_4$ orientation $E \parallel C_4$ with slightly poorer ones at $E \perp C_4$. An even longer KGW crystal demonstrates a much higher threshold and considerably lower slope efficiency (about 45%) in the same experimental scheme.

The Raman laser efficiency of $SrWO_4$ SRS crystal was studied in Ref. [73] under similar conditions. The laser scheme differed from the one considered earlier by having a shorter cavity (70 mm), lower reflectivity of the output coupler ($R_{1.05-1.32} = 30 \pm 5\%$), twice longer focal length of the focusing lens ($f = 100$ cm) and the focal spot twice larger (Ø = 200 μm).

To prevent coupling between the SRS crystal (without any anti-reflection coatings), the Raman laser cavity and the pump laser cavity, they were misaligned by about 1° from each other.

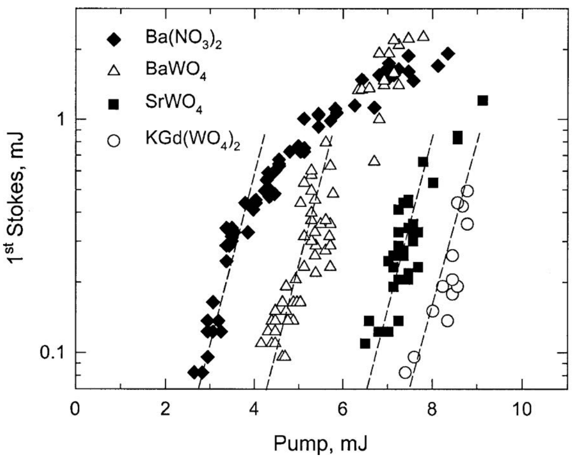

FIGURE 9.3 Dependences of the first Stokes output energy on the pump energy for $Ba(NO_3)_2$ 49-mm long (rhombs), $BaWO_4$ 43-mm long (triangles), $SrWO_4$ 47-mm long (squares) and $KGd(WO_4)_2$ 50-mm long (circles) crystals.

Figure 9.3 shows the Raman laser output energy *versus* the pump energy for the new $SrWO_4$ and $BaWO_4$ crystals in comparison with KGW and $Ba(NO_3)_2$. One can see that the $SrWO_4$ crystal has a lower threshold and an efficiency, which is approximately double (≈ 12%) that of KGW. In spite of poorer threshold, gain and output characteristics of $SrWO_4$ in comparison with those of $BaWO_4$ and $Ba(NO_3)_2$ crystals, the $SrWO_4$ crystal allows rather high levels of rare-earth doping, which makes it promising for many applications as a multi-functional non-linear (SRS) active material.

SRS self-conversion of laser radiation inside an $Nd^{3+}:SrWO_4$ laser crystal was first observed under flashlamp pumping in a Q-switched regime [74]. With high reflectivity cavity mirrors at the fundamental wavelength of 1.06 μm, the first Stokes oscillation at 1.18 μm wavelength was recorded with an output energy of 3 mJ. The first Stokes oscillation of this Raman laser combined two oscillation mechanisms: the broad-band stimulated emission of F_2^- colour centres and SRS inside the laser medium. This combination allowed SRS at lower intracavity energy density, i.e. it reduced the SRS threshold. Under alexandrite laser pumping such intracavity SRS conversion schemes provide the first Stokes radiation with a peak power of 440 kW at a pulse duration of about 3 ns [75].

9.10 $BaWO_4$ Yellow Raman Shifters and Lasers

The yellow SRS in a $BaWO_4$ crystal 33 mm long under green (532 nm) pumping was studied in Ref. [76] in comparison with the $KGd(WO_4)_2$ crystal. The pumping thresholds for different orientations of the beam propagation vector $\boldsymbol{K}$ and polarization vector $\boldsymbol{E}$ in respect to the C_4-axis of the $BaWO_4$ crystal were measured to be 240 (for $\boldsymbol{K} \perp C_4$ and $\boldsymbol{E} \parallel C_4$) and 200 MW cm^{-2} (for $\boldsymbol{K} \perp C_4$ and $\boldsymbol{E} \parallel C_4$). These values are much lower than 340 MW cm^{-2} for the KGW crystal (for $\boldsymbol{K} \perp C_2$ and $\boldsymbol{E} \perp C_2$ and $\boldsymbol{E} \parallel C_2$) and point to a much higher gain in the new $BaWO_4$ crystal for both orientations.

In the single-pass Raman shifting arrangements without laser cavities, the conversion efficiency for the KGW crystal was up to 15% in the first Stokes (λ = 559 nm) and up to 5% in the second Stokes (λ = 589 nm). The conversion efficiency of the $BaWO_4$ crystal was almost double (30%) for the first Stokes (λ = 560 nm) and 6% for the second Stokes (λ = 590 nm) under the same pumping conditions.

In the double-pass scheme [77] with one reflecting back mirror, which increased the length of the light–crystal interaction by a factor of two (to 66 mm), the SRS threshold was equal to 95 MW cm^{-2}, which is half as high as in the single-pass scheme and the conversion efficiency was increased up to 45%.

Measurements of the SRS temporal profile have shown that the SRS pulse is two to three (and more) times shorter than the pump pulse duration when the pump energy exceeded the threshold value by a factor of approximately three. With a 5.1 ns pump pulse, the first Stokes pulse duration was 2 ns and the second Stokes pulse had a duration of 1.5 ns. These measurements show that it is possible to have the Raman frequency shift virtually without loss of peak power.

A pulsed yellow $BaWO_4$ Raman laser operated at a high repetition rate was studied in Ref. [78] under Nd:YLF high-power green (527 nm) pumping. The first (544 nm) and second (583 nm) Stokes radiation were obtained with an output power of 130 and 22 mW at 70% and 50% output coupler reflectivity, respectively. Strong SRS pulse shortening, from 400 to 10 ns, was observed. The slope efficiency for the frequency conversion from the pumping to the first Stokes was measured to be as high as 15%.

9.11 $BaWO_4$ Picosecond Raman Frequency Shifters

A comparative study of picosecond SRS in this new $BaWO_4$ crystal and in $KGd(WO_4)_2$ and $KY(WO_4)_2$ crystals in a single-pass scheme was fulfilled in Refs. [76,79–82] for 28 and 40 ps pulses with wavelengths of 532 and 1064 nm, respectively. With visible green light pumping, the picosecond Raman gain coefficient calculated for the $BaWO_4$ crystals from the pump threshold measurements by the formula $g_{\text{exp}} = 25/I_p l$, was equal to 14.4 cm GW^{-1}, which is 30% higher than that of KGW (11.5 cm GW^{-1}) but 30% lower than that of KYW (18.7 cm GW^{-1}).

In comparison with the steady-state regimes, where the $BaWO_4$ crystals show approximately a three times higher gain than KGW, this ratio at picosecond pumping is moderate, though the $BaWO_4$ still has a higher gain than the KGW crystal. This is caused by the deeper transient behaviour of $BaWO_4$ due to its smaller linewidth and longer T_R (= 6.6 ps).

A much stronger difference can be found when comparing the $BaWO_4$ crystal with $Ba(NO_3)_2$. With nanosecond pumping (steady-state regime), $BaWO_4$ has only a 20%–30% lower Raman gain (40 cm GW^{-1} against 52 cm GW^{-1}) [76,77] but in the picosecond mode, its gain is about three times higher (see Table 9.2).

For 1064 nm picosecond pumping, the $BaWO_4$ Raman gain reaches 3.8 cm GW^{-1}, which is slightly lower than that for KYW (4.7 cm GW^{-1}) but higher than for KGW (3 cm GW^{-1}). The maximum conversion efficiency for a 30-mm long $BaWO_4$ crystal under 532 nm picosecond pumping was 30% for the first Stokes frequency. This is much higher than the 18% efficiency of an even longer (40 mm) KGW crystal. For the second Stokes scattering, both crystals show a similar efficiency of about 15%.

Optimization of the pump-to-output conversion efficiency for the best pumping orientation gives a similar first Stokes (560 nm) efficiency (~50%) for $BaWO_4$ and KGW crystals and the $BaWO_4$ second Stokes (590 nm) efficiency of up to 20% [76].

The study of picosecond SRS temporal behaviour reveals an approximately twofold shortening of the SRS pulse (18 ps) with respect to the pump pulse duration (35 ps). Hence, keeping in mind the 50% conversion efficiency of $BaWO_4$, we can conclude that the efficiency of peak power conversion from green to yellow radiation is 100%. A detailed study of $BaWO_4$ SRS under 1.06-μm, 50-ps pulsed pumping [73] allowed the authors to obtain the first Stokes radiation at 1180 nm with a conversion efficiency of 25% in the single-pass and 35% in the double-pass regimes. Placing the $BaWO_4$ crystal into a short (3.8 cm) cavity with an optimized output coupler provided a

TABLE 9.2

Comparative SRS and Thermo-Mechanical Characteristics of $Ba(NO_3)_2$, $KGd(WO_4)_2$, $SrWO_4$ and $BaWO_4$ Crystals

	Raman Crystal			
Characteristic	**$Ba(NO_3)_2$**	**$KGd(WO_4)_2$**	**$SrWO_4$**	**$BaWO_4$**
Raman frequency shift ν_R (cm^{-1})	1047	901; 767	922	924
Raman linewidth $\Delta\nu_R$ (cm^{-1})	0.4	5.4; 6.4	2.74	1.6
Dephasing time T_R (ps)	28	2.0	4	6.6
Gain coefficients:				
g(0.53 μm) steady-state (ns)	47	11		36–40
g(0.53 μm) transient (20 ns)	4.7	11		14.4
g(1.06 μm) steady-state (ns)	11	4	5	8.5
g(1.06 μm) transient (30–50 ps)	1.1	3		3.8
g(1.3 μm) steady-state (ns)				5.8
Transparency range (μm)	033–1.8	0.3–5	0.25–5	0.255–5
Moisture resistance	Low	High	High	High
Thermal conductivity at 25°C, W K^{-1}m^{-1}	1.17	2.5–3.4	3	3.0
Thermal expansion coefficient α, 1°C^{-1}	13×10^{-6}	$(1.6–8.5) \times 10^{-6}$		6×10^{-6}
Hardness	19.2 ($NaNO_3$ Knoop)	4–4.5 (Mohs)	4 (Mohs)	4 (Mohs) 400 (Knoop)

55% pump-to-first-Stokes conversion efficiency with an output energy as high as 3 mJ.

Thus, we can conclude that $BaWO_4$ is the first universal crystal, which shows an almost record high gain, both in the nanosecond and picosecond modes of operation.

9.12 $PbWO_4$ SRS Shifters and Raman Lasers

Another interesting SRS crystal was used in Raman laser development. This is a well-known scintillating material, $PbWO_4$, with a scheelite structure similar to that of $BaWO_4$. Analogous to other tungstates, one can expect a high integral cross section for the $PbWO_4$ crystal, but the measured linewidth of the totally symmetrical A_{1g} 904 cm^{-1} Raman vibration shows a rather high value of 5.6 cm^{-1} for a polycrystalline sample [17] close to KGW. A detailed study of the A_{1g} Raman line broadening at different temperatures up to the melting point shows that similar to $CaWO_4$ and $SrWO_4$, lead tungstate $PbWO_4$ has a rather high Davydov splitting (ΔE_{DS} = 32 cm^{-1}) caused by a strong $[WO_4]^{2-}$–$[WO_4]^{2-}$ intermolecular interaction [23]. This value is one or two orders of magnitude higher than that in $BaWO_4$ and $Ba(NO_3)_2$ crystals (with a record high peak value of gain) ΔE_{DS} = 0–1 cm^{-1}. The high density of acoustic phonon states leads to fast dephasing and large Raman line broadening $\Delta\nu_R$ (300 K) = 4.7 cm^{-1} (for a single crystal) due to the direct relaxation processes between the DS components with single-phonon absorption or emission.

The study of $PbWO_4$ crystals using picosecond SRS spectroscopy techniques and under nanosecond Raman laser pumping was first reported in Refs. [83–85]. The authors presented the measured data on the gain coefficient (8.4 cm GW^{-1} at 532 nm and 3.1 cm GW^{-1} at 1064 nm) and some other characteristics of the $PbWO_4$ single crystal. They observed 18 different spectral lines of SRS Stokes and anti-Stokes radiation in the 485.5–1117 nm spectral region under pumping by 1064 nm Nd:YAG laser pulses with a duration of 100 ps and by its second harmonic (532 nm) with a pulse duration of 80 ps.

Raman laser oscillation in $PbWO_4$ crystals under external pumping by 100 ps pulses of an Nd:YAG laser at 1064 nm was studied in Refs. [83,84]. In the 200-mm long plane-concave laser cavity with a spherical (r = 0.5 m) output coupling mirror with a reflectivity of 78%, the first Stokes radiation energy of 1 mJ with a slope efficiency as high as 40% was obtained at a pump energy of 5 mJ. In these experiments, the pump beam was focused inside the 30-mm long $PbWO_4$ crystal by a lens with a focal length of 12 cm. Data are also presented on the steady-state Raman gain measured in visible light under pumping by 30 ps pulses of the frequency-doubled radiation of an Nd:YAG laser. The authors concluded that the gain coefficient of $PbWO_4$, measured to be 8.4 cm GW^{-1}, is slightly higher than the 8 cm GW^{-1} of KGW crystal, measured by the same technique.

A linear Raman cavity 110 mm long with one flat mirror serving as the pump input coupler and another concave mirror with a radius of curvature of 10 m as an output coupler with 46% transmission at the first Stokes wavelength were used. Two $PbWO_4$ crystalline samples, each 45 mm long, were placed inside the cavity. Under external pumping by nanosecond (5–7 ns) 532 nm radiation, collimated inside the crystal to the beam diameter of 1.1 mm, the output energy of the first Stokes beam (558.9 nm) was 1 mJ with a conversion efficiency of 13%. Laser damage on the crystal surface was observed with a pump fluence of 5.1 J cm^{-2}. The IR Raman lasing by one or two 45-mm long $PbWO_4$ crystals was studied in a ring Raman laser cavity 285 mm long with two highly reflecting mirrors and one output coupler with a reflectivity of 27% for the first Stokes wavelength [85]. The Raman crystals were pumped by an Nd:YAG laser (1064 nm) beam 2.1 mm in diameter with a pulse duration of 7 ns. At a pumping energy of 36 mJ (close to the Raman crystal laser damage threshold), the output energy of the first Stokes radiation was as high as 5.3 mJ for one $PbWO_4$ crystal. The highest conversion efficiency reached 20% for two SRS crystals in the cavity. The authors noted that the laser damage threshold for IR radiation was surprisingly low, about 2 J cm^{-2}, which is more than twofold lower than that for visible radiation.

The $PbWO_4$ crystal can also be easily activated by Nd^{3+} ions [83]. The first attempt to develop a diode-pumped passively Q-switched Nd^{3+}:$PbWO_4$ Raman laser with self-frequency conversion was described in Refs. [86]. An active and SRS Nd(0.5 at%):$PbWO_4$ crystal with the dimensions of 3 × 3 × 15 mm was transversely pumped by a 100 W GaAlAs quasi-cw diode laser array (λ = 808 nm) with a pulse duration of 160 μs and a repetition rate of 20 Hz. In a highly-reflective cavity 24 mm long, passively Q-switched by a Cr:YAG saturable absorber with T = 95%, under a pump energy of 4.5 mJ, the Raman output energy at 1170 nm was rather low, 2.5 μJ, with an efficiency of 0.6% and a threefold output pulse shortening to 8 ns.

Comparative data on the energy, pulse duration, power and efficiency of SRS radiation are given in Table 9.3 along with the pump laser parameters, Raman shifter and laser optical schemes and SRS crystal types.

The basic optical schemes for SRS generation are single-pass SRS, double-pass SRS, Raman laser with external pumping, Raman laser with synchronous pumping and Raman laser with intracavity pumping and self-conversion.

One can see that the wavelength range of SRS shifters and Raman lasers covers a wide spectral region, 0.5–2 μm, limited only by the fundamental absorption of the SRS material and the wavelengths of the pump sources. The SRS conversion efficiency comprises tens of per cents, reaching 90% for the intracavity scheme. For nanosecond pulses, SRS reaches the energy of hundreds of milliJoules and an average power of several watts. The SRS conversion of picosecond pulses is accompanied by pulse shortening by a factor of up to 10 and reaches sub-picosecond durations (0.9 ps).

9.13 Raman Laser Applications

As we discussed earlier, coupling an Nd-YAG pump with a barium nitrate Raman crystal results in Raman laser output at 1.56 μm. This is an optimum wavelength for atmospheric propagation and eye-safe operation. Therefore, this type of Raman laser is ideal as a transmitter for atmospheric LIDAR systems [46–48,68,69]. Since laser radars are used for many

TABLE 9.3

Pump and Output Characteristics of Solid-State SRS Shifters and Raman Laser

SRS Crystal, Raman Shift	Optical Scheme	Pump Laser and Wavelength (μm)	Pump Pulse Duration, Rep. rate	SRS Efficiency	SRS Energy, Power, Pulse Duration	SRS Wavelength (nm)	References
Green Nanosecond Pumping with Low Repetition Rate							
$Ba(NO_3)_2$, 1047 cm^{-1}	SRS shifter	Nd glass, 0.532	15 ns single pulse	26%	150 mJ	560	8
$Pb(NO_3)_2$	”	”	”	20%	70 mJ	”	
$NaNO_3$, 1066 cm^{-1}	”	”	”	17%	150 mJ	”	
$CaCO_3$ 1084 cm^{-1}	”	”	”	14%	120 mJ	”	
$Ba(NO_3)_2$, 1047 cm^{-1}	Raman laser	Nd:YAG 0.532	10 ns	40%–50%	60 mJ	560	10
				25%	20 mJ	598	
	SRS shifter	Nd:YAG 0.532	22 ps	25%		583	28
				5%		599	
	Raman laser, external pumping	Nd:YAG 0.532	8 ns (1–30 Hz)	40%–48%	25 mJ	563, 281	26
					32 mJ, 5 ns	599, 299	
	Oscill. + amplifier	Nd:YAG 0.532	5–7 ns	14%	3.5 mJ	563	27
$BaWO_4$, 926 cm^{-1}	Single-pass SRS	Nd:YAG 0.532	5.1 ns	30%	2 ns	560	76,77
				6%	1.5 ns	590	
	Double-pass SRS	”	”	45%		560	77
	Raman laser, external pumping	Nd:GGG 0.531	29 ns	50%	6 mJ	559.5	87,88
				30%	4 mJ	588.95	
$PbWO_4$, 904 cm^{-1}	Ring cavity Raman laser	Nd:YAG 0.532	5–7 ns	13%	1 mJ		89
KGW, 901.5 cm^{-1}	Backward single-pass SRS	Nd:YAG 0.532 μm	19 ps	30%	1 mJ, 1.6–1.7 ps	555	65
$BaWO_4$, 926 cm^{-1}	Single-pass SRS	0.532 μm	28–35 ps	30%–50%	18 ps	560	76
				15%–20%		590	
$Ba(NO_3)_2$, 1047 cm^{-1}	Single-pass SRS	Copper vapour laser 510.6; 578.2	15 ns (16 kHz)	38%	0.6 mW	539.4	25
				18%	0.3 W	615.4	
					0.01–0.08 W	203–308	
$BaWO_4$, 925 cm^{-1}	Raman laser	Nd:YLF 2ω, 527	400 ns (1 kHz)		130 mW	544	78
					22 mW	583	
IR Nanosecond Low Repetition Rate Pumping							
$Ba(NO_3)_2$, 1047 cm^{-1}	Single-pass shifter	LiF:F_2^- 1.08–1.28	15 ns, 20 Hz	60%	0.1 J	1230–1370	32
				20%	0.03 J	1430–1600	
	Raman laser	Nd:YAG 1.064 μm	12 ns, 10 Hz	39%	6 mJ	1197	35–38
				27%	4.6 mJ	1363	
				21%	3.5 mJ	1598	
		Nd:YLF 1047	10 Hz		150 mJ (1.5 ns)	1176	49
					90 mJ	588 (2ω)	
	Raman laser, external pumping	Nd:YAG 1.064	30 ns, 20 Hz	20%	2.8 mJ, 11 ns	1197	48

(Continued)

TABLE 9.3 (*Continued*)

Pump and Output Characteristics of Solid-State SRS Shifters and Raman Laser

SRS Crystal, Raman Shift	Optical Scheme	Pump Laser and Wavelength (μm)	Pump Pulse Duration, Rep. rate	SRS Efficiency	SRS Energy, Power, Pulse Duration	SRS Wavelength (nm)	References
				20%	2.7 mJ, 9.5 ns	1367	
				7%	8.5 mJ, 3.5 ns	1598	
			5 ns	30%	100 mJ, 3 ns	1197	90
					18.5 mJ	598.5	
			50 ns, 10–30 Hz	35%	32 mJ	1197	
				9%	16 mJ	1363	
			50 ns	19%	17.3 mJ, 2.6 W	1197	33
			5-pulse trains, 30 Hz	14.4%	32 mJ, 4.76 W	1197	
				8.5%	2.7 mJ, 0.4 W	1363	
	Raman laser, external pumping	Nd:YAG 1.318	64 ns	39%	5 mJ	1529	38
			64 ns	39%	5 mJ	1556	
			32 ns	52%	3 mJ	1556	
		Nd:YAP 1.341	60 ns	40%	5 mJ	1560	
	Raman laser, intracavity pumping	Nd:YAG 1.338	10–12 ns	90%	1.5 mJ	1556	39–42
		Nd:YAG 1.318–1.338	10 ns	48%	12 mJ	1529–1556	46,47
						1820–1860	
		Nd:YAP 1.341	1–10 Hz	44%	250 mJ	1529–1556	
	Single-pass SRS	Nd:YAG+LiF:F_2^-	12 ns	35%–50%	10–45 mJ, 20–45 ns	1197	43
		Nd:YAP+LiF:F_2^-				1216	
KGW, 901.5–767.3	Single-pass SRS	Nd:YAG 1.064	10 ns	70%	10 mJ	1St + 2St	67
KGW, 901.5 cm^{-1}	Single-pass SRS	LiF:F_2^- 1.1–1.23	8 ns	30%	6 mJ	1230–1370	32
				20%	4 mJ	1430–1600	
	Intracavity Raman laser	Nd:YAG+LiF:F_2^-	12 ns	50%	10–45 mJ, 20–45 ns	1180	44
		Nd:YAP+LiF:F_2^-					
Nd:KGW, 901.5 cm^{-1}	Raman laser, intracavity self-conv.	Nd:KGW LD pumping	40 ns		1–6 mJ, 40 ns	1538	68,69
					13.5–15 mJ, 12 ns	1538	
	SRS self-conversion	Diode pumping 1.067	140 ns		0.1 mJ, 50 ns	1162	70
					0.03 mJ, 16 ns	581	
BaWO$_4$, 926 cm^{-1}	Raman laser, external pumping	Nd:GGG 1.062	20 ns	24%	15 mJ	1179.9	87,88
		Nd:YAG 1.064	12 ns	30%	2.4 mJ	1180	24,74
		Nd:YAG 1.318	50 ns, 3 Hz	12%–20%	1.8 mJ (300 K)	1501	33
				19%–35%	3 mJ (77 K)		
		Nd:GGG 1062	50 ns	20%	2 J	1178	91
			50 pul			1322	
			0.1 Hz				

(*Continued*)

TABLE 9.3 (*Continued*)

Pump and Output Characteristics of Solid-State SRS Shifters and Raman Laser

SRS Crystal, Raman Shift	Optical Scheme	Pump Laser and Wavelength (μm)	Pump Pulse Duration, Rep. rate	SRS Efficiency	SRS Energy, Power, Pulse Duration	SRS Wavelength (nm)	References
$SrWO_4$, 921 cm^{-1}	Raman laser, external pumping	Nd:YAG 1.064	12 ns	15%	1.3 mJ		74
Nd:$SrWO_4$, 921 cm^{-1}	Raman laser, intracavity self-conv.	Nd:$SrWO_4$ 1.06			3 mJ	1180	74
$PbWO_4$, 904 cm^{-1}		7 ns	17%–20%	5.3 mJ		84	
Nd:$PbWO_4$, 904 cm^{-1}	Raman laser intracavity self-conv.	Nd:$PbWO_4$ LD pumping		0.6%	2.5 μJ (8 ns)	1170	86
IR High Repetition Rate Nanosecond Pumping							
$LiIO_3$, 818 cm^{-1}	Raman laser, intracavity pumping	Nd:YAP 1.080	100 ns	77%	1.26 W (50 ns)	1180	50,51
					0.55 W (15 ns)	1310	
					0.9 W (4–8 ns) 7 kW peak	1180	
					0.2 W (2 ns) 100 kW peak	1310	
$LiIO_3$, 770 cm^{-1}	Raman laser, intracavity pumping	Nd:YAG 1.064	100 ps	57%	1.8 W (40 ns)	1179	53
			100 kHz		0.55 W	580	53
			15 kHz	42%	2.7 W	1155	54–56
					0.96–1.2 W (8 ns)	577	
					1.42 W (20 ns)	577	57
$CaWO_4$, 911 cm^{-1}	Raman laser, intracavity pumping	Nd:YAG 1.064	10 kHz	8 ns	0.5 W	1178	92
			8 kHz	2 ns	0.062 W	1320	
$Ba(NO_3)_2$	Raman laser, intracavity pumping	Nd:YAG 1.064	3–7 kHz		0.15–1.4 W	1197	93
Yb:KGW, 901 cm^{-1}	Raman laser, intracavity self-conv.	Diode-pumped Yb:KGW1.03			7 mW (17 kHz)	1139	71,72
					2 mW (49 kHz)		
IR Picosecond Low Repetition Rate Pumping							
$BaWO_4$, 921 cm^{-1}	Raman laser, external pumping	Nd:YAG 1.064	20–100 ns	35%–21%	6 W	1180	94
			150–300 Hz				
$LiIO_3$, 760 cm^{-1}	Raman laser	Phosphate glass 1.054	6–10 ns	40%	1 mJ (1 ps)	1143	52
Nd:KYW, 900 cm^{-1}	Raman laser, intracavity pumping	1.067	10–12 ps	<5%		947.9	58–64
	Self-conv. Raman laser	1.067	10–12 ps	37%	1.3 ps	1180.5	
				16%		1323.7	
	Raman amplifier		10–4 ps	40%	0.9 ps	1180	
			5–6 ps	40%	1.5–2.5 ps		
$BaWO_4$, 926 cm^{-1}	Single-pass SRS	1.06	50 ps	25%		1180	73
	Double-pass SRS	”	”	35%	3 mJ	”	
	3.8-cm laser cavity	”	”	55%		”	
$PbWO_4$, 904 cm^{-1}		Nd:YAG 1.064	100 ps	20%	1 mJ		83,84

different purposes, it is important to be able to make use of the design flexibility of Raman lasers to provide a transmitter with optimized operational parameters. For example, detecting atmospheric pollutants through backscattering from aerosols can be done with direct detection LIDAR systems. If measuring distance is important, range-gating techniques can be used and the temporal pulsewidth of the laser becomes important. As mentioned previously, Raman lasers can provide output pulses of 1 ns or less in duration, which results in a significant improvement in range resolution over normal Q-switched or cavity-damped lasers [45,77]. It is difficult to obtain this pulsewidth from any other type of solid-state laser. If it is important to identify the type of chemical species that is in the atmosphere, differential absorption techniques can be employed. In this case, the laser transmitter must operate at two different wavelengths, on and off a resonant absorption line of the chemical of interest. Raman lasers can easily be configured to meet this requirement through use of the pump and Raman wavelengths or the use of first-Stokes and second-Stokes output. Depending on the position of the chemical absorption lines, this may require laser emission anywhere in the spectral range from the near-ultraviolet to the near-infrared. Using Raman lasers in conjunction with other frequency-conversion techniques, all of these spectral regions can be reached. For applications requiring the measurement of the Doppler shift of the return signal due to wind or atmospheric turbulence, coherent LIDAR techniques are used. This requires a laser transmitter operating with high stability at a single frequency, so heterodyne detection can be used. Injection seeding of Raman lasers has been demonstrated to show the ability to obtain single frequency operation for use in this type of application [89].

Similar systems have been demonstrated for marine imaging LIDAR applications [49,95]. For these systems, the transmitter wavelength must be chosen to match the maximum transmission through the water. This changes from blue-green in open seawater to yellow or orange in the littoral zone due to the difference in the number of particulates and their effect on scattering light. In general, these systems are used to identify objects underwater such as types of fish or obstructions that might injure ships. High image quality and accurate range resolution require a laser transmitter with a short temporal pulsewidth and good beam quality. This is ideal for a solid-state Raman laser and excellent results have been obtained with marine imaging LIDAR systems employing Raman lasers [49,95].

Semiconductor processing applications need efficient, compact, all-solid-state sources with a high repetition rate of 10 kHz, good pulse-to-pulse stability and diffraction-limited beam quality. One of the important wavelengths is close to but longer than the silicon band-to-band and excitonic absorption at 1.12–1.153 μm [92]. As a device satisfying these requirements, the authors offered an end-pumped intracavity Raman laser. They used a 2 × 10 mm Nd:YAG rod longitudinally pumped by a 5 W diode bar via a fibre bundle 600 mm in diameter. A cavity, high-reflecting at 1064 nm and low-reflecting at 1178 nm, with a $CaWO_4$ SRS crystal of dimensions 4 × 4 × 22 mm and acousto-optical Q-switching, was calculated and optimized. This resulted in about 500 mW for the first Stokes (1178 nm) single-mode radiation with a repetition rate of 10 kHz and a pulse duration of 8 ns. At a lower repetition rate, 8 kHz, the cascaded second Stokes radiation at 1320 nm was observed with the average power of 62 mW and a much shorter pulse duration of about 2 ns. External frequency doubling by a 12-mm-long LBO crystal provided about 250 mW of 589 nm (visible–yellow) and 27 mW of 660 nm (visible–red) radiation. The yellow 589 nm radiation is of interest for pumping the sodium resonance line (D2), which can be applied in adaptive optic systems. The red frequency can be applied for photodynamical therapy.

An interesting application of SRS technology was proposed in Ref. [92]. The authors suggested using SRS radiation to form artificial guide stars in the 10-km deep mesoscopic layer situated 95 km from the earth's surface. In this case, a laser is projected through a telescope to the upper atmosphere, where it is resonantly absorbed by a layer of sodium atoms. The sodium fluorescence acts like an artificial star and the telescope detects the atmospheric distortion of its image. Then, using adaptive optics techniques, one of the optical elements of the telescope system is altered in such a way as to null out the atmospheric distortion of the image. With the optical system in this configuration, images of astronomical objects that are free of atmospheric distortion can now be obtained. The requirements for the laser to create an effective sodium guide star are quite stringent. To create the maximum photon return, the wavelength, temporal pulsewidth, spectral pulsewidth, energy per pulse and pulse repetition rate must all be exactly correct to get the maximum amount of light absorbed by the sodium atoms and emitted as fluorescence without the effects of saturation, radiation pressure or interference from multiple pulses. So far, this has proven to be a major challenge for the laser community and no acceptable solution is currently working in a telescope. However, a solid-state Raman laser appropriate for sodium guide star applications has been demonstrated in the laboratory [96,97]. A second type of Raman guide star laser based on a fibre as the Raman shifting element is also being developed in the laboratory [98]. This has the advantage of power scaling for non-astronomy adaptive optics applications.

The sodium atomic transition corresponds to a wavelength of 589.2 nm and has a radiative lifetime of 16 ns. A laser source for pumping the sodium resonance should be adjusted to this wavelength with accuracy better than 1 GHz and must operate in the burst pulsed mode or pulsed-periodic mode. All-solid-state, high efficiency and reliable laser systems based on a diode-pumped crystalline neodymium laser, solid-state Raman frequency shifter and non-linear frequency doubler could be promising for this type of application.

Such a system could consist of an Nd:YAG pump laser and a $CaWO_4$ SRS frequency shifter with subsequent doubling. However, this frequency matches the Na resonance only when the Nd:YAG crystal is cooled to below room temperature. At the same time, the $CaWO_4$ SRS crystal is not the best candidate for frequency shifting due to its strong Raman line broadening, low gain and high SRS threshold.

A different scheme of sodium Raman laser, based on the new best SRS crystal, $BaWO_4$, which has a line several times narrower ($1.6\,cm^{-1}$), higher gain and lower threshold, was proposed in Refs. [87,88]. In comparison with the $Ba(NO_3)_2$ crystal, with its record high value of nanosecond Raman gain, the $BaWO_4$ has almost the same gain but operates better in the sub-nanosecond and picosecond modes. The $BaWO_4$ crystal also has a much higher moisture resistance and a thermal conductivity at least twice as good.

As the pump source, the authors of Refs. [87,88] used an Nd:GGG solid-state laser, because its operation wavelength, λ = 1062.1 nm, shifted by ν_R = 925 cm^{-1} using the $BaWO_4$ crystal and then doubled, fits the Na resonance very well. The Nd:GGG laser crystal is well known as a good candidate for high-power solid-state lasers. In comparison with Nd:YAG lasers, it demonstrates a little longer metastable level lifetime (280 *versus* 250 µs) and a little wider linewidth (7.2 *versus* 5 cm^{-1}), which results in a smaller emission cross section, $\sigma = 1.7 \times 10^{-19}$ cm^2. The Nd:GGG crystal also has a 30% lower thermal conductivity and a 50% higher temperature derivative of the refractive index. At the same time, Nd:GGG crystals can be grown with a much higher speed and have a larger diameter and very high optical quality, free of central core defects. This is very important for the large disc, slab and zigzag geometry of high-power lasers.

The neodymium concentration in these crystals can be increased by a factor of three to five in comparison with Nd:YAG crystals. In addition, co-doping with Cr^{3+} and Ce^{3+} ions can provide much better sensitization and stability. As a result, the Nd:GGG lasers can have a doubled laser efficiency when pumped by flashlamps.

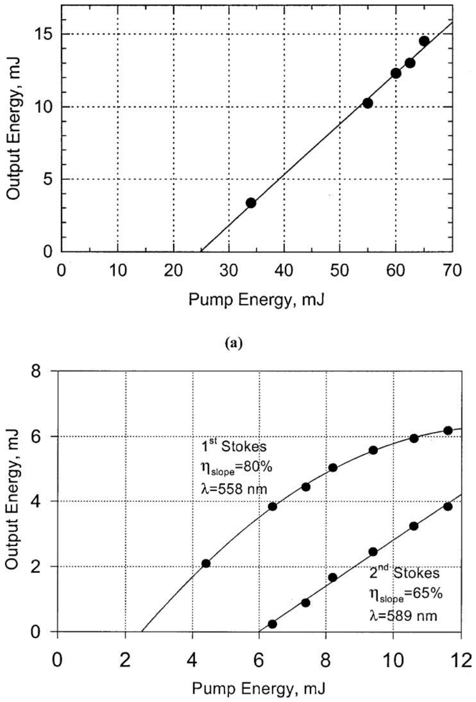

(a)

(b)

FIGURE 9.4 (a) The first Stokes (1179.9 nm) output energy of a $BaWO_4$ Raman laser *versus* 1062.1 nm pump energy of an Nd:GGG laser. (b) The first (559.5 nm) and second (588.95 nm) Stokes output energy of an Na-star Raman laser *versus* 531.05 nm pump energy of an Nd:GGG laser (second harmonic).

To prove this approach to the sodium resonance laser source, two laser schemes for an Na solid-state yellow Raman laser were tested in Refs. [87,88]. The first one was based on IR Raman shifting of the Nd:GGG laser fundamental wavelength λ_p = 1062.1 nm by the first Stokes $BaWO_4$ crystalline Raman laser to λ_{1St} = 1177.9 nm. This wavelength was then halved to λ_{SHG} = 588.95 nm by a second-harmonic generator on a $LiNbO_3$, LBO or KTP non-linear crystal. The results of the pump-to-output conversion in the $BaWO_4$ Raman laser are shown in Figure 9.4a, which demonstrates the more than 30% slope efficiency and the 15 mJ output energy. The second scheme was based on the Raman shifting of visible radiation. In this scheme, the 1062.1 nm radiation of an Nd:GGG laser is first transformed by a non-linear crystal, BBO or KTP, to the second harmonic, λ_{SHG} = 531.05 nm, which then serves as the pump radiation for the $BaWO_4$ visible Raman laser. In this case, the second Stokes output of the Raman laser oscillation was used to reach the Na resonance wavelength. As is seen from Figure 9.4b, this scheme gives more than 50 and 30% output-to-pump conversion efficiency of the first (λ_{1St} = 559.5 nm) and second Stokes (λ_{2St} = 588.95 nm), respectively. The 60% slope efficiency indicates that these characteristics can be improved. The better efficiency for the second scheme is caused by the higher Raman gain of the $BaWO_4$ crystal for green pumping ($g_{0.53} \approx 40$ cm GW^{-1}) than for IR pumping ($g_{1.06} \approx 8$ cm GW^{-1}). At the same time, as we discussed earlier, application of the intracavity IR pumping scheme of Raman laser allows one to increase the IR Raman conversion efficiency up to 100% (due to the use of the non-linear intracavity-dumping regime), to improve the spatial beam quality (beam clean-up) and to decrease the pulse duration with increasing peak power, which is important for the following second-harmonic generation. Another advantage is that the $BaWO_4$ Raman laser and the Nd:GGG solid-state pump laser permit some temperature wavelength tuning at around room temperature. This provides fine temperature adjustment of the oscillation wavelength in the vicinity of the sodium resonance without using a dispersive cavity. A long (up to 4 ms) pulse train of 50 giant pulses (50 ns each) of a high-energy (20 J in the train) Nd:GGG laser was used as a pump source for a $BaWO_4$ Raman Laser. As a result, an SRS train energy as high as 2 J was obtained, with a peak power of up to 1 MW and conversion efficiency reaching 20% [91]. A high average power (up to 6 W) of the SRS radiation was realized under self-phase-conjugated Nd:YAG pumping at the conversion efficiency of 15%–35% with a rather low thermal lensing (0.12 D) of the $BaWO_4$ SRS crystal [94]. The spectral range of output wavelengths and the variety of output configurations used in the applications described here demonstrate the potential for Raman lasers in military applications such as range finders, target designators and munitions guidance, in medical applications requiring specific wavelengths in the visible and near-infrared spectral regions and in material processing applications requiring high beam quality and precise wavelength selection [99].

Since Raman lasers can be based on a wide variety of combinations of pump lasers and active Raman crystals and they can be constructed in a variety of configurations using slabs or rods with normal Q-switching and mode-locking technology, it is possible to envision many more applications in the future.

9.14 Conclusions

In summary, high gain solid-state Raman materials provide infrared Raman shifting and lasing for tunable and fixed-frequency operation in the 1.1–2.2 μm spectral range and allow the development of high efficiency intracavity solid-state Raman lasers based on coupled resonator or shared resonator designs. These intracavity configurations take advantage of the third-order non-linear nature of SRS to provide for special operating characteristics, such as spatial beam clean up, leading to diffraction-limited output and pulsewidth control through nonlinear cavity damping. Important results have been reported on self-Raman shifting lasers in which the Raman crystal is also the host material for the rare-earth ions that are active in lasing. Tunable Raman laser emission can be obtained by using glass fibres as the active medium, by scattering from polaritons in polar crystals such as $LiNbO_3$, and by parametric interactions among different types of stimulated emission processes.

In spite of strong Raman gain decrease in the IR spectral region ($g_{0.53\,\mu m}/g_{1.06\,\mu m} \approx 4$), the unique features of $Ba(NO_3)_2$ crystals allowed for the development of a single-pass SRS cell and then a Raman laser for extending the tuning range of LiF:F_2^- solid-state colour-centre lasers. With nanosecond pulse pumping in the range of 1.10–1.25 μm, the steady-state SRS to the first and second Stokes components provided narrow line, broadly tunable laser oscillation in the 1.23–1.37 μm and 1.43–1.6 μm spectral regions with conversion efficiencies as high as 60% and 20%, respectively.

The special properties of solid-state Raman lasers make them useful in many different types of applications. The appropriate intracavity design employing a high Fresnel number pump cavity with conversion to a single-mode Raman laser output can provide lasers with extremely high wall-plug efficiencies. The third-order nature of the nonlinearity allows for efficient wavelength conversion without the requirement of a high spatial quality pump beam and strict acceptance parameters for wavelength, angle and temperature, as is the case for second-order non-linear effects used in harmonic generators and optical parametric oscillators. The stimulated Raman process in the cavity that acts to clean up the spatial quality of the laser beam is a mechanism similar to phase conjugation. High efficiency and excellent beam quality are important laser properties for any application. In addition, intracavity Raman laser configurations can be designed to operate with non-linear cavity damping to control the temporal properties of pulsed output. This allows for laser emission with pulsewidths of 1 ns or less without the complexity of mode-locking.

Acknowledgements

The research discussed in this article is based on work partially supported by ISTC and EOARD Partner project 2022p. The authors gratefully acknowledge the major contributions to the work described here by their many colleagues, especially P G Zverev, A A Sobol, L I Ivleva, M E Doroshenko, V V Osiko and A M Prokhorov of the General Physics Institute and James T Murray and William L Austin of Lite Cycles, Inc.

REFERENCES

1. Raman C V and Krishnan K S 1928 *Nature (London)* **121** 501.
2. Landsberg G S and Mandel'shtam L I 1928 *Zh. Rus. Fiz. Khim. Obshch.* **60** 335.
3. Woodbury E J and Ng W K 1962 *IRE* **50** 2367.
4. Levenson M D 1982 *Introduction to Nonlinear Laser Spectroscopy* (New York: Academic).
5. Murray J T, Powell R C and Peyghambarian N 1996*J. Luminesc.* 66&67 89.
6. Kaiser W and Maier M 1972 *Laser Handbook* vol 11, ed F T Arecchi and E O Shultz-Dubois (Amsterdam: North-Holland) p 1077.
7. Loudon R 1963 *Proc. R. Soc. A* **275** 218.
8. Eremenko A S, Karpukhin S N and Stepanov A I 1980 *Kvantovaya Elektron.* 7 196–7 (Engl. transl. 1980 *Sov. J. Quantum Electron.* **10** 113).
9. Karpukhin S N and Yashin V E 1984 *Kvantovaya Elektron.* 10 1992 (Engl. transl. 1984 *Sov. J. Quantum Electron.* **14** 1337).
10. Karpukhin S N and Stepanov A I 1986 *Kvantovaya Elektron.* 13 1572–7 (Engl. transl. *Sov. J. Quantum Electron.*).
11. Belevtseva L I, Voitsekhovskii V N, Nazarova N A, Romanova G I, Shvedova M V and Yakobson V E 1989 *Opt. Mekh. Promst.* 56 38 (Engl. transl. *Sov. J. Opt. Technol.*).
12. Voitsekhovskii V N, Karpukhin S M and Yakobson V E 1995*J. Opt. Technol.* **62** 770–6.
13. Zverev P G, Basiev T T, Osiko V V, Kulkov A M, Voitsekhovskii V N and Yakobson V E 1999 *Opt. Mater.* **11** 315–34.
14. Zverev P G, Basiev T T and Prokhorov A M 1999 *Opt. Mater.* **11** 335.
15. Zverev P G and Basiev T T 1995 *Kvantovaya Elektron.* 22 1241 (Engl. transl. *Sov. J. Quantum Electron.*).
16. Zverev P G, Jia W, Liu H and Basiev T T 1995 *Opt. Lett.* **20** 2378.
17. Basiev T T, Sobol A A, Zverev P G, Fedorov V V, Doroshenko M E, Ivleva L I, Polozkov N M, Osiko V V, Prokhorov A M and Hager G 1999 *Laser '98, Proc. Int. Conf. (Tucson AZ, 1998)* ed V J Corcoran and T A Goldman (McLean, VA: SRS Press) p 712; Basiev T T, Sobol A A, Zverev P G, Fedorov V V, Doroshenko M E, Ivleva L I, Polozkov N M, Osiko V V and Prokhorov A M 1999 Solid state Raman materials characterization for high average power 1.3 μm laser frequency shift *Technical Report LMTRC of GPI for EOARD*, Moscow, p 85.
18. Basiev T T, Sobol A A, Zverev P G, Voron'ko Yu K, Osiko V V and Powell R C 1998 *Advanced Solid State Lasers* vol 19, ed W R Rosenberg and M M Fejer (Washington, DC: OSA TOPS) p 546.
19. Basiev T T, Sobol A A, Zverev P G, Osiko V V and Powell R C 1999 *Appl. Opt.* **38** 594.
20. Basiev T T, Sobol A A, Zverev P G, Ivleva L I, Osiko V V and Powell R C 1999 *Opt. Mater.* **11** 307.
21. Basiev T T, Zverev P G, Sobol A A, Fedorov V V, Doroshenko M E, Skornyakov V V, Ivleva L I and Osiko V V 1999 *Novel Lasers and Devices—Basic Aspects Tech. Digest. Int. Conf. CLEO—Europe Focus Meeting '99 (Munich)* (Washington DC: Optical Society of America) p 160.

22. Basiev T T, Sobol A A, Zverev P G, Ivleva L I and Osiko V V 2000 *Laser material for stimulated Raman scattering* Patent RU 2178938.
23. Basiev T T, Sobol A A, Voron'ko Yu K and Zverev P G 2000 *Opt. Mater.* **15** 205–16.
24. Zverev P G, Basiev T T, Sobol A A, Skornyakov V V, Ivleva L I, Polozkov N M and Osiko V V 2000 *Quantum Electron.* **30** 55–9.
25. Vitsinskii S A, Isakov V K, Karpukhin S M and Lovchil L L 1993 *Kvantovaya Elektron.* 20 1555–8 (Engl. transl. *Sov. J. Quantum Electron.*).
26. Chuan H and Chyba T H 1997 *Opt. Commun.* **135** 273–8.
27. McCray C L, Lee S W and Chyba T H 1998 Measurements of stimulated Raman amplification and Raman shifts in barium nitrate *Advanced Solid State Lasers* vol 19, ed W B Bosenberg and M M Fejer (Washington DC: OSA TOPS) pp 550–4.
28. Zverev P G, Murray J T, Powell R C, Reeves R J and Basiev T T 1993 *Opt. Commun.* **97** 59–64.
29. Basiev T T, Voron'ko Yu K, Mirov S B, Osiko V V and Prokhorov A M 1982 *Izv. Akad. Nauk SSSR, Ser. Fiz.* **46** 1600–10.
30. Basiev T T 1985 *Izv. Akad. Nauk SSSR, Ser. Fiz.* 49 68–77 (Engl. transl. *Bull. Sov. Acad. Sci. USSR Phys. Ser.*).
31. Basiev T T, Osiko V V and Mirov S B 1988 *IEEE J. Quantum Electron.* **24** 1052.
32. Basiev T T, Voitsekhovskii V N, Zverev P G, Karpushko F V, Lyubimov A V, Mirov S B, Morozov V P, Mochalov I V, Pavlyuk A A, Sinitsyn G V and Yakobson V E 1987 *Kvantovaya Elektron.* 14 2452–3 (Engl. transl. 1987 *Sov. J. Quantum Electron.* **17** 1560–1).
33. Basiev T T, Fedin A V, Gavrilov A, Osiko V V and Smetanin S N 2003 Stimulated Raman scattering of high average power Nd:YAG laser radiation *Laser Physics J.* accepted.
34. Basiev T T and Mirov S B 1994 *Room Temperature Tunable Color Center Lasers (Laser Science and Technology Books Series)* (New York: Gordon and Breach Science/Harwood Academic).
35. Zverev P G and Basiev T T 1993 *Proc. All-Union Conference Optika Laserov* vol 2 (Leningrad) p 363.
36. Zverev P G and Basiev T T 1994 *J. Physique* **4** C4–599.
37. Zverev P G, Basiev T T and Prokhorov A M 1994 *Tech. Digest CLEO/Europe'94 94TH0614–8* (Amsterdam: IEEE) p 154.
38. Zverev P G, Basiev T T, Ermakov I V and Prokhorov A M 1994 *Laser Methods of Surface Treatment and Modification (Proc. SPIE2498)* (Bellingham: SPIE) p 164.
39. Basiev T T, Sigachev V B, Doroshenko M E, Zverev P G, Osiko V V and Prokhorov A M 1994 *Tech. Digest CLEOI Europe'94 94TH0614–8* (New Jersey: IEEE) p 125.
40. Basiev T T, Sigachev V B, Doroshenko M E, Zverev P G, Osiko V V and Prokhorov A M 1994 *Laser Methods of Surface Treatment and Modification (Proc. SPIE 2498)* (Bellingham: SPIE) p 171.
41. Zverev P G and Basiev T T 1995 *Advanced Solid State Lasers* vol 24, ed B H T Chai and S A Pain (Washington DC: OSA) p 288.
42. Zverev P G, Basiev T T, Jia V and Liu H 1996 *Advanced Solid State Lasers* vol 1, ed S A Pain and C Pollok (Washington DC: OSA TOPS) p 554.
43. Khulugurov V M, Ivanov N A, Inshakov D V, Oleinikov E A, Voitsekhovskii V N and Yakobson V E 1992 *Kvantovaya Electron.* **19** 162–3.
44. Khulugurov V M, Ivanov N A and Oleinikov E A 1994 Nanosecond lasers based on Raman converters with resonant excitation *Technical Digest CLEO'94 CtuK70* (Washington DC: Optical Society of America) p 126.
45. Murray J T, Austin W L, Powell R C and Peyghambarian N 1999 *Opt. Mater.* **11** 373.
46. Murray J T, Powell R C and Austin E L 1995 *Opt. Photon. News* **6** 32.
47. Murray J T, Powell R C, Peyghambarian N, Smith D, Austin W and Stolzenberger R A 1995 *Opt. Lett.* **20** 1017–19.
48. Kannari F and Takei N 1997 20-Hz Operation of an eye-safe cascade-Raman laser with a $Ba(NO_3)_2$ crystal *Proc. Int. Symp. On Lasers and Nonlinear Optical Materials* (Singapore, 3–5 November) pp 289–91.
49. Murray J T, Austin W L, Calmes L K, Powell R C and Quarles G J 1997 Nonlinear cavity-damped intracavity solid state Raman laser transmitters *OSA TOPs on Advanced Solid State Lasers* vol 20, ed St A Payne and C K Pollock (Washington DC: OSA) pp 72–6.
50. Ammann E O and Decker C D 1977 *J. Appl. Phys.* **48** 1973–5.
51. Ammann E O 1978 *Appl. Phys. Lett.* **32** 52–4.
52. Grigoryan G G and Sogomonyan S B 1989 *Kvantovaya Electron.* 16 2180–3 (Engl. transl. *Sov. J. Quantum Electron.*).
53. Pask H M and Piper J A 1998 *Opt. Comm.* **148** 285–8.
54. Pask H M and Piper J A 1999 *Opt. Lett.* **24** 1490–2.
55. Revermann M, Pask H M, Blows J L and Omatsu T 2000 Thermal lensing measurements in an intracavity $LiIO_3$ Raman laser *Advanced Solid State Lasers* ed H Injeyan, U Keller and Ch Marshal (Washington DC: OSA TOPS) pp 506–9.
56. Pask H M and Piper J A 2000 *IEEE J. Quantum Electron.* **36** 949–55.
57. Pask H M and Piper J A 2002 Design and operation of an efficient 1.4 W diode-pumped Raman laser at 578 nm *Advanced Solid-State Lasers Technical Digest Int. Conf. (Quebec City, 3–6 February)* (Washington DC: OSA) pp 1–3.
58. Andryunas K, Vishakas Yu, Kabelka V, Mochalov I V, Pavlyuk A A, Petrovskii G T and Syrus V 1985 *Pis. Zh. Ek. Teor. Fiz.* 42 333 (Engl. transl. 1986 *JETP Lett.* **42** 410–12); Andryunas K, Vishakas Yu , Kabelka V, Mochalov I V, Pavlyuk A A, Ionina N V and Syrus V 1984 A method of generation of picosecond pulses at a Raman frequency Patent of USSR # 1227074.
59. Ivanyuk A M, Ter-Pogosyan M A, Shakhverdov P A, Belyaev V D, Ermolaev V L and Tikhonova H P 1985 *Opt. Spectrosk.* 59 950–2 (Engl. transl. *Sov. Opt. Spectrosc.*).
60. Mikhailov A V, Mochalov I V and Lyubimov A V 1987 Raman scattering in KGW crystals *Lasers and Optical Nonlinearity* ed E K Maldutis (Vilnyus: Vilnyus University) pp 265–9 (in Russian).
61. Andryunas K, Barila A, Vishchakas Yu and Syrus V 1987 Investigation of pulse duration dynamics in a laser based on $KGd(WO_4)_2:Nd^{3+}$ and $KY(WO_4)_2:Nd^{3+}$ *Lasers and Optical Nonlinearity* ed E K Maldutis (Vilnyus: Vilnyus University) pp 43–50 (in Russian).

62. Andryunas K, Barila A, Vishchakas Yu, Mochalov I V, Petrovskii G T and Syrus V 1988 *Opt. Spektrosk.* 64 397–401 (Engl. transl. *Sov. Opt. Spectrosc.*).
63. Vishchakas Yu K, Mochalov I V, Mikhailov A V, Klevtsova R F and Lyubimov A V 1988 *Lietuvos fizikos rinkinys* **28** 224–34.
64. Mochalov I V 1997 *Opt. Eng.* **36** 1660–9.
65. Kurbasov S V and Losev L L 1999 *Opt. Commun.* **168** 227–32.
66. Ivanyuk A M, Sandulenko V A, Ter-Pogosyan M A, Shakhverdov P A, Chervinskii V G, Lukin A V and Ermolaev V L 1987 *Opt. Spektrosk.* 62 961–2 (Engl. transl. *Sov. Opt. Spectrosc.*).
67. Berenberg V A, Karpukhin S N and Mochalov I V 1987 *Kvantovaya Electron.* 14 1849–50 (Engl. transl. *Sov. Quantum Electron.*).
68. Kaminskii A A, Ustimenko N S, Gulin A V, Bagaev S N and Pavlyuk A A 1998 *Dokl. Akad. Nauk.* 359 179–83 (Engl. transl. *Sov. Phys. Docl.*).
69. Ustimenko N S and Gulin A V 2000 *Pribory i Tekhnika Eksperimenta* 3 99–101 (Engl. transl. *Sov. Instrum. Exp. Technol.*).
70. Fideisen J, Eichler N J and Peuser P 2000 *Opt. Commun.* **181** 129–33.
71. Lagatsky A A, Abdolvand A and Kuleshov N V 2000 *Opt. Lett.* **25** 616–18.
72. Grabtchikov A S, Kuzmin A N, Lisinetskii V A, Orlovich V A, Demidovich A A, Danailov M B, Eichler N V, Bednarkiewics A, Strek W and Titov A N 2002 Yb:KGW Microchip laser performance: fundamental frequency generation and Raman self-frequency conversion *Advanced Solid State Lasers, Technical Digest Int. Conf. (Quebec City,* 3–6 *February)* (Washington DC: OSA) pp 1–3.
73. Basiev T T, Zverev P G, Sobol A A and Osiko V V 2002 Search and characterization of new crystals for Raman lasers *Advanced Solid State Lasers MB10* (Washington DC: Optical Society of America) pp 1–3.
74. Cerný P, Jelínková H, Basiev T T and Zverev P G 2001 Properties of transient and steady-state stimulated Raman scattering in $KGd(WO_4)_2$ and $BaWO_4$ tungstate crystals *Growth, Fabrication, Devices and Applications of Laser and Nonlinear Devices (Proc. SPIE4268)* (Los Angeles CA: SPIE) pp 101–8.
75. Cerný P, Jelínková H, Šulc J, Zverev P G and Basiev T T 2001 Evaluation of $BaWO_4$ Steady-state Raman gain in single- and double-pass arrangement *Advanced Solid State Lasers (OSA TOPS, Seattle, WA)* vol 50 (Washington DC: Optical Society of America)..
76. Zverev P G, Basiev T T, Sobol A A, Ermakov I V and Gellerman W 2001 $BaWO_4$ crystal for quasi-cw yellow Raman laser *Advanced Solid-State Lasers (OSA Technical Digest)* (Washington DC: OSA) pp 124–5.
77. Cerný P, Zverev P G, Jelínková H and Basiev T T 2000 Opt. Commun. **177** 397–404.
78. Cerný P, Zverev P G, Jelínková H, Basiev T T, Ivleva L I and Osiko V V 2000 Comparison of stimulated Raman scattering of picosecond pulses in tungstate crystals *Nonlinear Materials, Devices, and Applications (Proc. SPIE* 3928*)* ed J W Pierce (Los Angeles CA: SPIE) pp 124–31.
79. Cerný P, Jelínková H, Zverev P, Basiev T and Kubecek V 2000 Picosecond Raman gain of $CaCO_3$, $KGd(WO_4)_2$ and $BaWO_4$ crystals *Book of Abstract CLEO/Europe, Int. Quantum Electronics Conf. 2000 (Nice)* paper no CthE14 (New Jersey: IEEE) p 94.
80. Cerný P, Jelínková H, Miyagi M, Basiev T T and Zverev P G 2002 Efficient picosecond Raman lasers on $BaWO_4$ and $KGd(WO_4)_2$ tungstate crystals emitting in 1.15 to 1.18-µm spectral region *LASE 2002, part of Photonics West Symp. (San Jose)* paper no 4630-17 (Los Angeles CA: SPIE).
81. Cherný P and Jelinkova H 2002 Picosecond stimulated Raman scattering in $BaWO_4$ crystal with close to quantum limit efficiency *Advanced Solid-State Lasers, Tech. Digest (Quebec City)* (Washington DC: Optical Society of America) pp 1–3.
82. Kaminskii A A, Eichler H J, Ueda K, Klassen N V, Redkin B S, Li L E, Findeisen J, Jaque D, Garcia-Sole J, Fernandez J and Balda R 1999 *Appl. Opt.* **38** 4533–46.
83. Findeisen J, Eichler H J and Kaminskii A A 1999 *IEEE J. Quantum Electron.* **35** 173–8.
84. Kaminskii A A, McCray C L, Lee H R, Lee S W, Temple D A, Chyba T H, Marsh W D, Barnes J C, Annanenkov A N, Legun V D, Eichler H J, Gad G M A and Ueda K 2000 *Opt. Commun.* **183** 277–87.
85. Chen W, Inagawa Y, Omatsu T, Tateda M, Takeuchi N and Usiki Y 2001 Self-stimulating, passively Q-switched, diode-pumped Nd^{3+}:$PbWO_4$ Raman laser *Advanced Solid-State Lasers (Technical Digest Int. Conf., January, Seattle, WA)* (Washington, DC: OSA).
86. Rawle C B, Ter-Mikirtychev V V, Kinnie I T and Sandle W J 2001 High-energy solid-state Raman laser based on barium nitrate crystal for near IR and visible spectral range *Advanced Solid-State Lasers (Technical Digest Int. Conf. 28–31 January, Seattle, WA)* (Washington, DC: OSA) pp 22/MB1-1–24/MB1–3.
87. Basiev T T, Doroshenko N E, Zverev P G and Prokhorov A M 2000 Solid-state laser of yellow spectral region Russian Patent Appl. No 2000110183/28(010974).
88. Zverev P G, Basiev T T, Doroshenko M E and Osiko V V 2000 Barium tungstate Raman laser—a new coherent source for sodium star experiments *Trends in Optics and Photonics Series* vol 34 ed H Injeyan, U Keller and C Marshall (Washington, DC: OSA) pp 348–354.
89. Murray J T, Austin W L and Powell R C 1998 End-pumped intracavity solid-state Raman lasers *Advanced Solid-State Lasers (OSA Trends in Optics and Photonics 19)* ed W R Bosenberg and M M Feiger (Washington DC: OSA) pp 129–35.
90. Pask H M, Blows J L, Piper J A and Omatsu T 2001 Thermal lensing in a barium nitrate Raman laser *Advanced Solid-State Lasers (Technical Digest Int. Conf. 28–31 January, Seattle, WA)* (Washington DC: OSA) 276/TuB15-1–278/TUB15-3.
91. Murray J T, Powell R C and Kock G 1996 *NASA Research Report.*
92. McLean J W and Murray J T 1998 *Laser Focus World (January)* (Los Angeles CA: SPIE) p 171; Murray J T, Austin W L, Calmes L K, Powell L K and Quarles G J 1997 *Advanced Solid State Lasers (OSA TOPS 10)* ed C R

Pollock and W R Bosenberg (Washington DC: OSA) p 72; Murray J T, Austin W L, Calmes L K, Powell R C, McLean J W and Brian L 1997 *Proc. SPIE* (Orlando FL: SPIE).

93. Murray J T, Roberts W T Jr, Austin W L, Powell R C and Angel J R 1998 *Proc. SPIE* (Los Angeles CA: SPIE).
94. Murray J T, Powell R C, Austin W L, Roberts W T Jr, Angel J R, Shelton C T and Sandler D G 1997 *Proc. ESO Laser Technology and Laser Guide Star Workshop (Garching, June)* (LosAngeles CA: SPIE).
95. Murray J T, Roberts W T Jr, Austin W L, Powell R C and Bonaccini D 1998 *Proc. SPIE* (Los Angeles, CA: SPIE).
96. Murray J T, Austin W L and Powell R C 1998 *Advanced Solid-State Lasers (OSA TOPS 11)* ed W R Bosenberg (Washington DC: OSA) p 82.
97. Basiev T T, Danileiko Yu K, Doroshenko M E, Fedin A V, Gavrilov A, Osiko V V and Smetanin S N 2003 High-energy $BaWO_4$ Raman laser pumped by a self-phased-conjugated Nd:GGG laser *Optics of Lasers Int. Conf. June* (St. Petersburg).
98. Basiev T T, Fedin A V, Gavrilov A, Osiko V V and Smetanin S N 2003 High-average-power $BaWO_4$ Raman laser pumped by a self-phase-conjugated Nd laser *CLEO-Europe, June,* (Munich).
99. Sulc J, Jelinkova H, Cerny P, Skornjakov V, Doroschenko M, Zverev P and Basiev T T 2003 Nd:SrWO4 Raman laser *Proceedings of Workshop* 2003 *Part A, CTU reports* vol 7, (Prague) pp 174–4.

FURTHER READING

Basiev T T 1999 *Sov. Phys.–Usp.* **42** 1051–62.

Bloembergen N 1967 *Am. J. Phys.* **35** 989.

Erckhart G 1966 *IEEE J. Quantum Electron.* QE-**2** 1.

Glass A 1967 *IEEE J. Quantum Electron.* QE-**3** 516–20.

Grasyuk A Z 1974 *Kvantovaya Elektron.* **3** 485 (Engl. transl. *Sov. J. Quantum Electron.*).

Kaiser W and Maier M 1972 *Laser Handbook* vol 11, ed F T Arecchi and E O Shultz-Dubois (Amsterdam: North-Holland) p 1077.

Loudon R 1964 *Adv. Phys.* **13** 423.

Lugovoi V N 1968 *Introduction to the Theory of Stimulated Raman Scattering* (Moscow: Nauka) in Russian.

Mochalov I V 1997 *Opt. Eng.* **36** 1660–9.

Murray J T, Powell R C and Peyghambarian N 1996*J. Luminesc.* 66&67 89.

Powell R C and Basiev T T 2000 Seventy years of Raman scattering *Advances in Laser Physics* ed V S Letokhov and P Meystre (Amsterdam: Harwood Academic) pp 55–66.

Zubov V A, Sushchinskii M M and Shuvalov I K 1964 *Usp. Fiz. Nauk* **83** 197 (Engl. transl. *Sov. Phys.–Usp.*) 7419.

Zverev P G, Basiev T T and Prokhorov A M 1999 *Opt. Mater.* **11** 335.

Zverev P G, Basiev T T, Osiko V V, Kulkov A M, Voitsekhovskii V N and Yakobson V E 1999 *Opt. Mater.* **11** 315–34

Taylor & Francis
Taylor & Francis Group
http://taylorandfrancis.com

10

Colour Centre Lasers

T. T. Basiev, P. G. Zverev, and S. B. Mirov

CONTENTS

10.1 Crystal Hosts for Active Elements of Colour Centre Lasers ... 151
10.2 Types of CCs in Ionic Crystals ... 153
10.3 Colour Centre Formation in Ionic Crystals ... 154
  10.3.1 Colour Centre Formation in Alkali-Halide Crystals under Ionizing Irradiation ... 155
  10.3.2 $\mathrm{LiF}:\mathrm{F}_2^-$ Active Elements Optimization ... 155
  10.3.3 $\mathrm{LiF}:\mathrm{F}_2^+$ Active Elements Optimization ... 156
10.4 CW and Quasi-cw CCL Operation ... 157
10.5 Pico- and Femtosecond Quasi-cw CCL Operation ($T = 77$ K) ... 158
10.6 Room-Temperature CCL Operation ... 159
  10.6.1 CW and Quasi-cw Regimes ... 159
  10.6.2 High-Peak-Power Room-Temperature CCL Operation in Pico- and Femtosecond Regimes ... 160
  10.6.3 High Energy and Power in Colour Centre Lasers ... 162
  10.6.4 Narrow-Line Tunable and Super-Broadband CCL Oscillation ... 162
10.7 CC Energy and Power Amplifier ... 163
10.8 Conclusions ... 164
References ... 164

10.1 Crystal Hosts for Active Elements of Colour Centre Lasers

Colour centres (CCs) exist in many types of crystalline solids, including both ionic and covalently bonded lattices. In Table 10.1, the major physico-chemical, optical and mechanical characteristics of the crystal hosts intended for CC laser-active elements are considered and compared with each other and with other well-known laser media. The most promising materials for developing CCs are crystals of alkali-halide metals, alkali-earth fluorides, oxides (for instance, sapphire) and covalent crystals (at present the only available representative is diamond).

The most widespread media with CCs—alkali-halide crystals—are optically transparent in a wide range of spectra (0.11–35 μm) and are widely used as optical materials for instruments in UV, visible and IR optical technology, optics and spectroscopy. The structure of the alkali-halide crystals refers to the Fm3m spatial group with a general cubic symmetry of the crystal lattice. Thus, the alkali-halide crystals are inherently isotropic, i.e. their refraction index does not depend upon the polarization or direction of light propagation. A simple, fast and available Kyropoulos technique enables the commercial growth of high-quality crystals with large cross sections and volumes (for instance, $\varnothing 400 \times 200\,\mathrm{mm}$) on a large scale. The crystal media so grown may be used for fabricating large active elements and Q-switches in powerful laser systems.

LiF and NaF crystals are the most outstanding among the alkali halides because of their low hygroscopicity. Their solubility in water is rather low and, hence, they are acceptable for practical applications under natural conditions. It is possible to use NaF crystals in a dry atmosphere. All the remaining alkali-halide crystals, without exception, cannot be used in damp air. Their facets become opaque without a special protective coating.

Of the alkali halides, LiF crystals have the smallest (close to $-1.2 \times 10^{-5}\,°\mathrm{C}^{-1}$) value for the temperature-derivative refractive index and a high thermal conductivity coefficient (14 W $\mathrm{m}^{-1}\mathrm{C}^{-1}$ at 300 K, even higher than the value of 13 W $\mathrm{m}^{-1}\mathrm{C}^{-1}$ for the YAG crystal). Thus, the critical thermal power P_{cr} ($P_{\mathrm{cr}} = \lambda K |\mathrm{d}n/\mathrm{d}t|^{-1}$) of an LiF crystal [1,2], for which the value of thermal aberration becomes comparable with the laser wavelength, amounts to 1.25 W at $\lambda = 1.06$ μm (for YAG:Nd^{3+} $P_{\mathrm{cr}} = 1.3$ W). Therefore, LiF must be considered as a promising laser lattice for high average-power laser operations at room temperature. A comparatively small non-linear refractive index, n_2, for LiF provides a high level of self-focusing critical power—0.46 MW, $\left(P_{\mathrm{cr}}^{\mathrm{s}} = \varepsilon_0 C \lambda^2 / 8\pi n_2\right)$—which exceeds the $P_{\mathrm{cr}}^{\mathrm{s}}$ of YAG crystals (0.30 MW) and is slightly lower than that for ED–2 glass $\left(P_{\mathrm{cr}}^{\mathrm{s}} = 0.69\,\mathrm{MW}\right)$. From this point of view as well as for their high (compared to the YAG crystal) laser-induced bulk damage threshold of 3.6 GW cm^{-2} (at 1.06 μm for 10 ns pulses), LiF crystals are also considered as prospective lattices for non-linear saturable absorbers and Q-switchers in resonators in powerful laser systems.

TABLE 10.1

Main Physico-Chemical, Mechanical and Optical Characteristics of the Most Promising Crystal Hosts with CCs [2]

Crystal	ρ (g cm^{-3})	d (Å)	H (kg mm^{-2})	(g/100g H_2O)	Solubility T_m (K)	K (W mK^{-1})	$\alpha \times 10^6$ (K^{-1})	E (kg mm^{-2})	M	S_T (kg mm^{-2})	R_T^* $\left(\mathrm{W\,m^{-1}}\right)$	$N10^5$ (K^{-1})	$dn/dT \times I_{thr} \times 10^{12}$ (Wm^{-2})	Transparency at $\alpha = 1\,\mathrm{cm}^{-1}$ level	Range
LiF	2.64	4.03	99–102	0.12	1121	14.2	33.7	8820	0.28	1.2–4.0	43–143	1.387	–2.9	3600	0.11–6.6
NaF	2.79	4.62	60	4.2	1270	9.2	32.2	8780	0.19	-	-	1.321	–1.8	1400	0.16–11.2
NaCl	2.17	5.64	15.2–18.2	36.0	1074	6.4	39.6	4360	0.20	-	-	1.53	–3.7	200	0.17–18.0
KF	2.50	5.35	-	94.9	1130	-	-	-	-	-	-	-	-	-	0.2–15.0
KCl	1.99	6.29	7.2–9.3	37.4	1049	6.0	37.0	3810	0.14	-	-	1.48	–3.3	700	0.18–23.0
KBr	2.75	6.60	6–7	70.9	1007	4.8	38.4	3290	0.32	-	-	1.54	3.2	500	0.21–28.0
KI	3.13	7.07	5	144.0	959	2.1	41.2	2550	0.14	-	-	1.64	4.5	200	0.3–35.0
RbCl	2.76	6.58	-	94.2	717	-	32.8	-	-	-	-	-	-	-	-
MgF_2	3.18	$a = 4.64$ $c = 3.06$	576	0.0076	1536	$21 \perp c$ $30 \parallel c$	$9.4 \perp c$ $13.4 \parallel c$	17 265	0.27	5.4	470	$n_0 = 1.373$ $n_c = 1.385$	11.2 5.8	1000	0.1–7.0
CaF_2	3.18	5.46	120–163	0.0016	1676	9.7	18.8	14 000	-	-	-	1.429	–1.05	>1000	0.13–9.4
SrF_2	4.24	5.79	144	<0.1	1190	-	19.6		-	-	-	-	-		0.1–9.0
Al_2O_3	3.974	$a = 4.76$ $c = 13.0$	2100	0	2313	35.0	$5.0 \perp c$ $6.7 \parallel c$	35 230	0.27	55.0	10 000	$n_0 = 1.765$ $n_c = 1.757$	1.3 0.97	1900	0.18–5.1
Diamond	3.515	3.57	8820	0	3770	900.0	1.0	58 000	-	-	-	2.40	0.4	12 000	0.24–2.7
$Y_3Al_5O_{12}$	4.55	12.0	1350	0	2223	13.0	7.8	31 275	-	20.0	790	1.815	1.05	2000	0.21–5.3
ED-2 glass	2.539	-	-	-	582	1.4	8.0	9190	0.24	10.0	140	1.56	0.3		-

The thermal shock parameter, R, characterizes the thermo-mechanical strength of the material. For instance, for a plate element with a thickness t, thermal power P_V, which may be absorbed by the medium with a parameter R_T without being damaged, $P_V = 12R_T/t^2$, where $R_T = S_T(1 - \mu)K/\alpha E$.

ρ, density (g cm^{-3}); d, lattice constant (Å); H, Knoop hardness (kg mm^{-2}); T_m, melting temperature (K); K, coefficient of thermal conductivity at 300 K (W m^{-1} K^{-1}); α, coefficient of linear expansion at 300 K (K^{-1}); E, Young's modulus (kg mm^{-2}); μ, Poisson's coefficient; S, compression (tension) or bending strength (kg mm^{-2}); R, thermal shock parameter (W m^{-1}); n, refractive index at $\lambda = 1$ μm; dn/dT, temperature derivative refractive index at $\lambda = 1$ μm (K^{-1}); I_{thr}, laser-induced bulk damage threshold at $\lambda = 1.06$ μm for 10 ns pulse duration.

As shown in Table 10.1, alkali-halide crystals have low Knoop hardness values, 10–200 times lower than those for Al_2O_3 and YAG crystals, which are the most widely used ones in laser technology. This makes it difficult to achieve and preserve highly polished surfaces during the process of preparation and application for all alkali-halide crystals except LiF and NaF.

The most durable of the alkali-halide crystals—LiF—has a tensile strength almost 20 times less than that for YAG, ten times less than for laser silica glasses and close to the strength of phosphate glasses. Moreover, alkali-halide crystals easily come to pieces along the [100] cleavage planes under impact. Therefore, they have to be carefully handled during exploitation and protected from appreciable thermal gradients and thermal and mechanical shocks.

Alkali-earth fluorides are of great interest as host crystals for active media with CCs. They are easily produced to have low hygroscopicity and high mechanical and thermal strength, in contrast to alkali-halide crystals.

Sapphire and diamond are also promising for application as CC active media. These crystals feature a unique combination of thermal and mechanical properties, which exceed (as seen in Table 10.1) the corresponding values for YAG crystals. However, they are not so readily accessible for technology as alkali halides. Since LiF can be grown as large crystals and has remarkable physical and optical properties (the best material for room temperature operation) and because of the extensive research on this material we will primarily focus on it for the rest of this chapter.

10.2 Types of CCs in Ionic Crystals

Table 10.2 shows the major types of CCs that can be used to achieve stimulated radiation. In general, the major crystals where laser-active CCs can be developed are the pure and impurity-doped fluorides and chlorides of Li, Na, K and Rb alkali metals [2–6] as well as CaF_2 and SrF_2 [7]. Laser oscillation has also been reported using CCs in Al_2O_3 [8,9], diamond [10], MgF_2 [11] and the compound fluorides, $KMgF_3$ [12] and $YLiF_4$ [13]. In the primal state, these crystals are optically transparent. Under irradiation with high-energy electrons, neutrons, γ-rays, X-rays or hard UV, or calcination in alkali metal vapour (additive colouration), anionic vacancies appear in the crystal lattice and serve to localize free electrons. The absorption bands of these (F) centres (vacancy + electron) give a typical colouring to the crystals.

The simplest of point defects is the anionic vacancy V, denoted in Table 10.2 by an empty square (empty circle in Figure 10.1) in place of an absent negative ion. The vacancy has an effective positive charge and, on capturing an electron, forms a defect whose electronic structure is similar to that of the hydrogen atom. Such an optical centre is referred to as an F centre and has absorption bands in the visible or UV spectral regions (for many reasons [6] F centres are not suitable for laser oscillation).

The other intrinsic electronic CCs on which oscillation has been obtained (see Table 10.2 and Figure 10.1) are complexes derived from F centres. For instance, the F_2^+ centre consists of two neighbouring anionic vacancies with one captured electron, the F_2 centre consists of two neighbouring vacancies with two captured electrons (an analogue of the hydrogen molecule) and the F_2^- centre is composed of a pair of vacancies with three captured electrons (see Table 10.2 and Figure 10.1).

The CCs denoted with a subscript A (besides their own defects) involve a neighbouring impurity ion replacing the positive ion in the nearest site of the cationic sublattice (for example, an Li impurity in Na or K sublattices or an Na impurity in K or Rb sublattices). The centres denoted by subscript B comprise an association of an anionic vacancy capturing one electron with two neighbouring impurity ions (see Table 10.2).

The principles of colour centre laser (CCL) operation can be accounted for using the Frank–Condon configuration diagram, which describes the optical properties of an electron system interacting with molecular or lattice vibrations; in particular, the optical transition of CCs. Pump radiation is absorbed in the wide band of the electric-dipole electron–vibrational transition 1 → 2. In a time of the order of 10^{-12}–10^{-13} s, radiationless relaxation to the minimum of the potential curve of the excited electronic state 2 → 3 occurs, accompanied by a mutual rearrangement of the neighbouring ions and by phonon emission. Then a radiative electron–vibrational transition (3 → 4) occurs with a probability of $A = 10^7$–$10^8\,s^{-1}$, followed by another rapid vibrational relaxation (4 → 1) to the potential curve minimum of the ground electronic state with a resetting of the spatial ion configuration. Disregarding the details, one may consider this scheme as the four-level laser scheme of oscillation.

TABLE 10.2
Colour Centre Representations

Type of Centre	Schematic Representation
F_2	
F_2^+	
F_2^-	
$(F_2^+)_A$	
$(F_2)_A$	
FA(II)	
FB(II)	

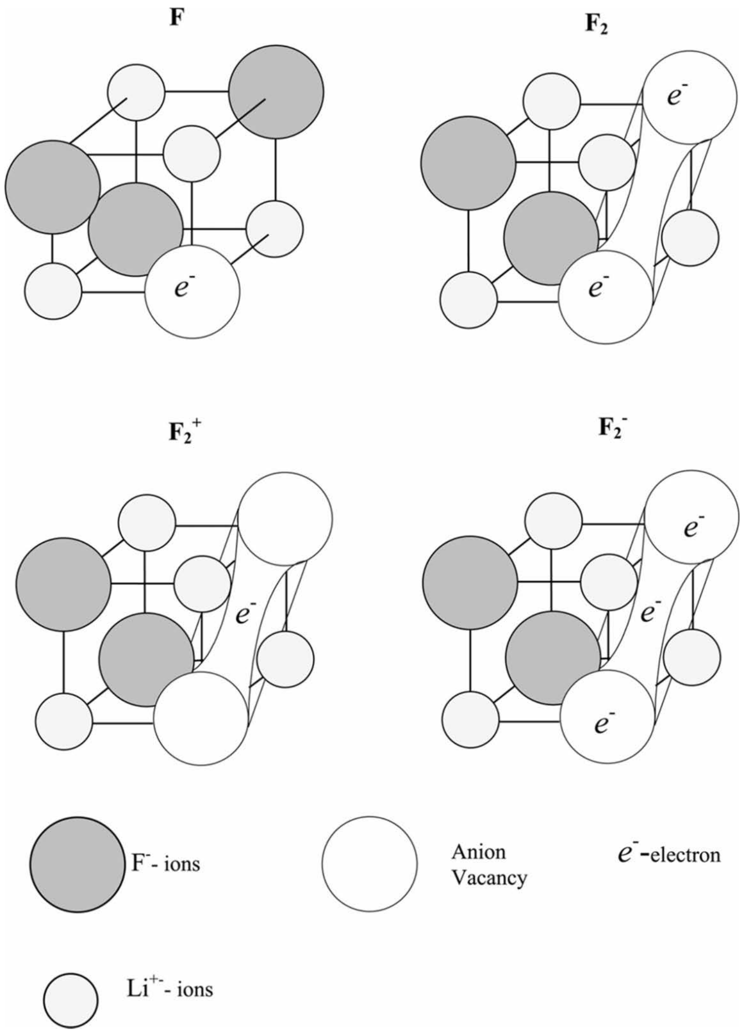

FIGURE 10.1 Structure of the simplest CCs in LiF crystals.

10.3 Colour Centre Formation in Ionic Crystals

CCs are formed in originally transparent crystals through ionic displacement caused by high-energy irradiation or through the creation of a stoichiometric excess of an alkali or alkali-earth metal in the crystal at an elevated temperature. The latter method is called additive colouration and provides CC with a longer lifetime.

The formation of aggregate CCs in alkali-halide crystals under ionizing radiation is a complicated process. It involves the emergence, separation and subsequent association of primary Frenkel defects into aggregate CCs as well as their recharging by electrons and band holes.

The necessary radiation damage can be produced by X-rays, γ-rays, neutrons, electrons or other charged particles. However, neutron beams are not readily available. The production of CCs using an electromagnetic field requires relatively long (days) exposure times but provides high homogeneity in the resultant CCs.

The readily available electron beam is a commonly used irradiation source for CC preparation. To penetrate through a crystal with a thickness of several millimetres, electrons with energies of 1–2 MeV are required and the crystal is usually exposed from both sides to provide sufficient homogeneity. The crystals are always irradiated at lower temperatures (77–177 K) with a current density of about 10 μA cm^{-2}. Irradiation time may vary from several minutes to a few hours depending on the crystal lattice and the type of centres to be produced [5].

The procedure for additive colouration consists of calcination of the crystal in metal vapour at a temperature between the crystal melting point and the temperature of colloid formation. For instance, for KCl the melting point is 768°C and the colloid formation is initiated at a temperature of 400°C. As a result of this procedure, the alkali-metal atoms are captured and become ionized on the crystalline surface, attracting the halogen ions. The latter diffuse towards the surface, forming anion vacancies in the bulk of the crystal. The electrons appearing as a result of alkali-metal atom ionization also diffuse to be captured by the vacancies, hence forming F centres. The crystal is then quickly cooled down to room temperature to avoid colloid formation. Further accumulation of the F_A, F_B and F_2^+ centres is stimulated by additional light treatment of the crystal. The technology for additive colouration in alkali-halide crystals was developed a long time ago. A detailed description of the relevant techniques and apparatus can be found in Ref. [14].

The technology for electrolytic colouration was also available rather a long time ago but it was only in 1987 that the first laser crystals were produced by this technique [15]. The procedure is as follows. A crystal is placed in a crucible and heated to the temperature of anion mobility, at which point 'thermal' anion vacancies also appear. A dc high-voltage electric field is applied to the crystal to drive an ionic current: anions move towards the anode and the cathode emits electrons. The latter are captured by the anion vacancies to form F centres. The next part of the crystal treatment, as in the case of additive colouration, involves rapid cooling and light treatment. Additive and electrolytic colouration techniques are better than radiation techniques because they produce more temperature- and light-resistant laser crystals. The disadvantages of the previously mentioned methods are the low colouring homogeneity, the poor optical quality of the crystals due to colloid formation and the inability to produce large-size active media.

10.3.1 Colour Centre Formation in Alkali-Halide Crystals under Ionizing Irradiation

The formation of aggregate CCs in alkali-halide crystals under ionizing radiation is a complicated process. It involves the emergence, separation and recombination of primary Frenkel defects, association into aggregate $F_2, (F_2)_A, F_2^+, (F_2^+)_A, F_2^-, F_3, F_3^+, F_3^-$, F_3 and other CCs and recharging of the CCs by electrons and band holes. Defect formation may occur rapidly or slowly. Decomposition of self-localized excitons into primary radiational defects and the recharging of CCs are relatively fast processes (10^{-12}–10^{-7} s). Slow processes occur because of either spatial diffusion of the defects and their associates or diffusion of self-localized holes (resulting in CCs recharging).

All these processes determine the efficiency with which any type of CC is formed. They depend upon the irradiation temperature, and crystal storage, impurity composition of the initial material, ionizing radiation dose power and irradiation dose.

Separated electrons and holes, free and self-localized excitons are generated in alkali-halide crystals under ionizing irradiation. Self-localized excitons decompose with the emergence of pairs of F centres and interstitial halogen atoms (H). Rapid recharging of these pairs under a flux of electrons gives rise to the simultaneous formation of anion vacancies V_a^+ and interstitial halogen ions I_a [16]:

$$e_s^0 \Rightarrow F + H \tag{10.1}$$

$$e_s^0 \Rightarrow V_a^+ + I_a^-. \tag{10.2}$$

The mechanisms for aggregate centre formation through the migration of anion vacancies have been studied by Delbecq [17]. According to him, charged F_2^+ centres first appear and then capture electrons to produce neutral F_2 centres:

$$V_a^+ + F \Rightarrow F_2^+ \tag{10.3}$$

$$F_2^+ + e \Rightarrow F_2. \tag{10.4}$$

Simultaneously with rapid electron capture, F_2^+ centres may take part in a slow temperature-dependent migration process. Colliding with the F, F_2^+ and F_2^- CCs, they form more complex CCs — F_3^+, F_4^+ and F_4, respectively:

$$F_2^+ + F \Rightarrow F_3^+ \tag{10.5}$$

$$F_2^+ + F_2 \Rightarrow F_4^+ \tag{10.6}$$

$$F_2^+ + F_2^- \Rightarrow F_4 \tag{10.7}$$

whose further aggregation leads to the appearance of colloid particles in the crystal. The processes for F_2 CC formation by the scheme in (10.3) and (10.4) compete with those for ionization due to a rapid capture of free electrons:

$$F_2 + e \Rightarrow F_2^- \tag{10.8}$$

or holes

$$F_2 + h \Rightarrow F_2^+ \tag{10.9}$$

or due to the diffusion processes involving mobile anion vacancies

$$V_a^+ + F_2 \Rightarrow F_3^+ \tag{10.10}$$

and self-localized holes

$$F_2 + V_k \Rightarrow F_2^+. \tag{10.11}$$

These processes (10.4, 10.8, 10.9 and 10.11), leading to recharging in the group of F_2, F_2^+ and F_2^- CCs, are also inherent in the group of F_3, F_3^+ and F_3^- CCs.

The ratio of the contributions of different reactions depends on the irradiation procedure and impurity composition in the irradiated crystal. The optimization of irradiation treatment to create F_2^- and F_2^+-stabilized CCs in doped LiF crystals is discussed later.

10.3.2 LiF : F_2^+ Active Elements Optimization

Here we use the LiF crystal with an F_2^- CC as an example to illustrate how irradiation parameters optimization overcomes the technological difficulties faced when producing an optically dense active medium.

LiF : F_2^- crystals, with their unique combination of modulation, thermal and operational characteristics, are now widely used as active media in tunable lasers and as nonlinear elements with saturable absorption for neodymium laser Q-switches. However, the available techniques for the preparation of such laser crystals fail to produce the optically dense, high-contrast media required for a series of applications. Usually, the value of the active absorption at the working wavelength does not exceed 0.4–0.6 cm^{-1} at a contrast (the ratio of the active absorption coefficient to the loss coefficient at $\lambda = 1.06$ μm) of 10–20. Under the action of γ-quanta commonly used for producing $\mathrm{LiF:F_2^-}$ laser crystals, the $\mathrm{F_2^+}$ CCs emerging by reaction (10.3) may be involved in one of three processes: (a) rapid electron capture to produce $\mathrm{F_2}$ (reaction (10.4)) and $\mathrm{F_2^-}$ (reaction (10.8)) CCs; (b) slow diffusion processes of aggregation of the type (10.5)–(10.7) and (c) dissociation on the F centre and anion vacancy $\mathrm{F_2^+ \Rightarrow F{+}V_a^+}$.

The rates of the various processes and the final concentration of CCs depend, as mentioned previously, on the impurity composition of the initial material, irradiation dose, power and crystal temperature. By varying the ratio of these parameters, one can essentially influence the processes of $\mathrm{F_2^-}$ CC formation in LiF.

When the procedure of LiF crystal treatment under ionizing irradiation is optimized so that processes (10.3) and (10.4) are efficient and (10.5)–(10.7) negligible, the maximum active absorption of $\mathrm{F_2^-}$ CCs at the wavelength 1064 μm exceeds 1.5 cm^{-1} at a contrast as high as 20–40.

10.3.3 $\mathrm{LiF:F_2^+}$ Active Elements Optimization

$\mathrm{LiF{:}F_2^+}$ is a high-gain active medium with large absorption and emission cross sections and a wide near-IR tuning range [2,6]. Unfortunately, the low thermal stability of 'pure' $\mathrm{F_2^+}$ centres at room temperature (half decay time ~ 12 h) made the $\mathrm{LiF{:}F_2^+}$ laser medium very inconvenient for use, as it could be operated only at temperatures <100 K [6].

To overcome the low thermostability of $\mathrm{LiF{:}F_2^+}$ active media, a technique for the two-step photoionization of neutral $\mathrm{F_2}$ centres in LiF was proposed [18]. However, in this case, the problem of low active element operational stability has only partially been solved. While the pumping beam is turned on, the $\mathrm{F_2^+}$ laser exhibits stable operation but, after the pumping beam is switched off, the active zone of the crystal becomes exhausted due to thermal degradation of the $\mathrm{F_2^+}$ centres after one day at $T = 300$ K. By thermoelectrically cooling an $\mathrm{LiF{:}F_2^+}$ CC crystal to –30°C to 0°C, the operation time can be extended to a few weeks or months.

In 1978, Khulugurov and Lobanov [19] discovered that the thermal stability of positively charged 'pure' $\mathrm{F_2^+}$ centres can be increased by co-doping LiF crystals with suitable anion or cation impurities, with the formation of complex $\mathrm{F_2^+}$-like centres. However, the improved thermostability of these centres at room temperature did not provide the appropriate photostability of the active media under powerful laser excitation at wavelengths ≤590 nm. For example, pumping the LiF crystals with $\mathrm{F_2^+}$-stabilized CCs by powerful radiation of the second harmonic of an Nd:YAG laser (532 nm) results in a significant fading in the CCL output [20], although at low levels of pumping (several tens of mJ), the CCL will operate relatively well [21]. The fading under high power excitation is caused by the photo-chemical process in the pumping channel of the crystal, which involves the two-step photoionization of neutral $\mathrm{F_2}$ centres $\left(\mathrm{F_2} + 2h\nu = \mathrm{F_2^+} + \mathrm{e}\right)$ and trapping of the released electron e by the positively charged $\mathrm{F_2^{+**}}$ centres $\left(\mathrm{F_2^{+**}} + \mathrm{e} = \mathrm{F_2^{**}}\right)$. The concentration of 'pure' $\mathrm{F_2^+}$ centres, which appeared due to photoionization of $\mathrm{F_2}$ centres, quickly reduces as $\mathrm{F_2^+}$ centres migrate through the crystal with the creation of $\mathrm{F_3^+}$ centres: $\mathrm{F_2^+ + F = F_3^+}$ [22].

In Refs. [21,23], the development of a high-power room-temperature photo- and thermostable tunable $\mathrm{LiF{:}F_2^{+**}}$ laser was reported. The optimized technology of thermostable $\mathrm{F_2^{+**}}$ CCs in LiF crystals and an appropriate choice for the pumping laser wavelength in Refs. [21,23] allowed for the simultaneous solution of the problems of photo- and thermostability of laser materials based on LiF crystals with $\mathrm{F_2^+}$-like CCs. The peculiarities of the technological preparation of $\mathrm{LiF{:}F_2^{+**}}$ crystals according to Refs. [21,23,24] are discussed later.

The crystals were grown by the Kyropoulos method in an argon atmosphere from nominally pure raw materials and doped with LiOH, $\mathrm{Li_2O}$ and $\mathrm{MgF_2}$. As-grown LiF crystals have an intense infrared absorption band at $\nu = 3730$ cm^{-1} (absorption coefficient ≃ 1.2 cm^{-1}) due to $\mathrm{OH^-}$ ions, which substitute for the fluoride in the anion node of the crystalline lattice, and intense bands with frequency maxima at 3560 and 3610 cm^{-1}, due to $\mathrm{Mg^{2+}OH^-OH^-V_c^-}$ complexes. The UV absorption spectra of the grown LiF crystals exhibit strong absorption bands in the region 200–270 nm that are due to the $\mathrm{O^{2-}}$–$\mathrm{V_a^+}$ as well as $\mathrm{O^{2-}}$–$\mathrm{Mg^{2+}}$ dipoles.

To obtain a high concentration of $\mathrm{F_2^{+**}}$ centres and a small concentration of colloids and parasitic aggregate CCs, as-grown crystals are subjected to a multi-step γ-irradiation treatment with a Co^{60} source.

At the first stage, the crystals are subjected to an ionizing treatment (γ-irradiation, 2–5 × 10^7 Rad) at temperatures lower than temperature $T\left(\mathrm{V_a^+}\right) = 240$ K of anion vacancy $\left(\mathrm{V_a^+}\right)$ mobility in LiF crystals.

The ionizing treatment creates a great number of free electrons and holes, which can form self-localized excitons after thermalization. These excitons localized near a specific anion node of the crystalline lattice may annihilate and the released energy can be used for shifting an anion from its node to the interstitial position, causing the formation of an anion vacancy and an F centre according to the schemes (10.1) and (10.2).

Simultaneously with primary defect formation according to (10.1) and (10.2), two processes of $\mathrm{(OH)^-}$ ions dissociation are taking place under the ionizing treatment [4]:

$$2\left(\mathrm{OH^-}\right) \Rightarrow \mathrm{O_2^-} + \mathrm{e} + \mathrm{V_a^+} + 2\mathrm{H_i^0} \tag{10.12}$$

and

$$2\left(\mathrm{OH^-}\right) + \mathrm{V_a^+} + \mathrm{e} \Rightarrow \mathrm{O^{2-}V_a^+} + \mathrm{O^-} + 2\mathrm{H_i^0} \tag{10.13}$$

where $\mathrm{O_2^-}$ is a molecular ion of oxygen, $\mathrm{O^-}$ is a single ionized atom of oxygen and $\mathrm{H_i^0}$ is an interstitial atom of hydrogen.

It is very important that there is no formation of aggregate CCs during the irradiation of the crystal at temperatures below the temperature of mobility of anion vacancies. $\mathrm{O^{2-}}$–$\mathrm{V_a^+}$ dipoles are accumulated in a high quantity, since they are photo- and thermostable under γ-irradiation. In addition to this, the ionizing treatment creates a high concentration of single ionized oxygen atoms and molecules due to a hydroxyl group dissociation. It is noteworthy to mention that one of the products of $\mathrm{OH^-}$ radiolysis—interstitial $\mathrm{H_i^0}$ atoms—are efficient traps of electrons:

$$\mathrm{H_i^0} + \mathrm{e} \Rightarrow \mathrm{H_i^-} \tag{10.14}$$

which prevent the electrons from being captured by the F_2^+ centre at the subsequent stages of the crystal preparation, thereby increasing the efficiency with which stable F_2^{+**} centres accumulate. The role of the Mg impurity can be explained as follows. F-centre formation is likely to occur near impurity-cation-vacancy dipoles $M^{2+}–V_c^-$. In accordance with the following reaction:

$$Mg^{2+}V_c^- + F \Rightarrow Mg^+ + V_a^+V_c^- \tag{10.15}$$

an F centre can give its electron to a divalent metal impurity forming Mg^+ and a pair of vacancies $V_a^+V_c^-$. Anion–cation dipoles, $V_a^+V_c^-$,, play an important role in the formation of F_2^+-perturbed CCs at the subsequent stages of the crystal preparation. However, an excessive concentration of the Mg dopant may play a negative role due to the decreasing concentration of the useful $O^{2-}V_a^+$ dipoles as they bond with oxygen and form $Mg^{2+}O^{2-}$ dipoles that do not take part in F_2^+-like CC formation.

At the second stage of the technological process, the crystals are heated up to $T_1 < T < T_2$, where T_1 (~240 K) is the threshold temperature of V_a^+ mobility and T_2 (~270 K) that of F_2^+, $V_a^+V_c^-$ and $O^{2-}V_a^+$ mobility in an LiF crystal, and stored at this temperature for some time. This temperature interval is chosen within these specific limits so that anion vacancies are mobile in the crystal and F_2^+ centres as well as $V_a^+V_c^-$ and $O^{--}V_a^+$ dipoles are immobile and cannot diffuse in the crystalline lattice. During this time, an important process in the formation of unperturbed F_2^+ CCs takes place due to the diffusion of mobile anion vacancies and their association with F centres:

$$V_a^+ + F \Rightarrow F_2^+. \tag{10.16}$$

Consequently, the concentration of F centres decreases due to their association with anion vacancies. This is a useful process which helps to increase the concentration of F_2^+-stabilized centres at the following stages and to decrease the concentrations of other aggregates and colloids. At the third stage, the crystals are re-irradiated at the temperature $T < T_1$ to increase the number of anion vacancies (that have been exhausted at the second stage) by ionizing the neutral F centres. After that, the crystals are again subjected to the procedure described for stage 2 to increase the number of pure F_2^+ centres due to the process (10.16).

At the fourth stage, the crystals are heated up to the room temperature and stored for some period of time, after which the crystals exhibit a stable concentration of the CCs of interest and are ready for use as a laser medium. The processes that take place at this stage are as follows.

1. The $O^{2-}V_a^+$ complexes are mobile at room temperature and their migration leads to the development of F_2^{+**} centres stabilized with the O^{2-} ion $\left(F_2^+O^{2-}\right)$:

$$O^{2-}V_a^+ + F \Rightarrow F_2^+O^{2-}. \tag{10.17}$$

2. Another very important reaction occurs due to the intrinsic mobility of F_2^+ centres at room temperature. The migration of these centres may lead to a useful process of association of F_2^+ centres with a single ionized oxygen atom O^- with the formation of $\left(F_2^+O^{2-}\right)$ centres:

$$F_2^+ + O^- + e \Rightarrow F_2^+O^{2-}. \tag{10.18}$$

3. Since at room temperature bi-vacancy dipoles $V_a^+V_c^-$ are also mobile ($V_a^+V_c^-$ start to be mobile at temperatures of about 273 K), they may associate with F centres and perturbed F_2^+ centres can occur:

$$V_a^+V_c^- + F \Rightarrow F_2^+V_c^-. \tag{10.19}$$

Due to the described multi-stage LiF crystal treatment, the optimum conditions for useful processes (10.17–10.19) of F_2^+-stabilized CC formation are provided and the efficiency of the parasitic processes ($F_2^+ + e \Rightarrow F_2, F_2 + e \Rightarrow F_2^-, F_2^+ + F \Rightarrow F_3^+$, $F_2^+ + F_2 \Rightarrow F_4^+, F_2^+ + F_2^- \Rightarrow F_4, V_a^+ + F_2 \Rightarrow F_3^+$), using the techniques responsible for formation of other aggregate and colloid centres, is suppressed.

Using the techniques developed in Refs. [21,23], LiF:F_2^{+**} crystals did not exhibit any photo-degradation when pumped by radiation in the 620–750 nm range at energy densities of up to ~5 J cm^{-2}. We estimate the lifetime of these CC crystals to exceed 10 years at room temperature. The real conversion efficiency of the LiF:F_2^{+**} laser exceeds 50% with a maximum output power of 100 mJ, limited only by the capabilities of the available pumping lasers.

Detailed descriptions of the laser oscillation in CCLs have been presented in several review papers [1,2,5,6,25]. Here, only the main features of specific operating regimes of CCLs will be described.

10.4 CW and Quasi-cw CCL Operation

Stationary CC oscillation was realized for the first time at the beginning of the laser era, in 1965, by Fritz and Menke [26], who obtained CC lasing at a cryogenic temperature under flashlamp pumping. Now there are many cw lasers that can be used as pumping sources for tunable CCLs, but the most popular are the widespread Ar^+ and Kr^+ ion gas lasers oscillating in the visible range and solid-state lasers on neodymium-doped yttrium aluminium garnet and perovskite, which effectively lase in the IR, at wavelengths of 1.06 and 1.3 μm. These lasers in the cw regime can provide an output power of several tens of watts for pumping CCLs.

From the laser threshold expression (see, for example, Equation (10.7) in Ref. [2]), one can see that a pump density of several kW cm^{-2} is needed to reach the threshold for CCL oscillation. This is easily achieved for pulsed pumping by a flashlamp emitting a few tens of joules during a millisecond pulse. In this case, the lasing volume of the CC crystal can be as large as 1 cm^{-3} or even more.

To get the same pump densities for cw laser pumping with a power of 0.1–10 W, the pump radiation has to be strongly focused and the CCL crystal placed at the focal point or cavity waist, 0.1–1 mm in diameter. The crystal length is limited by the confocal parameter of the focused beam and does not usually exceed 1 cm (typically it is a few millimetres).

The most popular optical scheme now used for cw CCL operation is the Kogelnik scheme with a Brewster-cut active element and a V or Z-shaped folded cavity to compensate for spherical lens or mirror astigmatism [27].

The relationship between the CC crystal thickness *t*, focal length $f = r/2$ of the spherical mirrors with radius *r* and folded angle of the cavity is given by the expression

$$\sin\theta\tan\theta\frac{n^4}{\left(n^2-1\right)\left(n^2+1\right)^{1/2}}=\frac{t}{f}. \qquad (10.20)$$

For a typical thickness, $t = 2\,\mathrm{mm}$, and the mirror curvature, $r = 50\,\mathrm{mm}$, the compensation angle 2θ is about 20°C and depends slightly on the refractive index *n*, which is typically 1.35–1.5 for alkali halides (Table 10.1).

The beam waist diameter, w_0, and confocal length, *b*, can be found from the following formulae:

$$w_0 = f\sqrt{\lambda/2\pi l_2} \qquad t \le b = f^2/l_2 \qquad \left(\frac{b}{f_2}=\frac{f}{l_2}\right), \qquad (10.21)$$

As one can see, such a strong focusing condition leads to strong local heating of the CC crystal pumped zone due to Stokes losses and can result in a strong thermal lens. Fortunately, deep cooling to liquid nitrogen temperature greatly increases the thermal conductivity of CC active crystals and leads to a decrease in thermal lensing.

There are two most popular regimes for operating in the cw mode. The first is narrow-line (single-frequency) broadly tunable CCL oscillation used for visible and IR spectroscopy, analytical application and fundamental metrology. The second is the mode-locked pico- and femtosecond pulse operating regime used for time-resolved transient spectroscopy, high-peak-power non-linear conversion and fast telecommunication systems.

Single-mode, single-frequency operation of a KCl:Li F_A(II) CCL under krypton ion laser pumping at 647 nm with a linewidth less than 260 KHz and tunability in the 2.5–2.9 µm spectral range using a pair of birefringent plates and an intracavity solid etalon was obtained in Ref. [28]. By active frequency stabilization, linewidths as low as 2 KHz were realized later [29]. To obtain single-mode operation and to improve linewidth and wavelength stability, ring cavity operation can also be applied [30,31]. The typical output power of an F_A(II) CCL varies from tens to hundreds of milliwatts in the 2.3–3.5 µm spectral region (Figure 10.2) [25].

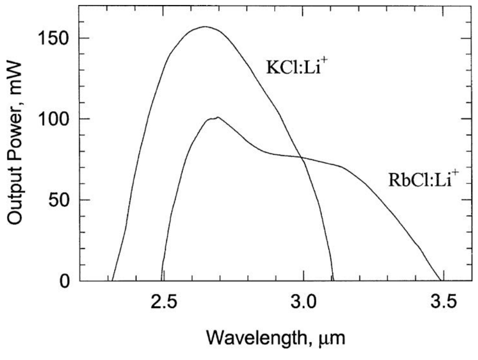

FIGURE 10.2 Tuning curves of KCL:Li$^+$ and RbCl:Li$^+$$F_A$(II) CCLs.

With the same pump source, $\mathrm{LiF:F_2^+}$, CCL operation with a very high slope efficiency of 60%, close to the physical limit (output-to-pump photon energy ratio) of 70%, was obtained. A wide tuning range, 0.84–1.04 µm, was covered with a cw output power of up to 1.1 W in the pure cw regime and under synchronous picosecond pumping [6]. In the last case, shortening by a factor of 25 from a 100 ps pump to a 4 ps CCL output was demonstrated. Optimal output coupling of the cw CCL varied from about 30% to 1%, depending on the gain. To work at the maximum of the tuning curve, where the gain is high, one usually uses low-output coupled laser cavities with a transmittance $T = 10\%–30\%$; however, when the tuning curve widens, a high-output coupling of $T = 1\%–3\%$ should be chosen.

One of the main problems of the $\mathrm{LiF}\left(\mathrm{F_2^+}\right)$ CCL is fast optical bleaching due to the orientational diffusion of $\mathrm{F_2^+}$ CCs [1]. The maximum cw lasing output (2.7 W) was recorded in a $\mathrm{KF}\left(\mathrm{F_2^+}\right)$ CCL under 1.064 µm Nd^{3+}:YAG pumping with a tuning range of 1.22–1.5 µm [25].

In the case of $\left(\mathrm{F_2^+}\right)$ A CCs, the KCL:Li crystal showed a very good performance: $P_{\mathrm{out}} = 400\,\mathrm{mW}$ under 1.32 µm cw Nd laser pumping and $E_{\mathrm{out}} = 2.3\,\mathrm{mJ}$ under 1.41 µm pulsed pumping with a tuning range of 2–2.5 µm [25].

The operation of $\left(\mathrm{F_2^+}\right)$ H CCs in NaCl crystals doped by OH$^-$ ions looks very promising. It was reported for the first time in Ref. [32] and then studied by many other groups [5,25]. An output power as high as 3.05 W at a slope efficiency of 33% was reported in Ref. [33] under 9 W pumping at 1.064 µm and 200 mW collinear auxiliary light of 514 nm. A very wide tuning range, 1.4–1.92 µm, important for telecommunications studies and tests with outputs of up to 1.3 W was obtained in Ref. [34] at 6 W 1.064-µm laser pumping and only 2 mW of 532 nm collinear auxiliary light. This laser can also easily operate in the mode-locked regime with picosecond pulses as short as 5 ps.

Stable cw laser operation without the use of auxiliary light was also obtained with the help of F_A(T1) CCs in KCl:Tl$^+$, KBr:Tl$^+$ and KBr:Tl$^+$ crystals. The first of these crystals provides about 1.4 W output at the maximum of the tuning curve with tunability from 1.4 to 1.6 µm at the absorbed pump power of ~3.5 W of a 1.064 µm Nd:YAG pump laser (Figure 10.3) [5]. What distinguishes these CCs from the others is their partially forbidden optical transitions, resulting in a lower gain and the longest radiative lifetime equal to 1.6 µs.

10.5 Pico- and Femtosecond Quasi-cw CCL Operation (T = 77 K)

One of the most interesting and important regimes of CCL operation is the mode-locked regime, when many longitudinal modes of a broadband laser radiate with a ‘coordinated phase’. According to the Fourier transformation, this multi-frequency cw laser operation leads to short-pulse high-peak-power

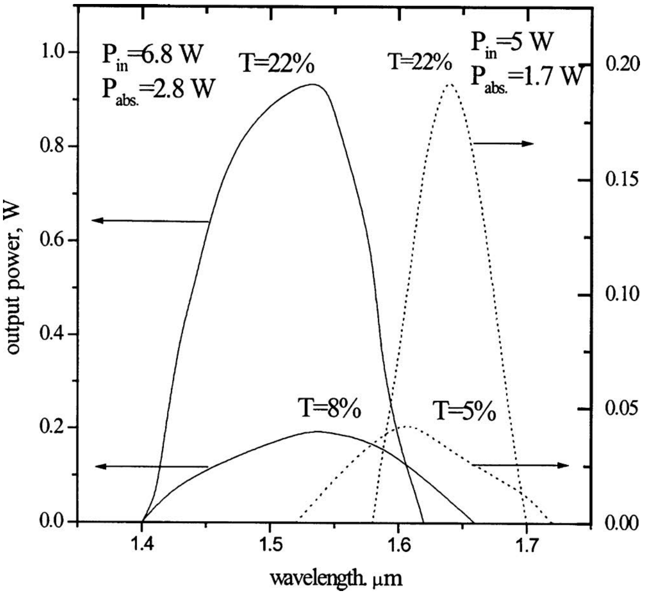

FIGURE 10.3 Tuning curves of an $F_A(T1)$ colour centre laser in KCl:Tl$^+$ (full curves) and KBr:Tl$^+$ (dashes) pumped by Nd:YAG laser radiation (1.064 μm). The increase in output coupler transmission from 5% to 22% results in a considerable increase in oscillation power accompanied by a narrowing of the overall spectral range

quasi-cw lasing with a pulse-to-pulse temporal interval equalling the laser cavity round-trip time and a pulse duration inversely proportional to the number of longitudinal modes operating in the mode-locking regime.

All types of the mode-locking techniques developed for dye lasers are applicable for developing mode-locked CCLs. CC mode-locked operation is quite similar to the dye laser mode-locking regime with only one distinction: the excited-state lifetime of a CC τ_{CC} is about 15–1500 ns and is usually larger than the laser cavity round-trip time, $\tau_{\text{cavity}} = 6–10$ ns, while for the dyes it is smaller ($\tau_{\text{dye}} = 3–5$ ns).

One of the most popular and effective techniques for realizing of pico- and femtosecond lasing is synchronous pumping, when the pump laser mode-locking regime is transferred to a CCL. In this case, the cavity round-trip times of both pump and CCLs should be synchronized and the synchronized CCL gain modulation results in pulsed CCL lasing and pulse shortening to a duration much shorter than the pump pulse duration. The expression for the pulsewidth [35] shows that it should be proportional to the pump and CCL cavities mismatch parameter Δ and inversely proportional to the logarithmic gain loss product

$$\tau_p \simeq \frac{\Delta}{\ln(G \cdot R)}.$$

This means that the shortest pulse duration in the CCL can be realized at the highest gain, pump energy and power. When using 90 ps pulsed krypton laser synch-pumping, the LiF : F_2^+ CCL pulses had a duration of 2–3 ps in linear cavities and 0.7 ps in ring cavities [36].

Similar results were obtained in linear cavities of $KF(F_2^+)$, $NaCl(F_2^+)$ and KCL:FA(Tl$^+$) lasers under Nd:YAG synch-pumping and for KCl:Li(F_A) and RbCl:Li(F_A) CCL under mode-locked argon laser pumping (see Ref. [5]).

In the passive mode-locking regime with a dye saturable absorber, a pulse duration of 180 fs was achieved in a LiF : F_2^+ CCL ring cavity at a lasing bandwidth of about 60 cm^{-1} [37]. Using a multiple-quantum-well saturable absorber, a $NaCl(F_2^+)$ CCL demonstrated 260 fs pulse operation with 50 cm^{-1} bandwidth [38].

By developing a new additive pulse mode-locking technique for pulse shortening, a pulse duration of 127 fs instead of 23 ps from KCl:Tl CCL was realized [39]. In a similar regime, 50 fs pulses have been generated by the so-called ‘soliton laser’ on KCL:Tl at 1.5 μm [40].

10.6 Room-Temperature CCL Operation

10.6.1 CW and Quasi-cw Regimes

Room-temperature tunable CCLs have a special importance in comparison with dye and cryogenic CCLs due to their compactness, simplicity and ease of use both for laboratory and field conditions. Lithium fluoride with F_2^- CCs is one of the most reliable active media for room-temperature tunable operation.

During the last two decades, only a few papers have been dedicated to the study of cw and quasi-cw laser operation on LiF:F_2^- crystals at $T = 300$ K [3,41–44]. Most of them used neodymium solid-state lasers as the pumping source. Due to the high absorption cross section of F_2^- CC in LiF crystals at Nd^{3+} wavelength (1.06 μm), which equals 2×10^{-17} cm^2 and which is much higher than the emission cross section ($10^{-19} \times 10^{-21}$ cm^2) of the Nd^{3+} ions wavelength, LiF : F_2^- CC crystals can be used not only as a gain medium but also as a crystalline saturable absorber for Nd laser Q-switching.

The first attempts to produce cw laser operation were made on a 4-mm long LiF:F_2^- crystal in a linear laser cavity. At a pump power of 6 W (cw YAG:Nd^{3+} laser), using a focusing lens with $f = 100$ mm, and a mechanical chopper, Gusev et al. [3] attained an output power of 60 mW; but because of optical feedback between the two resonators of the LiF : F_2^- and YAG : Nd_3^+ lasers, a repetitive passive Q-switching mode with a peak power much higher than the average power level of 6 W was observed. As a result, only a quasi-cw high repetition rate nanosecond pulsed operation was achieved.

Using a pitchless YAG:Nd^{3+} laser operating in a free-running mode with smooth 150 μs pulses as a pump and a quarter-wave quartz plate with Glan polarizers to decouple the cavities of the YAG:Nd^{3+} and LiF:F_2^- lasers, the authors [1] produced pitchless quasi-cw lasing on a 5-cm long LiF:F_2^- crystal with a pulse duration of 150 μs and an efficiency of 0.5%.

The application of a ring cavity for removing feedback enabled lasing on a 1-cm long LiF : F_2^- crystal with 60% absorption and a calculated diameter for the beam waist of 80 μm [3]. For a pump of 6 W and a tunable range of 1.14–1.19 μm, the output power was 80 mW. However, considerable thermo-optical distortions, which started manifesting themselves at an average pump power of more than 0.5 W, prevented the researchers from attaining a purely cw lasing mode without a mechanical chopper, because the lasing threshold was 2.5 W.

For the first time, pure cw LiF : F_2^- lasing has been attained using crystals with double the absorption coefficient; $k_{abs} = 1.3\,cm^{-1}$ at a pump wavelength of 1.064 µm and low losses ($K_L = 0.01\,cm^{-1}$) in the lasing region of 1.1–1.2 µm [43]. A ring cavity with a 1 m base and astigmatism compensation incorporated two plane mirrors (2 and 3) with 99.7% and 99% reflectance in the lasing region and two 100% reflectance spherical mirrors (1) with a curvature radius of 10 cm (see Figure 10.4). At a pump power higher than 0.5 W, lasing was disrupted. This can probably be attributed to a strong negative lens with a focal distance of less than 5 mm, which was induced in the sample during pumping. The induced lens was reduced by heating the sample surface to 20°C–40°C, or by slowly rotating it at 6 turns min^{-1}. As a result, pure cw LiF : F_2^- lasing was realized. For a pump power of 3 W, the lasing output power was 60 mW. These results were further improved: the maximum output cw power of a LiF : F_2^- laser exceeded 100 mW at a pump power of 5 W. The LiF : F_2^- active element preserved all its properties after a 30 h performance.

The first results on frequency tuning and picosecond generation at room temperature of cw LiF : F_2^- laser were obtained under synchronous pumping with a continuous train of picosecond pulses of a cw-pumped Nd^{3+}:YAG laser. The use of a ring cavity like that in Figure 10.4 and a Lyot filter as a dispersive element provided lasing over the 1.1–1.2 µm spectral region. LiF:F_2^- oscillation under Nd^{3+} :YAG laser synchronous pumping provided picosecond pulses with a duration of 10 ps and a 7 ns axial interval for a continuous train of pulses [44] (the pulsed mode-locking regime will be discussed later).

Because of a small Stokes shift between the energies of pump and lasing photons ($\nu_p - \nu_{osc} = 200–300\,cm^{-1}$ at room temperature), the investigation of the efficiency of LiF:F_2^- lasing under different pump wavelengths performed in Ref. [45] is very interesting. Pumping with a wavelength lying in the region of wide overlapping in the electronic–vibrational absorption and luminescence bands of the F_2^- CCs in addition to excitation or stimulated upward transitions gave rise to stimulated downward transitions and a corresponding deactivation of the excitation. As a result, the maximum concentration of the excited CCs in a crystal pumped by Nd^{3+}:YAG laser radiation ($\lambda_p = 1.064$ µm) could only reach 26% of the total concentration of these centres even under saturation conditions. Shortening the pump wavelength by replacing the Nd^{3+}:YAG pump laser with an Nd^{3+}:$YLiF_4$ laser ($\lambda_p = 1.047$ µm) increased the maximum concentration of the excited CCs up to 43% and, as calculations show, in the case of a Yb^{3+}:YAG laser ($\lambda_p = 1.029$ µm), this concentration rises to 62%. Therefore, the pump laser wavelength is an important parameter in attempts to increase CCL gain and efficiency.

In a non-selective cavity for the same peak pump power, the LiF : F_2^- laser was 2.5 times more efficient when pumped by the radiation of an Nd^{3+}:$YLiF_4$ laser [42]. Moreover, the efficiency did not reach its saturation value and could be further improved by increasing the peak pump power. The adoption of a shorter pump wavelength also resulted in a ten-fold reduction in the LiF : F_2^- lasing threshold.

Figure 10.5 shows the tuning curves of the LiF : F_2^- laser obtained in a selective cavity with a diffraction grating. The laser was pumped by an Nd^{3+}:$YLiF_4$ laser (1.047 µm) radiation at a pulse repetition rate of 1 kHz. The duration of the pump pulses was 450 ns and their peak power was 750 W. A tuning range of 1.07–1.27 µm was also obtained in a dispersive cavity with a high (45%) efficiency at the maximum of the tuning curve.

10.6.2 High-Peak-Power Room-Temperature CCL Operation in Pico- and Femtosecond Regimes

Since the middle 1970s, there have been many studies on the picosecond operation of F_2^+,$F_2^+O^-$,F_2^- and F_3^- CCs in LiF and NaF crystals at room temperature. Synchronous pumping by a train of picosecond pulses from ruby, Nd:YAG or Nd:glass lasers was used as the most effective scheme for CCL pulse shortening.

Fast CC gain switching (modulation) leads to an effective CCL pulse shortening depending on the degree to which the pump power exceeds threshold, the number of pulses and the length of the train. Here, we would mention only a few results on developing high peak power and high conversion efficiency LiF : F_2^- CCL with short (2–3 ps) picosecond and femtosecond pulse durations.

In the first case, a high optical density and high contrast LiF:F_2^- CC crystal was used in a semi-concentric cavity with a prism pair for dispersion compensation under pumping with an Nd-phosphate glass picosecond pulse train. The pump scheme was almost longitudinal with a transverse angle of

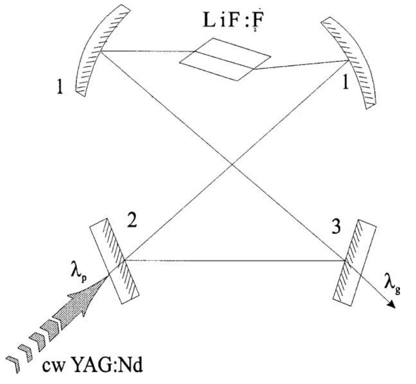

FIGURE 10.4 Typical cavity for cw or quasi-cw ring colour centre laser.

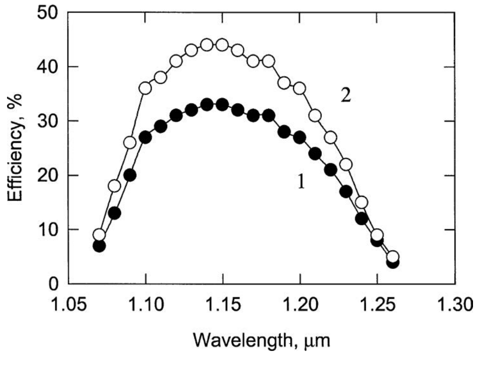

FIGURE 10.5 Tuning curves of quasi-cw oscillation of LiF:F_2^-CCL pumped by Nd^{3+}:YAG (1) and Nd^{3+}:$YLiF_4$ (2) lasers.

2°–3° of beams. The Brewster-cut LiF : F_2^- crystals had lengths of 60 and 160 mm. Precise matching of the resonator's lengths gave rise to LiF:F_2^- femtosecond oscillation with a pulse duration of less than 500 fs, at a full train duration of 300–400 ns and a train energy of 250 μJ [46].

The durations of the subpicosecond pulses were measured directly on the screen of the streak camera (8) with a resolution of 0.6–0.7 ps (Figure 10.6) as well as with an autocorrelator, which provided an average pulse duration in the LiF:F_2^- train of less than 0.5 ps. A conservative estimation of the peak power for 0.5 ps output pulses gives a minimum power of 10 MW, which greatly (by three to four orders) exceeds the standard peak power generated by ordinary quasi-cw femtosecond dye and CC lasers Stokes.

F_2^- CCs feature a long fluorescence decay time ($\tau = 55$ ns) that makes them very attractive for developing synchronously pumped mode-locked lasers. A highly efficient LiF:F_2^- lasing of high-power short picosecond pulses was realized under LiF:F_2^- synchronous pumping with a train of 50 pulses with 7 ps duration from a passively mode-locked neodymium phosphate glass laser ($\lambda = 1.055$ μm) [47]. The energy of the train was up to 6 mJ. The pump laser radiation was focused into an LiF:F_2^- CC crystal by a mirror (2) (see Figure 10.6). The Brewster-cut LiF:F_2^- CC crystal was 4 cm long. The initial absorption in this crystal at the pump wavelength was 0.7 cm^{-1}. The LiF:F_2^- laser cavity was formed by a plane mirror (1), a highly reflective spherical mirror (2) with a radius of curvature $r = 1500$ mm and a plane output mirror (3) whose reflection coefficient varied to ensure the optimal output energy. The group velocity dispersion was compensated for by introducing a pair of compensating prisms into one of the cavity arms.

The efficiency of LiF:F_2^- lasing versus the reflectivity of the output mirror is depicted in Figure 10.7. The maximum efficiency of conversion of the pump radiation to CCL output and output energy reached 35% and 1.4 mJ, respectively. The temporal parameters of the output radiation were measured directly by an IMACON-501 streak camera, coupled to a linear photodiode array. The time resolution of the apparatus was 3 ps.

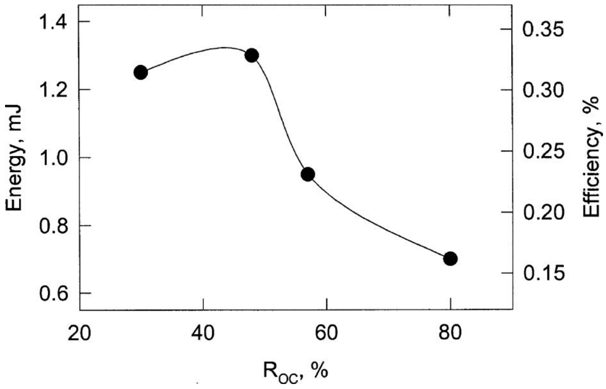

FIGURE 10.7 Energy and efficiency of a picosecond LiF:F_2^-CCL with respect to the reflectivity of the output coupler for 4 mJ energy in the pump pulse train.

Figure 10.8 presents the duration of the output pulses of CC laser. The minimum pulse duration was close to the time resolution of the recording system and was about 2 ps. The half-width, $\Delta\lambda$, of the lasing spectrum was 8 nm. Tuning the output wavelength over 1.10–1.22 μm range was performed by a birefringent filter or by moving the slit aperture across the optical axis of the cavity. We estimate that, in this scheme, 35% efficiency can be obtained for 2 ps pulses with a peak power as high as 100 MW. As mentioned before, short-wavelength (compared to 1.064 and 1.055 μm excitation) 1.047 μm Nd:YLiF$_4$ pump laser radiation provides a much higher gain in the LiF:F_2^- CC laser. In addition to this, Kerr lens mode-locking provided shorter picosecond pump pulses with a duration of about 4 ps each. This resulted in a cavity round-trip time of 10 ns and a train duration of 7–10 μs, which was 20–30 times longer than that noted earlier [47]. Average pump energy in each pulse was about 3–4 μJ with a slow decrease at the end of the pulse train. The 40-mm long LiF:F_2^- Brewster-cut crystal with an absorption coefficient of 0.7 cm^{-1} was longitudinally pumped by a focused (500 mm focal distance) radiation through a dichroic mirror. The pulse duration was measured by means of non-collinear second-harmonic generation with LiIO$_3$ non-linear crystal.

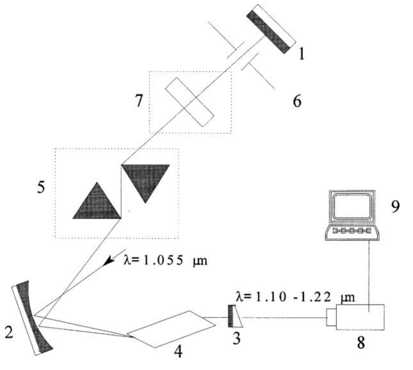

FIGURE 10.6 Experimental set-up of a picosecond LiF:F_2^-CCL : (1,2,3) end, spherical and cavity mirrors; (4) active element (LiF:F_2^-crystal); (5) prism compensator of the group velocity dispersion; (6) aperture; (7) Lyot filter; (8) streak camera and (9) PC.

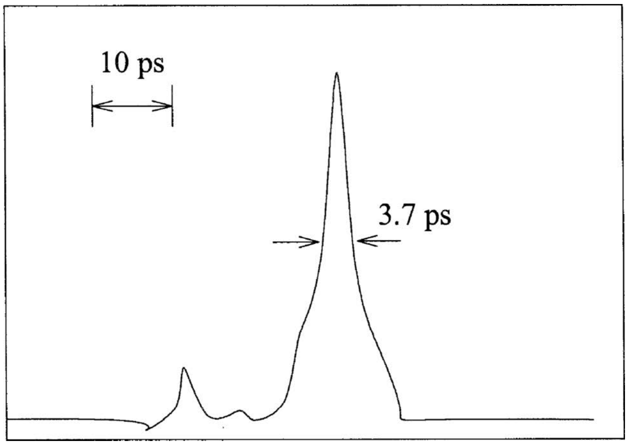

FIGURE 10.8 Temporal shape of the picosecond LiF:F_2^-CCL.

The minimum pulse duration of LiF:F_2^- CCL was measured to be 0.2–0.5 ps, assuming a Lorentzian pulseshape (Figure 10.9) that constitutes a 15-fold output pulse compression with respect to the pump pulse duration [48]. These results were obtained at a wavelength of 1.14 µm near the maximum of the gain curve when a 75% reflectivity output coupler was used. Figure 10.10 presents a CCL pulse duration dependence on the degree to which the pump energy exceeds that of the threshold. The minimum pulse duration corresponded to the maximum pump energy, which was three times higher than the threshold value. The pulse duration was very critical to a mismatch of more than 10 µm. The total energy conversion efficiency for the shortest pulses was measured to be 6%–8% with respect to the pump pulse energy. Peak power estimations show that, in this long pulse synchronous pumping scheme, one can obtain LiF:F_2^- femtosecond output pulses with a peak power exceeding 1 GW, which is many orders of magnitude higher than that from an Al_2O_3:Ti femtosecond laser pumped under similar conditions.

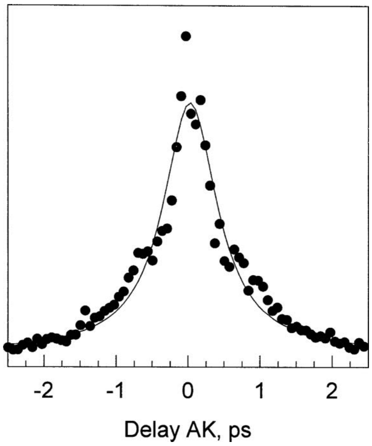

FIGURE 10.9 Autocorrelation curve of a pulse duration of synchronously pumped LiF:F_2^-CCL with 75% output coupler.

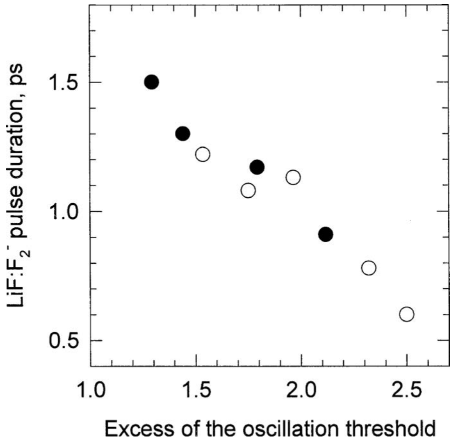

FIGURE 10.10 Dependence of the pulse duration of a synchronously pumped LiF:F_2^-CC laser with respect to pump threshold excess: filled circles, 50% reflectivity output coupler and hollow circles, 75%.

10.6.3 High Energy and Power in Colour Centre Lasers

Success in the growth of large size and good quality alkali-halide optical crystals and in the development of homogeneous, high-contrast colouration techniques gives rise to a unique opportunity to design large-scale high-power lasers and amplifiers based on CCLs. Using an LiF:F_2^- active crystal 50 × 50 × 50 mm in size and an initial transmittance of 8% for the 1.064 µm wavelength of an Nd-glass pump laser, an output energy as high as 20 J with a 23% pump-to-output conversion efficiency and a 100 ns pulse duration was obtained [49].

Developing large-scale homogeneously coloured LiF:F_2^- CC active crystals with a size of up to 40 × 80 × 200 mm with four large polished faces allows a huge (700 J in 120 ns pulse duration) pump energy from a multi-stage Nd:glass laser system. In a two-pass pumping scheme with a 5 J cm^{-2} pump energy density, transversely directed lasing of F_2^- CCs was realized in a non-selective 300 mm long Fabry–Pérot cavity with 50% output coupling. Under these conditions, the authors were able to reach the record output energy of 100 J and a peak power of 1 GW at 1.12–1.16 µm and 100 ns pulse duration.

For smaller (40 × 40 × 20 mm) LiF:F_2^- crystals in a transversal LiF and Nd:glass coupled cavity arrangement, the Nd laser pump-to-CCL output conversion efficiency was increased by up to 80% with a CCL output energy of 8 J at 1.15 µm [49].

10.6.4 Narrow-Line Tunable and Super-Broadband CCL Oscillation

The main advantage of a CCL is the possibility of obtaining coherent radiation tunable over a wide near-IR spectral range. The oscillating wavelength can be roughly selected by choosing an appropriate CC active medium. In a non-dispersive cavity, the oscillation occurs at wavelengths near the maximum of the fluorescence curve. The width of the oscillating spectra can be up to several hundreds of cm^{-1}. The radiation of CCLs in dispersive cavities is tunable when prisms, diffraction gratings, Fabry–Pérot etalons, Lyot filters and other wavelength-selective elements are utilized.

As an example, we consider a nanosecond LiF:F_2^+ CCL pumped by the second-harmonic radiation of an Nd^{3+}:YAG laser. The use of a selective cavity with a single glass prism enables the radiation to be tunable over 0.84–1.1 µm with a spectral width of 20 cm^{-1}. Utilization of three dispersive prisms narrows the output spectrum to 5–7 cm^{-1}. A diffraction grating with 1200 lines mm^{-1} provides radiation with a 1–3 cm^{-1} spectral width tunable over the 0.84–1.1 µm spectral region. An additional intracavity Fabry–Pérot etalon provides a further ten-fold reduction in the oscillating linewidth of up to 0.1–0.3 cm^{-1}. A narrow-line single-frequency laser oscillation regime is of special interest for numerous applications. The use of a grazing incidence scheme with a diffraction grating operating simultaneously as an intracavity telescope and dispersive element allows the linewidth of nanosecond high-peak-power lasers to be reduced to the level of 0.03–0.01 cm^{-1} and to realize a single-frequency oscillation [1].

A narrow line tunable LiF:F_2^-CCL system with a nanosecond powerful amplifier with up to 50 mJ output pulse energy was developed in Refs. [50,51]. The master oscillator with synchronous scanning of autocollimation grating and dielectrically coated quarts Fabry–Pérot etalon ($d = 1$ cm) provided stable (more than 20 min) single-frequency operation (<300 MHz) smoothly and continuously tunable in 1 cm^{-1} frequency region. This system allowed the authors to investigate and optically pump HCl, HBr molecular gases in the wide spectral range of 1.1–1.25 μm. As an example, mid-IR HCl gas laser operation at 3.88 μm at (3,2) P(5)–(2,1) P(6) optical transition was demonstrated under single frequency CC laser optical pumping [51].

A new type of laser, specifically a super-broadband colour centre laser was proposed for LiF:F_2^- and LiF:F_2^+ CC active elements. It provides two types of laser radiation: simultaneous super-broadband lasing over the whole amplification band (about 1000 cm^{-1}) of the active medium (0.85–1.1 and 1.1–1.25 μm for LiF:F_2^+ and LiF:F_2^- lasers, respectively) and multi-frequency or spectrally controlled laser oscillation (20 lines simultaneous oscillation) [52]. The basic idea of super-broadband lasing is the suppression of mode competition and the creation of a number of independent channels in the cavity, each lasing at different wavelengths within the amplification band of the active medium. As a result, super-broadband operation of an LiF CCL provided 'low-coherence' easily collimated high-intensity laser radiation with a spectral width of 1400 Å centred at 0.96 and 1.14 μm, correspondingly.

By simultaneous second-harmonic generation in one nonlinear crystal, the oscillation in the visible (blue-green (0.43–0.53 μm) and green-red (0.55–0.62 μm)) spectral ranges was obtained in both regimes for LiF:F_2^+ and LiF:F_2^- CCLs and can be called rainbow or 'sun-colour' lasers. Super-broadband lasing can be of great interest for fast fluorescence and absorption spectroscopy, two-photon non-linear spectroscopy, nanosecond colour photography, optical communication systems, information coding and other scientific and technical areas.

Free-running pulsed room-temperature tunable operation of a LiF:F_2^- laser pumped by an InGaAs laser diode has been described in Ref. [53]. In the free-running mode, with a non-selective resonator, the LiF:F_2^- laser showed a 4% slope conversion efficiency and a measured 2.5% pumping-to-lasing efficiency at the maximum of the tuning curve for tunable narrow-band operation. The LiF:F_2^- oscillator was tunable in the 1122–1201 nm range.

Pulsed operation of a tunable LiF:F_2^{+*} CCL has been obtained at room temperature under pumping by a 680-nm fibre-coupled linear array of laser diodes [54]. Tunable operation in the 880–995 nm spectral region has been demonstrated with an efficiency of 2% in the maximum of the tuning curve when a birefringent plate was utilized as a cavity dispersive element.

10.7 CC Energy and Power Amplifier

In many cases, it is necessary and convenient to amplify a weak laser radiation with special spectral, spatial or temporal properties to a high-energy or peak power values. The four-level energy diagram describing the electronic–vibrational transitions of CCs together with a considerable Stokes shift and the quasi-homogeneous nature of their wide absorption and fluorescence bands, as well as a high quantum efficiency and a large amplification cross section, are very favourable factors for tackling this amplification task. CC crystal can be effectively used in master oscillator power amplifier schemes or for pico- and femtosecond pulse amplification in near-IR spectral regions.

The high emission cross section ($\sigma_{\text{em}} = 7 \times 10^{-17}\,\text{cm}^2$) and long lifetime ($\tau = 100$ ns) of F_2^- CCs promise a high amplification gain and efficiency for an LiF:F_2^- amplifier. Compared to dye solutions, the concentration of an F_2^- CCs in LiF crystal is rather low. Due to this, a longitudinally pumped amplifier scheme is preferable for good spatial overlapping of the pump and probe radiation in the bulk CC crystal with a 40–80 mm length.

The experimental set-up included a pulsed Nd^{3+}:YAG pump laser with an output energy of up to 200 mJ, a 3 Hz pulse repetition rate and a 10 ns pulse duration. It was used to pump both a CC master oscillator and a CC power amplifier. A tunable LiF:F_2^- CCL provided a low divergence, tunable nanosecond probe beam with a spectral linewidth of less than 1 cm^{-1}.

The output energy and gain dependences of single-pass amplification in an LiF:F_2^- CC crystal 40 mm long with an initial absorption coefficient $K_0^{(1.064)} = 0.67\,\text{cm}^{-1}$ and 40 mJ pump pulse energy are shown in Figure 10.11. The highest values of the amplification gain, $G = 12$, and amplification coefficient, $\alpha = 0.62\,\text{cm}^{-1}$, were obtained for a low-energy probe pulse ($E_{\text{input}} = 0.06$ mJ). An increase in the probe pulse energy to 1 mJ resulted in gain saturation with a corresponding lowering of the amplification gain and gain coefficient to $G = 4$ and $\alpha = 0.35\,\text{cm}^{-1}$, respectively, on increasing the amplified output energy to 4 mJ per pulse. This value corresponded to about 10% energy conversion efficiency for the LiF:F_2^- CC power amplifier [55].

Due to the limited concentration of F_2^- CCs in an LiF crystal, an increase in the interaction length by using longer crystals or multi-pass amplifier schemes is of great importance. A two-pass LiF:F_2^- CC amplifier scheme utilized the reflection from the back HR mirror located close to the LiF crystal. Figure 10.12 shows the results from the amplification in a LiF:F_2^- CC crystal 88 mm long with $K_0^{(1.064)} = 0.5\,\text{cm}^{-1}$ for a 40-mJ pump pulse. For a low input energy of 0.08 mJ, a high

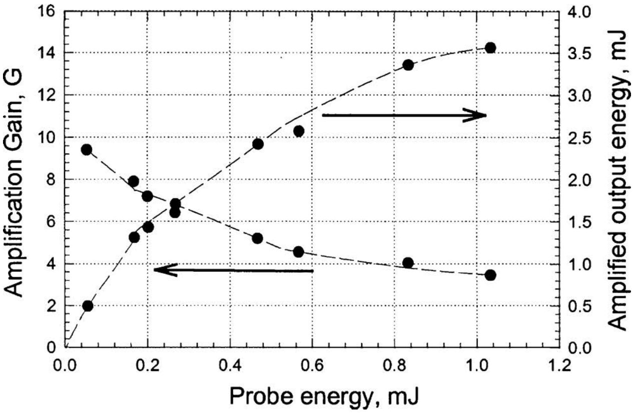

FIGURE 10.11 Energy dependences of the amplification gain and output energy of an LiF:F_2^- single-pass CCL amplifier with a 40 mJ pump pulse.

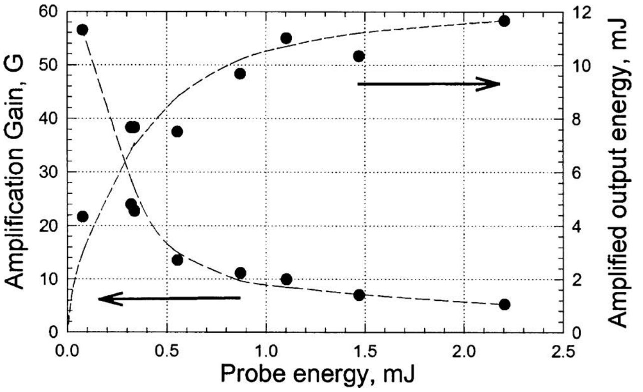

FIGURE 10.12 Energy dependences of the amplification gain and output energy of an LiF:F_2^- two-pass amplifier with a 40 mJ pump pulse.

amplification gain of 56 ($\alpha = 0.26\,\text{cm}^{-1}$) was realized with an output energy of 4.2 mJ and an efficiency of about 10%. For a higher energy input beam (2.2 mJ), the CCL amplifier output energy was increased to 12 mJ with a pump conversion efficiency of up to 30%, which is close to the best values for CCL conversion efficiency [55].

The utilization of a LiF:F_2^- double-pass amplifier with an 80 mJ Nd^{3+}:YLiF$_4$ laser with a more efficient, shorter pumping wavelength (1047 nm) provided the highest gain coefficient ($G = 300$) for a low-energy probe pulse of 0.1 mJ. The maximum amplified output energy of 34 mJ with amplification gain $G = 90$ and an energy conversion efficiency of 45% was obtained for a high-energy probe pulse of 0.6 mJ.

The experimental results on LiF:F_2^- CC crystal amplification have shown that this crystal is a promising candidate for developing both high-gain and high-power optical amplifiers for low-divergence, short-pulse or narrow-line laser radiation in the 1.1–1.25 µm spectral region.

The feasibility of amplifying the broadband radiation of diode lasers and light-emitting diodes with the aid of LiF:F_2^+ CC crystals was demonstrated in Ref. [56]. A single-pass amplifier configuration was used. The active centres were excited by the second harmonic ($\lambda_p = 532\,nm$) of a multi-mode-pulsed Nd^{3+}:YAG laser emitting pulses of 10 ns duration. A GaAs laser diode generated 85 ns radiation pulses with a linear polarization at the wavelength of 900 nm (close to the maximum of the fluorescence spectrum of F_2^+ CCs) with the spectral width being about 55 cm^{-1}.

In this experiment, single-pass gains (G) of 5 in the short crystal ($l = 0.8\,\text{cm}$) and 20 in the long crystal ($l = 2\,\text{cm}$) were reached with a pump pulse energy of 1 mJ. No saturation of the gain relative to the energy of the amplified radiation from the laser diode was observed. The optical gain was constant when the pump energy was in the range of 0.1–1 mJ and the energy of the amplified IR radiation was 0.4–33 nJ.

In the second case, the pump beam was split into two beams of equal intensities, which pumped the active element from opposite sides. An increase in the pump energy to 5 mJ per pulse and focusing of the pump radiation behind the exit end of the crystal enhanced the optical gain in the short 0.8 cm crystal up to eight per single pass. Hence, in this case, the gain coefficient, α, was at least 2.6 cm^{-1}.

The high stability and good laser performance of LiF CCLs with O^{2-} and OH$^-$-stabilized F_2^+ CC have been demonstrated at room temperature [21,23,57]. Stabilized F_2^+ CCs have a broad absorption band with a spectral width of more than 3500 cm^{-1} with a maximum of about 600 nm. The room temperature fluorescence spectrum is centred at 890 nm with a bandwidth of more than 2300 cm^{-1}. The complexity of tunable cavity development for such broadly tunable CCLs arises from the necessity to use several sets of mirrors to obtain oscillation at the edges of the tuning curves. The use of different kinds of dichroic cavity mirrors in these CCLs reduced two-pass superfluorescence and provided an extremely wide tunable range (800–1200 nm) with a conversion efficiency of 12%–25% in the maximum of the tuning curve.

10.8 Conclusions

In this chapter, we have reviewed the progress in the physics of LiF CC formation and stabilization and demonstrated developments in dramatically improved LiF CC lasers providing stable, room temperature, broadly tunable, near-infrared, optical output and operating efficiently in all known modes of operation. We believe that now, when the merits and shortcomings of tunable lasers based on impurity-doped crystals are clearly understood and the new merits of CC lasers are clearly demonstrated, the interest in CC lasers will be renewed.

LiF CC active elements have a unique combination of spectroscopic, oscillation, thermo-optic, and operational properties and the lasers based on them have many of the positive features of a solid-state dye-like laser. These advantages include high gain coefficients, broad homogeneous gain profile, low threshold and highly efficient single-mode operation with extremely narrow spectral outputs, wide wavelength tunability, compactness, long operational lifetime, rigidity, ease of handling and insensitivity to the quality of the cavity's optical elements, and to the spatial angular and spectral characteristics of the pump source. The system also exhibits virtually no temporal delay between pump and output pulses. This temporal overlap between the pump and generated CC laser pulses for the entire range of tunability provides an easy extension to the UV, visible and middle-IR region through sum and difference frequency generation of the pump and CCL output. The described developments are expected to result in LiF CC lasers finding widespread acceptance in research laboratories throughout the world and generating an abundance of activity in different areas of science.

REFERENCES

1. Basiev T T, Mirov S B and Osiko V V 1988 IEEE J. Quantum Electron. **24** 1052–69.
2. Basiev T T and Mirov S B 1994 *Room Temperature Tunable Colour Centre Lasers (Laser Science and Technology Book Series 16)* ed V S Letokhov et al. (New York: Gordon and Breach Science/Harwood Academic) pp 1–160.
3. Gusev Yu L, Marennikov S I and Chebotaev V P 1980 Bull. Acad. Sci. USSR, Phys. Ser. **44** 15.

4. Parfianovich I A, Khulugurov V M, Lobanov B D and Maksimova N T 1979 Bull. Acad. Sci. USSR, Phys. Ser. **43** 20–7.
5. Gellermann W 1991 J. Phys. Chem. Solids **52** 249.
6. Mollenauer L F 1987 Colour centre lasers *Tunable Lasers* vol 59, ed L F Mollenauer and J C White (Berlin: Springer) pp 225–77.
7. Archandelskaya V A and Feofilov P P 1980 Sov. J. Quantum Electron. **7** 657.
8. Martynovich E F, Baryshnikov V I and Grigorov V A 1985 Opt. Commun. **53** 257–8.
9. Voytovich A P, Grinkevich V A, Kalinov V S and Mikhnov S A 1988 Kvant. Electron. 15 318–20 (Engl. transl. Sov. J. Quantum Electron.).
10. Rand S C and DeShazer L G 1985 Opt. Lett. **10** 481–3.
11. Shkadarevich A P and Yarmolkevich A P 1985 New laser media on colour centre compound fluoride *Preprint* Inst. Phys. AN BSSR, Minsk, USSR, p 24.
12. Horsch G and Paus H J 1986 Opt. Commun. **60** 69–73.
13. Basiev T T, Vakhidov, F A and Mirov S B 1988 Kratkie Soobsheniya po Fizike 7 3–5 (Engl. transl. Sov. Phys. Lebedev Inst. Rep. **7** 1–5).
14. Mollenauer L F 1979 *Colour Centre Lasers in Quantum Electronics Part B* vol 15 ed C L Tang (New York: Academic) ch 6.
15. Rzepka R E, Bernard M, Lefrant S, Dubost H, Charneau R and Galaup Y P 1987 Opt. Commun. **62** 174–8.
16. Lushchik Ch B, Vitol I K and Elango M A 1977 Uspehi Fizicheskih Nauk **122** 223–52 (Engl. transl. Sov. Achievements Phys. Sci.).
17. Delbecq C J 1963 Z. Phys. **171** 560–81.
18. Basiev T T, Voron'ko Yu K, Mirov S B, Osiko V V and Prokhorov A M 1979 Pis'ma v JETP **30** 661–5 (Engl. transl. 1979 Sov. JETP Lett. **30** 626–9).
19. Khulugurov V M and Lobanov B D 1978 Sov. Tech. Phys. Lett. **4** 595–6.
20. Basiev T T, Konyushkin V A, Mirov S B and Ter-Mikirtychev V V 1992 Sov. J. Quant. Electron. 22 128.
21. Basiev T T, Ermakov I V, Fedorov V V, Konushkin V A and Zverev P G 1994 Laser oscillation of LiF:F$_2^+$—stabilized colour centre crystals at room temperature *Proc. Int. Conf. on Tunable Solid State Lasers* (Minsk, Inst. Mol. and Atom. Phys.) p 64.
22. Nahum J 1967 Phys. Rev. **158** 814.
23. Dergachev A Yu and Mirov S B 1998 Opt. Commun. **145** 107–12.
24. Mirov S B and Dergachev A Yu 1997 Proc. SPIE **2986** 162–73.
25. German K R 1989 *Handbook of Solid State Lasers* ed P K Cheo (New York: Marcel Dekker) ch 5.
26. Fritz B and Menke E 1965 Solid State Commun. **3** 61.
27. Kogelnik H W, Ippen E P, Dienes A and Shank C V 1972 IEEE J. Quantum Electron. QE-**8** 373.
28. Beigang R, Liftin G and Welling H 1977 Opt. Commun. **22** 269.
29. Breant Ch, Baer T, Nesbitt D and Hall J L 1983 *Laser Spectroscopy* vol VI, ed H P Weber and W Luthy (Berlin: Springer) p 138.
30. Johnston T F and Proffitt W 1980 IEEE J. Quantum Electron. QE-**16** 483.
31. Pollock C R and Jennings D A 1982 Appl. Phys. B **28** 308.
32. Rong F, Yang Y and Luty F 1989 Cryst. Latt. Def. Amorph Mater. **18** 1.
33. Beigang R and Wynne J J 1981 Opt. Lett. **6** 295.
34. Pinto J F, Stratton E and Pollock C R 1985 Opt. Lett. **10** 384.
35. Yasa Z A 1983 Opt. Lett. **8** 277.
36. Langford N, Smith K and Sibbett W 1987 Opt. Commun. **64** 274.
37. Langford N, Smith K and Sibbett W 1987 Opt. Lett. **12** 903.
38. Islam M N, Sundermann E R, Bar-Joseph I, Sauer N and Chang T Y 1989 Appl. Phys. Lett. **54** 1203.
39. Mark J, Liu L Y, Hall K L, Haus H A and Ippen E P 1989 Opt. Lett. **14** 48.
40. Mollenauer L F and Stolen RH 1984 Opt. Lett. **9** 13.
41. Gellermann W, Muller A, Wandt D, Wilk S and Luty F 1987 J. Appl. Phys. **61** 1297.
42. Basiev T T, Zverev P G, Papashvili A G, Konyushkin V A and Osiko V V 1997 Quantum Electron. **27** 759.
43. Basiev T T, Gusev Yu L, Kruzhalov S V, Mirov S B and Petrunkin V Ya 1988 Sov. J. Quantum Electron. 12.
44. Basiev T T, Gusev Yu L, Kruzhalov S V, Mirov S B and Petrunkin V Ya 1988 *Abst. Rep. XIII Inter. Conf. Coherent Nonlinear Opt.* Minsk, USSR, Part 2, 256.
45. Basiev T T, Zverev P G, Papashvili A G and Fedorov V V 1997 Quantum Electron. **27** 574.
46. Babushkin A V, Basiev T T, Vorob'ev N S, Mirov S B, Prokhorov A M, Serdyuchenko Yu N and Shchelev M Ya 1986 Sov. J. Quantum Electron. **16** 1492.
47. Basiev T T, Dergachev A Yu, Karasik A Ya, Fedorov V V and Shubochkin R L 1996 Quantum Electron. **26** 1042.
48. Zverev P G, Basiev T T and Laubereau A 1999 *Novel Lasers and Applications—Basic Aspects, OSA Technical Digest* (Washington DC: OSA) p 57.
49. Basiev T T, Dolzhenko S V, Ershov B V, Kravtsov S B, Mirov S B, Spiridonov V A and Fedorov V B 1988 Bull. Acad. Sci., USSR **52** 164.
50. Basiev T T, Doroshenko M E, Kravtsov C B, Skornyakov V V, Zverev P G, Vasiliev S V, Alimpiev S S, Nikiforov S M and Hager G 2003 Quantum Electronics **33** 210.
51. Basiev T T, Papashvilli A G, Fedorov V V, Vasiliev S V and Gellermann W 2003 Laser Phys.
52. Basiev T T, Zverev P G, Fedorov V V and Mirov S B 1997 Appl. Opt. **36** 2515.
53. Ter-Mikirtychev V V 1998 Appl. Opt. **37** 6442.
54. Ter-Mikirtychev V V 1998 IEEE Photon. Technol. Lett. **10** 1395.
55. Basiev T T, Doroshenko M E, Zverev P G, Skornyakov V V and Hager G 2001 Laser amplifier on LiF:F$_2^-$ colour centre crystal for 1.1–1.25 μm spectral region *Advanced Solid State Lasers, OSA Technical Digest* (Washington DC: OSA) pp 54–5.
56. Basiev T T, Mirov S B and Ter-Mikirtychev V V 1992 Proc. SPIE Int. Soc. Opt. Eng. **1839** 227.
57. Jenkins N W, Mirov S B and Fedorov V V 2000 J. Luminescence **91** 147–53

Taylor & Francis
Taylor & Francis Group
http://taylorandfrancis.com

11

Laser Diodes: Section Introduction

Ian White

The laser diode has proved to be an enduring device. Whilst at the most fundamental level its operation is very simple, using a two-level transition normally within a p–n junction, the device has proved to be complex to develop. As a result, despite being invented not long after the first laser, room-temperature continuous-wave operation took several years to develop and robust single-mode operation was only achieved using distributed feedback structures yet later.

Since then, a large number of variants of the basic laser diode structure have been developed. A wide range of materials has been used to enable lasing action across a range of wavelengths and the use of quantum wells and dots within active regions has generated many technological advances. Advanced laser structures have been developed for ensuring high-performance laser diode operation in terms of spectral and beam quality of the laser output. A key feature of the diode laser is its ability to allow high-speed direct modulation and, hence, a range of structures has been developed to allow both short-pulse and high-frequency modulation.

The result of this period of development is that laser diodes now find widely varying applications. They are the dominant optical sources in optical communications and storage and are increasingly being used in sensing and in high-power applications.

A full treatment of the laser diode must consider many aspects and, hence, in this section, following a treatment of the basic principles of the device, chapters concentrate on spectral control in laser diodes and their high-speed and high-power operation. Special attention is then given to laser devices able to operate in the red, in the blue and at long wavelengths, where unipolar devices have been demonstrated. Finally, advanced laser diode devices, able to carry out signal-processing functions, are reviewed and novel silicon-based diode lasers are described.

Taylor & Francis
Taylor & Francis Group
http://taylorandfrancis.com

12

Basic Principles of Laser Diodes

Niloy K. Dutta

CONTENTS

12.1 Introduction 170
  12.1.1 Basic Laser Diode 170
  12.1.2 Materials 170
  12.1.3 Epitaxy 171
  12.1.4 Lightwave System Applications 171
12.2 Principles of Operation 171
  12.2.1 The Dielectric Waveguide 171
  12.2.2 Threshold Condition 172
  12.2.3 Condition for Stimulated Emission 172
  12.2.4 The pn Junction Laser 173
12.3 Radiative Recombination 173
  12.3.1 Gain Calculation 174
  12.3.2 Spontaneous Emission Rate 175
  12.3.3 Threshold Current Calculation 175
12.4 Non-Radiative Recombination 176
  12.4.1 Auger Effect 176
  12.4.2 Surface Recombination 178
  12.4.3 Recombination at Defects 178
12.5 Laser Designs and Performance 178
  12.5.1 Laser Designs 178
  12.5.2 Laser Performance 179
12.6 Quantum Well Lasers 180
  12.6.1 Energy Levels 181
  12.6.2 Quantum Well Laser Performance 182
  12.6.3 Strained Quantum Well Lasers 183
12.7 Distributed Feedback Lasers 184
  12.7.1 Distributed Feedback Laser Design and Fabrication 184
  12.7.2 Laser Performance 185
  12.7.3 Phase Noise and Intensity Noise 185
12.8 Surface-Emitting Lasers 185
  12.8.1 Surface-Emitting Laser Designs 186
12.9 Visible and Quantum Cascade Lasers 187
  12.9.1 Visible Lasers 187
  12.9.2 Quantum Cascade Lasers 187
12.10 Quantum Wire, Quantum Dot and Nanostructure Lasers 188
  12.10.1 Quantum Wire and Quantum Dot Lasers 188
  12.10.2 Nanostructure Lasers 189
12.11 Laser Reliability 190
12.12 Summary and Future Challenges 191
References 191

12.1 Introduction

Since its invention in 1962 [1–4], the semiconductor injection laser has emerged as an important device in many optoelectronic systems such as optical recording, high-speed data transmission through fibres, optical sensors, high-speed printing and guided wave signal processing. Perhaps the most important impact of semiconductor lasers is in the area of lightwave transmission systems where the information is sent through encoded light beams propagating in glass fibres. These lightwave transmission systems, which are currently being installed throughout the world, offer a much higher transmission capacity at a lower cost than coaxial copper cable transmission systems.

The advantages of semiconductor lasers over other types of lasers—gas lasers, dye lasers and solid-state lasers—lie in their considerably smaller size and lower cost and their unique ability to be modulated at gigahertz speeds simply by modulation of the injection current. These properties make the laser diode an ideal device as a source in several optoelectronic systems, especially optical fibre transmission systems.

12.1.1 Basic Laser Diode

The concept of a semiconductor laser diode is a unique blend of semiconductor device physics and quantum electronics. The basic laser diode chip consists of two parallel-cleaved facets, which form an optical cavity (Figure 12.1). The other two edges are saw cut. The device has a pn junction near the light-emitting region (active region) for effective current injection. The typical cavity length is about 200–400 μ*m*.

The light–current characteristics of a laser diode are shown in Figure 12.2. As the injected current is increased beyond a certain value (threshold current), the light output from the facet increases dramatically. Associated with this is a narrowing of the spectral emission from ~600 Å in the below-threshold region to ~30–40 Å in the above-threshold region. The light below threshold is emitted spontaneously as the injected electrons and holes recombine in the active region. Above threshold, stimulated emission into a low divergence beam characteristic of laser action is observed. For digital lightwave systems, the light signal is encoded by modulating the injection current, which generally switches the laser between the 'on' state (stimulated emission regime) and the 'off' state (spontaneous emission regime).

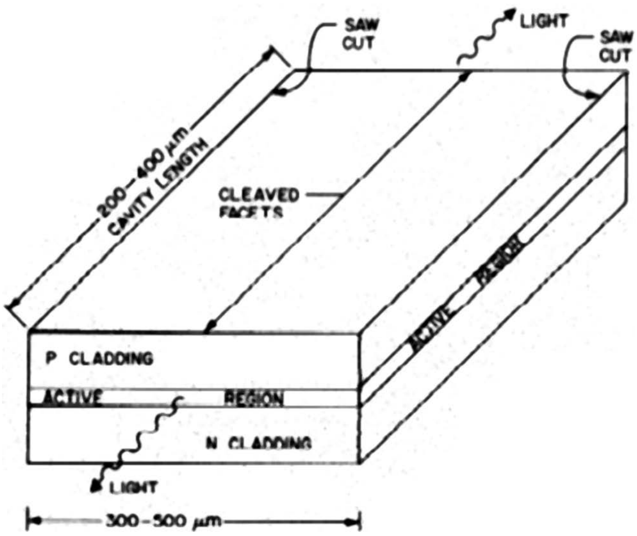

FIGURE 12.1 Schematic diagram of the basic semiconductor laser diode.

A close relative of the injection laser is the light-emitting diode (LED) [5]. The LED is a spontaneous emission device: its emission characteristics are similar to those of lasers below the threshold. LEDs generally emit lower power and have a broader spectral emission and lower modulation speed than lasers. The basic concepts, the physics of semiconductor lasers and semiconductor laser designs are described in this chapter. The semiconductor laser is essentially an oscillator where the feedback is provided by the cleaved mirror facets and the amplification (or gain) is provided by electron–hole radiative recombination in the active region. The condition for sustained oscillation (laser action) is that gain equals loss.

12.1.2 Materials

The choice of materials for semiconductor lasers is principally determined by the requirement that the probability of radiative recombination should be sufficiently high and that there is enough gain to overcome the cavity losses. This is usually satisfied for 'direct-gap' semiconductors. The various

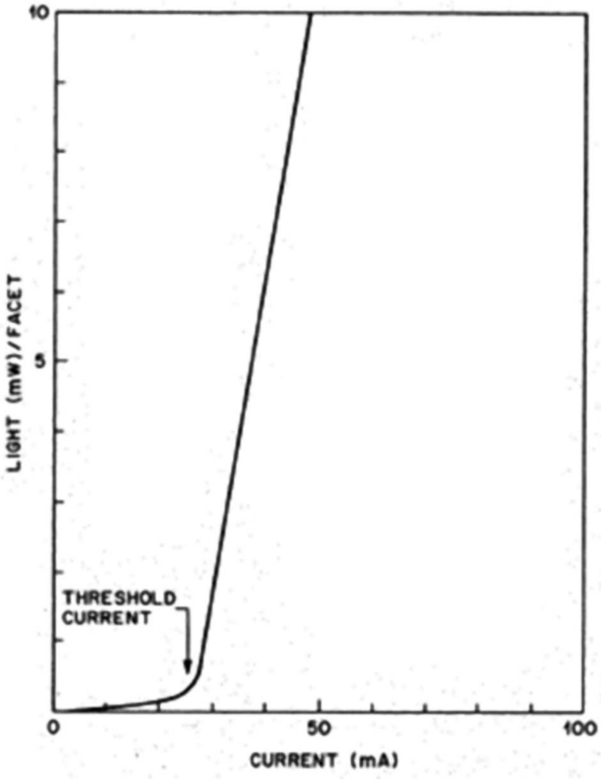

FIGURE 12.2 Light emitted from the facet versus the injected current for a semiconductor injection laser. The device is a proton-stripe GaAs laser.

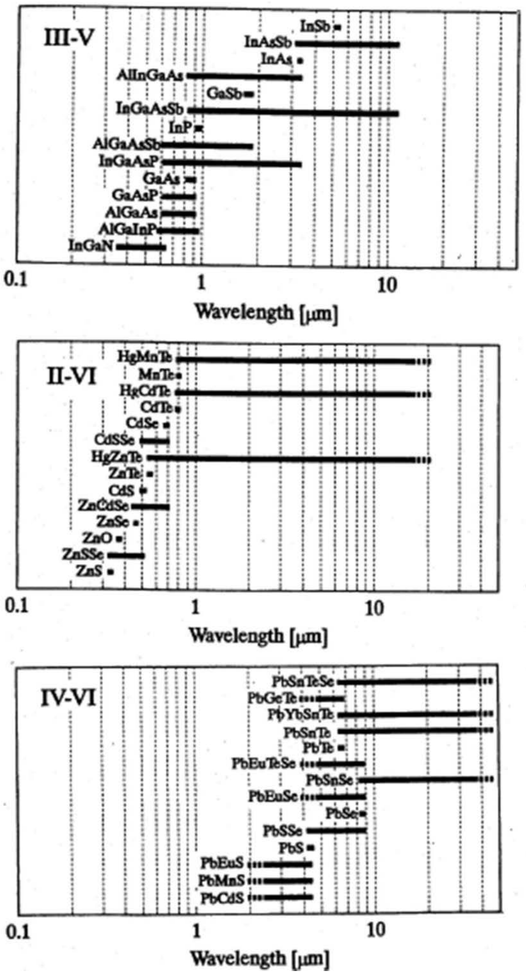

FIGURE 12.3 Semiconductor materials used in laser fabrication at different regions of the spectrum. The three figures refer to compound semiconductors formed using group III and group V elements (III–V), group II and group VI elements (II–VI) and group IV and group VI elements (IV–VI) of the periodic table (after Eliseev [6]). The quantum cascade lasers are fabricated using III–V semiconductors and they operate on intraband transitions in a quantum well.

semiconductor material systems along with their range of emission wavelengths are shown in Figure 12.3. Many of these material systems are ternary (three-element) and quaternary (four-element) crystalline alloys that can be grown lattice-matched over a binary substrate.

12.1.3 Epitaxy

The lattice-matched crystalline growth of one semiconductor over another is called epitaxy. The development of sophisticated epitaxial growth techniques has been of major significance in the development of high-quality reliable semiconductor lasers. The commonly used techniques are liquid-phase epitaxy (LPE) [7], vapour-phase epitaxy (VPE) [8] and molecular epitaxy (MBE) [9].

In LPE, the epitaxial layer is grown by cooling a saturated solution of the component of the layer to be grown while that solution is in contact with the substrate. In VPE, the epitaxial layer is grown by the reaction of gaseous elements or compounds at the surface of a heated substrate. The VPE technique has also been called chemical vapour deposition (CVD) depending on the constituents of the reactants. A variant of the technique is metal–organic chemical vapour deposition (MOCVD) [10], which has been very successful for lasers in which metal alkyls are used as the compound source. In MBE, the epitaxial layer growth is achieved by the reaction of atomic or molecular beams of the constituent elements (of the layer to be grown) with a crystalline substrate held at high temperature in ultrahigh vacuum.

12.1.4 Lightwave System Applications

As mentioned previously, one of the principal applications of semiconductor lasers is in the area of lightwave transmission systems. These systems have been made possible by two major technological advances: the development of low-loss silica (glass) fibres, which act as a transmission medium, and the development of high-performance reliable semiconductor lasers. Early lightwave systems used multimode fibres and an operating wavelength of about 0.85 μm. AlGaAs semiconductor lasers are used as sources for these systems. Current systems using single-mode fibres and an operating wavelength near 1.3 μm offer longer repeater spacing because of the lower silica fibre loss near 1.3 μm than at ~0.85 μm. Even larger repeater spacing is allowed for an operating wavelength near 1.55 μm, where the fibre loss is minimum. Semiconductor lasers fabricated using the InGaAsP material system are, by and large, the only sources for commercial high-data-rate long-haul lightwave systems operating near 1.3 and 1.55 μm. Because of its substantial impact on lightwave technology, a large portion of semiconductor laser research and development has been on A1GaAs ($\lambda \sim 0.85$ μm) and InGaAsP ($\lambda \sim 1.3$ and 1.55 μm) lasers. For the same reason, we shall use AlGaAs and InGaAsP material systems as examples to illustrate the concepts in semiconductor lasers. Early work in the area of semiconductor lasers has been extensively reviewed in three books [11–13].

12.2 Principles of Operation

12.2.1 The Dielectric Waveguide

Conceptually, stimulated emission in a semiconductor laser arises from electron–hole radiative recombination in the active region, and the light generated is confined and guided by a dielectric waveguide (Figure 12.4). The active region has a slightly higher index than the p- and n-type cladding layers and the three layers form a dielectric waveguide. The energy distribution of the fundamental mode of the waveguide is also sketched in Figure 12.4. A fraction of the optical mode is confined in the active region. Two types of fundamental transverse modes can propagate in the waveguide: the transverse electric (TE) and the transverse magnetic (TM) modes. The confinement factor (Γ), the fraction of mode in the active region, has been previously calculated [12, Part A, p 34]. Figure 12.5 shows the calculated Γ as a

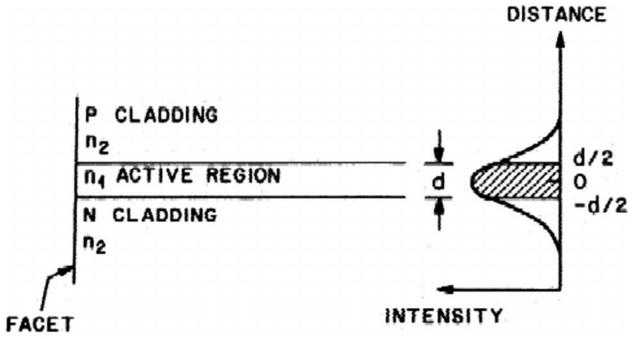

FIGURE 12.4 The dielectric waveguide of the semiconductor laser. n_2 is the refractive index of the cladding layers and n_1 that of the active region: $n_1 > n_2$. The cladding layers are of a higher bandgap material than the active region. The intensity distribution of the fundamental mode is shown. The cross-hatched region represents the fraction of the mode (Γ) within the active region.

function of active layer thickness for the TE and TM modes for the $\lambda = 1.3$ μm InGaAsP double heterostructure (DH) with p-InP and -InP cladding layers.

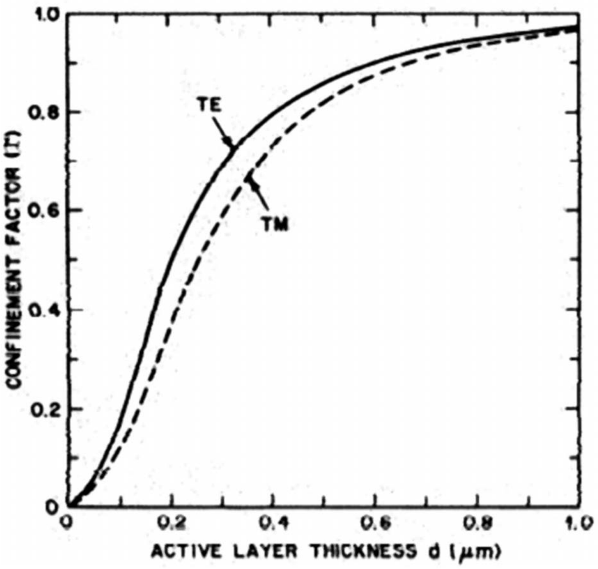

FIGURE 12.5 Confinement factor of the fundamental TE and TM modes for a waveguide with an InGaAsP ($\lambda = 1.3$ μ*m*) active layer and InP cladding layers as a function of the thickness of the active region. The refractive indices of the active and cladding region are 3.51 and 3.22, respectively.

12.2.2 Threshold Condition

At the threshold, the optical gain equals the total optical loss in the laser cavity. The condition for threshold (gain = loss) is

$$\Gamma g_{\mathrm{th}} = \alpha_{\mathrm{a}}\Gamma + (1-\Gamma)\alpha_{\mathrm{c}} + \frac{1}{L}\ln\frac{1}{R} \tag{12.1}$$

where g_{th} is the threshold gain in the active region; α_{a} and α_{c} are the absorption losses in the active and cladding regions, respectively; L is the cavity length and R is the mirror facet reflectivity. Typically, $L \sim 300$ μm and $R \sim 0.3$. For a 0.2 μm-thick active layer, Γ (TE) is ~0.47 (from Figure 12.5) and using $\alpha_{\mathrm{a}} \simeq 30\,\mathrm{cm}^{-1}$, the calculated $g_{\mathrm{th}} \simeq 150\,\mathrm{cm}^{-1}$. This compares with a value of 10^{-2}–$10^{-3}\,\mathrm{cm}^{-1}$ for HeNe lasers [14].

12.2.3 Condition for Stimulated Emission

Sufficient numbers of electrons and holes must be excited in the semiconductor for stimulated emission or net optical gain. The condition for net gain at photon energy E is given by [15]

$$E_{\mathrm{f_c}} + E_{\mathrm{f_v}} = E - E_{\mathrm{g}} \tag{12.2}$$

where $E_{\mathrm{f_c}}$ and $E_{\mathrm{f_v}}$ are the quasi-Fermi levels of electrons and holes, respectively, measured from the respective band edges (positive into the band) and E_{g} is the bandgap of the semiconductor. For zero net gain (transparency), this condition becomes $E_{\mathrm{f_c}} + E_{\mathrm{f_v}} = 0$. For an undoped material at a temperature T, the quasi-Fermi energy $E_{\mathrm{f_c}}$ is related to the injected carrier (electron or hole) density n by

$$n = N_{\mathrm{c}}\frac{2}{\sqrt{\pi}}\int\frac{\mathrm{d}\varepsilon}{1+\exp\left(\varepsilon-\varepsilon_{\mathrm{f_c}}\right)} \tag{12.3}$$

with $N_{\mathrm{c}} = 2(2\pi m_{\mathrm{c}}kT/h^2)^{3/2}$ and $\varepsilon_{\mathrm{f_c}} = E_{\mathrm{f_f}}/kT$, where k is the Boltzmann constant, h is Planck's constant, T is the temperature and m_{c} is the effective mass of the electrons in the conduction band. A similar equation holds for holes.

Figure 12.6 shows the variation of the injected carrier density for transparency n_{t} as a function of temperature for undoped $\lambda = 1.3$ μm InGaAsP. The parameter values used in the calculation are $m_{\mathrm{c}} = 0.061m_0$, $m_{\mathrm{hh}} = 0.45m_0$ and $m_{\mathrm{lh}} = 0.08m_0$, where m_0, m_{hh} and m_{lh} are the free-electrons, heavy-hole and the light-hole mass, respectively. Figure 12.6 shows that n_{t} is considerably smaller at low temperatures. The threshold carrier density is ~20%–30% higher than n_{t}.

The high carrier densities needed for gain can be generated by optical excitation or current injection. The first injection laser operation was demonstrated in 1962 [1–3]. The injection laser utilized the unique characteristics of the pn junction to confine carriers near the depletion region under forward bias.

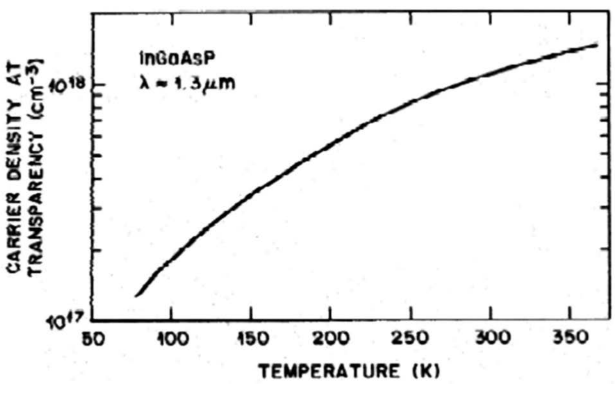

FIGURE 12.6 The calculated injected carrier density for transparency as a function of temperature for undoped $\lambda = 1.3$ μm InGaAsP.

12.2.4 The pn Junction Laser

Under high current injection through a pn junction, a region near the depletion layer can have a high density of electrons and holes. These electrons and holes can recombine radiatively if the interfaces are free of traps. The device will lase if the threshold condition (Equation 12.2) is satisfied.

The energy-band diagram of a pn junction between two similar semiconductors (homojunction) at zero bias is shown in Figure 12.7. The broken line represents the Fermi level. Under forward bias, both electrons and holes are present near the depletion region. This region can have a net gain if the electron and hole densities are sufficiently high. However, the thickness of the gain region is very small (~100 Å), which makes the confinement factor (Γ) for an optical mode very small. Hence, from Equation (12.1), it follows that the threshold gain and, hence, the threshold current are high for a homojunction laser.

The threshold current of an injection laser was historically reduced using a DH for carrier confinement, which increased the size of the region of optical gain [16,17]. The DH laser utilizes a pn heterojunction for carrier injection. A heterojunction is a junction in a single crystal between two dissimilar semiconductors. Thus, the fabrication of heterojunctions had to wait until the development of epitaxial growth techniques. The energy-band diagram of a DH laser at zero bias is shown in Figure 12.8. The device consists of a narrow-gap semiconductor (p-type, n-type or undoped) sandwiched between higher gap p- and n-type semiconductors. The narrow-gap semiconductor is the light-emitting region (active region) of the laser. The broken line represents the Fermi level. For the purpose of illustration, we have chosen the active region to be p-type in Figure 12.8. The band diagram under forward bias is shown in Figure 12.8b. Electrons and holes are injected at the heterojunction and are confined in the active region. Thus, the region of optical gain is determined by the thickness of the active region in lasers. In addition, the refractive index of the lower-gap active region is higher than that for the n- and p-type higher-gap confining (also known as cladding) layers. These layers form a waveguide for the lasing optical mode, as discussed previously.

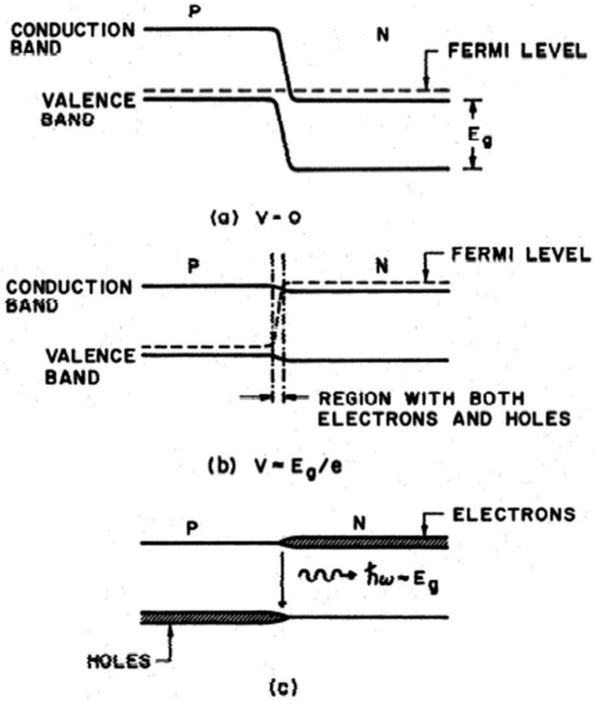

FIGURE 12.7 Energy-band diagram of a pn junction at (a) zero bias and (b) forward bias ($V \approx E_g/E$). (c) Schematic representation of electrons and hole densities under forward bias ($V \approx E_g/e$).

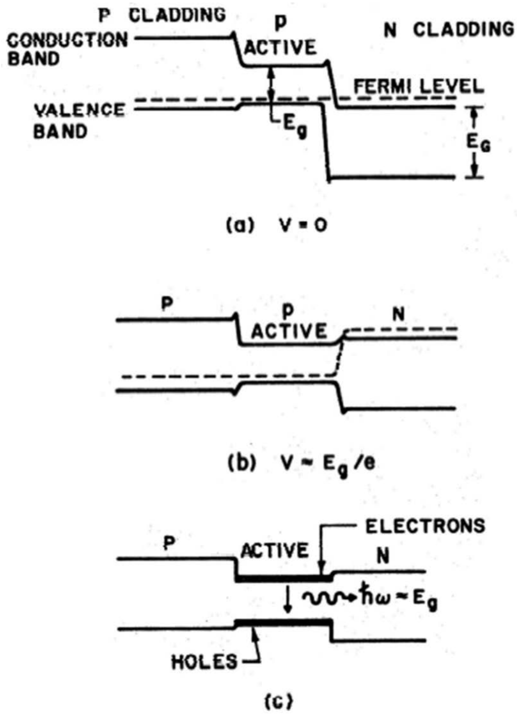

FIGURE 12.8 Energy-band diagram of a double heterostructure laser at (a) zero bias and (b) forward bias ($V \approx E_g/e$).

The active region thickness of DH lasers is typically in the range of 0.1–0.3 μm. Within the past two decades, with the development of MBE and MOCVD growth techniques, it has been possible to fabricate very thin epitaxial layers (<300 Å) bounded by higher-gap cladding layers. These double heterostructures are called quantum well (QW) double heterostructures because the kinetic energy for carrier motion along the thickness of the active region is quantized, similar to that for a one-dimensional potential well [18]. The modification of the electron–hole recombination characteristics (which is the basis for laser action) in QWs is described in Section 12.5. In this chapter, a laser device with an active layer thickness greater than 300 Å is termed a DH laser, and a laser with a smaller active layer thickness is termed a QW laser.

12.3 Radiative Recombination

The basis of light emission in semiconductors is the recombination of an electron in the conduction band with a hole from the valence band; the excess energy is emitted as a photon (light quantum). The process is called radiative recombination, The

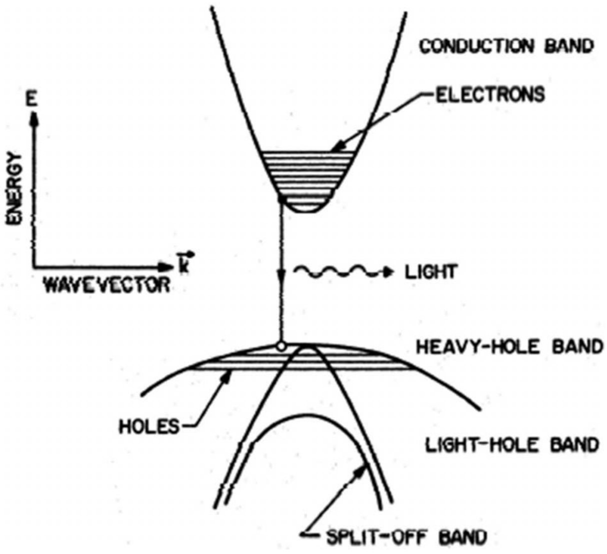

FIGURE 12.9 Energy versus wavevector of the four major energy bands for a zinc-blende type of direct-gap semiconductor.

energy versus wave–vector diagram of the electrons and holes in a cubic (zinc-blende type) semiconductor is shown in Figure 12.9. For direct-gap semiconductors, the bottom of the conduction band and the top of the valence band are at the same point in momentum space or $\boldsymbol{k}$ space ($\boldsymbol{k} = 0$ in Figure 12.9).

This allows both energy and momentum conservation in the process of photon emission by electron–hole recombination. For indirect-gap semiconductors (e.g. silicon), the momentum conservation can be achieved with the assistance of a phonon (lattice vibration), which significantly decreases the probability of radiative recombination. The valence band in many III–V semiconductors is represented by three major sub-bands. These are the heavy-hole band, the light-hole band and the spin–split-off band. The radiative transitions occurring near bandgap energies are due to the recombination of electrons with heavy holes and light holes. A heavy hole, as the name implies, has a larger effective mass than a light hole, which makes the density of states (and also the available number of heavy holes for a given Fermi level) larger than that for light holes.

12.3.1 Gain Calculation

The quantities associated with a radiative recombination are the absorption spectrum, emission spectrum, gain spectrum and total radiative emission rate. The optical absorption or gain for a transition between the valence band and the conduction band at an energy E is given by [12, part A, p 129]

$$\alpha(E) = \frac{e^2 h}{2\varepsilon_0 m_0^2 c n E} \int_{-\infty}^{+\infty} \rho_c(E')\rho_v(E'')\left|M(E',E'')\right|^2 \left[f(E''=E'-E) - f(E')\right] \mathrm{d}E' \qquad (12.4)$$

where m_0 is the free-electron mass, e is the electron charge, ε_0 is the permittivity of free space, E is the photon energy, n is the refractive index at energy E and ρ_c and ρ_v are the densities of state per unit volume per unit energy in the conduction and valence band, respectively. $f(E')$ is the probability that a state of energy E' is occupied by an electron and M is the effective matrix element between the conduction-band state of energy E' and the valence-band state of energy. Hwang [19] has shown that the contribution of the band-tail impurity states can be significant for photon energies near the band edges. Several models for the density of states and matrix element for the transition between band-tail states exist (e.g. [11, part A, Chap 3]). The latest of such models that take into account the contributions of the parabolic bands and impurities is a Gaussian fit of the Kane form to the Halperin–Lax model of band tails. This was first proposed by Stern [20] and used to calculate the gain and recombination rate in GaAs.

The matrix element M may be expressed as a product of two terms: $M = M_b M_{env}$. The quantity M_b arises from the band-edge Bloch functions and M_{env} arises from the envelope wave functions. For III–V semiconductors using the Kane model [22],

$$\left|M_b\right|^2 = \frac{m_c^2 E_g}{12 m_c} \frac{E_g + \Delta}{E_g + \frac{2}{3}\Delta} \qquad (12.5)$$

where m_c is the conduction-band effective mass, E_g is the energy gap and Δ is the spin–orbit coupling. The envelope matrix element for the band-tail states has been calculated by Stern.

The calculated spectral dependence of absorption or gain at various injected carrier densities is shown in Figure 12.10

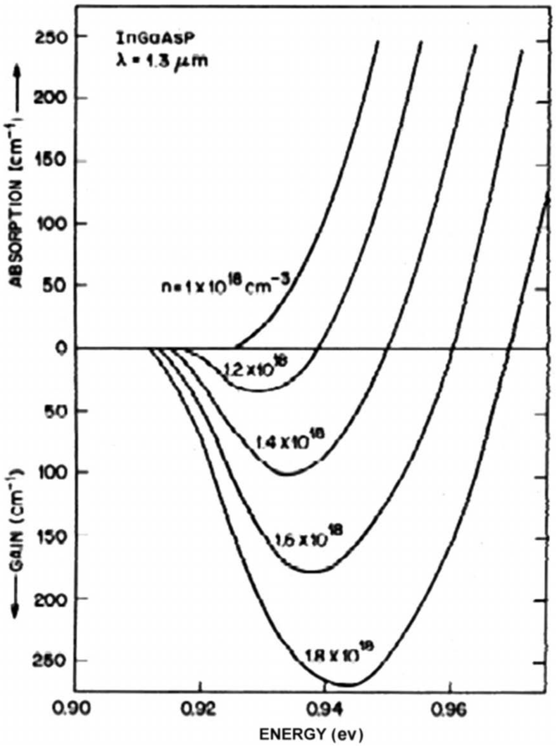

FIGURE 12.10 Calculated gain or absorption as a function of photon energy for $\lambda = 1.3$ μm ($E_g = 0.9$ eV) InGaAsP at various injected carrier densities (after Dutta [21]).

for InGaAs ($\lambda \simeq 1.3$ μm) with acceptor and donor concentrations of $2 \times 10^{17}\,\text{cm}^{-3}$. The calculation was done using Gaussian Halperin–Lax band tails and Stern's matrix element. The material parameters used in the calculation are $m_c = 0.061m_0$, $m_{hh} = 0.45m_0$, $m_{lh} = 0.08m_0$, $\Lambda = 0.26\,\text{eV}$, $E_g = 0.96\,\text{eV}$ and $\varepsilon = 11.5$. Figure 12.10 shows that the gain peak shifts to higher energies with increasing injection.

Figure 12.11 shows the maximum gain as a function of injected carrier density at different temperatures. Note that a considerably lower injected carrier density is needed at a lower temperature to achieve the same gain; this is the origin of the lower threshold current at low temperature. It is often convenient to use a linear relationship between the gain g and the injected carrier density n of the form

$$g = a(n - n_0) \tag{12.6}$$

where a is the gain coefficient and n_0 is the injected carrier density at transparency.

12.3.2 Spontaneous Emission Rate

At unity quantum efficiency, the total spontaneous radiative recombination rate R equals the excitation rate. The latter is usually expressed in terms of the nominal current density J_n [20,21]:

$$J_n\left[\text{A}\cdot\text{cm}^2\cdot\mu\text{m}^{-1}\right] = eR \tag{12.7}$$

with $R = \int r_{\text{spon}}(E)\text{d}E$, where e is the electron charge and the thickness of the active region is assumed to be 1 μm. $r_{\text{spon}}(E)$ is the spontaneous emission rate at a photon energy E. It is given by [21]

$$r_{\text{spon}}(E) = \frac{4\pi n e^2 E}{m^2 \varepsilon_0 h^2 c^3}\int_{-\infty}^{+\infty} \rho_c(E')\rho_v(E'')\left|M(E',E'')\right|^2 \times f(E')\left[1 - f(E'')\right]\text{d}E' \tag{12.8}$$

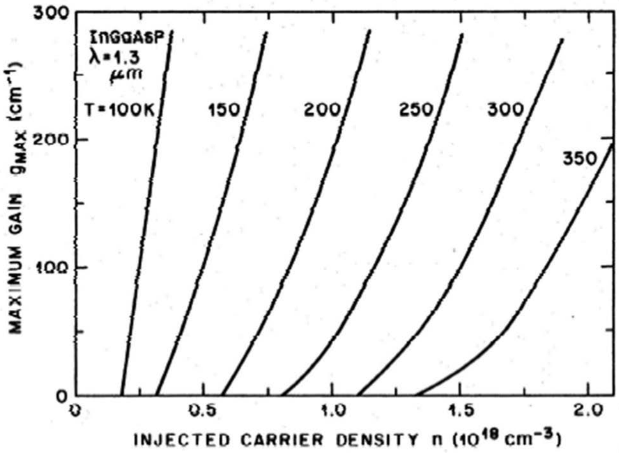

FIGURE 12.11 The maximum gain as a function of injected carrier density for undoped InGaAsP ($\lambda = 1.3$ μm) at different temperatures (after Dutta and Nelson [23]).

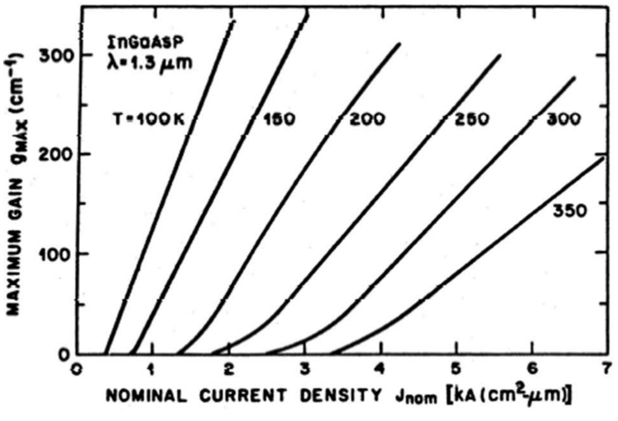

FIGURE 12.12 The maximum gain as a function of nominal current density for InGaAsP ($\lambda = 1.3$ μm) at different temperatures (after Dutta and Nelson [23]).

The calculated maximum optical gain g as a function of the nominal current density at various temperatures is shown in Figure 12.12 for InGaAsP ($\lambda \simeq 1.3$ μm). The calculation is for an undoped lightly compensated material with $10^{17}\,\text{cm}^{-3}$ of acceptors and donors, respectively. Note that gain varies linearly with J_n above a certain gain.

The total spontaneous radiative recombination rate R can be approximated by

$$R = Bnp \tag{12.9}$$

where B is the radiative recombination coefficient and n and p are the electron and hole densities, respectively. For undoped semiconductors, Equation (12.9) becomes $R = Bn^2$. For GaAs, the measured $B = 1 \times 10^{-10}\,\text{cm}^3\text{s}^{-1}$. Calculation of the radiative recombination rate shows that B decreases with increasing carrier density [20]. This has been confirmed by Olshansky and coworkers [24] using carrier lifetime measurements.

12.3.3 Threshold Current Calculation

In DH lasers, the injected carriers can recombine by both radiative and non-radiative recombination. The injected current density J is simply the sum of the radiative R and non-radiative R_{nr} recombination rates in the absence of carrier leakage:

$$J = e(R + R_{nr})d = J_r + J_{nr} \qquad (J_r = J_n d) \tag{12.10}$$

where e is the electron charge, d is the active layer thickness and J_r and J_{nr} are the radiative and non-radiative components of the current density, respectively.

For a GaAs DH laser where the quantum efficiency is believed to be close to unity, i.e. most of the injected carriers recombine radiatively, $J \simeq J_r$. The relation between the optical gain and the nominal current density for a GaAs material system has been calculated by Stern [20]. It is given by

$$g = 0.045(J_{\text{nom}} - 4222)\,\text{cm}^{-1} \tag{12.11}$$

where J_{nom} is expressed in amperes per square centimetre per micrometre. The threshold current of a 250-μm-long

GaAs–A1GaAs DH laser with 2 × 0.2 µm active region can now be calculated using Equations (12.1) and (12.11). The calculated $\Gamma \simeq 0.6$ for a 0.2 µm-thick $\mathrm{GaAsAl_{0.36}Ga_{0.64}As}$ double heterostructure. Assuming $R = 0.3$ and $\alpha_a = \alpha_c = 20\,\mathrm{cm^{-1}}$, we get $g_{th} = 114\,\mathrm{cm^{-1}}$, $J_{th} = 1.35$ kA cm^2 and a threshold current of 6.7 mA. This compares well with the experimentally observed threshold currents in the range of 5–10 mA for GaAs–A1GaAs DH lasers with good current confinement. Figure 12.12 shows that the current density needed to achieve a certain optical gain increases with temperature that is the threshold current density of a laser is expected to increase with increasing temperature. It is experimentally observed that the threshold current density J_{th} of a laser varies with the temperature T as $J_{th} = J_0 \exp(T/T_0)$, where T_0 is a characteristic temperature determining the temperature sensitivity. For $g = 114\,\mathrm{cm^{-1}}$, the calculated $T_0 \simeq 210\,\mathrm{K}$ from Figure 12.12 in the temperature range of 300–350 K. This agrees well with the measured values for GaAs lasers.

For InGaAsP lasers, a significant amount of non-radiative recombination is believed to be present at carrier densities comparable to the lasing threshold near room temperature. Non-radiative recombination can increase the threshold current density as discussed in the next section.

12.4 Non-Radiative Recombination

An electron–hole pair can recombine non-radiatively, meaning that the recombination can occur through any process that does not emit a photon. In many semiconductors—for example, pure germanium or silicon—non-radiative recombination dominates radiative recombination. The measurable quantities associated with non-radiative recombination are internal quantum efficiency and carrier lifetime. The variations of these quantities with parameters such as temperature, pressure and carrier concentration are, by and large, the only way to identify a particular non-radiative recombination process.

The effect of non-radiative recombination on the performance of injection lasers is to increase the threshold current. If τ_{nr} is the carrier lifetime associated with the non-radiative process, the increase in threshold current density is given approximately by

$$J_{nr} = \frac{e n_{th} d}{\tau_{nr}} \tag{12.12}$$

where n_{th} is the carrier density at threshold, d is the active layer thickness and e is the electron charge. The non-radiative recombination processes described in this section are the Auger effect, surface recombination and recombination at defects or traps.

12.4.1 Auger Effect

Since the pioneering work by Beattie and Landsberg [25], it is generally accepted that Auger recombination can be a major non-radiative recombination mechanism in narrow-gap semiconductors. Recent attention to the Auger effect has been in connection with the observed higher temperature of threshold current of long-wavelength InGaAsP lasers compared to short-wavelength AlGaAs lasers [23,26–29]. It is generally believed that the Auger effect plays a significant role in determining the observed high-temperature sensitivity of the threshold current in InGaAsP lasers emitting near 1.3 and 1.55 µm.

There are several types of Auger recombination processes. The three major ones are the band-to-band process, the phonon-assisted Auger process and the trap-assisted Auger process. The band-to-band Auger processes in direct-gap semiconductors are shown in Figure 12.13. The three processes are labelled CCCH, CHHS and CHHL, where C stands for the conduction band and H, L and S stand for heavy-hole, light-hole and split-off valence-band hole, respectively. The CCCH mechanism involves three electrons and a heavy hole and is dominant in n-type materials. The process was first considered by Beattie and Landsberg [25]. The CHHS process involves one electron, two heavy holes and a split-off band hole. The CHHL process is similar to the CHHS process except that it involves a light hole. The CHHS and CHHL mechanisms are dominant in p-type material. Under the high injection conditions present in lasers, all these mechanisms must be considered.

Band-to-band Auger processes are characterized by a strong temperature and bandgap dependence, the Auger rate decreasing rapidly either for low temperature or for high bandgap materials. These dependencies arise from the energy

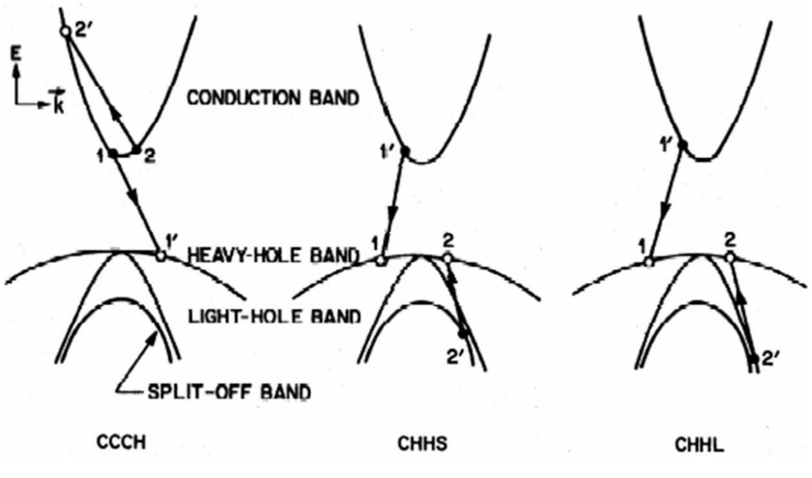

FIGURE 12.13 Band-to-band Auger recombination processes in a direct-gap semiconductor.

and momentum conservation that the four free-particle states involved (1, 2, 1′ and 2′ in Figure 12.13) must satisfy. This may be seen in the following way for the CCCH process. The momentum and energy conservation laws give rise to a threshold energy E_T for each of the processes. For the CCCH process, if we assume $E_1 \simeq E_2 = 0$, only holes with energies greater than ~$(E_T - E_g) = \delta E_g$ can participate (δ is a constant that depends on the effective masses). The number of such holes varies approximately as $\exp(-\delta E_g/kT)$ for non-degenerate statistics and, thus, the Auger rate varies as $\exp(-\delta E_g/kT)$ in the non-degenerate case. In the absence of momentum conservation, there is no threshold energy E_T. Thus, the strong temperature dependence does not appear if the individual particle states are not states of definite momentum, for example, if they are trap states or if momentum conservation is satisfied through phonon assistance. Examples of a CCCH-type phonon-assisted process and a shallow-donor-trap-assisted process are shown in Figure 12.14.

The Auger rate R_A in n-type semiconductors with a carrier concentration n_0 varies as [25]

$$R_A = Cn_0^2\delta p \tag{12.13}$$

where $\delta p \ll n_0$ is the injected minority carrier (hole) density and C is the Auger coefficient. Thus, the minority carrier lifetime is given by

$$\tau_A = \frac{R_A}{\delta p} = \frac{1}{Cn_0^2}. \tag{12.14}$$

The calculated τ_A for n-InGaAsP with a carrier concentration of 10^{18}cm^{-3} is shown in Figure 12.14. The phonon-assisted process dominates at high bandgap and the band-to-band processes dominate for low bandgap semiconductors. The active region of an InGaAsP laser is nominally undoped. Under high injection, the Auger rate R_A varies approximately:

$$R_A = Cn^3 \tag{12.15}$$

where n is the injected carrier density. Calculations of the Auger coefficient using the Kane band model [22] yield a value of 10^{-28}cm^{6}s^{-1} for $\lambda \simeq 1.3$ μm InGaAsP. Haug [29] has calculated a value of ~2.5×10^{-29}cm^{6}s^{-1} for $\lambda \approx 1.3$ μm InGaAsP using a different model for the band structure. The experimental values of the Auger coefficient for this material are in the range of 2–7×10^{-29}cm^{6}s^{-1}. For GaAs, $C \simeq 10^{-31}$cm^{6}s^{-1}. From Equations (12.10) and (12.15), the current lost to Auger recombination at threshold is given by

$$J_A = edCn^3 \tag{12.16}$$

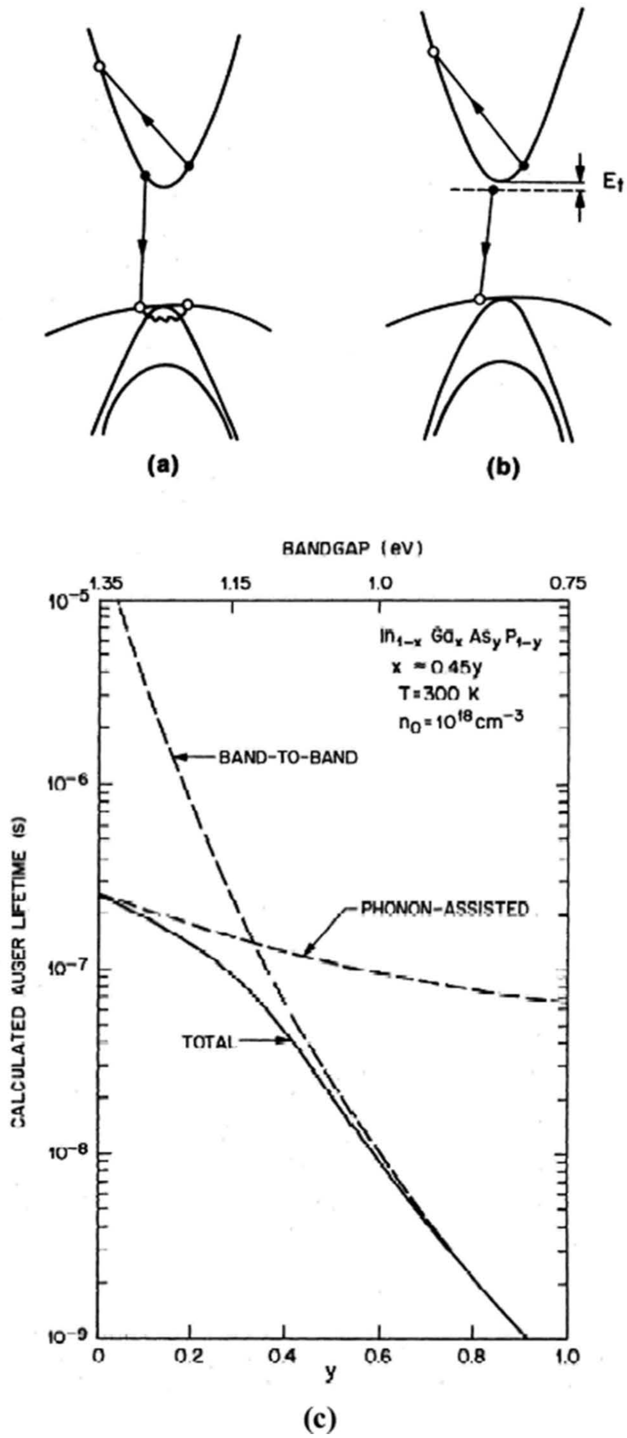

FIGURE 12.14 (a) Photon-assisted CCCH-type Auger recombination process. (b) Auger recombination process using a donor trap. (c) The calculated Auger lifetime for n-InGaAsP with a carrier concentration of 10^{18}cm^{-3} (after Dutta and Nelson [23]).

Thus, the effect of Auger recombination on the threshold current of GaAs lasers is small compared to that for InGaAsP lasers because the Auger coefficient in GaAs is smaller by two orders of magnitude. Since the threshold carrier density increases with increasing temperature, the carrier loss to the non-radiative Auger effect increases with increasing temperature, which results in a more rapid increase in threshold current with increasing temperature (low T_0) for long-wavelength InGaAsP lasers than for AlGaAs lasers. The measured variation in threshold current density as a function of temperature for InGaAsP lasers can be expressed by the relation $J_{th} = J_0 \exp(T/T_0)$ with $T_0 = 50$–70 K in the temperature range 300–350 K. Auger recombination plays a significant role in determining the smaller T_0 values of InGaAsP ($\lambda \simeq 1.3$ and

1.55 μm) lasers compared to the shorter wavelength ($\lambda \simeq 0.85$ μm) AlGaAs lasers.

12.4.2 Surface Recombination

In an injection laser, the cleaved facets are surfaces exposed to the ambient surroundings. In addition, in many index-guided laser structures, the edges of the active region can be in contact with curved surfaces, which may not be a perfect lattice. A surface, in general, is a strong perturbation of the lattice, creating many dangling bonds that can absorb impurities from the ambient. Hence, a high concentration of defects that can act as non-radiative recombination centres can occur. Such localized non-radiative centres, in addition to increasing the threshold current, can cause other performance problems (e.g. sustained oscillations) in lasers.

The recombination rate of carriers at the surface is expressed in terms of a surface recombination velocity S. If A is the surface area and n_{th} the threshold carrier density, then the increase in threshold current, ΔI_{th}, due to surface recombination, is given by

$$DI_{\text{th}} = en_{\text{th}}SA \tag{12.17}$$

where e is the electron charge. The surface recombination velocity for an InP surface exposed to air is about two orders of magnitude smaller than that for GaAs.

12.4.3 Recombination at Defects

Defects in the active region of an injection laser can be formed in several ways. In many cases, they are grown in during the epitaxial growth process. They can also be generated, multiplied, or propagated, during a stress ageing test [30]. Defects can propagate along a specific crystal axis in a strained lattice. The well-known dark line defect (DLD—dark region of linear aspect) is generally believed to be responsible for the high degradation rate (short life span) of early AlGaAs lasers. Defects, in general, produce a continuum of states in a localized region. Electrons or holes that are within a diffusion length from the edge of the defect may recombine non-radiatively *via* the continuum of states. The rate of recombination at a defect or trap is usually written as

$$R = \sigma \upsilon N_{\text{t}} \tag{12.18}$$

where σ is the capture cross section of the trap, N_{t} is the density of traps and υ is the velocity of the electrons or holes. A trap can preferentially capture electrons or holes. The study of recombination at defects in semiconductors is a vast subject—a detailed discussion is beyond the scope of this chapter.

12.5 Laser Designs and Performance

A schematic diagram of a typical DH used for laser fabrication is shown in Figure 12.1. It consists of n-InP, undoped $\text{In}_{1-x}\text{Ga}_x\text{P}_y\text{As}_{1-y}$, p-InP and p-InGaAsP grown over a (100) oriented n-InP substrate. The undoped $\text{In}_{1-x}\text{Ga}_x\text{P}_y\text{As}_{1-y}$ layer is the light-emitting layer (active layer). It is lattice matched to InP for $x \sim 0.45y$. The bandgap of the $\text{In}_{1-x}\text{Ga}_x\text{P}_y\text{As}_{1-y}$ material (lattice matched to InP) that determines the laser wavelength is given by

$$E_g(\text{eV}) = 1.35 - 0.72y + 0.12y^2 \tag{12.19}$$

12.5.1 Laser Designs

For lasers emitting near 1.3 μm, $y \simeq 0.6$. The DH material can be grown by the LPE, gas source molecular beam epitaxy (GSMBE) or MOCVD growth technique. The DH material can be processed to produce lasers in several ways. Perhaps the simplest is the broad area laser (Figure 12.1), which involves putting contacts on the p- and n-sides and then cleaving. Such lasers do not have transverse-mode confinement or current confinement which leads to high threshold and non-linearities in light versus current characteristics. Several laser designs have been developed to address these problems. Among them are the gain-guided laser, the weakly index-guided laser and the buried heterostructure (BH) (strongly index-guided) laser. Typical versions of these laser structures are shown in Figure 12.15. The gain-guided structure uses a dielectric layer for current confinement. The current is injected in the opening in the dielectric (typically 6–12 μm wide), which produces gain in that region and, hence, the lasing mode is confined to that region.

The weakly index-guided structure has a ridge etched on the wafer and a dielectric layer surrounds the ridge. The current is injected in the region of the ridge and the optical mode overlaps the dielectric (which has a low index) in the ridge. This results in weak index guiding. The BH design shown in Figure 12.15 has the active region surrounded (buried) by lower index layers. The fabrication process for a double channel planar buried heterostructure laser involves growing a double heterostructure, etching a mesa using a dielectric mask and then regrowing the layer surrounding the active region using a second epitaxial growth step. The second growth can be a single Fe-doped InP (Fe:InP) semi-insulating layer or a combination of p-InP, n-InP and Fe:InP layers. Generally, the MOCVD growth process is used for the growth of the regrown layer. Researchers have often given different names to the particular BH laser design that they have developed. For the structure in Figure 12.16, the Fe-doped InP layer provides both optical confinement to the lasing mode and current confinement to the active region. BH lasers are generally used in communication system applications because a properly designed strongly index guided BH design has superior mode stability, higher bandwidth and superior linearity in light versus current (L versus I) characteristics compared to the gain and weakly index guided designs. Early recognition of these important requirements for communication grade lasers led to intensive research on InGaAsP BH laser designs all over the world in the 1980s. It is worth mentioning that BH lasers are more complex and difficult to fabricate compared to the gain and weakly index guided lasers.

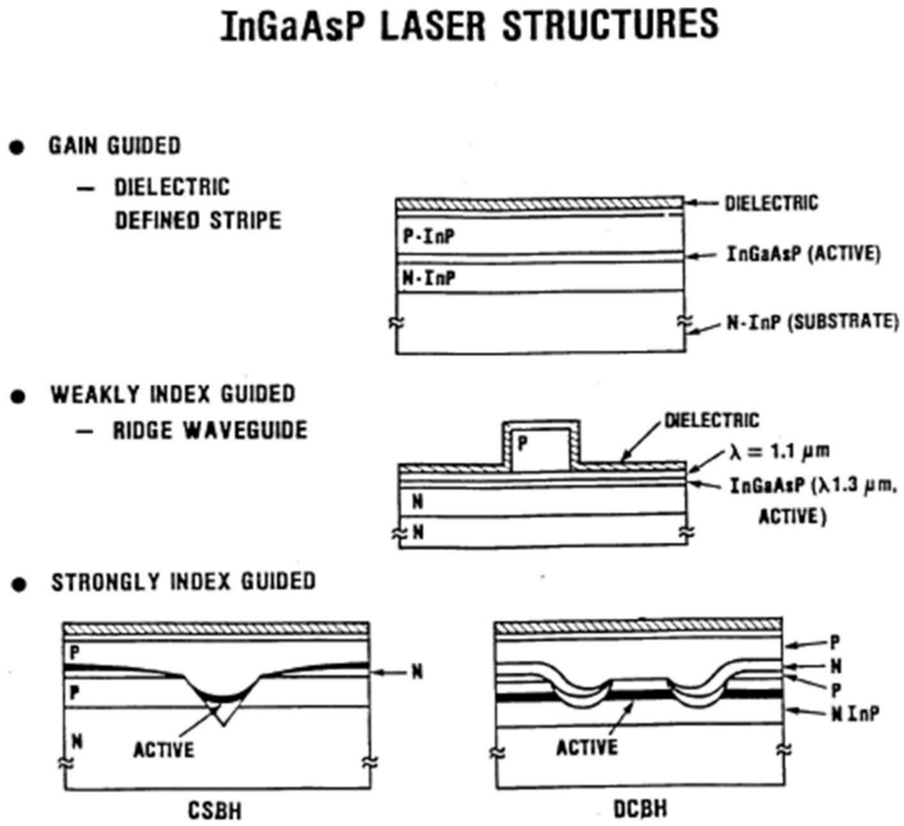
InGaAsP LASER STRUCTURES
● GAIN GUIDED
— DIELECTRIC DEFINED STRIPE
DIELECTRIC
P-InP
InGaAsP (ACTIVE)
N-InP
N-InP (SUBSTRATE)
● WEAKLY INDEX GUIDED
— RIDGE WAVEGUIDE
P
DIELECTRIC
λ = 1.1 μm
InGaAsP (λ1.3 μm, ACTIVE)
N
N
● STRONGLY INDEX GUIDED
P
N
P
N
ACTIVE
CSBH
P
N
P
N InP
ACTIVE
DCBH

FIGURE 12.15 Schematic diagram of various laser designs using the InGaAs/InP materials system.

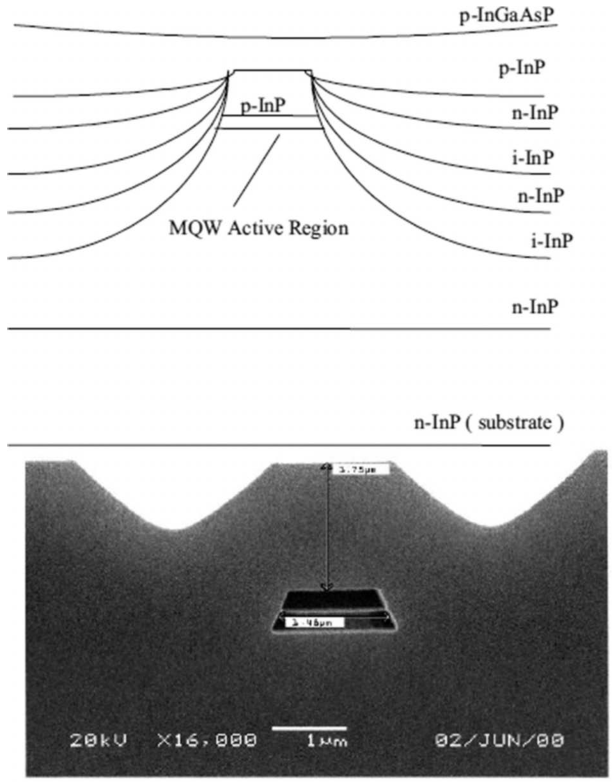
p-InGaAsP
p-InP
p-InP
n-InP
i-InP
n-InP
MQW Active Region
i-InP
n-InP
n-InP (substrate)
20kV ×16,000 1μm 02/JUN/00

FIGURE 12.16 Schematic diagram and scanning electron photomicrograph of a buried heterostructure (BH) laser.

A scanning electron micrograph of a capped mesa buried heterostructure (CMBH) laser along with the laser structure is shown in Figure 12.16. The current-blocking layers in this structure consist of i-InP (Fe-doped InP), n-InP, i-InP and n-InP layers. These sets of blocking layers have the lowest capacitance and are, therefore, needed for high-speed operation. An optimization of the thickness of these layers is needed for highest-speed performance. The laser fabrication involves the following steps. Mesas 1 μm wide are etched on the wafer and the current-blocking layers consisting of i-InP, n-InP i-InP and n-InP layers are grown on the wafer with an oxide layer on top of the mesa in place. The oxide layer is then removed and a third growth of a p-InP cladding layer and a p-InGaAs contact layer is carried out. The wafer is then processed using standard lithography, metallization and cleaving techniques to produce the lasers.

12.5.2 Laser Performance

The light versus current characteristics at different temperatures of an InGaAsP BH laser emitting at 1.3 μm are shown in Figure 12.17. A typical threshold current for a BH laser at room temperature is in the 5–10 mA range. For gain and weakly index guided lasers, typical room temperature threshold currents are in the 25–50 and 50–100 mA range, respectively. The external differential quantum efficiency defined as the derivative of the L versus I characteristics above threshold is ~0.25 mW mA^{-1} facet^{-1} for a cleaved uncoated laser emitting near 1.3 μm.

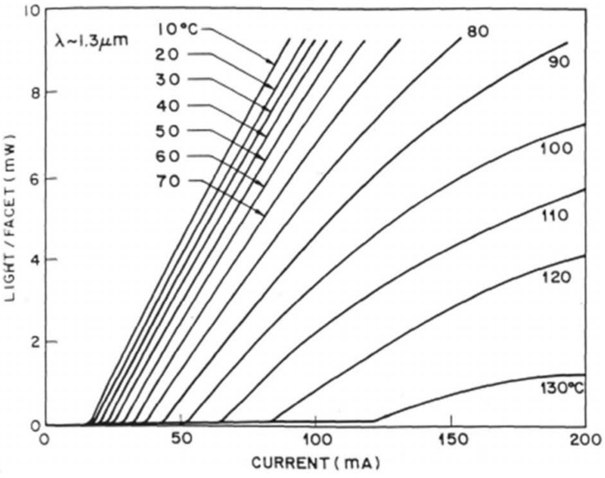

FIGURE 12.17 Light versus current characteristics at different temperatures of a typical buried heterostructure (BH) laser.

An important characteristic of the semiconductor laser is that its output can be modulated easily and simply by modulating the injection current. The relative magnitude of the modulated light output is plotted as a function of the modulation frequency of the current in Figure 12.18 at different optical output powers. The laser is of the BH type (shown in figure 12.15), has a cavity length of 250 μm and the modulation current amplitude was 5 mA. Note that the 3-dB frequency to which the laser can be modulated increases with increasing output power and the modulation response is at a maximum at a certain frequency (ω_r). The resonance frequency, ω_r, is proportional to the square root of the optical power. The modulation response determines the data transmission rate capability of the laser, for example, for 10 Gb s^{-1} data transmission, the 3-dB bandwidth of the laser must exceed 10 GHz. However, other system level considerations, such as allowable error-rate penalty, often introduce much more stringent requirements on the exact modulation response of the laser.

A semiconductor laser with cleaved facets generally emits in a few longitudinal modes of the cavity. A typical spectrum of a laser with cleaved facets is shown in Figure 12.19. The discrete emission wavelengths are separated by the longitudinal cavity mode spacing, which is ~10 A for a laser ($\lambda \simeq 1.3$ μm) with 250 μm cavity length. Lasers can be made to emit in a single frequency using frequency-selective feedback, for example using a grating internal to the laser cavity as described later.

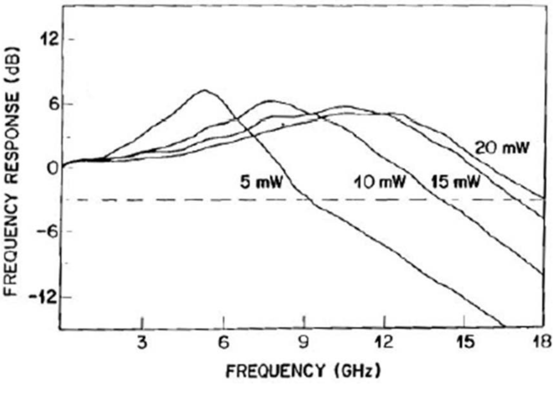

FIGURE 12.18 Frequency response, i.e. modulated, output power as a function of modulation frequency at different output powers.

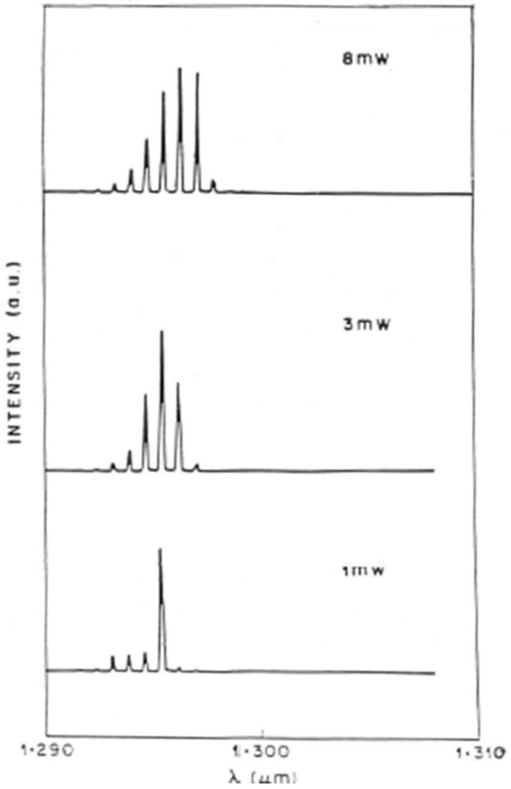

FIGURE 12.19 Typical Fabry–Pérot laser spectrum at different output powers.

The active region waveguide dimensions of a semiconductor laser are typically comparable to or smaller than the wavelength of emission. This results in diffraction of the light as it emerges from the facet. The diffraction leads to a divergence of the emitted light. The magnitude of the divergence depends on the waveguide dimensions, index of refraction and wavelength of emission. The measured far-field patterns parallel and perpendicular to the junction plane at different output powers of a typical laser are shown in Figure 12.20. The figure shows that the laser operates in the fundamental transverse mode in the entire operating power range from threshold to 60 mW. The full width at half maximum of the beam divergences parallel and normal to the junction plane are 40° and 30°, respectively.

12.6 Quantum Well Lasers

As shown in Figure 12.1, a conventional DH laser consists of an active layer sandwiched between higher-gap cladding layers. The active layer thickness is typically 0.1–0.5 μm. Over the last decade, DH lasers have been fabricated with an active layer thickness of ~100 Å or less. The carrier (electron or hole) motion normal to the active layer in these structures

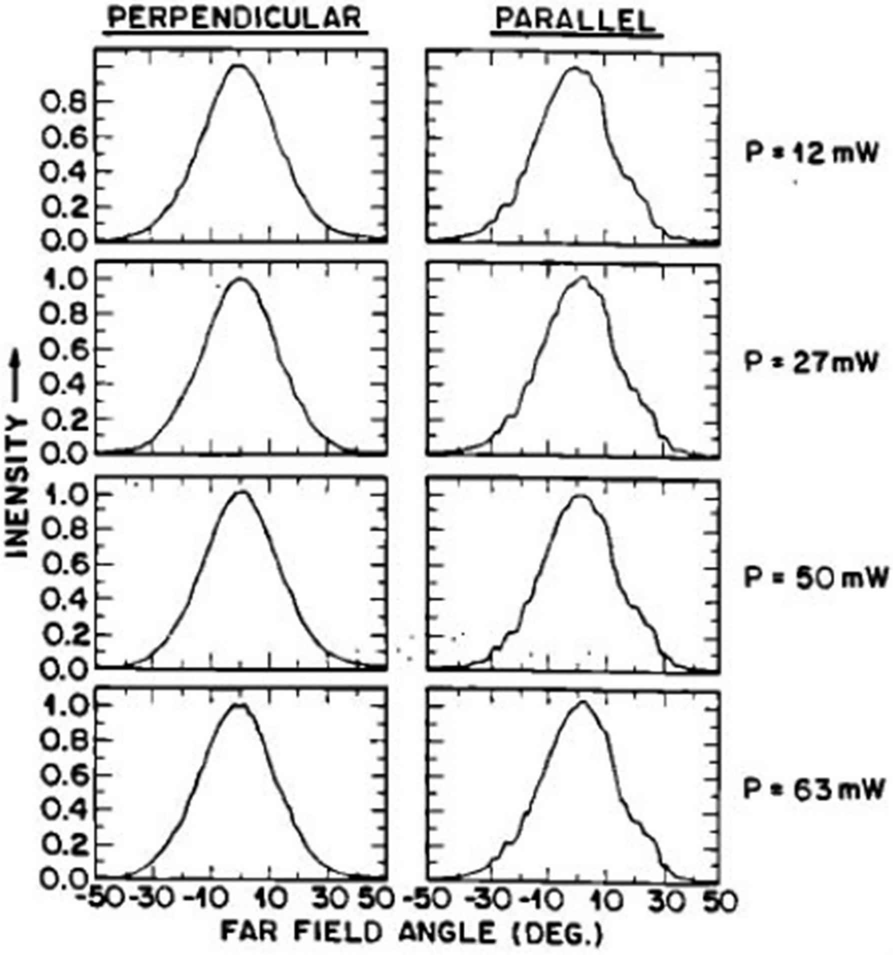

FIGURE 12.20 Typical beam divergence characteristics of a semiconductor laser parallel and perpendicular to the junction plane.

is restricted. This may be viewed as carrier confinement in a one-dimensional potential well and, hence, these lasers are called QW lasers [31,32].

12.6.1 Energy Levels

When the thickness L of a narrow-gap semiconductor layer confined between two wide-gap semiconductors becomes comparable to the de Broglie wavelength ($\lambda \simeq h/p \simeq L_z$), quantum-mechanical effects are expected to occur. The energy levels of the carriers confined in the narrow-gap semiconductor can be determined by separating the Hamiltonian into a component normal to the layer (z component) and into the usual (unconfined) Bloch function components (x, y) in the plane of the layer. The resulting energy eigenvalues are:

$$E\left(n,k_x,k_y\right) = E_n + \frac{\hbar^2}{2m_n^*}\left(k_x^2 + k_y^2\right) \tag{12.20}$$

where E_n is the n_{th} confined-particle energy level for carrier motion normal to the well. m_n^* is the effective mass of the n_{th} level, ħ is Planck's constant and k_x and k_y are the usual Bloch wavevectors in the x and y directions. Figure 12.21 shows schematically the energy levels E_n of the electrons and holes confined in a QW. The confined particle energy levels E_n are denoted by $E_{1\text{c}}$, $E_{2\text{c}}$ and $E_{3\text{c}}$ for electrons; $E_{1\text{hh}}$ and $E_{2\text{hh}}$ for heavy holes, and $E_{1\text{lh}}$ and $E_{2\text{lh}}$, for light holes. The calculation of these quantities is a standard problem in quantum mechanics for a given potential barrier (ΔE_c, ΔE_v). For an infinite potential well, the following simple result is obtained:

$$E_n = \frac{h^2 n^2}{8L_z^2 m_n^*}. \tag{12.21}$$

Since the separation between the lowest conduction-band level and the highest valence-band level is given

$$E_\text{q} = E_\text{g} + E_{1\text{c}} + E_{1\text{hh}} \approx E_\text{g} + \frac{h^2}{8L_z^2}\left(\frac{1}{m_\text{c}} + \frac{1}{m_\text{h}}\right) \tag{12.22}$$

It follows that in a QW structure, the energy of the emitted photons can be varied simply by varying the well width L_z. For the realistic case of a finite well, the Schrödinger equation for a finite well needs to be solved to get more accurate values for the sub-band energy levels in the conduction and valence band and, hence, the emission energy in a QW [33]. The infinite potential model overestimates the value of E_n in

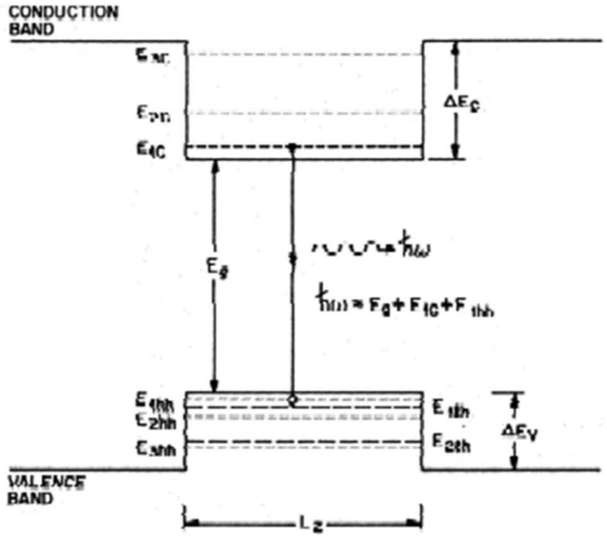

FIGURE 12.21 Energy levels in a quantum well structure (after Holonyak et al. [32]).

Equation (12.22). Figure 12.22 shows the experimental results [34] for an InGaAs QW bounded by InP cladding layers.

The discrete energy levels result in a modification of the density of states in a QW to a 'two-dimensional-like' density of states. This modification of the density of states results in several improvements in the laser characteristics such as lower threshold current, higher efficiency, higher modulation bandwidth and lower continuous wave (cw) and dynamic spectral width. All of these improvements were first predicted theoretically and then demonstrated experimentally [23–32,35,36].

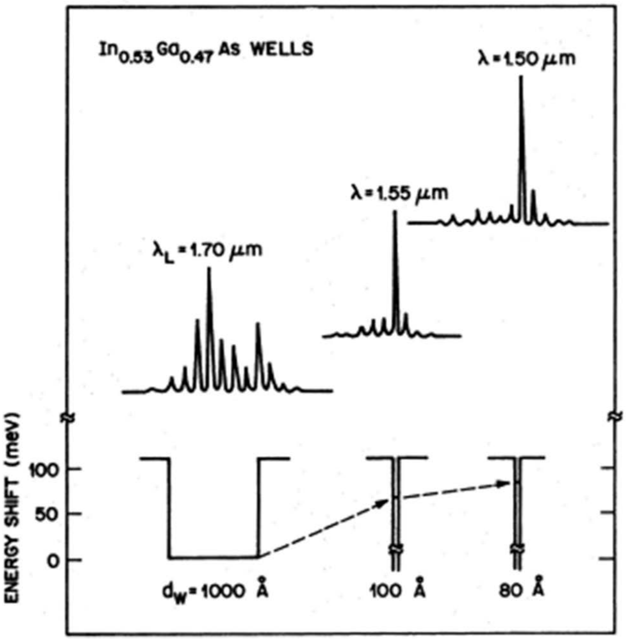

FIGURE 12.22 The laser spectrum for different well widths for InGaAs single quantum well structures.

12.6.2 Quantum Well Laser Performance

The development of InGaAsP QW lasers were made possible by the development of MOCVD and GSMBE growth techniques. The transmission electron micrograph of a multiple QW laser structure is shown in Figure 12.23.

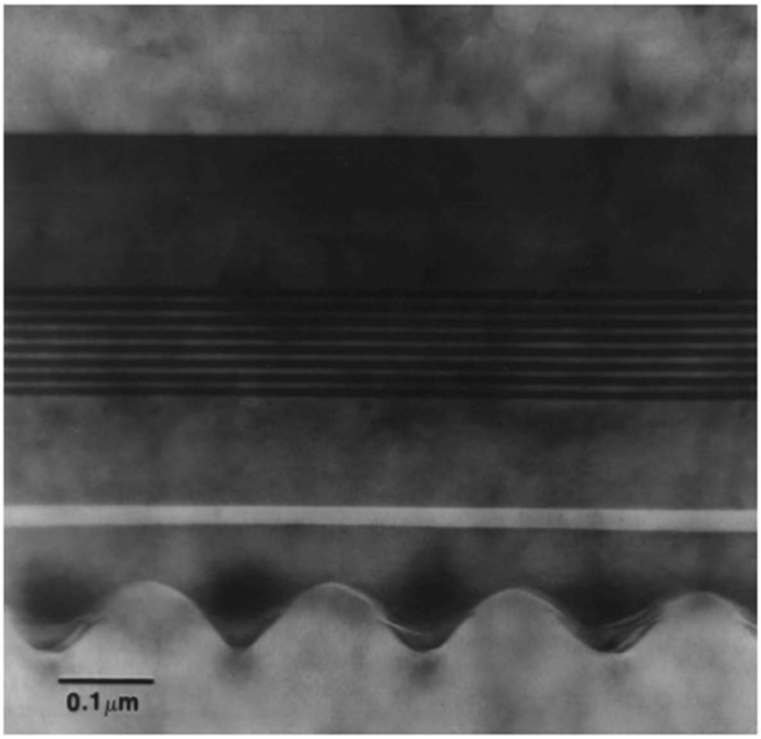

FIGURE 12.23 Transmission electron micrograph of a quantum well structure fabricated over a substrate with a grating.

Shown are four InGaAs QWs grown over an n-InP substrate. The well thickness is 70 Å and they are separated by barrier layers of InGaAsP ($\lambda \simeq 1.1$ μm). Multiquantum well (MQW) lasers with threshold current densities of 600 A cm^{-2} have been fabricated [35]. MQW BH lasers have also been fabricated. The composition of the InGaAsP material from the barrier layers to the cladding layer (InP) is gradually varied in this structure over a thickness of ~0.1 μm. This produces a graded variation in index (GRIN structure), which results in a higher optical confinement of the fundamental mode than that for an abrupt interface design. The larger mode confinement factor results in a lower threshold current. Many BH lasers utilize an MQW active region and Fe-doped semi-insulating (SI) InP layers for current confinement and optical confinement. The light versus current characteristics of an MQW BH laser are generally similar to those of other BH lasers except for a lower threshold current. In addition, the two-dimensional-like density of states of the QW lasers makes the transparency current density of these lasers significantly lower than that for regular DH lasers [30]. This allows the fabrication of very low threshold lasers using high-reflectivity coatings.

The optical gain (g) of a laser at a current density J is given by

$$g = a\left(J - J_0\right) \tag{12.23}$$

where a is the gain constant and J_0 is the transparency current density. Although a logarithmic dependence of gain on current density [37] is often used in order to account for gain saturation, a linear dependence is used here for simplicity. The logarithmic relationship between gain (g) and current density (J) for decoupled QWs is given by

$$g = N\Gamma B ln\left(J/J_0\right) \tag{12.23a}$$

where N is the number of QWs in the active region, Γ is the coupling factor, B is a constant and J_0 is the current needed for transparency.

The cavity loss α is given by

$$\alpha = \alpha_c + \ (1/L)\ ln\left(1/R_1R_2\right) \tag{12.24}$$

where α_c is the free carrier loss, L is the length of the optical cavity and R_1 and R_2 are the reflectivities of the two facets. At threshold, gain equals loss; hence, it follows from Equations (12.23) and (12.24) that the threshold current density (J_{th}) is given by

$$J_{th} = \alpha_c/a + \left(1/La\right)\ ln\left(1/R_1R_2\right) + J_0 \tag{12.25}$$

Thus for a laser with high-reflectivity facet coatings ($R_1, R_2 \simeq 1$) and with low loss ($\alpha_c \simeq 0$), $J_{th} \simeq J_0$. For a QW laser, $J_0 \simeq 50$ A cm^{-2} A cm^{-2} and for a DH laser, $J_0 \simeq 700$ A cm^{-2}; hence, it is possible to get a much lower threshold current using QWs as the active region.

The light versus current characteristic of a QW laser with high-reflectivity coatings on both facets is shown in Figure 12.24 [33]. The threshold current at room temperature is ~1.1 mA.

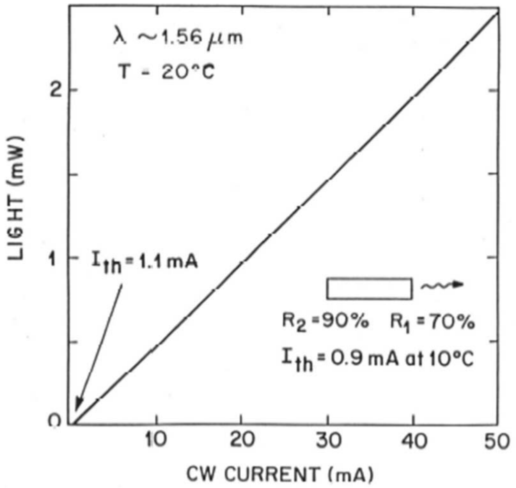

FIGURE 12.24 Light versus current characteristic of a low-threshold quantum well laser fabricated using high-reflectivity coatings.

The laser is 170 μm long and has 90% and 70% reflective coating at the facets. This laser has a compressively strained MQW active region. For lattice-matched MQW active regions, a threshold current of 2 mA has been reported [34].

Such low-threshold lasers are important for array applications. Recently QW lasers have been fabricated which have a higher modulation bandwidth compared to a regular DH laser. Current and optical confinement in this laser is carried out using MOCVD-grown Fe-doped InP lasers. The laser structure is then further modified by using a small contact pad and etching channels around the active region mesa. These modifications are designed to reduce the capacitance of the laser structure. The modulation response of the laser is shown in Figure 12.25. A 3-dB bandwidth of 25 GHz is obtained [38].

12.6.3 Strained Quantum Well Lasers

QW lasers have also been fabricated using an active layer whose lattice constant differs slightly from that of the substrate and cladding layers. Such lasers are known as strained QW lasers. Over

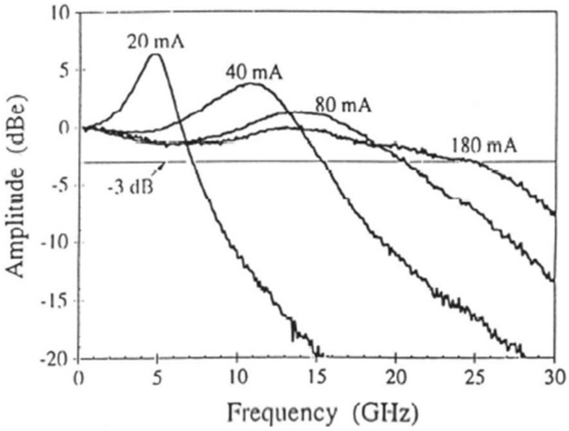

FIGURE 12.25 Modulation response of a quantum well buried heterostructure laser fabricated using Fe:InP current-blocking layers.

the last few years, strained QW lasers have been extensively investigated all over the world [39–46]. They show many desirable properties such as (i) a very low threshold current density and (ii) a lower linewidth than regular MQW lasers, both under cw operation and under modulation. The origin of the improved device performance lies in the band-structure changes induced by the mismatch-induced strain [47,48]. Strain splits the heavy- and light-hole valence bands at the Γ-point of the Brillouin zone, where the bandgap is minimum in direct bandgap semiconductors.

Two material systems have been widely used for strained QW lasers: (i) InGaAs grown over InP by the MOCVD or CBE growth technique [39–43] and (ii) InGaAs grown over GaAs by the MOCVD or MBE growth technique [44–46]. The former material system is of importance for low-chirp semiconductor lasers for lightwave system applications, while the latter has been used to fabricate high-power lasers emitting near 0.98 µm, a wavelength of interest for pumping erbium-doped fibre amplifiers.

The alloy $In_{0.53}Ga_{0.47}As$ has the same lattice constant as InP. Semiconductor lasers with an $In_{0.53}Ga_{0.47}As$ active region have been grown on InP by the MOCVD growth technique.

Excellent material quality is also obtained for $In_{1-x}Ga_xAs$ alloys grown over InP by MOCVD for non-lattice-matched compositions. In this case, the laser structure generally consists of one or many $In_{1-x}Ga_xAs$ QW layers with InGaAsP barrier layers whose composition is lattice matched to that of InP. For $x < 0.53$, the active layer in these lasers is under tensile stress, while for $x > 0.53$, the active layer is under compressive stress.

BH lasers have been fabricated using compressive- and tensile-strained MQW lasers. Lasers with compressive strain have a lower threshold current than that for lasers with tensile strain [49]. This can be explained by the light and heavy-hole bands splitting under stress [50,51].

Strained QW lasers fabricated using $In_{1-x}Ga_xAs$ layers grown over a GaAs substrate have been extensively studied [44,46,52–57]. The lattice constant of InAs is 6.06 Å and that of GaAs is 5.654 Å. The $In_{1-x}Ga_xAs$ alloy has a lattice constant between these two values and, to a first approximation, can be assumed to vary linearly with x. Thus, an increase in the In mole fraction x increases the lattice mismatch relative to the GaAs substrate and, therefore, produces larger compressive strain on the active region.

A typical laser structure grown over the n-type GaAs substrate is shown in Figure 12.26 [44] for this material system. It consists of a MQW active region with one to four $In_{1-x}Ga_xAs$ wells separated by GaAs barrier layers. The entire MQW structure is sandwiched between n- and p-type $Al_{0.3}Ga_{0.7}As$ cladding layers, and the p-cladding layer is followed by a p-type GaAs contact layer. Variations of this structure with different cladding layers or large optical cavity designs have been reported. The emission wavelength depends on the In composition, x. As x increases, the emission wavelength increases and for x larger than a certain value (typically ~0.25), the strain is too large to yield a high-quality material. For $x \simeq 0.2$, the emission wavelength is near 0.98 µm, a wavelength region of interest for pumping fibre amplifiers [49]. Threshold current densities as low as 47 A cm^{-2} have been reported for $In_{0.2}Ga_{0.8}As$/GaAs strained MQW lasers [55]. High-power lasers have been fabricated using an $In_{0.2}Ga_{0.8}As$/GaAs MQW active region. Single-mode output powers of greater than 400 mW have been demonstrated using a ridge-waveguide-type laser structure.

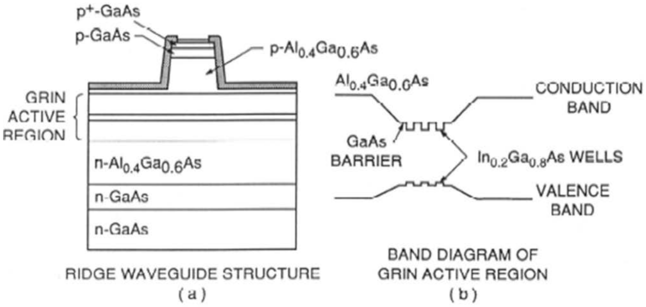

FIGURE 12.26 Schematic diagram of a ridge waveguide-type InGaAs/GaAs laser.

12.7 Distributed Feedback Lasers

Semiconductor lasers fabricated using the InGaAsP material system are widely used as sources in many lightwave transmission systems. One measure of the transmission capacity of a system is the data rate. Thus, the drive towards higher capacity pushes systems to higher data rates where the chromatic dispersion of the fibre plays an important role in limiting the distance between regenerators. Sources emitting in a single wavelength help reduce the effects of chromatic dispersion and are, therefore, used in most systems operating at high data rates (>1.5 Gb s^{-1}).

The single-wavelength laser source used in most commercial transmission systems is the distributed feedback (DFB) laser where a diffraction grating etched on the substrate close to the active region provides frequency-selective feedback which makes the laser emit in a single wavelength. This section reports on the fabrication, performance characteristics and reliability of DFB lasers [58].

12.7.1 Distributed Feedback Laser Design and Fabrication

A schematic diagram of a DFB laser structure is shown in Figure 12.27. The fabrication of the device involves the following steps. First, a grating with a periodicity of 2400 Å (for ~ 1.55 µm emission) is fabricated on a (100) oriented n-InP substrate using optical holography and wet chemical etching. Four layers are then grown over the substrate. These layers are (i) an n-InGaAsP ($\lambda \simeq$ 1.3 µm) waveguide layer, (ii) an undoped InGaAsP ($\lambda \simeq$ 1.55 µm) active layer, (iii) a p-InP cladding layer and (iv) a p-InGaAsP ($\lambda \simeq$ 1.3 µm) contact layer. Mesas are then etched on the wafer using a SiO_2 mask and wet chemical etching. Fe-doped InP semi-insulating layers are grown around the mesas using the MOCVD growth technique. The semi-insulating layers help confine the current to the active region and also provide index guiding to the optical mode. The SiO_2 stripe is then removed and the p-InP cladding layer and a p-InGaAsP contact layer are grown on the

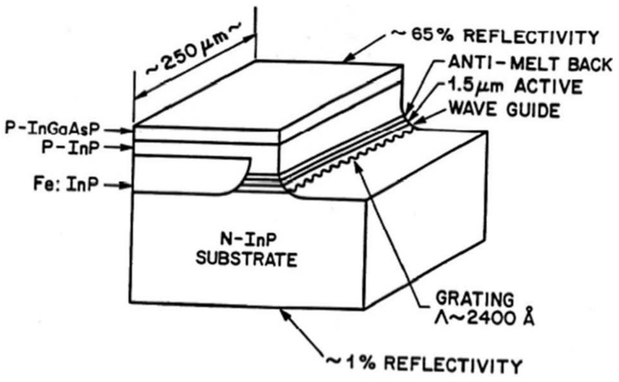

FIGURE 12.27 Schematic diagram of a distributed feedback (DFB) buried-heterostructure laser.

wafer using VPE. The wafer is then processed to produce 250-μm long laser chips using standard metallization and cleaving procedures. The final laser chips have anti-reflection coating (<1%) at one facet and high-reflectivity coating (~65%) at the back facet. The asymmetric facet coatings help remove the degeneracy between the two modes in the stopband.

12.7.2 Laser Performance

The cw light versus current characteristics of a laser are shown in Figure 12.28. Also shown is the measured spectrum at different output powers. The laser emits near 1.3 μm. The threshold current of these lasers is in the 10–15 mA range. For high fibre coupling efficiency, it is important that the laser emits in the fundamental transverse mode.

Tunable single-wavelength semiconductor lasers are needed for many applications. Examples of application in lightwave transmission systems are (i) wavelength-division multiplexing (WDM) where signals at many distinct wavelengths are simultaneously modulated and transmitted through a fibre and (ii) coherent transmission systems where the wavelength of the transmitted signal must match that of the local oscillator. Several types of tunable laser structures have been reported in the literature [59–64]. The two principal schemes are (i) the multisection DFB laser and (ii) the multisection distributed Bragg reflector (DBR) laser. The multisection DBR lasers generally exhibit higher tunability than that for the multisection DFB lasers. The three sections of a multisection device are (i) the active region section that provides the gain, (ii) the grating section that provides the tunability and (iii) the phase-tuning section that is needed to access all wavelengths continuously. The current through each of these sections can be varied independently. The tuning mechanism can be understood by noting that the emission wavelength, λ, of a DBR laser is given by $\lambda = 2n\Lambda$, where Λ is the grating period and n is the effective refractive index of the optical mode in the grating section. The latter can be changed simply by varying the current in the grating section.

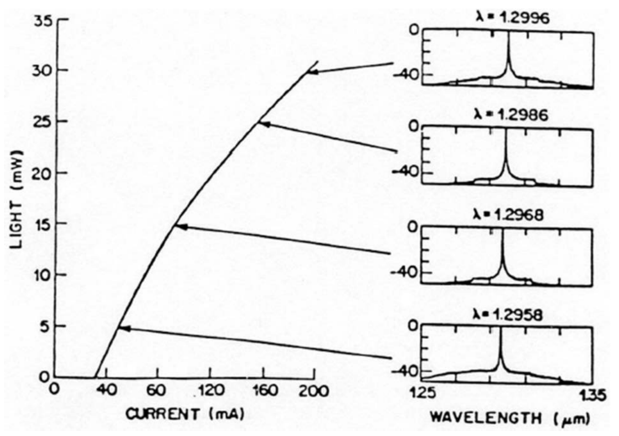

FIGURE 12.28 Light versus current characteristics and spectrum at different powers of a distributed feedback laser.

12.7.3 Phase Noise and Intensity Noise

The coupling of the spontaneous emission to the stimulated emission in a semiconductor laser leads to phase and intensity noise in the laser output. The phase noise manifests itself as a finite spectral width of the laser even for cw operation. Low phase noise is needed for lasers used in coherent transmission. The intensity noise arises from the coupling of the electrons in the semiconductor and the photons in the electric field. The intensity noise is generally characterized by the relative intensity noise (RIN). The RIN value must be sufficiently small if the laser is used in analogue or subcarrier-based transmission systems. Typical RIN values for DFB lasers are in the range of –150 to –160 dB Hz^{-1}.

An important characteristic of lasers for applications requiring a high degree of coherence is the spectral width (linewidth) under cw operation. The cw linewidth depends on the rate of spontaneous emission in the laser cavity. For coherent transmission applications, the cw linewidth must be quite small. The minimum linewidth allowed depends on the modulation format used. For differential phase-shift keying transmission, the minimum linewidth is approximately given by $B/300$ where B is the bit-rate. The linewidth varies inversely with the output power at low powers (<10 mW) and shows saturation at high powers. Typical cw linewidths are in the 1–10 MHz range, the lowest reported value being ~200 kHz.

12.8 Surface-Emitting Lasers

Semiconductor lasers described in the previous sections have cleaved facets that form the optical cavity. The facets are perpendicular to the surface of the wafer and light is emitted parallel to the surface of the wafer. For many applications requiring a two-dimensional laser array or monolithic integration of lasers with electronic components (e.g. optical interconnects), it is desirable to have the laser output normal to the surface of the wafer. Such lasers are known as surface-emitting lasers (SELs). A class of SELs also have their optical cavity normal to the surface of the wafer [65–72]. These devices are known as vertical-cavity surface-emitting lasers in order to distinguish them from other surface emitters.

12.8.1 Surface-Emitting Laser Designs

A generic SEL structure utilizing multiple semiconductor layers to form a Bragg reflector is shown in Figure 12.29. The active region is sandwiched between n- and p-type cladding layers, which are themselves sandwiched between the two n- and p-type Bragg mirrors. This structure is shown using the AlGaAs/GaAs material system, which has been very successful in the fabrication of SELs. The Bragg mirrors consist of alternating layers of low-index and high-index materials. The thickness of each layer is one quarter of the wavelength of light in the medium. Such periodic quarter-wave-thick layers can have very high reflectivity. For normal incidence, the reflectivity is given by [73].

$$R = \frac{\left(1 - n_4/n_1\left(n_2/n_3\right)^{2N}\right)^2}{\left(1 + n_4/n_1\left(n_2/n_3\right)^{2N}\right)^2} \tag{12.26}$$

where n_2 and n_3 are the refractive indices of the alternating layer pairs, n_4 and n_1 are the refractive indices of the medium on the transmitted and incident sides of the DBR mirror and N is the number of pairs. As N increases, R increases. Also for a given N, R is larger if the ratio of n_2/n_3 is smaller. For an $AlAs/Al_{0.1}Ga_{0.9}As$ set of quarter-wave layers, typically 20 pairs are needed for a reflectivity of ~99.5%. Various types of AlGaAs/GaAs SELs have been reported [74–82].

For an SEL to have a threshold current density comparable to that of an edge-emitting laser, the threshold gains must be comparable for the two devices. The threshold gain of an edge-emitting laser is ~100 cm^{-1}. For an SEL with an active-layer thickness of 0.1 μm, this value corresponds to a single-pass gain of ~1%. Thus, for the SEL device to operate with a threshold current density comparable to that of an edge emitter, the mirror reflectivities must be >99%. The reflectivity spectrum of an SEL structure is shown in Figure 12.30. The reflectivity is >99% over a 10 nm band. The drop in reflectivity in the middle of the band is due to the Fabry–Pérot mode.

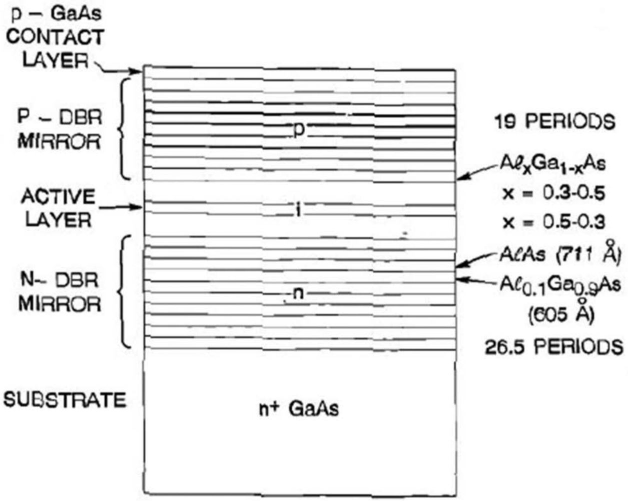

FIGURE 12.29 Schematic diagram of the layers of an AlGaAs/GaAs surface-emitting laser.

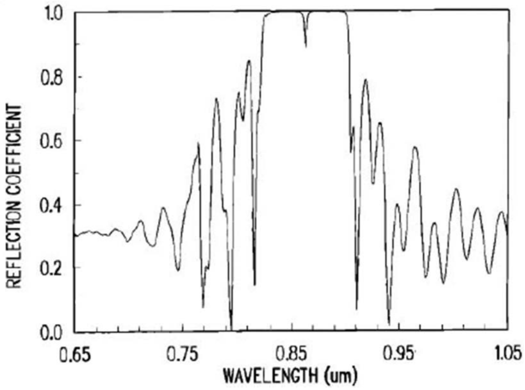

FIGURE 12.30 Reflection spectrum of a typical surface-emitting laser structure.

The number of pairs needed to fabricate a high-reflectivity mirror depends on the refractive index of layers in the pair. For large-index differences, fewer pairs are needed. For example, in the case of CaF_2 and ZnS for which the index difference is 0.9, only six pairs are needed for a reflectivity of 99%. By contrast, for an InP/InGaAsP ($\lambda \simeq 1.3$ μm) layer pair for which the index difference is 0.3, more than 40 pairs are needed to achieve a reflectivity of 99%.

An important SEL structure for the AlGaAs/GaAs material system is the oxide aperture device [81] (Figure 12.31). AlAs oxidizes rapidly in the presence of oxygen to aluminium oxide, which forms an insulating layer. Thus, by introducing a thin AlAs layer in the device structure, it is possible to confine the current to a very small area. This allows the fabrication of very low threshold (<0.2 mA) and high bandwidth (~14 GHz) lasers.

Central to the fabrication of low-threshold SELs is the ability to fabricate high-reflectivity mirrors. In the late 1970s, Soda et al. [83] reported on a SEL fabricated using the InP material system. The surfaces of the wafer form the Fabry–Pérot cavity of the laser. Fabrication of the device involves the growth of a DH on an n-InP substrate. A circular contact is made on the p-side using an SiO_2 mask. The substrate side is polished making sure that it is parallel to the epitaxial layer and ring electrodes (using an alloy of Au–Sn) are deposited on the n-side.

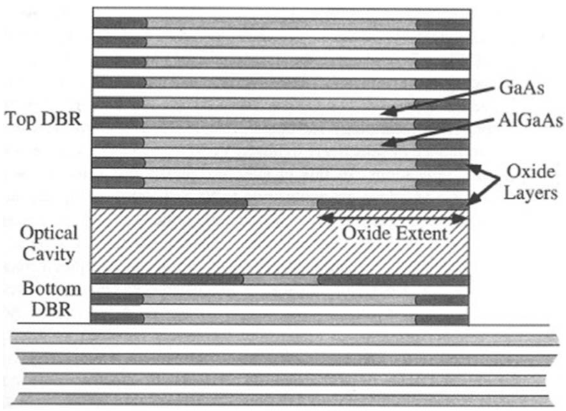

FIGURE 12.31 Schematic diagram of an oxide-aperture AlGaAs/GaAs surface-emitting laser structure.

The laser had a threshold current density of ~11 kA cm^{-2} at 77 K and operated at output powers of several milliwatts.

12.9 Visible and Quantum Cascade Lasers

12.9.1 Visible Lasers

For visible and shorter wavelength operation, several material systems have been studied. Both III–V and II–VI-based materials have been studied. Most of the initial work on visible semiconductor lasers were based on the InAlGaP system. The typical laser design consists of an InGaP active region bounded by n- and p-type InAlGaP cladding layers and a p-GaAs contact layer. The entire structure is grown over a GaAs substrate. The typical emission wavelength is ~630–670 nm [84]. Both gain and index-guided lasers have been reported. The shortest wavelength that can be reached using this system is ~600 nm at room temperature.

Shorter wavelength operation using II–VI-based materials such as Zns, ZnSe, ZnSSe and CdZnSe [85,86] has been reported. A typical laser design may consist of a CdZnSe active region bounded by n-ZnSe, n-ZnSSe and p-ZnSe, p-ZnSSe layers grown over an n-GaAs substrate. Laser operation at ~490 nm has been observed. The reliability of II–VI lasers needs to be improved considerably.

Nitride-based (GaN, AlGaN, InGaN and AlInGaN) laser technology has been developed extensively over the last two decades [87,88]. Blue lasers and LEDS have been realized using a strained InGaN active region. The lasers are grown on an n-SiC substrate and have n- and p-AlGaN cladding layers. Stimulated emission from InGaN SQW was observed under pulse operation in 1996 [87,88]. Laser emission under pulsed operation using InGaN MQW structure fabricated from III–V nitride materials was demonstrated by Nakamura et al. [87]. The laser design is shown in Figure 12.32. The semiconductor layers are grown over a sapphire substrate.

The active region of the lasers has 26 periods of 30 A wide $In_{0.2}Ga_{0.8}N$ wells with 50 A wide $In_{0.05}Ga_{0.95}N$ barriers. Since sapphire is insulating, the n-contact is formed on the top by etching down past the active region. This laser produced 215 mW at 2.3 A of pulsed current. The laser emission wavelength is 417 nm. Lasers emitting in the blue region with cw output powers greater than 100 mW have been demonstrated. Nitride-based blue lasers are commercially available.

12.9.2 Quantum Cascade Lasers

Quantum cascade lasers (QCLs), which emit in the infrared, are based on intraband transitions in a QW. QCLs were first demonstrated by Faist and Capasso at Bell Laboratories in 1994 [89]. The operation of the QCL is illustrated with the aid of Figure 12.33. The QCL relies upon unipolar injection of electrons into quantum states in a three-level system formed in coupled QW composed of AlInAs/InGaAs layers grown on an InP substrate by MBE. The emitted photon energy in the QCL is determined by the energy difference between the quasi-confined energy states in the QWs. These QW states can

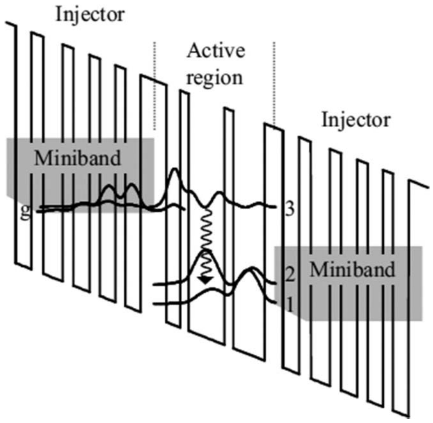

FIGURE 12.33 Conduction-band profile of one active region with the two adjacent injector regions under an applied electric field of 55 kV cm^{-1}. The moduli squared of the relevant wave functions are labelled 1, 2, 3 and g. The wavy arrow denotes the laser transition. The shaded region in the injectors represents a band-like manifold of states. This 'miniband' extracts electrons from levels 1 and 2 of a previous active region and injects them into state 3 of the following downstream active region. An energy range with a low density of states above the miniband prevents electrons from tunnelling out of level 3. Electrons traverse the structure from left to right. The QW material is InGaAs and the barrier material is AlInAs; both are grown lattice matched to InP. The band offset is assumed as 520 meV. The length of one period of active region and injector is 43.4 nm; 32 periods were grown.

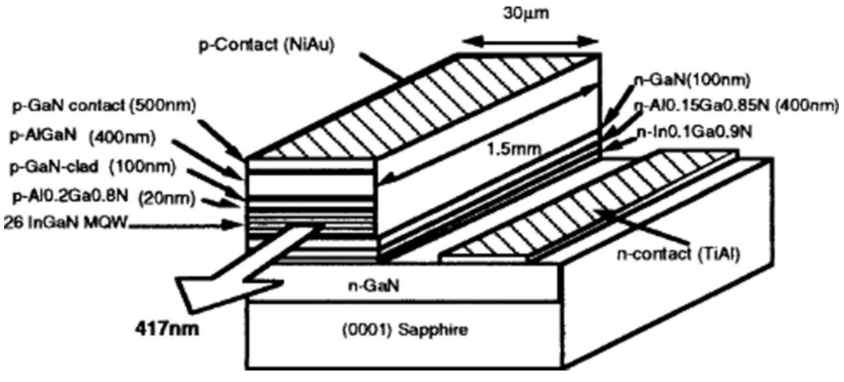

FIGURE 12.32 Schematic of a blue light-emitting GaN/InGaN/AlGaN laser diode.

be tuned over a very broad range by 'band gap engineering' through appropriate selection of the thickness and bandgap of the constituent semiconductors that form the superlattice. The QCL typically contains multiple periods (typically 30) of the QW injection and active emission regions in order to obtain useful laser gains and low-threshold current densities. The operating wavelengths of the QCL have been demonstrated over the range of 3–17 μm [90–93]. The ability to specifically design the operating wavelength of the QCL for spectroscopic detection of gas molecules is the key reason why the QCL is the laser of choice for gas sensor applications.

The operation of unipolar electron injection in a QCL to obtain laser oscillations is quite different compared to the normal operation of pn-diode semiconductor lasers. The photon energy in conventional semiconductor lasers results from direct radiative recombination of electrons and holes and is determined by the difference in the conduction- and valence-band energy levels, which is simply the semiconductor bandgap. Therefore, the emission wavelength in pn-junction lasers is fixed by the direct semiconductor bandgap.

MBE growth technology is generally used in synthesizing QCL structures to meet the precise layer thickness and interface abruptness that determines the QW electron states and, hence, the emission wavelength. Figure 12.32 shows a schematic diagram of a QCL-active region grown by MBE. The material system is InGaAs/InAlAs grown over n-InP. These devices have been fabricated into wide-stripe lasers and have operated with peak powers of ~200 mW at 200 K.

For improved performance, designs based on double-phonon resonance [92] and a bound to continuum resonance [93] have been used. The former has recently been used to demonstrate cw lasers [92]. The active region consists of four InGaAs/InAlAs QWs designed so that the lasing transition takes place from level 4 to 3 in one QW and has three coupled lower energy levels separated from each other by one phonon energy (Figure 12.33). The fast interband transition in the lowest subbands leads to a high population inversion at room temperature. The active also has a narrow QW barrier to increase the injection efficiency to the upper laser level (level 91).

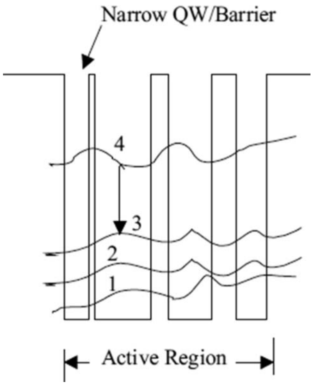

FIGURE 12.34 Schematic diagram of one period of a QCL-active region that operated cw at room temperature. The laser transition is from level 4 to level 3. The moduli-squared wave functions in the four-QW active region are shown. The separation between levels 3 and 2 and that between 2 and 1 equals one phonon energy, which helps depopulate the lower laser level (level 3).

The active region is fabricated by the MBE technique using InGaAs/InAlAs material over an n-InP substrate. The entire active region consists of 25–30 periods of the type shown in Figure 12.34. Each period will have an n-type injector region and an undoped four QW light-emitting (active) region. The entire active region structure is bounded by an InGaAs layer followed by an InP layer. These layers form the waveguide. The estimated gain for a QCL is $\sim 10\,\text{cm}^{-1}/(\text{kA cm}^{-2})$.

Room-temperature CW operation has also been demonstrated using a ridge waveguide geometry using long cavity length which reduces the thermal impedance (Figure 12.35) [92]. The laser is bonded epi-side down on a diamond heat sink. The threshold current density is 1.1 kA cm^{-2}. Using a ridge width of 200 mm, 34 W of pulsed output power has been reported [92]. The laser uses a double-channel geometry to form the ridge as shown in the scanning electron micrograph of Figure 12.35b.

12.10 Quantum Wire, Quantum Dot and Nanostructure Lasers

12.10.1 Quantum Wire and Quantum Dot Lasers

The electron motion is restricted further in quantum wire and quantum dot structures compared to that for a QW [94–100]. For QWR structures, the electron motion is restricted in two directions and in QD structures, the electron motion is restricted in all directions. Using a similar procedure, as for

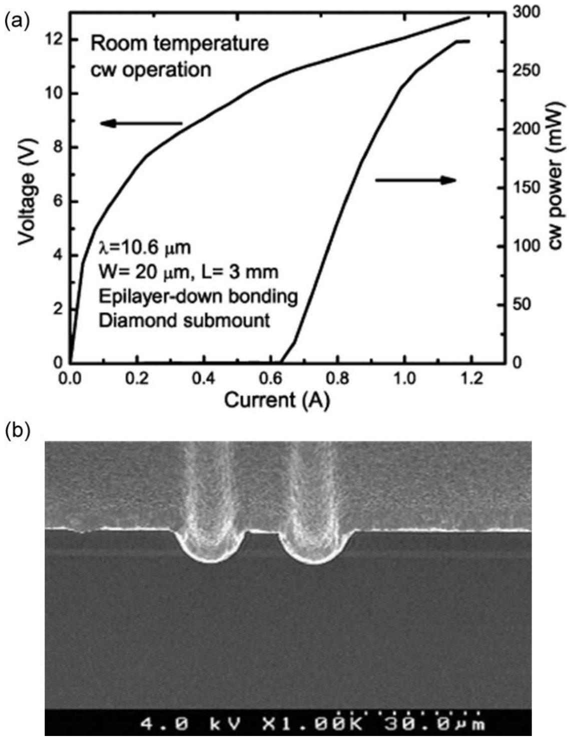

FIGURE 12.35 (a) L-I-V characteristics of a QCL emitting near 10.6 mm. The ridge width and cavity length are 20 and 3 mm, respectively. (b) Scanning electron photomicrograph of double channel geometry.

QWs, the density of states of QWR and QD structures is given by [94]

$$\rho_{\text{QWR}} = \sum_n \sum_m \frac{1}{2\pi}\left(\frac{2m}{\hbar^2}\right)^{1/2} n_{\text{QWR}}\left(E - E_{n,m}\right)^{1/2} \quad (12.27)$$

$$\rho_{\text{QD}} = \sum_n \sum_m \sum_l 2n_{\text{QD}}\delta\left(E - E_{n,m,l}\right) \quad (12.28)$$

where n_{QWR} (cm^{-1}) and n_{QD} (cm^{-2}) are the density of quantum wires and quantum dot, respectively, and the summation is over the discrete energy levels. The density of states for regular bulk materials, QW, QWR and QD materials, is sketched in Figure 12.36 [94].

For QWR the density of states has a sharp maximum at the position of the each of the discrete energy states and for QD the density of states is large at only the discrete energy states. As discussed previously for QW structures, the density of states for QWR and QD structures are not sharp in practice, they get broadened by the interband carrier relaxation time for QWR structures and for distribution of dot sizes and interaction with surrounding material for QD structures. The broadening for QWR structures is given by the following Lorentzian form:

$$L\left(E - E_{n,m,l}\right) = \frac{\hbar}{2\pi\tau_{\text{in}}} \frac{1}{\left(E - E_{n,m,l}\right)^2 + \left(\dfrac{\hbar}{2\tau_{\text{in}}}\right)^2} \quad (12.29)$$

where τ_{in} is the intraband relaxation time. Based on the density of states, QD lasers are expected to have a low threshold current.

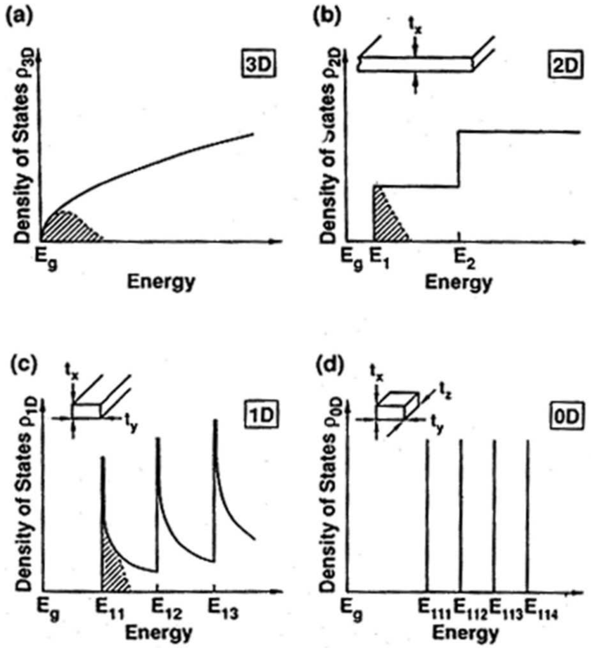

FIGURE 12.36 Schematic description of the density of states for regular bulk semiconductor, quantum well (QW), quantum wire (QWR) and quantum dot (QD) structures. The dimensionalities of each of these types are bulk (3D), QW (2D), QWR (1D) and QD (0D).

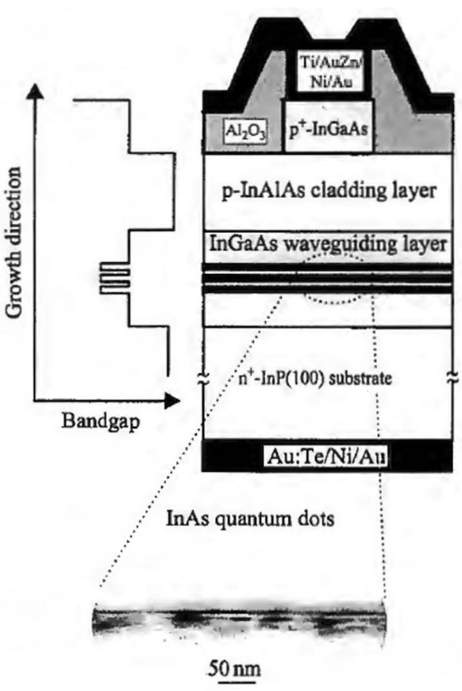

FIGURE 12.37 Schematic of an InAs QD laser and the transmission electron micrograph of the InAs dot region.

The structure of a quantum-dot laser along with the scanning electron photomicrographs of the QD active region is shown in Figure 12.37 [101]. The quantum-dot layers consist of InAs QDs embedded in an InGaAs waveguiding layer. The cladding layers are InAlAs. The InGaAs and InAlas layers are lattice matched to the InP substrate. The InAs dots are embedded in the InGaAs matrix.

The lateral dimension (*W*) is provided by etching the InGaAs contact layer. The lasers were cleaved to a cavity length (*L*) of 240 µm. The laser with a 100-µm stripe width has a threshold current of 25 mA (~108 A cm^{-2}).

12.10.2 Nanostructure Lasers

Various types of photonic crystal-based nanostructure lasers have been reported [102–105]. The two-dimensional photonic crystals are formed on a regular multiple QW-like layer structure by etching air holes in a regular pattern using reactive ion beam etching. Example of a photonic crystal ring laser is shown in Figure 12.38 [102]. The hexagonal ring waveguide is formed by reactive ion beam etching and standard photolithographic techniques [102].

The ring laser operated under optical pumping using a 980 nm pump laser at a pump power of ~3 mW. A low threshold current-pumped photonic crystal laser has been reported using the InGaAsP/InP material system built on a p-InP substrate. In this case, a post (p-InP) connects the photonic crystal material with air holes to the substrate. A submicron wire contact is made on the n-side. The schematic of the device along with the layer structure is shown in Figure 12.39 [103]. Laser action is observed with a threshold current of 260 µA.

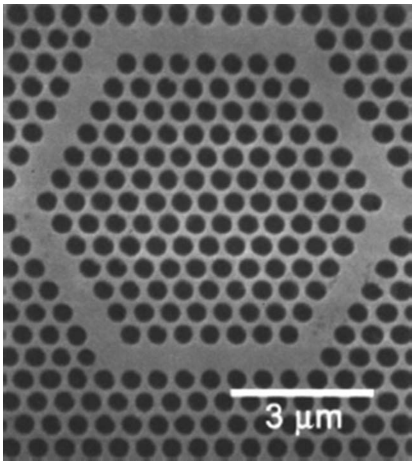

FIGURE 12.38 Scanning electron photomicrograph of a photonic crystal ring laser fabricated using an InGaAsP/InP material system.

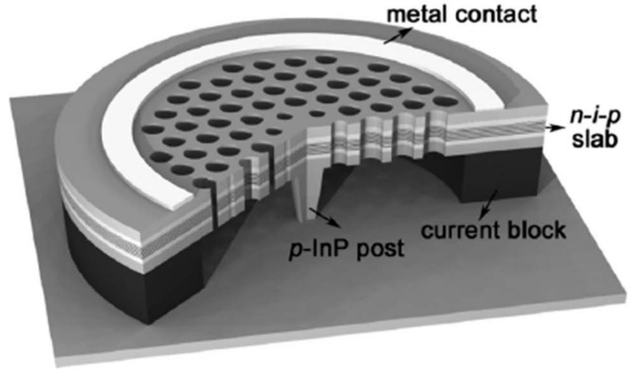

(a)

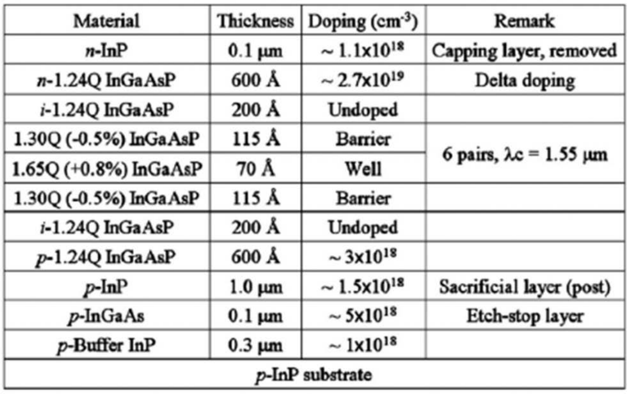

Material	Thickness	Doping (cm^{-3})	Remark
n-InP	0.1 μm	~ 1.1x10^{18}	Capping layer, removed
n-1.24Q InGaAsP	600 Å	~ 2.7x10^{19}	Delta doping
i-1.24Q InGaAsP	200 Å	Undoped	
1.30Q (-0.5%) InGaAsP	115 Å	Barrier	6 pairs, λc = 1.55 μm
1.65Q (+0.8%) InGaAsP	70 Å	Well	
1.30Q (-0.5%) InGaAsP	115 Å	Barrier	
i-1.24Q InGaAsP	200 Å	Undoped	
p-1.24Q InGaAsP	600 Å	~ 3x10^{18}	
p-InP	1.0 μm	~ 1.5x10^{18}	Sacrificial layer (post)
p-InGaAs	0.1 μm	~ 5x10^{18}	Etch-stop layer
p-Buffer InP	0.3 μm	~ 1x10^{18}	
p-InP substrate			

(b)

FIGURE 12.39 (a) Schematic of the nanostructure photonic crystal device. (b) The epitaxial layer structure used for fabrication.

12.11 Laser Reliability

The performance characteristics of injection lasers used in lightwave systems can degrade during their operation. The dominant mechanism responsible for the degradation is determined by any or all of the several fabrication processes including epitaxial growth, wafer quality, device processing and bonding [106–116]. In addition, the degradation rate of devices processed from a given wafer depends on the operating conditions, i.e. the operating temperature and the injection current. Although many of the degradation mechanisms are not fully understood, extensive empirical observations exist in the literature, which have allowed the fabrication of InGaAsP laser diodes with extrapolated median lifetimes over 25 years at an operating temperature of 20°C [106].

The detailed studies of the degradation mechanisms of optical components used in lightwave systems have been motivated by the desire to have a reasonably accurate estimate of the operating lifetime before they are used in practical systems. Since for many applications, the components are expected to operate reliably over a period in excess of 10 years, an appropriate reliability assurance procedure becomes necessary, especially for applications such as an undersea lightwave transmission system, where the replacement cost is very high. The reliability assurance is usually carried out by operating the devices under a high stress (e.g. high temperature), which enhances the degradation rate so that a measurable value can be obtained in an operating time of a few hundred hours. The degradation rate under normal operating conditions can then be obtained from the measured high-temperature degradation rate using the concept of an activation energy [106]. The light output versus current characteristics of a laser change after stress ageing. There is generally a small increase in threshold current and a decrease in external differential quantum efficiency following the stress ageing. Ageing data for 1.3 μm nGaAsP lasers used in the first submarine fibre optic cable are shown in Figure 12.40 [106].

Some lasers exhibit an initial rapid degradation after which the operating characteristics of the lasers are very stable. Given a population of lasers, it is possible to quickly identify the 'stable' lasers by a high-stress test (also known as the purge test) [106,117]. The stress test implies that operating the laser under a set of high stress conditions (e.g. high current, high temperature or high power) would cause the weak lasers to fail and stabilize the possible winners. Observations on the operating current after stress ageing have been reported by Nash et al. [106]. It is important to point out that the determination of the duration and the specific conditions for stress ageing are critical to the success of this screening procedure. The expected operating lifetime of a semiconductor laser is generally determined by accelerated ageing at high temperatures and using an activation energy. The lifetime (t) at a temperature T is experimentally found to vary as $\exp(-E/kT)$, where E is the activation energy and k is the Boltzmann constant [106]. The operating current of good lasers increases at a rate of less than $1\%/kh$ of ageing time at 60°C operating temperature. Assuming a 50% change in operating current as the useful lifetime of the device and an activation energy of 0.7 eV, this ageing rate corresponds to a light-emitting lifetime of greater than 100 years at 20°C.

A parameter that determines the performance of the DFB laser is the side-mode suppression ratio (SMSR), i.e. the ratio of the intensity of the dominant lasing mode to that of the next most intense mode [118,119]. The SMSR of good DFB lasers does not change significantly after ageing, which confirms the spectral stability of the emission.

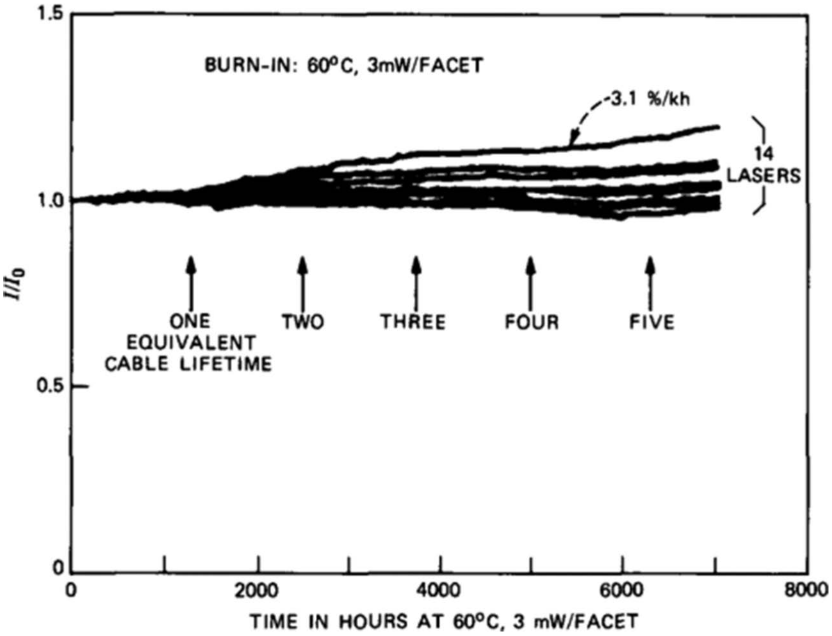

FIGURE 12.40 Ageing data of lasers used in the first submarine cable application in 1988.

There have been a significant number of developments in the technology of optical integration of semiconductor lasers and other related devices on the same chip. These chips allow higher levels of functionality than that achieved using single devices. For example, laser and optical modulators have been integrated, serving as simple monolithic transmitters.

12.12 Summary and Future Challenges

Tremendous advances in semiconductor lasers have occurred over the last decade. The advances in research and many technological innovations have led to the worldwide deployment of fibre optic communication systems that operate near 1.3 and 1.55 μm and compact storage discs that utilize lasers for read/write purposes. Although most of these systems are based on digital transmission, lasers have also been deployed for carrying high-quality analogue cable TV transmission systems. However, many challenges remain.

The need for higher capacity is pushing the deployment of WDM-based transmission, which needs tunable or frequency-settable lasers. The development of lasers with a very stable and settable frequency will continue to be an important research area. The integration of many such lasers on a single substrate would provide the ideal source for WDM systems.

Laser-to-fibre coupling is also an important area of research. Recent developments in spot size converter integrated lasers are quite impressive but some more work, perhaps, needs to be done to make them easy to manufacture. This may require more process developments.

Although WDM technology is currently being considered for increasing transmission capacity, the need for sources with very high modulation capability still remains. Hence, research on new mechanisms for very high-speed modulation is important.

The SEL is very attractive for two-dimensional arrays and for single-wavelength operation. Several important advances in this technology have occurred over the last few years. An important challenge is the fabrication of a device with characteristics superior to that of an edge emitter.

QW lasers have shown that lower dimensionality (two-dimensional-like density of states) leads to improved performance. Further performance improvement is expected and has been demonstrated to some extent using quantum wire and quantum dot structures. These lower-dimensional systems require further investigation before they become commercial realities. Lasers based on inter-sub-band transitions in QW, quantum cascade lasers have been developed over the last decade. Further improvements, such as cw operation at high temperature, will continue to be important for wide commercial use.

Finally, much of the advances in laser development would not have been possible without the advances in materials and processing technology. The challenges of current laser research are intimately linked with the challenges in materials growth, which include not only the investigation of new material systems but also improvements in existing technologies to make them more reproducible and predictable.

REFERENCES

1. Hall R N, Fenner G E, Kingley J D, Soltys T J and Grlson R O 1962 *Phys. Rev. Lett.* **9** 366.
2. Nathan M I, Dumke W P, Burns G, Dill F H Jr and Lasher G 1962 *Appl. Phys. Lett.* **1** 63.
3. Quist T M, Rediker R H, Keyes R J, Krag W E, Lax B, McWhorter A L and Ziegler H J 1962 *Appl. Phys. Lett.* **1** 91.
4. Holonyak N Jr and Bevacqua S F 1962 *Appl. Phys. Lett.* **1** 82.
5. Burrus C A and Dawson R W 1970 *Appl. Phys. Lett.* **17** 97.

6. Eliseev P G 1998 *Semiconductor Lasers* vol II, ed E Kapon (New York: Academic) ch 2.
7. Nelson H 1963 *RCA Rev.* **24** 603.
8. Finch W F and Mehal E W 1964 *J. Electrochem. Soc.* **111** 814.
9. Cho A Y 1971 *J. Vac. Sci. Technol.* **8** 531.
10. Dupuis R D 1981 *J. Crystal Growth* **55** 213.
11. Kressel H and Butler J K 1977 *Semiconductor Lasers and Heterojunction LEDs* (New York: Academic).
12. Casey H C Jr and Panish M B 1978 *Heterostructure Lasers* (New York: Academic).
13. Thompson G H B 1981 *Physics of Semiconductor Laser Devices* (New York: Wiley).
14. Yariv A 1976 *Quantum Electronics* 2nd edn (New York: Wiley) p 306.
15. Bernard M G A and Duraffourg G 1961 *Phys. Status Solidi* **1** 699.
16. Alferov Zh I, Andreev V M, Portnoi E L and Trukan M K 1970 *Sov. Phys. Semicond.* **3** 1107.
17. Hayashi I, Panish M B, Foy P W and Sumski S 1970 *Appl. Phys. Lett.* **17** 109.
18. Dingle R, Wiegman W and Henry C H 1974 *Phys. Rev. Lett.* **33** 827.
19. Hwang CJ 1970 *Phys. Rev. B* **2** 4117.
20. Stern F 1973 *J. Appl. Phys.* **47** 5382; Stern F 1973 *IEEE J. Quantum Electron.* **QE-9** 290.
21. Dutta N K 1980 *J. Appl. Phys.* **51** 6095; Dutta N K 1981 *J. Appl. Phys.* **52** 55.
22. Kane E O 1957 *J. Phys. Chem. Solids* **1** 249.
23. Dutta N K and Nelson R J 1981 *Appl. Phys. Lett.* **38** 407; Dutta N K and Nelson R J 1982 *J. Appl. Phys.* **53** 74 and references therein.
24. Olshansky R, Su C B, Manning J and Powaznik W 1984 *IEEE J. Quantum Electron.* **QE-20** 838.
25. Beattie A R and Landsberg P T 1959 *Proc. R. Soc. A* **249** 16; Beattie A R and Landsberg P T 1960 *Proc. R. Soc. A* **258** 486.
26. Horikoshi Y and Furukawa Y 1979 *Japan. J. Appl. Phys.* **18** 809.
27. Thomson G H B and Henshall G D 1980 *Electron. Lett.* **16** 42.
28. Sugimura A 1981 *IEEE J. Quantum Electron.* **QE-17** 627.
29. Haug A 1983 *Appl. Phys. Lett.* **42** 512.
30. DeLoach B C Jr, Hakki B W, Hartman R L and D'Asaro L A 1973 *Proc. IEEE* **61** 1042.
31. Dingle R 1975 *Festkorperprobleme* **XV** 21–47.
32. Holonyak N Jr, Kolbas R M, Dupuis R D and Dapkus P D 1980 *IEEE J. Quantum Electron.* **QE-16** 170.
33. Agrawal G P and Dutta N K 1992 *Semiconductor Lasers* (Dordrecht: Kluwer Academic) ch 9.
34. Kazmierski C, Ougazzaden A, Blez M, Robien D, Landreau J, Sermage B, Bouley J C and Mirca A 1991 *IEEE J. Quantum Electron.* **27** 1794–7.
35. Hess K, Vojak B A, Holonyak N Jr, Chin R and Dapkus P D 1980 *Solid State Electron.* **23** 585.
36. Dutta N K 1982 *Electron. Lett.* **18** 451; Dutta N K 1982 *J. Appl. Phys.* **53** 7211.
37. Arakawa Y and Yariv A 1985 *IEEE J. Quantum Electron.* **QE-21** 1666.
38. Morton P, Logan R A, Tanbun-Ek T, Sciortino P F Jr, Sergent A M, Montgomery R K and Lee B T 1993 *Electron. Lett.* **29** 1429–30.
39. Thijs P J A, Tiemeijer L F, Kuindersma P I, Binsma J J M and van Dongen T 1991 *IEEE J. Quantum Electron.* **27** 1426.
40. Thijs P J A, Tiemeijer L F, Binsma J J M and van Dongen T 1994 *IEEE J. Quantum Electron.* **QE-30** 477–99.
41. Temkin H, Tanbun-Ek T and Logan R A 1990 *Appl. Phys. Lett.* **56** 1210.
42. Tsang W T, Yang L, Wu M C, Chen Y K and Sergent A M 1990 *Electron. Lett.* **26** 2033.
43. Laidig W D, Lin Y F and Caldwell P J 1985 *J. Appl. Phys.* **57** 33.
44. Fischer S E, Fekete D, Feak G B and Ballantyne J M 1987 *Appl. Phys. Lett.* **50** 714.
45. Yokouchi N, Yamanaka N, Iwai N, Nakahira Y and Kasukawa A 1996 *IEEE J. Quantum Electron.* **QE-32** 2148–55.
46. Beernik K J, York P K and Coleman J J 1989 *Appl. Phys. Lett.* **25** 2582.
47. Loehr J P and Singh J 1991 *IEEE J. Quantum Electron.* **27** 708.
48. Corzine S W, Yan R and Coldren L A 1993 Optical gain in III–V bulk and quantum well semiconductors *Quantum Well Lasers* ed P Zory (New York: Academic).
49. Temkin H, Tanbun-Ek T, Logan R A, Coblentz D A and Sergent A M 1991 *IEEE Photon. Technol. Lett.* **3** 100.
50. Adams A R 1986 *Electron. Lett.* **22** 249.
51. Yablonovitch E and Kane E O 1986 *J. Lightwave Technol.* **LT-4** 50.
52. Wu M C, Chen Y K, Hong M, Mannaerts J P, Chin M A and Sergent A M 1991 *Appl. Phys. Lett.* **59** 1046.
53. Dutta N K, Lopata J, Berger J R, Sivco D L and Cho A Y 1991 *Electron. Lett.* **27** 680.
54. Kuo J M, Wu M C, Chen Y K and Chin M A 1991 *Appl. Phys. Lett.* **59** 2781.
55. Chand N, Becker E E, van der Ziel J P, Chu S N G and Dutta N K 1991 *Appl. Phys. Lett.* **58** 1704.
56. Choi H K and Wang C A 1990 *Appl. Phys. Lett.* **57** 321.
57. Dutta N K, Wynn J D, Lopata J, Sivco D L and Cho A Y 1990 *Electron. Lett.* **26** 1816.
58. Agrawal G P and Dutta N K 1992 *Semiconductor Lasers* (New York: Van Nostrand) ch 7 (1st edn 1985).
59. Koch T L, Koren U, Gnall R P, Burrus C A and Miller B I 1988 *Electron. Lett.* **24** 1431.
60. Suematsu Y, Arai S and Kishino K 1983 *J. Lightwave Technol.* **LT-1** 161.
61. Koch T L and Koren U 1991 *IEEE J. Quantum Electron.* **QE-27** 641.
62. Dutta N K, Piccirilli A B, Cella T and Brown R L 1986 *Appl. Phys. Lett.* **48** 1501.
63. Liou K Y, Dutta N K and Burrus C A 1987 *Appl. Phys. Lett.* **50** 489.
64. Tanbun-Ek T, Logan R A, Chu S N G and Sergent A M 1990 *Appl. Phys. Lett.* **57** 2184.
65. Soda H, Iga K, Kitahara C and Suematsu Y 1979 *Japan. J. Appl. Phys.* **18** 2329.
66. Iga K, Koyama F and Kinoshita S 1988 *IEEE J. Quantum Electron.* **24** 1845.
67. Jewell J L, Harbison J P, Scherer A, Lee Y H and Florez L T 1991 *IEEE J. Quantum Electron.* **27** 1332.
68. Chang-Hasnain C J, Maeda M W, Stoffel N G, Harbison J P and Florez L T 1990 *Electron. Lett.* **26** 940.

69. Geels R S, Corzine S W and Coldren L A 1991 *IEEE J. Quantum Electron.* **27** 1359.
70. Geels R S and Coldren L A 1990 *Appl. Phys. Lett.* **5** 1605.
71. Tai K, Hasnain G, Wynn J D, Fischer R J, Wang Y H, Weir B, Gamelin J and Cho A Y 1990 *Electron. Lett.* **26** 1628.
72. Tai K, Yang L, Wang Y H, Wynn J D and Cho A Y 1990 *Appl. Phys. Lett.* **56** 2496.
73. Born M and Wolf E 1977 *Principles of Optics* (New York: Pergamon) section 1.6.5, p 69.
74. Jewell J L, Scherer A, McCall S L, Lee Y H, Walker S J, Harbison J P and Florez J P 1989 *Electron. Lett.* **25** 1123.
75. Lee Y H, Tell B, Brown-Goebeler K F, Jewell J L, Leibenguth R E, Asom M T, Livescu G, Luther L and Mattera V D 1990 *Electron. Lett.* **26** 1308.
76. Tai K, Fischer R J, Seabury C W, Olsson N A, Huo D T C, Ota Y and Cho A Y 1989 *Appl. Phys. Lett.* **55** 2473.
77. Ibaraki A, Kawashima K, Furusawa K, Ishikawa T, Yamayachi T and Niina T 1989 *Japan. J. Appl. Phys.* **28** L667.
78. Schubert E F, Tu L W, Kopf R W, Zydzik G J and Deppe D G 1990 *Appl. Phys. Lett.* **57** 117.
79. Geels R S, Corzine S W, Scott J W, Young D B and Coldren L A 1990 *IEEE Photon. Technol. Lett.* **2** 234.
80. Vakhshoori D, Wynn J D, Liebenguth R E 1994 *Appl. Phys. Lett.* **65** 144.
81. Deppe D and Choquette K 2000 *Vertical Cavity Surface Emitting Lasers* ed J Cheng and N K Dutta (New York: Gordon and Breach) chs 1 and 2.
82. Dutta N K, Tu L W, Zydzik G J, Hasnain G, Wang Y H and Cho A Y 1991 *Electron. Lett.* **27** 208.
83. Soda H, Iga K, Kitahara C and Suematsu Y 1979 *Japan. J. Appl. Phys.* **18** 2329.
84. Valster A, van der Pol C J, Finke M N and Boermans M J B 1992 *Electron. Lett.* **28** 144.
85. Drenton R, Petruzzello J and Haberern K 1995 *Phillips J. Res.* **49** 225.
86. Nurmikko A V and Gunshor R L 1994 *IEEE J. Quantum Electron.* **QE-30** 619.
87. Nakamura S, Senoh M, Iwasa N and Nagahama S 1996 *Japan. J. Appl. Phys.* **35** L74.
88. Nakamura S and Fasol G 1997 *The Blue Laser Diode—GaN Based Light Emitters* (Berlin: Springer).
89. Faist J et al. 1994 *Science* **264** 553.
90. Capasso F et al. *2002 IEEE J. Quantum Electron.* **38** 511.
91. Gmachl C et al. 2002 *IEEE J. Quantum Electron.* **38** 569.
92. Razeghi M 2009 *IEEE J. Selec Areas Quantum Electron* **15** 941.
93. Faist J et al. 2001 *Appl. Phys. Lett.* **78** 147.
94. Kapon E 1993 Chapter 10 *Quantum Well Lasers* ed P. Zory (New York: Academic Press).
95. Arakawa Y and Sasaki H 1982 *Appl. Phys. Lett.* **40** 939.
96. Asada M, Miyamoto Y and Suematsu Y 1986 *IEEE J. Quantum Electron.* **QE-22** 1915.
97. Yariv A 1988 *Appl. Phys. Lett.* **53** 1033..
98. Miyamoto Y, Miyake Y, Asada M and Suematsu Y 1989 *IEEE J. Quantum Electron.* **QE-25** 2001.
99. Asada M, Miyamoto Y and Suematsu Y 1985 *Japan. J. Appl. Phys.* **24** L95.
100. Cao M, Miyake Y, Tamura S, Hirayama H, Arai S, Suematsu Y and Miyamoto Y 1990 *Trans. IEICE* **E73** 63.
101. Ustinov V M, Zhukov A E, Egorov A, Yu A, Kovsh A R, Zaitsev S V, Alferov Zh I and Bimberg D 1998 *Electron. Lett.* **34** 670.
102. Kim S, Ryu H, Park H, Kim G, Choi Y and Lee Y 2002 *Appl. Phys. Lett.* **81** 2499.
103. Park H, Kim S, Seo M, Ju Y, Kim S and Lee Y 2005 *IEEE J. Quantum Electron.* **QE-41** 1131.
104. Inoshita K and Baba T 2003 *IEEE J. Sel. Topics Quantum Electron.* **9** 1347.
105. Park H G, Kim S K, Kwon S H, Kim G H, Kim S H, Ryu H Y, Kim S B and Lee Y H 2003 *IEEE Photon. Technol. Lett.* **15** 1327.
106. Nash F R, Sundburg W J, Hartman R L, Pawlik J R, Ackerman D A, Dutta N K and Dixon R W 1985 *AT&T Tech. J.* **64** 809.
107. The reliability requirements of a submarine lightwave transmission system are discussed in a special issue of 1985 *AT&T Tech. J.* **64** 3.
108. DeLoach B C Jr, Hakki B W, Hartman R L and D'Asaro L A 1973 *Proc. IEEE* **61** 1042.
109. Johnston W D and Miller B I 1973 *Appl. Phys. Lett.* **23** 1972.
110. Petroff P M, Johnston W D Jr and Hartman R L 1974 *Appl. Phys. Lett.* **25** 226.
111. Matsui J, Ishida R and Nannichi Y 1975 *Japan. J. Appl. Phys.* **14** 1555.
112. Petroff P M and Lang D V 1977 *Appl. Phys. Lett.* **31** 60.
113. Ueda O, Umebu I, Yamakoshi S and Kotani T 1982 *J. Appl. Phys.* **53** 2991.
114. Ueda O, Yamakoshi S, Komiya S, Akita K and Yamaoka T 1980 *Appl. Phys. Lett.* **36** 300.
115. Yamakoshi S, Abe M, Wada M, Komiya S and Sakurai T 1981 *IEEE J. Quantum Electron.* **QE-17** 167.
116. Mizuishi K, Sawai M, Todoroki S, Tsuji S, Hirao M and Nakamura M 1983 *IEEE J. Quantum Electron.* **QE-19** 1294.
117. Gordon E I, Nash F R and Hartman R L 1983 *IEEE Electron. Device Lett.* **ELD-4** 465.
118. Joyce W B, Liou K Y, Nash F R, Bossard P R and Hartman R L 1985 *AT&T Tech. J.* **64** 717.
119. Hartman R L and Dixon R W 1975 *Appl. Phys. Lett.* **26** 239.

Taylor & Francis
Taylor & Francis Group
http://taylorandfrancis.com

13

Spectral Control in Laser Diodes

Markus-Christian Amann

CONTENTS

13.1 Introduction 195
13.2 Single-Mode Laser Diodes 197
  13.2.1 Distributed Bragg Reflector Laser 197
  13.2.2 Distributed Feedback Laser 199
  13.2.3 Spectral Linewidth 200
13.3 Wavelength-Tunable Laser Diodes 201
  13.3.1 Continuously Tunable Monolithic Devices 203
  13.3.2 Wavelength-Tunable Vertical-Cavity Surface-Emitting Lasers 204
  13.3.3 Discontinuously Tunable Monolithic Devices 204
  13.3.4 External Cavity Tunable Laser Diodes 206
13.4 Multiwavelength Laser Diodes 206
References 206
Further Readings 208

13.1 Introduction

The purpose of this chapter is to present an introduction into the various techniques for the control of the spectral properties of laser diodes and to investigate the most important device parameters that determine the spectral performance. The relevant characteristic hence is the laser spectrum and its variation with time. It should be noted that—strictly speaking—the laser spectrum should not be time dependent because it is defined as the Fourier transform of the time-dependent laser signal. Restricting the integration of the Fourier transform to finite time intervals, however, we may define time-dependent laser spectra.

It is well known that because of the large resonator length with respect to the optical wavelength, lasers in general but even laser diodes with their small dimensions tend to operate in several longitudinal modes. However, the transverse and lateral dimensions of laser diodes can be made small enough to provide the transverse and lateral single-mode operation. Let i denote the longitudinal mode number, the wavelength of the ith longitudinal mode is given as

$$\lambda_i = \frac{2n_{\text{eff}}(\lambda_i)L}{i} \tag{13.1}$$

where n_{eff} is the effective refractive index describing the transverse and lateral waveguide characteristics, L is the laser length and the longitudinal mode number i (typically 1000–10 000) equals the number of nodes of the intensity distribution along the laser axis.

The spacing $\Delta\lambda_{\text{m}}$ between adjacent longitudinal modes around mode i is

$$\Delta\lambda_{\text{m}} \simeq \frac{\lambda_i^2}{2n_{\text{g,eff}}L} \tag{13.2}$$

where $n_{\text{g,eff}}$ is the effective group index that takes into account the wavelength dependence of n_{eff}

$$n_{\text{g,eff}} = \left.\frac{\mathrm{d}(k_0 n_{\text{eff}})}{\mathrm{d}k_0}\right|_{\lambda_i} = n_{\text{eff}}(\lambda_i) - \lambda_i \left.\frac{\mathrm{d}n_{\text{eff}}}{\mathrm{d}\lambda}\right|_{\lambda_i}. \tag{13.3}$$

Since the effective refractive index usually decreases with increasing wavelength, the effective group index is commonly larger than the effective refractive index. In InGaAsP/InP laser diodes operated in the 1.3–1.55 μm wavelength regime, n_{eff} is typically of the order of 3.3 and $n_{\text{g, eff}} \simeq 4$. A schematic representation of a longitudinal mode spectrum of a Fabry–Pérot laser diode is shown in Figure 13.1.

Accordingly, for a well-controlled laser spectrum, it is most important to force the laser operation in one single longitudinal mode. The physical parameter defining the quality of the single-mode operation is the side-mode suppression ratio (SSR), which is the power ratio between the dominant and second strongest laser mode. With P_i being the output power of the dominant mode i per mirror in a symmetric laser, the SSR is

$$SSR = \frac{2P_i\Delta g}{h\nu v_{\text{g}} n_{\text{sp}} \alpha_{\text{tot}} \alpha_{\text{m}}} \tag{13.4}$$

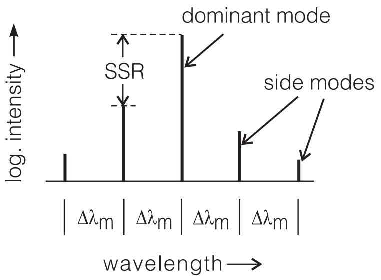

FIGURE 13.1 Longitudinal mode spectrum of a multi-mode Fabry–Pérot laser diode.

where Δg is the mode gain difference between the dominant mode and the second strongest mode, h is Planck's constant, v is the optical frequency (hv is photon energy), n_{sp} is the spontaneous emission factor (typ. 2), α_{tot} is the total optical loss and α_m is the mirror loss. While single-mode operation may more easily be achieved in the vertical-cavity surface-emitting laser (VCSEL) diodes because of their small cavity length, considerable effort has to be spent in the more usual edge-emitting laser diodes to achieve a sufficiently large suppression of side modes ($SSR > 30\,\text{dB}$). The techniques to achieve single-mode operation in edge-emitting laser diodes are described in detail in Section 13.2.

After accomplishing the transverse and longitudinal single-mode operation of a laser diode, the next relevant spectral characteristic is the spectral linewidth of the lasing mode, which usually is in the megahertz regime. The spectral linewidth represents the power spectrum of the laser output, which because of the carrier density dependence of the refractive index in semiconductor lasers may change during modulation and/or relaxation processes. In practice, this effect manifests itself as a parasitic frequency modulation (chirping of the laser frequency) during amplitude modulation. As with the laser linewidth, the amount of chirping strongly depends on the amplitude–phase coupling in laser diodes, which is usually described by the α-factor α_H [1].

Finally, the spectral purity of laser diodes is significantly affected by feedback of the laser output as caused, for instance, by reflections at coupling lenses or remote reflectors such as fibre couplers. Because of the marked sensitivity of the laser diodes to feedback and because of possible deterioration of their static and dynamic performance in demanding applications, one usually applies optical isolators with isolation above 30 dB. The effect of optical feedback can be investigated by means of a simplified illustration in Figure 13.2. Besides the remote reflectivity r_3, the amplitude external reflection coefficient r_{ext} includes the coupling efficiency η_c between the laser diode and external components (e.g. a fibre), and the optical losses α_{ext} along the external cavity of length L_{ext}:

$$r_{ext} = \eta_c^2 r_3 e^{-\alpha_{ext} L_{ext}}. \tag{13.5}$$

The rate equation analysis of the external optical feedback shows that the different feedback regimes can conveniently be described by the feedback parameter

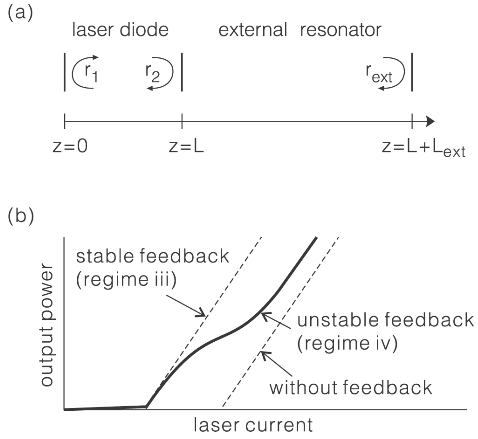

FIGURE 13.2 Schematic illustration of a laser diode with external optical feedback (a) and light characteristic for various degrees of external optical feedback (b).

$$C = \frac{\tau_{ext}}{\tau_1}\frac{r_{ext}}{r_2}\left(1-|r_2|^2\right)\sqrt{1+\alpha_H^2} \tag{13.6}$$

where τ_1 and τ_{ext} denote the round-trip times in the laser diode and external resonator. Depending on C and the power reflectivity given by the external reflection $R_{ext} = |r_{ext}|^2$, we may distinguish five regimes for a single-mode laser diode [2]:

a. For $C < 1$, the laser operates in single mode and the external feedback may only affect the spectral linewidth.
b. For $1 < C \leq 2$ and $R_{ext} < 3 \times 10^{-4}$, mode jumps and hysteresis effects may occur.
c. For still larger feedback up to $R_{ext} = 10^{-4}$, the laser operates relatively stably with a *reduced* spectral linewidth.
d. For $R_{ext} > 10^{-4}$, strong instabilities occur (coherence collapse) with large linewidth broadening.
e. For an external reflection that exceeds the reflection at the laser facet the instabilities cease and the laser with external feedback operates like a laser with a combined length $L_{ext}+L$ with an internal perturbation by mirror 2 (r_2).

The light–current characteristics of laser diodes with different external optical feedback are shown in Figure 13.2b.

Once the single-mode operation has been established, one may want to tune the laser wavelength over a certain wavelength range. This may either be required in wavelength division multiplex applications, in measurements and sensing or to fix the laser wavelength precisely to a given value. Depending on the application, the wavelength tuning should be continuous, i.e. without mode jumps, or quasicontinuous, so that over the tuning range, each wavelength may be addressed by at least one of the longitudinal modes. The established methods for electronic wavelength tuning of laser diodes using current or voltage variations at additional electrodes are compiled in Section 13.3 together with the corresponding device structures and performance.

Furthermore, laser diodes may also be suited for applications where simultaneous operation at several wavelengths is needed. The corresponding laser diode arrays are presented in Section 13.4.

13.2 Single-Mode Laser Diodes

Truly single-longitudinal-mode laser diodes with high performance were first realized in the InGaAsP/InP material system with anticipated applications in fibre optical communications. State-of-the-art single-mode laser diodes in the 1.55 μm wavelength range exhibit an SSR of at least 30 dB and spectral linewidth of the order of several MHz at a few (≃5) mW of optical output power [3].

The most successful technique to achieve single-mode operation is to introduce strongly wavelength-dependent cavity loss or gain to favour one single longitudinal mode. In practice, this is usually done by integrating a Bragg grating into the laser cavity that replaces one or both mirrors by the distributed feedback (DFB) along the periodic refractive index changes. The Bragg grating thereby acts like a pile of pairs, each $\lambda/4$ thick, of alternating dielectric layers with different refractive index yielding a strong reflection at the Bragg wavelength

$$\lambda_B = 2\Lambda\bar{n}_{\text{eff}} \tag{13.7}$$

where Λ is the grating period and $\bar{n}_{\text{eff}}$ is the average effective refractive index.

As shown in Figure 13.3, the Bragg grating filters can be arranged either outside the active region at one or both ends of the laser cavity and act then as wavelength-selective reflectors (distributed Bragg reflector (DBR)) [4] or can be collocated with the active region along the entire laser cavity yielding a DFB [5] structure. The longitudinal index variation is thereby introduced by periodic thickness variation of the grating layer with refractive index n_1, which covers a semiconductor region with different refractive index n_0. Since, in the type 1 DBR laser, the DBR acts as a wavelength-selective reflector through which the outcoming light must pass, optimum reflectivity and output efficiency cannot be obtained at the same time. Consequently, the type 2 DBR laser is advantageous because output coupling and wavelength selective reflection occur at different ends of the laser cavity. In the DFB laser the distribution of the optical feedback along the entire laser length allows various designs with high output efficiency and wavelength selectivity. Furthermore, by the application of anti-reflection and/or high-reflection coatings onto the end facets, the laser performance may be tailored to the anticipated application.

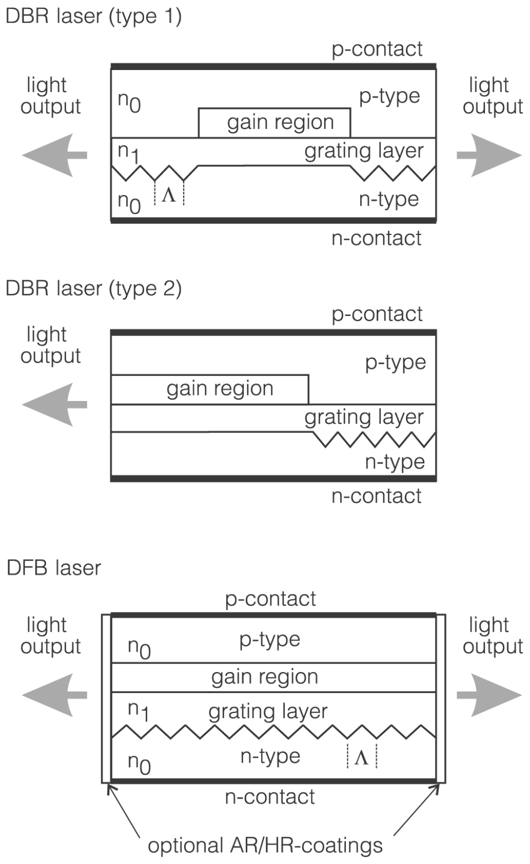

FIGURE 13.3 Schematic longitudinal sections of DBR and DFB laser diodes.

It should be noted that for an effective reflectivity of the grating, it is *not* necessary that the index variations occur stepwise; even a soft periodic index transition, e.g. by a sine-like function, may provide strong and wavelength-selective feedback [5]. Since these index perturbations occur only within a part of the transverse mode profile, their effect on the effective refractive index n_{eff} of the composite waveguide structure is weakened. The modulation of n_{eff} is determined by the product of the index difference $n_1 - n_0$ and the confinement factor within the grating area.

In DBR and DFB lasers, the grating-induced refractive index perturbations lead to a coupling between the forward and backward propagating waves of the particular laser mode throughout the entire grating region. Therefore, the optical feedback is not localized at the cavity end facets but is distributed over the entire laser cavity (DFB) or only part of it (DBR). The analysis of these devices, therefore, requires the investigation of wave propagation and wave coupling in periodic structures. This is usually accomplished by means of coupled-mode theory.

13.2.1 Distributed Bragg Reflector Laser

First, we will consider the DBR laser, which effectively represents a Fabry–Pérot laser, whose mirrors are replaced by DBRs so that the mirror reflectivities become wavelength dependent. Accordingly, the characteristics of the DBRs decisively determine the device performance, particularly the spectral purity.

A schematic model for a DBR is shown in Figure 13.4 with a sine-like z-dependence of n_{eff}.

The DBR extends from $z = 0$ to $z = L_B$ and the z-dependent effective index reads as

$$n_{\text{eff}}(z) = \bar{n}_{\text{eff}} + \frac{\Delta n_{\text{eff}}}{2}\sin k_g z \tag{13.8}$$

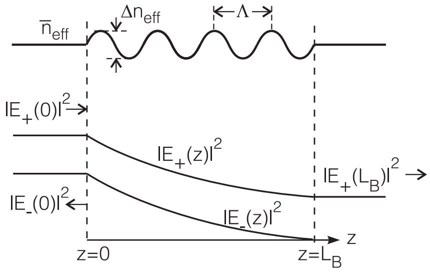

FIGURE 13.4 Forward and backward propagating waves in DBR.

where $\bar{n}_{\text{eff}}$ and Δn_{eff} denote the average effective refractive index and the effective refractive index difference (peak to peak). The grating wavevector k_g is related to the grating period Λ as

$$k_g = \frac{2\pi}{\Lambda}. \tag{13.9}$$

As indicated in Figure 13.4, the periodic feedback leads to a decay in the incoming wave E_+ and produces a backward travelling (reflected) wave E_-, which starts with zero amplitude at the grating end $z = L_B$. The reflection is not complete and a fraction of the forward travelling wave escapes from the Bragg grating at $z = L_B$. The amplitude reflection at $z = 0$ is usually complex and is defined as

$$r = \frac{E_-(0)}{E_+(0)}. \tag{13.10}$$

Analysis by coupled-mode theory requires a coupling coefficient κ which describes the strength of the DFB

$$\kappa = \frac{\pi\,\Delta n_{\text{eff}}}{2\lambda}. \tag{13.11}$$

The reflectivity of the Bragg grating is furthermore dependent on the grating length L_B, so that the product κL_B can be used to concisely describe the grating. The result of coupled-mode theory for the simple grating structure shown in Figure 13.4 with no reflection at both ends of the grating yields for the amplitude reflectivity at wavelength $\lambda_B + \Delta\lambda$ [4]:

$$r(\Delta\lambda) = \frac{-j\kappa \sin h(\gamma L)}{\gamma \cos h(\gamma L) + j\Delta\beta \sin h(\gamma L)} \tag{13.12}$$

where

$$\Delta\beta = \frac{2\pi\,\Delta\lambda}{\lambda^2} \tag{13.13}$$

$$g^2 = k^2 - \Delta\beta^2 \tag{13.14}$$

and $\Delta\lambda$ is the deviation from the Bragg wavelength. At the Bragg wavelength, where $\Delta\lambda = 0$, the amplitude reflection is

$$r = -j \tan h(kL_B) \tag{13.15}$$

Plots of the power reflectivity $|r(\Delta\lambda)|^2$ are shown in Figure 13.5 with the κL_B product as a parameter.

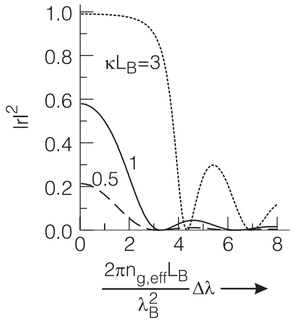

FIGURE 13.5 Power reflectivity $|r|^2$ of DBR as a function of $\Delta\lambda$ with the κL_B product as parameter.

As can be seen, reasonable power reflection is achieved for κL_B larger than unity. At the same time, the filter bandwidth increases and the shape of the filter characteristic approaches that of a bandpass filter.

As mentioned earlier, the amplitude reflectivity at $z = 0$ is complex, which indicates a phase shift of the reflected wave E_- with respect to the incoming wave E_+ and can be interpreted by a longitudinal displacement of the reflecting plane from $z = 0$ to an effective penetration depth into the Bragg reflector $z = L_{\text{eff}}$. Near the Bragg wavelength, therefore, Equation (13.12) can be written as

$$r(\Delta\lambda) \simeq \tan h(\kappa L_B)\, e^{j4\pi\bar{n}_{\text{eff}} L_{\text{eff}}\,\Delta\lambda/\lambda_B^2} \tag{13.16}$$

with an effective penetration depth

$$L_{\text{eff}} = \frac{\tan h(\kappa L_B)}{2\kappa}. \tag{13.17}$$

The bandwidth $\Delta\lambda_{\text{DBR}}$ of the DBR increases with κ as

$$\Delta\lambda_{\text{DBR}} \simeq \frac{\kappa \lambda_B^2}{\pi n_{g,\text{eff}}}. \tag{13.18}$$

A small bandwidth with a large reflectivity is obtained for long DBRs (large L_B) and small coupling coefficients κ. Even though the bandwidth can be made smaller than the longitudinal mode spacing $\Delta\lambda_m$, DBR lasers have not been successfully commercialized as single-mode laser diodes. This is because the wavelengths of the longitudinal modes are still given by the phase condition (see Equation (13.1)), where the effective length of the DBR(s) has to be included in the total laser length L. Hence, the wavelengths of the longitudinal laser modes are independent of the DBR parameters and any relative position of the longitudinal comb-mode spectrum may occur with regard to the Bragg wavelength, where the reflection is maximum. This is particularly crucial if the wavelength changes due to temperature and laser current changes are taken into account. Therefore, the unfortunate case in which two longitudinal modes are placed exactly symmetrically to the Bragg wavelength with a spacing of $\Delta\lambda_m/2$ each so that both modes attain equal reflection and oscillate simultaneously may not be excluded. This results in a two-mode laser with poor spectral behaviour and strong mode competition noise worse than those in multi-mode lasers with many longitudinal modes.

For a truly single-mode laser diode with a stable single-mode emission, it is necessary that the longitudinal comb-mode spectrum is stably synchronized with the Bragg wavelength. As will be seen in the next section, this goal can conveniently be achieved with DFB lasers.

13.2.2 Distributed Feedback Laser

In contrast to the DBR laser, in a DFB laser (see Figure 13.3), the gain and DFB are not longitudinally separated but homogeneously extend over the entire laser axis. Technologically, therefore, DFB lasers are simpler to fabricate because no longitudinal integration of gain and DBR sections is required. Moreover, the longitudinal inhomogeneity of the DBR laser may yield unintentional reflections at the junctions of gain and DBR section that may deteriorate the spectral performance. However, the mathematical treatment of DFB lasers is more complicated because the amplitude and phase are not separable as in the case of the DBR laser.

Numerous types of DFB lasers have been proposed and these essentially differ in the grating structure and the treatment of the reflection at the end facets [6]. A selection of the most common DFB laser grating structures is compiled in Figure 13.6. First of all, the simplest 'pure' DFB laser is shown in Figure 13.6a. Practically, this structure can be realized by applying anti-reflection coatings onto both end facets. Depending on the facet-to-grating phase, however, even small residual reflections at the end facets may significantly affect the DFB laser spectral performance. Since a DFB laser structure without anti-reflection-coated end facets would be advantageous for technological reasons, we will also consider the DFB laser structure with two reflecting end facets as shown in Figure 13.6b. In this case, it is found to be technologically impossible to control the phase relationships between the two end facets and the grating, as indicated by the offsets Δz_1 and Δz_2. Accordingly, a random-phase relationship has to be taken into account and the laser performance (SSR, yield of single-mode lasers) may be predicted only statistically [7,8]. Optimum single-mode performance with a high device yield can be achieved with either a grating with a Λ/2-shift near the centre (see Figure 13.6c) [9,10] and with a gain/loss-grating (see Figure 13.6d) [11] in which that is not the real part of the refractive index but its imaginary part, namely the mode gain or loss, that is longitudinally modulated.

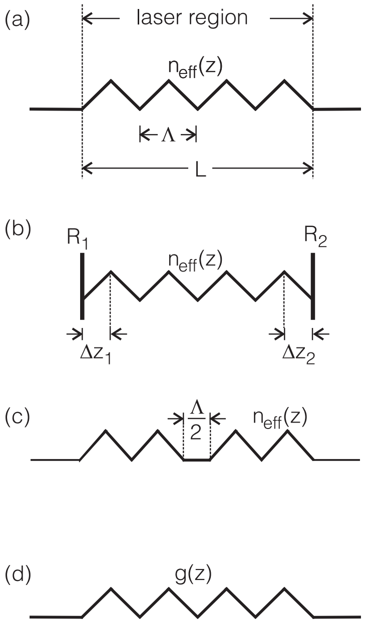

FIGURE 13.6 Various grating structures for single-mode DFB lasers: (a) 'pure' DFB laser, (b) DFB laser with two reflecting end facets with random phase offsets Δz_1 and Δz_2, (c) quarter-wave shifted DFB laser and (d) gain/loss-coupled DFB laser.

Even for the relatively simple 'pure' DFB laser (Figure 13.6a), coupled-mode solutions can only be obtained numerically [5]. These solutions give the threshold gain that is to be supplied by the active region for the various longitudinal modes. In the DFB laser, the mode with the smallest threshold gain will start lasing and the gain difference to the neighbouring modes determines the SSR. Due to the grating, a strong variation of the threshold gain can be observed around the Bragg wavelength. This is illustrated in Figure 13.7, where the product of threshold gain and laser length is plotted *versus* the wavelength for the longitudinal modes nearest to the Bragg wavelength.

As can be seen, the threshold gain spectrum is symmetric with respect to λ_B and shows a minimum threshold gain for the modes nearest to λ_B as well as an effective gain discrimination. The spacing between the two modes nearest to the Bragg wavelength is called the stop band and has a width of

$$\Delta\lambda_s \simeq \Delta\lambda_m \sqrt{1+\left(\frac{\kappa L}{\pi}\right)^2}. \tag{13.19}$$

In the limit of small κL products, the stop bandwidth approaches the longitudinal mode spacing of a Fabry–Pérot laser diode with equal length.

The threshold gain can be decreased for all modes by increasing the κL product. In the case of large κL, the threshold gain for the two modes nearest to the Bragg wavelength can be approximated by

$$g_{th} = \frac{2}{L}\left(\frac{\pi}{\kappa L}\right). \tag{13.20}$$

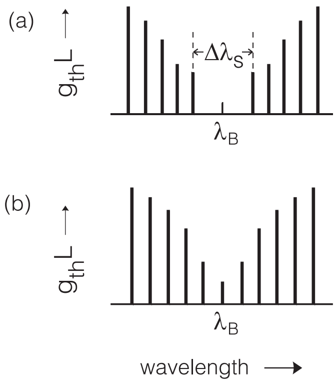

FIGURE 13.7 Threshold gain spectra for (a) a pure DFB laser and (b) quarter-wave-shifted and gain/loss-coupled DFB laser.

Theoretically, the symmetry of the threshold gain spectrum would result in exactly a two-mode operation of this type of DFB laser with bad spectral performance. Owing to spatial hole burning because of the longitudinal inhomogeneous intensity distribution, however, the degeneracy of the threshold gain breaks and one of the two modes becomes dominant to a certain degree. Nevertheless, this DFB laser type can hardly be considered as a reproducibly single-mode laser.

The threshold gain spectra strongly change if the end facets are reflecting (Figure 13.6b). In this case, the symmetry of the threshold gain spectrum is usually broken and one of the longitudinal modes is preferred. From the fabrication point of view, this represents a considerable advantage, because no anti-reflection coating has been applied to the laser end facets, yielding an end facet reflectivity of the order of 30% in InP-based devices. However, the random-phase relationship(s) between mirror positions and grating require that, after laser fabrication, well-performing devices have to be selected using a spectral measurement. Statistically, a high yield of single-mode lasers can be achieved if one facet is anti-reflection coated while the other one is high-reflectivity coated [7].

A deterministic approach to single-mode DFB lasers is the application of the quarter-wave-($\Lambda/2$)-shifted Bragg grating and no reflection at the end facets. In this structure, the threshold gain spectra exhibit one mode with its minimum threshold gain located exactly at the Bragg wavelength [5,12]. The field distribution within the laser peaks at the phase shift and exponentially decays towards the end facets. This means a large resonator quality factor and a narrow spectral linewidth; however, the optical output power may be small. Optimum laser performance therefore requires that the κL product is not too large (i.e. <2) in order to provide a good balance between spectral linewidth and output power and positioning of the phase shift near one of the end facets [13].

While the fabrication of the quarter-wave shift requires considerable effort (e.g. electron beam lithography), a similar performance can be achieved with the complex-coupled DFB lasers in which a gain/loss Bragg grating or a mixed refractive index and gain/loss grating is incorporated [11,14]. The technological realization usually employs a loss grating because the fabrication of a structured active region requires the partial removal of the active region with a subsequent overgrowth that may reduce the active region gain and induce degradation. The loss grating is usually made by placing a grating with an absorbing low-bandgap material (e.g. InGaAs with $E_g = 0.75$ eV in 1.55 μm lasers) near to the active region. As has already been indicated in the first DFB laser theory [5], the gain/loss Bragg grating shows an equivalent threshold gain spectrum to that of the quarter-wave-shifted DFB laser. More detailed theoretical work as well as experimental investigations furthermore showed that the axial field distribution is more strongly fixed yielding additional stability, particularly with respect to external optical feedback [15].

13.2.3 Spectral Linewidth

The spectral linewidth $\Delta\nu$ of a single-mode laser diode is ultimately limited by the phase noise input due to spontaneous emission into the lasing mode [16,17]. Here single-mode operation means a suppression of side modes (SSR) of at least 30 dB, otherwise mode competition effects may severely broaden the spectrum and dominate the spectral linewidth of the modes [18,19]. Due to the gain clamping mechanism in lasers, the spontaneous emission saturates above threshold, while the photon number in the laser cavity as well as the optical output power increase further with current. Accordingly, the spectral linewidth decreases with optical output power as described by the Schawlow–Townes–Henry linewidth formula for laser diodes:

$$\Delta\nu = \frac{h\nu v_g^2 \alpha_{\mathrm{tot}} \alpha_{\mathrm{m}} n_{\mathrm{sp}}}{8\pi P}\left(1+\alpha_{\mathrm{H}}^2\right). \tag{13.21}$$

Here, $h\nu$ is the photon energy (e.g. 0.8 eV for 1.55 μm wavelength), v_g is the group velocity of light in the laser, α_{tot} is the total loss of the laser cavity, α_{m} is the mirror loss, n_{sp} ($\simeq 2$) is the spontaneous emission coefficient that takes into account the non-complete inversion and P is the optical output power per facet by assuming a symmetric structure. The occurrence of α_{H}^2 in the linewidth formula is a speciality of laser diodes that, with α_{H}-values of 2–7, significantly affects the spectral linewidth of laser diodes. It originates from the fact that the gain characteristic of laser diodes is not symmetric with respect to frequency as is usually the case in other laser types, where the gain profiles are usually Lorentzian (homogeneous broadening) or Gaussian (inhomogeneous broadening).

The Kramers–Kronig relation shows that in the case of non-symmetric gain characteristics in laser diodes, gain changes during relaxation processes induce refractive index changes that directly broaden the line as described by the α_{H}-factor. Since the α_{H}-factor is smaller for wavelengths smaller than the gain peak wavelength, negative detuning of the DFB laser wavelength using the grating pitch results in a significant improvement of the spectral linewidth [20]. A detuning of the order of −30 nm is therefore usually accomplished in state-of-the-art DFB laser diodes in the 1.55 μm regime.

Typical values of the spectral linewidth for laser diodes in the 1.3–1.55 μm wavelength range at a few mW of optical output power are of the order of several hundred kHz to a few MHz. The reciprocity between output power and linewidth usually ceases at very high output powers or high currents, respectively, as shown schematically in Figure 13.8. As can be seen, a reduction of $\Delta\nu$ with increasing P changes into a steep increase of the linewidth, which is attributed to the appearance

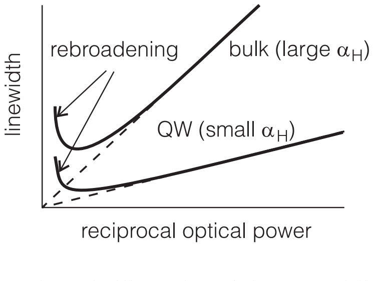

FIGURE 13.8 Schematic illustration of the spectral linewidth *versus* reciprocal optical power for bulk and QW single-mode lasers. The broken line is the theoretical relationship according to Equation (13.21).

of side modes because of strong longitudinal hole burning by the dominant mode [21]. The smallest linewidth reported for monolithic semiconductor lasers is 3.6 kHz [22].

13.3 Wavelength-Tunable Laser Diodes

Electronically wavelength-tunable single-mode laser diodes are required for numerous applications in optical communications, measurement and sensing [23,24]. In particular, advanced optical communication techniques such as optical heterodyning and wavelength division multiplexing rely on the availability of these sources [25]. A comparative review on widely tunable laser diodes for wavelength-division-multiplexed applications in the 1.55 μm region can be found in Ref. [26]. After the development of truly single-mode DFB and DBR lasers, therefore, the realization of electronically wavelength-tunable laser diodes represents an additional gain in device functionality.

The principal function of an idealized tunable single-mode laser is displayed in Figure 13.9. The wavelength control requires at least one control current (I_t), while the output power should be adjusted by I_l. For practical reasons, a clear separation of the control functions for the output power and wavelength tuning is highly desirable, as indicated in the figure. However, since all of the available physical mechanisms for wavelength control also introduce varying (additional) optical losses, the output power usually changes during tuning. By a simultaneous adjustment of the power control current, the output power variations can, in principle, be eliminated. However, the output power variation via I_l changes the refractive index (e.g. because of temperature variations), which in turn affects the laser wavelength. As a consequence, the complete separate control of output power and the emission wavelength is practically impossible and compromises must be found.

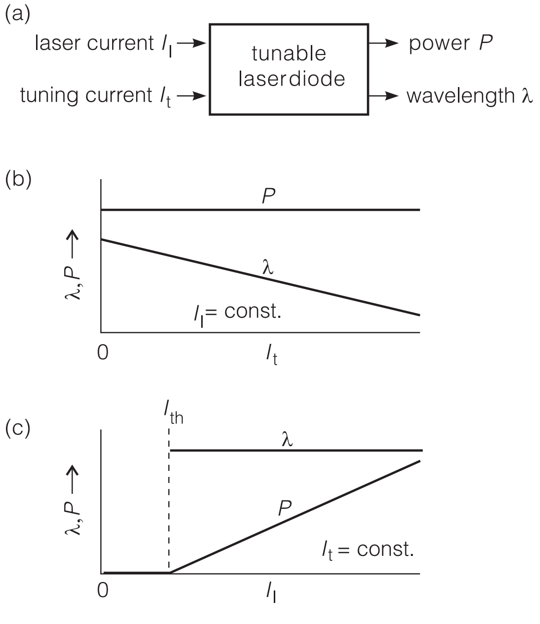

FIGURE 13.9 Schematic illustration of an idealized tunable laser diode (a). The wavelength and light power can be controlled independently by the two control currents I_t (b) and I_l (c), respectively.

For most applications, continuous tuning with a high spectral purity is demanded [25,27,28]. In contrast to microwave oscillators, for instance, the continuous tuning of laser oscillators is rather difficult to achieve because of the large cavity dimensions compared to the light wavelength. This is true even for comparatively small laser diodes with cavity lengths of only several hundreds of micrometres.

Depending on the operating principle, three different tuning modes (shown in Figure 13.10) may be distinguished. Besides continuous wavelength tuning, in which any wavelength within the covered wavelength band can be achieved, one may observe discontinuous tuning, in which discrete wavelength jumps occur, and quasicontinuous tuning, in which overlapping intervals of each continuously tunable regimes appear. The wavelength jumps in the discontinuous tuning mode stem from longitudinal mode jumps corresponding to the longitudinal mode spacing $\Delta\lambda_m$. The continuously tunable intervals in the quasicontinuous tuning mode each correspond to operation in a certain longitudinal mode that can be continuously tuned over an interval exceeding $\Delta\lambda_m$. While in the discontinuous tuning mode not any wavelength within the tuning range can be addressed, the quasicontinuous mode allows access to all wavelengths by a proper choice of the corresponding control currents. Apparently, the tuning effort is largest in the discontinuous tuning mode requiring at least two current (or voltage) controls for the wavelength setting. Correspondingly, quasicontinuous tuning can be performed reasonably only by using a microprocessor control with look-ahead tables that are obtained by a detailed characterization of each device.

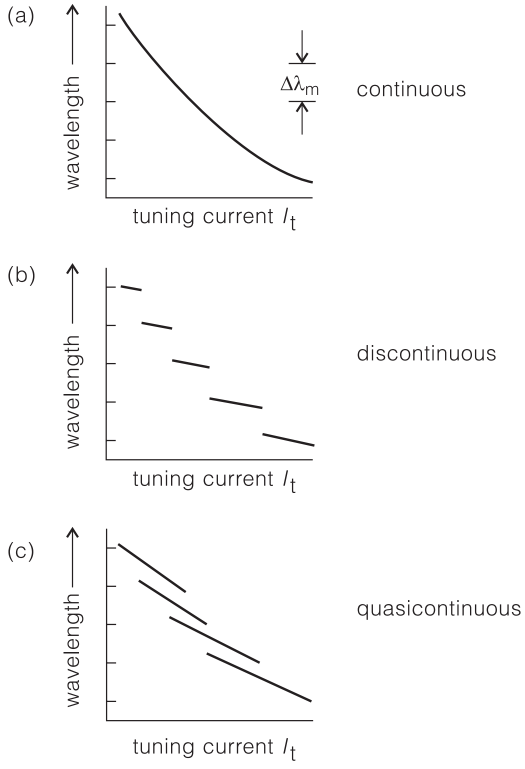

FIGURE 13.10 Tuning characteristics for the continuous (a), discontinuous (b) and quasicontinuous (c) tuning mode.

Electronic wavelength control requires the integration of additional controls into the laser cavity for the variation of the total wavelength-dependent cavity gain. This integration can either be performed longitudinally [29] or transversely [30] as shown in Figure 13.11. As can be seen, in the longitudinal integration one replaces one (or both) of the laser mirrors that usually are not wavelength selective, by wavelength-selective elements, the centre wavelength of which can be controlled electronically. In practice, these elements are DBR-grating reflectors equipped with electronic control of the refractive index.

Likewise, the transverse integration scheme (Figure 13.11b) comprises a DFB laser structure that provides single-mode operation and an additional electronic control mechanism for the effective refractive index of the transverse waveguide structure. In both approaches, the Bragg condition $\lambda_B = 2n_{eff}\Lambda$ yields the wavelength variation $\Delta\lambda$ due to the effective index change Δn_{eff}:

$$\Delta\lambda = \lambda_0 \frac{\Delta n_{eff}}{n_{g,eff}}. \tag{13.22}$$

Whether the tuning is performed continuously or discontinuously depends on whether the optical cavity length $n_{eff}L$ scales simultaneously with the centre wavelength of the wavelength-selective element. This is illustrated in Figure 13.12a, where discontinuous tuning via the shift of the filter curve of the Bragg reflector in a longitudinally integrated tunable laser is shown. Since the spectral positions of the longitudinal (Fabry–Pérot) modes remain unchanged, the otherwise continuous shift of the centre wavelength of the Bragg grating results in jumps from one longitudinal mode to the next. If, however, the longitudinal mode spectrum can be shifted synchronously (Figure 13.12b), the continuous tuning mode can be achieved. For the transverse integration scheme of Figure 13.10b, an inherently continuous tuning behaviour is obtained because the shift of Bragg wavelength and optical cavity length that determines the wavelengths of the longitudinal modes occur synchronously.

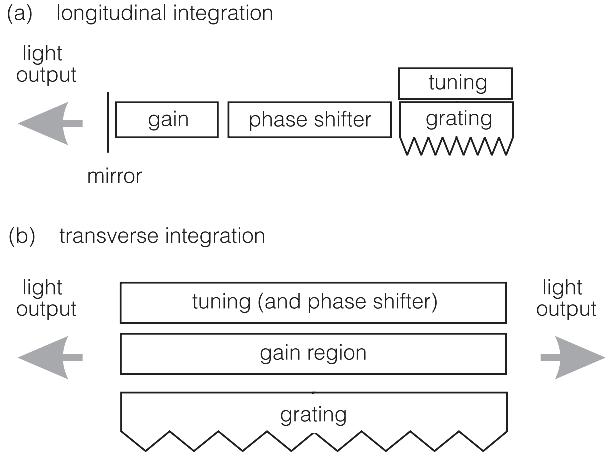

FIGURE 13.11 Longitudinally (a) and transversely (b) integrated wavelength-tunable laser diodes.

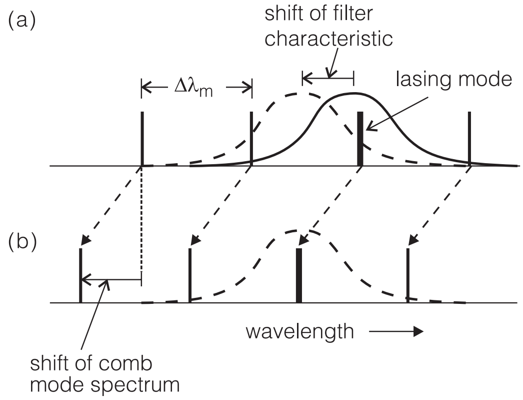

FIGURE 13.12 Discontinuous and continuous tuning. Tuning only the filter characteristic results in discontinuous tuning with mode jumps from one longitudinal mode to the next one (a). The simultaneous tuning of filter characteristic and comb mode spectrum results in continuous tuning (b).

The practically relevant physical mechanisms for electronic wavelength control are:

- the free-carrier plasma effect [31,32],
- the quantum-confined Stark effect (QCSE) [33,34] and
- the temperature dependence of the refractive index [35,36].

For the plasma effect, the injection of an electron–hole plasma into a heterostructure reduces the refractive index leading to a redshift of the laser wavelength. The refractive index change Δn is proportional to the injected carrier density N:

$$\Delta n = \beta_{p1} N \tag{13.23}$$

where

$$\beta_{p1} = -\frac{e^2\lambda^2}{8\pi^2 c^2 n\epsilon_0}\left(\frac{1}{m_e} + \frac{1}{m_h}\right) \tag{13.24}$$

and m_e and m_h denote the effective masses of the injected electrons and holes, respectively, and n is the refractive index of the semiconductor. Note that β_{p1} is negative so that the refractive index and the wavelength both decrease by using the plasma effect for tuning. In addition to the real part, the imaginary part of the refractive index also changes, yielding an additional optical loss

$$\alpha_{p1} = \frac{e^3\lambda^2}{4\pi^2 c^3 n\epsilon_0}\left(\frac{1}{m_e^2\mu_e} + \frac{1}{m_h}\right)N \tag{13.25}$$

where μ_e and μ_h are the mobilities of the electrons and holes, respectively. Δn can be as large as ~ −0.03 with an optical loss α_{pl} of around 30 cm^{-1} at 1.5 μm wavelength in InGaAsP/InP heterostructures. While the plasma effect represents the strongest mechanism for electronic wavelength tuning, it suffers from the disadvantage that, due to recombination, a sustained current flow is needed that leads to significant heat generation. The latter not only degrades the laser performance (power) but also yields an inverse wavelength shift that markedly reduces the magnitude of the combined refractive index change.

The QCSE occurs if a reverse electric field is applied onto a pn-junction comprising a multiple quantum-well structure [33]. In this way, the effective bandgap energy decreases and the electron and hole wavefunction overlap changes. Accordingly, the dipole matrix element changes as well resulting in a refractive index change. Either a red or blue shift may be obtained with the QCSE depending on the quantum-well design. The amount of index change is rather small; however, no sustained current flow is required and additional heat generation can be neglected. Also, the QCSE allows a fast change of the refractive index and is thus well suited for high-speed tuning or FM modulation in the GHz regime.

The refractive index variation by temperature change is essentially based on the temperature dependence of the bandgap energy of semiconductors. This shifts the absorption edge which, by means of the Kramers-Kronig dispersion relation, indirectly changes the refractive index. Thereby, the decrease of the bandgap energy with temperature yields an increase of the refractive index resulting in a redshift of the laser wavelength. In 1.55 μm wavelength InGaAsP/InP lasers, the slope of the λ *versus* T characteristic is $\simeq 0.1\,\text{nm K}^{-1}$ [35]. It should be noted that thermal tuning exhibits the slowest tuning speed (μs to ms regime) among the relevant wavelength control mechanisms. Admitting a maximum temperature change of 50 K, therefore, a tuning range of the order of 5 nm (0.3%) can be achieved by thermal tuning of InP-based laser diodes in the 1.55 μm wavelength region. However, heating laser diodes degrades many important laser parameters such as the output power, threshold current, spectral linewidth, modulation bandwidth and long-term reliability.

13.3.1 Continuously Tunable Monolithic Devices

The technologically simplest approach for a wavelength-tunable laser diode is the multi-section (typically two or three sections) DFB laser [37–39] shown in Figure 13.13. Referring to Figure 13.11, the three-section DFB laser is a longitudinally integrated device. With respect to reproducibility and single-mode yield, the symmetrical three-section DFB laser with a quarter-wave-shifted DFB grating and anti-reflection-coated end facets performs particularly well with the largest continuous tuning ranges around 5 nm [40]. The anti-reflection coating is important because of the unknown and uncontrollable phase relation between the end facet and grating, which results in random device performance and reduced device yield.

Wavelength tuning is induced by an inhomogeneous biasing of the centre and side regions. Considering the gain-clamping mechanism in laser oscillators that keeps the total mode gain constant above threshold, it appears surprising that inhomogeneous biasing may lead to a wavelength shift. In fact, at equal total current, no tuning occurs in an inhomogeneously biased Fabry–Pérot laser. In the case of DFB lasers, however, the longitudinally varying complex-field amplitudes yield longitudinally varying amplitude-phase coupling. As a consequence, constant total gain may be maintained by a change of the round-trip phase that performs the wavelength shift. In summary, wavelength tuning in all-active multi-section DFB lasers is a rather complex mechanism, also comprising spatial hole-burning effects.

A distinct disadvantage of this laser type is that the controls of output power and wavelength are not separated, i.e. both currents I_1 and I_2 simultaneously affect output power and oscillation wavelength. The result is an increased complexity of the device control, particularly because of possible longitudinal-mode jumps for certain I_1–I_2 combinations. Despite their relatively simple device technology, therefore, the multisection DFB lasers have become less important as continuously tunable laser diodes than other approaches.

A more convenient handling with an effective separation between power and wavelength control offers the three-section DBR laser [29,41,42] shown in Figure 13.14, which is also a longitudinally integrated device. In this laser, the current into the active region (I_l) mainly determines the output power, while wavelength tuning is essentially accomplished with currents I_B and I_p. Referring to Figure 13.14, the Bragg region current I_B determines the Bragg wavelength, i.e. the wavelength where the total cavity gain exhibits its maximum. The phase current I_p controls the effective refractive index in the phase section and thus the optical cavity length ($n_{\text{eff}}L$ product). The latter is relevant for the comb spectrum of the longitudinal modes and small changes of $n_{\text{eff}}L$ essentially affect the positions of the modes, rather than the spacings. Accordingly, the positions of the comb modes can be controlled by the phase current, so that continuous tuning can be achieved in the way shown in Figure 13.12 by a proper mutual adjustment with the Bragg

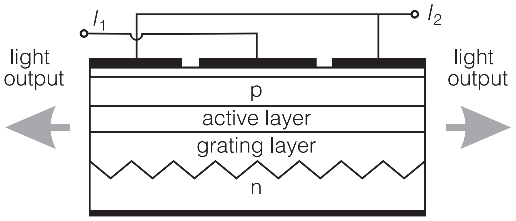

FIGURE 13.13 Schematic longitudinal view of a three-section DFB laser.

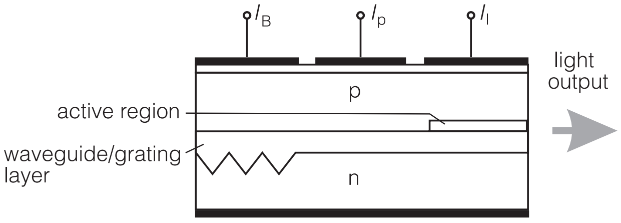

FIGURE 13.14 Schematic longitudinal view of a three-section DBR laser.

region. Otherwise, by a solitary change of either I_B or I_p, the tuning behaviour is essentially discontinuous.

The continuous tuning range of the three-section DBR laser is usually limited by the tunability of the phase section, because the tuning of the phase section has to match the optical cavity changes including the active section that is not tuned. With well-designed devices, a continuous wavelength tuning over some 5 nm [42,43] and a discontinuous tuning up to 8 nm [44] can be achieved in InP-based lasers at 1.55 µm wavelength. Again, however, the wavelength setting requires considerable effort with respect to device characterization and control of the three currents and temperature. In particular, it is important that mode jumps are avoided, which usually requires device control via microprocessors and look-ahead tables.

The most convenient handling performance can be achieved with the transversely integrated structures, such as the tunable twin-guide (TTG) laser [45–47], shown in Figure 13.15, or the striped heater DFB lasers [48]. This is because, in these devices, the refractive index change is applied homogeneously along the entire laser axis so that the optical cavity length changes are automatically synchronized with the Bragg wavelength changes. Consequently, the tuning behaviour of these devices is inherently continuous. As can be seen for the case of the TTG laser, carriers injected into the tuning layer lead to a longitudinally homogeneous reduction of the refractive index resulting in a blue shift. Also, only two control currents I_l and I_t are required for the output power and wavelength control. As indicated by the subscripts, current I_l controls the output power and current I_t essentially controls the wavelength. Both controls, however, are not strictly orthogonal to each other, so that the output power is affected also by I_t because of the additional loss by the injected carriers and the wavelength is influenced also by I_l because of temperature changes.

Since the tuning layer extends over the entire laser length, and not only part of it as in the phase control section in the three-section DBR laser, the tuning effect is stronger in the transversely integrated devices. Accordingly, the largest continuous tuning ranges reported so far (≃13 nm) have been achieved with TTG laser diodes [49] while the thermal tuning of DFB lasers yields up to some 4 nm of continuous tuning at 1.55 µm wavelength [48].

Besides the laser wavelength, the electronic wavelength tuning influences other laser characteristics. First of all, the optical power usually decreases because of the additional loss (plasma effect) or the larger threshold current (thermal tuning). The reduction of the optical power, in turn, leads to an increased spectral linewidth according to the Schawlow–Townes–Henry formula (Equation (13.21)). In case of the most often used plasma effect, the linewidth generally shows distinct additional broadening, denoted $\Delta\nu_t$, because of shot-noise in the tuning region(s) [50]. This contribution to the linewidth amounts to

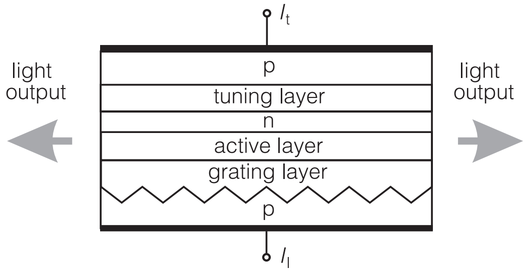

FIGURE 13.15 Schematic longitudinal section of a transversely integrated tunable twin-guide (TTG) laser diode.

$$\Delta\nu_t = 4\pi e \frac{c^2}{\lambda^4}\left(\frac{\mathrm{d}\lambda}{\mathrm{d}I_t}\right)^2 I_t \tag{13.26}$$

in TTG laser diodes and

$$\Delta\nu_t = 4\pi e \frac{c^2}{\lambda^4}\left\{\left(\frac{\partial\lambda}{\partial I_p}\right)^2 I_p + \kappa L_B \left(\frac{\partial\lambda}{\partial I_B}\right)^2 I_B\right\} \tag{13.27}$$

in three-section DBR laser diodes. Apparently, this broadening is proportional to the tuning efficiencies squared so that the wider tunable devices show the larger broadening. In TTG laser diodes with tuning ranges of the order of 7 nm at 1.55 µm wavelength, $\Delta\nu_t$ can be up to several 10 MHz, while in three-section DBR lasers with their smaller continuous tuning ranges, $\Delta\nu_t$ can generally be kept below about 10 MHz [50].

13.3.2 Wavelength-Tunable Vertical-Cavity Surface-Emitting Lasers

Continuous wavelength tuning can also be accomplished with VCSELs. Longitudinal-single-mode operation and the efficient suppression of other longitudinal modes because of the short cavity length ease the mode control considerably. VCSELs may be tuned either externally by using a piezoelectric transducer actuator [51] or with an integrated micromechanically moveable top mirror [52]. Tuning ranges around 40 nm have been reported for the wavelength ranges from 950 nm [53] to 1.3 µm [51].

13.3.3 Discontinuously Tunable Monolithic Devices

The continuous electronic wavelength tuning is ultimately limited by the maximal achievable effective refractive index change (see Equation (13.22)). With maximum refractive index changes of the order of 1% and maximum confinement factors of the tuning regions around 50%, therefore, the continuous tuning range is limited to about 0.5%–1% of the wavelength. Significantly larger tuning ranges can be achieved if discontinuous or quasicontinuous tuning can be accepted. In this case the tuning range is enhanced by mode jumps from one longitudinal mode to the next one. Again, electronic tuning is induced by refractive index changes exploiting the physical mechanisms discussed in the preceding section. Thereby, largest discontinuous and/or quasicontinuous tuning range around 22 nm was achieved by combining the free-carrier plasma effect and thermal heating [54].

To obtain a large tuning effect, one exploits the Vernier effect, by which small relative refractive index changes can be used to yield large relative wavelength changes. The application of the Vernier effect in tunable laser diodes is illustrated in Figure 13.16 for the case of the longitudinal integration technique. The essential device components are the two mirrors with comb reflection spectra exhibiting different pitch $\Delta\lambda_a$ and $\Delta\lambda_b$, respectively. Typically, $\Delta\lambda_a$ and $\Delta\lambda_b$ differ only by 3%–10%. The comb reflection spectra may be achieved, for instance, by spatially modulated Bragg gratings (sampled gratings, superstructure gratings and chirped gratings). As shown in Figure 13.16b and c, lasing can occur only at wavelength λ_1, where both mirrors exhibit non-vanishing reflection. By a small shift $\delta\lambda$ of the comb reflection spectrum of mirror B, using the free-carrier plasma effect, the 'resonance' at λ_1 breaks and lasing can now take place at wavelength λ_2. Consequently, the wavelength tuning by $\Delta\lambda_a$ from λ_1 to λ_2 is much larger than $\delta\lambda$ because of the Vernier effect provided by the two comb reflection spectra with a slightly different pitch.

The schematic structure of the corresponding laser in the longitudinal integration technique [55–57] is shown in Figure 13.17 and includes a phase-shift section [58] to enable the quasicontinuous tuning mode. This type of device may have up to four control currents including the current into the gain section for power control, two tuning currents into the mirrors for adjusting the comb reflection spectra and a phase control current into the phase shift section to adjust the Fabry–Pérot modes to enable quasicontinuous tuning.

Practically, the amplification factor due to the Vernier effect,

$$T = \frac{\Delta\lambda_a}{\Delta\lambda_a - \Delta\lambda_b} \tag{13.28}$$

can be of the order of 10–100, so that the maximum discontinuous tuning range is now finally limited by the gain bandwidth of the laser gain region. The latter is of the order of 10% of the laser wavelength for the usual III/V laser diodes and discontinuous and quasicontinuous tuning ranges around 100 nm were achieved in InGaAsP/InP laser diodes at 1.55 μm wavelength [59,60].

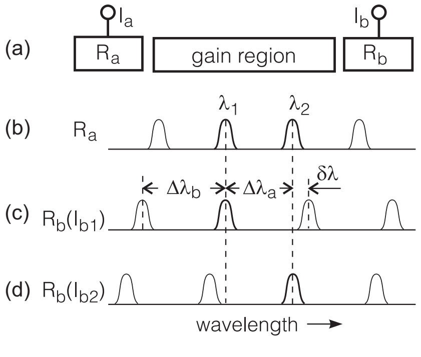

FIGURE 13.16 Schematic illustration of widely tunable laser diodes exploiting the Vernier effect (a). Both mirrors exhibit comb reflection spectra (b and c) with different pitches $\Delta\lambda_a$ and $\Delta\lambda_b$. Lasing can occur at wavelength λ_1, where both mirrors yield reflection. By a small shift $\delta\lambda$ of the reflection spectrum of mirror B, the laser wavelength shifts by a much larger amount, $\Delta\lambda_a$, to λ_2, where now both mirrors reflect (d).

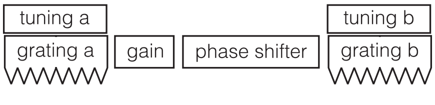

FIGURE 13.17 Schematic longitudinal section of longitudinally integrated tunable laser diode exploiting the Vernier effect.

The Vernier effect can also be applied to transversely integrated structures such that the small differences in optical pathlength of the interfering modes of a twin waveguide are tuned [61,62]. In this way, the wavelength for constructive interference, i.e. the laser wavelength, can be tuned widely by small changes of the optical path difference

$$\left(n_{\text{eff},1} - n_{\text{eff},2}\right)L \tag{13.29}$$

where $n_{\text{eff},1}$ and $n_{\text{eff},2}$ are the effective refractive indices of the participating transverse modes. The resulting wavelength change is

$$\Delta\lambda = \lambda \frac{\Delta\left(n_{\text{eff},1} - n_{\text{eff},2}\right)}{n_{\text{g,eff},1} - n_{\text{g,eff},2}} \tag{13.30}$$

where $\Delta(n_{\text{eff},1} - n_{\text{eff},2})$ denotes the change of the difference of the effective refractive indices of the two modes. The comparison with Equation (13.22) shows that the amplification factor of the transversely integrated structures due to the Vernier effect is

$$T = \frac{n_{\text{g,eff},1}}{n_{\text{g,eff},1} - n_{\text{g,eff},2}}. \tag{13.31}$$

While $n_{\text{g,eff},1}$ is of the order of 3–4, $n_{\text{g,eff},1} - n_{\text{g,eff},2}$ is typically less than 0.1 and T is larger than 30, even small changes $\Delta(n_{\text{eff},1} - n_{\text{eff},2})$ may cause large changes of the laser wavelength. The schematic longitudinal section of a representative device is shown in Figure 13.18. The tuning in this device is done by the vertical coupler filter, in which the superposition of the two guided transverse mode gives a power transfer from waveguide 1 (WG 1) to waveguide 2 (WG 2) only at the coupling wavelength. The latter can be tuned by current I_t which, by the plasma effect, dominantly changes the effective refractive index of the mode in the upper waveguide and thus the difference $n_{\text{eff},1} - n_{\text{eff},2}$ occurring in Equation (13.30). The tuning ranges achievable with the transversely integrated devices are again of the order of 50–100 nm for 1.55 μm lasers [61]. Particular performance with tuning ranges exceeding 100 nm at 1.55 μm wavelength [63] and spectral linewidth below

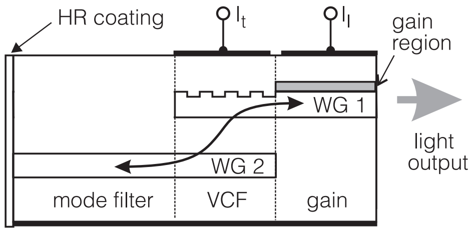

FIGURE 13.18 Schematic longitudinal section of a discontinuously tunable laser diode in the transverse integration technique. VCF laser, vertical cavity filter.

4 MHz [64] can be obtained by combining the longitudinal integration scheme with the transverse one.

Only a few data have been reported on the spectral properties of discontinuously tunable laser diodes. This is mainly because the linewidth strongly changes during tuning, showing singularities near the mode jump regimes. In linewidth-sensitive applications, therefore, care has to be taken to avoid the operation of discontinuously as well as quasicontinuously tunable devices near to longitudinal mode jumps.

13.3.4 External Cavity Tunable Laser Diodes

The use of an external cavity for a tunable laser diode [65,66] may yield significant advantages; the efforts in adjustment and control, however, may be considerable. For a proper operation of a laser diode in an external cavity, it is necessary that the reflection of at least one of the end facets be sufficiently well suppressed to avoid multiple cavity effects or, still worse, to establish an optical feedback configuration with reduced or unpredictable stability. The main advantages of external cavity diode lasers with respect to tuning are the smaller spectral linewidth due to the smaller spontaneous emission input into the laser mode, and the possibility to tune the wavelength precisely by means of mechanical movements. However, the mechanical and thermal stability of the external cavity may be a problem in practice.

The principal configuration of a simple external cavity tunable laser diode is shown in Figure 13.19. In this device the laser wavelength is determined by the inclination of the grating reflector, because only at the wavelength

$$\lambda = 2\Lambda \sin\phi \tag{13.32}$$

does reflection back into the diode occur. Changing the angle ϕ allows discontinuous wavelength tuning with mode jumps equal to the (small) longitudinal mode spacing of the external cavity. With this technique, large tuning ranges can be achieved: the maximum tuning range reported so far is around 240 nm in the 1.3–1.55 μm wavelength regime [67]. Continuous tuning is also possible by choosing the axis for the grating rotation appropriately [68]. In this way, the length of the external cavity is changed simultaneously with the laser wavelength, which is the prerequisite for continuous tuning.

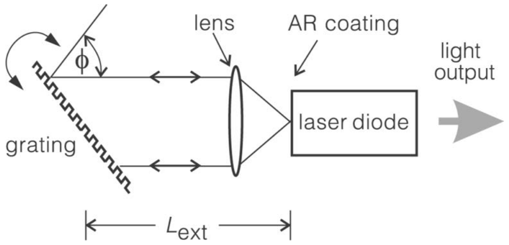

FIGURE 13.19 Principal setup of external-cavity tunable laser diode with a wavelength-selective grating reflector.

13.4 Multiwavelength Laser Diodes

In many applications, such as WDM, an array of laser diodes is required in which each laser operates at a well-defined wavelength, usually in equidistant wavelength channels. For proper device operation it is necessary for each laser to be tunable over a certain wavelength range. If the tuning range of each element exceeds the wavelength difference between the elements these devices may cover a huge wavelength range without a gap, making these devices particularly attractive as spare light sources. Simple multiwavelength laser arrays exhibit separate outputs for each laser. Most often, however, it is necessary to combine the outputs of all elements into one output, e.g. a single optical fibre. In the latter case the multiwavelength laser array represents a considerably integrated photonic device comprising a combiner. Multiwavelength laser diodes can essentially be of the following four types:

- simple arrays [69,70],
- laser arrays integrated with a combiner [71],
- multi-stripe grating cavities [72] or
- phased arrays [73].

Multiwavelength laser diodes are also useful in applications where multiple wavelengths in a fixed channel spacing must rapidly be accessed. Devices with 40 wavelengths spaced by 100 GHz in the 1.55 μm wavelength range based on a chirped waveguide grating router have successfully been demonstrated [74].

REFERENCES

1. Osiński M and Buus J 1987 Linewidth broadening factor in semiconductor lasers—an overview *IEEE J. Quantum Electron.* **23** 9–29.
2. Petermann K 1995 External optical feedback phenomena in semiconductor lasers *IEEE J. Selected Topics Quantum Electron.* **1** 480–9.
3. Kojima K and Kyuma K 1990 Multi-quantum well distributed feedback and distributed Bragg reflector lasers *Semicond. Sci. Technol.* **5** 481–93.
4. Suematsu Y, Arai S and Kishino K 1983 Dynamic single-mode semiconductor lasers with a distributed reflector *IEEE J. Lightwave Technol.* **1** 161–76.
5. Kogelnik H and Shank C V 1972 Coupled-wave theory of distributed feedback lasers *J. Appl. Phys.* **43** 2327–35.
6. Carroll J, Whiteaway J and Plumb D 1998 *Distributed Feedback Semiconductor Lasers* (Stevenage: IEE).
7. Buus J 1986 Dynamic single-mode operation of DFB lasers with phase shifted gratings and reflecting mirrors *IEE Proc.* **133** 163–4.
8. Matsuoka T, Yoshikuni Y and Nagai H 1985 Verification of the light phase effect at the facet on DFB laser properties *IEEE J. Quantum Electron.* **21** 1880–6.
9. Utaka K, Akiba S, Sakai K and Matsushima Y 1986 λ/4-shifted InGaAsP/InP DFB lasers *IEEE J. Quantum Electron.* **22** 1042–51.

10. Sasaki T, Takano S, Henmi N, Yamada Y, Kitamura M, Hasumi H and Mito I 1988 1.5 µm $\lambda/4$ shifted multiple quantum well distributed feedback laser diodes *Electron. Lett.* **24** 1408–9.
11. Luo Y, Nakano Y, Tada K, Inoue T, Hosomatsu H and Iwaoka H 1990 Purely gain-coupled distributed feedback semiconductor lasers *Appl. Phys. Lett.* **56** 1620–2.
12. Utaka K, Akiba S, Sakai K and Matsushima Y 1984 Analysis of quarter-wave-shifted DFB laser *Electron. Lett.* **20** 326–7.
13. Usami M and Akiba S 1989 Suppression of longitudinal spatial hole-burning effect in $\lambda/4$-shifted DFB lasers by nonuniform current injection *IEEE J. Quantum Electron.* **25** 1245–53.
14. Borchert B, David K, Stegmüller B, Gessner R, Beschorner M, Sacher D and Franz G 1991 1.55 μm gain-coupled quantum-well distributed feedback lasers with high single-mode yield and narrow linewidth *IEEE Photon. Technol. Lett.* **3** 955–7.
15. Hui R, Kavehrad M and Makino T 1994 External feedback sensitivity of partly gain-coupled DFB semiconductor lasers *IEEE Photon. Technol. Lett.* **6** 897–9.
16. Henry C H 1982 Theory of the linewidth of semiconductor lasers *IEEE J. Quantum Electron.* **18** 259–64.
17. Henry C H 1986 Phase noise in semiconductor lasers *IEEE J. Lightwave Technol.* **4** 298–311.
18. Pan X, Olesen H and Tromborg B 1990 Spectral linewidth of DFB lasers including the effects of spatial hole burning and nonuniform current injection *IEEE Photon. Technol. Lett.* **2** 312–15.
19. Pan X, Tromborg B and Olesen H 1991 Linewidth rebroadening in DFB lasers due to weak side modes *IEEE Photon. Technol. Lett.* **3** 112–14.
20. Ogita S, Kotaki Y, Kihara K, Matsuda M, Ishikawa H and Imai H 1988 Dependence of spectral linewidth on cavity length and coupling coefficient in DFB laser *Electron. Lett.* **24** 613–14.
21. Kitamura M, Yamazaki H, Sasaki T, Kida N, Hasumi H and Mito I 1990 250 kHz spectral linewidth operation of 1.5 µm multiple quantum well DFB-LDs *IEEE Photon. Technol. Lett.* **2** 310.
22. Okai M, Suzuki M, Taniwatari T and Chinone N 1994 Corrugation-pitch-modulated distributed feedback lasers with ultranarrow spectral linewidth *Japan. J. Appl. Phys.* **33** 2563–70.
23. Park C A and Williams P J 1989 Single-mode laser sources for FSK systems *IEE Proc.* **136** 18–21.
24. Strzelecki E M, Cohen D A and Coldren L A 1988 Investigation of tunable single frequency diode lasers for sensor applications *IEEE J. Lightwave Technol.* **6** 1610–18.
25. Koch T L and Koren U 1990 Semiconductor lasers for coherent optical fiber communications *IEEE J. Lightwave Technol.* **8** 274–93.
26. Delorme F 1998 Widely tunable 1.55-μm lasers for wavelength-division-multiplexed optical fiber communications *IEEE J. Quantum Electron.* **34** 1706–16.
27. Kotaki Y and Ishikawa H 1991 Wavelength tunable DFB and DBR lasers for coherent optical fibre communications *IEEE Proc.* **138** 171–7.
28. Dieckmann A and Amann M C 1995 FMCW-LIDAR with tunable twin-guide laser diode *Trends in Optical Fibre Metrology and Standards* (Dordrecht: Kluwer) pp 791–802.
29. Coldren L A and Corzine S W 1987 Continuously-tunable single-frequency semiconductor lasers *IEEE J. Quantum Electron.* **23** 903–8.
30. Amann M C and Thulke W 1990 Continuously tunable laser diodes: longitudinal versus transverse tuning scheme *IEEE J. Selected Areas Commun.* **8** 1169–77.
31. Bennet B, Soref R and DelAlamo J 1990 Carrier-induced change in refractive index of InP, GaAs, and InGaAsP *IEEE J. Quantum Electron.* **26** 113–22.
32. Weber J P 1994 Optimization of the carrier-induced effective index change in InGaAsP waveguides—application to tunable Bragg filters *IEEE J. Quantum Electron.* **30** 1801–16.
33. Miller D A B, Chemla D S, Damen T C, Gossard A C, Wiegmann W, Wood T H and Burrus C A 1984 Band edge electroabsorption in quantum well structures: the quantum confined Stark effect *Phys. Rev. Lett.* **53** 2173–6.
34. Susa N and Nakahara T 1992 Enhancement of change in the refractive index in an asymmetric quantum well *Appl. Phys. Lett.* **60** 2457–9.
35. Chinen K, Gen-Ei K, Suhara H, Tanaka A, Matsuyama T, Konno K and Muto Y 1987 Low-threshold 1.55 μm InGaAsP/InP buried heterostructure distributed feedback lasers *Appl. Phys. Lett.* **51** 273–5.
36. Woodward S L, Koren U, Miller B I, Young M G, Newkirk M A and Burrus C A 1992 A DBR laser tunable by resistive heating *IEEE Photon. Technol. Lett.* **4** 1330–2.
37. Horita M, Tsurusawa M, Utaka K and Matsushima Y 1993 Wavelength-tunable InGaAsP-InP multiple-$\lambda/4$-shifted distributed feedback laser *IEEE J. Quantum Electron.* **29** 1810–16.
38. Tohyama M, Onomura M, Funemizu M and Suzuki N 1993 Wavelength tuning mechanism in three-electrode DFB lasers *IEEE Photon. Technol. Lett.* **5** 616–18.
39. Ishii H, Kondo Y, Kano F and Yoshikuni Y 1998 A tunable distributed amplification DFB laser diode (TDA-DFB-LD) *IEEE Photon. Technol. Lett.* **10** 30–2.
40. Tohyama M, Funemizu M, Onomura M, Takakuwa C and Suzuki N 1995 Mechanism of wavelength tuning and frequency modulation in three-electrode DFB lasers *IEEE J. Selected Topics Quantum Electron.* **1** 416–26.
41. Caponio N P, Goano M, Maio I, Meliga M, Bava G P, Destefanis G and Montrosset I 1990 Analysis and design criteria of three-section DBR tunable lasers *IEEE J. Selected Areas Commun.* **8** 1203–13.
42. Murata S, Mito I and Kobayashi K 1987 Over 720 GHz (5.8 nm) frequency tuning by a 1.5 μm DBR laser with phase and Bragg wavelength control regions *Electron. Lett.* **23** 403–5.
43. Murata S, Mito I and Kobayashi K 1988 Tuning ranges for 1.5 μm wavelength tunable DBR lasers *Electron. Lett.* **24** 577–9.
44. Koch T L, Koren U, Gnall R P, Burrus C A and Miller B I 1988 Continuously tunable 1.5 μm multiple-quantum-well GaInAs/GaInAsP distributed-Bragg-reflector lasers *Electron. Lett.* **24** 1431–3.

45. Amann M C, Illek S, Schanen C and Thulke W 1989 Tunable twin-guide laser: A novel laser diode with improved tuning performance *Appl. Phys. Lett.* **54** 2532–3.
46. Amann M C 1995 Broad-band wavelength-tunable twin-guide lasers *Optoelectron—Devices Technol* **10** 27–38.
47. Yamamoto E, Hamada M, Suda K, Nogiwa S and Oki T 1992 Wavelength tuning characteristics of tunable twin-guide lasers with improved current-injection structures *Appl. Phys. Lett.* **60** 805–6.
48. Sakano S, Tsuchiya T, Suzuki M, Kitajima S and Chinone N 1992 Tunable DFB laser with a striped thin-film heater *IEEE Photon. Technol. Lett.* **4** 321–3.
49. Wolf T, Illek S, Rieger J, Borchert B and Amann M C 1994 Extended continuous tuning range (over 10 nm) of tunable twin-guide lasers *Conf. on Lasers and Electro-Optics (CLEO '94)* (Anaheim, CA) p CWB 1.
50. Amann M C and Schimpe R 1990 Excess linewidth broadening in wavelength-tunable laser diodes *Electron. Lett.* **26** 279–80.
51. Hsu K, Miller C M, Babic D, Houng D and Taylor A 1998 Continuously tunable photopumped 1.3 μm fiber Fabry-Pérot surface-emitting lasers *IEEE Photon. Technol. Lett.* **10** 1199–201.
52. Tyebati P, Wang P, Vakhshoori D, Lu C C, Azimi M and Sacks R N 1998 Half-symmetric cavity tunable micromechanical VCSEL with single spatial mode *IEEE Photon. Technol. Lett.* **10** 1679–81.
53. Wang P, Tayebati P, Vakhshoori D, Lu C C, Azimi M and Sacks R N 1999 Half-symmetric cavity micromechanically tunable vertical cavity surface emitting lasers with single spatial mode operating near 950 nm *Appl. Phys. Lett.* **75** 897–8.
54. Öberg M, Nilsson S, Klinga T and Ojala P 1991 A three-electrode distributed Bragg reflector laser with 22 nm wavelength tuning range *IEEE Photon. Technol. Lett.* **PTL-3** 299–301.
55. Tohmori Y, Yoshikuni Y, Tamamura T, Ishii H, Kondo Y and Yamamoto M 1993 Broad-range wavelength tuning in DBR lasers with super structure grating (SSG) *IEEE Photon. Technol. Lett.* **5** 126–9.
56. Mason B, Fish G A, DenBaars S P and Coldren L A 1998 Ridge waveguide sampled grating DBR lasers with 22 nm quasi-continuous tuning range *IEEE Photon. Technol. Lett.* **10** 1211–13.
57. Jayaraman V, Chuang Z M and Coldren L A 1993 Theory, design, and performance of extended tuning range semiconductor lasers with sampled gratings *IEEE J. Quantum Electron.* **29** 1824–34.
58. Ishii H, Tanobe H, Kano F, Tohmori Y, Kondo Y and Yoshikuni Y 1996 Broad-range wavelength coverage (62.4 nm) with superstructure-grating DBR laser *Electron. Lett.* **32** 454–5.
59. Tohmori Y, Yoshikuni Y, Tamamura T, Yamamoto M, Kondo Y and Ishii H 1993 Over 100 nm wavelength tuning in superstructure grating (SSG) DBR lasers *Electron. Lett.* **29** 352–4.
60. Jayaraman V, Heimbuch M E, Coldren L A and DenBaars S P 1994 Widely tunable continuous-wave InGaAsP/InP sampled grating lasers *Electron. Lett.* **30** 1492–4.
61. Kim I, Alferness R C, Koren U, Buhl L L, Miller B I, Young M G, Chien M D, Koch T L, Presby H M, Raybon G and Burrus C A 1994 Broadly tunable vertical-coupler filtered tensile-strained InGaAs/InGaAsP multiple quantum well laser *Appl. Phys. Lett.* **64** 2764–6.
62. Amann M C and Illek S 1993 Tunable laser diodes utilizing transverse tuning scheme *IEEE J. Lightwave Technol.* **11** 1168–82.
63. Rigole P J, Nilsson S, Bäckbom L, Klinga T, Wallin J, Stålnacke B, Berglind E and Stoltz B 1995 114 nm wavelength tuning range of a vertical grating assisted codirectional coupler laser with a super structure grating distributed Bragg reflector *IEEE Photon. Technol. Lett.* **7** 697–9.
64. Saavedra A A, Rigole P J, Goobar E, Schatz R and Nilsson S 1998 Relative intensity noise and linewidth measurements of a widely tunable GCSR laser *IEEE Photon. Technol. Lett.* **10** 481–3.
65. Lee B L and Lin C F 1998 Wide-range tunable semiconductor lasers using asymmetric dual quantum wells *IEEE Photon. Technol. Lett.* **10** 322–4.
66. Mehuys D, Mittelstein M, Yariv A, Sarfaty R and Ungar J E 1989 Optimized Fabry-Pérot (AlGa)As quantum-well lasers tunable over 105 nm *Electron. Lett.* **25** 143–5.
67. Bagley M, Wyatt R, Elton D J, Wickes H J, Spurdens P C, Seltzer C P, Cooper D M and Devlin W J 1990 242 nm continuous tuning from a GRIN-SC-MQW-BH InGaAsP laser in an extended cavity *Electron. Lett.* **26** 267–9.
68. Favre F and Le Guen D 1991 82 nm of continuous tunability for an external cavity semiconductor laser *Electron. Lett.* **27** 183–4.
69. Okuda H, Hirayama Y, Furuyama H, Kinoshita J I and Nakamura M 1987 Five-wavelength integrated DFB laser arrays with quarter-wave-shifted structures *IEEE J. Quantum Electron.* **23** 843–8.
70. Nakao M, Sato K, Nishida T and Tamamura T 1990 Distributed feedback laser arrays fabricated by synchrotron orbital radiation lithography *IEEE J. Selected Areas Commun.* **8** 1178–82.
71. Young M G, Koren U, Miller B I, Chien M, Koch T L, Tennant D M, Feder K, Dreyer K and Raybon G 1995 Six wavelength laser array with integrated amplifier and modulator *Electron. Lett.* **31** 1835–6.
72. Asghari M, Zhu B, White I H, Seltzer C P, Nice C, Henning I D, Burness A L and Thompson G H B 1994 Demonstration of an integrated multichannel grating cavity laser for WDM applications *Electron. Lett.* **30** 1674–5.
73. Zirngibl M, Joyner C H, Doerr C R, Stulz L W and Presby H M 1996 An 18-channel multifrequency laser *IEEE Photon. Technol. Lett.* **8** 870–2.
74. Doerr C R, Joyner C H and Stulz L W, 1999 40-wavelength rapidly digitally tunable laser *IEEE Photon. Technol. Lett.* **11** 1348–50

FURTHER READINGS

Amann M C and Buus J 1998 *Tunable Laser Diodes* (Norwood, MA: Artech House).

A survey over fundamentals, device structures and performance, and applications of monolithic tunable laser diodes.

Buus J 1991 *Single Frequency Semiconductor Lasers* (Bellingham, WA: SPIE).

A comprehensive introduction into theory and device structures of single mode laser diodes.

Carroll J, Whiteaway J and Plumb D 1998 *Distributed Feedback Semiconductor Lasers* (Stevenage: IET).

Covering all aspects of DFB lasers including theory, modelling, system aspects. Provides also a useful set of simulation programs (MATLAB).

Coldren L A and Corzine S W 1995 *Diode Lasers and Photonic Integrated Circuits* (Chichester: Wiley).

An extensive textbook proceeding from the fundamentals of diode lasers to advanced photonic devices.

Ikegami T, Sudo S and Sakai Y 1995 *Frequency Stabilization of Semiconductor Laser Diodes* (Norwood, MA: Artech House)

A rather complete compilation of the various techniques for frequency stabilization of laser diodes and their practical performance.

Morthier G and Vankwikelberge P 1997 *Handbook of Distributed Feedback Laser Diodes* (Norwood, MA: Artech House)

A detailed monography on distributed feedback laser diodes with particular emphasis on the theoretical description and design.

Ohtsu M 1996 *Frequency Control of Semiconductor Lasers* (Chichester: Wiley).

A useful book on theory and performance of frequency control techniques for laser diodes.

Taylor & Francis
Taylor & Francis Group
http://taylorandfrancis.com

14

High-Speed Laser Diodes

Peter P. Vasil'ev

CONTENTS

14.1 Introduction 211
14.2 Dynamics of Laser Diodes 212
    14.2.1 Review of Rate Equations for Study of Dynamics 212
    14.2.2 Modulation Bandwidths and Damping 213
    14.2.3 Frequency Chirp and Spectral Control 215
    14.2.4 Noise 216
14.3 High-Speed Laser Diode Design 216
    14.3.1 Device Optimization 216
    14.3.2 Microwave Propagation Effects 217
14.4 External Modulation 217
14.5 Ultrashort Pulse Generation 218
    14.5.1 Gain and Q-Switching 218
    14.5.2 Mode Locking of Laser Diodes 220
    14.5.3 Femtosecond Superradiant Pulse Generation 221
14.6 Future Trends in High-Speed Diode Lasers 222
References 223

14.1 Introduction

A wide range of potential applications for high-speed optical pulse sources includes fibre optic communications, high-speed sampling and signal processing, ultrafast analogue to digital conversion, terahertz wave generation, microwave and millimetre-wave measurement, optical time division multiplexed transmission, optical clock distribution and acquisition, ultra-high-speed logic and fibre radio. Diode lasers capable of being modulated at very high bit rates are key requirements for many of these applications. The major feature of the laser is its ability to generate modulated optical signals as a result of the direct injection of electrical currents. Hence, the dynamic response and modulation behaviour of lasers are of great importance for many applications and have been extensively studied for many years.

High-speed modulation can be realized either internally or externally. Directly modulated laser diode systems are simpler to implement compared with external modulation. They can be fabricated in conjunction with the drive electronics of the transmitter circuitry on the same wafer to make up optoelectronic integrated circuits. A number of external modulators, including electroabsorption and electrorefractive modulators, can be used for ultrafast external modulation and data encoding, which can often provide less frequency chirp than that under direct modulation.

In principle, two aspects to designing high-speed diode lasers exist. The first one is the physical aspect which involves the optimization of the laser active area, taking into account an enhancement of the differential gain, decreasing the threshold current, minimizing the carrier transport effects in quantum well (QW) lasers, etc. The other is the device aspect, which involves the fabrication of a structure and a laser cavity, minimization of the parasitic capacitance and series resistance, etc. Both these aspects are thought to be of equal importance for the realization of practical high-speed diode lasers and are discussed here.

Very high bit rate communication systems with a capacity of 160 Gbit s^{-1} and higher require sources of ultrashort optical pulses. Laser pulses shorter than 10 ps with minimum possible bandwidths (bandwidth-limited pulses) are necessary to ensure such speeds of data transmission and processing. Both gain/Q-switching and mode-locking (ML) techniques have been widely used to generate picosecond and femtosecond optical pulses from diode lasers. A relatively new technique, namely superradiance (SR), allows for generating ultra-high power femtosecond pulses on demand. A number of methods for external optical pulse compression, including the soliton effect, have been often utilized to produce even shorter pulses than lasers can generate themselves.

14.2 Dynamics of Laser Diodes

14.2.1 Review of Rate Equations for Study of Dynamics

The dynamics of diode lasers, including laser modulation and ultrashort pulse generation, have been conventionally modelled using a set of a few coupled first-order differential equations [1–4]. The simplest rate equations consist of just two equations, one for the carrier density n in the active area and the other for the photon density S in the laser cavity

$$\frac{\mathrm{d}n}{\mathrm{d}t} = \frac{j(t)}{ed} - g_0\left(n - n_\mathrm{t}\right)S - \frac{n}{\tau_\mathrm{S}} \tag{14.1}$$

$$\frac{\mathrm{d}S}{\mathrm{d}t} = \Gamma g_0\left(n - n_\mathrm{t}\right)S - \frac{S}{\tau_\mathrm{ph}} + \frac{\beta\Gamma n}{\tau_\mathrm{S}} \tag{14.2}$$

where n_t is the transparency density, g_0 is the differential gain coefficient, β is the spontaneous coupling factor, e is the electron charge, d is the active layer thickness, j (t) is the current density, Γ is the optical confinement factor and τ_s and τ_ph are the carrier and photon lifetimes. Here, the optical gain is assumed to be proportional to the carrier concentration. These simple equations are written on the assumption that the laser operates in a single longitudinal and transverse mode, that is, they do not take into account the distribution of S between any multiple cavity modes. τ_ph is given as [1]

$$\tau_\mathrm{ph} = 1\big/\left[\upsilon_\mathrm{g}\left(\alpha_\mathrm{m} + \alpha_\mathrm{i}\right)\right] \tag{14.3}$$

where υ_g is the group velocity of light and α_m and α_i are the mirror and internal loss, respectively.

To take the frequency dependence of the optical gain into account and to simulate multi-mode laser dynamics, the rate equations can be modified to the form [2,4],

$$\frac{\mathrm{d}n}{\mathrm{d}t} = \frac{j(t)}{ed} = \sum g_m S_m - \frac{n}{\tau_\mathrm{S}} \tag{14.4}$$

$$\frac{\mathrm{d}S_m}{\mathrm{d}t} = \Gamma g_m S_m - \frac{S_m}{\tau_\mathrm{ph}} + \frac{\beta\Gamma n D_m}{\tau_\mathrm{s}} \tag{14.5}$$

where $g_m = g_0(D_m n - n_\mathrm{t})$, S_m is the photon density in the mth laser mode and D_m is the line shape factor, which is defined, say, for Lorentzian shape as

$$D_m = \frac{\delta\lambda\big/\left(\pi\Delta\lambda_\mathrm{g}\right)}{1 + \left[\left(\lambda_m - \lambda_0\right)\big/\Delta\lambda_\mathrm{g}\right]^2} \tag{14.6}$$

where $\delta\lambda$ is the longitudinal mode spacing, $\Delta\lambda_\mathrm{g}$ is the gain bandwidth, λ_0 and λ_m are the wavelengths of the central and mth laser cavity mode. The total photon density is thus given by $S(t) = \Sigma S_m$. The evaluation of these multi-mode rate equations often gives more accurate results than those obtained using the single-mode Equations (14.1) and (14.2).

The linear dependence of the optical gain on the carrier density which is assumed in Equations (14.1)–(14.2) and (14.4)–(14.5) is an approximation. In fact, an additional non-linear dependence of the optical gain upon the photon density is observed [2]. In particular, the gain non-linearity manifests itself in long-wavelength InP/InGaAsP lasers and QW lasers. A number of physical processes, the most important of which are spectral hole burning, spatial hole burning and carrier heating, are generally thought to be responsible for gain non-linearity in diode lasers [2,3]. An analytical expression of gain $g(n, S)$, accounting for the effects of photon density, is generally written as

$$g(n,S) = \frac{g_0\left(n - n_t\right)}{\left(1 + \varepsilon S\right)^m} \tag{14.7}$$

where ε is the non-linear gain compression coefficient [3] and m is a fitting constant, which is often thought to take a value of either unity or a half. Non-linear gain effects play a significant role in laser diode dynamics. They impact on the modulation bandwidth of lasers and other modulation properties and determine the minimum achievable pulse widths and maximum peak power levels of ultrashort pulses from diode lasers.

The carrier density variations across the laser active region and the associated effects of lateral carrier diffusion on the dynamic properties have been neglected in the rate equations (14.1)–(14.2) and (14.4)–(14.5). This is thought to be a good approximation in high-speed diode lasers because they have typically active regions, which are sufficiently narrow in the lateral dimension. In contrast, carrier transport effects in the direction of current injection (the transverse direction) are very important in modern QW high-speed lasers and should be included [3,5]. QW lasers are different from bulk ones, where the entire undoped region is the active area and the carrier transport effects are not significant. For instance, electron and hole transport in QW lasers with a separate confinement heterostructure (SCH) consists basically of two parts. The first is the transport of carriers across the SCH from the doped cladding layers to the QW region, whereas the second is carrier capture by the QW. Thermionic emission or the thermally activated carrier escape from the QW and tunnelling between the QWs are other transport mechanisms, which strongly affect high-speed laser dynamics.

The rate equation model derived for high-speed multiple QW (MQW) lasers, taking into account all carrier transport effects, is based upon the equations describing the dynamics of the carrier densities in the QW N_w and in the SCH layer N_b, and the photon density dynamics in the laser cavity. They can be written as follows [5]

$$\frac{\mathrm{d}N_\mathrm{b}}{\mathrm{d}t} = \frac{I(t)}{eV_\mathrm{SCH}} - \frac{N_\mathrm{b}}{\tau_{\mathrm{n}_1}} + \frac{N_\mathrm{w}}{\tau_\mathrm{e}}\frac{V_\mathrm{W}}{V_\mathrm{SCH}} \tag{14.8}$$

$$\frac{\mathrm{d}N_\mathrm{w}}{\mathrm{d}t} = -\frac{G\left(N_\mathrm{w}\right)S}{1 + \varepsilon S} - \frac{N_\mathrm{w}}{\tau_\mathrm{e}} - \frac{N_\mathrm{w}}{\tau_{\mathrm{n}_2}} + \frac{N_\mathrm{b}}{\tau_\mathrm{tr}}\frac{V_\mathrm{SCH}}{V_\mathrm{w}} \tag{14.9}$$

$$\frac{\mathrm{d}S}{\mathrm{d}t} = \frac{\Gamma G\left(N_\mathrm{W}\right)S}{1 + \varepsilon S} - \frac{S}{\tau_\mathrm{ph}} + \frac{\beta\Gamma N_\mathrm{W}}{\tau_{\mathrm{n}_2}} \tag{14.10}$$

where V_SCH is the volume of the SCH, V_w is the volume of the QW, τ_{n_1} and τ_{n_2} are the carrier recombination lifetimes in the SCH and active regions, respectively, τ_tr is the carrier transport time across the SCH region which also includes the local capture time at the QW, τ_e is the carrier thermionic emission time from the QW into the SCH layer and $G(N_w)$ is the carrier-density-dependent gain. Note that the non-linear gain has been taken into consideration here using Equation (14.7) with $m = 1$.

Much progress in ultrafast diode lasers has been recently made with the use of quantum dot (QD) lasers [6]. QD material has proved especially well suited to short pulse generation due to its broadband gain spectra and ultrafast carrier dynamics. High-speed QD lasers are often modelled as three-level systems comprising a wetting layer (WL), a QD-excited state (ES) and a QD ground state (GS). Here, the SCH layer is not included as it is thought that the important carrier dynamics take place in the WL and the QDs. Carriers injected into the WL are first captured into the QD ES with a time constant τ_c, and then they relax into the QD GS with a time constant τ_0. The carrier escape occurs due to thermal excitation at rates $\tau_{esc}{}^{G}$ and $\tau_{esc}{}^{E}$ for the GS and ES, respectively. The carrier rate equations are similar to Equations (14.8) and (14.9) and are [7]

$$\frac{\mathrm{d}N_\mathrm{W}}{\mathrm{d}t} = \frac{\eta I}{eV_\mathrm{W}} + \frac{N_\mathrm{E}}{\tau_\mathrm{esc}^\mathrm{E}}\frac{V_\mathrm{D}}{V_\mathrm{W}} - N_\mathrm{W}\frac{1-f_\mathrm{E}}{\tau_\mathrm{c}} - \frac{N_\mathrm{W}}{\tau_\mathrm{r}^\mathrm{W}} \tag{14.11}$$

$$\frac{\mathrm{d}N_\mathrm{E}}{\mathrm{d}t} = N_\mathrm{W}\frac{1-f_\mathrm{E}}{\tau_\mathrm{c}}\frac{V_\mathrm{W}}{V_\mathrm{D}} + N_\mathrm{G}\frac{1-f_\mathrm{E}}{\tau_\mathrm{esc}^\mathrm{G}} - \frac{N_\mathrm{E}}{\tau_\mathrm{esc}^\mathrm{E}} - N_\mathrm{E}\frac{1-f_\mathrm{G}^\mathrm{e}}{\tau_0} - \frac{N_\mathrm{E}}{\tau_\mathrm{r}^\mathrm{E}} \tag{14.12}$$

$$\frac{\mathrm{d}N_\mathrm{G}}{\mathrm{d}t} = N_E\frac{1-f_\mathrm{G}^\mathrm{e}}{\tau_0} - N_\mathrm{G}\frac{1-f_\mathrm{E}}{\tau_\mathrm{esc}^\mathrm{G}} - \frac{N_\mathrm{G}}{\tau_\mathrm{r}^\mathrm{EG}} - v_\mathrm{g}g\left(f_\mathrm{G}^\mathrm{e} + f_\mathrm{G}^\mathrm{h} - 1\right)S \tag{14.13}$$

The photon rate equation is given by

$$\frac{\mathrm{d}S}{\mathrm{d}t} = v_\mathrm{g}g\left(f_\mathrm{G}^\mathrm{e} + f_\mathrm{G}^\mathrm{h} - 1\right)S + \beta\frac{N_\mathrm{G}}{\tau_\mathrm{sp}} - \frac{S}{\tau_\mathrm{ph}} \tag{14.14}$$

Some dynamic regimes of high-speed diode lasers, including Q-switching and ML of multiple contact lasers, in particular, require travelling-wave rate equations rather than 'space-averaged' ones. Indeed, those lasers have a nonuniform distribution of driving current along the laser cavity axis or unpumped passive sections, which result in inherently nonuniform distributions of both carrier and photon densities along the cavity axis. To account for these space distributions, one needs to include spatial coordinates into the equations. This is particularly important when the generation of ultrashort light pulses with a spatial length smaller than or about the cavity length is described. Travelling-wave rate equations, which become partial differential equations, are often written as follows [2]:

$$\frac{\partial S^+}{\partial t} + \upsilon_\mathrm{g}\frac{\partial S^+}{\partial z} = \frac{\Gamma g_0\left(n - n_\mathrm{t}\right)S^+}{1 + \varepsilon\left(S^+ + S^-\right)} - \upsilon_\mathrm{g}\alpha_\mathrm{i}S^+ + \frac{\beta n}{\tau_\mathrm{s}} \tag{14.15}$$

$$\frac{\partial S^-}{\partial t} - \upsilon_\mathrm{g}\frac{\partial S^-}{\partial z} = \frac{\Gamma g_0\left(n - n_\mathrm{t}\right)S^-}{1 + \varepsilon\left(S^+ + S^-\right)} - \upsilon_\mathrm{g}\alpha_\mathrm{i}S^- + \frac{\beta n}{\tau_\mathrm{s}} \tag{14.16}$$

$$\frac{\partial n}{\partial t} = \frac{j(z,t)}{ed} - g_0\left(n - n_\mathrm{t}\right)\left(S^+ + S^-\right) - \frac{n}{\tau_\mathrm{s}} \tag{14.17}$$

where $S^+(z, t)$ and $S^-(z, t)$ are forward and backward travelling waves (photon densities), respectively.

Boundary conditions are now necessary to solve the partial differential equations (14.15)–(14.17). The boundary conditions should include reflections of light at the laser facets and look like

$$S^+(0,t) \ = R_1 S^-(0,t)\ S^-(L,t) = R_2 S^+(L,t)$$

where R_1 and R_2 are the power reflectivities at the chip facets and L is the cavity length. Since all the rate equations are non-linear ones, it is very difficult to solve them analytically and numerical computations are generally required. However, equation linearization and small-signal analysis can be used to study laser dynamics in some cases. For instance, the modulation properties of high-speed lasers can be readily established analytically using the latter approach.

14.2.2 Modulation Bandwidths and Damping

The overall dynamic response of a laser includes the response of the package parasitics, the parasitics associated with the laser chip and the intrinsic laser, i.e. the active region and the cavity. The parasitics cause a high-frequency roll-off in the small-signal response of the laser, which slows down the fast transients of drive current waveforms. The small-signal response of the intrinsic laser is obtained by linearizing equations (14.1) and (14.2) using

$$I(t) = I_0 + i\mathrm{e}^{\mathrm{i}\omega t} \quad N(t) = N_0 + n\mathrm{e}^{\mathrm{i}\omega t} \quad S(t) = S_0 + s\mathrm{e}^{\mathrm{i}\omega t}$$

with

$$i \ll I_0, n \ll N_0, s \ll S_0,$$

where $I(t)$ is the small-signal current modulation and N_0 and S_0 are the steady-state (average) carrier and photon densities, respectively. The small-signal analysis of the rate equations gives the intrinsic frequency response $R_\mathrm{int}(\omega) = |M(\mathrm{j}\omega)/M(0)|$ as

$$R_\mathrm{int}(\omega) = \frac{\omega_0^4}{\left(\omega^2 - \omega_0^2\right)^2 + \omega^2\gamma^2} \tag{14.18}$$

where $\gamma = g_0 S_0$ is the damping rate and the resonant frequency ω_0 is given by

$$\omega_0^2 = \frac{g_0 S_0}{\tau_\mathrm{ph}}. \tag{14.19}$$

Figure 14.1 illustrates the general form of $R_\mathrm{int}(\omega)$ for two values of S_0. A resonance in modulation response at ω_0 is known as the relaxation oscillation and its strength depends on the spontaneous emission factor, carrier diffusion, carrier transport effects, etc. Typical values of $\omega_0/2\pi$ are in the range of 1–10 GHz. Above the resonance peak, the magnitude of the intrinsic response approaches asymptotically a slope of −40 dB/decade. A parameter $f_{3\,\mathrm{dB}} = \omega_{3\,\mathrm{dB}}/2\pi$ is widely referred to as the maximum modulation bandwidth of the laser. The 3-dB bandwidth is defined by setting $R(\omega) = 1/2$.

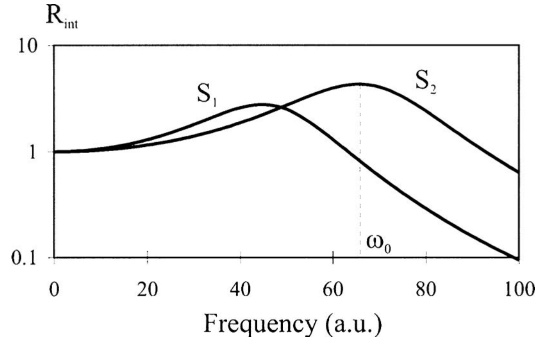

FIGURE 14.1 Small-signal AM response of a diode laser for two values of the photon density S_1 and S_2, $S_2 > S_1$.

There is a universal relationship between the resonant frequency and the damping rate. It has been demonstrated both experimentally and theoretically that γ varies linearly with $f_0^2 = (\omega_0/2\pi)^2$. The proportionality constant is called the *K*-factor [2]. The *K*-factor was originally defined given by $\gamma = Kf_0^2$. However, a dc offset is always observed and, hence, a better definition is $= Kf_0^2 + \gamma_0$. From this definition and using the small-signal solution of the rate equations, the *K*-factor is given by $K = 4\pi^2\tau_{ph}$. The *K*-factor is often taken as a figure of merit for high-speed lasers since the maximum possible intrinsic modulation bandwidth f_{max} (3-dB bandwidth) is determined solely by this factor [8]:

$$f_{max} = \sqrt{2}\left(2\pi/K\right) \approx 8.88/K. \tag{14.20}$$

In fact, the *K*-factor depends not only on the photon lifetime but it is also significantly affected by non-linear gain effects and carrier transport effects (in QW lasers). From the small-signal analysis of Equations (14.8)–(14.10) and for negligible τ_{n_1} and $\tau_n = \tau_{n_2}$, one obtains, for the resonant frequency and damping rate, the following analytical approximations [5]

$$\omega_0^2 = \frac{(g_0/\chi)S_0}{\tau_{ph}(1+\varepsilon S_0)}\left\{1 + \frac{\varepsilon}{g_0\tau_n}\right\} \tag{14.21}$$

$$\gamma = \frac{(g_0/\chi)S_0}{1+\varepsilon S_0} + \frac{\varepsilon S_0}{\tau_{ph}(1+\varepsilon S_0)} + \frac{1}{\chi\tau_n} \tag{14.22}$$

where the carrier transport factor χ is given by $\chi = 1 + \tau_{tr}/\tau_e$. The *K*-factor in this case is given by

$$K = 4\pi^2\left(\tau_{ph} + \frac{\varepsilon}{g_0\chi}\right). \tag{14.23}$$

There are a number of laser parameters to optimize if one wants to design a laser with the maximum possible modulation bandwidth. More specifically, the differential gain g_0, the photon density S_0 and the carrier escape time τ_e should be maximized, whereas the carrier transport time τ_{tr}, the photon lifetime τ_{ph}, the gain compression factor ε and device parasitics should be as small as possible. The use of QWs, wires and QDs instead of bulk materials for the active layers of high-speed diode lasers has been predicted to increase the differential gain strongly. It has been demonstrated [2,5,9,10] that, in contrast to bulk lasers, g_0 in QW lasers is a structure-dependent parameter, i.e. it is not only determined by the material parameters of the active layer but also influenced by the dimensions of the QW and barrier layers, optical confinement factor and carrier injection and confinement processes. Wavelength detuning is considered to be a promising method of differential gain enhancement in laser structures, where the lasing wavelength can be fixed independently of the peak wavelength of the material gain, for instance, in distributed feedback (DFB) lasers. The differential gain is larger on the 'blue' wavelength side of the gain distribution. Thus, negative detuning of the lasing wavelength from the material gain peak is often exploited in both bulk and QW DFB lasers.

Strained-layer QW structures have recently received a lot of attention since an in-plane comprehensive strain can reduce the valence-band effective masses, which leads to further enhancement of differential gain. P-doping and modulation doping of the active layer have been predicted and demonstrated to enhance the differential gain and decrease the *K*-factor of high-speed QW lasers. p-doped lasers demonstrate very efficient high-speed direct modulation. A maximum possible intrinsic bandwidth of 63 GHz (a *K*-factor of 0.14 ns and the value of $\varepsilon = 4.6\times10^{-17}\text{cm}^3$) has been reported in strained InGaAs/GaAs MQW lasers [11]. In 1.5 µm InGaAsP/InP MQW strained p-doped lasers, an f_{max} as high as 40 GHz has been demonstrated [12]. The actual 3 dB modulation bandwidth of 25 GHz has been limited by the parasitics of the devices.

The photon density S_0 is related to the driving current I_0 (by the total output optical power) as follows

$$S_0 = \left(\frac{\Gamma}{V}\right)\frac{\eta(I_0 - I_{th})}{e\upsilon_g(\alpha_m + \alpha_i)} \tag{14.24}$$

where V is the volume of the active region, η is the injection efficiency and I_{th} is the threshold current. Although high output power levels of a high-speed diode laser are highly desirable for large modulation bandwidths, it is the optical mode volume V/Γ that determines the photon density within the laser resonator. As a result, a large modulation bandwidth laser structure requires tight optical confinement within the laser cavity. Facet passivation and application of special coatings on device facets can substantially increase the power level of the optical damage of the facets and allows for an enhancement of values of S_0.

The effects of carrier transport on the modulation bandwidth are evident from Equations (14.21)–(14.23). The first effect consists in a parasitic-like roll-off in the modulation response, which would significantly limit the 3-dB modulation bandwidth for large τ_{tr}. This limitation, which originates from the finite transport time across the SCH, is indistinguishable from the parasitics [5]. The second effect is the reduction of the effective differential gain by a factor of χ. This leads to the reduction of the resonance frequency for the same power levels. To optimize the high-speed performance of QW lasers, the transport time across the SCH has to be minimized. A narrower SCH should result in shorter τ_{tr}. However, decreasing the SCH width below an optimum point will also lead to a drop in the optical confinement factor and an increase of the internal loss. This, in turn, results in a higher carrier density at threshold and, consequently, a lower differential gain, which originates from rapid gain saturation in QW lasers.

It has been demonstrated that vertical-cavity surface-emitting lasers (VCSELs) have a very large modulation bandwidth of over 70 GHz. The physical reason for such enormous increase in the bandwidth is that VCSELs have very short cavity lengths, which result in a substantial reduction of the photon and electron lifetimes.

The direct modulation bandwidth can be extended considerably by introducing a supplementary high-frequency resonance of the laser. Photon–photon resonance (PPR) is one of the ways to achieve a large modulation bandwidth as an alternative to conventional carrier-photon resonance, which has been discussed above. The PPR has been obtained by the interaction of two longitudinal modes in dual-mode multi-section DFB lasers. In addition, several candidates that utilize PPR, including the transverse-coupled-cavity VCSELs, DFB lasers with a laterally corrugated ridge waveguide, the intracavity loss modulation laser diodes, distributed Bragg reflector (DBR) lasers with antireflection coatings at the grating end facet and active multi-mode interferometer laser diodes, have been proposed [13]. The PPR technique allows for increasing the modulation bandwidth of diode lasers by a few GHz. A design procedure to exploit the PPR effect to extend the modulation bandwidth in DBR lasers has been presented and validated in Ref. [14]. It allows precise positioning of the required PPR frequency.

14.2.3 Frequency Chirp and Spectral Control

Carrier density variations which occur under high-speed modulation result in a corresponding change in the refractive index in the laser cavity. This change, in turn, causes a variation in the lasing wavelength (or the oscillation frequency) which is referred to as wavelength chirping. Enhanced linewidth and frequency chirp under dc modulation can also originate from the finite difference in the carrier density between the 'on' and 'off' states of the laser. The chirping response of a laser can be determined by means of the rate equations with an additional differential equation describing the evolution of the optical phase $\phi(t)$, which is given by [2]

$$\frac{\mathrm{d}\phi}{\mathrm{d}t} = \frac{1}{2}\left\{\frac{\Gamma g_0(N - N_\mathrm{t})S}{1 + \varepsilon S} - \frac{1}{\tau_\mathrm{ph}}\right\} \tag{14.25}$$

where α is the linewidth enhancement factor. The linewidth enhancement factor, describing the coupling between the carrier-induced variation in the real $\mu(n)$ and imaginary $g(n)$ parts of the optical susceptibility, can be defined as [15]

$$\alpha = -2k\frac{\mathrm{d}\mu/\mathrm{d}n}{\mathrm{d}g/\mathrm{d}n} \tag{14.26}$$

where $k = 2\pi/\lambda$ is the free-space wavenumber. Since $\mathrm{d}\mu/\mathrm{d}n$ is negative, α is positive.

The frequency chirp is defined as $\Delta\nu(t) = (1/2\pi)\mathrm{d}\phi/\mathrm{d}t$. Using Equation (14.25), the chirp can be related directly to the output laser power $P(t)$ as

$$\Delta\nu(t) = \frac{\alpha}{4\pi}\left\{\frac{\mathrm{d}\ln P(t)}{\mathrm{d}t} + \frac{2\Gamma\varepsilon}{V\eta\hbar\omega}P(t)\right\} \tag{14.27}$$

where η is the laser differential quantum efficiency. The magnitude of the chirp represented by the first term in Equation (14.27) may be large during high-speed turn-on and turn-off transients, while being relatively small at the on and off levels. By contrast, the second term results in frequency offset between the on and off levels owing to a difference in the steady-state values of the carrier density. Under digital pulse modulation when zeros of the pulse sequence are close to threshold, shoulders can be apparent on both the long-wavelength and short-wavelength side of the optical spectrum. The former is caused by the relaxation oscillation and light present in the trailing edges and nominal zeros of the pulse stream, while the latter results from the relaxation oscillation at turn on.

From Equation (14.27), it is clear that the α-factor is a key parameter in obtaining low-chirp emission from high-speed directly modulated lasers. Hence, lasers with lower values of α should exhibit lower wavelength chirp under high-speed modulation. Typical values of α in most lasers lie in the range of 3–5 [2,3]. The development of laser structures with $\alpha < 2$ has attracted considerable attention in recent years. According to Equation (14.26), α is inversely proportional to the differential gain of the laser medium. Since the differential gain is enhanced in QW lasers, the α parameter has been predicted and observed to be reduced in this type of laser. Consequently, QW lasers are the most promising for low-chirp operation under high-speed modulation. However, α is a structure-dependent parameter and a parameter α_eff should be used in Equation (14.27) for the chirp evaluation. In the case of QWs, laser carrier transport, particularly carrier density variation in the SCH region, has a significant impact on α_eff and frequency chirping leads to enhanced values of it. An expression for α_eff can be written as

$$\alpha_\mathrm{eff} = \frac{4\pi}{g_0\lambda}\left[\frac{\partial n}{\partial N_{\mathrm{w}_0}} + \left(\frac{1}{\Gamma} - 1\right)\left(\frac{V_\mathrm{w}}{V_\mathrm{SCH}}\right)(\chi - 1)\left(\frac{\tau_\mathrm{b}}{\tau_\mathrm{b} + \tau_\mathrm{tr}}\right)\frac{\partial n}{\partial N_{\mathrm{b}_0}}\right] \tag{14.28}$$

where N_{w_0} is the steady-state carrier density in the QW, N_{b_0} is the steady-state carrier density in the SCH region and τ_b is the barrier transport time.

Strained-layer QW lasers exhibit lower values of α_eff when compared with their unstrained counterparts. For example, the α_eff parameter of an unstrained MQW DFB laser was estimated to be 3.1 at the 1.55 μm wavelength, while a similar laser structure with a compressive strain of 1.9% had a linewidth enhancement factor as low as 1.1 [16]. P-type modulation doping of QWs also results in decreasing the α-factor. Reduced wavelength chirp is thus expected in these lasers as a result of a reduction in the α_eff parameter. Since α_eff depends on wavelength, the frequency chirp of a laser can be controlled by detuning the lasing wavelength with respect to the gain profile peak.

14.2.4 Noise

Noise in diode lasers originates from both carrier density fluctuations and photon density fluctuations. The relative intensity noise (RIN) spectrum is commonly used to analyse the noise properties of high-speed diode lasers and to determine the modulation bandwidth [5,10]. The RIN is defined as the ratio of the intensity fluctuations to the averaged intensity. The RIN spectrum of a laser can be derived using the same formalism of the rate equations as before. The RIN spectrum can be written as

$$\mathrm{RIN}(f) = \frac{4}{\pi}(\delta f)_{\mathrm{ST}} \frac{f^2 + \left(\gamma^*/2\pi\right)^2}{\left(f_0^2 - f^2\right)^2 + \left(\gamma/2\pi\right)^2 f^2} \qquad (14.29)$$

where $(\delta f)_{\mathrm{ST}}$ is the intrinsic Schawlow–Townes linewidth, which derives from spontaneous emission and γ^* is given by

$$\gamma^* = \frac{\left(g_0/\chi\right)S_0}{1+\varepsilon S_0} + \frac{1}{\chi \tau_{\mathrm{n}}}.$$

The γ term is very close to γ^* at sufficiently low powers and small ε. It is commonly believed that the RIN spectrum measurement is a parasitic-free means of determining the actual modulation performance of high-speed diode lasers. However, significant transport effects can strongly affect the results of RIN spectrum measurements.

Typical RIN spectra for two values of S_0 are shown in Figure 14.2. The RIN spectra have been plotted on a relative scale and do not give the actual noise level of the laser. The resonance frequency f_0 and damping γ can be defined from the RIN spectrum with a high degree of accuracy.

14.3 High-Speed Laser Diode Design

The device aspects of the requirements and techniques employed to design high-speed diode lasers comprise a variety of means, including decreasing the photon lifetime, decreasing the device size to eliminate microwave propagation effects, reduction of parasitic capacitance and series resistance, using semi-insulating substrates, etc. Device structures with low parasitics are considered to be of great importance since, in practice, the dominant limit to the modulation response of high-speed diode lasers is the device parasitics.

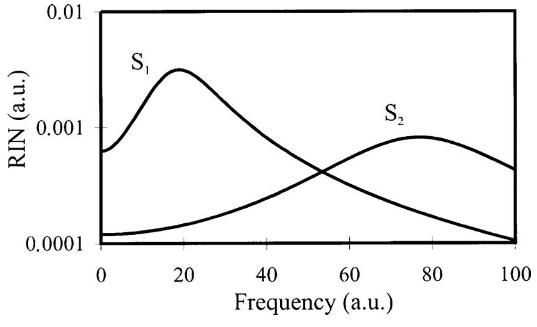

FIGURE 14.2 Typical RIN spectra for a diode laser.

14.3.1 Device Optimization

To disclose the effects of parasitics on device optimization, one should treat the laser as an electrical element and establish an equivalent circuit for the intrinsic laser in conjunction with the bond wire, the mount elements, the transmission line used for impedance matching, etc. A simplified equivalent circuit of a diode laser is shown in Figure 14.3a [2]. It includes the bond wire inductance L_{p}, the series resistance of the layers above and below the active layer R_{s}, the capacitance between the top and the bottom contact in the area outside the lasing region C_{p} and the intrinsic laser diode.

A more practical equivalent circuit should include additional *R*, *L* and *C* elements, which describe the parasitic elements of each particular device accurately. Figure 14.3b shows an example of an equivalent circuit of a double-heterostructure laser with an oxide isolation layer and blocking layers. The circuit includes a contact resistance R_{c}, an effective resistance in series with the active layer R_{a} and the blocking layer R_{b}, a parallel effective capacitance comprising the oxide isolation layer in series with either blocking layer C_{i}, a capacitance of the blocking layer C_{b} and the diffusion capacitance of the device C_{j}.

The input resistance of the intrinsic laser is approximately given by $2kT/eI_0$ and is typically less than 1 Ω [3] at currents I_0 above threshold due to clamping of the Fermi levels. Typical values of R_{s} for high-speed diode lasers can be in the range of 2–4 Ω [4]. The use of p-type substrates instead of the typical n-type has been proposed for the fabrication of lower resistance high-speed lasers. The actual device resistance is constrained by the maximum doping in the cladding for acceptable levels of loss due to free-carrier absorption and the minimum cladding layer thickness required for good transverse optical confinement.

The *RC* constant characterizing the parasitic roll-off in the overall response is given by the product of R_{s} and the effective shunt capacitance C_{i}. In some lasers C_{i} was measured to be as large as 40 pF while in low-parasitic devices it can be as low as 1–3 pF. To minimize the parasitic capacitance, a number of structures have been developed [2–4]. They include polyimide-buried ridge waveguide geometry structures, undercut 'mushroom' mesa-type structures, devices with

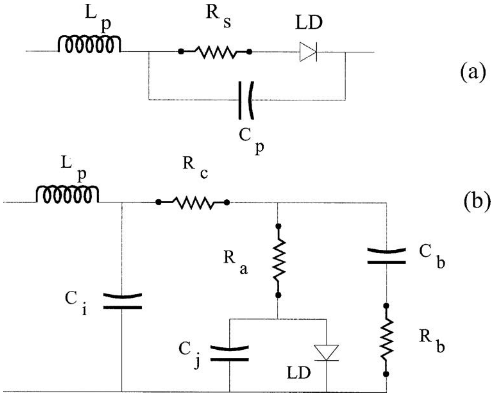

FIGURE 14.3 Equivalent circuits of a laser diode: (a) simplified circuit and (b) small-signal circuit of a double-heterostructure laser.

isolation channels in a buried heterostructure configuration and Fe-doped semi-insulating InP-based structures.

If the bond wire inductance L_p is less than 0.2 nH, it has little effect on the laser response up to 20 GHz. L_p depends on the length of the wire, its diameter and its proximity to the ground plane. Low inductance can be achieved using a short (<1 mm) wire or with a tape or mesh instead of the usual thin wire. An inductance L_p above 1 nH results in significant roll-off in the laser response at frequencies above 6 GHz. The R_sC_i product of the chip dominates in the case of small L_p and these parasitics must be minimized if a high-speed operation is to be achieved.

14.3.2 Microwave Propagation Effects

As the modulation speed increases above 20–30 GHz, the laser size becomes very critical. Conventional designs that treat a laser diode as a lumped electrical element as presented in Figure 14.3 are valid only when the laser cavity length is much smaller than the modulation wavelength. This is not the case for modulation frequencies of 25–30 GHz and higher and cavity lengths of about 300 μm. In addition, at very high frequencies, the time delay from the feed point of the modulation current to the far end of the laser can be a significant fraction of the modulation period. The high-frequency current injection and the optical modulation response are, thus, modified by the distributed microwave nature of the laser. It is thought that microwave propagation effects put an ultimate limit on the modulation bandwidth.

The distributed circuit laser model shown in Figure 14.4 was proposed as a first-order estimation of the propagation effects [17]. The total current flowing into the device is a sum of all currents flowing through the distributed resistors R_s (injection current) and through the distributed capacitors C_s (displacement current). The active region laser impedance is Z_d. A sizeable frequency-dependent current loss and change of the phase velocity caused by the microwave propagation effects which must be taken into consideration in laser design at very high frequencies exist. As the frequency increases, the loss increases as well. This, in turn, leads to a roll-off in the current injection into the active region. The estimated 3-dB roll-off frequency happens at approximately 25 GHz for a 300-μm long laser when the device is fed at the centre of the laser stripe. This is considered to be the optimal feeding condition since waves can propagate in either direction from the centre of the cavity.

14.4 External Modulation

An alternative approach to high-speed modulation of semiconductor laser emission is to use an external modulator instead of internal modulation. An external modulator can be either monolithic (integrated) or a separate device. External modulation of laser emission has significant advantages over direct modulation because frequency chirping is low and modulation at very high frequencies (>40 GHz) is possible. Electroabsorption (EA) and electrorefraction (ER) modulators are the most commonly utilized types of external modulators for high-speed modulation and data encoding [18,19]. Among various designs of external modulators for practical applications, waveguide (in-plane) and surface-normal (transverse) devices are the most widely used configurations. Waveguide devices tend to provide low drive voltages since the electric field is applied perpendicular to the light propagation direction. At the same time, the coupling of the light into the modulator waveguide adds some complexity to practical implementation. However, surface-normal devices exhibit much higher drive voltages due to their shorter interaction lengths [19].

Highly efficient modern EA and ER modulators exploit either the Franz–Keldysh effect in bulk semiconductor materials or the quantum-confined Stark effect in MQW heterostructures. The latter refers to the redshift of the exciton absorption peak of the QW when an electric field is applied in the perpendicular direction. Extremely large absorption changes of 5×10^3–$10^4\,\text{cm}^{-1}$ are readily achievable in MQW waveguide modulators at reasonably low electric fields and small drive powers [19]. By virtue of their small dimensions, the speed of devices may be very high because the *RC* time constant is small.

In an EA waveguide modulator, the transmitted optical power coupled into the waveguide is attenuated by a factor of $\exp\{-\alpha(V)L\}$ which is dependent on the absorption coefficient α at the applied voltage V and the length of the device L. The efficiency of the modulator depends on how close the optical wavelength is to the EA peak. However, there will always be substantial insertion loss in well-designed EA waveguide modulators. A typical EA modulator structure is schematically shown in Figure 14.5. It consists of an EA modulator section with a semi-insulating buried heterostructure and a DFB laser section. Both the active layer and absorption layer consist of either bulk or SCH MQW structures with slightly different material compositions and thicknesses. An additional buffer

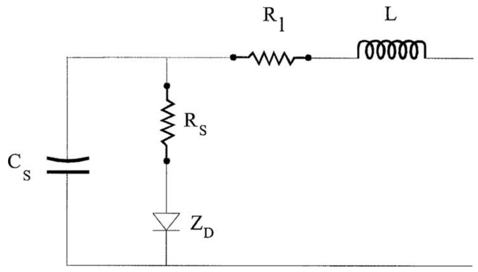

FIGURE 14.4 Distributed equivalent circuit of a diode laser.

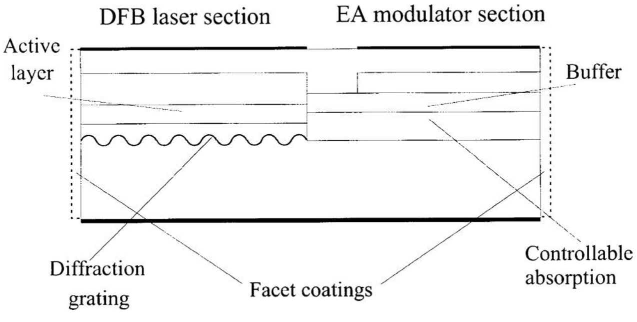

FIGURE 14.5 Electroabsorption modulator integrated with a DFB laser.

layer is often introduced between the upper cladding layer and the modulator waveguide layer to reduce the hole pile-up effect at high optical power levels. The modulating electric field is created by applying a voltage to the pin structure of the modulator section, the MQWs being enclosed in the i-region. Lengths of the EA modulator section and the DFB laser section are typically 100–250 and 200–450 μm, respectively. Antireflection coatings on the facets are used for optimizing the output power. The electrical isolation resistance between the two sections usually exceeds 1 MΩ [19]. Typical driving voltages for a 10-dB extinction ratio can be as low as 1.0–3.0 V_{p-p}. In principle, *RC*-limited bandwidths of over 30–40 GHz with a very low drive voltage ranging from 1–2 V can be achieved by optimizing both material and waveguide design simultaneously. It has been recently demonstrated over the 50-Gb s^{-1} operation with a 200-μm-long EA modulator section [20].

14.5 Ultrashort Pulse Generation

The generation of ultrashort optical pulses is another important field of applications of semiconductor lasers. A wide gain bandwidth of a semiconductor medium potentially allows optical pulses as short as 50–100 fs to be generated [2]. A number of methods for the generation of picosecond and femtosecond pulses in diode lasers have been developed. The main techniques include gain-switching, Q-switching, different types of mode locking and SR.

14.5.1 Gain and Q-Switching

The idea of gain switching was initially conceived as a result of early observations of the relaxation oscillations generated by a diode laser simply being turned on from below threshold by electrical pulses with a fast leading edge. Gain switching therefore consists of exciting the first pulse of a relaxation oscillation and then terminating the electrical pulse before the onset of the next optical relaxation pulse. Typical pulse widths of electrical pulses are in the range of 50–1000 ps. Alternatively, modulation of a laser biased below threshold with a large sinusoidal signal at sub-GHz or GHz frequencies can result in gain-switched optical pulses.

Dc bias I_0 and pulsed I_1 currents are assumed to be applied to the laser under gain switching. I_0 can be set to be below the laser threshold level. The lasing does not thus occur until the electrical pulse I_1 causes the carrier density in the laser to increase to above the device threshold density. Above this level, the carrier density reaches its maximum value n_i. Then lasing starts and represses the increase in carrier density and, consequently, $n(t)$ is pulled down to its minimum value n_f. Using the rate equations (14.1) and (14.2), one can approximately describe a gain-switched pulse as a combination of two exponential curves with the time constant τ_r on the rising edge of $S(t)$ and τ_f on the trailing edge. According to Equation (14.2), for a sufficiently small value of S, gain compression is negligible and $S(t)$ increases exponentially as a result of stimulated emission:

$$\frac{1}{S}\frac{\mathrm{d}S}{\mathrm{d}t}=\frac{1}{\tau_r}=g_0\Gamma\left(n_i-n_{th}\right). \tag{14.30}$$

The trailing edge of the optical pulse also exhibits an exponential decay constant and, normally, τ_f approximately equals (Equations (14.2) and (14.3)) τ_r or $\tau_f = \tau_r + \tau_{ph}$. The full-width at half-maximum (FWHM) of the pulse can be roughly estimated by the sum $\tau_f + \tau_r$. As a result, the pulse duration is limited by the rate of energy transfer between electron and photon populations. From Equation (14.30), it is clear that there is a corresponding improvement in the temporal response of gain-switched pulses if g_0 increases.

In practice, the generated optical pulse widths are of the order of several cavity round-trip times. It has been observed that the pulse width decreases and the peak power increases with increasing rf power until a point at which a second relaxation oscillation pulse appears. For most standard devices, pulse widths as low as 7–12 ps can be achieved at repetition rates of the order of 1 GHz for GaAs/AlGaAs lasers and 25–30 ps at the 1.5 μm wavelength. It is thought that gain-switched optical pulses generated in InGaAsP lasers are longer than pulses in the 0.85 μm wavelength region due to enhanced non-linear gain compression in quaternary lasers.

The peak powers of gain-switched pulses typically lie in the range of 0.1–1 W at the approximately 850 nm wavelength and from 10 to 100 mW for 1.3 or 1.5 μm InGaAsP lasers. Again, the peak powers for the InGaAsP systems are lower because of enhanced non-linear gain compression. More recently, gain switching of VCSELs has been demonstrated, the shortest pulse durations being below 15 ps.

Pulse-to-pulse timing jitter is an important parameter of gain-switched pulses as, for many applications, the timing jitter may affect dramatically the performance of a system where the laser is used. The timing jitter of gain-switched pulses originates from random fluctuations of the photon density in the laser cavity caused by the spontaneous emission. Typical values of timing jitter lie in the range of 1–10 ps. The jitter decreases as the ratio I_1/I_{th} increases and it can be less than 1 ps in multi-mode Fabry–Pérot lasers, where large levels of spontaneous emission act to reduce the turn-on jitter effect.

The optical bandwidth of picosecond pulses is another key parameter that plays a crucial role in a number of applications of gain-switched lasers. For instance, an excessive emission bandwidth results in a significant dispersion penalty in optical communication systems and can be the limiting factor in their performance. In Fabry–Pérot gain-switched lasers, a larger number of longitudinal modes are generated under gain switching than in steady-state operation as a consequence of the dynamic overshoot of electron concentration. This can occur even if the laser emission is single mode at a steady state. If a single-frequency laser is used for gain switching, a multi-mode operation can be avoided. However, the bandwidth under gain switching exceeds the bandwidth under cw operating conditions. Due to wavelength chirp, gain-switched pulses have a time-bandwidth product $\Delta\tau\Delta\nu$, which is often far from the theoretical limit for bandwidth-limited pulses. Gain-switched lasers can be used for robust, high-speed random number generation; for frequency comb generation, they can be readily amplified up to MW-level peak powers [21].

Picosecond optical pulses may also be generated in a semiconductor laser by a Q-switching technique. Here, current is applied to the gain section of a multi-section laser in which at least one section acts to switch the Q-factor of the cavity. While the laser population inversion is building up, the Q-switch is held in the 'off' or high-loss state, ensuring a low Q. As the carrier density in the laser reaches its peak, the cavity is suddenly switched to the high-Q condition and the stored energy is rapidly emitted in an output optical pulse. If the switching is caused by external influence, the technique is called active Q-switching. However, pulse generation can also be achieved by passive Q-switching by using an optically saturable absorber as the Q-switching element. Unlike other types of lasers, it is possible simply to divide the diode into several sections and apply different currents to them. The parts of the laser with high current injection act as the gain medium, while the unpumped sections or sections with a low pumping rate act as absorbers. Active Q-switching can be realized by modulation of the loss in the cavity. The modulation of loss in diode lasers is realized by shifting the band edge in the modulator section using the Franz–Keldysh effect or the quantum-confined Stark effect in MQW lasers caused by an applied electric field.

It can be shown that the Q-switched pulse parameters are drastically dependent on the photon life-time τ_{ph} and on the initial inversion level n_{i}. One can deduce this from consideration of the basic rate equations (14.1) and (14.2). When the ultrashort pulse is emitted, stimulated emission is the dominant mechanism and the contributions of all other processes, including spontaneous emission, carrier pumping and recombination, are negligible. Thus, using Equations (14.1) and (14.2), one can derive the following relation between carrier and photon densities in the laser cavity [2]:

$$S(t) = n_{\mathrm{i}} - n(t) - \frac{1}{g_0 \tau_{\mathrm{ph}}} \ln \frac{n_{\mathrm{i}} - n_{\mathrm{t}}}{n(t) - n_{\mathrm{t}}}. \tag{14.31}$$

By introducing the inversion ratio r and the energy extraction efficiency η as [1,2]

$$r = g_0 \tau_{\mathrm{ph}} (n_{\mathrm{i}} - n_{\mathrm{t}}) \quad \text{and} \quad r = \frac{1}{\eta} \ln \frac{1}{1-\eta}$$

the peak power of the Q-switched pulse is given by

$$S_0 = \frac{r - 1 - \ln r}{g_0 \tau_{\mathrm{ph}}} \tag{14.32}$$

and the pulse width of the pulse is

$$\tau_{\mathrm{Q}} = r \eta \tau_{\mathrm{ph}} \big/ \left(r - 1 - \ln r \right). \tag{14.33}$$

To obtain the shortest pulses, the initial inversion should be maximized, whereas the photon lifetime should be minimized.

Passive Q-switching is known as one of the simplest techniques for generating picosecond optical pulses in lasers. A difference between active and passive Q-switching is that, in contrast to active Q-switching, no external electrical or optical modulation is required for self-Q-switching to produce ultrashort optical pulses. Additionally, in the case of active Q-switching, the pulse repetition frequency is set by an external rf drive signal, whereas for passive Q-switching, the frequency is governed by the laser parameters and pumping conditions. As a result of the non-linear transmission characteristics of the absorber, the absorption of the leading edge of the pulse is typically larger than that of the trailing edge. This results in the generation of asymmetric pulses.

To generate self-Q-switched pulses, the saturable absorber in the laser cavity must satisfy a number of conditions. The most important parameters which affect the dynamic behaviour of the laser are the ratio of the differential loss, da/dn, of the absorber to the differential gain, dg/dn, of the amplifier section and the ratio of the carrier lifetime in the gain τ_{g} and the absorber τ_{a} sections. It can be shown [2] that for the generation of high-quality Q-switched pulses, the condition

$$\frac{\mathrm{d}a/\mathrm{d}n}{\mathrm{d}g/\mathrm{d}n} > 1 \tag{14.34}$$

must be satisfied. Owing to the dependence of gain and absorption on carrier concentration in lasers, the values of dg/dn and da/dn can be readily controlled by using different currents applied to different sections of the laser. As a result, the output performance is also dependent on the driving currents. The parameters of Q-switched pulses are dependent on the photon lifetime and the absorber recovery rate. Although the photon lifetime can be set by cavity design, the recovery of the absorber is due to the spontaneous recombination of excited electron–hole pairs. A number of techniques for decreasing τ_{a} have been developed. For example, proton or ion bombardment has been used to introduce a small region of saturable absorption having a very short carrier lifetime. Alternatively, a reverse bias can be applied on the absorber section of a multiple contact Q-switched laser to reduce τ_{a} [22]. Optical loss in the cavity can be changed by a reverse dc bias applied to the absorber section. The location of the absorber section at the middle between the gain regions and application of the reverse bias on the absorber result in the improvement of the pulse parameters generated by three section lasers as compared with the results for two-section devices.

Passive Q-switching exhibits relatively poor timing jitter. This is due to the influence of random spontaneous photons during the build-up of an ultrashort pulse in the laser cavity. The turn-on of a Q-switched pulse relies upon amplification of random spontaneous photons. In addition, the repetition rate of Q-switched pulses is very sensitive to variation in the applied bias currents; this also causes enhanced timing jitter. Many longitudinal modes of a Q-switched laser cavity may be excited as a consequence of the variation of carrier density during the emission of optical pulses. Self-Q-switched lasers normally have a spectral bandwidth as wide as 3–5 nm and thus generate picosecond pulses with time–bandwidth products that exceed, by several orders of magnitude, those for bandwidth-limited pulses. To reduce the spectral bandwidth of Q-switched pulses, single-frequency lasers such as DBR and DFB devices should be used. Using such devices, bandwidth-limited Q-switched operation can be achieved.

There exists another type of self-Q-switching in multiple-contact DFB lasers. It is called dispersive self-Q-switching because the Q-factor of the laser cavity is varied by dispersive effects in this case. Self-Q-switching can occur when the lasing wavelength coincides with a negative slope of the reflectivity of a DFB section. Through the linewidth enhancement factor α, an amplitude modulation causes a wavelength and feedback modulation. This type of Q-switching results in very high repetition rates of optical pulses in the range of 10–100 GHz [23].

14.5.2 Mode Locking of Laser Diodes

It is well known [1,2] that laser emission can be considered as a set of resonator modes ω_m, $m = 1, 2, 3...$, separated by $\delta\omega = \pi c/(\mu_g L)$, where μ_g is the group refractive index. The number of modes, which oscillate is limited by the spectral bandwidth $\Delta\omega_g$ over which the laser gain exceeds the cavity loss. The output therefore consists of the sum of oscillating modes and its electric field is given as (without taking into account the spatial distribution)

$$E(t)=\sum_{m} A_m \exp\left\{i\left[\left(\omega_0+m\delta\omega\right)t+\phi_m\right]\right\} \qquad (14.35)$$

where A_m and ϕ_m represent the amplitude and phase of the mth mode. In general, the relative phases between the modes are randomly fluctuating. If nothing fixes the phases ϕ_m, the laser output varies randomly in time, Alternatively, if the modes are forced to maintain a fixed phase and amplitude relationship, then the output of the laser has a periodic function of time, i.e.

$$E(t)=A_0\frac{\sin\left[(k+1)\delta\omega t_1/2\right]}{\sin\left[\delta\omega t_1/2\right]}\mathrm{e}^{i\omega_0 t} \qquad (14.36)$$

where k is the number of locked modes and $t_1 = t + \delta\phi/\delta\omega$. The operating conditions given by Equation (14.36) result in the generation of a train of regularly spaced optical pulses with a width of $\Delta\tau$, which is proportional to $1/\Delta\omega_g$. The pulse train has a temporal periodicity of $T = 2L\mu/c$ and the ratio of the period T to the pulse width is equal to the number of locked modes k. This dynamic regime is called mode locking. It is also possible to produce ML with several pulses inside the cavity spaced by a multiple of $c/2L\mu$. The basic advantage of ML is that much shorter pulses are generated than those produced using gain/Q-switching. ML can be realized using a number of techniques including active, passive and hybrid methods.

Active ML is achieved by modulation of the loss or gain of a laser at a frequency which is equal to the mode spacing $\delta\nu$ of the laser cavity. As a result, the phases of the modes are locked by the external modulation. Because of the very small dimensions of the lasers (the length of a cavity is typically 250–400 µm), $\delta\nu$ is very large (more than 100 GHz). Consequently, it is quite difficult to modulate the gain at such a frequency. A straightforward solution to this problem is, therefore, to increase the cavity length. If the cavity length is increased by placing the laser in an external resonator or using an extended monolithic cavity up to several millimetres long, the mode spacing is decreased and active ML can easily be realized.

The simplest method for realizing active ML is to place a laser in an external cavity, the most commonly used configurations of external resonators being shown schematically in Figure 14.6. ML in semiconductor lasers can also be achieved using phase-conjugate optical feedback. Phase-conjugate feedback, in contrast to ordinary feedback, directly couples pairs of longitudinal modes of a multi-mode laser. For certain strengths of phase-conjugate reflectivities, the phases and beat frequencies of various longitudinal modes become locked and the laser produces ultrashort pulses even though the laser is pumped continuously.

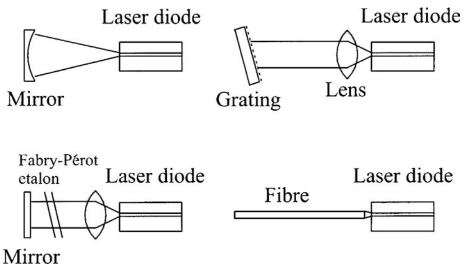

FIGURE 14.6 External cavity configurations of mode-locked diode lasers.

Unless special precautions are taken, the time–bandwidth product of ML pulses exceeds considerably the theoretical values for bandwidth-limited pulses. A number of methods for the restriction of the optical spectrum to a single mode of the laser have been used in external cavity lasers. Placing a Fabry–Pérot etalon in the cavity or using a diffraction grating as the external reflector, as shown in Figure 14.6, restricts the lasing spectrum considerably and leads to the generation of bandwidth-limited pulses. In this case, values of $\Delta\tau\Delta\nu$ lie in the range of 0.3–0.6. As mentioned earlier, Bragg reflectors can be integrated into the laser cavity, both in monolithic extended-cavity lasers and single-mode fibre composite cavity lasers for the same purpose.

In a similar manner to gain or Q-switched pulses, ML pulses exhibit wavelength chirping. The chirp leads to excessive values of the time–bandwidth product for ML pulses. Although the temporal variation of the instantaneous wavelength of the ML pulses is complex, the chirp is approximately linear near the peak of the pulses. The frequency chirp observed in actively ML lasers is of the opposite sign to that exhibited by passively ML lasers. This has been accounted for in terms of the different magnitudes and signs of the gain/refractive index coupling in the gain and absorber sections of the lasers. The frequency chirp, however, has been widely used for further pulse compression by external means.

Ultrashort pulse generation by a passively ML laser is schematically illustrated in Figure 14.7. The cavity configuration and the time-dependent gain and absorption loss in the laser are shown. The laser is driven by a dc and no external modulation is used. Before the arrival of the optical pulse, the loss and gain are approaching their steady-state values (broken curves in Figure 14.7), the loss being larger than the gain. Thus, the leading edge of the pulse experiences loss. In a passively ML laser the loss must saturate more quickly than the gain. When the gain becomes saturated below the unsaturated loss (due to mirror transmission, internal losses), the trailing edge of the pulse again experiences a loss. If the recovery time of the absorber is faster than that of the amplifier, then the loss remains greater than the gain everywhere except near the peak of the pulse. Spontaneous emission is not able

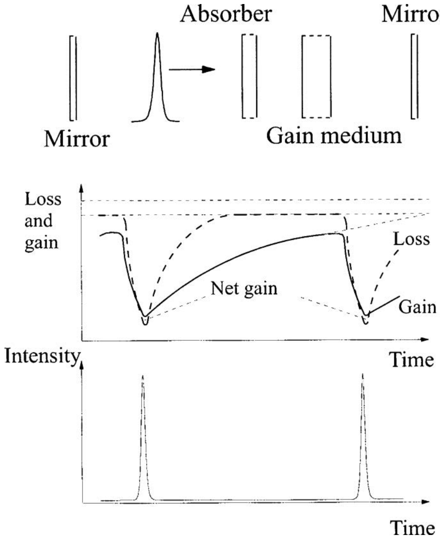

FIGURE 14.7 Passive mode locking with a saturable absorber: cavity configuration, gain and loss dynamics and optical output.

to build up between pulses. The unsaturated gain must also be greater than the unsaturated loss so that the laser oscillation can build up when the laser is turned on. On each round trip in the cavity, the combined action of the gain and loss saturation is to shorten the pulse by amplifying the peak of the pulse and attenuating the leading and trailing edges. In the steady state, this shortening is balanced by broadening mechanisms (detuning, dispersion and self-phase modulation). It is necessary to have substantial changes in both gain and loss during the passage of a pulse. Thus, it is desirable for the pulse repetition rate to be of the order of the gain or loss recovery time. Passive ML is a self-starting process and output pulses are formed from spontaneous fluctuations. The fundamental difference between passive ML and passive Q-switching is that in contrast to Q-switching where the pulse repetition rate is set by amplitudes of applied currents, the repetition rate of passive ML pulses is determined by the round-trip time of the laser cavity and is not dependent on the pumping conditions.

Colliding pulse mode (CPM) locking is an effective technique for generating ultrashort pulses in the femtosecond range [1,2,6]. This method is based upon the interaction of two counter-propagating optical pulses inside the saturable absorber of a laser with a linear or ring resonator. Coherent interaction of the pulses builds up a transient standing-wave optical field and a periodic saturation modulation in the absorber. This, in principle, should result in shorter pulses when compared with passive ML pulses obtained from the same laser. The counter-propagating pulses form transient standing waves in the absorber. The carrier generation rate is high at the peak of the standing wave while it is low at the nulls of the standing wave. The carrier density absorption grating facilitates the saturation of the absorber. The rigorous theory of the pulse collision effects in CPM lasers predicts the pulse width to be four times shorter at best than that for passive ML with the same absorber and gain medium and without pulse collisions [2,24]. It should be noted that the pulse collision effectively shortens ML pulses in thin saturable absorbers only, i.e. when the length of the absorber is less than the spatial dimension of the pulses. CPM can be obtained with a laser cavity configuration where a saturable absorber is placed near a highly reflecting mirror. In this case the transient absorber grating is formed by the interference of the incident and reflected pulses (self-colliding pulse configuration). Pulses as short as 500–600 fs can be produced in external cavity CPM diode lasers.

Monolithic cavity ML laser structures are very compact and do not exhibit the mechanical instabilities associated with optical elements in an external cavity [25]. Overall cavity lengths of monolithic ML lasers range typically from 0.25 to 7.0 mm, the corresponding repetition rates of the ML pulses varying from 5.5 to 350 GHz. Passive ML of cw monolithic lasers results in generating optical pulses with typical FWHM pulse widths of 0.6–2 ps ($\Delta\tau\Delta\nu$ of around 1) and peak powers in the range of 10–30 mW at repetition rates well above 100 GHz [26,27].

Hybrid ML of a monolithic laser can be achieved with the addition of a separate gain modulation section. Because of parasitics of the device, it is difficult to couple the modulation signal to a laser at very high frequency. As a result, the cavity length of hybridly ML lasers is longer than that of passively ML and CPM lasers. Since saturable absorption is the dominant mechanism for obtaining very short pulses, the requirements on the electrical modulation waveform are reduced in hybridly ML lasers. Here it is not as important to have an extremely short electrical modulation waveform as in actively ML lasers where the pulse-shortening mechanism is conditioned by the curvature of the electrical waveform. Harmonic passive monolithic ML can produce transform-limited ultrashort pulses at repetition rates of over 1.5 THz.

The peak power of ultrashort pulses is another key parameter which strongly affects potential applications of these pulses in various fields. The main means of enhancing peak power currently consists of increasing the emitting area of diode lasers. This can be done in a number of ways, including fabrication of structures with flared (tapered) waveguides, bow-tie devices or using laser arrays. A flared waveguide expands the optical mode from a narrow region, which gives a single lateral optical mode to a wider multi-mode region for higher pulse saturation energy. A promising approach for increasing the output power of optical pulses is the use of tapered-strip travelling-wave semiconductor amplifiers in conjunction with ML or gain/Q-switched lasers. Tapered single-pass amplifiers allow for increasing energies of ultrashort pulses because the saturation energy can be made relatively large at the flared output end of the device. A master oscillator power amplifier (MOPA) configuration has been considered one of the most promising for high-power generation in diode lasers [28].

14.5.3 Femtosecond Superradiant Pulse Generation

There exists another technique for ultrashort pulse generation, namely SR or cooperative spontaneous emission [29,30]. A physical principle is illustrated in Figure 14.8. SR pulses are generated in an e-h system at much larger carrier densities than those of spontaneous emission and lasing. A very short and powerful SR pulse is observed at a certain delay from the onset

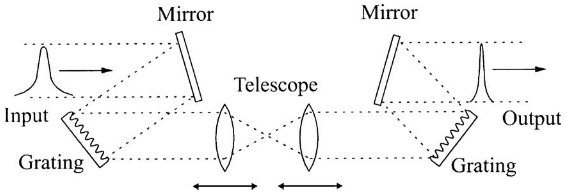

FIGURE 14.8 Comparison of spontaneous emission, lasing and superradiance.

of the pump pulse. An essential feature of SR is the mutual phasing of emitters involved in radiative emission. In case of a semiconductor, the self-organization in the e-h ensemble originates from an interplay of two processes, namely (i) the generation of resonant photons via the annihilation of e-h pairs and (ii) the generation of e-h pairs via the annihilation of the photons [31]. The most striking result of these interactions is the appearance of a distinctive form of emission as a consequence of an active medium whose collective and ordered behaviour bears little resemblance to that expected from a material dominated by independent e-h pairs. The pulse width of an SR pulse from N e-h pairs and its peak power is proportional to τ_s/N and N^2, respectively. For a typical semiconductor laser, τ_s is a few nanoseconds at room temperature and for a reasonably large number N, typical pulse widths of SR pulses are expected to be in the femtosecond range. Indeed, SR pulses have been generated from a large number of 0D, 2D and 3D multiple contact semiconductor structures of different compositions at 408, 880, 1280 and 1580 nm wavelengths [32]. Typical pulse widths range from around 1 ps down to below 200 fs. Peak powers of SR pulses exceed by a few orders of magnitude those of gain-switched and mode-locked pulses generated from lasers with similar material composition and cavity designs. The maximum peak power of SR pulses achieved so far is over 200 W [30].

The self-organization of emitters during SR emission generation results in regular 1D (grating-like) or 2D (chequerboard-like) spatial distributions of the inverted populations. Likewise, two counterpropagating SR pulses burn a periodic modulation or ‘grating’ into the inverted population distributions, the period of the modulation being half the optical wavelength. This lattice or grating results in a backscattering and pulse correlation. A distinctive feature of population gratings in semiconductor materials is that they result in strong refractive index gratings, which result in a change in the group velocity of light and superluminal pulse propagation [33].

14.6 Future Trends in High-Speed Diode Lasers

The ultrafast picosecond and femtosecond diode systems seem, at present, to be in an advanced state. Extensive experimental and theoretical work is in progress to take full advantage of all the possibilities offered by ultrafast diode lasers. At present, extremely high repetition rates of several hundred GHz of femtosecond pulses can be generated by CPM monolithic diode lasers. However, the weaknesses of ultrashort pulse generation by diode lasers are small pulse energies and longer pulse widths when compared with mode-locked solid-state and fibre lasers. Thus, the goal is to increase peak pulse power and to decrease pulse width without using nonsemiconductor (solid-state, fibre, etc.) components.

Fourier synthesis of optical harmonics is another good candidate for producing ultrashort optical pulse trains. Exploiting saturable absorbers based on novel advanced materials such as graphene and nano-wires as well as external cavity linear or non-linear dispersion management can result in the generation of mode-locked pulses below 100 fs from semiconductor lasers.

The generation of optical combs has recently attracted a great deal of interest. Stabilized optical frequency combs, particularly those centred at a wavelength of 1550 nm, are on the verge of having a strong impact on signal processing, coherent communications and astronomy. Harmonically mode-locked semiconductor-based lasers can be used as high repetition rate ultralow noise pulse train and optical frequency comb sources [34].

Another potentially important technique for the generation of ultrashort pulses with an ultrahigh repetition rate is Fourier synthesis of the laser emission. Indeed, optical pulses can be Fourier-synthesized using independent cw semiconductor lasers. Because there is no fundamental limitation on a wider frequency separation or on the laser material, Fourier synthesis is particularly suitable for the generation of ultrafast optical pulse trains. For instance, it is possible to produce pulses having an FWHM as short as 170 fs at a repetition rate of around 1.8 THz using three cw diode lasers and a non-linear phase-locking scheme [35].

The maximum modulation bandwidth achieved so far (30–40 GHz) can be increased by putting forward and realizing novel ideas on how to beat the present limits set by the device parasitics and device size. New fabrication techniques and device structures with cavity lengths less than 50–100 μm are required to solve the problem. Development of potentially chirpless high-speed laser structures is also very important for applications in long-haul high-bit-rate optical fibre communication systems. Different types of optical TDM and WDM systems utilizing all the advantages of high-speed diode lasers can provide very high bit rates above 100 Gb s^{-1}.

Superradiant emission from semiconductor media has been considered as a promising technique for the generation of femtosecond pulses on demand. What make SR pulses especially advantageous within the community of semiconductor optical sources are their large peak powers and femtosecond pulse widths. High peak powers at low pulse energies allow for the creation of localized disruption in delicate, for instance, biological tissues and materials. SR emission generators look also more promising as compared to other semiconductor lasers in different imaging applications in biology and medicine based on non-linear two-photon processes. SR emission can provide a competitive source for noninvasive techniques of fluorescent microscopy in tissues and 3D reconstruction. On the other hand, ultrafast recombination of the macroscopic polarization during the SR emission and observed THz coherent beating opens a possibility of the THz beam generation from semiconductor structures.

There exists a problem for applications of SR emission at present. Being one of the most remarkable features of SR, the stochastic nature of the cooperative emission manifests itself in macroscopic fluctuations of pulse intensity and turn-on times of SR pulses (timing jitter). Fluctuations are particularly large due to very small values of the polarization relaxation time in semiconductor media. An obvious and straightforward way for overcoming the problem of enhanced jitter of SR pulses is to use an optical feedback or technique of optical self-seeding. They are often used for increasing of stability of optical emission. The optical feedback allows for triggering of an SR pulse by injecting into the laser structure a tiny portion of the previous SR pulse in a train. On the other hand, macroscopic quantum coherence of the e-h system in SR semiconductor structures is a characteristic feature which makes them different from other optoelectronic and photonic devices. Further studies of e-h quantum coherence may result in the development of a novel type of quantum semiconductor photonic devices.

REFERENCES

1. Siegman A E 1986 *Lasers* (Mill Valley CA: University Science Books).
2. Vasil'ev P 1995 *Ultrafast Diode Lasers: Fundamentals and Applications* (Norwood MA: Artech House).
3. Agrawal G P and Dutta N K 2001 *Semiconductor Lasers* (New York: Van Nostrand Reinhold).
4. Petermann K 1988 *Laser Diode Modulation and Noise* (Dordrecht: Kluwer Academic).
5. Nagarajan R, Ishikawa M, Fucushima T, Geels R S and Bowers J E 1992 High speed quantum-well lasers with carrier transport effects *IEEE J. Quantum Electron.* **28** 1990–2007.
6. Avrutin E A, Cataluna M A and Rafailov E U 2011 *Ultrafast Lasers Based on Quantum-Dot Structures* (Weinheim: Wiley).
7. Markus A and Fiore A 2004 Modeling carrier dynamics in quantum-dot lasers *Phys. Stat. Sol. A* **201** 338–344.
8. Olshansky R, Hill P, Lanzisera V and Powazinik W 1987 Frequency Response of 1.3 μm InGaAsP high speed semiconductor lasers *IEEE J. Quantum Electron.* **23** 1410–18.
9. Hwang S K, Liu J M and White J K 2004 35-GHz intrinsic bandwidth for direct modulation in 1.3-mu m semiconductor lasers subject to strong injection locking *IEEE Photon. Tech. Lett.* **16** 972–974.
10. Tatham M C, Lealman I F, Seltzer C P, Westbrook L D and Cooper D M 1992 Resonance frequency, damping, and differential gain in 1.5 μm multiple quantum-well lasers *IEEE J. Quantum Electron.* **28** 408–14.
11. Ralston J D, Weisser S, Esquivias I, Larkins E C, Rosenzweig J, Tasker P J and Fleissner J 1993 Control of differential gain, nonlinear gain, and damping factor for high-speed application of GaAs-based MQW lasers *IEEE J. Quantum Electron.* **29** 1648–59.
12. Morton P A, Logan R A, Tanbun-Ek T, Sciortino P F Jr, Sergent A M, Montgomery P K and Lee B T 1992 25 GHz bandwidth 1.55 μm InGaAsP p-doped strained multiple quantum well lasers *Electron. Lett.* **28** 2156–7.
13. Kitano T, Uddin M N, Hong B, Tajima A, Jiang H and Hamamoto K 2016 Demonstration of photon–photon resonance peak enhancement by waveguide configuration modification on active multimode interferometer laser diode *Japan. J. Appl. Phys.* **55** 08RD04.
14. Bardella P and Montrosset I 2013 A new design procedure for DBR lasers exploiting the photon–photon resonance to achieve extended modulation bandwidth *IEEE J. Sel. Top. Quantum Electron.* **19** 1502408.
15. Henry C H 1982 Theory of the linewidth of semiconductor lasers *IEEE J. Quantum Electron.* **18** 259–64.
16. Yasaka H, Takahata K and Naganuma M 1992 Measurement of gain saturation coefficient in strained-layer multiple quantum-well distributed feedback lasers *IEEE J. Quantum Electron.* **28** 1294–304.
17. Tauber D A, Spickermann R, Nagarajan R, Reynolds T, Holms A L and Bowers J E 1994 Inherent bandwidth limits in semiconductor lasers due to distributed microwave effects *Appl. Phys. Lett.* **64** 1610–12.
18. Agrawal G P 2010 *Fiber-Optic Communication Systems* (New York: Wiley).
19. Dagli N 2007 *High-Speed Photonic Devices* (New York: Taylor & Francis).
20. Hasebe K, Sato T, Takeda K, Fujii T, Kakitsuka T and Matsuo S 2015 High-speed modulation of lateral p-i-n diode structure electro-absorption modulator integrated with DFB laser *IEEE J. Lightwave Tech.* **33** 1235–40.
21. Fang Y C, Chaki T, Hung J H, Yamada H and Yokoyama H 2016 1 MW peak-power subpicosecond optical pulse source based on a gain-switched laser diode *Opt. Lett.* **41** 4028–31.
22. Vasil'ev P P 1993 High-power high-frequency picosecond pulse generation by passively Q-switched 1.55 μm diode lasers *IEEE J. Quantum Electron.* **29** 1687–92.
23. Sartorius B, Mohrle M, Reichenbacher S, Preier H, Wunsche H-J and Bandelow U 1997 Dispersive self-Q-switching in self-pulsating DFB lasers *IEEE J. Quantum Electron.* **33** 211–18.
24. Vasil'ev P P, Morozov V N, Popov Yu M and Sergeev A B 1986 Subpicosecond pulse generation by a tandem-type AlGaAs DH laser with colliding pulse mode locking *IEEE J. Quantum Electron.* **22** 149–52.
25. Vasil'ev P P and Sergeev A B 1989 Generation of bandwidth-limited 2 ps pulses with 100 GHz repetition rate from multisegmented injection laser *Electron. Lett.* **25** 1049–50.
26. Avrutin E and Rafailov E 2012 Advances in Mode-Locked Semiconductor Lasers, *Advances in Semiconductor Lasers, Semiconductors and Semimetals* (Eds. Coleman J.J., Catrina Bryce A., and Jagadish C., Elsevier Inc., Amsterdam), vol. 86 pp. 93–147.
27. Keller U and Tropper A C 2006 Passively modelocked surface-emitting semiconductor lasers *Phys. Rep.* **429** (2), 67–120.
28. Thompson M G, Rae A, Sellin R L, Marinelli C, Penty R V, White I H, Kovsh A R, Mikhrin S S, Livshits D A and Krestnikov I L 2006 Subpicosecond high-power mode locking using flared waveguide monolithic quantum-dot lasers *Appl. Phys. Lett.* **88** 133119.
29. Vasil'ev P P 1997 Superfluorescence in semiconductor lasers *Quantum Electron.* **27** 860–5.

30. Vasil'ev P P 2009 Femtosecond superradiant emission in inorganic semiconductor *Rep. Prog. Phys.* **72** 076501.
31. Vasil'ev P P 2004 Conditions and possible mechanism of condensation of e–h pairs in bulk GaAs at room temperature *Phys. Stat. Solidi (b)* **241** 1251–60.
32. Vasil'ev P P, Penty R V and White I H 2013 Superradiant emission in semiconductor diode laser structures *IEEE J. Sel. Top. Quantum Electron.* **19** 1500210.
33. Vasil'ev P P, Penty R V and White I H 2016 Pulse generation with ultra-superluminal pulse propagation in semiconductor heterostructures by superradiant phase transition enhanced by transient coherent population gratings *Light: Sci. & Appl.* **5** e16086.
34. Quinlan F, Ozharar S, Gee S and Delfyett P J 2009 Harmonically mode-locked semiconductor-based lasers as high repetition rate ultralow noise pulse train and optical frequency comb sources *J. Opt. A* **11** 103001.
35. Hyodo M, Abedin K S and Onodera N 2001 Fourier synthesis of 1.8 THz optical-pulse trains by pulse locking of three independent semiconductor lasers *Opt. Lett.* **26** 340–2.

15

High-Power Laser Diodes and Laser Diode Arrays

Peter Unger

CONTENTS

15.1 Introduction 225
15.2 Mechanisms Limiting Output Power and Beam Quality of Laser Diodes 225
    15.2.1 Thermal Issues 225
    15.2.2 Filamentation 226
    15.2.3 Facet Damage 226
15.3 Vertical Waveguide Design for High-Power Operation 227
    15.3.1 Material Systems 227
    15.3.2 Graded-Index Separate-Confinement Heterostructure 228
    15.3.3 Broad-Width Vertical Optical Waveguide 228
15.4 Lateral Design of High-Power Laser Diodes 228
    15.4.1 Broad-Area Laser Diodes 229
    15.4.2 Tapered Laser Devices 229
    15.4.3 Unstable Resonator Lasers 230
    15.4.4 α-DFB Lasers 230
15.5 High-Power Laser Diode Arrays 231
15.6 Mounting of High-Power Laser Diodes and Diode Arrays 231
15.7 Reliability of High-Power Laser Diodes 232
15.8 Conclusion and Future Trends 232
References 232
Further Reading 233

15.1 Introduction

Laser diodes providing high optical output power show numerous advantages in comparison to conventional high-power laser systems. Superior features are high electrical-to-optical power conversion efficiency, small size, reliable operation and low price. The main uses of high-power laser diodes include optical pumping for solid-state lasers and fibre amplifiers, optical data storage, free-space data communication, material treatment, medical applications and infrared illumination. Depending on the specific application, the laser diodes are optimized with regard to high optical output power, spectral and spatial beam quality or emission wavelength. In this chapter, the basic criteria for the design of high-power laser diodes and laser diode arrays are discussed together with a presentation of state-of-the-art device implementations.

15.2 Mechanisms Limiting Output Power and Beam Quality of Laser Diodes

There are three important mechanisms that limit the output power of semiconductor laser diodes. The first effect is the heating of the device during operation leading to an increase in laser threshold current and a decrease in the differential efficiency. The second problem, usually called filamentation, is the distortion of the beam profile at high output power levels. The third phenomenon is catastrophic optical mirror damage (COMD), which is an irreversible destruction of the laser mirror facet.

15.2.1 Thermal Issues

The electrical-to-optical conversion efficiency of laser diodes is typically around 50% approaching record values close to 70% [1,2]. Thus, a significant amount of heat is generated in the device. Depending on the thermal resistance R_{therm}, which is defined by

$$R_{\mathrm{therm}} = \frac{\Delta T}{P_{\mathrm{el}} - P} \tag{15.1}$$

where P_{el} is the electrical input power and P is the optical output power, the active region of the laser diode experiences a temperature rise ΔT. The thermal resistance, also called the thermal impedance, can be influenced by the geometry and the thermal conductivity of the different materials and layers in the device. Another factor that governs thermal resistance is the mounting and packaging technology (see Section 15.6). The elevated temperature leads to a degradation of the output power P versus operating current I characteristic of the device. This characteristic is usually characterized by the threshold current I_th, where laser operation starts, and the differential quantum efficiency η_d. The differential quantum efficiency can be determined from the slope $(\mathrm{d}P)/(\mathrm{d}I)$ of the linear part of the characteristic above threshold using the equation

$$\eta_\mathrm{d} = \frac{e}{\hbar\omega}\frac{\mathrm{d}P}{\mathrm{d}I} = \frac{(\mathrm{d}P)/(\hbar\omega)}{(\mathrm{d}I)/e} \tag{15.2}$$

where $e = 1.602\,189 \times 10^{-19}\mathrm{C}$ is the elementary charge and $\hbar\omega$ is the photon energy of the emitted light. Thus, the differential efficiency η_d can be interpreted as the differential increase in emitted photons per unit time $(\mathrm{d}P)/(\hbar\omega)$ divided by the differential increase in injected electrons per unit time $(\mathrm{d}I)/e$ above laser threshold [3].

Increasing the temperature T of the device leads to an increase in the non-radiative recombination processes and a reduced carrier confinement in the active region, which results in a higher threshold current and a lower differential efficiency. Usually, the temperature behaviour of the output characteristic of a laser is phenomenologically described by two characteristic temperatures T_0 and T_1 for the threshold current I_th and the differential efficiency η_d, respectively, according to the following equations:

$$I_\mathrm{th} \propto \exp\left(\frac{T}{T_0}\right) \quad \text{and} \quad \eta_\mathrm{d} \propto \exp\left(-\frac{T}{T_1}\right). \tag{15.3}$$

As an example, the output power characteristics of a ridge-waveguide laser are shown in Figure 15.1 for different temperatures. If the active region gets extremely hot, thermal rollover is observed. In this case, a further increase in threshold current results in a decrease in output power, as shown in the left-hand side diagram of Figure 15.3.

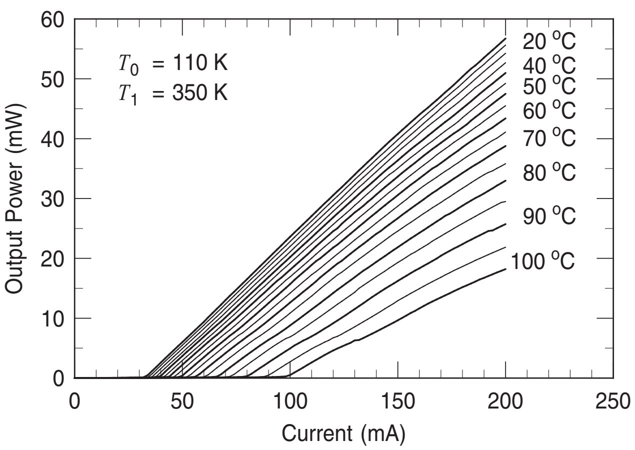

FIGURE 15.1 Continuous-wave (cw) output characteristics of a ridge-waveguide laser diode at different temperatures. At higher temperatures, the threshold current increases and the differential efficiency decreases. This behaviour is phenomenologically described by the characteristic temperatures T_0 and T_1.

15.2.2 Filamentation

At high optical output levels, the beam profile of semiconductor laser diodes deteriorates. The reason for this phenomenon, which is usually called filamentation, is the interaction between the optical wave and the electronic carriers in the active region of the device. A high optical power density leads to spatial hole burning, which locally increases the refractive index, resulting in self-focusing of the optical wave. Figure 15.2 shows an example of these filamentations for two broad-area laser amplifiers having different power densities inside the active region.

A detailed discussion of the filamentation effect is provided by the articles of Lang et al. [4,5], Hess et al. [6], Dai et al. [7] and Mullane and McInerney [8]. According to these publications, the complex refractive index $n(N)$ in the active region as a function of the electronic carrier density N is the sum of the carrier independent refractive index n_0 and a complex part originating from the modal optical gain $g_\mathrm{m}(N)$.

$$n(N) = n_0 - \frac{1}{2k_0} g_\mathrm{m}(N)\alpha_\mathrm{H} + \frac{i}{2k_0}\left[g_\mathrm{m}(N) - \alpha_\mathrm{i}\right]. \tag{15.4}$$

In this equation, $k_0 = 2\pi/\lambda$ is the vacuum wavenumber, α_i is the intrinsic optical modal loss inside the cavity and α_H is the Henry factor, which considers the influence of the optical gain on the refractive index via the Kramers–Kronig transformations [9,10]. To reduce filamentation effects in high-power lasers, it is therefore necessary to enlarge the optical mode volume and to reduce the modal gain [11,12].

15.2.3 Facet Damage

Another very important effect limiting the output power is COMD. An example of this phenomenon is shown in Figure 15.3. When a device is properly cooled, the output power limitation is caused by an irreversible and spontaneous

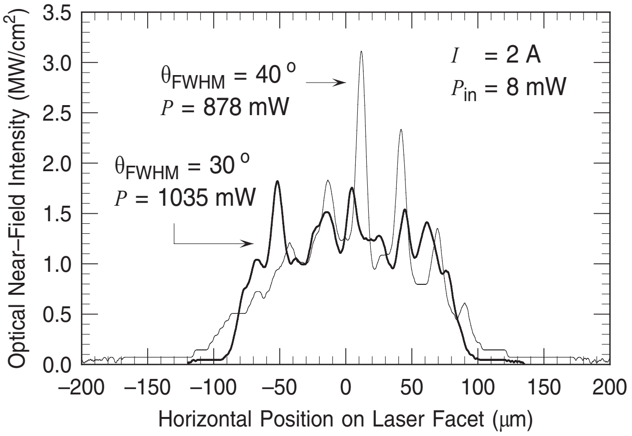

FIGURE 15.2 Optical near field intensity at the laser facet of two broad-area laser amplifiers having different optical power densities inside the active region. The device with low optical density has a smaller full-width at half-maximum angle Θ_FWHM of the vertical far-field pattern and shows less filamentation although the overall optical output power P is larger. The laser amplifier is driven by an electrical current of $I = 2$ A and an optical input power of $P_\mathrm{in} = 8\,\mathrm{mW}$.

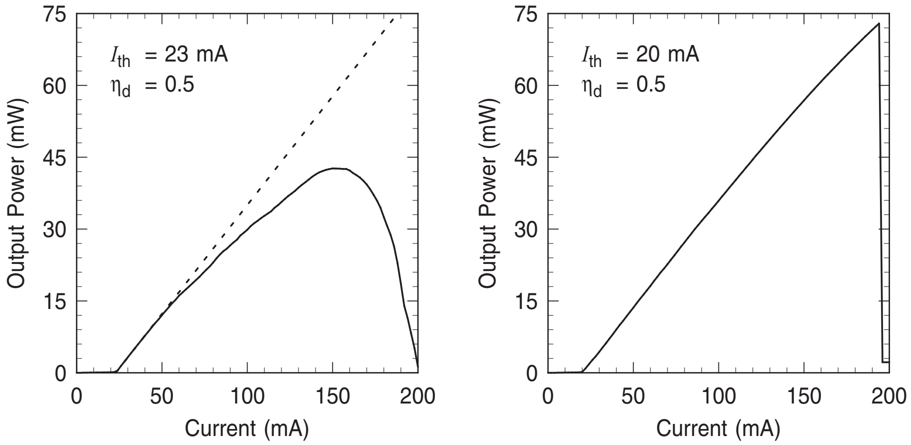

FIGURE 15.3 Optical output power versus operating current for two ridge-waveguide lasers. The output power of the device on the left-hand side is limited by thermal rollover, whereas the device on the right-hand side is destroyed by catastrophic optical mirror damage (COMD). Unlike COMD, thermal rollover is a reversible process, since it is normally not associated with a destruction or degradation phenomenon.

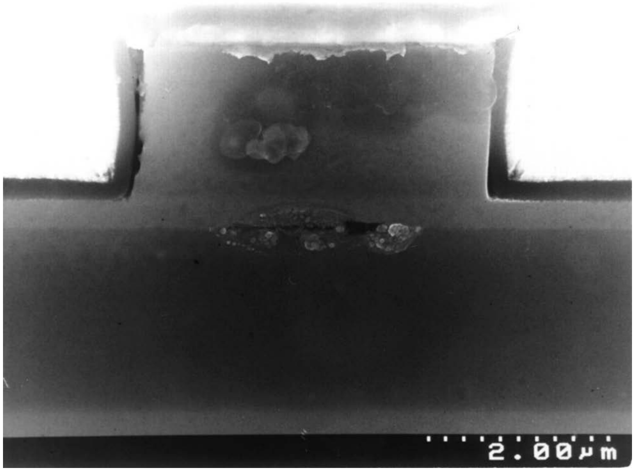

FIGURE 15.4 Scanning electron micrograph of the facet region of a ridge-waveguide laser, where the facet has been destroyed by catastrophic optical mirror damage. The pattern of the single-mode optical near-field distribution can be clearly identified.

destruction of the facet. A scanning electron micrograph of a facet after COMD is shown in Figure 15.4. The dynamics of this type of degradation is described in detail in Moser et al. [13], Brugger and Epperlein [14], Moser and Latta [15] and Fukuda [16]. The COMD can be reduced by lowering the optical power density on the laser facet using a suitable design of the vertical optical waveguide. With the help of sophisticated facet coatings, the COMD effect can be drastically reduced or even completely eliminated.

15.3 Vertical Waveguide Design for High-Power Operation

15.3.1 Material Systems

The vertical multilayer structures of laser diodes are fabricated using epitaxial growth techniques. The following list gives an overview of material systems commonly used for high-power operation.

- $Al_xGa_{1-x}As$ grown on GaAs is the classical material for high-power laser diodes. Since the radii of gallium and aluminium ions are nearly equal, $Al_xGa_{1-x}As$ can be grown lattice-matched for any composition x, and laser emission in the wavelength range of 700–870 nm can be realized.
- Using an InGaAs quantum well, the emission range of the AlGaAs/GaAs system can be extended to longer wavelengths. Since an indium ion has a larger radius than a gallium ion, the lattice parameter of GaInAs is higher than the lattice parameter of GaAs. Therefore, only thin GaInAs quantum-well layers containing compressive mechanical strain can be grown keeping lattice matching. The emission wavelength can be adjusted in the range of 800–1100 nm by varying the thickness and indium content of the strained quantum well.
- The same wavelength range can be covered using the strained GaInAs quantum well in combination with GaInAsP separate-confinement layers and $Ga_{0.51}In_{0.49}P$ cladding layers. Like GaInAs-AlGaAs/GaAs, this system is also lattice-matched to GaAs but is completely aluminium free [1,17].
- The visible-red short-wavelength range of 600–700 nm can be accessed using $(Al_xGa_{1-x})_{0.5}In_{0.5}P$. Again, this material is lattice-matched to GaAs for any aluminium concentration x since the ion radii of aluminium and gallium are approximately equal.

As mentioned previously, it is highly recommended to use a vertical epitaxial waveguide structure providing a low optical power density and a reduced optical modal gain. There are two major approaches for the vertical waveguide design to fulfil these requirements, a graded-index separate-confinement heterostructure (GRINSCH) having a narrow waveguide or a structure with a broad-width vertical waveguide.

Both waveguide designs, which are discussed in the next two sections in more detail, provide a number of advantages compared to conventional vertical waveguide structures which are used for low-power devices like laser diodes for fibre communication.

- The beam quality at high output power is improved due to reduced filamentation effects caused by spatial hole burning and self-focusing (see Figure 15.2).
- The device reliability is improved since regions with increased optical density and increased temperature (hot spots) leading to degradation effects are avoided.
- The localized power density at the laser facet is reduced resulting in less spontaneous device failures caused by COMD.
- A waveguide with a low optical power density in the active region has a rather broad optical mode profile. Since the optical far field is the Fourier transform of the optical mode profile, the vertical far-field angle Θ_{FWHM} is smaller (see Figure 15.5). As a consequence, lens and fibre coupling is easier due to the lower numerical aperture in the fast optical axis.

15.3.2 Graded-Index Separate-Confinement Heterostructure

An example of a GRINSCH structure having a narrow vertical waveguide is shown in Figure 15.5. The active region of the device is a single compressively strained quantum well with a typical thickness of 5–10 nm, allowing laser emission in the range of 900–1000 nm. The quantum well is surrounded by $Al_xGa_{1-x}As$ graded-index (GRIN) regions. This core-waveguide GRINSCH region is sandwiched between p- and n-doped cladding layers. Since the core region of the vertical waveguide is rather narrow, the resulting optical near-field intensity distribution is broad. The near-field distribution shown in Figure 15.5 has been calculated from the refractive-index profile using the one-dimensional Helmholtz equation. As a consequence, the full-width at half-maximum angle Θ_{FWHM} of the vertical far-field pattern is reduced compared to conventional vertical waveguide structures.

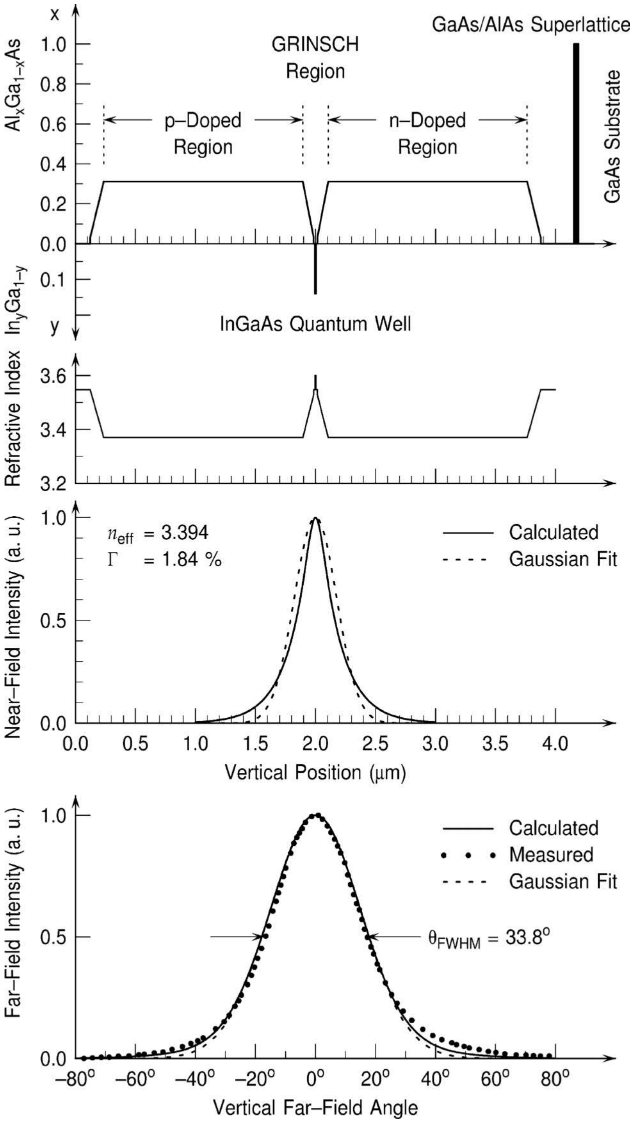

FIGURE 15.5 A vertical GRINSCH laser structure for high-power operation. The material composition is shown in the top diagram. The centre diagrams show the vertical refractive-index profile and the calculated optical near-field intensity together with a Gaussian fit. Listed also are the effective refractive index n_{eff} of the vertical waveguide and the optical confinement factor Γ, which is the overlap of the near-field intensity with the quantum well. In the diagram at the bottom, the calculated and measured far-field patterns and a Gaussian fit are plotted. Θ_{FWHM} is the full-width at half-maximum angle of the far-field distribution.

15.3.3 Broad-Width Vertical Optical Waveguide

An alternative approach to the epitaxial structure of high-power laser uses a broad-width vertical optical waveguide to achieve a broad near-field intensity distribution. These structures, which are also called large-optical-cavity (LOC) structures, are mainly used in the InGaAs/GaInAsP/GaInP material system where a grading of the refractive index in the optical waveguide is hard to achieve. In such a broad-width waveguide, the first- and second-order modes can also propagate. Since the first-order mode has a node at the quantum well, its confinement factor Γ is close to zero and thus the modal optical gain is negligible. The second-order mode is drastically reduced because its near-field distribution has a significant intensity in the GaInAsP cladding layers and therefore, it suffers from radiation losses due to the width of these layers and absorption losses at the p-side metal contact. A detailed discussion of the design of this type of structure can be found in Botez [11].

15.4 Lateral Design of High-Power Laser Diodes

A lateral fundamental-mode output beam can be achieved by choosing a narrow-stripe index- or gain-guided lateral waveguide having a typical width in the range of 4–8 μm. For this kind of device, a maximum single-mode output power of a few

100 mW has been reported limited by a deterioration of the beam profile or by COMD. Applications for lateral-waveguide single-mode lasers are mainly optical data storage and pumping of fibre amplifiers. To achieve higher output power levels, the lateral aperture width of the laser output facet has to be enlarged. In the following sections, different types of wide-aperture devices are discussed.

15.4.1 Broad-Area Laser Diodes

A rather simple approach to achieve high output powers uses broad-area laser diodes having a broad stripe design which allows the propagation of a very large number of different lateral modes. These devices are widely employed for applications where single-mode beam profiles are not required, such as infrared illumination, material treatment and solid-state laser pumping. Electrical-to-optical conversion efficiencies of more than 50% can be achieved, making broad-area lasers the most efficient technical light sources. Record output powers of around 10 W for lasers with cavity lengths of 2 mm and lateral stripe widths of 100 μm have been reported for the InGaAs/AlGaAs material system [18,19] as well as for aluminium-free InGaAs/GaInAsP/GaInP lasers [20] (Figure 15.6). An example for the characteristics of a broad-area InGaAs/AlGaAs laser diode is shown in Figure 15.7. For pumping solid-state lasers, several broad-area lasers are usually combined to a monolithically integrated bar having a typical width of 1 cm. When properly cooled, such bars yield continuous output power levels in the range of 50–200 W.

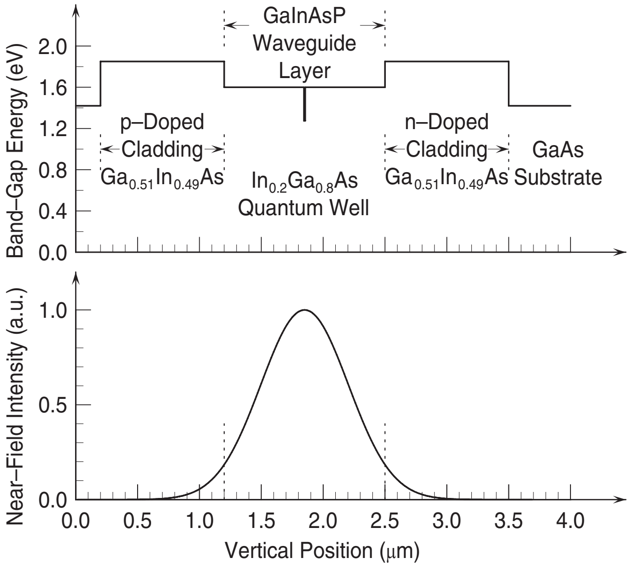

FIGURE 15.6 Aluminium-free broad vertical waveguide structure for 970 nm emitting high-power laser diodes. The waveguide consists of a 1.3-μm-wide undoped GaInAsP waveguide having a band-gap energy of 1.6 eV. In the centre of the broad-waveguide layer, one or two compressively strained InGaAs quantum wells are located. The cladding layers consist of $Ga_{0.51}In_{0.49}P$ having a band-gap energy of 1.85 eV. In the diagram at the bottom, the fundamental optical vertical mode intensity of the waveguide is plotted. The full-width at half-maximum vertical far-field angle of this structure was reported to be $\Theta_{FWHM} = 36°$ (after Al-Muhanna et al. [20]).

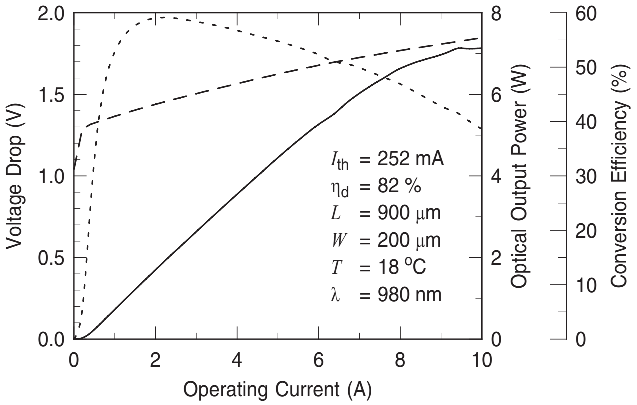

FIGURE 15.7 CW characteristics of a broad-area InGaAs/AlGaAs semiconductor laser diode having a vertical epitaxial layer structure as shown in Figure 15.5. Plotted are the optical output power (full curve), the voltage drop (dashes) and the electrical-to-optical power conversion efficiency (dots). Listed are the threshold current I_{th}, the differential quantum efficiency η_d (determined according to Equation (15.2) from the slope of the output power characteristic), the cavity length L, the lateral width of the active region W, the temperature of the heat sink T and the emission wavelength λ (after Deichsel et al. [21]).

15.4.2 Tapered Laser Devices

With tapered laser devices, the beam quality of wide-aperture laser diodes at high output powers can be significantly improved in comparison to broad-area devices. In Figure 15.8, three examples for tapered lateral designs are presented.

A tapered travelling-wave laser amplifier has a narrow-aperture input facet and a wide-aperture output facet. Both mirror facets are covered with antireflection coatings to suppress any optical resonances. The basic function of the device is the amplification of a low-power beam profile from an external master-oscillator laser while maintaining its beam properties. The master oscillator can be any type of laser having an excellent beam profile, usually another low-power single-mode laser diode. During amplification inside the tapered travelling-wave amplifier area, the beam propagates freely in the lateral direction. Therefore, the taper angle must be properly adjusted to the diffraction angle of the propagating beam. According to Gehrig and Hess [25], the mode pattern of the output beam is very sensitive to the coupling accuracy of the input beam, the quality of the antireflection coatings and the taper geometry. Figure 15.9 shows a typical example for the output power characteristics of a tapered amplifier.

Tapered laser oscillators with wide output apertures consist of a tapered gain region and a lateral waveguide section at the narrow-aperture mirror facet. The output facet is typically antireflection coated to a reflectivity of less than 1%; therefore, only a small part of the output light is reflected back towards the waveguide section which works like a spatial mode filter. Cavity-spoiling grooves around the waveguide, which are tilted against the output facet, suppress any further Fabry–Pérot oscillations. A detailed discussion on the design of tapered lasers can be found in Williams et al. [26].

The third example for a tapered laser design shown at the right-hand side of Figure 15.8 is a monolithically integrated master-oscillator power amplifier (MOPA). Again there is a

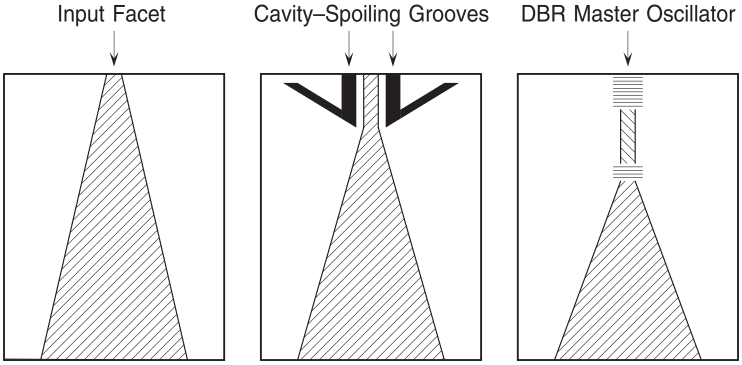

FIGURE 15.8 Lateral design of the active area for different types of tapered laser diodes with wide-aperture output facets. At the left-hand side, a tapered travelling-wave amplifier is shown (after Goldberg et al. [22]). The drawing in the centre illustrates a tapered laser oscillator having cavity-spoiling grooves at the narrow end of the taper (after Choi et al. [23]). The device sketched at the right-hand side is a monolithically integrated master-oscillator power amplifier (after O'Brian et al. [24]).

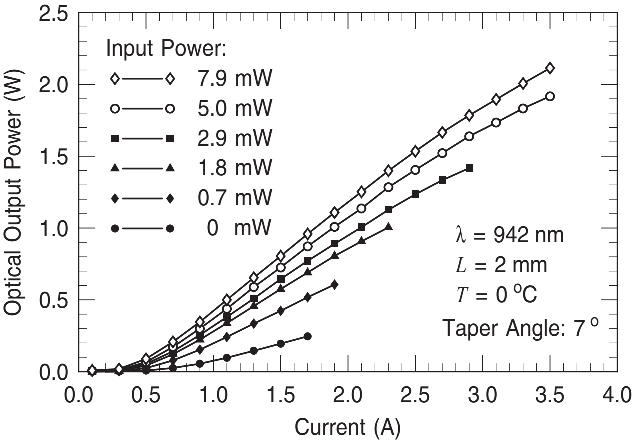

FIGURE 15.9 CW characteristics of a tapered semiconductor laser power amplifier with a taper angle of 7° for different input powers from the master-oscillator laser. Listed are the emission wavelength λ, the propagation length of the travelling-wave amplifier L and the heat-sink temperature T.

tapered gain region with an antireflection coating at the wide-aperture output facet. At the narrow end of the taper, a master laser with a single-mode waveguide is monolithically integrated into the chip. The resonator mirrors of the master laser are realized using distributed Bragg reflectors (DBRs).

15.4.3 Unstable Resonator Lasers

Considerable interest has been generated in semiconductor device research to realize unstable-resonator designs. The most promising approaches use curved mirror facets [21,27–29]. To produce these devices, a reliable dry-etching process for vertical, flat and smooth mirror facets is required [30,31]. In Figure 15.10, two examples for unstable resonator designs using curved mirrors are shown. The curved mirrors create a high-loss resonator through the introduction of lateral divergences in the oppositely propagating wavefronts reflected by the curved mirror surfaces. The design of the mirror curvature has to be optimized so that the lowest-loss mode will produce a single-lobed output beam and all higher-order modes are strongly suppressed because of their substantially higher losses.

15.4.4 α-DFB Lasers

A new class of broad-area lasers called grating-confined broad-area lasers has been demonstrated in which angled gratings are used to support broad-area laser ring modes. The most promising candidate of this class is the angled-grating distributed-feedback (α-DFB) laser [32], which provides near-Gaussian near and far fields, a high side-mode-suppression ratio and a strong suppression of the amplified spontaneous emission. The device illustrated in Figure 15.11 uses an angled

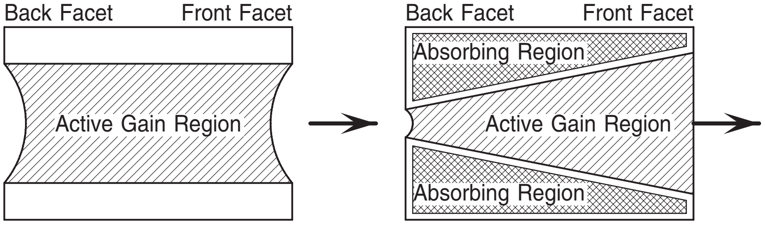

FIGURE 15.10 Two possible examples for lateral designs of unstable-resonator semiconductor lasers with dry-etched curved mirrors. On the left-hand side, a broad-area laser with curved mirrors is sketched, the right-hand side shows a design having a tapered active area and lateral absorber regions to suppress parasitic laser oscillations. Front and back facets of the devices are equipped with low- and high-reflectivity coatings, respectively.

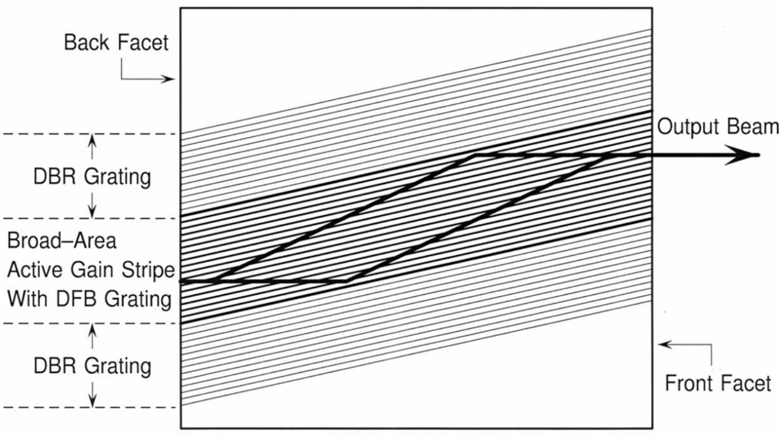

FIGURE 15.11 Schematic illustration of an α-DFB laser (after Lang et al. [32]). The broad-area active gain stripe is misorientated against the cleaved facets. The gain stripe is covered by a lateral DFB grating and is embedded between DBR gratings orientated parallel to the stripe. The front and back facets of the device are equipped with a low- and high-reflectivity coating, respectively.

DBR grating to generate ring modes. The active region consists of a broad-area gain stripe with a lateral DFB grating embedded between the DBR gratings. The angled grating supplies feedback and spatial filtering, enforcing single-spatial-mode and single-longitudinal-mode oscillation.

15.5 High-Power Laser Diode Arrays

Monolithic integration of laser diodes can be easily performed by arranging the individual devices onto the chip in the form of a one-dimensional array. If the distance between the individual emitters is large enough, no optical coupling is observed and the emission of each laser is independent of the emission of its neighbours. Typical array devices of this type are the 1-cm-wide bars, which are used for the pumping of solid-state lasers. Common emission wavelengths are 808 and 940 nm for the pumping of Nd:YAG and Yb:YAG, respectively. Commercially available 1-cm-wide laser bars with a cavity length of 900 μm are specified for continuous optical output powers of 50 W at operating currents of approximately 70 A. Although such devices can be driven to output powers of more than 100 W, the lifetime is drastically reduced under such conditions. When operated under specified conditions, lifetimes up to 10 000 h have been reported. Another example of broad-area laser arrays is individually addressable arrays of single-mode lasers used for laser printers.

If the single emitters are arranged in close proximity, the optical field generated by each element of the array is coupled to other elements. Typical arrays of this type consist of a single-mode index- or gain-guided waveguides, which are closely spaced. These devices are called phase-locked laser arrays, because there is a fixed phase correlation between the individual emitters. Optical coupling can occur either via evanescent waves or leaky modes (radiation modes). The nature of the coupling strongly depends on the geometry of the waveguides and the effective refractive index step from the waveguide regions to the regions that mediate the optical coupling between the waveguides. For evanescent-type array modes, the fields are peaked in the high-effective-index regions, whereas for leaky-type array modes, the fields are peaked in the low-index array regions. Evanescent-wave arrays have propagation constants between the low and high refractive-index level, while leaky modes have values for the propagation constant below the low effective refractive index. The modes are said to be ‘in-phase’ when there is no phase shift for the fields of each waveguide and are called ‘out-of-phase’ when the fields of adjacent waveguides show a phase shift of π.

Generally, evanescent-wave arrays tend to operate in the out-of-phase mode resulting in a double-lobed far field. The reason for this behaviour is the better field overlap of the out-of-phase mode with the gain regions because this mode has zero intensity in the regions between the waveguides. Another disadvantage of evanescent-wave arrays is the limitation in the effective refractive-index step between the waveguides and the inter-element regions since a high index step will allow the propagation of higher-order modes in the individual waveguide elements. This low index step makes the device sensitive to spatial hole burning resulting in deteriorated beam properties at high output-power levels.

In leaky-mode arrays, the optical gain is provided in the low-index regions. Unlike evanescent-wave arrays, there is no limitation in the refractive index step resulting in stable operation at high output power. When properly designed, leaky-mode arrays operate in phase and exhibit a single-mode beam profile at output power levels in the range of 1–2 W. A detailed treatment of phase-locked arrays can be found in the book edited by Botez and Scifres (1994).

15.6 Mounting of High-Power Laser Diodes and Diode Arrays

A proper cooling of laser diodes is essential to obtain high output power and reliable operation. To provide a low thermal resistance, the devices are usually mounted junction-side down, which is a rather sophisticated process because of the requirements in positional accuracy, the risk of injury to the laser facet and reliability problems attributed to the solder material. For small chips having dimensions below 2 mm, eutectic Au/Sn solder can be used, which provides a rather durable connection. In many cases, the chip is first soldered onto a heat spreader consisting of a low-thermal-resistivity material like diamond, boron nitride, silicon carbide or copper before being soldered into the device package. For larger chips like laser bars having a typical width of 1 cm, either a heat sink having the same thermal expansion coefficient as the chip or a flexible and soft solder material like indium has to be implemented to avoid cracks in the chip caused by the thermal expansion during operation [33]. Laser bars are mostly mounted onto water-cooled heat sinks having microchannels of some 100 μm dimension directly below the heat-sink surface to provide an efficient and homogeneous heat transfer [34].

15.7 Reliability of High-Power Laser Diodes

Depending on the application, different specifications for the device reliability of high-power lasers are expected by the customer. For consumer electronics, typical lifetimes are some thousands of hours. For pumping solid-state lasers, devices with lifetimes in the range of 5000–10 000 h are commercially available. For telecommunications applications, guaranteed lifetimes of 300 000 h are required.

For single-mode ridge-waveguide or narrow-stripe lasers, which have output powers of some 100 mW, the lifetime-limiting effect is a COMD at the mirror facet. Since the internal temperature is low compared to broad-area laser diodes and laser bars, degradation of the bulk material is normally not observed. To achieve the device reliability required in the telecommunications market, e.g. for pumping of fibre lasers, sophisticated processes are used to passivate and coat the laser facet [16].

For broad-area lasers and laser bars, the active fraction of the device area is much larger in comparison to ridge-waveguide or narrow-stripe lasers. In this case, the device reliability is governed by the excess heat produced in the device and a gradual degradation is typically observed. Important factors influencing the reliability and degradation behaviour are the defect density of the epitaxial material, the diffusion stability of the doping profiles at elevated temperatures and the mounting technology.

15.8 Conclusion and Future Trends

Semiconductor diode lasers providing high optical output powers are attractive devices for applications where a small size, a high electrical-to-optical power conversion efficiency, reliable operation and a low price are desired. Broad-area laser devices and laser diode bars exhibit optical output powers up to 100 W and are widely used for pumping solid-state lasers, material treatment, medical applications and infrared illumination. Due to filamentation effects, the beam quality of these devices is rather poor. State-of-the-art single-mode devices like ridge-waveguide and narrow-stripe lasers are limited to output power levels of several 100 mW.

A considerable part of the ongoing research activities on high-power lasers is attributed to approaches that allow high optical output powers and diffraction-limited beam profiles at the same time. Devices of this kind have tapered lateral designs, implement unstable resonator concepts, stabilize the mode by lateral-angled gratings or use coupled arrays of single-mode waveguides.

In future, the wavelength range of 600–1100 nm for commercially available high-power laser diodes will be extended towards longer wavelengths, e.g. using InGaAsN quantum wells [35]. An example of a new and promising device concept is the optically pumped semiconductor disc laser [36,37]. This type of laser, which is also called vertical external cavity surface-emitting laser, has excellent beam properties, is scalable in output power and allows intracavity frequency doubling.

REFERENCES

1. Botez D, Mawst L J, Bhattacharya A, Lopez J, Li J, Kuech T F, Iakovlev V P, Suruceanu G I, Caliman A and Syrbu A V 1996 66% cw wallplug efficiency from Al-free 0.98 μm-emitting diode lasers *Electron. Lett.* **32** 2012–13.
2. Jäger R, Heerlein J, Deichsel E and Unger P 1999 63% wall-plug efficiency MBE grown InGaAs/AlGaAs broad-area laser diodes and arrays with carbon p-type doping using CBr_4*J. Crystal Growth* **201/202** 882–5.
3. Smowton P M and Blood P 1997 The differential efficiency of quantum-well lasers *IEEE J. Selected Topics Quantum Electron.* **3** 491–8.
4. Lang R J, Hardy A, Parke R, Mehuys D, O'Brian S, Major J and Welch D 1993 Numerical analysis of flared semiconductor laser amplifiers *IEEE J. Quantum Electron.* **29** 2044–51.
5. Lang R J, Mehuys D, Welch D F and Goldberg L 1994 Spontaneous filamentation in broad-area diode laser amplifiers *IEEE J. Quantum Electron.* **30** 685–94.
6. Hess O, Koch S W and Moloney J V 1995 Filamentation and beam propagation in broad-area semiconductor lasers *IEEE J. Quantum Electron.* **31** 35–43.
7. Dai Z, Michalzik R, Unger P and Ebeling K J 1997 Numerical simulation of broad-area high-power semiconductor laser amplifiers *IEEE J. Quantum Electron.* **33** 2240–54.
8. Mullane M P and McInerney J G 1999 Minimization of the linewidth enhancement factor in compressively strained semiconductor lasers *IEEE Photon. Technol. Lett.* **11** 776–8.
9. Henry C H, Logan R A and Merritt F R 1980 Measurement of gain and absorption spectra in AlGaAs buried heterostructure lasers *J. Appl. Phys.* **51** 3042–50.
10. Henry C H, Logan R A and Bertness K A 1981 Spectral dependence of the change in refractive index due to carrier injection in GaAs lasers *J. Appl. Phys.* **52** 4457–61.
11. Botez D 1999 Design considerations and analytical approximations for high continuous-wave power, broad-waveguide diode lasers *Appl. Phys. Lett.* **74** 3102–4.

12. Mikulla M, Chasan P, Schmitt A, Morgott S, Wetzel A, Walther M, Kiefer R, Pletschen W, Braunstein J and Weimann G 1998 High-brightness tapered semiconductor laser oscillators and amplifiers with low-modal gain epilayer-structures *IEEE Photon. Technol. Lett.* **10** 654–6.
13. Moser A, Latta E E and Webb D J 1989 Thermodynamics approach to catastrophic optical mirror damage of AlGaAs single quantum well lasers *Appl. Phys. Lett.* **55** 1152–4.
14. Brugger H and Epperlein P W 1990 Mapping of local temperatures on mirrors of GaAs/AlGaAs laser diodes *Appl. Phys. Lett.* **56** 1049–51.
15. Moser A and Latta E E 1992 Arrhenius parameters for the rate process leading to catastrophic damage of AlGaAs–GaAs laser facets *J. Appl. Phys.* **71** 4848–53.
16. Fukuda M 1996 Reliability of high power pump lasers for erbium-doped fibre amplifiers *Int. J. High Speed Electron. Syst.* **7** 55–84.
17. Mawst L J, Bhattacharya A, Lopez J, Botez D, Garbuzov D Z, DeMarco L, Connolly J C, Jansen M, Fang F and Nabiev R F 1996 8 W continuous wave front-facet power from broad-waveguide Al-free 980 nm diode lasers *Appl. Phys. Lett.* **69** 1532–4.
18. He X, Srinivasan S, Wilson S, Mitchell C and Patel R 1998 10.9 W continuous wave optical power from 100 μm aperture InGaAs/AlGaAs (915 nm) laser diodes *Electron. Lett.* **34** 2126–7.
19. O'Brian S, Zhao H, Schoenfelder A and Lang R J 1997 9.3 W CW (In)AlGaAs 100 μm wide lasers at 970 nm *Electron. Lett.* **33** 1869–71.
20. Al-Muhanna A, Mawst L J, Botez D, Garbuzov D Z, Martinelli R U and Connolly J C 1998 High-power (> 10 W) continuous-wave operation from 100-μm-aperture 0.97-μm-emitting Al-free diode lasers *Appl. Phys. Lett.* **73** 1182–4.
21. Deichsel E, Jäger R and Unger P 2002 High-brightness unstable-resonator lasers fabricated with improved dry-etching technology for ultra-smooth laser facets *Japan. J. Appl. Phys. Part I* **41** 4279–82.
22. Goldberg L, Mehuys D, Surette M R and Hall D C 1993 High-power, near-diffraction-limited large-area traveling-wave semiconductor amplifiers *IEEE J. Quantum Electron.* **29** 2028–43.
23. Choi H K, Walpole J N, Turner G W, Eglash S J, Missaggia L J and Connors M K 1993 GaInAsSb–AlGaAsSb tapered lasers emitting at 2 μm *IEEE Photon. Technol. Lett.* **5** 1117–19.
24. O'Brian S, Lang R, Rarke R, Major J, Welch D F and Mehuys D 1997 2.2-W continuous-wave diffraction-limited monolithically integrated master oscillator power amplifier at 854 nm *IEEE Photon. Technol. Lett.* **9** 440–2.
25. Gehrig E and Hess O 2001 Spatio–temporal dynamics of light amplification and amplified spontaneous emission in high-power tapered semiconductor laser amplifiers *IEEE J. Quantum Electron.* **37** 1345–55.
26. Williams K A, Penty R V, White I H, Robbins D J, Wilson F J, Lewandowski J J and Nayar B K 1999 Design of high-brightness tapered laser arrays *IEEE J. Selected Topics Quantum Electron.* **5** 822–31.
27. Biellak S A, Fanning C G, Sun Y, Wong S S and Siegman A E 1997 Reactive-ion-etched diffraction-limited unstable resonator semiconductor lasers *IEEE J. Quantum Electron.* **33** 219–30.
28. Unger P, Boegli V, Buchmann P and Germann R 1993 Fabrication of curved mirrors for visible semiconductor lasers using electron-beam lithography and chemically assisted ion-beam etching *J. Vacuum Sci. Technol. B* **11** 2514–18.
29. Unger P, Boegli V, Buchmann P and Germann R 1994 High-resolution electron-beam lithography for fabricating visible semiconductor lasers with curved mirrors and integrated holograms *Microelectron. Eng.* **23** 461–4.
30. Deichsel E, Eberhard F, Jäger R and Unger P 2001 High-power laser diodes with dry-etched mirror facets and integrated monitor photodiodes *IEEE J. Selected Topics Quantum Electron.* **7** 106–10.
31. Vettiger P, Benedict M K, Bona G L, Buchmann P, Cahoon E C, Dätwyler K, Dietrich H P, Moser A, Seitz H K, Voegeli O, Webb G J and Wolf P 1991 Full-wafer technology—a new approach to large-scale laser fabrication and integration *IEEE J. Quantum Electron.* **27** 1319–31.
32. Lang R J, Dzurko K, Hardy A A, Demars S, Schoenfelder A and Welch D F 1998 Theory of grating-confined broad-area lasers *IEEE J. Quantum Electron.* **34** 2196–210.
33. Endriz J G, Vakili M, Browder G S, DeVito M, Haden J M, Harnagel G L, Plano W E, Sakamoto M, Welch D F, Willing S, Worland D P and Yao H C 1992 High power diode laser arrays *IEEE J. Quantum Electron.* **28** 952–65.
34. Beach R, Benett W J, Freitas B L, Mundinger D, Comaskey B J, Solarz R W and Emanuel M A 1992 Modular microchannel cooled heatsinks for high average power laser diode arrays *IEEE J. Quantum Electron.* **28** 966–76.
35. Egorov A Y, Bernklau D, Livshits D, Ustinov V, Alferov Z I and Riechert H 1999 High power cw operation of InGaAsN lasers at 1.3 μm *Electron. Lett.* **35** 1643–4.
36. Kuznetsov M, Hakimi F, Spargue R and Mooradian A 1999 Design and characteristics of high-power (>0.5-W CW) diode-pumped vertical-external-cavity surface-emitting semiconductor lasers with circular TEM_{00} beams *IEEE J. Selected Topics Quantum Electron.* **5** 561–73.
37. Schiehlen E, Golling M and Unger P 2002 Diode-pumped semiconductor disk laser with intracavity frequency doubling using lithium triborate (LBO) *IEEE Photon. Technol. Lett.* **14** 777–9.

FURTHER READING

Botez D and Scifres D R (ed) 1994 *Diode Laser Arrays* (Cambridge: Cambridge University Press).

A multi-author book providing a comprehensive overview of the fundamental principles and applications of semiconductor diode laser arrays.

Carlson M M 1994 *Monolithic Diode-Laser Arrays* (New York: Springer).

This book presents and analyses the results of work in the development of high-brightness diode-laser arrays.

Casey H C and Panish M B 1978 *Heterostructure Laser—Part A: Fundamental Principles, Part B: Materials and Operating Principles* (Orlando, FL: Academic).

A comprehensive treatment of the general aspects of modern semiconductor lasers including theory, fabrication technology and characterization of these devices.

Coldren L A and Corzine S W 1995 *Diode Lasers and Photonic Integrated Circuits* (New York: Wiley).

A modern textbook on semiconductor lasers primarily written for students.

Diehl R (ed) 2000 *High-Power Diode Lasers—Fundamentals, Technology, Applications (Topics in Applied Physics 78)* (Berlin: Springer).

A multi-author book covering various aspects of semiconductor diode lasers including theory, microscopic dynamic effects, epitaxial growth, beam properties and packaging. Also applications of these devices like frequency conversion and pumping of solid-state lasers are discussed.

16

Visible Laser Diodes: Properties of III–V Red-Emitting Laser Diodes

Peter Blood

CONTENTS

16.1 Introduction 235
  16.1.1 Background 235
  16.1.2 Fundamental Trends with Wavelength 236
  16.1.3 The AlGaInP Material System 237
  16.1.4 Quantum Confinement 237
  16.1.5 AlGaInP Quantum Wells 239
  16.1.6 InP/AlGaInP Quantum Dots 240
16.2 III–V Red-Emitting Quantum Well Laser Diodes 240
  16.2.1 Design of the Quantum Well Structure 240
  16.2.2 Intrinsic Gain and Recombination Characteristics 241
  16.2.3 Threshold Current 242
  16.2.4 Carrier Leakage 243
  16.2.5 Vertical-Cavity Surface-Emitting Lasers (VCSELs) 244
16.3 Quantum Dot Lasers 245
  16.3.1 Motivation 245
  16.3.2 Dot Structure and Optical Gain 246
  16.3.3 Devices 247
16.4 Summary 247
Acknowledgements 247
References 247
Further Reading 249

16.1 Introduction

This chapter is an account of the material structure and basic performance characteristics of diode lasers fabricated in the AlGaInP material system using quantum wells and dots and covering the wavelength range from about 635 to 740 nm. This introduction provides background information on material properties and quantum confinement. The two major sections that follow deal specifically with quantum well and quantum dot devices.

16.1.1 Background

In a semiconductor, light is produced by electrons making *radiative* transitions across the *direct* energy gap (E_g), with the energy lost by each electron being given up by the creation of a photon. The wavelength of the emitted light is determined by the magnitude of the direct energy gap and for short-wavelength emission, we require a wide-gap semiconductor: 650 nm corresponds to a photon energy of 1.91 eV. However, as illustrated in Figure 16.1, other energy gaps exist, which are termed *indirect* because the electron has to change its wavevector, denoted by the symbol $\mathbf{k}$ ($\hbar\mathbf{k}$ has dimensions momentum and is called the crystal momentum), as well as its energy in making a transition. The wavevector associated with a photon is small and cannot compensate for the wavevector difference between initial and final states of a transition across the indirect gap (a process which can loosely be thought of as momentum conservation). The radiative transition rate across the indirect gap is therefore very small because another ‘particle’ such as a phonon must also be involved in the process to conserve wavevector, consequently the dominant indirect recombination processes are non-radiative and take place via defect states, producing heat rather than light. If the conduction band minimum of the indirect gap is lower than that of the direct gap then most of the electrons will reside in the indirect minimum and will not be available to make direct radiative transitions. Thus, the direct energy gap can only be exploited for light emission, where it

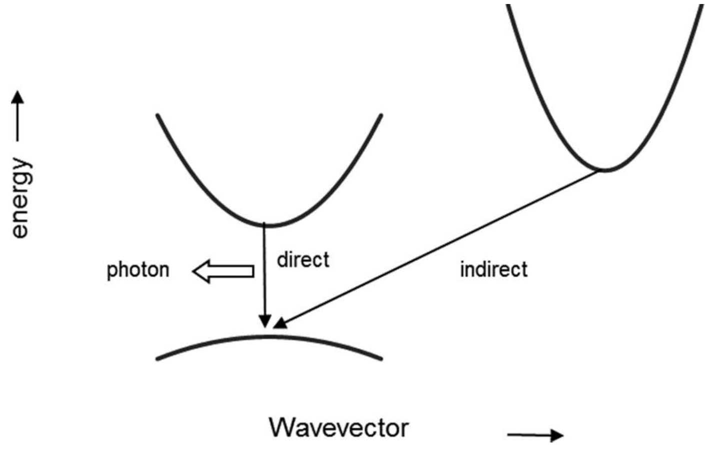

FIGURE 16.1 Diagram of energy versus wavevector for electrons in a crystalline semiconductor illustrating the direct and indirect energy gaps. An indirect transition requires the electron to change both energy and wavevector. Because photons have a very small wavevector they are produced most effectively by direct transitions.

lies below the indirect gap. The indirect gap has a major influence on the design of red-emitting devices.

In the elemental semiconductors Si and Ge, the indirect gap has the lowest energy so these are not effective light-emitting materials. The most common direct gap, light-emitting semiconductors are formed from elements in columns III and V or II and VI of the periodic table. Although compounds such as GaAs and ZnS have a defined composition and energy gap (E_g = 1.41 and 3.6 eV, respectively) it is possible to obtain a range of energy gaps by alloying compounds together. For example, by alloying AlAs with GaAs, effectively replacing the group III element Ga on some sites with Al, it is possible to vary the direct gap from 1.42 to 3.03 eV by changing the composition; however, the indirect gap at about 2 eV restricts the useful range for light emission. Semiconductor alloys are the key component in engineering laser diode structures, providing the basis for tailoring the emission energy and enabling multiple-layer heterostructures to be built in which the band gap changes with distance to confine the carriers and provide a waveguide for the emitted light. The double heterostructure (see Casey and Panish, 1978) is the essential element in realizing continuous operation of diode lasers at room temperature and its inventors, Kroemer and Alferov, were recipients of the Nobel Prize for Physics in 2000.

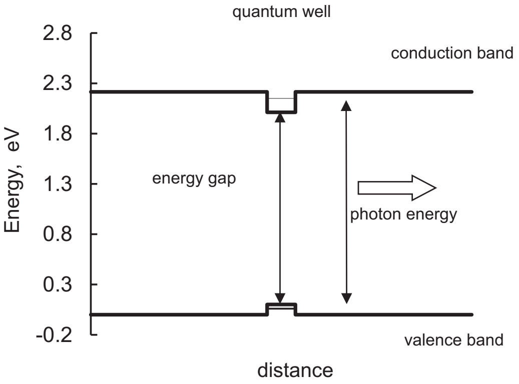

FIGURE 16.2 Illustration of the energy bands of a quantum well. As the well width is reduced, the confined states in the well move toward the band edges of the barrier material and the energy of the emitted photon is increased above the band gap of the well material. The maximum photon energy is set by the band gap of the barrier material. (This diagram is drawn to the energy scale of the GaInP well in Figure 16.6.)

In principle, it is possible to fabricate devices emitting at 700 nm using the $Al_xGa_{1-x}As$ alloy system but, at the Al content required ($x \cong 0.28$), the radiative efficiency of the material is poor and the threshold current for laser action is prohibitively high. In a given material system, the energy of recombination can be increased by confining electrons in a thin quantum well as illustrated in Figure 16.2 (the thinner the well, the greater the electron energy). A quantum well offered a more promising means of reducing the emission wavelength from GaAs and lasers operating at about 710 nm have been made in this way (Woodbridge et al., 1984), but the threshold currents were large and strongly temperature sensitive due to the leakage of carriers from the quantum well to the adjacent barrier material. This is because the confined states are near the top of the quantum well (Blood et al., 1989) in very short wavelength devices and the reduction in wavelength is ultimately limited by the band gap of the barrier material (Figure 16.2). To fabricate low threshold red-emitting lasers it is necessary to use a material system that provides a wider gap barrier to enable the photon energy to be increased while still providing strong localization of carriers within the quantum well. These requirements have been met using the AlGaInP system, which is more correctly termed a ternary alloy of the III–V compounds AlP, GaP and InP. Further refinements to the structure have been made more recently using quantum confinement in all three dimensions: quantum dots.

Before describing this material system and quantum confinement, we briefly consider general trends in the properties of semiconductor lasers with band gap to put the particular features of red-emitting lasers into a wider context.

16.1.2 Fundamental Trends with Wavelength

Properties of different III–V materials follow systematic trends with band gap; for example, as the gap increases from one material to another the effective mass of the electrons increases and the dielectric constant decreases. Consequently there are trends in laser characteristics (Blood, 2015, Appendix A), which apply to devices from the near-infrared (e.g. 1.55 μm communications lasers) through GaAs-based lasers (e.g. 780 nm CD lasers) to red (650 nm) and blue (430 nm) emitting devices. There are two intrinsic processes, which contribute to the threshold current: radiative recombination across the direct gap producing incoherent spontaneous emission and Auger recombination, in which the recombining electron excites another electron, which then gives up the excess energy as heat (see Agrawal and Dutta, 1986). Auger recombination is undesirable because it reduces the fraction of the current, which is used to produce light. The Auger coefficient is large in narrow-gap materials but decreases with increasing gap such that the Auger current is negligible in the wide gap materials used for red-emitting devices. The spontaneous recombination rate increases with increasing band gap so there is a trend for the threshold current to increase with band gap; therefore, we should not expect red-emitting lasers to have threshold currents as low as 870 nm GaAs lasers, for equivalent structures.

Most of the theories used to design laser diodes treat the electrons as independent, non-interacting particles. However, the Coulomb interactions between electrons become stronger as the band gap is increased due to the higher mass and lower dielectric constant. In addition to an increase in optical gain for a given carrier density, these interactions increase the rate of recombination per electron contributing a further increase in threshold current density. It is possible to take account of these effects within non-interacting, "single-particle" theories by means of phenomenological models but these are poor approximations for first-principles calculations in red-emitting lasers (see Chow et al., 1997a, for an example) and blue-emitting lasers.

16.1.3 The AlGaInP Material System

Red-emitting lasers are made using the $(Al_xGa_{1-x})_yIn_{1-y}P$ material system, which provides variation in the direct band gap from 1.9 eV to about 2.5 eV. To avoid formation of unwanted crystal defects it is necessary that the layer structure of the laser is grown with the same lattice parameter as the substrate material. The lattice parameter is determined chiefly by the ratio of [Al+Ga] to [In], the parameter y. The band gap can be changed by substituting [Al] for [Ga] with very little change in lattice parameter, or by changing y, which also causes the lattice parameter to change. (For a survey of AlGaInP band-gap parameters, see Smowton and Blood, 1997b.) This material can be grown lattice-matched to a GaAs substrate with $y = 0.51$. If the device structure cannot be grown lattice-matched to the substrate, the extended defects produced by the mismatch have a deleterious effect on both the operating current and lifetime of the devices. The availability of a suitable substrate material is the major factor, which determines the viability of a material system for laser diode manufacture, a problem which plagued the development of blue-emitting wide gap nitride laser diodes.

Figure 16.3 shows the variation of the direct and indirect band gaps as functions of the Al/Ga ratio (the composition x) for AlGaInP material lattice-matched to GaAs. The variation of the direct gap is given by

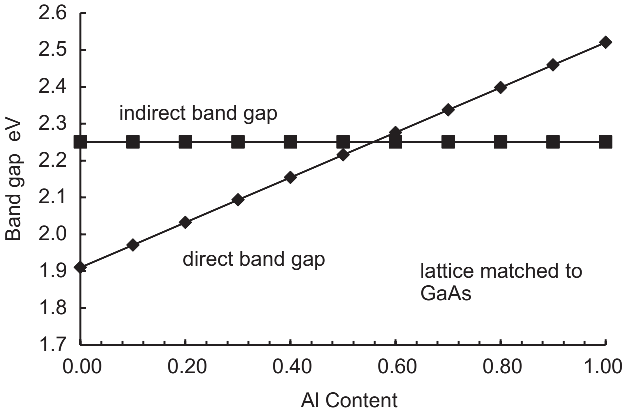

FIGURE 16.3 Direct and indirect energy gaps of $(Al_xGa_{1-x})_yIn_{1-y}P$ as a function of Al composition (x) for $y = 0.51$ corresponding to the lattice matched to the GaAs substrate.

$$E_g(x) = 1.91 + 0.61x\,[\text{eV}]. \tag{16.1}$$

The maximum useful direct gap is limited to about 2.25 eV ($x < 0.55$) because the minimum gap becomes indirect at higher compositions. In practice this material has been used to make laser diodes of reasonable performance down to about 625 nm (photon energy of about 2 eV).

It is assumed that the different atomic species of a semiconductor alloy are distributed randomly over the appropriate lattice sites. However, in AlGaInP, there is a tendency for the distribution of In on the group III sites to be ordered such that a periodic In distribution is produced along the ⟨111⟩ direction (see, for example, Kondow et al., 1989 and Okuda et al., 1989). In GaInP, there is a tendency to form alternating (111) planes of InP and GaP. This has the effect of reducing the band gap below that given by Equation (16.1). The degree of ordering depends upon the growth conditions and, unless these are well controlled, there is poor control over the emission wavelength. In developing red-emitting lasers, considerable effort was devoted to suppressing this ordering process by the choice of the growth temperature or by growth on substrates with orientation other than ⟨100⟩ (Chen et al., 1990). By suppressing ordering, the maximum band gap is obtained and the emission wavelength is reproducible.

16.1.4 Quantum Confinement

In the absence of quantum confinement the electrons in a semiconductor occupy very closely spaced states spread over energy bands: of principal interest are the conduction and valence bands. The density of these states in bulk material in the conduction band, per unit energy, increases proportional to $E^{1/2}$ as illustrated in Figure 16.2. The valence band state density increases similarly going down in energy from the valence band edge. Laser action takes place between a very small number of conduction and valence band states at energies near the edges of the gap, where the carrier population is inverted but carrier recombination, and hence current flow, takes place between carriers distributed over several multiples of the thermal energy, k_BT. The recombination current between these non-lasing states is unnecessary as far as laser action is concerned.

Consideration of Schrödinger's equation for a thin one-dimensional potential well shows that the energy of the lowest confined state is increased above that of the bottom of the well and, due to unconfined motion in the other two dimensions, the allowed states form a series of sub-bands as illustrated in Figure 16.4 (Blood, 2015, Chapter 8). It can be seen that the number of states available for occupation by electrons is reduced from that in unconfined material and this reduces the current associated with non-lasing states, as well as reducing the temperature dependence of the intrinsic threshold current.

Confinement in all three dimensions results in a set of widely spaced discrete energy states as illustrated in Figure 16.4 and in principle if their spacing is many multiples of the thermal energy, then only the pair of states with the lowest energy separation, the ground states, are occupied and a recombination current only flows between the states which are lasing and in these circumstances the threshold current is small and should be temperature independent. This idealized quantum dot system is not realized in practice, chiefly because of variability in dot dimensions which produces an inhomogeneous distribution of energy states and also because the states above the ground state, called excited states, may be occupied and contribute a recombination current. Nevertheless, both quantum-confined well and dot structures offer device improvements due to reduction in the active region volume and the effects of confinement.

Quantum dots are formed by self-assembly from a very thin layer of semiconductor material grown on an underlying layer chosen such that the deposited layer is highly strained (Bimberg et al., 1999); the strain is relieved by formation of flat pyramidal islands of material with the height of a few nanometres and lateral dimensions of the order of 10 nm or so, leaving a continuous thin layer of material contiguous with the dots, called the wetting layer, which can be represented as a quantum well. This is known as the Stranski–Krastanov growth mode. A further layer of wider gap material is deposited to form a potential well at the dots in all three directions as illustrated in Figure 16.5. In some cases, the dots are grown within a quantum well producing a dot-in-a-well or DWELL structure.

Quantum dot lasers were first developed in the InGaAs material system, formed by depositing strained InAs layers, for emission at communication wavelengths at 1.3–1.55 μm; however, more recently, InP dots have been produced to extend the wavelength range accessible in the AlGaInP system out to 750 nm, where good tissue penetration makes them attractive for biomedical applications.

The next section provides specific details of AlGaInP quantum well structures; InP dots are described in Section 16.1.6.

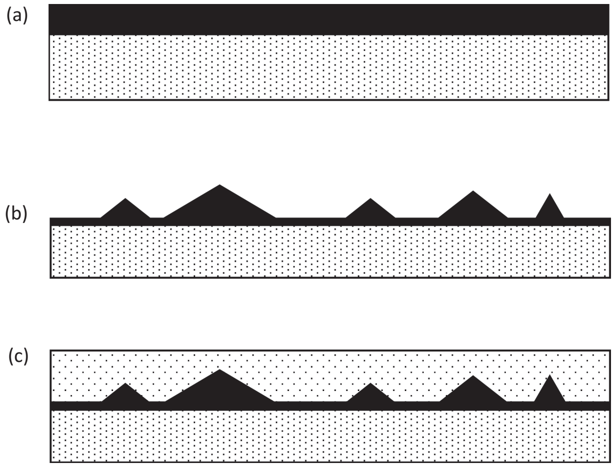

FIGURE 16.5 Illustration of the process of formation of quantum dots by self-assembly. (a) A thin layer of strained material deposited on an underlying epitaxial layer of wider gap, barrier material; (b) the relief of strain by formation of dots leaving a thin wetting layer of material and (c) the dots capped with a wider gap barrier layer.

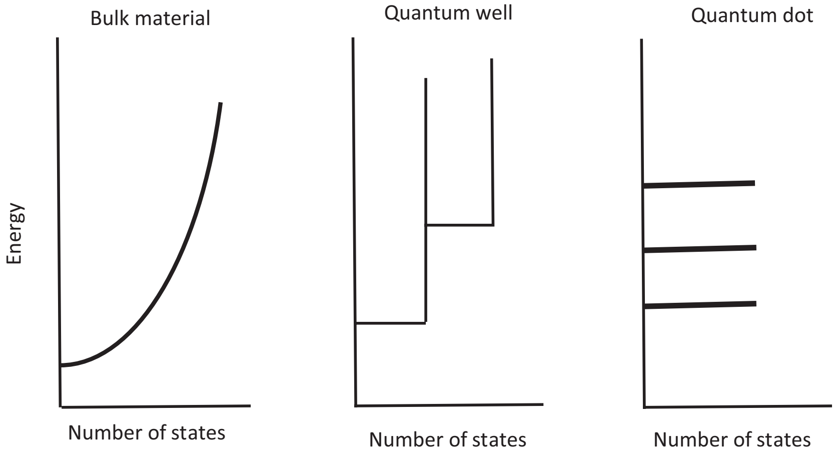

FIGURE 16.4 Schematic diagram showing how the number of states (horizontally) varies with increasing energy (vertically) for a bulk material (number increases parabolically with energy), a quantum well (a step at the confinement energy for each sub-band) and an ensemble of identical dots (discrete atom-like states).

16.1.5 AlGaInP Quantum Wells

The layer structure of a typical lattice-matched $(\text{Al}_x\text{Ga}_{1-x})_y\text{In}_{1-y}\text{P}$ quantum well laser ($y = 0.51$) is shown in Figure 16.6 as a plot of the variation of band gap of the layers with distance from the surface. In this example there is a single GaInP quantum well (5–8 nm thick) within a barrier layer with $x = 0.5$ and of overall width 200 nm, surrounded by outer cladding layers, each about 1 μm thick and having $x = 0.8$. Since the cladding layers have a lower refractive index than the inner barrier material they provide a waveguide which serves to localize the optical mode in the region of the well, which provides the optical gain. The structure has GaAs contact and buffer layers. The substrate is n-type and the structure is doped n-type through the lower cladding layer. The barrier and well region is undoped and the upper cladding and contact is p-type to form the junction necessary for carrier injection into the well to achieve population inversion and laser action. The emission wavelength can be tailored by choice of the width of the well.

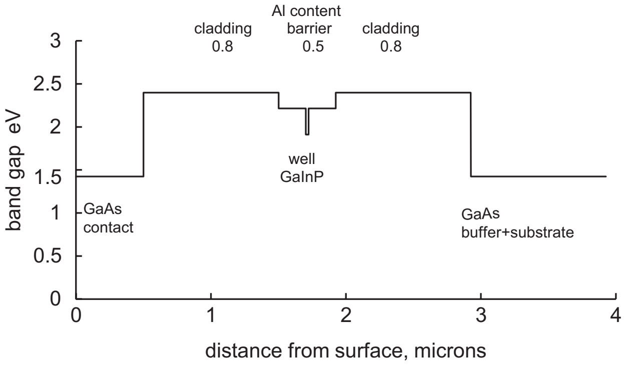

FIGURE 16.6 Schematic diagram of the energy gap through a typical AlGaInP laser structure with a single GaInP quantum well. There are GaAs contact layers at the surface and adjacent to the substrate. The Al content of the cladding and barrier layers is indicated.

While it is necessary that the overall device structure is lattice-matched to the substrate, it is possible to accommodate a limited amount of strain elastically in the thin GaInP quantum well. This enables the composition (y) of the $\text{Ga}_y\text{In}_{1-y}\text{P}$ well to be varied in addition to the width so that a wider range of emission wavelengths can be engineered. The composition dependence of the band gap of 'bulk', unstrained $\text{Ga}_y\text{In}_{1-y}\text{P}$ is given by:

$$E_g(y) = 1.35 + 0.73y + 0.70y^2\,[\text{eV}]. \tag{16.2}$$

With $y < 0.51$, the band gap is reduced below that of unstrained material but the compressive strain brought about by the increase in lattice parameter produces a small increase in gap above that given by Equation (16.2). Conversely with $y > 0.51$, the band gap is increased and tensile strain is introduced to the layer producing a small decrease in gap from that given by Equation (16.2).

The shaded area in Figure 16.7 defines the combinations of well composition (y) and width (L_z), which satisfy the criterion for elastic deformation according to the Matthews–Blakeslee condition (Matthews and Blakeslee, 1974). Outside the shaded region, the strain cannot be accommodated elastically and extended defects form. As well as allowing greater freedom in the choice of well composition, the presence of strain can also reduce the threshold current of the device through strain-induced modification of the electronic structure of the well material (O'Reilly, 1989) as well as being the driver for formation of dots.

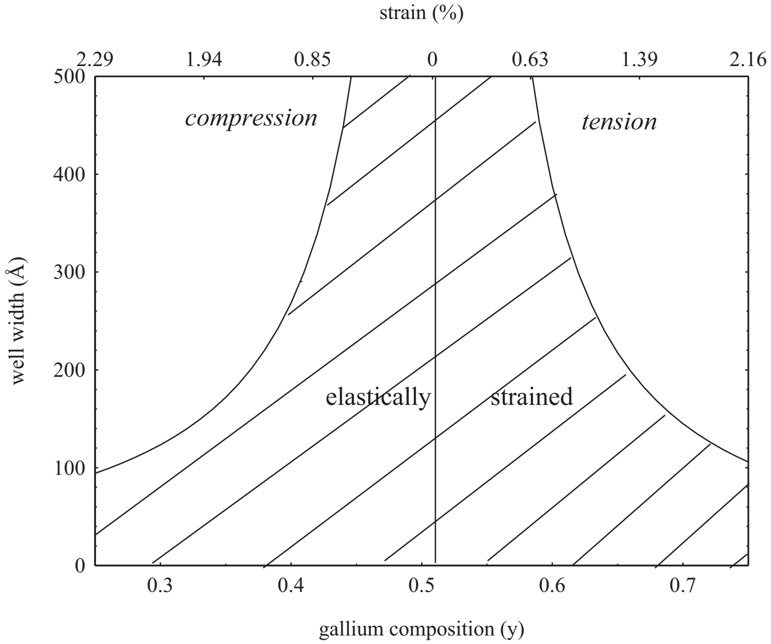

FIGURE 16.7 For the combinations of Ga composition (y) and well width within the shaded area of this diagram, the strain of the $\text{Ga}_y\text{In}_{1-y}\text{P}$ layer can be accommodated elastically. Outside this region, dislocations are formed (Smowton and Blood, 1997b, in chapter 4 of Optoelectronic properties of semiconductors and superlattices, ed M O Manasreh, Gordon and Breach, Fig. 4).

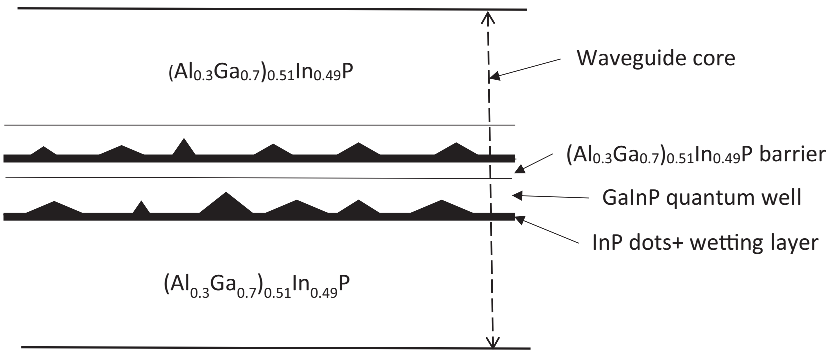
$(Al_{0.3}Ga_{0.7})_{0.51}In_{0.49}P$
Waveguide core
$(Al_{0.3}Ga_{0.7})_{0.51}In_{0.49}P$ barrier
GaInP quantum well
InP dots+ wetting layer
$(Al_{0.3}Ga_{0.7})_{0.51}In_{0.49}P$

FIGURE 16.8 A laser active region comprising a double-layer dot-in-a-well structure showing InP dots and wetting layer on $(Al_{0.3}Ga_{0.7})_{0.51}In_{0.49}P$ lattice matched to a GaAs substrate within a GaInP lattice-matched well. In a device, this structure is embedded in the waveguide core.

AlGaInP is used to make diode lasers over the red region of the spectrum, from 620 to 690 nm, and we concentrate on devices with the generic structure shown in Figure 16.6. Their design exploits the wider parameter space made available by strained quantum wells, with attendant benefits in performance. The proximity of the indirect and direct gaps in the cladding layer places a serious restriction on the realization of short wavelength lasers because the indirect gap is responsible for the leakage of electrons from the active region. The high electrical and thermal resistance of the wide-gap cladding layer also pose serious thermal problems for high-power devices.

AlGaInP quantum well lasers are described in Section 16.2.

16.1.6 InP/AlGaInP Quantum Dots

Dots have been made in the AlGaInP system, formed by deposition of a few monolayers of mismatched InP on AlGaInP, which is itself lattice matched to the underlying materials and the GaAs substrate. A typical dot layer structure is illustrated in Figure 16.8, having two layers of InP dots each deposited on lattice-matched $(Al_{0.3}Ga_{0.7})_{0.51}In_{0.49}P$ and covered with $Ga_{0.51}In_{0.49}P$, placing the dot and wetting layer within a quantum well. This is a DWELL structure. $(Al_{0.3}Ga_{0.7})_{0.51}In_{0.49}P$ also forms the waveguide core, which is within $Al_{0.51}Ga_{0.49}P$ cladding layers. The complete laser structure comprises a waveguide of similar form to that in Figure 16.6 with the multiple DWELL system replacing the well. Since the dots are formed by a random process of self-assembly, their dimensions are not uniform and they have a distribution of size about a mean. This distribution is largely determined by the amount of material deposited and the growth conditions such as temperature and it has an impact upon the magnitude of the peak gain and the form of the gain spectra.

InP quantum dot lasers are described in Section 16.3.

16.2 III–V Red-Emitting Quantum Well Laser Diodes

16.2.1 Design of the Quantum Well Structure

With a lattice-matched $Ga_{0.51}$ $In_{0.49}P$ quantum well emission can be obtained at wavelengths from the practical lower limit of about 625 nm in a thin well to 650 nm in a wide well, set by the band gap of the well material itself (1.91 eV). However, by using compressively strained GaInP it is possible to reduce the band gap of the well to extend this to longer wavelengths. For example, the Ga composition can be reduced to about 0.25 giving a minimum direct gap of about 1.63 eV (760 nm) in the well. However, Figure 16.7 shows that at this composition, the well must be thinner than 10 nm to avoid dislocation formation and the resulting quantum confinement increases the transition energy, resulting in a wavelength of about 725 nm. In practice, devices operating at room temperature can only be made using strains of up to about 1% because at higher compressive strain the GaInP well material becomes inhomogeneous, forming clusters rather than a continuous epitaxial layer. These clusters may be on a dimensional scale similar to the wavelength of light and scatter light out of the laser mode leading to a high internal optical loss, which ultimately prevents the laser working (Mogensen et al., 1998). In using tensile-strained GaInP layers to increase the photon energy and reduce the wavelength, quantum confinement arising from the need to keep the layer thin to accommodate the strain serves to contribute a further increase to the transition energy. In this case, the lower wavelength limit is set by the loss of carriers to the indirect energy gap.

As well as using strain to access a wider range of wavelengths, it is also possible to use different combinations of well width and well composition to achieve the same transition energy. Figure 16.9 shows two possible quantum well structures for emission at 633 nm. The compressively strained well has $y = 0.41$ and a width of 3 nm, while the tensile strained well has $y = 0.56$ giving a much larger band gap, so the well is wider at 12.5 nm to reduce the effects of quantum confinement. The question then arises as to which structure gives the ‘best’ device performance. Valster and coworkers (1992) have investigated the effect of strain at the fixed wavelength of 633 nm (Figure 16.10) and these data show that about 0.5% compressive and tensile strain reduces the threshold of these devices, with tensile strain giving the greatest effect. Smowton and coworkers (1994) have investigated the choice of well width/strain combinations for optimum 670 nm lasers. Small amounts of tensile or compressive strain initially reduce the threshold current but to maintain a fixed wavelength under compressive strain, the well width must be reduced and monolayer variations in well width broaden the gain spectrum

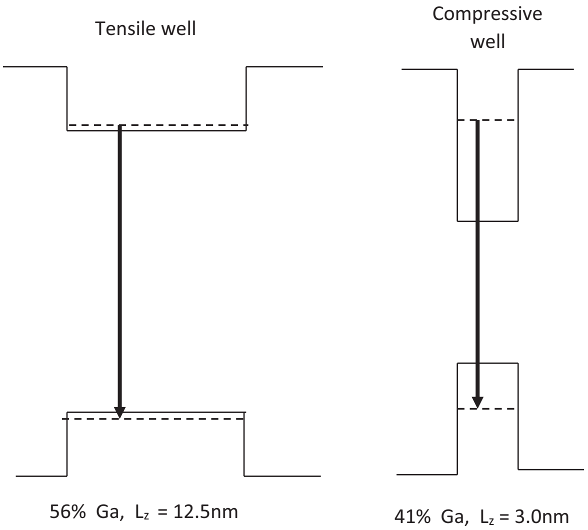

FIGURE 16.9 Illustration of compressive and tensile strained quantum well structures, both of which provide a transition energy of 633 nm (Data from: Smowton et al., 1995). The wide tensile-strained well will have further sub-bands at higher electron and hole energies.

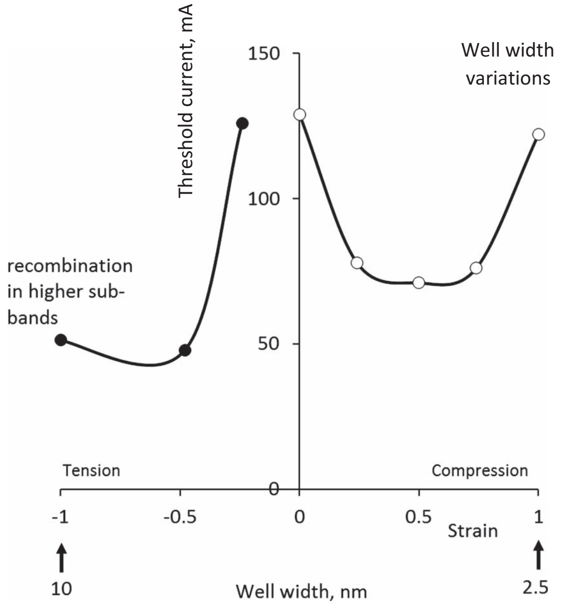

FIGURE 16.10 Experimental variation of the room temperature threshold current of 633 nm lasers with different combinations of well widths and compositions/strain. (Data from Valster et al., 1992.)

causing an increase in threshold as the strain is increased further. Under increasing tensile strain, the well width must be increased, which reduces the sub-band separation such that the higher sub-bands contribute to the current, also increasing the threshold. These features are apparent in Figure 16.10. Furthermore, from a practical standpoint, it is difficult to achieve wavelength reproducibility in very thin wells (a monolayer change in well width changes the transition wavelength of a 3-nm wide well by about 5 nm), therefore wider tensile strained wells may be preferred.

16.2.2 Intrinsic Gain and Recombination Characteristics

The modal optical gain (G) is defined as the fractional increase in energy in a specific optical mode per unit path length (Blood, 2015, Section 4.3). Because the mode is only partially coupled to the gain-generating region of the well it is usual to define a local (or material) gain (g) for the well itself (the well is much thinner than one optical wavelength) which is related to the modal gain by the optical confinement factor (Γ) as $G = \Gamma g$. The gain necessary for laser action is produced by stimulated transitions of electrons from the conduction band to the valence band across the direct gap. An account of the theory of optical gain, treating the electrons as non-interacting particles, is given in textbooks such as Blood (2015). Gain is produced over a range of photon energies and, for a given quantum well, its magnitude is determined by the separation of the quasi Fermi levels for electrons and holes, which is equal to the internal voltage of the device. In an edge-emitting device, laser action occurs when the optical gain just matches the optical losses from the cavity (due to scattering of light out of the guided mode and due to light emitted from the laser for external use), so threshold is determined by the peak value on the gain spectrum. Through the gain process, the optical loss determines the position of the quasi-Fermi levels at threshold and these are important in controlling the carrier leakage from the active region.

Current must be supplied to the well to maintain the threshold carrier density and internal voltage against recombination processes across the gap. In the absence of extrinsic non-radiative processes and carrier leakage, the current at and below threshold is due to spontaneous emission (Figure 16.11); it is usual to suppose that the photon density at threshold is sufficiently small that the stimulated recombination rate is negligible at *threshold*. Consequently, the intrinsic threshold current density is given by the integral of the spontaneous emission spectrum:

$$J_{\text{spon}}^{\text{th}} = -e\int R_{\text{spon}}(hv)\,\mathrm{d}hv \tag{16.3}$$

where $R_{\text{spon}}(hv)$ is the spontaneous recombination rate per unit area at photon energy hv, at threshold.

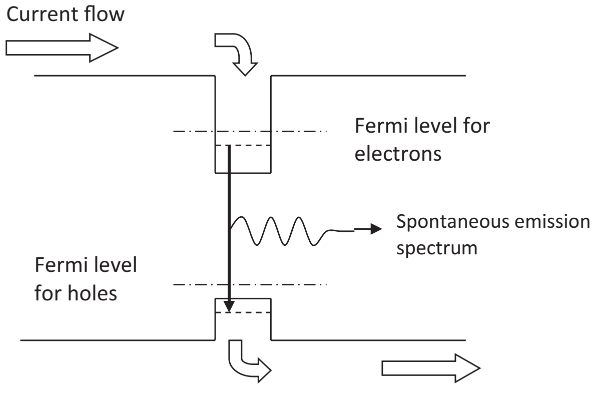

FIGURE 16.11 Band diagram of a quantum well showing the recombination current path at a given Fermi level separation.

It is necessary to take account of the broadening of the individual transitions due to dephasing by carrier collisions not included in a single-particle treatment and due to the effects of inhomogeneous broadening by monolayer variations in thickness along the quantum well. The former process is often incorporated as spectral broadening by a lineshape function (often a Lorentzian) defined by a fixed dephasing lifetime or, more realistically, by a lifetime which is calculated for the specific carrier density and transition energy. However using a simple lifetime it is not possible to obtain agreement between theoretical and experimental gain spectra; good agreement is obtained using the quantum kinetic equations (Chow et al., 1997a).

The variation in well width within a device can have a significant effect when the wells are thin and it is an important factor in determining the optimum well width (Smowton et al., 1994). The effect of broadening processes is to widen both the gain and emission spectra, reducing their peak values; consequently it is necessary to drive the device to a higher internal voltage and carrier density to generate the required peak gain, increasing the threshold current compared with that calculated in the absence of broadening. In a thin well (2.5 nm), the current needed to achieve a given value of gain is increased by these fluctuations by about 25%, whereas the effect is negligible for the thicker well.

A general characteristic of the variation of peak gain with current for quantum wells is that it saturates at high current for recombination between the lowest pair of sub-bands. The relation between optical gain g and current density J for a single pair of sub-bands can be written in the form (McIlroy et al., 1985)

$$g = g_{\mathrm{t}} \ln\left(\frac{J}{J_{\mathrm{t}}} + 1\right) \tag{16.4}$$

where g_{t} and J_{t} are parameters that describe the $g(J)$ relation of specific structures and are defined as the point where a line through the origin is a tangent to the $g(J)$ curve. If these parameters are known from theoretical calculations, then these relations enable the gain–current relations to be reconstructed. They also enable analytic expressions to be derived for threshold *current* as a function of cavity length for optimization of device designs with respect to cavity length and mirror reflectivity (McIlroy et al., 1985, 18 and Blood, 2015, Section 15.6). Because the gain-current density curve is non-linear, there is a minimum in the threshold current as a function of cavity length (Blood, 2015, Section 15.6, McIlroy et al., 1985 and Figures 26 and 27 of Zory et al., 1986). Typical values for the gain parameters for GaInP quantum wells are given in Table 16.1.

A strained structure offers a considerable choice of well width and composition/strain for emission at a specific wavelength and one use of gain–current curves is to provide guidance in the choice of an appropriate structure. As an example, Figure 16.12 shows calculations of the intrinsic threshold current density of 450 μm long, 670 nm lasers as a function of well width (lower axis), with the composition/strain being adjusted as indicated on the upper axis to maintain the same transition energy. The curve has a minimum at a well width of about 3.5 nm indicating that there is a specific structure which will provide a minimum threshold current. The details of optimization of 670 nm devices have been discussed by Smowton et al. (1994). The upturn of this curve for narrow wells is due to the spectral broadening by well-width fluctuations as shown for compressively strained devices in Figure 16.10 (Blood and Smowton, 1995).

16.2.3 Threshold Current

The gain–current curves discussed in the previous section enable the *intrinsic* threshold current to be calculated for a specific device. However, in real lasers, there are further *extrinsic* current paths, which also contribute to the total threshold current. In red lasers, the chief extrinsic processes are non-radiative recombination via defects in the quantum well, which provides a parallel current path (J_{nr}) to the spontaneous recombination in Figure 16.11, and thermally activated carrier

TABLE 16.1

Theoretical and Experimental Data for Gain–Current Parameters (Equation (16.4)) of GaInP Quantum Wells

Well Width (nm)	Composition Ga, *y*	Wavelength (nm)	Comments	g_{th} (cm^{-1}) (Material Gain)	J_t (A cm^{-2}) (Spontaneous Current)
2.5	0.25	670	No well fluctuations[a]	5100	275
2.5	0.25	670	With well fluctuations[a]	4800	335
6.8	0.41	670	[a,b]	1600	371
6.8	0.41	670	[a,c]	1850	470
Experimental Data at 160 K[d]				Modal Gain (cm^{-1})	(Total Current)
12.5	0.56	637	Tensile strain	62 ± 4	344 ± 12
3.0	0.41	637	Compressive strain	69 ± 9	426 ± 34
12.0	0.42	675	Compressive strain	60 ± 7	399 ± 30

[a] Data from (Smowton and Blood, 1997b).

[b] The effect of well width fluctuations is small at this well width.

[c] This is the result of a full 'many-body' calculation as described by Smowton et al. (2000). The effect of well width fluctuations is negligible at this well width and fluctuations have not been included in the calculation.

[d] Experimental data from Smowton et al. (1995). These results are for modal gain (local gain × optical confinement factor) and the current is that due to all paths through the structure. The measurements are at 160 K, where carrier leakage is thought to be negligible but there may be a non-radiative contribution within the well. The intrinsic current parameter J_{t} increases approximately linearly with temperature.

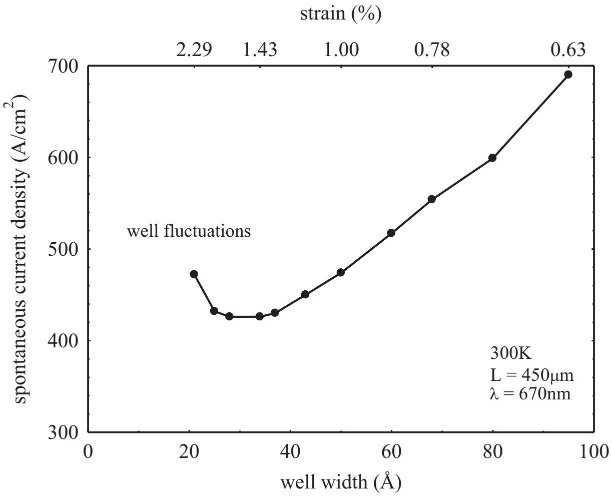

FIGURE 16.12 Calculations of the threshold current density of 450 μm long compressively strained 670 nm GaInP lasers as a function of well width with the composition/strain adjusted to keep the same transition energy. The calculation uses an energy- and density-dependent dephasing time and includes well-width variations. The up-turn in threshold current for the very thin well is due to the broadening of the gain spectrum by well-width variations (Smowton and Blood, 1997b, in chapter 4 of Optoelectronic properties of semiconductors and superlattices, ed M O Manasreh, Gordon and Breach, Fig. 18 (line a)).

leakage (J_l) through the cladding layer (see Figure 16.6); this process is discussed in more detail below. Thus, the total current at threshold is

$$J_{\mathrm{th}} = J_{\mathrm{spon}}^{\mathrm{th}} + J_{\mathrm{nr}} + J_{l}. \tag{16.5}$$

The extrinsic currents depend upon the material quality and the details of the specific structure and the non-radiative current in particular is difficult to predetermine. Sometimes these currents are lumped together into an unknown radiative quantum efficiency (η) defined as the ratio of the radiative current to the total current so that

$$J_{\mathrm{th}} = \frac{J_{\mathrm{spon}}^{\mathrm{th}}}{\eta}. \tag{16.6}$$

We issue a word of warning that the term ‘quantum efficiency’ is used in a variety of inconsistent ways in the literature, for example it is often erroneously interchanged with the differential quantum efficiency (or slope efficiency). The definitions of efficiency are set out in Section 5.5 of Blood (2015) (see also Smowton and Blood, 1997a, for an analysis of these issues in red-emitting lasers). The “bottom line” is that the efficiency η in Equation (16.6) may vary from one device to another and is very difficult to measure directly. A value of 0.33 has been reported for a 670 nm GaInP laser determined from a measurement of gain and emission spectra using a special device with segmented contacts (Blood et al., 2003).

An illustration of the form of the temperature dependence of threshold current density is shown in Figure 16.13. This form is typical of quantum well and quantum dot devices above about 200 K. At low temperatures the threshold current increases linearly with temperature due to recombination current in the quantum well, then at higher temperature carriers are thermally activated to populate the barriers alongside the wells and the waveguide cladding layers. Usually, the composition of the cladding layers is such that the lowest conduction band is the indirect minimum and electrons leak away from the active region through this p-type cladding to the top contact (Bour et al., 1993, Smowton et al., 1995). These thermally activated processes are particularly strong in short-wavelength devices, where the quasi-Fermi level at threshold is high in the well whereas carrier leakage through the cladding is weak in 670 nm devices up to about 80°C. However at these wavelengths there is evidence of thermal population of the barrier material where the potential barrier is not as high as that of the cladding and the recombination current is dominated by non-radiative recombination via defects in Al-containing material.

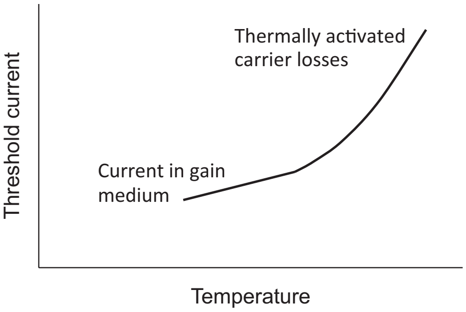

FIGURE 16.13 Illustration of the form of the temperature dependence of threshold current for quantum well lasers and quantum dot lasers above about 200 K.

Many applications of red-emitting lasers demand high output power and this is an area where there have been steady improvements in power conversion efficiency, optical power out divided by electrical power in. Power performance is very much related to the operating wavelength and the finer details of the device structure and mounting, as illustrated by the work of Sumpf et al. (2007). To minimize voltage drops in the structure, high doping levels are required in the cladding layers, but at high density, Zn has a tendency to diffuse into the structure and degrade the well. This can be overcome using a p-cladding layer of AlGaAs, which can be doped with C, which is less prone to diffusion. Power output of about 3 W has been obtained from such a 650 nm asymmetric single well laser 100 μm wide and 1.5 mm long (larger area decreases the thermal resistance to the heat sink) with anti-reflection front facet coating (4%) and high reflection rear facet coating (94%) (most of the light is emitted from the front), mounted p-side down (the heat-generating region is near the heat sink) on a diamond heat sink (high thermal conductivity).

16.2.4 Carrier Leakage

The strong temperature dependence of threshold current in GaInP lasers is due primarily to the leakage of electrons through the p-cladding layer (Bour et al., 1993, Smowton and Blood, 1995, Wood et al., 2000). The process is illustrated schematically in Figure 16.14 which shows the energies of the conduction and valence bands as functions of distance through a 670-nm double-well laser at threshold. The band edge of the n-type cladding layer is flat due to good electrical

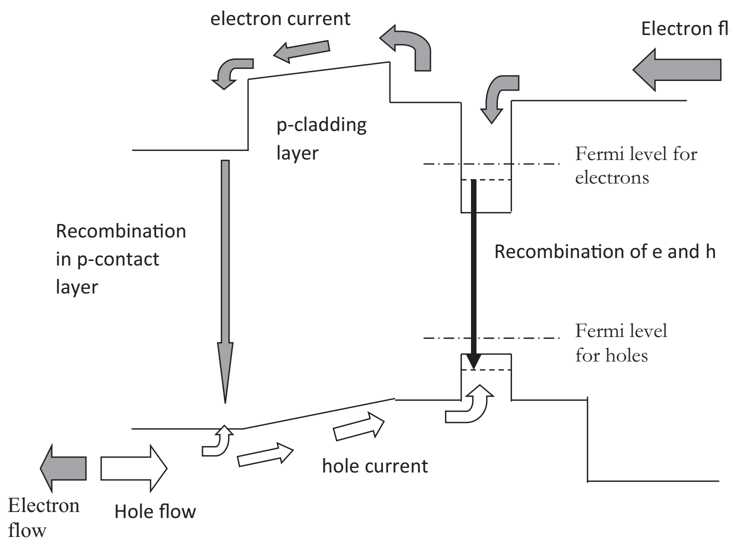

FIGURE 16.14 Schematic diagram showing current flow through a laser structure. Electrons leak as minority carriers through the p-cladding layer to recombine with holes in the p-contact layer. The hole current to the well generates an electric field across the resistive p-cladding layer, which assists the flow of electrons away from the active region.

conductivity, whereas there is a significant electric field across the p-cladding layer due to its high electrical resistivity caused by a low hole mobility and difficulties in achieving high concentrations of electrically active acceptors in the cladding material. This field is generated primarily by the majority carrier (hole) current which flows through the valence band of cladding layer to the active region. In the conduction band of the p-cladding layer, the indirect X conduction band edge lies below the direct minimum (see Figure 16.3) and electrons leak from the active region through this X-conduction band. Due to the high electric field established by the hole current electrons are swept through the cladding layer to the p-contact layer, a drift process. There is also a current contribution by electron diffusion due to their concentration gradient. Drift leakage is particularly deleterious because the electric field is proportional to the majority carrier current supplying the lasing process in the quantum well. As the temperature increases, the number of electrons able to escape increases exponentially; furthermore, the intrinsic hole current through the well needed to maintain a fixed gain increases with temperature and this also increases the leakage by increasing the field in the p-cladding, adding to the increase in total current with temperature. Self-consistent calculations of the energy bands through GaInP laser structures are described by Foulger et al. (1997).

Electron leakage is substantial in this material because of the low energy of the indirect conduction band edge (which determines the number of electrons able to escape), and because the field in the cladding layer is large (which increases the rate at which they can escape). Possible strategies to decrease this thermally activated current include efforts to increase the p-doping density in the cladding layer to reduce the field, keeping the hole current through the cladding layer as small as possible by minimizing the gain requirement (a long cavity and/or coating the mirrors and/or maximizing coupling between the well and the optical field) and increasing the height of the potential barrier seen by the electrons. There is little opportunity to increase the band gap of the cladding layer to increase the barrier height because the indirect gap is insensitive to alloy composition (Figure 16.3). However, there have been attempts to increase the effective height of the barrier by making a quantum mechanical reflector (Iga et al., 1986) providing an effective barrier up to twice the height of the electrostatic barrier (Takagi et al., 1991). The layers required are very thin (four to six monolayers) and although attempts to employ such structures in GaInP lasers (e.g. Raisch et al., 1999) have achieved reductions in threshold current it is difficult to attribute these unambiguously to an increase in the effective barrier height.

These actions may have other consequences for the performance of the laser. For example, the waveguide design influences the divergence of the external beam, affecting the coupling into an optical system (a plastic fibre for example), as well as the optical confinement factor (Elliott et al., 2006).

16.2.5 Vertical-Cavity Surface-Emitting Lasers (VCSELs)

Conventional diode lasers are in the form of a chip typically 300 μm square and with an active stripe region of about 5 μm wide. To realize a laser device it is necessary to cleave the wafer to produce reflecting end facets; consequently, the light is emitted from the end of the chip. These are termed edge-emitters. This geometry has several disadvantages: special mounting arrangements are needed because the light is emitted in a direction perpendicular to the plane on which the device is bonded, it is not easy to produce arrays of devices (for example, for high-power sources) and it is necessary to go through the labour intensive process of cleaving the wafer into chips before the device performance can be assessed. Edge-emitters also have an elliptical far-field pattern.

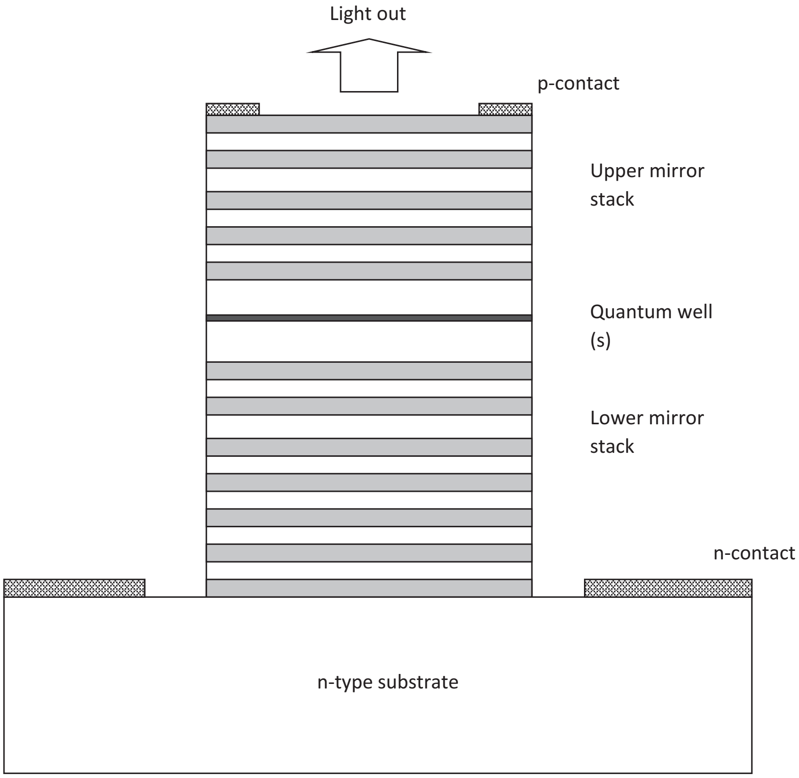

FIGURE 16.15 Schematic diagram of a vertical-cavity surface-emitting laser (VCSEL).

Iga et al. (1988) proposed the vertical-cavity geometry, where the light is emitted in a direction normal to the plane of the wafer, which has since evolved to use multilayer epitaxial mirrors to take the form illustrated in Figure 16.15. This has many advantages by allowing on-wafer testing before dicing into discrete chips, easier mounting due to the planar structure, fabrication of arrays and a circular far field. The device is usually made by growing a lower epitaxial multilayer dielectric Bragg reflector of alternating layers of semiconductors with different dielectric constant, then the laser cavity with a quantum well active region followed by an upper Bragg mirror. The cavity is very short, usually a few optical wavelengths, so the mirrors must have a high reflectivity (typically 0.996 or higher) so that the optical loss can be matched by the gain of the active region. These are termed VCSELs. Accounts of the current status of VCSELs are given in Wilmsen et al., 1999; Michaizik, 2013. While there is a general drive to utilize the generic advantages of VCSELs in red-emitters, the ability to make arrays is particularly attractive for high-speed laser printers.

The major issue which had to be addressed in making AlGaInP red-emitting VCSELs was the fabrication of the mirrors (Schneider and Lott, 1993). The variation of refractive index with composition is weaker in AlGaInP compared to AlGaAs, consequently, more layer pairs are needed to achieve similar values of reflectivity, and the band of high reflectivity is narrower. This puts greater demands on the control of the growth process and introduces more electrical and thermal resistance into the structure. For this reason, some red-emitting VCSELs combined an AlGaInP well and barrier system with AlGaAs multilayer mirrors (Schneider et al., 1995). As with edge-emitters, thermally activated carrier loss is an important issue and it is desirable to achieve a low electrical resistance in the mirror stack (Schnieder et al., 1995); however, because of the strong coupling to the optical field this introduces a higher free-carrier optical loss, increasing the gain requirement. In early devices lateral current confinement was provided by ion implantation, but confinement by lateral oxidation of high-Al-content layers has been shown to be a better approach (Choquette et al., 1995 and Jager et al., 1997). A comprehensive account has been given by Chow et al. (1997b).

16.3 Quantum Dot Lasers

16.3.1 Motivation

Although quantum dot lasers have not fulfilled all initial, optimistic expectations they do have a number of attractive features such as low threshold current density (but also lower gain) and a wide gain spectrum (due to inhomogeneous broadening), which can be exploited to produce ultra-short pulses (ps and below) by mode-locking. Development of InP/AlGaInP quantum dot lasers (Zundel et al., 1998) has been motivated principally by two application areas. Silicon-based single-photon detectors used in free-space quantum cryptography and quantum computing have their maximum efficiency in the region of 675 nm and red-emitting dot lasers provide single-photon sources in this range

(Zwiller et al., 2003). Second, the tolerance of quantum dots to comparatively high lattice mismatch enables devices to be made emitting at 740 nm providing good tissue penetration for biomedical applications (Shutts et al., 2014).

16.3.2 Dot Structure and Optical Gain

The height of self-assembled dots is usually much smaller than the dimensions of their base so this dimension is the principal factor determining the energy of the dot states. Detailed studies of InP dots, without the upper layer capping the dots, by atomic force microscopy, reveal a bimodal distribution of dot sizes, that is height distributions about two mean values as illustrated in Figure 16.16; in the measurements of Porsche et al. (2000), these are centred on heights of 5 and 20 nm. These distributions, and the dot densities, are controlled by the growth conditions (Schulz et al., 2009) and result in inhomogeneously broadened optical spectra, producing several series of peaks for ground and excited-state transitions in the optical absorption spectra (AlGhamdi et al., 2011). This inhomogeneous broadening has a much greater impact on the gain than fluctuations in the width of quantum wells.

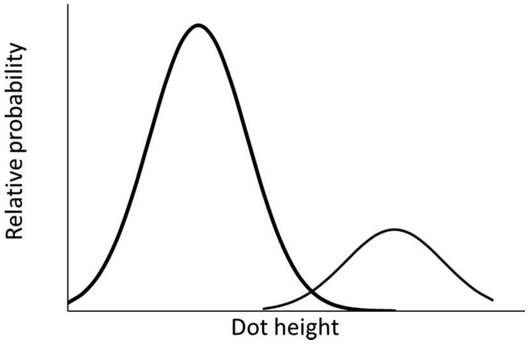

FIGURE 16.16 Illustration of a bimodal distribution in dot height. The measurements of Porsche et al. (2000) show two distributions centred on heights of 5 and 20 nm. Usually the dot height is smaller than the base dimensions and is the principal factor that determined the energy of the combined states.

The gain usually originates in the group of dots with the greatest height since these have confined states at the lowest energies and are the first to be inverted. The magnitude of the gain is determined by the density of dots in the group, which, for a fixed dot density, decreases with increasing width of the size distribution: the wider the distribution, the smaller the gain at the spectral peak. An illustration of modal gain spectra for a mono-modal distribution of ground and excited states is shown in Figure 16.17. Multiple layers of dots are used to increase the dot density and hence the available gain. The maximum peak modal ground state gain for multiple layers of dots is in the region of 10–40 cm^{-1}, which is smaller than for quantum well systems at similar current densities, which are in the region of 120 cm^{-1} for a single well. Devices are usually designed to operate on the ground state and quantum dot lasers have longer cavities, typically 2 mm, to give a smaller distributed optical loss per unit length, small enough to be matched by the available gain.

Because the carriers are thermally spread across the inhomogeneous and bimodal state distributions, the number of dots contributing to the gain is only a small fraction of the number contributing to the current. Inversion of the dots is also limited by the population of the high density of available states in the wetting layer (Matthews et al., 2002). As in quantum wells, the gain–current relation saturates at high current, although a different functional approximation has been adopted for dots of the form (Zhukov et al., 1999)

$$G_{\text{pk}} = G_0 \left\{ 1 - \exp\left[\frac{-\gamma (J - J_{\text{trans}})}{J_{\text{trans}}} \right] \right\} \tag{16.7}$$

where G_{pk} is the peak gain at current density J, and G_0, γ ($\approx$1) and J_{trans} are parameters that characterize the relation for

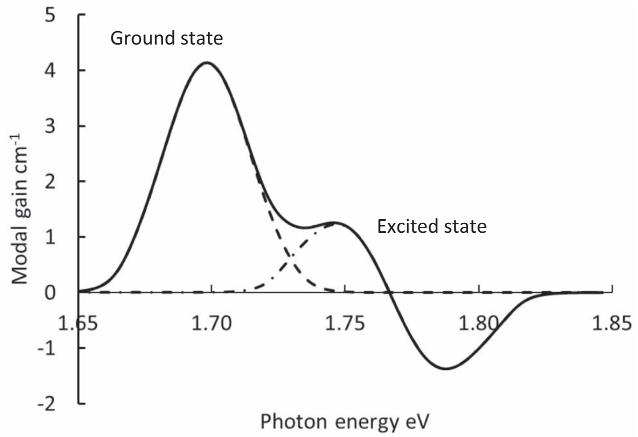

FIGURE 16.17 Illustration of the modal gain spectrum of a quantum dot laser with mono-modal size distribution showing the contributions from the ground and excited states. The quasi Fermi energy separation is about 1.765 eV, so all the ground states are inverted and provide gain, whereas the higher energy excited states are not inverted and are absorbing. Although absorption spectra from bimodal InP dot structures show two interlaced sets of ground and excited states (Al Ghamdi et al. 2011), these details are often smeared out in the gain spectra by the thermal occupation distribution across the states.

a particular structure, the latter being the current density at transparency. This analytic form has not been as widely used as that for quantum wells, possibly because the properties of a particular structure are difficult to quantify and are sensitive to the details of the growth conditions. Nevertheless, the form of the relation has similar consequences with regard to optimization of device structures (e.g. with respect to cavity length) as quantum wells. Since individual quantum dots are smaller than the wavelength of light with which they interact the concept of local or material gain must be used with care: usually it refers to a layer of dots (Blood, 2015, Section 9.4). Modal gain is often the preferred measure of the gain of a dot system.

16.3.3 Devices

The structure and principles of operation of quantum dot lasers are similar to quantum well devices, with the dot and wetting layer replacing the well in Figure 16.6. Reported values of the threshold current density at room temperature of InP dot lasers were initially much higher than their longer wavelength InAs counterparts, several kA cm^{-2}, but with attention to the growth conditions a value of 190 A cm^{-2} was reported for a 2-mm long device with uncoated facets emitting at 741 nm (Smowton et al., 2005). This improvement was ascribed to elimination of a group of very large dots and the defects associated with them. Further reductions to 138 A cm^{-2} have been achieved by use of strained layers of $Ga_{0.58}In_{0.42}P$ above each dot layer (Smowton et al., 2005). Estimates have been made of the efficiency of 2-mm long dot-in-a-well laser structures emitting at about 745 nm using spectrally resolved, calibrated measurements of spontaneous emission from dots and wells (Smowton et al., 2011): the ratio of the spontaneous recombination current in the dots to the external current was found to be 0.2. Since these devices operate at longer wavelengths than their quantum well counterparts heterobarrier leakage is not such a severe problem; nevertheless, the recombination current in the wells (and/or wetting layer) alongside the dots increases rapidly with temperature, following a form similar to that in Figure 16.13, contributing about one-third of the total current at room temperature and being responsible for the strong temperature dependence of threshold in these lasers. At low temperatures, below about 250 K, the threshold current of quantum dot lasers increases with a further decrease in temperature due to a transition for thermal population of dots around room temperature to random population at low temperature (see Blood, 2015, Chapter 10 for an account of this behaviour and further references).

Quantum dots offer particular advantages for dual-wavelength lasers because laser action in one size group is not strongly affected by laser action at a different wavelength in a different size group. For example, simultaneous emission at 686 and 720 nm has been demonstrated in a two-section device with distributed Bragg reflectors (Shutts et al., 2015). Such sources have potential application in read/write devices form optical storage and a range of bio-photonic processes, exploiting the good tissue penetration at these wavelengths.

16.4 Summary

The design and performance of red-emitting AlGaInP laser diodes can be summarized as follows.

- The availability of a ternary alloy system, which can be lattice matched to GaAs substrates, enables device designs to be optimized through the independent choice of well width and well composition, with the latter determining the degree of elastic strain.
- The indirect band gap at about 2.25 eV imposes a fundamental limit on the range of wavelengths, which can be engineered in this system, even though the direct gap can be increased to about 2.5 eV.
- Carrier leakage through the indirect conduction band minimum is exacerbated by the electric field caused by the relatively high electrical resistivity of the p-type cladding layer due to the low hole mobility and hole density. This introduces a strong temperature dependence to the threshold current, particularly at the shortest wavelengths.
- This alloy system permits only small changes in refractive index, which means that many periods are required for effective AlGaInP Bragg reflectors for VCSELs.
- AlGaInP has a lower thermal conductivity than AlGaAs, causing a higher temperature rise in the active regions with implications for the design of high-power devices.
- Quantum dot lasers have been developed by deposition of thin, highly strained layers of InP on AlGaInP providing devices operating at wavelengths out to the region of 740 nm with good tissue penetration, suitable for biomedical applications. While these longer wavelength devices are not subject to serious heterobarrier leakage, the threshold current is temperature dependent due to recombination in the wetting layer.

Acknowledgements

The author thanks his colleagues in Cardiff, also Weng Chow, David Bour and Steve Bland for their contributions to research activities on GaInP lasers, provision of material and valuable discussions. Funding for the Cardiff research activities was provided by the Engineering and Physical Sciences Research Council.

REFERENCES

Agrawal G P and Dutta N K 1986 *Long Wavelength Semiconductor Lasers* (New York: Van Nostrand Reinhold).

Al-Ghamdi M S, Smowton P M, Blood P and Krysa A B 2011 Dot density effect by quantity of deposited material in InP/AlGaInP structures *IEEE Photon. Technol. Lett.* **23** 1169–71.

Bimberg D, Grundman M and Ledentsov N. N 1999 *Quantum Dot Heterostructures* (Chichester: Wiley).

Blood P 2015 *Quantum Confined Laser Devices* (Oxford: Oxford University Press).

Blood P, Fletcher E D, Woodbridge K, Heasman K C and Adams A R 1989 Influence of the barriers on the temperature dependence of threshold current in GaAs/AlGaAs quantum well lasers *IEEE J. Quantum Electron.* **25** 1459.

Blood P, Lewis G M, Smowton P M, Summers H D, Thomson J and Lutti J 2003 Characterization of semiconductor laser gain media by the segmented contact method *IEEE J. Selected Topics Quantum Electron.* **9** 1275–82.

Blood P and Smowton P M 1995 Strain dependence of threshold current in fixed-wavelength GaInP laser diodes *IEEE J. Selected Topics Quantum Electron.* **1** 707–11.

Bour D P, Treat D W, Thornton R L, Geels R S and Welch D F 1993 Drift leakage current in AlGaInP quantum well lasers *IEEE J. Quantum Electron.* **29** 1337–43.

Casey H C Jr and Panish M B 1978 *Heterostructure Lasers* (San Diego, CA: Academic).

Chen G S, Jaw D H and Stringfellow G B 1990 Effects of substrate misorientation on ordering $InGaAs_{0.5}P_{0.5}$ grown by organometallic vapor phase epitaxy *Appl. Phys. Lett.* **57** 2475–7.

Choquette K D, Schneider R P, Crawford M H, Gleib K M and Figiel J J 1995 Continuous room temperature operation of 640–660 nm selectively oxidized AlGaInP vertical cavity lasers *Electron. Lett.* **31** 1145–6.

Chow W W, Choquette K D, Crawford M H, Lear K L and Hadley G R 1997b Design, fabrication, and performance of infrared and visible vertical-cavity surface-emitting lasers *IEEE J. Selected Topics Quantum Electron.* **33** 1810–24.

Chow W W, Smowton P M, Blood P, Girndt A, Jahnke F and Koch S W 1997a Comparison of experimental and theoretical GaInP quantum well gain spectra *Appl. Phys. Lett.* **71** 157–9.

Elliott S N, Smowton P and Berry G 2006 Optimisation of high power AlGaInP laser diodes for optical storage applications. *IEE Proc. Optoelectron.* **153** 321–5.

Foulger D L, Smowton P M, Blood P and Mawby P A 1997 Self-consistent simulation of AlGaInP visible lasers *IEE Proc. Optoelectron.* **144** 23–9.

Iga K, Koyama F and Kinoshita S 1988 Surface emitting semiconductor lasers *IEEE J. Quantum Electron.* **24** 1845–55.

Iga, K, Uenohara H and Koyama F 1986 Electron reflectance of multiquantum barrier (MQB) *Electron. Lett.* **22** 1008–9.

Jager R, Grabherr M, Jung C, Michalzik R, Reiner C, Weigl B and Ebeling K J 1997 57% wall-plug efficiency oxide confined 850 nm wavelength VCSELs *Electron. Lett.* **33** 330–1.

Kondow M, Kakibayashi H, Tanaka T and Minagawa S 1989 Ordered structure in $Ga_{0.7}In_{0.3}P$ alloy *Phys. Rev. Lett.* **56** 884–6.

Matthews D R, Summers H D, Smowton P M and Hopkinson M 2002 Experimental investigation of the effect of wetting layer states on the gain-current characteristic of quantum-dot lasers *Appl. Phys. Lett.* **81** 4904–06.

Matthews J W and Blakeslee A E 1974 Defects in epitaxial multilayers: I. Misfit dislocations *J. Crystal Growth* **27** 118.

McIlroy P W A, Kurobe A and Uematsu Y 1985 Analysis and application of theoretical gain curves to the design of multiple quantum well lasers *IEEE J. Quantum Electron.* **21** 1958–63.

Michaizik R 2013 *VCSELs: Fundamentals, Technology and Applications of Vertical Cavity Surface Emitting Lasers,* (Berlin: Springer).

Mogensen P C, Hall S A, Smowton P M, Bangert U, Blood P and Dawson P 1998 The effect of high compressive strain on the operation of AlGaInP quantum well lasers *IEEE J. Quantum Electron.* **34** 1652–9.

O'Reilly E P 1989 Valence band engineering in strained-layer structures *Semicond. Sci. Technol.* **4** 121–37.

Okuda H, Anayama C, Tanahashi T and Nakajima K 1989 X-ray investigation of the ordered structure of AlGaInP quaternary alloys *Appl. Phys. Lett.* **56** 731–3.

Porsche J, Ost M, Scholz F, Fantini A, Phillipp F, Riedl T and Hanglieter A 2000 Growth of self-assembled InP quantum islands for red-light-emitting injection lasers *IEEE J. Selected Topics Quantum Electron.* **6** 482–90.

Raisch P, Winterhoff R, Wagner W, Kessler M, Schweitzer H, Reidl T, Wirth R, Hangleiter A and Scholz F 1999 Investigations on the performance of multiquantum barriers in short wavelength (630 nm) AlGaInP laser diodes *Appl. Phys. Lett.* **74** 2158–60.

Schneider R P Jr, Hagerott Crawford M, Choquette K D, Lear K L, Kilcoyne S P and Figiel J J 1995 Improved AlGaInP-based red (670–690 nm) surface emitting lasers with novel C-doped short cavity epitaxial design *Appl. Phys. Lett.* **67** 329–31.

Schneider R P Jr and Lott J A Jr 1993 InAlP/InAlGaP distributed Bragg reflectors for visible vertical cavity surface emitting lasers *Appl. Phys. Lett.* **62** 2748–50.

Schulz W-M, Roßbach R, Reischle G J, Beirne G J, Bommer M, Jetter M and Michler P 2009 Optical and structural properties of InP quantum dots embedded in $(Al_xGa_{1-x})_{0.51}In_{0.49}P$ *Phys. Rev. B*, **79** 035329.

Shutts S, Elliott S N, Smowton P M and Krysa A B 2015 Exploring the wavelength range of InP/AlGaInP QDs and application to dual-state lasing *Semi. Sci. Technol.* **30** 044002.

Shutts S, Smowton P M and Krysa A B 2014 Dual wavelength InP quantum dot lasers *Appl. Phys. Lett.* **104** 241106.

Smowton P M and Blood P 1995 GaInP–(Al_yGa_{1-y})InP 670 nm quantum well lasers for high temperature operation *IEEE J. Quantum Electron.* **31** 2159–64.

Smowton P M and Blood P 1997a The differential efficiency of quantum well lasers *IEEE J. Selected Topics Quantum Electron.* **3** 491–8.

Smowton P M and Blood P 1997b Visible-emitting AlGaInP laser diodes *Strained Layer Quantum Wells and their Applications* ed M O Manasreh (New York: Gordon and Breach) pp 431–87.

Smowton P M, Blood P and Chow W W 2000 Comparison of experimental and theoretical gain-current relations in GaInP quantum well lasers *Appl. Phys. Lett.* **76** 1522–4.

Smowton P M, Blood P, Mogensen P C and Bour D P 1995 Role of sublinear gain-current relationship in compressive and tensile strained 639 nm GaInP lasers *Int. J. Optoelectron.* **10** 383–91.

Smowton P M, Elliott S N, Shuts S, Al-Ghamdi M S and Krysa A B 2011 Temperature-dependent threshold current in InP quantum dot lasers *IEEE J. Selected Topics Quantum Electron.* **17** 1343–8.

Smowton P M, Lutti J, Lewis G M, Krysa A B, Roberts J S and Houston P A 2005 InP-GaInP quantum dot lasers emitting between 690–750nm *IEEE J. Selected Topics Quantum Electron.* **11** 1035–40.

Smowton P M, Summers H D, Rees P and Blood P 1994 Threshold current of 670 nm AlGaInP strained quantum well lasers *IEEE Photon. Technol. Lett.* **6** 910–12.

Sumpf B, Zorn Z, Staske R, Fricke J, Ressel P, Ginolas A, Paschke K, Erbert G, Weyers M and Tränkle G 2007 3-W Broad area lasers and 12 W bars with conversion efficiencies up to 40% at 650 nm *IEEE J. Selected Topics Quantum Electron.* **13** 1188–93.

Takagi T, Koyama F and Iga K 1991 Design and photoluminescence study on a multiquantum barrier *IEEE J. Quantum Electron.* **27** 1511–9.

Valster A, van der Poel C J, Finke M N and Boermans M J B 1992 Effect of strain on the threshold current of GaInP/AlGaInP quantum well lasers emitting at 633 nm *13th Int. IEEE Semiconductor Laser Conf.* (Takamatsu, Japan) (Conference Digest).

Wilmsen C W, Temkin H K and Coldren L A 1999 *Vertical-Cavity Surface Emitting Lasers* (Cambridge: Cambridge University Press).

Wood S A, Molloy C H, Smowton P M, Blood P and Button C C 2000 Minority carrier effects in GaInP laser diodes *IEEE J. Quantum Electron.* **36** 742–50.

Woodbridge K, Blood P, Fletcher E D and Hulyer P J 1984 Short wavelength (Visible) GaAs quantum well lasers grown by molecular beam epitaxy *Appl. Phys. Lett.* **45** 16–18.

Zhukov A E, Kovsh A R, Egorov A Yu, Ledentsov N N, Tsatsulikov A F, Maximov M V, Shernyakov Yu M, Kopchatov V I, Lunev A V, Kopev P S, Bimberg D and Alferov Z I 1999 Gain characteristics of quantum dot lasers *Semicond. Sci. Technol.* **14** 118–23.

Zory P S, Reisinger A R, Mawst L J, Costrini G, Zmudzinski M A, Emanuel M A, Givens M E and Coleman J J 1986 Anomalous length dependence of threshold for thin quantum well AlGaAs diode lasers *Electron. Lett.* **22** 475–6 (Retrospectively use of the word anomalous in the title of this paper is misleading. The effect reported was certainly unusual at the time, but as an understanding of quantum wells advanced it became clear that this is exactly what should happen in such structures.).

Zundel S K, Jin-Phillipp, N Y, Phillipp F, Eberl K, Riedl T, Fehrenbacher E and Hanglieter A 1998 Red-emitting injection laser based on InP/GaInP self-assembled quantum dots *Appl. Phys. Lett.* **73** 1784–6.

Zwiller V, Aichele T, Seifert W, Persson J and Benson O 2003 Generating visible single photons on demand with single InP quantum dots *Appl. Phys. Lett.* 82 1509–11.

FURTHER READING

Bastard G 1988 *Wave Mechanics Applied to Semiconductor Structures [Les Editions de Physique]* (New York: Halstead)

An advanced quantum mechanical treatment of quantum well structures at undergraduate/graduate level.

Bour D P 1993 AlGaInP quantum well lasers *Quantum Well Lasers* ed P S Zory (San Diego, CA: Academic)

A book chapter providing an introductory research review on GaInP lasers.

Chow W W and Koch S W 1999 *Semiconductor Laser Fundamentals* (Berlin: Springer)

A serious text on the theory of semiconductor lasers at a post-graduate level. Deals with the electronic structure of bulk materials and quantum wells and many-body theories of gain.

Chuang S L 2009 *Physics of Photonic Devices* (New York: Wiley)

A comprehensive text at the advanced graduate and post-graduate level. In this book the derivations of equations are given in detail: no recourse to 'it can be shown that' in this text. Covers the basics of semiconductors and quantum mechanics and waveguiding, as well as full accounts of the physics of lasers.

Coldren L A, Corzine S W and Mashanovitch M L 2012 *Diode Lasers and Photonic Integrated Circuits* 2nd ed. (New York: Wiley)

A comprehensive account of the physics of quantum well laser structures at fourth-year undergraduate or first-year post-graduate level, including the basic physics of quantum well structures.

Fox M 2001 *Optical Properties of Solids* (Oxford: University Press)

A useful introduction to the basic physics at the undergraduate level.

Weisbuch C and Vinter B 1991 *Quantum Semiconductor Structures* (San Diego, CA: Academic)

A research review of the fundamental physics and applications of semiconductor quantum well structures.

Wolfe C M, Holonyak N Jr and Stillman G 1989 *Physical Properties of Semiconductors* (Englewood Cliffs, NJ: Prentice-Hall)

A valuable account of the physics of semiconductors including crystal structure, electronic band structure, carrier distributions, minority carrier behaviour, optical properties and heterostructures at final year undergraduate level.

Taylor & Francis
Taylor & Francis Group
http://taylorandfrancis.com

17

Visible Laser Diodes: Properties of Blue Laser Diodes

Robert Martin

CONTENTS

17.1 Introduction 251
17.2 The Development of Blue LEDs and Laser Diodes 251
    17.2.1 InGaN-Based LEDs 251
    17.2.2 The First GaN-Based Laser Diodes 253
    17.2.3 The Structure and Performance of State-of-the-Art GaN-Based LDs 253
    17.2.4 Advancing GaN-Based LDs to Higher Power 255
    17.2.5 Extending the Wavelength Range of GaN-Based Blue Laser Diodes 257
        17.2.5.1 ‘True Blue’ and Longer Wavelengths 257
        17.2.5.2 UV Laser Diodes 258
    17.2.6 Mode Structure and Control 258
17.3 Stimulated Emission Mechanisms in GaN and Related Materials 258
    17.3.1 Stimulated Emission in GaN 258
    17.3.2 Stimulated Emission in InGaN 259
17.4 Non-GaN Blue Lasers 259
    17.4.1 ZnO 259
    17.4.2 Frequency Doubling 259
    17.4.3 II–VI Materials 259
17.5 Extension of Lasing Emission beyond the Blue/UV, Green and Yellow Laser Diodes 259
17.6 Conclusion and Outlook 260
References 260

17.1 Introduction

The fact that the demonstrations of red and infrared laser diodes (LDs) in the early 1960s were not quickly followed by the development of similar shorter wavelength devices was not due to a lack of desirability and commercial attractiveness but rather due to the difficult nature of the wide bandgap semiconductors. Despite early work on II–VI compounds, GaN and ZnO, the technology and quality of epitaxial structures composed from these materials lagged far behind that of narrower gap materials such as GaAs. High-brightness blue light-emitting diodes (LEDs) and lasers were not developed until the 1990s and followed major advances in the fabrication of group III-nitride (AlGaInN) structures. This chapter presents an outline of these developments and then proceeds to a description of the current status and performance of GaN-based blue LDs. The extension of the lasing wavelength in GaN-based lasers to both shorter (UV) and longer (blue/green) wavelengths is described along with the competing technologies: namely ZnO-based structures and frequency doubled systems for the blue and II–VI semiconductor structures for the green/yellow spectral region.

Note that the performance, range, and applications of short-wavelength LDs (and LEDs) are still improving rapidly with time, and this chapter represents the situation in spring 2002. For a deeper understanding of the development and properties of blue LEDs and lasers, the reader is directed to several books [1,2] and conference proceedings [3,4].

17.2 The Development of Blue LEDs and Laser Diodes

17.2.1 InGaN-Based LEDs

The commercialization of the first short-wavelength LDs (violet, 400–410 nm emission) by the Nichia Corporation in February 1999 was the culmination of a dramatic series of research successes. The work within Nichia, under the leadership of Shuji Nakamura, spanned almost a decade and has been well documented (e.g. [1]). It included demonstrations of ultrabright UV, blue, green, and amber InGaN/GaN LEDs and rapid progress in improving the operating characteristics and longevity of violet LDs.

These achievements built on notable research successes by Akasaki and others in overcoming the main problems that had thwarted the development of GaN-based devices following the demonstration of metal–insulator–semiconductor LEDs in the 1970s [5]. The two main problems were the poor crystalline quality of GaN and the lack of a viable route to p-type material. High-quality GaN crystalline films were first grown in the late 1980s by metal–organic vapour-phase epitaxy (MOVPE) using low-temperature-grown buffer layers of A1N [6] or GaN [1]. These layers helped to isolate a region of high-quality GaN from the nitride–substrate interface, where lattice and thermal mismatches generate severe dislocations and defects. Nakamura made a further significant improvement in GaN epitaxy through the development of a novel two-flow MOVPE reactor [1]. The quality of MOVPE-grown III-nitrides has continued to improve at a rapid rate. As discussed later, additional dramatic reductions in dislocation densities were essential for laser development and were achieved using lateral epitaxial overgrowth techniques. The doping problem was also solved by Akasaki's group who produced p-type GaN by irradiating Mg:GaN with low-energy electrons and fabricated the first electroluminescent GaN pn diode GaN [7]. Nakamura subsequently showed that thermal annealing in a nitrogen ambient was a better method of p-doping, with advantages including speed, reliability, and homogeneous conversion of the full depth of a layer [1]. By early 1991, Nakamura was fabricating homojunction GaN LEDs emitting 430-nm blue light with output powers and external quantum efficiencies approximately ten times greater than commercial SiC blue LEDs at that time [8]. The light emission originated from an impurity transition related to the magnesium dopant within the p-GaN and rapid progress was made on changing to the use of band-edge emissions in InGaN. The Nichia Corporation was the first to succeed in the commercial production of high-brightness blue LEDs, starting in November 1993. Toyoda Gosei Co., Ltd also pioneered similar devices, starting commercial production in October 1995.

The performance of GaN-based LEDs improved rapidly with the incorporation and improvement of InGaN quantum wells in the active region. The main features of GaN-based LEDs on sapphire substrates are as follows: following the deposition of GaN nucleation layers, several micrometres of n-type Si-doped GaN are grown. Next comes the active region incorporating InGaN quantum wells (typically 1–4 nm) with either GaN or low-InN fraction InGaN barriers and, finally, a p-type GaN layer. The Mg dopants must be activated and are contacted with Ni/Au. For LEDs on sapphire substrates, the underlying n-type material is exposed by etching through the top layers and contacted using Ti/Al.

Nichia has LEDs incorporating multiple InGaN quantum wells with room-temperature external quantum efficiencies of approximately 20% in the blue (11 mW with a forward current of 20 mA, 50 A cm^{-2}) and green (8 mW, current as before) [9]. Figure 17.1 plots the external quantum efficiency against LED emission wavelength, showing the fall-off either side of the blue/green region. Measurements as a function of temperature for a 400-nm emitter indicate a considerable (more than double) improvement in efficiency on cooling to ~100 K [9]. These LEDs contain remarkably high densities of dislocations threading through the active region (~10^{10} cm^{-2}) [10]. Comparisons with LEDs fabricated on laterally overgrown GaN with considerably reduced dislocation densities (<10^{7} cm^{-2}) show virtually no improvement for blue LEDs [11] and only a slight improvement (~25%) for UV LEDs [9,12]. Such results are indicative of the origin of the InGaN luminescence, which results from radiative recombination within localizing InN-rich nanometre-scale regions [13–15]. This spontaneous extreme localization isolates the carrier recombination from the non-radiative recombination centres at the dislocations and leads to a surprising independence of luminescence efficiency from dislocation density. The low InN mole fraction in UV InGaN LEDs does allow for some improvement due to the limited number and depth of the localized states.

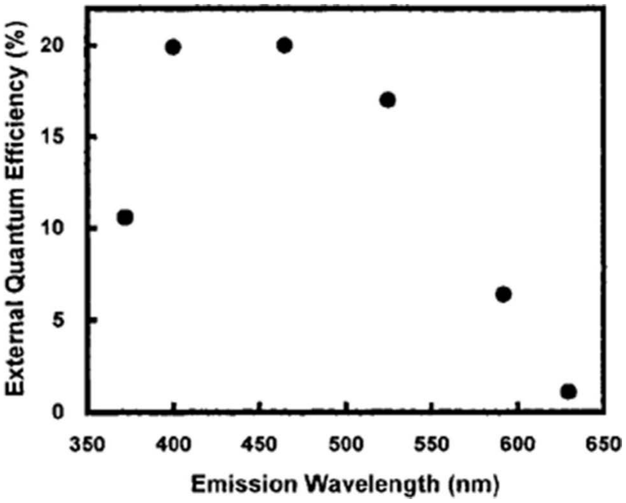

FIGURE 17.1 The dependence of the external quantum efficiency of InGaN LEDs on the emission wavelength. (From Ref. [9], reproduced with permission from P*hysica* S*tatus* S*olidi*.)

Several other groups soon followed Nichia and Toyoda Gosei in the fabrication of high-brightness blue/green LEDs, including a number of variations on the general scheme outlined earlier. Use of conducting substrates, such as 6H-SiC, offers a number of advantages: principally, the use of a vertical geometry with a back contact. Different approaches to metal–organic chemical vapor deposition (MOCVD) growth reactors have been successfully employed, and InGaN LEDs have also been fabricated using molecular beam epitaxy, although not of commercial quality.

Currently (spring 2002), the best InGaN LEDs emit 30 lumen W^{-1}, but the performance continues to improve at a rate indicating that over 100 lumen W^{-1} is achievable (this is to be compared with 15 lumen W^{-1} for conventional incandescents and 50 lumen W^{-1} for conventional fluorescents). One of the leaders in the development of high-power LEDs, Lumileds Lighting, has advanced flip-chip Luxeon devices showing record external quantum efficiencies of ~30% and optical powers in excess of 1 W (at 425 nm) in a 2×2 configuration of LEDs [16,17]. CREE Inc. has high-brightness 'Xbright' LEDs on SiC emitting at 470, 505 (11 mW) and 525 nm (9 mW) [18]. White GaN-based LEDs can also be fabricated using a number of routes. Devices emitting ~20 lumen W^{-1} are available using a blue LED coated with a yellow phosphor, which partially transmits the blue light. The impressive performance of III-nitride LEDs is exemplified by the demonstration of headlights using white Lumileds Luxeon LEDs on a concept car unveiled at the 2002 Geneva Motor Show.

17.2.2 The First GaN-Based Laser Diodes

The bright InGaN/GaN LEDs produced by Nakamura's MOCVD process and with p-type material resulting from thermal activation of Mg donors were the forerunners of the violet LDs. However, additional problems would have to be overcome to achieve reliable lasers. The fabrication of mirrors for a diode laser's optical cavity is generally achieved by cleaving, which is not practical for the c-face sapphire substrates used for InGaN LEDs. Early InGaN lasers contained relatively rough mirror facets created by reactive ion etching [19]. Shortly afterward, Nakamura also demonstrated InGaN lasers on a-face (1120) sapphire substrates, where mirror facets could be formed by cleaving, although no reduction in threshold current was achieved [20].

The implementation of two additional features was significant for the extension of the laser lifetime and a reduction in the operating voltage. First was the inclusion of modulation-doped strained layer superlattice (MDSLS) cladding layers above and below the active region of the lasers. These GaN/AlGaN MDSLSs reduced cracking within the laser structure, improved optical confinement and lowered the operating voltage. The second was the implementation of lateral overgrowth on patterned silica substrates [21,22]. Stripes of silica, typically 4 μm wide and 12 μm apart, are deposited on a GaN surface prior to growth of a thick GaN layer. Above the mask, the GaN grows laterally and soon coalesces to form a flat surface with, most importantly, approximately 10^4 fewer dislocations cm^{-2} in the regions above the silica stripes. In simple terms, the silica mask has almost eradicated the memory of the GaN/substrate interface for these regions. The structure of one of these layer diodes is represented schematically in Figure 17.2. Further improvement of the lasers was achieved by removing the sapphire substrate from beneath several micrometres of overgrown GaN to create 'GaN substrates', which are easily cleaved and have the extra benefit of higher thermal conductivity [23,24].

The first reports of violet LD operation at room temperature under pulsed conditions [19] and then with continuous-wave (cw) operation [25] came from Nakamura in 1996. Using the steps previously described, the lasing lifetime was improved dramatically over a short period of time; with 30 h in December 1996, 300 h in May 1997 and accelerated lifetime tests indicating achievement of the 'magical' 10 000 h lifetime in December 1997 [22]. The dramatic progress made by Nakamura in the late 1990s clearly shows the importance of minimizing dislocations for increasing the lasing lifetime. The degradation of InGaN LDs is also linked to the generation of heat within the p-cladding and contact layers, and there is a report suggesting a contribution of catastrophic optical damage to the failure mechanism [26].

17.2.3 The Structure and Performance of State-of-the-Art GaN-Based LDs

Following the previously described development, the Nichia Corporation proceeded to commercialize violet (~405 nm)-emitting GaN LDs with ~5 mW output in February 1999. Subsequently higher power (30 mW) versions (see Section 6.2.4) and extended wavelength (450 nm) LDs (see Section 6.2.5) were added to their product range.

Following Nichia's lead, violet GaN-based lasers have been demonstrated by a growing list of other companies and universities, with early players including Toyoda Gosei, University College of Santa Barbara (UCSB), CREE Inc., Samsung and Xerox. These devices share a number of similarities—they all employ MOCVD crystal growth, with some approach to a reduction in threshold density (lateral growth, low-temperature interlayers, etc.); they are grown p-side up due to the relative difficulty in doping and require some approach to lateral current spreading within the p-layer. Differences between them include the use of a variety of substrates, with

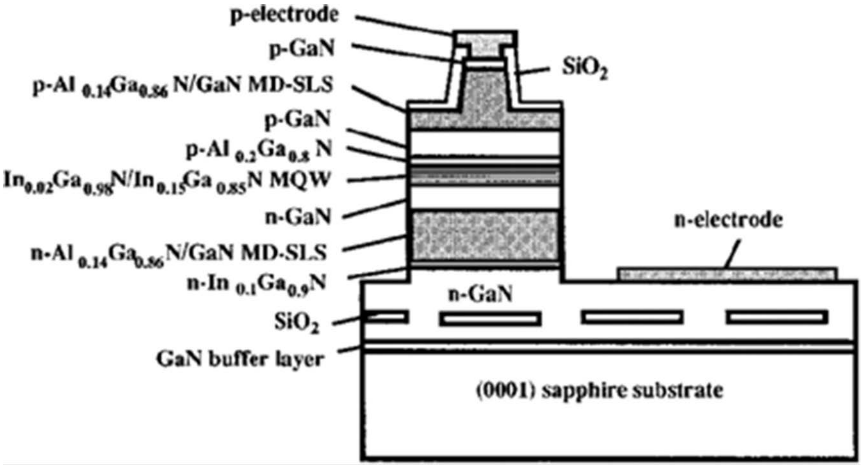
p-electrode
p-GaN
$\mathrm{SiO_2}$
p-$\mathrm{Al_{0.14}Ga_{0.86}N/GaN}$ MD-SLS
p-GaN
p-$\mathrm{Al_{0.2}Ga_{0.8}N}$
$\mathrm{In_{0.02}Ga_{0.98}N/In_{0.15}Ga_{0.85}N}$ MQW
n-GaN
n-electrode
n-$\mathrm{Al_{0.14}Ga_{0.86}N/GaN}$ MD-SLS
n-$\mathrm{In_{0.1}Ga_{0.9}N}$
n-GaN
$\mathrm{SiO_2}$
GaN buffer layer
(0001) sapphire substrate

FIGURE 17.2 Schematic diagram of the layer structure of one of the early ELOG GaN-based laser diodes from the Nichia Corporation. (From Ref. [22], reproduced with permission from the American Institute of Physics.)

the most notable variations being SiC (e.g. CREE Inc.), bulk GaN crystals (UNIPRESS [27]) or conductive ‘free-standing GaN’ (e.g. NEC [28]), which all allow use of a back-side contact. Note that Nakamura has reported lasing on a variety of substrates (including a-face sapphire [20], $MgAl_2O_4$ [29] and ‘free-standing GaN’ [23]). There are a number of variations in the lateral overgrowth technique for which a range of names and acronyms exist—ELOG, lateral epitaxial overgrowth (LEO), pendeoepitaxy™ [30], facet-induced epitaxial lateral overgrowth (FIELO) [28], lateral overgrowth from trenches (LOFT).

The structure and performance of the Nichia devices will now be summarized. Operating specifications and illustrative figures for Nichia’s devices are available on the company’s website [31]. All of their devices are based on a similar epitaxial layer structure, which can be generalized as follows. Starting with the reduced-defect-density GaN layer, a thick n-type GaN (or low-A1 A1GaN) layer is followed by an n-type MDSLS, then an undoped GaN (or low-InN InGaN) layer containing InGaN quantum wells, then a p-type MDSLS and, finally, a thin p-type GaN layer. A more detailed layer structure reported for lasers [9] is represented schematically in Figure 17.3. These layers are deposited on a low-defect density GaN layer produced by a lateral overgrowth of GaN. Nichia has detailed the fabrication of LDs by ELOG on sapphire and also ‘ELOG on GaN’ [32]. The ELOG on sapphire utilizes 100 nm thick SiO_2 masks on ~2.5 µm of GaN. The masks are patterned into 8 µm stripe windows with 20 µm periodicity. Approximately 15 µm of GaN is then grown, giving a flat surface with very low defect density above the SiO_2 stripes and a so-called ELOG substrate. A thick (200 µm) layer of GaN is deposited on this, using hydride vapor phase epitaxy (HVPE) with a high growth rate of 40 µm h^{-1}. The sapphire substrate, ELOG GaN and some HVPE GaN were then removed by polishing to obtain a free-standing GaN substrate. LDs are fabricated using the low-defect-density regions above the silica stripes. For the ‘ELOG on GaN’ substrates, the ELOG process is repeated to give a further reduction in the defect density. The dark spot density is reduced to $1\times10^6 cm^{-2}$ for ELOG on sapphire and $7\times10^5 cm^{-2}$ for ‘ELOG on GaN’. The n-InGaN serves to counteract the build-up of strain and prevents crack formation within the structure. The MDSLSs act as cladding layers to confine carriers and also serve to maintain crystal quality and reduce operating voltage.

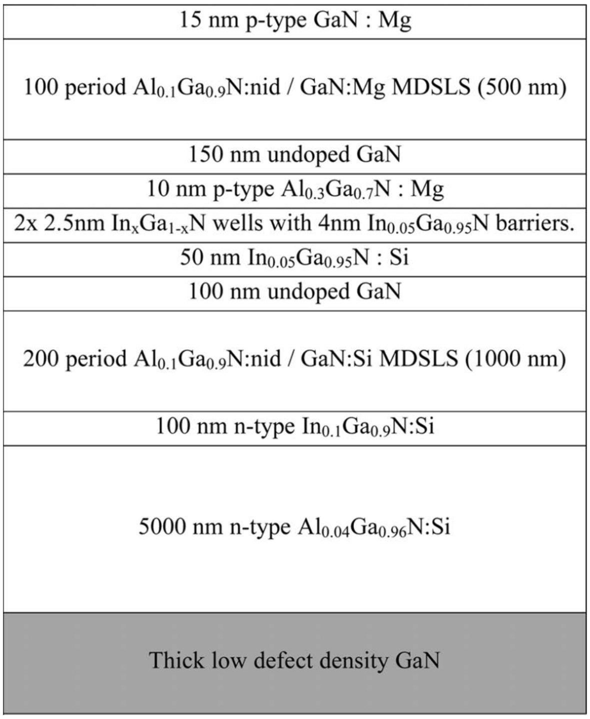
15 nm p-type GaN : Mg
100 period $Al_{0.1}Ga_{0.9}N$:nid / GaN:Mg MDSLS (500 nm)
150 nm undoped GaN
10 nm p-type $Al_{0.3}Ga_{0.7}N$: Mg
2x 2.5nm $In_xGa_{1-x}N$ wells with 4nm $In_{0.05}Ga_{0.95}N$ barriers.
50 nm $In_{0.05}Ga_{0.95}N$: Si
100 nm undoped GaN
200 period $Al_{0.1}Ga_{0.9}N$:nid / GaN:Si MDSLS (1000 nm)
100 nm n-type $In_{0.1}Ga_{0.9}N$:Si
5000 nm n-type $Al_{0.04}Ga_{0.96}N$:Si
Thick low defect density GaN

FIGURE 17.3 Schematic diagram of the layer structure of GaN-based LDs from the Nichia Corporation.

The LDs have a ridge geometry (typically 2.5×650 µm). In Nichia’s case, a ZrO_2 coating is used to define the ridge by refractive index confinement of the laser beam [9]. For LDs fabricated on ‘ELOG on GaN’ substrates, the facets are formed by cleaving, while for ELOG on sapphire, the facets are formed by reactive ion etching. Coating the facets, for example with TiO_2/SiO_2 multilayers, enhances device performance. Ni/Au is used for the p-contact and Ti/Al for the n-contact.

The laser emission wavelength is tuned mainly by control of the InN fraction within the wells, with a lesser effect from the width of the wells (see Ref. [33]). An optimization process for violet LDs resulted in a preferred well width of 2.5 nm, with wider wells resulting in increasing forward leakage currents and rising threshold current. With the choice of 2.5 nm well and 4 nm barrier layers, a second optimization showed a minimum threshold current for two wells (also a peak in emission wavelength) [32].

For the 405 nm, 5 mW LD, the quoted performance parameters are operating voltage (4.5±1.0) V, operating current (50±20) mA, and slope efficiency 0.7 W A^{-1}. The beam divergence (FWHM) is 10° and 28° for directions perpendicular and parallel to the growth direction. The LD spectrum reproduced in Figures 17.4 and 17.5 shows the output optical power plotted against forward current. The operating temperature is quoted as –10°C to 60°C, and Figure 17.6 plots the dependence of the peak wavelength on case temperature.

CREE Inc have been developing blue/violet GaN lasers using SiC substrates and in February 2002 announced that their 405-nm, 3-mW blue LDs exhibited a projected lifetime exceeding 10 000 h at room temperature.

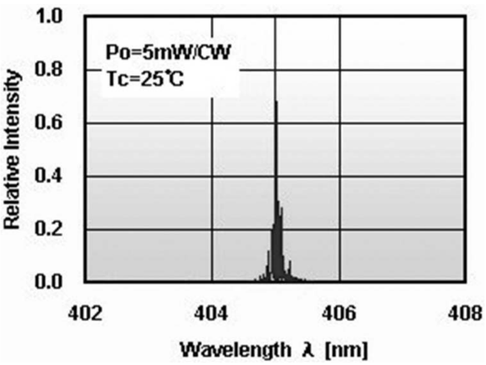

FIGURE 17.4 Lasing spectrum for the Nichia Corporation’s 5-mW diode. (Copyright Nichia Corporation [31].)

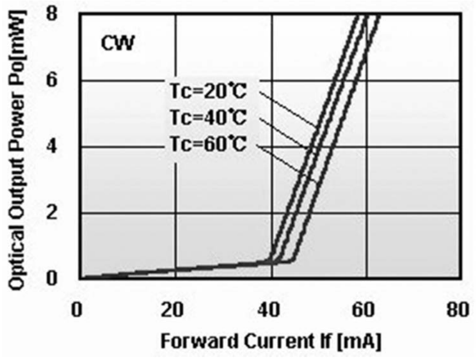

FIGURE 17.5 Output power against forward current for the Nichia Corporation's 5-mW diode. (Copyright Nichia Corporation [31].)

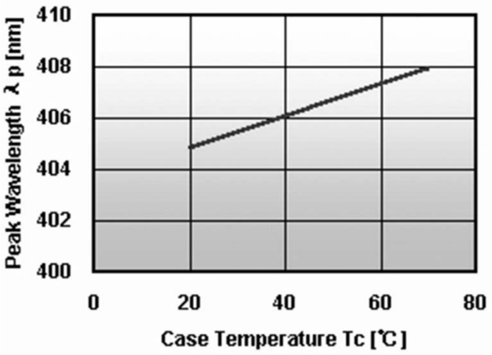

FIGURE 17.6 The dependence of laser peak wavelength on case temperature for the Nichia Corporation's 5-mW diode. (Copyright Nichia Corporation [31].)

All the demonstrations of laser action in the III-nitrides feature efforts to reduce the number of dislocations resulting from the lack of an ideal substrate material. As described earlier, high-performance LDs have been fabricated using free-standing GaN substrates produced by the removal of an alien substrate (usually sapphire) following growth of a thick low-defect-density GaN layer. The availability of high-quality large crystals of bulk GaN promises dislocation densities that are orders of magnitudes lower than in any other GaN and, consequently, a possible significant improvement in laser performance. However, the growth of bulk crystals of GaN is an immense challenge, due to the extremely high melting point (~2500°C) and equilibrium pressure at melting (~45 000 atm!). The team at the High Pressure Research Centre, Polish Academy of Sciences (UNIPRESS) is alone in producing such crystals and has demonstrated a blue LD fabricated by MOCVD on a substrate cut from a GaN crystal [27]. The laser is a separate confinement heterostructure device containing five InGaN quantum wells. Dislocation densities in the n-type-conducting substrates are as low as 10–100 cm^{-2}, and fully strained MOCVD structures can be grown with no evidence for the formation of additional dislocations. Pulsed operation of the first laser at −40°C showed a threshold at 1.7 A. The preparation of the bulk GaN substrates is clearly a highly technical challenge, but the rewards for overcoming it are similarly great. This is evidenced by reports of large improvements in performance of lasers grown at the Nichia Corporation in 1999 when Nakamura was provided with a small number of Polish bulk substrates (×10 increase in lifetime, ×2 increase in power over corresponding devices on sapphire) [27]. A number of alternative routes to 'bulk-like' GaN are actively being researched and show promise for the future.

17.2.4 Advancing GaN-Based LDs to Higher Power

The first commercial violet LDs had an output power of 5 mW, but for some major applications, e.g. DVD writers, higher power and longer lifetimes are necessary. (In February 2002, nine companies jointly announced the establishment of the basic specifications for a next-generation optical disc dubbed the 'Blu-ray Disk', designed for the recording, rewriting and playback of 27 Gbits of data on a single-sided single-layer CD/DVD size disc using a 405-nm blue-violet laser.) For optical disc writers, laser powers of 30 mW or above are required, and further increases in power are necessary for other applications, including laser-based display technologies, printing and certain medical applications. Additional desirable characteristics for high-power LDs include low operating voltage, the elimination of 'kinks' in the *L–I* curves, improved far-field patterns by reduction of the aspect ratio of the emitting region, low noise, long life, etc.

The Nichia Corporation has improved the reliability of their high-power LDs by use of free-standing GaNs and has commercially available 30 mW lasers. These higher power ~408 nm devices have the same operating voltage (4.5 V) as their commercial 5 mW devices, and the typical operating current is only slightly higher, at 70 mA. Plots of the forward voltage and output power against forward current are shown in Figures 17.7 and 17.8. The slope efficiency has increased to 1.2 W A^{-1}, and the lateral spread (FWHM) decreased to 8° and 23° for directions perpendicular and parallel to the epitaxial growth direction (Figure 17.9). Results for 55 mW lasers at 60°C show lifetimes (defined as a 50% increase in current) exceeding 4000 h for devices with both cleaved and etched facets, although productivity is improved by the latter.

NEC have developed high-power (>30 mW) devices using a ridge by a selective regrowth (RiS-) LD structure [34,35] on a low-dislocation laterally grown GaN (FIELO) [28], as

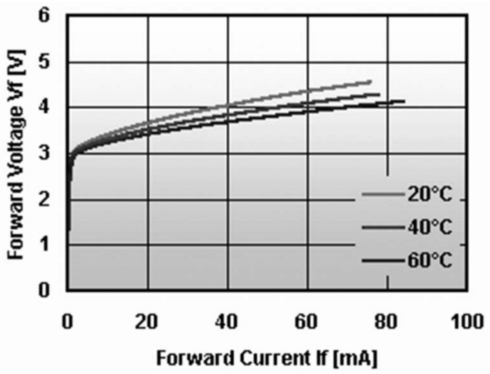

FIGURE 17.7 Forward voltage against forward current for the Nichia Corporation's 30-mW diode. (Copyright Nichia Corporation [31].)

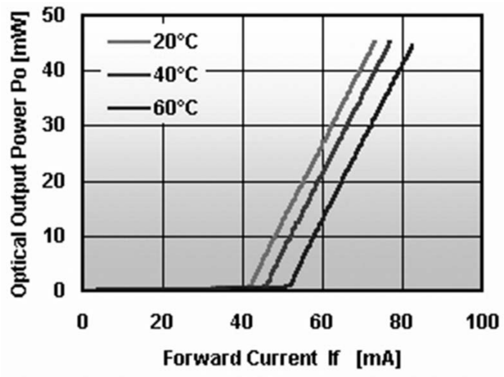

FIGURE 17.8 Output power against forward current for the Nichia Corporation's 30-mW diode. (Copyright Nichia Corporation [31].)

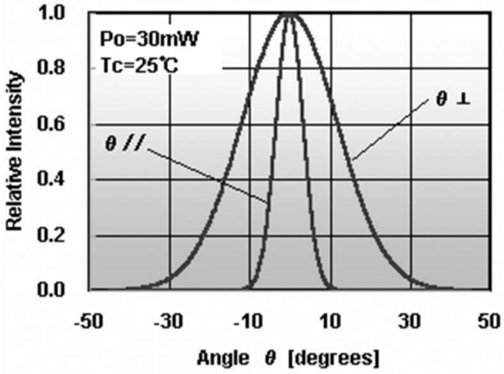

FIGURE 17.9 Beam spread for the Nichia Corporation's 30-mW diode. (Copyright Nichia Corporation [31].)

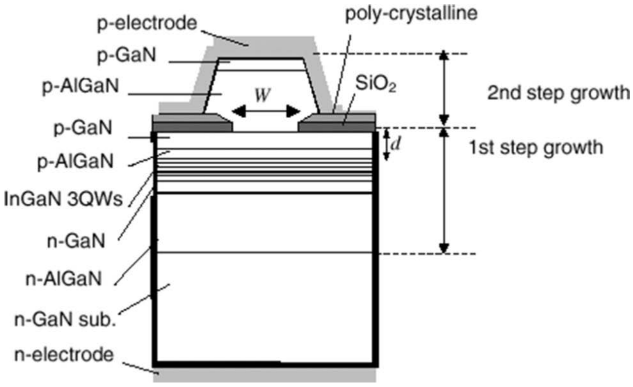

FIGURE 17.10 Schematic diagram of the layer structure of NEC's RiS laser diode fabricated on a FIELO n-GaN substrate. (From Ref. [35], reproduced with permission from P*hysica* S*tatus* S*olidi*.)

shown schematically in Figure 17.10. The RiS-LD initially suffered from internal losses caused by light absorption in the region of the regrowth boundary for the upper ridge, but performance has been improved by reducing the internal loss to as low as 26 cm^{-1}. The main source of loss was identified as Si contamination at the regrowth boundary, the effect of which was minimized by shifting the optical field deeper into the structure using a thick low-Al content n-AlGaN cladding layer. The result was superior laser performance with a threshold current as low as 10 mA (J_{th} = 1.6 kA cm^{-2}) with highly reflective-coated facets, as shown in Figure 17.11. The large differential gain and suppressed non-radiative recombination in these structures may be associated with the lack of a dry etching step in the fabrication process. An impressively low aspect ratio, 2.0, is achieved in the 30 mW lasers also benefitting from the extension of the optical mode vertically in the lower cladding layer [35].

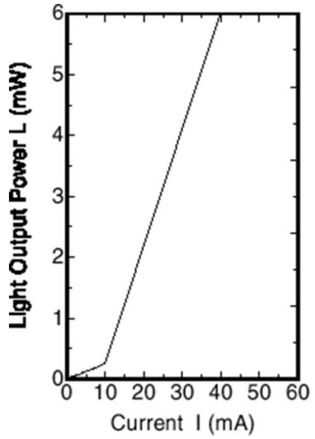

FIGURE 17.11 Light output power plotted against forward current for NEC's RiS laser diode with highly reflective facet coatings. (From Ref. [35], reproduced with permission from P*hysica* S*tatus* S*olidi*.)

Extremely impressive progress in high-power GaN-based lasers has been reported by Sony [36–38]. They have developed blue LDs emitting in excess of 100 mW and demonstrated a 4.2 W LD array consisting of 44 individual lasers (11 laser chips each with four monolithically integrated laser stripes). Deviation between the individual emitters is the key limitation here, but the power performance is impressive with a wall-plug efficiency approaching 10%. The 1 W cw lifetime of these laser arrays exceeded 1000 h at the time of writing. Figure 17.12 reproduces the *L–I* and *V–I* characteristics and lifetime data as presented at the ISBLLED2002 symposium in March 2002 [38]. It is noteworthy that the power consumption of an individual 100 mW blue laser (>20% wall-plug efficiency) is less than half that of an equivalent red LD. The Sony lasers use a licensed lateral overgrowth technique, based on pendeo-epitaxy [30], to reduce the dislocation density. 'Kink-free' *L–I* curves have been demonstrated for powers in excess of 100 mW with lateral beam spreads of 8° and lifetimes (defined by a 20% increase in operating current) in excess of 15 000 h. The kinks are associated with an increase in higher transverse modes, whose suppression is discussed in Section 6.2.6.

Improving the laser output aspect ratio by increasing the angular spread parallel to the layers ($\theta_{\parallel}$) will lead to the kinks discussed earlier, and thus, any improvement in the far-field pattern can preferably be achieved by reducing the angular spread along the growth direction ($\theta_{\perp}$). Raising the thickness of the guiding layer is associated with an increased threshold current (due to less confinement), and so the reduction of $\theta_{\perp}$ has been achieved by setting the active layer back from the p-AlGaN using an undoped spacer layer. An aspect ratio of

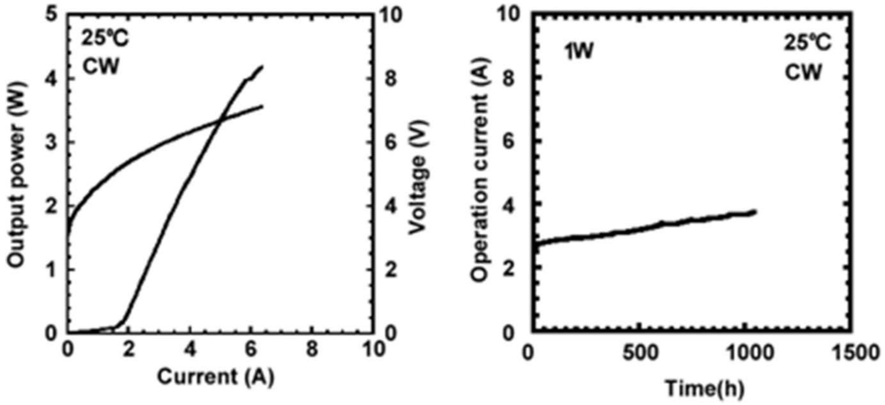

FIGURE 17.12 Output power and forward voltage as a function of forward current for Sony's 44 stripe GaN LD and lifetime data for an array running at 1 W. (From Ref. [38], reproduced with permission from P*hysica* S*tatus* S*olidi*.)

2.3 has been reported with no degradation in threshold current. The spacer layer is also found to have a beneficial impact on the internal losses (down to 10 cm^{-1}) due to the reduced absorption within the Mg-doped layers [38].

17.2.5 Extending the Wavelength Range of GaN-Based Blue Laser Diodes

Figure 17.1 illustrated the falling luminescence efficiency for LEDs emitting outside of the violet–blue–green spectral range. For LDs, this characteristic of InGaN emitters imposes more severe limitations on the achievable emission wavelengths. Early GaN-based LDs were limited to the 390–420 nm spectral range, which includes the 405 nm selected for next-generation optical discs. However, longer and shorter wavelengths are very desirable, and considerable progress is being made to this end.

17.2.5.1 'True Blue' and Longer Wavelengths

Nichia Corporation has reported results on GaN-based lasers with emission wavelengths ranging from 425 to 454 nm, achieved by changes in the InGaN well-growth temperature [9]. The variation in threshold current is reproduced in Figure 17.13 and highlights the problems to be overcome in raising the lasing wavelength. At this time, cw lasing was not achieved above 455 nm, due to the reduced quality of the layers with a higher indium nitride fraction and the damaging effects of band-tail states.

Spectra for LDs emitting at 402, 422 and 447 nm are illustrated in Figure 17.14 as a function of excitation current density [32]. The 402 nm laser shows a red-shifting peak (~5 nm) due to heat generation. However, the 422 and 447 nm samples both show a blue shift (~10 and 15 nm), attributed to screening of the in-built piezoelectric fields for current densities below 0.25 kA cm^{-2} and thereafter dominated by the band-tail filling. Ref. [32] also shows microscope images revealing deterioration of the quality of the ELOG material as the wavelength increases from 440 to 460 nm, which may be related to dissociation of the InGaN during growth of the p-type cladding layers.

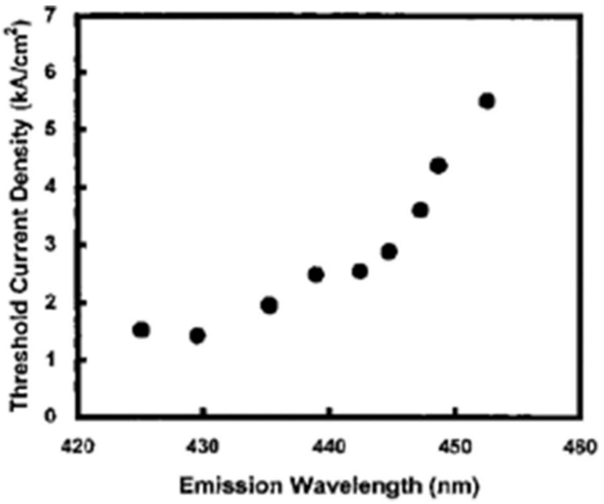

FIGURE 17.13 Emission wavelength dependence of the threshold current density of blue GaN-based laser diodes. (From Ref. [9], reproduced with permission from P*hysica* S*tatus* S*olidi*.)

Despite the difficulties, progress has been steady and the Nichia Corporation has been offering a commercial LD emitting at a wavelength of 440 nm for some time. The specifications are not dissimilar to those of the commercial 405 nm 5 mW LD, although the typical operating voltage and current are increased to 5 V and 55 mA, respectively [31].

By mid-2001, Nichia had published details of InGaN LDs with emission wavelengths in excess of 460 nm [39]. The room-temperature threshold current density of the device emitting at 460 nm was 3.3 kA cm^{-2} and the estimated lifetime approximately 3000 h. The improvement in material quality using the 'ELOG on GaN' substrates described earlier has proved significant for enhancing the performance of the longer-wavelength GaN-based LDs [32]. The Nichia Corporation achieved GaN-based room-temperature cw lasing at 488 nm, and further extensions of wavelength are sure to follow, albeit with declining performance characteristics [40].

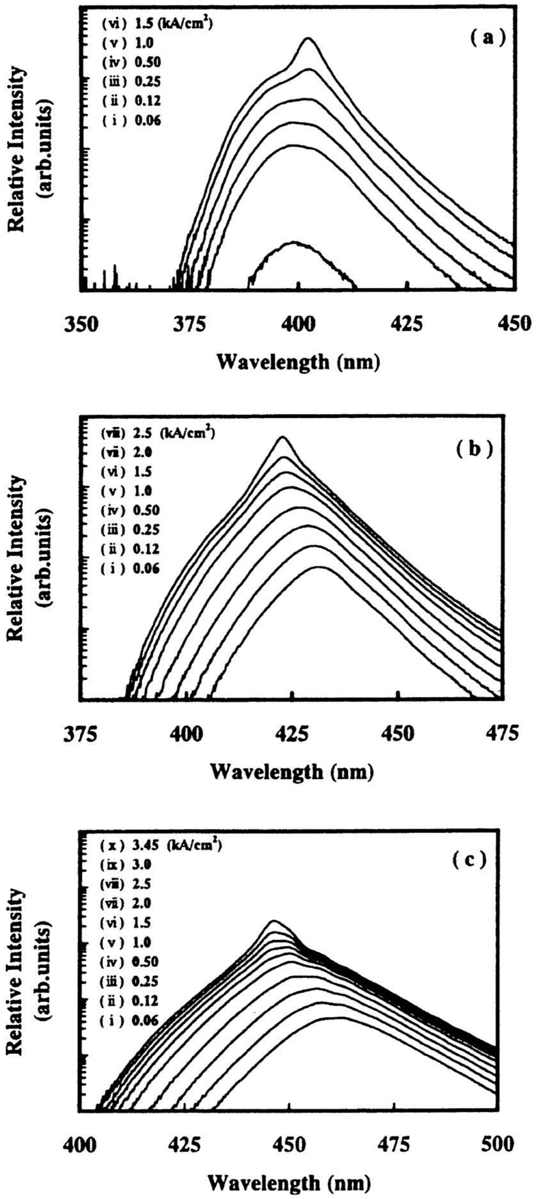

FIGURE 17.14 Emission spectra of lasers diodes with lasing wavelengths of (a) 402 nm, (b) 422 nm and (c) 447 nm at different forward current densities. (From Ref. [32], reproduced with permission from the *Japanese Journal of Applied Physics*.)

17.2.5.2 UV Laser Diodes

The Nichia Corporation has also demonstrated laser emission at shorter wavelengths using either GaN [41] or AlInGaN [42] active regions. Lasing at 367 nm (pulsed) or 369 nm (cw) was demonstrated using a 10 nm well of binary GaN. For $Al_{0.03}In_xGa_{(0.97-x)}N$ wells, room-temperature cw lasing was achieved below 370 nm. In both cases, threshold current densities as low as 3.5 kA cm^{-2} and lifetimes up to 2000 h were reported. For the AlInGaN wells, the threshold current rises with the increasing AlN fraction, required for shorter wavelengths, due to deteriorating crystal quality. Improvements in the performance of these and similar UV diode lasers will doubtlessly follow in the near future.

17.2.6 Mode Structure and Control

Early GaN lasers with ridge widths above 3 μm gave outputs with multiple transverse modes for moderate powers. These are highly undesirable for optical storage and high-resolution spectroscopic applications but by narrowing the ridge widths, Nakamura achieved lasers with only the fundamental transverse mode for variable operating current [43].

When increasing the power of GaN-based lasers, kinks are sometimes seen in the *L–I* traces, which are generally associated with a change in the transverse mode structure. ‘Kink-free’ operation has been demonstrated for powers in excess of 100 mW by suppression of higher transverse modes. For example, the conventional ridge structure has been replaced with one including layers of silicon or ‘spin-on-glass’ that preferentially absorb the first mode [37,38].

Similar suppression of higher modes can be achieved by fabrication of distributed feedback (DFB) gratings, as described in Refs. [44] and [45]. Such gratings are defined by periodic variations in the refractive index, such as by etching trenches, laterally coupled to the optically active region. This also enables the emission wavelength to be tuned across the gain spectrum. For example, the use of DFB gratings with periods between 160 and 170 nm results in a 10 nm tuning range for a ~400-nm GaN-based LD, with single-mode behaviour [44].

17.3 Stimulated Emission Mechanisms in GaN and Related Materials

As previously mentioned, the remarkable luminescence efficiency of the dislocation-ridden InGaN LEDs appears to be related to the spontaneous formation of strongly localizing In-rich regions [13–15,33]. These regions result from segregation of InN and GaN and have a quantum-dot-like nature, which concentrates excitonic recombination away from the non-radiative centres. Strong strain variations and intense piezoelectric fields are associated with these composition variations and have major effects on the characteristics of the luminescence. However, many or all of the localized states will be filled in the stimulated emission (SE) regime controlling the operation of the LDs and different mechanisms will become dominant.

17.3.1 Stimulated Emission in GaN

SE from GaN was first reported as early as 1971 by Dingle et al. [46], using single-crystal GaN needles at 2 K. Later studies have demonstrated SE in GaN at temperatures up to 700 K [47]. The large excitonic binding energy in GaN means that exciton effects persist to high temperatures as can be observed, for example, in measurements of optical absorption at elevated temperatures [48]. SE, however, involves much higher excitation densities than in these demonstrations and the contribution of excitons will depend on the degree of screening of the Coulomb interaction by the carriers. Bidnyk et al. [49] reported a temperature dependence (20–700 K) of the SE threshold in GaN epilayers grown on sapphire and SiC substrates. Figure 17.15 shows the measured SE threshold

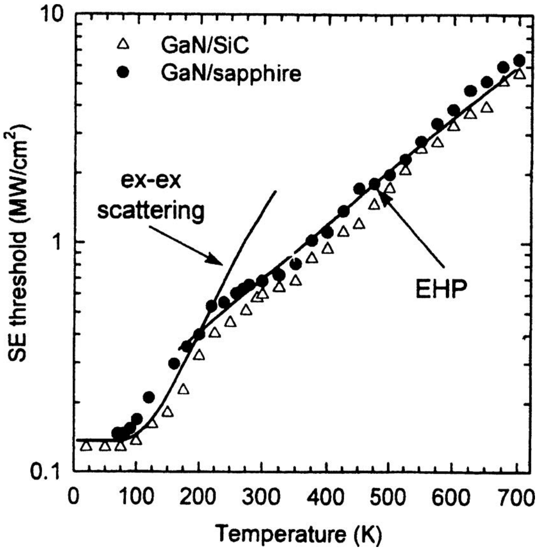

FIGURE 17.15 Threshold of stimulated emission as a function of temperature for GaN thin films. (From Ref. [47], reproduced with permission from the American Institute of Physics.)

increasing rapidly up to ~200 K, and in this range, inelastic exciton–exciton scattering appears to be the dominant gain mechanism. Exciton effects can, thus, still operate above the carrier densities required for SE at low temperatures. At higher temperatures, however, the dominant gain mechanism is electron–hole plasma (EHP) recombination, characterized by a strong red-shift of the SE peak relative to that of spontaneous emission due to bandgap renormalization.

Note that in ZnO-based devices (see Section 6.4.1), exciton–exciton scattering persists up to higher temperatures due to the stronger exciton binding energy, and ZnO-SE due to bi-excitonic processes has also been demonstrated [50,51].

17.3.2 Stimulated Emission in InGaN

In comparison to the situation in GaN, a discussion of the origin of SE in the InGaN layers present in almost all of the LDs discussed previously in this chapter is complicated by InN–GaN segregation, disorder, composition fluctuations, piezoelectric fields, and strain effects. Furthermore, measurements of InGaN SE have sometimes revealed two distinct SE peaks with quite different characteristics that compete for gain [52,53]. Further work is required to explain the mechanism of SE in InGaN.

17.4 Non-GaN Blue Lasers

17.4.1 ZnO

ZnO is a wide bandgap ($E_g = 3.37$ eV at 300 K) semiconductor with similarities to GaN (e.g. wurtzite structure) but also a number of potential advantages. These include the extremely large excitonic binding energy (at ~60 meV, considerably larger even than for GaN); there is the possibility that lattice-matched heterostructures using $Mg_yZn_xCd_{1-x-y}O$ compounds and the availability of more closely matched substrates will be available. For example, homoepitaxy is possible using ZnO substrates [54] and $ScAlMgO_4$ substrates are almost lattice-matched to ZnO [55]. ZnO is naturally n-type but, as in the development of GaN devices, progress towards ZnO-based light emitters has been held up by the difficulty of doping p-type materials. However, Eagle Picher Technologies have demonstrated p-ZnO layers doped with Mg giving carrier densities of ~10^{18} cm^{-3} (although at very low mobility) [54]. Given the advantages listed here, further progress with p-type ZnO could be expected to result in the emergence of high-performance LEDs and, possibly, lasers. Nevertheless, it remains to be seen whether the spontaneous segregation and large polarization fields within the III-nitrides are the key to success in these areas.

17.4.2 Frequency Doubling

An alternative approach to semiconductor-based blue lasers involves frequency doubling of high-power infrared diodes. Both Matsushita and Coherent have second harmonic generation (SHG) blue lasers emitting 20–30 mW. Matsushita has demonstrated a 31% power conversion efficiency using SHG in a periodically poled MgO:$LiNbO_3$ waveguide by frequency doubling an AlGaAs LD [56] and has a 410-nm emitter suitable for writing to optical discs. Coherent's devices employ an 810-nm diode to optically pump a vertical external cavity surface emitting GaAs-based laser and use different gain regions for devices emitting at 460 and 488 nm.

The size of the resulting device is an issue but Matsushita has reduced the package for their SHG laser to an impressive 0.3 cm^3, which may be suitable for optical disc writers [57].

17.4.3 II–VI Materials

ZnSe-based blue lasers have been demonstrated with room temperature lasing at 463 nm (pulsed mode, binary ZnSe quantum well [58]) and 490 nm (cw mode, CdZnSe quantum well [59]). A major obstacle to the development of II–VI lasers remains the limited lifetime, largely resulting from the formation of dislocation networks in the active region, and the significantly higher lifetimes demonstrated for GaN-based lasers mean that ZnSe-based structures are very unlikely to compete in the blue region. However, as discussed in Section 6.5 the II–VIs retain pole position for diode lasing at wavelengths above 500 nm, where InGaN proves more problematic.

17.5 Extension of Lasing Emission beyond the Blue/UV, Green and Yellow Laser Diodes

As described in Section 6.2.5, the longest lasing wavelength demonstrated for GaN-based LDs is currently 488 nm. Researchers on III-nitride lasers will continue to work on increasing this value, but experience thus far indicates that progress will be hard won. Thus far, diode lasers operating in the 510–520 nm green spectral region have only been demonstrated in ZnSe-based devices, including CdZnSe quantum wells. For these devices, optimization of the point defect density within the active layer enabled researchers at Sony to report a ~400 h cw lifetime at 20°C in 1998 [60], although that result still retains the record for longevity.

Conventionally, ZnSe-based LDs are grown on conductive (n-type) GaAs substrates allowing back contacting [60,61]. The active region is composed of CdZnSe or CdZnSSe quantum well(s), typically 3–4 nm wide. A separate confinement structure is employed using MgZnSSe cladding layers and ZnSSe waveguiding layers. The p-type contact can be formed by a ZnTe/ZnSe multi-quantum-well structure although there are other schemes with potential advantages. Indeed, achieving a reliable low-voltage ohmic p-contact remains one of the challenges for ZnSe-based lasers and appears to limit the lifetime [62]. The degradation of II–VI lasers is mostly due to a gradual process involving the development of dark spot defects which align and propagate as dark line defects, although failure by catastrophic optical damage has been observed.

As mentioned earlier ZnSe-based lasers are unable to compete with the III-nitrides for blue emission but are currently superior in the green/yellow area. Careful optimization of CdZnSSe quantum wells has led to the demonstration of yellow laser emission (560 nm [63]). The increased Cd content of the wells required for such emission tends to lead to high strains when using GaAs substrates, which would be expected to impair lasing severely. The addition of S to give the quaternary wells has allowed high structural and optical quality to persist even with Cd contents of up to >40% [63]. In some respects, the characteristics (e.g. higher resistance to catastrophic optical damage with 560 nm, powers exceeding 1 W in pulsed mode) of the yellow lasers exceeds that of the shorter-wavelength ZnSe-based structures. This reflects the improved carrier confinement at the longer wavelengths since the bandgap of the MgZnSSe cladding material is similar in both cases.

The development of ZnSe substrates offers an alternative homoepitaxial route to ZnSe-based diode lasers with a number of potential advantages, including reduced defect densities and absorption losses. Very low thresholds (current densities as low as 176 A cm^{-2} [64]) have been demonstrated for II–VI gain-guided LDs on ZnSe substrates and attributed to the reduction in the internal losses occurring in a non-transparent substrate such as GaAs. However, Wenisch et al. [65] describe a comparison of the characteristics of devices grown on GaAs and ZnSe substrates and report some similarities in the propagation of defects, although they have a relatively high defect density in the homoepitaxial lasers.

17.6 Conclusion and Outlook

The rapid development of III-nitride semiconductor devices in the past decade has produced high-performance LDs covering the UV to blue/green spectral region with more than 30 mW available in commercial 400–420 nm emitting devices. The rate of progress remains high, both in increasing power and extending the wavelength range. Schemes to minimize dislocations have been shown to be important in all of the GaN-based LDs. The most attractive of these would be the use of true bulk GaN substrates, for which the demonstration of lasers has been described. The difficulty of producing such GaN substrates remains extremely hard, however. ZnO-based devices may yet compete with the III-nitrides for blue LDs, with the availability of matched substrates a considerable advantage, but the development is at a very early stage. LDs based on the II–VIs will almost certainly not be able to compete in the blue spectral region, but they still hold the ground for use in green/yellow LDs. It remains to be seen whether the success of the III-nitrides in the UV and blue can be extended into these longer wavelength regions.

REFERENCES

1. Nakamura S, Pearton S and Fasol G 2000 *The Blue Laser Diode* 2nd edn (Berlin: Springer).
2. Gil B (ed) 2002 *Low Dimensional Nitride Semiconductors* (Oxford: Oxford University Press).
3. *Proceedings of the International Conferences on Nitride Semiconductors*; e.g. ICNS3 Montpellier; 1999 *Phys. Status Solidi a* **176**; 1999 *Phys. Status Solidi b* 216; 1999 and ICNS4 Denver; 2001 *Phys. Status Solidi a* **188**; 2001 *Phys. Status Solidi b* 228.
4. *Proceedings of the International Symposia on Blue LEDs and Lasers*; e.g. Berlin; 2000 *Phys. Status Solidi a* **180**; Cordoba 2002 Phys. Status Solidi a 192.
5. Pankove J I, Miller E A, and Berkeyheiser J E 1971 *RCA Rev.* **32** 383.
6. Amano H, Sawaki N, Akasaki I and Toyoda Y 1986 *Appl. Phys. Lett.* **48** 353.
7. Akasaki I, Amano H, Kito M and Hiramatsu K 1989 *Japan. J. Appl. Phys.* **28** L2112.
8. Nakamura S, Mukai T and Senoh M 1991 *Japan. J. Appl. Phys.* **30** L1998.
9. Nagahama S et al. 2001 *Phys. Status Solidi a* **188** 1.
10. Lester S D, Ponce F A, Craford M G and Steigerwald D A 1995 *Appl. Phys. Lett.* **66** 1249.
11. Mukai T, Takekawa K and Nakamura S 1998 *Japan. J. Appl. Phys.* **37** L839.
12. Mukai T and Nakamura S 1999 *Japan. J. Appl. Phys.* **38** 5735.
13. Chichibu S, Azuhata T, Sota T and Nakamura S 1996 *Appl. Phys. Lett.* **69** 4188.
14. Narukawa Y, Kawakami Y, Funato M, Fujita Sz, Fujita Sg and Nakamura S 1997 *Appl. Phys. Lett.* **70** 981.
15. O'Donnell K P, Martin R W and Middleton P G 1999 *Phys. Rev. Lett.* **82** 237.
16. Kim A Y, Götz W, Steigerwald D A, Wierer J J, Gardner N F, Sun J, Stockman S A, Martin P S, Krames M R, Kern R S and Steranka F M 2001 *Phys. Status Solidi a* **188** 15.
17. Krames M R, Bhat J, Collins D, Gardner N F, Gotz W, Lowery C H, Ludoweise M, Martin P S, Mueller G, Mueller-Mach R, Rudaz S, Steigerwald D A, Stockman S A and Wierer J J 2002 *Phys. Status Solidi a* **192** 237.
18. http://www.cree.com/products/led/.
19. Nakamura S et al. 1996 *Japan. J. Appl. Phys.* **35** L74.
20. Nakamura S et al. 1996 *Japan. J. Appl. Phys.* **35** L217.
21. Zheleva T S et al. 1997 *Appl. Phys. Lett.* **71** 2472; Sakai A et al. 1997 *Appl. Phys. Lett.* **71** 2259.
22. Nakamura S et al. 1998 *Appl. Phys. Lett.* **72** 211.

23. Nakamura S, Senoh M, Nagahama S, Iwasa N, Yamada T, Matsushita T, Kiyoku H, Sugimoto Y, Kozaki T, Umemoto H, Sano M and Chocho K 1998 *Appl. Phys. Lett.* **72** 2014.
24. Nakamura S et al. 1998 *Japan. J. Appl. Phys.* **37** L309.
25. Nakamura S et al. 1997 *Appl. Phys. Lett.* **70** 868.
26. Cohen D A, Margalith T, Abare A C, Mack M P, Coldren L A, DenBaars S P and Clarke D R 1998 *Appl. Phys. Lett.* **72** 3267.
27. Grzegory I et al. 2001 *Acta Phys. Polon. A* **100** 57, 229.
28. Usui A et al. 1997 *Japan. J. Appl. Phys.* **36** L899.
29. Nakamura S et al. 1996 *Appl. Phys. Lett.* **68** 2105.
30. Zheleva T S, Smith S A, Thomson D B, Gherke T, Linthicum K J, Rajagopal P, Carlson E, Ashmawi W M and Davis R F 1999 *MRS Internet J. Nitride Semicond. Res.* **4S1** G3.38.
31. Nichia. http://www.nichia.co.jp/.
32. Nagahama S, Yanamoto T, Sano M and Mukai T 2001 *Japan. J. Appl. Phys.* **40** 3075.
33. Martin R W, Edwards P R, Pecharroman-Gallego R, Liu C, Deatcher C J, Watson I M and O'Donnell K P 2002 *J. Phys. D: Appl. Phys.* **35** 604.
34. Kuramoto M et al. 2001 *Japan. J. Appl. Phys.* **40** L925.
35. Kuramoto M, Sasaoka C, Futagawa N, Nido M and Yamaguchi A A 2002 *Phys. Status Solidi a* **192** 329.
36. Miyajima T et al. 2001 *J. Phys.: Condens. Matter* **13** 7099.
37. Kijima S et al. 2001 *Phys. Status Solidi a* **188** 55.
38. Takeya M, Tojyo T, Asano T, Ikeda S, Mizuno T, Matsumoto O, Goto S, Yabuki Y, Uchida S and Ikeda M 2002 *Phys. Status Solidi a* **192** 269.
39. Nagahama S et al. 2001 *Appl. Phys. Lett.* **79** 1948.
40. Mukai T, Nagahama S, Yanamoto T and Sano M 2002 *Phys. Status Solidi a* **192** 261.
41. Nagahama S et al. 2001 *Japan. J. Appl. Phys.* **40** L785.
42. Nagahama S et al. 2001 *Japan. J. Appl. Phys.* **40** L788.
43. Nakamura S et al. 1998 *Japan. J. Appl. Phys.* **37** L1020.
44. Hofman R et al. 1996 *Appl. Phys. Lett.* **69** 2068.
45. Hofstetter D, Thornton R L, Kneissl M, Bour D P and Dunnrowicz C 1998 *Appl. Phys. Lett.* **73** 1928.
46. Dingle R, Shaklee K L, Leheny R F and Zetterstrom R B 1971 *Appl. Phys. Lett.* **19** 5.
47. Bidnyk S, Little B D, Schmidt T J, Krasinski J and Song J J 1998 Proc. *SPIE* **3419** 35.
48. Fischer A J et al. 1997 *Appl. Phys. Lett.* **71** 1981.
49. Bidnyk S, Schmidt T J, Little B D and Song J J 1999 *Appl. Phys. Lett.* **74** 1.
50. Sun H D et al. 2000 *Appl. Phys. Lett.* **77** 4250.
51. Sun H D et al. 2000 *Appl. Phys. Lett.* **78** 3385.
52. Deguchi T, Azuhata T, Sota T, Chichibu S, Arita M, Nakanishi H and Nakamura S 1998 *Semicond. Sci. Technol.* **13** 97.
53. Schmidt T J et al. 1999 *Appl. Phys. Lett.* **73** 3689.
54. http://www.epcorp.com/press/64.asp.
55. Ohtomo A et al. 2000 *Appl. Phys. Lett.* **77** 2204.
56. Sugita T, Mizuuchi K, Kitaoka Y and Yamamoto K 1999 *Opt. Lett.* **24** 1590.
57. Kitaoka Y, Yokoyama T, Mizuuchi K and Yamamoto K 2000 *Japan. J. Appl. Phys.* **39** 3416.
58. Grillo D C et al. 1994 *Electron. Lett.* **30** 2131.
59. Nakayama N et al. 1993 *Electron. Lett.* **29** 2194.
60. Kato E, Noguchi H, Nagai M, Okuyama H, Kijima S and Ishibashi A 1998 *Electron. Lett.* **34** 282.
61. Klude M et al. 2000 *Phys. Status Solidi a* **180** 21.
62. Kijima S et al. 1998 *Appl. Phys. Lett.* **73** 235.
63. Klude M et al. 2002 *Phys. Status Solidi b* **229** 935.
64. Katayama K et al. 1998 *Appl. Phys. Lett.* **73** 102.
65. Wenisch H et al. 1999 *Japan. J. Appl. Phys.* **38** 2590.

Taylor & Francis
Taylor & Francis Group
http://taylorandfrancis.com

18

Long-Wavelength Laser Diodes

S. Anders, G. Strasser, and E. Gornik

CONTENTS

18.1 Introduction ... 263
18.2 Lead-Salt Lasers ... 264
18.3 Antimonide-Based Lasers ... 265
18.4 Mercury–Cadmium–Telluride-Based Lasers ... 265
18.5 Quantum Cascade Lasers ... 265
  18.5.1 Distributed Feedback QCLs ... 268
  18.5.2 Terahertz (Far-Infrared) QCLs ... 268
  18.5.3 Continuous-Wave Operation ... 269
18.6 Summary ... 270
References ... 271
Further Reading ... 272

18.1 Introduction

Optoelectronics relies on emitters and detectors of electromagnetic radiation. The most widely used mechanism to generate light from a semiconductor is the recombination of electrons and holes across the bandgap of a semiconducting material. Soon after the invention of the laser, this photon-emitting process was used to demonstrate the first semiconductor lasers based on GaAs [1–3]. The bandgap of GaAs (1.4–1.5 eV) sets the emission wavelength in the near infrared (~800 nm). Considerable effort has been undertaken to develop semiconductor lasers that operate at longer and at shorter wavelengths. For short wavelengths, cheap and efficient diode lasers based on GaAs and InP are available. A breakthrough has occurred by solving the technological problems of wide-gap semiconductors. Green, blue and ultraviolet current injection lasers based on II–VI compounds (ZnSe [4]) as well as on III–V compounds (GaN [5]) have been developed. For wavelengths in the mid-infrared (MIR, also called 'long wavelengths'), narrow-gap semiconductor lasers were demonstrated in the 1960s [6]. The most prominent example is lead-salt compounds with an emission range from below 3 μm to about 30 μm. A gap exists in the far-infrared, while wavelengths beyond 1 mm can be readily generated by high-frequency oscillators. Figure 18.1 presents an overview of the emission ranges of various types of lasers. While the near-infrared range is well covered by commercially available lasers, quantum cascade lasers (QCLs) are very promising sources for the mid- and far-infrared range.

Steady progress has been made to fill gaps in the emission wavelengths that are not conveniently accessible. The advance in epitaxial layer growth and band structure engineering led to improvements of MIR sources that have been available for decades. In particular, these are lead-salt lasers, antimonide-based lasers and mercury–cadmium–telluride-based lasers. Most notably, molecular beam epitaxy (MBE) allowed the realization of QCLs [7]. QCLs are unipolar lasers based on transitions between quantum levels in ultrathin layers.

The emission range of the MIR (wavelength range: 3–30 μm) is interesting for several industries. Compact, cheap and reliable coherent sources are useful for a wide spectrum of applications ranging from IR astronomy to the automobile and telecommunication industries and to chemical sensing applications.

Many small molecules have their fundamental absorption bands in the MIR. Therefore, this frequency range is sometimes called the fingerprint region of molecules. Applications in gas sensing have been shown as early as 1998 [8]. An overview of near- and mid-infrared lasers as optical sensors for gas analysis is presented in the work of Werle et al. [9]. The designable wavelength of QCLs makes it possible to install a detection system for literally any organic molecule. Environmental control, the food industry, pollution and contamination control applications will most probably make use of these coherent sources once the product is established. A number of dedicated QCL 'mini-spectrometers' installed at strategic points in any process line (like, e.g. semiconductor industries) would ensure that any process failures are rapidly detected, thereby reducing redundant processing and minimizing product loss.

Other potential applications are in IR astronomy and remote sensing collision avoidance radars. The atmospheric windows in the MIR spectral range—from 3–5 to 8–12 μm—make coherent MIR sources favourable to telecommunications [10–12], because these wavelengths are not strongly scattered by fog, smog and dust particles suspended in the atmosphere.

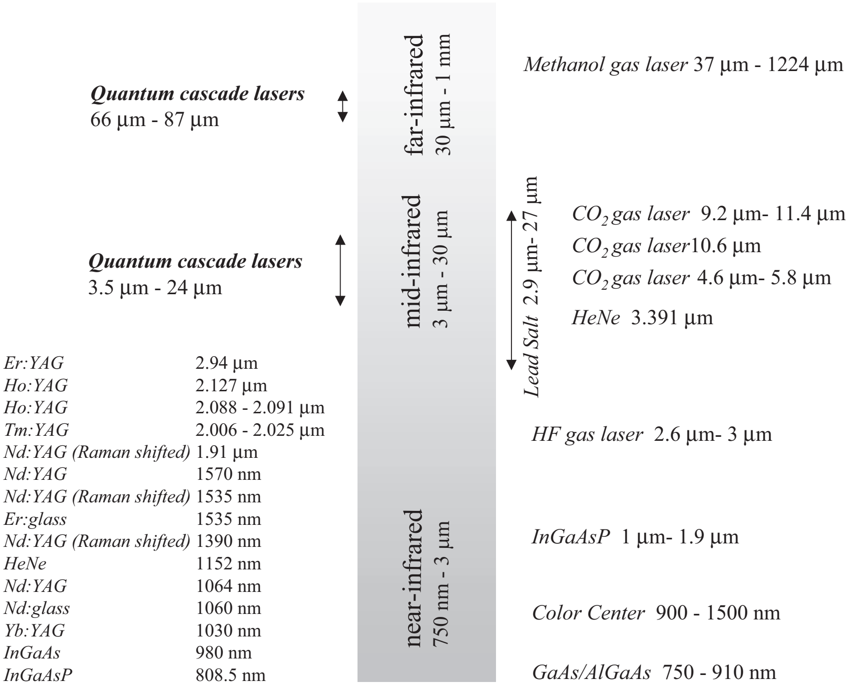
Quantum cascade lasers
66 µm - 87 µm
far-infrared
30 µm - 1 mm
Methanol gas laser 37 µm - 1224 µm
Quantum cascade lasers
3.5 µm - 24 µm
mid-infrared
3 µm - 30 µm
Lead Salt 2.9 µm- 27 µm
CO2 gas laser 9.2 µm- 11.4 µm
CO2 gas laser 10.6 µm
CO2 gas laser 4.6 µm- 5.8 µm
HeNe 3.391 µm
Er:YAG 2.94 µm
Ho:YAG 2.127 µm
Ho:YAG 2.088 - 2.091 µm
Tm:YAG 2.006 - 2.025 µm
Nd:YAG (Raman shifted) 1.91 µm
Nd:YAG 1570 nm
Nd:YAG (Raman shifted) 1535 nm
Er:glass 1535 nm
Nd:YAG (Raman shifted) 1390 nm
HeNe 1152 nm
Nd:YAG 1064 nm
Nd:glass 1060 nm
Yb:YAG 1030 nm
InGaAs 980 nm
InGaAsP 808.5 nm
HF gas laser 2.6 µm- 3 µm
InGaAsP 1 µm- 1.9 µm
near-infrared
750 nm - 3 µm
Color Center 900 - 1500 nm
GaAs/AlGaAs 750 - 910 nm

FIGURE 18.1 Overview of the emission ranges of various types of lasers. The wavelength axis is not to scale. (*The Photonic Spectrum Reference Wall Chart* Photonics Spectra 2000.)

This would allow a replacement of microwave RF links by MIR systems that are smaller and directional and can be easily focused. Furthermore, high-speed applications of actively and passively mode-locked QCLs are being developed [13]. Emission in the mid- to far-infrared is well suited for law enforcement (concealed weapons detection) and applications in medicine and biology [14].

This chapter will describe selected MIR emitters, namely lead-salt lasers, antimonide-based and mercury–cadmium–telluride-based lasers, and QCLs. Most of the space is dedicated to QCLs. They are relatively new and considered most exciting by researchers in the field because an extended quantum mechanical structure is grown in a controlled fashion, and because of their potential for applications. For more extensive reviews about the established lasers, the reader may refer to the literature suggested as further reading.

18.2 Lead-Salt Lasers

Lead-salt lasers cover the emission range from below 3 to almost 30 µm [15–17]. Continuous emission is observed at temperatures that can be achieved with thermoelectric coolers, while pulsed operation is possible above room temperature [18]. For more than two decades, lead-salt lasers have been commercially available. Their high sensitivity and selectivity makes them well suited for MIR gas analysis. Once a single-mode emitter with an emission near the target absorption energy has been selected and tuned, it can be operated for years with reproducible performance.

In principle, emitters with long wavelengths are possible by decreasing the bandgap of the material. However, as the bandgap is decreased, the non-radiative Auger recombination drastically increases. Especially at the high electron and hole densities needed to achieve lasing action at non-cryogenic temperatures, Auger recombination severely limits the gain of the active material. Lead-salt lasers circumvent this hindrance to some extent. The amount of Auger recombination depends, among other things, on the band structure. The direct bandgap minimum of lead-salt compounds is not located at the Γ point like in III–V band shapes, but rather there are four minima located at the L-points. The band structure influences energy and momentum conservation of an Auger process. Thus, it becomes clear why Auger processes are less likely in some band structures. The inhibited Auger recombination is the reason why conventional III–V diode lasers cannot compete with lead-salt lasers for wavelengths longer than about 3.5 µm.

Examples of lead-salt components are PbS (one of the few naturally occurring semiconductors), PbTe, PbSe, PbSnTe, PbSnSe, PbCdSe and PbSSe [19]. The infrared dielectric constant of these materials is quite high and, as usual, increases with decreasing bandgap. Thus, one can combine the materials to obtain a structure that confines the carriers and guides the light. A disadvantage for lasing operation is that the lead-salt components have a low thermal conductance. Lead-salt lasers were made early on by chemical or vapour deposition with a curing step. Furthermore, epitaxially grown (liquid phase, hot wall and MBE is used) and single crystal lead-salt lasers have been fabricated. Vertical-cavity surface-emitting lasers based on lead-salt components have also been demonstrated [20,21].

18.3 Antimonide-Based Lasers

Lasers fabricated from antimony-containing III–V compounds are developed for emission wavelengths of 2–5 μm. Before 1990, antimonide-based lasers were mostly grown by liquid phase epitaxy. Room-temperature continuous-wave operation was reported at 2.3 μm [22]; however, at longer wavelengths, lasing operation was restricted to cryogenic temperatures. Liquid-phase epitaxy cannot be used to grow sophisticated structures such as strained quantum well lasers that can potentially reduce Auger recombination. Therefore, the use of molecular beam and organometallic vapour-phase epitaxy improved the performance of antimonide-based lasers.

So far, GaInAsSb/AlGaAsSb quantum well lasers have shown the best performance between 1.9 and 3 μm. Room-temperature pulsed operation has been observed up to 2.9 μm [23], while continuous-wave operation has been obtained at 2 μm [24,25]. Using InAsSb as the active layer allows emission beyond 3 μm, however, well below room temperature because of Auger recombination.

In addition to these type I lasers, type II lasers have been demonstrated. In type II lasers, conduction and valence band minima are physically separated. In principle, the wavelength can now be extended beyond the values given by the bandgap of each alloy. Also, Auger recombination can be reduced by proper design. Type II lasers with GaInSb/InAs superlattices or quantum wells have emission wavelengths between 2.7 and 5.2 μm. Optically pumped type II lasers function at higher temperatures (350 K [26]) than electrically pumped type II lasers (255 K [27]). Both maximum operating temperatures are for an emission wavelength of 3.2 μm. Operation at 27 μm is proposed [28].

18.4 Mercury–Cadmium–Telluride-Based Lasers

Mercury–cadmium–telluride compounds have been studied for a long time [29,30]. The $Cd_xHg_{1-x}Te$ alloy is the only semiconductor that can be grown with any bandgap of 0–1.48 eV. Zero bandgap is reached for $x = 0.15$. The lattice parameter varies only by 3×10^{-3} for this composition range, and the energy band structure is of the direct type. Even though these are attractive properties for MIR emitters, so far this compound has been mostly used for the fabrication of infrared detectors and detector arrays.

The best optically pumped lasers were grown by MBE. They were designed to emit at 3.2 μm by using a composition of $x = 0.38$ and a quantum well thickness of 20 nm. The cladding layers had a composition of $x = 0.5$ and a thickness of 1 μm. The devices worked up to 154 K and had an external quantum efficiency of 7.5% at 80 K [31]. For electrical pumping, the active material has to be inserted into a p–i–n junction with doping levels in excess of 10^{17} cm^{-3} for the doped regions. Non-radiative recombination (mostly Auger recombination) appears to limit the performance of the electrically pumped lasers produced so far to operating temperatures below 100 K [32–34]. Improvements are expected by incorporating quantum wells into the recombination region because carrier confinement strongly modifies the Auger recombination [35–37].

18.5 Quantum Cascade Lasers

In contrast to bandgap lasers, which are based on electron–hole recombination, unipolar lasers are based on *intersubband* transitions. The lasing transition occurs between sublevels of the same polarity (see Figure 18.2). Electronic levels are used for InP- and GaAs-based QCLs, because the conduction band offset in these materials is larger than the valence band offset. Because the electrons that are involved in the optical transition are still available after the transition, the operation of several light-emitting stages in series is possible. One electron passing through the device can thus emit several photons (‘electron recycling’). This boosts the optical output to several hundred mW, depending on the temperature, the type of operation (pulsed or continuous mode) and the material. *Interband* cascade lasers are also possible; here, we focus on intersubband cascade lasers. The unipolar nature of these lasers means that, as long as non-parabolicity effects are excluded, all initial and final states have the same curvature. The joint density of states is sharp; the gain linewidth does not directly depend on the temperature. The gain is only limited by the amount of current that can be driven through the structure.

The light-emitting cascades consist of a multiple-quantum well heterostructure. Figure 18.3 shows the conduction band with an applied field for two QCL designs. The wavefunctions are obtained by solving Schrödinger’s equation. To illustrate the transition probabilities, the squared wavefunctions are plotted at the energy of the electronic states. In a superlattice design (Figure 18.3a), the active region consists of several wells and barriers such that the lower lasing level is emptied by tunnelling of the electrons into a miniband. For three-well designs, the thicknesses of the wells and barriers in the active region are chosen such that the lasing transition occurs between the wavefunctions labelled ‘3’ and ‘2’ in Figure 18.3b. The lower lasing level ‘2’ is emptied efficiently because the energy difference between level ‘2’ and ‘1’ corresponds to one longitudinal optical phonon energy, 30–40 meV depending on the material. For both three-well and superlattice designs, the active regions are separated by injector regions. These serve as charge reservoirs and contain doped layers. Injectorless QCLs have

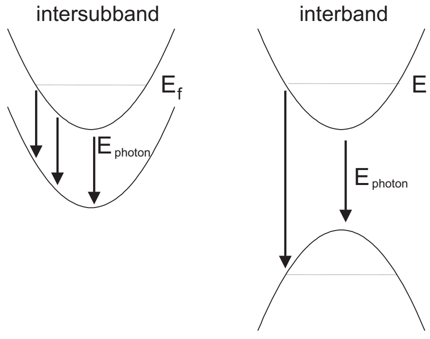

FIGURE 18.2 Schematic diagrams of interband and intersubband optical transitions.

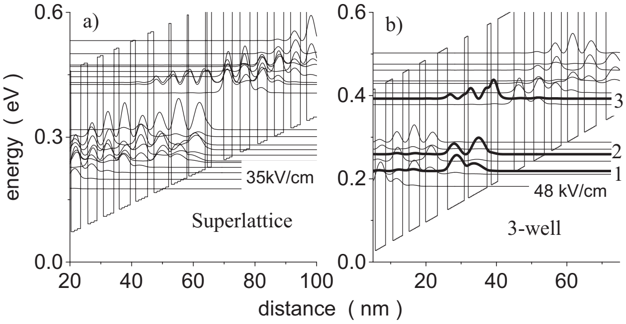

FIGURE 18.3 Band diagram and squared wavefunctions of a (a) superlattice and (b) a three-well quantum cascade structure.

been fabricated by using an appropriately designed chirped superlattice active region [38].

The main difficulty in the realization of an intersubband laser is the achievement of population inversion, which is not an intrinsic property like in interband lasers, but a result of properly designed scattering times. The dominant scattering mechanism between subbands separated by more than one optical phonon energy is the emission of optical phonons [39,40]. This limits the non-radiative lifetimes of the excited states to the order of a picosecond. Lifetime measurements [41] on InGaAs/InAlAs show that, in general, the lifetime of an excited state has a minimum (~0.25 ps) for a subband spacing equal to the energy of the optical phonons. It increases monotonically up to a few picoseconds for subband spacings of about 300 meV. In the far-infrared (or terahertz) regime, where the subband spacing is well below an optical phonon energy, a different mechanism to establish population inversion had to be found.

For a three-well intersubband emitter, the active region consists of a three-level scheme, designed to ensure population inversion between level 3 and level 2. In a simple model, the inversion condition is reduced to $\tau_{32} > \tau_2$. Here, $1/\tau_{32}$ denotes the non-radiative scattering rate from level 3 to level 2, and $1/\tau_2$ denotes the total scattering rate out of level 2. The transition $3 \rightarrow 1$ is, in coupled quantum wells, not negligible. This leads to an inversion condition of $\tau_3 > \tau_2$ (total lifetimes). A characterization for the $3 \rightarrow 2$ transition is given by the strength of the wavefunction overlap of these two states. For a strong overlap, the transition is called vertical; in a regime with a weak overlap, the term diagonal transition is used.

Generating infrared radiation based on the electronic transitions between minibands in a superlattice has some advantages compared to coupled quantum well systems. The main advantage is the high oscillator strength of the radiative transitions between two minibands. The oscillator strength has a maximum at the mini-Brillouin zone boundary ($k_z = \pi/d$). The injected electrons are located in the upper miniband, while in the lower miniband in properly designed and carefully doped structures the states at the zone boundary are empty. This is called 'natural inversion'.

In weakly coupled superlattices, transport proceeds by sequential resonant tunnelling and is usually accompanied by the formation of electric field domains. Applying external electric fields breaks superlattice structures into high- and low-field domains, where the energy levels lock in resonances [42]. In a laser, it is necessary to have a homogenous and stable electric field distribution. Therefore, doping is inserted into the QCL to compensate the total negative charge in the active region by positive ions (impurities). This prevents charge build-up even for strong injection. Also, the operating point of a QCL structure has to be stable to avoid field domain formation. The active region is normally left undoped, since impurity atoms in the active region reduce the lifetimes of the excited states. Dopants in the active region broaden and red-shift the lasing transitions [43]. The doping is usually inserted in the centre of the injectors, where scattering increases the relaxation probability and, thus, enhances the injection efficiency.

In addition to a radiative transition combined with a population inversion in a quantum cascade structure, a cavity is necessary to achieve lasing. In the simplest approach, the cleaved side facets of a laser bar act as mirrors. Optical confinement within these mirrors is, like in bandgap lasers, achieved by dielectric waveguides. The main requirement for an optical waveguide, apart from guiding the light, is to have low optical losses. In QCLs, the waveguide losses are predominantly controlled by free carrier absorption and can be described by a Drude model [44,45]. In contrast to near-infrared lasers, mid-infrared QCLs have to deal with high internal losses and rather thick cladding layers. The total thickness of the waveguide structure is limited because the growth time should not be excessive and because the defect density should be kept minimal. Also, the thermal transport across the layers needs to be as efficient as possible.

A plasmon enhanced waveguide may be used for mid-infrared-emitting lasers. The first plasmon-enhanced waveguide for a QCL was demonstrated in the InGaAs/InAlAs system in 1995 [46] and in the GaAs/AlGaAs system in 1999 [47]. In this waveguide design, the refractive index variations are based on changes in the doping concentration n or on interfaces between different materials. The plasma frequency ω_p of the highly doped n^{++} layers is shifted close to the laser frequency. Especially for the GaAs system, plasmon-enhanced GaAs waveguides are preferred to AlGaAs cladding layers for a variety of reasons. First, the refractive index of GaAs is higher than the effective refractive index of the active material. Hence, in contrast to the InGaAs/InAlAs/InP system, the substrate does not support the waveguiding. From the technological point of view, the growth of thick GaAs layers is much more reliable than the growth of thick AlGaAs layers with high A1 contents, where residual strain limits the total thickness. Furthermore, ternary alloys such as AlGaAs have a poor thermal conductivity compared to binary materials such as GaAs. Figure 18.4 shows the refractive indices of a double-plasmon-enhanced waveguide together with the optical intensity. For the plasmon-enhanced waveguides, the overlap between the n^{++} layers and the optical mode needs to be minimized to avoid very high waveguide losses. This is done with 3- to 4-μm-thick low-doped (some $10^{16}\,\mathrm{cm}^{-3}$) GaAs layers.

A QCL consists of several tens of cascades, each containing an active region and an injector, embedded in the waveguide. The total thickness of MBE-grown material adds up to several micrometres. Figure 18.5 shows a TEM image of a cross

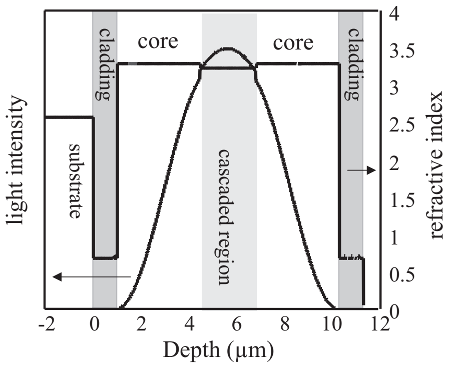

FIGURE 18.4 Refractive index and light intensity of a double-plasmon-enhanced waveguide.

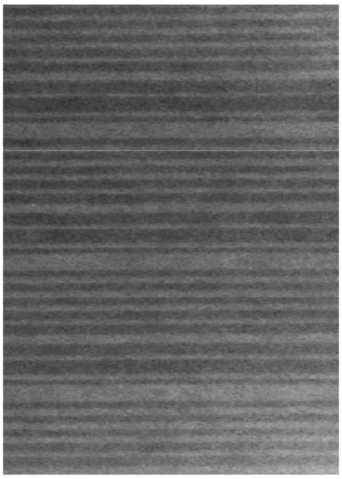

FIGURE 18.5 TEM image of a cascaded structure.

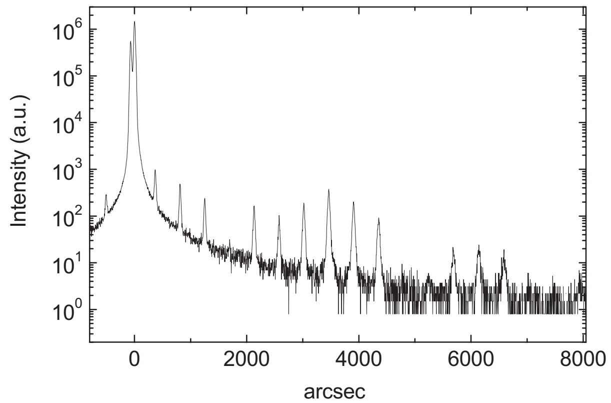

FIGURE 18.6 X-ray scan of a cascaded structure.

section of several layers. Figure 18.6, a $\omega/2\theta$ scan, shows an X-ray scan along the (004) plane of GaAs.

Compared to bandgap lasers, the major advantage of QCLs is that their emission energy is not fixed by the bandgap of the utilized materials but can be tailored by band structure engineering. This allows a wide emission range in the mid-infrared, currently from 3.5 [48] to 24 μm [49] and from 66 [50] to 87 μm [51].

Lasing in a cascaded structure was first proposed in 1971 [52]. In this work, electrons tunnel from a quantum well ground state to an excited state of the neighbouring well by photon-assisted tunnelling. After the photon emission, the electrons non-radiatively relax into the ground state and are injected into the next stage. The population inversion necessary for lasing action is obtained here because of a long non-radiative transition time (≥10 ps) in the 'diagonal' transition compared to the short intrawell transition time. The first intersubband emission data were observed in an electron gas at a Si/SiO$_2$ interface [53]. The first intersubband luminescence spectrum in a GaAs/AlGaAs superlattice pumped by resonant tunnelling was demonstrated in 1988 [54]. Because of the stringent requirements on the layer thicknesses and interface quality, the growth of QCLs was only possible after the advent of MBE [55]. In 1994, the first QCL was built [7]. It was based on the InGaAs/InAlAs material system. Four years later, the AlGaAs/GaAs system was the second system that showed lasing [56]. This material system potentially has a number of key advantages, including a more mature materials technology, amenability to dry etching for improved device fabrication, good lattice matching over the entire range of alloy compositions, and the possibility to realize extremely long wavelength emission. Disadvantages arise due to the lower conduction band offset in this material system [57], which places a lower limit on the lasing wavelength (~7 μm) and decreases the confinement of the upper lasing state. However, mostly because the InGaAs/InAlAs material system is better explored, continuous-wave operation at room temperature has been demonstrated only for this system so far [58]. Products based on the InP/InGaAs/AlInAs technology are already commercially available [59]. While there is some effort to develop SiGe-based QCL structures [60], to date, InP and GaAs remain the only two material systems that show quantum cascade lasing.

The processing of electrically pumped laser cavities from the MBE-grown heterostructure is done by photolithography. Typically, the laser cavity consists of a ridge that is about 1 mm long and several tens of micrometres wide (see Figure 18.7 for an SEM image). The lateral confinement can be done either by wet-chemical or, if a straight profile is desired, by reactive-ion etching (RIE). Due to the unipolar nature of QCLs, surface recombination is, in contrast to bandgap lasers, not an issue. To complete the most simple device, metallization is deposited on top of the ridge as well as on the back of the device. Alternatively, extended top contacts for improved current homogeneity can be fabricated. SiN or SiO may be used as isolation. The metal contacts can be processed either as Schottky contacts or, if less heat dissipation is desired, as alloyed ohmic contacts. Here, care must be taken not to alloy too deep into the waveguide, since a high charge concentration close to the light field is detrimental to the light output power.

The end facets are frequently left as-cleaved. For higher reflectivity, a coating of, for example, ZnSe and Au may be applied to one of the mirrors. Another approach is to process a Bragg mirror with a focused ion beam. This can decrease the threshold current by up to 40% [61]. Microcylinder-shaped cavities do not need mirrors because the light propagates mostly by total internal reflection (see Figure 18.8 for an example of a ring-shaped laser) [62,63].

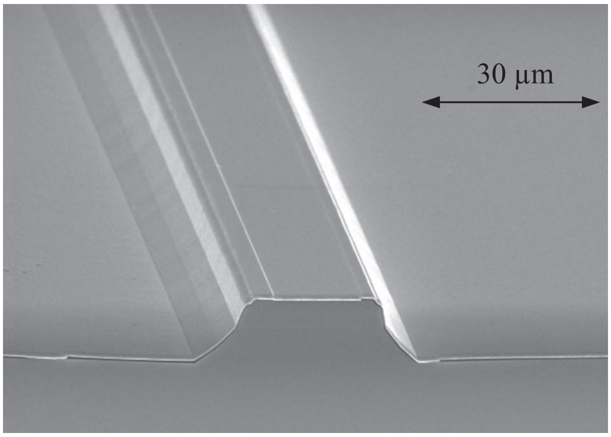

FIGURE 18.7 SEM image of a Fabry–Pérot laser cavity.

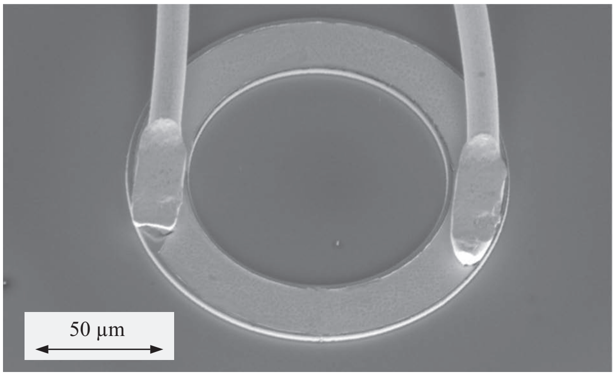

FIGURE 18.8 SEM image of a ring-shaped laser cavity.

18.5.1 Distributed Feedback QCLs

For several applications, it is desirable to have a single-mode emitter. While conventional ridge cavities emit a Fabry–Pérot spectrum (see Figure 18.9), the fabrication of a grating on top of the laser ridge fixes the emission wavelength to a desired value. The first 'distributed feedback (DFB) laser' was introduced in 1997. Figure 18.10 shows an SEM image of a grating that was defined by photolithography. For gratings with a period of less than about 1 µm, holographic lithography may be used. Figure 18.11 demonstrates the good sideband suppression of a DFB laser. Figure 18.12 shows that the emission energy can be tuned by temperature, thus allowing it to sweep across, for example, a chemical absorption spectrum.

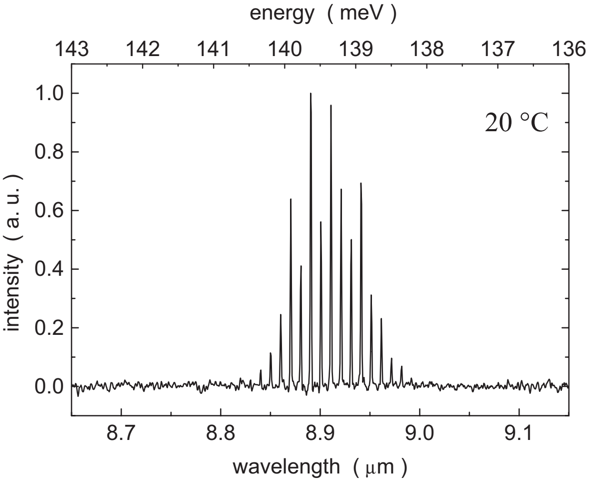

FIGURE 18.9 Emission spectrum of a QCL with Fabry–Pérot cavity.

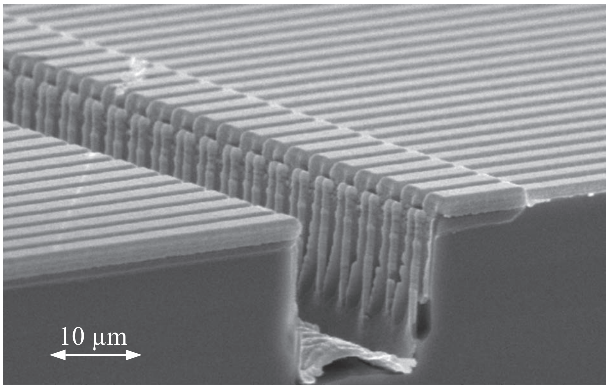

FIGURE 18.10 SEM image of a DFB grating. The grating extends across the trench that defines the laser cavity. The SiN isolation (300 nm thick) is visible.

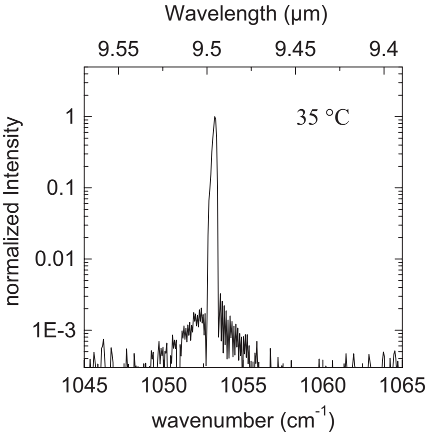

FIGURE 18.11 Single-mode emission spectrum of a DFB laser.

18.5.2 Terahertz (Far-Infrared) QCLs

The emission range of QCLs has been extended into the terahertz range [64]. This is a particularly important feat since it is the first versatile approach to bridge the 'terahertz gap'. Already in 1984 lightly doped germanium has been shown to show lasing action under crossed electric and magnetic fields [65]. However, the properties of this semiconductor laser were fixed by the bulk material. The great advantage of a QCL terahertz emitter is that the design is flexible. Terahertz sources are beneficial for applications in astronomy, telecommunications, medical imaging and concealed weapon detection. The terahertz gap is approached from the high-energy side by semiconductor lasers that can operate at frequencies no lower than 30 THz (about 10 µm). On the low-energy side, transistors

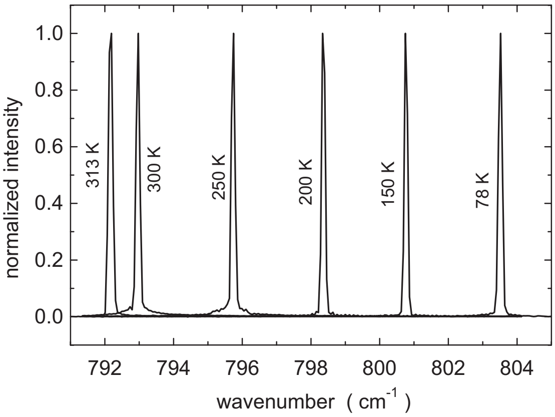

FIGURE 18.12 Temperature tuning behaviour of a DFB laser.

deliver frequencies not higher than about 300 GHz. Between the two technologies, the conversion of electrical power into electromagnetic radiation poses several difficulties. Free-carrier absorption losses increase quadratically with the wavelength, and the optical mode scales with the wavelength so that a sufficiently large (or clever) waveguide must be designed. Furthermore, the lifetime of the upper lasing level is short because of much electron–electron scattering between the closely spaced energy levels. For the first terahertz QCL, Köhler et al. developed a hybrid waveguide between a 'metallic microwave strip-line' and a 'surface plasmon waveguide'. A chirped superlattice heterostructure has been used to achieve fast depopulation of the lower lasing level as well as efficient depletion of the upper level. Figure 18.13 shows a lasing spectrum of the first functioning terahertz QCL together with spontaneous emission spectra at currents below threshold. The spectra were taken at 8 K. Improvements of terahertz lasers with power output and maximum operating temperature moving towards commercial terahertz technology are already underway [50,66].

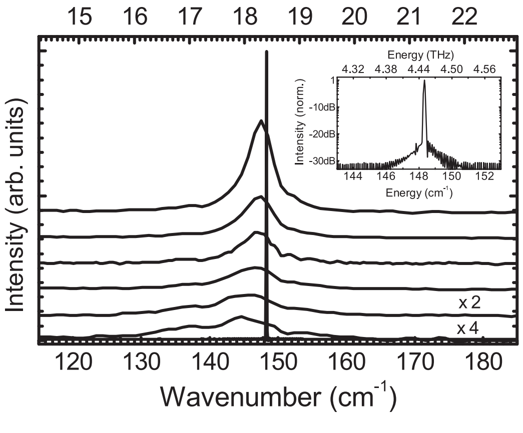

FIGURE 18.13 Terahertz emission from a 1.24 mm long and 180 µm wide device recorded at 8 K. Shown are spectra below and above lasing threshold. Currents are 300, 450, 600, 700, 750, 850 and 1240 mA. Inset: single-mode emission with a side-mode suppression ratio of 20 dB. (Reproduced by permission of Nature Publishing Group from Köhler R, Tredicucci A, Beltram F, Beere H E, Linfield E H, Davies A G, Ritchie D A, Iotti R C and Rossi F 2002 *Nature* **417** 156.)

18.5.3 Continuous-Wave Operation

Considerable progress has been made as the first QCL operating continuous wave at room temperature was introduced [58]. This QCL emits at 9.1 µm. The output power is 17 mW at 20°C. Because no cooling is needed and the linewidth can be narrower than the 0.1 cm^{-1} that limits pulsed lasers, such a laser is a milestone for applications in high-resolution spectroscopy and free-space optical communication.

Compared with bandgap lasers, the thresholds of even the best QCLs are rather high because of the large fraction of non-radiative recombination. Threshold current densities of several kA cm^{-2} dissipate several tens of kW cm^{-2}. This is enough heat load to substantially raise the laser temperature above the ambient temperature. If the coupling to the heat sink is poor, the laser temperature of a continuous-wave-driven QCL can easily be 100 K above the heat sink temperature. Pulsed laser operation circumvents this problem by allowing the laser to cool in between pulses. Figure 18.14 shows the phase shift of a detection laser beam that illuminates the laser ridge. The phase shift is proportional to the temperature change. Thus, Figure 18.14 illustrates how the temperature in the laser ridge increases during a 100 ns long pulse. After the pulse, the temperature decreases exponentially. The decrease can be fitted by assuming heat conductivities of 0.25 W K^{-1}cm^{-1} parallel to the layers and 0.015 W K^{-1}cm^{-1} perpendicular to the layers [67].

For room-temperature continuous-wave operation, sufficient thermal coupling is thus essential. Furthermore, the characteristic temperature T_0, which describes the temperature dependence of the threshold $J_{\text{th}} = J_0 \exp(T/T_0)$, should be large. In the approach of Beck et al. [58], the active region consisted of four quantum wells (see Figure 18.15). The lower three energy states are separated roughly by one longitudinal optical phonon energy each. A narrow quantum well and barrier separate the injector region from the active region. This increases the magnitude of the upper-state wavefunction locally and enhances the injector efficiency.

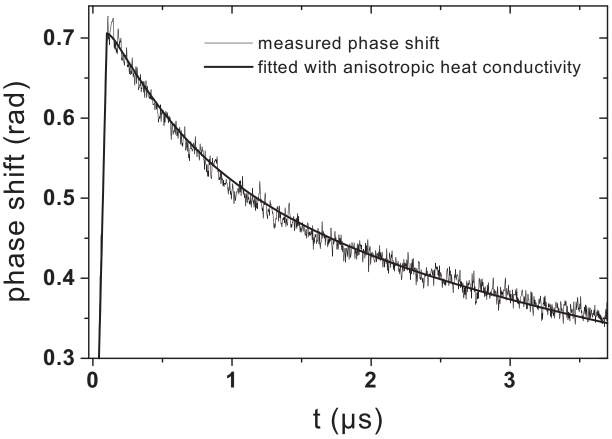

FIGURE 18.14 Phase shift of a detection laser beam that illuminates the QCL ridge from the back. The phase shift is proportional to the temperature increase of the QCL while it is driven with a 100 ns long pulse.

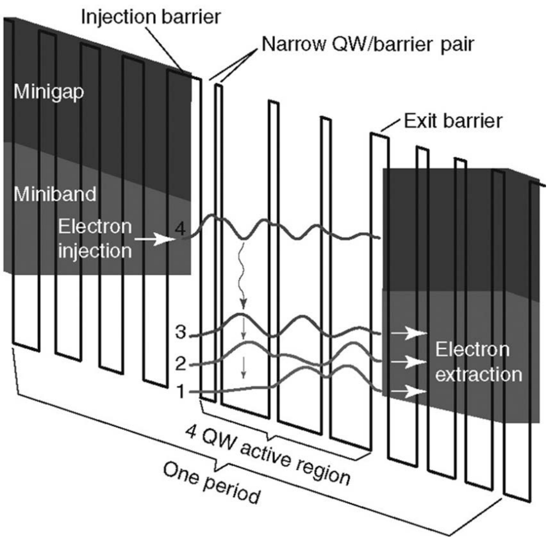

FIGURE 18.15 Four-well design of the structure that emitted continuous wave at room temperature. (Reprinted with permission from Beck M, Hofstetter D, Aellen T, Faist J, Oesterle U, Ilegems M, Gini E and Melchior H 2001 *Science* **295** 310. Copyright 2002 American Association for the Advancement of Science.)

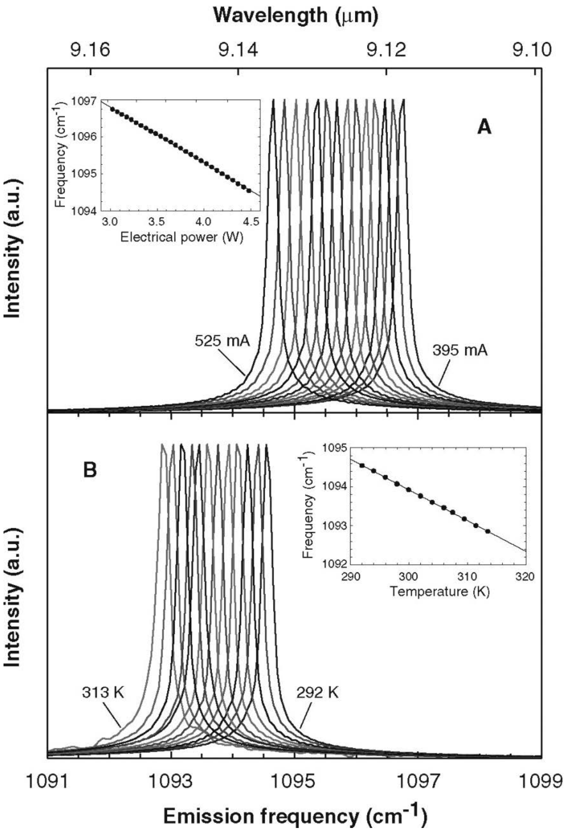

FIGURE 18.16 (a) High-resolution continuous-wave spectra for various injection currents. Inset: emission frequency as a function of the electrical input power. (b) Spectra of a continuous-wave QCL at various temperatures around room temperature. Inset: temperature tuning behaviour. (Reprinted with permission from Beck M, Hofstetter D, Aellen T, Faist J, Oesterle U, Ilegems M, Gini E and Melchior H 2001 *Science* **295** 310. Copyright 2002 American Association for the Advancement of Science.)

The devices were processed in a narrow-stripe, planarized and buried heterostructure geometry, all of which serve to enhance the heat flow. Continuous-wave operation was observed up to 39°C, which is quite a jump from the previously observed record of −30°C where junction-down-mounted devices were used. The threshold current density at room temperature was 4.3 kA cm^{-2} at a voltage bias of 7.6 V. Figure 18.16 shows high-resolution spectra at various currents and temperatures.

18.6 Summary

A remarkable number of new concepts and contributions demonstrate the scientific and industrial relevance of new or improved mid- and far-infrared sources. Thinking in a timescale of 1–5 years, steady process in the performance of the already existing mid- and far-infrared sources will lead to an increased wavelength range as well as to improved temperature and power output performance. The continuing efforts put into the understanding, and the technology of crystal growth techniques such as MBE and metal–organic chemical vapour deposition (MOCVD) will increase the number of possible material combinations.

Improvements of material knowledge and technology will allow further development of all the discussed laser types. For lead-salt lasers, there is no theoretical argument that makes continuous-wave room-temperature operation impossible. These lasers, widely commercially available, will probably remain, for a while, the workhorse of mid-infrared gas analysis with high-resolution spectroscopy. For mercury-cadmium-telluride-based lasers, the use of sophisticated heterostructures led to better performance. Better material quality of antimonide-based lasers resulted in larger output power and higher operating temperatures.

In the 5–12 μm range, InP-based QCL structures currently show the best performance in terms of high output power, aging, single mode emission, and temperature performance. Nevertheless, there is room for improvement. First, the design of the active region and of the waveguide can be further improved, including new solutions for low loss optical confinement. To extract the heat from the active region as effectively as possible, regrowth of InP, most likely by a MOCVD technique, will become state of the art. Junction-down mounting and high reflectivity mirrors (done by, for example, coatings, Bragg reflectors or photonic band-gap structures) will further improve the high-temperature performance.

Similar improvements are feasible for GaAs-based QCLs. Continuous-wave operation at room temperature has yet to be demonstrated. Comparing GaAs- with InP-based QC lasers, the lower-band offset of the GaAs-based lasers may well be compensated by the higher degree of freedom in the design of the active region, as well as by the amenability to RIE techniques. Limiting the losses at long wavelengths allowed the realization of a GaAs/AlGaAs terahertz QCL. Further improvements in the far-infrared emission range with respect to output power and maximum operating temperature are certainly just around the corner.

REFERENCES

1. Hall R N, Genner G E, Kingsley J D, Soltys T J and Carlson R O 1962 *Phys. Rev. Lett.* **9** 366.
2. Nathan M I, Dumke W P, Burns G, Dill F J Jr and Lasher G J 1962 *Appl. Phys. Lett.* **1** 62.
3. Quist T M, Rediger R H, Keyes R J, Krag W E, Lax B, McWorther A L and Zeigler H J 1962 *Appl. Phys. Lett.* **1** 91.
4. Gaines J M, Drenten R R, Habern K W, Maeshall T, Mensz P and Petruzello J 1993 *Appl. Phys. Lett.* **62** 2462.
5. Nakamura S, Mukai T and Senoh M 1993 *Appl. Phys. Lett.* **64** 1687.
6. Horikoshi Y 1985 *Semiconductors and Semimetals* vol 22C, ed W T Tsang (Orlando, FL: Academic).
7. Faist J, Capasso F, Sivco D L, Sirtori C, Hutchinson A L and Cho A Y 1994 *Science* **264** 553.
8. Namjou K et al. 1998 *Opt. Lett.* **23** 219.
9. Werle P, Slemr F, Maurer K, Kormann R, Muecke R and Jaenker B 2002 *Opt. Lasers Eng.* **37** 101.
10. Faist J and Capasso F 1997 *Quantum Cascade Laser (McGraw-Hill Yearbook of Science and Technology)* (New York: McGraw-Hill).
11. Martini R, Gmachl C, Falciglia J, Curti F G, Bethe C G, Capasso F, Whittaker E A, Paiella R, Tredicucci A, Sivco D L and Cho A Y 2001 *Electron. Lett.* **37** 111.
12. Blaser S, Hofstetter D, Beck M and Faist J 2001 *Electron. Lett.* **37** 778.
13. Paiella R, Capasso F, Gmachl C, Sivco D L, Baillargeon J N, Hutchinson A L, Cho A Y and Liu H C 2000 *Science* **290** 1739.
14. Waynant R W, Ilev I K and Gannot I 2001 *Phil. Trans. R. Soc. A* **359** 635.
15. Tacke M 2001 *Phil. Trans. R. Soc. A* **359** 547.
16. Bauer G, Kriechbaum M, Shi Z and Tacke M J 1995 *Nonlinear Opt. Phys. Mater.* **4** 283.
17. Katzir A, Rosman R, Shani V, Bachem K H, Boettner H and Preier H M 1989 Tunable lead-salt lasers *Handbook of Solid State Lasers* ed P K Cheo (New York: Dekker) pp 227–347.
18. Schiessl U P and Rohr J 1999 *Infrared Phys. Technol.* **40** 328.
19. Holloway H and Walpole J N 1979 *Prog. Cryst. Growth Charac.* **2** 49.
20. Heiss W, Schwarzl T, Springholz G, Biermann K and Reimann K 2001 *Appl. Phys. Lett.* **78** 862.
21. Zhao F, Wu H, Jayasinghe L and Shi Z 2002 *Appl. Phys. Lett.* **80** 1129.
22. Bochkarev A E, Dolginov L M, Drakin A E, Eliseev P G and Sverdlov B N 1988 *Sov. J. Quantum Electron.* **18** 1362.
23. Lee H, York P K, Menna R J, Martinelli R U, Garbuzov D Z, Naryan S Y and Connolly J C 1995 *Appl. Phys. Lett.* **66** 1942.
24. Garbuzov D Z, Martinelli R U, Lee H, York P K, Menna R J, Connolly J C and Naryan S Y 1996 *Appl. Phys. Lett.* **69** 2006.
25. Garbuzov D Z, Martinelli R U, Lee H, Menna R J, York P K, DiMarco L A, Matarese M G, Naryan S Y and Connolly J C 1997 *Appl. Phys. Lett.* **70** 2931.
26. Malin J I, Felix C L, Meyer F R, Hoffmann C A, Pinto J F, Lin C H, Chang P C, Murry S J and Pei S S 1996 *Electron. Lett.* **32** 1593.
27. Miles R H and Hasenberg T C 1997 *Antimonide-Related Strained-Layer Heterostructures* ed O Manasreh (New York: Gordon and Breach).
28. Vurgaftman I and Meyer J R 1999 *Appl. Phys. Lett.* **75** 899.
29. Willardson R K and Beer A C (ed) 1981 *Mercury Cadmium Telluride, Semiconductors and Semimetals* vol 18 (New York: Academic).
30. Capper P (ed) 1994 *Properties of Narrow Gap Cadmium-Based Compounds (EMIS Data Review Series 10)* (London: INSPEC).
31. Le H Q, Arias J M, Zandian M, Zucca R and Singh J 1994 *Appl. Phys. Lett.* **65** 810.
32. Zucca R, Zandian M, Arias J M and Gill R V 1992 *J. Vac. Sci. Technol. B* **10** 1587.
33. Million A, Colin T, Ferret P, Zanatta J P, Bouchut P, Destefanis G L and Bablet J 1993 *J. Cryst. Growth* **127** 291.
34. Arias J M, Zandian M, Zucca R and Singh J 1993 *Semicond. Sci. Technol.* **8** S255.
35. Jiang Y, Teich M C and Wang W I 1991 *J. Appl. Phys.* **69** 6869.
36. Vurgaftman I and Meyer J R 1998 *Opt. Express* **2** 137.
37. Yang R, Yang B H, Zhang D, Lin C-H, Murry S J, Wu H and Pei S S 1997 *Appl. Phys. Lett.* **71** 2409.
38. Wanke M C, Capasso F, Gmachl C, Tredicucci A, Sivco D L, Hutchinson A L, Chu S N G and Cho A Y 2001 *Appl. Phys. Lett.* **78** 3950.
39. Price P J 1981 *Ann. Phys.* **133** 217.
40. Ferreira R and Bastard G 1989 *Phys. Rev. B* **40** 1074.
41. Faist J, Capasso F, Sirtori C, Sivco D L, Hutchinson A L, Chu S-N G and Cho A Y 1993 *Appl. Phys. Lett.* **63** 1354.
42. Grahn H T, Schneider H and von Klitzing K 1990 *Phys. Rev. B* **41** 2890.
43. Faist J, Capasso F, Sirtori C, Sivco D L, Hutchinson A L and Cho A Y 1994 *Appl. Phys. Lett.* **65** 94.
44. Drude P 1900 *Ann. Physik* **1** 566; Drude P 1900 *Ann. Physik* **3** 369.
45. Jensen B 1985 *Handbook of Optical Constants* ed E D Palik (Orlando, FL: Academic).
46. Sirtori C, Faist J, Capasso F, Sivco D L, Hutchinson A L and Cho A Y 1995 *Appl. Phys. Lett.* **66** 3242.
47. Sirtori C, Kruck P, Barbieri S, Page H, Nagle J, Beck M, Faist J and Oesterle U 1999 *Appl. Phys. Lett.* **75** 3911.
48. Faist J, Capasso F, Sivco D L, Hutchinson A L, Chu S-N G and Cho A Y 1998 *Appl. Phys. Lett.* **72** 680.
49. Colombelli R, Capasso F, Gmachl C, Hutchinson A L, Sivco D L, Tredicucci A, Wanke M C, Sergent A M and Cho A Y 2001 *Appl. Phys. Lett.* **78** 2120.
50. Rochat M, Ajili L, Willenberg H, Faist J, Beere H, Davies G, Linfield E and Ritchie D 2002 *Appl. Phys. Lett.* **81** 1381.
51. Williams B S, Callebaut H, Kumar S, Hu Q and Reno J L 2003 *Appl. Phys. Lett.* **82** 1015.
52. Kazarinov R and Suris R 1971 *Fiz. Tekh. Poluprov.* **5** 797.
53. Gornik E and Tsui D C 1976 *Phys. Rev. Lett.* **37** 1425.
54. Helm M, England P, Colas E, DeRosa F and Allen S J Jr 1988 *Phys. Rev. Lett.* **63** 74.
55. Cho A Y (ed) 1994 *Molecular Beam Epitaxy* (Woodbury, NY: American Institute of Physics).
56. Sirtori C, Kruck P, Barbieri S, Collot P, Nagle J, Beck M, Faist J and Oesterle U 1998 *Appl. Phys. Lett.* **73** 3486.
57. Adachi S 1985 *J. Appl. Phys.* **58** R1; Adachi S 1989 *J. Appl. Phys.* **66** 6030.

58. Beck M, Hofstetter D, Allen T, Faist J, Oesterle U, Ilegems M, Gini E and Melchior H 2002 *Science* **295** 301.
59. http://www.alpeslaser.ch.
60. Dehlinger G, Diehl L, Gennser U, Sigg H, Faist J, Ensslin K, Gruetzmacher D and Mueller E 2002 *Science* **290** 2277.
61. Hvozdara L, Lugstein A, Finger N, Gianordoli S, Schrenk W, Unterrainer K, Bertagnolli E, Strasser G and Gornik E 2000 *Appl. Phys. Lett.* **77** 1241.
62. Anders S, Schrenk W, Gornik E and Strasser G 2002 *Appl. Phys. Lett.* **80** 4094.
63. Faist J, Gmachl C, Capasso F, Sirtori C, Sivco D L, Baillargeon J N and Cho A Y 1997 *Appl. Phys. Lett.* **70** 2670.
64. Köhler R, Tredicucci A, Beltram F, Beere H E, Linfield E H, Davies A G, Ritchie D A, Iotti R C and Rossi F 2002 *Nature* **417** 156.
65. Andronov A A et al. 1984 *JETP Lett.* **40** 804.
66. Menon V M, Goodhue W D, Karakashian A S, Naweed A, Plant J, Ram-Mohan L R, Gatesman A, Badami V and Waldman J *2002 Appl. Phys. Lett.* **80** 2454.
67. Pflügl C, Litzenberger M, Schrenk W, Pogany D, Gornik E and Strasser G 2003 *Appl. Phys. Lett.* **82** 1664.
68. Hofstetter D, Beck M, Aellen T, Faist J, Oesterle U, Ilegems M, Gini E and Melchior H 2001 *Appl. Phys.* **78** 1964.

FURTHER READING

Capasso F, Paiella R, Martini R, Colombelli R, Gmachl C, Myers T L, Taubman M S, Williams R M, Bethea C G, Unterrainer K, Hwang H Y, Sivco D L, Cho A Y, Sergent A M, Liu H C and Whittaker E A 2002 Quantum cascade lasers: Ultrahigh-speed operation, optical wireless communication, narrow linewidth, and far-infrared emission *IEEE J. Quantum Electron.* 38 511

Gmachl C, Capasso F, Sivco D L and Cho A Y 2001 Recent progress in quantum cascade lasers and applications *Rep. Prog. Phys.* 64 1533

Helm M (ed) *Long Wavelength Infrared Emitters Based on Quantum Wells and Superlattices* (New York: Gordon and Breach)

Liu E H C and Capasso F 2000 *Intersubband Transitions in Quantum Wells (Physics and Device Applications II)* (San Diego, CA: Academic)

19

Semiconductor Lasers and Optical Amplifiers for Switching and Signal Processing

Hitoshi Kawaguchi

CONTENTS

19.1 Introduction....273
19.2 Semiconductor Optical Amplifiers....274
  19.2.1 Ultrafast Dynamics in SOAs....274
  19.2.2 Designs for High-Power Operation....274
19.3 Wavelength Conversion....275
  19.3.1 Converters Based on Optically Controlled Gates....275
    19.3.1.1 Cross-Gain Modulation Gates....275
    19.3.1.2 Cross-Phase Modulation Gates....276
  19.3.2 Four-Wave Mixing....276
    19.3.2.1 Principle of Four-Wave Mixing in SOAs....276
    19.3.2.2 Dispersion Compensation Using Optical Phase Conjugation....277
    19.3.2.3 Wavelength Conversion of Coherent Signals with Advanced Modulation Formats....277
    19.3.2.4 Ultrafast All-Optical Switching for Wavelength Routing....277
    19.3.2.5 Phase-Sensitive Amplification....278
19.4 Optical Bistability in LDs and SOAs....278
  19.4.1 Absorptive Bistability and Dispersive Bistability....278
  19.4.2 Two-Mode Bistability through Gain Saturation....279
    19.4.2.1 General Considerations....279
    19.4.2.2 Non-linear Optical Gains and Rate Equation Analysis....279
    19.4.2.3 Polarization Bistability in VCSELs....280
  19.4.3 Flip-Flop Operations of Bistable VCSELs....280
    19.4.3.1 Switching Power and Speed....280
    19.4.3.2 Consumption Power....281
    19.4.3.3 Bit Error Rate of Flip-Flop Operation....281
  19.4.4 Other Types of Bistable Devices....282
19.5 Applications of Polarization-Bistable VCSELs....283
  19.5.1 All-Optical Format Conversion, Demultiplexing and Retiming....283
  19.5.2 Optical Memories....283
    19.5.2.1 High-Bit-Rate Operation....284
    19.5.2.2 Shift Register Operation and Multi-bit Memories....284
  19.5.3 Header Recognition....284
19.6 Future Directions....284
References....285
Further Reading....286

19.1 Introduction

Optical non-linearities of semiconductor lasers and semiconductor optical amplifiers (SOAs) create many different types of optical devices with new functions. These devices are expected to become the key devices in optical communication and signal processing systems. The great advantage of these functional devices is that they have optical gain. Thus, the device can be operated by optical control signals with low power. The output signals are stronger than those of input signals in many cases. In addition, some mechanisms for these non-linearities have ultrafast response times, which enable the optical functional devices to operate with very high speed. Optical bistability is a unique phenomenon which can be applied to all-optical memory operation.

In the present lightwave transmission systems, signal processing is mainly carried out by using electronic devices.

It is considered that the speed limitation of electronic devices will be about 100 Gb s^{-1}. For signal processing at higher speed, the use of all-optical devices will be inevitable. In the ideal all-optical networks, the data signals are carried completely as the optical signals to remove the electronics bottleneck. Although some of the all-optical devices have the great potential in signal processing, optical signals are only used for the transmission of signals at the present moment. The amount of data traffic is growing rapidly every year. To meet this demand, the realization of all-optical networks is the important and exciting target.

This chapter describes the non-linear optical characteristics of SOAs and laser diodes (LDs) and their applications for switching and signal processing. In Section 19.2, ultrafast dynamics in SOAs is briefly reviewed. Section 19.3 describes wavelength conversion. Optical bistability is reviewed in Section 19.4. Section 19.5 describes applications of polarization-bistable vertical-cavity surface-emitting lasers (VCSELs) to all-optical signal processing including optical memory operation. Future directions are described from the device-level point of view in Section 19.6.

19.2 Semiconductor Optical Amplifiers

19.2.1 Ultrafast Dynamics in SOAs

The SOA is similar to a semiconductor laser [1]. The laser has both a gain medium and an optical feedback mechanism. On the other hand, a travelling-wave (TW)-type SOA has only a gain medium. The optical gain is generated by the recombination of electrons and holes which are injected into these devices by the driving current. This subsection briefly describes ultrafast dynamics of carriers in SOAs, which acts as the essential mechanisms of ultrafast optical non-linearities [2].

The non-linear gain (and absorption) of SOAs strongly depends on the carrier dynamics in their energy bands. One important mechanism is spectral hole burning (SHB). In a gain medium, short optical pulses at a specific wavelength cause stimulated transitions only between specific energy levels. Thus, stimulated transitions deform the Fermi distribution of carriers in a semiconductor. The width of the spectral hole depends on the dephasing rate. Figure 19.1 shows the temporal change in the energy dependency of the carrier density [3]. At $0 < t < \tau_1$ (τ_1 is the lifetime of SHB, typically ~60 fs), in the gain region, an optical input pulse stimulates emission and decreases the carrier density for a limited energy range. In the absorption regime, an optical pulse generates carriers for a limited energy range. These localized non-uniformities in the carrier distributions continue until the carrier–carrier scattering redistributes the total carrier density into a new Fermi distribution.

Another non-linearity is caused by carrier heating (CH). After τ_1, the carriers become a Fermi distribution. However, the temperature of this distribution is still different from the lattice temperature until τ_h (see Figure 19.1b, $\tau_1 < t < \tau_{h;}\tau_h$ is the lifetime of CH, typically ~700 fs). When electron and hole distributions are heated relative to the lattice, the optical gain in the active semiconductor medium is decreased, and the gain peak is shifted to longer wavelengths.

The saturated output energy of SOAs for ultrashort optical input pulses becomes lower than for longer optical input pulses because of the non-linear gain. For optical pulses longer than ~10 ps, SHB and CH non-linearities have negligible influence on the gain. Thus, the saturation behaviour of the SOA becomes pulsewidth independent for these longer optical pulses. As described in Section 19.3.2, the conversion efficiency of four-wave mixing (FWM) signal is governed by these ultrafast mechanisms, when the frequency difference between the pump wave and the signal wave is large.

19.2.2 Designs for High-Power Operation

Although the output power of SOAs is not a critical issue in switching and signal processing applications, many applications, such as laser fabrication and LiDAR (light detection and ranging or laser imaging detection and ranging), require large values of the output saturation power. Thus, this subsection briefly describes the designs for high-power operation [4,5]. The methods of increasing saturation intensity are as follows. The first one is increasing the carrier density by increasing the injection current. However, when the injection current is increased, the single-pass gain increases, and the resonance effect caused by the residual reflectivity of the facets appears. Therefore, a reduction in reflectivity of the facets is the most important device design to increase the saturation output power. Another method is lowering the optical confinement factor to the active layer. When the carrier density is increased, the gain coefficient increases. However, if the confinement factor or the SOA length is reduced by the same degree, the

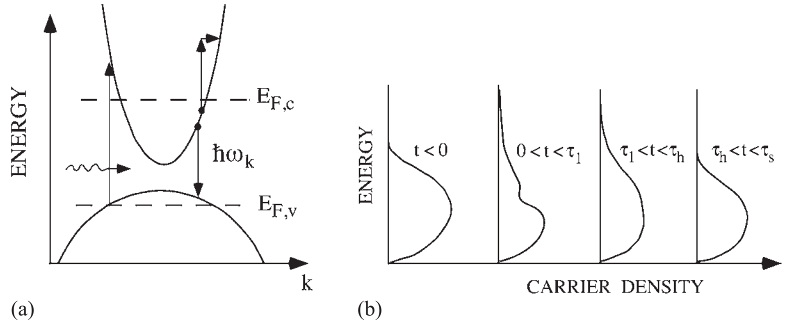

FIGURE 19.1 (a) Schematic diagram of interactions between semiconductor and optical field. (b) Temporal change of carrier density in the semiconductor after interaction with a short optical pulse. Typical values for GaAs SOAs are $\tau_1 = 60$ fs, $\tau_h = 700$ fs, $\tau_s = 200$ ps [3].

single-pass gain is unchanged; thus, resonance effects are suppressed.

The proper selection of the light input wavelength against the gain spectrum of SOA is also important. When the carrier number decreases, the gain peak wavelength shifts towards the longer wavelength. Due to this characteristic, even the carrier number is decreased by a strong optical input, the reduction in the gain value at longer wavelengths is small and strong saturation does not occur. This is especially clear in a multi-quantum well (MQW) SOA. Due to its characteristic band structure, there are conditions that signal gain almost does not change even if the carrier density changes. Thus, high saturation output power can be obtained by the introduction of an MQW structure.

Laser sources require high output power stronger than 1 W in some applications. Such power levels are difficult to obtain from a single-semiconductor laser directly due to a relatively small volume of the active region. Thus, increase of the mode cross section is very beneficial. However, in the device having the large mode cross section, the mode profile tends to become unstable or cause the filamentation, if there is no careful waveguide design. An approach based on this consideration is to unfold the waveguide width towards the output facet (see Figure 19.2a). The mode field area is larger at the output side, and a high saturation output power is obtained.

Master oscillator power amplifiers (MOPAs) generated beams with high power and a good beam quality [4]. The output power is about 5 W for pulsed or continuous-wave (cw) operation. The output of a low-power semiconductor laser, which acts as a master oscillator, is amplified in a TW-type SOA acting as a power amplifier (see Figure 19.2b). If the master oscillator and the SOA are integrated monolithically on the same chip, this integrated device can operate with the power in the range of 1–10 W. The devices maintain single-mode operation with a good beam quality even for such strong output power.

Filament formation is the most difficult problem to create high-power semiconductor lasers and amplifiers [5]. The origin of the filamentation can be attributed to the following reasons: (i) fluctuation of light beam intensity causes spatially non-uniform carrier depletion; (ii) the variation of carrier density changes the refractive index profile, and then the optical field is distorted due to the self-focusing effect and (iii) the temperature distribution across the waveguide in tapered and broad-area semiconductor lasers is not uniform. This spatial temperature distribution causes both carrier density and refractive index non-uniformity. The possibility of reducing the filamentation by changing the intrinsic property of the semiconductor material was also discussed [5].

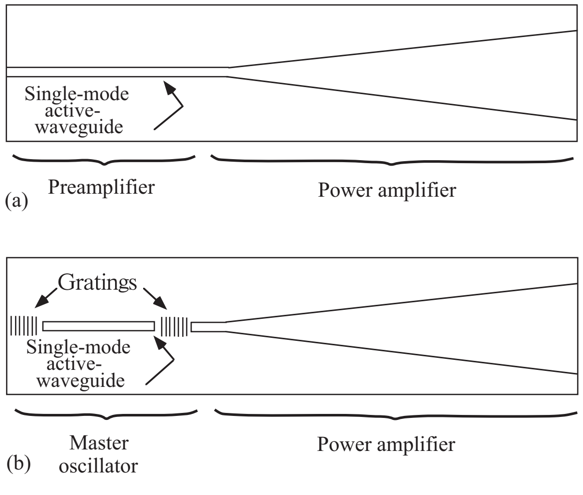

FIGURE 19.2 Two types of tapered structures for high power operation: (a) a single-mode preamplifier section coupled to a tapered gain region and (b) the MOPA structure [4].

A MOPA including a distributed feedback LD (DFB LD) and a tapered optical amplifier on a single chip was demonstrated [6]. The maximum cw power of the MOPA was about 12 W at about 1064 nm. Short optical pulses (pulse width, 84 ps; peak power, 42 W and spectral width; 160 pm) were obtained when nanosecond current pulses were injected into both the DFB LD and the tapered optical amplifier.

19.3 Wavelength Conversion

Wavelength converters transform information on the lightwave with one wavelength (λ_1) to the one with another different wavelength (λ_2) [7,8]. There are four types of wavelength converters. These are optoelectronic converters, laser converters, converters based on optically controlled optical gates and coherent converters using FWM. Optoelectronic (O/E/O) conversion is a straightforward solution. This approach has the big advantage that it can be implemented with existing technology. Fast optoelectronic converters now operate around at 40 Gbit s^{-1}. In the future, higher-speed converters will be needed in high-speed optical networks. However, the bandwidth will be limited by the power consumption and the speed limit of electronic circuitry. Therefore, improvement of all-optical converters is highly expected. As described in this section, wavelength conversion using an LD or an SOA has the advantages of wide tunability and fast operation. Another advantage is that the wavelength conversion can be directly obtained by using an LD or an SOA only.

19.3.1 Converters Based on Optically Controlled Gates

The input light at λ_i controls the gating of cw light at λ_c in this type of converters. Thus, the wavelength of the data is converted from λ_i to λ_c. The cw light generates from a light source with either a fixed or a tunable output wavelength depending on the application of the converter. Depending on the configurations of the converters, they have positive or negative slope transfer function. The converted signal becomes in-phase or inverted relative to the input. Two types of gates, cross-gain modulation (XGM) gates and cross-phase modulation (XPM) gates, are introduced in this section.

19.3.1.1 Cross-Gain Modulation Gates

A simple optical gate is realized by using an SOA. An optical input signal controls the gain in the SOA. As the result, the transmission of the signal through the SOA gate is controlled. The converter, also called a XGM converter, is extremely simple to assemble. It is polarization-insensitive if the polarization-independent SOA is used. However, the signal is inverted relative to the input signal and the extinction ratio for the converted signal degrades when the signal wavelength becomes longer. The converted signal has also a relatively large frequency chirp. Despite such non-ideal properties, the converter has been used with good results in a number of switch-block experiments.

The conversion speed is determined by the relatively slow interband carrier recombination. The use of longer cavity lengths is a very effective method for the high speed conversion. A 100 Gbit s^{-1} wavelength conversion was achieved by a XGM converter in a 2-mm-long SOA. To extend the conversion bandwidth, a grating was used for frequency modulation (FM) to amplitude modulation (AM) conversion of the chirped output [9]. All-optical wavelength conversion of non-return-to-zero (NRZ) signal was demonstrated based on XGM in an SOA that is integrated on a silicon substrate. The SOA is 500 μm long. For all-optical wavelength conversions of 12.5 and 40 Gbit s^{-1} signals, both wavelength up and down conversions were realized [10].

19.3.1.2 Cross-Phase Modulation Gates

Wavelength converters with a better performance are obtained by the integration of two SOAs into the Mach-Zehnder interferometer (MZI) (Figure 19.3a) [11]. This device is usually called SOA-MZI. The optical input signal changes the phase difference between the two interferometer arms through the XPM. The input signal changes the carrier density in the SOA, and as a result, the refractive index is also changed. Then, cw light intensity is modulated by the input signal. For creating the phase difference between the two arms, the input signal is coupled into only one of the SOAs.

Faster operation can be achieved by controlling both arms of the interferometer in a differential way. This device is called a symmetric Mach-Zhender switch. In the differential operation with an appropriate time delay, ultrafast gating can be achieved [12]. Both switch-on and switch-off time are not limited by the slow carrier lifetime in SOAs. Due to this great advantage, this technique is widely used in the field of optical signal processing.

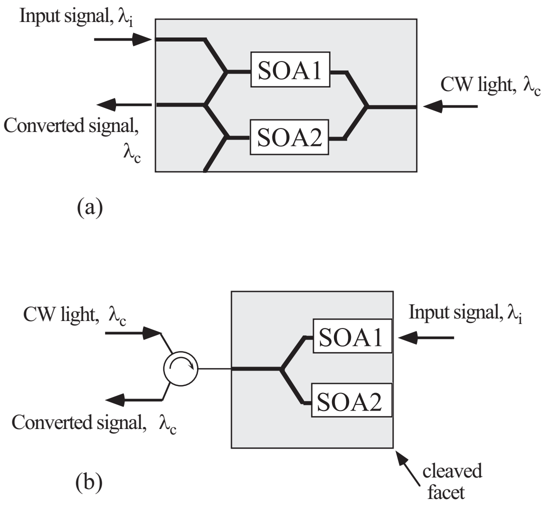
Input signal, λ_i
SOA1
SOA2
CW light, λ_c
Converted signal, λ_c
(a)
CW light, λ_c
Input signal, λ_i
SOA1
SOA2
Converted signal, λ_c
cleaved facet
(b)

FIGURE 19.3 Wavelength conversion principle using MZI (a) and MI structures (b) with SOAs [7].

Michelson interferometric converters (MIs) shown in Figure 19.3b have a simpler structure [13]. Because the input signal is coupled directly to the SOA, a high-modulation bandwidth is obtained thanks to the strong input signal power.

The radio-over-fibre system is an attractive candidate for a broadband wireless communication system. To reduce the signal attenuation caused by the chromatic dispersion of fibre, an all-optical single-sideband (OSSB) frequency upconverter was examined. The upconverter consists of an arrayed waveguide grating (AWG) and an SOA-MZI. The generated OSSB radio frequency (RF) signal was transmitted through single-mode fibres. Degradation of the phase noise was negligible for the upconverted electrical RF signal of 48 GHz [14].

19.3.2 Four-Wave Mixing

19.3.2.1 Principle of Four-Wave Mixing in SOAs

FWM in SOAs has been used as an efficient and practical wavelength conversion mechanism, because it has the following grate advantages: compactness, high conversion efficiency and transparency to bit-rate and modulation formats [15]. Especially, FWM in SOAs is paid attention to the mechanism for wavelength conversion of coherent signals with advanced modulation format. As shown in Figure 19.4, a pump wave and a signal wave are injected into the SOA with the same polarization. The angular frequencies are ω_p and ω_s, and the optical input powers are $P_p(0)$ and $P_s(0)$ for pump and signal wave, respectively. The beating of these two waves in the SOA generates modulation of refractive index and optical gain in the active layer of the SOA. The interaction of the injected waves with these modulations generates new frequency components, the FWM signals. If the pump signal frequency detuning Δf (= $|\omega_p - \omega_s|/2\pi$) is small, FWM is mainly caused by carrier density pulsation (CDP). The response time of the CDP is the effective carrier lifetime. When the detuning Δf becomes large, FWM generates through three mechanisms (CDP, CH and SHB) up to a few THz. The converted FWM signal $P_c(L)$ has the optical angular frequency $\omega_c = 2\omega_p - \omega_s$.

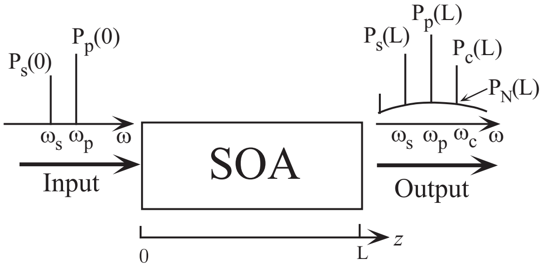
$P_s(0)$
$P_p(0)$
ω_s ω_p ω
Input
SOA
$P_s(L)$
$P_p(L)$
$P_c(L)$
$P_N(L)$
ω_s ω_p ω_c ω
Output
0
L
z

FIGURE 19.4 Schematic diagram of FWM signal generation in an SOA.

19.3.2.2 Dispersion Compensation Using Optical Phase Conjugation

Transmission of 1.55 μm optical time-division multiplexing (OTDM) signals in a standard single-mode fibre (SSMF) needs compensation of chromatic dispersion in the fibre. This is because the zero-dispersion wavelength is at about 1.3 μm, not 1.55 μm. One method is the use of a mid-span optical phase conjugation (OPC) technique. An 80 Gbit s^{-1} return-to-zero (RZ) and carrier-suppressed RZ (CS-RZ) OTDM signal transmission over a 208 km SSMF was demonstrated. To generate the OPC signal, the FWM in SOAs was used [16]. In the CS-RZ signal, the phase relation of the neighbouring pulses is out-of-phase. This carrier phase maintained after the transmission.

Figure 19.5a shows a diagram of chromatic dispersion compensation obtained by a mid-span OPC. The optical pulse is temporally broadened by the chromatic dispersion. If the relation of $\beta_2(1)\,L_1 = \beta_2(2)\,L_2$ is satisfied, the dispersion in the fibre can be compensated. Here, $\beta_2(1)$ and $\beta_2(2)$ are second-order dispersions in region 1 and 2, and L is the fibre length. This is because the dispersion of the broadened optical pulse is reversed by spectral inversion through the FWM process. The spectrum of an optical-phase-conjugated wave is inverted, and the frequency shifts (see Figure 19.5b).

19.3.2.3 Wavelength Conversion of Coherent Signals with Advanced Modulation Formats

The spectral efficiency of binary modulation formats is limited to 1 bit/s/Hz/polarization. This is called the Nyquist limit. The use of modulation formats with M bits of information per symbol can achieve up to the spectral efficiency of M bit/s/Hz/polarization. Figure 19.6a shows the waveforms and constellation diagrams for On–Off keying and 16-quadrature amplitude modulation (16-QAM). Coherent systems use spectrally efficient advanced modulation formats to obtain higher channel capacity. Examples are quadrature phase-shift keying (QPSK), 16-QAM and 64-QAM formats. Using the coherent detection technique, we can select one signal from the multiplexed signals in the spectral domain without optical wavelength filters. These networks are improved by the use of wavelength conversion to optimize wavelength allocation. Wavelength converters are also important building blocks for optical routers in data centres. For both these cases, the performance of future all-optical networks will depend on the efficiency of wavelength converters.

Wavelength conversion of QAM signals was demonstrated based on FWM in an SOA [17]. The conversion range can be extended over the broad gain spectrum of the SOA when two pump waves are used. By using two copolarized pumps, wavelength conversion of 16 Gbaud 16-QAM signals over the entire C-band was demonstrated. Low power penalty at the forward error correction (FEC) threshold was obtained for a wide range of input optical-signal-to-noise-ratio (OSNR). In a single pump wave configuration with different pump wavelengths, wavelength conversion of 5-Gbaud 64-QAM signals was demonstrated with bit error rate (BER) below the FEC threshold over the entire C-band. The measured BER as a function of the received power and constellation diagrams of input signal and wavelength converted signals are shown in Figure 19.6b. Here, λ_s and λ_c are the wavelengths of the original signal and converted signals, respectively. BER below the FEC threshold ($= 2.2 \times 10^{-3}$) is possible over a 32 nm bandwidth.

19.3.2.4 Ultrafast All-Optical Switching for Wavelength Routing

Time-division switching and wavelength conversion are required for the wavelength routing in high-speed OTDM networks. Fast all-optical switching makes it possible to realize fine-granularity routing. The ultimate goal is bit-by-bit switching of the OTDM signal. The FWM in SOAs is very suitable for this purpose.

All-optical bit-by-bit switching of an OTDM signal was experimentally demonstrated by using FWM in an SOA [18]. To achieve 1 × 2 switching, two pump pulses with different wavelengths and timings were used. The generated two FWM signals have different wavelengths. Therefore, two signals can be separated into two different channels by using an optical band pass filter. Very short FWM signals with a pulse width of 1.7 ps were generated in the experiment. This is sufficiently short for multiplexing to a 160 Gbit s^{-1} signal. The results show that high-speed switching of the OTDM signal is possible using this method.

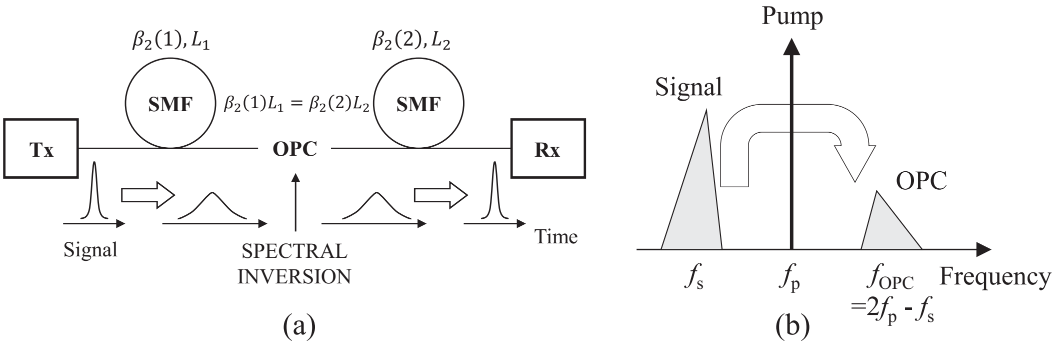

FIGURE 19.5 Principle of chromatic dispersion compensation by using mid-span optical phase conjugation [16]. Implementation (a) and frequency diagram of optical phase conjugation (b).

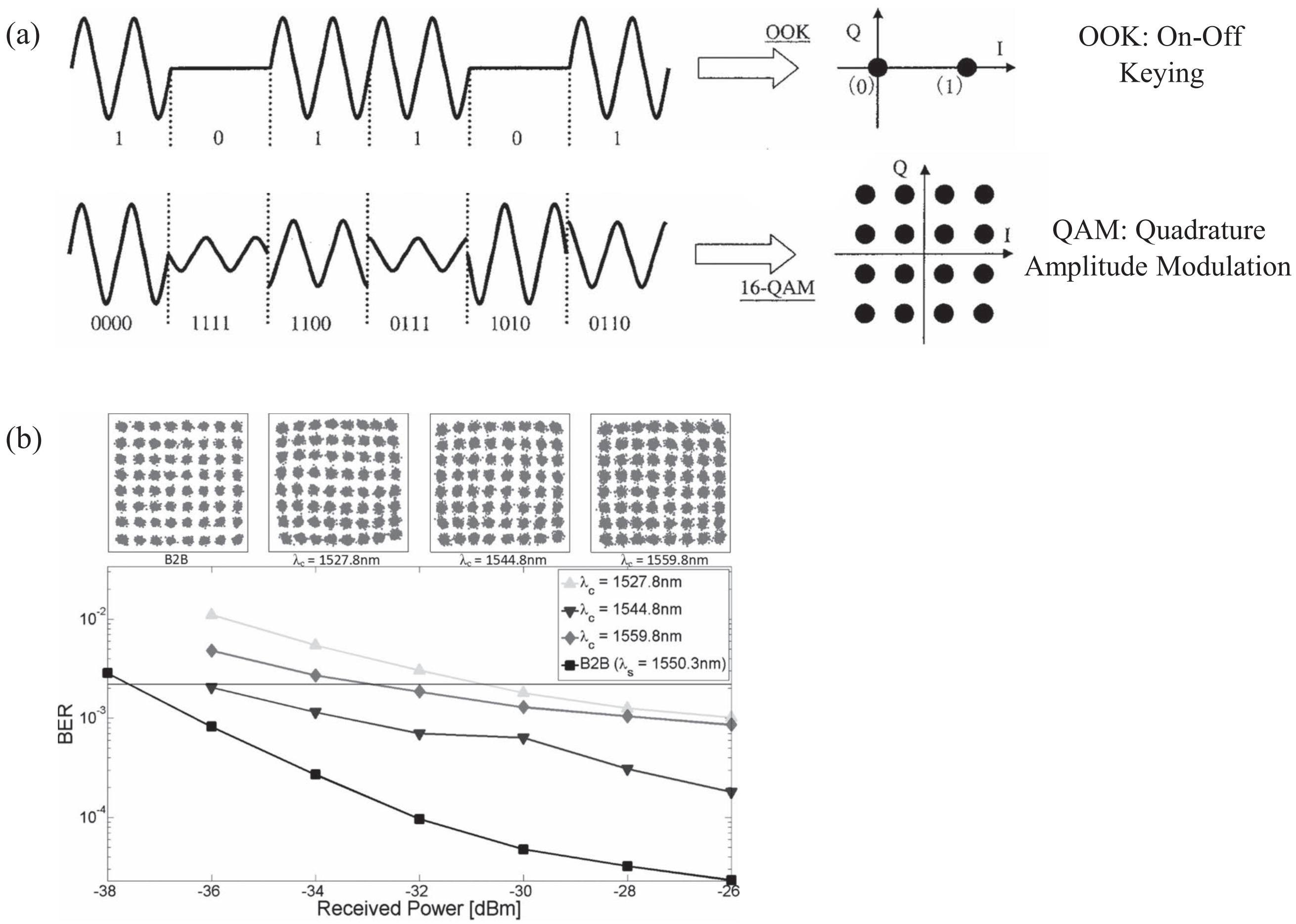

FIGURE 19.6 (a) Waveforms and constellation diagrams for On–Off keying and 16-QAM. (b) Constellation diagrams and BER as a function of received power of 64-QAM. (Reprinted with permission from Ref. [17] © The Optical Society.)

19.3.2.5 Phase-Sensitive Amplification

Realization of noiseless amplification by optical phase-sensitive amplifiers (PSAs) is highly expected. Conventional phase-insensitive amplifiers (PIAs) have the inherent minimum noise figure of 3 dB. On the other hand, PSAs can amplify only one of the two quadrature phase components in a signal and attenuate the other component. In the optical transmission system, PSAs may realize the phase regeneration to reduce the phase and time jitters.

The PSA was experimentally demonstrated by using FWM in a highly saturated SOA. A monolithically integrated photonic PSA chip was fabricated on an InP/InGaAsP platform [19]. Experiments successfully demonstrated PSA with phase-sensitive on-chip gain.

19.4 Optical Bistability in LDs and SOAs

In the optically bistable operation, for single-input states, there are two different stable output states which depend on the initial conditions [20–23]. The following two conditions are needed to create optical bistability: (i) the existence of an appropriate parameter which depends on the optical input intensity, for example, the absorption or gain coefficient or refractive index, and (ii) the existence of a feedback mechanism. Various types of bistability appear in LDs or SOAs, which depend on their configurations and operation conditions. Hysteresis occurs both in a counterclockwise sense and in a clockwise sense. These types of hysteresis are called S-shape bistability. As will be described in the next section, another type of bistability appears in two-mode LDs. This is called pitchfork bifurcation bistability.

19.4.1 Absorptive Bistability and Dispersive Bistability

If LDs include saturable absorbers in their cavity, the LDs show bistability. When the high intensity light is injected into a semiconductor, the absorption decreases, and it is called saturable absorber. In the *off* state of a bistable LD, there is no laser action. On the other hand, in the *on* state, the device operates as a laser. The carriers in the absorber are increased by optical pumping from the gain region so that it becomes essentially transparent to the laser radiation. This situation can be created by the simple two-section LD. These two states of the device are usually stable.

This absorptive bistability was observed in the 1.55 μm InGaAsP DFB LD [20]. The p-type electrode was divided into three parts to inject the driving current into each region independently. The region with low bias current acts as a saturable absorber, and the LD shows bistable characteristics as shown in Figure 19.7a. A clear hysteresis loop is seen in the curve. When the bias current is set at a value just below the turn-off threshold, the optical output *versus* input curve shows bistability as shown in Figure 19.7b. When the bias current is set within the bistability range, the bistable LD is still lasing and even input optical power is reset to zero. Thus, the bistable LD acts as an optical memory device.

A resonant-type SOA with a cavity can act as a non-linear cavity and shows bistability in the optical input–output characteristics [24]. This is because the active layer refractive index changes by light injection. The characteristics of this dispersive bistable device strongly depend on the bias current of the SOAs and the wavelength detuning of the injection light from the resonant wavelength of the cavity.

19.4.2 Two-Mode Bistability through Gain Saturation

19.4.2.1 General Considerations

If a laser is oscillating in two different modes, the cross-effect between these two modes arises through gain saturation [25]. The saturated gain $\bar{g}_i(I_i)$ of a particular mode of (i) is related to the unsaturated gain g_{i0} through the mode intensity I_i and saturation parameter $1/\varepsilon_{ii}$ as follows;

$$\bar{g}_i(I_i) = g_{i0}(1 - \varepsilon_{ii} I_i). \tag{19.1}$$

If we consider two modes, the rate of change of one-mode intensity also depends on the intensity of the other:

$$\frac{dI_1}{dt} = g_1 I_1 (1 - \varepsilon_{11} I_1 - \varepsilon_{12} I_2) \tag{19.2}$$

$$\frac{dI_2}{dt} = g_2 I_2 (1 - \varepsilon_{21} I_1 - \varepsilon_{22} I_2) \tag{19.3}$$

where ε_{11} and ε_{22} are self-saturation and ε_{12} and ε_{21} are cross-saturation coefficients.

There are two possible characteristic situations, i.e. weak coupling and strong coupling. If $\varepsilon_{11}\varepsilon_{22} > \varepsilon_{12}\varepsilon_{21}$ (weak coupling), two-mode operation is possible. Bistability will occur if $\varepsilon_{21}\varepsilon_{12} > \varepsilon_{11}\varepsilon_{22}$ (strong coupling). In this strong coupling case, only one of the modes oscillates and the other mode is suppressed. Which of the bistable states is reached is dependent on the initial conditions.

19.4.2.2 Non-linear Optical Gains and Rate Equation Analysis

The linear gain dependency on the photon energy was simulated for an InGaAsP bulk VCSEL and a quantum well (QW) VCSEL [20,22]. We consider two orthogonal optical fields (mode 1 and mode 2). The gains in mode 1 (g_1) and mode 2 (g_2) are identical for both VCSELs. The QW VCSEL has two gain peaks, which correspond to the electron–heavy hole transition and the electron–light hole transition, respectively.

To examine the potentiality of bistable operation, the values of $\varepsilon_{11} \times \varepsilon_{22}$ and $\varepsilon_{12} \times \varepsilon_{21}$ were calculated. In the bulk VCSEL, the bistable operation condition ($\varepsilon_{12} \times \varepsilon_{21} > \varepsilon_{11} \times \varepsilon_{22}$) is satisfied for all spectral region, where the VCSEL has optical gain. On the other hand, in the QW VCSEL, the bistable operation condition is also satisfied in most of the spectral region. Because the linear gains are the same for the two orthogonal modes, polarization-bistable operation is achieved in both the bulk and QW VCSELs. When the QW VCSEL and the bulk VCSEL are compared around the gain peak wavelength, the difference between $\varepsilon_{12} \times \varepsilon_{21}$ and $\varepsilon_{11} \times \varepsilon_{22}$ is greater for the QW VCSEL. Thus, the QW VCSEL structure is more suitable for achieving the polarization-bistable operation.

The behaviours of the polarization bistable operation in VCSELs can be analysed using the rate equations. From the inherent intraband relaxation processes, without any additional mechanisms such as a saturable absorber, the pitchfork bifurcation bistability is observed as shown in Figure 19.8.

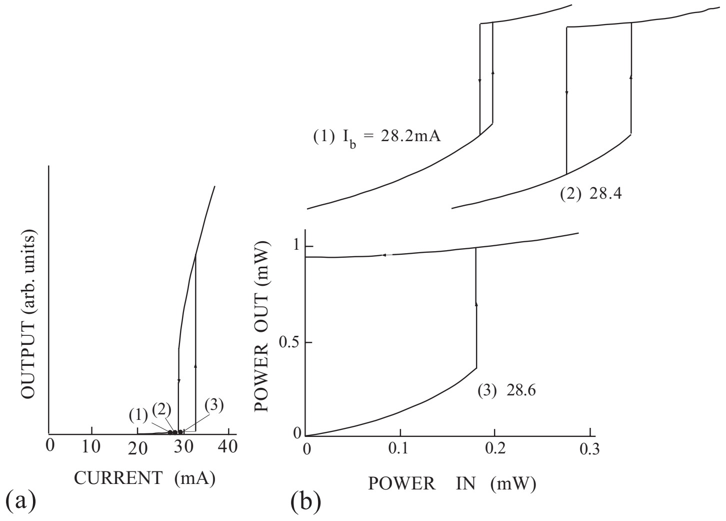

FIGURE 19.7 Output characteristics of absorptive bistable DFB LD; light output *versus* current curve (a) and optical output *versus* input curve (b). Bias current values are indicated by the closed circles (1)–(3) in (a) [20].

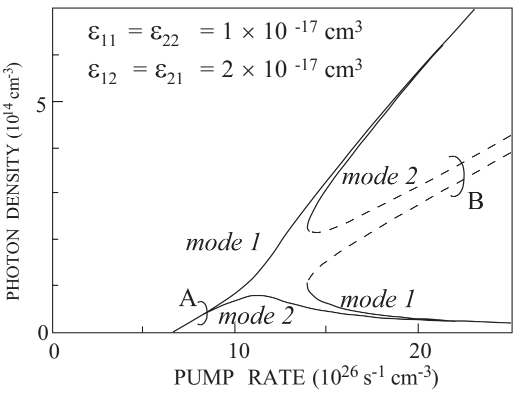

FIGURE 19.8 Pitchfork bifurcation polarization bistability (simulated result) [22].

Here, we assume $\varepsilon_{11} = \varepsilon_{22}$ and $\varepsilon_{12} = \varepsilon_{21} = 2\varepsilon_{11}$. In this case, as the pump rate is increased from zero, the output intensities of the 0° and 90° polarizations (mode 1 and mode 2) bifurcate at a critical point and form branch A. Injection of the 90° polarization trigger input switches the lasing polarization from the state of branch A to the state of branch B.

19.4.2.3 Polarization Bistability in VCSELs

In this subsection, experimental results showing the pitchfork bifurcation polarization bistability in VCSELs are described [20–23]. The VCSEL consists of In$_{0.2}$Ga$_{0.8}$As active layers and AlAs-GaAs distributed Bragg reflector mirrors. The top mesa is 6 μm square. The lasing polarization direction was controlled through this square mesa shape. The VCSEL showed a polarization switching between around 0° and 90°.

The polarization-resolved *L–I* curve is shown in Figure 19.9a. No polarization switching was observed, and the lasing light was linearly polarized at 100°. Pitchfork bifurcation polarization bistability was observed, when light input was injected as shown in Figure 19.9b. A 10° polarized trigger light pulse was injected into the VCSEL at a bias current of 3.52 mA. The polarization of the VCSEL changed to the same polarization (10°) as that of the incident light. Even when the incident light was blocked, the polarization of the VCSEL remained unchanged (10°). This experimental result clearly shows the pitchfork bifurcation polarization bistability, which is theoretically predicted in Figure 19.8.

After this pioneering experiment, different types of VCSELs with a square mesa structure have been developed. A mesa-structure VCSEL embedded in a polyimide layer [22] and a VCSEL with an oxide current-confinement structure show polarization-bistable characteristics at 980 nm [26]. Polarization-bistable characteristics were obtained at 1.55 μm in InAlGaAs/InP VCSELs with a square mesa structure [27].

19.4.3 Flip-Flop Operations of Bistable VCSELs

19.4.3.1 Switching Power and Speed

All-optical flip-flop operation is realized by injection of trigger optical pulses (set and reset pulses) into the polarization-bistable VCSEL with a square cross-sectional waveguide, as schematically shown in Figure 19.10 [28]. The VCSEL has two lasing modes of 0° and 90° polarizations. A set pulse of 90° polarization switches the lasing polarization from 0° to 90°. The lasing polarization of 90° is maintained until a reset pulse of 0° polarization is injected. If an injection pulse has the same polarization as the lasing polarization, the lasing polarization remains unchanged. In this way, all-optical reset–set flip-flop operation is obtained by bidirectional polarization switching and an ability to maintain the polarization when the trigger pulse is not injected.

Generally, the lasing wavelengths of the 0° and 90° polarizations do not exactly the same. This wavelength difference may be caused by a small asymmetry of the shape of square waveguide or the mechanical stress in the VCSEL. The detuning characteristics of the injection pulses from the VCSEL

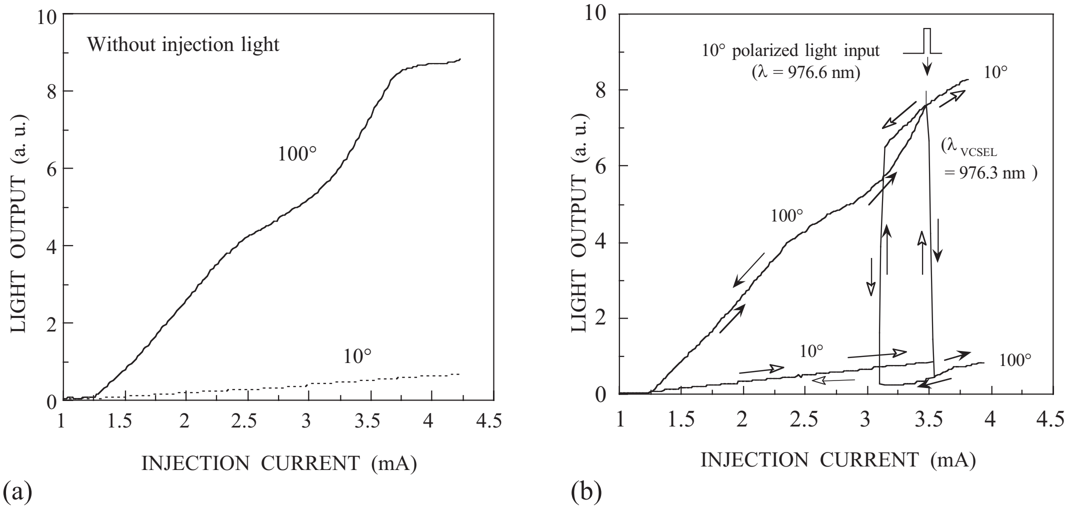

FIGURE 19.9 Polarization resolved *L–I* curves (a) and polarization resolved *L–I* curves for when 10° polarization light pulse is injected into the VCSEL at *I* = 3.52 mA (b) [21].

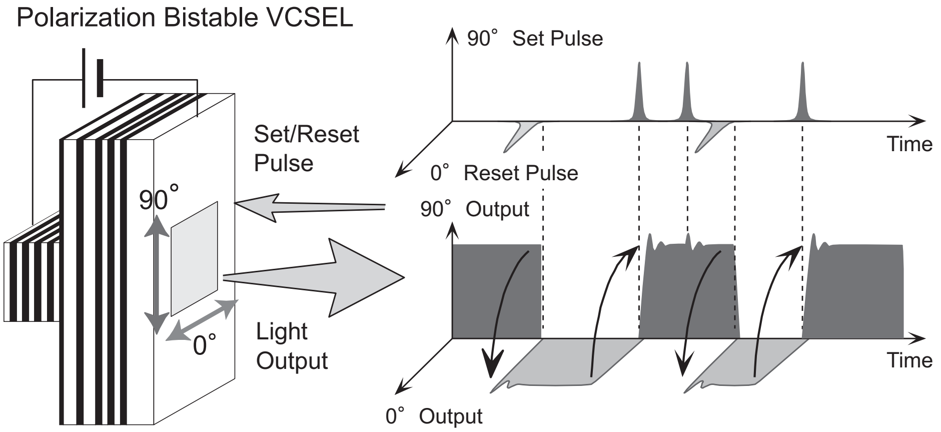

FIGURE 19.10 Schematic diagram of all-optical flip-flop operation using a polarization bistable VCSEL [28].

oscillation frequency were measured to achieve the minimum switching power [29]. The switching power becomes the minimum, when the wavelength of the injection pulse is around the resonant wavelength for the same polarization. The wavelength tolerances of the set pulse and the reset pulse were wider on the longer wavelength side. Bidirectional switching was obtained by the two orthogonal set and reset pulses, which have the same wavelength. Much lower switching power can be obtained by independently adjusting the wavelengths of the set and the reset pulses.

The relationship between the pulsewidth/switching frequency of set/reset optical pulses and the switching power for all-optical flip-flop operation is shown in Figure 19.11 [29]. The minimum injection energy for the operation is almost constant (~0.3 fJ) for long pulses. When the pulsewidth becomes less than about 1 ns, the energy increases. Ultrafast flip-flop operation with a switching time of 7 ps was demonstrated using 1-ps set/reset pulses at a repetition frequency of 80 MHz [21]. These pulse energies are much bigger than those for the case with wider pulse width. The main reason is considered as follows: the wavelength tolerances of set and reset pulses are about 1 GHz for obtaining the low switching power. The spectral envelope width of the 1-ns pulse train is about 1 GHz. This is close to the width of the high-sensitivity wavelength region. Thus a higher pulse energy is required.

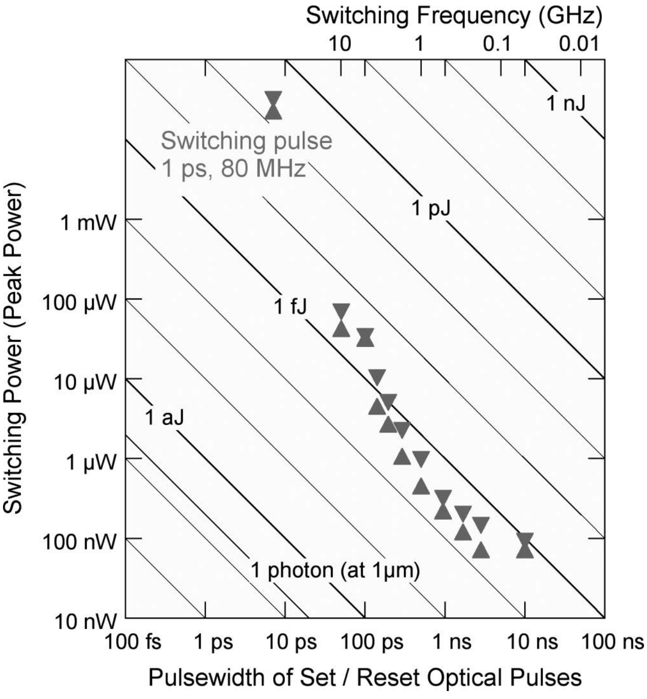

FIGURE 19.11 Pulsewidth dependence of minimum switching power for polarization-bistable switching [29].

19.4.3.2 Consumption Power

Consumption power of bistable VCSELs is almost determined by their bias current. To reduce the power consumption, we can use the similar fabrication process, which is used for usual LDs with a low threshold current. Using an oxide current-confinement structure, all-optical flip-flop operation was obtained at a very low bias current of 0.85 mA in the 980-nm region [26]. The VCSELs have a current aperture of 3 μm square at the centre of the mesa to reduce the lasing threshold current.

All-optical flip-flop operation was successfully performed using this VCSEL with a bias current of 0.85 mA; power consumption corresponds to 1.7 mW. Its output power was 258 μW. The polarization of the VCSEL switched bistably by injection of trigger optical pulses with a 3.6 μW power and 200 ps duration. Thus, the flip-flop operation had large optical gain.

19.4.3.3 Bit Error Rate of Flip-Flop Operation

For the digital signals, the measurement of the BER is essential to evaluate the signal quality. The BER of all-optical flip-flop operation was evaluated using a 1.55-μm polarization-bistable VCSEL [28]. Polarization-bistable flip-flop operations were obtained by injection of optical set and reset pulses. Clearly opened eyes and BERs better than 1×10^{-9} were obtained up to 1 Gbit s^{-1} [28].

The BER of flip-flop operation with AND gate functionality for the data and set pulses was also measured [30]. The arrangement and timing chart are schematically illustrated in Figure 19.12a and b. All input pulses had a 1-ns duration, which

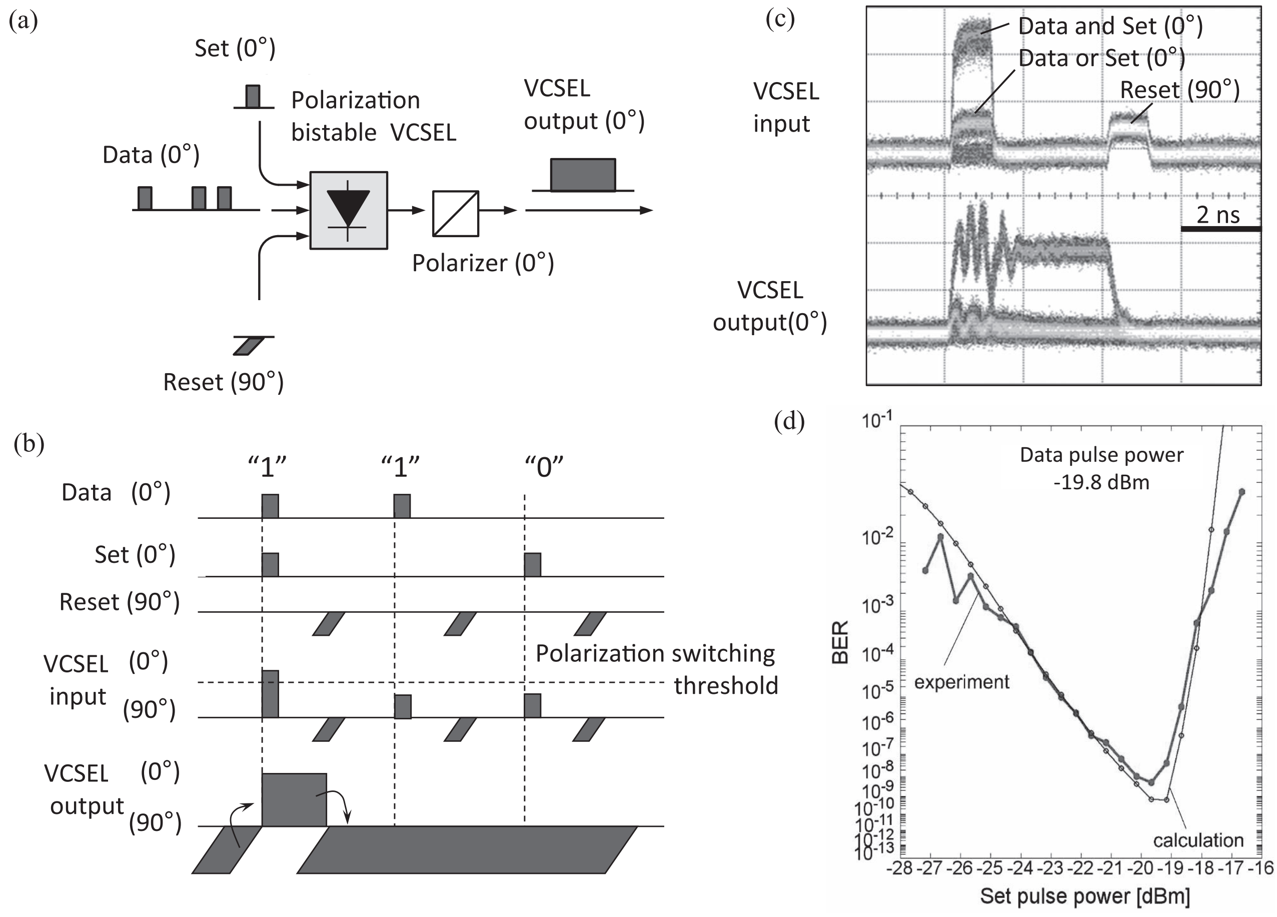

FIGURE 19.12 Implementation (a), timing chart (b) and eye diagram (c) of optical flip-flop operation with AND gate functionality, and experimental and calculated BER variations for set pulse power under fixed data pulse power of –19.8 dBm (d) [30].

corresponded to 500 Mbit s^{-1} RZ signals. The data pulses had a format of 2^{11}-1 pseudo-random bit sequence (PRBS), and the set and reset pulses had a repetitive pattern. The AND gate functionality is obtained on the following conditions: the total injection power of the data signal and that of the set pulse exceed the polarization switching threshold, but each power of these inputs does not exceed the threshold.

The BER of this flip-flop operation was measured as a function of the set pulse power [30]. The best condition for the stable flip-flop operation was obtained when the data and set pulse have almost the same power. As shown in Figure 19.12c and d, the clearly opened eye diagram and the best BER of 5.0×10^{-9} were obtained. For the BER simulation, we take into account fluctuations of the sum of data and set pulse power as well as the polarization-bistable switching threshold. The result shows good agreement with the measured one.

19.4.4 Other Types of Bistable Devices

Many types of optical bistable devices have been reported so far, for example, absorptive bistable LDs, dispersive bistable SOAs/LDs, injection-locking LDs and two-mode bistable LDs. Some devices are reviewed in the previous section. Here, two different types of the devices are introduced briefly.

A bistable device is also created by two microscopic ring lasers connected by a waveguide as shown in Figure 19.13a [31]. In state A, clockwise (CW) light from laser A is injected into laser B through the waveguide and is amplified significantly in laser B, if the resonant frequencies of the two laser cavities are close (Figure 19.13a(i)). This injected light competes with the laser B self-oscillation. If the injected light power is sufficient, the gain of the laser B is decreased below the lasing threshold. Thus, the laser B stops its self-oscillation, and the light circulates only in the CW direction in the laser B. This switching is caused by small amounts of light from laser A, because of the strong resonant amplification. In the reverse situation (state B), the light from laser B locks laser A. The light circulates in the anticlockwise (ACW) direction (Figure 19.13a(ii)). These two states are stable when two lasers are equally pumped. The switching between state A and state B is obtained by injection of CW or ACW input pulses.

Although the details are not shown here, similar results of bistable operation between CW and counterclockwise laser oscillations were reported by many researchers based on a single micro-ring laser.

A hybrid-integrated all-optical flip-flop based on two coupled MZIs was also reported [32]. The device layout is schematically shown in Figure 19.13b. The flip-flop device consists of two coupled MZIs (MZI 1 and MZI 2). Each MZI has an

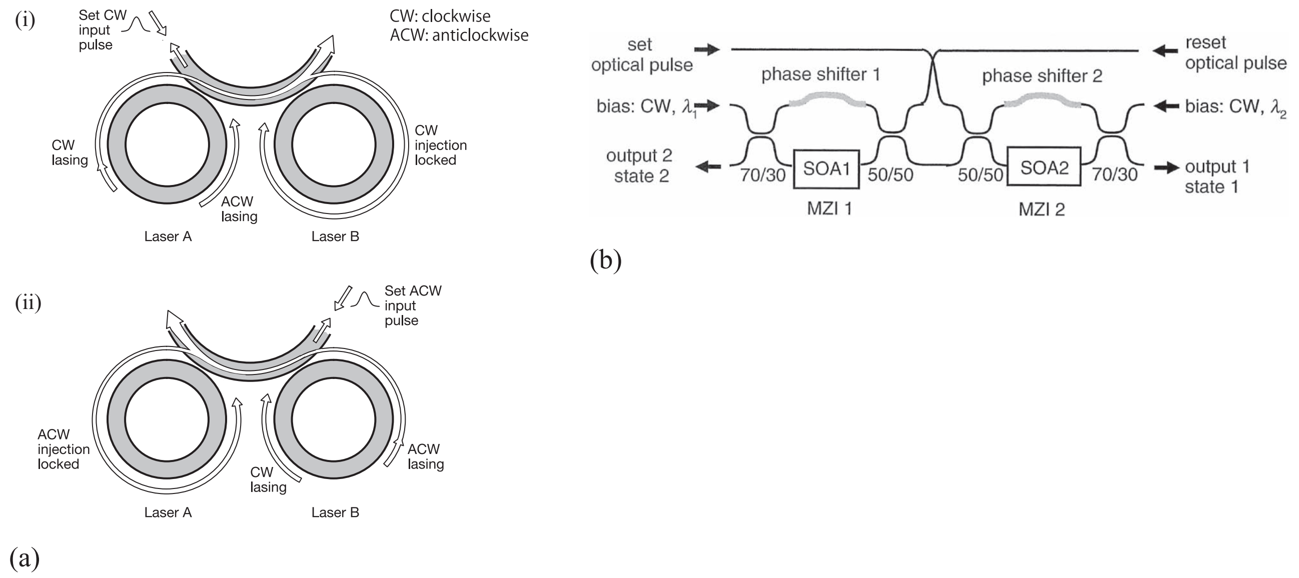

FIGURE 19.13 (a) Coupled micro-ring laser. (Reprinted by permission from Nature Publishing Group: Nature [31], Copyright (2004).) (b) Hybrid integrated two coupled MZIs [32]. (Reproduced by permission of the Institution of Engineering & Technology.)

SOA in one arm as the optical non-linear element. A cw bias light with wavelength λ_1 is injected into MZI 1. The MZI 1 output is injected into MZI 2. The MZI 2 has the same structure as MZI 1 but is biased by a cw light with a different wavelength, λ_2. The MZI 2 output is also injected into MZI 1. The device has two possible states. In state 1, the MZI 1 output suppresses output from MZI 2. Thus the output 1 with wavelength of λ_1 becomes dominant. On the contrary, in state 2, the MZI 2 output suppresses output from MZI 1, and the output 2 with wavelength of λ_2 becomes dominant. These two states are stable. The set and reset optical pulses are injected into the device through the input waveguides. The bistable switching between these two states is obtained.

An all-optical static random access memory (SRAM) cell was experimentally demonstrated [33]. It consists of a monolithic InP set–reset flip-flop chip and a single hybridly integrated SOA-MZI-based access gate. The configuration of the flip-flop chip is the same as the one which is shown in Figure 19.13b. Error-free random access memory (RAM) operation was demonstrated at 5 Gbit s^{-1} for both read and write functionalities. The theory predicts that this memory will be able to operate as a RAM with memory speed well beyond 40 GHz.

19.5 Applications of Polarization-Bistable VCSELs

19.5.1 All-Optical Format Conversion, Demultiplexing and Retiming

Optically bistable devices based on SOAs and LDs have very important characteristics such as optical gain, thresholding, AND gate function and memory function. Using these functions of the polarization-bistable VCSEL, many types of all-optical signal processing can be obtained.

Format conversion between different transmission schemes may become an important function for future optical networks. All-optical format conversions from RZ to NRZ and NRZ to RZ were achieved [34]. All-optical demultiplexing (DEMUX) with a signal-bit width conversion function was obtained from high-bit-rate multiplexed signals [35]. A simulation shows that 5 Gbit s^{-1} demultiplexed output signals are selected once every 10 bits from a 50 Gbit s^{-1} optical input signal [35].

All-optical retiming of optical signals was also performed by using the functions of AND gate and bistable memory operation [23]. For the AND gate operation, an optical clock pulse was added to the input data signal. The timing jitter of the regenerated signal can be reduced by optimizing the injection power ratio of these two optical inputs. Here, the clock pulses with very small timing jitter are used as the set and reset pulses of the flip-flop operation for the retiming. In this operation the rise and fall timings of the output signal are mainly determined by the injection timings of the clock pulses, even when the data signal has timing jitter. Thus, the timing jitter of the data signal is suppressed by the all-optical signal regeneration. In addition, this all-optical signal regeneration also has signal reshaping function, because the polarization switching has both thresholding and bistable memory characteristics. The mesa-structure VCSEL embedded in a polyimide [22] was used in the experiment. The peak-to-peak timing jitter in the data signal was reduced from 2 to 0.7 ns in the regenerated optical output signal.

19.5.2 Optical Memories

Optical-packet switching system is a potentially important candidate for the future optical networks. An optical-packet switch node is a key part in this system, and the node routes the arrived optical signals to its destination. To improve the switching speed in the system, the use of all-optical signal processing is expected. The node should have the two functions:

header recognition and memory. These important functions can be created by using optical flip-flop memories.

Using the AND gate function and memory function of bistable LDs described in Section 19.4.4.3 (see Figure 19.12), one data bit from the data signal row is selectively memorized by adjusting the timing of the set pulse. The stored ‘0’ or ‘1’ signal of the target bit can be read out using an optical gate device at any timing. A novel optical buffer memory with a shift register function will be realized using a two-dimensional (2D) array of polarization-bistable VCSELs. The information of the optical signal, ‘0’ or ‘1’, is stored in each VCSEL as a lasing linear polarization, 0° or 90° [36].

19.5.2.1 High-Bit-Rate Operation

The operation speed of the optical memories strongly depends on the operating condition of the bistable LDs. Increase in the frequency detuning between the cavity resonant frequency and carrier frequency of the data signal is important, when the bit length of the data is long, because the remaining time of the data signals in the laser cavity is determined by the detuning. Large detuning is favourable for the fast operation. Reduction in cavity Q-factor of VCSELs, such as a decrease in the cavity reflectivity, is also effective for high-speed operation. However, this method has a drawback of increase in the lasing threshold of the bistable LD.

The 980-nm VCSEL described in reference [22] was used to carry out a 1-bit memory operation for 20-Gbit s^{-1}, 2^6-1-bit PRBS RZ data signals [37,38]. The memory operation was successfully demonstrated for 20 Gbit s^{-1} RZ data signals using the polarization-bistable VCSEL. This all-optical memory was operated with an optical gain even for such a high data rate. A similar memory operation was also demonstrated for 6-bit 40-Gbit s^{-1} NRZ signals.

19.5.2.2 Shift Register Operation and Multi-bit Memories

If we connect the polarization-bistable VCSELs in series, a shift register operation can be achieved [22]. Input data are first stored as the lasing polarization state of a VCSEL1. This stored polarization state is then transferred to next VCSEL2. To construct the shift register, there are two methods: one is write-after-erase method and the other is overwrite method. In case of the write-after-erase method, VCSEL2 is erased by the reset pulse, and then VCSEL1 output is injected into VCSEL2. A more elegant method for transferring the polarization state is the overwrite method, which does not need to erase VCSEL2.

Using four 1.55-μm VCSELs, a 4-bit optical buffer memory was constructed from two optical buffer memory sets with shift register function [39]. To realize the shift register function, write-after-erase method was used. The two shift registers are connected in parallel between a time-to-space converter and a space-to-time converter to increase the memory size. In the experiment, the four bits of the data signal, which corresponds to 500-Mbit s^{-1} RZ signals, were stored in the four VCSELs at the same time. The input power of the 4-bit data signal and the output power of the 4-bit memory were estimated to be 12 and 24 μW, respectively. These results demonstrate the technical feasibility of multi-bit optical buffer memory without optical amplifiers.

The all-optical shift register operation was achieved using 1.55 μm polarization-bistable VCSELs formed in a one dimensional (1D) monolithic array [40]. This is the important step to realize a compact and stable all-optical shift register. To compensate for the non-uniformity in the lasing wavelengths of the arrayed devices, the lasing wavelengths were tuned by adjusting the driving current of each VCSEL. A VCSEL in the array showed polarization flip-flop operation by injection of the set–reset input pulses with orthogonal polarization. By injection of the VCSEL output light into another VCSEL in the same array, the second VCSEL also showed polarization flip-flop operation according to the polarization state of the first VCSEL. The shift register operation was successfully demonstrated using two adjacent VCSELs in the array.

19.5.3 Header Recognition

Optical packet switching is a potentially important technology as described in the former section. Many types of non-linear optical signal processing have been investigated so far. The use of the optical AND gate functionality of a polarization-bistable VCSEL makes possible to recognize 1-bit in a multi-bit header [41]. The concept is similar to the memory operation shown in Figure 19.12. The header signal is selected by the AND gate operation and used to control the optical switch for change the output port. Thus, depending on the state of 1 bit in the header, 1 or 0, the output of the payload is switched between two output ports.

All-optical 2-bit header recognition and packet switching were experimentally demonstrated [42]. Two 1.55-μm polarization-bistable VCSELs and three $LiNbO_3$ optical switches were used as the memory device and the route switch device, respectively. The header signals consist of 4-bit 1-ns pulses. Optical packets including 40-Gbit s^{-1} NRZ PRBS 2^{11}-1 payloads were successfully sent to one of four ports according to the state of 2 bits in the headers.

19.6 Future Directions

Results described in this chapter show the high potential of all-optical signal processing based on non-linearities in SOAs and LDs. The progress in all-optical functional devices and semiconductor lasers over the past several decades is summarized in Figure 19.14. The advances of optical functional devices strongly depend on the semiconductor laser technology.

With improving in the technology for SOAs and LDs, it is expected that the operation speed of all-optical signal processing becomes much faster. For example, a high modulation bandwidth of 30 GHz has been reached for a 3.5-μm-oxide aperture 850-nm VCSEL [43]. XGM in optically bistable quantum-dot vertical-cavity SOAs was theoretically studied. A high-speed XGM response up to 200 GHz has been predicted by this analysis [44]. Consumption energy will also be drastically reduced using nano-LDs [45].

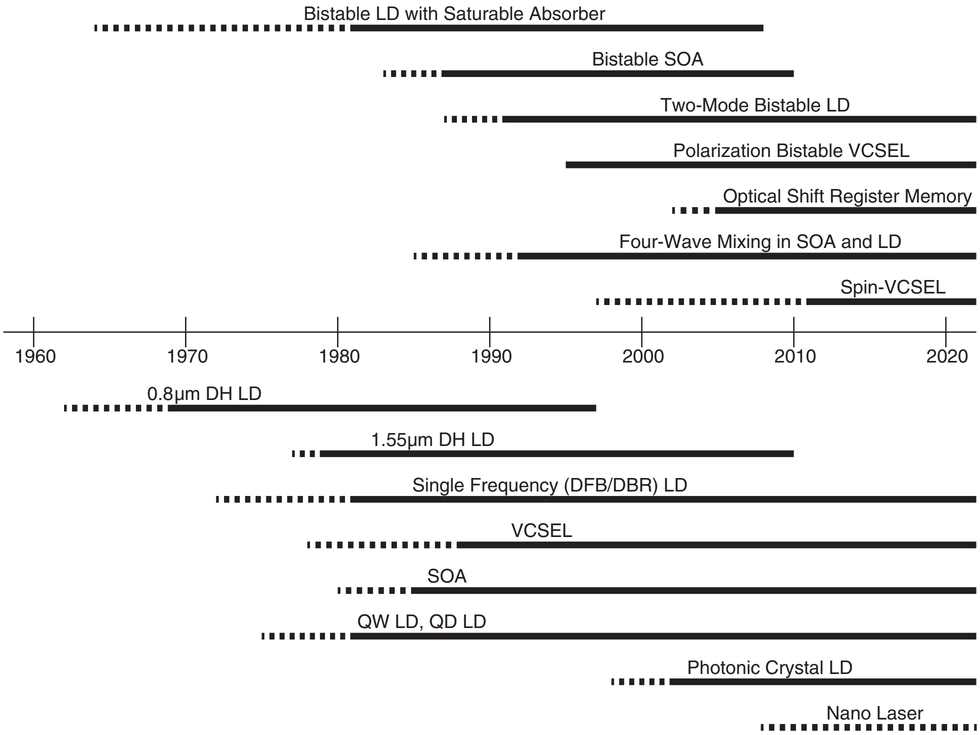

FIGURE 19.14 Development timeline of all-optical functional devices (upper half) and LDs (lower half).

Integration on a Si or silicon-on-insulator (SOI) substrate is one of the most important trends for realization of sophisticated functions and multi-bit memory [46]. A photonic crystal (PhC) nanolaser based on the heterogeneous integration of a III–V PhC nanocavity on SOI and its operation as set–reset flip-flop were reported [47]. Optically bistable memory operation with 6.4 fJ/bit switching energies and response times of faster than 53 ps was demonstrated by injection locking. Bit-level set–reset flip-flop memory operation was evaluated at 5 Gbit s^{-1}, and error free operation was obtained. This device can carry out fundamental logic functions, such as switching and latching. It may provide a building block for functional optical SRAM cells [48].

In a 2D array of polarization-bistable VCSELs, optical connection through in-plane optical waveguides is a valuable method to realize multi-bit optical memory. A VCSEL equipped with a high-index-contrast subwavelength grating (HCG) mirror is suitable for this purpose. The HCG acts as both a cavity mirror and coupler to the waveguide. A conventional HCG is polarization sensitive by its nature of 1D periodicity. A straightforward solution to realize the polarization-independent HCGs for achieving polarization bistability is the use of 2D structurer, such as an island type or a cross-stripe type. A VCSEL having a polarization-independent HCG coupled with two orthogonal in-plane output waveguides was proposed [49]. The output waveguide can be switched by changing the lasing polarization. A VCSEL with a polarization-independent HCG mirror on SOI was fabricated for a novel polarization-bistable device on a Si substrate.

The use of the electron spin as an information carrier is expected. Spin lasers might provide superior characteristics. For example, they have faster modulation dynamics and lower lasing threshold. The lasing circular polarization can be switched very fast by optical spin injection. The polarization modulation bandwidth has been extended to higher than 240 GHz very recently [50]. Spin VCSELs might also have new possibilities. Using chiral microlasers, bistability between two modes having different orbital angular momentum was demonstrated [51].

We are seeking faster speed and lower power consumption operation for optical functional devices. Along this line, many interesting researches are now conducting. Integration on Si is a very important method to make the device compact and stable. The development of all-optical functional devices always needs support from innovations in the fundamental research.

REFERENCES

1. Dutta N. K. and Wang Q. 2013 *Semiconductor Optical Amplifiers* 2nd ed. (Singapore: World Scientific).
2. Hall K L, Thoen E R and Ippen E P 1999 Nonlinearities in active media Nonlinear Optics in Semiconductors vol II, ed E Garmire and A Kost (San Diego: Academic Press) pp 83–160.
3. Spano P 1995 Nonlinear optical effects in active semiconductor devices Nonlinear Optical Materials and Devices for Applications in Information Technology ed A Miller et al. (Dordrecht: Kluwer Academic) pp 183–205.
4. Walpole J N 1996 *Opt. Quantum Electron.* **28** 623–45.
5. Lai J-W and Lin C-F 1998 *IEEE J. Quantum Electron.* **34** 1247–56.
6. Wenzel H, Schwertfeger S, Klehr A, Jedrzejczyk D, Hoffmann T and Erbert G 2012 *Opt. Lett.* **37** 1826–28.

7. Stubkjaer K E, Kloch A, Hansen P B, Poulsen H N, Wolfson D, Jepsen K S, Clausen A T, Limal E and Buxens A 1999 *IEICE Trans. Electron.* **E82-C** 338–48.
8. For a review of wavelength conversion in SOAs see, e.g. Wiesenfeld J M 1996 Gain Dynamics and Associated Nonlinearities in Semiconductor Optical Amplifiers *Current trends in optical amplifiers and their applications* ed T P Lee (Singapore: World Scientific) pp 179–222.
9. Ellis A D, Kelly A E, Nesset D, Pitcher D, Moodie D G and Kashyap R 1998 *Electron. Lett.* **34** 1958–9.
10. Wu Y, Huang Q, Keyvaninia S, Katumba A, Zhang J, Xie W, Morthier G, He J-J and Roelkens G 2016 *Opt. Express* **24** 20318–23.
11. Durhuus T, Joergensen C, Mikkelsen B, Pedersen R J S and Stubkjaer K E 1994 *IEEE Photon. Technol. Lett.* **6** 53–5.
12. Tajima K, 1993 *Jpn. J. Appl. Phys.* **32** L1746–49.
13. Mikkelsen B, Du Durhuus T, Joergensen C G, Mikkelsen B, Pedersen R J S and Stubkjaer K E rhuus T, Joergensen C, Pedersen R J S, Danielsen S L, Stubkjaer K E, Gustavsson M, van Berlo W and Janson M 1994 *ECOC '94: 20th European Conference on Optical Communication* (*Firenze, Italy*) vol 4, pp 67–70 (Firenze: Instituto Internazionale delle).
14. Kim D-H, Lee J-Y, Choi H-J and Song J-I 2016 *Opt. Express* **24** 20309–17.
15. For reviews of four-wave mixing in SOAs see, e.g. Vahala K J, Zhou J, Geraghty D, Lee R, Newkirk M and Miller B 1996 Four wave mixing in semiconductor travelling-wave amplifiers for wavelength conversion in all-optical networks *Current Trends in Optical Amplifiers and Their Applications* (Singapore: World Scientific) pp 153–77; Guekos G (ed) 1999 *Photonic Devices for Telecommunications* (Berlin: Springer).
16. Inoue J, Sotobayashi H, Chujo W and Kawaguchi H 2003 *IEICE Trans. Commun.* **E86-B** 1555–61.
17. Filion B, Ng W C, Nguyen A T Rusch L A and LaRochelle S 2013 *Opt. Express* **21** 19825–33.
18. Mori T and Kawaguchi H 2004 *IEICE Trans. Electron.* **E87-C** 2189–92.
19. Li W, Lu M, Mecozzi A, Vasilyev M, Arafin S, Dadic D, Johansson L A and Coldren L A 2016 *IEEE J. Quantum Electron.* **52** 0600212.
20. Kawaguchi H 1994 *Bistabilities and Nonlinearities in Laser Diodes* (Norwood, MA: Artech House).
21. Kawaguchi H 1997 *IEEE J. Selected Topics Quantum Electron.* **3** 1254–70.
22. Kawaguchi H 2009 *Opto-Electron. Review* **17** 265–74.
23. Kawaguchi H 2015 Chapter 1 Recent progress in polarization-bistable VCSELs and their applications to all-optical signal processing pp1-17 in Shulika and Sukhoivanov, eds., *Advanced Lasers* (Dordrecht: Springer).
24. Adams M J 1985 *IEE Proc. Pt. J* **132** 343–8.
25. Tang C L, Schremer A and Fujita T 1987 *Appl. Phys. Lett.* **51** 1392–4.
26. Katayama T, Yanai A, Yukawa K, Hattori S, Ikeda K, Koh S and Kawaguchi H 2011 *IEEE Photon. Technol. Lett.* **23** 1811–3.
27. Katayama T, Sato Y, Mori T and Kawaguchi H 2007 *Jpn. J. Appl. Phys.* **46** L1231–L1233.
28. Hayashi D, Takahashi H, Katayama T and Kawaguchi H 2014*J. Lightwave Tech.* **32** 2671–7.
29. Mori T, Yamayoshi Y and Kawaguchi H 2006 *Appl. Phys. Lett.* **88** 101102-1–3.
30. Hayashi D, Nakao K, Katayama T and Kawaguchi H 2015 *IEICE Electron. Express* **12** 1220150479-1–12.
31. Hill M T, Dorren H J S, de Vries T, Leijtens X J M, den Besten J H, Salbrugge B, Oei Y-S, Binsma H, Khoe G-D and Smit M K 2004 *Nature* **432** 206–9.
32. Liu Y, McDougall R, Hill M T, Maxwell G, Zhang S, Harmon R, Huijskens F M, Rivers L, Dorren H J S and Poustie A 2006 *Electron. Lett.* **42** 1399–400.
33. Pitris S, Vagionas C, Tekin T, Broeke R, Kanellos G T and Pleros N 2016 *IEEE Photon. J.* **8** 0600207.
34. Kawaguchi H, Yamayoshi Y and Tamura K 2000 in *Conference on Lasers and Electro-Optics*, OSA Technical Digest (Optical Society of America, Washington DC, 2000), pp 389–90.
35. Kawaguchi H, Yamayoshi Y, Tamura K 1999 *ECOC'99 (25th European Conference on Optical Communication* (Niece, France) pp II-268–9.
36. Kawaguchi H, Mori T, Sato Y and Yamayoshi Y 2006 *Jpn. J. Appl. Phys. Express Lett.* **45** L894–7.
37. Sakaguchi J Katayama T and Kawaguchi H 2010 *Opt. Express* **18** 12362–70.
38. Sakaguchi J, Katayama T and Kawaguchi H 2010 *IEEE J. Quantum Electron.* **46** 1526–34.
39. Katayama T, Ooi T and Kawaguchi H 2009 *IEEE J. Quantum Electron.* **45** 1495–504.
40. Katayama T, Hayashi D and Kawaguchi H 2016 *IEEE Photon. Technol. Lett.* **28** 2062–5.
41. Katayama T, Okamoto T and Kawaguchi H 2013 *IEEE Photon. Technol. Lett.* **25** 802–5.
42. Hayashi D, Nakao K, Katayama T and Kawaguchi H 2015 *Opt. Express* **23** 8357–64.
43. For example Haglund E, Westbergh P, Gustavsson J S, Haglund E P, Larsson A, Geen M and Jeol A 2015 *Electron Lett.* **51** 1096–7.
44. Qasaimeh O 2017 *IEEE Photon. Technol. Lett.* **29** 342–5.
45. For example Hill M T 2010*J. Opt. Soc. Am.* **27** B36–44.
46. For example Liang D and Bowers J E 2010 *Nature Photon.* **4** 511–7.
47. Fitsios D, Alexoudi T, Bazin A, Monnier P, Raj R, Miliou A, Kanellos G T, Pieros N and Raineri F 2016 *Opt. Express* **24** 4270–7.
48. Alexoudi T, Fitsios D, Bazin A, Monnier P, Raj R, Miliou A, Kanellos G T and Pleros N 2016 *IEEE J. Selected Topics Quantum Electron.* **22** 4901410.
49. Tsunemi Y, Ikeda K and Kawaguchi H 2013 *Appl. Phys. Express* **6** 092106-1–4.
50. Lindemann M, Xu G, Pusch T, Michalzic R, Hafmann M R, Žutic I, Gerhardt N C 2019 *Nature* **568** 212–5.
51. Zambon N C, St-Jean P, Lemaître A, Harouri A, Le Gratiet L, Sagnes I, Ravets S, Amo A, Bloch J 2019 *Opt. Lett.* 44 4531–4.

FURTHER READING

For another review of optical switching in SOAs see, e.g. Tarek S. El-Bauab 2006 *Optical Switching* (New York: Springer).

For another review of all-optical signal processing see, e.g. Stetan Wabning and Benjamin J. Eggleton eds. 2015 *All-Optical Signal Processing* (Switzerland: Springer).

20

Silicon-Based Lasers

Qiang Li, Bei Shi, and Yu Han

CONTENTS

20.1 Introduction 287
20.2 Quantum Dot Lasers on Silicon 287
  20.2.1 Physical Properties of Quantum Dots 287
  20.2.2 Self-Assembled Quantum Dot Growth 288
  20.2.3 High-Performance 1.3-µm In(Ga)As/GaAs Quantum Dot Lasers on Si 289
  20.2.4 1.55-µm Quantum Dot Lasers on Si 291
20.3 Nano-lasers on Si 292
  20.3.1 Nanowire Lasers Grown on (111) Si 292
  20.3.2 Nano-ridge Lasers Grown on (001) Si 294
20.4 Challenges and Discussions 296
References 296

20.1 Introduction

The global data traffic is going up with an unprecedented growth rate over the years. While the continuous scaling of silicon (Si) electronic devices pushes ever higher computational speed, high dissipation electrical interconnects quickly become the bottleneck. The use of photonic integrated circuits (PICs) in communication systems is under extensive investigation, boosting the development of silicon photonics technology. In order to leverage the massive manufacturing capability and cost reduction provided by silicon foundries, it is of significant interest to realize the full suite of optical components with group IV semiconductors. However, despite the great electronic and waveguide properties, silicon cannot emit light efficiently due to its indirect bandgap properties. The lack of high-performance, long-lifetime and electrically injected silicon-based lasers continues to pose a major roadblock. In contrast to group-IV semiconductors (such as Si or Ge), most of the III-V compound semiconductors possess a direct bandgap with excellent photon absorption and emission efficiencies. Integrating a reliable electrically pumped III–V laser on Si would be ideal to overcome silicon's deficiency. Yet the challenges are also enormous, primarily arising from differences in the lattice, thermal mismatch and crystal polarities, which result in severe non-radiative recombination and device early failures in lasers grown on silicon. Recent advances in advanced heteroepitaxy technologies have opened new opportunities to tackle these challenges associated with material incompatibility. In this chapter, we review progress in III–V quantum dot (QD) lasers and nano-lasers monolithically grown on silicon, together with a discussion of state-of-the-art device implementations towards PICs.

20.2 Quantum Dot Lasers on Silicon

Proposed in 1982 by Arakawa and Sakaki [1], QD semiconductor lasers are predicted to outperform conventional double heterostructure quantum well (QW) lasers in terms of temperature stability. Owing to the unique "delta-function-like" discrete density of state in those three-dimensional quantum confined nano-structures, more advantageous laser characteristics, such as low thresholds, narrow linewidth and high-speed modulation, have been theoretically studied and experimentally demonstrated. One unique property exhibited by QDs is their in-plane carrier strongly suppressing carrier diffusion in laser devices, which can be exploited for integration on lattice-mismatched substrates like silicon. In this section, we discuss III–V QD lasers epitaxially grown on silicon emitting at the strategically important datacom and telecom wavelengths, with an aim to address one of the most enduring challenges in photonics integration.

20.2.1 Physical Properties of Quantum Dots

The reduced dimensionality of a semiconductor can have profound impacts on the electronic density of states of charge carriers, as shown in Figure 20.1. The three-dimensional confinement in QDs leads to quantized energy levels resembling the discrete energy levels in atoms [2]. Generally, the energy eigenvalues of QDs $\left(E_{n_{x,y,z}}\right)$ are given as

$$E_{n_{x,y,z}} = \frac{\hbar^2\pi^2}{2m}\left(\frac{n_x^2}{L_x^2} + \frac{n_y^2}{L_y^2} + \frac{n_z^2}{L_z^2}\right), \quad n = 1,2,3,...... \qquad (20.1)$$

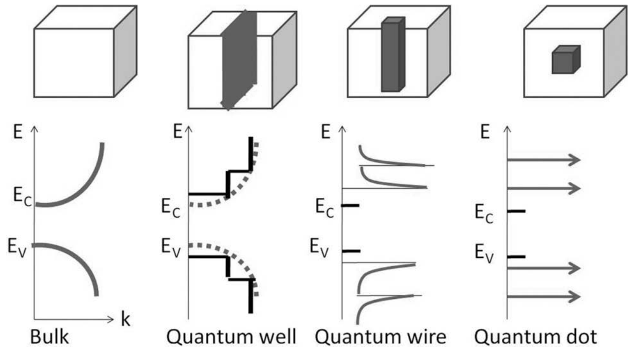

FIGURE 20.1 Charge carriers are confined in a semiconductor (red) with a smaller bandgap than the cladding semiconductor. E_c and E_v are the conduction-band and valence-band edge of a 3D semiconductor, respectively [3]. (© 2015 Jasim K E. Published in *Quantum dots solar cells* under CC BY 3.0 license. Available from: http://dx.doi.org/10.5772/59159.)

where n stands for energy state numbers, L is the QD size in three dimensions and $\hbar$ is the reduced Planck's constant [3]. One must also specify the effective mass m_e for electrons and m_h for holes. Consequently, the energy separation between the ground state and excited states of QDs strongly depends on the QD sizes. For example, InAs/GaAs QDs with a typical dot diameter of ~20 nm would have larger intraband separations than the InAs/InP QDs (or quantum dashes) with a diameter of 40–60 nm.

Previous studies have revealed suppressed in-plane carrier diffusion in In(Ga)As/GaAs QDs as compared to an InGaAs/GaAs QW structure [4]. Attributed to the carrier localization and quantum confinement, QDs tend to be "more forgiving" to crystalline defects than their QW counterparts. Figure 20.2 compares room-temperature (RT) photoluminescence (PL) of the QW and QDs on GaAs native substrate and silicon substrate [5]. Despite a relatively high defect density of $3 \times 10^8\,\text{cm}^{-2}$ on silicon, a comparably strong PL intensity was obtained from the QDs grown on silicon and GaAs, in sharp contrast to the PL quenching observed in the QW on Si.

20.2.2 Self-Assembled Quantum Dot Growth

Although initial theoretical studies on QD lasers were based on lattice-matched materials such as GaAs/AlGaAs, realistic QD lasers with superior properties were demonstrated using strongly strained heterostructures. The Stranski–Krastanov (SK) layer-plus-island growth mode is widely adopted to form high-quality self-assembled QDs.

In principle, the QDs should fulfil the following requirements to be suitable in device applications at RT [6]:

a. Sufficiently deep localizing potential and small QD size are prerequisites for observation and exploitation of the zero-dimensional quantum confinement effects.
b. QD ensembles should show high uniformity and a high-volume filling factor.
c. The material should be coherent without defects such as dislocations.

In practical QD laser applications, the density of QDs is normally in the range of 10^{10}–$10^{11}\,\text{cm}^{-2}$. The uniformity of QDs directly correlates to the inhomogeneous broadening of the emission spectra by tens of meV, and consequently, only a portion of the QDs can effectively contribute to the laser operation. Controlling the overgrowth process is crucial to form defect-free QDs. Various methods, such as thermal anneal on the QDs with cap layer [7], growth interruption after the assembling of QDs [8] and introducing strain reducing layer [9], have been reported in the past for defect elimination. Figure 20.3a and b show the elimination of pinhole-like defects in a multistack QD structure by introducing growth interruptions in the GaAs spacer layer and performing thermal annealing after the GaAs cap layer. Figure 20.3c shows schematically the use of partial overgrowth to leave those defective islands exceeding a critical thickness uncovered and then evaporated in the subsequent annealing process.

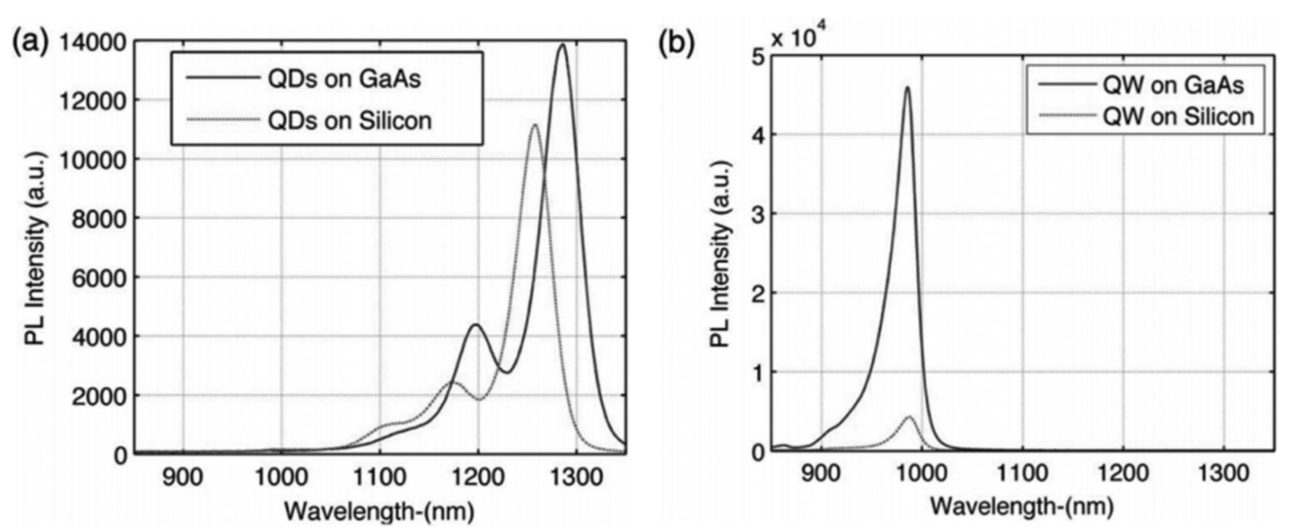

FIGURE 20.2 Room-temperature PL comparison of (a) single InAs quantum dot (QD) layer and (b) single 8-nm $In_{0.2}Ga_{0.8}As$ quantum well (QW) grown on GaAs versus silicon substrates. (Reprinted/adapted with permission from Ref. [5]. © 2015 Chinese Laser Press.)

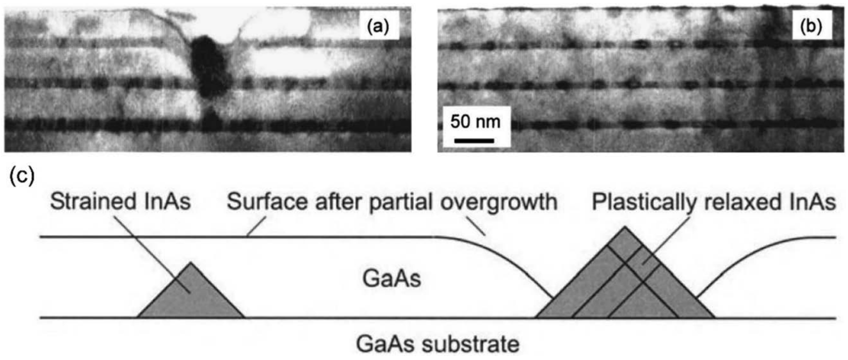

FIGURE 20.3 Cross-sectional transmission electron microscopic images of three-stack QDs (a) without and (b) with growth interruption after QDs are capped. (Reproduced from Ref. [8], with the permission of AIP Publishing. Available from: https://doi.org/10.1063/1.2202195.) (c) Schematic of partial overgrowth of islands. Subsequent annealing evaporates the uncapped QDs [7]. (© 2004 by John Wiley & Sons, Inc.)

20.2.3 High-Performance 1.3-µm In(Ga)As/GaAs Quantum Dot Lasers on Si

Since the first demonstration of self-organized $In_{0.4}Ga_{0.6}As$ QD lasers grown on an offcut (001) silicon by Linder et al. in 1999 [10], tremendous efforts have been made towards high-performance O-band QD lasers on Si substrates with low lasing thresholds, high temperature operation and long device lifetime. Figure 20.4 shows the historical development of QW and QD lasers on different substrates [11]. Yang et al. reported $In_{0.5}Ga_{0.5}As$/GaAs QD lasers using a GaAs/Si buffer with QD-based dislocation filter layers. Pulsed lasing up to 85°C was achieved with lasing peak wavelength around 1 µm [12]. In 2011, Wang et al. demonstrated the first 1.3-µm InAs/GaAs QD laser epitaxially grown on silicon by adopting strained layer superlattice (SLS) dislocation filters and applying a dot-in-well active structure. RT pulsed lasing was obtained with a reduced threshold of 725 A cm^{-2} [13]. To enable RT continuous-wave (CW) operation, further improvement of QD growth with a higher gain is a prerequisite. In 2014, Liu et al. demonstrated high-performance 1.3-µm QD lasers on a Ge-on-Si substrate with a lasing threshold as low as 16 mA, output power exceeding 176 mW, lasing up to 119°C and over 2700 h CW operation at 30°C [14,15]. In 2016, Chen et al. further improved the device performance with a record-low threshold current density, a high operation temperature up to 120°C and over 3100 h RT CW lasing [11], as shown in Figures 20.4 and 20.5. The significant improvement in device performance results from an optimized QD growth condition and a GaAs-on-Si buffer with an ultralow dislocation density on the order of $10^5 cm^{-2}$. The well-optimized InGaAs/GaAs SLS played an important role in bending and filtering the threading dislocations (see Figure 20.5b). Thanks to the uniform QD size distribution shown in the inset of Figure 20.5c, the ground-state envelope of QDs is narrow and strong. It is noteworthy that all these works were accomplished based on molecular beam epitaxy (MBE) growth. QD lasers on Si by metal–organic chemical vapour deposition (MOCVD), a more practical technique for manufacturing, have been much less reported. The use of a high temperature for the AlGaAs upper cladding of QDs in MOCVD could lead to a significant blue-shift of QD emission. In 2018, Wang et al. demonstrated all-MOCVD-grown 1.3-µm QD laser on miscut Si substrates with an InGaP upper cladding grown at a low temperature (550°C). The fabricated Fabry-Perot (FP) lasers exhibit a RT CW threshold of 737 A cm^{-2} and single facet output power of 21.8 mW [16].

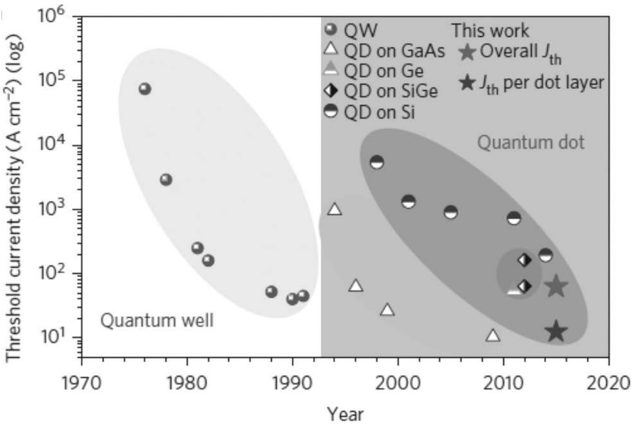

FIGURE 20.4 Historical development of low-dimensional heterostructure lasers, showing the record-low threshold current densities. (Reproduced from Ref. [11], with the permission of NPG. Available from: https://doi.org/10.1038/nphoton.2016.21.)

To improve the compatibility of the epitaxial QD lasers with existing silicon photonics and microelectronics foundries, growing 1.3-µm InAs QD laser on on-axis (001) silicon substrates has attracted a great deal of attention. This requires overcoming antiphase domain boundaries (APBs) arising from the growth of polar materials on non-polar substrates without using miscut silicon wafers to create “double-step” atomic terraces on the Si surface. Several methods, including the use of V-groove-patterned silicon substrates (see Figure 20.6a) [17], well-optimized GaP-on-Si virtual substrates [18] and special treatments of nominal (001) silicon wafers with a minimal offcut angle [19], have been developed for QD lasers on silicon. The silicon V-groove-patterned growth circumvents APB generation by initiating III–V nucleation on etched (111) silicon surface. Norman et al. [20] reported deeply etched ridge lasers with the active materials grown on a 2-µm-thick GaAs-on-V-grooved Si (GoVS) template. These lasers with high-reflection coatings exhibited low-threshold lasing up to 80°C. For the commercially available GaP/Si (001) substrate,

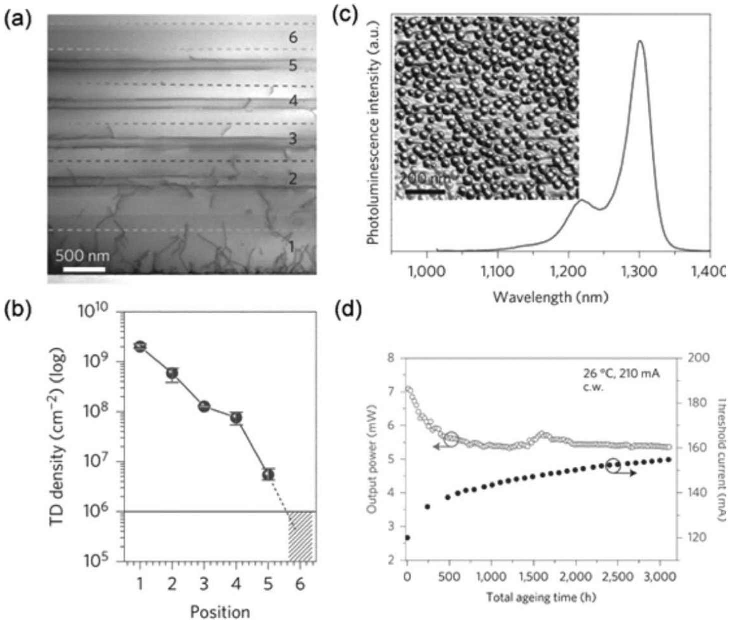

FIGURE 20.5 (a) Bright-field scanning transmission electron microscopic image of dislocation filters. (b) Dislocation density measured at different positions, as indicated in (a). (c) Photoluminescence spectrum for a QD active region grown on silicon. Inset: representative atomic force microscopy image of an uncapped QD sample grown on silicon. (d) Ageing data for the InAs/GaAs QD laser on silicon at a constant heatsink temperature of 26°C and CW drive current of 210 mA. (Reproduced from Ref. [11], with the permission of NPG. Available from: https://doi.org/10.1038/nphoton.2016.21.)

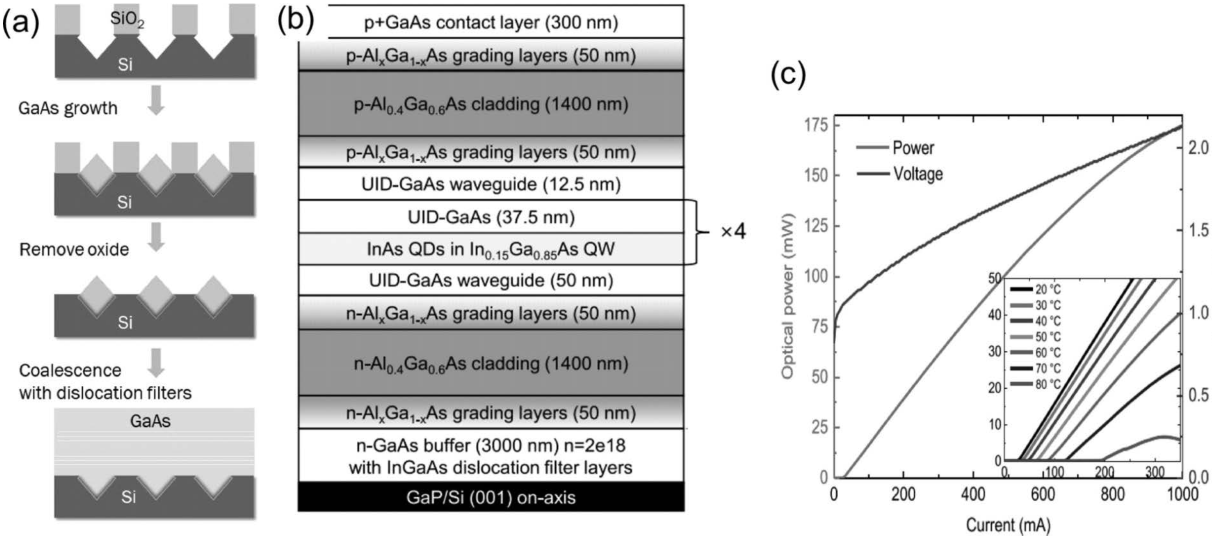
(a)
SiO_2
Si
GaAs growth
Remove oxide
Coalescence with dislocation filters
GaAs
(b)
p+GaAs contact layer (300 nm)
p-$Al_xGa_{1-x}As$ grading layers (50 nm)
p-$Al_{0.4}Ga_{0.6}As$ cladding (1400 nm)
p-$Al_xGa_{1-x}As$ grading layers (50 nm)
UID-GaAs waveguide (12.5 nm)
UID-GaAs (37.5 nm)
InAs QDs in $In_{0.15}Ga_{0.85}As$ QW
×4
UID-GaAs waveguide (50 nm)
n-$Al_xGa_{1-x}As$ grading layers (50 nm)
n-$Al_{0.4}Ga_{0.6}As$ cladding (1400 nm)
n-$Al_xGa_{1-x}As$ grading layers (50 nm)
n-GaAs buffer (3000 nm) n=2e18 with InGaAs dislocation filter layers
GaP/Si (001) on-axis
(c)
Power
Voltage
Optical power (mW)
Voltage (V)
Current (mA)
20 °C
30 °C
40 °C
50 °C
60 °C
70 °C
80 °C

FIGURE 20.6 (a) Schematic of growing GaAs on V-grooved silicon. (b) A cross-sectional schematic of the InAs QD laser structure grown on a GaP/Si substrate. (c) Single-side CW LIV curves at 20°C from a 2600 × 8 μm^2 laser with as-cleaved facets. The inset shows temperature-dependent single-side CW LI curves from 20°C to 80°C. (Reproduced from Ref. [21], with the permission of AIP Publishing. Available from: https://doi.org/10.1063/1.4993226.)

the APB issue is resolved by performing annealing cycles on the homoepitaxial Si-buffer and low-temperature GaP nucleation via flow-rate modulated epitaxy [18]. Using such GaP/Si templates, high-efficiency low-threshold current QD lasers have been fabricated, as shown in Figure 20.6b and c [21]. Recent studies also revealed that, under certain conditions, it is possible to grow APB-free GaAs on nominal (001) silicon wafers without any substrate patterning or GaP/Si intermediate buffers. Chen et al. [22] demonstrated electrically pumped CW QD lasers on a MOCVD-grown 400-nm GaAs-on-nominal (001) Si template with a 0.15° Si misorientation, which is considered small enough to be compatible with the complementary metal oxide semiconductor (CMOS) process. Kwoen et al. showed that a single-domain GaAs can be achieved on (001) Si by optimizing an $Al_{0.3}Ga_{0.7}As$ nucleation layer. An all-MBE-grown QD laser on Si was fabricated on the template, and high-temperature CW operation was reported [23].

There are continuing efforts to study the impact of threading dislocation density (TDD) on the lifetime of III–V lasers grown on Si. Highly efficient long-wavelength lasers are the most sensitive monitors of the quality of III–V/silicon hetero-integration. Early work of growing GaAs-based QW lasers on Si often reveals rapid device degradation and poor lifetimes. This was traced back to dislocation climb and multiplication enhanced by the carrier recombination process, which generates high-density dark line defects. Up to date, the achievement of III–V QW lasers epitaxially grown on Si that can simultaneously exhibit high performance and long lifetime remains elusive. Thanks to the in-plane carrier confinement, QD lasers are much less sensitive to threading dislocations and could potentially achieve good device lifetime with less demanding crystalline quality. Nevertheless, the improvement in the crystalline quality of III–V/Si buffer layers is still of paramount importance. Figure 20.7a compares the lifetime of QD lasers in aging test and the TDD of GaAs buffers grown on Si. By reducing TDD from 2.8×10^8 to $7.3 \times 10^6 \text{cm}^{-2}$, the laser lifetime was improved by about five orders of magnitude under a certain device aging condition [24]. An extracted lifetime value of more than 10^6h highlighted the great potential of the monolithic QD lasers. For practical on-chip operations, the working ambient could be more stringent, and the chip temperatures may go beyond 80°C. To achieve a better temperature stability as well as a reliable device operation at high temperatures, p-type modulation doping (pMD) can be used to compensate the closely packed hole levels and mitigate thermal hole broadening [25]. The pMD QDs have demonstrated higher characteristic temperature (T_0) values than those undoped QDs counterparts. Figure 20.7b shows the advantage of pMD over undoped QD lasers in high temperature (60°C) and current (1.6 kA cm^{-2}) aging test. The much longer extrapolated lifetime for pMD QD laser here is speculated to be related with a suppressed recombination-enhanced dislocation growth after the p-doping [26].

20.2.4 1.55-μm Quantum Dot Lasers on Si

There is a lot of interest in extending the operation wavelength of Si-based QD lasers to 1.55 μm where long-haul fibre communication and free spacer communication can benefit from the least attenuations in fibres and silicon waveguides. This requires developing InP-based semiconductor lasers on silicon that incorporate self-organized InAs QD as active gain materials. Due to the reduced lattice mismatch in the SK mode and the anisotropic surface diffusion of indium adatoms, it remains challenging to grow circular-shaped InAs QDs on InP with high optical qualities. In addition, the growth of low-dislocation density InP on silicon is hampered by the 8% lattice mismatch and the polarity difference between the two materials. Most of existing research studies on InAs QD lasers at this wavelength have been performed on native III–V substrates, such as using metamorphic InGaAs buffers on GaAs [27], GaAsSb buffers on GaAs [28], InAs/GaAs QDs with a GaAsSb capping layer [29] and InAs/InP-based QDs [30]. Comprehensive reviews on recent advances towards high-performance InAs/InP QD and quantum-dash-based lasers are also available [31]. In principle, realization of 1.55-μm InAs QD lasers on silicon by epitaxial growth should be possible, if the good-quality QD active structures can be preserved with suitable buffer designs on silicon.

To explore the monolithic integration approach, Shi et al. developed MOCVD-grown InAs QDs grown on both InP substrates and metamorphic InP buffers on (001) Si substrates [32]. Optically pumped InAs/InAlGaAs QD microdisk laser (MDL) on nominal (001) Si substrates was demonstrated, as seen in Figure 20.8a and b [32]. In these devices, QDs are used in both the active laser medium and the dislocation filter layers in the buffer. By combining the gain contributed from QDs and the high-quality whispering gallery modes, the 4-μm-diameter MDLs can successfully achieve CW lasing at liquid helium temperature with a low threshold of 1.6 mW. RT pulse operation was later demonstrated from a 1.5-μm-diameter disk [33]. By further improving crystalline quality of the InP buffer on

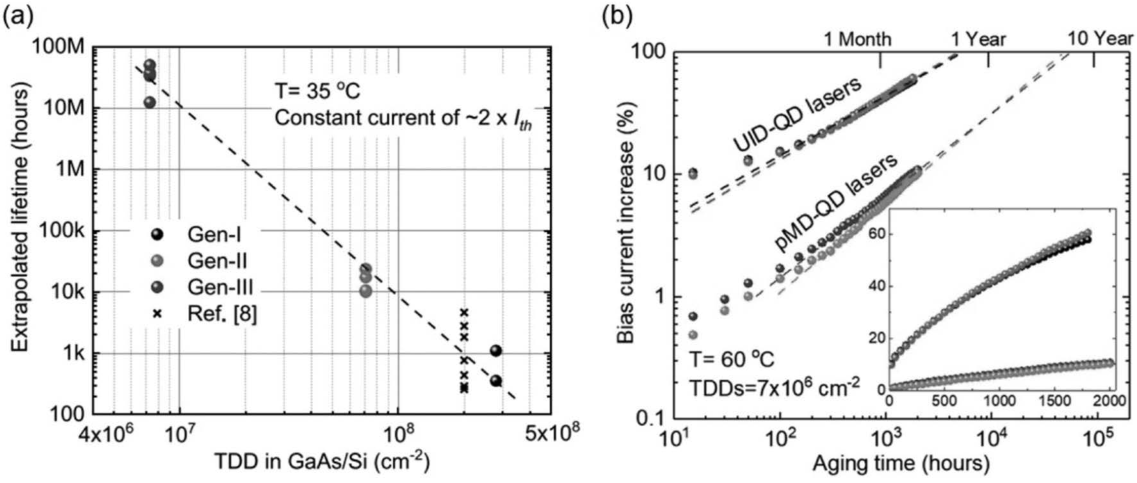

FIGURE 20.7 (a) Extrapolated quantum dot laser lifetime versus the threading dislocation density. (Reproduced from Ref. [24], with the permission of AIP Publishing. Available from: https://doi.org/10.1063/1.5026147.) (b) Bias current increases for 10 mW output power versus ageing time for undoped and pMD lasers at 60°C ageing. Inset shows linear–linear plots. (Reproduced from Ref. [26], © 2019 by John Wiley & Sons, Inc. Available from: https://doi.org/10.1002/pssa.201800602.)

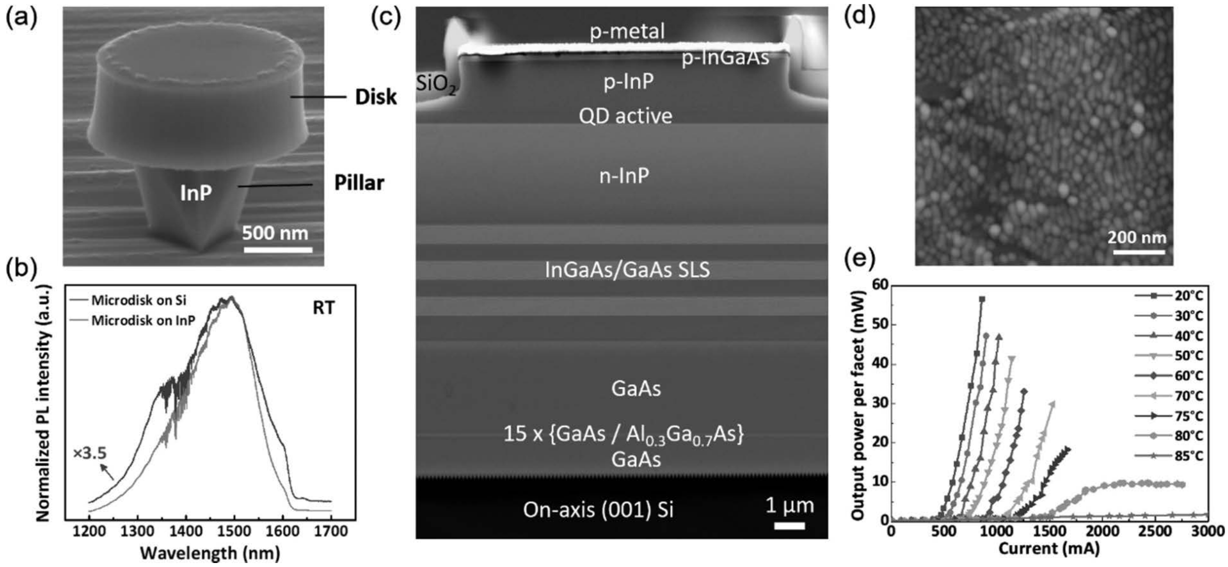

FIGURE 20.8 (a) An SEM image of the optically pumped 1.55-μm-subwavelength microdisk laser. (b) Room-temperature photoluminescence spectra of QD microdisks on InP and Si. (c) Colour-enhanced cross-sectional scanning electron microscopy image of MOCVD-grown 1.55-μm electrical injection. (d) An AFM image of MOCVD-grown multilayer InAs quantum dots on InP buffer on Si, showing a density of $4.5\times10^{10}\,\text{cm}^{-2}$. (e) Light output power versus current for a 20 μm × 1 mm Fabry-Perot ridge waveguide laser at various temperatures. (Reproduced from Refs. [33] and [34], with the permission of AIP Publishing. Available from: https://doi.org/10.1063/1.4979120 and https://doi.org/10.1063/1.5055803.)

a V-groove-patterned Si substrate and carefully optimizing QD growth conditions, electrically injected QD lasers were also implemented [34]. Figure 20.8c shows an scanning electron microscopic (SEM) image of the complete structure after the ridge waveguide FP laser fabrication [34]. The V-groove-patterned (001) Si substrate was used to avoid the generation of APBs and partially confine the threading dislocations. A GaAs intermediate buffer was grown to alleviate the large lattice mismatch between InP and Si. After the introduction of $In_{0.6}Ga_{0.4}As$/InP SLSs, the dislocation density of the InP buffer was further reduced to $1.5\times10^{8}\,\text{cm}^{-2}$ as determined by plan-view transmission electron microscopy (TEM) characterization. An atomic force microscopic (AFM) image of an uncapped QD layer on top of MOCVD-grown five-stack InAs QDs on InP buffer on Si is shown in Figure 20.8d. The dot density is around $4.5\times10^{10}\,\text{cm}^{-2}$. The QDs remain coherent during the multilayer stacking without generation of large clusters. Under pulsed current injection, multimode lasing occurs, and the lasers can sustain up to 80°C (see Figure 20.8e).

20.3 Nano-lasers on Si

In analogy to the relentless miniaturization of state-of-the-art silicon transistors governed by Moore's law, scaling laser footprint to nanometre scale brings benefits such as high integration density and low energy consumption in PICs. As device size approaches wavelength scale, nano-lasers could unlock new applications inaccessible to traditional macroscopic lasers, such as ultra-dense data storage, super resolution imaging, sensing and optical probing [35]. The bottom-up III–V nano-structures can support axially guided optical modes and stimulated light oscillation with feedback provided by end facets [36]. Their small cross section and unique strain relaxation mechanisms allow for direct heteroepitaxy on highly lattice/thermal mismatched substrates. Research of III–V nano-lasers flourished in the early 2010s. Stimulated emission has been demonstrated in various III–V nanowires such as GaAs, InP, InGaAs InAs and GaSb [37]. To attain sufficient optical feedback and thus lasing operation, these III–V nanowires were usually removed from the as-grown substrates and transferred onto a low-index substrate for optical excitation. However, the orientations of the transferred nano-lasers are completely random, making it challenging to precisely manipulate the direction and position of these tiny light emitters. Practical applications, however, require on-chip nano-lasers with better control over material growth and fabrication process.

Direct growth of III–V nano-lasers on Si substrates presents a promising path towards ultra-compact, high-functionality, and low-cost Si-based PICs [38]. Nano-lasers with various compositions, architectures and emission wavelengths have been experimentally demonstrated on Si substrates. In this section, we will review recent efforts in integrating III–V nano-lasers on both (111)- and (001)-oriented Si wafers. Discussion will focus on the design and processing of the nano-lasers for achieving lasing behaviour on Si.

20.3.1 Nanowire Lasers Grown on (111) Si

Vertical III–V nanowires grown on (111)-oriented Si substrates have been extensively studied [39]. The elastic relaxation in lateral directions leads to a significant increase in critical thickness and enables dislocation-free axial and core–shell structures. While these air-cladded III–V nanowires can support strongly confined transverse modes, optical feedback from the III–V/Si interface is too trivial to sustain laser oscillation, due to the small refractive index difference between III–V and Si (e.g. the refractive index of Si and GaAs is 3.6

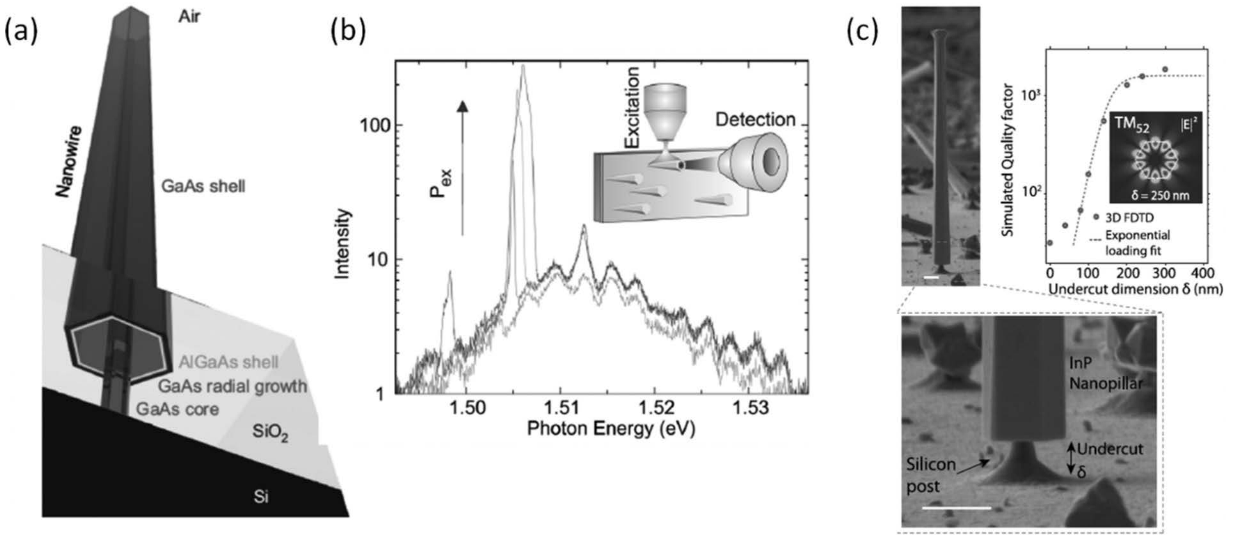

FIGURE 20.9 (a) Schematic of the GaAs/AlGaAs nanowire laser grown on (111)-oriented Si substrate. (b) Emission spectra of the nanowire laser under optical pumping at 10 K. (Reprinted with permission from Ref. [40]. Copyright © 2015 ACS Publications.) (c) SEM image of InP nano-pillar laser grown on (111)-oriented silicon-on-insulators. (Reprinted/adapted with permission from Ref. [41], Optical Society of America.)

and 3.5 at 1000 nm, respectively). Therefore, special cavity designs are usually required to achieve sufficient reflections from the III–V/Si interface for stimulated light emission. Mayer et al. circumvented this issue by inserting a tailored dielectric interlayer between the epitaxial GaAs and the Si substrate, as indicated in Figure 20.9a [40]. With the oxide mask layer, they first grew the GaAs inner core by solid-source MBE. The GaAs core evolved axially into a nanowire with a diameter of 80 nm and a length of 19 µm. Then growth conditions were tuned to favour radial growth and form GaAs/AlGaAs core–shell structure with a diameter of 470 nm. The as-grown nano-laser has a FP cavity with light reflections from the top nanowire/air interface and the bottom nanowire/oxide interface. The refractive index difference between GaAs (around 3.5 at 1000 nm) and SiO$_2$ (around 1.4 at 1000 nm) is adequate for strong optical feedback. Stimulated emission was observed under optical excitation at 10 K. As illustrated by the PL spectra in Figure 20.9b, lasing behaviour is attested by the strong peak at 824 nm and the clamping of spontaneous emission around threshold. III–V nano-lasers have also been demonstrated on silicon-on-insulator (SOI) substrates [41]. As shown by the SEM images and calculated mode profiles in Figure 20.9c, the quality factor of the nano-cavity is greatly improved through undercutting the Si layer between the InP nano-pillar and the buried oxide layer. With embedded InGaAs QWs as active gain media, reflections from the top and bottom InP/air interfaces support RT lasing at 1200 nm.

Laing oscillation can be sustained inside III–V nano-pillars supporting unconventional optical modes. Figure 20.10a shows InGaAs/GaAs nano-pillars directly grown on Si exhibiting a hexagonal cross section and a reducing dimension from the bottom to the top [42]. Thanks to the glancing angle

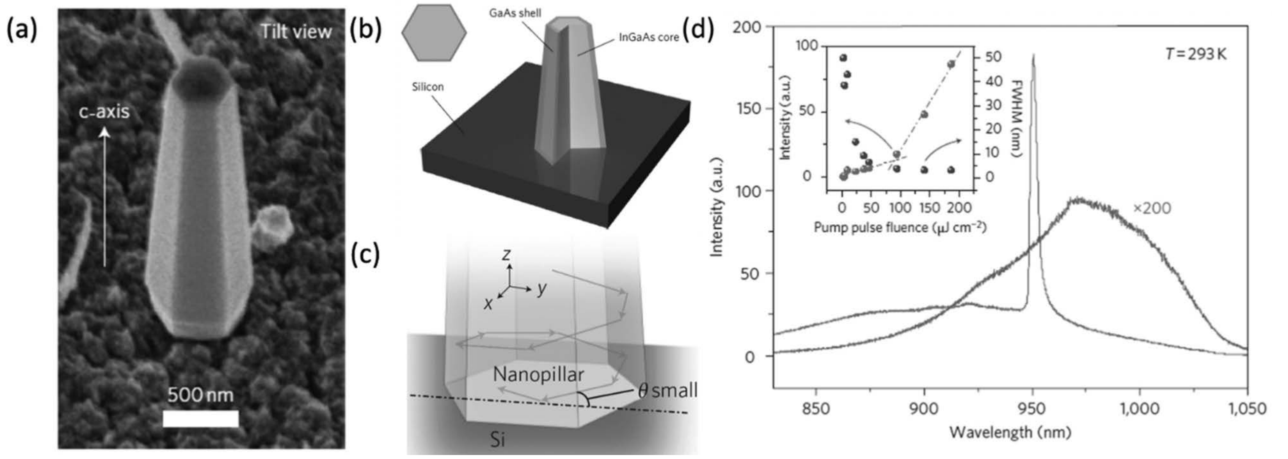

FIGURE 20.10 (a) GaAs/InGaAs nano-pillar grown on Si substrate. (b) Schematic of the designed nano-pillar laser. (c) Schematic showing the helically propagating modes and optical feedback from the III–V/Si interface. (d) Emission spectra of the nano-pillar measured at room temperature. (Reproduced from Ref. [42], with the permission of NPG. Available from: https://doi.org/10.1038/nphoton.2010.315.)

incidence (see Figure 20.10b and c), strong reflection exists at the InGaAs/Si interface and sustains light circulation inside the nano-pillar cavity and thereby unique helically propagating cavity modes. The authors observed RT lasing from the as-grown InGaAs/GaAs nano-pillars (see Figure 20.10d) with wavelength range from 890 to 950 nm by tuning the indium composition of the InGaAs core.

Instead of lasing from a single nanowire, lasing can also be supported from well-aligned nanowire arrays forming a photonic crystal cavity. High quality factors can be realized by tailoring the position and the dimension of each nanowire [43]. As shown by the schematic in Figure 20.11a and the calculated modes in Figure 20.11b, Kim et al. designed InGaAs/InGaP nano-beam lasers on (111) SOI substrates with one-dimensional photonic crystal cavity [44]. Tightly confined optical modes, both vertically and laterally, were formed within the central nanowires. Figure 20.11c and d displays tilted-view SEM images of the as-grown nanowire array with hexagonal cross sections. Under optical excitation, single-mode lasing behaviour was detected from these nano-beam lasers, and the emission wavelength can be tuned from 1100 to 1440 nm via tailoring the cavity parameters and the indium fractions of the InGaAs/InGaP nanowires, as shown in Figure 20.11e.

20.3.2 Nano-ridge Lasers Grown on (001) Si

The request to integrate lasers on CMOS-compatible Si substrates has driven the development of in-plane zinc-blende III–V nano-ridge lasers on (001) Si using the V-groove aspect ratio trapping (ART) technique [45]. In the V-groove ART epitaxy process, III–V layers are deposited in oxide-confined trenches. A high aspect ratio allows for an efficient defect filtering, whereas the {111} facets of the Si V-groove prevents antiphase domains. In contrast to vertical III–V nanowires where the cavity length hinges on growth parameters and is normally less than 20 µm, III–V nano-ridges grown by the ART approach are lithographically defined with lengths varying from a few microns to hundreds of microns. In addition, the in-plane configuration is also more compatible with the well-established planar fabrication processing. While optical feedback can be readily achieved by etching end facets or creating gratings atop the nano-ridges, light leakage into the underlying Si substrates needs to be addressed so that the transverse optical modes are confined inside the nano-ridges. This can be achieved by removing the Si layer underneath to suspend the InP nano-ridges, defining DFB gratings for laser oscillation and fabricating output gratings to couple light out, as indicated in Figure 20.12a [46]. Under optical excitation, single-mode lasing was demonstrated, with tunable lasing peak via altering the parameters of the DFB gratings, which allows for high-capacity wavelength-division multiplexing applications (see Figure 20.12b). By incorporating InP/InGaAs QW in the InP nano-ridge, emission wavelength can be extended to 1360 nm (see Figure 20.12c) [47].

Another approach to get around the leakage loss into the Si substrate was demonstrated by growing III–V nano-ridge structures out of narrow oxide trenches. In principle, the effectiveness of the ART mechanism is the best with tiny trench designs and large depth-to-width aspect ratios. However, the resultant small material volume limits device implementation with insufficient mode confinement in laser cavities. Kunert et al. surpassed this limitation by growing the initial GaAs nano-ridges inside the oxide trench and then scaling up the ridge dimension outside of the oxide trench (see the SEM images in Figure 20.13a) [48]. The air-cladded GaAs nano-ridges could effectively guide optical modes thanks to the reduced light leakage into the Si substrate. The morphology and dimension of the GaAs nano-ridges can be carefully controlled by the epitaxial parameters. InGaAs/GaAs nano-ridge lasers with etched DFB gratings were fabricated, as shown by the SEM images in Figure 20.13b [49]. RT lasing around 1020 nm was observed under optical pumping, as evidenced by the emission spectra below and above threshold in Figure 20.13c.

Another approach to minimize light leakage into Si substrates has been achieved by growing nano-ridge lasers on (001)-oriented SOI wafers. Han et al. demonstrated telecom

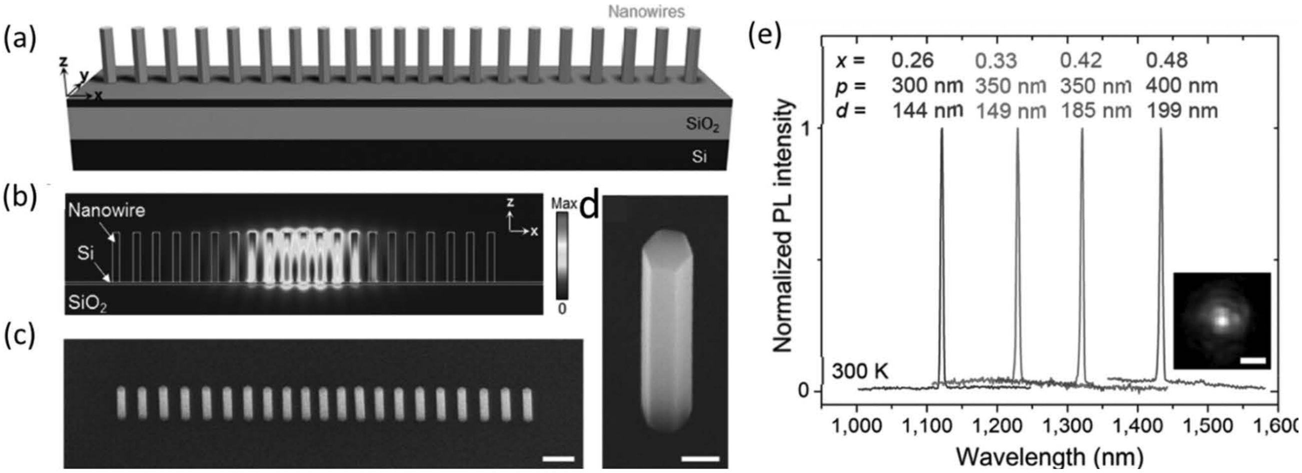

FIGURE 20.11 (a) Schematic of the nanowire-formed one-dimensional photonic crystal cavity. (b) Calculated modes supported inside the photonic crystal cavity. (c) Tilted-view SEM image of the as-grown InGaAs/InGaP nano-beam laser. (d) Zoomed-in SEM image of one nanowire. (Reprinted with permission from Ref. [43]. Copyright © 2017 ACS Publications.) (e) Room-temperature emission spectra of nano-beam lasers with different cavity parameters and indium compositions. (Reprinted with permission from Ref. [44]. Copyright © 2017 ACS Publications.)

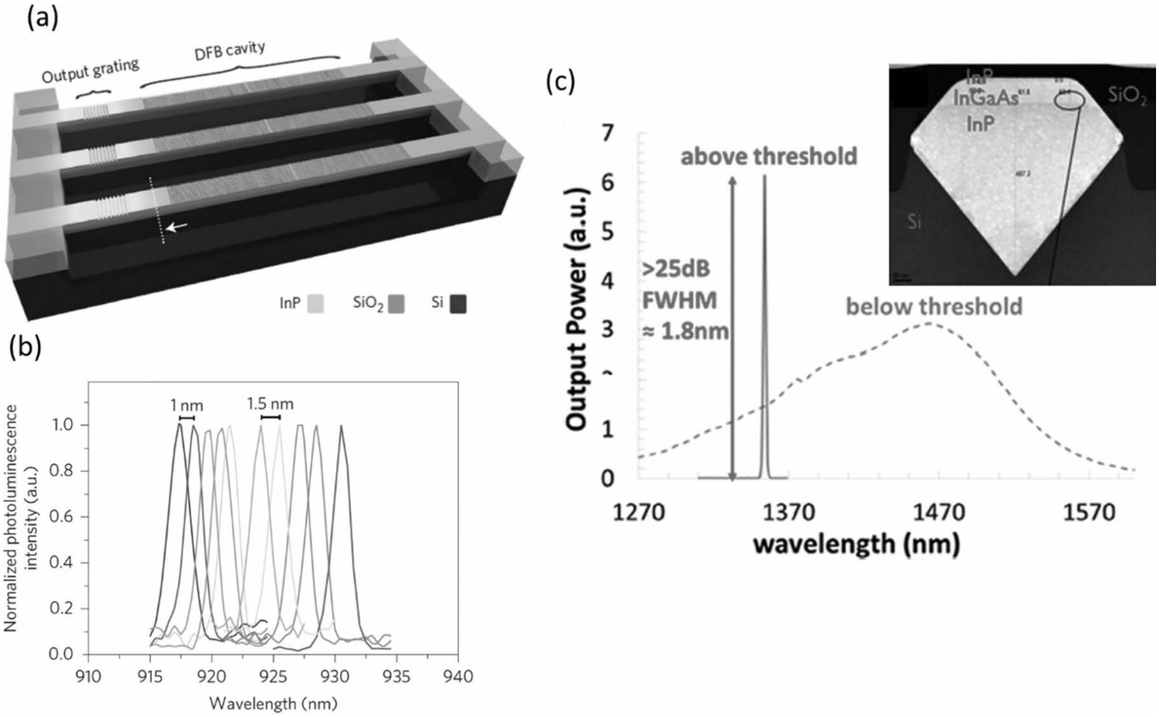

FIGURE 20.12 (a) Schematic of the InP DFB laser grown on Si. Optical modes are confined within the InP nano-ridges by etching away the Si underneath and achieving suspended nano-ridges in the air. (b) Emission spectra of one InP nano-ridge laser measured at room temperature. (Reproduced from Ref. [46], with the permission of NPG. Available from: https://doi.org/10.1038/nphoton.2015.199.) (c) Emission spectra of one InP/InGaAs nano-ridge laser measured at room temperature. The inset shows the TEM image of InP/InGaAs nano-ridges. (Reprinted with permission from Ref. [47]. Copyright © 2016 ACS Publications.)

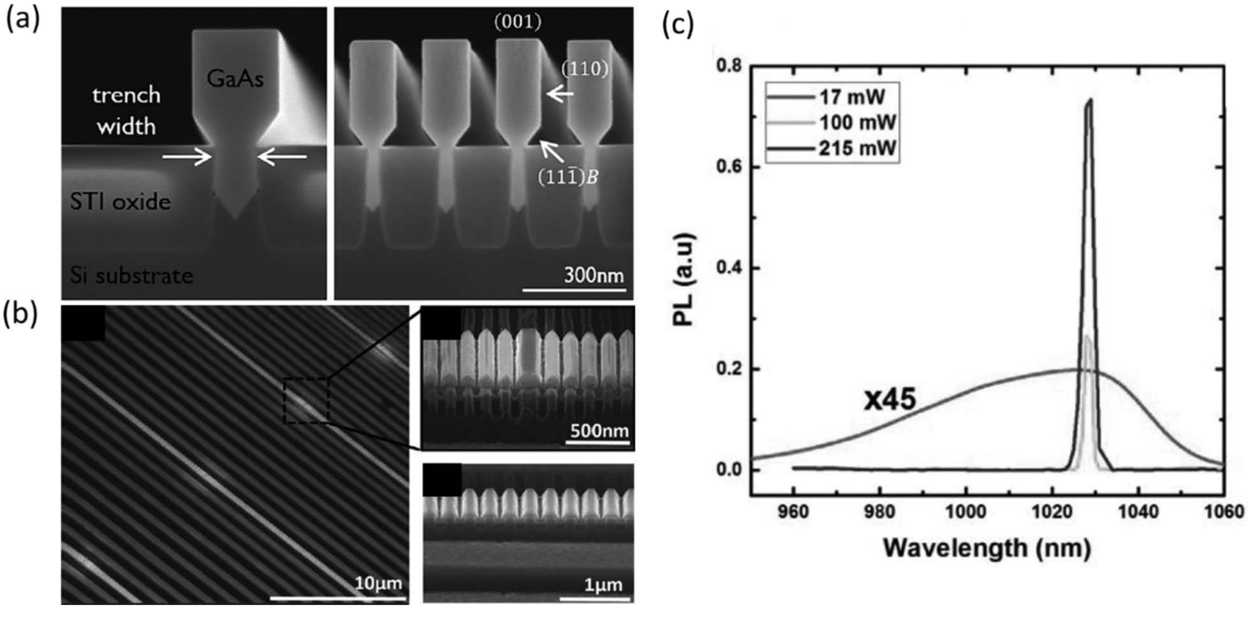

FIGURE 20.13 (a) SEM images of GaAs/InGaAs nano-ridges grown out of narrow nano-scale Si trenches on Si wafers. (Reproduced from Ref. [48], with the permission of AIP Publishing. Available from: https://doi.org/10.1063/1.4961936.) (b) Tilted-view SEM image of the fabricated GaAs/InGaAs nano-ridge laser. Inset shows details of the grating. (c) Emission spectra of one GaAs/InGaAs nano-ridge laser measured at room temperature. (Reprinted/adapted with permission from Ref. [49], Optical Society of America.)

InP/InGaAs nano-laser array on SOI substrates (see Figure 20.14a) [50]. Hybrid FP nano-cavities consisting of a top InP/InGaAs nano-ridge and a bottom supporting Si pedestal were fabricated, as shown by the SEM image in Figure 20.14b. The Si pedestal was formed via anisotropic wet etching, and the dimension was carefully controlled to ensure a strong mode confinement inside the InP nano-ridge and a robust mechanical stability. Under optical excitation, RT lasing at the 1.5 μm

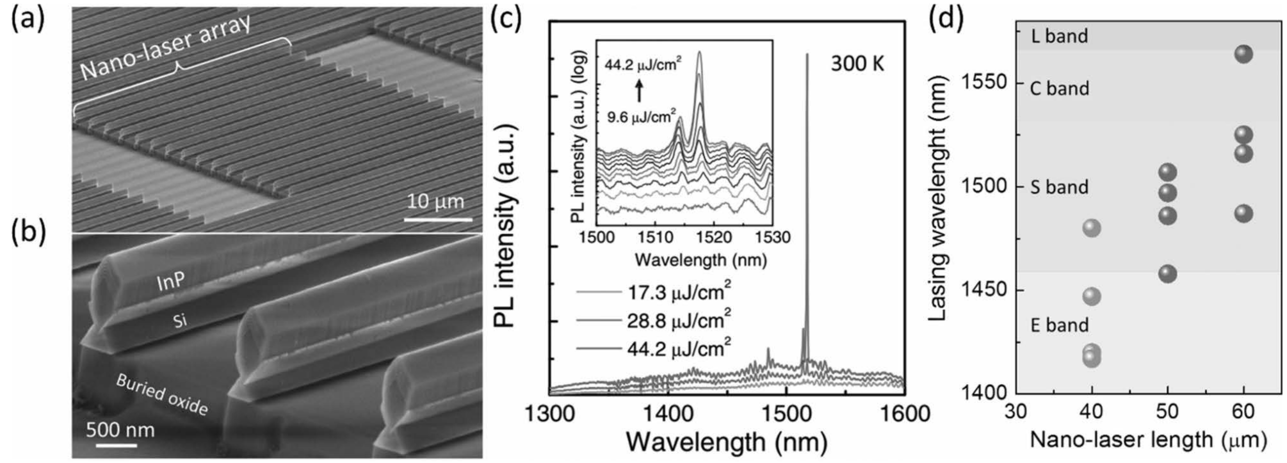

FIGURE 20.14 (a) Tilted-view SEM images of InP/InGaAs nano-laser array grown on SOI. (b) Zoomed-in SEM image of the end facets of three nano-ridge lasers. (c) Emission spectra of one InP/InGaAs nano-ridge laser measured at room temperature. (d) The lasing peak exhibits a strong dependence on the length of the nano-cavity. (Reprinted/adapted with permission from Ref. [50], Optical Society of America.)

band was observed from nano-lasers with a cavity length of 60 µm, as evidenced by the emission spectra in Figure 20.14c. It is intriguing that the lasing peak exhibits a strong dependence on the length of the nano-cavity. As indicated in Figure 20.14d, the lasing peak shifts from 1450 to 1550 nm when the laser cavity length is increased from 40 to 60 µm. The demonstration of telecom-emitting nano-lasers on Si-photonics standard (001) SOI platforms presents an important step towards fully integrated Si-photonics circuits.

20.4 Challenges and Discussions

Achieving high-performance, long-lifetime and electrical injection Si-based lasers will open enormous opportunities in photonic integration technologies. Recent progress in developing III–V lasers monolithically grown on the Si platform has been enabled by advances in epitaxy techniques yielding low dislocation density materials and well-controlled nanostructures. The demonstration of reliable and efficient 1.3 µm QD laser on silicon is attracting tremendous attention for practical applications such as optical interconnects in data centres. Improving 1.55 µm QD laser on silicon requires further reduction of the dislocation densities of InP-based metamorphic buffers as well as perfecting circular QDs with high optical gain. The eventual photonics integration would need all optical components integrated on the same platform through a CMOS-compatible process. The use of thick and complex buffers in QD lasers grown on Si could pose a challenge for coupling light from the active device to the underlying silicon waveguides. Butt-joint or evanescent coupling through selective area growth or selective etching might provide possible solutions, which, however, has not received sufficient investigations so far. In terms of nano-lasers on Si, most of the demonstrated devices operate under pulse optical pumping conditions at RT. CW operation at RT requires efficient heat dissipation and careful design of the heat sinking techniques. The realization of electrically driven nano-lasers on Si put additional stipulations on the growth and processing technologies. The unique morphology and growth modes of III–V nano-structures, especially vertical III–V nanowires on (111) Si wafers, complicate the formation of doped structures and require carefully designed metallization process for efficient carrier injection. Significant research is therefore needed to address these challenges towards practical applications.

REFERENCES

1. Arakawa Y and Sakaki H 1982 Multidimensional quantum well laser and temperature dependence of its threshold current *Appl. Phys. Lett.* **40** 939–941.
2. Bimberg D and Pohl U W 2011 Quantum dots: promises and accomplishments *Mat. Today* **14** 388–397.
3. Jasim K E 2015 Quantum dots solar cells. In Leonid A. Kosyachenk, ed., *Solar Cells-New Approaches and Reviews* IntechOpen, pp. 303–331.
4. Fiore A, Rossetti M, Alloing B et al. 2004 Carrier diffusion in low-dimensional semiconductors: A comparison of quantum wells, disordered quantum wells, and quantum dots *Phys. Rev. B* **70** 205311.
5. Liu A Y, Srinivasan S, Norman J, Gossard A C and Bowers J E 2015 Quantum dot lasers for silicon photonics *Photon. Res.* **3** B1–B9.
6. Bimberg D, Grundmann M and Ledentsov N N 1999 *Quantum Dot Heterostructures* John Wiley & Sons.
7. Shchukin V, Ledentsov N N and Bimberg D 2004 *Epitaxy of Nanostructures* Springer Science & Business Media.
8. Liu W S, Chang H, Liu Y S and Chyi J I 2006 Pinholelike defects in multistack 1.3 µm InAs quantum dot laser *J. Appl. Phys.* **99** 114514.
9. Nishi K, Saito H, Sugou S and Lee J S 1999 A narrow photoluminescence linewidth of 21 meV at 1.35 µm from strain-reduced InAs quantum dots covered by $In_{0.2}Ga_{0.8}As$ grown on GaAs substrates *Appl. Phys. Lett.* **74** 1111–1113.
10. Linder K K, Phillips J, Qasaimeh O et al. 1999 Self-organized $In_{0.4}Ga_{0.6}As$ quantum-dot lasers grown on Si substrates *Appl. Phys. Lett.* **74** 1355–1357.

11. Chen S, Li W, Wu J et al. 2016 Electrically pumped continuous-wave III–V quantum dot lasers on silicon *Nat. Photon.* **10** 307.
12. Yang J, Bhattacharya P and Mi Z 2007 High-performance $In_{0.5}Ga_{0.5}As$/GaAs quantum-dot lasers on silicon with multiple-layer quantum-dot dislocation filters *IEEE Trans. Electron Dev.* **54** 2849–2855.
13. Wang T, Liu H, Lee A, Pozzi F and Seeds A 2011 1.3-µm InAs/GaAs quantum-dot lasers monolithically grown on Si substrates *Opt. Express* **19** 11381–11386.
14. Liu A Y, Zhang C, Norman J et al. 2014 High performance continuous wave 1.3 µm quantum dot lasers on silicon *Appl. Phys. Lett.* **104** 041104.
15. Liu A Y, Herrick R W, Ueda O, Petroff P M, Gossard A C and Bowers J E 2015 Reliability of InAs/GaAs quantum dot lasers epitaxially grown on silicon *IEEE J. Sel. Top. Quant. Electron.* **21** 690–697.
16. Wang J, Hu H, Yin H et al. 2018 1.3 µm InAs/GaAs quantum dot lasers on silicon with GaInP upper cladding layers *Photon. Res.* **6** 321–325.
17. Li Q, Ng K. W and Lau K M 2015 Growing antiphase-domain-free GaAs thin films out of highly ordered planar nanowire arrays on exact (001) silicon *Appl. Phys. Lett.* **106** 072105.
18. Volz K, Beyer A, Witte W et al. 2011 GaP-nucleation on exact Si (001) substrates for III/V device integration *J. Cryst. Growth* **315** 37–47.
19. Alcotte R, Martin M, Moeyaert J et al. 2016 Epitaxial growth of antiphase boundary free GaAs layer on 300 mm Si (001) substrate by metalorganic chemical vapour deposition with high mobility *APL Mat.* **4** 046101.
20. Norman J, Kennedy M J, Selvidge J et al. 2017 Electrically pumped continuous wave quantum dot lasers epitaxially grown on patterned, on-axis (001) Si *Opt. Express* **25** 3927–3934.
21. Jung D, Norman J, Kennedy M J et al. 2017 High efficiency low threshold current 1.3 µm InAs quantum dot lasers on on-axis (001) GaP/Si *Appl. Phys. Lett.* **111** 122107.
22. Chen S, Liao M, Tang M et al. 2017 Electrically pumped continuous-wave 1.3 µm InAs/GaAs quantum dot lasers monolithically grown on on-axis Si (001) substrates *Opt. Express* **25** 4632–4639.
23. Kwoen J, Jiang B, Watanabe K and Arakawa Y 2019 High-temperature continuous-wave operation of directly grown InAs/GaAs quantum dot lasers on on-axis Si (001) *Opt. Express* **27** 2681–2688.
24. Jung D, Herrick R, Norman J et al. 2018 Impact of threading dislocation density on the lifetime of InAs quantum dot lasers on Si *Appl. Phys. Lett.* **112** 153507.
25. Deppe D G, Huang H and Shchekin O B 2002 Modulation characteristics of quantum-dot lasers: The influence of p-type doping and the electronic density of states on obtaining high speed *IEEE J. Quant. Electron.* **38** 1587–1593.
26. Jung D, Norman J, Wan Y et al. 2019 Recent advances in InAs quantum dot lasers grown on on-axis (001) silicon by molecular beam epitaxy *Phys. Status Solidi (a)* **216** 1800602.
27. Karachinsky L Y, Kettler T, Novikov I I et al. 2006 Metamorphic 1.5 µm-range quantum dot lasers on a GaAs substrate *Semicond. Sci. Technol.* **21** 691.
28. Liu H Y, Qiu Y, Jin C Y, Walther T and Cullis A G 2008 1.55 µm InAs quantum dots grown on a GaAs substrate using a GaAsSb metamorphic buffer layer *Appl. Phys. Lett.* **92** 111906.
29. Liu H Y, Steer M J, Badcock T J et al. 2006 Room-temperature 1.6 µm light emission from InAs/GaAs quantum dots with a thin GaAsSb cap layer *J. Appl. Phys.* **99** 046104.
30. Gilfert C, Ivanov V, Oehl N, Yacob M and Reithmaier J P 2011 High gain 1.55 µm diode lasers based on InAs quantum dot like active regions *Appl. Phys. Lett.* **98** 201102.
31. Lelarge F, Dagens B, Renaudier J et al. 2007 Recent Advances on InAs/InP Quantum Dash Based Semiconductor Lasers and Optical Amplifiers Operating at 1.55 µm *IEEE J. Sel. Top. Quant. Electron.* **13** 111–124.
32. Shi B, Zhu S, Li Q, Wan Y, Hu E L and Lau K M 2017 Continuous-wave optically pumped 1.55 µm InAs/InAlGaAs quantum dot microdisk lasers epitaxially grown on silicon *ACS Photon.* **4** 204–210.
33. Shi B, Zhu S, Li Q et al. 2017 1.55 µm room-temperature lasing from subwavelength quantum-dot microdisks directly grown on (001) Si *Appl. Phys. Lett.* **110** 121109.
34. Zhu S, Shi B, Li Q and Lau K M 2018 1.5 µm quantum-dot diode lasers directly grown on CMOS-standard (001) silicon *Appl. Phys. Lett.* **113** 221103.
35. Ma R-M and Oulton R F 2019 Applications of nanolasers *Nat. Nanotechnol.* **14** 12–22.
36. Johnson J C, Choi H J, Knutsen K P et al. 2002 Single gallium nitride nanowire lasers *Nat. Mat.* **1** 106.
37. Zhang Y, Saxena D, Aagesen M et al. 2019 Toward electrically driven semiconductor nanowire lasers *Nanotechnol.* **30** 192002.
38. Liang D and Bowers J E 2010 Recent progress in lasers on silicon *Nat. Photon.* **4** 511.
39. Tomioka K, Kobayashi Y, Motohisa J et al. 2009 Selective-area growth of vertically aligned GaAs and GaAs/AlGaAs core–shell nanowires on Si (111) substrate *Nanotechnol.* **20** 145302.
40. Mayer B, Janker L, Loitsch B et al. 2015 Monolithically integrated high-β nanowire lasers on silicon *Nano Lett.* **16** 152–156.
41. Lu F, Bhattacharya I, Sun H et al. 2017 Nanopillar quantum well lasers directly grown on silicon and emitting at silicon-transparent wavelengths *Optica* **4** 717–723.
42. Chen R, Tran T D, Ng K W et al. 2011 Nanolasers grown on silicon *Nat. Photon.* **5** 170.
43. Kim H, Lee W J, Farrell A C et al. 2017 Monolithic InGaAs nanowire array lasers on silicon-on-insulator operating at room temperature *Nano Lett.* **17** 3465–3470.
44. Kim H, Lee W J, Farrell A C et al. 2017 Telecom-wavelength bottom-up nanobeam lasers on silicon-on-insulator *Nano Lett.* **17** 5244–5250.

45. Merckling C, Waldron N, Jiang S et al. 2014 Heteroepitaxy of InP on Si (001) by selective-area metal organic vapor-phase epitaxy in sub-50 nm width trenches: The role of the nucleation layer and the recess engineering *J. Appl. Phys.* **115** 023710.
46. Wang Z, Tian B, Pantouvaki M et al. 2015 Room-temperature InP distributed feedback laser array directly grown on silicon *Nat. Photon.* **9** 837.
47. Tian B, Wang Z, Pantouvaki M et al. 2016 Room temperature O-band DFB laser array directly grown on (001) silicon *Nano Lett.* **17** 559–564.
48. Kunert B, Guo W, Mols Y et al. 2016 III/V nano ridge structures for optical applications on patterned 300 mm silicon substrate *Appl. Phys. Lett.* **109** 091101.
49. Shi Y, Wang Z, Van Campenhout J et al. 2017 Optical pumped InGaAs/GaAs nano-ridge laser epitaxially grown on a standard 300-mm Si wafer *Optica* **4** 1468–1473.
50. Han Y, Ng W K, Xue Y et al. 2019 Telecom InP/InGaAs nanolaser array directly grown on (001) silicon-on-insulator *Opt. Lett.* 44 767–770.

21

Gas/Vapour Lasers: Section Introduction

Julian Jones

For many readers, perhaps their first sight of laser radiation was from a helium–neon lasers, the subject of Alan White and Lisa Tsufura's chapter (Chapter 22). The helium–neon laser was first demonstrated in 1961; it was the prototype of all gas lasers, and the first laser of any kind to be operated continuous-wave (cw), first in the near-infrared (IR) at 1.15 µm and then—by White and Rigden—at the familiar red wavelength of 633 nm. Production of the helium–neon laser peaked in the 1980s at more than 750 000 units per annum, for applications from holography to printing and barcode scanning. Since then it has been displaced in many areas by semiconductor diode lasers (see Chapter 11) but still has sales exceeding 200 000 each year, more than for any type other than the diode laser.

A subclass of the discharge-pumped gas lasers is those in which the active medium is a metal. The helium–cadmium laser, the subject of William Silfvast's chapter (Chapter 23), is one of the most widely used metal–vapour lasers, with emission at 325, 354 and 442 nm and with principal applications in stereolithography and printing. The stereolithographic technique involves forming three-dimensional solid objects by scanning a laser beam to produce photopolymerization of a liquid monomer. Photosensitivity is more easily achieved at the short wavelength of the helium–cadmium laser.

Copper and gold vapour lasers are the subject of Colin Webb's chapter, 24. They are examples of cyclic, or self-terminating lasers, efficiently generating short pulses. The copper vapour laser is more common, with fundamental wavelengths in green (511 nm) and yellow (578 nm), typically generating pulses of a few mJ, 10 ns duration and—most importantly—at very high repetition rates of perhaps 10–30 kHz. Copper vapour lasers first found use in isotope separation. Since then, their visible wavelength and short, high repetition rate pulses have made them very useful in high speed imaging and in material processing (Chapter 1 of Volume 3). The gold vapour laser is in many respects similar, with wavelengths in the red (628 nm) and UV (312 nm).

The helium–neon laser is one of a large class of devices in which the pumping mechanism is by means of an electrical discharge in a gas mixture. It was soon joined by the argon ion and krypton ion lasers, the subject of Chapter 25 (Malcolm Dunn and Tony Gutierrez). Ion lasers have fundamental wavelengths spanning the UV to near-IR, from 275 nm to 1.09 µm, and with frequency-doubling can be used efficiently in the deep-UV, from 229 to 264 nm. Their range of applications is exceptional: holography, printing, imaging, spectroscopy and non-destructive testing. A major application has been in the pumping of other lasers, such as the Ti:sapphire (see Chapter 6), although there has often been displaced by solid-state pump sources. The frequency-doubled Nd:YAG laser (Chapter 4) has become a convenient substitute for applications, e.g. in instrumentation, requiring a visible laser source. Nevertheless, ion lasers are attractive in the UV, violet and red, having excellent coherence properties, and where cw solid-state lasers are not available.

The highest-average-power gas laser is the carbon dioxide laser, operating at a wavelength of 10.6 µm, described in Denis Hall's chapter, 26. The CO_2 laser has many applications but is perhaps best known for its use in laser material processing (D1), in which its high power, high efficiency and reliability are decisive advantages. Only the Nd:YAG laser (Chapter 4) is used in a comparable volume of laser processing applications, where an advantage that it has over the CO_2 laser is its shorter wavelength, 1.06 µm, compatible with delivery by fused silica optical fibres.

There has always been a strong drive towards the development of shorter-wavelength lasers. One reason was to enable better spatial resolution in photolithographic applications, notable in the manufacture of microelectronics. Excimer gas lasers are the subject of Chapter 27 by W. J. Wittemann. The excimer lasers (notably the rare-gas halide lasers XeCl, KrF, ArF) and the similar F_2 lasers became the sources of choice for high-resolution photolithography, at progressively shorter wavelengths as feature sizes reduced. The chapter covers also the related N_2 and H_2 lasers. The recent progress in application of high-brightness excimer lasers is described in Chapter 28.

The concentration of molecular vibrational spectra in the mid-IR led to an obvious need for sources in that region suitable for spectroscopy, satisfied by the optically pumped NH_3 and C_2H_2 lasers described by Mary Tobin in Chapter 29, with wavelengths in the 8–20 µm range. The ammonia laser is usually pumped by CO_2 lasers, and frequency-doubled CO_2 lasers are suitable for pumping C_2H_2. The ammonia laser dominates in applications, one of which is for differential absorption LIDAR (light detection and ranging), for atmospheric monitoring.

The development of far-IR lasers opened up a new range of spectroscopic applications, previously hampered by the inadequate performance of the only sources previously available, which were thermal. HCN and H_2O lasers are the subject of Chapter 30, by Wilhelm Prettl. The 337 µm line of the HCN laser is the strongest of any discharge-pumped far-IR laser, with powers typically of a few mW. The H_2O laser offers over 100 emission lines, from 7 to 220 μm.

Diode-pumped alkali lasers attract growing interest of researchers because of their potential to produce high laser power in an excellent quality beam, and thus, they can compete with the best currently available high-power laser systems. Since the first DPAL demonstration in 2005, a significant progress in this field has been achieved. Chapter 31 presents a historical review of the alkali laser research and development and discussion of the most important achievements in this field.

22

Atomic Gas Lasers: Helium–Neon Lasers

Alan D. White and Lisa Tsufura

CONTENTS

22.1 Introduction 301
22.2 The Glow Discharge in Rare Gases 302
22.3 Population Inversion, Optical Gain and Oscillation 303
22.4 HeNe Laser Tube Construction 304
22.5 The Evolution of Expectations 305
22.6 HeNe Laser Manufacturing Processes and Technology 306
22.7 'Single-Frequency' HeNe Lasers 306
22.8 HeNe Lasers: Typical Performance Characteristics 307
22.9 HeNe Lasers: The Future 308
References 308
Further Reading 308

22.1 Introduction

The helium–neon gas laser was the first gas laser to be developed and the first truly continuous-wave (cw) laser of any kind. It is a textbook example of light amplification by stimulated emission of radiation from free atoms, in which population inversion occurs by selective excitation of the upper level through resonant energy transfer.

The initial demonstration in 1961 by Javan, Bennett and Herriott of Bell Telephone Laboratories [1] of laser oscillation on the infrared transition of Ne at 1.15 µm was followed shortly afterwards by the demonstration of laser oscillation on the 632.8-nm red transition by White and Rigden [2] also at Bell Labs. From that time to the present day, the helium neon (HeNe) laser has been a mainstay of scientific, industrial, medical and commercial laser applications. At its peak in the late 1980s, HeNe laser manufacturers were shipping more than 750 000 units a year for applications as diverse as holography and barcode scanning, biological cell counting, metrology, construction alignment, printing and reprographics, medical and industrial pointing and light shows. The overall numbers have dropped considerably, but even today, nearly 10 years after the 'death' of the HeNe, it is predicted as a result of advances in semiconductor diode laser technology, approximately 200 000 are sold annually—more than all other lasers combined (excluding, of course, diode lasers).

The oscillating fields in the HeNe laser match very closely the classical description of light modes in a resonant optical cavity. Its output beam when operating in its lowest transverse mode approximates very closely that of a coherent Gaussian beam with an M^2 value, typically smaller than 1.02. This is largely a consequence of the optical homogeneity of gas-phase light-amplifying media at low-pressure and low-power dissipation. In precision scanning applications such as recording, imaging, defect measurement and reprographics and in biotechnology applications including microscopy and cytometry, it is critical for the beam to have a known, repeatable energy distribution and an M^2 value close to unity in order to properly calculate, create or measure artefacts with extremely high accuracy and resolution. A particular advantage over many types of diode lasers that HeNe lasers possess is the polarization extinction ratio. This is of value in applications such as ellipsometry where precise measurements of relative phase changes are made. HeNes can obtain extinction ratios on the order of 500:1, 1000:1 or higher without additional cost of polarization elements.

Plasma tube life is typically greater than 10 000 h, and many systems in the field have been operating 50 000 h or more without a tube replacement. The lasers are small in size (relative to other gas-laser sources) and convection cooled and can be operated on normal household power. Lower-power lasers can be operated easily from batteries, making them ideal sources for field equipment including theodolites, laser levels and other construction alignment equipment. HeNe lasers are low in cost; in single-unit quantities, purchase prices range from a few hundred to a few thousand dollars. For original equipment manufacturer quantities, the prices are much lower. Finally, in addition to the familiar red (633 nm) output, HeNes with orange (612 nm), yellow (594 nm), green (543 nm) and infrared (1523 nm) output became commercially available in the early 1980s finding fluorescence applications in microscopy, cytometry, genomics and other applications.

HeNe lasers are low-power devices, with output ranging from 0.1 mW or less to about 40 mW for the largest

TABLE 22.1

Output Power Characteristics of Commercial HeNe Lasers

Laser Wavelength (nm)	Power Range (mW)
1523 near infrared	0.25–1.0
633 red	0.25–40
612 orange	0.25–7.0
594 yellow	0.25–4.0
543 green	0.10–3.0

practical tube. This limitation makes them unsuitable for most materials-processing applications or for pumping other laser sources (e.g. dye lasers).

About a dozen visible transitions and perhaps 15 times as many infrared transitions of the neon atom have been reported as showing either laser oscillation or optical gain [3]. However, the most common wavelengths for which HeNe lasers are commercially available are listed in Table 22.1.

In this chapter, we shall deal primarily with the 633-nm red HeNe laser. With some obvious changes, the discussion applies to all the visible and infrared transitions which originate from the same upper level (3s in Paschen notation) of the neon atom and therefore compete with it. Similar considerations apply to a group of infrared transitions which originate from the 2s group of levels about 0.9 eV below the 3s levels of Ne (see Section 22.3).

22.2 The Glow Discharge in Rare Gases

The active medium of the HeNe laser is a glow discharge in a mixture of the ‘rare’ or ‘noble’ gases such as helium and neon. For that reason it is worthwhile at this point to review briefly the main features of the discharge physics relevant to the excitation and inversion mechanisms of the laser [3–5].

The term glow discharge refers to a specific manifestation of electrical conduction in low-pressure gas, in which sufficient charge carriers and excited states are created in the gas by electron impact to establish a low current self-sustaining discharge. Figure 22.1 illustrates such a discharge in a long narrow tube provided with a planar cold cathode and anode, and filled with one of the rare gases at a pressure of a few Torr (1 torr = 1.32 mbar).

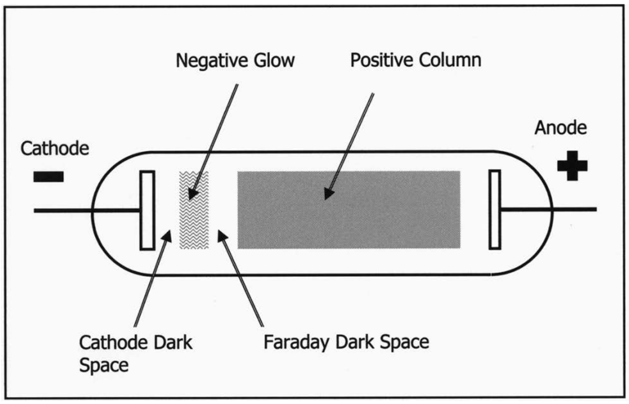

FIGURE 22.1 The glow discharge.

The region adjacent to the cathode, termed the cathode fall or sheath, is strongly accelerating for electrons leaving the cathode. Within this region, and extending into the light and dark regions just beyond, fast electrons make ionizing collisions with gas atoms, creating large numbers of ion–electron pairs. Ions drifting back to the cathode under the influence of the field produce secondary electrons in an Auger process. Each secondary electron must generate enough ions (usually three to five) in traversing the cathode sheath to produce its Auger replacement at the cathode, and the cathode fall voltage (typically 100–300 V) adjusts until this criterion is met. Beyond the cathode region and extending to the anode is the uniform, strongly luminous region known as the positive column. Though characterized by a much smaller electric field than the cathode region, a similar criterion applies: enough ions, electrons and excited atoms must be generated by electron impact within the positive column to supply the loss of energetic particles through diffusion and recombination at the wall, and to radiation and gas heating.

Electrons gain energy continuously from the electric field in the positive column since they make only elastic collisions with gas atoms until they acquire sufficient energy to excite or ionize. The electron population tends to thermalize as a group (electrons colliding with other electrons share their energy) and, to an approximation, may be characterized by a Maxwellian energy distribution at some high temperature, T_e. Ions, on the other hand, share their energy on collision with other ions and neutral atoms, the net effect of which is to raise the gas temperature slightly. Except at the tube wall, where a negative sheath is created by fast electrons, charge equality is closely maintained. One way of looking at the positive column, which relates it to the external discharge parameters, is to note that an energy balance exists throughout its length, such that the power input per unit length (product of tube current and voltage gradient) equals the power dissipated per unit length [4].

Electrons at the end of the column are collected at the anode. Depending on whether the electron diffusion current to the anode is larger or smaller than the tube current, the (usually small) anode sheath becomes negative or positive with respect to the adjacent positive column. The dynamic resistance of a glow discharge is negative, which, if discovered empirically, may lead to an entirely different regime, termed the destructive arc discharge.

The source of light in neon signs, and the seat of HeNe laser action, is the positive column. In order to examine some of the properties of a specific positive column in detail, we choose as an example the typical 1–2-mW HeNe laser shown in Figure 22.2.

Here the cold cathode is an aluminium cylinder, close-fitting within the tube envelope, which surrounds the 1 mm precision bore capillary tube defining the positive column. The mirrors are hard-sealed to metal end caps, one of which serves as an anode. The tube voltage and current are 1450 V and 6 mA, respectively.

The cathode sheath voltage drop is 200 V. The length of the positive column is typically 15 cm, the positive column voltage

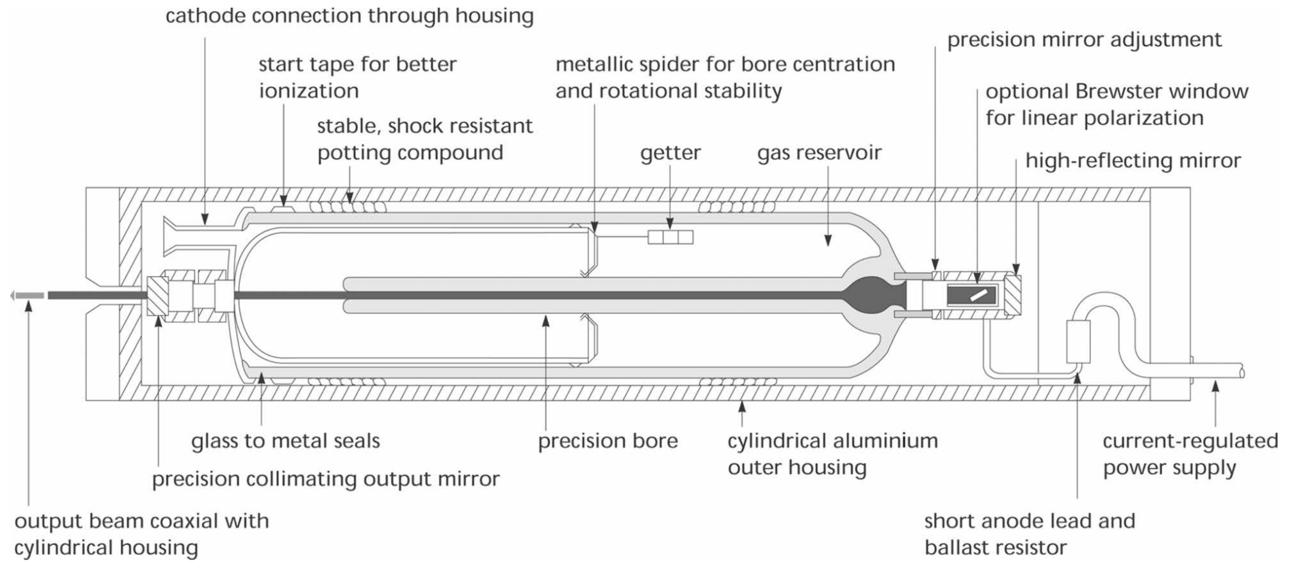
cathode connection through housing
start tape for better ionization
stable, shock resistant potting compound
metallic spider for bore centration and rotational stability
getter
gas reservoir
precision mirror adjustment
optional Brewster window for linear polarization
high-reflecting mirror
glass to metal seals
precision collimating output mirror
output beam coaxial with cylindrical housing
precision bore
cylindrical aluminium outer housing
current-regulated power supply
short anode lead and ballast resistor

FIGURE 22.2 Construction of a modern commercial HeNe laser. (Courtesy: Melles Griot Inc.)

gradient is 90 V cm^{-1} and the current density in the capillary is 0.7 A cm^{-2}. The gas fill is a 5:1 mixture of helium 3 (see Section 22.3) and neon to a total pressure of 4 torr. With these operating parameters, the electron and the positive ion densities in the positive column plasma are in the range 10^{11} cm^{-3}, representing fractional ionization of less than one part in 10^6. With some significant exceptions, discussed later, all excited states, including ions, are created by single- or multiple-step inelastic collisions with hot electrons, characterized by a temperature, $T_e \sim 80\,000$ K (10 eV average electron energy).

22.3 Population Inversion, Optical Gain and Oscillation

In the discharge, both helium- and neon-excited state populations are comparable with electron and ion populations. However, the helium metastable populations are likely to be an order of magnitude higher because they are unable to relax to the ground state by photon emission. Decay from the $1s2s^3S_1$ and $1s2s^1S_0$ first excited levels of He to the $1s^{21}S_0$ ground state by electric dipole transitions is rigorously forbidden by the parity selection rule.

In order to realize population inversion and optical gain, some departure from electron thermal excitation equilibrium must occur. In the HeNe discharge, this departure from equilibrium is a result of fortuitously close energy coincidence between the triplet 2^3S and singlet 2^1S metastable levels of helium and the $2s_2$ and $3s_2$ levels of neon, respectively [6].

The two upper laser levels in Ne are $3s_2$ and $2s_2$ and have quite short radiative lifetimes (10–20 ns) since both can decay via fast transitions in the vacuum ultraviolet back to the ground state. However, at any neon pressure above 0.05 torr, the probability of resonance radiation photons in these transitions being reabsorbed by ground-state atoms before they can escape discharge is so high that the decay paths in the transitions from $3s_2$ and $2s_2$ to the ground state may be considered as fully blocked. Thus, the *effective* lifetimes of $3s_2$ and $2s_2$ are determined entirely by their slower decay in visible transitions ($\tau_{eff} \sim 96$ ns for $2s_2$, $\tau_{eff} \sim 110$ ns for $3s_2$). The two lower levels $3p_4$ and $2p_4$ can decay by reasonably fast UV transitions to levels in the $1s_2$–$1s_5$ block with lifetimes of order 20 ns. Thus, the He–Ne system has a $\tau_{upper}:\tau_{lower}$ ratio very much in its favour on all three laser transitions.

The other desirable factor, selective excitation of the *upper* laser levels, is ensured by the presence of the helium. By two completely unrelated accidents of nature, the energy of the He 2^3S lies within 0.049 eV of $2s_2$ Ne (a coincidence of one part in 500) and that of 2^1S He coincides with $3s_2$ Ne to within 0.039 eV (better than 1 part in 400). When a discharge is run in pure He at low pressure (1 torr, say), electron collisions with ground-state He will excite some atoms directly (and by cascade from higher levels) to both metastable levels from which they can only escape by collision with the wall or by making an ionizing collision with an electron.

A reservoir of excited He atoms in these two long-lived levels builds up to steady values of the order of 10^{11}–10^{12} atoms cm^{-3}. If now a small quantity of Ne is added to the discharge (not enough to change its character as a discharge governed by the properties of He), selective transfer of energy to the Ne $2s_2$ and $3s_2$ levels can occur in the reactions:

$$\mathrm{He}\left(2^3\mathrm{S}_1\right) + \mathrm{Ne}(1\mathrm{s}_1) \rightarrow \mathrm{He}\left({}^1\mathrm{S}_0\right) + \mathrm{Ne}(2\mathrm{s}_2) + 0.04\ \mathrm{eV} \qquad (22.1)$$

and

$$\mathrm{He}\left(2^1\mathrm{S}_0\right) + \mathrm{Ne}(1\mathrm{s}_1) \rightarrow \mathrm{He}\left({}^1\mathrm{S}_0\right) + \mathrm{Ne}(3\mathrm{s}_2) - 0.05\ \mathrm{eV} \qquad (22.2)$$

Note that because atom–atom interactions occur via short-range forces, transfer of excitation will be appreciable only for those states of Ne close enough to exact resonance that thermal energy (kT ~ 0.03 eV at 350 K) can make up the difference. Because of the accidental energy resonances already mentioned, the transfer of excitation is selective in exciting predominantly the $3s_2$ and $2s_2$ levels of neon and creating inversions of population with respect to the $3p_4$ and $2p_4$ lower levels.

The reactions (22.1) and (22.2) can also go backwards, but since neon atoms in $3s_2$ and $2s_2$ either radiate spontaneously or are stimulated out of these levels fairly promptly, the backward reaction rate is not serious.

Excitation through energy transfer from the helium 2^1S metastable is the dominant process populating the $3s_2$ level. There is experimental evidence that it is 70–90 times the excitation rate to the same level by direct electron impact. The three other levels in the 3s group (despite similarly close energy coincidence) are excited to a much smaller extent by energy transfer, a circumstance that is attributed to the fact that those interactions do not conserve spin. The transfer process reaches a broad maximum with the helium to neon ratio in the range 7:1. By employing the lighter helium isotope, ^3He, a 10%–20% increase in excitation transfer is realized. Several factors contribute to this increase, but the most important appear to be increased frequency of energy transfer collisions and increased electron temperature, T_e.

With such strong pumping to the upper $3s_2$ level, population inversion and optical gain is obtained for all nine permitted visible transitions to the 2p group, as well as all the permitted transitions to the 3p group. Small signal gain for the $3s_2$–$2p_4$ red line in a typical 1 mm bore capillary at optimum conditions is 0.4%–0.6% cm^{-1}. For all other visible lines, the gain is smaller. The highest gain line is the $3s_2$–$3p_4$ transition at 3.39 µm, where a gain of 50 dB m^{-1} has been measured.

Excitation energy transfer from the triplet 2^3S helium metastable level to the $2s_2$ neon level, though not as dramatic as the 2^1S to $3s_2$ transfer, is 10–20 times the electron excitation rate. However, this transfer is distributed more uniformly over the 2s group, so that inversion also occurs between other 2s levels and various 2p levels. The strongest oscillation occurs on the $2s_2$–$2p_4$ transition at 1.1529 µm.

Given a suitable optical cavity and gain medium, optical transitions with sufficient gain to overcome cavity loss will oscillate. When several transitions having a common upper level show gain, the line with the largest excess gain will dominate and, through oscillation, deplete the upper level to the point where competing lines are no longer inverted. This situation exists with the $3s_2$–2p group of lines, where the 632.8 nm line dominates. By introducing a wavelength-selective device, such as a prism, into the cavity to suppress all wavelengths but one, other visible lines in the $3s_2$–2p group can be made to oscillate. As mentioned before, the $3s_2$–$3p_4$ line at 3.39 µm has an extremely high gain approaching 50 dB m^{-1}. This gain is high enough to achieve oscillation with uncoated mirrors. To make the stronger point, it is almost impossible to suppress oscillation at 3.39 µm without the use of special mirrors having very low reflectivity at this wavelength.

Oscillation will build up in the cavity until the net gain (gain minus loss and transmission) approaches zero at the frequency of oscillation. The steady-state output power depends in a complex manner on cavity properties, atomic lifetimes and the rate at which the upper level is pumped. Unlike homogeneously broadened lasers, which ‘burn’ the gain profile uniformly, the HeNe laser is Doppler-broadened and each axial mode burns two ‘holes’ in the gain profile (corresponding to atoms moving in opposite directions whose frequency is Doppler-shifted to match the frequency of the cavity resonance). In the case of a single axial mode at atomic line centre, the two holes coincide, resulting in a power dip (Lamb dip). The hole width depends on the intensity of the field within the cavity; higher fields extract power from a wider spectrum of atoms. For this reason, reducing the mirror loss so as to increase the field intensity is crucial for maximizing the output power of single axial mode lasers.

There are several similarity relations [5] pertinent to the HeNe laser discharges, which have some theoretical justification and which have, to a considerable degree, received empirical substantiation by many years of engineering practice. For optimum power output, changes in capillary diameter require an inverse change in filling pressure such that the product $p \cdot D$ of pressure (p in torr) and diameter (D in mm) remains about 3.6 torr mm. Optimum discharge current is nearly proportional to tube diameter throughout the range 1.5–8 mm when $p \cdot D$ is held constant. Optical gain is found to be inversely proportional to tube diameter and proportional to discharge length.

22.4 HeNe Laser Tube Construction

Until the late 1960s, the capillary bore and glass bottle were constructed from ‘soft’ glasses. Unfortunately, these were permeable to helium, limiting life to a few hundred operating hours. Modern HeNe lasers are made from ‘hard’ borosilicate glass, which is impermeable to helium.

Many cathode designs have been tried, but virtually all HeNe lasers now use the interior surface of a cylindrical aluminium cold cathode that has been oxidized by running an oxygen discharge during the initial processing of the plasma tube. The overall life of the plasma tube is determined by the quality of the cathode processing and the configuration of the plasma tube. To maximize life, the discharge should utilize the maximum possible cathode area. A tightly confined discharge, or a discharge that reaches a sharp edge of the cathode, will significantly degrade operating life. To keep the discharge away from edges, the cathodes are usually quite long. Likewise, the diameter of the cylinder should be as large as practicable to allow the discharge to expand as it leaves the bore. Since the only task of the anode is to collect electrons, the drop in potential near the anode is much smaller than that near the cathode, and the impact of electrons is insufficient to cause sputtering. Thus, unlike the cathode whose concave geometry acts to confine sputtered material, the configuration of the anode is usually not critical.

As was true with most gas lasers, the resonator (mirror) structure that enables lasing action was mounted external to the plasma tube on early HeNe lasers, with light entering and exiting the plasma tube through Brewster windows. However, with the development of damage-resistant laser coatings, it quickly became apparent that the mirrors could be mounted directly to the ends of the plasma tube as part of the gas-confinement structure. This had two major advantages: the cost of the external resonator support structure was eliminated, and the problem of mirror and Brewster window contamination was eliminated. If linearly polarized output was required, it could be obtained by inserting a piece of glass, in the beam path, at Brewster's angle, inside the tube itself. Today, most HeNe lasers incorporate internal mirrors. External mirror lasers with Brewster windows are available, however, that provide access to up to 100 W of recirculating laser power within the laser cavity. Such lasers are used extensively in high-speed small-particle counting applications because of their predictable energy profiles and excellent reliability.

HeNe lasers are operated by a current-controlled dc supply. The operating characteristics vary with the size and configuration of the plasma tube, but typical configurations would have an output current ranging from 4 to 8 mA and an output voltage of 1000–3000 V. The tube is ignited by a voltage multiplier (Crockcroft–Walton) circuit, which quickly rises to 8 kV or more to break down the discharge and then immediately drops to operating tube voltage.

The illustration of Figure 22.2 shows a cross section of a commercial HeNe laser head. The entire plasma tube assembly is mounted in an aluminium cylinder using a shock-resistant potting compound. Inside the tube, a metallic support (spider) is attached to the cathode to support the narrow bore discharge capillary tube, preventing droop and reducing the effects of shock and vibration. A contaminant-absorbing flashless getter is installed in the tube to maximize shelf and operating life.

The glow discharge in a HeNe laser operates at negative impedance, meaning that, as the tube current increases, the voltage across the tube decreases. Since the power supplies require positive impedance across their output for proper current regulation, a ballast resistor is added to the package to compensate for the effects of the laser tube.

22.5 The Evolution of Expectations

One of the reasons for the continued success of the HeNe laser has been its ability to evolve over time to meet the ever-increasing demands of sophisticated customers. In the early years of the laser (the first commercial HeNe lasers became available in 1963), obtaining red light was sufficient. The main concern was lifetime, because early HeNes lasted only a few hundred hours at most as the helium leaked out through the glass envelopes. Once this problem was solved (circa 1965), customers began to focus on the output parameters—mode, divergence, power fluctuations and optical noise. This meant that manufacturers had to increase attention to bore straightness and diameter; precisely define and control mirror curvature, mirror transmission properties and mirror spacing; as well as improve structural designs to provide uniform heat loading (to minimize power drift) and improve the control electronics in the power supplies (to decrease noise).

In the mid-1970s, the intensity and location of satellite beams, the extraneous beams caused by reflections between the front and back surfaces of the output coupler, became a major issue for many customers. Although the total power in all of the satellite beams was rarely more than a few per cent of the power in the main beam, the increased sensitivity of detection electronics, coupled with cosmetic and quality perceptions of customers, demanded that these extraneous effects should be eliminated. This required laser manufacturers to work with optics manufacturers to improve dramatically the quality of the antireflection coatings used on output couplers and put stringent requirements on the centration and wedge angle of the optics themselves.

In the early 1980s, HeNe manufacturers had to meet their greatest challenge—the requirements of the barcode scanning industry. Although flatbed scanner installations in supermarkets were becoming commonplace, the major growth opportunity was in handheld barcode scanners for general-purpose merchandising, an extremely cost-sensitive application. Because traditional HeNes were too large and too expensive, the manufacturers literally went back to the drawing board to develop new designs amenable to semiautomated processing techniques. They were successful. The volume of lasers sold annually went from approximately 150 000 per year to well over 750 000, and average unit prices dropped from approximately $500 to $150. In high volume, some HeNe plasma tubes were selling for less than $50.

By 1990, the barcode tide was receding as HeNe lasers were replaced with red diode lasers operating at 650 nm. However, the requirements for shorter-wavelength HeNes were growing strong, particularly for the 543-nm (green) wavelength, which was especially suited to a wide variety of biotechnology applications. Because of the low gain of these lasers, processing requirements were much more stringent than for the red HeNes, and severe demands were made on optics vendors to develop extremely low-loss, scatter-free, damage-resistant coatings at these wavelengths. Once again, the industry came through and, today, 30% of unit HeNe sales are for non-red lasers (Figure 22.3).

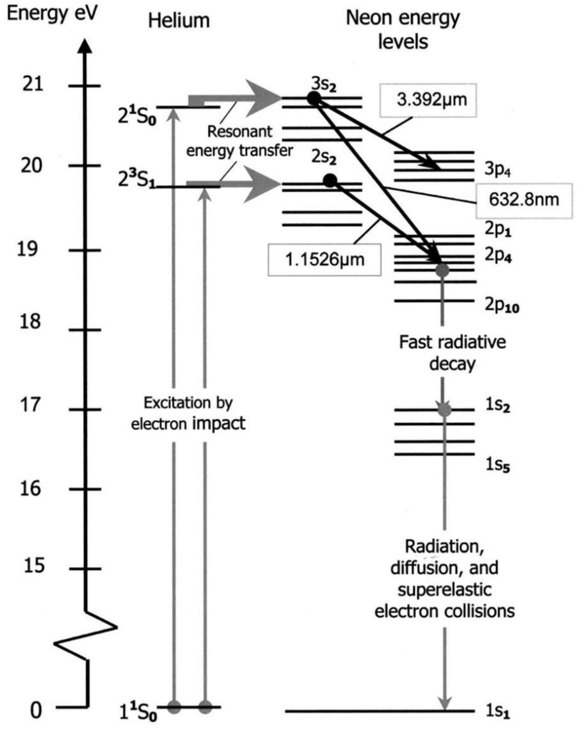

FIGURE 22.3 Energy level diagrams of He and Ne.

22.6 HeNe Laser Manufacturing Processes and Technology

The basic techniques used to manufacture HeNe lasers have not changed significantly over the past 50 years, although processes and testing procedures have been refined extensively in order to meet the ever-more-stringent customer demands. The bulk of the manufacturing process is 'hands-on'. Only tube processing and some testing procedures are semiautomated.

The manufacturing procedure begins with the cleaning and degreasing of all the plasma tube components. This step is particularly important because even the smallest particulate, lodged in the laser bore, can cause severe power or beam quality degradation, particularly in the lower-gain lasers.

Once cleaned, the plasma tube (sans mirrors) is assembled. Historically, some manufacturers have used frits (mixtures of powdered glasses and ceramic that melt to form a vacuum-tight seal) to attach the metallic components to the glass envelopes, but these have proved to be susceptible to vibration. Today, most HeNe laser plasma tubes are assembled with traditional glass-to-metal seals.

In the next step, mirrors are applied to the metallic mirror mounts on each end of the tube with a frit. The seal is made by placing the components in an oven with a highly controlled multistage heating cycle designed for the specific frit. At this point, the tube is ready to be placed on the processing station.

Processing of the plasma tube occurs in three stages. In the first stage, the tube is baked, under vacuum, to remove any impurities that could cause outgassing. In the second stage, the tube is filled with oxygen, and a discharge is struck. This develops a stable aluminium oxide layer on the cathode which will act as an electron emitter in the finished tube. It also oxidizes any residual contaminants in the tube. Finally, the tube is evacuated and filled with the helium and neon lasing mixture, and a discharge is ignited.

Depending on the tube configuration and the process requirements, these steps may be repeated several times. Overall processing time can vary from 3 to 8 h or more. Once processing is completed, the getter is activated, and the tube is pinched off from the processing station. At this point, the mirrors are aligned so that the plasma tube can produce laser light. A technician deforms the metallic end pieces with a tool to move the mirrors into the proper position. Because the laser cavity is designed with relatively short-radius mirrors, this can be accomplished easily. A skilled technician can fully align a plasma tube in 1 or 2 min.

Finally, the aligned plasma tube is 'burned in' for 24–48 h to allow the tubes to stabilize and to isolate any premature failures. At the end of this period, the tubes are tested (see Figure 22.4) to determine their operating parameters and then sorted for output power.

22.7 'Single-Frequency' HeNe Lasers

Some of the earliest uses of HeNe lasers were in holography, laser ranging and metrology applications requiring very narrow linewidths ($\Delta\nu$) and long coherence lengths ($c/\Delta\nu$). Consequently, various schemes were devised to narrow the frequency spread of these lasers. The red HeNe laser discharge has a gain (amplification) curve that is approximately 1.4 GHz wide (full width at half maximum) centred at 632.8 nm. If the laser is operating in the fundamental Gaussian mode, the laser resonator (mirror structure) can only support output at specific, equally spaced, frequencies (longitudinal modes) which are determined uniquely by the mirror spacing. The actual output of the laser is a comb of frequencies that coincide with the intersection of the resonator modes and the laser gain curve. The greater the separation of the resonator mirrors, the more frequencies will be present in the laser output. Conversely, the shorter the distance between the mirrors, the fewer frequencies will be present. It is possible to make the laser short enough that only a single frequency will be present, with an instantaneous linewidth of a few kilohertz.

FIGURE 22.4 Testing HeNe lasers.

In a gas laser, the laser gain is fixed by the parameters of the discharge, but the frequency of a longitudinal mode is determined by the effective mirror spacing, which can vary significantly as a function of alignment, ambient temperature, vibration, barometric pressure and many other environmental factors. Since it takes only 0.6 μm of change in spacing to sweep a single longitudinal mode completely through the HeNe gain curve, it is imperative to control the laser cavity length precisely in a stabilized single-frequency laser. The precision of control will determine the effective linewidth.

Several techniques have been developed to determine the frequency of a laser and to provide feedback information to adjust the cavity length. Early methods with true single-frequency lasers focused on stabilizing the cavity frequency around the Lamb dip found in the gain curve which occurs when single-isotope gases are used. However, the very short lasers required for true single-mode operation limited output power to a small fraction of a milliwatt.

An approach embodied in commercially available stabilized single-frequency lasers takes advantage of the fact that adjacent longitudinal modes are cross-polarized. The overall laser length is increased to allow two adjacent modes to lase, as shown in Figure 22.5. As the laser cavity length changes, the modes move through the gain curve, changing in both frequency and amplitude. As one mode increases in power, the other decreases and *vice versa*. To stabilize the system, the two modes are separated into two beams by polarization components, and their amplitudes are compared electronically. The cavity length is then adjusted to maintain the proper relationship between the modes. Only one beam is allowed to exit the system. Even though as much as half the power is not utilized, the increase in overall gain obtained from lengthening the laser provides significantly more output in the remaining beam than could be obtained from a laser that only oscillates in a single mode.

A significant advantage of the two-beam system is that, by adjusting the ratio of power in one beam with respect to the other, the output frequency can be swept 300 MHz or more, while maintaining a 1 MHz linewidth. Since the ratio of power in the two beams is completely independent of the output power itself, excellent frequency stability can be maintained over long periods of time, regardless of power fluctuations or long-term power degradation. Since cavity fluctuations are a major contributor to power fluctuations in a HeNe laser, this stabilization technique has the added advantage of reducing overall system noise. Typical frequency and noise characteristics of a stabilized HeNe laser are shown in Figure 22.6.

The cavity length of a stabilized HeNe laser can be controlled by placing the discharge tube in an oven and relying on the expansion properties of the glass plasma tube to change the cavity length, or by providing a dynamically adjustable mirror on one end of the tube. The advantage of the oven approach is that it uses a standard, off-the-shelf plasma tube, but its overall response is slower, due to the thermal mass of the system.

The adjustable mirror approach is somewhat more complex and requires a special plasma tube, but it can reach the frequency lock point in about 10 min compared with approximately 30 min for the temperature-controlled systems. In addition to the aforementioned applications, single-frequency HeNe lasers are used for wavelength calibration and for a wide variety of interferometric applications.

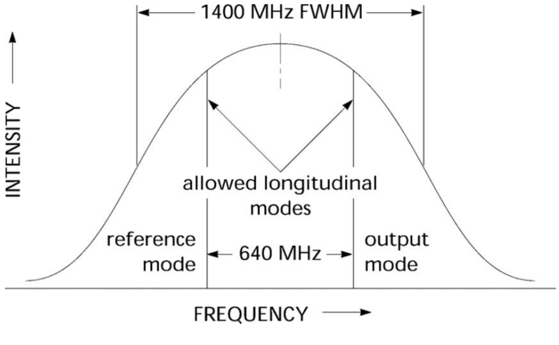

FIGURE 22.5 HeNe gain curve showing two orthogonally polarized modes.

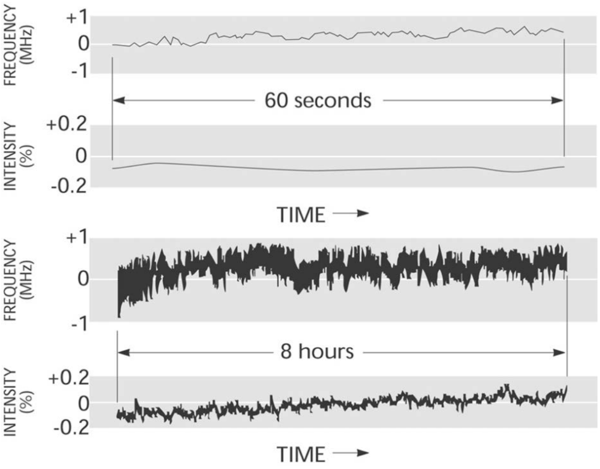

FIGURE 22.6 Short- and long-term frequency and intensity stability of a commercial frequency-stabilized HeNe laser. (Courtesy: Melles Griot Inc.)

22.8 HeNe Lasers: Typical Performance Characteristics

As mentioned before, the chief operational characteristics of a HeNe laser are superb beam quality, long life and low power consumption. Depending on the laser, output power ranges from 0.25 mW to more than 40 mW. Other characteristics of these lasers bear mentioning and include the following:

- Polarization. The basic HeNe laser is randomly polarized, but by inserting a Brewster's angle window into the beam path between the resonator mirrors, the laser can be linearly polarized with a 500:1 polarization ratio. If the laser is to be used with any polarizing elements in the optical path, it is recommended that a linearly polarized laser is used. Randomly polarized lasers can cause unexpected shifts and amplitude fluctuations when used with beamsplitters and other polarizing elements.
- Mode sweeping. As already mentioned, when the length of the laser changes as a result of environmental conditions or changes in temperature, the longitudinal modes sweep across the gain curve causing fluctuations in output power. A very short laser with a single longitudinal mode can fluctuate from maximum power to zero power and back to maximum as the temperature changes—the longer the laser, the smaller the fluctuations. A 7-inch-long laser typically will have mode-sweeping fluctuations of 10%. A 14-inch-long laser will normally have a mode-sweeping fluctuation of less than 2%. These fluctuations are particularly noticeable while the laser is warming up. Once equilibrium is reached, the frequency of the fluctuations decreases dramatically. By stabilizing the temperature of the laser, fluctuations can be eliminated completely.

- No automatic power control. HeNe lasers operate as normal glow discharges with negative impedance. Unfortunately, with these lasers, there is not a direct, linear relationship between output power and discharge current. Increasing discharge current may increase output power, decrease output power or have no effect. This makes it very difficult to provide an economically attractive method to adjust or control output power.

22.9 HeNe Lasers: The Future

For virtually all consumer applications (e.g. DVD and CD players) and many commercial applications (e.g. barcode scanning), the red semiconductor diode laser with its small size, low cost and low power consumption is the better choice. On the other hand, for applications requiring exceptional mode quality, narrow linewidth or output at shorter wavelengths (orange, yellow, green), the HeNe laser is the only low-cost choice, and there exist no other technologies that will supplant it in the foreseeable future.

In addition to the demand for lasers for new systems, there is a huge replacement market. Today, there are several million HeNe lasers still in use around the world. In many cases, when these units fail, it is more cost-effective to replace the laser plasma tube for a few hundred dollars than to replace the instrument for many thousands of dollars.

REFERENCES

1. Javan A, Bennett W R Jr and Herriott D R 1961 *Phys. Rev. Lett.* **6** 106.
2. White A D and Rigden J D 1962 *Proc. IRE* **50** 1697.
3. Willett C S 1974 *Introduction to Gas Lasers: Population Inversion Mechanisms* (Oxford: Pergamon) ch 43.
4. Webb C E 1975 The fundamental discharge physics of atomic gas lasers *High Power Gas Lasers 1975 (IOP Conf. Series 29)* ed R Pike (Bristol: IOPP) ch 1.
5. Francis G 1956 The glow discharge at low pressure *Handbuch der Physik Vol XXII Gas Discharges* ed S Flugge (Berlin: Springer).
6. Moore C E 1949 *Atomic Energy Levels (NBS Circular 467)* vol 1 (Washington, DC: US Government Printing Office).

FURTHER READING

For introductory level texts on gas lasers see, e.g.

Davis C C 1996 *Lasers and Electro-Optics—Fundamentals and Engineering* (Cambridge: Cambridge University Press) Section 9.7 ISBN 0-521-30831-3.

Silfvast W T 1996 *Laser Fundamentals* (Cambridge: Cambridge University Press) Section 13.2 ISBN 0-521-55424-1.

For a more advanced text, with an extensive and detailed coverage of HeNe lasers see:

Willett C S 1974 *Introduction to Gas Lasers: Population Inversion Mechanisms* (Oxford: Pergamon) ch 4 ISBN 0-08-017803-0.

23

Metal vapor Lasers: Helium–Cadmium Laser

William T. Silfvast

CONTENTS

23.1 General Description 309
23.2 Energy Levels and Laser Transitions 309
23.3 Pumping or Excitation Techniques 310
23.4 Uniform Vapour Distribution—Cataphoresis 310
23.5 Role of Helium 310
23.6 Laser Gain—Isotope Distribution 311
23.7 Gain, Saturation Intensity and Output Power 312
23.8 Long-Life Operation—He Clean-Up 312
23.9 Structural Arrangement 312
23.10 Discharge Tube Design 313
23.11 Applications 313
References 313

23.1 General Description

The continuous-wave He–Cd laser is perhaps the best known and most widely used metal vapour laser. It produces visible laser output in the blue at 441.6 nm [1] and ultraviolet output at 354.0 and 325.0 nm [2]. The blue transition produces the most power output [3], while the 354 nm transition is the weakest. A number of other lasers in the green and red portions of the spectrum have been observed in various types of He–Cd discharges. However, these lasers are not available in the commercial He–Cd laser that operates in a positive column type of dc discharge, similar to that of the He–Ne laser. Hence, these other visible transitions will not be dealt with further in this discussion.

23.2 Energy Levels and Laser Transitions

Laser action occurs on transitions within the singly ionized (Cd^{+}) species. To understand the nature of these transitions, we must first consider the neutral Cd atom. The ground state has an outer electronic configuration of $4d^{10}5s^{2}\,{}^{1}S_{0}$. The removal of a 5s electron leaves the atom in the ground state of the ion ($4d^{10}5s\,{}^{2}S_{1/2}$) as indicated in Figure 23.1. The electronic structure of the upper laser levels is relatively unique in that it involves the removal of an inner shell d electron from the Cd atom leaving the atom ionized in the $4d^{9}5s^{2}\,{}^{2}D_{5/2}$ and ${}^{2}D_{3/2}$ levels as also seen in Figure 23.1. The laser transition involves decay from the upper laser level to the $4d^{10}5p\ {}^{2}P^{o}_{3/2}$ and ${}^{2}P^{o}_{1/2}$ excited

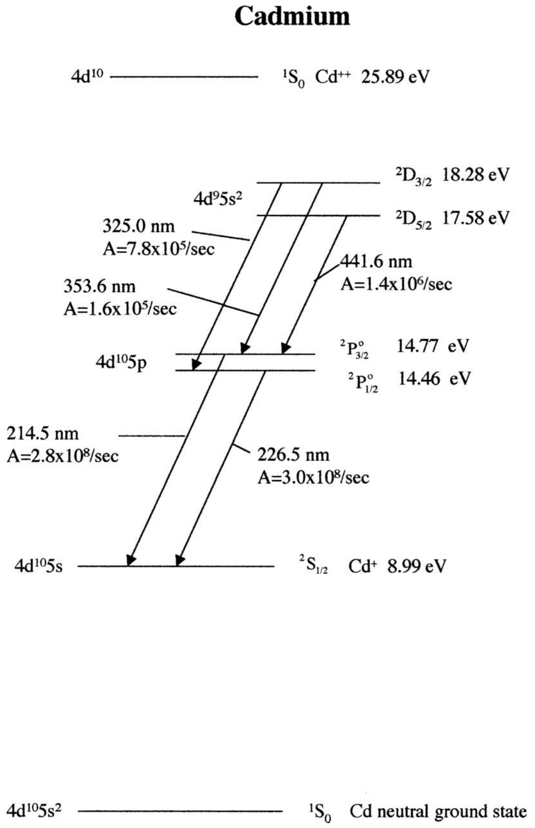
Cadmium
4d¹⁰
¹S₀ Cd⁺⁺ 25.89 eV
4d⁹5s²
²D₃/₂ 18.28 eV
²D₅/₂ 17.58 eV
325.0 nm
A=7.8x10⁵/sec
441.6 nm
A=1.4x10⁶/sec
353.6 nm
A=1.6x10⁵/sec
4d¹⁰5p
²P°₃/₂ 14.77 eV
²P°₁/₂ 14.46 eV
214.5 nm
A=2.8x10⁸/sec
226.5 nm
A=3.0x10⁸/sec
4d¹⁰5s
²S₁/₂ Cd⁺ 8.99 eV
4d¹⁰5s²
¹S₀ Cd neutral ground state

FIGURE 23.1 Energy level diagram for the He–Cd laser.

ion levels which then rapidly decay to the ion ground state as shown in Figure 23.1. The relevant transition probabilities are shown for the laser transitions as well as for the transitions on which the lower levels decay. It can easily be seen how the population inversion is established due to the much more rapid decay rates of the lower laser levels compared with those of the upper laser levels.

23.3 Pumping or Excitation Techniques

There are three excitation mechanisms that have been proposed for the excitation of the Cd laser as indicated in Figure 23.2. The first one involves the transfer of energy *via* Penning ionization from He metastable levels to the Cd upper laser levels [4]. This is similar to the process for the excitation of the He–Ne laser except that, since the Cd upper laser level is an ion level, the exact energy coincidence is not necessary. The electron emitted in the ionization process takes up the energy difference between the He metastable energy and the Cd upper laser level energy (approximately 12 eV). The second process is electron excitation from the Cd ion ground state to the upper laser level [5]. The third process, which can be shown to represent only a few per cent of the total excitation for the conditions of the He–Cd laser discharge, involves photoionization of the Cd atoms to populate the upper laser level *via* emission from the 50–60 nm transitions of the excited He atoms radiating within the discharge [6]. A paper with additional experimental results supports the dominance of Penning ionization [7].

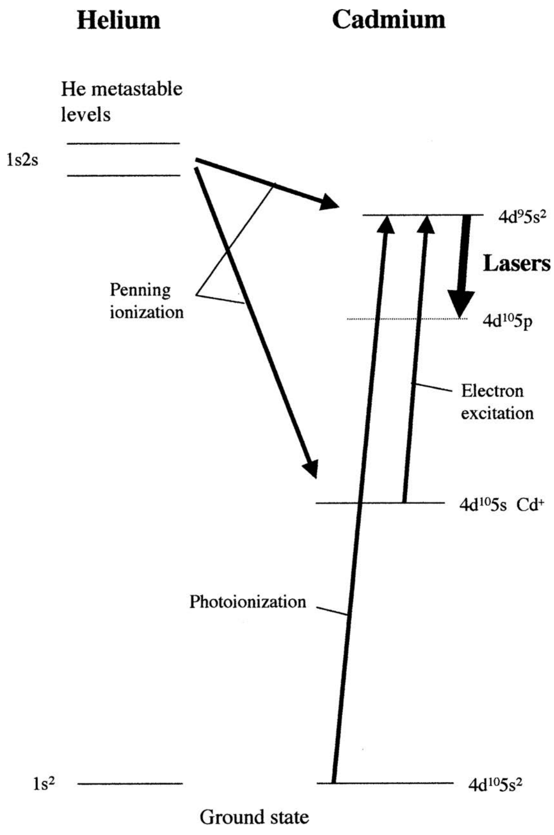

FIGURE 23.2 Excitation process for the He–Cd laser.

23.4 Uniform Vapour Distribution—Cataphoresis

Normally a uniform vapour is obtained within a chamber by placing the vapour source (either liquid or solid) within the chamber and heating the entire chamber uniformly. In the case of Cd, the chamber would have to be heated to a temperature of approximately 260°C. However, in the He–Cd laser, this would be very impractical. The only region that is necessary to be heated is the region of the discharge capillary bore where the excitation and amplification occur. It is much more desirable to have the laser windows, mirrors, electrodes, etc. at or near room temperature. This is achieved by using a process known as cataphoresis to control the Cd vapour distribution [8]. In this process, the Cd metal is heated and vapourized at the anode (positive potential) end of the discharge and is transported towards the cathode end (negative potential) of the discharge by the electric field acting upon the Cd ions that are produced by the discharge current. The Cd atoms then condense in the cathode region. The laser species is essentially 'flowing' down the capillary, albeit at a very slow rate of approximately 1–2 g/5000 h. The discharge current heats the gain region sufficiently so that Cd does not condense in that region while it is being transported down the capillary.

The cataphoresis process is sensitive to the fractional degree of ionization of the desired species (in this case Cd) to be transported through the discharge region [8]. A fractional ionization of the order of 1% is required to produce the uniform distribution throughout the entire length of a long discharge capillary such as that used in the He–Cd laser. In the case of Cd, this unusually high fractional ionization is produced primarily due to the process of Penning ionization, previously mentioned as one of the excitation processes. The highest Penning ionization cross section to produce a specific Cd^+ level is to the ion ground-state $4d^{10}5s^2S_{1/2}$ [9]. The second highest Penning ionization cross section is to the upper laser level species ($4d^95s^2$) in the $^2D_{5/2}$ and $^2D_{3/2}$ levels. Penning ionization cross sections to all other Cd ion levels are significantly lower since the process would require the removal of one electron and the change of another electron, whereas the two states mentioned require only the removal of one electron with no change of another electron.

Hence, whether Penning ionization from He metastable atoms or electron excitation from the Cd ion ground state is the dominant excitation mechanism to the Cd upper laser levels, the Penning ionization process plays a major role in producing the high degree of ionization of the Cd atom. This allows either of the excitation mechanisms to occur by providing the necessary uniform vapour distribution along the gain region of the capillary bore. It also provides a high-density source of Cd ions in the ion ground state from which electron collisional excitation could occur.

23.5 Role of Helium

The importance of the helium metastable atoms involved in the Penning ionization process was described both by producing excitation directly to the Cd upper laser levels and by providing the high percentage (1%) of ionization of Cd necessary to obtain a uniform vapour distribution *via* cataphoresis. The He metastable density population is of the order of 10^{12}cm^{-3} within the discharge bore region, whereas the population of the most excited levels in both He and Cd are of the order of 10^{9}–10^{10}cm^{-3}. Hence, the He metastables are the dominant excited species within the discharge gain region, and consequently, the rate of energy transfer from them *via* Penning ionization can be quite large. In addition, the presence of He serves to maintain a relatively high electron temperature in the discharge, favourable for all of the mentioned excitation processes.

23.6 Laser Gain—Isotope Distribution

The laser is typically operated with a naturally occurring mixture of Cd isotopes, which includes Cd 106, 108, 110, 111, 112, 113, 114 and 116. This natural isotope mixture favours Cd 112 and Cd 114, each contributing approximately 1/4 of the Cd atoms within the discharge. For most gas laser transitions, Doppler broadening dominates over natural broadening, as is the case for the He–Cd laser. However, when using the Cd natural isotope mixture, isotope broadening becomes the dominant broadening process. Each of the even isotopes has a 1.1 GHz emission linewidth (full width at half maximum) on the laser transitions, and the series of even isotopes are separated by approximately 1.5 GHz to produce an emission spectrum as indicated in Figure 23.3. Also included in that spectrum are the distributed spectra of the odd isotopes Cd 111 and Cd 113. The odd isotopes have a nuclear spin, and thus, each of them divides into three spectral components with a distribution spread out enough that those isotopes do not have a major impact upon the emission spectrum at any specific wavelength as indicated in Figure 23.3. With the natural isotope mixture, the laser operates over a bandwidth of approximately 3 GHz, the width of Cd 112 and Cd 114 combined (as shown in Figure 23.3), since the other isotopes have a gain too low to contribute significantly to laser output. However, the laser can also be operated with a single even isotope of Cd (at a significant additional expense) to produce approximately a factor of two more power output and a much narrower emission bandwidth than that of the natural mixture. The higher power is obtained since the gain is higher and the energy is concentrated in fewer longitudinal modes.

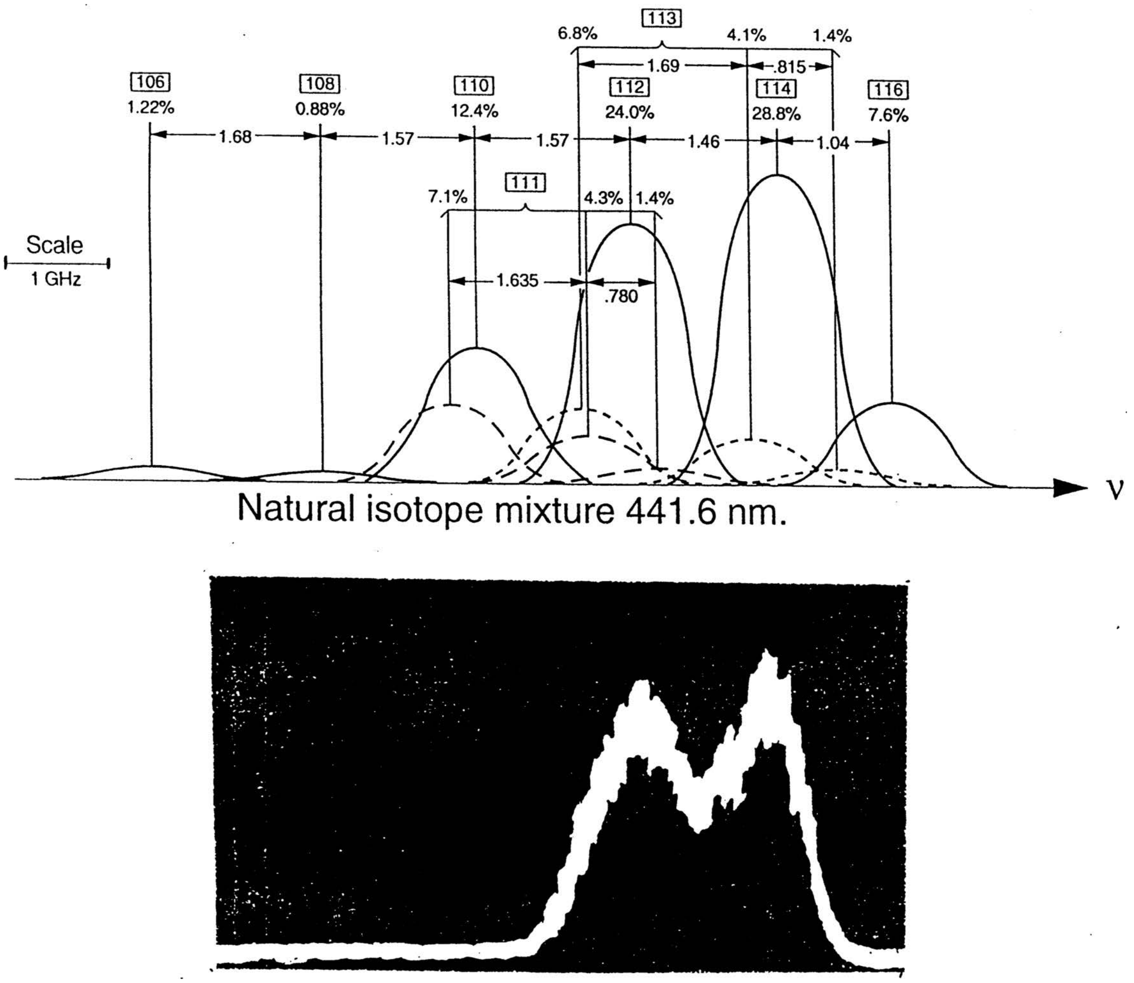

FIGURE 23.3 Natural isotope distribution and typical laser emission spectrum for 441.6-nm Cd laser transition.

23.7 Gain, Saturation Intensity and Output Power

The laser gain coefficient for the 441.6 nm laser transition is of the order of 0.3 m^{-1} for a laser that uses naturally occurring Cd as the Cd vapour source, as indicated in Table 23.1. Hence, for a discharge tube having a gain length of 30 cm, the single pass gain within the discharge would be approximately 11%/pass. The saturation intensity of this laser is 0.4 W cm^{-2}. Thus, assuming a laser system that has losses of the order of 0.2%/pass, and assuming that a high reflecting mirror is located at the rear of the laser tube, the optimum mirror transmission for the output mirror would be approximately 2.2%. Inserting these values into a well-known expression for laser power output suggests an optimum output power of 24 mW, which is approximately what is experimentally achieved.

TABLE 23.1

Typical Helium–Cadmium Laser Parameters

Laser Wavelengths	441.6, 353.6, 325.0 nm
Laser transition probability	$1.4 \times 10^6 s^{-1}$, $1.6 \times 10^5 s^{-1}$, $7.8 \times 10^5 s^{-1}$
Upper laser level lifetime	7.1×10^{-7} s (1.1×10^{-6} s)
Stimulated emission cross section	$8 \times 10^{-18} m^2$
Emission linewidth and laser gain bandwidth for each isotope	$1.5 \times 10^9 s^{-1}$, $1.4 \times 10^9 s^{-1}$, $1.5 \times 10^9 s^{-1}$
Inversion density	$4 \times 10^{16} m^{-3}$
Small signal gain coefficient	0.3 m^{-1}
Laser gain medium length (*L*)	0.25–1.5 m
Single pass gain	0.07–0.45
Gas pressure	5–10 torr He
Gas mixture	100:1, He:Cd
Operating temperature	Tube bore 350°C, Cd temp. 260°C
Pumping method	Electrical discharge
Electron temperature	5–7 eV
Gas temperature	300°C
Output power	10–200 mW
Mode	TEM_{00} or multimode

23.8 Long-Life Operation—He Clean-Up

In the He–Cd laser, helium is gradually lost within the laser system both by leaking through the glass structure of the laser tube and by being buried underneath the Cd as the Cd condenses in the form of a metallic coating at the cathode end of the laser tube [10]. Thus, a He reservoir (ballast) is provided as part of the laser system. At the end of the ballast is a separate reservoir (bottle) that is initially filled with helium at approximately atmospheric pressure and is separated from the ballast region by a thin membrane that allows He gas to leak slowly through from the high-pressure He bottle into the low-pressure ballast region. The amount of He leakage through the membrane is temperature sensitive and is controlled with a pressure sensor and an active feedback control system. This system is able to maintain a constant He pressure within the laser tube over the lifetime of the laser.

23.9 Structural Arrangement

There are typically two versions of this laser including a long discharge tube with a bore length (gain region) of the order of 60–75 cm, and a shorter version with a bore length of the order of 25–35 cm. The longer version comprises either one long bore or two shorter bores within the same laser cavity. The lasers are installed within air-cooled housings (some use cooling fans) with lateral dimensions of the order of 15 cm and an overall length that is approximately 40 cm longer than the bore length. A small power supply is separate from the tube assembly. The larger lasers produce up to 200 mW multimode at 441.6 nm and 100 mW multimode at 325 nm. A 10-mW single TEM_{00} mode blue laser is also produced from a 25–30 cm bore length. A diagram of the small version of a commercial He–Cd laser is shown in Figure 23.4. The heated Cd reservoir is located at the anode end of the laser discharge bore region. A metal vapour trap is located beyond the cathode to prevent metal vapour from condensing on the laser window or mirror. The ballast is a region within the tube that provides a large reservoir of He gas to help maintain the proper

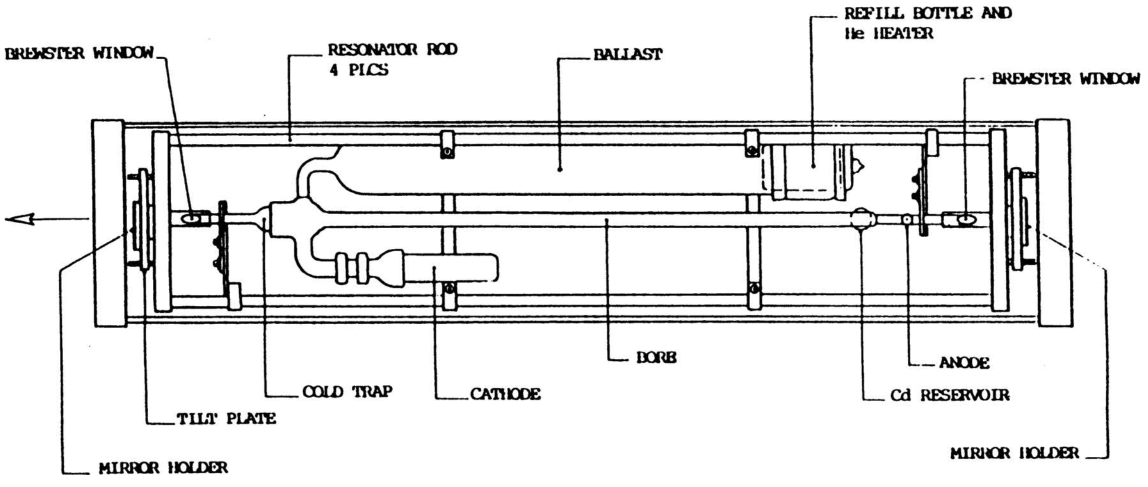

FIGURE 23.4 Structural arrangement of the He–Cd laser. (Courtesy of LiCONix, Inc.)

He pressure. Beyond the reservoir is a bottle containing He at high pressure. The He in that bottle is diffused into the reservoir region as needed to maintain the proper He pressure. The rigid cavity structure is used to maintain the mirror alignment with respect to the fixed location of the laser bore.

23.10 Discharge Tube Design

The lasers operate within a 1–2-mm bore glass discharge tube. The tube contains He gas at a pressure of several torr and a partial pressure of Cd that is approximately 1% of that of He. A dc discharge is operated within the tube at currents in the range of 60–100 mA. The lasers typically operate for a lifetime of the order of 4000–5000 h with a loading of 1 or 2 g of Cd metal in the anode reservoir. The general properties of the laser are summarized in Table 23.1.

23.11 Applications

Applications of these lasers include stereolithography, printing, making CD masters, microchip inspection, flow cytometry, lithography and fluorescence analysis. Stereolithography is a process that uses the ultraviolet laser to make computer-generated models in a plastic material. The blue wavelength is used for printing on photosensitive materials in which the short-wavelength blue photons react more readily with many photosensitive materials. In flow cytometry, the He–Cd laser is most favourable in some situations where the short wavelength is desired from either the standpoint of scattering or absorption of the light by the material. Also, for fluorescence analysis, the short wavelengths of the He–Cd laser are often more useful than for the other visible lasers. The lasers are also used extensively for inspection of electronic circuit boards.

REFERENCES

1. Silfvast W T, Fowles G R and Hopkins B D 1966 Laser action in singly ionized Ge, Sn, Pb, In, Cd, and Zn *Appl. Phys. Lett.* **8** 318–19.
2. Silfvast W T 1969 New cw metal–vapor laser transitions in Cd, Sn, and Zn *Appl. Phys. Lett.* **15** 23–5; Goldsborough J P 1969 A continuous laser oscillation at 3250 A in the Cd ion *IEEE J. Quantum Electron.* QE-**5** 133.
3. Silfvast W T 1968 Efficient cw laser oscillation at 4416 A in cadmium *Appl. Phys. Lett.* **13** 169–71.
4. Silfvast W T 1971 Penning ionization in a He–Cd dc discharge *Phys. Rev. Lett.* **27** 1489–92.
5. Goto T, Shimizu Y, Hattori S and Sakurai T 1983 Quantitative interpretation of radial profiles of Cd(II) lines in the positive column He–Cd laser discharge *J. Phys. D: Appl. Phys.* **16** 261–8.
6. Silfvast W T, Macklin J J and Wood O R II 1983 High gain inner-shell photoionization laser in Cd vapor pumped by soft-x-ray radiation from a laser-produced plasma *Opt. Lett.* **8** 551–3.
7. Ivanov I G, Latush E L and Sem M F 1966 *Metal Vapor Ion Lasers—Kinetic Processes and Gas Discharges* ed C Little (Chichester: Wiley).
8. Sosnowski T P 1969 Cataphoresis in the helium–cadmium laser discharge tube *J. Appl. Phys.* **40** 5138–44.
9. Cermak V 1971 Penning ionization electron spectroscopy III, ionization of cadmium *Coll. Czechoslovakian Chem. Commun.* **36** 948–50.
10. Sosnowski T P and Klein M B 1971 Helium cleanup in the helium–cadmium laser discharge *IEEE J. Quantum Electron.* QE-**7** 425–6.

Taylor & Francis
Taylor & Francis Group
http://taylorandfrancis.com

24

Copper and Gold Vapour Lasers

Colin Webb

CONTENTS

24.1 Atomic Physics and Excitation Mechanisms of Copper Vapour Lasers 315
24.2 Development of the Copper Vapour Laser 316
24.3 Elemental CVLs—Practical Considerations 317
24.4 Copper Halide Lasers 318
24.5 Effect of Additive Hydrogen 319
24.6 Copper HyBrID Lasers 320
24.7 CVL Cavities and Beam Quality 320
24.8 MOPA CVLs 321
24.9 Kinetically Enhanced CVLs 322
24.10 The Gold Vapour Laser 322
References 323
Further Reading 324

24.1 Atomic Physics and Excitation Mechanisms of Copper Vapour Lasers

Historically, the first of the ‘self-terminating’ or ‘cyclic’ class of laser systems was the 723-nm atomic lead laser [1] demonstrated by Fowles and Silfvast in 1965. In 1966, Walter et al. [2] reported oscillation on the 511 and 578 nm transitions of the copper atom Cu, a system belonging to the same generic type as the Pb laser, and the one that has become the best known of the entire class. The operating principles can best be understood by reference to Figure 24.1, which shows the low-lying energy levels of atomic copper.

The $^2S_{1/2}$ ground state of Cu arises from the configuration $3d^{10}4s$. Promotion of the outer electron to successively higher orbitals $3d^{10}4p$, $3d^{10}5p$ gives rise to a series of ^2P levels connected to the ground state by strong resonance transitions (whose first members are 328 and 325 nm) analogous to the principal series in alkali atoms.

However, in contrast to the alkalis, in Cu, there exists an alternative configuration ($3d^9 4s^2$) that happens to be almost as low in energy as the ground state—indeed, it misses being the ground state by only about 1.5 eV. This configuration gives rise to $^2D_{3/2}$ and $^2D_{5/2}$ levels, which are fully metastable because radiative transitions from them to the $^2S_{1/2}$ ground state are rigorously forbidden by the parity rule for electric dipole radiation. Emission from the ^2P levels of the $3d^{10}4p$ configuration to the ^2D levels of $3d^9 4s^2$ would be forbidden by the electric dipole selection rule that allows only one electron at a time to change orbital. However, a slight mixing of other configurations in Cu is sufficient to allow this rule to be violated to some extent, because the levels of the real atom are not rigorously described by the quantum numbers implied by the pure LS description.

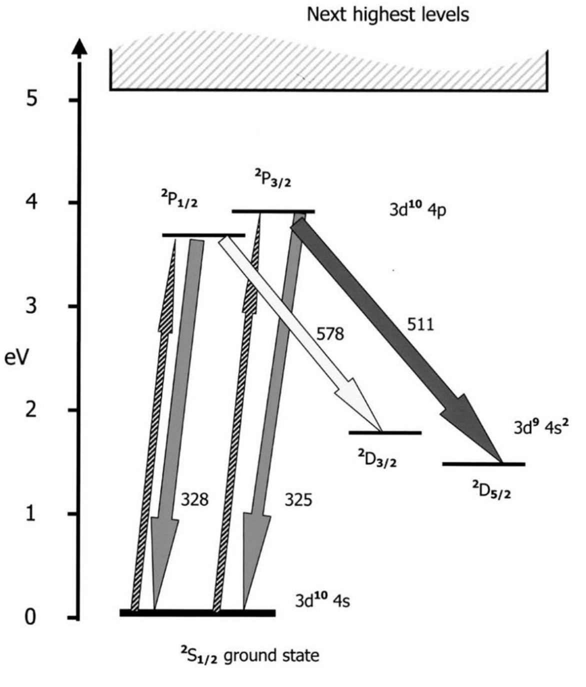

FIGURE 24.1 First few levels of atomic copper.

Thus, while free Cu atoms in the $3d^{10}4p^2P$ levels can relax to the $^2S_{1/2}$ ground state with untrapped lifetimes of the order of 7 ns, they do have a finite probability (with $A_{21} \sim 2\times10^6\,s^{-1}$ [3]) for decay to the ^2D levels in these 'forbidden' transitions. Furthermore, at the vapour densities appropriate to laser action in the copper vapour laser (CVL), decay from the $3d^{10}4p^2P$ upper laser levels direct to the ground state does not represent a significant loss since the 328 and 325 nm transitions are subject to strong radiation trapping. Thus, the only effective radiative decay route is *via* the laser transitions to the ^2D levels.

Now, if a fast rising current pulse is applied to a discharge containing copper vapour, Cu atoms are more likely to be promoted to the levels of the $3d^{10}4p$ configuration than they are to the $3d^94p^2$. This is because the 4s outer electron of the ground state Cu atom presents a bigger target than one of the $3d^{10}$ electrons, at least for electrons of more than a few eV energy. The result is that, provided T_e (the temperature of the electron energy distribution) exceeds about 3.5 eV, the $3d^{10}4p$ levels are populated faster than the $3d^94p^{2\,2}D$ levels, and a large population inversion can be created transiently.

In Cu vapour, the wanted excitation of the $3d^{10}4p^2P$ upper laser levels provides by far the largest inelastic collision cross section for plasma electrons, just as the wanted process of excitation of the $3p^2P$ resonance levels from the $3s^2S_{1/2}$ ground state of the Na atom dominates all other electron energy-loss processes in the sodium vapour lamp. For the same reason that sodium vapour makes an efficient lamp, the CVL is an efficient laser—more than ten times as efficient as the argon ion laser, with over 1% true wall-plug efficiency available from present commercial systems.

Electric dipole optical transitions from the ^2D lower laser levels back to the ^2S ground state are rigorously forbidden since both the configurations $3d^94s^2$ and $3d^{10}4s$ are of even parity. Because of this, the lower levels are truly metastable, and the Cu vapour laser fails to satisfy the minimum condition for CW lasing:

$$A_{21}^{-1} > \left(g_2/g_1\right)\tau_1 \tag{24.1}$$

in which A_{21} is the Einstein coefficient for spontaneous emission on the laser transition, g_2 and g_1 are the statistical weights of upper and lower levels, respectively, and τ_1 is the lower level lifetime. The gain on the 511 and 578 nm transitions is sufficiently strong (e.g. ~50 000 per pass in the case of 511 nm) that the laser can produce substantial output power even without an optical cavity. With a cavity, oscillation builds up in a very small number of cavity round trips. By the time this has occurred, stimulated emission is dumping population into the ^2D metastable lower levels, which have no means of disposing of it on the timescale of 100 ns. This, together with the decrease in electron temperature as the current pulse develops, precipitates a rapid switch in the behaviour of the active medium—from high gain to high loss—and the laser action self-terminates well before the end of the current pulse. It is then necessary to wait until the lower-level population has been reduced to a much smaller value before the next excitation pulse can be applied and the cycle of events repeated.

It is important to point out that the processes acting to de-excite atoms in the ^2D lower laser levels by collisions with buffer gas atoms or with the tube wall are not very effective in emptying the lower level of population. If there were no other mechanisms, the rate at which laser pulses could be repeated would be very slow. Experiments by Lewis [4] showed unambiguously that the population of the ^2D levels in Cu during the 100 μs interval between excitation pulses becomes clamped after about 10 μs to that of the ^2S ground state. The clamping mechanism is the kinetically balanced two-way exchange of population brought about by inelastic collisions of electrons with ground-state ^2S atoms, which excites them to ^2D and the thermodynamic inverse process of de-excitation from ^2D to ^2S in superelastic collisions:

$$\mathrm{Cu}\left({}^2S_{1/2}\right) + \mathrm{e(fast)} \Leftrightarrow \mathrm{Cu}\left({}^2D_{3/2}, {}^2D_{5/2}\right) + \mathrm{e(slow)}. \tag{24.2}$$

Although the cross section for these optically forbidden processes tends to be much smaller than those for the allowed processes, which excite the upper laser levels from the ground state, the electron density in the interpulse period remains high enough to ensure that the forward and reverse rates in Equation (24.2) are the dominant processes affecting the ^2D population in elemental CVLs without gas additives.

The pulse repetition frequency limitation in practical CVLs is due not so much to the population remaining in the metastable lower laser levels from one excitation current pulse to the next—the superelastic de-excitation rate is usually sufficient to ensure this. Rather it is the remnant electron density which causes the discharge to remain conducting after the discharge pulse and prevents the electron temperature rising to the required high values at the onset of the next pulse of applied voltage.

The characteristic features of the term diagram of a 'self-terminating' or 'cyclic' laser are thus an upper laser level connected by strong transitions to the ground state but by less allowed transitions to the lower levels which are themselves optically forbidden to decay the ground state. These features are exemplified by Pb, Au, Cu and several other atomic systems.

24.2 Development of the Copper Vapour Laser

The first CVL of Walter in 1966 employed an alumina discharge tube of 10 mm internal diameter and 800 mm length. The tube contained metallic copper beads and helium at a few mbar pressure. To achieve its working temperature of 1500°C (sufficient to give enough ground-state copper density for trapping on the resonance lines to be effective), it employed an external oven.

The next major advance in CVL development was reported by workers in Russia. In 1972, Isaev et al. [5], using a discharge tube surrounded by a thick layer of thermal insulator, showed that the heat generated by the pulsed discharge was sufficient to maintain the elemental copper at the CVL working temperature and obtained 15 W at 1% true efficiency.

Development of elemental copper lasers continued in the late 1970s and 1980s in the United States, prompted largely by the requirements of the Atomic Vapor Laser Isotope

Separation (AVLIS) program at the Lawrence Livermore National Laboratory (LLNL).

The scaling-up of CVL power was based on the demonstration in 1978 by Smilanski et al. [6] in Israel that the CVL could be operated in tubes of relatively wide bore (up to 40 mm) and with neon as buffer gas at a pressure of 180 mbar. The surprising feature of Smilanski's experiments was the excellent uniformity with which the Ne + Cu discharge filled the cross section of the discharge tube. Discharges in rare gases above a few mbar pressure in wide bore tubes tend to be self-constricted columns following tortuous and irreproducible paths between electrodes. Later work by Gabay and Smilanski [7] has provided the explanation by showing that ionization remaining from one laser pulse to the next is able to provide enough seeding to make the discharge current flow in a uniform fashion across the tube cross section.

With the proof that the CVL power could be scaled by increasing the size of the discharge device, rapid progress was made at LLNL so that by 1991 that laboratory was able to report that CVL amplifiers of 80 mm tube diameter with extractable powers of 650 W per unit were entering production and were qualified to install in a full-scale isotope enrichment facility at LLNL [8].

TABLE 24.1

Properties of a Typical Commercial CVL

Average Power on 511 and 578 nm Combined 45 W	Green/Yellow Power Ratio 2:1
Pulse energy (max), 3 mJ	Pulse width (FWHM), 25 ns (nominal)
Peak power, 200 kW	Pulse repetition frequency, 10–30 kHz
Timing jitter, < 2 ns RMS	Beam diameter, 23 mm
Beam divergence, 4 mrad (plane–plane cavity) 75 µrad (unstable resonator fitted)	
Power consumption for normal running, 4 kW	Cooling water requirement, 5 L min^{-1}
Gas supply, neon/HCl premix	Gas consumption, 0.5 L atm h^{-1} (running)

CVL, chemical vapour laser; FWHM, full width at half maximum

By 1980, the development of elemental CVLs was well under way in the Clarendon Laboratory at the University of Oxford, and in 1982, a commercial 25 W CVL was introduced by Oxford Lasers Ltd based on the Clarendon Laboratory design.

Typical performance figures for a modern commercial 45-W CVL (Oxford Lasers model LM100-X) are shown in Table 24.1.

24.3 Elemental CVLs—Practical Considerations

Most commercial CVLs for scientific and industrial (non-nuclear) applications operate with output powers in the range 10–100 W. Figure 24.2 shows a schematic diagram of the construction of a typical elemental CVL, i.e. one employing thermal evaporation of metallic copper as the source of the vapour. The discharge tube (typically an alumina ceramic tube of 20–40 mm internal diameter and 1 m length) is surrounded by a layer of ceramic fibre material for thermal insulation. The entire discharge tube and thermal insulator assembly is contained within a gas envelope of pyrex or silica closed at each end by silica windows set tilted a few degrees from the normal to the laser tube axis. One of the two cylindrical electrodes at either end of the discharge tube is electrically connected to a metal tube enclosing the discharge tube which acts both as a heat sink (to absorb the heat radiated by the discharge tube) and as a coaxial current return path. Small pellets of copper are placed at intervals down the length of the discharge tube that also contains a buffer gas, usually neon, at a pressure of 20–200 mbar. Both the efficiency and beam quality are improved if a small amount of hydrogen (typically ~0.5%–3%) is added to the buffer gas (see Section 24.5).

During the period from initial switch-on, the heat generated by the repetitively pulsed discharge (carried by the buffer gas) raises the temperature in the discharge tube until it reaches its stable working temperature of about 1500°C. This occurs

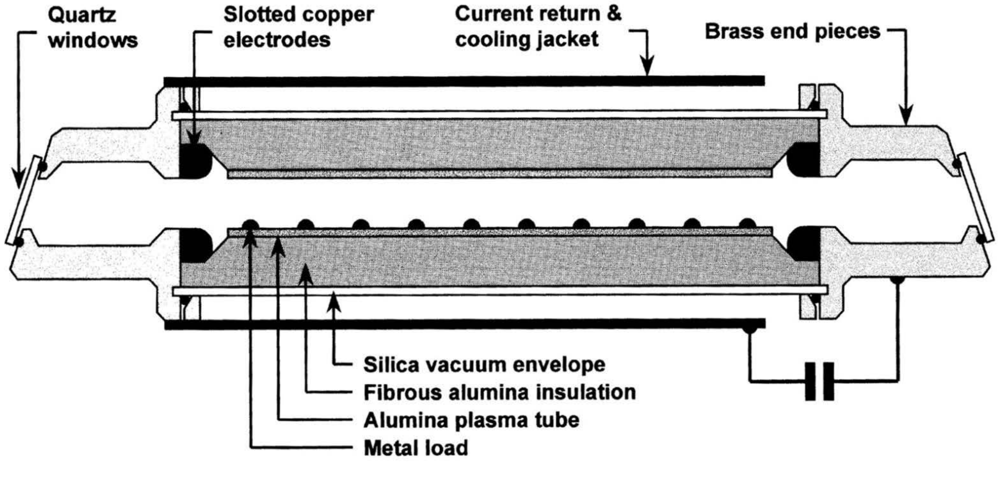
Quartz windows
Slotted copper electrodes
Current return & cooling jacket
Brass end pieces
Silica vacuum envelope
Fibrous alumina insulation
Alumina plasma tube
Metal load

FIGURE 24.2 CVL discharge tube, schematic illustration.

when the heat lost by radiation through the end windows and conduction radially outwards is sufficient to balance the power input to the discharge. At this temperature, the vapour pressure of copper is 0.3 mbar, and the discharge in the heated zone is dominated by the copper vapour component with the buffer gas playing only a minor role.

During hundreds of hours of operation, the copper fill slowly migrates from the hot region to condense in the cold regions at each end of the tube, and laser power will thus eventually decrease. For this reason, if the laser tube is permanently sealed off (as in the case of 3–10 W devices manufactured for many years by the Russian firm, Istok), it is necessary to replace the complete tube assembly at roughly 1000 h intervals of operating time. An alternative approach is to provide demountable window sections on the tube so that one or both can be removed at appropriate servicing intervals to remove the copper condensed in the catcher regions at each end of the tube and to recharge the central region of the tube with a new load of metallic copper. In the CVL, unlike the Ar^+ laser, there is no problem in exposing the electrodes to air since the electrodes are not coated with chemically reactive materials. The CVL tube can simply be connected permanently to a source of low-pressure neon and supplied with a trickle flow of the gas to purge continuously any impurities. The copper refill procedure also provides the opportunity to clean the laser tube windows if necessary, although the buffer gas in the end regions very effectively protects the windows from becoming coated with copper.

A basic version of the circuit which powers the laser is shown in Figure 24.3. It comprises a high-voltage supply capable of resonantly charging the storage capacitor C *via* the inductor L_H to a voltage between 10 and 20 kV. When a low-voltage trigger pulse is applied to the control grid of the thyratron T, the tube conducts and allows the charge on the storage capacitor C to be transferred to the peaking capacitor C_P mounted close to the laser tube assembly and connected directly across the two electrodes. To avoid damage to the thyratron, the initial switching current through the thyratron is limited by the saturable inductor L_S. As the voltage on the peaking capacitor rises, the gas in the main discharge tube undergoes breakdown and the peaking capacitor rapidly discharges through the low-inductance circuit comprising the gas discharge and the external coaxial current return path.

The thyratron is a gas-filled hot-cathode tube containing hydrogen. Once conducting, it can only be restored to the non-conducting state by removing the voltage across it or even applying a slightly negative voltage for a short period while the hydrogen ions recombine. With a suitable choice of thyratron, operation at several tens of kilohertz is possible. The upper limit on frequency of operation is set by kinetic processes within the laser medium itself. Power supplies incorporating all solid-state switching elements and magnetic pulse compression techniques offer an alternative to the use of gas-filled tube technology, but the efficiency, power handling capability and low-timing jitter associated with thyratron-switched circuits make them still highly competitive.

24.4 Copper Halide Lasers

In the years following the first demonstration of the CVL, the warm-up time needed to bring a self-heated CVL into operation (usually about 1 h, depending on the size of the laser) and the fact that the tube operated at high temperature were seen as problems, which would inhibit the widespread adoption of the technology. In fact, the high tube temperature, although it does restrict the choice of construction materials, has not proved to be a barrier to the attainment of long-term reliability. Modern elemental CVLs operate for many tens of thousands of hours without experiencing tube failure. However, the idea of making a CVL which could operate at lower temperature (even room temperature) was an important motivation for testing many molecular compounds of copper which could be used as donors of copper atoms.

As early as 1966, Walter et al. [9] had suggested the use of volatile compounds as a source of atomic copper. Although in 1973–1974 Liu et al. [10] reported observation of 'superradiance' (i.e. amplified spontaneous emission) in discharges containing copper halide compounds, the first successful operation of a laser containing a He–CuCl mixture at temperatures in the range of 500°C–600°C was reported by Chen et al. [11] in 1974. Their device, in common with many in the years immediately following, used a system of double pulse excitation in which the first pulse of the pair served to dissociate the molecular copper donor compound in the volume of the tube. Laser action was achieved on the second pulse of each pair. This strategy avoided the problems of discharge stability to which longitudinally excited discharges in gases containing electronegative components are prone. The tendency of such discharges to knot themselves into self-constricted and

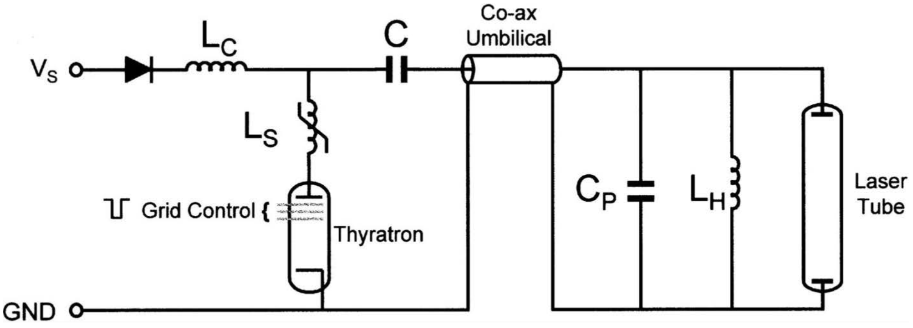

FIGURE 24.3 CVL discharge circuit.

tortuous filaments associated with the build-up of excess free halogen compounds in the tube was ameliorated by operating the devices either with low repetition rate pulse trains of double pulses in short bursts of high repetition rate pulses.

Steady progress in the development of copper halide lasers (particularly the CuBr system which they pioneered) was made in the years from 1974 onwards by the group headed by Sabotinov [12] at the Institute of Solid State Physics in Sofia, Bulgaria. The characteristic feature of many of the laser tube designs they developed, which could be run in a truly pulse repetitive mode, was, as indicated in Figure 24.4a, a series of discharge confining silica discs spaced at intervals along the wide bore silica gas envelope. Narrow apertures in discs served to confine the discharge along the axis of the tube, while the wide pockets between neighbouring discs allowed the copper bromide density to be regulated independently from discharge heating.

By providing traps containing copper filings in the electrode regions, as in Figure 24.4b, or by other means, the build-up of excess bromine can be avoided, and these lasers can be run in a truly pulse repetitive fashion at pulse repetition frequencies typically in the range 10–20 kHz. Although powers of over 120 W have been reported from CuBr lasers [13], most commercial CVLs such as those marketed by the Australian company, Norseld (whose designs are based on the Bulgarian work), have typically been for devices in the power range up to 10 W on 511 and 578 nm combined. Tube lifetimes are of the order of 1000 h for these sealed-off tubes.

24.5 Effect of Additive Hydrogen

As early as 1980, Bokhan et al. [14] reported evidence of the beneficial effect of adding a small proportion (typically 0.3%–0.6%) of hydrogen to the neon buffer gas in an elemental CVL. Other workers at first found the effect difficult to reproduce. This was largely because the amount of hydrogen needed to obtain a positive effect is small enough that the optimum concentration was already provided by the dissociation of water vapour from the atmosphere permeating the flexible plastic hoses connecting the laser tube to the buffer gas supply. Another source of water vapour is the alumina used both for the thermal insulation and for the discharge tube itself. One form of alumina is $Al_2O_3(5H_2O)$, and the amount of this compound in the construction materials of the laser depends on the manufacturing process. At elevated temperatures, the water leaves the alumina and enters the discharge where it is dissociated. The oxygen forms oxides and leaves the laser gas mixture, while the hydrogen concentration continuously builds up in the tube unless a steady purge of gas is maintained.

However, the beneficial effect of adding hydrogen is certainly real and results in an increase in output power by some 50%–70% in discharge gas mixtures containing 0.5% H_2 in neon when compared with the power obtained with a buffer gas of pure neon. A similar power enhancement with addition of hydrogen is also observed in copper halide lasers [15].

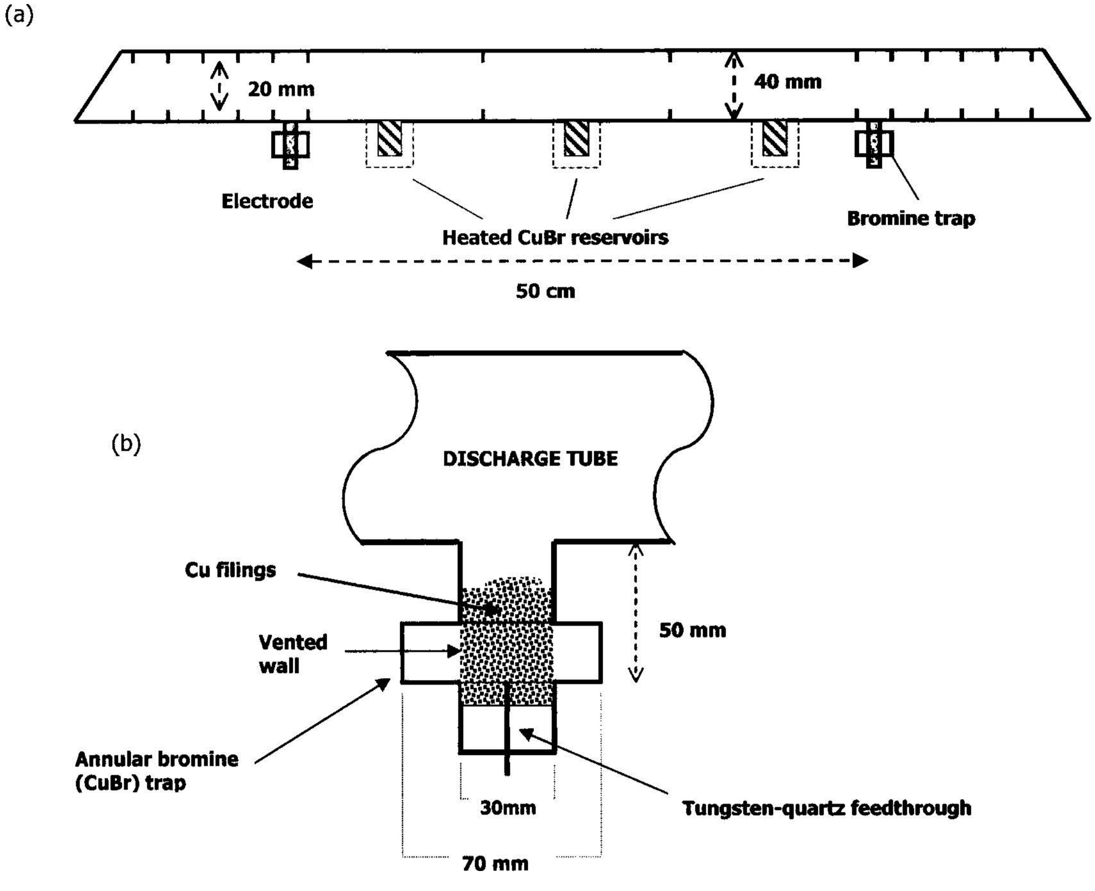

FIGURE 24.4 Copper bromide laser tube. (After Sabotinov [12].)

The beneficial effect of adding hydrogen is threefold. Not only does it allow the laser to be run at a higher pulse repetition frequency, but the energy per pulse is increased. Even more importantly, as shown by Withford et al. [16], by optimizing both the total neon buffer gas pressure and the hydrogen concentration, the radial dependence of gain early in the gain period can be manipulated to advantage. Without hydrogen, the gain and emission rises first in the outer regions of the discharge tube near the tube walls. This annular pattern of radiation seeds the growth of the beam by stimulated emission and causes the final output beam to have a highly undesirable doughnut shape in the far field. (For this reason some early CVL designs [17] employed off-axis unstable resonators to take advantage of the rise in gain near the discharge wall in the early part of the pulse to build up a low-divergence beam which could extract power from the axial regions later in the pulse.) However, with optimized neon and hydrogen concentrations, the gain rises first on the tube axis, and a much more desirable axially peaked output beam results. CVLs of modern design employ on-axis unstable resonators, with beneficial effects on the symmetry and divergence properties of the output beam.

The mechanisms by which added hydrogen affects the discharge kinetics is discussed in detail in the encyclopaedic treatise on metal vapour lasers by Little [18]. The H_2 molecules, with their myriad of closely spaced rotational and vibrational levels, act to provide a rapid means of cooling the electrons in the period immediately following the discharge current pulse. This rapid decrease of electron temperature not only reduces the population in the lower lasers levels more rapidly than would otherwise be the case but even more importantly promotes rapid recombination of the electrons and ions because of the sensitive dependence (typically $T_e^{-9/2}$) of recombination rate upon electron temperature.

24.6 Copper HyBrID Lasers

A radical innovation in CVL design was introduced by Maitland, Little, Jones and co-workers at St Andrews University in the early 1990s [19]. Although these (Ne–HBr–CuBr) lasers employ a copper halide to achieve adequate densities of copper atoms, they differ from the copper bromide (Ne–H_2–CuBr) lasers by generating the CuBr *in situ* in the discharge tube by the reaction of HBr gas with annular strips of metallic copper placed at intervals along the bore of the discharge tube. The copper component is transported from the cooler regions near the tube wall into the axial region by the same kind of mechanism operating in tungsten–halogen filament lamps. The halogen scavenges copper by forming CuBr at the lower temperature of the wall region and then migrates to the axis of the tube where it is dissociated into its atomic components.

These so-called HyBrID (Ne–HBr–CuBr) take their name from the slightly awkward acronym **hy**drogen **br**omide **i**n **d**ischarge. They have proven capable of high efficiency (3%), high repetition rate (20 kHz in large bore devices) and average powers of up to 280 W [20], at the same time operating at moderate temperatures in the range 600°C–700°C. The lower operating temperature range not only brings advantages in shortening the warm-up period before full laser power is obtained but also gives the laser designer greater freedom in the choice of materials for laser tube construction. In particular, the entire laser tube assembly can be made from fused silica by conventional glassblowing techniques.

To date, CVLs of the HyBrID design do not appear to have been made commercially. Perhaps one reason for this is the susceptibility of the lasers to form 'dendrites'—tree-like accumulations of metallic copper—which hang from the walls in the cooler regions at the ends of the tube and may ultimately block the optical path of the beam inside the cavity.

24.7 CVL Cavities and Beam Quality

When oscillating in the usual plane–plane resonator cavity, the seed radiation determining the form of the output beam from a CVL typically diverges with an angle determined by the geometric value representing the aspect ratio of the discharge tube. Matters can be improved significantly by providing a confocal unstable resonator such as that shown schematically in Figure 24.5.

The large concave high-reflectance mirror at one end of the cavity returns incident spontaneous emission back through

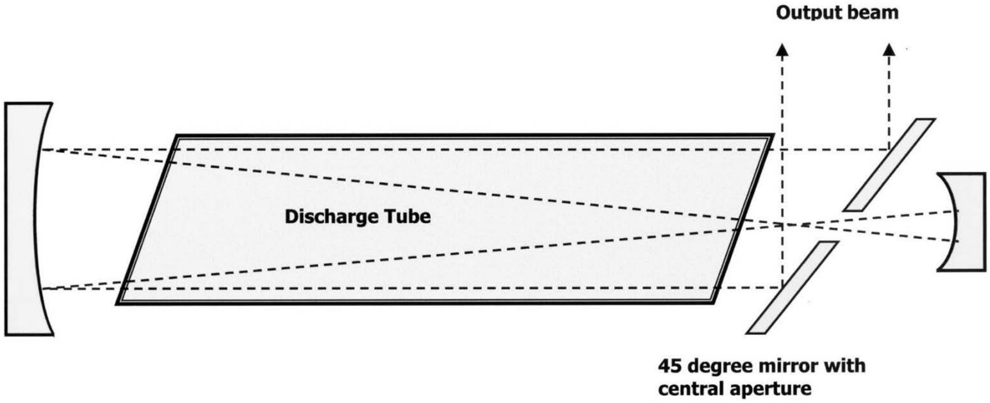

FIGURE 24.5 Confocal unstable resonator.

the amplifying medium towards the beam splitter—a high-reflectance flat plate at 45° to the cavity axis with a small hole at its centre. The radiation returning towards the large mirror *via* this hole after reflection at the small concave mirror (of short focal length) therefore appears to diverge from a point close to where the two mirrors have their common focal point. After making a further double transit of the discharge tube, most of this beam exits from the cavity in the form of an annular beam having been reflected from the outer region of the beam splitter plate. The remaining central part of the beam continues through the hole and is reflected again at the smaller mirror. However, now the returning beam appears to diverge from a source point even closer to the common focal point of the mirrors. Thus, the beam which exits from the cavity after a further round trip (reflection at the large mirror and the beam splitter) is of much lower divergence. This iterative process continues as long as the gain pulse lasts, with the apparent source point approaching arbitrarily close to the common focus and the divergence correspondingly decreasing until (ideally) diffraction sets a limit. In a cavity of magnification 100, approximately 0.01% of the output beam is fed back from the small mirror and the flux divergence decreases by a factor of about 100 on each round trip.

For the 45-W laser described in Section 24.2, the output beam divergence with a plane–plane cavity is some 4 mrad, but use of an unstable resonator reduces this below 75 μrad. In conventional CVLs with hydrogen addition, the time taken to build up the low divergence signal corresponds to two round trips. However, the maximum gain occurs early in the pulse. The result is that only the last part of the laser pulse, containing about 30%–60% of the total energy, is of the low divergence form.

24.8 MOPA CVLs

The problem of extracting power over the full duration of the gain pulse in a stand-alone CVL oscillator is associated with the finite time taken to build up a radiation distribution inside the unstable resonator cavity corresponding to the steady-state low divergence. One method of solving this problem is to inject low-divergence laser light into an amplifier unit just as its excitation pulse rises. The optical layout of such a master oscillator power amplifier (MOPA) scheme used by Coutts et al. [21] is shown in Figure 24.6.

The narrow bore (12 mm) master oscillator laser tube is enclosed in its own unstable resonator. Its unpolarized output is transmitted *via* a rotatable polarizing beam splitter and an adjustable iris to be focused by a 500 mm achromatic lens through the 1 mm central hole in the 45° coupling mirror into the double-pass amplifier. After traversing the gain tube once, a mirror of 2 m radius of curvature produces a collimated beam of 25 mm diameter that is returned for a second pass through the gain medium, this time extracting power efficiently. The double-pass output exits by reflection at the 45° coupling mirror and is finally transmitted through a second, fixed, polarizing beam splitter cube. By rotating the first polarizing beam splitter, full control over the power output of the MOPA CVL

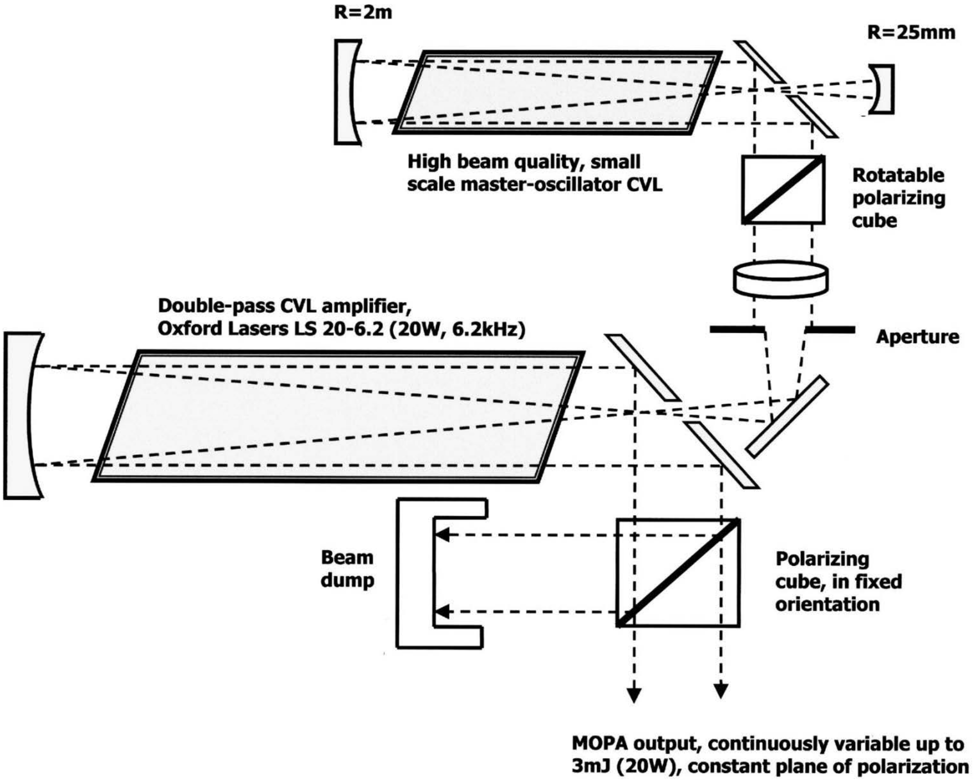
R=2m
R=25mm
High beam quality, small scale master-oscillator CVL
Rotatable polarizing cube
Double-pass CVL amplifier, Oxford Lasers LS 20-6.2 (20W, 6.2kHz)
Aperture
Beam dump
Polarizing cube, in fixed orientation
MOPA output, continuously variable up to 3mJ (20W), constant plane of polarization

FIGURE 24.6 Master oscillator power amplifier (MOPA) CVL configuration.

is obtained without variation of any other beam parameter. The divergence of the final beam for an output power of 19 W was measured to be 27 µrad(full width at half maximum), only 1.3 times the diffraction-limited value.

24.9 Kinetically Enhanced CVLs

The development of kinetically enhanced CVLs (KE-CVLs) by Piper and co-workers [22] at the Centre for Lasers and Applications at Macquarie University, Australia, has resulted in a doubling of the power output capability of elemental CVL of a given size. The enhancement is brought about by adding a mixture of H_2 and HCl to the neon buffer gas of a high-temperature elemental CVL. The philosophy that led to this advance was the idea of decoupling the effect of the halide additives on the enhanced relaxation of electron and metastable densities from its role as the provider of ground-state copper which it has in the low-temperature HyBrID concept. The behaviour of KE-CVLs suggests that besides the increased cooling rate the electrons experience in the interpulse period due to the presence of H_2, the process of dissociative attachment of electrons with the hydrogen halide plays a dominant role in reducing the prepulse electron density [23]. The increased decay rate of the electron density combined with the efficient reformation of HCl in the plasma region has allowed very dramatic improvements in repetition rate capability as well as specific output power to be demonstrated. Operation of a KE-CVL with 9 W of output power at a pulse repetition rate of 100 kHz has been reported by Marshall et al. [24]. Another benefit is that mutual neutralization of (positive) copper ions with negative hydrogen and halide ions benefits the replenishment of ground-state copper atoms near the axis of the tube, which otherwise would be depleted due to the migration of copper ions to the wall by ambipolar diffusion. The result is that, early in the discharge pulse, the gain rises to high values on axis. This is most important for the beam quality that the laser is able to achieve, since the effects of axial depletion of copper ground-state density combined with the skin effect tend to produce a gain profile which rises first near the walls with the deleterious effects noted in Section 24.5.

24.10 The Gold Vapour Laser

The gold vapour laser is another member of the class of self-terminating neutral metal vapour lasers. It is closely analogous to the copper system; indeed, gold is the only element in the whole periodic table which has exactly the same arrangement of low-lying energy levels as those of the copper atom. As shown in Figure 24.7 where the term diagrams of copper and gold are drawn side by side, the ground state of Au is $^2S_{1/2}$ and arises from the configuration $5d^{10}6s$. The ^2P upper laser levels lie about 5 eV above the ground state, and the $J=3/2$ and $J=1/2$ levels are separated by a much greater interval than in the case of Cu, as are the ^2D lower levels, owing to the much greater spin–orbit splitting in the heavier element. Thus, while the $^2D_{3/2}$ lower level of the red 628 nm transition (analogous to the yellow 578 nm transition of Cu) at 2.8 eV is higher in energy than the corresponding state of Cu (1.5 eV), the opposite is true of the $^2P_{5/2}$ level which, in Au, lies only 1 eV above the ground state.

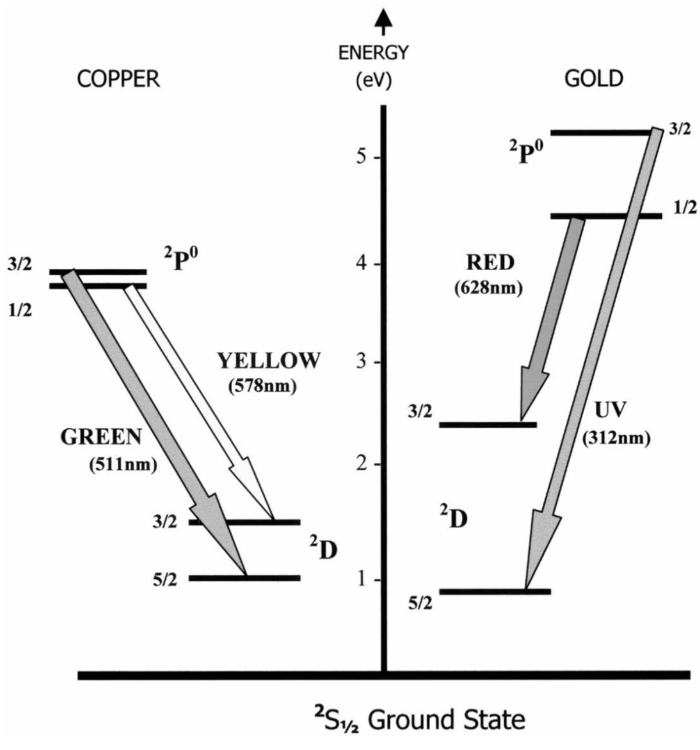

FIGURE 24.7 Low-lying energy levels of atomic copper and gold.

This has important consequences for the power capabilities of the ultraviolet 312 nm laser transition of Au. Because gold is less volatile than copper, the typical running temperature of a GVL is 1650°C as against 1500°C for the CVL. Even at these temperatures, thermal population of the $^2D_{5/2}$ is a problem to such an extent that relaxation of its population between pulses is not very effective and the 312 nm does not show oscillation at all in wide bore tubes at high repetition rates.

These same considerations also explain the lack of strong dependence of pulse energy with repetition rate displayed by the 628 nm transition of Au. The thermalization of the lower laser-level population to the Boltzmann fraction $\exp(-E_1/kT_e)$ of the ground-state population at T_e (the electron temperature) in the interpulse period and the fact that T_e can decay no further than T_{gas} is sufficient to explain the observed behaviour.

The $^2P_{1/2}$ upper level of the 628 nm transition in Au is significantly higher in energy than its counterpart in Cu. This may go some way to explaining why the GVL at 628 nm is not as efficient as the CVL operating on the analogous transition at 578 nm. In a laser of similar dimensions, the 628 nm transition of Au produces only 50% of the power available on the 578 nm transition of Cu. To date, the highest power recorded for the GVL is the 16 W of 628 nm output achieved by Lewis [4] at the Clarendon Laboratory in 1985. However, since, to obtain a vapour pressure of Au comparable with that of Cu in the CVL, the temperature of the discharge tube must be raised by a further 100°C, it is possible that simply problems associated with preventing discharge tube sag have limited GVL performance to date. Little development of GVLs has been reported in the 1990s; however, in view of the improvements made to CVL technology and performance over the past decade, it is interesting to speculate whether, by applying similar concepts to the GVL, significant improvements in performance might be realized in this laser system.

REFERENCES

1. Fowles G R and Silfvast W T 1965 High-gain laser transition in lead vapor *Appl. Phys. Lett.* **6** 236–7.
2. Walter W T, Piltch M, Solimene N and Gould G 1966 Pulsed laser action in atomic copper vapor *Bull. Am. Phys. Soc.* **11** 113.
3. Bielski A 1975 A critical survey of atomic transition probabilities for CuI *J. Quantum Spectrosc. Radiat. Transfer* **15** 463–72.
4. Lewis R R 1985 *DPhil Thesis* University of Oxford.
5. Isaev A A, Karayan M A and Petrash G G 1972 Effective pulsed copper-vapour laser with high average generation power *JETP Lett.* **16** 27–9.
6. Smilanski I, Kerman A, Levin L A and Erez G 1978 Scaling of the discharge heated copper vapour laser *Opt. Commun.* **25** 79–82.
7. Gabay S and Smilanski I 1980 Effect of preionization on a copper vapor laser *IEEE J. Quantum Electron.* **QE-16** 598–601.
8. Warner B E 1991 Status of copper vapor laser technology at Lawrence Livermore National Laboratory *Paper CFH4 in CLEO 1991 Technical Digest* (Washington DC: Optical Society of America) pp 516–8.
9. Walter W T, Piltch M, Solimene N and Gould G 1966 Efficient pulsed gas discharge lasers *IEEE J. Quantum Electron.* **QE-2** 474–9.
10. Liu C S, Sukov E W and Weaver L A 1973 Copper superradiant emission from pulsed discharges in copper iodide vapor *Appl. Phys. Lett.* **23** 92–3.
11. Chen C J, Nerheim N M and Russell G 1973 Double-discharge copper vapor laser with copper chloride as lasant *Appl. Phys. Lett.* **23** 514–5.
12. Sabotinov N V 1996 Copper bromide lasers *Pulsed Metal Vapour Lasers (NATO ASI Series 1)* vol 5, ed C E Little and N V Sabotinov (Dordrecht: Kluwer) pp 113–24.
13. Astadjov D N, Dimotrov K D, Jones D R, Kirkov V K, Little C E, Sabotinov N V and Vuchkov N K 1997 Copper bromide laser of 120 W average output power *IEEE J. Quantum Electron.* **33** 705–9.
14. Bokhan P A, Silant'ev V I and Solomonov V I 1980 Mechanism for limiting the repetition frequency of pulses from a copper vapour laser *Sov. J. Quantum Electron.* **10** 724–7.
15. Sabotinov N V, Vuchkov N K and Astadjov D N 1993 Effect of hydrogen in the CuBr and CuCl-vapour lasers *Opt. Commun.* **95** 55–6.
16. Withford M J, Brown D J W, Coutts D W and Piper J A 1995 Increased efficiency of high-quality beam extraction from a copper vapor laser with H_2–Ne admixtures *IEEE J. Quantum Electron.* **31** 898–902.
17. Webb C E 1991 High power dye lasers pumped by copper vapour lasers *High Power Dye Lasers (Springer Series in Optical Sciences 65)* ed F J Duarte (Berlin: Springer) ch 5.
18. Little C E 1999 *Metal Vapour Lasers: Physics, Engineering and Applications* (Chichester: Wiley).
19. Livingstone E S, Jones D R, Maitland A and Little C E 1992 Characteristics of a copper bromide laser with flowing Ne–HBr buffer gas *Opt. Quantum Electron.* **24** 73–83.
20. Le Guyadec E, Coutance P, Bertrand G and Peltier C 1999 A 280 W average power Cu–Ne–HBr laser amplifier *IEEE J. Quantum Electron.* **35** 1616–21.
21. Coutts D W, Wadsworth W J and Webb C E 1998 High average power blue generation from a copper vapour laser pumped titanium sapphire laser *J. Mod. Opt.* **45** 1185–97.
22. Withford M J, Brown D J W, Carman R J and Piper J A 1998 Enhanced performance of elemental copper-vapor lasers by use of H_2–HCl–Ne buffer gas mixtures *Opt. Lett.* **23** 706–8.
23. Webb C E and Hogan G P 1996 Copper laser kinetics—a comparative study *Pulsed Metal Vapour Lasers—Physics and Emerging Applications in Industry, Medicine and Science (NATO ASI Series 1)* vol 5, ed C E Little and N V Sabotinov (Dordrecht: Kluwer Academic) pp 29–42.
24. Marshall G D and Coutts D W 2000 Repetition rate scaling up to 100 kHz of a small scale (50 W) kinetically enhanced copper vapor laser *IEEE J. Selected Topics Quantum Electron.* **6** 623–8.

FURTHER READING

Little C E 1999 *Metal Vapour Lasers: Physics, Engineering and Applications* (Chichester: Wiley).

This is a truly encyclopaedic work on the subject of metal vapour lasers. It covers the history, science, practical construction details, performance, and applications of all types of metal vapour lasers, together with an exhaustive list of literature references on the subject.

Little C E and Sabotinov N V (ed) 1996 *Pulsed Metal Vapour Lasers—Physics and Emerging Applications in Industry, Medicine and Science (NATO ASI Series 1)* vol 5 (Dordrecht: Kluwer Academic).

This book is the proceedings of the NATO Advanced Research Workshop on Pulsed Metal Vapour Lasers held at the University of St Andrews in August 1995. The meeting brought together many of the pioneers of the subject and leading research specialists from around the world to discuss the latest advances in the science and applications of metal vapour lasers.

25

Ion Lasers: Argon and Krypton Ion Lasers

Malcolm H. Dunn and Tony Gutierrez

CONTENTS

25.1 Introduction 325
25.2 Early History 325
25.3 Basic Processes 326
  25.3.1 Energy Levels 326
  25.3.2 Transition Probabilities and Level Lifetimes 327
  25.3.3 Plasma Parameters of the Discharge 327
  25.3.4 Level Populations 329
  25.3.5 Excitation Mechanisms 329
25.4 Device Development to the Present Day 330
25.5 Present Systems and Capabilities 332
25.6 Ion Laser Applications 334
References 334
Further Reading 335

25.1 Introduction

Since its discovery in 1964, the argon ion laser (and the closely related krypton ion laser) has continued to be a valued ‘powerhouse’ of coherent radiation in the ultraviolet (UV), visible and near infrared (NIR). Continuous-wave (cw) powers of several tens of watts in the visible (450–530 nm) and of several watts in the ultraviolet (229–363 nm) are available from commercial devices providing both high beam quality and spectral refinement. In addition, devices have been demonstrated that generate hundreds of watts of cw power in the blue-green spectral region.

Despite being gas lasers and ones of poor electrical to optical conversion efficiency, the ion lasers have continued to hold their own on the technological scene despite the rapid development of diode–laser–pumped solid-state lasers. This is particularly the case with regard to their high-power capabilities in the UV and deep-UV (DUV) and their coverage of spectral ranges (e.g. red, violet) not accessible at present to solid-state cw sources.

This chapter covers the early history of ion lasers, particularly the argon ion laser (Section 25.2), basic processes involved in their operation (Section 25.3) and device development to the present day including contemporary capabilities and applications (Section 25.4).

A word on notation may be appropriate here. The conventional spectroscopic notation for neutral Ar is Ar I. The singly ionized species (which discharge physicists denote as Ar^+) in spectroscopic notation is denoted by Ar II, and the doubly ionized species (Ar^{++}) in spectroscopic notation is denoted by Ar III, etc.

25.2 Early History

In the spring of 1964, Bridges [1] and Convert et al. [2] reported pulsed laser oscillation on ten transitions of singly ionized argon in the range 450–530 nm, all but one of these transitions being from the levels of the (^3P) 4p to those of the (^3P) 4s configuration. This was soon followed by reports from Bennett et al. [3] and Gordon et al. [4] of quasi-continuous and true continuous laser oscillation on these transitions.

The active medium of the argon ion laser is the positive column region of a low-pressure (<1 mbar) DC discharge in argon. In the first generation of argon lasers, the positive column was constricted by a quartz capillary tube (bore 1–4 mm) to produce the high current densities (100 A cm^{-2}) necessary to create population inversions. The capillary was usually between 25 cm and 1 m long.

Since high currents have to be passed into the gas, hot oxide-coated cathodes were employed to keep discharge voltages and cathode sputtering to a minimum. Voltage gradients in the positive column are around 10 V cm^{-1} and so the power dissipation in the capillary, even at an operating current as low as 1 A, is around 10 W cm^{-1}. A power dissipation of 25 W cm^{-1} is sufficient to heat quartz discharge tubes (with these dimensions) to incandescence within a few seconds, so that, for prolonged running at high currents, water cooling of the constricted region of the discharge is essential.

For a 2-mm bore tube, the optimum argon filling pressure is about 0.5 torr (1 torr = 1.32 mbar) and varies only slightly between the different transitions. The E/p ratio for the positive column is therefore around 20 V cm^{-1} $torr^{-1}$.

TABLE 25.1

Wavelengths of Continuous-Wave Laser Transitions in Ar II (All Levels Have a ^{3}P Core Except Where Otherwise Indicated)

Wavelength in Air (nm)			Designation
437.1	(^{1}D)	4p	${}^2D^0_{3/2} - 3d^2D_{3/2}$
448.2		4p	${}^2D^0_{5/2} - 3d^2D_{5/2}$
454.5		4p	${}^2P^0_{3/2} - 4s^2P_{3/2}$
457.9		4p	${}^2S^0_{1/2} - 4s^2P_{1/2}$
472.7		4p	${}^2D^0_{3/2} - 4s^2P_{3/2}$
476.5		4p	${}^2P^0_{3/2} - 4s^2P_{1/2}$
488.0		4p	${}^2D^0_{5/2} - 4s^2P_{3/2}$
488.9		4p	${}^2P^0_{1/2} - 4s^2P_{1/2}$
496.5		4p	${}^2D^0_{3/2} - 4s^2P_{1/2}$
501.7	(^{1}D)	4p	${}^2F^0_{5/2} - 3d^2D_{3/2}$
514.2	(^{1}D)	4p	${}^2F^0_{7/2} - 3d^2D_{5/2}$
514.5		4p	${}^4D^0_{5/2} - 4s^2P_{3/2}$
528.7		4p	${}^4D^0_{3/2} - 4s^2P_{1/2}$
1090		4p	${}^2P^0_{3/2} - 3d^2D_{5/2}$

Considerable progress was made in improving the power outputs available from a fixed volume of active medium, both through the development of improved discharge tubes and through the use of longitudinal magnetic fields.

Bridges and Halstead [5] reported total output powers of up to 8.5 W from a 46 cm-long 4-mm bore quartz discharge tube at a current of 45 A (350 A cm^{-2}) in the presence of a longitudinal magnetic field of 0.1 T. In 1965 Labuda et al. [6] established that laser power output increases monotonically with increasing discharge current and that the power output is limited through the current limitation set by the destruction of the quartz capillary under positive ion bombardment (maximum power dissipation in quartz being approximately 140 W cm^{-2}).

By using a ceramic discharge tube (3.5 mm bore, 50 cm long), Paananen [7] was able to overcome the current limitation set by the quartz capillary and reported a total output of 14 W at a current of 75 A (800 A cm^{-2}) in the presence of a magnetic field. Using a similar discharge to one given earlier, Paananen [7] also reported cw oscillation in Ar III at 351.1 nm. An output power of 13 mW was obtained at a discharge current of 72 A.

Labuda et al. [6], Rigden [8], Hernqvist and Fendley [9] and McMahan [10] investigated a range of materials in attempts to replace quartz as the confinement material for the discharge. These included molybdenum, aluminium, tantalum and pyrolytic graphite. Since the wall of the discharge tube is electrically conducting when such materials are used, it must be constructed in the form of short segments, each segment being insulated by a suitable spacer material from its neighbours.

By going to larger bore quartz discharge tubes (10 mm) Boersch et al. [11] in July 1967 succeeded in producing continuous output powers of the order of 100 W at currents of the order of 300 A (400 A cm^{-2}) in the absence of a magnetic field.

In order to reach the current densities that produce saturation of power output in the large-bore tubes, Boersch et al. [12] devised an argon ion laser where the capillary was constructed in anodized aluminium segments (bore 12 mm). Power output was found to depend on the product of current density with tube radius (*JR*) and to reach a maximum value at around $JR = 170$ A cm^{-1} (280 A cm^{-2}). Maximum power output on all transitions of Ar II was 105 W m^{-1} at filling pressures around 1 torr. The saturation of power output for transitions of Ar II was found to correspond to the threshold for Ar III oscillation, and for *JR* values around 250 A cm^{-1} (420 A cm^{-2}), two Ar III transitions (351.1, 363.8 nm) produced a total coherent output power of 3.0 W.

If large total output powers (100 W) are required, then large-bore tubes with large discharge currents are used, but if more moderate powers are sufficient (tens of watts), the narrow-bore tube with axial magnetic field is more convenient.

Fourteen cw laser transitions of Ar II are listed in Table 25.1 together with level designations.

25.3 Basic Processes

25.3.1 Energy Levels

The configurations of Ar II of relevance to the argon ion laser are of the form $3s^2 3p^4 nl$. The parent configuration (Ar III), $3s^2 3p^4$, is essentially governed by *LS* coupling so that the designation of the parent levels is ${}^3P_{2,1,0}$, ${}^1D_2$ or ${}^1S_0$. When the outer electron of Ar II is added to the Ar III parent, its associated coupling energies are larger than the spin–orbit energy of the $3p^4$ core for the configurations of principal interest here (3d, 4s, 4p, 4d, 5s) and, hence, are describable by *LS* coupling.

In the argon ion laser, the configurations of particular interest are all associated with the ^{3}P parent term. The following are of particular interest (Figure 25.1): the $3p^4(^3P)4p$ configuration since it contains the majority of the upper laser levels of Ar II; the $3p^4(^3P)4s$ configuration since it contains the short-lived lower laser levels (doublet levels) as well as

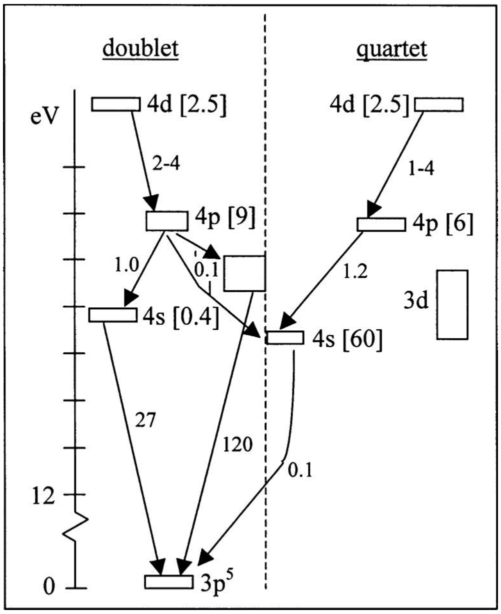

FIGURE 25.1 Electronic configurations in Ar II. All have the ^3P as parent term. The vertical extension of each block indicates the energy range associated with the levels of that configuration (units shown are electronvolts). The numbers at the arrows designate the radiative transition probabilities (spin conserved) in units of $10^8 s^{-1}$. Level lifetimes (in ns) are given in square brackets.

metastable levels of interest in relation to the pumping cycle (quartet levels); the $3p^4(^3P)3d$ configuration since it also contains metastable levels of relevance to the pumping cycle; the $3p^4(^3P)$ configurations since this is a source of cascade pumping to the 4p levels and finally the $3p^5$ ground configuration with levels $^2P_{1/2,3/2}$. The excited configurations contain both doublet and quartet terms.

25.3.2 Transition Probabilities and Level Lifetimes

Shortly after the discovery of the Ar II laser transitions in 1964, Statz et al. [13] calculated transition probabilities for transitions between levels of the $3p^4(^3P)4p$ and $3p^4(^3P)4s$ configurations and the $3p^4(^3P)4s$ and $3p^5$ configurations of Ar II. This was an extension of earlier work by Garstang [14]. In 1967, Rudko and Tang [15] extended the calculations of Statz et al. [13] to cover all transitions from the 4p levels (transitions to 3d levels now being included), as well as transitions from the 5s and 4d configurations to the 4p configuration (with the aim of assessing the part played by the 4d and 5s levels in cascade pumping of the 4p levels). In 1968, Koster et al. [16] published corrections to the original transition probabilities of Statz et al. [13] for transitions from the $3p^4(^3P)4s$ to the $3p^5$ configuration, finding that the transition probabilities for transitions from the 4s lower laser levels were a factor of five larger than originally thought. These calculations have been confirmed by Kitaeva et al. [17].

Experimental investigations on relative intensities of transitions in Ar II were first carried out by Olsen [18], and subsequently, Rudko and Tang [15] carried out detailed spectroscopic measurements of absolute spontaneous intensities. Bennett et al. [19] have determined experimentally total radiative lifetimes for the 4p states.

Average values of the lifetimes for the different configurations associated with Ar II are summarized in Figure 25.1 (for a more detailed consideration, the reader is referred to the original references cited earlier), where both transition probabilities between the configurations and level lifetimes within the configurations are indicated.

The following general statements regarding transition probabilities in the argon ion can be summarized from a consideration of Figure 25.1:

i. For transitions between the same pair of configurations, transition probabilities are roughly an order of magnitude smaller for transitions involving spin changes compared with transitions not involving spin changes. (The former only occur at all because of deviations from pure *LS* coupling.)
ii. In the $3p^4(^3P)4s$ configuration, the levels are $^2P_{1/2,3/2}$ and $^4P_{1/2,3/2,5/2}$. Since the ion ground states are doublet states, and since *LS* coupling is valid approximately, the decays of the quartet 4s states to ground states are slow compared with the decays of the doublet 4s states to the ground states. As a consequence, there are two orders of magnitude difference in radiative lifetime between quartet and doublet 4s states, the latter, but not the former, being short-lived enough to be lower laser levels for transitions from the 4p configuration.
iii. Transition probabilities for 4d–4p transitions are generally about half an order of magnitude greater than for 4p–4s transitions. (The influence of spin change considered in (i) applies to both these sets of transitions.)

It will be recognized from a comparison of Table 25.1 and Figure 25.1 that all of the laser transitions terminate on the short-lived doublet 4s states where lifetimes (0.4 ns) are considerably shorter than those (6–9 ns) associated with the upper (4p) states of these transitions, whereas none terminate on the much longer lived quartet 4s states whose lifetimes (30–90 ns) far exceed those of the 4p states. This is because population builds up on the latter of the 4s states, hence destroying population inversions but not on the former 4s states. The laser transitions at 514.5 and 528.7 nm are particularly interesting in that they involve spin changes. Despite the lower transition probabilities associated with these transitions, as a result, both show laser oscillation—indeed the transition at 514.5 nm delivers the highest power output of all the Ar II laser transitions and is probably the one most often selected for usage in applications of the laser.

25.3.3 Plasma Parameters of the Discharge

The basic plasma parameters of the argon discharge operating as the active medium of a laser are particularly important in evaluating excitation processes. It is appropriate to divide measurements into two groups: those carried out on small-bore laser discharges (diameter less than 6 mm), which were the first type to be investigated, and those carried out on larger bore systems (diameter greater than 6 mm). The former type of discharge has been extensively investigated by three groups: that under the direction of V F Kitaeva at the Lebedev Physics Institute, Moscow; that under the direction of W R Bennett Jr at Yale University, New Haven and that at Bell Telephone Laboratories, Murray Hill, involving A N Chester, E I Gordon, E F Labuda, R C Miller and C E Webb. Investigations on the large-bore systems have mainly been by G Herziger and collaborators at the University of Bern. In this brief review, we restrict our attention to electron density and electron temperature measurements alone since these are of particular significance in the context of excitation mechanisms.

Electron densities in the argon discharge have been determined by (i) measuring the Stark broadening of the H_α and H_β lines (Kitaeva et al. [20], Labuda et al. [21]); (ii) probe measurements (Labuda et al. [21], Kitaeva et al. [22]); (iii) microwave cavity techniques (Pleasance and George [23]) and (iv) Voigt analysis of the Ar I line profiles (Sze and Bennett [24]). In Figure 25.2, electron density has been plotted as a function of Jp_0, where J in the operating current density and p_0 is the argon filling pressure in torr, to allow the measurements of different investigations to be compared. A linear dependence on Jp_0 is to be noted. This observation is of particular importance in the subsequent discussion on excitation mechanisms since it means that an experimentally observed dependence of a level population on discharge current can immediately be interpreted as a similar dependence on electron density. There are, however, discrepancies in absolute magnitudes of electron density, most notably in the case of Sze and Bennett [24], where results are about a factor of ten greater than those of the other investigators.

Radial dependence of electron density has also been investigated using the probe technique developed by Kitaeva et al. [22].

Electron temperatures have been determined by (i) probe measurements (Labuda et al. [21], Kitaeva et al. [22]) and (ii) linewidth measurements on Ar II transitions (Sze and Bennett [24]). Results are summarized in Figure 25.3, where electron temperature is plotted as a function of discharge current with pressure as a parameter.

In order to deduce electron temperatures by linewidth or line-profile techniques, the broadening of Ar II transitions when viewed transverse to the discharge tube axis is measured. The additional broadening so observed is a consequence of a drift velocity superimposed on the ion random velocity by the strong radial electric field in the plasma. This radial electric field may be related to electron temperature—roughly speaking, the radial potential drop between tube axis and the beginning of the wall sheath is of the order of kT_e/e, where e is the electronic charge, but the exact details depend on the discharge model assumed.

As may be seen from Figure 25.3, there is reasonable agreement between the probe and linewidth measurements of Kitaeva et al. Sze and Bennett repeated the linewidth measurements using a Fabry–Pérot system of much higher finesse, so that detailed line profiles were obtained for the Ar II transitions. These measurements, also shown in Figure 25.3, indicate that although electron temperature increases initially with increasing current, it soon reaches a constant value for current densities above about 200 A cm^{-2}, at variance with the observations of Kitaeva et al. discussed previously. However, the findings of Sze and Bennett are more consistent with the probe measurements of Labuda et al., both with regard to the magnitude of electron temperature and its independence of current density.

The behaviour of electron temperature with discharge parameters, in particular current density, is therefore a region of some uncertainty. This is particularly unfortunate, as such knowledge is required to identify unequivocally the excitation mechanisms associated with the argon laser, as will become apparent shortly.

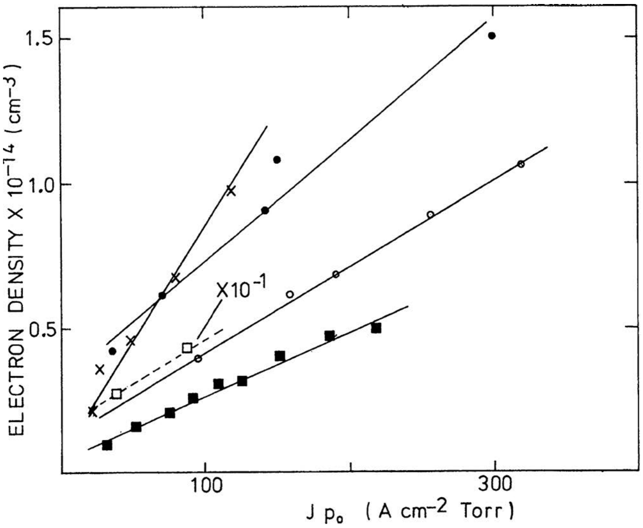

FIGURE 25.2 Electron density (cm^{-3}) as a function of $J\ p_0$ (A cm^{-2} torr): ○, Labuda et al. [21] (2 mm bore); ●, Pleasance and George [23] (2 mm bore); ■, Kitaeva et al. [20] (1.6 mm bore); □, Sze and Bennett [24] (2 mm bore); ×, Kitaeva et al. [22] (1 cm bore). (Reproduced from Dunn M H and Ross J N 1976 The argon ion laser *Prog. Quantum Electron.* **4** 233–69, with permission.)

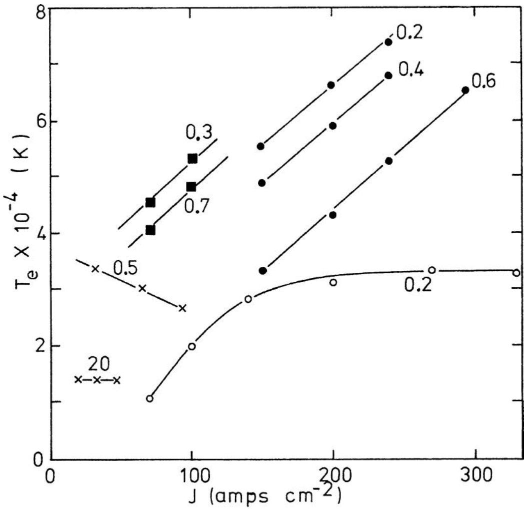

FIGURE 25.3 Electron temperature (K) as a function of discharge current (A cm^{-2}) with pressure as parameter (torr): ×, Labuda et al. [21] (2 mm bore, probe); ○, Sze and Bennett [24] (2 mm bore, line profile); ●, Kitaeva et al. [20] (1.6-mm bore, line profile); ■, Kitaeva et al. [22] (10 mm bore, probe). (Reproduced from Dunn M H and Ross J N 1976 The argon ion laser *Prog. Quantum Electron.* **4** 233–69, with permission.)

25.3.4 Level Populations

The dependence on discharge parameters of the population of 4p, 4s and 3d levels of Ar II and of neutral argon has been experimentally investigated by Gordon et al. [21,25], Webb [26], Rudko and Tang [15], Vladimirova et al. [27] and Ross [28]; radiating levels by emission spectroscopy and metastable levels by the Ladenburgh–Reiche line-absorption technique. The general conclusions that can be drawn about level populations from these observations are as follows.

i. The populations of the radiating levels of neutral argon are only weakly dependent on current density, showing a tendency to decrease slowly with increasing current density.
ii. Metastable level populations of neutral argon are only weakly dependent on current density, again showing a tendency to decrease with increasing current density.
iii. Populations of radiating levels of Ar II are a quadratic function of discharge current density.
iv. Metastable level populations of Ar II ($4s^4P$, $3d^4D$, $3d^4F$) are a linear function of discharge current density.

By a consideration of simple rate equations describing the steady-state populations of the excited levels, several important conclusions regarding excitation and relaxation mechanisms for these levels may be drawn. These may be summarized as follows:

v. Since the populations of both radiating and metastable levels of neutral argon effectively saturate with discharge current, electron collisional processes (including both superelastic collisional de-excitation and collisions which lead to ionization [26]) can be identified as the dominant loss mechanism for both. In the case of radiating levels it predominates over losses due to radiative decay, and in the case of metastable levels, it predominates over losses due to diffusion to the walls. These conclusions are based on the assumption that the electron temperature and, hence, also electronic excitation and de-excitation rates are independent of discharge current. (We have previously discussed the uncertainties in the dependence of the electron temperature with the current density in the discharge.)
vi. The linear dependence on discharge current of the populations of both the ion ground state and the ion metastable levels is consistent with the metastable levels being created by electron impact excitation from the ion ground level and being destroyed by electron collisions. In other words, the populations of the ion metastable levels are saturated relative to the population of the ion ground level, in just the same way as the populations of the neutral metastable levels are saturated relative to the population of the neutral ground level.
vii. The quadratic dependence of the populations of the radiating levels of the ion on discharge current is consistent with these levels being populated by electron impact excitation from the ion ground level, as before, but being destroyed by radiative decay. Since, like those of the ion ground level, the population of ion metastable levels is linearly dependent on current, the radiating levels could equally be created by electron impact excitation from metastable levels and still show a quadratic current dependence.
viii. Webb [27] has investigated the radial variation of Ar I and Ar II excited-state populations using a novel 'end-on' collimation technique. Measurements were made on tubes of 2 and 3 mm bore. His findings confirmed many of the previous observations while providing additional insights.

25.3.5 Excitation Mechanisms

Numerous excitation pathways have been proposed to explain the 4p–4s population inversions in the argon ion laser. It is convenient to consider five distinct mechanisms, although the active medium excitation probably involves more than one of these mechanisms. The proposed excitation pathways may be summarized as follows (Figure 25.4):

i. direct electron excitation from the $3p^6$ neutral argon ground state to the 4p upper laser level (mechanism I);
ii. electron excitation to an intermediate Ar I metastable state ($1s_{2-5}$) followed by electron impact excitation from this state to the 4p state (mechanism II);
iii. electron impact excitation to the Ar II ground state ($3p^5$) followed by electron impact excitation from this ion ground state to the 4p state (mechanism III);
iv. electron impact excitation to the Ar II ground state followed by electron impact excitation to a 4d or higher state, followed by radiative cascade to the 4p state (mechanism IV);

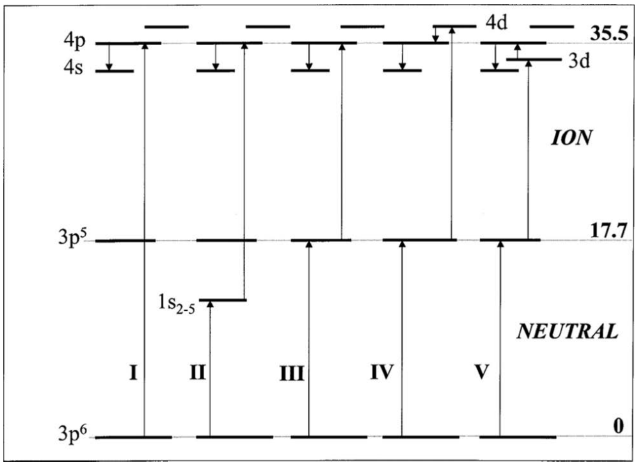

FIGURE 25.4 Excitation pathways for the 4p states of Ar II.

v. electron impact excitation to the Ar II ground state, followed by electron impact excitation to an intermediate ion metastable state (4s, 3d) followed by electron impact excitation to the 4p state (mechanism V).

Obviously, combinations of these excitation processes are possible (for example, IV and V).

As a consequence of the large electron energy required to reach threshold in the direct excitation process (35 eV) compared with the mean electron energy in the cw laser discharge (see Figure 25.3), the direct excitation process can be shown to make only a negligible contribution. (It is, however, much more significant in the case of the pulsed argon ion laser.)

Webb [26] has analysed excitation and destruction rates for the $1s_{2-5}$ metastable levels of Ar I, pertinent to pathway II. Under discharge conditions appropriate to the operation of the argon laser (electron temperature of the order of 1.5 eV), the predominant loss mechanism for these metastable levels is through ionization to the ground state of Ar II by electron collisions. Since the metastables are excited by electron collisions in the first place, the metastable populations of Ar I saturate with current, and indeed, this can be shown to occur even at very low currents. It can further be shown, using arguments relating to the dependences of relevant cross sections on electron temperature, that this two-step electron excitation of the Ar II ground state dominates by at least an order of magnitude over the single-step process.

Although excitation of the ion ground state is, therefore, predominantly a two-step process, its population is still expected to be a linear function of discharge current since the intermediate populations ($1s_{2-5}$ metastables) are saturated relative to the neutral ground state. The approximately linear dependence of electron density (and hence ion density) on discharge current that is observed experimentally is consistent with this excitation mechanism for the ion ground state (see Figure 25.2).

Excitation processes from the ion ground state can be either directly to the 4p upper laser levels or through intermediate levels. The populations of the upper laser levels (4p levels of Ar II) show a quadratic dependence on discharge current. However, it is not possible from this dependence alone to conclude, therefore, that the 4p levels are excited solely by direct electron excitation from the Ar II ground state, as opposed to *via* intermediate excitation to Ar II metastable states. This is because the metastable level populations of Ar II (quartet 4s, metastable 3d) are themselves saturated with respect to the ion ground state and hence show the same dependency on current as this ground state itself.

For both direct and indirect excitation processes, a quadratic dependence of 4p populations on discharge current is, hence, to be expected. However, Dunn [29,30] and Ross [31] have applied the technique of perturbation spectroscopy to a study of the excitation processes in argon, in particular to assess the roles of the quartet 4s and metastable 3d states. By measuring the changes in the populations of other 4p levels when the laser oscillates on a particular 4p–4s transition, Dunn has shown that an important excitation pathway for the 4p states is through the quartet 4s states. Ross has shown that under typical laser conditions 57% of the loss rate from the $3d^4F_{7/2}$ and 75% of the loss rate from the $3d^4F_{5/2}$ level are by electron excitation to the 4p levels. Circulation of populations between 4s, 3d and 4p states of Ar II, therefore, plays a significant role in creating the population inversions of the 4p–4s transitions.

Excitation by radiative cascade from above has been investigated experimentally by Rudko and Tang [32]. They have shown by comparing relative spontaneous emission intensities that, for example, 30% of the $4p^2D_{5/2}$ state population appears to be due to cascade from above.

Process II can be ruled out by the observed quadratic dependence of the 4p populations on discharge current—direct excitation from neutral metastable states ($1s_{2-5}$) implies a linear dependence on current, since these metastable populations are themselves saturated with respect to current.

In conclusion, all of the processes III–V are generally considered to play significant roles in determining the populations of the upper laser states of Ar II (4p states of argon II) and, hence, in determining the population inversions associated with the laser transitions.

25.4 Device Development to the Present Day

The ion laser tube represents the most costly component to the end user. Therefore, improvements in laser tube lifetime have been a major focus of device development. Coherent's Innova® Series V™ metal/ceramic plasma tube incorporates many improvements in tube design, as well as tube processing techniques that have evolved since 1981 when Coherent Inc. introduced metal/ceramic tube technology [33]. An example of a modern large-frame laser of this type is shown in Figure 25.5.

In the 1960s, the first commercially available plasma tubes were fabricated from either BeO or quartz/graphite. These plasma tubes had significant limitations in terms of performance and lifetime. However, hard sealing by metal/ceramic technology [34] eliminated a source of contamination and thus led to monumental increases in performance and lifetime.

In 1975, crystalline quartz windows replaced fused silica as Brewster window material. Crystalline quartz is more resistant than fused silica to changes in optical thickness due to densification [35] as a result of prolonged exposure to VUV radiation from the plasma discharge. In addition, crystalline quartz is less prone to colour centre formation. Both of these factors led to increases in available UV output power [36].

In 1981, Innova (metal/ceramic) plasma tube technology was introduced. In plasma tubes of this design, the discharge path is defined by a series of apertures in thin tungsten discs aligned to an accuracy better than 100 µm. Tungsten is used because of its resistance to sputtering and stable crystalline structure at temperatures up to 1400°C. Supporting the tungsten discs (which define the bore) are oxygen-free copper cups [37], to which the tungsten discs are brazed as shown in the cutaway view of Figure 25.6. The high thermal conductivity of copper makes it ideal for transferring heat to the ceramic tube envelope. It is this feature, removal of the heat flux generated by the discharge by conduction to the water-cooled alumina tube gas envelope, which differentiates the Innova design from the pioneering segmented-metal-disc plasma confinement structures developed by Labuda and Gordon in the 1960s, which were cooled by radiative transfer via a water-cooled silica tube gas envelope [6,37].

Sabre
COHERENT

FIGURE 25.5 A large-frame (25 W) Innova® Series V™ argon ion laser.

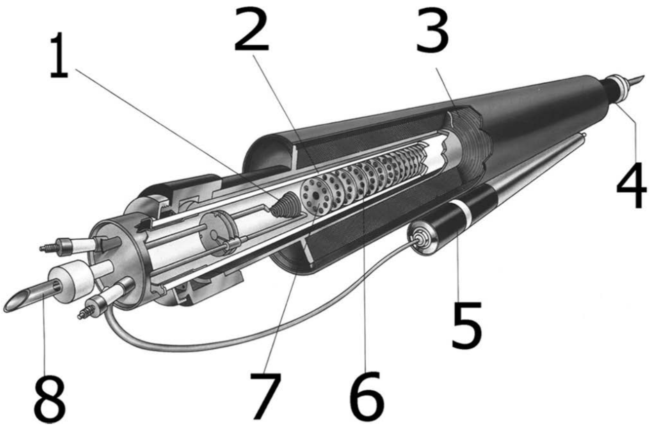

FIGURE 25.6 Innova ion laser tube: 1, thermionic cathode; 2, gas envelope (high conductivity ceramic); 3, solenoid magnet; 4, conduction-cooled anode; 5, gas reservoir for automatic pressure control; 6, internal gas return apertures; 7, tungsten discs supported in conduction-cooled copper cups; 8, hard-seal crystalline quartz Brewster windows.

The next major breakthrough in plasma tube development, however, occurred in 1985, when coated Brewster windows were introduced. The coated crystalline quartz windows further reduced colour centre formation and led to increases in UV tube lifetimes of more than 1000 h [38]. Also in 1985, gas pressure modifications were made inside the tube, increasing cathode lifetime and decreasing bore erosion. Increased pressure at the cathode allowed material sputtered off the cathode to redeposit onto it, thus increasing the usable lifetime of the cathode itself [39]. In 1989, sealed mirror tubes with no anode window were introduced. Elimination of the anode window increased lifetime by an additional 500 to 1000 h, depending on the type of plasma tube. UV plasma lifetimes also increased to more than 2000 h. Shortly thereafter, in 1991, new higher-strength ceramic materials were introduced. This improved the plasma tube's ability to withstand thermal stresses, thereby reducing a potential source of catastrophic failure. In 1994, a new braze alloy with better thermal uniformity and joint strength was introduced, further reducing sources of catastrophic failure due to thermal stresses within the plasma tube.

In 1995, Coherent, Inc. introduced the Series V™ plasma tubes with internal re-engineered gas pathways, which substantially improved cathode performance over a wide range of operating currents. With this improvement in cathode lifetime, cathode degradation was no longer considered a primary failure mechanism. UV plasma lifetimes also increased to more than 3500 h [33]. The working lifetime of tubes designed for output in the visible region increased to more than 5000 h [40].

Lifetime data taken from actual in situ field installations provide a useful metric for measuring tube lifetimes in conjunction with life-tested lasers. Life-tested lasers are usually operated 24 h a day at maximum currents while measurements are made of the output power, mode quality and other electrical and optical parameters. Although this type of life test data is useful, actual field data are more pertinent. This is true because the number of life-tested lasers that can be tested is much less than the actual number of lasers in the field. Also, lasers in the field are subject to actual usage patterns that are variable, depending on the installation. This variability in operating conditions, such as on-and-off cycling, operating powers and operating currents and extreme ambient conditions, provides useful information about the reliability and lifetimes of plasma tubes.

A summary (shown in Table 25.2) of tube lifetimes from 1990 to the present, based on the size, quasi-air-cooled cartridge, small frame, or large frame, tube type, dual Brewster window or tunable sealed mirror and wavelength, provides a useful guideline for laser selection.

Along with improvements in laser tube technology, productivity enhancements, such as PowerTrack™, an active power stabilization, mode optimization and noise-reduction system

TABLE 25.2

Argon Ion Laser Tube Lifetimes

Small or Large Frame/Output Wavelengths	Tube Type	Mean Lifetime (h)
Small/visible lines	Cartridge TSM	7100
Small/visible lines	DBW	6200
Small/UV lines	DBW	3500
Small/UV and visible	TSM	6200
Large/UV and visible	DBW	2500
Large/UV and visible	TSM	3300

DBW, dual Brewster window; TSM, tunable sealed mirror; UV, ultraviolet.

that operates by feedback control of the output coupler or the high-reflector mirror, have extended both ion laser performance and lifetime. PowerTrack also shortens the warm-up time for ion laser systems since users can operate the laser immediately upon turn-on. PowerTrack also maintains the optimal alignment of the optical beam through the resonator. This extends tube lifetime by minimizing bore erosion of the tube. Similarly, v-Track™, an active cavity, single-frequency stabilization system, enhances applications that require mode-hop-free operation. v-Track operates by a feedback circuit that monitors a temperature-controlled etalon, allowing the etalon to track a single longitudinal mode of the laser resonator and provide mode-hope-free operation.

Device development has also been focused on extending the fundamental wavelength regimes available from ion lasers. This is done by doubling the frequency of the visible lines to the corresponding DUV wavelengths by intracavity critically phase-matched BBO crystals [41].

25.5 Present Systems and Capabilities

Presently, air-cooled ion lasers with powers up to 500 mW are available commercially. Water-cooled units with multi-line powers ranging from 1 to 25 W are also on the market. Tables 25.3 and 25.4 show output power as a function of

TABLE 25.3

Output Power and Wavelengths from Commercially Available Argon Ion Lasers

	Output Power			
	25-W Main Frame (DBW25)	Frequency-Doubled 25-W Main Frame (Sabre MotoFRED)		Small-Frame Laser 610 (612)
	Multi-line Visible 25.0 W	Multi-line Ultraviolet 3.0 W		Multi-line Visible 1.00 W
Wavelength (nm)	(W)	(nm)[a]	(W)	(mW)
528.7	1.8	(264.3)	0.10	
514.5	10.0	(257.2)	1.00	350
501.7	1.8			
496.5	3.0	(248.2)	0.30	
488.0	8.0	(244.0)	0.50	200
476.5	3.0			
472.7	1.3			
465.8	0.8			
475.9	1.5	(229.0)	0.04	(80)[b]
454.5	0.8			
333.6–363.8	7.0			(Multi-line UV 100 mW)[b]
350.7				(40)[b]
351.1	1.8		1.0	
363.8	1.7		1.0	
351.1–385.8	4.4			
300.3–335.8	3.0			
275.4–305.5	1.6			
334.5	0.5			
302.4	0.38			
275.4	0.18			

Source: Courtesy Coherent Inc.

UV, ultraviolet.

[a] Frequency-doubled output wavelengths in brackets.

[b] Available with appropriate UV mirror cavity.

wavelength for a representative set of commercial water-cooled ion laser systems. These output power/wavelength tables include argon, krypton and mixed-gas (argon/krypton) ion laser systems. Table 25.5 lists a number of plasma tube parameters for typical small-frame and large-frame ion lasers [33].

Ion lasers are commercially available in a number of configurations. Examples include systems designed to provide multi-line operation, single-line operation and single-frequency operation (where a suitable etalon assembly is installed). Similarly, a number of active stabilization systems, diagnostics and computer-interfacing capabilities are commercially available. The stabilization systems can maintain constant power, constant frequency and constant transverse mode. Ion laser diagnostics currently available include power measurement, TEM_{00} transverse-mode detectors and wavelength indicators. The digital computer interfacing available today includes RS-232/RS-422 and/or IEEE-488. Digital remote control modules that allow remote operation of the laser systems are also available.

TABLE 25.4

Output Power and Wavelengths from Commercially Available Krypton Ion Lasers

	Output Power	
Wavelength (nm)	**Main-Frame Krypton (Model 302) Multi-line Red 1.0 W (W)**	**Mixed-Gas Krypton/Argon (Model 70—Spectrum) Multi-line 'Whitelight' 2.5 W (W)**
793.2–799.3	0.03	-
752.5–799.3	0.25	-
752.5	0.10	0.03
676.4	0.15	-
647.1	0.80	0.25
568.2	0.15	0.15
530.9	0.20	0.13
520.8	0.07	0.13
514.5 (Ar)	-	0.25
488.0 (Ar)	-	0.25
482.5	0.03	-
476.5 (Ar)	-	0.10
476.2	0.05	-
457.9 (Ar)	-	0.03
413.1	0.30	-
	Multi-line violet 0.60 W	
406.7	0.20	-
356.4	0.12	-
350.7	0.25	-
	Multi-line UV 0.5 W	Multi-line UV 0.05 W

Source: Courtesy Coherent Inc.

TABLE 25.5

Typical Plasma Tube Parameters of High-Power Large-Frame and Small-Frame Argon Ion Lasers. The Typical Powers Are for TEM_{00} or a Combination of TEM_{01} and TEM_{01} Modes [33]

Laser Parameter	Large Frame	Small Frame
Maximum tube current	65 A	60 A
Nominal tube voltage	535 V	235 V
Active tube length	1.11 m	0.41 m
Bore diameter	3.25 mm	3.15 mm
Current density	785 A cm^{-2}	779 A cm^{-2}
Heat load per cm	300 W cm^{-1}	320 W cm^{-1}
Typical output power (457.9–514.5 nm)	30 W	10 W
Typical output power (333.3–363.8 nm)	10 W	2 W
Efficiency (457.9–5145 nm)	0.08%	0.07%

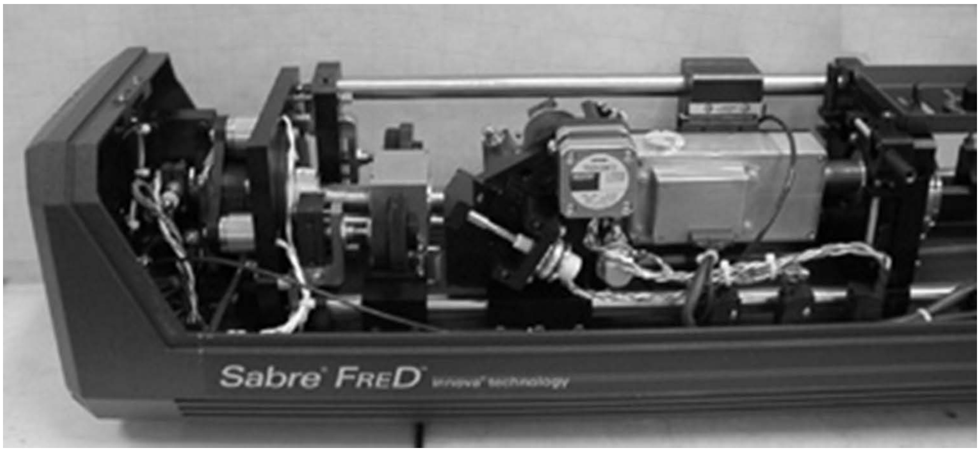

FIGURE 25.7 Motorized mount for doubling crystal in a frequency-doubled argon ion laser cavity.

Ion lasers are currently available with fundamental wavelengths that range from 275.4 to 1090 nm. Lasers generating DUV wavelengths, obtained by intracavity frequency doubling the fundamental wavelengths, are commercially available in the 229.0–264.3 nm range.

Figure 25.7 shows the intracavity frequency-doubling crystal section of a modern laser of this type (Sabre MotoFRED). The average tube lifetimes of today's ion lasers operating in the visible regime are greater than 6000 h. In contrast, an ion laser operating directly at fundamental wavelengths in the DUV region will have an average tube lifetime greater than 3500 h. Because frequency-doubled UV systems are designed so that the tube is exposed only to the visible fundamental laser wavelengths, average tube lifetimes are well over 6000 h.

25.6 Ion Laser Applications

Key applications currently for ion laser systems are holography, printing, digital imaging, nondestructive testing, spectroscopy, optical pumping, confocal microscopy, flow cytometry, compact disc and DVD mastering, basic R&D, photomask direct imaging, printed circuit board direct imaging, writing fibre Bragg gratings laser art and precision optics inspection. These applications require the use of argon, krypton and argon/krypton mixed-gas lasers, as well as frequency-doubled argon ion systems.

The technology of ion lasers is a mature one. Ion lasers are used in both scientific and commercial applications. At present, the scientific use of ion lasers accounts for approximately 20% of all new ion laser deployments. Solid-state lasers have replaced ion lasers in many traditional applications, such as laser-pumping cw and pulsed titanium:sapphire lasers, and pumping dyes. However, solid-state pumping has yet to provide a viable solution for pumping dyes in the UV. This is an application where the ion laser remains the laser of choice. Similarly, ion lasers are used in scientific and commercial applications, such as laser spectroscopy in the UV, DUV and red wavelengths, and violet wavelengths, all where solid-state cw solutions are not readily available.

REFERENCES

1. Bridges W B 1964 *Appl. Phys. Lett.* **4** 128.
2. Convert G, Armand M and Martinot-Lagarde P 1964 *C. R. Acad. Sci.* **258** 4467.
3. Bennett W R, Knutson J W, Mercer G N and Detch J L 1964 *Appl. Phys. Lett.* **4** 180.
4. Gordon E I, Labuda E F and Bridges W B 1964 *Appl. Phys. Lett.* **4** 178.
5. Bridges W B and Halstead A S 1966 *IEEE J. Quantum Electron.* QE-**2** 84.
6. Labuda E F, Gordon E I and Miller R C 1965 *IEEE J. Quantum Electron.* QE-**1** 273.
7. Paananen R 1966 *Appl. Phys. Lett.* **9** 34.
8. Rigden J D 1965 *IEEE J. Quantum Electron.* QE-**1** 221.
9. Hernqvist K G and Fendley J R Jr 1967 *IEEE J. Quantum Electron.* QE-3 66.
10. McMahan W H 1968 *Appl. Phys. Lett.* **12** 383.
11. Boersch H, Herziger G, Seelig W and Volland I 1967 *Phys. Lett. A* **24** 695.
12. Boersch H, Boscher J, Hoder D and Schafer G 1970 *Phys. Lett. A* **31** 188.
13. Statz H, Horrigan F A, Koozekanani S H, Tang C L and Koster G F 1965 *J. Appl. Phys.* **36** 2278.
14. Garstang R H 1954 *Mon. Not. R. Astron. Soc.* **114** 118.
15. Rudko R I and Tang C L 1967 *J. Appl. Phys.* **38** 4731.
16. Koster G F, Statz H, Horrigan F A and Tang C L 1968 *J. Appl. Phys.* **39** 4045.
17. Kitaeva V F, Osipov Yu I, Rubin P L and Sobolev N N 1968 On oscillation mechanisms in the CW ion argon laser, private communication.
18. Olsen H N 1963 *J. Quantum Spectroc. Radiat. Trans.* **3** 59.
19. Bennett W R Jr, Kindlmann P J, Mercer G N and Sunderland J 1964 *Appl. Phys. Lett.* **5** 158.
20. Kitaeva V F, Osipov Yu I and Sobolev N N 1967 *Sov. Phys. Dokl.* **12** 55.
21. Labuda E F, Webb C E, Miller R C and Gordon E I 1968 A study of capillary discharges in noble gases at high current densities Bell Telephone Laboratories private communication.
22. Kitaeva V F, Osipov Yu I, Sobolev N N, Shelekhov A L and Agheev V P 1974 *IEEE J. Quantum Electron.* QE-10 803.
23. Pleasance L D and George E V 1971 *Appl. Phys. Lett.* **18** 557.

24. Sze R C and Bennett W R Jr 1972 *Phys. Rev. A* **5** 837.
25. Miller R C, Labuda E F and Webb C E 1967 Excited level populations in high current density argon discharges *Bell Syst. Tech. J.* **46** 281–4.
26. Webb C E 1968 *J. Appl. Phys.* **39** 5441.
27. Vladimirova N M, Konkov I D, Rovinskii R E and Cheburkin N V 1971 *Opt. Spectrosc.* **31** 91.
28. Ross J N 1974 *J. Phys. D: Appl. Phys.* **7** 1426.
29. Dunn M H 1968 *IEEE J. Quantum Electron.* **QE-4** 43.
30. Dunn M H 1974 PhD Thesis University of St Andrews, Fife, Scotland.
31. Ross J N 1975 *J. Phys. B: At. Mol. Phys.* **8** 529.
32. Rudko R I and Tang C L 1996 *Appl. Phys. Lett.* **9** 41.
33. Arrigoni M, Spinelli L and Barker G 1991 Experimental methods for designing, testing, and producing high-power ion lasers *SPIE 1620 Laser Testing and Reliability* (Bellingham, WA: SPIE).
34. US Patent No 4,376,328.
35. Ginouves P T 1996 Longer lifetimes revive water-cooled ion lasers *Laser Focus World* (Tulsa, OK: Penwell) pp 69–74.
36. US Patent No 3,993,965.
37. US Patent No 3,531,734.
38. US Patent No 5,101,415.
39. US Patent No 4,378,600.
40. US Patent No 4,736,379.
41. Asher S A, Bormett R W, Chen X G, Lemmon D H, Cho N, Peterson P, Arrigoni M, Spinelli L and Cannon J 1993 UV resonance Raman spectroscopy using a new cw laser source: convenience and experimental simplicity *Appl. Spectrosc.* **47** pp 628–33.

FURTHER READING

At introductory level:.

Davis C C 1996 *Lasers and Electro-Optics—Fundamentals and Engineering* (Cambridge: Cambridge University Press) Section 9.7.

Silfvast W T 1996 *Laser Fundamentals* (Cambridge: Cambridge University Press) Section 13.2.

At research level:

Bridges W B 1982 Ionized gas lasers *Handbook of Laser Science and Technology* vol II, ed M J Weber (Boca Raton, FL: Chemical Rubber Company).

Bridges W B 2000 Ion lasers—the early years *IEEE J. Selected Topics Quantum Electron.* **6** 885–98.

Dunn M H and Ross J N 1976 The argon ion laser *Prog. Quantum Electron.* **4** 233–69.

Taylor & Francis
Taylor & Francis Group
http://taylorandfrancis.com

26

Carbon Dioxide Lasers

Denis R. Hall

CONTENTS

26.1 Introduction 337
26.2 Basic Physics of Excitation 338
  26.2.1 Introduction 338
  26.2.2 CO_2 Molecular Structure and Laser Excitation Issues 339
    26.2.2.1 Upper Laser Level Excitation 339
    26.2.2.2 Electron Excitation of N_2 and Resonant Energy Transfer to CO_2 340
    26.2.2.3 Direct Electron Collisional Excitation of CO_2 341
    26.2.2.4 Electron Excitation of CO and Resonant Energy Transfer to CO_2 341
    26.2.2.5 Lower-Laser-Level De-excitation Processes 342
  26.2.3 Optimization of CO_2 Laser Operating Parameters 342
    26.2.3.1 Selection of Gas Additives 342
    26.2.3.2 Optimization of Discharge Operating Conditions 343
26.3 Events in the Life of the Carbon Dioxide Laser 343
  26.3.1 DC-Discharge-Excited Lasers 344
  26.3.2 Convectively Cooled Lasers 346
  26.3.3 Transverse–Electric Discharge–Atmospheric Pressure CO_2 Lasers 346
  26.3.4 Waveguide CO_2 Lasers 348
26.4 Modern Era: CO_2 Lasers Excited by RF Discharges 349
  26.4.1 Introduction 349
  26.4.2 RF Gas Discharges 350
    26.4.2.1 Basic RF Discharge Structures 350
    26.4.2.2 RF Discharge Instability Processes 352
    26.4.2.3 Similarity and Parameter Scaling in RF Discharge Lasers 353
  26.4.3 Diffusion-Cooled RF-Excited Waveguide Lasers 354
    26.4.3.1 Linear RF Waveguide Lasers 354
    26.4.3.2 Power Scaling—Folded Waveguide Lasers 355
    26.4.3.3 Power Scaling—Waveguide Laser Arrays 355
    26.4.3.4 Power Scaling—Area Scaling in Planar Waveguide Lasers 356
    26.4.3.5 Annular Discharge Lasers 360
  26.4.4 Convectively Cooled Radio-Frequency-Excited Free-Space Radio Frequency Lasers 360
    26.4.4.1 Fast-Axial-Flow Transverse RF-Excited Lasers 360
    26.4.4.2 Transverse-Flow RF Lasers 362
References 362

26.1 Introduction

The study of the carbon dioxide laser and its spectacular portfolio of applications has been the topic of near continuous research and development. Although the physical principles underlying the basic operation of the CO_2 laser itself had become known and well understood within about a decade of its invention in 1964 [1], the ensuing three decades has seen huge activity worldwide in the development of diverse technological implementations of the basic laser physics. Many different types of excitation technology, as well as a wide variety of optical resonator designs required to accommodate the vastly different gain medium architectures and scales which have been invented to exploit the basic excitation physics, have been developed. This wide diversity of laser technologies developed for CO_2 lasers is capable of generating a *range* of laser beam characteristics that is probably unmatched by any other laser. These have been applied in many important applications to produce considerable practical impact in key areas of science, industry, and surgery and in the military sector. Moreover, despite the evident reduction in device research on CO_2 lasers, the scale and diversity of these applications, particularly in industrial manufacturing, continues to expand year-on-year despite the growth in competitive technologies such as solid-state and power diode array lasers. As a result, despite such 'competition', the CO_2 laser remains a basic workhorse of the laser industry, particularly where powerful and flexible beam sources are required for industrial applications.

Not only can the CO_2 laser be constructed in many different configurations, but it also has the virtue of being a highly efficient laser capable of ~20% electrical-to-optical conversion with near-diffraction-limited beam quality and able to be tuned to deliver more than ~200 discrete transitions in the 8–18 μm wavelength range. It is at its most powerful and useful in the 9–11 μm spectral region in two bands centred at 10.4 and 9.4 μm, where many important engineering materials absorb well and where there is a good transmission window in the atmosphere. Many different designs of CO_2 laser are commercially available with average powers in the range from a few watts to tens of kilowatts, and with MW peak power levels and with pulse duration in the nanosecond to microsecond range. Moreover, much more extreme performance levels in terms of peak power (TW in master oscillator power amplifier systems), pulse energy (~100 kJ) and average power levels (100s of kW) have been produced in the laboratory. Many different designs of CO_2 have been developed by companies large and small to match the attractive versatility in CO_2 laser beam characteristics, and although there has been considerable consolidation in the industry, this is a still a market where the scale and diversity of applications, particularly in the industrial sector, has sustained a highly competitive and expanding commercial environment. Over the years, there have also been very important CO_2 laser applications in certain surgical procedures, where compact, sealed laser sources have played an important role. In the military and aerospace sectors, CO_2 lasers have been the focus of very substantial research and development efforts as the active source for applications such as direct detection or coherent laser radar including laser ranging, designation, Doppler-based velocity measurement systems and directed energy. In addition, the atmospheric window, beam properties and eye safety features of CO_2 lasers make them suitable for many applications in atmospheric remote sensing. However, the most important market and key technology driver has been the industrial application sector. This has continued to grow at about 10% per annum throughout the last decade or so notwithstanding the well-documented travails of other parts of the photonics industry. There are many factors that have contributed to the growth of the CO_2 laser as a viable and productive modern industrial tool. Aside from the beam diversity and the strength of the basic laser device technologies, research on key laser–material interaction processes has been strong, often combining a sound science base with effective connections to industrial needs. In addition, certain key industries and notably machine tool and innovative automotive manufacturers embraced laser-based techniques at an early stage and integrated them into their production lines. This has stimulated significant growth in recognition of the commercial advantages of laser tools in manufacturing generally with respect to product design for manufacture, process optimization and just-in-time methodologies.

As a consequence of this high level of activity, there is considerable literature covering CO_2 laser physics device technology and applications, and many authoritative reviews (for example [2–8]) have been published over the years on most aspects of the topic. In an effort to minimize unnecessary repetition, this chapter will concentrate on CO_2 device physics and technology covering only the later period, while providing a brief coverage of the essential basic physics and a historical review of the key milestones that occurred in the first 20 years of technology development. The limitations of space inevitably mean that not all interesting and relevant topics can be adequately covered or even mentioned.

In Section 26.2 which covers the basic physics of the excitation of CO_2 laser, the aim is to provide a brief summary of the 'rules of the game' that one must appreciate in order to facilitate an understanding of the extraordinary developments in device technology that have occurred over the past years. Section 26.3 provides a rather brief historical review of the main developments over the first two decades of this technology development, covering the main events up until about 1980, while Section 26.3 covers the modern era of CO_2 lasers, which, as we will see, is based largely on the device technology opportunities made possible by the exploitation of high-power radio frequency (RF) discharges.

26.2 Basic Physics of Excitation

26.2.1 Introduction

Aside from the primary literature, many comprehensive treatments of the physics of CO_2 laser excitation have been published both in textbooks and in detailed review articles, e.g. [2–8]. The brief outline presented here is intended to provide sufficient background information on the fundamental excitation physics of the CO_2 laser to provide a basic 'underlay' for the device physics and technology covered in remainder of the chapter.

The CO_2 laser operates by virtue of energy exchanges between pairs of the low-lying rotational–vibrational energy states of the molecule. Molecules are excited to the upper energy state via collisions with energetic electrons in a gas discharge, leading subsequently to a transition that is induced or 'stimulated' by the radiation field to the lower energy state, accompanied by the generation of an IR photon with energy corresponding to the difference in energy between the two states. The rate at which such transitions can occur, and the corresponding laser output power is dependent on *both* the rate at which molecules can be excited to the upper state *and* the rate at which the lower level can be depopulated. The excitation rate of the upper level is dependent on the efficacy of the gas discharge in providing electrons with appropriate kinetic energy to preferentially excite ground-state CO_2 molecules to the upper level. As will be seen later, the efficiency of this process is hugely increased if nitrogen is added to the CO_2 laser gas mix. However, the second process essential for efficient laser action, namely, the de-excitation of the lower level, may be seriously impeded if the discharge gas temperature is allowed to rise too high, because of the thermally induced population of this level from the ground state. Thus, for gas temperatures above about 550 K, the rate of depopulation of the lower energy level becomes seriously impeded, resulting in reduced laser output power levels. Although the basic electrical-to-optical energy conversion efficiency of the CO_2 laser is high (for a laser!), with a basic quantum defect of 40% and demonstrated devices efficiencies of >20%, the difference between laser input power and laser output power appears as gas heating. It is, therefore, clear that the magnitude of the power that can be transferred to the laser discharge capable of high efficiency conversion to optical output is dependent on the rate at which waste heat can be removed from the system.

These two factors, namely, the excitation of the upper level usually by some form of gas discharge and the de-excitation of the lower level mediated via effective gas cooling, are at the very core of much of the technological innovation that has characterized different types of CO_2 laser developed over the past four decades. For excitation, various forms of gas discharge have been employed, including longitudinal dc and ac discharges, transverse RF discharges, pulsed dc discharge, electron beam discharges and a variety of hybrid excitation schemes. *Three* main options characterize the gas cooling issue. At a basic level, assuming no net heat removal from the system, the maximum input energy that can be achieved for *pulsed* systems is limited by the heat capacity of the laser gas itself to values of approximately 300 $\text{J} \cdot \text{l}^{-1}$ of laser gas at atmospheric pressure, with pulsed laser output capacity at the ~40 $\text{J} \cdot \text{l}^{-1}$ atmosphere level. The *second* and by far the simplest gas cooling method for continuous-wave (cw) or low-repetition-rate operation is passive and relies on the thermal conductivity of the gas and thermal transfer to the (cooled) vessel containing the discharge. However, much higher output power levels may be achieved by an active heat removal method where the hot gas itself is removed from the laser cavity by some form of 'fast gas flow' technique.

26.2.2 CO_2 Molecular Structure and Laser Excitation Issues

Carbon dioxide is a linear polyatomic molecule which probably because of its relative simplicity and importance in basic sciences has been studied extensively for more than 100 years [9]. Its principal axis of symmetry lies along the line of the nuclei, and it has a plane of symmetry perpendicular to this axis, as illustrated in Figure 26.1. The molecule has three vibrational degrees of freedom with vibrational modes corresponding to symmetric stretch (υ_1), where the oxygen atoms vibrate in a straight line in opposition to each other, the bending mode (υ_2), which is doubly degenerate because the oxygen atoms can oscillate in two planes perpendicular to the principal molecular axis, and the asymmetric stretch (υ_3), where the oxygen atoms are always moving in the same direction along the axis. The vibrational levels are characterized in terms of the quantum numbers, n_1, n_2, n_3, which refer to the number of quanta of energy in each of the vibrational modes. In addition, since the bending mode, υ_2, is twofold degenerate, the quantum number, n_2, has a superscript, l, which specifies the angular momentum quantum number. The relevant section of the energy level term diagram for CO_2 is shown in Figure 26.2, along with the lowest two energy levels for nitrogen. This simplified CO_2 diagram omits much of the rich spectroscopic structure, for example that which gives rise to 'hot bands' and 'sequence bands', where laser action is possible with some extra effort [10], because here we concentrate only on the molecular energy states which contribute to the most important laser emission bands centred at 9.4 and 10.4 μm. The upper laser level is the 00^01 excited state corresponding to a single quantum in the υ_3 asymmetric stretch mode with an energy, υ_3, of 2349 cm^{-1}. As indicated in Figure 26.2, there are two possible lower laser vibrational energy levels corresponding to the two emission bands referred to earlier. The first is the 00^01 energy state with a single quantum in the symmetric longitudinal mode υ_1 with a potential energy of 1388 cm^{-1}, where the energy difference gives rise to laser lines centres at 10.4 μm, while the second lower energy level is the 02^00 state, corresponding to two quanta in the bending mode and energy of 1285 cm^{-1}, with emission lines centred at 9.4 μm.

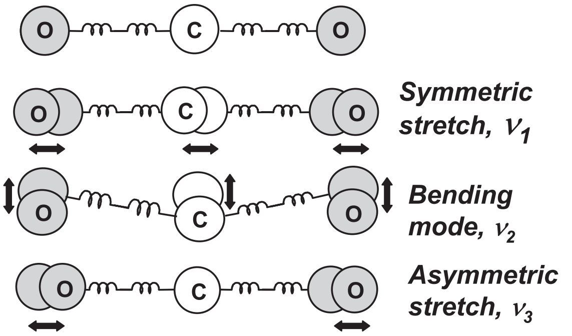

FIGURE 26.1 CO_2 molecular structure and three fundamental modes of vibration.

So far, we have only considered the vibrational character of the molecular motion, but it is clear that molecules are also free to rotate. The rotational energy of the molecule is characterized by a series of quantized rotational sublevels designated by the rotational angular momentum quantum number *J*, which may be either zero or a positive integer. The quantum mechanical selection rules for transitions between rotational–vibrational levels require that in emission $\Delta J = +1$ (describing the so-called P-branch) or $\Delta J = -1$ (giving the R-branch), as illustrated in Figure 26.3. Individual rot–vib transitions are then designated by the letter P or R for each branch followed by the *J* value of the *lower* level of the transition. For example, the strongest transition line under typical laser operating conditions is the line P(20) (at a wavelength of 10.59 μm) denoting a P-branch transition from the $J = 19$ upper level (of 00^01) and terminating on the $J = 20$ level of the 10^00 state—where for the P branch $\Delta J = +1$.

26.2.2.1 Upper Laser Level Excitation

Here, we consider the most important class of CO_2 lasers where the basic laser inversion is produced by energetic electrons produced in suitable electric *discharges*. The process of molecular excitation to the upper laser state, 00^01 may be

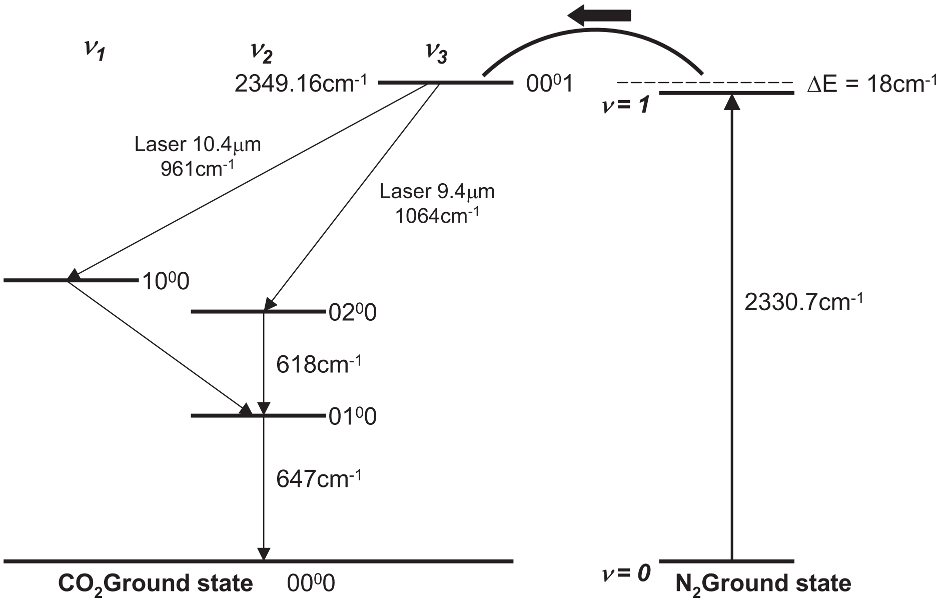
ν_1
ν_2
ν_3
2349.16cm^{-1}
00^{0}1
ΔE = 18cm^{-1}
ν= 1
Laser 10.4μm
961cm^{-1}
Laser 9.4μm
1064cm^{-1}
10^{0}0
02^{0}0
2330.7cm^{-1}
618cm^{-1}
01^{1}0
647cm^{-1}
CO$_2$Ground state 00^{0}0
ν= 0
N$_2$Ground state

FIGURE 26.2 CO_2 laser energy level diagram showing the lowest vibrational levels of the electronic ground state of the CO_2 and N_2 molecules.

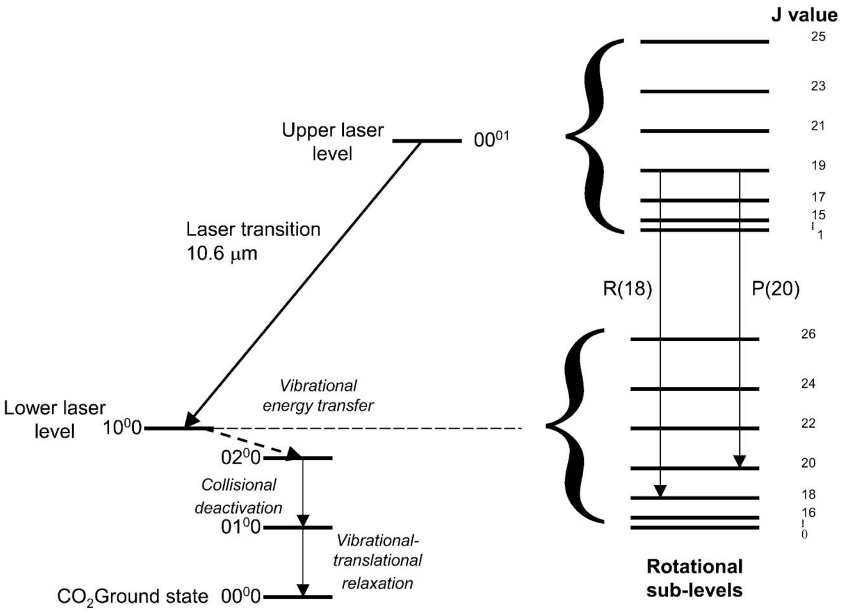
J value
25
23
21
19
17
15
1
Upper laser level
00^{01}
Laser transition 10.6 μm
R(18)
P(20)
26
24
22
20
18
16
0
Vibrational energy transfer
Lower laser level 10^{0}0
02^{0}0
Collisional deactivation
01^{1}0
Vibrational-translational relaxation
CO$_2$Ground state 00^{0}0
Rotational sub-levels

FIGURE 26.3 Some detail of the CO_2 laser (00^01–10^00) transition rotational spectrum.

achieved by three main ‘routes’, either direct excitation of the CO_2 molecules or via intermediate states in nitrogen or carbon monoxide.

26.2.2.2 *Electron Excitation of N_2 and Resonant Energy Transfer to CO_2*

Nitrogen is a diatomic molecule and therefore only has a single vibrational mode of which the two lowest states are shown in Figure 26.2. It can be seen that the potential energy of the first excited state ($\upsilon = 1$) of N_2 is 2330.7 cm^{-1} above the ground state and is in near-resonance (ΔE = 18 cm^{-1}) with the 00^01 state of CO_2. The energy difference between the two states is small compared with the value of kT of about 350 cm^{-1} for a typical discharge temperature of ~500 K. It follows that the probability of resonance energy transfer to the 00^01 state of CO_2 is high in the reaction

$$N_2(\upsilon=1)+CO_2\left(00^00\right)\leftrightarrow N_2(\upsilon=0)+CO_2\left(00^01\right) - \Delta E\left(18\ \text{cm}^{-1}\right). \tag{26.1}$$

Moreover, since radiative decay to the ground state is a forbidden process (metastable state) for a symmetric diatomic

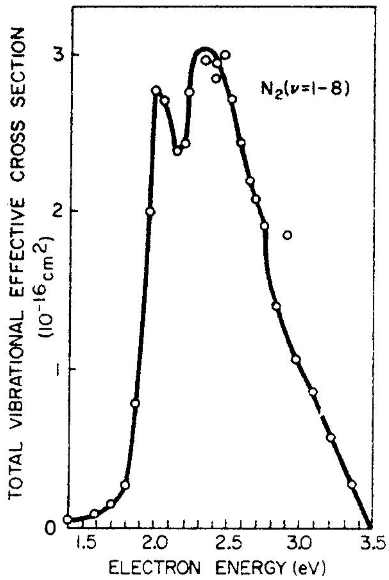

FIGURE 26.4 Total effective cross section for vibrational excitation by electron impact of N_2 for the v = 1–8 vibrational levels. (After [1].)

nitrogen molecule whereas the CO_2 (00^00) molecule can decay radiatively, the reaction proceeds predominantly in the *forward* direction, providing an efficient route for excitation of the upper laser level. However, the CO_2 lower energy level (10^00) is some 900 cm^{-1} below the highly populated N_2 ($\upsilon = 1$) level, which is too large an energy decrement for efficient collisional energy transfer to occur. Consequently, very little vibrational energy transfer occurs between these two levels, to the considerable benefit of CO_2 laser pumping efficiency. So far, we have seen that the coincidence of the energy states of CO_2 and nitrogen provides a potentially very efficient upper-level pumping route. But mother nature's contribution to the creation of a very efficient high power CO_2 laser does not end here. In addition, as first determined by Schultz et al. [11], the excitation cross sections of individual higher-lying vibrational states of nitrogen are comparable with each other and rather high for the first to the fourth level falling to 10% at the seventh and eighth levels. The net excitation effect can thus be reasonably approximated by looking at the sum to the eighth state, and as shown on Figure 26.4, the cross section for electron excitation to these levels is large ($>2 \times 10^{-16}$cm^2) for electron energies in the approximate range 2.0–2.7 eV. Moreover, the upper-lying vibrational levels N_2 decay rapidly to the $\upsilon = 1$ state, so completing an efficient set of excitation channels that funnel into the first vibrational level in N_2, as required for CO_2 laser pumping by this route.

26.2.2.3 Direct Electron Collisional Excitation of CO_2

The measured cross sections for direct electron collisional excitation of vibrational levels in CO_2 show a series of resonances associated with the three lowest asymmetric stretch, (υ_3) levels which occur for electron energies of < 1 eV [12]. However, although the value peak of the cross section for excitation of the 00^01 level is 3×10^{-16}cm^2 and occurs at an electron energy of 0.9 eV [13], it also has a high energy tail which extends to > 1.5 eV with $\sigma \sim 10^{-16}$cm^2. Consequently, the 00^01 upper laser level can be directly excited from the ground state via electron impact, according to the inelastic collision process described by

$$\mathrm{CO_2}\left(00^00\right)+e^-_{\text{fast}} \rightarrow \mathrm{CO_2}\left(00^01\right)+e^-_{\text{slow}}. \qquad (26.2)$$

In fact the electronic excitation of both N_2 and CO_2 are actually quite complex processes, which proceed via a series of intermediate steps involving negatively charged ions, and which have a significant effect on the energy threshold for the processes.

26.2.2.4 Electron Excitation of CO and Resonant Energy Transfer to CO_2

The coincidence of the near-resonance of the $\upsilon = 1$ vibrational state in nitrogen with the 00^01 state in CO_2 (and many of the corresponding excitation processes) is mirrored by a similar near-resonance involving carbon monoxide, since the energy of the $\upsilon = 1$ vibrational state in CO is within ~206 cm^{-1} of the CO_2 upper laser level. This has some impact on the excitation kinetics since, in practice, in typical gas discharges, a dissociation equilibrium is established very rapidly after switch-on in which a significant fraction of the CO_2 molecules dissociate into carbon monoxide and oxygen, so that CO molecules are available to participate in resonance energy transfer reactions. The physics of the excitation via CO is very similar to the processes mentioned earlier for nitrogen, including the involvement of a significant contribution to the excitation of $CO_2(00^01)$ via higher-lying states in CO. Excitation cross sections for low lying-levels in CO were also measured by Schultz [11] and Boness [13] and values observed to be $>4 \times 10^{-16}$cm^2 for electron energies in the range 1.5–2.3 eV. A major difference, however, is that the resonance transfer probability from CO is lower than from N_2, due to the much larger value of ΔE for CO.

Considering the overall situation for electron excitation of the upper laser level via each of the three channels indicated, it is clear that for efficient laser pumping, electron collision processes are required where the electron energies lie in the approximate range 1.5–2.5 eV. Fortunately for the creation of CO_2 laser excitation technologies, there is considerable choice in that the properties of several different types of self-sustained discharges are such that the energy range of electrons can be optimized to be in the appropriate range.

A very practical consequence of the effect of CO_2 and N_2 on CO_2 laser kinetics has been observed in research aimed at reducing the time constant for upper-state excitation in order to maximize the repetition rate achievable with direct pulsing of the laser discharge to achieve repetitively pulsed laser operation. The time constant for resonant energy transfer to the upper-state population from nitrogen imposes a repetition rate limit of a few tens of kHz in typical gas mixtures due to the time taken to 'exhaust' the energy 'trapped' in the vibrational states of nitrogen and CO. Efforts to 'beat' this limit by using nitrogenless gas mixes and aiming to rely only on direct excitation of the upper level (at some cost in terms of maximum power) are partly thwarted by the creation of CO in the discharge and 'locking-up' of upper-state population in CO near-resonant transfer.

It is important to also consider possible de-excitation routes from the upper laser level other than the desired one via either of the two possible lower laser levels as shown in Figure 26.2, since this would represent a net loss of inversion. One obvious possibility is radiative decay from the 00^01 level to the 00^00 ground state. However, for gas densities used in typical CO_2 lasers, the concentration of ground-state molecules is sufficient to ensure that radiation trapping effectively negates this loss-possible mechanism. Radiative lifetimes for molecular vibrational transitions are, in fact, very long, varying from milliseconds to seconds at typical gas pressures in the tens of torr range. Perversely the lifetime of the upper level laser in CO_2 is actually *shorter* than that of the lower laser level, so that under conditions where radiative decay dominates, laser action would be impossible. However, the important mechanisms in CO_2 laser kinetics are all collisional. Collisional lifetime effects dominate since, with values in the range 10^{-7}–10^{-8} s, they are many orders of magnitude shorter than those for spontaneous emission. Thus, spontaneous emission effects are usually ignored in setting up the kinetic rate equations and in kinetic process modelling.

26.2.2.5 Lower-Laser-Level De-excitation Processes

Radiative decay transitions from the lower laser levels $10^00 \rightarrow 01^00$ and $02^00 \rightarrow 01^00$ are both allowed, but, as mentioned previously, the corresponding spontaneous emission decay lifetimes are very long and the level population densities are dominated by collision effects. So far, we have considered the two lower laser levels, 10^00 and 02^00, as though they are completely independent of each other. In fact, the energy difference between the two levels is very small compared with kT and, furthermore, there is a coupling between the two levels (Fermi resonance) which results from the fact that the motion of the oxygen atoms in the bending mode vibration produces a degree of linear displacement of the oxygen molecules, which corresponds to symmetric stretch. The populations of the two lower laser levels are, thereby, effectively close-coupled together and to the 01^00 state via near-resonant collisions with ground state molecules as follows:

$$CO_2\left(10^00\right)+CO_2\left(00^00\right)\rightarrow CO_2\left(01^10\right)+CO_2\left(01^10\right)+\Delta E \tag{26.3}$$

$$CO_2\left(12^00\right)+CO_2\left(00^00\right)\rightarrow CO_2\left(01^10\right)+CO_2\left(01^10\right)+\Delta E'. \tag{26.4}$$

These two relaxation processes have a very high degree of probability since both energy decrements ΔE and $\Delta E'$ are much smaller than kT so, as a result, the three levels reach a state of thermal equilibrium in a very short time. The necessary process of depopulation of the lower laser levels thus reduces to processes which effect the decay of the 01^00 state to the ground state, if we are to avoid the build-up of the population and, hence, an effective 'bottleneck' in this state. However, this is the least energetic transition of any in the term diagram, and therefore, decay from the 01^00 state can only occur by means of the transfer of vibrational energy to the translational energy of the partners participating in the collision, the so-called vibrational–translational (*VT*) relaxation process. Since the probability of *VT* energy transfer in a collision is increased for light–atom collision partners, the use of helium in the laser gas mix, as noted later, is highly advantageous for efficient depopulation of the lower laser level. The use of He in the gas mix has additional significant benefits for CO_2 laser action, as we will see later.

26.2.3 Optimization of CO_2 Laser Operating Parameters

A key component of laser design is the optimization of operating conditions to maximize laser power and conversion efficiency. With the CO_2 laser, there are two particular parameter choices where optimization may be achieved, namely in the use of gas additives to the basic gas mixture and the selection of the operating conditions (particularly the *E*/*N* ratio) of the gas discharge.

26.2.3.1 Selection of Gas Additives

The use of selective gas additives in CO_2 laser gas mixtures is motivated by a combination of factors that unite to produce operational benefits and enhanced laser performance. These include the desire to increase the excitation rate of the upper level, to mediate more effective depopulation of the lower level, to reduce gas temperature and, thereby, produce a positive effect on the gas kinetics, to modify the electron energy distribution to produce increased population inversion and to reduce molecular decomposition and to stabilize the gas chemistry for stable long-life operation. We have already seen how the addition of *nitrogen* provides an alternative and highly effective pumping route for upper-laser-level excitation via electron impact to the $\upsilon = 1$ and higher-lying vibrational N_2 states, which channel their energy to the 00^01 state via collisional resonant energy transfer. Also, it has already been noted that the presence of *helium* in the gas mix can significantly increase laser gain and output power, as first observed by Moeller and Rigden [14]. Helium plays an important role in the relaxation of the lower laser levels via its role in mediating efficient *VT* collisional energy transfer processes and also in reducing electron temperature. Most importantly, helium has a crucial part to play in gas temperature control. Because its thermal conductivity is more than an order of magnitude greater than the values for CO_2 or N_2, its presence in the mix significantly enhances the rate of heat transfer to the discharge vessel walls, thus minimizing increases in temperature and, thereby, reducing the probability of a thermally induced population of the 01^00 intermediate energy state. Helium may also be used to good effect as a useful gas component in the optimization of the discharge *E*/*N* ratio for maximum fractional input power transfer to the resonant vibrational states of N_2 and CO_2, as described later. The presence of helium also cools the rotational levels as pointed out by Patel [15] and so enables these closely spaced levels to come to equilibrium with the gas temperature, thereby helping to determine the *J* line with the highest gain. This fast thermalization of the rotational manifold has the important effect of feeding energy into the lasing transition from all other neighbouring rotational transitions, which has the very important consequence that most of the energy in the upper vibrational state is extracted in a single line.

Xenon gas is frequently used as a CO_2 laser gas mix additive usually in small concentrations and for economic reasons, only in sealed-off devices. The addition of a few per cent Xe has been observed to produce increases in laser power of ~30% in both dc discharge [16] devices and RF lasers [17,18]. The presence of Xe in the gas mix is also observed to have beneficial effects on the operational lifetime of sealed-off lasers. To explain these effects, we first note that xenon has no energy levels that are resonant with vibrational levels in CO_2, CO or N_2 to produce any direct selective effects on population inversion, and as a heavy atom, it does not produce positive effects on gas cooling via its thermal conductivity properties or on thermalization of the rotational manifold. It is now widely believed that the observed benefits of the use of Xe in CO_2 lasers are a consequence of its effects on the discharge plasma properties, in particular its impact on driving the electron energy distribution to one that is more favourable for electron impact excitation of vibrational levels. For example, experiments [19] indicate that the presence of Xe produces fewer energetic electrons with energy above 2.5 eV and an increase in those with energy below this value, which explains the reduced dissociation observed, the increased pumping rates and higher gain. With RF discharges, the presence of Xe is observed to produce higher values of gain and lower measured electron temperatures and [18] and reduced discharge sheath thickness.

26.2.3.2 Optimization of Discharge Operating Conditions

In the previous discussions of optimization, we have referred rather loosely to the idea of average electron temperature. However, this is an oversimplification, and the distribution of electron energies in a molecular gas discharge is neither Maxwellian nor Druyvesteyn [20] and cannot be characterized by a single electron temperature. Here, we consider the main opportunities that exist to optimize laser performance by appropriate selection of the operating parameters of the gas discharges. In particular, we consider the optimization of the parameter *E*/*N*, which is the ratio of the electric field ($V \cdot cm^{-1}$) to the total neutral particle number density (cm^{-3}) and which is the most useful and frequently quoted optimization parameter. A number of authors have calculated the distribution electron energies for a range of relevant laser gas mixtures. However, perhaps the most useful results are those of Nighan and Bennett [21], who determined the fractional rate of energy transfer to the various excited states of CO_2 and nitrogen relevant to CO_2 laser operation as a function of *E*/*N*, as shown in Figure 26.5. They used an energy balance procedure that equates the rate of energy input to electrons from the electric field of the discharge to the rate of energy transfer from the electrons to the various molecular states that are excited by electron impact collisions. The calculations shown are for an 8:1:1 mixture of He, CO_2 and N_2 and demonstrate in a striking manner the sensitivity of the energy transfer processes to the value of *E*/*N*. In particular, it can be seen that for an *E*/*N* value of 10^{-16} V cm^2, nearly 65% of the available electron energy goes directly into pumping the CO_2 00^01 upper laser level and less than 8% into the 01^00 lower level. Virtually all energy available goes into vibrational states and nearly none into electronic states or ionization, so that discharges with these conditions are potentially extremely efficient for converting electricity into light. The calculated fractional power transfer values of ~50% coupled with the 41% CO laser quantum efficiency are in very good agreement with the experimentally observed laser efficiency values of >20% [22]. However, the selection of discharge conditions to provide the value of *E*/*N* that gives optimum laser excitation conditions is secondary to the primary requirement to produce a stable (self-sustaining) discharge and, in practice, one is usually faced with a complex iterative design and optimization process, since the conditions for ideal stable discharges with the desired physical scale are not always compatible with the requirements to optimize *E*/*N*.

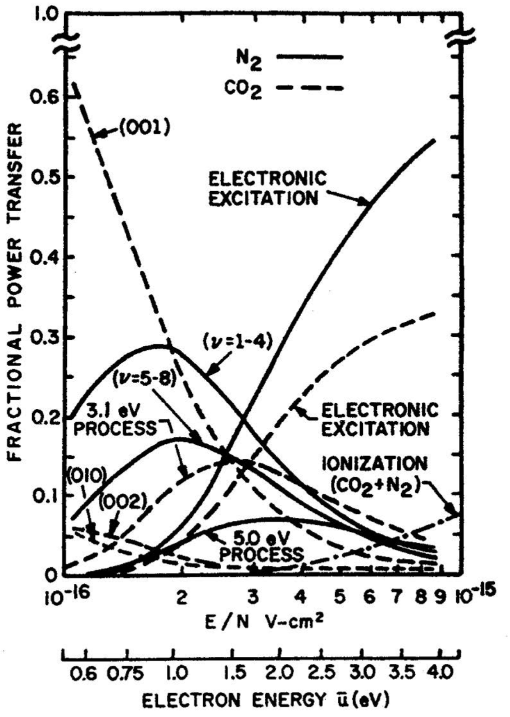

FIGURE 26.5 Fractional power transferred from electrons to vibrational and electronic excited states of CO_2 and N_2 as a function of *E*/*N* for a CO_2–N_2–He, 1:1:8 gas mixture. (After [21].)

26.3 Events in the Life of the Carbon Dioxide Laser

Although most of the key excitation physics underpinning the operation of the CO_2 laser were quite well understood after the first 10 years or so of its life, the ensuing 30 years or so has seen the growth of a very extensive literature devoted to laser device technologies and applications. As mentioned previously, the technology developments have been driven by a diverse application sector, dominated by industrial processing and military applications but also including applications in surgery, science and remote sensing. However, it is clear that most of the leading edge research particularly prior to 1980 was driven by military and aerospace requirements. To meet these needs, CO_2 lasers have been developed with the capability of producing a very wide range of laser beam characteristics and a correspondingly diverse range of disparate device *technologies*. In fact, of all lasers, the CO_2 laser probably has the widest diversity of laser output beam formats. Thus, different CO_2 laser technologies may operate in cw mode from mW to the MW range, in pulsed mode with pulse widths from millisecond to subnanosecond, with repetition rates to hundreds of kHz with pulse energies to the MJ range, and with >200 discrete lines in the 8–18 μm wavelength regions, that may be frequency stable to a few parts in 10^{-12}. Moreover, many of these laser technologies have been developed for commercial production for a very wide range of applications and proven to be very successful in the market.

Although, as will be seen later, technologies for CO_2 lasers may appear to be extremely dissimilar, they all have in common the key constituent elements of a gain medium excitation technique, a gas cooling method, an optical resonator design, a gas mixture control subsystem and a mechanical support system. Each of these may be realized in very different ways, but all are necessary for effective laser operation. Virtually all gain excitation techniques for CO_2 lasers involve some form of gas discharge, though excitation via rapid gas expansion through a nozzle is the basis of the gas dynamic laser, which had a relatively transient 'life' in the 1970s as a feasible but technically demanding route to very high average power levels [23]. Thus, discharges involving dc, ac or RF power generators, with cw or pulsed outputs, have all been developed as practical and effective pumping techniques, though only RF techniques have seen significant development in the 'modern era' since about 1980. In Section 26.2, the importance of controlling gas temperature rise has been emphasized, so effective gas cooling is a necessity. Techniques have included 'passive' cooling based on diffusion of the laser gases to water or air-cooled surfaces; selection of appropriate gas mixtures with effective transport properties is key here, and high helium content is usually important. To achieve higher power levels, gas transport cooling techniques have been developed which employ high-speed gas flow, which may be either transverse or co-axial with the laser optic axis.

The range of optical resonators and intracavity optical components selected for use with CO_2 lasers is also extensive, and it is usually the physical scale of the gain medium *transverse* aperture which is the key factor determining the design. Conventional stable free-space Gaussian resonators in linear or folded designs are an excellent match to many excitation schemes involving modest diameter (usually less than a few cm) cylindrical tubes to contain the gas discharge. For very small apertures, free-space resonators cannot be used and a distinct class of 'waveguide resonators' that incorporate a waveguide section are appropriate while for large aperture devices such as transverse–electric discharge–atmospheric pressure (TEA) lasers or electron-beam-excited lasers [24], unstable resonators are usually required. Hybrid designs, e.g. waveguide-unstable or stable–unstable, are often found to be suitable for lasers with large-aspect-ratio gain media, where the transverse and lateral dimensions are very different. Most CO_2 lasers operate in the 9–11 μm infrared wavelength range where there are few high transmission materials for use as substrates for optical components. Of these, zinc selenide has the lowest absorption loss and is the most frequently used material for output couplers, lenses, etc., although germanium and KCl have been used in the past. Optical coating technology is well developed for both high damage-threshold, low-loss high reflectors where reflectance values of >0.99 may be achieved and partially transmitting mirrors with low losses and effective antireflection coatings. For high reflectors, glass, semiconductor (silicon on GaAs) or metals (copper, beryllium–copper etc.) are in common use depending on the power levels. For high average power lasers, water cooling must be used to prevent surface distortion or damage in resonator mirrors and beam-forming optics [25]. Large-aperture mirrors for unstable resonators have been developed for high-power lasers, and there has been considerable progress in the development of high damage-threshold coatings. Reflective diffraction gratings with acceptably low losses are also available with the capacity to resolve adjacent rotational–vibrational lines and facilitate the design of single-line tunable lasers. Overall, the industry supplying optical components for use in CO_2 lasers has become very mature with a strong element of consolidation, as befits a well-established commercial marketplace for these lasers. Control of the gas chemistry and, in particular, the level of dissociation of the CO_2 gas is also a crucial requirement. In sealed lasers, such control also demands effective vacuum engineering, and several companies have developed proprietary processing regimes capable of producing equilibrium mixtures with adequate CO_2 concentration for particular discharge regimes to produce stable laser power levels sustained over lifetimes exceeding 10 000 h. The use of 'slow-flow' of the laser gas to remove dissociation products and to ensure constant gas composition is technically less demanding to achieve but requires the use of a consumable gas supply and vacuum pump and is usually unacceptable in modern commercial lasers. In some slow-flow systems and many 'fast-flow' convectively cooled laser designs, catalysts are employed to stabilize CO_2 dissociation and ensure constant gas composition. For all lasers, a suitable mechanical system is required to support and package the key operational elements of the device in a manner appropriate for the overall design. In particular, a detailed optomechanical design is an important (but sometimes neglected) requirement to ensure stable beam properties over the range of thermal and mechanical conditions that it may be anticipated that the laser will encounter.

26.3.1 DC-Discharge-Excited Lasers

The earliest form of CO_2 laser in common use employed longitudinal dc discharge excitation. A typical laser of this type involves the use of a cylindrical glass tube with a co-axial water jacket with anode and cathode structures often in side arms, as illustrated in Figure 26.6a. The dc discharge behaves as a negative impedance element, so the high-voltage dc power supply is required to provide discharge circuit stabilization, most simply via a series resistor as shown in the figure. The gas mixture may be static in a sealed-off configuration or operated in slow-flow mode with a mixture of CO_2, N_2 and He (with Xe included in sealed mode mixtures) at a total pressure of a few tens of torr. As a consequence of the law of 'similar discharges' (pd = Constant) [26,27], the optimum gas pressure is inversely proportional to the tube diameter, which is typically in the 10–20 mm range with gas pressures of a few tens of torr (760 torr = 1 bar = 1.013×10^5 Pa). The gas is cooled here by radial diffusion to the glass tube walls, with modest levels of heat transfer through the glass to the circulating water coolant. In general, the laser power output increases with current density until gas heating effects exceed the capacity of the cooling system and a thermal bottleneck in the lower laser levels occurs (corresponding to an axial gas temperature of ~ 600 K) whereupon it falls. Thus, the optimum value of current density is inversely proportional to tube diameter, though as dictated by discharge similarity principles, the output power of the laser depends only on tube length. In practice, laser powers of 50–100 W m^{-1} can be achieved, depending on the laser constructional details and degree of control of the gas chemistry. The development of sealed-off cw CO_2 lasers was a topic of major practical interest for many years, driven by application needs in military and space-borne systems. It was shown that careful attention is necessary in the choice of material and design for the cold-cathode structure coupled with the choice of gas additives [28].

Commercial versions of slow-flow lasers of this type began to be available in the late 1960s at power levels of tens of watts and were used for some industrial applications (e.g. ceramic scribing), as well as scientific and government research. The wavelength selectivity feature of the CO_2 laser was soon exploited by the use of a planar diffraction grating in the Littrow configuration as one of the laser mirrors, as illustrated in Figure 26.6b. Lasers with this basic tuning design are still in use for spectral applications that require unambiguous single-line operation at wavelengths away from the band centres. Frequency tuning within a given rotational–vibrational emission line may also be achieved via resonator length tuning, for example using a piezoelectric length transducer fitted to one of the resonator mirrors. However, for these lasers, operating pressures are low at a few tens of torr, so that the tuning range is limited to ~50–100 MHz.

Much higher power levels were soon achieved in experimental systems by geometric folding of the resonator. In one design developed at MIT Lincoln Laboratory, an average power of 1 kW was obtained from a device 230 ft in length, employed in such a planar folding system [29], while a year later in 1969, Horrigan reported a 750-ft-long folded laser which produced 8.8 kW [30]. Driven by demands from applications in industrial materials processing, commercial folded lasers at power levels to a few kW became available from the major laser suppliers during the early 1970s. Notable among these was a highly innovative and compact design from Ferranti Ltd in the United Kingdom, which employed a 3D folding system utilizing a Herriott cell which produced near-diffraction-limited beam quality at power levels of 400 W—and later to 2 kW [31]. A great deal of development work on longitudinal discharge lasers was carried out by numerous companies in Europe and North America, especially during the 1970s, to meet the rising demands for reliable lasers for the industrial processing market. During this period, considerable practical advances were made in discharge technology, folded resonator

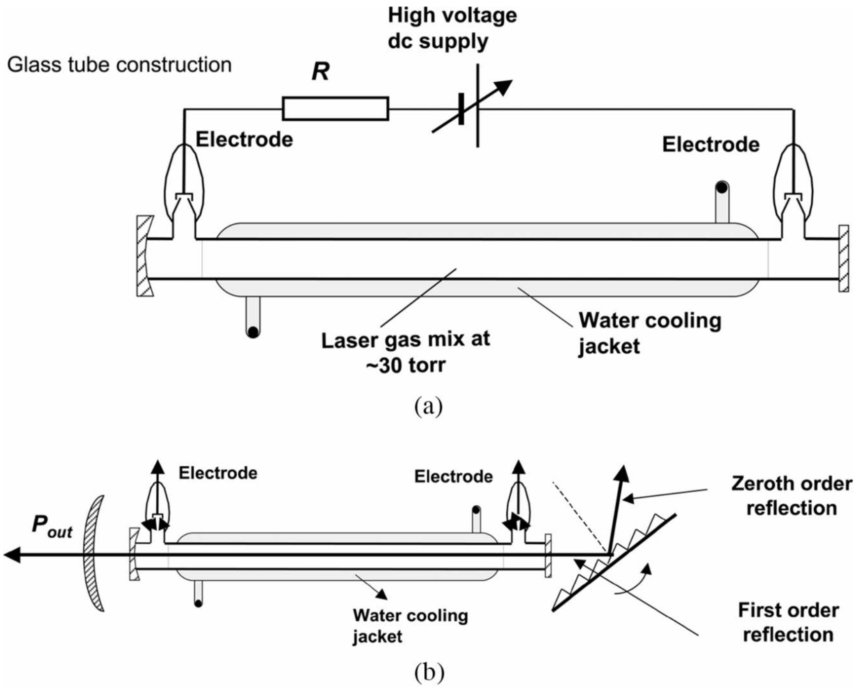

FIGURE 26.6 (a) Longitudinal dc-discharge-excited CO_2 laser tube and (b) line-tunable selectable CO_2 laser using diffraction grating tuning laser.

design, gas-handling systems and power supplies, so that this generation of lasers, though rather bulky, became reliable and important commercial workhorses for several generations of laser-based production systems.

26.3.2 Convectively Cooled Lasers

Although the CO_2 laser has an intrinsic capacity for high electrical-to-optical energy conversion efficiencies, as mentioned previously the output power is nevertheless limited by excess temperature rise of the gain medium. For diffusion-cooled dc-excited lasers, the average power extraction limit of <100 W m^{-1} limits laser power to a few kW usually in rather bulky slow-flow lasers that may be inconvenient for integration into processing systems. An alternative approach to achieving multi-kW laser outputs is to significantly improve the heat removal ability of the laser beyond the limited capacity of passive diffusion cooling in centimetre-scale dielectric tubes. This may be achieved by flowing the gas mixture out of the gain region at high speed (~100 m s^{-1}), so that the heat is removed from the active laser discharge gain region by simply removing the hot gas itself and replacing it with equivalent cool gas in a process termed *convective cooling.* The hot gas mixture removed by the flow system can then be cooled by a suitable heat exchanger unit within an external flow system, and the cooled gas subsequently returned to the discharge gain region. This approach provides much more effective cooling than the passive diffusion technique described earlier, and specific power output values of several kW m^{-1} can be achieved in practice. The maximum input power $P^{\mathrm{i}}_{\max}$ to the discharge under convectively cooled conditions is given by

$$P^{\mathrm{i}}_{\max} = (1-\eta)\dot{M}c_{\mathrm{P}}\Delta T \tag{26.5}$$

where η is the laser conversion efficiency, $\dot{M}$ is the mass flow rate, c_{P} is the specific heat and ΔT is the rise in the stagnation temperature (about 300 K). The laser efficiency is ~15%–20%, and the mass flow rate depends on the operating gas pressure and the volume rate of the gas blowers.

As illustrated in Figure 26.7, two types of convective cooling (fast-flow) systems have been developed for use in multikilowatt lasers: *axial-flow* systems involving gas flow along the optic axis of the laser and *transverse-flow* lasers, where the gas flow is transverse to the optical axis [32]. Longitudinal flow designs are much more commonly employed due to the simpler constructional arrangements that can be used, involving single or multiple discharge sections in cylindrical glass tubes a few centimetres in diameter, with in-line cylindrical electrodes. In addition, for axial-flow cooling, it is usually less complex to design lasers with high beam quality since any variations in gain medium particle density and refractive index are approximately radial. Since dc discharges in large bore tubes operate at gas pressures of only a few tens of torr, high mass flow rates demand large volume rates and, therefore, (large) high capacity blowers are required for the production of high laser powers. However, such blowers are not available with very high volume rates. In fast *axial*-flow devices, Roots blowers must be used in order to overcome the large pressure drop across the discharge tube, but unfortunately such blowers have limited volume flow capacity. Nevertheless, in practice, there are relatively few serious problems in extending the power levels of axial-flow lasers to ~5–10 kW range by multiple 'U' or 'V' folds, and many companies have developed such lasers for the industrial market, notably for high-speed flat-bed cutting.

By contrast for cross-flow lasers, gain medium density fluctuations are one-dimensional and occur in a direction transverse to the laser axis as shown in Figure 26.7b: optical resonators that provide effective compensation for these effects are, therefore, rather more difficult to design. However, blowers with simpler designs (such as single-stage compressors or radial fans) are available which are capable of high volume rates (and, therefore, higher laser powers) because of the much smaller pressure drops involved.

To achieve the stable long-term operation that is needed for most applications of fast-flow lasers, it is necessary to take account of molecular dissociation. To achieve this, it is usual to design flow-through catalysis units into the external gas-flow loop in order to control the level of dissociation and the concentration levels of the key gases. Over the years, considerable effort has gone into producing highly effective proprietary designs for flow loops for convectively cooled CO_2 lasers, although some degree of 'gas make-up' is often required. For obvious geometric reasons relating to the transit time of the laser gas through the gain region (see Figure 26.7a and b), the transverse-flow technique provides, *at least in principle*, a larger value of heat removal capacity than for axial flow, so that transverse-flow systems potentially offer advantages for very high average power lasers. For such lasers, it is advantageous to operate at higher values of gas pressures (~100 torr), that is five to ten times larger than the value typically used for axial lasers. In order to minimize the required inter-electrode separation, as well as other practical reasons, it is usual for cross-flow lasers to employ discharges that are maintained in a direction transverse to both the flow direction *and* the optic axis, as shown in Figure 26.7b. Transverse-flow lasers offering power levels in excess of 10 kW have been developed for material-processing applications such as thick section welding that require very high power levels and where the somewhat reduced beam quality is less important in practice.

26.3.3 Transverse–Electric Discharge–Atmospheric Pressure CO_2 Lasers

Although it is possible to operate longitudinal dc discharges of the type discussed earlier in a *pulsed* mode and thereby to produce pulsed laser radiation, the attainable peak powers and pulse energies are severely restricted by limitations in scaling the discharge in volume, gas pressure and power. However, beginning in about 1969, a series of discoveries occurred within a few years of each other, which completely changed the situation with regard to CO_2 laser scaling in peak power and pulse energy because of significant advances in scaling lasers to larger discharge volumes at high (atmospheric) pressures. It was realized that the key to success here is to use a transverse pulsed dc discharge architecture with essentially parallel plate electrodes. However, for several years, the missing technical

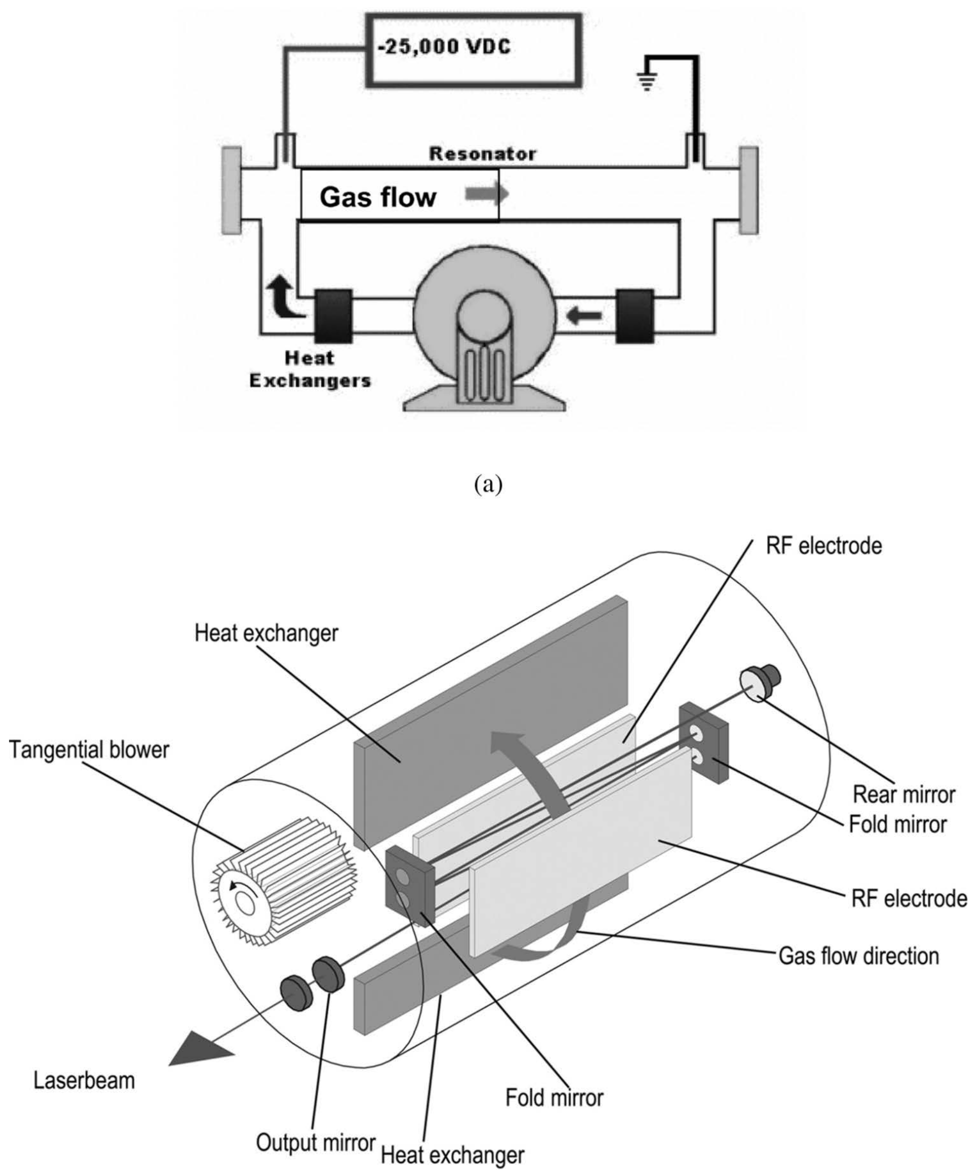

(a)

(b)

FIGURE 26.7 (a) Convectively cooled CO_2 laser employing fast axial gas flow and (b) convectively cooled RF-excited CO_2 laser employing fast transverse gas flow.

advance was the invention of some techniques to 'volume-stabilize' the discharge. First Beaulieu in Canada [33], then Dumanchin and Rocca Serra in France [34] and Lamberton and Pearson in the United Kingdom [35] succeeded with novel methods for controlling a transverse avalanche discharge in a high (atmospheric) pressure mixture of CO_2, N_2 and CO_2 and preventing the onset of instabilities and the triggering of arcs within the discharge. Thus was born the TEA laser, the acronym for transverse electrically excited, atmospheric pressure laser, a major landmark in CO_2 technological history. These inventions triggered a period of intense worldwide research activity in the race to 'control' larger and larger discharge volumes and to develop practical technologies for repetitively pulsed lasers [36,37]. This was seen as the route to scaling TEA lasers for very high peak powers and pulse energies and to produce effective and practical technologies for both low and high repetition rate laser devices.

A schematic diagram of a typical TEA laser of the modern era is shown in Figure 26.8. A pair of shaped metal electrodes is arranged in parallel and separated by ~1–5 cm with lateral dimension up to about 10 cm defining a (usually) rectangular cross-sectional discharge with length up to ~1 m. The electrode shape is determined by the requirement to control the discharge width and to ensure uniformity in the electric field and, thereby, in the discharge. In this design, pre-ionization of the main discharge volume is provided by the UV radiation emanating from two rows of running arc discharges between pairs of subsidiary pin electrodes positioned at intervals of 5–10 cm along the length and on each side of the main discharge. These arc discharges are supplied with electrical energy stored in the

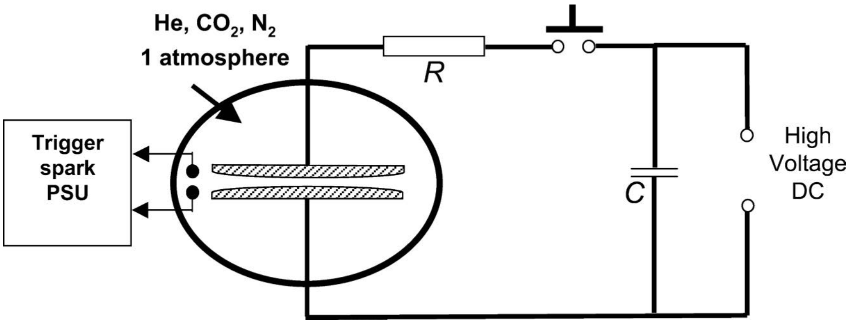

FIGURE 26.8 Schematic diagram of a TEA (transverse–electric discharge–atmospheric pressure) CO_2 laser.

ceramic capacitors that support the pin electrodes, as illustrated in the schematic diagram. The deep UV produced by the sparks produces the necessary ionization in the gas volume by both photoionization of constituents of the laser gas mixture and also photoionization of the electrode surface. Once the pre-ionization has become established within the whole laser volume, a fast high voltage switch (spark gap or hydrogen thyratron) is used to rapidly switch the energy from the main (~10–50 nF) capacitor, which can be repetitively charged to ~25–40 kV via appropriate pulse-forming circuitry. Other forms of pre-ionization that have been used include trigger wires, x-ray pre-ionization and electron beams, as described in Refs. [36,37].

Much of the early interest in TEA lasers was for military applications and as a source of high-peak power, short-pulse radiation for research on laser-generated plasmas. However, interest in the use of TEA laser systems for industrial applications and, in particular, for product marking began to increase in the late 1970s. The discharge electrode geometry is suitable for the generation of large relatively uniform multi-mode rectangular beams, which are used to illuminate a thin mask, usually of copper in which the mark/code/message to be marked has been etched. The image is then projected onto the product to be marked, for example as it passes on a production line. Typical TEA lasers for this application emit pulse energies of ~5 J in 1 μs and with pulse repetition rates up to ~50 Hz.

26.3.4 Waveguide CO_2 Lasers

Waveguide lasers can be distinguished from those employing 'conventional' resonators by the fact that over at least some part of the intracavity path, the laser radiation is guided and does not obey the laws of free-space Gaussian propagation. In the early 1970s, the demands of one particular NASA application led to a surge of interest in lasers with gain cells with cross-sectional dimensions which are too small for Gaussian beam propagation and where optical guiding can be exploited. The optical propagation laws [38] and resonator physics [39] for such lasers differ considerably from that of free-space devices and have been the subject of considerable subsequent research—see [8,40,41]. The NASA requirement was to produce continuous frequency tunability of ±500 MHz in heterodyne receiver local oscillator laser for use in wideband telecommunication links between satellites in earth orbit [42]. In typical CO_2 laser gas mixtures, collision effects produce line broadening at ~5 MHz torr^{-1}, so gas pressures of >150 torr are required to achieve the required continuous tuning range. Recalling the similarity rules gas discharges, this implies the use of tube diameters of <2 mm, which is not possible for conventional resonators of the required length. Earlier work with helium neon lasers [43] had demonstrated the concept of lasers based on hollow dielectric waveguides, and it was not long before the CO_2 waveguide lasers became a reality [26,44,45]. The potential of waveguide lasers to provide compact, stable sources of infrared laser light for applications in laser radar and other military/aerospace applications was rapidly recognized, and considerable development took place in the mid- and late 1970s. A typical sealed–off dc waveguide laser of the time, capable of 5 W cw, is shown in Figure 26.9. As with conventional diffusion-cooled free-space lasers, tubes for dc-discharge-excited waveguide lasers are usually cylindrical but may be fabricated from alumina (or, in extreme cases, beryllia [46]) instead of Pyrex glass, for improved thermal conductivity and reduced waveguiding losses and to meet demands for more rugged construction. The use of small-bore higher-pressure discharges requires the use of longitudinal high dc voltages, and the need for series ballast resistance means that twin 'central' electrodes are needed to permit electrically grounded mirror mounts as shown in the schematic diagram. Considerable research was devoted to investigating laser scaling laws in the spirit of discharge similarity principles [26,47] and to developing device technology for practical (field) applications. Technology limitations such as the maximum available length of (very straight) dielectric waveguide, excessively high dc voltages and/or the complexity of multiple high voltage dc discharges in restricted volumes put quite practical restrictions on cavity folding strategies and limited power levels to a few tens of watts. This matched several important military requirements but was generally too low for many key industrial applications of the time. Nevertheless, much of the research conducted on dc waveguide laser device physics laid the groundwork for future significant developments in the later life of the CO_2 laser. In particular, it prepared the way for the subsequent utilization of RF discharge excitation, which effectively solved most of the technical problems of dc discharge devices but, even more significantly, it opened the door to *planar waveguide* architectures and the huge device technology potential of *area scaling* to produce ultra-compact high-power high-brightness lasers, which is a main topic of Section 26.4.

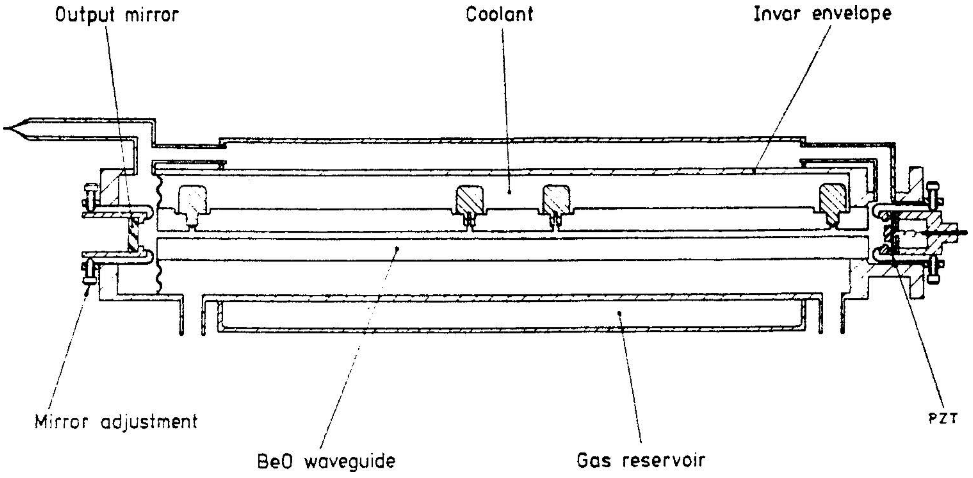

FIGURE 26.9 Schematic diagram of a 6-W dc-excited waveguide CO_2 laser. (After [47].)

26.4 Modern Era: CO_2 Lasers Excited by RF Discharges

26.4.1 Introduction

The onset of the 'modern era' in the progress of CO_2 laser technologies to their present state can be traced to an intensive burst of research activity that began to gain momentum around 1980, and which lasted for about a dozen years, underpinning a new generation of ultra-compact high-performance commercial lasers. The key factor that sparked this interest was the growing realization that transverse RF discharges offer significant advantages over dc discharges as an effective technique for the excitation of CO_2 in both diffusion-cooled and fast-flow formats. Aside from offering a series of important but incremental technology improvements over dc lasers, the major impact of RF technology has been in enabling *new laser device architectures*. Thus, the ability to control RF discharges over very large areas of *all-metal electrodes* at unprecedented power densities in relatively simple and inexpensive structures provides the basis for high average power lasers in ultra-compact sealed packages, using the planar waveguide or annular configuration. This feature, which has spawned a whole new generation of ultra-compact high-power sealed-off lasers, is not feasible with dc discharge excitation due to the onset of arcs and discharge filamentation. In addition, RF discharges can be modulated or switched at much higher frequencies than for dc discharges, so facilitating considerable benefits in terms of more flexible temporal formats, which is crucial for many important material-processing applications. Also, at a practical technological level, there are several important device engineering advantages of RF versus dc discharge excitation. These include the avoidance of high voltages and cathode processes for a reduced impact of gas chemistry effects on the sealed lifetime, an all-metal construction for more effective cooling, the avoidance of ohmic losses in series ballast resistors and simpler, more rugged and lower-cost construction opportunities. Convectively, cooled lasers share many of these advantages.

Research on high-frequency discharges can be traced back to the end of the 19th century [48], and indeed, RF discharge excitation was involved in a number of landmark experiments in the early days of gas laser physics. For example, the first gas (HeNe) laser and the first CO_2 laser were excited by RF discharges [49,50], and the first waveguide laser also employed RF fields [43]. However, despite several apparently promising results [51,52] obtained with RF and combinations of RF and dc fields, high-frequency excitation was largely ignored in favour of dc discharge pumping until the end of the 1970s. The resurgence of interest owes most to the pioneering work of Laakmann and co-workers at Hughes Aircraft Company [53–56] and of Chenausky et al. at United Technologies Research Center [57,58] in the United States and the Hull University, United States, group [59,60] following the first published report by Lachambre and colleagues at DREV in Quebec, Canada [61]. At about the same time, several Russian researchers including Raizer [62], Myshenkov [63] and Yatsenko [64] were active in fundamental studies of the structure and properties of transverse high-frequency discharges, and their work was to have a profound impact on the development of practical laser excitation technologies over the following decade.

After a few years, it became apparent that two distinct strands could be identified in the international research efforts in the area of RF excitation of CO_2 lasers. Thus, while most of the initial work was focused on RF discharges in hollow waveguide gain structures, aiming at higher-performance sealed lasers cooled by *diffusion*, a different orientation soon became apparent where researchers, mostly in Germany, began developing RF excitation technologies for fast-flow, *convectively* cooled lasers. This research led to the development of RF-excited lasers involving axial gas flow in glass tubes of diameter ~2–10 cm, with transverse RF discharges maintained between shaped external metal electrodes. In this configuration, the dielectric nature of the glass tube walls provides additional capacitative ballast, which *combines* with the internal stabilizing influence of the RF discharge sheaths to permit stable discharge operation at high power densities. These values are substantially higher than for equivalent dc discharge lasers (even when 'stabilized' by turbulent flow) where thermally induced arcs are the limiting factor, though they are significantly lower than for the all-metal 'thin' discharges of diffusion-cooled planar waveguide lasers mentioned earlier. However, the use of glass tubes and external electrodes is conveniently compatible with fast-flow cooling techniques and offers relatively simple laser engineering opportunities for folded cavity designs typical of those that had previously been developed for dc lasers. These designs were soon undergoing commercial development and were the forerunners of several successful families of commercial RF lasers.

This section of the chapter endeavours to provide a summary of the key device physics/technology features of each of these two types of transverse RF discharge laser. As a necessary introduction to this, we first introduce the underlying physics and operational characteristics of transverse RF discharges, since it is their distinct properties that are the essential enabling factor in the most significant developments in CO_2 laser engineering technologies over the past years.

26.4.2 RF Gas Discharges

26.4.2.1 Basic RF Discharge Structures

ac discharges differ from dc discharges because the polarity of the applied electric field reverses every half cycle, though at low frequencies the properties of ac discharges do not differ appreciably from those which are unidirectional. However, when the oscillation frequency increases sufficiently so that the electron ambit is smaller than the discharge dimensions, the situation is transformed and the discharge structure and physics for high-frequency discharges is very different from the dc case. Moreover, as discussed later, RF discharge excitation offers considerable fundamental and practical advantages for high-performance CO_2 lasers. The use of the terms 'high' or 'radio' frequency is somewhat imprecise, but, in the present context, they refer to frequencies in the approximate range 1–200 MHz, though for practical reasons, most research and all commercial RF lasers employ power generators with frequencies below ~100 MHz. Both 13.56 and 27.12 MHz are preferred industrial frequencies for larger electrode separation, non-waveguide lasers where frequencies at the low end of this range are required. At a very basic level, the physical phenomena involved in dc and ac discharges are not dissimilar. The main differences derive from the temporal interaction of the frequency of the applied field, the oscillation frequencies, collision frequencies and drift velocities of the charged and neutral particles, on the one hand, and the scale and geometry of the electrodes and/or containing vessel, on the other. Electrons gain energy from the applied field and transfer it to atoms and molecules via collisions, and collisions may result in electronic/molecular excitation or ionization of atoms or molecules or electron loss from the discharge depending on conditions. For example, electron multiplication may be produced by ionization processes in the bulk of the gas or following secondary emission following ion bombardment of the electrodes/walls or by a combination of both processes. For laser excitation, we look for electron collisions to produce excitation of atoms (molecules), while recognizing that as well as electron multiplication in the field, electron loss will occur by recombination with positive ions, by attachment to neutrals to form negative ions or simply by collision with the walls.

We consider a simple parallel plate metal electrode structure typical of RF lasers as illustrated in Figure 26.10a. A transverse RF electric field is applied between the plates in a vacuum enclosure containing gas at intermediate pressure (~10–300 torr). Assuming that only electron motion need be considered due to the high relative mass of atoms/molecules, the initiation of the discharge will result in potentially large electron loss to the electrodes due to the frequency-dependent and finite oscillatory electron motion in the applied field. This leads very rapidly (microseconds) to the creation of electron-depleted regions of high positive ion concentration or 'space charge layers' near each electrode. The resulting combination of space charge fields and applied RF field determines the spatial structure, dynamics and frequency dependence of the discharge for a given inter-electrode spacing. As described later, the space charge regions play a crucial stabilizing role in the role in RF discharge operation. Two stable forms of the RF discharge were identified by Levitskii [65] for this transverse-field situation. The first of these was designated the alpha (α) discharge, reflecting the fact that, in this case, the ionization is maintained largely by electron multiplication in the main volume, where the Townsend α-coefficient applies. The α-discharge is usually, though not always, characterized by low current densities; it has a positive net impedance characteristic and, in practice, is the only one of the two discharge types that is relevant to the pumping of molecular lasers such as CO_2. The second type, designated the gamma (γ) discharge, is associated with higher current densities and involves secondary electron emission from the electrode surfaces and, hence, the γ-designation consistent with the Townsend γ-coefficient describing electrode secondary emission. γ discharges have near-electrode regions which are RF analogues of the near-cathode regions (cathode sheath, negative glow and Faraday dark space) of the dc glow discharge. Although the γ-discharge may have a diffuse plasma column that may be quite uniform, the high power dissipation in the sheaths together with the low electron temperature in the plasma glow renders this type of discharge useless for molecular laser excitation [63,66]. Thus, in practice, the transition from an α-discharge to a γ-discharge may be considered as an 'instability' process, to be avoided at all costs.

Observation of the visible light emission from α RF discharges reveals significant transverse structure, with intense visible light emission ('striations') evident in the high-field 'sheath' regions close to but not immediately adjacent to each electrode [67], as illustrated in Figure 26.10a. The striations are caused by electronic excitation by energetic electrons accelerated by the high fields in the boundary layers, with the sheath regions effectively isolating the more diffusely emitting discharge plasma column from the electrodes. The α-discharge is characterized by a stable and positive impedance characteristic, and its plasma column can provide efficient laser excitation, while suffering low dissipative power losses in the sheath regions. The scale of the sheath regions depends on the operating conditions, and ideally, they occupy only a small fraction

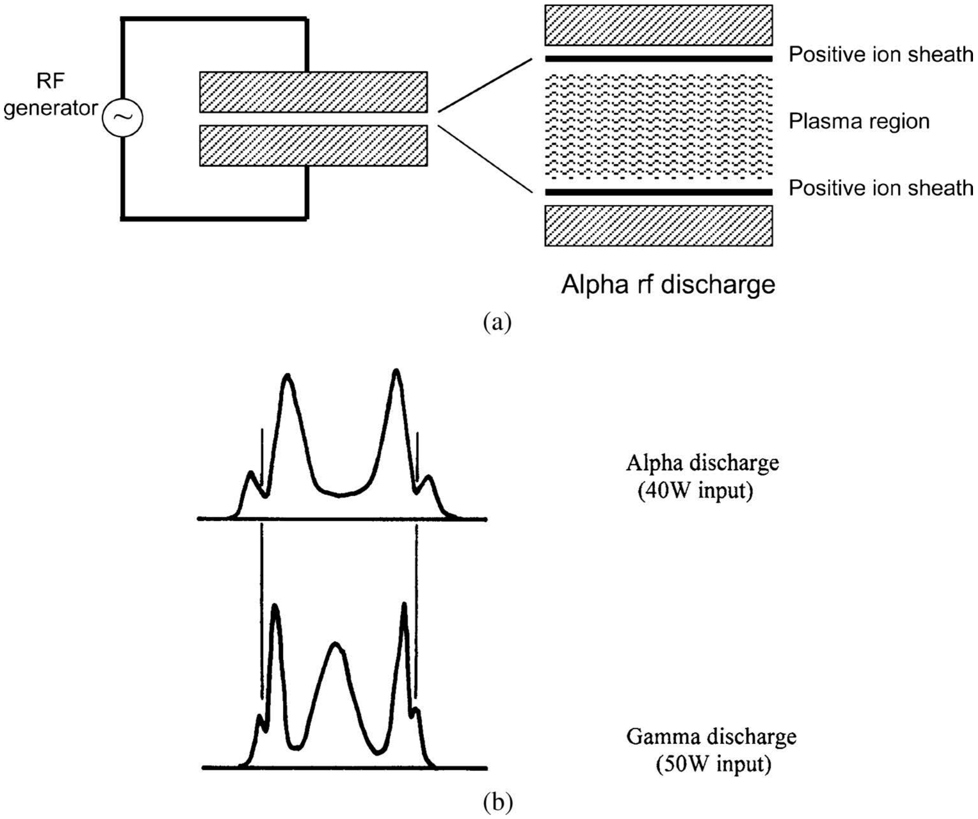

FIGURE 26.10 (a) Schematic diagram of transverse RF electrodes and α-discharge structure and (b) TV line scans of the visible emission from an RF discharge in the α and γ modes. (After [98].)

of the inter-electrode spacing since they do not contribute directly to laser excitation. Given the strong parametric dependencies of RF discharge properties, an issue of major practical importance is the optimization of RF discharge conditions for efficient laser operation. This applies both for the case of narrow-discharge 'waveguide-type' diffusion-cooled devices and also for larger electrode separation laser designs that are cooled by fast gas flow. However, first, we consider the more fundamental question of the instability processes to which α RF discharges are subject particularly under conditions of high power loading. The aim is to design devices such that the probability of instabilities occurring is minimized. From the earliest days of RF laser investigations, it had been observed that although in certain situations, the magnitude of the power density that can be maintained in the plasma column of a spatially uniform RF discharge may be large; nevertheless, it is limited. Above certain values, depending on the conditions, it is observed that the α RF discharge becomes unstable, producing significant observable changes in its structure and properties. In particular, for laser pumping, such instabilities result in the destruction of the inversion, and laser action ceases. Therefore, the challenge was to understand the key instability processes so that inappropriate operating conditions could be avoided. Perversely in this context, the basic question that confronted researchers for many years was to determine the origin of the high degree of *stability* that characterized RF discharges maintained between *metallic* electrodes, rather than specifically to understand how the instability occurs. In the early 1980s, Myshenkov and Yatsenko [63] had shown that the instability threshold depends critically on macro-parameters such as generator frequency, electrode separation and gas pressure and composition. Moreover, Kolesnychenko et al. [68] and Wester et al. [69] among others noted that the insertion of dielectric sheets (or glass tube walls) between the metal electrodes and the low-pressure gas produced an increased instability threshold. They correctly attributed this to the additional ballasting (current stabilizing) effects of the series capacitance of the dielectric sheet. However, the problem remained to explain the relatively high level of stability of α-discharges with no added series dielectric/capacitative ballast and to determine the instability threshold for situation where parallel all-metal electrodes are used. This is particularly relevant for laser design since the avoidance of dielectric sheets in an all-metal structure is highly desirable to enable efficient cooling and the attainment of high-power density excitation.

With a detailed analysis and a careful set of experiments on α RF discharges, Vitruk et al. [70] were able to determine for the first time the electrical properties of the sheath and plasma glow regions *separately*. Using the results of Smirnov [71], the thickness and, thereby, the capacitance of the sheath were determined using vector analysis of the equivalent circuit of the discharge, including the electrodes and associated structure. This allowed the determination for the first time of the current–voltage characteristics of the sheath and plasma regions separately, as shown in Figure 26.11a. Analysis of these data leads to important conclusions concerning the structure and stability of the α-discharge. For example, it is clear from this figure that the positive slope of the current–voltage characteristics of the α-type discharge is a consequence of the properties of the *sheath* rather than of the plasma glow region, and moreover that the high current densities and relatively low plasma voltages compared with the ion sheath voltages indicate that the α-discharge behaves almost as a capacitative load. Taking account of the thickness of the two sheaths, one can now compute the value of *E*/*N* averaged across the plasma region of the discharge, and this is plotted in Figure 26.11b. The values of the reduced field in the plasma are seen to be pressure dependent and to be comparable with the near-optimum values observed by Abrams and Bridges [26] for dc discharge waveguide lasers. This is not unexpected since for typical RF discharge laser conditions, the electron collision frequency is much higher than the excitation frequency [72].

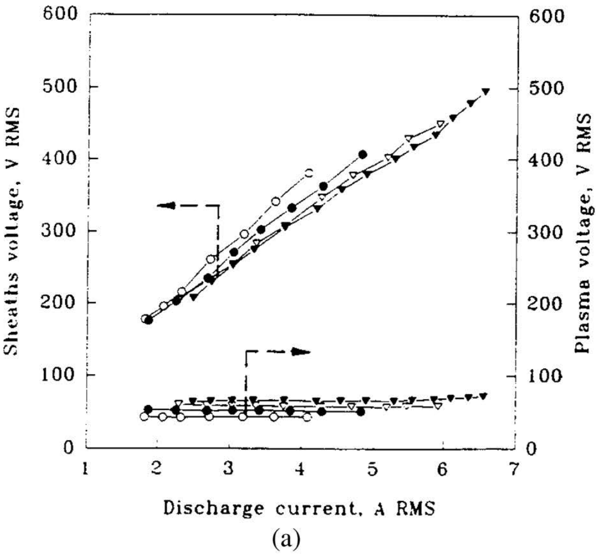

(a)

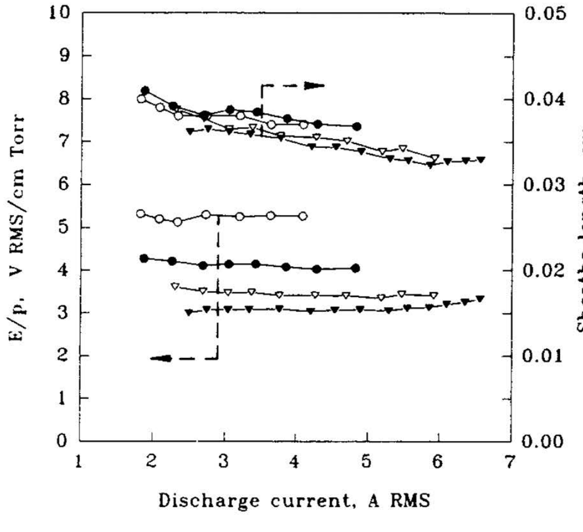

(b)

FIGURE 26.11 (a) Voltage–current characteristics of the sheaths and plasma region. (b) Plasma-reduced electric field and sheath length versus discharge current for different pressures. (From Ref. [70]).

26.4.2.2 RF Discharge Instability Processes

The susceptibility of RF discharges to instability processes is shared by many other types of gas discharges, and such instabilities can be generally categorized as either thermal or ionic in origin. For most designs of diffusion-cooled laser that employ all-metallic electrode systems, the α-to-γ transition, which is an example of an ionic instability, is the most important type to consider. However, for fast-flow RF lasers that have a larger electrode separation, the thermal instability process is usually dominant since series dielectric ballast (e.g. the glass tube structure) is usually employed and heat removal is much less efficient than for narrow-gap diffusion-cooled lasers [73]. Let us consider the sequence of events in the initiation of an α-type discharge and the transition instability to the γ-type. For an all-metal parallel electrode geometry with a separation of a few mm, the application of RF power via a suitable impedance matching network triggers the initiation of an α-type discharge, the area of which may be less than the full electrode area. Increase in the RF power supplied causes the discharge to expand to cover the entire electrode surface area, after which further increases cause the discharge current density to increase and the visible discharge glow to intensify, reflecting the positive impedance characteristic of the discharge under these conditions. As the RF power is further increased, a threshold is reached where a sudden transition to the γ-type discharge occurs, accompanied by a reduction in discharge area and an increase in current density. The visible transverse profiles of the α- and the γ-type discharges are shown in Figure 26.10b. The γ-discharge has a bright central region with spectral emission from both ionized and dissociated molecules being present in the typical CO_2 laser gas mixture, and the electrodes are covered with a bright glow, similar in appearance to that of a dc-voltage-excited cold cathode surface. The electrical changes occurring in the α/γ transition in a small test cell are illustrated in Figure 26.12 [74]. Following ignition, the positive impedance characteristic of the α-type discharge with

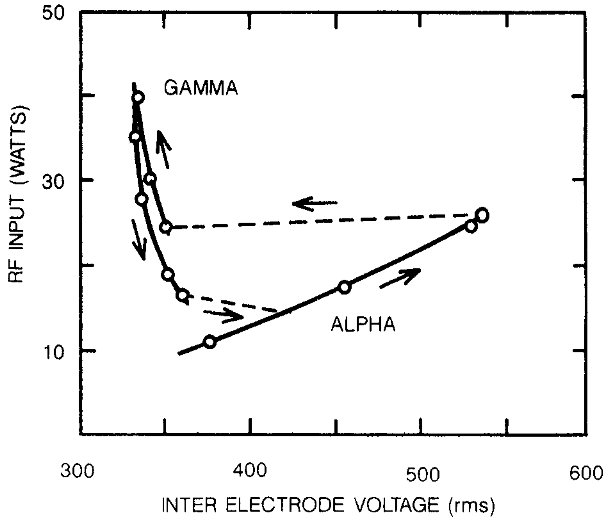

FIGURE 26.12 Electrical characteristics of a 6 mm gap RF discharge, showing the α and γ regions and the bistable switching effect: He, N_2, CO_2, 3:1:2+5% Xe at 15.5 MHz. (After [98].)

inter-electrode voltage increasing with RF power is observed, and large areas of discharge can be uniformly excited so long as the electrode voltage is uniform across the electrode area. At a well-defined value of the power density, which is dependent on the generator frequency, gas mixture and pressure and the electrode material and gap size, a discontinuous switch to the γ-type discharge occurs. The transition is usually accompanied by a slight decrease in the power coupled to the discharge due to the changed impedance characteristic of the γ discharge, and the *I–V* curve is observed to be slightly negative. Figure 26.12 also shows the 'bistable effect' where a considerable reduction in applied RF power must be made in order to return the discharge to the a-mode. The conditions in the central region of the γ-discharge are akin to those in the dc discharge negative glow, with high ion densities being sustained by hot electrons being 'injected' from the boundary layers, high gas temperatures and significant molecular dissociation. As mentioned, these conditions are highly inimical to CO_2 laser excitation. Consequently, a good understanding of this instability process is required to facilitate laser designs that, for good cooling and low cost reasons, employ all-metallic electrodes, so that the transition and latching into the γ-discharge can be avoided. Figure 26.11a shows that the net positive slope of the *I–V* characteristic is a consequence of the behaviour of the *sheath* regions while the slope of the plasma column is never observed to be positive [70]. We can conclude from this that the capacitative sheaths perform the crucial role in stabilizing the plasma in an α-type RF discharge and behave as an *internal* ballast element in series with the plasma 'load' which has a non-positive *I–V* characteristic. Thus, the onset of the α/γ transition instability is very unlikely to occur when the plasma voltage is small compared with the sheath's voltage. Moreover, experiments [70] indicate that the threshold for the α/γ transition instability is the point when the sheath voltage exceeds a critical threshold value linked to the α/γ transition, and this value increases with increased frequency as explained by the model proposed in Ref. [70].

26.4.2.3 Similarity and Parameter Scaling in RF Discharge Lasers

The experimental optimization of discharge parameters usually aimed at maximizing the laser power extraction involves a complex interplay between many intrinsic and extrinsic factors. The study of parametric dependencies or scaling for dc discharge lasers has been investigated within the framework of the so-called *similarity laws* for such discharges [75,76]. Gas heating in the discharge plasma is seen to play an important role in the definition of a series of invariant parameters of the system. Comparing the situation for RF discharges, the principal additional parameter where optimization is required is the generator frequency. Vitruk et al. [77] have extended the similarity principles for dc discharges to include frequency effects and have included the key structural features of the α RF discharge. Bringing together earlier data on the optimization of the generator frequency with inter-electrode spacing indicates that these parameters are linked by the simple relationship that the (frequency × spacing) product *f d*~280 mm MHz. The results of their theoretical analysis of similarity in α RF discharges are compared with experimental data on the current–voltage–power characteristics of these discharges over a wide range of generator frequencies, *f*, gas pressures, *p*, and inter-electrode distances, *d*, for a typical CO_2 laser gas mix. The analysis results in a set of invariant parameters and the formulation of a set of scaling and similarity laws for RF discharges. These relations extend the laws developed for dc discharges to include the generator frequency and the impact of varying *f* on key parameters relevant to the stability of the α RF discharge. These rules may be applied to the design of discharge structures and impedance-matching networks. Moreover, the scaling laws for plasma and sheath voltages are particularly useful in defining the frequency and power limits of discharge scalability, as illustrated by the operational 'map' [77] shown in Figure 26.13. Thus, for large-gap discharges at low excitation frequencies, the sheath voltage may become large enough such that there is significant risk that the α/γ transition instability may occur. The frequency at which the α-discharge sheath voltage becomes comparable with the α/γ transition sheath voltage defines the low frequency limit of stability for unballasted metal electrodes. For the typical CO_2 gas mixture used, the transition voltage is about 400 Vrms [70], and hence, the frequency scalability limit is predicted to be ~40–50 MHz, as shown in Figure 26.13. These predictions are in excellent agreement with experimental observations. A second reason to avoid low excitation frequencies arises from a consideration of the RF power losses in the sheaths. The ratio of power dissipation in the sheaths (which produces unwanted gas heating) to desirable plasma power dissipation is proportional to $1/f^2$. The relatively high observed values of lasing efficiency at high frequencies with high power loading may be due to very low power losses in the sheaths at such frequencies. There is a high frequency limit on excitation that occurs here at about 300 MHz when the sheath and plasma voltage curves cross and the net discharge impedance is then

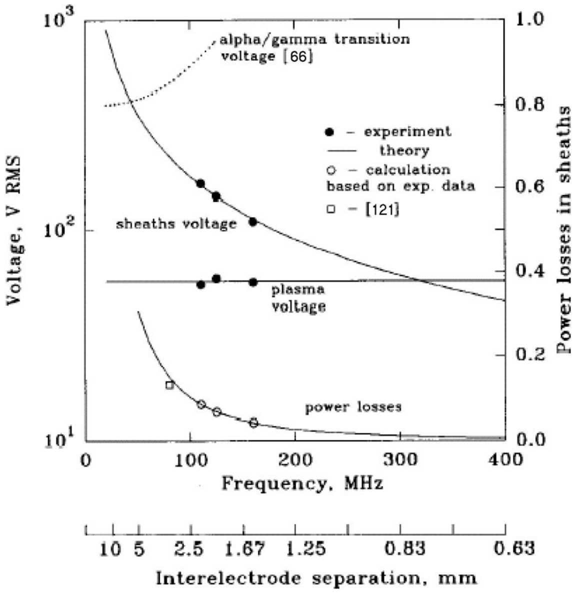

FIGURE 26.13 Frequency dependencies of some of the α 'similar discharge' parameters for $He:N_2:CO_2 = 3:1:1 + 5\%$ Xe gas mixture.

only barely positive. This leads to increasing current density non-uniformities along the electrodes even for cases where the applied inter-electrode voltage uniformity is constant. Finally, for high-power pulsed RF discharges with metal electrodes that are required for generating high peak power laser pulses from planar waveguide devices [78] (see later), Figure 26.13 indicates that high frequencies (>100 MHz) are preferable for stable discharges, though a compromise at, say, 80 MHz provides very good performance. This is because the value of V_s can be maintained below the α/γ transition voltage even for electrical power density inputs of ~1 kW cm^{-3}. This is key information for the development of enhanced pulsed (so-called 'ultra-super-pulse' [USP]) lasers [78].

As previously mentioned, the modern era of CO_2 laser research has spawned two parallel technology development tracks that have been driven, to a large extent, by the requirements of different laser market sectors. These two topic areas, namely, (i) diffusion-cooled RF waveguide lasers and (ii) convection-cooled free-space lasers, are the main subjects for the remainder of this chapter.

26.4.3 Diffusion-Cooled RF-Excited Waveguide Lasers

26.4.3.1 Linear RF Waveguide Lasers

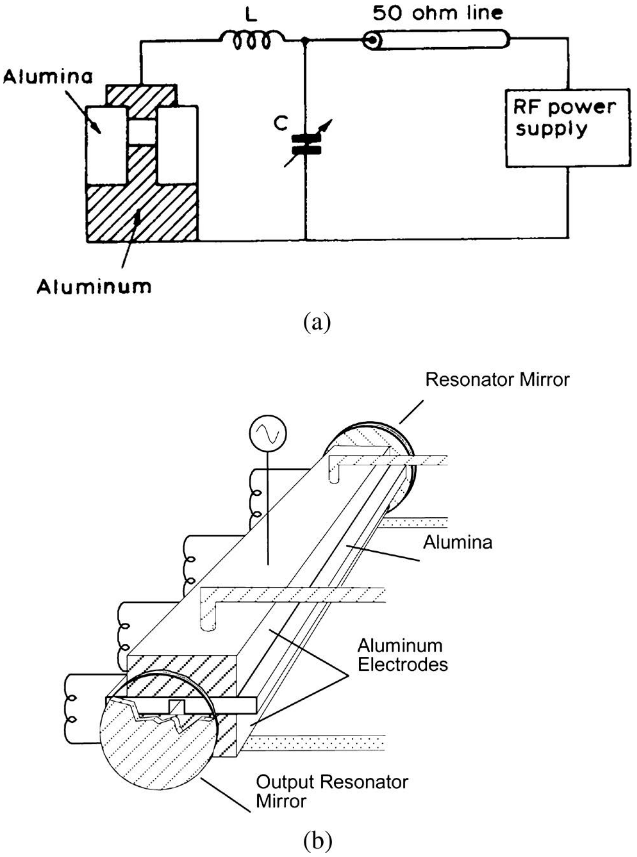

(a)

(b)

FIGURE 26.14 (a) Cross section and electrical schematic diagram of an RF-excited waveguide CO_2 laser. (b) Schematic diagram of an RF-excited waveguide CO_2 laser showing inductors in parallel resonance configuration.

In many ways, a *linear* RF waveguide laser represents a direct progression from the dc discharge waveguide lasers developed in the early 1970s, employing similar optical cavity designs (typically dual case I resonators, see Refs. [39–41]) but with RF excitation technology providing a number of important performance advantages. A typical RF waveguide laser discharge cross section shown in Figure 26.14a is designed around a metal/ceramic sandwich structure where the inter-electrode spacing is typically ~2 mm and waveguide length is less than 0.5 m. The lower electrode is grounded, and the entire electrode structure and vacuum envelope is maintained near room temperature by water cooling or forced air. A pair of planar dielectric-coated mirrors is used in a simple waveguide case I resonator with output coupling usually <10%. A typical gas mixture is 3:1:1 helium, nitrogen and CO_2 with 5% xenon added at a total pressure of ~100 torr (the optimum value depends on electrode separation). Power is delivered from an RF power generator often via a 50 Ω cable, though lasers with integrated RF power supplies have been developed commercially. The laser can be considered as an electrical load comprising a complex impedance consisting of the mechanical structure combined with the RF discharge. Power transfer efficiency to the discharge is a key feature for laser operation, and this is made more complicated by the fact that the RF discharge behaves as a *power-dependent* impedance element. Moreover, at the high frequencies (>50 MHz) where RF waveguide laser performance is optimized, unacceptable longitudinal variations of the inter-electrode voltage occur due to transmission line effects caused by the RF electrical properties of the laser structure of parallel metal conductors (electrodes) separated by high dielectric ceramic spacers. To solve this problem, compensation techniques producing distributed impedance matching have been developed [8,56,58,79], and such designs are used to minimize linear variations in the inter-electrode voltage and the consequent triggering of the α/γ transition, which would otherwise limit the discharge power density that can be achieved. The schematic diagram in Figure 26.14b shows one approach that involves distributed resonant matching with an array of inductors that is designed to compensate for the effects of the structure capacitance by achieving parallel resonance at, or near, the generator frequency. Beginning with the first reported RF waveguide laser of Lachambe et al. in 1978 [61], laser performance in terms of power extraction and conversion and efficiency increases significantly over the next few years. This is evident from the increase achieved over a 5-year period in a frequently-quoted figure of merit for linear lasers, the specific power, P_L, measured in W cm^{-1} of the discharge length. Reported values of P_L showed an increase from the earliest value of 0.04 W cm^{-1} achieved by Lachambre to the value of 0.83 W cm^{-1} reported by He and Hall who in 1983 obtained a cw power output of 30.6 W and a maximum efficiency of 13% from a 37 cm RF discharge operated at 125 MHz in a 3:1:1 mixture of He, CO_2 and N_2 with the addition of 5% xenon at a total pressure of 110 torr [60]. These power increases were due in the main to increased recognition of the design requirement to optimize the generator frequency [80], to ensure negligible longitudinal variation in the transverse RF voltage and to maximize heat transfer to the all-metal electrodes. The use of trace quantities of Xe in CO_2 laser mixtures is well known to have several beneficial effects including increased laser power and increased sealed-off lifetime [16,81]. A 24% increase in laser power was observed with 5% Xe [82], and this observation is linked to gain increases [83] by spatially resolved measurements of electron temperature, T_e, using an electrostatic double-probe technique. These measurements show T_e falling to 1.5 eV for 5% Xe concentration, a value where vibrational pumping of N_2 and CO (formed by CO dissociation) has a peak cross section with corresponding maximum gain, and under near-optimized condition, Vidaud et al. [84] achieved efficiency values 20%. Diffusion-cooled RF lasers became available commercially as sealed-off devices in the early 1980s at power levels of ~5–50 W from several companies including Laakmann Electro-optics Inc. in the United States and Laser Applications Ltd in the United Kingdom, who developed a folded RF laser design producing >50 W for applications in surgical and industrial systems. These new laser technologies produced a rapid increase in diverse applications of laser-based ‘table-top’ systems in medicine, science and industry. In addition, there was a parallel series of RF laser device developments that were aimed largely at military, aerospace and remote sensing applications, for example at United Technologies Research Centre and Ferranti Ltd in the United Kingdom. With these rapid developments under way, it became apparent by the mid-1980s that there were very large potential markets for sealed CO_2 lasers at power levels of tens to hundreds of watts, particularly for surgical and industrial manufacturing applications.

26.4.3.2 Power Scaling—Folded Waveguide Lasers

Because of its volumetric power efficiency and technical convenience, RF waveguide laser technology was seen as a prime candidate for further development, but the key question was how best to achieve the necessary power scaling. Many laboratories around the world became interested in the challenge of how to scale CO_2 lasers to the kilowatt power range while maintaining beam brightness, sealed-off operation, compactness and ease of usage, given that the intrinsic efficiency and power extraction capability of CO_2 lasers are limited by discharge-dependent excitation kinetics, gas chemistry and gas heating. Thus, the specific laser power, P_L, is limited to an optimum value of <100 W m^{-1} for linear sealed or slow-flow RF lasers, so the only realistic line of attack for power scaling is to somehow increase the gain volume. Clearly, the simplest conceptual approach is to employ longer gain lengths. However, there are problems with fabricating very long waveguides with sections in the range ~1–3 mm, especially if a machined ceramic is used to define all or part of the waveguide, since the imperative of low waveguiding losses imposes quite stringent fabrication conditions of waveguide surface straightness and finish. In practice, this limits single-section waveguides to maximum lengths of ~0.5 m. A linear series of multiple sections is possible in principle, but mutual alignment problems and excessive overall device length make this an unattractive option. An alternative is to deploy an optical folding system using multiple parallel waveguides with a series of ‘U’ folds or else ‘V’ folds with multiple waveguides in a folded zigzag arrangement. When repeated, these folding arrangements can be used to concatenate several metres of an active gain medium into a compact structure, with the advantage that a single pair of planar metal electrodes and a single RF power generator can be employed. However, the design of low-loss optical folds is, of course, complicated by the problem of the beam passing repeatedly from one waveguide section to another via a folding mirror positioned a non-negligible distance away, so that mode-coupling losses and beam effects associated with multiple waveguide/free-space transitions become a major issue. Jackson et al. [85] compared several types of waveguide folding designs and produced a compact folded waveguide laser of 60 W in a compact design. Newman and Hart [86] developed the folding concept considerably further, and this work became the basis for a successful commercial range of RF-excited folded waveguide lasers developed by DeMaria ElectroOptics Systems Inc. and operated either cw or with an internal Q-switching element [87].

26.4.3.3 Power Scaling—Waveguide Laser Arrays

However, it was apparent that linear resonator waveguide lasers with multiple folds were likely to be too complex to permit effective power scaling to the desirable levels of 100 W^{-1} kW. Nevertheless, the potential power-scaling capacity of multiple parallel waveguides in a monolithic *array* structure had been noted earlier and proposed as a route for the realization of high-power dc waveguide lasers [88]. The additional potential benefit of successfully phase-locking the elements of such arrays for the production of a coherent output and the possibility of high-speed beam scanning via differential phase modulation, by analogy with radar antenna technology, was also recognized. However, the practical limitations of high-voltage dc technology prevented the development of effective high-power laser arrays. By contrast, the benefits of transverse RF excitation techniques employing a single RF generator to excite multiple waveguides in a planar structure, cooled efficiently by diffusion to cooled metal/ceramic surfaces (as illustrated in Figure 26.15a), appeared as a most attractive option, at least in terms of ‘raw’ power. The parallel quest for the necessary high beam quality drove considerable research on phase-locking techniques for RF waveguide laser arrays. Youmans [89] showed the principle of phase-locking between a pair of adjacent waveguides separated by a plate of optically transparent zinc selenide, and Newman et al. [90] soon demonstrated higher-power phase-locked operation, using a hollow-bore ridge waveguide structure. Subsequently, other techniques were devised and demonstrated by the Heriot Watt University group for coherent coupling (phase-locking) of linear waveguide laser arrays, including intracavity four-wave mixing [91], distributed coupling [92] and the use of the waveguide-confined Talbot effect [93]. However, the realization of a *practical* phase-locking technique capable of extending array power towards the kilowatt region was seriously hindered by the difficulties in ensuring adequate phase uniformity across the array in the face of variations in element-to-element RF power deposition and cooling across the array. Thus, heterodyne measurements indicated [94] that these effects produce frequency shifts of 1 MHz W^{-1}, thereby

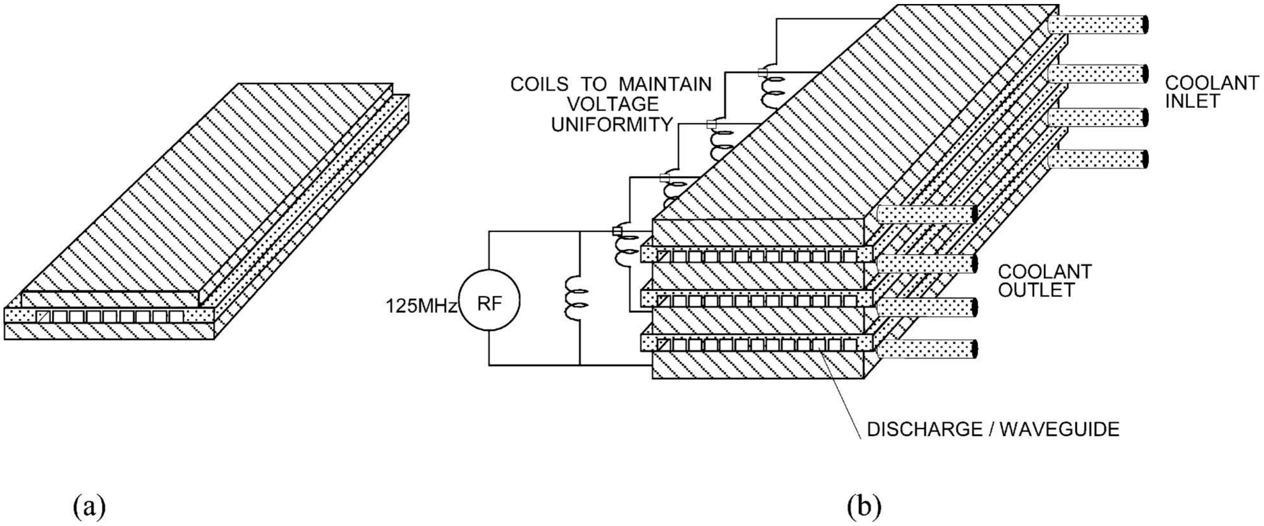

FIGURE 26.15 Schematic diagram of RF-excited CO_2 waveguide array laser gain media: (a) one-dimensional array and (b) two-dimensional array. (After [95].)

imposing severe challenges to the locking range of any candidate coherent coupling technique. Nevertheless, large planar and two-dimensional array lasers (see Figure 26.15b), deliberately designed to be incoherent with respect to each other to avoid interference effects, have been demonstrated with power levels >2 kW with the excellent individual element beam quality and the capacity for array beam reformatting to produce useful beam shapes at high average power levels for industrial applications [95,96].

26.4.3.4 Power Scaling—Area Scaling in Planar Waveguide Lasers

The planar waveguide laser concept can fully exploit the enormous (power scaling) benefit that RF discharges can be *area* rather than length scaled. Large-area RF discharges can be operated in a stable manner at high power densities and efficiently cooled by diffusive heat flow to concentric or plane parallel metallic electrodes, as illustrated in Figure 26.16. If we consider a uniform RF discharge maintained between metallic electrodes of width, ω, length, L, and spacing, d, then the total power that can be extracted from the volume is given by [97]:

$$P = fP_L(\omega/d)L = fP_L(A/d) \qquad (26.6)$$

where P_L is the specific power (~80 W m^{-1}) and A is the electrode area, as illustrated in Figure 26.17. The numerical factor f is a number <1, which takes account of the difference between two-dimensional heat flow in a linear laser and one-dimensional flow in planar devices. Geometric arguments suggest that $f \sim 2/\pi$, and this is confirmed by experiment [97]. We can thus arrive at a very simple *area* scaling law and define a figure of merit, P_A, for area-scaled lasers:

$$P_L = P/A = fP_L/d. \qquad (26.7)$$

The huge potential of the area scaling concept and the importance of the (1/d) factor were demonstrated by a simple plot [97,98] based on Equation (26.7) and reproduced in Figure 26.18. This shows a plot of laser output power per unit area of electrode, P_A, measured in kW m^{-2} that can be expected from a large-area discharge with one-dimensional heat flow, plotted against electrode separation for three slightly different operating modes. The upper line relates to a slow-flow mode where helium-rich mixtures can be used to give maximum

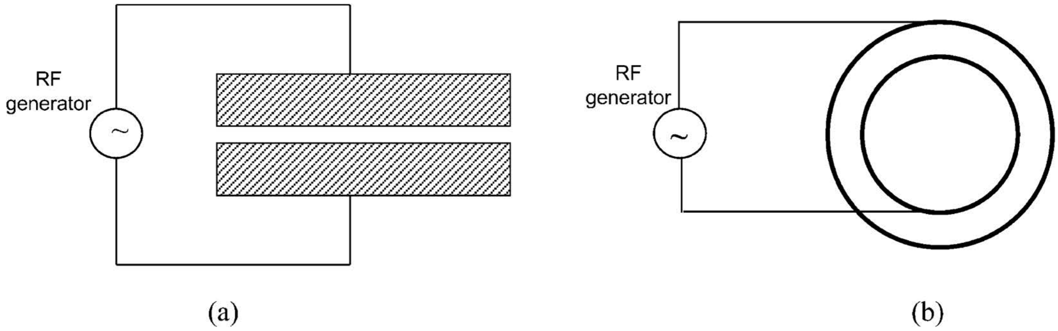

FIGURE 26.16 Schematic diagram of a large area diffusion-cooled laser using (a) planar or (b) annular electrode geometry.

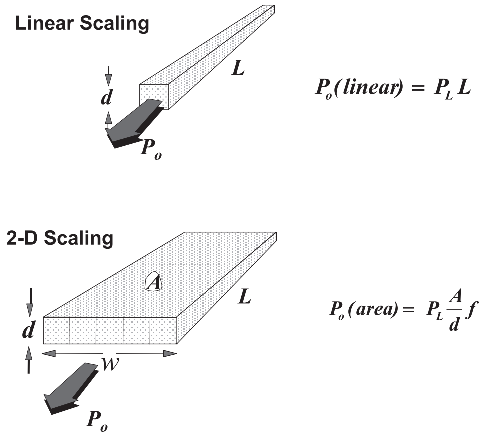

FIGURE 26.17 Schematic diagram illustrating two-dimensional (area) power scaling for planar lasers.

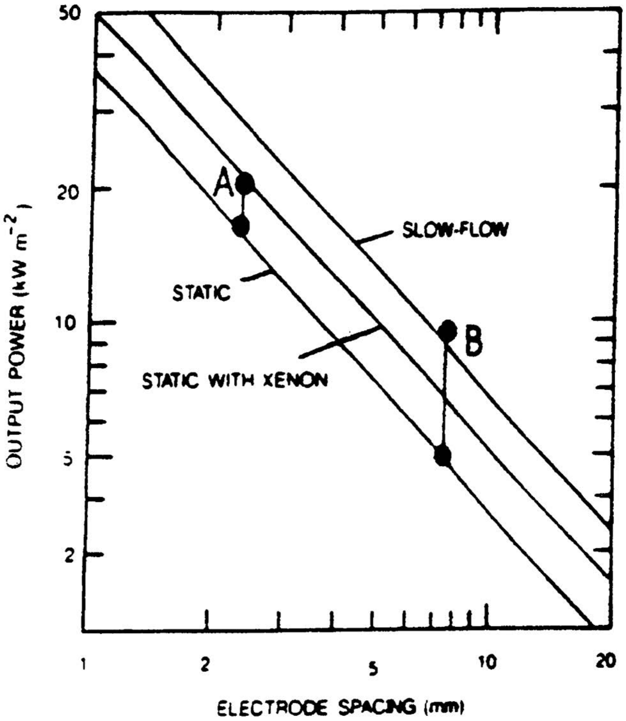

FIGURE 26.18 Scaling of laser power per unit area of large-area discharges with an electrode gap. Experimental points A are from a 2.25-mm device with a static gas fill. Points B are for a 7.5-mm device with slow flow and a static gas. (After [98].)

thermal conductivity and provide the highest output for all relevant electrode spacings. For static gas/sealed mode operation, the higher molecular gas content in the mixture of helium, nitrogen and CO_2 necessary to stabilize dissociation for a long gas lifetime reduces the gas conductivity, and laser power output falls by about 50% compared with slow flow. The middle line indicates the expected power levels obtained when ~5% xenon is added to the mix. These projections were extremely exciting, predicting laser power generation scaling at 1/*d* and reaching levels in excess of 20 kW m^{-2} for inter-electrode spacings of ~2 mm, characteristic of optical waveguiding for 10 µm radiation. These projections were based on the assumption that the discharge is optimized in terms of the RF drive frequency and the achievement of efficient power transfer and uniform power deposition throughout the structure. The experimental data points shown are from measurements of multi-mode laser output from two different types of planar structure that confirm the power scaling behaviour of large-area discharges. The first set was obtained with a discharge gap of 2.25 mm forming a one-dimensional waveguide with an electrode area of 66 cm^2, while the second was measured using an electrode pair with area 320 cm^2 and a gap of 7.5 mm operating as a free space resonator device [99]. The power scaling data for the more interesting small gap (waveguide) data are presented in greater detail in Ref. [97], along with experimental evidence for the key feature which is the transition from two-dimensional to one-dimensional discharge cooling. The data in Figure 26.18 confirm that these power scaling laws based on thermal conduction limits are, indeed, realistic and demonstrate quite dramatically the power scaling opportunities available with this 2-D laser concept. The attainment [97] of 20 kW m^{-2} from a large-area discharge under conditions that are suitable for long-term sealed-off operation was a particularly exciting result, which heralded the subsequent development of a new generation of ultra-compact lasers with average powers in the multi-kilowatt range. Later research [100] further investigated the validity of the (1/*d*) scaling law down to electrode gap sizes of 0.5 mm. This research showed that for values of *d* below about 1.5 mm, the power per unit value was seen to depart from the 1/*d* dependency and to show a peak value of 30 kW m^{-2} for a gap of ~1.2 mm as shown in Figure 26.19. The departure from 1/*d* can be expected because of the increased waveguiding losses of the machined aluminium alloy electrodes, which scale as ~d^{-3} and increase mirror–guide coupling losses, as well as an increased impact of ion sheath losses in the discharge for very small gaps [77].

The extraordinary potential benefits of the ‘thin’ laser idea for producing ultra-compact laser designs could perhaps be best realized by considering the input power density

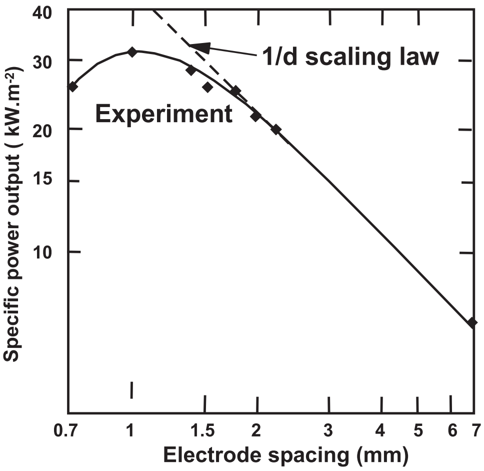

FIGURE 26.19 Dependence of specific laser output power (power per unit area of electrode (kW m^{-2})) on electrode spacing, demonstrating the 1/*d* scaling law. (After [100].)

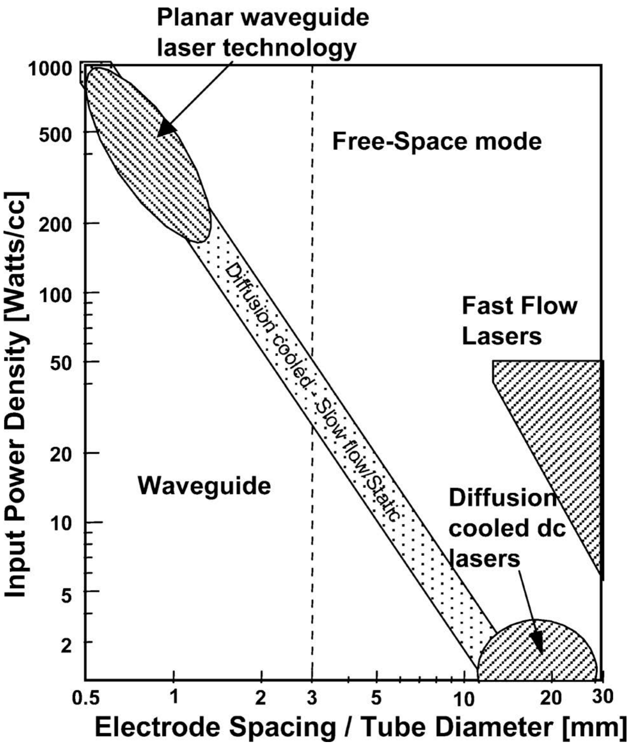

FIGURE 26.20 Dependence of discharge electrical power density for efficient laser power extraction on electrode spacing/tube diameter output power, indicating the × 10 advantage of RF planar waveguide lasers. (After [98].)

map, first presented at the 1988 GCL Conference and shown in Figure 26.20 [98,101]. This map shows—as the diagonal band—the input power density which the laser gain medium can 'tolerate' while still maintaining high laser conversion efficiency (corresponding to an axial gas temperature <600 K), as a function of the gain medium thickness. Also shown for comparison are the 'allowed' input power density values that are representative of both (passive) diffusion-cooled non-waveguide lasers and (active) convectively cooled devices of the day. What emerges from considering Figure 26.20 is that the planar waveguide laser technology is capable of operating, with high electrical-to-optical power conversion efficiency, even at power density levels which are more than 100 times greater than diffusion-cooled, conventional geometry lasers and 10–50 times higher than even the much more complex and bulky fast-flow convectively cooled lasers. Much later, it has been shown [78] that stable discharges at power density values to 1 kW cm^{-3} can be used to produce high peak powers in pulsed operation in the so-called USP mode (see later).

In the quest for high-*brightness* lasers, a challenge of equal importance to the development of these new diffusion-cooled gain medium structures was the design of effective optical resonators capable of combining diffraction-limited beam quality with high power extraction to produce high-brightness beams in ultra-compact devices. The benefits of the very high values of P_A that are associated with the use of narrow electrode gaps offer particular rewards for diffraction-limited resonators that can efficiently incorporate waveguide gain structures. The most suitable resonator so far developed for such planar waveguide gain structures was proposed by Jackson et al. [102]. This is a *hybrid* design based on the use of classical waveguide resonators [39] for mode control in the narrow (transverse) dimension and a confocal unstable resonator for beam control in the wide (lateral) direction. The resonator they proposed is illustrated in Figure 26.21a. It consists of a pair of spherical mirrors of radius R_1 and R_2 spaced by a distance, L, and arranged in a confocal setting with $R_1 - R_2 = 2L$. This design provides a magnification factor $M = R_1/R_2$ and a geometric output coupling fraction, $\delta = 1 - 1/M$. The concave (back) mirror R_1 completely 'covers' the discharge width, a_0, while the 'front' mirror R_2 has a diameter and position selected to project a distance, d_0, into the active discharge region such that the magnified edge-coupled output beam matches the discharge width, a_0 such that $Md_0 = a_0$. This resonator design permits the use of quite large radius of curvature mirrors (5 and −4.22 m) for the confocal unstable resonator to produce lateral beam control. Simultaneously, such reflectors behave as 'pseudo-planar' mirrors in a near-case I waveguide resonator design to produce low-loss waveguide–mirror coupling in the transverse direction. In the experiment, a stable α-type discharge at 125 MHz was maintained in a static 3:1:1 He, N_2 CO_2, gas mixture with 5% Xe between water-cooled electrodes (380 × 45 mm) separated by 22.25 mm. A maximum laser power of 240 W was obtained at a conversion efficiency of 12% and a value of specific power extraction, P_A of 14 kW m^{-2}. This reduced value of P_A is a consequence mostly of the reduced volume overlap in the unoptimized resonator. The *negative* branch hybrid waveguide–confocal unstable resonator shown in Figure 26.21b has the advantage of a higher optical stability against the effects of mechanical misalignments, though the fill factor is usually lower. The *x–y* hybrid nature of the resonator design means that beam divergence in the *X* and *Y* directions are usually not identical. Moreover, the laser near-field beam pattern shows small ripples deriving from diffraction at the edge of the coupling mirror. However, subsequent experiments showed that a simple extra-cavity optical transformation with spherical lenses or mirrors and the judicious positioning of a one-dimensional spatial filter produces a beam which is circular and has identical divergence in the *X* and *Y* directions. Optical losses as low as 5% are achievable using fixed passive optics, and the net result is a near-perfect beam with values of $M^2 < 1.2$.

As mentioned already, the use of a positive-branch type of unstable resonator [102,103] permits the use of large-radius mirrors, which are most convenient for rapidly planned experiments but which provided only a modest degree of waveguide mode discrimination. A further refinement of this resonator design involving the use of the negative-branch confocal unstable resonator has several useful advantages. First, as pointed out for example by Seigmann [104], the negative-branch resonator produces considerable enhanced optical beam pointing stability against resonator mirror misalignment due to thermal/vibration effects or other mechanical factors. In addition, it is possible to select radii of curvature that, satisfying the conditions for the confocal negative-branch design, simultaneously match the radius of curvature of the fundamental waveguide mode at a specified distance from the end of the discharge waveguide. Following this demonstration of

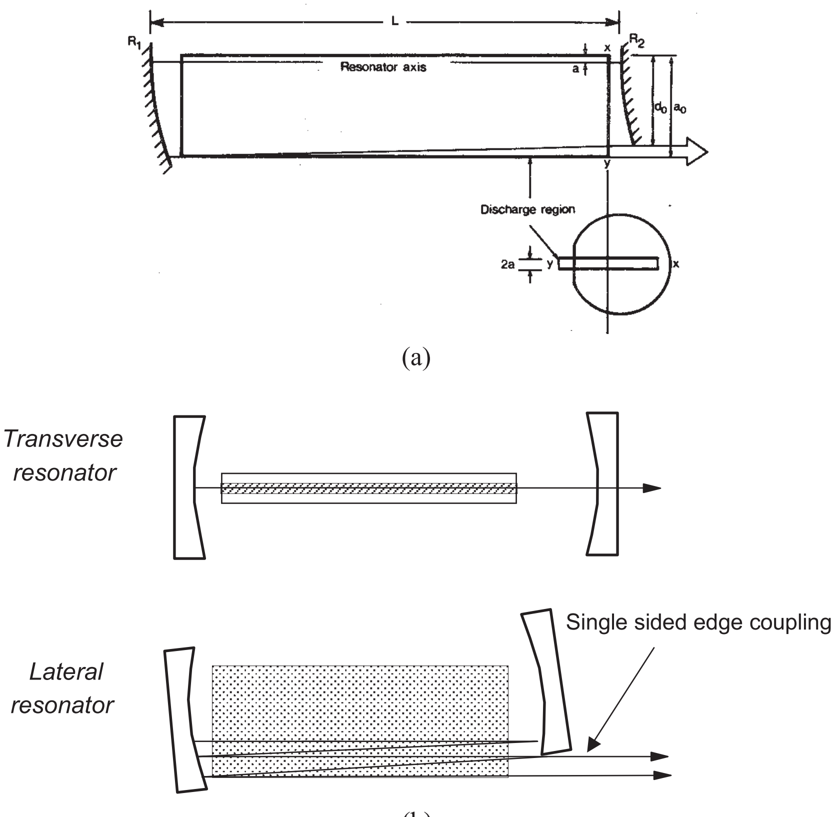

(a)

(b)

FIGURE 26.21 (a) Hybrid waveguide–positive-branch confocal unstable resonator. (After [102].) (b) Hybrid resonator for a planar waveguide CO_2 laser waveguide in the transverse direction and negative-branch confocal unstable in the lateral direction.

planar waveguide sealed lasers at the 250 W level, area scaling was applied to take the laser power to the 1 kW as reported by Nowack et al. [105] from the DLR lab in Stuttgart and Colley et al. [106] at Heriot-Watt University with the demonstration of 1.1 kW in the device shown in Figure 26.22. At the same time, parallel development of commercial versions of these lasers occurred at Rofin Sinar GmbH in Hamburg, who aimed largely at the flat-bed cutting market with lasers at >1 kW, and Coherent Inc. in Hull, United Kingdom, and California, where focus was on compact sealed technology at power levels to 500 W. Considerable development has occurred in the ensuing years, with compact hard-sealed long-life planar waveguide lasers with all solid-state power supplies being available at power levels up to >600 W for 'table-top' industrial and medical systems, while static gas, refillable planar waveguide lasers with power levels up to 6 kW being supplied into the material-processing industrial markets by Rofin Sinar GmbH. These lasers also feature excellent (near-diffraction-limited) beam quality and attractive modulation characteristics.

One final planar waveguide laser development is worthy of note. Although offering many advantages as power sources for industrial processing, two particular limitations of 'conventional' planar waveguide laser 'operating space' are evident for some applications. First, conventional planar waveguide lasers offer only a very modest value (of ~3) in the ratio of attainable peak-to-average power; second, pulse widths are restricted to values larger than ~100 μs at full operating efficiency. However, some applications are best served with shorter pulses with higher peak power levels, and this problem was addressed by Villarreal et al., who demonstrated the

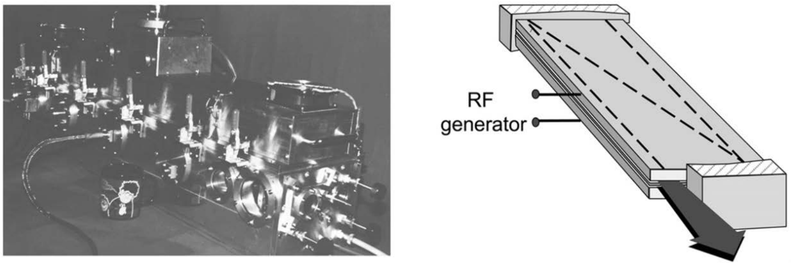

FIGURE 26.22 Photograph and schematic diagram of a sealed 1.1-kW CO_2 planar waveguide CO_2 laser (Heriot-Watt University). (After [106].)

so-called ‘ultra-super-pulse (USP)’ mode of operation with peak power of 3.8 kW and pulses to 10 μs at kHz repetition rates, while maintaining high efficiency and a slight *increase* in average output power from 100 to 120 W in compact sealed devices [78]. Such lasers offer clear performance advantages for applications including microvia drilling for advanced PCB fabrication [107] and rapid melting of metal surfaces for increased corrosion resistance [108].

26.4.3.5 Annular Discharge Lasers

Annular gain medium lasers with radial RF discharges between coaxial electrodes offer the key advantage of large cross-sectional areas (large gain volumes) without the need for excessive inter-electrode distances that would otherwise necessitate low gas pressures. Thus, coaxial lasers provide the opportunity to employ large electrode areas in compact (rolled-up planar) structures for efficient diffusion cooling, as well as utilizing cylindrical geometries that are convenient for manufacture. An early and prescient example of RF CO_2 laser design (one of the first RF CO_2 lasers on record) was that of Crocker and Wills at SERL, United Kingdom, who used an annular discharge to produce what appeared to be a very promising result in 1969 with a device at 200 W [51]. However, the design of high beam quality resonators with good azimuthal mode discrimination for the annular geometry, low misalignment sensitivity and efficient volumetric power extraction represented a significant challenge. Several approaches were investigated including toric resonators [109] and multipass resonators based on the Herriott cell optical folding system [110] to produce a single-mode Gaussian beam, though the discharge fractional utilization and corresponding value of P_A was quite low. The Herriott multi-fold system has also been applied to the *planar* electrode design, offering good beams at reasonable values of P_A [31,99]. Subsequently, a compact annular *waveguide* coaxial discharge laser was developed at the 500 W level [111], but such designs are seriously hampered by the extreme mechanical precision and tight tolerances demanded of annular waveguide structure and resonator mirrors, so that the full benefit of $1/d$ scaling that waveguiding requires cannot easily be achieved and, to date, it appears not to have been possible to develop practical resonators for annular *waveguide* devices that are capable of the high beam quality necessary for modern lasers.

In the more tractable non-waveguide stable resonator regime, promising designs of transverse RF-excited annular laser construction at the kilowatt level were demonstrated at ILT, Aachen, in Germany [112]. This led to the design and demonstration of a novel hybrid resonator that is stable in the radial direction and unstable in the azimuthal direction that uses a specially manufactured helical mirror. With this resonator, near-diffraction-limited beam output was obtained at power levels of 2 kW and 10% efficiency from a coaxial gain length of 1.8 m [113].

26.4.4 Convectively Cooled Radio-Frequency-Excited Free-Space Radio Frequency Lasers

As mentioned earlier, the exploitation of transverse RF discharges for innovation in diffusion-cooled CO_2 laser technologies in the 1980s was paralleled by important new developments in convectively cooled (fast-flow) lasers. The main driver for research in combining fast-flow gas cooling techniques with transverse RF discharges was the relatively buoyant market for multi-kilowatt lasers required for an increasing range of industrial material-processing applications. Although dominated numerically by metal-cutting applications, the development of higher-power lasers (>5 kW) has resulted in a steady increase in the use of industrial CO_2 lasers for welding and, to a lesser extent, for the surface treatment of metals. As workpiece handling and system control hardware for laser-cutting systems have improved and competition intensified, the industrial market has demanded ever higher processing speeds and better finished product quality. This has driven industrial laser manufacturers to seek ever higher average laser powers to match required production rates, combined with better optical quality beams in ever more reliable and low-cost laser systems. For instance, whereas in the past lasers for cutting typically operated at the 1.0–1.5 kW range, modern requirements, for example, for fine cutting applications are for lasers at 5 kW and above with near-diffraction-limited beam quality.

By 1980, fast-flow dc/ac lasers had been under development for about 10 years, with axial-flow lasers meeting many industrial laser needs at power levels of up to ~5 kW. However, as previously mentioned, RF discharges are stable at higher values of power density and gas pressure than dc discharges. In addition, they can be modulated at higher frequencies and operated with electrodes external to the gas discharge vessel, thereby avoiding electrode sputtering reducing gas consumption. dc-excited lasers with *transverse* flow are often capable of higher average power levels than axial devices but are usually viewed as being technically more complex, often with inferior beam quality and lower levels of reliability. Today, after 20 years or so of further development, the situation is not dissimilar. Partly because RF technology is highly compatible with longitudinal flow structures, axial fast-flow lasers now dominate the industrial laser scene and power outputs from folded cylindrical designs have kept pace with industrial market demand for power levels up to ~20 kW.

26.4.4.1 Fast-Axial-Flow Transverse RF-Excited Lasers

Most fast-axial-flow (FAF) RF-discharge-excited lasers are based on the use of metal/dielectric electrodes, where the metal electrode is separated from the discharge by a sheet of dielectric material as illustrated in Figure 26.23a and b, which shows the version of this concept that is commonly used in RF-excited FAF lasers [73]. The RF electric field is applied to the metal electrodes, and there is a voltage drop that is proportional to the current density across the capacitative dielectric layer. As previously mentioned, the use of dielectric sheets in series with the discharge acts to supplement the stabilizing influence of the internal RF discharge sheaths [69] and to increase the power density threshold for the onset of α-to-γ instabilities. This added stabilizing effect of the dielectric layers is particularly important given that tube diameters of several centimetres are called for (values of ~2–8 cm are common) to achieve effective gas flow, and such inter-electrode distances are associated with *low* frequency operation for optimized operation, where α-to-γ transition instabilities are more probable (see Figure 26.13 and Ref. [77]). The use of series dielectric ballast permits the use of desirable industrial frequencies at 13.56 or 27.12 MHz, and these are the two most commonly used generator frequencies for fast-flow lasers. The impact of the selected frequency, f, (and material) on the effectiveness of the dielectric ballast can also be seen from the voltage drop across the glass wall ballast in Figure 26.23b, which is given by $V_{\mathrm{b}} = 2t\ J/\varepsilon\varepsilon_0\omega$ where t is the dielectric thickness and J is the current density [98]. For a 1 mm wall thickness in a typical FAF laser, the voltage drop across the glass walls is ~2000 V at 13.6 MHz, compared with only ~30 V at 126 MHz. Thus, for the low-frequency case, the ballast voltage is significantly larger than the discharge voltage, which helps to inhibit the onset of γ discharges.

However, in order to maintain the high level of transverse homogeneity of the RF discharge needed to produce high beam quality, more complex electrode designs than the simple matched-diameter cylindrical shape shown in Figure 26.23b are necessary. Viewed from the tube end, the discharge with electrodes that are shaped and positioned such as in Figure 26.23b shows evidence of the expected electrode sheath regions (of thickness ~a few mm) close to each electrode. There is also clear evidence of localization of the transverse current density in the highest field regions corresponding to the shortest inter-electrode distances. Electrode optimization using electric field calculations and experiments [114] have produced shapes such as that shown schematically in Figure 26.23c which have been shown to produce very uniform visible luminosity across the tube diameter at right angles to the field direction [115]. For the (usual) case of multiple discharges that are optically in series, residual non-uniformities can be further reduced by rotating the electrode pairs by an appropriate angle about the tube axis. In practice, proper attention to these issues enables excellent phase homogeneity in the gain medium and permits circularly symmetric high-quality laser beams to be obtained. However, there is a remaining problem that the spatially averaged gain profile may have a minimum value on axis which makes the achievement of TEM_{00} mode operation rather difficult. Such lasers often are designed to operate in the TEM_{01} 'doughnut' mode.

One has also to be concerned with non-uniformities in the longitudinal, axial flow direction since as the gas proceeds through the discharge region (usually some tens of cm in length) its temperature rises, resulting in a density (and discharge impedance) gradient in the direction of the flow. Thus, assuming a constant inter-electrode electric field, the transverse current density will vary in the axial direction if the electrode spacing is constant along the tube. This effect may be countered, for example, by tilting the electrodes so that the separation increases appropriately in the direction of the flow [116]. With the design refinements mentioned, RF excitation of FAF lasers can operate very effectively. For RF lasers this is true even without the highly turbulent flow and consequent high values of pressure drop that are characteristic of dc lasers, so that turbo-blowers can be substituted for Roots pumps allowing the design of very compact lasers with integrated blowers [117]. Nevertheless, it is necessary to fully understand power deposition uniformity issues, including the effects of generator frequency, gas conductivity and gas flow conditions since, as with all discharges, hot spots can occur and lead to thermal instabilities, discharge filamentation and destructive arcs [69]. The demand for higher power levels has stimulated a need to understand power scaling in terms of gas pressure, tube length and diameter and electrical issues where the limit is usually the onset of discharge instabilities [118]. Considerable effort has been devoted to theoretical and experimental research on discharges and gas flow systems for the optimization of spatial uniformity of gain in FAF RF lasers, for example using the CARS techniques [115]. The resulting technology combining RF excitation and FAF gas cooling can provide an excellent 'building block' for scaling to very high powers in a modular fashion. As with diffusion-cooled lasers, such scaling is multi-stage involving multiple (as many as 16) discharge sections and optically folded resonators.

Since heat is removed by convection, a second type of power scaling is available, which seeks to extract higher powers per unit length of discharge by using larger tube diameters (~65 mm) and higher gas pressures (100 mbar). This approach exploits the flow conditioning and discharge homogenization techniques developed by modelling and experiment [119] and leads to designs that are capable of average power levels to >20 kW, [120,121]. In one experiment at ILT Aachen, a large-diameter high-pressure laser was constructed with eight-discharge sections that incorporated four radial compressors for gas flow with a volume rate of 3300 $\mathrm{m}^3\mathrm{h}^{-1}$. With a power input of 160 kW from a pair of 100 kW generators operating at 27.12 MHz, a laser power of >25 kW was obtained, with the expectation that power could be scaled further towards 40 kW [119].

The need for process quality and competition in the industrial laser sector means that near-perfect beam quality is an

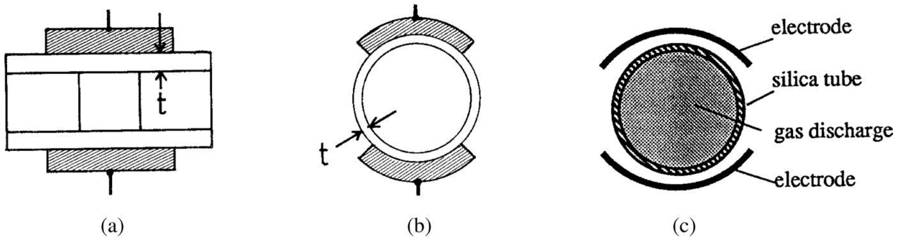

FIGURE 26.23 Schematic cross section of electrode system for fast axial flow lasers, showing reactive ballast of dielectric layers: (a) planar structure, (b) glass tube structure and (c) illustration of optimized metal electrode shape.

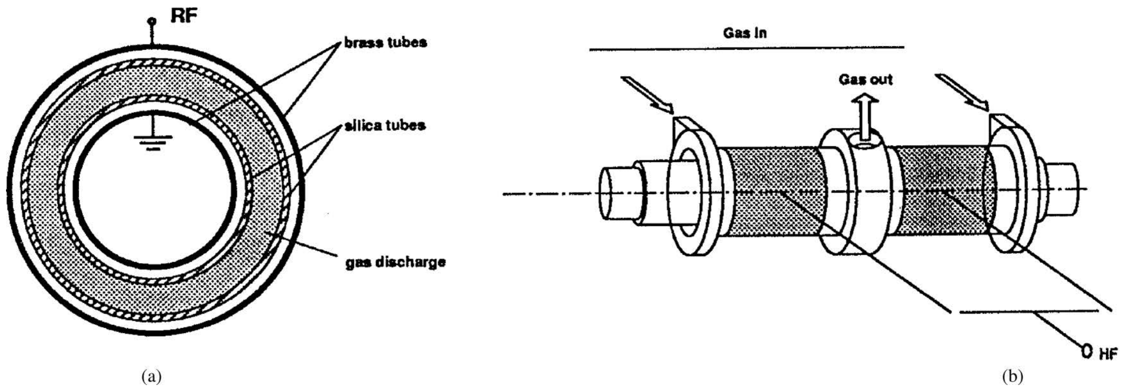

FIGURE 26.24 (a) Coaxial electrode structure and annular RF discharge. (b) Schematic diagram of a two-section coaxial fast-flow laser. (After [119].)

indispensable requirement in modern industrial lasers. The key to achieving this for FAF RF lasers is the achievement of a high degree of optical homogeneity in the gain medium by attention to optimized electrode design and flow conditioning. Failure to do this results in strong negative lensing and large aberration effects and laser beam quality that is inadequate for modern lasers. However, with an optimized electrode configuration, only small negative lens effects remain due to transverse heat conduction gradients, and for normal operation, their influence on beam quality is quite low [122]. Optical transient effects may also occur. For example, transient statistical phase distortions associated with turbulent flow in the medium may cause optical effects, which may have to be taken into account. Nevertheless, a high degree of uniformity of the gain medium refractive index can be achieved; excellent laser beam quality at multi-kilowatt power has been demonstrated using either stable or unstable cavities and folded designs depending on the overall laser length and aspect ratio. This type of FAF laser technology is available from several companies including Trumpf GmbH and Rofin Sinar GmbH.

As has been shown for diffusion-cooled lasers, an alternative to discharge-length scaling as a route to very high power lasers is area scaling, and the annular RF discharge with coaxial electrodes offers a very promising route to very high average power lasers since it offers a large effective cross section for gas flow coupled with a relatively small gap, high gas pressure and, therefore, high mass flow, as illustrated in Figure 26.24 [119]. This system uses two silica tubes as dielectric layers, with a grounded inner metal electrode and an outer metal cylinder to which the RF is applied, to provide a discharge with inner and outer diameters of 95 and 117 mm, respectively, and a total discharge length (two sections) of 0.4 m. A Roots blower with a 1700 m^{2}h^{-1} maintains the fast gas flow, and a hybrid stable azimuthal unstable resonator was employed [114]. In initial experiments, more than 2 kW of laser power was obtained at ~10% efficiency with a high optical quality beam which, after extracavity beam transforming optics, was measured as $M^2 < 1.2$.

26.4.4.2 Transverse-Flow RF Lasers

In the renaissance period of RF laser development since 1980, there has been considerable work on transverse-flow RF-excited lasers. The main thrust of much of this work has concentrated on the integration of the requirements of transverse RF discharges with the technology for handling high-speed gas flow in the transverse direction, gas recirculation and cooling. Although transverse systems are superficially attractive in providing very short transit distances through the active discharge medium, as mentioned earlier the main (intrinsic) deficiency relates to the transverse density (refractive index) gradients which have deleterious effects on the optical beam quality and pointing stability. Although these effects may be compensated to some degree for cw lasers, for repetitively pulsed or modulated lasers which are required for some applications, the transient moving density gradients produce non-stationary phase-front distortions and steering which it is not possible to correct. Nevertheless, the use of RF technology permits significantly increased discharge power density ≤ 30 W cm^{-3} for pseudo-cw excitation within and up to 100 W cm^{-3} for 'superpulsed' operation [123]. Such lasers have been demonstrated at power levels of >10 kW, but the limitations in terms of achievable beam quality limit the use of these lasers to some of those uses (e.g. some welding and heat treatment applications) where imperfect beam quality can be sometimes tolerated. The relative decline in interest in transverse-flow laser technologies has been particularly accentuated by the development of highly compact and lower-cost FAF technologies at power levels to >25 kW with superior beam quality. The latter have become highly competitive in the commercial market for high-power CO$_2$ lasers.

REFERENCES

1. Patel C K N 1964 *Phys. Rev. Lett.* **13** 617–19.
2. Witteman W J 1986 *The CO$_2$ Laser (Springer Verlag Series in Optical Sciences)* (Berlin: Springer).
3. Cheo P K 1971 CO$_2$ lasers *Advance in Lasers* vol 3, ed A K Levine and A J De Maria (New York: Dekker) ch 2.
4. Sobelev N N and Sokovikov V V 1967 *Sov. Phys.–Usp.* **10** 153.
5. Willett C S 1974 *An Introduction to Gas Lasers: Population Inversion Mechanisms* (Oxford: Pergamon).
6. Tyte D C 1970 Carbon dioxide lasers *Advances in Quantum Electronics* vol 1 ed D W Goodwin (London: Academic).
7. De Maria A J 1976 Review of high power CO$_2$ lasers *Principles of Laser Plasmas* ed G Bekefi (New York: Wiley) ch 8.

8. Hall D R and Hill C A 1987 Radiofrequency discharge excited CO_2 lasers *Handbook of Molecular Lasers* ed P Cheo (New York: Dekker) ch 3.
9. Herzberg G 1964 *Molecular Spectra and Molecular Structure* vol 2 (Princeton, NJ: Van Nostrand).
10. Reid J and Siemson K 1976 *Appl. Phys. Lett.* **29** 250.
11. Schultz G J 1959 *Phys. Rev.* **116** 1141.
12. Hake R D and Phelps A V 1967 *Phys. Rev.* **158** 70.
13. Boness M J W and Schultz G J 1968 *Phys. Rev. Lett.* **21** 1031.
14. Moeller G and Rigden G D 1965 *Appl. Phys. Lett.* **7** 274.
15. Patel C K N 1964 *Phys. Rev. A* **136** 1187.
16. Clark P O and Wada J Y 1968 *IEEE J. Quantum Electron.* **QE-4** 263.
17. He D and Hall D R 1984 *J. Appl. Phys.* **56** 856.
18. Vidaud P and Hall D R 1985 *J. Appl. Phys.* **57** 1757.
19. Novgorodov M Z, Sviridov A G and Sobolev N N 1971 *IEEE J. Quantum Electron.* **QE-7** 508.
20. Willett C S 1974 *An Introduction to Gas Lasers: Population Inversion Mechanisms* (Oxford: Pergamon) p 280.
21. Nighan W L and Bennett J H 1969 *Appl. Phys. Lett.* **14** 240.
22. Vidaud P, He D and Hall D 1985 *Opt. Commun.* **56** 185.
23. Anderson J D 1976 *Gas Dynamic Lasers: An Introduction* (New York: Academic).
24. Fenstermacher C A, Nutter M J, Leyland K and Boyer K 1972 *Appl. Phys. Lett.* **20** 56.
25. Dyson D J 1989 Resonators for high power CO_2 lasers *The Physics and Technology of Laser Resonators* ed D R Hall and P E Jackson (Bristol: Adam Hilger) ch 13.
26. Abrams R L and Bridges W B 1973 *IEEE J. Quantum Electron.* **QE-9** 940.
27. Vitruk P, Baker H J and Hall D R 1994 *IEEE J. Quantum Electron.* **QE-30** 1623.
28. Hochuli U and Sciacca T P 1974 *IEEE J. Quantum Electron.* **QE-1** 239.
29. Miles P A and Lotus J W 1968 *IEEE J. Quantum Electron.* **QE-4** 811.
30. Horrigan F 1969 *Microwaves* **8** 68.
31. Baker H J 1989 Multifold laser resonators *The Physics and Technology of Laser Resonators* ed D R Hall and P E Jackson (Bristol: Adam Hilger) ch 5.
32. Tiffany W B, Targ T R and Foster J D 1969 *Appl. Phys. Lett.* **15** 91.
33. Beaulieu A J 1970 *Appl. Phys. Lett.* **16** 504.
34. Dumanshin R and Rocca-Serra J 1970 *C. R. Acad. Sci.* **269** 916.
35. Lamberton H M and Pearson P R 1971 *Electron. Lett.* **7** 141.
36. Brown R T 1987 CO_2 TEA lasers in *Handbook of Molecular Lasers* ed P Cheo (New York: Dekker) ch 2.
37. Figueira J 1987 High energy short-pulse CO_2 lasers *Handbook of Molecular Lasers* ed P Cheo (New York: Dekker) ch 4.
38. Marcatili E A J and Schmeltzer R A 1964 *Bell. Syst. Tech. J.* **43** 1783.
39. Degnan J J and Hall D R 1973 *IEEE J. Quantum Electron.* **QE-8** 901.
40. Degnan J J 1976 *Appl. Phys. Lett.* **11** 1.
41. Hill C A 1989 Theory of waveguide laser resonators *The Physics and Technology of Laser Resonators* ed D R Hall and P E Jackson (Bristol: Adam Hilger) ch 3.
42. Hall D R, Peruso C, Johnson E, Schiffner G, McElroy J H and McAvoy N 1972 *Opt. Eng.* **11** 77.
43. Smith P W 1971 *Appl. Phys. Lett.* **19** 132.
44. Bridges T J, Burkhardt E G and Smith P W 1972 *Appl. Phys. Lett.* **20** 403.
45. Abrams R L 1974 *Appl. Phys. Lett.* **25** 304.
46. Burkhardt E G, Bridges T J and Smith P W 1972 *Opt. Commun.* **6** 193.
47. Hall D R, Jenkins R M and Gorton E K 1978 *J. Phys. D: Appl. Phys.* **11** 859.
48. Thomson J J 1891 *Phil. Mag.* **32** 321.
49. Javan A, Bennett W R Jr and Herriott D R 1961 *Phys. Rev.* **6** 106.
50. Patel C K N 1964 *Phys. Rev. A* **136** 1187.
51. Crocker A and Wills M S 1969 *Electron. Lett.* **5** 33.
52. Brown C O and Davis J W 1972 *Appl. Phys. Lett.* **21** 480.
53. Laakmann K D 1978 *Proc. Lasers '78 Conf.* (Orlando, FL).
54. Laakmann K D 1979 *Proc. Lasers '79 Conf.* (Orlando, FL) pp 741–3.
55. Sutter L V 1980 *Proc. SPIE 227* (Washington, DC).
56. Griffiths G A 1980 *Proc. SPIE 227* (Washington, DC) pp 6–11.
57. Chenausky P P 1980 Paper TUKK4 *Conf. on Lasers and Electro-optic Systems* (San Diego, CA).
58. Chenausky P P, Drinkwater E H and Laughman L 1982 US Patent 4,363,126.
59. Allcock G and Hall D R 1981 *Opt. Commun.* **37** 49.
60. He D and Hall D R 1983 *Appl. Phys. Lett.* **43** 726.
61. Lachambre J L, MacFarlane J, Otis G and Lavigne P 1978 *Appl. Phys. Lett.* **32** 652.
62. Raizer Y P 1979 *Sov. J. Plasma Phys.* **5** 232.
63. Myshenkov V I and Yatsenko N A 1981 *Sov. J. Quantum Electron.* **11** 1297.
64. Yatsenko N A 1982 *Sov. Phys. Tech. Phys.* **27** 741.
65. Levitskii S M 1958 *Sov. Phys. Tech. Phys.* **2** 887.
66. Vidaud P, Durrani S M and Hall D R 1988 *J. Phys. D: Appl. Phys.* **21** 57.
67. He D, Baker C J and Hall D R 1984 *J. Appl. Phys.* **55** 4120.
68. Kolesnychenko F Yu, Matyukhin V D, Murv'ev V F and Smaznov S I 1979 *Dokl. Akad. Nauk. SSSR* **246** 1091.
69. Wester R, Siewert S and Wagner R 1991 *J. Phys. D: Appl. Phys.* **24** 1796.
70. Vitruk P, Baker H J and Hall D R 1992 *J. Phys. D: Appl. Phys.* **25** 1767.
71. Smirnov A S 1984 *Sov. Phys.–Tech. Phys.* **29** 34.
72. Baker C J, Hall D R and Davies A R 1984 *J. Phys. D: Appl. Phys.* **17** 1597.
73. Wester R, Herziger G and Schulke H 1987 *SPIE* **81** 14.
74. Durrani S M A 1988 Optimization of rf discharges for CO_2 laser excitation *PhD Thesis* (Edinburgh: Heriot Watt University).
75. Konyukhov V K 1971 *Sov. Phys.—Tech. Phys.* **15** 1283.
76. Muehe C E 1974 *J. Appl. Phys.* **45** 82.
77. Vitruk P, Baker H J and Hall D R 1994 *IEEE J. Quantum Electron.* **QE-30** 1623.
78. Villarreal F, Murray P, Baker H J and Hall D R 2001 *Appl. Phys. Lett.* **78** 2276.
79. He D and Hall D R 1983 *J. Appl. Phys.* **54** 4367.
80. He D and Hall D R 1984 *IEEE J. Quantum Electron.* **QE-20** 509.

81. Siemson K J 1980 *Appl. Opt.* **19** 818.
82. He D and Hall D R 1984 *J. Appl. Phys.* **56** 856.
83. Vidaud P and Hall D R 1985 *J. Appl. Phys.* **57** 1757.
84. Vidaud P and Hall D R 1985 *Opt. Commun.* **56** 185.
85. Jackson P E, Hall D R and Hill C A 1989 *Appl. Opt.* **28** 935–41.
86. Newman L A and Hart R A 1987 *Laser Focus* **18** 80.
87. Spacht D P and DeMaria A J 2001 *Laser Focus World* **37** 397.
88. Corcoran V J and Crabbe I A 1974 *Appl. Opt.* **13** 1755.
89. Youmans D G 1984 *Appl. Phys. Lett.* **44** 365.
90. Newman L A, Hart R A, Kennedy J T, Cantor A J, DeMaria A J and Bridges W B 1986 *Appl. Phys. Lett.* **48** 1701.
91. Abramski K, Colley A D, Baker H J and Hall D R 1992 *Opt. Commun.* **90** 61.
92. Abramski K, Colley A D, Baker H J and Hall D R 1992 *Appl. Phys. Lett.* **60** 530.
93. Baker H J, Hornby A and Hall D R 1993 *Appl. Phys. Lett.* **63** 2591.
94. Abramski K M, Colley A D, Baker H J and Hall D R 1991 *IEEE J. Quantum Electron.* **QE-27** 1939.
95. Abramski K M, Baker H J, Colley A D and Hall D R 1996 *IEEE J. Quantum Electron.* **32** 304.
96. Villarreal F, Baker H J, Abram R, Jones D and Hall D R 1999 *IEEE J. Quantum Electron.* **QE-35** 267.
97. Abramski K M, Colley A D, Baker H J and Hall D R 1989 *Appl. Phys. Lett.* **54** 1833.
98. Hall D R and Baker H J 1988 *Proc. Gas Flow and Chemical Laser Symposium* Proc SPIE 1031 (Vienna) p 60.
99. Zhang X, Baker H J and Hall D R 1993 *J. Phys. D: Appl. Phys.* **26** 359.
100. Shackleton C, Baker H J and Hall D R 1992 *Opt. Commun.* **89** 423.
101. Hall D R and Baker H J 1989 *Laser Focus World* **25** 77.
102. Jackson P E, Baker H J and Hall D R 1989 *Appl. Phys. Lett.* **54** 1950.
103. Tulip J 1988 US Patent 4,719,639.
104. Siegman A E 1986 *Lasers* (Oxford: Oxford University Press) ch 22.
105. Nowack R, Opower H, Schaefer U and Wessel K 1990 *Proc. SPIE* **1276** 18.
106. Colley A D, Baker H J and Hall D R 1992 *Appl. Phys. Lett.* **61** 136.
107. Baker H J, Villarreal F J and Hall D R 2002 *The 3rd Int. Symp. on Laser Precision Microfabrication LPM2002* (Osaka).
108. Tsagkarakis M, Villarreal F J, Baker H J and Hall D R 2003 *J. Laser Appl.* in press.
109. Ferguson T R 1984 *Appl. Opt.* **23** 2122.
110. Xin J G and Hall D R 1987 *Appl. Phys. Lett.* **51** 469–71.
111. Bethel J W, Baker H J and Hall D R 1998 *Opt. Commun.* **125** 352.
112. Erlichmann D, Habich U and Plum H-D 1993 *J. Phys. D: Appl. Phys.* **26** 183.
113. Erlichmann D, Habich U, Plum H-D, Loosen P and Herziger G 1994 *IEEE J. Quantum Electron.* **30** 1441.
114. Schwede H 1989 *Proc. 9th Int. Laser Congress (Munich)* (Berlin: Springer).
115. Loosen P 1992 *Proc. Gas and Chemical Laser Conf.* (Crete) SPIE 1810 p 26.
116. Hage H, Martinen H and Northemann T 1987 *Proc. High Power Lasers Conf.* Proc. SPIE 801 (The Hague) p 58.
117. Beck R 1987 *Appl. Phys. B* **42** 233.
118. Loosen P and Wester R 1995 *J. Phys. D: Appl. Phys.* **28** 849.
119. Habich U, Du K, Erlichmann D, Jarosch U, Niehoff J, Plum H-D, Meyer R, Wolf N, Loosen P, Beck T, Hertzler C and Wollermann-Windgasse R 1994 *Proc. Gas and Chemical Laser Conf.* (Friedrichshafen).
120. Habich U, Jarosch U, Maly H, Meyer R, Loosen P, Wolf N, Beck T, Hertzler C and Wollermann-Windgasse R 1996 *Proc. Gas and Chemical Laser Conf.* (Edinburgh: SPIE).
121. Habich U, Loosen P, Hertzler C and Wollermann-Windgasse R 1996 *Proc. SPIE* **2702** 374.
122. Loosen P 1992 *Proc. Gas and Chemical Laser Conf.* SPIE 1810 (Madrid: SPIE) p 26.
123. Schock W, Hall T, Wildermuth E, Wessel K, Gehringer E, Schnee P and Hadinger F 1988 *Proc. Gas and Chemical Laser Conf.* SPIE 1031 (Vienna: SPIE) p 76.

27

Excimer Lasers: F_2, N_2 and H_2 Lasers

W. J. Witteman

CONTENTS

27.1 Introduction 366
27.2 Historical Perspectives 367
27.3 Excitation Technique 367
  27.3.1 Electron-Beam Excitation 368
    27.3.1.1 Electron-Beam Geometries 368
  27.3.2 Self-Sustained Discharge Technology 369
    27.3.2.1 Pre-Ionization 370
    27.3.2.2 X-Ray Source with Corona Plasma 370
    27.3.2.3 Single-Discharge Pulse 371
    27.3.2.4 Prepulse–Main Pulse 371
    27.3.2.5 Resonant Overshoot Mode 373
    27.3.2.6 Photo-Triggered Mode 374
    27.3.2.7 Instrumental Design 374
27.4 Rare Gas Halogen Excimers 375
  27.4.1 Kinetics 376
27.5 KrF Laser (248 nm) 378
27.6 XeCl Laser (308 nm) 379
  27.6.1 The Discharge 380
  27.6.2 Parametric Studies 380
  27.6.3 High Average Power XeCl Laser 381
27.7 KrCl Laser (222 nm) 383
27.8 ArF Laser (193 nm) 384
  27.8.1 The Discharge 384
  27.8.2 Laser Performance 385
  27.8.3 Long Pulses 386
27.9 XeF Laser (351,353 and 486 ± 35 nm) 387
  27.9.1 The Spectroscopy 388
  27.9.2 The Discharge 389
  27.9.3 Broadband Blue–Green C → A Transition 389
27.10 F_2 Laser (157 nm) 391
  27.10.1 The Spectroscopy 392
  27.10.2 Laser Performance 392
  27.10.3 Long Pulses 393
27.11 Other Rare Gas Halide Lasers 394
27.12 N_2 Laser (337–406 nm and 741–1230 nm) 394
  27.12.1 The Discharge 395
27.13 H_2 Laser (140–165 nm and 100–120 nm) 396
  27.13.1 Lyman Band (140–165 nm) 397
  27.13.2 Werner Band (100–120 nm) 397
  27.13.3 Excitation Technique 397
Appendix 398
References 398

27.1 Introduction

In the field of laser development, researchers have always been challenged to move to the shorter-wavelength part of the spectrum. In the period shortly after the invention of the laser, research activities were mainly concentrated on systems operating in the visible and near-infrared part of the spectrum. This choice of spectrum is understandable if we look at the required instrumental conditions: in particular, the optical components and technology for the required input powers were already available. The appropriate excitation method and input power could be realized at that time with classical instruments available in any well-equipped laboratory. Furthermore, the excitation power for reaching the laser threshold decreases rapidly with longer wavelength. Some near-infrared lasers such as the CO_2 and Nd:YAG lasers could, therefore, be developed energetically as mature high-power instruments for large-scale applications in roughly one decade. Being so successful and driven by potential new applications, similar systems in the UV, VUV and even XUV were desired.

However, worldwide research efforts to unlock UV and VUV laser systems revealed the limitations of the available suitable materials, the complexity of excitation technologies and, last but not least, the threshold conditions. Up to now, the availability of these lasers has been rather limited. This is partly related to the required low absorption of the laser medium and optical components in this part of the spectrum. Nearly, all solids and liquids strongly absorb VUV radiation. Fortunately, the situation for some selected gases is much more favourable.

Another limiting factor is the required high input power of those lasers. This can be understood by the following analysis. The cross section for stimulated emission σ_{st} is described by

$$\sigma_{\text{st}} = \frac{c^2}{8\pi v^2} A g(v) \tag{27.1}$$

where c is the speed of light, v is the transition frequency, A is the decay rate of the spontaneous emission and $g(v)$ is the lineshape function of the transition. To obtain laser action the small signal gain α_0 should exceed the minimum required threshold gain α_{th} which is equal to the losses in the resonator (mainly mirror and medium absorption). Thus, we have the condition

$$\alpha_0^3 \alpha_{\text{th}} = \sigma_{\text{st}} \Delta N_{\text{th}} \tag{27.2}$$

where ΔN_{st} is the threshold inversion. For each photon, the input power has to produce at least one excited state with energy exceeding that of the transition. Let us assume, for the moment very conservatively, an excitation efficiency of 100%. The minimum input power P_{th} to produce the threshold inversion density is then

$$P_{\text{th}} > hvA\Delta N_{\text{th}} \tag{27.3}$$

Substituting equations (27.1) and (27.3) into equation (27.2), we have the condition

$$P_{\text{th}} > \frac{8\pi h v^3 \alpha_{\text{th}}}{c^2 g(v)} \tag{27.4}$$

Usually the lineshape $g(v)$ is expressed in terms of the linewidth $\Delta\lambda$ of the transition with the relation $g(v) = \lambda^2/c\Delta\lambda$ so that equation (27.4) becomes

$$P_{\text{th}} > \frac{8\pi hc^2 \alpha_{\text{th}} \Delta\lambda}{\lambda^5}. \tag{27.5}$$

It can be seen that the minimum required input power density increases very rapidly with decreasing wavelength, and it does not depend on the spontaneous decay rate of the transition. In most VUV lasers, the values for cavity losses and $\Delta\lambda/\lambda$ are higher—sometimes by several orders of magnitude—than for visible or infrared lasers. But even assuming comparable values for these quantities the power density increases with the fourth power of the wavelength ratio of the compared systems. For example, at 100 nm, a threshold gain of 1% per cm and a linewidth of $\Delta\lambda/\lambda = 10^{-2}$, we need at least 36 kW cm^{-3}. Usually the excitation efficiency is not 100% but a small fraction of it so that the minimum input power must be considered at least an order of magnitude higher. Thus, it is not the fast decay rates of the upper laser transitions but, in most cases, the broad line profiles and short wavelengths that are the principal reasons for very high input powers. These high powers are not realistic for continuous operation and can only be reached in pulsed systems.

For VUV lasers with very short lifetimes in the upper laser level, of the order of 1 ns or less, an additional complication arises if the system is self-terminating, i.e. the lifetime of the lower laser level is larger than that of the upper level. For such systems time-independent spatial homogeneity of the excitation pulse, even at the required high density, is catastrophic. Gain is only present for a period equal to the lifetime of the upper state. Stimulated emission is, therefore, only feasible if a high-power excitation pulse moves with the speed of the generated stimulated emission. The initially produced spontaneous emission will then be amplified by the generated gain, and this stimulated emission thus follows the propagating excitation pulse. The pulse duration is given by the lifetime of the upper state. The output power is amplified spontaneous emission (ASE). The molecular hydrogen laser is a typical example.

Successful pulsed operation of gas systems is based on either high-energy beams that penetrate the laser gas or a self-sustained glow discharge. In special cases a combination of both techniques turns out to be advantageous.

As mentioned already, the transparency for UV and VUV is often another serious handicap even for reaching threshold. Although there have been successful attempts at purifying suitable materials, this has so far only contributed to the improvement of such optical components as mirrors. For gases, the situation is more promising. The absorption can often be circumvented or reduced to an acceptable level when the composition, density and purity are well chosen. This, together with the high potential of discharge technology is the main reason why short-wavelength gas lasers have been successfully developed.

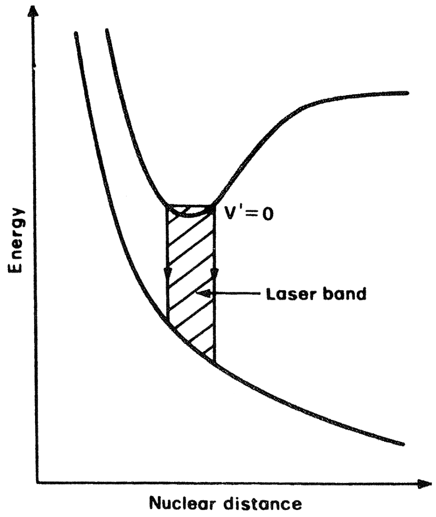

FIGURE 27.1 Energy states of an excimer molecule.

Of all known short-wavelength systems, the excimer lasers can be considered, with respect to output power and efficiency, as the champions. They represent an interesting and important class of molecular lasers involving electronic transitions between an excited bound state and an unbound or weakly bound ground state. They use rare gas molecules such as Xe_2 (172 nm), Ar_2 (126 nm) and Kr_2 (146 nm) or, more successfully, rare gas halogen molecules, for example ArF. This is schematically shown in Figure 27.1 with the potential energy curves for the upper and repulsive lower states of a diatomic molecule. The upper potential curve has a minimum so that the excited state exists, i.e. a vibrating molecule in an electronic state. Decaying to the lower state the molecule dissociates immediately because of the repulsive potential. For the vibrating molecule there is a broadband of transitions with different energies. The attractive feature for laser action is the absence of the lower level so that absorption from the ground state is absent. The system does not saturate by the laser process itself. Such systems are, in principle, good candidates for high output powers.

Electronic transitions with an unbound lower state have been known for decades in the field of gaseous electronics and spectroscopy of high-pressure rare gases. Gas discharges in multi-atmospheric rare gases producing excited molecules such as He_2, Ne_2 and Ar_2 are often used as high-intensity UV light sources. Since these molecules exist only in an excited electronic state, they are called excimers, a contraction from excited dimer. Later on, especially when other gases were studied as candidates for UV lasers, it was found that rare gas and halogen mixtures show similar behaviour with an unbound ground state. For that reason, they were also called excimers although, strictly speaking, we are not dealing with a dimer because they are composed from different atoms.

27.2 Historical Perspectives

The broadband emission of excimer molecules was already known around 1930 when the UV emission of He_2 was described [1]. Much later, other rare gas molecules such as Ar_2, Kr_2 and Xe_2 as well as metal vapours [2] such as Hg_2 and Cd_2 were reported [3]. Rare gas halogen compounds were probably observed for the first time around 1974 when the quenching of metastable states of rare gases was studied [4,5]. The idea to select excimers as an attractive medium for laser action because of the absence of a ground level came shortly after the invention of the laser [6]. However, at that time, the instrumental developments, i.e. the technology for high-pressure discharges to fulfil the laser conditions, were inadequate to realize excimer lasers. It took more than 10 years before the first excimer laser was reported [7]. It used stimulated emission from Xe_2 molecules obtained by electron-beam (e-beam) excitation of cryogenically cooled xenon.

The first experimental studies with excimer lasers go back to 1972 when a high-pressure xenon gas was excited by an e-beam [8]. Laser action in rare gas halogen excimers was reported for the first time in 1975 for XeBr and XeF [9,10]. Shortly after the first realizations of rare gas halogen excimer lasers all possible combinations of rare gases and halogens were thoroughly investigated as laser candidates. Practically, all combinations were successful, although some of them were superior with respect to output power and efficiency. This is especially true for XeCl, KrF, ArF and XeF.

It became clear at that time that, in general, the laser physics of excimers was understood to a great extent but not the technology for realizing good performing systems. Further development was, therefore, seriously hampered by the absence of the technical knowledge to realize stable discharges in large volumes of multi-atmospheric rare gas halogen mixtures. During the subsequent decade, there was a worldwide effort to find new technologies to improve discharge performance. This was also stimulated by the awareness of several potential applications of high-power UV lasers in industry, especially in the field of material processing and lithography. The found solutions were promising, and it even became a challenge to build very large systems with average output powers in the range of kilowatts. In order to pay for the costly developments, international collaboration was then strongly stimulated by national governments. This approach has, for instance, been very successful for the kilowatt XeCl laser. In a sense, this laser development has also had a strong technological push on the progress in high-density gas discharges containing species with negative ion formation.

27.3 Excitation Technique

Pulsed excitation technology for excimer lasers has developed along two different paths. The first, e-beam excitation, which can be successfully applied to all systems, is based on direct excitation with relativistic electrons. It offers the advantage of uniformly depositing large amounts of energy into any high-density gas mixture. The attractive feature is the possibility of separately studying the input energy transfer and the laser kinetic process for various gas compositions. Studies with this excitation technique have, therefore, contributed tremendously to a better understanding of excimer formation and its lasing potential. Moreover, this technique has been developed successfully to reach the highest output powers and efficiencies for excimer systems. The disadvantages, however, are its complexity, high costs and limited repetition rate.

The other more practical excitation technology is based on the self-sustained discharge of a laser gas. To limit the applied voltage for high-density gases, transverse discharge geometries were chosen. Large electrodes are parallel to the laser axis. The discharge electrons gain their kinetic energy from the applied electric field and lose it to the gas by excitation, ionization and elastic collisions. The discharge's behaviour depends strongly on the gas density and its composition. In most cases it is strongly inclined to unstable behaviour so that pulse durations are inherently limited. Such a discharge can be kept stable for a longer period with the help of a simultaneous excitation with a rather weak e-beam, say a combination of e-beam and gas discharge. Nevertheless, for practical reasons, one likes to avoid the complexity of e-beams. Therefore, many more attractive alternatives have been successfully worked out. Those techniques are very specific and refined. They are relatively cheap compared with e-beams and, in principle, suitable for high repetition rates so that high average output powers become available.

27.3.1 Electron-Beam Excitation

High-energy electrons to excite the laser gas are generated outside the laser in a vacuum chamber or diode compartment. The electrons are emitted from the cathode in this compartment, usually by field emission, and are accelerated by a high voltage. The high-energy electrons are then directed towards the anode and penetrate through a thin foil that separates the high-pressure gas from the vacuum chamber. The e-beam, with energies usually in the range of several 100 kV, excites and ionizes the laser gas. This direct transfer is then followed by a chain of kinetic reactions involving energy exchange between the ions and excited states with other gas constituents, eventually leading to the excited excimer molecules. For efficient excitation, the current density must be at least 10 A cm^{-2} over a length of at least 20 cm. The realization of such devices was energetically carried out thanks to the pioneering work in the AWRE Aldermaston Laboratory [11] in the 1960s. The required high voltage of several hundreds of kilovolts is usually achieved by means of a fast-switching Marx generator that charges a coaxial oil or water capacitor as a pulse-forming line. The principle of the Marx generator is based on the parallel charging of its capacitors with a relatively low-voltage power supply followed by decharging in series through spark gaps into the coaxial capacitor. The transfer to the pulse-forming coaxial capacitor is done because the high-voltage pulse of the switched Marx, especially in the case of large capacitors, is too slow to obtain a high current density. When the voltage of the coaxial capacitor has risen to a sufficiently high value, a low-inductance spark gap closes spontaneously transmitting the charge to the load, i.e. the laser chamber. In the case of impedance matching with the diode compartment, a short, clean, square pulse of high current density is obtained. The current pulse length is determined by the length of this coaxial capacitor and ranges, in practical systems, between 20 and 200 ns.

The high current density of the cathode is mostly obtained by field emission on a cold cathode. (Conventional thermionic electron emitters cannot be used for currents above 1 A cm^{-2} because of their limited yield.) The construction is very special to ensure high current fields. It contains tantalum knife edges, needles, carbon wedges or carbon felt. This is based on the strong enhancement of the electric field on a microscopic scale. The anode can be a grid supporting a thin metal foil often made of titanium, a metal with a high ratio of tensile strength and mass density. This foil separates the diode compartment from the laser vessel. For very high gas densities, say above 5 bar, some constructions have an additional foil with a support structure that contains holes or slots with a transparency of 70%–80%.

To achieve an optimum incoupling of the input energy the diode impedance must be matched as well as possible with the pulse-forming line. The maximum current density in the diode is space-charge limited according to the Child–Langmuir law [12]:

$$J = 2.37 \times 10^{2} \frac{V^{3/2}}{d^{2}} \tag{27.6}$$

where J is the current density (A cm^{-2}), V is the diode voltage [MV] and d is the anode–diode distance [cm]. The maximum obtainable pulse length depends on d, because at the onset of the vacuum current, a plasma is formed that moves across the gap with a velocity of a few cm per microsecond, decreasing the actual impedance [13]. Furthermore, for high current densities, pinching effects in the diode caused by the self-magnetic field or by the magnetic field of the return current can limit the freedom in designing diodes adapted to a more or less homogeneous excitation current in the laser vessel.

27.3.1.1 Electron-Beam Geometries

The most simple and commonly used diode configuration has a one-sided transversal geometry. A cross-sectional view is shown in Figure 27.2a. The electrons emitted from a cathode wedge in the vacuum diode (VD) penetrate through the supporting foil into the laser compartment (LC). The broken circle in LC indicates schematically the cross section of the laser beam in the cavity. The main drawback of this construction is its poor energy utilization by the excitation inhomogeneity of the laser beam. A more uniform deposition can be obtained with a guiding magnetic field [14] or with a symmetric construction where two identical beams on both sides are applied as shown in Figure 27.2b. The best way to obtain beam uniformity is a coaxial symmetry [15] (see Figure 27.2c). The anode is a self-supporting cylindrical foil tube with a high electron transmittance. The electrons are focused to the laser axis so that a uniform high excitation density can be performed. Using titanium foil 50 μm thick, the laser gas can be pressurized to at least 14 bar in cylinders of 1 cm diameter [16]. Scaling up this geometry to larger diameters and higher current densities, say 4 cm and 200 A cm^{-2}, the self-magnetic field of the current may cause current contractions near the cavity ends. This problem can be circumvented by an additional current return, parallel to the laser tube, as indicated in Figure 27.2d.

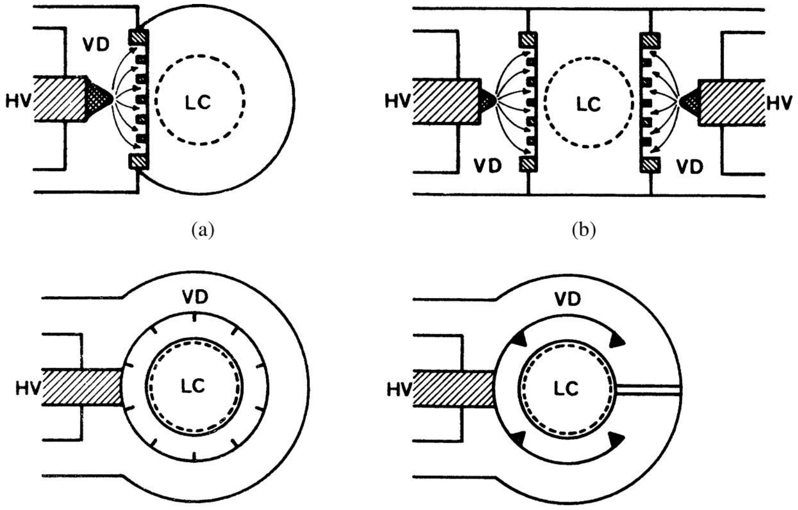

(a) (b)

(c) (d)

FIGURE 27.2 Different e-beam diode configurations. (a) One-sided transversal. (b) Two-sided transversal. (c) Coaxial (radial). (d) Pseudo-coaxial.

A relatively simple cylindrical construction for a laser tube 20 cm in length with a diameter of 1 cm has been successfully used to study various excimer systems. A cross section of this laser is shown in Figure 27.3 [17]. The coaxial vacuum diode is driven directly by a low-inductance ten-stage Marx generator. The spark gaps are UV-triggered, except for the first gap, which is triggered externally. Each stage is formed by eight pairs of $BaTiO_3$ capacitors of 1.8 nF each. The total capacitance per stage is 7.2 nF. It is seen that the generator is enclosed in a cylindrical vessel 1 m in height and with a diameter of 25 cm, filled with 4 bar SF_6 to prevent flash-over. The compact arrangement provides a low inductance and a fast risetime. The Marx generator is capable of providing 100 J at a maximum voltage of 600 kV. The spark gaps are flushed with dry air. The voltage is monitored by means of a differentiating voltage sensor [18] and by means of a self-integrating Rogowski coil [19]. The cathode consists of a 20-cm-long cylinder of diameter 5 cm with rounded ends to prevent flash-over to the vacuum chamber walls. Inside this cylinder, two graphite felt strips of $20 \times 0.7\,\text{cm}^2$ are mounted parallel to the axis. In this way, a two-sided transversal excitation in a radial symmetric electric field is obtained. The anode or laser tube is made of 25 μm thick titanium foil with a single electric weld along the axis. Titanium end-pieces are laser welded to this tube. The tube can stand gas pressures of up to 10 bar. This cathode configuration provides a good impedance matching to the Marx generator. The corresponding voltage and current waveforms are illustrated in Figure 27.4. The current pulsewidth is about 50 ns. Since most halogen components in the gas mixture are very aggressive, the total reflector is an MgF_2-coated aluminium mirror. As outcoupler, an uncoated plane-parallel suprasil or MgF_2 window is used.

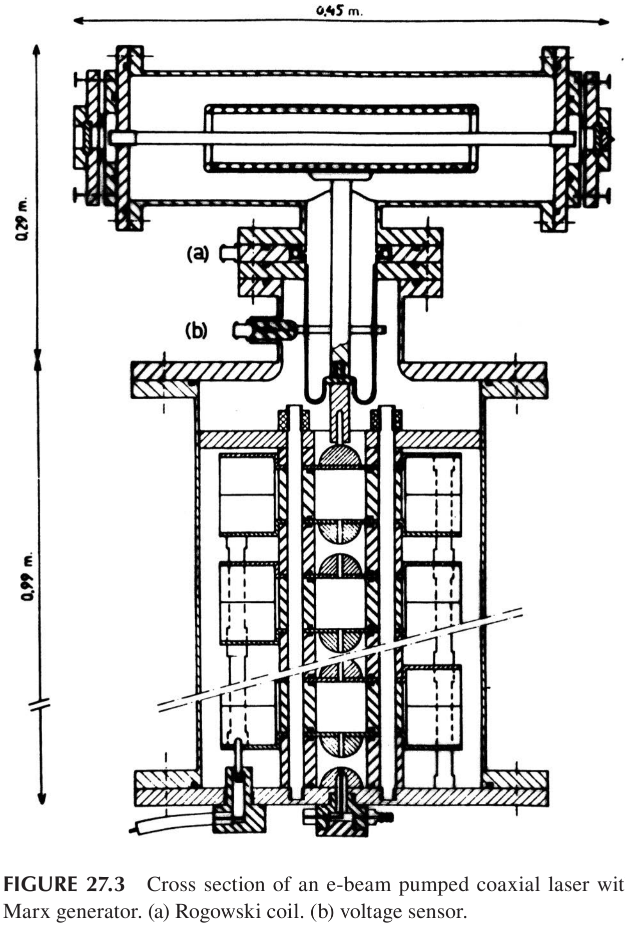

FIGURE 27.3 Cross section of an e-beam pumped coaxial laser with Marx generator. (a) Rogowski coil. (b) voltage sensor.

27.3.2 Self-Sustained Discharge Technology

The chain of kinetic reactions leading to the formation of excimer molecules in gas discharges is based on three-body collisions. For those collisions to be effective, it is requisite to consider multi-atmospheric gas densities. This fundamental condition has a strong impact on the discharge technology for the relevant gas mixtures. Most multi-atmospheric self-sustained discharge systems are, by nature, unstable, and the presence of the halogen constituent with its negative ion formation intensifies the instability process. As pointed out earlier, the laser conditions can only be fulfilled with pulsed systems.

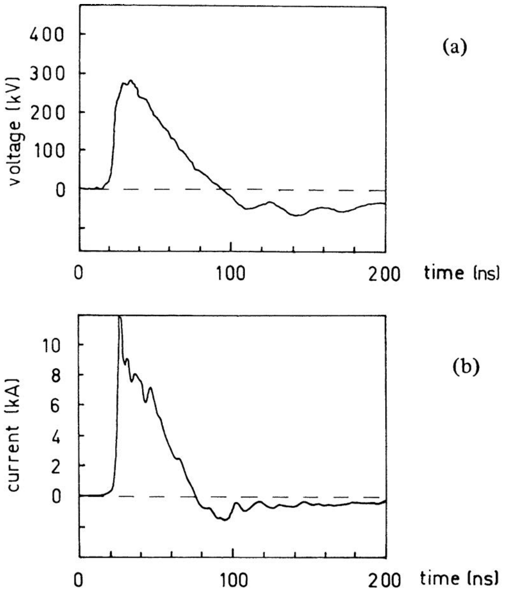

FIGURE 27.4 Voltage and current pulse of the vacuum diode as a function of time.

Therefore, the technological development of the discharge is focused on slowing down or temporarily suppressing instability formation in an initially stable pulsed discharge. For this purpose, several innovations have been pioneered. They all have in common that the quality of the discharge of any excimer laser depends, among other things, strongly on the initial electron density and its distribution by the pre-ionization source. Furthermore, all these developments are based on a fast transverse discharge geometry (perpendicular to the laser axis). The average electron energy in this kind of discharge is only a few electronvolts so that the production of excited states and ions and the subsequent formation of excimer molecules are less efficient than in e-beam systems. However, this discharge technique can operate at a high repetition rate. The systems are then also capable of delivering high average powers.

27.3.2.1 Pre-Ionization

Operation of high-pressure gas lasers in a self-sustained discharge regime demands a proper pre-ionization technique to obtain a uniform glow discharge. This can be performed by direct e-beam interaction, by UV or by X-ray irradiation of the laser gas. Both UV and e-beam have their own shortcomings for high-pressure gases. Those for UV pre-ionization arise mainly due to high absorption of the UV radiation in the laser gas. The main limitation of e-beam pre-ionization is its window. Since it must be transparent for the electrons, a thin metal foil is used. The strength requirements for this thin foil separating the vacuum diode from the high-pressure laser chamber are not compatible with high transmission. For X-ray pre-ionization, the situation is much more favourable. Medium-energy X-rays (50–100 kV) already have a high penetration depth, and relatively thick windows can be constructed. Therefore, the X-ray technique has been successfully applied to excimer lasers.

In general, medium-energy X-rays with high peak powers and short risetimes are required. This is especially the case for X-ray switched single discharges [20,21] where the applied discharge voltage is relatively high compared with the quasi-steady-state discharge voltage. After switching a fast electron avalanche, a uniform glow discharge free from streamers is obtained, provided the X-ray peak power is sufficiently high and uniform with a short risetime. A premature electron avalanche due to a long risetime of the X-ray pulse causes a non-uniform unstable discharge.

27.3.2.2 X-Ray Source with Corona Plasma

A very successful development for obtaining a short intense X-ray pulse with a fast risetime is based on a corona plasma cathode that supplies the X-ray-producing electrons [22]. A cross-sectional view and its electrical circuit are shown in Figure 27.5. The anode consists of a tantalum foil, and the cathode contains two corona plasma tubes each 80 cm in length. These tubes are made of quartz tubes of 1 cm diameter with the inside metal bars acting as trigger electrodes, and outside thin tungsten, wires wound around them. When a fast-rising positive-voltage pulse reaches these trigger electrodes, a negative charge accompanied by a corona plasma along these quartz tubes is formed. The plasma is produced by the interaction of the accelerated electrons along field lines on the quartz surface with (impurity) molecules adsorbed to the quartz surface. The plasma electrons are then extracted from the surface and accelerated to the anode by the anode voltage. The distance between the cathode and the anode is 3.5 cm. The anode is connected to a pulse transformer by means of an 80-cm-long, 25-Ω coaxial cable. The primary storage capacitor of 17 nF is charged to 20 kV. The trigger voltage for the corona on the quartz tube surface taken from a tab of the pulse transformer passes a 180-cm-long shock line to compress and to delay the pulse [23]. Figure 27.6 shows the

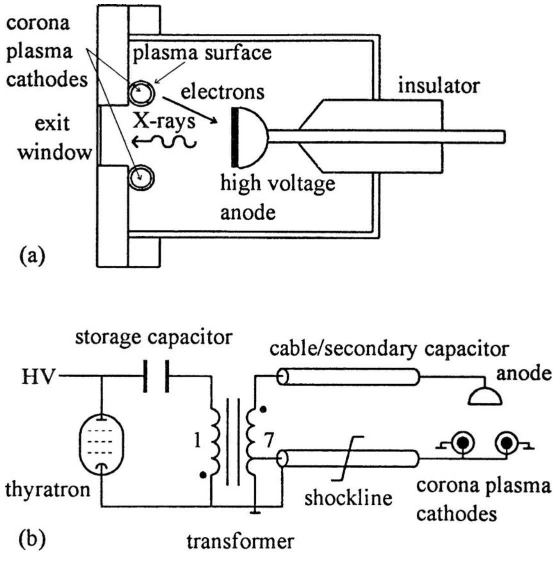

FIGURE 27.5 Cross-sectional view of the X-ray generator and its electrical circuit.

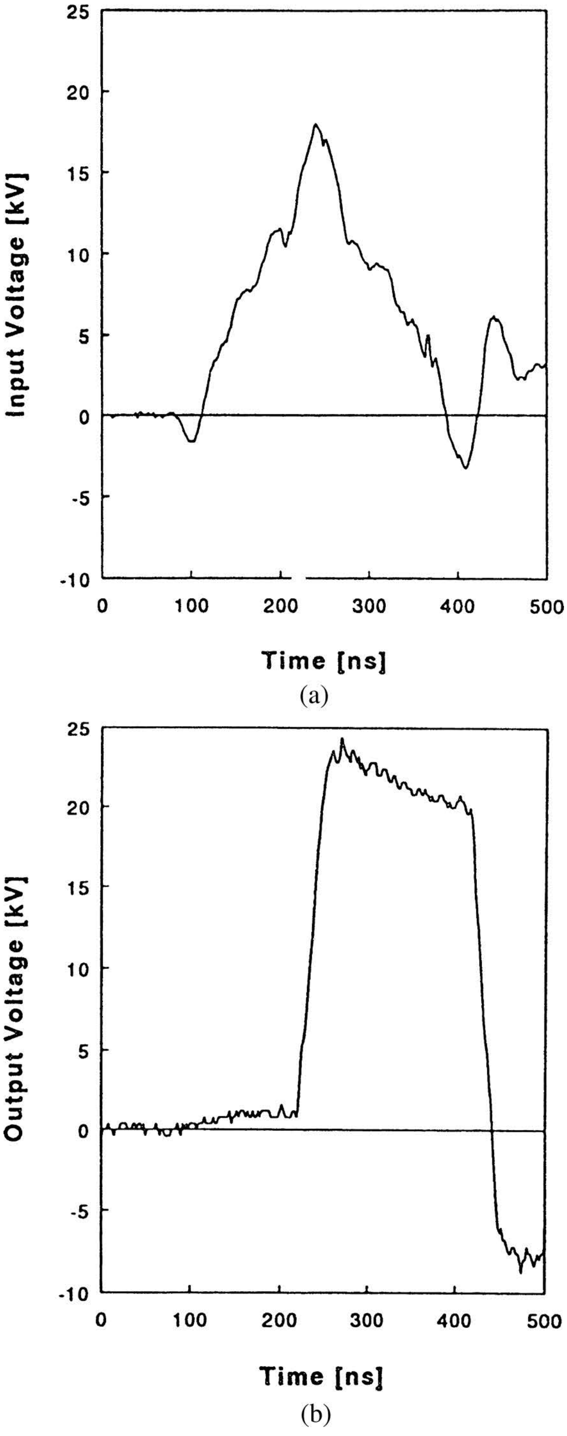

FIGURE 27.6 Input (a) and output (b) voltages of the ferrite shock line.

waveforms of the input and output pulses. It is seen that the risetime is reduced from 100 ns to less than 20 ns and delayed by about 100 ns. During this delay, the acceleration voltage pulse reaches the anode. Thus, as soon as the trigger pulse is applied, the plasma electrons are accelerated and bombard the tantalum foil producing X-rays. Figure 27.7 shows the waveforms of the anode voltage, current and X-ray pulses. These X-ray pulses with fast risetimes are successfully applied to prepulse–main pulse excited excimers.

27.3.2.3 Single-Discharge Pulse

After the initial low electron density obtained by the X-ray pulse, the discharge implies the sudden application of a strong electric field that causes electron multiplication in the laser gas. In order to avoid the formation of filamentary arcs, i.e. an unstable irregular discharge, it is necessary to start with an initially homogeneous electron density of at least of the order of 10^8 electrons cm^{-3} and a fast risetime, of the order 10 ns, of the applied electric field. The fast risetime leads to the formation of a dense hot-spot structure on the cathode which enhances the homogeneity of the discharge [24]. If the discharge is formed by an applied electric field, the plasma resistivity decreases rapidly with increasing plasma density. In this way the discharge will reach the so-called steady-state conditions for which the voltage U_B across the discharge gap varies, from now on, relatively little with increasing current. The impedance across the discharge gap will then become lower than the driving circuit's output impedance. When this occurs, the discharge will go into an oscillatory mode, which immediately destroys the stability necessary for the laser kinetic process. The circuit is schematically shown in Figure 27.8 where the electrodes are shown in a cross-sectional view perpendicular to the laser axis. The energy storage capacitor is connected to the electrodes in series with a switch [25–28]. To increase the initial electric field of the discharge, a small peaking capacitor is used so that at the onset twice the charging voltage is applied to the electrodes. The first phase before the current reversal of an initially stable discharge is most effective for the laser process. In the appendix it is shown that for efficient energy transfer from the capacitor into the discharge, the charging voltage should be twice the steady-state discharge voltage. This condition is not consistent with the required high-voltage breakdown of the discharge. Hence, for such a system, the voltage and current show circuit ringing, and only during the short period of the first oscillation is laser power generated.

27.3.2.4 Prepulse–Main Pulse

Since the impedance before breakdown of the discharge is high compared with its steady-state value and the voltage required for rapid breakdown is not consistent with efficient impedance matching of the electric circuit, using separate electric circuits for the avalanche breakdown (prepulse) and the quasi-steady-state discharge (main pulse), respectively, has been proposed [29–31]. The energy of the prepulse is kept low, in most cases only a few joules at a voltage, depending on the specific excimer, of roughly six times the steady-state value U_B. This low prepulse energy facilitates the realization of the desired fast current rise for obtaining a dense hot-spot structure on the cathode, as discussed earlier, resulting in a high overvoltage and a rapid breakdown of the gas. The sustainer capacitor for the main pulse will then be charged to twice the steady-state voltage U_B for optimum impedance matching (see appendix). With such a circuit, there are, in principle, two modes of operation: the switch mode and the diode mode as will be described in the next paragraph. The diode mode is not attractive because the polarities of the two pulses are equal,

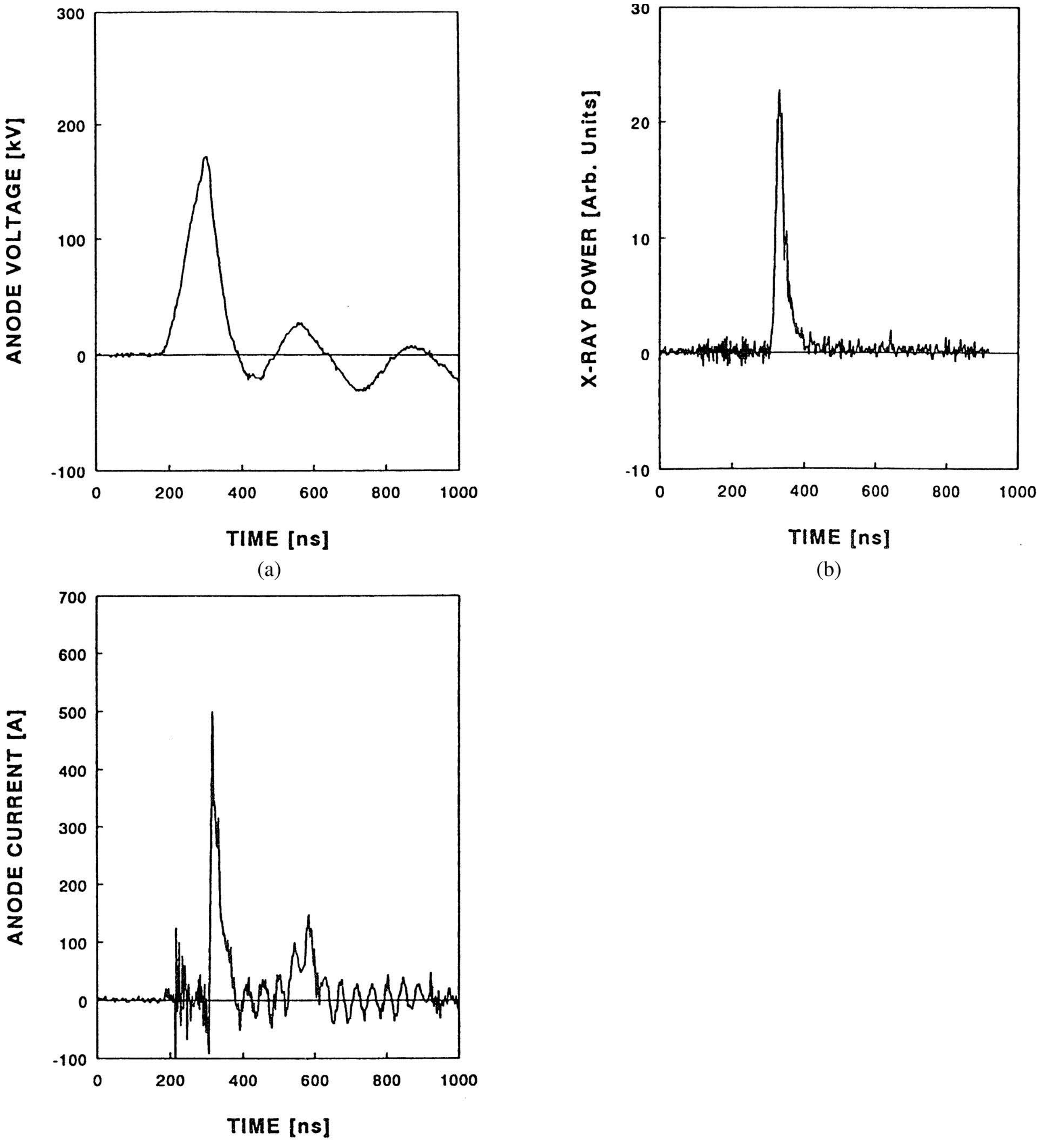

(a)

(b)

(c)

FIGURE 27.7 Waveforms of the anode voltage (a), current (b) and X-ray power (c) of the X-ray generator.

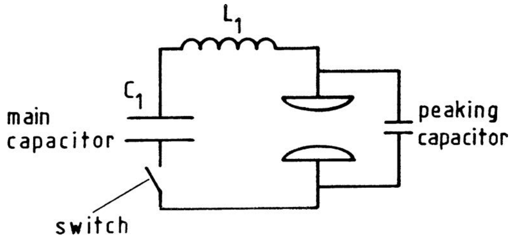

FIGURE 27.8 Scheme for a single discharge.

and consequently, there will be a time delay between the two pulses due to the inductance of the main pulse circuit. Since the mechanism for forming streamers or filamentary arcs is always present and time-dependent, any delay should be avoided. The situation is much more favourable for the switch mode.

An attractive way to separate the two circuits is by the use of a saturable magnetic isolator. The principle is shown in Figure 27.9. For the essential requirement of fast discharging into the laser gas, during their discharge, the inductances of

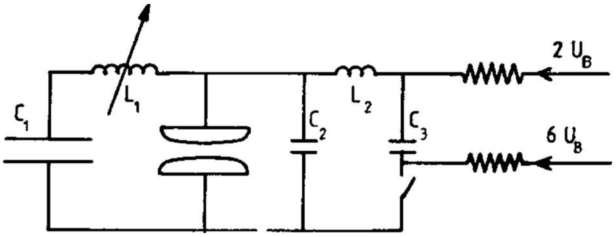

FIGURE 27.9 Scheme for a prepulse–main pulse discharge in switch mode.

the circuits are as low as possible. Therefore, the sustainer capacitor C_1 charged at $2U_B$ is connected to the laser head by a metal plate surrounded by a race track made of low-loss ferrite bricks. The prepulse circuit consists of a small peaking capacitor C_2 in series with a capacitor C_3 of equal size and a spark gap. The capacitor C_3 can be positively (switch mode) or negatively (diode mode) charged with respect to the main capacitor. For the switch mode, one side of C_3 is connected to C_1 with the voltage $2U_B$, whereas the other side is connected with a voltage source of about $6U_B$. Directly after firing the X-ray pulse, the prepulse circuit is switched so that the voltage across C_3 becomes $-4U_B$ which will be directly transferred to the peaking capacitor C_2. Then this voltage is also across the electrodes causing, during several tens of nanoseconds, the breakdown of the discharge. In the meantime, this prepulse also saturates the magnetic switch so that after the avalanche process of the prepulse, the main pulse will automatically maintain the discharge by delivering, in principle, all its energy.

The inductive state of the saturable ferrite inductor of the main switch can be described with the *BH* curve as shown in Figure 27.10. After charging the main capacitor C_1, the ferrites are, for increasing *H*-values, in a high inductive state, indicated by point A. During the firing of the prepulse, the ferrites remain in this high inductive state while passing the section from A to B. When the gas breaks down at point B, the ferrites are almost saturated, and the main current with still increasing *H* values starts immediately at point C in a low inductive state. At the end of the pulse, the current is zero, and the state of the ferrite reaches point D. Charging C_1 again the left-hand part of the loop with negative *H*-values is followed, finally reaching point A again for zero current.

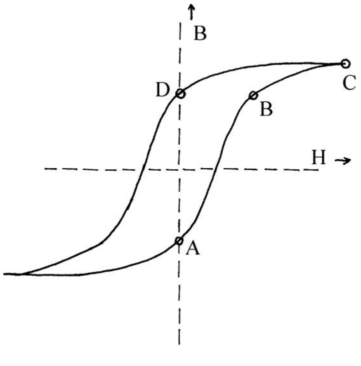

FIGURE 27.10 *B H* curve of the saturable ferrite inductor showing the inductive states of the pulsed current operation.

It should be noted that when the main pulse starts there is a current reversal in the discharge and that the saturating voltage across the switch is $6U_B$. It may happen that in order to obtain a faster avalanche and a stabler discharge, depending on the specific excimer, the charging voltages, especially of the prepulse circuit, are somewhat different.

Since there is a current reversal through the laser, the anode and cathode functions of the electrodes are interchanged. It is well known in discharge physics that the electron emission of the cathode is accompanied by material sputtering. With X-ray pre-ionization, the thin plate that transmits the X-rays is, therefore, chosen as the anode for the main pulse. However, during the prepulse, this electrode is the cathode so that material is sputtered. Therefore, this mode of operation limits the lifetime of this thin electrode. This mode of operation with the present construction is therefore not suitable for high repetition operation.

27.3.2.5 Resonant Overshoot Mode

The resonant overshoot mode [32] is, at first glance, very similar to switch-mode operation. The schematic diagram is shown in Figure 27.11. It is essential for obtaining fast current rise to replace L_2 by a saturable inductor [33]. Furthermore, the difference in operation is set by the specific values of the chosen components. We have the additional requirement that the resonance time τ_1 of the current flow from C_1 to C_2 just after the saturation of L_1 is shorter than the resonance time τ_2 of a reversed current flow from C_3 to C_2.

The principle of operation is as follows. The capacitors C_1 and C_2 are also charged to $2U_B$, and the connected voltage to C_3 is, in this case, only $4U_B$ as shown in the figure. After pre-ionization, the prepulse is again fired within a few microseconds after charging C_1, C_2 and C_3. After switching, the voltage drop over C_3 is now $-2U_B$ so that the voltage over C_2 will subsequently change from $2U_B$ to $-2U_B$, which is too low to start the avalanche. Thus, the laser gas does not break down at this phase. In the meantime, the magnetic switch L_1 saturates by its voltage drop of $4U_B$ and allows a current flow from the main capacitor C_1 to the small peaking capacitor C_2 which results in an overshoot by reaching, at most, $6U_B$. The increasing voltage on the peaking capacitor in this charge transfer will now reach such a level that a fast avalanche breakdown in the discharge will occur to be directly followed by the main discharge.

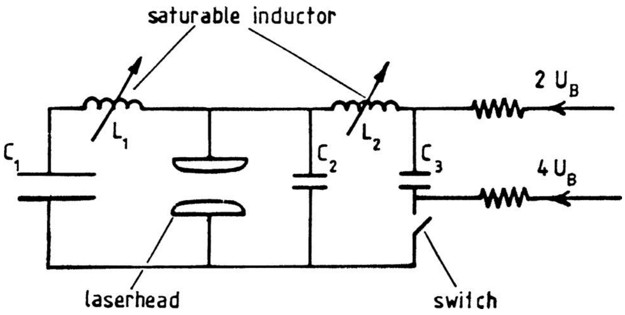

FIGURE 27.11 Resonant overshoot circuit scheme.

The inductive state of the saturable ferrite inductor L_1 can also be described with the *B H* curve shown in Figure 27.10. Following the *B H* curve we start after the charging of C_1 at point A. After switching C_3 and charging C_2 at $-U_B$, we reach point B. Next the ferrites will further saturate as C_2 is now charged by the main capacitor C_1. After breakdown, a large current flows through the inductor and, for increasing current, point C will be reached. At the end of the discharge, when the current again becomes zero, point D of the upper part of the curve is reached. By charging C_1 again, the current flows in the opposite direction, bringing the ferrites back in the high inductive state indicated by point A.

It is important that, just after switching the prepulse, the resonance charging of C_2 from $2U_B$ to $-2U_B$ occurs very rapidly because the size of the magnetic main switch L_1 is proportional to the switching time. The inductor L_2 is, during this resonance charging of C_2, in a saturated state so that for a current reversal between C_2 and C_3, the inductor L_2 is unsaturated and the condition that τ_1 is shorter than τ_2 is easily fulfilled.

We note that, because of a voltage drop of only $4U_B$ over the main magnetic switch, less ferrite bricks are needed for the race-track construction and that the current to be switched by the prepulse between C_3 and C_2 is only two-thirds of that described earlier for the switch mode. We also note that, in this case, there is no current reversal in the discharge. This means that the thin X-ray transmitting anode will, in principle, not be damaged. This all makes this mode of operation attractive for high repetition operation.

27.3.2.6 Photo-Triggered Mode

For the photo-triggered mode, an X-ray beam starts the discharge, and hence, this mode is often called the X-ray-triggered mode. In this mode of operation, the laser gas discharge itself is used as the switch in a single discharge circuit. Thus, the laser discharge is triggered by the pre-ionization pulse instead of a prepulse as in the previous case. This breakdown, now initiated by the pre-ionization pulse after the high voltage pulse has been applied over the electrodes, has a strong impact on the discharge physics. The closing time of the laser discharge as switch, which is equal to the formative time of the discharge, depends on the voltage applied to the electrodes and on the electron production rate of the pre-ionizer. Usually, the charging voltage of the circuit capacitor is considerably higher than twice the steady-state voltage, in order to obtain a rapid avalanche in the electron multiplication process from the pre-ionization density of, say, $10^8\,\text{cm}^{-3}$ to a steady-state value of about $10^{14}\,\text{cm}^{-3}$. The high charging voltage leads to a current oscillation of which only the first phase before the current reversal will be stable. Consequently, the conversion efficiency will be low. However, each photo electron will immediately gain sufficient ionization energy so that the multiplication remains, in principle, spatially homogeneous, while in the previous case, some pre-ionization electrons drifted away from the cathode due to the presence of the main voltage across the electrodes, thereby making the discharge less homogeneous.

The absence of a prepulse, of course, also has several advantages. The system becomes simpler. The thyratron switch, power supply and trigger circuit of the prepulse as well as the magnetic switches of the main circuit and prepulse compressor are not needed. This mode of operation has been successfully developed for XeCl lasers [20,21].

27.3.2.7 Instrumental Design

The most promising discharge technique for the rare gas halide excimer lasers is the prepulse–main pulse technology with resonant overshoot, although it is more complicated than the single-discharge technique. Most attractive are the better conversion efficiency, the longer output pulses, less system poisoning by electrode sputtering and wear-out of the thin X-ray transmitting electrode and the suitability for high repetition rate operation.

A successful prepulse–main pulse design for a self-sustained excimer laser requires spatial homogeneities, pulse compressions and fast risetimes for all input quantities of the discharge. A cross-sectional view of such a system and a scheme for its electrical circuit are shown [34] in Figures 27.12 and 27.13, respectively. A pulsed collimated X-ray beam (described in Section 27.3.2.2) enters the discharge chamber through a 2 × 60 cm aluminium window 1 mm thick. The electrode gap is 2.5 cm. The pulse compression network of the prepulse also serves to keep the current of the thyratron below its maximum

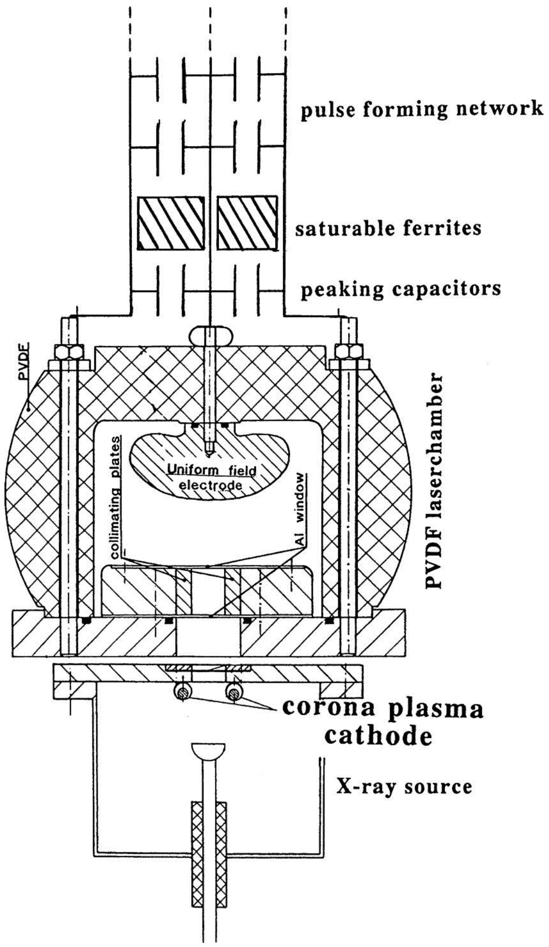

FIGURE 27.12 Cross-sectional view of a pulsed excimer laser system

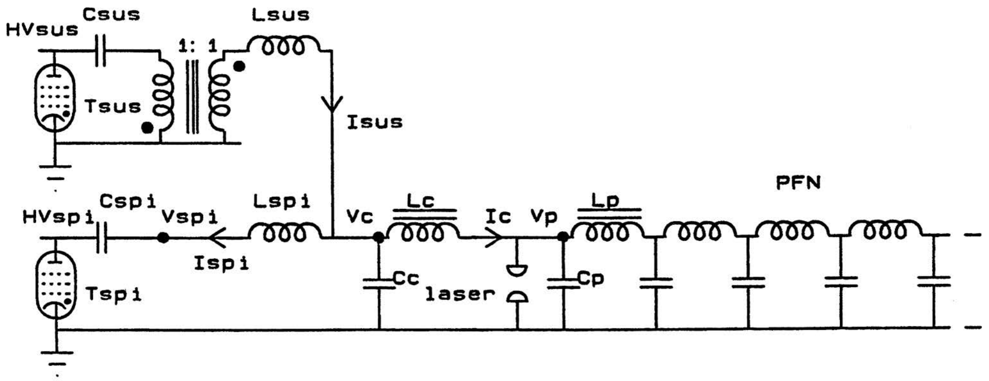

FIGURE 27.13 Scheme of the prepulse–main-pulse circuit with thyratron switches. The subscript 'sus' refers to the sustainer and the subscript 'spi' to the prepulse or spiker pulse.

allowable value. The saturable inductor of the prepulse circuit consists of six rings of CMD 5005 high-frequency ferrite from Ceramic Magnetics with a total cross section of 26.4 cm^2. The pulse-forming network (PFN) capacitor of the main pulse circuit consists of eight double-plate transmission lines connected in parallel to the laser head. Each line contains 20 TDK capacitors of 2.7 nF each resulting in a total capacity of 432 nF. The saturable inductor of the main switch is constructed in a rectangular shape in order to reach minimum inductance after saturation. It has a 2 mm slit in the middle to be used for the conducting plate that connects the laser chamber with the PFN capacitor. The inductor is made of CMD 5005 ferrite blocks with a total cross section of 12 cm^2. The peaking capacitor is 2.8 nF. In general, the prepulse will be chosen as high as possible without a discharge breakdown during its negative voltage swing. The risetime of the resonance voltage just before breakdown is given by $\pi(C_p L_{p,\,sat})^{1/2} = 24$ ns, where $L_{p,\,sat}$ is the residual inductance of the saturated ferrite blocks.

Applying this system, for example, to a XeCl laser system by using a mixture of 1 mbar HCl, 20 mbar Xe and 4 bar Ne and charging voltages of 10 and 20 kV for the PFN and prepulse capacitor, respectively; typical waveforms are shown [34] in Figure 27.14. Thanks to fast risetimes and impedance matching, the discharge stability for this XeCl system of 4 bar is 500 ns, whereas the output pulse follows the current pulse closely.

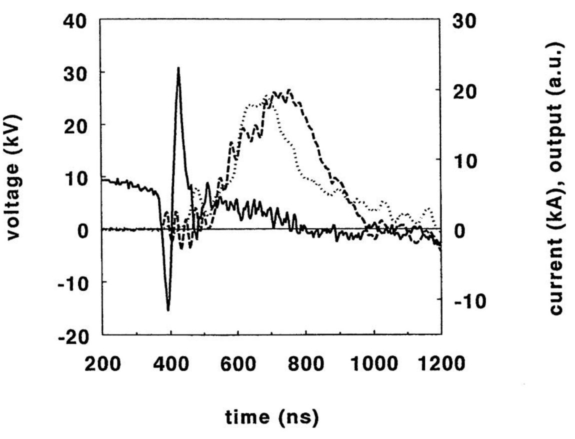

FIGURE 27.14 Waveforms of the discharge voltage (full), current (dashes) and optical output (dots) for the resonant overshoot mode of an XeCl laser.

The stability of the inherently unstable excimer systems depends on both gas composition and instrumentation parameters. For usual gas compositions, the stability deteriorates very rapidly even after appropriate starting conditions with increasing risetimes of the various circuits and with improper matching. Stated differently, the stability period of an excimer discharge can be extended by shorter risetimes in the circuits. It should be noted that the discussed instrumental principles apply to practically all self-sustained discharge excimers, although the values for circuit components and electrical parameters may differ widely.

27.4 Rare Gas Halogen Excimers

The rare gas halogen excimer has received most attention in the field of excimer lasers. They are highly developed and are currently the most powerful lasers in the UV. Several systems are well engineered, and there is a great deal of understanding about the discharge physics and the kinetic chain for the formation of the lasing molecules. In particular, the properties of XeCl (308 nm), KrF (248 nm), ArF (193 nm) and XeF (351 and 353 nm) have been studied extensively.

The spectroscopy of the rare gas halide molecules exhibits a general structure which is shown in Figure 27.15 [35]. The ground state is covalently bonded and correlates to ground state ^1S rare gas and ^2P halogen atoms at infinite internuclear separation. The ground-state manifold of the halogen atom with the orbital angular momentum of one consists of two states. The $^2\Sigma$ state has the lowest energy since in this configuration the single occupied halogen orbital is directed toward the rare gas atom. Since it forms the ground state, it is referred to as the X state [36]. This state is generally nearly flat or, at most, weakly bound as in the case of XeCl (255 cm^{-1}). The exception is XeF which has a binding of approximately 1065 cm^{-1} [37]. The $^2\Pi$ state of the ground-state manifold is always repulsive. Since it forms the first state above the ground state it is referred to as the A state. The upper state is a charge transfer state between the positive rare gas atom and

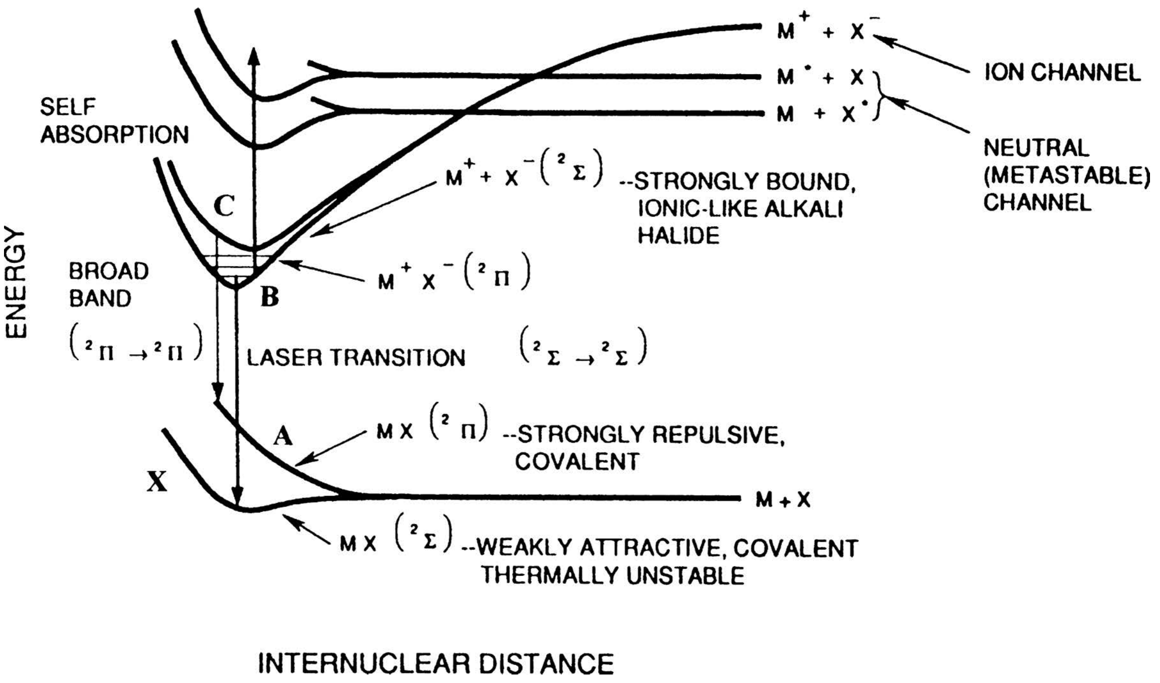
M⁺ + X⁻
ION CHANNEL
M* + X
M + X*
NEUTRAL (METASTABLE) CHANNEL
SELF ABSORPTION
M⁺ + X⁻ (²Σ) --STRONGLY BOUND, IONIC-LIKE ALKALI HALIDE
C
ENERGY
BROAD BAND
(²Π → ²Π)
M⁺ X⁻ (²Π)
B
LASER TRANSITION
(²Σ → ²Σ)
A
M X (²Π) --STRONGLY REPULSIVE, COVALENT
X
M + X
M X (²Σ) --WEAKLY ATTRACTIVE, COVALENT THERMALLY UNSTABLE
INTERNUCLEAR DISTANCE

FIGURE 27.15 Schematic potential energy diagram for a diatomic rare gas halide molecule showing the dominant B → X transition and the less efficient C → A transition.

the negative halogen atom with the ^2P and ^1S state, respectively, at infinite separation distance. Beginning at an energy equal to the ionization potential of the rare gas less the electron affinity of the halogen, the potential of the state of this system formed by the two particles follows a Coulomb curve which crosses, in the adiabatic sense, the covalent curves correlating to excited states of the rare gas atom and the halogen atom. The crossings generally occur at large internuclear separation where the overlap between orbitals centred on the rare gas and the halogen is small, so that the interactions will be small at the crossing points. At close internuclear separation, the potential energy curve splits into $^2\Sigma$ and $^2\Pi$ states. The structure of the upper-level manifold is similar to that of the ground-state manifold, again with the $^2\Sigma$ state lying lowest as indicated. By convention, this is referred to as the B state. In the interesting cases, the Coulomb curve crosses all the excited covalent curves, and the ionic state forms the lowest excited state. The emission spectrum of the rare gas halides consists of several bands. The strongest band is the $B(^2\Sigma) \rightarrow X(^2\Sigma)$ transition and gives rise to a laser transition. Other transitions have, in general, a much higher input energy threshold value if they will lase at all.

27.4.1 Kinetics

The kinetics of the rare gas halide lasers are rather complex. The laser gas mixtures are at multi-atmospheric densities and consist of a high percentage of a lighter rare gas, called a buffer gas (He, Ne or Ar), a small amount, less than 10%, of a lighter donor rare gas (Ar, Kr or Xe) and about 1% of a halogen or halogen-bearing gas. The electrical excitation of the gas mixture results mainly in the formation of excited atoms and atomic ions of the dominant lighter rare gas. The formation of the desired excimer molecule occurs at the end of the kinetic reaction chain. This reaction chain consists of charge transfer processes and recombination processes such as collisions between charge carriers of opposite sign and the dimerization of excited atoms with neutral atoms. The internal energy must decrease as a result of each reaction; otherwise, the reaction is not possible. For instance, in the case of atomic ions forming the excimer molecule, the energy decrease is equal to the sum of the ionization energy of the positive ion and the electron affinity of the negative ion minus the excitation energy of the excimer. Once the oppositely charged ions or excited particles begin to interact, the ability of the system to dispose of this excess energy determines the probability that recombination occurs or reaction products are obtained. The requirement that linear and angular momentum be conserved in the reaction makes it almost impossible to dispose of the recombination energy by an increase in the kinetic energy of the recombining ions. However, the energy release can be achieved through an increase in the kinetic energy of a neutral particle that is also involved in this interaction process. Then, we are dealing with three-body collisions. The three-body collisions take place in several reactions and are essential in the formation of the lasing excimer molecules. This means that for obtaining sufficient fast recombination or energy transfer, the density of neutral particles (buffer gas) must be at least at atmospheric density.

The predominantly excited and ionized buffer gas atoms may then lead rapidly to the excimer molecule. Although the excited buffer atoms are initially in different states, at high gas density these states are rapidly quenched to lower states and by far most of the excited atoms will then be found in the lowest metastable state. These atoms will dimerize by three-body collisions:

$$X^* + 2X \rightarrow X_2^* + X \tag{27.7}$$

where X is the buffer atom. Then the energy of the excited states is transferred between the buffer gas and the heavier donor rare gas (Y). Reactions of the type $X^* + Y \rightarrow X + Y^*$ are relatively slow unless there is a near resonance between the initial and final states. The rate depends very sensitively on the closeness of the resonance. Reactions of the type

$$X_2^* + Y \rightarrow 2X + Y^* \tag{27.8}$$

are much more rapid because the excess energy can be disposed of in the dissociation products.

Also, the ions formed by the electrical excitation rapidly dimerize by three-body collisions of the type

$$X^+ + 2X \rightarrow X_2^+ + X \tag{27.9}$$

where X^+ is directly produced by the high-energy electrons of e-beam pumping or, in the case of discharge pumping, in a two-step process. The first step is the formation of the metastable state X^* followed in the next step by the ionization of X^*. This happens because the average electron energy in the discharge is low (a few eV), only relatively few electrons are able to ionize directly and much more can reach the metastable level. The metastable state density can be relatively large in a gas discharge. Furthermore, the cross section for ionization of a metastable state is orders of magnitude larger than the cross section for ground-state ionization.

Direct charge transfer between the buffer gas ion and the neutral-donor rare gas atom is generally very slow like the reaction of the excited buffer atom with the donor gas. However, charge transfer from the dimer ion to the donor atom is generally very fast in a reaction like

$$X_2^+ + Y \rightarrow 2X + Y^+. \tag{27.10}$$

The excited-donor rare gas atom reacts directly with the halogen (Z_2) or halogen-bearing molecule (ZM) as

$$Y^* + Z_2\,(\text{or ZM}) \rightarrow YZ^* + Z(\text{or M}) \tag{27.11}$$

where YZ^* is the excited rare gas halide molecule. These kinds of reaction have large cross sections and are often called *harpooning* in analogy with reactions between alkali atoms and halogen molecules. If other reaction products do not occur, reaction (27.11) is said to have a unit branching ratio. This formation process is often called the metastable or neutral channel.

The forming of an excited rare gas halide may also follow the ion channel. The negative halide ion is produced in a fast exothermic dissociative attachment reaction such as

$$Z_2 + e^- \rightarrow Z^- + Z \tag{27.12}$$

or

$$ZM + e^- \rightarrow Z^- + M \tag{27.13}$$

In spite of the strong Coulomb attraction between the negative halogen atom and the positive donor rare gas atom, a recombination in the absence of collisions with a third body is not possible because linear and angular momentum are not conserved. The recombination is, therefore, mainly achieved by a three-body process such as

$$Y^+ + Z^- + X \rightarrow YZ^* + X \tag{27.14}$$

which is very fast at high buffer gas densities.

So far, we have discussed, in general, the main kinetics in the formation process. A full description, including all species produced in the discharge, may deal, depending on the specific excimer, with more than 60 different reactions, and as numerical simulation has shown, most of them have a negligible effect on the production rate of the lasing excimer molecule. For instance, the reactions of the excited and ionized buffer gas atoms with the halogen molecules and halogen ions, similar to reactions (27.11) and (27.14), are much less likely with an appropriate choice for the partial pressures of the system. There are, however, fast quenching processes of the excited excimer. Direct quenching takes place by all gas components, and they are most effective by the halogens. This may result in the dissociation of the excited excimer or in the formation of triatomic species of the type

$$YZ^* + Y + X \rightarrow Y_2Z^* + X \tag{27.15}$$

This process is found to be very effective.

Although several of the quenching processes are very rapid, they do not, in general, give serious problems for well-engineered laser systems. In such systems, the excited excimer molecule is also subjected to the radiation field in the laser cavity, so there is a finite stimulated emission lifetime which, if the optical field is strong enough, can be made shorter than the quenching lifetime. The quenching losses are then negligible. However, the intracavity absorption may become a dominant loss mechanism. For optimizing the output, there will be a trade-off between these processes.

The significance of these kinetics depends strongly on the initial excitation of the gas. When we are dealing with e-beam pumping, the energy of the incident electrons is so high that they mainly ionize the particles and transfer high energy to the secondary electrons which, in turn, further ionize the gas by slowing down. They also create excited atoms, although these atoms will be ionized as well. This means that in e-beam systems, the excimer production rate is mainly given by the ionization channel, i.e. reactions (27.9), (27.10) and (27.14). The metastable route is less significant here. In contrast, the discharge-pumped systems produce mainly along the metastable channel described by reactions (27.7), (27.8) and (27.11). This is because the average electron energy in the discharge is much smaller than the first excited state and certainly not enough to reach direct ionization. Only a small fraction of the discharge electrons are capable of exciting the gas, and a relative small amount of ions is then produced in a two- or multistep process. This also counts for the much lower efficiency that is obtained with discharge systems compared with e-beam systems.

27.5 KrF Laser (248 nm)

The first reported KrF laser was based on e-beam pumping [10,38–40]. Around this time, discharge pumping for this system was demonstrated [41–43]. The high electron energy density and plasma stability that is imposed by e-beam excitation resulted in the successful development of this laser. The usual gas mixture of an e-beam system is 2–6 mbar F_2 or NF_3, 100–300 mbar Kr and 2–4 bar Ar. In the formation kinetics, both metastable atoms and ions are produced by the e-beam electrons interacting mainly with the buffer gas. When Ar is the buffer gas, on average, approximately 26 eV is deposited in the gas for each produced electron–ion pair. Some of it is transferred to the emitted secondary electron which, in turn, excites atoms and finally, through successive atomic collisions, rapidly cools to about a few eV. Of all e-beam pumped excimer lasers, the highest intrinsic efficiency (about 10% [44–47]) and an output power density of more than 60 J l^{-1} [48] have been reported for KrF. The reason for the high efficiency comes from the relatively low ionization energy of the buffer gas, a few potential energy crossings of the Coulomb curve of the Kr^+ and F^- ions covalent curves correlating to excited states of Kr and F atoms and the relatively low intracavity radiation absorption.

The KrF emission spectrum consists of several bands. The strongest band with the B → X transition is observed as the lasing transition. The linewidth is about 2 nm, and the X state is weakly repulsive. The upper state has a large number of overlapping vibrational and rotational states at the usual high gas density. This homogeneous line broadening also has a favourable effect on the efficiency. The lifetime of the upper state is found to be 9 ns [49]. The cross section becomes $2.4 \times 10^{-16} cm^2$ as follows from equation (27.1).

The Kr ions for forming KrF^* are either produced directly by the interaction of the e-beam with Kr or by the reaction with Ar_2^+ according to reaction (27.10). The secondary electrons from the ionization process undergo easily attachment with F_2 to form F^- ions according to reaction (27.12). The ions recombine in three-body collisions:

$$Kr^+ + F^- + Ar \to KrF^* + Ar \qquad (27.16)$$

This process is rapid because the ions attract each other with the long-range Coulomb interaction. Although for e-beam pumping there is also, in principle, a metastable channel, it is not important because only a fraction (15%–20%) of the electron energy is transferred to the metastable atoms. Moreover, the sequence reactions in this neutral channel are much slower than those with ions so that an even smaller part of the electron energy goes through the metastable channel. The KrF^* molecules also undergo quenching reactions with the laser gas and electrons [50]. These quenching losses in the laser are in competition with the stimulated emission process and are determined by the optical quality of the cavity. However, intracavity absorption by discharge species such as Ar_2^+, Kr_2^+, F^- and F_2 increases with the cavity field. For an optimized system, for the outcoupling mirror of the laser, there is a trade-off between these competing processes.

Analysing the kinetic process, it is found that a limited number of reactions play a critical role in calculating the laser parameters. The quenching of KrF^* determines critically the optimized gas densities, especially the Ar density. F_2 is less critical, and the additional F_2 concentration that compensates for the burn-up loss during the excitation has practically no effect on the output power when the excitation pulse length is increased. At optimized conditions, of the KrF^* produced about 50% is lost by quenching, about 20% is lost by absorption and about 30% is correlated to the outcoupled beam [51]. Experiments have confirmed that the output power follows the input power at least up till 500 ns [52]. In the Figures 27.16 and 27.17, the output powers are plotted as a function of, respectively, the Ar and Kr density with an average ionization rate of an Ar atom, $P[s^{-1}]$, as parameter [53]. It is seen that the optimized densities of Ar and Kr increase with the pumping power as indicated by P. For instance at $P = 4 \times 10^3$ which corresponds to an e-beam current density of 70 A cm^{-2}, the observed optimized densities for Ar and Kr are, respectively, 4 bar and 160 mbar and the output power density is 100 MW l^{-1}.

Higher output power densities for a given input current of the e-beam are obtained when the buffer gas is increased with a mixture of Ar and Ne. This effect can be attributed to the fact that the quenching by Ne is less effective so that the optimization occurs at higher density and that the energy deposited in the Ne buffer is efficiently transferred to the Kr species. The metastable Ne atoms are formed in so-called Penning

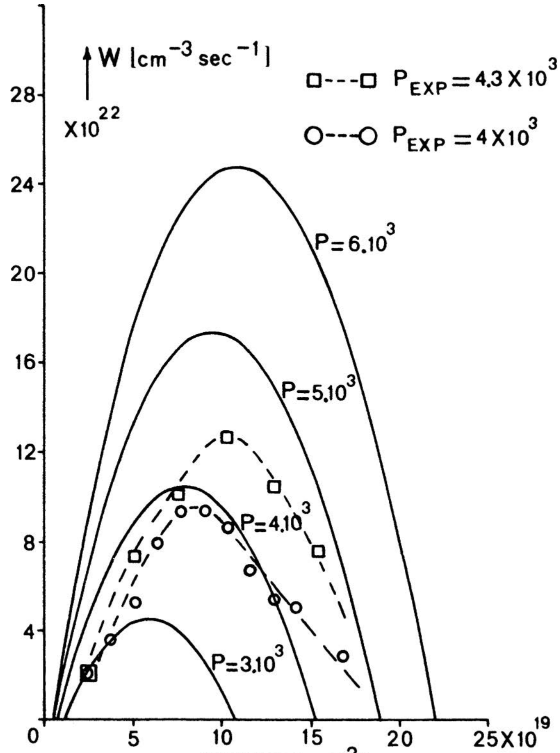

FIGURE 27.16 The measured and calculated extracted photon density rate as a function of the Ar density for Kr and F_2 densities of 3×10^{18} and 6×10^{16} cm^{-3}, respectively. The parameter P is the average number of ionizations of an Ar atom per second.

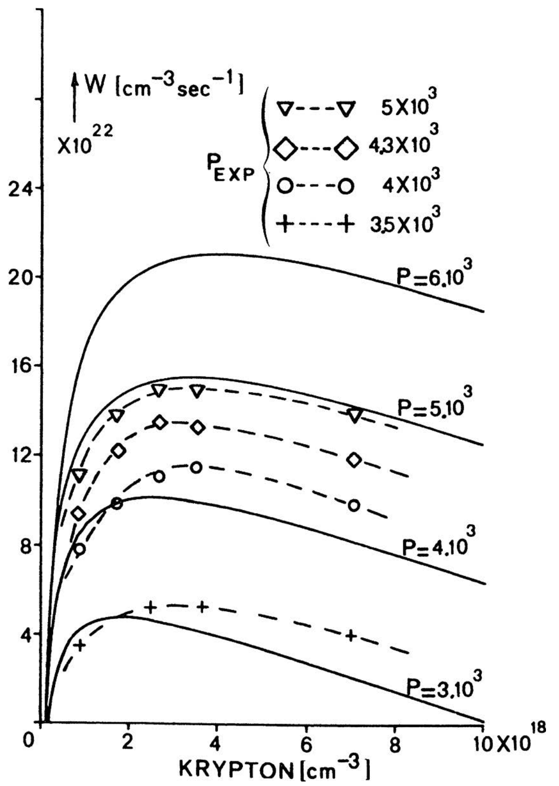

FIGURE 27.17 The measured and calculated extracted photon density rate as a function of the Kr density for Ar and F_2 densities of 6.5 $\times 10^{19}$ and 6×10^{16} cm^{-3}, respectively. The parameter *P* is the average number of ionizations of an Ar atom per second.

reactions with Ar^+ and Kr^+ [54]. The effect of Ne as a buffer gas becomes even more pronounced at higher input powers. At an e-beam current of 400 A cm^{-2}, the optimized Ar density is 5 bar in the Ar–Kr–F_2 mixture. Replacing Ar by Ne, the laser output scales linearly with the Ne density over the range 2–14 bar [55]. For the high-density regime, the addition of Ar has no beneficial effect. This range was limited by the strength of the anode foil of the e-beam. At 14 bar, the output with the Ne–Kr–F_2 mixture exceeds the optimized Ar–Kr–F_2 mixture by a factor of 4.5. The dimerization of Ne^+ and Ne^* proceeds at a speed 3–20 times slower than the corresponding processes in a mixture with Ar as the buffer gas [56]. So it is expected that the dimer densities in the Ne mixture are relatively low which is favourable since the absorption coefficient of Ne_2^+ at 248 nm is at least an order of magnitude higher than for Ar_2^+.

The impressive performance of the e-beam-pumped KrF with its highest output density and efficiency at relatively short wavelengths was a strong encouragement for developing huge systems with energies above 10 kJ to study laser fusion by means of inertial confinement [57].

For discharge KrF lasers, the kinetic processes and system technology are very similar to those in ArF systems to be discussed later. For KrF the same gas mixture is used except that Ar is replaced by Kr. The buffer gas is again He or Ne. Usually, He is used as the buffer gas [28,58–60]. However, it is expected that when the risetime of the prepulse discharge is small, say 10 or less nanoseconds, the use of Ne will lead to longer pulses and higher output energies, as will be discussed for ArF. A discharge-pumped KrF laser needs less pumping power and yields more output than the ArF laser under identical circumstances.

27.6 XeCl Laser (308 nm)

The first reported XeCl laser was based on e-beam pumping [38]. The high electron energy is, as mentioned earlier, advantageous for obtaining an efficiency as high as 8% [61]. The more interesting development in this field is based on gas discharge excitation for reasons explained in Section 27.3. However, the efficiency of discharge pumping is lower than that of e-beam pumping. The highest reported value is 5% [32].

For the laser process the main upper levels are the B and C states which have a strong bond. The lower A state is strongly repulsive whereas the X state is loosely bound. The energy needed to break the X state is so small that the thermal vibrational energy of the molecule is sufficient to break it. The strongest laser lines at 307.9 and 308.2 nm involve the B → X transition with a bandwidth of $\Delta\lambda = 0.5$ nm [36]. The B state has a rotational–vibrational structure. In the XeCl formation process, the inversion is spread over these levels. Between these levels, the vibrational energy can be transferred by collisions. There is, however, competition between this relaxation process and the stimulated emission process. The depleted strongest laser line will be filled with less populated levels if the collision process is faster than the stimulated emission process of these levels. So it may happen that one strong transition is fed by all excited vibrational levels. If, however, the radiation field is weak (lower pumping power) and the relaxation process is sufficiently slow (lower gas density), several lines oscillate simultaneously. Also, the loosely bound X state has some vibrational levels so that transitions can, in principle, take place between different upper levels and different lower levels. The strongest transition is then determined by the population inversion as well as by the corresponding Franck–Condon factor. It was found that, for a non-selective cavity, the 0 → 1 and the 0 → 2 vibrational transitions are the strongest [62,63]. The C → A transition, which emits at $\lambda = 345$ nm, has, due to its strong repulsive lower state, a large linewidth of 20 nm so that the cross section for stimulated emission is much smaller than for the B → X transition. Since the upper states are also strongly coupled normally only the B → X transition will oscillate.

A typical gas mixture of the discharge laser contains 1 mbar HCl, 10 mbar Xe and Ne as the buffer gas with a total pressure of 5 bar. In the past, He has also been used as a buffer gas but less successfully. The halogen-bearing molecules BCl_3, CCl_4, CH_2Cl_2, CCl_2F_2, $CFCl_3$ and $CHCl_3$ were also tried, but the best results are obtained with HCl. The partial pressures of HCl and Xe can be very controllably kept constant by means of a cold trap gas purifier. Since the optimized HCl density depends on the discharge current and its pulse length, it is convenient to regulate the partial pressure by the cold trap temperature. Furthermore, the purifier controls the vapour pressures, and the surplus is frozen in the cold trap. In particular, this buffer takes care that the HCl consumed during operation will be supplied. This happens because the discharge dissociates the HCl and the chlorine ions attach themselves to the electrodes and other metal parts of the laser head. The H ions eventually form H_2 molecules. Thus, there is a loss of HCl. Another advantage of a cold trap gas purifier is that it freezes in contaminants such as the H_2O and CO_2 released from the walls. A typical temperature for the purifier is 122 K.

Detailed kinetic modelling of the laser process requires a thorough understanding of the reactions and their cross sections. The main kinetics for the inversion production are

$$\mathrm{Xe}^+ + \mathrm{Cl}^- + \mathrm{Ne} \rightarrow \mathrm{XeCl}^* + \mathrm{Ne} \tag{27.17}$$

$$\mathrm{Xe}_2^+ + \mathrm{Cl}^- \rightarrow \mathrm{XeCl}^* + \mathrm{Xe} \tag{27.18}$$

$$\mathrm{Xe}^* + \mathrm{HCl}_{v=1,2} \rightarrow \mathrm{XeCl}^* + \mathrm{H} \tag{27.19}$$

where Xe^+, Xe_2^+ and Xe^+ are formed in reactions with dimer ions and metastable dimers of the buffer gas as pointed out in Section 27.4.1.

The ionization of Xe occurs *via* excited states because the average electron energy of only a few electron volts is too small. The discharge instability is strongly enhanced by the dissociative attachment of electrons to HCl by the reaction

$$\mathrm{HCl} + \mathrm{e}^- \rightarrow \mathrm{Cl}^- + \mathrm{H} \tag{27.20}$$

The higher the HCl concentration is, the higher the attachment rate of the electrons and the faster the growth of instability will be. The formation reaction for HCl from H and Cl is very slow so that the HCl must be replenished. During the discharge many other reactions take place [64].

27.6.1 The Discharge

Shortly after a homogeneous pre-ionization, with an initial electron density of at least $10^7\,\mathrm{cm}^{-3}$, is obtained, a quasi-stable discharge can be maintained for a period up to 1 µs depending on the discharge parameters. During this period, instabilities are building up, and these will eventually short-circuit the discharge. Thus, there is a transit time during which the discharge remains uniform and useful for the laser process.

The discharge physics is as follows. The high electron density of about $10^{14}\,\mathrm{cm}^{-3}$ for reaching the quasi-steady state is obtained by a fast high voltage prepulse. The initial electrons are accelerated in an avalanche process. The shorter the risetime is, the longer the acceleration voltage will remain much higher than the quasi-steady-state voltage and the faster the avalanche will be. The short risetime also has a favourable effect on the formation of a dense hot-spot structure on the cathode which enhances the discharge homogeneity [24]. The electrons move toward the positive electrode and leave the slow ions behind. In this way, each initial electron is creating a cone of positive charges behind it. If there is sufficient pre-ionization, the created cones will overlap and will form a homogeneous plasma moving to the anode. If, however, the pre-ionization is insufficient, an individual cone will reach the anode much faster than the overlapping cones forming a narrow channel (called a streamer) with a high plasma density between the anode and cathode. The streamer short-circuits the discharge. In the case of sufficient pre-ionization and a fast avalanche process, the ions shield the acceleration field for the electrons by forming a positively charged ion layer, which increases its own acceleration field so that the ions acquire sufficient energy to bombard the cathode and thereby release fresh electrons (secondary emission) to maintain the discharge. It may also happen that some emission from the cathode is due to field emission by microscopic protrusions on the surface. Anyhow a quasi-steady state might be produced. However, the cathode will not emit uniformly and, after a short time, so-called hot spots are formed on the cathode surface, which are small areas where the electron emission is very dense and which develop to filamentary arcs destroying the homogeneity of the discharge. This process is strongly enhanced by the electron attachment to the HCl molecules. The quasi-steady time period, more or less the time needed for the filamentary arcs to reach the anode, must be used for the laser process. The question then is how much pumping energy can be supplied. Since the discharge voltage in the quasi-steady state is more or less independent of the current, the inversion production is then proportional to the current. Therefore, the highest output power and pulse energy will be obtained for the highest current that can be reached in the stable period. This is possible either by increasing the charging voltage of the circuit or by decreasing the inductance of the circuit. The former has been successfully performed in the photo-triggered mode (X-ray triggering). High output energies of 1.2 [20], 0.5 [65] and $3.5\,\mathrm{J\,l}^{-1}$ [66] at efficiencies of 1.7%, 0.9% and 1.6%, respectively, have been obtained. Increasing the voltage to double the steady-state value leads to current ringing, and because only the first half current wave is stable, this is not the most efficient energy conversion. Higher efficiencies with no current ringing and better performance are obtained with prepulse–main-pulse excitation [29,30]. With the so-called switch mode, an output energy of $3.3\,\mathrm{J\ l}^{-1}$ at 4% efficiency [31] has been reported. For the resonant overshoot mode, the best reported results are $3.6\,\mathrm{J\ l}^{-1}$ at 5% efficiency [32]. The disadvantage of the prepulse–main-pulse technique is the high voltage of the main pulse across the electrodes, which may initiate a slow avalanche of the pre-ionization electrons and therewith hampering an effective avalanche process by the prepulse. A fast risetime for the prepulse and a low inductance for the main pulse to obtain high current density are, therefore, the best conditions for high output energy.

27.6.2 Parametric Studies

We consider the resonant overshoot mode. The effects of various parameters have been studied for a system 60 cm in length and with an electrode gap of 2.5 cm [67]. The discharge width at optimum performance is 2 cm. The laser construction is shown in Figure 27.12. The gas mixture used is 1 mbar HCl, 10 mbar Xe and Ne as buffer gas with a total pressure of 5 bar. The scheme of the electrical circuit is shown in Figure 27.18. It consists of a prepulse and a main-pulse circuit. The saturable inductor of the main-pulse circuit is a race-track transformer to conduct the prepulse to the laser head. The prepulse circuit contains the capacitors $C_{\mathrm{pp}} = 5.1$ nF and $C_{\mathrm{pc}} = 3.4$ nF. For the

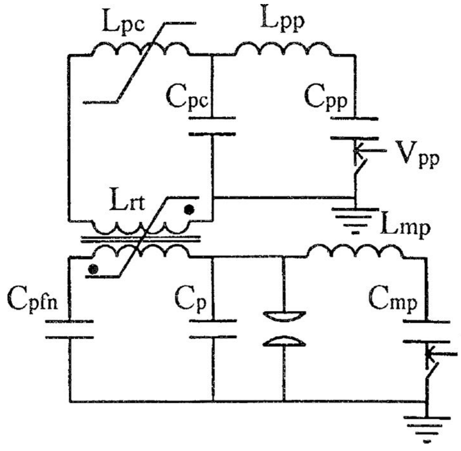

FIGURE 27.18 Scheme for the electrical circuit of an XeCl laser with a race-track transformer.

main circuit, C_p = 3.6 nF and C_{pfn} = 389 nF. After charging C_{pp}, its energy is switched to C_{pc} while it saturates L_{pc} in order to compress the prepulse passing through the transformer. The cross sections of both the ferrites of the magnetic pulse compressor and the main switch must be adjusted to hold off the required amount of volt-seconds. The relatively low current of the prepulse compressor is switched with eight ferrite rings having a total cross section of 35.2 cm^2. The low inductance race-track transformer, built from ferrite bars, has a length equal to the discharge and a cross section of 24 cm^2. It is observed that these cross sections are not critical for optimum performance.

The energy of the storage capacitor C_{pp} is transferred in about 130 ns to C_{pc}. Then, after saturating the ferrites, the energy is rapidly transferred to C_p in about 25 ns. Because of energy losses by transfer and saturation of the ferrites, the subsequent capacitors become smaller each time. The energy needed for the prepulse can be estimated by calculating the minimum ionization energy that is required to produce an ion density of 10^{13}–10^{14} cm^{-3}. Having an ionization potential of 22 eV for Ne and a discharge volume of 300 cm^3, we find 0.01–0.1 J. Since the efficiency for ionization is low, the required energy will be in the range of 1 J. This has indeed been observed. Using peaking capacitors in the range 2.8–4 nF and charges in the range 20–30 kV, satisfactory results are obtained.

As already mentioned, the main capacitor is charged to twice the quasi-steady-state voltage in order to avoid ringing of the discharge current. If the voltage is higher only, the first half-cycle of the current pulse is effective for the laser process and the intrinsic efficiency, defined as the output energy divided by the deposited energy of both prepulse and main pulse, will be less (see appendix). The dependence of output energy and intrinsic efficiency on the deposited energy are plotted in Figure 27.19. The plotted results are optimized with respect to the HCl density. The smaller the value of C_{pfn} and the smaller the current pulse, the higher the HCl density becomes. This can be understood from the fact that for a shorter current pulse, a faster growth for the instabilities caused by HCl, i.e. a higher HCl density, is allowed. A higher HCl density gives higher output power. Thus, for optimized conditions, the HCl density is adjusted in such a way that the discharge remains stable up till the end of the current pulse. The optical pulse will then closely follow the current pulse. Typical waveforms of the discharge current, voltage and output power for optimized conditions are shown in Figure 27.20. It is seen that the output power does not terminate before the current pulse. If we increase the current pulse by increasing the inductance of the main circuit, the optical pulse will follow this extension, provided the HCl density is sufficiently reduced. Laser pulses up to 1 µs can be obtained in this way. However, the total output energy will always be reduced by extending the pulse. As a general observation, it is found that a shorter current pulse gives a higher HCl density and a higher output energy. The maximum energy for short pulses is above 1 J l^{-1}.

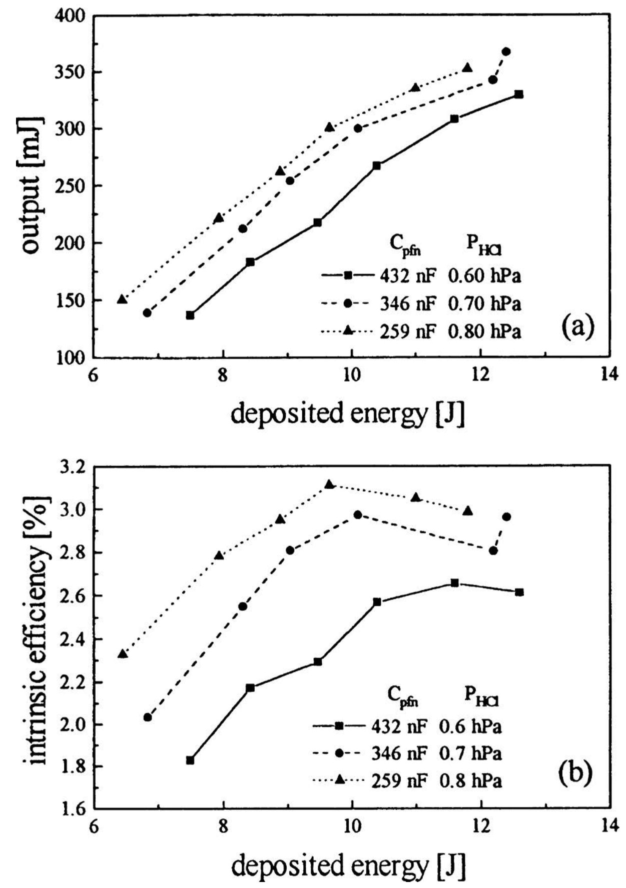

FIGURE 27.19 Optical output (a) and intrinsic efficiency (b) as a function of the deposited energy for different values of the pulse-forming network capacitor.

27.6.3 High Average Power XeCl Laser

The development of high-repetition-rate XeCl lasers in the kilowatt range can be considered as a logical extension of successful single-pulse experiments. In principle, it can be performed with a fast-flowing circulating laser gas with a homogeneous velocity profile and thin boundary layers near the electrodes of the laser discharge. The flow speed is then determined by the condition of gas renewal after each pulse. However, although for repetition rates up to 1 kHz the

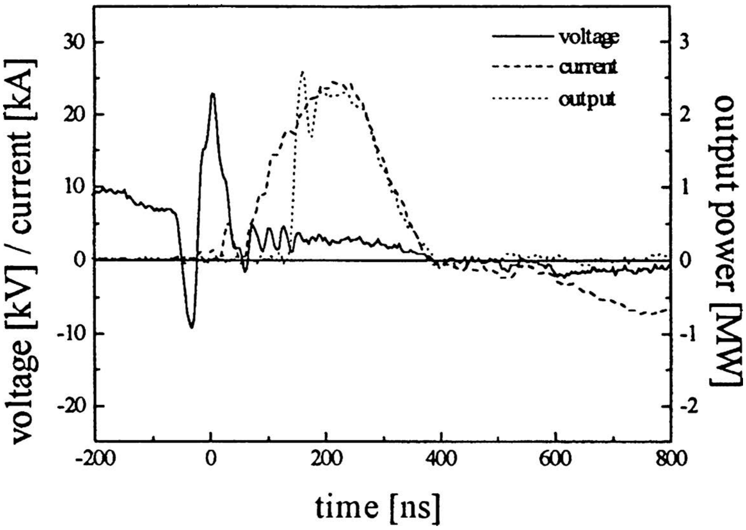

FIGURE 27.20 Voltage, current and output power of the XeCl laser with a PFN of 346 nF containing 17 J stored energy (10 kV).

pulse discharge time is much shorter than the time interval in between pulses, the flow pattern can be disturbed by discharge shock waves which, in turn, may have a detrimental effect on the homogeneity of the discharge and output beam. Furthermore, the optical elements and circuit components of the discharge have to be compatible with high repetition rate and long lifetime. For instance, fast-switching circuits with low heat production are required. The heat consumption of the saturable magnetic switches and its cooling is critical since the operational temperature range for high-quality ferrites is about 50°C above room temperature. This may set a limit to the repetition rate. Also the reliability of a short-pulse, high-repetition-rate X-ray pre-ionizer requires new developments in its high voltage performance and materials with long lifetimes.

The efforts to realize a high average power system were driven by various potential applications. In the middle of the 1980s, large national and international projects were started to reach the kilowatt power level with discharge systems. Depending on the application, the interest was in high pulse energy of the order of 10 J at low frequency or about 1 J at a much higher frequency. In Europe several companies in close collaboration with university groups or institutes participated in the Eureka programs. In Japan, it was coordinated by the Advanced Material Processing and Technology Research Association (AMMTRA). The Kurchatov Institute of Atomic Energy in Moscow and Rand Afrikaans University in Johannesburg also became involved.

The development carried out by the Nederlands Centrum voor Laser Research (NCLR) in collaboration with the University of Twente involves a repetition rate of 1 kHz, a pulse energy of 1 J and a pulse duration of 250 ns [68]. The gas mixture consists of 2 mbar HCl, 20 mbar Xe and 4 bar Ne. The distance between the electrodes is 2.5 cm; the discharge width and length are, respectively, 2 and 80 cm. On both sides of the discharge region, there are spaces to prevent mirror damage. For a general performance, the stable resonator has a 5 m radius of curvature end mirror with maximum reflectivity and a flat outcoupling mirror with 70% reflectivity. An output energy of 1 J is reached. The system also operates with an unstable resonator.

The laser system includes a gas circulation unit with a heat exchanger to remove the discharge and flow friction heat of the circulating gas. A cross-sectional view of the system is shown in Figure 27.21. In order to minimize flow inhomogeneity and turbulence in the discharge chamber, a settling chamber containing honeycombs and screens is placed in front of the contraction section. Passing the contraction section, the flow speed is increased to reach 60 m s^{-1} in the discharge section. With a discharge width of 2 cm, the volume flow between two pulses is then three times the discharge volume. This clearing ratio of three is conservative, and with the chosen impedance-matched discharge technique, it may be reduced. After the discharge region, the flow passes the diffuser to reduce the speed and therefore the friction losses. The contraction and diffusor walls connect smoothly to the uniform-field [69] high-voltage electrode and to the flat thin ground electrode that also acts as the entrance window for the X-ray pre-ionization. Current returns are placed both upstream and downstream to minimize the self-inductance of the laser chamber. The insulator of the high-voltage feed-through and the parts of the contractor and diffusor near the high voltage electrode were made of alumina. A gas purification unit with a cold trap and a hot reactor is incorporated into the gas-handling system to remove contaminations mainly produced by interaction with long-living discharge species and the walls. A constant HCl density is maintained by regulating the temperature of the cold trap. In this way the HCl losses by wall adsorption are replenished.

The X-ray source used (discussed in Section 27.3.2.2) is based on a corona plasma cathode. An additional advantage of the chosen X-ray illumination through the thin anode is the separation of the source and the laser system. The operation condition requires a homogeneous short X-ray pulse with a very short risetime. The short pulse is not only beneficial for the discharge build-up, but it also reduces the heat consumption of the plasma cathode. The lifetime of the plasma cathode at

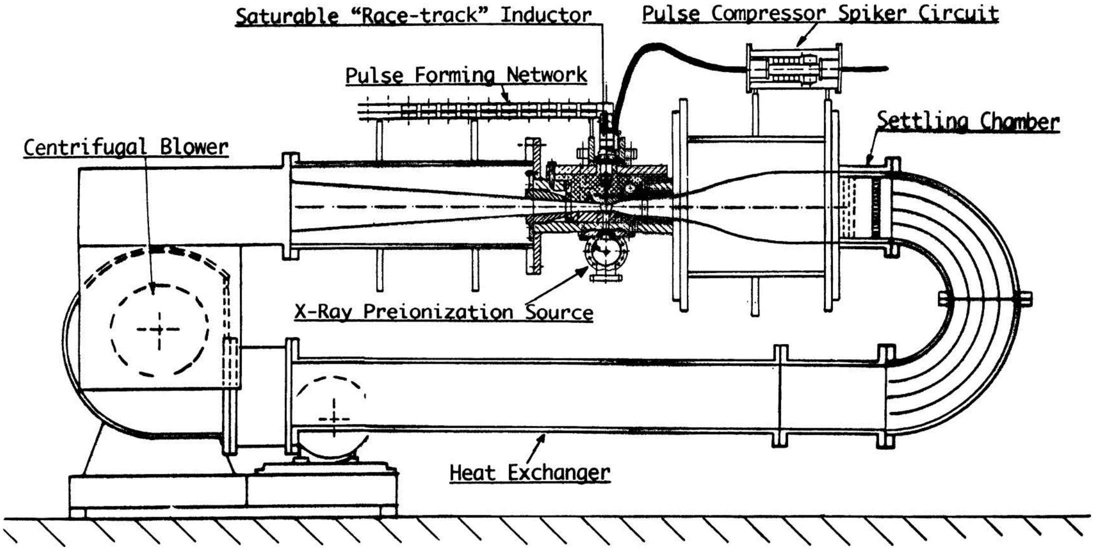
Saturable "Race-track" Inductor
Pulse Compressor Spiker Circuit
Pulse Forming Network
Settling Chamber
Centrifugal Blower
X-Ray Preionization Source
Heat Exchanger

FIGURE 27.21 Schematic drawing of a 1-kW average power XeCl laser.

high repetition rate is limited to the order of magnitude of 10^8 pulses, mainly caused by material wear-out and surface sputtering. An alternative may be a thermionic X-ray source with high-yield (scandate) dispenser cathodes [70], which are well known for their long lifetime.

The discharge uses the resonant overshoot mode with the prepulse–main-pulse circuitry schematically shown in Figure 27.13. As pointed out before, this technique requires the lowest amount of energy that can be switched as fast as possible. Furthermore, the main pulse is impedance matched to the laser discharge so that current oscillations do not occur. Sputtering from the X-ray transmitting electrode is also avoided. Thyratrons are the best choice for high-voltage switching at high repetition rates, provided the average current and its change in time are limited. This is no problem for charging the PFN of the main discharge up to 10 kV, about twice the steady-state discharge voltage. The PFN consists of eight double-plate transmission lines connected in parallel to the laser chamber. Using 160 ceramic capacitors of 2.7 nF each, resulting in a total capacity of 432 nF, the charged energy is 20 J. In the resonant overshoot mode, the voltage of the prepulse capacitor after the swing becomes $6U_B$. With a capacity of 4.5 nF, the prepulse energy is 2 J.

For a pulse duration of 100 ns, the average current is about 1.5 kA and dI/dt of the order of 10^{10} A s^{-1}, which are within the specifications of the thyratron. This prepulse is further compressed to 25 ns with a saturable inductor. A good choice for a saturable high-frequency material is ferrite CMD 5005 from the company Ceramic Magnetics. The flux swing is about 0.5 T, the magnetic field intensity to reach saturation, H_S, is 2 kA m^{-1} and the field intensity to achieve μ–$5\mu_0$ is about 5 kA m^{-1}, whereas the dissipation losses are reported as only 100 J m^{-3}. This inductor contains six rings with a total flux area of 21.6 cm^2.

The saturable inductor that connects the PFN with the laser chamber is, due to the large current, made from eight blocks with the dimensions 2.5 × 2.4 × 40 cm of the same ferrite material. They are arranged in a rectangular configuration with a 2-mm central slit for the high-voltage conductor. Optimum performance of the laser was achieved with a cross section of 12 cm^2. Both saturable inductors are reset after each pulse by charging the PFN for the next one. Because of the considerable amount of dissipated saturation energy at 1 kHz, both inductors must be effectively cooled with a flowing oil circuit. Since the ferrite material itself is a poor heat conductor, copper-supporting structures with forced convection flows reaching the inner volume were made.

It should be noted that the application of a very short prepulse, limited by the smallest inductance of the laser head, is not only a requirement for pulse stability, it also reduces the amount of saturable ferrite material. For high repetition rates, it is crucial to minimize the amount of ferrite material because of costs, saturation energy losses and effective cooling.

27.7 KrCl Laser (222 nm)

The first lasing of this system was again observed with e-beam pumping [71,72]. The performance of the e-beam-pumped KrCl system may be compared with that of KrF. The gas mixture also contains 100–300 mbar Kr, 2–4 bar Ar and 2–6 mbar Cl_2 instead of F_2. Ar as the buffer gas again gives the highest output energy. However, the observed output energy and efficiency of KrCl are both considerably lower than in the case of KrF under equal e-beam-pumping conditions. This is due to the different loss processes such as relatively high medium absorption at the laser wavelength and quenching of KrCl by the gas components.

The discharge pumping is straightforward. It has been studied for both single-discharge short pulses [73] and double-discharge long pulses with prepulse–main-pulse discharges [74]. The behaviour of the KrCl laser operating in the long-pulse discharge mode may also be compared with the XeCl laser. Both the kinetics of the laser process and the system technology are very similar. Self-sustained discharge pumping and the technology described for XeCl are appropriate.

In fact, if for a XeCl prepulse–main-pulse system the Xe is replaced by Kr and the mirror reflectivities are adjusted for a 222 nm wavelength with an outcoupling percentage about half the value used for XeCl, only the pulse energies have to be increased to reach the optimum performance. A typical gas mixture contains 3–4 bar Ne, 100–150 mbar Kr and 1–2 mbar HCl. Because of the relatively mild attachment rate of HCl compared with other halogen donor gases, the discharge stability allows also for relatively long pulses up to 500 ns without substantial loss of total energy. The gain, output energy density and the intrinsic efficiency are all 30%–40% lower than that of the XeCl laser.

27.8 ArF Laser (193 nm)

The first ArF was realized with e-beam pumping [40]. Shortly afterwards, the first paper on discharge pumping appears [41]. The intrinsic efficiency, defined as the optical output energy divided by the electrical energy delivered to the laser medium, of the e-beam-pumped system is reported to be as high as 8% [75], whereas discharge pumping is less than 4% [76]. This system has also been examined very thoroughly in the past.

The development of the e-beam system was very similar to that of the KrF laser, and its prospects for high energy systems to be used for inertial confinement studies were also considered [77–79]. A mixture of only Ar and F_2 where Ar is both donor and buffer gas does not work [16]. The best results are obtained with Ar and F_2 as donors and Ne as the buffer gas. Like other excimer lasers, it is found that a high e-beam current density gives higher optimized gas densities. At a high current density of 375 A cm^{-2} in a small coaxially pumped e-beam system, the optimum output does not saturate even at 14 bar, similar to KrF. Using a mixture of 28 mbar F_2, 280 mbar Ar and 14 bar Ne, an output energy of 8.1 J l^{-1} was obtained for a pulse of 40 ns [16].

In spite of the successful e-beam studies, much more attention is, like several other excimer systems, given to discharge pumping because of its relative simplicity, higher development potential and more promising applications. A laser gas of a discharge system with densities in the range 2–5 bar contains about 1% F_2 or fluorine-bearing gas and about 5% Ar in a mixture with He or Ne as the buffer gas. The laser has been operated with NF_3 as the fluorine donor. As in the KrF system, the main kinetics for the formation of the ArF* molecule are

$$\mathrm{Ar}^+ + \mathrm{F}^- + \mathrm{X} \rightarrow \mathrm{Arf}^* + \mathrm{X} \tag{27.21}$$

where Ar^+ is formed in the reaction of Ar with the dimer ion of the buffer gas as given by Equation (27.10), X is the buffer gas atom and along the metastable channel

$$\mathrm{Ar}^* + \mathrm{F}_2 \rightarrow \mathrm{ArF}^* + \mathrm{F} \tag{27.22}$$

The F^- ions are formed in the dissociative attachment of electrons to F_2, i.e.

$$\mathrm{F}_2 + \mathrm{e}^- \rightarrow \mathrm{F}^- + \mathrm{F}. \tag{27.23}$$

For e-beam pumping, the ionization channel followed by reaction (27.21) is dominant; whereas for discharge pumping with an average electron energy of only a few electron volts, the metastable channel and the formation by reaction (27.22) are most productive. In modelling the kinetic process many reactions have been considered for e-beam [80] as well as for discharge systems [75,81,82]. Parallel to the formation channel there are also several reactions that channel energy away from the desired path or which quench the ArF^* molecule itself. The quenching is in competition with the stimulated emission and can be minimized by a cavity design that imposes a stimulated emission lifetime that is shorter than that of the quenching. Besides the losses by quenching, laser photons are absorbed by F^-, Ar^+ and rare gas dimers in the discharge plasma [75,83]. Furthermore, photons are also absorbed by impurities such as O_2. However, this can be avoided by using a cold trap gas purifier and a thorough passivation of the laser vessel. Satisfactory purification is obtained by continuously flowing the gas mixture through a liquid nitrogen gas purifier with a cold trap of 90 K to freeze out the impurities [84].

The ArF^* molecule exists in two very closely lying B and C upper states. The mixing between these states is so strong that they act as a single state with a lifetime of 4.2 ns [85]. The lower states, A and X, are also strongly mixed. Therefore, the radiative transitions between the upper and lower levels are a structureless continuum [85].

27.8.1 The Discharge

A major problem for maintaining a quasi-stable discharge is the dissociative electron attachment to fluorine. The attachment rate is of the order of $10^{-9} cm^3 s^{-1}$ so that, for an F_2 concentration of $10^{17} cm^{-3}$, the free electron lifetime is only 10 ns. This means that the discharge pulse or prepulse must have an overlap with the pre-ionization pulse by starting the multiplication process. Furthermore, as pointed out for the XeCl excimer, the continuity of the discharge current is governed both by the field emission of microscopic protrusions on the surface of the cathode and dominantly by secondary emission of the cathode. Near the cathode, a positively charged ion layer is formed, which is accompanied by a high electric field near the cathode so that ions from this layer will bombard the cathode with sufficient energy to release electrons for the current continuity. In the used gas mixture with electronegative fluorine, the discharge instabilities develop in a few nanoseconds from minor pre-ionization inhomogeneities and cathode hot spots. This instability process depends strongly on the initial electron density near the cathode and the risetime of the acceleration voltage. A fast risetime for the current leads to the formation of a dense hot spot structure, which enhances the homogeneity and favours stability. The absence of electrons or a low density near the cathode is very favourable for instabilities. This happens, for instance, in the resonant overshoot mode where the main voltage is across the electrodes before the pre-ionization pulse starts. Some of the pre-ionization electrons will then drift away from the cathode before the prepulse of the discharge is applied, and since the attachment rate in F_2 is much faster than in HCl, the electron depletion near the cathode will become too strong. Thus, for

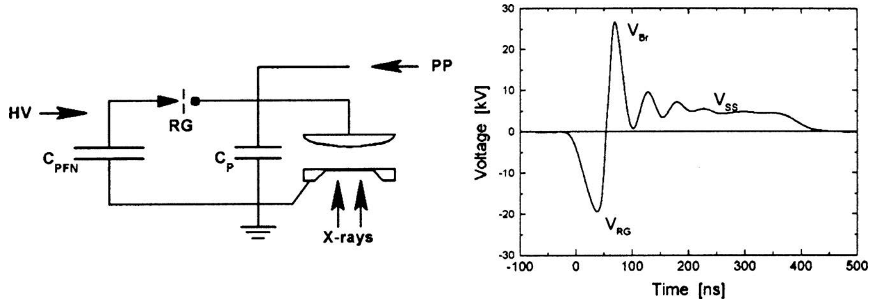

FIGURE 27.22 Scheme for a prepulse–main-pulse excitation circuit for a field-free medium during the pre-ionization. pp, prepulse; RG, rail gap switch; V_{br}, breakdown voltage of laser; V_{RG}, breakdown voltage of rail gap; V_{SS}, steady-state voltage of discharge.

mixtures containing F_2, the stability period becomes shorter, if present at all, than in mixtures containing HCl. There will be at least a loss of potential laser energy. This has, indeed, been observed when the resonant overshoot mode has been applied to mixtures containing F_2 in ArF and KrF lasers. The cathode depletion problem can be circumvented with the discharge scheme shown in Figure 27.22 [84]. It is very similar to the resonant overshoot mode except for the absence of the main voltage across the electrodes before pre-ionization.

Even if good pre-ionization conditions exist, the fast attachment rate still requires a very fast electron multiplication process or avalanche process. This can be performed by minimizing the current risetime of the prepulse. The self-inductance of the prepulse circuit should, therefore, be as short as possible. A successful construction is shown in Figure 27.23 where the peaking capacitance is placed within the laser vessel [84]. The decrease in current risetime results in a denser hot spot structure on the cathode surface and therewith to a more homogeneous discharge, longer pulses and more output.

27.8.2 Laser Performance

In the past several authors have discussed the ideal buffer gas option for optimizing the ArF laser. Some of them found the best results with He, while others had better results with Ne or a mixture of these gases. However, the general impression has, for a long time, been that it does not make much difference which choice is made. It has been suggested that, with Ne, the formation kinetics of the lasing molecule is much more efficient, whereas the optical extraction efficiency, limited by intracavity absorption, is favoured by a He gas medium with the result that both options are effectively more or less equal [85,86].

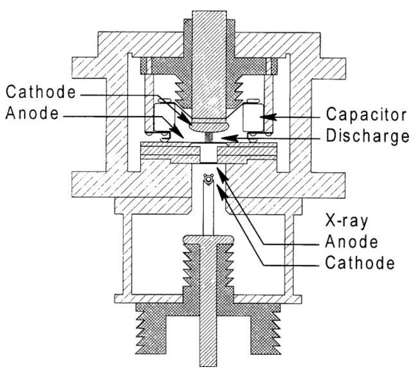

FIGURE 27.23 Cross-sectional view of a laser head with peaking capacitors and current return rods inside the laser head to reduce self-inductance.

In a He buffer gas mixture, the electron multiplication process and breakdown are faster than in a Ne mixture, because of the lower inductance by less scattering losses and therewith higher current. However, the more effective electron losses by three-body volume recombination in Ne buffered mixtures such as

$$\mathrm{ArNe^+ + e^- \rightarrow Ar + Ne} \tag{27.24}$$

offer a current control mechanism which helps to stabilize the discharge. In the case of He, the production rate of $ArHe^+$ is much smaller because of the higher ionization energy and the lower *E*/*p* value which is related to the average electron energy. Since instability growth is very fast in mixtures containing electronegative fluorine, it follows that the choice of buffer gas depends on the current risetime of the prepulse discharge. Using a system with minimized inductance, as shown in Figure 27.23, the difference between the two buffer gases is substantial. Experiments have been performed with the following parameters [84]. The discharge length is 60 cm, the electrode gap is 1.2 cm and the discharge width, determined by the pre-ionization area, is about 0.7 cm so that the active medium is about 50 cm^3. The peaking circuit is formed by 10 ceramic capacitors with a total value of $C_p = 460$ pF. To reduce the self-inductance of the main circuit, the laser vessel is fitted with additional current returns. These peaking capacitors and current returns are distributed evenly along the cathode length. In this way, the inductance of the laser vessel is about 8 nF. The main circuit has a capacitance of $C_{pfn} = 162$ nF and is charged to 32 kV. The switch gap together with C_p is very fast charged by means of a mini-Marx generator with an effective output capacitance of 0.6 nF delivering a 120-kV pulse with a risetime of 2 ns. For a gas mixture that consists of 3 mbar F_2, 250 mbar Ar and 4.75 bar He, the optimum pulse length of this system is 32 ns (full width at half maximum (FWHM)), as shown in Figure 27.24, and the output energy is 1.9 J l^{-1}. In a mixture of 3 mbar F_2, 250 mbar Ar, 60 mbar He and 4.7 bar Ne, the pulse length becomes 48 ns (FWHM), as shown in Figure 27.25, and the output is 3.6 J l^{-1}. These output energies are in the range 2–5 J l^{-1} as is also obtained with

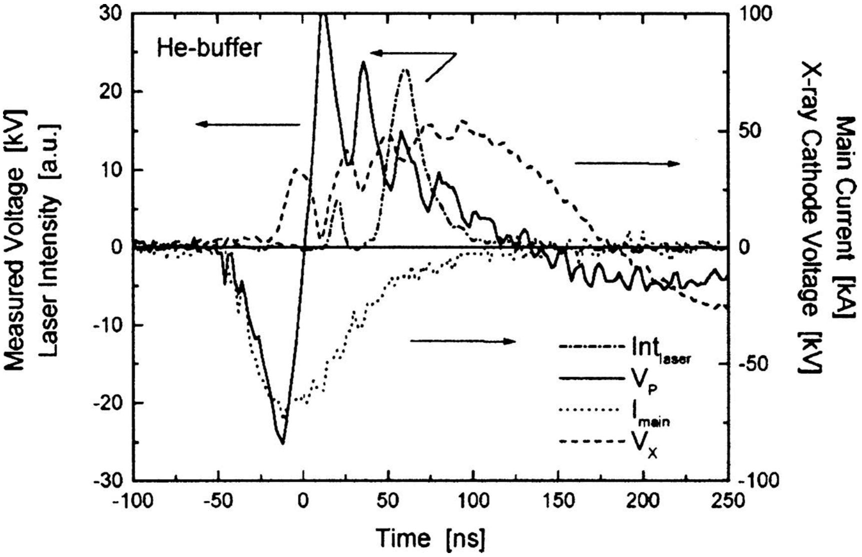

FIGURE 27.24 Waveforms of the ArF laser using He as the buffer gas.

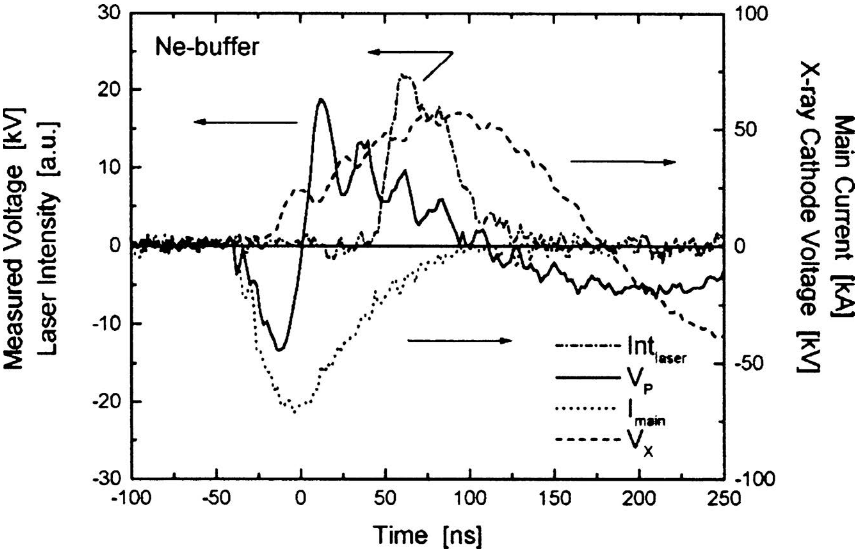

FIGURE 27.25 Waveforms of the ArF laser using Ne as the buffer gas.

single-discharge systems producing pulse lengths of no more than 12 ns [87–90].

27.8.3 Long Pulses

Since the fast growth of the instabilities is mainly induced by the electronegative fluoride gas, it is expected that pulse elongation can be obtained by reducing the fluoride content, i.e. with lean mixtures. This has indeed been observed. However, it has also been observed that the strongly reduced self-inductance of the laser vessel, as shown in Figure 27.23, is also essential [84]. The usual systems with circuit components outside the laser vessel performing much longer current risetimes are not appropriate for minimizing the instabilities. Unfortunately, the fluorine reduction also affects the laser power and pulse energy, and an extension of the quasi-stable discharge period is found at the expense of laser power and total energy. The reduced gain requires a higher output coupler reflector that has to increase to at least 90% instead of the usual 60%–70% for the previously described high-energy systems.

An advantage of operational systems with long pulses and lean mixtures is that, due to the reduced electron attachment rate, the more convenient resonant overshoot mode with a saturable magnetic ferrite switch can be successfully applied. The experiments have been performed with the following parameters [84]. The gas mixture consists of 1 mbar F_2, 20 mbar He, 50 mbar Ar and 5 bar Ne. The main circuit capacitance C_{pfn} = 427 nF. The peaking capacitance C_p(= 460 nF) placed inside the laser vessel is again charged very fast by the mini-Marx with an output capacitance of 0.6 nF and delivering a 120-kV pulse with a risetime of 2 ns.

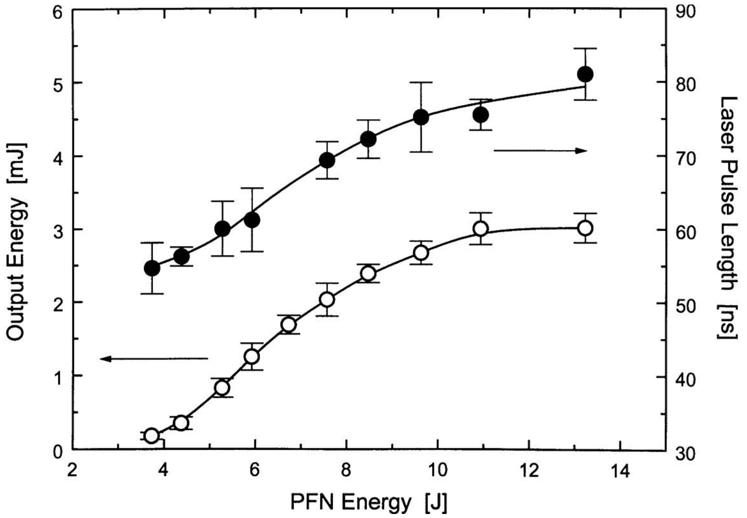

FIGURE 27.26 Output energy and pulse duration of an ArF laser as a function of the energy stored in the PFN.

If the charging voltage of C_{pfn} is varied between 4.1 and 7.9 kV with a corresponding energy variation between 3.7 and 13.2 J, both the pulse length and output energy increase as shown in Figure 27.26. Having a discharge volume of about 50 cm^3, the output reaches 60 mJ l^{-1}.

The pre-ionization timing is a very critical parameter in this laser system. The first condition for discharge stability is a homogeneous pre-ionization with an electron density of at least 10^8 cm^{-3}. If this pre-ionization is too early, too many electrons are lost by attachment and fast instabilities will develop when the discharge starts. If the pre-ionization is too late, there is too little time left for electron multiplication. In Figure 27.27, the output energy and corresponding pulse duration (FWHM) are shown as a function of the pre-ionization time delay, defined as the time between the onset of the X-ray pre-ionization pulse and the discharge breakdown. The pulse length is, as expected, dependent on the fluorine content. This is plotted in Figure 27.28 where the other gas components are as previously described.

27.9 XeF Laser (351,353 and 486 ± 35 nm)

Like most excimer systems, the first XeF(B → X) excimer laser was realized with e-beam pumping [39]. Although the system is complex, this was an attractive way to get some understanding of the potentials of this excimer [91,92]. The instabilities, which are inherent to the simpler discharge systems, can be avoided so that the choice of gas composition can be totally based on kinetic considerations. Shortly afterwards, papers on discharge-pumped XeF(B → X) lasers appeared [93,94]. Although the efficiency and output energy density are much less than with e-beam pumping, the continuing research is mainly carried out on discharge systems because of their relative simplicity, higher development potential and more promising applications. The gas mixture consists of a few mbar F_2 or NF_3, a few mbar Xe and several bars of He or Ne as buffer gas. The discharge stability sets stringent limitations on gas composition and densities, especially for the halogen donor

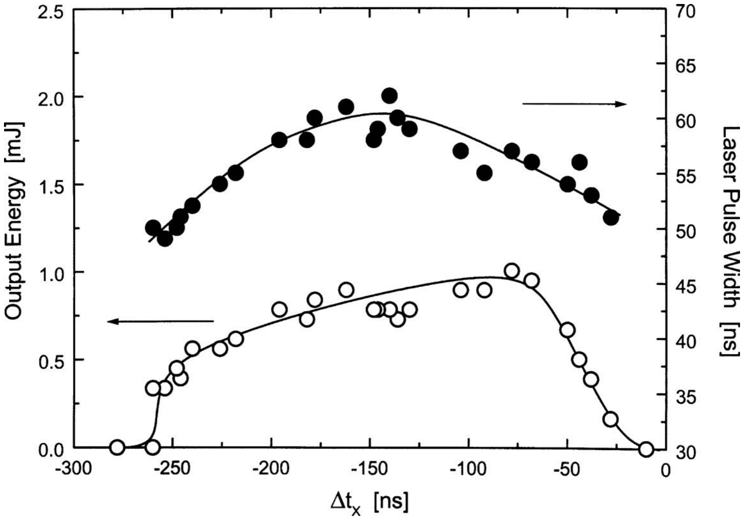

FIGURE 27.27 Pulsewidth (FWHM) and output energy of an ArF laser as a function of the pre-ionization delay time.

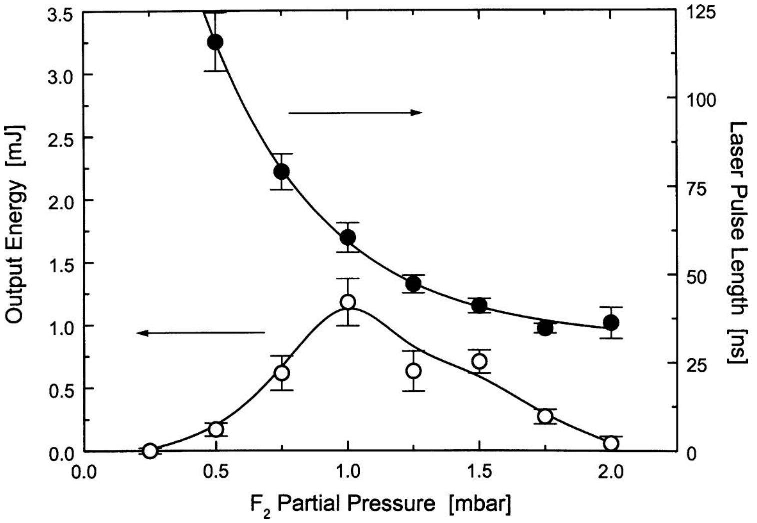

FIGURE 27.28 Pulsewidth (FWHM) and output energy of an ArF laser as a function of the F_2 density.

gas. Detailed kinetic modelling of the laser process requires a thorough understanding of the reactions and their cross sections. The most important reactions are similar to those of other excimers. For the ionic channel, we have

$$Xe^+ + F^- + X \rightarrow XeF^* + X \qquad (27.25)$$

where X is the buffer gas atom. As described in Section 27.4.1, Xe^+ is formed in a charge transfer reaction with dimer ions of the buffer gas. The metastable channel has the formation reaction

$$Xe^* + F_2 \rightarrow XeF^* + F \qquad (27.26)$$

or

$$Xe^* + NF_3 \rightarrow XeF^* + \text{fragments} \qquad (27.27)$$

where Xe^* is mainly formed in a reaction with the metastable dimer of the buffer gas as indicated in Section 27.4.1. The F^- is formed by the dissociative attachment of the electrons to NF_3 or F_2.

For e-beam pumping, the ionic channel followed by reaction (27.25) is dominant, whereas for discharge pumping, the metastable channel with the reaction (27.26) or (27.27) is most productive.

The attachment rate has a great impact on the stability of the discharge. This rate is different for NF_3 and F_2 [95], which means that the discharge behaviour depends on the choice of halogen donor gas. It is found that for the XeF system NF_3 is the better choice. The main reason is the rather large absorption cross section of the F_2 molecules for the laser radiation. Furthermore, with F_2, the discharge becomes unstable more quickly compared with NF_3-based gas mixtures, although the total output energy remains more or less equal [96].

Once the XeF^* is formed, it can easily be quenched by all gas constituents and discharge electrons. The quenching process will be in strong competition with the stimulated emission so that a high radiation field density in the cavity is required. However, there is also optical absorption, mainly photoionization of the dimer states Xe_2^+, Xe_2^* and Ne_2^* as well as photodissociation of F^- and F_2. For an optimized laser system, there will be a trade-off between quenching and absorption losses.

27.9.1 The Spectroscopy

The bottom of the C state of the excimer potential curve as a function of the internuclear separation distance is approximately 0.08 eV lower than that of the B state as indicated in Figure 27.29. The A state is repulsive while the X state is weakly bound. The binding energy of the X state of 0.15 eV is rather strong compared with other excimers. The bottom of this potential curve is situated at shorter internuclear separation than the bottom of the potential curve of the B state. Because of the weakly bound lower state, the emission in the B → X band has a complex structure [97], starting on the lower vibrational levels of the B state and terminating on high vibrational levels of the X state. The strongest lines are at 351.1

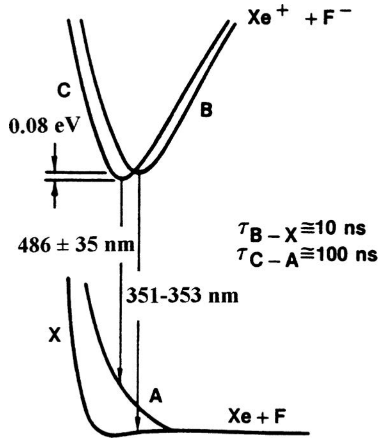

FIGURE 27.29 Schematic potential energy diagram of XeF showing both the B → X and the C → A transitions.

and at 353.1 nm, which are due to the 1–4 and 0–3 vibrational bands, respectively. The linewidths of these bound–bound B → X transitions are of the order of 0.1 nm. The bound-free C → A transition is much broader with a bandwidth of about 70 nm centred at 486 nm. Tunability, as will be discussed later, reaches from 454 to 525 nm. The radiative lifetime of the B state is about 10 ns, while the C state has a radiative lifetime of 100 ns. The effective lifetime of the X state is about 1 ns for the usual gas composition and densities. The cross sections for stimulated emission for the strongest transitions of the XeF excimer laser are, for the usual gas conditions, estimated as 4.5×10^{-16}cm^2 for the B → X band and 7.4×10^{-18}cm^2 for the C → A band, respectively [98]. Because of the much smaller cross section for stimulated emission of the C → A band, which is due to its large linewidth, the laser action will always occur in the B → X band unless special measures are taken.

27.9.2 The Discharge

A straightforward approach to a XeF(B → X) laser is the use of a single self-sustained discharge; with a conventional single-discharge circuit with a spark gap switch and UV pre-ionization, laser pulses of 20 ns with a specific output of 1.2 J l^{-1} have been reported [99]. A further improvement is obtained with X-ray pre-ionization, and a single-discharge circuit that includes a low-inductance multichannel spark gap for fast switching. By increasing the charging voltage of the circuit capacitor, the discharge current can be enhanced to obtain higher output energy. In this way, laser pulses of 85 ns and a specific output energy of 4.7 J l^{-1} have been obtained for a gas density of 6 bar [100]. In such a discharge, the driving voltage of the circuit is much higher than twice the steady-state voltage so that the discharge will go into an oscillatory mode, of which only the first phase before the current reversal will be stable. The efficiency, in this case 0.5%, is therefore inherently low. Furthermore, this technique is not suitable for high repetition rates.

A much better performance is obtained with the overshoot mode of the prepulse–main-pulse technique [101]. The system has the following parameters. The gas mixture used contains 1 mbar NF_3, 5 mbar Xe and 4 bar Ne. The cavity discharge length is 60 cm, the electrode gap is 1 cm and the discharge width is 1.25 cm. The PFN capacitor of the main circuit of 108 nF has a charging voltage of 17.4 kV. The capacitance of the prepulse circuit of 5.6 nF is charged to 20 kV. The output energy and pulsewidth have broad maxima with respect to the delay time between the pre-ionization and the prepulse [101], as shown in Figure 27.30. For good performance, the delay of the prepulse after the onset of the pre-ionization should be more than the attachment lifetime of the electrons in the gas mixture and less than the pre-ionization pulsewidth. The maximum output energy is 180 mJ or 2.4 J l^{-1} with a pulse length of 70 ns. It should be noted that the pulse length, similar to that of the ArF laser, can be extended at the expense of the output energy if the halogen content is reduced.

The risetime of the prepulse taking care of the avalanche electron multiplication must be, as pointed out in section 27.3.2.7, as short as possible. In the previously mentioned results, this risetime is about 50 ns. By placing a magnetic pulse compression (MPC) circuit just before the charging of the prepulse, this risetime can be further reduced to 20 ns. The output enhancement is remarkable. This is seen in Figure 27.31 where the effect of the prepulse risetime is shown by plotting the output energy as a function of the charging voltage of the main capacitor (PFN). The highest output energy for the mentioned gas mixture is 275 mJ or 3.7 J l^{-1}.

27.9.3 Broadband Blue–Green C → A Transition

Most excimer lasers operate on the relatively narrow-band transitions between the B and the nearly flat or at most weakly bound X state. Transitions between the C and the strongly repulsive A state are relatively broad because, even with a small deviation from the bottom of the potential well of the C-state

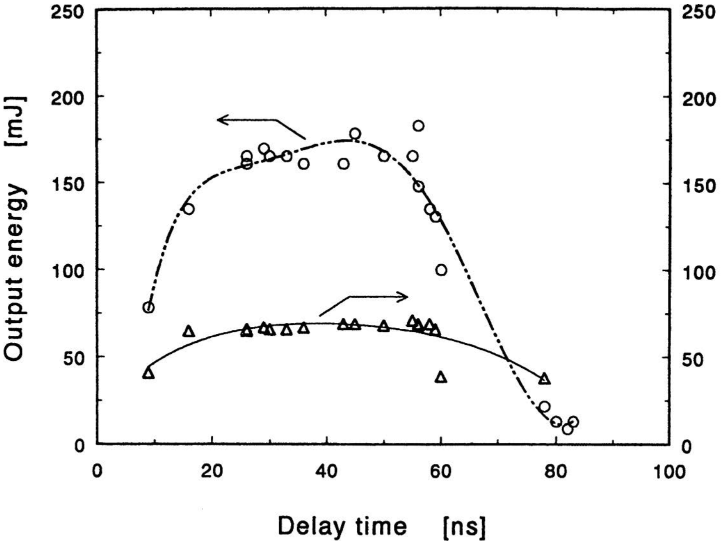

FIGURE 27.30 Pulsewidth (FWHM) and output energy of a XeF laser as a function of the pre-ionization delay time.

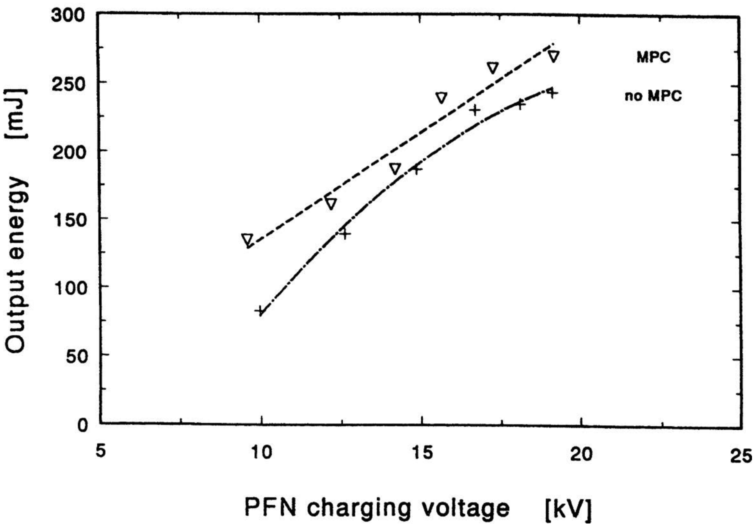

FIGURE 27.31 Output energy as a function of the charging voltage with and without magnetic pulse compression (MPC) of the prepulse.

energy curve, a considerable wavelength shift will occur, and therefore, this transition exhibits a much smaller cross section for stimulated emission than the B → X transition. Moreover, most excimers have a C state sufficiently higher than the B state so that, at room temperature for the gas, it is essentially empty. (During the discharge and laser pulse, the gas temperature does not increase substantially. The discharge energy is initially mainly transferred to electronic excitation and ionization processes. Some of this energy will then be transferred to thermal motion after the laser pulse.) This means that the B → X transition is the only one observed for most excimers.

The XeF system is, in this respect, exceptional because the C state lies 0.08 eV below the B state as indicated in Figure 27.29. At high buffer gas density, the B and C states are coupled by collisional mixing. The buffer gas will thermalize the state densities in times shorter than the radiative lifetime of the B state. The C state may therefore have a considerably larger population density which is favourable for satisfying the laser threshold condition. Nevertheless, the small signal gain equal to the product of the upper state density and its cross section of stimulated emission is smaller than for the B → X transition so that, in order to get laser oscillations on the C → A transition, special measures must be taken. This can be done with mirrors that are highly reflective for the region around 486 nm and less reflective in the region of 351 nm. To make the system tunable over the entire blue–green region, highly reflective dispersive optical elements like a Littrow prism or a diffraction grating can be used as end reflectors. The output coupler can then be a highly reflective mirror with a few per cent transmission.

Laser oscillation on the C → A transition has been reported by a number of investigators with e-beam excitation [102,103]. Typical gas mixture contains 1–3 mbar NF_3, 3–10 mbar Xe and 2–8 bar Ar. The addition of 0.1–1 bar Kr has a favourable effect on the laser performance by suppressing the UV of the B → X transition. Small amounts of F_2 are also beneficial. Using a mixture of 6 bar Ar, 0.5 bar Kr, 8 mbar NF_3, 10 mbar Xe and 2 mbar F_2 excited by 1 MeV electrons of 250 A cm^{-2} and a pulse duration of 10 ns, a pulse output energy of more than 2 J l^{-1} at an intrinsic efficiency of 1.5% has been obtained [104]. Scalable and continuously tunable e-beam-pumped systems covering the blue–green region of the spectrum has been described by several authors [105–109].

Nearly simultaneously discharge-pumped systems operating on the C → A transition have been obtained [110,111]. Because of the small cross section for stimulated emission, intense electric pumping is needed. The first report [110] described an output density of 0.56 mJ l^{-1} which was achieved in a short-pulse UV pre-ionized single discharge with an input power of 11 MW cm^{-3} and a gas mixture of 3 bar He, 4 mbar Xe and 2.7 mbar NF_3. Using a mixture of 2.2 bar He, 7 mbar Kr, 3.5 mbar NF_3 and an input energy of 2.7 MW cm^{-3}, an output energy of 9 mJ l^{-1} was reached [112]. These intense discharges with high electron densities contribute to the mixing of the B and C states, which has a detrimental effect on the C-state density because the average kinetic electron energy is much higher than that of the laser gas. Strong pumping may also increase the production of absorbers of the C → A radiation. Furthermore, the applied short single-pulse UV pre-ionized discharge leads to considerable difficulties in optical energy extraction because the available build-up time for stable cavity oscillation is short for this excitation technique. For e-beam devices, one has the advantage of generating higher gain to prolong its period and to minimize the absorbers by choosing the gas composition and its density independently from the discharge parameters so that laser oscillations on the C → A transition have been successfully generated even for short e-beam pulses. An approach to solve this problem for short-pulse discharges is to apply external injection of a suitable dye laser pulse into a discharge laser to provide an enhanced optical flux in the cavity that is much higher than the C → A spontaneous emission flux. In this way, the entire blue–green line can be tuned by tuning the injection source. This has been successfully demonstrated by injection into both a stable [113] and an unstable [114] XeF discharge system.

A very promising principle [115] for obtaining XeF(C → A) lasers with long pulses and high output energy is optical pumping by photodissociation of XeF_2 vapour. The XeF_2 vapour can be conveniently produced from solid crystalline XeF_2 kept in a separate container closely attached to the laser tube. In this photolysis process, the components XeF(B) and F are formed. Efficient energy transfer from the B to the C state occurs by atomic and molecular collisions. In the first experiments, it was demonstrated by using e-beam-excited fluorescence of Xe_2^* at 172 nm as the photodissociation source. Nearly simultaneously, broadband optical pumping of XeF_2 with the exploding wire technique was successfully applied [116]. Further development has led to multijoule laser pulses of several microseconds [117,118]. For obtaining repetitively operating devices, surface discharges are used [119,120]. By means of ferrite surface plasmas [121], selective radiation production can be obtained in the spectrum region below 220 nm that coincides with the dissociation absorption continuum of XeF_2, which lies between 140 and 200 nm. With high-current surface discharges on ferrite rods placed near the wall of the laser tube, effective illumination is obtained. Each rod is initially conditioned by burning a conductive path into its surface by discharging a current pulse through a thin aluminium wire taped to the surface of each rod. The thus-formed narrow track on each surface then becomes a line light source from the narrow high-current surface discharge when a capacitor is fired in a fast circuit. Using two parallel rods of 76 cm length energized by a 6 μF capacitor at 50 kV and a gas filling of 450 torr Ar, 50 torr N_2 and 12 torr XeF_2 in an active volume of 11 an output energy of 8 J at 351 nm has been obtained [122]. A compact device with an output pulse energy of 225 mJ based on this ferrite surface plasma has also been described [123].

27.10 F_2 Laser (157 nm)

The halogen molecular laser F_2^* operating at 157 nm has, so far, been the only high-power laser operating in the VUV. As pointed out in the introduction, solid-state-based VUV laser systems are no alternative as the thermal loading of the laser crystals and the absorption of the frequency conversion crystals prohibit operation at comparable power levels. The F_2^* laser, like other halogen lasers, operates on transitions between molecular electronic states. At the usual gas densities, the lifetime of the lower state is smaller than that of the upper state. Strictly speaking, this laser does not belong to the class of excimer lasers, as they do not radiate to an unbound ground state. However, the formation kinetics and laser parameters resemble that of the rare gas halogen excimer lasers. The F_2 laser has, like the XeF laser, a weakly bound ground state, and the depopulation rate is, even at high output power densities, fast enough to prevent saturation of the radiation production. The gas composition is also very similar. The halogen lasers also have a multi-atmosphere rare gas density with a very small fraction of the lasing halogen gas.

A great deal of the F_2^* laser research was carried out with e-beam pumping [124–130]. The great advantage of e-beam pumping is, in principle, the detailed study of the kinetics for various input powers and gas densities without loss of homogeneity and input stability as is the case for discharge pumping. The observed very high gain is one of the most striking phenomena. In the absence of resonator mirrors, strong ASE will be observed, and optimized lasers may have output couplers with a few per cent reflection. For e-beam-pumped systems, a gain of more than 50% per cm has been measured for an input power density of 6 MW cm^{-3} in a gas of 8 bar He containing only 0.1% F_2. The gain even increases to more than 60% cm^{-1} if, for the same gas density, 60% of the He is replaced by Ne and the input power density with the same input current density changes to 11 MW cm^{-3} [131]. It is observed that the optical pulse duration is only limited by the e-beam duration, even at high input power. The lifetime of the stable ground state is, for the usual gas conditions, only a few nanoseconds. Any self-termination by the accumulation of the lower-level population has not been observed for pulses up to 160 ns. Both He and Ne have been used as buffer gases. Since the deposition of the e-beam energy in Ne is higher than in He, the gain and output power increase slightly if, for the same e-beam current, the Ne concentration is between 10% and 60%. With an e-beam pulse of 160 ns delivering an input energy of 400 J l^{-1}, an output energy of 1.8 J in a volume of 157 cm^3, corresponding to 11.4 J l^{-1}, was realized with an intrinsic efficiency of 2.8% for an Ne–F_2 mixture of 8 bar containing only 0.15% F_2 [131]. E-beam pumping yields, as for all excimer lasers, much higher power densities and efficiencies than discharge pumping. Nevertheless, the much simpler discharge pumping has attracted much more research efforts.

For discharge systems, the best performance is obtained with He as the buffer gas because of discharge stability. The development of this type of laser challenged previous successful advances in discharge technology for rare gas halogen excimer systems. Furthermore, it may also have been stimulated by its application potential. The high photon energy combined with high beam power discloses a new area of application, which could not be reached by the rare gas halogen excimers.

The first step of the reaction channel for reaching the excited electronic state of the upper laser level is the formation of the rare gas halogen excimer molecule by the Coulomb attraction between the F^- ions and the He^+ or He_2^+ ions. The F^- ions are produced by the dissociative attachment of discharge electrons to F_2 molecules according to reaction (27.23). The helium ions are produced by the interaction of discharge electrons with the buffer gas as described in Section 27.4.1. The initially highly vibrational excited excimer molecule relaxes towards its lower vibrational levels in collisions with the buffer gas. During this relaxation, several curve crossings with repulsive $He + F^*$ states occur, giving the excimer molecule a high probability to predissociate into ground-state helium and an excited fluorine atom [132] according to the reactions

$$He^+ + F^- + He \rightarrow HeF^* + HeF^* + 2He \qquad (27.28)$$

and

$$He_2^+ + F^- \rightarrow HeF^* + He \rightarrow F^* + 2He. \qquad (27.29)$$

When Ne is used as the buffer gas, the reactions are similar.

The formation of the $F_2(D', \upsilon)$ molecule in the upper laser level occurs during a three-body collision of F^* with a fluorine molecule and a buffer atom like:

$$F^* + F_2 + He \rightarrow F_2(D', \upsilon) + F + He. \qquad (27.30)$$

Excited F^* atoms will also be ionized in the discharge and subsequently recombine with F^- in three-body collisions to form the excited fluorine molecule according to

$$F^+ + F^- + He \rightarrow F_2(D', \upsilon) + He \qquad (27.31)$$

Highly vibrational excited $F_2(D', \upsilon)$ may relax to lower or lowest vibrational state in collisions with buffer atoms before the stimulated emission takes place. If the stimulated emission process is not fast enough, because of a low optical quality of the resonator, the $F_2(D', \upsilon)$ molecules are quenched in collisions with the gas and the discharge electrons, of which F_2 is the dominant quencher. The amount of F_2 is, therefore, critical. In principle, it should be enough for the production of the upper laser state during the excitation pulse. For lower concentrations, the output will also be relatively lower. (The regeneration process of fluorine molecules is too slow during the excitation pulse.) Moreover, the electron density will be higher due to the reduced loss of electrons by attachment, so that electron quenching becomes higher. However, too high a fluorine concentration results in too high a quenching rate by fluorine. With a longer excitation pulse, the trade-off with respect to the fluorine content becomes more critical.

The kinetics of the laser process are rather efficient. Some energy is lost by the radiative decay of HeF^* forming F^*. Minor losses in the discharge take place by radiative decays of various excited states of atoms and dimers. Although the radiative lifetime of F^* to the ground state is only a few nanoseconds, its radiation is trapped by ground-state fluorine atoms, which are produced in various reactions. The effective lifetime in the usual laser gas is estimated to be 100–200 ns [133]. The radiative decay of F^* runs parallel to the formation of the upper laser state $F_2(D', \upsilon)$. For the usual gas mixtures, the decay losses are relatively low.

There are also some minor absorption losses. The main losses are the photoionization of He^* and F^* and the electron photodetachment of F^-. However, the absorption cross sections are small. There may be some additional absorption from impurities like O_2, HF and CF_4 that are present in the fluorine gas. Furthermore, the resonator mirrors are usually made of coated or uncoated MgF_2, which also gives some absorption losses for the laser wavelength.

27.10.1 The Spectroscopy

The laser transition takes place between the $D'^3\Pi_g$ and the $A'^3\Pi_u$ states in molecular fluorine, as shown [134] in Figure 27.32. The spontaneous emission spectrum shows a complex structure containing many rotational–vibrational bands. At the usual high pressure of the laser gas, the vibrational and rotational relaxations are fast enough to assume a homogeneously broadened transition. The observed spontaneous emission is predominantly from its lowest vibrational level. The linewidth is approximately 0.3 nm. Laser oscillations are observed on two lines: a strong one at 157.63 nm which is always accompanied by a weaker line at 157.52 nm [62,135]. The energy gap between the two lines is attributed to a rotational splitting in the lower laser level. An additional weak line at 156.71 nm is observed in e-beam-pumped systems [136]. When helium is used as the buffer gas, the laser pulse is also accompanied by a red laser pulse, which originates from transitions of the higher energy levels in the atomic F^* manifold [124]. This is not observed when neon is used as the buffer gas and may be due to the fact that the predissociation of NeF^* mainly populates the lower energy levels of this manifold, which prevents laser inversion [125].

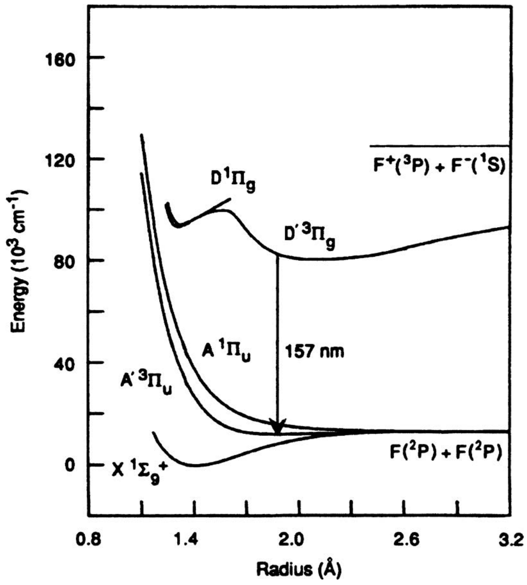

FIGURE 27.32 Schematic potential energy diagram for electronic levels in F_2 showing the laser transition.

The lower laser level of the F_2^* system is a covalently bound electronic state. It has practically the same small binding energy of about 0.15 eV as the lower laser level of the XeF^* laser. Such a small binding energy leads under the usual high gas density to an effective lifetime of the lower laser level of about 1 ns. This small lifetime prevents a substantial population build-up of the lower laser level that might lead, at high power densities, to an effective reduction in the inversion density. The laser process, similar to that in excimer lasers, is not hampered by the ground state. From a radiation lifetime of 3.7 ns for the upper state [134] and a linewidth of 0.3 nm, the stimulated emission cross section according to equation (27.1) becomes $\sigma_{st} = 6.8 \times 10^{-16} cm^2$. This relatively large cross section, compared with those found for most rare gas halogen excimer lasers, is due to its relatively narrow linewidth and explains the relatively high gain of the F_2^* laser.

27.10.2 Laser Performance

Discharge-pumped F_2^* lasers are commonly excited by a fast single-discharge circuit that allows a high pumping power density in a short pulse [127,137]. The output pulse durations are typically in the range 10–30 ns (FWHM). The limit on the pulse duration is imposed by the very fast growth of discharge instabilities, which are inherent for the high-pressure gas mixtures used. Filaments formed in the discharge absorb and scatter the laser field, and the laser oscillation may terminate before the end of the discharge pulse. Since the time is very limited, researchers have been looking to optimize the input power density. Performed systems with high pumping power exhibit very high gain, of the order of 10% per cm, and output beams that are dominated by ASE. The beam quality is rather poor with strong divergence up to a few mrad [138].

For good laser performance, it is crucial to use a short-pulse high-intensity X-ray pre-ionization source. This can be successfully done with a corona plasma cathode from which the electrons are emitted [22]. They are accelerated towards the anode with voltages ranging from 40 to 110 kV and are stopped in a 25-μm-thick tantalum foil to produce the X-rays [131]. The X-ray pulse has a sharp peak with a width of 25 ns (FWHM). The pre-ionization electron density in the laser gas is proportional to the X-ray dose entering the gas. A uniformity within 8% over the full entrance window can be obtained. It is essential that the inductance of the discharge circuit of the laser is minimized in order to get a fast current risetime and a high current density. This can be reached by placing a series of capacitors along the cathode as close as possible to the discharge. Following these principles, the following experiment can be described for a laser gas containing 0.1% F_2 in 5 bar He [131]. Using a discharge length of 42 cm, an electrode spacing of 1.5 cm and a discharge width of 2.4 cm, the inductance is 1.7 nH for a capacitance of 14 nF and 1.1 nH for 30 nF. The discharge width depends on the electrode spacing. Reducing the spacing to 0.8 cm the width becomes 1.5 cm. Setting the latter spacing and installing a capacitance of 14 nF charged at 20 kV, the observed waveforms are shown in Figure 27.33. While the capacitors are charged, the X-rays are injected. After typically 30–100 ns, the gas breaks down, and the discharge starts. The applied discharge voltage drops while the current rises very fast. Both the pump power pulse and the laser pulse are as short as 7.5 ns (FWHM). It was found that the onset of the X-ray pulse must occur during the voltage rise on the electrodes. If the pre-ionization is earlier, the electrons are already lost by attachment, and if it occurs near the end or after the full charging of the capacitors, the avalanche electron multiplication is not homogeneous.

The output energy density depends on the electrode spacing. If, for the same capacitance of 14 nF and inductance of 1.7 nH, the spacing is increased from 0.8 to 1.5 cm, the discharge width increases from 1.5 to 2.4 cm, whereas the maximum output as a function of the charging voltage increases from 10 mJ at 20 kV to 26 mJ at 35 kV. The maximum specific output energy density is $0.3\,\mathrm{J}\,\mathrm{l}^{-1}$ at an intrinsic efficiency of 0.3%. By increasing the electrode spacing to 1.5 cm, nearly a factor of 2, the breakdown voltage is expected also to increase by a factor of 2 so that the stored energy in the capacitor is about four times more. The simultaneously observed discharge width changes by a factor of 1.6. Then the input power density, within experimental error, was more or less constant. The output density seems to saturate only with the current density.

27.10.3 Long Pulses

The poor beam quality of the described short-pulse single-discharge systems can be improved when the number of cavity round trips can be increased. This means that the gain duration of the medium should be increased. The question is then to look for discharge parameters and technology that extend the stability duration of the discharge. One possibility is a reduction in the fluorine content which is accompanied by a reduction in the output. This reduction of output can be limited by the application of the resonant overshoot mode in a prepulse–main-pulse configuration, which has already been shown to improve the performance of rare gas halogen excimer lasers. Applied to the F_2^* laser system, it also resulted in relatively long output pulses. The system then may run without current reversal and opens the way to the development of high repetition systems. To obtain fast risetimes, the prepulse capacitors are again placed as close as possible to the electrodes. This technique with magnetic switching has been successfully demonstrated with the following parameters [131]. Using the same laser head construction as described in the previous section except that the main capacitor of 153 nF is now built as

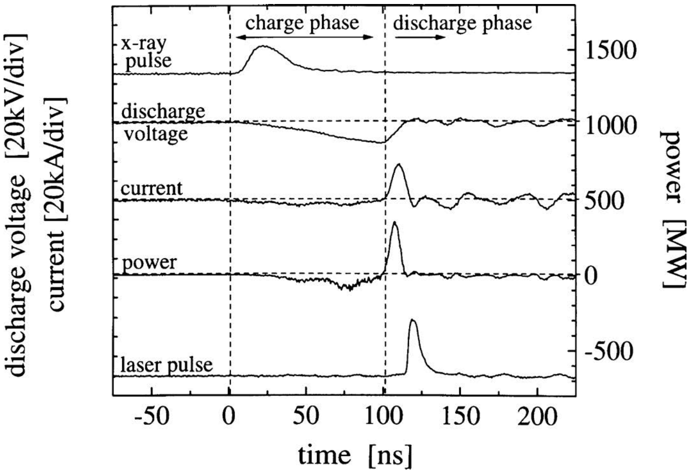

FIGURE 27.33 Typical waveforms of the F_2 laser showing the X-ray pulse, discharge voltage, laser current and output pulse.

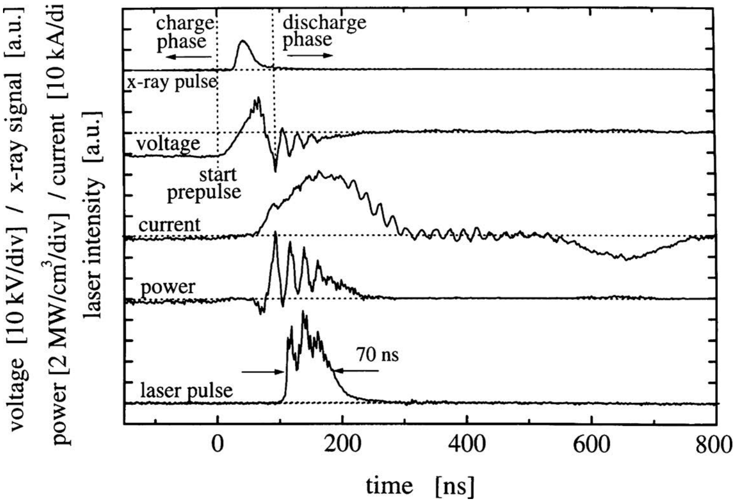

FIGURE 27.34 Typical waveforms of the long pulse F_2 laser showing the X-ray pulse, discharge voltage, laser current and output pulse.

a PFN consisting of nine rows of five low inductance ceramic capacitors, 1.7 nF each. The ten prepulse capacitors with a total capacitance of 3.6 nF are equally distributed along either side of the cathode. Its circuit inductance is about 3 nH. The series inductance of the saturated magnetic switch together with the main capacitance is about 12 nH. Typical waveforms for a discharge in a gas mixture of 2 bar He and 3 mbar F_2 are shown in Figure 27.34. The charging voltages of the main and prepulse capacitors are 12 and 20 kV, respectively. At the peak of the charging voltage, a positive prepulse is applied to the peaking capacitors. This creates a large voltage difference across the magnetic switch driving it from a high to a low inductance state. Next, the peaking capacitors are resonantly charged by the main capacitor. The voltage reverses and rises rapidly until the laser gas breaks down. The low inductance of the laser allows a fast rise in the current and, thus, a high power deposition from the prepulse capacitors during the start of the discharge. The fast risetime of the current leads to the formation of a dense hot-spot structure on the cathode, which enhances the homogeneity of the discharge [24] and favours the generation of long laser pulses. After this breakdown, the current from the main capacitor starts flowing through the low-impedance discharge driving the magnetic switch deep into saturation so that the stored energy in the main capacitor is very rapidly dissipated in the discharge. The oscillations on the voltage waveform are due to current oscillations in the circuit that is formed by the discharge, the laser head and the peaking capacitor.

The timing of the start of the pre-ionization is most effective between 5 and 85 ns after the start of the prepulse. For the described system, an output of a few mJ and a pulse duration of 70 ns have been demonstrated [131].

27.11 Other Rare Gas Halide Lasers

Apart from the previously discussed rare gas halide lasers, some more systems have shown stimulated emission. These are XeBr (281.8 nm) [9], KrBr (206.5 nm) [139], ArCl (169 and 175 nm) [140] and NeF (108 nm) [141]. These systems have been demonstrated with self-sustained discharges, except for NeF which was pumped by e-beam. The energies and efficiencies are low. This may explain the low interest in further development.

Next to diatomic excimers, polyatomic excimers have also been investigated. The broadband emission spectra, mostly in the visible part of the spectrum, observed in e-beam excitation of rare gas halide mixtures are assigned to triatomic excimers [142]. The large linewidths of those spectra with $\Delta\lambda/\lambda$ of the order of 10% provoked the development of high power lasers, tunable over these relatively broad spectral ranges. However, the experiments showed that it was difficult to reach threshold because of the low gain and high absorption of the emitted radiation. Using a high e-beam current density of 800 A cm^{-2} and a short pulse of 10 ns lasing has been found for Xe_2Cl at 520 nm with $\Delta\lambda = 30$ nm (FWHM) [143] and for Kr_2F in the range 380–480 nm [144]. The cross sections for stimulated emission are very small due to the large linewidths of the transitions. The studies have indicated that these complex molecules have a high laser threshold, high working pressure, low gain and low efficiency.

27.12 N_2 Laser (337–406 nm and 741–1230 nm)

Nitrogen is also an attractive medium for obtaining high output laser energy in the UV region of the spectrum. This laser was introduced as a simple operating self-sustained discharge system shortly after the invention of the first lasers [145,146]. More than 10 years later, when suitable e-beam technology became available, additional studies were carried out to obtain improved performances and a better understanding of the system [147,148]. Its high gain obtained with a simple *LC* circuit in the easily available N_2 gas made the system very popular as a home-made system to be used for various applications where intense UV radiation was required, for instance dye laser pumping and spectroscopy. The lasing scheme has some similarities with the excimers although the formation kinetics of the lasing molecule is different.

Laser action occurs on electronic vibrational transitions of the N_2 molecule. The electronic energy states with vibrational levels of the N_2 molecule are shown in Figure 27.35. The main UV transition takes place in the so-called second positive band, i.e. in the transition from the $C^3\Pi_u$ to the $B^3\Pi_g$ state at 337.1 nm. The upper state is formed by electronic excitation from the ground state of N_2. Since the lifetime of the lower state, about 10 μs, is much longer than the 40 ns of the upper state, the laser is self-terminating, and therefore, it operates only in the pulsed mode. As a consequence, during the laser process, there will be a strong population build-up of the $B^3\Pi_g$ state so that cascade laser transitions in the first positive band between the $B^3\Pi_g$ and $A^3\Sigma_u^+$ states in the near infrared (741–1230 nm) may also occur [146,149], which are also self-terminating because the lifetime of the $A^3\Sigma_u^+$ state is about 1 ms. Since the lifetime of the $C^3\Pi_u$ state is 40 ns, it follows that the excitation pulse is only effective within this period and that the radiation build-up time in the cavity must be much shorter than this lifetime. This means that the discharge pulse must be as short as possible to produce the high gain for a fast radiation build-up.

Initially, the N_2 molecules are at room temperature and practically all in the ground vibrational state of the ground electronic $X^3\Sigma_u^+$ state. The probability of exciting a vibrational state of a higher electronic state from this initial ground state and the subsequent radiative transition probability between states can be calculated quantum mechanically. It depends on the overlap of the wavefunctions of the respective states and is described by the Franck–Condon (FC) factor. The FC principle states that, during an electronic transition in a molecule induced by the influence of an external perturbation as in electronic impact, absorption or emission of radiation, the internuclear separation of the molecule and the velocity of the relative nuclear motion alter to a negligible extent. The transition takes place so quickly that the nuclei do not have time to move any appreciable distance. This is due to the fact that the impulse transfer to the relatively heavy nuclear mass of a molecule is very small. The transitions are then indicated by vertical lines in the molecular potential energy diagram. According to this FC principle, the electronic excitation of the N_2 molecules to the ground vibrational state of the $C^3\Pi_u$ manifold is more likely than to that of the $B^3\Pi_g$ manifold. This follows from the energy state diagram in Figure 27.35 where the potential minimum of the $B^3\Pi_g$ state relative to that of the ground state is shifted to a larger internuclear separation distance than in the case of the $C^3\Pi_u$ state.

27.12.1 The Discharge

The discharge system has a typical gas mixture of 1 bar He and 50–100 mbar N_2. The He contributes to the initial stability of the principally unstable discharge and not so much to collisional pumping of the laser. The discharge requires high electric fields of the order of 10 kV cm^{-1} or *E*/*p* values of about 10 V cm^{-1}mbar^{-1}. This is obtained by transverse electrodes similar to excimer laser constructions. The energy

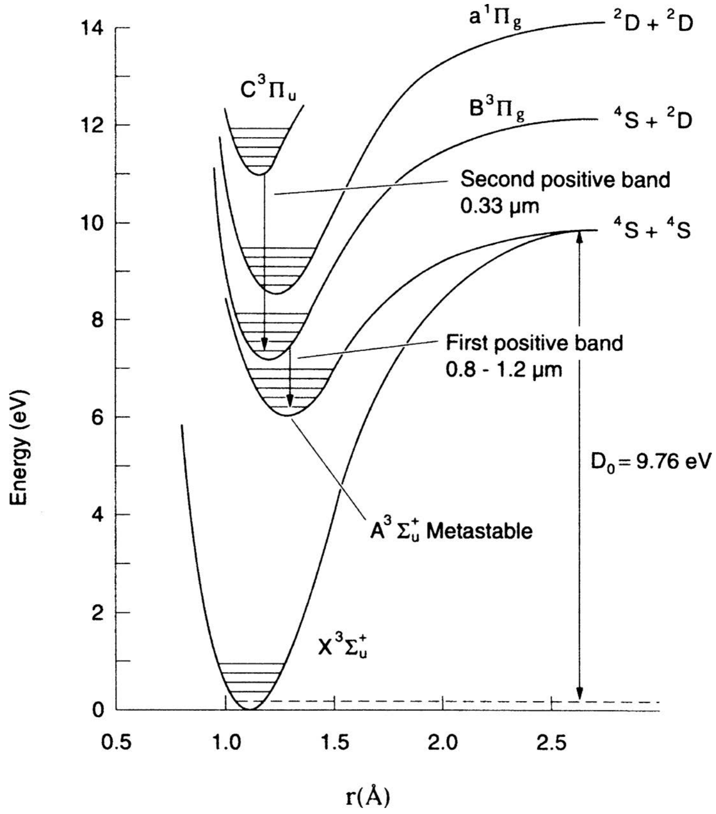

FIGURE 27.35 Potential energy diagram for electronic-vibrational levels in N_2 showing the first and second positive bands; D_0 is the dissociation energy.

needed to excite the upper laser level is about 11.7 eV so that discharge electrons with higher energy are desired. The initial quasi-stability of the discharge can be obtained with e-beam, X-ray or UV pre-ionization, similar to that in excimer lasers. The simplest constructions are based on UV pre-ionization by means of a row of spark plugs parallel to the laser axis, surface flashes or corona discharges. Once the more or less uniform pre-ionization is obtained, the discharge follows immediately. Since the discharge instabilities will build up rapidly and the lifetime of the upper level is only 40 ns, it is advantageous to have the current pulse as short as possible. The inductance of the circuit must then be as low as possible to obtain the required fast current risetime. This can be done by mounting parallel capacitors as close as possible to the discharge electrodes.

The initial voltage that is applied across the discharge gap just after switching is several times higher than the quasi-steady-state voltage that follows after breakdown. A faster switch gives a higher initial voltage and a higher electron energy of the initial discharge. Due to fast switching, a high electric field in the laser gas is maintained during the delay time to break down the discharge. This delay time is typically in the range 100 ns. Just after the break down, the *E*/*p* value drops very rapidly, say in about 5 ns, to its steady-state value. During this short period, the electrons have sufficient energy for laser pumping. The duration of the fast fall of the electric field depends on the gas components and their densities. It determines the laser pulse duration. The following quasi-steady-state discharge is not suitable for laser pumping because of its low average electron energy. Small amounts of electronegative gases such as SF_6, NF_3 and F_2 added to the laser gas increase the delay time before breakdown so that the maximum voltage just before breakdown is increased. The field strength during the transient time for pumping will increase, and higher output energies are obtained [150,151].

The gain of the N_2 discharge lasers is, in general, very high so that the short output pulse may be considered as ASE. Output powers above 1 MW are feasible. The optical beam quality is poor as a consequence of the short pulse durations, which do not allow sufficient cavity passes to reach coherence. Often a single mirror is used at one end to provide a unidirectional output beam. High repetition rate performance requires adequate electric circuitry. Spark gaps have limited repetition rates and lifetimes. Thyratrons are more suitable, although their current is limited. This can be circumvented by applying MPC before the current passes the discharge.

Higher output energies, longer pulses and higher intrinsic efficiencies [147,152] have been obtained with e-beam pumping where the discharge parameters are independent from the gas composition. Most successful is the addition of Ar as a buffer gas in multi-atmospheric systems. The accumulated excitation energy of Ar is transferred to the upper laser level of N_2 during molecular collisions in multi-atmospheric systems. It was also observed that the addition of He and Ne to the Ar–N_2 mixture has a further enhancing effect on the output energy, efficiency and pulse duration. Next to 337.1 nm, several additional wavelengths, e.g. 357.7, 380.5 and 405.9 nm, have been observed [152,153].

27.13 H_2 Laser (140–165 nm and 100–120 nm)

The molecular hydrogen laser has much in common with the nitrogen laser. The system is attractive for producing laser power in the vacuum ultraviolet region of the spectrum. The system was also suggested shortly after the invention of the laser [154]. Since the gain needed for laser action decreases drastically with wavelength, as we discussed in Section 27.1, extremely high pumping power densities are required. Fortunately, this condition can still be fulfilled for laser action in the Lyman band (140–165 nm) as well as for the Werner band (100–120 nm). Both high current electron beams [155,156] and very intense transverse discharges [157–159] have been applied successfully. The lasing scheme is very similar to that of the N_2 laser and has also similarities to the excimer lasers. Laser actions occur between the B and X states in the Lyman band and between the C and X states in the Werner band. The X state is the ground state and the B and C states are, respectively, the first and second excited electronic states of molecular hydrogen. Each electronic state can be further described by its vibrational and rotational energy distributions. The system is also self-terminating because the lifetime of the lower laser level, with its long rotational and vibrational relaxation times, is much longer than that of the excited B or C state. The selective kinetic paths in the laser processes are mainly determined by the FC principle, similar to what we have discussed for the N_2 laser. Figure 27.36 shows the potential energy diagram of molecular hydrogen with electronic and vibrational energy levels, excitation paths and radiative decay paths in the Lyman and Werner bands. The transitions according to the FC principle are indicated

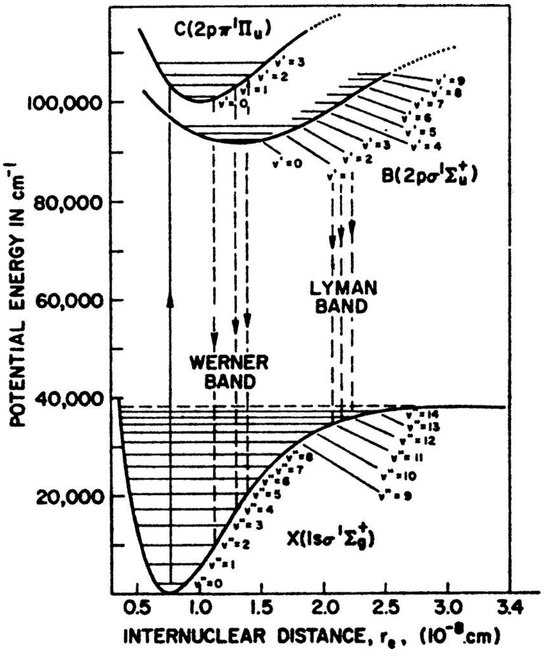

FIGURE 27.36 Potential energy diagram for electronic-vibrational levels in H_2 showing the Lyman and Werner bands and the electron impact excitation path [160].

by vertical lines. The upper vibrational levels being initially empty at room temperature have a very low probability of being excited because of the FC principle.

27.13.1 Lyman Band (140–165 nm)

The light hydrogen molecules are at room temperature in their ground vibrational state and have only a few rotational levels occupied, mainly the levels $J_2 = 0, 1, 2$ and 3 of which $J_2 = 1$ has the highest density. The excited B state will then, according to the FC principle, have the vibrational levels $\upsilon_1 = 2\text{–}11$ and preferentially $\upsilon_1 = 6$ and 8. The electronic excitation of these molecules results in even-numbered rotational levels in the B state ($J_1 = 0, 2$) with $J_1 = 2$ preferred. Since the upper vibrational levels of the X state are empty, the laser process is mainly observed between B($\upsilon_1 = 2\text{–}11$; $J_1 = 0, 2$) and X($\upsilon_2 = 9\text{–}14$; $J_2 = 1, 3$) states with intensities proportional to the FC factors. See Table 27.1.

27.13.2 Werner Band (100–120 nm)

In this laser process, the electronic excitation from the ground state occurs according to the FC principle to the low-lying vibrational levels ($\upsilon_1 = 0\text{–}4$) of the C state. Laser oscillation can then be obtained between these low-lying vibrational states and the high vibrational levels of the X state. The intensity distribution depends on the FC factors. The Q(1) line with $\Delta J = -1$ of the C($\upsilon_1 = 1$) to X($\upsilon_2 = 4$) transition is the strongest. Observed lines are shown in Table 27.2.

TABLE 27.1

Wavelengths and Vibrational Transitions of Observed Laser Lines in the Lyman Band [157]

Transition	Wavelength (nm)		
B(υ_1)–X(υ_2)	P(1)	P(3)	R(1)
2–9	157.18	-	
3–10	159.15	159.61	
4–11	160.47	160.86	
5–12		161.33	
6–13	160.74		
7–13		158.05	157.71
8–14	156.73		

TABLE 27.2

Wavelengths and Vibrational Transitions of the Strongest Observed Laser Lines in the Werner Band [156]

Transition	Wavelength (nm)	
C(υ_1)–X(υ_2)	Q(1)	P(3)
1–4	116.136	116.617
2–5	117.586	118.050
1–5	120.668	
2–6	121.900	122.358
3–7	123.004	
4–8	123.956	

The isotopes of hydrogen can also be successfully used. The observed stimulated emission spectrum of H_2, HD and D_2 shows tens of lines in both Lyman and Werner bands [161].

27.13.3 Excitation Technique

As pointed out in Section 27.1, the main difficulty encountered in obtaining laser action in the VUV spectral region is the required high pumping power density. Because of the very short radiative lifetime of the upper states of about 0.8 ns and the relatively long lifetime of the lower state, stimulated emission of this self-terminating system may occur on the order of 1 ns. The shortness of the upper state lifetime means that both optical feedback by cavity mirrors and excitation pulses longer than this lifetime are of no use. It even means that time-independent spatial homogeneity of the excitation pulse is catastrophic, which imposes an additional constraint on the applied excitation technology. Stimulated emission is only feasible when the medium is excited by an excitation pulse that moves with the speed of stimulated emission. The first reports on observed stimulated emission in H_2 describe an intense e-beam pulse propagating parallel to the stimulated emission system [155,156]. A short e-beam pulse of a few nanoseconds penetrates longitudinally, parallel to the axis of a cylinder containing H_2. The e-beam generator consists of a Marx circuit for obtaining high voltages followed by a Blumlein circuit for pulse compression, voltage doubling and pulsefront sharpening. A 3-ns e-beam pulse of 10 kA cm^{-2} with an acceleration voltage of 600 kV excites longitudinally this cylinder containing 20–100 torr H_2. In this way, stimulated emission in both Lyman and Werner bands has been observed. The short high-power e-beam pulse produces a large inversion density before the spontaneous emission can populate the upper vibrational levels of the ground electronic state. The gain is then high enough for stimulated emission in the direction of the propagating e-beam. The system then operates in the ASE mode, just as the molecular nitrogen laser does. The laser pulses, estimated to be about 1 ns, have power densities in the range 50–500 W cm^{-2}.

An attractive alternative technique for pumping the H_2 system is the short-risetime travelling-wave discharge. This type of discharge can be performed with a Blumlein transmission line connected to the discharge channel [162–164]. The required high input power density is further increased by a narrow channel for the laser discharge. The Blumlein construction consists, in principle, of two parallel plates, one is a continuous conducting plate and the other is interrupted by the laser discharge channel. The two plates are charged like a capacitor. If on one end of the two parallel plates a fast switch is used to short-circuit the plates, a short square voltage pulse of twice the charging voltage is applied to the channel. The switching time determines the voltage risetime; the length of the plates with the dielectric the pulse duration; the dielectric with the distance between the plates the current per unit length. The trick in obtaining the required travelling excitation-current pulse wave is to position the switch in a corner of the parallel plates and to shape the conducting plates in such a way by the angle relative to the discharge channel that a travelling-wave current pulse reaches the discharge channel. With the correct angle, the excitation pulse seen by the discharge moves with a velocity equal to that of ASE. Pulse durations of 1 ns are recorded at the end toward which the excitation pulse proceeds [157]. Using discharge channels with thicknesses of 50–1000 μm and H_2 densities 30–60 torr, pulse energies up to 20 μJ with a duration of 0.5 ns have been obtained at a high repetition rate [158].

Appendix

During the stable period of a pulsed discharge, there is an equilibrium between the production and loss of free electrons, i.e. a glow discharge is formed. This discharge is characterized by a more or less constant steady-state voltage between the electrodes, independent of the discharge current. The steady-state voltage depends strongly on the gas composition and density. The main pulse maintaining the steady state of the discharge can then be described by a simple *LC* circuit as shown in Figure 27.37. Starting with the main capacitor C_{pfn} charged at V_{pfn} and the constant voltage V_{SS} across the electrodes, the circuit current is described by the differential equation

$$LC_{\text{pfn}}\frac{\mathrm{d}^2 i}{\mathrm{d}t2}+i=0$$

with the initial conditions

$$\frac{\mathrm{d}i}{\mathrm{d}t}=\frac{V_{\text{pfn}}-V_{\text{SS}}}{L}$$

and $i = 0$ for $t = 0$. The solution of this equation is

$$i(t)=\left(V_{\text{pfn}}-V_{\text{ss}}\right)\left(\frac{C_{\text{pfn}}}{L}\right)^{1/2}\sin\left(\frac{t}{\sqrt{LC_{\text{pfn}}}}\right).$$

If we integrate the current over the first half-cycle, $\Delta t = \pi(LC_{\text{pfn}})^{1/2}$, the charge transfer from the capacitor becomes $2C_{\text{pfn}}\,(V_{\text{pfn}} - V_{\text{ss}})$. It is seen that for $V_{\text{pfn}} = 2V_{\text{SS}}$, the capacitor is empty, and no current reversal can occur. This is the so-called matched discharge situation. The energy delivered to the discharge during the first half-cycle becomes, by integrating $i(t)$ V_{SS}, equal to $2V_{\text{SS}}C_{\text{pfn}}(V_{\text{pfn}} - V_{\text{SS}})$.

The efficiency η defined as the energy delivered to the discharge during the first half-cycle divided by the energy stored on the capacitor is then

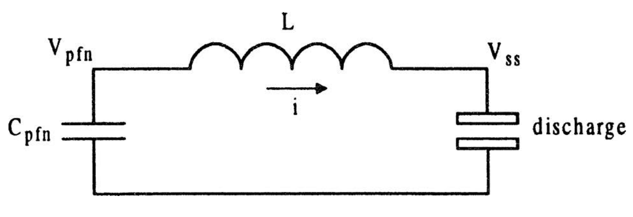

FIGURE 27.37 Single *LC* circuit of the main discharge.

$$\eta=4\frac{V_{\text{SS}}\left(V_{\text{pfn}}-V_{\text{SS}}\right)}{V_{\text{pfn}}^2}.$$

The efficiency reaches its maximum, $\eta = 1$, for $V_{\text{pfn}} = 2V_{\text{SS}}$.

REFERENCES

1. Hopfield J J 1930 Absorption and emission spectra in the region 60–110 nm *Phys. Rev.* **35** 1133–4.
2. Funkelnburg W 1938 *Kontinuierliche Spektren* (Berlin: Springer).
3. Tanaka Y 1955 Continuous spectra of rare gases in the vacuum ultraviolet region *J. Opt. Soc. Am.* **45** 710–13.
4. Golde M F and Thrush B A 1974 Vacuum UV emission from reactions of metastable inert gas atoms: Chemiluminescence of ArO and ArCl *Chem. Phys. Lett.* **29** 486–90.
5. Velazco J E and Setser D W 1975 Bound free emission spectra of diatomic xenon halides *J. Chem. Phys.* **62** 1990–1.
6. Houtermans F G 1960 *Helv. Phys. Acta* **33** 933.
7. Basov N G, Danilychev V A, Popov Y M and Khodkevich D D 1970 Laser operating in the vacuum region of the spectrum by excitation of liquid xenon with an electron beam *JETP Lett.* **12** 329–31.
8. Koehler H A, Ferderber L J, Redhead D L and Ebert P J 1972 Stimulated VUV emission in high pressure xenon excited by high current relativistic electron beams *Appl. Phys. Lett.* **21** 198–200.
9. Searles S K and Hart G A 1975 Stimulated emission at 281.8 nm from XeBr *Appl. Phys. Lett.* **27** 243–5.
10. Brau C A and Ewing J J 1975 354 nm laser action on XeF *Appl. Phys. Lett.* **27** 435–7; Brau C A and Ewing J J 1975 Emission spectra of XeBr, XeCl, XeF and KrF *J. Chem. Phys.* **63** 4640–7.
11. Fleischmann H H 1975 High current electron beams *Phys. Today* **28** 35–43.
12. Langmuir I 1913 Effect of space charge and residual gases on thermionic currents in high vacuum *Phys. Rev.* **II–6** 450–86.
13. Bradley L P 1976 *High Power Gas Lasers 1975 (Conference Series 29)* (Bristol: IOPP).
14. Hsia J C, Jacob, J H Mangano, J A and Rokni M 1977 Avco Everett Research Lab., Semiannual Report, DARPA 3125, NTIS Intermediar.
15. Bradley D J, Hull, D R, Hutchinson, M H R and McGeoch M W 1975 Coaxially pumped, narrow band, high power VUV xenon laser *Opt. Commun.* **14** 1–3.
16. Peters P J M, Fierkens I H T and Witteman W J 1987 Effect of Ne and Ar on the performance of a high pressure ArF laser pumped by a small coaxial electron beam *Appl. Phys. Lett.* **51** 883–5.
17. Kleikamp B M H H and Witteman W J 1984 High energy extraction of electron beam pumped KrF lasers at multi atmospheres *Opt. Commun.* **49** 345–8.
18. Ekdahl C A 1980 Voltage and current sensors of high density Z-pinch experiments *Rev. Sci. Instrum.* **51** 1645–8.
19. Pellinen D G and Spence P W 1971 A nanosecond risetime megampere current monitor *Rev. Sci. Instrum.* **42** 1699–701.
20. Lacour, B and Vannier C 1987 Phototriggering of a 1 J excimer laser using either UV or x-rays *J. Appl Phys.* **62** 754–8.

21. Bollanti S, Letardi T and Zheng C 1991 Effect of pre-ionization on uniformity of photo-triggered XeCl laser discharges: modeling and comparison with experimental results *IEEE Trans. Plasma Sci.* **19** 361–8.
22. van Goor F A 1993 Fast risetime x-ray pre-ionization source using a corona plasma cathode *J. Phys. D: Appl. Phys.* **26** 404–9.
23. Seddon N and Thornton E 1988 A high voltage short rise-time pulse generator based on a ferrite pulse sharpener *Rev. Sci. Instrum.* **59** 2497–8.
24. Makarov M 1995 Effect of electrode processes on the spatial uniformity of the XeCl laser discharge *J. Phys. D: Appl. Phys.* **28** 1083–93.
25. Levatter J I AND Bradford R S Jr 1978 Water dielectric Blumlein driven fast electric discharge KrF laser *Appl. Phys. Lett.* **33** 742–4.
26. Wang C P 1978 High repetition rate transverse flow XeF laser *Appl. Phys. Lett.* **32** 360–2.
27. Taylor R S, Sarjeant W J, Alcock A J and Leopold K E 1978 Glow discharge characteristics of a 0.8 J multi-atmosphere rare gas halide laser *Opt. Commun.* **25** 231–4.
28. Sze R C and Loree T R 1978 Experimental studies of a KrF and ArF discharge laser *IEEE J. Quantum Electron.* **14** 944–50.
29. Long W H, Plummer M J and Stappaerts E A 1983 Efficient discharge pumping of an XeCl laser using a high voltage pre-pulse *Appl. Phys. Lett.* **43** 735–7.
30. Taylor R S and Leopold K E 1985 Magnetically induced pulser laser excitation *Appl. Phys. Lett.* **46** 335–7.
31. Fisher C H, Kushner M J, DeHart T E, MCDaniel J P, Petr R A and Ewing J J 1986 High efficiency XeCl laser with spiker and magnetic isolation *Appl. Phys. Lett.* **48** 1574–6.
32. Gerritsen J W, Keet A L, Ernst G J and Witteman W J 1990 High efficiency operation of a gas discharge XeCl laser using a magnetically induced resonant voltage overshoot circuit *J. Appl. Phys.* **67** 3517–19.
33. Witteman W J, Ekelmans G B, Trentelman M and van Goor F A 1990 Discharge technology for excimer lasers of high average power *Eighth Int. Symp. on Gas Flow and Chemical Lasers (SPIE Volume 1397)* ed J M Orza and C Domingo (Bellingham, WA: SPIE) pp 37–45.
34. Timmermans J C M, van Goor F A and Witteman W J 1993 A new mode to excite a gas discharge XeCl laser *Appl. Phys. B* **57** 441–5.
35. Brau Ch A 1984 Rare gas halide excimers *Excimer Lasers (Topics in Applied Physics 30)* ed Ch K Rhodes (Berlin: Springer) p 88.
36. Tellinghuisen J, Hoffman J M, Tisone G C and Hays A K 1976 Spectroscopic studies of diatomic noble gas halides: analysis of spontaneous and stimulated emission from XeCl *J. Chem. Phys.* **64** 2484–90.
37. Tellinghuisen J, Tisone G C, Hoffman J M and Hays A K 1976 Analysis of spontaneous and laser emission from XeF *J. Chem. Phys.* **64** 4796–7.
38. Ewing J J and Brau C A 1975 Laser action on the ${}^2\sum^+_{1/2} \to {}^2\sum^+_{1/2}$ bands of KrF and XeCl *Appl. Phys. Lett.* **27** 350–2.
39. Ault E R, Bradford R S and Bhaumik M L 1975 High power xenon fluoride laser *Appl. Phys. Lett.* **27** 413–15.
40. Hoffman J M, Hays A K and Tisone G C 1976 High power noble gas halide lasers *Appl. Phys. Lett.* **28** 538–9.
41. Burnham R and Djeu N 1976 Ultraviolet pre-ionized discharged pumped lasers in XeF, KrF and ArF *Appl. Phys. Lett.* **29** 707–9.
42. Mangano J A and Jacob J H 1975 Electron beam controlled discharge pumping of the KrF laser *Appl. Phys. Lett.* **27** 495–8.
43. Sutton D G, Suchard S H, Gibb O L and Wang C P 1976 Fast discharge initiated KrF laser *Appl. Phys. Lett.* **28** 522–3.
44. Jacob J H, Hsia J C, Mangano J A and Rokni M 1979 Pulse shape and lasing energy extraction from e-beam pumped KrF *J. Appl. Phys.* **50** 5130–4.
45. Rice J K, Tisone G C and Patterson P L 1980 Oscillator performance and energy extraction from a KrF laser pumped by a high intensity relativistic electron beam *IEEE J. Quantum Electron.* **16** 1315–26.
46. Edwards C B, O'Neil F and Shaw M J 1980 60 ns e-beam excitation of rare gas halide lasers *Appl. Phys. Lett.* **36** 617–20.
47. Swingle J C, Schlitt L G, Rapopart W R, Goldhar J and Ewing J J 1981 Efficient narrow band electron beam pumped KrF laser for pulse compression studies *J. Appl. Phys.* **52** 91–6.
48. Peters P J M, Bastiaens H M J, Witteman W J and Gerber T 1987 A study of the electron quenching of excimers in a KrF laser *Appl. Phys. B* **43** 253–61.
49. Burnham R and Searles S K 1977 Radiative lifetime of KrF *J. Chem. Phys.* **67** 5967–8.
50. Mangano J A, Jacob J H, Rokni M and Hawryluk A 1977 Three body quenching of KrF by Ar and broadband emission at 415 nm *Appl. Phys. Lett.* **31** 26–7.
51. Witteman W J and Kleikamp B M H H 1984 On the electron-beam pumped KrF laser *J. Appl. Phys.* **55** 1299–307.
52. Peters P J M, Bastiaens H M J and Witteman W J 1984 Compact coaxially excited high energy density KrF laser *J. Appl. Phys.* **55** 1410–12.
53. Witteman W J and Oomen G L 1980 On the performance of an e-beam pumped KrF laser *Opt. Commun.* **32** 467–72.
54. Oomen G L and Witteman W J 1978 Electron beam pumped KrF laser with a neon-argon diluent *Appl Phys. Lett.* **33** 878–80.
55. Gerber T, Peters P J M, Bastiaens H M J and Witteman W J 1984 Enhancement of the specific output energy of an electron-beam pumped KrF laser using Ne as the main buffer gas *Appl. Phys. Lett.* **45** 356–7.
56. Ewing J J 1979 *Laser Handbook* vol 3 ed M K Stitch (Amsterdam: North-Holland) p 163f.
57. Inertial Confinement Fusion at Los Alamos 1989 *Progress in Inertial Confinement Fusion Since 1985* **1** 262.
58. Greene A E and Brau C A 1978 Theoretical studies of UV pre-ionized transverse discharge KrF and ArF lasers *IEEE J. Quantum Electron.* **14** 951–7.
59. Loree T R, Butterfield K B and Barker D L 1978 Spectral tuning of ArF and KrF discharge lasers *Appl. Phys. Lett.* **32** 171–3.
60. Zhupikov A A and Razhev A M 1998 Excimer KrF laser with He buffer gas, 0.8 J energy and 2% efficiency *Sov. J. Quantum Electron.* **28** 667–9.

61. Moody S E, Levin L A, Center R E, Ewing J J and Klosterman E L 1981 Measurements of laser performance and efficiency of e-beam pumped xenon chloride *IEEE J. Quantum Electron.* **17** 1856–61.
62. McKee T J 1985 Spectral narrowing techniques for excimer oscillators *Can. J. Phys.* **63** 214–19.
63. Efimovskii S V, Kurbasov S V, Novichkov A V and Palchikov K K 1996 Influence of the parameters of a Fabry–Pérot etalon on the output characteristics of a narrow band long optical pulse XeCl laser *Sov. J. Quantum Electron.* **26** 599–603.
64. Sorkina R, van Goor F A and Witteman W J 1992 Simulation studies of the pre-pulse main pulse XeCl discharge lasers with magnetic switching *Appl. Phys. B* **55** 478–84.
65. Bollanti S, Di Lazzaro P, Giordano G, Hermsen T, Letardi T and Zheng C E 1990 Performance of a ten liter electron avalanche discharge XeCl laser device *Appl. Phys. B* **50** 415–23.
66. Sentis M L, Delaporte P, Forestier B M and Fontaine B L 1991 Design and characteristics of high pulse repetition rate and high average power excimer laser systems *IEEE J. Quantum Electron.* **27** 2332–9.
67. Timmermans J C M 1995 Double discharge XeCl laser *PhD Dissertation* (University of Twente, Enschede, The Netherlands).
68. Witteman W J, van Goor F A, Ekelmans G B, Trentelman M and Ernst G J 1990 Design studies of a high pulse repetition rate excimer Eurolaser *High Power Gas Lasers (SPIE 1225)* ed P V Avizonis, C Freed, J J Kim and F K Tittel (Bellingham, WA: SPIE) pp 132–41.
69. Ernst G J 1984 Uniform field electrodes with minimum width *Opt. Commun.* **49** 275–77.
70. van Goor F A and Witteman W J 1994 High average power XeCl laser with x ray pre-ionization and spiker sustainer excitation *High-Power Gas and Solid State Lasers (SPIE 2206)* (Bellingham, WA: SPIE) pp 30–40.
71. Murray J R and Powell H T 1976 KCl laser oscillation at 222 nm *Appl. Phys. Lett.* **29** 252.
72. Eden J G and Searles S K 1976 Observation of stimulated emission of KrCl *Appl. Phys. Lett.* **29** 350–2.
73. Panchenko A N and Tarasenko V F 1995 Maximum performance of discharge pumped exciplex laser at λ = 222 nm *IEEE J. Quantum Electron.* **31** 1231–6.
74. Hueber J M, Fontaine B L, Bernard N, Forestier B M and Sentis M L 1992 Long pulse KrCl excimer laser at 222 nm *Appl Phys. Lett.* **61** 2269–71.
75. Boichenko A M, Derzhiev V I, Zhidkov A G and Yakovlenko S I 1992 Kinetic model of an ArF laser *Sov. J. Quantum Electron.* **22** 444–8.
76. Lo D, Shchedrin AI and Ryabtsev A V 1996 The upper energy limit of a self sustained discharge pumped ArF laser *J. Phys. D: Appl. Phys.* **29** 43–9.
77. Suda A, Obara M and Noguchi A 1986 Performance characteristics of the ArF excimer laser using a low pressure argon-rich mixture *J. Appl. Phys.* **60** 3791–3.
78. Mandle A 1986 ArF short pulse extraction studies *J. Appl. Phys.* **59** 1435–45.
79. Klementov A D, Morozov N V and Sergeev P B 1986 Electron beam excited ArF laser *Sov. J. Quantum Electron.* **16** 1139–42.
80. Maeda M, Nishitarumizu T and Miyazoe Y 1979 Formation and quenching of excimers in low pressure rare gas halogen mixtures by e-beam excitation *Japan. J. Appl. Phys.* **18** 439–45.
81. Akashi H, Sakai Y and Tagashira H 1994 Modelling of a self sustained discharge excited ArF excimer laser *J. Phys. D: Appl. Phys.* **27** 1097–106.
82. Akashi H, Sakai Y and Tagashira H 1995 Modelling of a self sustained discharge excited ArF excimer laser: the influence of photo-ionization and photodetachment by laser light on the discharge development *J. Phys. D: Appl. Phys.* **28** 445–51.
83. Nagai S, Sakai M, Furuhashi H, Kono A, Goto T and Uchida Y 1998 Effects of F^- ions and F_2 molecules on the oscillation process of a discharge pumped ArF excimer laser *IEEE J. Quantum Electron.* **34** 40–6.
84. Feenstra L 1999 On the long pulse operation of a discharge pumped ArF excimer laser *PhD Dissertation* (University of Twente, Enschede, The Netherlands).
85. Ohwa M and Obara M 1988 Theoretical evaluation of the buffer gas effects for a self sustained discharge ArF laser *J. Appl. Phys.* **63** 1306–12.
86. Nagai S, Furuhashi H, Uchida Y, Yamada J, Kono A and Goto T 1995 Formation dynamics of excited atoms in an ArF laser using He and Ne buffer gases *J. Appl. Phys.* **77** 2906–11.
87. Saito T, Ito S and Tada A 1996 Long lifetime operation of an ArF excimer laser *Appl. Phys. B* **63** 229–35.
88. Andrew J E, Dyer P E and Roebuck P J 1984 Improved energy output from discharge pumped ArF and KrCl lasers *Opt. Commun.* **49** 189–94.
89. Miyazaki K, Hasama T, Yamada K, Fukatsu T, Eura T and Sato T 1986 Efficiency of a capacitor transfer type discharge excimer laser with automatic pre-ionization *J. Appl. Phys.* **60** 2721–8.
90. Zhupikov A A and Razhev A M 1997 Excimer ArF laser with an output energy of 0.5 J and He buffer gas *Sov. J. Quantum Electron.* **27** 665–9.
91. Mandle A 1992 XeF(B-X) long pulse length laser studies *J. Appl. Phys.* **71** 1630–7.
92. Nishida N, Takashima T, Tittel F K, Kannari F and Obara M 1990 Theoretical evaluation of a short pulse electron beam excited XeF(B-X) laser using a low pressure, room temperature Ar/Xe/F_2 mixture *J. Appl. Phys.* **67** 3932–40.
93. Burnham R, Harris N W and Djeu N 1976 Xenon fluoride laser excitation by transverse electric discharge *Appl. Phys. Lett.* **28** 86–7.
94. Sarjeant W J, Alcock A J and Leopold K E 1977 A scalable multi-atmosphere high power XeF laser *Appl. Phys. Lett.* **30** 635–7.
95. Nighan W L 1978 Influence of electron F_2 collisions in rare gas halide laser discharges *Appl. Phys. Lett.* **32** 297–300.
96. Mei Q C, Peters P J M, Trentelman M and Witteman W J 1995 Optimisation of the pulse duration of a discharge pumped XeF(B → X) excimer laser *Appl. Phys. B* **60** 553–6.
97. Tellinghuisen J *Applied Atomic Collision Physics* vol 3, ed E C McDaniel and W L Nighan (London: Academic).

98. Sze R C, Sakai T, Vannini M and Sentis M L 1991 Time resolved studies of the C-A transition in avalanche discharges: fluorescence and gain-loss studies *IEEE J. Quantum Electron.* **27** 77–89.
99. Kumagai H and Obara M 1989 Output energy enhancement of discharge pumped XeF(B to X) lasers with the two component halogen donor mixtures *IEEE J. Quantum Electron.* **25** 1874–8.
100. Peters P J M, Trentelman M, Mei Q C and Witteman W J 1994 Gas discharge XeF(B → X) laser with high specific output power *Appl. Phys. B* **59** 533–5.
101. Trentelman M, Peters P J M, Mei Q C and Witteman W J 1995 Gas discharge XeF(B → X) laser excited by a pre-pulse main pulse circuit with magnetic switching *J. Opt. Soc. Am. B* **12** 2494–501.
102. Ernst W E and Tittel F K 1979 A new electron beam pumped XeF laser at 486 nm *Appl. Phys. Lett.* **35** 36–7.
103. Cambell J D, Fisher C H and Center R E 1980 Observations of gain and laser oscillation in the blue–green during direct pumping of XeF by microsecond electron beam pulse *Appl. Phys. Lett.* **37** 348–50.
104. Nighan W L, Tittel F K, Wilson W L, Nishida N, Zhu Y and Sauerbrey R 1984 Synthesis of rare gas halide mixtures resulting in efficient XeF(C → A) laser oscillation *Appl. Phys. Lett.* **45** 45–7.
105. Liegel J, Tittel F K and Wilson W L Jr 1981 Continuous broadband tuning of an electron beam pumped XeF(C → A) laser *Appl. Phys. Lett.* **39** 369–71.
106. Bischel W K, Ekstrom D J, Walker H C Jr and Tilton R A 1981 Photolytically pumped XeF(C-A) laser studies *J. Appl. Phys.* **52** 4429–34.
107. Mandle A and Litzenberger L N 1988 Efficient long pulse XeF(A → C) laser at moderate electron beam pump rate *Appl. Phys. Lett.* **53** 1690–2.
108. Hofmann Th, Yamaguchi S, Dane C B, Wilson W L Jr, Sauerbrey R, Tittel F K, Rubino R A and Nighan W L 1991 Wavelength agile operation of an injection controlled XeF(C → A) laser system *Appl. Phys. Lett.* **58** 565–7.
109. Peters P J M, Bastiaens H M J, Witteman W J, Sauerbrey R, Dane C B and Tittel F K 1990 Efficient XeF(C → A) laser excited by a coaxial electron beam at intermediate pumping rates *IEEE J. Quantum Electron.* **26** 1569–73.
110. Fisher C H, Center R E, Mullaney G L and McDaniel J P 1979 A 490 nm XeF electric discharge laser *Appl. Phys. Lett.* **35** 26–8.
111. Burnham R 1979 A discharge pumped laser on the C → A transition of XeF *Appl. Phys. Lett.* **35** 48–50.
112. Cheng Yong-kang, Yang Shao-peng, Wang Min-xiao and Ma Zu-guang 1993 Free running XeF(C-A) lasing at 2.2 atm in a commercial discharge excimer laser *Appl. Phys. Lett.* **62** 4–6.
113. Fisher C H, Center R E, Mullaney G J and McDaniel J P 1979 Multipass amplification and tuning of the blue-green XeF(C → A) laser *Appl. Phys. Lett.* **35** 901–3.
114. Voges H and Marowsky G 1988 Injection control of a discharge excited XeF(C → A) laser *IEEE J. Quantum Electron.* **24** 827–32.
115. Bischel W K, Nakana H H, Eckstrom D J, Mill R M, Huestis D L and Lorents D C 1979 A new blue–green excimer laser in XeF *Appl. Phys. Lett.* **34** 565–7.
116. Basov N G, Zuev V S, Kanaev A V, Mikheev L D and Stavrovskii D B 1979 Laser action due to the bound free C(3/2)-A(3/2) transition in the XeF molecule formed by photodissociation of XeF_2 *Sov. J. Quantum Electron.* **9** 629–32.
117. Eckstrom D J and Walker H C 1982 Multi-joule performance of the photolytically pumped XeF(C → A) laser *IEEE J Quantum Electron.* **18** 176–81.
118. Zuev V S, Mikheev L D and Stavrovskii D B 1984 Efficiency of an optically pumped XeF laser *Sov. J. Quantum Electron.* **14** 1174–8.
119. Zuev V S, Kashnikov G N, Kozlov N P, Mamaev S B, Orlov V K, Protasov Yu S and Sorokin V A 1986 Characteristics of an XeF(C-A) laser emitting visible light as a result of optical pumping by surface discharge radiation *Sov. J. Quantum Electron.* **16** 1665–7.
120. Zuev V S, Kashnikov G N, Kirilenko V V, Mamaev S B, Sorokin V A and Sukhorukov V F 1989 Photodissociation XeF laser emitting visible and ultraviolet radiation when pumped with radiation from a sectioned surface discharge *Sov. J. Quantum Electron.* **19** 748.
121. Watanaba K, Kashiwabara S and Fujimoto R 1987 Development of a formed ferrite flash plasma light source for gas laser applications *Appl. Phys. Lett.* **50** 629–31.
122. Gross R W F, Schneider L E and Amimoto S T 1988 XeF laser pumped by high-power sliding discharges *Appl. Phys. Lett.* **53** 2365–7.
123. Mitko S V, van Goor F A, Witteman W J and Ochkin V N 1996 Optical pumping and ferrite flash discharges *Proc. NATO Advanced Research Workshop ARW 950443 on Gas Lasers—Recent Developments and Future Prospects (Moscow, Russia, July 2–5, 1995) (Kluwer Academic Publishers Series 3: High Technology 10)* (Dordrecht: Kluwer Academic) p 185.
124. Kovacs M A and Ultee C J 1970 Visible laser action in fluorine *Appl. Phys. Lett.* **17** 39–40.
125. Huestis D L, Hill R M, Nakano H H and Lorents D C 1978 Quenching of Ne, F and F_2 in Ne/Xe/NF_3 and Ne/Xe/F_2 mixtures *J. Chem. Phys.* **69** 5133–9.
126. Bastiaens H M J, van Dam B M C, Peters P J M and Witteman W J 1993 Small signal gain measurements in an electron beam pumped F_2 laser *Appl. Phys. Lett.* **63** 438–40.
127. Bastiaens H M J, Peters P J M and Witteman W J 1997 *Eleventh Int. Symp. on Gas Flow and Chemical Lasers (SPIE 3092)* ed H J Baker (Bellingham, WA: SPIE) pp 374–7.
128. Kakehata M, Uematsu T, Kannari F and Obara M 1991 Efficient characterization of vacuum ultraviolet molecular fluorine laser (157 nm) excited by an intense electric discharge *IEEE J. Quantum Electron.* **27** 2456–64.
129. Yamada K, Miyazaki K, Hasama T and Sato T 1989 High power discharge pumped F_2 molecular laser *Appl. Phys. Lett.* **54** 597–9.
130. Lankhorst F T J L, Bastiaens H M J, Peters P J M and Witteman W J 1993 High specific laser output energy at 157 nm from an electron beam pumped He–Ne–F_2 gas mixture *Appl. Phys. Lett.* **63** 2869–71.
131. Bastiaens H M J 2000 On the long pulse operation of the molecular fluorine laser *PhD Dissertation* (University of Twente, Enschede, The Netherlands).

132. Rokni M and Jacob J H 1982 *Applied Atomic Collision Physics: Gas Lasers* vol 3 ed H S W Massey, E W McDaniel and B Bederson (New York: Academic) p 274.
133. Asinovskii E I, Vasilyak L M and Markovets V V 1983 Wave breakdown of gas filled gaps *High Temperature* **21** 293–305.
134. Diegelmann M, Hohla K, Rebentrost F and Kompa K L 1982 Diatomic interhalogen laser molecules: Fluorescence spectroscopy and reaction kinetics *J. Chem. Phys.* **76** 1233–47.
135. Ishchenko V N, Kochubei S A and Razhev A M 1986 High power efficient vacuum ultraviolet F_2 laser excited by an electric discharge *Sov. J. Quantum Electron.* **16** 707–9.
136. Woodworth J R and Rice J K 1978 An efficient, high power F_2 laser near 157 nm *J. Chem. Phys.* **69** 2500–4.
137. Kakehata M, Hashimoto E, Kannari F and Obara M 1990 High specific output energy operation of a vacuum ultraviolet molecular fluorine laser excited at 66 MW cm^3 by an electric discharge *Appl. Phys. Lett.* **56** 2599–601.
138. Kakehata M, Yang C H, Ueno Y and Kannari F 1993 Output characteristic of a discharge pumped F_2 laser (157 nm) with an injection seeded unstable resonator *J. Appl. Phys.* **74** 2241–6.
139. Waynant R W 1978 Inert gas halide VUV lasers *Sov. J. Quantum Electron.* **8** 1002–4.
140. Waynant R W 1977 A discharge pumped ArCl superfluorescence laser at 175 nm *Appl. Phys. Lett.* **30** 234–5.
141. Rice J K, Hays A K and Woodworth J K 1977 VUV emissions from mixtures of F_2 and the nobel gases. A molecular F_2 laser at 157.5 nm *Appl. Phys. Lett.* **31** 31–3.
142. Tittel F K, Marowsky G, Wilson W L and Smayling M C 1981 Electron beam pumped broadband diatomic and triatomic excimer lasers *IEEE J. Quantum Electron.* **17** 2268–81.
143. Tittel F K, Wilson W L, Stickel R E, Marowsky G and Ernst W E 1980 A triatomic Xe_2Cl excimer laser in the visible *Appl. Phys. Lett.* **36** 405–7.
144. Tittel F K, Marowsky G, Smayling M C and Wilson W L 1980 Blue laser action by rare gas halide trimer Kr_2F *Appl. Phys. Lett.* **37** 862–4.
145. Heard H G 1963 Ultraviolet gas laser at room temperature *Nature* **220** 667.
146. Mathias L E S and Parker J T 1963 Stimulated emission in the band spectrum of nitrogen *Appl. Phys. Lett.* **3** 16–18.
147. Searles S K and Hart G A 1974 Laser emission at 357.7 and 380.5 nm in electron beam pumped Ar–N_2 mixtures *Appl. Phys. Lett.* **25** 624–6.
148. Bychkov Yu I, Losev V F, Mesyats G A and Tarasenko V F 1977 Stimulated emission of three lines from an N_2+Ar laser *Sov. J. Quantum Electron.* **7** 789–90.
149. Tarasenko V F and Bychkov Yu I 1973 Nitrogen laser with a transverse discharge *Instrum. Exp. Techniques* **16** 221–2.
150. Junichi I, Kiichiro K and Yoshitake K 1975 Intense laser emission on 337.7 nm using N_2-SF_6 mixtures in a TE N_2 laser *Appl. Phys. Lett.* **27** 503–4.
151. Losev V F and Tarasenko V F 1976 Effect of SF_6 on characteristics of the N_2 laser *Sov. Phys. Technical Phys.* **21** 1295–7.
152. Chou M S and Zavarzkas G 1981 Long pulse N_2 UV lasers at 357.7, 380.5 and 405.9 nm in N_2–Ar–Ne–He mixture *IEEE J. Quantum Electron.* **17** 77–81.
153. Derzhiev V I, Losev V F and Skakun V S 1986 Effect of neon and helium impurities on the lasing energy of an Ar–N_2 laser *Opt. Spectrosc.* **60** 499–500.
154. Bazhulin P A, Knyazev I N and Petrash G G 1965 *Sov. Phys.–JETP* **21** 649.
155. Hodgson R T 1970 *Phys. Rev. Lett.* **25** 494.
156. Hodgson R T and Dreyfus R W 1972 Vacuum-UV laser action observed in H_2 Werner bands *Phys. Rev. Lett.* **28** 536–9.
157. Waynant R W, Shipman J D, Elton R C and Ali A W 1970 Vacuum ultraviolet laser emission from molecular hydrogen *Appl. Phys. Lett.* **17** 383–4.
158. Goldsmith J E M and Knyazev I N 1977 A simple compact high repetition rate hydrogen VUV laser for scientific applications *J. Appl. Phys.* **48** 4912–21.
159. Waynant R W 1972 Observations of gain by stimulated emission in the Werner band of molecular hydrogen *Phys. Rev. Lett.* **28** 533–5.
160. Waynant R W 1971 A travelling wave vacuum ultraviolet laser *Proc. Technical Program, Electro-Optical Systems Design Conference* (Anaheim) pp 1–5.
161. Dreyfus R W and Hodgson R T 1974 Molecular hydrogen laser: 109.8–161.3 nm *Phys. Rev. A* **9** 2635–48.
162. Shipman J D 1967 Travelling wave excitation of high power gas lasers *Appl. Phys. Lett.* **10** 3–4.
163. Schwab A J and Hollinger F W 1976 Compact high power N_2 laser: circuit theory and design *IEEE J. Quantum Electron.* **12** 183–8.
164. Wang C P 1976 Simple fast discharge device for high power pulsed lasers *Rev. Sci. Instrum.* **47** 92–5.

28

High-Brightness Excimer Lasers and Extreme Conditions They Produce

Sándor Szatmári

CONTENTS

28.1 Introduction 403
  28.1.1 Main Features of Excimer Molecules 404
  28.1.2 Architecture of Short Wavelength, High-Brightness Systems 405
  28.1.3 Brief History of Short-Pulse KrF Excimers 405
28.2 Energy Extraction Issues 406
  28.2.1 Effect of Nonsaturable Absorption 406
  28.2.2 Off-Axis Amplification 407
  28.2.3 Consequences of the Limited Storage Time 408
  28.2.4 Optical Multiplexing 408
  28.2.5 Picosecond Gain Dynamics of Excimers 408
28.3 Contrast Issues 410
  28.3.1 Plasma Mirror 411
  28.3.2 Non-linear Fourier-Filter 411
28.4 Amplifier Requirements, Design Considerations 412
28.5 Experimental Realizations 413
28.6 Outlook 414
References 416

28.1 Introduction

Lasers are outstanding tools to investigate materials in a large scale, spanning from material research of nanoparticles to model astrophysical phenomena. Laser research—including its application in micro- and macro processing of materials, life sciences, medicine and communication—have long become an indispensable and prominent part of research policy.

Laser–matter interactions in the vicinity of 10^{20} W cm^{-2}, for which the internal Coulomb-field of atoms can already be neglected with the electrons gaining relativistic velocities, represent a milestone in material research. The study of such interactions and the generation of the necessary intensities are in the frontiers of modern physics.

Lasers are known as light sources where the energy carried in the beam can efficiently be concentrated both spatially and temporally. Temporal and spatial resolution of physical systems/processes—monitored by electromagnetic radiation—scales with the minimum achievable spatial width of the pulse in the direction of propagation ($c{\cdot}\Delta\tau$) and perpendicular to that (d). The best concentration—corresponding to the equality in equations of $c \cdot \Delta\tau \geq \dfrac{\lambda}{\Delta\lambda}\lambda$ and $d \geq \lambda \cdot F$ (where F is the F-number of focusing)—can only be carried out, if the pulse has optimum quality (limited by the uncertainty principle and diffraction). This kind of quality of the pulse/beam is expressed by the so-called brightness (B), which is the intensity radiated in a unit solid angle and therefore gives the achievable intensity by an $F = 1$ focusing. Considering the spectral dependence of B ($B \sim \nu^3{\cdot}\Delta\nu/\nu$)—i.e. that for a fixed normalized bandwidth $\Delta\lambda/\lambda$ ($= \Delta\nu/\nu$)—the temporal compression of a pulse is theoretically proportional to the frequency (ν) and the spatial concentration scales with the square of the frequency—the maximum intensity (I) that can be achieved by a light pulse of a certain energy E scales with the third power of the frequency, as $I \sim E{\cdot}\nu^3$. In this respect, short-pulse UltraViolet (UV) excimer lasers have a unique potential. They offer high photon energy, thus significantly extending the energy range of interactions. This also decreases the necessary order of non-linear interactions for a given energy gap. UV excimer gas lasers (Rhodes 1979) have the advantage—based on their short wavelength and negligible optical distortion—that considerably high focused intensities ($I > 10^{19}$ W cm^{-2}) can be reached even with medium output pulse powers. Another fundamental advantage is a much better intensity contrast (signal-to-noise ratio) of the pulses. In high-field physics experiments, where the light–matter interaction is studied at relativistic intensities, a background radiation (noise) of small fraction of the peak intensity would already generate a hot plasma, thus preventing the possibility of making such experiments under controlled conditions.

Short-pulse, short-wavelength KrF lasers are preferential pumps for the generation of short X-ray pulses. Because of the pronounced absorption and reduced non-linearities in the plasma, the conversion of the short-wavelength radiation to X-rays (e.g. to the water window) can be very high.

Besides the above-detailed advantages/potentials of UV excimer lasers—based on the given frequency scaling of the temporal/spatial resolution and intensity—this scaling is only true as long as the pulse has large bandwidth and the maximum quality allowed by the uncertainty principle and diffraction, i.e. the pulse is transform- and diffraction-limited. However, it becomes more difficult to reach these limits as the wavelength becomes shorter. The basic reason for that lies in the well-known frequency scaling of the Einstein *A* and *B* coefficients, as $A \sim B\,\nu^3$. This is one of reasons, while in the last decades a significant part of the most important scientific breakthroughs in optics, especially in the field of the generation and application of ultrashort laser pulses were connected to solid-state laser systems, mainly to Ti:Sapphire lasers. This is the laser—having an optimum $\Delta\nu/\nu$ approaching 1/3—which allowed the generation of the shortest optical pulses and opened the attosecond regime. Also, this kind of laser—having a high saturation energy density (several J cm^{-2})—is capable to give very high peak powers. The short-pulse duration and the extremely high peak power make it possible to study laser–matter interaction in the presence of an extremely high electric field with femtosecond resolution. This, however, also gives way to obtain coherent radiation at even shorter wavelengths.

Although the first energetic, high-quality KrF excimer (Rhodes 1979) laser systems of nanosecond pulse durations were built long time ago, short-pulse, high-brightness excimer technology was underdeveloped for a long period. The other consequence of the third-order frequency scaling of *A* is the fast decrease of the excited-state lifetime as the wavelength is getting shorter. In three-level systems, this necessitates fast/intense pumping sources/techniques to compete with the fast spontaneous relaxation, when population inversion is to be reached. This stringent requirement is significantly relaxed by the use of four-level schemes (see Figure 28.1a). These schemes are ideally suited for pumping short-wavelength lasers, where pumping must span over large energy differences and spontaneous relaxation is fast. In these schemes, the lower lasing level is kept empty by a fast relaxation to the ground state, therefore almost "complete" population inversion is achieved/maintained even when pumping can only raise small fraction of the total population to the upper lasing state.

Similarly to three-level systems, pumping is realized through a state (or states) lying above the upper lasing level. If this level is broadened, not only monoenergetic (monochromatic) pumping is tolerated but also the pumping cycle accepts a broad energy range of excitation. This has great importance in case of electron beam pumping and discharge pumping, both are commonly used for excimers. It can be read from Figure 28.1a that this scheme is very efficient; even in case of slow pumping conditions, practically all the excited particles can be forced to stimulated emission if a quasi-continuous stimulating field is maintained during the pumping process, whose strength (*w*) can dominate the stimulated emission over the spontaneous one ($Bw \gg A$).

28.1.1 Main Features of Excimer Molecules

In the UV, an ideal four-level system can be realized by excimers. Excimers are "short living" molecules which only exist in the excited state; their potential curve is only bound in the excited state but repulsive in the ground state. The potential curve of such a molecule is shown in Figure 28.1b. The correlation between the excimer potential curves and the four-level system can easily be carried out by comparing the two figures: the finite relaxation times to the upper lasing level (Trelax) and from the lower lasing level (tdis). Both can have significant contribution to the efficiency (and contrast) of short-pulse amplification (see following sections). The first one limits the minimum effective pumping time (Teff), resulting in—with regard to the given value of the excited-state lifetime (τ)—the ratio of the accessible molecules by the short signal pulse. The finite value of tdis can turn this amplifying medium into a less efficient three-level system as the intense signal pulse can transiently populate the lower lasing level, leading to considerable reabsorption.

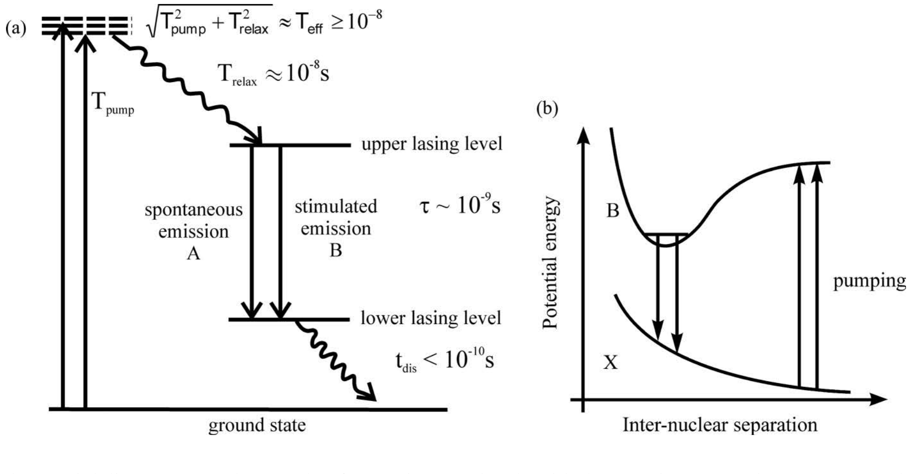

FIGURE 28.1 Typical potential diagram (a) and curve (b) of an excimer molecule with the most important time constants relevant to KrF excimer.

28.1.2 Architecture of Short Wavelength, High-Brightness Systems

Due to the “unfavourable” scaling of the A and B coefficients the gradual evolution of the temporal, spatial and spectral quality of the pulse through the many roundtrips in the laser cavity is not possible for the presently available UV-lasing materials. The only way to convert the optical energy of an UV-emitting material into a short-wavelength electromagnetic field of the highest possible spatial and temporal quality is optical amplification. Even this can only be realized with stringent limitations. These are the reasons why short-wavelength, high-brightness laser systems are generally dual-wavelength systems.

In dual-wavelength systems the high-quality pulses are generated in the long-wavelength region and shifted into the UV through frequency upconversion. UV gain modules are then used as optical amplifiers for the amplification of the frequency-converted pulses.

Such a scheme is shown in Figure 28.2a. After frequency conversion (usually frequency doubling or tripling), the short pulse is amplified in UV gain modules (Schwarzenbach 1986, Dick et al. 1987, Szatmári and Schäfer 1988, Békési et al. 2002, Alekseev et al., 2013), as shown schematically in the Figure 28.2a. This approach provides a great ability to control precisely the pulse parameters and therefore the characteristics of the system output. Moreover, the frequency converter can efficiently decouple the temporal noise of the long-wavelength front end and using a special technique—called as active spatial filtering (Szatmári et al. 1997)—both the directional and spectral properties of the main pulse can efficiently be controlled. The basic idea behind this method is that the frequency converter is positioned at the Fourier-plane of the beam, where it is mainly the more intense zeroth order which is efficiently converted, therefore the high-order spatial frequencies are removed from the beam. In this way, both the temporal and the spatial properties of the main pulse are reset in the “middle” of the system.

Using a pulsed dye laser, the KrF 248.5 nm wavelength can easily be reached through efficient frequency doubling (Szatmári and Schäfer 1988). Since this wavelength is also accessible—through frequency tripling of the widely used Ti:Sapphire wavelength—a hybrid Ti:Sapphire-excimer laser system has a potential for simultaneous generation of synchronized high-power UV and IR pulses, thus making pump-probe experiments with the extended wavelength range possible. The corresponding scheme of such a combined system is shown in Figure 28.2b.

28.1.3 Brief History of Short-Pulse KrF Excimers

KrF excimer is a high gain medium and best suited for short-pulse amplification in the UV (Szatmári et al. 2007). The KrF medium has a relatively narrow spectral bandwidth ($\Delta\lambda/\lambda \approx 1/300$), which limits the minimum achievable pulse duration. The low saturation energy density ($2\,\text{mJ cm}^{-2}$) compared to solid-state lasers necessitates larger cross section for the same energy, on the other hand, ensures the use of direct amplification of short pulses. The power amplification required to surpass the TW regime can be accomplished in the UV with large aperture electron beam-pumped (10–30 cm diameter) excimer amplifiers. This approach generally leads to bulky designs, which requires extremely precise control of the quality of the propagating beam to maintain the phase quality and to obtain high-brightness output pulses. Discharge pumping offers a more practical way for the realization of short-pulse excimer gain modules in a limited ($\sim 100\,\text{cm}^2$) aperture range. The low density gaseous media provides minimum phase-front distortions. As a consequence of the shorter wavelength, in case of proper phase-front control, short-pulse KrF excimer laser systems can reach $>10^{19}$ W cm^{-2} focused intensity (or $>10^{21}$ Wcm$^{-2}\cdot$sterad^{-1} brightness) despite the moderate level of output power (Borisov et al. 2016, Békési et al. 2002, Szatmári et al. 1996).

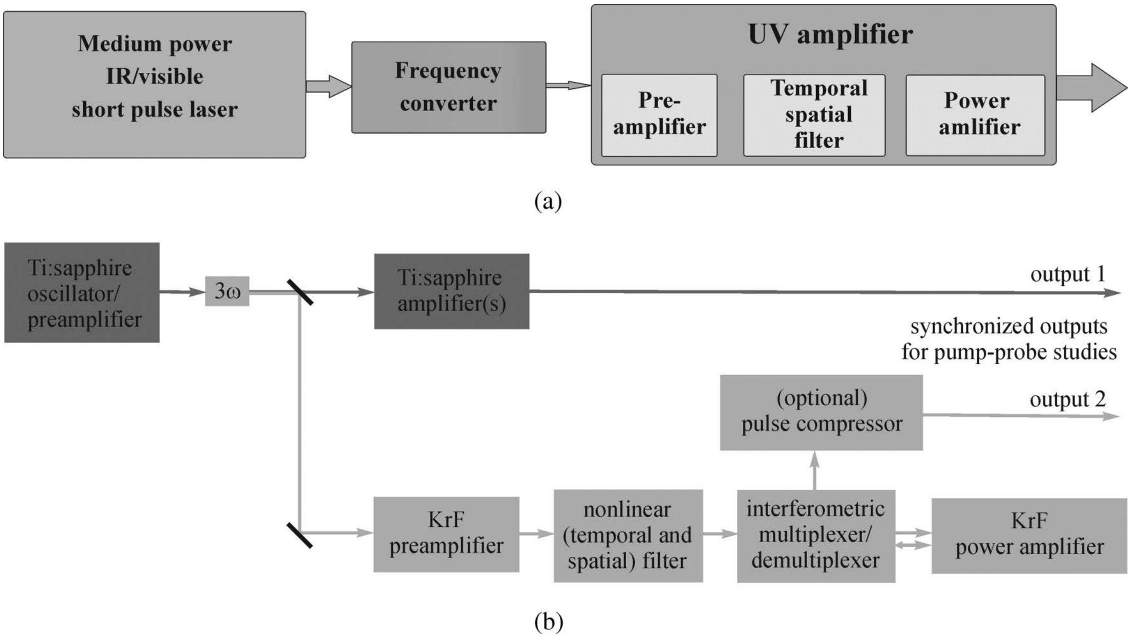

FIGURE 28.2 Possible approaches for the generation of high-brightness UV pulses on the TW level.

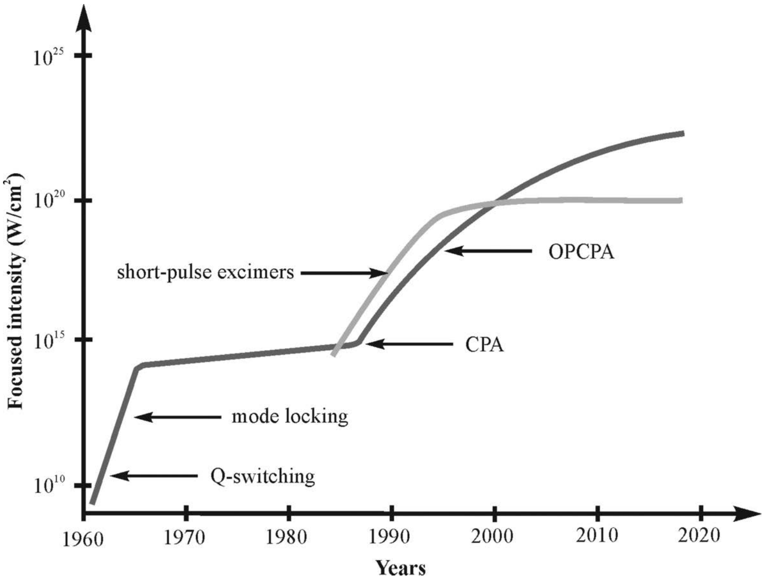

FIGURE 28.3 Laser intensity versus the years.

As a consequence of direct amplification of short pulses in excimers, relatively high intensity contrast can easily be reached, where the Amplified Spontaneous Emission (ASE)—as the only source of the noise—is homogeneously distributed both in the temporal and spatial domains.

Figure 28.3 shows the temporal evolution of the focused intensity achieved by lasers in the last decades. Fast rise in the curves can clearly be attributed to the invention of new techniques [like Q-switching, mode locking, chirped-pulse amplification (CPA)] or to the introduction of dual-wavelength short-pulse UV excimer lasers.

Up to now, the main figure of merit for comparison of large laser systems was the energy, peak-power and the focused intensity. Recently, high intensity laser–matter interaction experiments showed the pronounced importance of the temporal and spatial contrast of the pulses. This issue makes short-pulse excimers even more competitive.

28.2 Energy Extraction Issues

28.2.1 Effect of Nonsaturable Absorption

It is known from former studies (Szatmári and Schäfer 1987, Zhao et al., 1988) that KrF is a superior amplifying medium for short-pulse amplification compared to other excimers. Even for this medium optimum energy extraction, equal amplification for a short signal pulse and for the (long) ASE cannot be realized for several reasons. One reason is associated with the fact that KrF is an amplifying medium exhibiting considerable nonsaturable absorption (Tilleman and Jacob 1987. Szatmári et al. 2007). For such a medium, both the extraction efficiency and the ratio of the gain coefficients for signal and noise deteriorates rapidly with increasing energy density. This feature can be followed in Figure 28.4 (Almási et. al. 1992, Szatmári et al. 2007), where the dependence of the local efficiency

$$\eta(\varepsilon) = \frac{1}{g_0}\frac{\mathrm{d}\varepsilon}{\mathrm{d}z}$$

and of the contrast coefficient (the ratio of the effective gain coefficient g_{eff} for an "energetic" signal and for a "weak" noise)

$$c = \frac{g_{\text{eff}}}{g_0 - \alpha}$$

are shown as a function of the normalized energy density (ε^*), where g_0 is the small-signal gain coefficient, α is the absorption coefficient, and L is the length of the medium.

$$g_{\text{eff}} = \lim_{\Delta L \to 0} \ln\left(E_{\text{out}}/E_{\text{in}}\right)/\Delta L$$

$$\varepsilon^* = \varepsilon / \varepsilon_{\text{sat}}$$

It is seen from these curves that both requirements can never be fulfilled at the same time, one can only have a trade-off, when operating the amplifier close to the saturation energy density. In Figure 28.4, this condition is marked by X for a preamplifier, where the energy density is $\varepsilon_x \approx 1.1\varepsilon_{\text{sat}}$. In power amplifiers, extraction efficiency plays a more important role than gain contrast. Here, we set the optimum at $\varepsilon_y \approx 2.2\varepsilon_{\text{sat}}$, marked by Y in Figure 28.4 (Almási et al. 1992). This optimized operation can be best attained by an amplifier for which the overall increase of the local energy density is limited, corresponding to a limited gain-length product of $gL \leq 2$. This sets L to ~10 cm for a typical discharge-pumped amplifier, where $g_0 = 0.2\,\text{cm}^{-1}$ (Szatmári and Schäfer 1987). It is seen that from the optical point of view a "short" amplifier is ideal, on the other hand, the cross section is limited by the fast electric pump circuit. These requirements would certainly limit the active volume and therefore the maximum stored energy (linearly scaling with the volume) unless a transformation is found which properly converts the "geometrical" cross section

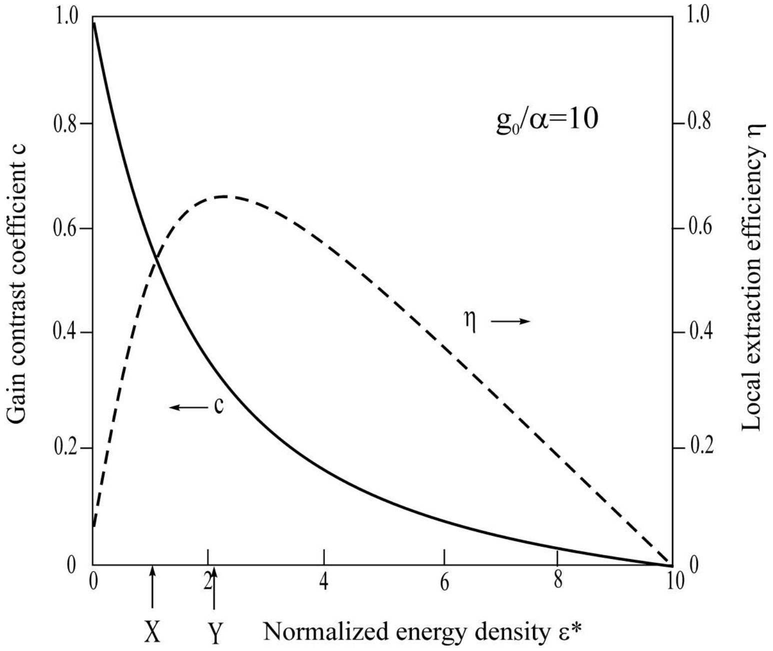

FIGURE 28.4 Local extraction efficiency η (dashed line) and gain contrast coefficient c (solid line) as a function of the normalized energy density in a KrF amplifier. The optimum operation with regard to both efficiency and contrast for a preamplifier and for a final amplifier is marked by X and Y, respectively.

and length of the amplifier into new ones, which are seen by the pulse to be amplified.

28.2.2 Off-Axis Amplification

Figure 28.5a shows a simple solution of the problem, where the effective cross section of the pencil-like discharge-pumped excimer amplifier is increased by tilting the input beam with respect to the geometrical axis of the amplifier (Szatmári et al. 1991, Almási et al. 1992). This off-axis arrangement is also capable of decreasing the *gL* product and of solving the inherent inhomogeneity problem of these amplifiers, caused by the inhomogeneous transversal distribution of the deposited energy in the discharge. In the off-axis mode, it is the more homogeneous longitudinal distribution, which is seen by the pulse, then mainly determines the intensity homogeneity of the output beam.

Another interesting feature of the off-axis amplification scheme is that it allows the optimization of the operational conditions for multiple passes using the same amplifier (Szatmári et al. 1991, Almási et al. 1992). A practical example for a three-pass arrangement is shown in Figure 28.5b, where the increasing beam diameter is always optimally matched to the increased effective cross section of the amplifier by proper choice of the divergence angle of the beam and the off-axis angles of the different passes. This makes it possible to

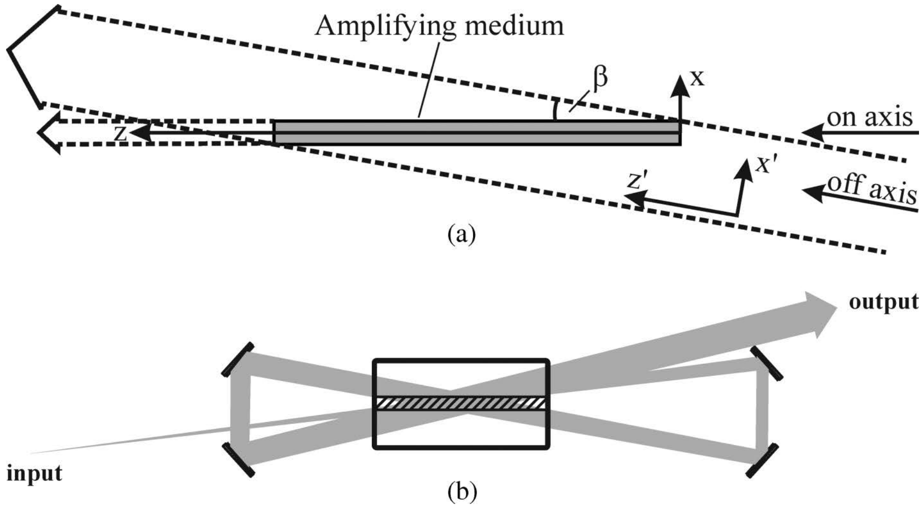

FIGURE 28.5 Illustration of the off-axis amplification geometry (a), realization of the three-pass off-axis amplification using a divergent signal beam (b).

optimally extract the stored energy of the same amplifier in limited subsequent steps. Since the ideal number of the successive amplification steps in KrF amplifiers is significantly more (see later), the off-axis amplification scheme only relaxes but does not solve the problem of energy extraction by a single short pulse.

28.2.3 Consequences of the Limited Storage Time

In the former part of this paper, it is pointed out that excimers provide an ideal four-level system for efficient laser operation in the UV. This however, is only true for long-pulse amplification; when the duration of the pulse is comparable to that of pumping. Considering the typical effective pumping times (see data in Figure 28.1a), this necessitates pulse durations ranging from 10 to 100 ns.

The bandwidth of the lasing transitions of most excimers allows the amplification of subpicosecond pulses (Szatmári and Schäfer 1988, Dick et al. 1987, Zhao et al. 1988). In such cases, the efficiency—the number of accessible molecules—is significantly decreased. It can be read from Figure 28.1a that—due to the short (several nanosecond) storage time (τ) of the upper lasing state referred to the gain window T (or to $T_{\text{eff}} \approx T \approx$ several 10 ns possible pumping times)—only small fractions of the pumped molecules are available on the upper laser level at the instant of the passage of the short pulse. For this reason, only a small fraction of the energy represented by all the excited molecules (E_{tot}) is available at a certain instant. This energy—called as momentarily stored energy ($E_{\text{mstored}} = \varepsilon_{\text{sat}} \cdot gLA$, where A is the cross section of the active volume)—is accessible by the short pulse and is the most important figure of merit of a short-pulse excimer amplifier. As a consequence, in excimer amplifiers—due to the $T/\tau \gg 1$ relation—successive replenishment of the momentarily stored energy is the only way to have access to the whole stored energy E_{tot} (Rhodes 1979, McIntyre and Rhodes 1991, Szatmári et al. 2007, Szatmári and Simon 1993), which is given roughly by $E_{\text{tot}} = E_{\text{mstored}} T/\tau$. Since for KrF $T/\tau \geq 10$ for most pumping conditions, significant increase of the extractable energy is expected by successive depletion of the gain (Szatmári et al. 2007). This can either be performed by multiple-pass amplification of a single pulse (Glownia et al. 1986, Schwarzenbach et al. 1986, Szatmári et al. 1987, Barr et al. 1988, Szatmári and Schäfer 1988, Watanabe et al. 1988) or by optical multiplexing (Watanabe et al. 1990, Szatmári and Simon 1993, Szatmári et al. 2007).

28.2.4 Optical Multiplexing

In optical multiplexing, the beam to be amplified is split into partial beams, which are arranged in the multiplexer to form a pulse train with a separation comparable to the recovery time of the amplifier. After amplification, the partial beams are recombined to form a single pulse again called as demultiplexing (Figure 28.6a). The key point of any kind of multiplexing is how accurately the recombination of the partial beams can be performed. In the conventional multiplexing schemes, recombination is far from that of interferometric accuracy, which imposes severe limitations on the focus ability of the final beam. Synchronism can generally be obtained only for longer than picosecond pulses (Rosocha et al. 1987), or in some cases, even no attempt has been made for beam recombination. The beam combination method based on Raman conversion (Shaw et al. 1993) is rather complex and best suited for longer than picosecond pulses.

For the above reasons, a multiplexing method has been introduced which does not suffer from the earlier listed shortcomings of the conventional ones. This novel method is based on a common optical arrangement used both for multiplexing and for demultiplexing (Figure 28.6b). In this way, automatic (phase-locked) synchronization of the partial beams is achieved for any alignment of the multiplexer (demultiplexer), and any kind of distortion and/or misalignment is automatically compensated. With this scheme, optimum focus ability and brightness are provided for the recombined beam (Szatmári et al. 2007, Szatmári and Simon 1993). Figure 28.7a and b show possible realizations for two multiplexed beams using a Sagnac interferometer with polarization (Figure 28.7a) or geometrical splitting (Figure 28.7b). Each arrangement can be scaled up to multiple beams and for multiple-pass (off-axis) amplification geometries (Szatmári and Simon 1993).

28.2.5 Picosecond Gain Dynamics of Excimers

Another issue leading to reduced gain and energy extraction for the signal pulse is connected to the gain dynamics of KrF, XeCl and XeF studied extensively in Szatmári and Schäfer (1987) and Zhao et al. (1988).

In Figure 28.8a–c, the logarithm of the gain is shown versus the delay between a saturating and a probe pulse for KrF, XeCl and XeF. In Figure 28.8a, the gain of KrF is followed over the first 300 ps after passage of the saturating pulse. After the initial drop, the gain recovers with a $\tau = 57$ ps time constant to 25% of its initial value. For comparison, the result of the same measurements for XeCl and XeF are seen in Figure 28.8b and c. Figure 28.8b shows that with XeCl, there is also a gain recovery with a similar time constant ($\tau = 53$ ps); however, its amplitude is much larger (65%). Compared to the previous two cases for XeF (Figure 28.8c), the gain recovers with larger time constant ($\tau = 85$ ps) and with larger amplitude (85%). In all cases, the short-term recovery of the gain is the evidence

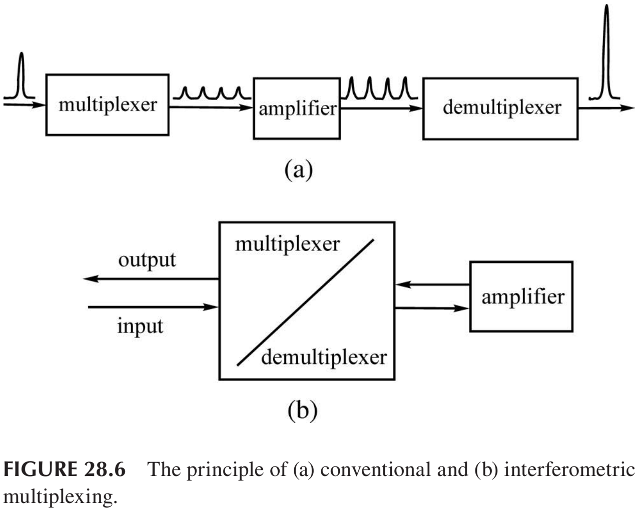

FIGURE 28.6 The principle of (a) conventional and (b) interferometric multiplexing.

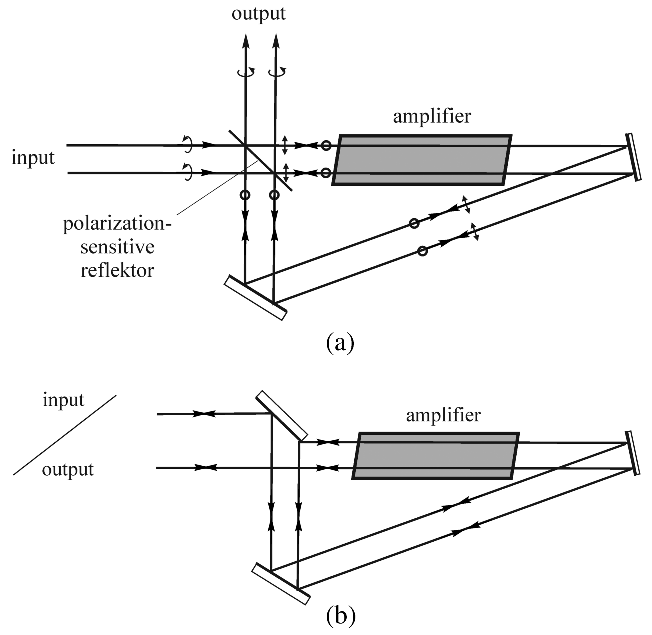

FIGURE 28.7 Possible realization of interferometric multiplexing using (a) polarization or (b) geometrical splitting.

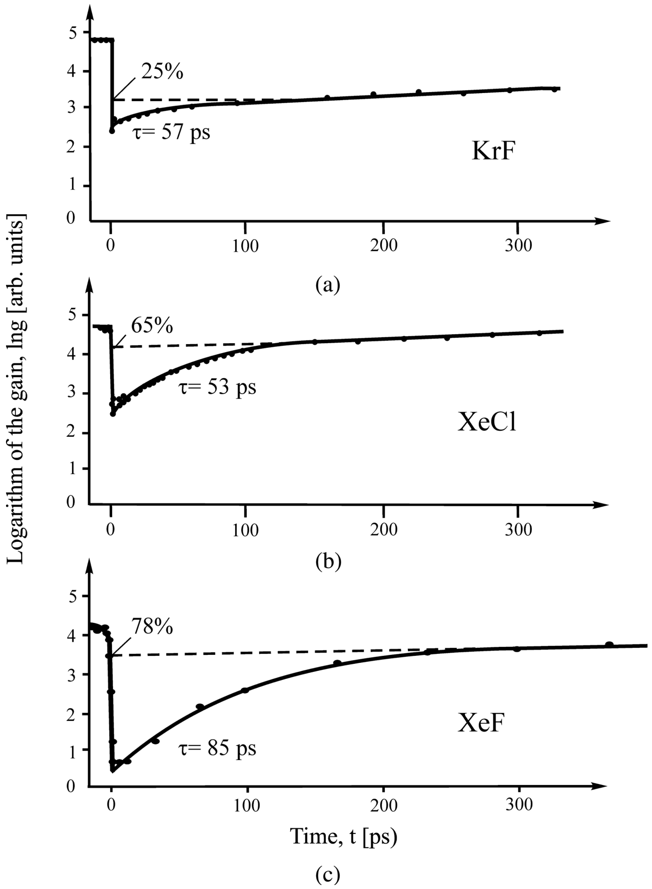

FIGURE 28.8 Logarithm of the gain in KrF (a) [Reprinted with permission from Szatmári and Schäfer 1987.], in XeCl (b) and in XeF (c) versus the delay between the saturating and the probe pulse, followed over 300 ps.

of left-over optical energy in the active medium; meaning that some part of the energy of the excited molecules is not accessible by subpicosecond pulses, only by pulses of sufficiently longer than several 100 ps duration. The observed gain recovery is attributed to rotational relaxation in the *B* state, with possible contribution of the incomplete relaxation in the *X* state (see Figure 28.1b). The latter assumption is applied mainly for XeCl and XeF, where the slightly bound *X* state can be populated by the short and intense saturating pulse; thus, its reabsorption also contributes to the limited energy extraction. Since the density of accessible molecules in the *B* state is coupled to the logarithm of the small signal gain, the gain coefficients for short and long pulses are expected to be different. For the calculation of their ratio (K), one has to compare the small-signal gain of the excimers for short and long pulses. From the input–output curves measured for all three excimers (Szatmári and Schäfer 1987; Zhao et al. 1988), and taking the typical (ASE limited) $gL = 11$ value of excimers (Ghani Moghadam and Farahbod 2016) different K values are obtained: $K_{\mathrm{KrF}} = 0.76$, $K_{\mathrm{XeCl}} = 0.53$ and $K_{\mathrm{XeF}} = 0.74$.

Having these values, correct interpretations of the gain dynamic curves and exact determination of the contribution of reabsorption of the finite population of the *X* state to the gain recovery become possible. For such calculations, let us assume an initial population density (n) in the *B* state is decreased to n' by the saturating pulse (followed by a gain recovery). Assuming that in both conditions the same part of the population is accessible by a short pulse (the K factor is the same), n' is defined by the relative amplitude of the recovery (by the amplitude of the recovery referred to that of the initial drop). From the curves of Figure 28.8

$$\left(\frac{n'}{n}\right)_{\mathrm{KrF}} = 0.25 \left(\frac{n'}{n}\right)_{\mathrm{XeCl}} = 0.65 \text{ and } \left(\frac{n'}{n}\right)_{\mathrm{XeF}} = 0.78$$

are obtained. In the KrF case—assuming no population in the *X* state during the process—the remaining population n' is the inaccessible part of the initial population, represented as

$$(1-K)\,n = n'.$$

This gives $K_{\mathrm{KrF}} = 0.75$, the same value as obtained from the small-signal gain measurements. This confirms the assumption that in KrF the *X* state has no influence on the energy extraction; Kn part of the initial population is extracted/removed by the saturating pulse.

However, in case of XeCl and XeF, the same way of calculations leads to contradiction; to a value significantly different from that of obtained from the gain measurements. In that cases—connected to the slightly bound feature of the *X* state—only partial extraction of the "accessible" population of the *B* state can be assumed due to remarkable population of the *X* state, whose balance value—in case of strong saturation—is determined by the ratio of the stimulated transition rates of the *B* and *X* states (or by the emission, σ_e and absorption cross section, σ_a). In this way, the remaining population (n') is the sum of the inaccessible initial population and a $(1-\alpha)$ fraction of the "accessible" initial population, as

$$(1-K)n+(1-\alpha)\ K\ n=n'$$

where $\alpha=\dfrac{\sigma_e}{\sigma_e+\sigma_a}$

In the XeCl case, substituting K_{XeCl} = 0.53 (obtained from the gain measurements) to this equation, α_{XeCl} = 0.66 is obtained. This gives σ_a/σ_e =0.5. While σ_e is known from the literature (Hokazono et al., 1984), this procedure gives a way to determine σ_a. Note, that with other methods, one can hardly obtain data for σ_a ($X \rightarrow B$) since the X state can only be populated for a short time through the B state.

From the measurements data obtained by (Zhao et al. 1988) for XeF, a similar calculation results in $K_{\mathrm{XeF}} \approx 0.8$; a value which is comparably high to that in KrF; however energy extraction is limited by the—rapidly populated—bound X state, which takes only α_{XeF} = 0.28 fraction, and leaves as high as $(1-\alpha) = 0.72$ fraction of the population in the B state, corresponding to a $\sigma_a/\sigma_e = 2.6$ ratio.

From the gain dynamics of the three excimers, a conclusion—similar to that of (Szatmári and Schäfer, 1987)—can be drawn: it is only KrF which behaves as a real four-level system and offers good energy extraction, resulting in preferable contrast for short pulses. Here, the only limitation for energy extraction and temporal contrast is imposed by the partial access to the excited molecules in the B state. However, in case of XeCl and XeF, not only the partial access in the B state but also absorption in the transiently populated X state limits the efficiency and contrast. Their relative contribution is different; in XeCl the former effect, in XeF the latter one are found dominant.

Then, the final ratio of effective gain coefficients for intense short pulses and weak long pulses (K^*) is the product of the gain coefficient c, K and α; as

$$K^*=c\ K \propto$$

The former considerations suggests, that even in KrF—as the best choice among short-pulse excimer amplifiers where $\alpha_{\mathrm{KrF}} \approx 1$—one must face to significant loss of efficiency and contrast, when operated as a short-pulse preamplifier or power amplifier. In such cases, the final ratio (K^*) is $K^*_{\mathrm{pre}} = 0.7\times0.76 = 0.53$ and $K^*_{\mathrm{power}} = 0.5\times0.76 = 0.38$ for KrF preamplifiers and power amplifiers, respectively.

28.3 Contrast Issues

The relatively low value of K^* is the indication of limited energy extraction in KrF for the short pulse; moreover it suggests much higher gain for the weak ASE, than for the intense subpicosecond signal pulse. The latter effect has significant impact on the achievable contrast (see later) since the noise develops more rapidly than the signal. It also means that similarly to the CPA schemes

- a temporal filter has to be used to compensate for the rapid increase of the noise,
- and the temporal filter should be as close to the end of the amplifier chain as possible, or preferably after the amplifier chain.

While in solid-state systems, even a minor amplification following the temporal filter necessitates the use of CPA (i.e. a subsequent use of a stretcher, an amplifier and a compressor), in KrF such amplification (of limited g_0L product) is feasible, without significant deterioration of the contrast. That is why the ideal position of the temporal filter in solid-state systems is exclusively after the CPA amplifier chain. Assuming a KrF amplifier—which typically allows the development of ASE in a solid angle $\Omega = 10^4$, as seen in Figure 28.1 (Ghani Moghadam and Farahbod 2016)—one can set a limit of $g_0L \approx 4$, where ASE remains in the slowly rising region. This, however, also limits the (short-pulse) gain-length product to $g_{\mathrm{short}}L \approx 1.5$, allowing an amplification not more than 5 for short pulses ($G_{\mathrm{short}} \approx 5$).

As discussed in detail in the next section of this paper, the most important features of temporal filters are their throughput and contrast enhancement. In a similar manner, a KrF amplifier can best be characterized by its short-pulse amplification (G_{short}) and by the associated deterioration of the contrast (D). From the former considerations, even "local" values (normalized to the unit length) can be defined. For the most important power amplifier case:

$$G_{\mathrm{short}}=e^{g_{\mathrm{short}}L}=e^{0.38g_{\mathrm{long}}L}$$

$$D=\frac{e^{g_{\mathrm{long}}L}}{e^{g_{\mathrm{short}}L}}=e^{\left(g_{\mathrm{long}}-g_{\mathrm{short}}\right)L}=e^{0.62g_{\mathrm{long}}L}$$

It is seen from the equations that a KrF power amplifier of a given gain coefficient deteriorates the contrast with twice larger "coefficient". A similar calculation for KrF preamplifiers yields $G_{\mathrm{short}} = D = e^{0.5g_{\mathrm{long}}L}$, i.e. a KrF preamplifier deteriorates the contrast with the same coefficient as it amplifies the short pulse.

Recently many experiments confirmed that the key parameter during laser–matter interactions is the temporal and spatial contrast of the pulses (Ceccotti et al. 2007). These experiments showed that prepulses of 10^7–10^8 W cm^{-2} intensity can influence/change laser–matter interactions considerably (Wharton et al. 2001). Considering that the focused intensity of present laser system already surpasses 10^{22} W cm^{-2}, the necessary intensity contrast is in the 10^{14}–10^{15} regime. Several techniques have been developed and successfully applied for the improvement of the temporal contrast of intense laser pulses. The most straightforward methods are the plasma mirror technique (Kapteyn et al. 1991, Thaury et al. 2007), or frequency conversion (Marcinkevicius et al. 2004) at the end of the laser system, or the use of XPW technique in a double-CPA arrangement (Kalashnikov et al. 2005). These techniques usually provide a temporal contrast approaching 10^{12} on the nanosecond scale. However, an inherent shortcoming of the CPA-based systems is that the coherent pedestal (on the intensity scale from 10^{-5} to 10^{-10}) in the picosecond temporal vicinity of the main pulse still remains (Wang et al. 2011, Wagner et al. 2014). It also means that by the use of the pulse cleaning techniques, where further amplification and the use of CPA are needed (like XPW), one has to face additional inherent deterioration of the temporal contrast. Energy scalable pulse cleaning methods, which can be used after amplification, like frequency conversion or plasma mirror technique, in principle can avoid this problem. In such cases, however, high-throughput operation is absolutely required since no additional amplification can compensate for the energy loss.

In contrast to solid-state systems, short-pulse UV laser systems are using direct amplification, therefore the only source of the temporal background is the ASE. As it was mentioned earlier, the short wavelength and the special gain dynamics of the KrF medium are causing a rapidly growing ASE. These features set the temporal contrast to ~10^{10} already for several times 10 mJ output energy at 248 nm. To reach higher output power/intensity, contrast improvement techniques are needed to be applied in (or preferably after) the amplifier chain. The former considerations can be recognized in Figure 28.2, where the UV amplifier chain is split into two parts (called as pre- and power amplifier) by the spatial/temporal filter. Based on the possible use of direct amplification in excimer amplifiers, the use of a power amplifier following the pulse cleaning element seems possible since—in contrast to CPA amplification schemes—deterioration of the temporal contrast in the power amplifier is expected to be moderate and is only originated by the development of ASE (see former predictions/calculations for *D*). For the above-detailed reasons, a pulse cleaning method with high contrast improvement and high throughput is needed for temporal filtering of UV short pulses. Because of the increased non-linear absorption and the poor contrast (extinction coefficient) of the presently available polarizers, methods based on polarization rotation cannot be used effectively for this wavelength regime. Because of the short wavelength (λ_{KrF} = 248.5 nm), no efficient frequency conversion is possible. The remaining methods are the plasma mirror and the recently used non-linear Fourier-filtering (NFF) techniques.

28.3.1 Plasma Mirror

Plasma mirror technique (Kapteyn et al. 1991) has been proven to be an efficient method to remove prepulses. The laser beam is focused onto an antireflection-coated transparent glass or quartz plate inside a vacuum chamber. The low intensity part of the beam arriving before the main pulse is transmitted through the plate. Only above the ionization threshold, an overdense plasma is generated, reflecting the laser beam of improved temporal contrast. Since reflectivities up to 80% were reached (Ziener et al. 2003), plasma mirrors even in a double arrangement are often used. Recently, reflectivity up to 97% was reached by Scott et al. (2015) using a prepulse some picoseconds before the main pulse of the PHELIX laser.

The plasma mirror effect was also demonstrated (Földes et al. 2010) for a short-pulse KrF laser. In an improved experiment, reflectivity up to 70%, corresponding to >10^2 contrast improvement is reached (Gilicze et al. 2016). It was found that the high reflectivity—while preserving the focus ability of the laser beam—could only be approached if the plasma mirror was situated in the Fourier plane of the focusing optics.

The plasma mirror technique, however, has the shortcomings that the contrast improvement is moderate (roughly two orders of magnitude) for a single use, a fresh interaction area is needed for each shot; moreover, the surface quality of the generated plasma can deteriorate the beam quality significantly.

28.3.2 Non-linear Fourier-Filter

To exceed the shortcomings of the plasma mirror technique, an alternative method, called NFF has been proposed for temporal filtering of intense UV pulses (Szatmári et al. 2016). In this arrangement, the separation of the intense main pulse from the noise is based on a non-linear interaction in the Fourier-plane and on the resulting directional modulation of the beam. The experimental realization uses a confocal telescope and a pair of conjugate filters, where middle and outer parts of the beam are filtered out at the input and output of the system, respectively (Figure 28.9). In this way, an annular beam is focused through a gas jet, where the low intensity temporal noise (ASE) is not or negligibly modulated and the same annular beam is imaged at the output, where the output diaphragm blocks the remaining part of the beam. However, for the intense main pulse, the self-generated plasma introduces selective non-linear phase-modulation of the diffraction

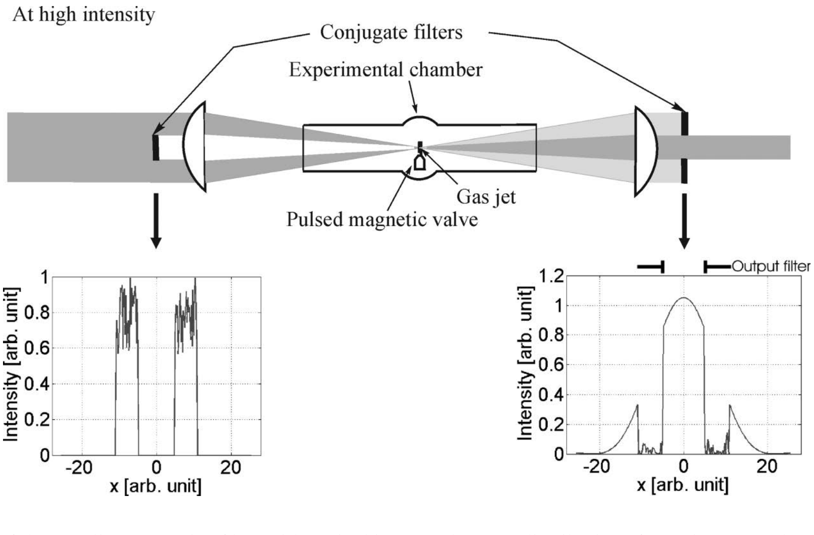

FIGURE 28.9 Schematic of the non-linear Fourier-filter with typical input and output distributions for an intense pulse.

orders of the beam which leads to modified directional properties and as a result significant throughput appears. In this way, the noise becomes spatially separable from the main pulse (see Figure 28.9). Important feature of this arrangement, that the temporal filtering is accompanied by efficient spatial filtering. As the simulation shows in Figure 28.9, the unwanted high spatial frequency components of the beam are transferred outside of the output aperture, therefore are completely blocked. Within the frame of geometric optics, this arrangement has no throughput.

First demonstration of this filtering technique (Szatmári et al. 2016) showed 10^3 temporal contrast improvement and >40% energy throughput with stable performance. Later investigations showed that the moderate value of contrast improvement is caused by the limited spatial contrast of "conventional" imaging of the input annular aperture. This limit is a consequence that the annular object contains (high) spatial frequency components that cannot be processed by the imaging system (Gilicze et al. 2017). To avoid this limitation, one must reduce the spatial frequency components of the object and to match to the "capabilities" of imaging of the Fourier-filter. This statement was confirmed both theoretically and experimentally; calculations predicted $>10^{10}$ contrast improvement, which experimentally was confirmed beyond 10^7. This means that the NFF is capable to provide significantly higher contrast improvement than the former techniques. One possible way is to use an apodized spatial filter to create a continuous descent at the edges of the object. Another possible and more preferable realization is to introduce an imaging of low numerical aperture (NA) prior to Fourier-filtering (called pre-imaging) to exclude the higher spatial frequencies of the intermediate picture created by this pre-image system. This image completed by a second annular beam block then serves as an apodized—but high contrast—object for the NFF. Schematic of such an arrangement is shown in Figure 28.10. Further advantage of this arrangement is that the amplification can be carried out simultaneously during the imaging (see Figure 28.10); moreover, the pre-imaging acts as a spatial filter at the same time, reducing the ASE coupling between the amplifiers.

The NFF uses subsequent image systems and ionization of noble gases, therefore expected to be energy scalable; moreover, is an excellent candidate for filtering short pulses in a wide wavelength range. The earlier discussed features of the gain dynamics of excimer amplifiers necessitate the use of the filtering technique close to the end of the amplifier chain. Since the extension of this technique towards larger energies and larger cross sections is technically challenging, integration of this method into a high-brightness KrF laser system has been carried out in subsequent steps.

28.4 Amplifier Requirements, Design Considerations

Considering the small (mJ cm^{-2}) saturation energy density of excimers and the moderate (≥100 ps) minimum pulse durations can be amplified, multi TW-class amplifiers can be accomplished with electron-beam-pumped excimer amplifiers of several times 10 cm aperture, that are technically available, but leading to a complicated and robust design.

For practical reasons, discharge-pumped excimer amplifiers are preferable to e-beam-pumped ones, when moderate output energies (up to several 100 mJ), high pulse-repetition rates and ease of operation are required (Glownia et al. 1986, Schwarzenbach et al. 1986, Szatmári et al. 1987, Barr et al. 1988, Szatmári and Schäfer 1988, Watanabe et al. 1988). In the conventional amplification schemes, the large cross section necessary for high-energy, short-pulse amplification was achieved by increasing both the gap separation (d) and the width (w) of the discharge of the discharge-pumped gain modules. This, however, necessarily increases the cross section of the discharge loop, thus limits the speed of electric excitation leading to enhanced instabilities and inhomogeneities of the discharge. Hence, in most cases, more complicated X-ray preionization is necessary for stable operation. With the off-axis amplification scheme, the size of the amplified beam can be significantly increased in one dimension. Therefore, large and square beam cross sections can be obtained even with discharges of small w/d aspect ratios. From the optical point of view a circular cross section is ideal, theoretically necessitating a discharge cross section of $w/d \approx 1$. If the off-axis scheme is applied for an amplifier of $w \cdot d$ original cross section for the amplification of a beam of d^2 cross section, comparison of the optimum short-pulse energy for the latter cross section with the momentarily stored energy of the discharge gives a $w/d \geq 1/3$ lower limit for the ratio of the dimensions of the discharge (Szatmári et al. 2007). Most of the commercial UV preionized, discharge-pumped excimer lasers have discharges of this aspect ratio. It means that commercial discharge units could effectively be used for short-pulse amplification, by the use of the off-axis amplification scheme. It is known that such

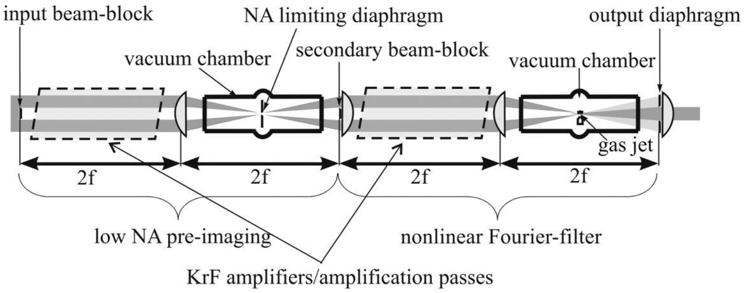

FIGURE 28.10 Schematic of the non-linear Fourier-filter completed by a low NA pre-imaging. Possible positions of the amplifiers are also indicated. (Reprinted with permission from Gilicze et al. 2017.)

discharges are more stable, the discharge loop can be made relatively small even for larger gap separations, allowing high-speed charging circuits and relatively low operational voltages. Under these circumstances, simple UV preionization is expected to be sufficient. Moreover, the charging circuit can be optimized for other parameters such as maximum momentarily stored energy, maximum efficiency, high stability, minimum temporal jitter of the gain, etc. The use of such excitation schemes also helps to reduce the effective pumping times, thus increasing the ratio of the momentarily stored energy and the pumped-in energy. It also means that for a given (needed) value of the accessible (momentarily stored) optical energy significantly relaxed energy has to be pumped-in (or through) the active medium. This minimizes the optical distortion which is a crucial parameter to maintain the diffraction limited feature of the beam during amplification.

Summarizing these requirements, pumping of excimer gain modules can only be realized by an efficient and temporally short pumping mechanism capable of homogeneously excite a large volume. However—even in this case—special considerations and corresponding steps are needed to homogeneously deposit large amount of electric energy in a short time into a gas-filled volume of well-defined dimensions (Szatmári and Schäfer 1987, Szatmári et al. 1987, Mizoguchi et al. 1991, Nodomi et al. 1991, Kovács and Szatmári 1994).

It is known from former gain dynamic studies (Szatmári et al. 2007), that it is only KrF and ArF which acts as a real four-level system when short-pulse amplification is needed, allowing good access to the momentarily stored energy. On the other hand, these are just the excimers where homogeneous excitation of the initial Fluorine-based gas mixture is the most critical; special measures are needed to ensure arc-free, homogeneous excitation of large volumes (Shields 1989). One needs a fast rising, temporally clean electric pulse to produce a highly uniform electric field together with a fast and efficient preionization of the gas characterized by a similarly uniform spatial distribution of the generated ions. Due to the strong halogen (Fluorine) attachment of the ions, their effective lifetime is shortened to several times 10 ns, which necessitates an intense and short preionization process, precisely synchronized to the main pumping pulse.

In spite of the fact that the off-axis amplification geometry makes possible to use discharges of low ($w/d < 1$) aspect ratio, the increase of the aspect ratio is desirable for two reasons; this necessarily leads to the increase of the pumped volume resulting in increased momentarily stored energy, moreover—because of the inherent nonsaturable absorption of the gas mixture—it minimizes the absorbing unpumped volume seen by the short signal pulse. A discharge of large aspect ratio, however, necessitates the use of X-ray preionization which is known to be capable of homogeneously ionizing large volumes (Midorikawa et al. 1984, Shields 1989, Tallman 1989, Mizoguchi et al. 1991).

28.5 Experimental Realizations

Among the numerous experimental realizations, the next section will show some examples of high-brightness KrF excimer systems. The first group of examples is, where the 248.5 nm KrF wavelength is reached by efficient frequency doubling of the 497 nm radiation of an excimer laser-pumped pulsed dye laser (Szatmári et al. 1987, Szatmári and Schäfer 1988, Békési et al. 2002, Gilicze et al. 2019). The latest version of such a system shown in Figure 28.11 is optimized for the maximum temporal contrast and beam quality, presently operational in the High Intensity Laser Laboratory (HILL) of the University of Szeged, Hungary. Here, for the first time the NFF was integrated into the short pulse, hybrid dye-KrF excimer laser system (Gilicze et al., 2019).

The seed pulse of several times 100 fs at 497 nm is generated by a special dye laser system pumped by a commercially available XeCl excimer laser (Szatmári et al. 1988). The pulses are frequency doubled using a BBO crystal placed in the Fourier-plane of the beam. The non-linear conversion result is not only temporal but also effective spatial filtering (Szatmári et al. 1997). As a consequence, high-contrast, nearly Gaussian UV pulses of ~20 μJ energy are available before the first KrF preamplifier. The NFF has been implemented after the first preamplifier, where the intensity-limit for the NFF is reached with stable spatial distribution of the beam. The following amplifiers compensate for the energy loss caused by the filter and by the associated UV optics. An annular beam block (called as first beam block) is placed after the first pass and imaged through a vacuum pinhole to exclude the higher spatial frequencies and the spatially incoherent background (marked as "low NA pre-imaging" in Figure 28.10). The image of the beam block complemented by a second annular beam block acts as an input for the NFF. In this way, the theoretically achievable highest contrast improvement is reached. After filtering, the beam is amplified in subsequent four passes to ~100 mJ. The final amplification stage having an effective cross section of ~$4 \times 4\,\text{cm}^2$ is used in a double-pass, two beam interferometric multiplexing arrangement (Szatmári and Simon, 1993, Békési et al. 2001). This setup gives access to higher portion of the energy of the amplifier. The two preamplifiers are driven by a common pumping circuit providing automatic synchronization. The pumping circuits of the XeCl pump laser, the preamplifiers and the final amplifier are synchronized by an active synchronization unit, which can compensate for the long-time drift.

Despite the fact that this system layout is far from the ideal (regarding the fast evolution of ASE in the multistage amplifier chain following the temporal filter), more than two orders of magnitude higher intensity contrast ($>10^{11}$) is achieved for the same output energy as in former cases (Békési et al. 2001). It is important to note that the ASE at the output of the system is measured to be generated exclusively by the amplifier chain following the temporal filter. In conclusion, short pulses of 100 mJ energy, ~700 fs pulse duration (positively chirped) ~two times limited by diffraction and 10^{11} focused intensity contrast are generated. This laser system with its unique parameters gives access to (and presently serves) laser–matter interaction experiments at the 10^{19} W cm^{-2} intensity level with high contrast at 248 nm.

In this system UV preionized, discharge-pumped KrF amplifier modules with "standard" discharge geometries ($w/d \approx 1/2.5$) were used in the off-axis amplification geometry.

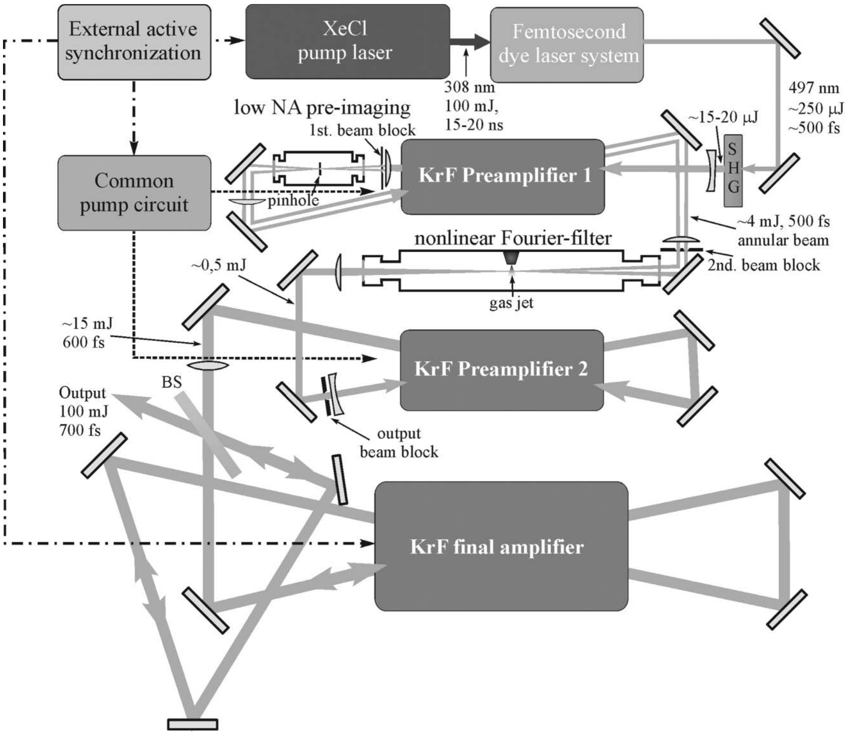

FIGURE 28.11 Schematic of the high-contrast, high-brightness KrF laser system of the University of Szeged. (Adopted with permission from Gilicze et al. 2019.)

The next realization is an example, where the KrF wavelength is reached by frequency tripling of the 745 nm radiation of a Ti:Sapphire laser and—in order to reach even larger output energies—an X-ray preionized power amplifier of larger aperture and correspondingly larger momentarily stored energy is used.

The arrangement shown in Figure 28.12 illustrates the practical implementation of the high-brightness UV laser system that operated in the X-ray Microimaging and Bioinformatics Laboratory of the University of Illinois at Chicago, USA. Here, the short (typically ~100 fs) pulses are generated by a Ti:Sapphire laser (operating at 745 nm) and by the following third harmonic generating (THG) crystals. In this case, a dual-channel KrF excimer preamplifier is used to boost the pulse energy to ~60 mJ. Relay imaging of the THG crystal to the output windows of the subsequent amplifier stages maintains high beam quality. A spatial filter positioned between the discharge tubes provides efficient ASE suppression. This system is followed by an X-ray preionized KrF amplifier of $10\times10\,\mathrm{cm}^2$ cross section (‘PROMETHEUS’) having a double discharge gain module. The parameters of this system represent the present limit of femtosecond high-brightness discharge-pumped KrF technology. The performance yields a maximum gain-length product of $g_0L \approx 2\times8$ over a duration of ~50 ns (FWHM). The maximal output energy allowed by the beam cross section (A) is $E_{\mathrm{out}} = 2.2\ \varepsilon_{\mathrm{sat}}A \approx 450\,\mathrm{mJ}$ (Almási et al. 1992). The nominal operating parameters are power $P \sim 1$–2 TW, pulse energy $E = 300$–500 mJ, pulse length 200–300 fs, and repetition rate ~0.1 Hz. With an off-axis f/2 parabolic mirror, the system can produce a focal spot of ~2 µm in diameter. This performance represents ~1.65 times the diffraction limit and enables focal intensities of ~ 6–$8\times10^{19}\ \mathrm{W\,cm^{-2}}$ to be produced, a value that corresponds to an electric field amplitude of ~40 (e/a_0^2).

With this system efficient X-ray generation at ~2.8 Å is reported by the multiphoton-induced 3d → 2p Xe(L) transition in Xe clusters (Boyer et al. 2005, Borisov et al. 2016).

28.6 Outlook

In spite of the excellent directional properties of the radiation of short-pulse excimer systems, the rapid saturation of the focused intensity achieved in the past by these lasers (see Figure 28.3) is mainly attributed to the limitations imposed by the short-pulse KrF amplifier-technology. The more practical discharge-pumping requires fast electric excitations, which can only be realized by small discharge loops thus limiting the optically usable cross sections. In this respect, some optical methods (like off-axis amplification, optical unification of more discharges, like the “back-to-back” design, etc.) can give a possibility to step forward in the future (Szatmári et al. 1991, Borisov et al. 2016).

In short-pulse excimer amplifiers, the main limitation on short-pulse energy extraction is connected to their limited energy storage capabilities. The storage time for solid-state materials is in the microsecond regime, allowing complete extraction of the stored energy by a single short pulse. This implies that the values for the maximum peak power, brightness and focused intensity of solid-state lasers correspond to almost complete energy extraction. On the other hand, in excimer amplifiers, due to the short (nanosecond) storage time

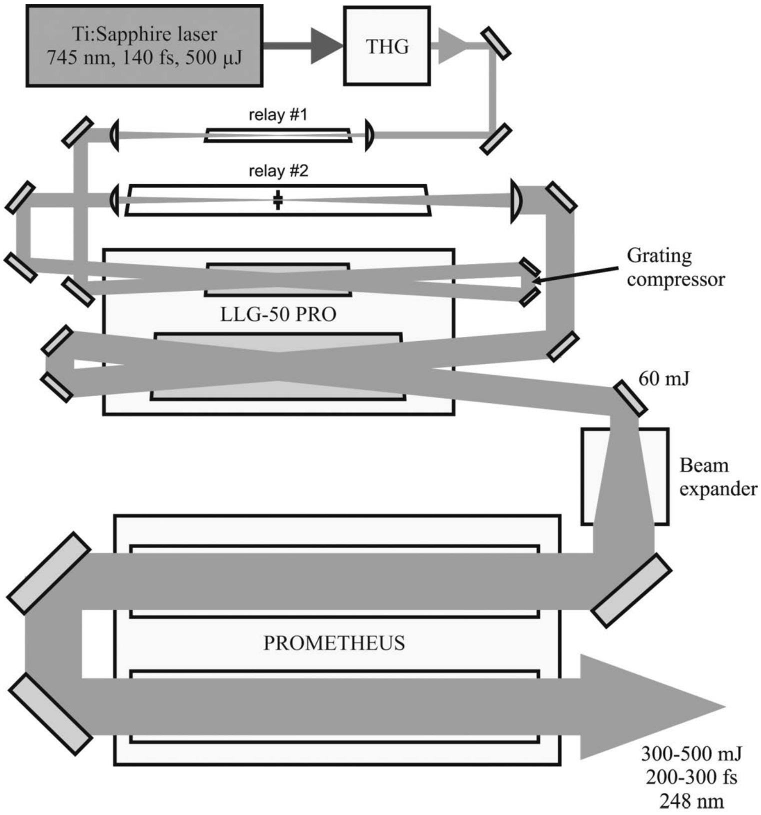

FIGURE 28.12 Schematic of the high-power KrF installation of the University of Illinois, Chicago.

of the active medium, only a small fraction (<1/10) of the overall energy is available for a single short pulse. Since no practical way has been found up to now for successive replenishment of the gain in excimers by optical multiplexing of subpicosecond pulses, the corresponding data for excimers were obtained mainly in single beam amplification experiments using not more than 10% of the available energy. If a generally applicable interferometric beam recombination method was found for optical multiplexing, it might solve the inherent energy extraction problem of excimers caused by their short storage time and low saturation energy density. This would be of an importance comparable to that of the CPA scheme used in short-pulse solid-state systems and could make the excimer-based, short-pulse laser systems competitive with solid-state ones.

As it is pointed out in the former sections, a possible way to increase the accessible optical energy of short-pulse Krf amplifiers (defined by the τ/T ratio) is to minimize the effective pumping time (T_{eff}). Since relaxation from the upper state is on the $T_{\text{rel}} \approx 10$ ns scale (see Figure 28.1a), the decrease of T_{pump} is only straightforward until ~10 ns. Beyond that, it is (the relatively long) T_{rel} which determines T_{eff}, thus limiting the ratio of accessible molecules to the maximum ~10% value. For longer T_{pump} values, extraction decreases even further to several per cent.

The possibility of direct amplification of subpicosecond pulses in excimers makes possible to produce intensities in excess of 10^{20} W cm^{-2} with very high temporal contrast. Most of recent experiments showed that the key parameter primarily is not the achieved peak intensity but the temporal and spatial quality (contrast) of the pulses. Unfortunately, inherent shortcoming of the CPA technique is the coherent temporal pedestal on the picosecond scale, which hardly can be eliminated by the conventionally used pulse cleaning techniques (such as plasma mirrors, XPW). On one hand the low saturation energy density of excimers requires large beam/amplifier cross sections, thus limiting the achievable peak power; on the other hand, direct amplification of subpicosecond pulses is possible, which avoids the use of CPA and the associated coherent temporal background.

The problem associated with the temporal and spatial contrast of high-power solid-state and excimer systems can be best explained by the comparison of the amplification schemes used in the two kinds of laser systems. In CPA amplification schemes, the high intensity—corresponding to the needed large energy density of solid-state amplifiers—is relaxed by expanding the pulse in the direction of propagation. In excimer systems the small energy density requires the expansion of the pulse in the directions perpendicular to the propagation. While incomplete compression in the perpendicular direction (incorrect focusing) does not have serious effect on the interaction (it only decreases the intensity in the focus), incomplete (not phase-locked) compression of the pulse in the direction of propagation (incorrect temporal compression) leaves a temporal background prior to the main pulse (both hitting the target at the same point), which can significantly change the physics of interaction.

In this way excimer laser systems—using direct amplification schemes—have inherently better temporal contrast. Moreover, their gaseous active media allows to maintain excellent spatial contrast as well.

As it is introduced in Section 28.1.1.2, short-pulse excimer systems are two-wavelength systems, where the temporal background is restricted to the ASE, exclusively originated in the second, short-wavelength part of the system. The ASE, however, grows more rapidly than the short, intense signal pulse (see Section 28.1.2.5), necessitating the use of pulse cleaning in the high energy part of the system, as close to the end of the amplifier chain as possible. The recently introduced NFF offers high throughput and contrast improvement even in the UV. Its use in the high energy part of the system, however, requires to prove its power-scalability in the multiterawatt range.

Intense, short-wavelength radiation has a unique potential in plasma generation; at high intensity it shows pronounced absorption and higher conversion to X-rays. The reason is that most of the non-linear processes scale with $I\lambda^2$, consequently unwanted, competing effects are of much less importance in the short-wavelength region. The observed high absorption is attributed to the anomalous absorption, i.e. that the mean free path of the electrons in the accelerating laser field is longer than the skin depth in the solid plasmas.

The pronounced absorption together with the good focus ability and excellent temporal contrast of high-brightness KrF lasers make them ideal pump sources in surface harmonic-generation experiments.

The high photon energy of KrF radiation, and the intensity which can be reached by high-brightness KrF systems, make it possible to step out of the conventional weak coupling regime and to enter the anomalous region of enhanced coherent coupling (defined by the $h\nu > 5\,\mathrm{eV}$ and $I > 3\times10^{15}$ W cm^{-2} parameters of excitation), opening a new regime of laser–matter interaction.

This anomalously enhanced coherent coupling definitely played an important role in the efficient generation of 4.5 keV and 1 keV X-rays by the multiphoton-induced 3d → 2p Xe(L) and 4f → 3d Xe(M) transitions in Xe clusters. Further study of such transitions by high-brightness KrF radiation is straightforward and can lead to future, most powerful X-ray laser schemes.

REFERENCES

Alekseev, S.V., Aristov, A.I., Grudtsyn, Ya.V. et al. 2013. Visible-range hybrid femtosecond systems based on a XeF(C–A) amplifier: state of the art and prospects. *Quantum Electronics* **43**(3): 190–200.

Almási, G., Szatmári, S., Simon, P. 1992. Optimized operation of short-pulse KrF amplifiers by off-axis amplification. *Optics Communications* **88**: 231–239.

Barr, J.R.M., Everall, N.J., Hooker, C.J. et al. 1988. High energy amplification of picosecond pulses at 248 nm. *Optics Communications* **66**: 127–132.

Békési, J., Marowsky, G., Szatmári, S. et al. 2001. A 100 mJ table-top short pulse amplifier for 248 nm using interferometric multiplexing. *Zeitschrift fürPhysikalische. Chemie* **215**: 1543.

Békési, J., Szatmári, S., Simon, P., Marowsky, G. et al. 2002. Table-top KrF amplifier delivering 270 fs output pulses with over 9 W average power at 300 Hz. *Applied Physics B* **75**(4): 521–524.

Borisov, A.B., McCorkindale, J.C., Poopalasingam, S. et al. 2016. Rewriting the rules governing high intensity interactions of light with matter. *Reports on Progress in Physics* **79**: 046401

Boyer, K., Borisov, A.B., Song, X. et al. 2005. Explosive super-saturated amplification on 3d→2p Xe(L) hollow atom transitions at λ ~ 2.7-2.9 Å. *Journal of Physics B: Atomic, Molecular and Optical Physics* **38**: 3055

Ceccotti, T., Lévy, A., Popescu, H. et al. 2007. Proton acceleration with high-intensity ultrahigh-contrast laser pulses. *Physical Review Letters* **99**: 185002.

Dick, B., Szatmári, S., Rácz, B. et al. 1986. Bandwidth limited amplification of 220 fs pulses in XeCl. *Optics Communications* **62**: 277–283.

Földes, I.B., Csáti, D., Szűcs, F.L. et al. 2010. Plasma mirror and temperature evolution for short pulse KrF lasers. *Radiation Effects and Defects in Solids* **165**: 429–433.

Ghani Moghadam, G., Farahbod, A.H. 2016. General formula for calculation of amplified spontaneous emission intensity. *Optical and Quantum Electronics* **48**: 227.

Gilicze, B., Barna, A., Kovács, Zs. et al. 2016. Plasma mirrors for short pulse KrF lasers. *Review of Scientific Instrument* **87**: 083101.

Gilicze, B., Dajka, R., Földes, I.B. et al. 2017. Improvement of the temporal and spatial contrast of the nonlinear Fourier-filter. *Optics Express* **25**: 20791–20797.

Gilicze, B., Homik, Zs., Szatmári, S. 2019. High-contrast, high-brightness ultraviolet laser system. *Optics Express* **12**: 17377–17386.

Glownia J.H., Misewich, J., Sorokin, P.P. 1986. Ultrafast ultraviolet pump-probe apparatus. *Journal of the Optical Society of America B* **3**: 1573–1579.

Hokazono et al. 1984.

Kalashnikov, M.P., Risse, E., Schonnagel, H. et al. 2005. Double chirped-pulse-amplification laser: a way to clean pulses temporally. *Optics Letters* **30**(8): 923–925.

Kapteyn, H., Murnane, M., Szoke, A. et al. 1991. Prepulse energy suppression for high-energy ultrashort pulses using self-induced plasma shuttering. *Optics Letters* **16**(7): 490–492.

Kovács, G., Szatmári, S. 1994. KrF gain module for short-pulse off-axis amplification. *Measurement Science and Technology* **5**: 127–137.

Marcinkevičius, A., Tommasini, R., Tsakiris, G.D. et al. 2004. Frequency doubling of multi-terawatt femtosecond pulses. *Applied Physics B* **79**(5): 547–554.

McIntyre, I.A., Rhohes C.K. 1991. High power ultrafast excimer lasers. *Journal of Applied Physics* **69**: R1.

Midorikawa, K., Obara, M., Fujioka, T. et al. 1984. X-ray preionization of rare-gas-halide lasers. *IEEE Journal of Quantum Electronics* **20**: 198–205.

Mizoguchi, H., Endoh, A., Jethwa, J. et al. 1991. Rapid discharge-pumped wide aperture X-ray preionized KrF laser. *Applied Physics B* **52**: 195–199.

Nodomi, R., Oeda, Y., Sajiki, K. et al. 1991. High repetition rate, wide-aperture KrF lasers for subpicosecond amplification. *IEEE Journal of Quantum Electronics* **27**: 441–447.

Rhodes, C.K. 1979. *Excimer Lasers*, Springer-Verlag, Berlin.

Rosocha, L.A., Hanlon, J.A., McLeod, J. et al. 1987. Aurora multikilojoule KrF laser system prototype for inertial confinement fusion. *Fusion Technology* **11**: 497.

Schwarzenbach, A.P., Luk, T.S., McIntyre, I.A. et al. 1986. Subpicosecond KrF* excimer-laser source. *Optics Letters* **11**: 499–501.

Scott G.G., Bagnoud, V., Brabetz, C. et al. 2015. Optimization of plasma mirror reflectivity and optical quality using double laser pulses. *New Journal of Physics* **17**: 033027.

Shaw et al. 1993.

Shields, H. 1989. X-ray preionization technology for high pressure gas discharge lasers. *SPIE Proceedings* **1046**: 15.

Szatmari, S., Almási, G., Feuerhake, M. et al. 1996. Production of intensities of 10^{19} W/cm^2 by a table-top KrF laser. *Applied Physics B* **63**: 463–466.

Szatmari, S., Almási, M., Simon, P. 1991. Off-axis amplification scheme for short-pulse amplifiers. *Applied Physics B* **53**: 82–87.

Szatmári, S., Bakonyi, Z., Simon, P. 1997. Active spatial filtering of laser beams. *Optics Communications* **134**: 199–204.

Szatmári, S., Dajka, R., Barna, A. et al. 2016. Improvement of the temporal and spatial contrast for high-brightness laser beams. *Laser Physics Letters* **13**(7): 075301.

Szatmári, S., Marowsky, G., Simon, P. 2007. Femtosecond Excimer Lasers and their Applications. In *Landolt–Börnstein - Group VIII* (Herziger, G., Weber, H., Poprawe, R. Eds.), **Vol. 1B1**: 215–253, Springer, Berlin.

Szatmári, S., Schäfer, F.P. 1987. Comparative study of the gain dynamics of XeCl and KrF with subpicosecond resolution. *Journal of the Optical Society of America B* **4**(12): 1943–1948.

Szatmári, S., Schäfer, F.P. 1988. Simplified laser system for the generation of 60 fs pulses at 248 nm. *Optics Communications* **68**(3): 196–202.

Szatmári, S., Schäfer, F.P., Müller-Horsche, E. et al. 1987. Hybrid dye-excimer laser system for the generation of 80 fs, 900 GW pulses at 248 nm. *Optics Communications* **63**: 305–309.

Szatmári, S., Simon, P. 1993. Interferometric multiplexing scheme for excimer amplifiers. *Optics Communications* **98**: 181–192.

Tallman, C. 1989. Preionization techniques for discharge lasers. *SPIE Proceedings* **1046**: 2.

Thaury, C., Quéré, F., Geinder, J-P. et al. 2007. Plasma mirrors for ultrahigh-intensity optics. *Nature Physics* **3**: 424–429.

Tilleman, M.M. and Jacob, J.H. 1987. Short-pulse amplification in the presence of absorption. *Applied Physics Letters* **50**: 121.

Wagner, F., João, C.P., Fils, J. et al. 2014. Temporal contrast control at the PHELIX petawatt laser facility by means of tunable sub-picosecond optical parametric amplification. *Applied Physics B*. **116**(2): 429–435.

Wang, Z., Liu, C., Shen, Z. et al. 2011. High-contrast 1.16 PW Ti:sapphire laser system combined with a doubled chirped-pulse amplification scheme and a femtosecond optical-parametric amplifier. *Optics Letters* **36**(16): 3194–3196.

Watanabe, M., Hata, K., Adachi, T. et al. 1990. High-repetition-rate terawatt excimer laser system with gated gain amplification. *Optics Letters* **15**: 845–847.

Watanabe, S., Endoh, A., Watanabe, M. et al. 1988. Terawatt XeCl discharge laser system. *Optics Letters* **13**: 580–582.

Wharton, K.B., Boley, C.D., Komashko, A.M. et al. 2001. Effects of nonionizing prepulses in high-intensity laser-solid interactions. *Physical Review E* **64**: 025401.

Zhao, Q., Szatmári, S., Schäfer, F.P. 1988. Gain dynamics of XeF and subpicosecond pulse generation at 351 nm. *Applied Physics B* **47**(4): 325–332.

Ziener, Ch., Foster, P.S., Divall, E.J. et al. 2003. Specular reflectivity of plasma mirrors as a function of intensity, pulse duration and angle of incidence. *Journal of Applied Physics* **93**: 768.

Taylor & Francis
Taylor & Francis Group
http://taylorandfrancis.com

29

Optically Pumped Mid-IR Lasers: NH_3, C_2H_2

Mary S. Tobin

CONTENTS

29.1 Introduction 419
29.2 Basic Spectroscopy of NH_3 and C_2H_2 419
29.3 Principle of Operation 421
29.4 Experimental Aspects 421
29.5 NH_3 Laser 423
29.6 Gain Models 426
29.7 Optically Pumped Laser Action in C_2H_2 and Its Isotopes 428
29.8 Applications and Future Prospects 429
References 429
Further Reading 432

29.1 Introduction

The development of mid-infrared (MIR) optically pumped gas lasers (MIROPLs) has been motivated by the concentration of molecular vibrational–rotational spectra in the MIR, with the consequential need for sources for spectroscopy and gas identification. Another source need is for selective excitation of vibrational modes to produce photochemical reactions, e.g. for isotope separation. The objective here is to provide an overview of the MIROPLs NH_3 and C_2H_2 and their isotopic variations, primarily in the 8–20 μm range. We differentiate MIR from far-infrared (FIR) lasers in that the MIROPL transitions occur between different vibrational bands, whereas FIROPL transitions generally occur on pure rotational transitions within a given vibrational mode at wavelengths mainly from 50 μm to 1 mm [1]. Much of the MIROPL development occurred in the 1970s and 1980s, and several reviews are available [2–6].

Electrical discharge pumping has produced MIR pulsed laser action in NH_3 [7,8]. Electrical excitation of H_2 with He or CO, followed by vibrational energy transfer, has produced laser action near 8 μm in C_2H_2 [9–11]. Optical pumping has advantages in that it does not dissociate the molecules, which in many cases allows continuous wave (cw) (as opposed to pulsed only) and sealed-off operation. Furthermore, it is energy-level selective and more efficient than electrical pumping. As in the FIR, the CO_2 laser is the major pump choice. A fundamental requirement of optical pumping is that the molecule must have an absorption transition in the spectral region of the pump laser. NH_3 is the most efficient, powerful and important of all the MIROPLs because of a combination of its fundamental properties and the near-coincidence of absorption lines with the CO_2 laser. There has been one report of an HF laser pumping an NH_3 laser [12]. The use of an isotopic species, e.g. $^{15}NH_3$, can sometimes provide a better match with the pump and produce many new laser lines. A complete list of close matches of CO_2 laser lines with ammonia lines is given by Frank et al. [13]. Whereas the CO_2 laser cannot directly pump C_2H_2, it can pump C_2D_2, with a performance that rivals NH_3 for some lines. In this chapter, we discuss these lasers including their simplest spectroscopy, the principles of operation, laser construction and current topics of interest.

29.2 Basic Spectroscopy of NH_3 and C_2H_2

The absorption and emission spectra of molecules in the MIR are related to vibrational and rotational motions of the electronic ground state. For a fundamental mode of vibration at frequency ν, the vibrational energy is $E_\upsilon^{\text{vib}} = h\nu\left(\upsilon + 1/2\right) +$ anharmonic terms, where υ is the vibrational quantum number. Acetylene is a linear molecule belonging to point group $D_{\infty h}$, which means it has a plane of symmetry perpendicular to the internuclear axis. Figure 29.1 indicates the five normal vibrational modes and fundamental frequencies for C_2H_2 and C_2D_2; ν_1, ν_2, and ν_3 are non-degenerate stretching modes and ν_4 and ν_5 are degenerate bending modes. Vibrational states of C_2H_2 can be denoted by the quantum numbers (υ_1, υ_2, υ_3, υ_4^{l4}, …). Bending modes have a vibrational angular momentum about the internuclear axis characterized by quantum number l_i, which are combined to give a total vibrational angular quantum number l. The notation Σ, Π, Δ refers to $l = 0, 1, 2$, respectively. The superscripts (+ and –) indicate the parity of the wave functions when the vibrational normal coordinates are reflected in a plane containing the molecular axis. The subscripts, g and u, indicate that the vibrational wave function

Mode	Frequency (cm^{-1})	Description	Symmetry	Normal Mode H C C H
ν_1	3374 (2700)	Sym. C-H stretch	Σ_g^+	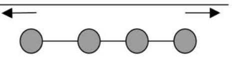
ν_2	1974 (1762)	C-C stretch	Σ_g^+	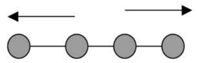
ν_3	3287 (2427)	Asym. C-H stretch	Σ_u^+	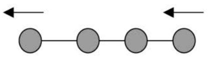
ν_4	612 (505)	Sym. bend	Π_g	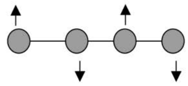
ν_5	729 (539)	Asym. bend	Π_u	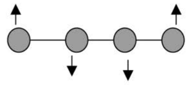

FIGURE 29.1 The fundamental modes and frequencies of C_2H_2 (frequencies of C_2D_2 in parentheses).

is +1 or –1, i.e. even (gerade) or odd (ungerade) upon inversion of the normal coordinates with respect to the molecule-fixed axis. The only infrared-active fundamental modes are ν_3 and ν_5; neither of these modes for C_2H_2 (or C_2D_2) overlaps the CO_2 laser emission.

Each vibrational level consists of many rotational levels. In the rigid-rotor harmonic oscillator approximation, the energy of a molecule can be considered as a sum of vibrational and rotational energy. For a linear molecule, $E_\upsilon^{\mathrm{rot}}(J) = B_\upsilon[J(J+1) - l^2] - [D_\upsilon J^2(J+1)^2]$ where l is included for degenerate levels, B_υ and D_υ are vibrational–rotational parameters and J is the angular momentum quantum number. Selection rules for transitions depend on whether the oscillating dipole moment is parallel ($\Delta l = 0$, $\Delta\upsilon = \pm1$, $\Delta J = \pm1$) or perpendicular ($\Delta l = \pm1$, $\Delta\upsilon = \pm1$, $\Delta J = 0, \pm1$) to the molecular axis.

For a symmetric top molecule such as NH_3, the rotational energy for a non-degenerate vibrational mode including centrifugal and Coriolis effects in the non-rigid molecule is

$$E_\upsilon^{\mathrm{rot}}(J) = B_\upsilon[J(J+1) - l^2] - [D_\upsilon J^2(J+1)^2] \qquad (29.1)$$

where B_υ, C_υ and the Ds are vibrational–rotational parameters, K is the projection of the rotational angular momentum number J on the molecular symmetry axis ($-J \le K \le J$). Radiative transitions follow dipole-like selection rules, $\Delta J = \pm1{,}0$; $\Delta K = 0$. The bands corresponding to $\Delta J = -1$, 0 and +1 are referred to as the P, Q and R branches, respectively, where the sign of the change in J is taken from the lower level to upper level for either absorption or emission. Therefore, the R, Q and P branches extend from higher to lower energy, respectively. Degenerate vibrations are more complicated to treat, and further details can be found in [14,15]. As in the case of FIROPLs, the gain for MIROPLs is preferentially parallel or perpendicular to the pump polarization depending on the type of pump and MIR transition [16].

NH_3 is a pyramidal molecule with threefold rotational symmetry (point group $C_{3\upsilon}$). It has four fundamental vibrational modes: $\nu_1 = 3337\,\mathrm{cm}^{-1}$ and $\nu_2 = 950\,\mathrm{cm}^{-1}$ are totally symmetric (species A_1), and $\nu_3 = 3414\,\mathrm{cm}^{-1}$ and $\nu_4 = 1628\,\mathrm{cm}^{-1}$ are degenerate (species E) [14]. The only fundamental mode that the CO_2 laser can pump is ν_2 (Figure 29.2). The lines are doubled by the inversion of the molecule, which corresponds to the two states that the N atom can take on opposite sides of the plane formed by the H atoms, and $950\,\mathrm{cm}^{-1}$ is the average of the two doublets due to passage through the potential barrier. The inversion removes the degeneracy in K and separates the levels

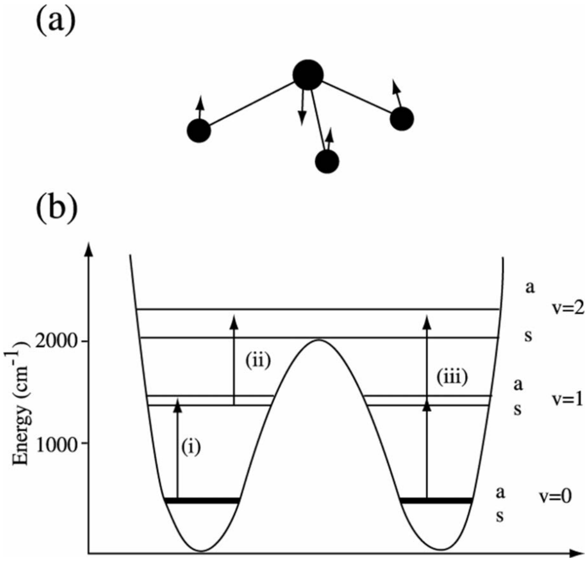

FIGURE 29.2 Schematic diagrams of (a) the ν_2 mode of NH_3 and (b) the potential function of the ν_2 mode indicating a double minimum and showing the possible pumping processes in NH_3: {i}, fundamental 0 → 1 {ii}, hot band 1 → 2 {iii}, two-photon (or two-step) pumping 0 → 2.

into symmetric (s) for the lower level and antisymmetric (a) for the upper level. Vibrational transitions can only occur between levels of opposite parity, i.e. $a \leftrightarrow s$. Another concept important in understanding the NH_3 laser is the concept of ortho- and para-NH_3. Rotational levels with $K = 3n$, so called ortho-NH_3, species A, have twice the statistical weight of the levels with $K = 3n \pm 1$, para-NH_3, species E; ortho-NH_3 cannot convert to para-NH_3 or *vice versa* by collisions.

The strength of a vibrational transition is proportional to the square of the vibrational transition dipole moment. The ν_2 transition dipole moments for NH_3 are about 0.24*D* for the fundamental and 0.28*D* and 0.42*D* for the overtone $2\nu_2 s$ and the $2\nu_2 a$ band, respectively [17]. These are relatively large and contribute to the success of the NH_3 laser.

29.3 Principle of Operation

Figure 29.3a indicates the basic principle of operation of the MIROPL. The pump laser radiation is absorbed on a vibrational–rotational transition $1 \rightarrow 2$, followed by laser action on vibrational–rotational transition $2 \rightarrow 3$ at a longer wavelength. Several types of transitions can occur. For the strongest NH_3 lines, 1 and 3 represent rotational levels of the ground vibrational state and 2 is of the fundamental ν_2 vibrational band. Pumping to an overtone band followed by lasing on a hot band can also occur, e.g. two-step pumping to the $2\nu_2$ band of NH_3. Pumping is also possible to a combination band (as for C_2D_2) with lasing on a hot band. The merits of various pumping schemes, based on the relative level populations and transition strengths, are compared in Harrison and Gupta [4]. The FIROPL shares the same excitation mechanism, but lasing occurs on a pure rotational transition. There are fewer MIROPL molecules and laser lines compared to FIROPLs. One reason is that the MIR transition is often back to the same (ground) vibrational state, and the relatively small population difference between the initial and final states can result in significant MIR self-absorption [18]. This absorption can be reduced by pumping far off-line centre (Raman lines) as was done for the first cw NH_3 laser [19], but this requires more pump power.

The dynamics of NH_3 lasers show the presence of two gain mechanisms, inversion and Raman [19–22]. For inversion gain, the pump is absorbed by a specific ammonia transition and the excitation may be transferred to other states via collisions: buffer gases such as N_2 and Ar can aid this process. The frequency of the pump does not determine the frequency of MIR emission. In contrast, Raman gain is a coherent process simultaneously involving two radiation fields and three molecular levels (Figure 29.3b). A pump photon at frequency $\omega_{21} - \delta\omega$ is converted to an emission photon with a corresponding offset at frequency $\omega_{23} - \delta\omega$, and the molecule is transferred directly from level 1 to level 3 where $\omega = 2\pi\nu$. In general, the gain can be expressed as a sum of population inversion and Raman gain:

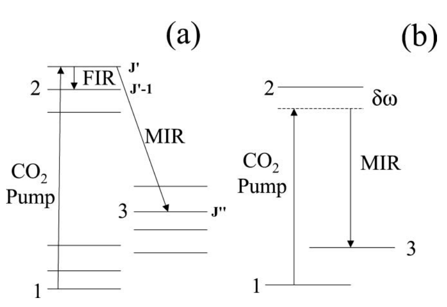

FIGURE 29.3 Energy-level schematic diagram to show (a) the basic principle of operation for MIROPLs (and FIROPLs) and (b) the Raman process, where the pump and emission frequencies are off-resonance from the molecular transitions.

$$g(\omega) = \sigma_{01}\left[S_I(n_2 - n_1) + S_R(n_1 - n_3)\right] \qquad (29.2)$$

where σ_{12} is the absorption cross section at frequency ω_{21}, S_I and S_R are lineshape factors for the inversion and Raman gain, respectively, and n_1, n_2 and n_3 represent populations of levels 1, 2 and 3, respectively. Raman gain only appears on laser transitions having one level in common with the pumped transition. Gain models are discussed further in Section 29.6.

29.4 Experimental Aspects

The major pump source for MIR- and FIROPLs is the CO_2 laser because of its large number of lines (approximately 80—see Figure 29.4) in the 9 and 10 μm molecular 'finger print' region. Isotopic variations and sequence band CO_2 lasers offer additional pump frequencies. The cw CO_2 laser is relatively inexpensive, easy to operate, has tunability of about 70 MHz, produces up to 50 W m^{-1} length and is about 20% efficient. The laser tube is water cooled and a flowing gas mixture of about 10–30 torr of a mixture of CO_2, N_2 and He is used. The laser can be sealed off, often with the addition of xenon. Waveguide cw CO_2 lasers exhibit higher operating pressure and greater tunability and have produced new FIROPL lines [23]. A cw CO_2 waveguide laser at 52 MHz above the 10R(24) line was used to pump an NH_3 waveguide MIROPL on the aP(4,0) transition but severe feedback problems, in the absence of an optical isolator, discouraged this approach [25].

Pulsed MIROPLs mainly use CO_2 pumps with transverse excitation at atmospheric pressure (TEA). The short transverse discharge paths of TEA lasers allow excitation of large volumes of gas at high pressures at reasonable voltages (20–50 kV). Pulse energies in the fraction to multi-joule range are obtained depending on gas and excitation conditions. Tunability ranges from about 1 GHz for a one-atmosphere to the entire R and P branches for a multi-atmosphere CO_2 TE laser [26]. Frequency-selective elements (e.g. gratings, etalons and apertures) or injection locking can be used to achieve single longitudinal and transverse mode operation. The TEA laser output typically consists of a 100–150 ns pulse followed by a tail, which contains most of the energy, of several microseconds duration. The initial peak can saturate the MIR absorption so that the pulse-tail transmits with little contribution. Biswas et al. [27] improved MIROPL efficiency 30% by redistribution of the energy within the pump pulse through choice of gas mixtures.

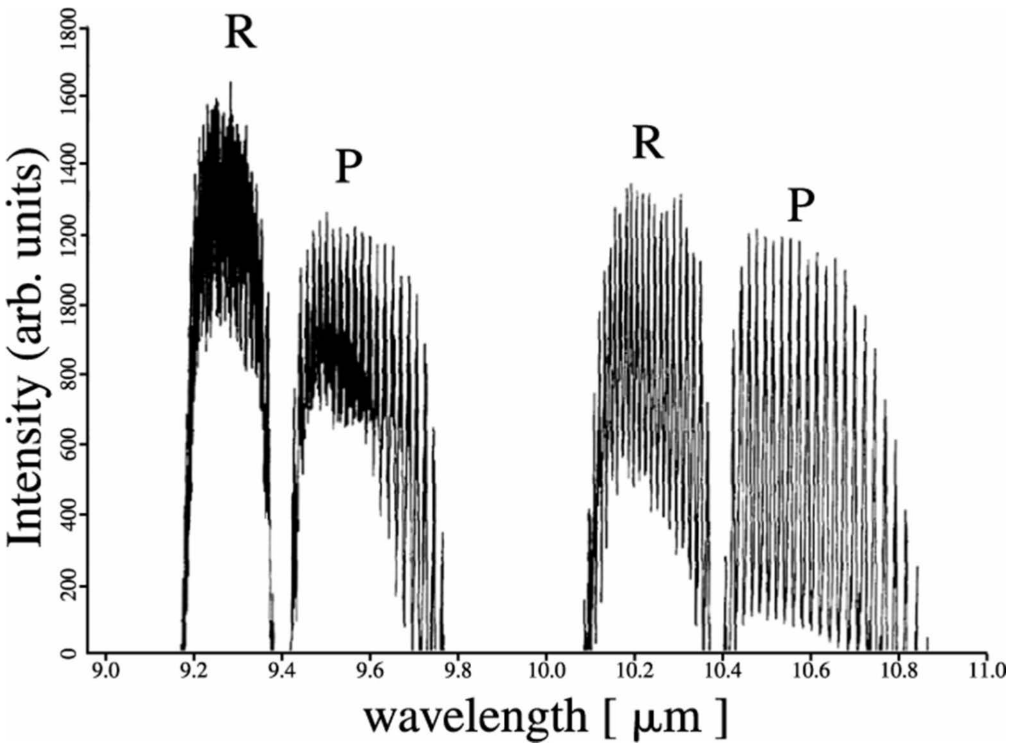

FIGURE 29.4 CO_2 laser tuning profile showing the R- and P-branches of the $00^{0}1$–$02^{0}0$ and $00^{0}1$–$10^{0}0$ bands in the 9 and 10 μm regions, respectively [112]. (Reproduced by permission of Elsevier.)

The MIR gas cell can be an oversized waveguide with dielectric or metallic walls with a cooling jacket. The cell is evacuated by a standard mechanical pump with a liquid nitrogen (LN_2) cold trap, then filled and sealed off. A superfluorescent laser consists of the pump laser and a single- or multi-pass gas cell [26,28]. Otherwise, the pump radiation must be admitted into the MIR cavity while maintaining good MIR resonator efficiency. Line selection, prevention of feedback into the pump laser and separation of the residual pump from the MIR output are all important. Optical alignment can be complicated by the different material optical properties in the MIR *versus* visible, e.g. germanium and silicon are opaque in the visible. Some MIR materials are toxic and some are hygroscopic. ZnSe optical windows and elements are frequently used, although they may be more expensive. These various requirements present challenges, as evidenced by the many papers that have addressed MIROPL designs over the years and continue to do so [29,30].

The pump beam can be injected into the MIR cavity off-axis through the Brewster angle window [31,32], or side-window of the gain tube [33] (as shown in Figure 29.5), and reflected down the MIR resonator by an oversized waveguide [34]. Such a design is relatively simple and inexpensive to make, the resonators can be independently optimized, there is little pump feedback and the pump beam is separated from the MIR output. However, for off-axis pumping, much of the gas can remain unexcited and contribute significant MIR loss, especially for lines terminating in the ground state, e.g. the NH_3 $\nu_2 \rightarrow 0$ lines. Hole coupling through the MIR mirror is

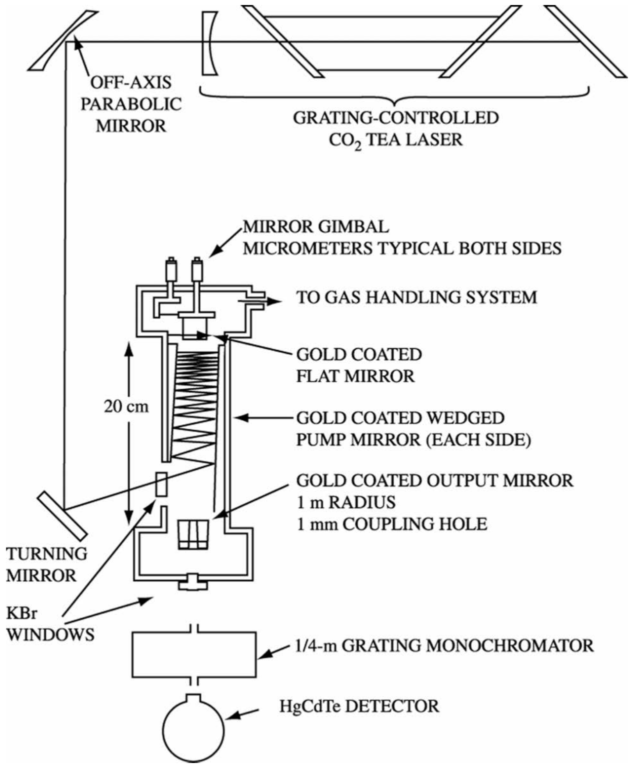
OFF-AXIS PARABOLIC MIRROR
GRATING-CONTROLLED CO2 TEA LASER
MIRROR GIMBAL MICROMETERS TYPICAL BOTH SIDES
TO GAS HANDLING SYSTEM
GOLD COATED FLAT MIRROR
20 cm
GOLD COATED WEDGED PUMP MIRROR (EACH SIDE)
GOLD COATED OUTPUT MIRROR
1 m RADIUS
1 mm COUPLING HOLE
TURNING MIRROR
KBr WINDOWS
1/4-m GRATING MONOCHROMATOR
HgCdTe DETECTOR

FIGURE 29.5 Experimental setup for off-axis pumping. Note the MIR elements of KBr windows and HgCdTe fast detector [33]. (Reproduced by permission of Elsevier.)

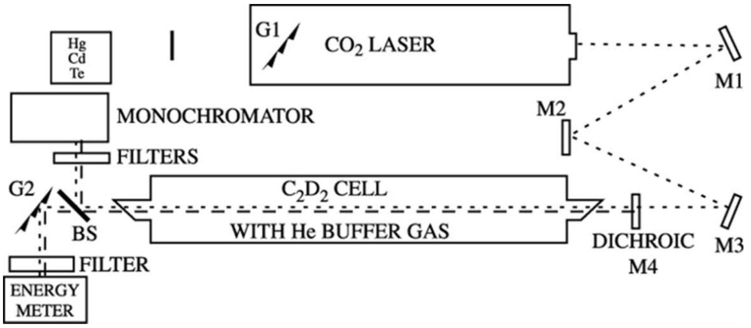

FIGURE 29.6 Experimental setup for on-axis pumping. Note use of dichroic mirror for input of pump into MIR cavity and use of the Littrow grating with output in zeroth order for MIR resonator [35]. (Reproduced by permission of the American Institute of Physics.)

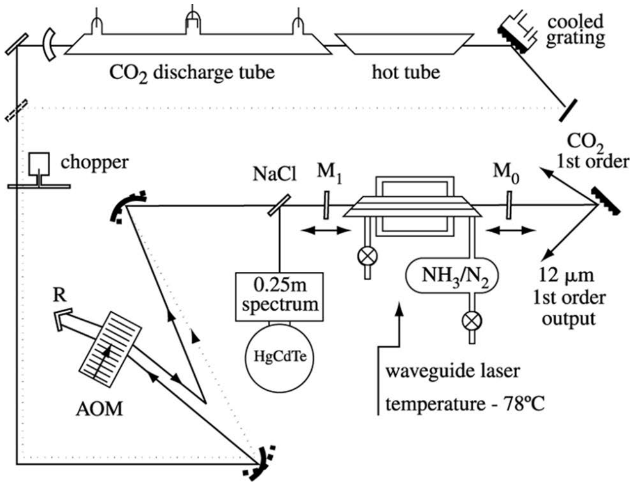

FIGURE 29.7 Experimental setup for on-axis pumping of a cooled MIR waveguide laser. The hot cell in the CO_2 cavity enables sequence-band operation. The full line shows the pump path when an AOM in the double-pass configuration is used. The dotted line is without AOM. M_1 and M_0 are dichroic mirrors. The grating is used to separate the 12 μm MIR output from the residual pump radiation [35]. (Reproduced by permission of the Optical Society of America.)

inexpensive but far from optimal with regard to power output and mode quality. Improvements are achieved by on-axis pumping and matching the pump with the MIR cavity mode. Dichroic optical elements, which can selectively transmit the pump but strongly reflect the generated MIR radiation, are frequently used as mirrors for collinear pumping (Figures 29.6 and 29.7).

Gratings are used in both pump and MIR lasers for wavelength selection. For light of wavelength λ, the grating equation is $m\lambda = d(\sin I + \sin R)$, where m is the diffraction order, d is the grating constant and I and R are the incident and reflection angles, respectively. Gratings are blazed and d can be selected for optimum performance at a given wavelength. Figures 29.5–29.7 demonstrate the Littrow configuration, whereby the grating replaces a CO_2 pump laser end mirror in which case $I = R$, $m\lambda_L = 2d \sin I$ and wavelength λ_L is reflected directly back on itself. Turning the grating does line selection. Some light is always reflected in zeroth order, and this can be used for the MIR output (Figure 29.6). Note this provides for inefficient pumping as only one pass of the CO_2 results and has the inconvenience that the output direction varies at twice the grating tuning angle. Radiation-damage-resistant original gratings can be used to reflect the pump in the first order for on-axis pumping while simultaneously providing for MIR line selection (Figure 29.8). A variety of other configurations have been reported [36,37] and reviewed by Harrison and Gupta [4].

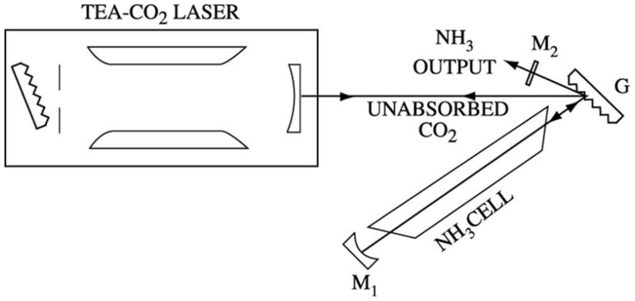

FIGURE 29.8 Schematic diagram of a TEA CO_2 laser pumped NH_3 laser. Grating G diffracts the pump energy in the first order into NH_3 cell and selects MIR frequency [27]. (Reproduced by permission of Elsevier.)

Acousto-optic modulators (AOMs) have application in frequency-shifting pump lines into coincidence with absorption lines [38]. In Figure 29.7, the full line demonstrates double pass through a 90 MHz AOM to achieve a 180 MHz downshift. The disadvantage of AOMs is that they are lossy (~40% loss per pass); however, a benefit is pump-feedback isolation. Polarization isolators, ring cavity configurations and single-pass configurations also provide isolation. An efficient cavity configuration was proposed in [30] which solves many problems including feedback, although it requires accurate focusing of the pump beam through a hole in the input mirror to the MIR cavity.

29.5 NH_3 Laser

The first MIROPL was NH_3 pumped by the 9R(16) CO_2 TEA laser, producing 5 kW at 12.81 μm for a 1.5 MW pump [34]. Many improvements have since been made through the resonator design, gas cooling and buffer gas use. There are now about 200 MIR laser transitions known for $^{14}NH_3$ and $^{15}NH_3$. Pulse energies have reached the 1 J range with peak powers in the MW range and energy conversion efficiencies greater than 20% [39]. Repetitively pulsed operation at 100 Hz can give 20 W average power [40]. CW operation over 10 W at 28% conversion efficiency has been reported [41]. Table 29.1 classifies the NH_3 laser in terms of the vibrational bands. Table 29.2 lists the pump wavelength, pump transitions and the pump offset for some of the more important NH_3 lines. Table 29.3 lists some specific results. The best-known NH_3 lines are associated with

TABLE 29.1

Summary of NH_3 and $^{15}NH_3$ Lasing Bands and Wavelengths

Molecule	Pump Information	No Lines	Lasing Band	Wavelength Range (μm)	References
$^{14}NH_3$	SPP	116	$\nu_2 \to 0$	9.3–13.8	[a]
	TPP 10P(24) and 10P(18)	2	$\nu_4 \to 0$	6.27, 6.69	[b]
	TPP (several combinations)	38	$2\nu_2 \to \nu_2$	11.5–21.3	[c]
$^{15}NH_3$	SPP–various lines	22	$\nu_2 \to 0$	10.8–13.5	[d]
	True TPP/single pump line 9R(46)	1	$2\nu_2 \to \nu_2$	13.9	[e]

[a] [42, Table 3.2.34a], [43, Table 3.2.3.4a], [16,33–35,38,44–51].

[b] [42, Table 3.2.3.4a], [54].

[c] [43, Table 3.3.2.3c], [17,52–57].

[d] [43, Table 3.3.2.3d], [58].

[e] [43, Table 3.3.2.3d], [59]

TABLE 29.2

CO_2 Pump Line/NH_3 Pumped Transition/Pump Offset for Well-Known NH_3 Lines. Unless Otherwise Designated, the Normal Isotopic Species Are Implied

CO_2 Pump/λ (μm)	NH_3 Pumped Transition(s)	Pump Offset ($\nu_{NH3} - \nu_{pump}$) (MHz)	NH_3 Emission (μm)
9R(40)/9.107	$^{15}NH_3$ sR(6,6)	–72	sP(8,6) at 12.476159130 [61,62]
9R(30)/9.22	sR(5,0)	–184[63]	sP(7,0) at 12.08 μm
	sR(5,1)	–336[63]	>70 lines 10.08–14.14 [39]
9R(16)/9.29	aR(6,0)	1355[64]	aP(8,0) at 12.812 [34]
9P(24)/9.59	2sR(4,3)	–475[64]	13 lines 15.9–21.3[17]
9P(34)/9.67	aR(4,2)	–5164[65]	aP(6,2) at 12.26[66]
10R(42)/10.11	$^{15}NH_3$ aR(2,0)	52.65[63]	aP(4,0) at 11.76[66]
			12 lines total 10.79–12.74[35,44]
$^{13}CO_2$ 9P(8)/8.89	aR(3,3)	76.8[63]	aP(4,0)/7 lines total [35]

The numbers in the square brackets are the relevant references.

TABLE 29.3

Some of the Strongest Results for cw and Pulsed NH_3

Pump	MIR Lambda (μm)	MIR Output	Parameters	Reference
TEA 9R (30) ~5 J pulse^{-1}	Over 70 lines 10.08–14.14	1 J pulse^{-1} on strongest lines	For $J \leq 7$, 0.2% NH_3/Ar at 170 torr/$T = 200$ K $J > 7$, 0.2% NH_3/Ar at 270 torr/$T = 300$ K	White et al. [39]
TEA 9R (16) ~120 mJ 80–160 ns	12.8	18 mJ pulse^{-1} from their Figure 29.3	For 250 cm cell	Gupta et al. [67]
CW9R(30) 37 W	12.08	10.2 W	Raman. Linear dry-ice cooled waveguide 1.2m/2.5 mm bore	Rolland et al. [41]
CW 9R(30) (AOM/-180 MHz) 18 W	41 total lines strongest are: 11.52–12.31	3.5 W Max	3.0 torr-NH_3/N_2 1.0 m/2.5 mm bore waveguide at 200 K	Kroeker and Reid [47]
CW 9R(30) (AOM/-360 MHz) ~6 W	para-NH_3 24 total lines strongest are: 11.98–12.25	90 mW Max	1 or 2% NH_3/Ar 1.0 m/1.5 mm bore waveguide at 200 K	Kroeker and Reid [47]
CW 10R(42) 8.8 W	12 lines 11–13	1.9 W max power	NH_3/Ar dry-ice cooled 1.0 m/2.5 mm waveguide	Chakrabarti and Reid [44]

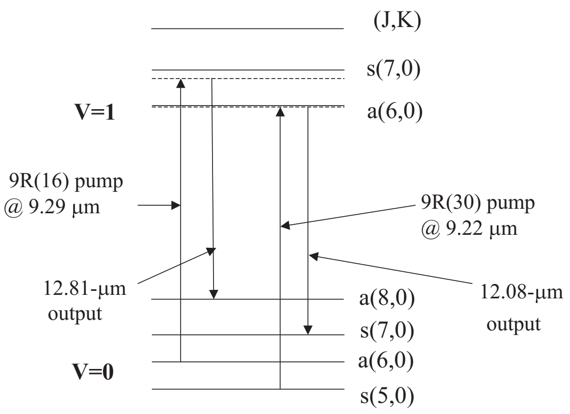

FIGURE 29.9 Energy-level schematic diagram showing two major NH_3 laser transitions. The $CO_2$9R(16) line pumps the aR(6,0) transition; lasing occurs on the aP(8,0) transition at 12.08 μm. Also, the $CO_2$9R(30) line pumps the sR(5,0) transition with emission on the sP(7,0) transition at 12.08 μm.

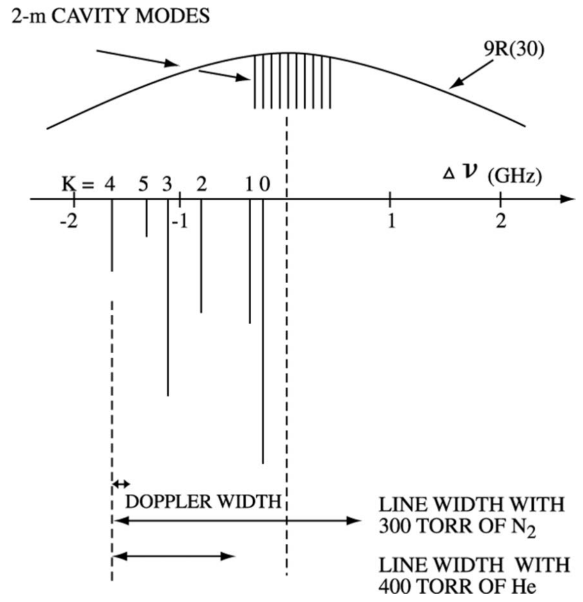

FIGURE 29.10 Pressure-broadened linewidths for comparison with CO_2 laser gain bandwidth. The position of the sR(5,K) multiplet is shown [60]. (Reproduced by permission of Springer.)

the CO_2 9R(30) and 9R(16) lines pumping the ν_2-fundamental with lasing at 12.06 and 12.82 μm, respectively, on the same band (Figure 29.9). In both cases, pumping occurs on an NH_3 R-branch line with lasing on a P-branch line, which is ideal for a molecule with a small moment of inertia [4].

Buffer gases and temperature are important in MIROPLs. Individually or in some combination, He, H_2, N_2 and Ar can increase the output and the lasing spectrum for the CO_2 TEA 9R(30) pumped line [33,49] by several mechanisms. First, pump absorption increases substantially, e.g. threefold [28] by pressure broadening of the NH_3 line. With 350 torr He, the sR(5,K), $K = 0.5$ multiplet lines merge into a single absorption band that can be pumped by the 9R(30) CO_2 TEA laser [48]. Figure 29.10 indicates the transition strengths of this multiplet and some relevant linewidths. Buffer gases also provide rotational relaxation, which allows tuning over much of the ν_2 band. With NH_3/Ar, White et al. [39] reported more than 70 vibrational band transitions between 10.08 and 14.14 μm for the single 9R(30) CO_2 TEA pump line. The optimum NH_3 concentration and pressure are transition dependent. Cooling the NH_3 tube with dry ice or LN_2 vapour increases power for some lines, as indicated in Table 29.3. The response to temperature can be explained through the Boltzmann distribution, which gives the populations of the rotational levels as a function of $E(J, K)$, the statistical weights, as well as the temperature. The buffer gas N_2 has ground-state rotational energy levels that are nearly resonant to those of NH_3, providing for possible collisional deactivation of the lower laser level [37], and results of Grasiuk et al. [2] show a correlation between those lines with close coincidences and best performance. The results from modelling the effects of buffer gases are discussed in Section 29.6.

In contrast to the 9R(30)-CO_2 pumped transition, buffer gases generally have little effect on the 9R(16) pumped 12.82 μm line. The pump laser is 1.355 GHz from the NH_3 aR(6,0) line so that pressure-broadening effects on absorption are insignificant. The limited tuning achieved with He is attributed to that fact the 12.82 μm line is Raman for a broad range of pressures and pump intensities [49]. However, with the high repetition rate pulsed laser, thermal effects become important. Baranov et al. [40] reported ~100% increase in output with He (or H_2) for the 9R(16) pumped line but no effect with N_2. These results are explainable by the high thermal conductivity of He, which is effective in removing heat. For comparison, output for 9R(30) pumped line increased 700%.

The initial cw NH_3 lasers were Raman type [19]. The offsets for the sR(5,0) and sR(5,1) NH_3 lines are 184 and 336 MHz, respectively, from the CO_2 9R(30) pump line (Table 29.2). The cw CO_2 laser can be frequency shifted with an AOM to obtain population inversion on either transition. Thereafter, collisions with buffer gas (either N_2 or Ar) thermalize the NH_3 rotational population, and gain can occur throughout the band for line tunable emission. If the $K = 0$ transition is pumped, gain occurs only on the ortho ($K = 3n$) transitions [38]. If the $K = 1$ transition is pumped, gain occurs only on the para ($K = 3n \pm 1$) transitions. Using appropriate AOMs to pump the sR(5,0) and sR(5,1) transitions and dry-ice cooling, Kroeker and Reid [47] reported line tunable cw emission on a total of 65 laser lines (41 in ortho-NH_3 and 24 in para-NH_3) in the 10.3–13.8 μm region.

CW operation, with thresholds below 1 W, is obtained without modulators with $^{15}NH_3$. The aR(2,0) line is offset 52.65 MHz from the CO_2 9R(42) line [35], which allows for direct pumping within the linewidth. Twelve line-tunable transitions in the 10.8–12.8 μm region were obtained using buffered $^{15}NH_3$/Ar or $^{15}NH_3/N_2$ [44]. Using a cooled hybrid waveguide and Fox-Smith mode selector, Wazen and Bourdet [68] showed 550 MHz tunability for the cw-pumped $^{15}NH_3$ aP(4,0) emission at 11.76 μm and 430 MHz for the collisionally pumped aP(4,2) emission at 11.76 μm. Both CO_2 sequence band and isotopic $^{13}CO_2$ lasers can also cw pump NH_3 and $^{15}NH_3$ [35]. Using a 3.4 W maximum power cw $^{15}NH_3$ MIROPL, Tachikawa and Evenson [69] sequentially pumped $^{15}NH_3$ to produce new FIROPLs.

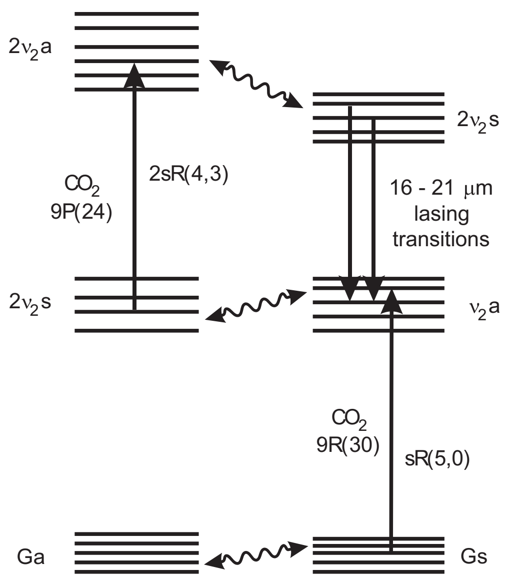

FIGURE 29.11 Partial energy-level schematic diagram of NH_3 indicating two-step pumping that leads to efficient emission in the 16–21 μm region [17]. (Reproduced by permission of the Optical Society of America.)

Simultaneous pumping with two pulsed TEA lasers, either as two-step or two-photon pumping, has extended the NH_3 laser operation to the 16–21 μm region ($2\nu_2 \rightarrow \nu_2$ band), as indicated in Table 29.1. Two-photon pumping with a single pump line has also been used [59]. Pumping with the combination of the 9R(30) and the 9P(24) TEA CO_2 lines (Figure 29.11) for buffered NH_3 has led to line tunable emission on 13 lines from 15.9 to 21.3 μm with 100 mJ maximum pulse energy [17].

Still more NH_3 lines can be pumped with a multi-atmosphere CO_2 TE laser, which can tune continuously ~10 cm^{-1} on each branch, compared to about 0.1 cm^{-1} per line for the usual TEA laser [46]. With a 20-atmosphere pump laser and a multi-pass Raman cell, Tillert et al. [26] obtained 52 emissions in the 11–50 μ region, including 37 MIR lines (25 new) in normal NH_3 and 15 MIR lines (14 new) in NH_3. These are not included in the number of lines in Table 29.1. The cavity was not optimal for wavelengths below 20 μm, leaving the possibility of more lines.

Optically pumped NH_3 produces amplification over a large bandwidth. White et al. [70] measured small signal gain near 7% and pump conversion efficiencies of 46% under saturated gain conditions for the CO_2 TE 9R(30) pumped NH_3 transition aQ(3,3) at 10.7 μm. Good performance is expected for many other transitions as well. CW amplifiers have also been investigated. Wazen et al. [71] investigated the cw 12 μm Raman amplifier pumped by the CO_2 9R(30) line and obtained amplifier power conversion efficiencies of 30%. Scaling relations indicate the practicality of a 150 W system.

The self-absorption of NH_3 at many lasing frequencies may be disadvantageous to the gain but can be used to good advantage for stabilization. The NH_3 laser output beam can be reabsorbed in a low-pressure NH_3 cell to produce strong saturation dips, which have been used to stabilize the laser frequency and accurately measure the line-centre frequencies [63]. The dispersion associated with this absorption (Kramers–Kronig) can lead to a sub-kilohertz spectral linewidth of the NH_3 laser under certain purely passive operating conditions [72,73].

Other interesting aspects of the NH_3 laser are self-pulsing instabilities [74] leading to chaos in the 12 μm emission, as predicted for a homogeneously broadened system by Haken [75]. Chaotic and periodic pulsation behaviour for the NH_3 12.8 μm aP(8,0) transition have been observed [76] and, under normal low-power conditions, for the sP(7,0) transition [77].

29.6 Gain Models

Rate-equation models [21,78–80], which treat level populations, can describe the dynamics of inversion gain. Such computer models successfully describe laser action in NH_3 in cw and pulsed operation particularly where buffer gases are used and particularly where population occurs through collisional transfer. It is assumed that (1) rotational populations are always thermalized except for the two levels of the pumped transition and (2) only one species ortho-NH_3 ($K = 3n$) or para-NH_3 ($K = 3n \pm 1$) is pumped, with no conversion between. Consider three levels, n_0, n_1 and n_2 are the ground, pumped state and final state populations, respectively, and $n = n_0+n_1+n_2$. Input to the equations [79] includes the pumping rate from the rotational level r_0 in n_0 to r_1 in n_1: $W_p \cdot \Delta r = (I_p/h\nu_p)\sigma[r_0 - r_1(g_0/g_1)]$, where I_p is the pump intensity at frequency, σ is the absorption cross-section and g_0 and g_1 are the degeneracies of r_0 and r_1.

Other input includes the *V–T* relaxation rate $(\tau_{VT})^{-1}$, which is given by $\left(k_{NH_3}p_{NH_3} + k_B p_B\right)$ where k is the rate and p is pressure of NH_3 or gas B. The rotational relaxation rates τ_0 and τ_1 are related to the pressure-broadened absorption linewidths. For steady-state pumping, the time derivatives to the rate equations are set to zero to obtain a numerical solution for the gain spectrum. Figure 29.12 compares theory and experiment for some cw lines for the aR(6,0)-pumped line [79]; the gain spectrum represents a thermalized distribution for the buffered NH_3/N_2 mixture. Morrison et al. [21] compared the effects of the three buffer gases N_2, Ar and He by a rate-equation analysis on the aR(1,1) system. Their results are included in Table 29.4. They conclude that the major effect of N_2 is the large pressure broadening relative to its *V–T* rate contribution, rather than the resonance deactivation, as discussed in Section 29.5.

For off-resonant pumping involving two-photon Raman processes, a quantum mechanical theory based on the density formalism is required. The original model developed for FIROPLs [24] is readily extended to MIROPLs [22,66,81,111]. This theory treats a coupled three-level system with mixed broadened transitions interacting with two travelling-wave fields of arbitrary strength. A numerical solution can be obtained for the small signal and saturated gain. Silva et al. [82] have extended the model to include the effect of a standing-wave MIR as would occur in a Fabry–Pérot cavity.

Morrison et al. [66] performed calculations and experiments for the 12.26 μm NH_3 aP(6,2) transition under

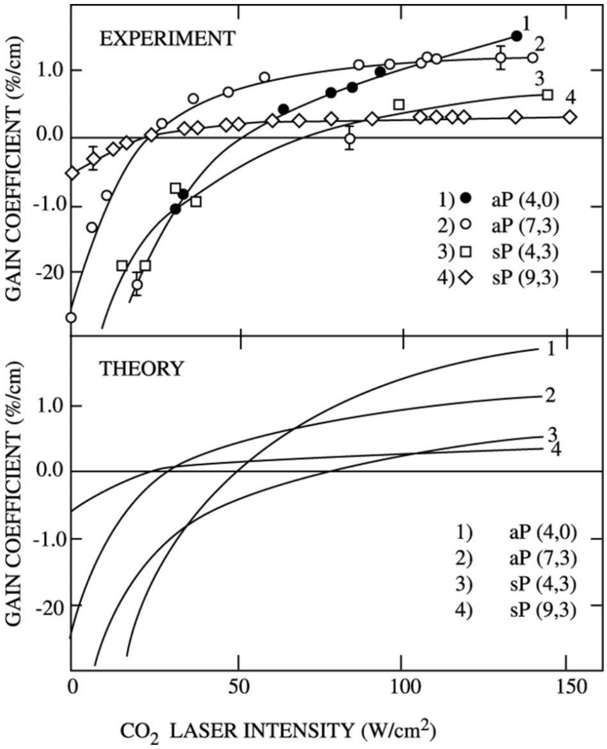

FIGURE 29.12 Comparison of gain coefficients: experiment (top) and rate-equation model (lower): The experiments and calculations are for a 1%NH_3/N_2 mixture at 5 torr. The NH_3 cw-pumped transition is aR(6,0) [79]. (Reproduced by permission of the Optical Society of America.)

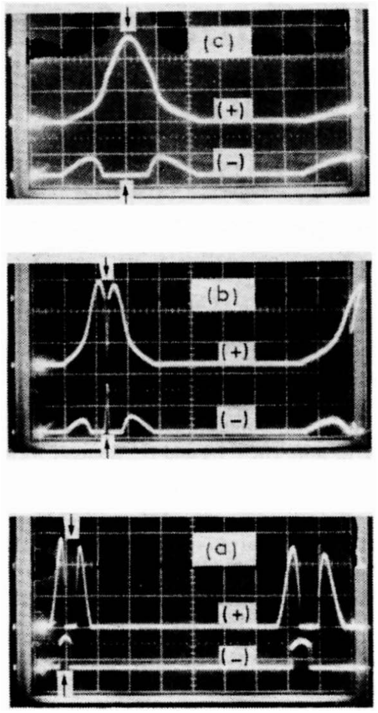

FIGURE 29.13 Experimentally observed tuning curves for $^{15}NH_3$ at 11.76 μm for co-propagation (+) and counter-propagation (–) of MIR and pump beams for total pressure of (a) 0.75, (b) 1.3 and (c) 3 torr, and for I_p = 150 W cm^{-2} [87] (©1991 IEEE). (Reproduced by permission of the IEEE.)

experimental conditions that avoid confounding effects such as population transfer, power broadening and ac Stark shifts. Their results show typical Raman gain characteristics: at low pressures, the gain is higher for the co-propagating case than for the counter-propagating case. Furthermore, the Raman linewidth is substantially narrower for the co-propagating case. For high pump intensities, the lasing-transition gain shape is strongly influenced by the coherent pump field through the dynamic Stark or Autler–Townes effect [84]. The pump levels are split by an amount equal to the Rabi frequency ($\omega_R = |\mu 20|\ E_2/\hbar$); this lead to a splitting of the MIR gain in the Doppler broadened regime for the case of co-propagation of MIR and pump beams. Although we tend to associate Raman lasers with large pump-frequency offsets, this is not necessarily the case. Wazen and Bourdet [85] investigated the Doppler broadened 11.76 μm $^{15}NH_3$ line optically pumped in a ring laser and found that, although the pumping occurs inside the Doppler width, Raman processes appear to be responsible for the emission. Figures 29.13 and 29.14 show experimental and calculated tuning curves for the co- and counter-propagating waves, respectively, for three different laser gas pressures for the cw 11.76 μm $^{15}NH_3$ line. For the (+) wave, the two-photon effect dominates, while for the (–) wave, population inversion dominates. Conditions can be chosen so that the laser operates unidirectionally in either direction. Co-propagating gain spikes were observed by Siemsen et al. [86] in a simple straight gain cell at low NH_3 pressure.

The very complicated dynamics is demonstrated by the NH_3 aR(6,0) pumped transition, which has a 1.355 GHz offset (Table 29.3) from the 9R(16) CO_2 pump but produces efficient lasing at 12.8 μm. Under conditions of single-mode 1 MW cm^{-2} pump intensity [22], the associated Rabi frequency is comparable to the offset of the pump from the absorbing transition. A variety of processes including

TABLE 29.4

Comparison of Buffer Gaser on a aR(1,1) for Equal Absorption Linewidth

	NH_3	N_2	Buffer gases Ar	He
$\Delta\nu/p$ (MHz torr^{-1})	19.8 ± 0.6[a]	4.34 ± 0.28[a]	1.91 ± 0.20[a]	1.15 ± 0.20[a]
k_{VT} (ms torr^{-1})	(1.3 ± 0.2) × 10^3 [b]	12 ± 1.3[b]	5.9 ± 0.7[b]	9.3 ± 1.0[b]
Partial pressure (torr)	1.0[a]	75[a]	170[a]	283[a]
Peak gain (% cm^{-1})		0.93[a]	0.90[a]	0.50[a]

[a] For 10R(14)-pump intensity of 1.0 MW cm^{-2} [21].

[b] Hovis and Moore [83].

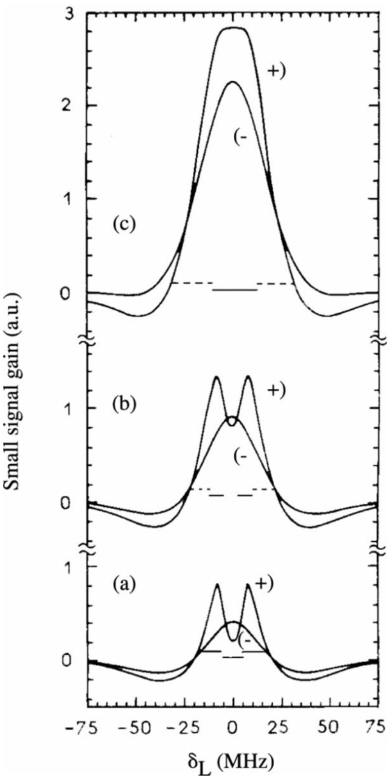

FIGURE 29.14 Calculated small-signal gain for $^{15}NH_3$ at 11.76 μm for co-propagation (+) and counter-propagation (–) of MIR and pump beams for total pressure of (a) 0.75, (b) 1.3 and (c) 3 torr, and for $I_p = 150$ W cm^{-2} [87] (©1991 IEEE). (Reproduced by permission of the IEEE.)

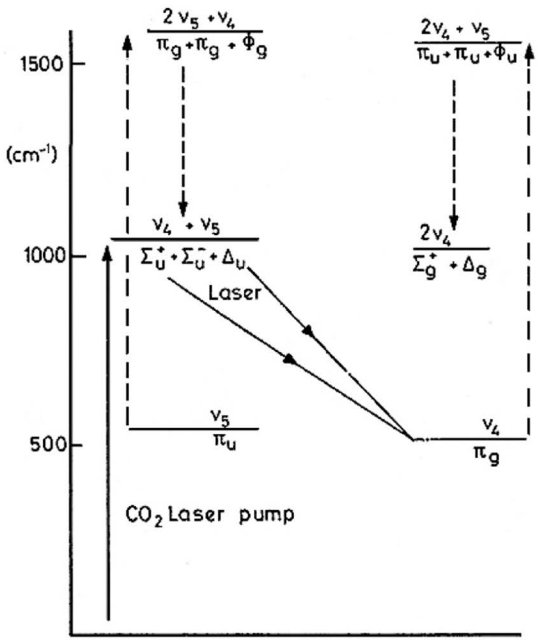

FIGURE 29.15 Partial energy-level diagram of C_2D_2 indicating bands leading to MIROPL emission [90]. (Reproduced by permission of Elsevier.)

population transfer occur. An interesting aspect of pumping this transition is that there are actually two different observed Raman transitions: the aP(8,0) shares the upper level with the pump and the aP(6,0) shares the lower level with the pump. However, the aP(6,0) is pumped indirectly because it first requires a large population transfer to the upper vibrational level. Raman gains of greater than 10% cm^{-1} and inversion gain greater than 2% cm^{-1} are observed and compared to a combined density-matrix and rate-equation model [22].

29.7 Optically Pumped Laser Action in C_2H_2 and Its Isotopes

The CO_2 laser cannot directly optically pump C_2H_2. However, the frequency-doubled 9P(24) TEA CO_2 laser can pump the CO (0 → 1) P(14) transition. Energy is then vibrationally transferred by collisions to the ν_2 level of C_2H_2. Lasing occurs on four lines [1243.08, 1243.75, 1244.12 and 1244.52 ± 0.04 cm^{-1} (vacuum)] of the $\nu_2 \rightarrow \nu_5$ band near 8 μm [88]. The addition of hydrogen improves performance through depopulation of the lower laser level. C_2H_2 was optically pumped with a tunable optically pumped oscillator (OPO) in [89]. The 3 μm OPO pumps C_2H_2 from the ground state to $(\nu_2+\nu_4+\nu_5)$; laser action occurs on transitions $(\nu_2+\nu_4+\nu_5) \rightarrow (\nu_2+\nu_5)$ and $(\nu_2+\nu_4+\nu_5) \rightarrow (\nu_4+\nu_5)$ at 13.6 and 15.7 μm, respectively. Super-radiant emission in both directions was obtained with total unidirectional output energy up to 20 μJ for 1 mJ pump energy for 100 mtorr C_2H_2.

The CO_2 9.6 μm laser can optically pump the C_2D_2 $(\nu_4+\nu_5)$ band (Figure 29.15) to produce MIR lasing for 29 total lines of the $(\nu_4+\nu_5) \rightarrow \nu_4$ transition (Table 29.5); the strongest lines are at 20 and 17.8 μm. Nine additional lines associated with other high-order bands have been reported. The C_2D_2 laser can be categorized according to type of pump laser: (i) TEA, (ii) repetitively pulsed TEA and (iii) multi-atmosphere TE. Only pulsed, not cw, operation has been reported. A total of seven lines from a tunable TEA laser produced 15 C_2D_2 emissions ranging from 17.4 to 20.5 μm [90]. The 9R(12) CO_2 pump produces the highest C_2D_2pulse energies, which are 380 mJ for the combined 20 and 17.8 μm lines with energy efficiencies up to 15% for a cooled cell at 160 K [91]. At 300 K, 130 mJ was obtained. Fischer and Wittig [92] observed rotationally relaxed, grating-tuned oscillation on seven C_2D_2 P-branch lines, in the 17.79–20 μm region, which was obtained with a C_2D_2/He mixture at 50 torr for the 9R(12) TEA CO_2 pumped line. To achieve tunability, superfluorescence and Q-branch oscillation had to be quenched by less than ideal conditions, such as short tube lengths and high pressure. When pumped with the 9R(12) CO_2 TEA laser repetitively pulsed at 100 Hz, ~1 MW peak power and ~5 W average power were obtained for the C_2D_2 17.8 μm line for a liquid-nitrogen-vapour cooled cell [93]. The dependence on pressure and repetition rate is shown in Figure 29.16. Lasing on the 20 μm line produced about one-fifth as much power. The addition of buffer gases (He, N_2 and CF_4) all led to a monotonic sharp drop in the output energy of the C_2D_2 laser [93]. Smith et al. [94] investigated the relaxation mechanisms of C_2D_2, but the modelling of this MIROPL has not been reported.

TABLE 29.5

Summary of Optical Pumping Results in C_2H_2 and Its Isotopes

Molecule	No Lines	Lasing Band	Wavelength Range (μm)	Reference
C_2H_2	4	$v_2 \rightarrow v_5^1$	About 8.04	Optical transfer pumping [88]
C_2H_2	2	$(v_2 + v_4 + v_5) \rightarrow (v_2 + v_5)$	13.6	OPO pump 3 μm [89]
		$\rightarrow (\nu_4 + \nu_5)$	15.7	
C_2D_2	21	$(v_4 + v_5)\Sigma_u^+ \rightarrow v_4$	17.5–20.3	[42, Table 3.2.3.4b], [90,95]
C_2D_2	2	$(v_4 + v_5)\Delta_u^+ \rightarrow v_4$	17.61, 19.67	[42, Table 3.2.3.2b], [90]
C_2D_2	9	Other higher bands	17.5–20.5	[42, Table 3.2.3.2b], [90]
C_2D_2	6	$(v_4 + v_5)\Sigma_u^+ \rightarrow v_4$	17.9–19.9	[43, Table 3.2.32b], [92]
$^{13}C_2D_2$	4		17.2–20.9	[91]
C_2HD	15	$(2v_4)\Sigma^+ \rightarrow v_4$	17.7–20.4	[43, Table 3.3.2.3b], [96]
	Total	$2v_4(\Delta_c) \rightarrow v_4$ and hot bands.		

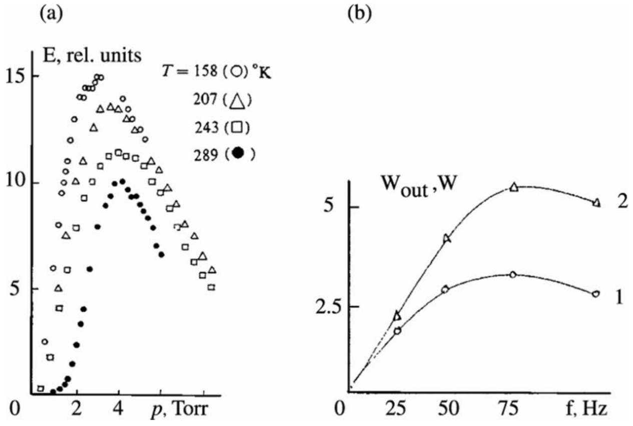

FIGURE 29.16 C_2D_2 laser results: (a) pulse output energy *versus* pressure at four temperatures [93]; (b) dependence of average MIR power on pump repetition frequency [97]. Curve 1 corresponds to a CO_2 short pump pulse of ~150 ns FWHM. Curve 2 corresponds to a CO_2pulse consisting of a 150 ns spike and ~3 μs tail that contains more than 50% of the energy. (Figures reproduced by permission of the American Institute of Physics).

Similarly as for NH_3, [95] used a continuously tunable multi-atmosphere CO_2 TEA laser to pump C_2D_2 and produced 16 additional lines, including a very strong line at 20 μm. The isotope $^{13}C_2D_2$ has produced a total of four lines in the 17–21 μm region for four different CO_2 pump lines [91]. Finally, 15 lines in the 17.7–20.4 μm region were obtained with C_2HD using eight pump lines from a 9 μm region CO_2 laser [96].

29.8 Applications and Future Prospects

The future prospects for the NH_3 and C_2H_2 MIROPLs and their isotopes will depend on the needs associated with applications and what alternative sources exist. Gas lasers have the attributes that they can be constructed in a laboratory with glass and vacuum capabilities. However, gas lasers suffer from their size and are replaced by solid-state lasers if one exists that meets the power and spectral requirements. The MIR quantum cascade (QC) semiconductor laser has come to the forefront and offers great promise as an efficient source for applications not requiring large powers, e.g. chemical sensing [98]. Such QC lasers based on GaInAs/AlInAs structures emit at wavelengths in the 3.4–20 μm region with peak output powers in the fraction of a watt range.

The NH_3 laser covers a spectral region not covered by the CO_2 laser or any other intense source. The very high spectral purity of an NH_3 laser has been used in spectroscopic investigation of the fine structure of a single trapped barium ion [99, 100]. Other applications of the NH_3 MIROPL include gas absorption measurements [101], laser spectrometers for analysis of gaseous mixtures [102], remote gas analyser [103], lidar [105,106], (sequential) optical pumping of the NH_3 FIR laser, i.e. using the 11–13 μm NH_3 laser to pump a FIR laser in the range of 60–400 μm [69], optical pumping an InSb spin-flip Raman laser [32], and multi-photon dissociation of molecules [107]. Mixing an ammonia laser with a CO_2 laser and microwave radiation has generated tunable FIR radiation for high-resolution spectroscopy [108]. High-repetition-rate pulsed gas lasers have their applications in chemistry and isotope separation [109], e.g. separation of tritium from deuterium [110].

Multi-frequency lasing makes the NH_3 laser attractive for differential-absorption lidar systems. The NH_3 laser has the unique effect that when it is pumped by a TEA CO_2 laser operating on the 9R(30) line, it can generate up to 30 lines *simultaneously* and co-linearly in the 12–14 μm region [102] with efficiencies of 20% [105]. Numerical simulations have been carried out to understand the simultaneous multi-frequency operation aspect of NH_3 [111], but this aspect has not been fully investigated [102].

Ammonia has clearly become the leading MIROPL; in comparison, there has been relatively little application reported for the C_2H_2 or C_2D_2 MIROPL; nonetheless, these sources offer alternative wavelengths should a need develop. Deuterated acetylene, in particular, has strong lines for applications in the 16 μm region; NH_3 also emits in this region but most of the lines require two pump sources.

REFERENCES

1. Chang T Y 1977 Optical pumping in gases topics *Nonlinear infrared Generation (Applied Physics 16)* ed Y R Shen (New York: Springer) pp 215–72.

2. Grasiuk A Z, Letokhov V S and Lobko V V 1980 Molecular infrared lasers using resonant laser pumping *Prog. Quantum. Electron.* **6** 245–93.
3. Gupta P K and Mehendale S C 1987 Mid-infrared optically pumped molecular lasers *Hyperfine Interact.* **37** 243–74.
4. Harrison R G and Gupta P K 1983 Optically pumped mid-infrared molecular gas lasers *Infrared and Millimeter Waves, Vol 7, Coherent Sources And Applications part II*, ed K J Button (New York: Academic).
5. Harrison R G and Gupta P K 1984 Mid infrared optically pumped molecular gas lasers *NATO Advanced Study institute on Physics of New Laser Sources (NATO ASI Series 132) (San Miniato)* (New York: Plenum Press) pp 201–16.
6. Jones C R 1978 Optically pumped mid-IR lasers 1978 *Laser Focus* **14** 68–74.
7. Akitt D P and Wittig C F 1969 Laser emission in ammonia *J. Appl. Phys.* **40** 902–3.
8. Mathias L E S, Crocker A and Wills M S 1965 Laser oscillations at wavelengths between 21 And 32 μm from a pulsed discharge through ammonia *Phys. Lett.* **14** 33–4.
9. Nelson L Y, Fisher C H, Hoverson S J, Byron S R, O'Niell F and Whitney W T 1977 Electron-beam -controlled excitation of a CO–C_2H_2 energy transfer laser *Appl. Phys. Lett.* **30** 192–5.
10. Shelton C F and Byrne F T 1970 Laser emission near 8 μm from a H_2_C_2H_2-He mixture *Appl. Phys. Lett.* **17** 436–7.
11. Stregack J A, Wexler B L and Hart G A 1976 CW CO-CS_2, CO-C_2H_2, CO-N_2O Energy-transfer lasers *Appl. Phys. Lett.* **28** 137–9.
12. Jones C R, Buchwald M I, Gundersen M and Bushnell A H 1978 Ammonia laser optically pumped with an HF laser *Opt. Commun.* **24** 27–30.
13. Frank E M, Weiss C O, Siemsen K, Grinda M and Willenberg G D 1982 Predictions of far-infrared laser lines from $^{14}NH_3$ and $^{15}NH_3$ *Opt. Lett.* **7** 96–8.
14. Herzberg G 1945 *Molecular Spectra and Molecular Structure, II. Infrared and Raman Spectra of Polyatomic Molecules* (New York: Van Nostrand).
15. Hollas J M 1998 *High Resolution Spectroscopy* 2nd edn (New York: Wiley).
16. Chang T Y and McGee J D 1976 Off-resonant laser action in NH_3 and C_2H_4 without population inversion *Appl. Phys. Lett.* **29** 725–7.
17. White J D and Reid J 1993 Efficient NH_3 laser operation in the 16 μm to 21 μm region *Appl. Opt.* **32** 2053–7.
18. Rolland C, Reid J, Garside B K, Jessop P E and Morrison H D 1983 Tunable-diode-laser measurements of gain in optically pumped NH_3 *Opt. Lett.* **8** 36–8.
19. Rolland C, Garside B K and Reid J 1982 CW optically pumped 12 μm NH_3 laser *Appl. Phys. Lett.* **40** 655–7.
20. Julien F, Wazen P, Lourtioz J-M and DeTemple T A 1983 The cw optically pumped 12.08 μm Raman laser—theory and experiments for high power conversion efficiency *IEEE J. Quantum Electron.* **QE-19** 1654–62.
21. Morrison H D, Garside B K and Reid J 1984 Dynamics of the optically pumped midinfrared NH_3 laser at high pump power—part I: inversion gain *IEEE J. Quantum Electron.* **QE-20** 1051–9.
22. Morrison H D, Garside B K and Reid J 1984 Dynamics of the optically pumped midinfrared NH_3 laser at high pump power—part II: Raman gain and ac Stark shifts *IEEE J. Quantum Electron.* **QE-20** 1060–4.
23. Tobin M S, Sattler J P and Daley T W 1982 New SMMW laser transitions optically pumped by a tunable CO_2 waveguide laser *IEEE J. Quantum Electron.* **QE-18** 79–86.
24. Heppner J, Weiss C O, Hubner U and Schinn G 1980 Gain in cw laser pumped FIR laser gases *IEEE J. Quantum Electron.* **QE-13** 392–401.
25. Siemsen K J 1986 Private communication.
26. Tillert T, Zimnas P and Renk K F 1996 Partly tunable mid-infrared NH_3 laser *Int. J. Infrared Millimeter Waves* **17** 1011–21.
27. Biswas D J, Sarkar S K and Nayak A K 1992 Improved performance of an NH_3 laser by temporal shaping of the CO_2 laser pulse *Opt. Commun.* **89** 249–52.
28. Midorikawa K, Matsuda I, Obara M and Fujioka T 1980 Efficient energy extraction by superradiant emission in NH_3 *Opt. Commun.* **32** 447–50.
29. Makowe J, Boyarkin O V and Rizzo T R 1998 Highly efficient optically pumped NH_3 laser with near diffraction limited output *Rev. Sci. Instrum.* **69** 4041–3.
30. Nilaya J P and Biswas D J 2001 Versatile cavity for optically pumped molecular lasers *Rev. Sci. Instrum.* **72** 1343–5.
31. Harrison R G and Al-Watban F A 1977 High power laser emission at 12.812 μm from an optically pumped ammonia laser *Opt. Commun.* **20** 225–8.
32. Miyazaki K, Kasada H and Ohtsuka M 1994 Tunable laser for sensing atmospheric transmission in the infrared region of 11–16 μm *Int J. Infrared Millimeter Waves* **15** 1669–74.
33. Fry S M 1976 Optically pumped multi-line NH_3 laser *Opt. Commun.* **19** 320–4.
34. Chang T Y and McGee J D 1976 Laser action at 12.812 μm in optically pumped NH_3 *Appl. Phys. Lett.* **28** 526–8.
35. Siemsen K J, Reid J and Danagher D J 1986 Improved cw lasers in the 11–13 μm wavelength region produced by optically pumping NH_3 *Appl. Opt.* **25** 86–91.
36. Shaw E D and Patel C K N 1978 Improved pumping geometry for high power NH_3 lasers *Opt. Commun.* **27** 419–22.
37. Vasil'ev B I, Grasyuk A Z, Dyad'kin A P, Sukhanov A N and Yastrebkov A B 1980 High-power efficient optically pumped NH_3 laser, tunable over the range 770–890 cm^{-1} *Sov. J. Quantum Electron.* **10** 64–8.
38. Rolland C, Reid J and Garside B K 1984 Line-tunable oscillation of a cw NH_3 laser from 10.7 to 13.3 μm *Appl. Phys. Lett.* **44** 380–2.
39. White J D, Chakrabarti A and Reid J 1990b High-power, high-efficiency optically pumped NH_3 lasers *Appl. Phys. B* **51** 371–3.
40. Baranov V Y, Kazakov S A, Pis'menny V. D, Starodubtsev A I, Velikhov E P, Gorokhov Y A and Letokhov V S 1978 Multiwatt optically pumped ammonia laser operation in the 12–13 μm *Appl. Phys.* **17** 317–20.
41. Rolland C, Reid J and Garside B K 1984 10 W cw optically pumped 12 μm laser *Appl. Phys. Lett.* **44** 725–7.
42. Weber M J (ed) 1985 *CRC Handbook of Laser Science and Technology, Volume 1: Lasers and Masers* (Boca Raton, FL: Chemical Rubber Company).
43. Weber M J (ed) 1991 *CRC Handbook of Laser Science and Technology, Supplement 1: Lasers* (Boca Raton, FL: Chemical Rubber Company).
44. Chakrabarti A and Reid J 1987 Simple cw NH_3 laser operating in the 11–13 μm region *Rev. Sci. Instrum.* **58** 1413–16.

45. Danielewicz E J, Malk E G and Coleman P D 1976 High-power vibration–rotation emission from 14 NH_3 optically pumped off resonance *Appl. Phys. Lett.* **29** 557–9.
46. Deka B K, Dyer P E and Winfield R J 1980a optically pumped NH_3 laser using a continuously tunable CO_2 laser *Opt. Commun.* **33** 206–8.
47. Kroeker D F and Reid J 1986 Line-tunable cw ortho- and para-NH_3 lasers operating at wavelengths of 11 to 14 μm *Appl. Opt.* **25** 2929–33.
48. Tashiro H, Suzuki K, Toyoda, K and Namba S 1980 Wide range line-tunable oscillation of an optically pumped NH_3 laser *Appl. Phys.* **21** 237–40.
49. Tiee J J and Wittig C 1978 Optically pumped molecular lasers in the 11–17 μm region *J. Appl. Phys.* **49** 61–4.
50. Yamabayashi N, Yoshida T, Miyazaki K and Fujisawa K 1979 Infrared multi-line NH_3 laser and its application for pumping an InSb laser *Opt. Commun.* **30** 245–8.
51. Znotins T A, Reid J, Garside B K and Ballik E A 1980 12 μm NH_3 laser pumped by a sequence CO_2 laser *Opt. Lett.* **5** 528–30.
52. Bobrovskii A N, Vedenov A A, Kozhevnikov A V and Sobolenko D N 1979 NH_3 laser pumped by two CO_2 lasers *JETP Lett.* **29** 536–9.
53. Eggleston J, Dallarosa J, Bischel W K, Bokor J and Rhodes C K 1979 Generation of 16 μm radiation in14NH3 by two-quantum excitation of the $2\nu_2^-$ (7,5) state *J. Appl. Phys.* **50** 3867–70.
54. Jacobs R R, Prosnitz D, Bischell W K and Rhodes C K 1976 Laser generation from 6 to 35 μm following two-photon excitation of ammonia *Appl. Phys. Lett.* **29** 710–2.
55. Lee W, Kim D, Mark E and Leap J 1979 Hot-band lasing in NH_3 *IEEE J. Quantum Electron.* **QE-15** 838–9.
56. Morrison H D, Reid J and Garside B K 1984c 16–21 μm line-tunable NH_3 laser produced by two step optical pumping *Appl. Phys. Lett.* **45** 321–3.
57. Pinson P, Delage A, Girard G and Michon M 1981 Characteristics of two-step and two-photon-excited emissions in $^{14}NH_3$*J. Appl. Phys.* **52** 2634–7.
58. Akhrarov M, Vasil'ev B I, Grasyuk A Z and Soskov V I 1984 Middle infrared laser utilizing isotopically substituted$^{15}NH_3$ ammonia molecules *Sov. J. Quantum Electron.* **14** 572–3.
59. Akhrarov M, Vasil'ev B I, Grasyuk A Z, Soskov V I and Yastrebkov A B 1986 $^{15}NH_3$ laser with two-photon optical pumping *Sov. J. Quantum Electron.* **16** 1016–19.
60. Pinson P, Girard G and Michon M 1982 Optically pumped$^{14}NH_3$ laser and its Stark tuning at 10.78 μm *Appl. Phys. B* **28** 55–62.
61. Siemsen K J, Madej A A and Whitford B G 1995a Frequency stabilized ammonia laser system for probing the 24 THz clock transition of a trapped barium ion *IEEE J. Quantum Electron.* **31** 1764–73.
62. Siemsen K J, Madej A A and Whitford B G 1995b Absolute frequency measurement of the sP(8,6) transition of $^{15}NH_3$*J. Mol. Spectrosc.* **174** 613–14.
63. Siemsen K J and Reid J 1985 Heterodyne frequency measurements of$^{14}NH_3$ and$^{15}NH_3$ ν_2-band transitions *Opt. Lett.* **10** 594–7.
64. Sattler J P, Miller L S and Worchesky T L 1981 Diode-laser heterodyne measurements on (NH-3)-N-14*J. Mol. Spectrosc.* **88** 347–51.
65. Sattler J P and Worchesky T L 1981 Additional diode-laser heterodyne measurements on ammonia *J. Mol. Spectrosc.* **90** 297–301.
66. Morrison H D, Garside B K and Reid J 1982 Raman gain in 12 μm NH3 lasers *Opt. Lett.* **7** 520–2.
67. Gupta P K, Kar A K, Taghizadeh M R and Harrison R G 1981a 12.8 μm NH_3 laser emission with 40–60% power conversion and up to 28% energy conversion efficiency *Appl. Phys. Lett.* **39** 32–4.
68. Wazen P and Bourdet G L 1989 CW MIR optically pumped ammonia laser with large frequency tunability *Opt. Commun.* **71** 81–4.
69. Tachikawa M and Evenson K M 1996 Sequential optical pumping of a far-infrared ammonia laser *Opt. Lett.* **21** 1247–9.
70. White J D, Bruce D M, Beckwith P H and Reid J 1990a Efficient optically pumped NH_3 amplifiers in the 10–12 μm region *Appl. Phys. B* **50** 345–54.
71. Wazen P, Lourtioz J-M, Julien F and DeTemple T 1987 High-power optically pumped cw 12 μm NH_3 amplifier systems *IEEE J. Quantum Electron.* **23** 623–32.
72. Siemsen K J, Williams E and Reid J 1987 Alternative approach to stable lasers: the optically pumped laser *Opt. Lett.* **12** 879–81.
73. Siemsen K J, Madej A A, Hanes G R and Reid J 1992 Improved frequency stability of the ammonia laser *Appl. Phys. B* **54** 126–31.
74. Harrison R G and Al-Saidi I A 1985 Experimental-evidence of self-pulsing and chaos in an optically pumped 12 μm NH_3 laser *Opt. Commun.* **54** 107–11.
75. Haken H 1975 Analogy between higher instabilities in fluids and lasers *Phys. Lett. A* **53** 77–8.
76. Biswas D J and Harrison R G 1985 Observation of optical turbulence in a single mode homogeneously broadened optically pumped molecular laser *Opt. Commun.* **54** 112–16.
77. Siemsen K J, Reid J and Weiss C O 1987 Self pulsing and chaos of a vibrational NH_3 laser *Opt. Commun.* **63** 415–16.
78. Gupta P K and Harrison R G 1981b Rate equation model for mid IR OPML having common pump and upper lasing level; application to 12.8 μm emission from NH_3 *IEEE J. Quantum Electron.* **QE-17** 2238–44.
79. Sinclair R L, Reid J, Morrison H D Garside B K, and Rolland C 1985 Dynamics of the line-tunable 12 μm continuous-wave NH_3 laser as measured with a tunable-diode laser *J. Opt. Soc. Am. B* **2** 800–5.
80. Morrison H D, Garside B K and Reid J 1985 Gain dynamics in pulsed 12 μm NH_3 lasers *J. Opt. Soc. Am.* **2** 535–40.
81. Luo X and Qui R 1997 Optimized operation of optically pumped NH_3 laser emission at 12.08 μm and 12.81 μm *Int. J. Infrared Millimeter Waves* **18** 641–52.
82. Silva F, Vilaseca R, and Corbalán R 1992 Theroretical gain spectrum of coherently pumped mid-infrared Fabry–Pérot lasers *Opt. Commun.* **94** 589–98.
83. Hovis F E and Moore C B 1980 Temperature dependence of vibrational energy transfer in NH_3 and $H_2^{18}O$ *J. Chem. Phys.* **72** 2397–402.
84. Delsalt C and Keller J-C 1978 The optical Autler–Townes effect in Doppler broadened three-level systems *J. Physique* **39** 350–60.
85. Wazen P and Bourdet G L 1989 Experimental investigation of the MIR optically pumped ammonia bidirectional ring laser *Appl. Phys. B* **49** 377–81.

86. Siemsen K J, Madej A A and Reid J 1991 Narrow gain spikes and frequency pulling in the midinfrared ammonia laser *IEEE J. Quantum Electron.* **27** 1199–206.
87. Wazen P and Bourdet G L 1991 Gain anisotropy and simultaneous bidirectional emission of a Doppler-broadened MIR optically pumped ammonia ring laser *IEEE J. Quantum Electron.* **27** 152–7.
88. Kildal H and Deutsch T F 1975 Optically pumped infrared V–V transfer lasers *Appl. Phys. Lett.* **27** 500–2.
89. Tapalian H C, Michaels C A and Flynn G W 1997 Midinfrared molecular gas lasers optically pumped by a continuously tunable infrared optical parametric oscillator *Appl. Phys. Lett.* **70** 2215–17.
90. Rutt H N and Green J M 1978 Optically pumped laser action in dideuteroacetylene *Opt. Commun.* **26** 422–6.
91. Rutt H N 1980 Development of the C_2D_2 laser: high energy, line-tuned, and 13C isotopic operation *Topical Meeting on Infrared Lasers: A Digest of Technical Papers Presented at the Topical Meeting on Infrared Lasers (Los Angeles, CA)* (Washington, DC: OSA).
92. Fischer T A and Wittig C 1982 Rotationally relaxed, grating tuned laser oscillations in optically pumped C_2D_2 *Appl. Phys. Lett.* **41** 107–9.
93. Baranov V Y, Dyad'kin A P, Pigul'skii S V and Starodubtsev A I 1989 Laser-pumped C_2D_2 laser *Sov. J. Quantum Electron.* **19** 715–18.
94. Smith N J G, Davis C C and Smith W M 1985 Relaxation of C_2D_2 (ν_4, ν_4) by vibration-rotation, translation energy transfer *J. Chem. Soc. Faraday Trans.* **2** 417–32.
95. Deka B K, Dyer P E and Winfield R J 1980b New 17–21 μm laser lines in C_2D_2 using a continuously tunable CO_2 laser pump *Opt. Lett.* **5** 194–5.
96. Rutt H N 1984 Optically-pumped laser action in monodeutero-acetylene (HCCD) *Infrared Phys.* **24** 535–41.
97. Baranov V Y, Dyad'kin A P, Kazakov S A, Pigul'skii S V and Starodubtsev A I 1987 Optically pumped pulse-periodic C_2D_2 laser *Sov. J. Quantum Electron.* **17** 771–2.
98. Capasso F, Gmachl C, Tredicucci A, Sivco D L, Baillargeon J N, Cho A Y and Liu H C 2000 New frontiers in quantum cascade lasers and applications *IEEE J. Selected Topics Quantum Electron.* **6** 931–46.
99. Madej A A, Siemsen K J, Sankay J D, Clark, R F and Vanier J 1993 High-resolution spectroscopy and frequency measurement of the midinfrared $5d^2D_{3/2}$–$5d^2D_{5/2}$ transition of a single laser-cooled barium ion *IEEE Trans. Instrum. Meas.* **42** 234–41 a review *Infrared Phys. Technol.* **36** 465–73.
100. Whitford B G, Siemsen K J, Madej A A, and Sankey J D 1994 Absolute-frequency measurement of the narrow-linewidth 24 THz D-D transition of a single laser-cooled barium ion *Opt. Lett.* **19** 356–8.
101. Benzerhouni K, Meyer F and Lourtioz J M 1986 Absorption-measurements using cw MIR NH_3 laser *Infrared Phys.* **26** 377–80.
102. Baranov V Y, Khakhlev A A, Maluta D D, Mezhevov V S, Petrushevich Y V and Poliakov G A 2000 Analysis of gaseous mixtures with multifrequency NH_3 laser spectrometer *Infrared Phys. Technol.* **41** 97–113.
103. Banakh V A, Ponomarev Y N, Smalikho I N, Firsov K M, Maluta D D and Poliakov G A 2000 Simulation of operation of multiwave remote gas-analyser based on NH_3-laser *Infrared Phys. Technol.* **41** 115–31.
104. Anan'ev V Y, Vasil'ev B I, Lobanov A N, Lytkin A P, Whang C C and Sung K J 2000 Two-frequency lidar based on an ammonium laser *Quantum Electron.* **30** 535–9.
105. Vasil'ev B I and Whan C C 2000 NH_3 Laser as a radiation source for a two-frequency lidar *Quantum Electron.* **30** 1105–6.
106. Makowe J, Boyarkin O V and Rizzo T R 2000 Collision-free infrared multiphoton dissociation of silane *J. Phys. Chem. A* **104** 11505–11.
107. Odashima H, Tachikawa M, Zink L R and Evenson K M 1997 Extension of tunable far-infrared spectroscopy to 7.9 THz *Opt. Lett.* **22** 822–4.
108. Baranov V Y 1983 High repetition rate pulsed gas lasers and their applications in chemistry and isotope separation *IEEE J. Quantum Electron.* **QE-19** 1577–87.
109. Nayak A K, Sarkar S K, Biswas D J, RamaRao K V S and Mittal J P 1991 Separation of tritium from deuterium by pulsed NH_3 laser-selective multiple photon dissociation of $CTCl_3$ *Appl. Phys. B* **53** 246–9.
110. Petrushevich Y V 1998 Theoretical computational investigation of an NH_3 laser subjected to intensive pulsed pumping *Quantum Electron.* **28** 3–8.
111. Rolland C, Reid J, Garside B K, Morrison H D and Jessop P E Investigation of cw optically pumped 12-μm NH_3 lasers using a tunable diode laser *Appl. Opt.* **23** 87–93.
112. Urban W 1995 Physics and spectroscopic applications of carbon monoxide lasers, a review *Infrared Phys. Technol.* **36** 465–73.

FURTHER READING

Barrow GM 1975 *Molecular Spectroscopy* (New York: McGraw-Hill).

This book is particularly recommended for the beginning spectroscopist.

Brown R T 1987 CO_2 TEA lasers *Handbook of Molecular Lasers* ed P K Cheo (New York: Marcel Dekker) ch 2, pp 93–164.

This gives information concerning TEA lasers.

Cheo P K 1987 Emission spectra of molecular lasers *Handbook of Molecular Lasers* ed P K Cheo (New York: Marcel Dekker) ch 1, pp 1–92.

This chapter describes the spectroscopy of the CO_2 molecule and lists the wavelengths for the various 12C16O2 laser transitions and the isotopic variations.

Gordiets B F, Osipov A I, Stupochenko E V, and Shelepin L A 1973 Vibrational relaxation in gases and molecular lasers *Sov. Phys.–Usp.* **15** 759–85.

This paper discusses the vibrational kinetics and mechanisms of lasers that are based on vibrational-rotational transitions and is the foundation for most of the rate-equation models for the NH_3 MIROPL.

Marcatili E A J and Schmeltzer R A 1964 Hollow metallic and dielectric waveguides for long distance optical transmission and lasers *Bell Syst. Tech. J.* **43** 1783–809

This paper gives the theory of oversized waveguides that are frequently used in MIROPLs.

Tobin M S 1985 A review of optically pumped NMMW lasers *Proc. IEEE* **73** 61–85

This paper reviews FIROPLs but addresses optical pumping issues that also relate to MIROPLs.

30

Far-IR Lasers: HCN, H_2O

Wilhelm Prettl

CONTENTS

30.1 Introduction 433
30.2 Laser Lines 433
30.3 HCN Laser 434
  30.3.1 Laser Mechanism 434
  30.3.2 Laser Fuels 435
  30.3.3 Wall Effects 435
30.4 H_2O Laser 436
30.5 Resonator 436
30.6 Glow Discharge and Additive Gases 437
30.7 Design and Operational Characteristics 437
30.8 Summary 438
References 438
Further Reading 439

30.1 Introduction

This chapter deals with electric discharge pumped far-infrared lasers. The discovery of the H_2O and the HCN laser by Gebbie et al. [1–3] opened up a new age of spectroscopy in the far-infrared, a spectral range which had been notoriously hampered by the low power of thermal radiation sources. Many laboratories took up research on glow discharge excited molecular lasers, and suddenly a substantial number of fairly strong laser lines in the far-infrared were available. Many measurements of fundamental importance could be carried out in various fields. In particular, in solid-state physics, a new technique, magneto-spectroscopy, evolved which made use of fixed frequency laser lines, tuning the energy levels of the object of investigation by an external magnetic field. For instance, after its feasibility was first demonstrated [4], most effective masses and band parameters of semiconductors were determined by this method [5,6].

Besides HCN, H_2O and the isotopic derivatives DCN and D_2O, a number of other polyatomic molecules have been found to be suitable for laser action in an electric gas discharge. Among them are NH_3, OCS and SO_2. However, the lifetime of these molecules in a high voltage electric discharge is very short. Electrons with average kinetic energy in the range of ~10 eV break chemical bonds and decompose molecules. Therefore, most polyatomic molecule lasers can only be operated in a pulsed mode with a duty cycle of the order of 1 cycle s^{-1}.

Among the many laser lines observed, there are a few strong laser lines in the cw mode lying in atmospheric windows. Today only these lines are of practical importance. These lines are currently used as an analytical tool in plasma diagnostics [7], to heat electrons in semiconductors [8] and in Stark spectroscopy on molecules [9]. Finally, it is interesting to note that one of the HCN laser lines belongs to about 100 cosmic laser transitions observed so far [10].

In this article, the basic physics, techniques and construction of HCN and H_2O lasers will be summarized.

30.2 Laser Lines

HCN and H_2O lasers may be electrically pumped in a longitudinal configuration of electrodes in the pulsed and cw mode of operation as well as transversely excited [11]. Laser action of HCN by HF pumping and for both lasers by flash lamp excitation has also been observed. However, today only longitudinally pumped cw lasers are in practical use.

Under longitudinal excitation, the gain bandwidth of both lasers is for practically all lines smaller than the frequency separation of the subsequent fundamental longitudinal modes or longitudinal and higher transverse modes. Hence, the output intensity as a function of the resonator length is modulated with sharp peaks at resonance between the molecular transition frequency and the resonances of the resonator. Therefore, a good estimate of the wavelength of an emission can easily be performed by monitoring the laser intensity as a function of the resonator length, a technique which has been termed resonator interferometry [12]. In many cases, more than one laser line or more than one mode can oscillate under the same operational conditions. Tuning the resonator length here is also a useful tool with which to obtain single-line and single-mode emission.

TABLE 30.1

Strong cw Laser Lines of the HCN and the H_2O Laser. The Highest Reported Power Is Given

	Wavelength Approximate	Wavelength High Resolution	Frequency	Power
	(μm)	(μm)	(GHz)	(mW)
HCN	337	336.5578[a]	890.7607[a]	250[b]
H_2O	28	27.971[c]	10 718.073[e]	150[c]
	78	78.442[c]	3821.755 (4)	12[c]
	119	118.59[c]	2527.9528[d]	52[c]

[a] Ref. [17].
[b] Ref. [18].
[c] Ref. [19].
[d] Ref. [20].
[e] Ref. [21].

The laser wavelengths were determined with high accuracy by long path-difference Michelson interferometry [13]. Very high precision measurements of laser line frequencies were carried out by heterodyning the laser emission with the high harmonics of coherent microwave sources like the klystron [14].

The gain in energy per pulse due to transverse excitation is not much larger than that at longitudinal excitation; however, discharge instabilities occurring at high longitudinal currents are avoided. In addition, transverse excitation increases the gain bandwidth, which makes tuning and stabilization of the resonator length unnecessary.

With HCN as a laser medium essentially two groups, each of four or five laser lines, may be obtained. One group is around the strongest HCN laser line at $\lambda = 337$ μm (see Table 30.1) and the other is in the range of 130 μm. With DCN, a similar set of lines may be obtained around 190 μm. The longest wavelengths with an electric discharge pumped molecular laser were observed by Steffen et al. with ICN at 538 μm [15] and at 774 μm [16]. These lines had not been assigned until then.

The 337 μm line of HCN is the strongest far-infrared laser emission of an electrically pumped molecular laser. It may yield cw power around 250 mW [18].

With the water vapour laser in the pulsed mode more than 100 laser lines and over a dozen lines in the cw mode have been found in the wavelength range 7–220 μm. In addition to these lines attributed to the isotopic species $H_2{}^{16}O$, a comparable number of laser lines have been obtained with $H_2{}^{18}O$ and $D_2{}^{16}O$. The molecular transitions of most but not all of these lines have been identified. A list of the wavelengths is given in [22,23].

The wavelengths of the strong lines in the cw mode of the H_2O laser are 28, 78 and 119 μm, as summarized in Table 30.1. Only these lines are of practical importance. An exhaustive list of experimentally observed lines of glow discharge pumped far-infrared lasers is given in [24].

30.3 HCN Laser

30.3.1 Laser Mechanism

The history of the identification of the energy levels involved in the far-infrared transitions of the HCN and the H_2O laser and even the recognition of the laser active molecules illustrates the complexity of molecular spectra and molecular kinetics. The striking feature of these triatomic molecular lasers is that there is no regularity in the emission-line spectra as in the case of the CO_2 or CO laser. It took three years of controversial discussions in the literature until Lide and Maki [25] succeeded in assigning the strong 337 μm line and the neighbouring line at 311 μm of the HCN laser correctly.

The essential physical background of laser transitions comprises the resonance perturbations in the vibrational–rotational system due to the Coriolis force acting in the frame of the rotating molecule and anharmonic resonances like the Fermi resonance [26]. The electric discharge creates a population inversion between low-lying predominantly stretching modes and bending modes. Laser action occurs by rotational–vibrational inter-mode transitions. In the harmonic approximation, inter-mode transitions are forbidden; therefore, anharmonicity of the molecular vibrations is important for laser action.[1] The transition probabilities between different vibrational modes are usually too small to give sufficient gain for laser oscillation. However, if two molecular states belonging to the same symmetry species come accidentally close in energy, their wavefunctions may mix. The mixing of vibrational states of identical symmetry occurs due to anharmonicity. A coupling of vibrational states of differing symmetry may be accomplished by the Coriolis interaction of nearly degenerate rotational–vibrational states if the overall symmetry species are the same. In particular, the angular momentum quantum number *J* and the parity of the interacting rotational states must be identical. In some sense, the inter-mode vibrational transition borrows oscillator strength from rotational transitions. If laser oscillation occurs between two different modes, rotational states in the individual modes are populated and depopulated. Hence, laser action may also occur by cascades of purely rotational transitions. Therefore, HCN as well as H_2O lasers have a tendency towards simultaneous multi-line emission.

In the case of the linear molecule HCN laser, the mixing of different vibrational modes due to the Coriolis force is possible between almost degenerate states of the same angular momentum *J* and parity. The mixing of these states allows optical inter-mode transitions. In the electric discharge of a HCN laser, the molecule is formed with a high amplitude for the stretching mode $(\nu_1\ \nu_2\ \nu_3)=(100)$ which is mostly made up of CN vibrations. This is due to the fact that the (100) state is practically metastable [27]. Vibrational transitions from (100) to the (000) ground state are almost three orders of magnitude slower than the (010)–(000) and (001)–(000) transitions [28]. In the gas discharge of HCN laser, molecules are distributed over all vibrational states which are quickly depopulated by spontaneous emission cascading down the vibrational levels to the ground state. The metastable (100) state and all combinations based on it become overpopulated compared to other vibrational modes. Such combinations are obtained by adding one or two quanta of the bending mode ν_2 yielding a combination of the vibrational states (110) and (120) which are very close in energy to the pure bending modes (040) and (050), respectively. The bending and stretching combination states give the upper laser levels whereas the purely bending states represent the lower laser levels. This is due to faster relaxation of the bending modes compared to stretching–bending equilibrations [29].

---

[1] In fact, all electric discharge pumped molecular infrared gas lasers are based on inter-mode transitions made possible by anharmonicity.

The pumping mechanism is not very effective as the majority of the molecules relax back to the ground state without passing through the laser transitions. This correlates to the low small-signal gain of the order of 0.1 dB m^{-1} and the correspondingly moderate output power of the order of magnitude of 10–100 mW.

In the case of HCN transitions around the strong 337 μm line, two rotational levels of the combined stretching and bending mode (11^10) and the bending mode (04^00) having the same rotational quantum number and parity, $J^+(10)$, lie sufficiently close together that the Coriolis interaction relaxes the selection rule of forbidden inter-mode transitions. In addition, the inter-vibrational transitions pump purely rotational transition cascades at 284, 310, 335 and 373 μm. High-precision measurements of the frequencies of these laser lines support this level assignment. The sum of the frequencies of the 311 and 335 μm lines differ by less than one part in 10^6 from the sum of the frequencies of the 310 and 337 μm lines [17]. A schematic energy-level diagram and the corresponding laser transitions are displayed in Figure 30.1.

The same mechanism can be assumed for other groups of laser lines. In the HCN laser, the coupling of $J=26$ rotational states of the 12^00 and the 05^10 vibration ladders leads to an emission of laser lines in the region of ~130 μm and in the DCN laser, a similar perturbation occurs between $J=21$ states of the (22^00) and (09^10) vibrations generating laser emission in the vicinity of 190 μm.

30.3.2 Laser Fuels

HCN molecules are not stable in the glow discharge. They are decomposed by the impact of high-energy electrons and form again in excited vibrational–rotational states. Thus, the HCN laser is a chemical laser. In fact, it is not necessary to use poisonous HCN as a laser medium but almost any compound or mixture of molecules containing C, N and H, with a sufficient excess of H, may produce HCN in the gas discharge and generate laser action. Several chemical reactions have been discussed, making population inversion conceivable [30].

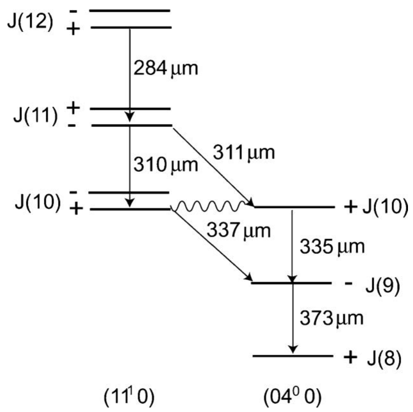

FIGURE 30.1 Rotation–vibration energy-level diagram around the Coriolis resonance (curly line) of (11^10) and (04^00) vibrational states and laser transitions (arrows) leading to the strong 337 μm line and the lines in the vicinity of 337 μm. The energy levels are about 2900 cm^{-1} above the ground state. J and ± denote the angular momentum and the overall parity of the states. The plotted l-type doubling of the rotational levels of (11^10) is largely exaggerated.

Gas mixtures are selected from the point of view of high output power and small polymer deposition on the resonator wall (see later). A standard fuel is the gas mixture N_2+CH_4 in volume ratios ranging from 1:1 to 1:3. Other laser media are CH_3N, C_2H_5CN and CH_4+NH_3. Remarkably, $C_2H_2+N_2$ is laser inactive but may be activated by adding H_2 [31].

30.3.3 Wall Effects

Physical and chemical processes at the inner walls of the discharge tube are of central importance for the operation of an HCN laser. A characteristic feature of the HCN laser is the deposit of a polymer layer on the discharge tube and on the mirrors of the resonator. The deposited film, coloured between yellow and dark brown, causes a substantial reduction in output power and, if the layer gets too thick, laser emission ceases. The deposit can be removed by running the discharge with H_2O for several hours. Adding oxygen speeds up the process of converting the deposit into gaseous products.

Chemical analysis and infrared spectroscopy showed that the main constituent of the electric discharge polymerized material is $(CN)_x$ [32]. Laser emission of the 337 μm HCN line may be obtained in a discharge tube with the polymer deposit running the discharge with pure H_2O, H_2 or NH_3. Laser action occurs because HCN molecules are formed in sufficient concentration by the discharge from the wall deposit.

The generation of laser active molecules at the walls leads to a surprising dependence of the gain on the laser tube as a function of the distance from the tube axis. In typical low-pressure gas lasers, the gain drops rapidly as it approaches the discharge tube walls. Atoms or molecules excited in the volume diffuse to the wall and lose their energy there. In contrast, the gain in the HCN laser is almost constant over the whole cross section of the discharge tube [33]. This unusual behaviour was explained by taking the volume and wall processes in the plasma into account simultaneously [32].

30.4 H_2O Laser

The physical mechanisms and operating conditions of the water vapour laser are very similar to those of the HCN laser. Both Coriolis and Fermi resonances yield the transition probability between different vibrational modes. The coupling occurs between rotational levels of the (100) and (001) vibrational states of the ν_1 and ν_3 modes, respectively, and the first overtone (020) of the symmetric bending mode of frequency ν_2. The strong interaction is caused by large anharmonicity and the fact that the frequencies of the symmetric (ν_1) and antisymmetric (ν_3) OH stretching modes are almost exactly twice the frequency of the bending fundamental vibration (ν_1). Symmetry analysis [27] shows that Fermi resonances cause perturbations of rotational levels in (100) and (020), whereas the Coriolis force is responsible for the interaction between (020) and (001).

As an asymmetric top molecule, the rotational energy-level structure of H_2O is considerably more complex than that of the linear molecule HCN. A very detailed discussion of the water vapour laser and an assignment of a large number of observed laser lines is given in [22]. In Figure 30.2, part of the energy-level scheme of H_2O is shown which accounts, among other lines, for the stronger laser lines given in Table 30.1. A concise discussion of the inversion mechanism is given in [34].

The H_2O laser is very convenient to operate as there are no problems of wall depositions in the laser tube and the lifetime of the molecule is quite long. In contrast to the HCN laser, H_2O is directly excited in the glow discharge without being dissociated. This was concluded from the observation that, in the pulsed mode of operation, H_2O lases during the exciting current pulse and decays rapidly when the excitation terminates. HCN and other molecular species lase with characteristic temporal delay in the afterglow of the current pulse [35].

30.5 Resonator

The glow discharge and the resonator mirrors of electrically pumped far-infrared lasers are usually confined in glass or Pyrex tubes. Typical dimensions of laser resonators are several centimetres in radius a and a few metres in length b. These units result in Fresnel numbers $N=a^2/\lambda b \approx 1$ where λ is the laser wavelength. This is in contrast to lasers in the visible or near-infrared which have Fresnel numbers much larger than one. Thus, taking into account the low gain, diffraction losses cannot limit the laser threshold. This fact was first recognized by Schwaller et al. [36] who pointed out the discrepancy between diffraction-selected resonator modes and actually observed modes. Steffen and Kneubühl [12] showed that, in fact, the resonator works like an oversized leaky waveguide. Instead of diffraction, the losses are due to reflection at the dielectric resonator walls. The attenuation in a low-index leaky guide decreases with increasing radius like $\propto(\lambda/a)^3$ [37]. The loss of fundamental longitudinal modes is vanishingly small in oversized resonators due to the almost grazing incidence of radiation on the wall. The curvature of the mirrors is still important as it affects the mode volume [38].

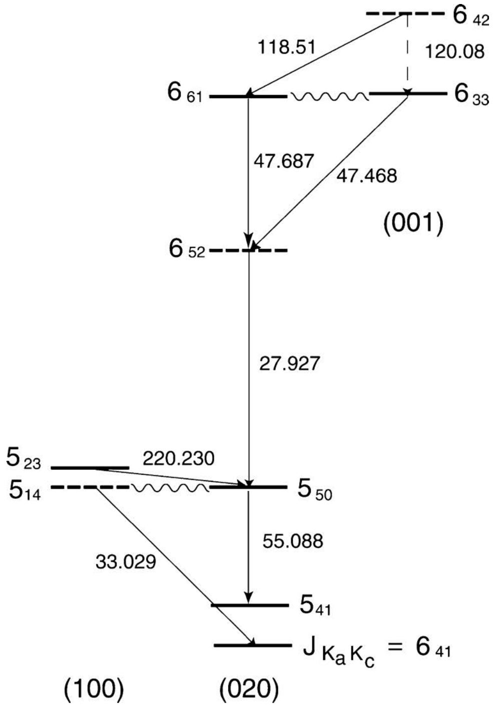

FIGURE 30.2 Part of the rotation–vibration energy-level diagram and laser transitions of $H_2{}^{16}O$, among them the lines listed in Table 30.1. The laser levels shown are between 2500 and 4500 cm^{-1} above the ground state. The transitions are indicated by their wavelength in µm. Energy levels are shown for the case of strong transitions of statistical weight 3 (parallel orientation to the hydrogen proton spins). The Fermi resonance ((100) ⇔ (020)) and the Coriolis resonance ((020) ⇔ (001)) are indicated by curly lines. J is the total angular momentum, K_a and K_c are the K values in the limit of prolate and oblate tops, respectively, where K is the angular momentum along the symmetry axis of a symmetric top. Levels of symmetry classes ++ and +– are plotted as full lines, classes – + and – – are shown as dashes. The ± are parities of two two-fold rotations in physical space around two independent principal axes of the moment of inertia. For more details, see Ref. [22].

Partially reflecting loss-free solid-state mirrors, such as those used as output reflectors in optical lasers, do not exist in the far-infrared due to phonon absorption at room temperature. Therefore, there is no standard scheme to couple radiation from the resonator. Several coupling systems have been developed and applied. The most used among them include hole coupling, coupling with a thin dielectric film, coupling with a Michelson interferometer and coupling by a metallic mesh.

Coupling through a hole in the centre of one of the resonator mirrors is technically simple and thus mostly applied. The disadvantage is the diffraction widening of the beam and the need for an individual hole diameter for each laser line in order to optimize output. The latter requirement is in fact nowadays no real restriction as most discharge-pumped lasers are used with one line only.

Coupling is performed by mounting a thin (5–20 µm) Mylar or polyethylene film with a tilt angle of 45° to the resonator axis. Absorption losses in the thin films can be ignored. The reflection coefficient is independent of the wavelength in a wide wavelength range, but it is polarization dependent. Thus, the output beam is polarized. Two output ports may be used yielding two low-divergence beams of the same cross section as the resonator.

A Michelson interferometer with a dielectric film, usually Mylar, as beamsplitter is very reliable making the operation of a laser on different lines easier. By varying the length of one interferometer arm, the output can be tuned and optimized for different laser lines.

Thin metallic meshes represent low-loss partial reflectors in the far-infrared [39] and have been frequently used [40,41]. The advantage is that they retain the laser beam and the linear structure of the resonator. The pitch has to be adapted to the particular laser line. Using two parallel metallic meshes with adjustable spacing gives the arrangement of a Fabry–Pérot interferometer. As an output coupler, it allows the reflectivity and selection of single laser lines to be tuned [12].

Films of Mylar or polyethylene as well as sheets of TPX or crystalline quartz are used as window materials.

30.6 Glow Discharge and Additive Gases

The optimum radiation power of a longitudinally pumped cw laser is obtained with a pressure in the range of 0.2–0.8 mbar. The output power of the laser increases with rising current until it assumes a maximum and drops on further increase in current. The optimum current is in the range 1–3 A, yielding a voltage drop of about 2–4 kV. The peak output is found with a wall temperature between 100°C and 150°C. The wall temperature has been controlled by thermostatically temperature-stabilized oil flowing in a jacket around the laser tube. In the case of the HCN laser, a higher temperature is advantageous even if the power is not optimal because it reduces the wall deposit rate. The glow discharge of a cw laser is in the diffusion-dominated regime where the positive column fills almost the whole plasma tube. In the positive column, striations are formed which become unstable at higher currents causing large fluctuations of the laser output power. This process limits the current and radiation power of stable laser operation. Stronger striations affect the lower frequency lines of HCN more than those of H_2O at higher frequencies as the refractive index fluctuations of the plasma decrease with the distance of the laser frequency to the plasma frequency.

A common method for improving stability is to introduce additive gases. Among the different chemical species investigated in the past [42], He, H_2 and H_2O are of importance. Due to its small mass and its high mobility, He reduces the temperature and the radial temperature gradient. This supports the maintenance of inversion and improves the homogeneity and stability of the discharge. Addition of He shifts the current of maximum output power to higher values or, in turn, lowers the required discharge voltage for a given current. H_2 and H_2O have a similar effect on the discharge. In addition, H_2 may compensate for a shortage of hydrogen in the laser fuel and it helps to relax the energy of the lower laser level bending mode by hydrogen bonding effects.

30.7 Design and Operational Characteristics

In Figure 30.3, a standard design of a cw HCN laser is shown. The characteristic data are given in Table 30.2.

The laser oscillates on the 337 µm line only. The gain of the laser is too small to obtain other HCN lines. The length of the laser tube is made of glass (Schott Duran 50) and is thermally stabilized by four invar rods. Sufficient thermal stability is achieved after running the laser for about 1 h. The temperature at the wall of the tube is then 150°C. The stability of the laser also depends critically on the electrode configuration. As an anode, a stainless steel ring 7 cm wide attached concentrically onto the inner wall of the discharge tube and as a cathode, a hollow copper cylinder in a side arm of the tube have proved to provide a stable discharge. The cathode is cooled by water flow. Another important parameter with respect to stability is the gas pressure. The discharge runs smoothly below about 0.6 mbar forming stable mushroom-like striations. Above this pressure, the striations start irregular motions and mixing until any regular pattern in the discharge disappears. In this state, the output power strongly fluctuates; however, the average power is two to three times higher than in the smoothly running mode. Adding small amounts of water vapour to the discharge increases stability, adding He does not have much effect.

Making full use of the waveguide effect of rather thin discharge tubes, similar but more compact cw laser designs have been reported by Belland and Veron [38], Véron et al. [43] and Bruneau et al. [44]. In these devices, the temperature of the tube wall could be actively controlled by the flow of oil in an outer jacket around the tube. This gives another parameter at hand to optimize laser operation.

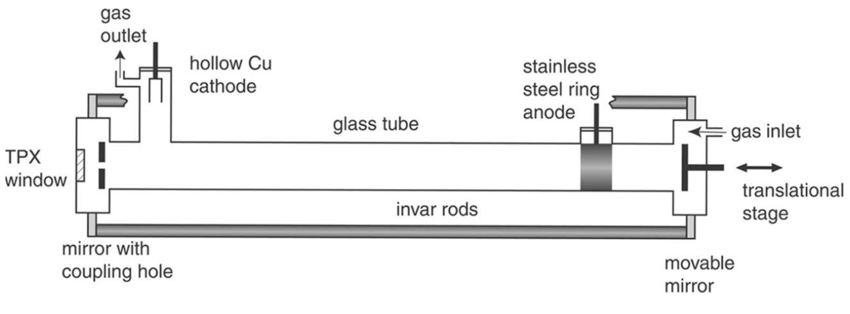

FIGURE 30.3 Design of a cw HCN laser.

TABLE 30.2

The characteristic data of HCN laser.

Resonator	
Length	2.4 m
Curvature of movable mirror	4 m
Curvature of coupling mirror	∞
Hole coupling, bore	15 mm
Output window	TPX sheet, 3 mm thick
Thermal stabilization	4 invar rods, 25 mm diameter
Discharge	
Laser gas	CH_4 and N_2, 1:1
Optical additive gases	H_2O, He
Pressure	0.4. . . 0.6 mbar
Flow rate	500 $cm^3 min^{-1}$
Anode	Stainless steel ring, 70 mm wide
Cathode	Hollow copper structure 50 mm diameter, water cooled
Voltage	1.0. . . 2.5 kV
Current	0.5. . . 1.5 A
Load resistor	600 Ω
Power	
Gain	0.5 dB m^{-1}
Output power	5 mW

30.8 Summary

Glow discharge lasers were coherent sources of substantial intensity which bridged the gap between the microwave range and near-infrared. The revolution in the field of coherent far-infrared sources was concluded by the discovery of the CO_2 laser pumped molecular laser by Chang and Bridges [45] and approached maturity with the advent of the free-electron laser [46]. Optically pumped molecular lasers deliver thousands of laser lines in the far-infrared, they may be operated as cw or pulsed, they produce short pulses or extremely high intensities when transversely excited atmospheric pressure (TEA)-CO_2 lasers are applied as the pump source. To all these the free-electron laser adds tunability in a wide wavelength range. Thus, these laser concepts superseded the electrically pumped far-infrared laser in most cases. However, there are still areas of research where it is reasonable to apply H_2O and HCN lasers. Both lasers are low cost, reliable and of simple construction. In the cw mode, they are easy to handle due to direct electrical excitation and deliver on a few lines with a rather high power.

REFERENCES

1. Crocker A, Gebbie H A, Kimmit M F and Mathias L E S 1964 Stimulated emission in the far-infrared *Nature (London)* **201** 250–1.
2. Gebbie H A, Stone NWB and Findlay F D 1964 Interferometric observations on far infra-red stimulated emission sources *Nature (London)* **202** 169–70.
3. Gebbie H A, Stone NWB and Findlay F D 1964 A stimulated emission source at 0.34 millimetre wave-length *Nature (London)* **202** 685.
4. Button K J, Gebbie H A and Lax B 1966 Cyclotron resonance in semiconductors with far infrared laser *IEEE J. Quantum Electron.* **QE-2** 202–7.
5. von Ortenberg M 1980 Submillimeter magnetospectroscopy of charge carriers in semiconductors by use of the strip-line technique *Infrared and Millimeter Waves* vol 3, ed K J Button (New York: Academic) pp 275–345.
6. Otsuka E 1980 Cyclotron resonance and related studies of semiconductors in off-thermal equilibrium *Infrared and Millimeter Waves* vol 3, ed K J Button (New York: Academic) pp 347–416.
7. Jie Y X, Gao X, Cheng Y F, Yang K and Tong X D 2000 Multi-channel FIR HCN laser interferometer on HT-7 Tokamak *Int. J. IR MM-Waves* **21** 1375–80.
8. Golubev V G and Prettl W 1991 FIR photoconductivity at filamentary current flow in n-GaAs in a magnetic field *Solid State Commun.* **79** 1035–8.
9. Jackson M, Sudhakaran G R and Gansen E 1996 Lees R M 1999 Far-infrared laser Stark spectroscopy of $^{13}CD_3OD$ *J. Mol. Spectrosc.* **176** 439–1.
10. Schilke A, Mehringer D M and Menten K M 2000 A submillimeter HCN laser in IRC +10216 *Astrophys. J.* **528** L37–40.
11. Sturzenegger Ch, Vetsch H and Kneubühl F 1979 Transversely excited double-discharge HCN laser *Infrared Phys.* **19** 277–96.
12. Steffen H and Kneubühl F K 1968 Resonator interferometry of pulsed submillimeter-wave lasers *IEEE J. Quantum Electron.* **QE-4** 922–1008.

13. Daneu V, Hocker L O, Javan A, Ramachandra Rao D, Szöke A and Zernike F 1969 Accurate laser wavelength measurement in the infrared and far infrared using a Michelson interferometer *Phys. Lett. A* **29** 319–20.
14. Hocker L O, Javan A and Ramachandra Rao D 1967 Absolute frequency measurement and spectroscopy of gas laser transitions in the far infrared *Appl. Phys. Lett.* **10** 147–9.
15. Steffen H, Steffen J, Moser J F and Kneubühl F K 1966 Stimulated emission up to 0.535 mm wavelength from cyanic compounds *Phys. Lett.* **20** 20–1.
16. Steffen H, Steffen J, Moser J F and Kneubühl F K 1966 Comments on a new laser emission at 0.744 mm wavelength from ICN *Phys. Lett.* **21** 425–6.
17. Hocker L O and Javan A 1967 Absolute frequency measurements on the new cw HCN submillimeter laser lines *Phys. Lett. A* **25** 489–90.
18. Belland P, Veron D and Whitbourn L B 1976 Scaling laws for cw 337-μm HCN waveguide lasers *Appl. Opt.* **15** 3047–53.
19. Sentz A 1983 Operating conditions of a cw water vapour laser at 28, 47, 78, 79, and 119 µm *Infrared Phys.* **23** 9–14.
20. Frenkel L, Sullivan T, Polack M A and Bridges T J 1967 Absolute frequency measurement of the 118.6-μm water-vapor laser transition *Appl. Phys. Lett.* **11** 344–5.
21. Evenson K M, Wells J S, Matarrese L M and Elwell L B 1979 Absolute frequency measurement of the 28- and 78-μm cw water vapor laser lines *Appl. Phys. Lett.* **16** 159–62.
22. Benedict W S and Pollack M A 1969 The water-vapor laser *IEEE J. Quantum Electron.* **QE-5** 108–24.
23. Mathias L E S and Crocker A 1964 Stimulated emission in the far-infrared from water vapour and deuterium oxide discharges *Phys. Lett.* **13** 25–36.
24. Kneubühl F K and Sturzenegger C 1980 Electrically excited submillimeter-wave lasers *Infrared and Millimeter Waves* vol 3, ed K J Button (New York: Academic) pp 220–60.
25. Lide D R and Maki A G 1967 On the explanation of the so-called CN laser *Appl. Phys. Lett.* **11** 62–4.
26. Mills I M 1972 Vibration–rotation structure in asymmetric- and symmetric-top molecules *Molecular Spectroscopy: Modern Research* ed K N Rao and C W Mathews (New York: Academic) pp 115–40.
27. Herzberg G 1945 *Molecular Spectra and Molecular Structure II: Infrared and Raman Spectra of Polyatomic Molecules* (Princeton, NJ: Van Nostrand Reinhold) p 279.
28. Kim K and King W T 1979 Integrated intensities in hydrogen cyanide *J. Chem. Phys.* **71** 1967–72.
29. McGarvey J A Jr, Friedmann N E and Cool T A 1977 Vibrational energy transfer in HF-HCN, DF-HCN, and H_2-HCN mixtures *J. Chem. Phys.* **66** 3189–96.
30. Pichamuthu J P 1974 The excitation mechanism of the HCN laser *J. Phys. D: Appl Phys.* **7** 1096–100.
31. Schötzau H J and Kneubühl F K 1975 Mass spectroscopy of the HCN-laser plasma *IEEE J. Quantum Electron.* **QE-11** 817–22.
32. Schötzau H J and Veprek S 1975 Wall processes and the radial gain of the cw HCN laser *Appl. Phys.* **7** 271–7.
33. Strafsudd O M and Yeh Y C 1969 The CW characteristics of several gas mixtures at 337 µm *IEEE J. Quantum Electron.* **QE-5** 377.
34. Pollack M A 1969 Far-infrared laser gain resulting from rotational perturbations *IEEE J. Quantum Electron.* **QE-5** 558–62.
35. Coleman P D 1973 Far-infrared molecular lasers *IEEE J. Quantum Electron.* **QE-9** 130–8.
36. Schwaller P, Steffen H, Moser J F and Kneubühl F K 1967 Interferometry of resonator modes in submillimeter wave lasers *Appl. Opt.* **6** 827–9.
37. Ulrich R and Prettl W 1973 Planar leaky light guides and couplers *Appl. Phys.* **1** 55–68.
38. Belland P and Veron D 1973 A compact cw HCN laser with high stability and power output Opt. Commun. **9** 146–8.
39. Ulrich R 1967 Far-infrared properties of metallic mesh and its complementary structure *Infrared Phys.* **7** 37–55.
40. Bruneau J L, Belland P and Veron D 1978 A cw DCN waveguide laser of high volumetric efficiency *Opt. Commun.* **24** 259–64.
41. Prettl W and Genzel L 1966 Notes on the submillimeter laser emission from cyanic compounds *Phys. Lett.* **23** 443–4.
42. Pichamuthu J P 1983 Submillimeter lasers with electrical, chemical, and inciherent optical excitation *Infrared and Millimeter Waves* vol 7, ed K J Button (New York: Academic) pp 166–241.
43. Véron D, Belland P and Beccaria M J 1978 Continuous 250 mW gas discharge DCN laser at 195 µm *Infrared Phys.* **18** 465–8.
44. Chang T Y and Bridges T J 1970 Laser action at 452, 496, and 541 µm in optically pumped CH_3F *Opt. Commun.* **1** 423–6.
45. Elias L R, Ramian G, Hu J and Amir A 1986 Observation of single-mode operation in a free-electron-laser *Phys. Rev. Lett.* **57** 424–7.
46. Ulrich R, Bridges T J and Pollack M A 1970 Variable metal mesh coupler for far infrared lasers *Appl. Opt.* **9** 2511–16..

FURTHER READING

Chantry G W 1984 *Long-Wave Optics* (London: Academic)

A concise textbook presentation of the inversion mechanism and energy-level scheme of the HCN and H_2O laser (Vol 1: *Basics*, pp 150–3) and technical performance (Vol 2: *Applications*, pp 570–3) in the context of other infrared lasers.

KneubühlF K and Sturzenegger C 1980 Electrically excited submillimeter-wave lasers *Infrared and Millimeter Waves* vol 3, ed K J Button (New York: Academic) pp 220–60.

Kneubühl pioneered submillimetre glow discharge lasers. This review was written after understanding of the physics background was settled and after the technology had approached a certain technological maturity. Coverage of all excitation mechanisms (cw, pulsed longitudinal, transversely excited).

Pichamuthu J P 1983 Submillimeter lasers with electrical, chemical, and inciherent optical excitation *Infrared and Millimeter Waves* vol 7, ed K J Button (New York: Academic) pp 166–241.

A review with emphasis on the kinetic and transport processes in the laser plasma. A very thorough discussion of chemical processes, excitation and relaxation in the plasma and rate equation models.

Taylor & Francis
Taylor & Francis Group
http://taylorandfrancis.com

31

Diode-Pumped Alkali Lasers (DPALs)

Boris Zhdanov and Randall Knize

CONTENTS

31.1 Introduction ... 441
31.2 Achievements in DPAL Research and Development ... 443
  31.2.1 First Demonstration of Efficient Lasing of an Alkali Vapour Laser ... 443
  31.2.2 Demonstration of the Highly Efficient Optically Pumped Alkali Laser ... 443
  31.2.3 Experiments with Alexandrite Laser Pump ... 444
  31.2.4 First DPAL Demonstration ... 444
  31.2.5 DPAL Efficiency Increase with the Use of a Narrowband Pump ... 444
  31.2.6 Power Scaling of Alkali Lasers ... 444
  31.2.7 Transverse Pumping ... 446
31.3 Conclusions ... 447
References ... 447

31.1 Introduction

Diode-Pumped Alkali Lasers (DPALs) attract growing interest of researchers during the past 15 years because of their potential to produce high laser power in an excellent quality beam and, thus, they can compete with the best currently available high-power laser systems. But, the history of alkali laser started much earlier, in 1958, even before the first laser demonstration was performed (ruby laser, T.H. Maiman, 1960). In 1958, Schawlow and Townes published their paper “Infrared and optical masers” [1] in which they proposed an optically pumped alkali (Potassium) vapour laser. They called it “optical maser” as the word “laser” was introduced by Gordon Gould later in 1959. Unfortunately, they did not experimentally demonstrate proposed alkali laser at that time. Laser gain in an optically pumped Cs vapour was first demonstrated and measured in 1961 [2], and the first laser action in alkali atoms (Cs) at 7.18 μm was observed in 1962 [3] using an RF-powered helium lamp as a pump source. The lasing efficiency in these experiments was very low, and the output power did not exceed 50 μW. All these experiments were a kind of “prehistory” of DPAL because no diode laser pumping was used that time and output power and efficiency of these lasers were very low.

After these initial experiments with alkali vapours, there were various demonstrations of stimulated emission, gain, amplified spontaneous emission (ASE) and lasing with low power and efficiency in alkali vapours over the next 40 years (see, for example Refs. [4–8]). Numerous theoretical and experimental studies of energy transfer, energy levels mixing and a three-level lasing in alkalis were performed during that time (see, for example Refs. [9–15]), though, an absence of powerful enough narrowband tunable pump laser sources did not allow efficient lasing in alkali vapours and, thus, limited interest to such lasers. However, as a result of these initial research efforts in the field of optically pumped alkali lasers, the basic principles and techniques for creation of population inversion, gain and lasing on D1 transition of an alkali atomic vapour ($nP_{1/2} \rightarrow nS_{1/2}$) using optical pumping of the D2 line ($nS_{1/2} \rightarrow nP_{3/2}$) were developed. To provide fast population transfer from $nP_{3/2}$ to $nP_{1/2}$ and create population inversion on lasing transition (D_1 line), a buffer gas has to be used (usually ethane, methane or He). That is a standard pumping scheme (see Figure 31.1) utilized in all DPALs nowadays.

Using this approach, a concept of DPAL was introduced by Krupke in 2001 [16], when high-power and highly efficient diode lasers appeared in the market. As a proof of this concept, the first really efficient optically pumped alkali laser based on Rb vapour [17] was demonstrated by Krupke and his coworkers in 2003 using a Ti:Sapphire laser for optical pumping, and then, in 2004, they successfully repeat this experiment for Cs vapour [18] with the same pump source. The first true DPAL demonstration [19] based on Cs vapour was performed in 2005.

The first successful demonstration of efficient alkali vapour laser operation convinced several research groups in the United States and abroad to start extensive experimental and theoretical studies of all aspects of DPAL operation and its potential for scaling to high powers (see, for example Refs. [20–26]). Experiments performed during the past decade brought very positive and promising results. A slope efficiency of 81% and an optical efficiency of 63% were demonstrated for a CW operating Cs laser [27] with a Ti:Sapphire laser pump.

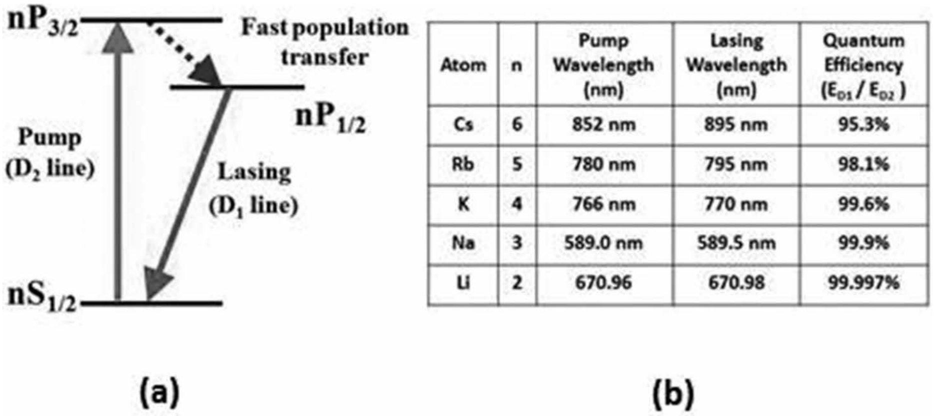

Atom	n	Pump Wavelength (nm)	Lasing Wavelength (nm)	Quantum Efficiency (E_{01} / E_{02})
Cs	6	852 nm	895 nm	95.3%
Rb	5	780 nm	795 nm	98.1%
K	4	766 nm	770 nm	99.6%
Na	3	589.0 nm	589.5 nm	99.9%
Li	2	670.96	670.98	99.997%

FIGURE 31.1 A standard three-level pump scheme for all optically pumped alkali lasers (a). Table (b) shows operating wavelengths and quantum efficiencies for corresponding alkali atoms.

(The "slope efficiency" is the slope of the line obtained by plotting the laser output power versus the pump power after threshold. The "optical efficiency" is the ratio of the laser output power to the pump power.) The first DPAL [19] based on the Cs-ethane mixture had only 130 mW output power because of limited diode laser pump power. The way to significantly increase the output power of alkali laser and, at the same time, the total wall plug efficiency is to use high-power laser diode bars [also called laser diode arrays (LDAs)] or stacks of arrays for optical pumping of alkali lasers.

There are, however, some problems in using diode lasers for alkali lasers pumping, mainly connected with the relatively broad spectral line width of diode lasers (~1 THz) compared to the absorption line of the alkali vapour gain medium (~10 GHz at atmospheric pressure of buffer gas). To achieve an efficient coupling of the pump radiation into the alkali vapour gain medium, it is necessary to match the pump line width and the alkali absorption line width. This requires either spectral line narrowing of the pump radiation or alkali absorption line broadening, or both. Currently, there are two approaches for DPAL development explored by different groups. First approach utilizes low-pressure buffer gas (about 1 atm) and requires spectral narrowing of the pump diode laser emission line to the value about 10–20 GHz. Another approach, so called high pressure approach, requires moderate narrowbanding of the diode laser pump to the value about 100–200 GHz but has to use high-pressure buffer gas (10–20 atm) and higher gain medium temperatures (200°C–250°C). Both approaches have their pros and cons and are under extensive study by researchers. Illustration of the first approach is presented in Ref. [28], where the authors used a Volume Bragg Grating (VBG) [29] to narrow the diode laser bar emission line width to about 0.2–0.3 nm that was still much broader than the alkali absorption line broadened by a buffer gas with a pressure of several atmospheres. The relatively broad line width of the pump sources in this experiment limited the absorption efficiency, and the slope efficiency for the Cs laser was only 1.8% [28]. There were several other experiments in which the authors used diode laser bars or stacks narrowbanded by VBG to the value of about 0.3–0.5 nm for DPAL pumping. The optical-to-optical efficiencies achieved in these experiments were less than 10% because of bad matching of pump and absorption line widths. Further research on VBG development [30] showed that VBGs can provide much better narrowbanding (below 0.03 nm) for LDAs with a power of several tens of watts. However, implementing VBGs for high-power diode laser stacks can meet technical problems because of their high thermal sensitivity.

Another technique for line narrowing of diode laser bars was developed (Ref. [31]) and provided line narrowing up to 0.03 nm. This allowed demonstration of an efficient CW operation of the Cs laser [32] with 10 W output power, a slope efficiency of 68%, and a total optical efficiency of 63%. Using this narrowbanding technique, the same authors performed a series of scaling experiments with longitudinal [33] and transverse [34,35] pumping using multiple LDAs and both stable [35] and unstable [36] configurations of the laser cavity. This allowed for an increase of the output power of these alkali lasers to a level of tens of Watts, which was again limited by the available pump power. However, these experiments also demonstrated that at power level higher than several tens of Watts, the DPAL efficiency can be affected by such limiting issues as thermal effects [33] and/or photoionization [37]. These problems can, probably, be mitigated by flowing the gain medium through the laser cavity, what was studied in several publications [38,39]. Recent published experiments on power scaling DPAL with flowing gain medium demonstrated output power close to 1 kW for Cs DPAL [40] and about 1.5 kW for K DPAL [41].

Such an extensive research and development of DPALs during the past decade was stimulated by their potential to achieve high power in a high-quality beam as these properties are very desirable for various important applications in science, technology and national security areas. The DPALs have a number of positive features as compared to other high-power lasers (chemical, solid-state and fibre lasers) and do not have the problems which exist in other high-power laser systems that limit their applications. The most important features of alkali laser systems are the following:

High quantum efficiency: 95.3% for Cs, 98.1% for Rb and 99.6% for K as compared to 76% for a 1.06 μm Nd:YAG laser. High quantum efficiency is not only a promising factor for the high overall laser efficiency but also important for minimizing heating problems since the energy defect is usually converted into heat released into the gain medium.

1. *Gaseous gain medium* is a very important feature because it can be very homogeneous and has excellent optical quality with reduced aberrations, absorbing and scattering centres and refraction index fluctuations. Generally, laser beams generated in a gaseous gain medium have excellent quality and diffraction limited divergence.
2. *Reduced thermal problem* is one more advantage of a gaseous gain medium. The thermal effects existing, for example, in solid-state lasers and causing aberrations and thermal lensing that degrade the beam quality. The thermal problems in a gaseous gain medium can be significantly reduced or even eliminated by flowing the gain medium.
3. Use of *diode laser pumping* of the alkali gain medium allows an increase of the total wall plug efficiency of the DPAL system because of very high efficiency of the diode lasers as compared to other pump sources.
4. *CW operation* is possible for DPALs which is important when high average power is required for the specific application.
5. *Scalability to high power* is possible by increasing the volume of the gain medium and number of pump diode laser sources. Thus, scaling to high power does not necessarily lead to the high light intensity inside the gain medium, like in fibre lasers. Operating at lower intensities suggests that non-linear optical effects and optical damage will probably not be limiting factors for alkali lasers.
6. *Operating wavelengths* of all DPALs lie within atmospheric transmission windows (see for example Ref. [41]), which is essential for any directed energy application of DPALs in atmosphere.
7. *No hazardous expendable chemicals* required for DPAL operation that is a great advantage compared to chemical lasers. In addition, alkali lasers have no chemical waste as they can be constructed in a sealed cell or closed cycle flowing system, eliminating the need for vacuum pumping and discharge of chemicals.

All these properties and features of alkali lasers show that they can be a successful alternative to the most developed high-power laser systems and may even exceed them in many parameters.

There are numerous publications and reviews describing basic principles of the DPAL operation (see, for example Ref. [22,25,43]), which interested readers can study. In this chapter, we present the most important reported experiments and results achieved in the field of DPAL research and development in more detail.

31.2 Achievements in DPAL Research and Development

31.2.1 First Demonstration of Efficient Lasing of an Alkali Vapour Laser

The first experimental demonstration of a really efficient lasing in optically pumped Rb [17] and Cs [18] lasers was performed by W. F. Krupke et al. in 2003–2004. A standard for an optically pumped alkali laser three-level pump scheme (see Figure 31.1 above) with Ethane buffer gas was used in both experiments. An optical pump source was a tunable narrowband Ti:Sapphire laser with an output power up to 500 mW. A laser cavity design utilized a widely used so call "L-shape" geometry (see Figure 31.2) with separation of the pump and lasing beams by Polarization Beam Splitter. A slope efficiency of 54% and an optical-to-optical efficiency of 16% for Rb laser and 59% slope efficiency and 34% optical efficiency for Cs laser were demonstrated in these experiments. The efficiencies reported in these experiments were "relative to the absorbed power", and the real efficiencies (relative to the pump power) were several times lower because the line width of the pump laser (30–50 GHz) was broader than the absorption line of the alkali vapour (about 10 GHz for buffer gas pressure about 1 atm). These experiments also showed the importance of narrowbanding the diode laser pump source to match its line width to the alkali atom absorption line.

31.2.2 Demonstration of the Highly Efficient Optically Pumped Alkali Laser

To demonstrate the potential of alkali lasers to operate with extremely high efficiency, an experiment with Cs vapour laser, for which all important parameters affecting its efficiency were optimized was performed [27]. As a pumping source, a Coherent MBR 110 Ti:Sapphire laser operating at 852 nm (corresponding to the D2 line of Cs atom) in single longitudinal and transverse modes was used. A line width of this laser output was less than 1 MHz, which is much narrower than the Cs vapour absorption line broadened by a 1 atm of ethane buffer gas (10 GHz). The density of the Cs vapour (or its temperature), the output coupler reflectivity and the pump beam matching to the laser cavity mode were experimentally optimized. Lasing

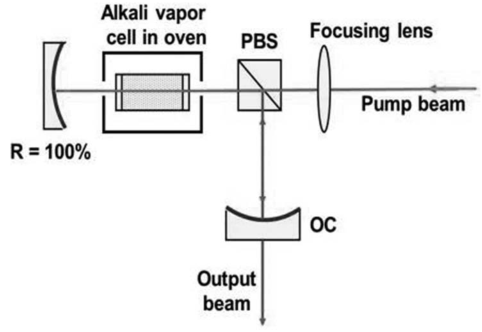

FIGURE 31.2 A diagram of the alkali laser cavity design.

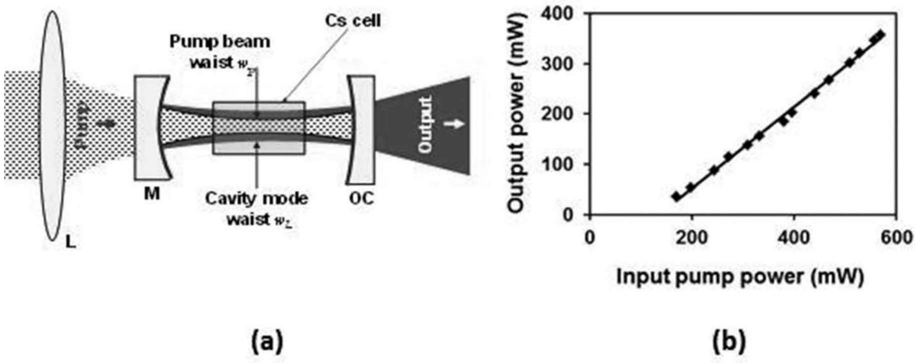

FIGURE 31.3 Diagram of the experiment (a) and the dependence of the Cs laser output power on the input pump power (b).

occurred on the Cs D1 transition with a wavelength 895 nm. Figure 31.3 presents the experimental setup diagram and the dependence of the Cs laser output power on the input pump power showing 81% slope efficiency and 63% overall optical efficiency for the output power relative to the input power.

The output power of this laser was not very high (about 360 mW) because of limited pump power (570 mW), but the slope efficiency demonstrated in this experiment is very close to the calculated value (86%) and is still a world record for optically pumped alkali lasers.

31.2.3 Experiments with Alexandrite Laser Pump

Tunable Alexandrite lasers can cover a spectral range that includes the pumping wavelength for Rubidium (780 nm) and Potassium (766 nm) alkali vapour lasers. Using of a pulsed Alexandrite laser for pumping the alkali vapours can demonstrate alkali laser operation under conditions of a high intensity pump, which could not be achieved with the CW Ti:Sapphire laser. Such experiments with a pulsed Alexandrite laser as a pump source were performed by Zweiback et al. [44] for both Rb and K vapour lasers. This pump laser had a bandwidth of 0.15 nm, produced about 300 ns pulses at 10 Hz repetition rate and provided a maximum peak power up to 75 kW. The pulse duration of 300 ns is long enough for the alkali lasers to operate as a CW laser because of a very short laser cavity build-up time. On other hand, the pulsed operation with low repetition rate allows to eliminate thermal effects, which can strongly affect laser operation at high average power (see, for example Ref. [33]). In these experiments authors used a longitudinal pumping geometry or, so called, end pump (similar to presented on Figure 31.2) and stable resonator. Optical-to-optical efficiencies of 64% for Rb and 60% for K lasers were demonstrated (see Figure 31.4), promising efficient operation of alkali lasers when scaling to high-power levels.

31.2.4 First DPAL Demonstration

The first real DPAL i.e. alkali laser operating with a diode laser pump was demonstrated in 2005 using a Cs-Ethane mixture [19]. A narrowband diode laser operating at 852 nm (SDL-8630 with a line width less than 1 MHz was used to pump a 5 cm long Cs vapour cell with 100 torr of Ethane buffer gas. The gain medium was longitudinally pumped through the one of the cavity mirrors. A maximum slope efficiency of 41% and a maximum output power of 130 mW were obtained in this experiment. The efficiency of this laser could be higher if the pump beam (which had an elliptical cross section) would better match the laser cavity mode. And output power of this DPAL was low because of the limited pump power. The way to increase DPAL output power is to use high-power diode laser bars and stacks with narrowbanded emission line.

31.2.5 DPAL Efficiency Increase with the Use of a Narrowband Pump

The first experiment on pumping Cs vapour laser by narrowband diode laser bar [32] (line width about 10 GHz) demonstrated an optical-to-optical efficiency of 62% with a slope efficiency of 68%. The laser cavity arrangement was similar to the one presented in Figure 31.4. The L-shape 51 cm long laser cavity consisted of a flat output coupler (20% reflectivity at 894 nm) and a high reflective 50 cm radius concave back mirror. A 2 cm long cell with antireflection coated windows was filled with metallic cesium and 500 torr Ethane and placed in a heated oven with a temperature 92°C. An output power of 10 W was obtained using 16 W of an incident LDA pump. These CW efficiencies and output power were about an order of magnitude higher than the previous results obtained for diode laser bar pumped pulsed alkali laser [28] and were related to the total pump power, not to the “absorbed power”.

31.2.6 Power Scaling of Alkali Lasers

Scaling of alkali lasers to higher powers requires using multiple diode laser sources for pumping. First scaling experiments using longitudinal pumping of alkali gain medium from two sides of the alkali cell [33] were performed using two LDAs for Rb DPAL (see Figure 31.5a) and four LDAs for Cs DPAL (Figure 31.5b). In these experiments, an output power up to 17 W with slope efficiency 53% for Rb DPAL and 48 W with slope efficiency 52% for Cs DPAL were demonstrated.

It is worth noting that the experiment presented in Figure 31.5b also demonstrated for the first time that DPAL power scaling can suffer from some parasitic effects limiting their output power. Figure 31.6 presents results of measurement of the Cs DPAL output power for two modes of operation:

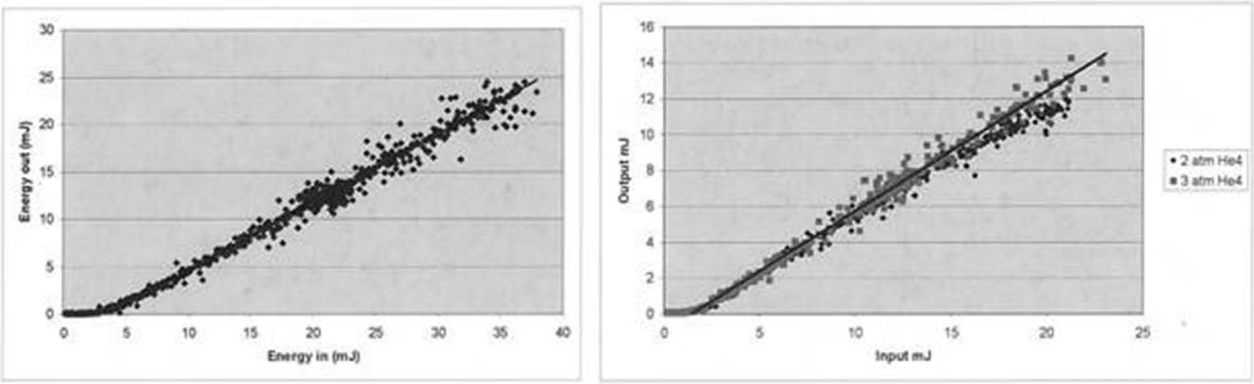

(a)

(b)

FIGURE 31.4 Plots of performance for the Rb laser with 1 atm of methane (a) and for the Potassium laser with Helium-4, and Helium-3 (b) as a function of pump pulse energy. (Adopted from Ref. [44].)

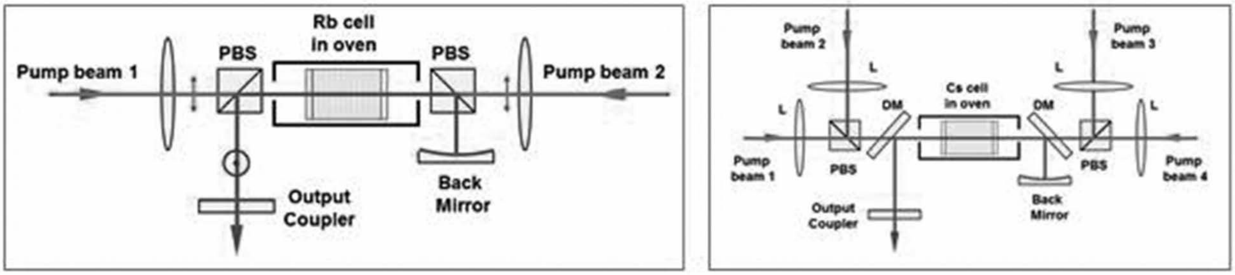

(a)

(b)

FIGURE 31.5 Schematic of the experimental setups for DPALs with longitudinal pumping by two LDAs (a) and four LDAs (b).

CW and pulsed with pulses duration of 100 msec and repetition rate of 1 Hz. In the pulsed mode, the Cs laser output power grows linearly with the pump power and reaches 48 W at 98 W pump power that results in 52% slope efficiency and overall optical efficiency of 49%. In the CW mode, the relationship between the pump power and output power is no longer linear as starting from 30 W pump power it rolls over and even drops at higher pump powers. Such behaviour can be explained by thermal effects created by the heat released into the Cs vapour gain medium due to the energy defect between the D1 and D2 Cs lines (554 cm^{-1}). The quantum efficiency of the Cs laser is $\lambda_{D1}/\lambda_{D2}=95.3\%$, which means that 4.7% of the pump power is released as heat into the gain medium. Another possible limiting effect that can cause the efficiency decrease is ionization of the gain medium in the high intensity pump and lasing beams [37], resulting in decrease of neutral alkali atoms density and, thus, the gain. To mitigate both these limiting effects, the flowing of the gain medium is required. The flow can both remove the excessive heat and replenish density of neutral alkali atoms required for gain and lasing.

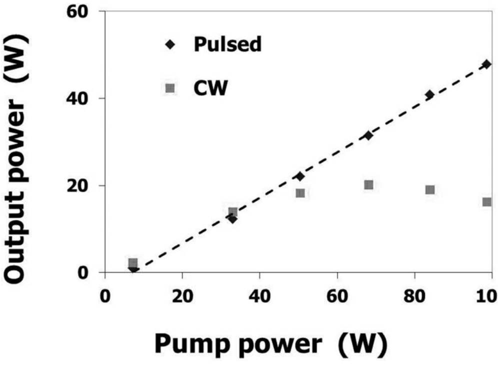

FIGURE 31.6 Cs laser with four LDAs pump output power performance in pulsed and CW regimes.

An experiment on Cs vapour laser with flowing gain medium, performed by the Russian group in 2012 [40], demonstrated about 1 kW output power with 48% optical-to-optical efficiency that showed effective mitigation of the limiting effects mentioned above. The authors of this work used longitudinal pumping of the gain cell from both sides by multiple diode laser stacks (see Figure 31.7). The combined spectral width of the pump radiation from all diodes was about 0.7 nm (or about 300 GHz). The gain medium was a mixture of Cs vapour with He and Methane (CH_4) at total pressure from 1 to 5 atm and it was kept at about 150°C. The partial pressure of methane varied in the range 0.1–1 atm. The gain medium

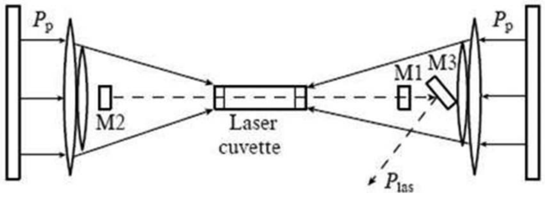

FIGURE 31.7 Experimental setup diagram of the Cs laser with flowing gain medium. (Adopted from Ref. [40].)

was flown through the cell with a flow rate about 20 m s^{-1}. According to the data provided in this paper, matching of the pump spectral line width to the absorption band of Cs vapour broadened by buffer gas was not perfect because even at 5 atm pressure, the Cs absorption line width is about 80 GHz, which is four times less than the pump radiation band. At the lower pressures, this ratio is even worse. In spite of this, the optical efficiency demonstrated in this work was high enough, but, probably could be higher with better matching of the pump and absorption line widths.

31.2.7 Transverse Pumping

A transverse pumping geometry, which is widely used in solid-state lasers, has many advantages for high-power lasers compared to the longitudinal pumping. First of all, it only has technical limitations on the number of pump sources used that allows coupling much higher pump power into a gain medium compared to the longitudinal pumping. Then, there is no problem with spatial separation of the pump and lasing beams because they use different windows of the gain cell. The downside of the transverse pumping is that it is more difficult to match the pump and laser mode volumes, especially when the stable laser resonator is used. An unstable resonator can solve this problem because the laser mode of such resonator can fill the whole gain medium.

To study the operation of DPAL with transverse pumping, an experiment [34] with a Cs vapour laser transversely pumped by 15 narrowband LDAs with total power of about 200 W through the side of the gain cell (see Figure 31.8a) was performed. A Cs vapour cell with 100 torr of Ethane and 500 torr of He mounted inside a cylindrical white diffuse reflector was placed inside a temperature-controlled oven. Both the reflector and the oven had a 2 mm×50 mm side slit for coupling the pump beams into the cell. The stable laser cavity was made by a 50 cm concave back mirror and a flat output coupler with 20% reflection at 894 nm.

To avoid thermal effects in cesium vapour that was observed previously [33], the Cs laser was pumped by pulses with duration of 500 μs and repetition rate of 20 Hz. A maximum output power about 28 W with a slope efficiency of 15% and maximum optical efficiency of 14% were demonstrated in this experiment. The lower value of the slope efficiency compared to the longitudinally pumped Cs laser (68% in Ref. [32]) can be caused by a poor pump coupling efficiency: the laser cavity mode size inside the Cs cell was about 600 μm and the size of the diffuse reflector was 1 cm. To increase the pump efficiency, the laser cavity must have a mode size close to the illuminated volume inside the reflector filled with gain medium. This can be performed by using an unstable laser resonator.

A Cs laser with an unstable resonator and transverse pumping of the gain medium was explored in Ref. [35] (see Figure 31.8b). In this experiment, the Cs cell diameter was increased to 7 mm to better fill the diffuse reflector volume compared to design used in Ref. [34] (Figure 31.8a). The unstable confocal laser resonator was constructed of concave and convex high reflecting mirrors and the laser output beam, which was the light that escapes the cavity around the perimeter of the small concave mirror, had a doughnut shape with external diameter about 7 mm (the Cs cell internal diameter) and the hole diameter about 2.8 mm (convex mirror diameter). An effective output coupler reflectivity was approximately 16%. In this experiment, a maximum output power of 49W with the slope efficiency of 43% was obtained when being pumped with 160W. The maximum optical-to-optical efficiency was 31%. The efficiencies achieved in this experiment are more than twice of that in the previous experiment utilizing the transversely pumped Cs laser with a stable resonator [34]. This increase in performance can be contributed to the better overlap between the lasing mode and pumped volume of the gain medium when using the unstable cavity geometry. However, the slope efficiency of this system is still lower than that for longitudinal pumping (81% for Ti:Sapphire pump [27]

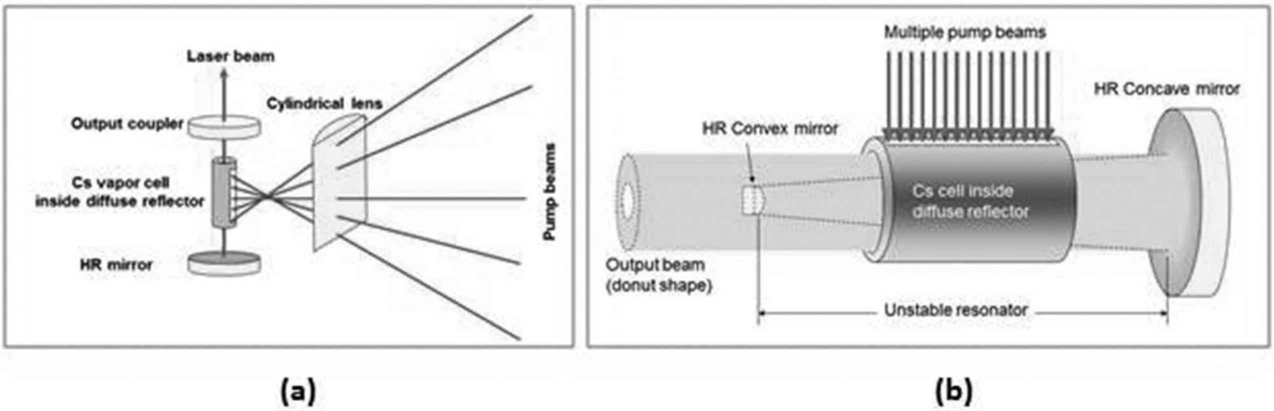

FIGURE 31.8 Schematic diagram of the transverse pumped Cs laser with stable (a) and unstable (b) resonator.

and 68% for diode laser pump [32]). This difference can be due to nonhomogenious pumping of the whole volume of the gain medium through the narrow slit. This assumption is supported by the observed output beam profile, which had elliptical doughnut shape instead of circular. In addition, there can be pump power losses because of multiple reflections of pump beams off the diffuse reflector. Improvements in the design of the transverse pumping system may result in an increase of the laser pumping efficiency.

31.3 Conclusions

We presented a historical prospective of DPAL research and development and a review of the main achievements in this field, demonstrating the high potential of alkali lasers as a scalable source of high-power laser radiation in the near-infrared range. The remarkable proprieties of these lasers, such as high wall plug efficiency, high beam quality, scalability and no consumables make DPAL systems very attractive for many important scientific, medical, technological and military applications. At the same time, we have to note that there are several challenges in DPAL high-power scaling, which need to be addressed and investigated. Among them, we can mention chemical interaction of alkali vapour with buffer gases and other elements of the DPAL system, damage of alkali cell windows, ionization of the gain medium and others.

REFERENCES

1. A.L. Schawlow and C.H. Townes, "Infrared and optical masers," *Phys. Rev.* **112**(6), 1940–1949 (1958).
2. S. Jacobs, G. Gould, and P. Rabinowitz, "Coherent light amplification in optically pumped Cs vapor," *Phys. Rev. Lett.* **7**(11), 415–417 (1961).
3. P. Rabinowitz, S. Jacobs, and G. Gould, "Continuous optically pumped Cs laser," *Appl. Optics* **1**(4), 513–516 (1962).
4. S.N. Atutov, A.I. Plekhanov, and A.M. Shalagin, "Superluminosity on the resonant transition of Na atoms under optical excitation," *Opt. Spectrosc. (USSR)* **56**(2), 134–137 (1984).
5. M.E. Movsesyan, T.O. Ovakimyan, and S.V. Shmavonyan, "Stimulated processes in a mixture of rubidium vapor and buffer gas under two-photon excitation," *Opt. Spectrosc. (USSR)* **61**(3), 285–287 (1986).
6. A.A. Dabagyan, et al., "Laser resonance radiation at the atomic-potassium D_1 line," *Opt. Spectrosc. (USSR)* **66**(5), 686–687 (1989).
7. A.A. Dabagyan, et al., "Stimulated processes in potassium vapor in the presence of a buffer gas," *Sov. Phys. JETP* **58**(4), 700–702 (1983).
8. A.A. Apolonsky et al., "Lasing on the D_2 line of sodium in a helium atmosphere due to optical pumping on the D_1 line (up-conversion)," *Phys. Rev. A* **61**, 033408–1–033408–4 (2000)
9. B.A. Glushko, M.E. Movsesyan, and T.O. Ovakimyan, "Processes of stimulated electronic Raman scattering and stimulated resonance emission in potassium vapor in the presence of buffer gas," *Opt. Spectrosc. (USSR)* **52**(4), 458–459 (1982).
10. J. Czub, J. Fiutak, and W. Miklaszewski, "Influence of resonant pulse propagation on collision-induced stimulated effect in the $S_{1/2}$-$P_{1/2,3/2}$ system," *Phys. Rev. A* **54**(1), 746–754 (1996).
11. Z. Konefal, "Observation of collision induced processes in rubidium-ethane vapour," *Opt. Comm.* **164**, 95–105 (1999).
12. L. Krause, "Collisional excitation transfer between the2P1/2 and2P3/2 levels in alkali atoms," *Appl. Opt.* **5**(9), 1375–1382 (1966).
13. I.N. Siara, E.S. Hrycyshyn, and L. Krause, "Sensitized fluorescence in vapors of alkali atoms. XIII.. $6^2P_{1/2-}6^2P_{3/2}$ excitation transfer in Rubidium, induced collisions with noble gas atoms," *Can. J. Phys.* **50**, 1826–1832 (1972).
14. I.N. Siara and L. Krause, "Inelastic collisions between excited alkali atoms and molecules. VIII. $6^2P_{1/2-}6^2P_{3/2}$ mixing and quenching in mixtures of rubidium with H_2, HD, D_2, N_2, CH_4, and CD_4," *Can. J. Phys.* **51**, 257–265 (1973).
15. E. Walentynowicz, R.A. Phaneuf, and L. Krause, "Inelastic collisions between excited alkali atoms and molecules. X. Temperature dependence of cross sections for 2P3/2-2P1/2 mixing in Cs, induced in collisions with deuterated hydrogens, ethanes, and propanes," *Can. J. Phys.* **52**, 589–591 (1974).
16. W.F. Krupke, "Diode Pumped Alkali Laser," U.S. patent No. 6,643,311.
17. W.F. Krupke, et al., "Resonance transition 795-nm rubidium laser," *Opt. Lett.* **28**, 2336–2338 (2003).
18. R.J. Beach, et al., "End-pumped continuous-wave alkali vapor lasers: experiment, model, and power scaling," *J. Opt. Soc. Am. B* **21**(12), 2151–2163 (2004).
19. T. Ehrenreich, et al., "Diode pumped cesium laser," *Elect. Lett.* **41**(7), 47–48 (2005).
20. Y. Zheng, M. Niigaki, and H. Kan, "Efficient operation of a Cesium-vapor laser longitudinally pumped by a fine-tunable bandwidth-narrowed laser-diode bar," *Jpn. J. Appl. Phys.* **40**(12), 7768–7770 (2007).
21. W.F. Krupke, et al., "DPAL: a new class of CW, near-infrared, high-power diode-pumped alkali (vapor) lasers," *Proc. SPIE* **5334**, 156 (2004).
22. C.D. Lewis, D.E. Weeks, and G.P. Perram, "Diode pumped alkali laser kinetics: comparison of theory and experiment," *Proc. SPIE* **8381**, 83810A-1–83810A–11 (2012).
23. D.A. Hostutler, G.D. Hager, and M.C. Heaven, "Collisional quenching and radiation trapping kinetics for Rb(5p) in the presence of ethane," *Proc. SPIE* **7005**, 700522 (2008).
24. G.A. Pitz, C.D. Fox, and G.P. Perram, "Transfer between the cesium 62*P*1/2 and 62*P*3/2 levels induced by collisions with H2, HD, D2, CH4, C2H6, CF4, and C2F6," *Phys. Rev. A* **84**, 032708–1–032708–6 (2011).
25. G.D. Hager and G.P. Perram, "A three level analytic model for alkali vapor lasers: Part I. Narrow band optical pumping," *Appl. Phys. B* **101**, 45–56 (2010).
26. M.C. Heaven, "Potential energy surfaces for the interactions of excited Rb and Cs atoms with methane," *Proc. SPIE* **8238**, 823808 (2012).
27. B.V. Zhdanov, T. Ehrenreich, and R.J. Knize, "Highly efficient optically pumped cesium vapor laser," *Opt. Comm.* **260**(2), 696–698 (2006).
28. Y. Wang, et al., "Cesium vapor laser pumped by a volume-Bragg-grating coupled quasi-continuous-wave laser-diode array," *Appl. Phys. Lett.* **88**, 141112 (2006).

29 A.L. Glebov, O. Mokhuna, A. Rapaport, S. Vergnole, V. Smirnov, L.B. Glebov, “Volume Bragg gratings as ultranarrow and multiband optical filters,” *Proc. SPIE* **8428**, 84280C1–84280C11 (2012).

30. A. Podvyaznyy, et al., “250W diode laser for low pressure Rb vapor pumping,” *Proc. SPIE* **7583**, 758313 (2010).

31. B.V. Zhdanov, T. Ehrenreich, and R.J. Knize, “Narrowband external cavity laser diode array,” *Elec. Lett.* **43**(4), 221–222 (2007).

32. B.V. Zhdanov and R.J. Knize, “Diode-pumped 10 W continuous wave cesium laser,” *Opt. Lett.* **32**(15), 2167–2169 (2007).

33. B.V. Zhdanov, J. Sell, and R.J. Knize, “Multiple laser diode array pumped Cs laser with 48 W output power,” *Elec. Lett.* **44**(9), 582–583 (2008).

34. B.V. Zhdanov, et al., “Cesium vapor laser with transverse pumping by multiple laser diode arrays,” *Opt. Comm.* **281**, 5862–5863 (2008).

35. B.V. Zhdanov, M.K. Shaffer, and R.J. Knize, “Cs laser with unstable cavity transversely pumped by multiple diode lasers,” *Opt. Express* **17**(17), 14767–14770 (2009).

36. B.V. Zhdanov, M. K. Shaffer, and R.J. Knize, “Scaling of diode pumped Cs laser: transverse pump, unstable cavity, MOPA,” *Proc. SPIE* **7581**, 75810F–1 (2010).

37. R.J. Knize, B.V. Zhdanov, and M. K. Shaffer, “Photoionization in alkali lasers,” *Opt. Express* **19**(8), 7894–7902 (2011).

38. Z. Yang, et al., “Modeling, numerical approach, and power scaling of alkali vapor lasers in side-pumped configuration with flowing medium,” *J. Opt. Soc. Am. B* **28**, 1353–1364 (2011).

39. B.D. Barmashenko and S. Rosenwaks, “Detailed analysis of kinetic and fluid dynamic processes in diode-pumped alkali lasers,” *JOSA B* **30**(5), 1118–1126 (2013).

40. A.V. Bogachev, et al., “Diode-pumped caesium vapour laser with closed-cycle laser-active medium circulation,” *Quantum Electron.* **42**(2), 95–98 (2012).

41. G.A. Pitz et al., “Advancements in flowing diode pumped alkali lasers,”, *Proc. SPIE* **9729**, 972902-1–972902-8 (2016); C.A. Rice and G.P. Perram, “Atmospheric transmission for cesium DPAL using TDLAS,” *Proc. SPIE* **8238**, 82380I (2012).

42. G.A. Pitz, et al., “Atmospheric propagation properties of various laser systems,” *Proc. SPIE* **8380**, 83800V (2012).

43. W.F. Krupke, “Diode pumped alkali lasers (DPALs) – a review,” *Progress Quantum Electron.* **36**(1), 4–28 (2012).

44. J. Zweiback and W.F. Krupke, “High power diode pumped alkali vapor lasers,” *Proc. SPIE* **7005**, 700525-1–700525-8 (2008).

32

Chemical Lasers: Section Introduction

Julian Jones

Quite different from all other lasers in this book are those pumped by chemical reactions, rather than by electrical or optical means. The chemical iodine oxygen, COIL, laser (Chapter 33, Boris Barmashenko and Samit Rosenwaks) is the only known example of a high-power chemically driven electronic transition laser. The reaction of gaseous chlorine with basic hydrogen peroxide solution produces enormous (multi-megawatt) power at 1315 nm and 30% chemical efficiency. Its development was driven by military applications, but it is also suitable for some material processing applications, such as in the heavy cutting needed in some nuclear decommissioning work. In Chapter 34, Lee Sentman describes HF and DF chemical lasers, with wavelengths of 2.8 and 3.8 μm, respectively, or in the range 1.3–1.4 μm for the HF overtone laser. Small-scale lasers with power outputs in the range of tens to hundreds of watts are available commercially.

Taylor & Francis
Taylor & Francis Group
http://taylorandfrancis.com

33

Chemical Lasers: COIL

B. D. Barmashenko and S. Rosenwaks

CONTENTS

33.1 Principle of Operation 451
33.2 Construction and Components 455
33.3 Cavity Design and Extraction Efficiency 459
33.4 Operating Characteristics, Performance and Modes of Lasing 460
33.5 Conclusions 462
References 463
Further Reading 465

33.1 Principle of Operation

The chemical oxygen iodine laser (COIL) [1] is the only known example of a high-power chemically driven electronic transition laser. Unlike other chemical lasers (e.g. HF (hydrogen fluoride) and DF (deuterium fluoride) lasers), which operate on rotational–vibrational transitions of molecules, the COIL operates on an atomic electronic transition. At present the COIL is the shortest wavelength chemical laser system [2,3]. Figure 33.1 shows the electronic states of the species participating in the pumping process of the COIL. The laser transition, at 1315 nm, takes place between the spin-orbit levels of the ground-state configuration of the iodine atom, $I(5p^{5\,2}P_{1/2}) \rightarrow I(5p^{5\,2}P_{3/2})$. Basic chemical reactions taking place in the COIL are presented in Table 33.1 [4,5]. The iodine atoms are pumped by a near-resonant energy transfer from oxygen molecules in the excited singlet delta state, $O_2(a^1\,\Delta_g)$ (reaction 1, Table 33.1). $O_2(^1\Delta)$ is a metastable molecule with a very long radiative lifetime (76 min) [6] and a pronounced stability against collisional deactivation processes in many environments. Hence, it can be used as the energy carrier for the COIL. Mixing of chemically produced $O_2(^1\Delta)$ with I_2 molecules results in dissociation of molecular iodine to atomic iodine which is subsequently excited *via* reaction 1 (Table 33.1).

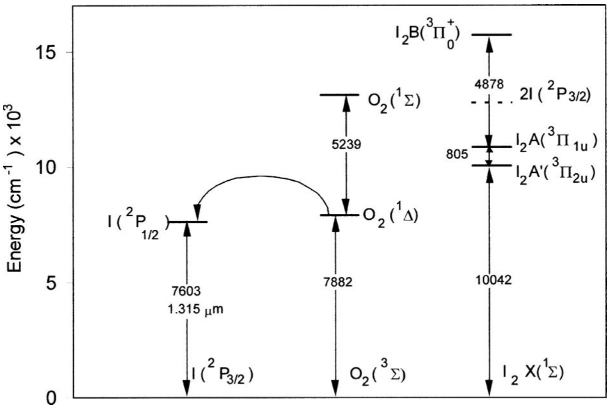

FIGURE 33.1 Low-lying electronic states of O_2, I_2 and I. Energy gaps are given in cm^{-1}.

$O_2(^1\Delta)$ is produced in a chemical generator by the reaction of gaseous chlorine with basic hydrogen peroxide (BHP) solution. BHP is prepared by mixing an aqueous solution of H_2O_2 with aqueous alkali metal hydroxide MOH (M≡Na or K). The mixing results in formation of HO_2^- ions in reaction 2 (Table 33.1). Due to the large value of the equilibrium constant of reaction 2 the BHP is composed of HO_2^-, H_2O_2 and H_2O with very little OH^-. The BHP solutions used in the COIL are 6–8 molar in HO_2^-, 1–3 molar in H_2O_2 and about 50% wt H_2O [2,7]. Since reaction 2 is extremely exothermic ($\Delta H = -50$ kJ mole^{-1}), the BHP has to be cooled down during preparation and is kept at −10°C to −30°C. The chlorine molecules are transferred from the gas–phase to the gas/liquid interface and then enter the liquid. $O_2(^1\Delta)$ is then produced in the liquid (mainly in a layer that extends 100 nm from the interface) *via* reactions 3a–c (Table 33.1) with the overall reaction 3 between the chlorine and HO_2^- [8,9]. The $O_2(^1\Delta)$ product diffuses back to the interface and emerges from the liquid, some fraction of $O_2(^1\Delta)$ being quenched in the liquid by reaction 4. Key parameters of the $O_2(^1\Delta)$ chemical production are the $O_2(^1\Delta)$ yield Y and chlorine utilization U defined as

$$Y = \left[O_2\left(^1\Delta\right)\right] \big/ \left[O_2\right]_{\text{total}} \tag{33.1}$$

and

$$U = \left[O_2\right]_{\text{total}} \big/ \left[Cl_2\right] \tag{33.2}$$

respectively, where $[O_2]_{\text{total}} = [O_2(^1\Delta)] + [O_2(^1\Sigma)] + [O_2(^3\Sigma)]$ and $[Cl_2]$ is the chlorine density prior to its reaction with the BHP. Although the $O_2(^1\Delta)$ yield in reaction 3 is near one [8,10], the

TABLE 33.1

Basic Chemical Reactions in the COIL [4,5]. $I^* \equiv I(^2P_{1/2})$, $I \equiv I(^2P_{3/2})$ $I_2^\dagger$ is the intermediate state of I_2.

No	Reaction	Rate Constant (cm^3s^{-1}) or Equilibrium Constant (K_e)
	Energy Transfer Pumping Reaction	
1	$O_2(^1\Delta) + I \leftrightarrow O_2(^3\Sigma) + I^*$	$k_{1f} = 7.8 \times 10^{-11}$, $k_{1b} = k_{1f}/K_{e1}$, $K_{el} = 0.75 \exp(402/T)$
	Liquid Phase $O_2(^1\Delta)$ Production	
2	$OH^- + H_2O_2 \leftrightarrow HO_2^- + H_2O$	$K_{e2} = 4 \times 10^4$
3a	$HO_2^- + Cl_2 \rightarrow HOOCl + Cl^-$	$k_{3a} = 4.5 \times 10^{-14}$
3b	$HO_2^- + HOOCl \rightarrow ClO_2^- + H_2O_2$	$k_{3b} = \infty$
3c	$ClO_2^- \rightarrow Cl^- + O_2(^1\Delta)$	$k_{3c} = 10^7 s^{-1}$
3	$Cl_2 + 2H_2O^- \rightarrow O_2(^1\Delta) + 2Cl^- + H_2O_2$	
4	$O_2(^1\Delta) \rightarrow O_2(^3\Sigma)$	$k_4 = 5 \times 10^5 s^{-1}$
	I_2 Dissociation by O_2 (1Σ)	
5	$O_2(^1\Delta) + O_2(^1\Delta) \rightarrow O_2(^1\Sigma) + O_2(^3\Sigma)$	$k_5 = 2.7 \times 10^{-17}$
6	$O_2(^1\Delta) + I^* \rightarrow O_2(^1\Sigma) + I$	$k_6 = 1.1 \times 10^{-13}$
7	$O_2(^1\Sigma) + H_2O \rightarrow O_2(^1\Delta) + H_2O$	$k_7 = 6.7 \times 10^{-12}$
8	$I_2(X) + O_2(^1\Sigma) \rightarrow I + I + O_2(^3\Sigma)$	$k_8 = 4 \times 10^{-12}$
	Heidner's Auto Catalytic Mechanism of I_2 Dissociation	
9	$O_2(^1\Delta) + I_2 \rightarrow O_2(^3\Sigma) + I_2^{\dagger\dagger}$	$k_9 = 7 \times 10^{-15}$
10	$I^* + I_2 \rightarrow I + I_2^{\dagger\dagger}$	$k_{10} = 3.8 \times 10^{-11}$
11	$O_2(^1\Delta) + I_2^{\dagger\dagger} \rightarrow O_2(^3\Sigma) + 2I$	$k_{11} = 3 \times 10^{-10}$
12	$I^* + H_2O \ \Sigma \ I + H_2O$	$k_{12} = 2 \times 10^{-12}$
13	$I_2^{\dagger\dagger} + M \rightarrow I_2 + M(M = H_2O, O_2, He)$	$k_{13H_2O} = 2 \times 10^{-12}$, $k_{13O_2} = 5 \times 10^{-11}$, $k_{13He} = 4 \times 10^{-12}$
	HLAHP Mechanism of I_2 Dissociation	
14	$O_2(^1\Delta) + O_2(^1\Delta) \rightarrow O_2(^1\Sigma, v = 2) + O_2(^3\Sigma)$	$k_{14} = 9.5 \times 10^{-28} T_{eff}^{3.8} \exp(700/T_{eff})^a$
15	$O_2(^1\Delta) + O_2(^1\Delta) \rightarrow 2O_2(^3\Sigma, v = 3)$	$k_{15} = 1.7 \times 10^{-17}$
16	$O_2(^1\Sigma) + H_2O \rightarrow O_2(^1\Delta, v = 3) + H_2O$	$k_{16} = 6.7 \times 10^{-12}$
17	$O_2(^1\Delta\ v = 1 - 3) + I_2 \rightarrow O_2(^3\Sigma) + I_2(A', A)$	$k_{17}(v = 1) = 1.9 \times 10^{-11} \exp(-897/T)$ $k_{17}(v = 2) = 3.0 \times 10^{-11}$, $k_{17}(v = 3) = 1.0 \times 10^{-11}$
18	$O_2(^1\Delta) + I_2(A', A) \rightarrow O_2(^3\Sigma) + 2I$	$k_{18} = 3.0 \times 10^{-10}$
19'	$I^* + I_2 \rightarrow I + I_2^{\dagger\dagger}$	$k_{19} = 3.8 \times 10^{-11}\ \Gamma$, $\Gamma = 0.25$
19"	$I^* + I_2 \rightarrow I + I_2^\dagger$	$k_{19} = 3.8 \times 10^{-11} (1 - \Gamma)$
20	$O_2(^1\Delta) + I_2^\dagger \rightarrow O_2(^3\Sigma) + I_2(A')$	$k_{20} = 2 \times 10^{-11}$

yield obtained at the exit of the singlet oxygen generator (SOG) is usually smaller than unity, ranging from 0.5 to 0.7 [11,12] for the high-pressure SOGs used in the modern COIL devices (see Section 33.2). $O_2(^1\Delta)$ losses are due to both liquid-phase and gas-phase (reaction 5) quenching. For high pressures in the SOG, the liquid-phase losses are enhanced by HO_2^- depletion near the gas–liquid interface, which results in the reaction zone shifting into the bulk of the liquid and an increase in the $O_2(^1\Delta)$ transport time to the interface. To estimate the values of Y and U, taking into account all the aforementioned processes, one can use simple analytical expressions [13–15]. Unlike Y, the utilization U is close to unity for almost all types of the SOG.

The mechanism by which $O_2(^1\Delta)$ dissociates I_2 is one of the most complex and least understood aspects of COIL chemistry. Since the loss of excited $O_2(^1\Delta)$ molecules in the iodine mixing–dissociation zone results in a decrease of laser power, this process is very important for the COIL operation. Three mechanisms have been suggested for iodine dissociation. The first [16] involves I_2 dissociation by energy transfer from $O_2(^1\Sigma)$ (reaction 8), which has sufficient energy to dissociate I_2 (see Figure 33.1). $O_2(^1\Sigma)$ is initially formed by the energy-pooling reaction 5 and then (once an appreciable density of I is formed) strongly supplemented by the pooling reaction 5, where I^* (= $I(^2P_{1/2})$) is formed by the pumping reaction 1. However, dissociation in COIL devices, where significant water concentrations severely reduce the steady-state density of $O_2(^1\Sigma)$ by the quenching reaction 7, is too fast to be attributed solely to this mechanism. Hence, reaction 8 is important only at the initiation stage of dissociation when a small fraction of I_2 is dissociated to atoms.

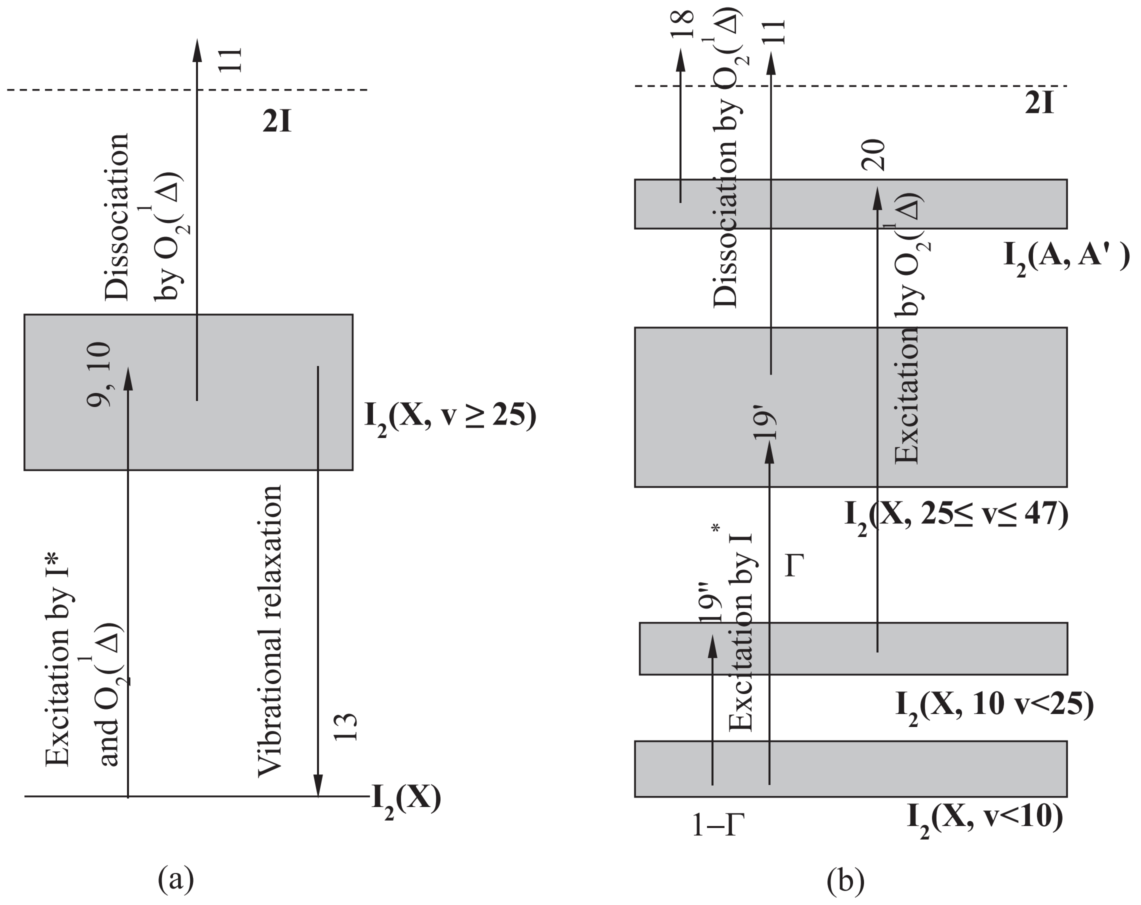

FIGURE 33.2 Schematic diagram of iodine dissociation mechanisms in the COIL: (a) Heidner's mechanism; (b) HLAHP mechanism. The arrows show excitation and relaxation pathways and the labels near the arrows denote the number of the process in Table 33.1.

The second and most celebrated mechanism of iodine dissociation was suggested by Heidner et al. [4] (which for brevity will be referred to as Heidner's mechanism). They found that iodine dissociation is an autocatalytic chain reaction accelerated by I^*. A schematic representation of the dissociation mechanism is shown in Figure 33.2a. The dissociation is a two-step process. In the first step, I_2 is excited to an intermediate state $I_2^{\dagger\dagger}$ by reaction 9 and the more rapid reaction 10. Then, excited $I_2^{\dagger\dagger}$ molecules are dissociated by $O_2(^1\Delta)$ in reaction 11. The dissociation rate is controlled by the rates of the excitation reactions 9 and 10. The slow reaction 9 initiates the process but after the buildup of I atoms (excited to I* in reaction 1), the much faster reaction 10 dominates. Consequently, the rate of iodine dissociation is dependent on the number density of I_2 in the flow. Although the iodine intermediate $I_2^{\dagger\dagger}$ was not observed directly, there is evidence that it is vibrationally excited I_2 (X, $\upsilon > 25$) and not one of the low-lying triplet I_2 electronic states shown in Figure 33.1 [4,17].

Subsequent kinetic studies have raised doubts concerning Heidner's mechanism. As discussed in Refs. [18–20], the values of several reaction rate constants suggested in Heidner's mechanism, and in particular the rate constant of reaction 9 which initiates the dissociation process, are substantially different from the directly measured values of these constants. To check the validity of Heidner's mechanism, a three-dimensional (3D) computational fluid dynamics (CFD) modelling of a low-pressure supersonic COIL was carried out in Ref. [20]. Comparison between the calculated and experimental results (also obtained in Ref. [20]) showed that Heidner's mechanism underestimates the dissociation rate of I_2 at the early initiation stage. As a result, the calculated small signal gain *g*, the temperature *T* and the I_2 dissociation fraction *F* were significantly different than those measured experimentally. As shown in Refs. [21,22], *g*, *F*, *T* and the lasing power *P* for different types of COIL can be predicted over the entire range of checked parameters using the Heidner–Lilenfeld–Azyazov–Heaven–Pichugin (HLAHP) mechanism [21,23], where pathways involving the excited species $I_2(X\ ^1\Sigma_g^+, 10 \le v < 25)$, $I_2(X\ ^1\Sigma_g^+, 25 \le v \le 47)$, $I_2(A'\ ^3\Pi_{2u})$, $I_2(A\ ^3\Pi_{1u})$, $O_2(X\ ^3\Sigma_g^-$, v), $O_2(a\ ^1\Delta_g$, v), $O_2(b^1\ \Sigma_g^+, v)$ and $I(^2P_{1/2})$ as intermediate reactants are included.

Table 33.1 lists the most important reactions considered in the modelling and their rate constants, the full list of reactions being presented in Refs. [21,22]. In the HLAHP mechanism, iodine dissociation involves at least three steps where $O_2(^1\Delta)$ is consumed: first in reactions that lead to production of $O_2(^1\Delta, v = 1–3)$ by the sequence of $O_2(^1\Delta)$ energy-pooling (reactions 14 and 15) and $O_2(^1\Sigma)$ quenching by water (reaction 16), second in I_2 excitation to $I_2(A', A)$ ($\equiv I_2(A'\ ^3\Pi_{2u}, A\ ^3\Pi_{1u})$) by energy transfer from $O_2(^1\Delta, v)$ via reaction 17 and third in

$I_2(A', A)$ dissociation to I atoms via interaction with $O_2(^1\Delta)$ (reaction 18); this is the initiation stage of I_2 dissociation.

At the later stage of dissociation, when a substantial number of I atoms have been formed, an additional rapid three-step dissociation mechanism takes over, as shown in the schematics presented in Figure 33.1. In the first step of the rapid dissociation phase, I* atoms (formed from I by reaction 1) excite I_2 molecules to vibrational states via reaction 19 that splits to two channels: (19′) a small fraction $\Gamma \approx 0.25$ of I_2 molecules is excited to high vibrational levels $I_2^{\dagger\dagger}$ ($\equiv I_2(X, 25 \leq v \leq 47)$) which, in turn, dissociate via reaction 11; and (19″) a larger fraction $1 - \Gamma$ (≈ 0.75) of I_2 is excited first to lower vibrational states, $I_2^{\dagger}$ ($\equiv I_2(X, 10 \leq v \leq 25)$), then to $I_2(A', A)$ by O_2(a) via reaction 5 which is the second step and finally $I_2(A', A)$ is dissociated by another O_2(a) via reaction 18, just as in the above-mentioned initiation stage.

Zagidullin et al. revisited the values of some rate constants shown in Table 33.1 [24,25]. They claimed that according to their experimental observations, the rate constants of reactions 5 and 6, responsible for $O_2(^1\Sigma)$ production, and reaction 8, responsible for I_2 dissociation by $O_2(^1\Sigma)$, are several times larger than the standard values presented in the table and concluded that the contribution of the of I_2 dissociation by $O_2(^1\Sigma)$ is the same as that of Heidner's mechanism. Note that neither the revisited I_2 dissociation mechanism by $O_2(^1\Sigma)$ [23,24] nor Heidner's mechanism can explain the results of the measurements of the gain and iodine dissociation fraction in the supersonic COIL [20] since, as mentioned above, Heidner's model and hence the mechanism of I_2 dissociation by $O_2(^1\Sigma)$ (which has a rate close to that predicted by Heidner's model) strongly underestimate the iodine dissociation rate in typical supersonic COILs. At the same time, the supersonic COIL parameters predicted by the aforementioned HLAHP model are very close to the measured values.

The condition for the existence of population inversion between the levels involved in the $I(^2P_{1/2}) \rightarrow I(^2P_{3/2})$ transition is

$$\frac{[I(^2P_{1/2})]}{[I(^2P_{3/2})]} > 0.5. \tag{33.3}$$

Taking into account that fast equilibrium between I* and $O_2(^1\Delta)$ is established in reaction 1, one can determine the yield Y_{th} necessary to achieve threshold population inversion in the O_2–I system:

$$Y_{th} \equiv \frac{1}{2K_{e1} + 1} \tag{33.4}$$

where K_{e1} is the equilibrium constant. At room temperature ($T = 300$ K), $Y_{th} = 0.15$.

TABLE 33.2

Wavelengths of Transitions between the Hyperfine Sublevels of $^2P_{1/2}$ and $^2P_{3/2}$ States of I [26]

Transition	Wavelength in Vacuum (nm)
3 → 4	1315.2463
3 → 3	1315.2220
3 → 2	1315.2106
2 → 3	1315.3360
2 → 2	1315.3246
2 → 1	1315.3204

To find the small signal gain, it is necessary to take into account that the upper laser level $^2P_{1/2}$ is split into two hyperfine sublevels with total angular momentums of the I atom $F = 2$ and 3 and the lower level $^2P_{3/2}$ consists of four hyperfine sublevels with $F = 1$, 2, 3 and 4. Possible transitions between these sublevels and their wavelengths in vacuum are shown in Table 33.2. The largest value of the Einstein coefficient $A = 5\ s^{-1}$ corresponds to the $F = 3 \rightarrow F = 4$ which is the lasing transition. The gain coefficient for this transition is given by

$$g = \frac{7}{12}\sigma_{34}\left(\left[I\left(^2P_{1/2}\right)\right] - 0.5\left[I\left(^2P_{3/2}\right)\right]\right) \tag{33.5}$$

where $\sigma_{34} = 1.29 \times 10^{-17}(300/T)^{1/2}\text{cm}^2$ is the stimulated emission cross section for Doppler broadening [27]. Taking into account the aforementioned assumption of the equilibrium between I* and $O_2(^1\Delta)$, the following equation for g is derived [27]:

$$g = \frac{7}{12}\sigma_{34}\frac{I_{total}}{2}\frac{(2K_{e1} + 1)Y - 1}{(K_{e1} - 1)Y + 1} \tag{33.6}$$

where $[I]_{total} = [I(^2P_{1/2})] + [I(^2P_{3/2})]$. Hence, the gain increases with increasing iodine density and decreasing temperature and weakly depends on the yield Y. At room temperatures and $Y = 0.5$–0.8, $g\ (\text{cm}^{-1}) = (5$–$7) \times 10^{-18}\ [I]_{total}$, where $[I]_{total}$ is in cm^{-3}. Hence, to get gain around 10^{-3}–10^{-2}cm^{-1}, the iodine densities in the COIL active medium should be around 10^{14}–10^{15}cm^{-3}.

The lasing power P can be estimated with the aid of an energy book-keeping methodology such as the COIL heuristic equation [28]:

$$P = 91\left(\text{kJ mole}^{-1}\right)nCl_2U\left(Y_{plen} - Y_{diss} - Y_{th}\right)\eta_{mix}\eta_{ext} \tag{33.7}$$

where 91(kJ mole^{-1}) is the energy of I*, nCl_2 is the chlorine molar flow rate and Y_{plen} is the $O_2(^1\Delta)$ yield just upstream of the iodine injection,

$$Y_{diss} = NF\frac{nI_2}{nCl_2\eta_{mix}} \tag{33.8}$$

is the $O_2(^1\Delta)$ loss during iodine dissociation, η_{mix} is the mixing efficiency defined as the fraction of $O_2(^1\Delta)$ mixed with iodine, η_{ext} is the optical extraction efficiency of the resonator, F is the iodine dissociation fraction and N is the number of $O_2(^1\Delta)$ molecules lost in the region of iodine dissociation per I_2 molecule. From energy considerations, N cannot be less than two. However, analytical and numerical computations [28,29] and experimental measurements [19,30] show that N can be appreciably larger, typically in the range 4–6. Exact value of N was determined experimentally in [20,31] where direct measurements of the dissociation of I_2 molecules in the supersonic COIL were carried out: it is 4.5 ± 0.4 for typical conditions and I_2 densities applied for optimal operation of the COIL but increases at lower I_2 densities. The expressions for η_{ext} for different types of optical resonators are presented later in Section 33.3. A very important parameter of the COIL is the chemical efficiency η_{chem}, defined as the number of emitted photons per number of chlorine molecules passed through the generator of $O_2(^1\Delta)$ and, hence, given by

$$\eta_{\text{chem}} \equiv \frac{P}{91(\text{kJ mole}^{-1})n\text{Cl}_2} = U(Y_{\text{plen}} - Y_{\text{diss}} - Y_{\text{th}})\eta_{\text{mix}}\eta_{\text{ext}}. \quad (33.9)$$

High values of the chemical efficiency can be achieved for efficient SOG with large values of U and Y_{plen}, good mixing and optical extraction corresponding to large η_{mix} and η_{ext}, small dissociation losses Y_{diss} and low temperature in the resonator corresponding to small Y_{th}.

There are two types of COILs: subsonic and supersonic. The first COIL [1] used subsonic flow of the reagents in the resonator. Due to small flow velocities, low densities of iodine are needed to provide for the total dissociation of I_2 and to extract energy $O_2(^1\Delta)$ while maintaining a reasonable laser mode volume [32]. Small values of the iodine density and, hence, of the small signal gain forces the laser beam region to become unbearably long. For example, the first 100–500 W class subsonic devices [33,34] had a gain length of 0.5 to 2 m, and an output power of 4.6 kW was eventually obtained from a 4 m gain-length device [2]. In the supersonic COILs, the flow is brought to supersonic velocity *via* expansion in a converging–diverging nozzle. The supersonic COILs, which have been intensively studied during the last decade, have several advantages over the subsonic devices. Most importantly, the low temperature achieved by supersonic expansion (predicted to be 150 K for typical devices) displaces the equilibrium of reaction 1 (Table 33.1) in favour of I* production. The equilibrium constant increases from $K_{e1} = 2.88$ at room temperature to 10.9 at 150 K. Using Equation (33.4), one obtains that the threshold yield Y_{th} falls to 0.044; hence, both the gain and power, given by Equations (33.6) and (33.7), respectively, rise. Also, supersonic flow stretches the gain region, which facilitates power extraction from the optical cavity. In addition, the low temperature reduces the Doppler linewidth of the lasing transition, thereby increasing the gain at the line-centre. These advantages were demonstrated in a supersonic COIL with a 25 cm length nozzle, which yielded powers comparable to the 4 m subsonic device mentioned earlier [2].

33.2 Construction and Components

A block diagram of a typical COIL is shown in Figure 33.3. The major components of the COIL are the SOG, water vapour trap (WVT) for H_2O removal (in most modern COILs, this trap is not used), iodine supply system, iodine–oxygen mixing system, optical resonator and reactant exhaust system.

Figure 33.4 shows four main types of SOGs: bubbler (or sparger), wetted wall with rotating discs, jet and aerosol generators. In a bubbler or sparger generator (Figure 33.4a), $O_2(^1\Delta)$ is produced by bubbling (sparging) of the Cl_2 gas through a batch of pre-cooled BHP. Cl_2 is injected into the BHP through small orifices in a plate located in the lower part of the generator. Chlorine bubbles formed in this way float up and react with the BHP. The chlorine is absorbed by the solution and reacts in the liquid phase generating $O_2(^1\Delta)$, which in its turn is transferred from the liquid to the interior of the bubble. This generator has a very simple configuration and a very high specific surface area for the gas–liquid interface, S (the area per active unit volume in the generator), which can reach 300 cm^{-1} and ensures high utilization of chlorine (close to 100%). However, the yield is sufficiently high (above ~0.3) only when the partial pressure of oxygen in the generator is relatively low ~1–2 torr.

In a wetted wall SOG, the gaseous Cl_2 reacts with a thin film of the BHP solution on the surface of packing placed inside the SOG. This generator evolved from falling film generators [35] to the current rotating-disc generator, as shown in Figure 33.4b [36]. In this generator, closely spaced discs rotate through a pool of BHP producing a set of parallel-plate surfaces coated with a

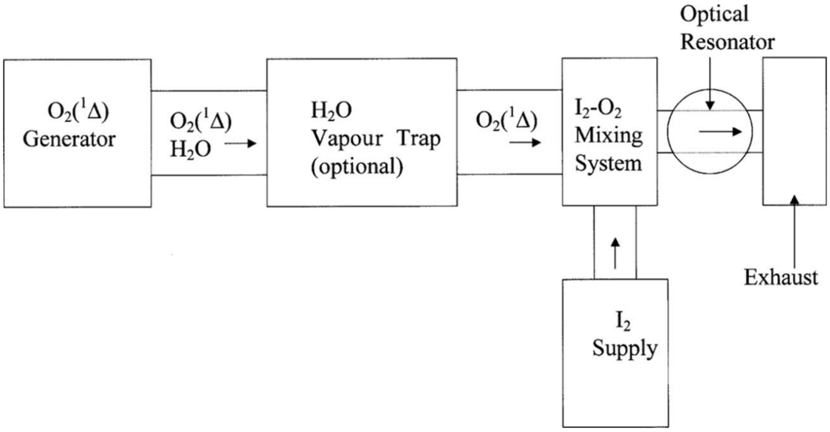
Optical Resonator
$O_2(^1\Delta)$ Generator
$O_2(^1\Delta)$ H_2O →
H_2O Vapour Trap (optional)
$O_2(^1\Delta)$ →
I_2-O_2 Mixing System
Exhaust
I_2 Supply

FIGURE 33.3 Block diagram of a typical COIL.

thin BHP film. The Cl_2 gas is forced through the discs, producing $O_2(^1\Delta)$. This generator operates better at higher pressures, the chlorine utilization and $O_2(^1\Delta)$ yield being about 0.9 and 0.5–0.55 [12], respectively, at a partial oxygen pressure of 11.5 torr. The specific surface *S* for disc generators reaches 10 cm^{-1}.

The third type of the SOG shown in Figure 33.4c is a jet generator [37]. The BHP is pushed through holes of 0.6–0.8 mm diameter in a perforated plate into the generator, producing jets at a velocity of 6 m s^{-1} in the reaction zone. Cl_2 is delivered into the reaction zone at the lower part of the generator and flows at a velocity of 10 m s^{-1} between the BHP jets, against their flow direction, to the generator exit. Most of the Cl_2 (80%–90%) reacts with the BHP to produce singlet oxygen at a yield of 0.6–0.7 [11] and a partial oxygen pressure of 20–30 torr. An increase in the velocity of the jets to 20 m s^{-1} and of the chlorine to 30 m s^{-1} enables the oxygen pressure to be increased to 100 torr, and the yield is then about 0.6 [38].

In aerosol SOGs, the gaseous Cl_2 reacts with the BHP delivered in the form of droplets. The best design is the uniform droplets SOG [39], as shown in Figure 33.4d. Just as in the jet SOG, BHP is sprayed through a large number of holes in an injector plate located at the top of the generator. The plate is vibrated by a piezoelectric actuator at a frequency of 4 kHz to generate a field of uniformly sized 0.5 mm diameter droplets at a velocity 12 m s^{-1}. Mutual orientation of the chlorine and droplet flows of 90°, as suggested and analysed by Barmashenko et al. [13], is employed in this generator. Application of a uniform droplet field and 90° orientation in this SOG enables the separation of the droplets from the gas flow to be precluded.

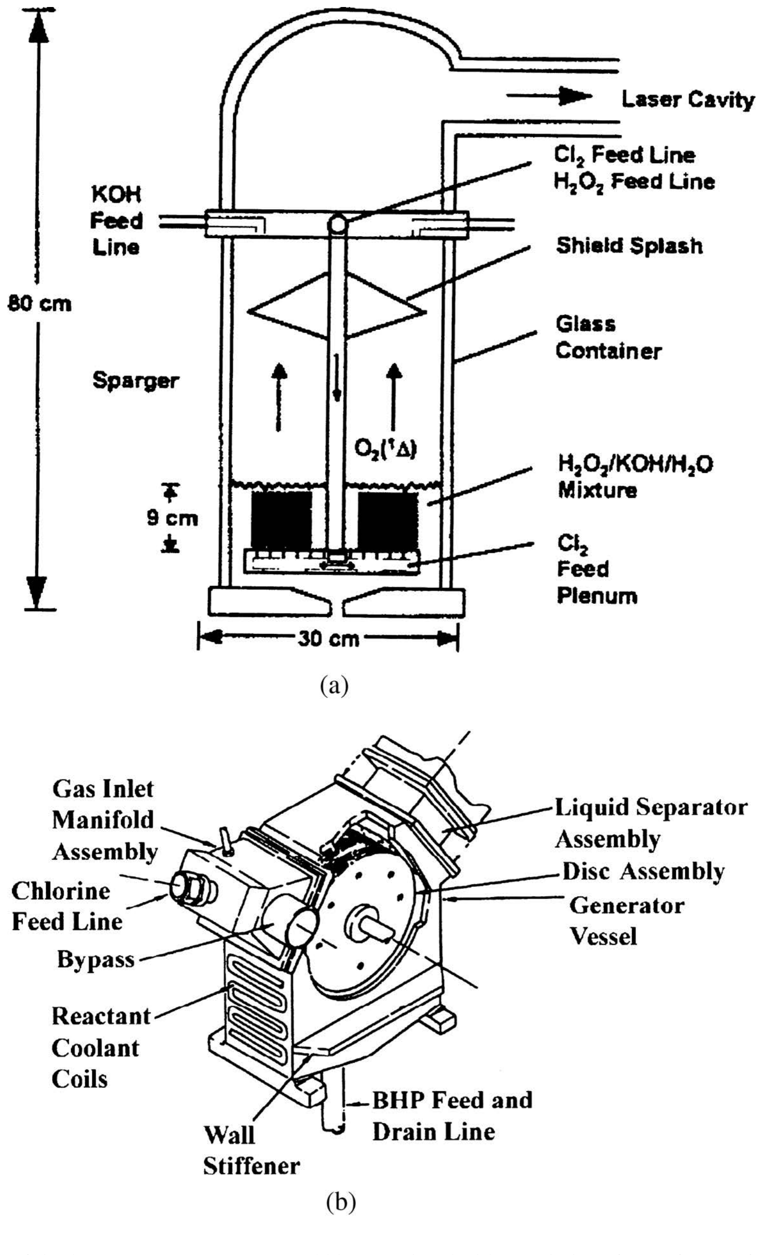
Laser Cavity
Cl₂ Feed Line
H₂O₂ Feed Line
KOH Feed Line
Shield Splash
80 cm
Glass Container
Sparger
O₂(¹Δ)
H₂O₂/KOH/H₂O Mixture
9 cm
Cl₂ Feed Plenum
30 cm
(a)
Gas Inlet Manifold Assembly
Chlorine Feed Line
Bypass
Reactant Coolant Coils
Wall Stiffener
Liquid Separator Assembly
Disc Assembly
Generator Vessel
BHP Feed and Drain Line
(b)

FIGURE 33.4 Different types of singlet oxygen generators. (a) Bubble. (Reprinted with permission of SPIE from Ref. [5]). (b) Wetted wall with rotating discs. (Reprinted with permission of SPIE from Ref. [5]).

(*Continued*)

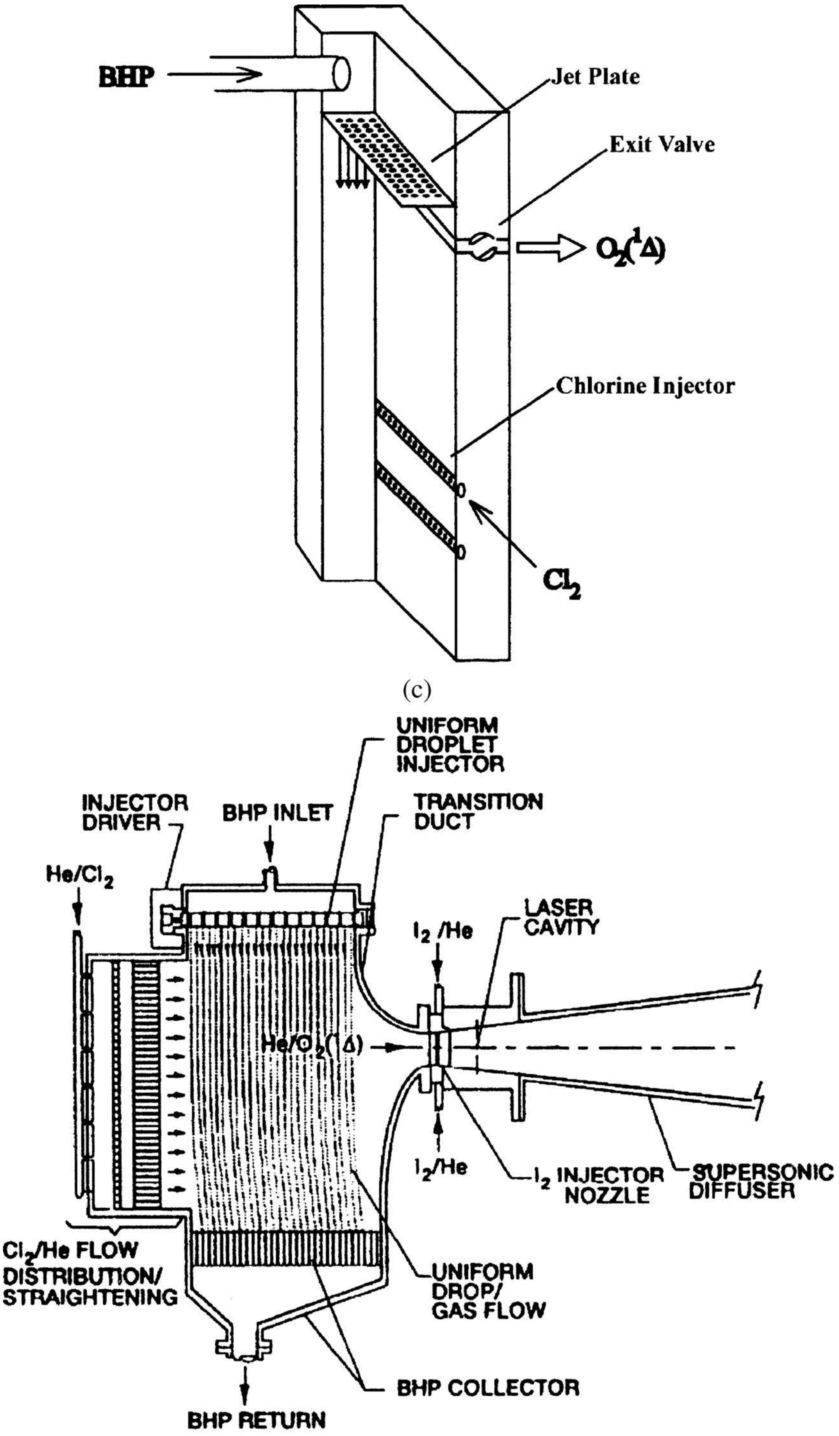
BHP
Jet Plate
Exit Valve
$O_2(^1\Delta)$
Chlorine Injector
Cl_2
UNIFORM DROPLET INJECTOR
INJECTOR DRIVER
BHP INLET
TRANSITION DUCT
He/Cl_2
LASER CAVITY
I_2/He
He/$O_2(\Delta)$
I_2/He
I_2 INJECTOR NOZZLE
SUPERSONIC DIFFUSER
Cl_2/He FLOW DISTRIBUTION/ STRAIGHTENING
UNIFORM DROP/ GAS FLOW
BHP COLLECTOR
BHP RETURN

(c)

(d)

FIGURE 33.4 (*CONTINUED*) (c) Jet [37]. (d) Aerosol with uniform droplets. (Originally published in Ref. [39]. Copyright © 1994/2000 by the Am. Inst. Aeronaut. and Astronaut, Inc. Reprinted with permission.)

At the nominal conditions of 10 torr partial oxygen pressure, the chlorine utilization and $O_2(^1\Delta)$ yield are 0.8 and 0.7, respectively. The uniform droplet SOG is used in the multi-megawatt COIL for the US Air Force Airborne Laser [40].

The flow emerging from the SOG contains water vapour that strongly quenches both I* and $I_2^\dagger$ by reactions 13 and 14 (Table 33.1) and, hence, decreases laser power. To minimize this effect, two approaches have been used: (1) WVT to freeze the water downstream of the SOG; and (2) lower BHP temperature to minimize water vapour formation [41]. The first approach works well for the bubble SOG used in subsonic COILs, where pressure is low and losses of $O_2(^1\Delta)$ due to the pooling reaction 5 (Table 33.1) are small. Different types of WVTs are used: cold-finger-style WVTs [5], finned WVT [5] and rotational/scraping finned cold traps [42] to remove the ice forming on the trap walls. The WVT temperature is usually about 200 K. For the disc, jet and aerosol SOGs used mainly in supersonic COILs, the pressure is significantly higher and, therefore, the WVT cannot be used due to large $O_2(^1\Delta)$ losses. In this case, the second approach is employed and the BHP is kept at –15°C to 30°C. It is worth noting that the harmful effect of the water on the COIL operation is determined by the ratio $[H_2O]/[O_2(^1\Delta)]$ rather than by the absolute H_2O vapour density [9]. In the case of high $O_2(^1\Delta)$ partial pressure, this ratio just after the generator is not larger than that after the WVT in the case of low $O_2(^1\Delta)$ pressure. That means that COILs using high-pressure SOG can work without WVT.

The I_2 supply system uses the following two methods of iodine vapour production: (i) sublimation of solid I_2 into a carrier gas (Ar, He or N_2) by heat lamps or circulating oil heater [5,43,44] and (ii) iodine boilers where I_2 is swept out of molten iodine by heated carrier gas [45,46]. The tubes delivering the iodine vapours to the iodine–oxygen mixing system are heated to avoid I_2 condensation.

Subsonic and supersonic COILs use different kinds of iodine–oxygen mixing systems. For subsonic COILs, the primary stream emerging from the WVT, and typically carrying the oxygen and a diluent (buffer) gas, flows in a rectangular duct with constant cross section. The secondary stream carrying the iodine and additional diluent is injected into the primary stream through either small (~0.5 mm diameter) holes, uniformly distributed across the primary flow (with a distance of several millimetres between adjacent holes), or a narrow slit in metal (brass or stainless steel) tubes. Due to low pressure and flow velocity, almost total mixing is achieved several centimetres downstream of the injection location.

In supersonic COILs, as previously mentioned (Section 33.1), the primary stream is expanded in a supersonic nozzle with ~2:1 area ratio and ~10:1 pressure ratio [2]. Both slit mono-nozzles [46] (see Figure 33.5) and grid nozzles, i.e. arrays of several supersonic nozzles [2,45] (see Figure 33.6), are used. The secondary flow is injected into the primary flow at some location in the nozzle, i.e. in the subsonic, transonic or supersonic part of the flow (see Figure 33.5). Usually one or two rows of small injection holes, uniformly distributed across the flow, are drilled in each side of the nozzle wall. Most of the supersonic COILs operating with He primary diluent use a subsonic mixing scheme [2,46]. In subsonic mixing, He is preferred due to the high velocity of flows diluted with He. For conditions where a nitrogen buffer gas or no primary buffer gas is used, this scheme is not optimal and transonic [44] or quasi-transonic (with injection holes located several millimetres upstream of the critical cross section [47,48]) mixing schemes are employed. A supersonic mixing scheme uses either iodine injection in the diverging section of a slit nozzle [7,49], or supersonic mixing of parallel jets of O_2 and of I_2/N_2 with Mach number Ma $\simeq$ 1.5 [50] created by a two-dimensional conical nozzle array, referred to as a Cassady grid nozzle [51].

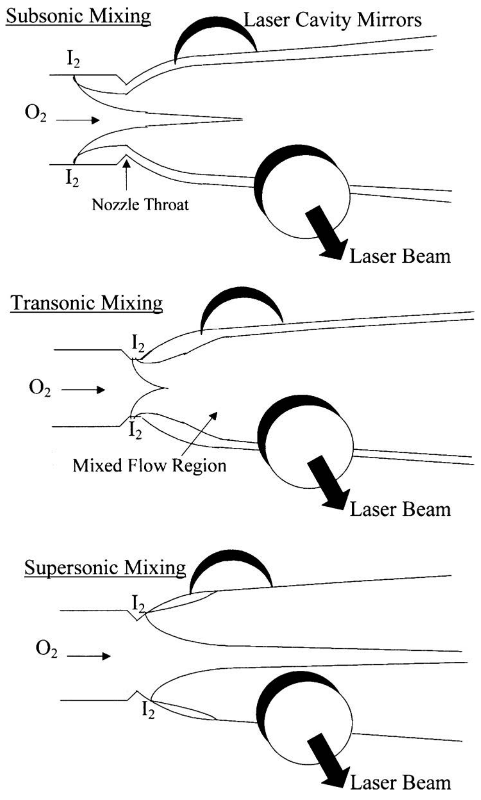

FIGURE 33.5 Subsonic, transonic and supersonic injection schemes (in slit nozzles).

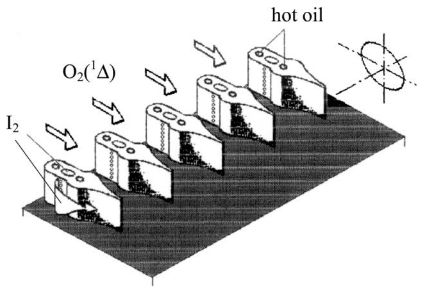

FIGURE 33.6 Grid nozzle with subsonic injection. Either hot oil or electrical heating is used to heat the nozzle blades to preclude I_2 clogging.

Another concept of ejector COIL also uses supersonic mixing [52,53]. In order to achieve good pressure recovery and effective exhaust of the laser gas into the atmosphere, it is necessary to increase the stagnation pressure at the supersonic section of the flow, which usually is less than 100 torr. To this end special grid nozzles were designed where a transonic (Ma = 1) oxygen flow is mixed with hypersonic (Ma = 4–5) I_2/N_2 flow, the N_2 flow rate being five to ten times larger than that of the oxygen. If the total momentum of the N_2 stream is much larger than the momentum of oxygen stream, the latter is pulled into the laser cavity by the nitrogen flow and the stagnation pressure of completely mixed stream is determined mainly by the $N_2 + I_2$ flow. Figure 33.7 shows one such mixing nozzle with separate supplies of N_2 and I_2 [52]. The ejector COIL operates at stagnation pressure in the cavity of 200 torr and a Mach number of about 3 and, hence, is able to ensure a good pressure recovery using small pumping rates.

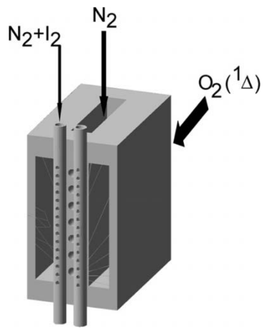

FIGURE 33.7 Fragment of the nozzle bank of the ejector COIL. (Originally published in Ref. [52]. Copyright © 1994/2000 by Am. Inst. Aeronaut. and Astronaut. Inc. Reprinted with permission.)

The optical resonator where the energy of $O_2(^1\Delta)$ is converted into the laser radiation is located several centimetres downstream of the iodine injectors. The optical axis of the resonator is usually transverse to the flow direction. The design and extraction efficiency of the resonators are discussed later in Section 33.3.

The laser effluent is then exhausted into a diffuser-pumping system where the pressure is recovered to the atmospheric pressure [54]. The pumping system usually consists of one or two Roots stages on the vacuum side followed by a rotary pump [45]. Sometimes a cryogenic trap is installed upstream of the pumps to remove iodine and residual chlorine from the exhaust gas in order to prevent corrosion in the pumps. For high stagnation pressures in supersonic COILs, ejectors can be used for pressure recovery [54].

Considerable heat release downstream of the supersonic nozzle (and thus in the optical cavity) driven by the water deactivation of the excited iodine atoms (reaction 13, Table 33.1) has a direct impact on the hardware design of the supersonic part of the flow channel and on the performance of the gas recovery system. To preclude a temperature rise in the gas the floor and the ceiling of the supersonic flow duct usually diverge at an angle of 4°–8° [28,55]. Calculations of the shape of the flow duct for the supersonic diffuser should also take into account the aforementioned heat release [56].

33.3 Cavity Design and Extraction Efficiency

The measured values of the small signal gain are typically smaller than 1–1.5 and $0.15\,\text{m}^{-1}$ in supersonic [7,46,57] and subsonic [58,59] COILs, respectively. Hence, stable resonators have been commonly used in these lasers. The mirror separation depends on the gain length L of the COIL and is usually in the range of 0.5–3 m, the mirror radius of curvature being 2–10 m. The outcoupling mirror transmissions for supersonic COILs with large gain length are about 10%–20%, whereas for subsonic COILs a typical transmission coefficient does not exceed 5%. The mirrors are isolated from the gas flow by ducts purged with He or N_2 to protect the mirror coatings from BHP contamination as well as to prevent iodine from entering the ducts. To extract most of the energy stored by $O_2(^1\Delta)$, the aperture of the mirrors in the flow direction should be 3–10 cm, hence, 5 or 10 cm diameter mirrors are typically used in COILs. Since each iodine atom is repumped and cycled many times throughout the flow field during the lasing process, the saturation characteristics of the COIL are different than in other lasers. To find the extraction efficiency η_{ext} appearing in Equation (33.7) for the laser power, simple models for gain saturation and power extraction in the COIL should be used [29,60,61]. In particular, if the mirror's aperture is much larger than the $O_2(^1\Delta)$ energy extraction distance along the flow, the efficiency η_{ext} for Fabry–Pérot resonator is given by

$$\eta_{\text{ext}} = \frac{t}{t+a}\frac{\left(1-\frac{g_{\text{th}}}{g}\right)}{\left[1-\frac{g_{\text{th}}}{g}\frac{Y-1/(2K_{\text{el}}+1)}{Y+1/(K_{\text{el}}+1)}\right]} \tag{33.10}$$

where t and a are the transmission and loss of the mirrors, respectively, and $g_{\text{th}} \equiv (t+a)/2L$ is the threshold gain of the resonator. The values of η_{ext} of stable and unstable resonators are shown to be higher than those of a Fabry–Pérot resonator [29,61].

The COIL using stable resonator with mirror aperture of several centimetres has a large Fresnel number and, hence, oscillates on high-order transverse modes. Therefore, it has a large mode volume and is well suited for the extraction of high power. However, this advantage is associated with a large beam divergence and, thus, with a beam quality that is far from what is required for the general applications of such a laser. This problem can be solved by using an unstable resonator which, on the one hand, has a large mode volume and, on the other hand, is capable of discriminating the high-order transverse modes [62]. A conventional confocal unstable resonator consists of either concave and convex (positive branch) or two concave (negative branch) spherical mirrors. The most important parameter of this kind of resonator is the magnification M, which is equal to the ratio between the mirror apertures. M describes the outcoupled fraction of the mode volume by simple geometry, being also a measure of the amount of power (intensity) that can be concentrated in the central peak of the far-field mode pattern. In addition to the central peak, this pattern has also side diffraction maxima. Low power in the side maxima is obtained only for large M. However, for small- and medium-sized COILs, only a small fraction of the intracavity power can be coupled out without a serious loss in the total lasing power. For small values of M (close to unity), the radiation field forms a narrow ring with only a small fraction of power in the central peak and the beam divergence is large. This means that a conventional unstable resonator is unable to provide for high lasing power and good quality of the laser beam. In experiments carried out in China [63], an output power of 7.1 kW was achieved at a chlorine flow rate of 450 mmole s^{-1} for a 1 m gain-length COIL a using confocal, conventional unstable resonator with $M = 1.39$. However, the experimental beam divergence angle was almost six times larger than the beam diffraction angle, defined as the divergence of a filled-in beam with uniform amplitude and phase; and the aforementioned ring intensity profile pattern was

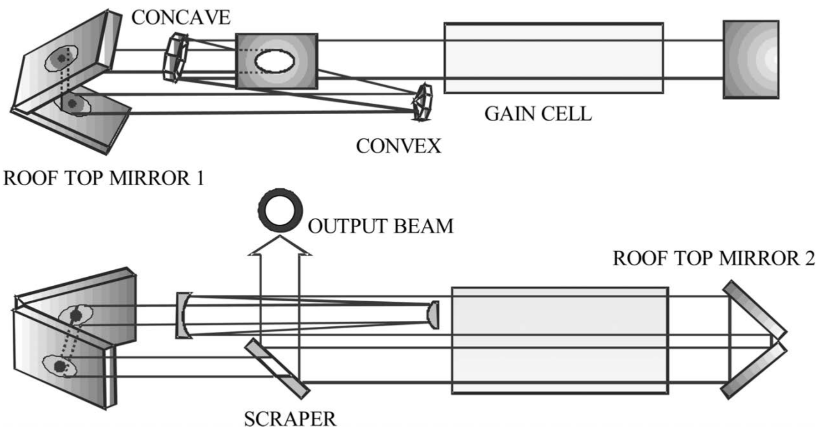

FIGURE 33.8 Unstable resonator with 90° phase rotation [56].

observed in the near field. One way for improving this situation was suggested by Anan'ev et al. [64] and investigated for the COIL by Latham et al. [65]. Their resonator utilizes an oblique roof-top reflector to turn the phase by 90° with each path (Figure 33.8). This resonator (named UR-90) was used to obtain a uniform intensity profile pattern in the near field. The same output power as for a conventional unstable resonator was obtained with a beam divergence angle only twice the beam diffraction angle. Another unstable double-pass resonator of the hybrid, confocal type was designed for outcoupling the radiation of a 10 kW class COIL with a gain length of 20 cm developed at the Deutsche Zentrum fur Luft und Raumfahrt (DLR) in Germany [62]. This positive branch unstable resonator uses two cylindrical mirrors with $M = 1.17$. While being unstable in the flow direction, it is of the common Fabry–Pérot type in the other direction. Predicted mode field distribution shows excellent beam quality in the far field with over 95% of the outcoupled power in the central peak with 0.3×0.5 mrad divergence. Further experimental studies of DLR 10 kW class COIL operation with hybrid resonator and other kinds of unstable resonators were reported in [66–68].

33.4 Operating Characteristics, Performance and Modes of Lasing

Operating characteristics and performance of different cw COIL devices are shown in Table 33.3. The first lasers, starting with the 4 mW COIL (No 1, Table 33.3) demonstrated in 1977 [1], used subsonic velocity gas in the laser cavity. After an initial scaling from the milliwatt level to 100 W by Benard et al. [33], the subsonic COIL was further scaled to 4.6 kW (No 2, Table 33.3 [5]). The chemical efficiencies of these COILs were smaller than 10%. Much higher values of the efficiencies were achieved at the end of the 1980s in Japan. In particular, a COIL with extremely high efficiency of 42% (No 3, Table 33.3), was demonstrated by Yoshida et al. [69]. The highest reported chemical efficiency of both subsonic and supersonic COILs is 42%. The same authors developed the first subsonic industrial COIL (No 4, Table 33.3) with a power of 1 kW and a highest efficiency of 23% at the same power level. Long-term stable operation was demonstrated with the output power kept within 3% at 1 kW for over 1 h [70,71].

As has already been mentioned in Section 33.1, most subsonic devices have a very large gain length and, therefore, are inconvenient for operation and upscaling. The first compact, 10 cm gain length subsonic COIL [72] was developed in Israel (No 5, Table 33.3). In spite of relatively high efficiency, low (~0.5 torr) pressure in the cavity resulted in a very small output power. Later 5–7.5-cm gain-length compact subsonic COILs with an output power of several hundred watts (No 6, Table 33.3) have been developed in Russia and Japan [73,74]. Unlike the first COIL devices, these COILs are energized by jet SOGs and have chemical efficiencies larger than 20%. To increase the efficiency of these compact COILs, pre-cooling of the primary buffer gas, previously demonstrated by Blayvas et al. [75] for supersonic COIL, was employed.

From the end of the 1980s, the emphasis of COIL research switched to the supersonic devices first demonstrated in 1982 in the Phillips Laboratory in Albuquerque, NM [2]. For the VertiCOIL (shown in Figure 33.9), RADICL and RotoCOIL devices (Nos 7–10, respectively, Table 33.3) power larger than 1, 10 and 30 kW, respectively, were achieved. Both VertiCOIL and RADICL used slit supersonic nozzles, whereas a grid nozzle array was employed in the 54-cm gain-length RotoCOIL. Very high chemical efficiency of 29.6%, was obtained for the RADICL device energized by the jet SOG, (No 9, Table 33.3). These COILs served as the prototypes for the multi-megawatt supersonic COIL (No 11, Table 33.3) employed in the US Air Force Airborne Laser [40,78]. The multi-megawatt COIL used the aforementioned uniform droplet SOG (shown in Figure 33.4d) and subsonic injection of the I_2/He mixture into the helium-singlet delta oxygen mixture. Then, the oxygen / helium / Iodine mixture accelerates through a supersonic nozzle and enters the laser cavity [78].

Two 10 kW class supersonic COIL devices operating with a grid nozzle array were developed at the DLR in Germany and in China (Dalian) (Nos 12 and 13, respectively, Table 33.3). The aforementioned supersonic COILs used He as the diluent gas and, hence, a subsonic mixing scheme (see Section 33.2). In order to obtain high gas velocity and a low partial stagnation pressure for $O_2(^1\Delta)$, the He molar flow rates were three to five times higher than that of the chlorine.

TABLE 33.3

Operating Characteristics and Performances of Different CW COILs

No	Name of the COIL and Comment	Type of the SOG	Gain Length (cm)	Cl_2 Flow Rate (mmole s^{-1})	Power, (W)	Chemical Efficiency (%)	Reference
				Subsonic COILs			
1	The first COIL	Bubble	70	4	0.004	10^{-5}	[1]
2	COIL-IV	Bubble	400	600	4600	8.4	[5]
3	Extremely efficient COIL	Bubble	35	5	192	42	[69]
4	Industrial COIL	Bubble	100	69	1015	16	[70,71]
5	Compact subsonic COIL	Bubble	10	0.4	5	13.7	[72]
6	High pressure subsonic COIL	Jet	7.5	19.7	448	25	[73]
				Supersonic COILs			
7	VertiCOIL with primary He	Disc	5	70.8	1730	27	[46]
8	RADICL	Disc	25	500	12 790	28.1	[76,77]
9	RADICL	Jet	25	509	13 690	29.6	[77]
10	RotoCOIL	Disc	54.1	1800	39 000	24	[2]
11	COIL for Airborne Laser	Uniform droplet	-	-	$> 10^6$	-	[78]
12	DLR (Germany) 10 kW class	Disc	20	500	9700	21.3	[79]
13	Dalian (China) 10 kW class COIL	Jet	100	450	8800	21.4	[80]
14	VertiCOIL with primary N_2	Disc	5	23.8	490.6	23	[47]
15	Compact COIL with primary N_2	Jet	5	75	1408	20.7	[82]
16	Ejector COIL	Jet	5	39.2	700	19.7	[52]
17	COIL without primary buffer gas	Jet	5	17.4	517	32.7	[83]
18	COIL with efficiency approaching the theoretical limit	Jet	5	17.4	627	39.6	[84]
19	COIL with precooling of primary N_2	Jet	7.5	20	599	32.9	[85]

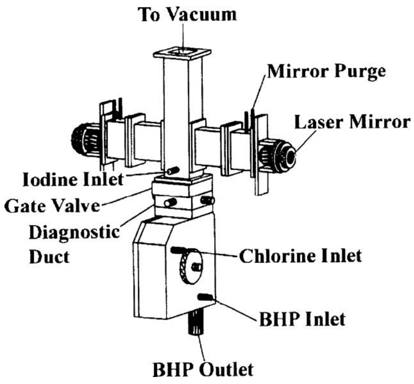

FIGURE 33.9 Three-dimensional view of VertiCOIL generator, duct and cavity hardware. (Reprinted with permission from Ref. [39]. Copyright © 1999 IEEE.)

For industrial applications, the use of large amounts of He is expensive. Therefore, supersonic COILs with a nitrogen diluent (which is more readily available and cheaper than He) or without a primary buffer gas were developed at the end of the 1990s. A supersonic COIL with N_2 buffer gas using subsonic mixing scheme was first demonstrated by Blayvas et al. [75], the chemical efficiency being only about 13%. Much higher chemical efficiencies (over 20%) were achieved by moving the mixing location downstream to the nozzle throat, i.e. by using quasi-transonic mixing scheme [47,48]. Twenty-three per cent chemical efficiency with a room-temperature nitrogen diluent was obtained by Carroll et al. [47] using a VertiCOIL with modified iodine injector blocks (No 14, Table 33.3). A higher efficiency, with room-temperature N_2, 24.6%, was obtained by Endo et al. [81]; however, in these experiments a much larger gain length, 22.5 cm, was employed. The highest power, with room-temperature nitrogen, 1.4 kW, was achieved by Zagidullin et al. [82] using a 5-cm gain-length supersonic COIL (No 15, Table 33.3). A highly efficient ejector COIL (No 16, Table 33.3) has been demonstrated by Nikolaev et al. [52]. Efficient supersonic COILs without any primary diluent applying either transonic or supersonic mixing schemes have been demonstrated in Ben-Gurion University, Israel [44,49,55]. The maximum chemical efficiencies were 18% and 21% for transonic [55] and supersonic [49] mixing schemes, respectively. Later even higher values of the efficiencies were achieved at this laboratory [83,84]. By carefully studying and optimizing the operation of the chemical generator, 0.73 yield of singlet oxygen was obtained for conditions corresponding to the highest efficiency. As a result, 30% efficiency was exceeded for the first time and ~33% efficiency was achieved [83] (No 17, Table 33.3). Then, further optimization of the supersonic nozzle and iodine temperature made it possible to achieve ~40% efficiency (No 18, Table 33.3) [84], the highest reported value of any supersonic COIL, and the closest to the theoretical limit. Also, ~ 33% efficiency was obtained using a COIL with a supersonic mixing scheme where the primary buffer gas was pre-cooled by liquid nitrogen (No 19, Table 33.3) [85] (pre-cooling leads to ~20% power increase [75]).

The range of applications of the COIL can be extended considerably by pulsed or pulse-periodic operation. A cw COIL can be transformed into a pulse-periodic laser by using either gain-switching (which is similar to Q-switching) or mode-locking methods.

The design of a pulsed COIL is practically identical to that of a cw laser. This means that all the characteristic features of the operation of a COIL associated with dissociation of molecular iodine and relaxation are still retained. The advantage of this method is that there is no need to alter the laser design in going over from pulsed to cw operation, i.e. both may be achieved in the same device. The principle of gain switching, first suggested by Schmiedberger et al. [86], is based on magnetic suppression or modulation of the gain by means of applying strong (hundreds of Gauss) magnetic field directly to the COIL cavity. Increasing the magnetic field in the range 1–500 G causes splitting of the hyperfine levels of the I atom due to the Zeeman effect and a significant monotonic decrease in the gain coefficient on the strongest $F = 3 \rightarrow F = 4$ transition. Modulation of the gain of a kilowatt-class COIL was demonstrated in the Phillips Laboratory in Albuquerque, NM [87]. Initially, a static magnetic field of 400 G was applied to the cavity of a supersonic COIL with an output power of 3 kW. An alternating magnetic field, directed opposite to the static field, compensated the latter at certain moments and the lasing pulse appeared at these moments. The peak power in the pulse, 39 kW, was about 13 times larger than the average power corresponding to cw operation, the pulse duration and repetition rate being of 10–20 μs and 500 Hz, respectively.

The mode-locking experiments were carried out at the Phillips Laboratory using the RADICL device [88]. To achieve mode locking, an acousto-optic modulator was inserted into the resonator and lasing was demonstrated on the $TEM_{(00)}$ mode with a small intracavity aperture. A dc magnetic field was used to increase the number of axial modes. The field broadened the gain by weakly splitting the Zeeman components of the $I(^2P_{1/2}, F = 3) \rightarrow I(^2P_{3/2}, F = 4)$ hyperfine transition. A peak power of 2.5 kW was reached with a pulse width of 2.1 ns at a repetition rate of 43.68 MHz.

Pulsed operation in COILs can also be obtained in a flowing gas mixture containing $O_2(^1\Delta)$ and an iodide (CH_3I, CF_3I or C_3F_7I) exposed to a pulse (e.g. a light flash) which generates iodine atoms throughout the whole volume [3]. Optimization of the laser performance made it possible to generate 4.4 J pulses of 15 μs duration, which corresponds to a pulse power of 300 kW [3]. This is the highest value reported so far. These results were obtained at a chlorine flow rate of 17 mmole s^{-1}, when under the best circumstances the cw output power could be 680 W (assuming that the laser chemical efficiency is 40%). Thus, the power of a pulsed COIL (with flash formation of iodine) was over 400 times higher than the cw power. Different methods of the pulsed operation of the COIL have been comprehensively analysed by Yuryshev [3].

The high power of both the cw and pulsed COIL devices makes it possible to generate second harmonics in these devices. The frequency doubling of 1315 nm radiation is very important since chemical lasers in the visible wavelength region have not yet been constructed. Different research groups have carried out both intra- and extra-cavity frequency-doubling experiments. The maximum second-harmonic power was obtained in a series of extracavity frequency-doubling tests performed using the output from a RotoCOIL at the Phillips Laboratory [89]. The diffraction-limited radiation of 6.8 kW power was focused into an $LiIO_3$ crystal. Conversion efficiencies of 8% were achieved resulting in visible (657 nm) cw outputs of nearly 700 W. It was found that the optical strength of the non-linear crystals was insufficient: it fractured after 1 s exposure to a focused beam. Intracavity frequency-doubling experiments was carried out using both $LiIO_3$ [90] and LBO crystals [91], the maximum conversion efficiency being about 8% [90].

An interesting alternative to the COIL is the electrically driven oxygen-iodine laser (ElectricOIL), which was first demonstrated by Carroll et al. [92]. This laser operates on the same electronic transition of the iodine atom at 1315 nm as does COIL. The lasing state I* in the ElectricOIL is also produced by near-resonant energy transfer from the singlet oxygen metastable $O_2(^1\Delta)$; however in this case the $O_2(^1\Delta)$ is generated by an "electric" discharge rather than via a "chemical" reaction (as is the case of the COIL). The highest reported output power of ElectricOIL was 481 W [93].

33.5 Conclusions

Since the invention of the COIL in 1977, this laser has made impressive progress and is now one of the most powerful and efficient lasers. It can operate at multi-megawatt power levels with 30% chemical efficiency at a wavelength of 1315 nm, favourable for fibre and atmospheric transmission. Employment of unstable resonators offers excellent beam quality. Development of COILs with a small consumption of a nitrogen diluent makes their operation inexpensive. These characteristics make COIL an ideal laser for both military and industrial applications, in particular for laser cutting, decommissioning of nuclear power facilities and the removal of space debris [19]. COIL technology culminated with the Advanced Tactical Laser demonstrating penetration of the hood of a moving truck [94], and the Airborne Laser successfully shooting down a ballistic missile in the boost phase [94]. However, despite the successful demonstration, the range for shooting down the missiles was too short and to reach the program goals, the onboard COIL had to be by an order of magnitude more powerful which made the program too expensive and impractical; as a result it was eventually discontinued [95].

COILs have higher investment and operation costs than the classical CO_2 and Nd:YAG lasers if they are compared on the basis of equal power [96]. However, the advantages of the COIL, which has a much better beam quality than the Nd:YAG laser and a much shorter wavelength and, hence, a much higher material processing speed than the CO_2 laser, may more than compensate for these higher costs.

In spite of the progress in laser technology, some fundamental processes in the COIL active medium are not still properly understood. In particular, one of the more critical issues, the kinetics of iodine dissociation, is still obscure. Other important issues are understanding the hydrodynamics in the supersonic COIL and finding new mixing schemes resulting in minimal losses of singlet oxygen and ensuring a good mixing efficiency.

REFERENCES

1. McDermott W E, Pchelkin N R, Benard D J and Bousek R R 1978 An electronic transition chemical laser Appl. Phys. Lett. **32** 469–70.
2. Truesdell K A, Helms C A and Hager G D 1995 A history of COIL development in the USA SPIE **2502** 217–37.
3. Yuryshev N N 1996 Chemically pumped oxygen–iodine laser Quantum Electron. **23** 583–600.
4. Heidner R F III, Gardner C E, Segal G I and El-Sayed T M 1983 Chain reaction mechanism for I_2 dissociation in the $O_2(^1\Delta)$-I atom laser J. Phys. Chem. **87** 2348–60.
5. Truesdell K A and Lamberson S E 1993 Phillips laboratory COIL technology overview SPIE **1810** 476–92.
6. Newman S M, Lane IC, Orr-Ewing A J, Newnham D A and Ballard J 1999 Integrated absorption intensity and Einstein coefficients for the O_2 (0, 0) transition: a comparison of cavity ringdown and high resolution Fourier transform spectroscopy with a long-path absorption cell J. Chem. Phys. **110** 10749–57.
7. Furman D, Bruins E, Rybalkin V, Barmashenko B D and Rosenwaks S 2001 Parametric study of a small-signal gain in a slit nozzle, supersonic chemical oxygen–iodine laser operating without primary buffer gas IEEE J. Quantum Electron. **37** 174–82.
8. Held A M, Halko D J and Hurst J K 1978 Mechanisms of chlorine oxidation of hydrogen peroxide J. Am. Chem. Soc. **100** 5732–40.
9. Storch D M, Dymek C J and Davis L P 1983 MNDO study of the mechanism of $O_2(^1\Delta)$ formation by reaction of Cl_2 with basic H_2O_2J. Am. Chem. Soc. **105** 1765–9.
10. Avizonis P V and Truesdell K A 1995 Chemical oxygen–iodine laser (COIL) SPIE **2502** 180–203.
11. Furman D, Barmashenko B D and Rosenwaks S 1999 Diode-laser based absorption spectroscopy diagnostics of a jet-type generator for chemical oxygen-iodine lasers IEEE J. Quantum Electron. **35** 540–7.
12. Kendrick K R, Helms C A and Quillen B G 1999 Determination of singlet-oxygen generator efficiency on a 10-kW class supersonic chemical oxygen iodine laser IEEE J. Quantum Electron. **35** 1759–64.
13. Barmashenko B D, Kochelap V A and Mel'nikov L Yu 1985 Singlet oxygen generator of the atomizer type (for O_2–I chemical laser) Sov. J. Quantum Electron. (USA) **15** 1346–52.
14. Barmashenko B D and Rosenwaks S 1993 Theoretical modelling of chemical generators producing $O_2(^1\Delta)$ at high pressure for chemically pumped iodine laser J. Appl. Phys. **73** 1598–611.
15. Copeland D A, McDermott W E, Quan V and Bauer A H 1993 Exact and approximate solutions of the utilization and yield equations for $O_2(^1\Delta)$ generators Am. Inst. Aeronaut. Astronaut. **93** 3220.
16. Arnold S J, Finlayson N and Ogryzlo E A 1966 Some novel energy-pooling process involving $O_2(^1\Delta_g)$ J. Chem. Phys. **44** 2529–30.
17. Van Benthem M H and Davis S J 1986 Detection of vibrationally excited I_2 in the iodine dissociation region of chemical oxygen–iodine lasers J. Phys. Chem. **90** 902–5.
18. Kommisarov A V, Goncharov V and Heaven M C 2001 Chemical oxygen iodine laser (COIL) kinetics and mechanisms SPIE **4184** 7–12.
19. Heaven M C 2001 Chemical dynamics in chemical laser media Chemical Dynamics in Extreme Environments (Advanced Series in Physical Chemistry) ed R A Dressler (Singapore: World Scientific) ch 4, pp 138–205.
20. Waichman K, Rybalkin V, Katz A, Dahan Z, Barmashenko B D and Rosenwaks S 2007 Toward understanding of the dissociation of I_2 in chemical oxygen-iodine lasers: combined experimental and theoretical studies J. Appl. Phys. **102** 013108.
21. Waichman K, Barmashenko B D and Rosenwaks S 2009 Kinetic-fluid dynamics modeling of I_2 dissociation in supersonic chemical oxygen-iodine lasers J. Appl. Phys. **106** 063108.
22. Waichman K, Barmashenko B D and Rosenwaks S 2010 Comparing modeling and measurements of the output power in chemical oxygen-iodine lasers: a stringent test of I_2 dissociation mechanisms J. Chem. Phys. **133** 084301.
23. Azyazov V N, Pichugin S Yu and Heaven M C 2009 On the dissociation of I_2 by $O_2(a\ ^1\Delta$**:** Pathways involving the excited species $I_2(A'^3\Pi_{2u}, A\ ^3\Pi_{1u})$, $I_2(\boldsymbol{X}\ ^1\Pi, v)$, and $O_2(a^1\Delta, v)$ J. Chem. Phys. **130** 104306.
24. Zagidullin M V, Khvatov N A, Malyshev M S and Svistun M I 2012 Dissociation of molecular iodine in a flow tube in the presence of $O_2(^1\Sigma)$ molecules J. Phys. Chem. A **116** 1050–53.
25. Zagidullin M V, Khvatov N A, Malyshev M S and Svistun M I 2016 Experimental results on the dissociation of molecular iodine in the presence of singlet oxygen molecules Quantum Electron. **46** 706–12.
26. Engelman R Jr, Keller R A and Palmer B A 1980 Hyperfine structure and isotope shift of the 1.3 μm transition of ^{129}I Appl. Opt. **19** 2767–70.
27. Avizonis P V, Hasen G and Truesdell K A 1990 The chemically pumped oxygen-iodine laser SPIE **1225** 448–74.
28. Hon J, Plummer D N, Crowell P G, Erkkila J, Hager G D, Helms C A and Truesdell K A 1996 Heuristic method for evaluating COIL performance Am. Inst. Aeronaut. Astronaut. **43** 1595–603.
29. Barmashenko B D and Rosenwaks S 1996 Analysis of the optical extraction efficiency in gas-flow lasers with different types of resonator Appl. Opt. **35** 7091–101.
30. Churassy S, Bacis R, Bouvier A J, Pierre dit Mery C, Erba B, Bachar J and Rosenwaks S 1987 The chemical oxygen–iodine laser: comparison of a theoretical model with experimental results J. Appl. Phys. **62** 31–5.
31. Rybalkin V, Katz A, Waichman K, Vingurt D, Dahan Z, Barmashenko B D and Rosenwaks S 2006 How many $O_2(^1\Delta)$ molecules are consumed per dissociated I_2 in chemical oxygen-iodine lasers? Appl. Phys. Lett. **89** 021115.
32. Scott J E, Shaw J L R, Truesdell K A, Hager G D and Helms C A 1994 Design considerations for the chemical oxygen–iodine supersonic mixing nozzle Am. Inst. Aeronaut. Astronaut. **94** 2436.
33. Benard D J, McDermott W E, Pchelkin N R and Bousek R R 1979 Efficient operation of a 100-W transverse-flow oxygen–iodine chemical laser Appl. Phys. Lett. **34** 40–1.
34. Wiswall C E, Bragg S L, Reddy K V, Lilenfeld H V and Kelley J D 1985 Moderate-power cw chemical oxygen–iodine laser capable of long duration J. Appl. Phys. **58** 115–18.

35. Richardson R J, Wiswall C E, Carr PGA, Hovis F E and Lilenfeld H V 1981 An efficient singlet oxygen generator for chemically pumped iodine laser J. Appl. Phys. **52** 4962–9.
36. Harpool G M, English W D, Berg G D and Miller D J 1992 Rotating disc oxygen generator Am. Inst. Aeronaut. Astronaut. **92** 3006.
37. Zagidullin M V, Kurov A Y, Kupriyanov N L, Nikolaev V D, Svistun MI and Erasov N Y 1991 Highly efficient jet generator Sov. J. Quantum Electron. **21** 747–53.
38. Azyazov V N, Zagidullin M V, Nikolaev, V D, Svistun M I and Khvatov N A 1994 Jet $O_2(^1\Delta)$ generator with oxygen pressures up to 13.3 kPa Quantum Electron. **24** 120–3.
39. Thayer W J III and Fisher C H 1994 Comparison of predicted and measured output from a transverse flow uniform droplet singlet oxygen generator Am. Inst. Aeronaut. Astronaut. **94** 2454.
40. Lamberson S E, Schall H and Shattuck P 2006 The airborne laser SPIE **6346** 63461M.
41. Takeshita K, Kikuchi T and Uchiyama T 1988 Laser operation of chemical oxygen–iodine laser without water vapor trap J. Appl. Phys. **63** 1785–6.
42. Fuji H, Yoshida S, Iizuka M and Atsuta T 1989 Long-term stability in the operation of a chemical oxygen–iodine laser for industrial use J. Appl. Phys. **66** 1033–7.
43. Elior A, Barmashenko B Dº, Lebiush E and Rosenwaks S 1995 Experiment and modelling of a small-scale, supersonic chemical oxygen–iodine laser Appl. Phys. B **61** 37–47.
44. Furman D, Barmashenko B D and Rosenwaks S 1997 An efficient supersonic chemical oxygen–iodine laser operating without buffer gas and with simple nozzle geometry Appl. Phys. Lett. **70** 2341–3.
45. Handke J, Werner A, Bohn W J and Schall W O 1995 Multikilowatt supersonic chemical oxygen–iodine laser SPIE **2502** 266–71.
46. Rittenhouse T L, Phipps S P and Helms C A 1999 Performance of a high efficiency 5-cm gain length supersonic chemical oxygen–iodine laser IEEE J. Quantum Electron. **35** 857–66.
47. Carroll D L, King D M, Fockler L, Stromberg D, Solomon W C, Sentman L H and Fisher C H 2000 High-performance chemical oxygen–iodine laser using nitrogen diluent for commercial applications IEEE J. Quantum Electron. **36** 40–51.
48. Zagidullin M V, Nikolaev V D, Svistun M V, Hvatov N A and Ufimtsev NI 1997 Highly efficient supersonic chemical oxygen–iodine laser with a chlorine flow rate of 10 mmole/s Quantum Electron. **27** 195–9.
49. Rosenwaks S, Rybalkin V, Katz A and Barmashenko B D 2003 Comparative studies of different schemes of iodine injection in a high efficiency supersonic COIL Am. Inst. Aeronaut. Astronaut. **2003** 302.
50. Azyazov V N, Zagidullin M V, Nikolaev V D and Safonov V S 1997 Chemical oxygen–iodine laser with mixing of supersonic jets Quantum Electron. **27** 491–4.
51. Cassady P E, Newton J F and Rose P H 1976 A new mixing gasdynamic laser Am. Inst. Aeronaut. Astronaut. **76** 343.
52. Nikolaev V D, Zagidullin M V, Hager G D and Madden T J 2000 An efficient supersonic COIL with more than 200 torr of the total pressure in the active medium Am. Inst. Aeronaut. Astronaut. **2000** 427.
53. Yang T T, Hsia Y C, Moon L F and Dickerson R A 2000 Advanced mixing nozzle concepts for COIL SPIE **3931** 116–30.
54. Walter R F and O'Leary R A 1993 Pressure recovery in supersonic gas lasers SPIE **1810** 328–33.
55. Furman D, Barmashenko B D and Rosenwaks S 1998 Parametric study of an efficient supersonic chemical oxygen–iodine laser/jet generator system operating without buffer gas IEEE J. Quantum Electron. **34** 1068–74.
56. Malkov V M, Boreysho A S, Savin A V, Kiselev I A and Orlov A E 2001 About choise of working parameters of the pressure recovery systems for high power gas flow chemical lasers SPIE **4184** 419–22.
57. Gruenwald K M, Handke J and Duschek F 2001 Small signal gain and temperature profiles in supersonic COIL SPIE **4184** 75–8.
58. Schmiedberger J, Kodymova J, Kovar J, Spalek O and Trenda P 1991 Magnetic modulation of gain in a chemical oxygen–iodine laser IEEE J. Quantum Electron. **27** 1262–4.
59. Watanabe K, Kashiwabara S, Sawai K, Toshima S and Fujimoto R 1983 Small-signal gain and saturation parameter of a transverse-flow cw oxygen–iodine laser IEEE J. Quantum Electron. **19** 1699–2609.
60. Hager G D, Helms C A, Truesdell K A, Plummer D, Erkkila J and Crowell P 1996 A simplified analytic model for gain saturation and power extraction in the flowing chemical oxygen–iodine laser IEEE J. Quantum Electron. **32** 1525–36.
61. Barmashenko B D, Furman D and Rosenwaks S 1998 Analysis of lasing in gas flow lasers with stable resonators Appl. Opt. **37** 5697–705.
62. Schall W O, Hall T and Handke J 2001 Unstable resonator for COIL SPIE **4184** 461–4.
63. Bailing Y 1998 Latest advances in COIL in Dalian SPIE **3574** 281–9.
64. Anan'ev Yu A, Kuprenyuk V I and Sherstobitov V E 1979 Properties of unstable resonators with field rotation Sov. J. Quantum Electron. **9** 1105–10.
65. Latham W P, Paxton A H and Dente G C 1990 Laser with 90 degree rotation SPIE **1224** 265–82.
66. Handke J, Schall W O, Hall T, Duschek F and Grünewald K M 2006 Appl. Opt. **45** 3831–8.
67. Pargmann C, Hall T, Duschek F, Grünewald K and Handke J 2008 Hybrid resonator in a double-pass configuration for a chemical oxygen iodine laser Appl. Opt. **47** 6644–9.
68. Pargmann C, Hall T, Duschek F, Grünewald K and Handke J 2011 Off-axis negative branch unstable resonator in rectangular geometry Appl. Opt. **50** 11–16.
69. Yoshida S, Endo M, Sawano T, Amano S, Fuji H and Fujioka T 1988 Chemical oxygen iodine laser of extremely high efficiency J. Appl. Phys. **65** 870–2.
70. Fuji H and Atsuta T 1992 Current status of industrial COIL development SPIE **1980** 148–52.
71. Shimizu K, Sawano T, Tokuda T, Yoshida S and Tanaka I 1991 High-power stable chemical oxygen–iodine laser J. Appl. Phys. **69** 79–83.
72. Bachar J and Rosenwaks S 1982 An efficient, small scale chemical oxygen–iodine laser Appl. Phys. Lett. **41** 16–18.
73. Wani F, Endo M and Fujioka T 1999 High-pressure, high-efficiency operation of a chemical oxygen–iodine laser Appl. Phys. Lett. **75** 3081–3.

74. Zagidullin M V, Nikolaev V D, Svistun M I and Khvatov N A 1998 Comparative characteristics of subsonic and supersonic oxygen–iodine lasers Quantum Electron. **28** 400–2.
75. Blayvas I, Barmashenko B D, Furman D, Rosenwaks S and Zagidullin M V 1996 Power optimization of small-scale chemical oxygen–iodine laser IEEE J. Quantum Electron. **32** 2051–7.
76. Helms C A 2001 Review of the US Air Force research laboratory's 10-kW RADICL laser SPIE **4184** 13–18.
77. Yang T T, Copeland D A, Bauer A H, Quan V, McDermott W E, Cover R A and Smith D M 1997 Chemical oxygen–iodine laser performance modelling Am. Inst. Aeronaut. Astronaut. **97** 2384.
78. Truesdell K 2006 Recent airborne laser - laser results SPIE **63436** 63461L.
79. Handke J, Grunewald K M, Schall W O and Entress-Fursteneck L 1998 Power extraction investigations for a 10 kW-class supersonic COIL SPIE **3574** 309–14.
80. Fengting S, Bailing Y and Qi Z 2001 Chemical oxygen–iodine laser research in China SPIE **4184** 27–31.
81. Endo M, Kazuyoku T, Sugimoto D, Nanri K, Uchiyama T and Fujioka T 2001 Development of a prototype COIL for decomissioning and dismantlement SPIE **4184** 23–6.
82. Zagidullin M V, Nikolaev V D, Svistun M I and Khvatov N A 2000 Supersonic oxygen–iodine 1.4-kW laser with a 5 cm gain length and a nitrogen-diluted active medium Quantum Electron. **30** 161–6.
83. Rybalkin V, Katz A, Barmashenko B D and Rosenwaks S 2003 A 33% efficient chemical oxygen–iodine laser with supersonic mixing of iodine and oxygen Appl. Phys. Lett. **82** 3838–40.
84. Rybalkin V, Katz A, Barmashenko B D and Rosenwaks S 2004 Nearly attaining the theoretical efficiency of supersonic chemical oxygen-iodine lasers Appl. Phys. Lett. **85** 5851–3.
85. Endo M, Osaka T and Takeda S 2004 High-efficiency chemical oxygen–iodine laser using a streamwise vortex generator Appl. Phys. Lett. **84** 2983–5.
86. Schmiedberger J, Kodymova J, Spalek O and Kovar J 1991 Experimental study of gain and output coupling characteristics of a cw chemical oxygen–iodine laser IEEE J. Quantum Electron. **27** 1265–70.
87. Hager G D, Kopf D, Plummer D, Salsich T and Crowell P 1993 Demonstration of a repetitively pulsed magnetically gain-switched chemical oxygen–iodine laser chemical Phys. Lett. **204** 420–9.
88. Phipps S P, Helms C A, Copland R J, Rudolph W, Truesdell K A and Hager G D 1996 Mode locking of a cw supersonic chemical oxygen–iodine laser IEEE J. Quantum Electron. **32** 2045–50.
89. Hager G D, Hanes S A and Dreger M A 1992 Continuous wave frequency doubling of a high-energy 1315 nm laser IEEE J. Quantum Electron. **28** 2573–6.
90. Frolov M P, Ishkov D V, Kryukov P G, Pazyuk V S and Yurishev N N 1992 A frequency-doubled pulsed chemical oxygen–iodine laser Appl. Phys. B **54** 490–1.
91. Baba T, Tezuka T, Ito D, Uchiyama T and Fuji H 1995 Intracavity 2nd-harmonic generation of chemical oxygen–iodine laser-emission using a LBO crystal Appl. Phys. B **60** 369–73.
92. Carroll D L, Verdeyen J T, King D M, Zimmerman J, Laystrom J, Woodard B, Benavides G, Kittell K, Stafford D, Kushner M J and Solomon W C 2005 Continuous-wave laser oscillation on the 1315 nm transition of atomic iodine pumped by $O_2(^1\Delta)$ produced in an electric discharge Appl. Phys. Lett. **86** 111104.
93. Benavides G F, Zimmerman J W, Woodard B S, Day M T, King D M, Carroll D L, Palla A D, Verdeyen J T and Solomon W C 2012 Discharge-driven electric oxygen-iodine laser superlinear enhancement via increasing g_0L Opt. Lett. **37** 1409–11.
94. Carroll D L 2011 Overview of high energy lasers: past, present, and future? Am. Inst. Aeronaut. Astronaut. **2011** 3102.
95. Boeing YAL-1 Accessed January 16, 2017 https://en.wikipedia.org/wiki/Boeing_YAL-1.
96. Von Bulow H and Schall W O 1995 Oxygen–iodine lasers for industrial applications SPIE **2502** 258–65.

FURTHER READING

Avizonis P V and Truesdell K A 1995 Chemical oxygen-iodine laser (COIL) SPIE **2502** 180–203.

Basic principles of the COIL operation are presented; the main equations for the gain and power are derived.

Basov N G 1990 *Chemical Lasers* 1st edn (Berlin: Springer).

Main principles of the chemical lasers operation are described, theoretical description of different processes in the COIL is given.

Davis S J, McDermott W E and Heaven M C 2007 Atomic iodine lasers *Gas Lasers* eds M Endo and R F Walter (New York: CRC Press) pp. 413–48.

Overview of photolytic iodine lasers, COILs, COIL diagnostics, singlet oxygen yield, the all gas-phase iodine laser and electric oxygen-iodine laser.

Kodymova J 2007 Overview on the chemical oxygen-iodine laser technology SPIE **6346** 634609.

The overall COIL technology is considered as a sequence of coexistent technologies of main laser components with a mutual impact: a technology of the singlet oxygen generator, gasdynamic mixing and expansion nozzle, energy extraction and optical resonator and the exhaust and pressure recovery systems.

Taylor & Francis
Taylor & Francis Group
http://taylorandfrancis.com

34

Chemical Lasers: HF/DF

Lee H. Sentman

CONTENTS

34.1 F-Atom Generators 467
34.2 Mixing Nozzles 468
34.3 Optical Resonators 470
34.4 Exhaust Systems 471
34.5 Laser Performance 471
34.6 HF Overtone Laser 472
34.7 Line-Selected Performance of the HF Laser 473
34.8 Concluding Remarks 473
References 473
Further Reading 474

The HF/DF chemical lasers are based on the cold and hot pumping reactions:

$$F + H_2 \rightarrow HF(v, J) + H \quad v = 1,2,3 \qquad 34\ \text{kcal mol}^{-1}\ \text{'cold reaction'}$$

$$H + F_2 \rightarrow HF(v, J) + H \quad v = 1-8 \qquad 102\ \text{kcal mol}^{-1}\ \text{'hot reaction'}$$

$$F + D_2 \rightarrow DF(v, J) + H \quad v = 1,2,3,4 \qquad 34\ \text{kcal mol}^{-1}\ \text{'cold reaction'}$$

$$D + F_2 \rightarrow DF(v, J) + F \quad v = 2-9 \qquad 102\ \text{kcal mol}^{-1}\ \text{'hot reaction'}$$

which produce the excited species HF(v, J) or DF(v, J) in a population inversion from which energy is extracted as a laser beam at 2.8 µ for HF or 3.8 µ for DF. These lasers have been extensively developed since their inception in 1967. Both the continuous wave (cw) and pulsed versions of these lasers were pursued. Since the cw device is the laser of choice for high-power applications, this chapter will concentrate on this type of HF/DF laser.

A schematic diagram of a typical HF/DF laser is shown in Figure 34.1. The HF/DF laser consists of an F-atom generator, a nozzle array to accelerate the F-atom stream and reduce its pressure and temperature, a device to inject H_2 or D_2 and promote their mixing with the F atom stream, an optical resonator to extract the laser beam and a pressure recovery system because these lasers operate at subatmospheric pressures. The power produced by these lasers scales with the flow rates of the reactants: to double the power, the flow rates are doubled.

34.1 F-Atom Generators

At the present time, small-scale devices that operate at tens to hundreds of watts are commercially available from Helios Inc. (1822 Sunset Place, Longmont, CO 80501, USA). These lasers use a low-pressure arc to partially dissociate SF_6 to produce

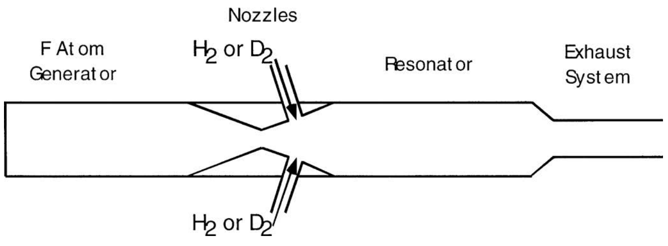

FIGURE 34.1 A schematic diagram of a typical HF/DF chemical laser.

F atoms. If a high-pressure, high-temperature arc was used, these lasers would produce several kilowatts at the same flow rates. The hundreds of kilowatts to several megawatts lasers react to NF_3 with a small amount of D_2 or H_2 to raise the temperature in the combustor high enough to thermally dissociate the remaining NF_3. This results in F atoms, N_2 and some DF or HF flowing through the primary nozzles at the exit of which H_2 or D_2 is mixed with the primary stream to form the lasing species, HF or DF.

34.2 Mixing Nozzles

Once the F atoms have been produced, the power of the laser is determined by the effectiveness with which the F atoms and the H_2 or D_2 are mixed. The physical–chemical characteristics of the HF/DF systems determine the design of the mixing nozzles. The pumping reactions that produce the population inversions are very fast, of the order of microseconds. If the chemicals were premixed, the width of the laser beam would be of the order of a millimetre which results in very large intensities which windows and mirrors could not survive. The exothermicity of the pumping reactions raises the temperature which increases the rates of deactivation of the excited HF/DF. The problems of the heat release and the width of the lasing zone are solved by introducing He and expanding the F atom/He stream through a nozzle. For combustor and high-pressure, high-temperature arc-produced F-atoms, the nozzles must be supersonic nozzles. Typically these will be Mach 5 nozzles which produce 2–10 torr exit pressures and gain zones that are several centimetres long [1]. For low-pressure, high-voltage arc-produced F-atom flows, either supersonic or subsonic nozzles may be used. These nozzles typically produce exit pressures of 2–10 torr and gain zones that are 3–12 mm long. In the supersonic case, they are typically Mach 2 nozzles [2].

The original HF/DF lasers employed alternating primary (F atom) and secondary (H_2 or D_2) slit nozzles at the exits of which the two streams begin mixing [3]. Because the pressures are so low, the mixing is two-dimensional and diffusive with the mixing layer growing as $x^{1/2}$, where x is the distance downstream measured from the nozzle exit plane. Flow field photography showed that the mixing was slow and that the primary and secondary streams were not fully mixed before the fluid exited the resonator. One of the most successful schemes developed to increase the rate of mixing injected interleaved jets of He near the exits of the primary and secondary nozzles. These jets, called trip jets, caused a rapid increase in the rate of mixing and about a factor of two increase in power. With laser-induced fluorescence, Driscoll [4–6] showed that the trip jets introduced fluid element stretching which dramatically increased the surface area of contact between the primary and secondary streams which increased the rate at which they mixed. Driscoll showed that the same effect could be obtained by putting alternating, interleaved solid ramps at the exits of adjacent nozzles. With this understanding of the fluid dynamic mechanism responsible for the increased mixing due to the side-wall injection in these low-pressure nozzles, the logical development of the trip jet concept led to eliminating the secondary nozzle and injecting the H_2 directly into the primary flow near the exit of the nozzle. To shield the H_2 from the primary flow until it exited the nozzle, a He jet was placed immediately upstream of the H_2 jets. This is illustrated by the TRW HYLTE nozzle [7]; see Figure 34.2.

Another efficient mixing scheme is called the double axisymmetric nozzle. This is a conical hole primary nozzle around the exit of which the H_2 or D_2 is injected from a circular slit.

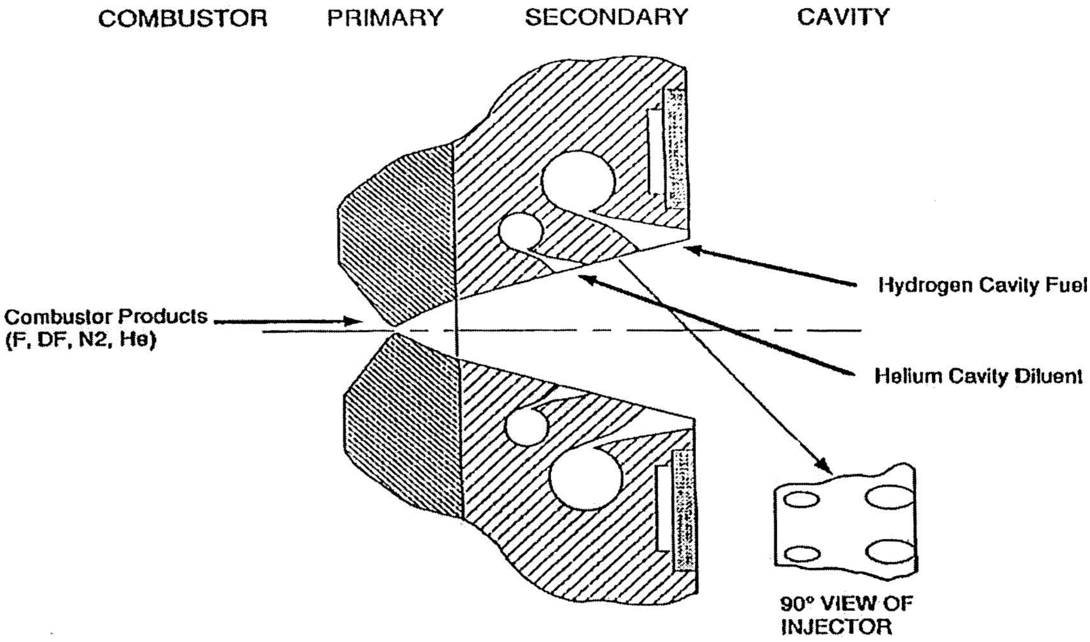

FIGURE 34.2 A schematic diagram of the TRW HYLTE nozzle. (This figure was originally published in Ref. [7], copyright © 1991 by the AIAA, reprinted with permission.)

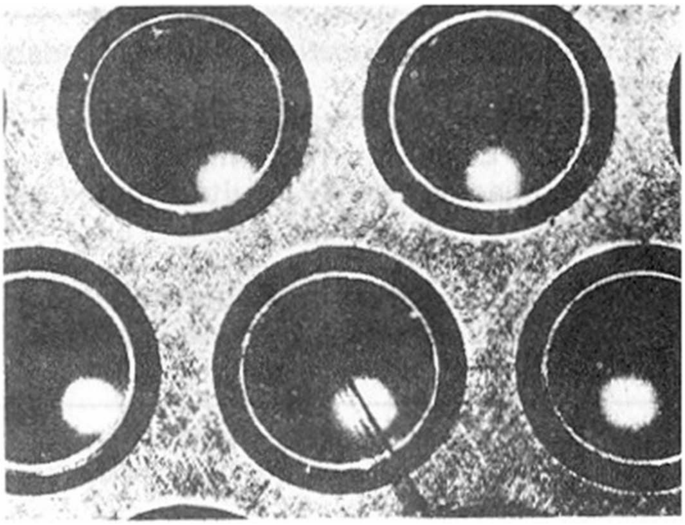

FIGURE 34.3 A photograph of the face of the Bell Aerospace Textron double axisymmetric BCL-13 nozzle. The primary conical nozzle is surrounded by the conical secondary nozzle. The diameter of the exit of the primary nozzle is of the order of 0.12 inches.

This is illustrated by the Bell Aerospace Textron BCL-13 nozzle, Figure 34.3 [8]. These nozzles are excellent performers.

The choice of nozzle depends upon the mission of the laser. If space and volume constraints do not drive the design, rectangular nozzle banks are usually used. The flow system is linear, with the fluid flowing from the combustor through the nozzle bank to the laser cavity and out through the exhaust system. When space and volume constraints are critical, cylindrical gain generators are used. An example is the TRW Alpha laser which is a prototype for a space-based laser system [9]. In this case, the nozzle bank is wrapped around the surface of a cylinder, see Figure 34.4. The centre of the cylinder is the combustor which produces the F atoms. The fluid flows radially out through the nozzles and the resonator to the exhaust ducts and out to space. The choice of nozzle geometry for the cylindrical gain generator is heavily influenced by manufacturing considerations.

HF/DF laser nozzles typically have throat widths that are 0.10 inch or less. The secondary He and H_2 injection holes are of the order of 0.020 inch diameter spaced several millimetres apart and are staggered on opposite nozzle walls. Since these are low-pressure nozzles, the boundary layers are quite thick,

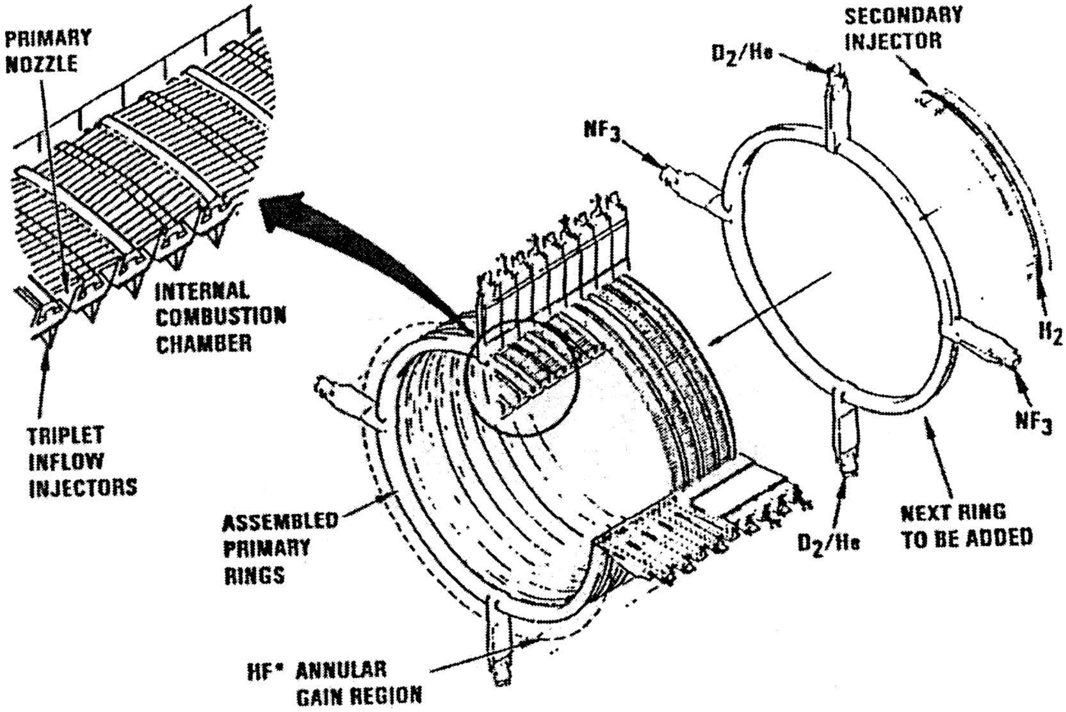

FIGURE 34.4 TRW hypersonic wedge nozzles on the surface of the ALPHA laser cylindrical gain generator. (This figure was originally published in Ref. [9], copyright © by the AIAA, reprinted with permission.)

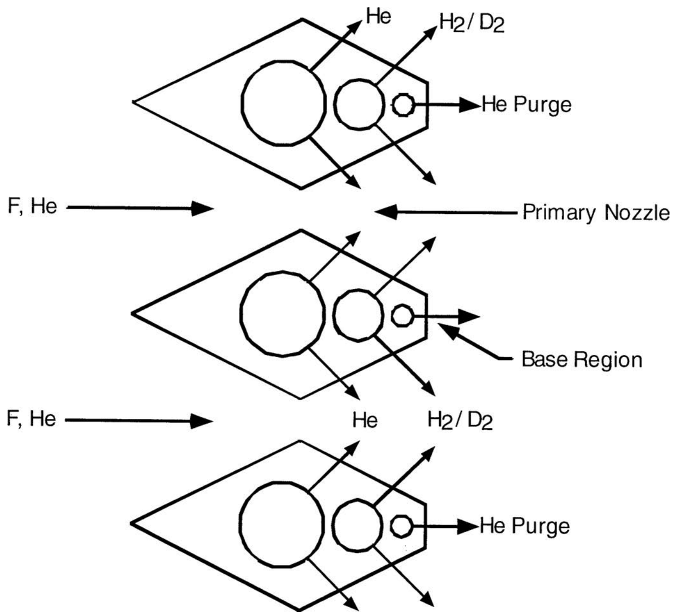

FIGURE 34.5 A schematic diagram of a nozzle bank showing the side-wall injection of H_2 and He and the base region He purge.

typically up to 50% of the nozzle exit area. The side-wall injection of the H_2 and He partially blocks the primary nozzle, further reducing its effective area ratio. These effects must be taken into account when designing the nozzle so that the desired exit pressure will be obtained.

With the side-wall injection of the secondary He and H_2, the manifolds for these fluids usually determine the thickness of a nozzle blade. The size of the base area between adjacent primary nozzles may become large enough to provide a recirculation region for ground-state HF/DF, see Figure 34.5. In this case, the base region must be purged with He to prevent the buildup of ground-state HF/DF. If this is not done, up to 50% of the laser power may be lost. The He base purge flow rates are determined experimentally to maximize the power.

34.3 Optical Resonators

Each of the three types of resonators, Fabry–Pérot (two plane, parallel mirrors), stable and unstable, have been used to extract power from the HF/DF chemical laser. Since it generally produces the least power, the Fabry–Pérot resonator is only used for special studies. Normally, the stable or unstable resonator is used to extract power. Since the stable resonator extracts power through a partially transmitting mirror, the stable resonator is usually used when the power is less than tens of kilowatts. At higher power levels, partially transmissive mirrors cannot handle the radiative fluxes that occur. For powers of tens of kilowatts and larger, power is extracted with an unstable resonator which employs all reflective optical elements. The outcoupled beam from an unstable resonator generally has a hole in it so that some of the radiation can be fed back into the resonator to keep the lasing process going. The problem is to design the unstable resonator to produce an outcoupled beam with a uniform phase so that it can be focused to a spot in the far field. Since diffraction effects play a major role in the performance of an unstable resonator, the resonator must be designed with a wave optics code. As a minimum, these models are two-dimensional, and in most cases, a three-dimensional wave optics model is used.

The rotational non-equilibrium kinetic-fluid dynamic model must be coupled with the wave optics model of the unstable resonator or the geometric optics model of the stable resonator. Since the flow and optical axes are perpendicular to each other, the computer models are coupled in an iterative fashion [10]. An initial guess at the intensity distribution on each line is used to run the fluid dynamic-kinetic model to obtain the gain distribution on each line. Then, the optics model propagates the initial guess of the intensity distribution on each line one round trip through the resonator. Each time the optical wave passes through the gain medium, the intensity distribution is modified by the gain distribution from the preceding fluid dynamic-kinetic calculation. After the round trip through the resonator, the new intensity distribution is used in the fluid dynamic-kinetic model to recalculate the gain. When the changes in I and α are less than some small number ε, the procedure has converged. The resulting power, spectra and intensity distributions agree very well with data. With appropriate fluid dynamic, kinetic and optical models, it is possible, in theory at least, to predict laser performance as various aspects of the laser design are changed.

When choosing the outcoupling fraction and the location for the optical axis for an unstable resonator, knowledge of the gain distribution on each of the lasing lines is important. If the optical axis is placed so that the saturated gain distribution of some of the lasing lines does not fill the resonator, a time-dependent oscillation may occur on those lines [11]. The period of the oscillation increases as the magnification of the resonator decreases and the amplitude increases as the fraction of the resonator filled by the line decreases [12]. The oscillations do not occur if the gain medium is strongly coupled to the optical fields diffractively, the Fresnel number $N_F = (D^2/4\lambda L) < 3$, or geometrically, the number of round trip

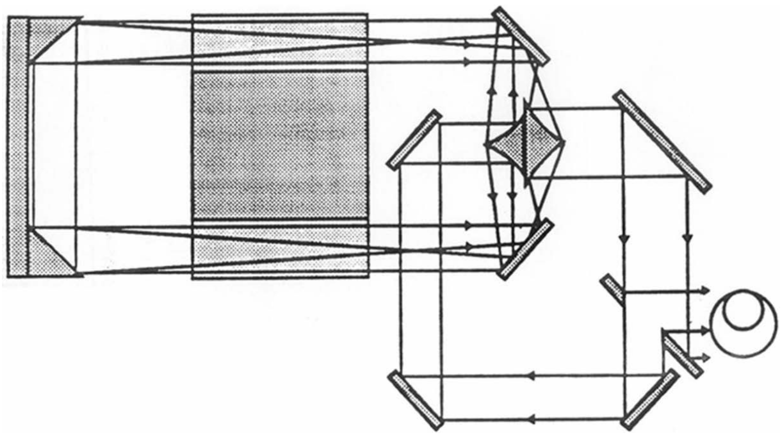

FIGURE 34.6 A schematic view of the HEXDARR resonator used to extract power from the cylindrical gain generator of the ALPHA laser. The dark shaded region is the cylindrical combustor and the light shaded region is the gain zone of the cylindrical laser. (This figure was originally published in Ref. [14], copyright © 1993 by SPIE, reprinted with permission.)

passes required for a wave to exit the resonator after leaving the Fresnel core $n_p = [\ln\{MD_s/2(\lambda L)^{1/2}\}]/\ln M > 3.8$, where D is the diameter of the large mirror, D_s is the diameter of the small mirror, λ is the wavelength, M is the resonator magnification and L is the distance between the mirrors.

Prior to the development of the cylindrical gain generator, HF/DF lasers were rectangular and the optical resonators were developed to extract power from rectangular gain regions. The cylindrical gain region produced by the cylindrical gain generator required the development of an entirely new resonator to extract the power. This resulted in a class of resonators, denoting the high extraction efficiency decentred feedback annular ring resonator (HEXDARR) [13,14]. A schematic view of the HEXDARR resonator is shown in Figure 34.6. Testing of the TRW Alpha laser has demonstrated good performance for the HEXDARR resonator [15].

For all laser geometries, the mirrors that form the resonator must be protected from the lasant flow. This is accomplished with He purges (jets of He) that are positioned to prevent the laser fluids from entering the mirror cavity. Improperly placed or missing purges will result in ground-state HF/DF building up in the mirror boxes which reduces the laser power and degrades the mirror coatings. The mirror purge flow rates are experimentally optimized to maximize the power.

34.4 Exhaust Systems

The exhaust system depends upon the application for the laser. For power levels up to tens of kilowatts, blowers backed by mechanical pumps are used. The pump exhaust is scrubbed before discharge to the atmosphere. For hundreds of kilowatts power levels, the laser effluent is pumped with a steam ejector jet pump system [16–18] which also scrubs the exhaust.

34.5 Laser Performance

HF/DF laser performance is characterized by the power of the laser beam and by the spectral content of the laser beam or the power spectral distribution. The power of the laser is determined by the flow rates of the reactants and the effectiveness of the mixing nozzles. The power scales linearly with the flow rates of the reactants. For fixed flow rates, an efficient mixing nozzle may double the power obtained with an inefficient mixing nozzle.

The HF laser operates on several (υ, J) transitions (wavelengths) simultaneously, with the spectra generally peaked around $J=6$, 7, 8 in both $v=2 \rightarrow 1$ and $\upsilon=1 \rightarrow 0$ vibrational bands. Since rotational relaxation is the fastest collisional deactivation mechanism, the original models of laser performance (e.g. [19–21]) assumed that the HF was in rotational equilibrium. These models were capable of predicting the correct power in each vibrational band. However, they allowed only one (υ, J) transition in each vibrational band to lase at a time. They predicted a sequential shift as lasing progressed from low-J to high-J lines. In the early 1970s, Polanyi and Woodall, and Polanyi and Sloan performed a comprehensive set of experiments on the hydrogen halides, including HF, that measured the fraction of product molecules that were formed in each (υ, J) state for both the cold and hot reactions [22,23]. The data showed that the product molecules were produced in a decidedly non-equilibrium distribution over both rotational and vibrational states. A kinetic model that treats each (υ, J) state of the HF molecule as a separate species where the nascent distribution was measured by Polanyi and coworkers was set up. This approach was implemented by Hough and Kerber in 1975 for the pulsed laser and by Sentman in 1975 for the cw laser [24,25]. For the cw case, 21 J states in $\upsilon=0$, 1, 2, that is 63 states for the lasing molecule, are followed. The results of these models were the prediction of simultaneous lasing on many (υ, J) lines in each vibrational band, in agreement with experiment. When the rotational relaxation rate constants in these models are increased by a factor of 10^6 above the measured values, the rotational non-equilibrium models reproduce the results of the rotational equilibrium models.

The computer models still predicted significant power in the higher vibrational bands populated by the hot reaction. Particularly in the HF cw case, under certain conditions some power is observed in the $3 \rightarrow 2$ band, but generally no power occurs in the $4 \rightarrow 3$, $5 \rightarrow 4$ or $6 \rightarrow 5$ bands. Bartoszek, Manos and Polanyi [26] performed a set of chemiluminescence depletion with mass spectrometry experiments that allowed them to measure the relative rates for the deactivation reactions:

$$\mathrm{HF}(v,J)+\mathrm{D}\rightarrow \mathrm{F}+\mathrm{HD}\ \text{and}\rightarrow \mathrm{H}+\mathrm{DF}\ \text{for}\ v=3,4,5,6.$$

These measured rates showed that these reactions deactivated the HF (v=3–6) as fast or faster than the pumping reactions produced it. When these reactions were incorporated into the kinetic models, the predictions of which vibrational bands lased were in agreement with data.

Before the collisional decomposition reactions were incorporated into the computer models of the HF laser, these models predicted large increases in performance if the laser could be operated to emphasize the hot reaction by increasing F_2 in the flow [27]. Unfortunately, the experimental data did not come close to the theoretical predictions. When the collisional decomposition reactions are included in the computer models, the predicted performance is in reasonable agreement with the experimental data [28].

The power spectral distribution of the HF laser is primarily determined by the rotational non-equilibrium produced by the pumping reactions and the fact that the lasing process is faster than rotational relaxation which results in many (v, J) transitions lasing simultaneously in each vibrational band.

The essential rotational non-equilibrium kinetics required to model the HF laser are:

Pumping Reactions

$$\mathrm{F}+\mathrm{H}_2\rightarrow \mathrm{HF}(1,J)+\mathrm{H}$$

$$\mathrm{F}+\mathrm{H}_2\rightarrow \mathrm{HF}(2,J')+\mathrm{H}$$

$$\mathrm{F}+\mathrm{H}_2(0)\Leftrightarrow \mathrm{HF}(3)+\mathrm{H}$$

$$\mathrm{F}+\mathrm{H}_2(1)\rightarrow \mathrm{HF}(3)+\mathrm{H}$$

$$\mathrm{F}_2+\mathrm{H}\rightarrow \mathrm{HF}(3)+\mathrm{F}$$

The H_2 in the first two pumping reactions is $H_2(0)+H_2(1)$.

Collisional Deactivation Reactions

$$\mathrm{HF}(1,J)+M\Leftrightarrow \mathrm{HF}(0,J''')+M$$

$$\mathrm{HF}(2,J')+M\Leftrightarrow \mathrm{HF}(1,J)+M$$

$$\mathrm{HF}(3)+M\Leftrightarrow \mathrm{HF}(2,J')+M$$

$$\mathrm{H}_2(1)+\mathrm{H}\Leftrightarrow \mathrm{H}_2(0)+\mathrm{H}$$

where M=HF, F, H, H_2 and DF

Multiquantum Deactivation Reactions

$$\mathrm{HF}(2,J')+M\rightarrow \mathrm{HF}(0,J''')+M$$

$$\mathrm{HF}(3)+M\rightarrow \mathrm{HF}(1,J)+M$$

$$\mathrm{HF}(3)+M\rightarrow \mathrm{HF}(0,J''')+M$$

where M=HF, F, H and DF

Collisional Decomposition Reaction

$H+HF(3) \rightarrow H_2+F$

VV Transfer Reactions

$$\mathrm{H}_2(1)+\mathrm{HF}(2,J')\Leftrightarrow \mathrm{H}_2(0)+\mathrm{HF}(3)$$

$$\mathrm{H}_2(1)+\mathrm{HF}(1,J)\Leftrightarrow \mathrm{H}_2(0)+\mathrm{HF}(2,J')$$

$$\mathrm{H}_2(1)+\mathrm{HF}(0,J''')\Leftrightarrow \mathrm{H}_2(0)+\mathrm{HF}(1,J)$$

$$\mathrm{HF}(1,J)+\mathrm{HF}(2,J')\Leftrightarrow \mathrm{HF}(0,J''')+\mathrm{HF}(3)$$

$$\mathrm{HF}(2,J')+\mathrm{HF}(2,J')\Leftrightarrow \mathrm{HF}(1,J)+\mathrm{HF}(3)$$

$$\mathrm{HF}(1,J)+\mathrm{HF}(1,J)\Leftrightarrow \mathrm{HF}(0,J''')+\mathrm{HF}(2,J')$$

Rotational Relaxation Reactions

$$\mathrm{HF}(2,J')+M\Leftrightarrow \mathrm{HF}(2,J)+M$$

$$\mathrm{HF}(1,J)+M\Leftrightarrow \mathrm{HF}(1,J'')+M$$

$$\mathrm{HF}(0,J''')+M\Leftrightarrow \mathrm{HF}(0,J')+M$$

where M=HF, F, H, H_2, F_2, DF, He, Q

The species denoted by Q is included to take account of any other combustion or dissociation products that may be present in the mixture and which would contribute to the rotational relaxation but not the collisional deactivation of the lasing species.

34.6 HF Overtone Laser

The cw HF overtone laser operates on the first overtone $\Delta v=2(v=2 \rightarrow v=0)$ transitions between 1.3–1.4 μ [29,30]. An extensive series of experiments [7,29,31] demonstrated that 60%–90% of the fundamental power is obtainable on the overtone, and the overtone is optimized by the same flow rates as the fundamental and overtone efficiency is independent of mode volume and whether the mixing is slow or fast. Since the overtone is a low gain system, $\alpha_{\mathrm{OT}}\approx(1/80)\alpha_{\mathrm{FUND}}$, to suppress fundamental lasing, mirror coatings must be less than 1% reflective over the fundamental wavelengths and highly reflective (>99%) over the overtone wavelengths. Optimization of the output power [32] requires careful selection of the reflectivity of the resonator mirrors in terms of their absorption/scattering losses. The overtone mirror design problem led to the development of uncooled silicon optics. Measurements of the fundamental gain while lasing on the overtone [$P_{20}(7)$, $P_{20}(8)$, $P_{20}(9)$, $P_{20}(10)$] [33] showed that lasing on the overtone suppressed the gains of the low J lines $P_1(4–6)$ and $P_2(4–6)$ by 41%–96% and suppressed the gains of the high J lines $P_1(7–9)$ and $P_2(7–9)$ by 3%–44% for a well-saturated overtone laser. The high J lines are suppressed because their upper or lower levels are directly involved in overtone lasing. The upper levels of the $P_2(7–9)$ lines are depopulated and the lower levels of the $P_1(7–9)$ lines are populated by overtone lasing, which decreases their gains. The low J P_2 lines are suppressed [34] because overtone lasing depopulates the high $Jv=2$ states which blocks the rotational relaxation that populates the low $Jv=2$ states which decreases the gains of the $P_2(4–6)$ lines. The low J P_1 lines are suppressed because overtone lasing populates the high $Jv=0$ states which increases the rotational relaxation that populates the $v=0$ low J states which decreases the gains of the $P_1(4–6)$ lines.

34.7 Line-Selected Performance of the HF Laser

To operate the HF laser in a multiple line-selected mode, a grating is incorporated into the resonator in the off-Littrow orientation [35]. In an unstable resonator, the feedback mirrors are placed at the locations of the positive first-order diffraction peaks of the desired lines. In a stable resonator, one line can be selected in the Littrow orientation and the remaining lines selected by placing mirrors at the locations of the positive first-order diffraction peaks of the desired lines. The possible line combinations are dictated by the grating equation. The grating characteristics, ruling and blaze angle, are selected to permit only first-order diffraction and to ensure that the grating incident angle does not exceed the limit for high grating efficiency [36]. For first-order diffraction peaks of the HF wavelengths of interest, the maximum grating incident angle must be less than 57°. For incident angles greater than this, the grating begins to behave as a grazing optic. Experiments by Chodzko, Gordon et al. and Sentman et al. [37–39] have shown that 55%–80% of the multiline power can be obtained by operating the HF laser in the line-selected mode on two to four lines.

34.8 Concluding Remarks

The fundamental processes responsible for the performance, power, spectra and beam quality of cw HF/DF chemical lasers are reasonably well understood. An HF/DF laser can be designed with confidence to meet the requirements of an application. The rotational non-equilibrium distribution produced by the pumping reactions is primarily responsible for the power spectral distribution of these lasers. The basic kinetic processes are fairly well understood. The rate constants for the major kinetic processes are known although some of the energy transfer/redistribution rate constants are less well known. Mixing is the mechanism primarily responsible for the power of the HF/DF laser and the basic fluid dynamic mechanism that controls the mixing is fluid element stretching. Resonator designs that efficiently extract the energy from the gain medium in a beam that can be focused to a spot in the far field have been developed for rectangular and cylindrical gain media. Efficient HF overtone lasing has been demonstrated. The processes responsible for the suppression of the fundamental gain while lasing on the overtone have been identified. The grating characteristics required for efficient line-selected operation of the HF laser have been identified. Line-selected operation of the HF laser has been demonstrated for both stable and unstable resonators.

REFERENCES

1. Spencer D J, Mirels H and Durran D A 1972 Performance of cw HF chemical laser with N_2 or He diluent J. Appl. Phys. **43** 1151–7.
2. Sentman L H, Theodoropoulos P T, Nguyen T, Carroll D L and Waldo R E 1989 An economical supersonic CW HF laser testbed *AIAA Preprint 89-1898, AIAA 20th Fluid Dynamics, Plasma Dynamics and Lasers Conf.* (June 12–14).
3. Durran D A and Spencer D J 1970 Axisymmetric mixing nozzle for supersonic diffusion laser Technical Report TOR-0059 (6756-02)-1, The Aerospace Corporation, Los Angeles, CA.
4. Driscoll R J 1984 Effect of reactant-surface stretching on chemical laser performance AIAA J. **22** 65–74.
5. Driscoll R J 1986 Mixing enhancement in chemical lasers, part I: Experiments AIAA J. **24** 1120–6.
6. Driscoll R J 1987 Mixing enhancement in chemical lasers, part II: Theory AIAA J. **25** 965–71.
7. Duncan W, Patterson S, Graves B and Holloman M 1991 Recent progress in hydrogen fluoride overtone chemical lasers *AIAA Preprint 91-1480, AIAA 22nd Fluid Dynamics, Plasma Dynamics and Laser Conf.* (June 24–26, Honolulu, Hawaii).
8. Raymonda J W, Subbiah M, Schimke J T, Zelazny S W and Sentman L H 1979 Advanced HF and DF chemical laser performance modelling vol I The CNCDE/Blaze rotational equilibrium code Technical Report DRCPM-HEL-CR-79-7, Bell Aerospace Textron, Buffalo, NY.
9. Horkovich J A and Pomphrey P J 1997 Recent advances in the alpha high power chemical laser program *AIAA Preprint 97–2409, AIAA 28th Plasmadynamics and Lasers Conf.* (June 23–25, Atlanta, GA).
10. Sentman L H 1978 Chemical laser power spectral performance: a coupled fluid dynamic, kinetic and physical optics model Appl. Opt. **17** 2244–9.
11. Sentman L H, Nayfeh M H, Townsend S W, King K, Tsioulos G and Bichanich J 1985 Time-dependent oscillations in a cw chemical laser unstable resonator Appl. Opt. **24** 3598–609.
12. Sentman L H, Gilmore J and Carroll D 1989 Mechanism for time-dependent oscillations in a cw HF chemical laser unstable resonator *AIAA Preprint 89*–1897*, AIAA* 20th *Fluid Dynamics, Plasma Dynamics and Laser Conf.* (June 12–14, Buffalo, NY).
13. Wade R C 1998 Chemical lasers with annular gain media Optical Resonators-Science and Engineering ed R Kossowsky et al. (Dordrecht: Kluwer Academic) pp 211–23.
14. Wade R C 1993 Annular resonators for high-power chemical lasers Proc. *of Laser Resonators and Coherent Optics: Modelling, Technology and Applications* vol 1868, ed A Bhowmik (Bellingham, WA: SPIE).
15. Horkovich J A, Nefzger C L, Platt B C, Hyver G A, Pomphrey P J, Jacoby J L and Loomis D N 1998 Space-based laser programs high power testing progress *AIAA Preprint 98–2661, AIAA 29th Plasmadynamics and Lasers Conf.* (June 15–18, Albuquerque, NM).
16. Emanuel G 1976 Optimum performance for a single-stage gaseous ejector AIAA J. **14** 1292–6.
17. Emanuel G 1982 Comparison of one-dimensional solutions with Fabri theory for ejectors Acta Mech. **44** 187–200.

18. Taylor D and Toline F R 1968 Summary of exhaust gas ejector-diffuser research, AEDC-TR-68-84, Arnold Engineering Development Center, Tullahoma, TN.
19. Emanuel G 1971 Analytical model for a continuous chemical laser J. Quant. Spectrosc. Radiat. Trans. **11** 1481–520.
20. Emanuel G, Adams W D and Turner E B 1971 RESALE-1: A chemical laser computer program, TR-0172(2776)-1, The Aerospace Corporation, July.
21. Mirels H, Hofland R and King W S 1973 Simplified model of CW diffusion-type chemical laser AIAA J. **11** 156–64.
22. Polanyi J C and Sloan J J 1972 Energy distribution among reaction products, VII. $H+F_2$J. Chem. Phys. **57** 4988–98.
23. Polanyi J C and Woodall K B 1972 Energy distribution among reaction products, VI. $F+H_2$, D_2J. Chem. Phys. **57** 1574–86.
24. Hough J J T and Kerber R L 1975 Effect of cavity transients and rotational relaxation on the performance of pulsed HF chemical lasers: a theoretical investigation Appl. Opt. **14** 2960–70.
25. Sentman L H 1975 Rotational nonequilibrium in cw chemical lasers J. Chem. Phys. **62** 3523–37.
26. Bartoszek F E, Manos D M and Polanyi J C 1978 Effect of changing reagent energy. x. vibrational threshold energies for alternative reaction paths $HF(\upsilon)+D \rightarrow F+HD$ and $\rightarrow H+DF$ J. Chem. Phys. **69** 933–5.
27. Cummings J C, Broadwell J E, Shackleford W L, Witte A B, Trost J E and Emanuel G 1977 H_2–F_2 chain reaction rate investigation J. Quant. Radiat. Spectrosc. Trans. **17** 97–116.
28. Sentman L H and Detweiler G L 2002 The possibility of hot reaction enhancement of CW HF laser performance, AAE TR 02-02, UILU ENG 02–0502 Aeronautical and Astronautical Engineering Dept., University of Illinois, Urbana, IL, March.
29. Jeffers W Q 1989 Short wavelength chemical lasers AIAA J. **27** 64–6.
30. Jeffers W Q 1988 United States Patent 4,760,582 July 26.
31. Carroll D L, Sentman L H, Theodoropoulos P T, Waldo R E and Gordon S J 1993 Experimental study of continuous wave hydrogen-fluoride chemical laser overtone performance AIAA J. **31** 693–700.
32. Carroll D L and Sentman L H 1993 Maximizing output power of a low-gain laser system Appl. Opt. **32** 3930–41.
33. Theodoropoulos P T, Sentman L H, Carroll D L, Waldo R E, Gordon S J and Otto J W 1996 Continuous wave hydrogen fluoride overtone lasing saturation effects on fundamental gain suppression AIAA J. **34** 1216–23.
34. Theodoropoulos P T and Sentman L H 1996 Fundamental gain suppression mechanisms in a continuous wave hydrogen fluoride overtone laser AIAA J. **34** 1589–94.
35. Chodzko R A 1974 Multiple-selected-line unstable resonator Appl. Opt. **13** 2321–5.
36. Petit R 1980 *Electromagnetic Theory of Gratings* (Berlin: Springer).
37. Chodzko R A 1993 Multiple line selection in cw HF/DF chemical lasers, Report Number ATR-92(2732)-1, The Aerospace Corp., Los Angeles, CA.
38. Gordon S J, Sentman L H, Jenkins D S and Eyre A J 1997 A study of line selection in cw HF lasers, AAE TR 97-02, UIUL ENG 97–0502, Aeronautical and Astronautical Engineering Dept, University of Illinois, Urbana, IL, March.
39. Sentman L H, Cassibry J T, Wootton B P and Eyre A J 1999 Influence of grating design on cw HF laser line selected performance, AAE TR 99-08, UILU ENG 99–0508, Aeronautical and Astronautical Engineering Dept., University of Illinois, Urbana, IL.

FURTHER READING

Bott J F and Gross R W F (ed) 1976 *Handbook of Chemical Lasers* (New York: Wiley).

Excellent review of all aspects of chemical lasers as of the date of publication. This is probably the best reference for an introduction to the field of chemical lasers.

Lacour B 2003 Recent advances in pulsed HF/DF lasers *Proc. XIV Int. Symp. Gas Flow Chemical Lasers and High Power Lasers* SPIE vol 5120 ed K Abramski, E Plinski and W Wolinski (Bellingham, WA: SPIE).

Meinzer R A 1987 HF/DF chemical lasers *Handbook of Molecular Lasers* ed P K Cheo (New York: Marcel Dekker) pp 393–493.

Powers R B 1963 Steam-Jet Air Ejectors: Specification, Evaluation and Operation, ASME Paper 63-WA-143.

This is a comprehensive review of steam ejectors with an extensive reference list.

Shellan J B, Smith W and Wade R C 1990 Novel resonators for high power HF overtone lasers *Proc. Optical Resonators (SPIE 1224)* ed D A Holmes (Bellingham, WA: SPIE) pp 302–11.

Solomon W C 1991 Chemical lasers *Encyclopedia of Lasers and Optical Technology* ed A Meyers (New York: Academic) pp 1–8.

Ultee C J 1979 Chemical and gas dynamic lasers *Laser Handbook* vol 3, ed M L Stitch (Amsterdam: North-Holland).

35

Fiber and Waveguide Lasers: Section Introduction

R. C. Powell

One of the major technological advances in laser systems was the development of fibre optics [1]. This allowed laser light to be accurately and efficiently delivered to distant targets over ranges from several millimetres to many kilometres. The combination of laser sources and fibre optic delivery systems has led to important applications such as modern telecommunication systems and non-invasive laser surgery. The next step in this technology development is to combine the fibre delivery system and the laser into one device. Since fibres are made out of glass, they can act as the host material for rare earth laser ions to make fibre lasers. All of the fundamental science and technology of rare-earth-doped glass laser materials discussed in Chapter 1 are relevant for fibre lasers. The major difference is that the length of a single pass of light in a fibre laser is much longer than in a rod or slab laser. This requires significantly different resonator design techniques.

The basic spectroscopic properties discussed in Chapter 1 and the waveguide theory discussed in Chapter 24 form the basis for fibre lasers. Because of the length of the gain media, non-linear optical effects play an important role in fibre lasers. Non-linear optical processes can be the limiting factor in determining the power output of a fibre laser. At the same time, non-linear processes such as stimulated Raman scattering can form the basis of the fibre laser itself.

The development of the technology to produce fibres with special shapes and properties has led to the ability to make fibre lasers with very low loss over very long distances. By controlling the core size and shape, and using Bragg gratings for distributed feedback, the power, mode structure, dispersion and wavelength of the laser can be designed. Rare-earth-doped fibre amplifiers have become standard devices in optical telecommunication systems. All of these topics are discussed in this section.

REFERENCE

1. Yeh C 1990 *Handbook of Fiber Optics* (San Diego, CA: Academic).

Taylor & Francis
Taylor & Francis Group
http://taylorandfrancis.com

36

Fibre Lasers

Wei Shi, Shijie Fu, and Qiang Fang

CONTENTS

36.1 Introduction 477
36.2 Features of Fibre Lasers 478
  36.2.1 High Gain and Low Threshold 478
  36.2.2 High Efficiency 478
  36.2.3 Broad Gain-Linewidth 478
  36.2.4 Robust Modal Characteristics 479
  36.2.5 Monolithic All-Fibre Construction 479
  36.2.6 Capability of Generating High-Power High-Brightness Laser Beam 479
36.3 Basic Principles and Formulae 479
36.4 Energy Level and Optical Spectra Properties of Rare-Earth Ions in Optical Fibre 481
36.5 Laser Performance 485
36.6 Future Prospects 485
References 485
Further Reading 487

36.1 Introduction

Fibre laser is one of the lasers using fibre as the gain medium. So far, laser emissions have been successfully demonstrated with glass fibres, polymer fibres, single-crystal fibres and even gas-filled hollow-core fibres. The rare-earth (RE)-doped glass fibre laser is the main form of the fibre lasers.

Since the birth of the first glass fibre laser demonstrated by Snitzer and co-workers in 1964 [1], fibre lasers have seen progressive developments in all aspects of the laser performance and their application range has expanded significantly. Nowadays, the emission wavelengths of fibre lasers range from ultraviolet to visible/near-infrared and even to mid-infrared. Because of the excellent heat dissipation capability and the inherent long gain length of optical fibre, continuous wave (CW) output power as high as 100 kW has been generated with a single multimode fibre [2] and 10 kW diffraction-limited output has been obtained from a single large-mode area fibre [3]. In pulsed fibre lasers, tens of multi-joule nanosecond pulses [4–6], femtosecond pulses with multi-joule pulse energy, gigawatt (GW) peak power, and over 800 W average power [7,8], and ultrashort pulses as short as sub-10 fs [9] have been achieved. Due to the high gain of highly doped optical fibres and their compatibility to fibre Bragg gratings, stable and robust single-frequency operation can be achieved with short-fibre-cavity lasers. Low-noise single-frequency fibre lasers with linewidth as narrow as several kilohertz or even sub-kilohertz have been demonstrated [10]. Single-frequency multi-joule -level laser pulses have been recently obtained in an all-fibre master oscillator and power amplifier (MOPA) laser system [11]. These outstanding performances of fibre lasers and their inherent attractive advantages, including compactness, robust operation, easy thermal management, excellent beam quality, free alignment and convenient maintenances, have facilitated extensive applications of fibre lasers in the industry (material welding, cutting, soldering, marking, cleaning), medicine, research, defence and security [12].

Among fibre lasers there is a wide variety of fibre geometries, resonator designs and pumping arrangements. Some of these variants will be described later in this chapter and in companion chapters. First, we describe the canonical fibre laser design since this illustrates the salient characteristics of fibre lasers in general.

This basic structure (see Figure 36.1) is essentially the same as that of a conventional optical fibre as used in telecom applications, i.e. with a central glass core surrounded by a glass

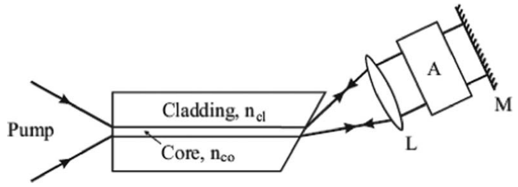

FIGURE 36.1 An end-pumped fibre laser. The resonator shown has feedback provided on the left by Fresnel reflection from the end-face of the fibre, and on the right by a separate mirror, M. Light emerging from the right-hand end of the fibre is collimated by a lens, L. Intracavity components can be inserted at A. Unwanted feedback from the right-hand end-face of the fibre can be reduced by cleaving or polishing the end of the fibre at an angle, as shown.

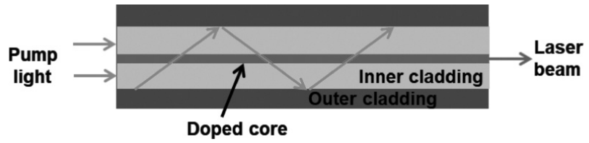

FIGURE 36.2 Schematic of cladding-pumping principle of operation.

cladding, whose refractive index, n_{cl}, is less than that of the core, n_{co}, thus ensuring guidance of light within the core. Unlike in conventional fibres, the core contains laser-active dopant ions which, when suitably pumped, provide amplification at wavelengths corresponding to a transition of the dopant ion. So far, laser action has been confined to the RE. Pumping is achieved optically, e.g. by launching the pump light directly into the exposed core at the end of the fibre (see Figure 36.4). Thus, the core not only guides the amplified laser light but also the pump light. The final ingredient, needed to complete the laser, is provision of a resonator for feedback, thus converting the amplifier to an oscillator. In its simplest form, relying on the very high gains that can be achieved in active fibres, this feedback can be provided by Fresnel reflections from the fibre ends. Often a more sophisticated feedback arrangement is used, with the laser light emerging from a fibre end and then passing through a region of free space before being fed back, (see Figure 36.1). This then allows a range of different components, such as filters and modulators, to be inserted into the resonator for control of the spectral and temporal characteristics of the laser output.

The core-pumping scheme is adopted in the fibre laser, as shown in Figure 36.1. It is difficult to couple much low-brightness pump power into the highly restrictive fibre active core to get high-power fibre lasers. The cladding-pumping scheme (see Figure 36.2) promotes the revolutionary development of fibre lasers in terms of output power and pulse energy [13]. In this pumping scheme, the high-power low-brightness pump light is launched into the fibre inner-cladding with a larger size and larger numerical aperture (NA). The pump light could be gradually absorbed by the active fibre core and transformed to the much brighter laser when they propagate in the fibre inner-cladding and cross the active core.

We now briefly survey some of the main features of fibre lasers, before elaborating on these and giving them a quantitative basis in Section 36.3.

36.2 Features of Fibre Lasers

36.2.1 High Gain and Low Threshold

The basis for these two connected features is the small cross-sectional area of the core, typically in the range 10^{-11}–10^{-10}m^2, corresponding to core diameters in the range 4–10 μm. This area is a factor of 2–3 orders of magnitude smaller than the typical pumped area involved in an end-pumped bulk laser. Hence, this same factor increases the gain for a given pump power, or conversely decreases the threshold for a given resonator loss. Submilliwatt threshold pump powers and gains of 10 dB mW^{-1} are not uncommon for the active-fibre devices.

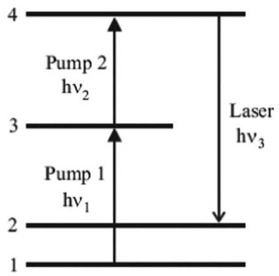

FIGURE 36.3 An upconversion laser. Sequential absorption of two pump photons of energy $h\nu_1$, $h\nu_2$ (these may be identical for a suitable energy-level scheme) takes ions to the excited level 4, and subsequent laser emission to level 2 produces laser photons that are more energetic than the pump photons.

These high gains led to a number of important possibilities, of which high-gain amplifiers for telecom have been the most prominent [14–16], while more generally it provides very convenient MOPA schemes for power scaling of a wide variety of laser sources, including diode lasers and fibre lasers [17].

Related to the fact that modest pump powers can lead to high pump intensities in the core, is the result of very strong saturation (or ‘bleaching’) of the absorbing ions, i.e. most of the ions can be pumped out of the ground state into an excited state. This population of excited ions can then easily be subjected to a second or even a third pumping stage that takes them to yet higher excited states. Laser action can then take place from these highly excited states with the emission of photons that are more energetic than the pump photons (see Figure 36.3). This is referred to as an upconversion laser, and while upconversion lasers were first demonstrated in a bulk laser geometry, a dramatic improvement in performance and practicality resulted when a fibre laser geometry was adopted, leading to CW visible lasers directly pumped by near-infrared diode lasers [18].

36.2.2 High Efficiency

The excellent modal overlap between pump and laser modes over the entire length of the laser medium contributes to the typically very high efficiency. Also, the high gains and the low background losses of the host (for silica, a few dB km^{-1}) allow one to ensure that the output coupling is the dominant loss, i.e. essentially no laser photons are wasted. The ability to use a three-level laser effectively, by virtue of the high pump intensity in the core, has given prominence to the ytterbium (Yb^{3+}) ion. This ion offers no significant channels for parasitic loss of excitation from the upper laser level, and essentially 100% quantum efficiency (~80% power efficiency) can be achieved [19].

36.2.3 Broad Gain-Linewidth

In a fibre, the host medium being glass (silica is commonly used), the dopant ions occupy a wider range of environments than in the ordered lattice of a crystal host. This results in a significant broadening of the transition linewidths, including that of the amplifying transition. As an example, Figure 36.4 shows a typical spontaneous-emission spectrum of an erbium-doped

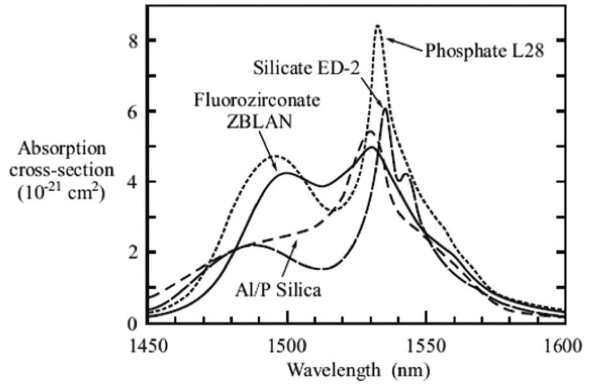

FIGURE 36.4 The spontaneous-emission spectrum of erbium at ~1500 nm in various glass hosts [20].

silica fibre in the 1.5 μm spectral region, indicating a bandwidth of ~4 THz or 25 nm. This is more than an order of magnitude broader than the same transition would exhibit in a typical crystalline host. Other REs show similarly broad, and in the case of the important ions Yb^{3+} and Tm^{3+} even broader, linewidths.

The broad gain profile implied by Figure 36.4 has an important application in optical telecom. The fact, that the gain for a given pump power varies inversely with the emission bandwidth, is easily accommodated by the gain-enhancement conferred by the waveguide geometry. More generally, the broad linewidths offer significant scope for tuning fibre lasers and for ultrashort pulse mode-locked operation. The Er gain-bandwidth is sufficient to support mode-locked pulses of ~100 fs duration, as has been widely demonstrated [21] and Yb has produced even shorter pulses [22]. In the context of mode-locked operation, one should also note two other features of the fibre that play an important role. These are the dispersion, which can be significant as a result of a long length of medium, and self-phase modulation (SPM) [23], which can be as strong as a result of the combination of high peak intensity and long path length.

36.2.4 Robust Modal Characteristics

If the core diameter is chosen small enough, so as to support propagation of just the lowest-order mode, the fibre laser will ensure a single-spatial mode output despite the fibre being subjected to major disturbances, such as bending of the fibre and thermal variations either of the environment or due to pump-induced heat load. This contrasts with the much more critical behaviour of typical bulk lasers.

36.2.5 Monolithic All-Fibre Construction

The practicality of fibre lasers and their further prospects benefit enormously from the monolithic all-fibre construction. For one thing, the gain medium for fibre lasers is the RE-doped fibre. For the other thing, there are a number of robust fibre components available including the fibre Bragg gratings and fibre-couplers. Take fibre Bragg grating [24] as an example. This can be optically written directly into the core of the fibre (usually silica) and can serve as a mirror or filter. Not only does it have superior characteristics of stability and robustness compared to bulk counterparts but also have much greater functionality, e.g. allowing it to fulfil sophisticated pulse-shaping functions that enhance the fibre laser's role as a source of ultrashort pulses. The grating can be made to extend over the full length of the gain medium, thus resulting in a distributed feedback (DFB) laser [25,26], a very convenient source with an output that is robustly single-frequency (single-longitudinal mode). Another example of a simple and stable component is the fibre-coupler, obviating the need for bulk beam splitters. Figure 36.5 shows a typical example of how fibre lasers can have an all-fibre construction by incorporating various fibre components.

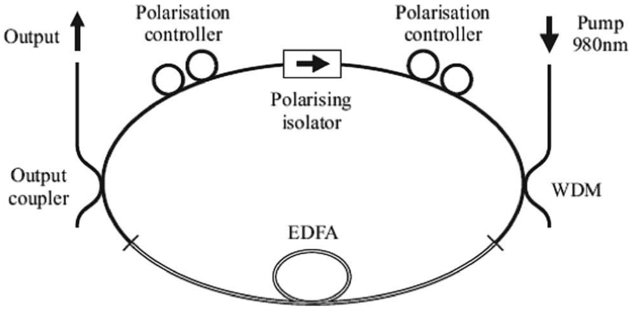

FIGURE 36.5 A stretched-pulse mode-locked Er-doped fibre laser (after Ref. [27]) using an all-fibre construction in a unidirectional ring configuration. Pump light enters at the wavelength division multiplexer (WDM) and pumps the erbium-doped fibre amplifier (EDFA). Output is taken via the fibre output coupler. Tightly wound fibre loops are used to control the polarization state. The constituent fibre lengths and dispersion values, positive and negative, are chosen to achieve the desired stretching and compression of the pulses.

36.2.6 Capability of Generating High-Power High-Brightness Laser Beam

RE-doped glass fibre is an outstanding laser gain medium to achieve a high-power laser with high brightness [28–30] because, first, the geometry of the glass fibre enables very high surface-to-volume ratio, which facilitates the heat dissipation to the surroundings (air, coolant, heat sinks); second, because of the inherent long action length, glass fibres can provide very large single-pass gain, offering the option of MOPA scheme for the effective power scaling; third, the waveguide nature of the fibre provides significant freedom to well control the beam quality of a fibre laser and strong immunity from the thermally induced spatial mode distortion. Other factors include the developments of high-brightness semiconductor diode lasers (pump sources), novel fibre designs, new pumping schemes and high-power fibre components.

36.3 Basic Principles and Formulae

For simplicity we assume that the fibre has a so-called step-index profile (uniform refractive index, value n_{co} in the core and n_{cl} in the cladding). The NA of the fibre defines the maximum incidence angle θ_m ('acceptance-angle') at the endface of the fibre core, for subsequent guidance to take place in the core, with θ_m given by, $\sin \theta_m = \text{NA}$. The NA is given by [31]

$$\text{NA} = \left(n_{\text{co}}^2 - n_{\text{cl}}^2\right)^{1/2}. \tag{36.1}$$

It is customary to define a quantity referred to as the V value, given by

$$V = 2\pi a(\text{NA})/\lambda \tag{36.2}$$

where a is the core-radius and λ is the (vacuum) wavelength of the guided wave. For the fibre to be monomode at wavelength λ, (i.e. for the LP_{11} and higher-order modes to be cut off, allowing only the LP_{01} mode to propagate), V must be less than 2.4. Thus, substituting in Equation (36.2), a wavelength of 1 μm and a typical NA of 0.15, one finds that for $V = 2.4$, a has the value 2.5 μm, implying a maximum diameter of 5 μm for monomode propagation at this wavelength. One can see from Equation (36.2) that monomode operation can be maintained at larger diameters provided the NA is appropriately reduced to keep V below 2.4. There are however, practical limits to this procedure since, e.g., the reduced index difference, $n_{\text{co}} - n_{\text{cl}}$, makes the fibre more liable to bending losses.

Conversely, to increase gain for a given pump power, or equivalently to reduce the threshold power, one needs to minimize the mode areas for pump and laser modes. This can be achieved, up to a point, by reducing the core size. However, it is important to note that, while it is a reasonable approximation to identify the LP_{01} mode area with core area for V values around 2.4, this is not in general true and, for small V values, ($V < 2$) the mode size increases as V is further reduced. Hence, reduction in core size must be accompanied by a corresponding increase in NA (to keep V from decreasing below ~2) if reduced mode volume is to result. Thus, assuming $V \sim 2.4$, so that mode-area ≅ core-area, then Equation (36.2.) implies that gain is proportional to $(\text{NA})^2$.

If one now considers a four-level laser, i.e. with an empty lower-laser level (see Figure 36.6a), assuming $V = 2.4$ and equating core area to the mode area, then the gain, expressed in dB mW^{-1} of absorbed pump power, is given by

$$\text{Gain} = (\text{NA})^2 \phi \big/ \left(10^4 \Delta\nu h\nu_{\text{p}}\right) \tag{36.3}$$

Here, $\Delta\nu$ is the linewidth (FWHM) of the amplifying transition, ν_{p} is the pump frequency and ϕ is the product of ϕ_{p}, the pump-quantum efficiency, i.e. the fraction of absorbed pump photons that produce an ion in the upper-laser level, and ϕ_{r}, the radiative quantum efficiency, i.e. the fraction of spontaneous decays of ions in the upper-laser level that occur as radiative emission via the amplifying transition. Insertion of typical numbers for the case of Nd^{3+} ions [0.8 μm pump, $\lambda_{\text{p}} \sim 1$ μm, $\phi_{\text{p}} = 1$, $\phi_{\text{r}} = 0.5$ (radiative decay also occurs via the 0.94 μm, and 1.3 μm, channels), $\Delta\nu = 3$ THz] and assuming an NA of 0.15, gives a gain of 1.5 dB mW^{-1}. A somewhat higher figure has been achieved in Er-doped fibre at ~1.5 μm, where $\phi \sim 1$, and by deliberately using a larger NA, a gain of 11 dB mW^{-1} has been achieved [32]. The expression of Equation (36.3) cannot be applied directly to the case of the Er^{3+} ion, however, as this exhibits a three-level scheme, i.e. the lower-laser level is also the ground level (see Figure 36.6b). An approximate analytical treatment of the three-level case leads to Equation (36.3) being modified by insertion of the factor $(I/I_{\text{sat}} - 1)/(I/I_{\text{sat}} + 1)$ into the right-hand side, where I_{sat} is the saturation intensity of the pump transition, $I_{\text{sat}} = h\nu_{\text{p}}/\sigma_{\text{p}}\tau$. Here, σ_{p} is the pump-absorption cross-section and τ is the lifetime of the upper-laser level. When $I \gg I_{\text{sat}}$, a condition that is easily achieved in a fibre since it may typically need only ~milliwatt power levels, then the three-level case approaches that of the four level, as expected, since this corresponds to most of the ground-state population having been promoted to the upper-laser level. In general, however, the treatment of the three-level case is more complicated analytically than that of the four level since the ratio I/I_{sat} decreases progressively along the fibre as the pump intensity is decreased by absorption (for $I < I_{\text{sat}}$, this factor indicates that the medium has negative gain, i.e. is absorbing). Furthermore, a number of laser transitions involve a lower-laser level that is somewhat above the ground level, although still containing a significant thermally-excited population. This is often referred to as a quasi-three-level transition. Further complications arise from the fact that the nature of a transition may in fact be continuously graded from effectively three level at the short-wavelength end of the emission spectrum, to the four level at the long-wavelength end since the longer emission wavelengths correspond to emission into higher-lying sublevels of the ground manifold (see Figure 36.6b).

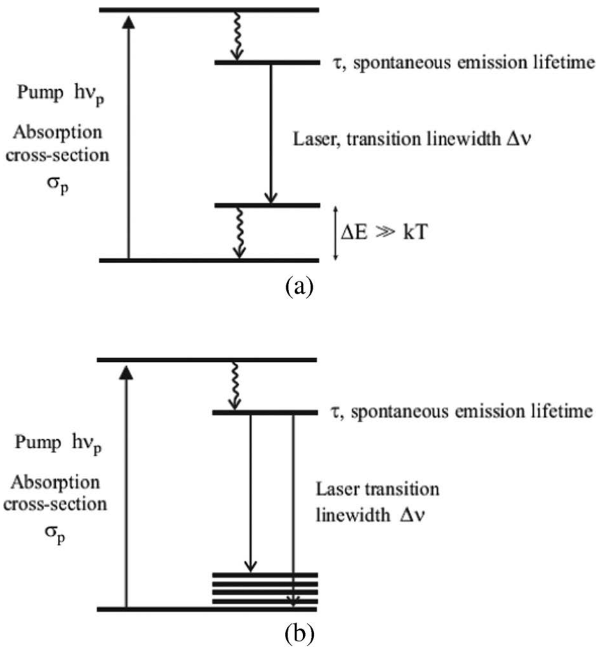
τ, spontaneous emission lifetime
Pump $h\nu_{\text{p}}$
Absorption cross-section σ_{p}
Laser, transition linewidth Δν
ΔE ≫ kT
(a)
τ, spontaneous emission lifetime
Pump $h\nu_{\text{p}}$
Absorption cross-section σ_{p}
Laser transition linewidth Δν
(b)

FIGURE 36.6 (a) A four-level transition in which the lower laser level is several KT above the ground level. (b) A three-level transition in which the lower laser level is the ground level. Wiggly arrows indicate nonradiative decays. The multilevel nature of the ground manifold is explicitly indicated in (b) illustrating the fact that longer wavelength emission has some 'four-level' character as it involves higher-lying and therefore less populated sublevels.

To complete this brief survey of basic principles, an indication is given of the role played by amplified spontaneous emission (ASE) in limiting the maximum achievable gain and thus also limiting the maximum energy that can be stored (and subsequently extracted, e.g. in the form of a Q-switched pulse). Photons created by spontaneous emission at one end of the fibre and then guided over the fibre's length will be amplified, thereby causing some reduction of the population inversion and hence of the gain. This ASE process therefore acts as a limiter, reducing the achievable gain even in the absence of any feedback, to a level that, in practice, is typically 40 dB over a single pass. ASE for example, provides the ultimate limit on tuning range achievable from a fibre laser. Thus, when tuning to the extreme wings of a transition, where the gain is low, while one can, in principle, compensate the low gain by pumping harder, this can raise the gain at line-centre to a level that induces strong ASE. This therefore limits the tuning range that can be covered. ASE also limits the energy stored in the population inversion. The relation between gain and stored energy is

$$\text{Gain}[\text{dB}]/(\text{Stored energy}) = 4.34/E_{\text{sat}} \qquad (36.4)$$

where $E_{\text{sat}}=A_{\text{core}}\ F_{\text{sat}}$, with A_{core} being the area of the core and F_{sat} the saturation fluence, given by $h\nu_1/\sigma_1$, where ν_1 and σ_1 are the laser frequency and emission cross-section, respectively. The maximum stored energy, limited by the onset of ASE, is found by inserting a gain of ~40 dB in Equation (36.4). The effect of a small core diameter is immediately apparent as the stored energy, for a given gain, is proportional to A_{core}. Typical values for Nd^{3+} for a 5 μm core diameter are ~3 dB μJ^{-1}, thus the ASE-limited energy is ~10 μJ. For Er^{3+}, with a much smaller σ_1, corresponding to the much longer τ_1 than for Nd^{3+} (~30×), there is a correspondingly greater energy-storage capability. Further increases in the energy storage are achievable by scaling up the core area.

36.4 Energy Level and Optical Spectra Properties of Rare-Earth Ions in Optical Fibre

As the main luminescent elements, RE ions play an important role in the development of fibre laser. In periodic table of elements, the RE ions employed in active fibre are mainly focused on lanthanides, which are characterized by the filling of the 4f shell. The Ionization process to RE ions removes the electrons on the 6s and 5d shell preferentially, and the corresponding electronic configuration can be taken as the xenon structure plus a certain number of electrons on the 4f shell. Since the trivalent level of ionization is the most stable state for lanthanide ions, most of RE ions in active fibres are trivalent. Stark splitting of the energy level is generally formed due to the interactions including electron–electron and electron–host.

In addition to laser transitions accompanied with emission of photons, an excited RE ion can decay nonradiatively by means of phonon emission, resulting from the interaction with vibrations of host material. If the energy levels are separated in one or two phonon energy, nonradiative transition to lower electronic state occurs rapidly through emission of phonons. For energy gaps much larger than the phonon energy, the nonradiative decay rate is inversely proportional to the exponential of energy gaps [33]. Moreover, due to the large variation of vibrational spectra for different materials, the nonradiative decay is extremely host-dependent. For silica host, which obtains a phonon energy around 1100 cm^{-1}, the infrared transparency is limited by absorption loss due to the excitation of phonons in the glass lattice to ~2 μm. This forms the multiphonon edge of silica glass. Wavelength transparency to longer wavelength can be obtained under glass host with lower phonon energy, such as fluoride and chalcogenide glass. Especially, the heavy metal fluoride glass, ZBLAN (ZrF_4-BaF_2-LaF_3-AlF_3-NaF), with phonon energy of 600 cm^{-1}, has been studied with more efforts on lasing wavelength extended to mid-IR because of the benefits including high allowable doping levels, relatively high strength and low background loss.

The RE ions in glasses possess spectroscopic parameters similar to that in crystals. But, unlike crystal, in which the RE ions exhibit absorption and emission transitions with discrete lines, the glass is a disordered material that the inhomogeneous broadening of spectral lines results in broadband spectra of absorption and emission transitions.

In the following section, we provide the major energy levels and spectroscopic parameters of the most used RE ions in the development of fibre lasers.

Neodymium. Since the first demonstration of fibre laser with Nd-doped glass fibre in 1964 [1], Nd^{3+} has attracted intense attention for the development of fibre lasers in the early stage. Figure 36.7 shows the main energy levels of Nd^{3+} for most important laser transitions. Strong absorption around 800 nm has been employed as the main pump scheme with an energy-level transition from $^4I_{9/2} \rightarrow {}^4F_{5/2}$. While the laser transitions between energy levels: $^4F_{3/2} \rightarrow {}^4I_{9/2}$,$^4F_{3/2} \rightarrow {}^4I_{11/2}$ and $^4F_{3/2} \rightarrow {}^4I_{13/2}$ correspond to the three emission peaks of Nd^{3+} at 930, 1060 and 1340 nm, respectively, among them, the four-level transition around 1060 nm has been well exploited for both glass and crystalline hosts, especially to achieve high-power and high-energy laser due to the large emission cross-section. Afterwards, the Nd^{3+} is gradually replaced by a more powerful RE ion, Yb^{3+} for the development of high-power fibre laser around 1 μm, which will be introduced in the next part.

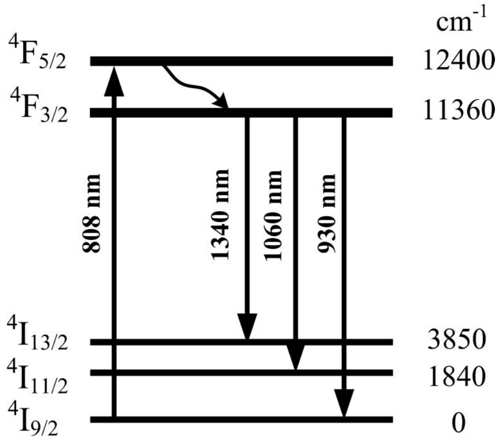

FIGURE 36.7 The energy-level diagram of regular laser transitions of Nd^{3+}.

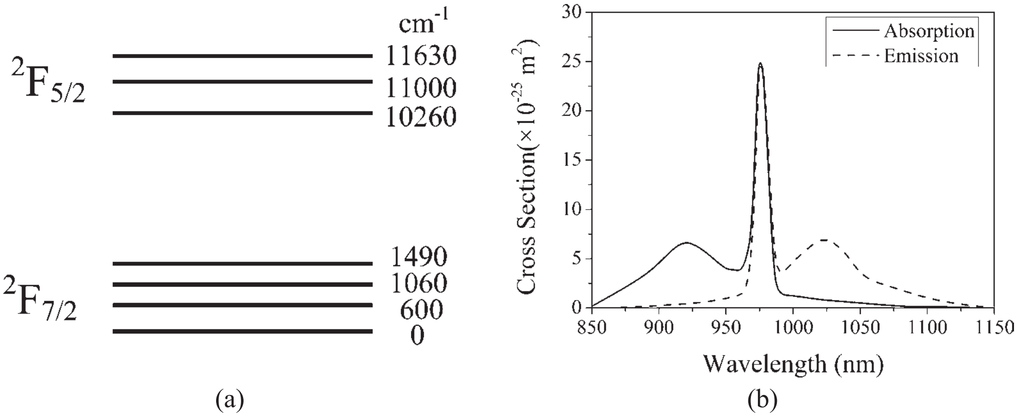

(a) (b)

FIGURE 36.8 (a) The energy levels of Yb^{3+} ion. The Stark sublevels of the ground manifold $^2F_{7/2}$ and excited manifold $^2F_{5/2}$ are indicated with approximate energies. (b) Absorption and emission cross-section of Yb^{3+} in silica fibre. (Data is provided by Thorlabs.)

For $^4F_{3/2} \rightarrow {}^4I_{13/2}$ transition, within the optical communications window around 1300 nm, it had been investigated for fibre amplifiers to fill in this window. Except for the low emission intensity, the excited-state absorption (ESA) between energy levels $^4F_{3/2}$ and $^4G_{7/2}$ limits the lasing performance in this band. Another transition of Nd^{3+}, $^4F_{3/2} \rightarrow {}^4I_{9/2}$, corresponds to the three-energy-level lasing for wavelength between 900 and 950 nm, which provides the possibility to achieve blue laser through non-linear frequency conversion. The main challenge for this laser transition comes from the gain competition with the other two four-energy-level transitions.

Ytterbium energy-level diagram of Yb^{3+} is illustrated in Figure 36.8a, which consists of simple two Stark manifolds (ground $^2F_{7/2}$ state and excited $^2F_{5/2}$ state). Compared with traditional Nd^{3+}, the Yb^{3+} exhibits the advantages on longer upper-energy-level lifetime (~1 ms), small quantum defect, and absence of ESA. Figure 36.8b shows the typical absorption and emission spectra of Yb^{3+} in silica fibre. The strong and wide absorption bands near 915 and 976 nm, corresponding to the transition from the lowest Stark sublevel of the ground $^2F_{7/2}$ state to the second and the first Stark sublevels of excited $^2F_{5/2}$ state, facilitate efficient pump with InGaAs laser diodes for high-power operation. Furthermore, Yb-doped silica fibre possesses a broad emission band, from 950 to 1200 nm, which offers a convenient way to achieve versatile laser source in this broad emission range [19].

All the features mentioned earlier, together with the advantages of fibre laser scheme, make the Yb^{3+} become the most powerful RE ion for the high-power and high-efficiency fibre laser system. Since the first Yb^{3+}-doped fibre laser demonstrated by Hanna et al. in 1988 [34], significantly progress in scientific research, and commercialization have been made with this ion in fibre lasers. One of remarkable results is reported by IPG Photonics Inc. in 2009 in which single-mode 1070 nm Yb-doped fibre laser with a record power of 10 kW has been developed in all-fibre scheme using a number of hundred-watts 1018 nm fibre lasers as pump laser [3].

Erbium. Because of the broad applications in the area of optical communication, Er-doped fibre lasers and amplifiers have been extensively investigated in the past few decades. The energy-level diagram of Er^{3+} is shown in Figure 36.9a with typical energy transition for both pump and laser. Similar to Yb^{3+}, Er^{3+} can be pumped with a laser diode at 980 nm, but the corresponding absorption cross-section is much smaller, as shown in Figure 36.9b. In addition, Er^{3+} can also be directly in-band pumped to the upper levels of $^4I_{13/2}$ at a wavelength around 1480 nm, through which the quantum defect can be significantly alleviated compared to pump at 980 nm. The emission spectrum of Er^{3+} covers the whole C-band, which motivates its applications in optical signal transmission, whereas power scaling of the Er-doped fibre laser is constrained by low doping concentration due to pair-induced quenching, which lowers the laser efficiency and deteriorates the output stability [35]. Co-doping of Er^{3+} with Yb^{3+}, which has a higher doping concentration (generally more than 10 times higher than that of Er^{3+}), provides an effective solution. The operating mechanism can be understood with Figure 36.10: Yb^{3+} in ground state $^4F_{7/2}$ absorbs a pump photon at 980 nm to transit to upper state $^4F_{5/2}$ and then transfers the energy to Er^{3+}, raising it to the excited state $^4I_{11/2}$. Since output power for the co-doping system is still limited by the parasitic lasing of Yb^{3+} at a wavelength of ~1.1 μm, optimization of co-doping concentration ratio between Er^{3+} and Yb^{3+} should be addressed for efficient energy transfer [37].

Thulium. A Tm-doped fibre laser has become the most mature fibre laser system around 2 μm after broad investigation and development in recent 10 years. Figure 36.11 shows the relevant energy-level transitions for lasing around 1.9 μm. For pump at 793 nm, corresponding to energy-level transition from ground-state $^3H_6$ to excited-state $^3H_4$, Tm^{3+} has the highest absorption cross-section. Efficient pump can be realized with high-power commercially available diode laser at 0.8 μm. In addition, a cross relaxation process occurs when the doping concentration of Tm^{3+} reaches 3–5 wt% [38]. It means that two excited Tm^{3+} can be obtained at the upper level with only one pump photon at 793 nm absorbed, which may double the quantum efficiency in theory. Additionally, Tm-doped fibre can be in-band pumped by the laser at 1570 nm, which can be provided by the well-developed high-power Er-doped fibre laser. The majority of works on Tm-doped fibre lasers are focused on lasing a wavelength around 1.9 μm, where Tm^{3+} has the largest emission cross-section, as shown in Figure 36.11b. As the wavelength increases, emission intensity of Tm^{3+} drops

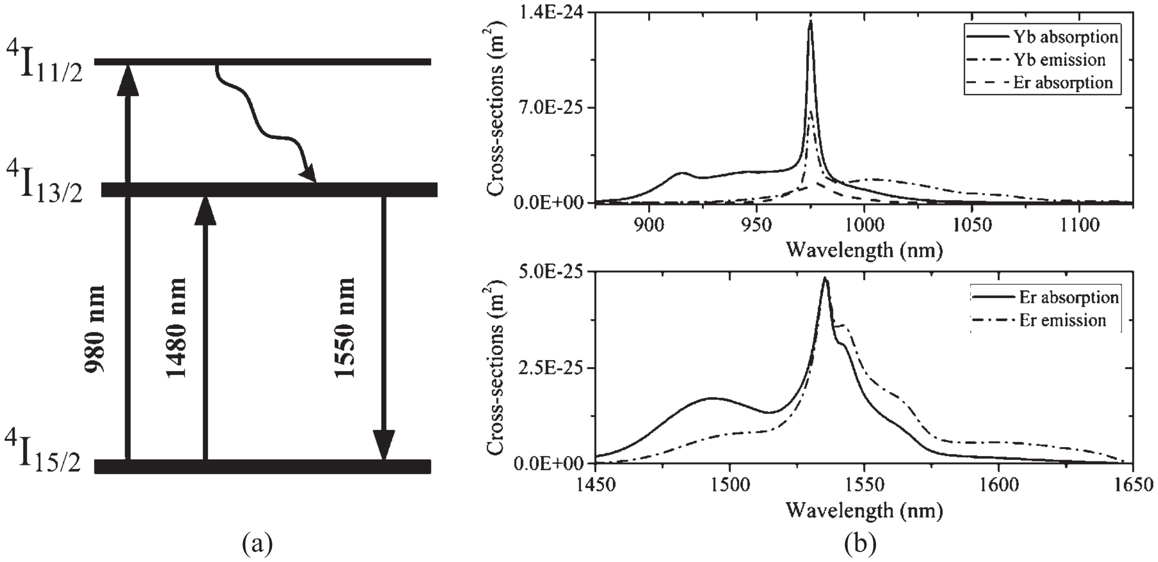

FIGURE 36.9 (a) The energy levels of Er^{3+}. Pump at 980 nm and In-band pump at 1480 nm correspond to the energy transition from ground state $^4I_{15/2}$ to excited state $^4I_{11/2}$ and $^4I_{13/2}$. (b) Up: Absorption and emission cross-section of Yb^{3+} as well as absorption cross-section of Er^{3+} at the wavelength from 875 to 1125 nm; Bottom: Absorption and emission cross-section of Er^{3+} at wavelength from 1450 to 1650 nm in Er-Yb co-doped fibre [36].

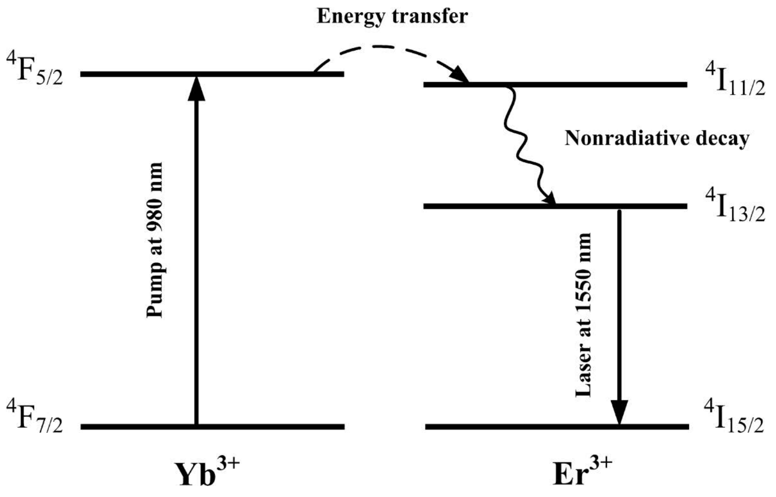

FIGURE 36.10 Energy-level diagram of Er-Yb co-doped fibre. The Er^{3+} is excited by the following two steps: the Yb^{3+} is excited to upper level under pump at 980 nm, and then the excited Yb^{3+} transfers energy to an Er^{3+} in ground-state $^4I_{15/2}$, raising it to excited-state $^4I_{11/2}$.

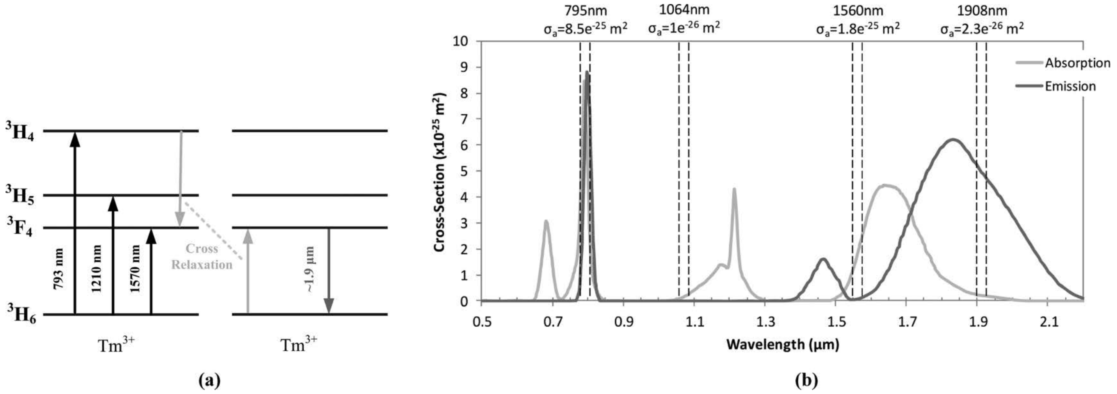

FIGURE 36.11 (a) Lower-energy levels of Tm^{3+}. Process of cross relaxation occurs under the pump at 793 nm, which can double the quantum efficiency in theory. (b) Absorption and emission cross-section of Tm-doped silica fibre. Dashed lines indicate common pumping regions for Tm-doped fibres. (Reprinted with permission from Ref. [39], OSA.)

gradually. Recently, with the development of fabrication techniques on high-quality Tm-doped fibre and fibre devices around 2 μm, various demonstrations in Tm-doped fibre lasers, including high-power CW laser to kilowatt [40], single-frequency operation with linewidth in kilohertz [41], and ultrafast operation with pulse duration shorter to 27 fs [42], have been presented by the researchers.

Holmium. Extending operating wavelength of fibre laser to >2.1 μm with Ho-doped fibre has attracted more attention for its distinctive applications involving atmospheric transmission window in this wavelength region. The energy levels of Ho^{3+} are shown in Figure 36.12a. The Ho^{3+} can be pumped to upper level $^5I_6$ with a high-power diode laser or Yb-doped fibre laser at 1.12 μm for three-level lasing at 2.1 μm. While the small absorption cross-section requires long active fibre for efficient lasing, which introduces more background loss for silica fibre. As shown in Figure 36.12b, the absorption loss due to silica and hydroxyl contamination becomes significant for the wavelength region >2.1 μm. The other option of the pump scheme is in-band pump at 1.95 μm, where much higher absorption avoids serious background loss with long fibre. This has been realized with well-developed Tm-doped fibre laser as a high-power pump source. Furthermore, similar to Er-Yb co-doped fibre, Tm-Ho co-doped fibre is employed to exploit the favourable absorption properties of Tm^{3+}. The resonant energy transfer from Tm^{3+} to Ho^{3+} motivates the performance improvement of Ho^{3+} on laser emission at 2.1 μm.

RE Ions in ZBLAN Fiber. The main discussion of energy levels and spectra properties above is based on the RE ions in silica host. As we mentioned at the beginning of the section, although the silica host has outstanding properties on low loss, strong mechanical strength and mature fibre devices fabrication techniques, the high phonon energy limits the lasing wavelength to ~2 μm. With nearly half of the phonon energy, ZBLAN fibre attracts intense attention for the development of mid-IR as well as upconversion ultraviolet and visible fibre laser [44]. For mid-IR lasing with Er^{3+}, through ground-state absorption and ESA, energy-level transition $^4I_{11/2} \rightarrow {}^4I_{13/2}$ can

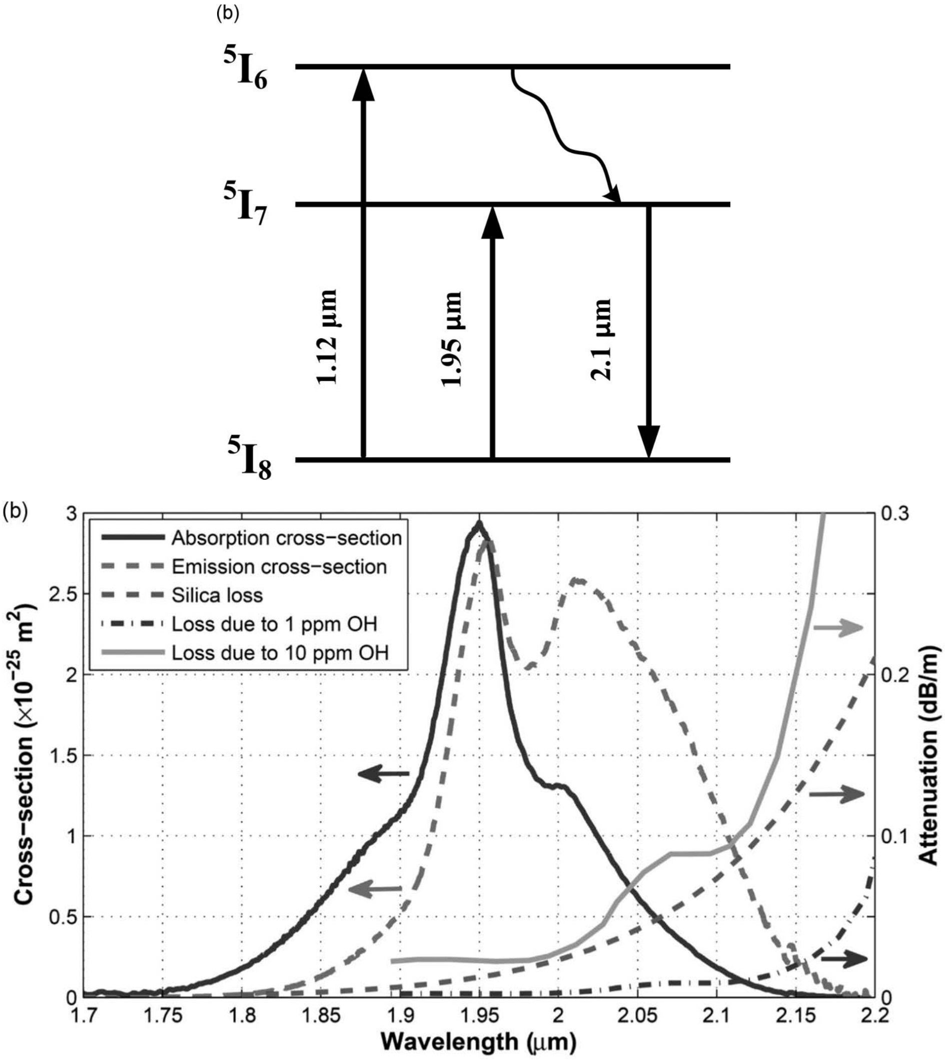

FIGURE 36.12 (a) The energy-level diagram, as well as common pump and lasing transitions of Ho^{3+} in silica host. (b) Absorption and emission cross-section of Ho-doped silica fibre in the wavelength range of 1.7–2.2 μm. The silica and hydroxyl absorptions in this wavelength region are also shown. (Reprinted with permission from Ref. [43], OSA.)

produce an emission of 2.7 μm, and $^4F_{9/2} \rightarrow {}^4I_{9/2}$ can produce an emission of 3.45 μm. For Ho-doped ZBLAN fibre, 2.9, 3.2, and 3.9 μm emissions can be achieved from the transitions, $^5I_6 \rightarrow {}^5I_7$, $^5F_4 \rightarrow {}^5F_5$, and $^5I_5 \rightarrow {}^5I_6$, respectively. Furthermore, RE ions such as Er^{3+}, Tm^{3+}, Ho^{3+} and Nd^{3+} have also been employed in the upconversion fibre laser [43]. Among them, an impressive result on CW ultraviolet laser operating at 284 nm has been achieved with Tm-doped ZBLAN fibre for transition between energy level $^1I_6$ and $^3H_6$ [45]. An output power of 42 μW was obtained at the pump power of 590 mW.

36.5 Laser Performance

Fibre lasers have built up a fruitful system with operating regimes including CW, Q-switched, mode-locked, single-frequency and wavelength-tunable. Some of these will be introduced in detail in companion chapters of this handbook. Here, to emphasize the unique properties of fibre lasers, a brief discussion of laser performance on three aspects of fibre laser operation is addressed, involving high-power fibre laser with MOPA configuration, mode-locked fibre laser, and single-frequency fibre laser with DBR structure.

RE-ion-doped glass fibre provides an outstanding gain medium for high-power lasers, due to the unique geometry of optical fibre, whose high surface-to-volume ratio allows for superior capability of heat dissipation under high-power condition. To achieve high laser power, fibre sources are generally realized with MOPA configuration as the bulk lasers in which a high-performance, low-power oscillator is served as the seed and followed by a series of amplifier stages to realized power scaling. The MOPA configuration provides an excellent solution for power amplification while preserving the desirable characteristics obtained from the seed. With the development of high-brightness semiconductor diode lasers, novel high-gain active fibres and high-power fibre components, output power of fibre lasers has reached 100 kW in multimode and 10 kW in single mode. As we mentioned above, the first 10-kW single-mode fibre amplifier was realized with MOPA configuration. The master oscillator provides an output power of 1 kW and then amplified under one stage of amplifier with 15 m of Yb-doped fibre. By using several hundred-watts fibre lasers at 1018 nm as the pump source, 10 kW output power in a single mode was demonstrated eventually.

Mode-locked fibre lasers capable of producing ultrafast laser pulses (picosecond and femtosecond pulses) with compact fibre configuration provide the peak powers several orders of magnitude higher than that in the CW mode. Development with robust and compact designs motivates the applications in the areas such as ophthalmology, micromachining, medical imaging and precision metrology [46]. As the commercially available fibre components allow for all-fibre mode-locked laser constructed via simple fibre splicing routines, nowadays commercialization of mode-locked fibre laser is gradually mature in the wavelength regimes of 1, 1.5 and even 2 μm.

Single-frequency fibre laser, which maintains the laser running with a single-longitudinal mode, has become an ideal laser source for the applications such as high-resolution spectroscopy, coherent lidar, and interferometric sensing due to the outstanding properties on low noise, narrow linewidth, and the resulting long coherence length [47]. Among the different configurations, distributed Bragg reflector (DBR) fibre laser, which combines a pair of narrowband FBGs with a short piece of RE-doped fibre, shows attractive properties on simplicity and compactness. With the development of soft glass fibres, which possess high RE-ion solubility, high optical gain coefficient of several decibels per centimetre can be achieved. This facilitates efficient operation of compact single-frequency DBR fibre lasers, where output power up to hundreds of milliwatts can be realized with ~2-cm long active fibre. With the DBR fibre laser as high-performance single-frequency seed, output power of hundreds of watt in a single-longitudinal mode has been presented in 1–2 μm with all-fibre MOPA configurations. Moreover, to meet the need of practical applications, such as coherent lidar, pulsed single-frequency fibre amplifiers have been demonstrated with pulse energy in the multi-joule level.

36.6 Future Prospects

Fibre laser technology has developed over 50 years with the laser performance improved significantly. In the family of lasers, fibre laser attracts great attention in recent years due to the unique properties on compactness, robustness and free of maintenance, which allows for it to displace some of the laser systems gradually. New operating wavelengths, higher power/energy, narrower linewidth (single-frequency), shorter pulse duration, and wider tunable wavelength range, have become the eternal pursuit for the development of fibre lasers.

Silica fibre has been maintaining the dominant place due to the superior mechanical and optical characteristics. High-power operation of fibre lasers still relies on silica glass host, while further power scaling requires to deal well with the photodarkening and mode instability effect. The former one is focused on the material itself in which optimization of glass component needs to be addressed. The later one can be taken as a result of the combination of photodarkening and waveguide structure. Therefore, strategies can also be directed to waveguide structure design and operating environment adjustment under high-power operation. Novel fibre-based functional devices, such as filter, multiplexer/demultiplexer, and saturable absorber, are deserved to be developed with the exploration of fibre structures to enrich the performance of fibre lasers. Furthermore, as the research in wavelength regime of 1–2 μm is maturing gradually, wavelength extension to mid-IR, visible and UV for fibre lasers are required to meet the need for practical applications. Alternative hosts with desirable mechanical and spectroscopic properties and corresponding fibre devices are anticipated to develop.

REFERENCES

1. Koester C J and Snitzer E 1964 Amplification in a fiber laser *Appl. Opt.* **3** 1182–6.
2. Optics.org. 2012. IPG set to ship 100 kW laser. http://optics.org/news/3/10/44.

3. Stiles E 2009 New developments in IPG fiber laser technology *Proceedings of the 5th International Workshop on Fiber Lasers*, Dresden, Germany: Fraunhofer-Institute.
4. Cheng M Y, Chang Y C, Galvanauskas A, Mamidipudi P, Changkakoti R and Gatchell P 2005 High-energy and high-peak-power nanosecond pulse generation with beam quality control in 200 μm core highly multimode Yb-doped fiber amplifiers *Opt. Lett.* **30** 358–60.
5. Stutzki F, Jansen F, Liem A, Jauregui C, Limpert J and Tünnermann A 2012 26 mJ, 130 W Q-switched fiber laser system with near-diffraction-limited beam quality *Opt. Lett.* **37** 1073–5.
6. Fang Q, Qin Y, Wang B and Shi W 2013 11 mJ all-fiber-based actively Q-switched fiber master oscillator power amplifier *Laser Phys. Lett.* **10** 115103.
7. Eidam T, Rothhardt J, Stutzki F, et al. 2011 Fiber chirped pulse amplification system emitting 3.8 GW peak power *Opt. Express* **19** 255–60.
8. Eidam T, Hanf S, Seise E, et al. 2010 Femtosecond fiber CPA system emitting 830 W average output power *Opt. Lett.* **35** 94–6.
9. Krauss G, Lohss S, Hanke T, Sell A, Eggert S, Huber R and Leitenstorfer A 2010 Synthesis of a single cycle of light with compact erbium-doped fiber technology *Nature Photon.* **4** 33–6.
10. Spiegelberg C, Geng J, Hu Y, Kaneda Y, Jiang S and Peyghambarian N 2004 Low-noise narrow-linewidth fiber laser at 1550 nm *J. Lightwave Technol.* **22** 57–62.
11. Fang Q, Shi W, Kieu K, Petersen E, Chavez-Pirson A and Peyghambarian N 2012 High power and high energy monolithic single frequency 2 μm nanosecond pulsed fiber laser by using large core Tm-doped germanate fibers: experiment and modeling *Opt. Express* **20** 16410–20.
12. Shi W, Fang Q, Zhu X, Norwood R A and Peyghambarian N 2014 Fiber lasers and their applications *Appl. Opt.* **53** 6554–68.
13. Zervas M N and Codemard C A 2014 High power fiber lasers: a review *IEEE J. Sel. Topics Quantum Electron.* **20** 1–23.
14. Mears R J, Reekie L, Jauncey I M and Payne D N 1987 Low noise, erbium-doped fibre amplifier operating at 1.54 μm *Electron. Lett.* **23** 1026–8.
15. Desurvire E 1994 *Erbium-Doped Fibre Amplifiers* (New York: Wiley).
16. Sudo S 1997 *Optical Fibre Amplifiers: Materials, Devices and Applications* (Boston MA: Artech).
17. Höfer S, Liem A, Limpert J, et al. 2001 Single-frequency master-oscillator fibre power amplifier system emitting 20 W of power *Opt. Lett.* **26** 1326–8.
18. Baney D M, Rankin G and Kok-Wai C 1996 Blue Pr^{3+}-doped ZBLAN fibre up-conversion laser *Opt. Lett.* **21** 1372–4.
19. Pask H M, Carman R J, Hanna D C, et al. 1995 Ytterbium-doped silica fiber lasers: versatile sources for the 1-1.2 μm region *IEEE J. Sel. Top. Quantum Electron.* **1** 2–13.
20. Miniscalco W J 2001 Optical and electronic properties of rare earth ions in glasses *Rare-Earth Doped Fibre Lasers and Amplifiers* 2nd edn ed M J F Digonnet (New York: Marcel Dekker) pp 17–112.
21. Tamura K, Nelson L E, Haus H A and Ippen E P 1994 Soliton versus nonsoliton operation of fibre ring lasers *Appl. Phys. Lett.* **64** 149–51.
22. Cauterts V, Richardson D J, Paschotta R and Hanna D C 1997 Stretched pulse Yb3+: silica fibre laser *Opt. Lett.* **22** 316–8.
23. Agrawal GP 1995 *Nonlinear Fibre Optics* 2nd edn (San Diego, CA: Academic).
24. Kashyap R 1999 *Fibre Bragg Gratings* (San Diego, CA: Academic).
25. Asseh H, Storoy H, Kringlebotn J T, Margulis W, Sahlgren B and Sandgren S 1995 10 cm long Yb^{3+} DFB fibre laser with permanent phase shifted grating *Electron. Lett.* 31 969–70.
26. Loh W H and Laming R I 1995 1.55 μm phase-shifted distributed feedback fibre laser *Electron. Lett.* **31** 1440–2.
27. Tamura K, Ippen E P, Haus H A and Nelson L E 1993 77-fs pulse generation from a stretched-pulse mode-locked all-fibre ring laser *Opt. Lett.* **18** 1080–2.
28. Jeong Y E, Sahu J K, Payne D N and Nilsson J 2004 Ytterbium-doped large-core fiber laser with 1.36 kW continuous-wave output power *Opt. Express* **12** 6088–92.
29. Khitrov V, Minelly J D, Tumminelli R, Petit V and Pooler E S 2014 3 kW single-mode direct diode-pumped fiber laser *Proc. SPIE* **8961** 89610V.
30. Fang Q, Li J, Shi W, et al. 2017 5 kW Near-diffraction-limited and 8 kW high-brightness monolithic continuous wave fiber lasers directly pumped by laser diodes *IEEE Photon. J.* **9** 1506107.
31. Snyder A W and Love J D 1983 *Optical Waveguide Theory* (London: Chapman and Hall).
32. Shimizu M, Yamada M, Horiguchi M, Takeshita T and Okayasu M 1990 Erbium-doped fiber amplifiers with an extremely high gain coefficient of 11.0 dB mW^{-1} *Electron. Lett.* **26** 1641–2.
33. Layne C B, Lowdermilk W H and Weber M J 1977 Multiphonon relaxation of rare-earth ions in oxide glasses *Phys. Rev. B* **16** 10–20.
34. Hanna D C, Percival R M, Perry I R, et al. 1988 Continuous-wave oscillation of a monomode ytterbium-doped fibre laser *Electron. Lett.* **24** 1111–3.
35. Delevaque E, Georges T, Monerie M, Lamouler P and Bayon J F 1993 Modeling of pair-induced quenching in erbium-doped silicate fibers *IEEE Photon. Technol. Lett.* **5** 73–5.
36. Han Q, Yan W, Yao Y, Chen Y and Liu T 2016 Optimal design of Er/Yb co-doped fiber amplifiers with an Yb-band fiber Bragg grating *Photonics Res.* **4** 53–6.
37. Yahel E and Hardy A A 2003 Modeling and optimization of short Er^{3+}/Yb^{3+} codoped fiber lasers *IEEE J. Quantum Electron.* **39** 1444–51.
38. Jackson S D 2004 Cross relaxation and energy transfer upconversion processes relevant to the functioning of 2 μm Tm^{3+}-doped silica fibre lasers *Opt. Commun.* **230** 197–203.
39. Creeden D, Johnson B R, Rines G A and Setzler S D 2014 High power resonant pumping of Tm-doped fiber amplifiers in core-and cladding-pumped configurations *Opt. Express* **22** 29067–80.
40. Ehrenreich T, Leveille R, Majid I, Tankala K, Rines G and Moulton P 2010 1-kW, all-glass Tm:fiber laser *Proc. SPIE* **7580** 758016.
41. Fu S, Shi W, Lin J, Fang Q, Sheng Q, Zhang H, Wen J and Yao J. 2015 Single-frequency fiber laser at 1950 nm based on thulium-doped silica fiber *Opt. Lett.* **40** 5283–6.

42. Herda R and Zach A 2013 All-fiber generation of few-cycle pulses at 1950 nm by triple-stage compression of a Thulium-doped laser system *IEEE Photonics Conference*, Bellevue, WA: IEEE, pp 621–2.
43. Simakov N, Hemming A, Clarkson WA, Haub J and Carter A 2013 A cladding-pumped, tunable holmium doped fiber laser *Opt. Express* **21** 28415–22.
44. Zhu X and Peyghambarian N 2010 High-power ZBLAN glass fiber lasers: review and prospect *Adv. OptoElectron.* **2010** 1–23.
45. El-Agmy R M 2008 Upconversion CW laser at 284 nm in a Nd:YAG-pumped double-cladding thulium-doped ZBLAN fiber laser *Laser Phys.* **18** 803–6.
46. Fermann M E and Hartl I 2013 Ultrafast fibre lasers *Nature Photon.* **7** 868–74..
47. Fu S, Shi W, Feng Y, et al. 2017 Review of recent progress on single-frequency fiber lasers *J. Opt. Soc. Am. B* **34** A49–62.

FURTHER READING

Agrawal G 2013 *Nonlinear Fiber Optics* 5th edn (San Diego CA: Academic).

Covers a range of non-linear optical processes that occur in fibres. It formats the foundation of the development of fiber lasers, such as mode-locked fiber lasers, Raman fibre lasers and Brillouin fibre lasers.

Digonnet M J F 2001 *Rare-Earth-Doped Fiber Lasers and Amplifiers* 2nd edn (New York: Marcel Dekker).

The most comprehensive treatment of fiber lasers, comprising a multiauthor collection of chapters each written by acknowledged experts, covering fabrication, spectroscopy, fiber components, silica and fluoride fiber lasers in various modes of operation and amplifiers.

Shi W, Fang Q, Zhu X, Norwood R A and Peyghambarian N 2014 Fiber lasers and their applications *Appl. Opt.* 53 6554–68.

The advanced progress in the area of fiber lasers is reviewed systematically with various regimes. Corresponding applications for different kinds of fiber lasers are addressed in detail.

Svelto O 1998 *Principles of Lasers* 5th edn (New York: Plenum).

Covers the basic principles of lasers. While not explicitly dealing with fiber lasers, it gives good coverage of material needed for an understanding of fiber lasers, such as the principles of optically pumped solid-state lasers and mode-locking of lasers.

Ter- Mikirtychev V V 2014 *Fundamentals of Fiber Lasers and Fiber Amplifiers* (New York: Springer).

More detail about different glass hosts and challenge for rare-earth-doped fiber lasers are introduced. High-power fiber laser and their industrial applications are also included.

Taylor & Francis
Taylor & Francis Group
http://taylorandfrancis.com

37

High-Power Fibre Lasers

Christophe A. Codemard and M. N. Zervas

CONTENTS

37.1 Introduction 489
37.2 Fundamentals 490
  37.2.1 Cladding Pumping 490
    37.2.1.1 Principle 490
    37.2.1.2 Cladding Absorption 490
    37.2.1.3 Brightness Enhancement in Cladding-Pumped Lasers 491
    37.2.1.4 Cladding-Pumping Schemes 491
  37.2.2 Active Ion Spectroscopy 492
  37.2.3 Fibre Laser Cavity Configurations 493
    37.2.3.1 Main Fibre Laser Configurations 493
    37.2.3.2 Diode Pump Sources 493
  37.2.4 Beam Quality 494
  37.2.5 Fibre Types 494
    37.2.5.1 Active Fibres 495
    37.2.5.2 Passive Fibres 496
37.3 High-Power Fibre Lasers 496
  37.3.1 Single Fibre, Single-Mode Continuous-Wave (CW) Output 496
  37.3.2 Challenges 497
References 498

37.1 Introduction

Fibre lasers [1] were proposed and studied as a promising laser configuration soon after the discovery and first laser demonstration by Maiman [2]. Ever since lasers have played a central role in the development of the rapidly expanding field of Photonics, which in turn has revolutionized existing, as well as, enabled entire new scientific and industrial sectors.

Lasers exploit the quantum effect of stimulated emission to generate light. Typically, they consist of an active medium to provide gain, an optical cavity to enhance and control the optical field and a pumping source to provide the energy [3]. In comparison to other laser technologies such as bulk-optic lasers based on gas-filled tubes, crystal rods and discs, fibre lasers can be monolithic, readily power scalable, highly efficient, simple and compact. With their large surface-to-volume ratio, fibre lasers provide better thermal management and total elimination of thermal lensing, which plagues solid-state crystal counterparts. In addition, the well-controlled spatial distribution of the signal, provided by the guidance of the fibre core, results in superior beam quality and stability, while small quantum defect, as well as, low cavity and transmission losses result in record wall-plug efficiencies.

Since fibre lasers are commonly based on rare-earth-doped silica glass doped core, they benefit from the glass amorphous nature that produces inhomogeneously broadened active-ion emission and absorption spectra, which are much wider than they would be in crystals [4]. This enables fibre lasers to be spectrally widely tuneable and to work efficiently from continuous-wave (CW) operation to ultrashort optical pulses. They show high gain, which enables master-oscillator power amplifier (MOPA) and cascaded amplifier configurations and makes them suitable for average power scaling. However, the small saturation energy, associated with the relatively small—compared to solid-state rod counterparts—fibre diameter compromises the energy storage capabilities and high energy operation.

Thanks to their unique attributes and features, fibre lasers have been fast increasing their penetration in all sectors of industrial, medical and directed energy application space while enabling numerous new applications. Over the last decade, the performance advances in fibre lasers have been spectacular making fibre lasers a successful, fast increasing commercial business currently worth over \$800M per year, with compound annual growth rate of about 13%—the highest among the different laser technologies. Key for the power scaling of high-power fibre lasers are developments in major technologies, such as high-quality passive and active fibres, high-power passive fibre components, including, beam combiners, fibre Bragg gratings (FBG), isolators, cladding mode strippers and end caps, and bright diode laser pump modules.

37.2 Fundamentals

Fibre laser based on silica glass consists generally of a core with a higher refractive index than the surrounded glass cladding that allows the signal to be guided and transported along the fibre length. Under optical pumping, the additional rare-earth dopants present in the core amplify the signal through stimulated emission.

37.2.1 Cladding Pumping

37.2.1.1 Principle

In his seminal paper [1] E. Snitzer states that "the major disadvantage (of the fibre laser) is that of getting the pump power into the fibre. However, it should be possible to overcome this difficulty with proper design of the fibre and the illuminating optics". Subsequently in 1988 E. Snitzer proposes an elegant solution to this problem in the form of cladding pumping [5] which has proven to be the most powerful enabling technique for power scaling fibre lasers.

In cladding pumping (see Figure 37.1), instead of launching the pump power into the highly restrictive in terms of size and numerical aperture (NA) active core, high-power low-brightness pump light is launched into the much larger in size (typically in the range of 50 μm to 1 mm diameter), and numerical aperture, cladding. As the pump light rays propagate down the highly multimoded fibre cladding they cross and get absorbed gradually by the active core, as shown schematically in Figure 37.1. However, the generated light is efficiently trapped inside the much smaller size and lower-numerical aperture core, and as a result the cladding-pumped amplifier or laser output is much brighter and intense. In this respect, cladding-pumped fibre lasers are extremely efficient brightness converters

The maximum pump power that can be launched into a circular fibre cladding is given by:

$$P_{\mathrm{p}}^{\mathrm{in}} = B_{\mathrm{p}}\left(\pi r_{\mathrm{cl}}^2\right)\left(\pi \mathrm{NA}_{\mathrm{cl}}^2\right) = B_{\mathrm{p}}\lambda_{\mathrm{p}}^2 N_{\mathrm{p}} \qquad (37.1)$$

The launched power is proportional to the brightness of the pump source (B_{p}), the square of the cladding radius (r_{cl}), and numerical aperture ($\mathrm{NA}_{\mathrm{cl}}$). Alternatively, the maximum launched pump power is proportional to the number of supported pump modes $N_{\mathrm{p}} = \frac{V_{\mathrm{cl}}^2}{2}$, where V_{cl} is the cladding V-number. Therefore, power scaling in fibre lasers relies on the development of high brightness pump modules, and fibres with high cladding NA and large cladding area. However, the launched pump power cannot be increased indefinitely due to limitations imposed by the practically achievable NA, the fibre dimension, the onset of non-linear effects and brightness of the pump source.

37.2.1.2 Cladding Absorption

The overall cladding-pumped fibre laser and amplifier length depends on the pump absorption coefficient (α_{CP}), which scales as $\alpha_{\mathrm{CP}} = \eta_{\mathrm{S}}\alpha_{\mathrm{co}}\left(\frac{A_{\mathrm{co}}}{A_{\mathrm{cl}}}\right)$, where α_{co} is the small-signal pump absorption when launched into the core, and as $\alpha_{\mathrm{CP}} = \eta_{\mathrm{S}}\alpha_{\mathrm{co}}\left(\frac{A_{\mathrm{co}}}{A_{\mathrm{cl}}}\right)$ is the doped core area. η_{S} is a coefficient, which defines the effectiveness of modal absorption of the various mode scrambling techniques. $\eta_{\mathrm{S}}=1$ implies that all cladding modes are excited equally, overlap equally with the doped core and are absorbed uniformly along the fibre length. This can only be achieved by a cladding shape that fully scrambles the pump modes [6] during propagation. To improve the overall pump absorption, several fibre designs have been proposed which break the cladding rotational symmetry and increase the fraction of cladding modes overlap with the active core. Equivalently, we can consider that these improved designs "scatter" skew rays towards the active core.

Figure 37.2 shows the most commonly used cladding-pumped fibre cross-sections. The pump NA is defined by the choice of the outer cladding material. Typically, these fibres use fluorinated polymer, fluorosilicone or Teflon outer cladding coating giving NAs of ~0.46–0.6. In this case, in high-power operation special cooling arrangements are required to avoid excess heating of the polymer. Fluorinated polymers are typically limited to operate in the range of 60°C–80°C. To overcome these problems, novel jacketed-air clad (JAC) fibre designs have been developed, which rely on a row of cylindrically arranged air holes to provide effectively a glass/air interface with NAs >0.8 [7].

The choice of the cladding perturbation should be considered judiciously to maximize mode scrambling while avoiding excess pump scattering loss. It was found, for example, that for the same material compositions, the effective NA of rectangular fibres is smaller than that of circular fibres and the pump light propagation loss in rectangular inner-cladding fibres is larger [8]. The cladding perturbation elements can be placed inside the cladding. This is the case in cladding pumped birefringent fibres where borosilicate stress-applying elements are inserted in the cladding to maintain the polarization of the

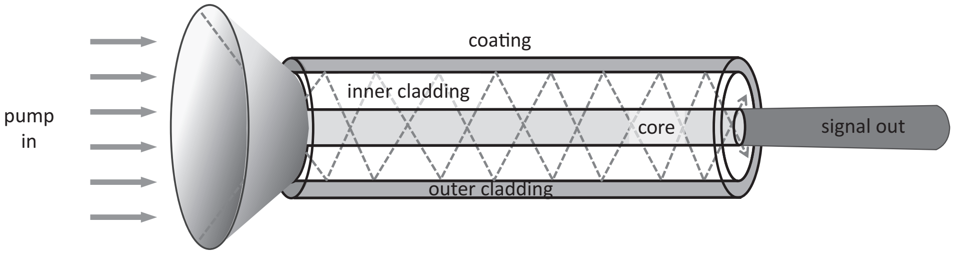

FIGURE 37.1 Schematic of cladding pumping principle of operation.

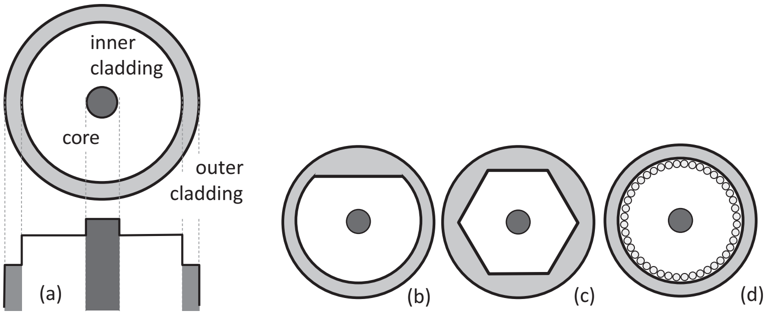

FIGURE 37.2 Cladding-pumped fibre cross-sections: (a) circular, (b) D-shape, (c) octagonal shape and (d) jacketed-air clad (JAC).

signal in the core. The low refractive index of the stress rod ensures that pump light will not be trapped in these elements, and their presence along with the applied stresses scrambles helical modes within the inner cladding [9].

In most practical cases, breaking the cladding cross-section rotational symmetry alone is not enough to absorb effectively the launched pump power over the entire fibre length and over all wavelengths. In order to increase the pump absorption close to its limiting value, given by core over cladding area ratio, the modes should be continuously mixed over the entire length, which is achieved by properly perturbing the fibre along its length [10], using periodic/quasiperiodic fibre bending [11] or fibre tapering [12].

Figure 37.3 plots the cladding pump absorption calculated by the beam propagation method, for a circular and octagonal shaped cladding of same area, with various coiling shape, as a function of length. It is shown that in the case without broken cross-section rotational symmetry and without periodic fibre bending, the absorption quickly saturates with fibre length. Mode mixing increases considerably the pump absorption and restores to large extend the absorption (in dB) linearity with length. In Ref. [13], it is also shown the higher absorption wavelengths saturate quickly than low absorption wavelength and thus require stronger mode mixing. This non-linear pump absorption effect affects the signal evolution and overall efficiency in fibre laser cavities. In practice, a fixed overall pump absorption results in highly non-uniform heat generation along the fibre length, with most of the heat generated over short length at the launching side.

37.2.1.3 Brightness Enhancement in Cladding-Pumped Lasers

Cladding pumping enables power scaling of the amplified signal with a beam quality output and provides extraordinary brightness conversion. The brightness enhancement factor is given by:

$$\eta_{\mathrm{B}} = \frac{B_{\mathrm{s}}^{\mathrm{out}}}{B_{\mathrm{p}}^{\mathrm{in}}} = \eta_{\mathrm{oo}} \left(\frac{\lambda_{\mathrm{p}}}{\lambda_{\mathrm{s}}}\right)^{2} \frac{\dfrac{V_{\mathrm{cl}}^{2}}{2}}{\dfrac{V_{\mathrm{co}}^{2}}{2}} \approx \eta_{\mathrm{oo}}^{*} \frac{N_{\mathrm{cl}}}{N_{\mathrm{co}}} \tag{37.2}$$

where $B_{\mathrm{s}}^{\mathrm{out}}$ and $B_{\mathrm{p}}^{\mathrm{in}}$ are the brightness of the output amplified signal (at the wavelength λ_{s}) and input pump (at the wavelength λ_{p}), respectively. $\eta_{\mathrm{oo}} = \dfrac{P_{\mathrm{s}}^{\mathrm{out}}}{P_{\mathrm{p}}^{\mathrm{in}}}$ is the optical-to-optical power conversion efficiency, where $P_{\mathrm{s}}^{\mathrm{out}}$ and $P_{\mathrm{p}}^{\mathrm{in}}$ are the output signal and input pump powers, respectively. N_{cl} (N_{co}) is the total number of cladding (core) modes (including degenerate spatial orientations and orthogonal polarizations). The maximum brightness enhancement factor is simply proportional to the ratio of the cladding pump mode to signal core mode numbers.

37.2.1.4 Cladding-Pumping Schemes

Over the years, a number of different cladding pumping schemes have been proposed in pursue for higher fibre laser output power. These schemes can be broadly classified into

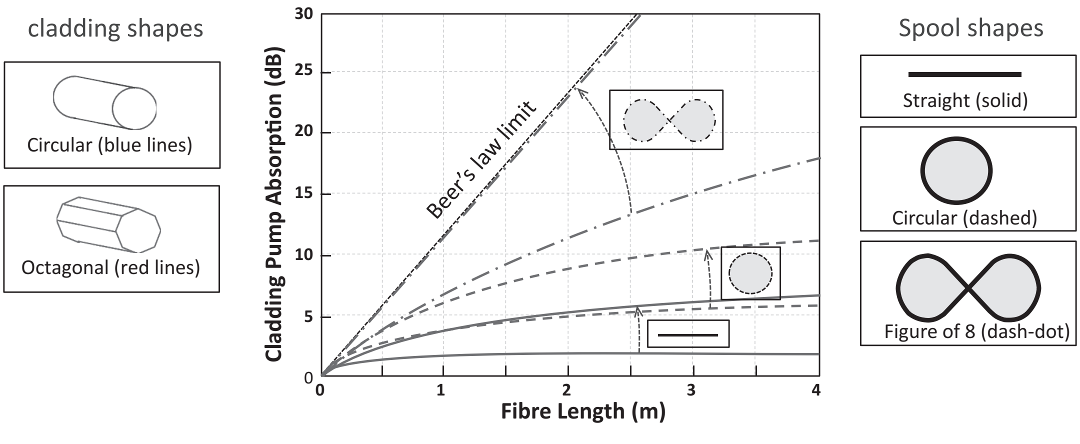

FIGURE 37.3 Effect of longitudinal mode mixing and wavelength on pump absorption.

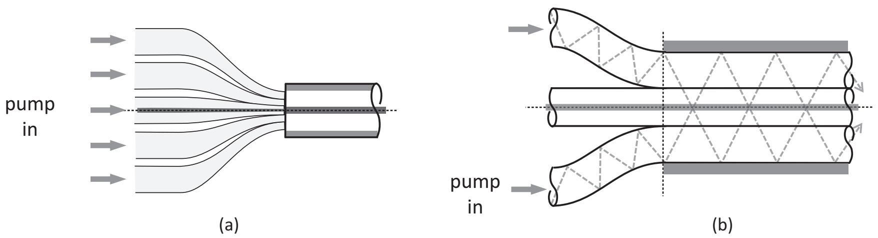

FIGURE 37.4 Cladding-pumping schemes (a) end-pumping with a taper fibre bundle (b) side-pumping.

two main categories of end-pumping and side-pumping. Figure 37.4 shows the main pumping technique used to-date in commercial industrial fibre laser. Figure 37.4a shows schematically the main end-pumping scheme based on tapered fibre bundles (TFB) [14]. The number of combined free space or fibre-coupled pump modules depends on the cladding diameter and NA and is restricted by the étendue conservation principle [13]. In the geometric combination schemes such as in Figure 37.4a, the brightness of the combined pump module is usually lower than the brightness of the contributing pump modules. It is equal in the lossless case.

In conventional end-pumping scheme the signal is usually injected into or extracted from the active fibre through a fibre that is intertwined with the pump-combiner fibres in a tapered fibre bundle. In a TFB, special care should be taken to minimize signal losses in the taper region and to thermally manage possible excess losses.

Figure 37.4b shows the most prevalent side-pumping technique based on a multi-fibre assembly in optical contact surrounded and held together by a common low-index polymer cladding, applied the usual way during the drawing (trade name GTWave™ [15]). Removing part of the polymer overcladding frees the individual fibre members, which then can be accessed independently. Such fibre assembly provides multiple ports for pump power to be injected into the cladding and be absorbed by the core of the optically coupled signal fibre. A variant of this scheme uses multiple bare pump and signal fibres fused together during the fibre drawing process. In the side-pumping schemes, the signal path is kept separate from the pump injection paths. This simplifies the optical design and enhances the overall laser robustness. In this pumping scheme, some pump brightness is lost because of the area of the additional signal fibre.

Finally, the side-pumping scheme, based on evanescently-coupled, has the additional advantage of distributing the pump power mode uniformly along the fibre length, resulting in better heat management.

37.2.2 Active Ion Spectroscopy

A number of rare-earth dopants have been incorporated successfully into silica optical fibres, using the modified chemical vapour deposition (MCVD) process [16], to form lasers. They include Nd^{3+}, Er^{3+}, Er^{3+}/Yb^{3+}, Yb^{3+}, Tm^{3+} and Ho^{3+} (see references within Ref. [13]). It is also possible to use different glass host [17]. From the extended range of dopants used in fibre lasers, we consider here only the Yb^{3+} ions in silica fibre, which so far have shown excellent power scaling with output powers exceeding 1 kW.

Yb^{3+} comprises a simple two-level system and provides efficient lasing around the 1 µm window. Figure 37.5a shows a typical energy diagram of Yb^{3+} ions in silica, with indicative sub-level Stark splitting. The exact sub-level splitting depends on the glass composition and Yb^{3+} concentration [18]. Figure 37.5b plots typical emission and absorption cross-sections in aluminosilicate and phosphosilicate fibres [19]. The emission and absorption spectra details and level lifetimes depend on the host material. Although phosphosilicate glasses reduce considerably the emission and absorption cross-sections, they allow for much larger dopant concentrations, without significant

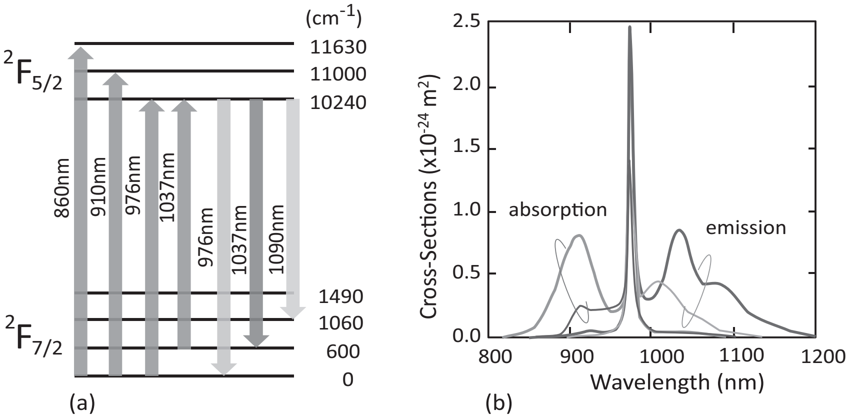

FIGURE 37.5 (a) Typical energy level diagram of Yb^{3+} ions in silica. (b) Typical emission and absorption cross-sections in aluminosilicate (thicker lines) and phosphosilicate (thinner lines) fibres. (From Ref. [13].)

clustering effects, and eliminate photo-darkening effects (see Section "Challenges"). The simplicity of the Yb^{3+} energy-level structure also eliminates other efficiency reducing effects, such as excited-state absorption, multi-phonon non-radiative decay and concentration quenching.

Yb^{3+} shows a broadband absorption spectrum, extending from ~850 to ~1080 nm, enabling multi-pump or multi-wavelength pumping schemes, which in turn facilitate power scaling. The broadband absorption spectrum also enables the use of broad linewidth unstabilized and low-cost pumps, simplifying the design and reducing the overall cost and long-term stability of high-power fibre lasers. Interestingly, the small but finite absorption in the 1010–1020 nm band enables in-band (or tandem) pumping with high brightness fibre lasers, which is key for the power scaling to multi-kW levels [20]. In addition, the broadband emission spectrum enables wide wavelength coverage and tunability, from 980 to about 1100 nm and short pulse (down to few 10s of fs) amplification.

37.2.3 Fibre Laser Cavity Configurations

The gain in fibre lasers is provided by fibres of various types with cores doped with active ions, such as ytterbium, erbium, thulium, or holmium. The cavity is formed either by bulk mirrors placed on either fibre end, or fibre Bragg gratings [21] written directly inside the fibre core. The pumping is achieved by combining laser diodes (single emitters, bars or stacks) and launching either in the core or cladding of the fibre using end- or side-pumping.

37.2.3.1 Main Fibre Laser Configurations

Several different configurations have been used for fibre laser demonstrations, depending on the active fibre and pumping technology availability.

The main fibre laser configurations are shown in Figure 37.6 for (a) an end-pumped and (b) side-pumped cavity. The laser cavity is formed by using a high reflector (HR) mirror with R >99% at one end of the active fibre in order to maximize the signal feedback to the cavity, and by a lower reflectivity output coupler (OC) on the other end for extracting the signal out of the cavity, as well as providing the signal feedback to the cavity. In Figure 37.6a, the mirrors are intra-core FBGs and the combined pumps are launched through the FBGs. This configuration puts extra stress on the FBGs as they are subjected to strong pump and signal power and special care should be taken to protect them. Finally, Figure 37.6b shows an all-fibre configuration with intra-cavity pump launching, which alleviates some of these issues. FBGs are usually written in single-mode fibres, which in addition to fixing the operating wavelength can also determine the output beam modality.

Free space mirrors can be used in high-power laser if the mirrors are butt-coupled or directly deposited onto the fibre facet. Such approaches are more suitable for multimode operation or for academic research. All fibre configurations as in Figure 37.6, on the other hand, are preferable if all the benefits of the fibre technology are to be harnessed, and such systems are currently deployed in most industrial fibre laser.

In some cases, some performance characteristics are not readily available directly from fibre laser oscillators, e.g. in terms of linewidth or pulse duration, which will require to use more complex configurations known as master-oscillator power-amplifier. In a fibre MOPA configuration, a seed laser is amplified in a cladding-pumped fibre optical amplifier to boost the output average/peak power while retaining the properties of the seed lasers. In a MOPA, the optical amplifier typically provides gain in excess of 10 dB, more generally about 20 dB, making it sensitive to back-reflections, as the backward propagating power is feedback into the oscillator. This can be alleviated by using an optical isolator after the amplifier.

37.2.3.2 Diode Pump Sources

The brightness of the semiconductor pump laser diode required for pumping fibre laser is typically achieved by spatially and polarization combination of single emitters coupled into a delivery fibre. The delivery fibre has typically a 105 or 200 μm diameter core with a 0.22 NA. There are small core size variations from vendor to vendor due to their brightness optimization between brightness of the single emitters and efficiency of the imaging coupling optics. The electrical-optical efficiency of fibre pigtailed high brightness laser diode can now exceed 60% [13]. Figure 37.7 shows the brightness against power from commercial laser diodes with 105 and 200 μm diameter core in the wavelength 915–960 nm and for 976 nm wavelength locked with a volume Bragg Grating (VBG).

The brightness from VBG-locked laser diodes follow the same trends as unlocked lasers diode albeit with a lower brightness because of the additional loss that occurs from the VBG and from the difficulty to wavelength locked a larger number of emitters.

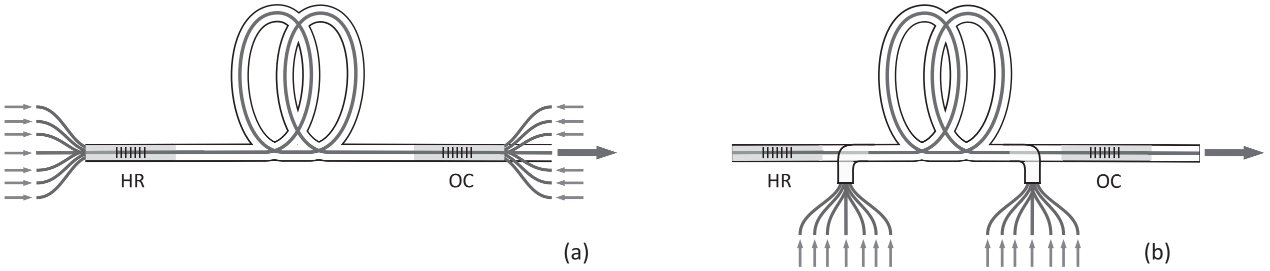

FIGURE 37.6 Cladding-pumped fibre laser cavity configurations (a) co- and counter end-pumped through TFBs (b) all-fibre side-pumped.

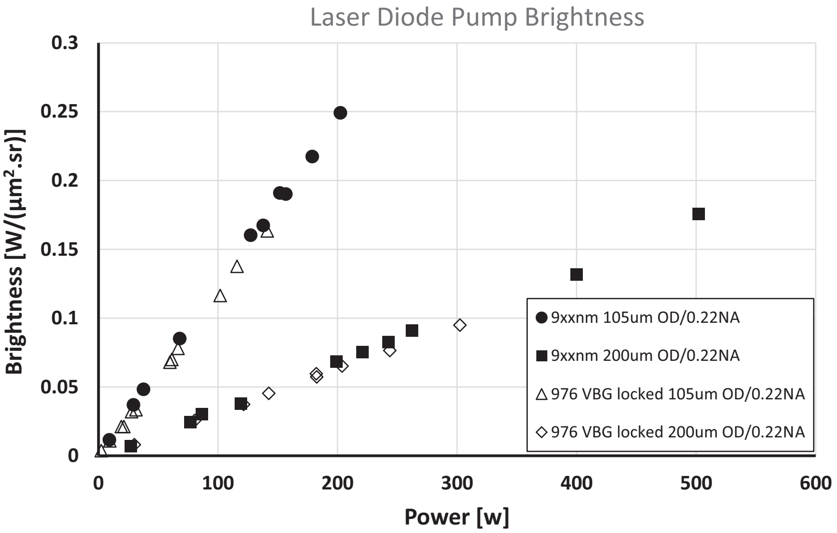

FIGURE 37.7 Brightness versus power of commercial multimode laser diodes.

37.2.4 Beam Quality

Laser beam quality can be defined in a number of different ways but the M^2 definition, based on the second moment of the beam intensity profile, is the most commonly used method [22]. From a practical point of view, though, the "quality" of a laser beam depends on the specific application for which the beam is intended for. The M^2 parameter denotes also how many times faster the beam diverges compared to a diffraction-limited Gaussian beam with the same waist diameter. Therefore, it can be defined as the ratio of the beam-parameter product ($\mathrm{BPP_B}$) of the beam in question divided by the $\mathrm{BPP_G}$ of a diffraction-limited Gaussian beam, namely,

$$M^2 = \frac{\mathrm{BPP_B}}{\mathrm{BPP_G}} = \frac{\omega_\mathrm{B}\theta_\mathrm{B}}{\omega_\mathrm{G}\theta_\mathrm{G}} = \frac{\pi}{\lambda}\omega_\mathrm{B}\theta_\mathrm{B}, \tag{37.3}$$

where ω_B and θ_B are the mode-field radius and far-field divergence of the beam. For diffraction limited, Gaussian beams $M^2=1$, while for any other practical beam $M^2>1$. The beam quality of a fibre laser output can be tailored by proper fibre design.

Figure 37.8 shows the M^2 variation, calculated by the second moment of the corresponding mode intensity profile, as a function of the normalized frequency (V number) of a step-index fibre, for different modes. The M^2 of the fundamental mode $\mathrm{LP_{01}}$ is shown to depart considerably from 1 for $V<1.5$. This is due to the increased evanescent extension into the cladding and departure from the Gaussian profile. It follows closely the $\mathrm{LP_{01}}$ mode-to-core radius ratio variation with V number, as approximated by the Marcuse formula [23]. The same behaviour is observed for all modes as they approach cut-off and their field extends deep into the cladding. The $\mathrm{LP_{pq}}$ mode can be defined by a same composite mode number $m=p+2q-1$, as in graded-index profile core [24]. Modes with the same composite mode number have the same propagation constant. Interestingly, the M^2 parameter is approximately ~m, even in step-index fibre, as shown in Figure 37.8. In the case of real fibres with complex refractive-index profiles (RIPs), the mode intensity distributions differ from the corresponding mode distributions of the step-index fibre and, therefore, show different values of M^2.

The M^2 of an incoherent multimode beam is given by the weighted average of the M^2 of the participating modes. In this case, the centroid of the beam is stationary. Using simple arguments applicable to multimode fibres [24], it can be shown that the weighted-average $\langle M^2 \rangle$ of a multimode beam can be approximated by $M^2 \approx \frac{\pi(2p_{\max}+1)}{12} = \frac{\pi}{12} + \frac{V}{3}$ where $p_{\max}=2V/\pi$ and both polarizations are counted [25]. The weighted-average $\langle M^2 \rangle$ is obtained when all supported modes are equally excited.

In practice, the number of modes and their relative power depends on the gain saturation level, their overlap with the active region and effective modal reflectivities [26]. For relatively low V numbers ($V<8$) the lower-order modes dominate and the M^2 remains small. For higher V-number fibres, though, the higher-order modes attain substantial power and the output beam quality approaches the equipartition $\langle M^2 \rangle$ value.

A drastically different situation arises in the case of coherent multimode beams in large mode area fibres. Even with large higher-order mode (HOM) content (e.g. 30% $\mathrm{LP_{11}}$) the resulting M^2 can be deceptively low ($M^2<1.1$), depending on the relative phase between $\mathrm{LP_{01}}$ and HOMs. However, significant changes in beam shape, peak intensity, and pointing stability can occur by varying the relative phase of the constituent fibre modes [27] such as when bending the fibre.

37.2.5 Fibre Types

High-power fibre lasers require the development of active and passive large mode area (LMA) fibres, in order to reduce peak intensities and diminish non-linear effects. In most occasions, these fibres end up being multimoded (MM), and they are operated in the single-mode (SM) or low-mode (LM) regime by introducing enough higher-order mode differential losses, without increasing significantly the fundamental mode

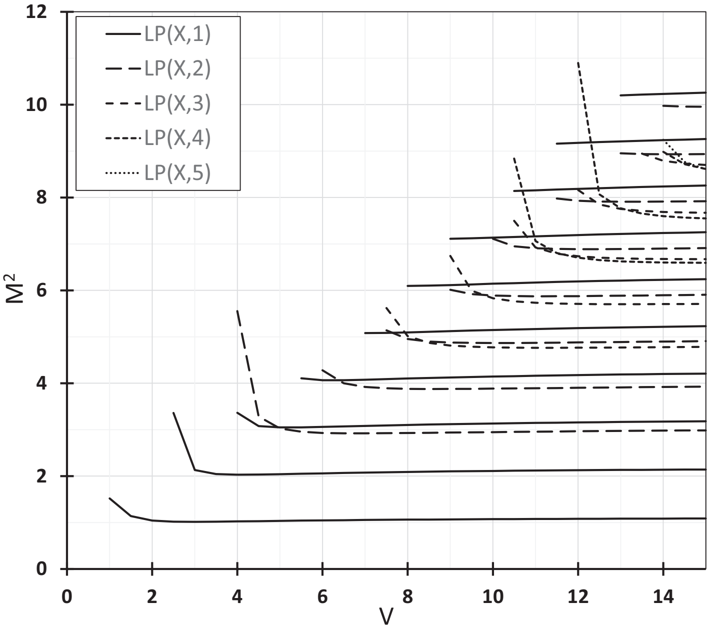

Modes	**M^2 LP_{pq} ~ (p+2q-1)**
LP_{72} LP_{91}	10
LP_{05} LP_{24} LP_{43} LP_{62} LP_{81}	9
LP_{14} LP_{33} LP_{52} LP_{71}	8
LP_{04} LP_{23} LP_{42} LP_{61}	7
LP_{13} LP_{32} LP_{51}	6
LP_{03} LP_{22} LP_{41}	5
LP_{12} LP_{31}	4
LP_{02} LP_{21}	3
LP_{11}	2
LP_{01}	1

FIGURE 37.8 Beam quality for different modes as a function of *V* number of step-index fibre, and their theoretical approximation.

(FM) loss. This becomes increasingly challenging as the fibre dimensions increase and the mode effective index differences decrease. Additionally, in the presence of unavoidable small external perturbations, such as fibre drawing or packaging-induced microbending, small modal effective index differences enhance modal cross-coupling between FM and HOMs. This results in efficiency and beam quality deterioration.

37.2.5.1 Active Fibres

In order to operate MM LMA or LM fibre in the SM regime, it is generally important to matching the fundamental mode at the input [28], either launching through a mode-field adapter (MFA) [29] or a mode matched splice. Intrinsic modality in multimode LMA fibres is generally controlled by properly engineering the gain and/or loss of the HOM in the core. Advanced fibre designs by tailoring the dopant distribution inside the core can provide gain and favour predominantly the fundamental mode [30]. For example, the core can be doped with active ions only in its centre in such a way to have good overlap with the fundamental mode but almost none with the HOMs. Mode selection can be enhanced by selective loss mechanism for the HOMs, for example by placing an absorber in the cladding that causes high losses to higher-order modes but almost no losses for the fundamental mode. In practice, HOM loss is provided by properly bending the fibre [31]. However, care should be taken to avoid excessive bending, which exceeds the safe bend-induced stresses level. This level depends on the fibre outer diameter. Depending on the core radius and NA in active fibres, bending does not always reduce modality or improves output beam quality. This is due to induced mode coupling, modal deformation and modal gain competition [32]. Furthermore, in high-power lasers and amplifiers short LMA active fibre lengths and small cladding diameters are needed in order to maximize pump absorption and minimize length-dependent non-linear effects. However, small cladding diameter and low-NA LMA fibres have the disadvantage of being extremely sensitive to external perturbations, which has adverse effects on efficiency and optical beam quality.

Another issue associated with low-NA, LMA active fibres is related to the uniformity of the refractive index across the core area. Making low NA, highly doped Yb^{3+} fibres requires high phosphorous concentration to increase dopant solubility. This, in addition to increasing the core refractive index, results usually in refractive index central dips due to uncontrolled phosphorous evaporation in MCVD fabricated fibres. Such refractive index feature can deteriorate the beam quality and power stability of LMA fibre lasers.

An alternative method has been demonstrated, which places much less stringent requirements on the MCVD process. Solid rod has been fabricated, with small index step and quasi-uniform doping to form the core region of a LMA photonic crystal fibre (PCF) laser, by repeated stacking and drawing of Yb^{3+}-doped and undoped silica. The ensemble therefore can form an effective-index medium with $V<1.3$. The composite doped rod has been then stacked along with silica capillaries to form a PCF in the usual manner [33]. Solid active fibres with similar novel core structures composed of small doped cores to give a LMA structure with a low effective core NA and without a central dip have also been demonstrated [34]. In another approach, based on PCF technology, by adjusting the hole size and spacing of the air-holes around the LMA doped core, effectively single mode operation has been achieved for core diameters up to 100 μm [35].

Fibre lasers based on gain-guided, index anti-guiding mechanism are another interesting approach to achieving LMA operation and power scaling. These waveguides, though, are fundamentally leaky and additional measures should be taken to manage the leaking power during high-power operation.

37.2.5.2 Passive Fibres

LMA passive fibres play an important role in the construction of high performance, high-power fibre lasers, particularly in delivering efficiently the generated power into the work-piece. In some applications, delivery fibres up to 10–20 m long are required or even longer. Optical power LMA delivery fibres should be designed properly to avoid excessive spectral broadening and onset of temporal instabilities due to non-linear interactions, such as stimulated Raman scattering (SRS), stimulated Brillouin scattering (SBS), self-phase modulation and four-wave mixing, as well as, beam quality degradation due to modal scrambling.

Standard step-index (SI) fibres with core diameters of ~30 μm and effective areas ~360 μm^2 can be SM at a 5 cm bending radius with numerical aperture (NA) of ~0.06, which is considered to be the lowest limit that can be achieved repeatedly and it is manufacturable with current fibre fabrication techniques. Recently, it was demonstrated possibility to use highly multimode SI fibres with core size of about 50 μm to transport near-diffraction limited beam ($M^2 \sim 1.3$–1.5) over several hundred meters thanks to careful adiabatic launch [36].

A number of different fibre designs have been proposed and experimentally demonstrated, which extend the fundamental mode area well beyond the SI capabilities. These fibres are fundamentally multimoded but utilize different techniques to filter out higher order modes (HOMs). An early example is the W-type fibre, which uses a refractive-index dip around the core to drive the second-order mode beyond cut-off into leakage [37] or LMA segmented-cladding fibres, which leak out HOMs [38]. Recently more advanced leakage-channel fibres (LCFs) have been demonstrated using a small number of air holes inserted in the silica cladding, providing differential loss for the higher-order modes. LCFs with core diameters in the range of 170 μm have been demonstrated, with effective areas in excess of 10 000 μm^2 [39]. In another approach, modal filtering is achieved by inserting small cores around the main multimode core, which are resonant to the higher-order modes. The HOMs are then leaking out of the main core through evanescent coupling [40].

Lately, state-of-the-art hollow microstructured fibres have been used for high peak power delivery. In such fibres optical non-linearities are contained effectively, since the vast majority of the power (>99%) is guided in air. Hypocycloid core Kagome lattice microstructured fibres have been used for delivering high beam quality, high peak power 500 fs, 1 mJ pulses over 10 m length, without beam quality degradation. The energy threshold damage was found to be >10 mJ, with output power density after focusing approaching TW cm^{-2}. This opens up the possibility of using such fibres for practical high peak power delivery.

37.3 High-Power Fibre Lasers

So far it is shown that that fibre technology is quite diverse and can provide an excellent platform for fabricating high performance laser systems. The core and cladding structures can be tailored appropriately to control the beam modality, optical non-linearities and scale-up the power.

37.3.1 Single Fibre, Single-Mode Continuous-Wave (CW) Output

Thanks to fibre technology advancements, the power of fibre lasers has increased over the years to reach unprecedented levels compared to other industrial lasers. Figure 37.9 shows the power evolution of single mode near diffraction-limited, low multimoded ($M^2 \sim 2$) as well as, multimode fibre laser outputs with time. Following the crash of the telecom “bubble” in 2000, new higher brightness pump modules were developed

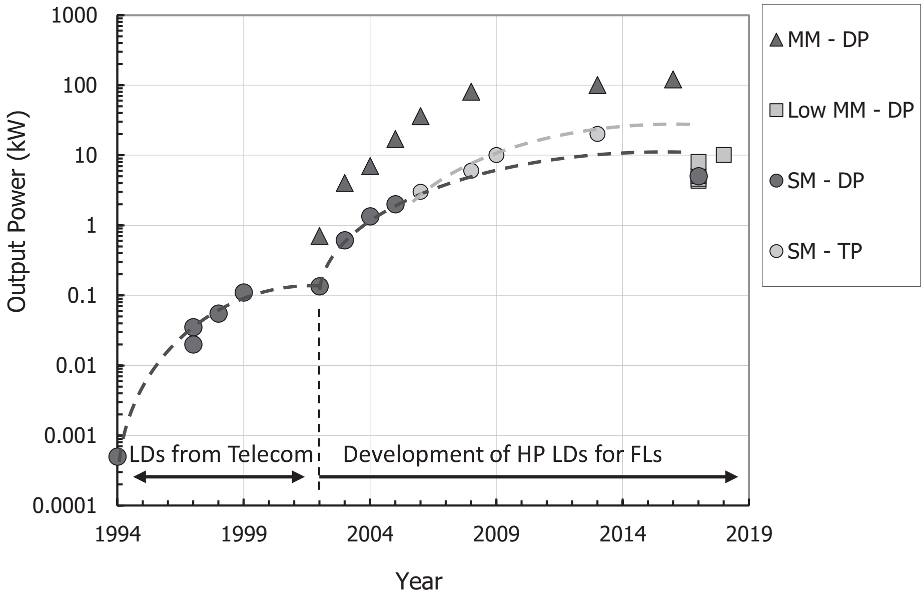

FIGURE 37.9 Power evolution with time from high-power Yb-doped cladding-pumped fibre lasers. MM-DP, multimode direct diode pumped; Low MM—DP, low M^2 (M^2~2) direct diode pumped; SM-DP, single-mode direct diode pumped; SM-TP, single-mode tandem pumped.

to address the fibre laser markets. This transition from low brightness diodes to combined high-brightness diode modules resulted to an sharp increase of single-mode outputs to 6 kW [20]. It has been predicted that if the fibre's MFD could be increased arbitrarily, about 36 kW [41] of diffraction-limited power could be obtained from single fibre lasers or amplifiers. This power limit is determined primarily by thermal and SRS effects. Recently, transverse mode instability (TMI) has been found to be the limiting factor for further power scaling of fibre lasers. This explains the curtailing of the output power from laser diode pumped SM fibre laser despite the pumps getting brighter at the same time. The brighter diodes pump can produce output power in excess of 10 kW but only with low multimoded beam.

A technique to reduce thermal effects and TMI, is to use tandem pumping where high-power high brightness fibre laser are combined together to pump a double clad fibre amplifier. With this approach the first 10 kW SM fibres were demonstrated using 1018 nm fibre laser as pump source [42]. Later, near diffraction-limited output has increased to reach 20 kW [43].

MM output has been achieved by geometric incoherent combination of SM outputs, and has currently reached the 120 kW level in industrial lasers. The main limitation of MM lasers is the electrical power available. Such power levels promise even higher fibre laser penetration into the industrial and directed energy application space.

37.3.2 Challenges

As mentioned above further fibre laser power scaling been hindered by a new non-linear effect, namely, transverse modal instability [44]. TMI in high-power lasers amounts to a sudden, threshold-like output beam fluctuation and beam quality deterioration above a certain power level. This threshold can be particularly low when large core diameter amplifying fibres are used, such as in the case of high peak power applications.

In high average power operation, the origin of this effect is predominantly thermal and a number of theoretical models have been introduced to explore the nature and investigate the characteristics of TMI. Theoretical models so far have considered the interaction of two propagating modes and studied the power exchange between the modes and TMI threshold through either Stimulated Thermal Rayleigh Scattering (STRS) static or dynamic mode interactions. It has also been shown that at small core diameters (<15 μm) and low output powers (<100 W), TMI is attributed predominantly to population inversion effects. In an alternative approach, TMI has been studied by considering the stability of the amplified fibre fundamental mode (FM) in the presence of transverse perturbations [45]. TMI, along with stimulated Raman scattering, pump brightness, and bend-induced mechanical reliability, is shown to be limiting the power scalability in high-power fibre lasers. The TMI power threshold is influenced by a number of fibre and laser system parameters, such as core/cladding diameter, dopant confinement, higher-order mode differential losses, photodarkening, choice of pump wavelength, pumping direction, input signal level, and gain saturation (see references within Ref. [45]). In addition, TMI power threshold is affected significantly by the seed coherence properties and linewidth. This dependence is more severe for larger core diameters [13].

Figure 37.10 shows the SM fibre laser power limits due to pump brightness, SRS and TMI, in the case of (a) diode pumping and (b) tandem pumping as a function of the fibre length and core diameter. It is shown that SM outputs in excess of 25 and 50 kW is achievable with diode and tandem-pumping, respectively. However, to achieve these power levels, new single-mode fibres with core diameters in the 45–55 μm range should be developed along with improved fibre manufacturing techniques.

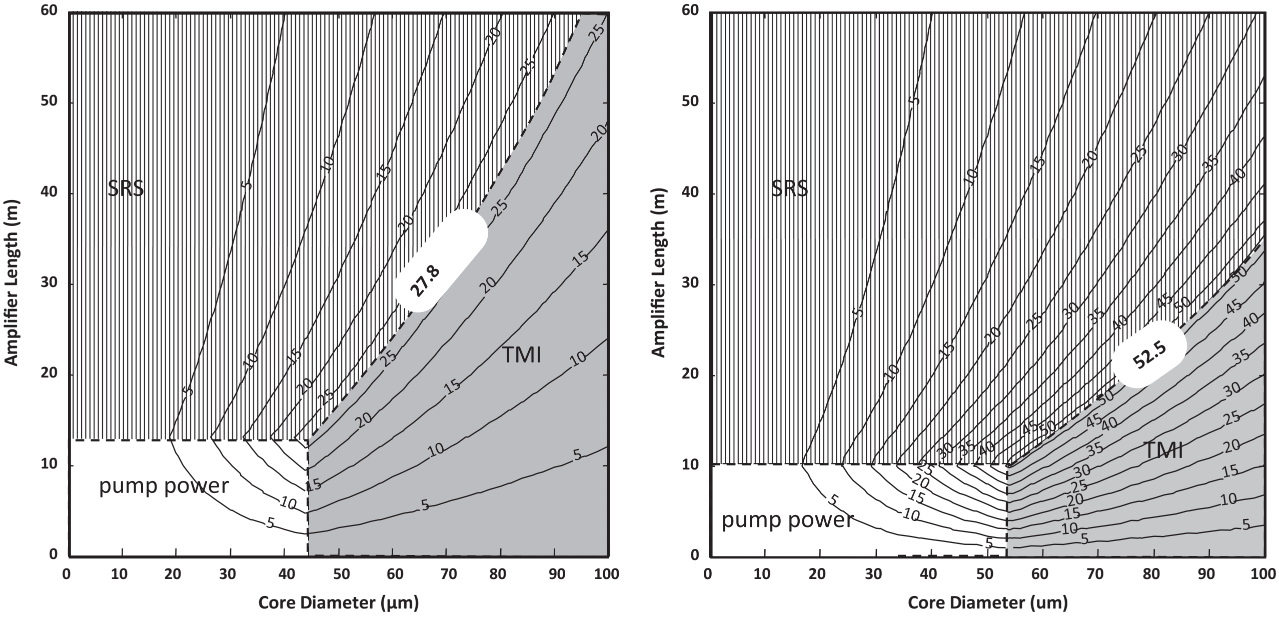

FIGURE 37.10 SM fibre laser power limits due to pump brightness, SRS and TMI, in the case of (a) diode pumping and (b) tandem pumping.

SRS can be mitigated by novel fibre designs that provide distributed or localized SRS filtering [46] or by developing novel glasses with tailored non-linear properties [47]. A number of experimental techniques have been demonstrated for increasing the TMI threshold in high-power fibre amplifiers. They include input signal dithering, and pump power modulation, in order to smear-out thermally generated index gratings. Lately, it has been shown that in the case of pump modulation, the TMI threshold shows a much more complex dependence on pump power and can actually be much lower than the CW case, indicating that relative shifts between the FM/HOM interference pattern and the induced refractive index long period grating can play a significant role in defining the onset of TMI. In an alternative approach, optical fibre lanterns have been used to apply appropriate phase shifts into and/or to control the amount of excited HOMs at the fibre amplifier input and have been proposed as a technique to mitigate TMI in high-power fibre lasers.

In addition, despite the tremendous progress, high-power fibre lasers based on Yb^{3+}-doped silicate glasses are known to suffer from light-induced optical losses, known as photodarkening (PD). Photodarkening also decreases considerably the TMI threshold. The optical losses are believed to be due to formation of colour centres in the glass matrix, which increase the background loss and reduce the output power. The exact colour-centre formation mechanisms are still under debate. There have been a number of studies showing that the PD rate and saturated level are dependent on the Yb^{3+} inversion [48]. The order of the inversion dependence, however, varies between 3.5 and 7. It has also been observed that photodarkening in LMA fibres is non-uniformly distributed over the fibre cross-section. The PD-induced loss is also non-uniformly distributed along the length of the active fibre, following closely a dependence to the calculated Yb^{3+} inversion to the power of 2. However, the occurrence of PD is entirely dependent on the materials composing the fibre core [49]. The Yb^{3+} concentration and co-dopants such as aluminium, phosphorous or cerium can reduce significantly or even eliminate PD [13].

REFERENCES

1. C.J. Koester and E. Snitzer, “Amplification in a fiber laser,” *Appl. Opt.* 3, 1182–1186 (1964).
2. T.H. Maiman, “Stimulated optical radiation in ruby,” *Nature* 187, 493–494 (1960).
3. A.E. Siegman, *Lasers* (University Science Books, CA, 1986).
4. E. Snitzer, “Glass lasers,” *Appl. Opt.* 5, 1487 (1966).
5. E. Snitzer, H. Po, F. Hakimi, R. Tumminelli, and B.C. McCollum, “Double-clad, offset core Nd fiber laser,” *Proc. Optical Fiber Communication Conf.*, paper PD5 (1988).
6. M.H. Muendel, “Optimal inner cladding shapes for double-clad fiber lasers,” *Conf. Lasers and Electro-Optics – OSA Tech. Dig. Series*, vol. 9, Washington DC, 1996, p. 209.
7. J.K. Sahu, C.C. Renaud, K. Furusawa, et al., “Jacketed air-clad cladding pumped ytterbium-doped fibre laser with wide turning range,” *Electron. Lett.* 37, 1116–1117 (2001).
8. A. Liu and K. Ueda, “Propagation losses of pump light in rectangular double-clad fibers,” *Opt. Eng.* 35, 3130–3134 (1996).
9. C. Pare, “Influence of inner cladding shape and stress-applying parts on the pump absorption of a double-clad fiber amplifier,” *Proc. SPIE* 5260, 272–277 (2003).
10. D. Gloge, “Bending loss in multimode fibers with graded and ungraded core index,” *Appl. Opt.* 11, 2506–2513 (1972).
11. J. Nilsson, S.-U. Alam, J.A. Alvarez-Chavez, et al., “High power and tunable operation of erbium-ytterbium co-doped cladding-pumped fiber lasers,” *IEEE J. Quantum Electron.* 39, 987–994 (2003).
12. V. Filippov, Y. Chamorovskii, J. Kerttula, et al., “Double clad tapered fiber for high power applications,” *Opt. Express* 16, 1929–1944 (2008).
13. M.N. Zervas and C.A. Codemard, “High power fiber lasers: a review,” *IEEE J. Select. Topics Quantum Electron.* 20(5), 219–241.
14. D.J. DiGiovanni and A.J. Stentz, “Tapered fiber bundles for coupling light into and out of cladding-pumped fiber devices,” U.S. Patent 5,864,644 (1999).
15. A.B. Grudinin, D.N. Payne, P.W. Turner, et al., “Multi-fibre arrangements for high power fiber lasers and amplifiers”, US patent 6,826,335 (2000).
16. S.B. Poole, D.N. Payne, and M.E. Fermann, “Fabrication of low-loss optical fibres containing rare-earth ions,” *Electron. Lett.* 21(17), 737–738 (1985).
17. W.C. Wang, B. Zhou, S.H. Xu, Z.M. Yang, Q.Y. Zhang, “Recent advances in soft optical glass fiber and fiber lasers,” *Prog. Mat. Sci.* 101, 90–171 (2019).
18. P. Barua, E.H. Sekiya, K. Saito, and A.J. Ikushima, “Influences of Yb^{3+} ion concentration on the spectroscopic properties of silica glass,” *J. Non-Cryst.* Solids 354, 4760–4764 (2008).
19. H.M. Pask, R.J. Carman, D.C. Hanna, et al., “Ytterbium-doped silica fiber lasers: versatile sources for the 1-1.2 μm region,” *IEEE J. Select. Topics Quantum Electron.* 1, 2–13 (1995).
20. D. Gapontsev, “6kW CW Single mode ytterbium fiber laser in all-fiber format”, *21st Annual Solid State and Diode Laser Technology Review*, p 258 (2008).
21. J-L. Archabault and S.G. Grubb, “Fiber gratings in lasers and amplifiers,” *J. Lightwave Technol.* 15(8), 1378–1390 (1997).
22. A.E. Siegman, “How to (maybe) measure laser beam quality,” in *DPSS Lasers: Applications and Issues*, M. W. Dowley, Ed. Washington, DC: OSA, 1998, pp. 184–199.
23. D. Marcuse, “Loss analysis of single-mode fiber splices,” *Bell System Techn.* J. 56(5), 703–718 (1977).
24. D. Gloge, “Optical power flow in multimode fibers,” *Bell System Techn.* J. 51, 1767–1783 (1972).
25. M.N. Zervas, “High power ytterbium-doped fiber lasers — fundamentals and applications,” *Int. J. Mod. Phys.* B 28(12), pp. 1442009-1–35.
26. Z. Jiang and J.R. Marciante, “Impact of transverse spatial-hole burning on beam quality in large-area Yb-doped fibers”, *J. Opt. Soc. Am.* B 25, 247–254 (2008).
27. H. Yoda, P. Polynkin, and M. Mansuripur, “Beam quality factor of higher order modes in a step-index fiber,” *J. Lightwave Technol.* 24, 1350–1355 (2006).
28. M.E. Fermann, “Single-mode excitation of multimode fibers with ultrashort pulses,” *Opt. Lett.* 23, 52–54 (1998).
29. Y. Jung, Y. Jeong, G. Brambilla, and D.J. Richardson, “Adiabatically tapered splice for selective excitation of the fundamental mode in a multimode fiber,” *Opt. Lett.* 34, 2369–2371 (2009).

30. J.R. Marciante, "Gain filtering for single-spatial-mode operation of large-mode-area fibre amplifiers," *IEEE J. Select. Topics Quantum Electron*. 15, 30–36 (2009).
31. J.P. Koplow, D.A.V. Kliner, and L. Goldberg, "Single-mode operation of a coiled multimode fiber amplifier," *Opt. Lett*. 25, 442–444 (2000).
32. R.T. Schermer, "Mode scalability in bent optical fibers," *Opt. Express* 15, 15674–15701 (2007).
33. W.J. Wadsworth, R.M. Percival, G. Bouwmans, J.C. Knight, and P.St.J. Russell, "High power air-clad photonic crystal fibre laser," *Opt. Express* 11, 48–53 (2003).
34. G. Canat, S. Jetschke, S. Unger, et al., "Multifilament-core fibers for high energy pulse amplification at 1.5 µm with excellent beam quality," *Opt. Lett*. 33, 2701–2703 (2008).
35. F. Di Teodoro, M.K. Hemmat, J. Morais, and E.C. Cheung, "High peak power operation of a 100µm-core Yb-doped rod-type photonic crystal fibre amplifier," *Proc. SPIE 7580, Fiber Lasers VII: Technology, Systems, and Applications*, p 758006 (February 17, 2010).
36. C. Röhrer, C. Codemard, G. Kleem, et al., "Preservation of Good Beam Quality over Several Hundred Meters in Highly Multimode Fibers," in *Advanced Photonics 2018 (BGPP, IPR, NP, NOMA, Sensors, Networks, SPPCom, SOF), OSA Technical Digest* (online), paper SoW4H.2, Optical Society of America (2018)
37. S. Kawakami and S. Nishida, "Characteristics of a doubly clad optical fiber with a low-index inner cladding," *IEEE J. Quantum Electron*. 10, 879–887 (1974).
38. V. Rastogi and K.S. Chiang, "Propagation characteristics of a segmented cladding fiber," *Opt. Lett*. 26, 491–493 (2001).
39. L. Dong, T.W. Wu, H.A. McKay, et al., "All-glass large-core leakage channel fibers," *IEEE J. Select. Topics Quantum Electron*. 15, 47–53 (2009).
40. J.M. Fini, "Design of solid and microstructure fibers for suppression of higher-order modes," *Opt. Express* 13, 3477–3490 (2005).
41. J.W. Dawson, M.J. Messerly, R.J. Beach, et al., "Analysis of the scalability of diffraction-limited fiber lasers and amplifiers to high average power," *Opt. Express* 16, 13240–13266 (2008).
42. E. Stiles, "New developments in IPG fiber laser technology," *5th International Workshop on Fiber Lasers*, Dresden, Germany (2009).
43. B. Shiner, "The impact of fiber laser technology on the world wide material processing market", *CLEO: Appl. Technol*., (2013).
44. T. Eidam, C. Wirth, C. Jauregui, F. Stutzki, F. Jansen, H.-J. Otto, O. Schmidt, T. Schreiber, J. Limpert, and A. Tünnermann, "Experimental observations of the threshold-like onset of mode instabilities in high power fiber amplifiers," *Opt. Express* 19(14), 13218–13224 (2011).
45. M.N. Zervas, "Transverse mode instability, thermal lensing and power scaling in Yb^{3+}-doped high-power fiber amplifiers," *Opt. Express* 27, 19019–19041 (2019).
46. X. Ma, I-N. Hu, and A. Galvanauskas, "Propagation-length independent SRS threshold in chirally-coupled-core fibers," *Opt. Express* 19, 22575–22581 (2011).
47. P.D. Dragic, M. Cavillon, J. Ballato, "Materials for optical fiber lasers: A review," *Appl. Phys. Rev*. 5, 041301 (2018).
48. J. Koponen, M. Söderlund, H. Hoffman, D. Kliner, and J. Koplow, "Photodarkening measurements in large mode area fibers," *Proc. SPIE* 6453, 64531E (2006).
49. S. Jetschke, S. Unger, A. Schwuchow, M. Leich, and J. Kirchhof, "Efficient Yb laser fibers with low photodarkening by optimization of the core composition," *Opt. Express* 16, 15540–15545 (2008).

Taylor & Francis
Taylor & Francis Group
http://taylorandfrancis.com

38

Raman Fibre Lasers

Igor Bufetov and Sergey Babin

CONTENTS

38.1 Introduction 501
38.2 Stimulated Raman Scattering and Scheme of Fibre Raman Laser 502
38.3 Optical Fibre as Raman Gain Medium 503
38.4 Operational Spectral Regions of Fibre Raman Lasers 504
  38.4.1 Silica Based RFLs 505
  38.4.2 Mid-IR Range Raman Fibre Lasers 506
  38.4.3 Mid-IR Gas Raman Fibre Lasers 507
38.5 Raman Fibre Lasers with Random Distributed Feedback via Rayleigh Backscattering 509
38.6 Raman Fibre Lasers Directly Pumped by Multimode Laser Diodes 512
38.7 Spectral Broadening 515
38.8 Conclusions 516
References 517

38.1 Introduction

Raman fibre lasers (RFLs) are based on a non-linear process of stimulated Raman scattering in optical fibres. RFLs are applied for a laser light generation at new wavelengths. At most cases, RFL converts a single-mode pump radiation into a single-mode output radiation at increased wavelength. However, it was recently demonstrated that an almost single-mode radiation can be generated by the RFL based on a multi-mode fibre. Moreover, this multi-mode fibre was pumped by a multi-mode radiation. Thus, RFLs can increase the brightness of radiation: the RFL output radiation is much brighter than the pump. In this respect, RFLs are similar to usual double clad rare-earth lasers. The value of the frequency shift of the RFL radiation with respect to the pump (the Raman shift) is mainly determined by three factors. Those are properties of the core material, properties of a pump radiation and the scheme of RFL. In particular, it is possible to increase the resulting value of the Raman shift with the use of a cascaded scheme of the RFL.

RFLs can be created using a standard scheme with an optical resonator, as well as using a single-pass scheme without a resonator (in the case of high Raman gain). Fibre Bragg gratings (FBGs) of refraction index in the fibre core are usually used as mirrors of fibre laser resonators. FBGs allow us to develop high-Q optical resonators based on low loss fibres. As a result, the threshold power of RFLs (P_{th}) can be reduced to tenths of a watt. Such values of P_{th} are usual for fibre lasers based on standard silica fibres.

The wavelength range of RFL operation is determined by the transparency band of the fibres used as Raman gain medium and by the availability of the pump sources with necessary properties. Currently, lasers based on silica, fluoride, tellurite, chalcogenide fibres, hollow core fibres filled with various gases and liquids were experimentally demonstrated. These lasers can generate in the wavelength range 360 nm–4.4 μm. The current maximal CW output power of a RFL is around 4 kW.

For silica fibres with minimal losses of 0.2 dB km^{-1} near 1.5 μm, it appears possible to obtain Raman lasing in ultra-long cavity (up to 270 km) with well-resolved longitudinal mode structure, but at further lengthening (~300 km) the mode structure is washed out. In this case, Rayleigh backscattering is responsible for positive feedback resulting in narrowband Raman lasing in such a long cavity. Further endeavours focused on Raman lasing based on pure Rayleigh backscattering-based random distributed feedback (RDFB) resulted in high-efficiency high-power generation in short (several hundred metres) fibre at appropriate pumping, which may be also broadly tunable at cascaded operation.

One of important features of Raman lasers is their relatively large spectral broadening. Due to long cavity, they are characterized by large values of both the group velocity dispersion and Kerr non-linearity. The number of longitudinal cavity modes is also large reaching millions in kilometres long RFL. To describe the spectral broadening in RFLs, the weak wave turbulence theory has been modified which treats non-linear interaction of multitude cavity modes at the presence of dispersion. As a result, the shape of generation spectrum is shown to be hyperbolic secant and its width grows non-linearly with power. Moreover, such a behaviour is similar in normal and RDFB cavities, where the modes have random phases and random frequencies, respectively.

38.2 Stimulated Raman Scattering and Scheme of Fibre Raman Laser

The first RFL was demonstrated in 1970 [1] with the use of a hollow core fibre filled with liquid. Soon the silica-based RFL was developed [2]. Afterwards, a large number of RFLs based on various types of fibres in a broad wavelength range (approximately 360 nm–4.4 μm) were demonstrated; see reviews [3,4].

Physical phenomena, which take place at spontaneous Raman scattering in a material medium, can be illustrated by the scheme Figure 38.1a. A photon with energy $\hbar\omega_P$ interacts with a material system in a ground state. The system has no absorption at the pump frequency ω_P. An exciting photon $\hbar\omega_P$ moves the system to the virtual energy level and afterwards the system returns to an excited level while emitting Stokes photon with energy $\hbar\omega_S < \hbar\omega_P$. An opposite process is also possible (Figure 38.1c). However, if a medium does not contain excited states, one can neglect this process of anti-Stokes scattering. As a Raman material medium one deals with core glass in ordinary fibres or with gas (or liquid) filling the hollow core fibre. In general, the Stokes photon can be scattered into any mode of a radiation field with probability of spontaneous scattering w_{sp}. But if a mode already contains n photons, then, according to Bose–Einstein statistics, the probability of the next photon scattering into this mode w_{n+1} is $(n+1)$-times more than the probability of spontaneous scattering.

$$w_{n+1} = (n+1) w_{sp} = w_{sp} + w_{st} \tag{38.1}$$

Thus, the probability of a spontaneous scattering w_{sp} of one photon to a mode is proportional to the flux of pump photons, i.e. $w_{sp} \sim I_P$. The second term in Equation (38.1) $nw_{sp} = w_{st}$ is proportional to the pump flux I_P and the flux of scattered radiation I_S: $w_{st} \sim I_P I_S$. This term is equal to the probability of the stimulated Raman scattering (Figure 38.1b). If this probability is greater than the probability of a photon loss (in other words, if a Raman gain is higher than an absorption of the medium), then the Raman laser generation is possible. The Raman shift between the frequency of pump and Stokes radiation is determined by the properties of the fibre core and can be within the range from tens to thousands of inverse centimetres. This provides a lot of opportunities for a laser radiation frequency conversion in the range from UV to mid-IR.

If the Raman gain coefficient of a fibre is high enough for sufficient conditions of a Raman laser generation to hold [5], then it is possible to reach the pump threshold power for RFL. Currently both RFLs with resonators and single-pass RFLs (without resonators) were developed. For example, in Ref. [6], the Raman conversion $1.064\,\mu\text{m} \rightarrow 1.239\,\mu\text{m}$ in a single-pass scheme (see Figure 38.2) was obtained. CW 1.064 μm radiation was launched into a high germanium fibre of length 0.5 km. The 1.239 μm radiation of the third cascade of stimulated Raman scattering was observed at the output of the high germanium fibre. The output power was up to 300 mW. This possibility was earlier considered in Ref. [7] (see Figure 38.2).

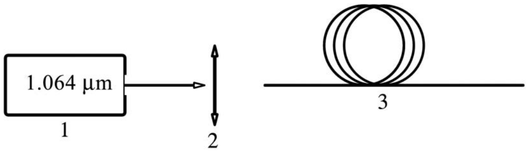

FIGURE 38.2 The RFL scheme for three-cascaded single-pass generation 1.064 → 1.239 μm. 1—CW Nd:YAG laser at 1.064 μm; 2—micro-objective; 3—fibre of 0.5 km length and 20 mol% concentration of GeO_2 in the core. (Adapted from Ref. [6].)

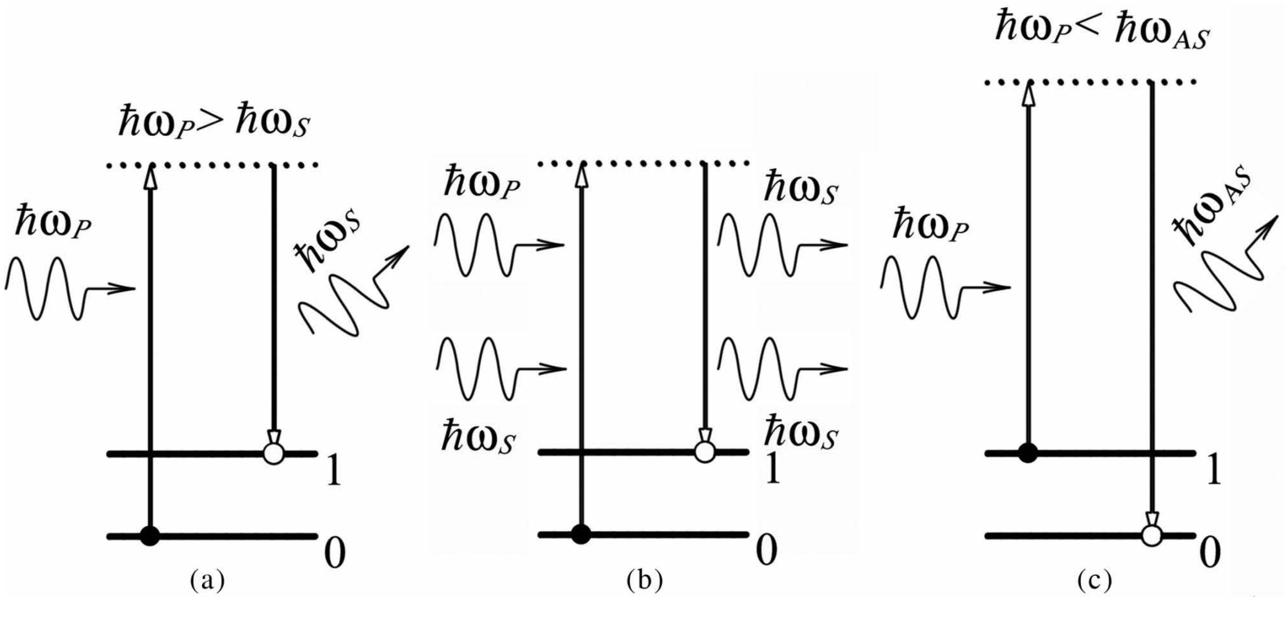

FIGURE 38.1 Raman scattering of light. 1—excited state of the system. 0—ground state. (a) Scheme of the spontaneous Raman scattering. (b) Scheme of the stimulated Raman scattering. (c) Spontaneous Raman anti-Stokes scattering. Dotted line: virtual states.

In Ref. [8], an all-fibre resonator scheme of RFL was demonstrated. This scheme then found wide applications in technology. The effective Raman generation was obtained there by using the cascaded Raman lasers with a system of nested resonators. FBGs written directly in the core of germanosilicate fibre [9] were used as mirrors of resonators (see Figure 38.4). The 800 m long germanosilicate fibre was used as a Raman gain medium. It enabled one to abruptly reduce the radiation losses in the scheme and to reach a high efficiency. The slope efficiency of the Raman conversion 1.06 μm → 1.24 μm was as high as 61%. The ytterbium double clad fibre laser was used as a pump source.

After that, 1.48 μm five cascaded Raman lasers based on germanosilicate fibres were developed [10]. The RFL efficiency was 38%, the slope efficiency was around 45%, the 1.48 μm output power was 1.5 W. More powerful lasers of similar scheme (output power 8.5 W, wavelength 1.472 μm, efficiency 47%) were demonstrated later in [11]. These experiments showed that Raman lasers with large number of cascades can be used for an effective Stokes components generation.

In the subsequent works, the output power of RFLs based on silica fibres in the near-IR range reached hundreds of watts (150 W, [12]) and even several kilowatts [13].

38.3 Optical Fibre as Raman Gain Medium

In the most simple case, the process of CW Raman conversion can be described in the following way [14]:

$$\frac{dI_S}{dz} = g_R I_P I_S - \alpha_S I_S \tag{38.2}$$

$$\frac{dI_P}{dz} = -\frac{\omega_P}{\omega_S} g_R I_P I_S - \alpha_P I_P \tag{38.3}$$

As typical for non-linear processes, essential parameters in these equations are intensities: intensity of pump radiation I_P and intensity of Stokes radiation I_S. The Raman gain properties of the medium are described by the Raman gain coefficient of

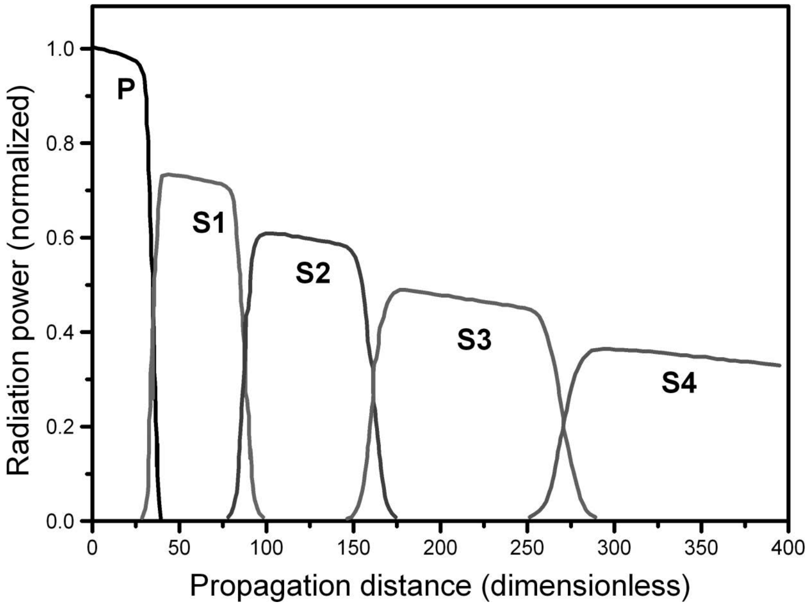

FIGURE 38.3 The cascaded generation of Stokes components of the Raman scattering under a pump radiation propagation through non-linear medium (single-pass scheme). P, pump power; S1–S4, corresponding Stokes powers [7].

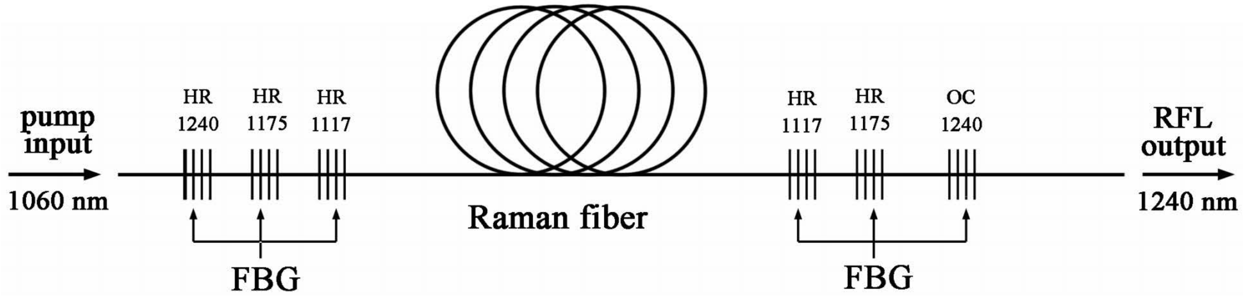

FIGURE 38.4 Scheme of three-cascaded RFL based on a germanosilicate fibre. (Adapted from Ref. [8].)

the medium g_R. Optical losses at the wavelength of pump and Raman generation are α_P and α_S. ω_P and ω_S are frequencies of a pump radiation and a Stokes component. g_R somewhat depends on the pump wavelength (in a rough approximation, $g_R \sim \omega_P$ [15]). Mainly, the behaviour of g_R is determined by the value of the Raman shift $\omega_P - \omega_S$. The spectrum of the Raman gain $g_R(\omega_P - \omega_S)$ for a fixed pump wavelength can be calculated with the use of the measured spectrum of the spontaneous Raman scattering [15]. For example, such a spectrum for silica is shown in Figure 38.5. Raman gain coefficients for fused silica at 440 and 490 cm^{-1} main maxima turned out to be around $g_R \approx 10^{-13}\,\mathrm{m\,W^{-1}}$ (pump wavelength 1.0 μm) [15].

RFL frequency shift (or a frequency shift in each cascade of a cascaded RFL) is in the vicinity of the Raman shift $\omega_P - \omega_S$ corresponding to the maximal value of $g_R(\omega_P - \omega_S)$ of the core material.

Equations (38.2) and (38.3) are written for one-cascaded Raman conversion. They can be easily generalized to the case of several cascades (see, e.g. Ref. [16]). In an active Raman medium is an optical fibre, Equations (38.2) and (38.3) can be written not for intensities but for the powers of pump and Stokes radiation propagating along the fibre:

$$\frac{dP_S}{dz} = g_0 P_P P_S - \alpha_S P_S \tag{38.4}$$

$$\frac{dP_P}{dz} = -\frac{\omega_P}{\omega_S} g_0 P_P P_S - \alpha_P P_P \tag{38.5}$$

Here, g_0 is the Raman gain coefficient of the fibre. It can be measured experimentally (see, e.g. Ref. [17]). One can find an expression for g_0 using Equations (38.2)–(38.5):

$$g_0 = \int_\Gamma g_R(\vec{r}) f_S(\vec{r}) f_P(\vec{r})\, ds(\vec{r}) \tag{38.6}$$

where $\vec{r}$ is a position in a cross section of the fibre Γ, the integral is taken over a whole cross section, f_S and f_P are normalized distribution functions of the pump and Stokes powers over a cross section of the fibre. $g_R(\vec{r})$ is a Raman gain coefficient of the core material at the Stokes wavelength. It often significantly depends on $\vec{r}$, e.g. due to a variation of the glass composition in the core. $ds(\vec{r})$ is an element of area in the cross section. If $g_R(\vec{r})$ is constant, then g_0 can be written as g_R/A_{eff}, where A_{eff} is the effective cross-sectional area of the fibre core determined with respect to the process of Raman amplification. In this case,

$$A_{\text{eff}} = \frac{1}{\int_\Gamma f_S(\vec{r}) f_P(\vec{r})\, ds(\vec{r})} \tag{38.7}$$

If $g_R(\vec{r})$ is not constant, A_{eff} cannot be uniquely determined.

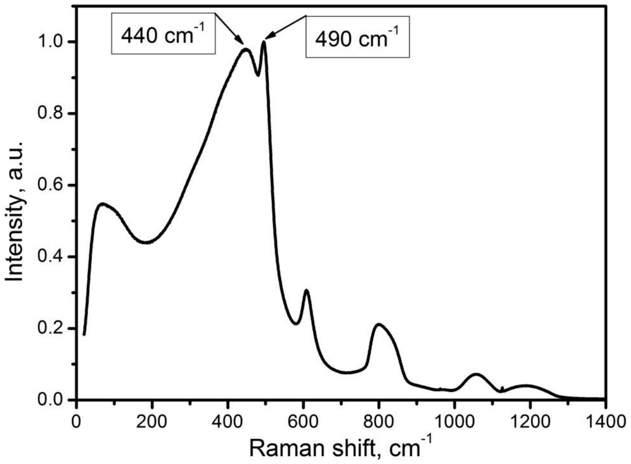

FIGURE 38.5 Spectrum of spontaneous Raman scattering in silica fibre (normalized).

Systems of equations which describe RFLs are typically solved by numeric methods (see, e.g. Ref. [18]). But using some approximations, it is possible to show that the quality of fibre as Raman gain medium can be analytically characterized by a single parameter P_F (kind of figure of merit, FOM). This parameter has dimensionality of power and is determined by properties of the fibre only [19]. The FOM of a fibre has a physical sense of the pump threshold power of the Raman laser based on this fibre with a high enough Q factor resonator. For a one cascade RFL, the FOM value P_{F1} has a simple expression:

$$\boldsymbol{P}_{F1} = \left(\sqrt{\frac{\alpha_0}{\boldsymbol{g}_0}} + \sqrt{\frac{\alpha_1}{\boldsymbol{g}_0}}\right)^2 \tag{38.8}$$

Equations (38.4), (38.5), and (38.8) imply that properties of a fibre as a Raman active medium for a one cascade RFL are determined by the fibre Raman gain coefficient g_0 and values of optical losses α_S, α_P. In the case of multi-cascaded RFL with N cascades the expression for FOM includes values of fibre Raman gains for each cascade g_{i-1}, optical losses at the pump wavelength α_P and at each of Stokes wavelengths α_{Si} (where i is a number of a cascade, $i = 1\ldots N$, see Ref. [19]).

The expressions P_F for two- and three-cascaded RFLs are more cumbersome and can be found in Ref. [19]. Expression (38.8) and analogous ones for multi-cascaded RFLs determine the contributions of optical losses at the pump wavelength and wavelengths of different Stokes components into FOM of a Raman fibre. This is especially interesting if fibre Raman gain coefficients and optical losses vary significantly in different cascades of RFLs.

38.4 Operational Spectral Regions of Fibre Raman Lasers

Most of the current RFLs use optical fibres of doped silica as a Raman active medium. With the help of such RFLs, a Raman generation is obtained in the entire transparency region of silica, from 360 nm to 2.2 μm. For RFLs intended for the operation outside this spectral band, optical fibres made of glasses having low optical losses in the corresponding spectral region are required. Figure 38.6 shows an approximate transmission and Raman gain spectra of such glasses. Fluoride, tellurite, and chalcogenide glasses a are transparent in parts of the mid-IR range and can be used for RFLs in these regions.

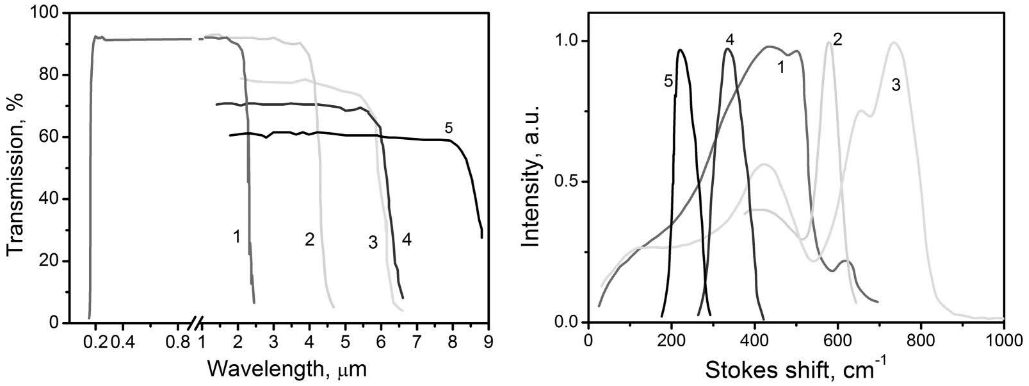

(a) (b)

FIGURE 38.6 (a) Transmission spectra of various types of glasses. (b) Normalized spectra of Raman gain for various types of glasses. Notation: 1—silica glass; 2—fluoride glass; 3—tellurite glass; 4 and 5—chalcogenide glasses, 4—As-S; 5—As-Se. (Data are taken from Refs. [20–22].)

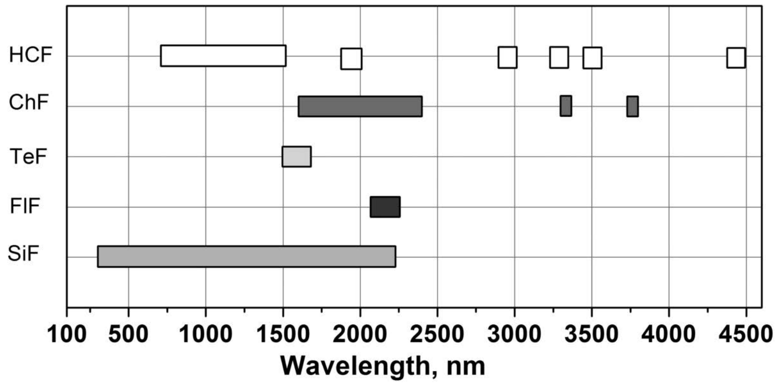

FIGURE 38.7 Wavelength ranges of RFL for various types of fibres. Notation: ChF, chalcogenide fibres; FlF, fluoride fibres; HCF, hollow core fibres, filled with gases; SiF, silica fibres; TeF, tellurite fibres.

Additional possibilities for a development of RFLs in the mid-IR range are provided by hollow-core optical fibres [23]. In this case, various light gases filling a hollow-core of the fibre are used as an active Raman medium [24]. Figure 38.7 shows wavelengths obtained by a generation of RFLs based on various types of fibres.

38.4.1 Silica Based RFLs

As an active Raman medium of RFLs in visible and near-IR regions silica communication fibres and specialty silica fibres are used. The former ones have extremely low optical losses in the near-IR. The latter ones typically have higher optical losses in the near-IR, but better suited for special Raman lasers, e.g. with a large Raman shift, operating in UV. All these fibres have silica core with various dopants, such as P_2O_5, GeO_2, B_2O_3, and even N_2. Dopants allow not only to design the core index profile, but also to change the spectrum and intensity of the Raman scattering. For example, a doping of the silica core with phosphorus oxide ($P_2O_5 + SiO_2$) results in an additional peak in Raman spectrum. The peak is shifted by 1330 cm^{-1} from the pump frequency. This enables the three-times reduction of the number of cascades in a RFL converting wavelengths 1.06 → 1.24 μm (and 1.06 → 1.48 μm), and, consequently, to simplify the RFL scheme and to increase its efficiency. Raman gain spectra of various types of fibres based on silica glass are shown in Figure 38.8.

Silica-based fibres have the maximal value of g_0 in the range 400–490 cm^{-1}. This determines the frequency shift between a pump and a generation in silica-based RFLs. The maximum of g_0 in the range 400–490 cm^{-1} is observed in all types of fibres shown in Figure 38.8. However, phosphosilicate fibres reveal an additional maximum of g_0 at the Raman shift of 1330 cm^{-1}. It appears due to the presence of the double bond P=O in the structure of phosphosilicate glass. Thus, phosphosilicate RFLs have a three-times higher Raman shift than germanosilicate RFLs. Moreover, phosphosilicate RFLs allows to have significantly different values of Raman shifts in different Raman laser cascades (in this case, ≈440 and ≈1330 cm^{-1}). This greatly enhances possibilities of RFLs. For example, in such a way a three-cascaded phosphosilicate RFL was developed for the 1062 → 1407 nm wavelength conversion [26]. The scheme of this laser is shown in Figure 38.9.

Ordinary communication fibres have the value of g_0 around 5 dB km^{-1}·W^{-1}) (see Figure 38.8, spectra 2 and 3). In comparison, high germanium doped fibres have a much higher g_0 value – approximately 40 dB km^{-1}·W^{-1}). A calculation of P_F shows that the FOMs of these fibres are roughly equal to each other. The increase of g_0 with the increase of GeO_2 concentration in the core is balanced by higher optical losses

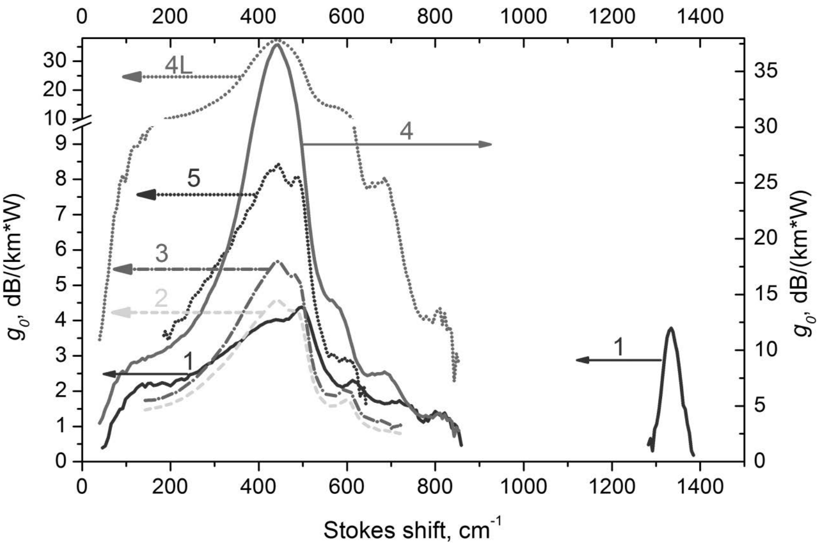

FIGURE 38.8 Spectra of the fibre Raman gains g_0 for various types of silica fibres. 1, P-doped fibre (≈10 mol% P_2O_5 in a core); 2, LEAF communication optical fibre; 3, NZ DSF communication optical fibre; 4L and 4, high Ge-doped fibre (≈25 mol GeO_2), left and right axis, correspondingly; 5, nitrogen doped fibre ($\Delta n \approx 0.01$). The data are obtained for the pump wavelength 1.24 μm. (Adapted from Ref. [25].)

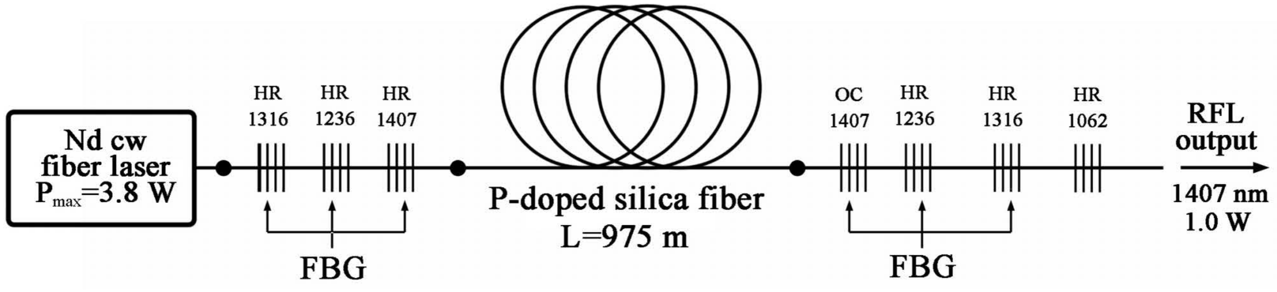

FIGURE 38.9 Scheme of the 1407 nm P-doped silica fibre-based Raman laser.

TABLE 38.1

Parameters of Certain Silica-Based Raman Fibres

	g_0 (dB km^{-1} W^{-1})	α_p (dB km^{-1})	α_s (dB km^{-1})	P_F (W)
$\lambda_p = 1407\,nm;\ \lambda_s = 1500\,nm$				
HGDF	18.9	1.46	1.06	0.265
NZ DSF	3.1	0.31	0.20	0.325
LEAF	2.8	0.34	0.24	0.411
$\lambda_p = 1229\,nm;\ \lambda_s = 1300\,nm$				
HGDF	23.3	2.03	1.63	0.313
NZ DSF	5.8	0.48	0.36	0.288
LEAF	4.8	0.49	0.36	0.352

(see Table 38.1, adapted from Ref. [17]). Therefore, the increase of GeO_2 doping does not result directly in a higher efficiency of RFLs. However, the use of high germanium doped fibres as a Raman medium enables one to reduce significantly the length of RFLs: the optimal value of the fibre for RFL can be as low as 3 m long [27].

Even more importantly, high germanium optical fibres have lower optical losses in the vicinity of 2 μm in comparison with silica fibres. For this reason, RFLs with lasing at wavelengths >2 μm (up to 2.2 μm) were developed using high germanium doped fibres [27].

Ordinary germanium doped optical fibres cannot be used for the RFLs in the UV. The presence in these fibres of germano-oxygen deficient centres with the maximum of the absorption band at 240 nm essentially increase optical losses in the short wavelength range [28]. Therefore, for UV RFLs, it is necessary to use special fibres with reduced optical losses in this region. For example, one can use silica fibres with a core doped with nitrogen (see Figure 38.8, spectrum 5). Using this fibre in a single-pass RFL scheme the Raman generation of 6 Stokes in the wavelength range 360–390 nm was demonstrated [29]. Note once more that currently most powerful RFLs (with output power up to kilowatts) with efficiency close to the quantum limit were developed using precisely silica fibres [13].

38.4.2 Mid-IR Range Raman Fibre Lasers

A possibility of a RFL development at a certain wavelength is determined by availability of (i) a low loss Raman fibre with a high fibre Raman gain coefficient at this wavelength (in other words, with a low value of P_F), and (ii) pump unit of required wavelength and power. High optical losses in silica-based fibres prevent the propagation of mid-IR radiation. For this reason, another types of glass optical fibres: fluoride, chalcogenide, tellurite fibres are used as active Raman media for this wavelength region.

Parameters of certain such fibres are given in Table 38.2. In the last row the data of a communication silica fibre (for the wavelength 1.5 μm) are given for a comparison. The last column shows P_F values of these fibres for a one cascade Raman conversion. One can see from the table that currently IR glass fibres have higher optical losses than silica fibres. However, chalcogenide glasses have much higher values of the Raman gain coefficient g_R compared to silica glasses. This balances the difference in FOM P_F values and in threshold pump powers of RFLs. Indeed, P_F for a certain fibre is a rough estimation of the threshold power of the RFL based on this fibre. A significant increase of P_F (up to tens and hundreds watts, see Table 38.2) is observed for chalcogenide fibres with large core diameter (65 μm). However, chalcogenide RFLs with a reduced core diameter have the threshold pump power significantly lower 1 W [33], and estimation for tellurite fibres gives values of the threshold power at the level of 10 mW. All this indicates a large potential of these types of fibres.

In the last several years a number of publications addressed fluoride and chalcogenide RFLs. Fluoride fibre RFLs demonstrated 3.7 W CW output power at the wavelength 1231 nm [35]. A two-cascaded RFL at the wavelength 3.77 μm was developed with the use of a chalcogenide fibre [36]. In comparison with tellurite fibres, fluoride and chalcogenide fibres have lower energies of phonons. For this reason, the transparency region of these fibres may be well beyond 5 μm. However, tellurite fibres in 2–5 μm region have a significantly higher fibre Raman gain coefficient and a significantly higher value of the Raman shift, which might help to reduce P_{th} and the number of cascades in a Raman conversion scheme.

All fibres from Table 38.2 have a Raman shift of the order of hundreds cm^{-1}. This means that RFLs based on these fibres need sources of pump radiation which do not differ much in wavelength. The longest wavelength glass RFLs in the mid-IR use as a pump unit an erbium fluoride fibre laser which generates at around 3 μm [30].

38.4.3 Mid-IR Gas Raman Fibre Lasers

Solid-core fibres made of soft glasses have some inevitable restrictions in terms of optical strength, resistance to thermal loads and humidity. This fact is a serious limitation for development of mid-IR non-silica fibre lasers, especially for high power and ultrashort pulse applications.

The development of hollow core microstructured optical fibres paved the way to RFL with gas as a Raman gain medium. An important advantage of such fibres is a possibility to use molecules of light gases with high energy of vibrational quanta. Raman shifts in such gases are as high as 4155 cm^{-1} (light hydrogen), 2987 cm^{-1} (deuterium), 2917 cm^{-1} (methane). All these values are much higher than the maximal Raman shift in glass fibres (1330 cm^{-1}). For example, one cascaded RFL based on vibrational transition in$^1H_2$ molecules can provide a wavelength conversion 1.06 → 1.9 μm. Starting with 1.56 μm one cascaded Raman conversion allows to directly obtain a laser generation at 4.4 μm. Therefore, a significant progress in mid-IR range Raman lasers can be achieved with the use of well-established near-IR fibre lasers as pump units.

For the first time HC-PCF RFL with the use of a vibrational transition in$^1H_2$ molecule (conversion 535HM → 683HM) was demonstrated in 2002 [24]. The hydrogen pressure in HC-PCF was 17 bar. RFL was pumped by a 6 ns pulse radiation. Hydrogen RFL can also use rotational transitions of the molecule. In this case, Raman frequency shift is 587 cm^{-1} [37]

Efficient SRS was also demonstrated in hydrogen-filled HCFs pumped around 1 μm [38,39]. In those works quantum conversion efficiency as high as 80% [38] and 60% [39] was achieved for Raman generation at 1.8 and 1.9 μm, respectively. Using 1.56 μm pump radiation, 4.4 μm RFL has been recently realized in similar scheme with molecules of the lightest hydrogen isotope $^1H_2$ (protium) as an active medium [40].

Hollow core optical fibres are mainly made of silica due to its excellent technological properties. The contribution of own optical absorption of silica to the optical losses of the hollow core fibre depends on a light localization mechanism of the fibre.

Note that the waveguiding mechanism of HC-PCF is based on a considerable penetration of radiation into the microstructured reflecting cladding on several periods of cladding structure. Thus, silica-based HC-PCF lose their excellent properties in the wavelength region $\lambda > 3$ μm. A substantial increase of silica optical absorption in this region results in an increase of optical losses in HC-PCF [41]. Therefore, an

TABLE 38.2

Comparison of Certain Soft Glass Fibres

Glass Type	Composition	Minimum Loss Achieved (dB km^{-1})	Raman Shift (cm^{-1})	Peak Raman Gain g_R at 3 μm (10^{-14}m W^{-1})	Core Diameter (μm)	P_F (W) (at ~3 μm)
Fluorozirconate [31]	ZrF_4, HfF_4, LaF_3, BaF_2, NaF, AlF_3	~1 (at 2.5 μm)	572	2.2	6.5	1.4 W
As_2S_3 [32]	As_2S_3	95 (at 3.4 μm)	340	125	65	235 W
As_2S_3 [33]	As_2S_3	100 (3.34 μm)	340	~125	4	~1 W
As_2Se_3 [32]	As_2Se_3	~200 (at 5 μm)	230	890	65	70 W
Tellurite [34]	-	20 (at 1.55 mm)	750	~570	2.2	0.01 W
Silica fibre (LEAF, [17])	$SiO_2 + GeO_2$	0.2 (at 1.55 μm)	440	~10 (1 μm)	13	0.5 W (at 1.5 μm)

Source: Adapted from Ref. [30].

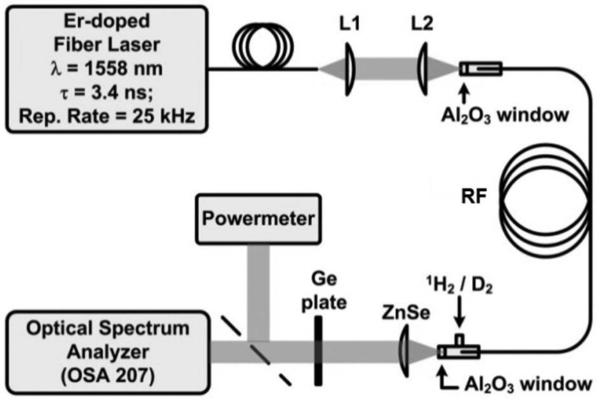

FIGURE 38.10 Scheme of the experimental setup. L1 and L2, aspheric fused silica lenses; RF, revolver fibre; Al_2O_3, sapphire windows of the gas cells at the HCF ends; ZnSe, collimating lens made of zinc selenide; Ge, 2-mm-thick germanium plate.

another type of HCF should be used for lasers in mid-IR. A good choice is HCF which use antiresonant waveguiding mechanism [42] and, additionally, have core cladding boundary with negative curvature [43]. In particular, hollow core revolver fibres meet these conditions well [41]. RFL-based on revolver fibres enabled one to generate a single-mode radiation at the wavelength 4.4 µm with quantum efficiency more than 50% [44]. This RFL was pumped by the ns pulse erbium fibre laser with average output power of 1 W. Its scheme is shown in Figure 38.10.

A cross section of the revolver fibre and the dependence of the average output power on the pump power are shown in Figure 38.11.

Raman lasers based on gas-filled revolver fibres can become a versatile tool for generation at new wavelengths in mid-IR, because various Raman-active gases and their mixtures can be implemented. For example, another hydrogen isotope, deuterium D_2, can be used to achieve Raman generation around 3 µm. Figure 38.12 shows an output spectrum of a RFL with revolver fibre filled with a mixture of $^1H_2$ and D_2. Its scheme is similar to the one shown in Figure 38.10, but the revolver fibre has a slightly different size of the cross section, that results in proper positions of transparency bands of the revolver fibre for 1.55 and 3 µm radiation. The radiation at the output of the laser contains the Stokes components that arise as a result of Raman generation on the vibrational and rotational transitions of both gases (Figure 38.12b).

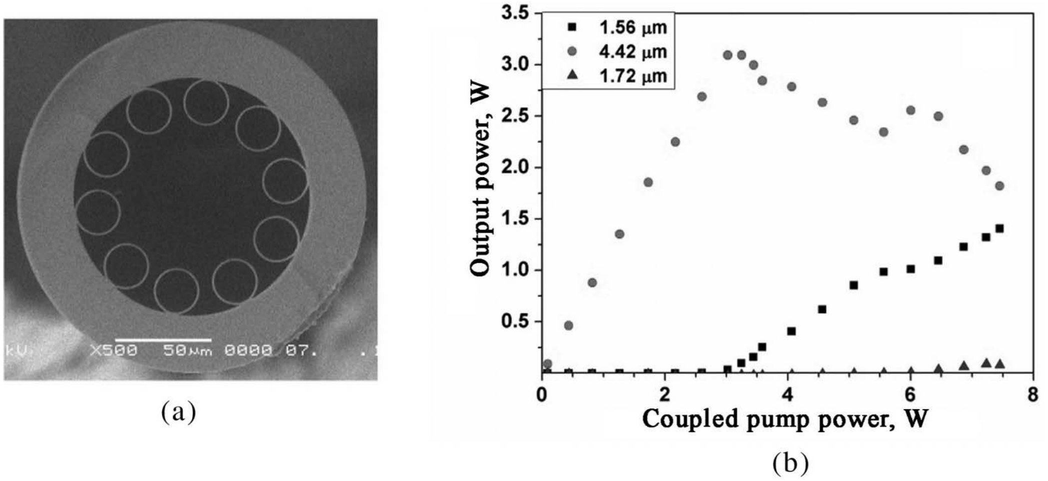

(a)

(b)

FIGURE 38.11 (a) SEM picture of the revolver fibre cross section. The hollow core diameter is 75 µm. (b) The average power at the RFL output vs. pump power launched into the hollow core. Red dots, non-converted pump $\lambda = 1.56$ µm. Black squares, vibrational Stokes radiation $\lambda = 4.42$ µm. Blue triangles, rotational Stokes radiation $\lambda = 1.72$ µm.

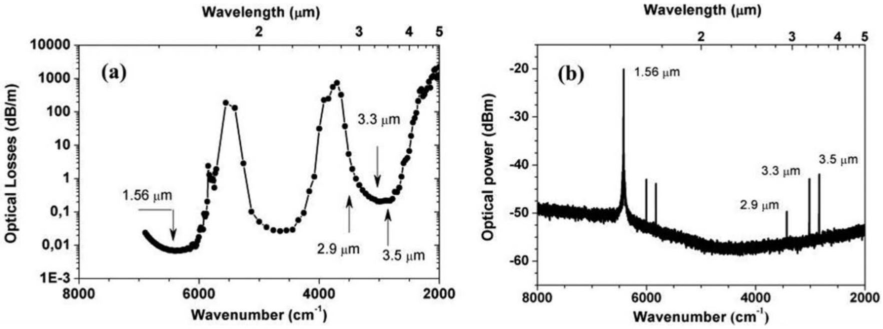

FIGURE 38.12 (a) Calculated spectrum of optical losses for revolver fibre that was developed to realize RFL for 2.9–3.5 µm spectral region. (b) Output spectrum of the gas RFL. Peak pump power at $\lambda = 1.56$ µm coupled into the revolver fibre core was 14 kW. A mixture of $^1H_2$ and D_2 at partial pressures of 2 and 28 atm, respectively, was used as an active medium.

38.5 Raman Fibre Lasers with Random Distributed Feedback via Rayleigh Backscattering

It is known that the lower limit for the loss coefficient in silica fibres $\alpha \sim 0.2$ dB/km is reached in telecom window around 1.55 μm (see Table 38.2). This value is defined by Rayleigh scattering on naturally present random refractive index fluctuations arising due to sub-micron irregularities of the silica glass structure. Such a low losses make it possible to increase the length of silica fibre Raman lasers with FBG cavity [9] operating at 1.55 μm to several hundred kilometres [45]. The measured radio-frequency (RF) spectrum exhibits beatings of longitudinal modes for the cavity lengths up to 270 km thus proving the formation of standing wave in such a long cavity. However, increasing the distance between the cavity FBGs beyond this value (to ~300 km) results in "washing out" the mode structure although the Raman lasing is still observed. It has been shown [45] that in such ultra-long RFL the distributed Rayleigh backscattering (~2×10^{-3} of scattered light comes back into the fibre) prevails the point reflection from the FBG at the opposite fibre end.

As a next step, a RFL operating completely via Rayleigh backscattering has been demonstrated in Ref. [46]. In this case, a conventional telecom fibre without any point reflectors (either FBGs or Fresnel reflection at the fibre end facet which was eliminated by its cleaving at an angle of >10°). Though the RDFB is very weak, it appears to be sufficient for lasing in a 80-km long passive fibre given that the integral Raman gain is proportional to the effective length and pump power. The threshold pump power at bi-directional pumping of two 40-km fibre arms from the centre is

$$P_{\rm in}^{\rm th}(\lambda)=\frac{1}{2}\times\frac{\alpha\exp(\delta_1)\left[\ln(1/R)+\alpha L\right]}{g_0(\lambda)\left(1-\exp\left[-\alpha L/2\right]\right)}. \tag{38.9}$$

where δ_1 is the pump coupling loss, L is the total length ($L/2$ is the length of one arm), $R \sim 2\cdot\times 10^{-3}$ is the integral Rayleigh back-reflection coefficient. The threshold power is estimated to be about 1.8 W for $L = 80$ km, this value is well confirmed by the measured threshold in the experiment [46]. Near the threshold, the RDFB Raman laser power and spectrum consist of irregular spikes, similar to those induced by double Rayleigh scattering in high-gain Raman amplifiers [47]. However, well above the threshold the spiky behaviour is changed to the quasi-continuous regime with constant power and smooth narrow spectrum localized near two main Raman gain spectral maxima (see Figure 38.13) (adapted from Ref. [46]). At increasing power, one peak becomes dominating, at that the generation linewidth (~1 nm) at –3 dB level becomes much narrower than the Raman gain bandwidth. Note that the measured RF spectrum has no longitudinal mode structure meaning that the generated spectrum is quasi-continuous consisting of the random frequencies.

The optical-to-optical efficiency of RDFB RFL may be evaluated in frames of the balance model [48]:

$$\eta=\frac{P_{\rm out}}{P_{\rm in}}=\exp(-\alpha L)\frac{\lambda_{\rm P}}{\lambda_{\rm S}}\left[1-\exp\left(g_0\left(P_{\rm in}^{\rm th}-P_{\rm in}\right)\frac{1-\exp(-\alpha L)}{\alpha}\right)\right]. \tag{38.10}$$

where $\lambda_{\rm P}$ and $\lambda_{\rm S}$ are the pump and Stokes wavelengths, $P_{\rm in}$ and $P_{\rm in}^{\rm th}$ are the input pump power and threshold pump power, respectively. Experimental test confirms the specific behaviour with exponential approach to the stationary value (see Figure 38.14) (adapted from Ref. [48]). This limiting value is defined by the linear attenuation along the fibre $\exp(-\alpha L)$ (taken equal for the pump and Stokes waves in the model). So, the efficiency may be increased by shortening the fibre if the pump power is enough to exceed the lasing threshold.

Another important feature is that the efficiency well above the threshold does not depend on the operating wavelength, as the formula (38.10) is almost independent of wavelength well above the threshold, $P_{\rm in} \gg P_{\rm in}^{\rm th}$. It was also checked in Ref. [48]

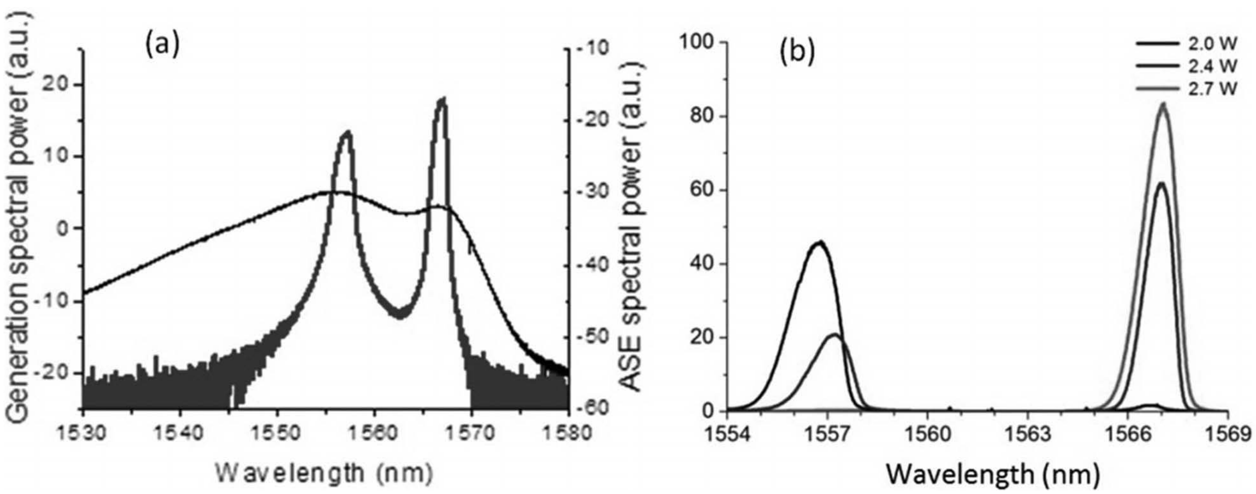

FIGURE 38.13 RDFB Raman fibre laser power spectrum below and above the threshold in logarithmic scale (a) and in linear scale at different output powers (b). (Adapted from Ref. [46].)

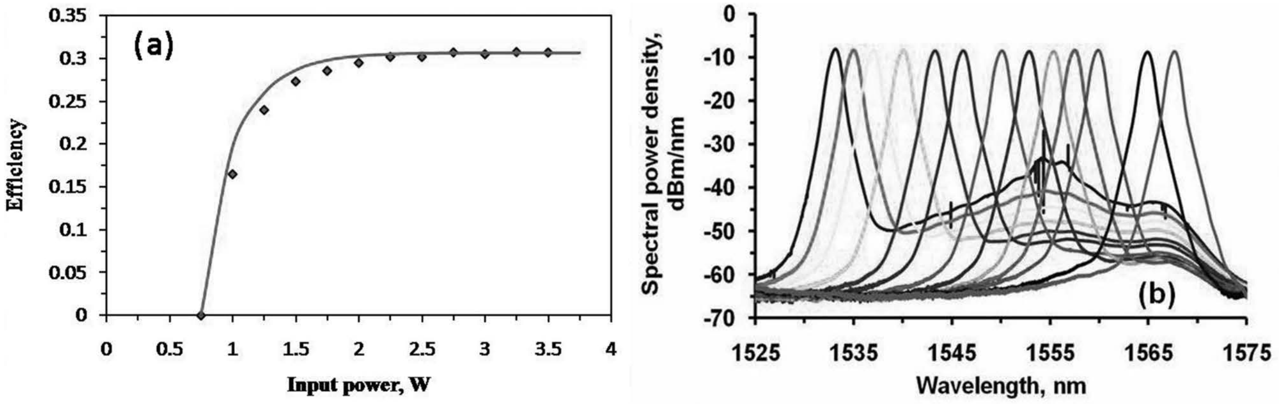

FIGURE 38.14 (a) The optical-to-optical efficiency η of RDFB Raman fibre laser with two 20-km arms as a function of one-arm input pump power (experimental points and fitting curve according to Equation (38.10)). (b) RDFB Raman fibre laser spectra at different wavelengths are shown at one-arm input pump power of 3 W. (Adapted from Ref. [48].)

that the inserting of a tunable filter in the scheme provides very flat tuning characteristic with power variation as low as 0.1 dB at laser tuning in the range 1535–1570 nm (see Figure 38.14). As power inside the RDFB Raman laser varies much strongly as compared to conventional RFL, the filter may be inserted in low-power part thus enabling high-power operation with the use of low-power filtering components. This approach was further applied for spectrum narrowing by means of Fabry-Perot spectral filter resulting in laser bandwidth reduction to 0.02 nm [49].

All the first experiments discussed above were performed in the symmetric scheme with two fibre arms and two pumps directed from the centre to the output ends, so that two pump and two output beams are co-propagating. Equivalent scheme may be realized with the use of only one arm and one highly reflective mirror instead of the second arm (so called half-open scheme) (see Figure 38.15). At that, the pump beam may be directed from the mirror to open fibre end as shown in figure (forward pumping), or from the output end to the mirror (backward pumping). As a highly reflective mirror, either broadband fibre loop or narrowband FBG or their combination with other spectrally selective or tunable elements may be used.

In the half-open scheme with backward pumping, a multi-wavelength operation of RDFB RFL has been also demonstrated with the use of FBG array with different wavelengths as a complex mirror. As a result, 22 lines separated by ~0.8 nm (100 GHz) nearly corresponding to ITU grid is generated in the range of 1552–1570 nm [50]. At that, a comparison of angled cleaved output end with normally cleaved output end (4% Fresnel reflection) shows that the RDFB scheme is more efficient (Figure 38.16a), suppresses the line competition and provides much better power equalization between the lines as compared with the conventional linear cavity (Figure 38.16b).

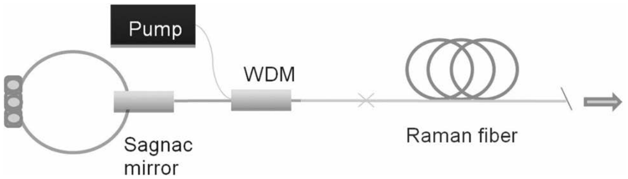

FIGURE 38.15 Half-open RDFB laser scheme with Sagnac mirror and forward pumping through WDM.

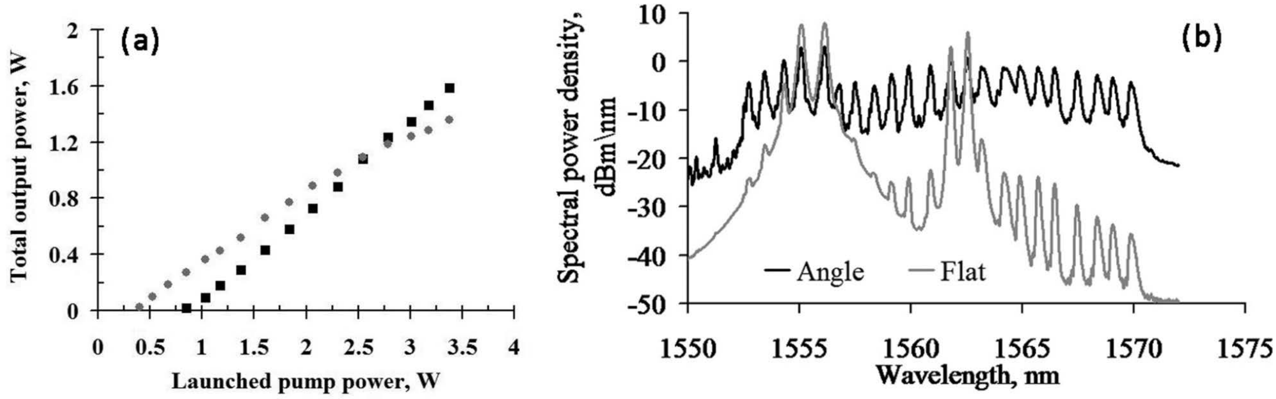

FIGURE 38.16 Output power of half-open RFL with an array of 22 FBGs and 20-km fibre as a function of backward pump power (a) and corresponding generation spectrum at 0.3 W output power (b) for RDFB cavity with angled fibre cleaving (black) and linear cavity with 4% Fresnel reflection from flat end (grey). (Adapted from Ref. [50].)

The half-open forward-pumped scheme (Figure 38.15) is the simplest one and enables higher efficiency with shorter fibres according to Equation (38.10). In such scheme with relatively short (800 m) P-doped silica fibre and fibre loop mirror, pump radiation of 10-W 1.1 µm Yb-doped fibre laser is converted into the 1.3 µm first Stokes radiation with optical-to-optical efficiency of more than 70% nearly corresponding to the pump attenuation in the fibre (Figure 38.17) [51]. The RDFB laser output power is well described by the balance model (red) and sufficiently differ from both the 4% linear cavity (green) and single-pass SRS generation (grey line) (see Figure 38.17b). Another sufficient difference of the RDFB laser scheme from the single-pass SRS generation shown in Figure 38.2, Figure 38.3 is a much narrower laser spectrum that is formed due to the random feedback (see e.g. Figure 38.13). Lengthening of P-doped fibre to 1.5 km in the same scheme and the same pumping level [52], results in second Stokes generation near 1.4 µm in the absence of nested FBG cavities necessary for cascaded operation of conventional RFL scheme shown in Figure 38.9. The conversion efficiency of pump to second Stokes radiation amounts to ~50% that also corresponds to fibre attenuation in the RDFB laser scheme.

Shortening of conventional (Ge-doped) silica fibre to 300 m [53] and then to 120 m in combination with one FBG [54] supported by corresponding increase of pump power, results in random Raman lasing with output power of more than 100 W at 1.17 µm with pump-to-Stokes conversion efficiency of 89%. Further increase of pump power coupled to large mode area (LMA) passive fibre enables the first Stokes Raman lasing in such scheme at 0.5 kW level with excellent beam quality and stability [55].

The RDFB RFLs employing conventional single-mode fibres (SMF) under depolarized pumping generate depolarized (or randomly polarized) light [46–55]. The first attempt to govern the polarization state of the random RFL explores linearly polarized pumping of SMF [56] that results in generation of partially polarized output radiation. The RDFB laser characteristics (threshold, output power, efficiency, and degree of polarization) appear to be significantly influenced by the polarization state of pump radiation. In the opposite case, depolarized forward pumping of a 500 m polarization-maintaining (PM) fibre in the half-open cavity configuration with a highly reflecting FBG connected to one fibre end [57] leads to generation of linearly polarized Stokes radiation with a 14 dB polarization extinction ratio (PER) at low output powers (<3 W) if special measures (strongly coiled piece of fibre inserted) are taken for the polarization selection. Herewith, the polarization state almost fully degrades (PER < 3 dB) when the output power approaches to 9 W, at that the maximum conversion efficiency is also rather low (~40%).

The half-open fibre configuration with Sagnac mirror (Figure 38.15) at linearly polarized pumping and all-PM performance enables generation of linearly polarized Stokes radiation with high PER (~25 dB) in the full range of the obtained powers [58]. Moreover, it exhibits superior stability and high optical efficiency (87%) at relatively low pump power (~10 W) that requires moderate (~500 m) PM fibre length. Using longer PM fibre (1 km) at the same pump level, efficient cascaded generation appears feasible [59] in such scheme with broadband fibre loop mirror (Figure 38.15) used instead of complicated nested FBG cavities in conventional cascaded Raman laser scheme shown in Figure 38.4. Nearly equal pump-to-Stokes efficiency for all Stokes orders has been obtained (amounting to about 70%), which corresponds to pump attenuation in such fibre. At that, higher orders appear at the output consequently at increasing pump power and/or fibre length taking also specific power distribution along the fibre in accordance with balance model (Figure 38.18), that is similar to that one at single-pass SRS (see Figure 38.3).

Further increase of fibre length and/or pump power in this PM fibre scheme results in generation of the next Stokes orders shifting the laser output to longer wavelengths [60], but the process stops near zero dispersion wavelength (ZDW) amounting to ~1.4 µm in silica fibres, where enormous spectral broadening of Stokes radiation prevents to the generation of the next Stokes orders. Similar effect has been observed in non-PM fibre scheme of cascaded RDFB Raman laser [61]. To overcome this problem, 2-km specialty SMF with ZDW

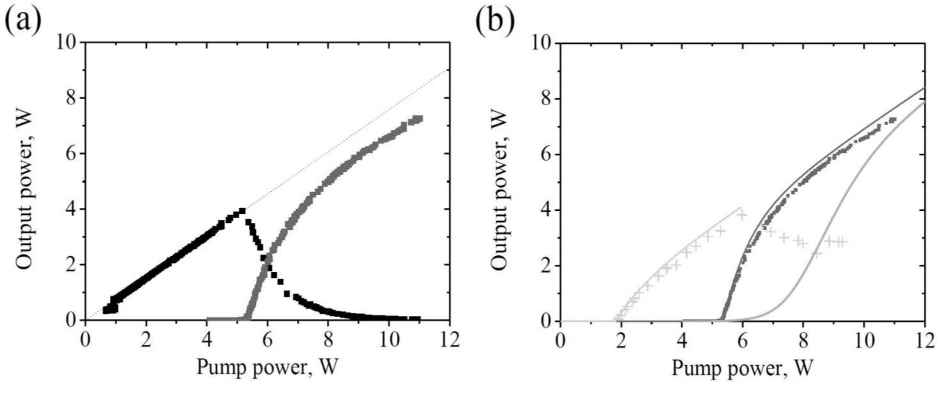

FIGURE 38.17 (a) The output power at 1308 nm (red points) together with the pump power at 1115 nm (black points). The dashed black line is the transmitted output pump power under assumption of Raman gain absence. (b) The comparison of the output power of the short random DFB fibre laser in experiment (red dots) and numerics (red curve) with the output power of the same system without random Rayleigh scattering feedback (grey curve, numerics) and with the output power of the laser with 4% broadband mirror (green crosses, experiment, and green curve, numerics). (Adapted from Ref. [51].)

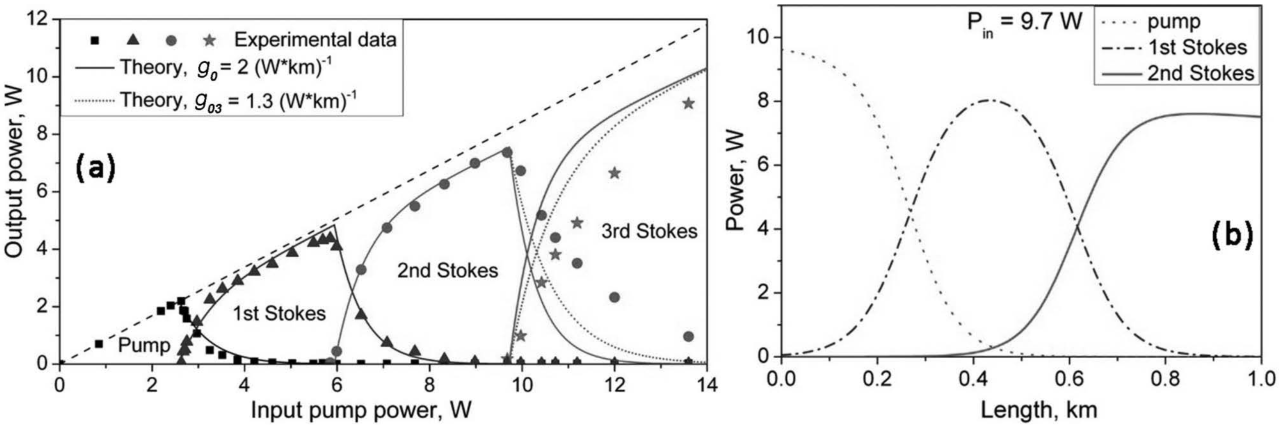

FIGURE 38.18 Output power of the cascaded PM RDFB Raman laser as a function of input pump power. Points correspond to experimental data for transmitted pump (squares) and generated first Stokes (triangles), second Stokes (circles) and third Stokes (stars) orders. Solid and dotted lines show the balance model calculated at Raman gain coefficients $g_0 = 2(\mathrm{m}\cdot\mathrm{W})^{-1}$ for all Stokes components and $g_{03} = 1.3(\mathrm{m}\cdot\mathrm{W})^{-1}$ for 3rd Stokes component, respectively (a). Corresponding power distribution at 9.7 W input pump power (b). (Adapted from Ref. [59].)

shifted to longer wavelength (~2 μm) has been explored [62]. Such RDFB fibre laser is shown to be continuously tunable from 1 to 1.9 μm (see Figure 38.19) utilizing ten Stokes orders of cascaded operation for rough tuning and tunable Yb doped fibre pump laser for fine tuning.

Another possibility to avoid the problem of ZDW at cascaded operation in RDFB Raman laser scheme with single broadband mirror is to use P-doped silica fibre with large P-related Stokes shift that makes possible to "jump" over the ZDW area. It has been demonstrated in Ref. [63] that such laser with 700-m PM fibre is able to generate 9 W at 1515 nm with PER of 27 dB and ~50% pump conversion efficiency when pumped by linearly polarized 1080-nm Yb-doped fibre laser.

Another important development of RDFB fibre laser regimes includes its pulsed operation via internal intensity modulation [64], active [65] or passive [66] Q-switching, and quasi mode locking of random modes [67]. More details about physical principles, operation regimes and potential applications of random fibre Raman lasers one can find in review papers [68,69].

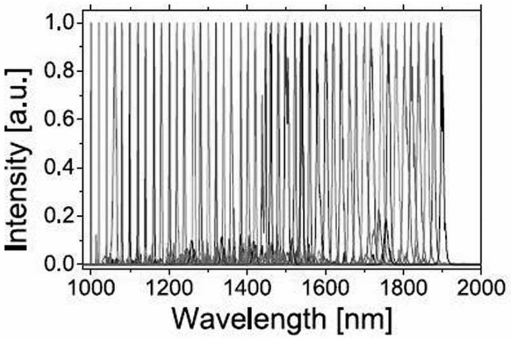

FIGURE 38.19 RDFB Raman laser spectra plotted for every 20 nm at tuning from 1 to 1.9 μm. (Adapted from Ref. [62].)

38.6 Raman Fibre Lasers Directly Pumped by Multimode Laser Diodes

As discussed above, RFLs are usually pumped into the passive fibre core by rare-earth (RE) doped fibre lasers (mostly Yb-doped ones) operating in fundamental transverse mode. In their turn, high-power RE-doped fibre lasers are usually cladding-pumped by multimode laser diodes (LDs). Such complex pumping scheme leads to a rather complicated design of RFLs. An interesting possibility to simplify the RFL design is its direct pumping by cheap and reliable high-power multimode LDs, similar to the LD-pumped RE-doped fibre lasers [70]. To continue the analogy, it is possible to employ cladding pumping, but this technique requires development of special double-clad passive fibres. In this way, Raman lasing at 1120 nm with output power of 100 W and beam quality parameter $M^2 \sim 1.6$ was demonstrated with a multimode YDFL as a pump source [71], whereas at direct diode pumping only 6 W output power was obtained [72].

From technical and economical points of view, it is more attractive to use standard graded-index (GRIN) multimode fibres which currently have high quality and low cost due to their wide use in telecom. In this case, one can directly couple the multimode radiation of high-power LDs into the multimode GRIN fibre core. In addition, using commercially available multimode LDs with operating wavelengths of 915–940 nm, it is possible to obtain high-power Raman lasing in wavelength range of 950–1000 nm, which is problematic for powerful Yb-doped fibre lasers (YDFLs). At the same time, output beam quality of the multimode RFL may be high enough due to the beam clean-up effect at Raman conversion of CW radiation in GRIN fibres [73]. Since the power of relatively bright (beam quality parameter $M^2 \sim 20$) commercial laser diodes operating at ~915 and ~976 nm has reached 100 W level for a single unit pigtailed by a 105 μm core fibre, the multimode RFL with direct LD pumping became feasible.

The concept of LD-pumped GRIN-fibre-based RFLs has been recently developed in two directions. First one explores high-power operation based on free-space pump coupling and bulk mirrors cavity [73–75], whereas second one aims at high-quality beam generation using FBGs as cavity mirrors [76–79]. In the first case, up to 154 W of output power is reported [75]. However, Raman output obtained at ~1020 nm in this case is not as interesting, because much higher power at this wavelength is available from Yb-doped fibre lasers [70]. In addition, in spite of significant improvement of the output beam quality in comparison with that for the pump beam (M^2 ~20) due to the clean-up effect in GRIN fibres, output beam parameter deteriorates from 4 to 8 with the increasing output power.

The second approach, started from an attempt of a 940-nm multimode LD pumping of telecom GRIN fibre with 62.5 μm core resulted in ~3 W 980-nm output of much better beam quality provided by UV-inscribed multimode FBG in combination with 4% Fresnel output reflector [76]. Using angled cleaving of the output fibre end, random lasing of such LD-pumped GRIN fibre laser has been shown to be also possible [77]. As a next step, a linear cavity consisting of two UV-inscribed FBGs (highly reflective and output one) was employed with a 62.5 μm GRIN fibre at 915-nm LD pumping enabling generation of 954-nm Stokes radiation [78]. Implementation of a special output FBG inscribed by a point-by-point femtosecond (FS) technique in the central part of the 62.5 μm GRIN fibre core results in nearly single-mode Raman lasing ($M^2 \sim 1.2$) with output power of 10 W at 954 nm [79]. Such FBG has typical dimensions 1×10 μm and plays a role of a fundamental mode selector with ~10 dB suppression of higher order transverse modes (seen at short-wavelength tail of reflection spectrum), see Figure 38.20a and b.

As a next step, coupling of several LDs through the multimode fibre pump combiner allows one to increase the coupled pump power and to develop an all-fibre design of the multimode Raman laser [80] (see Figure 38.21). This configuration has obvious advantages such as compactness, ease of operation, low cost, reliability, long-term stability in combination with flexibility of output fibre end and results in nearly diffraction limited ($M^2 \sim 1.3$) Stokes radiation with higher output power (~18 W at 954 nm).

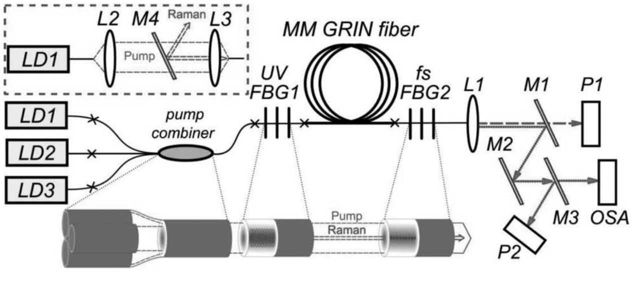

FIGURE 38.21 All-fibre scheme of MM GRIN fibre Raman laser with LD pumping and cavity formed by HR UV FBG1 and output fs FBG2 with LD pumping through the fibre pump combiner (bulk-optic pump coupling scheme is shown in the inset).

The obtained power for the 1.1-km 62.5 μm GRIN RFL with pump coupling via bulk optics and fibre spliced combiner are compared in Figure 38.20c. The generation threshold increases from ~40 to ~50 W in the all-fibre configuration, but the slope efficiency also increases (from 40% to 47%) while the 2nd Stokes threshold increases from 10 to 16 W of the generated power. The reason of the second threshold increase is the elimination of Fresnel reflection at the input fibre facet after the modification from the free-space to the all-fibre pump coupling scheme. Nevertheless, the second Stokes wave can lase even with the fibre pump coupling due to the random distributed feedback via Rayleigh backscattering in the 1.1-km long GRIN fibre, similar to the RDFB lasers treated in the previous paragraph.

The next steps performed with the all-fibre scheme shown in Figure 38.21 include the study and comparison of Raman lasing in the GRIN fibres of different core diameters (62.5, 85 [80] and 100 μm [81] with corresponding FBGs inscribed in them), when three 915-nm laser diodes and pump combiner are kept the same. As the pump combiner has the GRIN output fibre of 100 μm core diameter, the pump coupling losses are reduced with the increasing the GRIN fibre core diameter and amount to about 75%, 59% and 25% for 62.5, 85 and 100 μm

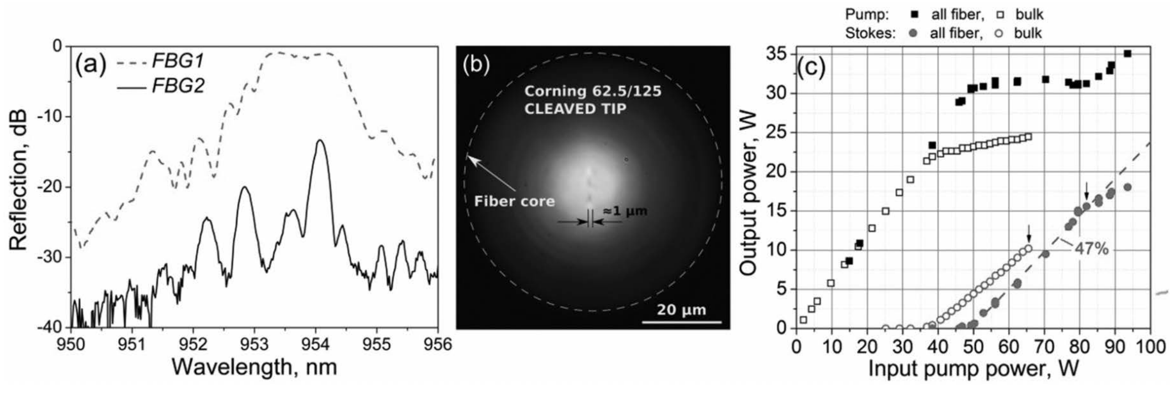

FIGURE 38.20 (a) Reflection spectrum of UV-inscribed FBG1 (dashed line) and fs-inscribed FBG2 (solid line) in 62.5 μm GRIN fibre. (b) Microscope image of fs modification area in the core of GRIN fibre for FBG2 [79]. (c) Power of residual pump (squares) and generated Stokes (circles) waves as a function of input pump power for the free-space (empty symbols) [79] and all-fibre (filled symbols) [80] pump coupling to the same 62.5 μm GRIN fibre with FBGs.

core, respectively. The coupled pump power increases correspondingly. The output power at 954 nm obtained in different GRIN fibres of optimal length (for available pump power) is compared in Figure 38.22.

A comparison of the all-fibre configuration based on the 62.5 μm GRIN fibre with that for the 85 and 100 μm GRIN fibres of optimal lengths (1.5 and 1.1 km, respectively) shows that the threshold pump power grows nearly proportionally to the core area increase (see Figure 38.22a) reaching ~110 W for the 100 μm GRIN fibre. At the same time, the slope efficiency of pump-to-Stokes conversion also increases amounting to 47%, 67% and 84% for 62.5, 85 and 100 μm GRIN fibre, respectively, in spite of sufficiently stronger integral pump attenuation for larger core fibres. The maximum output power of 62 W at 954 nm is reached for 100 μm GRIN fibre, which is characterized by the lowest coupling losses and the highest coupled pump power (beyond 200 W) from the same three diodes. However, quality parameter M^2 of the generated beam worsens for larger core fibres. The measured value for the 85 μm GRIN fibre Raman laser is $M^2 = 2.6$ near power maximum that is almost two times of the quality factor for the 62.5 μm fibre laser ($M^2 \sim 1.3$). It is further increased for 100 μm GRIN fibre, amounting to about 3 at maximum power. At that, the measured parameter M^2 for the transmitted pump radiation amounts to $M^2 \sim 30$. The measured M^2 value of output beam is only slightly (<10%) varying with power in all operating range of corresponding RFL. The shape of generated spectrum is close to the hyperbolic secant with exponential wings, just like the spectrum of conventional Raman lasers based on single-mode fibres. The only sign of higher-order transverse mode impurities consists in visible asymmetry of the line (Figure 38.22b). The 3-dB linewidth at maximum power (0.4 nm) is nearly the same for three core sizes in spite of different maximum power (due to larger effective mode area at larger core diameter). The linewidth remains to be smaller than the distance between the neighbouring groups of transverse modes of GRIN fibre. In case of 100 μm GRIN fibre the laser spectrum is unstable at low powers, but stabilizes at high powers (quite opposite to mode instability in rare-earth-doped fibre lasers [70]). At that, both the spectrum (Figure 38.22b, lower picture) and beam profile (Figure 38.22c) exhibit the signs of higher transverse mode appearance time to time.

To clarify the mechanism of the low-power mode instability, Raman generation with FBGs centred at 950 and 958 nm (slightly shifted from the Raman gain maximum to the short and to the long wavelengths, respectively) was also tested. It has been found that the unstable behaviour with random generation of higher-order transverse modes is observed in different power domains. The spectrum stabilizes at >35 W for 958 nm, at >18 W for 954 nm, and >8 W for 950 nm thus demonstrating that the transverse mode competition depends on the FBG wavelength position within the Raman gain spectral profile. The weakest instability effect is observed at the short-wavelength slope of Raman gain where the gain coefficient for higher order modes is lower than that for the fundamental one. In spite of the impurity of higher modes, the beam spectrum and profile become stable at high powers and do not vary significantly with power thus indicating a formation of a stable group of coupled low-index modes.

The proposed approach based on the development and integration of three key technologies—LD pump coupling through the multimode fibre pump combiner, core pumping of GRIN fibre and in-core cavity made of 3D-shaped fs-inscribed FBGs—opens the door to new type of LD-pumped high-power high-beam-quality CW fibre lasers which may operate at almost any wavelength defined by available LDs. Note that these are only the first steps demonstrating basic principles of the new type of CW high-power laser. The next steps towards a better pump coupling at higher powers and a better fundamental mode selection will result in further improvements in optical efficiency, output power and brightness of such source. This makes it very attractive for applications, such as efficient/bright source for pumping solid-state/fibre lasers, second harmonic generation, laser displays, bio-medical imaging. Interesting fundamental challenges also appear, e.g. investigation of mode instability in graded-index fibres, which may behave differently from that in step-index fibres, thus breaking the existing limits of high-power fibre lasers.

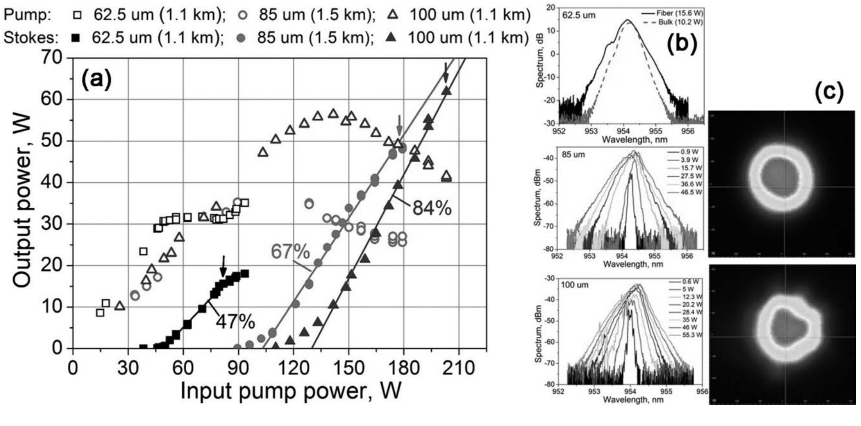

FIGURE 38.22 Transmitted pump power at 915 nm (empty symbols) and output Stokes power at 954 nm (filled symbols) of the LD-pumped Raman fibre laser shown in Figure 38.21 (a) and corresponding output spectra (b) for different GRIN fibre core diameters. At panel (c) the unstable (bottom) and stable (top) beam profiles are shown for 100 μm GRIN fibre laser at low and high output powers, correspondingly.

38.7 Spectral Broadening

In comparison with rare-earth-doped fibre lasers, RFLs are characterized by the absence of hole burning but much stronger Kerr non-linearity and group velocity dispersion effects, as their cavity length is usually much longer. So, the spectrum of RFLs is usually significantly broader at the same power level due to non-linear power broadening. In case of FBG cavity with relatively narrow reflection spectrum, the Raman laser linewidth broadening with power may even exceed the FBG spectral width thus leading to significant reduction of their reflection coefficient. This effect is more important in cascaded RFLs with highly reflecting intermediate FBG cavities, its influence on the power characteristics of the cascaded RFL may be described phenomenologically in frames of the balance model by introducing the effective FBG reflection coefficient [82].

The generated RFL spectrum consists of multiple cavity modes with spacing $\delta\nu = c/2nL$ (in linear cavity of length L). The number of generated longitudinal modes is proportional to the RFL cavity length and estimated to be about one million in several hundred metres long RFL operating at wavelength near 1 μm. At that, the longitudinal modes exhibit dephasing with increasing power due to the interplay of Kerr-induced self/cross phase modulation and group velocity dispersion resulting in the randomization of mode phases, see Ref. [83] and citation therein. Supposing Gaussian statistics for mode phases and relatively weak non-linearity (and dispersion correspondingly), a wave kinetic equation of the weak wave turbulence theory has been applied with corresponding modifications for the description of RFL spectrum consisting of multiple cavity modes [83]. As a result of multiple four-wave mixing process between the modes with different frequencies in the presence of their group velocity dispersion result in specific hyperbolic secant shape of the generated RFL spectral profile, which is non-linearly broadened with increasing power [83].

In random RFLs, not only the phases but also the initial frequencies of longitudinal modes are random. In this case, a more general theory based on the weak wave turbulence kinetic equation has been developed [84] which has been then compared with the experimental data for short half-open RDFB laser (Figure 38.15) but with backward pumping providing better compliance with the applicability conditions in the whole fibre, namely non-linearity (dispersion) is (much) less than the Raman gain, $\gamma P_S L < g_0 PL$ and $\beta\Delta^2 L \ll g_0 PL$, respectively. Here P and P_S are pump and Stokes power, γ and β are the nonlinearity and dispersion coefficient, Δ is the linewidth. Since the fibre loop mirror is broadband, the spectral filtering effect at each roundtrip is provided by the Raman gain of bandwidth Δg. So, near the threshold the RDFB Raman laser exhibits linear Shawlow-Townes narrowing, whereas well above the threshold the spectrum becomes to be broadened due to the non-linear effects (see Figure 38.23). The shape of the spectrum is described by the hyperbolic secant function with the width growing nearly linearly with increasing power (if the dispersion effect is much smaller than the non-linear Kerr effect):

$$F_\omega \propto \frac{1}{\cos h\left[(\omega-\omega_0)/\Delta\right]} \tag{38.11}$$

$$\Delta = \frac{2}{\pi}\Delta_g\left(\frac{\gamma P_S}{g_0 P}\right)\sqrt{1/g_0 PL} \tag{38.12}$$

It should be noted that slight non-linearity of linewidth-power dependence in Figure 38.23b is defined by the pump depletion with increasing Stokes power which was also taken into account.

When the dispersion effects become dominating, $\beta\Delta^2 L \gg g_0 PL$ (e.g. at broader spectrum in forward-pumped RDFB scheme), the linewidth-power dependence becomes strongly non-linear. Generalizing the kinetic theory for cascaded RDFB RFL operation, one can obtain the

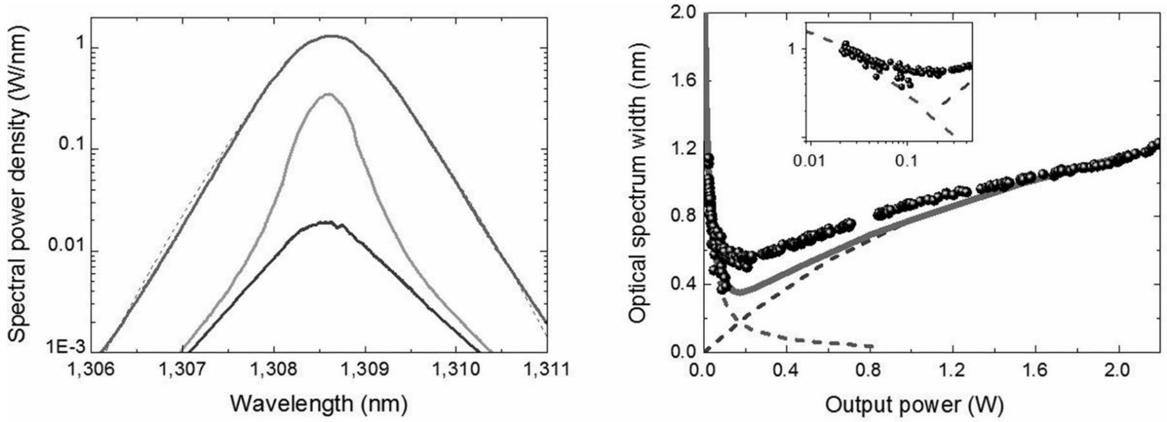

(a) (b)

FIGURE 38.23 (a) Experimentally measured optical spectrum: near the generation threshold (blue curve, RDFB laser power is 0.025 W), slightly above the generation threshold (green curve, 0.2 W), well above the generation threshold (red curve, 1.5 W). The optical spectrum predicted by the wave kinetic equation, for laser power 1.5 W is shown by dashed red line. (b) Spectrum width as a function of the RDFB laser's output power in theory and experiment. Experimental data is shown by black circles. The prediction for spectrum broadening from non-linear kinetic theory based on wave kinetic equation is shown by blue dashed line. The prediction for spectrum narrowing from modified linear kinetic Schawlow-Townes theory. Red line is a sum of non-linear and linear contributions. Inset show the data near the threshold in a logarithmic scale [84].

root-mean-square linewidth for *j*th order Stokes component in the following form [59]:

$$\Delta_{\mathrm{RMS}(j)} = \left[\frac{\gamma_{\mathrm{SPM}} P_j(L) \Delta_{g1/2(j)}}{\beta_{(j)} \sqrt{2 g_0 L \left(P_j^{\mathrm{th}} - P_{j-1}^{\mathrm{th}}\right)\left(\lambda_0/\lambda_{j-1}\right)}} \right]^{1/3} \quad (38.13)$$

$$\Delta_{\mathrm{XPM}(j)} = 2\sqrt{\frac{2\ln 2 \gamma_{\mathrm{XPM}} P_{\mathrm{P}(j-1)} \Delta_{g1/2(j)}}{\Delta\beta_j \sqrt{P_{\mathrm{P}(j-1)} L g_0}}} \quad (38.14)$$

Here in addition to the main self-phase modulation (SPM) effect, the influence of cross-phase modulation (XPM) is also evaluated, γ_{SPM} and γ_{XPM} are the Kerr non-linearity coefficients for the SPM and XPM processes, β_j and $\Delta\beta_j$ are the second-order dispersion and dispersion walk-off coefficients, respectively, $P_{\mathrm{P}(j-1)}$ is the maximum power of the $(j-1)$th order Stokes wave (or pump wave if $j = 1$) corresponding to the *j*th Stokes generation threshold, and $\Delta g_{(j)}$ is the HWHM width of the corresponding Raman gain spectral peak. A comparison of the theory with experimentally measured spectra of the cascaded RDFB RFL [59] demonstrate their very good agreement for all Stokes orders (see Figure 38.24). The laser bandwidth grows with increasing order, but it is almost independent of power in the 1–10 W range amounting to ~1, ~2 and ~3 nm for orders 1–3, respectively. Such a behaviour is defined by cubic-root broadening law for SPM at strong dispersion. The impact of XPM is rather small but it should be included for better quantitative correspondence of the theory and experiment.

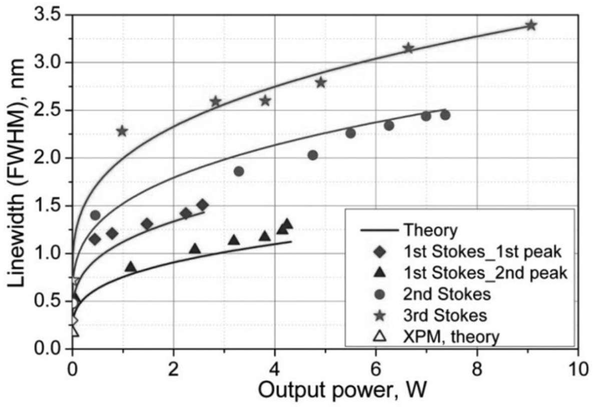

FIGURE 38.24 Spectral width (FWHM) of the individual Stokes line of cascaded RDFB RFL as a function of its power. Points correspond to experimental data for the first Stokes wave generated at 440 cm^{-1} (diamonds) and 490 cm^{-1} (triangles) Raman peaks, second Stokes (circles) and third Stokes (stars) components. Solid lines show the analytical model of spectral bandwidth including XPM input.

If one uses FBG instead of broadband fibre loop mirror, the Raman gain bandwidth in Equations (38.13) and (38.14) will be replaced by FBG bandwidth (which is much narrower) and generated spectrum will be narrower according to the cubic-root law Equation (38.13). When the dispersion and non-linearity are of the same order, a square-root law may be obtained as a solution of the wave kinetic theory, for example RFL with linear cavity of intermediate length and power shows such a dependence, see Ref. [83].

As it was mentioned in previous paragraph, RFLs with direct LD pumping which generate nearly diffraction limited beam exhibit the same spectral hyperbolic secant shape and non-linear power broadening law as the conventional single-mode RFL. Moreover, even the RFL output beam contains some impurity of higher-order transverse modes, it also exhibits nearly the same behaviour. In Figure 38.25, the experimental results at different GRIN fibre lengths are well fitted by the power law x^a with fitting parameter $a = 0.39$ (1.5 and 2 km), 0.37 (1.3 km), and 0.34 (1.1 km) that is close to the cubic root low observed in case of single-mode RFL with relatively large dispersion. At that the spectral shape is close to hyperbolic secant.

Thus, the hyperbolic secant shape with exponential tales and non-linear power broadening of the linewidth are common features of all RFLs.

38.8 Conclusions

In conclusion, let us briefly discuss the main directions of further development of the RFL concept.

During the last decade the progress in the development of RFLs technology was related to (i) improvement of existing optical fibres transparent in mid-IR range, (ii) development of

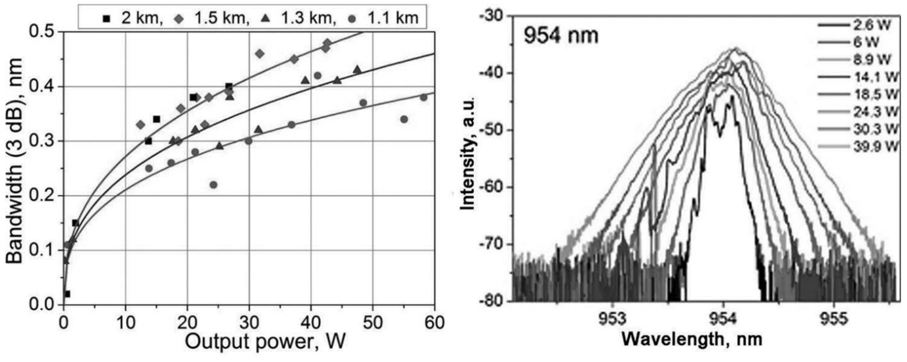

(a) (b)

FIGURE 38.25 Output linewidth (at –3 dB level) of the RFL at different lengths of the 100 µm GRIN fibre versus output power at 954 nm: experiment (points) and fitting curves (solid lines) and corresponding spectra for 1.1-km length at different powers.

new types of optical fibres (hollow core optical fibres filled with various gases), (iii) new technologies of optical elements for RFLs (FBGs written by femtosecond laser pulses). Also new schemes of RFLs were developed (random RFLs). One can expect that further progress in RFLs will continue in similar ways.

More specifically, it seems that in term of efficiency and performance, directly LD pumped RFLs based on GRIN fibres have a great potential. Its combination with random distributed feedback will make their design even more simple and reliable. As for potential of RFLs to operate in new spectral ranges, the hollow core micro-structured optical fibres filled by gases with different energy of vibrational quanta open the way to ultra-broadband operation.

Another possibilities which has been already demonstrated include using long (~1 m) regular phase-shifted FBG with DFB [85] or random FBG [86] and FBG array [87] for single-frequency (≤1 MHz kHz) low-power operation or narrowband (≤1 GHz) high-power operation, as well as ultrashort pulse generation at synchronous pumping of Raman lasers by pulsed RE-doped fibre lasers in common [88] or external [89] cavity that enables ~200 fs pulses with energy of ~10 nJ at new wavelengths (not available for RE-doped fibre lasers).

REFERENCES

1. Ippen, E.P. 1970. Low-power quasi-cw Raman oscillator. *Applied Physics Letters* 16: 303–5.
2. Stolen, R.H., Ippen, E.P., Tynes, A.R. 1972. Raman oscillation in glass optical waveguide. *Applied Physics Letters* 20: 62–4.
3. Yan Feng, ed. 2017. *Raman Fiber Lasers*, Springer Series in Optical Sciences, vol 207.
4. Supradeepa, V.R., Feng, Y., Nicholson, J.W. 2017. Raman fiber lasers. *Journal of Optics* 19: 023001.
5. Silfvast, William T. 2004. *Laser Fundamentals*. Cambridge, New York, Melbourne, Madrid, Cape Town, Singapore, Säo Paulo, Delhi: Second Edition. Cambridge University Press. Chapter 7: Conditions for producing a laser-population inversion, gain and gain saturation, p. 225–254.
6. Dianov, E.M., Fursa, D.G., Abramov, A.A. et al. 1994. Raman fibre-optic amplifier of signals at the wavelength of 1.3 μm. *Quantum Electronics* 24: 749–51.
7. Shen, Y.R., Bloembergen, N. 1965. Theory of stimulated Brillouin and Raman scattering. *Physical Review* 137: A1787–805.
8. Grubb, S., Erdogan, T., Mizrahi, V. et al. 1994. “1.3 μm Cascaded Raman Amplifier in Germanosilicate Fibers,” In: *Optical Amplifiers and Their Applications*, Vol. 14 of 1994 OSA Technical Digest Series (Optical Society of America, 1994), paper PD3.
9. Kashyap, R. 1999. *Fiber Bragg Gratings*. San Diego: Academic Press, p 458.
10. Grubb, S.G., Strasser, T., Cheung, W.Y. et al. 1995. Highpower 1.48 μm cascaded Raman laser in Germanosilicate fibers. In: *Optical Amplifiers and Their Applications*, Vol. 18 of 1995 OSA Technical Digest Series (Optical Society of America, 1995), paper SaA4.
11. Innis, D., DiGiovanni, D.J., Strasser, T.A. et al. 1997. Ultrahigh-power single-mode fiber lasers from 1.065 to 1.472 μm using Yb-doped cladding-pumped and cascaded Raman lasers. In: *Conference on Lasers and Electro-Optics*, D. Killinger, G. Valley, C. Chang-Hasnain, and W. Knox, eds., Vol. 11 of OSA Technical Digest (Optical Society of America, 1997), paper CPD31.
12. Feng, Y., Taylor, L.R., Calia, D.B. 2009. 150 W highly-efficient Raman fiber laser. *Optics Express* 17: 23678–83.
13. Xiao, Q., Yan, P., Li, D. et al. 2016. Bidirectional pumped high power Raman fiber laser. *Optics Express* 24: 6758–68.
14. Agraval, Govind P. 2013. *Nonlinear Fiber Optics*. Amsterdam, Boston, Heidelberg, London, New York, Oxford, Paris, San Diego, San Francisco, Singapore, Sydney, Tokyo: Fifth Edition. Academic Press.
15. Stolen, R.H. 1980. Nonlinearity in fiber transmission. *Proceedings of the IEEE* 68: 1232–6.
16. Jackson, S.D., Muir, P.H. 2001. Theory and numerical simulation of *n*th-order cascaded Raman fiber lasers. *Journal of the Optical Society of America B* 18: 1297–306.
17. Bufetov, I.A., Bubnov, M.M., Neustruev, V.B. et al. 2001. Raman gain properties of optical fibers with a high content of germanium and standard optical fibers. *Laser Physics* 11: 130–3.
18. Rinia, M., Cristiania, I., Degiorgioa, V., Kurkov, A.S., Paramonov, V.M. 2002. Experimental and numerical optimization of a fiber Raman laser. *Optics Communications* 203: 139–44.
19. Bufetov, I.A., Dianov, E.M. 2000. A simple analytic model of a cw multicascade fibre Raman laser. *Quantum Electronics* 30: 873–7.
20. Sanghera, J.S., Shaw, L.B., Florea, C.M. et al. 2010. Nonlinear Properties of Chalcogenide Glass Fibers. In: *Frontiers in Guided Wave Optics and Optoelectronics* ed. Bishnu Pal 29–48 Published by InTech (Rijeka, Croatia) DOI: 10.5772/3033 ISBN: 978-953-7619-82-4.
21. Petersen, C., Dupont, S., Agger, C., Thøgersen, J., Bang, O., Keiding, S.R. 2011. Stimulated Raman scattering in soft glass fluoride fibers. *Journal of the Optical Society of America B* 28: 2310–13.
22. Zhu, G., Geng, L., Zhu, X. et al. 2015. Towards ten-watt-level 3-5 μm Raman lasers using tellurite fiber. *Optics Express* 23: 7559–73.
23. Russell, P. 2003. Photonic crystal fibers. *Science* 299: 358–62.
24. Benabid, F., Knight, J.C., Antonopoulos, G., Russell, P.St.J. 2002. Stimulated Raman scattering in hydrogen-filled hollow-core photonic crystal fiber. *Science* 298: 399–401.
25. Dianov, E.M. 2002. Advances in Raman fibers. *Journal of Lightwave Technology* 20: 1457–62.
26. Dianov, E.M., Bufetov, I.A., Bubnov, M.M, Grekov, M.V., Vasiliev, S.A., Medvedkov, O.I. 2000. Three-cascaded 1407-nm Raman laser based on phosphorus-doped silica fiber. *Optics Letters* 25: 402–4.
27. Dianov, E.M., Bufetov, I.A., Mashinsky, V.M. et al. 2005. Raman fibre lasers based on heavily GeO_2-doped fibres. *Quantum Electronics* 35: 435–41.
28. Skuja, L. 1998. Optically active oxygen-deficiency-related centers in amorphous silicon dioxide. *Journal of Non-Crystalline Solids* 239: 16–48.

29. Bufetov, I.A., Grekov, M.V., Golant, K.M., Dianov, E.M., Khrapko, R.R. 1997. Ultraviolet-light generation in nitrogen-doped silica fiber. *Optics Letters* 22: 1394–6.
30. Fortin, V., Bernier, M., Caron, N. et al. 2013. Towards the development of fiber lasers for the 2 to 4 µm spectral region. *Optical Engineering* 52: 054202.
31. Fortin, V., Bernier, M., Carrier, J., Vallée, R. 2011. Fluoride glass Raman fiber laser at 2185 nm. *Optics Letters* 36: 4152–54.
32. White, R.T., Monro, T.M. 2011. Cascaded Raman shifting of high-peakpower nanosecond pulses in As_2S_3 and As_2Se_3 optical fibers. *Optics Letters* 36: 2351–53.
33. Bernier, M., Fortin, V., Caron, N. 2013. Mid-infrared chalcogenide glass Raman fiber laser. *Optics Letters* 38: 127–9.
34. Deng, D., Liu, L., Cheng, T. et al. 2015. Widely tunable Raman laser in a tellurite fiber ring cavity. *CLEO:2015* JW2A.98.
35. Fortin, V., Bernier, M., Faucher, D., Carrier, J., Vallee, R. 2012. 3.7 W fluoride glass Raman fiber laser operating at 2231 nm. *Optics Express* 20: 19412–9.
36. Bernier, M., Fortin, V., El-Amraoui, M., Messaddeq, Y., Vallee, R. 2014. 3.77 µm fiber laser based on cascaded Raman gain in a chalcogenide glass fiber. *Optics Letters* 2239: 2052–5.
37. Benabid, F., Bouwmans, G., Knight, J.C., Russell, P.St.J. 2004. Ultrahigh efficiency laser wavelength conversion in a gas-filled hollow core photonic crystal fiber by pure stimulated rotational Raman scattering in molecular hydrogen. *Physical Review Letters* 94: 123903.
38. Benoit, A., Beaudou, B., Debord, B., Gérôme, F., Benabid, F. 2017. High power Raman-converter based on H_2-filled inhibited coupling HC-PCF. *Proc. SPIE, Nonlinear Freq. Gener. Convers., Mater. Devices XVI*, 10088: 100880H.
39. Gladyshev, A.V., Kolyadin, A.N., Kosolapov, A.F. et al. 2015. Efficient 1.9 µm Raman generation in a hydrogen-filled hollow-core fiber. *Quantum Electronics* 45: 807–12.
40. Gladyshev, A.V., Kosolapov, A.F., Khudyakov, M.M. et al. 2017. 4.4-µm Raman laser based on hollow-core silica fibre. *Quantum Electronics* 47: 491–4.
41. Bufetov, I.A., Kosolapov, A.F., Pryamikov, A.D. et al. 2018. Revolver hollow core optical fibers. *Fibers* 6: 39.
42. Litchinitser, N.M., Abeeluck, A.K., Headley, C., Eggleton, B.J. 2002. Antiresonant reflecting photonic crystal optical waveguides. *Optics Letters* 27: 1592–4.
43. Pryamikov, A.D., Biriukov, A.S., Kosolapov, A.F. et al. 2011. Demonstration of a waveguide regime for a silica hollow - core microstructured optical fiber with a negative curvature of the core boundary in the spectral region > 3.5 µm. *Optics Express* 19: 1441–8.
44. Astapovich, M.S., Gladyshev, A.V., Khudyakov, M.M. et al. 2019. Watt-Level Nanosecond 4.42-µm Raman Laser Based on Silica Fiber. IEEE Photonics Technology Letters 31: 78–81.
45. Turitsyn, S.K., Ania-Castañón, J.D., Babin, S.A. et al. 2009. 270-km ultralong Raman fiber laser. *Physical Review Letters* 103: 133901–4.
46. Turitsyn, S.K., Babin, S.A., El-Taher, A.E., et al. 2010. Random distributed feedback fibre laser. *Nature Photonics* 4: 231–5.
47. Chen, C., Lee, H., Cheng, Y. 2003. Instability in Raman amplifiers caused by distributed Rayleigh reflection. In: *Optical Fiber Communication Conference*, Technical Digest (Optical Society of America, 2003), paper TuC2.
48. Babin, S.A., El-Taher, A.E., Harper, P., Podivilov, E.V., Turitsyn, S.K. 2011. Tunable random fiber laser. *Physical Review A* 84: 021805(R).
49. Sugavanam, S., Tarasov, N., Shu, X., Churkin, D.V. 2013. Narrow-band generation in random distributed feedback fiber laser. *Optics Express* 21: 16466–72.
50. El-Taher, A.E., Harper, P., Babin, S.A. et al. 2011. Effect of Rayleigh-scattering distributed feedback on multiwavelength Raman fiber laser generation. *Optics Letters* 36: 130–2.
51. Vatnik, I.D., Churkin, D.V., Podivilov, E.V., Babin, S.A. 2014. High-efficiency generation in a short random fiber laser. *Laser Physics Letters* 11: 075101.
52. Babin, S.A., Vatnik, I.D., Laptev, A.Y., Bubnov, M.M., Dianov, E.M. 2014. High-efficiency cascaded Raman fiber laser with random distributed feedback. *Optics Express* **22**: 24929–34.
53. Zhang, H., Zhou, P., Xiao, H., Xu, X. 2014. Efficient Raman fiber laser based on random Rayleigh distributed feedback with record high power. *Laser Physics Letters* 11: 075104.
54. Du, X., Zhang, H., Wang, X., Zhou, P., Liu, Z. 2016. Short cavity-length random fiber laser with record power and ultrahigh efficiency. *Optics Letters* 41: 571–4.
55. Zhang, H., Huang, L., Zhou, P. et al. More than 400 W random fiber laser with excellent beam quality. *Optics Letters* 42: 3347–50.
56. Wu, H., Wang, Z.N., Churkin, D.V., Vatnik, I.D., Fan, M.Q., Rao, Y.J. 2015. Random distributed feedback Raman fiber laser with polarized pumping. *Laser Physics Letters* 12: 015101.
57. Du, X., Zhang, H., Wang, X., Zhou, P., Liu, Z. 2015. Investigation on random distributed feedback Raman fiber laser with linear polarized output. *Photonics Research* 3: 28–31.
58. Zlobina, E.A., Kablukov, S.I., Babin, S.A. 2015. Linearly polarized random fiber laser with ultimate efficiency. *Optics Letters* 40: 4074–7.
59. Babin, S.A., Zlobina, E.A., Kablukov, S.I., Podivilov, E.V. 2016. High-order random Raman lasing in a PM fiber with ultimate efficiency and narrow bandwidth. *Scientific Reports* 6: 22625.
60. Zlobina, E.A., Kablukov, S.I., Babin, S.A. 2016. Generation of linearly polarised light near 1.4 µm in a cascaded, random distributed feedback Raman laser. *Quantum Electronics* 46: 1102–5.
61. Zhang, L., Jiang, H., Yang, X., Pan, W., Feng, Y. 2016. Ultra-wide wavelength tuning of a cascaded Raman random fiber laser. *Optics Letters* 41: 215–8.
62. Zhang, L., Jiang, H., Yang, X., Pan, W., Cui, S., Feng, Y. 2017. Nearly-octave wavelength tuning of a continuous wave fiber laser. *Scientific Reports* 7: 42611.
63. Lobach, I.A., Kablukov, S.I., Babin, S.A. 2017. Linearly polarized cascaded Raman fiber laser with random distributed feedback operating beyond 1.5 µm. *Optics Letters* 42: 3526–9.

64. Bravo, M., Fernandez-Vallejo, M., Lopez-Amo, M. 2013. Internal modulation of a random fiber laser. *Optics Letters* 38: 1542–4.
65. Kuznetsov, A.G., Podivilov, E.V., Babin, S.A. 2015. Actively Q-switched Raman fiber laser. *Laser Physics Letters* 12: 035102.
66. Tang, Y., Xu, J. 2015. A random Q-switched fiber laser. *Scientific Reports* 5: 9338.
67. Ma, R., Zhang, W.L., Zeng, X.P. et al. 2016. Quasi mode-locking of coherent feedback random fiber laser. *Scientific Reports* 6: 39703.
68. Turitsyn, S.K., Babin, S.A., Churkin, D.V. et al. 2014. Random distributed feedback fibre lasers. *Physics Reports* 542: 133–93.
69. Churkin, D.V., Sugavanam, S., Vatnik, I.D. et al. 2015. Recent advances in fundamentals and applications of random fiber lasers. *Advances in Optics and Photonics* 7: 516–69.
70. Richardson, D.J., Nilsson, J., Clarkson, W.A. 2010. High power fiber lasers: current status and future perspectives. *Journal of the Optical Society of America B* 27: B63–92.
71. Codemard, C.A., Ji, J., Sahu, J.K., Nilsson, J. 2010. 100 W CW cladding-pumped Raman fiber laser at 1120 nm. *Proceedings of SPIE* 7508: 75801N.
72. Yao, T., Harish, A.V., Sahu, J.K., Nilsson, J. 2015. High-power continuous-wave directly-diode-pumped fiber Raman lasers. *Applied Sciences* 5: 1323–36.
73. Baek, S.H., Roh, W. 2004. Single-mode Raman fiber laser based on a multimode fiber. *Optics Letters* 29: 153–5.
74. Glick, Y., Fromzel, V., Zhang, J. 2016. High power, high efficiency diode pumped Raman fiber laser. *Laser Physics Letters* 13: 065101.
75. Glick, Y., Fromzel, V., Zhang, J., Ter-Gabrielyan, N., Dubinskii, M. 2017. High efficiency, 154 W CW, diode-pumped Raman fiber laser with brightness enhancement. *Applied Optics* 56: B97–B102.
76. Kablukov, S.I., Dontsova, E.I., Zlobina, E.A., Nemov, I.N., Vlasov, A.A., Babin, S.A. 2013. An LD-pumped Raman fiber laser operating below 1 µm. *Laser Physics Letters* 10: 085103.
77. Babin, S.A., Dontsova, E.I., Kablukov, S.I. 2013. Random fiber laser directly pumped by a high-power laser diode. *Optics Letters* 38: 3301–3.
78. Zlobina, E.A., Kablukov, S.I., Skvortsov, M.I., Nemov, I.N., Babin, S.A. 2016. 954 nm Raman fiber laser with multimode laser diode pumping. *Laser Physics Letters* 13: 035102.
79. Zlobina, E.A., Kablukov, S.I., Wolf, A.A., Dostovalov, A.V., Babin, S.A. 2017. Nearly single-mode Raman lasing at 954 nm in a graded-index fiber directly pumped by a multimode laser diode. *Optics Letters* 42: 9–12.
80. Zlobina, E.A., Kablukov, S.I., Wolf, A.A. et al. 2017. Generating high-quality beam in a multimode LD-pumped all-fiber Raman laser. *Optics Express* 25: 12581–7.
81. Evmenova, E.A., Kablukov, S.I., Nemov, I.N. et al. 2018. High-efficiency LD-pumped all-fiber Raman laser based on a 100-µm core graded-index fiber. *Laser Physics Letters* 15: 095101.
82. Babin, S.A., Churkin, D.V., Podivilov, E.V. 2003. Intensity interactions in cascades of a two-stage Raman fiber laser. *Optics Communications* 226: 329–35.
83. Babin, S.A., Churkin, D.V., Ismagulov, A.E., Kablukov, S.I., Podivilov, E.V. 2007. FWM-induced turbulent spectral broadening in a long Raman fiber laser. *Journal of the Optical Society of America B* 24: 1729–38.
84. Churkin, D.V., Kolokolov, I.V., Podivilov, E.V. et al. 2015. Wave kinetics of random fibre lasers. *Nature Communications* 6: 6214.
85. Westbrook, P.S., Abedin, K.S., Nicholson, J.W., Kremp, T., Porque, J. 2011. Raman fiber distributed feedback lasers. *Optics Letters* 36: 2895–97.
86. Gagné, M., Kashyap, R. 2014. Random fiber Bragg grating Raman fiber laser. *Optics Letters* 39: 2755–58.
87. Skvortsov, M.I., Abdullina, S.R., Vlasov, A.A. et al. 2017. FBG array-based random distributed feedback Raman fibre laser. *Quantum Electronics* 47: 696–700.
88. Babin, S.A., Podivilov, E.V., Kharenko, D.S. et al. 2014. Multicolour nonlinearly bound chirped dissipative solitons. *Nature Communications* 5: 4653.
89. Churin, D., Olson, J., Norwood, R.A., Peyghambarian, N., Kieu, K. 2015. High-power synchronously pumped femtosecond Raman fiber laser. *Optics Letters* 40: 2529–32.

Taylor & Francis
Taylor & Francis Group
http://taylorandfrancis.com

39

Solitons and Dissipative Solitons for Ultrafast Lasers

Ph Grelu

CONTENTS

39.1 Introduction 521
39.2 Passive Mode Locking of Fibre Lasers 522
39.2.1 Saturable Absorber Materials 522
39.2.2 Virtual Saturable Absorbers 523
39.2.3 Non-linear Loop Mirrors 523
39.2.4 Figure-8 Lasers and Variants 523
39.2.5 Non-linear Polarization Evolution Mode Locking 524
39.3 The Soliton Laser: Advantages and Limitations 525
39.3.1 Soliton Energy 525
39.3.2 Dispersive Wave Radiation 526
39.3.3 Multi-Pulsing Instability 527
39.4 The Concept of Dissipative Solitons 527
39.4.1 Beyond Conventional Solitons 527
39.4.2 The Dissipative Soliton Paradigm 527
39.4.3 Dissipative Solitons in the Normal Propagation Regime 528
39.4.4 Dissipative Soliton and Frequency Chirping 528
39.4.5 Dissipative Soliton Molecules 528
39.5 Applications of Dissipative Solitons 529
39.5.1 The Quest of High-Energy Pulses from Laser Oscillators 529
39.5.2 Innovative Chirped-Pulse Laser Architectures 529
39.5.3 Peculiar Laser Pulses 530
39.6 Prospects 530
References 531
Further Reading 533

39.1 Introduction

From the user point of view, ultrafast lasers can be simply defined as lasers generating pulses whose temporal profile cannot be easily monitored in real time. Namely, when the optical pulses are shorter than the electronic response time of the direct optical detection scheme based on a fast photodiode connected to an oscilloscope. Owing to the tremendous progress in fast electronics during the past two decades, this practical definition has been shifting the ultrashort pulse duration border from, typically, below 100 to below 10 ps. But from the laser engineering point of view, ultrafast lasers are laser cavities where dispersive and non-linear effects do affect intracavity propagation significantly, owing to, respectively, the large optical bandwidth and the high peak power associated with ultrashort pulses. In this respect, there will be large quantitative differences according to the laser architecture. In bulk lasers, such as in the celebrated titanium–sapphire laser, the dispersive and non-linear effects accumulate every cavity roundtrip through, typically, a few-millimetre-long dense gain medium: they will become a significant issue to generate sub-picosecond pulses. In contrast, fibre lasers are usually several metres long, so that pulses of tens of picoseconds can experience major dispersive and non-linear effects during a single cavity roundtrip.

The Soliton Laser. The concept of an optical soliton, originated in the early 70s (Zakharov and Shabat 1972, Hasegawa and Tappert 1973) provides an elegant solution to the handling of both chromatic dispersion and Kerr non-linearity effects. The optical Kerr effect produces a self-phase modulation (SPM) of the optical pulse. Alone, SPM alters the optical spectrum, generating longer (resp. shorter) wavelengths at the pulse leading (resp. trailing) edge. A precise balance between anomalous dispersion and SPM allows the fundamental optical soliton to maintain a chirp-free temporal waveform of minimal duration while it propagates. In 1980, the optical soliton propagation regime was evidenced experimentally in a passive optical fibre link (Mollenauer et al. 1980). Four years later, the soliton pulse shaping effect was introduced inside a mode-locked laser cavity, by coupling a length of optical fibre to a bulk colour-centre laser cavity: the so-called *soliton laser* had been invented (Mollenauer et al. 1984). This seminal work also predicted that, when a suitable fibre gain medium would become available, *the soliton laser would probably take the form of a single loop of fibre closed upon itself. The simplicity and low cost of such devices would make them most attractive.* Since then, fibre laser technology has been developed at a tremendous rate, whereas the soliton laser concept has been considered as a safe guideline for ultrafast laser engineering. Nevertheless, in practice, laser cavities may be quite far from presenting the ideal conditions for the implementation of the soliton laser concept.

Implementation Issues. First, the laser may operate at wavelengths where the propagation medium features normal dispersion. As a matter of fact, normal dispersion is typical of most bulk materials in the visible and near infrared optical domains, such as silica for wavelengths shorter than 1.27 μm. At first sight, it seems that such a laser cavity would hardly support ultrashort pulses, due to the lack of balance between non-linear and dispersive effects. Indeed, the longer (resp. shorter) wavelengths at the pulse leading (resp. trailing) edge generated by SPM, together with the faster propagation of the longer wavelengths in normal dispersion, entails an accentuated spreading of the temporal wave packet. Therefore, dispersion compensation has become the standard procedure, through the engineering of adequate amount of geometric dispersion, which can take the form of gratings, prisms or waveguides that can be incorporated into the laser cavity. In bulk lasers, dispersion management has culminated in the design of chirped multilayer dielectric mirrors allowing the direct generation of few-cycle optical pulses out of the laser oscillator. Dispersion management in fibre lasers displays an even greater diversity. As it will be shown in the following sections, the cavity dispersion map determines the generation of specific ultrafast internal dynamics that unfold within the cavity roundtrip. Understanding the variety of these ultrafast dynamics requires to go well beyond the conventional soliton concept, calling in particular for the broader conceptual framework of *dissipative solitons*.

Second, in addition to the chromatic dispersion and the Kerr non-linearity, an ultrafast laser includes other physical effects that contribute to the pulse shaping. Besides Kerr non-linearity, passive mode locking requires a fast-saturable absorber. The gain medium features saturation, as well as wavelength dependence that contributes to an overall spectral filtering effect. Therefore, non-linear gain and loss are always acting. Their importance over shaping the pulse dynamics depends on the laser architecture, and associated cavity parameters. Dissipative non-linear effects become significant in lasers having relatively large gain and loss contributions during a roundtrip pulse propagation. In such situation, which is typical of the majority of ultrafast fibre laser architectures, it is unlikely that the pulse dynamics will merely follow the conventional soliton dynamics, defined by the simple balance between chromatic dispersion and Kerr non-linearity. Nevertheless, what can be first seen as a difficult challenge turned out to be a fantastic opportunity to test original laser cavity architectures supporting new types of solitary waves in the dissipative cavity regime, namely, a variety of *dissipative optical solitons*. Such exploration has been particularly prominent since the early 2000s.

The Dissipative Soliton. Dissipative solitons are localized formations of an electromagnetic field that are balanced through an energy exchange with the environment in presence of non-linearity, dispersion and/or diffraction (Grelu and Akhmediev 2012). Their growing use in the area of passively mode-locked lasers is remarkable: the concept of a dissipative soliton provides an excellent framework for understanding complex pulse dynamics and stimulates innovative cavity designs. Reciprocally, the field of mode-locked lasers serves as an ideal playground for testing the concept of dissipative solitons and revealing their unusual dynamics.

In the sections that follow, the focus will be on the ultrafast soliton and dissipative soliton dynamics of fibre lasers that employ a passive saturable absorber mechanism. Therefore, Section 39.2 provides a brief technical overview of the passive mode-locking techniques adapted to the fibre laser arena. Then, Section 39.3 discusses the soliton laser advantages and limitations. The conceptual framework of dissipative solitons is presented in Section 39.4, with important applications for ultrafast lasers developed in Section 39.5. To conclude, a few remarkable prospects are presented in Section 39.6.

39.2 Passive Mode Locking of Fibre Lasers

Regardless for the moment of the fibre cavity dispersion map and the type of ultrafast dynamics that unfolds, it is instructive to scan the popular fibre laser mode-locking techniques, which intend to follow the general philosophy of the fibre laser platform: compactness, fibre integration, low-cost and reliability. There are two major options: to resort on the fast-saturable absorption of an engineered localized material that will be inserted in the cavity, or to employ non-linear interferences based on the optical Kerr effect that accumulates along with propagation in the optical fibres.

39.2.1 Saturable Absorber Materials

There has been a considerable evolution of saturable absorber materials during the past two decades. First, the design of semiconductor saturable absorber mirrors based on a Bragg multilayered structure, or *SESAM*, has rapidly come to maturity (Keller 2003, Okhotnikov et al. 2004). A SESAM is engineered for a specific wavelength range and, in its fibre-integrated version, for a specific laser fluence. Its fabrication requires a relatively complex and expensive clean-room manufacturing process. The SESAM has become one component of choice for commercial mode-locked fibre lasers produced in series. As alternatives to SESAM, there has been a surge of investigation of the saturable absorber properties of one and two-dimensional (2D) materials. Indeed, several such materials demonstrated an ultrafast relaxation time, a wideband operation, and a relatively large damage threshold. Among them, single-walled carbon nanotubes (Set et al. 2004) and graphene (Sun et al. 2010) have become quite popular for fibre laser mode locking. In particular, as a Dirac gapless 2D material, graphene displays an ultrawideband optical absorption, suitable to cover the major wavelengths of interest in current rare-earth-doped fibre lasers, namely the 1 μm (ytterbium), 1.5 μm (erbium) and 2 μm (thulium, holmium) emission bands. For their integration, 2D materials can be simply deposited on a fibre ferrule and sandwiched between two connectors, though the contrast of saturable absorption will be relatively low, of the order of a few per cent. A 2D material can also be integrated as a coating of a tapered optical fibre, or as a planar film deposited onto a side-polished D-shaped fibre: in these cases, a significant fraction of the evanescent optical field interacts with the saturable absorber material over a properly designed length. Other saturable absorber materials recently investigated include topological insulators (Jung et al. 2014) and black phosphorus (Sotor et al. 2015).

39.2.2 Virtual Saturable Absorbers

Until now, no single engineered material has shown to combine the large non-linear absorption contrast of a SESAM with the wideband operation, ultrashort relaxation time of graphene, together with a large damage threshold. However, the fibre laser platform naturally presents several options to build a laser cavity architecture where such efficient saturable absorption becomes readily available for mode locking. These options resort to the use of the distributed third-order Kerr non-linearity to create non-linear interferences that affect the overall cavity losses, a strategy initially called *additive-pulse mode locking* (APM) (Ippen et al. 1989). To circumvent the difficulty in stabilizing interferometric devices in general, two self-consistent fibre cavity architectures have become popular among the fibre laser physicists. The first one includes a non-linear asymmetric Sagnac interferometer—or one of its variants. The second one consists in a unidirectional fibre ring laser wherein non-linear polarization evolution takes place during field propagation. Based on the dispersive Kerr effect, there will not be a real saturable absorption effect within the material, this is why APM is also said to employ a *virtual*, or *artificial* saturable absorber effect, in contrast to the *real* saturable absorber effect of the materials introduced in the previous paragraph. The APM strategy takes advantage of the quasi-instantaneous response time of the Kerr effect in glass materials (in the femtosecond range), as well as its ultrabroadband applicability (for silica, from the visible to the near infrared) and very large intrinsic damage threshold. As a drawback, the transfer function associated with the related *artificial* saturable absorber effect will not be a monotonous function of the optical intensity, since resulting from interferences.

39.2.3 Non-linear Loop Mirrors

The non-linear asymmetric Sagnac interferometer is better known under the acronym of *NOLM*, which stands for *non-linear optical loop mirror*, following its initial proposition as a fibre-integrated all-optical switch (Doran and Wood 1988). Whereas the original Sagnac interferometer is symmetric so that it acts as a mirror—or as an inertial rotation sensor from its inception (Sagnac 1913), by breaking the optical intensity symmetry between the two counterpropagating waves, these two waves will accumulate different non-linear phase shifts. That phase shift difference dictates the outcome of the wave interference that takes place when the two waves recombine after propagation through the loop. Therefore, the NOLM output features a transmission that oscillates as a function of the input optical intensity, namely, a sinusoidal non-linear transfer function. To break the symmetry between the counterpropagating beams, there are several possibilities. In the original proposition (Doran and Wood 1988), the NOLM is based on an asymmetric coupler (Figure 39.1a). It is also possible to induce different non-linear phase shifts for counterpropagating beams by inserting a segment of highly-dispersive fibre asymmetrically, namely, to make a dispersion-imbalanced NOLM, or *DI-NOLM* (Figure 39.1b) (Wong et al. 1997). Another alternative is to insert an optical amplifier within the loop, followed by a length of passive fibre: this geometrical gain asymmetry also leads to asymmetric non-linear phase shifts. Indeed, whereas one direction of propagation will first meet the amplifier, enhancing the non-linear phase shift in the subsequent passive fibre link, the counterpropagating wave will first propagate through the passive fibre at a lower optical intensity before meeting the amplifier at the end of the loop, see Figure 39.1c. Such active NOLM option has been termed *Non-linear Amplifying Loop Mirror*, or *NALM* (Fermann et al. 1990). In the NALM, the non-linear transfer function of the loop mirror can be adjusted by varying the gain, which provides one useful additional degree of freedom to control the non-linear transfer function and to adjust the mode-locking operation of the NALM laser (Nakazawa et al. 1991).

39.2.4 Figure-8 Lasers and Variants

The so-called *figure-of-eight laser* (F8L) represents the typical cavity architecture that incorporates a non-linear loop mirror within a fibre ring laser, see Figure 39.1d. One important issue of the F8L is that it does not easily lead to a self-starting mode-locked operation. This can be understood by noting that the non-linear transmission of the NOLM or the NALM part grows as a sinusoidal function of the optical intensity, namely with a flat initial slope that will not easily enhance the higher field fluctuations, up to some extent. Such issue can be circumvented by using standard—i.e. non-polarization-maintaining—optical fibres and incorporating polarization controllers within the loop: this introduces a tunable phase bias, which helps promoting the self-starting mode-locked operation. Nevertheless, using long lengths of standard fibres in a fibre laser cavity will make the laser operation quite sensitive to environmental perturbations (temperature drift, mechanical noise), so that a preferred option is nowadays to design polarization-maintaining (PM) F8Ls that include a flexible control of the effective saturable absorber. For instance, this can be achieved by inserting a second gain medium in the cavity (Runge et al. 2014), or by using a non-reciprocal phase bias. The latter can be obtained through a combination of Faraday rotators and retarding waveplates (Jiang et al. 2016). With a complete control of the phase bias range, it is possible to make a virtual saturable absorber from either the transmission or the reflection output port of the non-linear loop mirror. This has

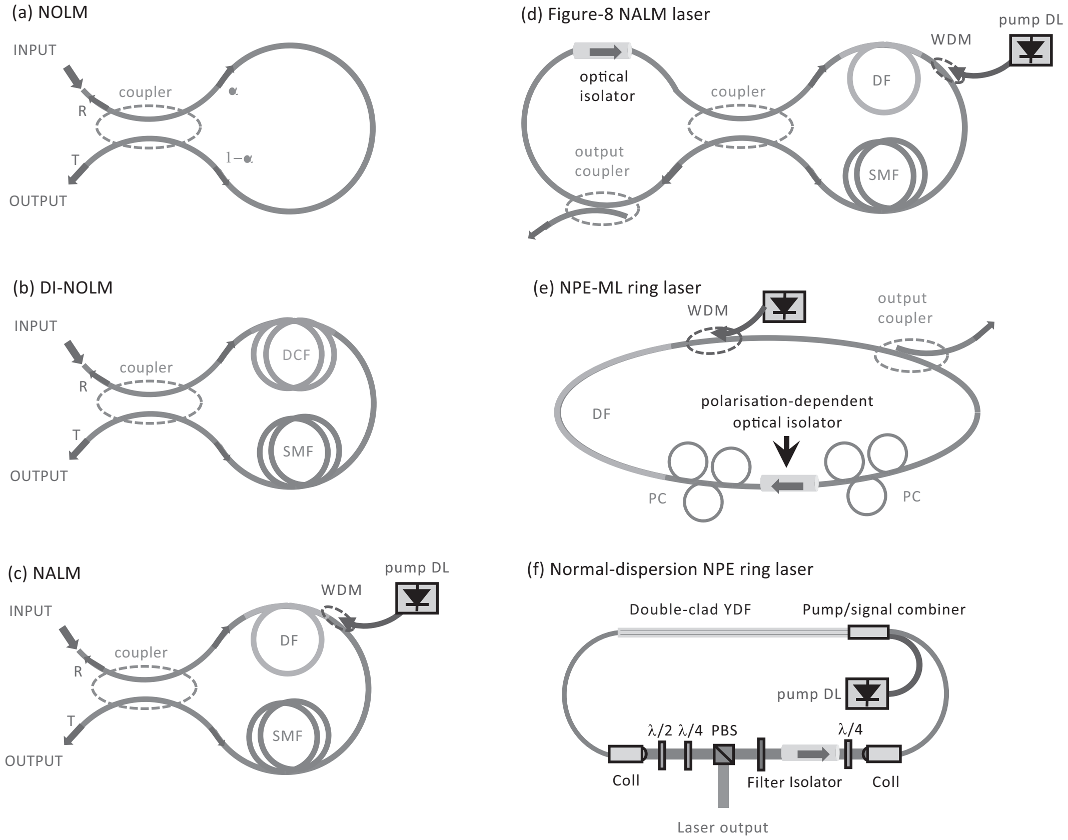
(a) NOLM
INPUT
coupler
R
T
α
1−α
OUTPUT
(b) DI-NOLM
INPUT
coupler
R
T
DCF
SMF
OUTPUT
(c) NALM
INPUT
coupler
R
T
DF
SMF
WDM
pump DL
OUTPUT
(d) Figure-8 NALM laser
optical isolator
coupler
output coupler
DF
SMF
WDM
pump DL
(e) NPE-ML ring laser
WDM
output coupler
DF
polarisation-dependent optical isolator
PC
PC
(f) Normal-dispersion NPE ring laser
Double-clad YDF
Pump/signal combiner
pump DL
λ/2 λ/4 PBS
λ/4
Coll
Filter Isolator
Coll
Laser output

FIGURE 39.1 Non-linear loop mirrors and passively mode-locked fibre lasers. (a) NOLM. (b) Dispersion-imbalanced NOLM. (c) NALM. (d) Figure-8 laser. (e) Unidirectional fibre ring laser mode-locked through non-linear polarization evolution (NPE). (f) All-normal-dispersion fibre laser including a free-space cavity section. Coll, collimator; DCF, dispersion-compensation fibre; DF, rare-earth doped fibre; DL, diode laser; PC, fibre polarization controller; PBS, polarizing beam splitter; SMF, standard single-mode fibre; WDM, wavelength-division multiplexer; YDF, ytterbium-doped fibre.

led to the development of a compact, environmentally stable, reflection variant of the PM-fibre loop-mirror laser cavity, whose architecture has been dubbed *figure-9 laser* (Hänsel et al. 2017).

39.2.5 Non-linear Polarization Evolution Mode Locking

Alternatively, a fibre ring laser is a simpler laser architecture, as a mirrorless serial loop of optical fibres and components. Endowed with an optical isolator, it becomes a unidirectional fibre ring cavity, where the APM mechanism can be readily implemented by using the polarization degree of freedom of the optical field that propagates through standard (non-PM) single-mode optical fibres, as sketched in Figure 39.1e. Since 1964, the non-linear coupling between orthogonal polarization components in an isotropic Kerr medium is known to entail the rotation of an elliptic polarization input (Maker et al. 1964). Such non-linear polarization rotation (NPR) effect is proportional to the difference of the polarization components intensities in the circular polarization basis and to the propagation distance. By discriminating the amount of polarization rotation with a polarizing element, a non-linear transmission function is obtained. The latter can be conveniently adjusted by orienting retarding waveplates placed before the polarizer. Therefore, the implementation of an NPR-based virtual saturable absorber within a fibre ring laser appears to be fairly simple. The intracavity waveplates constitute the practical degrees of freedom used to shape up the required non-linear transfer function enabling the self-starting mode locking of the laser cavity. The main non-linear transmission features, namely contrast, initial slope, and peak intensity can be varied widely, allowing to explore a large range of pulse dynamics within a given fibre ring laser setup. For these practical reasons, NPR has become one of the most popular mode-locking techniques among fibre laser physicists, since its experimental implementation in the early 90s (Matsas et al. 1992). NPR operates ideally within an isotropic Kerr medium, which is not exactly the case of standard optical fibres, which have a small amount of random birefringence. The associated beat length is in the few-metre range for standard SMF fibres, but may be significantly shorter for rare-earth doped fibres—to which the stress-induced birefringence brought by fibre coiling or splicing may add. Therefore, instead of NPR, a better description of the mechanism at play is *non-linear polarization evolution* (NPE), where the polarization beat length varies non-linearly with the optical intensity (Winful 1985). NPE followed by polarization discrimination makes an efficient virtual saturable absorber, provided that the non-linear length remains smaller than or comparable to the polarization beat length. This is generally the case with standard optical fibres but the above criterion obviously precludes the use of PM fibres. One drawback of NPE is that it is extremely difficult, if not impossible, to make an accurate modelling of the polarization evolution within the fibre cavity, owing to the presence of random birefringence. But the major inconvenient is a practical one: the NPE mode-locked laser cavity will generally remain sensitive to environmental perturbations. Nevertheless, note that in the case of rod-type glass fibres (Deslandes et al. 2013), the approximation of an isotropic Kerr medium may become valid again, and a genuine NPR effect may take place, allowing for a precise modelling of the non-linear transmission through the polarizer as a function of the orientation of the waveplates.

39.3 The Soliton Laser: Advantages and Limitations

In the 1990s, the development of ultrafast fibre lasers in the 1.5 µm window was accompanied by the fast expansion of high-bit-rate optical communications, benefiting from the newly available optical amplifier and efficient fibre-integrated components, whose cost has been dramatically reduced. The 1.5 µm spectral window combines the ultralow loss of silica with the anomalous dispersion of standard single-mode fibres (SMF) and the broadband gain (~25 nm) of erbium-doped silica glass. These conditions have favoured the development of passively mode-locked erbium-doped fibre lasers generating ultrashort soliton pulses.

39.3.1 Soliton Energy

Soliton pulse shaping takes place within the length of passive SMF that is part of the fibre cavity. When the SMF length is larger than the other characteristic propagation lengths, namely the non-linear and the dispersive length, the pulse may reach a fundamental soliton profile, where SPM exactly balances the anomalous chromatic dispersion. The fundamental soliton yields a bell-shaped hyperbolic-secant-square (sech^2) pulse intensity profile, whose duration is Fourier-transform limited, namely, with a constant-phase profile across the pulse. The fundamental soliton energy E and duration T_0 are constrained by the soliton area theorem:

$$E = \frac{2|\beta_2|}{\gamma\ T_0}, \tag{39.1}$$

where β_2 is the second-order chromatic dispersion of the optical waveguide, and γ its effective non-linear coefficient. We recall that β_2 combines both material and geometrical dispersion, which can be engineered. The non-linear coefficient γ is proportional to the Kerr non-linearity coefficient of the material n_2 and inversely proportional to the effective mode area A_{eff} and to the optical wavelength λ_0, as follows: $\gamma = \dfrac{2\pi\ n_2}{\lambda_0 A_{\text{eff}}}$. Note that the soliton duration parameter T_0 is related to the full-width pulse duration at half maximum (FWHM) by: $T_{\text{FWHM}} \approx 1.76\ T_0$.

However, we can see that the soliton model does not predict the pulse energy or temporal duration, but only fixes the relationship between them. Technically, this reflects the fact that non-linear propagation, as modelled by the non-linear Schrödinger (NLS) equation (Zhakarov and Shabat 1972), admits a whole family of soliton solutions, as pictured in Figure 39.2. An additional constraint needs to be included to yield a specific soliton solution within a given fibre laser cavity. Such constraint comes from the gain and loss cavity contributions (Kutz 2006). One constraint is obtained by

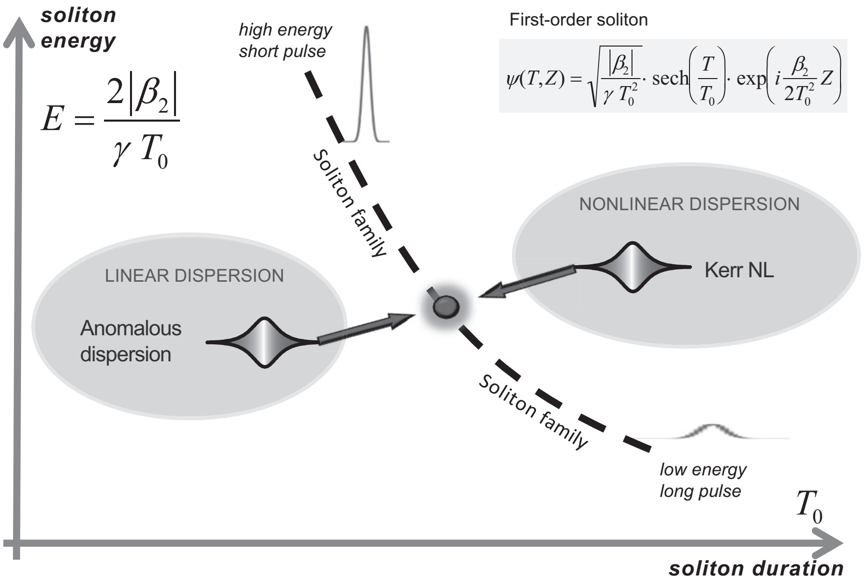

FIGURE 39.2 The soliton family. For a given optical waveguide, the balance between the anomalous dispersion β_2 and the non-linearity γ defines a soliton family, which has the soliton duration T_0 as free parameter. Represented by the dotted line, the family spans from high-energy short pulses to low-energy long pulses. The temporal field profile ψ of the fundamental (first order) soliton is given in the upper-right formula as a function of the local time T in the pulse reference frame, and the propagation distance Z.

the following reasoning. The mode-locked pulses tend to use the available gain bandwidth, which fixes the pulse duration, assuming Fourier-transform limited pulses. Given the amount of anomalous dispersion, this fixes the pulse energy. However, the main constraint can originate from the saturable absorber, which fixes the pulse peak power. This in turn determines the pulse duration and energy compatible with the soliton area theorem. That is why the adjustment of saturable absorbers such as those relying on non-linear interference (NALM, NPE) can lead to a wide range of pulse parameters within a given laser cavity setup.

Let us provide some typical orders of magnitude. With a laser gain bandwidth of 25 nm, soliton pulses can be as short as 100 fs (T_{FWHM}). By using a standard SMF fibre at 1.55 µm, with dispersion $\beta_2 = -0.021\ \mathrm{ps^2 m^{-1}}$ and non-linearity $\gamma = 1.2 \times 10^{-3}\mathrm{W^{-1} m^{-1}}$, and assuming that the saturable absorber saturation intensity is appropriate, the fundamental soliton has an energy of 0.6 nJ. The output pulse energy will be a fraction of that, say, around 0.1–0.2 nJ. This is the typical energy limitation that results from soliton pulse shaping, by using SMF fibres in the 1.5 µm spectral window. Note that the soliton energy limitation is higher by nearly an order of magnitude in thulium-doped fibre lasers operating at ~2 µm, as a result of larger anomalous dispersion, wavelength and mode area in standard SMF. Actually, the most efficient way to increase the fundamental soliton energy is through the engineering of large mode area fibres (LMA), which can gain more than two orders of magnitude in the mode area scaling (Richardson et al. 2010).

39.3.2 Dispersive Wave Radiation

Nevertheless, the overall pulse propagation within a fibre laser cavity is quite far from the propagation experienced in a single passive fibre. The large saturated-gain of the rare-earth doped fibre compensates for the losses of the optical components (optical isolator, multiplexer etc.), their coupling (splices, connectors), and the major losses resulting from the saturable absorber and the output coupler. Altogether, these losses can typically amount to ~10 dB per cavity roundtrip. In addition, the rare-earth doped fibre generally has a different mode area than that of the passive fibre, so that the waveguide dispersion contributions can differ widely. Therefore, the pulse will experience major, periodic, soliton-like reshaping, which entails the emission of *dispersive waves*. Dispersive waves are low-amplitude radiated waves that propagate linearly. The amount of such radiation depends on the ratio between the average non-linear length and the cavity length. When this ratio is large, the soliton evolution will not be able to follow closely the propagation medium landscape, so that an *average soliton* propagation can prevail, leading to a moderate level of dispersive wave radiation (Hasegawa and Kodama 1990, Kelly et al. 1991). Noting that a fibre laser cavity is generally not so short, with a length of several metres, that ratio will be typically of the order of unity or smaller: in such a case, the amount of radiation will be large, leading to a spreading oscillating pulse pedestal in the temporal domain (Gordon 1992), and to a specific spectral signature featuring high-amplitude sidebands (Noske et al. 1992). As a consequence, the pulse temporal profile can deviate significantly from the sech^2 profile of a conventional soliton, while the spectral sidebands can contribute to a significant fraction of the intracavity energy.

Gordon-Kelly Sidebands. The existence of specific radiation sidebands, as opposed to a radiation continuum, is linked to the periodicity of the perturbation undergone by the circulating pulse. Such phenomenon was predicted by Gordon in the context of periodic optical transmission lines (Gordon 1992), and by Kelly for ultrafast fibre lasers (Kelly 1992). Resonant wave mixing occurs between dispersive waves and soliton spectral components when their phase matching is satisfied after each period of the propagation landscape. Such phase matching condition yields resonant sidebands that are symmetric with respect to the soliton spectrum and unevenly spaced (see Figure 39.3a), with a spectral distribution that follows:

$$\Delta\nu_{\mathrm{N}} = \frac{\pm 1}{2\pi}\sqrt{\frac{1}{-\beta_2}\left(\frac{4\pi N}{L} - P_0\gamma\right)} \qquad (39.2)$$

where L is the propagation period, N is the sideband order (absolute value), β_2 is the path-averaged second-order chromatic dispersion (here, negative), γ is the average non-linearity, and P_0 the average soliton peak power. These sidebands are very familiar to fibre laser physicists, who dub them *Kelly sidebands*, or better, *Gordon-Kelly sidebands*, see Figure 39.3(a). By fitting their location, it is possible to measure the

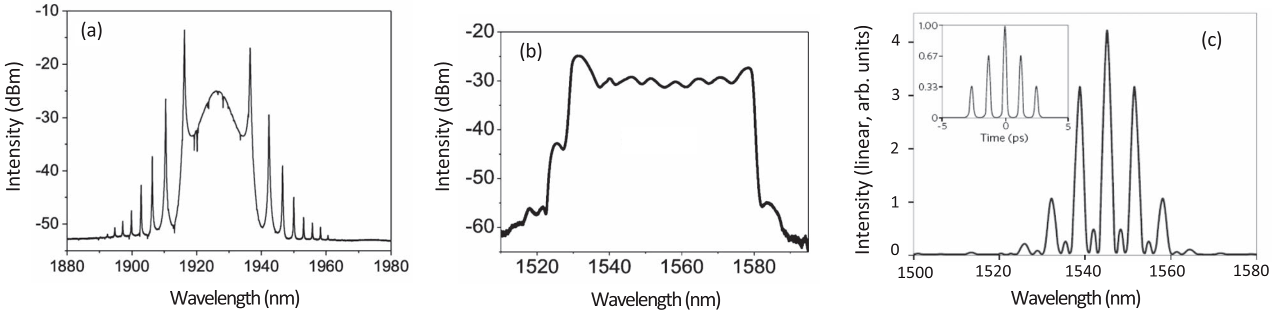

FIGURE 39.3 Some typical spectral features observed with passively mode-locked fibre lasers. (a) Spectral sidebands superimposed on the soliton spectrum, in the anomalous-dispersion regime. (b) Rectangular spectral profile obtained in the normal-dispersion regime. (c) Modulated soliton spectrum of a stable three-soliton molecule laser output, also confirmed in the temporal domain by the optical autocorrelation (inset).

average cavity dispersion. Note that the sidebands become asymmetrically located whenever third-order dispersion is no longer negligible with respect to the second-order dispersion. In addition, as quasi-continuous wave components, the sidebands can be subjected to modulation instability at sufficiently high power, leading to a more complex sideband distribution across the pulse spectrum (Tang et al. 2001a).

39.3.3 Multi-Pulsing Instability

In soliton fibre lasers, the spectral sidebands tend to grow along the increase of the pumping power, until a multi-pulsing instability develops. The latter is responsible for the generation of one or several additional pulses within the cavity (Komarov et al. 2005, Liu 2010). These multiple pulses generally share the same field profile and thus carry the same energy, giving the sense of an energy quantization within the laser cavity (Grudinin et al. 1992). After one such multi-pulse transition has occurred, the energy taken by the dispersive waves is reduced (Gutty et al. 2001). Such scenario can go on repeatedly as the pumping power is increased. For a fibre laser operated in the anomalous dispersion regime under multi-Watt pumping power, several hundreds of identical pulses can circulate simultaneously round the cavity (Haboucha et al. 2008, Lecaplain and Grelu 2013). These pulses will always interact, since being regenerated one roundtrip after another, they have virtually an infinite time to express the variety of their interaction processes, even in the case of faint interaction (Sanchez et al. 2014, Weill et al. 2016). Therefore, a wide range of pattern formations can take place, according to the hierarchy of pulse interactions that in turn depends precisely on the set of cavity parameters. Common patterns range from passive harmonic mode locking (HML) (Grudinin and Gray 1997), which is dominated by repulsive interactions (Kutz et al. 1998), to pulse bunching, dominated by attractive ones (Richardson et al. 1991). In particular, HML appears as a very promising option to multiply the pulse repetition rate within the relatively long fibre cavity, and therefore reach the multi-GHz repetition rate that is otherwise typical from the semiconductor laser platform, while benefitting from the higher optical power and shorter pulse duration delivered by the fibre laser platform (Pang et al. 2015). Among pulse bunching cases, stable bound states can form, called *soliton molecules*, which will be explained in the following section. Nevertheless, multiple pulsing is generally considered as a major setback that hampers the scaling of the pulse energy with the pump power, owing to the limitation imposed by the soliton area theorem.

Whereas we have seen that a laser cavity poses a number of issues to implement the soliton dynamics, one can also take advantage of the subsequent propagation after the laser output to improve the pulse features in accordance to the applicative needs. By using an optimized passive fibre link connected to the laser output, it is indeed possible to benefit from well-known solitonic effects, such as soliton compression to get shorter pulses and higher peak power (Chernikov et al. 1993, Travers et al. 2007), or soliton self-frequency shift to obtain a widely tunable pulse source (Mitschke and Mollenauer 1986, Nishizawa et al. 2000).

39.4 The Concept of Dissipative Solitons

39.4.1 Beyond Conventional Solitons

In the multiple-pulse regime, the rich pattern-forming dynamics that is found experimentally in fibre lasers cannot be explained by the conventional soliton dynamics that applies to the passive optical fibres. First, the formation of multiple identical ultrashort pulses within the laser cavity involves the repeated action of an attracting state of dissipative nature (Grelu and Akhmediev 2012). This is opposed to the generation of a soliton family comprising pulses of various duration and energy from passive optical fibre rings (Schwache and Mitschke 1997). Second, understanding the self-formation of peculiar pulsed laser outputs such as the ubiquitous *soliton molecules* (Gutty et al. 2001, Tang et al. 2001b) requires going beyond the conventional soliton propagation model, which does not predict a stable equilibrium between interacting pulses (Gordon 1983).

Besides, the generation of stable ultrashort pulses in the normal-dispersion cavity regime appears counterintuitive, as it opposes the view of the chromatic dispersion balancing the accumulated self-phase modulation. Nevertheless, it dawned theoretically as early as in 1991 that a laser including dispersion management could be advantageously shifted into the net-normal-dispersion regime, to increase the pulse energy, albeit at the expense of its time-bandwidth product (Haus et al. 1991). This prediction was validated a couple of years later (Tamura et al. 1993), leading to a substantial research activity on the stretched-pulsed dynamics generated within dispersion-managed lasers, which also inspired additional innovative laser architectures (Ilday et al. 2004). Another decisive step was taken with the theoretical prediction that stable frequency-chirped pulses could be formed within an entirely normal propagation medium, i.e. without the need for dispersion compensation (Soto-Crespo et al. 1997). Such laser regime was validated experimentally a few years later (Chong et al. 2006), demonstrating an advantageous pulse energy scaling beyond 30 nJ, see the sketch of the normal-dispersion ring cavity architecture in Figure 39.1f (Kieu et al. 2009).

39.4.2 The Dissipative Soliton Paradigm

The above paradoxical ultrafast laser regimes find their interpretation within the conceptual frame of dissipative solitons (Grelu and Akhmediev 2012, see also Further Reading). As represented in the sketch of Figure 39.4a, the composite balance involving non-linear gain and loss, dispersive non-linearity and diffraction/dispersion provides a fixed soliton solution, instead of the soliton family of a passive transmission line. Such soliton, whose profile is therefore defined by the laser cavity parameters, is called a *dissipative soliton*. It acts as an attracting state: as long as energy is pumped into the system, any initial field condition belonging to the basin of attraction will converge toward the fixed dissipative soliton profile. This provides a simple way to understand the stability of mode-locked lasers, where an ultrashort pulse is able to propagate during hours or, equivalently, through billions of kilometres. Such a feat is impossible for conventional solitons, owing to

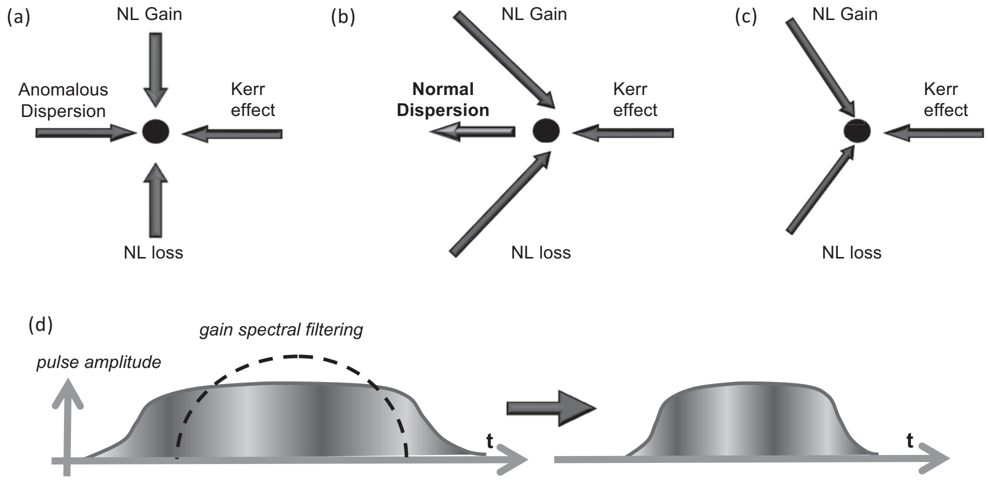

FIGURE 39.4 Dissipative soliton concepts. The dissipative soliton as a composite balance (a) in anomalous-dispersion cavity regime, (b) in the normal-dispersion cavity regime, (c) for a dispersion-less laser. (d) Explanation, from the temporal domain, of the stabilisation of the propagation of dissipative solitons in a normal-dispersion laser cavity, by using spectral filtering.

unavoidable losses and noise perturbation along any practical passive transmission line. Here, the losses are compensated, and the noise is eaten by the dissipative processes—by the saturable absorber in particular—so that its accumulation remains bounded.

39.4.3 Dissipative Solitons in the Normal Propagation Regime

The dissipative soliton paradigm applies to modelocked lasers in general, but it is particularly relevant for fibre lasers and other photonic systems where pulses experience significant amounts of non-linear gain and loss (see Further Reading). The composite balance then allows for a larger freedom in handling the contributions of the physical effects involved. Besides the double-balance extension of the soliton laser concept in Figure 39.4a, it is also possible to balance the normal chromatic dispersion, as sketched on Figure 39.4b. Tilting the arrows that represent the gain and loss terms means physically that we introduce a large level of gain/loss dispersion. Obviously, by continuity, dispersion is not a prerequisite to stable pulse propagation (Figure 39.4c). To understand better how pulses can be stabilized in the normal dispersion, Figure 39.4d represents the action of a strong spectral filtering on a highly-chirped pulse: owing to the dissipation, the extended pulse wings are clipped off, which combats the temporal broadening due to normal dispersion accentuated by self-phase modulation. Such possibility was anticipated by Haus et al. (1991): *For positive GVD, the chirp parameter can become quite large (...) Gain dispersion, instead of lengthening the pulse, shortens it. At first sight, this may seem paradoxical. However, if a pulse is chirped, frequency filtering can, in fact, shorten it, if it shaves off the high- and low-frequency wings. (…) The pulse is kept in balance by a lengthening due to positive GVD. Of course, the gain dispersion also narrows the pulse spectrum. This spectral narrowing is compensated for by SPM* (Haus et al. 1991).

Consequently, ultrashort pulses generated from laser cavities that are operated in the normal dispersion regime always present a large amount of frequency chirping. This is precisely one efficient way to circumvent the pulse energy limitation applying to soliton lasers. Owing to a reduced peak power, a chirped pulse can propagate without suffering breakup instabilities, at a much higher pulse energy. In essence, the strategy is similar to that of chirped-pulse amplification (CPA) (Strickland and Mourou 1985), except that it is implemented inside of the laser cavity. Therefore, the energetic chirped pulses need to be compressed after the laser output (Kieu et al. 2009).

39.4.4 Dissipative Soliton and Frequency Chirping

A dissipative soliton pulse always presents frequency chirping. Fundamentally, recalling that energy flows through phase gradients, the non-uniform phase profile of the pulse is dictated by the necessary energy redistribution resulting from the action of non-linear gain and loss. Therefore, in addition to a linear chirp part, the pulse generally presents non-linear frequency chirping that is more difficult to compensate. Dissipative soliton pulses can therefore present temporal profiles that are very different from the sech^2 shape of an NLS soliton, as well as from the typical Gaussian shape of a linearly-chirped pulse. For instance, flat-top pulse profiles are common in the normal-dispersion regime. Naturally, this is also reflected in the spectral domain, where the optical spectra of modelocked pulses in normally-dispersive laser cavities present a plateau with steep edges, see Figure 39.3b. The spectrum often includes broad bounces right before these edges, which make an "M-shaped" spectral profile (Kieu et al. 2009).

39.4.5 Dissipative Soliton Molecules

The dissipative soliton nature reveals itself in other situations, including for lasers operating in the anomalous-dispersion regime. For the latter, the conventional soliton theory can only be considered as a first approach to describe optical pulses having a small amount of frequency chirping. The limit of the conventional soliton theory is met when soliton pulses interact to form a stable optical soliton molecule. Soliton molecule formation is a universal behaviour observed among the whole range of ultrafast lasers operating in the multiple pulse regime (Grelu and Akhmediev 2012). The soliton-pair molecule is the simplest one: it consists of a bound state of two mutually-trapped optical pulses at a temporal separation of a few pulse widths. It results from a complex pulse attractor, which explains the self-assembly and subsequent stability of the soliton molecule. The experimental characterization of self-phase-locked soliton molecules has yielded sub-femtosecond timing jitter for the relative separation between the two ultrashort pulses (Shi et al. 2018). Molecules comprising higher number of pulse constituents are also commonly observed. In general, soliton molecules can be analysed from the spectral domain, since the interference among multiple pulses produces spectral fringes of high contrast, see Figure 39.3c. In the soliton-pair molecule case, the temporal separation between the two solitons is simply the inverse of the spectral interfringe, whereas the offset of the fringe pattern with respect to the central wavelength yields the relative phase between the solitons.

39.5 Applications of Dissipative Solitons

Beyond providing a consistent frame to understand the complex dynamics of ultrafast lasers, the dissipative soliton paradigm has stimulated the creative design of new mode-locked laser architectures, bypassing the former prerequisites of a low-loss cavity and dispersion compensation. Note that this conceptual margin has been possible thanks to the large gain available from the rare-earth doped fibres.

39.5.1 The Quest of High-Energy Pulses from Laser Oscillators

Increasing the output pulse energy is the most recurrent objective with fibre lasers, which confronts the pulse breakup issue at higher pump powers. The overdrive of the saturable absorber, the excess of self-phase modulation, and/or other higher-order effects (Raman effect, thermal mode instability, component damage) can either lead to multiple pulsing or to the disruption of mode locking. There are two main remediation directions. The first one is to act on the spatial (transverse) domain: the larger the effective mode area, the less the nonlinear impairments, so the larger the pulse energy. This is efficient and scalable, but remains highly technical, involving for instance either LMA fibres, rod-type fibres (Ortaç et al. 2007) or thin-disk lasers (Marchese et al. 2008). Note that coherent beam combining is the current step forward in this direction, leading to millijoule-class ultrafast fibre laser oscillator systems of kW average optical power (Kienel et al. 2016). The second direction is to act on the temporal domain: by stretching the pulse, thus limiting peak optical intensities, high-energy pulses can be generated. As explained above, this is precisely the chosen field of dissipative solitons, with various laser cavity architectures possibilities, as introduced below. Naturally, the two approaches can be combined, paving the way for unprecedented pulse energy levels directly out of robust fibre or waveguide laser oscillators, leading after pulse compression to MW-level peak powers (Baumgartl et al. 2010).

39.5.2 Innovative Chirped-Pulse Laser Architectures

The Stretched-Pulse Fibre Laser. The original stretched-pulse fibre laser cavity developed in the early 90s is based on a concatenation of optical fibres having opposite dispersion signs, so as to present an average dispersion close to zero (Tamura et al. 1993). Such contrast between the local and the average dispersion is responsible for a large temporal breathing of the laser pulse that repeats twice per roundtrip (Turitsyn et al. 2012). Consequently, there are two locations where the pulse duration is close to the Fourier-transform limit. Elsewhere in the cavity, the pulse is stretched, with a stretching factor that can be in excess of 10. Using standard optical fibres and components, the laser can generate pulses with energies in the few-nJ range and peak power around 20 kW after external pulse compression (Lenz et al. 1995). Compared with conventional soliton lasers, dispersion-managed lasers achieve a typical ten-fold increase of the pulse energy.

Self-Similar Evolution. Is it possible to improve the stretched-pulse strategy? The existence of two locations within the cavity where the pulse is compressed remains a weak point, as instabilities are prone to develop around these locations of highest peak power. It is desirable to develop a larger pulse stretching, while limiting the peak power where the pulse is at its minimum duration. Self-similar propagation is one interesting solution in that respect. In the normal dispersion regime, a pulse can acquire a monotonic chirp and evolve toward a self-similar parabolic profile that avoids pulse breakup (Anderson et al. 1993, Fermann et al. 2000). In 2004, this propagation regime was implemented in a fibre laser cavity and subsequently developed (Ilday et al. 2004, Oktem et al. 2010). Self-similar propagation allows to gain nearly another order of magnitude in the pulse energy, while parabolic pulses can be easily compressed. Implementing such a marked internal evolution within the laser cavity requires to reset the pulse after every cavity roundtrip: this is the *self-consistency* issue. Self-consistency is here obtained by inserting a relatively narrow spectral filter, which shrinks the chirped pulse in both temporal and spectral domains, allowing for the subsequent roundtrip self-similar evolution. Again, such a strategy opposes the conventional handling of cavity losses, but finds its full justification within the dissipative soliton concept: high losses, if deeply associated with the non-linear dynamics, can be useful to define a suitable attracting pulse state. Similarly, spectral filtering is essential for the consistency of the roundtrip propagation in the all-normal-dispersion lasers, as explained earlier.

Ultralong All-Normal Cavities. Higher frequency chirping can be provided in ultralong fibre laser cavities operating in the normal-dispersion regime (Kelleher et al. 2009). For a given allocated pump power, which limits the average laser output power, increasing the cavity length allows for an increased pulse energy. In 2008, by using a 3.8-km long fibre, researchers achieved an additional increase of the dissipative-soliton energy by two orders of magnitude, generating 3-ns highly-chirped pulses with a 3.9 μJ energy (Kobtsev et al. 2008). Note that long fibre cavities generally require additional stabilization, as they are more sensitive to environmental perturbations. It is also important to mention that propagation of wideband energetic pulses in long fibre cavities favours *stimulated Raman scattering*. The latter may convert the excess energy out of the coherent dissipative soliton into a noisy Raman pulse, thus limiting its energy (Aguergaray et al. 2013). However, it has been shown that an appropriate two-track feedback scheme allowed for the formation of a coherent two-color Raman dissipative soliton (Babin et al. 2014).

39.5.3 Peculiar Laser Pulses

Dissipative Soliton Resonance. Normal dispersion may not be always required to generate ultralong energetic pulses. Within an ultrafast laser, a specific balance among dissipative and dispersive physical effects can lead to the formation of ultralong rectangular pulses carrying high energy. This phenomenon, which is accentuated within a limited range of cavity parameters, is called *dissipative soliton resonance* (DSR), and can take place in both dispersion regimes (Grelu et al. 2010). It makes an interesting alternative to ultralong cavities for the generation of ns-long pulses with μJ energy level (Seeman et al. 2016). However, in practice, the temporal coherence of experimental DSR pulses needs to be investigated further, as such parameter resonance can become unstable in presence of perturbations, leading to the formation of *noise-like* rectangular pulses.

Noise-Like Pulses. Under higher pumping power, a peculiar instability can take place. Instead of either generating additional dissipative soliton pulses, or completely disrupting the short-pulse laser operation, the laser can sustain the propagation of a high-energy optical burst, or *noise-like pulse* (Horowitz et al. 1997). This regime looks paradoxical, as the pulse is subjected at a same time to a strong instability and to a strong temporal localization that maintains its short duration—*picosecond* to *nanosecond*, typically. Since it propagates round the cavity, and generates a broad averaged optical spectrum, it resembles to mode locking. However, shot-to-shot spectral measurements confirm the pulse incoherence (Runge et al. 2013). This regime leads to a generalization of the dissipative soliton concept to incoherent pulses, this time with the presence of a *chaotic attractor*. Noise-like pulses could be used in a few applications requiring low coherence and high pulse energy, such as in optical coherence tomography and laser ranging.

39.6 Prospects

Ultrafast fibre laser development has been continuously expanding over the past two decades, stimulated by novel soliton concepts and fuelled by major advances in materials and integrated components. Obviously, laser applications are always eager to implement one or several of the following upgrades: higher pulse energy, higher pulse-repetition rate, new spectral window, shorter pulse duration. In near future, some applications may also request more agility, versatility, and self-starting resilience from the ultrafast laser source itself, in the wake of the early development of *smart lasers*, i.e. lasers combining dissipative soliton dynamics, automated ultrafast measurement and machine learning (Andral et al. 2015, Woodward and Kelleher 2016, Winters et al. 2017).

Soliton energy scalability will benefit from the ongoing development of ultrafast lasers operated in the transverse multimode regime. Indeed, the discovery of novel spatiotemporal propagation regimes reenables the transverse degree of freedom for dissipative soliton waveguide and fibre lasers. This represents a wide margin to increase the transverse effective area of the guided pulse, and support the propagation of higher-energy solitons (Wright et al. 2017, Guenard et al. 2017, Qin et al. 2018). The generalization of the optical temporal soliton to the transverse spatial dimensions is also called a *light bullet*, which could find applications in parallel all-optical processing. Beyond mode-locked laser cavities, other oscillator architectures involving stable attracting states can also be developed. Such is the case with *Mamyshev oscillators*, based on *Mamyshev regenerators* (MR) (Mamyshev 1998). A MR combines a high amount of SPM followed by a strong spectral filtering to regenerate optical pulses at a carrier wavelength that is significantly offset from the initial central wavelength by, say, $\Delta\lambda$. By adding a spectrally-symmetric MR, namely an optical regenerator that regenerates optical pulses at a carrier wavelength offset by $-\Delta\lambda$, and operating within an optical amplifying loop, a stable roundtrip propagation can be obtained. That stable pulse propagation is attributed to a special type of dissipative soliton attractor, which tolerates a large amount of SPM and therefore circumvents efficiently the pulse breakup at high optical intensity (Regelskis et al. 2015, Fu et al. 2018). Note that Mamyshev oscillators cannot be truly considered as mode-locked lasers, as in most configurations, these are not lasing in quasi-continuous wave and therefore do not sustain cavity modes. These oscillators require an optical injection to initiate the pulse propagation, or in the language of non-linear dynamics, to enter the basin of attraction of the dissipative soliton.

Besides the quest of higher-energy dissipative solitons, there is also an intense research activity focused on special soliton patterns generated from mode-locked fibre lasers. This research encompasses the study of soliton molecules, which has been accentuated by the recent availability of real-time ultrafast characterization techniques. Among these techniques, the time-stretch dispersive Fourier-transform technique has become the most popular, as it allows to monitor single-shot optical spectra from low-power laser oscillators within a simple experimental setup (Goda and Jalali 2013). Therefore, various ultrafast dynamics of soliton molecules can be precisely monitored and interpreted (Krupa et al. 2017, Herink et al. 2017). Whereas this research remains fundamental so far—the fibre laser platform serving as a universal testbed of non-linear dynamics—some applications of pulse patterns could appear in future, such as for optical data encoding in multilevel schemes (Rohmann et al. 2012). In addition, understanding better and controlling dissipative soliton interactions in a laser cavity could lead to passively mode-locked laser sources at high harmonics (multi-GHz repetition rates) with unprecedented stability. To this goal, hybrid laser cavities combining the respective advantages of the optical fibre and those of the planar waveguide technology represent an interesting possibility (Peccianti et al. 2012). Finally, by considering further polarization, carrier wavelength and spatial modes, possibly in combination, and their non-linear coupling, the possibilities of soliton and dissipative soliton dynamics in fibre and waveguide lasers seem limitless.

REFERENCES

Aguergaray C, Runge A, Erkintalo M and Broderick N G R 2013 Raman-driven destabilization of mode-locked long cavity fiber lasers: fundamental limitations to energy scalability *Opt. Lett.* **38** 2644.

Anderson D, Desaix M, Karlsson M, Lisak M and Quiroga-Teixeiro M L 1993 Wave-breaking-free pulses in nonlinear-optical fibers *J. Opt. Soc. Am. B* **10** 1185.

Andral U, Si Fodil R, Amrani F, Billard F, Hertz E and Grelu P 2015 Fiber laser mode locked through an evolutionary algorithm *Optica* **2** 275.

Babin S A et al. 2014 Multicolour nonlinearly bound chirped dissipative solitons *Nat. Commun.* **5** 4653.

Baumgartl M, Ortaç B, Lecaplain C, Hideur A, Limpert J and Tünnermann A 2010 Sub-80 fs dissipative soliton large-mode-area fiber laser *Opt. Lett.* **35** 2311.

Chernikov S V, Dianov E M, Richardson D J and Payne D N 1993 Soliton pulse compression in dispersion-decreasing fiber *Opt. Lett.* **18** 476.

Chong A, Buckley J, Renninger W and Wise F 2006 All-normal-dispersion femtosecond fiber laser *Opt. Express* **14** 10095.

Deslandes P et al. 2013 Picosecond to femtosecond pulses from high power self-mode–locked ytterbium rod-type fiber laser *Opt. Express* **21** 10731.

Doran N J and Wood D 1988 Nonlinear-optical loop mirror *Opt. Lett.* **13** 56.

Fermann M E, Haberl F, Hofer M and Hochreiter H 1990 Nonlinear amplifying loop mirror *Opt. Lett.* **15** 752.

Fermann M E, Kruglov V I, Thomsen B C, Dudley J M and Harvey J D 2000 Self-similar propagation and amplification of parabolic pulses in optical fibers *Phys. Rev. Lett.* **84** 6010.

Fu W, Wright L G, Sidorenko P, Backus S and Wise F W 2018 Several new directions for ultrafast fiber lasers *Opt. Express* **26** 9432.

Goda K and Jalali K B 2013 Dispersive Fourier transformation for fast continuous singleshot measurements *Nat. Photon.* **7** 102.

Gordon J P 1983 Interaction forces among solitons in optical fibers *Opt. Lett.* **8** 596.

Gordon J P 1992 Dispersive perturbations of solitons of the nonlinear Schrödinger equation *J. Opt. Soc. Am B* **9** 91.

Grelu Ph and Akhmediev N 2012 Dissipative solitons for mode-locked lasers *Nat. Photonics* **6** 84.

Grelu Ph, Chang W, Ankiewicz A, Soto-Crespo J M and Akhmediev N 2010 Dissipative soliton resonance as a guideline for high-energy pulse laser oscillators *J. Opt. Soc. Am. B* **27** 2236.

Grudinin A B and Gray S 1997 Passive harmonic mode locking in soliton fiber lasers *J. Opt. Soc. Am. B* **14** 144.

Grudinin A B, Richardson D J, and Payne D N 1992 Energy quantization in figure eight fibre laser *Electron. Lett.* **28** 67.

Guenard R et al. 2017 Kerr self-cleaning of pulsed beam in an ytterbium doped multimode fiber *Opt. Express* **25** 4783.

Gutty F, Grelu Ph, Huot N, Vienne G, and Millot G 2001 Stabilisation of modelocking in fibre ring laser through pulse bunching *Electron. Lett.* **37** 745.

Haboucha A, Leblond H, Salhi M, Komarov A and Sanchez F 2008 Analysis of soliton pattern formation in passively mode-locked fiber lasers *Phys. Rev. A* **78** 043806.

Hänsel W et al. 2017 All polarization-maintaining fiber laser architecture for robust femtosecond pulse generation. *Appl. Phys. B* **123** 41.

Hasegawa A and Kodama Y 1990 Guiding center soliton in optical fibers *Opt. Lett.* **15** 1443.

Hasegawa A and Tappert F 1973 Transmission of stationary nonlinear optical pulses in dispersive dielectric fibers I—anomalous dispersion *App. Phys. Lett.* **23** 142–4.

Haus H A, Fujimoto J G and Ippen E P 1991 Structures for additive pulse mode locking *J. Opt. Soc. Am. B* **8** 2068.

Herink G, Kurtz F, Jalali B, Solli D R and Ropers C 2017 Real-time spectral interferometry probes the internal dynamics of femtosecond soliton molecules *Science* **356** 50.

Horowitz M, Barad Y and Silberberg Y 1997 Noiselike pulses with a broadband spectrum generated from an erbium-doped fiber laser *Opt. Lett.* **22** 799.

Ilday F Ö, Buckley J R, Clark W G and Wise F W 2004 Self-similar evolution of parabolic pulses in a laser *Phys. Rev. Lett.* **92**, 213902.

Ippen E P, Haus H A and Liu L Y 1989 Additive pulse mode locking *J. Opt. Soc. Am. B* **6**, 1736.

Jiang T, Cui Y, Lu P, Li C, Wang A and Zhang Z 2016 All PM fiber laser mode locked with a compact phase biased amplifier loop mirror *IEEE Phot. Technol. Lett.* **28** 1786.

Jung M et al. 2014 A femtosecond pulse fiber laser at 1935 nm using a bulk-structured Bi_2Te_3 topological insulator *Opt. Express* **22** 7865.

Kelleher E J R et al. 2009 Generation and direct measurement of giant chirp in a passively mode-locked laser *Opt. Lett.* **34** 3526.

Keller U 2003 Recent developments in compact ultrafast lasers *Nature* **424** 831.

Kelly S M J 1992 Characteristic sideband instability of periodically amplified average soliton *Electron. Lett.* **28** 806.

Kelly S M J, Smith K, Blow K J and Doran N J 1991 Average soliton dynamics of a high-gain erbium fiber laser *Opt. Lett.* **16** 1337.

Kienel M, Müller M, Klenke A, Limpert J and Tünnermann A 2016 12 mJ kW-class ultrafast fiber laser system using multidimensional coherent pulse addition *Opt. Lett.* **41** 3343.

Kieu K, Renninger W H, Chong A and Wise F W 2009 Sub-100 fs pulses at watt-level powers from a dissipative-soliton fiber laser *Opt. Lett.* **34** 593.

Kobtsev S, Kukarin S and Fedotov Y 2008 Ultra-low repetition rate mode-locked fiber laser with high-energy pulses *Opt. Express* **16** 21936.

Komarov A, Leblond H and Sanchez F 2005 Multistability and hysteresis phenomena in passively mode locked fiber lasers *Phys. Rev. A* **71** 053809.

Krupa K, Nithyanandan K, Andral U, Tchofo-Dinda P and Grelu P 2017 Real-time observation of internal motion within ultrafast dissipative optical soliton molecules *Phys. Rev. Lett.* **118** 243901.

Kutz J N 2006 Mode-locked soliton lasers *SIAM Rev.* **48**, 629.

Kutz J N, Collings B C, Bergman K and Knox W H 1998 Stabilized pulse spacing in soliton lasers due to gain depletion and recovery *IEEE J. Quantum Electron.* **34** 1749.

Lecaplain C and Grelu Ph 2013 Multi-gigahertz repetition-rate-selectable passive harmonic mode locking of a fiber laser *Opt. Express* **21** 10897.

Lenz G, Tamura K, Haus H A and Ippen E P 1995 All-solid-state femtosecond source at 1.55 μm *Opt. Lett.* **20** 1289.

Liu X 2010 Hysteresis phenomena and multipulse formation of a dissipative system in a passively mode locked fiber laser *Phys. Rev. A* **81** 023811.

Maker P D, Terhune R W and Savage C M 1964 Intensity-dependent changes in the refractive index of liquids *Phys. Rev. Lett.* **12** 507.

Mamyshev P V 1998 All-optical data regeneration based on self-phase modulation effect *24th European Conference on Optical Communication* (ECOC ’98 IEEE Cat. No. 98TH8398) p 475.

Marchese S V et al. 2008 Femtosecond thin disk laser oscillator with pulse energy beyond the 10-microjoule level *Opt. Express* **16** 6397.

Matsas V J, Newson T P, Richardson D J and Payne D N 1992 Selfstarting passively mode-locked fibre ring soliton laser exploiting nonlinear polarization rotation *Electron. Lett.* **28** 1391.

Mitschke F M and Mollenauer L F 1986 Discovery of the soliton self-frequency shift *Opt. Lett.* **11** 659.

Mollenauer L F, Stolen R H and Gordon J P 1980 Experimental observation of picosecond pulse narrowing and solitons in optical fibers *Phys. Rev. Lett.* **45** 1095–8.

Mollenauer L F and Stolen R H 1984 The soliton laser *Opt. Lett.* **9** 13–5.

Nakazawa M, Yohida E and Kimura Y 1991 Low threshold, 290 fs erbium-doped fiber laser with a nonlinear amplifying loop mirror pumped by InGaAsP laser diodes *Appl. Phys. Lett.* **59** 2073.

Nishizawa N, Okamura R and Goto T 2000 Widely wavelength tunable ultrashort soliton pulse and anti-Stokes pulse generation for wavelengths of 1.32–1.75 μm *Japan. J. Appl. Phys.* **39** L409.

Noske D U, Pandit N and Taylor J R 1992 Source of spectral and temporal instability in soliton fiber lasers *Opt. Lett.* **17** 1515.

Okhotnikov O, Grudinin A and Pessa M 2004 Ultrafast fibre laser systems based on SESAM technology: new horizons and applications *New J. Phys.* **6** 177.

Oktem B, Ülgüdür C and Ilday F Ö 2010 Soliton-similariton laser *Nat. Photon.* **4** 307–11.

Ortaç B, Schmidt O, Schreiber T, Limpert J, Tünnerman A and Hideur A 2007 High-energy femtosecond Yb-doped dispersion compensation free fiber laser *Opt. Express* **15** 10725.

Pang M. et al. 2015 Stable subpicosecond soliton fiber laser passively mode-locked by gigahertz acoustic resonance in photonic crystal fiber core *Optica* **2** 339.

Peccianti M, Pasquazi A, Park Y et al. 2012 Demonstration of a stable ultrafast laser based on a nonlinear microcavity *Nat. Commun.* **10** 1038.

Qin H, Xiao X, Wang P and Yang C 2018 Observation of soliton molecules in a spatiotemporal mode-locked multimode fiber laser *Opt. Lett.* **43** 1982.

Regelskis K, Želudevičius J, Viskontas K and Račiukaitis G 2015 Ytterbium-doped fiber ultrashort pulse generator based on self-phase modulation and alternating spectral filtering *Opt. Lett.* **40** 5255.

Richardson D J, Laming R I, Payne D N, Matsas V J and Phillips M W 1991 Pulse repetition rates in passively self-starting femtosecond soliton laser *Electron. Lett.* **37** 157.

Richardson D J, Nilsson J and Clarkson W A 2010 High power fiber lasers: current status and future perspectives *J. Opt. Soc. Am. B* **63** 27.

Rohmann P, Hause A and Mitschke F 2012 Solitons beyond binary: possibility of fibre-optic transmission of two bits per clock period *Sci. Rep.* **2** 866.

Runge A F J, Aguergaray C, Broderick N G R and Erkintalo M 2013 Coherence and shot-to-shot spectral fluctuations in noise-like ultrafast fiber lasers *Opt. Lett.* **38** 4327.

Runge A F J, Aguergaray C, Provo R, Erkintalo M and Broderick N G R 2014 All-normal dispersion fiber lasers mode-locked with a nonlinear amplifying loop mirror *Opt. Fib. Technol.* **20** 657.

Sagnac G 1913 *Sur la preuve de la réalité de l’éther lumineux par l’expérience de l’interférographe tournant C.R. Acad. Sci.* 157 1410.

Sanchez F et al. 2014 Manipulating dissipative soliton ensembles in passively mode-locked fiber lasers *Opt. Fiber Technol.* **20** 562.

Schwache A and Mitschke F 1997 Properties of an optical soliton gas *Phys. Rev. E* **55** 7720.

Seeman G et al. 2016 Generation of high energy square-wave pulses in all anomalous dispersion Er:Yb passive mode locked fiber ring laser *Opt. Express* **24** 8399.

Set S Y, Yagushi H, Tanaka Y and Jablonski M 2004 Laser mode locking using a saturable absorber incorporating carbon nanotubes *J. Lightwave Technol.* **22** 51.

Shi H, Song Y, Wang C, Zhao L and Hu M 2018 Observation of subfemtosecond fluctuations of the pulse separation in a soliton molecule *Opt. Lett.* **43** 1623.

Sotor J et al. 2015 Ultrafast thulium-doped fiber laser mode locked with black phosphorus *Opt. Lett.* **40** 3885.

Soto-Crespo J M, Akhmediev N N, Afanasjev V V and Wabnitz S 1997 Pulse solutions of the CQGLE in case of normal dispersion *Phys. Rev. E* **55** 4783.

Strickland D and Mourou G 1985 Compression of amplified chirped optical pulses *Opt. Commun.* **56** 219.

Sun Z et al. 2010 Graphene mode-locked ultrafast laser *ACS Nano* **4**(2) 803.

Tamura K, Ippen E P, Haus H A and Nelson L E 1993 77 fs pulse generation from a stretched-pulse mode-locked all-fiber ring laser *Opt. Lett.* **18** 1080.

Tang D Y, Fleming S, Man W S, Tam H Y and Demokan M S 2001a Subsideband generation and modulational instability lasing in a fiber soliton laser *J. Opt. Soc. Am. B* **18** 1443.

Tang D Y, Man W S, Tam H Y and Drummond P D 2001b Observation of bound states of solitons in a passively mode-locked fiber laser *Phys. Rev. A* **64** 033814.

Travers J C et al. 2007 Optical pulse compression in dispersion decreasing photonic crystal fiber *Opt. Express* **15** 13203.

Turitsyn S K, Bale B G, and Fedoruk M P 2012 Dispersion-managed solitons in fibre systems and lasers *Phys. Rep.* **521**(4) 135.

Weill R, Bekker A, Smulakovsky V, Fischer B and Gat O 2016 Noise-mediated Casimir-like pulse interaction mechanism in lasers *Optica* **3** 189.

Winful H G 1985 Self-induced polarization changes in birefringent optical fibers *Appl. Phys. Lett.* **47** 213.

Winters D G, Kirchner M S, Backus S J and Kapteyn H C 2017 Electronic initiation and optimization of nonlinear polarization evolution mode-locking in a fiber laser *Opt. Express* **25** 33216.

Wong W S, Namiki S, Margalit M, Haus H A and Ippen E P 1997 Self-switching of optical pulses in dispersion-imbalanced nonlinear loop mirrors *Opt. Lett.* **22** 1150.

Woodward R I and Kelleher E J R 2016 Towards ‘smart lasers’: self-optimisation of an ultrafast pulse source using a genetic algorithm *Sci. Rep.* **6** 37616.

Wright L G, Christodoulides D N and Wise F W 2017 Spatiotemporal mode-locking in multimode fiber lasers *Science* **358** 94.

Zakharov V E and Shabat A B 1972 Exact theory of two-dimensional self-focusing and one-dimensional self-modulation of wave in nonlinear media *J. Experim. Theor. Phys.* **34** 62.

FURTHER READING

2013 Nature Photonics Issue on Fiber Lasers **7**(11) 841–82.

A special issue with emphasis on high-power fibre lasers.

Agrawal G P *Nonlinear Fiber Optics* (4th Edition, Academic Press, New-York, 2007).

The reference book to understand the variety of nonlinear effects relevant in fiber optics and apprehend the conditions under which they exert and can be utilized.

Akhmediev N and Ankiewicz A (ed) 2005 *Dissipative Solitons* (Springer, Berlin Heidelberg); 2008 *Dissipative Solitons: from Optics to Biology and Medicine* (Springer Verlag, Berlin Heidelberg).

These two multi-authored volumes unfold the background and applications of dissipative solitons applied to various research fields, in photonics and other disciplines of nonlinear science.

Delavaux J M, Grelu Ph, Pu W, and Ilday F Ö (eds) 2014 Special issue on short-pulse fiber lasers. *Opt. Fiber Technol.* **20**(6) 561.

A special issue covering various pulse emission regimes and wavelength.

Grelu Ph (ed) 2016 *Nonlinear Optical Cavity Dynamics: From Microresonators to Fiber Lasers* (Wiley-VCH, Weinheim).

A multi-authored review presenting many aspects of soliton dynamics from various platforms in photonics.

Okhotnikhov O (ed) 2012 *Fiber Lasers* (Wiley-VCH Verlag, Weinheim).

A multi-authored review covering high-power fibre lasers and amplifiers, and extension of wavelength coverage. Presents a variety of advanced fibre technology and fibre laser architectures.

Taylor & Francis
Taylor & Francis Group
http://taylorandfrancis.com

40

Bismuth-Doped Fibre Lasers and Optical Amplifiers

Evgeny Dianov, Mikhail Melkumov, and Sergei Firstov

CONTENTS

40.1 Introduction 535
40.2 Distinctive Features of Bismuth as an Active Element and the Nature of Bismuth-Related NIR Active Centres in Glasses 536
40.3 NIR Luminescence Properties of Bi-Doped Fibres (BDFs) 539
40.4 Excited State Absorption (ESA) in BDFs 542
40.5 Continuous-Wave Bi-Doped Fibre Lasers (CW BDFLs) 544
  40.5.1 Bi-Doped Aluminosilicate Fibre Lasers 545
  40.5.2 Bi-Doped Phosphosilicate Fibre Lasers 546
  40.5.3 Bi-Doped Germanosilicate Fibre Lasers (Small Concentration of GeO_2) 547
  40.5.4 Bi-Doped Germanosilicate Fibre Lasers (Large Concentration of GeO_2) 548
40.6 Bi-Doped Optical Fibre Amplifiers (BDFAs) 549
  40.6.1 Bi-Doped Phosphosilicate and Germanosilicate (with Low Ge Content) Fibre Amplifiers 550
  40.6.2 Bi-Doped Germanosilicate Fibre Amplifier (Large Concentration of GeO_2) 550
40.7 Bismuth-Doped Superfluorescent Fibre Sources 551
40.8 Conclusions 552
References 553

40.1 Introduction

Since the appearance of the first lasers in 1960, great attention has been paid to the search for and the fabrication of novel active laser materials which made it possible to improve the performance of existing lasers and to create new ones. This area of new laser materials research continues to attract great attention because of a constant demand for novel lasers and optical amplifiers for various applications.

In the last 10–15 years there appeared a growing interest in Bi-doped glasses and optical fibres. These materials demonstrate intensive and long lifetime luminescence in a spectral region of 1000–1800 nm. It is important that this region includes the ranges from 1150 to 1500 nm and from 1600 to 1800 nm, where efficient rare-earth fibre lasers and optical amplifiers are absent. But these spectral regions are very promising for a number of important applications, such as advanced optical communication, medicine, astrophysics and spectroscopy. In particular, Bi-doped optical fibres with amplification in extended transmission bands have a potential to meet growing demands of both existing and forthcoming optical fibre communication systems [16]. At present, modern commercial long-haul transmission systems have per-fibre capacities of up to 10 Tbit s^{-1} using a narrow transmission band of 80 nm (1530–1610 nm) determined by the gain band of erbium-doped fibre amplifiers (EDFAs). The data rate in experimental systems has reached ~100 Tbit s^{-1}. This is a tremendous success in the development of optical fibre communication systems, but now the demand for information in the developed countries increases by 30%–60% every year [97]. This means that in 10 years data transmission at petabit rates will be highly required. A number of approaches to solve this problem were discussed in the literature (see e.g. Ref. [70]). One of the possibilities is to extend the spectral range of data transmission using the transmission bands 1300–1500 nm and 1600–1700 nm (see e.g. Ref. [15]) where the optical losses of silica-based fibres are under 0.4 dB km^{-1} (Figure 40.1). But there are no efficient fibre lasers and optical amplifiers in these spectral bands. That is why the discovery of broadband near IR (NIR) luminescence from Bi-doped silica glass in 2001 [51] caused a noticeable interest and the appearance of a number of papers devoted to the investigations of NIR luminescence in various Bi-doped glasses. Intensive broadband luminescence was observed in these glasses confirming the perspective of Bi-doped glasses as an active material for the NIR region (see e.g. Refs. [78,79,68,77,67]).

The interest in Bi-doped materials increased greatly after the creation of the first Bi-doped optical fibres [34,55] and the demonstration of the first Bi-doped fibre laser (BDFL) in 2005 [23]. Until now, several hundred papers concerning the NIR luminescence characteristics of various Bi-doped materials—glasses, crystals, liquids, optical fibres, films—have been published. The results of the non-fibre materials investigations can be found in the review papers [17,57,95]. The most

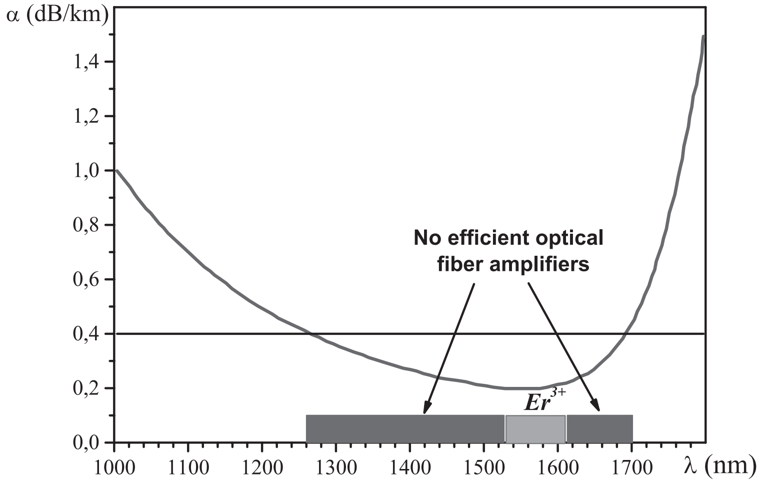

FIGURE 40.1 The low-loss spectrum of silica-based optical fibres and the spectral regions: green—the EDFA gain band, used for high-bit-rate transmission; red—promising as low-loss (<0.4 dB km^{-1}) extended transmission bands [16].

interesting and promising for applications results have been obtained on the development and investigation of various Bi-doped silica-based fibres and the creation of new fibre lasers and optical amplifiers on their base.

The first Bi-doped optical fibres were fabricated using the modified chemical vapour deposition (MCVD) technique that is typically used for fabrication of low-loss optical fibres. The core of these fibres consisted of Bi-doped aluminosilicate glass. Bi and Al were incorporated into the core by a solution technique. Later, various types of Bi-doped optical fibres were developed including fibres with the cores consisting of Bi-doped SiO_2, GeO_2, P_2O_5-SiO_2, GeO_2-SiO_2 and P_2O_5-GeO_2-SiO_2 glasses. The first BDFL was constructed using a Bi-doped aluminosilicate fibre and the cw laser generation with a slope efficiency of 10% was achieved in a spectral range 1150–1215 nm. A Nd:YAG laser with a wavelength of 1064 nm was used as a pump source. The demonstration of the first Bi-doped aluminosilicate fibre laser initiated the active development and investigations of such lasers. A number of BDFLs were constructed including cw lasers with higher efficiency [2,80,27,58,33], yellow frequency-doubled bismuth fibre lasers [27,33,22,87,31] and mode-locked lasers [26,62]. Later on, much successful effort was made to develop BDFLs and BDFAs (bismuth-doped fibre amplifiers) for longer wavelengths. BDFLs and optical amplifiers were demonstrated in a spectral range of 1260–1775 nm using Bi-doped phosphogermanosilicate, germanosilicate (with small and large amount of GeO_2) fibres [24,8,25,43,35,10,48].

The investigations carried out and the results obtained have shown that despite great success in developing the technology of Bi-doped fibres (BDFs) and creating BDFLs, some problems are not solved yet. The main problem is that we do not know exactly the nature of the bismuth NIR emitting centres [18]. This prevents one from solving some other problems which are associated, to a considerable extent, with the distinctive features of bismuth as an active element.

In this paper we first discuss the distinctive features of bismuth as an active element and the nature of Bi-related active centres (BACs) in glasses. Then, we present NIR luminescence properties of various BDFs. One of the possible reasons for the low efficiency of some BDFLs is the excited state absorption (ESA). The results of the measurements of the ESA in various Bi-doped fibres are described. Subsequently, recent results on the creation of cw BDFLs, and BDFAs operating in a spectral region of 1150–1800 nm are reported. Besides, the results on the development of Bi-doped superfluorescence fibre sources are provided. In the conclusion, we will underline key scientific and technological problems which should be solved to improve the efficiency of BDFLs.

40.2 Distinctive Features of Bismuth as an Active Element and the Nature of Bismuth-Related NIR Active Centres in Glasses

Bismuth is a polyvalent element with four oxidation states: Bi^{5+}, Bi^{3+}, Bi^{2+} and Bi^{+}. Usually bismuth oxide Bi_2O_3 or some salts (with Bi oxidation state 3+) are used as raw materials in Bi-doped glass synthesis. It is well known that Bi^{3+} and Bi^{2+} ions emit visible luminescence and no NIR luminescence [75,82,54,94]. The results of many experiments demonstrate clearly that NIR luminescence in Bi-doped glasses is observed because of the reduction of Bi^{3+} ions to a lower oxidation state.

Polyvalent ions in molten glass are in reduction/oxidation (redox) equilibrium, as described by the equation:

$$\mathrm{Me}^{x+n} + \frac{n}{2}\mathrm{O}_2 \leftrightarrow \mathrm{Me}^{x} + \frac{n}{4}\mathrm{O}_2 \tag{40.1}$$

where Me^{x+n} and Me^{x} are polyvalent ions in the oxidation and reduction states, respectively, and n represents the number of transferred electrons. Generally, the redox equilibrium of metal ions moves toward the reduction side with the increase of melting temperature.

Bismuth is “the wonder metal”: with no other element do reduction reactions proceed so extensively and produce such a variety of products [13]. With the increase of melting temperature of Bi-doped glasses the following change in the valent state of bismuth takes place [60]:

$$Bi^{3+} \rightarrow Bi^{2+} \rightarrow Bi^{+} \rightarrow Bi/Bi_2,\ Bi_2-,\ Bi_3,\ \text{etc.} \rightarrow (Bi)_n \tag{40.2}$$

where Bi_2, Bi_2-, Bi_3, etc. are Bi clusters and $(Bi)_n$ is metallic colloid

This process depends strongly on the melting temperature, the glass composition, the atmosphere and the concentration of polyvalent elements. An extensive reduction reaction makes it difficult to control the Bi^{3+} reduction to the necessary oxidation state. Excessive reduction results in the formation of Bi clusters and colloids and in the increase of the unsaturable absorption of active media. So an efficient operation of BDFLs takes place at the low initial Bi concentrations (≤0.01 at.%), and laser generation has not been obtained in bulk samples of Bi-doped glasses.

The indicated distinctive features of bismuth, especially those leading to low Bi concentration in active medium, makes it difficult to determine the valence state of Bi and the exact nature of Bi-related NIR emitting centres in glasses. At present, there are following hypotheses concerning the origin of the NIR emission from Bi-doped glasses: Bi^{5+}, Bi^0, Bi^+, Bi clusters, BiO, dimer ions Bi_2, Bi_2-, Bi_2^{2-}, point defects. But none of them has been directly confirmed. These hypotheses have been analysed in detail in Ref. [76]. Now only some brief comments will be made. Bi^{5+} could not be a source of NIR luminescence in glasses, it was shown convincingly in Ref. [76]. The authors of the paper [89] measured luminescence spectra of germanate glasses doped with various p-elements (1 mol.% of Bi_2O_3, PbO, SnO_2 and Sb_2O_3) and codoped with 12 mol.% of AlF_3 on excitation at 514, 680, 800 and 980 nm. All glasses showed similar luminescence spectra what, in the authors' opinion, indicated similarity of NIR emitting centres. On the base of this result the authors made a conclusion that centres responsible for NIR luminescence are most likely point defects or localized states in the host medium but not the dopant ion itself. But the authors did not suggest any definite structure of the NIR emitting centres.

On the other hand, our recent results show that the NIR luminescence spectra of the same fibres doped with Bi, Pb and Te are not similar [6,20].

The molecule BiO was proposed as a source of NIR luminescence in Bi-doped glasses because NIR luminescence from BiO molecules in the gas phase was so similar to that from the Bi-doped alkaline-earth metal silicate glass [83]. But it is doubtful that the properties of BiO molecules dispersed in glasses are similar to those of BiO molecules in the gas phase.

The rest of hypotheses include Bi^+ ion, Bi atom and clusters of several Bi atoms—Bi_2, Bi_2^-, Bi_2^{2-}. We doubt that these hypotheses can explain all properties of NIR luminescence in Bi-doped glasses.

We suggest a new approach to determine the origin of NIR luminescence in Bi-doped glasses based on the results of the extensive research on the luminescence spectra and lasing performance of crystals doped with Tl and Pb. These elements are bismuth's neighbours in the sixth period of the Periodic Table, and all three have many similar properties. These results allow one to draw a more definite conclusion regarding the origin of NIR luminescence in Bi-doped glasses and glass optical fibres [19]. The identified optically active Tl and Pb centres, containing anion vacancies, have the NIR luminescence bands in a range of 900–1700 nm at the excitation wavelengths from 400 to 1000 nm [69,1,50]. Given that the NIR bismuth luminescence bands practically in all bismuth-doped glasses are also located in this spectral region, and that Tl^0, Pb^+ and Bi^{2+} are isoelectronic with each other ($6s^26p^1$), there are good grounds to suppose that the NIR Bi emitting centres in glasses have a structure similar to those of Tl and Pb centres in crystals, that is, include oxygen vacancies. It is very important to note here that Bi-doped silica-based glasses and optical fibres contain noticeable quantity of oxygen vacancies, their number depending on the fabrication conditions and the glass compositions.

For example, the following three emitting centres were identified in SrF_2:Pb^{2+} X-ray irradiated at 300°K: Pb^+ ion + anion vacancy, Pb^+–Pb^{2+} dimer with ions adjacent to anion vacancy, Pb atom flanked by a pair of anion vacancies (Figure 40.2) [50]. So it was predicted that the following BACs could be a source of NIR luminescence [19]: Bi^{2+} ion + oxygen vacancy, Bi^{2+}–Bi^{3+} dimer with Bi ions adjacent to oxygen vacancy and Bi^+ ion flanked by a pair of oxygen vacancies. It was also underlined that, depending on the glass composition and the fabrication conditions, only some of the above-mentioned centres may be formed. On the other hand, some other active centres are not excluded.

Some results of our recent experiments could be explained by a structure of BACs which includes oxygen vacancies [14,53,30]. Besides, the first-principle study of possible Bi active NIR centres in SiO_2 and GeO_2 glass model hosts shows that BACs, which include oxygen deficiency centres ODC (I) [93] or ODC (II) [92], can be formed. Here, ODC (I) is attributed to the neutral oxygen vacancy ("Si-Si bond" or "relaxed oxygen vacancy") with the absorption band at 7.6 eV. ODC (II) was initially attributed to another oxygen vacancy ("non-relaxed oxygen vacancy" or "B_2 centre"). Now, it is widely accepted that ODC (II) is a two-fold-coordinated Si atom (Si^0_2 centre) or Ge atom (Ge^0_2 centre) with the absorption

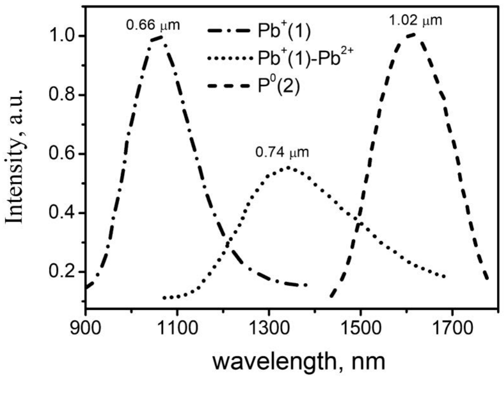

FIGURE 40.2 The emission spectra of Pb optical defect centres in SrF_2:Pb^{2+}, X-ray irradiation at 300 K [19]. The wavelengths of the excitation of corresponding luminescence bands are also shown.

band around 5 eV (242–244 nm) [91]. The foregoing results of our experimental and theoretical investigations show only a possible structure of Bi active centres consisting of Bi ions and oxygen deficiency centres. But it is desirable to have the direct experimental confirmation of such structures. We carried out the following experiments to confirm directly the suggested idea that the structures of Bi active NIR centres contain oxygen deficiency centres [48].

Bi-doped germanosilicate optical fibres with a high GeO_2 content (~50 mol.%) and a small Bi concentration (≤0.1 at.%) were used in these experiments. Fibre preforms were fabricated by the MCVD technique. It is well known that there are two types of BACs in a Bi-doped germanosilicate fibre associated with Si and Ge and two long lifetime luminescence bands at 1430 and 1700 nm correspondingly. The detailed investigations of the luminescence properties of these BACs have shown the structure identity of these centres. Thus, for simplicity we carried out the experiment for the BAC associated with Ge. Figure 40.3 shows the optical loss spectrum of this fibre and the emission and excitation spectra of this active centre.

Oxygen deficiency centres ODC (II) in germanosilicate glasses have the absorption band at 242 nm. Photoexcitation of this absorption band transforms ODCs (II) to the E′-centres, partially bleaching the ODCs (II) absorption band [91]. If our supposition about the nature of active centres is correct the number of NIR Bi centres will decrease under irradiation at 244 nm leading to the decrease of the absorption and luminescence intensities of these centres. We treated the fibre with 244 nm radiation and observed the luminescence and absorption properties of the BAC. Figure 40.4a shows the luminescence spectra of the fibre pumped at 1460 nm before and after photoexcitation at 244 nm with a dose of 1 kJ cm^{-2}. It is seen that the 1700 nm luminescence intensity greatly decreased. The inset shows the experimental dependence of the luminescence intensity on the irradiation dose. Figure 40.4b shows the absorption spectra of the fibre before (curve 1) and after (curve 2) photoexcitation at 244 nm. The background loss level

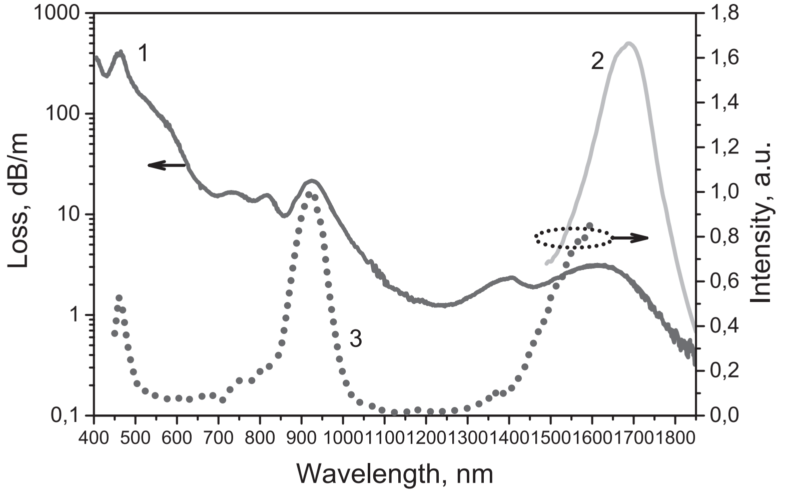

FIGURE 40.3 The spectra of optical losses (1), luminescence (2) and excitation (3) of Bi-doped optical fibres with high GeO_2 content [48].

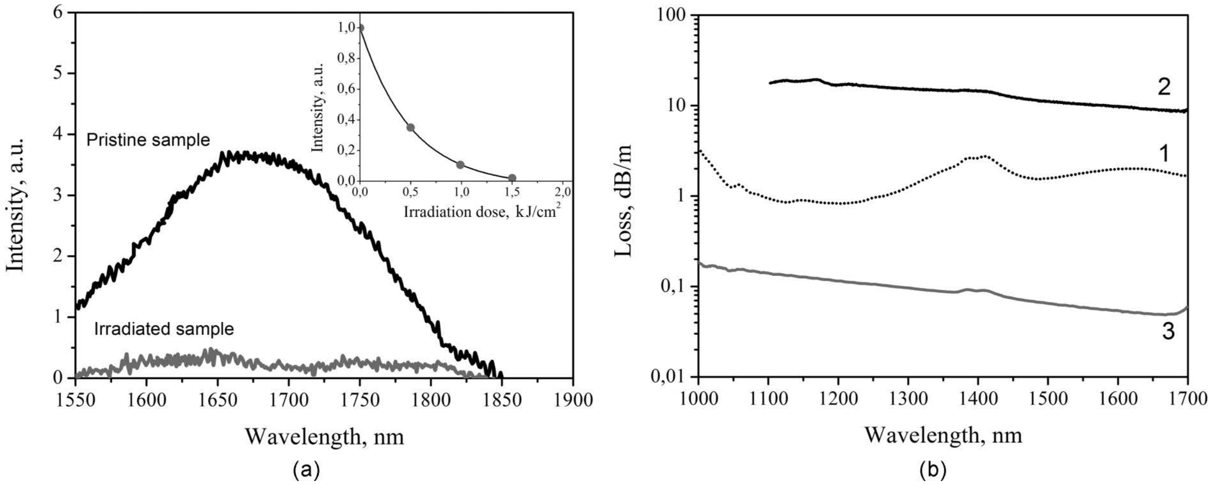

FIGURE 40.4 Optical properties of the pristine and irradiated Bi-doped germanosilicate fibre. (a) The emission spectra of the fibre (before and after irradiation). Inset: the dependence of the intensity of 1700 nm luminescence on the irradiation dose at 244 nm. (b) The absorption spectra of the fibre before (1) and after irradiation (2). Curve (3) shows the loss spectrum of a pristine germanosilicate fibre without Bi [48].

is strongly induced by a 244 nm irradiation. The growth of the background losses is probably caused by the UV absorption bands belonging to E′-centres and other induced defects [91]. The obtained absorption spectra of the fibre after irradiation (curve 2) and a fibre without Bi are similar. Therefore, the characteristic absorption bands of the NIR bismuth active centre, as well as the emission band, have greatly decreased under irradiation. The results of these experiments are described in detail in [48].

In conclusion of this section, new experimental data obtained for Bi-doped germanosilicate fibres with a small concentration of Bi (≤0.01 at.%) confirm our previous conclusion that Bi-related NIR emitting centres associated with Ge are clusters consisting of Bi ions and oxygen deficiency centres but not Bi ions themselves. As both active centres in germanosilicate fibres have the similar structure, we can conclude that the structure of BACs associated with Si also contains oxygen deficiency centres. Further research is necessary to get reliable results on the nature of Bi-related NIR emitting centres in Bi-doped glasses and optical fibres of various compositions with both small and large Bi concentrations.

40.3 NIR Luminescence Properties of Bi-Doped Fibres (BDFs)

A review of the recent results concerning the luminescent properties of the bismuth-doped optical fibres is presented in this section. Here, we will focus on the bismuth-doped pure SiO_2 and GeO_2 glass fibres and more complex Al_2O_3-SiO_2, GeO_2-SiO_2 and P_2O_5-SiO_2 glass fibres which were used for lasing and studied in detail.

Bismuth (Bi) having the electronic configuration of (Xe)$4f^{14}5d^{10}6s^26p^3$ belongs to p-elements group. As it was previously mentioned, bismuth can exist in different oxidation states, but only Bi^{3+} and Bi^{2+} can show luminescence which has been repeatedly observed in crystals and glasses [100]. It was revealed that blue luminescence corresponds to the $^3P_1 \rightarrow {}^1S_0$ transition belonging to Bi^{3+} [3] and red luminescence originated from Bi^{2+} ($^2P_{3/2} \rightarrow {}^2P_{1/2}$ transition) [52]. The reliable experimental data about the observation of luminescence from other oxidation states of bismuth have not been found (Figure 40.5).

Unusual luminescence in near IR region from bismuth-doped glasses has also been observed for the first time in 1999 [71]. However, oxidation state of Bi responsible for IR luminescence and nature of active IR centre in general is still under discussion.

The development of Bi-doped optical fibres was a new stage which led to increase an interest to study their features (Ref. [16] and references therein). The BDFs have been paid more attention because of the first demonstration of laser generation in them. That is why we will examine features of Bi-doped fibres in detail.

One of the characteristic peculiarities of all bismuth-doped materials, including fibres, is a strong dependence of their luminescent properties on the chemical glass composition. Obviously, it is due to the fact that the optically active electrons (s- and p-electrons) of bismuth are unsheltered unlike f-elements. As a result, emission bands can become wider and significantly overlap each other. It can be seen clearly in the contour plots of luminescence intensity for four types of BDFs presented in Figure 40.6 [16,45]. Combined excitation-emission spectroscopy is applied for the obtaining of presented contour plots. To construct the contour plots of luminescence intensity, 2D luminescence spectra with a variation of excitation wavelength at step of 10 nm have been measured. In fact, the obtained contour plots show luminescence intensity as a function of the excitation and emission wavelengths. The luminescence intensity is determined by the colour palette. The background corresponds to black colour. All the graphs demonstrate diagonal straight line corresponding to the scattered excitation radiation.

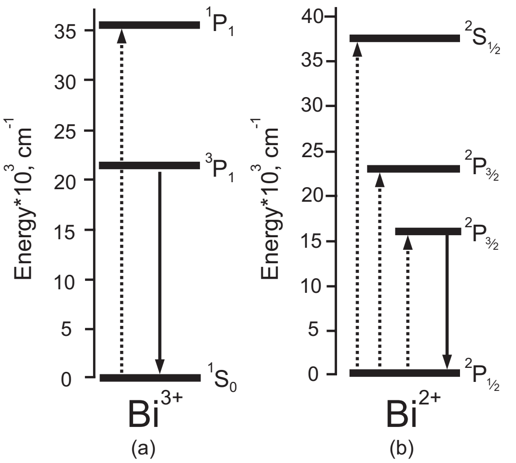

FIGURE 40.5 Transitions between energy levels of Bi^{3+} (a) and Bi^{2+} (b) ions corresponding to excitation and emission bands are shown with dashed and solid arrows, respectively.

Among the presented plots, the simplest view has the figure belonging to the bismuth-doped pure silica fibre (Figure 40.6a). Two characteristic bands of IR luminescence peaking at 830 and 1430 nm were observed repeatedly [9,81,44]. First one can be excited at 420 and 820 nm and another one at ~420, ~820 and ~1400 nm. Lifetimes of the luminescence at 830 and 1430 nm are 40 and 640 μs, correspondingly. Many experimental results indicated (e.g. [45,30]) that both luminescence bands originate from the radiative transitions between energy levels of the same BAC associated with Si (BAC-Si). In addition to the NIR luminescence, the well-known red luminescence of Bi^{2+} ion at 600 nm takes place under excitation near 500 nm [94].

Figure 40.6b demonstrates the luminescent properties of a Bi-doped fibre with a glass core containing >90 mol.% GeO_2. This type of BDF also features a set of peaks which are situated in a similar order observed for bismuth-doped pure silica fibre but are shifted a little toward longer excitation and emission wavelengths. In such case, there are two luminescence bands at 950 and 1650 nm with the corresponding lifetimes of ~30 and ~500 μs. The both luminescence bands are assigned to BAC-Ge. Also, the presence of the luminescence bands which are characteristic for BAC-Si can be observed in bismuth-doped high-germania glass core fibre. Their appearance may

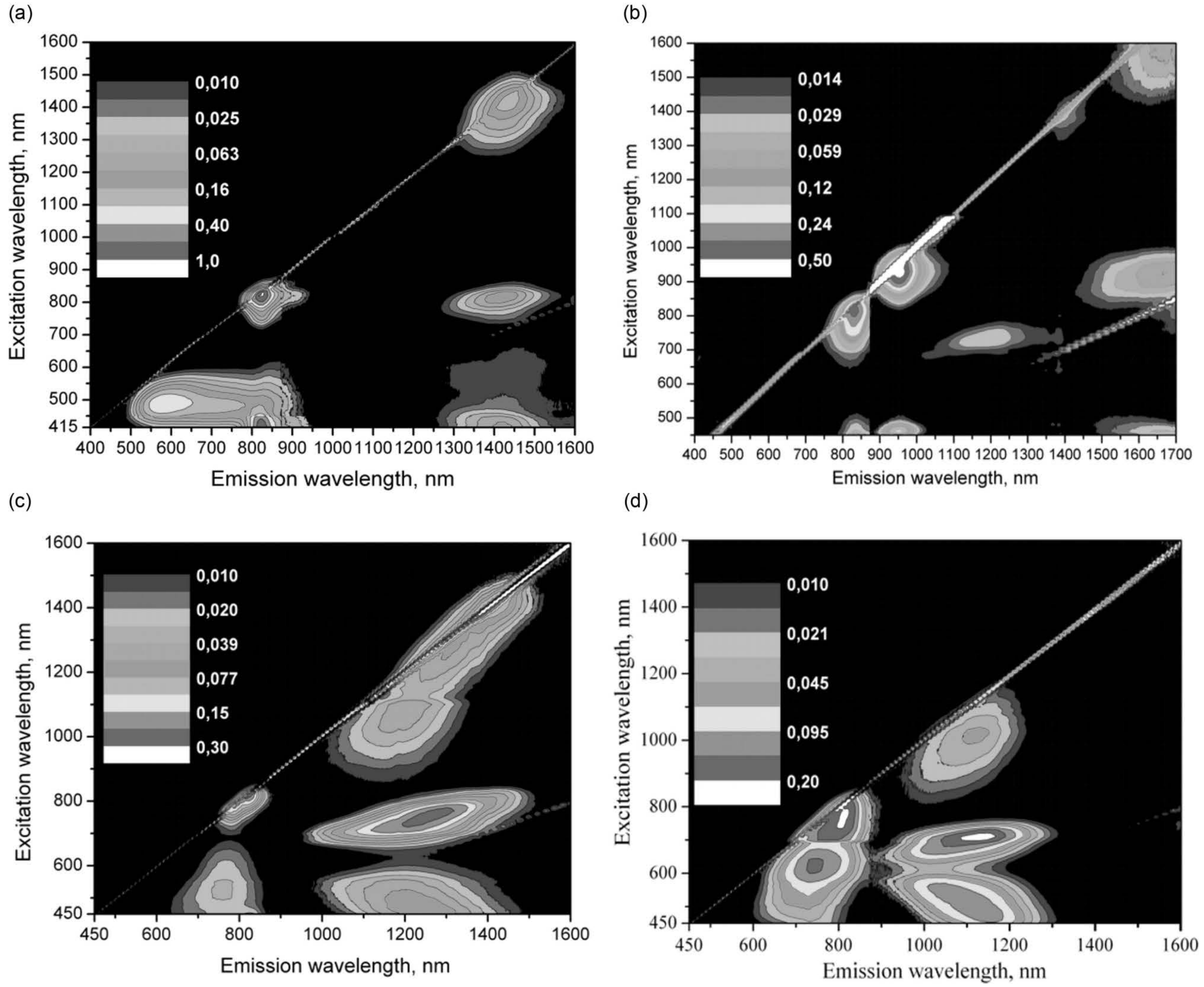

FIGURE 40.6 Contour plots of luminescence intensity of bismuth-doped fibres with different glass core compositions at the room temperature [16]. The luminescence intensity is determined by the colour palette. (a) Bi:SiO_2. (b) Bi:GeO_2. (c) Bi:(P_2O_5–SiO_2). (d) Bi:(Al_2O_3–SiO_2).

be explained as a result of diffusion processes of SiO_2 from the cladding into the high-germania glass core of the fibre and Bi ions from the fibre core into the cladding during the fabrication of the fibre [45]. It is worth noting that there is no visible luminescence.

The more complex fibre glass composition is, the more intricate contour plots of luminescence intensity become. A bright example of it is the luminescence intensity maps of the Bi-doped phosphosilicate and aluminosilicate fibres shown in Figure 40.6c and d, respectively. In both cases, a much stronger dependence of the luminescence spectrum on the excitation wavelength for the most of the luminescence bands is observed. Nevertheless, it was identified that the typical NIR luminescence spectrum has a maximum at 1300 nm for Bi-doped phosphosilicate fibres and 1140 nm for Bi-doped aluminosilicate fibres. The excitation spectra of NIR luminescence for these fibres are similar and consist of three bands peaking in the regions of ~400–500, ~700 and ~1100–1300 nm. The lifetimes of NIR luminescence are about 700–850 μs. Moreover, there are the short-wavelength luminescence bands at 700–750 nm with shorter lifetimes of 3–5 μs [43]. The results of detailed investigations of luminescent properties of Bi-doped phosphosilicate fibre show that the luminescence at ~700 nm is complex and consists of two overlapping bands arising from Bi^{2+} and BAC associated with P (BAC-P). It should also be noted that complexity of luminescence maps is connected to the coexistence of several BACs with different spectral characteristics. In particular, luminescence bands belonging to BAC-Si and BAC-P are clearly observed in Bi-doped phosphogermanosilicate fibres which have been investigated in detail [43]. As illustrated in Figure 40.7, at excitation of 1230 nm the luminescence spectra of these fibres consist of two emission bands peaking at ~1300 and ~1400 nm associated with BAC-P and BAC-Si. The luminescence intensity at 1300 nm monotonically decreased with reducing of P content in fibre. In this case, the germanium probably plays role of glass component providing conditions suitable for the enhanced formation of BAC-Si with luminescence at 1400 nm.

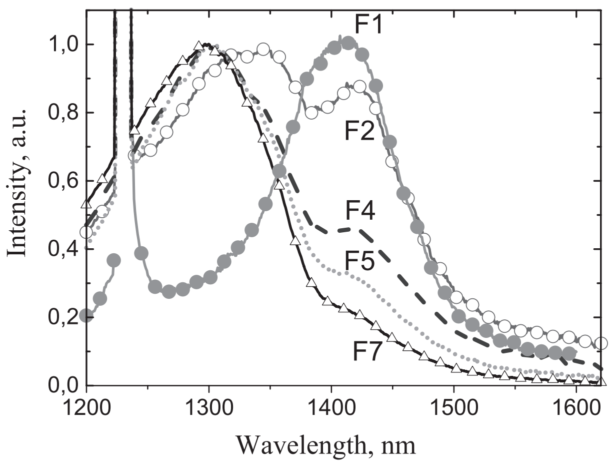

FIGURE 40.7 The luminescence spectra of Bi-doped phosphogermanosilicate fibres at 1230-nm excitation. (F1 and F7 are Bi-doped germanosilicate and phosphosilicate fibres, correspondingly.) The decreasing of Ge and increasing of P simultaneously takes place from F2 to F5 [43].

In addition, the BAC-Si responsible for luminescence band at 1400 nm was also found in Bi-doped aluminosilicate and high-germania fibres [35,42,40]. In both cases, lasing in this region has been demonstrated successfully.

Taking into consideration the experimentally obtained contour plots of luminescence intensity in UV range [49], the energy level schemes of three kinds of the BACs have been determined (Figure 40.8). As it is observed that the energy-level schemes of the BACs are similar, the corresponding BAC-Ge/BAC-P energy levels lie lower/higher than those of the BAC-Si. An accuracy of the determination of the energies of GE_4 and GE_5 levels was lower than others because of the strong absorption bands belonging to germanium oxygen-deficient centres. The fact of the similar energy-level schemes of three kinds of the BACs points on their same structure of them. However, the same accordance for the BAC in Bi-doped aluminosilicate fibres has not been found.

Obviously, the obtained energy level schemes of the BACs are different than those of Bi^{2+} and Bi^{3+}. There are a number of papers in which Bi^+ has been suggested as an IR active centre in crystals and some glasses (more in detail in Ref. [95]). As for BDFs, a comparison of calculated spectral properties of bismuth-related centres (BAC-Si and BAC-Ge) with the experimental data shows that the IR luminescence is most likely caused by a Bi ion and an oxygen-deficient defect [93]. Some experimental results confirming this suggestion have been obtained recently [48,41].

As can be seen in Figure 40.9, the summarized spectral region which can be covered with emission bands from Bi-doped fibres extends from 900 to over 1800 nm.

Besides, visible anti-stokes luminescence (ASL) of BDFs excited by NIR radiation was also observed [46,98,7]. Typical ASL spectra of different BDFs are presented in Figure 40.10.

The ASL spectra of Bi-doped pure silica and germania fibres consist of two visible bands peaking at 420, ~530 nm

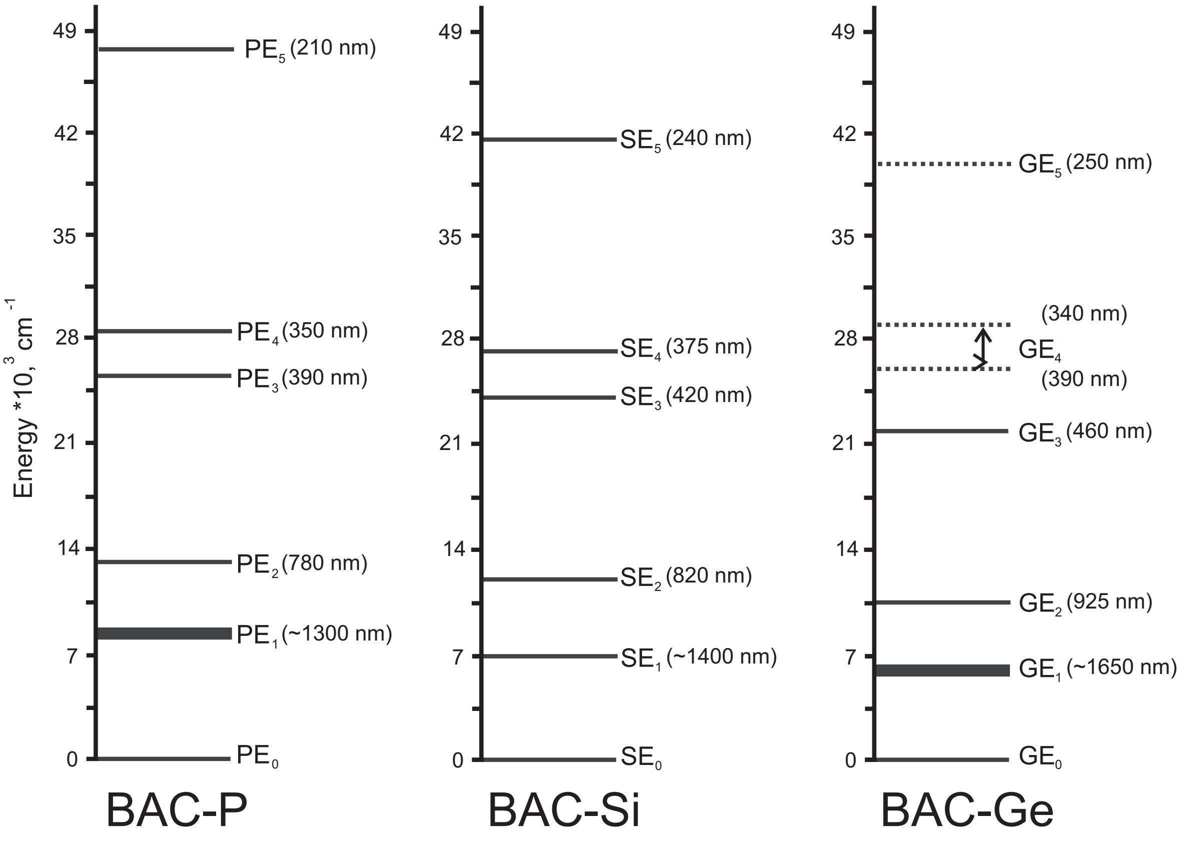

FIGURE 40.8 Experimentally determined energy level schemes of various BACs. The GE_4 and GE_5 levels are shown using the dashed lines because of lower accuracy of determination of their energies than for other levels [49].

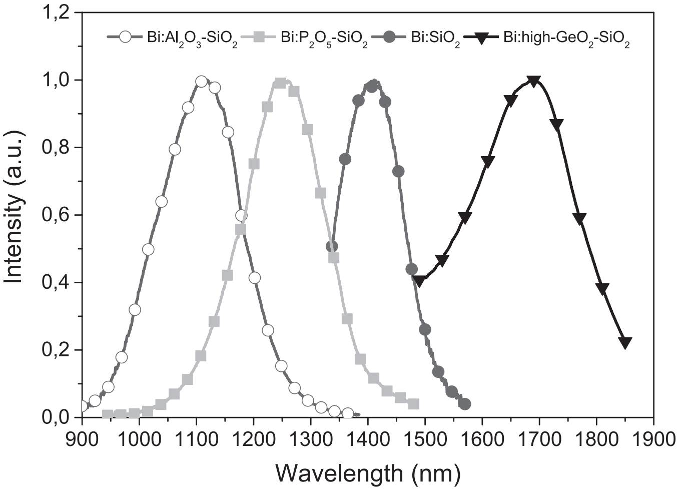

FIGURE 40.9 The normalized emission spectra of various Bi-doped fibres [39].

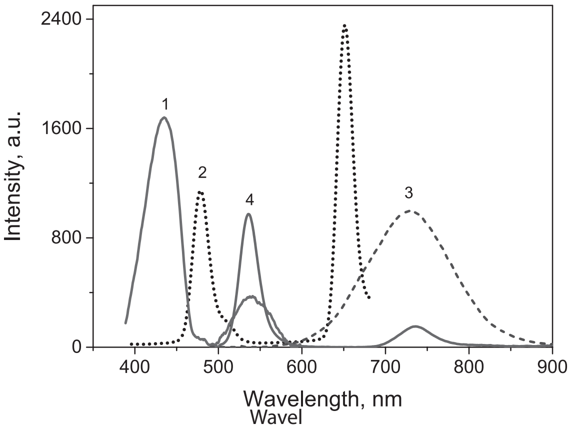

FIGURE 40.10 Anti-Stokes luminescence of various bismuth-doped fibres. 1, Bi:SiO$_2$ (λ_{exc} = 830 nm; T = 77 K); 2, Bi:GeO$_2$ (λ_{exc} = 920 nm; T = 77 K); 3, Bi:(P$_2$O$_5$–SiO$_2$) (λ_{exc} = 1058 nm; T = 300 K); 4, Bi:(Al$_2$O$_3$–SiO$_2$) (λ_{exc} = 1058 nm; T = 300 K).

and 460, 650 nm, correspondingly. The intensity of these bands sharply increased at nitrogen temperature (~77 K). As concerns the Bi-doped pure silica and germania fibres, the occurrence of visible bands in ASL spectra is explained as a result of the radiative transitions between high-lying energy levels belonging to the BAC-Si and BAC-Ge [46]. In particular, luminescence bands at 420 and 530 nm assigned to the BAC-Si occur due to the transitions SE$_3$ → SE$_0$ and SE$_3$ → SE$_1$, correspondingly (Figure 40.8). Similarly to the BAC-Si, the transitions of GE$_3$ → GE$_0$ and GE$_3$ → GE$_1$ originated from BAC-Ge are responsible for an appearance of the luminescence bands peaking at 460 and 650 nm. These emission bands can be observed under excitation of BACs to E$_3$ state as a result of either absorption of one photon or two photons from E$_0$ state via intermediate excited E$_1$, E$_2$ states. The presence of these transitions has been determined using wavelength-scanning radiation for an excitation of active fibres [46].

The green luminescence with a maximum at 530 nm is characteristic of Bi-doped aluminosilicate fibres. The 730-nm luminescence band can be observed in Bi-doped aluminosilicate fibres as well as in Bi-doped phosphosilicate fibres at excitation of 1058 nm. It is worth noting that the Bi-doped phosphosilicate fibres at excitation of 1058 nm have no anti-Stokes emission bands in the visible region even at 77 K.

An origin of ASL in Bi-doped aluminosilicate and phosphosilicate fibres are still exactly unidentified. But ASL in all Bi-doped fibres appeared due to ESA process or cooperative processes, including up-conversion, cross-relaxation etc., which can reduce the optical amplification. The detailed results concerning investigation of ESA processes are listed in the next section.

40.4 Excited State Absorption (ESA) in BDFs

For the first time, ESA in Bi-doped aluminosilicate fibres for the wavelength range of 900–1250 nm was measured in Ref. [58]. The authors found significant ESA at the wavelength range of 900–1000 nm under 1047 nm pumping. In Ref. [61], the ratio of ESA to ground state absorption (GSA) cross-section was estimated based on measurement of the NIR fluorescence kinetics and dependencies of the fibre transmission on the signal power. Later in Ref. [84] the ESA has been measured from 750 to 1700 nm in bismuth doped fibres with various hosts and BAC concentrations with emphasis on the aluminosilicate fibres. Also, the effect of temperature of the fibre on the ESA was examined. Here, we present some results from this work.

Measurements of GSA, ESA and net gain were performed in BDFs with different compositions. The measurements were fulfilled for germanosilicate (GSB) with low concentration of Ge, aluminosilicate (ASB) and phosphosilicate (PSB) BDFs to characterize their amplifying properties. In ASB and PSB fibres the properties of BAC-Al and BAC-P were studied, respectively. In contrast, properties of BAC-Si were investigated in GSB fibres with small amount of Ge (~5–7 mol.%).

All the investigated fibres were fabricated by MCVD and solution doping. Fibres with various BAC concentrations were used. The BAC concentration was characterized by the absorption value $\alpha(\lambda)$ at the wavelength λ_{max} of the NIR absorption band of each fibre. Thus, for the ASB, PSB and GSB fibres λ_{max} is 1.0, 1.24 and 1.4 µm, correspondingly. For simplicity the fibres were marked in the following way: {type of fibre}—{$\alpha(\lambda_{max})$ (dB m^{-1})} (e.g. ASB—1.6—aluminosilicate fibre with absorption 1.6 dB m^{-1} at 1.0 µm).

A similar experimental arrangement as described in Ref. [99] was used to measure the ESA. Authors measured spectra of the optical loss $\alpha(\lambda)$ and spectra of the loss under pumping $\alpha_p(\lambda)$ in the BDFs and calculated the difference $\Delta\alpha(\lambda) = (\alpha_P(\lambda)—\alpha(\lambda))$ (transmission change). The pumping was performed at 1.32 µm in GSB, 1.24 µm in PSB and at 1.06 µm in ASB with powers ~200–500 mW.

Figure 40.11 shows the measured spectra for two GSB fibres with high concentrations of BAC (GSB-17). The net gain in fibre GSB-17 is observed in a spectral region of 1355–1490 nm. Some noticeable ESA (up to ~2 dB m^{-1}) is observed in a spectral region of 950–1200 nm (Figure 40.11, Curve “Transmission change”). In GSB fibres with high BAC concentration, amplification dominates over ESA in the range of 1.35–1.5 µm, but ESA could reduce the gain and hence the efficiency of lasers and amplifiers. In fibres with low and middle BAC concentration in Ge-doped fibres, the measured transmission under pumping is always higher than when pump is off. Thus, there is no any significant ESA in these fibres in the spectral range 850–1700 nm.

Figure 40.12 shows the measured spectra for the PSB-0.7 fibre. The net gain in this fibre is observed in a spectral region of 1250–1400 nm, the maximum value being at λ = 1320 nm. In this case essential difference in the spectra shapes of $\alpha_p(\lambda)$ and $\alpha_p(\lambda)-\alpha(\lambda)$ were observed in contrast to GSB fibres. The ESA is practically absent in a spectral region of 1100–1700 nm. From this one can conclude that in PSB with low concentration of BACs the ESA is absent outside the active centre transitions and in the range of laser transitions is either absent or negligible. It should be noted that we did not measure ESA in PSB fibres with the high BACs concentration.

Since the effect of the ESA is most pronounced in ASB fibres, a series of six ASB fibres with different bismuth concentration were used in experiments. The optical absorption α at 1.0 µm varied from $\alpha_{1.0}$ = 1.5 to $\alpha_{1.0}$ = 50 dB m^{-1}. The loss spectra of the fibres are shown in Figure 40.13. There are three strong absorption bands at 0.5, 0.7 and 1.0 µm related to the IR BACs in ASB fibres. Also, the luminescence excitation spectrum is shown in Figure 40.13 (λ_{em}=1.15 µm).

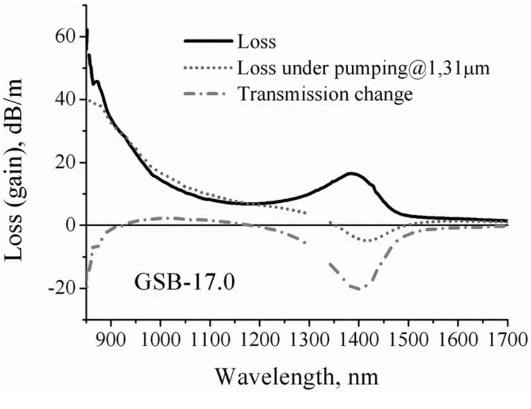

FIGURE 40.11 Optical losses and transmission change of GSB-17.0 [84].

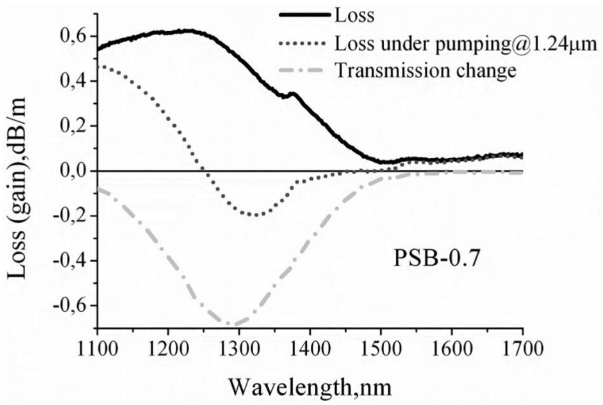

FIGURE 40.12 Optical losses and transmission change of PSB-0.7 [84].

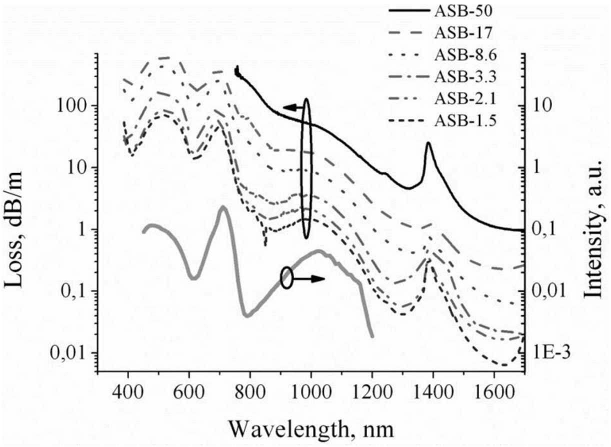

FIGURE 40.13 The loss spectra of the ASB fibres and luminescence excitation spectrum (λ_{em} = 1.15 µm) [84].

Figure 40.14 shows pump induced losses (gain) of the ASB fibres with different BAC concentration. The spectra were normalized to the absorption of each fibre at 1000 nm.

It is worth noting that $\Delta\alpha(\lambda)$ excludes the impact of grey losses and characterizes only the transitions of the active centres from the ground and excited levels. So, it includes change in the transmission due to the BAC transitions between ground and first excited levels – $g(\lambda)$ and changes due to ESA – $\alpha_{esa}(\lambda)$. Thus, ESA spectra could be determined by

$$\alpha_{esa}(\lambda) = \Delta\alpha(\lambda) + g(\lambda). \tag{40.3}$$

Let’s assume that spectral shape of $g(\lambda)$ is close to Gaussian, and it does not depend on the BAC concentration while the peak value of $g(\lambda)$ increases proportional to it. In this case varying Gaussian coefficients we were adding $g(\lambda)$ to $\Delta\alpha(\lambda)$ (for ASB-3.3) until monotonous and smooth spectrum of $\Delta\alpha(\lambda)-g(\lambda)$ had been obtained. Resulted $g(\lambda)$ was normalized with BAC absorption at 1.0 µm and calculated for each fibre. Then, $\alpha_{esa}(\lambda)$ spectra were calculated for all fibre samples.

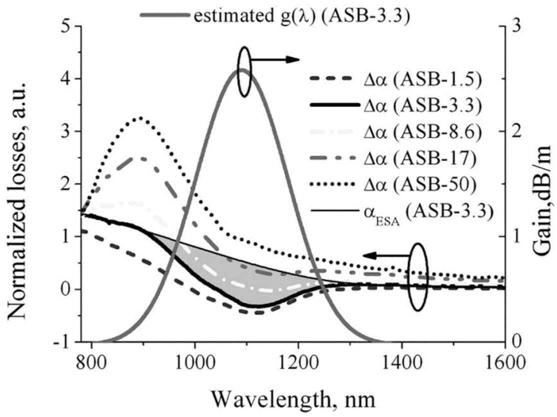

FIGURE 40.14 The spectra of the pump induced losses at room temperature normalized on absorption at 1000 nm and estimated gain spectrum of ASB-3.3 [84].

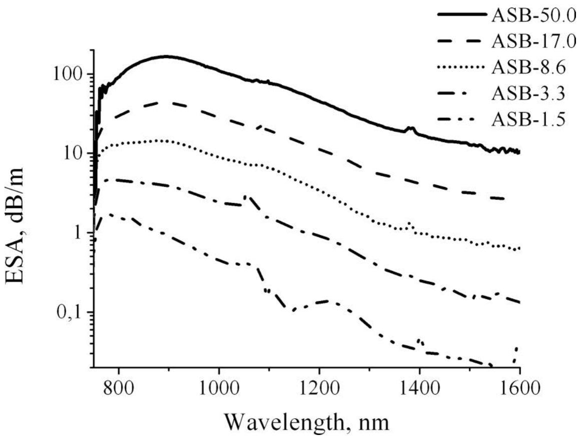

FIGURE 40.15 The estimated ESA spectra of the ASB fibres [84].

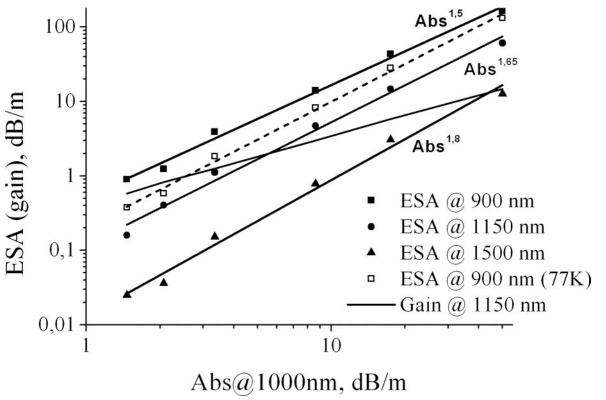

FIGURE 40.16 Dependencies of the ESA at various wavelengths on the absorption at 1.0 μm (Abs) at room temperature and at 77 K (for 900 nm) [84].

Resulting graphs are shown in Figure 40.15. These spectra relate exclusively to the ESA and they exclude grey losses and transitions between the ground and the laser levels. It should be noted that the ESA spectra were obtained for the maximum population inversion at a given wavelength of the pump. Spectrum roughness in the area of 1150 nm for the sample ASB-1.5 are related to the inaccuracy in the gain estimates. ESA spectra monotonically decrease from 900 nm, any characteristic peaks are not observed. Slope of the curves is approximately the same, and slightly decreases with BAC concentration increase.

The dependencies of the ESA on the concentration of BAC at various wavelengths are shown in Figure 40.16. The ESA level depends essentially on the BACs concentration. The increase of the ESA can be estimated as ~(α(1.0 μm))^x practically in all wavelength range 800–1700 nm. It is worth noting that the nature of the dependencies is same at wavelengths where $\Delta\alpha(\lambda)$ involves $g(\lambda)$ (1150 nm) and where it does not (900 and 1500 nm). This fact indicates that the $g(\lambda)$ extraction and ESA estimation was done correctly.

In conclusion of this section, the ESA in various Bi-doped fibres was measured in the 750–1700 nm wavelength range. In GSB and PSB fibres with low BAC concentration the ESA was not detected in the 1100–1700 nm region. In GSB fibres with high BAC concentration ESA peaked at 1000 nm was observed, but with magnitude ~2 dB m^{-1} which is lower than the gain ~5 dB m^{-1} peaked at 1420 nm. This agrees with a high efficiency of the BDFLs based on these fibres [10]. The main mechanism of efficiency reduction with the increase of BAC concentration in P-doped and Ge-doped fibres is a non-linear (related to BACs concentration) growth of background losses associated with BACs.

The ESA in the aluminosilicate fibres is significant in the 750–1700 nm wavelength range at any BAC concentration. Significant dependence of the ESA on the BAC concentration and the temperature of the fibre were found. The ESA in ASB fibres increases with BACs concentration as ~(α(1.0 μm))$^{1.7}$. This can explain (at least, partially) comparatively low efficiency of Bi-doped aluminosilicate fibre lasers [61] and remarkable decrease of their efficiency with the increase of BAC concentration. The reduction of efficiency in ASB fibres due to increase of background loss associated with BACs also takes place, but mechanism associated with ESA dominates at high concentrations of BACs.

40.5 Continuous-Wave Bi-Doped Fibre Lasers (CW BDFLs)

As it was shown in Section 40.3 (NIR luminescence properties of Bi-doped fibres), the luminescence spectra of Bi-doped fibres depend on the fibre core glass composition. Thus, one need to use various types of Bi-doped fibres to get laser generation in different spectral regions. The thorough research of luminescence and laser properties of various Bi-doped fibres allowed one to select four types of Bi-doped fibres for the construction of efficient BDFLs covering a spectral region of 1140–1800 nm. Table 40.1 contains the core glass composition of these Bi-doped fibres and corresponding spectral regions of laser generation (LG).

Below the main characteristics of the corresponding BDFLs, laboratory samples will be presented and possible applications and some difficulties to get efficient operation will be discussed.

TABLE 40.1

Spectral Regions of Laser Generation for Bi-Doped Fibres with Different Core Glass Compositions

BDF Types	Al_2O_3-SiO_2	P_2O_5-SiO_2	GeO_2-SiO_2 (Small Content of GeO_2)	GeO_2-SiO_2 (Large Content of GeO_2)
LG spectral region (nm)	1140–1215	1260–1360	1370–1540	1625–1775

40.5.1 Bi-Doped Aluminosilicate Fibre Lasers

As it was noted in the introduction much attention was paid to the first Bi-doped aluminosilicate fibre laser. A number of detailed studies [7,61,84,99,32,2,80,27,58,33] focused on the influence of parameters of active aluminosilicate fibres, with emphasis on the pump and lasing wavelengths and bismuth concentration, on the laser efficiency. A large fraction of nonsaturable absorption was found at the pump wavelength λ_p [27,58,33]. The absorption depends on λ_p and increases with increasing bismuth concentration. An increase in bismuth concentration leads to clustering of bismuth-related active centres as was confirmed by a nonexponential luminescence decay at relatively high bismuth concentrations. It was shown that the excited-state absorption (ESA) and upconversion (UC) processes are responsible for a growth of nonsaturable absorption [58,7,61,32]. All these phenomena limit the efficiency of lasers. So that a very low bismuth concentration (of the order of 0.01 at.%) have to be used in order to improve the laser efficiency. Low bismuth concentrations are a drawback to these lasers because they require long lengths (50–100 m) of active fibres and make cladding pumping of fibre lasers impossible. Note in passing that it is necessity of using very low bismuth concentrations for efficient lasing which accounts for the failure of attempts to achieve lasing in bulk bismuth-doped glasses.

An inherent drawback of Bi-doped aluminosilicate fibre lasers is the narrow spectral range of their lasing. To date, laser generation has been achieved in the range 1150–1215 nm. The laser design was typical of cw fibre lasers: use was made of a 83-m length of Bi-doped aluminosilicate fibre and two fibre Bragg gratings (FBGs) fusion-spliced to the ends of the Bi-doped fibre (Figure 40.17). The reflectance of one grating was about 100%, and as the output coupler, a 50% reflective grating was used. The pump source used was a Yb fibre laser with the output power up to 80 W. At the pump wavelength λ_p = 1070 nm, the laser efficiency at 1150 and 1160 nm was 19% and 21%, and the output power was 13 and 15 W respectively. At the wavelengths 1205 and 1215 nm the efficiency was ~ 7%–13% [27]. The highest efficiency 28% was reached at 1179 nm under pumping at 1090 nm [32]. The dependence of the output power of Bi-doped aluminosilicate fibre lasers on the fibre temperature was measured in a range of 0°C–60°C. This dependence is nearly linear and shows the 40% reduction of the output power with the temperature increase from 0°C to 60°C [27].

A considerable interest was shown in the creation of narrow linewidth BDFLs, in particularly operating in the spectral range 1160–1180 nm [27,33,87,59]. It is known that the 570–590 nm band is very promising for ophthalmology and dermatology applications [4,88]. There is also a very interesting and important application of high-brightness 589 nm sources in astronomy to generate laser guide stars for adaptive optics correction of large telescopes [64]. Bi-doped aluminosilicate fibre lasers give one a good opportunity for yellow light generation as second harmonic of these lasers [27,33,22,88,31]. The first experiments on the yellow light generation at 573 and 580 nm using cw and pulsed BDFLs were carried out in 2006 and the results were presented at ECOC'2006 [22]. Frequency doubling with a quite low efficiency was accomplished by KTP crystal. The higher efficiency was obtained in [27,33] using a commercial 30-mm-long periodically poled lithium niobate crystal with a fibre input. Table 40.2 contains the parameters of narrow linewidth cw BDFLs used for the second harmonic generation and characteristics of yellow light obtained in [27,33,87]. The authors expect that using polarization maintaining, large-mode area and shorter-length Bi-doped fibres will allow to obtain yellow light with the watt-level power.

Very interesting results were reported in Ref. [31] where all-fibre laser operating at 580 nm was realized by

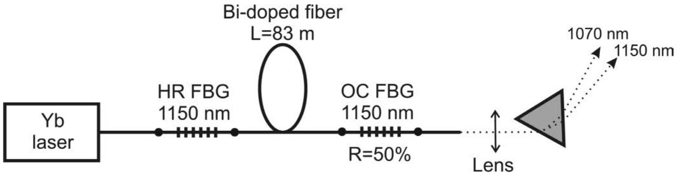

FIGURE 40.17 The scheme of a Bi-doped fibre laser [10].

TABLE 40.2

Parameters of Bi-Doped Aluminosilicate Fibre Lasers and Characteristics of Yellow Light

Wavelength of BDFL (nm)	Fibre Length (m)	Output Power (W)	Polarization	Linewidth (nm)	Yellow Light Wavelength (nm)	Yellow Light Power (mW)
1160 [27]	78	12	Non-polarized	0.3	580	300
1160 [33]	55	4.5	Non-polarized	0.3	580	200
1178 [87]	80	6.4	Non-polarized	0.2	589	125

frequency-doubling of the Bi-doped laser radiation in a periodically poled optical fibre. The obtained results show that such lasers are promising for creation of compact all-fibre visible light sources.

Now we will consider one more result connected with Bi-doped aluminosilicate fibres. It concerns the creation of a Bi-doped aluminosilicate fibre amplifier at 1180 nm using a commercially available 1120 nm LD as a pump source [96]. The amplifier performance was compared for a novel pumping wavelength of 1120 nm with the pumping wavelength of 1047 nm. About 70% increase in gain was observed for 1120 nm pumping. Higher gain in case of 1120 nm pumping is connected with a value of the unsaturable loss which was 35% and 65% of the total small signal loss for 1120 and 1047 nm pump wavelengths, respectively. A maximum gain of 8 dB was obtained for 100 m-long fibre. BDFAs at 1180 nm are of considerable interest because of the serious demand for an efficient source for laser guide star application [64]. It is expected that solving some problems of Bi-doped fibre technology will lead to a further improvement in the amplifier performance.

40.5.2 Bi-Doped Phosphosilicate Fibre Lasers

Despite the considerable progress in creating BDFLs for a spectral region of 1140–1215 nm the most important task was the development of efficient BDFLs and optical amplifiers for a wavelength range of 1300–1500 nm. It was recognized that this spectral region is promising for advanced optical fibre communication systems [16]. The first results in this direction were obtained by creating a Bi-doped phosphogermanosilicate fibre laser pumped at 1230 nm. The laser operated at the wavelengths 1310 and 1345 nm with the output powers 400 and 30 mW and the slope efficiencies 3.2% and 0.8% correspondingly [24]. It was turned out that the luminescence spectrum of Bi-doped phosphogermanosilicate fibres depends on the concentration ratio of GeO_2 and P_2O_5. The increase of the GeO_2 concentration leads to the shift of the long wavelength luminescence spectrum end towards the longer wavelength side, up to the 1500 nm region. So, laser generation was demonstrated in the wavelength regions 1300–1470 nm and 1470–1550 nm using a Bi-doped phosphogermanosilicate fibre which the larger concentration of GeO_2 [8,25]. We investigated the luminescence spectra of Bi-doped phosphogermanosilicate fibres of the different compositions, including Ge-free and P-free fibres [43]. We revealed that the luminescence spectra of Bi-doped phosphogermanosilicate fibres consisted of two overlapping bands, centred at 1300 and ~ 1420 nm, which belong to bismuth active centres associated with P and Si correspondingly. The bismuth active centres associated with Si are activated by Ge content, so the intensity of the luminescence band at 1420 nm grows with the increase of the Ge concentration. The mechanism of the activation of the bismuth active centre associated with Si by Ge content will be discussed in the Section 40.5.3.

Thus, one should use a Bi-doped phosphosilicate fibre with a small content of Ge (<1 at.%) to obtain efficient laser generation in the spectral region near 1300 nm. A small content of Ge improves the optical quality of phosphosilicate glasses. Using this approach we demonstrated Bi-doped phosphogermanosilicate fibre lasers operating at 1280, 1330, 1340 and 1360 nm with the 10 watt-level output power (Figure 40.18). As a pump source we used a Raman fibre laser with the output power 30 W at 1230 nm [10].

We also present here the properties of a BDFL operating at 1270 nm. This laser is of interest in various applications, including medicine [63] and remote sensing measurements of atmospheric oxygen [72]. Besides, the second harmonic of such laser can be used for the substitution of the He-Ne gas laser. We used a 95-m Bi-doped phosphogermanosilicate fibre as a gain medium. A Raman fibre laser at the wavelength

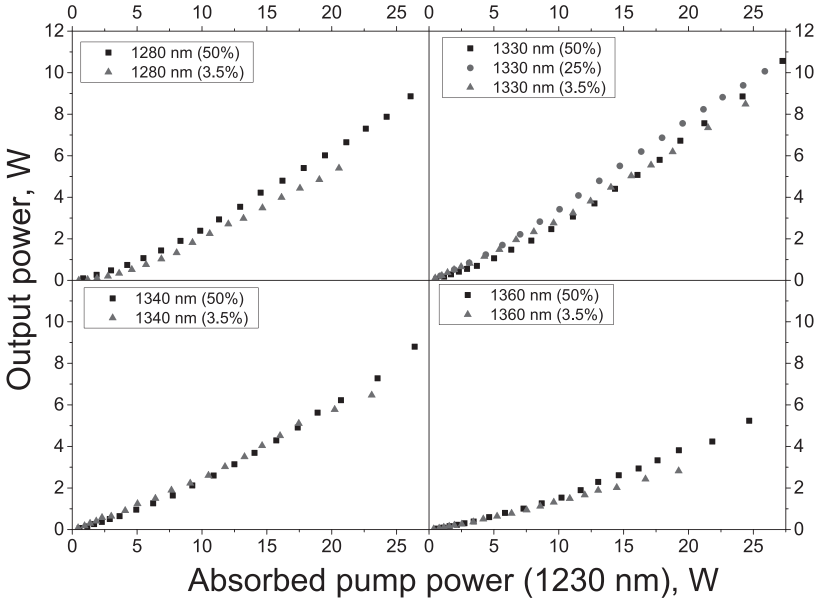

FIGURE 40.18 The output power *versus* the absorbed power for Bi-doped fibre lasers at different lasing wavelengths. Lasing wavelengths and the output coupler reflectivity are indicated in each graph [10].

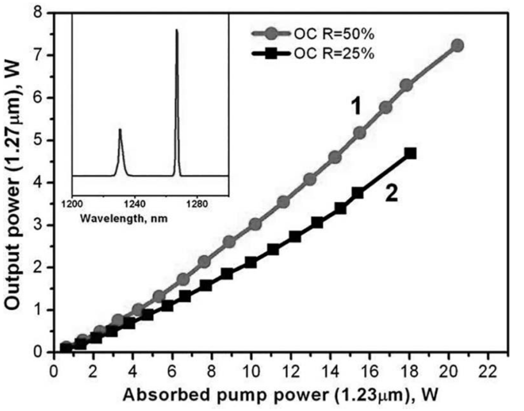

FIGURE 40.19 The output power of the 1270 nm fibre laser as a function of the absorbed pump power for the output Bragg grating reflectivity 50% (1) and 25% (2) [16].

1230 nm with the output power 25 W was used as a pump source. Figure 40.19 shows the output power of the laser as a function of absorbed pump power [11,16].

40.5.3 Bi-Doped Germanosilicate Fibre Lasers (Small Concentration of GeO_2)

As we have shown in the previous paragraph laser generation in a spectral region of 1400–1550 nm can be achieved using Bi-doped silica-based fibres (phosphogermanosilicate or aluminosilicate) which contain BACs-Si [8,25,35]. It is clear that it is possible to use Bi-doped SiO_2 fibres for laser generation in this spectral region.

The first results on laser generation in Bi-doped fibres free of other dopants were published in [9,28,101]. But the efficiency of such lasers was not high, the output power was less than 1 W. We have mentioned in the previous paragraph that BACs-Si are activated by GeO_2 content. The addition of GeO_2 results in the large increase of the ODC number [91] and therefore in the increase of the BAC-Si number, as discussed in Section 40.2.

So to develop high-power, efficient BDFLs for a spectral region of 1390–1530 nm we used a germanosilicate fibre containing no more than 0.01 at.% Bi and 4 mol.% GeO_2 [21,47,90,5]. The luminescence band of the fibre had a 3 dB width of 150 nm with the peak emission wavelength near 1430 nm. The fibre length was 95 m. Figure 40.20 shows the configuration of a laser emitting at 1460 nm. The pump source used (λ_p = 1340 nm) was a phosphosilicate fibre Raman laser, which was in turn pumped by an Yb-doped fibre laser at 1137 nm.

Figure 40.21a shows the output power of the bismuth laser as a function of pump power. The highest output power was 22 W, and the pump efficiency was 50%. Figure 40.21b shows the temperature dependencies of the efficiency for bismuth-doped aluminosilicate, phosphogermanosilicate and germanosilicate fibre lasers.

The efficiency of the bismuth-doped germanosilicate fibre laser is seen to be a weak function of temperature. The broad luminescence band of the bismuth-doped germanosilicate fibre, with a peak emission wavelength near 1430 nm, suggests that lasing can be achieved at various wavelengths within this band. Lasing with several watts of output power and 30%–65% efficiency was achieved at 1390, 1480, 1500 and 1538 nm (Figure 40.22) [90]. Thus, the first bismuth doped germanosilicate fibre laser with the output power above 20 W and 50% efficiency at 1460 nm has been demonstrated. Its efficiency decreases only slightly with increasing temperature. Lasing in the spectral range 1390–1540 nm showed rather high efficiency.

Besides, a BDFL with a linear polarization output was developed in Ref. [90]. We have already mentioned in paragraph 5.1 that frequency doubling in a periodically poled optical fibre is very promising for creation of compact all-fibre visible light sources. It was shown that this approach allows one to double the frequency of NIR radiation with the efficiency as high as 15%–20% [12]. Using a NIR fibre laser with linearly polarized radiation gives the two times increase of power conversion efficiency. We fabricated a PANDA-type Bi-doped fibre preform with borosilicate rods to obtain a fibre with high birefringence. The measured beat length in the fibre was ~ 2.5 mm at the wavelength 650 nm. As a pump source, we used the Raman fibre laser at 1340 nm. The dependence of the output power on the launched pump power for the PM laser at 1460 nm is presented in Figure 40.23. The slope efficiency *versus* the launched power was ~41%; the polarization extinction ratio was >15 dB. The laser line is shown in the inset of Figure 40.23. It is seen that FWHM was < 0.06 nm (resolution of our optical spectrum analyser).

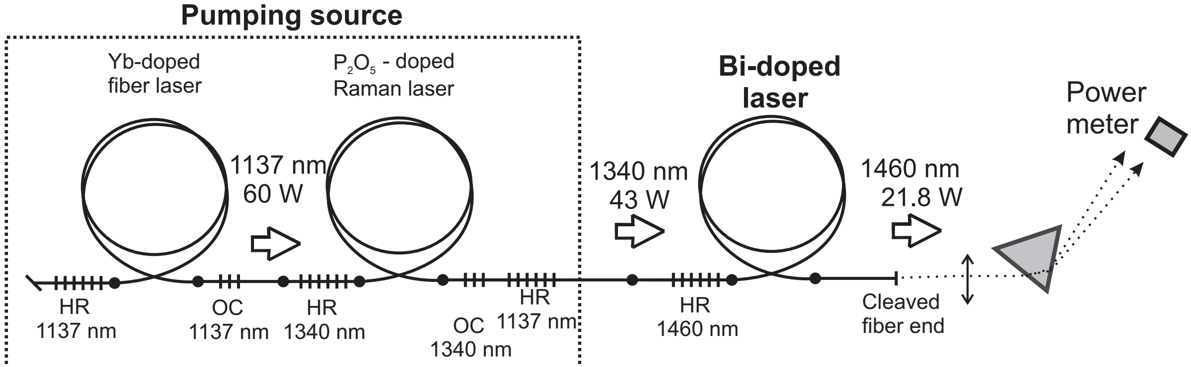

FIGURE 40.20 The scheme of the Bi-doped germanosilicate fibre laser operating near 1460 nm [5].

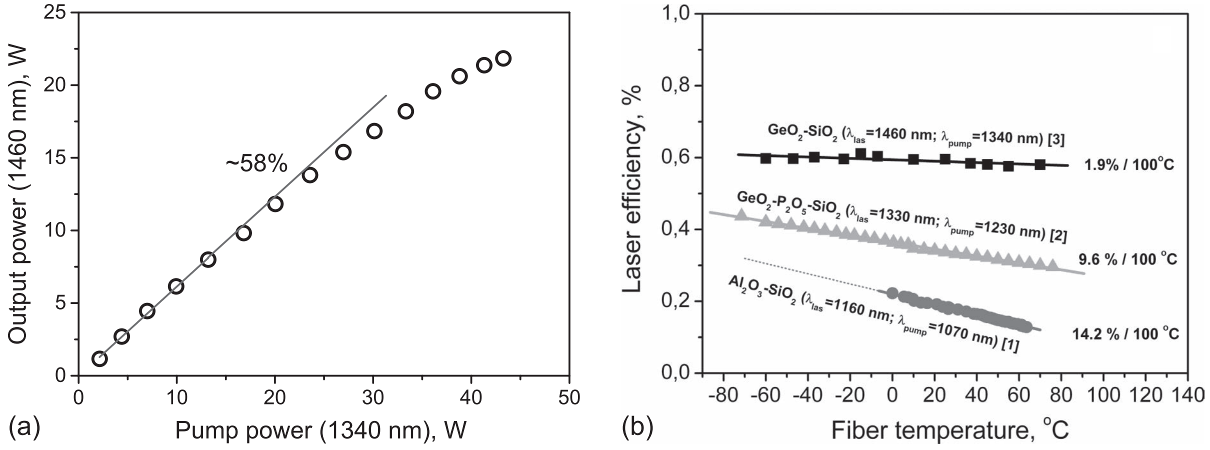

FIGURE 40.21 The output power at 1460 nm in dependence on the pump power (a) and the efficiency of various Bi-doped fibre lasers as a function of temperature (b). On the right side of picture "b" the laser efficiency changes (in %) per 100 temperature change are shown for fibre lasers with different core glass composition [5].

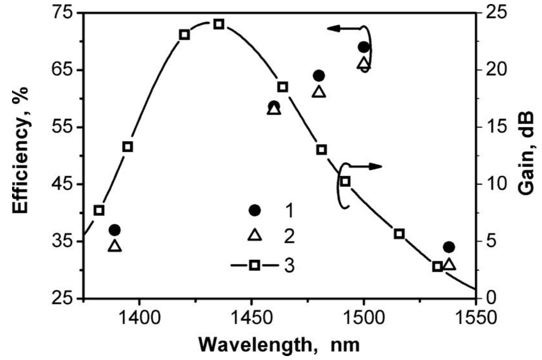

FIGURE 40.22 The dependence of slope efficiency (1), power conversion efficiency (2) and gain spectra (3) on lasing wavelengths [5].

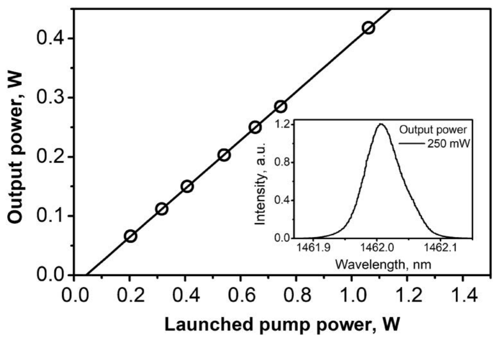

FIGURE 40.23 The dependence of the output power on the launched pump power for PM laser at 1460 nm. Inset: the output laser spectrum [90].

40.5.4 Bi-Doped Germanosilicate Fibre Lasers (Large Concentration of GeO$_2$)

Here, we present the results on the development of Bi-doped germanosilicate fibres with the large concentration of GeO$_2$ and BDFLs for a spectral region of 1600–1800 nm [48,42]. Bismuth-doped optical germanosilicate fibres with ≈50 mol. % GeO$_2$ content were used as active media. The bismuth concentration in this fibre was less than 0.1 mol.%. Fibre preforms were fabricated by a MCVD technique. The single-mode fibres with $\lambda_{cut\text{-}off} \approx 1.2$ μm were drawn from these preforms. The selection of core glass composition and parameters of the fabrication process made it possible to obtain efficient luminescence in the 1600–1800 nm region.

The absorption spectrum of the fibre prepared is shown in Figure 40.24. As it is seen, two absorption bands centred at 1400 and 1650 nm with the similar values of peak absorption—2.5 dB m^{-1} are presented. BAC-Si and BAC-Ge formed in Bi-doped germanosilicate fibres are responsible for the absorption bands at 1400 nm (BAC-Si) and 1650 nm (BAC-Ge). Figure 40.24 contains also the gain spectrum of this fibre. The gain bands at 1400 and 1700 nm were measured upon excitation at 1240 and 1460 nm respectively. First, we demonstrated that BAC-Si in Bi-doped high-germania fibres excited by a Raman fibre laser at 1340 nm can also be used to obtain laser generation at 1410 nm. Now we focus on laser properties of BAC-Ge which are less studied than those of BAC-Si.

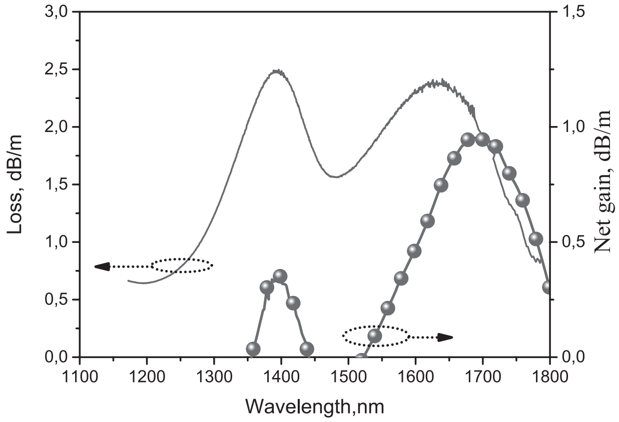

FIGURE 40.24 The loss (solid line) and gain (line with balls) spectra of the bismuth-doped germanosilicate fibre with a large concentration of Ge. The gain bands at 1400 and 1700 nm were measured upon excitation at 1240 and 1460 nm correspondingly [40].

The decay of luminescence at 1700 nm under pumping at 975 nm has a single-exponential shape with the lifetime 500 μs. We also determined an unsaturable loss value at 1568 nm which was found to be ~ 0.3 dB m^{-1}. The gain spectrum width (FWHM) reaches 150 nm (Figure 40.24). This made it possible to obtain laser generation in a range of 1625–1775 nm. All the BDFLs were constructed using the common linear scheme. An Er-Yb co-doped fibre laser operating at 1568 nm was used as a pump source. All details of the laser construction can be found in paper Ref. [42]. Figure 40.25 shows the output power of the 1700 nm laser versus the launched pump power for a 60-m long fibre with the 100%–4% cavity. The highest slope efficiency achieved was 30%.

In conclusion, for the first time Bi-doped germanosilicate fibres having the net gain bandwidth 150 nm in a spectral region of 1600–1800 nm have been developed and laser generation in the region 1625–1775 nm has been obtained. CW 33% efficient BDFL with the output power 1.05 W at 1700 nm was demonstrated. The possibility of laser generation at 1410 nm using Bi-doped germanosilicate fibres with the large GeO$_2$ concentration was also demonstrated.

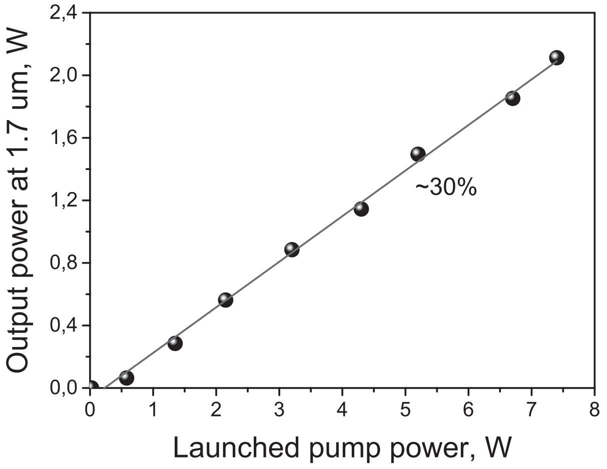

FIGURE 40.25 The output power near 1700 nm *versus* the launched pump power [40].

40.6 Bi-Doped Optical Fibre Amplifiers (BDFAs)

BDFAs are promising candidate for upgrade of future telecom and datacom optical networks for higher capacity. In 2017 using germanosilicate BDFA with low content of GeO$_2$ the first demonstration of error-free data transmission over 80 km long fibre link (TrueWave) with data rate of 10.6 Gb s^{-1} per channel in the E-band (1441–1453 nm) was reported in Ref. [65]. This chapter devoted to description of the latest progress on development of BDFAs in the range 1260–1750 nm.

The luminescence spectra of BDF of various compositions were shown above in Figure 40.9. The spectra are quite broad and cover the range 1.1–1.8 μm. Figure 40.26 shows normalized spectra of the net gain in BDF of various compositions. It is seen that amplification bands are narrower than luminescence but still quite broad. In spite of similar shape of amplification in Bi-doped fibres with different compositions, other properties such as maximal gain per meter, power conversion efficiency, noise figure and gain efficiency can be quite different.

So far, maximal achieved gain per meter at room temperature depends on fibre composition and reaches ~0.23 dB m^{-1} at 1150 nm in ASB fibre [96], 0.2 dB m^{-1} near 1330 nm in PSB fibre [56], ~5 dB m^{-1} around 1430 nm in GSB fibre [74] and ~1 dB m^{-1} at 1700 nm in high-germanium concentration (~50%) silica fibre doped with Bi (HGSB) [42]. The best power conversion efficiency among bismuth amplifiers was demonstrated by amplifier based on BAC-Si in bismuth-doped germanosilicate fibre where >60% of efficiency was achieved at 1430 nm [66]. At the moment commercially available single mode laser diodes can be successfully used for pumping of Bi-doped amplifiers in any range (1100–1800 nm). The required pump power lies within 50–500 mW range for BDFA with 20 dB small signal gain.

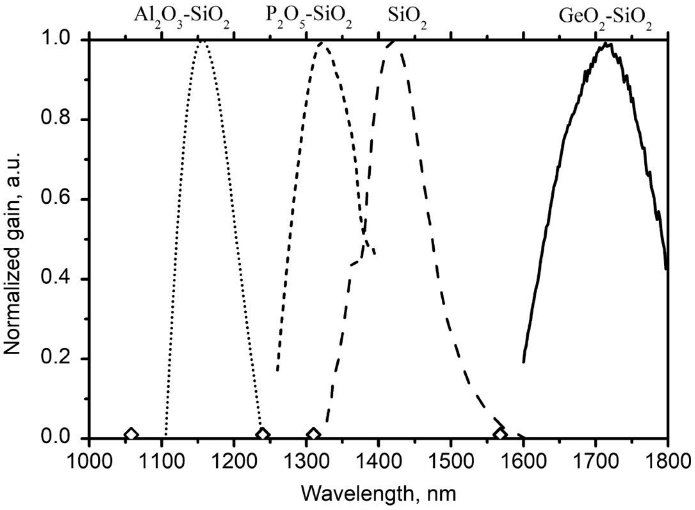

FIGURE 40.26 Lines—normalized gain in Bi-doped fibres of various compositions, points—corresponding pump wavelengths.

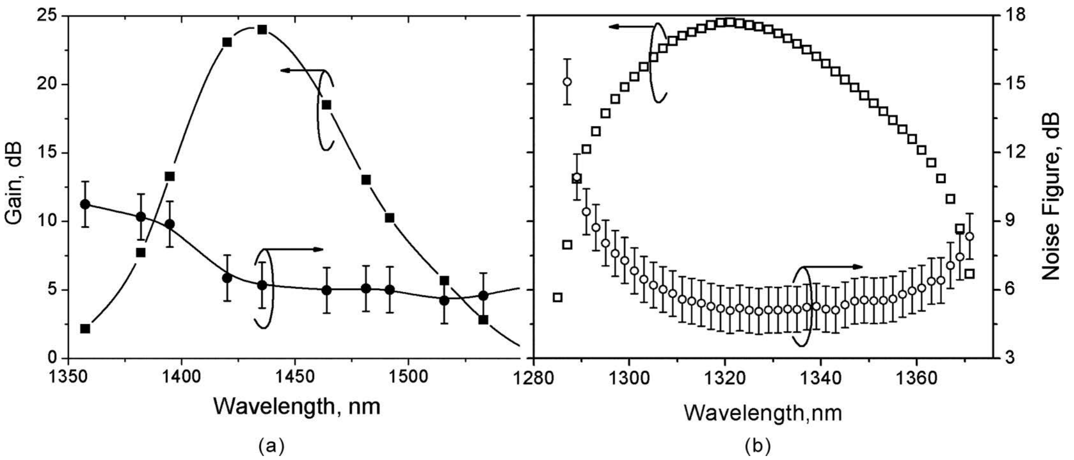

(a) (b)

FIGURE 40.27 Net gain (left scale) and noise figure (right scale) for: LD pumped GSB fibre amplifier, pump power 65 mW (a); PSB fibre amplifier, pump power 460 mW (b) [5].

40.6.1 Bi-Doped Phosphosilicate and Germanosilicate (with Low Ge Content) Fibre Amplifiers

Figure 40.27a shows gain spectra and noise figure (NF) of the GSB amplifier pumped by laser diode at $\lambda = 1310$ nm [66]. The launched pump power was near 65 mW. The unabsorbed pump power for a 65 mW input power was ~20 mW. The peak gain of 24 dB was observed near 1427 nm, 3 dB bandwidth was $\Delta\lambda_{1/2} =$ 36 nm and NF was ≈6 dB. Gain flattening filters were not used to smooth the gain spectra. As shown in Figure 40.27a a positive gain in GSB amplifier was observed in the wavelength range between 1350 and 1550 nm. The maximum gain of 34 dB was measured at $\lambda_s = 1427$ nm for the pump power of 180 mW (not shown in Figure 40.27a).

Net gain and noise figure spectra of PSB fibre amplifiers at a pump power level of 460 mW are presented in Figure 40.27b [10]. The net gain was positive in the wavelength range 1283–1372 nm. The gain maximum was near 1321 nm, reaching 24.5 dB. The 3 dB bandwidth of the net gain was ~37 nm.

Figure 40.28 shows the gain as a function of pump power near the peak gain wavelength for GSB [66] and PSB [10] amplifiers. The input signal power here was lower than −20 dBm. The maximum gain coefficient is $G = 0.4$ dB mW^{-1} for GSB and $G = 0.09$ dB mW^{-1} for PSB. The G value achieved for GSB fibres is one order of magnitude lower than that for typical Er-doped fibre amplifier, but one order of magnitude higher than that of Raman fiber amplifier and two to four times higher than that of Tm-doped fibre amplifiers. It should be noted that these results were obtained at room temperature.

The possibility of lasing at 1320 nm in PSB fibre with pumping at the shorter excitation band at 808 nm has been demonstrated in Ref. [8]. The optical amplification at 1310 nm in the similar fibre with 810 nm pumping was investigated in Ref. [73]. On/off gain amounted to 2 dB at pump power of 350 mW was observed. Thus, it was shown that using 0.8 μm absorption band for pumping of PSB optical fibre amplifiers is not efficient in comparison with 1.3 μm band.

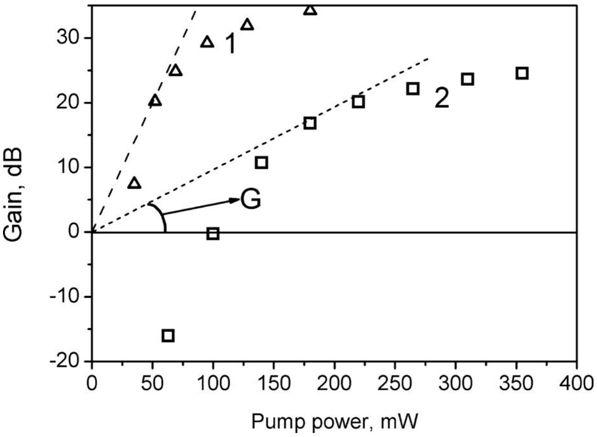

FIGURE 40.28 Dependence of the net gain on the launched pump power for: 1, GSB fibre amplifier at λ_s = 1427 nm and λ_p = 1320 nm; 2, PSB fibre amplifier at λ_s = 1318 nm and λ_p = 1230 nm [5].

In conclusion of this section: Bismuth-doped fibre amplifiers at 1.33 and 1.43 μm are able to provide more than 20 dB gain and NF ~6 dB in a single stage, which could be important for telecommunication systems. Commercially available single mode laser diodes can be used for pumping of such amplifiers. Next paragraph gives some details on BDFA on HGSB operating in the region between 1650 and 1760 nm.

40.6.2 Bi-Doped Germanosilicate Fibre Amplifier (Large Concentration of GeO_2)

For a long period of time the range between 1625 and 1750 nm was uncovered by amplifiers based on active fibres. Part of this region falls into the low-loss transparency window in silica-based glass fibres located between 1270 and 1700 nm where optical losses lower than 0.4 dB km^{-1}. Thus, this region may be important for increase of optical network capacity.

In 2015 the first BDFA operating between 1650 nm and 1760 nm have been demonstrated [36]. The active fibre

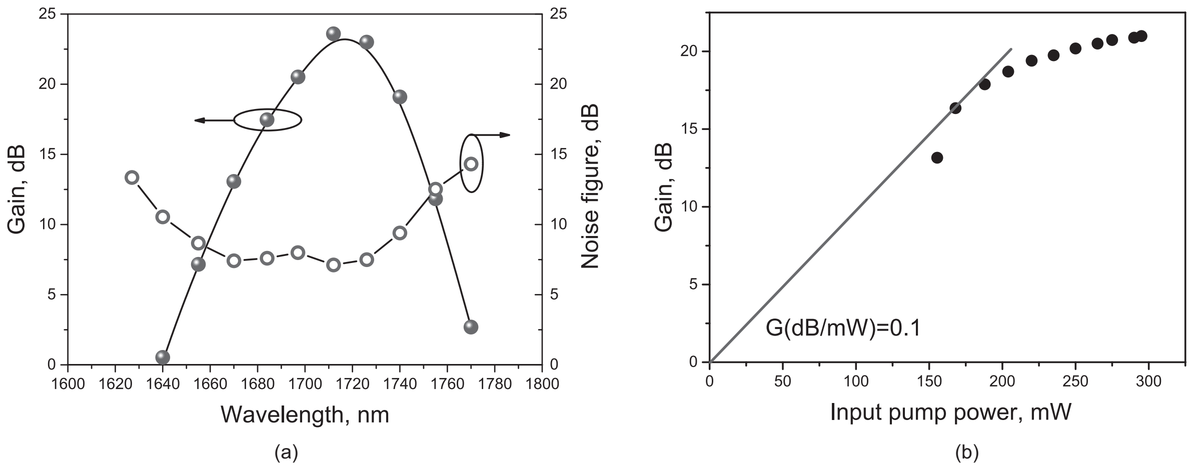

FIGURE 40.29 Gain and noise figure spectra of BDFA (a); Dependence of gain at 1700 nm on pump power at 1550 nm (b) [40].

used was highly doped with GeO_2 (>50 mol.%), the bismuth concentration in the core was ~0.02 weight %. the cladding and the core diameter—125- and 2-µm correspondingly, a cutoff wavelength ~1.2 µm and numerical aperture (NA) ~0.45. The bismuth absorption and unsaturable loss at 1550 nm was ~2 dB m^{-1} and ~0.2 dB m^{-1} respectively. BDFA with the gain of 23 dB peaked at 1710 nm consists of 60 m long active fibre bi-directionally pumped in the core by two laser diodes (LD) operating at 1550 nm with an output power up to 150 mW each.

The measured BDFA gain and noise figure are shown in Figure 40.29a. The input signal did not exceed –20 dBm. The 3 dB bandwidth of the amplifier was ~40 nm and probably partially shortened by a fused WDM served as a pump/signal combiner. The noise figure of the amplifier within 3 dB bandwidth was ~7 dB. The measured dependence of the net gain at 1700 nm on input pump power from both ends is plotted in Figure 40.29b. During the measurements the power of co-directional pump was fixed at 150 mW whereas the contra-directional pump power was varied from 0 to 150 mW. The maximum gain coefficient of the BDFA reached ~0.1 dB mW^{-1}. In Refs. [37,40] authors also investigated the dependence of the gain coefficient on active bismuth concentration in the fibre core and revealed that maximal gain coefficient was observed in the fibre with the absorption ~2 dB m^{-1} at 1650 nm.

The dependencies of the BDFA gain and power conversion efficiency at 1700 nm for pump power of 300-mW are shown in Figure 40.30. The 3 dB gain compression observed at the input signal power of –13 dBm. The maximum power conversion efficiency with respect to launched pump power reached ~3% at the input signal power of +7 dBm. It is worth noting that due to quite small core diameter of the BDF with high GeO_2 content the splice losses between active fibre and standard fibre are quite high (~1 dB or higher), that is why the pump and the signal radiation experiences quite large attenuation and launched pump power significantly lower than initial pump power.

It is important to note that unlike BDFAs at 1330 and 1430 nm bismuth amplifier at 1710 nm requires bi-directional pumping to achieve >20 dB gain with reasonable pump power (on the order of hundreds of mW). The main reason for that is quite high unsaturable loss at pump and signal wavelength, the same reason is responsible for quite low power conversion efficiency for BDFA at 1710 nm. Nevertheless, even for this region it is possible to use commercially available single mode laser diodes for pumping which is important for creation of low cost commercial amplifiers for telecom and datacom applications. The main optical characteristics of BDFA at 1710 nm—gain (>20 dB), noise figure (~7 dB), bandwidth (~40 nm), required pump power (~300 mW) and saturation output signal power (~5 dBm) are high enough for effective commercial utilization in telecom networks. Of course, the obtained parameters are not as good as in EDFA but in comparison with RFA (Raman fibre amplifiers) and TDFA (thulium-doped fibre amplifier) BDFA at 1710 nm require much less pump power and has quite large bandwidth and thus may be more cost effective for certain applications.

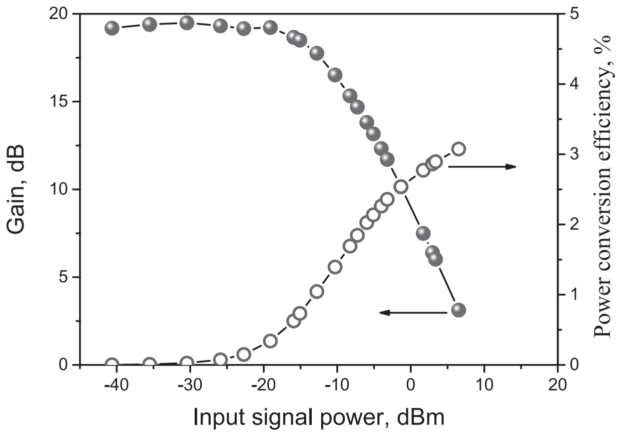

FIGURE 40.30 Dependence of gain and power conversion efficiency on input signal power [40].

40.7 Bismuth-Doped Superfluorescent Fibre Sources

Superfluorescent fibre sources (SFSs) find wide application including fibre-optic gyroscopes, ophthalmology, optical time-domain reflectometry, optical telecommunications and other devices that need a signal with low temporal and high spatial coherence. Requirements for SFS stem from the application they are intended for. Most of the requirements are met by superfluorescent rare-earth-doped fibre sources, the most widespread of which are erbium-, ytterbium-, thulium- and neodymium-doped ones [29]. There are still enough room for new SFS at new wavelengths with broader spectrum and better line shape. One of promising candidates to substitute or at least complement the rare-earth-doped sources is a bismuth-doped SFS. The bismuth-doped optical fibres having a fairly wide band of the laser transition in the range uncovered by rare-earth-doped lasers and relatively high efficiency. An additional advantage is that in the various glass hosts bismuth active centres provide gain at different wavelengths.

Recently a Bismuth-doped SFS peaked at 1.43 μm was demonstrated using GSB fibre [85]. A single stage double-pass backward pumped configuration was used. The slope efficiency reached 38%. The spectrum FWHM decreased with the pump power increase and amounted to 24 nm at 260 mW pump power. The output power reached ~85 mW. Important feature of SFS based on Bi-doped fibres is a Gaussian-like shape of output spectra (see GSB SFS spectra in Figure 40.31). According to measurement results the temperature stability of peak wavelength of GSB SFS was ~3.5 nm in the temperature range −55°C to +65°C.

First SFS based on PSB fibres with a mean output wavelength of 1336 nm was demonstrated in Ref. [86]. Due to lower efficiency of the fibre the double stage scheme was used. Bandwidth of 26 nm FWHM and output power of 48 mW were achieved at the highest pump power of 600 mW. Output spectrum has again nearly Gaussian shape (a fit of its spectrum by a Gaussian at a pump power of 320 mW is shown in Figure 40.32).

Next progress in SFS based on BDFs was taken in 2016 [38] where authors realized single stage SFS at 1730 nm using fibre with high GeO_2 content (~50 mol.%) and with bismuth concentration <0.1 weight %. Being pumped with power ~300 mW at 1460 nm the active fibre demonstrated maximum gain of 1 dB m^{-1} at 1700 nm. The SFS consist of 60 m long active fibre counter pumped with radiation from Er-Yb laser at 1568 nm. The threshold and the maximum pump power was 50 and 650 mW correspondingly. The spectra of output radiation for different pump power are represented in Figure 40.33. It is seen that Gaussian approximation fitted experimental spectrum at maximal output power of 7 mW very good. The FWHM bandwidth of the spectra reduces from 55 nm at threshold pump power to ~50 nm at the highest pump value.

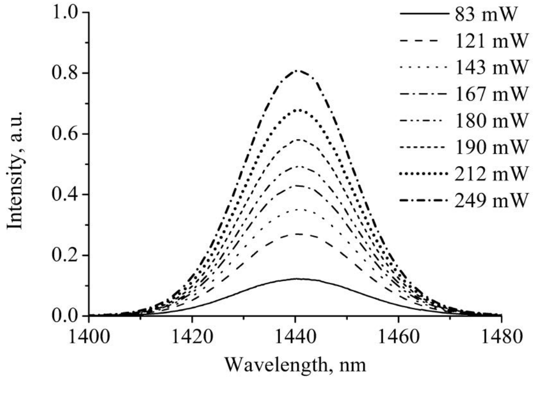

FIGURE 40.31 The output spectra of GSB-based SFS at various pump powers [85].

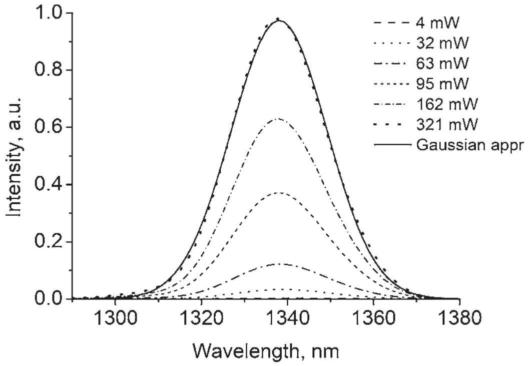

FIGURE 40.32 Output spectra of the PSB-based SFS at various pump powers [87].

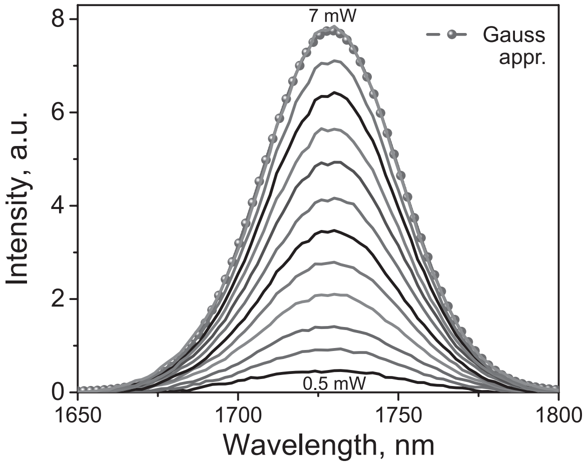

FIGURE 40.33 SFS output spectra at pump power from 0.5 to 7 mW [40].

The efficiency of the SFS at 1730 nm was quite low ~1% but authors notes that optimization of the optical scheme and active fibre may significantly improve it. Nevertheless, even at this level of efficiency the SFS can be pumped by commercially available laser diodes at 1.45–1.55 μm.

SFS based on GSB, PSB and Hi-Ge GSB fibres demonstrate high enough efficiency, output power from several mW to several tens of mW, quite broad spectral bandwidth ~ 25–55 nm FWHM and perfect Gaussian-like shape without any filters. These SFS could successfully be used in a number of applications including high precision fibre gyroscopes, optical coherent tomography, microscopy, optical time-domain reflectometry, optical telecommunications and many other.

40.8 Conclusions

The results obtained confirm that Bi-doped optical fibres have a great potential as NIR laser materials. Various types of Bi-doped silica-based optical fibres emitting luminescence in a spectral region of 800–1800 nm have been developed. BDFLs operating at 1150–1550 and 1625–1775 nm have been created. Despite the great progress in the development of various Bi-doped optical fibres and BDFLs several problems remain to be solved. The main problem is that we do not know exactly the nature of the Bi-related NIR emitting centres. This prevents one from solving some other problems, in particular three very important ones:

- The efficient operation of BDFLs has been achieved only at very low bismuth concentration (~ 0.01 at.%)
- The efficiency of BDFLs reached at present is lower than that of the conventional rare-earth-doped fibre lasers
- We could not yet eliminate bismuth clustering in fibres with Bi concentration in excess of 0.01–0.05 at.%

Further fundamental research is needed to understand the nature of BACs and to solve other problems that will allow one to improve the characteristics of BDFLs.

REFERENCES

1. Ahnlers, F.J.; Lohse, F.; Spaeth, J.-M. Identification of a Tl dimer centre in alkali halides by ODMR. *J. Phys. C: Sol. State. Phys.* **1985**, *18*, 3881–3890.
2. Bigot, L.; Razdobreev, I.; Pureur, V.; Bouwmans, G.; Douay, M. Broadband and efficient bismuth fiber laser around 1.2 µm. In *Proceedings of the Europhoton Conference*, Pisa, Italy, 10–15 September 2006, ThE6.
3. Blasse, G.; Bril, A. Investigation on Bi3+ - activated phosphors. *J. Chem. Phys.* **1968**, *48*, 217–222.
4. Blody, C.F.; Russel, S.R.; Padilo, J.S.; Folk, J.C. Direct and feeder vessel photocoagulation of retinal angiograms with die yellow laser. *Ophthalmology.* **1990**, *97*, 791–797.
5. Bufetov, I.A.; Melkumov, M.A.; Firstov, S.V.; Riumkin, K.E.; Shubin, A.V.; Khopin, V.F.; Guryanov A.N. and Dianov, E.M. Bi-doped optical fibers and fiber lasers. *IEEE J. Sel. Topics Quantum Electron.* **2014**, *20*(5), 0903815.
6. Bufetov, I.A.; Firstov, S.V.; Khopin, V.F.; Abramov, A.N.; Guryanov, A.N.; Dianov, E.M. Luminescence and optical gain in Pb-doped silica-based optical fibers. *Opt. Express.* **2009**, *17*, 13487–13492.
7. Bufetov, I.A.; Firstov, S.V.; Khopin, V.F.; Guryanov, A.N.; Dianov, E.M. Visible luminescence and upconversion processes in Bi-doped silica-based fibers pumped by IR radiation. In *Proceedings of the European Conference on Optical Communication*, Brussel, Belgium, 21–25 September 2008, Tu.3.B.4.
8. Bufetov, I.A.; Firstov, S.V.; Khopin, V.F.; Medvedkov, O.I.; Guryanov, A.N.; Dianov, E.M. Bi-doped fiber lasers and amplifiers for a spectral region of 1300–1470 nm. *Opt. Lett.* **2008**, *33*, 2227–2229.
9. Bufetov, I.A.; Melkumov, M.A.; Firstov, S.V.; Shubin, A.V.; Semenov, S.L.; Vel'miskin, V.V.; Levchenko, A.E.; Firstova, E.G.; Dianov, E.M. Optical gain and laser generation in bismuth-doped silica fibers free of other dopants. *Opt. Lett.* **2011**, *36*, 166–168.
10. Bufetov, I.A.; Melkumov, M.A.; Khopin, V.F.; Firstov, S.V.; Shubin, A.V.; Medvedkov, O.I; Guryanov, A.N; Dianov, E.M. Efficient Bi-doped fiber lasers and amplifiers for the spectral region 1300–1500 nm. In *Proceedings SPIE 7580, Fiber Lasers VII: Technology, Systems, and Applications*, 17 February 2010, 758014-1–9.
11. Bufetov, I.A.; Shubin, A.V.; Firstov, S.V.; Melkumov, M.A.; Khopin, V.F.; Guryanov, A.N.; Dianov, E.M. High-power cw 1.27 µm Bi-doped fiber laser. In *Proceedings of the Conference on Lasers and Electro-Optics Europe and 12th European Quantum Electronics Conference*, Munich, Germany, 22–26 May 2011, CJ8.2.
12. Canagasabey, A.; Corbari, C.; Gladyshev, A.V.; Liegeois, F.; Guillemet, S.; Hernandez, Y.; Yashkov, M.V.; Kosolapov, A.; Dianov, E.M.; Ibsen, M.; Kazansky, P.G. High-average-power second-harmonic generation from periodically poled silica fibers. *Opt. Lett.* **2009**, *34*, 2483–2485.
13. Corbett, J.D. Homopolyatomic ions of the post-transition elements – synthesis, structure and bonding. In *Progress in Inorganic Chemistry*; Lippard S.J. ed.; New York: John Wiley and Sons Inc. 1976; Volume 21, pp. 129–158.
14. Denker, B.I; Galagan, B.I.; Osiko, V.V.; Shulman, I.L.; Sverchkov, S.E.; Dianov, E.M. Factors affecting the formation of near infrared-emitting centers in Bi-doped glasses. *Appl. Phys. B.* **2010**, *98*, 455–458.
15. Desurvire, E. Optical communications in 2025. In *Proceedings of the European Conference on Optical Communication*, Glasgow, Scotland, 25–30 September 2005, pp. 5–6.
16. Dianov, E.M. Amplification in extended transmission bands using Bismuth-doped optical fibers. *J. Lightwave Technol.* **2013**, *31*, 681–688.
17. Dianov, E.M. Bi-doped glass optical fibers: is it a new breakthrough in laser materials. *J. Non-Crystal. Solids.* **2009**, *355*, 1861–1864.
18. Dianov, E.M. Nature of Bi-related near IR active centers in glasses: state of art and first reliable results. *Laser Phys. Lett.* **2015**, *12*, 095106.
19. Dianov, E.M. On the nature of new IR emitting Bi centers in glass. *Quantum Electron.* **2010**, *40*, 283–285.
20. Dianov, E.M.; Alyshev, S.V.; Shubin, A.V.; Khopin, V.F.; Guryanov, A.N. IR luminescence of tellurium-doped silica-based optical fiber. *Quantum Electron.* **2012**, *42*, 189–191.
21. Dianov, E.M.; Bufetov, I.A.; Firstov, S.V.; Medvedkov, O.I.; Melkumov, M.A. Bismuth-doped silica-based fiber lasers operating near 1460 nm. In *Proceedings of the European Conference on Optical Communication*, Geneva, Switzerland, 18–22 September 2011, Tu 3.Le Cervin.3.
22. Dianov, E.M.; Dvoyrin, V.V.; Mashinsky, V.M.; Medvedkov, O.I. Yellow frequency-doubled bismuth fiber laser. In *Proceedings of the European Conference on Optical Communication*, Cannes, France, 24–28 September 2006, Th2.3.1.
23. Dianov, E.M.; Dvoyrin, V.V.; Mashinsky, V.M.; Umnikov, A.A; Yashkov, M.V.; Guryanov A.N. CW bismuth fiber laser. *Quantum Electron.* **2005**, *35*, 1083–1084.
24. Dianov, E.M.; Firstov, S.V.; Khopin, V.F.; Guryanov, A.N.; Bufetov, I.A. Bi-doped fiber lasers and amplifiers emitting in a spectral region of 1.3 µm. *Quantum Electron.* **2008**, *38*, 615–617.

25. Dianov, E.M.; Firstov, S.V.; Khopin, V.F.; Medvedkov, O.I; Guryanov, A.N; Bufetov, I.A. Bi-doped fiber lasers operating in the range 1470–1550 nm. *Quantum Electron*. **2009**, *39*, 299–301.
26. Dianov, E.M.; Krylov, A.A.; Dvoyrin, V.V.; Mashinsky, V.M.; Kryukov, P.G.; Okhotnikov, O.G.; Guina M. Mode-locked Bi-doped fiber laser. *J. Opt. Soc. Am. B*. **2007**, *27*, 1807–1808.
27. Dianov, E.M.; Shubin, A.V.; Melkumov, M.A.; Medvedkov, O.I.; Bufetov, I.A. High-power cw bismuth fiber lasers. *J. Opt. Soc. Am. B*. **2007**, *24*, 1749–1755.
28. Dianov, E.M.; Vel'miskin, V.V.; Firstov, S.V.; Semenov, S.L.; Shubin, A.V.; Bufetov, I.A. Bi:SiO_2 optical fibers –a possible way to understand the nature of Bi-related emitting centers. In *Proceedings of the Optical Fiber Communication Conference*, Los Angeles, CA, 6–10 March 2011, OTuC6.
29. Digonnet M.J.F. *Rare-Earth-Doped Fiber Lasers and Amplifiers*. New York*:* Marcel Dekker, Inc. 2001.
30. Dvoretsky, D.A.; Bufenov, I.A.; Velmiskin, V.V.; Zlenko, A.S.; Khopin, V.F.; Semjonov, S.L.; Guryanov, A.N.; Denisov, L.K.; Dianov, E.M. Optical properties of Bi-doped silica-based fibers in a temperature range of 300–1500 K. *Quantum Electron*. **2012**, *42*, 762–773.
31. Dvoyrin, V.V.; Gladyshev, A.V.; Mashinsky, V.M.; Dianov, E.M.; Canagasabey A.; Corbari, C.; Ibsen, M.; Kazansky, P.G. Yellow all-fiber Bi Laser. In *Proceedings of the European Conference on Optical Communication*, Brussels, Belgium, 21–25 September 2008, Tu1.B.1.
32. Dvoyrin, V.V.; Kir'yanov, A.V.; Mashinsky, V.M.; Medvedkov, O.I; Umnikov, A.A.; Guryanov, A.N.; Dianov, E.M. Absorption, gain and laser action in bismuth-doped aluminosilicate optical fibers. *IEEE J. Quantum Electron*. **2010**, *46*, 182–190.
33. Dvoyrin, V.V.; Mashinsky, V.M.; Dianov, E.M. Efficient bismuth-doped fiber lasers. *IEEE J. Quantum. Electron*. **2008**, *44*, 834–840.
34. Dvoyrin, V.V.; Mashinsky, V.M.; Dianov, E.M.; Umnikov, A.A.; Yashkov, M.V.; Guryanov, A.N. Absorption, fluorescence and optical amplification in MCVD Bismuth-doped silica glass optical fibers. In *Proceedings of the European Conference on Optical Communication*, Glasgow, Scotland, 25–30 September 2005, Th.3.3.5.
35. Dvoyrin, V.V.; Medvedkov, O.I.; Mashinsky, V.M.; Umnikov, A.A.; Guryanov, A.N.; Dianov, E.M. Optical amplification in 1430–1495 nm range and laser action in Bi-doped fibers. *Opt. Express*. **2008**, *16*, 16971–16976.
36. Firstov, S.V.; Alyshev, S.V.; Riumkin, K.E.E.; Khopin, V.F.; Melkumov, M.A.; Gurjanov, A.N.; Dianov, E.M. Bismuth-doped fibre amplifier operating between 1600 and 1800 nm. *Quantum Electron*. **2015**, *45*(12), 1083.
37. Firstov, S.V.; Alyshev, S.V.; Riumkin, K.E.; Khopin, V.F.; Guryanov, A.N.; Melkumov, M.A.; Dianov, E.M.A. 23-dB bismuth-doped optical fiber amplifier for a 1700-nm band. *Sci. Rep*. **2016**, *6*, 28939.
38. Firstov, S.V.; Riumkin, K.E.E.; Khopin, V.F.; Alyshev, S.V.; Mel'kumov, M.A.; Gur'yanov, A.N.; Dianov, E.M. Superluminescent bismuth-doped fibre IR source for the range. *Quantum Electron*. **2016**, *46*(9), 787.
39. Firstov, S.V.; Alyshev, S.V.; Kharakhordin, A.V.; Riumkin, K.; Dianov, E.M. Laser-induced bleaching and thermo-stimulated recovery of luminescent centers in bismuth-doped optical fibers. *Opt. Mater. Express*. **2017**, *7*, 3422–3432.
40. Firstov, S.V.; Alyshev, S.V.; Riumkin, K.E.; Khegai, A.M.; Kharakhordin, A.V.; Melkumov, M.A.; Dianov, E.M. Laser-active Bi-doped fibers for a spectral region of 1.6 – 1.8 um. *IEEE J. Sel. Top. Quantum*. Electron. **2018**, *24*(5), 0902415.
41. Firstov, S.; Alyshev, S.; Khopin, V.; Melkumov, M.; Guryanov, A.; Dianov, E. Photobleaching effect in bismuth-doped germanosilicate fibers. *Opt. Express*. **2015**, *23*, 19226–19233.
42. Firstov, S.V.; Alyshev, S.V.; Riumkin, K.E.; Melkumov, M.A.; Medvedkov, O.I.; Dianov E.M. Watt-level, continuous-wave bismuth-doped all-fiber laser operating at 1.7 μm. *Opt. Lett*. **2015**, *40*, 4360–4363.
43. Firstov, S.V.; Bufetov I.A.; Khopin, V.F,; Shubin, A.V.; Smirnov, A.M.; Iskhakova, L.D.; Vechkanov, N.N.; Guryanov, A.N; Dianov, E.M. 2W bismuth-doped fiber lasers in the wavelength range 1300–1500 nm and variation of Bi-doped fiber parameters with core composition. *Laser Phys. Lett*. **2009**, *6*, 665–670.
44. Firstov, S.V.; Girsova, M.A.; Dianov, E.M.; Antropova, T.V. Luminescent properties of thermoinduced active centers in quartz-like glass activated by bismuth, *Glas. Phys. Chem*. **2014**, *40*, 521–525.
45. Firstov, S.V.; Khopin, V.F.; Bufetov, I.A.; Firstova, E.G.; Guryanov, A.N.; Dianov, E.M. Combined excitation-emission spectroscopy of bismuth active centers in optical fibers. *Opt. Express*. **2011**, *19*, 19551–19561.
46. Firstov, S.V.; Khopin, V.F.; Velmiskin, V.V.; Firstova, E.G.; Bufetov, I.A.; Guryanov, A.N.; Dianov, E.M. Anti-Stokes luminescence in bismuth-doped silica and germania-based fibers. *Opt. Express*. **2013**, *21*, 18408–18413.
47. Firstov, S.V.; Shubin, A.V.; Khopin, V.F.; Mel'kumov, M.A.; Bufetov, I.A.; Medvedkov, O.I.; Guryanov, A.N.; Dianov, E.M. Bismuth-doped germanosilicate fiber laser with 20 W output power at 1460 nm. *Quantum Electron*. **2011**, *41*, 581–583.
48. Firstov, S; Alyshev, S; Melkumov, M; Riumkin, K; Shubin, A; Dianov, E. Bismuth-doped optical fibers and fiber lasers for a spectral region of 1600–1800 nm. *Opt. Lett*. **2014**, *39*, 6927–6930.
49. Firstova, E.G.; Bufetov, I.A.; Khopin, V.F.; Velmiskin, V.V.; Firstov, S.V.; Bufetova, G.A.; Nishchev, K.N.; Guryanov, A.N.; Dianov, E.M. Luminescence properties of IR-emitting bismuth centres in SiO_2-based glasses in the UV to near-IR spectral region. *Quantum Electron*. **2015**, *45*(1), 59–65.
50. Fockele, M.; Lohse, F.; Spaeth, J.-M.; Bartram, R.H. Identification and optical properties of axial lead centers in alkaline-earth fluorides. *J. Phys.: Condens. Matter*. **1989**, *1*, 13–26.
51. Fujimoto, Y.; Nakatsuka, M. Infrared luminescence from bismuth-doped silica glass. *Jpn. J. Appl. Phys*. **2001**, *40*, L279–L281.
52. Gaft, M.; Reisfeld, R.; Panczer, G.; Boulon, G.; Saraidarov, T.; Erlish, S. The luminescence of Bi, Ag and Cu in natural and synthetic barite $BaSO_4$. *Opt. Mat*. **2001**, *16*, 279–290.

53. Galagan, B.I.; Denker, B.I.; Hu, L.; Sverchkov, S.E.; Shulman, I.L.; Dianov, E.M. Effect of variable valence impurities on the formation of bismuth-related optical centers in silica glass. *Quantum Electron*. **2012**, *42*, 940–942.
54. Hamstra, M.A.; Folkerts, H.F.; Blasse, G. Red bismuth emission in alkaline-earth-metal sulfates. *J. Mater. Chem*. **1994**, *4*, 1349–1350.
55. Haruna, T.; Kakui, M.; Taru, T.; Ishikawa, S.-H.; Onishi, M. Silica-based bismuth-doped fiber for ultra broad light source and optical amplification around 1.1 μm. In *Proceedings of the Optical Amplifiers and Their Applications (OAA) Topical Meeting*, Budapest, Hungary, 7–10 August 2005, MC3.
56. Heikkinen, J.; Gumenyuk, R.; Rantamäki, A.; Leinonen, T.; Melkumov, M.; Dianov, E.M.; Okhotnikov, O.G. A 1.33 μm picosecond pulse generator based on semiconductor disk mode-locked laser and bismuth fiber amplifier. *Opt. Express*. **2014**, *22*(10), 11446–11455.
57. Jiang, X.; Su, L.; Yu, P.; Guo, X.; Tang, H.; Xu, X.; Zheng, L.; Li, H.; Xu, J. Broadband photoluminescence of Bi_2O_3 – GeO_2 binary systems: glass, glass-ceramics and crystals. *Laser Phys*. **2013**, *23*, 105812–105824.
58. Kalita, M.P.; Yoo, S.; Sahu, J. Bismuth-doped fiber laser and study of unsaturable loss and pump induced absorption in laser performance. *Opt. Express*. **2008**, *16*, 21032–21038.
59. Kelleher, E.J.R.; Travers, J.C.; Golant, K.M.; Popov, S.V.; Taylor, J.R. Narrow linewidth bismuth-doped all-fiber ring laser. *IEEE Photon. Tech. Lett*. **2010**, *22*, 793–795.
60. Khonthon, S.; Morimoto, Sh.; Arai, Y.; Ohishi, Y. Redox equilibrium and NIR luminescence of Bi_2O_3-containing glasses. *Opt. Mater*. **2009**, *31*, 1262–1268.
61. Kir'yanov, A.V.; Dvoyrin, V.V.; Mashinsky, V.M.; Barmenkov, Yu.O.; Dianov, E.M. Nonsaturable absorption in aluminosilicate bismuth-doped fibers. *J. Appl. Phys*. **2011**, *109*, 023113-1–8.
62. Kivistö, S.; Puustinen, J.; Guina, M.; Okhotnikov, O.G.; Dianov, E.M. Tunable mode-locked bismuth-doped soliton fiber laser. *Electron. Lett*. **2008**, *44*, 1456–1457.
63. Krasnovsky, A.A.; Drozdova, N.N.; Ivanov, A.V.; Ambartsumian R.V. Activation of molecular oxygen by infrared radiation in pigment-free aerobic systems. *Biochemistry (Moscow)*. **2003**, *68*, 963–966.
64. Max, C.E.; Oliver, S.S.; Friedman, H.W.; An, J.,; Avicola, K.; Becman, B.V.; Bissinger, H.D.; Brase, J.M.; Erbert, G.V.; Gavel, D.T.; Kanz, K.; Liu, M.C.; Macintosh, B.; Neeb, K.P.; Patience, J.; Waltjen, K.E. Image improvement from a sodium-layer laser guide star adaptive optics system. *Science*. **1977**, *277*, 1649–1651.
65. Melkumov, M.A.; Mikhailov, V., Khegai, A.M.; Riumkin, K.E, Westbrook, P.S.; DiGiovanni, D.J.; Dianov, E.M. E-band data transmission over 80 km of non-zero dispersion fibre link using bismuth-doped fibre amplifier. *Electron. Lett*. **2017**, *53*(25), 1661–1663.
66. Melkumov, M.A.; Bufetov, I.A.; Shubin, A.V.; Firstov, S.V.; Khopin, V.F.; Guryanov, A.N.; Dianov, E.M. Bismuth-doped optical fiber amplifier for 1430 nm band pumped by 1310 nm laser diode. In *Proceedings of the Optical Fiber Communication Conference*, Los Angeles, California, 6–10 March 2011, OMH1.
67. Meng, X.-G.; Qiu, J.-R.; Peng, M.-Y.; Chen, D.-P.; Zhao, Q.-Z.; Jiang, X.-W.; Zhu, C.S. Near infrared broadband emission of bismuth-doped aluminophosphate glass. *Opt. Express*. **2005**, *13*, 1628–1634.
68. Meng, X.-G.; Qiu, J.-R.; Peng, M.-Y.; Chen, D.P.; Zhao, Q.-Z.; Jiang, X.-W.; Zhu, C.S. Infrared broadband emission of bismuth-doped barium-aluminum borate glasses. *Opt. Express*. **2005**, *13*, 1635–1642.
69. Mollenauer, L.F.; Vieira, N.D.; Szeto, L. Optical properties of the Tl^0 (1) center in KCl. *Phys. Rev. B*. **1983**, *27*, 5332–5346.
70. Morioka, T. New generation optical infrastructure technologies: "EXAT initiative" towards 2020 and beyond. In *Proceedings of the Optoelectronics and Communications Conference (OECC)*, Hong Kong, China, 13–17 July 2009, FT4.
71. Murata, K.; Fujimoto, Y.; Kanabe, T.; Fujita, H.; Nakatsuka, M. Bi-doped SiO_2 as a new laser material for an intense laser. *Fusion Eng. Design* **1999**, *44*, 437–439.
72. Nagel, J.A.; Temyanko, V.; Dobler, J.; Dianov, E.M.; Biriukov, A.S.; Sysoliatin, A.A.; Norwood, R.A.; Peyghambarian, N. High-power narrow-linewidth continuous-wave Raman amplifier at 1.27 μm. *IEEE Photon. Tech. Lett*. **2011**, *23*, 585–587.
73. Norizan, S.F.; Chong, W.Y.; Harun, S.W.; Ahmad, H. O-band bismuth-doped fiber amplifier with double-pass configuration. *IEEE Photon. Tech. Lett*. **2011**, *23*(24), 1860–1862.
74. Noronen, T.; Melkumov, M.A.; Stolyarov, D; Khopin, V.F.; Dianov, E.M.; Okhotnikov, O.G. All-bismuth fiber system for femtosecond pulse generation, compression, and energy scaling. *Opt. Lett*. **2015**, *40*, 2217–2220.
75. Parke, S.; Webb, R.S. The optical properties of thallium, lead and bismuth in oxide glasses. *J. Phys. Chem. Solids*. **1973**, *34*, 85–95.
76. Peng, M.; Dong, G.; Wondraczek, L.; Zhang, L.; Zhang, N.; Qju, J. Discussion on the origin of NIR emission from Bi-doped materials. *J. Non-Cryst. Solids*. **2011**, *357*, 2241–2245.
77. Peng, M.; Qiu, J.; Chen, D.; Meng, X.; Zhu, C. Broadband infrared luminescence from Li_2O – Al_2O_3 – ZnO – SiO_2 glasses doped with Bi_2O_3. *Opt. Express*. **2005**, *13*, 6892–6898.
78. Peng, M.Y.; Qiu, J.R.; Chen, D.P.; Meng, X.G.; Yang, I.Y.; Jiang, X.W.; Zhu, C.S. Bismuth-and aluminum-codoped germanium oxide glasses for super-broadband optical amplifiers. *Opt. Lett*. **2004**, *29*, 1998–2000.
79. Peng, M.Y.; Qiu, J.-R.; Chen, D.P.; Meng, X.G.; Zhu, C.S. Superbroadband 1310 nm emission from bismuth and tantalum codoped germanium oxide glasses. *Opt. Lett*. **2005**, *30*, 2433–2435.
80. Razdobreev, I.; Bigot, L.; Pureur, V.; Favre, A.; Bouwmans, G.; Douay, M. Efficient all-fiber bismuth-doped laser. *Appl. Phys. Lett*. **2007**, *90*, 031103-1–3.
81. Razdobreev, I.; Hamzaoui, H.El.; Ivanov, V.Yu.; Kustov, E.F.; Capoen, B.; Bouazaoui, M. Optical spectroscopy of bismuth-doped pure silica fiber preform. *Opt. Lett*. **2010**, *35*, 1341–1343.

82. Reisfeld, R.; Boehm, L. Optical properties of bismuth in germanate, borax and phosphate glasses. *J. Non-Cryst. Solids*. **1974**, *16*, 83–92.
83. Ren, J.; Yang, L.; Qiu, J.; Chen, D.; Jiang, X.; Zhu, C. Effect of various alkaline-earth metal oxides on the broadband infrared luminescence from Bi-doped silicate glasses. *Solid State Commun*. **2006**, *140*, 38–41.
84. Riumkin, K.E.; Melkumov, M.A.; Varfolomeev, I.A.; Shubin, A.V.; Bufetov, I.A.; Firstov, S.V.; Khopin, V.F.; Umnikov, V.F.; Guryanov, A.N.; Dianov, E.M. Excited-state absorption in various bismuth-doped fibers. *Opt. Lett*. **2014**, *39*, 2503–2505.
85. Riumkin, K.E.; Melkumov, M.A.; Bufetov, I.A.; Shubin, A.V.; Firstov, S.V.; Khopin, V.F.; Guryanov, A.N.; Dianov, E.M. Superfluorescent 1.44 μm bismuth-doped fiber source. *Opt. Lett*. **2012**, *37*, 4817–4819.
86. Riumkin, K.E.; Melkumov, M.A.; Shubin, A.V.; Firstov, S.V.; Bufetov, I.A.; Khopin, V.F.; Guryanov, A.N.; Dianov, E.M. Superfluorescent 1.34 μm bismuth-doped fiber source. *Quantum Electron*. **2014**, *44*, 700–702.
87. Rulkov, A.B.; Ferin A.A.; Popov S.V.; Taylor J.R.; Razdobreev I.; Bigot L.; Bouwmans G. Narrow-line 1178 nm cw Bismuth-doped fiber laser with 6.4 W output for direct frequency doubling. *Opt. Express*. **2007**, *15*, 5473–5476.
88. Sadick N.S.; Weiss R. The utilization of a new yellow light laser (578 nm) for the treatment of class I, red telangiectasia of the low extremities. *J. Dermatol. Surg*. **2002**, *28*, 21–25.
89. Sharonov, M.Yu.; Bykov, A.B.; Petricevic, V.; Alfano, R.R. Spectroscopic study of optical centers formed in Bi-, Pb-, Sb-, Sn-, Te- and In-doped germanate glasses. *Opt. Lett*. **2008**, *33*, 2131–2133.
90. Shubin, A.V.; Bufetov, I.A.; Melkumov, M.A.; Firstov, S.V.; Medvedkov, O.I.; Khopin, V.F.; Guryanov, A.N.; Dianov, E.M. Bismuth-doped silica-based fiber lasers operating between 1389 and 1538nm with output power of up to 22 W. *Opt. Lett*. **2012**, *37*, 2589–2591.
91. Skuja L. Optically active oxygen-deficiency-related centers in amorphous silicon dioxide. *J. Non. Cryst. Solids*. **1998**, *239*, 16–48.
92. Sokolov, V.O.; Plotnichenko, V.G.; Dianov, E.M. Origin of NIR luminescence in $Bi_2O_3 - GeO_2$ and $Bi_2O_3 - SiO_2$ glasses: first-principle study. *Opt. Mater. Express*. **2015**, *5*, 163–168.
93. Sokolov, V.O.; Plotnichenko, V.G.; Dianov, E.M. The origin of near-IR luminescence in bismuth-doped silica and germania glasses free of other dopants: first-principle study. *Opt. Mater. Express*. **2013**, *3*, 1059–1074.
94. Srivastava, A.M. Luminescence of divalent bismuth in M^{2+} BPO_5 ($M^{2+}=Ba^{2+}$, Sr^{2+} and Ca^{2+}). *J. Lumin*. **1998**, *78*, 239–243.
95. Sun, N.T.; Zhou, J.; Qiu, J. Recent advances in bismuth activated photonic materials. *Prog. Mater. Sci*. **2014**, *64*, 1–72.
96. Thipparapu, N.K.; Jain, S; Umnikov, A.A.; Barua, P.; Sahu, J.K. 1120 nm diode-pumped Bi-doped fiber amplifier. *Opt. Lett*. **2015**, *40*, 2441–2444.
97. Tkach, R. Scaling optical communications for the next decade and beyond. *Bell Labs Tech. J*. **2010**, *14*, 3–9.
98. Xie, W.; Qiu, Y.; Wang, Y. Upconversion fluorescence of bismuth doped silica fibers. *Laser Phys*. **2013**, *23*, 015702.
99. Yoo, S.; Kalita, M.P.; Nilsson, J.; Sahu, J.; Excited state absorption measurement in the 900–1250 nm wavelength range for bismuth-doped silicate fibers. *Opt. Lett*. **2009**, *34*, 530–532.
100. Zhou, Sh.; Jiang, N.; Zhu, B.; Yang, H.; Ye, S.; Lakshminarayana, G.; Hao, J.; Qiu, J. Multifunctional bismuth-doped nanoporous silica glass: from blue-green, orange, red, and white light sources to ultra-broadband infrared amplifiers. *Adv. Funct. Mater*. **2008**, *18*, 1407–1413.
101. Zlenko, A.S.; Dvoyrin, V.V.; Mashinsky, V.M.; Denisov, A.N.; Iskhakova, L.D.; Mayorova, M.S.; Medvedkov, O.I.; Semenov, S.L.; Vasiliev, S.A.; Dianov, E.M. Furnace chemical vapor deposition bismuth-doped silica-core holey fiber. *Opt. Lett*. **2011**, *36*, 2599–2601.

41

Erbium and Other Doped Fibre Amplifiers

Kevin Cordina

CONTENTS

41.1 Introduction ... 557
41.2 Amplifier Topology ... 558
41.3 Gain Spectra ... 559
  41.3.1 Dynamic Gain Tilt ... 560
  41.3.2 Variable Gain Amplifiers ... 561
  41.3.3 Gain Flattening ... 561
41.4 Noise in EDFAs ... 561
41.5 Amplifier Pumping ... 563
  41.5.1 Influence on Amplifier Performance ... 563
  41.5.2 980 nm Pumping ... 563
  41.5.3 1480 nm Pumping ... 564
  41.5.4 Pump Distribution Schemes ... 564
41.6 Doped Fibre Amplifiers for Other Telecoms Windows ... 565
  41.6.1 1450–1500 nm ... 565
  41.6.2 1300 nm ... 565
41.7 Inhomogeneous Effects ... 566
  41.7.1 Polarization Hole Burning ... 566
  41.7.2 Polarization-dependent Gain ... 566
  41.7.3 Spectral Hole Burning ... 566
41.8 The EDFA in a Communication System ... 566
  41.8.1 Line Amplifiers ... 566
  41.8.2 Pre-amplifiers ... 567
  41.8.3 Narrow Band Amplifiers ... 567
41.9 Amplifier Control ... 567
  41.9.1 Total Output Power Control ... 567
  41.9.2 Gain Control ... 567
  41.9.3 Transient Control ... 567
41.10 Alternatives to EDFAs ... 568
  41.10.1 Erbium-doped Waveguide Amplifiers ... 568
  41.10.2 Semiconductor Optical Amplifiers ... 568
  41.10.3 Raman Fibre Amplifiers ... 568
41.11 Amplifier Measurement ... 569
41.12 EDFA Modelling ... 569
  41.12.1 Gain Tilt Modelling ... 569
  41.12.2 Rate Equation Modelling ... 569
References ... 569
Further Reading ... 570

41.1 Introduction

The erbium-doped fibre amplifier (EDFA) has become a vital part of optical communication systems, enabling the economic transmission of multiple wavelengths through a single fibre over very long distances.

The EDFA is a member of the doped fibre amplifier (DFA) family, which extends to cover any amplifier which achieves gain via excitation and decay of electrons in ions within the material through which the light is passing. Typically these ions are rare earth elements which have been included as dopants within the material during its production. Different ions and materials provide gain at different wavelengths.

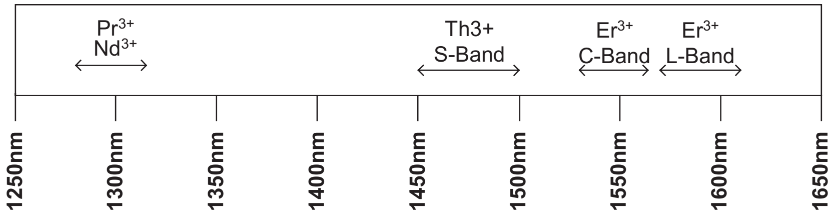

FIGURE 41.1 Rare earth dopants and their gain bands for telecom applications.

Figure 41.1 shows the dopants and amplification bands that have been demonstrated for use in telecoms applications.

The EDFA has become the most commonly utilized DFA due to the fact that its gain spectrum coincides with the third transmission window (ca 1550 nm) of silica optical fibre. Whilst this chapter will focus directly on EDFAs all of the principles discussed are applicable to other dopants and types of DFA. Where there are important differences, these are cited within the text.

Fibre amplifiers in telecommunications are desirable for a number of reasons:

- no requirement for optical to electrical conversion;
- amplification is achieved within the fibre;
- high efficiencies can be attained;
- low noise figures (NFs) can be achieved;
- broad gain window enabling wavelength division multiplexed (WDM) transmission;
- low cost;
- compact.

Optical-to-electrical conversion within a system is undesirable as it adds significant cost and complexity to the system. Therefore, the ability to amplify signals without this conversion is very important in communication systems.

The fact that amplification is achieved within the fibre is a key performance benefit – first no coupling is required from the input fibre, into the amplifier and then in reverse at the output, minimizing losses, costs and construction difficulties associated with the transition from fibre to other amplification media. Since the light is principally confined within the core of the fibre, very high cross section overlaps can be achieved between the amplifying medium and the signal to be amplified, hence leading to high efficiencies.

It has been demonstrated that amplifiers with an NF tending towards the ‘quantum limit’ [1] of 3 dB can be achieved in the laboratory [2]. This high level of performance is achieved without paying a premium in other aspects of the device. The fact that a single amplifier can be used to amplify many channels in a WDM system is a key commercial consideration, and it contrasts with the fact that an independent electrical repeater would be needed for every channel.

41.2 Amplifier Topology

Figure 41.2 shows the topology of a very basic EDFA.

A simple amplifier actually only requires three components – doped fibre, a pump multiplexer and a source of pump light. The pump multiplexer is generally a wavelength selective device which couples the signal and pump lights together into a single fibre, with only a small loss to both signal and pump (throughout we assume operation with single-mode fibres only). Within the doped fibre the pump and signal lights interact with the dopant ions to provide gain to the signal. At the output of the amplifier, there will be a small amount of residual pump light (typically <0.1% of input pump light), the amplified signal and a broadband noise radiation referred to as amplified spontaneous emission (ASE). As will be discussed later, there are merits to utilizing a more complicated structure in order to improve the performance of the amplifier. The structure of a typical commercial telecoms EDFA is shown in Figure 41.3. Multiple pump sources are used to achieve superior noise performance, and also due to the fact that there is a limit to the optical power that can be obtained from a single laser diode.

Optical isolators are utilized in the design for a number of reasons. The isolator at the input to the amplifier prevents backward travelling noise from leaving the amplifier, which can degrade system performance and the isolator at the output

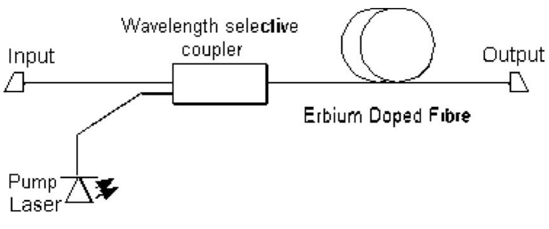

FIGURE 41.2 Topology of a simple EDFA.

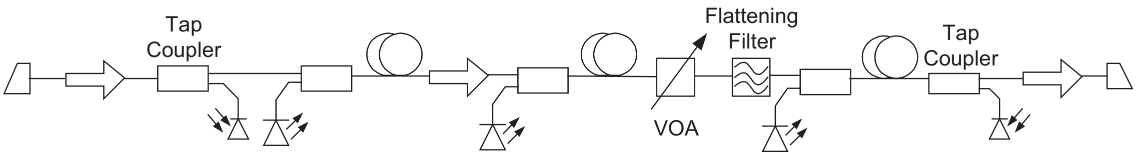

FIGURE 41.3 Topology of a typical commercial EDFA.

prevents backward travelling light entering the amplifier and leading to a degradation of its performance. The isolators within the amplifier break up the length of doped fibre and prevent accumulation of backward travelling noise which may degrade performance. Detailed consideration to these requirements will be given later. The inherent gain spectrum of erbium-doped fibre (EDF) is not flat and, therefore, for operation in WDM systems filters are required to flatten the gain spectrum.

41.3 Gain Spectra

The exact gain spectrum of an EDFA is dependent ultimately on the net cross section of the amplifier, which is defined by the inversion level and the absorption and emission cross sections of the doped fibre being used. If we know the net cross section we can calculate the gain spectrum that will be obtained from a given amplifier. Whilst the cross sections can be measured for a given fibre type, calculating the inversion level is very difficult. Figure 41.4 shows typical absorption and emission cross sections. The doped fibre cannot be considered to have zero length, and therefore the flow of signal, pump and ASE power in both forward and backward directions must be considered. All of these powers are also a function of wavelength, which must be taken into account. The problem cannot be solved analytically and must be tackled numerically. Section 41.12 gives consideration to the modelling approaches commonly used.

Whilst it is very hard to determine the inversion level, we can use the cross section and inversion level as a starting point to discuss gain shapes that can be achieved with an EDFA. Figure 41.5 shows the net cross section versus wavelength for a range of inversion levels for a typical erbium-doped silica glass. The net cross section of a fibre is given by Equation (41.1):

$$\sigma_{\text{net}} = \frac{\sigma_e N_2}{N} - \frac{\sigma_a N_1}{N} \tag{41.1}$$

where σ_{net} is the net cross section; σ_e is the emission cross section; σ_a is the absorption cross section; N_2 is the population of the upper energy level; N_1 is the population of the lower energy level; and N is the total ion population.

The upper and lower lines (labelled 1 and 0) are the emission and absorption cross sections, respectively. The net cross section can be considered to be equivalent to gain per unit length, with a net cross section of 0 being a gain of unity, negative values being losses and positive values being gains. The net cross section therefore offers a route to predicting an amplifier's performance as a function of inversion level.

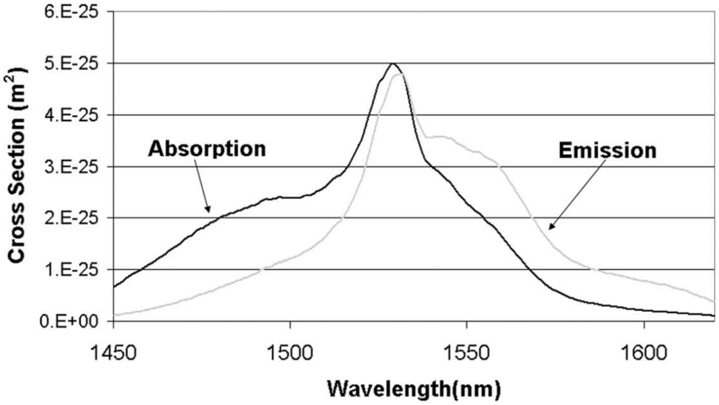

FIGURE 41.4 Typical absorption and emission cross sections.

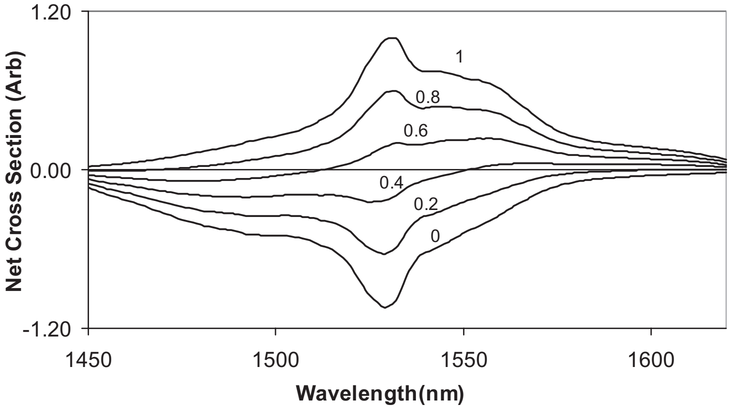

FIGURE 41.5 Net cross sections for varying inversion levels.

Figure 41.5 suggests that gain may be achieved from 1450 nm to beyond 1650 nm. However, in practically realizable amplifiers a sufficiently high inversion level cannot be obtained. The band from 1528 to 1560 nm is known as the C-band, and amplifiers can be constructed in this region with an inversion level of around 0.8. Whilst an amplifier with this inversion does provide gain to longer and shorter wavelengths, the discrepancy from the peak gain is such that the gain is not useful.

Another area of interest is the L-band extending from 1565 to 1610 nm, which can be accessed using inversion levels of around 0.4. The net cross section in this case is significantly smaller than for the C-band; hence, the gain per unit length is much lower in an L-band amplifier and, to achieve useful gains, much longer lengths of fibre are used (up to 100 m). The maximum wavelength at which gain can be attained is generally limited by excited state absorption (ESA) of the signal. In conventional silica fibre, this limits the edge of the L-band to approximately 1610 nm; however, special glass compositions have pushed the band out to beyond 1620 nm [3].

The natural gain spectrum obtained in the L-band is substantially flatter than the natural shape in the C-band. For comparison, Figure 41.6 shows typical unflattened C- and L-band gain shapes. The flatter shape is desirable as it makes gain flattening easier; however, unfortunately, L-band amplifiers have yet to rival C-band amplifiers in terms of performance and cost.

The long lengths of fibre required for L-band amplifiers (up to 100 m) are undesirable as they add cost and reduce amplifier performance (due to background loss and other fibre impairments). In an effort to improve the performance of L-band amplifiers, highly doped fibre has been utilized [4]. These have successfully reduced fibre length by a factor of 2, and, consequently, performance improvements have been realized. The level of doping that can be achieved in a fibre is limited by cooperative energy transfer (CET) effects that become significant when doping densities are high (due to the closer proximity of rare earth ions and the formation of clusters within the glass). The CET effects compete with the gain process and hence limit amplifier performance.

41.3.1 Dynamic Gain Tilt

Dynamic gain tilt (DGT) is a method of describing changes in the gain spectrum of a given amplifier as the inversion level changes. Figure 41.7 shows a set of gain curves obtained by varying the inversion level.

As can be seen each of the curves is comparable, having been 'tilted' around a point to the long wavelength edge of the gain spectrum. This predictable dependence of gain spectrum on inversion level (and hence on signal and pump powers) can be used to model the behaviour of an amplifier under changing conditions. A set of values for DGT versus wavelength are calculated from gain spectra measurements and can then be used

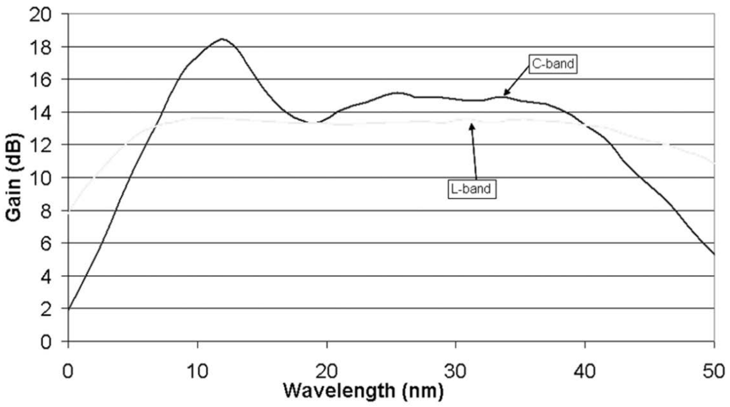

FIGURE 41.6 C-band and L-band gain spectra.

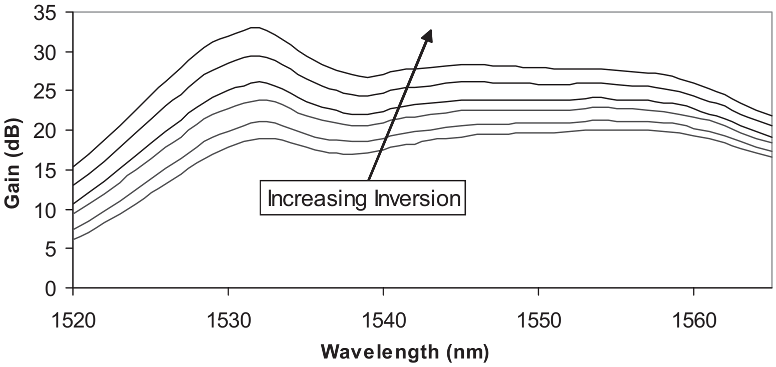

FIGURE 41.7 Gain spectrum demonstrating gain tilt.

to predict gain spectra under different conditions. The DGT parameter is defined in Equation (41.2):

$$\mathrm{DGT}(\lambda) = \frac{\Delta_g(\lambda_1)}{\Delta_g(\lambda_2)} \tag{41.2}$$

if $\lambda_1 < \lambda_2$ then $\mathrm{DGT} > 1$.

41.3.2 Variable Gain Amplifiers

If we wish to change the gain of an amplifier for a given set of input conditions, the only parameter we have control over is the inversion level (via the pump power). However, from Figure 41.7 (and the fact that $\mathrm{DGT} \neq 1$), we know that changing the inversion level also changes the gain spectrum, which implies that it is not possible to produce a variable gain amplifier that maintains a flat gain spectrum as its gain is changed.

In practice, we obtain a variable gain amplifier by operating the amplifier at a fixed inversion level and including a variable optical attenuator (VOA) in the design. There are a number of locations within the amplifier in which the VOA can be placed, and here we consider the trade-offs involved.

To describe the operation of a variable gain amplifier, we introduce the terms 'internal gain' and 'external gain'. The internal gain is the gain spectrum provided by the EDF, whilst the external gain is the gain from the input to the output, including all other optical components. Since we have said that the inversion level must be fixed, the internal gain spectrum must also be fixed. If a VOA is placed at the output of the amplifier, its loss can be adjusted to directly vary the external gain of the amplifier without affecting the operation of the doped fibre. The drawback of this approach is that it is inefficient, as the attenuation is performed where the powers are highest. The most efficient position for the VOA would be at the input of the amplifier where powers are at a minimum. The input, however, is the worst position from an NF perspective – any loss before gain adds directly to the NF.

A compromise is therefore reached whereby the VOA is 'buried' along the length of EDF. This allows a significant amount of gain to be achieved before the VOA, but reduces signal powers at the VOA and hence improves efficiency. The key consideration in selecting the position of the VOA is that the gain seen by the signals before the VOA is much larger than the maximum loss of the VOA to avoid any impact on the NF.

41.3.3 Gain Flattening

Amplifiers in a WDM system require a flat gain spectrum, which is not provided by EDF and therefore gain flattening filters (GFFs) must be included to flatten the gain spectrum. These filters are usually buried along the length of the doped fibre, according to the same compromises as the VOA discussed previously.

Many technologies are employed for the flattening filters; however, dielectric components are the most common. The erbium gain shape is a complex one and, hence, the filter technology chosen must be capable of generating arbitrary shapes. Also, since the filters are often placed within a gain medium, it is important that the technology employed is not reflective (e.g. Bragg gratings), as the reflected light would result in a degradation of the amplifier performance.

Dielectric filters are cheap when purchased in large quantities; however, the design and prototyping phase is expensive. Other technologies such as blazed gratings and tapered fibre filters have been developed to provide a cheaper alternative to dielectric filters; however, the performance of dielectric filters means that they have yet to be replaced in commercial amplifiers.

Although it is possible to produce an amplifier with a very flat gain spectrum under one set of operating conditions, the gain spectrum is affected by a number of factors. The cross sections of erbium fibre are affected by temperature and can change over the lifetime of the fibre. Other components within the amplifier may also change their spectral shape, further affecting the gain shape. The most significant change is that of gain spectrum with temperature, and this has been tackled in a number of ways, for example controlling the temperature of the erbium fibre, or manufacturing filters whose shape changes in the same manner as the erbium fibre.

As the performance of optical communication systems has advanced the requirements for flat gain have become tighter, and this has led to the development of dynamic gain flattening technology. This technology utilizes filters whose shapes can be changed on a continual basis, which, when combined with spectral monitoring, can be used to provide a continuously flat amplifier.

Two approaches have been employed – continual filter shapes and per channel power control. The former utilizes a filter whose shape can be changed to flatten the gain spectrum. This can be accomplished utilizing a set of sinusoidal filters to generate a Fourier series [5]. By changing the characteristics of the filters, the resulting filter shape can be defined. Figure 41.8 shows a typical C-band gain spectrum being successively flattened with up to five sinusoidal filters.

The per channel power control system controls the power of each channel by de-multiplexing the channels, passing them through a VOA and then re-multiplexing them. This is less desirable as the de-multiplexing–multiplexing process degrades system performance; however, the devices are cheaper and easier to control.

41.4 Noise in EDFAs

Gain is achieved in an EDFA via a two- or three-level laser system, in which electrons are excited to an upper energy level by a pump source and are then available for stimulated emission when they interact with the light to be amplified. Electrons in the upper state are also available for spontaneous emission, and it is this process that leads to the creation of noise in an EDFA.

The photons emitted spontaneously from an ion will be travelling in a random direction and a small proportion of them will be captured by the numerical aperture (NA) of the fibre, and hence are guided along the fibre. These photons experience gain as they propagate along the fibre giving rise to ASE.

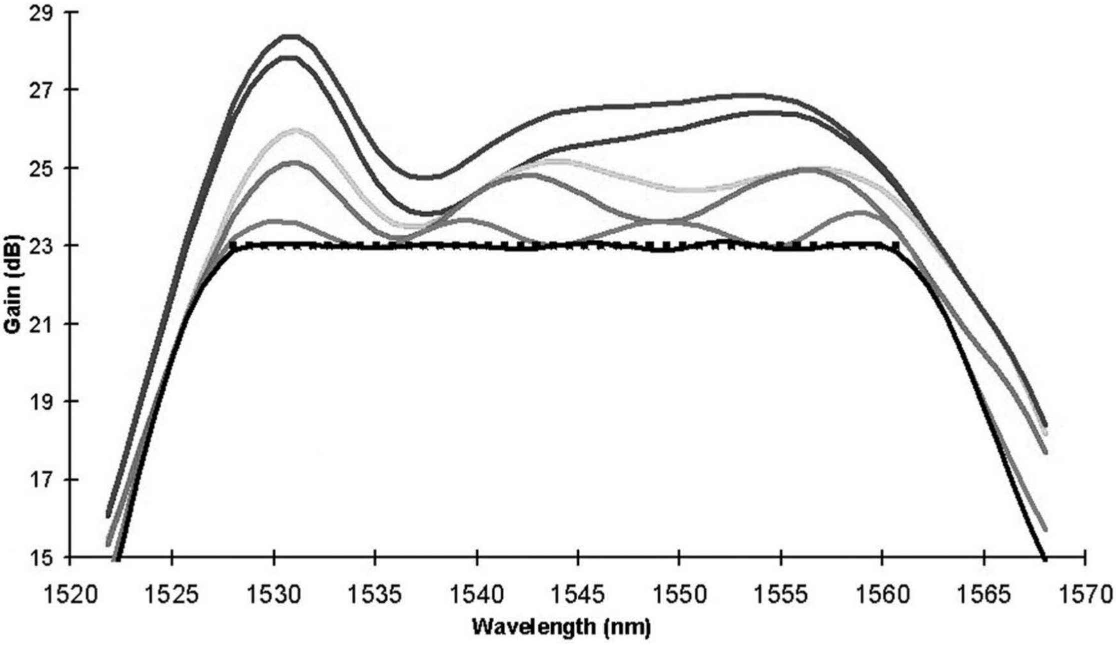

FIGURE 41.8 C-band gain spectrum successively flattened by up to five sinusoidal Fourier filters.

As well as providing the amplifier with a finite NF, ASE also degrades the amplifier performance, as discussed later.

It can be shown that the NF of an EDFA is given by Equation (41.3)

$$\mathrm{NF}(\lambda) = \frac{\rho_{\mathrm{ASE}}(\lambda)}{h\nu G(\lambda)} + \frac{1}{G(\lambda)} \tag{41.3}$$

where ρ is the ASE power spectral density; G is the linear gain; h is Planck's constant; and ν is the optical frequency at λ. Furthermore, in the case of high gain amplifiers, we can show that the NF is approximated by:

$$\mathrm{NF} \approx 2N_{\mathrm{sp}} \tag{41.4}$$

where N_{sp} is the spontaneous emission factor. For the case of three-level pumping, as occurs at 980 nm, the emission cross section is zero and, hence, the minimum value of N_{sp} is unity. This gives a minimum achievable NF for a 980 nm pumped EDFA of 3 dB [6]. This is borne out in simulation and experiment, where amplifiers tending to a 3 dB NF have been demonstrated [2]. The figure of 3 dB is often referred to as the quantum limited NF.

In the case of two-level pumping (around 1480 nm), the minimum value of N_{sp} is increased and is ultimately determined by the pump and signal cross sections. For signals in the C-band, typical values of $N_{\mathrm{sp}}^{\mathrm{min}}$ are 1.3–1.5, which correspond to minimum NF of 4.1–4.7 dB.

In an ideal case the ASE is small at all points in comparison to the signals and does not affect the inversion level and, hence, gain spectrum of the amplifier. Unfortunately, this is not the case and steps must be taken to manage the ASE within an amplifier to avoid degradation of performance. The first point to note is that since spontaneous emission occurs in all directions from an ion, the captured spontaneous emission, and hence propagating ASE, will be travelling both forward and backward through the amplifier. Assuming that a sensible design of amplifier has been chosen, the power of the forward propagating ASE will be substantially smaller than the signal at all points in the amplifier and hence will have little effect on the performance of the amplifier.

Counterpropagating ASE, on the other hand, behaves very differently to the signals – in fact, the power profile of counterpropagating ASE is broadly the opposite of the signals – it is smallest at the output end of the amplifier and grows towards the input of the amplifier. This can mean that the power of the ASE at the input end of the amplifier is significant in comparison to the signal and, hence, may decrease the inversion of the amplifier. This will lead to an increase in the NF of the amplifier as the gain per unit length at the input of the amplifier will be lower. The conversion efficiency of the amplifier will also be reduced as power will be preferentially transferred to ASE, rather than the signals.

The backward travelling ASE must therefore be managed along the length of the fibre to ensure that it never becomes significant with respect to the signal. This is achieved by the insertion of optical isolators along the length of doped fibre which serve to block the backward propagating light, whilst allowing the forward propagating signals (and ASE) to pass though. Figure 41.9 shows inversion level versus length for amplifiers with and without an isolator placed at the peak of the backward propagating ASE. All other parameters for the amplifiers remained consistent.

A consequence of inserting isolators in the doped fibre is that they themselves may decrease performance. The loss of the isolator must be compensated for by a higher gain, and the loss may also degrade the NF if the gain before the isolator

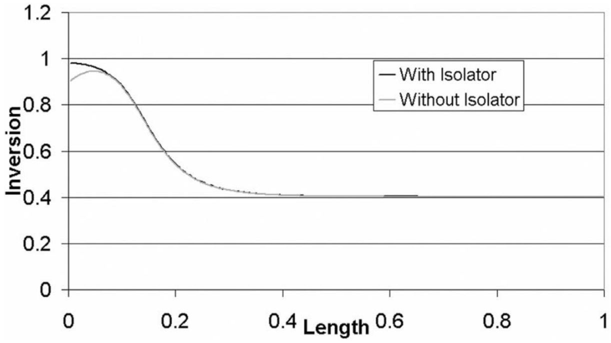

FIGURE 41.9 Inversion level with and without a buried optical isolator.

is not much larger than the loss. Isolators designed to work at signal wavelengths will not pass 980 nm pump light and, hence, a system to bypass the pump around the isolator must be introduced. This adds further loss (to both the signals and pump) and increases complexity and cost. To obtain the benefits of an isolator it is often, therefore, placed at a point where the vast majority of the pump light has been absorbed and so a pump bypass is not required. Another pump is then inserted after the isolator. There is often a trade-off between position for optimum noise performance and that required to minimize complexity and pump loss.

41.5 Amplifier Pumping

Erbium in a silica host glass has a number of absorption bands which can be used to pump an EDFA to provide gain in the 1550 nm optical transmission window. Figure 41.10 shows the absorption cross section with potential pumping wavelengths highlighted, along with regions of ESA. Of the possibilities, two wavelengths have emerged as the favoured ones – 980 and 1480 nm (not shown on diagram).

The energy levels ($^4I_{11/2}$) of the 980 nm absorption band reside in a different multiplet to those corresponding to the 1550 nm amplification band ($^4I_{13/2}$), and we therefore obtain a true three-level laser system. The non-radiative spontaneous decay time from the $^4I_{11/2}$ to the $^4I_{13/2}$ level is of the order of 10 μs, giving effectively no spontaneous emission to the ground state from the $^4I_{11/2}$ level. This allows the creation of very high inversion levels using a 980 nm pump. In contrast, the energy levels of the 1480 nm band ($^4I_{13/2}$) reside in the same multiplet as the amplification levels, and the amplification system can be considered a two-level system. Due to the thermal equilibrium within each multiplet, the population of the pump level will not necessarily be zero and is dependent upon the distance of the given level from the bottom of the multiplet. There will, hence, be spontaneous and stimulated emission at the pump wavelength. The weaker absorption cross section at 1480 nm, and the emission that occurs, means that it is not possible to achieve arbitrarily high inversion levels. As has been discussed previously this limits the minimum NF that can be achieved with 1480 nm pumping.

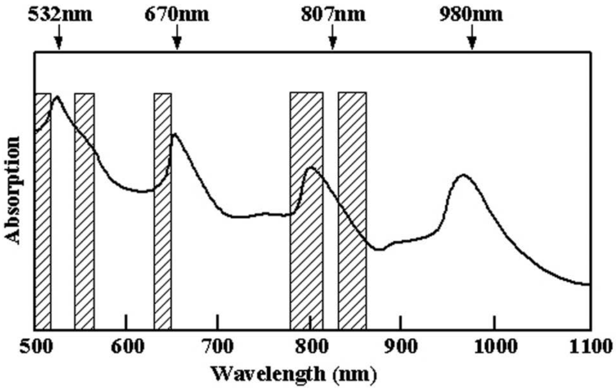

FIGURE 41.10 Erbium absorption spectra, regions of significant ESA (hatched boxes) and possible pumping wavelengths.

41.5.1 Influence on Amplifier Performance

A plot of inversion level versus length can be used to understand the relative merits and issues of the two pumping wavelengths. Figure 41.11 shows this plot for a simple amplifier with a single copropagating pump. As can be seen the inversion levels peak near the input end of the amplifier and then tail off towards the output end, where there is little pump power left. This shape of inversion curve is desirable for good noise performance – the signals entering the amplifier immediately see a high gain, which is key to achieving a low NF. The decrease in inversion at the very front of the amplifier is due to counterpropagating noise and, as shown in Figure 41.9, it can be dealt with the use of a buried isolator. Whilst the 980 and 1480 nm curves follow the same pattern, there are quantitative differences between them, which are discussed in the following sections.

41.5.2 980 nm Pumping

Due to the high absorption cross section and zero emission cross section, a 980 nm pump can achieve a very high level of inversion in the fibre, which will provide a high level of gain per unit length for the optical signals. This is desirable at the input of the amplifier as it means the signals will experience gain immediately upon entering the amplifier and, hence, the noise performance is optimized.

Since the 980 nm absorption band is very strong, the pump light is absorbed very quickly and, hence, the inversion level

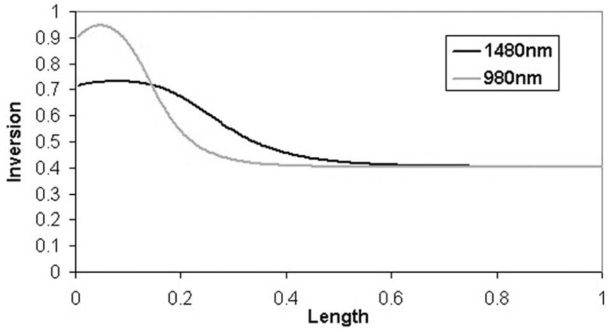

FIGURE 41.11 Inversion versus length for copropagating 980 and 1480 nm pumps.

of the amplifier decreases rapidly after the initial region where almost all of the pump is absorbed. Since the gain spectrum is dependent on the average inversion of the fibre, gain shapes which require low average inversion (e.g. L-band amplifiers) are hard to achieve with good performance using a 980 nm pump, as they require a long length of fibre with a very low inversion level to counteract the high inversion at the input end. This fibre will absorb signal photons, which are then either spontaneously emitted as noise, or are lost non-radiatively, thus reducing efficiency.

The efficiency of a pumping scheme can be quantified using either power conversion efficiency (PCE) or quantum conversion efficiency (QCE). For practical amplifier design, the PCE is the more useful figure as we are interested in the amount of pump power that will be required to produce an amplifier with a given signal output power.

Pumping at 980 nm is less efficient than at 1480 nm and an experimental figure of 50% PCE has been reported [7], in contrast to 75.6% for a 1480 nm pumped amplifier. Interestingly, the vast majority of this difference is due to the differences in photon energy as the QCE figures are similar (78.9% versus 79.4%).

An effect cited as pump-mediated gain inhomogeneity has been reported for pumping in the 980 nm band. It has been shown [8] that significant changes in the gain spectrum occur with only small changes in the pump wavelength, when an amplifier is pumped near to 980 nm. Figure 41.12 shows results for the short and long wavelength edges of a C-band amplifier. Changes of over 2 dB are seen at the short wavelength end of the spectrum when the pump wavelength is changed over a range of 4 nm.

The gain spectrum of commercial EDFAs is specified very tightly; therefore, due to pump-mediated gain inhomogeneity, it is vital that if 980 nm pumps are utilized, their wavelength is specified tightly. This will add cost to the devices and is therefore a factor in the choice of pump wavelength for commercial amplifiers.

The main advantage of 980 nm pumping is the superior noise performance, which has been discussed in Section 41.4.

41.5.3 1480 nm Pumping

As can be seen from Figure 41.11, the 1480 nm pump does not achieve such a high peak inversion level as the 980 nm pump; however due to the lower absorption the pump penetrates further into the amplifier giving a more even inversion level along the amplifier.

The lower inversion level at the input to the amplifier causes the noise performance of the 1480 nm pumped amplifier to be poorer than that of the 980 nm pumped amplifier; however, there are a number of other advantages to 1480 nm pumping. As mentioned in the previous section, the efficiency of 1480 nm pumping is substantially higher than 980 nm and so less pump power is required to achieve an amplifier with a given output power. The 1480 nm pumps are therefore utilized where efficiency is a more important parameter than noise performance.

The more even inversion profile of a 1480 nm pumped amplifier is desirable for L-band amplifiers which require a low average inversion. It is also possible to pump away from the peak of the absorption band to achieve still lower absorption which may be useful in some situations, such as amplifiers requiring gain out to ultra-long wavelengths (beyond ca 1610 nm).

Amplifiers with mixed pump wavelengths are commonly used: a 980 nm pump is used at the input to the amplifier to provide good noise performance, with 1480 nm pumps being employed towards the output to provide efficiency.

41.5.4 Pump Distribution Schemes

Pump distribution schemes can be broadly categorized into three families: copropagating, counterpropagating and bidirectional pumping. In the small signal regime where the signal powers are too small to influence the inversion level, the co- and counterpropagating pump schemes are equivalent; however, the bidirectional pumping scheme can deliver higher gains. Since all practical amplifiers are operated in a saturated regime we will only consider that situation in detail here.

In the saturated regime, the signal powers have a significant impact on the inversion level of the amplifier at any given

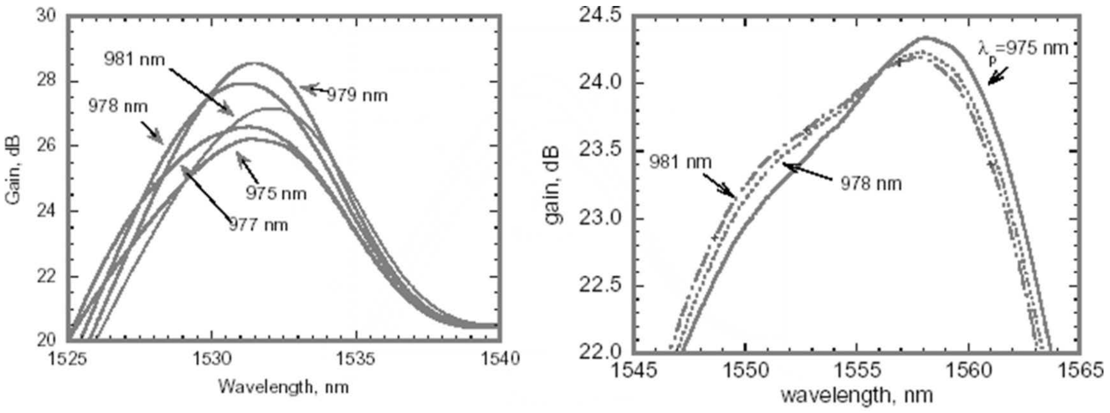

(a) (b)

FIGURE 41.12 Pump-mediated gain inhomogeneity. (a) Short wavelength edge of the C-band. (b) Long wavelength edge of the C-band. (From Ref. [3].)

point along the fibre and, hence, the relative pump, ASE and signal powers at each point through the amplifier play a role in determining the gain available to the signal. The two key performance factors that are optimized by the choice of pumping scheme are gain (and hence output power) and NF. Unfortunately, these two factors often demand opposite actions to optimize them and hence any design is ultimately a compromise.

A copropagating pump is invariably the preferred choice when optimizing an amplifier for noise performance, since the inversion, and hence gain per unit length, is highest at the input of the amplifier. In the counterpropagating case the inversion is lowest at the input of the amplifier, and the lower gain per unit length is the equivalent of having some loss before the signal undergoes amplification, resulting in an increased NF. The difference in NF for co- and counterpropagating pumps is lessened for 1480 nm pumping as the pump penetrates further towards the input to the amplifier, increasing the inversion there and reducing the NF.

As a signal propagates through an amplifier its power increases such that, in a well-designed amplifier, it is at a maximum level at the end of the doped fibre. With a copropagating pump, the pump power follows the inverse pattern to the signal, whereas with a counterpropagating pump, the pump power follows the same pattern as the signal powers. The counterpropagating pump is therefore more efficient.

41.6 Doped Fibre Amplifiers for Other Telecoms Windows

Doped fibre amplifiers have also been developed in other areas of the optical spectrum of interest to optical communications. This section summarizes two of the areas which have received attention and generated positive results.

41.6.1 1450–1500 nm

Thulium-doped fibre amplifiers (TDFAs) have been widely investigated as a source of amplification in the 1450–1500 nm range, which is an area of interest to telecoms, being known as the S-band.

The performance of TDFAs has yet to reach that of EDFAs; however, practical amplifiers have been constructed. Different glass hosts are utilized for thulium-doped fibre, as the high phonon energy of silica makes thulium-doped silica impractical. This has led to a number of challenges in the production of useable amplifiers since the glass used as the host must be mechanically reliable and capable of joining efficiently to silica-based fibres.

A further difference is that the energy levels of interest are part of a quasi-four-level laser system, as opposed to the two- or three-level system of erbium amplifiers. Figure 41.13 shows the energy levels of a thulium ion along with typical lifetimes when a fluoride-based glass is used as the host.

As can be seen the lifetime of the lower energy level is substantially longer than the upper level, which is undesirable in a lasing or amplification material and has implications for the pumping scheme employed. A number of pumping schemes have been demonstrated, typically utilizing an upconversion pumping process [9–11].

41.6.2 1300 nm

Two rare earth dopants have been proposed in this wavelength range – neodymium and praseodymium. Both of these dopants

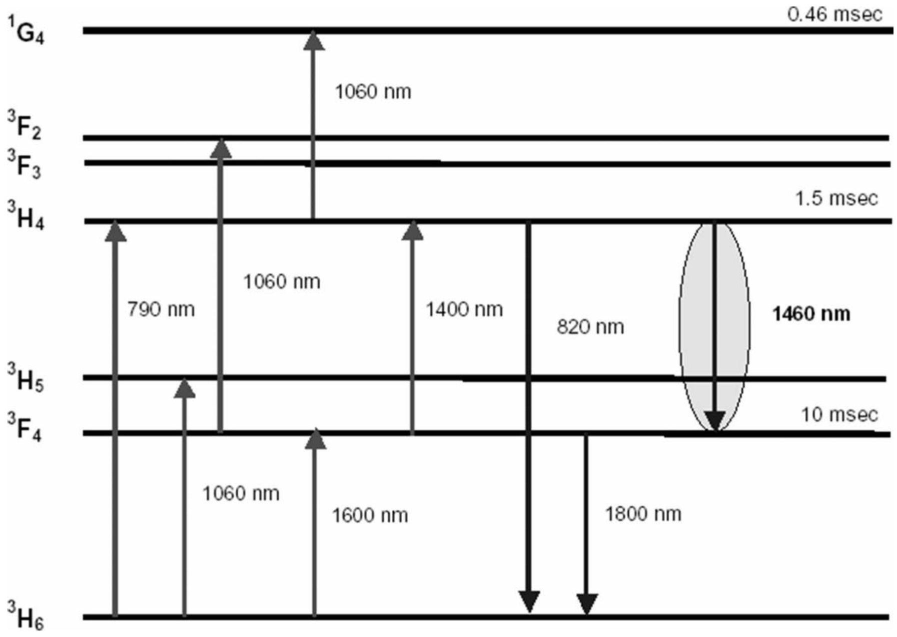

FIGURE 41.13 Energy levels in thulium, with the transition of interest to telecoms applications highlighted.

require non-silica hosts and work has concentrated on fluoride glasses. Whilst practical amplifiers have been developed, a number of mechanical issues with fluoride fibres remain, and the lack of commercial interest in the 1300 nm region has prevented their further development.

41.7 Inhomogeneous Effects

Inhomogeneous effects are those that result from restricting the set of ions available for interaction with signal photons to a subset of the total population. This occurs in both the polarization and wavelength domains. The principle inhomogeneous effects are summarized in this section.

41.7.1 Polarization Hole Burning

The absorption and emission cross sections of an ion are a function of the polarization of light in relation to the symmetry axis of the sites around the ions. Polarized light will therefore preferentially interact with a subset of the total ion population, causing preferential saturation in that subset.

ASE propagating in the orthogonal polarization state to the signal will interact with the orthogonal subset of ions, which have been depleted less by the signal and will therefore see a higher gain than would normally be expected. This results in a poorer NF than would be predicted if PHB is not taken into account.

PHB is a small effect of the order of 0.1 dB in a single amplifier [12]; however, the underestimate of ASE will accumulate between amplifiers and hence may be significant in systems with many amplifiers.

41.7.2 Polarization-dependent Gain

The relative polarizations of pump and signal photons in an amplifier can cause a change in the gain experienced by the signal. The gain is maximum when the polarizations are aligned and minimum when they are orthogonal. This is a very small effect and reports in the literature have shown dependencies of <0.1 dB [13]. The effect is generally masked by the polarization-dependent loss (PDL) of other components in the amplifier and is very hard to measure experimentally.

41.7.3 Spectral Hole Burning

Energy-level broadening within the erbium ion in glass hosts has an inhomogeneous component which can affect the gain spectrum of the amplifier under certain loading conditions. The result of inhomogeneous broadening is that only a subset of the total ion population is available to provide gain at a certain wavelength, and hence the inversion level is a function of wavelength. If a high-power wavelength is present in an amplifier, the inversion level local to that wavelength may be reduced and, hence, the channel will see a reduced gain. This reduction in inversion will also affect wavelengths close to the high-power wavelength and the effect will appear as depressions in the gain spectrum – this effect is known as spectral hole burning (SHB) [14].

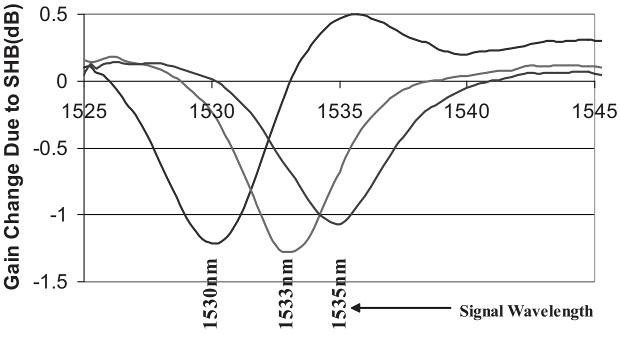

FIGURE 41.14 Gain change due to spectral hole burning (SHB).

Figure 41.14 shows the changes in the gain spectrum where a spectral hole has been created. The characteristics of the holes are a function of wavelength – the holes become deeper and narrower to the short wavelength edge of the C-band (1530 nm) and wider and shallower to longer wavelengths. Non-localized SHB has also been reported, whereby a spectral hole is burnt at a wavelength different to the saturating signal wavelength [15].

41.8 The EDFA in a Communication System

When deploying amplifiers in a system detailed consideration must be given to the specification of the devices to ensure that the system performs as desired.

As has been shown the performance of EDFAs can be optimized around a number of parameters (gain, NF, efficiency, bandwidth), each of which assumes a different level of importance depending upon the amplifier's purpose in the network. For example, in the case of an optical pre-amplifier the requirement is for a low-noise device, whereas the optical bandwidth is not important as only a single channel passes through the amplifier. Figure 41.15 shows the typical locations of amplifiers in a network. Each of the locations has a set of distinctive requirements that govern the specification of the amplifier.

41.8.1 Line Amplifiers

These amplifiers are responsible for compensating for the loss of the fibre within the communication system, thus ensuring that sufficient signal gets to the receiver to enable data transmission. The amplifier's performance must be such that it can amplify all of the channels to a relatively high-power level for transmission through the next fibre span. The bandwidth of the amplifier is therefore of key importance, as is the gain flatness. Many line amplifiers are cascaded along the length of the system, and therefore, any penalties associated with each one are multiplied through the system.

Typical span losses require line amplifiers to have a gain of approximately 20 dB, and current channel counts may require output powers over +17 dBm. In order to avoid excessive heat dissipation, the efficiency of the amplifier is very important.

The line amplifier is generally the most challenging amplifier to design as every facet of its performance is important to the system.

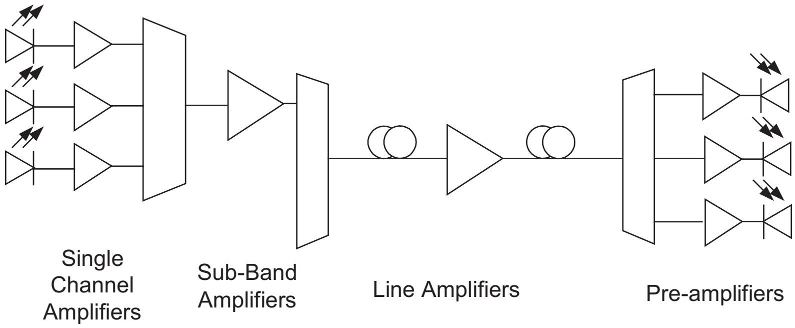

FIGURE 41.15 Amplifiers in an optical communication system.

41.8.2 Pre-amplifiers

It is widely known that an optically pre-amplified receiver can give superior performance to a receiver with an electrical post amplifier, and therefore, the optical pre-amplifier plays a vital role in the system.

The main requirement of this amplifier is that it is a low-noise device. Only one channel will be propagated through the amplifier, and hence, the bandwidth and output power requirements are not significant. This also removes the need for gain flattening filters. Since one amplifier is needed for every receiver (sometimes, pre-amplifiers are shared but it is not desirable), the cost of the amplifier is also important.

41.8.3 Narrow Band Amplifiers

Narrow band amplifiers are used to amplify signal levels at switch nodes and multiplexing sites before they are combined onto the transmission fibre. Typically, these amplifiers will be used to amplify four to eight channels.

Since many of these amplifiers may be used in a network the cost and physical size of them is important. The output power and bandwidth requirements are limited by the fact that they only have to amplify a small number of channels. By careful design of these amplifiers it may be possible to remove the need for gain flattening filters and this has an impact on the cost of the devices.

41.9 Amplifier Control

In order to operate reliably and with good performance, the amplifier must be controlled correctly throughout its lifetime. In an ideal situation, an amplifier will be set up at the time of installation and left running with the defined pump powers until the system is switched off. In reality, this is not possible as many parameters are likely to change during the lifetime of the system. Consideration must be given to changes in the number of channels operated on the system, in span losses and in variation in the operating environment of the amplifier.

Some form of autonomous control is required to enable amplifiers to operate over a long period of time. Two main forms of control system are used in optical amplifiers: total output power (TOP) control and gain control (GC).

41.9.1 Total Output Power Control

In TOP control the amplifier monitors its output power and adjusts the pump powers to achieve the desired output power. As parameters change the amplifier will continually update the pump powers to maintain the required output power. This method of control works well under steady-state conditions as the performance of a system is generally defined using the power launched into each span.

Problems arise however when the number of channels passing through an amplifier changes. Since we have fixed the total output power, the per channel power (which is what is important to system performance) is dependent upon the number of channels passing through the amplifier. Thus, if channels are added, the per channel power is reduced and the system may stop operating. Therefore, the amplifier set points must be modified each time the channel count in a system is changed.

TOP control is achieved by using a broadband photodiode at the output of the amplifier to monitor the total power, and then the pump powers are controlled by an analogue or digital controller. At the output of the amplifier, both signals and ASE are present; and in order that the signal powers are set to the desired level, an adjustment is often provided in the control system to account for the ASE power.

41.9.2 Gain Control

In this mode, the amplifier's operating point is controlled based on the optical gain provided by the amplifier. This is generally achieved by monitoring the total input and output powers and maintaining a constant ratio between them. This mode is preferential to TOP as it ensures that the channel powers are independent of the number of channels present.

41.9.3 Transient Control

It is possible that the channel count or channel powers will change very quickly due to failures within the optical network. If this occurs it is undesirable for the changes to impact other channels unconnected with the original failure.

If amplifiers are being operated in TOP mode and some channels rapidly disappear, the other channels will rapidly increase in power. In addition to failure of the system, damage to components can also occur.

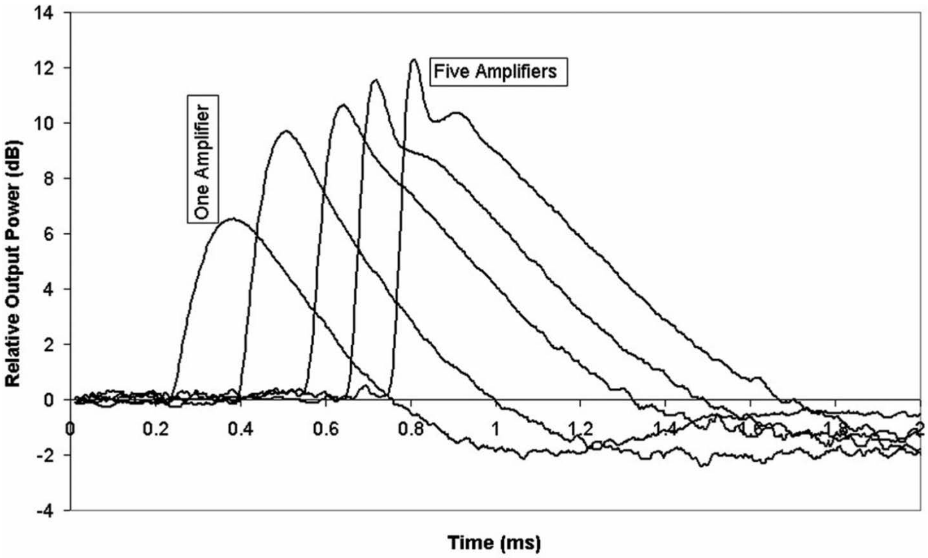

FIGURE 41.16 Transient propagating through six gain-controlled optical amplifiers.

Gain control solves transient control issues – the per channel powers are not dependent on the number of channels, and therefore, the remaining channels are not affected by the failure. Failures can occur on very short timescales, down to 1 μs for certain types of fibre cut and so control systems must be capable of tracking these changes. If the control loop does not respond fast enough, changes in the power of surviving channels will occur.

A key factor in transient control is that behaviour can accumulate as the transient passes through successive amplifiers, and can therefore be very large by the time the signals get to the receiver. Figure 41.16 shows an example of a transient passing through up to five gain controlled amplifiers. As can be seen the gain control is not fast enough to control the amplifier, and hence some deviation is seen.

With the move towards optical switching in networks, the control of transients will become more important as rapid changes in channel count will occur as the network is reconfigured.

41.10 Alternatives to EDFAs

This section gives brief consideration to alternative types of amplifiers.

41.10.1 Erbium-doped Waveguide Amplifiers

Erbium-doped waveguide amplifiers (EDWAs) utilize the same amplification mechanism as EDFAs; however, the dopant is placed in a planar waveguide grown on a substrate as opposed to within an optical fibre. The advantages of this are seen as the ability to integrate many amplifiers onto a single substrate, and the possibility of constructing all parts of the amplifier in one growth process, creating significant production cost savings.

EDWAs have yet to match the performance of EDFAs; however, progress is being made continuously. The main limitations are low-output powers due to poor efficiency obtained in waveguide glasses, and also poor NFs due to coupling losses. EDWAs are unlikely to form a competitor to line amplifiers, however may find a market in narrow band amplifiers where many low-power devices are needed in one location.

41.10.2 Semiconductor Optical Amplifiers

Semiconductor optical amplifiers (SOAs) utilize the same amplification mechanism and structure as semiconductor laser diodes, however without the mirrors that cause lasing.

High-output powers are hard to achieve and, again, coupling losses limit the NF. There is also a significant issue due to channel–channel crosstalk which can occur due to the very short carrier lifetimes. SOAs have found application as preamps and as single-channel booster amplifiers for transmitter lasers, where only modest output powers are required.

41.10.3 Raman Fibre Amplifiers

The Raman effect can be utilized to obtain gain for signal wavelengths within standard transmission fibre. Raman amplifiers simply consist of a high-power pump of a shorter wavelength than the signals. This pump is inserted into the optical fibre via a wavelength selective coupler and allowed to propagate the signals (often counterpropagating Raman pumps are used as they have performance benefits over copropagating pumps), the signal wavelengths then experience gain via energy transfer from the pump wavelength(s).

Two types of Raman amplifier have been utilized – discrete and distributed. Discrete amplifiers are operated in a very similar way to EDFAs, as stand-alone amplification modules between spans. In contrast, a distributed Raman amplifier utilizes the fibre spans as the gain media and, thus, the span losses are reduced. Distributed Raman amplifiers are advantageous in extending the distances over which systems can operate as the reduced span loss improves signal-to-noise ratios.

Discrete Raman amplifiers have not seen widespread deployment due to poorer performance and efficiency than EDFAs. An advantage of Raman amplifiers is that their gain bandwidth is not restricted by the availability of suitable rare earth dopants; therefore, gain can be produced at any wavelength. This may be important as the demand for capacity pushes signal wavelengths outside of the wavelengths accessible with DFAs.

41.11 Amplifier Measurement

Here we will consider the measurement of the gain and NF spectra of EDFAs.

The measurement of the gain spectrum would appear to be a relatively simple task; however, a complication arises due to the presence of ASE in the output spectrum. A direct measurement of the output spectrum will include the ASE and hence we are not measuring the true signal powers. We must therefore measure the ASE and subtract this from the output spectrum to obtain the true signal powers.

ASE measurement can be performed utilizing a method known as time domain extinction (TDE). EDFAs have a relatively long time constant (ca 10 ms) and, hence, the input signals can be modulated at a high frequency (>50 kHz) without affecting the inversion level and, hence, operating point of the amplifier. The input signals are modulated, and then a gating method is used to govern when the output spectrum is sampled. Figure 41.17 shows such a measurement system. The optical switches allow the device under test (DUT) to be bypassed such that the system can be calibrated.

Two measurements are taken – one when the signals are present and one when the signals are switched off, measuring the full output spectra and the ASE respectively. We now have a measure of the ASE at the signal wavelengths and can hence calculate the actual signal output powers, gain and NF. Alternative methods utilizing interpolation have been used; however, the TDE method has been shown to give the most accurate results [16].

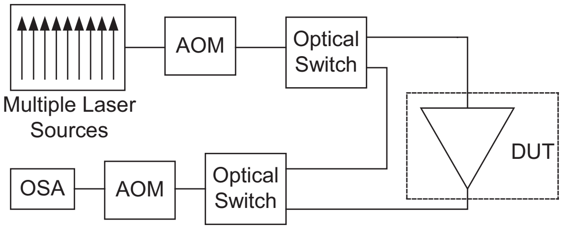

FIGURE 41.17 The EDFA measurement system.

41.12 EDFA Modelling

An accurate method of modelling EDFAs is essential to their successful development. A brief introduction to two methods is given here; however, no actual mathematical details are provided can be found in the referenced literature.

41.12.1 Gain Tilt Modelling

The DGT parameter discussed previously can be used to predict the gain shape at different operating points as signal powers, pump powers and fibre lengths are changed. The method, however, does not provide any information on the noise properties of the resulting amplifier and only considers homogeneous effects.

Despite these limitations, the method is very useful for understanding how a given amplifier will perform under changing conditions, and is often used for predicting gain shape changes as conditions change. The model is a very simple analytical expression and, hence, generates results rapidly.

41.12.2 Rate Equation Modelling

In order to accurately model an EDFA, including noise and inhomogeneous effects, one must develop a numerical model based on the rate equations applicable to the amplification process. The solution process is complex and must take into account the wavelength and directions of power at each wavelength.

Data on the fibre being modelled can be captured either as absorption and emission cross sections, or as part of a ‘Giles’ dataset which contains the fibre data in a more readily measurable form. (See Desuvires’ book, referenced in the Further Reading section, for an in-depth study of EDFA modelling.)

REFERENCES

1. Simon J C 1982 Semiconductor laser amplifiers for single-mode optical fiber communications *J. Opt. Commun.* **4** 51.
2. Cordina K, Jolley N and Mun J 1999 Ultra low noise long wavelength EDFA with 3.6 dB external noise figure *OFC*.
3. Ellison A J G 2001 Extending the L-band to 1620 nm using MCS fiber *OFC* TuA2.
4. Ishikawa S et al. 1998 High gain per unit length Silica based Erbium doped fiber for 1580nm band amplification *OAA* TuC4.
5. Parry S, King J P, Roberts K B, Jolley N E, Keys R and Mun J 1999 Dynamic gain equalization of EDFAs with Fourier filters *OAA*.
6. Oleshanky R 1988 Noise figure for erbium doped optical fibre amplifiers *Electron. Lett.* **24** 1363.
7. Massicott J F, Wyatt R, Ainslie B J and Craig-Ryan S P 1990 Efficient, high power, high gain, Er^{3+} doped silica fibre amplifiers *Electron. Lett.* **26** 1038.
8. Bennet K, Davis, F, Jakobson P A, Jolley N, Keys R, Newhouse M A Sheih S-J and Yadlowsky M J 1997 980 nm

band pump wavelength tuning of the gain spectrum of EDFAs *OAA*.

9. Roy F, Leplingard F, Lorcy L, Le Sauze A, Baniel P and Bayart D 2001 48% power conversion efficiency in a single-pump gain-shifted thulium-doped fiber amplifier *OFC* PD2.
10. Roy F, Le Sauze A, Baniel P and Bayart D 2001 0.8 mm and 1.4 mm pumping for gain-shifted TDFA with power conversion efficiency exceeding 50% *OAA* PD4.
11. Aozasa, M. H, Ono H, Sakamoto Y, Kanamori T, Ohishi Y and Shimizu M 2001 1480–1510 nm band Tm doped fiber amplifier (TDFA) with a high power conversion efficiency of 42% *OFC* PD1.
12. Taylor M G 1993 Observation of new polarization dependence effect in long haul optically amplified system *IEEE Phot. Tech. Lett.* **5** 1244.
13. Mazurczyk V J and Zyskind J L 1994 Polarisation dependent gain in EDFAs *IEEE Phot. Tech. Lett.* **6** 616.
14. Aizawa Y, Sakai T, Wada A and Tamauchi R 1999 Effect of spectral hole burning on multi channel EDF gain profile *OFC* WG1-1.
15. Rudkevich E, Baney M, Simple J, Derickson D and Wang G 1999 Nonresonant spectral hole burning in erbium doped fiber amplifiers *IEEE Photon. Tech. Lett.* **11** 542–4.
16. Jolley N and Cordina K 1999 A modification of the time domain extinction measurement technique for erbium doped fibre amplifiers with improved accuracy *OAA*.

FURTHER READING

Becker P C, Olsson N A and Simpson J R 1999 *Erbium Doped Fiber Amplifiers—Fundamentals and Technology* 1st edn (New York: Academic).

Covers all aspects of EDFAs, particularly considering the practical implications and impact on real-world applications of each aspect.

Desurvire E 1994 *Erbium Doped Fibre Amplifiers—Principles and Applications* 1st edn (New York: Wiley).

A thorough and complete reference on EDFAs. Mainly theoretical work, covering all areas of EDFAs.

42

High-Power Planar Waveguide Lasers

J. I. Mackenzie and D. P. Shepherd

CONTENTS

42.1 Introduction 571
42.2 Coupling of High-Power Diode Pump Sources to Planar Waveguides 572
  42.2.1 In-plane Pumping 572
  42.2.2 End-Pumping 572
  42.2.3 Side-Pumping 573
  42.2.4 Face-Pumping 574
42.3 Thermal Management Properties 575
42.4 Spatial-Mode Selection 575
  42.4.1 Double-Clad Waveguides 575
  42.4.2 Self-Imaging Waveguides 576
  42.4.3 Tapered Waveguides 577
  42.4.4 External Resonator Waveguides 577
42.5 Waveguide Laser Performance 578
  42.5.1 End-Pumping 578
  42.5.2 Side Pumping 580
  42.5.3 Face Pumping 580
42.6 Future Prospects 580
References 581
Further Reading 583

42.1 Introduction

Dielectric planar waveguides can be fabricated in a wide range of crystal and glass materials by many methods. These include modification of the material refractive index, typically at or near the surface, through such techniques as ion-exchange (Ramaswamy and Srivastava 1988), ion-implantation (Chandler et al. 1991), ion-diffusion (Schmidt and Kaminow 1974), and optical writing (Svalgaard et al. 1994, Okhrimchuk et al. 2005). Alternatively, a waveguide may be formed by adhesion (Brown et al. 1997), deposition (Kawachi 1990), or growth (Chartier et al. 1992) of one material on another of different refractive index. These techniques generally lead to waveguides in the form of a planar thin film or, if some patterning technique is used, a planar array of channel waveguides (see Figure 42.1).

The optical confinement afforded by these structures, even if only in one plane in the case of the thin film, leads to smaller pump and laser mode sizes than would be the case in an equivalent bulk laser. Thus, high optical gains can be achieved, and if the additional propagation losses due to the waveguide are not too high, low lasing thresholds are possible. For most planar devices, the lengths involved are on the centimetre scale and the propagation losses are just a few tenths of a dB. The optical confinement also tends to give a good spatial overlap of the population inversion and the laser mode, leading to high efficiency for low-loss waveguides.

The very large range of fabrication techniques means that many different laser hosts can be used in the planar waveguide format (Grivas 2011). These include high-gain materials such as rare-earth-doped garnets and sesquioxides (Chartier et al. 1992, Parsonage et al. 2015); broadly tuneable materials with potential for ultrafast operation such as Ti:sapphire (Anderson et al. 1997) and Yb:Glass (Shepherd et al. 2016); non-linear and electro-optic materials such as $LiNbO_3$ (Becker et al. 2000); low-phonon-energy materials such as LaF_3 (Bhutta et al. 2001, Bolanos et al. 2012); and many different glasses, some of which may be difficult to produce in the form of an optical fibre.

Recently, the advantages of the planar geometry have been applied to the production of multi-kW-class laser devices (Filgas et al. 2012). First, there is a natural compatibility with high-power diode pump lasers, as these also have a planar format, simplifying the coupling optics required and allowing very compact laser devices (Bonner et al. 2000). Secondly, the planar waveguide is an extreme case of the slab geometry, commonly used in high-power bulk lasers (Hodgson et al. 2002), and consequently has analogous excellent thermal power

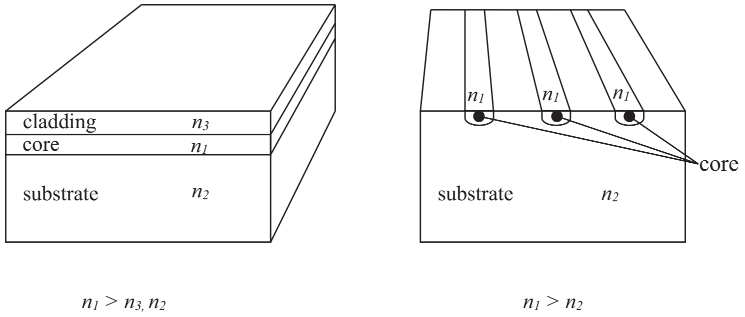

FIGURE 42.1 Typical planar and channel waveguide structures.

handling capabilities. The aim of this section is to describe how these geometric advantages can be combined with those of optical guidance to make compact and robust, high average power, diode-pumped laser devices.

42.2 Coupling of High-Power Diode Pump Sources to Planar Waveguides

The spatial properties of a typical high-power diode pump source are asymmetric, non-diffraction-limited, and of high divergence. This makes coupling to a solid-state laser medium a major issue, and many different techniques have been used in bulk and fibre lasers. These have included pre-conditioning optics such as fibre-coupling (Graf and Balmer 1993), lens ducts (Beach 1996), and beam-shaping (Clarkson and Hanna 1996); beam-confining techniques such as cladding-pumping (Snitzer et al. 1988), tapered fibre bundles (DiGiovanni and Stentz 1999), total internal reflection (Bibeau et al. 1998), and reflective pumping chambers (Faulstich et al. 1996), as well as beam-combining methods (Fan 2005). Many of these techniques may be used in the case of a waveguide, but it is also possible to use straightforward cylindrical focusing optics or direct proximity coupling of linear diode-laser arrays.

The geometry of the planar waveguide suggests three possible pumping arrangements (see Figure 42.2), each suited to different types of diode pump laser and waveguide structure.

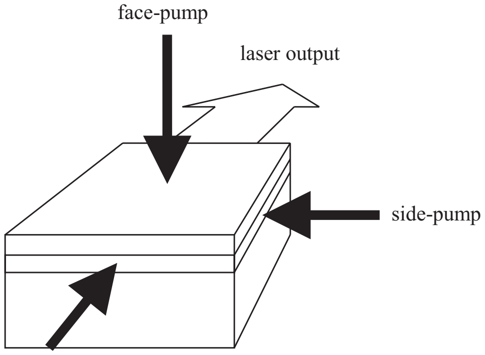

FIGURE 42.2 Pumping configurations for a planar waveguide.

42.2.1 In-plane Pumping

Both side- and end-pumping of waveguides fall into the category of in-plane pumping techniques and so have some common requirements. If a waveguide laser is to be in-plane pumped by a beam with a divergence in the guiding axis M^2 times greater than the diffraction limit, then the depth, D, and the numerical aperture, NA, of the waveguide must be chosen such that,

$$\text{NA} \geq \frac{\lambda M^2}{D} \qquad (42.1)$$

This condition is shown graphically in Figure 42.3, assuming a pump wavelength of $\lambda = 1$ μm. For single diode units (broad stripe or diode bar) it is possible to arrange to have the near-diffraction-limited fast axis coincide with the guiding axis of the waveguide so that relatively low-NA structures can be used. The larger-NA waveguides can be used to confine higher-M^2 beams, such as that from a beam-shaped or fibre-coupled diode bar, the slow axis of a broad-stripe diode, or the fast axis of a diode stack (a vertical array of diode bars). The high-NA waveguides can also allow direct proximity coupling of a single diode unit to the waveguide with no focusing optics, allowing a very compact system. However, the slow axis of a diode bar or diode stack can be >1000 times diffraction limited and so is normally aligned to be in a non-guided axis.

To make high-NA guides of >10 μm depth, it is usually necessary to combine two different materials through a deposition, growth, or adhesion technique. The example waveguides given in Figure 42.3 can both be fabricated by the adhesion technique of direct bonding (Brown et al. 1997), as this relies on the intermolecular forces between two highly polished surfaces and is thus very broadly applicable. In contrast, epitaxial growth techniques are more limited in the materials that they can combine, as a near lattice match is required between the two crystals. Nevertheless, some examples of high-NA epitaxial waveguides have been successfully demonstrated, such as GGG on YAG structures fabricated by pulsed-laser deposition (PLD) (Bonner et al. 1997; Beecher et al. 2017).

42.2.2 End-Pumping

End-pumping implies focusing on the plane of the waveguide, as well as coupling into the guided axis, and so tends to give the most intense pumping and the best spatial overlap of the

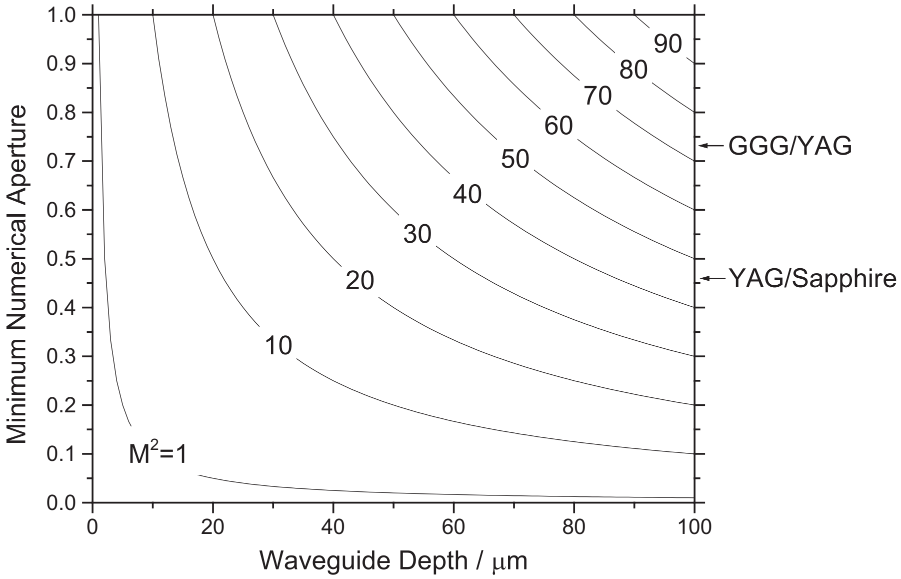

FIGURE 42.3 Graph of minimum waveguide NA, for a given depth D, required to confine beams of M^2 up to 90. Example waveguide NAs are also given.

inversion profile and the laser mode. Thus, low thresholds and high efficiency can be achieved. The relatively small pumping mode sizes also make it easier to obtain diffraction-limited output from a compact cavity. However, the number of pumping units is limited and so this scheme is not as easily scalable in power as side or face pumping. Broad-stripe diodes are well suited to end-pumping, having powers of several Watts, near-diffraction-limited fast-axis divergence, and ~10–40 times diffraction-limited divergence in the slow axis. In general, only one of the pumping and/or lasing axes is guided and reported configurations have included: guiding of only the diode slow axis in relatively large waveguides (Griebner et al. 2000); guidance of only the diode and laser fast axes in smaller waveguides (Mackenzie and Shepherd 2002) (see Figure 42.4); and, one-axis guiding of both the pump and the laser using a beam-shaped diode source (Ng and Mackenzie 2012). In all cases, relatively simple cylindrical focusing can be used to couple the diode light into the waveguide and pumping power of several hundred Watts is possible.

42.2.3 Side-Pumping

Side-pumping is more suited to high-power pumping, as it is compatible with the use of high-power diode bars and can be scaled by adding further pumping units, vertically or horizontally, and on both sides. It also allows independent optimization of the lasing, pumping, and heat removal, as these three processes occur along different axes. Despite these advantages, there is a disparity in the spatial distributions of the pump and cavity-mode fields, which implies a limited achievable overlap, unless exploiting appropriate cavity configurations (Thomson et al. 2011).

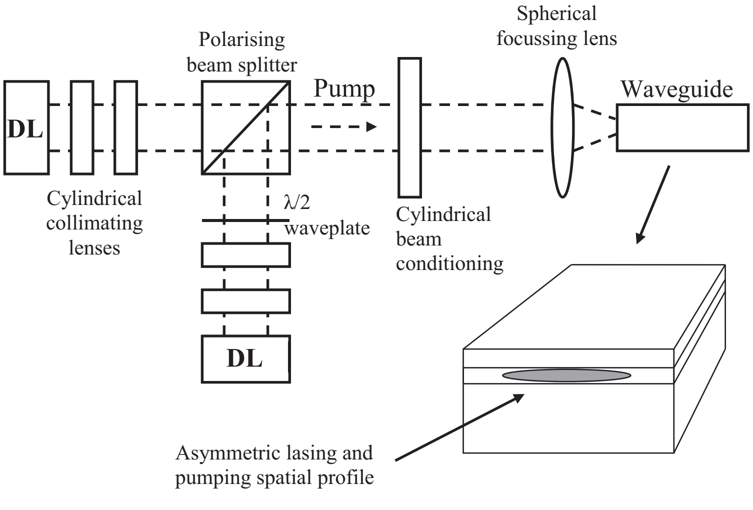
Spherical focussing lens
Polarising beam splitter
Pump
Waveguide
DL
Cylindrical collimating lenses
λ/2 waveplate
Cylindrical beam conditioning
DL
Asymmetric lasing and pumping spatial profile

FIGURE 42.4 Typical configuration for end-pumping waveguide lasers with two polarization coupled broad-stripe diode lasers (DL) with guidance of the pump and laser modes in one axis (after Mackenzie and Shepherd 2002).

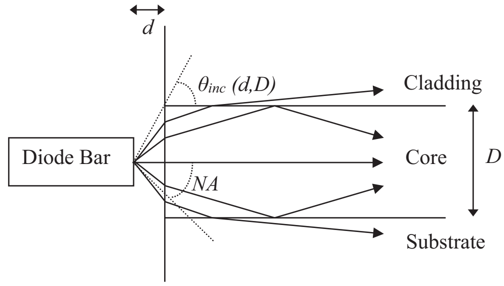

FIGURE 42.5 Side-pumping with proximity-coupled diode bars.

Side-pumping of high-NA guides can be achieved in a very compact fashion by simply proximity coupling the diode bars to either side of the waveguide (see Figure 42.5). The delivery efficiency, η_{del}, of such a coupling scheme is given by (Mackenzie et al. 2002),

$$\eta_{\text{del}} = \frac{\displaystyle\int_{-\min\left(\vartheta_{\text{inc}},\sin^{-1}(\text{NA})\right)}^{+\min\left(\vartheta_{\text{inc}},\sin^{-1}(\text{NA})\right)} \exp\left[-\ln(16)\left(\frac{\theta}{\theta_{\text{FWHM}}}\right)^2\right]\text{d}\theta}{\displaystyle\int_{-90}^{+90} \exp\left[-\ln(16)\left(\frac{\theta}{\theta_{\text{FWHM}}}\right)^2\right]\text{d}\theta} \tag{42.2}$$

where θ is the angle of propagation (in degrees) of the divergent diode beam with respect to the axis of the planar waveguide and θ_{FWHM} is the full-width half-maximum divergence of the diode fast-axis. If the half-angle subtended by the waveguide core to the diode emission aperture, θ_{inc}, is smaller than the angular acceptance of the waveguide, $\sin^{-1}$ (NA), then (42.2) describes the overlap of the diverging pump beam with the physical aperture of the core. Any light incident on the waveguide outside this aperture is lost. If the angular acceptance of the waveguide is less than θ_{inc}, then (42.2) describes the fraction of the diverging pump beam that is contained by the numerical aperture of the waveguide. Figure 42.6 shows how the delivery efficiency varies with the core depth, *D*, and waveguide NA for typical experimental values of coupling distance $d = 20$ μm and diode divergence $\theta_{\text{FWHM}} = 35°$. It can be seen that high efficiencies (>80%) are obtained for waveguides with NA ≥ 0.4 and $D \geq 15$ μm. As diode bars with powers of ~200 W continuous wave (CW) are now available, total pumping power of ~400 W per cm length of waveguide is quite feasible.

If focusing optics are used it can be seen from Figure 42.3 that a high-NA waveguide, such as a YAG/Sapphire structure, of a few tens of microns thickness could easily be pumped by a ~20 times diffraction-limited diode beam. This is compatible with the fast-axis of a micro-lensed vertical diode stack of ~3 bars, i.e. exploiting combining techniques pumping powers in excess of 1 kW per cm length of waveguide are feasible.

42.2.4 Face-Pumping

Face-pumping avoids the restrictions placed on the waveguide NA imposed by in-plane pumping and is an area-scalable scheme compatible with pumping by large diode stacks. As the pumping direction is perpendicular to the plane of the waveguide, a relatively large waveguide core ($D > 100$ μm) and a reflective pumping chamber are required to achieve high absorption efficiency. Current demonstrations have used a pumping chamber with narrow slots through which

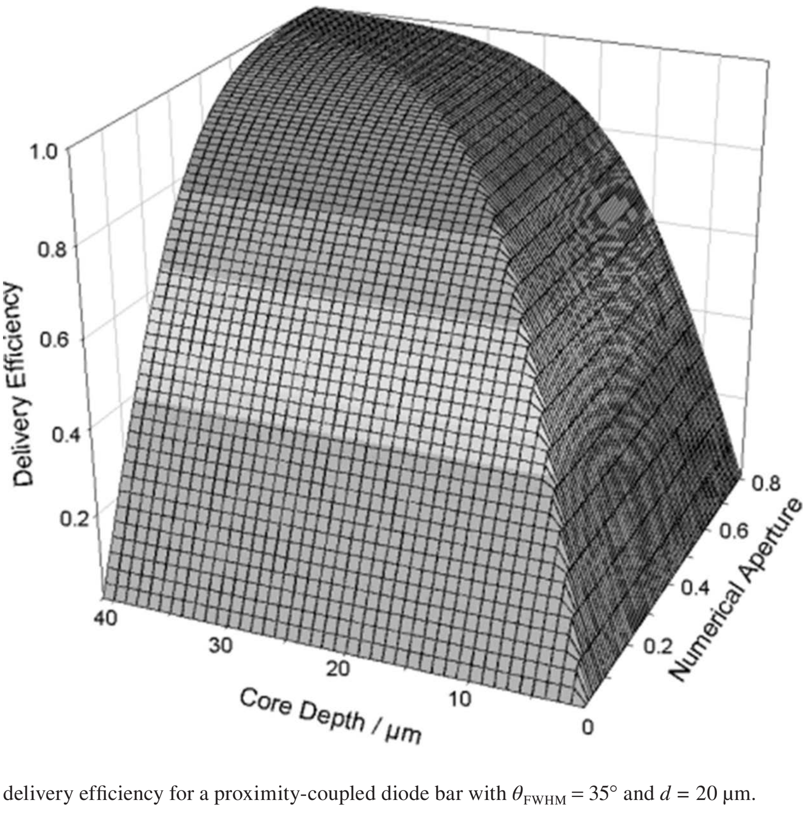

FIGURE 42.6 Theoretical delivery efficiency for a proximity-coupled diode bar with $\theta_{\text{FWHM}} = 35°$ and $d = 20$ μm.

the divergent light from the individual bars of a diode stack could pass with high efficiency and then be effectively trapped within the chamber, multi-passing through the thin bulk or waveguide slab to achieve efficient and uniform pump absorption (Faulstich et al. 1996). Later developments included the integration of water-cooling in the same package, as shown in Figure 42.7 (Lee 2002a). In this way pumping with over 400 W was demonstrated with a 10-bar diode stack and a 6 cm-long, 1.1 cm-wide, waveguide consisting of a 200 μm-thick Nd:YAG core and 400 μm-thick YAG claddings.

42.3 Thermal Management Properties

The thermal loading associated with high-power operation of solid-state lasers can lead to optical distortions such as thermal lensing and birefringence, and eventually to thermal stress fracture. High-power pumping can be achieved with face or side-pumping, and both can give a relatively uniform thermal loading of the slab-like doped-core. For an ideal, uniformly pumped slab (of infinite extent), a one-dimensional heat-flow is obtained by cooling both large faces, leading to well-defined stress-induced birefringence axes, and light polarized either in the plane, or at 90° to it, will not suffer from depolarization loss (Koechner 1996). In a bulk slab, the focusing effects of the strong, birefringent, cylindrical lens associated with the stress and temperature profiles can be eliminated by taking a zigzag optical path, using total internal reflection off the slab faces (Eggleston et al. 1984). In the case of a waveguide, the thermally induced focusing is overcome by the guidance properties of the structure, even for the thicker waveguides used in the case of face-pumping (Baker et al. 2001, Lee 2002b). For the slab waveguide shown in Figure 42.8, the temperature at the centre of the waveguide, T, and the maximum thermal power per unit cooling area before stress fracture occurs, $P_{\text{a max}}$, are given by (Shepherd et al. 2002),

$$T = \frac{P_\text{a}}{2}\left(\frac{1}{\lambda_\text{t}} + \frac{(2t - D)}{4k}\right) + T_\text{C} \tag{42.3}$$

$$P_{\text{a max}} = \frac{8R_\text{s}}{\left(t - \dfrac{D^2}{3t}\right)} \tag{42.4}$$

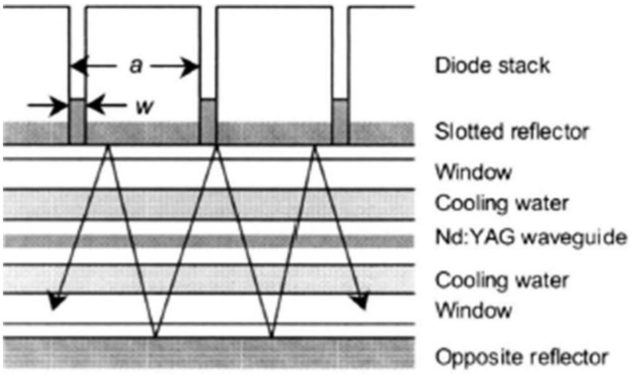

FIGURE 42.7 Schematic of face-pumping and cooling (after Lee et al. 2002).

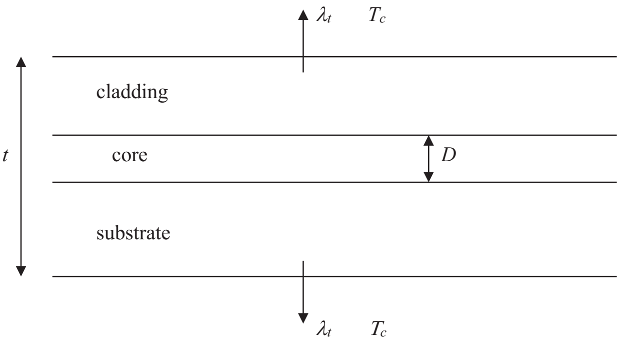

FIGURE 42.8 Symmetric slab waveguide used for thermal model (after Shepherd 2001).

where λ_t is the surface heat-transfer coefficient, k is the thermal conductivity (for simplicity assumed to be the same in all regions of the waveguide), T_c is the coolant temperature, and R_s is the thermal shock parameter (Koechner 1996). These equations reduce to those for a uniformly pumped slab when $D = t$ (Eggleston et al. 1984). Thus, a 100 μm-thick YAG waveguide (R_s = 790 W m^{-1}) with a 50 μm-thick doped region can handle a thermal load per unit cooling area of up to 6.9 kW cm^{-2}. However, it should be noted that the same waveguide has a maximum temperature rise of 85°C for a thermal load per unit area of just 100 W cm^{-2} (using λ_t = 6000 W m^{-2} K^{-1} and k = 13 W m^{-1} K^{-1}). Assuming that the main contribution to the thermal load is due to the energy difference between the pump and laser photons, then a thermal load per unit area of 100 W cm^{-2} corresponds to over 1 kW cm^{-2} of actual pump power for the Yb:YAG system. As such, very compact, kW power level, devices would appear to be a possibility. A theoretical comparison of power scaling in face and side-pumped slabs has been made for the case of quasi-three-level bulk lasers (Rutherford et al. 2000), which include the important high-power material Yb:YAG, and it was found that the greater freedom of choice over the thickness and doping level in the case of side-pumping is advantageous.

42.4 Spatial-Mode Selection

The need to confine non-diffraction-limited diode pump sources in the case of in-plane pumping, and the need to use relatively thick cores in the case of face-pumping, both lead to the use of multi-mode waveguides in terms of power-scaling requirements. In the non-guided plane, both face and side-pumping (and the need for effective cooling) tend to lead to relatively large pumping mode sizes of 0.5–1 cm, which again tends to lead to multi-mode laser output. Various methods of spatial-mode control have thus been applied in both axes.

42.4.1 Double-Clad Waveguides

A standard solution to the conflicting requirements of needing a multi-mode waveguide for confinement of the pump, while simultaneously desiring a single-spatial-mode laser output, is to embed a single-mode lasing core within a much larger

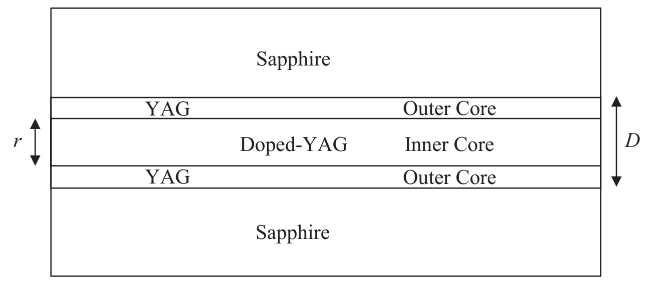

FIGURE 42.9 Double-clad planar waveguide for spatial-mode selection.

multi-mode pump guide (Snitzer et al. 1988). Widely used in high-power fibre lasers, this cladding-pumping technique also increases the length of the active medium required to efficiently absorb the pump. A similar double-clad structure can be used for mode selection in planar waveguides, but the design must be such that the increase in the absorption length is moderated by the fabrication limitations for typical device dimensions. By doping a central portion of a multi-mode waveguide only (see Figure 42.9), mode-selection can be achieved by the gain profile rather than by its index profile. For a uniformly pumped medium, the gain exponent for a particular mode with a spatial profile $\phi_p(x, y, z)$, relative to that for a lasing mode, φ (x, y, z), is given by (Bhutta et al. 2002)

$$G_{\mathrm{rel}} = \iiint \frac{\mathrm{d}(x,y,z)\varphi_{\mathrm{p}}(x,y,z)}{\left(1+S\varphi(x,y,z)\right)\left[\iiint \frac{\mathrm{d}(x,y,z)\varphi(x,y,z)}{1+S\varphi(x,y,z)}\,\mathrm{d}V\right]}\,\mathrm{d}V \tag{42.5}$$

where $d(x, y, z)$ is the spatial profile of the doping and S gives a measure of the degree of saturation due to the intracavity laser power. For a centrally doped waveguide, the fundamental mode reaches threshold first as it has the best spatial overlap with the doped region. Figure 42.10 then shows how G_{rel} varies for the ten lowest order modes of a step-index waveguide for conditions of high saturation. As shown, for a doping ratio of up to 60%, that is, the core thickness over that of the multi-mode step-index waveguide gives preferential gain for the fundamental mode and that, when lasing on the fundamental mode, the higher-order modes cannot reach threshold, even under conditions of high saturation (Bhutta et al. 2002). In this way, the absorption length is increased by less than a factor of two and fundamental-spatial-mode output is robustly selected. Mode fidelity can be easily maintained as coupling between the lasing fundamental mode and higher-order modes is very inefficient due to the short and straight nature of the planar waveguide.

One limitation to this gain-selection technique is that it assumes that there is no refractive index change at the core interfaces. It is known that rare-earth doping typically induces an increment in the refractive index of a material; thus the inner-core numerical aperture must be kept below the level at which this region becomes an independent waveguide (Mackenzie 2007). Furthermore, for thicker and higher-power waveguides, care must be taken of the index profile associated with the temperature profile across the core, which can produce a thermally induced waveguide (Baker et al. 2002).

42.4.2 Self-Imaging Waveguides

Another technique of use for mode selection in the guided axis is that of self-imaging (Bryngdhal 1973, Ulrich and Ankele 1975). This technique relies on the fact that an optical beam of a given spatial profile will periodically re-image within a multi-mode step-index waveguide with a period,

$$L = \frac{4n_1D^2}{\lambda} \tag{42.6}$$

Given typical waveguide-laser laser device lengths are less than 10 cm and noting that axially symmetric profiles re-image for the first time at $L/4$ (see Figure 42.11), implies effective use for core depths of up to a few hundred microns. This is an order of

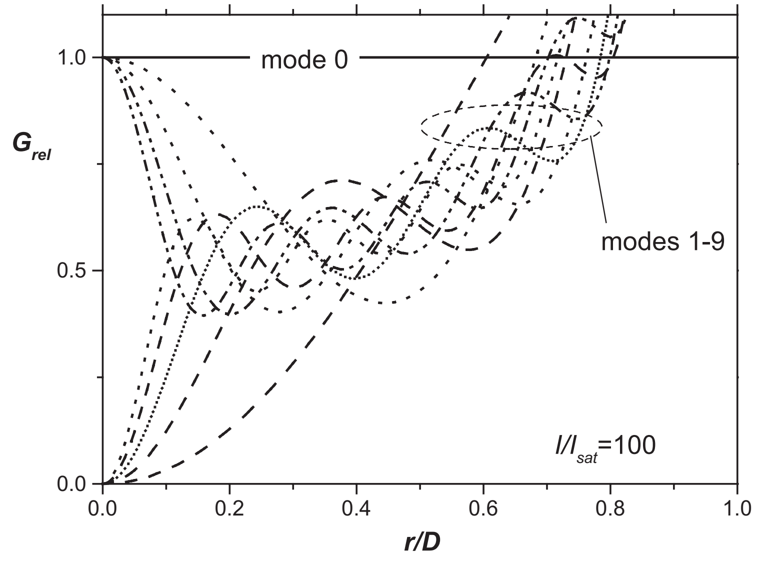

FIGURE 42.10 Relative gain for the ten lowest order modes against doping fraction, for a heavily saturated gain region (after Bhutta 2002).

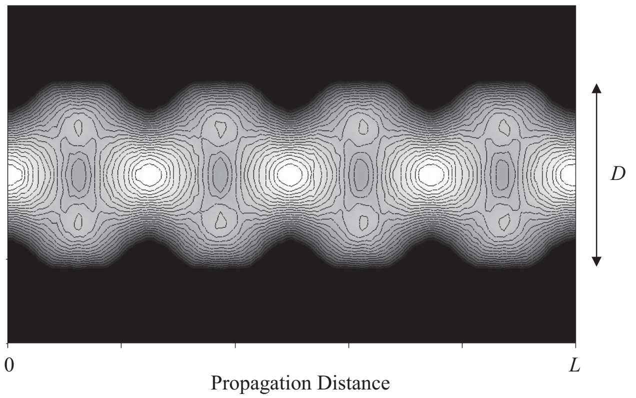

FIGURE 42.11 Theoretical plot for the field contours of a self-imaging, multi-mode, step-index waveguide.

magnitude larger in scale than double-clad structures have currently reached, and the design also maintains the normal pump absorption length. Self-imaging can be applied in practice to amplifiers (Lee et al. 2001, Baker et al. 2002) and laser oscillators (Pelouch et al. 2002) by launching an undersized, diffraction-limited, Gaussian beam at one end of the waveguide, which will couple to higher-order modes and efficiently sweep out the uniformly pumped core, before re-imaging to a diffraction-limited output at the end of the guide. Some degradation of the re-imaging process may occur in high-power systems due to the effects of gain saturation and thermal lensing, as well as simple misalignment of the input beam, but with careful design these effects can be minimized (Baker et al. 2002).

42.4.3 Tapered Waveguides

One technique that can provide diffraction-limited output in both axes is to use a tapered waveguide. The basic principle (see Figure 42.12) is that a multi-mode broad-stripe guide, compatible with diode pumping, is connected to a single-mode channel via a taper (in the lateral axis) designed to give minimal mode coupling between the fundamental mode and higher-order modes (Hettrick et al. 2000). Thus low-loss laser operation is obtained in the fundamental mode, while efficiently pumping with multi-mode diode sources. A design condition, set to minimize mode coupling in a parabolic-shaped horn, has been given as (Milton and Burns 1977)

$$L = \frac{n_1 {D_{\max}}^2}{2\lambda} \tag{42.7}$$

where D_{max} is the maximum width that the taper can open out to in a length L. This has a similar form to the self-imaging condition of Equation 42.6 and imposes much the same sort of restriction, i.e. if the device is a few cm long then the taper can only open to a few hundred microns. Thus, this sort of waveguide is most suited to end-pumping with broad-stripe diodes, with the diode slow axis arranged to coincide with the broad width of the taper and the diffraction-limited axis coinciding with the depth. It should be noted that end-pumping of monolithic thin-film waveguides with broad-stripe diode sources can give multi-Watt diffraction-limited output without any need for structuring in the non-guided plane, as the focused pump can be kept small enough to give a good match to the fundamental mode size (Mackenzie et al. 2003). Thus, the use of a tapered structure is perhaps most useful to produce an integrated laser source fabricated on the same substrate as, and connecting to, further waveguide circuits.

42.4.4 External Resonator Waveguides

An external resonator can be useful in controlling the mode of the waveguide laser in both axes, but is especially useful for the non-guided axis in face or side-pumped waveguide lasers, where the large pump mode size leads to multi-mode operation in monolithic devices. Figure 42.13 shows a stable extended cavity applied to a side-pumped, double-clad, Nd:YAG waveguide laser. In the fast axis of the waveguide, the fundamental mode selected by the double-clad structure is simply collimated onto an external plane mirror, and diffraction-limited output ($M^2 < 1.2$) is easily obtained. In order to achieve a large

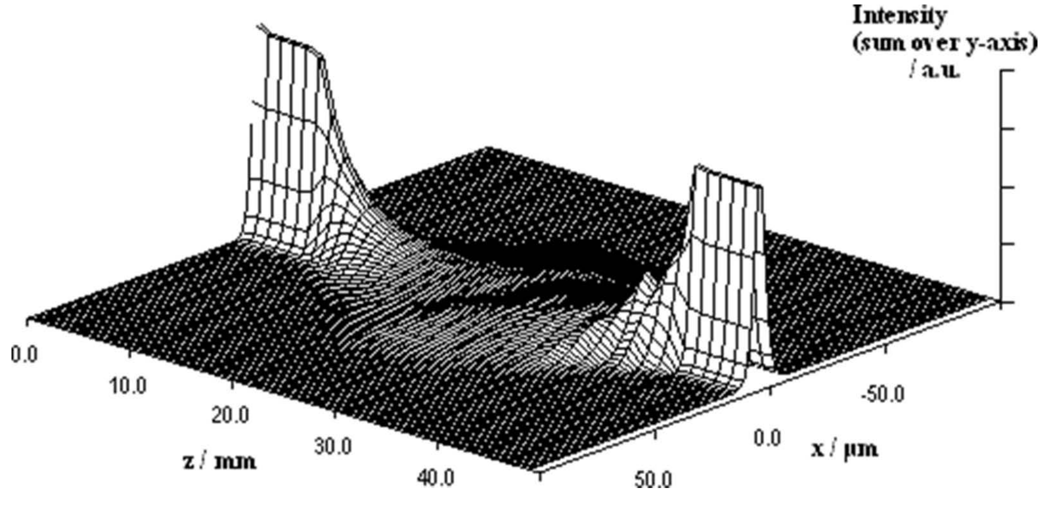

FIGURE 42.12 Theoretical plot of the mode propagation in a double-pass of a tapered planar waveguide laser (after Shepherd 2001).

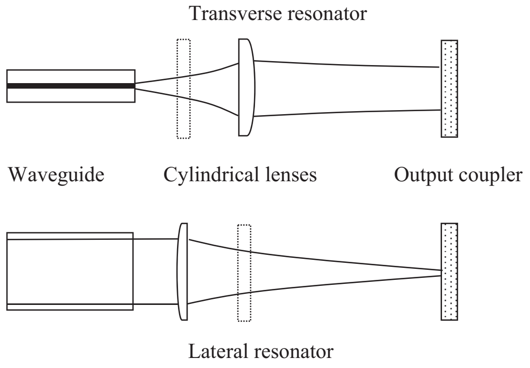

FIGURE 42.13 Schematic of an extended stable cavity waveguide laser.

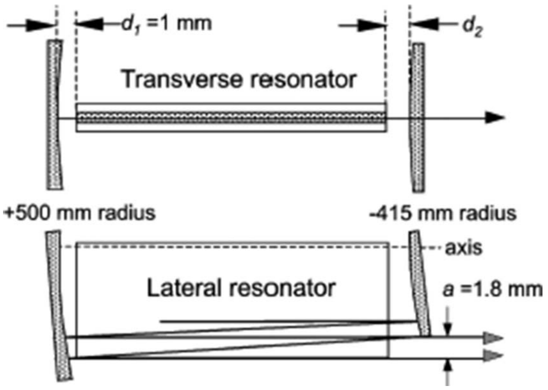

FIGURE 42.15 Hybrid waveguide-unstable resonator (after Baker 2001).

fundamental mode size that efficiently sweeps out the gain in the 5 mm-wide, non-guided axis of the waveguide, the cavity has to operate relatively close to instability. Nevertheless, as shown in Figure 42.14, the M^2 of the output can be reduced to <3 in this axis. Further improvement in laser performance can be realized with an end-pumped configuration (Ng and Mackenzie 2012, 2013), in which case there is an improved overlap between the pump and in-plane cavity mode. Stable extended resonators have also been applied to side-pumped, multi-mode, channel waveguide lasers (Griebner and Schönnagel 1999), where the free-space propagating resonator mode is closely matched to the fundamental mode size of the large channel, again leading to low-M^2 output.

Alternatively, a hybrid waveguide-unstable resonator design can be used (Baker et al. 2001), as shown in Figure 42.15. In this scheme, low-order guided (transverse) mode operation is selected, as the low-order modes have the lowest re-coupling loss from the waveguide to the mirrors and back. In the non-guided (lateral) axis, the cavity corresponds to an off-axis, positive branch, confocal unstable resonator. For this configuration, the mirror radii are related by

$$R_1 - R_2 = 2\left(\frac{L}{n_1} + d_1 + d_2\right) \tag{42.8}$$

and the effective output coupling is given by $(1-R_1/R_2)$. This type of resonator has been used at output powers >100 W, sweeping out a gain width of ~1 cm, and delivering M^2 values of 4.4 in the unguided-axis and 8.6 in the guided axis (Lee 2002a, Thomson et al. 2011).

42.5 Waveguide Laser Performance

42.5.1 End-Pumping

Fully diffraction-limited, multi-Watt, performance is most easily achieved via the end-pumped configuration. Using a 10 W beam-shaped broad-stripe diode source at 807 nm (M^2 = 17 in both axes), a monolithic, Nd:YAG double-clad waveguide laser has delivered the performance shown in Figure 42.16 (Mackenzie et al. 2003). The high slope efficiency (~60%) for

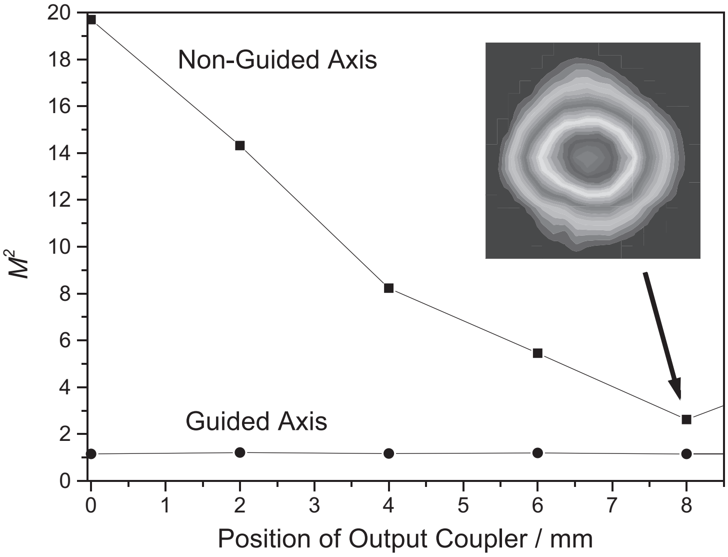

FIGURE 42.14 Plot of M^2 against position of output coupler for the extended stable cavity and CCD image of the collimated output spatial profile.

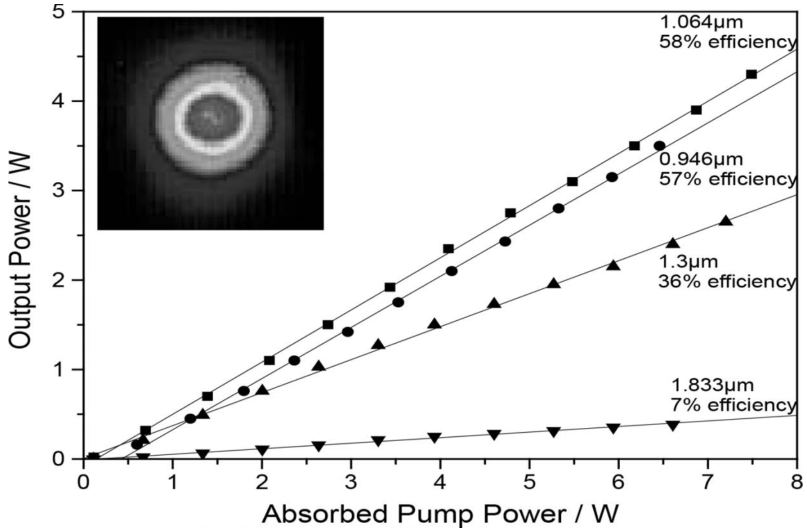

FIGURE 42.16 Output power characteristics of an end-pumped double-clad Nd:YAG waveguide laser, and CCD image of the collimated, near-diffraction-limited, output profile.

the 1.064 µm and 946 nm transitions and the low M^2 values (1.0 by 1.3) are characteristic of end-pumped waveguides. Further power scaling of a monolithic cavity to 105 W at 946 nm was demonstrated with multiple-diode-bar pumping, again with good optical efficiency, 50% (Ng and Mackenzie 2012). While enhanced radiance was achieved with an extended cavity and an output with near-diffraction-limited beam quality (Ng and Mackenzie 2013). The fact that the same double-clad structure can provide fundamental-mode selection across a wide range of wavelengths is an interesting feature. It can also be seen that the high gain provided by the waveguide structure allows laser operation of rather weak transitions, such as 1.833 µm in Nd:YAG, scaled to over 1 W of output in a compact cavity (Mackenzie et al. 2015). This can be said to be true of single-clad waveguides as well, e.g. Tm:YLF waveguides grown by liquid-phase epitaxy (LPE), with 76% slope efficiency (Bolanos et al. 2012), or, Yb:YAG grown by PLD with 70% slope and 16 W of output (Beecher et al. 2017). Additionally, a pump-guiding waveguide has been exploited in a Master Oscillator Power Amplifier (MOPA) configuration, using Yb:YAG as the active core, to produce multi-kW average powers (Filgas et al. 2012).

Passively Q-switched operation has also been demonstrated in the end-pumped configuration in both Nd and Yb-doped YAG, monolithic, double-clad waveguide lasers (Mackenzie and Shepherd 2002). Using a similar direct-bonded structure to that shown in Figure 42.9, but with a small part of the doped inner core being replaced by a Cr^{4+}-doped section to act as a saturable absorber, the results shown in Figure 42.17 were obtained for the Yb:YAG guide. Although the double-clad design is strictly based upon cw operation, the output was still found to be near-diffraction-limited with M^2 values of 1.3 (guided-axis) by 1.5. In this way, peak powers of up to 18 kW were available (30 µJ pulses with 1.6 ns duration) in a linearly polarized beam.

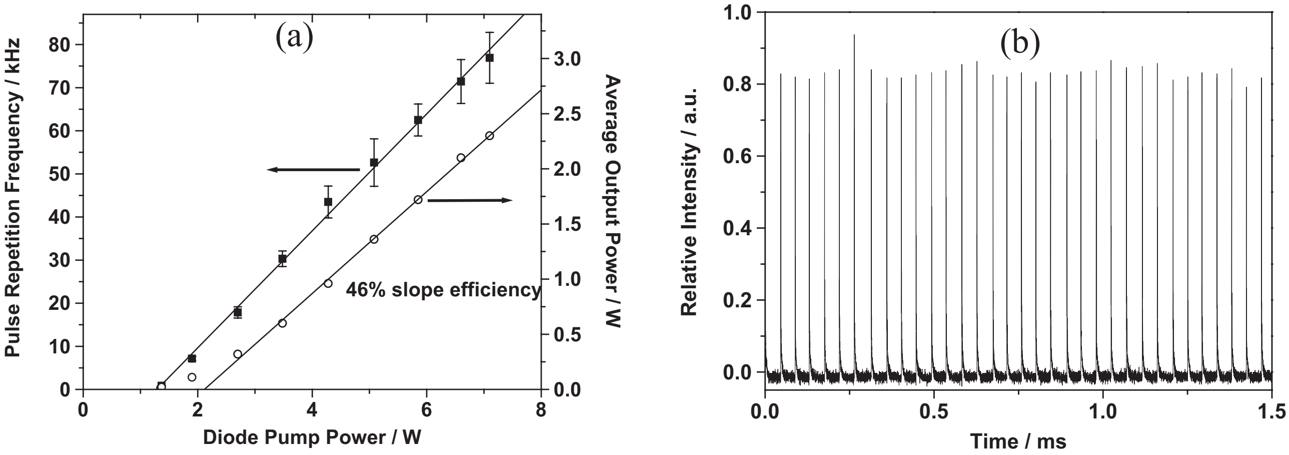

FIGURE 42.17 Output performance characteristics of an end-pumped passively Q-switched Yb:YAG waveguide laser (after Mackenzie and Shepherd 2002). (a) Repetition rate and output power against diode pump power. (b) Typical output pulse train.

42.5.2 Side Pumping

Initially side-pumping was restricted to pumping with diode bars rather than diode stacks, due to the low NA of the waveguide structures. At that time pump power of up to 40 W, pumping both sides of 1 cm-long waveguides with 20 W diode bars, was achieved. First demonstrations of side pumping were carried out using Nd:YAG guides fabricated by LPE (Hanna et al. 1992), but since then most work has used double-clad waveguides fabricated by direct bonding. Side-pumping has been demonstrated in Nd, Yb, and Tm-doped YAG, double-clad, waveguides in various configurations. The proximity-coupled results for Tm at 2.02 μm (Mackenzie et al. 2001) and Yb at 1.03 μm (Beach et al. 2001) are shown in Figure 42.18, with both demonstrating high efficiencies with respect to incident diode power. Using a monolithic cavity, the output is diffraction-limited in the guided axis but >100 times diffraction limited in the non-guided axis. Side-pumped passively Q-switched operation has also been demonstrated using a similar guide to that discussed in the previous section but based on Nd rather than Yb-doped YAG. Once again using proximity coupling of two diode bars and a monolithic laser cavity, average powers up to 8 W were obtained with peak pulse powers of nearly 30 kW (Beach et al. 2001). Thomson et al. (2011) illustrated the performance could be scaled to stacked diode-bar pumping, with 400 W output from a stable-unstable external resonator.

An extended stable cavity of the design shown in 42.13, based on a side-pumped Nd:YAG double-clad waveguide operating at 1.064 μm, gave the performance shown in Figure 42.19. These results show how implementing near-diffraction-limited performance can reduce the slope efficiency due to the fact that the now near-Gaussian laser mode has a worse spatial overlap with the uniformly pumped slab than the highly multi-mode case. In order to avoid this effect, a stable cavity could be designed that takes a zigzag path through the unguided axis to efficiently sweep out the gain, as has been demonstrated in bulk systems (Snell et al. 2000). Similar slope efficiencies and low output M^2 have been obtained with side-pumped, Yb:YAG, multi-mode channel (Griebner and Schönnagel 1999) and thin-film waveguides (Griebner et al. 1999) using extended stable cavities.

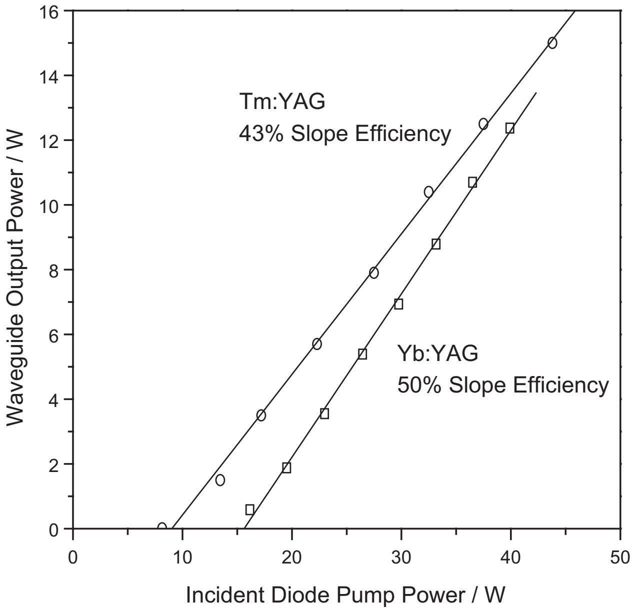

FIGURE 42.18 Output power against incident diode-pump power for proximity-coupled, side-pumped double-clad waveguide lasers (after Shepherd 2001).

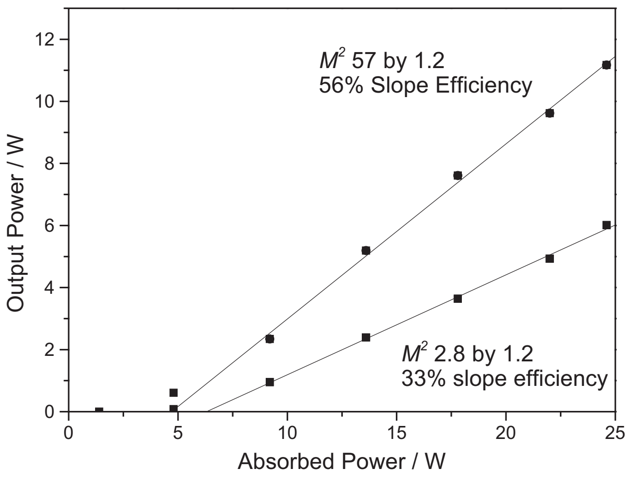

FIGURE 42.19 Output power against absorbed diode pump power for an extended stable cavity, side-pumped, double-clad waveguide laser, with the cavity length set for multi-mode and single-mode operation.

42.5.3 Face Pumping

During the early years of developing high-power planar waveguide lasers, the highest output powers were obtained from the face-pumped configuration shown in Figure 42.7. Using plane resonator mirrors placed near to the end faces of the Nd:YAG waveguide (6 cm long, 1.1 cm wide, and 200 μm-thick core), a maximum of 150 W of multi-mode output was obtained for 430 W of pump power (Lee et al. 2002a). Employing a hybrid waveguide-unstable resonator cavity as shown in Figure 42.15, the M^2 values were reduced to 8.6 (guided) by 4.4 for output powers of up to 110 W. A comparison of the multi-mode and unstable-resonator output power performance is shown in Figure 42.20, indicating that ~88% of the multi-mode output power can be converted into the high-brightness beam. In subsequent work, using a hybrid-unstable resonator of the negative branch confocal type, M^2 values as low as 1.8 by 1.3 have been obtained at powers of 110 W (Lee et al. 2002).

42.6 Future Prospects

Rapid development in the power scaling of planar slab waveguides was demonstrated in the first decade of the 21st century. Output powers in the kW regime were obtained in MOPA configurations, with expectations to be able to push to the 100 kW levels in the near future. Primarily due to the excellent power handling capabilities of ultra-thin, uniformly pumped

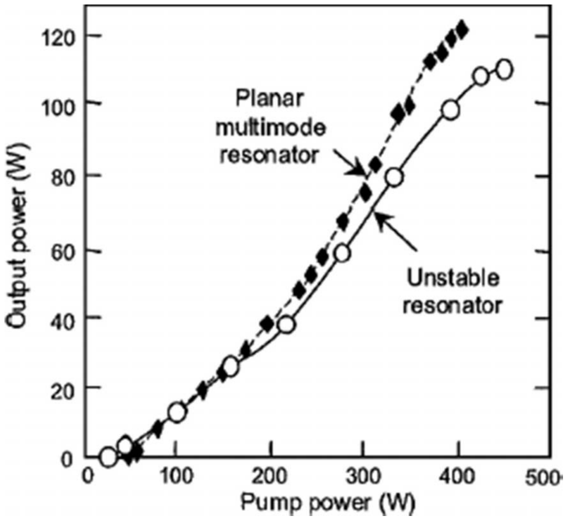

FIGURE 42.20 Comparison of the output power for a multi-mode plane mirror and unstable resonator configurations for a face-pumped Nd:YAG waveguide laser (after Lee et al. 2002a).

slabs, this gain-media geometry is a complementary technology for high-power fibre lasers, whereby the additional degree of freedom to scale the beam size opens a broader range of potential operating conditions. Clearly to continue power-scaling it is a requirement to use multi-mode waveguides, for which, as discussed, there are several technologies that exist that can deliver high-brightness output beams with good optical efficiencies. These include waveguiding techniques such as tapers, double-cladding, and self-imaging, as well as the use of stable and unstable external resonators and finally MOPA configurations. The high gains generated in the thin planar films can cause problems with amplified spontaneous emission and parasitic lasing, and so these structures would appear to be more suited to cw or high-repetition-rate pulsed outputs than for high-energy storage. The natural compatibility of the planar waveguide geometry with high-power diode bars and stacks allows rather compact gain modules and relatively simple coupling optics. Thus waveguide lasers operating in the multi-kW power regime should find numerous uses in scientific, industrial, and military applications, while waveguides of a few Watts to a few hundred Watts may find application in efficient operation of unusual low-gain transitions and integrated laser sources for data communications systems.

REFERENCES

Anderson A. A., Eason R. W., Hickey L. M. B., et al. 1997. Ti:Sapphire Planar Waveguide Laser Grown by Pulsed Laser Deposition. *Opt. Lett.* **22** 1556–1558.

Baker H. J., Chesworth A. A., Pelaez Millas D, et al. 2001. A Planar Waveguide Nd:YAG Laser with a Hybrid Waveguide-Unstable Resonator. *Opt. Commun.* **191** 125–131.

Baker H. J., Lee J. R., and Hall D. R. 2002. Self-Imaging and High-Beam-Quality Operation in Multi-Mode Planar Waveguide Optical Amplifiers. *Opt. Express* **10** 297–302.

Beach R. J. 1996. Theory and Optimisation of Lens Ducts. *Appl. Opt.* **35** 2005–2015.

Beach R. J., Mitchell S. C., Meissner H. E., et al. 2001. Continuous Wave and Passively Q-Switched Cladding-Pumped Planar waveguide lasers. *Opt. Lett.* **26** 881–883.

Beecher S. J., Grant-Jacob J. A., Hua P, et al. 2017. Ytterbium-doped-garnet crystal waveguide lasers grown by pulsed laser deposition. *Opt. Mat. Expr.* **7** 1628–1633.

Becker C., Oesselke T., Pandavenes J., et al. 2000. Advanced Ti:Er:LiNbO$_3$ Waveguide Lasers. *IEEE J. Quantum Electron.* **6** 101–113.

Bhutta T., Chardon A. M., Shepherd D. P., et al. 2001. Low Phonon Energy, Nd:LaF$_3$ Channel Waveguide Lasers Fabricated by Molecular Beam Epitaxy. *IEEE J. Quantum Electron.* **37** 1329–1337.

Bhutta T., Mackenzie J. I., Shepherd D. P., et al. 2002. Spatial Dopant Profiles for Transverse-Mode Selection in Multi-Mode Waveguides. *J. Opt. Soc. Am. B* **19** 1539–1543.

Bibeau C., Beach R. J., Mitchell S. C., et al. 1998. High-Average-Power 1-µm Performance and Frequency Conversion of a Diode-End-Pumped Yb:YAG Laser. *IEEE J. Quantum Electron.* **34** 2010–2019.

Bolanos W., Starecki F., Benayad A., et al. 2012. Tm:LiYF$_4$ planar waveguide laser at 1.9 µm. *Opt. Lett.* **37** 4032–4034.

Bonner C. L., Anderson A. A., Eason R. W., et al. 1997. Performance of a Low-Loss Pulsed-Laser-deposited Nd:Gd$_3$ Ga$_5$O$_{12}$ Waveguide laser at 1.06 and 0.94µm. *Opt. Lett.* **22** 988–990.

Bonner C. L., Bhutta T, Shepherd D. P., et al. 2000. Double-Clad Structures and Proximity Coupling for Diode-Bar-Pumped Planar Waveguide Lasers. *IEEE J. Quantum Electron.* **36** 236–242.

Brown C. T. A., Bonner C. L., Warburton T. J., et al. 1997. Thermally Bonded Planar Waveguide Lasers. *Appl. Phys. Lett.* **71** 1139–1141.

Bryndhal O. 1973. Image Formation using Self-Imaging Techniques. *J. Opt. Soc. Am.* **63** 416–418.

Chandler P. J., Zhang L., and Townsend P. D. 1991. Ion-Implanted Waveguides in Laser Host Materials. *Nucl. Instrum. Meth. B* **59** 1223–1227.

Chartier I, Ferrand B, Pelenc D, et al. 1992. Growth and Low-Threshold Laser Oscillation of an Epitaxially Grown Nd:YAG Waveguide. *Opt. Lett.* **17** 810–812.

Clarkson W. A. and Hanna D. C. 1996. Two-Mirror Beam-Shaping Technique for High-Power Diode Bars. *Opt. Lett.* **21** 375–377.

DiGiovanni D. J., Stentz A. J. 1999. *Tapered Fiber Bundles for Coupling Light into and Out of Cladding-Pumped Fiber Devices.* US patent US5864644A.

Eggleston J. M., Kane T. J., Kuhn K, et al. 1984. The Slab Geometry Laser – Part I: Theory. *IEEE J. Quantum Electron.* **20** 289–301.

Fan T. Y. 2005. Laser Beam Combining for High-Power, High-Radiance Sources. *IEEE J. Sel. Tops. Quantum Electron.* **11** 567–577.

Faulstich A, Baker H. J., and Hall D. R. 1996. Face-Pumping of Thin, Solid-State Slab lasers with Laser Diodes. *Opt. Lett.* **21** 594–596.

Filgas D, Clatterbuck T, Cashen M, et al. 2012. Recent Results for the Raytheon RELI Program. *Proc. SPIE Laser Technology for Defense and Security VIII.* **8381** 83810W.

Graf T. and Balmer J. E. 1993. High-Power Nd:YLF Laser End Pumped by a Diode-Laser Bar. *Opt. Lett.* **18** 1317–1319.

Griebner U. and Schönnagel H. 1999. Laser Operation with nearly Diffraction-Limited Output from a Yb:YAG Multi-mode Channel Waveguide. *Opt. Lett.* **24** 750–752.

Griebner U., Grunwald R., and Schönnagel H. 1999. Thermally Bonded Yb:YAG Planar waveguide. *Laser Opt. Commun.* **164** 185–190.

Griebner U., Grunwald R., Schönnagel H., et al. 2000. Laser with Guided Pump and Free-Propagating Resonator Mode using Diffusion-Bonded Rectangular Channel Waveguides. *Appl. Phys. Lett.* **77** 3505–3507.

Grivas C. 2011. Optically pumped planar waveguide lasers, Part I: Fundamentals and fabrication techniques. *Prog. Quantum Electron.* **35** 159–239.

Hanna D. C., Large A. C., Shepherd D. P. et al. 1992. A Side-Pumped Nd:YAG Epitaxial Waveguide Laser. *Opt. Commun.* **91** 229–235.

Hettrick S. J., Mackenzie J. I., Harris R. D. et al. 2000. Ion-Exchanged Tapered Waveguide Laser in Neodymium-Doped BK7 Glass. *Opt. Lett.* **25** 1433–1435.

Hodgson N, Ter-Mikirtychev V. V., Hoffman H. J., et al. 2002. Diode-Pumped, 220W Ultra-Thin Slab Nd:YAG Laser with Near-Diffraction-Limited Beam Quality. *Advanced Solid-State Lasers*, M. E. Fermann and L. R. Marshall eds., Vol. 68 OSA Trends in Optics and Photonics Series (Optical Society of America, Washington, DC), 552–557.

Kawachi M. 1990. Silica Wave-Guides on Silicon and their Application to Integrated-Optic Components. *Opt. Quantum Electron.* **22** 391–416.

Koechner W. 1996. *Solid-State Laser Engineering*, 4th edn (New York: Springer-Verlag)

Lee J. R., Baker H. J., Friel G. J., et al. 2002a. High-Average-Power Nd:YAG Planar waveguide Laser that is Face Pumped by 10 Laser Diode Bars. *Opt. Lett.* **27** 524–526.

Lee J. R., Baker H. J., and Hall D. R. 2002b. Thermal Guiding, Birefringence and Brightness Scaling of High Average Power, Planar waveguide Devices. *Advanced Solid-State Lasers*, M. E. Fermann and L. R. Marshall eds., Vol. 68 OSA Trends in Optics and Photonics Series (Optical Society of America, Washington, DC, 2002), 529–534.

Lee J. R., Friel G. J., Baker H. J., et al. 2001. A Nd:YAG Planar Waveguide Laser Operating at 121W Output with Face-Pumping by Diode Bars, and its Use as a Power Amplifier. *Advanced Solid-State Lasers*, C. Marshall ed., Vol. 50 OSA Trends in Optics and Photonics Series (Optical Society of America, Washington, DC, 2001), 36–40.

Mackenzie J. I. 2007. Dielectric Solid-State Planar Waveguide Lasers: A Review. *IEEE J. Sel. Tops. Quantum Electron.* **13** 626–637.

Mackenzie J. I., Li C., and Shepherd D. P. 2003. Multi-Watt, High-Efficiency, Diffraction-Limited Nd:YAG Planar Waveguide. *Laser IEEE J. Quantum Electron.* **39** 493–500.

Mackenzie J. I., Li C, Shepherd D. P., Beach R. J. et al. 2002. Modeling of High-Power Continuous-Wave Tm:YAG Side-Pumped Double-Clad Waveguide Lasers. *IEEE J. Quantum Electron.* **38** 222–230.

Mackenzie J. I., Mitchell S. C., Beach R. J. et al. 2001. 15W Diode-side-Pumped Tm:YAG Waveguide Laser at 2μm. *Electron Lett.* **37** 898–899.

Mackenzie J. I. and Shepherd D. P. 2002. End-Pumped, Passively Q-switched Yb:YAG Double-Clad Waveguide Laser. *Opt. Lett.* **27** 2161–2163.

Mackenzie J. I., Szela J. W., Beecher S. J. et al. 2015. Crystal Planar Waveguides, a Power Scaling Architecture for Low-Gain transitions. *IEEE J. Sel. Tops. Quantum Electron.* **21** 1601610-1–10

Milton A. F. and Burns W. K. 1977. Mode Coupling in Optical Waveguide Horns. *IEEE J. Quantum Electron.* **13** 828–835.

Ng S. P. and Mackenzie J. I. 2012. Power and Radiance Scaling of a 946 nm Nd:YAG Planar Waveguide Laser. *Las. Phys.* **22** 494–498.

Ng S. P. and Mackenzie J. I. 2013. Planar Waveguide Laser Optimization and Characterization Employing Real-Time Beam Quality Measurement. *IEEE J. Quantum Electron.* **49** 146–153.

Okhrimchuk A. G., Shestakov A. V., Khrushchev I. et al. 2005. Depressed Cladding, Buried Waveguide Laser Formed in a YAG:Nd^{3+} Crystal by Femtosecond Laser Writing. *Opt. Lett.* **30** 2248–2250.

Parsonage T. L, Beecher S. J., Choudhary A., et al. 2015. Pulsed Laser Deposited Diode-Pumped 7.4W Yb:Lu$_2$O$_3$ Planar Waveguide Laser. *Opt. Express.* **23** 31691–31697.

Pelouch W. S., Smith D. D., Koroshetz J. E. et al. 2002. Self Imaging in Waveguide Lasers and Amplifiers. *Advanced Solid-State Lasers*, M. E. Fermann and L. R. Marshall, eds., Vol. 68 OSA Trends in Optics and Photonics Series (Optical Society of America, Washington, DC), 6–9.

Ramaswamy R. V. and Srivastava R. 1988. Ion Exchanged Glass Waveguides: A Review. *IEEE J. Lightwave Technol.* **6** 984–1002.

Rutherford T. S., Tulloch W. M., Gustafson E. K., et al. 2000. Edge-Pumped Quasi-Three-Level Slab Lasers: Design and Power Scaling. *IEEE J. Quantum Electron.* **36** 205–219.

Schmidt R. V. and Kaminow I. P. 1974. Metal-Diffused Optical Waveguides. *Appl. Phys. Lett.* **25** 458–460.

Shepherd D. P., Choudhary A., Lagatsky A. A., et al. 2016. Ultrafast High-Repetition-Rate Waveguide Lasers. *IEEE J. Sel. Tops. Quantum Electron.* **22** 16–24.

Shepherd D. P., Hettrick S. J., Li C., et al. 2002. High-Power Planar Dielectric Waveguide Lasers *J. Phys. D: Appl. Phys.* **34** 2420–2432.

Snell K. J., Lee D., Wall K. F., et al. 2000. Diode-Pumped, High-Power CW and Modelocked Nd:YLF Lasers. *Advanced Solid-State Lasers*, H. Injeyan, U. Keller, and C. Marshall, eds., Vol. 34 OSA Trends in Optics and Photonics Series (Optical Society of America, Washington, DC), 55–59.

Snitzer E., Po H., Hakimi F., et al. 1988. Double-Clad Offset Core Nd Fibre Laser. *Dig. Conf. On Optical Fibre Sensors.* paper PD5.

Svalgaard M., Poulsen C. V., Bjarklev A., et al. 1994. Direct UV Writing of Buried Single Mode Channel Waveguides in Ge-Doped Silica Films. *Electron. Lett.* **30** 1401–1403.

Thomson I. J., Monjardin F. J. F., Baker H. J., et al. 2011. Efficient Operation of a 400 W Diode Side-Pumped Yb:YAG Planar Waveguide. Laser *IEEE J. Quantum Electron.* **47** 1336–1345.

Ulrich R. and Ankele G. 1975. Self-Imaging in Homogeneous Planar Optical Waveguides. *Appl. Phys. Lett.* **27** 337–339.

FURTHER READING

Koechner W 1996 *Solid-State Laser Engineering*, 4th edn. (Berlin: Springer Verlag). Thorough coverage of characteristics, design and performance of a wide variety of solid-state lasers, including a good coverage of thermo-optic effects and heat removal.

Lee D L 1986 *Electromagnetic Principles of Integrated Optics* (New York: Wiley). Develops the concepts and principles of guided wave optics starting from Maxwell's equations and includes a useful introduction to many waveguide fabrication techniques and devices.

Siegman A E 1986 *Lasers* (Sausalito: University Science Books). A comprehensive textbook giving a detailed treatment of laser physics.

Taylor & Francis
Taylor & Francis Group
http://taylorandfrancis.com

43

MEMS-Based Swept Laser Source

John O. Gerguis, Yasser M. Sabry, Haitham Omran, and Diaa Khalil

CONTENTS

43.1 Introduction 585
 43.1.1 Wavelength-swept Source 585
 43.1.2 Principle of Operation of Swept Laser Sources 585
43.2 Scanning Techniques 586
 43.2.1 Wavelength Scanning 586
  43.2.1.1 Grating and Polygon Mirror 586
  43.2.1.2 Fabry–Perot Tunable Etalon 587
  43.2.1.3 Acousto-optic Filter 587
  43.2.1.4 Other Common Techniques 587
 43.2.2 Output Beam Position Scanning 587
43.3 MEMS Technology 588
 43.3.1 SOI and DRIE Overview 588
 43.3.2 Comb-drive Actuator 589
43.4 MEMS-based Swept Fibre-ring Laser Source 590
 43.4.1 MEMS Filter with Bragg Mirrors 590
  43.4.1.1 The Performance of the MEMS Filter 590
  43.4.1.2 The Performance Enhancement Using Lensed Fibres 591
 43.4.2 MEMS-based Swept Laser Source System 592
 43.4.3 The Dynamic Behaviour of the Swept Laser Source 593
43.5 Summary 596
References 596

43.1 Introduction

43.1.1 Wavelength-swept Source

Wavelength-tunable light sources are very essential elements in many biomedical imaging [1–3], biochemical sensing [4], gas sensing and enhanced spectroscopy techniques [5–7], fibre-optic sensing [8–10], and industrial applications [11]. There are two main approaches to build a wavelength-tunable source with a narrow linewidth. The first approach is "post-filtering", where a broad-band white source is used such as a super luminescent diode or a short-pulsed laser to produce a white spectrum, then it is filtered by the means of a band-pass filter of the desired narrow linewidth. The second approach is the "cavity-tuning", where the spectral filtering process occurs inside a laser's cavity. The lasing action occurs within the transmission window of the filter only. The main advantage here is that the output light usually has higher power than the previous approach because the energy lost during the filtering process is compensated by the repetitive lasing gain. Besides, the effective linewidth becomes narrower than that of the filter, due to the mode-competition in the laser at reasonable sweeping speeds of operation. However, the limitations for the laser cavity tuning are not only determined by the maximum frequency of the filter but by the time constant to build up a saturated lasing as well.

43.1.2 Principle of Operation of Swept Laser Sources

Swept laser source (SLS) is one of the most famous tunable light sources. It is a laser source which can be tuned over a wide range of wavelengths. Conventionally, SLSs are multi-longitudinal modes (MLM) lasers consisting of a gain medium, a large cavity with small free spectral range (FSR) modes, and a small cavity with wide FSR modes. The small cavity acts as a window that sets the wavelength span in which the gain exceeds the losses, thus allows the building up of a saturated lasing from the amplified spontaneous emission (ASE) of the gain medium as shown in Figure 43.1. By tuning this window, the wavelength of the output laser can be tuned. The spectral width of the output laser is defined by the envelope of the laser active modes of the large cavity.

Multi-mode lasers have shorter coherence lengths compared to single-mode lasers due to their broader spectral widths. Besides, they have higher relative intensity noise (RIN) than single-mode lasers, which limits their sweeping rates and

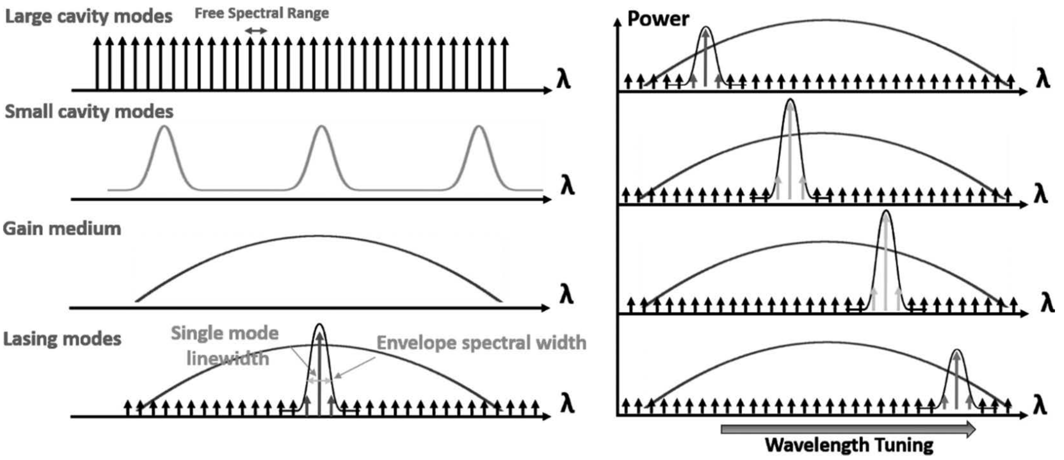
Large cavity modes
Free Spectral Range
λ
Small cavity modes
λ
Gain medium
λ
Lasing modes
Single mode linewidth
Envelope spectral width
λ
Power
λ
λ
λ
λ
Wavelength Tuning

FIGURE 43.1 Principle of operation of the SLS.

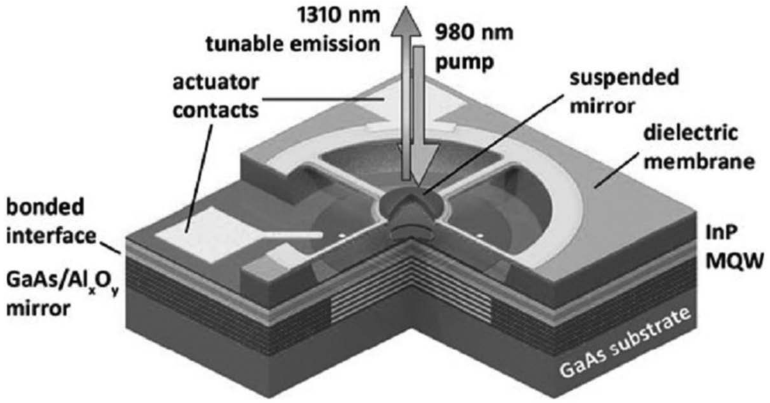
1310 nm tunable emission
980 nm pump
actuator contacts
suspended mirror
dielectric membrane
bonded interface
InP MQW
GaAs/Al$_x$O$_y$ mirror
GaAs substrate

FIGURE 43.2 3-D cutaway view of a MEMS VCSEL with optical pumping at 980 nm [16]. (Reproduced by permission of the Institution of Engineering & Technology.)

dynamic coherence lengths [12]. Swept sources based on vertical-cavity surface-emitting lasers (VCSELs) were developed for the purpose of providing single-mode swept sources, with variable repetition rates from the kHz range up to the MHz range [13–15]. It is a type of lasers based on the perpendicular emission from the top surface through a dielectric tunable mirror, contrary to the conventional in-plane side-emitting lasers. The short micron-scale of the VCSEL cavity is promising for a single-mode lasing operation and rapid build-up time. Wide-tunable lasers with wavelength tuning ranges (>100 nm) are allowed thanks to the large longitudinal mode spacing. Figure 43.2 shows a VCSEL based on a micro-electro-mechanical system (MEMS) tunable mirror with optical pumping at 980 nm [16].

43.2 Scanning Techniques

43.2.1 Wavelength Scanning

In this section, we present a review on some of the most common wavelength-scanning filters.

43.2.1.1 Grating and Polygon Mirror

One of the first developed filters was the polygon-based scanning filter. It enables a wide tuning range, a high sweep rate, and a narrow linewidth [17]. A schematic of the filter is shown in Figure 43.3. It consists of a diffraction grating, a telescope which consists of two lenses in an infinite-conjugates configuration, and a polygonal mirror scanner. The direction of wavelength tuning is determined by the beam's orientation, its angle of incidence, and the direction of rotation of the polygon mirror.

The main advantage of the polygon filter is the unidirectional scanning operation, which can be exploited for the forward scanning (towards longer wavelengths) which is advantageous over the backward scanning (towards shorter wavelengths) due to the non-linearities in the gain medium, as will be explained later in this chapter. Besides, it provides flexibility in varying the tuning speed, the resolution, the range, or the wavelength simply by controlling the rotational speed, the magnification of the telescope, or the grating angle. A drawback for this filter is the relatively bulk, moving polygonal mirror.

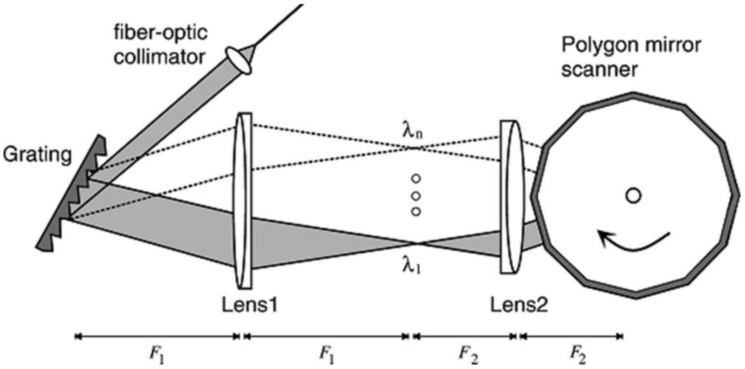

FIGURE 43.3 Schematic for the polygon-based scanning filter. (Reprinted with permission from Ref. [17]. © The Optical Society.]

43.2.1.2 Fabry–Perot Tunable Etalon

A Fabry–Perot (FP) tunable etalon is a filter constructed of a pair of mirrors of high reflectivity, separated by a distance that can be tuned as shown in Figure 43.4. A fibre-based small FP etalon enables wavelength scanning over its entire FSR, at high frequencies up to tens of kHz [18]. The main advantage of the Fabry–Perot filter is its relatively small size, while a drawback is its bidirectional tuning curve.

43.2.1.3 Acousto-optic Filter

Acousto-optic tunable filter (AOTF) is a kind of optical filters in which the wavelength tuning is electrically controlled through an applied RF signal [19]. The acousto-optic diffraction operation is demonstrated in Figure 43.5. Upon applying the RF signal, an acoustic wave is generated that modulates the refractive index, thus allowing the input light to diffract within some range of optical frequencies. Looking at the diffracted beam, one obtains a band-pass filter, while looking at the transmitted beam one obtains a band-stop filter. They are attractive because of their non-mechanical actuation and fast response time. However, currently available devices do not provide sufficiently high tuning speeds or narrow spectral widths.

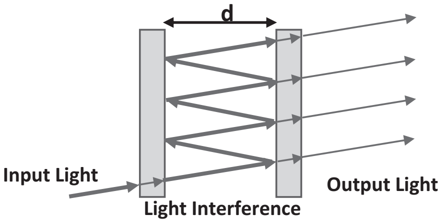

FIGURE 43.4 Fabry–Perot etalon.

43.2.1.4 Other Common Techniques

Other sweeping techniques are introduced in the literature based on using tunable filters manufactured by different technologies such as integrated optics [20], tunable liquid crystals [21,22], fibre Bragg gratings [23], out-of-plane MEMS with VCSELs [13,15,24], and in-plane silicon-on-insulator (SOI) MEMS technology [14,25]. The in-plane MEMS technology combines the advantages of self-alignment and ease of integration with single-mode (SM) fibres in a miniaturized manner with the high-speed operation of the MEMS [26,33]. Deep reactive ion etching (DRIE) of silicon technology enables the fabrication of multi-layer deeply etched mirrors with high reflectivity and wide spectral bandwidth.

43.2.2 Output Beam Position Scanning

SLS may be integrated, as well, with micro-scanners to allow the deflection of its output beam in order to form multi-dimensional images, like in OCT. MEMS is good candidate for integrable on-chip micro-scanners. Figure 43.6 shows a dual-fibre OCT probe in which the output of the SLS from

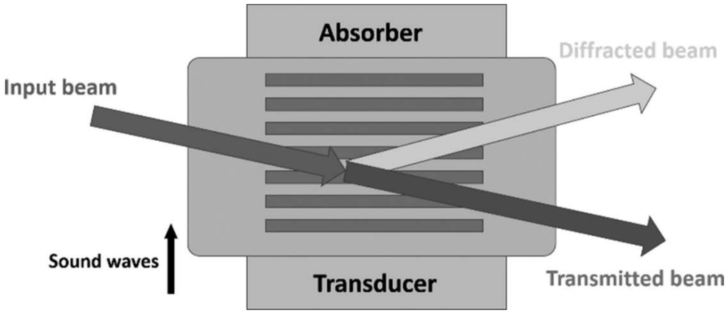

FIGURE 43.5 Schematic of the acousto-optic filter and the diffraction process.

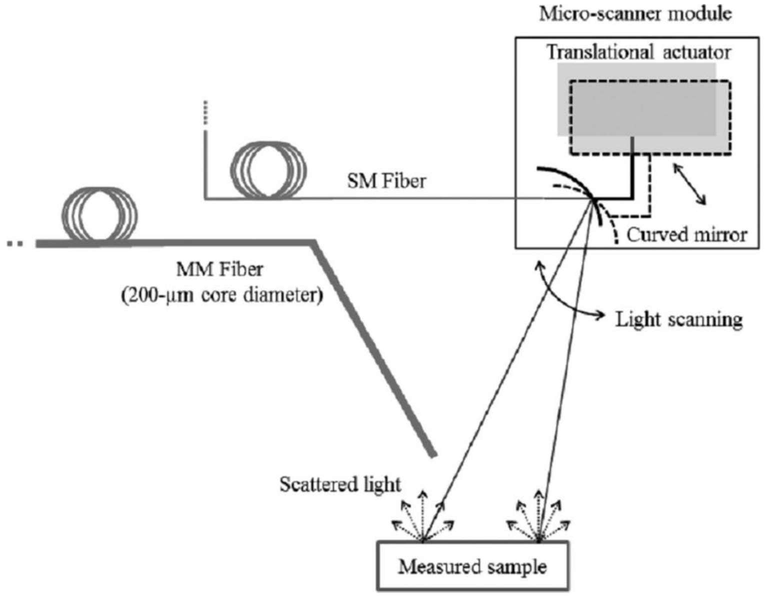

FIGURE 43.6 Dual-fibre OCT probe integrated with a curved micro-mirror 1-D MEMS scanner [27].

the SM fibre is combined with a movable curved silicon acylindrical-shaped micro-mirror [27], enabling ultra-wide angular deflection of the output beam, while the scattered light from the sample is collected by a MM fibre.

43.3 MEMS Technology

MEMS is a technology that enables the integration of micro-actuators with other micro-components to produce miniaturized systems on a single chip. Optical MEMS utilizes this technology in the fabrication of optical components, like mirrors and lenses for the production of optical systems on a silicon platform. The excellent and the well-known optical properties of silicon in the IR wavelength range, as well as the flexibility of the silicon fabrication owing to the vast spread of the CMOS fabrication process, participated in the booming of the optical MEMS technology. This technology provides light-weight, miniaturized-dimensions, high-speed, low-cost products due to the batch processing, with respect to the bulky optomechanical systems.

In this section, we present an overview on the SOI technology and the fabrication process based on DRIE technology, as well as the electrostatic comb-drive actuation mechanism on which the tunability of the optical filter (will be explained later) is based.

43.3.1 SOI and DRIE Overview

SOI stands for silicon-on-insulator technology. It is the starting material used to shape monolithic silicon micromechanical devices, shown in Figure 43.8. It consists of a silicon device layer (typically 80 μm), a buried oxide (BOX) layer (typically 3 μm), and a handle layer (typically 500 μm) that acts as the support for the whole system. The device layer is the one in which the desired micromechanical device is sculptured, while the BOX layer acts as a sacrificial layer that is removed to produce hanging structures that are free to move for the fabrication of MEMS sensors; besides, it acts as an etch-stop layer. SOI-based batch fabrication process introduces small, reliable, and lasting monolithic silicon structures.

DRIE technology is a highly anisotropic dry etching technology used for the fabrication of steep structures with a high aspect ratio (i.e. etch depth/feature width) [28]. It is widely used in fabricating deeply etched optical components, such as mirrors with good optical characteristics.

The Bosch DRIE technology is named after the German company Robert Bosch GmbH [29] who invented it. Demonstration of the process is shown in Figure 43.7a. It is a cyclic process switching between two alternate short cycles: the etching cycle in which the silicon is etched in an isotropic manner, and the passivation cycle in which the etched walls are protected during the etching step in the next cycles. A depassivation process is done at the beginning of each etching process, where ion bombardment selectively removes the passivation layer at the bottom of the trenches while keeping that on the walls. The periods of the etching and passivation cycles during the DRIE process, as well as the processing conditions, control the amplitude of the scallops, formed during the cycling process, as shown in Figure 43.7a. The main parameters that define the quality of the DRIE process, as shown in Figure 43.7b, are the scalloping amplitude (s), the verticality of the trench (β), the lateral undercut under the mask (U), the etching depth (D), the resulting trench width (W), and the resulting line critical dimension (CD).

A typical etched structure using the DRIE Bosch process with a scalloping depth of 160 nm and undercut of 0.3 μm is shown in Figure 43.7c.

SOI-based DRIE fabrication process steps, as shown in Figure 43.8, are:

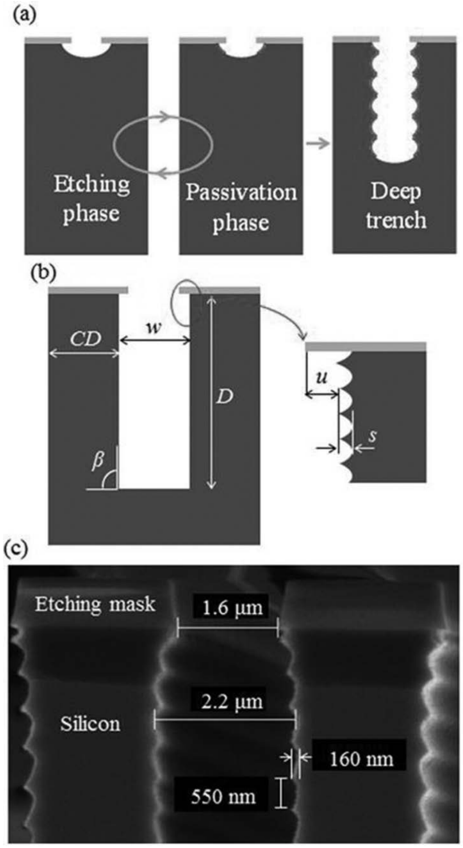
(a)
Etching phase
Passivation phase
Deep trench
(b)
CD
w
D
β
u
s
(c)
Etching mask
1.6 μm
Silicon
2.2 μm
160 nm
550 nm

FIGURE 43.7 (a) Demonstration for the DRIE Bosch process. (b) DRIE profile parameters. (c) Scanning electron microscope (SEM) image for a typical etched structure using DRIE Bosch process [28].

1. Forming a hard mask from Al or SiO_2 for DRIE through sputtering.
2. Spanning a resist material over the hard-mask layer and then pattering it.
3. Transferring the pattern on the resist material to the hard mask through dry etching, then etching the silicon of the device layer by means of DRIE.
4. Performing a post-processing step for sidewall smoothing.
5. Removing the BOX layer under the movable structures such as moving mirrors, springs, and comb fingers to release them.
6. Selective metallization of the micro-mirrors and creating electrical connection pads using the shadow mask, which protects the other surfaces (as beam splitters) from metallization.

43.3.2 Comb-drive Actuator

The micro-comb actuators were first introduced by Tang [30]. These actuators are usually used with MEMS due to their reliable operation and simple construction. They provide reasonable displacements up to 100 μm, while the driving forces are small and insufficient to drive huge loads. Thus, they are suitable for micro-opto-electro-mechanical system applications.

Figure 43.9a shows the schematic of the comb-drive actuator. It consists of two interleaved fingers sets: a fixed set (stator) and a movable set (rotor). When a voltage is applied across the two sets, an electrostatic attraction force is developed between them, thus moving the movable set towards the fixed one.

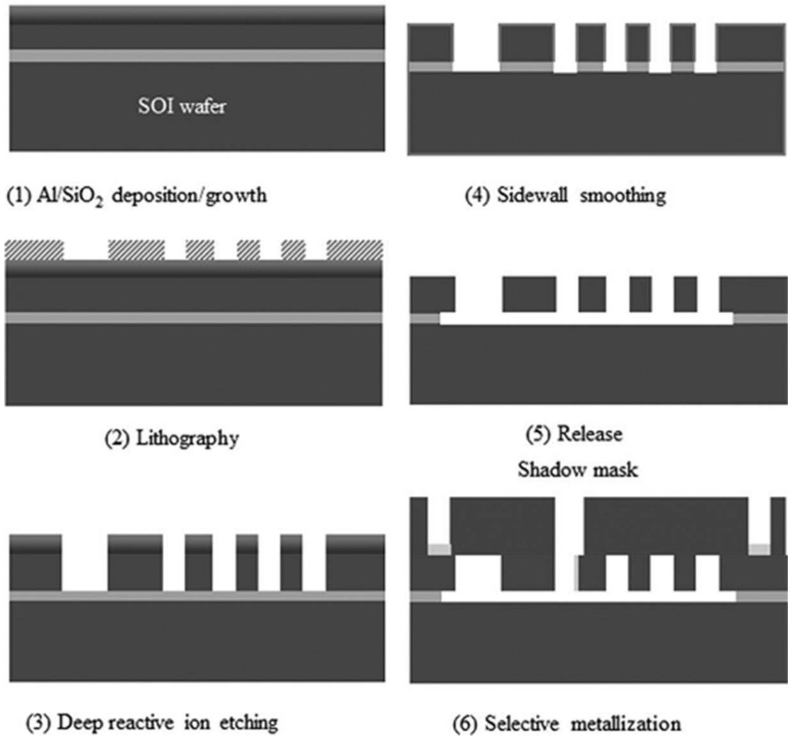
SOI wafer
(1) Al/SiO2 deposition/growth
(2) Lithography
(3) Deep reactive ion etching
(4) Sidewall smoothing
(5) Release
Shadow mask
(6) Selective metallization

FIGURE 43.8 SOI-based micro-optical bench fabrication steps [28].

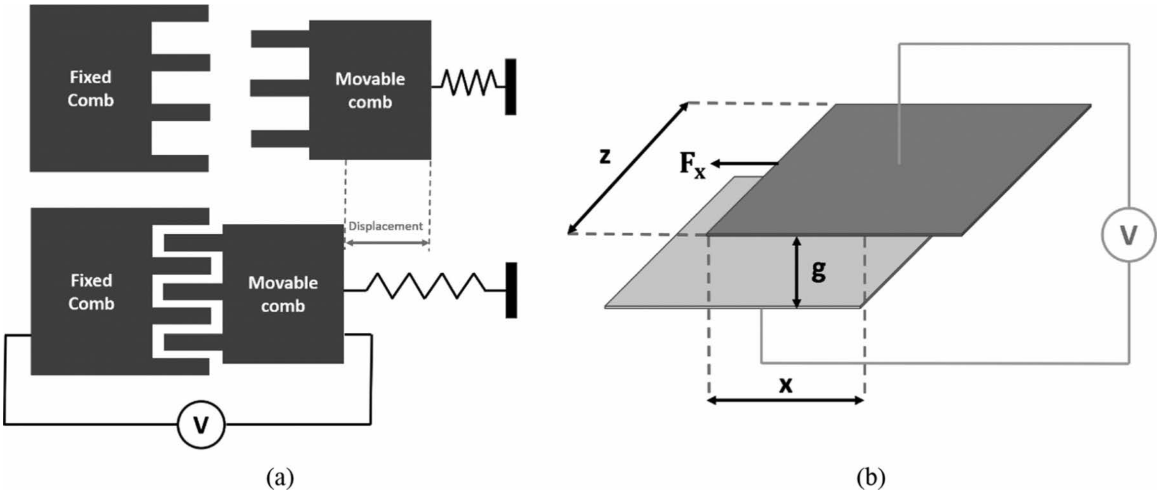

FIGURE 43.9 (a) Schematic of the comb-drive actuator. (b) Transverse force developed in parallel plate capacitor.

The rotor is attached to a spring to apply a mechanical force that balances the developed electrostatic force, and thus reaching an equilibrium state. A ground plate is placed below the combs which are normally connected to the rotor to eliminate the electrostatic pulling-down forces of the rotor towards the substrate.

For a parallel plate capacitor, shown in Figure 43.9b, the energy stored in the capacitor is given by:

$$E = \frac{1}{2} C V^2 \tag{43.1}$$

where V is the applied voltage across the plates of the capacitor, and C is the capacitance, which is given by:

$$C = \varepsilon \frac{zx}{g} \tag{43.2}$$

where x and z are the overlap length and the widths of the plates, respectively; g is the gap between the two plates; and ε is the permittivity of the dielectric material between the plates.

A lateral electrostatic force (F_x) is developed in the capacitor that tends to align the plates, and it is given by:

$$F_x = \frac{V^2}{2} \frac{\partial C}{\partial x} = \varepsilon \frac{z V^2}{2g} \tag{43.3}$$

For a comb drive with N fingers, a height of t, and a gap of g between every two fingers, then the total developed force is given by:

$$F_{\text{comb}} = N \frac{\varepsilon t}{g} V^2 \tag{43.4}$$

43.4 MEMS-based Swept Fibre-ring Laser Source

In this section, we will present one of the most common configurations of the swept source, the ring laser source with a tunable optical band-pass filter. The system of the ring SLS is shown in Figure 43.10. It consists of a single-mode (SM) fibre-ring loop, a semiconductor optical amplifier (SOA) as a gain medium, a MEMS tunable Fabry–Perot filter to tune the swept laser wavelength, a tap directional coupler to couple power out of the loop, an isolator to allow a unidirectional operation of the laser, and a fibre polarization controller to control the polarization state inside the fibre loop.

43.4.1 MEMS Filter with Bragg Mirrors

In this section, we present the MEMS optical band-pass filter. It is a Fabry–Perot filter, constructed from deeply etched 80 μm height multi-layer Bragg mirrors as shown in Figure 43.11a. The deep Bragg layers are fabricated by DRIE of SOI wafer. The Bragg mirrors allow high reflectivity (>96%) over a wide spectral bandwidth (>220 nm) [28,31–33]. The filter consists of two mirrors: one is fixed, while the other is free to move. The free-to-move mirror is attached to an electrostatic comb-drive actuator, consisting of a fixed and a movable combs. By applying a voltage across the two combs, an electrostatic force is developed between the two sides, leading to the attraction of the movable comb towards the fixed one, thus tuning the air gap between the two mirrors, and hence the peak-transmission wavelength of the filter. Figure 43.11b shows a scanning electron microscope (SEM) image for the MEMS filter. The filter is fed through two cleaved SM fibres: one is placed at the side of the fixed mirror, while the other is placed at the side of the movable mirror.

43.4.1.1 The Performance of the MEMS Filter

The in-plane MEMS SOI technology allows the fabrication of high-performance, reliable filters with acceptable finesse for SLS applications and a wide tuning range. Figure 43.12 shows the performance of a MEMS filter with Bragg mirrors, as introduced by Omran et al. [26,33,40]. The 3-dB bandwidth of the Bragg mirrors is shown in Figure 43.12a for both cases; the measurement (red line) and the simulation (blue line), where

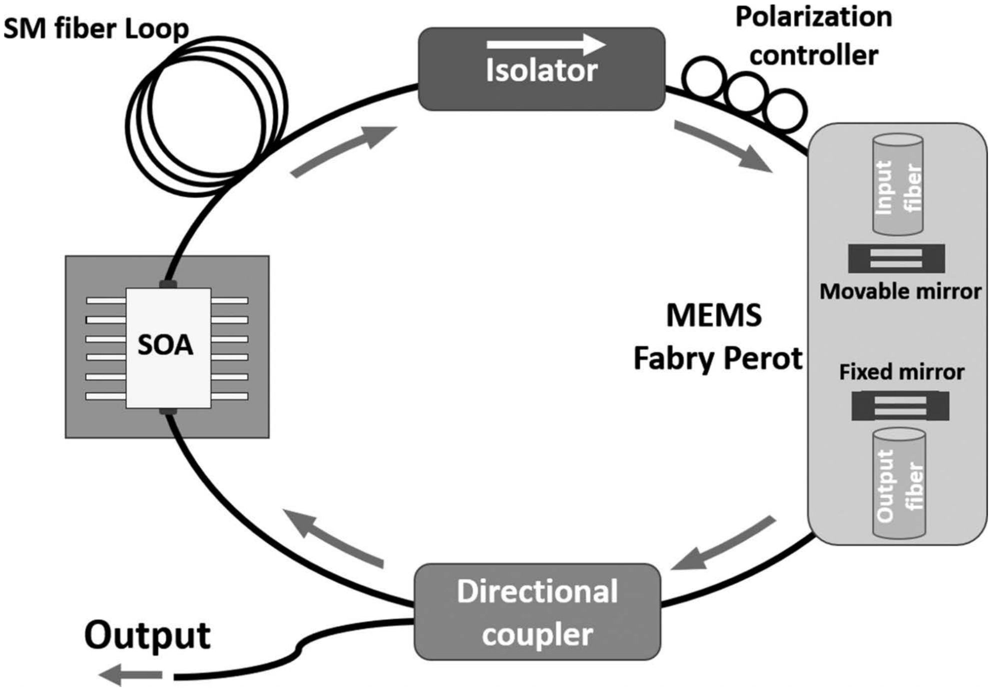
SM fiber Loop
Isolator
Polarization controller
Input fiber
Movable mirror
MEMS Fabry Perot
Fixed mirror
Output fiber
SOA
Directional coupler
Output

FIGURE 43.10 The MEMS-based ring swept laser source system.

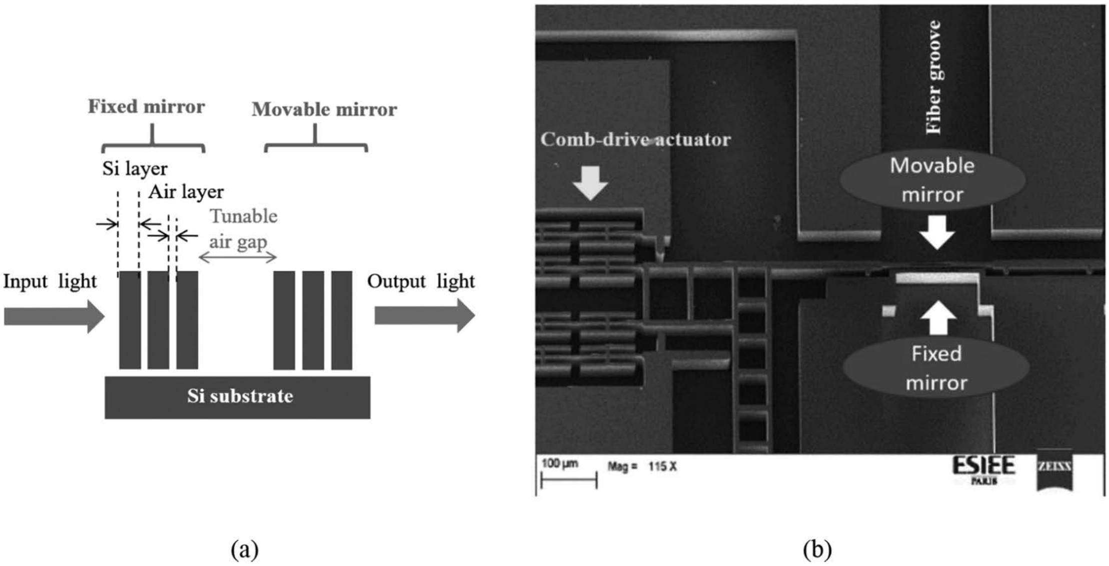
Fixed mirror
Movable mirror
Si layer
Air layer
Tunable air gap
Input light
Output light
Si substrate
Fiber groove
Comb-drive actuator
Movable mirror
Fixed mirror
100 μm
Mag = 115 X
ESIEE PARIS
ZEISS

(a) (b)

FIGURE 43.11 (a) Schematic for the MEMS filter with Bragg mirrors. (b) An SEM photo for the MEMS filter.

a measured 3-dB bandwidth of up to 230 nm was reported. Figure 43.12b shows the filter response at different applied dc voltages, where a tuning range of up to 125 nm was reported as well. The filter has a minimum full width at half maximum (FWHM) of about 4 nm.

43.4.1.2 The Performance Enhancement Using Lensed Fibres

One of the main challenges that faces the hybrid MEMS-fibre filter is the beam divergence of light during the free space propagation between the input and the output fibres. This results in a high insertion loss (IL) of the filter due to the coupling losses between the two fibres. Besides, the divergences of the beam during multiple reflections between the mirrors result in the degradation of the finesse of the filter. Different solutions were suggested to enhance the performance of the filter. Some of them depend on using curved mirrors to collimate the propagating beam between the two mirrors [34,35]. Other techniques depend on using lensed fibres with the MEMS filter, to increase the output beam waist of the fibre, in order to decrease its divergence. Here, we will present a

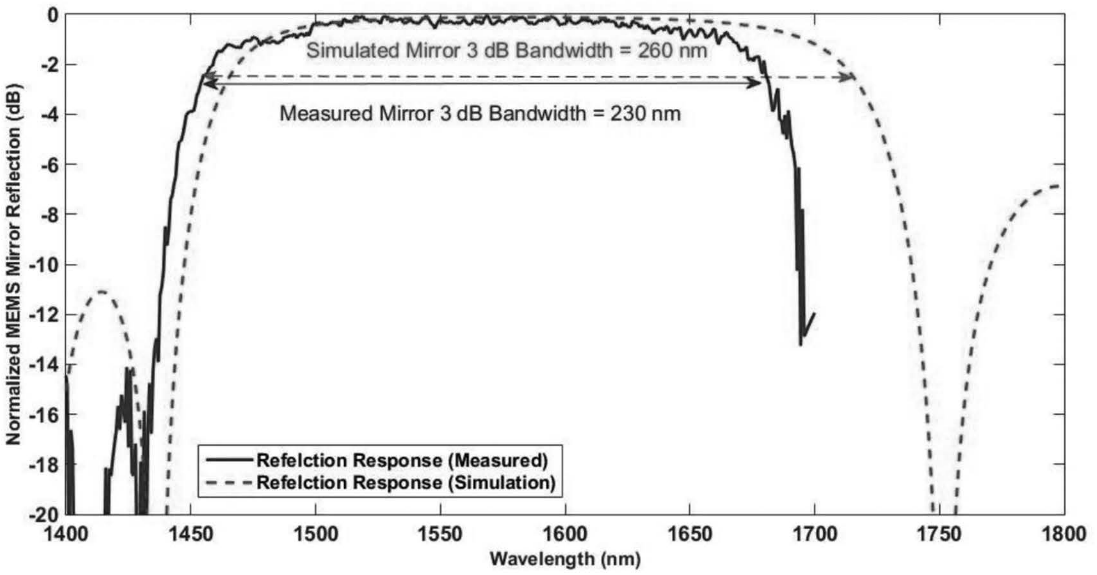

(a)

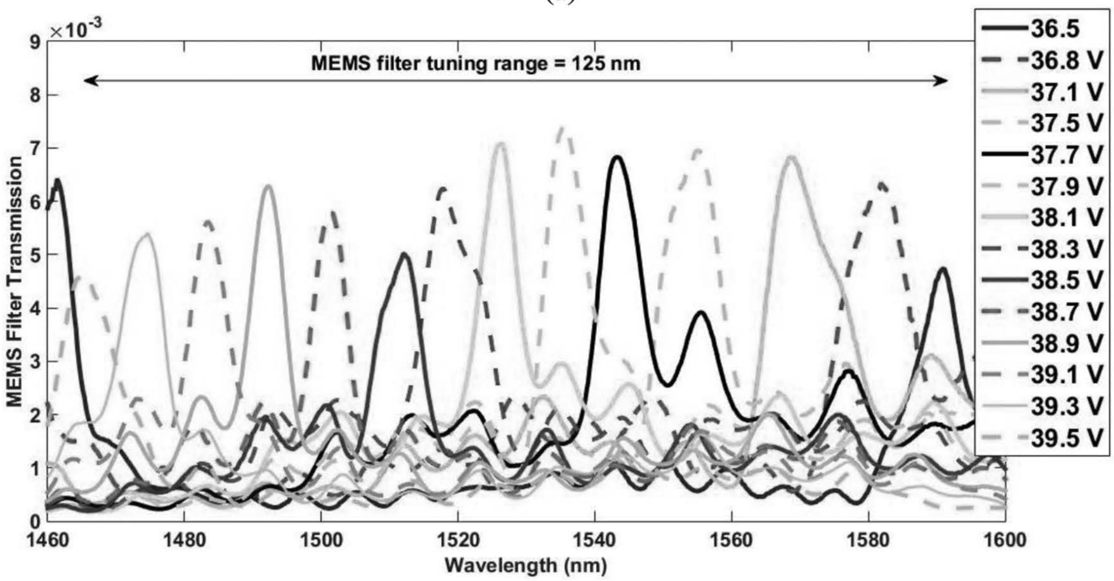

(b)

FIGURE 43.12 (a) The measured (red line) and simulation (blue line) 3-dB bandwidth of the Bragg mirror. (b) The response of the MEMS filter at different applied dc voltages.

comparison between the MEMS filter response using cleaved SM fibres and lensed fibres. The lensed fibres are fabricated using graded-index (GRIN) multi-mode (MM) fibre sections spliced at the tip of the SM fibres [36]. An increase in the output beam waist of the lensed fibre of up to 11.8 μm was reported, compared to the 5 μm waist of the cleaved SM fibre. Then, the MEMS filter is fed by the lensed fibres, and its performance is compared with that in the case of the cleaved SM fibres. Figure 43.13 depicts the comparison between the two cases where an enhancement of up to 5.1 dB in the IL was reported in Figure 43.13a, and a decrease in the FWHM from 9 to 5 nm was reported in Figure 43.13b. A decrease in the threshold current of the swept source was also reported, accompanied by an increase in the output power on using the lensed fibres with the MEMS filter as a result of the reduced filter IL. Figure 43.14 depicts the peak output power of the MEMS-based SLS for the two fibres' cases at a pumping current of 200 mA, showing a maximum increase of 7.5 dB in the output power when applying the lensed fibres.

43.4.2 MEMS-based Swept Laser Source System

In this section, we present the performance of the fibre-ring laser source comprising the in-plane MEMS filter.

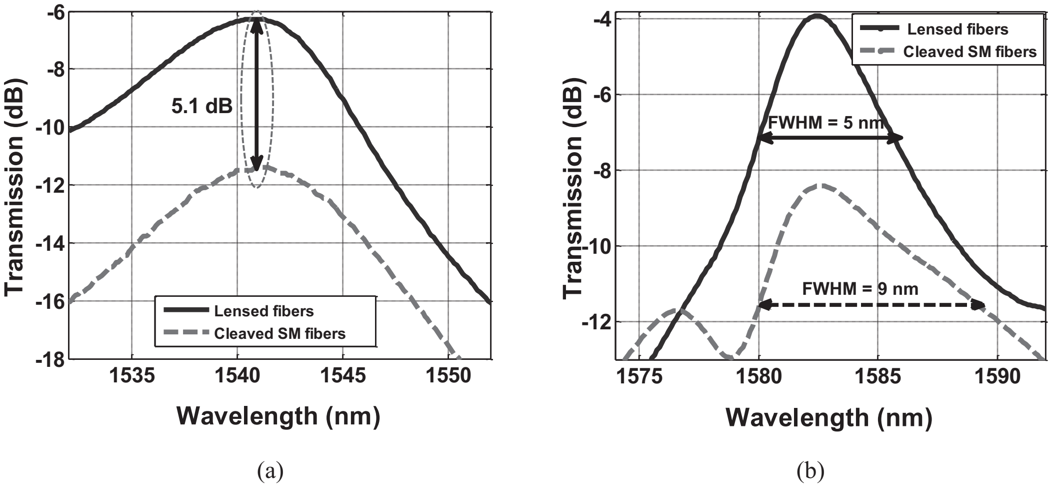

(a) (b)

FIGURE 43.13 Comparison between the filter response on using with cleaved SM fibres (dashed-green curves) versus the lensed fibres (solid-brown curves). (a) Maximum IL enhancement. (b) Maximum FWHM enhancement.

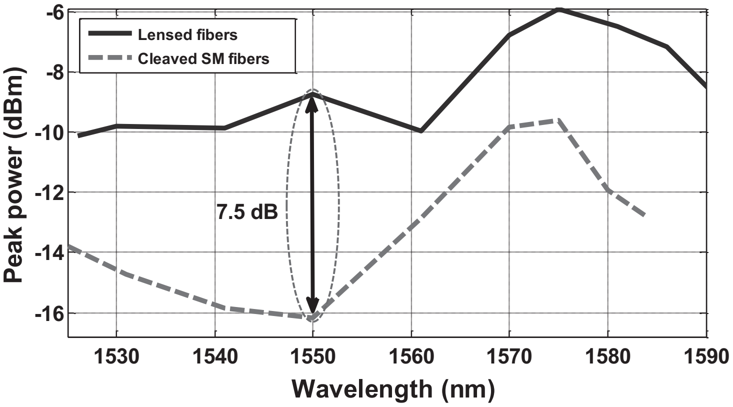

FIGURE 43.14 Comparison between the peak output power of the SLS on using cleaved SM fibres (dashed green curves) versus the lensed fibres (solid brown curves) at a pumping current = 200 mA.

A wide tuning range of up to 100 nm was reported [26,33] for the SLS as shown in Figure 43.15. The best recorded 3-dB linewidth for the laser source was 0.13 nm [33], as shown in Figure 43.16, which is about 30 times narrower than the 4 nm spectral width of the filter. The narrowing of the laser output with respect to the MEMS filter is due to the lasing action which results from the positive feedback and the mode-competition [37].

43.4.3 The Dynamic Behaviour of the Swept Laser Source

In this section, we explore the dynamic behaviour of the SLS based on an SOA gain medium during the sweep of the filter. The SOA tends to downshift the energy towards the lower frequencies, leading to a hysteresis in the performance of the SLS during sweeping in the different directions [18]. This hysteresis is demonstrated in Figure 43.17 for the forward scanning (traveling towards longer wavelengths) and the backward scanning (traveling towards shorter wavelengths) of the filter. For an SLS with a filter peak at λ_0 (the dark-gray one), a red shifting of the optical signal occurs after passing by the gain medium, thus the lasing action occurs at a longer wavelength than λ_0. For a sweeping filter, the photons will experience higher transmission through the filter in case of the forward scanning (the red one) than that in case of the backward scanning (the blue one) after a round trip. Thus, the power will favour the sweep towards longer wavelengths than that towards shorter wavelengths because the forward scanning is in line with the red shifting.

The characterization of the SLS while sweeping is very important as the performance of the sensing and the imaging applications depends on the instantaneous output power and the linewidth of the laser [37–39]. Conventional optical spectrum analysers (OSAs) may not be suitable for capturing the spectrum of high-speed swept sources (with sweep rates of tens of kHz). The SLS characterization is done by means of a simple method introduced in Ref. [38], as demonstrated in Figure 43.18. It is based on sampling the sweeping unknown spectrum of the SLS by a narrow filter gate with a reference response, then detecting the output on an oscilloscope. The unknown spectrum can be computed from the output signal

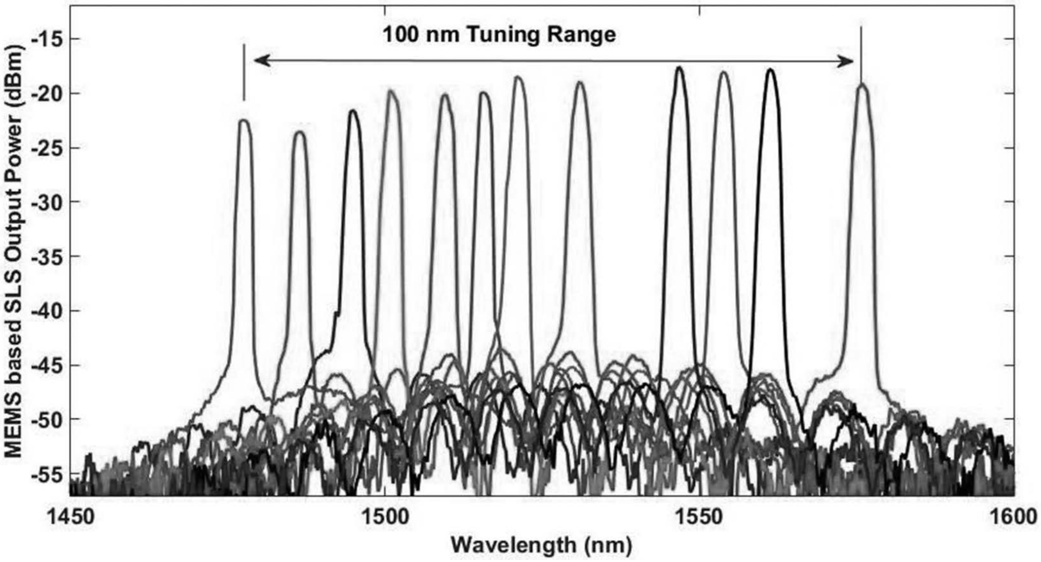

FIGURE 43.15 The measured tuning range of the MEMS-based SLS.

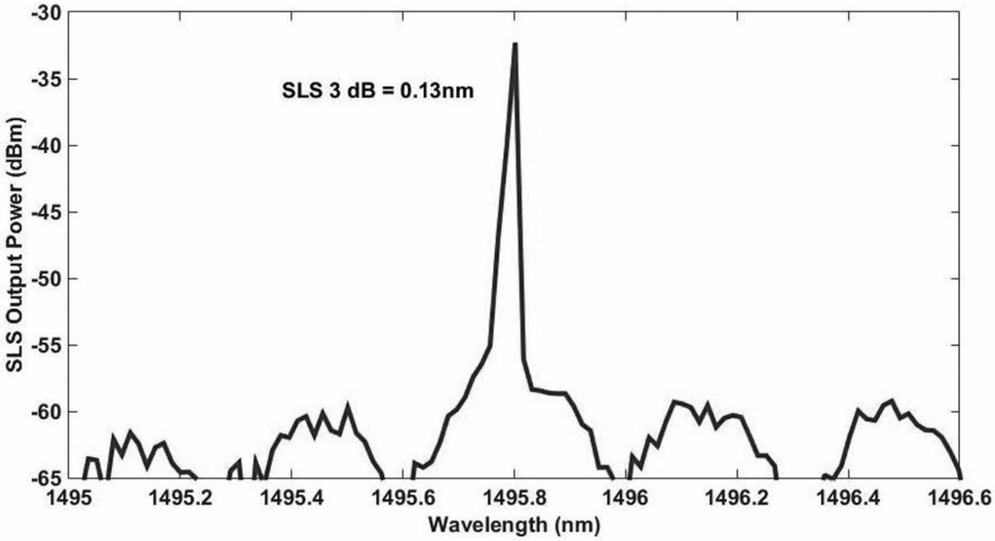

FIGURE 43.16 The measured 3-dB spectral linewidth of the MEMS-based SLS.

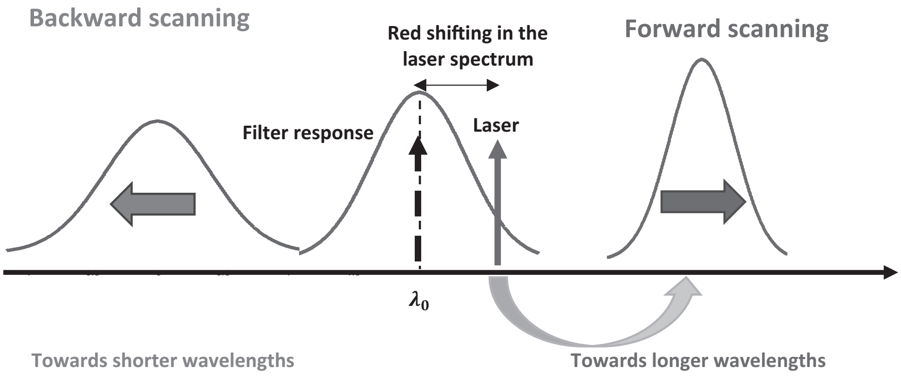
Backward scanning
Red shifting in the laser spectrum
Forward scanning
Filter response
Laser
λ_0
Towards shorter wavelengths
Towards longer wavelengths

FIGURE 43.17 Demonstration of the effect of the red shifting due to the gain medium on the spectrum of the swept source during sweeping in the forward (shown in red) and the backward (shown in blue) directions.

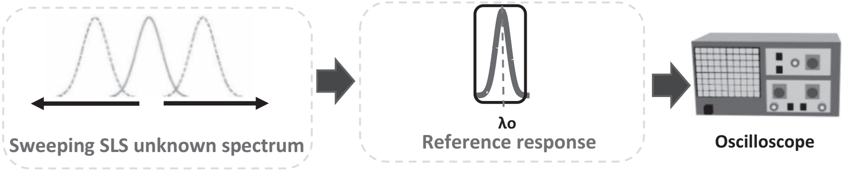

FIGURE 43.18 Demonstration of the characterization method which is used to extract the instantaneous spectrum of the high-speed SLS.

detected on the oscilloscope by deconvoluting the output signal by the reference filter response.

The dynamic peak power variation with the pumping current is depicted in Figure 43.19 for both the forward scanning (red solid line) and the backward scanning (blue dashed line) around $\lambda = 1560$ nm, for an SLS with a fibre loop length of 20 m and a sweep rate of 1 kHz. The output power is higher for the forward scanning than that for the backward scanning, and the gap between them increases with increasing the pumping current due to the increase in gain non-linearity at higher currents.

The variation of the output spectral width of the SLS with the scanning speed is depicted in Figure 43.20 for the forward scanning (red solid line) and the backward scanning (blue dashed line) directions around $\lambda = 1570$ nm, for an SLS with a fibre loop length of 80 m and a pumping current of 300 mA. Figure 43.20a shows the relative peak power versus the scanning speed, where it is higher for the forward scanning than the backward scanning, and the power for both cases decreases with increasing the scanning speed. Figure 43.20b shows the laser 3-dB spectral width versus the scanning speed, where it is broader for the backward scanning than the forward scanning, and the spectral width for both cases increases with increasing the scanning speed. The deterioration of the SLS performance at higher scanning speeds is due to the decrease of the sweeping period compared to the required time to build up a saturated lasing action [18,37].

The variation of the output spectrum of the SLS with the fibre loop length is depicted in Figure 43.21 for both the forward scanning (red solid line) and the backward scanning (blue dashed line) around $\lambda = 1570$ nm, for an SLS at a pumping current of 300 mA and a sweep rate of 1 kHz. Figure 43.21a shows the relative peak power versus the

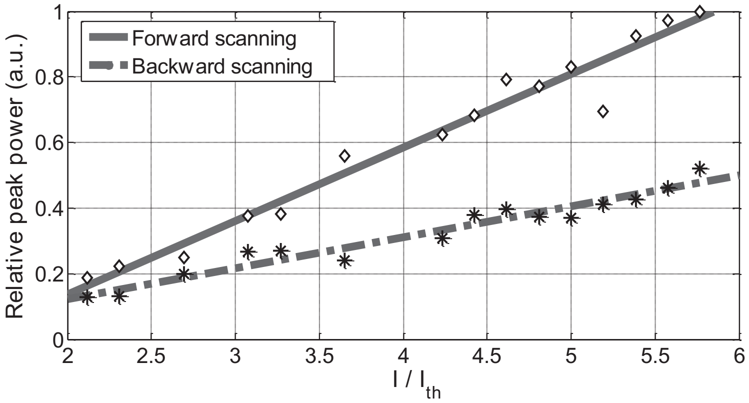

FIGURE 43.19 Dynamic I-P characteristics of the SLS for the forward scanning (red solid line) and the backward scanning (blue dashed line).

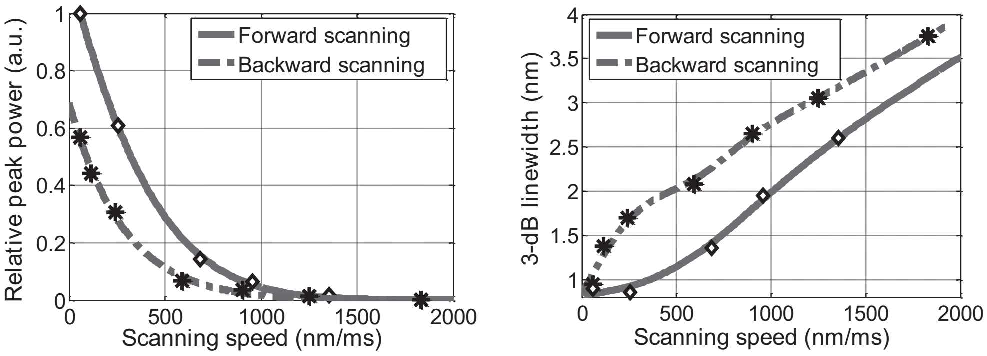

(a) (b)

FIGURE 43.20 The variation of the SLS output spectrum with the scanning speed for the forward scanning (red solid line) and the backward scanning (blue dashed line). (a) Relative peak power versus scanning speed. (b) 3-dB linewidth versus scanning speed.

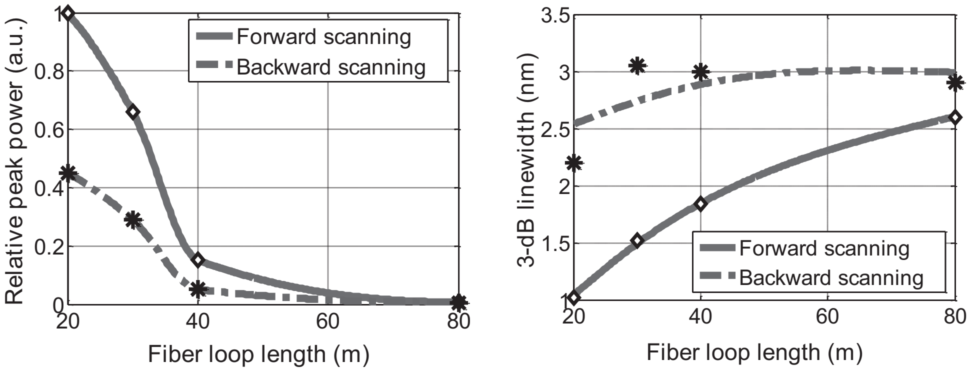

(a)

(b)

FIGURE 43.21 The variation of the SLS output spectrum with the fibre loop length for the forward scanning (red solid line) and the backward scanning (blue dashed line). (a) Relative peak power versus the fibre loop length. (b) 3-dB linewidth versus the fibre loop length.

fibre loop length, where the power decreases with increasing the fibre loop length. Figure 43.21b shows the laser 3-dB linewidth versus the fibre loop length, where the linewidth increases with increasing the fibre loop length. The deterioration of the performance at longer loop lengths is due to the increase of the roundtrip period, and consequently the swept laser building up time.

43.5 Summary

In this chapter, we presented an overview on the MEMS-based SLS. First, we reviewed the wavelength-tunable light sources and their classification; besides, we reviewed the most common sweeping techniques. Then, we gave a quick review on the MEMS technology, by reviewing the SOI and DRIE technologies, as well as the comb-drive actuation. Finally, we presented the MEMS-based SLS system based on the fibre-ring configuration. We began by introducing the MEMS tunable Fabry–Perot filter, showing the best reported performance, as well as the suggested techniques to overcome the drawbacks of the beam divergence. Then, we introduced the MEMS SLS system, showing the best reported performance. We terminated by discussing the dynamic performance of the SLS, revealing the hysteresis during sweeping in the different directions, as well as the variations in the spectrum with the pumping current, the scanning speed, and the fibre loop length.

REFERENCES

1. S. R. Chinn, E. A. Swanson, and J. G. Fujimoto, “Optical coherence tomography using a frequency-tunable optical source,” *Opt. Lett.*, vol. 22, no. 5, pp. 340–342, 1997.
2. M. A. Choma, M. V Sarunic, C. Yang, and J. A. Izatt, “Sensitivity advantage of swept source and Fourier domain optical coherence tomography,” *Opt. Express*, vol. 11, no. 18, pp. 2183–2189, 2003.
3. S. H. Yun, G. J. Tearney, J. F. de Boer, N. Iftimia, and B. E. Bouma, “High-speed optical frequency-domain imaging,” *Opt. Express*, vol. 11, no. 22, pp. 2953–2963, 2003.
4. L. A. Kranendonk et al., “High speed engine gas thermometry by Fourier-domain mode-locked laser absorption spectroscopy,” *Opt. Express*, vol. 15, no. 23, pp. 15115–15128, 2007.
5. J. O. Gerguis, Y. M. Sabry, H. Omran, and D. A. Khalil, “Spectroscopic Gas Sensing Based on a MEMS-SOA Swept Fiber Laser Source,” *J. Light. Technol.*, vol. 37, no. 20, pp. 5354–5360, 2019.
6. M. A. Selim, Y. M. Sabry, G. A. Adib, and D. Khalil, “Active fiber-ring enhanced absorption gas spectroscopy using multi-longitudinal mode tunable laser in the NIR,” *Proc.SPIE*, vol. 10925, 2019.
7. M. A. Selim, G. A. Adib, Y. M. Sabry, and D. Khalil, “Incoherent gain-assisted ring enhanced gas absorption spectroscopy,” *IEEE J. Quantum Electron.*, vol. 55, no. 1, pp. 1–8, 2019.
8. E. J. Jung et al., “Characterization of FBG sensor interrogation based on a FDML wavelength swept laser,” *Opt. Express*, vol. 16, no. 21, pp. 16552–16560, 2008.
9. Y. Nakazaki and S. Yamashita, “Fast and wide tuning range wavelength-swept fiber laser based on dispersion tuning and its application to dynamic FBG sensing,” *Opt. Express*, vol. 17, no. 10, pp. 8310–8318, 2009.
10. M. Y. Jeon, J. W. Park, and M. O. Ko, “Wavelength-swept laser based on semiconductor optical amplifier for dynamic optical fiber sensors,” in 2016 *International Conference Laser Optics (LO)*, 2016, pp. R3-29.
11. G. Song and K. Harding, “OCT for industrial applications,” 2012, vol. 8563, p. 85630N–8563-10.
12. W. Drexler and J. G. Fujimoto, Optical Coherence Tomography. 2015.
13. T. Ansbæk, I. Chung, E. S. Semenova, O. Hansen, and K. Yvind, “Resonant MEMS Tunable VCSEL,” *IEEE J. Sel. Top. Quantum Electron.*, vol. 19, no. 4, p. 1702306, 2013.
14. V. Jayaraman et al., “Rapidly swept, ultra-widely-tunable 1060 nm MEMS-VCSELs,” *Electron. Lett.*, vol. 48, no. 21, pp. 1331–1333, 2012.
15. G. D. Cole, E. Behymer, T. C. Bond, and L. L. Goddard, “Short-wavelength MEMS-tunable VCSELs,” *Opt. Express*, vol. 16, no. 20, pp. 16093–16103, 2008.
16. V. Jayaraman, G. D. Cole, M. Robertson, A. Uddin, and A. Cable, “High-sweep-rate 1310 nm MEMS-VCSEL with 150 nm continuous tuning range,” *Electron. Lett.*, vol. 48, no. 14, pp. 867–869, Jul. 2012.

17. S. H. Yun, C. Boudoux, G. J. Tearney, and B. E. Bouma, “High-speed wavelength-swept semiconductor laser with a polygon-scanner-based wavelength filter,” *Opt. Lett.*, vol. 28, no. 20, p. 1981, 2003.
18. R. Huber, M. Wojtkowski, K. Taira, J. Fujimoto, and K. Hsu, “Amplified, frequency swept lasers for frequency domain reflectometry and OCT imaging: design and scaling principles.,” *Opt. Express*, vol. 13, no. 9, pp. 3513–3528, 2005.
19. P. F. Wysocki, M. J. F. Digonnet, and B. Y. Kim, “Broad-spectrum, wavelength-swept, erbium-doped fiber laser at 1.55 μm,” *Opt. Lett.*, vol. 15, no. 16, pp. 879–881, 1990.
20. K. Chen, F. Duan, and Y. Yu, “High-performance thermo-optic tunable grating filters based on laterally supported suspended silicon ridge waveguide,” *Opt. Express*, vol. 26, no. 15, pp. 19479–19488, 2018.
21. A. Sneh, K. M. Johnson, and J. Liu, “High-speed wavelength tunable liquid crystal filter,” *IEEE Photonics Technol. Lett.*, vol. I, no. 4, pp. 13–15, 1995.
22. C. A. S. Toltzfus, R. U. B. Arbour, and D. A. A. Therton, “Micro-sized tunable liquid crystal optical filters,” *Opt. Lett.*, vol. 42, no. 11, pp. 2090–2093, 2017.
23. A. Iocco et al., “Bragg grating fast tunable filter for wavelength division multiplexing,” *J. Light. Technol.*, vol. 17, no. 7, pp. 1217–1221, 1999.
24. T. Gruendl et al., “50 nm continuously tunable MEMS VCSEL devices with surface micromachining operating at 1.95 μm emission wavelength,” *Semicond. Sci. Technol.*, vol. 28, no. 1, p. 12001, 2013.
25. Y. M. Sabry, Y. M. Eltagoury, A. Shebl, M. Soliman, M. Sadek, and D. Khlail, “In-plane deeply-etched optical MEMS notch filter with high-speed tunability,” *J. Opt.*, vol. 17, no. 12, p. 125703, 2015.
26. H. Omran, Y. M. Sabry, M. Sadek, K. Hassan, M. Y. Shalaby, and D. Khalil, “Deeply-etched optical MEMS tunable filter for swept laser source applications,” *IEEE Photonics Technol. Lett.*, vol. 26, no. 1, pp. 37–39, 2014.
27. A. Elhady, Y. M. Sabry, M. Yehia, and D. Khalil, “Dual-fiber OCT measurements,” *Proc. SPIE*, vol. 8934, 2014.
28. Y. M. Sabry, D. Khalil, and T. Bourouina, “Monolithic silicon-micromachined free-space optical interferometers onchip,” *Laser Photonics Rev.*, vol. 24, no. 1, pp. 1–24, 2015.
29. F. Laermer and A. Schilp, “Method of anisotropically etching silicon,” US5501893A, 1996.
30. W. Tang, T.-C. H. Nguyen, and R. T. Howe, Laterally driven polysilicon resonant microstructures, vol. 20. 1989.
31. H. Omran, Y. M. Sabry, K. Hassan, and D. Khalil, “Deeply-etched 1 micron-thick silicon layers enabling 170-NM bandwidth highly-reflective Bragg mirrors,” in 2014 International Conference on *Optical MEMS and Nanophotonics*, 2014, pp. 137–138.
32. M. N. Ali, Y. M. Sabry, F. Marty, T. Bourouina, K. A. Kirah, and D. Khalil, “In-plane coupled Fabry-Perot micro-cavities based on Si-air Bragg mirrors: a theoretical and practical study,” *Appl. Opt.*, vol. 57, no. 18, pp. 5112–5120, Jun. 2018.
33. H. Omran, Y. M. Sabry, M. Sadek, K. Hassan, and D. Khalil, “Wideband subwavelength deeply etched multilayer silicon mirrors for tunable optical filters and SS-OCT applications,” *IEEE J. Sel. Top. Quantum Electron.*, vol. 21, no. 4, pp. 157–164, 2015.
34. Y. Sabry, D. Khalil, B. Saadany, and T. Bourouina, “In-plane optical beam collimation using a three-dimensional curved MEMS mirror,” *Micromachines*, vol. 8, p. 134, Apr. 2017.
35. Y. M. Sabry, D. A. M. Khalil, B. A. Saadany, and T. E. Bourouina, “Aspherical optical surfaces and optical scanners,” U.S. Patent 9,158,109, issued October 13, 2015.
36. J. O. Gerguis, Y. M. Sabry, A. M. Hassanen, H. Omran, and D. Khalil, “MEMS swept laser source with enhanced performance,” in Proc.SPIE - MOEMS and Miniaturized Systems XVIII, 2019, vol. 10931.
37. H. Omran and D. Khalil, “Accessing rapidly scanning swept laser source instantaneous spectral width using a multimode rate equation model,” *IEEE J. Sel. Top. Quantum Electron.*, vol. 21, no. 6, pp. 714–721, 2015.
38. J. O. Gerguis, Y. M. Sabry, and D. A. Khalil, “Capturing the Instantaneous Spectral Response of a MEMS Swept Laser Source Using a Quasi-Static Tunable Filter,” *IEEE J. Sel. Top. Quantum Electron.*, vol. 25, no. 6, p. 1, 2019.
39. H. Omran and D. Khalil, “Parameter Extraction of Wide Band SOA Targeting Rapidly Swept Source Sensing Applications,” in Imaging and Applied Optics 2016, OSA technical Digest (online) (Optical Society of America, 2016), paper JW1F.5.
40. Haitham Omran, Yasser M. Sabry, Mohamed Sadek, Khaled Hassan, Mohamed Y. Shalaby, Diaa Khalil, “MEMS optical tunable filter based on free-standing subwavelength silicon layers,” Proc. SPIE 8977, MOEMS and Miniaturized Systems XIII, 89770V (7 March 2014); https://doi.org/10.1117/12.2040767

Taylor & Francis
Taylor & Francis Group
http://taylorandfrancis.com

44

Dye Lasers: Section Introduction

Colin Webb

Before the advancement of broadband and tunable solid-state lasers, the workhorse tunable laser, available in both cw and pulsed forms, has been the liquid dye laser. The dye laser does not convert electrical power directly into laser radiation but relies on radiation from a fixed wavelength laser or a flashtube for excitation. Though reviled by many for the messiness involved in making up and replacing the dye solution, the fact that the thermally perturbed laser medium is bodily transported out of the lasing region to be replaced by optically uniform, cool medium means that the power-handling capability of the dye laser can be scaled up to several kW of average power. Dye lasers of different types have been available to cover the spectral region from near UV through the visible to the near infrared, and the ability of a single dye-pump laser combination to tune across a spectral region 40–100 nm wide enabled them to gain an early hold as the laser of choice for many physical chemistry laboratories. Today, dye lasers have been practically replaced by various forms of tunable solid-state laser (such as Ti:sapphire) whose fundamental, harmonically and parametrically generated tunable ranges cover most the same spectral region.

The idea of encapsulating the dye medium in a solid host (plastic or porous glass), which is clean to handle and does not require the circulating pump and plumbing associated with liquid dye systems, is attractive from several points of view. True, the inability of the solid-state hosts to dissipate heat does tend to limit both the repetition rate capability and useful lifetime of such devices compared to their liquid dye counterparts. However, there are particular applications in which these features are not overwhelming considerations, and for which the solid-state dye laser provides a simple low-cost answer.

Taylor & Francis
Taylor & Francis Group
http://taylorandfrancis.com

45

Liquid Lasers

David H. Titterton

CONTENTS

45.1 Introduction ... 601
45.2 General Characteristics ... 602
  45.2.1 Gain Medium ... 602
  45.2.2 Pumping Options ... 603
  45.2.3 Dye Solutions ... 604
  45.2.4 Spectral Control ... 604
  45.2.5 Control of ASE ... 606
  45.2.6 Temporal Control ... 606
  45.2.7 Flashlamp-Pumped Devices ... 607
  45.2.8 Laser Head ... 608
  45.2.9 Dye Cell Configuration ... 609
  45.2.10 Multicolour Operation ... 611
  45.2.11 Laser-Resonator Design ... 611
  45.2.12 Other Beam-quality Enhancement Techniques ... 613
  45.2.13 Flashlamp-pumped Laser Performance ... 614
  45.2.14 Safe Operation ... 614
45.3 Dye-Lasers Pumped by Pulsed Lasers ... 615
  45.3.1 Dye Cells ... 615
  45.3.2 Pump Angle ... 615
  45.3.3 Pumping Configuration ... 616
  45.3.4 Linear Cavities ... 616
  45.3.5 Efficiency ... 617
  45.3.6 Mode Locking ... 617
  45.3.7 Performance of Laser-Pumped Devices ... 617
45.4 Dye Lasers Pumped by cw Lasers ... 617
45.5 Cavity Designs ... 618
  45.5.1 Mode Locking ... 618
  45.5.2 Broadband Emission ... 619
  45.5.3 Performance ... 619
References ... 619
Further Reading ... 621

45.1 Introduction

The first liquid laser was demonstrated in 1966 [1], using a solution of organic dye molecules[1] as its gain medium: it was pumped by a ruby laser. There have been research studies using rare earth ions, such as neodymium, in various solvents, but the emission performance of these lasers has been disappointing [2]. Consequently, the remainder of this chapter will focus on liquid-phase dye laser technology.

Operation of a liquid dye laser relies on the optical excitation of organic dye molecules dissolved in a suitable solvent. The optical excitation can be coherent from another laser or incoherent, using the energy from a flashlamp or arc lamp. An alternative approach involves the use of light from a surface discharge [3]. More than 50 laser dyes are available for use in the gain medium, enabling energy to be emitted from the ultraviolet to the near infrared, simply by using a different dye—this is wavelength diversity. Additionally, many dyes can be tuned over many tens of nanometres. A dye molecule requires a number of characteristics, such as strong fluorescence and low loss, to be suitable for laser operation. It is often possible to have a choice of solvents, as many laser dyes can be dissolved in a number of liquids. In fact, the solvent can have a very strong influence on the emission, governing the output power as well as influencing the rate of degradation of the dye solution [4].

---

[1] Dye molecules are characterized by having a backbone of carbon atoms connected by alternating single and double bonds, with an overlapping set of π-orbitals running along the length of the carbon atom backbone, in which the electrons are effectively de-localized.

The optical set-up of liquid dye lasers can be extremely simple [5], which leads to their flexibility and general versatility. However, this does have a cost in mechanical complexity if sustained output is required, along with some of their other attributes, such as narrow linewidth, high repetition rate and high power. In this case, a circulation pump will be required to circulate the dye solution from a reservoir and additional elements in the cavity, such as an etalon, birefringent filter or set of prisms for reducing the spectral width, as well as a dispersive element for tuning, in addition to the resonant cavity.

Dye lasers are attractive for many applications, owing to their simplicity; versatility; very broad spectral emission capability, including simultaneous multicolour emission; and energy scalability. A big advantage of this technology, compared with solid-state devices, is the ease of removal of heat from the gain medium. However, care is required in the design of the circulation system to achieve a compact arrangement that allows an easy and clean procedure for changing the dye solution; otherwise, it can become a messy configuration.

These features have made this source the laser of choice for a wide range of applications, and not only as a research tool in the laboratory. Industrial applications include inspection and laser isotope separation (LIS) [6–8] to enrich uranium, with less emphasis on use as a manufacturing tool [9]. In medicine, the scope of their application appears to be growing rapidly: embracing skin treatment, including tattoo removal; diagnostic measurements; lithotripsy; and activation of photosensitive drugs for photodynamic therapy [10,11]. Spectroscopy is an application where dye lasers have been employed extensively in the past, but optical parametric oscillators now offer an alternative source. Other applications include communications, particularly underwater [12], bathymetry [13] and creation of guide stars [14,15] for reference in an adaptive optical system.

45.2 General Characteristics

45.2.1 Gain Medium

It is quite easy and cheap to make a gain medium with high optical quality by forming a laser dye solution. The laser head will have a cell, containing this solution, for use as the active medium. The great flexibility of this laser is provided by the range of organic compounds suitable for use in the gain medium. Many techniques have been demonstrated [16–21] to give simultaneous multicolour operation by direct laser action. Alternatively, a number of cells can be 'ganged together' [22], one for each colour. Furthermore, if energy from a flashlamp is used to create the population inversion in the organic molecules, then the laser head may also have an additional cell for fluorescence conversion to enhance efficiency [23].

Generally, laser dyes are quite large and complex molecules, containing a number of ring structures [24], which lead to complex absorption and emission spectra [25]. Many dyes are suitable for use in a laser: they can be categorized into classes or families by virtue of their structures that are chemically similar. Common examples are the coumarins, xanthenes and pyrromethenes. Xanthenes, for example, have a three-ring structure, the central ring containing oxygen. The differences between the absorption and emission spectra, associated available tuning ranges and physical behaviour of members within these broad classes, result from the substitution of specific chemical groups on the edges of the basic ring structures. Examples of three classes of dye molecules are shown in Figure 45.1.

Optical energy from an external source is absorbed by the organic molecules raising them to an excited state. To a first approximation the wavelength absorbed by the molecules is proportional to the length of the 'backbone' of carbon atoms that form the chain structure [26]. Owing to the complex nature of the structures of these organic compounds, the energy level structure is very complex. However, a simplified generic diagram can be drawn to illustrate the principal interactions. Such a diagram is shown in Figure 45.2.

It is essentially a four-level system where the upper and lower energy levels have an extended span, which leads to the broad absorption and tunability. The electronic states form the basic structure and transitions between these states lead to emission

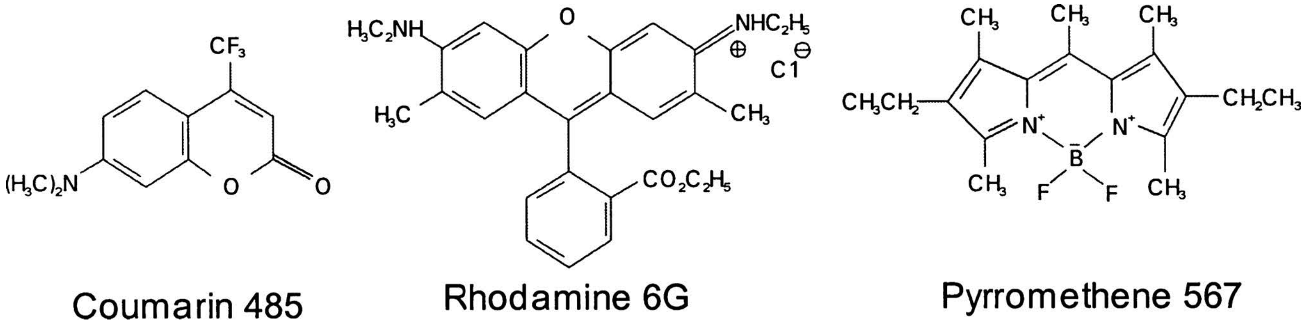

Coumarin 485 Rhodamine 6G Pyrromethene 567

FIGURE 45.1 Structures of dye molecules.

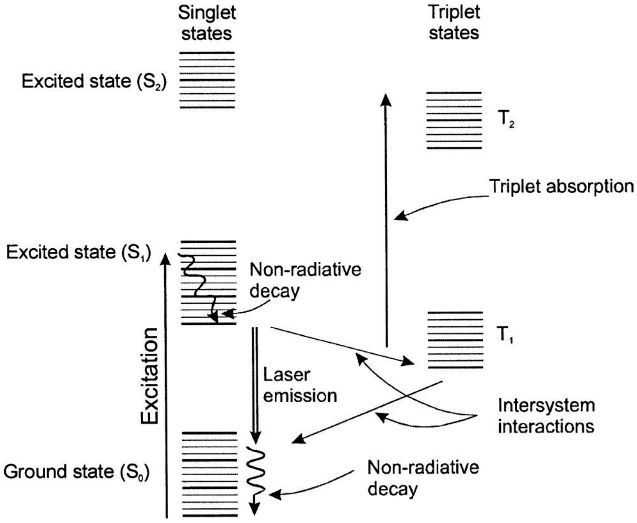

FIGURE 45.2 Simplified energy level structure diagram of a generic laser dye.

in, or close to, the visible part of the spectrum. The energy difference between the states which leads to the visible band emission ranges from ~3.1 eV to 1.65 eV. The diagram shows that these electronic levels have other substates superimposed on them, resulting from the vibrational and rotational motion within the molecule. Energy differences caused by rotational motion are small, and when the other line-broadening mechanisms are included [27], a continuum of states emerges, both for absorption and emission. The diagram shows a continuum of energy levels that enables a laser dye to absorb energy, as well as emit light over a broad range of wavelengths, particularly in comparison with other types of laser. Emission bands of 10–20 nm or more are possible, as shown schematically in Figure 45.3.

Figure 45.2 also shows the processes leading to laser action, with the population inversion being created in the bottom group of 'excited states'. A stimulated transition to a lower energy state provides the coherent light in the singlet manifold of states. Figure 45.3 shows that a typical molecule can emit spontaneously through fluorescence over a broad band of wavelengths, the highest probability being at the centre of the curve. In the case of a free-running resonant cavity, the excess of gain is greatest where the difference between absorption and emission is largest and determines the position of the peak of the laser gain curve. Use of a tuning element controls the loss over a narrow spread of wavelengths and consequently determines the band where amplification can occur.

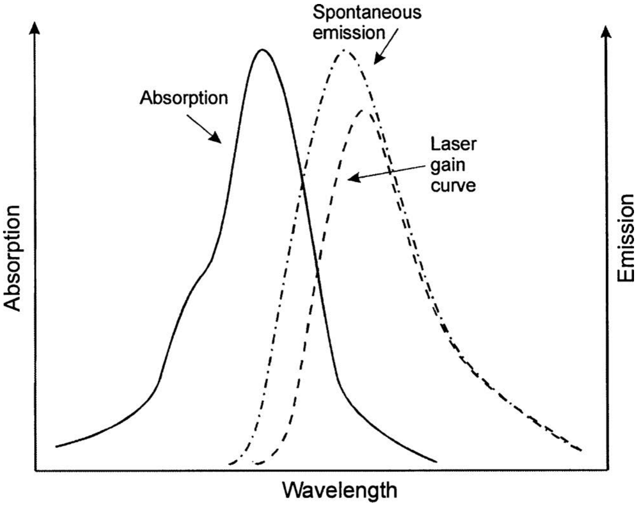

FIGURE 45.3 Absorption and emission spectra of a generic laser dye.

The lifetime of these states is very short, of the order of a few nanoseconds, so there is very little energy storage; hence, Q-switching is not a viable option for generating high-intensity short-duration pulses. Consequently, the temporal-emission profile is closely related to that of the excitation source, particularly for short-duration excitation pulses. However, the broad bandwidth of the lasing emission does lend itself to the generation of ultra-short pulses via the mode-locking technique.

In addition to the singlet states, there is a parallel set of energy bands, known as triplets, which have a slightly lower energy than the corresponding singlets. Triplets arise because the bonding of electrons in organic molecules occurs in pairs. In a singlet state, the electron pair occupies the same energy level with their spins aligned in exactly opposite directions, as happens in the ground state. Triplet states are characterized by a pair of electrons having parallel spins. Since the electric field associated with a light wave does not act upon the magnetic dipole represented by a spin, the change from singlet to triplet cannot be induced easily by light (or put another way, the transition is forbidden by electric dipole selection rules). The build-up of population in any triplet state is detrimental since, owing to their long lifetimes, triplet states act as traps for molecules taking them out of the laser population circulation loop. Furthermore, the detrimental processes are compounded by the fact that the absorption process $T_1 \rightarrow T_2$ overlaps the emission $S_1 \rightarrow S_0$ and so can reduce the efficiency of both pumping and lasing.

Because the build-up of population in the lowest triplet state takes a finite time, triplet-state losses tend not to cause too many problems during 'short-pulse' operations in the range up to a few microseconds. In the case of 'long-pulse' operations, a triplet-quenching agent, such as cyclo-octatetraene, will need to be added to the dye solution to enhance the performance of the gain medium. 'Triplet quenchers' [28] reduce the lifetime of the triplet states through collisional de-excitation.

The very large gain bandwidth of laser dye solutions makes them very attractive candidates for ultrashort pulse generation. The large tuning range of laser-pumped rhodamine 6G implied that pulses of less than 10 fs duration are possible. Furthermore, the large homogeneously broadened bandwidth of these dyes suggests that linear amplification is feasible.

45.2.2 Pumping Options

Many different pump sources have been used to excite the gain medium, ranging from flashlamps to lasers, and surface discharges [3,29,30]. Tables 45.1 and 45.2 show some of the common options.

The incoherent sources tend to offer a cheaper system with greater flexibility to exploit the full range of emissions from various dyes with a single pump source. Laser-pumped configurations can offer a simpler dye laser arrangement, as the pump source is directed into the dye cell, so the dye laser is essentially a wavelength conversion module. Longer-wavelength laser pumping also offers the prospect of greater longevity of the laser dye solution, as there is no UV energy to cause photodegradation.

45.2.3 Dye Solutions

Many solvents are available for creating a laser dye solution: alcohols and ethylene glycol are commonly used, although some are soluble in water, but a surfactant may be needed to prevent dimerization. Dimerization occurs when there is a strong affinity between two or more molecules, leading to large structures with suppressed fluorescence. The solvent used to make the solution can have a significant influence on the optical properties of the laser gain medium and the longevity or usefulness of the dye solution. For example, solvents containing the deuterium isotope of hydrogen tend to have a lower transmission loss than those based on ‘common hydrogen’.

As noted earlier, the pump light can cause the dye molecules to decompose, but for broadband pumping the use of additives in the dye can ameliorate the effects of unwanted shorter wavelength energy. Furthermore, the use of a dye solution between the pump source and the gain medium can absorb the harmful shorter wavelength photons and convert their wavelengths, via fluorescence conversion [23], to match the absorption band of the active dye. Caffeine can also be added to this solution to block the UV.

Photodegradation-causing mechanisms are complex. Studies [4,31] have shown that the formation of singlet oxygen in the solution is particularly detrimental. Elimination of oxygen enhances the longevity of the solution, but an alternative triplet-quenching agent will be needed. Figure 45.4 indicates how a solution’s longevity varies with different operational conditions [4].

Many flashlamp-pumped dye lasers operate efficiently with dye solutions, having a concentration of the order of 10^{-4}–10^{-5} molar. Laser-pumped systems often use a higher concentration, around 10^{-3} molar. The aim is to optimize the use of the pump photons in the gain volume, so that all the pump photons are absorbed by the dye solution throughout the dye cell. There is the flexibility to trade-off concentration, pumping efficiency and beam quality.

Some organic dyes are considered to be toxic, so data sheets must be consulted to establish whether or not special handling precautions are necessary. It is normal to wear a ‘dust mask’ and prepare the dye solution in a fume cupboard (or hood). Great care is recommended during handling and its use in the laser system. When the dye solution is no longer required, it must be disposed of as a toxic waste by a method approved by the local ‘Health and Safety’ service. Further guidance is given in Section 45.2.14 on the safe operation of flashlamp-pumped dye lasers.

45.2.4 Spectral Control

Spectral control of the emission is possible because of the broad gain bandwidth and the homogeneous broadening

TABLE 45.1

Incoherent Pump-source Characteristics

Incoherent	λ (μm)	τ (μs)	PRF (kHz)	
Flashlamp–linear	UV to IR	~5–10^4	To ~1	Broadband, high flexibility, limited PRF, high energy, high average power, lifetime up to 10^6 pulses.
Flashlamp–coaxial	UV to IR	~0.5–5	To ~0.001	Broadband, very limited PRF, high energy, lifetime up to 10^4 pulses, longer duration pulses possible.
Surface discharge	UV to IR	~0.15	~1	Discrete lines, high efficiency, high PRF, high energy, high average power, long life, non-thermal.
Explosive	-	Long	-	Broadband, single shot!, high energy.

TABLE 45.2

Coherent Pump-source Characteristics

Coherent	λ (nm)	τ (ns)	PRF (kHz)	
Copper vapour	511 and 578	~10–60	3 ~ 20	511 and 578 nm, high PRF, high average power, longer wavelengths.
Nd:YAG (2ν)	532	~5	To cw	Variable PRF to cw, short-pulse operation.
Nd:YAG (3ν)	355	~5	To cw	Variable PRF to cw, short-pulse operation.
Ion (Ar, Kr, . . .)	UV to green and red	~0.18 (mode locked)	To cw	Various lines, high PRF to cw, short wavelength emission, low average power, low efficiency.
Nitrogen	337	~2–10	0.01 to ~0.3	Low average power, low efficiency, short-pulse operation.
Excimer	Various in UV (157^+)	~10–200	~0.5–3	Various lines in UV (e.g. 308 nm), high PRF, high average power, short-pulse operation, large pump source.
Diode	Red to IR	Long	To cw	Long wavelength pump, high PRF to cw.

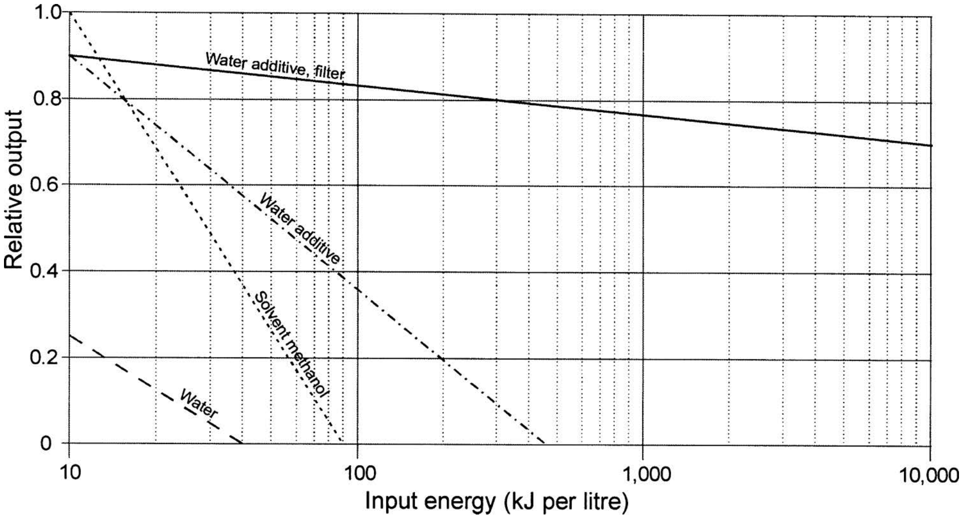

FIGURE 45.4 Dye solution longevity enhancement.

of the transition, which enables the power (or energy) to be extracted at a single wavelength. A number of approaches can be applied, which rely on increasing the cavity losses at the unwanted wavelengths, resulting in only one or a few wavelengths oscillating. There is a subtle difference between narrowing an existing line and forcing the laser to oscillate on a single line. In the latter case, gain is extracted over a narrow spectral region, rather than discarding the unwanted wavelengths, hence offering superior efficiency.

Schematic representations of spectral control schemes are shown in Figure 45.5. In the case of the filter technique, this could use a range of devices: examples include a birefringent (Lyot) filter, a Fabry–Pérot etalon, a dielectric filter, coloured glass or a dielectric mirror with a narrow-band coating. It is vital that low loss devices, such as ‘birefringent filters’ (also known as ‘Lyot’ filters) and etalons, are used in continuous wave sources, owing to their lower gain. In contrast, high gain (pulsed) systems can use many different types of more lossy tuning elements, including gratings with amplified spontaneous emission suppression.

Full exploitation of the spectral properties of this technology requires the use of wavelength-selective elements in the resonant cavity, such as prisms, a diffraction grating, a birefringent filter or Fabry–Pérot etalons. Prisms are attractive as they are relatively cheap and durable, but a single prism gives limited line narrowing. Use of an etalon, which is relatively expensive, with the appropriate finesse (equivalent to quality) gives enhanced line narrowing. A diffraction grating can provide excellent spectral control, including tunability, but great care is needed during high-power operation.

An effective and low-cost configuration, which is suitable for a flashlamp-pumped system, is to use a series of prisms for selection of a very narrow range of wavelengths to pass along the optical axis of the cavity; the remaining wavelengths are dispersed. An etalon can then be used for further line narrowing, usually with a finesse of about five. Additional line narrowing may be achieved by the use of more etalons; in this case the finesse may be up to 10, depending on the beam quality and laser aperture. This approach is inefficient but can be very effective, particularly if the parasitic reflections from the

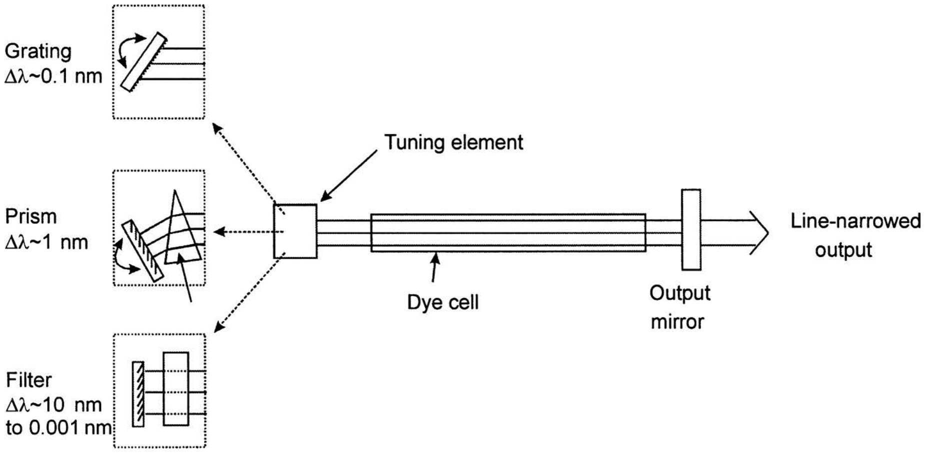

FIGURE 45.5 Tuning schemes.

dye-cell wall are controlled, for example, by inserting a helical spring inside the cell [32].

Tuning and line narrowing can be accomplished with a diffraction grating by using it as the 'high reflector' (Littrow grating configuration) [33,34], as shown in the 'grating arrangement' of Figure 45.5, with equal angles of incidence and diffraction on the same side of the normal. Adjusting the orientation of this grating gives the desired resonant condition. Many commercial systems use this technique and a series of prisms to expand the beam prior to incidence on a diffraction grating. The original demonstration [35] of this approach used a Cassegrain telescope to provide the beam expansion needed to take advantage of the available resolving power, but commercial systems now favour a prismatic system [33]. An alternative technique involves a fixed prismatic arrangement to expand and a near-grazing-incidence mirror to disperse the beam, movement of the feedback mirror providing tunable emission [36], shown schematically in Figure 45.6.

Similar results can be achieved with a birefringent element or a tuning wedge. In the former case, a birefringent plate is mounted at Brewster's angle inside the laser cavity and oriented to act as a waveplate. There is no reflection at the plate surfaces for suitably polarized light. However, at most wavelengths, a fraction of the light passing through the filter is transformed into the orthogonal polarization and then partially reflected out of the cavity. At the resonant wavelength, the retardation of the plate is an integer number of waves, the polarization is unchanged and the plate is loss-free. The resonant wavelength can be tuned by rotating the plate in its own plane. The tuning wedge uses interference as the discriminator by creating a Fabry–Pérot cavity. Translation of the wedge alters the separation of the plates of the interferometer.

Use of line-narrowing elements[2] has enabled linewidths as small as 5 GHz (sub-0.01 nm) to be achieved with a flashlamp-pumped dye laser. A laser-pumped system is capable of achieving 100 MHz, but with the application of special techniques this linewidth can be reduced to better than 1 MHz from a single-mode pulsed source. In the case of an injection-locked cw source, values of 1 kHz or better have been demonstrated; it is projected that 1 Hz could be achieved [33].

Some applications need a broad spectral output, and this may be achieved by the use of dispersive elements to make different parts of the dye cell oscillate at different wavelengths within a dye's gain curve [37]. This has been used to extend the linewidth to beyond 30 nm, using the scheme shown in Figure 45.7.

45.2.5 Control of ASE

One of the common problems of dye lasers is the control of amplified spontaneous emission (ASE), which produces an incoherent 'pedestal' of broadband energy around the laser line. This is shown in Figure 45.8. Use of multiple-prism beam-expanding configurations, in a closed-cavity arrangement with a Littrow grating [38], led to a significant reduction in ASE. A further attraction of prismatic cavities is the stability of alignment and also the prospect of a compact laser configuration.

45.2.6 Temporal Control

As noted earlier, the upper state lifetime of dye molecules is a few nanoseconds, so unlike the rare earth ion lasers, there is very little scope for modifying the temporal characteristics by Q-switching. If very short duration pump pulses cannot be achieved, as may be the case with flashlamp excitation, or a suitable pump pulse is not available, then the cavity-dumping technique [39,40] approach can be applied. In this case, the energy is stored in the optical cavity[3] and released by altering the polarization of the travelling wave. Creation of a high-Q cavity during the millisecond pump-pulse operation, where many thousands of cavity round-trips occur, demands mirrors with very high reflectivity (better than 99.999%). Hence, unwanted optical activity must be eliminated to avoid leakage of energy during this storage phase. A cavity-dumping scheme for the high reflecting element is shown in Figure 45.9: the

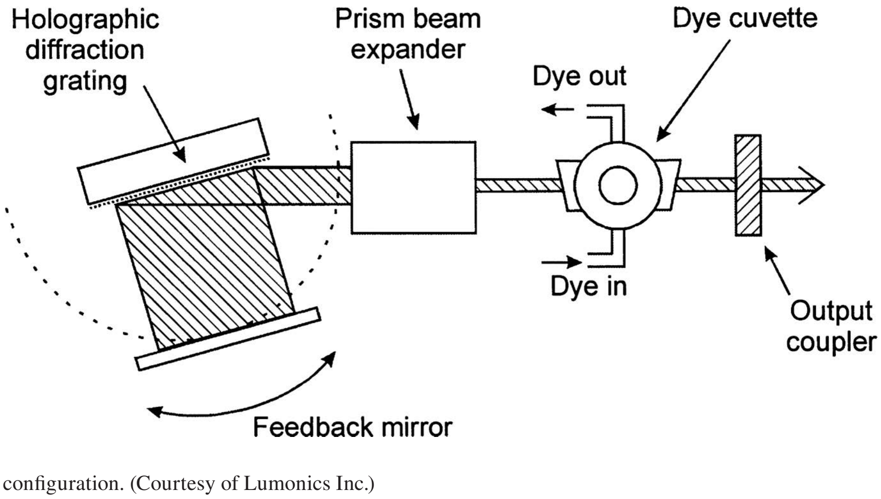

FIGURE 45.6 Tuning configuration. (Courtesy of Lumonics Inc.)

---

[2] The spread in frequency ($\Delta\nu$) and wavelength ($\Delta\lambda$), at a given wavelength (λ), is related by: $\Delta\nu = -c\Delta\lambda/\lambda^2$.

[3] The pulse length in seconds (τ), assuming two passes of the cavity of length (l m), is given by: $(2/3) \times l \times 10^{-8}$; hence for τ expressed in nanoseconds, this reduces to $(20l)/3$.

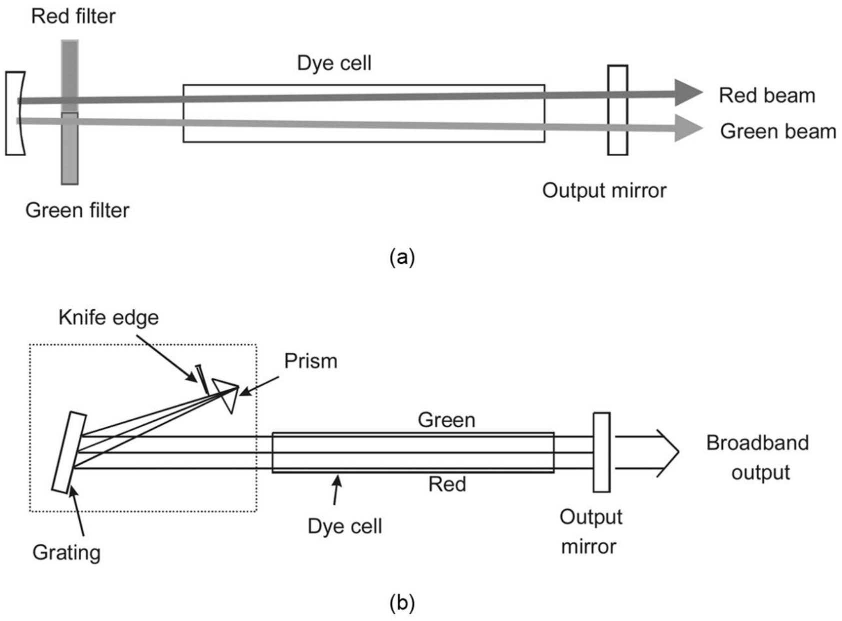
Red filter
Dye cell
Red beam
Green beam
Green filter
Output mirror
(a)
Knife edge
Prism
Green
Broadband output
Red
Dye cell
Output mirror
Grating
(b)

FIGURE 45.7 Broadband laser scheme. (a) Basic broadband laser scheme. (b) Broadband laser cavity design.

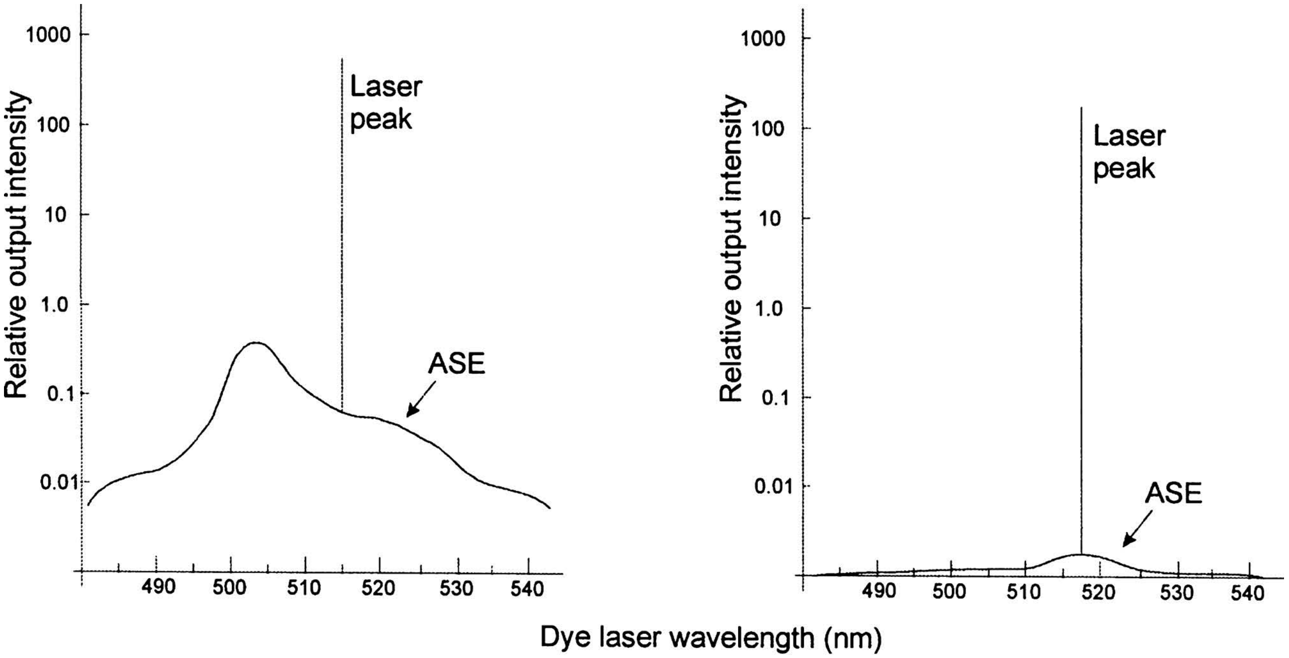

FIGURE 45.8 ASE reduction. (From Ref. [38].)

remainder of the laser cavity is to the right, but is not shown. Pulses with a duration as short as 8 ns [40] have been demonstrated from a flashlamp-pumped source.

Ultra-short pulses have been generated from a self-mode-locking flashlamp-pumped dye laser with a saturable absorber [41], using an organic dye solution. Continuous wave dye lasers have been passively mode-locked [42]. The colliding-pulse concept has been applied to a ring dye laser [43] by including a saturable absorber in the ring cavity to give pulses of a duration of 90 fs. This concept may also be realized by placing the saturable absorber close to the high reflector. Further reduction in pulse length has been achieved by the application of dispersion compensation to produce a pulse length of the order of 50 fs [44]. Further enhancement and compensation with extra-cavity compression has led to the generation of a pulse length of 6 fs [45].

45.2.7 Flashlamp-Pumped Devices

The first flashlamp-pumped devices were demonstrated in 1967 [46,47] and have seen steady development to enable mature systems to be manufactured.

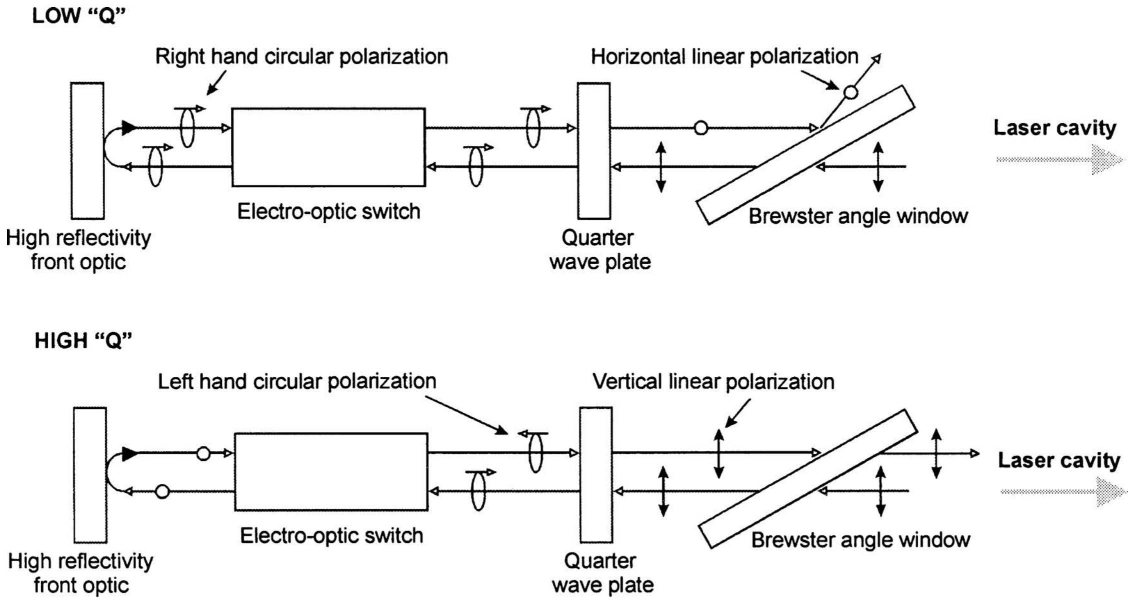
LOW "Q"
Right hand circular polarization
Horizontal linear polarization
Laser cavity
Electro-optic switch
Brewster angle window
High reflectivity front optic
Quarter wave plate
HIGH "Q"
Left hand circular polarization
Vertical linear polarization
Laser cavity
Electro-optic switch
Brewster angle window
High reflectivity front optic
Quarter wave plate

FIGURE 45.9 Cavity-dumping scheme (high reflector arrangement).

45.2.8 Laser Head

Flashlamps are essentially broadband emitters that are isotropic radiators, which can produce pulses of energy of a duration from about a microsecond to tens of milliseconds, depending on the impedance of the pulse-forming network [48]. In the case of a multi-lamp system, the flashlamps may be connected in series or parallel. A parallel arrangement tends to give short-duration pulses and longer lamp-life [49]. Schematic circuit diagrams of pulse-forming networks (PFN) are shown in Figure 45.10.

It is important to have a rapid rise in the radiated power from the flashlamp in order to avoid unwanted triplet state formation. The following argument illustrates the problem for rhodamine 6G. Once the laser starts to oscillate, the value of the upper level population N_1 is clamped at N_{1CR}, the critical value it has at the threshold of laser oscillation, since stimulated emission depletes the entire S_1 level at a rate faster than the spontaneous emission rate. During laser oscillation, the rate at which the triplet state is fed depends on k_{ST}, the rate constant for singlet to triplet conversion and the value of N_{1CR}:

$$\frac{dN_T}{dt} = N_{1CR}k_{ST} - \frac{N_T}{\tau_T} \cong N_{1CR}k_{ST} \qquad (45.1)$$

because the timescale for triplet decay (τ_T) is effectively infinite compared with other timescales. Within a single pulse, the triplet population at time t is given by:

$$N_T(t)\sigma(\lambda_L) = N_{1CR}k_{ST}t \qquad (45.2)$$

Now, lasing at wavelength λ_L will extinguish at t_f, such that for triplet absorption and emission cross sections σ_T and σ_e, respectively,

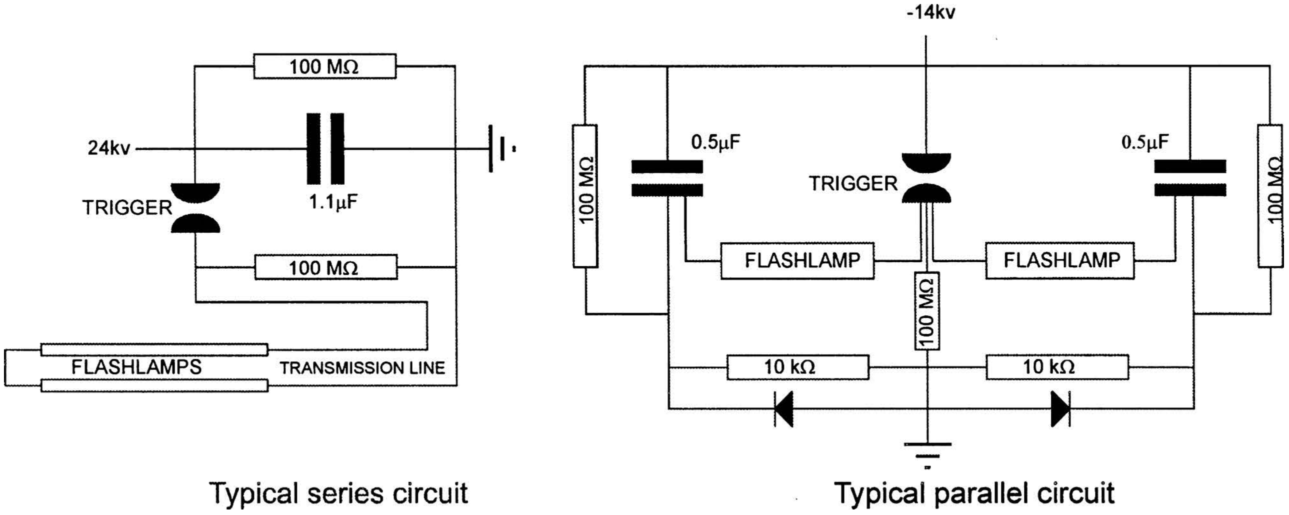
100 MΩ
24kv
1.1μF
TRIGGER
100 MΩ
FLASHLAMPS
TRANSMISSION LINE
-14kv
100 MΩ
0.5μF
TRIGGER
0.5μF
100 MΩ
FLASHLAMP
FLASHLAMP
100 MΩ
10 kΩ
10 kΩ

Typical series circuit

Typical parallel circuit

FIGURE 45.10 Flashlamp drive circuits.

$$N_{\mathrm{T}}(t)\sigma_{\mathrm{T}}(\lambda_{\mathrm{L}}) = N_{1\mathrm{CR}}\sigma_{\mathrm{e}}(\lambda_{\mathrm{L}}). \tag{45.3}$$

For a typical dye molecule, such as rhodamine 6G, the triplet absorption cross section σ_T is related to σ_e as $\sigma_T \sim 0.1\ \sigma_e$ for wavelengths in the spectral band of interest, the laser pulse will end when

$$N_{\mathrm{T}}(t_{\mathrm{f}}) \sim 10 N_{1\mathrm{CR}} \tag{45.4}$$

so

$$t_{\mathrm{f}} < 10/k_{\mathrm{ST}} \sim (3.3\,\mu\mathrm{s\ for\ rhodamine\ 6G}) \tag{45.5}$$

Consequently, the pulse-forming network should be designed to provide a rapid rise time of the order of a microsecond, which was a significant challenge in the early days of lasers and encouraged the development of alternative switches and new flashlamp designs. Failure to achieve full radiated power in more than a few microseconds, as described, results in energy not being used for pumping, but merely heating the dye solution and degrading the optical quality. Triplet quenching agents [28] are required to avoid these effects if long-pulse operation is required and are essential if efficient operation is required over a sustained period.

A flashlamp's envelope can be doped to modify its emitted spectrum, in order to match the spectral emission to the absorption spectrum of the dye. This can provide a modest enhancement to the longevity of the laser dye solution.

A linear flashlamp is essentially a cylindrical envelope with electrodes at either end: a discharge is created between them in the gas. The other common form of flashlamp is the coaxial device, which has an annular-section active region, with the gain medium inserted along its hollow core. In the latter case, there is little need for any structure to direct the optical energy into the dye cell, as many of the photons are travelling towards the dye cell, whilst the remainder would need to cross the plasma in the discharge tube in order to pump the dye solution. Little will be gained from attempting to couple this energy from the discharge into the cell.

The situation with linear flashlamps is somewhat different: there is a smaller barrier created by the plasma. Two distinct pump-chamber designs have been developed and are in common use. They are distinguished by the techniques used to couple the excitation energy from the discharge into the dye cell, namely, specular or diffuse reflecting surfaces. These alternative approaches have an impact on the design of the pumping chamber.

Use of specular reflections from the outer walls of the pumping chamber usually dictates the need for a curved reflector 'behind' each flashlamp. In the case of a single flashlamp, the pumping chamber can be elliptical. A flashlamp is located at one focus and the dye cell at the other. The situation is normally more complex for a multiple lamp configuration [50]. It is common for a pumping chamber to be faceted to make a compact design and to avoid directing the reflected energy back into the plasma. However, in this case, the 'rearward directed' energy may make multiple bounces before entering the dye cell, which may modify the duration of the pump pulse slightly, depending on the configuration. This type of pumping chamber tends to be quite expensive to produce and could be relatively heavy.

It is possible to make the entire pumping chamber from a diffuse-reflecting material, such as the resinous substance known as spectralon. In this case, the flashlamps can be placed very close to the dye cell in what is known as a close-coupled configuration, enabling a compact and lightweight design to be achieved. Alternatively, a metal structure can be fabricated and the inner surface sprayed with a diffuse-reflecting material with a high albedo, such as barium sulphate. Attempts have also been made to include dyes in this layer to provide some fluorescence conversion of the diffusely reflected energy, but this appeared to add little to the pumping efficiency. The shape of the inner surface of the pumping chamber is less critical than that for a specular reflector, so a curved surface has tended to be used with a cylindrical dye cell and a plane reflector with a rectangular-section dye cell. The close-coupled approach has been used extensively in dye lasers developed in the UK [5].

An alternative arrangement, known as the inverted configuration, has been investigated. A linear flashlamp is at the core of the pumping chamber, and the dye cell has an annular cross section, which surrounds the flashlamp. The need for a reflector to enhance the pumping efficiency is less critical in this configuration, as the concentration of the dye solution may be manipulated to ensure optimum absorption of the energy radiating outwards from the flashlamp. Alternatively, a reflecting sleeve can be placed over the outer surface of the dye cell. This design is shown schematically in Figure 45.11, along with the other approaches previously described.

45.2.9 Dye Cell Configuration

Design of the dye cell is an important aspect of achieving optimum performance: it is made of transparent material, such as quartz or sapphire. To minimize self-absorption losses in the dye solution, resulting from the overlap of the absorption and emission spectra (shown in Figure 45.3), its length is matched to that of the flashlamps. Normally, less than 5% of the gain-length is unpumped. Fresnel losses are minimized by using broadband anti-reflection coatings, matched to the anticipated band of emitted wavelengths, on the ends of the cell (windows): it is also possible to use 'Brewster windows'. The dye is shielded from acoustic shocks by surrounding each flashlamp with a water-cooling jacket, which also helps to provide a uniform thermal environment, needed for good beam quality.

The size of the dye cell is an important parameter in determining the output power of the laser, along with the emission efficiency of the chosen dye and the optical energy coupled into the cell from the flashlamp(s). An empirical rule-of-thumb is that a good dye, such as a xanthene or a pyrromethene, will allow about 0.25 J cc^{-1} to be extracted. Jensen [51] describes analytical techniques for accurate assessment of the size required for a given output performance.

If the laser is required to operate for more than a few 'shots', then it will be necessary to circulate the dye solution through the dye cell to maintain consistent laser efficiency and beam quality. As the temperature of the solution rises, efficiency

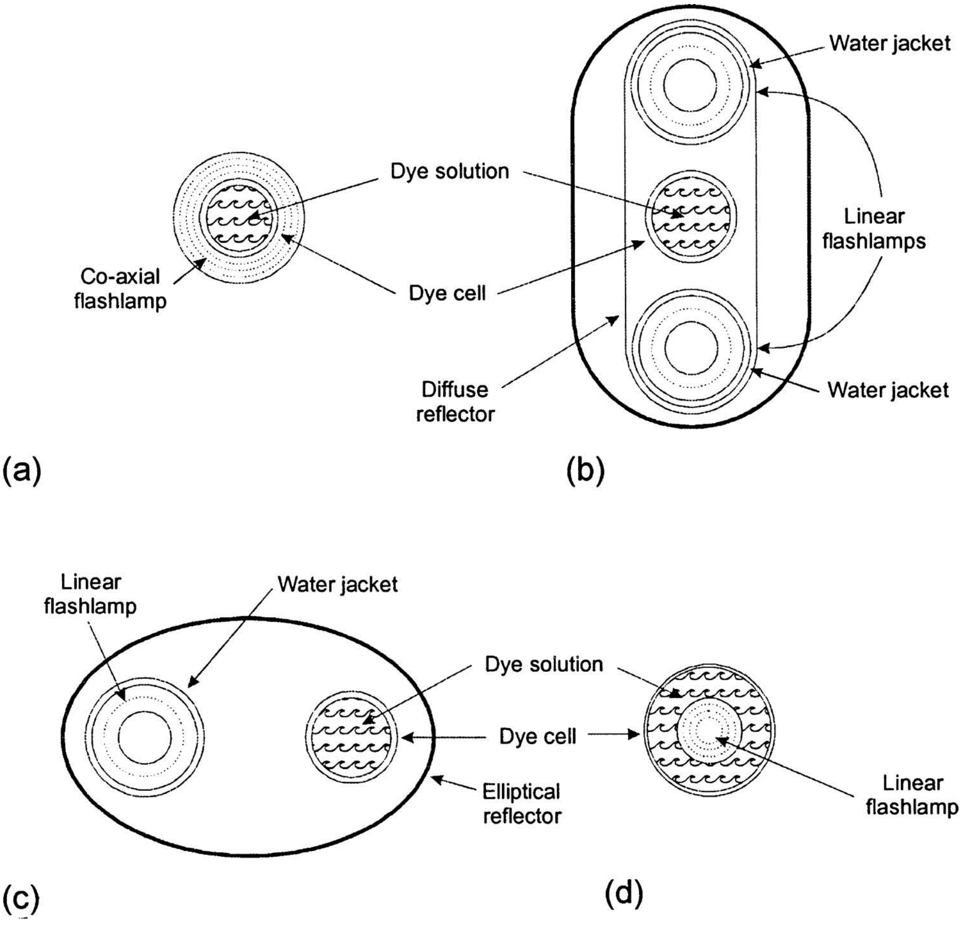

FIGURE 45.11 Cross-sectional schematic diagrams of laser head designs. (a) Co-axial flashlamp laser. (b) Close-coupled linear flashlamp laser. (c) Specular linear flashlamp. (d) Inverted laser.

degrades rapidly, owing to the thermal population of the lower laser level. Additionally, thermal gradients across the dye cell degrade the beam quality. Another empirical rule-of-thumb indicates the need for a 'flushing ratio (flush factor) of 2:1' of fluid in the cell between laser pulses to give an optimum trade-off between emission characteristics (particularly beam quality and dye solution longevity) and the volume of the circulated solution. The magnitude of the pumped volume therefore determines the size of the circulation pump required to meet the flushing ratio. Two common forms of flow geometry are used to pass the dye solution through the dye cell, namely, longitudinal and transverse flow.

Longitudinal flow allows a reasonably simple coupling of the circulating dye solution into the dye cell, and creation of a uniform flow throughout the cell. However, it can take a relatively long time for a given volume to be 'changed', particularly for a long dye cell. Hence, this geometry tends to be used when the repetition rate requirement is low, typically 15 Hz or less, in order to achieve the optimum flushing-ratio easily. Cylindrical section cells are common. A filter is included in the circulation system to suppress the formation of bubbles, which would degrade the optical quality, generating increased optical scatter. Typically, a 0.2 μm pore filter is used, as this provides a good compromise between flow resistance and required pump capacity.

In contrast, transverse flow across a cell is commonly used with higher repetition rates, as it allows large volumes of dye solution to be rapidly flushed through the cell. The one drawback of a transverse-flow arrangement is the design of the manifolds to ensure that the fluid maintains a uniform flow across the dye cell. These cells usually have a rectangular cross section. The formation of eddy currents or the creation of any non-uniform flow degrades the optical quality of the gain medium, thus having a direct impact on laser performance. Similarly, the formation of stagnation zones rapidly diminishes the performance of the laser head. It is normal in a transverse flow scheme to pump the solution vertically up through the cell to prevent the formation of air locks and similar voids in the system. A bubble-suppression filter is usually incorporated into the circulation system, as already noted, for longitudinal flow. Laminar-flow boundary layers along the dye cell walls must be minimized: fully developed, small-scale pipe flow is required to produce an even flow distribution [52].

Repetition rates of the order of a kilohertz are possible with a transverse scheme, the limit being determined by the recovery time of the flashlamp and PFN. This restriction could well be eliminated by the use of a surface discharge pump source. These flow schemes are illustrated in Figure 45.12.

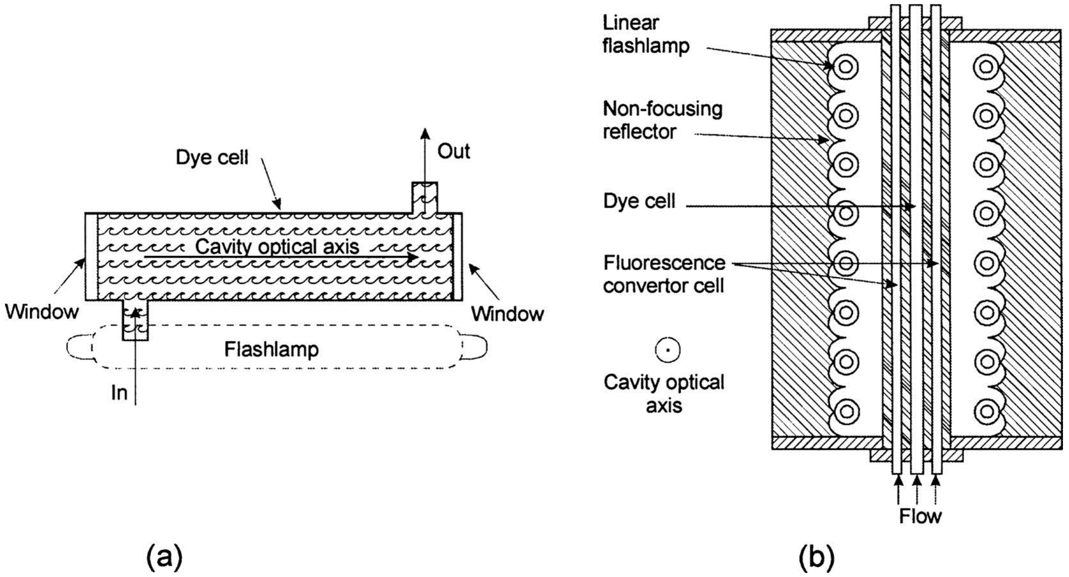
Dye cell
Out
Cavity optical axis
Window
Window
Flashlamp
In
(a)
Linear flashlamp
Non-focusing reflector
Dye cell
Fluorescence convertor cell
Cavity optical axis
Flow
(b)

FIGURE 45.12 Dye cell flow schemes. (a) Longitudinal flow close-coupled cavity, and (b) transverse flow with faceted specular cavity. (From Ref. [59].)

45.2.10 Multicolour Operation

There have been many demonstrations [16–22] of multicolour output. In the case of a longitudinal-flow scheme, this can readily be achieved by having a series of annular cells co-axial within the central cell. Managing the separate circulation systems and the respective inlet and outlet ports becomes a significant design issue with more than three cells, although more are feasible. The approach is to arrange the dyes so that the fluorescence from one dye will pump the dye in its inner cell, so the longest wavelength emission is at the centre. A schematic diagram of a three-colour source is shown in Figure 45.13.

A stack of rectangular-section dye cells can achieve a similar result for a transverse-flow laser head, as shown in Figure 45.12b. A photograph of a 'multicolour' laser head is shown in Figure 45.14.

Many applications find it easier to exploit the wavelength diversity of a laser head by simply using a different dye in the solvent. Provided suitable broadband anti-reflection coatings have been applied to the optical elements in the resonator, then the same laser head can be used to generate light from the UV to the near IR. Carbon filters have been used to remove one organic laser dye from solution [4], leaving a few parts per million in solution after a few minutes' normal circulation. At this level of contamination, the solvent appears 'clear'. A dye concentrate can then be injected to create a new solution with the appropriate concentration of laser dye to provide the desired new spectral properties. The range of laser dyes offered by a single dye manufacturer is shown in Figure 45.15.

45.2.11 Laser-Resonator Design

The choice of resonator configuration has a significant impact on the key performance parameters: beam divergence and extracted energy. Consequently, different arrangements have been investigated [53,54] in order to enhance some aspect of performance, especially beam quality in the case of a flashlamp-pumped dye laser. One approach is to have a long

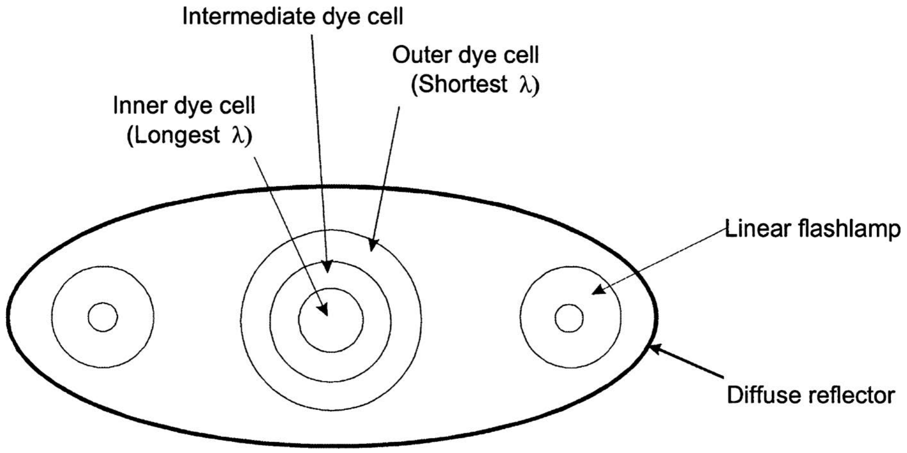
Intermediate dye cell
Outer dye cell (Shortest λ)
Inner dye cell (Longest λ)
Linear flashlamp
Diffuse reflector

FIGURE 45.13 Multicolour longitudinal flow laser head schematic diagram.

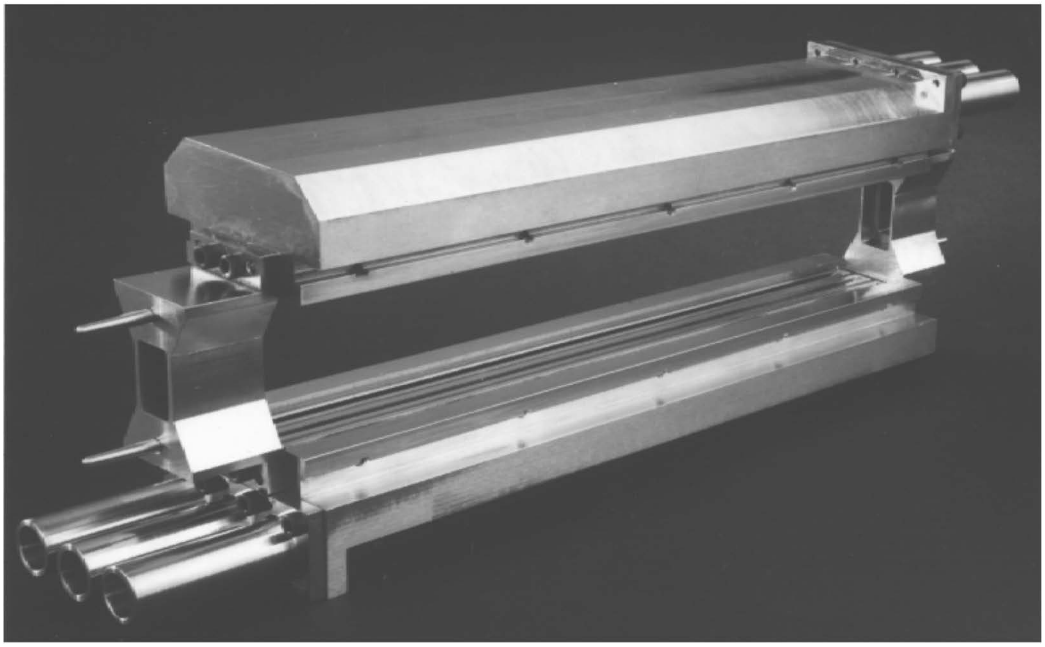

FIGURE 45.14 A transverse-flow multicolour dye laser head.

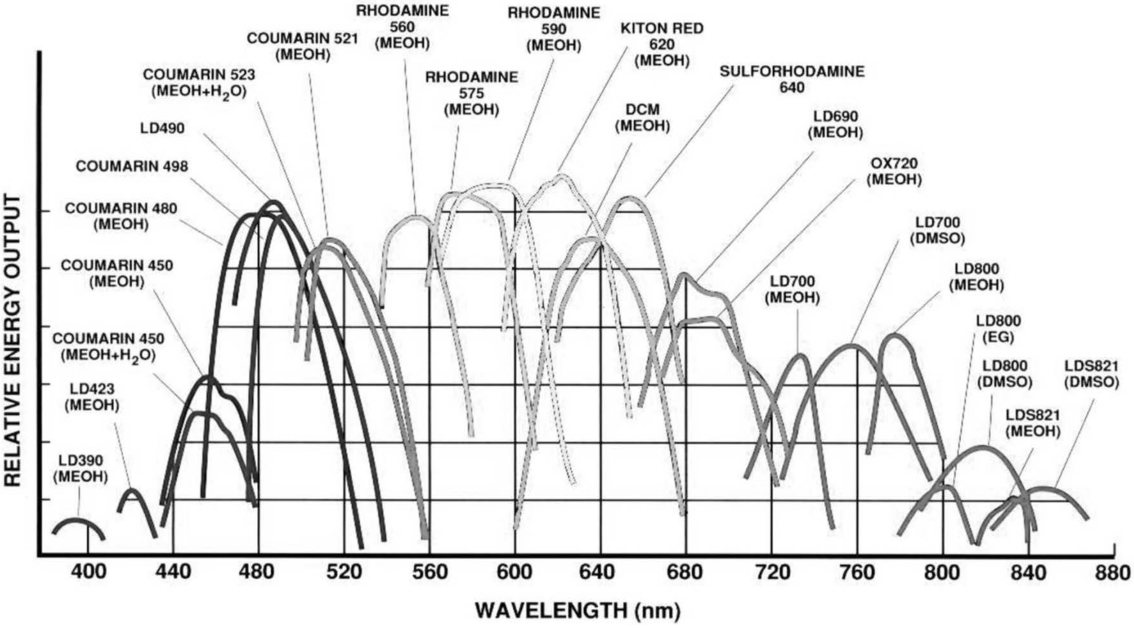

FIGURE 45.15 Dye spectral emission characteristics. (Courtesy of Exciton Ltd.)

laser so that the Fresnel number[4] is small, thus only the lowest order modes can resonate. However, this is often not practical, as many dye cells have a diameter of about 10 mm; moreover, it usually leads to inefficient light generation.

Positive branch unstable resonators with a magnification of about two have been exploited to optimize laser power extraction and simultaneously achieve high beam quality. In this case, the magnification reduces the (modified) Fresnel number,[5] allowing optimum power extraction from the dye cell. Graded-reflectivity mirrors [55] have been available to form resonators, permitting better beam quality to be maintained over a range of performance parameters.

The transmission of the output coupler (mirror) needs to be matched to the emission performance of the laser dye in the gain medium. With a high-gain lasing medium, it is beneficial to use a low-reflectivity output coupler. The converse is also true, but in this case if the energy extraction is too large, then the oscillator may fail to operate! Figure 45.16 shows the improvements that can be achieved by optimizing the output coupler reflectivity of a flashlamp-pumped dye laser.

---

[4] Fresnel number (F) = $a^2/(\lambda\ L)$, where a is the radius of the limiting aperture, λ is the wavelength of operation and L is the length of the resonator.

[5] Modified Fresnel number = $\{(M-1)/2\}\ F$, where M is the magnification.

Phase conjugation techniques offer another approach for enhancing beam quality. A self-starting resonator scheme with a primary and secondary cavity has been used to enhance beam brightness [5]. This scheme, shown schematically in Figure 45.17, improved the brightness by a factor of 100, compared with a plane-plane cavity.

45.2.12 Other Beam-quality Enhancement Techniques

A number of factors, other than the size of the gain volume, contribute to the degradation of the optical quality of the gain medium, causing excessive divergence of the emerging beam. The principal factors contributing to the reduction in beam quality are thermal gradients across the dye cell and non-uniform flow, including boundary-layer effects. The former effect can be reduced by a suitable choice of solvents with a high thermal conductivity and matched thermal characteristics, similar to those of the cell. Table 45.3 shows the thermo-optical parameters [56] of a few common solvents and their influence on beam brightness.

A number of different approaches, using standard ‘fluid-dynamical-flow principles’, have been suggested for reducing the boundary-layer effects of the fluid and parasitic reflections as it flows through a dye cell. A helical insert was proposed for use in gas lasers [32] to reduce these effects, consequently improving beam quality, and may be applied here. It is also anticipated that short duration pulses will reduce induced thermal effects, thereby enhancing beam quality. Finally,

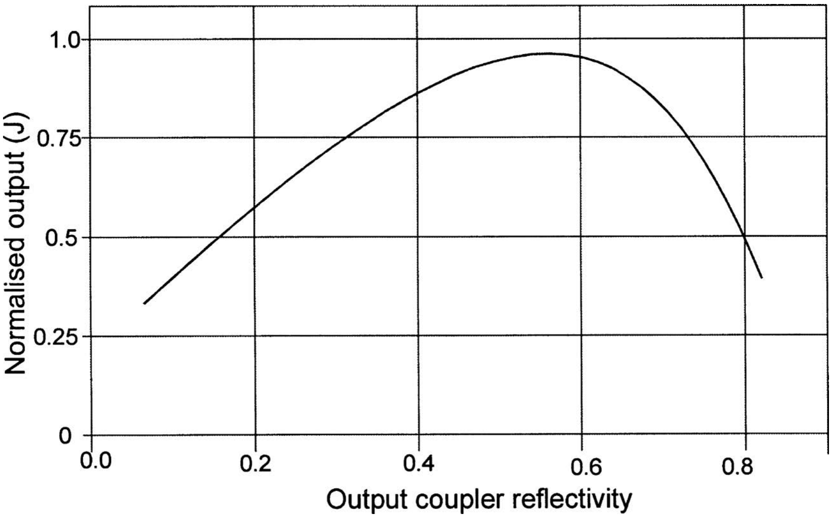

FIGURE 45.16 Output energy optimization.

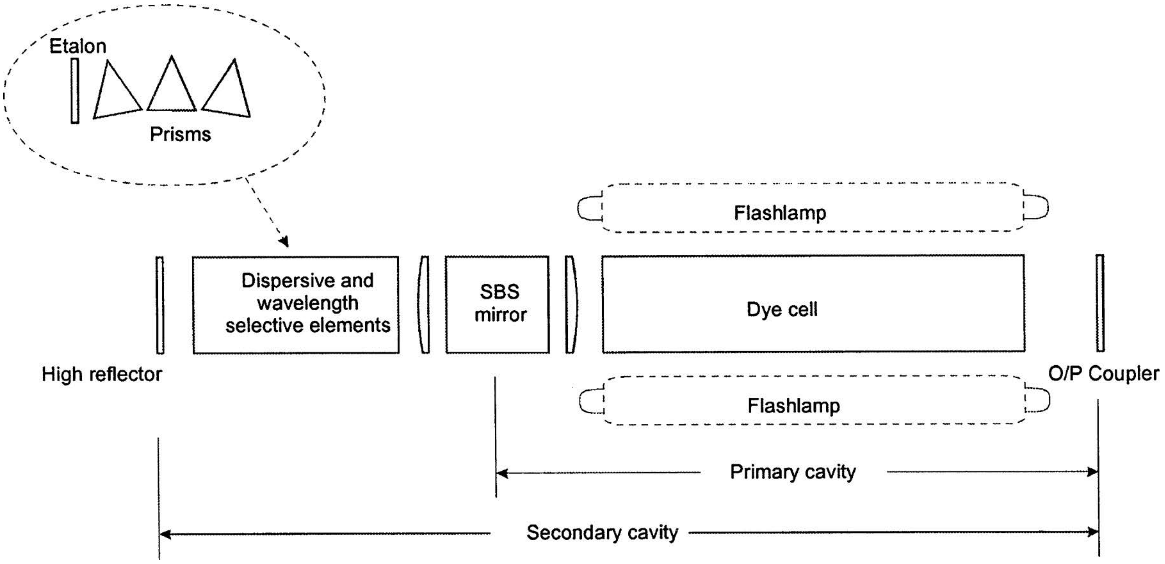

FIGURE 45.17 Schematic of self-starting phase conjugate resonator.

TABLE 45.3

Thermo-optical Parameters of Typical Dye Solvents

Solvent	($W\,m^{-1}\,K^{-1}$) Thermal Cond'y	(K^{-1}) (dn/dT) $\times 10^{-3}$	Rel. Divergence	Rel. Brightness
Water	0.561	0.08	1	1
Methanol	0.223	0.36	1.75	0.45
50% mixture	0.392	0.44	1.5	0.4

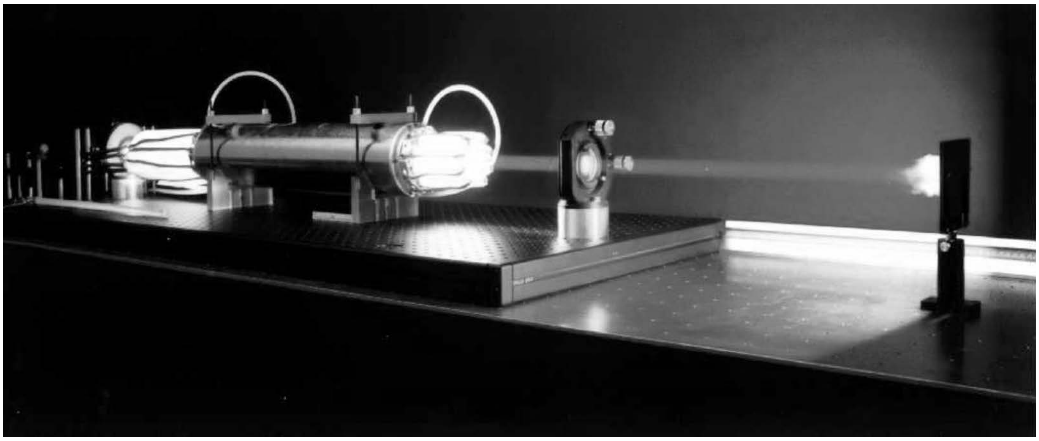

FIGURE 45.18 A 35 J laser in operation.

zigzag-pumping configurations have been demonstrated [57,58], which average out thermally induced effects in a dye cell.

45.2.13 Flashlamp-pumped Laser Performance

These lasers are usually operated as simple oscillators, because high average-power performance is readily achievable. Average output power in excess of several kilowatts has been demonstrated [50,59]. In some cases, this was from a low repetition rate (of approximately 10 Hz) string of high-energy pulses. Repetition rates of the order of a kilohertz have been demonstrated [6,60] for this power class. Devices to produce 1 kJ per shot have been designed, but it has not been possible to confirm achieved performance. In principle, this should be possible as flashlamp-pumped dye lasers are average-power devices. Hence, a 100 J/10 Hz device is equivalent to one emitting 1 kJ at 1 Hz. Figure 45.18 shows a high-energy source in operation. This performance is available from the UV to the near IR. However, it is dependent on the efficiency of the dyes, with the most efficient dyes tending to emit in the visible.

Miniature devices have been demonstrated using the same technology with average power of the order of a watt [60]. Scaling rules have been devised, enabling maximum use to be made of this technology. In general, it is easier to 'scale-up' a device than to reverse the process. One of the reasons for the scalability of this technology is the ease of removal of waste heat from the gain medium via a cooling circulation system.

Many techniques can be applied to modify the spectral and temporal characteristics. A formula[6] [61] relating the trade-off between the shortest possible duration of a pulse ($\Delta\tau$) and its linewidth ($\Delta\nu$) has been derived. It is not possible to combine a narrow linewidth in a very short pulse.

Linewidths of the order of 1 GHz have been demonstrated from flashlamp-pumped dye technology, whilst maintaining efficient operation. Pulse lengths are usually in the range of 1–5000 μs, although pulses as short as 1 ps have been reported [62], using passive mode-locking at the end of the pulse.

The efficiency of these lasers is in the region of 1%–2% (wall plug) [59,63] for the best dyes in medium- to high-power systems.

The *bête noire* of this technology has been the beam quality and the short useful life of the dye solution, particularly during high-power operation, which means the dye reservoir needs frequent replenishment. Use of unstable resonators with graded-reflectivity mirrors has enabled high-brightness beams to be produced. The beam size is dominated by the diameter of the cell: it is typically of the order of 10 mm or more. The use of carefully designed cocktails of solvents, blocking of the unwanted hard-UV, preventing singlet oxygen generation and having optimum pump emission matched to a range of dyes, has enabled longevity to be enhanced by many orders of magnitude [4], as shown in Figure 45.4.

Virtues of this technology are its simplicity, reliability and inherent low cost. The performance of this laser technology, particularly efficiency, is likely to be revolutionized by the application of surface discharge pump sources [3,30].

45.2.14 Safe Operation

Some dyes may need to be dissolved in a volatile flammable solvent. Additionally, large voltages with rapid rising currents are used to pulse the flashlamp, thus there is a danger of an explosion under some combinations of circumstances. For example, if the solvent is very volatile with low viscosity, enabling it to penetrate joints in the circulation system, this risk can be mitigated by using ‘metal plumbing’, with compression fittings, and physical separation of the hazards. This is possible because many solvents are heavier than air. However, use of efficient water-based solvents eliminates this hazard [4]. A schematic arrangement for safe operation with a hazardous solvent is shown in Figure 45.19.

---

[6] The relationship between pulse length ($\Delta\tau$) and linewidth ($\Delta\nu$) is given by: $\Delta\tau\,\Delta\nu \geq 0.441$.

Safe handling, use and disposal of laser dye solutions, as well as the constituent chemicals, are discussed in Section 45.2.3.

45.3 Dye-Lasers Pumped by Pulsed Lasers

Radiation emitted by a visible- or near-UV pulse laser is an ideal technique for exciting dye lasers and was used in the first liquid laser demonstration [1,64]. Many different types of lasers, as indicated in Table 45.2, are capable of delivering a very high intensity pulse of radiation, the peak power of which can reach 100 kW or more in a pulse lasting a few nanoseconds. The use of very short pumping pulses avoids the inefficiencies associated with triplet formation. Additionally, this method avoids distortion of the gain medium from acoustic effects.

In this case the dye laser becomes a wavelength-conversion module, enabling the user to select the emission wavelength. Clearly, there is an optimum pump wavelength for each type of laser dye molecule, as the pump-radiation’s wavelength must be within the region of high absorption, not too far away from the fluorescence region, although its exact wavelength is not critical. In some circumstances, with a pump laser that has a multiple-wavelength emission, it may be necessary to select one wavelength to achieve efficient use of the pump light. For example, with a copper-vapour pump laser, the green line could be used to excite one dye and the yellow line used for another.

The laser head for this type of excitation is usually very much simpler than that used for incoherent (flashlamp) pumping, although many of the techniques described relate directly to achieving the desired spectral output.

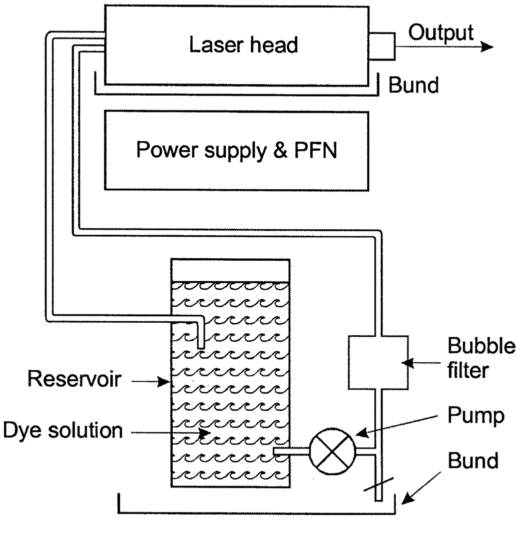

FIGURE 45.19 Scheme for safe operation.

45.3.1 Dye Cells

Laser pumping offers high optical conversion efficiency, owing to the large absorption and emission cross sections of many laser dye molecules, which leads to a small interaction volume. Hence, the dye cells can be very small: the lower limit is often set by the damage threshold of dye-cell windows, particularly with oscillator-amplifier configurations.

The shape of a dye cell [2,62] can have a significant effect on the spectral characteristics of the beam generated in the gain volume. For example, a broadband output can be generated from a rectangular cell that is excited transversely. In contrast, narrow linewidth emission from a similar configuration would require a reduction in parasitic reflections. This can be achieved by tilting the emission windows at an angle to an axis in the plane of propagation normal to the resonator axis.

Alternative approaches include those with a parallelogram-shaped section and rectangular cells skewed at an angle on the plane formed by the optical axis of the resonator, and the axis normal to the plane of laser-light propagation. Prismatic-shaped cells have been used for uniform mode extraction, as have conical cells. These cells offer more uniform pumping of the dye solution by taking advantage of total internal reflections within the cell. Figure 45.20 illustrates some of the cell shapes often used.

As described before for the flashlamp-pumped dye laser, the effects of parasitic reflection may be reduced further by the use of anti-reflection coatings.

The pulse repetition rate (PRF) of the desired output and required duration of the emission determine whether it will be necessary to circulate the dye solution through the cell. A low-PRF emission, sustained over a lengthy period, will require the solution to flow through the cell with a low velocity. In this configuration there is a choice of longitudinal or transverse flow. A typical dye cell cross-section for low average power emission is of the order of 1 cm^2.

A high-PRF laser output will demand rapid circulation of the solution through the cell, according to the 2:1 flushing ratio ‘rule-of-thumb’ described in Section 45.2.9. For very high PRFs, it may be necessary to reduce the cross-sectional area to achieve the desired flow velocity with a pump of reasonable proportions and to avoid the phenomenon of cavitation. For example, cells with cross-sectional dimensions of 15 × 0.5 mm have been used for multikilohertz emissions. It is quite common to use longitudinal pumping with this operational regime, as the dye solution flowing through a cell moves faster in the centre. Judicious shaping of components in the cell can minimize the boundary layer effect and produce a flat, turbulent velocity profile necessary for good optical homogeneity in the cell, leading to good beam quality.

45.3.2 Pump Angle

The pump beam may be directed into the dye cell at a range of angles, depending on pump power and the laser configuration [65]. Use of high-peak-power pulses of energy enables

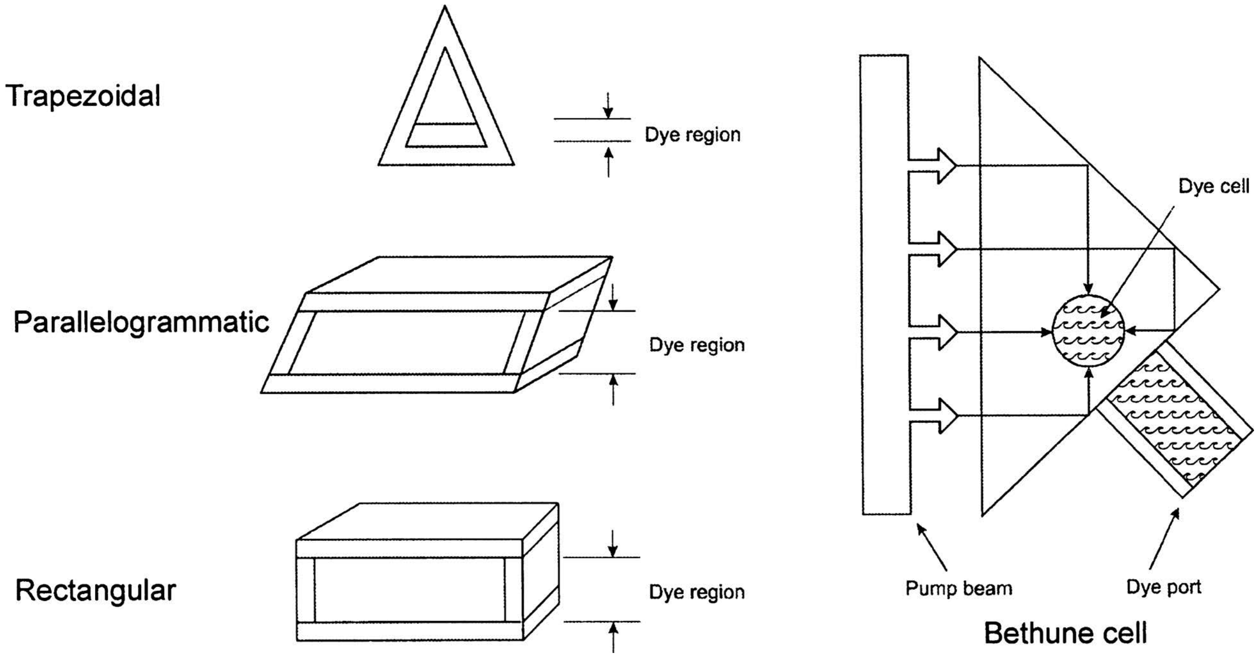

FIGURE 45.20 Dye cell shapes.

'transverse pumping' to be used, i.e. the pump beam illuminates the dye cell orthogonal to the resonator's optical axis. This technique simplifies alignment requirements, but there is some sacrifice of efficiency. Provided that the pump powers are high, then it will not be necessary to use any optical elements to focus the beam into the dye cell.

Transverse pumping is usually employed in an oscillator-amplifier configuration, which is commonly used to reduce the effects of ASE. In this case, the beam from a single-pump laser can be divided and directed transversely into both the oscillator and one or more amplifiers [62]. The use of a delay line may be required to achieve the optimum time-of-arrival of the pump pulses throughout the system, particularly at the amplifier to compensate for the build-up time in the oscillator.

Directing the pump beam along the optical axis of the cavity, or close to it, is known as longitudinal pumping. This approach tends to be used to improve the efficiency of low-gain systems, and it also helps to improve beam quality by providing a good match between the pump and gain modes. An additional advantage of longitudinal pumping is that optimum use can be made of the faster (Newtonian) flow along the centre of the dye cell, so enhancing the 'flushing ratio' for a given size of circulation pump. A practical configuration of this pumping technique has the pump beam directed at a small angle to the 'resonator axis', just avoiding one of the cavity mirrors, hence dispensing with the complication of using dichroic mirrors in the laser resonator.

45.3.3 Pumping Configuration

Laser pumping allows many configurations to be implemented, as the gain of the dye medium in a pulse-pumped system can be very high, owing to the peak intensity of the pump beam. Hence, the use of dispersive optic elements within the cavity, which have appreciable losses, can be tolerated without significantly reducing performance. Oscillator-amplifier configurations have been demonstrated: in the case of the LIS facility in America [8], chains of amplifiers were used, pumped by banks of copper-vapour lasers.

The LIS system demonstrated the use of master oscillator power amplifier (MOPA) chains with three or four amplifiers in series: the first two being high gain pre-amplifiers to give sufficient power to saturate the following power amplifiers. This system showed that several copper-vapour pump-lasers (CVL) could be combined, with staggered timing to elongate the oscillator pulse prior to amplification. This system also demonstrated the multiplexing of CVLs to increase the PRF of the output. Additionally, it was necessary to control the path lengths through the various banks of amplifiers to maintain temporal coincidence between the pump and dye pulses at each amplifier [8].

Other arrangements have seen the use of optical fibres [66–68] to deliver the pump energy to the dye cell. This approach is particularly useful for operation in a hazardous environment, or to ease the alignment requirements of the pump beam. Furthermore, an anamorphic telescope can be used to transform a circular beam emerging from a fibre into an elongated footprint, leading to optimum overlap of the pump beam with the resonated beam.

45.3.4 Linear Cavities

This configuration offers the simplest arrangement, but can be used to generate a tunable emission. Figure 45.21 shows the arrangement for generating a tuned output from a dye laser pumped with a nitrogen laser.

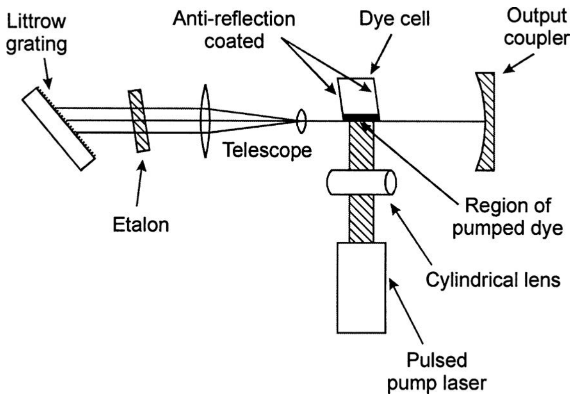

FIGURE 45.21 Pulse-pumped dye laser.

45.3.5 Efficiency

One important consideration with the laser-pumped configuration is to match the emission of the pump to the absorption bands of the laser dyes. With dyes such as the pyrromethenes and a well-matched pump-laser, it is possible to achieve conversion efficiencies well in excess of 50%, but this does not take into account the efficiency of the pump source. In some cases, this can be as high as 40% with a diode-pumped frequency-doubled neodymium laser, whereas other lasers are comparatively inefficient, of the order of 1% or 2%.

45.3.6 Mode Locking

Generation of ultrashort pulses from a dye laser, operated in a broadband mode, is possible with some form of mode-locking. Synchronous pumping of a dye laser is usually undertaken with a dye-jet configuration, enabling a string of very short pulses to be generated. This is considered further in Section 45.5.1.

45.3.7 Performance of Laser-Pumped Devices

In theory, a very broad spectral emission is possible by merely changing the dye in the solution and, where necessary, the pump source or using a tunable source. However, the spectral coverage capability of a given configuration may well be limited by the resonator's optics. Usually the low-loss coatings on mirrors cover a broader spectral range than the gain bandwidth of any single dye, but the advantage of the AR coatings may be lost when a substantially different colour is generated. However, broadband coatings are available. Similarly, the use of wavelength-selecting elements for limiting the linewidth of the output can restrict the efficient emission to the spectral range of a single dye, or to dyes whose wavelength is close to the primary dye wavelength. Generally, the simpler the configuration, the greater the possible range of wavelengths that can be generated using a range of dyes, without the need to change optical elements.

Laser-pumped devices can generate a tunable output over a spectral range of many nanometres from a given dye. Increasing the reflectivity of the output mirror increases the tunable bandwidth. Use of additional elements in the resonator enables a beam of high spectral purity to be emitted of better than 1 MHz with single-mode emission, but more commonly of the order of 100 MHz, ($\Delta\lambda \sim 10^{-4}$nm) [25,33,62]. Alternatively, use of mode-locking techniques has enabled very short pulses to be generated, of the order of 6 fs.

Pulsed lasers can give a few tens of watts of average power [65] close to the peak of the gain curve for efficient dyes, such as the xanthenes or the pyrromethenes. However, this value decreases as the wavelength is 'tuned' away from the peak of the gain curve. A MOPA system developed for LIS in the United States has demonstrated many kilowatts of average power with high spectral purity, from what is probably the largest dye laser in the world [8].

The temporal profile tends to follow, or be marginally shorter than, the pump pulse. This type of laser will give a very broad spectrum of pulse lengths from the very short to continuous, depending on the pump laser. Similar remarks apply to the pulse repetition rate. A range of pump lasers is available as discussed in Section 45.2.2 to provide the desired output. For example, copper vapour lasers have pulse lengths of about 20 ns and a PRF of 3–20 kHz, whereas nitrogen lasers have a pulse length of a few nanoseconds and a typical PRF of up to 300 Hz: the characteristics of frequency-doubled solid-state lasers is similar to the latter, although PRFs of many tens of kilohertz are possible.

The beam quality of this class of dye laser is generally somewhat better than that from a flashlamp-pumped device, owing to less waste heat being generated in the laser head. In this case, the pump source and the design of the resonant cavity have a strong influence on the performance. However, in general, beam quality is often a secondary consideration. The divergence of the emitted beam is usually substantially less than 10 mrad, often better than 1 mrad. The beam size is usually less than 10 mm, typically in the range 1–3 mm.

Linearly polarized energy is generated if a tuning grating is included in the cavity. This also occurs if any component is oriented at Brewster's angle. Additional components can be included, either intracavity or extracavity, to enhance the polarized output.

The coherence length can be defined in various ways, but can be estimated from:

$$\text{Coherence length} = \text{Speed of light frequency bandwidth.}$$

45.4 Dye Lasers Pumped by cw Lasers

The first cw dye laser was demonstrated in 1970 [69] using a cell with a flowing dye solution and excited by an ion laser. This was followed in 1972 by the introduction of the dye-jet laser [70], also pumped by an ion laser. Developments have seen these lasers pumped with frequency-doubled cw neodymium sources (Nd:YAG and Nd:YLF). Dye-jet lasers have also been excited using diodes: a number of studies [71–73] report the use of red or near infrared diodes for producing compact cw dye lasers. In this case, the laser emission is generally in the near infrared.

Population of triplet states dominates the design of continuous wave dye lasers. There is also the problem of the pump laser sources, as noted in Table 45.2, which are of modest power typically of the order of 10 W. Consequently, as the gain of a cw dye laser is very low, of the order of a few per cent per pass, the cavity must be designed to keep optical losses to an absolute minimum. Gratings therefore cannot be used, but a combination of a birefringent filter and one or more tilted etalons is a feasible spectral control configuration.

The gain region of these lasers is in the form of a parallel-sided, thin stream of dye solution forced as a laminar flow jet through a slit-like nozzle by a high-pressure pump. Longitudinal pumping is often used in dye-jet lasers. In this case, optical elements are needed to focus the pump energy to a spot, typically a few micrometres in diameter, to broach the laser threshold. In order to avoid causing optical damage to windows, the dye usually flows from a nozzle to a receiver in an open configuration.

The use of a high-quality pump beam enables a common waist to be shared by both the pump beam and the dye-laser cavity. The diameter of such a waist is of the order of 15 µm, so with a dye-flow velocity of 10 ms^{-1} it means that a molecule only spends about 1.5 µs in the pump beam; hence, the triplet-state population cannot build up to impair the efficiency of the laser action. If necessary, additional quenching agents can be used to augment the effects of atmospheric oxygen entrained in the dye jet.

45.5 Cavity Designs

Several cavity designs have been used for generating tunable cw operation. The diagrams in Figure 45.22 show a simple two-way linear cavity and a ring cavity. Both contain frequency-selective elements (FSE), such as birefringent filters, to give coarse control of the oscillation and tilted etalons to restrict the spread of oscillation even further.

Line narrowing of the oscillation in a linear cavity is limited by the characteristics of the standing wave in a two-way cavity. The standing wave is spatially pinned with respect to the cavity mirrors, and the upper-level population is depleted more strongly at the antinodes of the electric-field pattern than at the nodes. This leads to the possibility of unwanted cavity modes developing, by scavenging the population inversion not accessed by the 'spatial hole burning' of the dominant mode.

The ring cavity, introduced in the late 1970s [74], avoids this drawback by creating travelling waves, so there are no nodes with unused gain that could support additional (unwanted) modes. In a simple configuration, laser energy can be generated in either of the two directions around the ring. The first to resonate will oscillate at the expense of the other, thus suppressing the second resonance. However, the direction of preference is random, which is unsatisfactory, as brief fluctuations in the cavity loss can cause the direction of propagation to be reversed. This presents problems for extracting the cavity flux, so an additional element is placed in the cavity that has a direction-dependent loss, giving a preferred propagation direction. A common technique is to use a Faraday rotator and standard polarizer, acting as a unique direction device (UDD). Consequently, only one travelling wave is established as the dominant mode and avoids spatial hole burning, leading to single mode emission.

45.5.1 Mode Locking

Synchronous pumping of a dye-jet laser enables a string of ultra-short pulses, in the femtosecond regime, to be generated, provided sophisticated techniques are applied to the laser configuration [43–45,75]. An absorber is used for providing the non-linearity to phase-lock the cavity modes. [43]. The general rule is the shorter the pulses, the broader the emission bandwidth needs to be.

The basic arrangement is to focus a continuous wave laser on to a dye laser jet in a linear cavity to provide the gain. The beam inside the cavity has another focal spot on an absorber dye, such as 3,3-diethyloxadicarbocyannine iodide (DODCI). Saturation of a dye in the absorbing element is used as the non-linearity to phase-lock the cavity modes. Use of the colliding pulse technique [75] has enabled pulses of the order of 300 fs to be generated. Use of ring cavity configurations enabled this duration to be reduced to about 65 fs. More sophisticated techniques and compensation enabled this to be reduced by an order of magnitude [45,76].

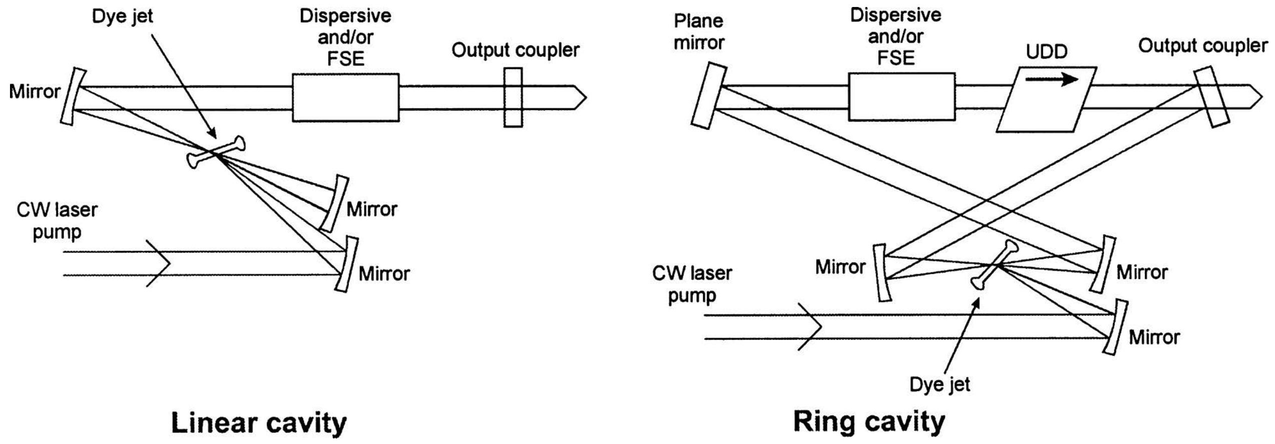

FIGURE 45.22 cw dye-laser arrangements.

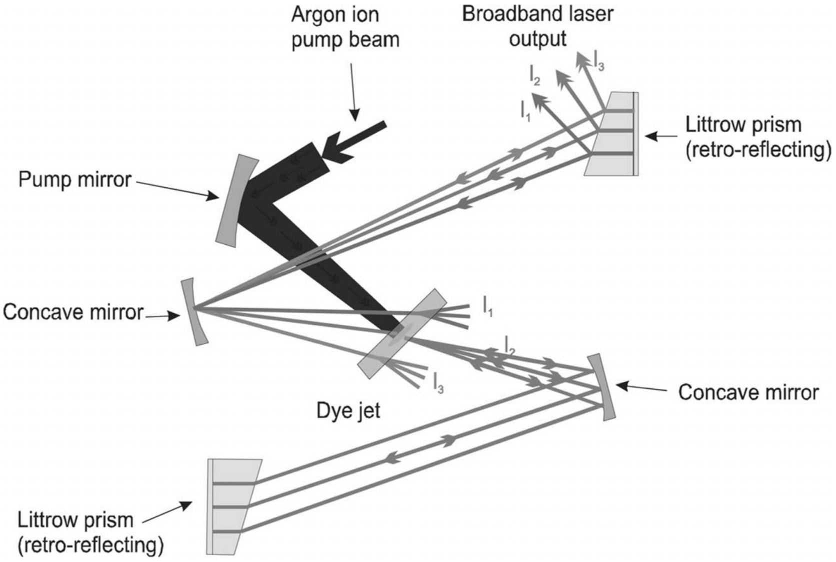

FIGURE 45.23 cw broadband dye-laser configuration.

45.5.2 Broadband Emission

Broadband emission is feasible from a dye-jet laser, and a scheme is shown in Figure 45.23. A mode-narrowing control aperture is required at the concave mirror, i.e. where the various beams intersect. The angles between the colours have been exaggerated for the purposes of illustrating the technique.

45.5.3 Performance

The performance of cw dye lasers is comparable with laser-pumped sources in terms of the beam quality and spectral characteristics, with frequency stability or linewidths of the order of 1 kHz being demonstrated by injection seeding. The spectral emission range is comparable with other dye lasers, stretching 365–1000 nm. This range can be extended further into the UV and near IR by the use of non-linear techniques.

This class of laser is capable of emitting beams with power in the 'watt class'. For special applications, the power has been extended to give tens of watts of tunable light. Developments with diode-pumping and the use of diode-pumped solid-state lasers have seen the efficiency of the complete cw dye laser system increase substantially, compared with the classic ion-laser pump source. Diode pumping has been used for near infrared emission [71].

The development of ring laser cavities has led to the generation of beams with high spectral purity. Mode locking has enabled very short duration pulses to be emitted in the femtosecond regime.

REFERENCES

1. Sorokin P P and Lankard J R 1966 Stimulated emission observed from an organic dye, chloro-aluminum phthalocyanine *IBM J. Res. Develop.* **10** 162–3.
2. Samelson H 1982 *Handbook of Laser Science Technology* vol 1, ed M L Weber (Boca Raton, FL: Chemical Rubber Company) pp 397–422.
3. Fulker D J et al. 1999 The evolution of pulsed discharges over PTFE in the presence of various cover gases *Proc. 12th IEEE Int. Pulsed Power Conf. (Monterey)* (Piscataway, NJ: IEEE) pp 1071–4.
4. Winstanley P A et al. 1998 Enhancements achieved in the performance of liquid and solid-state dye laser technology *Proc. SPIE Solid State Lasers Conference (San Jose, CA)* vol 3265 (Bellingham, AW: SPIE) pp 42–50.
5. Titterton D H et al. 1994 Studies to enhance the beam quality from flashlamp-pumped dye lasers *Proc. SPIE Solid State Lasers Conference (Los Angeles)* vol 2115 (Bellingham, WA: SPIE) pp 219–30.
6. Morton R G and Draggoo V G 1981 Reliable high average power high pulse energy dye laser *J. Quantum Electron.* **17** 222.
7. Ackerman D A 1990 Dye-laser isotope separation *Dye Laser Principles with Applications* ed F J Duarte and L W Hillman (Boston, MA: Academic) ch 9.
8. Bass I L et al. 1992 The high-average-power dye laser at Lawrence Livermore National Laboratory *Appl. Opt.* **31** 6993–7006.
9. Klick D 1990 Industrial applications of dye lasers *Dye Laser Principles with Applications* ed F J Duarte and L W Hillman (Boston, MA: Academic).
10. Wheeler M D 1999 Photonics in medicine-cancer in the crosshairs *Photon. Spectra* **33** 86.
11. Itzkan I and Izatt J A 1994 Medical uses of lasers *Encyclopaedia Appl. Phys.* **10** 33–59.
12. Pacheco D P et al. 1990 A high-average-power blue-green laser for underwater communications *Proc. Int. Conf. on Lasers '89* (McLean, VA: STS) pp 376–82.
13. Estep L 1993 A review of airborne lidar hydrographic (ALH) systems *Hydrographic J.* **67** 25–43.
14. Hogan G P et al. 1997 Designing a scaleable laser guide star system: the Oxford approach *Proc. ESO Workshop on Laser Technology for Laser Guide Star Adaptive Optics Astronomy Garching bei München, Germany* ed N Hubin, no 55, pp 92–8.

15. Friedman HW et al. 1997 Design of a laser guide star system for the Keck II telescope *Proc. ESO Workshop on Laser Technology for Laser Guide Star Adaptive Optics Astronomy Garching bei München, Germany* ed N Hubin, no 55, pp 138–44.
16. Alden M et al. 1984 Application of a two colour dye laser in CARS experiment *Appl. Opt.* **23** 2053–5.
17. Burlamacchi P et al. 1979 Characterization of a multicolour dye laser *Opt. Commun.* **34** 185–8.
18. Hilborn R C and Brayman H C 1974 Simultaneous two-wavelength output from multiple-dye pulsed tunable dye lasers *J. Appl. Phys.* **45** 4912.
19. Nair L G 1979 A double wavelength nitrogen-laser-pumped dye laser *Appl. Phys.* **20** 97–9.
20. Saito Y et al. 1985 Simultaneously tunable three-wavelength dye laser *Appl. Opt.* **24** 2477–8.
21. Williams S W et al. 1983 Simultaneous two-wavelength tunable dye laser with no mode competition and with a wavelength separation of more than 200 nm *Opt. Commun.* **45** 112–4.
22. Malikechi N and Allen L 1987 A two wavelength dye laser with broadband tunability *J. Phys. E: Sci. Instrum.* **20** 558–9.
23. Pacheco D P et al. 1989 The use of special conversion to increase the efficiency of flashlamp-pumped dye lasers *Proc. Int. Conf. on Lasers '88* (McLean, VA: STS) pp 410–19.
24. Griffiths J 1976 *Colour and Constitution of Organic Molecules* (London: Academic).
25. Hecht J 1992 Dye lasers *The Laser Guidebook* 2nd edn (New York: McGraw-Hill) ch 17.
26. Schäfer F P 1973 Principles of dye laser operation *Dye Lasers* (Berlin: Springer) ch 1.
27. Koechner W 1992 *Solid-State Laser Engineering* (Berlin: Springer).
28. Marling J B 1970 Chemical quenching of the triplet state in flashlamp-excited liquid organic lasers *Appl. Phys. Lett.* **17** 527–30.
29. Tuema F A et al. 1999 The spectral properties of UV radiation from pulsed surface discharges *Proc. 12th IEEE Int. Pulsed Power Conf. (Monterey)* (Piscataway, NJ: IEEE) pp 1106–9.
30. Fulker D J 2002 The development and application of surface discharges for the pumping of dye lasers PhD thesis University of Strathclyde.
31. Miller A W et al. 1995 Investigation into the photo-degradation products affecting the dye life in flashlamp pumped dye laser *Proc. SPIE Conf. on UV and Visible Lasers and Laser Crystal Growth (San Jose)* vol 2380 (Bellingham, WA: SPIE) pp 364–273.
32. Bradley D J et al. 1974 Megawatt VUV xenon laser employing coaxial electron-beam excitation *Opt. Commun.* **11** 335–8.
33. Duarte F J 1990 Narrow-linewidth pulsed dye laser oscillators *Dye Laser Principles with Applications* ed F J Duarte and L W Hillman (Boston, MA: Academic) ch 4.
34. Hansch T W 1972 Repetitively pulsed tunable dye laser for high resolution spectroscopy *Appl. Opt.* **11** 895–8.
35. Beiting E J and Smith K A 1979 An on-axis reflective beam expander for pulsed dye laser cavities *Opt. Commun.* **28** 355–8.
36. Titterton D H and Stokoe C 1995 Progress with a flashlamp-pumped titanium sapphire laser *Proc. SPIE Conf. on UV and Visible Lasers and Laser Crystal Growth (San Jose)* vol 2380 (Bellingham, WA: SPIE) pp 115–26.
37. Danilov M B and Kristov I P 1986 Novel method of ultra-broadband laser generation *Opt. Commun.* **73** 235.
38. Duarte F J and Piper J A 1980 A double-prism beam expander for pulsed lasers *Opt. Commun.* **35** 100–4.
39. Morton R G et al. 1978 Efficient cavity dumped dye laser *Appl. Opt.* **17** 3268–75.
40. Leslie S G et al. 1984 Efficient cavity dumped HgBr laser *Appl. Opt.* **23** 36–9.
41. Schmidt W and Schäfer F P 1968 Self-mode-locking of dye-lasers with saturable absorbers *Phys. Lett. A* **26** 558–9.
42. Ippen E P et al. 1972 Passive mode locking of the cw dye laser *Appl. Phys. Lett.* **21** 348–50.
43. Fork R L et al. 1981 Generation of optical pulses shorter than 0.1 psec by colliding pulse mode locking *Appl. Phys. Lett.* **38** 671–2.
44. Dietel W et al. 1983 Intracavity pulse compression with glass: a new method of generating pulses shorter than 60 fs *Opt. Lett.* **8** 4–6.
45. Fork R L et al. 1987 Compression of optical pulses to six femtoseconds by cubic phase compression *Opt. Lett.* **12** 483–5.
46. Sorokin P P and Lankard J R 1967 Flashlamp excitation of organic dye lasers: a short communication *IBM J. Res. Dev.* **11** 148.
47. Schmidt W and Schäfer F P 1967 Blitzlampengepumpte Farbstofflaser *Z. Naturf. a* **22** 1563–6.
48. Markiewicz J P and Emmett J L 1966 Design of (a) flash-lamp driving circuit *J. Quantum Electron.* **2** 707–11.
49. Miller A W et al. 1998 Factors affecting the life of dye laser flashlamps *Proc. SPIE Solid State Lasers Conference (San Jose)* vol 3265 (Bellingham, WA: SPIE) pp 21–8.
50. Klimek D E and Aldag H R 1994 10 Hz kilowatt-class dye laser system *Proc. SPIE Conf. on Intense Laser Beams and Applications (Los Angeles)* vol 1871 (Bellingham, WA: SPIE) p 11.
51. Jensen C C 1991 Pulsed dye laser gain analysis and amplifier design *High-Power Dye Lasers* ed F J Duarte (Berlin: Springer).
52. Schlichting H 1960 *Boundary Layer Theory* (New York: McGraw-Hill).
53. Hall D R and Jackson P E 1989 *The Physics and Technology of Laser Resonators* (Bristol: Hilger).
54. Siegman A W 1986 *Lasers* (Oxford: Oxford University Press).
55. Morin M 1998 National Optics Institute (Canada) GRM resonator design: a tutorial *Proc. SPIE Conf. on Laser Resonators (San Jose)* vol 3267 (Bellingham, WA: SPIE) p 6.
56. Kaye G W C and Laby T H 1986 *Tables of Physical Constants* (Singapore: Longman).
57. Klimek D E and Mandl A 1995 Single mode, diffraction-limited operation of a zig-zag dye laser *Proc. SPIE Conf. on UV and Visible Lasers and Laser Crystal Growth (San Jose)* vol 2380 (Bellingham, WA: SPIE) pp 256–63.
58. Dearth J J et al. 1988 A flashlamp-pumped zig-zag slab dye laser *Proc. Int. Conf. on Lasers '87* (McLean, VA: STS) pp 320–9.

59. Aldag H R 1996 Efficient high average power dye laser *Proc. SPIE Conf. on Gas Lasers (laser Optics '95) (St Petersburg)* vol 2771 (Bellingham, WA: SPIE).
60. Sierra R 1988 Flashlamp-excited dye lasers achieve new performance levels *Laser Focus/Electro-Opt.* 76–92.
61. Svelto O 1982 *Principles of Lasers* 2nd edn (New York: Plenum).
62. Duarte F J 1990 Technology of pulsed dye lasers *Dye Laser Principles with Applications* ed F J Duarte and L W Hillman (Boston, MA: Academic) ch 6.
63. Everett P N et al. 1986 Efficient 7-J flashlamp-pumped dye laser at 500 nm wavelength *Appl. Opt.* **25** 2142–7.
64. Schäfer F P et al. 1966 Organic dye solution laser *Appl. Phys. Lett.* **9** 306–9.
65. Hecht J 1992 Versatility keeps dye lasers alive *Laser Focus World* 59–74.
66. Anderson D J et al. 1996 Fiber-optic-bundle delivery system for high peak power laser particle image velocimetry illumination *Rev. Sci. Instrum.* **67** 2675–9.
67. Anderson D J et al. 1995 An optical-fiber delivery system for pulsed-laser particle image velocimetry illumination *Meas. Sci. Technol.* **6** 804–14.
68. Booth H 1998 Guide star lasers *High Power Fibre Optic Laser Beam Delivery* University of Oxford, DPhil Thesis, ch 4.
69. Peterson O B 1970 cw operation of an organic dye solution laser *Appl. Phys. Lett.* **17** 245–7.
70. Runge P K and Rosenburg R 1972 Unconfined flowing-dye films for cw dye lasers *IEEE J. Quantum Electron.* **8** 910–1.
71. Scheps R 1995 Near-IR dye laser for diode-pumped operation *IEEE J. Quantum Electron.* **31** 126–34.
72. Scheps R 1993 Low threshold dye laser pumped by visible diodes *IEEE Photonics Tech. Lett.* **5** 1156–8.
73. Scheps R 1995 Laser diode-pumped dye laser *Proc. SPIE Conference on UV and Visible Lasers and Laser Crystal Growth (San Jose)* vol 2380 (Bellingham, WA: SPIE) pp 274–84.
74. Schröder H W et al. 1977 A high-power single-mode cw dye ring laser *Appl. Phys.* **14** 377–80.
75. Ruddock I S and Bradley D J 1976 Bandwidth-limited subpicosecond pulse generation in mode-locked cw dye lasers *Appl. Phys. Lett.* **29** 296–7.
76. Diels J-C 1990 Femtosecond dye lasers *Dye Laser Principles with Applications* ed F J Duarte and L W Hillman (Boston, MA: Academic) ch 3.

FURTHER READING

Duarte F J (ed) 1991 *High-Power Dye Lasers* (Berlin: Springer).

Duarte F J and Hillman L W (ed) 1990 *Dye Laser Principles with Applications* (Academic).

Griffiths J 1976 *Colour and Constitution of Organic Molecules* (London: Academic).

Hecht J 1992 *The Laser Guidebook* 2nd edn (New York: McGraw-Hill).

Maeda M 1984 *Laser Dyes* (New York: Academic) 1951; *Fluoreszenz Organizcher Verbindungen* (Göttingen: Vanderhöck and Ruprecht).

Pavlopoulos T G 2000 Laser dyes *Encyclopaedia of Materials Science and Engineering, Section on Colors, Paints and Dyes* (New York: Wiley) ch 7.

Schäfer F P 1973 *Dye Laser* (Berlin: Springer).

Taylor & Francis
Taylor & Francis Group
http://taylorandfrancis.com

46

Solid-State Dye Lasers

David H. Titterton

CONTENTS

46.1 Introduction 623
46.2 Solid-state Dye-doped Host Preparation 624
  46.2.1 General Characteristics 624
  46.2.2 Pre-doped Hosts 624
    46.2.2.1 Sol-gel-derived Silicates 625
    46.2.2.2 Poly-(Methyl Methacrylate) 625
    46.2.2.3 Organically Modified Silicates 625
    46.2.2.4 Optical Epoxy 625
    46.2.2.5 Polyacrylamide Gel 626
    46.2.2.6 Fluorophosphate Glasses 626
    46.2.2.7 Other Media 626
  46.2.3 Post-doped Hosts 626
    46.2.3.1 Densified Sol-gel 626
    46.2.3.2 Microporous Glass 626
    46.2.3.3 Polycomposite Glass 626
    46.2.3.4 Polymer-filled Microporous Glass 627
  46.2.4 Additives 627
46.3 Gain Media 627
  46.3.1 General Considerations 627
  46.3.2 Fabrication of Laser Media 627
  46.3.3 Optical Coatings 628
  46.3.4 Damage Threshold 628
  46.3.5 Photostability 628
46.4 Laser Dyes 629
  46.4.1 Absorption/Fluorescence Characteristics 629
46.5 Laser-pumped Solid-state Dye Lasers 629
  46.5.1 Performance 629
46.6 Flashlamp-pumped Solid-state Dye Lasers 631
  46.6.1 Performance 632
46.7 Choice of Host 634
References 634

46.1 Introduction

The broad spectral emission from a single laser cavity containing a dye-based gain medium makes these sources attractive for many applications. A single laser configuration can be used to produce light from the ultraviolet to the near-infrared by merely changing the laser dye in the gain medium. In addition, it is possible to tune the wavelength of the light from a given laser dye over a narrow spectral range, often over a few tens of nanometres.

Traditionally, dye lasers have used a liquid gain medium but dye-doped materials, such as polymers and glasses, are now becoming established [1–24] with flashlamp-pumped configurations [15–24] as well as laser-pumped devices. The development of new laser dyes [25–30] over the last 15 years, offering greater photostability and potential for enhanced gain, has provided the catalyst for the development of dye-doped solid-state lasers. During this period, there has also been a significant improvement in the optical quality as well as the range and stability of host materials. However, other limitations in the physical characteristics of the gain materials, such as the thermal degradation of the dye, along with thermal expansion of the gain element and its impact on the cavity stability, will limit the linewidth performance that can be achieved from this class of laser. Hence, solid-state dye lasers cannot be expected to supersede the liquid laser in all of its established applications, particularly those requiring high spectral purity, such as spectroscopy. For many other applications such as medical or military ones, which generally require energetic pulses of coloured light, the solid-state dye laser is most attractive owing to its greater simplicity.

Laser action from a dye gain medium was first demonstrated in 1966 [31,32]. In these studies, solutions of the phthalocyanine class of organic laser dyes formed the gain medium, which was pumped by photons from a ruby laser. Soon afterwards flashlamp-pumped dye lasers were demonstrated [33,34], and the same year saw the first laser action from a dye-doped polymer [35]. The following year, 1968, saw the demonstration of a flashlamp-pumped dye-doped polymer [36]. The conversion efficiency of these early devices was poor but was improved with the use of transfer dyes to improve conversion efficiency in dye-doped poly-(methyl methacrylate) [37].

During the latter part of the 1980s, there was an upsurge in interest in solid-state dye lasers [1,2,15], particularly for medical applications [10]. The combination of better dyes being incorporated into host matrices with lower optical losses resulted in the dye-doped polymer hosts being very effective sources. Various hosts have been developed, including polymers and glass-like materials. The laser-pumped devices have routinely exhibited conversion efficiencies of the order of 70%, or more, for some dyes [2,11–13,17], and results with flashlamp-pumped rods have seen emissions with energy in excess of 1 joule per pulse [22,24]. Currently, there appears to be little prospect of sustained continuous-wave (cw) emission, although quasi-cw devices have been demonstrated [38].

Research has also been directed towards increasing the so-called ‘service life’ of the dye-doped solid-state gain medium [7,12,14], which relates the number of useful pulses of light that can be obtained from a gain element. Various criteria can be used to express the ‘useful performance’: a typical cut-off point is when the current output performance (such as energy per pulse) has fallen to 70% of its initial value.

A major *bête noire* of a liquid-phase laser is the need to circulate the laser-dye solution in order to remove heat, molecules in their triplet state and any dye molecules that have degraded from the gain volume. A dye-doped gain medium experiences similar performance-limiting effects, resulting from the trapping of pump light but their impact can be mitigated through careful design of the gain element and choice of laser dye. Several schemes have been designed to simulate dye flow by moving the dye-doped matrix in the resonant cavity, either by rotation, translation or a combination of both, which are somewhat simpler than a dye-circulation system. This approach has enabled enhanced ‘service life’ to be achieved, resulting in many tens of thousands of laser pulses to be emitted from a single dye-doped gain element without significant loss in performance. In some cases, well in excess of 500 000 shots have been reported from a small disc, of the order of 20 mm diameter. Developments indicate that this performance may be achievable without the need to move the gain element [14].

46.2 Solid-state Dye-doped Host Preparation

A few companies produce dye-doped materials for sale. However, good quality materials can be made relatively easily in a laboratory equipped for polymer or glass technology experiments. No particularly sophisticated equipment is required and the techniques that have been developed by various laboratories are quite straightforward; hence, research groups and other source developers can produce their own samples. Many different types of host [39] have been demonstrated and techniques for the production of various hosts are outlined in the following sections, the references providing details on experimental procedures.

46.2.1 General Characteristics

The use of conventional solid glass materials doped with laser dyes is quite attractive, as they have low optical scatter and low distortion, are hard and stable and can be polished to be smooth and flat. However, it is usually impossible to use such a host, owing to the need to heat the constituent materials to temperatures in excess of 1000°C during production, thereby destroying the laser dye. Consequently, alternative host materials and techniques for fabrication at a lower temperature have been sought.

There are two major approaches: synthesizing polymer or ‘glassy materials’ at low temperature or producing a glass with a porous structure. The former technique allows a laser dye to be added to the constituent chemicals and is known as pre-doping. A porous structure allows a dye solution to be introduced into the structure to impregnate it by diffusion and is termed post-doping of the solid matrix.

Pre-doped hosts usually produce solid materials with good optical quality and uniform dye concentration. These dye-doped solids can have properties approaching those of glass but tend to be somewhat softer, which can have an adverse impact on performance, particularly if high-energy performance is required. In contrast, post-doped materials are usually more ‘glass-like’, with many of the excellent bulk properties of glass but the material can be susceptible to losses owing to excessive optical scatter from the pores in the host matrix. Clearly, there is a trade-off between ensuring that the average pore size is large enough to absorb the dye solution, to achieve a good concentration, and still have very good optical quality with low losses, particularly optical scatter.

46.2.2 Pre-doped Hosts

In this case, a solution of the chosen laser dye is mixed with one of the constituent chemicals used to form the host matrix, which is normally a thermoplastic polymer with a linear molecular structure. Consequently, successful application of this technique is dependent on limiting the temperatures used in the polymerization, condensation or curing processes invoked, to produce the solid material, to less than a few hundred degrees Celsius. This process has been used successfully by many teams to produce dye-doped sol-gel [40], poly-(methyl methacrylate) (PMMA) [6], ormosil [41–43] and polyacrylamide gels [44], with dye concentrations of the order of 2×10^{-4} molar.

One of the snags with the pre-doping technique is that the laser dye may not be soluble in the basic constituent chemicals, such as the monomer—use of a co-polymer solves this problem [45]. An example is the popular dye rhodamine 6G, which is insufficiently soluble in methyl methacrylate. In this case, it is normal to use a hydroxylic co-monomer, e.g. 2-hydroxypropyl acrylate/methyl methacrylate, in order to produce rhodamine 6G-doped PMMA.

The curing process can take from a few tens of minutes for polyacrylamide gels to many weeks for ormosils: PMMA takes 5–10 days. Careful thermal control is necessary in order to prevent the build-up of stresses during the formation of the host matrix as the volume can shrink by about 80% in some cases, for example with a sol-gel. Various strategies have been developed to alleviate the stress formation, including the use of drying control chemical additives; however, some additives can be difficult to remove.

46.2.2.1 Sol-gel-derived Silicates

This matrix is produced [40] by a low temperature (less than 100°C) hydrolysis of tetramethoxysilane with water in a solvent, such as methyl alcohol, with subsequent poly-condensation. Following hydrolysis of the tetramethoxysilane, the poly-condensation reaction occurs to produce a sol of colloidal silica particles in suspension. This reaction continues to inter-link the sol particles to produce a rigid gel matrix. Further strengthening of the matrix results from additional reaction time and drying to remove the solvent and excess water. Such matrices are commonly known as xerogels.

The xerogel structure usually consists of a network of pores, their sizes being of the order of 1–10 nm. The pore surface is populated by silanol groups, Si–OH and is very polar. These silanol groups are suitable sites for hydrogen bonding with dye molecules inside the pore system.

46.2.2.2 Poly-(Methyl Methacrylate)

The fundamental unmodified host is produced from the polymerization of the monomer methyl methacrylate [6], in which a suitable dye is dissolved. This reaction is generally started by a radical initiator, such as benzoyl peroxide, or azo-bis-isobutyronitrile. Again, this is a low-temperature reaction with the mixture heated to about 50°C; it is also quite quick, producing samples within a few days. This host is often regarded as the standard for pre-doped solid-state dye media.

The use of co-polymer mixtures [3,8,17,45], such as methyl methacrylate/hydroxy propylacrylate and methyl methacrylate/hydroxyethyl methacrylate, to produce host matrices has been successful. This modified PMMA material (m-PMMA) has some attractions as, for example, it allows polar dyes to be used such as rhodamine 6G.

A common modification is to use a low-molecular weight additive [46–48], which plasticizes the polymer and increases the laser-induced damage threshold. The modest damage threshold of the unmodified host is a serious disadvantage for high-average-power operation.

46.2.2.3 Organically Modified Silicates

This host material is commonly known as ormosil, which has some similarities in its fabrication with sol-gels but produces an organic–inorganic composite substance on the molecular scale [49,50]. The silicate structure is prepared by a low-temperature sol-gel technique, and it is possible to produce materials where the PMMA is covalently bonded to the silicate network, producing a non-porous structure.

During the reaction, tetramethoxysilane (TMOS) undergoes acid catalysed hydrolysis and condensation reactions to form a silicate structure with loss of methyl alcohol. A second precursor, trimethoxysilylpropyl-methacrylate (TMSPM), undergoes partial hydrolysis and condensation to allow it to link into the developing silicate structure but its Si–C group is not hydrolysed, so it retains a methacrylate tail. This methacrylate tail allows the structure to bond to the third precursor, methyl methacrylate, which itself undergoes polymerization reactions, to form PMMA. This matrix is doped with a dye by adding a solution of laser dye in methyl alcohol to the reactants, for example after the initial rapid hydrolysis under acid catalysis.

The fabrication process can be somewhat lengthy, taking up to several weeks to produce a large fully cured matrix with negligible stress. The use of carefully controlled cooling methods (typically about 1°C per day) and curing techniques has led to the production of samples with very good optical quality, comparable with that of PMMA. Generally, this host is somewhat harder than PMMA.

46.2.2.4 Optical Epoxy

Optical epoxy polymer samples are fabricated [51,52] from two constituent parts: usually an epoxy oligomer and a polyamine hardener. These two components are mixed together according to the manufacturer's instructions and cured to give a thermoset epoxy polymer matrix. A suitable laser-dye solution is added to the two components prior to the curing process, which is conducted in an appropriate mould. These cured polymers tend to have a yellow colouration, because of the absorption of the matrix in the blue-violet region of the spectrum.

A Ukrainian group developed a matrix [53] formed by the radical photo-polymerization of oligomers, such as oligourethane acrylate. In this case, they used benzophenone as the initiator and it was introduced into the initial oligomer composition.

Epoxy materials are cheap and easy to manufacture and have high thermal resistance and damage threshold. Other advantages that are often cited, compared with PMMA, are a higher elastic modulus, a lower temperature coefficient of refractive index and better resistance to photochemical degradation. Moreover, during the curing process this type of host matrix only shrinks by a small percentage of the initial volume; hence, the dye concentration can be carefully controlled.

46.2.2.5 Polyacrylamide Gel

This laser gain medium, with high optical quality, can be produced [44] in about 20 minutes and is made up from three constituents: gel buffer, an acrylamide gel and an ammonium persulphate solution. The dye solution is added to the gel buffer prior to adding to the other constituent solutions, mixed quickly and allowed to set at room temperature in a quartz cuvette.

This dye-doped host degrades over time owing to the loss of water, and eventually, it becomes opaque. Loss of water from the matrix can be retarded by sealing the cuvette with a silicon rubber compound.

46.2.2.6 Fluorophosphate Glasses

A family of glasses in the lead-tin fluorophosphate system, which has viscosity characteristics that enable melting to occur at a temperature which does not cause thermal decomposition of many organic dyes, has been reported [54]. The dye-doped samples are prepared by melting batch materials at about 400°C in a vitreous carbon crucible and allowed to cool to 300°C. The composition is such that the viscosity at this temperature allows dyes to be thoroughly mixed with the host. The samples are then allowed to cool in air followed by annealing at around 50°C. In this case, the dye is incorporated into the matrix and is unaffected by the glass transition process.

Glasses within this class appear to be an ideal host for organic laser dyes. The hosts are transparent in the visible and near-infrared bands, with the onset of the ultraviolet absorption edge at around 350 nm.

46.2.2.7 Other Media

A range of other materials has been investigated, such as polystyrene, lavsan, di- and tri-acetate cellulose, polyvinyl ether and polycarbonate. In general, these hosts have tended to be less successful for dye-laser applications than the matrix materials just described in detail, or the glass-like materials considered later.

46.2.3 Post-doped Hosts

The use of this technique enables genuine glass-like materials to be produced, using elevated temperatures to strengthen the matrix. A porous structure can be generated either through a chemical reaction or by selective etching of a solid glass matrix. The resulting porous material can then be doped with a suitable laser-dye solution; however, it is usually difficult to calculate the exact dye concentration in the host matrix. Thus, it can be difficult to optimize the dye concentration for a given pump source. One common method is to estimate the amount of dye solution taken up by the host matrix from the difference in dye solution at the beginning and end of the doping or impregnation process. Hence, the doping concentration can be estimated. The other major drawback is the problem of achieving an optical-grade polish on the surfaces after the doping process, owing to the porous structure.

46.2.3.1 Densified Sol-gel

An undoped xerogel matrix produced by the hydrolysis process, described in Section 46.2.2.1, may be modified by heating to about 800°C [6]. This produces a stronger and denser matrix with smaller pores, which has thicker pore walls. During this process, the xerogel shrinks to about 50% of its original volume. Heating to higher temperatures results in a further reduction in pore size until, at about 1200°C, a non-porous structure is produced. This host is usually doped [6] by standing the partially densified matrix in a solution of laser dye for a couple of weeks at an ambient temperature of around 45°C–50°C. Subsequently, the material is dried, using vacuum techniques.

46.2.3.2 Microporous Glass

The porous glass host can be created through selective etching of a particular glass matrix, which has at least two skeletal structures. It is necessary for each to have a different reaction to a given solvent, so that one structure can be removed to leave the other intact, thus creating a porous matrix.

Vycor is a sodium borosilicate glass which, when heated above its glass transition temperature, forms a liquid–liquid phase separation. The sodium borate glass phase can be leached out at room temperature in acid to leave an interconnected sponge-like structure of more or less pure silica glass. The matrix can be impregnated with laser dye: this has been demonstrated in wet and dry forms [55–57]. In the former case, the dye is in solution in a suitable solvent, such as an alcohol or an ester, and the dye-doped microporous matrix is sealed between quartz plates, for example. In the latter case, the solvent is removed by warming. Generally, the 'wet fill' has superior optical performance, owing to reduced optical scatter.

The overall porosity (pore volume density) and the average pore size can be controlled by varying the ratio of the two phases in the original matrix to give a structure optimized to receive a dye solution. Pore sizes in the range 1–10 nm are usually achieved and a pore volume density of $0.15–0.2\,\text{cm}^3\,\text{g}^{-1}$. The presence of a continuous glass structure, together with the relatively small pores, allows efficient heat dissipation throughout the entire structure and its subsequent extraction during laser action.

46.2.3.3 Polycomposite Glass

In this case, a sol-gel matrix has its pores impregnated with a refractive-index-matched material [6,58] to reduce the optical scatter from the pores and, hence, improve the optical quality of the material. It is possible to use PMMA to 'index match' with silica glass, using an in situ polymerization of methyl methacrylate [6], producing a sol-gel–PMMA composite known as polycomposite (or polycom) glass. In this case, a solution of the monomer methyl methacrylate containing the laser dye and an initiator is permitted to diffuse into the pore network, then the polymerization is initiated at an ambient temperature of 40°C for a couple of days.

One snag with this approach is the progressive microfracturing of the host owing to the mismatch in the thermal properties of the two components within the composite structure.

46.2.3.4 Polymer-filled Microporous Glass

This has some similarities with polycomposite glass; in this case, a microporous glass [14,59] forms the fundamental matrix of the host. As previously noted, the host-fabrication process can be controlled to give a porous structure optimized to receive the monomer containing the dye dopant and initiator. Moreover, the porous structure can filter the monomer during the impregnation process, which leads to purification and enhances the damage threshold of the polymer content.

46.2.4 Additives

Studies have shown [46] that it has been possible to enhance the damage threshold of the host matrix and increase the resilience of the laser dye by clearing the initial monomer compositions of foreign inclusions and by doping PMMA with low-molecular-weight additives. It is recommended that the methyl methacrylate and the modifying additives are purified, by use of standard methods, to not less than 99.8 wt% of the main product.

Dye photostability [46] can be increased by doping a polymer with modifying additives that suppress the generation and branching of radical chains through cross-relaxation between the vibrational levels of the polymer macromolecules and those in the introduced additives. The function of these additives is to restrict the formation of radicals, which have a far lower ionization potential than the macromolecules. Elimination of these radicals and their products is vital for good 'service life' as they interact readily with the dye molecules in their first excited singlet (S_1) states and subsequently leads to the destruction of the dye molecules. These radical interactions have been postulated as the principal destruction mechanism.

46.3 Gain Media

46.3.1 General Considerations

One of the attractions of this class of laser source is that effective gain media, with good optical quality and low cost, can be made easily to match the requirement or application. With the exception of the polyacrylamide gels, the dye-doped material requires careful cutting and polishing before it is suitable for use in a laser cavity. As noted in Table 46.1, the shape of the gain medium is determined by the pump source configuration.

An important requirement of any gain medium is that its optical properties, such as refractive index, should be stable with varying environmental conditions, particularly temperature, humidity or water intake. Stress in the host matrix can not only lead to fracture but also to the creation of a lens within the material, which can be equally disruptive. As the material relaxes, this can lead to a variation in the focal length of the lens [24], which can prevent the effect being compensated or corrected.

Poor thermal conductivity, exhibited by some hosts, contributes to the bleaching of the dye and also distorts the gain medium, thus this class of gain medium will not be suitable for applications requiring high stability in the output beam. Hence, materials with poor thermal characteristics need careful heat control and management to avoid quickly changing optical properties. Changes to the optical properties can result in rapid fluctuations in laser performance, which may lead to a premature termination of laser action. Some hosts do have better thermo-optical characteristics than others, as shown in Table 46.2. A combination of hosts with good thermal properties and suitable geometrical shape can be used to mitigate some of the effects of waste heat deposited in the matrix. Rotation or translation of the gain medium can also help to reduce the effects of thermal gradients and the bleaching effects of the pump energy [48]. Rotation of the gain medium can help to increase the 'service life' of dye-doped media. Reports [7,13,48] suggest that more than 60 000 pulses can be emitted from a small rotating disc, of the order of 25 mm (diameter), with the possibility of up to an order of magnitude more at low pump fluences.

46.3.2 Fabrication of Laser Media

The fundamental approach is to mould the dye-doped material to the appropriate size, using a container of the approximate shape allowing for shrinkage and cutting to the required shape and size. The container can be made of any suitable inert substance, usually polythene or glass. Care is required during the curing or condensation processes to avoid introducing stress into the host and achieving a uniform density. It is essential to ensure that the polymer is fully cured before the machining of the pre-form is undertaken, which is dependent on the host. A range of techniques can be used to cut the sample to the approximate size and finish by diamond turning

TABLE 46.1

Characteristics of Solid-state Dye Laser Gain Media

Gain Shape	Typical Dimensions	Excitation	Host
Disc	Thickness: few to 20 mm Diameter: <10–100s of mm	Pulsed laser	Most pre-doped hosts except polyacrylamide gels. All post doped.
Cuboids	Side: few to 10s of mm	Pulsed laser	All.
Rods	Diameter: 4–15 mm Length: 20–250 mm	Short rods—pulsed laser Long rods—flashlamp	As discs. Mainly pre-doped to date.
Slabs	Up to 150×50×3 mm	Pulsed laser, flashlamp and surface discharge [60]	Most, except polyacrylamide gels.

TABLE 46.2

Thermo-optical Properties of Some Hosts

Host	105 × d*n*/d*T* $(°C^{-1})$	*K* $(W\ m^{-1}\,°C^{-1})$
PMMA	–0.85	0.21
Epoxy-filled MPG	–0.75	≈0.80
Silicate glass	0.30	1.3
Phosphate glass	–0.05	0.84

Source: From Ref. [14].

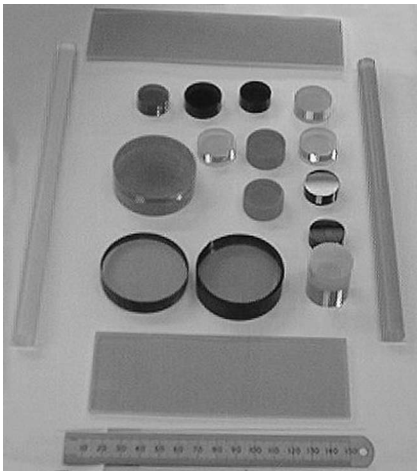

FIGURE 46.1 Dye-doped gain media.

and/or polishing. A photograph of various dye-doped gain media is shown in Figure 46.1.

46.3.3 Optical Coatings

Application of anti-reflection (AR) coatings to the dye-doped gain medium is important if high performance is to be achieved from the gain medium. The durability of ‘coatings’ is a problem with many materials, especially if the material to be ‘coated’ is soft or deforms easily. Sol-gel coatings have been spun on to a polymer [12], which enhanced the performance substantially. Motheye coatings [61,62] developed by the Defence Evaluation Research Agency (Malvern, UK) have been applied to PMMA to control parasitic reflections. This form of coating is attractive as it is effective over a wide range of incidence angles. A magnified photograph of this modification to the surface texture is shown in Figure 46.2 in which the pitch of the pattern is 400 nm.

46.3.4 Damage Threshold

The damage threshold of the plastic materials in an unmodified form is usually of the order of 2 J cm^{-2}, but this can be increased by a factor of 5 or so by the use of additives [10], as noted earlier. The porous glasses tend to have an inherent laser-induced damage threshold that is in the region of 26 J cm^{-2}, with the value for ormosils of the order of 20 J cm^{-2}. Polycom glass is quoted [13,63] as having a damage threshold of about 26 J cm^{-2}. Polyacrylamide gels potentially have a high damage threshold as they have some mobility within the matrix, so can be ‘self-healing’ [44].

Bulk damage effects can be mitigated by careful purification of the constituent chemicals used to create the host, particularly the exclusion of dust and other foreign particles, including moisture and bubbles.

46.3.5 Photostability

The ‘service life’ of a dye-doped element is dependent on the photostability of the laser dye, which depends on the number of photons absorbed by each laser dye molecule [10], and the damage threshold of the host: both aspects are a function of the incident pump fluence. Some molecules are more resilient than others, for example pyrromethene 597 is much better than pyrromethene 650, which, in turn, is much more resilient than

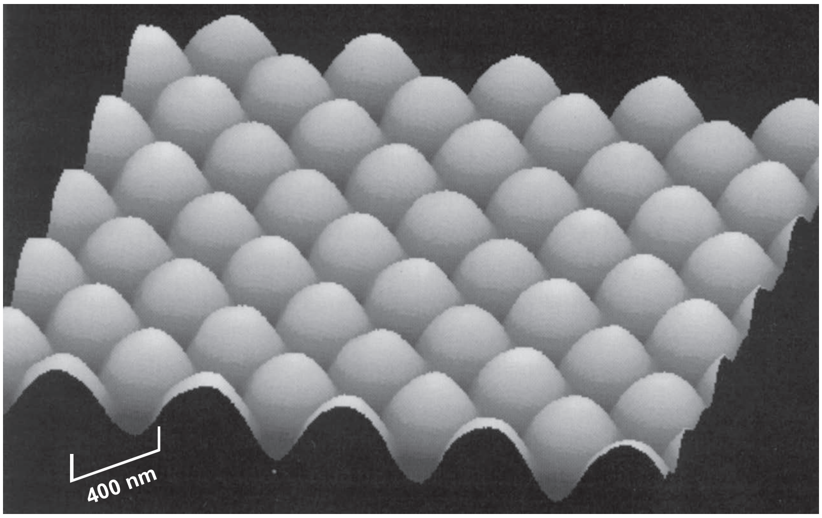

FIGURE 46.2 Motheye AR coating.

rhodamine 11B [10]. Photo-destruction results from excited dye molecules in a triplet state (see Figure 46.2) being excited from the lowest triplet energy state (T_1) into higher states (T_n). Having absorbed two light quanta, these molecules undergo chemical reactions, which may involve rearrangement of their chemical bonds, other reactions with dissolved impurities or residual solvent or oxygen from the atmosphere. The laser efficiency can be reduced significantly because the 'photoproducts' often absorb in the same part of the spectrum as the laser emission.

Good photostability may be achieved if the laser–host combination has high laser efficiency. Studies have reported [10] that dye-doped modified PMMA was superior to a modified acrylic co-polymer, which was much better than 'pure' PMMA. In the case of an inefficient combination, a significant proportion of the pump light will be trapped in the matrix, which leads to local heating and stresses resulting in destruction of laser dye molecules in this zone. Thus the trapped energy assists the photodegradation processes.

The photostability of a laser dye in a sol-gel matrix can be enhanced by increasing the organic character of the surrounding silica cage [50]. Additives to other hosts have also demonstrated enhanced service life. For example, use of 1,4-diazobicyclo[2,2,2] octane (DABCO) more than doubled the lifetime of pyrromethene 567 in PMMA and resulted in more than half a million shots being emitted from a small disc for a pump fluence well below the damage threshold [64].

46.4 Laser Dyes

46.4.1 Absorption/Fluorescence Characteristics

It is natural to assume that the spectral characteristics of the laser dyes in a solid matrix are dependent not only on the intermolecular interactions between individual dye molecules but also on intermolecular interactions between dye molecules and macromolecules. The intermolecular interactions may crucially affect the lasing characteristics of the dye molecules. These characteristics are determined by the degree of overlap between a laser-dye's absorption and fluorescence bands, as well as the luminescence quantum yield. The quantum yield may depend on the tendency of the dyes in weakly polar media to form dimers or other higher-order aggregates, which are usually weakly fluorescent.

A number of studies [65,66] have been conducted comparing the spectroscopic and photophysical properties of dyes in the liquid and solid states. The absorption and fluorescence spectra of dyes in the solid state are found to be similar to their analogous liquid counterparts (see Figure 46.3). The spectral properties of the dye pyrromethene 567 have been found [65] to be governed by polarity and specific hydrogen bonding ability of the solvent. There is a bathochromic (red) shift in less polar solvents.

It has been reported [66] that the fluorescence lifetime of dyes in solid hosts is higher than in a liquid solution. In common with viscous solvents, the fluorescence emission from dyes in solid-state hosts is anisotropic. This is because the rotational diffusion of the dye molecules embedded in the solid is slow in comparison with the lifetime of the singlet S_1 state.

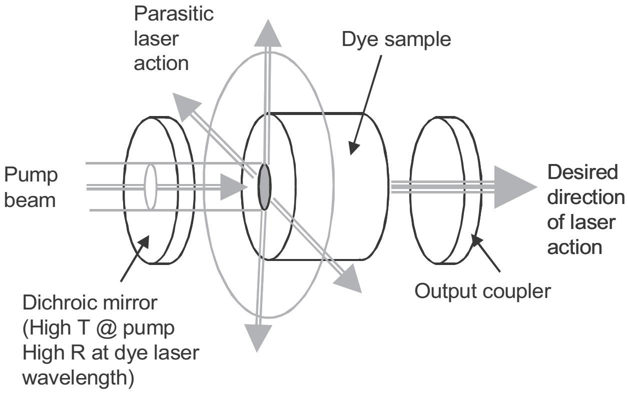

FIGURE 46.3 Parasitic effects in a dye-doped disc.

A study reported [15] similar fluorescence quantum yields for a number of dyes in solution and in a PMMA host, with the pyrromethene dyes having a superior performance in the solid host, compared with liquid hosts.

46.5 Laser-pumped Solid-state Dye Lasers

Pump lasers providing Q-switched pulses with durations of order 10 ns permit pump fluxes of the order of 100 MW cm^{-2} to be achieved from an energy density of about 1 J cm^{-2}. This is well within the operational limits of most host materials but is well in excess of that needed for fluorescence saturation (~1 MW cm^{-2}) of most dyes, so enabling the efficient extraction of laser energy from the gain medium. For these short pump pulses, the triplet state population is minimal and thermal-lensing effects should be small, particularly at low repetition rates.

A relatively simple configuration can be used for achieving laser action from a dye-doped disc, using an off-axis pumping arrangement. This approach avoids the need to use a dichroic mirror, which will transmit the pump energy but reflect the laser emission. A small penalty is paid in conversion efficiency, owing to the poor overlap of the pump energy and the resonant beam. In this arrangement, the reflectivity of the output coupler is usually in the range of 30%–50%. End pumping is common but transverse pumping [7] is also feasible.

The modern dye-doped materials offer high optical gain, which can lead to parasitic laser action establishing both transverse and longitudinal modes: these effects are illustrated in Figure 46.3. These parasitic effects result in loss of energy and poor tunability. Longitudinal parasitic laser action can be suppressed by using a 'motheye' anti-reflection coating [61,62] on the faces of the disc. Transverse parasitic laser action can damage the cylindrical surface of the gain medium. This action can be suppressed by roughening and 'blackening' the curved surface of the disc.

46.5.1 Performance

Table 46.3 shows the performance of three pyrromethene dyes in different hosts, when longitudinally pumped with a frequency doubled Q-switched Nd:YAG source. 'Uncoated'

TABLE 46.3

Solid-state Dye Laser Performance Data

	Laser Performance Data	
Laser Material	**Peak λ (nm)**	**Slope Efficiency (%)**
Pyr 567 in PMMA	554	85 (64)
Pyr 567 in ormosil	552	80 (67)
Pyr 567 in MeOH	557	>80
Pyr 580 in PMMA	563	86 (69)
Pyr 580 in MeOH	556	>80
Pyr 597 in PMMA	581	86 (58)
Pyr 597 in ormosil	578	80 (62)
Pyr 597 in MeOH	585	~80

discs were used with typical sizes of about 25 mm diameter and 6–8 mm thick: the dye concentration was of the order of 2×10^{-4} molar. The figures in brackets are for off-axis pumping of 'uncoated' discs with 5 ns pulses. Data are also included for dyes in a methanol solution for comparison.

The threshold energy for laser action is typically in the range of 100 μJ of pump energy for the range of dyes in the hosts quoted in Table 46.3. Owing to the small threshold energy, there is little difference between the slope efficiency and the overall efficiency with a high energy per pulse output.

In the short-pulse regime, pyrromethene dyes show better conversion efficiency than xanthenes or other dyes. A review [13] indicated that pyrromethene dyes showed a similar performance in solid-state and liquid hosts. Furthermore, those laser dyes, which show good efficiency, also tend to show good photostability, as this avoids detrimental thermally induced stress, as described earlier. An additional observation was that there had been little improvement in the performance of solid hosts doped with xanthenes over the last 15 years, despite the improvement in the host materials. This feature indicates that the limitation is dominated by the dye rather than the host: excited state absorption is probably the limiting loss mechanism with this class of dye. Optical epoxy hosts doped with pyrromethene dyes were found to have poorer laser efficiency and lifetime in comparison with analogous modified PMMA samples when tested [11].

Laser pumping of dye-doped materials with short pulses (nanoseconds) can provide output pulses with energy of 500 mJ pulse^{-1} when using high-performance dyes. The spectral range for this high performance is typically 550–650 nm. The performance when emitting pulses of microsecond duration tends to be inferior, owing to the increased triplet-state losses and the low-peak power of the excitation source. The spectral emission range can extend from the UV to the near IR. An efficient route to the UV is frequency doubling of yellow light [67]. A photograph of this form of arrangement is shown in Figure 46.4.

The pulselength of the emitted energy is closely related to that of the pump, in the short-pulse regime up to about a microsecond. For longer pulselengths, triplet state population becomes the dominant factor, which can lead to premature cessation of laser action.

The spectral emission bandwidth from a dye-doped host can extend over many tens of nanometres, often significantly more than is observed with the identical dye in a solution [6,13]. Figure 46.5 shows the emission bandwidth of two dyes in a PMMA host.

Studies [14] report a 'service life' of more than 60 000 pulses from a pyrromethene-doped microporous glass when pumped with a power density of 25 MW cm^{-2}. This value reduced to about 45 000 shots when the fluence increased to 50 MW cm^{-2}.

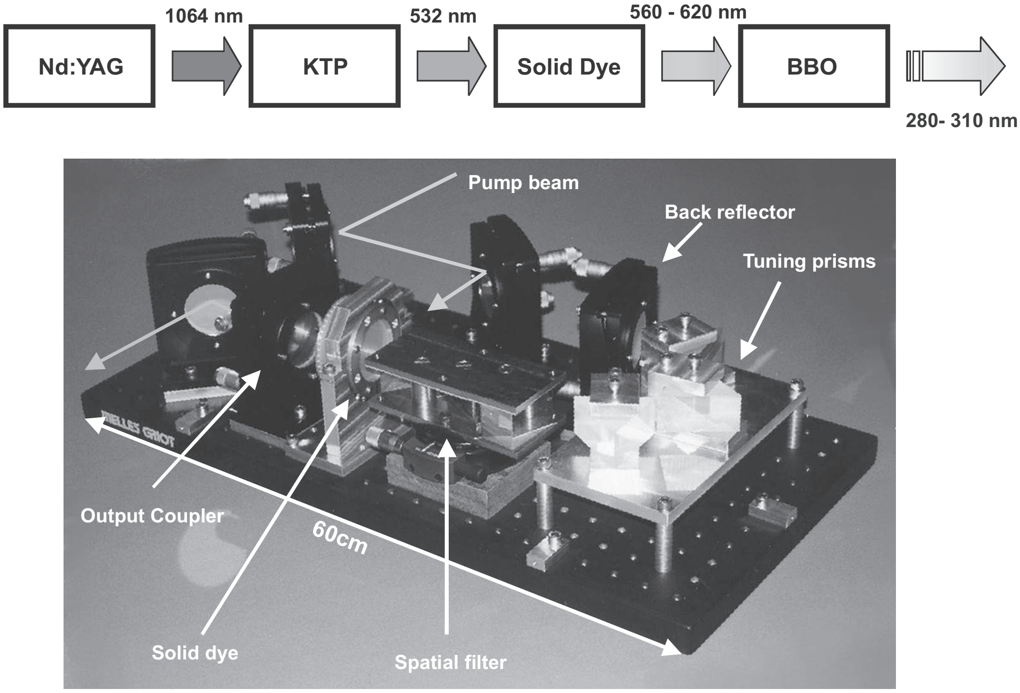

FIGURE 46.4 Laser-pumped dye laser.

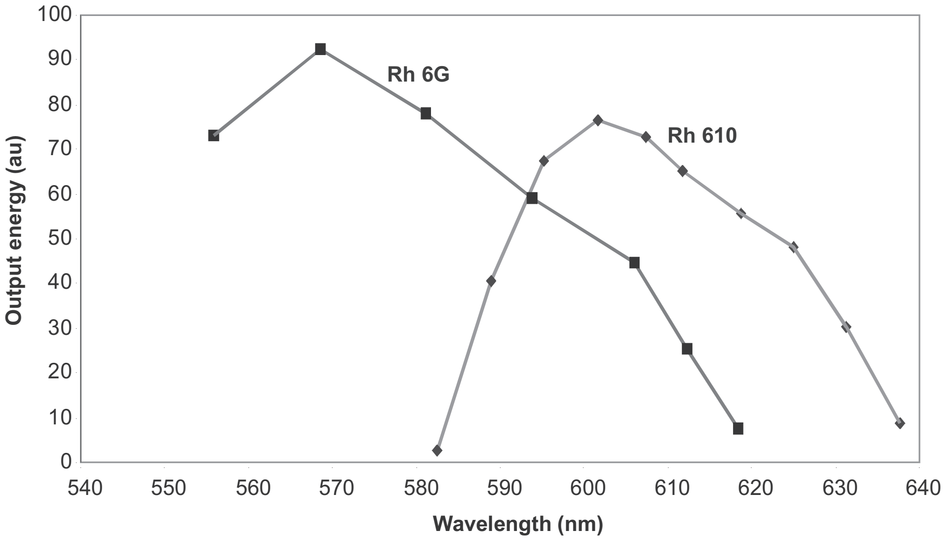

FIGURE 46.5 Laser dye emission bandwidth in PMMA.

The identical host doped with rhodamine 11B dye gave a service life of about 110 000 pulses. However, this dye has a somewhat lower efficiency than the pyrromethene dyes. For all of these studies, the 'service life' was defined as the point where the output energy fell to 70% of its initial value. The tests were undertaken by irradiating a single site in the gain medium and were limited by the photo-bleaching of the dye in the host and not by damage to the host. 'Service lifetimes' of many tens of thousands of shots have been recorded from dyes in ormosil and PMMA hosts [17,20].

The pulselength of the excitation influences the 'service life' as a high fluence is required to achieve laser action in the long-pulse regime, which, of course, is energy dependent. Consequently, the 'service life' for long-pulse operation is often in the realm of a few thousand pulses from a given site, although this value can be increased by moving the sample.

Short-pulse operations [68] with pulselengths of 30 ps have been demonstrated with dye-doped gain media pumped with the second harmonic from a mode-locked neodymium laser (Nd:YAG). Single pulse and pulse trains were obtained from materials doped with pyrromethene 580 and rhodamine 11B.

Studies [6] have shown that the peak of the laser output from a given dye experiences a hypsochromic (blue) shift as the host is changed from an organic polymer, such as PMMA, to a partially organic matrix (ormosil) and finally to an inorganic glass host. These wavelength shifts reflect changes in the dye–host interactions, with increased interaction in inorganic hosts with hydrogen bonding sites, leading to dye absorption occurring. Some laser dyes, such as the perylenes, are relatively non-polar in their ground state and more polar in an excited state, and experience a redshift in sol–gel glass, as their interaction with the inorganic host is very weak [6]. Wavelength shifts can also occur during the degradation of a dye-doped host during operation, owing to the creation of photodegradation products, which have an absorption profile coinciding with the laser emission band. This acts in a similar way to the spectral control filter described for liquid lasers, by creating an additional loss at the emission wavelength and forcing the emission to a different wavelength with a better excess gain. Of course, this does not occur if the degradation products are transparent. Figure 46.6 shows comparative output spectra of a pyrromethene dye in various hosts, reflecting the modified dye–host interactions.

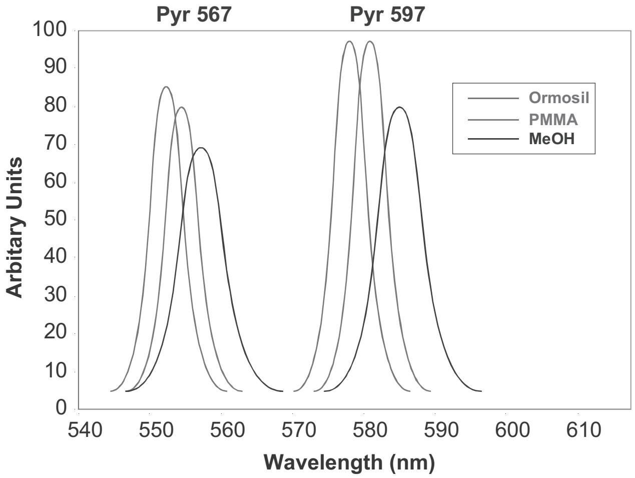

FIGURE 46.6 Lasing spectra of a pyrromethene dye in various hosts.

Dye-doped solid-state materials can be used in place of liquid phase dye cells in a range of laser-pumped systems, with the exception of the very high power devices, where bulk damage would be a serious issue and where very high spectral purity is required. For many applications, this gain medium offers a more convenient alternative to the liquid-phase device, particularly for those with low-power requirements.

46.6 Flashlamp-pumped Solid-state Dye Lasers

Progress with the performance of flashlamp-pumped dye-doped rods has been significant in the last few years [17,19,21–24]. One of the major problems with flashlamp-pumping has been producing rods which are large enough to match the extended pumped volume, whilst exhibiting good optical quality and low losses. It has been estimated [16] that bulk losses should not exceed 0.5% cm^{-1} for satisfactory laser performance. The major breakthrough has been a refinement of the production method that has led to the reduction in optical scatter in the rods and control of the refractive index profile which, in the past, has led to strong lensing within the rod.

A relatively simple arrangement with a coaxial flashlamp can be used to create laser action. For example, a dye-doped rod may be inserted into the annulus of the lamp, with suitable mirrors arranged to form the resonant cavity. A schematic arrangement is shown in Figure 46.7. For the best performance, it is necessary to match the length of the dye-doped rod to that of the flashlamp, as is common with liquid dye lasers.

The use of a flashlamp source presents a number of issues that need careful consideration, such as the triplet-excitation problem and the creation of a dynamical thermal lens in the rod. The triplet problem can be mitigated by use of relatively short flashlamp pulses or energy from a surface discharge and additives that collide with the excited dye molecules in the host. Consequently, the additives will only solve this problem if they can be arranged to be in very close proximity to the dye. The thermal lens can be controlled through careful design to avoid a thermal gradient. An additional problem is generating a sufficiently large flux in the cavity to ensure fluorescence saturation without exceeding the damage threshold of the host matrix. As previously noted, fluxes of the order of 1 MW cm^{-2} are required for efficient energy extraction from the cavity. However, when using long-pulse excitation, this would require pulses with a fluence of the order of 10 J cm^{-2}. Unfortunately, this fluence is well beyond the damage threshold of most polymeric and some glass-like hosts; hence, lower efficiency operation is necessary to achieve reliable and repeatable performance.

46.6.1 Performance

In addition to thermally induced focusing characteristics, a dynamic lens has been noted in polymer rods [24]: Figure 46.8 shows how the stress-induced lens of a pyrromethene-doped PMMA rod changed over a 40-day observation period.

The number of high-energy pulses that can be generated from a rod is still limited and the output decreases with the number of pulses, as shown in Figure 46.9. In the case of the low repetition rate, the interval between pulses was between 1 and 8 minutes. As can be seen for the 1 Hz case, the decline in performance was more rapid, owing to the heat not being able to be dissipated and, hence, allowing the creation of a thermally induced lens, in addition to triplet excitation. If the gain medium is not excited for a few minutes, the gain medium recovers and the original performance is re-established.

The temporal characteristics recorded from a similar dye-doped PMMA rod closely follow the flashlamp pulse, as

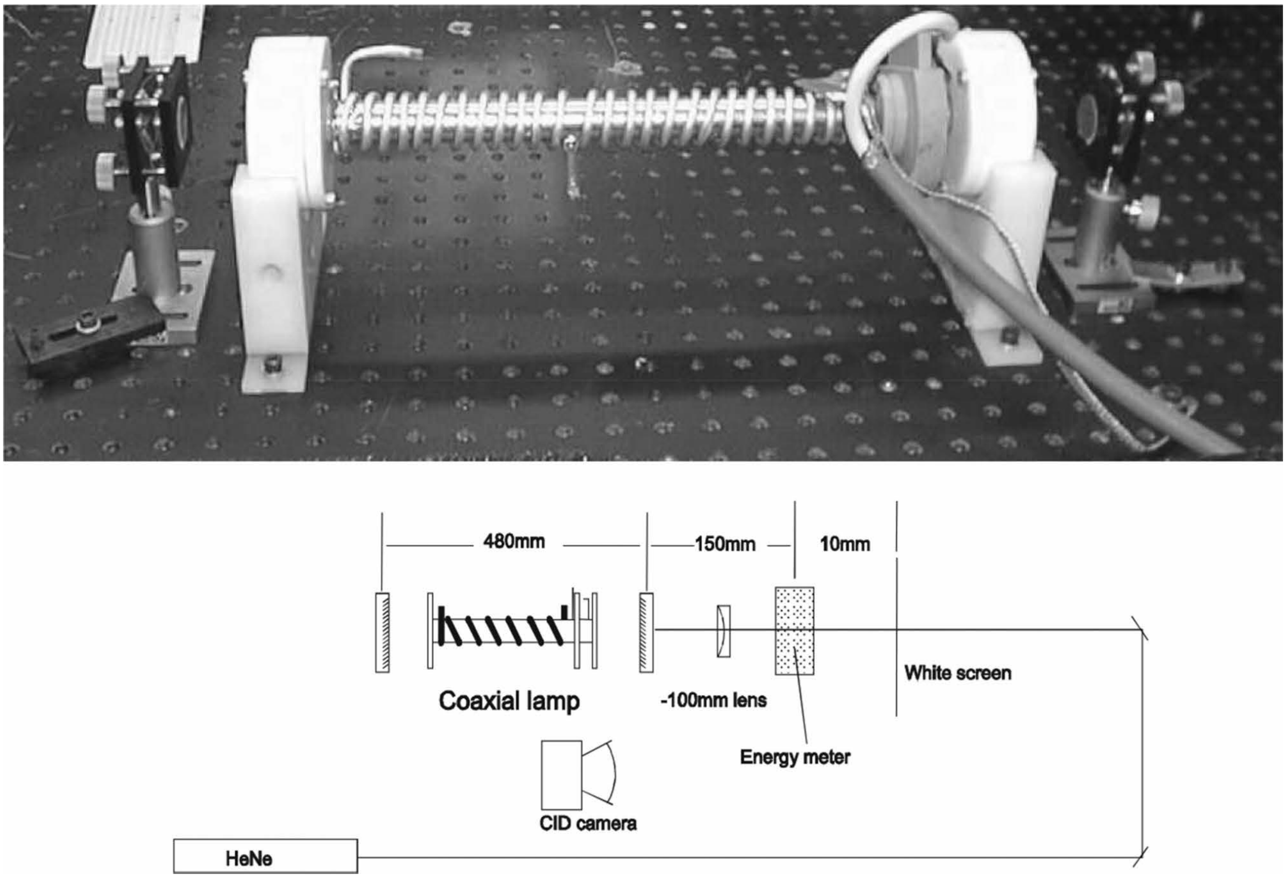

FIGURE 46.7 A schematic diagram of a flashlamp-pumped polymer rod test.

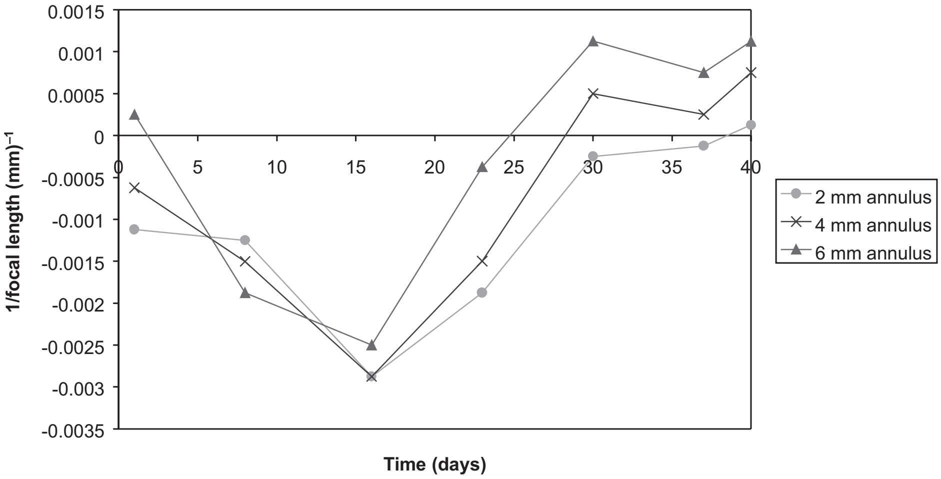

FIGURE 46.8 Variation of focal length of a polymer rod.

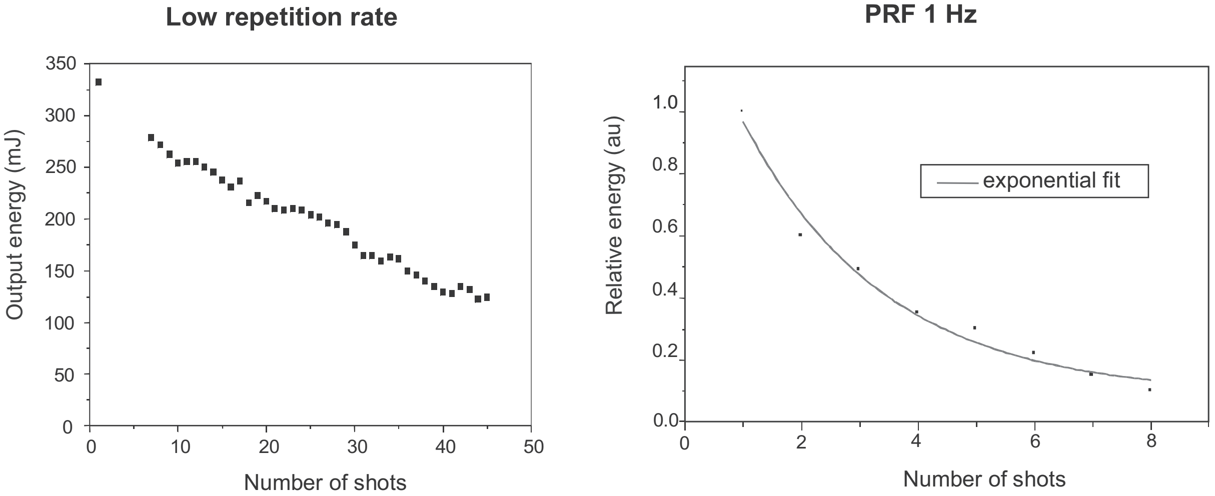

FIGURE 46.9 Degradation of output with shot number.

shown in Figure 46.10. The output trace is quite symmetrical and illustrates that there is no obvious indication of a premature termination of lasing, such that may result from dynamic thermal lensing in the rod or excessive triplet-state absorption.

Figure 46.11 shows the performance of three polymeric rods (PMMA), each doped with a different pyrromethene dye. The laser threshold was of the order of 100 J for each of them, with a slope efficiency of up to ~0.5% and an overall conversion efficiency of ~0.3%. Later results [22,24] have reported an output energy of 1.1 J per pulse with a conversion efficiency close to 0.5%: in this case, the dye dopant was pyrromethene 567. The same study reports that pyrromethene 567 exhibits better laser efficiency than pyrromethene 580, which, in turn, is better than pyrromethene 597. All of the pyrromethene-doped rods outperform those doped with rhodamine 6G. The divergence from these dye-doped laser rods is of the order of 10 mrad.

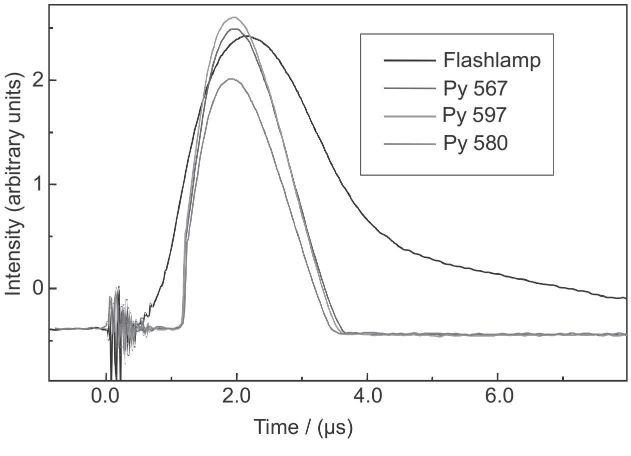

FIGURE 46.10 Temporal output of flashlamp and laser.

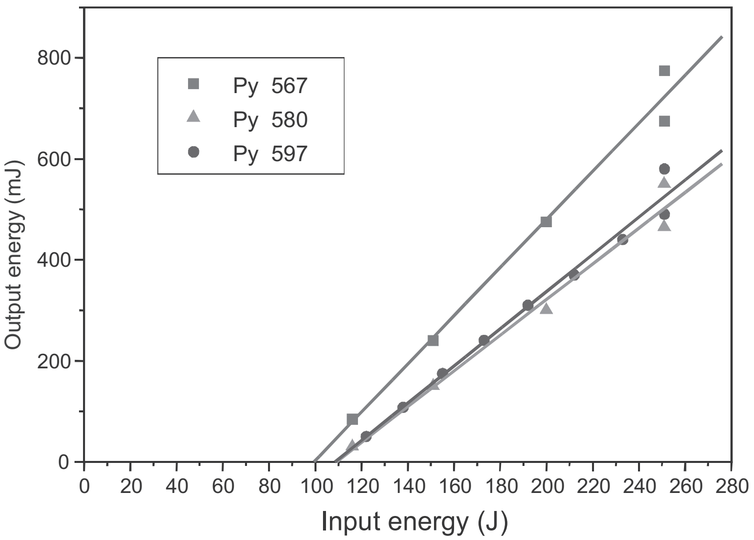

FIGURE 46.11 Comparative laser performance of dye-doped PMMA rods.

Long-pulse operation presents issues with the gain–loss balance and the need for a high fluence to generate a peak intensity above threshold. This can result in more damage to plastic hosts than other media, as the main damage mechanisms are energy related rather than power dependent. In addition, management of the triplet-state build-up is a considerable challenge for long-pulse operation. This process acts not only as a loss mechanism but can also provide a route to singlet oxygen generation, leading to rapid photodegradation of the laser dye.

Spectral emission is readily achieved in the visible band. The most energetic pulses are in the green to orange part of the spectrum. Pulselengths are of the order of a microsecond, and the spectral width is about 4 nm.

46.7 Choice of Host

As previously noted, excited-state absorption is an important loss mechanism in laser dyes but it should be independent of the host matrix, as it is only dependent on the energy levels in the dye molecule. Hence, there should be little difference between using a given laser dye in a polymer or glass-like host, except for small changes in the peak lasing wavelength. Other considerations are likely to determine the choice of host, such as the laser-induced damage threshold of the host, thermal environment or the repetition rate of the pulses. Thermal degradation is independent of the generation of excited states, although an increase in ambient temperature may increase the photodegradation rates as many processes are diffusion controlled; hence, it is important to match the thermo-optical parameters of the host to the operational environment.

Owing to the very low efficiency of flashlamp-pumped systems, it is critical that the gain medium has low loss and negligible optical distortion. To date, these characteristics have been most easily achieved with polymeric hosts, although it should be possible to use other hosts, such as the epoxy-filled microporous glasses. Other considerations tend to dominate the choice of host for short-pulse laser-pumped devices as a result of the ease with which fluorescence saturation may be achieved leading to high laser emission efficiency. Some of those considerations will include potential ‘service life’, desired operational configurations and laser damage threshold of the matrix.

Polymeric hosts have a number of advantages over the porous materials, such as better chemical compatibility with the organic dye molecules [50] and their suitability for inexpensive fabrication. However, dye-doped silica gels may offer superior photostability and better laser performance.

The geometry of the gain medium is usually dictated by mechanical mounting or service/replacement requirements for laser-pumped sources. In the case of high-performance laser-pumped systems, the shape of the gain medium becomes important for controlling the thermal balance of the system. Rods are popular for flashlamp pumping and slabs may be used for either form of excitation. Moreover, slabs may also be ideal for surface-discharge-pumped devices [60].

REFERENCES

1. Salin F et al. 1989 Efficient tunable solid-state laser near 630 nm using sulforhodamine 540-doped silica gel Opt. Lett. **14** 785–7.
2. Hermes RE et al. 1993 High-efficiency pyrromethene doped solid-state dye lasers App. Phys. Lett. **63** 877–9.
3. Hermes R E 1994 Lasing performance of pyrromethene-BF2 laser dyes in a solid polymer host *Conference on Visible and UV Lasers Los Angeles (Proc. SPIE 2115)* (Bellingham, WA: SPIE) pp 178–83.
4. Sastre R and Costela A 1995 Polymeric solid-state dye lasers Adv. Mater. **7** 1998–2002.
5. Canva M et al. 1995 Perylene- and pyrromethene-doped xerogel for a pulsed laser Appl. Opt. **34** 428–31.
6. Rahn M D and T A King 1995 Comparison of laser performance of dye molecules in sol-gel, polycom, ormosil and poly (methyl methacrylate) host media Appl. Opt. **34** 8260–71.

7. Rodriguez M et al. 1995 A simple rotating system to avoid early degradation of solid-state dye lasers Meas. Sci. Technol. **6** 971–8.
8. Costela A et al. 1996 Polymeric solid state dye lasers: new rhodamine 6G copolymers and terpolymers *Conf. on Solid State Lasers V San Jose (Proc. SPIE 2698)* (Bellingham, WA: SPIE) pp 17–22.
9. Faloss M et al. 1996 Pyrromethene-doped xerogels for solid state dye laser systems *Conf. on Solid State Lasers V San Jose (Proc. SPIE 2698)* (Bellingham, WA: SPIE) pp 2–7.
10. Anderson R S et al. 1998 Photo-stability of dye doped modified polymers at extremely high intensities: Medlite TM laser systems *Proc. Solid State Lasers San Jose VII (Proc. SPIE 3265)* (Bellingham, WA: SPIE) pp 13–20.
11. Pacheco D P and Aldag H R 1998 Comparison of the laser performance of solid-state dye media under long- and short-pulse excitation *Proc. Solid State Lasers VII San Jose (Proc. SPIE 3265)* (Bellingham, WA: SPIE) pp 2–12.
12. Nechitailo V S et al. 1999 Polymer dye lasers with exceptional performance *Proc. Solid State Lasers VIII San Jose (Proc. SPIE 3613)* (Bellingham, WA: SPIE) pp 105–11.
13. Rahn M D and King T A 1999 Comparison of solid-state dye laser performance in various host media *Proc. Solid State Lasers VIII San Jose (Proc. SPIE 3613)* (Bellingham, WA: SPIE) pp 94–105.
14. Aldag H R et al. 2000 Efficient solid-state dye lasers based on polymer-filled micro-porous glass *Proc. Solid State Lasers XI San Jose (Proc. SPIE 3929)* (Bellingham, WA: SPIE) pp 133–4.
15. Pacheco D P et al. 1988 A solid-state flashlamp-pumped dye laser employing polymer hosts *Proc. Int. Conf. on Lasers '87* ed F J Duarte (McLean, VA: STS) pp 330–7.
16. Minnigh S W et al. 1996 Performance of a flashlamp-pumped solid-state dye laser *Proc. Solid State Lasers V San Jose (Proc. SPIE 2698)* (Bellingham, WA: SPIE) pp 55–64.
17. Titterton D H 1997 Performance of plastic dye lasers in the UK *Conf. of Solid State Lasers VI San Jose (Proc. SPIE 2986)* (Bellingham, WA: SPIE) pp 132–40.
18. Calderon OG et al. 1997 Laser emission of a flash-lamp pumped Rhodamine 6 G solid copolymer solution Appl. Phys. Lett. **70** 25–7.
19. Finlayson A J et al. 1998 Flashlamp pumped polymer rod dye laser *Proc. Int. Conf. on Lasers '97* (McLean, VA: STS) pp 252–5.
20. Finlayson A J et al. 1998 Flashlamp pumped polymer dye laser containing Rhodamine 6G Appl. Phys. Lett. **72** 2153–5.
21. Winstanley P A et al. 1998 Enhancements achieved in the performance of liquid and solid-state dye laser technology *Conf. on Solid State Lasers VII San Jose (Proc. SPIE 3265)* (Bellingham, WA: SPIE) pp 42–50.
22. Finlayson A J et al. 1999 Flashlamp pumped solid-state dye laser incorporating pyrromethene 597 Appl. Phys. Lett. **75** 457–9.
23. Mandl A and Klimek D E 1999 Flashlamp pumped thin slab solid state plastic dye zig-zag laser *Proc. Solid State Lasers VIII San Jose (Proc. SPIE 3613)* (Bellingham, WA: SPIE) pp 119–24.
24. Finlayson A J and Venner M R W 2000 Flashlamp pumped polymer dye laser studies *Conf. on Solid State Lasers IX San Jose (Proc. SPIE 3929)* (Bellingham, WA: SPIE) pp 154–62.
25. Pavlopoulos T G et al. 1988 Laser action from a tetramethylpyrromethene-BF2-complex Appl. Opt. **27** 4998–9.
26. Pavlopoulos T G et al. Efficient laser action from 1,3,5,7,8-penta-methylpyrromethene-BF2-complex and its 2,6-disulphonate derivative Opt. Commun. 70 425–7.
27. Pavlopoulos T G et al. Laser action from 2,6,8-trisubstituted 1,3,5,7-tetramethylpyrromethene-BF2-complex: part 1 Appl. Opt. **29** 3885–6.
28. Boyer J H et al. Laser action from 2,6,8-trisubstituted 1,3,5,7-tetramethylpyrromethene-BF2-complex: part 2 Appl. Opt. **30** 3788–9.
29. Pavlopoulos T G et al. 1998 Laser action from a 2,6,8-trisubstituted 1,3,5,7-tetramethylpyrromethene-BF2-complex: part 3 Appl. Opt. **37** 7797–800.
30. Pavlopoulos T G 1999 Photostability of some pyrromethene laser dyes *Conf. on Solid State Lasers VIII San Jose (Proc. SPIE 3613)* (Bellingham, WA: SPIE) pp 112–8.
31. Sorokin P P and Lankard J R 1966 Stimulated emission observed from an organic dye, chloro-aluminum phthalocyanaine IBM J. Res. Dev. **10** 162–3.
32. Schäfer F P et al. 1966 Organic dye solution laser Appl. Phys. Lett. **9** 306–9.
33. Sorokin P P and Lankard J R 1967 Flashlamp excitation of organic dye lasers: a short communication IBM J. Res. Dev. **11** 148.
34. Schmidt W and Schäfer F P 1967 Blitzlampengepumpte Farbstofflaser Z. Naturforsch. a **22** 1563–6.
35. Soffer B H and McFarland B B 1967 Continuously tunable, narrowband, organic dye lasers Appl. Phys. Lett. **10** 266–7.
36. Peterson O G and Snavely B B Stimulated emission from flashlamp-excited organic dyes in polymethyl methacrylate Appl. Phys. Lett. 12 238–40.
37. Drake J M et al. 1972 The use of light converters to increase the power of flashlamp-pumped dye lasers IEEE J. Quantum Electron. QE-**8** 92–4.
38. Bank P W et al. 1995 High average power quasi-cw tunable polymer laser *Conf. on Visible Lasers and Laser crystal Growth San Jose (Proc. SPIE 2380)* (Bellingham, WA: SPIE) pp 292–7.
39. Duarte F J 1995 Opportunity beckons for solid-state dye lasers Laser Focus World **31** 187–9.
40. Hench L L and West J K 1990 The sol gel process Chem. Res. **90** 32–72.
41. Schmidt H 1984 *Better Ceramics through Chemistry* ed C J Brinker, D E Clarck and D R Ulrich (New York: North-Holland) p 327.
42. Schmidt H 1989 Organic modification of glass structure—new glasses or new polymers J. Non. Cryst. Solids **112** 419–23.
43. Altman J C et al. 1991 Solid-state laser using a rhodamine-doped silica gel compound IEEE Photon. Technol. Lett. **3** 189–90.
44. Kessler W et al. Novel solid state dye laser host *Conf. on Visible and UV lasers Los Angeles (Proc. SPIE 2115)* (Bellingham, WA: SPIE) pp 190–5.

45. Maslyukov A et al. 1995 Solid-state dye laser with modified poly(methylmethacrylate)-doped active elements Appl. Opt. **34** 1516–18.
46. Dyumaev A A et al. 1992 Dyes in modified polymers: problems of photostability and conversion efficiency at high intensities J. Opt. Soc. Am. B **9** 143–51.
47. Dyumaev K M et al. 1981 Transparent polymers as a new class of optical materials for lasers, laser induced damage in optical materials NBS Spec. Publ. **638** 31–40.
48. Nechitailo V S 1996 Recent advances in polymer dye lasers *Proc. Solid State Lasers V San Jose (Proc. SPIE 2698)* (Bellingham, WA: SPIE) pp 8–16.
49. Knobbe E T et al. 1990 Laser behaviour and photostability characteristics of organic dye doped silicate gel materials Appl. Opt. **29** 2728–33.
50. Seddon A B 1997 Potential of organic-inorganic hybrid materials, derived by sol-gel, for photonic applications. *Sol-Gel and Polymer Photonic Devices (Critical Reviews of Optical Science and Technology 68)* ed M P Andrews and S I Najofi (Bellingham, WA: SPIE) pp 143–71.
51. Jones G and Pacheco D P 1998 Fluorescence and lasing properties of pyrromethene dyes in epoxy solid host media *Conf. on Solid State Lasers VII San Jose (Proc. SPIE 3265)* (Bellingham, WA: SPIE) pp 51–8.
52. Cazeca M J et al. 1997 Epoxy matrix for solid-state dye laser applications Appl. Opt. **38** 4965–8.
53. Bezrodny V I et al. 1982 Active and passive laser elements on the basis of polymers with organic dyes Kvantovaya Elektron. 9 2455 (in Russian).
54. Tompkin W R 1987 Non-linear optical properties of lead tin fluorophosphate glass containing acridene dyes J. Opt. Soc. Am. **4** 1030–4.
55. Al'tshuler GB et al. 1983 Output characteristics of a laser utilizing rhodamine 6G in micro-porous glass Quantum Electron. **10** 784–8.
56. Efendiev T S et al. 1984 Tunable distributed-feedback laser-based on dye-doped micro-porous quartz glass Appl. Phys. B **33** 167–9.
57. Al'tshuler G B et al. 1985 Field-induced transport of laser dyes in porous glass matrices Sov. Phys. Tech. Phys. **30** 941–2.
58. Rahn M D and King T A 1994 Lasers based on dye-doped sol-gel composite glasses *Proc. Sol-Gel Optics III San Diego (Proc. SPIE 2288)* (Bellingham, WA: SPIE) pp 382–91.
59. Meshkovskii I K et al. 1995 Solid state dye laser *Conf. on Visible Lasers and Laser Crystal Growth San Jose (Proc. SPIE* 2380*)* (Bellingham, WA: SPIE) pp 292–305.
60. Fulker D J 2002 The development and application of surface discharges for pumping dye lasers PhD thesis University of Strathclyde.
61. Bernhard C G 1967 Structural and functional adaptation in a visual system Endeavour **26** 79–84.
62. Wilson S J and Hutley M C 1982 The optical properties of moth eye antireflection surfaces Opt. Acta **29** 993–1009.
63. Rahn M D and King T A 1998 High-performance solid-state dye laser based on perelene-orange doped polycom glass J. Mod. Opt. **45** 1259–67.
64. King T A et al. 2000 Dye triplet state and singlet-oxygen quenching effects in solid-state dye lasers *Conf. on Solid State Lasers IX San Jose (Proc. SPIE 3929)* (Bellingham, WA: SPIE) pp 145–53.
65. Arbeloa F L et al. 1998 Photophysical and lasing properties of pyrromethene 567 dye in liquid solution. Environment effects Chem. Phys. **236** 331–41.
66. Yariv E and Reisfeld R 1999 Laser properties of pyrromethene dyes in sol-gel glasses Opt. Mater. **13** 49–54.
67. Chandra S et al. 1997 Tunable ultraviolet laser source based on solid-state dye laser technology and $CsLiB_6O_{10}$ harmonic generation Opt Lett. **22** 209–11.
68. Garnov S V 1998 Ultra short pulse generation in solid state dye lasers *Proc. Solid State Lasers VII San Jose (Proc. SPIE 3265)* (Bellingham, WA: SPIE) pp 306–8.

47

Other Lasers: Section Introduction

Colin Webb, Subhash Chandra Singh, and Chunlei Guo

To explore the spectral regions where most atoms and molecules have their strongest absorption transitions—e.g. those due to electrons changing orbitals—has required the development of sources which are tunable in the UV, XUV and X-ray regions. Likewise, to explore the regions where transitions between different vibrational and/or rotational levels of molecules cause absorption requires sources tunable in the infrared and far-infrared regions.

One type of source which has the potential to provide radiation tunable over this entire range of wavelengths is the synchrotron and its closely related laser counterpart, the free-electron laser (FEL). Because both synchrotrons and FELs depend on fairly large and expensive electron accelerator technology, they tend to be built as shared national or regional facilities although there is some prospect that more affordable versions may become available in the future. Free electron lasers and synchrotron light sources are discussed in chapter 48.

The ability to generate X-rays in the form of short pulses of narrowband laser output on specific transitions of highly ionized atoms, pumped by radiation from conventional high-power near-visible laser sources, has been realized at several national laboratories. With the advent of commercial ultrashort-pulsed laser and amplifier systems, the prospect of tabletop versions of these systems, within the financial reach of many university laboratories, is now becoming a reality. Chapter 49 discusses recent advancements in X-ray lasers.

The other spectral domain of significant importance is between the radio and infrared frequencies, the so-called far-infrared or terahertz radiation. The laser in this frequency domain is described in the chapter of terahertz lasers by Taiichi Otsuji (Chapter 50). This chapter also discusses the most recent advancements of quantum cascade and graphene-based THz lasers.

Taylor & Francis
Taylor & Francis Group
http://taylorandfrancis.com

48

Free-Electron Lasers and Synchrotron Light Sources

P. G. O'Shea and J. B. Murphy

CONTENTS

48.1 Introduction 639
48.1.1 History and Basic Principles of FELs 639
48.2 Physics of FELs 640
48.2.1 Spontaneous Emission 641
48.2.2 FEL Lasing 641
48.2.3 FEL Gain and Saturation 641
48.2.3.1 Low-gain Oscillators 642
48.2.3.2 High-gain FELs 642
48.3 Technology for FELs 643
48.4 FEL Applications 644
48.5 Future Directions for FELs 645
48.6 Synchrotron Light Sources 646
48.6.1 Introduction 646
48.6.2 Brief History of Synchrotron Light Sources 646
48.6.3 Operational Characteristics of Synchrotron Light Sources 647
48.6.4 Electromagnetic Radiation from Charged Particles 647
48.6.4.1 Synchrotron or Bending Magnetic Radiation 648
48.6.4.2 Insertion Devices 650
48.7 Future Directions for Synchrotron Light Sources 651
References 652

48.1 Introduction

For many years, it has been a goal of optical researchers to produce coherent radiation at wavelengths where existing sources are weak. Free-electron lasers (FELs) are rapidly filling voids in the electromagnetic spectrum left by more conventional sources. FELs are attractive because of their potential to produce both high peak and high average power and because of their wavelength flexibility. When compared to conventional lasers, FELs are neither simple nor inexpensive. FELs can, however, produce intense coherent light at wavelengths where other sources are either weak or non-existent. This makes them the ideal choice when one moves away from the visible region of the spectrum to the far IR, or to the vacuum UV, X-ray and beyond. At present FELs operate over a broad spectrum from millimetre waves to the vacuum ultraviolet and at average power levels from watts to several kilowatts. No single device spans this entire range of wavelength or power. In spite of having the same underlying physical principles, the technology behind mm-wave FELs is quite different from that of UV devices.

The development of synchrotron radiation (SR) light sources has, until recently, been independent of the development of FELs. Therefore, for the most part, FELs and SR sources are treated independently in this chapter. Heretofore, FELs and synchrotron sources have not been in direct competition because they have occupied different regions of the electromagnetic spectrum. X-ray FELs currently proposed will offer direct competition to synchrotron sources (see Sections 48.5 and 48.6). Such X-ray FELs are now often referred to as 'fourth-generation synchrotron light sources'. Therefore, it is likely that the distinction between FELs and SR sources will become increasingly blurred, particularly at X-ray wavelengths.

48.1.1 History and Basic Principles of FELs

FELs are a marriage of accelerator and laser technology. The essential technical elements are an electron accelerator, a magnetic undulator (or wiggler)[1] and photon optics. FEL operation is based on a fundamental radiative mechanism—that of an oscillating electron in a sinusoidal magnetic field of an undulator magnet—which we call spontaneous emission

---

[1] The terms *wiggler* and *undulator* are often used interchangeably in the FEL community; however, they have quite specific meaning in the SR community, see Figure 48.7.

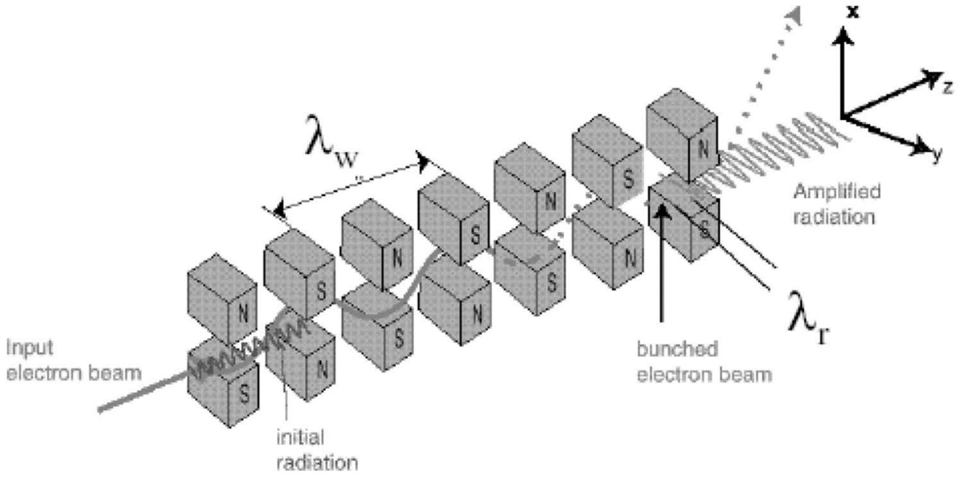

FIGURE 48.1 The FEL radiative process: As the electron beam moves in a magnetic undulator, it radiates light (full line with long undulations). Initially, the electron beam is unstructured on a scale comparable to the wavelength of emission. The electron emitters are randomly phased with respect to the optical wave and so incoherent or spontaneous emission results. As the electrons progress along the wiggler, their interaction with the optical field in the presence of the undulator field results in microbunching of the electrons (broken line). At saturation, the electrons become tightly bunched in clumps spaced one optical wavelength (λ) apart. Once the electrons are bunched, the emission becomes coherent and laser-like. After passage through the undulator, the electrons are separated from the light by a bending magnet (not shown).

(see Figure 48.1). This radiation is enhanced or amplified by the modulation of the electron beam density. In low-gain systems, an optical cavity provides the feedback and the optical mode selection necessary for proper performance; in high-gain FELs, an optical cavity is often unnecessary. Typical undulators in use today are 1–5 m long and have less than 100 magnetic periods, each several centimetres long. Future undulators for X-ray FELs may be as long as 100 m.

The history of FELs can be traced back to microwave tubes, which were the first sources of coherent radiation from free electrons in vacuum. Such early devices relied on slow-wave structures with closely coupled boundary conditions and were limited to long wavelengths. The possibility of producing coherent radiation from electrons bending in a magnetic field without the necessity of boundary structures was first postulated by Schwinger in relation to SR [1]. In the 1950s, Motz [2] performed a series of experiments with a high-energy electron beam passing through an undulator-like device. These experiments produced incoherent emission in the visible. Between 1957 and 1964, Phillips demonstrated an FEL-like microwave tube called the ubitron (for ‘undulating beam interaction’) in which a bunched electron beam in an undulator produced 150 kW of coherent radiation at a wavelength of 5 mm [3]. In 1971, Madey [4] proposed an optical wavelength device, subsequently referred to as an FEL, which included a conventional optical resonator. Madey’s proposal led directly to a series of seminal experiments that demonstrated FEL amplification [5] and oscillation [6] at near-IR wavelengths.

Is the FEL a laser? This question was originally addressed by Motz [7]. There is no doubt that the FEL mechanism is quite different from that of a conventional laser. FEL light output is, however, narrow band, transversely coherent and has well-defined spatial and temporal mode structures. In the optical region of the spectrum, FEL light looks very similar to conventional laser light. Madey originally coined the term free-electron laser to describe a device operating in the optical region with an optical resonator [8]. Today, the use of the term has been extended to include almost any device that produces coherent radiation from free electrons at any wavelength and which does not use closely coupled resonant structures.

48.2 Physics of FELs

In an FEL, electron energy transitions occur in a continuum. Consequently, the discrete level transitions that exist in conventional lasers are not a factor. The decoupling of the FEL mechanism from the constraints of atomic and molecular media allows for a light source that is continuously tunable and potentially capable of both high peak and high average power. Note that in a conventional laser the thermal energy associated with heating of the lasing medium is carried away at acoustic velocities ($\approx 10^3\,\mathrm{m\ s^{-1}}$), whereas in an FEL the heat is carried away at the speed of the electrons ($>10^8\,\mathrm{m\ s^{-1}}$). Therefore, if sufficient electron beam power is available, FELs should be capable of extremely high average power operation.

The key step in an FEL is the generation of ‘spontaneous emission’. In an FEL, the ‘lasing medium’ is the electron bunch (10^8–10^{10} electrons typically). Consider a relativistic electron travelling in the $\hat{z}$ direction encountering a region with a transverse sinusoidal magnetic field $B = B_0 \sin(k_u z)\hat{x}$, as shown in Figure 48.1. The undulator period ($\lambda_u = 2\pi/k_u$) is typically a few cm, and B_0 is usually in the range of 0.1–0.5 T. In this chapter, we consider only planar undulators, as shown in Figure 48.1. Planar undulators made with permanent magnets or electromagnets are by far the most common variety. The electrons wiggle in the $\hat{y}$ direction as they move through the field region. In the electron rest-frame, the undulator field is transformed into an intense virtual photon field with orthogonal electric and magnetic fields.

These virtual photons become real photons by Compton scattering off the relativistic electrons and are Doppler shifted to short wavelength when viewed in the laboratory frame. In the laboratory frame the real photons have wavelength:

$$\lambda_r \approx \frac{\lambda_u}{2h\gamma^2}(1+a_u^2) \tag{48.1}$$

where $h = 1, 2, 3, \ldots$ is the harmonic number, $a_u = \left(eB_0/\sqrt{2}mck_u\right)$ is known as the rms normalized vector potential of the undulator (a_u is usually of order unity) and γ is the electron energy divided by the rest energy of the electron. For a 50 MeV electron, $\gamma \approx 100$; the light wavelength is a factor of 10^4 smaller than the undulator period. Most FELs operate at harmonic number $h = 1$; however, a number of FELs have operated successfully at the third ($h = 3$) and fifth ($h = 5$) harmonic. A second-harmonic FEL has been demonstrated, but because the spontaneous emission and gain functions are zero on the electron beam axis, lasing was quite difficult to achieve [9].

48.2.1 Spontaneous Emission

The spontaneous emission is generally not very intense. A 50 MeV electron beam with a peak current of 100 A in a pulse several picoseconds long will produce a peak spontaneous emission power of the order of 1 W in a typical undulator. The intensity of the spontaneous radiation *on axis* near the fundamental ($h = 1$) resonant wavelength is given by [10]

$$\frac{d^2I}{d\omega\, d\Omega} = \frac{N_u^2 e^2 \gamma^2}{2\pi\varepsilon_0 c}\frac{a_u^2}{\gamma(1+a_u^2)}\left(\frac{\sin(\pi N_u \Delta\lambda/\lambda_r)}{\pi N_u\, \Delta\lambda/\lambda_r}\right)^2 F^2[1,\xi]. \tag{48.2}$$

where $F[1, \xi] = J_0(\xi) - J_1(\xi)$, J_x is a Bessel function of order x and $\xi = a_u^2/2(1+a_u^2)$.

The bandwidth of the emission ($\Delta\lambda/\lambda$) is approximately $1/2N_u$. The effective angular aperture is $\theta = \sqrt{\lambda_r/\lambda_u N_u}$, and the source radius is $\omega = \sqrt{\lambda_r \lambda_u N_u}/4\pi$. The number of photons per electron, per pass through the undulator within the angular aperture and bandwidth is given by

$$N_p = \frac{\pi}{2}\alpha\frac{a_u^2}{(1+a_u^2)}F^2\left[1,\xi\right] \tag{48.3}$$

where α is the fine structure constant. For the case of $a_u = 0.5$, $N_p = 2 \times 10^{-3}$ photons are emitted per electron per pass.

For a bunch of electrons, whose bunch length is much longer than λ, the total intensity is proportional to the number of electrons N_e in a bunch; typically, $N_e \approx 10^9$. If the electrons were grouped into bunches approximately λ apart in the longitudinal direction, the number of photons emitted by the bunch would be proportional to N_e^2. Such a process results in 'coherent emission' of photons.

48.2.2 FEL Lasing

The essence of the FEL mechanism is the conversion of spontaneous emission into narrow-band coherent emission by means of a feedback mechanism involving the interaction of the spontaneous photons and the electrons in the presence of the undulator magnetic field. The electrons either gain or lose energy depending on their phase with respect to the optical field. This results in a longitudinal clumping of the electrons. In the typical case where the electron pulselength (l) is much greater than the optical wavelength, the electron pulse will become modulated into l/λ_r micropulses spaced approximately λ_r apart. This modulation results in a narrowing of the spectrum and an increase in the output power, i.e. lasing. In low-gain systems, the optical feedback is provided by a resonator cavity, just as in conventional laser oscillators. In high-gain FELs, self-amplified spontaneous emission (SASE) occurs without the necessity of an optical cavity.

In an FEL the gain in the optical field depends on the peak current and the average optical power output depends on the average current. The quality of the electron beam is critical to FEL performance. For optimum gain, the electron beam must overlap well with the optical mode. Poor electron beam quality will result in poor overlap and reduced FEL performance.

In order to go from spontaneous emission to saturation, a total gain of the order of 10^8 is often required. Typically, low-gain oscillators can take up to several tens of passes to saturate, while high-gain amplifiers can achieve saturation in a single pass. In all cases, there is an incentive to have a large electron beam brightness, i.e. high peak current and small emittance (see Section 48.3), so as to optimize gain.

The efficiency of FELs depends on the details of the undulator used. For a low-gain FEL with a simple undulator with constant period and constant magnetic field amplitude and N_u magnetic periods, η, the efficiency of conversion of electron energy into light, is approximately $\eta \approx 1/(4N_u)$, a number comparable to the fractional width of the spontaneous emission spectrum. Typically, for simple FEL systems, $\eta \approx$ 1%–2%. If the undulator period or magnetic field amplitude is tapered to compensate for the reduction in electron-beam energy as power is extracted from the electrons, then much higher efficiencies can, in principle, be obtained. The present record for FEL efficiency at optical wavelengths is 5% at a wavelength of 10 μm [11]. In principle, efficiencies up to 20% appear feasible. The effective system efficiency can be enhanced by energy recovery of the electron beam in storage rings or in recirculating linac systems.

48.2.3 FEL Gain and Saturation

We present here a set of formulae that will allow the reader to estimate FEL performance in two particular cases: (i) low-gain oscillators and (ii) high-gain SASE or amplifiers. In both cases, we deal only with the Compton regime where plasma oscillations of the beam are not important. This regime is representative of almost all short-wavelength FELs. When plasma oscillations are important, the term Raman regime is used. The Raman regime is important for long-wavelength FELs driven by low-energy electron beams.

Figure 48.2 shows idealized FEL spontaneous emission and gain functions. The independent variable is $\Omega = N_u\pi\,(\omega - h\omega_r)/\omega_r$, where $\omega = 2\pi c/\lambda$. The spontaneous emission peaks at the FEL resonant wavelength λ_r, and the width of the spectrum to the first zero is $2/(hN_u)$. The gain function is given by the derivative of the spontaneous emission function. The peak optical

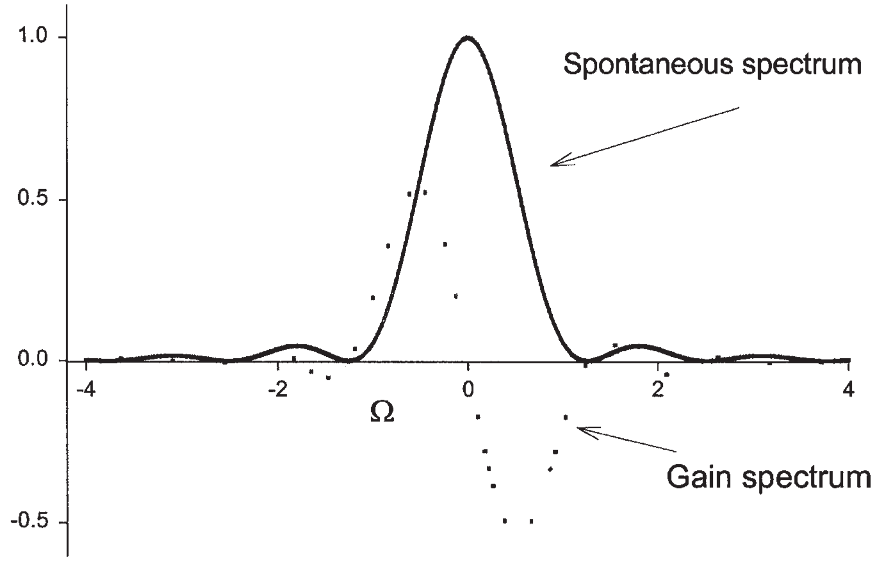

FIGURE 48.2 Distribution of the spontaneous emission and gain functions versus $\Omega = N_u\pi(\omega - h\omega_r)/\omega_r$, where $\omega = 2\pi c/\lambda$. Note that the peak of the gain function occurs at a longer wavelength than the FEL resonant wavelength.

gain occurs at a wavelength detuned on the long-wavelength side of resonance by

$$\frac{\Delta\lambda}{\lambda} = \frac{1}{hN_u}. \tag{48.4}$$

The negative side of the gain function corresponds to a situation where electrons gain energy from the optical field. An FEL operating on the negative side of the gain function is called an inverse FEL (IFEL), and IFELs have been proposed as electron accelerators.

48.2.3.1 Low-gain Oscillators

In a low-gain oscillator, optical power (P) builds up through many passes of the electron beam through the undulator. The gain length (L_G) for the growth of the optical power is such that $L_G \gg N_u\lambda_u$ (the undulator length). The small signal power gain per pass is denoted by δ, with $\delta \ll 1$. In the small signal regime where $P \ll P_{sat}$, where P_{sat} is the saturation power, we have

$$P = P_0(1 + \delta - \Gamma)^n, \tag{48.5}$$

where P_0 is the spontaneous emission power and Γ represents the fractional loss of power per pass resulting from out coupling and internal cavity losses.

The peak value of $\delta = \delta_0$ is given by

$$\delta_0 = 1.3 \times 10^{-3} \frac{h^2 a_u^2 f}{\gamma(1 + a_u^2)} I_e N_u^2 F^2[h,\xi] \tag{48.6}$$

where I_e is the peak electron current and f is a unitless quantity called the 'filling factor' that varies between 0 and 1 and depends on the degree of overlap between the optical mode and electron beam (with $f = 1$ corresponding to perfect overlap); and

$$\begin{aligned} F[h,\xi] &= J_0(\xi) - J_1(\xi) && \text{for } h = 1 \\ &= J_{\frac{(h-1)}{2}}(h\xi) - J_{\frac{(h+1)}{2}}(h\xi) && \text{for } h = 3,5,7,\ldots \end{aligned} \tag{48.7}$$

The spectral width of the gain function is shown in Figure 48.2.

The expression of δ_0 is valid in the case of a perfect electron beam with zero emittance and no energy spread. In practice, however, imperfections in the electron beam, such as finite emittance and energy spread, reduce the gain so that the small-signal gain is given approximately by [12]

$$\delta_s \approx \frac{g_0}{\left(1 + \dfrac{4N_u a_u \varepsilon_n}{\gamma^2 \lambda_r}\right)(1 + 27h^2 N_u^2 \sigma_\gamma^2)} \tag{48.8}$$

where ε_n is the rms normalized emittance and σ_γ is the rms fractional energy spread of the electron beam. Lasing on the higher harmonics is difficult because of the increased sensitivity of the terms in the denominator of the expression for δ_s to ε_n and σ_γ as the harmonic number h increases.

In the low-gain regime, the optical mode structure is largely governed by the details of the optical cavity design. Many FELs use linear near-concentric cavities, with the Rayleigh range (z_R) being chosen to match the electron and optical beam sizes at the centre of the undulator. To maximize the output power, the optimum outcoupling is usually chosen to be approximately one-third of σ_s. The maximum saturated power output is given by $P_{sat} \approx P_{ebeam}/N_u$.

48.2.3.2 High-gain FELs

The behaviour of high-gain FELs is quite different from that of low-gain devices. In contrast to the low-gain regime, the gain may be sufficiently high to saturate the FEL in a single pass through the undulator [13]. The high-gain regime is of particular interest in regions of the spectrum where high reflectivity mirrors do not exist, such as in the X-ray region. The optical power grows exponentially over most of the undulator distance z, except near the beginning and close to saturation. For an ideal beam, in the exponential gain regime at the fundamental wavelength,

$$P(z) = P_0 \exp(z/L_G) \tag{48.9}$$

where $P_0 \approx \rho^2 mc^3 (\gamma/\lambda_r)$ and $L_G = 0.046\lambda_u/\rho$ and the parameter

$$\rho = 5.7 \times 10^{-3} \left\{ \left(\frac{a_u F_1 \lambda_u}{\gamma} \right)^2 \frac{I_e}{\gamma R_e^2} \right\}^{\frac{1}{3}} \tag{48.10}$$

is referred to as the 'Pierce (or FEL) parameter', with R_e the electron beam rms radius. The saturated power is given by $P_{sat} \approx \rho\, P_{ebeam}$. Typically, saturation is achieved after a length approximately equal to 20 L_G. For the FEL to perform as described by the simple 1D equations above the following conditions must be met:

i. $L_G/z_R \ll 1$ (little diffraction over a gain length)
ii. $4\pi\varepsilon_n/\lambda_r\gamma \ll 1$ (small electron beam emittance)
iii. $\sigma_\gamma/\rho \ll 1$ (small energy spread).

When these conditions are not met, the gain is reduced and a more complicated set of equations is required [14] to calculate the performance. For short wavelengths, e.g. UV and X-ray, the requirement on the electron-beam emittance is the most difficult to meet (see later).

48.3 Technology for FELs

The type of accelerator used to drive an FEL depends very much on the lasing wavelength. Because the wavelength scales inversely as the square of the electron energy, short-wavelength devices tend to be driven by large and sophisticated accelerators, whereas long-wavelength FELs are driven by smaller and simpler accelerators. It is interesting to note that this size scaling is opposite to that of conventional microwave and rf generators, i.e. in an FEL the wavelength of emission scales inversely with the square of the electron energy; therefore, short-wavelength FELs are generally bigger than longer-wavelength devices. Note that the gain of an FEL scales approximately inversely with electron energy.

The type of FEL configuration, e.g. oscillator or amplifier, also scales with wavelength. Table 48.1 gives a summary of accelerator technology in relation to FELs.

At the longest wavelengths, the FEL gain is usually so high that the devices can operate from spontaneous emission to saturation in the amplifier mode (self-amplified spontaneous emission or SASE). At intermediate wavelengths (near-IR, visible and near-UV), the gain is lower; therefore, oscillators with optical cavities dominate. At present, storage-ring-driven FEL oscillators are leading the way to short UV wavelengths. At the shorter wavelengths (<100 nm), mirrors become impractical and so one has to consider linear-accelerator-driven SASE amplifiers with very long undulators designed to achieve saturation in a single pass. Linear accelerators are better suited as drivers for very-short-wavelength FELs rather than storage rings. This is because in a high-energy linear accelerator, higher electron beam peak current and lower beam emittance can be achieved than in a ring of equivalent energy.

At hard X-ray and γ-ray wavelengths, even SASE systems are likely to become impractical. Such photons can be produced by Compton backscattering of FEL-generated photons against the electron beam [15,16].

A measure of electron beam quality is the rms normalized emittance

$$\varepsilon_n \approx \gamma R_e \theta_e \tag{48.11}$$

where R_e is the rms electron beam radius and θ_e is the rms electron beam divergence angle. High electron beam brightness $(B \approx I_e/\varepsilon_n^2)$ corresponds to high peak current and low emittance. One of the goals of accelerator development for FELs is to have I_e as high as possible while keeping ε_n as low as possible. In order to work well, the electron and optical beams must overlap effectively. Note that the product of the optical beam radius w and the emission angle θ_0 is given by $w\theta_0 = \lambda_r/4\pi$. Effective overlap of the beams requires $R_e\theta_e < w\theta_0$, or in terms of the emittance,

$$\frac{\varepsilon_n}{\gamma} < \frac{\lambda_r}{4\pi}. \tag{48.12}$$

The current state of the art corresponds to $I_e \approx 100$ A with $\varepsilon_n \approx 2$ μm. The requirements of X-ray FELs are such that this low emittance value will have to be maintained at currents of several kA. The generation and transport of an electron

TABLE 48.1

FEL Accelerator Technology Is Wavelength Dependent

Wavelength Range	Accelerator Type	FEL Configuration
Far-IR(mm)	Induction linac, van de Graaff, Pulse-line accelerator	SASE amplifier, oscillator
Near-IR	rf linac, microtron	Oscillator
Visible	rf linac, storage ring	Oscillator
UV > 100 nm	Storage ring, rf linac	Oscillator
XUV	rf linac, storage ring	Amplifier, harmonic generation
1 keV–MeV	rf linac, storage ring	SASE (keV), Compton backscatter (keV–MeV)

beam from its source to the undulator involves a considerable amount of manipulation of the electrons. Maintaining the quality of the electron beam (i.e. keeping the emittance low and current high) is the subject of extensive research in the FEL community.

At optical wavelengths, considerable effort has been put into developing compact cost-efficient FELs, and also toward improving the quality of electron beams, particularly in regard to electron sources for rf linacs [17]. The technology of choice, which both enhances the performance and reduces the size of the FEL, is the rf electron gun, operated either in the thermionic mode or in the laser switched mode. Typically FELs require peak currents (I_e) in the range of 100 A for low-gain oscillators to several kA for high-gain amplifiers. In the case of low average power devices, increasing the electron beam brightness has the effect of making the accelerator more compact by allowing short-wavelength lasing at lower electron energy than would otherwise be possible, e.g. 370 nm using a 45 MeV electron beam [18].

48.4 FEL Applications

Because of their cost and complexity, FELs are most competitive at wavelengths where other sources are weak. In order for FELs to be of continued interest to users, they must deliver a performance that far surpasses conventional sources in brightness, power and wavelength range. At present, most applications-orientated FELs operate in the near- to mid-IR and near-UV regions of the spectrum.

In the following description of some FEL applications, we highlight applications that have great practical utility but which still require work to reach maturity. Any application requiring average optical power in excess of a few tens of watts should be considered speculative at this time. Table 48.2 gives a list of FELs that are operated as user facilities. Further details of these and other operating and proposed FELs can be found elsewhere [19,20].

Medicine is a very rich field for FEL applications [21]. Medical applications generally require rather modest average power levels of the order of several watts.

In the area of laser surgery, there is considerable interest in finding wavelengths at which tissue can be cut cleanly with little collateral damage. Ablation of tissue with high-peak power laser pulses in the IR and UV is of particular interest. There is some preference for the use of IR wavelengths because of the potential reduced risk of photochemical effects (with possible persistent collateral damage or genetic modifications) compared to UV wavelengths.

Studies at the Vanderbilt University FEL have shown that wavelengths near 6.45 μm, corresponding to the amide II absorption band of proteins, are particularly well suited for

TABLE 48.2

A Selection of FELs Intended as User Facilities. The Performance Numbers Are Subject to Change

Country	Institution	Device Name	Wavelength (μm)	Micropulse Length (ps)	Peak Power (MW)	Average Power (W)
China	Institute for High Energy Physics	-	10–16	4	20	2
France	Université de Paris-Sud	SuperACO	0.3–0.69	20	12	0.8
		CLIO	3–50	1.5–6	10	9
Germany	DESY	TESLA-FEL*	(0.0001–0.001)	(0.2)	(37 000)	(210)
The Netherlands	FOM-Institute for Plasma Physics	FELIX-2	5–30	0.5–10	2	1
		FELIX-1	25–110	1–10	2	0.5
Japan	iFEL	FELI 1	5–22	2	5	2
		FELI 2	1–6	2	5	0.5
		FELI 3	0.23–1.2	2	5	0.5
		FELI 4	20–80	2	5	1
		FELI 5	50–100	2	2	1
USA	Duke University	OK-4	0.19–0.4	10	1000	1
		Mark III	3–10	3	2	3
	Jefferson Laboratory	IR Demo	3–6.6	1–2	10	2000
		IR-Upgrade*	(1–15)			(10 000)
		UV-FEL*	(0.3–1)			(3000)
	University of Maryland*	MIRFEL	(10–150)	(4)	(4)	(0.5)
	Stanford University	FIREFLY	19–65	1–5	0.3	0.4
		SCA	3–10	0.7	10	1.2
	University of California, Santa Barbara		150–2000	10^6	0.004	0.08
	Vanderbilt University	MKIII	2–10	2	10	10
	SLAC*	LCLS-2*	(0.00015–0.0015)	(0.3)	(20 000)	(1.5)
	BNL	DUVFEL	0.266	2	50	N/A

The asterisk indicates facilities that are proposed or under construction; numbers in parentheses indicate design goals.

soft tissue surgery [22]. Remarkable results have been achieved in ocular and neural tissue, where extremely clear cuts were made with little collateral damage. In some cases, collateral damage extended only to a depth of 10 μm into the tissue from the cut boundary. Human studies are now underway.

The FEL is particularly suited for bulk materials processing because of its tunability for optimum wavelength, potential for scaling to high average power and low cost per unit of light energy. Because of the large investment of capital equipment and operating personnel, FELs are not cost effective for industrial processing at low average power levels. As the average power level increases, however, the cost effectiveness of the FEL as a photon source improves dramatically. Studies have shown that at average power levels in the 100–200 kW range, the cost of UV photons delivered should be less than \$0.0002 kJ^{-1} [23].

A general category of material processing involves surface modification. An example is the alteration of the surface characteristics of various fibres to make fabric less shiny, more hydroscopic, softer or more accepting of dyes [24]. Such an application would require approximately 100 kW of 193 nm light per min per 1000 m^2 of fabric. Other examples include improving the adhesion properties of material to reduce the requirement for glues and enhancing the antimicrobial properties of nylon by converting the amide groups to amines.

In the gas phase, infrared photochemistry by multiple-photon dissociation has been the subject of promising FEL research [25]. The IR excitation process that leads to molecular dissociation occurs by the successive absorption of a few tens of IR photons near a strong IR resonance. The particular features of the FEL make it a very appropriate device as a driver for bond-selective photochemistry. The FEL offers easy tunability to match molecular absorption resonances and the high-peak power necessary for multi-photon processes.

In general, the wavelength range covered by existing FELs is not far removed from that of conventional lasers. In many cases, FEL applications have been extensions of work already begun with other lasers. New opportunities exist at very short wavelengths (i.e. very high photon energies), where the only existing sources are incoherent.

The development of tunable, hard X-ray FELs such as the linac coherent light source (LCLS) at the Stanford Synchrotron Radiation Laboratory and the TESLA FEL facility at the Deutsches Elektronen Synchrotron (DESY) in Germany are commonly being referred to as ‘fourth-generation light sources’ [26]. This contrasts with the previous three generations of incoherent synchrotron light sources. The major advantage of FELs is that they produce a coherent beam with a peak brightness many orders of magnitude higher than that possible from synchrotrons (see Figure 48.12). Consequently, applications of light sources in the X-ray region will undergo an explosion similar to that experienced in the visible region brought on by the invention of the laser.

The proposed X-ray FELS will have the spatial and temporal resolution to observe features on the angstrom length scales of molecular bonds and the sub-picosecond time scales of molecular vibrations. This would allow chemists to directly observe reaction processes such as the photo-dissociation of isolated gas-phase molecules, photochemically induced bond breakage and recombination and structural transformations in photosynthetic processes. Studies of nanoscale dynamics involve the overlap of different time and length scales. Techniques that will be possible include X-ray photon correlation spectroscopy; X-ray transient grating spectroscopy; and the study of the dynamics of entangled polymers, glassy dynamics and collective mode dynamics in liquids and gases.

Very high-energy ($\gg$10 keV) photons can be generated by Compton backscattering of FEL photons against high-energy electrons. The head-on collision results in a pencil-like beam of hard photons whose energy is closely correlated with scattering angle. The highest energy photons are on the scattering axis, with energy falling monotonically as the scattering angle increases. Such a source is quite different in character from a conventional bremsstrahlung source in which photon energy is only loosely correlated with angle. Though the photon beam is incoherent, the correlation of photon energy with angle allows the collimation of the photon beam into a narrow beam with a small energy spread. Experiments have shown that a quasi-monochromatic beam of multi-MeV γ-rays could be produced by scattering near-UV FEL photons against 500 MeV electrons circulating in a storage ring [16]. Such beams will have many applications [27] in nuclear physics studies [28] and radiographic imaging [29].

48.5 Future Directions for FELs

Developments in both high average power and short wavelength have fuelled a tremendous increase in interest in FELs.

The demonstration of 2 kW average optical power in the near-IR by the Jefferson laboratory group using a superconducting energy recovery linac (Figure 48.3) has opened the door for high average power applications in materials processing. Continued development of high-power FEL technology in the UV should produce considerable interest from industry.

Ultrashort-wavelength FELs will be an important component in the next generation of light sources that will produce coherent, short-pulse radiation at soft and hard X-ray wavelengths. The technical challenges are particularly great in this region where high-reflectivity optics are not available. Developments in linear accelerator and storage ring technology and SR research, however, have made the new frontiers both alluring and reachable [26,30]. An example of a proposed device is the linac coherent light source [26]. The LCLS

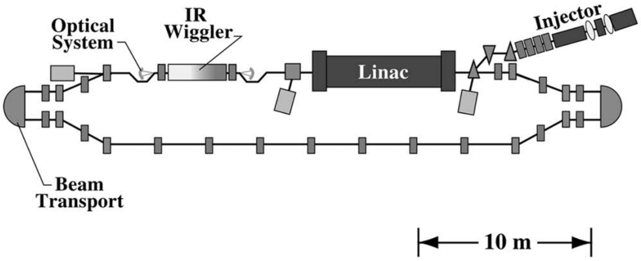

FIGURE 48.3 Thomas Jefferson National Accelerator Facility 50 MeV energy recovery linac and infrared FEL light source. (Courtesy Lia Merminga, TJNAF.)

is designed to operate from 0.15 to 2.5 nm and will require a 15 GeV electron beam with a peak current of $I_e > 3000$ A and a normalized emittance of 1–2 μm feeding a 100-m long undulator. The LCLS will produce an X-ray beam with a peak brightness of 10^{33} photons (s mm^2 mrad^2 0.1% bandwidth)$^{-1}$ in sub-picosecond pulses (see Figure 48.12). Such a device would have a peak spectral brightness several orders of magnitude greater than existing synchrotron sources. Another X-ray FEL designed to operate at longer wavelengths than the LCLS is under construction at DESY in Germany [26]. Figure 48.12 shows a comparison of the performance of these proposed FELs and existing synchrotron light sources.

Another spectral region that is ripe for FEL development is the far-IR at wavelengths of several tens to several hundred micrometres. In this region lie many molecular resonances of biological interest that have not yet been investigated. Unlike the X-ray FELs, far-IR devices can be very compact and can be driven by electrons that are a few MeV in energy. It is anticipated that far-IR devices will fit on an optical bench, and will be suitable for individual investigator use. For further details on FELs, the reader is referred to [31–36].

48.6 Synchrotron Light Sources

48.6.1 Introduction

A synchrotron light source typically consists of an electron storage ring which produces both SR in the bending magnets of the ring and wiggler or undulator radiation in the insertion devices installed in the straight sections of the ring. A detailed discussion of the properties of synchrotron, wiggler and undulator radiation will be given in a later section. As an example of a synchrotron light source, the schematic layout of part of the National Synchrotron Light Source at Brookhaven National Laboratory is shown in Figure 48.4.

The key elements of a synchrotron light source are the electron storage ring and the electron injection system:

The 'electron storage ring' stores 10^{12} electrons for 5 h and has the following components:

- dipole magnets which bend electrons in a circular orbit and produce SR;
- quadrupole magnets which provide focusing of the electron beam;
- rf cavity which replenishes the electron energy lost to SR;
- a vacuum system which reduces ring pressure to ~10^{-7} Pa;
- straight sections which are typically ~5 m of empty space to accommodate insertion devices; and
- beamlines providing an optical transport line (~5–30 m) to take the SR from the ring to the experimental end stations.

The 'electron injection system' has the following components:

- electron gun which is the electron source;
- linac which pre-accelerates the electrons to 50–100 MeV; and
- a booster ring which accelerates the electrons to the energy of the storage ring (500–8000 MeV).

48.6.2 Brief History of Synchrotron Light Sources

In the literature one often reads that light sources are classified in terms of 'generations' as follows:

- First Generation: SR is obtained parasitically from bending magnets in a high-energy physics ring (*circa* 1970s);
- Second Generation: dedicated storage rings producing SR from bending magnets with a only a few insertion devices of moderate brightness (*circa* 1980s);

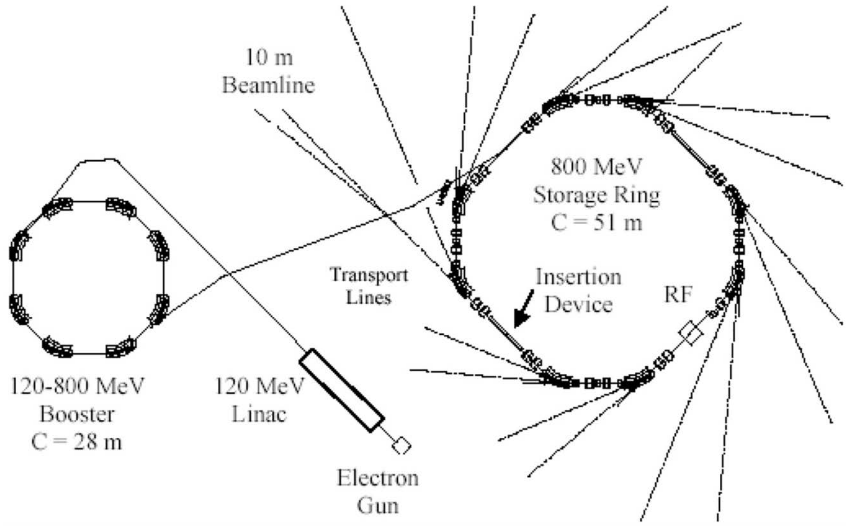

FIGURE 48.4 Schematic layout of a generic synchrotron light source.

- Third Generation: dedicated storage rings optimized for many insertion devices yielding very high brightness (*circa* 1990s); and
- Fourth Generation: an open research topic and possibly not a storage ring at all but an FEL on a linear accelerator *(circa* 2000s)!

At present, most of the first-generation light sources have been replaced by dedicated storage rings. There are more than 50 second- and third-generation rings in operation around the world with new rings being brought on line each year (see Table 48.3).

The rings in Table 48.3 are grouped into three ranges according to the energy of the electron beams. Using the formulae in the next section for synchrotron and undulator radiation, it can be shown that the rings of a particular energy produce photon beams as follows:

- 0–1.5 GeV rings: infrared, ultraviolet photon beams (less than 2 keV);
- 1.5–3 GeV rings: soft X-ray photon beams (1–10 keV); and
- 6–8 GeV rings: hard X-ray photon beams (10 keV and beyond).

48.6.3 Operational Characteristics of Synchrotron Light Sources

Typical stored currents in an electron storage ring are 750 mA for low-energy rings and 200 mA for high-energy rings; this corresponds to the order of 10^{12} electrons circulating in the ring. It should be noted that the electrons are not distributed uniformly around the ring; they are formed into circulating bunches with free space in between. The length of the electron bunch depends on the arrangement of the magnets, the energy of the ring and the voltage and frequency of the rf system. Bunch lengths typically range from 1 to 5 cm (rms). The number of electron bunches in a particular ring can range from one to several hundreds depending on the design of the ring and desires of the experimenters.

The operation of a generic ring proceeds as follows. All the hardware (magnets, rf, etc) is powered to the appropriate setpoints. An electron beam is emitted from a thermionic cathode and accelerated in the linear accelerator to low energy (~50–100 MeV). This beam is injected into a booster ring that cycles at a rate of 1–30 Hz and the energy of the electron is raised to the level of that in the storage ring (~500–8000 MeV). The electron beam is ejected from the booster ring into a transport line and injected into the storage ring. The circulating electron beam generates radiation when it is bent in the dipole magnets of the ring or in one of the insertion devices in a straight section of the ring. The electron beam is stored for roughly 5–12 h. The electrons are lost from the ring due to Coulomb collisions among electrons in a bunch and also due to collisions with residual gas molecules in the ring. To prolong the storage time, the vacuum in the storage ring should be very good (~10^{-7} Pa). This operation cycle is simply repeated throughout the life of the ring.

TABLE 48.3

Approximate Number of Synchrotron Light Source Rings Worldwide as a Function of Ring Energy

Region	0–1.5 GeV	1.5–3 GeV	6–8 GeV	Approximate Total
Asia	13	5	1	19
Europe	3	7	1	11
India	1	1		2
Middle East	1			1
North America	5	5	2	12
Russia	2	3	1	6
South America		1		1

One of the key figures of merit of a synchrotron light source is the emittance of the electron beam. The Holy Grail is to produce a light beam without any measurable effects on the electron beam. Since a zero emittance electron beam is not possible, the desire is to reduce the emittance, such that $\varepsilon_n/\gamma \sim \lambda/4\pi$, the so-called ‘diffraction limited emittance’. Figure 48.5 displays the horizontal emittance of the electron beam versus energy of the electron beam for many existing and planned synchrotron light sources.

The main factors determining the emittance of a light source are the energy of the ring and the layout of the quadrupole and dipole magnets that make up the ring, the so-called ‘lattice’. The lattice is usually constructed from basic cells as displayed in Figure 48.6; the number of cells in the full ring is termed the superperiodicity, N_s. The emittance, ε_n, of a ring depends on the energy of the ring and the number of superperiods: $\varepsilon_n \propto E^2/N_s^3$ [36].

Thus, for a ring of particular energy, one varies the number of cells to obtain the desired emittance. Of course the circumference of the ring increases as the superperiodicity is increased. A ring with an energy of 1 GeV will have a circumference of roughly 75 m, a 3 GeV ring ranges from 170 to 350 m, while a 6–8 GeV ring grows to 1–2 km.

48.6.4 Electromagnetic Radiation from Charged Particles

When an electron circulates in an electron storage ring designed as a synchrotron light source, there are three types of radiation that are of interest to the experimentalist who makes use of this light:

- synchrotron or bending magnetic radiation;
- wiggler magnet radiation; or
- undulator magnet radiation.

In Figure 48.7, we give a schematic diagram of the three radiation processes showing the electric field as a function of time and the intensity as a function of frequency for radiation from a single electron. In general, the radiation from the electrons is not coherent so the total intensity is simply given by the sum of the intensity for each electron. In the succeeding sections, we shall discuss the properties of each type of radiation and provide some formulas in ‘practical units’ to facilitate rapid calculations.

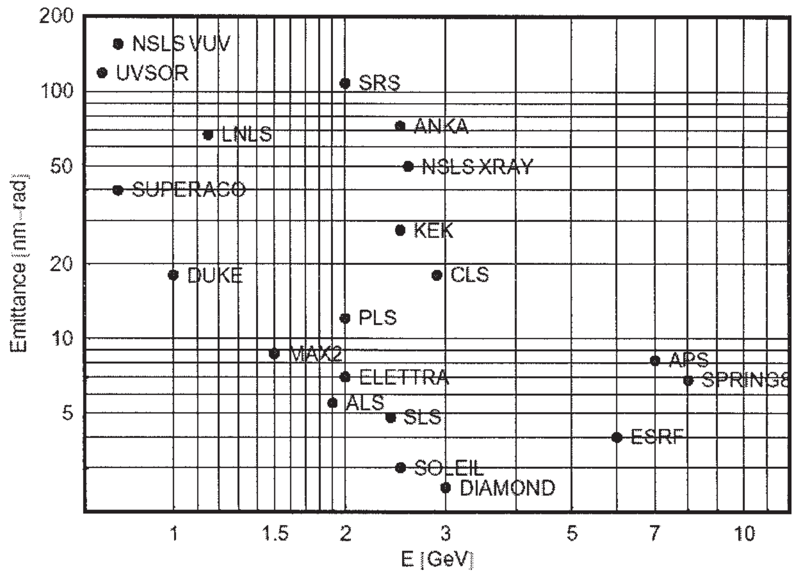

FIGURE 48.5 Horizontal electron beam emittance versus electron energy for several existing and planned synchrotron light sources worldwide.

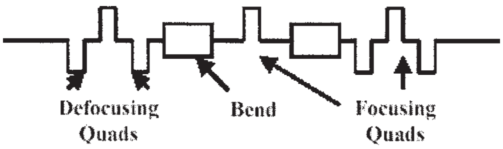
Defocusing Quads
Bend
Focusing Quads

FIGURE 48.6 Basic building block of a light source lattice: the Chasman–Green double-bend achromat cell.

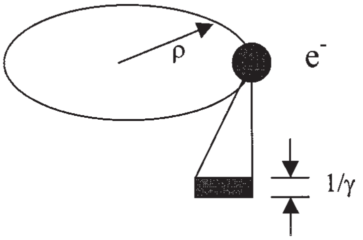

FIGURE 48.8 Schematic diagram for the emission of synchrotron radiation by a relativistic electron on a curved trajectory.

48.6.4.1 Synchrotron or Bending Magnetic Radiation

When an electron moves in a transverse magnetic field, the accelerated electron emits electromagnetic radiation known as synchrotron radiation (SR), as shown schematically in Figure 48.8. SR has a very broad spectrum for low photon energies and falls off exponentially above a critical photon energy, $E_c = \hbar\omega_c = 3\hbar c\gamma^3/2\rho$, where $\gamma = E/m_e c^2 = E$ [MeV]/0.511 [37–40]. ρ is the bending radius of the electron in the dipole magnetic field and is related to the electron energy and the dipole magnetic field, ρ [m] = E [GeV]/0.3B [T]. SR was first experimentally observed at the General Electric Corporation in 1947.

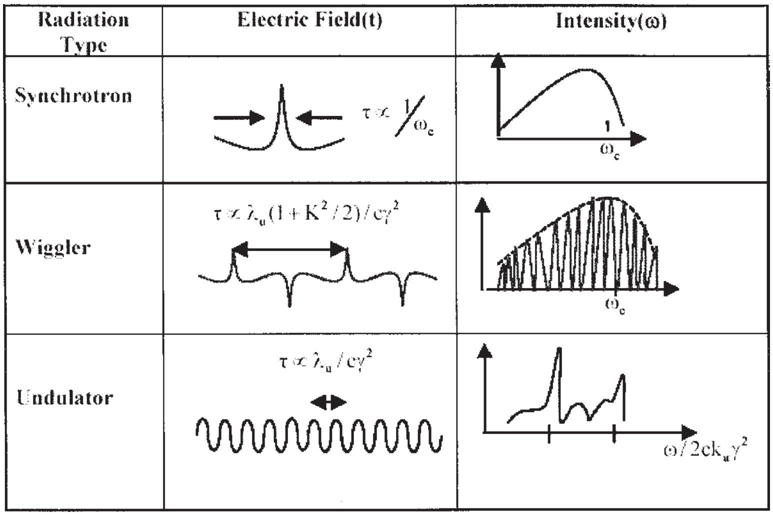
Radiation Type
Electric Field(t)
Intensity(ω)
Synchrotron
τ ∝ 1/ω_c
ω_c
Wiggler
τ ∝ λ_u(1 + K²/2)/cγ²
ω_c
Undulator
τ ∝ λ_u/cγ²
ω/2ck_uγ²

FIGURE 48.7 Schematic diagram of the three radiation processes of interest in a synchrotron light source. The second column displays the electric field as a function of time, and the third column displays the intensity as a function of frequency.

In practical units, the critical photon energy or wavelength can be written in terms of the electron energy and the dipole magnetic field as

$$E_c[\text{keV}] = 0.665B\,[\text{T}]E^2\,[\text{GeV}] \tag{48.13}$$

$$\lambda_c\,\overset{\circ}{\text{A}} = \frac{18.64}{B[\text{T}]E^2[\text{GeV}]} \tag{48.14}$$

Half of the total SR power is radiated above the critical photon energy and half below. Due to the relativistic motion of the electron, the SR is highly collimated in the forward direction with a characteristic vertical opening angle [37],

$$\psi(\omega) \approx \begin{cases} \dfrac{1}{\gamma}\left(\dfrac{\omega_c}{\omega}\right)^{1/3} & \omega \ll \omega_c \\ \dfrac{1}{\gamma} & \omega \approx \omega_c \\ \dfrac{1}{\gamma}\left(\dfrac{\omega_c}{\omega}\right)^{1/2} & \omega \gg \omega_c. \end{cases} \tag{48.15}$$

The spectral and angular distribution of the number of photons (flux) is given by [37–40]

$$\frac{\mathrm{d}N}{\mathrm{d}\Omega} = \frac{3\alpha\gamma^6}{4\pi^2}\left(\frac{\omega}{\omega_c}\right)^2\left(\frac{1}{\gamma^2}+\psi^2\right)^2 \times\left[K_{2/3}^2(x)+\frac{\psi^2}{1/\gamma^2+\psi^2}K_{1/3}^2(x)\right]\frac{I}{e}\frac{\Delta\omega}{\omega} \tag{48.16}$$

with units of photons s^{-1} sr^{-1}, $\alpha = 1/137.04$, I in amperes, $e = 1.6 \times 10^{-19}$C, $K_{2/3}$ is a Bessel function of fractional order and where $\chi \equiv \omega(1 + \gamma^2\psi^2)^{3/2}/2\omega_c$. The first term in the square brackets corresponds to radiation with the electric field vector polarized in the plane of the orbit and the second term to radiation polarized perpendicular to the plane.

In the forward direction ($\psi = 0$), the previous equation can be written in practical units as

$$\frac{\mathrm{d}N}{\mathrm{d}\Omega} = 1.325\times10^{16}E^2[\text{GeV}]I[\text{A}]H_2(y,\,0)\frac{\Delta\omega}{\omega} \tag{48.17}$$

with units photons s^{-1} mrad θ^{-1} mrad ψ^{-1}, $y \equiv \omega/\omega_c = \lambda_c/\lambda$ and $H_2(y,0) = y^2K_{2/3}^2(y,2)$ is plotted in Figure 48.9.

If the angular distribution is integrated over all vertical angles, one obtains the flux per milliradian of horizontal arc (θ),

$$\frac{\mathrm{d}N}{\mathrm{d}\theta} = \frac{\sqrt{3}\alpha\gamma}{2\pi\times10^3}\frac{\Delta\omega}{\omega}\frac{I}{e}\left(\frac{\omega}{\omega_c}\right)\int_{\omega/\omega_c}^{\infty}K_{5/3}(x)\mathrm{d}x \tag{48.18}$$

with units of photons s^{-1} mrad θ^{-1}, I in amperes and $e = 1.6 \times 10^{-19}$C.

In practical units, this can be written as

$$\frac{\mathrm{d}N}{\mathrm{d}\theta} = 2.457\times10^{16}E[\text{GeV}]I[\text{A}]G_1(y)\frac{\Delta\omega}{\omega} \tag{48.19}$$

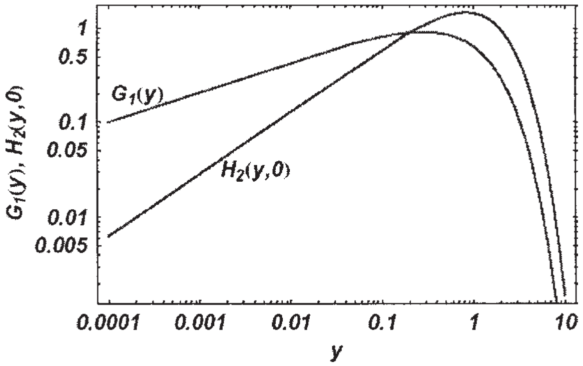

FIGURE 48.9 Plot of G_1 (y) and H_2 (y, 0) versus y.

with units of photons s^{-1} mrad θ^{-1} and where

$$G_n(y) = y^n\int_y^{\infty}K_{5/3}(x)\mathrm{d}x \tag{48.20}$$

Figure 48.9 is a plot of the functions $H_2(y,\ 0)$ and G_1 (y). Figure 48.10 is a plot of dN/dθ as a function of photon energy for radiation from a representative range of storage rings.

The spectral power per horizontal angle but integrated over all vertical angles is given in practical units by

$$\frac{\mathrm{d}P}{\mathrm{d}\theta}\left[\frac{\text{mW}}{\text{mrad}\,\theta}\right] = 8.73\times10^3\frac{E^4[\text{GeV}]}{\rho[\text{m}]}I[\text{A}]G_2(y)\frac{\Delta\omega}{\omega} \tag{48.21}$$

Finally, the total power radiated by a circulating current I is given in SI units by

$$P_T = \frac{4\pi r_e mc^2}{3e}\frac{\gamma^4}{\rho}I \tag{48.22}$$

or in practical units by

$$P_T[\text{kW}] = \left[\frac{88.5E^4[\text{GeV}]}{\rho[\text{m}]}\right]I[\text{A}]. \tag{48.23}$$

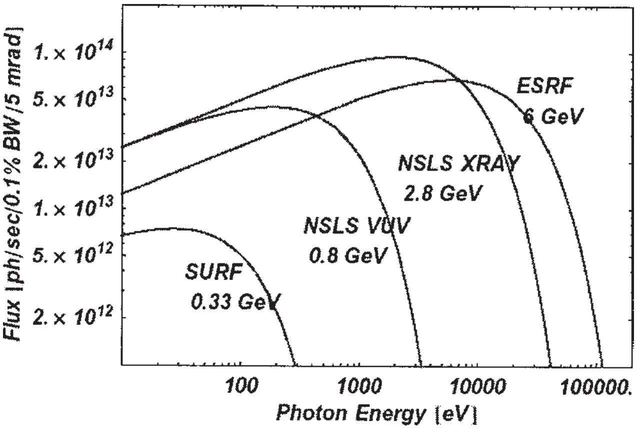

FIGURE 48.10 SR flux integrated over all vertical angles and for 5 mrad of horizontal angle versus photon energy for several synchrotron light sources of different energies.

48.6.4.2 Insertion Devices

To enhance the performance of synchrotron light sources beyond what is available from the dipole magnet radiation, so-called insertion devices are used in the straight sections of the electron storage ring. As mentioned in Section 48.2, an insertion device is characterized by a periodic magnetic field $B_x[z] = B_0 \sin[2\pi z/\lambda_u]$, and it is constructed from alternating polarity permanent magnets as shown in Figure 48.11. Although FELs do exist in a few storage rings, the radiation from insertion devices in synchrotron light sources is simply spontaneous emission.

The figure of merit of an insertion device is the 'K parameter' given by [40],

$$K = \frac{eB}{mck_u} = 0.934B[\mathrm{T}]\lambda_u[\mathrm{cm}]. \tag{48.24}$$

Note that the K parameter is simply related to the rms normalized vector potential introduced in Section 48.2 as $a_u \equiv K/\sqrt{2}$. In the literature on synchrotron light sources, 'K' is the mostly widely used notation; however, we shall use 'a_u' to make the notation consistent throughout this chapter.

For $a_u \le \sqrt{2}$, the insertion device is termed an undulator, and for $a_u > \sqrt{2}$, the device is termed a wiggler. Note that $a_u = 2$ is not a threshold: there is a continuous transition from an undulator to a wiggler. Schematically, the difference between an undulator and wiggler is shown in Figure 48.7, where the electric field as a function of time and the intensity as a function of frequency are given.

Wiggler Radiation: For a wiggler, the electric field as a function of time is simply a periodic train of pulses similar to those of ordinary SR. In the frequency domain, the intensity is then given by a large number of lines with an overall envelope given by ordinary SR but increased by twice the number of periods in the insertion device. This is the key advantage of a wiggler. By wiggling, the particle back and forth many times one can greatly enhance the amount of flux compared to that available from, say, 5 mrad of arc in a dipole magnet. Another use of a wiggler is to shift the critical photon energy to higher values by using superconducting coils instead of permanent magnets to produce fields of 5–10 T.

The total power radiated in a wiggler is given by

$$P_T[\mathrm{W}] = \frac{8\pi^2 r_e m_e c^2 a_u^2 \gamma^2 N_u}{3\lambda_u}\frac{I}{e} \tag{48.25}$$

$$= \frac{14.5E^2[\mathrm{GeV}]I[\mathrm{A}]N_u a_u^2}{\lambda_u\,[\mathrm{cm}]} \tag{48.26}$$

where N_u is the number of periods in the wiggler.

Undulator Radiation: For $a_u \le \sqrt{2}$, the electric field as a function of time is roughly sinusoidal giving rise to an intensity with a single peak in the frequency domain at

$$\omega = \frac{2ck_u\gamma^2}{(1+a_u^2)} \tag{48.27}$$

with an intensity proportional to N_u^2 and a bandwidth given by $\Delta\omega/\omega \approx 1/N_u$, as given in Section 48.2.1. As a_u is increased, the number of lines in the frequency domain increases but for $a_u \le \sqrt{2}$ the spectrum is still characterized by a few distinct lines. The narrow line structure arises from the interference between light emitted in successive periods. The very high intensity in a narrow spectral bandwidth is the signature feature of an undulator source. The formula given for the total power radiated in a wiggler also applies for an undulator. Thus, one additional feature of an undulator is that the total power incident on the beamline optical elements is greatly reduced as compared to a wiggler since $P \propto a_u^2$.

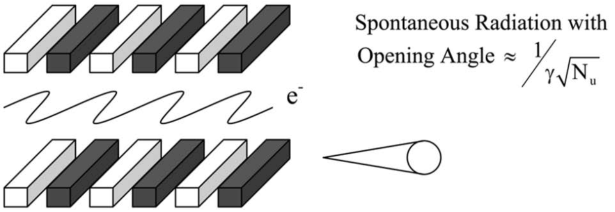
Spontaneous Radiation with
Opening Angle ≈ $1/\gamma\sqrt{N_u}$
e$^-$

FIGURE 48.11 Schematic diagram of an electron undulating as it traverses an insertion device and emitting spontaneous radiation.

Radiation in the forward direction occurs at odd harmonics of the frequency ω of Equation (48.27),

$$\omega_h = \frac{2hck_u\gamma^2}{(1+a_u^2)} \tag{48.28}$$

with a linewidth of

$$\frac{\Delta\omega_h}{\omega_h} = \frac{1}{hN_u}. \tag{48.29}$$

In contrast to most FELs, the higher harmonics of undulator and wiggler radiation are widely used in synchrotron light sources. For completeness, we generalize the expression for the spectral angular intensity in the forward direction given in Section 48.2.1 to include higher 'odd' harmonics and an electron beam with a current I. The intensity in units of photons s^{-1} sr^{-1} is then given by

$$\left.\frac{\mathrm{d}N_h}{\mathrm{d}\Omega}\right|_{\theta=0} = \alpha N_u^2\gamma^2 \frac{I}{e}\frac{\Delta\omega}{\omega}\frac{2h^2a_u^2}{\left(1+a_u^2\right)^2}F^2[h,\xi]\frac{\sin^2(x_h/2)}{(x_h/2)^2} \tag{48.30}$$

with I in amperes, $h = 1, 3, 5, \ldots$, $x_h = 2\pi hN_u(\omega - \omega_h/\omega_h)$ and $F[h, \xi]$ was given in Section 48.2.3.1.

Again generalizing the results in Section 48.2.3, the most useful part of the radiation is confined to a central cone about the forward direction within an angular divergence given by [40],

$$\sigma_r' \approx \frac{1}{\gamma}\left[\frac{\left(1+a_u^2\right)}{2hN_u}\right]^{1/2} = \left[\frac{\lambda_h}{L}\right]^{1/2} \tag{48.31}$$

Using this definition of the radiation opening angle, the spectral and angular distribution in the forward direction at $\omega = \omega_h$ can be rewritten as [40],

$$\left.\frac{\mathrm{d}N_h}{\mathrm{d}\Omega}\right|_{\omega=\omega_h} = \frac{N_h}{2\pi\sigma_r'^2} \tag{48.32}$$

where

$$N_{\mathrm{h}} = \pi\alpha N_{\mathrm{u}}\frac{I}{e}\frac{\Delta\omega}{\omega}\frac{2ha_{\mathrm{u}}^2}{\left(1+a_{\mathrm{u}}^2\right)}F^2\left[h,\xi\right] \tag{48.33}$$

is the intensity of photons in the central cone. It is interesting to note that this quantity does not depend explicitly on the energy of the electron!

A critical figure of merit for an undulator source is the on-axis peak brightness of the undulator radiation at $\omega = \omega_{\mathrm{h}}$ defined as [40]

$$B_{\mathrm{h}} = \frac{N_{\mathrm{h}}}{4\pi^2\,\Sigma_x\,\Sigma'_x\,\Sigma_y\,\Sigma'_y} \tag{48.34}$$

where $\Sigma_{x,y} = \sqrt{\varepsilon_{x,y}\beta_{x,y} + \lambda L/(4\pi)^2}$ is the effective rms beam size of the combined electron beam $\sigma_{x,y} = \sqrt{\varepsilon_{x,y}\beta_{x,y}}$ and photon beam $\sigma_{x,y}^{\mathrm{ph}} = \sqrt{\lambda L/(4\pi)^2}$ and, similarly, for the rms angular divergence $\Sigma'_{x,y} = \sqrt{\varepsilon_{x,y}/\beta_{x,y} + \sigma_{\mathrm{r}}'^2}$.

Figure 48.12 displays the average and peak brightness of several synchrotron light sources and FELs.

48.7 Future Directions for Synchrotron Light Sources

With more than 50 rings in existence and more under construction and in the planning stages, storage-ring-based synchrotron light sources will continue to serve the largest user base for decades to come. For high average brightness, from the infrared portion of the spectrum to the hard X-ray regime, with pulse-lengths in the range of 50–500 ps, electron storage rings are the source of choice at present. If higher peak brightness and/or sub picosecond pulses are required then the source of choice is an FEL.

It must be noted that the underlying physics of electron storage rings means it will be difficult, if not impossible, to continue increasing the brightness significantly as the rings are simply becoming too large [41,42]. One should note a paper entitled 'Towards the Ultimate Storage Ring-Based Light Source' [43]. New technologies will be needed to continue the trend of ever increasing brightness.

A candidate for a future light source that is beginning to appear on the drawing boards of machine designers is the so-called energy recovery linac (ERL), shown schematically in Figure 48.3 [44–49]. This device uses a superconducting linear accelerator and a pair of half arcs to return the accelerated beam back through the linac with a 180° phase shift to recover the energy in a bunch before the spent beam is dumped at an energy of the order of 10 MeV. At present, the ERL at the Thomas Jefferson National Accelerator Facility is the only machine in operation. It has an energy of 50 MeV, a circulating current of 5 mA, and it also contains a high average power infrared FEL [50]. Machines of higher energy (0.6–6 GeV) and average currents similar to that in ring (100 mA) are being explored for feasibility and should be possible in the next decade.

Potential advantages of an ERL-based light source are as follows [46]:

- diffraction limited electrons beams for 10 Å and below;

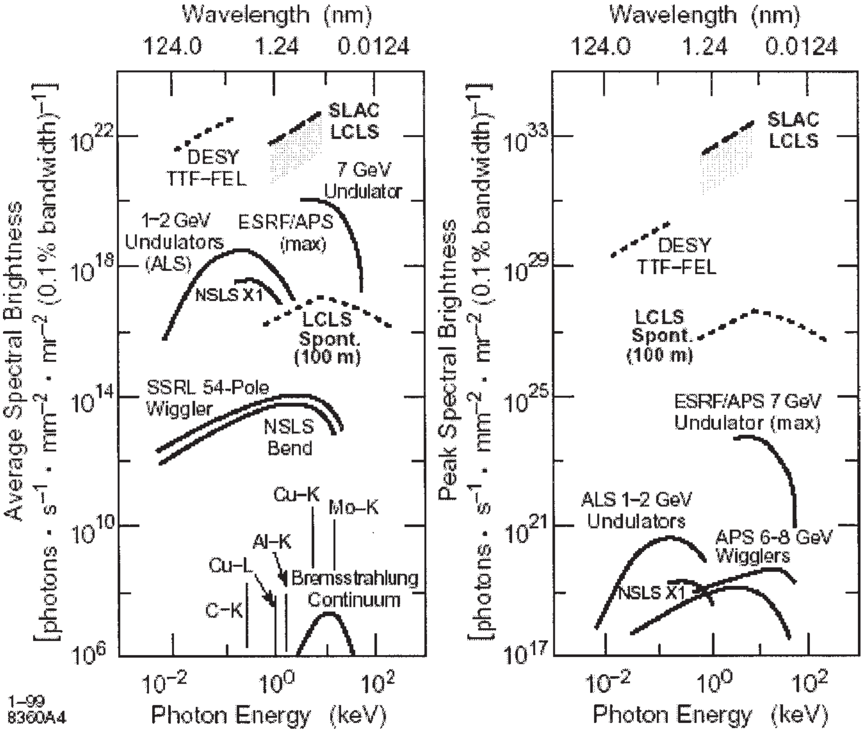

FIGURE 48.12 Average and peak brightness versus photon energy for several synchrotron light sources and FELs. (Courtesy of J Galayda/SLAC.)

- average brightness exceeding that of existing storage rings;
- sub-picosecond electron bunches;
- round electron beams;
- virtual ‘top off’ operation; and
- SC linac can serve as an FEL driver.

REFERENCES

1. Schwinger J 1949 *Phys. Rev.* **75** 1912–25.
2. Motz H, Thon W and Whitehurst R 1953 *J. Appl. Phys.* **24** 826–33.
3. Phillips R M 1988 *Nucl. Instrum. Methods A* **272** 1–9.
4. Madey J M J 1971 *J. Appl. Phys.* **42** 1906–13.
5. Elias L R, Fairbank W M, Madey J M J, Schwettmen H A and Smith T I 1976 *Phys. Rev. Lett.* **36** 717–20.
6. Deacon D A G, Elias L R, Madey J M J, Ramian G J, Schwettmen H A and Smith T I 1977 *Phys. Rev. Lett.* **38** 892–436.
7. Motz H 1979 *Phys. Lett. A* **71** 41–3.
8. Madey J M J, Fairbank W M, Schwettman H A 1973 *IEEE Trans. Nucl. Sci.* **NS-20** 980–3.
9. Neil G R et al. 2001 *Phys. Rev. Lett.* **87** 084801.
10. Brau C A 1990 *Free-Electron Lasers* (San Diego, CA: Academic).
11. Feldman D W et al. 1989 *Nucl. Instrum. Methods A* **285** 11–16.
12. Dattoli G, Letardi T, Madey J M J and Renieri A 1984 *IEEE J. Quantum Electron.* **QE-20** 637–46.
13. Bonifacio R, Pellegrini C and Narducci L M 1984 *Opt. Commun.* **50** 359–78.
14. Kim K J and Xie M 1993 *Nucl. Instrum. Methods A* **331** 359–64.
15. Carroll F E 1990 *Invest. Radiol.* **25** 465–72.
16. Litvinenko V N et al. 1997 *Phys. Rev. Lett.* **7** 4569–72.
17. O’Shea P G and Bennett H E (ed) 1997 Free-electron laser challenges *Proc. SPIE 2988.*
18. O’Shea P G et al. 1993 *Phys. Rev. Lett.* **71** 3661–4.
19. Freund H P and Granatstein V L 1999 *Nucl. Instrum. Methods A* **429** 37–40.
20. Colson W B 1999 *Nucl. Instrum. Methods A* **429** 33–6.
21. Carroll F and Brau C 1995 Medical applications of the free-electron laser *Tunable Laser Applications* ed F J Duarte (New York: Marcel Decker).
22. Edwards G et al. 1994 *Nature* **371** 416–19.
23. Neil G R 1996 *Proc. 1995 Particle Accel Conf.* (Piscataway, NJ: IEEE) pp 137–9.
24. Kelley M J *Free-Electron Laser Challenges (Proc. SPIE 2988)* ed P G O’Shea and H E Bennett (Bellingham, WA: SPIE) pp 240–4.
25. Petrov A K et al. 1998 *Nucl. Instrum. Methods B* **144** 203–10.
26. Nuhn H-D and Rossbach J 2000 *Synchrotron Radiation News* **13** 18–32.
27. O’Shea P G 1996 *Nucl. Instrum. Methods A* **375** 530–4.
28. Carman T S et al. 1996 *Nucl. Instrum. Methods A* **378** 1–20.
29. Schreiber E C and O’Shea P G 1997 *Proc. SPIE* **3154** 94–102.
30. Poole M 2000 *Synchrotron Radiation News* **13** 4–17.
31. Freund H P and Neil G R 1999 *Proc. IEEE* **87** 782–803.
32. Brau C A 1990 *Free-Electron Lasers* (San Diego, CA: Academic).
33. Freund H P and Antonsen T M 1996 *Principles of Free-Electron Lasers* 2nd edn (London: Chapman and Hall).
34. O’Shea P G and Freund H P 2001 *Science* **292** 1853.
35. Colson W B et al. 2002 *Phys. Today* **55** 35.
36. Sands M 1970 SLAC Report 121.
37. Jackson J D 1998 *Classical Electrodynamics* 3rd edn (New York: Wiley).
38. Green G K 1976 BNL Internal Report 50522.
39. Hofmann A 1986 SSRL ACD Note 38.
40. Kim K J 1989 *AIP Conf. Proc. 184* (New York: American Institute of Physics) p 565.
41. Laclare J L 1998 *Proc. EPAC 1998* (Bristol: Institute of Physics) p 78.
42. Wrulich A F 1999 *Proc. IEEE PAC 1999* (Mulhouse: European Physical Society) p 192.
43. Ropert A et al. 2000 *Proc. EPAC 2000* (Piscataway, NJ: IEEE) p 83.
44. Kulipanov G N, Skrinsky A N and Vinokurov N A 1998 *J. Synchrotron Rad.* **5** 176.
45. Bazarov I et al. 2001 *Proc. IEEE PAC 2001* (Piscataway, NJ: IEEE) p 230.
46. Ben-Zvi I et al. 2001 *Proc. IEEE PAC 2001* (Piscataway, NJ: IEEE) p 350.
47. Corlett J et al. 2001 *Proc. IEEE PAC 2001* (Piscataway, NJ: IEEE) p 2635.
48. Clarke D T et al. 2001 *Proc. IEEE PAC 2001* (Piscataway, NJ: IEEE) p 253.
49. Levi B G 2002 *Phys. Today* **55** 23.
50. Neil G R et al. 2000 *Phys. Rev. Lett.* **84** 662–5.

49

X-Ray Lasers

Jorge J. Rocca

CONTENTS

49.1 Introduction 653
49.2 Amplification and Pump Power Requirements 654
49.3 Soft X-Ray Laser Characteristics 655
  49.3.1 Wavelength 655
  49.3.2 Output Pulse Energy 655
  49.3.3 Pulse Duration 655
  49.3.4 Peak Power 655
  49.3.5 Average Power 655
  49.3.6 Beam Divergence 655
  49.3.7 Temporal Coherence 655
  49.3.8 Spatial Coherence 656
  49.3.9 Peak Spectral Brightness 656
  49.3.10 Average Spectral Brightness 656
49.4 Other Methods for the Generation of Coherent X-Ray Radiation 656
49.5 X-ray Laser Schemes 657
  49.5.1 Collisional Electron Excitation Lasers 657
    49.5.1.1 Quasi-steady-state Lasers 657
    49.5.1.2 Transient Collisional Lasers 659
    49.5.1.3 Travelling-wave Excitation 660
    49.5.1.4 Collisionally Excited Capillary Discharge Lasers 661
  49.5.2 Collisional Recombination Lasers 662
    49.5.2.1 Mechanisms 662
    49.5.2.2 Gain in Discharge-pumped Recombination Systems 664
    49.5.2.3 Recombination Lasing in Transitions to the Ground State 665
  49.5.3 Photoionization Lasers 666
References 667
Further Reading 670

49.1 Introduction

Specific proposals for excitation schemes for X-ray lasers date back to 1967, when the possibility of achieving amplification by photoionization pumping was first suggested by Duguay and Rentzepis [1]. This was followed by proposals for X-ray lasers based on the two population inversion mechanisms on which the present day's soft X-ray lasers are based: electron impact excitation schemes [2–5] and collisional recombination [6–9].

Several experiments realized during the 1970s and early 1980s yielded the observation of population inversions and gain [10–16]. Nevertheless, the experimental demonstration of large amplification at soft X-ray wavelengths was not realized until 1984, when Matthews et al. [17] and Suckewer et al. [18] observed amplification from the generation of population inversions in plasmas by collisional electron excitation and collisional electron–ion recombination, respectively. Subsequent experiments greatly expanded the number of laser transitions, achieved soft X-ray laser operation in the saturated regime for the first time [19–25] and realized proof-of-principle demonstrations in several applications [26–30]. However, the large size, cost and low-repetition rate of these lasers were barriers to their widespread utilization. Much progress has been achieved in the development of compact soft X-ray lasers. This is the result of advances in pump sources that include the development of compact multi-terawatt ultrashort pulse optical laser systems based on chirped pulse amplification [31–35], and fast capillary discharges capable of generating highly ionized plasma columns with high axial uniformity and length-to-diameter aspect ratios of 1000 to 1 [36–46]. Also contributing to the progress towards practical tabletop

X-ray lasers is the implementation of excitation mechanisms that take full advantage of the high intensity and ultrashort pulsewidth of new optical laser systems. The field is rapidly approaching the stage at which soft X-ray lasers sufficiently compact to fit onto a normal optical table (frequently described as 'tabletop' lasers) will be routinely utilized in science and technology.

Several articles have reviewed the progress in X-ray laser development [47–52]. The book by Elton discusses the developments up to 1990 [53]. A detailed account of the progress realized since that time[1] can be found in the proceedings of two biannual conferences that focus on soft X-ray lasers [54,55]. The advances in tabletop lasers have also been reviewed [56].

49.2 Amplification and Pump Power Requirements

In contrast to most optical lasers, the duration of the gain in soft X-ray lasers is usually shorter than the time required for the effective use of an optical cavity. This is the result of either the rapid self-terminating nature of the population inversion in transient schemes [57–66] or the difficulty in maintaining the stringent plasma conditions necessary for amplification in quasi-cw schemes for a sufficient period of time. Consequently, soft X-ray lasers normally operate with single- or double-pass amplification of the spontaneous emission through the gain medium. In such amplifiers, I, the spectrally integrated intensity of the laser line, increases as a function of l, the plasma length, as

$$I = \frac{E}{g}(\mathrm{e}^{gl} - 1)^{3/2}(gl\,\mathrm{e}^{gl})^{-1/2} \tag{49.1}$$

where g is the small-signal gain coefficient (assumed to be constant along the plasma column) and E is a constant proportional to the emissivity [67]. The product gl of the small-signal gain coefficient and the length of the amplifier (known as 'the gain–length product') have been widely used in the literature as a figure of merit to describe the level of amplification achieved.

A gain–length product greater than 5, commonly measured by monitoring the growth of the laser line intensity as a function of plasma length, is usually a clear indication that lasing is taking place. However, there are, in the literature, quite a large number of X-ray amplification experiments that measured products less than 4. In these cases, the data should be treated with significant caution, as such, phenomena such as for example plasma column end effects, could be responsible for the apparent enhancement of the line intensity. Ideally, the nearly exponential amplification continues until the intensity approaches the saturation intensity, as illustrated in Figure 49.1, for a 46.9 nm Ne-like Ar capillary-discharge-pumped laser [37]. At this intensity, the stimulated emission is sufficiently strong to extract the majority of the energy stored in the population inversion, depleting the population inversion and the gain. In collisionally excited lasers, gain saturation typically occurs [21–24,63] with $gl \simeq 14$–20. Consequently, to achieve saturated soft X-ray amplification in a single- or double-pass amplifier, the gain coefficient must be, depending on the length of the plasma, one to three orders of magnitude larger than those typically encountered in visible gas lasers which use optical cavities [68]. Moreover, the physics of the generation of amplification by stimulated emission determines a dramatic upward scaling of the power density deposition required to obtain substantial gain at ultrashort wavelengths. Consider a transition at wavelength λ from an upper level of degeneracy g_2 and population N_2 to a lower level of population N_1 and degeneracy g_1. The small-signal gain coefficient is the product of σ, the stimulated emission cross section and the population inversion density, N^*:

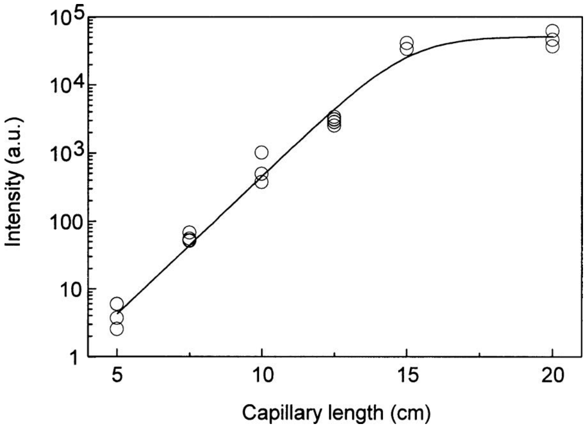

FIGURE 49.1 Integrated intensity of the 46.9 nm line of Ne-like Ar as a function of plasma column length in a capillary discharge amplifier. The exponential increase of the intensity ceases at $l \simeq 15$ cm, where the saturation intensity is reached. (From Rocca et al. [39].)

$$N^* = \left(N_2 - \frac{g_2}{g_1}N_1\right) \tag{49.2}$$

and

$$g = \sigma N^* \cong \frac{A_{21}\lambda^2}{8\pi\Delta\nu}\left(N_2 - \frac{g_2}{g_1}N_1\right) \tag{49.3}$$

in which A_{21} is the Einstein coefficient for spontaneous emission and $\Delta\nu$ is the linewidth of the transition.

Now, A_{21} scales along an isoelectronic sequence as $A_{21} \propto \lambda^{-2}$. Considering, as an example, the case of a naturally broadened unbranched transition with linewidth $\Delta\nu \propto A_{21}$, we obtain:

$$g \infty N\lambda^2. \tag{49.4}$$

In turn, $P_{\min}$, the minimum pump power density required to maintain a certain upper laser level population density N_2, scales as

$$P_{\min} = N_2 A_{21}\frac{hc}{\lambda}. \tag{49.5}$$

---

[1] The field of x-ray laser research is a rapidly advancing one. The present chapter includes only material published before the date of submission of the first draft (September 2000).

It results from the two previous equations that the power density required to obtain a certain gain coefficient in a naturally broadened transition scales as

$$P_{\min} \propto g\lambda^{-5} \tag{49.6}$$

Consideration of the case of Doppler broadening, the line-broadening mechanism most frequently dominant under soft X-ray laser operating conditions, leads to a different but also dramatic scaling of the power requirement. In this case,

$$P_{\min} \propto g\lambda^{-4}\sqrt{\frac{k_B T_i}{M_i}} \tag{49.7}$$

in which T_i is the kinetic temperature of the emitting species which has atomic mass M_i.

Nevertheless, using the case of natural broadening for purposes of illustration, the operation of a saturated, mirrorless laser at 50 nm would require an estimated pump power density 10^7 times larger than that necessary for a 500 nm blue-green laser, while one operated at 5 nm would require an estimated pump power density 10^{12} times larger than that for the blue-green. In making these estimates, it is assumed that the use of the cavity for the 500 nm laser reduces the gain requirement for lasing by a factor of 100. In addition, the pump power required for lasing at soft X-ray wavelengths is often further increased by refraction losses that reduce the effective gain coefficient.

49.3 Soft X-Ray Laser Characteristics

49.3.1 Wavelength

To date, saturated soft X-ray lasers have been developed at wavelengths ranging from 5.8 [21] to 46.9 nm [37,44]. Significant amplification has been observed at wavelengths as short as 3.56 nm [20].

49.3.2 Output Pulse Energy

The output pulse energy generated by soft X-ray lasers exceeds, by several orders of magnitude, that of other sources of coherent short wavelength radiation. Saturated collisional lasers pumped by large optical lasers have achieved energies of several mJ (e.g. 8 mJ at 15.5 nm [24]), and an 18.2 nm recombination laser has been reported to emit 3 mJ pulses [18]. A highly saturated 46.9 nm tabletop discharge pumped laser has produced millijoule-level pulses at a repetition rate of 4 Hz [45]. Transient collisional lasers pumped by relatively compact optical lasers have produced picosecond laser pulses with energies of the order of 10 μJ [64].

49.3.3 Pulse Duration

The pulsewidth of presently available soft X-ray lasers ranges from a fraction of a nanosecond to several nanoseconds for lasers operating in a quasi-steady-state regime, to several picoseconds for transient collisional excitation lasers [59–66] and recombination lasers in transitions to the ground state [57,58]. Future photoionization X-ray lasers will generate femtosecond pulses.

49.3.4 Peak Power

Quasi-cw collisional electron excitation lasers have produced peak output powers of several tens of MW [69], and recombination lasers have reached peak powers of the order of 0.1 MW [18]. Very compact capillary discharge tabletop collisional lasers have reached peak powers up to 0.6 MW [45], and transient collisional lasers have generated powers of up to ~1 MW [64].

49.3.5 Average Power

Most soft X-ray lasers demonstrated to date have produced low-average power due to the low-repetition rate used in the majority of the experiments that have produced significant output pulse energies (typically less than one shot every few minutes). An exception is a 4 Hz tabletop capillary discharge laser operating 46.9 nm that produced an average power of 3.5 mW [45]. The average power of soft X-ray lasers can be expected to increase dramatically during the next decade as a result of the development of efficient high-repetition-rate tabletop pump sources.

49.3.6 Beam Divergence

In the presently available soft X-ray lasers, the beam divergence is dominantly determined by refraction and typically ranges from 1 to 10 mrad. Refraction bends the amplified X-rays out of the gain volume as a result of the transverse variation of the index of refraction due to the large electron density gradients.

49.3.7 Temporal Coherence

Since presently available soft X-ray lasers do not employ optical resonators, their temporal coherence depends on the atomic linewidth of the laser transition. In most of these single- or double-pass amplifiers, the dominant line-broadening mechanism is the Doppler effect. Taking into account the fact that amplification narrows the output by a factor of $(gl)^{-1/2}$ below that of spontaneous emission from a thin source, the value of the linewidth $\Delta\nu_{\text{FWHM}}$ can be estimated as

$$\Delta\nu_{\text{FWHM}} = \nu_0\sqrt{\frac{8k_B T_i \ln 2}{M_i c^2}}\frac{1}{\sqrt{gl}}. \tag{49.8}$$

For values of gl above saturation ($gl \simeq 14$–20 in collisional lasers), some line re-broadening may occur. This linewidth determines l_{coh}, the longitudinal coherence length, and τ_{coh}, the coherence time, via

$$l_{\text{coh}} = c\tau_{\text{coh}} = \frac{c}{\Delta\nu_{\text{FWHM}}}\sqrt{\frac{2\ln 2}{\pi}} = \frac{0.66c}{\Delta\nu_{\text{FWHM}}}. \tag{49.9}$$

A few measurements of the linewidth of saturated collisional excitation lasers have been reported [70,71] and correspond to $l_{\text{coh}} \simeq 0.1$–$0.2$ mm.

49.3.8 Spatial Coherence

Several authors [72–74] have theoretically analysed the spatial coherence of soft X-ray amplifiers. Single-pass soft X-ray amplifiers can sustain a large number of spatial modes and, therefore, have poor spatial coherence [75,76]. However, significant improvements can be obtained by increasing the length of the plasma column [77] or by operating in a double-pass amplification [78]. The spatial coherence of a capillary discharge laser was measured to increase monotonically with plasma column length to reach nearly fully spatial coherence for plasma columns 36 cm in length [79]. This is the result of a decreasing number of spatial modes along the plasma column due to gain guiding and refraction anti-guiding.

49.3.9 Peak Spectral Brightness

Soft X-ray lasers are among the brightest soft X-ray sources available. Both laser-excited [64] and discharge-pumped collisional excitation lasers have reached brightness values that exceed 1×10^{25} photons mm^{-2} mrad^{-2}s^{-1} (0.01%BW)$^{-1}$ [79]. Figure 49.2 compares the peak spectral brightness of some of the brightest soft X-ray lasers with other sources of coherent short-wavelength radiation.

49.3.10 Average Spectral Brightness

Due to their low-repetition rate, most of presently available saturated soft X-ray lasers produce low-average brightness. An exception is a capillary discharge 46.9 nm laser [79] that produced an estimated spatially coherent average output power of nearly 1 mW within a relative spectral bandwidth $(\Delta\lambda/\lambda) < 1 \times 10^{-4}$, a spectral purity that exceeds that of some undulators at third-generation synchrotrons. The average spectral brightness of laser-pumped soft X-ray lasers can be expected to increase significantly in the near future as compact high-repetition rate optical laser pumps become available and more efficient target configurations are used to couple the laser pump energy to the plasma.

49.4 Other Methods for the Generation of Coherent X-Ray Radiation

The direct amplification of radiation in plasmas is not the only means by which coherent soft X-ray radiation can be generated. Alternative methods include high-order harmonic generation from the output of high-power optical lasers [80–84], synchrotron sources [85–88], free-electron lasers (FELs) and up-conversion of optical laser pulses by scattering with energetic electron beams [89–92]. Synchrotron sources are large multi-user facilities based on the radiation emitted by high-energy electron beams. They have the advantages of broad tunability and high-average power. However, they fall

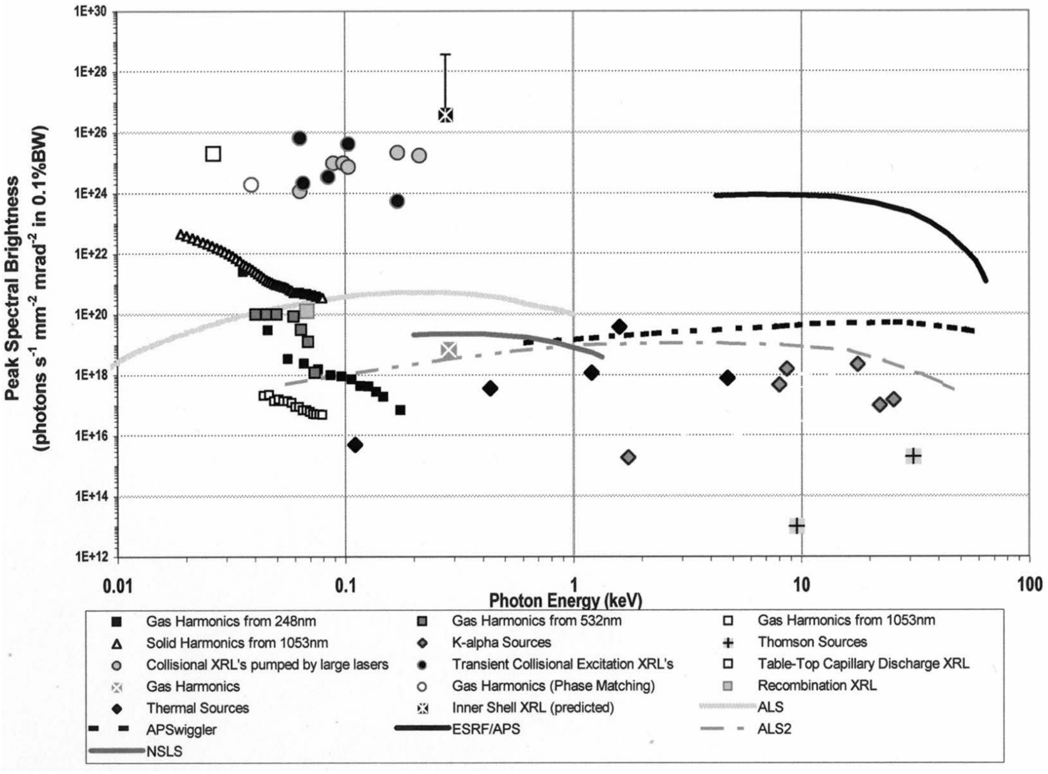

FIGURE 49.2 Peak spectral brightness of X-ray lasers compared to other X-ray sources. (The data are courtesy of Smith and Key [211].)

short of the high peak brightness needed in applications such as the study of non-linear phenomena at ultrashort wavelengths [93,94] and the diagnostics of dense plasmas [29,30,95,96]. Another alternative, also based on accelerator technology, is the use of self-amplified spontaneous emission in an FEL [88,89]. In a soft X-ray FEL, an electron beam would radiate at much higher powers and with better coherence than it does due to spontaneous synchrotron radiation. Several single-pass ultrashort-wavelength FELs have been proposed or are under construction [88,90]. Nevertheless, these lasers will also constitute large facilities that will not be tabletop ones.

Alternatively, soft X-ray coherent radiation can also be generated using non-linear optical techniques for frequency up-conversion of optical laser radiation. Harmonic up-conversion of intense ultrashort pulse tabletop optical laser systems has been reported to generate radiation at wavelengths as short as 2.7 nm [80]. Presently, fairly optimized conditions in non-phase-matched configurations typically yield a conversion efficiency of about 10^{-6} in the range of 10–40 eV (of the order of 10^9 photons per pulse) and 10^{-8} in the 40–150 eV range (10^6–10^7 photons per pulse) [81]. The highest energy reported for a high-order harmonic pulse, 60 nJ at about 50 eV, was obtained using a powerful glass laser [82]. The demonstration of phase-matched harmonic conversion of visible light into soft X-rays with a generation efficiency of 10^{-5}–10^{-6} in the 40–70 eV spectral region was reported [83,84]. Soft X-ray pulses with an energy >0.2 nJ pulse^{-1} per harmonic order were produced at a repetition frequency of 1 kHz utilising 20 fs optical pulses [83].

49.5 X-ray Laser Schemes

49.5.1 Collisional Electron Excitation Lasers

49.5.1.1 Quasi-steady-state Lasers

Collisional electron impact excitation of Ne-like and Ni-like ions has resulted in some of the most robust soft X-ray lasers available. In the traditional implementation of these lasers, the generation of a population inversion occurs in a quasi-cw regime by strong collisional monopole electron excitation of the upper level aided by the very favourable ratio between the radiative lifetime of the upper and lower levels. The upper levels are metastable with respect to radiative decay to the ground state, and the lower levels are depopulated by strong dipole-allowed transitions. The first successful demonstration of a collisional soft X-ray laser was realized at Lawrence Livermore National Laboratory and involved the $2p^53p \rightarrow 2p^53s$ transitions in Ne-like Se and Ne-like Y [17]. Lasing has been extended to nearly all of the Ne-like ions with an atomic number between Si [97] and Ag [98] at wavelengths ranging from 87 to 9.93 nm.

Figure 49.3 shows a simplified energy-level diagram for a typical Ne-like system (GeXXIII) illustrating the laser transitions and the dominant processes involved in the generation of amplification. The 3p upper levels are dominantly populated by electron monopole collisional excitation (E_0) from the Ne-like ion ground state and by cascades from higher energy levels. The population inversions are maintained by the very rapid

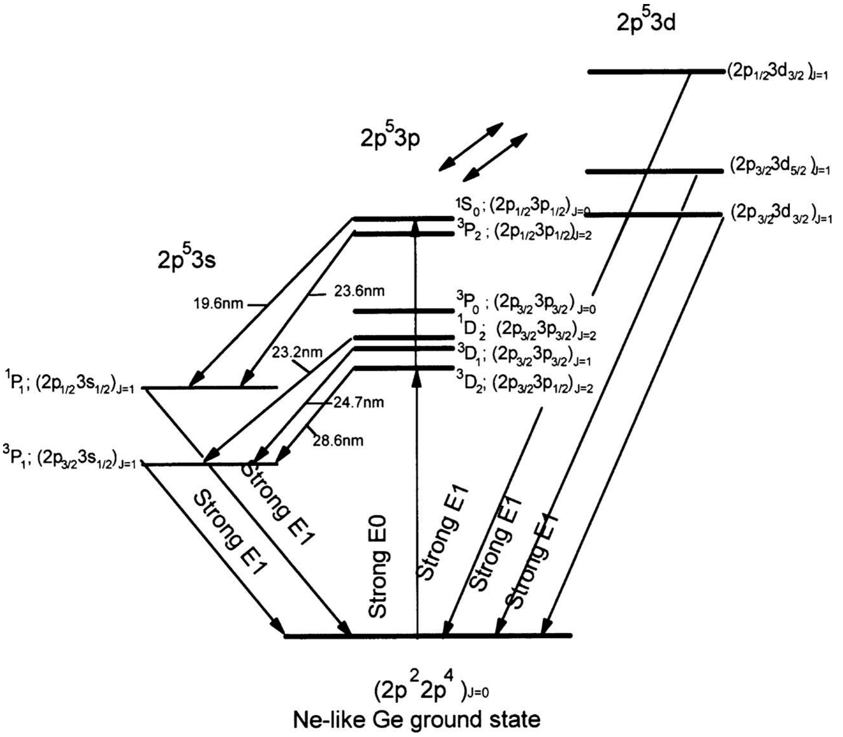

FIGURE 49.3 Simplified energy-level diagram of Ne-like Ge showing the laser transitions of interest and the dominant excitation and de-excitation processes responsible for the creation of population inversions between the 3p and 3s levels. The laser levels are labelled in both *LS* and *j j* notations. (From Keane [50].)

radiative decay of the 3s lower levels to the ground state of the ion through strong dipole-allowed transitions (E_1). Therefore, operation of these lasers in a quasi-cw regime requires the plasma to be optically thin for the transitions originating from the lower level.

Lasers in the $3d^94d \rightarrow 3d^94p$ transitions of Ni-like ions are direct analogues to lasers in $2p^53p \rightarrow 2p^53s$ transitions in closed-shell Ne-like ions but have the advantage of producing amplification at shorter wavelengths for a given state of ionization. This higher quantum efficiency significantly reduces the pumping energy required to achieve lasing of a selected wavelength. Ni-like soft X-ray lasers were first demonstrated in 1987 in an Eu-laser-created plasma, producing amplification with a $gl \simeq 4$ at 7.1 nm [99]. Subsequently, the scheme was isoelectronically extrapolated to other ions with laser wavelengths as short as 3.56 nm in Ni-like Au [100]. Gain-saturated operation has been obtained at wavelengths as short as 5.8 nm [21]. Hagelstein first proposed the use of low-Z Ni-like ions to develop tabletop collisional lasers at wavelengths near 20 nm and computed a significant gain for overheated plasma conditions [101]. Gain has also been observed in Co-like ions [100], and the use of the Nd-like sequence has also been proposed [101].

The collisionally excited soft X-ray lasers developed before 1990 consisted of line focus plasmas generated by optical laser pulses with energies ranging from several hundred joules to several kilojoules and, therefore, involved the use of very large facilities [17,20,97–100,102–106]. One such laser is schematically illustrated in Figure 49.4. Much progress has been made in improving laser efficiency. Strong refraction of the amplified beam caused by the large electron density gradients in the amplifier was early recognized as a major obstacle to the generation of efficient soft X-ray lasers with good beam quality. Methods implemented to mitigate refraction have included the use of foil targets [48,107–110], opposite-gradient and curved targets and, in particular, the use of one or multiple pre-pulses [111–130]. In the pre-pulse technique, the first pulse is used to create a plasma with an optimized density for amplification and with reduced density gradients for improved beam propagation. The subsequent pulses which are absorbed more efficiently in the gain region to heat the plasma to lasing conditions lead to the observation of large amplification in a large number of elements with dramatic increase in the $(J=0) \rightarrow (J=1)$ line intensity and reduced excitation energy.

Another important step in the reduction of the pump energy has been the use of shorter excitation pulses. Daido et al. [131,132] reported lasing in several lanthanide ions in the spectral range 5.8–14 nm using a three-pre-pulse sequence and a main excitation pulse of 100 ps and ~250 J of energy. A subsequent series of experiments conducted at the Rutherford Laboratory obtained saturation in several transitions [129,133–135] with wavelengths as short as 5.86 nm (Ni-like Dy [136]) using sequences of 75 ps pulses with about 100 J of energy saturation. Balmer et al. have used a relatively compact Nd:glass laser to demonstrate saturated lasing in Ne-like Fe (25.5 nm), Ni-like Ag (14.0 nm) and Ni-like Pd (14.7 nm) with driver energies below 30 J in a 100 ps pulse [137,138]. In terms of improving the soft X-ray output beam characteristics, double-pass amplification experiments have demonstrated increased spatial coherence and reduced beam divergence.

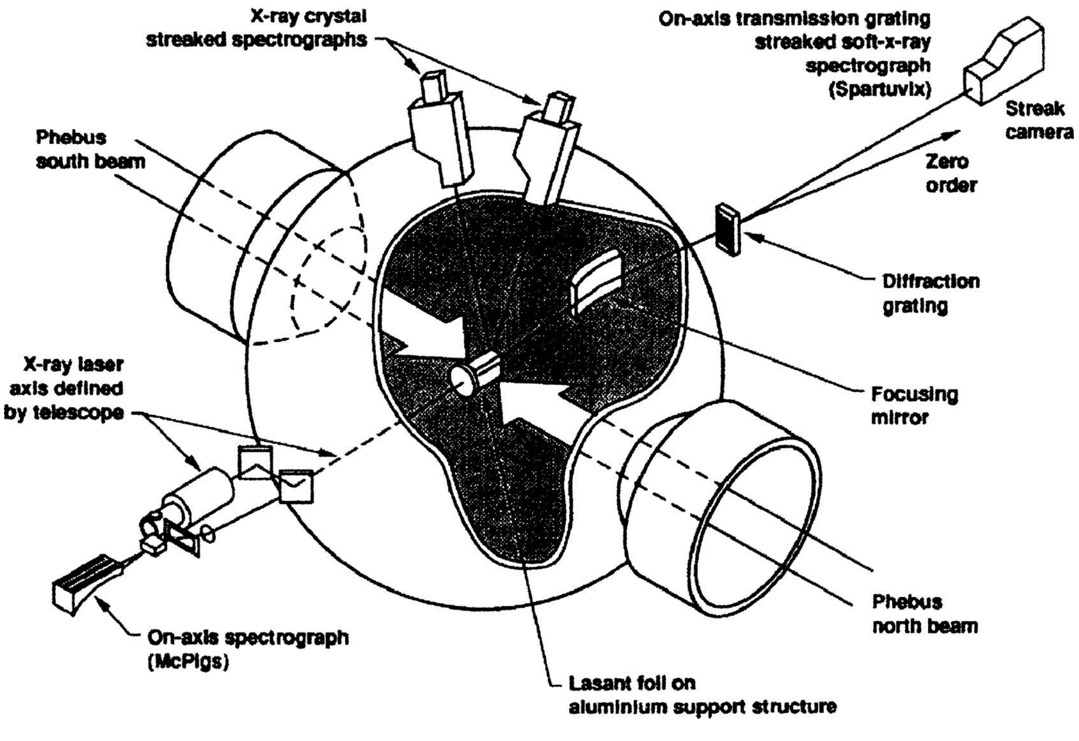
X-ray crystal streaked spectrographs
On-axis transmission grating streaked soft-x-ray spectrograph (Spartuvix)
Streak camera
Phebus south beam
Zero order
Diffraction grating
X-ray laser axis defined by telescope
Focusing mirror
Phebus north beam
On-axis spectrograph (McPigs)
Lasant foil on aluminium support structure

FIGURE 49.4 Schematic representation of a typical experimental set-up used to produce and diagnose a collisionally excited soft X-ray laser of the first generation. Two laser beams from an optical laser are line-focused onto a target to create the plasma column that constitutes the amplification medium. (From Keane et al. [101].)

49.5.1.2 Transient Collisional Lasers

The collisional electron excitation scheme described earlier is intrinsically a quasi-steady-state scheme in which lasing can occur for as long as the plasma conditions necessary for the generation of a population inversion can be maintained. It was first recognized by Afanasiev and Shlyaptsev [139] that one to two orders of magnitude larger gain coefficients could be produced for a short period of time (typically subpicosecond to tens of picoseconds) by heating the plasma at a rate faster than the relaxation rate of the excited states. The larger gain coefficients are mainly the consequence of the larger rate of excitation of the upper level from the ion ground state by electron collisions that result in a large population inversion before collisions have time to redistribute the populations. Another phenomenon that contributes to an increased gain is the increased rate of electron excitation in an overheated plasma. Transient gains in excess of $100\,\mathrm{cm}^{-1}$ have been predicted theoretically [139,140]. In the transient regime, there is no need to limit the transverse dimension of the plasma in order to ensure optical transparency of the laser lower level radiation. A main advantage of the transient excitation scheme for the realization of tabletop X-ray lasers is the greatly reduced pump energy required for excitation.

The availability of multi-terawatt ultrashort pulsed optical laser systems with output energies of several joules has provided the opportunity to demonstrate soft X-ray lasing by transient electron collisional excitation [60–66]. The implementation is based on a two-step excitation sequence. First, a long pulse (typically of nanosecond duration) is used to produce a plasma containing the desired active ions, which are usually closed-shell Ne-like or Ni-like. The temperature of this pre-plasma must be sufficiently high to produce a ground-state population of these ions but it does not need to reach the values necessary to populate the upper level. The plasma is allowed to expand hydrodynamically to reach the desired degree of ionization, optimum electron density and minimum possible electron density gradient. Second, the plasma is rapidly heated with a picosecond or subpicosecond laser pulse to increase the electron temperature rapidly to values that exceed the excitation energy of the upper level. The ionization balance is not significantly altered and a large transient population inversion is generated by electron excitation.

The first demonstration of amplification by transient inversion was realized by Nickles et al. in the 32.6 nm line of Ne-like Ti [60]. The experiment used a hybrid chirped-pulse amplification (CPA) Ti:sapphire/Nd:glass pump delivering synchronized long and short pulses of ~1.2 ns and 0.7 ps duration and energy of 3 and 2 J, respectively. The soft X-ray pulse duration was measured to be less than 20 ps. The results were analysed to correspond to an average gain of $19\,\mathrm{cm}^{-1}$ and to $gl \simeq 9.5$ [60]. Weaker lasing was also observed in a line near 30 nm, identified as the $3d(J=1) \to 3p(J=1)$ transition of Ne-like Ti. These results were improved and extended to other Ne-like ions, such as Fe and Ge, in subsequent experiments conducted at several laboratories [61–66].

The transient collisional scheme has also been extended to shorter wavelengths utilizing the Ni-like sequence [61–66]. Dunn et al. reported a gain of up to $35\,\mathrm{cm}^{-1}$ and $gl \simeq 12.5$ in the $4d^1S_0 \to 4p^1P_1$ line of Ni-like Pd at 14.7 nm and large amplification in several other Ni-like ions [61] using the relatively compact laser system illustrated in Figure 49.5. The pump laser occupies two 1.2×3.6 m optical tables with a total area of less than $10\,\mathrm{m}^2$. This 15 TW hybrid laser system consists

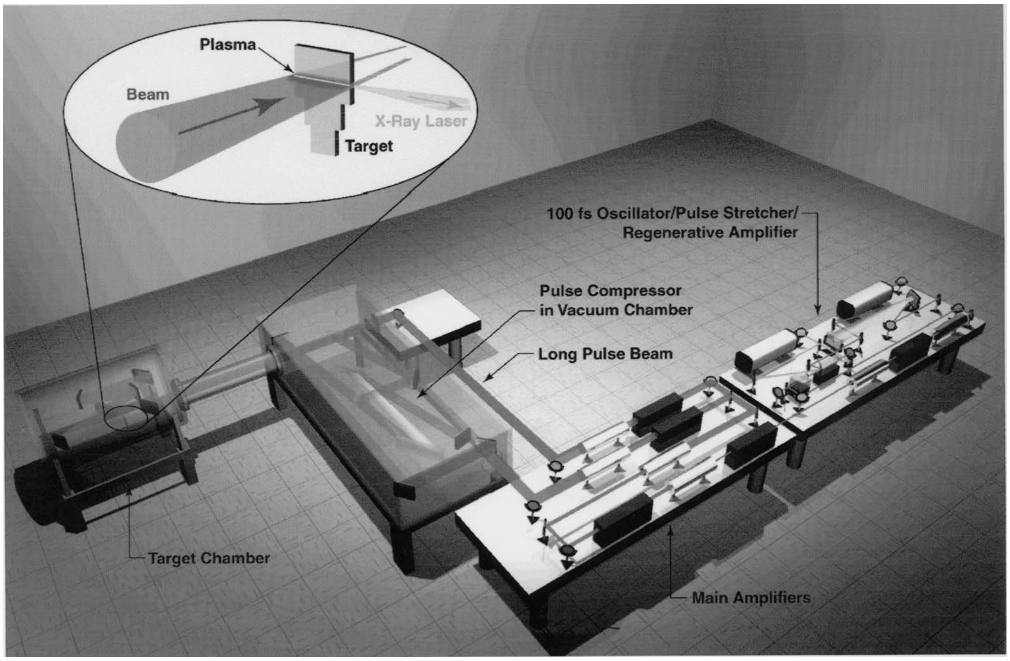

FIGURE 49.5 Schematic illustration of the CPM pump laser system and target chamber used to produce transient inversion collisional soft X-ray lasers at Lawrence Livermore National Laboratory. The pump laser occupies two standard optical tables of dimensions 1.2×3.6 m with total area less than $10\,\mathrm{m}^2$. The system can be fired once every 4 min. (Courtesy of J Dunn, Lawrence Livermore National Laboratory.)

of a Ti:sapphire oscillator tuned to 1050 nm, and four-stage Nd-phosphate glass amplifiers. It generates two synchronized laser pulses of 7.5 J in 500 fs and 15 J in 600 ps at a repetition rate of one shot every 4 min. Typically 50 shots on target are achieved in a day. The full circles in Figure 49.6b show the measured increase of the Ni-like Pd 14.7 nm line intensity for target lengths between 2 and 9 mm. The gain coefficient for lengths between 1 and 2 mm is about 35 cm^{-1} but continuously decreases to reach a value of 3.9 cm^{-1} for target lengths above 7 mm. This smooth decrease in gain with target length has been observed in all non-travelling-wave transient collisional excitation experiments and resembles gain saturation. However, it is mainly caused by the short duration of the gain and by refraction. Gain saturation with the transient excitation scheme was first demonstrated on the Ne-like scheme for the 32.6 nm line of Ne-like Ti and the 19.6 nm line of Ne-like Ge at the Rutherford Laboratory [63]. However, these experiments utilized a total reported excitation energy of 32 and 60 J, respectively, which is not available in smaller facilities. To achieve gain saturation with smaller excitation energy, travelling-wave excitation schemes have been implemented at several laboratories.

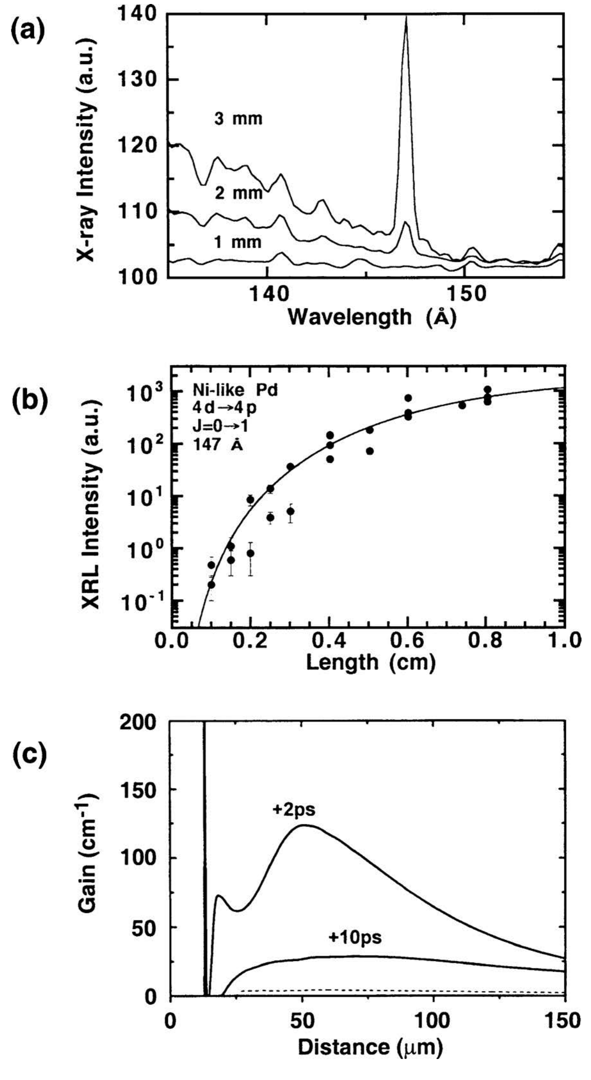

FIGURE 49.6 Results of transient inversion soft X-ray amplification experiment in the 4d–4p $J=0$–1 line of Ni-like Pd at 14.7 nm. (a) Spectra showing the increase of the intensity of the laser line as a function of target length. The intensity increases by more than three orders of magnitude when the target length is increased from 1 to 3 mm. (b) Measured intensity of the laser line as a function of target length. The continuous line is a guide through the experimental points. The data show the decrease of the transient gain as the X-ray laser propagates along the plasma column. (c) Computed transient gain profiles as a function of time measured from the arrival of a l ps excitation pulse. (From Dunn et al. [61].)

49.5.1.3 Travelling-wave Excitation

In these transient systems, the shortness of τ_g, the gain duration, limits the amplification length to $l < c\tau_g$ (where c is the speed of light in the plasma), unless travelling-wave excitation is used to maintain the excitation in phase with the amplified X-ray pulse. The travelling-wave system was used to demonstrate gain saturation in Ni-like Pd at 14.7 nm with 1.8 J of long pulse energy and 5.2 J of short pulse. Figure 49.7 illustrates the advantage of travelling-wave excitation and corresponds to a 20–100-fold increase in X-ray laser intensity compared to the configuration without travelling-wave excitation [65]. The soft X-ray laser output energy with travelling-wave excitation was estimated at ~10 µJ. Strong amplification was also obtained in Ni-like ions ranging from Mo (18.9 nm) to Sn (11.9 nm) [63]. A different travelling-wave method was also used at the Rutherford Laboratory to obtain gain saturation in several Ne-like ions and in Ni-like Sm at 7.3 nm [65]. Experiments conducted at CEA-Limeil yielded saturation of the 13.9 nm laser line of Ni-like Ag and also observed strong amplification at 16.05 nm in a 4f–4d transition in the same ion [66]. Table 49.1 compares the characteristics of soft X-ray lasers driven by the transient collisional scheme at a facility with a relatively compact multi-terawatt laser with those of the quasi-steady-state collisional lasers pumped by the Nova laser facility [64]. Future improvements in pumping efficiency resulting from optimized target configurations and travelling-wave excitation can be expected to lead to saturated transient inversion

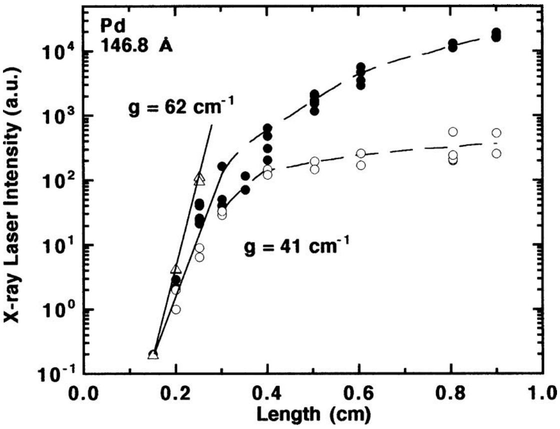

FIGURE 49.7 Comparison of the X-ray laser intensity versus plasma column length for the Ni-like Pd 4d–4p laser line at 14.7 nm with travelling wave (closed circles) and without travelling wave (open circles). The excitation energy consisted of a 1.8 J long pulse and a 5.2 J short pulse. (From Dunn et al. (2000) [64].)

TABLE 49.1

Characteristics Transient Inversion Collisional Laser Pumped by a Compact Multi-terawatt Laser, as Compared with Quasi-Steady-State Collisional Laser Pumped by NOVA (after Dunn et al. [141])

	COMET	NOVA
Size (sq. ft)	100	>40 000
Cost ($)	1 M	>100 M
Pump energy (J)	<10	$5–10 \times 10^3$ (2 beams, 1ω)
XRL gain (cm^{-1})	30–65	1–8
XRL output (J)	$>10 \times 10^{-6}$ (at 146.8 Å)	5×10^{-3} (at 155 Å)
Shot rate (per day)	50–100	4–6
XRL wavelength (Å)	119–330	35–330
Pulse duration (ps)	5–10	45–200
Brightness (ph mm^{-2} $mrad^{-2}$ s^{-1} (0.01% BW)$^{-1}$	10^{24}	10^{24}
Cost/shot ($)	50–100	10 000–20 000

soft X-ray lasers occupying a single optical table and to tabletop lasers that operate at shorter wavelengths.

Another method for pumping collisional lasers in which travelling-wave excitation is intrinsic was demonstrated by Lemoff et al. in Pd-like Xe utilising optical field ionization. In this scheme, an intense circularly polarized femtosecond laser pulse is used to simultaneously create closed-shell ions and hot pumping electrons by tunnelling ionization [59]. An amplification of $gl \simeq 11–12$ in the 41.8 nm line of Pd-like Xe was measured by axially pumping a Xe gas cell up to 8.4 mm in length with 70 mJ pulses from a Ti:sapphire laser operating at 10 Hz.

49.5.1.4 Collisionally Excited Capillary Discharge Lasers

Direct excitation of plasma columns with an electrical discharge has the advantage of generating soft X-ray lasers that are very efficient and compact. Fast-discharge excitation of capillary plasmas has produced the highest soft X-ray laser average power to date [44,45]. In these lasers, the electromagnetic forces of a fast rising current pulse flowing through a capillary channel rapidly compresses the plasma to a size of about 300 μm diameter. The fast current rise time minimizes the amount of material that is ablated from the capillary walls before the magnetic field detaches it from the walls [36–39]. The first observation of large soft X-ray amplification in a discharge-created plasma was realized in 1994 by Rocca et al. in the 46.9 nm line of Ne-like Ar [37,38]. In that initial experiment, illustrated in Figure 49.8, the fast capillary discharge set-up (generating current pulses of 60 ns half-cycle duration and ~40 kA peak current) was used to excite Ar plasma columns in 4 mm diameter capillary channels up to 12 cm in length. As indicated in Figure 49.9, the capillary was placed in the axis of a 3 nF liquid- dielectric capacitor that was pulse-charged by a Marx generator. The capillary loads were excited by discharging the capacitor through a spark-gap switch pressurized with SF_6. A small gain was also observed in the $(J=2) \rightarrow (J=1)$ line of Ne-like Ar at 69.8 nm [38,136]. The optimum conditions for lasing occur several nanoseconds before stagnation, when the first compression shock wave reaches the axis. Lasing by collisional electron excitation of Ne-like Ar ions takes place at a time when the electron density is rapidly increasing and reaches ($0.3–1 \times 10^{19} cm^{-3}$), when the electron temperature is 60–80 eV [40]. The pulsewidth is approximately 1 ns [40,43]. Subsequent experiments employing longer plasma columns under better optimized discharge conditions yielded an effective gain–length product of 27 and resulted in the first observation of gain saturation in a tabletop soft X-ray amplifier [40]. Saturation of the laser intensity was observed at products of about 14 [40].

A very compact, high-repetition rate, saturated 46.9 nm laser of a size comparable to that of many widely utilized visible and ultraviolet gas lasers has been developed [44,45]. Figure 49.10 illustrates the size of this capillary discharge soft X-ray laser in comparison to a 1 J Nd:YAG laser. The soft X-ray laser occupies a surface space of about 1 m by 0.4 m on an optical table. This laser was operated with capillaries 18.2 cm in length at a repetition rate of 7 Hz to produce an average output pulse energy of 135 μJ, corresponding to an average laser power of 1 mW [44]. Increasing the plasma column length to 35.4 cm resulted in the generation of 0.88 mJ laser pulses at a repetition rate of 4 Hz [45], corresponding to an average power of 3.5 mW as shown in Figure 49.11. The spatially coherent average output power per unit bandwidth emitted by this compact laser at 26.5 eV is comparable to that generated by a beam-line at a third-generation synchrotron facility, while its peak coherent power per unit bandwidth exceeds that of the synchrotron by several orders of magnitude [44,45]. Table 49.2 summarizes the characteristics of the 46.9 nm Ne-like capillary discharge laser. These capillary-discharge-pumped tabletop lasers were successfully used in several applications, including high-resolution soft X-ray laser interferometry and shadowgraphy of plasmas [95,96,142,143], the measurements of XUV optical constants of materials [144] and the demonstration of laser ablation with a focused soft X-ray beam [145].

The Ne-like Ar results were extended to Ne-like S (60.8 nm) [42] and Ne-like Cl (52.9 nm). To obtain amplification in Ne-like S, the discharge set-up illustrated in Figures 49.8 and 49.9 was modified to allow for the injection of the sulphur vapour into the capillary channel through a hole in the ground electrode. The sulphur vapour was produced, ablating the wall of an auxiliary capillary channel, drilled in a sulphur rod, with a slow current pulse. Model computations indicate that, in this

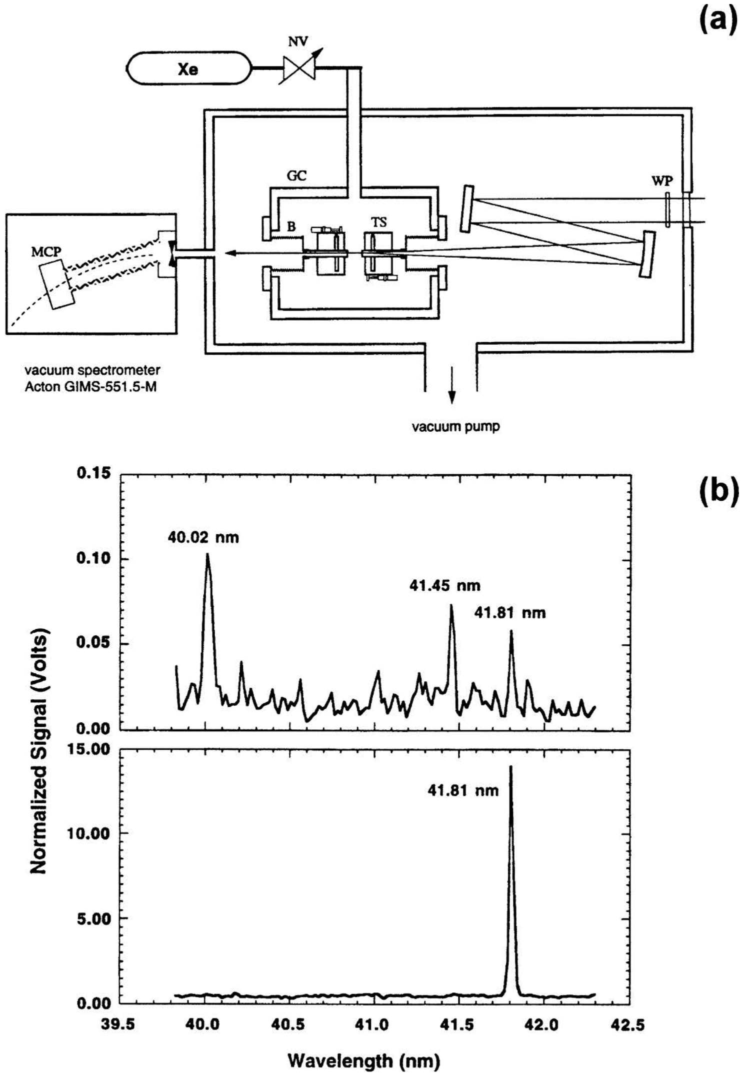

FIGURE 49.8 (a) Schematic illustration of the gas target set-up used to obtain lasing in Pd-like Xe at 41.8 nm in a plasma created by optical-field-induced ionization. Excitation was provided by circularly polarized laser pulses with an energy of 70 mJ and a duration of 40 fs from a CPA Ti:sapphire laser operating at 10 Hz. (b) Spectra illustrating the dramatic increase in the intensity of the 41.8 nm laser line observed when the pressure is increased from 3 torr (top spectrum) to 12 torr (lower spectrum). (From Lemoff et al. [59].)

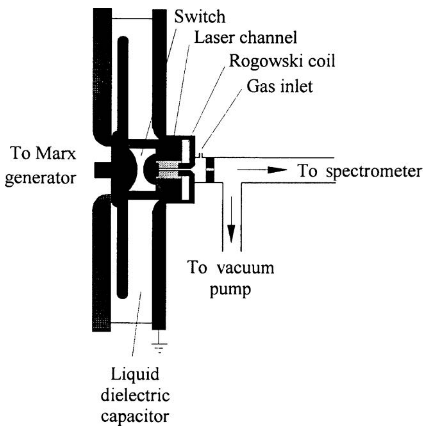

FIGURE 49.9 Schematic diagram of the capillary discharge set-up used to obtain saturated amplification of the 46.9 nm line of Ne-like Ar. (From Rocca et al. [37,38,40]).

case, transient population effects increase the gain by 20%–40% [42]. The scaling of plasma conditions and pump requirements for lasing at wavelengths as short as 10 nm have been estimated [38]. Current pulses of up to 200 kA peak amplitude and ~10 ns rise time were used to explore the generation of capillary plasma columns with the conditions necessary for amplification at shorter wavelengths [146].

49.5.2 Collisional Recombination Lasers

49.5.2.1 Mechanisms

In this population inversion scheme, first suggested by Gudzenko and Shelepin [147], the upper level is populated following the recombination of ions of atomic species A with a charge $Z+1$ with an electron, through a three-body interaction described as collisional or three-body recombination:

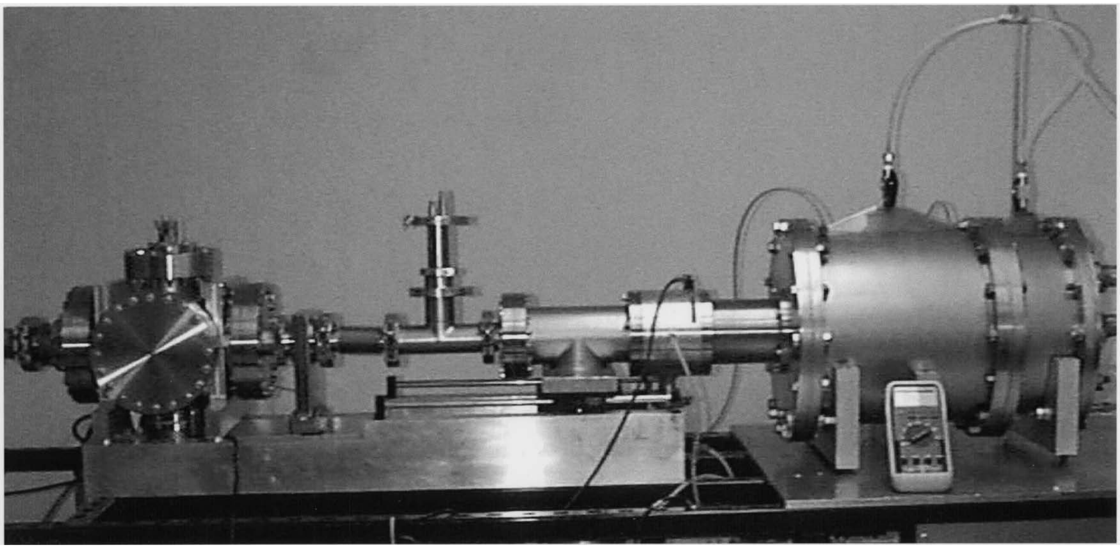

FIGURE 49.10 Photograph a of high-average power tabletop 46.9 nm capillary discharge (right) and applications chamber (left). The multimeter provides a reference for the size of the laser. (From Colorado State University.)

$$\left(\mathrm{A}^{Z+1}\right) + 2\mathrm{e} \rightarrow \left(\mathrm{A}^{Z}\right)^{*} + \mathrm{e}. \qquad (49.10)$$

This process preferentially populates highly excited bound levels $(\mathrm{A}^{Z})^*$ of the ion of charge Z, favouring the generation of population inversion. The collisional recombination rate is proportional to the square of the electron density. The recombination rate is also extremely sensitive to T_e, the electron temperature, following a dependence on $T_e^{-4.5}$. Therefore, the generation of large population inversions by recombination requires a dense and relatively cold plasma.

Hydrogen-like ions have a very favourable energy-level structure for the generation of population inversions by collisional recombination. In principle, several transitions can be inverted but, initially, much of the attention focused in the very favourable 3 → 2 transition. Figure 49.12 shows the atomic processes involved in the generation of population inversion in the 3 → 2 transition of H-like C at 18.2 nm. When the plasma cools, collisional recombination populates highly excited states and electron collisions rapidly transfer the population to levels of lower energy. Since collisional electron de-excitation is inversely proportional to the square root of the energy difference between the levels, this electronic cascade reaches a level at which electron de-excitation is no longer dominant over radiative decay. At this level, the bottleneck that is produced in the cascade creates a population inversion with respect to a lower level that is de-excited by very rapid radiative decay to the ion ground state.

The amplification of soft X-rays by plasma recombination would seem to require conflicting plasma conditions: a very highly ionized plasma and a very cold electron temperature. In practice, the problem has been traditionally solved utilizing a two-step process. First, a hot and dense plasma with a large population of A^{Z+1} ions is generated by a heating pulse. Second, the plasma is rapidly cooled by an adiabatic expansion [10,11,16,148–155], by electron heat conduction to a nearby wall or colder neighbouring plasma [156] or by radiation from high-Z ions introduced as impurities into the plasma [157,158]. All three cooling mechanisms, or combinations of them, have been utilized experimentally to generate gain at soft X-ray wavelengths by collisional electron–ion recombination.

Important efforts have been devoted to amplification in the 18.2 nm 3 → 2 line of H-like C. Initial experiments observed population inversions in plasmas generated by ablating solid carbon targets or carbon fibres with high-power laser pulses and cooled by adiabatic expansion [10,11,14–16]. Large amplification was first observed by Suckewer et al. in an experiment in which a 300 J pulse from a $\mathrm{CO_2}$ laser with about 75 ns pulsewidth was used to generate a nearly totally ionized carbon plasma column by bombarding a carbon solid target immersed in a strong solenoidal magnetic field [18]. The magnetic confinement allowed the maintenance of a high electron density while the plasma was cooled by radiation and electron heat conduction to adjacent cooling blades. Laser pulses of about 3 mJ were generated at an efficiency of 10^{-5}. Amplification has also been demonstrated in numerous experiments in which line focus plasmas were cooled by free adiabatic expansion [30,149–154]. Gain has been reported in H-like Na ions [152], in the 4f → 3d and 5f → 3d lines of Li-like ions [153,154] and in Be-like and Na-like ions [159].

Several experiments have been mostly conducted toward the realization of a small-scale recombination laser [160–167]. In 1989, Kim et al. reported a gain of about 8 $\mathrm{cm^{-1}}$ in the 18.2 nm line of CVI using a 25 J pump pulse of 3 ns duration, line-focused into a 5 mm-long solid carbon target [160]. Later experiments obtained similar gain coefficients target with only 4 J of laser excitation energy using a multi-fin carbon target [162]. However, difficulties were found in increasing the amplification over $gl \simeq 5$. One of the latest attempts to increase the product in this line utilized a polyethylene microcapillary as target [163]. A Nd:YAG laser (2.5 J, 1.5 ns pulsewidth) was focused at the entrance of the microcapillary with the motivation of guiding the pump beam, plasma confinement and plasma cooling by heat conduction to the walls. A product of

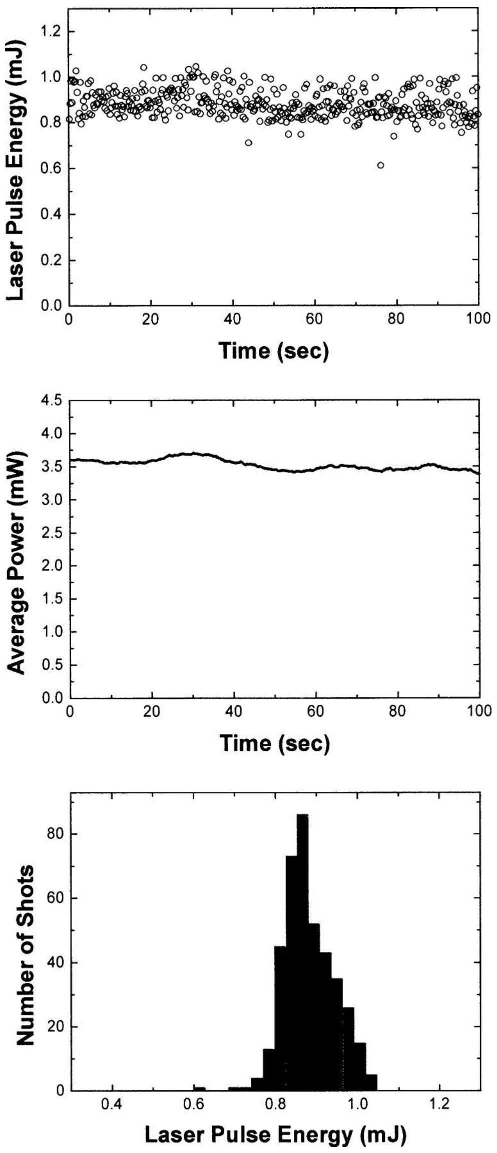

FIGURE 49.11 Measured output pulse energy and average output power of a tabletop capillary discharge 46.9 nm laser operating at a repetition frequency of 4 Hz. (a) Shot-to-shot laser output pulse energy. (b) Average output power computed as a walking average of 60 contiguous laser pulses. (c) Distribution of the output pulse energy. The average pulse energy is 0.88 mJ, corresponding to an average power of 3.5 mW. (From Macchietto et al. [46].)

TABLE 49.2

Characteristics of Capillary-discharge-pumped Tabletop 46.9 nm Laser in Ne-Like Ar

Laser Parameters		Ref.
Pulse energy	0.88 mJ at 4 Hz	[46]
Average pulse power	3.5 mW	[46]
Peak pulse power	0.6 MW	[46]
Divergence	≈4.6 mrad	[45,46]
Pulsewidth	1.2–1.5 ns	[45,46]
Peak spectral brightness	2×10^{25} photons s^{-1} mm^{-2} $mrad^{-2}$ (0.01% bandwidth)$^{-1}$	[79]

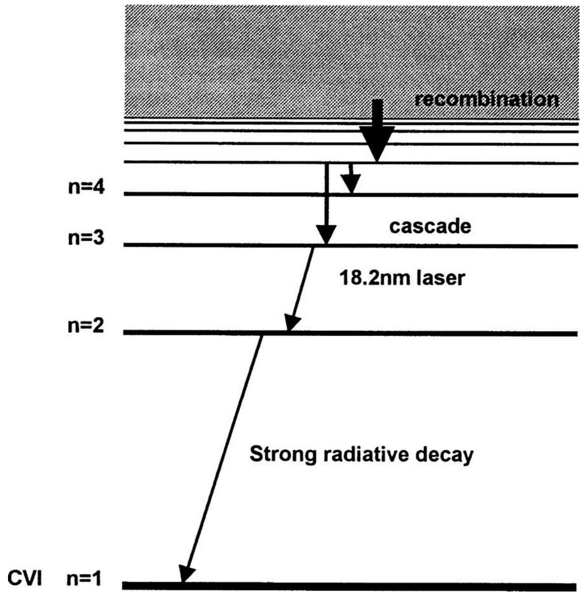

FIGURE 49.12 Simplified Grotrian diagram of H-like C showing the processes responsible for the generation of population inversion between the $n=3$ and $n=2$ levels in the 18.2 nm CVI recombination laser.

about 5 was inferred from the intensity ratio of lines in the axial and perpendicular direction. A similar experiment conducted in B_2O_3 resulted in a gain of $gl \simeq 5$ in the $3 \rightarrow 2$ transition of H-like B at 26.2 nm [167]. A pre-plasma was created by a 20 ns, 0.2 J KrF laser; and the excitation was produced by a 0.4 J, 8 ns Nd:YAG laser operating at 1 Hz. Hara et al. have utilized multiple-pulse excitation from a pulse train with the objective of developing a compact soft X-ray recombination laser based on a train of 100 ps pulses produced by a tabletop Nd:YAG laser [164–166]. Experiments conducted utilising 1.5–2 J of laser pulse energy to excite an 11 mm long Al slab target were reported to produce a gain coefficient of 3.2 cm^{-1} in the 15.5 nm line of Li-like Al [166] but the amplification was small.

An advantage of the recombination scheme with respect to the collisional excitation scheme involving $\Delta n=0$ transitions is its more rapid scaling to shorter wavelengths with nuclear charge Z. However, recombination lasers have suffered the problem of not scaling adequately with plasma column length, a problem possibly related to the very high sensitivity of the gain in recombination schemes to the variation of the plasma parameters. The largest product achieved to date is 8 [18].

49.5.2.2 Gain in Discharge-pumped Recombination Systems

The possibility of obtaining amplification by collisional recombination in capillary discharge plasmas was proposed by Rocca et al. in 1988 [168]. Evidence of gain has been reported in several discharge-pumped recombination laser experiments [169–175]. However, in all cases, only small exponentiation ($gl < 4$) has been observed to date, with the line intensity remaining of the same order as that of surrounding non-lasing lines emitted by the plasma.

49.5.2.3 Recombination Lasing in Transitions to the Ground State

Jones and Ali [9] demonstrated theoretically that large transient gains could be generated in the 2 → 1 transitions of H-like ions following recombination of a totally ionized plasma of arbitrarily low temperature. This kind of laser in a transition to the ground state is very attractive to rapidly scale recombination lasers to very short wavelengths. However, for lasing to occur in a transition to the ground state, recombination has to be very rapid to allow for the generation of large upper level populations before the ion ground-state level is significantly populated. The recombination time must then be shorter than the radiative lifetime of the upper level which is, for example, 26 and 1.6 ps for the $n=2$ level of H-like Li and H-like C, respectively. These time scales are shorter than the time required to cool a hot plasma before the ground state is significantly populated. Burnett and Corkum [176] recognized that a cold plasma of highly stripped ions in which recombination can occur in a very short time scale can be created by optical-field-induced ionization (OFI) using linearly polarized light and proposed the realization of ultrashort wavelength lasers utilizing this approach. Several theoretical studies analysed different aspects of the implementation of soft X-ray recombination lasers based on OFI [177,178].

The first report of amplification following plasma recombination of an OFI plasma corresponds to an experiment 13.5 nm in the 2 → 1 transition of H-like Li realized by Nagata et al. in 1993 utilizing the set-up illustrated in Figure 49.13a. [57]. A cold plasma of totally ionized Li ions was generated in two steps. First, a plasma of singly -ionized Li ions was produced by line-focusing a 20 ns KrF laser pulse with an energy of 200 mJ onto a rotating lithium target. Second, after a selected time delay, the plasma was optical-field ionized with 50 mJ pulses from a linearly polarized subpicosecond (0.5 ps) KrF laser pulse focused to an intensity of $1\times10^{17}\,\mathrm{cm}^{-2}$. Figure 49.13b shows the measured variation of the 13.5 nm laser line intensity with plasma length, from which a gain coefficient of $20\,\mathrm{cm}^{-1}$ was deduced. The 13.5 nm radiation pulse was measured to have a FWHM duration of less than 20 ps, with the peak intensity occurring about 20 ns after the pump pulse. However, the maximum resulting product only reached four because the plasma length was limited to 2 mm by ionization-induced refraction. This limitation is the result of the confocal geometry that causes the beam to refract due to the convex electron density profile resulting from the maximum ionization on axis. Approaches to overcome this problem have been suggested and include the generation of very flat transverse intensity profiles [178] and the generation of plasma waveguides with a minimum density on axis [58,179–184].

Korobkin et al. [58] used the set-up illustrated in Figure 49.14a to increase the amplification length to 5 mm by pre-forming a plasma waveguide in an LiF microcapillary tube. A plasma with a minimum electron density on axis was generated by ablation of the capillary walls with a 100 mJ, 5 ns pulse of 1.06 μm wavelength radiation from a Nd:YAG laser loosely focused on the entrance of the microcapillary. Following a time delay of several hundred nanoseconds, the plasma was further ionized with a laser pulse of 50 mJ energy and 250 fs duration from a tightly focused KrF laser. The observed increase of the intensity of the 13.5 nm line of H-like Li as a function of length is shown in Figure 49.14b, and corresponds to $gl=5.5$ [57]. These results were obtained at a repetition rate of 2 Hz. Gain by recombination in an OFI plasma has also been reported in the $2p2s\,^3P \rightarrow 2p^2\,^3P$ transition of OIII ($\lambda=37.4$ nm) and in the $2p^23s\,^2P \rightarrow 2p^3\,^2D$ line of OII ($\lambda=61.7$ nm) [185]. The data suggest gain coefficients as high as $25\,\mathrm{cm}^{-1}$ but again the overall amplification was small due to the small length of the gas targets.

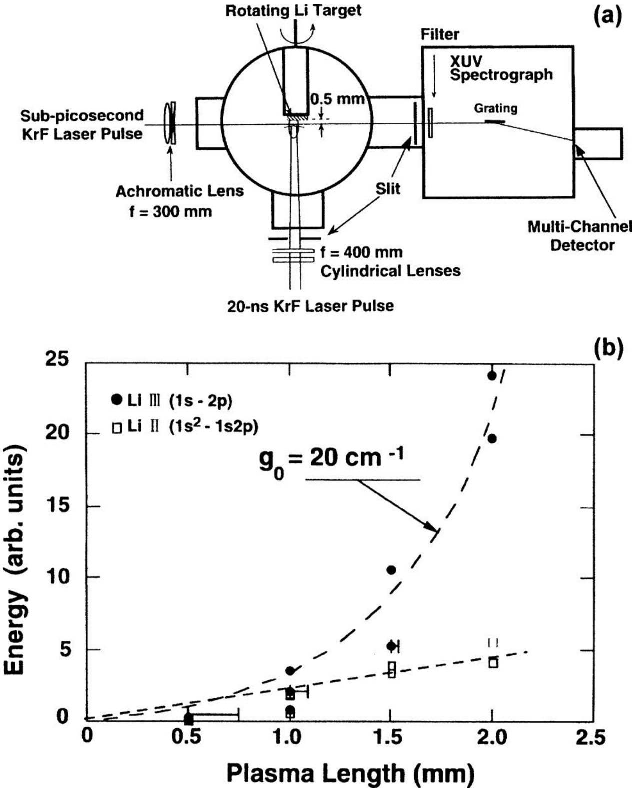

FIGURE 49.13 (a) Schematic illustration of the experimental set-up used at RIKEN in the observation of amplification in the 13.5 nm line of H-like Li in a plasma created by optical field induced ionization. (b) Results of amplification experiment in the 2 → 1 line of H-like Li in a plasma created by optical-field-induced ionization. Intensities of the 13.5 nm laser line of H-like Li and 19.9 nm line of He-like Li as a function of plasma column length. The broken curve is a calculated increase corresponding to a small-signal gain coefficient of $20\,\mathrm{cm}^{-1}$. (From Nagata et al. [57].)

The small excitation energies used in OFI soft X-ray laser experiments are compatible with the requirement for the generation of high-repetition-rate tabletop soft X-ray lasers. However, an increase in the product from the reported values of ~6.5 to the larger values is still required to achieve practical output energies. Predictions of the output pulse energies that can be expected from OFI lasers range from 1 μJ [178] to 10–20 μJ [186]. The OFI recombination scheme can, in principle, also be scaled to shorter wavelengths by using ions with higher charge and more intense optical fields, provided that parametric electron heating effects (mainly stimulated Raman backscattering) can be overcome.

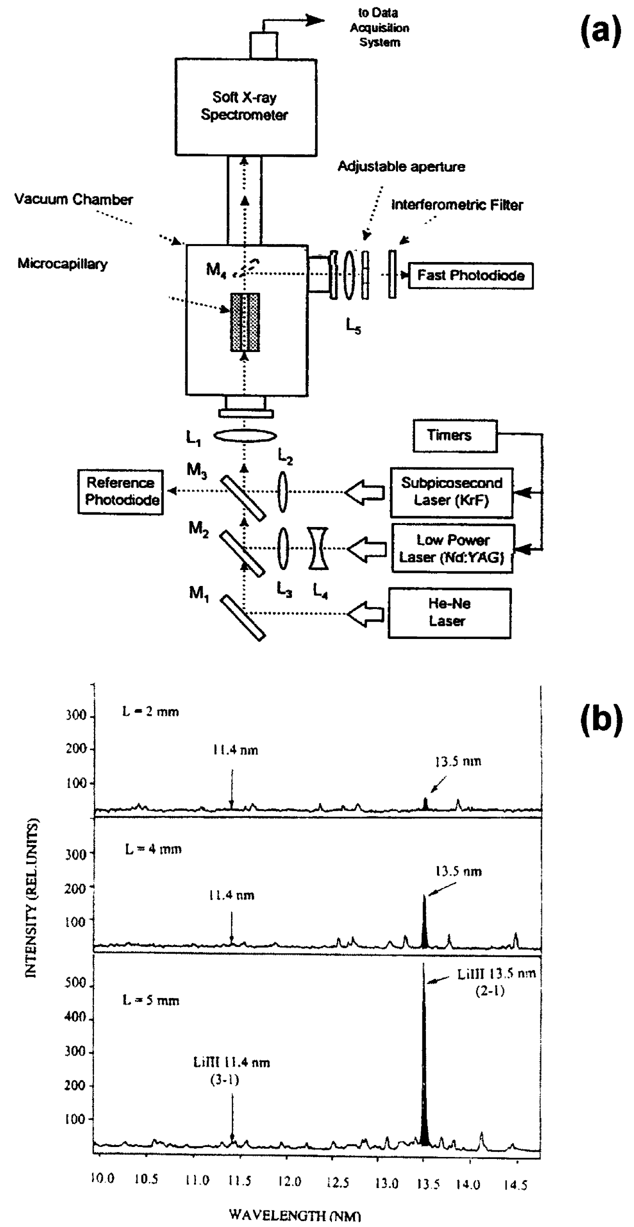
(a)
to Data Acquisition System
Soft X-ray Spectrometer
Adjustable aperture
Interferometric Filter
Vacuum Chamber
Microcapillary
M4
Fast Photodiode
L5
L1
L2
M3
Timers
Reference Photodiode
Subpicosecond Laser (KrF)
M2
Low Power Laser (Nd:YAG)
M1
L3
L4
He-Ne Laser
(b)
INTENSITY (REL.UNITS)
L = 2 mm
11.4 nm
13.5 nm
L = 4 mm
11.4 nm
13.5 nm
L = 5 mm
LiIII 11.4 nm (3-1)
LiIII 13.5 nm (2-1)
300
200
100
500
400
10.0
10.5
11.0
11.5
12.0
12.5
13.0
13.5
14.0
14.5
WAVELENGTH (NM)

FIGURE 49.14 (a) Schematic illustration of the experimental set-up used at Princeton in the creation of OFI plasmas in LIF microcapillaries for the observation of amplification in the 13.5 nm laser line of H-like Li. (b) Axial spectra of an OFI plasma created in a LiF microcapillary using the set-up shown in (a). The $n = 2$–1 transition of H-like Li at 13.5 nm is observed to increase as a function of plasma length with a gain coefficient of 11 cm^{-1}. (From Korobkin et al. [58].)

49.5.3 Photoionization Lasers

The generation of amplification following the selective X-ray photoionization of inner shell electrons was originally proposed by Duguay and Rentzepis in 1967 [1]. The generation of population inversions by this mechanism exploits the fact that at photon energies just above the threshold for inner-shell photoionization, the cross section is an order of magnitude larger for inner-shell electrons as compared to outer-shell electrons. This scheme has the potential advantage of leading to compact lasers with wavelengths shorter than 1.5 nm [187,188]. In principle, it can allow for operation at a low plasma temperature (<1 eV) with consequently less Doppler broadening and large gain coefficients. The incoherent X-ray photons that pump the laser media can be produced by a nearby plasma created by heating a high-Z target material, such as gold, with an intense ultrashort laser pulse. Photons at energy below the inner-shell binding energy can be removed from the pump with an appropriate filter to avoid pumping of the lower level.

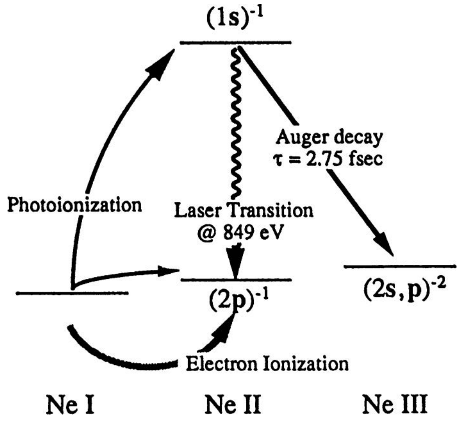
$(1s)^{-1}$
Auger decay
τ = 2.75 fsec
Photoionization
Laser Transition
@ 849 eV
$(2p)^{-1}$
$(2s,p)^{-2}$
Electron Ionization
Ne I
Ne II
Ne III

FIGURE 49.15 Simplified energy-level diagram of a proposed inner-shell photoionization laser in the Kα transition of Ne at 1.5 nm. X-rays photoionize the 1s electrons of the Ne atoms creating a population inversion and gain in the $(1s)^{-1} \rightarrow (2p)^{-1}$ transition of singly ionized Ne. Rapid Auger decay depletes the $(1s^{-1})$ upper level. Electron impact ionization populates the $(2p)^{-1}$ lower level limiting the duration of the gain. (From Kapteyn [188].)

The first proposal for inner-shell photoionization lasers at X-ray wavelengths [2] preceded by decades the development of sufficiently powerful ultrashort pulse laser drivers. McGuire proposed the production of population inversions by selective Auger decay [189]. In 1986 Kapteyn et al. demonstrated lasing at 108.9 nm in doubly ionized Xe by Auger decay following the photoionization of neutral Xe [190]. Output energies of several μJ in this transition were subsequently obtained at a 2 Hz repetition rate by Sher et al. utilizing travelling-wave excitation [191]. Amplification in the equivalent transition in Kr at 90.7 nm was also observed [192]. However, no demonstration of a photoionization laser at X-ray wavelengths has yet been realized. Nevertheless, the development of lasers capable of producing peak powers of up to 100 TW with ~20 fs pulse duration increases the likelihood that this type of X-ray lasers will soon be realized.

Kapteyn has analysed the possibility of obtaining lasing by preferentially photoionizing the K-shell electrons of low-Z elements [187], focusing in particular on the Kα line of Ne ($\lambda = 1.5$ nm). A main advantage of the Kα scheme is its scalability to very short wavelengths. The energy-level diagram of the Kα Ne laser is illustrated in Figure 49.15. The filtered X-rays from the pump primarily photoionize the inner-shell electrons, producing population inversion and gain in the allowed radiative transition between the $(1s)^{-1\,2}S$ and $(2p)^{-1\,2}P$ levels of the singly charged ion. Rapid Auger decay with a rate of $(2.7\,\mathrm{fs})^{-1}$ is the dominant mechanism of depopulation of the $(1s)^{-1}$ upper level. However, the self-terminating lifetime is not the dominant process that limits the duration of the gain.

Instead, the magnitude and duration of the gain is limited by electron collisional ionization of neutral neon atoms. The energetic electrons created in the lasing material by photoionization and Auger decay create predominantly ground-state Ne ions that are the lower level, destroying the gain. Therefore, this is intrinsically an ultrashort pulse X-ray laser. It has been estimated that lasing in the Kα transition of Ne at 1.5 nm could be produced by travelling-wave excitation using a pump laser generating ~10 J pulses of approximately 50 fs duration [187]. Eder et al. [178,188,193] calculated a scaling law relating the necessary laser pump energy E_L (J) to the wavelength λ (nm) that can be achieved. Assuming 20 fs X-ray pump pulses, they obtained $E_L = (4.5/\lambda)^2$ [194]. Calculations for lasing in C at 4.5 nm suggest that driving laser energy of the order of 1 J should be sufficient to produce a gain coefficient of 10 cm^{-1} and a large product [193].

The possibility of using inner-shell electrons to obtain lasing in 2p → 2s Ne-like ions and 3d → 3p Ni-like ion transitions has also been suggested [195,196]. Barty et al. and Kim et al. have discussed systems in which dominant Coster–Kronig decay of the laser lower level can overcome electron collisional filling of this state [197–204]. These systems are, therefore, more immune to secondary electron ionization. Computations show that, under certain conditions, inversions can be obtained with pumping by energetic electrons as well as X-rays. Conditions for inversion by Coster–Kronig lower level decay were analysed in several transitions in elements with nuclear charge up to $Z = 90$, and detailed computations of gain were published for the L_2M_1 transition in Ti ($Z = 22$) at 3 nm.

REFERENCES

1. Duguay M A and Rentzepis P M 1967 *Appl. Phys. Lett.* **10** 350.
2. Molchanov A G 1972 *Sov. Phys.–Usp.* **15** 124.
3. Elton R C 1975 *Appl. Opt.* **14** 97.
4. Zherikin A N, Koshelev K N and Letokhov V S 1976 *Sov. J. Quantum Electron.* **6** 82.
5. Vinogradov A V, Sobel'man I I and Yukov E A 1977 *Sov. J. Quantum. Electron.* **7** 32; Vainshtein L A, Vinogradov A V, Safranova V I and Skolev I Vu 1978 *Sov. J. Quantum Electron.* **8** 239; Vinogradov A V and Shlyaptsev V N 1980 *Sov. J. Quantum Electron.* **10** 753; Vinogradov A V and Shlyaptsev V N 1980 *Sov. J. Quantum Electron.* **13** 303.
6. Pert G J and Ramsden S A 1974 *Opt. Commun.* **11** 270.
7. Bohn W L 1974 *Appl. Phys. Lett.* **25** 15.
8. Konokov E Ya and Koshelev K N 1975 *Sov. J. Quantum Electron.* **4** 1340.
9. Jones W W and Ali A W 1975 *Appl. Phys. Lett.* **26** 450.
10. Irons F and Peacock N J 1974 *J. Phys. B: At. Mol. Phys.* **7** 1109.
11. Dewhurst R J, Jacoby D, Pert G J and Ramsden S A 1976 *Phys. Rev. Lett.* **37** 1265.
12. Kononov Y A, Koshelev K N, Levykin Yu A, Sidel'nikov Yu V and Churilov S S 1976 *Sov. J. Quantum Electron.* **6** 308.
13. Dixon R H and Elton R C 1977 *Phys. Rev. Lett.* **38** 1072.
14. Key M H, Lewis C L S and Lamb M J 1979 *Opt. Commun.* **28** 331.
15. Jaeglé P, Jamelot G, Carillon A and Wehenkel C 1978 *Japan. J. Appl. Phys.* **17** 483.
16. Jacoby D, Pert G J, Ramsden S A, Shorrock L D and Tallents G J 1981 *Optics Commun.* **37** 193; Jacoby D, Pert G J, Shorrock L D and Tallents G J 1982 *J. Phys. B: At. Mol. Phys.* **15** 3557.
17. Matthews D L 1985 et al. *Phys. Rev. Lett.* **54** 110; Rosen M D, Hagelstein P L, Matthews D L, Campbell E M, Hazi A U, Whitten B L, MacGowan B, Turner R E and Lee R W 1985 *Phys. Rev. Lett.* **54** 106.
18. Suckewer S, Skinner C H, Milchberg H, Keane C and Voorhees D 1985 *Phys. Rev. Lett.* **55** 1753; Suckewer S, Skinner C H, Kim D, Valeo E, Voorhees D and Wouters A 1986 *Phys. Rev. Lett.* **57** 1004.
19. Carillon A et al. 1992 *Phys. Rev. Lett.* **68** 2917.
20. MacGowan B J et al. 1992 *Phys. Fluids B* **4** 2326.
21. Smith R, Tallents G J, Zhang J, Eker G, McCabe S, Pert G J and Wolfrum E 1999 *Phys. Rev. A* **59** R47.
22. Koch J A et al. 1992 *Phys. Rev. Lett.* **68** 3291.
23. Rus B et al. 1994 *X-Ray Lasers* ed D C Eder and D L Matthews (New York: AIP).
24. DaSilva L B, MacGowan B J, Rowka S M, Koch J A, London R A, Matthews D L and Underwood J 1993 *Opt. Lett.* **18** 1174.
25. Wang S, Zhou G, Zhang G, Sheng J and Chunyu S 1994 *X-Ray Lasers* ed D C Eder and D L Matthews (New York: AIP) p 293.
26. Skinner C H, Dicicco D S, Kim D, Rosser R J, Suckewer S, Gupta A P and Hirshberg J G 1990 *J. Microsc.* **159** 51.
27. Da Silva L B et al. 1992 *Science* **258** 269.
28. Trebes J E et al. 1987 *Science* **238** 517.
29. Da Silva L B et al. 1995 *Phys. Rev. Lett.* **74** 3991; Wan A S, Barbee T W Jr, Cauble R, Celliers P, Da Silva L B, Moreno J C, Rambo P W, Stone G F, Trebes J E and Weber F 1997 *Phys. Rev. E* **55** 6293.
30. Cauble R, Da Silva L B, Barbee T W Jr, Celliers P, Moreno J C and Wan A S 1995 *Phys. Rev. Lett.* **74** 3816.
31. Backus S, Durfee C G III, Murnane M and Kapteyn H C 1998 *Rev. Sci. Instrum.* **1207** 69.
32. Barty C P J et al. 1996 *X-Ray Lasers* ed S Svanberg and C G Wahlstrom (Bristol: Institute of Physics Publishing) p 282.
33. Umstadter D P, Barty C, Perry M and Mourou G A 1998 *Opt. Photon. News* **9** 41.
34. Kato Y 1996 *X-Ray Lasers* ed S Svanberg and C G Wahlstrom (Bristol: Institute of Physics Publishing) p 274.
35. Yamakawa Y, Aoyama M, Matsuoka S, Kase T, Akahane V and Takuma H 1999 *Opt. Lett.* **23** 146.
36. Rocca J J, Cortázar O D, Szapiro B, Floyd K and Tomasel F G 1993 *Phys. Rev. E* **47** 1299.
37. Rocca J J, Shlyaptsev V, Tomasel F G, Cortázar O D, Hartshorn D and Chilla J L A 1994 *Phys. Rev. Lett.* **73** 2192–5.
38. Rocca J J, Tomasel F G, Marconi M G, Shlyaptsev V N, Chilla J L A, Szapiro B T and Guidice G 1995 *Phys. Plasmas* **2** 2547.
39. Rocca J J, Marconi M C, Chilla J L A, Clark D P, Tomasel F G and Shlyaptsev V N 1995 *IEEE J. Selected Topics Quantum Electron.* **945** 1.
40. Rocca J J, Clark D P, Chilla J L A and Shlyaptsev V N 1996 *Phys. Rev. Lett.* **77** 1476–9.
41. Tomasel F G, Rocca J J and Shlyaptsev V N 1996 *IEEE Trans. Plasma Sci.* **49** 24.
42. Tomasel F G, Rocca J J, Shlyaptsev V N and Macchietto C D 1997 *Phys. Rev. A* **55** 1437.

43. Benware B R, Moreno C H, Burd D J and Rocca J J 1997 *Opt. Lett.* **22** 796.
44. Benware B R, Macchietto C D, Moreno C H and Rocca J J 1998 *Phys. Rev. Lett.* **81** 5804.
45. Macchietto C D, Benware B R and Rocca J J 1999 *Opt. Lett.* **24** 1115.
46. Moreno C H, Marconi M C, Shlyaptsev V N, Benware B R, Macchietto C D, Chilla J L A, Rocca J J and Osterheld A 1998 *Phys. Rev. A* **58** 1509.
47. Waynant R W and Elton R C 1976 *Proc. IEEE* **64** 1059.
48. Hagelstein P L 1983 *Plasma Phys.* **25** 1345; Hagelstein P L 1984 *Atomic Physics* vol 9, ed R S Van Dyck Jr and E N Fortson (Singapore: World Science) p 382.
49. Keane C J 1991 *SPIE* **1551** 2.
50. Kapteyn H C, Da Silva L B and Falcone R W 1992 *Proc. IEEE* **342** 80.
51. Matthews D L 1995 *Nucl. Instrum. Methods Phys. Res. B* **98** 91.
52. Skinner C H 1991 *Phys. Fluids B* **3** 2420.
53. Elton R C 1990 *X-Ray Lasers* (Boston, MA: Academic).
54. Rocca J J and Da Silva L B (ed) 1999 *Soft X-Ray Lasers and Applications (Proc. SPIE 3776)* vol III (Bellingham, WA: SPIE).
55. Suckewer S (ed) 1991 *Ultrashort Wavelength Lasers (Proc. SPIE 1551)* (Bellingham, WA: SPIE).
56. Rocca J J 1999 *Rev. Sci. Instrum.* **70** 3799.
57. Nagata Y, Midorikawa K, Kubodera S, Obara M, Tashiro H and Tokoda K 1993 *Phys. Rev. Lett.* **71** 3774.
58. Korobkin D, Nam C H, Suckewer S and Golstov A 1996 *Phys. Rev. Lett.* **77** 5206.
59. Lemoff B E, Yin G Y, Gordon C L III, Barty C P J and Harris S E 1995 *Phys. Rev. Lett.* **74** 1576; 1996 *J. Opt. Soc. Am. B* **13** 180.
60. Nickles P V, Shlyaptsev V N, Kalashnikov M, Schnurer M, Will I and Sandner W 1997 *Phys. Rev. Lett.* **78** 2748.
61. Dunn J, Osterheld A L, Shepherd R, White W E, Shlyaptsev V N and Stewards R E 1998 *Phys. Rev. Lett.* **80** 2825.
62. Dunn J, Osterheld A L, Shepherd R, White W E, Shlyaptsev V N, Bullock A and Stewart R E 1997 *Soft X-Ray Lasers and Applications (Proc. SPIE 3156)* vol II, ed J J Rocca and L B Da Silva (Bellingham, WA: SPIE) p 114.
63. Kalachnikov M P et al. 1998 *Phys. Rev. A* **57** 4778.
64. Dunn J, Li Y, Osterheld A L, Nilsen J, Hunter J R and Shlyaptsev V N 2000 *Phys. Rev. Lett.* **84** 4834; Dunn J, Li Y, Osterheld A L, Nilsen J, Moon S J, Fournier K B, Hunter J R, Faenov A Ya, Pikuz T A and Shlyaptsev V N 1999 *Soft X-Ray Lasers and Applications (Proc. SPIE 3776)* vol III, ed J J Rocca and L B Da Silva (Bellingham, WA: SPIE) p 2.
65. Lewis C L S et al. 1999 *Soft X-Ray Lasers and Applications (Proc. SPIE 3776)* vol III, ed J J Rocca and L B Da Silva (Bellingham, WA: SPIE) p 292.
66. Miquel J L et al. 1999 *Soft X-Ray Lasers and Applications (Proc. SPIE 3776)* vol III, ed J J Rocca and L B Da Silva (Bellingham, WA: SPIE) p 24.
67. Linford G J, Peresini E R, Soor W R and Spaeth M L 1974 *Appl. Opt.* **13** 379.
68. For typical gains in visible gas lasers, see for example, Silfvast W T 1996 *Laser Fundamentals* (Cambridge: Cambridge University Press).
69. Jamelot J et al. 1999 *X-Ray Lasers* ed Y Kato, H Takuma and H Daido (Reading: IOPP) p 25.
70. Koch J A, MacGowan B J, DaSilva L B, Matthews D L, Underwood J H, Batson P J and Mrowka S 1992 *Phys. Rev. Lett.* **68** 3291; Koch J A, MacGowan B J, DaSilva L B, Matthews D L, Underwood J H, Batson P J and Mrowka S 1994 *Phys. Rev. A* **50** 1877.
71. Kato Y et al. 1991 *Ultrashort Wavelength Lasers (Proc. SPIE 1551)* ed S Suckewer (Bellingham, WA: SPIE) p 56.
72. London R A, Strauss M and Rosen M D 1990 *Phys. Rev. Lett.* **65** 563.
73. Feit M D and Fleck J J A 1991 *Opt. Lett.* **16** 76; Feit M D and Fleck J J A 1991 *J. Opt. Soc. Am. B* **7** 2048.
74. Hazak G and Bar A 1989 *Shalom Phys. Rev. A* **40** 7055.
75. Trebes J et al. 1992 *Phys. Rev. Lett.* **68** 588.
76. Burge R E, Slark G E, Browne M T, Yuang X C, Charalambous P, Cheng X H and Lewis C L S 1997 *J. Opt. Soc. Am. B* **14** 2742; Burge R E, Slark G E, Browne M T, Yuang X C, Charalambous P, Cheng X H and Lewis C L S 1998 *J. Opt. Soc. Am. B* **15** 1920; Burge R E, Slark G E, Browne M T, Yuang X C, Charalambous P, Cheng X H and Lewis C L S 1998 *J. Opt. Soc. Am. B* **15** 2515.
77. Marconi M C, Chilla J L A, Moreno C H, Benware B R and Rocca J J 1997 *Phys. Rev. Lett.* **79** 2799.
78. Jamelot G et al. 1995 *Soft X-Ray Lasers and Applications (Proc. SPIE 2520)* J J Rocca and P L Hagelstein (Bellingham, WA: SPIE) p 2.
79. Liu Y, Seminario M, Tomasel F G, Rocca J J, Chang C and Attwood D T 2001 *Phys. Rev. A* **63** 033802.
80. Chang Z, Rundquist A, Wang H, Murnane M M and Kapteyn H C 1997 *Phys. Rev. Lett.* **79** 2967.
81. L'Huillier A 1996 *X-Ray Lasers* ed S Svanberg and C G Wahlstrom (Bristol: Institute of Physics Publishing) p 444.
82. Ditmire T, Crane J K, Nyugen H, Da Silva L B and Perry M D 1995 *Phys. Rev. A* **51** R902.
83. Rundquist A, Durfee C G III, Chang Z, Herne C, Backus S, Murnane M and Kapteyn H C 1998 *Science* **280** 1412.
84. Tamaki T, Nagata Y, Obara M and Midorokawa K 1999 *Phys. Rev. A* **59** 4041.
85. Attwood D T, Halbach K and Kim N J 1985 *Science* **228** 1264.
86. Attwood D T, Sommargren G, Beguiristain R, Nguyen K, Boker J, Ceglio N, Jackson K, Koike M and Underwood J 1993 *Appl. Opt.* **32** 7022.
87. Coisson R 1995 *Appl. Opt.* **34** 904.
88. Attwood D T et al. 1999 *IEEE J. Quantum Electron.* **35** 709.
89. Rossback J P 1996 *X-Ray Lasers* ed S Svanberg and C G Wahlstrom (Bristol: Institute of Physics Publishing) p 436.
90. Feldhaus J, Krzywinski J, Saldin E L, Schneidmiller E and Yurkov M V 1999 *X-Ray Lasers* ed Y Kato, H Takuma and H Daido (Bristol: Institute of Physics Publishing) p 553.
91. Schoemlein R W et al. 1996 *Science* **274** 236.
92. Ditmire T, Cowan T E, LeSage G, Allen M, Hays G, Wharton K B, Perry M D, Powell H T and Rosenzweig J B 1999 *IEEE LEOS Annual Meeting Conf. Proc. (San Francisco, CA)* (Piscataway, NJ: IEEE) p 47.
93. Shkolnikov P L and Kaplan A E 1996 *X-Ray Lasers* ed S Svanberg and C G Wahlstrom (Bristol: Institute of Physics Publishing) p 512.
94. Muendel M H and Hagelstein P L 1991 *Phys. Rev. A* **44** 7573.
95. Rocca J J, Moreno C H, Marconi M C and Kanizay K 1999 *Opt. Lett.* **24** 240; Moreno C H, Marconi M C, Kanizay K, Rocca J J, Unspenskii Yu A, Vinogradov A V and Pershin Yu A 1999 *Phys. Rev. E* **60** 911.

96. Filevich J, Marconi M, Kanizay K, Chilla J L A and Rocca J 2000 *Opt. Lett.* **25** 356.
97. Li Y, Lu P, Pretzler G and Fill E E 1997 *Opt. Commun.* **133** 196.
98. Fields D J et al. 1992 *Phys. Rev. A* **46** 1606.
99. MacGowan B J, Maxon S, DaSilva L B, Fields D J, Keane C J, Matthews D L, Osterheld A L, Scofield J H, Shimkaveg G and Stone G F 1990 *Phys. Rev. Lett.* **65** 420.
100. MacGowan B J et al. 1990 *Phys. Rev. Lett.* **65** 2374.
101. Hagelstein P L 1988 *Proc. OSA Meeting on Short Wavelength Coherent Radiation: Generation and Applications* ed R W Falcone and J Korz (Washington DC: OSA); Shlyaptsev V N 1987 PhD Thesis P N Lebedev Physical Institute, Preprint FIAN #40.
102. MacGowan B J et al. 1987 *J. Appl. Phys.* **61** 5245.
103. MacGowan B J, Maxon S, Hagelstein P L, Keane C J, London R A, Matthews D L, Rosen M D, Scofield J H and Whelan D A 1987 *Phys. Rev. Lett.* **59** 2157.
104. Lee T N, McLean E A and Elton R C 1987 *Phys. Rev. Lett.* **59** 1185.
105. MacGowan B J, Maxon S, Keane C J, London R A, Matthews D L and Whelan D A 1988 *J. Opt. Soc. Am. B* **5** 1858.
106. O'Neill D M, Lewis C L S, Neely D, Uhomopbhi J, Key M H, MacPhee A, Tallents G J, Ramsden S A, Rogovski A and McLean E A 1990 *Opt. Commun.* **75** 406.
107. Lunney J G 1986 *Appl. Phys. Lett.* **46** 891.
108. Lewis C L S 1992 et al. *Opt. Commun.* **91** 71.
109. Kodama R, Neely D, Kato Y, Daido H, Murai K, Yuan G, MacPhee A and Lewis C L S 1994 *Phys. Rev. Lett.* **73** 3215.
110. Wanshiji et al. 1992 *J. Opt. Soc. Am. B* **9** 360.
111. Boehly I T et al. 1990 *Phys. Rev. A* **42** 6962.
112. Nilsen J, MacGowan B J, Da Silva L B and Moreno J C 1993 *Phys. Rev. A* **48** 4682.
113. Basu S, Hagelstein P L, Gooberlet J G, Muendel M H and Kaushik S 1993 *Appl. Phys. B.* **57** 203.
114. Nilsen J, Moreno J C, DaSilva L B and Barbee T W Jr 1997 *Phys. Rev. A* **55** 827.
115. Moreno J C, Nilsen J, Li Y L and Fill E E 1996 *Opt. Lett.* **21** 866.
116. Nilsen J and Moreno J C 1995 *Phys. Rev. Lett.* **74** 3376.
117. Jamelot G et al. 1995 *Soft X-Ray Lasers and Applications (Proc. SPIE 2520)* ed J J Rocca and L B Da Silva (Bellingham, WA: SPIE) pp 2–12.
118. Cairns G F et al. 1996 *Opt. Commun.* **124** 777–89.
119. Li Y, Pretzler G and Fill E E 1995 *Phys. Rev. A* **52** R3433, and Fill E E, Li Y, Schlögl D, Steingruber J and Nilsen J 1995 *Soft X-Ray Lasers and Applications (Proc. SPIE 2520)* ed J J Rocca and P L Hagelstein (Bellingham, WA: SPIE) p 134.
120. Daido H, Kodama R, Murai K, Yuan G, Takagi M, Kato Y, Choi I W and Nam C H 1995 *Opt. Lett.* **20** 61.
121. Rus B, Carillon A, Dhez P, Jaeglé P, Jamelot G, Klisnick A, Nantel M and Zeitoun P 1997 *Phys. Rev. A* **55** 3858.
122. Daido H, Ninomiya S, Imani T, Kodama B, Takagi M, Kato Y, Murai K, Zhang J, You Y, and Gu Y 1996 *Opt. Lett.* **21** 958.
123. Fill E E, Li Y, Schlögl D, Steingruber J and Nilsen J 1995 *Opt. Lett.* **20** 374.
124. Tallents G J 1997 *Soft X-Ray Lasers and Applications (Proc. SPIE 3156)* vol II, ed J J Rocca and L B Da Silva (Bellingham, WA: SPIE) p 30.
125. Moreno J C, Nilsen J and DaSilva L B 1994 *Opt. Commun.* **110** 585.
126. Nilsen J, Li Y, Lu P, Moreno J C and Fill E E 1996 *Opt. Commun.* **124** 287.
127. Zhang J et al. 1996 *Phys. Rev. A* **54** R4653.
128. Li Y L, Pretzler G, Lu P X, Fill E E and Nilsen J 1997 *Phys. Plasmas* **4** 479.
129. Yuang G, Murai K, Daido H, Kodama R and Kato Y 1995 *Phys. Rev. A* **52** 4861.
130. Zhang J et al. 1996 *Phys. Rev. A* **53** 3640.
131. Daido H et al. 1995 *Phys. Rev. Lett.* **75** 1074.
132. Daido H et al. 1996 *Opt. Lett.* **21** 958.
133. Zhang J et al. 1997 *Phys. Rev. Lett.* **78** 3856.
134. Zhang J et al. 1997 *Science* **276** 1097.
135. Zhang J et al. 1997 *Soft X-Ray Lasers and Applications (Proc. SPIE 3156)* vol II, ed J J Rocca and L B Da Silva (Bellingham, WA: SPIE) p 53.
136. Frati M, Seminario M and Rocca J J 2000 *Opt. Lett.* **25** 1022.
137. Prag A R, Loewenthal F and Balmer J E 1996 *Phys. Rev. A* **54** 4585.
138. Lowenthal F, Tommasini R and Balmer J E 1998 *Opt. Commun.* **154** 325.
139. Afanasiev Yu A and Shlyaptsev V N 1989 *Sov. J. Quantum Electron.* **19** 1606.
140. Shlyaptsev V N, Nickles P V, Schlegel T, Kalashnikov M R and Osterheld A L 1991 *SPIE* **1551** 111; Shlyaptsev V N, Rocca J J, Kalashnikov M P, Nickles P V, Sandner W, Osterheld A L, Dunn J and Eder D C 1997 *Soft X-Ray Lasers and Applications (Proc. SPIE 3156)* vol II, ed J J Rocca and L B Da Silva (Bellingham, WA: SPIE) p 93; Decker C D and London R A 1997 *Soft X-Ray Lasers and Applications (Proc. SPIE 3156)* vol II, ed J J Rocca and L B Da Silva (Bellingham, WA: SPIE) p 94; Nilsen J 1997 *Soft X-Ray Lasers and Applications (Proc. SPIE 3156)* vol II, ed J J Rocca and L B Da Silva (Bellingham, WA: SPIE) p 86.
141. Kato Y, Takuma H and Daido H (ed) 1999 *X-Ray Lasers* (Bristol: Institute of Physics Publishing).
142. Moreno C H, Marconi M C, Shlyaptsev V N and Rocca J J 1999 *IEEE Trans. Plasma Sci.* **27** 6.
143. Rocca J J, Moreno C H, Marconi M C and Kanizay K 1999 *Opt. Lett.* **24** 420; Filevich J, Kanizay K, Marconi M C, Chilla J L A and Rocca J J 2000 *Opt. Lett.* **25** 356.
144. Artioukov I A, Benware B R, Rocca J J, Forsythe M, Uspenskii Yu A and Vinogradov A V 2000 *IEEE. J. Selected Topics Quantum Electron.* **30** 328.
145. Benware B R, Ozols A, Rocca J J, Artioukov I A, Kondratenko V V and Vinogradov A V 1999 *Opt. Lett.* **24** 1714.
146. Gonzalez J J, Frati M, Rocca J J and Shlyaptsev V N 1999 *X-Ray Lasers* ed Y Kato, H Takuma and H Daido (Bristol: Institute of Physics Publishing) p 163; Gonzalez J J, Frati M, Rocca J J and Shlyaptsev V N 1999 *SPIE* **3776** 159.
147. Gudzenko G A and Shelepin L A 1963 *Zh. Ensp. Fiz.* **45** 1445 (Engl. transl. 1964 *Sov. Phys.–JETP* **18** 998).
148. Pert G J 1976 *J. Phys. B: At. Mol. Phys.* **9** 3301; Dave A K and Pert G J 1985 *J. Phys. B: At. Mol. Phys.* **18** 1027.
149. Seely J F, Brown C W, Feldman U, Richardson M, Yaakobi B and Behring W E 1985 *Opt. Commun.* **54** 289.
150. Grande M et al. 1990 *Opt. Commun.* **74** 309.
151. Boswell B, Shavarts D, Boehly T and Yaakobi B 1990 *Phys. Fluids B* **2** 436.

152. Azumma H et al. 1990 *Opt. Lett.* **15** 1011.
153. Jamelot G, Klisnick A, Carillon A, Guennov H, Sureau A and Jaeglé P 1998 *J. Phys. B: At. Mol. Opt. Phys.* **18** 4647.
154. Jaeglé P, Jamelot G, Carrillon A, Klisnik A, Sureau A and Guennov H 1987 *J. Opt. Soc. Am. B* **4** 563; Carillon A et al. 1990 *J. Phys. B: At. Mol. Opt. Phys.* **23** 147.
155. Chenais-Popovics C et al. 1987 *Phys. Rev. Lett.* **59** 2161.
156. Milchberg H, Skinner C H, Suckewer S and Voorhees D 1985 *Appl. Phys. Lett.* **47** 1151.
157. Suckewer S and Fishman H 1980 *J. Appl. Phys.* **51** 1922.
158. Keane C J and Suckewer S 1991 *J. Opt. Soc. Am. B* **8** 201.
159. Steingruber J, Chen S S and Fill E E 1992 *X-Ray Lasers* ed E E Fill (Bristol: Institute of Physics Publishing) p 115.
160. Kim D, Skinner C H, Umesh G and Suckewer S 1989 *Opt. Lett.* **14** 665.
161. Kim D, Skinner C H and Suckewer S 1991 *Proc. SPIE* **1551** 295.
162. Polonsky L, Park C O, Krushelnick K and Suckewer S 1976 *Proc. IEEE* **64** 75.
163. Morozov A, Polonsky L and Suckewer S 1995 *Soft X-Ray Lasers and Applications (Proc. SPIE 2520)* ed J J Rocca and P L Hagelstein (Bellingham, WA: SPIE) p 180.
164. Hara T, Ando K, Aoyagi Y, Kusakabe N and Yashiro H 1989 *Japan. J. Appl. Phys.* **28** L1010.
165. Yamaguchi N, Hara T, Fujikawa C and Hisada Y 1997 *Japan. J. Appl. Phys. Lett.* **36** L1297.
166. Hirose H, Hara T, Ando K, Negishi F and Aoyagi Y 1993 *Japan. J. Appl. Phys. Lett.* **32** L1538; Hara T, Ando K, Negishi-Tsuboi F, Aoyagi Y, Hirose H and Yashiro Y 1992 *Proc. SPIE.* **1627** 377.
167. Korobkin D, Goltsov A, Morozov A and Suckewer S 1998 *Phys. Rev. Lett.* **81** 1607.
168. Rocca J J, Beethe D C and Marconi M C 1988 *Opt. Lett.* **13** 565.
169. Steden C and Kunze H J 1990 *Phys. Lett. A* **151** 534.
170. Rocca J J, Marconi M C, Szapiro B T and Meyer J 1976 *Proc. IEEE* **64** 275.
171. Shin H J, Kim D E and Lee T N 1994 *Phys. Rev. E* **50** 1376.
172. Wagner T, Eberl E, Frank K, Hartmann W, Hoffmann D H H and Thotz R 1996 *Phys. Rev. Lett.* **76** 3124.
173. Glender S and Kunze H J 1994 *Phys. Rev. E* **49** 1586.
174. Böss T, Neff W, Boboc T, Weigand F, Bischoff R and Langhoff H 1998 *J. Phys. D: Appl. Phys.* **31** 2472.
175. Dussart R, Rosefeld W, Richard N, Hong D, Cachoncinlle C, Fleurier C and Pouvesle J M 1999 *X-Ray Lasers* ed Y Kato, H Takuma and H Daido (Bristol: Institute of Physics Publishing) p 171.
176. Burnett N H and Corkum P B 1989 *J. Opt. Soc. Am. B* **6** 1195.
177. Amendt P E and Eder D C 1991 *Phys. Rev. Lett.* **66** 2589; Eder D C, Amendt P and Wilks S C 1992 *Phys. Rev. A* **6761** 45.
178. Eder D C et al. 1994 *Phys. Plasmas* **1744** 1.
179. Durfee C G III, Lynch J and Milchberg H M 1995 *Phys. Rev. E* **51** 2368.
180. Milchberg H M, Durfee C G III and Lynch J 1995 *J. Opt. Soc. Am. B* **12** 731.
181. Durfee C G III, Lynch J and Milchberg H M 1994 *Opt. Lett.* **19** 1937.
182. Ehrlich Y, Cohen C, Zigler A, Krall J, Sprangle P and Erasay E 1996 *Phys. Rev. Lett.* **77** 4186.
183. Rocca J J, Tomasel F G, Marconi M C, Chilla J L A, Moreno C H, Benware B R, Shlyaptsev V N, Gonzales J J and Macchietto C D 1997 *Soft X-Ray Lasers and Applications (Proc. SPIE 3156)* vol II, ed J J Rocca and L B Da Silva (Bellingham, WA: SPIE) p 164.
184. Goltson A et al. 1999 *IEEE Sel. Top. Quantum Electron.* **5** 1453.
185. Chichkov B N, Egbert A, Eichmann H, Momma C, Nolte S and Wellegehausen B 1995 *Phys. Rev. A* **52** 1629.
186. Goltsov A, Korobkin D, Morozov A and Suckewer S 1998 *Proc. 1998 Int. Cong. on Plasma Physics and 25th EPS Conf. on Controlled Fusion and Plasma Physics* (Prague).
187. Kapteyn H C 1992 *Appl. Opt.* **31** 4931.
188. Strobel G L, Eder D L, London R A, Rosen M D, Falcone R W and Gordon S P 1993 Short pulse-high-intensity lasers and applications II *SPIE* **1860** 157.
189. McGuire E J 1975 *Phys. Rev. Lett.* **35** 844.
190. Kapteyn H C, Lee R W and Falcone R W 1986 *Opt. Phys. Rev. Lett.* **57** 2939.
191. Sher M H, Benerofe S J, Young J F and Harris S E 1991 *J. Opt. Soc. Am. B* **8** 114.
192. Kapteyn H C and Falcone R W 1988 *Phys. Rev. A* **37** 2033.
193. Moon S J, Eder D C and Strobel G L 1994 *X-Ray Lasers* ed D C Eder and D L Matthews (New York: AIP) p 262.
194. Matthews D L 1996 *X-Ray Lasers* ed S Svanberg and C G Wahlstrom (Bristol: Institute of Physics Publishing) p 32.
195. Lewis C L S et al. 1999 *X-Ray Lasers* ed Y Kato, H Takuma and H Daido (Bristol: Institute of Physics Publishing) p 1.
196. Moribayashi K, Sasaki A and Tajima T 1998 *Phys. Rev. A* **58** 2007.
197. Kim D, Toth C and Barty C P J 1999 *Phys. Rev. A* **59** R4129.
198. Rocca J J and Da Silva L B (ed) 1997 *Soft X-Ray Lasers and Applications (Proc. SPIE 3156)* vol II (Bellingham, WA: SPIE).
199. Svanberg S and Wahlstrom C G (ed) 1996 *X-Ray Lasers* (Bristol: Institute of Physics Publishing).
200. Rocca J J and Hagelstein P L (ed) 1995 *Soft X-Ray Lasers and Applications (Proc. SPIE 2520)* (Bellingham, WA: SPIE).
201. Eder D C and Matthews D L (ed) 1994 *X-Ray Lasers* (New York: AIP).
202. Suckewer S (ed) 1993 *Ultrashort Wavelength Lasers (Proc. SPIE 2012)* vol II (Bellingham, WA: SPIE).
203. Fill E E (ed) 1992 *X-Ray Lasers* (Bristol: Institute of Physics Publishing).
204. Tomassini R, Lowenthal F and Balmer J E 1999 *Phys. Rev. A* **59** 1577.

FURTHER READING

Attwood D T 1999 *Soft X-ray and Extreme Ultraviolet Radiation* (New York: Cambridge University Press); X-ray lasers 2000 *J. Physique IV.*

50

Terahertz Lasers

Taiichi Otsuji

CONTENTS

50.1 Introduction 671
50.2 Fundamental Physics and Constraints 672
50.3 THz Quantum Cascade Lasers 675
50.4 Graphene-based THz Lasers 677
50.5 Conclusions 681
References 681

50.1 Introduction

Exploitation of the terahertz (THz) electromagnetic resources is the fundamental need to envision real-world future smart society based on innovative information and communication technology (ICT) [1]. However, the THz region is yet to be well explored due to substantial physical limitations for both electron devices such as transistors and photonic devices such as lasers [1] (Figure 50.1). Then therefore, the development of compact, integrated, room-temperature operating novel solid-state THz laser devices is the critical demand for the brighter future society [2]. Among broad aspects and varieties of laser physics and device technology, THz frequency range constraints their applicability due to its low photon energy (on the order of meV to 100 meV) comparable to or rather weaker than the thermal energy at room temperature (~26 meV). Photon emission via interband radiative direct transitions of electrons in general semiconductor materials having bandgap energies above 100 meV does not meet the requirement for the THz lasers. Therefore, the THz lasers utilize the transitions of electrons in various fine structures of the energy bands such as absorption lines of gas molecules in gas lasers like He-Ne [3], CO_2 [4], and HCN [5], subbands where the degenerated states are split by spatial confinements in quantum wells in quantum cascade lasers (QCLs) [6,7], valence bands for heavy/light holes in p-Ge lasers [8–10], and Landau levels split by the application of magnetic fields in Landau lasers [11]. Another limiting factor is a so-called "phonon decoherency." The coherency of THz photons is easily broken in solid-state materials by the phonon scattering caused by thermally excited lattice vibrations (acoustic phonons) and/or electromagnetically excited lattice vibrations (optical phonons). To cope with this critical limit in the solid-state THz lasers, decrease of the operating temperature is a straightforward way. In fact, most of the currently existing solid-state THz lasers can only operate at cryogenic temperatures whose thermal energies are below the THz photon energies [1]. The THz p-Ge lasers are so-called inter-valence-band (IVB) transition-type THz lasers and exploit the direct transition of holes between the light hole (LH) valence band and the heavy hole (HH) valence band under high electric and magnetic fields to emit rather intense THz photons under cryogenic temperatures below ~20 K [8–10] (Figure 50.2). The THz QCLs are the most successful, industrialized current-injection-type laser devices that could be integrated into a single microchip and serve rather high wall-plug efficiency although still suffering

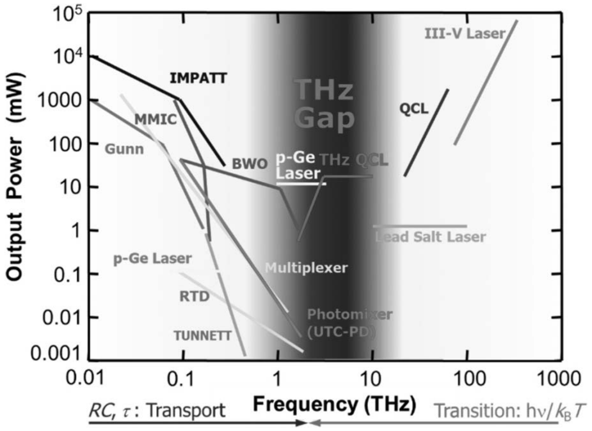

FIGURE 50.1 Maximum output power of various solid-state oscillators and light sources versus frequency. QCL, Quantum cascade laser; BWO, Backward-wave oscillator; RTD, Resonant tunnelling diode; UTC-PD, Uni-traveling carrier photo-diode; TUNNETT, TUNNElling transit-time diode; IMPATT, IMPact ionization avalanche transit-time diode; Gunn, Gunn diode; MMIC, Microwave monolithic integrated circuit. The left wing is the area of electron devices whose frequency response is substantially limited by the electron transit time τ and parasitic resistance-capacitance (RC) time constant, resulting in inverse triple power of frequency dependence of the output power. The right wing is the area of photonic laser devices whose frequency response is substantially limited by the phonon decoherency originated from the thermal energy k_BT (k_B is the Boltzmann constant and T is the absolute temperature). There still exists a technological gap in the THz range.

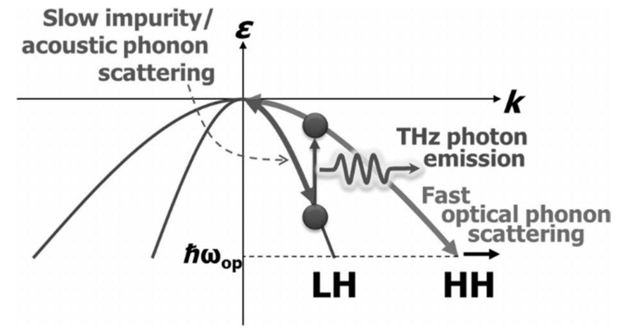

FIGURE 50.2 Band diagram of a p-Ge laser operation. Under an orthogonal pertinent electric and magnetic field applications, the heavy hole (HH) cannot be responsible for cyclotron motion but streaming recycle motion by emitting optical phonons which is a fast relaxation, whereas the light hole (LH) can be responsible for cyclotron motion so that it relaxes slowly via acoustic phonon and/or impurity scattering. Eventually the population of LH at an excited level (below the optical phonon energy) becomes higher than that of HH at the identical momentum (phase space), resulting in population inversion and spontaneous THz emission.

from the phonon decoherency [7,12,13]. The Landau lasers need external magnetic fields to split the degenerated Landau levels [11]. It is performed in THz p-Ge lasers as one lasing mode [9]. Due to their cryogenic temperature operation and the needs of external magnetic field, the physical size and volume of the THz Landau lasers as well as p-Ge lasers are large so that they could not have been well industrialized so far. New trends with graphene-based THz lasers have been recently emerging [11,14–17], and some experimental demonstrations have been reported in the last 3 years [18,19].

Historically, the CO_2 gas laser with optical pumping is the most popular among the THz lasers and is operable at room temperature, thanks to the gas nature free from the phonon decoherency so that it is well matured among broad industrial and military applications [20] (Figure 50.3). The CO_2 laser needs large physical volumes and consumes high power due to intense optical pumping so that it never be integrated into a tiny chip. On the other hand, free-electron lasers are a different type of THz lasers that does not utilize the interband direct transitions of photon emission but utilize the bunching of accelerated free electrons via periodically modulated resonant electromagnetic fields [21], providing high-energy coherent THz radiation in a gigantic synchrotron radiation system [22–24]. Semiconductor Raman lasers are the other optical-pumping-type THz solid-state lasers that do not utilize the interband transitions of photon emission but the stimulated Raman scattering in non-linear-optic semiconductor crystals [25]. Their quantum efficiencies are quite low (~10^{-5}), suffering from high pumping threshold intensity and preventing room temperature operation.

In the following subsections, first, fundamental physics and substantial and/or technological constraints are described. Then, the THz QCL is described as the most industrialized current-injection-type compact solid-state THz laser devices in detail. Finally an emerging THz laser device technology based on graphene is described.

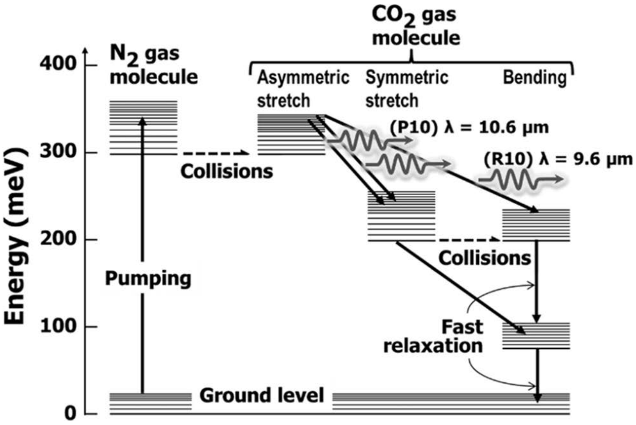

FIGURE 50.3 The band diagram showing a typical THz CO_2 gas laser operation. Optical pumping generates photoelectrons at the excited levels of fine band structure of N_2 gas molecules. The photoelectrons are injected to the excited levels of the fine band structure of the asymmetric stretch mode in CO_2 gas molecules via inter collisions. The electrons make direct radiative transitions to the lower state of the symmetric stretch mode and/or that of the bending mode, emitting spontaneous THz photon emission having wavelengths of 10.6 and 9.6 μm.

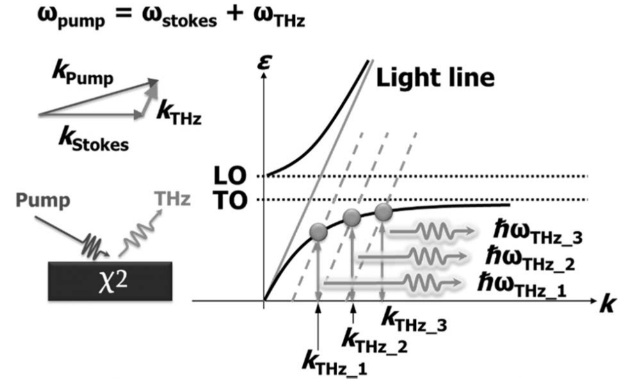

FIGURE 50.4 Semiconductor THz Raman laser [25]. The second-order susceptibility X^2 of a non-linear-optic semiconductor promotes the stimulated Raman scattering under optical pumping. The pumping photons interact with TO phonons, breaking up the light line of pumping photons to the upper branch and the lower branch. Then the pumping photons having an angular frequency ω_{pump} and a wave vector k_{pump} are split into the Stokes photons having ω_{stokes} and k_{stokes} and THz photons having ω_{THz} and k_{THz} in conditions of energy conservation and phase matching (momentum conservation).

50.2 Fundamental Physics and Constraints

Laser is the abbreviation of "Light Amplification by Stimulated Emission of Radiation." The substantial feature of the laser that is never obtained from any natural light sources is the coherency that is attributed to the action of the "stimulated" photon emissions. A pertinent material that gives an optical gain, which is called a gain medium, is prepared first. Its operation mechanism consists of (i) generation of incoherent spontaneous photon emission as a seed of the laser light and (ii) transformation of the incoherent spontaneous emission to the

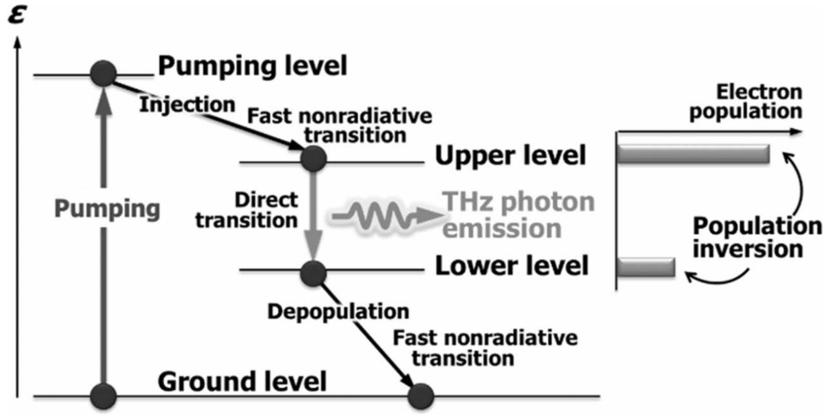

FIGURE 50.5 A four-level THz laser system. First electrons at the lowest level called "ground level" are optically or electrically pumped to the highest excited level called "pumping level." The electrons momentarily make fast non-radiative transitions to the second highest level called "upper level." The life time of electrons at the upper level is relatively long, and the electrons recombine with holes in the next lower level called "lower level" via direct radiative transitions to emit THz photons whose energy coincides with the band-gap between these two levels in a certain rate. The electrons transited to the lower level are momentarily evacuated (depopulated) to the ground level via fast non-radiative transitions. Due to the relatively long life time of electrons at the upper level and the fast transition from the lower level to the ground level the population of electrons between the upper and lower levels can be "inverted" as long as electrons are sufficiently pumped. This is the situation of "carrier population inversion" that is the fundamental condition to enable the lasing operation.

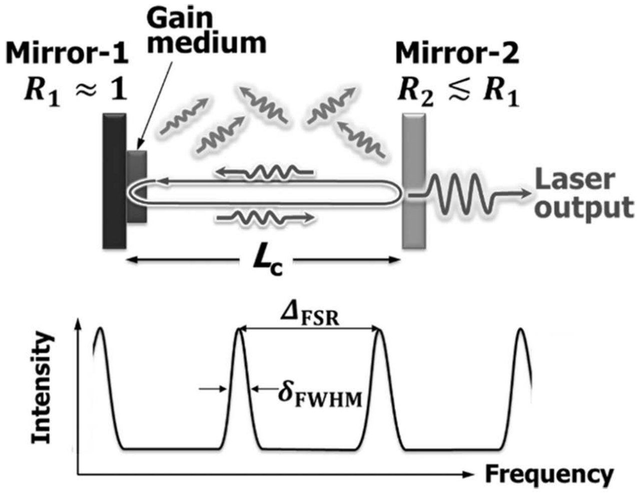

FIGURE 50.6 Fabry–Perot type laser cavity. Cross-sectional schematic (upper) and its frequency response (lower). THz photons are spontaneously generated from the gain medium inside the cavity. The photons emitted along the cavity direction can travel in a round-trip way between Mirror-1 and Mirror-2 with stimulating photon emission in every round-trip cycle, resulting in amplification of the photons by stimulated emission of radiation, that is the laser action. The lasing coherent photons are output from Mirror-2 having a bit low reflectance R_2. The spontaneously generated photons that are not directed along the cavity are spread outside the cavity to stray, resulting in ASE noise factor.

coherent stimulated emission. The process is further broken down into the following four steps. First, carriers are optically or electrically excited to make transition from an equilibrated low energy level to an upper energy level. This is called optical or electrical pumping. Second, thanks to the pumping the population of carriers between the adjacent two energy levels that allow the direct transition of electrons becomes "inverted." That is, the population of carriers at the upper energy level becomes larger than that of the lower energy level. In case of optical pumping, a four-level energy band system is generally utilized to obtain carrier population inversion efficiently. In the four-level system, electrons are first launched from the lowest level (called the ground level) to the highest level (called pumping level) by the pumping (Figure 50.5). The electrons excited to the pumping level are transferred soon to the second highest level (called the upper level) via fast indirect transitions where electrons are stacked for a while to increase their population. The electrons at the upper level recombine with holes at the secondly lower level (called the lower level) via direct transition. The electrons transit to the lower level is then evacuated to the ground level via fast indirect transition. In such consecutive processes, the population inversion condition between the upper and lower levels is maintained as long as the pumping is continued at a sufficient level. Third, the carrier population inversion gives rise to spontaneous photon emission whose energy coincides with the energy gap between the upper and lower levels. It is noted that this spontaneous emission is an incoherent emission. Fourth, by implementing a pertinent laser cavity structure, the spontaneously emitted photons travel along the cavity reflecting at the mirrors at the ends of the cavity and returning back to the gain medium after a fixed round-trip delay time (Figure 50.6). This photon is seldom absorbed to the gain medium if the carrier population inversion condition is preserved, but, instead, stimulates the recombination of an electron at the upper level and a hole at the lower level to create a new photon to emit. Thus, every returning back the spontaneously generated photon may stimulate the emission of a new photon at the deterministic fixed time period corresponding to the round-trip delay time of the cavity. This cavity-oriented action of stimulated emission gives coherency to the photon emission and substantially suppresses any parts of the incoherent photon emissions that have no correlation with the cavity resonant modes. As a result, coherent, stimulated photon emission occupies the most part of the entire photon emission. The residual incoherent spontaneous photon emission becomes a noise factor with respect to the main signal part of the coherent stimulated emission, which is called as an amplified spontaneous emission (ASE) noise. The signal-to-noise ratio of the stimulated coherent emission to the spontaneous incoherent emission is determined by the quality factor or the finesse of the laser cavity as well as by the level of carrier population inversion. The ASE noise causes fluctuations of the intensity and frequency of laser signal, giving rise to the fluctuation of laser output power. Thus the ratio of the fluctuation of optical power to the average optical power, which is called as relative intensity noise (RIN), is frequently utilized to characterize the noise performance of the laser.

Due to the broadening of the energy bands including the upper and lower levels originated from the quantum-mechanical uncertainties, the spontaneously emitted photons have a specific spectral width corresponding to the broadening. If no laser cavity is incorporated, the incoherent ASE is only obtained and its spectral width is rather broad. The laser cavity is a fundamental element to obtain the stimulated photon emission enabling the laser operation with spectral narrowing. When the facets of the solid-state laser mesa structure generally having mm's long are cleaved, they work as high reflectance mirrors. Thus, the main body of the laser structure itself works as a Fabry–Perot cavity. Due to its long cavity size with respect to the THz photon wavelength, multiple higher harmonic frequency resonant modes of the cavity may fall in the optical gain spectral range, resulting in multi-mode lasing. The lasing spectral width becomes narrower dramatically than that for the ASE according to the quality factor, Q, or the finesse, F, of the cavity that is determined by the reflectance of the mirrors, R_1 and R_2,

$$F = \frac{\Delta_{\text{FSR}}}{\delta_{\text{FWHM}}} = \frac{\pi\sqrt[4]{R_1R_2}}{1-\sqrt{R_1R_2}} \tag{50.1}$$

where Δ_{FSR} is the free spectral range and δ_{FWHM} is the spectral linewidth of each resonant mode in full-width value at a half maximal intensity [26]. Δ_{FSR} is the frequency difference between adjacent resonant modes, correspondingly the fundamental resonant mode frequency f_0,

$$\Delta_{\text{FSR}} = f_0 = c\big/2\sqrt{\varepsilon_{\text{r}}L_{\text{c}}} \tag{50.2}$$

where ε_{r} is the dielectric constant of the internal cavity, and L_{c} is the cavity length. For simplicity, assuming $L_{\text{c}} = 1\,\text{mm}$, $\varepsilon_{\text{r}} = 10$, and the reflectance of the two mirrors of 0.7 and 0.85, respectively, $\Delta_{\text{FSR}} = f_0 \sim 47\,\text{GHz}$ and $F \sim 10.6$. Then the spectral line width $\delta_{\text{FWHM}} \approx 4.5$ GHz. When the optical gain spectral width is 200 GHz at a central peak frequency of 3.000 THz (3000 GHz), this cavity gives multi-mode lasing at ~ 2.906, ~2.953, 3.0, 3.047, and 3.094 THz. To obtain a single-mode lasing, the THz laser needs a micro-size cavity whose feature size (electrical length) coincides with the THz photon wavelength of the order of 10s–100s of micrometres. As is implemented in general laser diodes (LDs) in visible or infrared frequencies, the distributed feedback (DFB) cavity is a practical structure to make the single-mode lasing in THz QCLs [12] (Figure 50.7).

The THz lasers are characterized by various aspects of performances like the quantum efficiency (QE), the wall-plug efficiency, the maximal output radiation power, the threshold injection current, the threshold operating temperature, the spectral purity (spectral linewidth), the RIN, as well as the physical volume. The QE of electrically (current-injection) pumped lasers is defined as the ratio of the emission rate of photons to the pumping rate (injection rate) of electrons, whereas the QE of optically pumped lasers is defined as the ratio of the emission rate of photons to the pumping rate of photons. 100% or unity of the QE is the idealistic lossless case in a single event of the laser action. If an electron can be recycled to contribute to make the cascade of photon emissions in case of electrically pumped lasers like QCLs, the total QE is multiplied by the number of the cascade so that it could well exceed "1." The wall-plug efficiency is the energy conversion efficiency of electrically pumped lasers that is defined as the ratio of the laser output power to the total consumed electric power.

Higher QE as well as higher wall-plug efficiency needs higher optical gain given by higher pumping efficiency and higher level of carrier population inversion. Generally, in case of electrical pumping, the electrons are injected to the upper level (states) for the radiative direct transition of photon emission from much higher initial levels (states) that are not responsible for the direct transitions. The transition from the initial level(s) to the upper level is performed via non-equilibrium electron energy relaxation dynamics associated with acoustic/optical phonon scattering as well as impurity scattering. The probability density of transition between the two states from the initial state to the final state is given by the Fermi's golden rule in good accuracy [26]. If there are other levels (states) near the upper level, the injected electrons may reach these levels (instead of the upper level), which reduce the injection efficiency. Such a stray leakage of undesirable electron transitions to the other

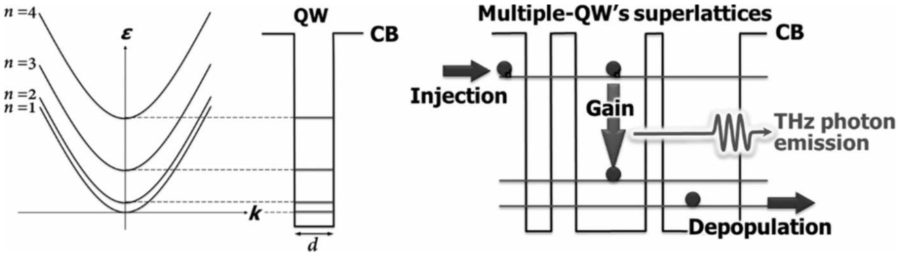

FIGURE 50.7 A subbands diagram for a QW having a thickness d (left) and a band diagram for a multiple-QW's superlattices (right) demonstrating an operation of intersubband THz photon emission.

surrounding levels (including the lower level) becomes significant in the THz frequency range due to overlapping the electron wave functions among these levels and also due to its weak photon energy comparable to or smaller than the optical phonon energy of the substance as well as the thermal energy. Also, there is non-zero probability of non-radiative transition via phonon and/or plasmon scattering that does not contribute to photon emission. The ratio of the number of electrons successfully reaches the upper level and contributes to the direct transition to the lower level to the number of total injected electrons is defined as the injection efficiency.

Electrons at the upper level recombine with holes at the lower level via direct radiative transitions to emit photons. This process is the normal route to get spontaneous THz photon emission. To constantly keep the photon emission via the direct transition, sufficiently large number of electrons must be injected at the upper level, and at the same time, sufficiently large number of unoccupied vacant states must be preserved at the lower level. This means the electrons recombined with holes at the lower level must be evacuated (depopulated) to the other energy level(s) as fast as possible. Otherwise, the recombined electrons are piled up in the lower level so that the population of electrons at the lower level increases, preventing population inversion. Thus, depopulation of electrons at the lower level is another key to maintain a high level of population inversion.

50.3 THz Quantum Cascade Lasers

As is described in former Fundamental Physics and Constraints section, to obtain the THz spontaneous emission in a solid-state semiconductor material, transitions of electrons in various fine structures of the energy bands. The THz QCL exploits the intersubband direct transition of electrons in QWs where the degenerated states are split into the subbands by its spatial confinement effect (Figure 50.8). For a simplest case with an infinitely deep potential well and a parabolic band dispersion, the subband energies (measured from the bottom of the conduction band) is given by

$$E_n = \frac{\pi^2\hbar^2}{2md^2}n^2$$

where d is the thickness of the well and n is the quantum number of the subband level. The THz QCL consists of a cascading stack of intersubband THz laser units based on multiple QW superlattices and incorporates a pertinent laser cavity structure. The intersubband THz laser unit consists of an electron injector section, a spontaneous photon emission section, and an electron depopulation (swept-out) section. The electron depopulation section works as the electron injector section of the successive unit. Such a cascading stack of the laser units emit incoherent THz photons via intersubband transitions of electrons in a cascading manner. Thanks to the laser cavity installed in the QCL, it eventually gives stimulated emission of coherent photon radiation.

The idea for the QCL was first discovered by Kazarinov and Suris in 1971 [27]. When a dc electric field is applied along an n-type doped multiple QW superlattices (MQW-SLs) structure so as to align the ground subband level in the $(n-1)$-th MQW-SL to the second subband level in the n-th MQW-SL, an electron at the ground subband in the $(n-1)$-th MQW-SL is driven to quantum-mechanically tunnel to the second subband level in the n-th MQW-SL, allowing direct

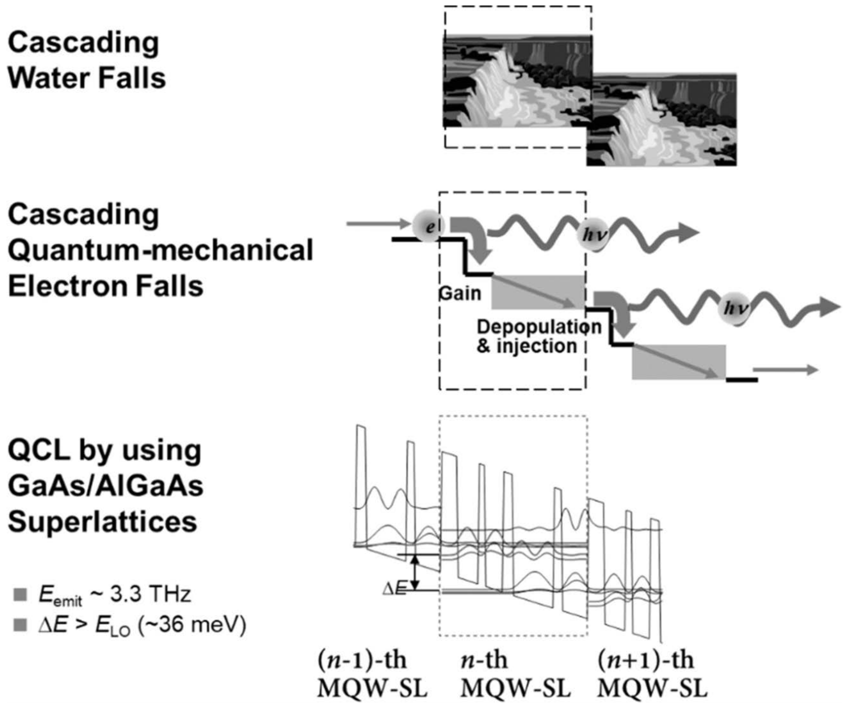

FIGURE 50.8 Concept and principle of operation for the QCL. As cascading waterfalls (upper) cascading quantum-mechanical electron falls (centre) can be configured by using multiple-QW superlattices (MQW-SLs) under application of a dc electric field (lower).

radiative transition to the ground subband level in the n-th MQW-SL to emit a THz photon whose energy coincides with the intersubband gap energy (Figure 50.8). Then the electron at the ground subband in the n-th MQW-SL is driven to tunnel to the second subband level in the $(n+1)$-th MQW-SL, allowing direct radiative transition to the ground subband level to emit another THz photon again. Such a series of (i) injection of electrons (from the ground subband in the $(n-1)$-th MQW-SL to the second subband in the n-th MQW-SL), (ii) intersubband transition to emit THz photons, and (iii) depopulation of the electrons at the ground subband in the n-th MQW-SL to the $(n+1)$-th MQW-SL, is taken place N times in a cascading manner over the entire MQW-SLs' structure. If the structure includes N cascade of the unit, a single electron can contribute to emit N photons, resulting in dramatically high QE. The QCL operation was first experimentally demonstrated in the mid-IR range using a GaInAs/AlInAs heterostructure material systems by Faist et al. in 1994 [6].

After 8 years passed since the first QCL worked in the mid-IR range, Kohler, Tredicucci, and their colleagues succeeded in the first THz QCL operation using a GaAs/AlGaAs heterostructure material system in 2002 [7]. As is described in former subsections, the weak THz photon energy of the order of 10's meV comparable to the environmental thermal energy, lattice phonon energy, and uncertainty (broadening) of electron wave function deteriorate the carrier injection efficiency as well as the population inversion due to the phonon decoherency as well as the thermal back filling. Thus, the THz QCLs generally operate at temperatures lower than the phonon-limiting temperatures. The difficulties in carrier injection to the upper level and in carrier depopulation from the lower level have been resolved by introducing novel quantum-mechanical physics with smart superlattices structures. The first operation of THz QCL was performed by introducing a so-called chirped superlattice structure into the carrier depopulation section in which the width of the QWs and barrier layers are designed to be chirped so that the minibands become flat bands under application of an operating fixed dc electric field [7] (Figure 50.9a). In such a situation, the electrons are injected to the ground level of the lowest miniband via longitudinal-optical- (LO-) phonon scattering, making radiative direct transition of THz photon emission to the topmost level of the miniband in the next carrier depopulation section. Then the electrons are depopulated to the ground level of the lower miniband via LO-phonon scattering in a recursive manner. This type of the THz QCLs utilizes LO-phonon scattering to organize the carrier depopulation from the topmost level of the upper minibands to the ground level of the lowest miniband thanks to its ultrafast relaxation rate. However, it is hard to exclusively interact the LO phonons with the electrons in the upper levels of minibands. Thus the electrons in the ground level of the lowest minibands (working as the upper level of direct radiative transition of electrons) are also scattered by the LO phonons, deteriorating the injection efficiency and the level of population inversion. The bound-to-continuum type THz QCL has been then developed in which an independent upper level is prepared just after the chirped superlattices section so as to improve the injection efficiency [28] (Figure 50.9b).

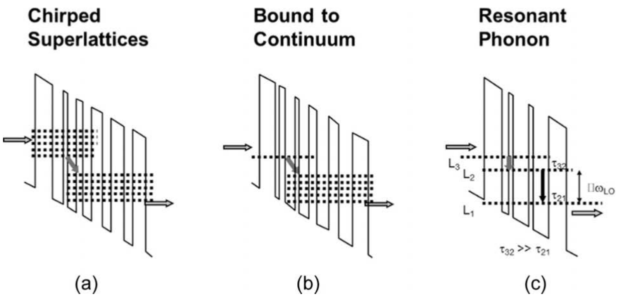

FIGURE 50.9 Electron injection and depopulation scheme in three types of the QCLs. (a) Chirped superlattices structure. (b) Bound-to-continuum structure. (c) Resonant phonon depopulation structure.

The resonant phonon depopulation (RPD) type THz QCL has been developed to cope with aforementioned LO-phonon issue [29] (Figure 50.9c). The RPD THz QCL introduces a new carrier depopulation mechanism in which a LO-phonon-assisted resonant tunnelling QW section is introduced just after the lower level of the THz photon emission section instead of the chirped superlattice minibands. In the LO-phonon-assisted resonant tunnelling QW, the level of the final state to which electrons transit is designed to be lower by the LO-phonon energy than that of the initial state (the lower level of the prior THz photon emission section). Therefore, the electrons at the initial state are assisted by the LO-phonon scattering to make the quantum-mechanical resonant tunnelling to the final state. In this regard, the electrons approaching the initial state just after radiative transition of THz photon emission can be exclusively depopulated via LO-phonon-assisted resonant tunnelling, resulting in improved higher levels of injection efficiency and population inversion than those for the other types of the THz QCLs. Thanks to the RPD mechanisms, this type of the QCLs demonstrate record-operating threshold temperatures in the wide THz frequency range with rather high output power approaching the level of 100's mW.

The early stage of the THz QCLs has incorporated Fabry–Perot cavity configured by the QCL mesa with the cleavage facets, resulting in multi-mode lasing (due to its mm-order long cavity length) with rather high output power [7,30]. To obtain a single-mode lasing, DFB cavity has been implemented in various structures [29,31–33]. The other critical limiting factor that strongly attenuates the emitted THz photons in THz QCLs is Drude free-carrier absorptions along the waveguide antenna structure. The Drude optical conductivity $\sigma(\omega)$ of a medium having a density of carrier n is given by

$$\sigma(\omega) = \frac{e^2 n\tau}{(1 - i\omega\tau)} = \frac{e^2 n\tau}{1+\omega^2\tau^2} + i\frac{e^2 n\omega\tau}{1+\omega^2\tau^2}\ , \tag{50.3}$$

where τ is the electron momentum relaxation time. The real part of $\sigma(\omega)$:

$$\mathrm{Re}\big[\sigma(\omega)\big] = \frac{e^2 n\tau}{1+\omega^2\tau^2} \tag{50.4}$$

gives the loss factor of free-carrier absorption. In general semiconductors, the τ value stays on the order of 10s of femtoseconds ~ sub-picoseconds at temperatures 100~300 K. Thus, in mid-IR or higher frequency range where $\omega\tau \gg 1$, the free-carrier absorption can be well suppressed. On the other hand, THz frequency range holds $\omega\tau \leq 1$ so that the free-carrier absorption becomes significant. How to suppress the free-carrier absorption in waveguiding the THz photon to the free-space radiation becomes a critical issue in the THz QCLs.

The standard QCL device structure consists of the active laser mesa on a base semiconductor substrate and the top metal electrode layer. The metal layer works as a high reflectance mirror to the THz radiation whereas the base substrate is made with a semiconductor whose refractive index should be lower than the mesa area in order to confine the THz photon field into the active mesa region of the gain medium, then minimizing the free-carrier absorption loss. However, in reality, the fraction of the refractive indices between the mesa area and the substrate could not be set largely due to material constraint, resulting in poor THz photon field confinement and suffering from the free-carrier absorption loss. To reduce the free-carrier absorption losses, two types of the waveguiding structures, the semi-insulating surface plasmon (SISP) waveguide [7,29] and the metal-metal (MM) waveguide [34,35], have been proposed. In the SISP waveguide structure, a heavily doped layer is introduced to the bottom of the mesa that can totally cut off the THz photon field, and the THz photons are attracted to the surface plasmon at the vicinity of the heavily doped layer. The base substrate gets a certain level of penetration of the evanescent modes of THz photons. To minimize the free-carrier absorption in the substrate, a semi-insulating substrate is utilized [29]. On the other hand, the MM waveguide is configured by transferring the mesa structure onto a metal-coated substrate. Then both the top and the bottom surface are covered by metal layers. Thanks to the highly reflectance mirror effect of the metal layers, the THz photon field is completely confined into the mesa area, resulting in dramatic reduction of the waveguide loss [35].

The lasing frequency in the THz QCLs is substantially limited by the LO-phonon Reststrahlen band of the material. The GaAs/AlGaAs material systems are the most popular for use in THz QCLs. Their lasing operation is inhibited at the frequencies between 5 and 12 THz due to the LO-phonon scattering of GaAs-based materials. GaN-based material systems are considered to be promising to cope with this substantial limit because the forbidden Reststrahlen band of the GaN-based materials lies between 17 and 22 THz so that they could extend the lasing operation frequencies beyond 5 THz till ~17 THz. The higher LO-phonon energies also give a strong benefit to suppress the thermal back-filling as well as phonon-related decoherency. This may lead to higher operating temperature as well as higher output power. GaN-based THz QCLs have suffered from poor crystallographic quality in their heteroepitaxial growth. Very recently, experimental demonstration of the lasing operation at 5~6 THz at ~5 K of a GaN/AlGaN THz QCL has been reported [36].

To date, the THz QCLs have covered the spectral range from 1 to 6 THz. Maximum operating temperature has been aggregated close to 200 K [37]. With regard to output power, a single state-of-the-art THz QCL could provide 1 W peak power in pulsed mode [38] and over 130 mW in CW mode [39] at 10 K heatsink temperature.

Optical parametric oscillation (OPO) [40] and optical rectification (OR) [41] using non-linear susceptibility in non-linear optic materials are other optical-pumping-type principles of THz coherent emission. Different frequency generation (DFG) is one type of OR that serves CW THz radiation [42,43]. When a mid-IR QCL is pumped with dual mid-IR laser lights whose frequency differs by the order of THz, the different frequency component of the incident dual laser beams is generated via OR due to non-linear optic effects of the gain media in the QCL, giving rise to another type of THz QCLs [12,44–47]. It is noted that this DFG THz QCL is not a simple current-injection type but a mixture of optically pumped and current-injection-pumped THz QCL, providing ~2 mW peak power in pulsed operation modes [47] and μW level average power in CW (continuous wave) operation modes [48]. This DFG THz QCL can only serve room-temperature operation and wide frequency tunability among semiconductor laser sources.

50.4 Graphene-based THz Lasers

Graphene, a monolayer of sp^2-bonded carbon atoms in a honeycomb crystal lattice, has attracted considerable attention due to its unique carrier transport and optical properties since it has been discovered [49]. The conduction band and the valence band of graphene take symmetrical conical shape and contact each other at the K and K′ point (Figure 50.10). Electrons and holes in graphene hold a linear dispersion relation with zero bandgap, resulting in extraordinary features like massless relativistic Dirac fermions with back-scattering-free ultrafast transport [50] as well as the negative-dynamic conductivity in the THz spectral range under optical or electrical pumping [13,15,51].

When the intrinsic graphene is optically pumped with a photon energy $\hbar\Omega$, where $\hbar$ is the reduced Planck constant and Ω is the angular frequency of the photon, interband transitions lead to the generation of "hot" photoelectron-photohole pairs in the distance equal to the photon energy at above and below the Dirac point for the electrons and holes, respectively (Figure 50.11). At room temperature, these photo-excited "hot" electrons and "hot" holes are quasi-equilibrated with the low-energy conduction electrons and valence holes around

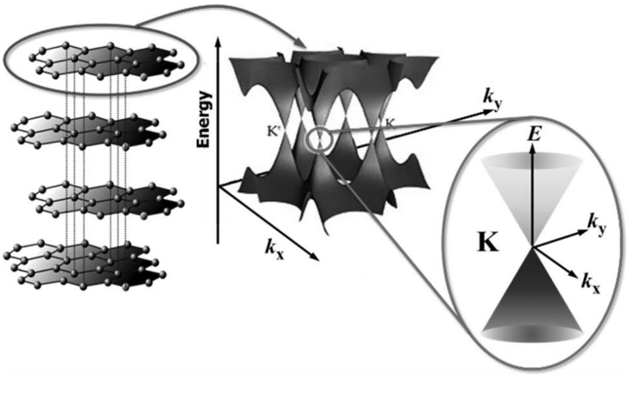

FIGURE 50.10 Graphene lattice and band structures. Graphene is a monolayer sp^2-bonded carbonaceous honeycomb lattice crystal. The energy band at the Brillouin zone edge, K and K′ points, takes conical and symmetric linear dispersion for conduction and valence bands touching each other.

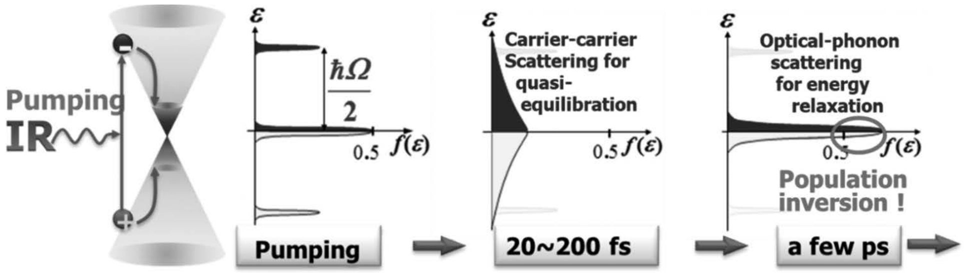

FIGURE 50.11 Carrier energy relaxation dynamics of optically pumped intrinsic graphene. When graphene is optically pumped with a photon energy $\hbar\Omega$, photoelectron-photohole pairs are generated at the level $\hbar\Omega/2$ above and below the Dirac point, and then followed by ultrafast carrier–carrier scattering and then optical phonon scattering.

the Dirac point at the ultrafast timescale of tens of femtoseconds due to the carrier–carrier scattering resulting in the quasi-Fermi distribution [15,52] (Figure 50.11). As a result, the quasi-Fermi level of electrons and holes split and shift *below* and *above* the Dirac point, respectively. At the same time, the high-energy electrons and holes lose their energy by emitting optical phonons. Thus the quasi-Fermi distribution, which is originally widely spread in the energy space, gets concentrated around the Dirac point. This results in a rapid recovery of the quasi-Fermi level on a picosecond time scale [52]. After the energy relaxation via the optical phonon emissions, the non-equilibrium electrons and holes may lose their energies via the "interband" optical phonon scattering, impurity/disordered scattering, as well as the acoustic phonon scattering, or they recombine. Compared to the aforementioned "intraband" optical phonon scattering, these scattering and recombination processes have much longer relaxation times. Therefore, the non-equilibrium carriers are piled up around the Dirac point if the pumping intensity is sufficiently high. This is the carrier population inversion, in which the quasi-Fermi levels for electrons and holes shift *above* and *below* the Dirac point, respectively (Figure 50.11). The Auger-type three-particle scattering processes are theoretically forbidden in the ideal graphene [53], but they might dominate in the disordered low-quality graphene and/or under an intense pumping leading to significant many-body effects [54]. Thus, the Auger-type scattering is recognized as a killer of the carrier population inversion [55]. However, the carrier population inversion in the THz frequency range has been experimentally observed in prolongated long time more than 1 ps after a rather intense pumping with a high photon energy (~1.5 eV) picosecond laser pulses even at room temperature in high-quality epitaxial graphene [56]. This result encouraged us to explore the creation of the graphene THz lasers/amplifiers.

Optical pumping suffers from a significant heating of the electron-hole plasma suppressing carrier population inversion. However, in case of the optical pumping with sufficiently low photon energies, the electron-hole plasma can be cooled down. Recently a rigorous theoretical modelling and calculation of the Auger scattering rate, including many-body effects of Coulomb interactions, reveal that the Auger scattering is substantially suppressed when carrier temperature is maintained at or below room temperature [57]. In this regard, current injection pumping is the idealistic way to suppress the carrier heating decreasing the pumping threshold because the pumping energy could be of the order of millielectron volts in a graphene p-i-n junctions structure [15,51]. A dual gate p-i-n structure using a dual-gate graphene-channel field-effect transistor (DG-GFET) has been proposed as a simplest current-injection THz graphene laser structure (Figure 50.12) [51]. The gate biasing ($\pm V_g$) controls the injection level, whereas the drain bias (V_{ds}) controls the level of population inversion. To minimize the undesired tunnelling current lowering the injection efficiency, the distance between the dual gate electrodes should be sufficiently long. The conductivity profiles calculated for the typical dimensions and applied bias conditions demonstrate the advantage of current-injection pumping compared to the optical pumping. The optical conductivity of graphene channel under the gates and drain biases is given by:

$$\sigma_\omega = \sigma_\omega^{\text{intra}} + \sigma_\omega^{\text{inter}}, \tag{50.5}$$

$$\sigma_\omega^{\text{intra}} \approx \frac{e^2 \varepsilon_F}{2\pi\hbar^2} \cdot \frac{\tau}{1+\omega^2\tau^2}, \tag{50.6}$$

$$\sigma_\omega^{\text{inter}} \approx \frac{e^2}{2\hbar} \cdot \exp\left(\frac{eV - 2e\sqrt{V_F V_g}}{2k_B T}\right) \cdot \sinh\left(\frac{\hbar\omega - eV_{ds}}{2k_B T}\right), \tag{50.7}$$

where $\sigma_\omega^{\text{intra}}$ and $\sigma_\omega^{\text{inter}}$ are the intraband and interband component of the conductivity, respectively; e is the elementary charge; ε_F is the Fermi energy reflecting the carrier doping level by applying V_g; τ is the carrier momentum relaxation time; k_B is the Boltzmann constant; and T is the temperature [51]. V_g determines the carrier injection level and the corresponding ε_F , whereas V_{ds} determines the level of the population inversion (the amount of shifting the quasi-Fermi levels of electrons and holes). When the carrier momentum relaxation time is rather long ($\tau = 2.0$ ps) and carrier injection level is pertinent at $V_g = 1.0$ V, an even weak V_{ds} produces a net gain (negative conductivity) in a wide THz frequency range (Figure 50.13a). The situation dramatically changes when the value of τ becomes short (down to 0.1 ps); in this case, the net gain almost disappears (Figure 50.13b). As a consequence, the high-quality graphene having a picosecond-order value of τ is mandatory to obtain a net gain in the THz range. It is noted that the maximal available negative conductivity is limited below $e^2/(4\hbar)$ corresponding to the interband absorption coefficient ($\alpha = \pi e^2/(c\hbar) \approx 2.3\%$) of monolayer graphene [50].

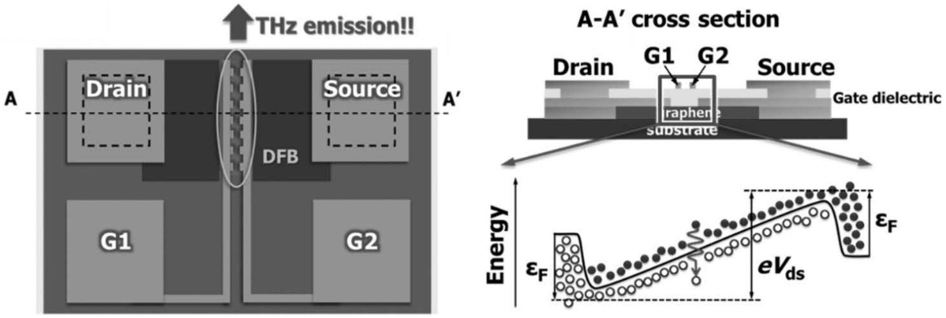

FIGURE 50.12 DG-GFET. Top view (left), cross-sectional view (right upper), and a band diagram under complementary dual gate bias and forward drain-source bias condition getting population inversion and resultant spontaneous THz emission (right lower). In this structure, a DFB laser cavity is incorporated in the toothbrush-shaped dual-gate electrodes in which the distance between the gates is periodically modulated to modulate the gain coefficient, producing resonant modes to the THz photons propagating along the DFB cavity (in plane DG finger direction). The DFB period gives the resonant mode frequencies, and the modulation depth and the number of periods give the quality factor of the cavity [19].

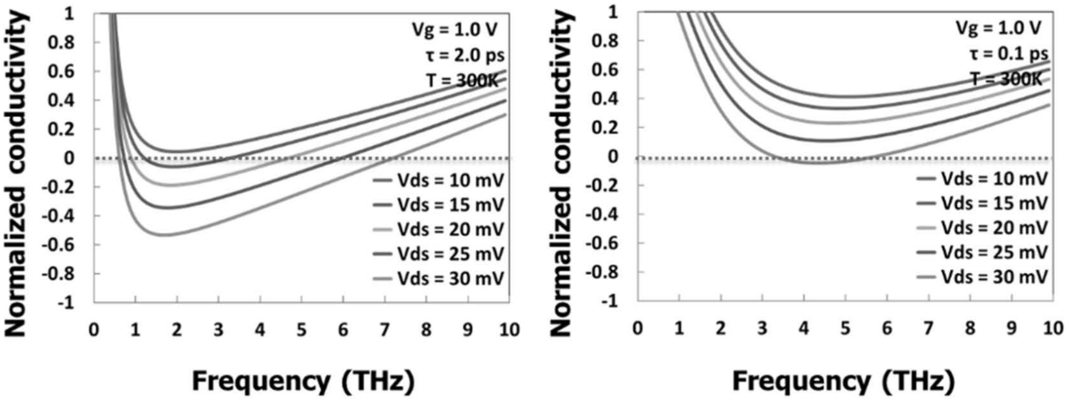

(a) (b)

FIGURE 50.13 Real part of the conductivity spectra of a complementary dual-gate-biased DG-GFET at 300 K for different drain-source bias voltages. The vertical axis is normalized to the fundamental conductivity (e^2/4h) corresponding to 2.3% absorbance of monolayer graphene. Vg (=–Vg1 = +Vg2) = 1.0 V. (a) $\tau = 2.0$ ps. (b) $\tau = 0.1$ ps.

Recently the DG-GFETs incorporating a DFB-type internal cavity have been reported demonstrating world-first observation of single-mode lasing from GFETs at 5.2 THz at 100 K [19] (Figure 50.14). The graphene used in the GFETs is non-Bernal-stacked a few layers of high-quality graphene synthesized by the thermal decomposition of a C-face 4H-SiC substrate. The GFET was fabricated using a standard photolithography and a gate stack with a SiN dielectric layer, providing an excellent intrinsic field-effect mobility exceeding 100 000 cm^2 V^{-1} s^{-1} at 300 K. A pair of toothbrush-shaped gate electrode was patterned to form a DFB cavity in which the active gain area and corresponding gain coefficient were spatially and periodically modulated. The THz single-mode lasing was observed at around 5.2 THz with a linewidth of 31 GHz under pertinent complementary DG biases ($\pm V_g$) and V_{ds} conditions serving the carrier population inversion in good agreement with numerical simulations. The emission power was weak as high as 0.1 μW. A different sample with the identical design on the same wafer exhibited an amplified spontaneous broadband emission ranging from 1 to 7.6 THz at 100 K with a maximal emission power of 80 μW. Such a variation stems from a poor THz photon field confinement and resultant weak gain overlapping. Numerical analysis well reproduces such a variation when a wide fraction of the carrier momentum relaxation time of graphene carrier under weak gain overlapping conditions is assumed [19]. Improvement on the gain overlapping by introducing a plasmonic waveguide for dense THz photon field confinement as well as on the cavity quality factor by increasing the number of the DFB periods, and the DFB modulation depth will lead to more intense lasing at higher temperatures approaching 300 K [19].

Introduction of graphene plasmon dynamics is a promising way to dramatically increase the THz net gain and QE of the GFET lasers due to the extremely slow-wave nature (by two orders slower than the speed of light) of the graphene plasmons [58,59]. Once THz photons couple with the graphene plasmons, photons may propagate along the population-inverted graphene as plasmon polaritons having the plasmon velocity so that the interaction between the THz photons and graphene carriers is dramatically enhanced in proportion to the ratio of the speed of photon to that of plasmon, well exceeding the aforementioned quantum-mechanical limit of 2.3% per layer of graphene [60]. A giant gain enhancement of up to 50 times as high as that without graphene plasmons has been experimentally observed in the THz range [61] (Figure 50.15).

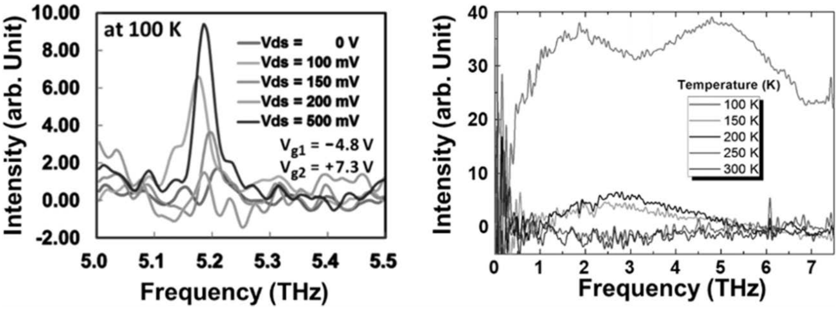

FIGURE 50.14 Measured emission spectra from fabricated DFB-DG-GFET samples [19]. (a) Single-mode emission at ~5.2 THz at 100 K with a ~0.1 μW and a minimal linewidth of ~31 GHz from one fabricated DFB-DG-GFET sample. (b) Amplified broadband spontaneous emission in a frequency range from 1 to 7.6 THz at 100 K from a different DFB-DG-GFET sample. The threshold operating temperature stays in between 100 and 150 K.

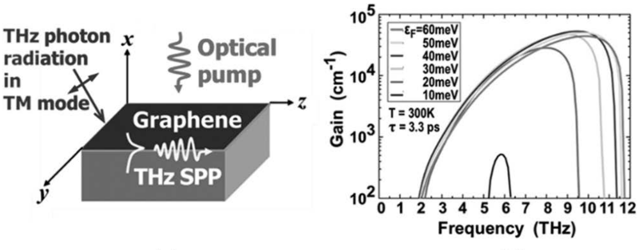

(a) (b)

FIGURE 50.15 The gain enhancement effect of surface plasmon polaritons (SPPs) on THz stimulated emission in optically pumped monolayer graphene [61]. (a) Experimental setup. Graphene is pumped by an IR laser light to set in carrier population inversion condition. Then a THz radiation in a TM mode is incident to the graphene from an oblique angle. The THz photons couple with graphene surface plasmons, getting into SPPs. The SPP travels along the gain medium of population-inverted graphene with extremely slow speed, leading to giant amplification by stimulated emission of THz SPPs. (b) Simulated frequency dependences of the SPP gain for monolayer population inverted graphene on a SiO_2/Si substrate at 300 K for different quasi-Fermi energies ε_F = 10, 20, 30, 40, 50, 60 meV. Carrier momentum relaxation time τ of τ = 3.3 ps in graphene is assumed. The results demonstrate giant THz gain (negative conductivity) of the order of $10^4 cm^{-1}$.

Graphene plasmon instability is another promising physics to promote giant amplification. When a dc current flows along the graphene channel in a GFET structure, plasma waves are excited as perturbative collective electron density waves and propagate onto the current flow. Since the electron density is spatially modulated (highest density at the ungated region at the source side, medium and chirped densities under the gate region, and lowest density at the ungated and depleted region at the drain side). This spatial charge density modulation spatially modulates the characteristic impedance. When the plasma wave travels forward to the drain side on the drift flow, its effective velocity is the sum of the plasma velocity s and the drift velocity v_d, $s+v_d$. It approaches the end of the gated region at the drain side, reflecting back to the source side in response to the high impedance boundary (due to the carrier depletion in ungated region at the drain side). The backward plasma wave propagates slowly with its effective velocity $s-v_d$, giving rise to compression of the wave with increase in the charge density δn, reflecting increase in the gate potential δV_g correlated via gate capacitance C_g as $\delta V_g = -e\delta n/C_g$ (Figure 50.16). Since the reflection at the source side end is almost equivalent to the one at the short-terminated end (due to highly dense electron concentration at the ungated region at the source side), preserving the energy and inverting the phase, every round-trip gives an increment of the gate potential δV_g, resulting in self-oscillation of plasmons at the resonant frequencies with the temporal period equal to the round-trip delay time or its N-th division (N is an integer). This is called Dyakonov–Shur instability, a Doppler shift-type instability [62]. Such a spatial charge density modulation also modulates the electron drift velocity spatially in order to preserve the current continuity along the channel. This velocity modulation causes bunching of electrons and plasma waves, giving rise to self-oscillation of plasmons. This is called Ryzhii–Satou–Shur instability, a transit-time-type instability [63]. There are several other types of plasmon instabilities like Cherenkov-type [64] and/or plasmonic-boom-type [65]. The self-oscillation of plasmon instability is a free-running oscillation whose quality factor is given by the quality factor (Q) of the graphene plasmons which is defined by the ratio of the electron momentum relaxation time to the round-trip delay time. In general, assuming a round-trip delay time of 0.2 ps (corresponding self-oscillation frequency of 5 THz) and a momentum relaxation time of 2 ps (practically obtainable in graphene electrons), the Q becomes 20, giving rise to rather broadband emission. Thus, the emission itself could not serve high coherency, but the emission of the free-running oscillation could work as a mean of amplification of stimulated emission of incoming coherent radiation like an output radiation of a THz DFB-DGGFET laser whose radiation frequency falls in the emission spectral range. This function is equivalent to those in semiconductor laser amplifier as well as optical fibre amplifier in which the spontaneous broadband emission is locked to the injected coherent radiation from a laser, outputting an amplified incoming laser signal. Recently, frequency tunable coherent THz light amplification up to 9% gain at 300 K by current-driven plasmon instabilities produced in GFETs has been experimentally demonstrated [66]. Integration of the graphene THz laser transistor and graphene plasmonic amplifier would be a possible way towards room-temperature operating current-injection pumped intense THz graphene laser device.

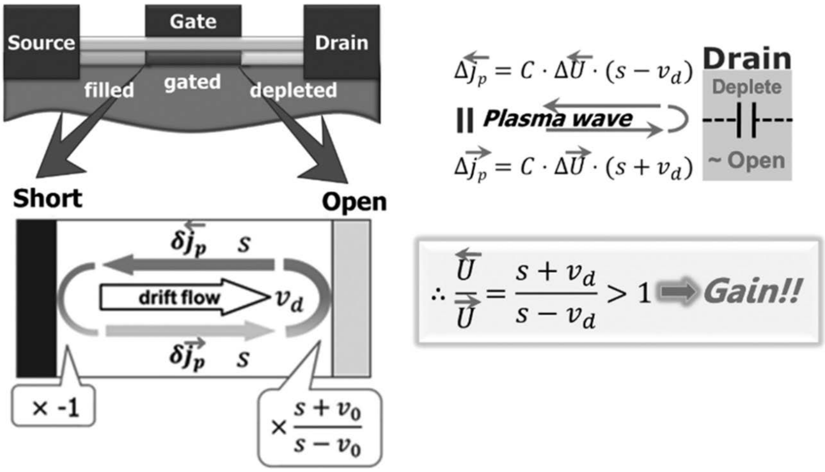
Gate
Source
Drain
filled
gated
depleted
Short
Open
$\delta\overleftarrow{j}_p$ s
drift flow v_d
$\delta\vec{j}_p$ s
× -1
$\times\frac{s+v_0}{s-v_0}$
$\Delta\overleftarrow{j}_p = C\cdot\Delta\overleftarrow{U}\cdot(s-v_d)$
Plasma wave
$\Delta\vec{j}_p = C\cdot\Delta\vec{U}\cdot(s+v_d)$
Drain
Deplete
~ Open
$\therefore \frac{\overleftarrow{U}}{\vec{U}} = \frac{s+v_d}{s-v_d} > 1$ Gain!!

FIGURE 50.16 Dyakonov–Shur Doppler-shift type plasmon instability in a 2D electron channel under source-terminated and drain-opened boundaries with dc current flow. The forward propagating plasma wave takes a velocity $s+v_\mathrm{d}$, whereas the backward wave propagating after reflection at the source-side boundary takes a relatively slow velocity $s-v_\mathrm{d}$. When the reflection coefficient is idealistically unity, the plasmon-responsible displacement current before and after the reflection, $\Delta\vec{j}_\mathrm{p}$ and $\Delta\overleftarrow{j}_\mathrm{p}$, must be conserved. As a result, the gate potential get an increment at every reflection. Such a reciprocal Doppler-shifting plasma waves reflecting at an asymmetric drain-opened boundary promote the increments of their intensity leading to self-oscillation of instability.

50.5 Conclusions

This chapter described the physics and technology of THz laser devices. First wide variety of THz lasers was overviewed, and their fundamental physics and constraints were discussed. Then attempt was focused on QCLs as currently industrialized current-injection pumping-type integrated solid-state THz lasers. The key technology to enable coherent intense THz lasing is maximizing the electron injection efficiency, minimizing phonon decoherency including thermal back-filling, and minimizing the waveguiding losses. Tremendous efforts have been made improving the operating threshold temperatures as well as output powers, still suffering from the phonon limit of $k_\mathrm{B}T$. Study on graphene-based THz lasers has been emerging due to its extraordinary carrier transport and optoelectronic properties. Recent experimental demonstration of single-mode THz lasing even at a low temperature and a weak emission intensity is encouraging the scientific community to proceed further getting steps ahead towards room-temperature intense THz lasing.

REFERENCES

1. Tonouchi M. 2007. Cutting-edge terahertz technology. *Nature Photon*. **1**: 97–105.
2. Sengupta K, Nagatsuma T, and Mittleman D M. 2018. Terahertz integrated electronic and hybrid electronic–photonic systems. *Nature Electron*. **1**: 622–35.
3. Patel C K N. and Kerl R J. 1964. Laser oscillation on X1 Σ+ vibrational-rotational transition of CO. *Appl. Phys. Lett*. **5**: 81–3.
4. Crocker A, Gebbie H A, Kimmitt M F, et al. 1964. Stimulated emission in the far infra-red. *Nature*. **201**: 250–1.
5. Gebbie H A, Stone N W B, and Findlay F D. 1964. A stimulated emission source at 0.34 millimeter wave-length. *Nature*. **202**: 685.
6. Faist J, Cappaso F, Sivco D L, et al. 1994. Quantum cascade laser. *Science*. **264**: 553–6.
7. Koeler R, Tredicucci A, Beltram F, et al. 2002: Terahertz semiconductor-heterostructure laser. *Nature*. **417**: 156–9.
8. Komiyama S, Iizuka N, and Arakawa Y. 1985. Evidence for induced far-infrared emission from p-Ge in crossed electric and magnetic fields. *Appl. Phys. Lett*. **47**: 958–60.
9. Andronov A A. 1986. Hot electrons in semiconductors and submillimeter waves (review). *Sov. Phys. Semicond*. **21**: 701–21.
10. Hiromoto N, Hosako I, and Fujiwara M. 1999. Far-infrared laser oscillation from a very small p-Ge crystal under uniaxial stress. *Appl. Phys. Lett*. **74**: 3432–4.
11. Aoki H. 1986. Novel Landau level laser in the quantum Hall regime. *Appl. Phys. Lett*. **48**: 559–61.
12. Williams B S. 2007. Terahertz quantum-cascade lasers. *Nature Photon*. **1**: 517–25.
13. Liang G, Liu T, Wang Q J. 2017. Recent developments of terahertz quantum cascade lasers. *IEEE J. Sel. Top. Quantum Electron*. **23**: 1200118
14. Ryzhii V, Ryzhii M, and Otsuji T. 2007. Negative dynamic conductivity of graphene with optical pumping. *J. Appl. Phys*. **83**: 083114.
15. Otsuji T, Boubanga-Tombet S A, Satou A, et al. 2013. Terahertz-wave generation using graphene: toward new types of terahertz lasers. *IEEE J. Sel. Top. Quantum Electron*. **19**: 8400209.
16. Tredicucci A and Vitiello M S. 2014. Device concepts for graphene-based terahertz photonics. *IEEE J. Sel. Top. Quantum Electron*. **20**: 8500109.
17. Hartmann R R, Kono J, and Portnoi M E. 2014. Terahertz science and technology of carbon nanomaterials. *Nanotechnol*. **25**: 322001.

18. Yadav D, Boubanga-Tombet S, Watanabe T, et al. 2016. Terahertz wave generation and detection in double-graphene layered van der Waals heterostructures. *2D Mater.* **3**: 045009.
19. Yadav D, Tamamushi G, Watanabe T, et al. 2018. Terahertz light-emitting graphene-channel transistor toward single-mode lasing. *Nanophoton.* **7**: 741–52.
20. Button Kenneth J. ed. 1984. *Reviews of Infrared and Millimeter Waves, Vol. 2 Optically pumped far-infrared lasers*. New York: Plenum Press.
21. Motz H. 1951. Applications of the radiation from fast electron beams. *J. Appl. Phys.* **22**: 527–35.
22. Oepts D, van der Meer A F G, and van Amersfoort P W. 1995. The free-electron-laser user facility FELIX. *Infrared Phys. Technol.* **36**: 297–308.
23. Ramian G. 1992. The new UCSB free-electron lasers. *Nucl. Instr. Meth.* **A318**: 225–9.
24. Nishimori N, Hajima R, Nagai R, et al. 2001. Sustained saturation in a free-electron laser oscillator at perfect synchronism of an optical cavity. *Phys. Rev. Lett.* **86**: 5707–10.
25. Nishizawa J and Suto K. 1980. Semiconductor Raman laser. *J. Appl. Phys.* **51**: 2429–31.
26. Siegman Anthony E. 1986. *Lasers*. Rev. Ed. Palo Alto, CA: University Science Books.
27. Kazarinov R F and Suris R A. 1971. Possibility of the amplification of electromagnetic waves in a semiconductor with a superlattice. *Sov. Phys.* **5**: 707–9.
28. Scalari, G, Ajili L, Faist J, et al. 2003. Far-infrared ($\lambda \simeq 87\,\mu$m) bound-to-continuum quantum-cascade lasers operating up to 90 K. *Appl. Phys. Lett.* **82**: 3165–7.
29. Biasco S, Garrasi K, Castellano F, et al. 2018. Continuous-wave highly-efficient low-divergence terahertz wire lasers. *Nature Commun.* **9**: 1122.
30. Slivken, S, Evans A, David J, et al. 2002. High-average-power, high-duty-cycle ($\lambda{\sim}6\,\mu$m) quantum cascade lasers. *Appl. Phys. Lett.* **81**: 4321–3.
31. Williams B S, Kumar S, Hu Q, et al. 2005. Distributed-feedback terahertz quantum-cascade lasers with laterally corrugated metal waveguides. *Opt. Lett.* **30**: 2909–11.
32. Ohtani K, Turčinková D, Bonzon C, et al. 2016. High performance 4.7 THz GaAs quantum cascade lasers based on four quantum wells. *New J. Phys.* **18**: 123004.
33. Khalatpour A, Reno J L, Kherani N P, et al. 2017. Unidirectional photonic wire laser. *Nature Photon.* **11**: 555–9.
34. Williams B S, Callebaut H, Kumer S, et al. 2003. 3.4-THz quantum cascade laser based on longitudinal-optical-phonon scattering for depopulation. *Appl. Phys. Lett.* **82**: 1015–7.
35. Williams B S, Kumar S, Callebaut H, et al. 2003. Terahertz quantum-cascade laser operating up to 137 K *Appl. Phys. Lett.* **83**: 5142–4.
36. Terashima W and Hirayama H. 2015. GaN-based terahertz quantum cascade lasers. *Proc. SPIE* **9483**: 948304.
37. Fathololoumi S, Dupont E, Chan I, et al. 2012. Terahertz quantum cascade lasers operating up to $\sim$ 200 K with optimized oscillator strength and improved injection tunneling. *Opt. Exp.* **20**: 3866–76.
38. Li L, Chen L, Zhu J, et al. 2014. Terahertz quantum cascade lasers with >1 W output powers. *Electron. Lett.* **50**: 309–11.
39. Williams B S, Kumar S, Hu Q, et al. 2006. High-power terahertz quantum-cascade lasers *Electron. Lett.* **42**: 89–91.
40. Minamide H, Ikari T, and Ito H. 2009. Frequency-agile terahertz-wave parametric oscillator in a ring-cavity configuration. *Rev. Sci. Instrum.* **80**: 123104.
41. Mu X, Zotova I B, and Ding Y J. 2008. Power scaling on efficient generation of ultrafast terahertz pulses. *IEEE J. Sel. Top. Quantum Electron.* **14**: 315–32.
42. Nishizawa J, Tanabe T, Suto K, et al. 2006. Continuous-wave frequency-tunable terahertz-wave generation from GaP. *IEEE Photon. Technol. Lett.* **18**: 2008–10.
43. Ragam S, Tanabe T, Saito K, et al. 2009. Enhancement of CW THz wave power under noncollinear phase-matching conditions in difference frequency generation. *J. Lightwave Technol.* **27**: 3057–61.
44. Belkin M, Cappaso F, Belyanin A, et al. 2007. Terahertz quantum-cascade-laser source based on intracavity difference frequency generation. *Nature Photon.* **1**: 288–92.
45. Pflugl C, Belkin M A, Wang Q J, et al. 2008. Surface-emitting terahertz quantum cascade laser source based on intracavity difference-frequency generation. *Appl. Phys. Lett.* **93**: 161110.
46. Vijayraghavan K, Adams R W, Vizbaras A, et al. 2012. Terahertz sources based on Čerenkov difference-frequency generation in quantum cascade lasers. *Appl. Phys. Lett.* **100**: 251104.
47. Lu Q Y, Bandyopadhyay N, Silvken S, et al. 2014. Continuous operation of a monolithic semiconductor terahertz source at room temperature. *Appl. Phys. Lett.* **104**: 221105.
48. Razeghi M, Lu Q Y, Bandyopadhyay N, et al. 2015. Quantum cascade lasers: from tool to product. *Opt. Exp.* **23**: 8462–75.
49. Novoselov K S, Geim A K, Morozov S V, et al. 2004. *Science*. **306**: 666.
50. Geim A K and Novoselov K S. 2007. The rise of graphene. *Nat. Mater.* **26**: 183–91.
51. Ryzhii M and Ryzhii V. 2007. Injection and population inversion in electrically induced p-n junction in graphene with split gates. *Jpn. J. Appl. Phys.* **46**: L151–L153.
52. Sano E. 2011. Monte Carlo simulation of ultrafast electron relaxation in graphene. *Appl. Phys. Exp.* **4**: 085101.
53. Foster M S and Aleiner I L. 2009. Slow imbalance relaxation and thermoelectric transport in graphene. *Phys. Rev. B.* **79**: 085415.
54. Winzer T and Malic E. 2012. Impact of Auger processes on carrier dynamics in graphene. *Phys. Rev. B.* **85**: 2410404(R).
55. Kim R, Pereveinos V, and Avouris P. 2011. Relaxation of optically excited carriers in graphene. *Phys. Rev. B.* **84**: 075449.
56. Someya T, Fukidome H, Watanabe H, et al. 2017. Suppression of supercollision carrier cooling in high mobility graphene on $\mathrm{SiC}(000\bar{1})$. *Phys. Rev. B.* **95**: 165303.
57. Alymov G, Vyurkov V, Ryzhii V, et al. 2018. Auger recombination in Dirac materials: A tangle of many-body effects. *Phys. Rev. B.* **97**: 205411.
58. Ryzhii V, Satou A, and Otsuji T. 2007. Plasma waves in two-dimensional electron-hole system in gated graphene heterostructures. *J. Appl. Phys.* **101**: 024509.

59. Grigorenko A N, Polini M, and Novoselov K S. 2012. Graphene plasmonics. *Nat. Photon*. **6**: 749–58.
60. Dubinov A A, Alehkin Y V, Mitin V, et al. 2011. Terahertz surface plasmons in optically pumped graphene structures. *J. Phys. Condens. Matter.* **23**: 145302.
61. Watanabe T, Fukushima T, Yabe Y, et al. 2013. The gain enhancement effect of surface plasmon polaritons on terahertz stimulated emission in optically pumped monolayer graphene. *New J. Phys*. **15**: 075003.
62. Dyakonov M and Shur M. 1993. Shallow water analogy for a ballistic field effect transistor: New mechanism of plasma wave generation by dc current. *Phys. Rev. Lett*. **71**: 2465–8.
63. Ryzhii V, Satou A, and Shur M S. 2012. Transit-time mechanism of plasma instability in high electron mobility transistors. *Phys. Status Solidi*. **202**: R113.
64. Mikhailov S A. 1998. Plasma instability and amplification of electromagnetic waves in low-dimensional electron systems. *Phys. Rev. B*. **58**: 1517–32.
65. Aizin G R, Mikalopas J, and Shur M. 2016. Current-driven plasmonic boom instability in three-dimensional gated periodic ballistic nanostructures. *Phys. Rev. B*. **93**: 195315.
66. Boubanga-Tombet S, Knap W, Yadav D, et al. 2020. Room-temperature amplification of terahertz radiation by grating-gate graphene structures. *Phys. Rev. X* 10: 031004.

Taylor & Francis
Taylor & Francis Group
http://taylorandfrancis.com

Index

Note: The locators in *italics* and **bold** represents *figures* and **tables**.

Abrams, R. L. 352
absorptive bistability 278–9
acousto-optic modulators (AOMs) 423
acousto-optic tunable filter (AOTF) 587
activation energy 21, 190
active ion spectroscopy 492–3
active Q-switching 219
active spatial filtering 405
adaptive optics techniques 144
additive colouration 154, 155
additive hydrogen 319–20
additive-pulse mode locking (APM) 523
adequate electric circuitry 396
Advanced Material Processing and Technology Research Association (AMMTRA) 382
Akasaki, I. 252
alexandrite laser crystal 17–18
alexandrite laser pump 444
Alferov, Zh. I. 236
AlGaInP material system 237
AlGaInP quantum wells *239,* 239–40
alkali-earth fluorides 153
alkali-halide crystals 151, 153
alkali laser cavity design *443*
amplified spontaneous emission (ASE) 77, 365, 406, 441, 480–1, 558, 585, 606, *607,* 674
amplifier 75
  design 75–6
  multipass 77
  multi-stage 77
  regenerative 76–7, *76*
amplifier control
  gain control 567
  TOP 567
  transient control 567–8
amplifier measurement 569, *569*
amplifier pumping
  influence 563
  pump distribution schemes 564–5
  980 nm *563,* 563–4
  1480 nm 564
amplifier requirements 412–13
amplifier topology *558,* 558–9
anionic group theory 117, 118
antimonide-based lasers 265
antiphase domain boundaries (APBs) 289
anti-stokes luminescence (ASL) 541, *542*
AOMs *see* acousto-optic modulators (AOMs)
APBs *see* antiphase domain boundaries (APBs)
aperture length 106
Arakawa, Y. 287
ArF laser
  discharge 384–5
  e-beam pumping 384
  intrinsic efficiency 384
  laser performance 385, *386*
  long pulses 386–7, *387*
  prepulse–main-pulse excitation *385*
argon/krypton ion lasers
  applications 334
  continuous-wave laser transitions **326**
  device development 330–2
  diode–laser–pumped solid-state lasers 325
  early history 325–6
  electronic configurations *327*
  energy levels 326–7
  excitation mechanisms 329–30
  level populations 329
  output power and wavelengths **332, 333**
  plasma parameters of the discharge 327–8
  present systems and capabilities 332–4
  spectroscopic notation 325
  transition probabilities and level lifetimes 327, **332**
arrayed waveguide grating (AWG) 276
ASE *see* amplified spontaneous emission (ASE)
aspect ratio trapping technique (ART) 294
astrophysical phenomena 403
atomic vapor laser isotope separation (AVLIS) 316–17
Auger effect *176,* 176–8, *177*
Auger-type scattering 678
AVLIS *see* atomic vapor laser isotope separation (AVLIS)

$Ba(NO_3)_2$ crystals
  infrared SRS shifters and Raman lasers 132–4
  optical scheme and characteristics *134*
  pump-to-output average power dependences *134*
  visible nanosecond SRS 131–2
BAC associated with P (BAC-P) 540
back transfer 86
Balmer, J. E. 658
band gap engineering 188
Barmashenko, B. D. 456
Bartoszek, F. E. 471–2
Barty, C. P. J. 667
basic hydrogen peroxide (BHP) 451
BDFL *see* Bi-doped fibre laser (BDFL)
beam divergence characteristics 180, *181*
Beattie, A. R. 176
Beaulieu, A. J. 347
Beck, M. 269
Bell Aerospace Textron double axisymmetric BCL-13 nozzle *469*
Belland, P. 437
Bennett, W. R. Jr. 301, 325, 327, 328
BER *see* bit error rate (BER)
BHP *see* basic hydrogen peroxide (BHP)
biaxial crystals 104–5, **105,** *105*
Bidnyk, S. 258
Bi-doped aluminosilicate fibre lasers **545,** 545–6
Bi-doped fibre laser (BDFL) 535, 536
Bi-doped fibres (BDFs) 539–42, *540, 542*
Bi-doped germanosilicate fibre lasers
  large concentration of GeO_2 548–9
  small concentration of GeO_2 *547,* 547–8
Bi-doped optical fibre amplifiers (BDFAs)
  Bi-doped germanosilicate fibre amplifier 550–1
  Bi-doped phosphosilicate and germanosilicate 550
  error-free data transmission 549
  gain and noise figure spectra *551*
  lines—normalized gain *549*
  luminescence spectra 549
Bi-doped phosphosilicate fibre lasers 546–7, *547*
biharmonic pumping 132
birefringence angle 105
birefringent filters (BRFs) 72, 73
Bi-related active centres (BACs) 536
bismuth-related NIR active centres 536–9
bistable effect 353
Biswas, D. J. 421
bit error rate (BER) 277
Blayvas, I. 461
blue laser diodes
  competing technologies 251
  development
    GaN-based (*see* GaN-based laser diodes)
    InGaN-based LEDs 251–3, *252*
  lasing emission 259–60
  non-GaN 259
  SE 258–9
  UV, green and yellow laser diodes 259–60
Boersch, H. 326
Bokhan, P. A. 319
bond-parameter models 116
Botez, D. 231
Bourdet, G. L. 425, 427
Boyd, G. D. 63
Brenier, A. 123
Brewster's angle crystal 72
Brewster windows 609
BRFs *see* birefringent filters (BRFs)
Bridges, T. J. 438
Bridges, W. B. 325, 326, 352
broadband laser scheme *607*
broad gain-linewidth 478–9
Brugger, H. 227
Bruneau, J. L. 437
buried heterostructure (BH) 178, *179*

Capasso, F. 187
capped mesa buried heterostructure (CMBH) 179
carbon dioxide lasers

- carbon dioxide lasers (*cont.*)
  - competitive technologies 338
  - designs 338
  - doppler-based velocity measurement systems 338
  - excitation technology 337
  - life events
    - applications 344
    - convectively cooled lasers 346
    - DC-discharge-excited lasers 344–6
    - disparate device technologies 344
    - gain medium excitation technique 344
    - optical resonators and intracavity optical components 344
    - reflective diffraction gratings 344
    - TEA 346–8, *348*
    - waveguide 348, *349*
    - waveguide resonators 344
  - limitations 338
  - physics of excitation
    - introduction 338–9
    - molecular structure and laser issues 339–42
    - operating parameters 342–3
  - RF discharges
    - annular discharge lasers 360
    - convectively cooled radio-frequency-excited free-space 360–2
    - electrical characteristics *352*
    - instability processes 352–3
    - introduction 349–50
    - linear waveguide lasers 354–5
    - power scaling 355–60
    - similarity and parameter scaling 353–4
    - structures 350–2, *351*
- Carnall, W. T. 111
- carrier density pulsation (CDP) 276
- carrier heating (CH) 274
- Carroll, D. L. 461
- cataphoresis 310
- catastrophic optical mirror damage (COMD) 225, 226, *227*
- cavity designs
  - broadband emission 619
  - line narrowing 618
  - mode locking 618
  - performance 619
  - ring cavity 618
- cavity-dumping scheme *608*
- cavity-tuning 585
- CDP *see* carrier density pulsation (CDP)
- central field Hamiltonian 4
- CET *see* cooperative energy transfer (CET)
- CH *see* carrier heating (CH)
- Chakrabarti, A. **424**
- Chang, T. Y. 438
- chaotic attractor 530
- chemical lasers 449
- chemical oxygen iodine laser (COIL)
  - basic chemical reactions **452**
  - block diagram *455*
  - cavity design and extraction efficiency 459–60
  - construction and components 455–9
  - grid nozzle with subsonic injection *458*
  - hyperfine sublevels **454**
  - iodine dissociation mechanisms *453*
  - low-lying electronic states *451*
  - nozzle bank *459*
  - operating characteristics, performance and modes of lasing 460–2, **461**
  - principle of operation 451–5
  - singlet oxygen generators *456–7*
  - subsonic and supersonic 455
  - unstable resonator *460*
  - VertiCOIL generator *461*
- chemical vapour deposition (CVD) 171
- Chenausky, P. P. 349
- Chen, C. J. 318
- Chen, S. 289, 290
- Chester, A. N. 328
- chirped-pulse amplification (CPA) 406, 528, 659
- chirped superlattice 676
- Chodzko, R. A. 473
- Chow, W. W. 245
- cladding 173
- cladding absorption 490–1, *491*
- cladding pumping
  - absorption 490–1, *491*
  - brightness enhancement 491
  - fibre cross-sections *491*
  - laser cavity configurations *493*
  - longitudinal mode mixing and wavelength *491*
  - principle 490, *490*
  - schemes 491–2, *492*
- CMBH *see* capped mesa buried heterostructure (CMBH)
- CMOS *see* complementary metal oxide semiconductor (CMOS)
- coherent detection technique 277
- coherent transmission systems 185
- coherent X-ray radiation 656–7
- COIL *see* chemical oxygen iodine laser (COIL)
- colliding pulse mode (CPM) 221
- colliding pulse technique 618
- collisional electron excitation lasers
  - collisionally excited capillary discharge lasers 661–2
  - quasi-steady-state lasers 657–8
  - transient collisional lasers 659–60
  - travelling-wave excitation 660–1
- collisional recombination lasers
  - capillary-discharge-pumped 664
  - discharge-pumped recombination systems 664
  - mechanisms 662–3
  - recombination lasing 665–6
- colour centre laser (CCL) 153
- colour centres (CCs)
  - active elements 151–3, **152**
  - CW and quasi-cw CCL operation 157–8
  - energy and power amplifier *163,* 163–4, *164*
  - ionic crystals
    - formation 154–7
    - types 153, **153,** *154*
  - pico- and femtosecond quasi-cw CCL operation 158–9
  - room-temperature CCL operation
    - CW and quasi-cw regimes 159–60, *160*
    - high energy and power 162
    - narrow-line tunable and super-broadband oscillation 162–3
    - pico- and femtosecond regimes 160–2, *161*
- colquiriite solid-state laser 18–23, **19**
- COMD *see* catastrophic optical mirror damage (COMD)
- commercial laser diodes **89**
- complementary metal oxide semiconductor (CMOS) 290
- conduction-band profile *187*
- configuration-coordinate diagram *10,* 10–11, 28, *28*
- confocal unstable resonator *320*
- continuous-wave Bi-doped fibre lasers (CW BDFLs)
  - Bi-doped aluminosilicate fibre lasers **545,** 545–6
  - Bi-doped germanosilicate fibre lasers (large concentration of GeO_2) 548–9
  - Bi-doped germanosilicate fibre lasers (small concentration of GeO_2) *547,* 547–8
  - Bi-doped phosphosilicate fibre lasers 546–7, *547*
  - characteristics 544
- continuous-wave operation 269–70
- contrast issues
  - CPA schemes 410
  - direct amplification 411
  - energy scalable pulse cleaning methods 410
  - frequency conversion/plasma mirror technique 411
  - improvement techniques 411
  - laser–matter interactions 410
  - NFF *411,* 411–12
  - plasma mirror 411
  - power amplifier 410
- convective cooling 346
- Convert, G. 325
- cooperative energy transfer (CET) 560
- copper bromide laser tube *319*
- copper halide lasers 318–19
- copper HyBrID lasers 320
- copper vapour lasers (CVL)
  - atomic physics and excitation mechanisms *315,* 315–16
  - cavities and beam quality 320–1
  - development 316–17
  - discharge circuit *318*
  - discharge tube *317*
  - kinetically enhanced 322
  - MOPA *321,* 321–2
  - practical considerations 317–18
  - properties **317**
- copper-vapour pump-lasers (CVL)
- coupled micro-ring laser *283*
- CPM *see* colliding pulse mode (CPM)
- CPM pump laser system *659*
- Cr^{3+} energy levels 7–10, *10*
- critical phase matching 106
- Crocker, A. 360
- cross-polarized wave (XPW) 77
- cross-relaxation process 112
- cryogenically cooled systems 77–8
- crystal-field splitting
  - Cr^{3+} energy levels 7–10, *10*
  - irreducible representations 8, **9**

  multiplets **9**
  octahedral symmetry site 6–7, *7, 8*
crystal-field strength ion 11, *12*
crystallophysical axes 105
crystal momentum 235
CVD *see* chemical vapour deposition (CVD)
CVL *see* copper vapour lasers (CVL)
cyclo-octatetraene 603
Czochralski crystal-pulling-from-the-melt technique 71
Czochralski method 14, 16, 35

Daido, H. 658
Dai, Z. 226
dark line defect (DLD) 178
Davydov splitting (DS) 131
DBR *see* distributed Bragg reflector (DBR)
deep reactive ion etching (DRIE) 587
demultiplexing 408
depolarization loss *vs.* phase difference *89*
Deutsches Elektronen Synchrotron (DESY) 645
device under test (DUT) 569
Dexter, D. L. 86
DGT *see* dynamic gain tilt (DGT)
dichroic optical elements 423
Dieke chart 84, *84, 85*
dielectric planar waveguides 571
dielectric waveguide 171–2, *172*
differential-absorption lidar systems 429
differential population inversion *vs.* ratio of loss to gain *95*
diffraction limited emittance 647
diode end-pumped lasers 109
diode-pumped alkali lasers (DPALs)
  alkali absorption line broadening 442
  concept 441
  features 442–3
  high pressure approach 442
  narrowbanding technique 442
  optical efficiency 442
  optical maser 441
  prehistory 441
  research and development
    alexandrite laser pump 444
    efficient lasing of alkali vapour laser 443
    first demonstration 444
    highly efficient optically pumped alkali laser 443–4
    longitudinal pumping *445*
    narrowband pump 444
    power scaling 444–6, *445*
    transverse pumping *446,* 446–7
  standard three-level pump scheme *442*
  VBG development 442
diode-pumped microchips 109
dipole–dipole interactions 11, 85
dipole–quadrupole interactions 11, 85
direct electron collisional excitation 341
discharge operating conditions 343
discontinuously tunable monolithic devices 204–6
dislocation densities 255
dispersive bistability 278–9
dispersive self-Q-switching 219
dispersive waves 526–7
dissipative soliton resonance (DSR) 530
dissipative solitons
  applications 529–30
  concept 522, 527–9, *528*
  vs. conventional solitons 527
  frequency chirping 528
  molecules 528–9
  normal propagation regime 528
  paradigm 527–8, *528*
distributed Bragg reflectors (DBRs) *197,* 197–9, *198,* 230
distributed equivalent circuit *217*
distributed feedback (DFB) *199,* 199–200, 268, 479
  buried-heterostructure laser *185*
  design and fabrication 184–5
  light *vs.* current characteristics and spectrum *185*
  lightwave transmission systems 184
  performance 185
  phase noise and intensity noise 185
  single-wavelength laser source 184
divalent rare-earth ion lasers *64,* 64–5
DLD *see* dark line defect (DLD)
Dmitriev, V. G. 123
dopants 1
Doppler-based velocity measurement systems 338
Doppler broadening 454
Doppler shift-type instability 680
double-clad waveguides 575–6, *576*
doublet 26, 86
DRIE *see* deep reactive ion etching (DRIE)
Drude model 266
DSR *see* dissipative soliton resonance (DSR)
dual-gate graphene-channel fieldeffect transistor (DG-GFET) 678
dual-wavelength systems 405
Dubinskii, M. A. 59
Dumanshin, R. 347
Duncan, R. C. 65
Dunn, J. 659
Dunn, M. H. 330
DUT *see* device under test (DUT)
Dyakonov–Shur Doppler-shift *681*
Dyakonov–Shur instability 680
dye cell configuration 609–10, *611*
dye gain medium 624
dye lasers 599
dye lasers pumped by cw lasers 617–18, *618, 619*
dye spectral emission characteristics *612*
dynamic gain tilt (DGT) 560–1

e-beam diode configurations *369*
Eder, D. C. 667
EDP *see* extraction during pumping (EDP)
EHP *see* electron-hole plasma (EHP)
Ehrlich, D. J. 58
electrically driven oxygen-iodine laser (ElectricOIL) 462
electroabsorption (EA) 217, *217*
electrolytic colouration 155
electromagnetic radiation 403
electron-beam excitation 367–9
electron-beam geometries 368–9
electron excitation
  CO 341–2
  N_2 340–2
electron–hole plasma (EHP) 259
electronic hyperpolarizability tensor 116–17
electron–phonon interaction
  configuration-coordinate diagram *10,* 10–11
  energy transfer processes 11–13
  optical band shapes 11
electrorefraction (ER) 217
Endo, M. 461
energy-band diagram 173
energy book-keeping methodology 454
energy extraction issues
  limited storage time 408
  nonsaturable absorption 406–7
  off-axis amplification *407,* 407–8
  optical multiplexing 408, *408*
  picosecond gain dynamics 408–10
energy recovery linac (ERL) 651
energy transfer parameter 86
energy transfer processes
  concentration-quenching processes 12–13
  radiative and non-radiative transitions 11–12
  self-quenching *13*
epitaxial growth techniques 173, 178, 227
epitaxy 171
Epperlein, P. W. 227
erbium *479,* 482
erbium-doped fibre amplifier (EDFA) *479*
  alternatives 568–9
  amplifier control 567–8
  amplifier measurement 569, *569*
  amplifier pumping 563–5
  amplifier topology *558,* 558–9
  communication system
    line amplifiers 566
    narrow band amplifiers 567
    pre-amplifiers 567
  gain spectra 559–61
  gain tilt modelling 569
  inhomogeneous effects
    polarization-dependent gain 566
    polarization hole burning 566
    spectral hole burning 566, *566*
  noise 561–3
  optical communication systems 557
  quantum limit 558
  rate equation modelling 569
  telecom applications *558*
  telecommunications 558
  telecoms windows
    1300 nm 565–6
    1450–1500 nm 565
erbium-doped fibre amplifiers (EDFAs) 535
erbium-doped waveguide amplifiers (EDWAs) 568
ESA *see* excited-state absorption (ESA)
evanescent-wave arrays 231
Evenson, K. M. 425
excimer lasers
  ArF laser (199nm) 384–7
  electronic transitions 367
  excitation technique 367–77
  F_2 laser (163nm) 391–4
  H_2 laser (140–165 nm and 100–120 nm) 396–8
  historical perspectives 367
  instrumental conditions 365

- excimer lasers (*cont.*)
  - KrCl laser (222 nm) 383–4
  - KrF Laser (248 nm) 378–9, *379*
  - magnitude 365
  - N_2 laser (337–406 nm and 741–1230 nm) 394–6
  - near-infrared lasers 365
  - rare gas halide lasers 394
  - rare gas halogen excimers 375–7
  - short-wavelength systems 367
  - steady-state voltage 398
  - time-independent spatial homogeneity 365
  - XeCl laser (308 nm) 379–7
  - XeF laser (351, 353 and 486 ± 35 nm) 387–9
- excimer molecules 404, *404*
- excitation technique
  - e-beam 367–9
  - H_2 laser 397–8
  - self-sustained discharge 368–75
- excited-state absorption (ESA) 26, 29–30, 56, 111, 482, 542–5
- exhaust systems 471
- experimental realizations 413–14
- external cavity tunable laser diodes 206
- external modulation 217–18
- external resonator waveguides 577–8, *578*
- extraction during pumping (EDP) 77

- F_2 laser
  - fluorine molecules 392
  - gas composition 391
  - high photon energy 391
  - kinetics 392
  - laser performance 392–3
  - long pulses *393,* 393–4, *394*
  - minor absorption losses 392
  - self-termination 391
  - spectroscopy 392
  - thermal loading 391
- Fabry–Pérot laser spectrum *180*
- Fabry–Perot type laser cavity *673*
- Faist, J. 187, 676
- farinfrared 637
- far-IR lasers
  - design and operational characteristics 437, **438**
  - glow discharge and additive gases 437
  - H_2O 436, *436*
  - HCN laser
    - design *437*
    - fuels 435
    - mechanism 434–5
    - wall effects 435–6
  - laser lines 433–4, **434**
  - magnetospectroscopy 433
  - plasma diagnostics 433
  - resonator 436–7
  - thermal radiation sources 433
- fast-axial-flow (FAF) 360–2, *361, 362*
- fast gas flow technique 339
- F-atom generators 467–8
- FBGs *see* fibre Bragg gratings (FBGs)
- FEC *see* forward error correction (FEC)
- femtosecond superradiant pulse generation 221–2
- Fendley, J. R. Jr. 326
- Feofilov, P. P. 60, 65
- Fermi resonance 434
- Fermi's Golden Rule 30
- fibre Bragg gratings (FBGs) 501, 545
- fibre laser cavity configurations
  - diode pump sources 493
  - main fibre laser configurations 493
- fibre lasers
  - advantages 477
  - basic principles and formulae 479–81
  - cladding-pumping principle *478*
  - core-pumping scheme 478
  - emission wavelengths 477
  - end-pumped *477*
  - energy level and optical spectra properties 481–5
  - features 478–9
  - functional devices 485
  - gain medium 477
  - heat dissipation capability 477
  - laser performance 485
  - rare-earth (RE)-doped glass 477
  - silica 485
  - spontaneous-emission spectrum *479*
  - stretched-pulse mode-locked Er-doped *479*
  - structure 477
- fibre optics 475
- fibre types
  - active 494
  - passive 496
- figure-of-eight laser (F8L) 523–4
- filamentation 225, 226, 275
- filling factor 642
- flame fusion technique 16
- flashlamp-pumped dye-doped polymer 624
- flashlamp-pumped polymer rod test 633
- flashlamp-pumped system 605
- flashlamp pumping 96, 98
- FLN *see* fluorescence line narrowing (FLN)
- fluid-dynamical-flow principles 613
- fluorescence line narrowing (FLN) 13
- fluorescence spectrum *44*
- fluorophosphate system 626
- Forster, T. 86
- forward error correction (FEC) 277
- Foulger, D. L. 244
- four-wave mixing (FWM) 11, 274, 496
  - coherent signals, modulation formats 277
  - OPC, dispersion compensation 277
  - principle 276
  - PSAs 278
  - ultrafast all-optical switching 277
- Fowles, G. R. 315
- Franck–Condon (FC) factor 395
- Frank–Condon configuration diagram 153
- Frantz–Nodvik equations 95
- freeelectron laser (FEL) 637
  - accelerator technology **643**
  - applications 644–5
  - developments 645–6
  - history/principle 639–40
  - peak brightness *vs.* photon energy *651*
  - physics 640–1
    - gain and saturation 641–2
    - high-gain 642–3
    - lasing 641
    - low-gain oscillator 642
    - spontaneous emission *641*
  - radiative process *640*
  - technology 643–4
  - user facilities **644**
- free-ion energy levels 4–6
- frequency-selective elements (FSE) 421, 618
- Fritz, B. 157
- Füchtbauer–Ladenburg (FL) equation 111
- Fukuda, M. 227
- full-width at half-maximum (FWHM) 218, 218
- FWM *see* four-wave mixing (FWM)

- Gabay, S. 317
- gain-clamping mechanism 203
- gain flattening filters (GFFs) 561
- gain medium 672
- gain spectra
  - absorption and emission cross sections *559*
  - C-band and L-band gain spectra *560*
  - DGT 560–1
  - gain flattening 561
  - net cross sections *559,* 560
  - upper and lower lines 559
  - variable gain amplifiers 561
- gain switching 90, 218–20, 462
- gain tilt modelling 569
- Galkin, L. N. 60
- GaN-based laser diodes
  - first 253
  - higher power 255–7
  - mode structure and control 258
  - structure and performance *253,* 253–5
  - wavelength range
    - true blue and longer wavelengths 257–9, *258*
    - UV laser diodes 258
- garnets **12**
- Garstang, R. H. 327
- gas source molecular beam epitaxy (GSMBE) 178
- gas/vapour lasers 299–300
- Gebbie, H. A. 433
- Gehrig, E. 229
- glow discharge *302,* 302–3
- gold vapour laser *322,* 322–3
- Gordon, E. I. 325, 328, 329
- Gordon-Kelly sidebands 526
- Gordon, S. J. 473
- Gould, G. 441
- graded-index separate-confinement heterostructure (GRINSCH) 227, 228, *228*
- graded-reflectivity mirrors *612*
- Graphene plasmon instability 680
- Grasiuk, A. Z. 425
- green problem 113, 121
- ground state absorption (GSA) 542
- GSB-17.0 *543*
- GSMBE *see* gas source molecular beam epitaxy (GSMBE)
- Gupta, P. K. **424**

- H_2 laser
  - electronic-vibrational levels *396*
  - excitation technique 397–8
  - lasing scheme 396
  - Lyman band (140–165 nm) 397, **397**
  - vacuum ultraviolet region 396

  - vibrational and rotational energy distributions 396
  - Werner band (100–120 nm) 397, **397**
- H_2O laser 436, *436*
- Haken, H. 426
- Hall, D. 299
- Halperin–Lax model 174
- Halstead, A. S. 326
- Han, Y. 294
- Hara, T. 664
- harmonic mode locking (HML) 527
- harpooning 377
- Hart, R. A. 355
- Haus, H. A. 528
- header recognition 284
- heat-exchanger method (HEM) 71
- heavy hole (HH) 671
- Heidner–Lilenfeld–Azyazov–Heaven–Pichugin (HLAHP) mechanism 453
- Heidner, R. F. III 453
- Heidner's mechanism 453–4
- helium–cadmium laser
  - applications 313
  - clean-up 312
  - description 309
  - discharge tube design 313
  - energy levels and laser transitions *309,* 309–10
  - gain, saturation intensity and output power 312
  - isotope distribution 311, *311*
  - parameters **312**
  - pumping/excitation techniques 310, *310*
  - role 310–11
  - structural arrangement *312,* 312–13
  - uniform vapour distribution—cataphoresis 310
- helium–neon lasers 299
  - ellipsometry 301
  - energy level diagrams *305*
  - evolution of expectations 305
  - future 308
  - glow discharge *302,* 302–3
  - laser manufacturing processes and technology 306
  - laser tube construction 304–5
  - light amplification 301
  - low-power devices 301
  - orthogonally polarized modes *307*
  - output power characteristics **302**
  - population inversion, optical gain and oscillation 303–4
  - scanning applications 301
  - semiconductor diode technology 301
  - short- and long-term frequency and intensity stability *307*
  - single-frequency 306–7
  - testing *306*
  - typical performance characteristics 307–8
- HEM *see* heat-exchanger method (HEM)
- hemispherical cavity 122
- Hernqvist, K. G. 326
- Herriott, D. R. 301
- Herziger, G. 328
- Hess, O. 226, 229
- HF/DF chemical lasers
  - cold and hot pumping reactions 467
  - exhaust systems 471
  - F-atom generators 467–8
  - laser performance 471–2
  - line-selected performance 473
  - mixing nozzles 468–70
  - nozzle bank *470*
  - optical resonators 470–1
  - overtone laser 472–3
  - power spectral distribution 473
  - schematic diagram *467*
  - TRW HYLTE nozzle *468*
- high-brightness systems 405
- higher-order modes (HOMs) 494, 496
- high extraction efficiency decentred feedback annular ring resonator (HEXDARR) 471, *471*
- High Intensity Laser Laboratory (HILL) 413
- high-power diode pump sources
  - end-pumping 572–3
  - face-pumping 574–5, *575*
  - in-plane pumping 572
  - pre-conditioning optics 572
  - pumping arrangements 572, *572*
  - side-pumping 573–4
- high-power fibre lasers
  - absorption spectra 489
  - attributes and features 489
  - challenges 497–8
  - fundamentals
    - active ion spectroscopy 492–3
    - beam quality 494
    - cladding pumping *490,* 490–2
    - fibre laser cavity configurations 493
    - fibre types 494–6
  - power scaling 489
  - quantum effect 489
  - single fibre, single-mode continuous-wave (CW) output 496–7
  - thermal lensing 489
- high-power KrF installation *415*
- high-power laser diodes
  - arrays 231
  - lateral design
    - aluminium-free broad vertical waveguide structure *229*
    - broad-area 229, *229*
    - tapered laser devices 229–30, *230*
    - unstable resonator lasers 230, *230*
    - α-DFB lasers 230–1, *231*
  - mounting, diode arrays 231–2
  - reliability 232
  - vertical waveguide design 227–8
- high-power planar waveguide lasers
  - advantages 571
  - high-power diode pump sources 572–5
  - optical confinement 571
  - planar and channel waveguide structures *572*
  - rapid development 580–1
  - refractive index 571
  - spatial-mode selection 575–8
  - thermal management properties 575, *575*
  - waveguide laser performance 578–80
- high repetition systems 393
- high-resolution laser spectroscopy technique 13
- high-speed laser diodes
  - design
    - device optimization 216–17
    - equivalent circuits *216*
    - microwave propagation effects 217
  - dynamics
    - frequency chirp and spectral control 215
    - modulation bandwidths and damping 213–15
    - noise 216
    - rate equations 212–13
  - electroabsorption and electrorefractive modulators 211
  - external modulation 217–18
  - optical pulse sources 211
  - soliton effect 211
  - trends 222–3
  - ultrashort pulse generation 218–22
- Hill, M. 328
- holmium 483–4, *484*
- Hough, J. J. T. 471
- Hovis, F. E. **427**
- Huang–Rhys factor 28
- Huang–Rhys parameter 10, *11*
- HVPE *see* hydride vapor phase epitaxy (HVPE)
- Hwang, C. J. 174
- hydride vapor phase epitaxy (HVPE) 254

- ICFD *see* intracavity frequency doubling (ICFD)
- Iga, K. 245
- III–V red-emitting laser diodes
  - AlGaInP material system 237
  - AlGaInP quantum wells *239,* 239–40
  - background 235–6
  - carrier leakage 243–4, *244*
  - fundamental trends with wavelength 236–7
  - InP/AlGaInP quantum dots 240
  - intrinsic gain and recombination characteristics *241,* 241–3, **242**
  - quantum confinement 237–8
  - quantum dot lasers 245–7
  - quantum well structure design 240–1, *241*
  - threshold current 242–3, *243*
  - VCSELs 244–5, *245*
- information and communication technology (ICT) 671
- infrared and optical masers 441
- infrared laser diodes 111
- InGaN-based LEDs 251–3, *252*
- injection locking 421
- Innova (metal/ceramic) plasma tube technology 330, *331*
- innovative chirped-pulse laser architectures 529–30
- InP/AlGaInP quantum dots 240
- insertion devices 650
- interconfigurational transition 8
- interferometric multiplexing *409*
- inter-mode vibrational transition 434
- inter-valence-band (IVB) 671
- intracavity frequency doubling (ICFD) 102
  - critical phase matching 118
  - diode end-pumped lasers 118–19
  - fibre-coupled laser-diode end-pumped lasers 119–20
  - Nd^{3+}-crystals as gain medium 107
  - non-linear crystals 107

intracavity frequency doubling (ICFD) (*cont.*)
  output power of second harmonics 107–8
  reabsorption, Nd^{3+} 946 nm laser emission 108–9
  resonator designs
    anti-reflection 121
    fibre-coupled diode pumping *123*
    hemispherical cavity 122
    microchip 122, *122*
    ring cavity 121
    self-doubling lasers 122–3
    three-mirror folded cavity 121, *121*
    types of 121
intracavity waveplates 524
intraconfigurational transition 8
inverse FEL (IFEL) 642
iodine–oxygen mixing systems 458
iodine vapour production 458
ion–host combination
  Nd^{3+} or Yb^{3+} dopants 115–16
  non-linear coefficients
    calculation of microscopic hyperpolarizability 117–18
    electronic hyperpolarizability tensor 116–17
    modelling chemical substitutions 117
ionic crystals
  active elements optimization 155–7
  alkali-halide crystals, ionizing radiation 155
IR-pumped LiIO$_3$ 134–5

Jackson, P. E. 355, 358
Jahn–Teller effect 21
Javan, A. 301
Jensen, C. C. 609
Jones, D. R. 320
Judd–Ofelt (JO) theory 111, 112

Kane band model 177
Kapteyn, H. C. 666
Kerber, R. L. 471
Keszler, D. A. 118
Keyes, R. J. 63
Khulugurov, V. M. 156
Kim, D. 663, 667
Kim, H. 294
kinetically enhanced CVLs (KE-CVLs) 322
Kiss, Z. J. 65
Kitaeva, V. F. 327, 328
Kneubühl, F. K. 436
Köhler, R. 269
Kolesnychenko, F. Y. 351
Korobkin, D. 665
Koster, G. F. 327
Kramers' degeneracy 85
Kramers–Kronig transformations 226
KrCl laser 383–4
KrF laser 378–9, *379*
Krishnan, K. S. 127
Kroeker, D. F. **424**
Krupke, W. F. 441, 443
Kunert, B. 294
Kwoen, J. 290
Kyropoulos method 151, 156

Laakmann, K. D. 349
Labuda, E .F. 326
Labuda, E. F. 326, 328
Lachambre, J. L. 349, 354
Ladenburgh–Reiche line-absorption technique 329
Lamberton, H. M. 347
Landsberg, G. S. 127
Landsberg, P. T. 176
Lang, R. J. 226
lanthanide series lasers
  advantages 83
  applications 83
  basic laser equations 92–5
  continuous/pulsed modes 83
  diffraction-limited beam 83
  energy transfer and diffusion 85–8
  energy transfer processes 83
  laser material properties **87,** 87–9
  laser performance 96–8
  pump and population inversion 89–92
  quantum mechanics and spectroscopy 84–5
  tuning 95–9
Laporte forbidden transition 63
large-optical-cavity (LOC) 228
laser-based display technologies 255
laser compartment (LC) 368
laser diode arrays (LDAs) 442
laser diodes
  advantages, semiconductor lasers 170
  designs 178
  distributed feedback lasers 184–5
  distributed feedback structures 167
  epitaxy 171
  high-power (*see* high-power laser diodes)
  LED 170
  light–current characteristics 170
  lightwave system applications 171
  materials 170–1, *171*
  multiwavelength 206
  non-radiative recombination 176–8
  optoelectronic systems 170
  output power and beam quality
    continuous-wave (cw) output characteristics *226*
    facet damage 226–7
    filamentation 226
    thermal issues 225–6
  parallel-cleaved facets 170
  performance 179–80
  principles of operation
    dielectric waveguide 171–2, *172*
    injected carrier density *172*
    pn junction laser 173, *173*
    stimulated emission condition 172
    threshold condition 172
  quantum well lasers 180–4
  quantum wire, quantum dot and nanostructure lasers 188–90
  radiative recombination 173–6
  reliability 190–1
  schematic diagram *170*
  SELs 185–7
  short-pulse and high-frequency modulation 167
  spectral control (*see* spectral control)
  visible and quantum cascade lasers 187–9
laser head designs *610*
laser-heated pedestal growth (LHPG) 13
laser intensity *vs.* years *406*
laser isotope separation (LIS) 602
laser material properties 69–71
laser–matter interactions 403
laser reliability 190–1
laser-to-fibre coupling 191
lasing emission 259–60
lasing spectrum *254*
lateral overgrowth technique 254, 256
Latham, W. P. 460
Latta, E. E. 227
lattice 647
Lawrence Livermore National Laboratory (LLNL) 52, 59
LDAs *see* laser diode arrays (LDAs)
lead-salt lasers 264
leakage-channel fibres (LCFs) 496
Lemoff, B. E. 661
Lewis, R. R. 316
LHPG *see* laser-heated pedestal growth (LHPG)
Lide, D. R. 434
light bullet 530
light-emitting diode (LED) 170
light hole (LH) 671
light sources 403
lightwave system applications 171
lightwave transmission systems 170
linac coherent light source (LCLS) 645
Linder, K. K. 289
linear flashlamp 609
line-narrowing elements 606
linewidth/line-profile techniques 328
liquid lasers
  absorption and emission spectra *603*
  applications 602
  cavity designs 618–19
  characteristics
    beam-quality enhancement techniques *613,* 613–14
    control of ASE 606
    dye cell configuration 609–10, *611*
    dye solutions 604
    flashlamp-pumped devices 607, *608*
    flashlamp-pumped laser performance 614
    gain medium 602–3
    laser head 608–9
    laser-resonator design 611–13
    multicolour operation 611, *611*
    pumping options 603–4
    safe operation 614–15
    spectral control 604–6
    temporal control 606–7
  dye lasers pumped by cw lasers 617–18, *618, 619*
  dye-lasers pumped by pulsed lasers
    copper-vapour pump laser 615
    dye cells 615, *616*
    efficiency 617
    linear cavities 616
    mode locking 617
    performance 617
    pump angle 615–16
    pumping configuration 616
    wavelength-conversion module 615
  dye molecules *602*
  dye solution longevity enhancement 605

  - generic laser dye *603*
  - incoherent pump-source characteristics **604**
  - nanometres 601
  - neodymium 601
  - optical set-up 602
  - thermo-optical parameters **614**
  - 35 J laser *614*
- liquid-phase dye laser technology 601
- liquid-phase epitaxy (LPE) 171
- liquid-phase laser 624
- LIS *see* laser isotope separation (LIS)
- Little, C. E. 320
- Liu, A. Y. 289
- Liu, C. S. 318
- LLNL *see* Lawrence Livermore National Laboratory (LLNL)
- Lobanov, B. D. 156
- LOC *see* large-optical-cavity (LOC)
- longitudinal integration technique 205
- long-wavelengths
  - antimonide-based lasers 265
  - fingerprint region of molecules 263
  - lead-salt lasers 264
  - mercury–cadmium–telluride-based lasers 265
  - MIR 263
  - optoelectronics 263
  - QCLs 263
  - quantum cascade lasers 265–9
- lower-laser-level de-excitation processes 342
- LPE *see* liquid-phase epitaxy (LPE)
- *L–S* coupling 5, *5*
- Lyman band 397, **397**
- Lyot filters 605

- Mach-Zehnder interferometer (MZI) 276
- magnetic pulse compression (MPC) 389, *390*
- Maiman, T. H. 3, 13, 489
- Maitland, A. 320
- Maker fringes 103
- Maki, A. G. 434
- Mamyshev oscillators 530
- Mamyshev regenerators (MR) 530
- Mandelshtam, L. I. 127
- manifolds 84
- Manos, D. M. 471–2
- Marshall, C. D. 59
- Marshall, G. D. 322
- master oscillator power amplifiers (MOPAs) 221, 229, 275, *321,* 321–2, 477, 489, 493, 616
- Matthews, D. L. 653
- MBE growth technology 188
- McGonigle, A. J. S. 59
- McInerney, J. G. 226
- McMahan, W. H. 326
- MCVD *see* modified chemical vapour deposition (MCVD)
- MDL *see* microdisk laser (MDL)
- MDSLS *see* modulation-doped strained layer superlattice (MDSLS)
- MEMS-based swept fibre-ring laser source
  - Bragg mirrors
    - filter performance 590–1, *591*
    - lensed fibres 591–2
- MEMS-based swept laser source system 592–3
- MEMS technology
  - comb-drive actuator 589–90, *590*
  - SOI and DRIE 588–9, *589*
- Menke, E. 157
- mercury–cadmium–telluride-based lasers 265
- metal/ceramic tube technology 330
- metallic microwave strip-line 269
- metal-metal (MM) 677
- metal–organic chemical vapor deposition (MOCVD) 171, 252, 270
- metal–organic vapour-phase epitaxy (MOVPE) 252
- metastable manifolds 88
- metastable/neutral channel 377
- MFA *see* mode-field adapter (MFA)
- Michelson interferometer 434, 436, 437
- microdisk laser (MDL) 291
- micro-electro-mechanical system (MEMS) 586
- microporous glass 626
- microwave propagation effects 217
- mid-infrared (MIR) *see* long-wavelengths
- mid-infrared (MIR) optically pumped gas lasers (MIROPLs) 419
- Miller, R. C. 328
- mini-spectrometers 263
- mixing nozzles 468–70
- MOCVD *see* metal–organic chemical vapor deposition (MOCVD)
- MOCVD growth technique 178
- mode-field adapter (MFA) 495
- mode-locking (ML) 159, 211, *220,* 220–1, *221,* 406, 462, 603, 618
- mode-overlap integrals 120
- modified chemical vapour deposition (MCVD) 492, 536
- modulation-doped strained layer superlattice (MDSLS) 253
- Moeller, G. 342
- molecular beam epitaxy (MBE) 171, 263, 270, 289
- monolithic all-fibre construction 479
- Moore, C. B. **427**
- MOPAs *see* master oscillator power amplifiers (MOPAs)
- Morrison, H. D. 426
- Moser, A. 227
- Motheye AR coating *628*
- Motz, H. 640
- mounting/packaging technology 226
- MOVPE *see* metal-organic vapour-phase epitaxy (MOVPE)
- MQW *see* multi-quantum well (MQW)
- MR *see* Mamyshev regenerators (MR)
- Mullane, M. P. 226
- Mulliken notation 7
- multicolour operation 611, *611*
- multi-longitudinal modes (MLM) 585
- multimode laser diodes 512–14
- multi-phonon relaxation 112, 116
- multiplets 5
- multi-pulsing instability 527
- multi-quantum well (MQW) 183, 275
- multisection DFB laser 185
- multisection distributed Bragg reflector (DBR) 185
- multiwavelength laser diodes 206
- Myshenkov, V. I. 349, 351

- N$_2$ laser
  - discharge 395–6
  - electronic-vibrational levels *395*
  - electronic vibrational transitions 395
  - FC principle 395
  - lasing scheme 394
  - radiative transition 395
  - self-sustained discharge system 394
- Nagata, Y. 665
- Nakamura, S. 187, 251–5, 258
- nano-lasers
  - nano-ridge lasers grown (001) 294–6
  - nanowires grown on (111) 292–4, *293*
  - stimulated emission 292
- nanostructure lasers 189–90
- narrowbanding technique 442
- Nash 190
- natural inversion 266
- nature of crystals 110–11
- Naval Research Laboratory (NRL) 59
- Nd^{3+} ion spectroscopy 111–12, **113**
- Nd:Cr:GSGG crystals 50–1
- Nd:Cr:YSGG crystals 50–1
- Nd:vanadate laser crystals
  - absorption and emission, Nd:GdVO$_4$ *47,* 47–8
  - cw diode-pumped quasi-three-level lasers **50**
  - disordered crystals 45
  - Nd:YVO$_4$ *vs.* Nd:GdVO$_4$ **46–7,** 46–50
  - pump-wavelength selection 45
  - Q-switched operation **49**
  - transition lines 48
- Nd:YAG laser crystal
  - 1064 nm properties 40
  - absorption spectra and pump levels 39, *39*
  - condition-cooled, end-pumped zigzag slab architecture *42*
  - diode-pumped *41,* **42**
  - emission cross sections 39
  - energy-level diagram *38*
  - energy levels 37–8
  - high neodymium doping levels 40–3
  - laser beam quality *42*
  - laser diode pumping and resonator configuration *41*
  - lifetime 38
  - Nd:YLF and Nd:YAlO$_3$ **36**
  - optical properties 35
  - output power *41*
  - parameters, side-pumped **41**
  - pump module and resonator configuration *43*
  - slab and rod sites *37*
  - structure 37
  - thermal expansion coefficients 37
- Nd:YLF laser crystal 45
- Nd:YVO$_4$ *vs.* Nd:GdVO$_4$ **46–7,** 46–50
- near to mid-infrared laser performance **97**
- Nederlands Centrum voor Laser Research (NCLR) 382
- neodymium 37, 481, *481*
- new-generation diode pump sources 49
- Newman, L. A. 355
- Ng, W. K. 127
- NH$_3$ laser 423–6, **424,** *425*
- NH$_3$ partial energy-level schematic diagram *426*

Nickles, P. V. 659
nitride-based laser technology 187
noise-like pulses 530
non-critical phase matching 106
non-GaN blue lasers
    frequency doubling 259
    II–VI materials 259
    ZnO 259
noninvasive techniques 222
non-linear effects
    frequency doublers 106, **107**
    ion–host combination 115–18
    operating characteristics 124–5
    physical background
        non-linear polarization 102
        phase matching 103–6
        SHG 102–3
    self-frequency doubled lasers *vs.* intracavity frequency doublers 106–15
    semiconductor laser diodes 102
    system configurations 118–23
non-linear Fourier-filter (NFF) *411,* 411–12
non-linear loop mirrors (NOLM) 523, *524*
non-linear optical gains 279–80
non-linear polarization 102
non-linear polarization evolution (NPE) 524
non-linear polarization evolution mode locking 524–5
non-linear polarization rotation (NPR) 524
non-radiative recombination
    Auger effect *176,* 176–8, *177*
    defects 178
    electron–hole pair 176
    surface 178
    threshold current 176
nonsaturable absorption 406–7
normalized absorption coefficient
    Cr:YAG *92*
    Er:YAG *91*
    Ho:YAG *90*
    Tm:YAG *91*
Norman, J. 290
Nowack, R. 359
NRL *see* Naval Research Laboratory (NRL)
Nyquist limit 277

octahedral sites 25, 26
octahedral symmetry site 6–7, *7, 8*
off-axis amplification *407,* 407–8
Olsen, H. N. 327
on–off keying 277, *278*
OPC *see* optical phase conjugation (OPC)
OPCPAs *see* optical parametric chirped pulse amplifiers (OPCPAs)
operational spectral regions
    hollow-core optical fibres 505
    mid-IR gas RFLs 507–8
    mid-IR range RFLs 506–7
    silica based RFLs 505–6, **506,** *506*
    soft glass fibres **507**
OPSLs *see* optically pumped semiconductor lasers (OPSLs)
optical bistability
    absorptive and dispersive 278–9
    all-optical memory operation 273
    bistable devices, types 282–3
    conditions 278
    flip-flop operations, VCSELs
        BER 281–2
        consumption power 281
        switching power and speed 280–1, *281*
    gain saturation
        general considerations 279
        non-linear optical gains and rate equation analysis 279–80
    output characteristics *279*
    polarization, VCSELs 280, *280, 281*
optical epoxy polymer 625
optical harmonic generation 106
optical isolators 558
optically pumped mid-IR lasers
    applications 429
    C_2H_2 and isotopes 428–9, **429,** *429*
    electrical discharge pumping 419
    energy-level schematic diagram *421*
    experimental aspects 421–2, *422, 423*
    gain models 426–8
    isotope separation 419
    NH_3 laser 423–6, **424,** *425*
    principle of operation 421
    spectroscopy, NH_3 and C_2H_2 419–21, *420*
optically pumped oscillator (OPO) 428, **429**
optically pumped semiconductor lasers (OPSLs) 71
optical memories
    high-bit-rate operation 284
    shift register operation and multi-bit memories 284
optical multiplexing 408, *408*
optical parametric chirped pulse amplifiers (OPCPAs) 77
optical parametric oscillation (OPO) 677
optical phase conjugation (OPC) 277
optical pumping 89
optical rectification (OR) 677
optical resonators 470–1
optical self-seeding 223
optical-signal-to-noise-ratio (OSNR) 277
optical spectrum analysers (OSAs) 593
optical telecommunication systems 475
optical time-division multiplexing (OTDM) 277
optical-to-optical threshold 96
optical transparency 93
optoelectronics 263
ormosil 625
OSAs *see* optical spectrum analysers (OSAs)
oscillators 71–3
OSNR *see* optical-signal-to-noise-ratio (OSNR)
OTDM *see* optical time-division multiplexing (OTDM)
output beam position scanning 587–6, *588*

Paananen, R. 326
passive mode locking 522
    evolution mode locking 524–5
    figure-8 lasers and variants 523–4
    non-linear loop mirrors 523, *524*
    saturable absorber materials 522–3
    virtual saturable absorbers 522–3
passive Q-switching 219
Patel, C. K. N. 343
Pauli exclusion principle 4
PCE *see* power conversion efficiency (PCE)
PCF *see* photonic crystal fibre (PCF)
PD *see* photodarkening (PD)
p-doping 252
peak absorption coefficient *44*
Pearson, P. R. 347
peculiar laser pulses 530
Pekarian function 28
periodically poled structures 115
Petawatt systems 77
PFN *see* pulse-forming network (PFN)
phase conjugation techniques *613*
phase-insensitive amplifiers (PIAs) 278
phase-locked laser arrays 231
phase-locking technique 355
phase matching
    biaxial crystals 104–5, **105,***105*
    coherence length 103
    doubling efficiency 105–6
    momentum conservation *103*
    uniaxial crystals 103, 104, **104,** *104*
phase-sensitive amplifiers (PSAs) 278
phonon decoherency 671
phonon–phonon interactions 128
photodarkening (PD) 498
photodegradation-causing mechanisms 604
photodissociation source 391
photodynamical therapy 144
photoionization lasers 666–7
photolithographic techniques 189
photonic crystal fibre (PCF) 495
photonic integrated circuits (PICs) 287
photonics 489
photon–photon resonance (PPR) 215
photon population density 94
photorefractive effect 116
photo-triggered mode 374
PIAs *see* phase-insensitive amplifiers (PIAs)
picosecond gain dynamics 408–10
PICs *see* photonic integrated circuits (PICs)
Piper, J. A. 322
pitchfork bifurcation bistability 278, *280*
plano-concave resonator 118
plasma mirror 411
pMD *see* p-type modulation doping (pMD)
pn junction laser 173, *173*
Polanyi, J. C. 471–2
polarization-bistable VCSELs
    all-optical format conversion, demultiplexing and retiming 283
    header recognition 284
    optical memories 283–4
polarization-dependent gain 566
polarization extinction ratio (PER) 511
polarization hole burning (PHB) 566
polarization-maintaining (PM) 523
poly-(methyl methacrylate) (PMMA) 625
polyacrylamide Gel 626
polycomposite glass 626–7
polycrystalline Nd:YAG ceramic laser 43–5
polyvalent ions 536
Porsche, J. 246
post-doped hosts 626–7
    densified sol-gel 626
    microporous glass 626
    polycomposite glass 626–7
    polymer-filled microporous glass 627
power conversion efficiency (PCE) 564
power scaling

  folded waveguide lasers 355
  planar waveguide lasers 356–60
  waveguide laser arrays 355–6, *356*
PowerTrack 332
PPR *see* photon-photon resonance (PPR)
PRBS *see* pseudo-random bit sequence (PRBS)
pre-doped hosts
  fluorophosphate system 626
  optical epoxy 625
  organic 625
  other materials 626
  poly-(methyl methacrylate) 625
  polyacrylamide Gel 626
  sol-gel-derived silicates 625
prepulse–main pulse 371–3, *373–5,* 389
pressure-broadened linewidths *425*
Prettl, W. 299
PSAs *see* phase-sensitive amplifiers (PSAs)
PSB-0.7 *543*
pseudo-random bit sequence (PRBS) 282
p-type modulation doping (pMD) 291
pulsed excitation technology 367
pulsed-laser deposition (PLD) 572
pulse-forming network (PFN) 375, 608
pulse-pumped dye laser *617*
pulse repetition rate (PRF) 615
pulse-shortening mechanism 221
pulse-to-pulse timing jitter 218
pump distribution schemes 564–5
pump-mediated gain inhomogeneity *564*
pump radiation 90
pyrromethene dye 631

QCE *see* quantum conversion efficiency (QCE)
QCLs *see* quantum cascade lasers (QCLs)
QPM *see* quasi-phase matching (QPM)
Q-switched modes 1
Q-switching 89, 94, 95, 211, 218–20, 406, 603
quadrature phase-shift keying (QPSK) 277
quadrupole–quadrupole interactions 11, 85
quantum cascade lasers (QCLs) 187–8, *188,* 671, 675–7
  band diagram and squared wavefunctions *266*
  concepts/principle *675*
  continuous-wave operation 269–70
  disadvantages 267
  distributed feedback 268
  dopants 266
  electrically pumped laser cavities 267
  electron injection *676*
  interband 265, *265*
  intersubband transitions 265, *265*
  lasing 267
  mini-spectrometers 263
  radiative transition 266
  refractive index and light intensity 266, *267*
  temperature tuning behaviour *269*
  terahertz (far-infrared) 268
quantum confinement 237–82
quantum conversion efficiency (QCE) 564
quantum dots (QD) 188–9, *189,* 213
  devices 247
  InGaAs material system 238
  InP/AlGaInP 240
  motivation 245–6
  silicon
    1.55-µm 291–2, *292*
    high-performance 1.3-µm In(Ga)As/GaAs 289–91, *290*
    low-dimensional heterostructure lasers *289*
    physical properties 287–8
    room-temperature PL comparison *288*
    self-assembled growth 288
  structure and optical gain *246,* 246–7
quantum efficiency (QE) 674
quantum mechanical interactions *84*
quantum numbers 4, **5**
quantum well (QW) 188–9, *189,* 211
quantum well (QW) double heterostructures 173
quantum well lasers
  energy levels 181–2, *182*
  performance *182,* 182–3
  strained 183–4
quantum wire (QWR) 188–9, *189*
quasi-four-level lasers 93, 95
quasi-four-level system 116
quasi-phase matching (QPM) 115
quasi-steady-state lasers 657–8
quest of high-energy pulses 529–30
Quist, T. M. 63

Racah parameters 5, 6
radiation-damage-resistant original gratings 423
radiative recombination
  defined 173
  energy *vs.* wavevector *174*
  gain calculation *174,* 174–5
  indirect-gap semiconductors 174
  spontaneous emission rate 175
  threshold current calculation 175–6
Raizer, Y. P. 349
Raman, C. V. 127
Raman fibre amplifiers 568–9
Raman fibre lasers (RFLs)
  gain medium 503–4
  minimal losses 501
  multi-mode fibre 501
  multimode laser diodes 512–14
  operational spectral regions 504–8
  optical resonator 501
  output linewidth *516*
  random distributed feedback via Rayleigh backscattering *509,* 509–12, *510*
  spectral broadening 501, 515–16
  stimulated Raman scattering *502,* 502–3, *503*
Raman scattering
  alkaline-earth metals 131
  applications 140, 144–5
  $Ba(NO_3)_2$ crystals 131–4
  $BaWO_4$
    picosecond shifters 139–40
    SRS crystals 137–8, **139**
    $SrWO_4$ 138
    yellow raman shifters and lasers 138–9
  four-phonon relaxation and dephasing process 129
  IR-pumped $LiIO_3$ 134–5
  KGW crystals
    nanosecond lasers 136–7
    picosecond shifters 135–4
  liquid media 128
  molecular gases 128
  monodirectional gain 128
  non-linear optical process 127
  non-pump-depletion region 128
  parameters 129, **130**
  PbWO4 SRS shifters 140
  phonon–phonon interactions 128
  picosecond pulse applications 129
  properties 127
  pump and output characteristics **141–3**
  resonance characteristics 127–8
  resonance enhancement effect 128
  steady-state regime 128
  symmetric breathing modes 129
  thermal energy (phonons) 127
random distributed feedback (RDFB) 501, *509,* 509–12, *510*
range-gating techniques 144
rare-earth-doped fibre amplifiers 475
rare-earth ion lasers (Nd^{3+})
  divalent 64–5
  electromagnetic spectrum 55
  Nd^{3+}-doped glass 51–2, **52**
  Nd:Cr:GSGG and Nd:Cr:YSGG crystals 50–1
  Nd:LSB crystal 51, **51**
  Nd:vanadate laser crystals 45–50
  Nd:YAG laser crystal 35–43
  Nd:YLF laser crystal 45
  polycrystalline Nd:YAG ceramic laser 43–5
  spectroscopic and laser properties 35
  trivalent activator ions 55
  trivalent cerium lasers 55–60
  trivalent uranium lasers 60–4
rare gas halide lasers 394
rare gas halogen excimers
  A state 375
  B state 376
  internuclear separation 376
  kinetics 376–7
  potential energy diagram 375, *376*
rate equation analysis 279–80
rate equation modelling 569
rate-equation models 426
Rayleigh backscattering 509–12
reactive-ion etching (RIE) 267
real-time ultrafast characterization techniques 530
reciprocity method 111, 112
refractive index 87, 266, *267*
refractive-index profiles (RIPs) 494
refractive indices measurements 113
Reid, J. **424**
relative intensity noise (RIN) 185, 216, *216,* 585, 674
relaxation oscillations 94
resonant energy transfer 340–2
resonant overshoot mode *373,* 373–4
resonant phonon depopulation (RPD) 676
resonator design techniques 475
resonator interferometry 433
RFLs *see* Raman fibre lasers (RFLs)
RIE *see* reactive-ion etching (RIE)
Rigden, G. D. 342
Rigden, J. D. 299, 301, 326
rigid-rotor harmonic oscillator approximation 420
RIN *see* relative intensity noise (RIN)

ring-cavity design 72, *72*
RIPs *see* refractive-index profiles (RIPs)
robust modal characteristics 479
Rocca, J. J. 661, 664
Rocca Serra, J. 347
Rolland, C. **424**
Ross, J. N. 329, 330
rotational non-equilibrium kinetic-fluid dynamic model 470
ruby laser
  absorption coefficient and cross section *14, 15*
  oscillator output *vs.* lamp *16*
  strong crystal-field model 13–16
  three-level scheme 13–16
Rudko, R. I. 327, 329, 330
Russell–Saunders approximation 5
Ryzhii–Satou–Shur instability 680

Sabotinov, N. V. 319
Sagnac interferometer 523
Sakaki, H. 287
saturable absorber 278, 522–3
SCH *see* separate confinement heterostructure (SCH)
Schäfer, F. P. 408
Schawlow, A. L. 441
Schawlow–Townes–Henry formula 204
Schmiedberger, J. 462
Schrodinger's equation 4
Schwaller, P. 436
Scifres, D. R. 231
Scott, G. G. 411
second-harmonic generation (SHG) 102–3, 109, 259
selective gas additives 342–3
self-amplified spontaneous emission (SASE) 641
self-frequency doubled lasers *vs.* intracavity frequency doublers 113–15
self-frequency doubling (SFD) 102, 106, 110, **115,** 122–3, **124–5**
self-imaging waveguides 576–7
self-phase modulation (SPM) 479, 496, 516, 521
self-similar evolution 529
self-sustained discharge
  instrumental design 374–5
  multi-atmospheric systems 369
  photo-triggered mode 374
  pre-ionization 370
  prepulse–main pulse 371–3, *373–5*
  resonant overshoot mode *373,* 373–4
  single-discharge pulse 371, *372*
  technological development 370
  X-ray source with corona plasma *370,* 370–1
Sellmeier equation 87, 113
SELs *see* surface-emitting lasers (SELs)
semiconductor lasers 1, 273
semiconductor optical amplifiers (SOAs) 568
  high-power operation 274–5, *275*
  optical non-linearities 273
  ultrafast dynamics 274
sensitizer 50
separate confinement heterostructure (SCH) 212
SFD *see* self-frequency doubling (SFD)
SFSs *see* superfluorescent fibre sources (SFSs)
SHB *see* spectral hole burning (SHB)
Sher, M. H. 666
SHG *see* second-harmonic generation (SHG)
Shi, B. 291
short-pulse excimer systems 414
short-pulse KrF excimers 405–6
short-risetime travelling-wave discharge 397
short wavelength 405
side-mode suppression ratio (SMSR) 190, 195
Siegmann, A. E. 358
Siemsen, K. J. 427
Silfvast, W. 299
Silfvast, W. T. 315
silica-based optical fibres *536*
silicon-based lasers
  challenges 296
  heteroepitaxy technologies 287
  nano-lasers 292–6
  QD 287–92
silicon-on-insulator (SOI) 285
silicon photonics technology 287
similarity laws 353
simplified Dieke diagram *92*
single-discharge pulse 371, *372*
single laser configuration 623
single-mode laser diodes
  DBR *197,* 197–9, *198*
  DFB *199,* 199–200
  spectral linewidth *200,* 200–1
singlet 86
singlet oxygen generator (SOG) 452
single wavelength operation 96
16-QAM *see* 16-quadrature amplitude modulation (16-QAM)
16-quadrature amplitude modulation (16-QAM) 277, *278*
Slater parameters 5
Sloan, J. J. 471
smart lasers 530
Smilanski, I. 317
Smirnov, A. S. 351
Smowton, P. M. 240, 242
SMSR *see* side-mode suppression ratio (SMSR)
Snitzer 477
Snitzer, E. 490
SOAs *see* semiconductor optical amplifiers (SOAs)
soft X-ray lasers
  average power 655
  beam divergence 655
  output pulse energy 655
  peak power 655
  peak spectral brightness 656
  pulse duration 655
  spatial coherence 656
  temporal coherence 655–6
  wavelength 655
SOG *see* singlet oxygen generator (SOG)
SOI *see* silicon-on-insulator (SOI)
solid-state amplifiers 415
solid-state dye lasers 624
  absorption/fluorescence characteristics 629
  flashlamp-pumped 631–2, *632*
    performance 632–4
    performance data **630**
    PMMA rods *634*
    polymer rod *633*
    rod test 633
    shot number *633*
    temporal output *633*
  gain media
    characteristics **627**
    damage threshold 628
    dye-doped *628*
    fabrication 627–8
    optical coatings 628
    photostability 628–9
  host preparation
    additives 627
    characteristics 624
    choice 634
    post-doped hosts 626–7
    pre-doped hosts 624–6
  laser-pumped *630*
    banwidth *631*
    emission bandwidth 631
    performance 629–31
    pyrromethene dye *631*
  parasitic effects *629*
  thermo-optical properties **628**
solid-state lasers 1
soliton laser
  advantages and limitations 525–7, *525*, *526*
  concept 521
  dispersive wave radiation 526–7
  energy 525–6, *525*
  multi-pulsing instability 527
Sorokin, P. P. 63, 65
spatial-mode selection
  double-clad waveguides 575–6, *576*
  external resonator waveguides 577–8, *578*
  self-imaging waveguides 576–7
  tapered waveguides 577
spectral broadening 515–16
spectral control
  amplitude–phase coupling 196
  edge-emitting laser diodes 196
  fibre couplers 196
  light–current characteristics 196
  longitudinal mode spectrum 195, *196*
  modulation/relaxation processes 196
  optical wavelength 195
  single-mode laser diodes 197–201
  SSR 195
  time-dependent laser signal 195
  wavelength-tunable laser diodes 201–6
spectral hole burning (SHB) 274, 566, *566*
spectral linewidth *200,* 200–1
spectralon 609
spin–orbit coupling *5,* 84
SPM *see* self-phase modulation (SPM)
spontaneous emission 641
SRAM *see* static random access memory (SRAM)
SRS *see* stimulated Raman scattering (SRS)
S-shape bistability 278
SSMF *see* standard single-mode fibre (SSMF)
standard perturbative theory 117
standard single-mode fibre (SSMF) 277
Stark effect 5
static electric theory 8

static random access memory (SRAM) 283
Statz, H. 327
steady-state regime (SRS) 132
Steffen, H. 434, 436
stereolithographic technique 299
Stern, F. 174, 175
Stevenson, M. J. 63, 65
stimulated Brillouin scattering (SBS) 496
stimulated emission (SE) 172
  GaN 258–9
  InGaN 259
stimulated Raman scattering (SRS) 127, 496, *502,* 502–3, *503,* 530
stimulated thermal Rayleigh scattering (STRS) 497
Stokes shift 11, 28
strained layer superlattice (SLS) 289
Stranski–Krastanov growth mode 238
stress ageing test 178
stretched-pulse fibre laser 529
subsonic mixing scheme 458, 460
Suckewer, S. 653, 663
Sugano, S. 8
superfluorescent fibre sources (SFSs) 551–2, *552*
surface-emitting lasers (SELs)
  defined 185
  designs 186–7
  reflection spectrum *186*
  vertical-cavity 185
surface plasmon polaritons (SPPs) *680*
surface plasmon waveguide 269
swept laser source 593–6
Swept laser source (SLS) 585–6, *586*
synchronism 408
synchrotron light source
  advantages 651
  approximate number **647**
  electron beam emittance *vs.* electron energy *648*
  electron circulates 647–8
  flux *649*
  generations 646–7
  history 646–7
  insertion device *650*
  insertion devices 650–1
  layout *646*
  magnetic field 648–9
  operational characteristics 647
  radiation processes *648*
synchrotron radiation (SR) 648
Szatmári, S. 408

Tachikawa, M. 425
Tanabe–Sugano diagram 9, *9,* 27, *28*
Tanabe, Y. 8
Tang, C. L. 327, 329, 330
tapered fibre bundles (TFB) 492
tapered waveguides 577
TDD *see* threading dislocation density (TDD)
TDE *see* time domain extinction (TDE)
TEA *see* transverse-electric discharge-atmospheric pressure (TEA)
Terahertz lasers (THz) 671–2
  band diagram *672*
  carrier energy relaxation dynamics *678*
  four-level system 673
  graphene-based 677–8
    DG-GFET 678
    dual-gate-biased 679
    emission spectra *680*
    optically pumped intrinsic 678
  graphene lattice *677*
  operation mechanism 672–3
  QCL (*see* quantum cascade lasers)
  semiconductor 672
  solid-state oscillators *671*
  subbands diagram 674
terahertz radiation 637
tetrahedral sites 25
tetramethoxysilane (TMOS) 625
thermal conductivities 88
thermal impedance 225
thermal management properties 575, *575*
third harmonic generating (THG) 414
Thomas Jefferson National Accelerator Facility *645*
Thomson, I. J. 580
threading dislocation density (TDD) 291
three-dimensional computational fluid dynamics (CFD) 453
three-mirror folded cavity 121, *121*
threshold condition 172
thulium 483, *483*
thulium-doped fibre amplifiers (TDFAs) 565
Tillert, T. 426
time domain extinction (TDE) 569
TIR *see* total internal reflection (TIR)
titanium sapphire lasers
  absorption and gain cross sections 70–1, *70*
  amplifiers 75–7, *76*
  ancestors 69
  cryogenically cooled systems 77–8
  dispersion management 74, *74*
  divalent transition metal ions 69
  frequency combs/carrier envelope phase 74rier *75*
  laser material properties 69–71
  material physics, properties and growth 71
  oscillators 71–3
  Petawatt systems 77
  physical properties 69, **70**
  ruby laser transition 69
  short-pulse laser 73, *73*
  spectroscopic properties 69, **70**
TMI *see* transverse mode instability (TMI)
Tobin, M. 299
total internal reflection (TIR) 42
total output power (TOP) 567
Townes, C. H. 441
transient collisional lasers 659–60
transition metal ion lasers (Cr^{3+})
  advantages 3
  colour characteristics 3
  Cr^{4+}, Cr^{2+}, Fe^{2+} and Mn^{5+} 26
  crystal-field splitting 6–10
  electron–phonon interaction 10–13
  free-ion energy levels 4–6
  operating characteristics **21**
  physical processes 3–4
  physics and engineering issues
    absorption and emission 27–9, *28*
    electronic structure 26–7
    ESA 29–30
    host properties **31,** 31–2
    laser gain and oscillation 31
    laser properties 26, **27**
    optical loss 30
    radiative rates and non-radiative losses 30, *30*
    tetrahedral/octahedral sites 26, ***27***
  strong crystal-field model and three-level scheme 13–16
  tabulation 26
  Ti^{3+} 25–6
  V^{2+}, Co^{2+} and Ni^{2+} 26
  weak crystal-field model and four-level scheme
    alexandrite laser crystal 17–18
    colquiriite solid-state laser 18–23, **19**
    excitation spectra *21*
    fluoride garnet and colquiriite crystals *21*
    laser output performances **20**
    laser-pumped laser configuration **17**
    output *vs.* input energy *18*
    spectroscopic approach 16–17, *17*
    x-fold cavity configuration *21*
transverse–electric discharge–atmospheric pressure (TEA) 344, 346–8, *348,* 421, *423*
transverse-flow multicolour dye laser head *612*
transverse-flow RF lasers 362
transverse integration technique *205*
transverse mode instability (TMI) 497, 498
transverse pumping *446,* 446–7
trapping effect 112
travelling-wave rate equations 213
trimethoxysilylpropyl-methacrylate (TMSPM) 625
triplet quenchers 603
triplets 603
trivalent cerium lasers
  absorption and fluorescence *58*
  applications 55
  Ce:YAG absorption and emission spectra *57*
  coupling flashlamp technologies 56
  crystal properties 56, **57**
  detrimental mechanisms 56
  identical pumping scheme 58
  intrinsic lattice defects 57
  isomorphs 59
  oxide hosts 57, **58**
  partial Ce^{3+} energy level diagram 56
  Russell-Saunders coupling approximations 56
  self-consistent field approximation 56
  spectroscopic and laser research 59
  spin–orbit coupling 56
  transition metal ions 56
trivalent uranium lasers
  absorption, fluorescence and laser transitions *61*
  diode-/laser-pumping 60
  diode-pumped solid-state laser *63,* 64
  electrons 61
  infrared laser transitions 61
  lanthanides 63

- trivalent uranium lasers (*cont.*)
  - minimal intrinsic/ground-state absorptive losses 61
  - oscillation wavelengths 63
  - polarization-dependent spectra 61
  - polarized absorption spectra *62*
  - pulse-pumped lasing 63
  - three-level *vs.* four-level laser 61
- TRW hypersonic wedge nozzles *470*
- Tsufura, L. 299
- TTG *see* tunable twin-guide (TTG)
- tunable cw lasers 71–3
- tunable twin-guide (TTG) 204
- tuning 95–6
- tuning configuration *606*
- tuning schemes 605
- Twyman–Green interferometer 37
- typical laser output energy *vs.* pump energy 93

- ubitron 640
- ultrafast all-optical switching 277
- ultrafast lasers
  - dissipative solitons 522
  - implementation issues 522
  - optical detection scheme 521
  - passive mode locking 522–5
  - soliton laser 525–7, *525*, *526*
  - upgrades 530–1
- ultralong all-normal cavities 529
- ultrashort pulse generation
  - femtosecond superradiant pulse generation 221–2
  - gain and Q-switching 218–20
  - mode locking *220,* 220–21, *221*
- ultrashort pulse mode-locked operation 479
- ultra-super-pulse (USP) 360
- uncertainty principle 29, 404
- uniaxial crystals 103, 104, **104,** *104*
- unipolar electron injection 188
- unique direction device (UDD) 618
- up-conversion 86, 112
- upconversion laser 478
- upper laser level excitation 339–40

- vacuum diode (VD) 368
- Valster, A. 240
- vapour-phase epitaxy (VPE) 171
- variable gain amplifiers 561
- variable optical attenuator (VOA) 561
- VCSEL *see* vertical-cavity surface-emitting laser (VCSEL)
- VCSELs *see* vertical-cavity surface-emitting lasers (VCSELs)
- Verneuil method 14
- Vernier effect 204–5, *205*
- Veron, D. 437
- vertical-cavity surface-emitting lasers (VCSELs) 185, 196, 215, 244–5, *245,* 274, 586
- vertical external cavity surface-emitting laser 232
- vertical waveguide design
  - broad-width 228
  - GRINSCH 228, *228*
  - material systems 227–8
- VertiCOIL generator *461*
- vibrational excitation *341*
- vibrational–translational (VT) relaxation process 342
- Villarreal, F. 359
- virtual saturable absorbers 523
- visible lasers 187
- Vitruk, P. 351, 353
- Vladimirova, N. M. 329
- VOA *see* variable optical attenuator (VOA)
- volume Bragg Grating (VBG) 493
- Volume Bragg Grating (VBG) 442
- VPE *see* vapour-phase epitaxy (VPE)

- walk-off effect 106, *106*
- Walter, W. T. 318
- Wang, J. 289
- Wang, T. 289
- water vapour trap (WVT) 455
- waveguide laser performance
  - end-pumping 578–9, *579*
  - face pumping 580
  - side-pumping 580
- wavelength chirping 215
- wavelength conversion
  - four-wave mixing 276–8
  - optically controlled gates
    - cross-gain modulation gates 275–6
    - cross-phase modulation gates 276
- wavelength-division multiplexing (WDM) 185, *479*
- wavelength scanning
  - AOTF 587
  - Fabry–Perot tunable etalon 587, *587*
  - grating and polygon mirror 586, *587*
  - sweeping techniques 587
- wavelength-swept source
  - cavity-tuning 585
  - post-filtering 585
  - scanning techniques
    - output beam position scanning 587–6, *588*
    - wavelength scanning 586–7
  - SLS 585–6, *586*
- wavelength-tunable laser diodes
  - continuously tunable monolithic devices 203–4
  - discontinuous and continuous tuning *202*
  - discontinuously tunable monolithic devices 204–6
  - external cavity 206
  - optical communication techniques 201
  - physical mechanisms *202*
  - power control current 201
  - QCSE 203
  - refractive index 203
  - transverse integration scheme 202
  - tuning characteristics *201*
  - vertical-cavity 204
- wavelength-tunable light sources 585
- wavelength-tunable vertical-cavity 204
- Wazen, P. 425, 426, 427
- Webb, C. 299
- Webb, C. E. 328, 329, 330
- Wenisch, H. 260
- Werle, P. 263
- Werner band 397, **397**
- Wester, R. 351
- White, A. 299
- White, A. D. 301
- White, J. D. **424,** 426
- Williams, K. A. 229
- Wills, M. S. 360
- Withford, M .J. 320
- Woodall, K. B. 471
- Woodbury, E. J. 127

- XeCl laser
  - discharge 380
  - e-beam pumping 379
  - high average power 381–3, *382, 383*
  - kinetic modelling 380
  - parametric studies 380–1
  - rotational–vibrational structure 379
- XeF laser
  - broadband blue–green C → A transition 389–91
  - discharge 389
  - discharge stability 387
  - excimer systems 387
  - metastable channel 388
  - quenching process 388
  - spectroscopy 388–9
- xenon gas 343
- XPW *see* cross-polarized wave (XPW)
- X-ray lasers 653–4
  - amplification 654–5
  - capillary discharge set-up *662,* **665**
  - coherent 656–7
  - energy-level diagram *657*
  - experimental set up *658, 666*
  - gas target set-up *662*
  - Grotrian diagram *664*
  - high-average power tabletop *663*
  - integrated intensity *654*
  - photoionization lasers 666–7
  - *vs.* plasma column *660*
  - pump power requirements 654–5
  - soft
    - average power 655
    - beam divergence 655
    - output pulse energy 655
    - peak power 655
    - peak spectral brightness *656*
    - pulse duration 655
    - spatial coherence 656
    - temporal coherence 655–6
    - wavelength 655
  - transient inversion collisional laser pumped **661**

- Yang, J. 289
- Yatsenko, N. A. 349, 351
- Yb^{3+} ion emission parameters 112–13, **114**
- Yb-doped fibre lasers (YDFLs) 512
- Youmans, D. G. 355
- Young, C. G. 22
- ytterbium 482

- zagidullin, M. V. 454, 461
- zero dispersion wavelength (ZDW) 511–12
- zero-phonon line (ZPL) 28
- Zhao, Q. 408
- Zweiback, J. 444